2017 Joint Conference of the European Frequency and Time Forum and IEEE International Frequency Control Symposium

(EFTF/IFCS)

PROCEEDINGS

July 9 –13, 2017
Micropolis Conference Center
Besançon, France



ISBN: 978-1-5386-2916-1

2017 Joint Conference of the European Frequency and Time Forum and IEEE International Frequency Control Symposium (EFTF/IFC)

Copyright and Reprint Permission: Abstracting is permitted with credit to the source. Libraries are permitted to photocopy beyond the limit of U.S. copyright law for private use of patrons those articles in this volume that carry a code at the bottom of the first page, provided the per-copy fee indicated in the code is paid through Copyright Clearance Center, 222 Rosewood Drive, Danvers, MA 01923. For reprint or republication permission, email to IEEE Copyrights Manager at pubs-permissions@ieee.org. All rights reserved. Copyright ©2017 by IEEE.

ISBN: 978-1-5386-2916-1

EFTF-IFCS 2017 TABLE OF CONTENTS

A1L-A Optical Clocks I

Date: Monday, July 10, 2017
Time: 10:40 - 12:20
Room: Amphitheatre
Chair(s): Ekkehard Peik; *PTB*

Direct Detection of the Elusive 229Thorium Isomer: Milestone Towards a Nuclear Clock 1
Peter Thirolf[5], Benedict Seiferle[5], Lars von der Wense[5], Jürgen Neumayr[5], Hans-Jörg Maier[5], Hans-Friedrich Wirth[5], Mustapha Laatiaoui[1], Christoph Mokry[4], C.E. Eberhardt[2], Christoph Düllmann[4], J. Runke[3], N.G. Trautmann[3]
[1]GSI Helmholtzzentrum f. Schwerionenforschung GmbH / Helmholtz-Institute Mainz, Germany; [2]Helmholtz-Institute Mainz, Germany; [3]Johannes-Gutenberg-Universität Mainz, Germany; [4]Johannes-Gutenberg-Universität Mainz / Helmholtz-Institute Mainz, Germany; [5]Ludwig-Maximilians-Universität München, Germany

Progress Towards a ^40Ca^+ Optical Clock with a Fractional Uncertainty at the 10^-18 Level 4
Yao Huang, Hua Guan, Kelin Gao
Chinese Academy of Sciences, China

A1L-B Space Systems

Date: Monday, July 10, 2017
Time: 10:40 - 12:20
Room: Room 2
Chair(s): Andreas Bauch; *PTB*

Ground-to-Space Time and Frequency Transfer Based on the "Virtual Clock" Method 6
Wenfang Jing[1], Xiaochun Lu[1], Shuo Liu[2]
[1]Chinese Academy of Sciences, China; [2]TimeTech GmbH, Germany

A1L-C Resonators I

Date: Monday, July 10, 2017
Time: 10:40 - 12:20
Room: Room 3 & 4
Chair(s): Dana Weinstein; *Purdue University*

Q-Boosting of Metal MEMS Resonators via Localized Anneal-Induced Tensile Stress 10
Alper Ozgurluk, Ruonan Liu, Clark T.-C. Nguyen
University of California, Berkeley, United States

Nonlinear Cancellation in Weakly Coupled MEMS Resonators 16
Milind Pandit, Chun Zhao, Aref Mustafazade, Guillermo Sobreviela, Ashwin Seshia
University of Cambridge, United Kingdom

The Effect of Elastic Anharmonicity on the Nonlinear Behavior of Waveguide-Based AlN Resonator 20
Mayur Ghatge, Roozbeh Tabrizian
University of Florida, United States

A1L-D Liquid Phase Sensing

Date: Monday, July 10, 2017
Time: 10:40 - 12:20
Room: Room 5, 6 & 7
Chair(s): Ashwin Seshia; *University of Cambridge*

Sensing Light and Sound Velocities of Fluids in PhoXonic Crystal 22
Yan Pennec, Yabin Jin, Bahram Djafari-Rouhani
Université Lille, France

Design Criteria for Plasticized Polymer Coatings for Long-Term Acoustic-Wave Sensor Measurements in Aqueous Phase 24
Pintu Adhikari[1], Florian Bender[1], Antonio Ricco[2], Fabien Josse[1]
[1]Marquette University, United States; [2]Stanford University, United States

Piezoelectric Transduction of a Button-Like Mode Disk Resonator for Enhanced Quality Factor in Water 26
Abid Ali, Joshua E.-Y. Lee
City University of Hong Kong, Hong Kong

Spin-Coated Piezoelectric-Polymer Composite Based Acoustic Resonators and Transducers 30
Pallabi Das, Siddharth Tallur
IIT Bombay, India

A2L-A Ultrastable Lasers
Date: Monday, July 10, 2017
Time: 14:00 - 15:40
Room: Amphitheatre
Chair(s): Rodolphe Le Targat; *OBSPM*

High-Stability Laser Using Ramsey-Bordé Interferometry 32
Judith Olson[3], Richard Fox[2], Roger Brown[2], Tara Fortier[2], Todd Sheerin[1], Chris Oates[2], Andrew Ludlow[2]
[1]Massachusetts Institute of Technology / Draper Laboratory, United States; [2]National Institute of Standards and Technology, United States; [3]University of Colorado Boulder, United States

A2L-B Time Scales
Date: Monday, July 10, 2017
Time: 14:00 - 15:40
Room: Room 2
Chair(s): Gerard Petit; *BIPM*

Estimating the Allan Variance from Frequency Measurements with Missing Data 34
Lorenzo Galleani[2], Ilaria Sesia[1]
[1]Istituto Nazionale di Ricerca Metrologica, Italy; [2]Politecnico di Torino, Italy

The Use of Fault-Tolerant Clock Synchronization Algorithms for Time Scales 38
Attila Kinali
Max-Planck-Gesellschaft, Germany

Application of GMDH Type Neural Network for Predicting UTC(k) Timescales Realized on the Basis of Hydrogen Masers 42
Łukasz Sobolewski
University of Zielona Góra, Poland

A2L-C Compact Atomic Clocks
Date: Monday, July 10, 2017
Time: 14:00 - 15:40
Room: Room 3 & 4
Chair(s): Gaetano Mileti; *Université de Neuchâtel*

Mesoscopic Physics in Vapor-Cell Atomic Clocks 47
James Camparo, Andrew Hudson
Aerospace Corporation, United States

Low-Power and Low-Profile Miniature Atomic Clock: Ceramic Based Flat Form Factor Miniature Atomic Clock Physics Package (C-MAC) 55
Jacques Haesler[1], Laurent Balet[1], Sylvain Karlen[1], Thomas Overstolz[1], Benjamin Gallinet[1], Steve Lecomte[1], Fabien Droz[1], Kari Kautio[3], Pentti Karioja[3], Markku Lahti[3], Antti Määttänen[2], Ossi Lahtinen[2], Ville Hevonkorpi[2]
[1]CSEM SA, Switzerland; [2]Primoceler Oy, Finland; [3]VTT Technical Research Centre of Finland Ltd, Finland

Impact of Static-Magnetic-Field-Gradients on Relaxation Times in a Rb Vapor Cell 57
Mohammadreza Gharavipour[1], Christoph Affolderbach[1], Florian Gruet[1], Gaetano Mileti[1], Ivan S. Radojičić[2], Aleksandar J. Krmpot[2], Brana M. Jelenković[2]
[1]Université de Neuchâtel, Switzerland; [2]University of Belgrade, Serbia

Microfabrication of Cs-Filled MEMS Cell Using Sequential Plasma Activated Bonding.....60
Kenta Terashima, Yoshikazu Hirai, Toshiyuki Tsuchiya, Osamu Tabata
Kyoto University, Japan

Cell-Based Stabilized Laser Sources and Light-Shifts in Pulsed Rb Atomic Clocks.....63
Nil Almat, William Moreno, Matthieu Pellaton, Mohammadreza Gharavipour, Florian Gruet, Christoph Affolderbach, Gaetano Mileti
Université de Neuchâtel, Switzerland

A2L-D Oscillators Design
Date: Monday, July 10, 2017
Time: 14:00 - 15:40
Room: Room 5, 6 & 7
Chair(s): Fabrice Sthal; *FEMTO-ST*
Jean-Pierre Aubry; *FEMTO-ST*

SPINTRONIC Based RF Components.....66
Ursula Ebels[1], Jérôme Hem[3], Anike Purbawati[3], Ana Ruiz Calafora[3], Chandrasekhar Murapaka[1], Laurent Vila[1], Karla Jaimes Merazzo[7], Erika Jimenez[7], Marie-Claire Cyrille[1], Ricardo Ferreira[2], Martin Kreissig[4], Rui Ma[4], Frank Ellinger[4], Romain Lebrun[6], Steffen Wittrock[6], Vincent Cros[6], Paolo Bortolotti[5]
[1]Commissariat à l'Énergie Atomique et aux Énergies Alternatives, France; [2]International Iberian Nanotechnology Laboratory, Braga, Portugal; [3]SPINTEC / Université Grenoble Alpes, France; [4]Technische Universität Dresden, Germany; [5]Thales Research & Technology, France; [6]Unite Mixte de Physique CNRS-Thales / Université Paris-Sud / Université Paris Saclay, France; [7]Université Grenoble Alpes / Commissariat à l'Énergie Atomique et aux Énergies Alternatives, France

A Fully Integrated Quartz MEMS VHF TCXO 68
Randall Kubena[1], Frederic Stratton[1], Hung Nguyen[1], Deborah Kirby[1], David Chang[1], Richard Joyce[1], Yook-Kong Yong[3], Jeffrey Garstecki[2], Matthew Cross[2], S. E. Seman[2]
[1]HRL Laboratories, LLC, United States; [2]Johns Hopkins University Applied Physics Laboratory, United States; [3]Rutgers University, United States

DORIS-Class Oscillator Under Radiations: the Jason Family of Satellites.....72
Alexandre Belli[2], Pierre Exertier[2], Christian Jayles[1], François Vernotte[3]
[1]Centre National d'Études Spatiales, France; [2]Géoazur / Université de Nice Sophia-Antipolis / Observatoire de la Côte d'Azur, France; [3]Université de Franche-Comté, France

High Precision Time Measurement Using a Self-Timed Ring Oscillator Based TDC 77
Assia El-Hadbi[2], Abdelkarim Cherkaoui[2], Oussama Elissati[1], Laurent Fesquet[2]
[1]Institut National des Postes et Télécommunications, Morocco; [2]Université Grenoble Alpes, France

A3L-A Microcombs

Date: Monday, July 10, 2017
Time: 16:00 - 18:00
Room: Amphitheatre
Chair(s): Thomas Sudmeyer; *Université de Neuchâtel*

Measuring Thermodynamic Noise in Optical WGM Microresonators 79
Jinkang Lim[2], Chee Wei Wong[2], Lute Maleki[1], Anatoliy A. Savchenkov[1], Elijah Dale[1], Wei Liang[1], Danny Eliyahu[1], Vladimir S. Ilchenko[1], Andrey B. Matsko[1]
[1]OEwaves Inc, United States; [2]University of California, Los Angeles, United States

In-Fibre Fabry-Pérot Microresonator with 100 Million Q-Factor 84
Ewelina Obrzud, Steve Lecomte, Tobias Herr
CSEM SA, Switzerland

A3L-B Network synchronization and fiber optics timing systems

Date: Monday, July 10, 2017
Time: 16:00 - 18:00
Room: Room 2
Chair(s): Javier Diaz; *Seven Solutions*

Time and Frequency Transfer Over a 500 km Cascaded White Rabbit Network 86
Namneet Kaur, Florian Frank, Paul-Eric Pottie, Philip Tuckey
Observatoire de Paris, France

A Novel Synchronization Method for WR System 91
Xu Yuan, Bo Wang
Tsinghua University, China

Ultra-Low Phase Noise Synchronization of Microwave Sources with Fiber-Optic Timing System 95
Aram Kalaydzhyan[1], Ming Xin[1], Kemal Şafak[1], Michael Peng[3], Kwangyun Jung[2], Wenting Wang[1], Jungwon Kim[2], Franz Kärtner[1]
[1]Deutsches Elektronen-Synchrotron, Germany; [2]Korea Advanced Institute of Science and Technology, Korea; [3]Massachusetts Institute of Technology, United States

Multichannel Precision Time Delay Measurement in Optical Fibers 98
Jingwen Dong, Bo Wang, Hongwei Si, Lijun Wang
Tsinghua University, China

A3L-C Fundamental Physics with Atomic Clocks

Date: Monday, July 10, 2017
Time: 16:00 - 18:00
Room: Room 3 & 4
Chair(s): Kurt Gibble;

Experimental Constraint on Dark Matter-Standard Model Coupling with Optical Atomic Clocks 100
Piotr Wcisło, Piotr Morzyński, Marcin Bober, Agata Cygan, Daniel Lisak, Roman Ciuryło, Michał Zawada
Nicolaus Copernicus University in Toruń, Poland; Nicolaus Copernicus University in Toruń , Poland

Mass Defect Effects in Atomic Clocks 102
Valeriy Yudin[1], Alexey V. Taichenachev[2]
[1]Novosibirsk State University, Russia; [2]Novosibirsk State University / Institute of Laser Physics SB RAS, Russia

Improving Phonon Sector Tests of Lorentz Invariance.....104
Maxim Goryachev[2], Eugene Ivanov[2], Michael Tobar[2], Philipp Haslinger[1], Holger Muller[1]
[1]University of California, Berkeley, United States; [2]University of Western Australia, Australia

Lorentz-Symmetry Test at Planck-Scale Suppression with a Spin-Polarized 133Cs Cold Atom Clock.....106
Hélène Pihan-Le Bars[3], Christine Guerlin[3], Raphaël-David Lasseri[4], Jean-Paul Ebran[1], Quentin Bailey[2], Sébastien Bize[3], Elias Khan[4], Peter Wolf[3]
[1]Commissariat à l'Énergie Atomique et aux Énergies Alternatives, France; [2]Embry-Riddle Aeronautical University, United States; [3]Observatoire de Paris, France; [4]Université Paris-Sud, France

A3L-D Measurement Methods
Date: Monday, July 10, 2017
Time: 16:00 - 18:00
Room: Room 5, 6 & 7
Chair(s): Enrico Rubiola; *FEMTO-ST*
Olivier Llopis; *LAAS*

An Additive Phase Noise Measurement Technique for Mixers with Non-DC IF in Large Signal.....108
Jason Breitbarth
Holzworth Instrumentation, United States

Next Generation 5G Radio Communication NW.....113
Ulrich Rohde[1], Ajay Poddar[4], Ignaz Eisele[3], Enrico Rubiola[2]
[1]Brandenburgische Technische Universität, Germany; [2]Franche-Comté Électronique Mécanique Thermique et Optique - Sciences et Technologies, France; [3]Fraunhofer Society, Germany; [4]Synergy Microwave Corp, United States

The Two-Edge Anti-Jitter Circuit for Phase Noise Reduction on Received Frequency Standards.....117
Michael Underhill
Underhill Research Limited, United Kingdom

Damped Sine Based Time Interval Counter.....121
Nicolas Boucquey[1], Attila Kinali[2]
[1]Institut Supérieur Industriel de Bruxelles, Belgium; [2]Max-Planck-Gesellschaft, Germany

B1L-A Combs I
Date: Tuesday, July 11, 2017
Time: 10:40 - 12:20
Room: Amphitheatre
Chair(s): Yann LeCoq; *OBSPM*

Analysis of the Carrier-Envelope Phase Noise of Passively Phase-Locked Er:fiber Frequency Combs Up to the Nyquist Frequency.....124
Andreas Liehl, David Fehrenbacher, Philipp Sulzer, Denis Seletskiy, Alfred Leitenstorfer
Universität Konstanz, Germany

Optical Frequency Comb Application in Time-Delay Interferometer.....126
Nan Yu, Ivan Grudinin, Massimo Tinto
Jet Propulsion Laboratory, United States

Rapid Electro-Optic Control of the Carrier-Envelope-Offset Frequency for Ultra-Low Noise Frequency Combs.....128
Wolfgang Hänsel[2], Michele Giunta[1], Marc Fischer[2], Matthias Lezius[2], Ronald Holzwarth[2]
[1]Max-Planck-Gesellschaft / Menlo Systems GmbH, Germany; [2]Menlo Systems GmbH, Germany

B1L-B Optical Time Transfer
Date: Tuesday, July 11, 2017
Time: 10:40 - 12:20
Room: Room 2
Chair(s): Gesine Grosche; *PTB*

Doppler-Tolerant Synchronization of Clocks Over Free Space at the Femtosecond Level 130
Hugo Bergeron[2], Jean-Daniel Deschênes[2], Laura Sinclair[1], William Swann[1], Isaac Khader[1], Esther Baumann[1], Nathan R. Newbury[1]
[1]National Institute of Standards and Technology, United States; [2]Université Laval, Canada

Femtosecond Atmospheric Frequency Transfer Using Diode Laser with Electronic Phase Compensation 132
Shijun Chen[2], Dawei Chen[2], Qiang Chen[2], Fuyu Sun[1], Jianguo Hu[1], Xianhe Huang[1], Dong Hou[1]
[1]University of Electronic Science and Technology of China, China; [2]ZTE Corporation, China

B1L-C Space Clocks
Date: Tuesday, July 11, 2017
Time: 10:40 - 12:20
Room: Room 3 & 4
Chair(s): Steven Wilkinson; *Raytheon*

Optically Pumped Cs Space Clock Development 136
Roman Schmeissner[6], Philippe Favard[6], Adel Douahi[6], Patrick Perez[6], Nicole Mestre[6], Michel Baldy[6], Andreas Romer[5], Frederic Chastellain[5], Willem Walter Coppoolse[5], Nicolas von Bandel[2], Michel Garcia[2], Michel Krakowski[2], Stéphane Guérandel[3], Yves Folco[4], Wolfgang Konrad[1]
[1]Arcosic Research, Austria; [2]III-V Lab, France; [3]Observatoire de Paris, France; [4]Thales Alenia Space, France; [5]Thales Alenia Space Switzerland, Switzerland; [6]Thales Electron Devices, France

B1L-D Microacoustic Signal Processing
Date: Tuesday, July 11, 2017
Time: 10:40 - 12:20
Room: Room 5, 6 & 7
Chair(s): Matteo Rinaldi; *Northeastern University*
Shuji Tanaka; *Tohoku University*

GHz Ultrasonics for on Chip Delay Lines, Communications, Timing, Memory, and Sensing 138
Amit Lal
Cornell University, United States

Acoustic Delay Lines to Measure Piezoelectricity in 4H Silicon Carbide 139
Pen-Li Yu, Sunil Bhave
Purdue University, United States

An SH0 Lithium Niobate Correlator for Orthogonal Frequency Coded Spread Spectrum Communications 143
Tomas Manzaneque, Ruochen Lu, Yansong Yang, Songbin Gong
University of Illinois at Urbana-Champaign, United States

Observation of Phononic Frequency Combs in a Micromechanical Resonator 148
Adarsh Ganesan, Cuong Do, Ashwin Seshia
University of Cambridge, United Kingdom

B2L-A Optical Clocks II
Date: Tuesday, July 11, 2017
Time: 14:00 - 15:40
Room: Amphitheatre
Chair(s): Jerome Lodewyck; *OBSPM*

The Collisional Frequency Shift of a Trapped-Ion Optical Clock 153
Amar Vutha[2], Tom Kirchner[3], Pierre Dubé[1]
[1]National Research Council Canada, Canada; [2]University of Toronto, Canada; [3]York University, Canada

Rydberg Spectroscopy for DC Stark Shift Characterisation in Optical Lattice Clocks.....154
William Bowden[2], Richard Hobson[2], Patrick Gill[2], Ian Hill[2], Paul Huillery[1], Matthew Jones[1]
[1]Durham University, United Kingdom; [2]National Physical Laboratory, United Kingdom

B2L-B Optical Fiber Links
Date: Tuesday, July 11, 2017
Time: 14:00 - 15:40
Room: Room 2
Chair(s): Per Olof Hedekvist; *SP Tech. Research Inst. of Sweden*
Przemysław Krehlik; *AGH University of Science and Technology*

The Italian Optical Link for Time and Frequency.....156
Davide Calonico, Cecilia Clivati, Alberto Mura, Anna Tampellini, Filippo Levi
Istituto Nazionale di Ricerca Metrologica, Italy

Hybrid Optical Link for Ultra-Stable Frequency Comparison 160
Dan Xu[2], Won-Kyu Lee[1], Fabio Stefani[2], Paul-Eric Pottie[2], Anne Amy-Klein[3], Olivier Lopez[3]
[1]Korea Research Institute of Standards and Science / Observatoire de Paris, PSL Research University, Korea; [2]Observatoire de Paris, France; [3]Université Paris 13, France

B2L-C CPT Clocks
Date: Tuesday, July 11, 2017
Time: 14:00 - 15:40
Room: Room 3 & 4
Chair(s): Christoph Affolderbach; *University of Neuchâtel*

The Medium and Long Term Stability of the NAC Atomic Clock.....162
Shemi Prazot, Avinoam Stern, Weiss Israel, Shlomo Marmor, Chagai Levi, Israel Yevilevich, Uriel Arad, Rony Man, Benny Levi
AccuBeat Ltd., Israel

Towards Miniaturization of a High Performance Coherent Population Trapping Clock.....169
Peter Enxue Yun[1], François Tricot[4], Emeric de Clercq[4], Stéphane Guérandel[4], Claudio Eligio Calosso[3], Salvatore Micalizio[3], Moustafa Abdel Hafiz[2], Rodolphe Boudot[2]
[1]Chinese Academy of Sciences, China; [2]Franche-Comté Électronique Mécanique Thermique et Optique - Sciences et Technologies, France; [3]Istituto Nazionale di Ricerca Metrologica, Italy; [4]Observatoire de Paris, France

Latest Achievements on the Pulsed CPT Clock 172
François Tricot[2], Peter Enxue Yun[1], Emeric de Clercq[2], Stéphane Guérandel[2]
[1]Chinese Academy of Sciences, France; [2]Observatoire de Paris, France

B2L-D Noise in oscillators

Date: Tuesday, July 11, 2017
Time: 14:00 - 15:40
Room: Room 5, 6 & 7
Chair(s): Jeremy Everard; *University of York*
Ajay Poddar; *Synergy Microwave Corporation*

Noise Sources Characterization and its Compact Modeling Based on Physical Device Simulations for Designing Low Phase Noise Oscillators 175
Jean-Christophe Nallatamby[1], Michel Prigent[1], David Cordeau[2], Jean-Marie Paillot[2]
[1]Université de Limoges, France; [2]Université de Poitiers, France

Investigation on Flicker Noise of Overtones and Anharmonic Modes of Ultra-Stables Quartz Crystal Resonators.....176
Alok Pokharel[3], Fabrice Sthal[2], Joël Imbaud[4], François-Xavier Esnault[1], Gilles Cibiel[1]
[1]Centre National d'Études Spatiales, France; [2]École Nationale Supérieure de Mécanique et des Microtechniques, France; [3]Franche-Comté Électronique Mécanique Thermique et Optique - Sciences et Technologies, France; [4]Franche-Comté Électronique Mécanique Thermique et Optique - Sciences et Technologies / ENS2M, France

First Search for Axions of Mass 110 μeV Using milliKelvin Cooled 26.6 GHz Microwave Resonator.....179
Ben McAlister, Justin Kruger, Graeme Flower, Jeremey Bourhill, Maxim Goryachev, Stephen Parker, Eugene Ivanov, Michael Tobar
University of Western Australia, Australia

A Crystal-Less Bluetooth Low Energy Radio Using a MEMS-Based Frequency Reference System.....181
Danielle Griffith, Ernest Ting-Ta Yen, Per Torstein Røine, Kaichien Tsai, Torjus Kallerud, Brian Goodlin
Texas Instruments, United States; Texas Instruments, Norway

B3P-E Student Paper Competition (see final program for full details)

Date: Tuesday, July 11, 2017
Time: 16:00 - 18:00
Room: Mezzanine
Chair(s): Francois Vernotte; *UTINAM-Observatory THETA-UBFC*

Mitigation of Lamplight-Induced Frequency Variations in Space Rubidium Clocks.....185
Valerio Formichella[2], Patrizia Tavella[2], James Camparo[1]
[1]Aerospace Corporation, United States; [2]Istituto Nazionale di Ricerca Metrologica, Italy

Ethernet Time-Transfer Based on Low Frequency White Rabbit Solution 186
Francisco Jesús Girela-López, Felipe Torres-González, Javier Díaz
Universidad de Granada, Spain

In-Situ Dispersion Measurement of a Coupled Optoelectronic Oscillator.....190
Oriane Lelièvre[2], Vincent Crozatier[2], Ghaya Baili[2], Pascale Nouchi[2], Daniel Dolfi[2], Loïc Morvan[2], Fabienne Goldfarb[3], Fabien Bretenaker[3], Olivier Llopis[1]
[1]Laboratoire d'analyse et d'architectures des systèmes / Centre National de la Recherche Scientifique, France; [2]Thales Research & Technology, France; [3]Université Paris-Sud, France

B3P-F Materials, Resonators & Resonator Circuits I

Date: Tuesday, July 11, 2017
Time: 16:00 - 18:00
Room: Poster Area
Chair(s): Ji Wang; *Ningbo University*
Sheng-Shian Li; *National Tsing Hua Univ.*

Material Parameters of Ca3TaGa3Si2O14 (CTGS) Piezoelectric Single Crystal at Extreme Temperatures 193
Andrei Sotnikov[3], Hagen Schmidt[3], Mohammad Hossein Haghighi[3], Yuriy Suhak[4], Holger Fritze[4], Mikhail Gorev[2], Sergey Sakharov[1]
[1]Fomos Materials, Russia; [2]Kirensky Institute of Physics, Russia; [3]Leibniz-Institut für Festkörper- und Werkstoffforschung Dresden, Germany; [4]Technische Universität Clausthal, Germany

Miniaturized VHF Quartz MEMS Resonator Design Methodology 198
Deborah Kirby[1], Randall Kubena[1], Yook-Kong Yong[3], Frederic Stratton[1], Hung Nguyen[1], Richard Joyce[1], David Chang[1], Jeffrey Garstecki[2]
[1]HRL Laboratories, LLC, United States; [2]Johns Hopkins University Applied Physics Laboratory, United States; [3]Rutgers University, United States

Capacitive Lamé Mode Resonator with Gap Closing Mechanism for Motional Resistance Reduction 203
Mohannad Elsayed[2], Frederic Nabki[1]
[1]Ecole de Technologie Superieure, Canada; [2]McGill University / Ecole de Technologie Superieure, Canada

HAL SAW Resonators Using LiTaO3 Thin Plate on Quartz Substrate 206
Michio Kadota, Shuji Tanaka
Tohoku University, Japan

Nonlinear Time Domain-FFT Study of the f – 2f Frequency Response of Lithium Niobate YX-127° SAW Resonators 210
Yook-Kong Yong, Xiangnan Pang
Rutgers University, United States

Buried Wave Devices 212
Victor Plessky[1], Julius Koskela[1], Bob Hammond[2]
[1]GVR Trade SA, Switzerland; [2]Resonant Inc., United States

Periodically Poled LiNbO3 Transducer on (YXl)/128° Cut for RF Applications 214
Alexandre Matic, Thomas Baron, Florent Bassignot
Franche-Comté Électronique Mécanique Thermique et Optique - Sciences et Technologies, France

DRIE of High Q-Factor Length-Extensional Mode Quartz Micro-Resonator 218
Paul Chapellier[2], Béatrice Verlhac[2], Pierre Lavenus[2], Bernard Dulmet[1]
[1]Franche-Comté Électronique Mécanique Thermique et Optique - Sciences et Technologies, France; [2]Office National d'Etudes et de Recherches Aérospatiales, France

B3P-G Oscillators, Resonators, and Noise

Date: Tuesday, July 11, 2017
Time: 16:00 - 18:00
Room: Poster Area
Chair(s): Joel Imbaud; *FEMTO-ST*

Extraordinary OCXO Solutions Based on the IHR Technology 222
Igor Abramzon, Vadim Tapkov, Aleksei Kornilov
Magic Xtal Ltd., Russia

The Design of a Novel Low Phase Noise Anti-Vibration OCXO 227
Songtao Jiang, Xu Wang
Chengdu Spaceon Electronics Co., Ltd., China

High Stability Miniature Size OCXO: Using a SC-Cut Crystal Resonator and Simultaneous Oscillations 231
Masato Ogawa, Manabu Ito, Kaoru Kobayashi, Manabu Ishikawa, Kazuo Akaike
Nihon Dempa Kogyo Co., Ltd, Japan

A Novel Design of Voltage Controlled Temperature Compensated Crystal Oscillator 235
Jianguo Hu, Xianhe Huang, Qi Zhou, Dong Liu, Wei Fu
University of Electronic Science and Technology of China, China

Limiting Factor for the Performance of High Stability Quartz Crystal Oscillators – the Residual Heat of Crystal Resonators 238
Xianhe Huang[2], Yuanlin Tang[2], Qi Zhou[2], Jianguo Hu[2], Wei Fu[2], Pingping Chen[1]
[1]Bowei Integrated Circuits Co.Ltd., China; [2]University of Electronic Science and Technology of China, China

Frequency Stabilization of a Quartz Oscillator by Using the Method of Delayed Differentiation of Ambient Parameters 241
Rimantas Miškinis[2], Dimitrij Smirnov[2], Emilis Urba[2], Eglė Baniulienė[2], Albin Czubla[1]
[1]Central Office of Measures, Poland; [2]State Research Institute Center for Physical Sciences and Technology, Lithuania

Concept and Main Results for Ultraprecise Low Noisy 10 MHz DOCXO Ensuring Allan Deviation of 1…2E-13 for 1…10 S 245
Yakov Vorokhovsky, Arkady Nikonov, Aleksandr Kotyukov, Alexey Kamochkin
Morion, Inc., Russia

10 GHz Low Timing-Jitter and Broadband Optical Comb Generation Based on an Optoelectronic Oscillator 250
Huanfa Peng, Yongchi Xu, Xiaofeng Peng, Cheng Zhang, Lixin Zhu, Weiwei Hu, Zhangyuan Chen
Peking University, China

Effect of Joule Heating on the Performance of a Piezoresistive Micromechanical Oscillator 253
Liu Xu[2], Xueyong Wei[2], Dong Pu[2], Zhuangde Jiang[2], Juan Ren[1]
[1]Chang'an University, China; [2]Xi'an Jiaotong University, China

Quantum Theory of 1/F Frequency Fluctuations 257
Peter Handel
University of Missouri–St. Louis , United States

Spectral Performance and Noise Theory of Nonlinear Transmission Line Frequency Multipliers 261
Jason Breitbarth[1], Zoya Popović[2]
[1]Holzworth Instrumentation, United States; [2]University of Colorado Boulder, United States

Ultra-Low Phase-Noise Microwave Oscillator Based on Electro-Optical Frequency Division 265
Jiang Li[2], Kerry Vahala[1]
[1]California Institute of Technology, United States; [2]hQphotonics Inc., United States

B3P-H Microwave Frequency Standards I

Date: Tuesday, July 11, 2017
Time: 16:00 - 18:00
Room: Poster Area
Chair(s): Fang Fang; *NIM*

Improving the Frequency Stability of Atomic Frequency Standard Basing on the Noise Asynchromism Correction 267
Qian Wang, Rong Wei, Richang Dong, Jinda Lin, Wenli Wang, Yuzhu Wang
Chinese Academy of Sciences, China

An Empirical Model of the Alkali rf-Discharge Lamp 271
James Camparo
Aerospace Corporation, United States

Theoretical and Experimental Study of Rb Coherent Population Trapping Atomic Clock with Phase Modulation Detection 277
Yuichiro Yano, Motoaki Hara, Masatoshi Kajita, Tetsuya Ido
National Institute of Information and Communications Technology, Japan

Ultrahigh-Contrast Saturated-Absorption Resonance to Enhance Stability of CPT Atom Clocks 278
Denis Brazhnikov[2], Moustafa Abdel Hafiz[1], Grégoire Coget[1], Alexey V. Taichenachev[3], Valeriy Yudin[2], Emeric de Clercq[4], Rodolphe Boudot[1]
[1]Franche-Comté Électronique Mécanique Thermique et Optique - Sciences et Technologies, France; [2]Novosibirsk State University, Russia; [3]Novosibirsk State University / Institute of Laser Physics SB RAS, Russia; [4]Observatoire de Paris, France

A Caesium Atomic Beam Microwave Clock Detected by Distributed Feedback Laser Diodes 282
Chang Liu[2], Shuhui Wang[2], Ziyu Chen[2], Yanhui Wang[2], Shimin Hou[2], Jinsheng Jia[1], Yong Sun[1], Bingqiang Zhang[1]
[1]China Building Materials Academy, China; [2]Peking University, China

Compact Vapor Cell Cesium Clock Based on Continuous Wave Optical Pumping 285
Jianhong Wan, Chang Liu, Yanhui Wang
Peking University, China

Simulation of the Ramsey Cavity Response 289
Fuyu Sun, Xianhe Huang, Jianguo Hu, Qingsong Bai, Dong Hou
University of Electronic Science and Technology of China, China

Study the Phase Transient of the RF Mach-Zehnder Interferometric Switch 292
Dandan Liu, Jun Ruan, Xinliang Wang, Yong Guan, Fengxiang Yu, Junru Shi, Hui Zhang, Rui Lin, Jiang Chen, Xiaofei Zhang, Shougang Zhang
Chinese Academy of Sciences, China

Reduction of Dick Effect in a Pulsed CPT Vapor Cell Clock by Interleaving Lock 294
Xiaolin Sun, Pengfei Cheng, Ya'Ni Zuo, Lijun Wang, Jianwei Zhang
Tsinghua University, China

Thermal Management of Microfabricated Vapor Cells for Chip Scale Atomic Clocks 296
Runqi Han, Zheng You, Fan Zhang, Yong Ruan
Tsinghua University, China

High Sensitively Coherent Population Trapping Magnetometer with Optically Pumped Degenerate Atoms 300
Ryo Maeda[1], Shigeyoshi Goka[2]
[1]Ricoh Co., Ltd., Japan; [2]Tokyo Metropolitan University, Japan

The Microwave Down Converted from Ultra-Stable Laser by an Optical Frequency Comb 302
Shaoyang Dai, Fang Fang, Shiying Cao, Nianfeng Liu, Rui Suo, Tianchu Li
Chinese Academy of Sciences, China

Design of Active All-Optical Magnetometer 305
Duo Pan, Tiantian Shi, Xiang Peng, Jingbiao Chen, Hong Guo
Peking University, China

Optimization of Frequency Modulation Parameters in Atomic Clocks Based on Coherent Population Trapping 307
Valeriy Yudin[1], Maksim Basalaev[1], Dmitriy Kovalenko[1], Alexey V. Taichenachev[2]
[1]Novosibirsk State University, Russia; [2]Novosibirsk State University / Institute of Laser Physics SB RAS, Russia

Retrace and Disciplining Time Constant Effects on Holdover Clock Drifts in Chip-Scale Atomic Clock 310
Yoonkee Kim, Christopher Walter
United States Army, United States

MEMS Atomic Vapor Cells for Gyroscope Applications 315
Sylvain Karlen, Gilles Buchs, Thomas Overstolz, Nicolas Torcheboeuf, Emmanuel Onillon, Jacques Haesler, Dmitri Boiko
CSEM SA, Switzerland

Preliminary Stability Analysis of Rb Fountains for Timescale Generation 317
Luca Lorini[2], Konstantin Pavlenko[4], Sébastien Bize[2], Bruno Desruelle[1], Guillaume Stern[1], Ilia Doronin[4], Yuri Pavlenko[4], Sergey S. Donchenko[3]
[1]Muquans, France; [2]Observatoire de Paris, France; [3]VNIIFTRI, Russia; [4]VREMYA-CH JSC, Russia

Generalized Electronics for Compact Atomic Clocks 322
Claudio Eligio Calosso[2], Michele Gozzelino[5], Elio Bertacco[2], Salvatore Micalizio[2], Bruno François[3], Rodolphe Boudot[1], Peter Yun[4]
[1]Franche-Comté Électronique Mécanique Thermique et Optique - Sciences et Technologies, France; [2]Istituto Nazionale di Ricerca Metrologica, Italy; [3]Istituto Nazionale di Ricerca Metrologica / FEMTO-ST Institute, France; [4]Observatoire de Paris, France; [5]Politecnico di Torino / Istituto Nazionale di Ricerca Metrologica, Italy

PIN Photodiode Spurious Noise Characterization 324
Roman Schmeissner, Antoine Maillard, Patrick Perez, Michel Baldy
Thales Electron Devices, France

Progress in Mexican Cesium Atomic Fountain-CsF1 Using an Ultra-Stable Laser 326
Carlos Andres Ortiz[2], Jose Mauricio López[1], Eduardo de Carlos López[3]
[1]Centro de Investigación y de Estudios Avanzados del Instituto Politécnico Nacional, Mexico; [2]Centro de Investigación y de Estudios Avanzados del Instituto Politécnico Nacional / Centro Nacional, Mexico; [3]Centro Nacional de Metrología, Mexico

Frequency Drift Detection Method Using Dual Alkali Gas for Coherent Population Trapping Atomic Clocks 328
Yota Furuse[1], Yuji Kase[1], Shigeyoshi Goka[2]
[1]Tokyo Metroplitan University, Japan; [2]Tokyo Metropolitan University, Japan

Magnetic Field Measurement by Stimulated Raman Transitions and Smoothing by Dynamical Compensation in Rubidium Fountain Clock 332
Wenli Wang[1], Richang Dong[1], Rong Wei[1], Tingting Chen[2], Qian Wang[1], Yuzhu Wang[1]
[1]Chinese Academy of Sciences, China; [2]Key Laboratory for Quantum Optics, Shanghai Institute of Optics and Fine Mechanics, Chinese Academy, China

B3P-J Sensors & Transducers I

Date: Tuesday, July 11, 2017
Time: 16:00 - 18:00
Room: Poster Area
Chair(s): Sid Tallur; *IIT Bombay*

Impact of the Environment on a Hygrometry Sensor Response 336
Marianne Sagnard[1], Thierry Laroche[2], Jean-Michel Friedt[1], Sylvain Ballandras[2]
[1]Franche-Comté Électronique Mécanique Thermique et Optique - Sciences et Technologies, France; [2]FREC'N'SYS, France

Three-Parameter Liquid Sensor Based on Surface and Plate Acoustic Waves 343
Natalia Voronova[2], Vladimir I. Anisimkin[1]
[1]Kotelnikov Institute of Radio Engineering and Electronics of RAS, Russia; [2]Kotelnikov's Institute of Radioengineering and Electronics Russian Academy of Sciences/IRE RAS, Russia

Elastic Properties of Graphene Oxide Films and Changes Due to Gas Phase Adsorption 345
Enrico Verona[1], Iren E. Kuznetsova[3], Vladimir I. Anisimkin[2], Sergey P. Gubin[4], Sergey V. Tkachev[4], Vladimir V. Kolesov[2], Vitaliy V. Kashin[2], Boris D. Zaitsev[3], Alexander M. Shikhabudinov[3]
[1]Consiglio Nazionale delle Ricerche, Italy; [2]Kotelnikov Institute of Radio Engineering and Electronics of RAS, Russia; [3]Kotelnikov Institute of Radio Engineering and Electronics of RAS / Yandex, Russia; [4]Kurnakov Institute of General and Inorganic Chemistry of RAS, Russia

SAW Torque Sensor for Marine Applications 347
Victor Kalinin[2], Arthur Leigh[2], Alexander Stopps[2], Stefan Blom Hanssen[1]
[1]Kongsberg Maritime, Norway; [2]Transense Technologies PLC, United Kingdom

Direct Integration of CNT Forests on Solidly Mounted Resonators and Their Influence on Device Performance 353
Teona Mirea, Jimena Olivares, Marta Clement, Jesús Sangrador, Enrique Iborra
Universidad Politécnica de Madrid, Spain

B3P-K Timekeeping, Time & Frequency Transfer, GNSS Applications I

Date: Tuesday, July 11, 2017
Time: 16:00 - 18:00
Room: Poster Area
Chair(s): Anne Amy-Klein; *Université Paris 13, CNRS*

Satellite Clock Offset Estimation and Analysis Based on Arc-Wise Observation Files 357
Meifang Wu, Baoqi Sun, Xuhai Yang, Hang Su
Chinese Academy of Sciences, China

GPS All in View Time Comparison Using Multi-Receiver Ensemble 362
Shinn Yan Lin[2], Zhiheng Jiang[1]
[1]International Bureau of Weights and Measures, France; [2]Telecommunication Laboratories Chunghwa Telecom Co., Ltd., Taiwan

Delay Compensation of 1 PPS Timetags in Fiber-Optic Time Distribution 366
Przemysław Krehlik, Michal Mazur, Łukasz Śliwczyński
AGH University of Science and Technology, Poland

Time and Frequency Transfer in Modern DWDM Telecommunication Networks 368
Krzysztof Turza[2], Artur Binczewski[2], Wojbor Bogacki[2], Przemysław Krehlik[1], Łukasz Śliwczyński[1]
[1]AGH University of Science and Technology, Poland; [2]Poznań Supercomputing and Networking Center, Poland

EFTF-IFCS 2017 TABLE OF CONTENTS

A Novel Real Time Cycle Slip Detection and Repair Method for a Single Dual-Frequency GNSS Receiver 371
Hang Yi, Hongbo Wang, Xueyun Wang, Shengkang Zhang, Haifeng Wang, Wenzhe Yang, Shuwei Wang
Beijing Institute of Radio Metrology and Measurement, China

Three Loops - a Method for Tracking a New TWSTFT Signal FBOC 375
Haifeng Wang, Xueyun Wang, Hongbo Wang, Hang Yi, Shuwei Wang, Wenzhe Yang, Shengkang Zhang
Beijing Institute of Radio Metrology and Measurement, China

Progress on the REFIMEVE+ Project for Optical Frequency Standard Dissemination 378
Etienne Cantin[4], Nicolas Quintin[5], Fabrice Wiotte[4], Christian Chardonnet[4], Anne Amy-Klein[4], Olivier Lopez[4], Paul-Eric Pottie[1], Giorgio Santarelli[3], Emilie Camisard[2]
[1]Observatoire de Paris, France; [2]Réseau National de Télécommunications pour la Technologie, l'Enseignement et la Recherche, France; [3]Université de Bordeaux / École Supérieure d'Optique, France; [4]Université Paris 13, France; [5]Université Paris 13 / RENATER, France

A Atomic Time Algorithm Based on Predictable Weighting and Wavelet Multi-Scale Threshold Denoising 381
Huijie Song, ShaoWu Dong, Jun Ruan, Tao Liu, Lili Qu, YanPing Wang, Yi Qi, Xiang Wang, Juan Hou
Chinese Academy of Sciences, China

EGNSS Based Robust Synchronization Service 385
Erik Dierikx[5], Anders Wallin[6], Mikko Merimaa[6], Roland Bauernfeind[4], Martti Kirkko-Jaakkola[3], Valeria Catalano[1], Kjell Arne Aarmo[2], Daniele Borio[2]
[1]European Global Navigation Satellite Systems Agency, Belgium; [2]European Union, Italy; [2]European Union, Belgium; [3]National Land Survey of Finland / Finnish Geospatial Research Institute, Finland; [4]NavCert GmbH, Germany; [5]VSL - Dutch Metrological Institute, Netherlands; [6]VTT Technical Research Centre of Finland Ltd, Finland

Clock Stability for Low Frequency Radar Tomography of Asteroids 388
Ricardo Granados, Alain Herique, Etienne Le-Coarer, Sylvain Rochat
Université Grenoble Alpes, France

A New TWSTFT Station in Warsaw 393
Michał Marszalec[3], Tomasz Kossek[3], Marzenna Lusawa[3], Albin Czubla[2], Piotr Szterk[2], Roman Osmyk[2], Przemysław Krehlik[1], Łukasz Śliwczyński[1], Marcin Lipiński[1]
[1]AGH University of Science and Technology, Poland; [2]Central Office of Measures, Poland; [3]National Institute ot Telecommunications, Poland

Time Delay Measurements: Estimation of the Error Budget 397
Marco Siccardi[2], Giovanni Daniele Rovera[1]
[1]Observatoire de Paris, France; [2]SKK Electronics, Italy

Some Approximated Methods of Calculation Sagnac Correction for Optical Fiber Time Transfer 399
Albin Czubla[2], Przemysław Krehlik[1], Łukasz Śliwczyński[1], Jacek Kołodziej[1], Artur Binczewski[3], Krzysztof Turza[3], Wojbor Bogacki[3], Piotr Rydlichowski[3]
[1]AGH University of Science and Technology, Poland; [2]Central Office of Measures, Poland; [3]Poznań Supercomputing and Networking Center, Poland

Analysis of Uncertainty in Time Traceability Links Using GPS Common View and Optical Fiber Techniques 402
Lingda Meng, Ya Liu, Feng Zhu, Xiaohui Li
Chinese Academy of Sciences, China

Global Time Synchronization Mechanism for Radio Interferometer Network 406
El Houssain Ait Mansour[2], Bruno Da Silva[2], Stéphane Bosse[2], Karl-Ludwig Klein[1]
[1]Observatoire de Paris, France; [2]Station de Radioastronomie de Nançay, France

Fractional Brownian Motion and its Application in the Simulation of Noise in Atomic Clocks.....408
Attila Kinali
Max-Planck-Gesellschaft, Germany

White-Rabbit-Enabled Data Acquisition System 410
José López-Jiménez, Miguel Jiménez-López, Javier Díaz, José Luis Gutiérrez-Rivas
Universidad de Granada, Spain

System of Comparison of Time Scales of Distant Objects via Optical Fiber.....417
Oleg V. Kolmogorov, Sergey S. Donchenko, Dmitrie V. Prokhorov
VNIIFTRI, Russia

B3P-L Optical Frequency Standards and Applications I

Date: Tuesday, July 11, 2017
Time: 16:00 - 18:00
Room: Poster Area
Chair(s): Nan Yu; *JPL*

Characterization of the Phase-Noise Induced by an Optical Frequency Doubler 419
Marion Delehaye, Jacques Millo, Pierre-Yves Bourgeois, Lucas Groult, Ahmed Bakir, Rodolphe Boudot, Enrico Rubiola, Vincent Giordano, Emmanuel Bigler, Yann Kersalé, Clément Lacroûte
Franche-Comté Électronique Mécanique Thermique et Optique - Sciences et Technologies, France

Inverted Crossover Resonances with ΔF=0 or 1: Inverted Crossover Resonances with the Intercombination Line of 171Yb 421
John McFerran[2], Emeric de Clercq[1]
[1]Observatoire de Paris, France; [2]University of Western Australia, Australia

Towards Doppler-Free Spectroscopy of O3 Isotopes at 28 THz with a Quantum Cascade Laser Locked to a Stabilized Frequency Comb Reference.....423
Thomas Zanon-Willette[1], Marco Minissale[2], Hadj Elandaloussi[1], Pascal Jeseck[1], Christian Rouillé[1], Corinne Boursier[1], Christof Janssen[1]
[1]Université Pierre-et-Marie-Curie, France; [2]Université Pierre-et-Marie-Curie / Aix-Marseille Université, France

Short-Length Homodyne Interferometer for Self-Stabilization of an Optical Frequency Comb 425
James Cahill[1], Weimin Zhou[1], Curtis Menyuk[2]
[1]United States Army Research Laboratory, United States; [2]University of Maryland, Baltimore County, United States

Resent Progresses of Dual-Wavelength Good-Bad Cavity Active Optical Clock.....427
Duo Pan, Tiantian Shi, Biao Xue, Jingbiao Chen
Peking University, China

Prospects for an Active Optical Clock Using Forbidden Transition in Trapped Ions 430
Georgy Kazakov, Thorsten Schumm
Technical University of Vienna, Austria

Deep Laser Cooling of Mg in Dipole Trap for Frequency Standard.....432
Oleg N. Prudnikov[1], Alexey V. Taichenachev[4], Valeriy Yudin[3], Ernst M. Rasel[2]
[1]Institute of Laser Physics SB RAS, Russia; [2]Leibniz Universität Hannover, Germany; [3]Novosibirsk State University, Russia; [4]Novosibirsk State University / Institute of Laser Physics SB RAS, Russia

Towards Black Body Radiation Shift Uncertainty in Optical Lattice Clocks at 10^-18 Level at Room Temperatures 437
Piotr Ablewski, Marcin Bober, Michał Zawada
Nicolaus Copernicus University in Toruń , Poland; Nicolaus Copernicus University in Toruń, Poland

Recent Progress of Neutral Mercury Lattice Clock in SIOM 439
Xiao Hu Fu[2], Su Fang[1], Ru Chen Zhao[1], Jian Fang Sun[1], Zhen Xu[1], Yuzhu Wang[1]
[1]Chinese Academy of Sciences, China; [2]Shanghai Institute of Optics and Fine Mechanics, Chinese Academy of Science, China

Thermal Noise Limited Ultra-Stable Laser at 1555 nm 444
Zhaoyang Tai, Lulu Yan, Yanyan Zhang, Wenyu Zhao, Xiaofei Zhang, Shougang Zhang, Haifeng Jiang
Chinese Academy of Sciences, China

Multiple Lasers Stabilization on a Single Three Color Optical Cavity 446
Gianmaria Milani[1], Benjamin Rauf[2], Piero Barbieri[1], Filippo Bregolin[1], Marco Pizzocaro[1], Pierre Thoumany[1], Filippo Levi[1], Davide Calonico[1]
[1]Istituto Nazionale di Ricerca Metrologica, Italy; [2]Istituto Nazionale di Ricerca Metrologica / National Physical Laboratory, Italy

Progress Towards a Two-Photon Clock Based on Laser-Cooled Calcium 448
Shreyas Potnis, Shira Jackson, Amar Vutha
University of Toronto, Canada

A Spectrograph to Characterize Comb Spectra 450
Rafael Probst[2], Tilo Steinmetz[3], Yuanjie Wu[3], Frank Grupp[4], Thomas Udem[1], Ronald Holzwarth[3]
[1]Max-Planck-Gesellschaft, Germany; [2]Max-Planck-Gesellschaft / Menlo Systems GmbH, Germany; [3]Menlo Systems GmbH, Germany; [4]Universitätssternwarte München, Germany

Methane Based Microwave Reference Oscillator 452
Mikhail Gubin[2], Alexey Kireev[2], Dmitri Tyurikov[2], Alexander Shelkovnikov[2], Anton Tausenev[2], Dmitriy Chernykh[2], Denis Shepelev[1], Alexander Konyashchenko[2]
[1]Avesta Ltd., Russia; [2]P.N. Lebedev Physical Institute of the Russian Academy of Sciences, Russia

Revisiting the Relation Between Laser Spectrum and Phase Noise Spectral Density with New Outcomes 456
Pierre Brochard, Stéphane Schilt, Thomas Südmeyer
Université de Neuchâtel, Switzerland

Photonic Microwave Generation at NTSC 458
Lulu Yan, Wenyu Zhao, Yanyan Zhang, Zhaoyang Tai, Pan Zhang, Xiaofei Zhang, Wenge Guo, Shougang Zhang, Haifeng Jiang
Chinese Academy of Sciences, China

High-Temperature Calcium Vapor Cell Construction and Spectroscopy 460
Nathan Lemke[1], Christopher Erickson[1], Kyle Martin[2], Jordan Armstrong[2], Jarom Jackson[3], Dallin Durfee[3]
[1]Air Force Research Laboratory, United States; [2]Applied Technology Associates, United States; [3]Brigham Young University, United States

G-LAS: a Ring Laser Goniometer for Angular Metrology 462
Jacopo Belfi[4], Nicolò Beverini[3], Giorgio Carelli[3], Angela Di Virgilio[1], Umberto Giacomelli[3], Enrico Maccioni[3], Milena Astrua[2], Marco Pisani[2], Marco Santiano[2]
[1]Istituto Nazionale di Fisica Nucleare, Italy; [2]Istituto Nazionale di Ricerca Metrologica, Italy; [3]Università di Pisa, Italy; [4]Università di Pisa / Istituto Nazionale di Ricerca Metrologica, Italy

C1L-A Transportable Optical Clocks

Date: Wednesday, July 12, 2017
Time: 10:40 - 12:20
Room: Amphitheatre
Chair(s): Steve Lecomte; *CSEM*

The Optical Rubidium Atomic Frequency Standard at AFRL 466
Nathan Lemke[1], Gretchen Phelps[1], John Burke[1], Kyle Martin[2], Matthew Bigelow[2]
[1]Air Force Research Laboratory, United States; [2]Applied Technology Associates, United States

Frequency Comb-Assisted QCL Stabilization for High Resolution Molecular Spectroscopy 468
Rosa Santagata[4], Dang Bao An Tran[4], Olivier Lopez[4], Bérengère Argence Argence[4], Sean K. Tokunaga[4], Benoît Darquié[4], Anne Amy-Klein[4], Daniele Nicolodi[2], Michel Abgrall[3], Yann Le Coq[3], Rodolphe Le Targat[3], Dan Xu[3], Won-Kyu Lee[1], Paul-Eric Pottie[3]
[1]Korea Research Institute of Standards and Science / Observatoire de Paris, PSL Research University, France; [2]National Institute of Standards and Technology / Observatoire de Paris, France; [3]Observatoire de Paris, France; [4]Université Paris 13, France

1.5 µm - Optical Frequency Standard Iodine Stabilized in the 10^-15 Range for Space Applications 471
Charles Philippe[2], Jonathan Gillot[2], David Holleville[2], Michel Lours[2], Rodolphe Le Targat[2], Peter Wolf[2], Ouali Acef[2], Thomas Lévèque[1], Roland Le Goff[3]
[1]Centre National d'Études Spatiales, France; [2]Observatoire de Paris, France; [3]SODERN, France

C1L-B Robust Timing and Synchronization Service

Date: Wednesday, July 12, 2017
Time: 10:40 - 12:20
Room: Room 2
Chair(s): Pierre Waller; *ESA*

The H2020 European Project DEMETRA: Experimental Time Services Based on European GNSS Signals 475
Patrizia Tavella[4], Ilaria Sesia[4], G. Cerretto[4], G. Signorile[4], Davide Calonico[4], R. Costa[4], Cecilia Clivati[4], E. Cantoni[4], C. De Stefano[4], Matteo Frittelli[4], Valerio Formichella[4], E. Biserni[1], V. Leone[1], E. Zarroli[1], D. Sormani[1], Pascale Defraigne[5], Q. Baire[5], M. Gandara[6], V. Hamoniaux[6], E. Varriale[6], Q. Morante[6], T. Widomski[2], J. Kaczmarek[2], J. Uzycki[2], K. Borgulski[2], P. Olbrysz[2], J. Kowalski[2], - et. al. [3]
[1]ANTARES, Italy; [2]ELPROMA, Poland; [3]et. al., Italy; [4]Istituto Nazionale di Ricerca Metrologica, Italy; [5]Observatoire Royal de Belgique, Belgium; [6]Thales Alenia Space, Italy; [6]Thales Alenia Space, France

C1L-C Cold-Atom Microwave Clocks

Date: Wednesday, July 12, 2017
Time: 10:40 - 12:20
Room: Room 3 & 4
Chair(s): Scott Crane; *U.S. Naval Research Laboratory*

Design and Performance of Cs Fountain Frequency Standards Constructed for Metrology Laboratories 477
Richard Hendricks[3], Filip Ozimek[3], Krzysztof Szymaniec[3], Scott Beattie[4], Bin Jian[4], Piotr Dunst[6], Bartłomiej Nagórny[6], Jerzy Nawrocki[1], Weilang Chen[2], Kurt Gibble[5]
[1]Borowiec Astrogeodynamic Observatory, Poland; [2]Chinese Academy of Sciences, China; [3]National Physical Laboratory, United Kingdom; [4]National Research Council Canada, Canada; [5]Pennsylvania State University, United States; [6]Space Research Centre, Poland

Cold-Atom-Based Commercial Microwave Clock at the 10^-15 Level 479
Bruno Pelle[1], Bruno Desruelle[1], Ramon Szmuk[2], David Holleville[2]
[1]Muquans, France; [2]Observatoire de Paris, France

Investigation of Dual Species Ions Cloud by Molecular-Dynamics Simulation for Microwave Clocks.....481
Ya'Ni Zuo, Pengfei Cheng, Xiaolin Sun, Lijun Wang, Jianwei Zhang
Tsinghua University, China

C1L-D Microwave Photonics I
Date: Wednesday, July 12, 2017
Time: 10:40 - 12:20
Room: Room 5, 6 & 7
Chair(s): Gilles Cibiel; *CNES*
Jean-Pierre Aubry; *FEMTO-ST*

High-Resolution Frequency Synthesizers Over X-Band Using SILPLL Opto-Electronic Oscillators 484
Tianchi Sun[1], Afshin Daryoush[1], Ajay Poddar[2], Li Zhang[2], Ulrich Rohde[2]
[1]Drexel University, United States; [2]Synergy Microwave Corp, United States

A Highly Stable OEO Using a Multi-Purpose Optical-Delay Stabilization System.....486
Luka Bogataj[3], Jurij Tratnik[3], Bostjan Batagelj[2], Uros Dragonja[1]
[1]InLambda BDT d.o.o., Slovenia; [2]University of Ljubljana, Slovenia; [3]University of Ljubljana / InLambda BDT d.o.o., Slovenia

COEO Phase Locking and Performance Optimisation.....489
Ramin Khayatzadeh, Vincent Auroux, Arnaud Fernandez, Olivier Llopis
Laboratoire d'analyse et d'architectures des systèmes / Centre National de la Recherche Scientifique, France

Low Phase Noise 10 GHz Coupled Optoelectronic Oscillator 493
Oriane Lelièvre[2], Vincent Crozatier[2], Ghaya Baili[2], Pascale Nouchi[2], Daniel Dolfi[2], Loïc Morvan[2], Fabienne Goldfarb[3], Fabien Bretenaker[3], Olivier Llopis[1]
[1]Laboratoire d'analyse et d'architectures des systèmes / Centre National de la Recherche Scientifique, France; [2]Thales Research & Technology, France; [3]Université Paris-Sud, France

C2L-A Optical Clocks III
Date: Wednesday, July 12, 2017
Time: 14:00 - 15:40
Room: Amphitheatre
Chair(s): Rachel Godun; *National Physical Laboratory*

Towards Magnesium Optical Lattice Clock: Spectroscopy with 40 Hz Linewidth 495
Nandan Jha, Steffen Rühmann, Dominika Fim, Klaus Zipfel, Steffen Sauer, Waldemar Friesen, Wolfgang Ertmer, Ernst M. Rasel
Leibniz Universität Hannover, Germany

Optical-Clock Local-Oscillator Universal Interrogation Protocol for Zero Probe-Field-Induced Frequency-Shifts 496
Thomas Zanon-Willette[3], Remi Lefevre[3], Alexey V. Taichenachev[2], Valera Yudin[1]
[1]Institute of Laser Physics SB RAS, Russia; [2]Novosibirsk State University / Institute of Laser Physics SB RAS, Russia; [3]Université Pierre-et-Marie-Curie, France

A Mercury Optical Lattice Clock with Improved Magic Wavelength Control 498
Changlei Guo[1], Maxime Favier[1], James Calvert[1], Valentin Cambier[1], Nicolas Galland[2], Luigi De Sarlo[1], Sébastien Bize[1]
[1]Observatoire de Paris, France; [2]Université Grenoble Alpes and CNRS / Institut NEEL / Observatoire de Paris, France

C2L-B MEMS & Advanced Processing

Date: Wednesday, July 12, 2017
Time: 14:00 - 15:40
Room: Room 2
Chair(s): Clark Nguyen; *U. C. Berkeley*

NEMS Infrared Detectors Based on High Quality Factor 50 nm Thick AlN Nano-Plate Resonators 500
Zhenyun Qian, Vageeswar Rajaram, Sungho Kang, Matteo Rinaldi
Northeastern University, United States

An Ultra-Sensitive Piezoelectric-on-Silicon Flapping Mode MEMS Lateral Field Magnetometer 502
Sagnik Ghosh, Joshua E.-Y. Lee
City University of Hong Kong, Hong Kong

Impact of Output Metric on the Resolution of Mode-Localized MEMS Resonant Sensors 506
Jerome Juillard[1], Pierre Prache[1], Pietro Maris Ferreira[1], Nuria Barniol[2]
[1]CentraleSupélec, France; [2]Universitat Autònoma de Barcelona, Spain

Closed-Loop Tracking of Amplitude and Frequency in a Mode-Localized Resonant MEMS Sensor 510
Milind Pandit, Chun Zhao, Guillermo Sobreviela, Aref Mustafazade, Ashwin Seshia
University of Cambridge, United Kingdom

Transparent Piezoelectric Transducers for Large Area Ultrasonic Actuators 514
Daniele Sette, Sebastjan Glinsek, Stéphanie Girod, Nicolas Godard, Emmanuel Defay
Luxembourg Institute of Science and Technology, Luxembourg

C2L-C Materials

Date: Wednesday, July 12, 2017
Time: 14:00 - 15:40
Room: Room 3 & 4
Chair(s): Thomas Baron; *FEMTO-ST*

Characterization of Single-Port SAW Resonators at 3.7 GHz Based on Epitaxial LiNbO3 Layers 516
Alexandre Clairet, Stefania Oliveri, Anthony Almirall, Thomas Baron, William Daniau, Ausrine Bartasyte
Franche-Comté Électronique Mécanique Thermique et Optique - Sciences et Technologies, France

AlN-Solidly Mounted Resonators Sustaining Up to 1000°C with TCF Compensation 519
Teona Mirea, Jimena Olivares, Marta Clement, José Luis Olivera, Jesús Sangrador, Enrique Iborra
Universidad Politécnica de Madrid, Spain

C2L-D Microwave Photonics II

Date: Wednesday, July 12, 2017
Time: 14:00 - 15:40
Room: Room 5, 6 & 7
Chair(s): Olivier Llopis; *LAAS*
Michael Underhill; *Underhill Research Limited*

Brillouin and Kerr-Based Whispering Gallery Mode Crystalline Fluoride-Type Resonators for Low Noise Microwave Source 523
Jean-Pierre Aubry, Souleymane Diallo, Romain Martinenghi, Yanne Chembo
Franche-Comté Électronique Mécanique Thermique et Optique - Sciences et Technologies, France

Soliton-Based Optical Kerr Frequency Comb for Low-Noise Microwave Generation.....530
Erwan Lucas[1], John Jost[1], Tobias Kippenberg[1], Katja Beha[2], Matthias Lezius[2], Ronald Holzwarth[2]
[1]Ecole Polytechnique Fédérale de Lausanne, Switzerland; [2]Menlo Systems GmbH, Germany

Optical Synthesis Using Kerr Frequency Combs 534
Shamsul Arafin[3], Arda Simsek[3], Seong-Kyun Kim[3], Mark J. Rodwell[3], Larry A. Coldren[3], Lute Maleki[2], Wei Liang[2], Vladimir S. Ilchenko[2], Anatoliy A. Savchenkov[2], Danny Eliyahu[2], Andrey B. Matsko[2], Gordon Morrison[1], Milan Mashanovitch[1], Leif Johansson[1]
[1]Freedom Photonics LLC, United States; [2]OEwaves Inc, United States; [3]University of California, Santa Barbara, United States

C3P-F Materials, Resonators & Resonator Circuits II
Date: Wednesday, July 12, 2017
Time: 16:00 - 18:00
Room: Poster Area
Chair(s): Olivier Le Traon; *Onera*
Jeffrey Pulskamp; *US Army Research Labs*

Perturbation Analysis of Nonlinear Signal Generation in Radio Frequency Bulk Acoustic Wave Resonators 538
Ken-Ya Hashimoto[1], Xinyi Li[2], Jingfu Bao[2]
[1]Chiba University, Japan; [2]University of Electronic Science and Technology of China, China

Improving Coupling Coefficient Distribution on BAW Filters Manufactured on 200mm Wafers 542
Sergey Mishin, Yury Oshmyansky
Advanced Modular Systems, Inc., United States

Use of Double-Raised-Border Structure for Quality Factor Enhancement of Type II Piston Mode FBAR.....547
Xinyi Li[3], Jingfu Bao[3], Yulin Huang[3], Benfeng Zhang[2], Gongbin Tang[2], Tatsuya Omori[1], Ken-Ya Hashimoto[1]
[1]Chiba University, Japan; [2]Shanghai Jiao Tong University, China; [3]University of Electronic Science and Technology of China, China

An Apodized 3-GHz Thin Film Piezoelectric on Substrate FBAR 551
Gayathri Pillai[2], Anurag A. Zope[2], Julius Ming-Lin Tsai[1], Sheng-Shian Li[2]
[1]InvenSense Inc., United States; [2]National Tsing Hua University, Taiwan

Analytical Modeling of Low-Loss Disk Flexure Resonators 554
Jonathan Puder[1], Jeffrey Pulskamp[3], Ryan Rudy[3], Ronald Polcawich[3], Sunil Bhave[2]
[1]Cornell University, United States; [2]Purdue University, United States; [3]United States Army Research Laboratory, United States

Fundamental Limits of Disk Flexure Resonators 558
Jonathan Puder[1], Jeffrey Pulskamp[3], Ryan Rudy[3], Ronald Polcawich[3], Sunil Bhave[2]
[1]Cornell University, United States; [2]Purdue University, United States; [3]United States Army Research Laboratory, United States

Substrate Texturing for Homogeneous Deposition of Tilted C-Axis AlN Films for Shear Mode Operation 561
Maria Sierra-Zapata, Marta Clement, Teona Mirea, Jimena Olivares, Enrique Iborra
Universidad Politécnica de Madrid, Spain

Properties of AlScN Thin Films for Hybrid BAW/SAW Resonator Fabrication.....565
Vladimir Pashchenko[1], Stefan Mertin[1], Fazel Parsapour[1], Jianing Li[1], Paul Muralt[1], Sylvain Ballandras[2]
[1]École Polytechnique Fédérale de Lausanne, Switzerland; [2]FREC'N'SYS, France

Temperature Coefficients of Quartz at Cryogenic Temperature.....567
Jérémy Bon, Roger Bourquin, Philippe Abbé, Xavier Vacheret, Serge Galliou
Franche-Comté Électronique Mécanique Thermique et Optique - Sciences et Technologies, France

Anti-Symmetric Shear-Extensional AlN Lamb-Wave Resonators with Kt^2 > 4% 570
Bumkyung Jo, Mayur Ghatge, Roozbeh Tabrizian
University of Florida, United States

C3P-G Digital Methods
Date: Wednesday, July 12, 2017
Time: 16:00 - 18:00
Room: Poster Area
Chair(s): Enrico Rubiola; *FEMTO-ST*

Wideband and Low Phase Noise Up-Converted Direct Frequency Synthesis Using High Frequency DAC and Oscillator 572
Jean-Marc Lesage, Jean-Francois Penn
Direction Générale de l'Armement, France

Dynamic Phase Shifting Method Utilized in the Enhanced Frequency Controlled Clock System.....575
Vladimir Stofanik[1], Adam Fibich[2], Tomas Bagala[2], Peter Kubinec[2]
[1]Slovak Academy of Sciences, Slovakia; [2]Slovak University of Technology in Bratislava, Slovakia

A Fully-Digital Realtime SoC FPGA Based Phase Noise Analyzer with Cross-Correlation 578
Pierre-Yves Bourgeois, Gwenhaël Goavec-Mérou, Jean-Michel Friedt, Enrico Rubiola
Franche-Comté Électronique Mécanique Thermique et Optique - Sciences et Technologies, France

Full Digital Phase Noise Measurement by Using Two Reference Oscillators and Multichannel ADCs 583
Takeshi Imaike
Nihon University, Japan

Frequency Synthesis Using Low-Pass Single-Bit Multi-Step Look-Ahead Sigma-Delta Modulators in Quadrature Upconversion Scheme 587
Charis Basetas[2], Paul Peter Sotiriadis[2], Nikos Temenos[1]
[1]National and Kapodistrian University of Athens, Greece; [2]National Technical University of Athens, Greece

Wide-Band Frequency Synthesis Using Hardware-Efficient Band-Pass Single-Bit Multi-Step Look-Ahead Sigma-Delta Modulators 591
Charis Basetas[2], Paul Peter Sotiriadis[2], Nikos Temenos[1]
[1]National and Kapodistrian University of Athens, Greece; [2]National Technical University of Athens, Greece

Phase Noise Measurements of Surface Acoustic Wave Resonators at 2.4 GHz.....595
Etienne Vaillant[2], Joël Imbaud[3], Fabrice Sthal[2], François-Xavier Esnault[1], Gilles Cibiel[1]
[1]Centre National d'Études Spatiales, France; [2]Franche-Comté Électronique Mécanique Thermique et Optique - Sciences et Technologies, France; [3]Franche-Comté Électronique Mécanique Thermique et Optique - Sciences et Technologies / ENS2M, France

Software Defined Radio Platform for Time and Frequency Metrology.....598
Nicolas Boucquey[1], Attila Kinali[2]
[1]Institut Supérieur Industriel de Bruxelles, Belgium; [2]Max-Planck-Gesellschaft, Germany

Noise Interaction with Time Quantization of TIC 600
Magnus Danielson
Net Insight AB, Sweden

32-QAM All-Digital RF Signal Generator Based on a Homodyne Sigma-Delta Modulation Scheme 603
Paul Peter Sotiriadis[2], Charis Basetas[2], Nikos Temenos[1]
[1]National and Kapodistrian University of Athens, Greece; [2]National Technical University of Athens, Greece

C3P-H Microwave Frequency Standards II
Date: Wednesday, July 12, 2017
Time: 16:00 - 18:00
Room: Poster Area
Chair(s): Stefan Weyers; *PTB*

The Portable CPT Atomic Clocks - Recent Developments 605
Zhenwei Zhang, Renfu Yang, Xueyun Wang
Beijing Institute of Radio Metrology and Measurement, China

Characteristics of Space Mini Passive Hydrogen Maser in Shanghai Astronomical Observatory 607
Yonghui Xie, Tao Shuai, Pengfei Chen, Yuxian Pei, Chao Shen, Xiaoyan Pan, Yang Zhao, Chuanfu Lin
Chinese Academy of Sciences, China

Progress Towards Chip-Scale Atomic Clock in Peking University 611
Jianye Zhao, Ruiyuan Liu, Hongling Meng, Ermeng Hu, Canbin He, Zhong Wang
Peking University, China

Analytical Expressions for Parameters of the Dark Resonance in a Vacuum Vapor Cell 614
Denis Brazhnikov[2], Moustafa Abdel Hafiz[1], Grégoire Coget[1], Rodolphe Boudot[1]
[1]Franche-Comté Électronique Mécanique Thermique et Optique - Sciences et Technologies, France; [2]Novosibirsk State University, Russia

An Electronic Controller Based on FPGA for the Ramsey-CPT Atomic Clock 616
Pengfei Cheng[2], Xiaolin Sun[2], Fengwei Liu[2], Daonong Zhang[1], Jianwei Zhang[2], Lijun Wang[2]
[1]North China Power Engineering CO., China; [2]Tsinghua University, China

A Merchandized Optically Pumped Cesium Atomic Clock 618
Yuanhong Cao[1], Xingwen Zhao[1], Wei Xie[1], Qiang Wei[1], Lin Yang[1], Haijun Chen[2], Shougang Zhang[3]
[1]Chengdu Spaceon Electronics Co., Ltd., China; [2]China Electronics Technology Group Corporation-12, China; [3]Chinese Academy of Sciences, China

Increasement of Effective Number of Detected Atoms in KRISS-F1(Cs) Fountain Clock by Optical Pumping 622
Sangmin Lee, Myoung-Sun Heo, Taeg Yong Kwon, Hyun-Gue Hong, Sang-Bum Lee, Sang Eon Park
Korea Research Institute of Standards and Science, Korea

Design of a Space Atomic Clock with Intracavity Cooling 623
Desheng Lü, Xiangkai Peng, Wei Ren, Qiuzhi Qu, Tang Li, Liang Liu
Chinese Academy of Sciences, China

MEMS Atomic Vapor Cells Sealed by Cu-Cu Thermocompression Bonding 625
Sylvain Karlen, Jacques Haesler, Thomas Overstolz, Giovanni Bergonzi, Steve Lecomte
CSEM SA, Switzerland

Preliminary Evaluation of the AOS-CsF1 Primary Frequency Standard 628
Piotr Dunst[4], Bartłomiej Nagórny[4], Dariusz Lemański[1], Paweł Nogaś[2], Jerzy Nawrocki[1], Richard Hendricks[3], Filip Ozimek[3], Krzysztof Szymaniec[3]
[1]Borowiec Astrogeodynamic Observatory, Poland; [2]Borowiec Astrogeodynamic Observatory / Piktime Systems, Poland; [3]National Physical Laboratory, United Kingdom; [4]Space Research Centre, Poland

Continuous Cold Atomic Beam in a Zerodur Chamber for Atom Interferometry 629
Myoung-Sun Heo[2], Taeg Yong Kwon[2], Sang Eon Park[2], Sang-Bum Lee[2], Hyun-Gue Hong[2], Sin Hyuk Yim[1], Kyu Min Shim[1]
[1]Agency for Defense Development, Korea; [2]Korea Research Institute of Standards and Science, Korea

A Low Phase Noise Raman Lasers System Based on Optical Injection and an Optical Phase-Lock Loop 631
Chenfei Wu[2], Xueshu Yan[2], Jianhui Tu[1], Peixian Miao[1], Pei Ma[1], Jianwei Zhang[2], Lijun Wang[2]
[1]Lanzhou Institute of Physics / China Academy of Space Technology, China; [2]Tsinghua University, China

First Results on Rb Fountain Rb304 Frequency Standard Developed at VNIIFTRI 633
Dmitry Kupalov, Viacheslav Baryshev, Igor Blinov, Alexandr Boiko, Yuri Domnin, Leonid Kopilov, Maxim Khromov, Olga Kupalova, Alex Novoselov
VNIIFTRI, Russia

Microfabricated Vapor Cells for Miniature Atomic Clocks Based on Post-Sealing Activated Cesium Dispensers 636
Vincent Maurice[1], Jaroslaw Rutkowski[1], Eric Kroemer[1], Sylwester Bargiel[1], Nicolas Passilly[1], Rodolphe Boudot[1], Ravinder Chutani[1], Serge Galliou[1], Christophe Gorecki[1], Luca Mauri[2], Marco Moraja[2]
[1]Franche-Comté Électronique Mécanique Thermique et Optique - Sciences et Technologies, France; [2]SAES Getters, Italy

Laser Intensity Noise Transfer for Pulsed Vapor-Cell Clocks with Optical Detection 638
Michele Gozzelino[2], Salvatore Micalizio[1], Filippo Levi[1], Aldo Godone[1], Claudio Eligio Calosso[1]
[1]Istituto Nazionale di Ricerca Metrologica, Italy; [2]Politecnico di Torino / Istituto Nazionale di Ricerca Metrologica, Italy

The NRC-FCs2 Primary Frequency Standard at the National Research Council Canada.....640
Scott Beattie[2], Bin Jian[2], John Alcock[2], John Bernard[2], Marina Gertsvolf[2], Richard Hendricks[1], Filip Ozimek[1], Krzysztof Szymaniec[1], Kurt Gibble[3]
[1]National Physical Laboratory, United Kingdom; [2]National Research Council Canada, Canada; [3]Pennsylvania State University, United States

Closed-Loop Characterization of Cesium Magnetometers Operating at Ambient Temperature 642
Janet Lou, Geoffrey Cranch
United States Naval Research Laboratory, United States

Compact Atom Interferometer Using a Single Laser 644
Sheng-Wey Chiow, Nan Yu
Jet Propulsion Laboratory, United States

A Large Mode Optical Resonator for Enhanced Atom Interferometry 646
Sapam Ranjita Chanu[1], Nicolas Mielec[1], David Holleville[1], Bess Fang[1], Arnaud Landragin[1], Remi Geiger[1], Isabelle Riou[2], Benjamin Canuel[2]
[1]Observatoire de Paris, France; [2]Université Bordeaux-IOGS-CNRS, France

C3P-J Sensors & Transducers II

Date: Wednesday, July 12, 2017
Time: 16:00 - 18:00
Room: Poster Area
Chair(s): Philip Feng; *Case Western Reserve University*

Liquid-Level Sensing by a Cylindrical Piezoelectric Resonator Operating in a Trapped-Energy Mode 647
Ken Yamada, Koki Watanabe
Tohoku-Gakuin University, Japan

A New Method for Measuring Properties of Liquid by Using a Single Quartz Crystal Microbalance 649
Feng Tan, Peng Ye, Duyu Qiu, Lianping Guo, Wuhuang Huang, Hao Zeng, Dong Hou
University of Electronic Science and Technology of China, China

Design and Characterization of Surface Acoustic Wave Resonance (SAR) System for in-Liquid Sensing 652
Kiryl Kustanovich, Ventsislav Yantchev, Aldo Jesorka
Chalmers University of Technology, Sweden

A Micromechanical Resonant Optical Power Meter 656
Xuan Chen, Dong Pu, Tianyi Zhang, Zhuangde Jiang, Xueyong Wei
Xi'an Jiaotong University, China

Piezoelectric Harvester Scavenges Energy from Cavity of Phononic Crystal 660
Hongping Hu[1], Yajun Zheng[1], Shan Jiang[1], Yuantai Hu[1], Vincent Laude[2]
[1]Huazhong University of Science and Technology, China; [2]Université Bourgogne Franche-Comté / FEMTO-ST Institute, France

Integration of Multilayered Graphene on AlN Based Resonators as a Functionalization Platform for Biosensors 662
Lorena Gordillo-Dagallier, Jimena Olivares, Bruno Marco-Dufort, José Luis Olivera, Jose Miguel Escolano, Teona Mirea, Marta Clement, Enrique Iborra
Universidad Politécnica de Madrid, Spain

C3P-K Timekeeping, Time and Frequency Transfer, GNSS Applications II

Date: Wednesday, July 12, 2017
Time: 16:00 - 18:00
Room: Poster Area
Chair(s): Philip Tuckey; *SYRTE*

Kalman Filter Approaches for a Mixed Clock Ensemble 666
Marion Gödel, Tobias Schmidt, Johann Furthner
Deutsches Zentrum für Luft- und Raumfahrt e.V., Germany

Two Way Time Comparison via Optical Fiber at BIRMM 673
Xueyun Wang, Wenzhe Yang, Hongbo Wang, Haifeng Wang, Hang Yi, shuwei wang, Shengkang Zhang, Zhenwei Zhang
Beijing Institute of Radio Metrology and Measurement, China

Fully and Optimally Use the Redundancy in a TWSTFT Network for Accurate Time Transfer 676
Zhiheng Jiang[1], Shinn Yan Lin[2], Wen-Hung Tseng[2]
[1]International Bureau of Weights and Measures, France; [2]Telecommunication Laboratories Chunghwa Telecom Co., Ltd., Taiwan

Fiber Optic Time Transfer Between PTB and Deutsche Telekom Using Multi-Link Redundant Topology 681
Łukasz Śliwczyński[1], Przemysław Krehlik[1], Jacek Kołodziej[1], Helmut Imlau[2], Horst Ender[2], Harald Schnatz[3], Dirk Piester[3], Andreas Bauch[3]
[1]AGH University of Science and Technology, Poland; [2]Deutsche Telekom Technik GmbH, Germany; [3]Physikalisch-Technische Bundesanstalt, Germany

A Cost-Efficient Regional Synchronization System 683
Ricardo Píriz[1], Pedro Roldán[1], Diego Sanz[1], Javier Díaz[3], Alejandro González[3], Thomas Polewka[2], Andreas Bauch[2]
[1]GMV Innovating Solutions, Spain; [2]Physikalisch-Technische Bundesanstalt, Germany; [3]Seven Solutions S.L., Spain

Research on Autonomous High-Precision Time Synchronization Method of UAVs Based on Side-Tone Signal 686
Tao Liu, Yonghui Hu, Yu Hua, Meifang Wu
Chinese Academy of Sciences, China

Accurate Time Transfer Based on Communication Satellite 690
Longxia Xu, Feng Zhu, Jingya Chen, Xiaohui Li
Chinese Academy of Sciences, China

The Study of Near Real-Time GPS/BDS Time Transfer 693
Hongbo Wang, Hang Yi, Shengkang Zhang, Haifeng Wang, Xueyun Wang, Wenzhe Yang, Shuwei Wang
Beijing Institute of Radio Metrology and Measurement, China

CLONETS – Clock Network Services: Strategy and Innovation for Clock Services Over Optical-Fibre Networks 697
Anne Amy-Klein[18], Artur Binczewski[15], Wojbor Bogacki[15], Davide Calonico[8], Fabiola Camargo[10], Emilie Camisard[16], Mauro Campanella[4], Ondřej Číp[7], Cecilia Clivati[8], Bruno Desruelle[10], Javier Díaz[17], Jiri Dostal[3], Elizabeth Laier English[11], Alessandro Galardini[5], Gesine Grosche[14], Ronald Holzwarth[9], František John[13], Przemysław Krehlik[1], Jochen Kronjaeger[11], Jean Lautier-Gaud[10], Maurice Lessing[9], Filippo Levi[8], Paweł Nogaś[2], Paul-Eric Pottie[12], Nicolas Quintin[19], Jan Radil[3], Simon Rerucha[7], - et. al. [6]
[1]AGH University of Science and Technology, Poland; [2]Borowiec Astrogeodynamic Observatory / Piktime Systems, Poland; [3]CESNET, Czech Rep.; [4]Consortium GARR, Italy; [5]Conzorzio Torino Piemont internet exchange, Italy; [6]et. al., Czech Rep.; [7]Institute of Scientific Instruments of the ASCR, v.v.i., Czech Rep.; [8]Istituto Nazionale di Ricerca Metrologica, Italy; [9]Menlo Systems GmbH, Germany; [10]Muquans, France; [11]National Physical Laboratory, United Kingdom; [12]Observatoire de Paris, France; [13]OPTOKON A.S., Czech Rep.; [14]Physikalisch-Technische Bundesanstalt, Germany; [15]Poznań Supercomputing and Networking Center, Poland; [16]Réseau National de Télécommunications pour la Technologie, l'Enseignement et la Recherche, France; [17]Seven Solutions S.L., Spain; [18]Université Paris 13, France; [19]Université Paris 13 / RENATER, France

Influence of UTC Parameters Generating Method on BDS Positioning Accuracy 699
Dandan Li, Longxia Xu, Xiaohui Li, Bo Li
Chinese Academy of Sciences, China

Monitoring of Time Signals Broadcast by EFR Long-Wave Transmitters at PTB 703
Bernhard Sbick[1], Klaus Katzmann[2], Egle Staliuniene[3], Dirk Piester[3], Andreas Bauch[3]
[1]EFR Europäische Funk-Rundsteuerung GmbH, Germany; [2]HKW-Elektronik GmbH, Germany; [3]Physikalisch-Technische Bundesanstalt, Germany

Calibration Method of TWSTFT Stations Equipped with SDR Receivers 705
Tung Thanh Thai[1], Alberto Mura[1], Ilaria Sesia[1], Joseph Achkar[2], Giovanni Daniele Rovera[2]
[1]Istituto Nazionale di Ricerca Metrologica, Italy; [2]Observatoire de Paris, France

Reference Signal Distribution for the ACES Microwave Link Ground Terminal at SYRTE 707
Michel Abgrall, Philippe Laurent, Giovanni Daniele Rovera
Observatoire de Paris, France

Modeling Time and Frequency Fiber Links with Bi-Directional Amplifiers Using Transmission Matrixes 710
Łukasz Śliwczyński, Przemysław Krehlik, Karol Salwik
AGH University of Science and Technology, Poland

Further Results of Time Transfer Through the Optical Fiber at NIM 712
Kun Liang[2], Aimin Zhang[2], Zhiqiang Yang[2], Ye Wang[1], Jian Wang[1], Xiangwei Zhu[3], Huaming Chen[3]
[1]Beijing Jiaotong University, China; [2]Chinese Academy of Sciences, China; [3]National University of Defense Technology, China

Enhanced Predictability of Hydrogen Maser Using Random Pursuit Strategy 719
Yuzhuo Wang, Yuan Gao, Aimin Zhang, Weibo Wang, Yige Lin
Chinese Academy of Sciences, China

The Possibility of Testing the Einstein Equivalence Principle (EEP) Using Two Way Satellite Time and Frequency Transfer (TW) and a Software Defined Receiver (SDR) 723
Wen-Hung Tseng[1], Demetrios Matsakis[2]
[1]Telecommunication Laboratories Chunghwa Telecom Co., Ltd., Taiwan; [2]United States Naval Observatory, United States

Anchor Stations for Inter-Satellite Link and Design for its Time Synchronization 728
Yan Bai, Xiaochun Lu, Wenfang Jing, Ke Zhang
Chinese Academy of Sciences, China

Observed Propagation-Phase/Frequency-Shift Theory with Impact on Time/Frequency Transfer and GNSS 733
Michael Underhill
Underhill Research Limited, United Kingdom

Initial Use of Galileo Signals in PTB 736
Andreas Bauch[2], Julia Leute[2], Thomas Polewka[2], Dirk Piester[2], Egle Staliuniene[2], Weijin Qin[1]
[1]Chinese Academy of Sciences, China; [2]Physikalisch-Technische Bundesanstalt, Germany

C3P-L Optical Frequency Standards and Applications II
Date: Wednesday, July 12, 2017
Time: 16:00 - 18:00
Room: Poster Area
Chair(s): John McFerran; *University of Western Australia*

Experimental Study of a Miniaturized Calcium Atomic Beam Tube for Small Optical Frequency Standard 737
Haijun Chen[1], Zhongzheng Liu[1], Shunlu Xiao[1], Haosen Shang[2], Shengnan Zhang[2], Jingbiao Chen[2]
[1]Beijing Vacuum Electronics Research Institute, China; [2]Peking University, China

A Small Calcium Beam Optical Frequency Standard with Fully-Sealed Vacuum Tube 740
Haosen Shang[2], Xiaogang Zhang[2], Shengnan Zhang[2], Jingbiao Chen[2], Haijun Chen[1]
[1]Beijing Vacuum Electronics Research Institute, China; [2]Peking University, China

New Clock Laser System for the Second Yb Optical Lattice Clock at KRISS.....744
Won-Kyu Lee[2], Chang Yong Park[1], Myoung-Sun Heo[1], Huidong Kim[1], Sang Eon Park[1], Dai-Hyuk Yu[1]
[1]Korea Research Institute of Standards and Science, Korea; [2]Korea Research Institute of Standards and Science / Observatoire de Paris, PSL Research University, Korea

Improved Absolute Frequency Measurement of the 1S0–3P0 Transition of 171Yb at KRISS 746
Huidong Kim[1], Myoung-Sun Heo[1], Won-Kyu Lee[2], Chang Yong Park[1], Hyun-Gue Hong[1], Sang-Wook Hwang[1], Dai-Hyuk Yu[1]
[1]Korea Research Institute of Standards and Science, Korea; [2]Korea Research Institute of Standards and Science / Observatoire de Paris, PSL Research University, Korea

A Strontium Optical Lattice Clock Apparatus for Precise Frequency Metrology and Beyond 748
Marco Giacinto Tarallo[2], Davide Calonico[2], Filippo Levi[2], Matteo Barbiero[3], Giacomo Lamporesi[1], Gabriele Ferrari[1]
[1]Istituto Nazionale di Ottica / Consiglio Nazionale delle Ricerche, Italy; [2]Istituto Nazionale di Ricerca Metrologica, Italy; [3]Politecnico di Torino, Italy

Production and Trapping of Th Ions for Nuclear Frequency Standard Development.....751
P.V. Borisyuk[1], S.P. Derevyashkin[1], K.Yu. Khabarova[2], N.N. Kolachevsky[2], Y.Y. Lebedinskii[1], Vitaly Palchikov[4], S.S. Poteshin[1], A.A. Sysoev[1], E.V. Tkalya[3], D.O. Tregubov[2], V.P. Yakovlev[1]
[1]National Research Nuclear University MEPhI, Russia; [2]P.N. Lebedev Physical Institute of the Russian Academy of Sciences, Russia; [3]Skobeltsyn Institute of Nuclear Physics Lomonosov Moscow State University, Russia; [4]VNIIFTRI, Russia

Polarizability and Magic Wavelength of Yb+ Clock Transition 2S1/2 → 2D3/2 753
Atish Roy[1], Subhadeep De[1], Bindiya Arora[2], Bijaya Kumar Sahoo[3]
[1]CSIR-National Physical Laboratory, India; [2]Dev University, India; [3]Physical Research Laboratory, India

Preparing a Frequency Measurement of the First Lattice Clock Based on Bosonic Magnesium 758
Steffen Sauer, Steffen Rühmann, Dominika Fim, Klaus Zipfel, Nandan Jha, Waldemar Friesen, Wolfgang Ertmer, Ernst M. Rasel
Leibniz Universität Hannover, Germany

Optical Sampling Analog-to-Digital Scheme for Broadband Microwave Signal Based on Atomic Resonator 759
Hongling Meng, Ruiyuan Liu, Jianye Zhao
Peking University, China

Precision Measurement of the Hyperfine Structure of the 85Rb 6P3/2 State 762
Shengnan Zhang[2], Xiaogang Zhang[2], Zhaojie Jiang[2], Haosen Shang[2], Pengyuan Chang[2], Jingbiao Chen[2], Jiqing Lian[1], Jianhui Tu[1], Shiyu Yang[1]
[1]Lanzhou Institute of Physics / China Academy of Space Technology, China; [2]Peking University, China

Frequency Stabilization of 423 nm Laser for Calcium-Beam Optical Frequency Standard 765
Shengnan Zhang[2], Xiaogang Zhang[2], Haosen Shang[2], Jingbiao Chen[2], Haijun Chen[1]
[1]Beijing Vacuum Electronics Research Institute, China; [2]Peking University, China

Spectroscopy of Samarium Colour Centres for a Solid-State Optical Frequency Reference 768
Graham Edge, Shreyas Potnis, Amar Vutha
University of Toronto, Canada

Frequency Stability Transfer by Optical Injection Locking Into a Semiconductor Frequency Comb 769
Amine Chaouche Ramdane, Pierre Grüning, Vincent Roncin, Frédéric Du-Burck
Université Paris 13, France

High Precision Phase and Frequency Measurements in Rare Earth Doped Crystals at Cryogenic Temperatures for Probing Nanoresonators Behavior 771
Nicolas Galland[4], Olivier Gobron[2], Kwangyun Jung[2], Alban Ferrier[1], Philippe Goldner[1], Signe Seidelin[3], Yann Le Coq[2]
[1]École Nationale Supérieure de Chimie de Paris, France; [2]Observatoire de Paris, France; [3]Université Grenoble Alpes and CNRS / Institut NEEL, France; [4]Université Grenoble Alpes and CNRS / Institut NEEL / Observatoire de Paris, France

Toward an Ultra-Stable Laser Based on Cryogenic Silicon Cavity 773
Baptiste Maréchal[1], Jacques Millo[1], Alexandre Didier[2], Pierre-Yves Bourgeois[1], Gwenhaël Goavec-Mérou[1], Clément Lacroûte[1], Enrico Rubiola[1], Yann Kersalé[1]
[1]Franche-Comté Électronique Mécanique Thermique et Optique - Sciences et Technologies, France; [2]Physikalisch-Technische Bundesanstalt, Germany

Compact Ultra-Stable Laser 775
Alexandre Didier[2], Jacques Millo[1], Baptiste Maréchal[1], Cyrus Rocher[1], Clément Lacroûte[1], Morvan Ouisse[1], Enrico Rubiola[1], Yann Kersalé[1]
[1]Franche-Comté Électronique Mécanique Thermique et Optique - Sciences et Technologies, France; [2]Physikalisch-Technische Bundesanstalt, Germany

D1L-A Combs II
Date: Thursday, July 13, 2017
Time: 09:00 - 10:20
Room: Amphitheatre
Chair(s): Helen Margolis; *NPL*

Simultaneous Spectral Purity Transfer at Three Optical Clock Transitions Using an Ultra-Low Noise Er:fiber Frequency Comb 777
Michele Giunta[1], Wolfgang Hänsel[2], Marc Fischer[2], Matthias Lezius[2], Ronald Holzwarth[2]
[1]Max-Planck-Gesellschaft / Menlo Systems GmbH, Germany; [2]Menlo Systems GmbH, Germany

Fully-Stabilized 1-GHz Optical Frequency Comb from a Diode-Pumped Solid-State Laser 779
Sargis Hakobyan[2], Valentin J. Wittwer[2], Pierre Brochard[2], Kutan Gürel[2], Stéphane Schilt[2], Thomas Südmeyer[2], Aline S. Mayer[1], Ursula Keller[1]
[1]Eidgenössische Technische Hochschule Zürich, Switzerland; [2]Université de Neuchâtel, Switzerland

Ultra-Short Optical Pulses Leading to Ultra-Stable Photonic Microwave Generation 781
Xiaopeng Xie[6], Romain Bouchand[6], Daniele Nicolodi[5], Michel Lours[6], Yann Le Coq[6], Pierre-Alain Tremblin[7], Giorgio Santarelli[7], Michele Giunta[3], Wolfgang Hänsel[4], Matthias Lezius[4], Ronald Holzwarth[4], Abhay Joshi[2], Shubo Datta[2], Christophe Alexandre[1]
[1]Conservatoire National des Arts et Métiers, France; [2]Discovery Semiconductors Inc., United States; [3]Max-Planck-Gesellschaft / Menlo Systems GmbH, Germany; [4]Menlo Systems GmbH, Germany; [5]National Institute of Standards and Technology / Observatoire de Paris, France; [6]Observatoire de Paris, France; [7]Université de Bordeaux / École Supérieure d'Optique, France

D1L-B GNSS

Date: Thursday, July 13, 2017
Time: 09:00 - 10:20
Room: Room 2
Chair(s): Pascale Defraigne; *Royal Observatory of Belgium*

Sub 10^-16 Frequency Transfer with IPPP: Recent Results 784
Gérard Petit[3], Julia Leute[4], Sylvain Loyer[2], Félix Perosanz[1]
[1]Centre National d'Études Spatiales, France; [2]CLS Collect Localisation Satellites, France; [3]International Bureau of Weights and Measures, France; [4]Physikalisch-Technische Bundesanstalt, Germany

Experimental Research on Beidou Time Transfer Using the NIM Made GNSS Time and Frequency Receivers at the BIPM in Euro-Asia Link 788
Kun Liang[2], Aimin Zhang[2], Zhiqiang Yang[2], Laurent Tisserand[3], Zhiheng Jiang[3], Gérard Petit[3], Felicitas Arias[3], Ye Wang[1]
[1]Beijing Jiaotong University, China; [2]Chinese Academy of Sciences, China; [3]International Bureau of Weights and Measures, France

D1L-C Atom Interferometry

Date: Thursday, July 13, 2017
Time: 09:00 - 10:20
Room: Room 3 & 4
Chair(s): John Kitching; *NIST*

High-Sensitivity Cold-Atom Gyroscope with Real-Time Vibration Compensation 798
Denis Savoie, Matteo Altorio, Bess Fang, Remi Geiger, Arnaud Landragin
Observatoire de Paris, France

Correction of Laser Wavefronts in an Atom Interferometer with a Deformable Mirror 800
Mehdi Langlois, Azer Trimeche, Sébastien Merlet, Franck Pereira Dos Santos
Observatoire de Paris, France

D1L-D Resonators II

Date: Thursday, July 13, 2017
Time: 09:00 - 10:20
Room: Room 5, 6 & 7
Chair(s): Songbin Gong; *Univ. of Illinois*

Quality Factor and Phase Noise Improvements in MEMS Resonators and Oscillators 802
Kimberly Foster[2], Brian Gibson[2], Kamala Qalandar[2], Gianluca Piazza[1], Cristian Cassella[1]
[1]Carnegie Mellon University, United States; [2]University of California, Santa Barbara, United States

Lowering Motional Resistance by Partially HfO2 Gap Filling in Double-Ended Tuning Fork MEMS Resonators 805
Mariazel Maqueda López, Emanuele Andrea Casu, Adrian Mihai Ionescu, Montserrat Fernández-Bolaños
École Polytechnique Fédérale de Lausanne, Switzerland

Orders of Magnitude Reduction in Acoustic Resonator Simulation Times via the Wide-Band Rapid Analytical-FEA Technique 807
Jonathan Puder[1], Jeffrey Pulskamp[3], Ryan Rudy[3], Ronald Polcawich[3], Sunil Bhave[2]
[1]Cornell University, United States; [2]Purdue University, United States; [3]United States Army Research Laboratory, United States

D2L-A Optical Clocks IV

Date: Thursday, July 13, 2017
Time: 10:40 - 12:20
Room: Amphitheatre
Chair(s): Dave Leibrandt; *NIST*

Absolute Frequency Measurement of the Electric Quadrupole Transition of 88Sr+.....811
Pierre Dubé, John Bernard, Marina Gertsvolf
National Research Council Canada, Canada

Absolute Frequency Measurement of the 171Yb Optical Lattice Clock at INRIM.....813
Marco Pizzocaro[1], Pierre Thoumany[1], Filippo Bregolin[1], Gianmaria Milani[1], Benjamin Rauf[2], María Del Carmen Vélez López[4], Cecilia Clivati[1], Giovanni A. Costanzo[3], Filippo Levi[1], Davide Calonico[1]
[1]Istituto Nazionale di Ricerca Metrologica, Italy; [2]Istituto Nazionale di Ricerca Metrologica / National Physical Laboratory, Italy; [3]Politecnico di Torino, Italy; [4]Real Instituto y Observatorio de la Armada, Spain

Contributing to TAI with Sr Optical Lattice Clocks.....815
Sławomir Bilicki, Eva Bookjans, Grégoire Vallet, Michel Abgrall, Rodolphe Le Targat, Jérôme Lodewyck
Observatoire de Paris, France

D2L-B GNSS and Calibration

Date: Thursday, July 13, 2017
Time: 10:40 - 12:20
Room: Room 2
Chair(s): Stefania Romisch; *NIST*

Timing Performance Evaluation of BDS IGSO-6 and GEO-7 Satellite Network: GNSS Timing Performance Evaluation Method and Characterization.....817
Feng Zhu, Xiaohui Li, Hui-Jun Zhang, Lu-Xi Huang, Longxia Xu
Chinese Academy of Sciences, China

Validation of the Inter-Frequency Calibration of Timing GNSS Receivers 821
Pascale Defraigne[2], Bruno Bertrand[4], Wei Huang[3], Giovanni Daniele Rovera[1]
[1]Observatoire de Paris, France; [2]Observatoire Royal de Belgique, Belgium; [3]Politecnico di Torino, Italy; [4]Royal Observatory of Belgium, Belgium

UTC Time Link Calibration in the Frame of APMP - Campaigns in 2014-2016.....826
Kun Liang[4], Aimin Zhang[4], Zhiqiang Yang[4], Jia-Lun Wang[8], Huang-Tien Lin[8], Ye Wang[2], Fan Yang[1], Jun Yang[1], Tadahiro Gotoh[6], Zhiwu Cai[3], Kun Liang[5], Zhiheng Jiang[5], Weihua Mou[7]
[1]Beijing Institute of Radio Metrology and Measurement, China; [2]Beijing Jiaotong University, China; [3]Beijing Satellite Navigation Center, China; [4]Chinese Academy of Sciences, China; [5]International Bureau of Weights and Measures, France; [6]National Institute of Information and Communications Technology, Japan; [7]National University of Defense Technology, China; [8]Telecommunication Laboratories Chunghwa Telecom Co., Ltd., Taiwan

D2L-C Microwave & Cryogenics

Date: Thursday, July 13, 2017
Time: 10:40 - 12:20
Room: Room 3 & 4
Chair(s): Serge Galliou; *FEMTO-ST*
Yann Kersalé; *FEMTO-ST*

Development of a Mobile HTS Cryogenic Oscillator 835
Olivier d'Allivy Kelly[2], Yves Lemaître[2], Bruno Marcilhac[2], David Chaudy[4], Jean-Michel Hode[3], Olivier Llopis[1]
[1]Laboratoire d'analyse et d'architectures des systèmes / Centre National de la Recherche Scientifique, France; [2]Thales Research & Technology, France; [3]Thales Systèmes Aéroportés, France; [4]Thales Systèmes Aéroportés / Laboratoire d'analyse et d'architectures des systèmes, France

Latest Results in the Development of an Ultra-Low Phase Noise Rb CPT Vapour Cell Atomic Clock 837
Tsvetan Burtichelov, Jeremy Everard
University of York, United Kingdom

Active Devices Choice and Design of an All Cryogenic Superconductor Resonator Oscillator 842
David Chaudy[4], Olivier Llopis[1], Bruno Marcilhac[2], Yves Lemaître[2], Olivier d'Allivy Kelly[2], Jean-Michel Hode[3]
[1]Laboratoire d'analyse et d'architectures des systèmes / Centre National de la Recherche Scientifique, France; [2]Thales Research & Technology, France; [3]Thales Systèmes Aéroportés, France; [4]Thales Systèmes Aéroportés / Laboratoire d'analyse et d'architectures des systèmes, France

D2L-D Wave Propagation

Date: Thursday, July 13, 2017
Time: 10:40 - 12:20
Room: Room 5, 6 & 7
Chair(s): Joshua Lee; *City University of Hong Kong*
Alexandre Reinhardt; *CEA-LETI*

Lithium Niobate Phononic Crystals for Radio Frequency SH0 Waves 846
Ruochen Lu, Tomas Manzaneque, Yansong Yang, Songbin Gong
University of Illinois at Urbana-Champaign, United States

Backward Acoustic Plate Waves: Features of Properties and Possible Applications in Microelectronic Devices 850
Vladimir Mozhaev[3], Iliya Nedospasov[1], Iren E. Kuznetsova[2]
[1]Kotelnikov Institute of Radio Engineering and Electronics of RAS, Russia; [2]Kotelnikov Institute of Radio Engineering and Electronics of RAS / Yandex, Russia; [3]Lomonosov Moscow State University, Russia

Nonreciprocal Reconfigurable Zero-Transmission Filters Through Nonreciprocal Coupling to Resonators 852
Christopher Peterson, Jennifer Bernhard, Gaurav Bahl
University of Illinois at Urbana-Champaign, United States

Direct detection of the Elusive ^{229}Thorium Isomer: Milestone Towards a Nuclear Clock

P.G. Thirolf, B. Seiferle, L. v.d. Wense, J.B. Neumayr, H.J. Maier, H.-F. Wirth
Faculty of Physics
Ludwig-Maximilians-Universität München
Garching, Germany

M. Laatiaoui
GSI Helmholtzzentrum für Schwerionenforschung GmbH
Darmstadt, Germany

M. Laatiaoui, C. Mokry, K. Eberhardt, C.E. Düllmann
Superheavy Elements
Helmholtz-Institute Mainz
Mainz, Germany

C. Mokry, J. Runke, K. Eberhardt, C.E. Düllmann, N.G. Trautmann
Institute for Nuclear Chemistry
Johannes-Gutenberg-Universität Mainz
Mainz, Germany

***Abstract*— Recently, the first direct detection of the long-searched low-lying isomeric first excited state of ^{229}Th could be realized via its internal conversion decay branch, which confirms the isomer's existence and lays the foundation for precise studies of its decay parameters, in particular its half-life and excitation energy. Follow-up studies confirmed the theoretically expected lifetime reduction by about 10^9 of neutral ^{229m}Th compared to charged isomers with τ~10 μs, thus emphasizing the need to efficiently suppress internal conversion when aiming for the detection of a potential photonic decay branch of ^{229m}Th. Work towards precisely determining the excitation energy of the thorium isomer is ongoing, preparing for an all-optical control of this potentially highly precise nuclear frequency standard transition.**

Keywords—^{229m}Th, isomer; direct detection; internal conversion;lifetime; nuclear clock

I. INTRODUCTION

Today's most precise time and frequency measurements are performed with optical atomic clocks. However, it has been proposed that they could potentially be outperformed by a nuclear clock, which employs a nuclear transition instead of an atomic shell transition. There is only one known nuclear state that could serve as a nuclear clock using currently available technology, namely, the isomeric first excited state of ^{229}Th, which exhibits the lowest nuclear excitation energy of all presently known about 176000 nuclear excited states. Fig. 1 illustrates the unique role of ^{229m}Th in the plane spanned by excitation energy and half-life. The blue dots represent all known nuclear isomers, while in red selected atomic transitions used for frequency metrology are shown.

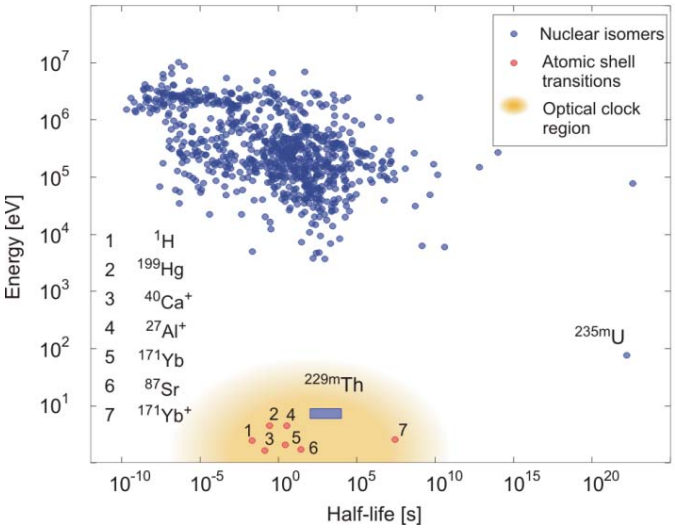


Fig. 1. Energy-half-life distribution of known nuclear isomeric states (blue) and selected atomic shell transitions used for frequency metrology (red). The orange region highlights the parameter space currently accessible for optical clocks [8].

Since 40 years nuclear physicists have targeted the identification and characterization of the elusive isomeric ground state transition of ^{229m}Th [1]. Evidence for its existence until recently could only be inferred from indirect measurements, suggesting an excitation energy of 7.8(5) eV [2,3]. With its expected radiative lifetime of about 10^4 s, the first excited state in ^{229}Th exhibits a relative linewidth $\Delta E/E \sim 10^{-20}$, thus rendering ^{229m}Th an ideal candidate for an ultra-precise nuclear clock with high resilience against external perturbations and promising a wealth of intriguing applications, e.g. studying potential temporal variations of fundamental constants like the fine-structure constant α [4].

This work was supported by DFG (TH956/3-1,TH956/3-2), by the European Union's Horizon 2020 research and innovation program under grant agreement No. 664732 "nuClock" and by the LMU department of Medical Physics via the Maier-Leibnitz Laboratory.

II. PREPARATION OF THE ^{229m}TH BEAM

The experimental concept pursued in our experiments builds on a spatial decoupling of population and deexcitation of the thorium isomer, using the 2% α-decay branch of a ^{233}U source placed inside a buffer-gas stopping cell, filled with 40 mbar of ultra-pure helium [5,6]. The α-recoil nuclei are stopped by the buffer gas, and guided by RF+DC fields in a funnel-like ring-electrode structure towards a Laval nozzle. Here an emerging supersonic gas jet drags the ions into the adjacent extraction vacuum chamber, housing a (segmented) radio-frequency quadrupole (RFQ) ion guide, buncher and phase-space cooler. Accompanying α-decay daughter products from the ^{233}U decay chain can be filtered in a subsequent quadrupole mass separator (QMS). The combined extraction and mass purification efficiency for ^{229}Th$^{1+,2+,3+}$ was determined as 0.34(7)%, 5.5(1.1)% and 10(2)%, respectively [7]. The corresponding parts of the mass spectra extracted from the gas cell for 1+ (a), 2+ (b) and 3+ (c) ions are illustrated in Fig. 2.

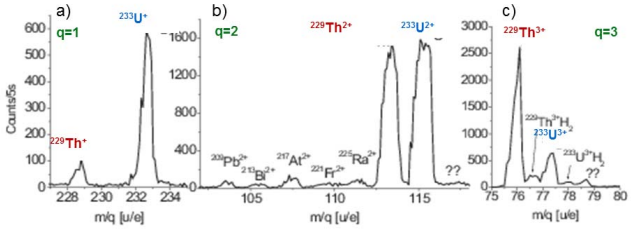


Fig. 2. Expanded parts of the extracted mass spectrum from the buffer-gas stopping cell after selection of singly (a), doubly (b) and triply charged (c) ions. Highlighted are the mass peaks of ^{229}Th and ^{233}U [7]. Eur. Phys. Jour. A 51, 29 (2015). Reprinted with permission of Springer.

Extracted and mass purified ions are then accumulated in 'soft landing' with low kinetic energy on an MCP detector surface (set to -25 V), in order to avoid ionic impact background signals by the remaining kinetic energy of the ions.

III. DIRECT IDENTIFICATION OF THE ^{229m}TH ISOMER

Due to the first ionization potential of ^{229}Th (6.31 eV) being smaller than the presumed isomer excitation energy, the internal conversion (IC) decay channel is energetically allowed for neutral ^{229}Th and will be the dominant de-excitation mode after neutralization of the impinging thorium isomers on the MCP surface. Fig. 3 shows the images obtained from electrons created in a low-noise MCP, and accelerated by + 6 kV towards a phosphor screen, which is monitored through an optical fibre-glass window by a CCD camera. Three different sources were used: a weaker ('source 1') and a stronger ('source 3') ^{233}U source, clearly showing signals from the ^{229m}Th isomer decay for doubly (column 1) and triply charged ^{229m}Th (column 3). The obtained signal was observed with a signal-to-background ratio of 8:1, the maximum signal intensity was 0.08 cts/ s mm^2 at a background rate of about 0.01 cts/ s mm^2. For comparison, also ^{233}U was extracted for the same charge states, however, as expected, no IC electron signals were observed in these cases. In order to exclude atomic shell effects as origin of the observed signals, also a ^{234}U source was studied, leading to ^{230}Th. No IC signals could be observed here either. Extensive verification studies were performed, allowing to exclude all possible sources of background and finally allowing to confirm that the measured signal can unambiguously be attributed to the de-excitation of the ^{229m}Th isomer.

.

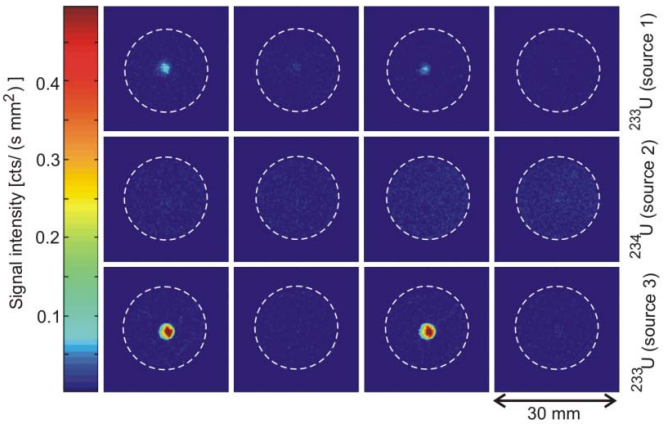


Fig. 3. Comparison of MCP signals obtained during accumulation of thorium and uranium in the 2+ and 3+ charge states, originating from ^{233}U (top and bottom rows) and ^{234}U sources (middle row), respectively. Columns 1 and 3 correspond to Th^{2+} and Th^{3+}extracted from the buffer-gas stopping cell , while columns 2 and 4 show similar measurements for U$^{2+,3+}$, respectively. Each image corresponds to an individual measurement of 2000 s integration time (20 mm diameter aperture indicated by dashed circles) [8].

IV. HALFLIFE OF ^{229m}TH

While the expected half-life regime of the charged thorium isomer with up to 10^4 s presently cannot be accessed with our technique due to the limited storage time in the RFQ, the half-life of neutral ^{229m}Th was measured via a bunched ion extraction from the RFQ (bunch width ca. 10 µs, ca. 400 ions/bunch). The ions were collected and the resulting IC electrons were measured with an MCP placed behind the QMS. The MCP was operated at low negative surface voltage to avoid background from ionic impact signals. In order to exclude chemical effects on the MCP surface as a signal origin, comparative measurements were performed with a ^{234}U source, providing ^{230}Th recoil ions. Fig. 4 displays the decay curve of ^{229m}Th (red) as compared to ^{230}Th (blue). A linear fit to the logarithmic decay curve reveals a half-life of 7(1) µs [10]. Considering the expected radiative lifetime of ca. 10^4 s, an internal conversion coefficient α_{ICC}~10^9 can be inferred, in agreement with theoretical expectations. This first half-life measurement constrains the relative strength of the radiative decay branch of ^{229m}Th to about 10^{-9} , thus emphasizing the need to efficiently suppress internal conversion when aiming for the detection of a potential photonic decay branch of ^{229m}Th.

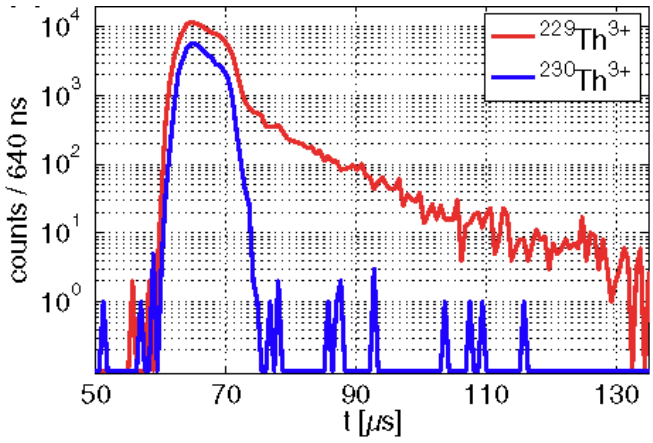


Fig. 4. Measurement of the isomeric decay with a bunched $^{229(m)}Th^{3+}$ ion beam (red curve). A comparative measurement with $^{230}Th^{3+}$ is also shown (blue curve) [9]. Reprinted with permission from B. Seiferle et al., Phys. Rev. Lett. 118, 042501 (2017). Copyright 2017 by the American Physical Society.

All this paves the way towards an all-optical control and thus the development of an ultra-precise nuclear frequency standard. Moreover, a nuclear clock promises intriguing applications in applied as well as fundamental physics, ranging from geodesy and seismology to the investigation of possible time variations of fundamental constants.

REFERENCES

[1] L.A. Kroger and C.W. Reich, "Features of the low energy level scheme of ^{229}Th as observed in the α decay of ^{233}U", Nucl. Phys. A 259, pp. 29-60, 1976.

[2] B.R. Beck et al., "Energy splitting of the ground-state doublet in the nucleus ^{229m}Th", Phys. Rev. Lett. 98, 142501 (2007).

[3] B.R. Beck et al., "Improved value for the energy splitting of the ground-state doublet in the nucleus ^{229m}Th", LLNL-PROC-415170 (2009).

[4] V.V. Flambaum, "Enhanced effect of temporal variation of the fine structure constant and the strong interaction in ^{229}Th", Phys. Rev. Lett. 97, 092502, 2006.

[5] J.B. Neumayr et al., "Performance of the MLL-Ion Catcher", Rev. Sci. Instr. 77, 065109, 2006.

[6] L. v.d. Wense, P.G. Thirolf, D. Kalb, M. Laatiaoui, "Towards a direct transition energy measurement of the lowest nuclear excitation in ^{229}Th", JINST 8, P03005, 2013.

[7] L. v.d. Wense, B. Seiferle, M. Laatiaoui, P.G. Thirolf, "Determination of the extraction efficiency for ^{233}U source α-recoil ions from the MLL buffer-gas stopping cell", Eur. Phys. Jour. A 51, 29, 2015.

[8] L. v.d. Wense et al., "Direct detection of the thorium-229 nuclear clock transition", Nature 533, pp. 47-51, 2016.

[9] B. Seiferle, L. v.d. Wense, and P.G. Thirolf, "Lifetime measurement of the ^{229}Th nuclear isomer", Phys. Rev. Lett. 118, 042501, 2017.

Progress Towards a $^{40}Ca^{+}$ Optical Clock with a Fractional Uncertainty at the 10^{-18} Level

Yao Huang, Hua Guan, and Kelin Gao*
Wuhan Institute of Physics and Mathematics
Chinese Academy of Sciences
Wuhan 430071, China
*klgao@wipm.ac.cn

***Abstract*—We recently reported a 5×10^{-17} level frequency comparison of two $^{40}Ca^{+}$ optical clocks, one of which has fractional frequency uncertainty of 3.4×10^{-17}, limited by the BBR effect. Here we present progress towards a $^{40}Ca^{+}$ optical clock with uncertainty at the 10^{-18} level. The differential static scalar polarizability $\Delta\alpha_0$ of the $^{40}Ca^{+}$ ion clock transition is obtained by precisely measuring the "*magic*" rf drive frequency. $\Delta\alpha_0$ is measured as $-7.2653(44)\times10^{-40}$ J m^2/V^2, the blackbody radiation shift is then calculated to be 0.3790(2) Hz at 300 K. The contribution of the blackbody shift coefficient to the uncertainty of the optical clock at room temperature is reduced to 5.6×10^{-19}, the excess micromotion induced clock uncertainty is also reduced to the 10^{-19} level by choosing the appropriate trap drive frequency. With a suppression of the BBR field temperature uncertainty to the sub-Kelvin level and improved clock stability, a robust, relatively low-cost $^{40}Ca^{+}$ ion clock with uncertainty at 10^{-18} level can be made.**

Keywords—optical clock; scalar polarizability; ion traps; blackbody radiation shift; micromotion

I. INTRODUCTION

The optical clocks with lowest fractional frequency uncertainties reported to date are the $^{171}Yb^{+}$ ion clock [1] and the ^{87}Sr optical lattice clock [2], both have reached uncertainty at the low 10^{-18} level. Since most of the clocks are running at the room temperature, the blackbody radiation effect contributes the largest frequency shift in most of state-of-artion or neutral atom optical clocks [1-4].

The blackbody radiation (BBR) shift at the room temperature is related to the differential static scalar polarizability $\Delta\alpha_0$. However, the state-of-art theoretical calculations of $\Delta\alpha_0$ only have uncertainty at the 1% level [5-8], which will contribute BBR shift uncertainty at the 10^{-17} level. $\Delta\alpha_0$ can be experimentally measured, which can give results with much higher precision. For neutral atom clocks, $\Delta\alpha_0$ of Yb [9] and Sr [10] are obtained by measuring the clock frequency shift due to applied dc electric fields, introduced by using precision parallel-plate capacitors. For the single-ion-based clocks, $\Delta\alpha_0$ of Yb^{+} is obtained by measuring clock shifts under near-infrared laser radiation with different wavelengths [1]; $\Delta\alpha_0$ of Sr^{+} is obtained by measuring the trap driving frequency at which the quadratic scalar Stark shift and the 2nd order Doppler shift due to the ion micromotion cancel each other [3].

The uncertainty of theoretically calculated $\Delta\alpha_0$ contributes 1.3×10^{-17} to our clock uncertainty. Via precisely measuring the "*magic*" trap drive frequency, $\Delta\alpha_0$ is experimentally measured with uncertainty of 0.06%, ~19 times better compared to the best atomic structure calculations with uncertainty of ~1.15% [5]. To our knowledge, our measurement of $\Delta\alpha_0$ currently has the lowest uncertainty over a variety of ion-based optical clocks.

II. EXPERIMENTAL SETUP

For a $^{40}Ca^{+}$ ion trapped in a Paul trap, at drive frequency of $\Omega_0 \approx \frac{e}{mc}\sqrt{-\frac{h\nu_0}{\Delta\alpha_0}}$, the total micromotion-related shift will be zero [3]. The frequency Ω_0 is so-called the "*magic*" trap drive frequency. Based on our previous work [11], improvements have been made. First of all, the rf driving source of the two clocks, called Clock1 and Clock2, are redesigned, the two clocks can both running at the "*magic*" rf driving frequency Ω_0. A variable capacitor is added with connection in parallel to the trap, the trap driving frequency can be continuously tuned from 22 to 27 MHz by adjusting the capacitance of the capacitor. The rf driving frequency can be changed while keeping the ion trapped. The working parameter of Clock1 is kept unchanged during the whole experiment. A dc offset voltage is added to the vertical compensation electrode of Clock2, producing a static electric field that will move the mean position of the ion vertically from the *E*-field free trap saddle point (trap center) to a new equilibrium position. Taking Clock1 as a frequency reference, the micromotion shifts can be measured by the frequency comparison of the two clocks. The rf trapping frequency of Clock2 is scanned for the study of "*magic*" trap frequency.

III. RESULTS

Fig. 1 shows the frequency difference of the two clocks as a function of the rf driving frequency of Clock2. The data were taken within ~ 2 weeks in a random order. The whole data sets are taken with the same ion loaded. Without firing the oven, very small change in stray electric fields can be observed during the experiments.

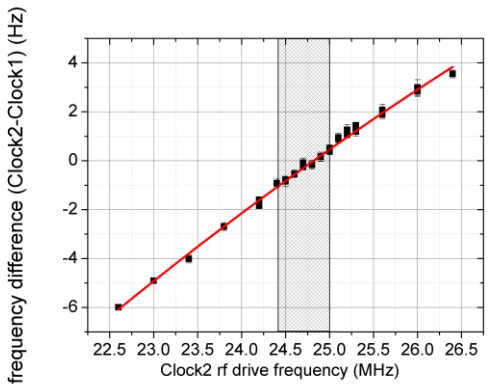


Fig. 1. Frequency difference between the two clocks as a function of the rf drive frequency of Clock2 with high micromotion levels. The shaded area illustrate the uncertainty of a theoretical result [5].

To reduce the measurement statistical uncertainty of Ω_0, the rf drive frequency of Clock2 is repeatedly and randomly scanned from 24.7~24.95 MHz. Linear fit are taken to obtain Ω_0 after each scan. After 15 of such scans, the inset shows the data taken in one of the scan and its linear fit. The corresponding weighted mean gives Ω_0=24.801(2) MHz.

To further determine $\Delta\alpha_0$ from Ω_0 with a higher accuracy, ion motions in Clock2 has to be studied [3]. By considering the motion harmonics at the frequencies of $n\Omega_0$, $\Delta\alpha_0$ is then calculated as $-7.2653(44)\times10^{-40}$ J m^2/V^2. The measurement of $\Delta\alpha_0$ reported here is in excellent agreement with the value $-7.31(8)\times10^{-40}$ J m^2/V^2 made by the recent theoretical calculations [5].

TABLE I. SIMPLIFIED UNCERTAINTY BUDGET OF THE $^{40}Ca^+$ OPTICAL CLOCK

Contribution	***Fractional frequency uncertainty***
BBR field evaluation (temperaturte)	1.9×10^{-17}
BBR coefficient ($\Delta\alpha_0$)	6×10^{-19}
Excess micromotion	6×10^{-19}
Second-order Doppler (thermal)	5.5×10^{-18}
ac Stark shift	1.3×10^{-18}
Residual quadrupole	3.6×10^{-18}
Zeeman effect	1.5×10^{-18}
Servo	1.9×10^{-17}
Total	2.8×10^{-17}

IV. CONCLUSION

With our measured value of $\Delta\alpha_0$ and the dynamic correction to the BBR shift of −0.0004 Hz calculated by Safronova *et al* [5], from Eq. (1) the BBR shift is calculated as 0.3790(2) Hz at 300 K. The contribution of the BBR coefficient to the $^{40}Ca^+$ ion clock is then reduced from a previously limiting value of 1.1×10^{-17} to 5.6×10^{-19}. With a suppression of the BBR field temperature uncertainty to sub-Kelvin level, the total fractional uncertainty will reach into the 10^{-18} level. For example, a BBR temperature uncertainty of 0.1 K would give a BBR shift uncertainty of 1.5×10^{-18}. In the meantime, the precisely measured "*magic*" rf drive frequency also helps suppress the overall micromotion induced frequency shift or uncertainty. By setting the trap drive frequency at the "*magic*" frequency Ω_0, the excess micromotion induced clock uncertainty can be easily reduced to the 10^{-19} level. A simplified uncertainty budget of the $^{40}Ca^+$ optical clock is shown in Table I.

The work reported here provides a significant improvement showing that the $^{40}Ca^+$ ion clock uncertainties caused by both the BBR shift coefficient and excess micromotion have been reduced to the 10^{-19} level. The servo error, primarily caused by statistical uncertainty of servo error signal data analysis, can be reduced by introducing the state preparation technique before the clock interrogations. The observed clock transition can be narrowed by using better clock lasers, smaller trap vibration, or weaker air turbulence. Narrower linewidth helps improving the clock stability thus suppressing the servo error. With a suppression of the BBR field temperature uncertainty to sub-Kelvin level, a robust, relatively low-cost $^{40}Ca^+$ ion clock with uncertainty at 10^{-18} level can be made.

REFERENCES

[1] N. Huntemann, C. Sanner, B. Lipphardt, C. Tamm and E. Peik, Phys. Rev. Lett. 116, 063001 (2016)

[2] T. L. Nicholson, S. L. Campbell, R. B. Hutson, et al. Nat. Commun. 6, 6896 (2015)

[3] P.Dubé, A. A. Madej, et al. Phys. Rev. Lett. 112, 173002(2014)

[4] G. P. Barwood, G. Huang, et al. Phys. Rev. A89, 050501(2014)

[5] M.S. Safronova et al. Phys. Rev. A 83, 012503 (2011)

[6] S. G. Porsev and A. Derevianko, Phys. Rev. A 74, 020502 (2006))

[7] D. Jiang, B. Arora, M. S. Safronova, and C. W. Clark, J. Phys. B 42, 154020 (2009)

[8] S. G. Porsev, A.D. Ludlow, M.M. Boyd, and J. Ye, Phys. Rev. A 78, 032508 (2008)

[9] J. A. Sherman, N. D. Lemke, N. Hinkley, M. Pizzocaro, R. W. Fox, A. D. Ludlow, and C. W. Oates, Phys. Rev. Lett. 108, 153002 (2012).

[10] T. Middelmann, S. Falke, C. Lisdat, and U. Sterr, Phys. Rev. Lett. 109, 263004 (2012)

[11] Y. Huang, H. Guan, P. Liu, W. Bian, L. Ma, K. Liang, T. Li, and K. Gao, Phys. Rev. Lett.116, 013001 (2016)

Ground-to-Space Time and Frequency Transfer based on the "Virtual Clock" method

Wenfang Jing[1,2], Xiaochun Lu[1,2,3]
1. National Time Service Center CAS, Xi'an, P.R.China
2. Key Laboratory for Precise Navigation, Positioning and Timing of the CAS, Xi'an, 710600, P.R.China
3. University of Chinese Academy of Sciences, Beijing
jingwf@ntsc.ac.cn

Shuo Liu
TimeTech GmBH
Stuttgart, Germany
Shuo.Liu@timetech.de

***Abstract*—We describe China Area Positioning System (CAPS) to transfer Time and Frequency between ground and space using a round-trip link via a transparent transponder onboard a satellite. The purpose is generation of navigation signals from ground, which appear to come from a non-physical "virtual" on-board clock, and its time modulation being close to UTC at the satellite transponder output. The system is synchronised to a high performance ground atomic clock via satellites in geosynchronous (GEO) and in inclined geo synchronous (IGSO) orbits is presented.**

Keywords—TWSTFT;VCLK;CAPS;TIMESYNC;CAPST

I. INTRODUCTION

Two-Way Satellite Time and Frequency Transfer (TWSTFT) via communication satellites is a time-proven method to link metrological laboratories via inter-continental bi-directional satellite links [1]. The method described here draws on these experiences to realize time and frequency transfer between ground and space based on CAPS. CAPS generates its navigation signals from ground uplink stations, being re-transmitted via the satellite's transponder. In this way, the signals appear as they would come from an on-board clock. The signals are synchronized to a ground reference clock, which itself is close to UTC, in order to generate a physical realization of an estimated UTC, virtual clock on-board the satellite (VCLK).

The main purpose of "Virtual clock" is generation of navigation signals, which appear to come from a non-physical, i.e. "virtual", clock on-board, for use in a novel GNSS system following these outline ideas:

A. Groud Clock versus Space Clock

The navigation signal locked to a high-performance ground clock is re-transmitted from space. By close-loop phase control, its stability is directly related to the high performance ground clock instead of a space clock. Also, the ground atomic clock is much easier to maintain and is less expensive compared to a clock in space at the same performance level.

B. C-Band versus L-Band

To improve frequency transfer stability by reduction of the absolute ionosphere delay, C-band is chosen as main signal frequency allocation instead of the traditional L-Band emissions.

C. User-defined Navigation Message

Additional corrective and ephemeris data is implemented. An open upload data interface covers the required corrective data e.g. Ionosphere [2], Troposphere model parameters and calibration delays.

D. Precise Time-tagged Measurement

The measuremnt data, i.e. code and carrier phase measurement, house-keeping and control messages are all timtagging precisely, according to the pulse per second (1PPS) input. In this case, the phase measurement error, which is caused by time-tagging error mutiplied by high doppler frequency is minimized to the best extent.

E. High Performance and Flexibility

The C-band signals are modulated at a rate of 10 MChips/s using Binary Phase Shift Keying (BPSK) with Pseudo-random Noise (PN) Codes. A precision of 10 ps has been achieved in code phase and 200 fs in carrier phase for a 1-second integration time. Satellite orbits include both GEO and IGSO orbits. The latter extends traditional TWSTFT operation to the conditions with significant relative velocity (up to 2 km/s), leading to high Doppler shift and Doppler rate.

The main challenge was to compensate the significant signal time-delay, inherent to the round-trip signal travel time, the significant relative velocity from satellite movement and unknown on-board transponder translation oscillator performance.

The tests have been conducted using the CAPS system operated by NTSC (National Time Service Center in Xi'an, China). The system architecture, the operations principle and test results for time and frequency synchronization will be presented.

II. SYSTEM DESIGN AND ARCHITECTURE

CAPS is a regional navigation system developed by China using normal communication satellite transponders (CST) to broadcast C-Band navigation signals via ground navigation stations to users, the system architecture is shown in Fig. 1.

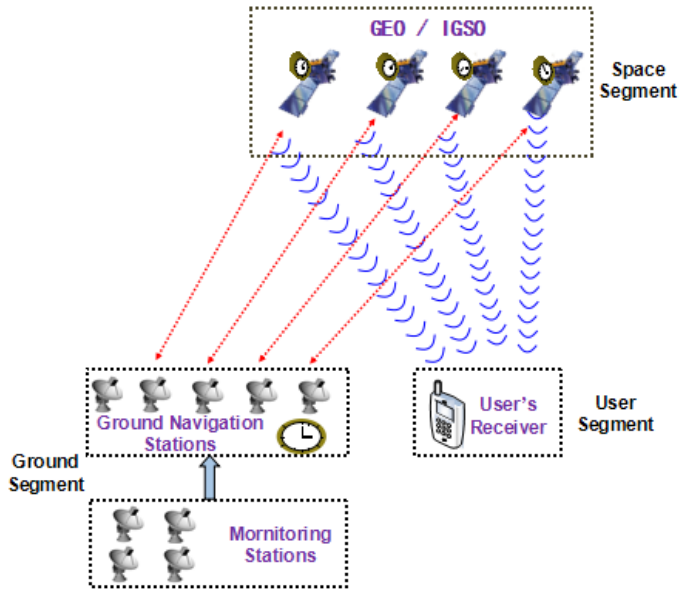


Fig. 1. System Architecture

Similar to a typical satellite navigation system, CAPS consists of three main segments, i.e. space segment, ground segment and user segment.

A. Space Segment

The space segment includes five satellites, with four GEOs located at 76.5°E, 87.5°E, 110.5°E, 148°E and one IGSO located at 95ºE.

B. Ground Segment

The ground segment consists of five ground navigation stations (GNS) equipped with 13m and 16m antennas (shown in Fig. 3) and monitoring stations (shown in Fig. 4) distributing throughout China mainland area (shown in Fig. 2). All measurements from monitoring stations are collected and processed in the master station located in X'an.



Fig. 2. Ground segment distribution inside China



Fig. 3. Ground navigation stations



Fig. 4. Monitoring and orbiting stations

In addition, the ground navigation stations are responsible of generation of reference signal with UTC tractability, generation of the uplink navigation message, and to monitor the health of all sub-systems' individual components.

C. User Segment

The user segment is C-Band user receiver (shown in Fig. 5), used to evaluate the navigation signal under normal signal condition (i.e. ~40dBHz) for the service of positioning, velocity and timing (PVT).

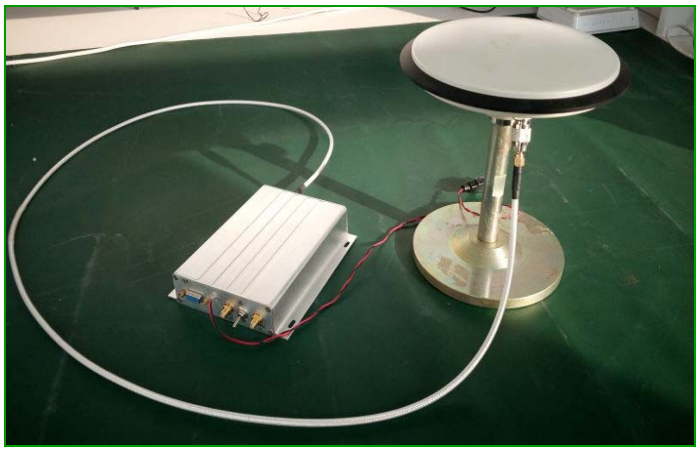


Fig. 5. C-Band user receiver

III. OPERATION PRINCIPLE

Different from typical navigation signals, the CAPS navigation signals are generated on ground. In this case, all CAPS navigation signals are highly coherent to the CAPS system time scale (i.e. CAPST).

The method of the "virtual clock" is shown in Fig. 6. By advancing a deterministic phase in the code and carrier phase separately, the "virtual clock" is physically realized, and accordingly, the time and frequency from ground atomic clock is transferred at the desired point, i.e. the phase center of the satellite transponder output.

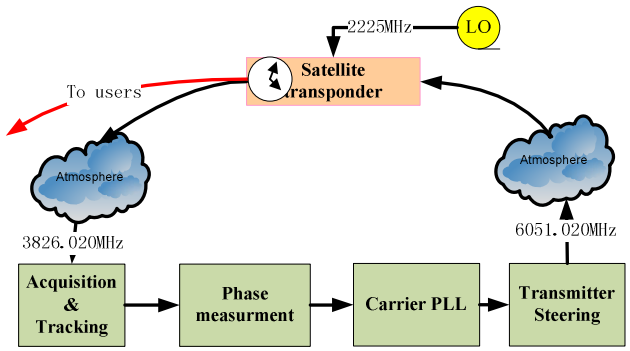


Fig. 6. Operation Principle

A. *Principle of CAPS-specific Time Transfer*

The time transfer is realized by pre-adjusting the transmitted code phase so that the phase of navigation data frame header changes at the same amount. The code control loop estimates and compensates the round-trip time delay continuously to achieve the navigation signal transmitted from the satellite output transponder at the time triggered by the CAPST. The CAPS-specific time transfer scheme is shown as follows in Fig. 7.

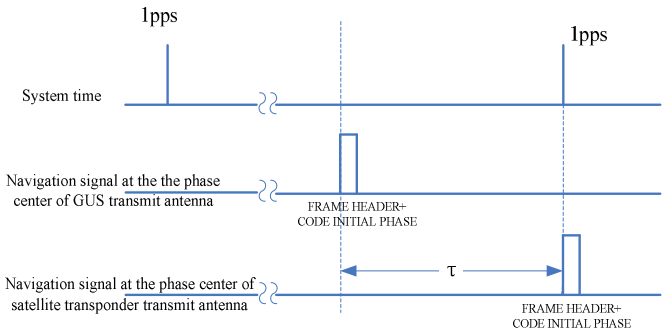


Fig. 7. Basics of CAPS-Specific Time Transfer

In above figure, τ indicates the total uplink time delay between GNS and the phase center of the satellite transponder antenna, which is to be compensated by the code control loop, when the uplink signal is generated. It can be expressed in the following formula.

$$\tau_i = \tau^i_{hw,up} + \tau^i_{tr,up} + \tau^i_{io,up} + \tau^i_{sag,up} + \rho^i_{gr,u} + \tau^i_{sat} \quad (1)$$

Where,

$\tau^i_{hw,up}$ is the uplink equipment time delay from the modem to the ground antenna phase center.

$\tau^i_{tr,up}$ is the time delay caused by uplink troposphere.

$\tau^i_{io,up}$ is the time delay caused by uplink ionosphere

$\tau^i_{sag,up}$ is the time delay caused by uplink sagnac [7]

$\rho^i_{gr,u}$ is the signal propagation delay from ground antenna phase center to the satellite transponder

τ^i_{sat} is the time delay from the satellite transponder.

Finally, the code phase control loop takes all kinds of time delay as inputs, sums them up with time-tagged code phase measurement from round trip delay and does the compensation.

B. *Principle of CAPS-specific Frequency Transfer*

Since the time is transferred to the phase center of the satellite's transponder output, a ground-to-space frequency transfer is achieved. Because the time and frequency reference is by-definition generated from the same source in the way, that the code and carrier phase is coherent. It is the on-board satellite oscillator that mainly changes the coherency between carrier phase and code phase after the navigation signal loops back, assumed that the ionosphere delay is known [2]. To recover the coherency, the integer ratio number in the downlink code and carrier frequency should be kept by imposing the same amount of phase change in both in any integral time.

In CAPS, the downlink carrier frequency is C-Band frequency around 3826.020 MHz and the code frequency is set to 10.23MHz for a modulation rate of 10.23Mchips/s , i.e. the ratio is 374. That is, in any integral time, due to the satellite movement the carrier phase in radians shall change 374 times more than the change in code phase.

But in reality, the code phase measurement is much noisy than the carrier phase. Therefore, we rely on very high carrier-to-noise ratio condition (~95dBHz) from large antennas, and implement a code tracking loop with less than 10ps @1s jitter in the downlink receiver. Filter algorithms are implemented to further stabilize the code phase measurement before it goes into the frequency control loop.

The carrier frequency control loop is then used to pre-adjust and compensate in advance the radians change induced by the on-board translation oscillator and downlink ionosphere, when the signal is transmitted from the ground navigation stations.

IV. EXPERIMENTS AND RESULTS

The experiment setup is shown in Fig.8. The user receiver is capable of switching its regulation source between its code and carrier phase measurement.

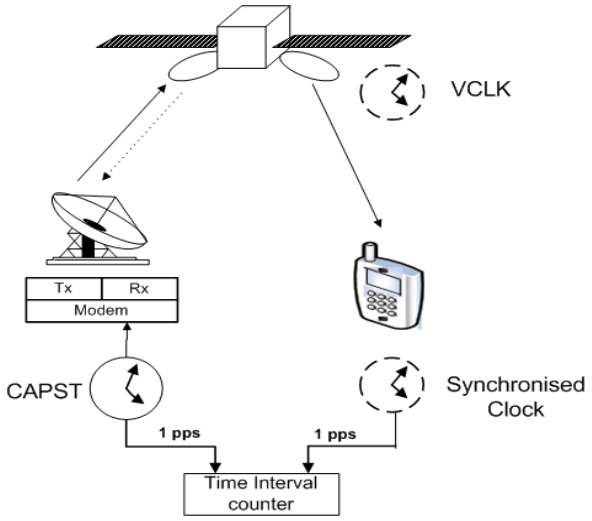


Fig. 8. Time Synchronization based on single satellite

The synchronized output pulse from the user receiver is compared with the CAPST externally by standard time interval counter, type SR620. The time delay measurement based on code and carrier phase regulation is shown in Fig. 9, the time deviation (TDEV) plot is shown in Fig. 10. It can be seen, that the bump visible in the time deviation around 100s is caused by internal regulation from the user receiver, while the long-term performance is roughly at the same level as the ground atomic clock.

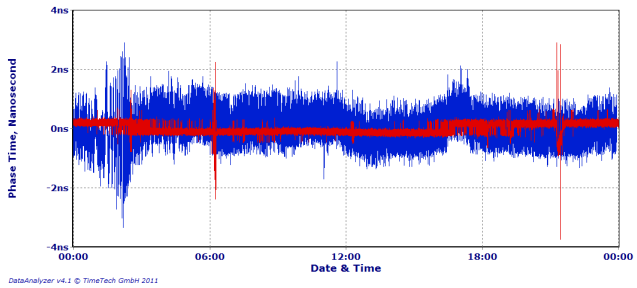


Fig. 9. Time delay measurement from synchronized output pulse versus CAPST based on code (blue) and carrier (red) phase

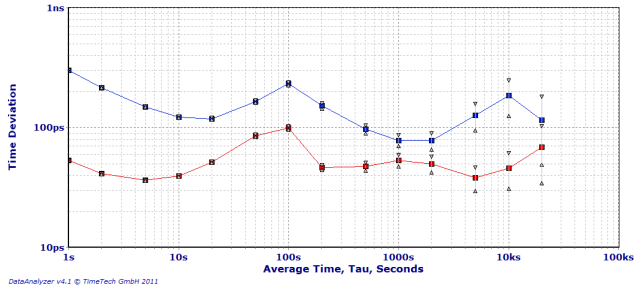


Fig. 10. Time deviation from synchronized output pulse versus CAPST based on code (blue) and carrier (red) phase

V. SUMMARY AND CONCLUSIONS

In this paper, we have presented the CAPS architecture, operation principle and test results on time and frequency synchronization by the user receiver under normal signal condition. The test results show time transfer stability ~40ps and frequency transfer stability 10^{-15} at 10000s based on "virtual clock" method.

Based on the advantages of CAPS that all navigation signals are generated from ground stations, the future research and development will focus on the topics of:

- Optimization of the control loop algorithm with aid from orbit knowledge
- Studies on the robustness of algorithms about carrier phase ambiguity solution under the conditions of GEO-and IGSO-satellite orbits
- Improvement of the "virtual clock" calibration and its traceability to UTC (NTSC)
- Construction of further differential ground stations to improve the wide area and long base-line time and frequency service

ACKNOWLEDGMENT

Current CAPS, as the 3rd generation, is built upon all lessons learned from previous generation [3] and inherits other NTSC groups for orbit determination from Prof. Dr. Xuhai Yang, time and frequency system from Prof. Dr. Xiaohui Li and maintenance for antenna, power and data processing. Thanks all the effort and contribution.

REFERENCES

[1] Bauch et al, Comparison between frequency standards in Europe and the USA at the 10-15 uncertainty level, Metrologia, 43-1, pp. 109-120, 2006

[2] Z. Li et al, Two-Way Satellite Time and Frequency Transfer Experiment via IGSO Satellite, FCS, DOI 10.1109/FREQ.2007.4319268, 2007

[3] G. X. Ai et al, A positioning system based on Communication Satellites and the Chinese Area Positioning System (CAPS), Chin. J. Astron. Astrophys., 8-6, pp. 611-630, 2008

[4] Hartl, P. et al 1983 High Accuracy Global Time Transfer Via Geosynchronous Telecommunication Satellites with Mitrex Z. Flugwiss. Weltraumforsch. 7 Heft 5.

[5] Salomon, C. et al 2001 Cold atoms in space and atomic clocks: ACES Comptes Rendus de l'Académie des Sci-ences - Series IV – Physics Vol. 2, Iss. 9 pp. 1313-1330.

[6] Recommendation ITU-R P.676-3 Attenuation by atmospheric gases.

[7] E.J. Post, "Sagnac Effect," Rev. Mod. Phys., vol. 39, no. 2, pp. 475-493, April 1967.

Q-Boosting of Metal MEMS Resonators Via Localized Anneal-Induced Tensile Stress

Alper Ozgurluk, Ruonan Liu, and Clark T.-C. Nguyen

Dept. of Electrical Engineering and Computer Sciences
University of California at Berkeley
Berkeley, California, USA
ozgurluk@eecs.berkeley.edu

***Abstract*— Introduction of tensile stress via localized Joule heating has yielded some of the highest metal MEMS resonator *Q*'s measured to date, as high as 48,919 for a 12-MHz ruthenium micromechanical clamped-clamped beam ('CC-beam'). The high *Q*'s continue into the VHF range, with *Q*'s of 7,202 and 4,904 at 61 and 70 MHz, respectively. These marks are substantially higher than the 6,000 at 10 MHz and 300 at 70 MHz previously measured for polysilicon CC-beams, defying the common belief that metal *Q* cannot compete with conventional micromachinable materials. The low-temperature ruthenium metal process, with highest temperature of 450°C and paths to an even lower ceiling of 200°C, further allows for MEMS post-processing directly over finished foundry CMOS wafers, thereby offering a promising route towards fully monolithic realization of CMOS-MEMS circuits, such as needed in communication transceivers. This, together with its higher *Q*, may eventually make ruthenium metal preferable over polysilicon in some applications.**

Keywords*— *MEMS, micromechanical resonator, ruthenium, localized annealing, quality factor, tensile stress, integration

I. Introduction

Oscillators referenced to high-*Q* micromechanical resonators that consume only 78 μW of power while attaining GSM-compliant phase noise performance have emerged as potential enablers for future low power autonomous wireless networks [1]. Although impressive, the bond-wired two-chip approach to realizing these MEMS-based oscillators inevitably incurs parasitic bond pad capacitances on the order of picofarads, thereby preventing these oscillators from realizing their true potential for power consumption [1]. Here, single-chip CMOS-MEMS integration to remove bond pad capacitance poses a nice solution. To date, however, high deposition temperatures for polysilicon or diamond MEMS materials hinder progress towards MEMS-last single chip integration alongside transistors. Their high structural and interconnect resistances also complicate applications that demand low loss, such as front-end filters. Structural and interconnect resistance also compromises MEMS-last integration approaches using SiGe structural material, which otherwise would meet temperature ceiling requirements for previous generation CMOS [2].

Ultimately, resistance needs might best be met by metal structural material options, many of which provide the added advantage of much lower deposition temperature making them more amenable to MEMS-last integration with CMOS. Unfortunately, to date metals post much lower *Q*'s than polysilicon, SiGe, or diamond counterparts [3]. If a metal is to replace these materials, some method is needed to enhance its *Q* without requiring transistor-damaging temperatures.

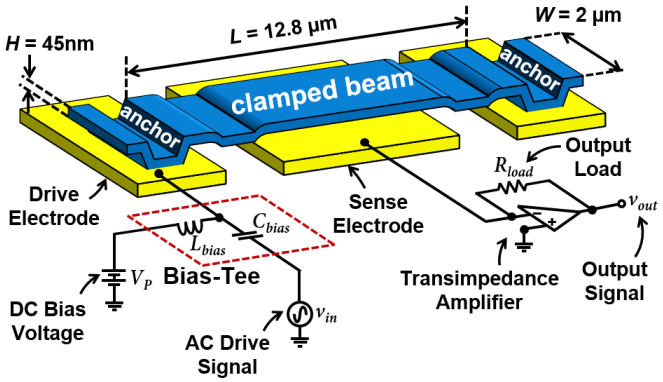


Fig. 1: Illustration of a single-electrode clamped-clamed (CC-beam) in a typical bias/excitation configuration.

Even without the draw of transistor-MEMS integration, there are burgeoning opportunities to apply high-*Q* metal structural material towards new all-mechanical circuits capable of detecting and demodulating RF signals while consuming no power when listening for inputs [4]. Such circuits can potentially obviate conventional sleep/wake methods intended to minimize sensor network power and in the process eliminate the clocks and computational overhead on which they rely. Here, the sensitivity, i.e., minimum detectable power, of such a circuit goes as the inverse of the *Q* of the resonator portion of the resoswitch they employ [4], which yet again, calls for a method for *Q* enhancement.

This paper demonstrates one such method that very effectively employs localized annealing to induce tensile stress in ruthenium clamped-clamped beam ('CC-beam') resonators and thereby raise their *Q*'s through mechanisms similar to those seen for nitride resonators [5], but with orders of magnitude lower thermal exposure for underlying transistors. Use of this method yields ruthenium resonator *Q*'s as high as 48,919 at frequencies approaching 12 MHz (to be compared with *Q* ~6,000 for polysilicon [6]); and retains high *Q* at VHF as indicated by *Q*'s of 7,202 and 4,904 at 61 and 70 MHz,

respectively (to be compared with Q ~300 at 70 MHz for polysilicon [7]).

II. Device Structure and Operation

Fig. 1 summarizes the CC-beam micromechanical resonator device [6] used as a vehicle in this work in a typical bias, excitation, and evaluation circuit. The CC-beam differs from previous renditions [6] in not only the material used, which is now Ru; but also in its dimensions, which are substantially smaller than previous ones in order to maximize sensitivity for a resoswitch-based receiver application [4]. Specifically, unlike previous polysilicon CC-beam dimensions on the order of of 40.8µm-long, 8µm-wide, and 1.9µm-thick to reach 7.81 MHz, a typical Ru design herein is 12.8µm-long, 2µm-wide, and 45 nm-thick, with dimensions 3.2, 4, and 42 times smaller, respectively. This reduces the mass and stiffness needed to achieve a given frequency, which improves (i.e., minimizes) sensitivity P_{sens} according to

$$P_{sens} = \frac{d_o^2 k_m \omega_0}{Q} \tag{1}$$

where k_m, d_o, and ω_0 are the mechanical stiffness, switch gap, and resonance frequency of the resoswitch, respectively. Note that smaller stiffness improves sensitivity, i.e., makes it smaller, by not only the direct stiffness term k_m in the numerator of (1), but also by reducing anchor dissipation, thereby raising the Q term in the denominator.

With Q as a focus, the devices herein were tested as resonators, rather than resoswitches, using the circuit of Fig. 1. Here, the bias-tee-combined AC-DC voltages of the drive and bias inputs together generate an amplified force at the frequency of the AC signal across the input-electrode-to-resonator gap. Sweeping the frequency of the AC source around the beam's resonance frequency generates vibrational motion that in turn creates a DC-biased time-varying capacitance across the electrode-to-resonator gap. A current then ensues, flowing through the structure and gap, out of the center electrode, and into the awaiting transimpedance amplifier detector.

As mentioned, this work boosts Q by introducing tension into the CC-beam. Of course, this tension affects not only Q, but also the resonance frequency. With tension added, the resonance frequency expression for the CC-beam becomes

$$f_0 = 1.03 \frac{H}{L^2} \sqrt{\frac{E}{\rho}} \sqrt{1 + \frac{SL^2}{3.4EH^2}} \tag{2}$$

where f_0 is resonant frequency, E is Young's modulus, ρ is density, S is tensile stress, and Fig. 1 identifies geometric parameters.

III. Fabrication

The choice of ruthenium as a metal for this work has more to do with the fact that its oxide is also conductive, making it useful for resoswitches [8] as well as resonators. The process used to achieve the device of Fig. 1 employs a surface micromachining process that uses Ru for interconnect, low-temperature LPCVD oxide as a sacrificial layer, and sputtered Ru (only 45 nm-thick) as the structural material. Fig. 2 summarizes the fabrication process.

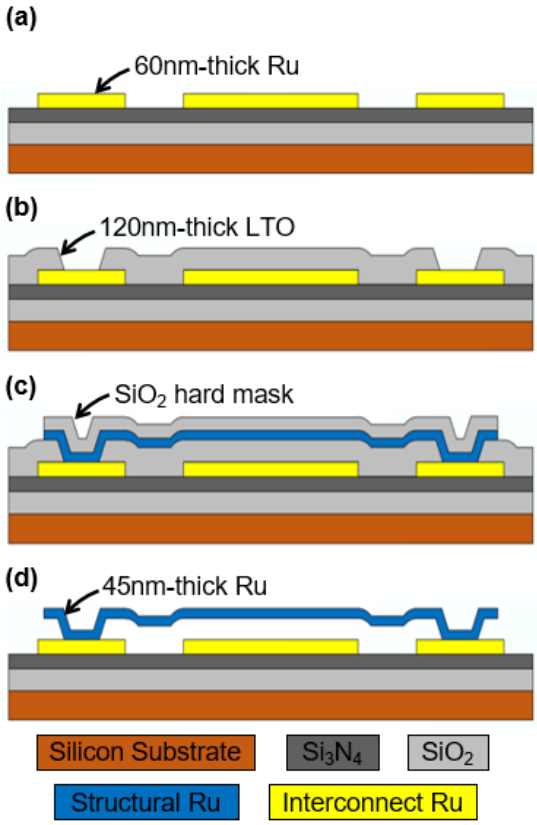


Fig. 2: Cross-sections describing the ruthenium metal CC-beam fabrication process flow after (a) patterning ruthenium interconnect and removing its etch hard mask; (b) depositing sacrificial layer and etching anchor openings; (c) depositing and patterning structural ruthenium; and (d) releasing the structure in HF.

The fabrication starts on 6″ blank p-type Si wafers with successive LPCVD depositions of 2µm LTO and 500nm silicon rich nitride at 450°C and 835°C, respectively, to serve as electrical isolation layers. Note that the silicon nitride could be replaced by a lower temperature material, such as alumina, if this process were actually run over CMOS, which it presently is not. Sputtering of 60nm-thick Ru and PECVD deposition at 350°C of 60nm-thick thick oxide then follow to serve as the interconnect layer and the oxide hard mask used in its etching, respectively. Lithography via a first mask and dry etch using Ar:CHF_3:CF_4 then transfers the interconnect layer pattern into the oxide hard mask. Next, a dry etch with Applied Materials Centura DPS etcher using gas flow rates of 90sccm of O_2 and 20sccm of Cl_2 at 20mTorr pressure with source and bias powers of 300W and 50W, respectively, delineates the interconnect layer as depicted in Fig. 2(a); followed by a 1 minute 5:1 buffered HF dip to remove the oxide hard mask layer.

Note that the need for a hard mask when etching the interconnect layer is not a consequence of the etch selectivity of the Ru dry etch chemistry over photoresist, which is actually quite adequate. Rather, it derives from a need to avoid cross-linking between Ru and photoresist observed at elevated temperatures [9]. In particular, even without hard- or UV-baking,

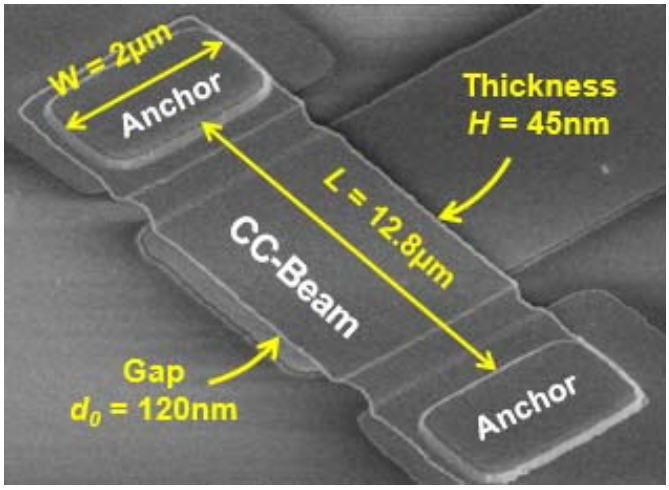


Fig. 3: SEM of a fabricated CC-beam resonator with key dimensions.

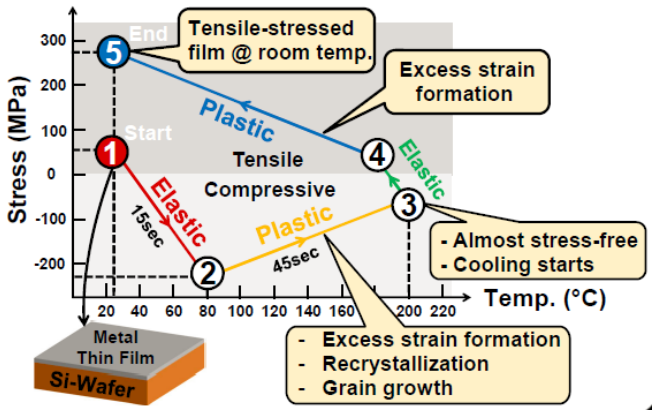


Fig. 4: A generic thermal annealing cycle for low-temperature sputtered metals atop Si substrate showing how film stress evolves during heating and cooling.

the temperature elevation that occurs during dry etching of Ru is enough to instigate cross-linking so strong that removal of photoresist after Ru layer patterning becomes very difficult.

After interconnect layer patterning, LPCVD deposition of low temperature oxide (LTO) at 450°C coats a sacrificial oxide layer that defines the 120nm capacitive actuation gap between the CC-beam and the underlying electrode. Anchor openings are then etched into the oxide sacrificial layer using Ar:CHF_3:CF_4 as illustrated in Fig. 2(b), followed by a sputtering of 45nm Ru to serve as the structural material. After depositing and patterning another oxide hard mask, the same chemistry that etched the interconnect layer delineates the structures as in Fig. 2(c). Here, a Ru etch chemistry comprised of mostly O_2 with a small amount of etch-rate enhancing Cl_2 provides good selectivity (> 10) over the underlying sacrificial LTO layer [9]. This degree of selectivity becomes ever more critical for beam type devices with very small actuation gaps, i.e. < 20nm, intended for highly sensitive resoswitches.

Completed wafers are diced and the resulting dies released (when needed) in 49 wt. % liquid HF that frees the resonators. Since the small size and stiffness of the devices make them more prone to stiction, criticial point drying (CPD) is generally needed after HF release to insure adequate yield. Fig. 2(d) presents the final cross-section of the device. Fig. 3 presents the SEM of a fabricated 12.8μm-long device.

IV. Tensile-Stressed Ruthenium CC-Beams

As shown in Fig. 5(a), immediately after fabrication, beams with dimensions shown in Fig. 1 post frequencies around 1.2 MHz with Q's on the order of only 180, which is quite low. These represent the nearly stress-free performance of the devices, or at least the performance before stress introduction.

Again, the strategy behind the present work is to introduce stress in order to attain higher Q. If previous work with nitride resonators holds [5], better Q should be possible via introduction of tensile stress. This previous work introduced stress mechanically, by tightening a pull system via turns of a screw.

Before presenting the localized anneal-based approach to tensile stress introduction that facilitates MEMS-last integration with transistors, we first confirm and gauge the degree to which tensile stress raises the Q's Ru CC-beams via rapid thermal annealing (RTA). Here, ruthenium CC-beams of different sizes were subjected to various rapid thermal anneals (RTAs) that generated tensile stress by stimulating structure reorganization and grain growth via plastic deformation [10], [11].

To better convey how tensile stress might ensue after an anneal cycle, Fig. 4 presents a plot of stress as a function of temperature and time during annealing and cooling periods. Initially, assuming the structural material thermal expansion coefficient is larger than that of the substrate, as the temperature rises the beam strain is predominantly elastic and compressive. When the temperature surpasses a certain value, a combination of excessive compressive strain and temperature induce recrystallization, which grows grains to relieve the stress, actually reduces the compressive stress and brings the total stress closer to zero at the end of the heating cycle.

When heating stops, the cooling process begins. Now the structure, with its relatively larger thermal expansion coefficient, shrinks faster than the substrate. Since the stress at the start of the cooling process was considerably smaller than if no recrystallization had occurred, very little of the beam shrinking during cooling goes towards compensation of compressive stress, so the beam goes into heavy tension. Tension values on the order of 700-900 MPa are typical in this work.

Using (2), curve fitting measured frequency versus beam length curves as in Fig. 6 yields the following values for material parameters: Young's modulus, E = 402.5 GPa and density ρ =13,420 kg/m^3.

Note that for large values of stress, (2) reduces to

$$f_0 \cong \frac{0.56}{L}\sqrt{\frac{S}{\rho}} \quad if \quad S \gg 3.4E\left(\frac{H}{L}\right)^2 \tag{3}$$

Here, the stress S becomes a principal determinant of resonance frequency. While on the one hand, some might argue

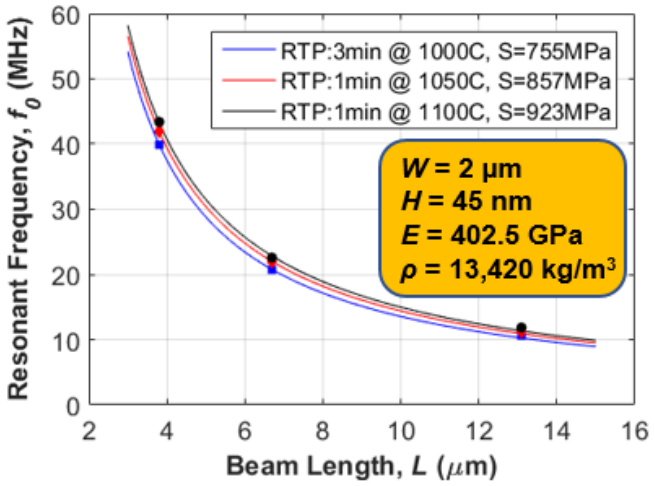


Fig. 6: Curve fitting measured frequency versus beam length where dots represent actual measured data and solid lines are analytically determined curves using (2).

that the frequency stability becomes too dependent on factors that might change the stress; others on the other hand might argue that this strong dependence on stress removes concern for instabilities in other parameters, such as Young's modulus and thickness. Ultimately, if the resonance frequency stability depends only on stress, then this might actually simplify strategies to maximize the stability of an oscillator referenced to this device, since one now need only find a method to stabilize stress. Yes, a tall order, but perhaps not an impossible one.

The dominance of stress as a determinant in (3) also suppresses the influence of non-idealities on resonance frequency. This can greatly facilitate design. For example, for the beams measured in this work, the large stress obviates the beam topography factor that would otherwise reduce the resonance frequency of a CC-beam from the theoretically expected value.

Returning to the influence of stress on Q, Table I documents the increase in frequency and Q experienced by beams

TABLE I. MEASURED Q'S AND RESONANT FREQUENCIES FOR CC-BEAMS OF DIFFERENT LENGTHS AFTER VARIOUS RTA CONDITIONS

Beam Length	Q and f_0 in Various RTA Conditions		
	1000°C, 3 min *S = 755 MPa*	*1050°C, 1 min* *S = 857 MPa*	*1100°C, 1 min* *S = 923 MPa*
L = 12.8 µm	Q = 8,617 f_0 = 10.5 MHz	Q = 9,872 f_0 = 11.3 MHz	Q = 46,066 f_0 = 11.7 MHz
L = 6.4 µm	Q = 6,210 f_0 = 20.5 MHz	Q = 7,652 f_0 = 21.7 MHz	Q = 16,040 f_0 =22.5 MHz
L = 3.5 µm	Q = 1,803 f_0 = 38.2 MHz	Q = 2,576 f_0 = 39.8 MHz	Q = 5,562 f_0 = 42.9 MHz

of different lengths under various amounts of RTA-induced tensile stress. As shown, introduction of tensile stress raises the frequency of the Fig. 5(a) device by almost 10 times. In addition, 923 MPa tensile stress provides an impressive 256 times increase in Q, taking the Q of the Fig. 5(a) device from 180 to 46,066!

V. LOCALIZED ANNEALING

Although the results of Table I are quite compelling, the RTA temperatures used therein could unfortunately degrade foundry CMOS transistors. This work circumvents this problem via use of localized Joule-heating, first demonstrated in [12], that raises only the MEMS resonator device to the needed stress-inducing temperature, keeping any underlying transistors near room temperature. Here, the circuit of Fig. 5(b) simply applies a voltage V_{ann} across the beam anchors, which then sends a current I_{ann} through the beam that Joule heats it to a desired temperature, generating tensile stress in the process. The tiny size of the device presents a correspondingly tiny thermal capacitance, allowing the beam to be heated to over 1000°C in milliseconds, which in turn allows fast pulsed annealing for more precise stress control.

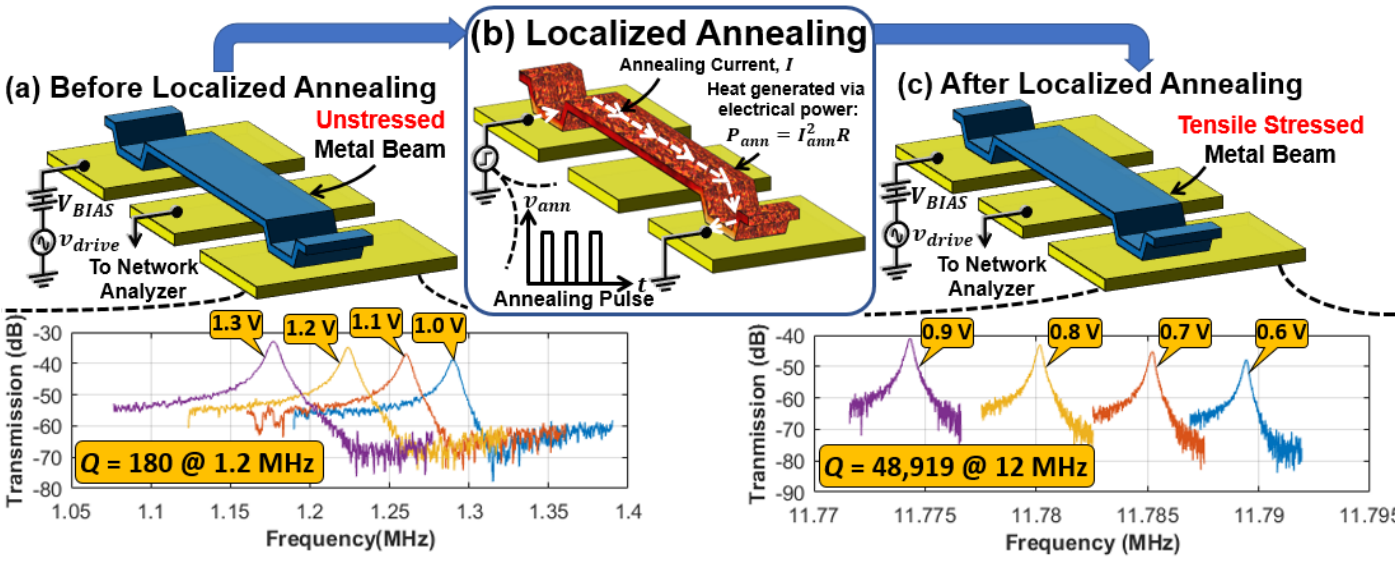


Fig. 5: Measured frequency response vs. DC bias voltage for a 12.8µm-long, 2µm-wide, 45nm-thick Ru CC-beam (a) before and (c) after localized anneal-stressing. (b) Schematic depicting the circuit needed for localized anneal-stressing.

VI. Localized Anneal-Induced Q-Boosting

Localized annealing experiments took advantage of the fast heating time constants characteristic at the micro-scale by heating via pulsed voltage train sequences, as shown in Fig. 7(a), which were applied across the beam annealing terminals. Here, (V_{ann}, τ_d, τ_b) sets describe specific pulse train types, where τ_d is pulse duration, and τ_b is spacing between pulses. A frequency response measurement to extract the resonance frequency and Q followed each pulse or pulse-train anneal step.

The measurement procedure was such that each device experienced successively stronger annealing each time it survived an anneal step. Specifically, if a device survives a first anneal set, the next anneal set raised the ante by either raising V_{ann} or adding pulses. This procedure continued until either excessive Joule heating destroys the beam or tensile stress breaks the beam or damages its anchors.

Fig. 5(c) presents frequency characteristics after localized anneal-induced stressing for a ruthenium metal CC-beam resonator with L = 12.8 µm, W = 2 µm, and H = 45 nm at various DC bias voltages. Here, the previous 1.2 MHz resonance frequency now approaches 12 MHz with a Q of 48,919 more than 272 times higher than the previous 180. Clearly, localized anneal-stressing is a game-changer for Ru metal CC-beams.

Fig. 7(b) gauges the efficacy of localized anneal-stressing as a function of resonator frequency by plotting measured Q versus frequency. As expected, an obvious drop in Q with increasing frequency occurs due to larger anchor loss at higher frequencies. Nevertheless, because these metal resonators are considerably thinner than previous CC-beam designs, their Q's remain high at higher frequencies, on the order of 7,202 and 4,904 at 61 and 70 MHz, respectively. These are considerably higher than the 300 typically measured for 2 µm-thick 70-MHz polysilicon CC-beams.

VII. Conclusions

By posting Q's of 48,919 at 11.8 MHz and 4,904 at 70 MHz, both many times higher than the 6,000 and 300 typical of 2 µm-thick polysilicon counterparts, the 45 nm-thick localized anneal-stressed ruthenium metal resonators demonstrated herein may soon enable oscillators with considerably better phase noise than achieved with previous polysilicon CC-beams. Although methods to insure adequate long-term stability, e.g., via alloying, still require exploration, the results reported herein certainly enhance the feasibility of MEMS-last CMOS-MEMS integration using metal structural material.

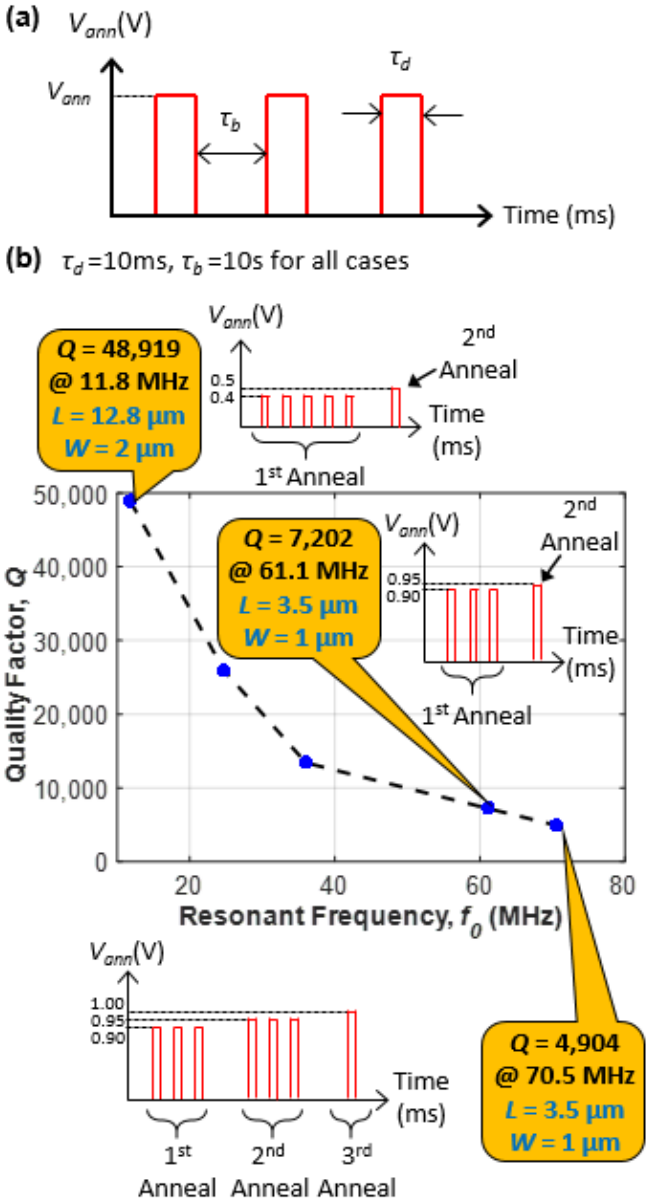


Fig. 7: (a) Pulse train localized annealing waveform used in this study. (b) Q after localized anneal-stressing as a function of beam frequency along with the localized annealing pulse conditions for certain frequencies.

Acknowledgment

This work was supported by DARPA N-ZERO program

References

[1] T. L. Naing, T. O. Rocheleau, E. Alon, and C. T.-C. Nguyen, "A 78-microwatt GSM phase noise-compliant pierce oscillator referenced to a 61-MHz wine-glass disk resonator," in *Proc. Joint IEEE Int. Frequency Control Symp. and European Freqeuency and Time Forum*, 2013, pp. 562–565.

[2] A. E. Franke, J. M. Heck, T.-J. King, and R. T. Howe, "Polycrystalline silicon-germanium films for integrated microsystems," *J. Microelectromech. Syst.*, vol. 12, no. 2, pp. 160–171, 2003.

[3] W.-L. Huang, Z. Ren, Y.-W. Lin, H.-Y. Chen, J. Lahann, and C. T.-C. Nguyen, "Fully monolithic CMOS nickel micromechanical resonator oscillator," in *Proc. 21st IEEE International Conference on Micro Electro Mechanical Systems (MEMS)*, 2008, pp. 10–13.

[4] R. Liu, J. N. Nilchi, Y. Lin, T. L. Naing, and C. T.-C. Nguyen, "Zero Quiescent Power VLF Micromechanical Communication Receiver," in *Dig. Tech. Papers 18th Int.*

Conf. Solid-State Sens., Actuators Microsyst. (TRANSDUCERS), 2015, pp. 129–132.

[5] S. S. Verbridge, J. M. Parpia, R. B. Reichenbach, L. M. Bellan, and H. G. Craighead, "High quality factor resonance at room temperature with nanostrings under high tensile stress," *J. Appl. Phys.*, vol. 99, no. 12, pp. 1–8, 2006.

[6] F. D. Bannon, J. R. Clark, and C. T.-C. Nguyen, "High- Q HF Microelectromechanical Filters," *IEEE J. Solid-State Circuits*, vol. 35, no. 4, pp. 512–526, 2000.

[7] K. Wang, A.-C. Wong, and C. T.-C. Nguyen, "VHF Free – Free Beam High-Q Micromechanical Resonators," *J. Microelectromech. Syst.*, vol. 9, no. 3, pp. 347–360, 2000.

[8] Y. Lin, R. Liu, W.-C. Li, M. Akgul, and C. T.-C. Nguyen, "A Micromechanical Resonant Charge Pump," in *Dig. Tech. Papers 17th Int. Conf. Solid-State Sens., Actuators Microsyst. (TRANSDUCERS)*, 2013, pp. 1727–1730.

[9] I.-R. Chen, "Novel Material Integration for Reliable and Energy-Efficient NEM Relay Technology.", Ph.D. dissertation, EECS, Univ. California, Berkeley, Tech. Rep. UCB/EECS-2014-227, 2014.

[10] P. A. Flinn, D. S. Gardner, and W. D. Nix, "Measurement and Interpretation of Stress in Aluminum-Based Metallization as a Function of Thermal History," *IEEE Trans. Electron Devices*, vol. ED-34, no. 3, pp. 689–699, 1987.

[11] T. C. Hodge, S. A. Bidstrup-Allen, and P. A. Kohl, "Stresses in thin film metallization," *IEEE Trans. Compon. Packag. Manuf. Technol. A*, vol. 20, no. 2, pp. 241–250, 1997.

[12] K. Wang, A.-C. Wong, W.-T. Hsu, and C. T.-C. Nguyen, "Frequency trimming and Q-factor enhancement of micromechanical resonators via localized filament annealing," in *Dig. Tech. Papers 9th Int. Conf. Solid-State Sens., Actuators Microsyst. (TRANSDUCERS)*, 1997, vol. 1, pp. 109–112.

Nonlinear cancellation in weakly coupled MEMS resonators

Milind Pandit, Chun Zhao, Aref Mustafazade, Guillermo Sobreviela and Ashwin A Seshia
Nanoscience Centre, Department of Engineering, University of Cambridge,
11 JJ Thomson Avenue , Cambridge CB3 0FF

***Abstract*—For the first time, this paper demonstrates the cancellation of nonlinear response in weakly coupled resonators. It has been observed that by working in the region where the mechanical nonlinearity of the resonators and the electrical nonlinearity of the electrostatic coupling cancel, the output current amplitudes are increased by 4x while the trend of vibration amplitude variation upon stiffness perturbations is preserved as seen in the linear regime of the resonators.**

I. Introduction

Weakly coupled MEMS resonators (WCRs) have been employed in device applications for electro mechanical signal processing [1] [2] and sensors [3][4] . In the context of sensing, a MEMS configuration consisting of weakly coupled resonators utilising the principle of vibration mode localization has been proposed. This technique has shown an improvement in sensitivity by orders of magnitude compared to the conventional single resonator devices using resonant frequency shifts as a readout [3]-[5]. The WCRs use amplitude ratio measurements instead of frequency shift measurements employed by the standard resonator systems to acheive common mode rejection capabilities that provide first-order response immunity to ambient temperature and pressure variations[6],[7].

In the context of sensing, WCRs have only been characterized in the linear regime at low vibration amplitudes so far. High vibration amplitudes allow for a higher output signal that in turn results in higher signal to noise ratio (SNR) in a system that is dominated by electrical noise of the readout electronics. However, at high vibration amplitudes, the nonlinearities of the system become considerable and higher order nonlinear effects, e.g. those that are often described by the Duffing equation, arise due to physical sources that are related to geometric and material properties, and from the electromechanical transduction scheme employed. These effects produce amplitude-frequency *(a-f)* dependency where multiple amplitudes and phase can be realized at a particular operating frequency. These nonlinearities limit the operation regime and power handling ability of the resonator system. Furthermore, they are undesirable in sensing applications due to their detrimental impact on the long-term stability of the resonators due to the up-mixing of low frequency noise in the form of close-to-carrier noise [8].

In this work, using the concept of nonlinearity cancellations shown for a single resonator[9],[10], electrical and mechanical nonlinearity were compensated in WCRs by tuning the coupling voltage. When operating in this regime, a higher output signal is achieved without compromising on the sensitivity to stiffness perturbations as compared to a linear response. Since the current measurement setup is dominated by electrical noise of the readout electronics, this allows for a greater Signal to Noise Ratio (SNR) and a pathway to higher resolution amplitude ratio measurements.

II. Theory

The WCRs can be schematically represented by a simple coupled spring-mass system as shown in Fig. 1. Such a system has two vibration modes - the in-phase mode and the anti-phase mode. Assuming a weak coupling ($K_c << K$), the anti-phase mode is separated from the in-phase mode by a factor proportional to the coupling stiffness. Since the coupling is negative in this case, the anti-phase mode has a lower eigenfrequency than the in-phase mode as expected of such a system.

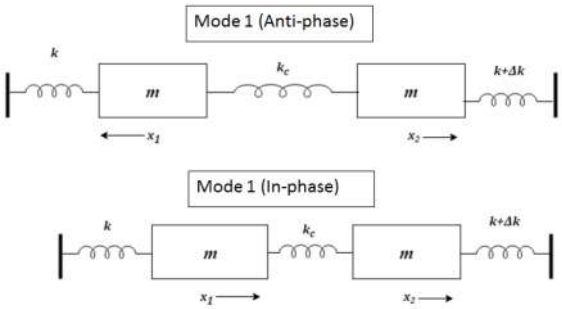


Fig. 1. Modes of Vibration for the coupled system.

The sources of mechanical nonlinearity in this system generally arise from the geometry and material properties of the resonators themselves. Mechanical nonlinearities in the WCRs are similar to those that arise in single resonator systems and effect all of the modes of the device. These nonlinearities cause spring stiffening and result in positive *a-f* effects. The nonlinear spring constant with mechanical nonlinearities for a DETF resonator can be approximated as [11]:

$$k(x) = k_0(1 + k_2x^2) \tag{1}$$

$$k_2 = \frac{0.767}{w^2} \tag{2}$$

Since the operating mode of the system is the anti-phase mode, it is assumed that a complete cancellation of the second order mechanical nonlinear term occurs in a DETF resonator.

Electrical nonlinearities on the other hand arise from the electrostatic force created by capacitive transduction, electrostatic forces and, coupling between the resonators. They cause spring softening and result in negative *a-f* effect. The nonlinearties arising due to capacitive transduction are similar to single resonator systems and affect all modes of the device. The nonlinear spring constant due to electrostatic forces can be derived as:

$$k_{en}(x_i) = -\frac{V_{DC}^2}{2}\frac{\partial^2 C}{\partial x_i^2} \quad i = 1, 2; \tag{3}$$

The electrostatic forces also affect both the modes equally. However, the nonlinearites arising from the capacitive coupling effect the anti-phase mode more than the in-phase mode. In the in-phase mode, the two capacitive plates are moving in-phase with each other and nonlinearities due to the coupling are suppressed However, in the anti-phase mode, due to the capacitive plates moving out of phase with each other, the nonlinearities due to electrostatic coupling force arise and act as an additional contributor to the electrical nonlinearities of that mode. This nonlinear coupling spring constant can be derived as:

$$k_{cn} = -\frac{V_{couple}^2}{2}\frac{\partial^2 C}{\partial (x_1 - x_2)^2} \tag{4}$$

Due to the selective effects of the nonlinearity of coupler on the anti-phase mode, this mode is used for all experiments and simulation. Since the strength of the coupler can be tuned with the coupling voltage, the sources of electrical nonlinearities can be tuned to cancel the mechanical nonlinearities sources at a particular range of coupling voltages in mode 1.

III. Simulation

A simulation was designed on Simulink® using the equations of motion of the nonlinear coupled resonator system driven from only one resonator:

$$m\ddot{x}_1 + c\dot{x}_1 + k_0 x_1 + k_2 x_1^3 + k_{en} x_1 + k_{cn}(x_1 - x_2) = F\cos(\omega t + \phi) \tag{5}$$

$$m\ddot{x}_2 + c\dot{x}_2 + k_0 x_2 + k_2 x_2^3 + k_{en} x_2 - k_{cn}(x_1 - x_2) = 0 \tag{6}$$

In Equation 5 and 6, it is assumed that the two resonators are identical thus resulting in the same linear and nonlinear mechanical stiffness terms. Furthermore, the coupling force is not split up into nonlinear terms but is used with a double differential term as shown in Equation 4 to preserve the effects of higher order nonlinear terms. The damping constant is chosen to have a quality factor of 10000 which, is similar to the experimentally observed quality factor. DC biasing voltage similar to that used in the experiment is applied to the resonators to simulate the experimental conditions.

A block diagram approach was used to represent the various forces being applied on the two resonators in terms of their displacements x_1 and x_2. The frequency response of resonator 1 at various coupling voltages driven at the same ac voltage of 125mV is shown in Fig. 2. A clear transition is seen with mechanical *a-f* effect observed at $V_{couple} = 12V$ to electrical *a-f* effect observed at $V_{couple} = 42V$ with the cancelled response at $V_{couple} = 27V$.

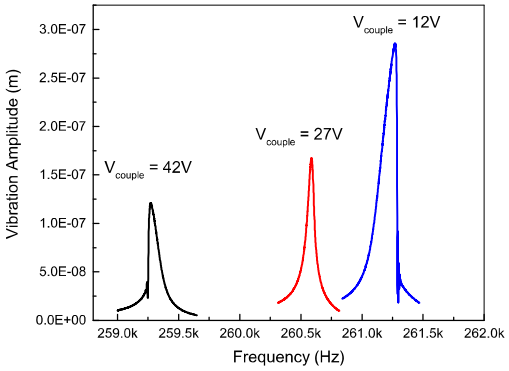


Fig. 2. Simulated frequency response curves of Mode 1 at 125mV AC drive voltage over three different coupling voltages showing mechanical nonlinearity, cancellation regime and electrical nonlinearity.

Although this simulation identifies the cancellation phenomenon, it also includes the occurrence of mode localisation where the amplitude of vibration of the resonator changes (in this case decreases) by tuning the coupling voltage. This would mean that the amplitude of vibration (x_1) at $V_{couple} = 27V$ is a lot lower than at $V_{couple} = 12V$ which leads to a lower nonlinear *a-f* behavior. To truly understand the nonlinear cancellation behavior in the WCRs, an experimental study of the power handling ability is done which is discussed in the reults section.

IV. Experiment

A. Device Description

The experiment is conducted using two identical, coupled double ended tuning fork (DETF) resonators. An optical micrograph of the device is shown in Fig. 3. The device was fabricated by MEMSCAP Inc. using SOIMUMPS, a commercial foundry process that uses silicon-on-insulator (SOI) wafers. The dimensions of the device are described in Table I.

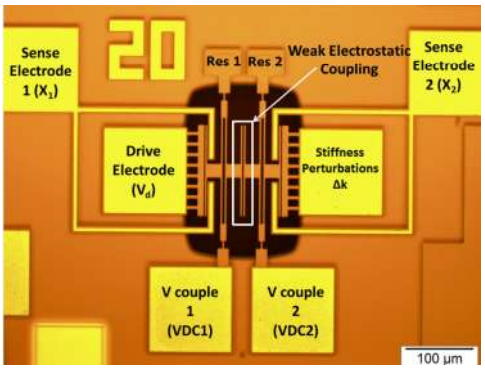


Fig. 3. Optical Micrograph of the device.

TABLE I
DEVICE PARAMETERS

Parameter	Dimensions
Beam Length	350 μm
Beam Width	6 μm
Electrode Length	260 μm
Electrode Width	6 μm
Device Layer Thickness	25 μm
Proof Mass (2 for each DETF)	40 μm $\times$ 40 μm
Electrode Gaps	2 μm

B. Measurement Setup

The experimental setup is shown in Fig. 4. and measurements are conducted in vacuum. Two DC voltages (VDC1, VDC2) were applied on the two resonators to achieve a negative coupling stiffness, which was tuned by varying the potential difference. A network analyzer (Agilent 4396B) was used to apply an AC drive voltage (V_d) along with a DC polarizing voltage on resonator 1. The DC polarising voltage for drive and sense transductions are kept constant throughout the experiment. The output motional current of each resonator is passed through a transimpedance Amplifier (TIA), then through a Band Pass Filter (BPF) and finally fed back into the network analyzer to calculate the transmission (S_{21}) parameter of the resonators. A negative stiffness perturbation relative to resonator 1 was applied on the perturbations electrode in the form of voltage differences for sensitivity measurements.

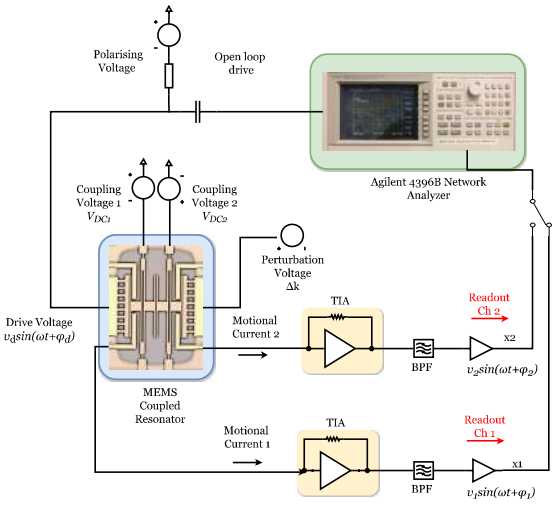


Fig. 4. Open loop measurement setup.

V. RESULTS AND DISCUSSION

To understand the effect of the coupling voltage on the cancellation regime, the motional current for each coupling voltage is measured. In this experiment, the ac drive voltage is not kept constant but is varied to achieve the critical amplitude before bifurcation occurs. Experimentally, the bifurcation point of the system is located when the resonant frequency of the response shifts greater than half of the 3dB bandwidth ($\Delta f_{peak}/\Delta f_{3dB} \geq 0.5$). From the point of bifurcation onwards, the *a-f* effect becomes considerable such that the amplitude response is multi-valued and a hysteresis is described in the frequency response. This regime is not considered for this study.

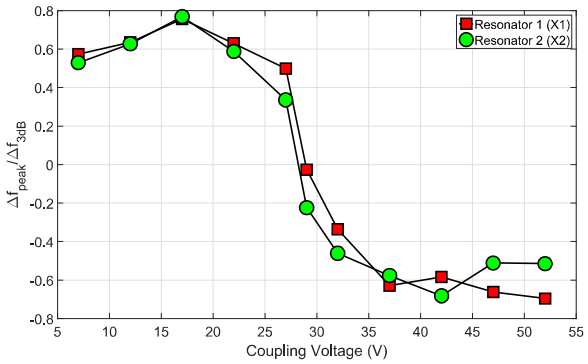


Fig. 5. Experimental ratio of peak frequency shift due to *a-f* effect and 3dB frequency (of the linear response at the same bias conditions) plotted over a swept coupling voltage in mode 1.

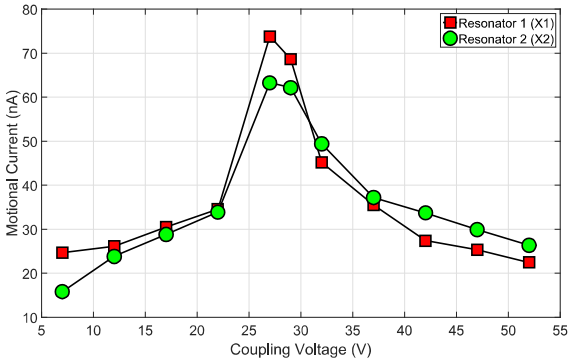


Fig. 6. Experimental motional current at critical displacement plotted against a swept coupling voltage showing non-linearity cancellation and enhancement in signal amplitude of mode 1. Peak motional current is observed between 25 and 35V coupling voltage at Vd=125mV.

The frequency response of the two resonator amplitudes (X_1 and X_2) were measured in open loop configuration. The maximum motional current and *a-f* effect at each coupling voltage were noted and plotted in Fig. 5 and Fig. 6. The *a-f* effect of mode 1 as seen in Fig. 5 reflects the cancellation occurring between 25V and 35V. At lower coupling voltages, the mechanical nonlinearities dominate the response and a positive *a-f* effect is seen. As the coupling voltage is increased, the electrical nonlinearities due to the coupler increase and compensate for the mechanical nonlinearites between 25V and 35V. Upon further increasing the coupling voltage, the electrical nonlinearities start to dominate in the system and a negative *a-f* effect is observed. Similarly Fig. 6 describes the highest motional current achieved at different coupling voltages before bifurcation occurs. Equivalent to Fig. 5, the peak motional current occurs between 25V and 35V where there is approximately 4x increase in the motional current (which translates to 12dB improvement in SNR) compared to extreme coupling voltages of 7V or 52V. Since the transduction voltages of drive and sense ports are kept constant throughout the experiment, the motional current is a good

indicator of the trend of the motional response of the two resonators.

It is to be noted that the coupling stiffness plays a significant role in the sensitivity of the WCRs. The sensitivity is inversely proportional to the coupling stiffness which signifies that it is beneficial to have a lower coupling voltages for sensing purposes. The resolution on the other hand is dependent on the amplitude of the output signal since the system is dominated by electrical noise from the amplifier circuit. Thus at lower coupling voltages, the system offers high sensitivity to stiffness perturbations but at the cancellation coupling voltage, the system offers higher output resolution. These two metrics are the most important specifications for sensor design and, in the case of WCRs, there is a tradeoff between the two metrics that needs to be considered before choosing the optimum coupling voltage for the application.

A final experiment was conducted to check the operation of the system as a sensor in the cancellation regime. The coupling voltage was set to 27V and negative stiffness perturbations in terms of voltage difference were added to resonator 2 at the perturbation port. The voltages corresponding to the motional current of both resonators were recorded at each perturbation voltage for two drive voltage levels of 12.8mV (linear drive) and 125mV (nonlinear drive). The results are shown in Figure 7.

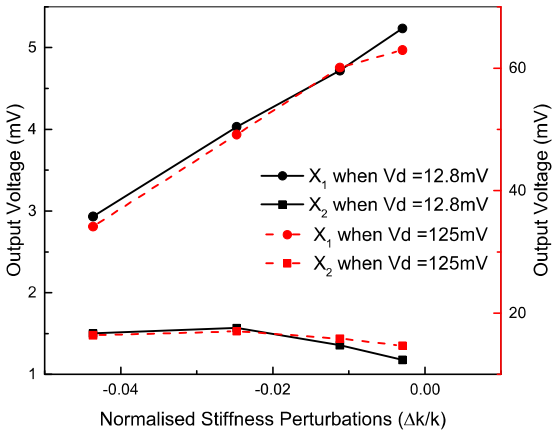


Fig. 7. Experimental amplitudes of vibration of the WCR in linear (12.8mV) and nonlinear AC drive (125mV) configurations. Output Voltage for nonlinear drive (in red and right axis) is higher than that of linear drive (in black and left axis) for both resonators X1 (circles) and X2 (squares).

The output voltage increases by a factor of 10x for both the resonators while conserving the trend of the change in amplitudes with respect to stiffness perturbations. When being used as a sensor, these stiffness perturbations can be a result of a force acting on one of the resonators due to change in tilt, acceleration or charge and thus, are a representative of any sensing applications these resonators will be used for. Since the output signal increased without compromising the sensitivity of the device, operating the system in the cancellation regime increases the signal to noise ratio and could be a potential gateway to higher resolution measurements.

VI. Conclusion and Future Work

In this work, we have demonstrated the concept of nonlinearity cancellation in WCRs through tuning the coupling voltage. The anti-phase mode is affected by the nonlinearities arising from the negative coupling while they are suppressed in the in-phase mode. It is seen that the motional current increases by a factor of 4x when the mechanical and electrical nonlinearities are compensated in the anti-phase mode. When being used as a sensor in the cancellation regime, the amplitude response for nonlinear drive is 10x higher than for a linear drive while conserving the trend of amplitude shift. This signifies a potential increase in the resolution of the amplitude measurements without compromising the sensitivity to stiffness perturbations.

Although open loop measurements allow for experimental characterization of the nonlinear cancellation phenomenon, a closed loop approach to tracking the resonant frequency is necessary for its application as a sensor or a timing reference. Parallel to this work, a closed loop approach for WCRs has been developed using a Phase Locked Loop approach and further characterizations are being made with respect to the optimum coupling for the best sensitivity and resolution.

VII. Acknowledgements

This work is supported by funding from Innovate UK and Natural Environment Research Council.

References

[1] S. Pourkamali and F Ayazi,"Electrically coupled MEMS bandpass filters: Part II. Without coupling element",*Sens. Actuators Phys.*, vol. 122, pp. 317-325, Aug. 2005.

[2] D. K. Agrawal, J. Woodhouse, and A. A. Seshia. "Observation of locked phase dynamics and enhanced frequency stability in synchronized micromechanical oscillators." *Phys. Rev. Lett.*, vol. 111, no. 8, p. 084101, Aug. 2013.

[3] H. Zhang, B. Li, W. Yuan, M. Kraft and H. Chang, "An Acceleration Sensing Method Based on the Mode Localization of Weakly Coupled Resonators," *J. Microelectromechanical Syst.*, vol. 25. no. 2,pp. 286-296, Apr. 2016.

[4] P. Thiruvenkatanathan, J. Yan, and A. A. Seshia, "Enhancing Parametric Sensitivity in Electrically Coupled MEMS Resonators," *J. Microelectromech. Syst.*, vol. 18, no. 5, pp. 10771086, Oct. 2009.

[5] C. Zhao, M. H. Montaseri, G. S. Wood, S. H. Pu, A. A. Seshia, and M. Kraft, "A Review on MEMS Coupled Resonators for Sensing Applications Utilizing Mode Localization," *Sens. Actuators Phys.*, vol. 249, no. 5, pp. 93-111, Oct. 2016.

[6] P. Thiruvenkatanathan, J. Yan and A. A. Seshia, "Differential amplification of structural perturbations in weakly coupled MEMS resonators," *IEEE Trans. Ultrason. Ferroelectr. Freq. Control*, vol. 57. no. 3,pp. 690-697, Mar. 2010.

[7] H. Zhang, J. Zhong, W. Yuan, J. Yang and H. Chang, "Ambient pressure drift rejection of mode-localized resonant sensors," in *2017 IEEE 30th International Conference on Micro Electro Mechanical Systems (MEMS)*, 2017, pp. 1095-1098.

[8] V. Kaajakari, J. K. Koskinen, and T. Mattila, "Phase noise in Capacitively Coupled Micromechanical Oscillators," *IEEE Trans. Ultrason. Ferroelectr. Freq. Control*, vol. 52. no. 12,pp. 2322-2331, Dec. 2005.

[9] M. Agarwal *et al.*, "Non-linearity cancellation in MEMS resonators for improved power-handling," *IEDM Technical Digest.*, 2005, pp. 286-289.

[10] M. Agarwal *et al.*, "Nonlinear Characterization of Electrostatic MEMS Resonators," *IEEE International Frequency Control Symposium and Exposition*, 2006, pp. 209-212.

[11] V. Kaajakari, T. Mattila,A. Oja, and H. Seppä, "Nonlinear Limits for Single-Crystal Silicon Microresonators," *J. Microelectromech. Syst.*, vol. 13. no. 5,pp. 715-724, Oct. 2004.

The Effect of Elastic Anharmonicity on The Nonlinear Behavior of Waveguide-Based AlN Resonator

Mayur Ghatge and Roozbeh Tabrizian
Electrical and Computer Engineering Department
University of Florida
Gainesville, USA
ruyam@ufl.edu; rtabrizian@ufl.edu

***Abstract*—This paper presents the effect of elastic anharmonicity in AlN film on the nonlinear performance of extensional AlN resonators. Elastic energy distribution is tailored through dispersion engineering of the waveguide to avoid boundary-induced nonlinearities and enable the study of the elastic anharmonicity contribution on the amplitude-frequency (A-f) characteristic. A 97MHz resonator with a Q of ~2,250 is demonstrated with a linear A-f coefficient of -3.47 ppm/μm² and a yield power of 5dBm. Excitation of the device beyond this yield power derives the AlN film into plastic regime and induces a hysteresis in resonator frequency response. A consistent Q over the elastoplastic cycling of the device suggests the dominant contribution of non-structural energy dissipation mechanisms.**

Keywords—elastic anharmonicity; nonlinear AlN resonator; amplitude-frequency effect.

I. Introduction

The application of aluminum nitride (AlN) Lamb-wave resonators for RF signal processing is limited by their finite dynamic range. This limit is imposed on the lower end by the relatively low Q of these resonators, and on the higher end by the performance nonlinearities. An intrinsic material property that fundamentally limits the dynamic range on either ends is the elastic anharmonicity, which is a result of nonlinear inter-molecular binding forces in solids. Elastic anharmonicity sets the energy dissipation rates through the interaction of elastic waves with thermal phonons. Also, besides nonlinearities induced by electromechanical transduction and non-ideal boundary conditions, elastic anharmonicity is partially responsible for limiting the linear operation range of AlN resonator. This paper serves as a first approach to study elastic anharmonicity and elastoplastic properties in sputtered AlN films, and the contribution of these fundamental properties on the performance of waveguide-based resonators.

II. Resonator Test-Vehicle Design

To study the effect of elastic anharmonicity, a waveguide-based resonator with tailored energy distribution is developed (Fig. 1-left). High-Q elastic energy trapping is realized through acoustic coupling of propagating and evanescent waves [1] across the length of a geometrically engineered waveguide. Proper dispersion engineering of the waveguide facilitates elastic energy localization at the central region of the waveguide and far from lateral boundaries (Fig. 1-right). This further obviates the need for narrow tethers to suspend the device [1]. These tethers are known as the major extrinsic source of the nonlinearities in bulk acoustic resonators [2].

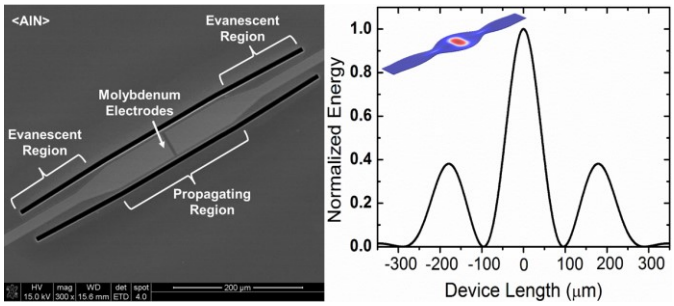


Fig. 1: The SEM of the waveguide-based AlN resonator (left) and the normalized energy distribution across device length (right). The COMSOL-simulated vibration mode shape is shown as the inset.

III. Elastic Anharmonicity Effect on Frequency

The frequency of a resonator can be related to its vibration amplitude X_0 through:

$$f_{0,non-linear} = f_{0,linear}(1 + \kappa X_0^2) \quad (1),$$

where κ, the amplitude-frequency (A-f) coefficient, represents the effect of elastic anharmonicity when the extrinsic nonlinear mechanisms (i.e. boundary-induced, transduction, etc.) are sufficiently suppressed. In such a case, κ can be related to the nonlinear elastic moduli through:

$$\kappa = \frac{9\pi^2 E_2}{16 E_0 W^2} - \frac{20 E_1^2}{3 W^2 E_0^2} \quad (2),$$

where W is the width of the waveguide in its central region and $E_{0,1,2}$ are the linear and nonlinear engineering elastic moduli of AlN (i.e. $\sigma/\epsilon = E_0 + E_1\epsilon + E_2\epsilon^2$).

IV. Resonator Characterization

Fig. 2 shows the frequency response of the waveguide-based AlN resonator. The resonance mode at ~97MHz with the desired elastic energy distribution shows a Q of 2,251, which is the highest among the three neighboring trapped width-extensional modes. As it is evident from Fig. 3, in-plane extensional AlN resonator shows spring softening effect with increased input power in elastic regime (i.e. P_{in} < 5dBm). The A-f characteristic of the resonator at this mode is extracted using digital

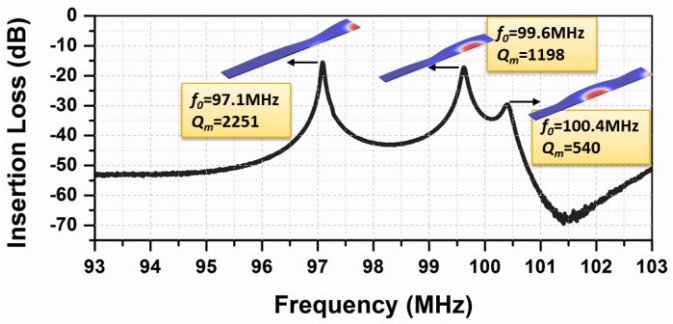


Fig. 2: The frequency response of the waveguide-based resonator indicating several resonance modes with different Q. The highest Q attributes to the desired mode with efficient energy trapping.

holographic microscope (DHM) and network analyzer, and through relating the frequency variations at different input powers to the maximum vibration amplitude as shown in Fig. 4. A κ of -3.47 ppm/μm^2 (-3.37e14 Hz/m^2) is measured through linear fitting in the elastic regime of operation (i.e. below 5dBm input power). The lower value of κ in AlN resonator compared to its undopped single crystal silicon counterpart [2] suggests the lower effect of elastic anharmonicity in sputtered AlN film on its waveguide based resonators. Application of an input power above 5 dBm (i.e. yield power) drives the device beyond the yield point of the film and into elastoplastic regime, where the frequency response is distorted around the peak (Fig. 5). Cycling the device back into the elastic linear regime results in a hystresis in the frequency response. While the shift in peak frequency can be attributed to the partial plastic deformation of the film during large excitation powers, the Q remains consistent over the elastoplastic cycling. Such a behavior is in contrary with the expected degradation in structural-dependent Q due to plastic transformation of the film and suggests the dominant effect of non-structural dissipation mechanisms [3] in limitting the Q of in-plane AlN resonators. The consistent Q, even after driving the device deep into the plastic regime, can also be attributed to the non-propagating and local elastoplastic behavior of the AlN film under in-plane elastic excitations.

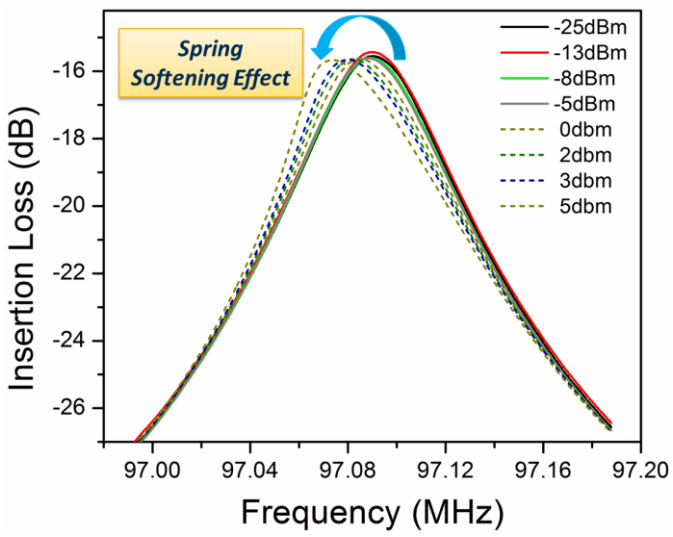


Fig. 3: The measured frequency response of the resonator for different input powers, operating in linear elastic regime.

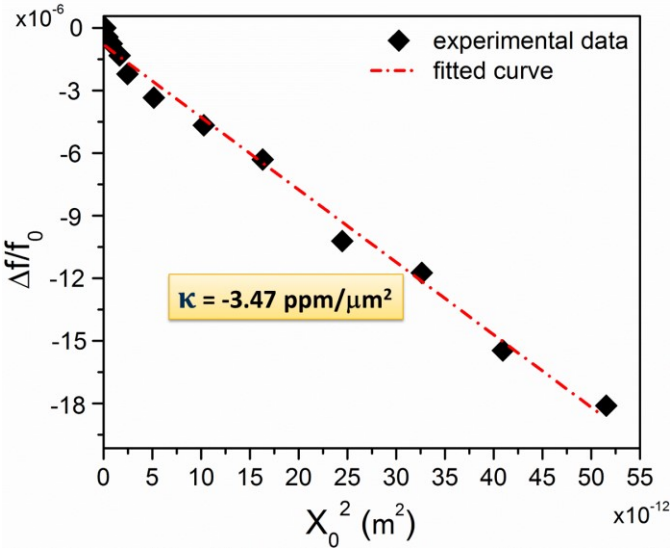


Fig. 4: The measured amplitude-frequency characteristic of the resonator. The slope of the fitted line gives the A-f coefficient κ.

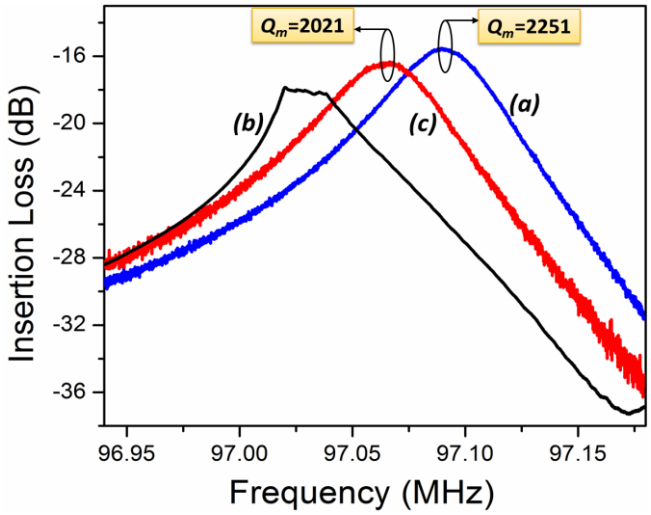


Fig. 5: The figure demonstrates the hysteresis effect observed in AlN resonators. (a) shows the frequency response at -25dBm with a Q of ~2251. The device is then forced into plastic regime of AlN with an input power of 6dBm (b). Cycling the device back into linear regime at -25dBm is shown in (c) with Q ~2021.

REFERENCES

[1] Ghatge, Mayur, Pratyusha Karri, and Roozbeh Tabrizian. "Power-insensitive silicon crystal-cut for amplitude-stable frequency synthesis." *Micro Electro Mechanical Systems (MEMS), 2017 IEEE 30th International Conference on*. IEEE, 2017.

[2] Yang, Yushi, et al. "Nonlinearity of Degenerately Doped Bulk-Mode Silicon MEMS Resonators." *Journal of Microelectromechanical Systems* 25.5 (2016): 859-869.

[3] Tabrizian, R., and M. Rais-Zadeh. "The effect of charge redistribution on limiting the kt 2. Q product of piezoelectrically transduced resonators." *Solid-State Sensors, Actuators and Microsystems (TRANSDUCERS), 2015 Transducers-2015 18th International Conference on*. IEEE, 2015.

Sensing light and sound velocities of fluids in phoXonic crystal

Y. Pennec, Y. Jin, B. Djafari-Rouhani

Institut d'Electronique, de Microélectronique et de Nanotechnologies, CNRS 8520, Université Lille, Villeneuve d'Ascq, France

***Abstract*—We discuss theoretically the new concept of dual phononic and photonic (phoxonic) crystal for sensing the light and sound velocities of fluidic analytes. We show that such a structure can support cavity modes with well confinement of both electromagnetic and acoustic fields with high quality factors. These modes give rise to peaks or dips in the transmission spectrum that are sensitive to both the acoustic velocity of sound and the optical index of refraction. Such an ultra compact structure is shown to be a label-free, affinity-based acoustic and optical nanosensor, useful for sensing applications in which the amount of analyte is often limited.**

Keywords; wave propagation; simulation; phononic; photonic; phoXonic cavity; Fano resonances; sensor

I. INTRODUCTION

Photonic crystals and their acoustic counterpart, the so-called phononic crystals, are now well-known for their ability to guide, control, and manipulate the propagation of optical and acoustic waves. These properties are mainly related to the possibility of band gaps in their band structure that allow the existence of localized modes and confined optical and acoustic waves. During the past few years, the potentiality of the phononic and photonic crystal has been gathered in a same structure, called phoXonic crystals, thus allowing dual confinement of phonons and photons. Using the simultaneous existence of phononic and photonic band gaps, defects have been introduced inside phoXonic crystal to create a cavity trap for both phonons and photons for the purpose of enhancing their optomechanical interaction [1]. These studies deal with the acoustic modulation of a confined photonic mode wavelength inside a cavity.

Our purpose is here to emphasis the potentiality of phoXonic crystal to be an efficient tool for sensing the light and sound velocities of liquids in a same structure. From the point of view of sensing applications, several papers have already shown the capability of photonic crystals for detecting small variations in the refractive index of gases and liquids and have opened the way to a platform for a new class of sensors. In contrast, phononic crystals have only been recently proposed as a possible platform for the investigation of the acoustic velocity of a liquid filling the hollow parts of the structure [2]. In this paper we discuss in details the new concept of dual phononic and photonic (phoxonic) crystal [3, 4] for sensing the light and sound velocities of fluidic analytes.

II. RESULTS

The first phoXonic structure is composed of a 2D infinite crystal made of holes drilled inside a silicon matrix. As seen in figure 1(a), all cylinders of radius r_1 are filled with air except one row of different radius r_2 in the middle of the structure which contains the fluid to be probed. In all calculations, the normalized radius of the inclusions constituting the perfect structure is fixed to $r_1/a = 0.25$ whereas r_2/a is chosen variable for the optimization of the sensor.

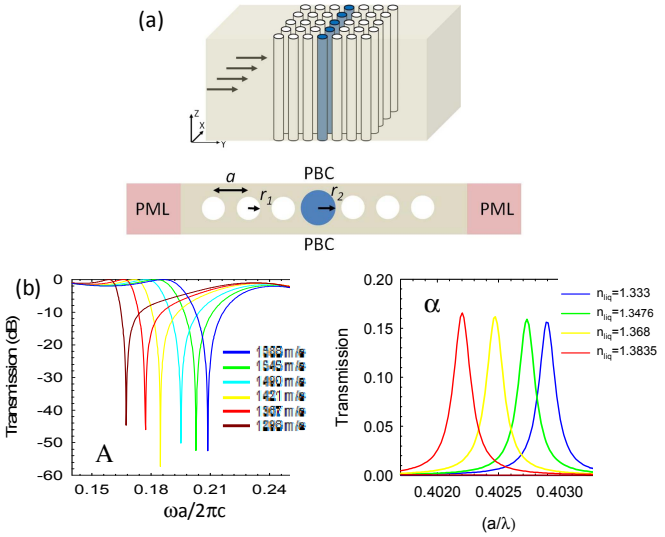


Fig. 1. Schematic representation of the 2D-phoxonic crystal containing one row of liquid filled cylinders perpendicular to the direction of propagation.

Fig. 1(b) shows the phononic and photonic transmissions coefficient through the water-filled structure when r_2/a=0.4a. The introduction of the water leads to well-defined sharp dips with high quality factors for both type of wave. In phononic, the corresponding modes are strongly confined in the water hole and solutions of the derivative of Bessel functions of an infinite water cylinder. The photonic transmission for TE modes displays peaks with a good quality factor and almost isolated in the middle of the band gap. The electromagnetic

field is not only well confined in the water-filled hole but also extend in the vicinity of the defect.

The size of the water hole has been tuned to design a structure in which the modes inside the phononic/photonic transmission spectra are well-defined and sufficiently isolated from each others. We then show that this structure can be used as a phoXonic sensor for separately sense the sound and light velocity of unknown liquids with a high sensitivity to the acoustic/optical parameters of the infiltrating liquid. The efficiency of the phoXonic sensor has been tested by changing the physical parameters of the liquid filling the central hole. We have considered a set of mixtures of water and 1-propanol at different molar ratio x. Fig. 1(b) gives respectively the evolution of the phononic (dip A) and photonic (peak α) as a function of the liquid filling the central hole (r_2/a = 0.4). The two features present clearly a shift in frequency by changing the nature of the liquid. We demonstrate that if we refer to the sound and light velocities, the acoustic and optical eigenmodes shift in the same way: an increase of the sound (light) velocity leads to a blue shift of the phononic (photonic) eigenfrequency. Finally, the efficiency of the dual phononic/photonic sensor has been tested using common parameters as the sensitivity and the figure of merit (FoM) for two sizes of the water filled cavity. We showed that, even if the two diameters can be chosen for probing the analyte, a higher sensitivity has been obtained for the smaller radius in phononic, while the larger diameter offers the higher one in photonic.

We then perform calculations on a finite phoXonic structure based on the transmissions of optical and acoustic waves normally impinging to a periodic perforated silicon plate when the embedded medium is a liquid (Fig. 2a) and show the existence of Fano-like resonances in both cases. This structure is going up the proof of concept and presents the advantage to be done experimentally. The signature of the resonances appears as well-defined asymmetric peaks in the phononic and photonic transmission spectra (Fig. 2b). We show that the origin of the Fano-like resonances is different with respect to the nature of the wave. In photonic, the origin comes from guided modes in the photonic plate while in phononic we show that it comes from the excitation of standing waves confined inside the cavity coming from the deformation of the water/silicon edges of the cylindrical inclusion. We finally use these features for sensing (Fig. 2b), and make the demonstration of the ultra-sensitivity of the dual phononic/photonic sensor to the light and sound velocities for different concentrations of analytes.

III. Conclusion

We have proposed a new class of phoXonic sensors which have the possibility to probe the light and sound velocity of unknown liquid in a same structure. Such mixed structures solid/fluid can also open the way to enhance the phonon-photon interactions with the simultaneous confinement of the phononic and photonic wave inside a same liquid cavity. We currently investigate the properties of phononic crystal plates with hollow pillars which exhibit confined whispering gallery modes around the hollow parts of the pillars [5] as sketched Fig. 3.

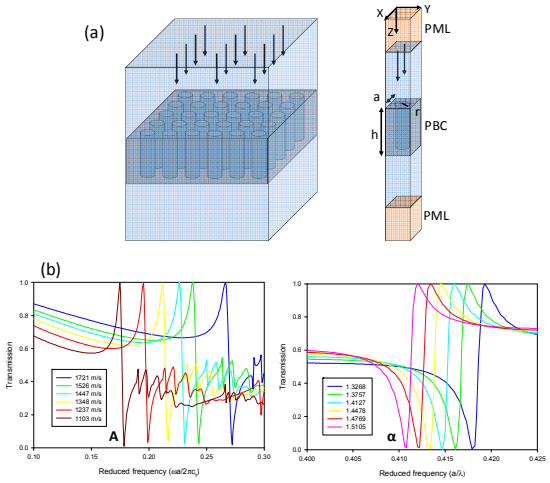


Fig. 2. (a) Three-dimensional schematic representation of a normal transmission through a silicon periodic plate embedded in a liquid. (b) (left):Evolution of the phononic transmission spectrum as a function of the acoustic velocities of the embedded medium. The inset indicates the different values of the longitudinal velocities of the probed analyte. (right): Evolution of the photonic transmission spectrum as a function of the refractive index of the liquid (*h/a=0.25* and *r/a=015*). The inset indicates the different values of the refractive index of the probed analyte

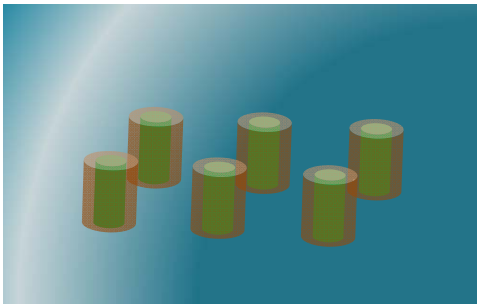


Fig. 3. Schematic view of a PnC consisting of hollow pillars deposited on top of a thin membrane, filled with water.

References

[1] Y.Pennec et al. Modeling light-sound interaction in nanoscale cavities and waveguides. *Nanophotonics*, *3*(6), 413-440 (2014)

[2] R. Lucklum, M. Ke, and M. Zubtsov, *Sens. Actuators,* B 271, 171 (2012)

[3] S. Amoudache et al., Simultaneous sensing of light and sound velocities of fluids in a two-dimensional phoXonic crystal with defects. *Journal of Applied Physics*, *115*(13), 134503, (2014)

[4] S. Amoudache et al. Optical and acoustic sensing using Fano-like resonances in dual phononic and photonic crystal plate. *Journal of Applied Physics*, *119*(11), 114502, (2016).

[5] Y. Jin, Y. Pennec, Y. Pan, & B. Djafari-Rouhani, Phononic Crystal Plate with Hollow Pillars Actively Controlled by Fluid Filling, *Crystals*, *6*(6), 64, (2016).

Design Criteria for Plasticized Polymer Coatings for Long-Term Acoustic-Wave Sensor Measurements in Aqueous Phase

Pintu Adhikari, Florian Bender, Antonio J. Ricco* and Fabien Josse
Department of Electrical and Computer Engineering, Marquette University
Milwaukee, Wisconsin 53201, United States
*Department of Electrical Engineering, Stanford University, Stanford, California 94305, United States
fabien.josse@marquette.edu

***Abstract*—This work investigates design criteria for an array of polymer-coated shear-horizontal surface acoustic wave sensors for detection of aromatic compounds directly in groundwater and wastewater. In addition to the sensitivity and selectivity issues, coating stability in water and long-term repeatability of the sensor response have been investigated. The compounds used in designing the coating have been selected according to their Hansen solubility parameters to ensure maximum chemical compatibility between the coating and the target analytes. The coatings' physical characteristics have been optimized to ensure high analyte uptake while maintaining low acoustic-wave attenuation and low spectrum distortion.**

Keywords—Plasticized polymer coatings; BTEX monitoring; groundwater monitoring; selectivity; repeatability

I. INTRODUCTION

The ultimate goal of this work is to develop a sensor system capable of long-term monitoring of groundwater, wastewater and surface water for organic contamination. Specifically, BTEX compounds (benzene, toluene, ethylbenzene, and xylene) have been selected for this study because these hazardous compounds are legally restricted in drinking water [1] and are good indicators of accidental releases of gasoline from underground pipes and storage tanks. On-site, automated, sensor-based monitoring for BTEX compounds eliminates the need for collection of groundwater samples, their shipment to a laboratory, and their analysis at an off-site location. The sensor system can be designed for installation in existing groundwater monitoring wells and allows frequent, regular measurement of BTEX concentrations in-situ in the aqueous phase.

The requirements for such sensors include low detection limits for some compounds [1], high selectivity to enable discrimination between chemically related compounds (such as BTEX) in multi-component mixtures of contaminants, and repeatability over a period of months to make this approach cost-effective over manual sampling protocols. It has been found in a previous study that only a small number of commercially available polymers exist that fulfill the above requirements when used as sensor coatings. This places a limit on the chemical selectivity that can be achieved with a sensor array. One approach taken to overcome this limitation is the design of novel sensor coatings, such as plasticized polymers [3]. In addition, it has been demonstrated that chemical selectivity can be greatly enhanced by the use of multi-variable sensor signal processing. Specifically, for a system employing shear-horizontal surface acoustic wave (SH-SAW) sensors, the combination of equilibrium frequency shift and sensor response time was found to enable high selectivity for multi-component analyte mixtures.

In the present study, SH-SAW sensor devices coated with appropriately plasticized polymers are characterized in long-term measurements by repeatedly exposing the devices to gasoline-range hydrocarbons in DI water or groundwater over the course of a few months. The changes in both equilibrium frequency shift and device insertion loss were monitored to gain insight into any physical or chemical changes that might occur in the sensor coating, such as formation of defects or loss of plasticizer from the polymer. Finally, results are presented on detection of BTEX compounds in water using plasticized and unplasticized polymer sensor coatings. It was found that the use of plasticized polymer coatings enhances the sensitivity of the sensor devices to all BTEX compounds. The highest chemical selectivity was obtained when combining plasticized and unplasticized coatings in a sensor array.

II. RESULTS AND DISCUSSION

Commercially available sensor coatings, poly(isobutylene) (PIB) and poly(epichlorohydrin) (PECH), have previously been identified as suitable for long-term BTEX monitoring directly in water [2]. Here, various plasticized polymer coatings are investigated for the same purpose. Both the polymer and the plasticizers were selected to match the Hansen solubility parameters of the BTEX compounds [3] as well as to ensure compatibility between plasticizer and polymer. The percentage of plasticizer in the coating was varied with the dynamic glass transition temperature of the blend in mind [4]. In brief, the dynamic glass transition temperature of the blend at low probing frequencies should be below ambient temperatures to enable rapid and efficient analyte uptake, but the dynamic glass transition temperature at the SH-SAW frequency (103 MHz in this case) should be above ambient temperatures to minimize acoustic-wave attenuation in the sensor coating [3],[4].

Fig. 1 shows the SH-SAW passband for a device coated with a 0.7 µm thick layer of polystyrene (PS) plasticized with 22.9% w/w diisooctyl azelate (DIOA). Coating thickness and plasticizer/polymer mixing ratio of the coatings were varied to find the best combination for high analyte sorption capacity and low acoustic-wave loss. This was done for two plasticizers, DIOA and DINCH (diisononyl cyclohexane-1,2-dicarboxylate), which show negligible solubility in water.

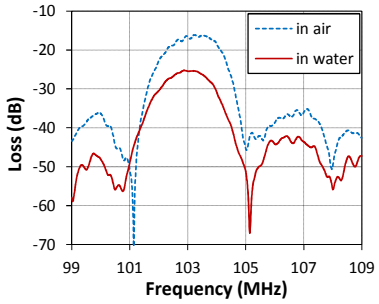


Fig. 1. Frequency spectra for an SH-SAW device coated with 0.7 µm 22.9% DIOA-PS in air and in water. The SH-SAW center frequency is 103 MHz.

Generally, the physical integrity of a sensor coating can be compromised in long-term measurements in aqueous phase. In the case of plasticized polymer coatings, no significant amount of plasticizer should be lost from the coating over its lifetime (i.e. negligible leaching). To test for both types of coating degradation, the sensor response to BTEX compounds as well as the insertion loss of the device were tracked over the course of a few months of use to determine the effects of the viscoelastic properties of the coatings. Both the frequency shift, Δf, and change in attenuation, $\Delta\alpha$, can be described as functions of the shear modulus: $\Delta f = g_1(\Delta m, \Delta G', \Delta G'')$ and $\Delta\alpha = g_2(\Delta G', \Delta G'')$ (m -mass density; G'-storage modulus; G" loss modulus). For various sensors and coatings, only small changes in sensor response (equilibrium frequency shift) over time were observed that are not deemed significant. This was different for the observed change in insertion loss over time, as shown for various DINCH-PS coatings in Fig. 2. Note that coating thickness is given in Fig. 2 in units of SH-SAW wavelength, $\lambda = 40$ µm, corresponding to absolute thicknesses of 0.8 – 1.3 µm. It was observed that an insertion loss of greater than about 35 dB resulted in excessive baseline noise; devices reaching this limit were therefore no longer used. The observed slow increase in insertion loss is probably related to polymer creep, which was found to lead to a slow formation of defects in the polymer over the course of months, as confirmed by optical microscopy.

Finally, measurements on detection of BTEX compounds were conducted using a variety of plasticized and unplasticized polymer coatings to see how the former can contribute to the chemical selectivity of a sensor array. An example is shown in Fig. 3. It can be seen that the ratios of frequency shifts of two coatings greatly differ among the different BTEX compounds if the ratio for a plasticized and an unplasticized coating is plotted, indicating that this combination of coating materials increases the chemical diversity of the sensor array. Generally, plasticized coatings also gave larger sensitivities to BTEX compounds than unplasticized coatings. In conclusion, it was shown that, following proper design guidelines, the use of plasticized polymer coatings in a sensor array greatly benefits the sensitivity and selectivity of the array while enabling long-term monitoring for aromatic compounds directly in aqueous phase. To further test the potential of this approach, actual measurements are planned on samples containing multiple analytes.

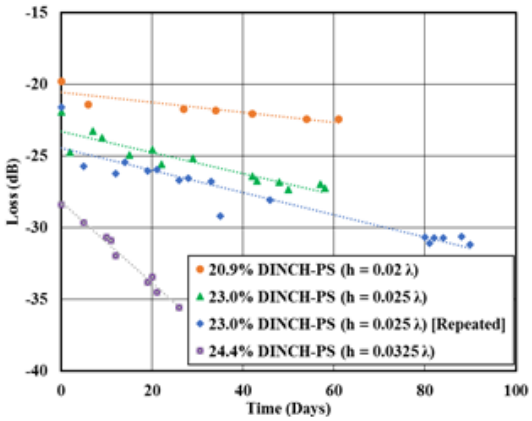


Fig. 2. Insertion loss (shown in negative dB) vs. time for SH-SAW sensors coated with DINCH-PS blends. Plasticizer-polymer mixing ratios and coating thicknesses (in units of the wavelength, $\lambda = 40$ µm) are indicated in the graph.

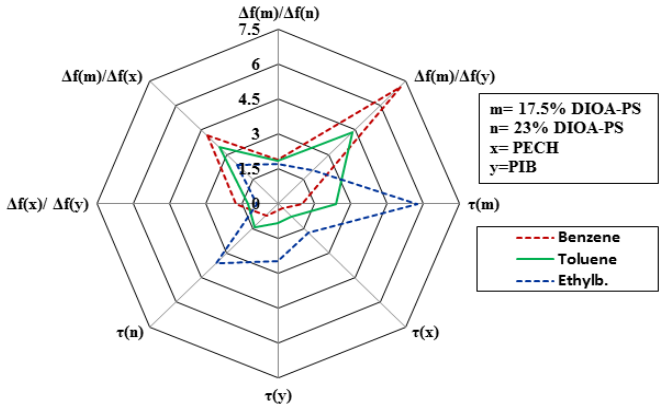


Fig. 3. Radial plot showing the response time constants, τ (in units of 100 s), and the ratios of equilibrium frequency shifts, Δf, for SH-SAW sensors for the coatings and analytes indicated in the graph.

ACKNOWLEDGMENT

The authors wish to thank Laura Alderson for valuable assistance with the measurements on DINCH-PS.

REFERENCES

[1] National Primary Drinking Water Regulations; United States Environmental Protection Agency: Washington, D. C., May 2009.

[2] F. Bender, R.E. Mohler, A.J. Ricco, and F. Josse, "Identification and Quantification of Aqueous Aromatic Hydrocarbons Using SH-Surface Acoustic Wave Sensors", Anal. Chem., vol. 86, pp. 1794–1799, 2014.

[3] P. Adhikari, L. Alderson, F. Bender, A.J. Ricco, and F. Josse, "Investigation of Polymer−Plasticizer Blends as SH-SAW Sensor Coatings for Detection of Benzene in Water with High Sensitivity and Long-Term Stability", ACS Sens., vol. 2, pp. 157–164, 2017.

[4] S.J. Martin, G.C. Frye, and S.D. Senturia, "Dynamics and Response of Polymer-Coated Surface Acoustic Wave Devices: Effect of Viscoelastic Properties and Film Resonance", Anal. Chem., vol. 66, pp. 2201–2219, 1994.

Piezoelectric Transduction of a Button-like Mode Disk Resonator for Enhanced Quality Factor in Water

Abid Ali, *Student Member, IEEE*
Department of Electronic Engineering, City University of Hong Kong, Kowloon, Hong Kong.
abidali2-c@my.cityu.edu.hk

Joshua E.-Y. LEE, *Senior Member, IEEE*
State Key Laboratory of Millimeter Waves, City University of Hong Kong, Kowloon, Hong Kong.
josh.lee@cityu.edu.hk

***Abstract*—We present a unique lateral bulk resonance mode with a lateral strain profile that resembles a shirt button that we transduce piezoelectrically in a MEMS disk resonator. This button-like (BL) mode offers the 3-fold benefits of (1) intrinsic feedthrough cancellation using fully-differential transduction, (2) strong piezoelectric coupling from the associated strain profile, and (3) higher quality (Q) factor compared to the fundamental wine glass (WG1) mode in water. These above features make the BL mode highly attractive when applying MEMS resonators to mass sensing in liquid. We demonstrate enhancements in Q factor by 68% to a Q factor of 265 and 41% increase in the coupling factor (k_t^2) relative to the WG1 mode when transducing in water, leading to a signal-to-background ratio (SBR) of 28.1 dB even in water.**

***Keywords*—Viscous damping, MEMS resonator, piezoelectric-on-silicon technology**

I. INTRODUCTION

Micro- and nano- electromechanical (M/NEM) resonant structures have been of interest for various biological sensing applications such as medical diagnosis, blood coagulation monitoring, mixture solution analysis and drug discovery [1-3]. But the electrical transduction of micro- and nano- scale resonators in liquids for bio-sensing is particularly challenging compared to ambient conditions in air [4-6]. Electrical transduction of MEMS resonators in liquids have two major challenges: (1) significant reductions in the resonant peak due to heavy damping of the quality (Q) factor, and (2) notable increases in background signal interference coupling between the drive and sense port of the device through the liquid that typically possesses a high dielectric constant [7]. These two factors combined greatly weaken the signal-to-background (SBR) ratio of the electromechanical signal output, presenting a challenge for tracking the resonance peak particularly when the SBR is low.

Pursuant to addressing the above issues, we here present a unique lateral resonance mode that we call the button-like (BL) mode due to the resemblance of its strain profile to a shirt button. The novel BL mode is based on a disk resonator, of which previous works have reported the piezoelectric transduction of the fundamental wineglass (WG1) mode [8]. Compared to the WG1 mode, the BL mode presented here offers both higher Q factor when limited by damping in water and higher electromechanical coupling factor (k_t^2). Besides, the BL mode retains the WG1 mode's benefit of feedthrough cancellation (to reduce background interference) using fully-differential transduction. The above benefits are experimentally demonstrated in the rest of this paper. For reference, we also present results for what we think resembles a second order wine glass (WG2) mode, which though shows higher Q factor suffers notable reduction in k_t^2 relative to the BL mode.

In the next section, we describe the simulated results of all three modes particularly with regards to the strain profile of the disk resonator. In Section III, we present the experimental results of measuring the various modes in water where the results of loading the water on the resonator from the front side and backside of the device are compared.

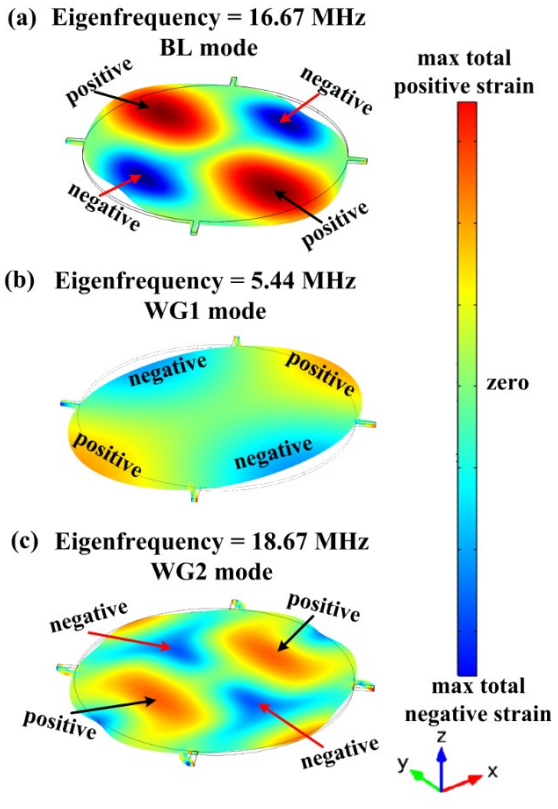


Fig. 1. Finite element (FE) simulation of the (a) button-like (BL), (b) fundamental wineglass (WG1), and (c) 2nd order wineglass (WG2) modes for a disk resonator with a radius of 400 µm. Color contours denote the sum of lateral strains: red for max positive, blue for max negative, and green for zero.

The work described in this paper was supported by a grant from the Research Grants Council of Hong Kong (*project number: CityU 11206414*).

II. Device Concept and Simulations

Fig 1 shows to the finite element (FE) simulation of the BL, WG1 and WG2 modes using COMSOL where the contours on the disk resonator denote the sum of lateral strains in the x (ε_x) and y (ε_y) axes. It can be seen that the net lateral strain ($\varepsilon_x + \varepsilon_y$) profile is anti-symmetric for all 3 modes. As such, all 3 modes offer the possibility of fully-differential electrical transduction (i.e. differential drive and differential sense) implemented with the electrode configuration shown in the micrograph given in Fig. 2. As seen from the micrograph of the fabricated disk resonator, the surface of the disk is divided equally into four quadrants, with one electrode covering one quadrant. Fully-differential transduction allows intrinsic cancellation of electric fields that couple between the piezoelectric transducers. We also see the basis of higher k_t^2 from the BL mode relative to the WG1 mode from the strain profiles. With reference to the modified Butterworth Van Dyke (MBVD) equivalent circuit model shown in Fig. 3, k_t^2 is approximated using the ratio of the motional capacitance (C_m) over the transducer capacitance (C_0) at either the input or output ports, i.e. $k_t^2 \approx C_m / C_0$. In the WG1 mode, the regions of maximum strain are limited to the edges of the disk.

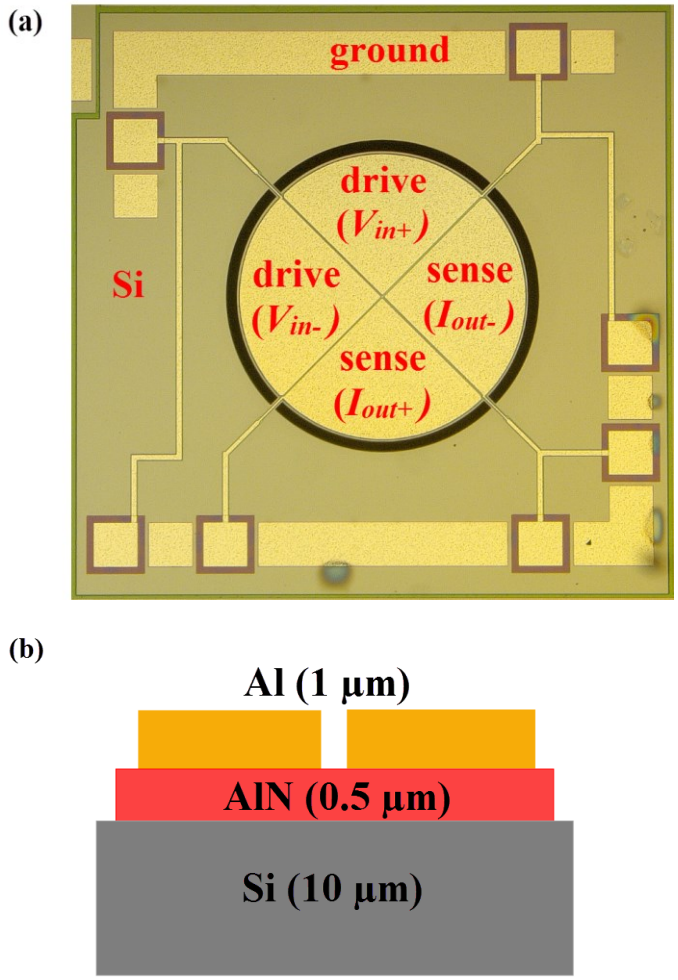


Fig. 2. (a) Micrograph of fabricated AlN on Silicon disk resonator labeled with the fully-differential transduction configuration; (b) Cross-sectional view showing the different film layers and their thickness.

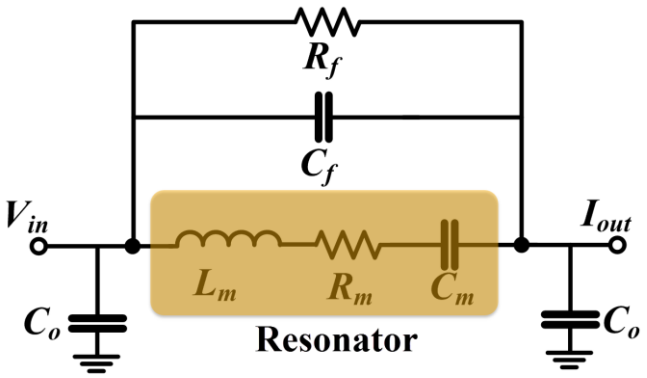


Fig. 3. Modified Butterworth Van Dyke (MBVD) equivalent circuit model of representing the key lumped parameters for electrical characterization of piezoelectric resonator in water.

In the BL mode, the regions of maximum strain center in each quadrant of the disk, thereby increasing the coupling area for maximum relative strain for the same static capacitance as seen by the piezoelectric transducers. This leads to higher k_t^2 in the BL mode compared to the WG1 mode. The WG2 mode, in contrast to the two other modes above, is marked by alternating regions of opposite strains along the x and y axes. As such, covering each quadrant of the disk with a single electrode as we have done here (Fig 2a) leads to some degree of mutual cancellation between opposite strains in the specific case of the WG2 mode. This effectively lowers k_t^2 for the WG2 mode as will be seen later from the experiments. The resonator was fabricated in an Aluminum Nitride (AlN) on Silicon-on-Insulator (SOI) micromachining process. As shown in Fig. 2b, a low resistivity silicon (Si) device layer acts as the ground electrode for the piezoelectric transducer stack comprising 1 µm Al, 0.5 µm AlN, and 10 µm Si.

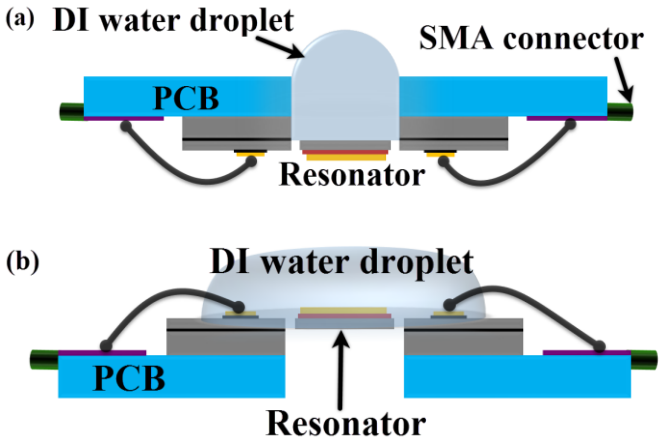


Fig. 4. Schematic cross-sectional view showing the piezoelectric AlN-on-Si MEMS disk resonator mounted and wire bonded on a custom-designed PCB with a DI water droplet loaded on the (a) back and (b) front side respectively.

III. Experimental Results

The fabricated die was mounted on a custom-designed printed circuit board (PCB) with wire bonds to connect between the bond pads on of the device and tracks on the PCB. As shown in Fig 4, a hole has been cut through the PCB where

the die is to be mounted. The hole in the PCB is sealed on the topside by the MEMS die. This setup exposes the backside of the resonator where contact with water can be made, thereby isolating the water droplet from the electrical contacts (Fig 4a) as opposed to adding the water droplet from the front side (Fig 4b). The device was transduced using the fully-differential configuration shown in Fig 2a with an RF input power of 0 dBm (applied to all subsequent measurements). It is worth noting that although the sides of the resonator are not sealed like a membrane, the surface energy between silicon and water as well as the surface tension at the water-air boundary is sufficient to prevent water from flowing through the gaps for the moderate volumes of water we are using (10-15 µl).

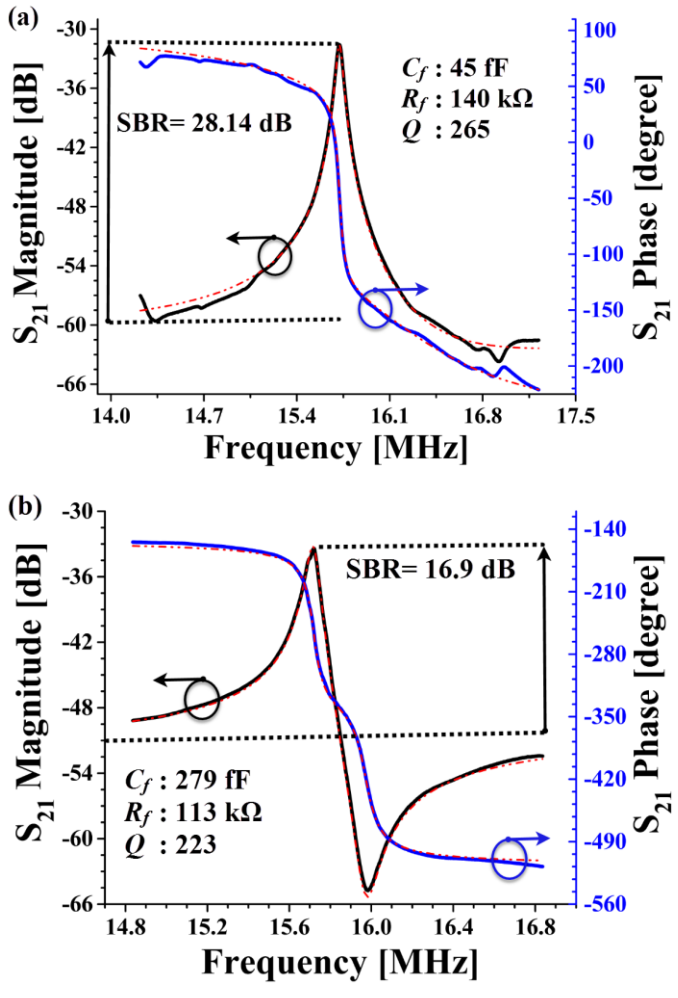


Fig. 5. Measured transmission S_{21} of the BL mode (the red broken lines represent the model curve fit based on a MBVD) when (a) water was added from the backside and (b) water was added from the front side.

Fig 5a shows the transmission S_{21} of the BL mode, measured using a network analyzer, with water added to the resonator from the backside. Due to the effective cancellation of feedthrough and strong coupling, we obtain an SBR of 28.1dB. The maximum feedthrough capacitance from three device samples measured is only 45 fF. To ensure that the bottom surface of the resonator is indeed in contact with water, we also measured the S_{21} with water added from the front side instead. From Fig 5b, we see that the SBR is only 16.9 dB when water was added from the front side due to the high feedthrough because of contact between the water droplet and electrical connections. The Q factors of the resonator measured with water added from the front side and backside are comparable, indicating that the viscous damping conditions are consistent. Fig 6a shows the measured S_{21} for the WG1 mode and Fig 6b for the WG2 mode when water was added from the backside. Comparing the WG1 mode to the BL mode, we see a reduction in the SBR (due to a lower C_m), a lower Q factor, and the appearance of nearby spurious modes. Comparing the WG2 to BL mode, we see a reduction in the SBR (due to a lower C_m) but higher Q factor.

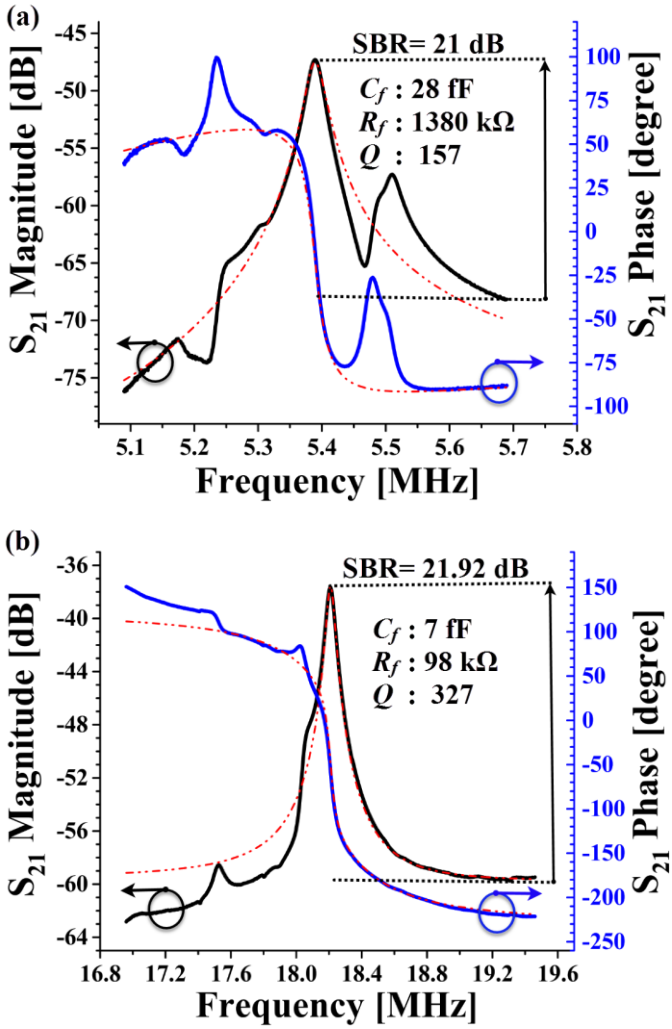


Fig. 6. Measured transmission S_{21} of the (a) WG1 mode and (b) WG2 mode when water has been added from the backside (the red broken lines represent the model curve fit based on a MBVD).

IV. Discussion

Three devices were measured for each of the modes in water from frontside and backside. The extracted results using the MBVD model (refer to Fig. 3) fit are summarized in Fig 7. It can be seen from Fig. 7 that C_m for the BL mode is 41% higher than the fundamental WG1 mode. Given that the static transducer capacitance (i.e. C_0) is the same for all mode, we

can conclude that k_t^2 for the BL mode is higher than then WG1 mode. Combined with 68% increase in Q factor for the BL mode over the WG1 mode, the BL mode offers an increase of 2.4 times in k_t^2Q. It is worth noting that the present electrode layout of the device has not been tailored specifically for the BL mode. As such, there is still room for further improving k_t^2 by modifying the electrode pattern to cover only the regions of maximum strain. As such, we can expect further increases in k_t^2Q. The significant decrease (64%) in k_t^2 for the WG2 mode relative to the WG1 mode is due to the poor match between the electrode design and the WG2 mode characterized by alternating bands of opposing strains. The WG2 mode offers a further 23% increase in Q factor over the BL mode. The k_t^2Q for the BL mode is 2.3 times higher than the WG2 mode. Based on previous observations of the effect of resonator size on Q factor for the WG1 mode damped in water [9], we envisage that Q factors of over 500 are achievable with the BL mode by reducing the disk radius.

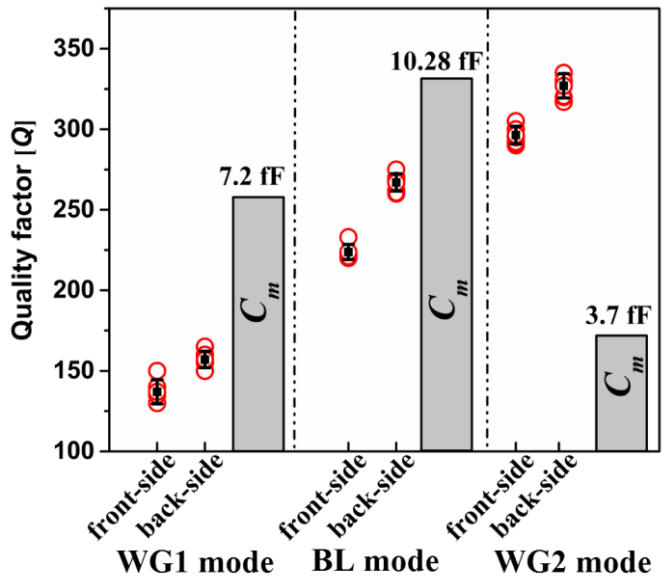


Fig. 7. Comparison of Q factors of BL, WG1, and WG2 modes electrically characterized in water with the water droplet added from either the front side or backside of the MEMS disk resonator.

V. CONCLUSION

In this work, we have proposed a unique lateral bulk resonance mode with a lateral strain profile that resembles a shirt button which we call the button-like (BL) mode. We have shown that the BL mode offers higher a coupling factor compared to the fundamental WG1 and higher order WG2 modes for the same disk resonator. The lateral strain profile of BL mode is well-suited for fully-differential transduction setup, allowing feedthrough cancellation to greatly improve the signal-to-background ratio (SBR). Apart from providing higher k_t^2, we have also shown that the BL provides a higher Q factor by 68% in water compared to the WG1 mode. In terms of k_t^2Q, the BL mode provides an enhancement of 2.4 times.

REFERENCES

[1] W. Xu, J. Appel and J. Chae, "Real-time monitoring of whole blood coagulation using a microfabricated contour-mode film bulk acoustic resonator," *J. Microelectromech. Syst.* vol. 2, pp. 302-307, 2012.

[2] L. Su, W. Jia, C. Hou, and Y. Lei, "Microbial biosensors: a review," *Biosens. and Bioelectr.,* vol. 26, no. 5, pp.1788-1799, 2011.

[3] P. S. Waggoner, and H. G. Craighead, "Micro-and nanomechanical sensors for environmental, chemical, and biological detection," *Lab on a Chip*, vol. 7, no. 10, pp. 1238-1255, 2007.

[4] F. Yu, J. Wang, P. Xu, and X. Li, "A tri-beam dog-bone resonant sensor with high-Q in liquid for disposable test-strip detection of analyte droplet," *J. Microelectromech. Syst.*, vol. 25, no. 2, pp. 244-251, 2016.

[5] D. Ramos, J. Tamayo, J. Mertens, M. Calleja, and A. Zaballos, "Origin of the response of nanomechanical resonators to bacteria adsorption," *J. App. Phys.*, vol. 100, no. 10, pp. 106105, 2006.

[6] A. Ali and J. E.-Y. Lee, "Single device on-chip feedthrough cancellation for enhanced electrical characterization of piezoelectric-on-silicon resonators in liquid," *Sens. Actuator A-Phys.* vol. 260, pp. 131-138, 2017.

[7] A. Ali and J. E.-Y. Lee, "Electrical characterization of piezoelectric-on-silicon contour mode resonators fully immersed in liquid," *Sens. Actuator A-Phys.* vol. 241, pp. 216-223, 2016.

[8] M.Y. Elsayed, P. V. Cicek, F. Nabki and M. N. El-Gamal, "Bulk mode disk resonator with transverse piezoelectric actuation and electrostatic tuning," *J. Microelectromech. Syst.* vol. 25, pp. 252-261, 2016.

[9] A. Ali and J. E.-Y. Lee, "Fully-differential AlN-on-Si wine glass mode resonator for enhanced characterization in water," *IEEE Sensors Conf.* pp. 1-3, 2016.

Spin-Coated Piezoelectric-Polymer Composite based Acoustic Resonators and Transducers

Pallabi Das and Siddharth Tallur
Department of Electrical Engineering, IIT Bombay
Mumbai, India
daspallabi@ee.iitb.ac.in, stallur@ee.iitb.ac.in

***Abstract*—We present a novel composite comprised of piezoelectric PMN-PT nanoparticles embedded in a SU8 polymer matrix that can be spin coated on any substrate to realize acoustic resonators and transducers. High Overtone Bulk Acoustic Resonators (HBARs) are fabricated using this novel composite on a low acoustic loss silicon substrate. Initial experimental results yield piezoelectric coefficient (d_{33}) as high as 216pm/V for the composite, indicating the possibility of designing efficient acoustic transducers.**

Keywords—Piezoelectric-polymer composite, PMN-PT, HBAR, polymer

I. Introduction

Surface Acoustic Wave (SAW) based devices form the basis of high resolution sensors in various applications [1]–[3]. Another common type of acoustic resonator used in bio-sensing in liquid environments is the thickness shear mode (TSM) resonator [4], [5]. The materials commonly employed for SAW devices and for sensors are quartz (SiO_2), lithium niobate ($LiNbO_3$), and lithium tantalate ($LiTaO_3$). The propagation of the SAW depends on the geometry of the substrate, and the crystal cut angle and quality of the film are important determinants of the sensor performance. While zinc oxide (ZnO) films sputtered at room temperature are efficient transducers for High Overtone Bulk Acoustic Resonators (HBARs) [6], other deposition techniques involve higher temperature processing or specialized equipment, in addition to specific requirements on the material and crystallographic orientation of the substrate.

In this paper, we present a novel approach based on fabricating polymer based high frequency acoustic transducers, by embedding nanoparticles of a piezoelectric material in the polymer. The piezoelectric-polymer composite can be deposited on a variety of substrates via spin coating, thus allowing us the flexibility to work with a broad range of materials. Here we report the fabrication of a silicon substrate HBAR using lead magnesium niobate-lead titanate (PMN-PT)/SU8 nanocomposite. Initial experimental results suggest a high d_{33} of 216pm/V for the composite, indicating that it could be a useful material for designing high efficiency transducers.

II. Device Design and Fabrication

HBARs are comprised of thin film piezoelectric materials sandwiched between metal electrodes which are solidly mounted on low acoustic loss substrates. We choose silicon as the low loss acoustic substrate, and chromium/gold bilayer for the metal electrodes. The PMN-PT/SU8 as the piezoelectric film, to study the efficiency of using a polymer based material for such a transducer. In our devices, we do not pattern the bottom metal. The PMN-PT/SU8 composite is patterned to define circular shaped transducers, and the top metal is patterned to align with the composite.

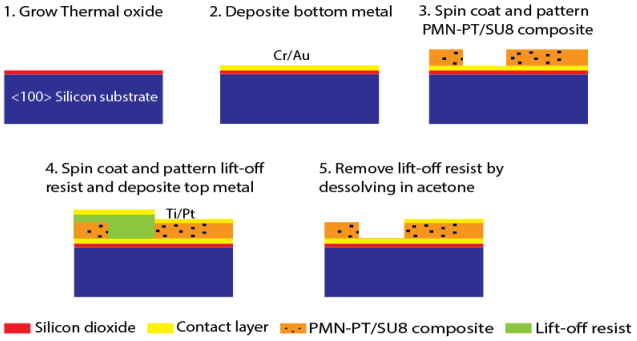


Fig. 1. Schematic of the fabrication process flow.

The composite solution is created by first ball-milling PMN-PT relaxor ferroelectric bulk crystals with SU8 2002 for 12 hours. This facilitates the PMN-PT powder to be dispersed in the solvent. Following this step, we probe sonicate the solution with SU8 thinner to get 7% by volume PMN-PT/SU8 composite. The fabrication process starts with growth of 200nm silicon dioxide on a <100> oriented double-side polished high resistivity n-type silicon wafer, to ensure no substrate leakage. Then we sputter 20nm/200nm chromium/gold as the bottom metal. The PMN-PT/SU8 composite is deposited on the bottom metal via spin coating to form a 3µm thick layer. SU8 is a negative photoresist, and hence the composite is patterned using photolithography and resist developer. For better dispersion of the composite layer on the gold we use Omnicoat as an adhesive layer. The top metal is deposited by sputtering 15nm/150nm thick chromium/gold, which is patterned by performing lift-off photolithography. Figure 1 shows a sketch of the fabrication process flow. Figure 2 shows the SEM image of the fabricated device and X-Ray Diffraction (XRD) spectrum of the composite, where the various crystalline planes of PMN-PT are visible in the matrix.

III. Experimental Results

We perform domain engineering (poling) of the piezoelectric PMN-PT particles in the polymer matrix using an Asylum MFP3D Origin conductive Atomic Force Microscope (c-AFM).

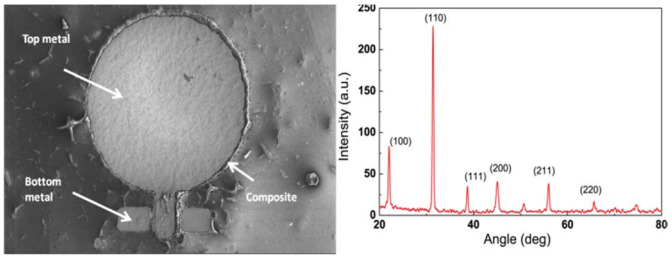


Fig. 2. (Left) Scanning electron micrograph (SEM) image of HBAR device. (Right) X-ray diffraction spectrum of PMN-PT/SU8 composite showing various crystalline planes of PMN-PT in the polymer matrix.

The tip is scanned repeatedly across the sample to align the domains in every particle to maximize the piezoelectric coefficient (d_{33}). The d_{33} is measured by performing Piezoresponse Force Microscopy (PFM) in the same setup. PFM is based on the detection of local deformation of a ferroelectric material induced by an external electric field. In our experiment, we apply 10V DC voltage to the tip and scan across a 20µm x 20µm area of the film. The d_{33} is obtained as slope of the PFM response curve, and is recorded following every scan. The largest d_{33} recorded on our sample was 216pm/V, as seen in Figure 3. Other values of bias voltage are to be explored to maximize the piezoelectric coefficient. RF experiment is performed after poling the device at 40V for 15 minutes using dc source meter. The reflection coefficient S_{11} was then obtained on a poled device by the use of a vector network analyser. The measured reflection coefficient in dB is shown in Figure 5. The sharp dips in the S_{11} data shows the resonance peaks at different frequencies.

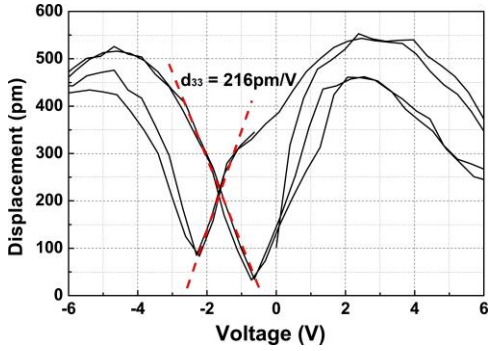


Fig. 3. High d_{33} of 216pm/V recorded on PMN-PT/SU8 composite.

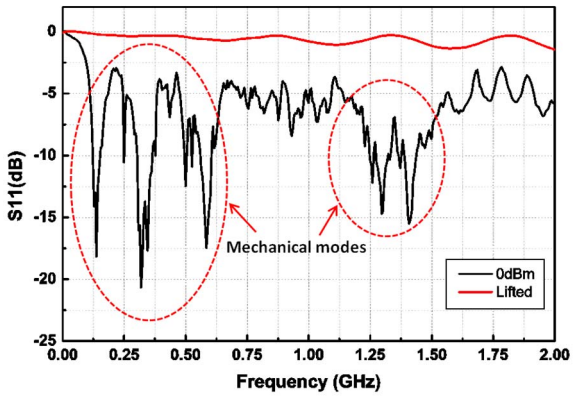


Fig. 4. Reflection coefficient S_{11} plotted as a function of frequency. The sharp dips show the resonant frequencies. To confirm this dips are indeed of mechanical origin we lifted the probe and performed the same measurement shown in red curve which doesn't show the resonances.

IV. Conclusion

We present a novel piezoelectric-polymer composite based on PMN-PT nanoparticles embedded in a SU8 polymer matrix. The polymer serves as a binder for the piezoelectric particles, and can be deposited via spin coating. The composite is also easily patternable via photolithography. Using a conductive AFM, we were able to successfully demonstrate domain engineering of the PMN-PT particles and recorded d_{33} as high as 216pm/V. We also successfully fabricated HBAR transducers using the composite film on a low acoustic loss silicon wafer substrate. RF measurements of this HBAR resonator using polymer film shows mechanical modes present at multiple-GHz frequencies.

Acknowledgment

We acknowledge the support of the Ministry of Electronics and Information Technology (MeitY) of the Government of India through the Centre of Excellence in Nanoelectronics (CEN) and IITBNF staff for help with fabrication.

References

[1] A. Pohl, "A Review of Wireless SAW Sensors," *IEEE Trans. Ultrason. Ferroelectr. Freq. Control*, vol. 47, no. 2, pp. 317–332, 2000.

[2] M. Thompson and G. L. Hayward, "Mass response of the thickness-shear mode acoustic wave sensor in liquids as a central misleading dogma," *Proc. Int. Freq. Control Symp.*, pp. 114–119, 1997.

[3] K. Länge, B. E. Rapp, and M. Rapp, "Surface acoustic wave biosensors: A review," *Anal. Bioanal. Chem.*, vol. 391, no. 5, pp. 1509–1519, 2008.

[4] R. D. Williams, A. K. Upadhyayula, and V. R. Bhethanabotla, "High frequency thickness shear mode devices for organic vapor sensing," *Sensors Actuators, B Chem.*, vol. 122, no. 2, pp. 635–643, 2007.

[5] M. Thompson, A. L. Kiplingt, and W. C. Duncan-hewitts, "Thickness-shear-mode Acoustic Wave Sensors in the Liquid Phase: A Review," *Analyst*, vol. 116, no. September, pp. 881–890, 1991.

[6] T. A. Gosavi, E. R. Macquarrie, and G. D. Fuchs, "HBAR as a High Frequency High Stress Generator," *Proc. - IEEE Ultrason. Symp. Taipei, Taiwan*, pp. 1–4, 2015.

High-stability laser using Ramsey-Bordé Interferometry

J. Olson, R. Fox, R. Brown, T. Fortier, Todd Sheerin, C. W. Oates, and A. D. Ludlow
Time and Frequency Division
National Institute of Standards and Technology
Boulder, CO USA
judith.olson@colorado.edu
ludlow@boulder.nist.gov

***Abstract*—We describe a system for high-performance laser stabilization using Ramsey-Borde interferometry with calcium.**

Keywords—optical clock, optical frequency standard, atomic clock, calcium, stabilized laser

I. INTRODUCTION

The conventional approach for state-of-the-art laser stabilization utilizes high-Q Fabry-Perot cavities. By frequency locking a laser to the optical mode of a carefully-designed and highly-isolated cavity, 10^{-16} laser frequency stability has been achieved over short timescales, making these stabilized oscillators very-well-suited to a wide range of applications, from optical clocks to low-noise-microwave generation. Present research efforts explore cryogenically-cooled optical cavities, as a way to reduce the thermal-mechanical fluctuations that typically limit the obtainable frequency stability. Here we report on a fundamentally distinct approach for realizing state-of-the-art laser stabilization, using high resolution spectroscopy of calcium in a Ramsey-Borde interferometer.

II. LASER STABILIZATION

Ramsey-Borde (RB) interferometry [1] is a powerful-spectroscopic tool that allows narrowband atomic and molecular resonances to be measured with high resolution in a Doppler-free configuration. Significantly, this technique can be applied to large atom samples with even a broad velocity distribution. RB spectroscopy on atomic calcium has a rich history spanning several decades of research on both thermal and laser-cooled systems (e.g. [2-5]). Here we employ RB spectroscopy to measure the frequency of the low-lying $^1S_0$-$^3P_1$ intercombination transition in a high-flux, collimated beam of thermal atomic calcium.

RB interferometry requires four laser-atom interaction zones, two each from opposing directions. High spectral resolution relies on sizeable distances between interaction zones, in order to achieve long Ramsey free-evolution-times. To realize this laser configuration with the strict angular tolerances required by RB interferometry, we utilize a monolithic, ultra-low-expansion (ULE) glass assembly which shares the same vacuum housing as the atomic beam. The ULE assembly includes optically contacted mirrors to generate the four laser interaction zones from a single input laser source. The resulting RB zones offer a ~1.5 kHz spectral linewidth for the thermal calcium beam utilized.

Measurement of the RB spectroscopic fringes can be made by monitoring photon fluorescence from natural decay out of the excited $^3P_1$ state. However, to reduce photon-shot-noise limitations in the fringe measurement, we employ a variant on electron-shelving detection with a 431nm cycling transition from the $^3P_1$ excited state to a doubly-excited $^3P_0$ state. This laser-induced-fluorescence offers orders-of-magnitude improved photon flux compared to natural decay from $^3P_1$, thus enhancing the measurement signal-to-noise.

Even though RB interferometry is a Doppler-free technique, it is known to suffer from residual first-order Doppler effects due to, for example, imperfect interferometer alignment. These residual first-order shifts can be large, and can thus compromise the achievable frequency stability at all timescales derived from a RB system. To mitigate these effects, our system employs dual, counter-propagating calcium beams, as well as independent detection of each atomic beam. Both atomic beams traverse the same laser-interaction zones, so that key residual Doppler shifts are equal and opposite for the opposing atomic beams. By stabilizing the laser frequency simultaneously to RB fringes from both atomic beams, residual first-order Doppler effects can thus be suppressed.

With a 657 nm laser stabilized to the RB calcium interferometer described above, we have observed laser frequency instability of 2×10^{-16} at 10 seconds. The frequency stability remains at or below the 5×10^{-16} level at all times from 1 to 1000 seconds. We are currently exploring ways to improve the resulting frequency stability towards the shot-noise limit, experimentally assessed to be in the 10^{-17} decade at just one second. This includes a detailed study of systematic drifts in the system which can impact frequency instability on both short and long timescales.

This work was supported by NIST and by DARPA through the QuASAR and STOIC programs.

REFERENCES

[1] Ch. J. Bordé, Ch. Salomon, S. Avrillier, A. Van Lerberghe, Ch. Bréant, D. Bassi, and G. Scoles, "Optical Ramsey fringes with traveling waves," Physical Rev. A, vol. 30, pp. 1836-1848, 1984.

[2] R. L. Barger, J. C. Bergquist, T. C. English, and D. J. Glaze, “Resolution of photon-recoil structure of the 6573-A calcium line in an atomic beam with optical Ramsey fringes,” Appl. Phys. Lett., vol. 34, pp. 850-852, 1979.

[3] P. Kersten, F. Mensing, U. Sterr, F. Riehle, “A transportable optical calcium frequency standard,” Appl. Phys. B, vol. 68, pp. 27-38, 1999.

[4] C.W. Oates, E.A. Curtis, and L. Hollberg, “Improved short-term stability of optical frequency standards: approaching 1 Hz in 1 s with the Ca standard at 657 nm,” Optics Letters, vol. 25, pp. 1603-1605, 2000.

[5] J. J. McFerran and A. N. Luiten, “Fractional frequency instability in the 10^{-14} range with a thermal beam optical frequency reference,” J. Opt. Soc. Am. B, vol. 27, pp. 277-285, 2010.

Estimating the Allan Variance from Frequency Measurements with Missing Data

Lorenzo Galleani
Politecnico di Torino
Torino, Italy
Email: galleani@polito.it

Ilaria Sesia
INRIM
Torino, Italy
Email: i.sesia@inrim.it

***Abstract*—The Allan variance is the key measure for stability analysis, a fundamental tool to establish the performances of atomic clocks, which are often critical elements in many applications, such as global navigation satellite systems (GNSS). In some applications, only frequency measurements with numerous missing data are available. Because of missing data, the resulting Allan variance can be dramatically different from the expected stability behavior. We have developed an Allan variance estimator which corrects this divergence. We show the effectiveness of our estimator by applying it to frequency measurements with up to 94.4% of missing data.**

I. Introduction

Among the many statistical tools used in atomic timing [1], such as, for instance, Bayesian analysis [2], random systems [3], and the Kalman filter [4], the Allan variance is the standard measure of stability for precise clocks and oscillators [5]-[8]. It is defined as

$$\sigma_y^2(\tau) = \frac{1}{2}\left\langle (\bar{y}(t+\tau) - \bar{y}(t))^2 \right\rangle \tag{1}$$

where $\langle\rangle$ indicates an average over the entire time axis, the average frequency deviation $\bar{y}(t+\tau)$ is defined as [9]

$$\bar{y}(t+\tau) = \frac{1}{\tau}\int_t^{t+\tau} y(t')dt' \tag{2}$$

and $y(t)$ is the normalized frequency deviation. In practical experiments we typically have N frequency measurements

$$y[n] = \frac{1}{\tau_0}\int_{(n-1)\tau_0}^{n\tau_0} y(t)dt, \qquad n = 1, \ldots, N \tag{3}$$

where τ_0 is the sampling time, and $n = t/\tau_0$ is the discrete time. Consequently, the Allan variance becomes

$$\sigma_y^2[k] = \frac{1}{2}\frac{1}{N-2k+1}\sum_{n=k}^{N-k} E\left[\left(\bar{y}_k[n+k] - \bar{y}_k[n]\right)^2\right] \tag{4}$$

where $k = \tau/\tau_0$ is the discrete observation interval, E is the expected value, and

$$\bar{y}_k[n+k] = \frac{1}{k}\sum_{m=1}^{k} y[n+m] \tag{5}$$

$$\bar{y}_k[n] = \frac{1}{k}\sum_{m=1}^{k} y[n-m+1] \tag{6}$$

The theoretical Allan variance (4) is estimated from experimental measurements by using the estimator

$$\hat{\sigma}_y^2[k] = \frac{1}{2}\frac{1}{N-2k+1}\sum_{n=k}^{N-k}\left(\bar{y}_k[n+k] - \bar{y}_k[n]\right)^2 \tag{7}$$

The Allan variance can be also evaluated from the time deviations $x[n]$, where $y[n] = (x[n]-x[n-1])/\tau_0$, and proper techniques must be used when data are missing [10]. In some situations, though, only the frequency measurements $y[n]$ are available, and the fraction of missing data can be high, as happens, for example, in some space applications involving atomic clocks. In such cases, missing data are typically due to telemetry failures, or to the limited visibility of the satellite carrying the clock, as happens in the atomic clock ensemble in space (ACES) experiment [11].

As a consequence of the missing frequency measurements $y[n]$, the Allan variance estimator (7) is biased, and, on the average, does not return the correct value (4), namely,

$$E\left[\hat{\sigma}_y^2[k]\right] \neq \sigma_y^2[k] \tag{8}$$

The bias $E\left[\hat{\sigma}_y^2[k]\right] - \sigma_y^2[k]$ can be very large when the missing data are many or follow certain patterns. Consequently, the estimate $\hat{\sigma}_y^2[k]$ is heavily distorted, and the consequent stability analysis is incorrect and misleading. This problem is critical, because stability analysis is a key element for assessing the performances of atomic clocks.

We have developed an Allan variance estimator which corrects the bias of (7) in case of missing frequency measurements. Our corrected estimator is unbiased, namely,

$$E\left[\hat{\sigma}_y^2[k]\right] (\text{Corrected}) = \sigma_y^2[k] \tag{9}$$

and it uses the available frequency measurements $y[n]$ only, without filling the gaps due to the missing data by using, for example, interpolation techniques. The basic idea behind it is given in Sect. II. The corrected estimator works with white frequency noise (WFN), white phase noise (WPN), and random walk frequency noise (RWFN), and it returns an estimate consistent with the theoretical Allan variance (4) even when a very high fraction of the data are missing, as the examples shown in Sect. III proves. The corrected estimator assumes knowledge of the noise type for the considered range of discrete observation intervals. The type of noise can be

978-1-5386-2916-1/$31.00 ©2017 IEEE

established from the clock specifications, or it can be identified by using the standard statistical methods.

II. Basic Idea

When missing data are present, the definition of the Allan variance (4) becomes

$$\sigma_y^2[k] = \frac{1}{2}\frac{1}{\#I(k)}\sum_{n\in I(k)} E\left[\left(\bar{y}'_k[n+k]-\bar{y}'_k[n]\right)^2\right] \quad (10)$$

where the average frequency deviations $\bar{y}'_k[n+k]$ and $\bar{y}'_k[n]$ are computed on the available data only, $I(k)$ is the set of discrete-time instants n at which the average frequency deviations $\bar{y}'_k[n+k]$ and $\bar{y}'_k[n]$ are both available for a given discrete observation interval k, whereas $\#I(k)$ is the number of elements of $I(k)$. If no data are missing, then $I(k) = k, \ldots, N-k$ and $\#I(k) = N-2k+1$. The corresponding Allan variance estimator is

$$\hat{\sigma}_y^2[k] = \frac{1}{2}\frac{1}{\#I(k)}\sum_{n\in I(k)} \left(\bar{y}'_k[n+k]-\bar{y}'_k[n]\right)^2 \quad (11)$$

It is the difference between the average frequency deviations $\bar{y}_k[n+k]$, $\bar{y}_k[n]$, obtained for the full data case, and $\bar{y}'_k[n+k]$, $\bar{y}'_k[n]$, for the missing data case, which generates the bias between the Allan variance for the full data case and the Allan variance for the missing data case.

To correct this bias, we modify the definition of the Allan variance for missing data as

$$\sigma_y^2[k] = \frac{1}{2}\frac{1}{\#I(k)}\sum_{n\in I(k)} \alpha^2[n,k] E\left[\left(\bar{y}'_k[n+k]-\bar{y}'_k[n]\right)^2\right] \quad (12)$$

where $\alpha^2[n,k]$ is a correction factor defined as

$$\alpha^2[n,k] = \sqrt{\frac{E\left[\left(\bar{y}_k[n+k]-\bar{y}_k[n]\right)^2\right]\ (\text{Full data})}{E\left[\left(\bar{y}'_k[n+k]-\bar{y}'_k[n]\right)^2\right]\ (\text{Missing data})}} \quad (13)$$

The corresponding Allan variance estimator is defined as

$$\sigma_y^2[k] = \frac{1}{2}\frac{1}{\#I(k)}\sum_{n\in I(k)} \alpha^2[n,k]\left(\bar{y}'_k[n+k]-\bar{y}'_k[n]\right)^2 \quad (14)$$

The correction factor $\alpha^2[n,k]$ is computed for every n and k values, and it depends on the pattern of the missing data, but it is a deterministic quantity independent from the different realizations of the frequency measurements. The correction factor can be analytically computed by first noting that

$$\begin{aligned} E\left[\left(\bar{y}_k[n+k]-\bar{y}_k[n]\right)^2\right] &= E\left[\bar{y}_k^2[n+k]\right] + E\left[\bar{y}_k^2[n]\right] \\ &\quad -2E\left[\bar{y}_k[n+k]\bar{y}_k[n]\right] \end{aligned} \quad (15)$$

and then by evaluating the three single terms for the case of full data and missing data. The value of such terms and the corresponding correction factor values change depending on the type of noise. We have computed the correction factor for WFN, WPN, and RWFN. We are currently preparing a journal paper where we describe the actual calculations of the correction factor and we give its value for these three fundamental noise components of precise clocks and oscillators.

III. Examples

We validate the proposed corrected estimator by simulating a WFN first with a pattern of missing data similar to the pattern of the expected ACES experiment data, then with uniformly distributed missing data. In both cases, despite the high percentage of missing data, the corrected estimator follows the expected Allan variance behavior.

A. The Case of the ACES Experiment

We consider a WFN with a pattern of missing data typical of the ACES experiment, where 5 minutes of frequency measurements of the ultra-stable atomic clocks onboard the international space station (ISS) are expected for every ISS pass, occurring every 90 minutes. Therefore, approximately 94.4% of the data are missing. We simulate $N = 1080$ frequency measurements $y[n]$, made by 20 blocks of 54 data each, where the first 3 frequency measurements of each block are available and correspond to WFN, whereas the subsequent 51 data are missing. Consistently with the ACES experiment, 94.4% of the simulated data are missing.

Figure 1 shows the simulated frequency measurements, whereas Fig. 2 shows the corresponding stability analysis. The solid blue line is the theoretical Allan deviation $\sigma_y[k]$ in (4), obtained when the full data set is available. The solid black line is the theoretical Allan deviation $\sigma_y[k]$ in (10), obtained for the specific pattern of frequency measurements and missing data shown in Fig. 1. Note that this Allan deviation is not merely an approximation of the full data case, but it is profoundly different, particularly for short-medium discrete observation intervals, where the curve is flat rather than decreasing with the correct $k^{-1/2}$ behavior. The dotted black line is the estimated Allan deviation $\hat{\sigma}_y[k]$ from (11) when no correction is applied. We see that this curve follows its expected value, the solid black line. The dotted red line is the estimated Allan deviation $\hat{\sigma}_y[k]$ from (14) when the correction is applied. Note that the corrected estimate follows the desired theoretical Allan deviation (blue line), even if the fraction of missing data is very large. The red circles are an approximation of the expected value of the corrected estimator obtained through Monte Carlo simulations. We note that they correspond to the true value $\sigma_y[k]$ indicated by the blue line. Finally, the red bars are 95% confidence intervals, obtained through Monte Carlo simulations. Although we only have 60 data out of 1080 total data, the confidence intervals are not too large.

B. The Case of Uniformly Distributed Missing Data

It is interesting to consider the case of missing data distributed with a uniform pattern. In Fig. 3 we show the simulated frequency measurements of a WFN when approximately 62% of the data are missing and follow such uniform pattern. The corresponding stability analysis is shown in Fig. 4. Again, the blue solid line represents the expect behavior of the Allan

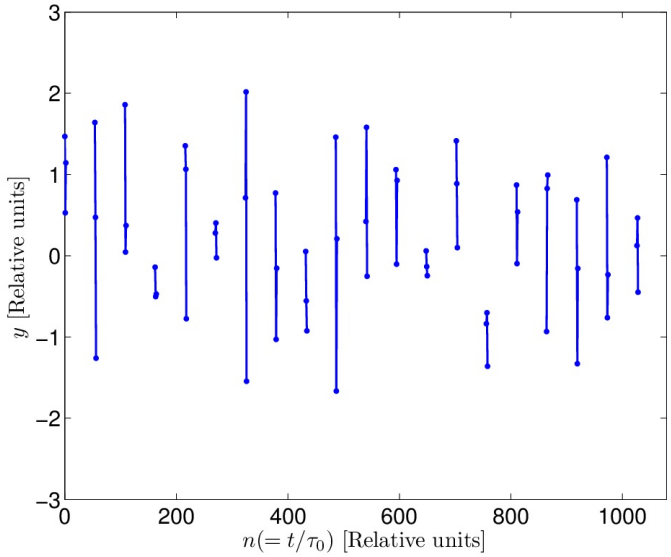


Fig. 1. Frequency measurements $y[n]$ with a WFN component and 94.4% of missing data.

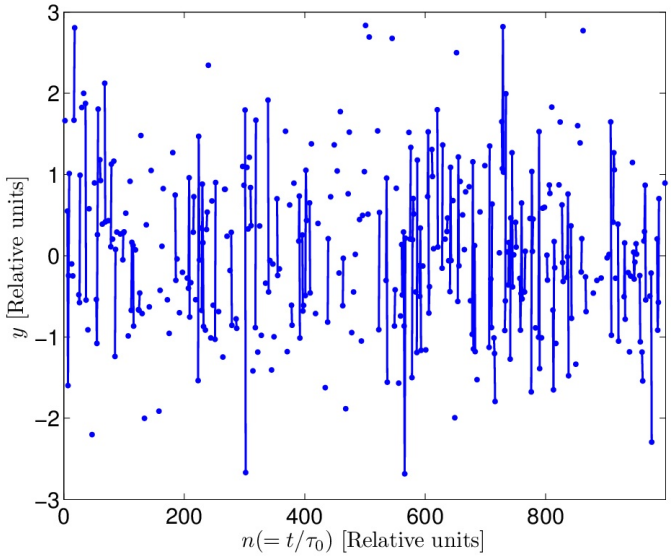


Fig. 3. Frequency measurements $y[n]$ with a WFN component and approximately 62% of uniformly distributed missing data.

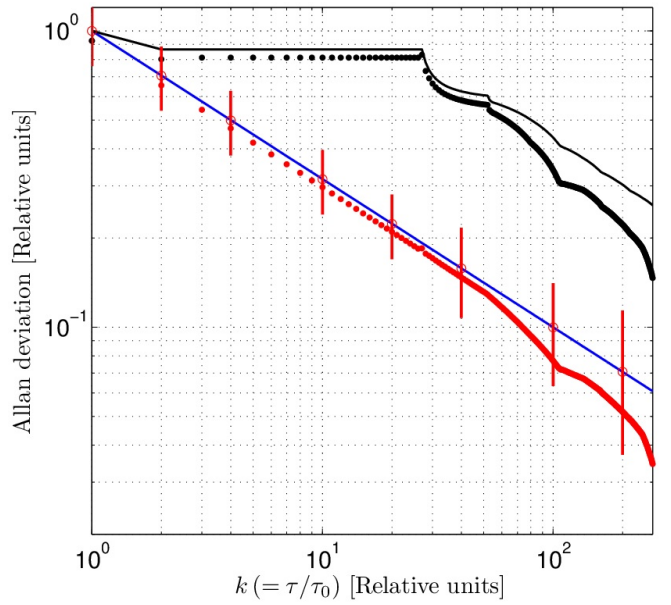


Fig. 2. Stability analysis of the frequency measurements in Fig. 1.

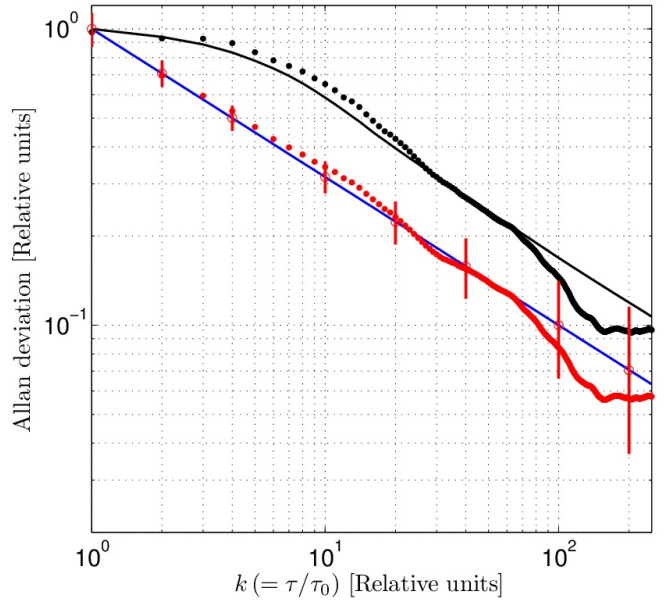


Fig. 4. Stability analysis of the frequency measurements in Fig. 3.

deviation obtained for the case of full data, the solid black line represents the Allan deviation for the case of missing data without correction, and the dotted black line is the corresponding estimate obtained with the estimator without the correction. The red dotted line is the corrected Allan deviation estimate, which follows the expected behavior indicated by the blue line. The red circles centered about the blue line confirm that, on average, we remove the bias, and the small 95% confidence intervals indicate that the corrected estimate is statistically reliable.

IV. Conclusions

We have developed an Allan variance estimator which works when frequency measurements only are available, and when a fraction of them is missing. In this case, the classical Allan variance estimator is biased because of the missing data. Our estimator uses a correction which eliminates the bias, even when the fraction of missing data is large. The corrected estimator guarantees therefore that the stability of atomic clocks can still be assessed even when a few measurements are available. The proposed estimator can be embedded in the dynamic Allan variance (DAVAR) [12]-[16], to evaluate how the clock stability changes with time when frequency measure-

ments with missing data are available. Such nonstationary tool is useful to monitor the integrity of global navigation satellite systems [17].

REFERENCES

[1] P. Tavella, "Statistical and mathematical tools for atomic clocks," *Metrologia*, vol. 45, no. 6, pp. S183-S192, December 2008.

[2] D. Calonico, F. Levi, L. Lorini, and G. Mana, "Use of Bayesian Statistics to reduce the density shift uncertainty in cesium fountain," *2010 IEEE International Frequency Control Symposium*, 1-4 June 2010, Newport Beach, CA, United States.

[3] C. Zucca and P. Tavella, "A mathematical model for the atomic clock error in case of jumps," *Metrologia*, vol. 52, no. 4, pp. 514–521, Aug. 2015.

[4] L. Galleani and P. Tavella, "Time and the Kalman Filter," *IEEE Control Systems*, vol. 30, no. 2, pp. 44-65, April 2010.

[5] D. W. Allan, "Statistics of atomic frequency standards," *Proc. IEEE*, vol. 54, no. 2, pp. 221-230, 1966.

[6] D. W. Allan, "Time and Frequency (Time-Domain) Characterization, Estimation, and Prediction of Precision Clocks and Oscillators," *IEEE Trans. Ultra. Ferro. Freq. Contr.*, vol. 34, no. 6, pp. 647-654, 1987.

[7] IEEE Standard Definitions of Physical Quantities for Fundamental Frequency and Time Metrology, IEEE Std. 1139-1999.

[8] ITU-R Recommendation TF 538-3, "Measures for random instabilities in frequency and time (phase)," *International Telecommunication Union – Radiocommunication ITU-R*, vol. 2000, TF Series, Geneva, 2001.

[9] P. Kartaschoff, *Frequency and time*, Academic Press, 1978.

[10] I. Sesia and P. Tavella, "The Allan variance for measurements with long periods of missing data and outliers," *Metrologia*, vol. 45, no. 6, pp. 134-142, Dec. 2008.

[11] L. Cacciapuoti and C. Salomon, "Atomic Clock Ensemble in Space," *Journal of Physics: Conference Series*, vol. 327, no. 1, pp. 1-13, 2011.

[12] L. Galleani and P. Tavella, "The Dynamic Allan Variance," *IEEE Trans. Ultra. Ferro. Freq. Contr.*, vol. 56, no. 3, pp. 450-464, 2009.

[13] L. Galleani, "The Dynamic Allan Variance II: A Fast Computational Algorithm," *IEEE Trans. Ultra. Ferro. Freq. Contr.*, vol. 57, no. 1, pp. 182-188, 2010.

[14] L. Galleani, "The Dynamic Allan Variance III: Confidence and Detection Surfaces," *IEEE Trans. Ultra. Ferro. Freq. Contr.*, vol. 58, no. 8, pp. 1550-1558, 2011.

[15] L. Galleani and P. Tavella, "The Dynamic Allan Variance IV: Characterization of Atomic Clock Anomalies," *IEEE Trans. Ultra. Ferro. Freq. Contr.*, vol. 62, no. 5, pp. 791-801, May 2015.

[16] I. Sesia, L. Galleani, and P. Tavella, "Application of the Dynamic Allan Variance for the Characterization of Space Clock Behavior," *IEEE Trans. Aero. Elec. Sys.*, vol. 47, no. 2, pp. 884-895, Apr. 2011.

[17] I. Rodríguez-Pérez, C. García-Serrano, C. Catalán Catalán, A. M. García, P. Tavella, L. Galleani, and F. Amarillo, "Inter-satellite links for satellite autonomous integrity monitoring," *Advances in Space Research*, vol. 47, no. 2, pp. 197-212, January 2011.

The Use of Fault-tolerant Clock Synchronization Algorithms for Time Scales

Attila Kinali,*
*Max Planck Institute for Informatics, Saarland Informatics Campus, Germany

***Abstract*—Clock ensembles are at the core of many applications in which precise time or frequency is required. The widely used time scale algorithms need cumbersome modifications when clocks can be potentially faulty. Fault-tolerant clock synchronization algorithms from distributed systems allow to build time scales without the need of special detection systems for anomalous behavior of the clocks. We present a short overview of the general principles underlying these algorithms and their advantages and disadvantages when being used for time scales.**

I. Introduction

A. Background

Conventional time scale algorithms compute a weighted average of the contributing clocks (see e.g. [1]). This averaging causes problems with continuity of the time scale when a clock is inserted or removed from the ensemble.

Detection of anomalous behavior is not supported by most time scale algorithms and has to be handled by an external wrapper, often requiring additional information on the internal state of the contributing clocks to be reliable. This not only makes the system quite complex, but also incurs a trade-off: false positives of the fault detection mechanism result in healthy clocks being excluded, while false negatives result in including faulty clocks. This becomes a problem especially if clocks show a lot of intermittent faults, which is typical for harsh environments like in space applications.

The distributed systems community has been employing clock synchronization algorithms which are fault-tolerant for some time. These algorithms do not try to detect erroneous behavior, but instead mask it, which allows having a single algorithm handling the ensemble without the need of any out-of-band information. In addition, this buys time for error detection and handling; it suffices to guarantee that, at no point in time, the number of faulty clocks exceeds the limit that can be sustained. The range of faults that the system can encounter is also defined much more broadly than is usually the case with time scale algorithms. Usually, very few assumptions are made about possible faults, allowing arbitrary faults (so-called Byzantine faults). One example of these algorithms is the Welch-Lynch algorithm [2]. This simple algorithm can handle any number of faults that is smaller than one third of the contributing clocks. Here, a fault can be *any* anomalous behavior of a clock, its associated computational logic, the communication links for incoming or outgoing signals, or any combination thereof. As long as the fault threshold is not reached, the output quality degrades only slightly. With accurate clocks, the dominant source of error is the uncertainty in the measurements of the relative phases between the clocks.

B. Our Contribution

We present an overview of how to implement a fault-tolerant distributed clock synchronization algorithm. We show how the fault-masking behavior can be used to build ensembles that are immune to phase and frequency jumps of any (sufficiently small) subset of the clocks, without the need for an explicit detection circuit.

We also give an overview of the problems arising from using these algorithms in the context of time scales, namely the deterioration of the absolute noise performance compared to traditional algorithms, and discuss possible solutions.

II. Fault Model

A. Classical Fault Models

Most electronics are designed with simple fault models that restrict the behavior of the faulty nodes. Quite a few of those can be summarized in the fail-stop model, i.e. the device either works correctly and it's output is valid or the device is faulty and its output invalid. In this model it is easy to detect faults and thus also easy to deal with them in globally consistent way.

The more interesting case is deterioration of the output, like phase or frequency jumps. If these jumps are small, then detecting them becomes hard. One big disadvantage of this model is, that it only models one specific type of event (jump in phase or frequency) for only one specific type of devices (clocks). It is not possible to use results derived from these models in a broader context.

B. Byzantine Fault Model

The fault model we use here, is a very broad and strong one: In a network of n nodes, at most f faulty nodes are allowed. Unlike in most electrical and electronic fault models, these faulty nodes are allowed to show inconsistent behavior to different non-faulty nodes. Additionally, the faulty nodes are granted the power to know the states of all nodes and may communicate with all other faulty nodes using a side channel with infinite capacity. Informally speaking, faulty nodes are omniscient beings that are allowed allowed to lie.

This fault model allows to capture a wide variety of faults, even those induced by outside disturbance. Unlike in the fail-stop model, it is not possible to reliably detect which nodes are faulty in the Byzantine fault model, without incurring a huge

978-1-5386-2916-1/$31.00 ©2017 IEEE

cost in either communication or convergence time. I.e. they can mimic a correctly working node to each non-faulty node and the only way to detect them is to communicate between all nodes and identify all faulty nodes at the same time. Mickens gives in [3] an humorous view on the difficulty of dealing with the Byzantine fault model.

Even though the fault model is very strong, it offers the possibility to capture faults that are otherwise hard to model. Any system that can deal with Byzantine faults is likely to be able to deal with any kind of fault that it encounters in reality. But one must be careful about this strength as well: Algorithms that work perfectly fine in reality might fail under these model assumptions. Hence it is important to show that useful result can still been achieved with such a strong model.

III. Fault Tolerant Algorithms Under Byzantine Faults

We will now look at how to deal with Byzantine faults. For this we first need to define the inputs, outputs and the required behavior of the system. As we are interested in synchronizing clocks, we are letting each node sending a pulse in regular intervals. Each node receives the pulses from all other nodes and corrects its own pulse timing such, that eventually all (correctly working) nodes agree on a common timing and pulse synchronously.

A. General Way of Dealing with Byzantine Faults

As it is not reliably possible to detect a faulty node, another approach must be chosen to work under such strict fault models. The general approach is not to try to detect them, but instead mask potentially faulty nodes in a way, that the faulty nodes that are not masked do not cause any trouble. After masking, the remaining nodes should be used in some way that will make all correctly working nodes either agree eventually or correct themselves in a way that converges to a common value.

This shifts the problem to which nodes and how many of them should be masked. A classic result from distributed computing is, that for Byzantine agreement requires that no more than one third of the nodes are faulty (i.e. $3f < n$). In this case, one can mask the the f nodes at the top and bottom extremes and work with the $n - 2f$ remaining nodes. The intuition here is, if any faulty nodes are left within the $n-2f$ nodes, then there is at least one correctly working node with a more extreme value, thus the faulty node left will not cause a degradation. Because, in the Byzantine fault model, faulty nodes are allowed to lie, correctly working nodes might have a different view and thus select a different group of $n - 2f$ nodes. It needs to be shown separately that these different views still allow a convergence of the algorithm.

The general implementation of a single node in a fault-tolerant clock synchronization system is depicted in Figure 1. Each node collects the output signals from all nodes, including its own. The timing of the signals are measured using either a TDC or a phase comparison system. The measured timing is then fed to the algorithm, which then controls the underlying clock and shifts its phase or frequency accordingly.

B. The Welch-Lynch Algorithm

Welch and Lynch described a simple, yet effective, Byzantine fault-tolerant clock synchronization algorithm in [2]. Informally, each node sends a pulse at regular intervals to every other node, including itself. The nodes receive the pulses, sort them by arrival time and drop the f earliest and f latest pulse arrival-times. The time span of the remaining $n - 2f$ pulse arrival-times is used to calculate where the nodes own pulse "should have been." The time difference between center of the time-span (i.e. the mean of the minimum and maximum of the time-span) the nodes own pulse arrival-time is used as correction value for the next round (see Figure 2). This algorithm, despite its simplicity, is Byzantine fault-tolerant. Intuitively, no matter what the faulty nodes do, the calculated center point calculated by each node, will be within the time span of the $n - 2f$ nodes. Thus, in the absence of noise, because the each correctly working node moves into the center of the span it sees, it will, in best case, halve the distance to the other correctly working nodes. Hence the nodes will converge and pulse together. A formal proof can be found in [4]. In a real implementation, the achievable synchronization is limited by uncertainty in the measurement of the arrival of the pulses (wire delay uncertainty and noise in the measurement) and difference in frequencies of the clock oscillators. The remaining skew between clocks is bounded by

$$\max \Delta t = 2\delta + \frac{\Delta f}{f}\tau$$

, where δ is the uncertainty in the pulse arrival time and Δf is the maximum difference in frequency, which is normalized over the nominal frequency f_0 and multiplied by the round length τ. If there are no faulty nodes, the skew reduces to [4]

$$\max \Delta t_{faultfree} = \delta + \frac{\Delta f}{f}\tau$$

.

IV. The Welch-Lynch Algorithm Applied to Atomic Clocks

A. Stability vs Synchroninity

The Welch-Lynch algorithm achieves a high level of synchronization, only limited by the precision of the relative phase measurement. Given that it is possible to compare local clocks with sub-picosecond precision, this should not pose a limitation in practice. But the Welch-Lynch algorithm applies a correction at each step. This correction is derived from noisy input, i.e. it is a random variable. Thus the correction itself is a random variable and hence the Welch-Lynch algorithm acts like an integrator of a random variable. Obviously, this will lead to degradation of the stability and a conversion from white phase noise to white frequency noise. To analyze this, we have simulated a 4 node/clock ensemble with no faulty nodes. In order to make the behavior of the algorithm under different noise process more clear, we performed different simulations

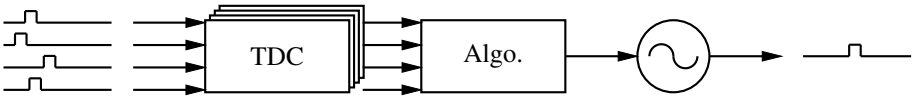


Figure 1. Design of a single node implementing a fault-tolerant clock synchronization algorithm. A TDC measures the timing difference between the different nodes. These values are fed to the algorithm which then controls underlying clock and shifts its phase or frequency. The output of the clock is distributed to all nodes.

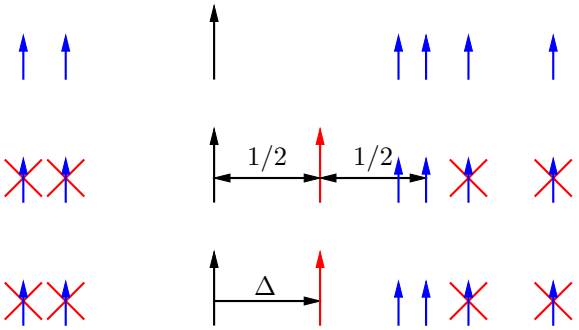


Figure 2. The Welch-Lynch clocksync algorithm. First receive all clock pulses from all nodes, including own pulse (long black arrow). Drop first $f = \lceil n/3 \rceil$ and last f received pulses (masking step). From the remaining pulses, calculate the center of the spanning time frame (long red arrow) which denotes where the pulse "should have been". Lastly, calculate the correction to be applied before the next round starts.

with only one single noise process. All 4 clocks have the same noise spectrum, but are otherwise independent. The algorithms period was chosen to be 1 s and phase corrections were applied instantaneously, i.e. before the next round starts. Measurement noise and uncertainty was set to zero, in order not to make analysis more complicated.

As can be seen in the modified Allan deviation plot Figure 4(a), the integration of the clock input noise leads to a noise process that is white frequency modulation, in the long term. Short term, below a τ of 3 s, the noise follows that of white phase modulation, though. A similar observation can be made for flicker phase modulation (Figure 4(b)), but the slope increase is smaller than for white phase modulation. This can be easily explained by the Welch-Lynch algorithm removing the outliers which get more pronounced as the low frequency components of the noise gets stronger. From white frequency modulation onwards (Figures 4(c), 4(d) and 4(e)) the slope does not degrade any further and there is only a slight degradation in stability.

Looking at the plots, one can see that there is a slight increase in slope between τ's between 1 s and about 3 s. The algorithm seems to be degraded by high frequency noise, which then ends up being integrated through the continuous corrections. Using this insight, we applied a first order IIR low-pass filter with a corner frequency of $1/100$ Hz corner frequency, at every input of each node. I.e. the phase measurements at each node are low pass filtered individually to dampen the high frequency components (Figure 3). As can be seen in Figure 4 ("LP100+WL" plots), the effect is quite tremendous improvement in stability of the ensemble. For white phase modulation, the low-pass filter brings the stability to what the underlying clocks have. For τ's longer than the filter bandwidth, the stability seems to even improve beyond what the clocks have themselves, but not much. This effect gets more pronounced for the higher exponent noise processes. While at τ's beyond the filter bandwidth, the ensemble slope is the same as the underlying clocks, at smaller τ the slope is much steeper and thus the stability improves quite considerably. Please note, that this behavior is different than a simple low pass filtered clock, where the maximum improvement is at the smallest τ (highest frequency), which the decreases until it reaches the clocks performance at the filters corner frequency. While here we have no stability improvement at lowest τ, but increasing improvement until the corner frequency is reached.

References

[1] J. Levine, "Invited review article: The statistical modeling of atomic clocks and the design of time scales," *Review of Scientific Instruments*, vol. 83, no. 2, p. 021101, 2012. [Online]. Available: http://dx.doi.org/10.1063/1.3681448

[2] J. L. Welch and N. A. Lynch, "A New Fault-Tolerant Algorithm for Clock Synchronization," *Information and Computation*, vol. 77, no. 1, pp. 1–36, 1988.

[3] J. Mickens, "The Saddest Moment," *login*, May 2013.

[4] P. Khanchandani and C. Lenzen, "Self-stabilizing byzantine clock synchronization with optimal precision," *CoRR*, vol. abs/1609.09281, 2016. [Online]. Available: http://arxiv.org/abs/1609.09281

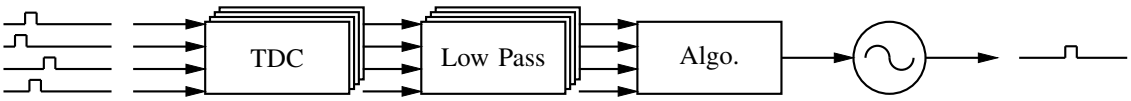
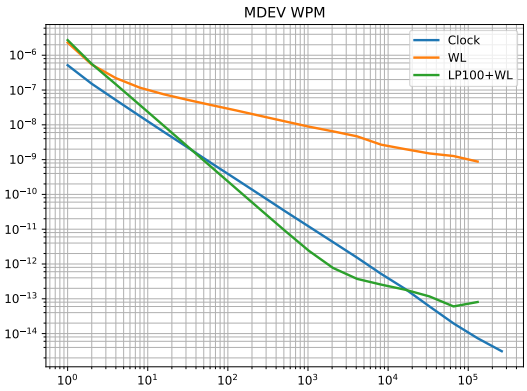
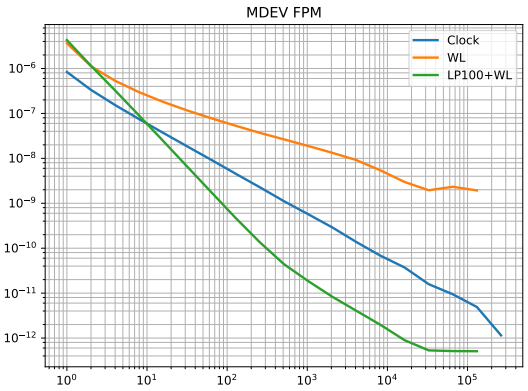


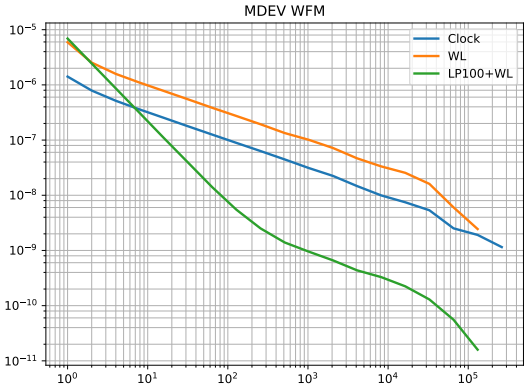
Figure 3. Additional low-pass filters between the TDC and the algorithm improves the performance of the system.



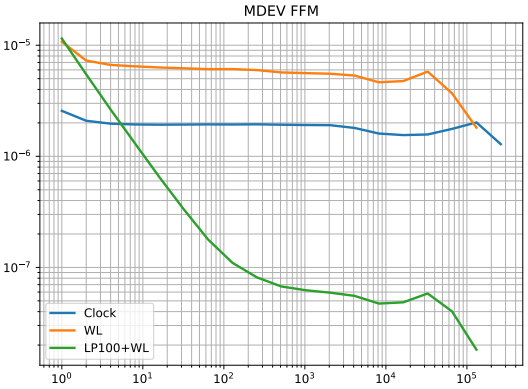
(a) White phase modulation.



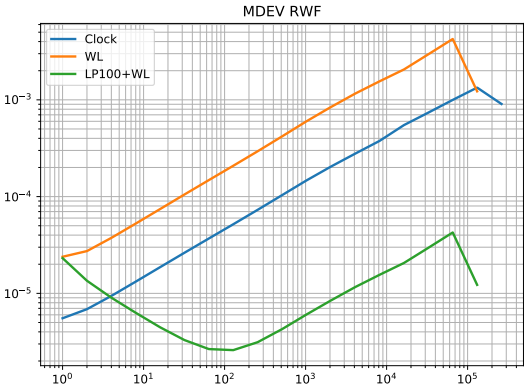
(b) Flicker phase modulation.



(c) White frequency modulation.



(d) Flicker frequency modulation.



(e) Random walk frequency.

Figure 4. Modified Allen deviation plots of a 4 node ensemble with different clock input noise spectra, but without any faulty clocks. The original clock noise ("Clock") gets slightly degraded by the Welch-Lynch algorithm. Applying a first order IIR filter with a corner frequency of $1/100\,\mathrm{Hz}$ to each nodes input ("LP100+WL) improves the stability of the time-scale of the ensemble quite considerably, especially for the higher exponent noise spectra.

Application of GMDH type neural network for predicting UTC(k) timescales realized on the basis of hydrogen masers

Łukasz Sobolewski
Institute of Metrology, Electronic and Computer Science
University of Zielona Góra
Zielona Góra, Poland
E-mail: L.Sobolewski@imei.uz.zgora.pl

***Abstract*—The article presents research results on predicting the deviations for UTC(AOS) timescale realized on the basis of hydrogen maser by means of GMDH type neural network. Input data are prepared in the form of two time series (TS1 and TS2). Time series TS1 is built on the basis of values of comparison between the UTC(AOS) timescale with a clock realizing this scale, and values of deviations determined according to UTC and UTC Rapid scales, published by the BIPM. Time series TS2 is built only on the basis of values of deviations determined according to UTC and UTC Rapid scales. Better quality of predicting the UTC(AOS) timescale is obtained for data prepared in the form of time series TS2. Obtained values of predictions differ from the deviations published by the BIPM at the same day of prediction by ±10 ns for time series TS1 and ±5 ns for time series TS2.**

Keywords—UTC(k) timescale; hydrogen maser; predicting [UTC – UTC(k)]; GMDH type neural network

I. INTRODUCTION

National timescales UTC(k) are physical realizations of the UTC timescale (Coordinated Universal Time). The organization responsible for determining the quality of UTC(k) timescales is the International Bureau of Weights and Measures BIPM (the French for Bureau International des Poids et Mesures). Each month BIPM determines the [UTC - UTC(k)] deviations for each UTC(k), which define the divergence of local timescale in relation to the UTC [1, 2, 3]. These deviations are determined with a five day interval as average values per day on MJD (Modified Julian Date) days ending with digit 4 and 9, and published in the "Circular T" bulletin. The process of calculating UTC scale is very complex and time-consuming. It requires a collection and proper preparation of measurement data from local and remote comparisons sent by an NMI (National Metrological Institutes) and the calculation of the UTC scale value by the BIPM. Due to publishing the BIPM "Circular T" bulletin between the 8th and 12th day of the following month, ensuring the highest compliance of the UTC(k) in relation to the UTC is only possible by predicting [UTC - UTC(k)] deviations. Taking into account the date of publication of [UTC - UTC(k)] deviations and the need to determine a prediction for the nearest MJD day ending with a digit 4 or 9 (to compare prediction values with the deviation values), the first day of prediction is between 10th and 20th day of a month. Part of NMI laboratories are predicting the deviations for UTC(k). The literature on the prediction of deviations presents method based on statistical models, for example [4, 5, 6 ,7], or methods based on artificial intelligence, for example [8, 9, 10, 11].

Delay in publication of the [UTC - UTC(k)] deviations by the BIPM adversely affect on the result of the prediction, and consequently on maintaining the best convergence of the UTC(k) with the UTC. Therefore, in order to expedite the transfer of information about the differences of the UTC(k) in relation to the UTC, BIPM on January 1, 2012 developed the "A Rapid UTC" project. On the basis of UTC Rapid (UTCr) scale, every Wednesday on the BIPMs ftp server the [UTCr - UTC(k)] deviations determined on each day for the previous week are published, for each clock realizing the UTC(k) scale. This allows to shorten the prediction horizon to several days. In this case, the day of the first prediction falls between 3rd and 7th day of the week and is considerably shorter than in the case of using values of deviations determined according to UTC scale.

Institute of Metrology, Electronics and Computer Science of the University of Zielona Góra, in collaboration with the Central Office of Measures GUM (the Polish for Główny Urząd Miar) has been working on the application of MLP (Multilayer Perceptron), RBF (Radial Basis Function), GRNN (Generalized Regression Neural Networks) and GMDH (Group Method of Data Handling) neural networks for predicting the values of deviations for the Polish Timescale UTC(PL) realized by the GUM on the basis of a single, commercial caesium atomic clock. The proposal of application of the neural networks stemmed from their properties. They can be used where there is a partial or total lack of knowledge of the rules that describe the objects or processes, i.e. a great complexity of problems occurs. Behavioural models created by a neural network have an internal structure and a working principle which corresponds to the behaviour of the original objects or processes. A unique feature of neural networks is their ability to build models via a method based solely on an analysis of specific examples, i.e. an inductive method. Neural networks are very good mathematical tool, used for solving problems of a nonlinear character [12, 13, 14, 15].

978-1-5386-2916-1/$31.00 ©2017 IEEE

The obtained research results, presented in papers [8, 9, 10, 11] confirmed the possibility of using MLP, RBF, GRNN and GMDH neural networks for predicting the deviations for the UTC(PL). The studies carried out for the above types of neural networks has shown that the best results in the prediction of deviations have a GMDH type neural network [9, 10].

GMDH neural network was subjected also to the research of predicting the deviations for the UTC(k) using the deviations values determined by BIPM based on the UTC and UTC Rapid scales. The results of research presented in [16], confirmed the possibility of application of the UTCr scale for predicting the values of [UTC - UTC(PL)] by means of GMDH type neural network. The conclusions from these research were the basis for developing an algorithm, which specifies the procedure of predicting the deviations for the selected local timescales UTC(k) by means of GMDH type neural network. This procedure takes into consideration the values of deviations for UTC(k) timescales published by the BIPM in relation to UTC and UTCr scales. The characteristics of the developed procedure and the results of the studies carried out for UTC(PL) were published in papers [17, 18]. In addition, the correctness of the developed procedure was verified for other selected UTC(k) timescales based on single, commercial caesium clocks. The results of these studies are presented in [19, 20].

The aim of the article is to examine the effectiveness of applying GMDH type neural network and the developed procedure for predicting UTC(k) timescales, which are realized on the basis of hydrogen masers. The hydrogen maser has different characteristics with respect to commercial caesium clocks. It has better short-term stability compared to caesium clocks, which are characterized by better long-term stability. The studies are conducted on the example of UTC(AOS) timescale which is realized by the Astrogeodynamic Observatory in Borovets near Poznan (Poland). The paper presents research results on predicting the [UTC - UTC(AOS)] deviations on the basis of data prepared in the form of two time series built on the basis of deviations determined according to UTC and UTCr scales.

II. Input Data Preparation for the GMDH Type Neural Network

Input data for the GMDH type neural network are prepared in the form of two time series. The basic elements of these time series are the [UTC - UTC(AOS)] deviations determined according to relation:

$$xb(t) = UTC(t) - UTC_{AOS}(t), \quad (1)$$

and [UTCr - UTC(AOS)] deviations determined by relation:

$$xbr(t) = UTCr(t) - UTC_{AOS}(t). \quad (2)$$

The first created time series TS1 consisted of two subsets of elements prepared according to the rules defined on Fig. 1. The first subset contains a group of data (from 1 to i) determined from relation:

$$x_1(t) = xa(t) + xb(t) = UTC(t) - clock_{AOS}(t), \quad (3)$$

published from day t_0 to day t_n, for which the last value of this time series before the publication day (t_{pub}) has been known. The values of $xa(t)$ are the historic results of the measurement of the phase time between 1 pps signals from $UTC_{AOS}(t)$ and the atomic clock realizing this scale ($clock_{AOS}$), determined on each day according to relation

$$xa(t) = UTC_{AOS}(t) - clock_{AOS}(t). \quad (4)$$

Set of $xb(t)$ values has been subjected to the PCHIP interpolation function (Hermite interpolation available in MATLAB). As a result, it is possible to determine the values of $xb(t)$ deviation for each day. The second subset is a complement of time series TS1 by a group of data between days t_n and t_{nr} containing the values determined on the basis of relation

$$x_2(t) = xa(t) + xbr(t) = UTCr(t) - clock_{AOS}(t), \quad (5)$$

The values of $xbr(t)$ deviations are published by the BIPM on day t_{pubr} (Fig. 1). The publication day of $xbr(t)$ deviations could also be the day (t_{pred}), on which the prediction of $xb(t)$ deviation, hereinafter referred to as $xb_p(t_{pred})$ is performed.

Each week, TS1 time series data are supplemented by new groups of data calculated from relation (5). Therefore, it is possible to determine the next values of $xb_p(t_{pred})$ predictions in the following weeks. At the time of publication of the new "Circular T" bulletin, which contains the values of $xb(t)$ deviations, a new group of data i+1 (Fig. 1) is created based on relation (3), which for the respective days replace the data determined according to relation (5).

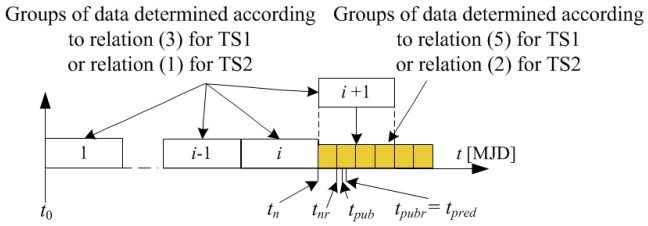


Fig. 1. Creation of time series TS1 and TS2

In certain situations, a need may arise to replace an atomic clock realizing the UTC(k) national timescale with another clock. Then, there may be a lack of the required number of the time series elements for determining $xb_p(t_{pred})$. Therefore, the second time series is the time series TS2 based only on the $xb(t)$ and $xbr(t)$ data published by the BIPM. This time series consists of two subsets prepared according to the principle described on Fig. 1.

III. Research Results

Predicting the deviations for the UTC(AOS) timescale have been carried out for a period of 17 months, from MJD 56204 (October 4, 2012) to MJD 56714 (February 26, 2014), on MJD days ending with a digit 4 and 9. The time series TS1 and TS2 applied at the input of the GMDH type neural network is created on the basis of historical $xb(t)$ data for the period from MJD 55629 (March 9, 2011) to MJD 56714 (February 26, 2014), and the $xbr(t)$ for the period from 56170 (August 31, 2012) to MJD 56714 (February 26, 2014). In case of using time

series TS1 at the output of the GMDH type neural network a value of $x_{1p}(t_{pred})$ prediction is obtained. Taking into account the value of $xa(t_{pred})$ measured on the prediction determining day, the $xb_p(t_{pred})$ prediction is calculated from the relation

$$xb_p(t_{pred}) = x_{1p}(t_{pred}) - xa(t_{pred}). \quad (6)$$

For time series TS2, the prediction determined value is simultaneously the determined value of predicted $xb_p(t_{pred})$ deviation. The determined values of prediction can constitute the basis for carrying out a UTC(AOS) timescale correction procedure.

Fig. 2 presents the values of $xb(t)$ and $xbr(t)$ deviations determined by the BIPM during the period of prediction. The performed analysis of $xb(t)$ and $xbr(t)$ deviations values designated by the BIPM for UTC(AOS) timescale showed a very good correlation between these deviations. The differences between $xb(t)$ and $xbr(t)$ deviations for the same day are on the level of only a few ns. In addition since April, 2013 $xb(t)$ deviations does not exceed the limit of ± 5ns. This has been the result of the correction process of the UTC(AOS) timescale.

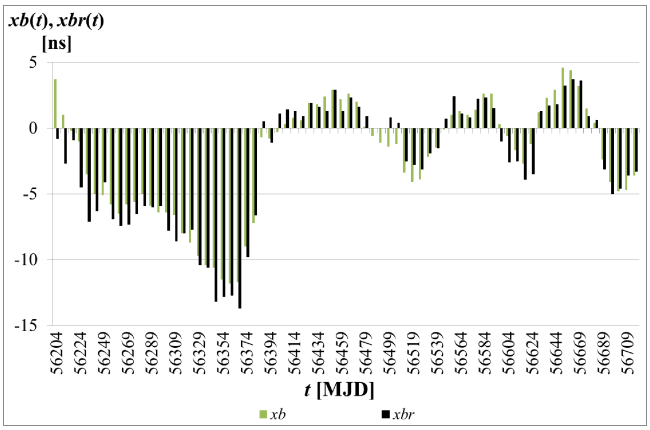


Fig. 2. Determined values of $xb(t)$ and $xbr(t)$ published by the BIPM for UTC(AOS)

Fig. 3 and 4 show determined by the GMDH type neural network values of $xb_p(t_{pred})$ predictions for UTC(AOS) timescale, which have been obtained for the prepared time series (TS1 and TS2), and a values of $xb(t)$ deviations determined by the BIPM on the same day of prediction (t_{pred}).

Fig. 5 and 6 present the values of residuals (r), so the differences between the predicted value of deviation and a $xb(t)$ deviation published by BIPM for the same day of prediction, calculated from relation:

$$r(t_{pred}) = xb(t_{pred}) - xb_p(t_{pred}). \quad (7)$$

The evaluation of the quality of $xb_p(t_{pred})$ predictions is carried out on the basis of following criteria: residuals, selected prediction quality measures [21, 22] and modified Allan deviations (MDEV) [23].

Based on the calculated residuals (r), the values of selected prediction quality measures is determined [21], which are presented in Table I. Presented in this Table three components of the MSE error [22] (MSE_1, MSE_2 and MSE_3) and their relative values (U_1, U_2 and U_3) determine the cause of this error. The MSE_1 component determines the inaccuracy of estimating by the prediction the average value of predicted variable, so it represents the prediction load. The MSE_2 component is associated with prediction insufficient flexibility, i.e. lack of estimation accuracy of the predicted variable fluctuations.

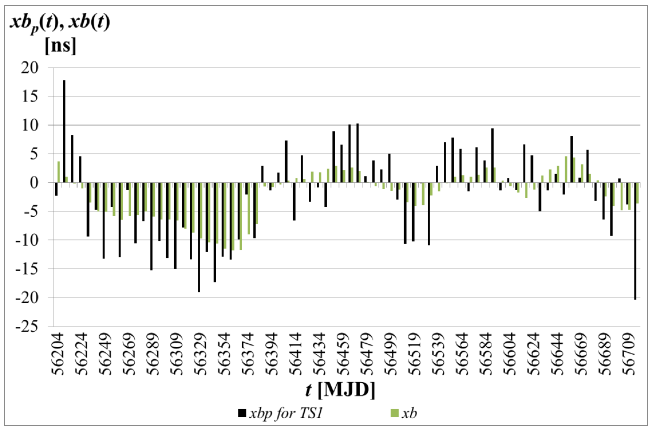


Fig. 3. Determined values of $xb_p(t)$ predictions based on the time series TS1 and values of $xb(t)$ deviations determined by the BIPM for UTC(AOS)

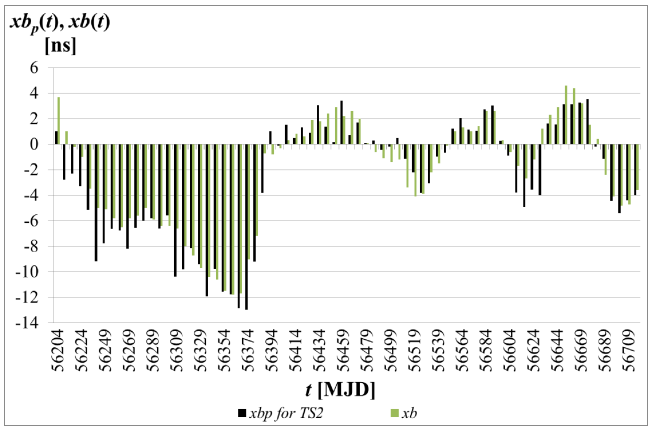


Fig. 4. Determined values of $xb_p(t)$ predictions based on the time series TS2 and values of $xb(t)$ deviations determined by the BIPM for UTC(AOS)

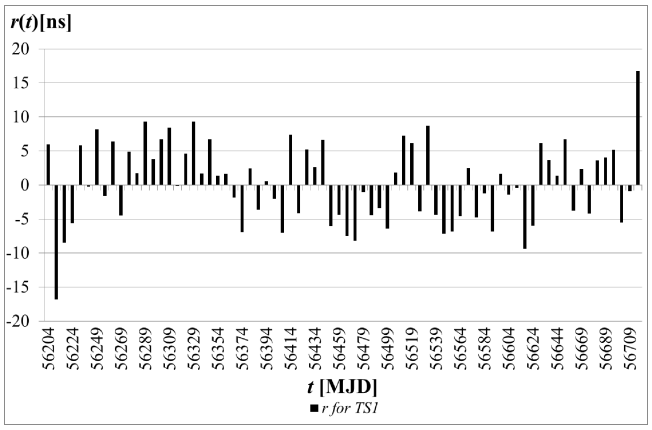


Fig. 5. Determined values of r residuals based on the time series TS1 for UTC(AOS)

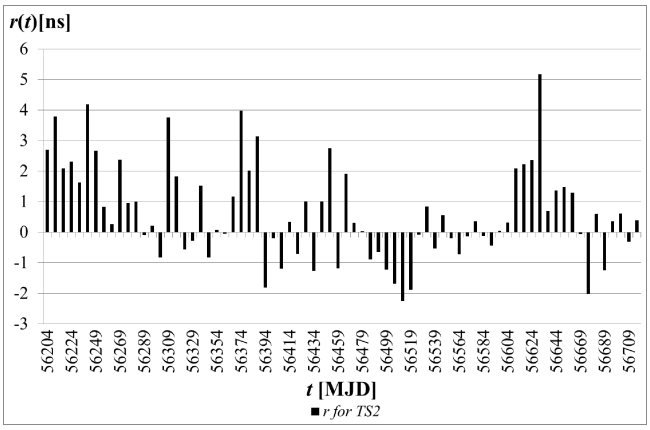


Fig. 6. Determined values of *r* residuals based on the time series TS2 for UTC(AOS)

TABLE I. VALUES OF SELECTED MEASURES OF QUALITY OF PREDICTIONS FOR UTC(AOS) FOR TIME SERIES TS1 AND TS2

Measure of quality of prediction	UTC(AOS) for TS1	UTC(AOS) for TS2
max [ns]	16.75	5.17
min [ns]	-16.82	-2.26
ME [ns]	0.2	0.6
MAE [ns]	4.9	1.3
MSE [ns^2]	34.4	2.87
MSE_1 [ns^2]	0.1	0.4
MSE_2 [ns^2]	15.3	0.12
MSE_3 [ns^2]	19.1	2.35
RMSE [ns]	5.9	1.7
U_1 [%]	0.1	14.1
U_2 [%]	44.3	4.0
U_3 [%]	55.6	81.9

The MSE_3 component signifies the error related to the insufficient compliance of the change in the direction of the prediction with the change in the direction of the predicted value. Fig. 7 shows a logarithmic comparison of the modified Allan deviation (MDEV) versus the averaged time (τ) for determined predictions by means of GMDH type neural network for the analysed time series TS1 and TS2.

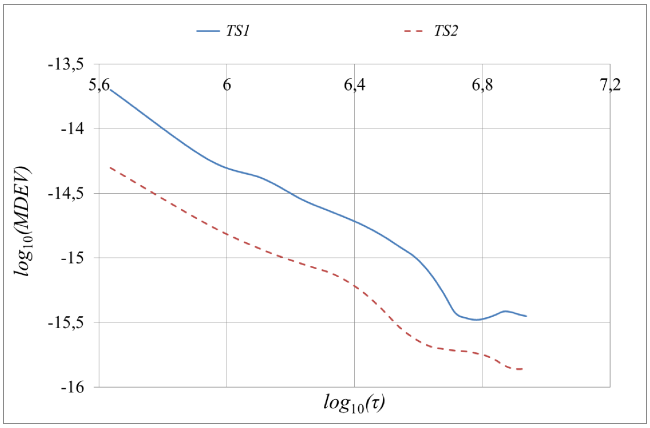


Fig. 7. The relationship log10(MDEV) of log10(τ) for GMDH NN with time series TS1 and TS2.

Based on the presented research results and carried out on its basis evaluation of the quality of predictions the following conclusions can be drawn:

1. From a comparison of the values of all prediction quality measures the best results of predicting the deviations is obtained for time series TS2.
2. In case of input data described by time series TS1 in 72 cases out of 74 the received values of residuals are in the range of ±10 ns. The highest absolute value of residuum is 16.82 ns. In case of data described by time series TS2 in 73 cases out of 74 the received values of residuals are in the range of ±5 ns. The highest absolute value of residuum is 5.17 ns (MJD 56634). This was due to the change in trend direction of the deviation values set by BIPM according to UTC scale.
3. Comparison of *ME*, *MAE* and MSE_1 errors for two time series shows that in the case of time series TS1 the predictions are unloaded. The observed values of residuals are multidirectional. In case of time series TS2 predictions are systematically underestimated. The obtained values of predictions are lower than the observed values.
4. The deviations predictions designated by the GMDH type neural network for time series TS2 characterize with the smaller values of MSE_2 error and its relative value U_2 in relation to time series TS1. This means better predicting the volatility of the predicted values relative to the volatility of observed values.
5. In the results obtained for time series TS1 and TS2 there are cases of high values of residuals. This is due to two factors. The first one is related to changes in the direction of the trend of $xb(t)$ deviations determined according to the UTC scale resulting from the time scale correction process. Hence, for these time series high value of the MSE_3 error component and its relative value U_3 occurred. The second factor is the variable prediction horizon, which varies from 3 to 7 days, depending on the date of prediction (t_{pred}), ending with a digit 4 or 9.
6. Obtained low values of residuals for time series TS2 allow to receive good result of time (1.24 ns/5d) and frequency ($4.98 \cdot 10^{-15}$ for τ = 5 days) stability of UTC(AOS) timescale.

IV. CONCLUSIONS

Obtained research results confirmed the possibility of predicting the values of [UTC - UTC(k)] deviations by means of GMDH type neural network on the basis of data prepared according to deviations determined by UTC and UTCr scales for UTC(k) time scales realized on the basis of hydrogen masers.

Publication of $xbr(t)$ deviations is delayed to three days in relation to several days delay in publication of $xb(t)$ deviations. This means better quality of prediction for UTC(k) timescales based on the deviation determined by the UTC Rapid scale than in the case of the predicting the deviations based only on the deviation determined by the UTC scale.

Better prediction quality of the UTC(AOS) timescale is achieved for input data prepared on the basis of time series TS2. This time series is based solely on the deviations determined according to UTC and UTCr scales. In the case of time series TS1, the measurement results of comparison of the UTC(AOS) scale with hydrogen maser realizing this scale have been used for its construction. These results show irregular high "jumps" in phase time values. This has resulted in poorer predictions results for the TS1 time series compared to the results obtained for the time series TS2.

REFERENCES

[1] BIPM Annual Report on Time Activities, vol. 9, Sevres BIPM, 2014.

[2] F. Arias, G. Panfilo and G. Petit, "Timescales at the BIPM," Metrologia vol. 48, no. 4, pp. 145-153, 2011.

[3] G. Panfilo, "The new prediction algorithm for UTC: application and results," in Proc. Eur. Frequency Time Forum, April 2012, pp. 242-246.

[4] L. G. Bernier, "Use of the Allan deviation and linear prediction for the determination of the uncertainty on time calibrations against predicted timescales," IEEE Transactions on Instrumentation and Measurement, vol. 52, no. 2, pp. 483-486, 2003.

[5] A. Czubla, J. Konopka, and J. Nawrocki, "Realization of atomic SI second definition in context UTC(PL) and TA(PL)," Metrology & Measurement Systems, vol. 12, no. 2, pp. 149-159, 2006.

[6] J. A. Davis, S. L. Shemar, and P. B. Whibberley, "A Kalman filter UTC(k) prediction and steering algorithm," in Proc. Joint IEEE FCS EFTF, May 2011, pp. 779-784.

[7] G. Panfilo and P. Tavella, "Atomic clock prediction based on stochastic differential equations," Metrologia, vol. 45, no. 6, pp. 108-116, 2008.

[8] J. Kaczmarek, W. Miczulski, M. Kozioł and A. Czubla, "Integrated system for monitoring and control of the national time and frequency standard," IEEE Transactions on Instrumentation and Measurement, vol. 62, no. 10, pp. 2828-2838, 2013.

[9] W. Miczulski and L. Sobolewski, "Influence of the GMDH neural network data preparation method on UTC(PL) correction prediction results," Metrology and Measurement Systems, vol. 19, no. 1, pp. 123-132, 2012.

[10] M. Luzar, L. Sobolewski, W. Miczulski and J. Korbicz, "Prediction of corrections for the Polish time scale UTC(PL) using artificial neural networks," Bulletin of the Polish Academy of Sciences: Technical Sciences, vol. 61, no. 3, pp. 589-594, 2013.

[11] L. Sobolewski, "Predicting the corrections for the Polish Timescale UTC(PL) using GMDH and GRNN neural networks," in Proc. Eur. Frequency Time Forum, June 2014, pp. 475-478.

[12] M. Norgard, O. Ravn, N. Poulsen, L. Hansen, Networks for Modelling and Control of Dynamic Systems, Springer Verlag, 2000

[13] R. Tadeusiewicz, "About usefulness of neural networks in electrical engineering problems," Electrical Review, no. 2, pp. 200-211, 2009.

[14] J. Korbicz, "Artificial neural networks and their application in electrical and power engineering," Electrical Review, no. 9, 194-200, 2009.

[15] O. Nelles, Nonlinear System Identification. From Classical Approaches to Neural Networks and Fuzzy Models, Springer Verlag, 2001

[16] L. Sobolewski, Predicting the Polish timescale UTC PL based on the corrections designated by the UTC and UTCr scale, in Proc. Joint UFFC, EFTF and PFM, July 2013, pp. 658-661.

[17] W. Miczulski and L. Sobolewski, "Algorithm for predicting [UTC-UTC(k)] by means of neural networks," IEEE Transactions on Instrumentation and Measurement, DOI: 10.1109/TIM.2017.2674778 , 2017.

[18] L. Sobolewski, "Application of the neural networks for predicting the corrections for the national timescale UTC(PL)", University of Zielona Gora Press, 2016.

[19] L. Sobolewski and W. Miczulski, "Application of neural networks for predicting selected time scales on the basis of UTC and UTCr scales," Electrical Review, no. 10, pp. 258-261, 2016.

[20] L. Sobolewski, "Predicting the Lithuanian Timescale UTC(LT) by means of GMDH neural network," unpublished

[21] R. B. Caldwell, "Performance metrics for neural network-based trading system development," NeuroVest Journal, vol. 3, pp. 22-26, 1995.

[22] R. S. Pindyck and D. C. Rubinfeld, Econometric Models and Economic Forecasts, Boston, USA: McGraw Hill, 1998.

[23] W. J. Riley, NIST Special Publication 1065, Handbook of Frequency Stability Analysis, National Institute of Standards and Technology, 2008.

Mesoscopic Physics in Vapor-Cell Atomic Clocks

James Camparo and Andrew Hudson
Physical Sciences Laboratories
Mail Stop: M2/253
The Aerospace Corporation, PO Box 92957, Los Angeles, CA 90009
james.c.camparo@aero.org

***Abstract* — In the early 1980s, it was common to hear that Rb atomic clocks were limited to $\sigma_y(\tau) = 10^{-11}/\tau^{1/2}$ at best, and that their ultimate frequency stability could never be better than low-parts of 10^{-13}. Twenty-first century Rb clocks put the lie to those pronouncements. Today, it is not uncommon for vapor-cell clocks to exhibit short-term stabilities at low-parts of $10^{-13}/\tau^{1/2}$, and ultimate stability levels in parts of 10^{-15}. Here, we discuss what it will take to improve those clocks further (*e.g.*, getting the long-term stability to break into the 10^{-16} range). Specifically, it is our contention that next steps will require a better understanding of *mesoscopic physics* in vapor-phase systems: atomic phenomena occurring on a scale between the microscopic level of quantum dynamics and the macroscopic level of vapor temperature and pressure. Though at present we have some understanding of mesoscopic physics and its effects, much more needs to be understood. Further, while past and present advances have been driven by "one-off" phenomenological discoveries, it is our opinion that rapid advancement will be best facilitated by a more overarching vision of mesoscopic vapor-phase physics, which at present is lacking.**

Keywords—Rb atomic clock, RAFS, vapor-cell clock, light-shift, position-shift, diffusion, mesoscopic

I. Introduction

In the early 1980s, in reviews of atomic clocks and predictions of future developments, one often heard claims that the vapor-cell atomic clock had reached its limit with regard to frequency stability: the device's short-term stability would never improve beyond $10^{-11}/\tau^{1/2}$, and the clock's ultimate stability could never be expected to get much below 10^{-13}. Figure 1 illustrates how wrong those claims were, as space applications of Rb clocks drove improvements in the device's frequency stability. Since 1978 the short-term performance of high-quality (*i.e.*, GNSS) Rb clocks has improved by two orders of magnitude, so that today $\sigma_y(\tau) \sim 2\times10^{-13}/\tau^{1/2}$ is not overly remarkable [1,2].

Timekeeping, of course, is rarely limited by the short-term frequency stability of a standard. Rather, it is the device's performance at averaging times of 10^4 seconds and longer that plays the primary role in a clock's time-error buildup. Figure 2 shows the evolution in stability of high-quality vapor-cell clocks at 10^4 seconds averaging time over the past decades; and though caution must be exercised in extrapolations of such data, there is nonetheless a clear suggestion that in the not-too-distant future the vapor-cell clock could break into 10^{-16} region. The issue we address in this correspondence is what it will take to achieve that goal.

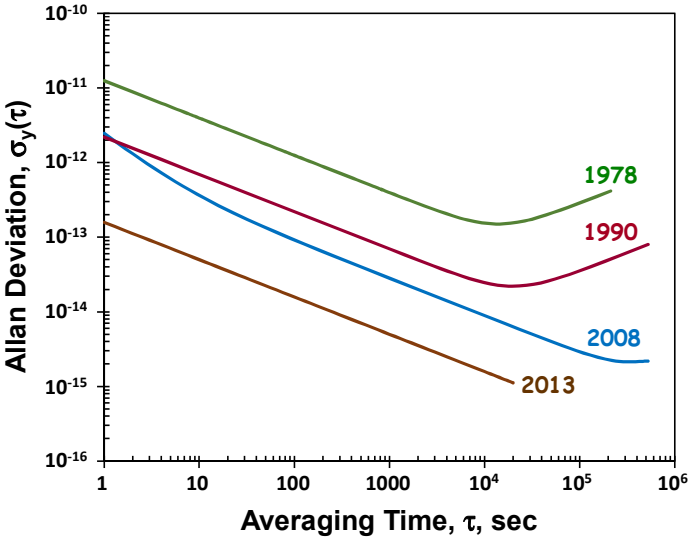


Figure 1: Improvement in the frequency stability of high-quality Rb atomic clocks over time: the curve labeled 1978 is the Allan deviation (ADEV) of a a GPS-I Rb clock [2], that labeled 1990 corresponds to a GPS-IIR clock [3], the 2008 curve is the ADEV of a GPS-IIF Rb clock [4], and the curve labeled 2013 shows results from a laboratory-version pulsed-optically-pumped Rb clock [5], which is a contender for next-generation GNSS missions [6]. As the figure shows, from 1978 to today, the white-noise frequency stability has improved by two orders of magnitude.

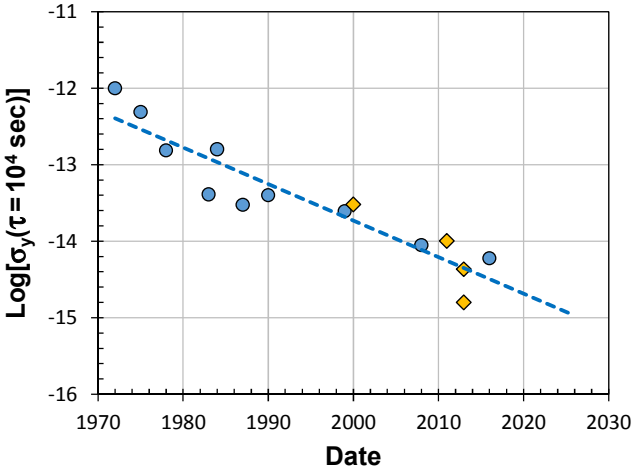


Figure 2: The Allan deviation at $\tau = 10^4$ sec for high-quality vapor-cell clocks over time [2-15]. Circles correspond to lamp-pumped clocks, while diamonds correspond to laser-pumped clocks.

Development of the vapor-cell atomic clock goes back to the 1950s [16], and since that time the device has been under continual improvement and modification [17]. Consequently, it would be reasonable to believe that there is little physics to discover regarding the vapor-cell clock, and that the device's improvement now relies solely on good solid engineering. "Don't we already know as much as we need to know about the light shift?" "Isn't optical pumping a much-studied area of atomic physics?"

It is our opinion that the answers to such questions is "yes… but." Specifically, there is no argument that we have a very good understanding of the *microscopic* atomic dynamics of vapor-phase systems: we can set up the density matrix equations for a multi-level atom, include perturbations on the atom of various type, and solve those equations numerically if necessary to predict the atom's behavior under any arbitrary set of conditions. However, evidence has been mounting over the years that there is another scale of physics that we only poorly understand, and which for lack of a better term we refer to here as the *mesoscopic* scale of physics.

By mesoscopic, we mean a scale larger than the atom's microscopic quantum dynamics, but smaller than the resonance cell volume, which confines the vapor. This scale is important, because in most vapor-phase systems the atoms are effectively frozen in place by buffer-gas collisions on time intervals long compared to the Rabi period of the resonant interaction. Thus, the atoms in the vapor's signal volume experience *local* perturbations, which combine nonlinearly to produce the device's overall atomic signal. Moreover, it is important to recognize what we are aiming for when we speak of "10^{-16} frequency stability levels at 10^4 seconds averaging time": we want to find the center of a ~ 10 GHz ground-state hyperfine resonance to μHz, and we want this determination of the atom's resonant frequency to not vary at that same level over time intervals of multiple hours… no matter how the environment of the signal volume might change.

In the next section we will provide several examples of mesoscopic physics and its influence on vapor-cell clock performance, illustrating the complexities that can arise. In Section III, we will outline our recent experiments to add to this data base. Finally, in Section IV we will sketch an overarching theory of mesoscopic physics for vapor-phase systems, the validity and details of which will need to be addressed by future research.

II. Mesoscopic Physics and the Vapor-Cell Clock's Atomic Signal

A. The Position Shift & Inhomogeneous Light Shift

One of the earlier examples of mesoscopic vapor-phase physics and its influence on Rb clock stability is the position-shift effect [18,19]. Due to the spatial variation of light intensity resulting from simple Beer's law absorption in the Rb clock's resonance cell, combined with the microwave field's mode geometry when the resonance cell is placed inside a microwave cavity, not all regions of the vapor contribute equally to the generation of the clock's atomic signal. Some regions of the vapor contribute more than others [20], and local perturbations (*e.g.*, the quadratic Zeeman shift) existing within those important regions play a dominant role in defining the overall clock's output frequency. When the microwave power changes, the dominant region can shift to a new location with a different local perturbation as illustrated in Fig. 3. This gives the Rb clock's output frequency a sensitivity to microwave power that is completely independent of the Bloch-Siegert shift [21,22]. Very generally, this shift appears to have a magnitude of 10^{-11}/dB [23].

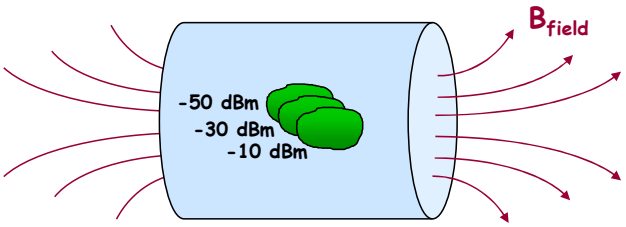
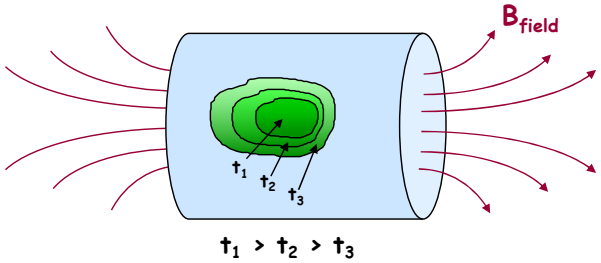


Figure 3: Illustration of the position-shift effect. In the vapor-cell clock, the atomic signal is not generated uniformly throughout the resonance cell. Rather, some regions contribute more than others, and local perturbations within those important regions play a dominant role in determining the clock's output frequency. In the case of the position-shift effect, if the microwave power changes the location of the dominant region will change, giving the clock's output frequency a sensitivity to microwave power.

Similar considerations give rise to the inhomogeneous light shift [24]. In that case, the source of the local perturbation is the ac-Stark shift or light-shift [25,26], which varies spatially due to: 1) Beer's law attenuation of the light as it propagates through the vapor, and 2) the light-field's radial profile. When the light intensity changes, the dominant region shifts to a new location with a different local light shift; and this gives the clock's output frequency a nonlinear dependence on light intensity.

B. The Pseudo Light Shift



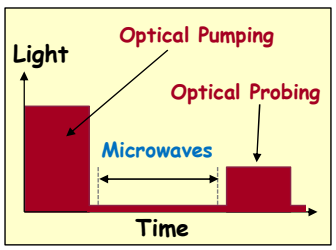


Figure 4: Illustration of the pseudo light shift. When the light is significantly attenuated, for probing of the atoms with the microwaves, the hyperfine polarization in the vapor relaxes. As the polarization relaxes, the shape of the dominant signal-generating region in the vapor changes with a subsequent change in the influence of local perturbations on the overall clock's signal.

Since the light shift is an important perturbation affecting the vapor-cell clock's signal, a number of researchers have proposed pulsed optical pumping as a means of circumventing the perturbation. Briefly, and in the most straightforward approach, the optical pumping light is turned on for a period of time long enough to allow hyperfine polarization to build up and reach steady-state. Of course, this hyperfine polarization will not have the same magnitude throughout the vapor, and certain regions will attain higher levels of polarization than others.

After the system reaches steady-state, the light is turned off (or significantly attenuated), and the atomic vapor interacts with a microwave field that drives the 0-0 hyperfine transition. Since the microwave transition is probed in the absence of light, there is in principle no light shift. However, in the absence of the optical pumping light, the hyperfine polarization relaxes as illustrated in Fig. 4, giving rise to a transient change in the dominant signal-generating region's shape. As the dominant signal-generating region's shape changes, so too does the integral of the local perturbations affecting the overall clock's signal (*e.g.*, the quadratic Zeeman shift). If the light intensity changes from one optical pumping cycle to another, the initial conditions on the dominant signal-generating region will be different. In other words the local perturbations for the atoms interacting with the microwaves will be different, and additionally the transient change in shape of the dominant signal-generating region may be different for the two cycles. Consequently, there can be a shift in the clock's output frequency that depends on light intensity, a "pseudo light-shift" [27], that occurs even though the atoms are probed with the microwave signal "in the dark." For the pulsed-laser optically-pumped Rb clock, this effect has been estimated at 10^{-13}/% [28].

C. Temperature-Gradient Shifts

In addition to confining the atoms to localized regions within the resonance cell, the buffer-gas also applies its own perturbation to the atom's energy-level structure via the so-called pressure shift. This is an unfortunate misnomer, as the phenomenon is more properly termed a collision shift, δy_{col}, which correctly implies that it is proportional to the *rate* of buffer-gas collisions and hence the buffer-gas number density (*i.e.*, not the buffer-gas pressure):

$$\delta y_{col} = [BG]\bar{v}\lambda_{col}. \qquad (1)$$

Here, [BG] is the number density of buffer-gas molecules in the vapor, $\bar{v}$ is the mean collisional speed, and λ_{col} is a collision-shift coefficient.

Under isobaric conditions, which must exist in the vapor under steady-state conditions, the pressure is a constant throughout the vapor. Thus, if we recognize that at *some* level there will always be a temperature gradient in the vapor, and we consider two regions at slightly different temperatures, then those two regions

$$P_1 = [BG]_1 kT_1 = [BG]_2 kT_2 = P_2, \qquad (2a)$$

which yields

$$\frac{\delta y_{col}(1)}{\delta y_{col}(2)} \cong \frac{T_2}{T_1},^{1} \qquad (2b)$$

where $\delta y_{col}(J)$ is the collision shift in region J.

Given a temperature gradient, there must be a buffer-gas density gradient in the vapor, which results in spatial variations of the atom's resonant frequency [29]. Conceptually, these spatial variations of the collision shift will act very much like spatial variations of the quadratic Zeeman shift due to an inhomogeneous C-field, and consequently can be expected to contribute to the position shift.

To put this "temperature-gradient shift" in context, we can rewrite Eqs. (1) and (2b) as

$$\delta y_{col}\left(\langle T\rangle + \delta T\right) = P_o \frac{\bar{v}\lambda_{col}}{k\langle T\rangle}\left(1+\frac{\delta T}{\langle T\rangle}\right)^{-1}, \qquad (3)$$

where P_o is the fill pressure of the buffer gas, $\langle T\rangle$ is the average temperature of the vapor over the signal volume, and δT is the difference in temperature from the average. Taking $^{87}Rb/N_2$ as an example and P_o in torr [30], and considering small temperature gradients, Eq. (3) yields

$$\delta y_{col}\left(\langle T\rangle + \delta T\right) - \delta y_{col}\left(\langle T\rangle\right) = -7.6\times10^{-8} P_o\left(\frac{\delta T}{\langle T\rangle}\right). \qquad (4)$$

In words, the collision shift puts a large lever arm on temperature gradients, so that if we consider a buffer gas pressure of 25 torr and an average signal-volume temperature of 50 ºC, then a temperature gradient of only 100 μK would produce a resonant frequency gradient of 6×10^{-13}. Consequently, to reach frequency stability levels of 10^{-16} under these conditions, this extremely small temperature gradient would need to be stabilized (over the long term of several hours) at levels of 0.1%. To illustrate the seriousness of this mesoscopic effect, this mechanism has been shown to play a dominant role in the long-term stability of laser-pumped Rb clocks [1,31].

D. Saturaton Broadening by Inhomogeneous Fields

In addition to clock-frequency shifts, mesoscopic phenomena can also affect the overall atomic-signal lineshape. In particular, for optimum signal-to-noise ratio and atomic line-Q, the atomic system should typically be close to saturation: if the resonant field's intensity is much lower than the saturation intensity, then there will be a degradation of signal-to-noise; if the resonant field's intensity is much higher than the saturation intensity, then there will be a loss of atomic line-Q due to saturation broadening. From a mesoscopic perspective, given an inhomogeneous field arising (for example) from the mode geometry of a microwave cavity, not all locations within the signal volume will saturate at the same input power level. This

[1] In addition to the difference in the two regions' buffer-gas densities, the difference in temperature implies that the collisional velocities and collision-shift coefficients will also be different in the two regions. We assume that these latter differences are small; hence the use of the approximately-equal sign.

can give rise to distorted overall atomic-signal lineshapes, and thereby anomalous behavior regarding the vapor-cell clock's short-term stability as a function of resonant field amplitude [32].

In the next section, we describe our experiments to expand this list of mesoscopic phenomena outlined above. In particular, we present our first results examining light-broadening in a vapor phase system when the interplay between optical-pumping light-beam geometry and resonance-cell geometry cannot be ignored as a consequence of mesoscopic considerations.

III. Mesoscopic Physics & Light-Broadening

A. Experiment

Figure 5 is a block diagram of our experimental arrangement. A VCSEL diode laser at 780 nm is locked to the $5^2S_{1/2}(F_g=2) \rightarrow 5^2P_{3/2}$ transition of ^{87}Rb in a cell containing isotopically enriched Rb and 10 torr of N_2 as a buffer gas. The laser light is also expanded and then apertured (to make a "top-hat" beam) before passing into our resonance cell, also containing isotopically enriched ^{87}Rb and 10 torr N_2. The beam diameter in the resonance cell is $2R_{laser} \cong 0.27$ cm; the cell has a diameter of $2R_{cell} = 2.5$ cm, and the cell length is L = 3.8 cm. The cell is located in an oven in which we can superimpose a temperature gradient along the cell length, and the oven sits inside a mu-metal tube to limit environmental magnetic fields to the axial direction. Magnetic field coils are placed outside the mu-metal tube in order to impose a controllable, axial quantization axis on the atoms.

Microwaves are derived from a frequency synthesizer; they pass through a variable attenuator, and then a +30 dB amplifier before passing to a horn that broadcasts the microwave signal to the atoms in the resonance cell. Additionally, we have the option of placing sidebands on the microwave signal at ± 10 MHz. The control voltage of the sidebands derives from a white-noise voltage source, which gives the sidebands stochastic character. If we tune one of the sidebands to the atoms' 0-0 hyperfine resonance (instead of the carrier), we then have the ability to study the interplay between stochastic fields and mesoscopic physics on vapor-cell clock signals.

The transmitted light intensity is detected with a Si photodiode, amplified, and recorded with an averaging oscilloscope. Additionally, if we modulate the microwave frequency (via the synthesizer's controls), we can pass the transmitted light to a lock-in amplifier and investigate the 1st and 2nd-harmonics of the clock signal. For the present study, we simply scanned the microwave frequency and investigated the 0-0 hyperfine transition linewidth as a function of optical-pumping laser intensity.

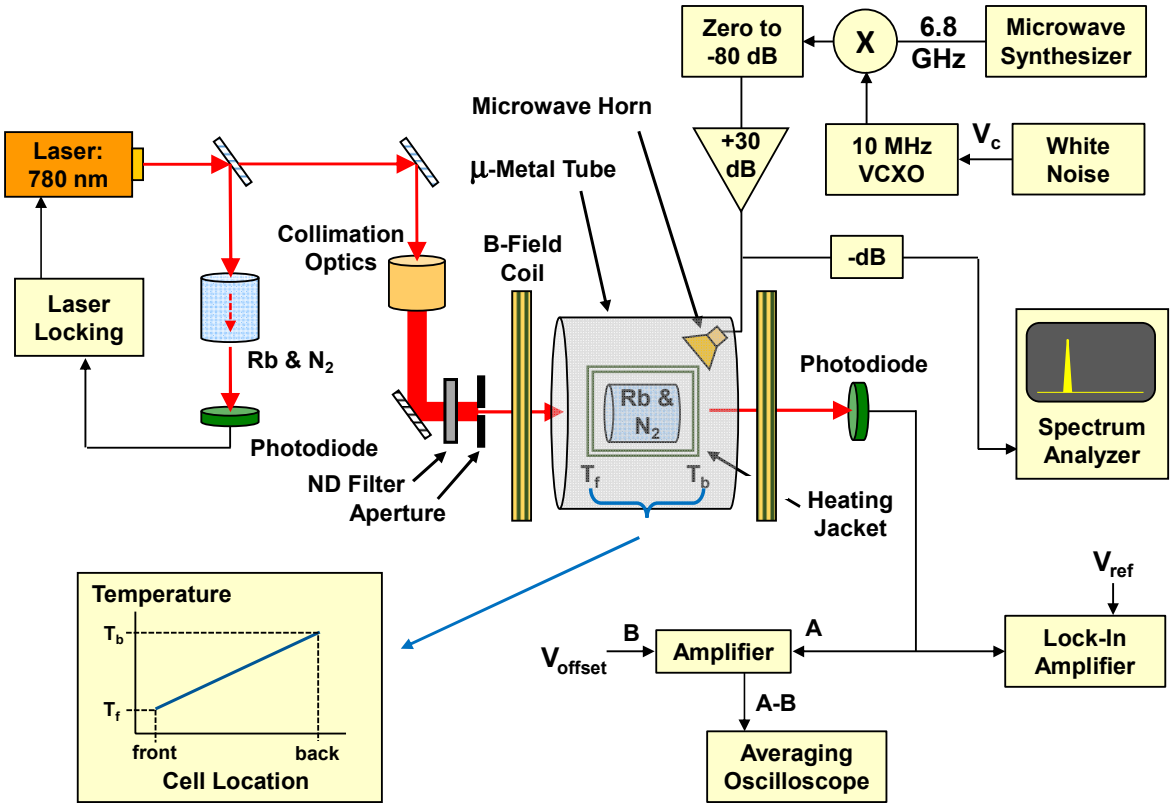


Figure 5: Block diagram of our experimental arrangement. For the present experiment, the signal passes from the photodiode to an amplifier and then an averaging oscilloscope. However, we also have the option (if the microwave frequency is modulated) of having the signal pass to a lock-in amplifier referenced to the microwave modulation frequency. If necessary, attenuation is placed in the microwave signal path to protect the spectrum analyzer's input.

B. First Results

Figure 6 shows the absorption spectrum of our resonance cell at room temperature taken with extremely low light intensity (*i.e.*, no optical pumping): $[Rb]\sigma L = \ln[V_o/V_L]$, where V_o and V_L are the photodiode voltages measured for the light far off-resonance and near-resonance, respectively, after passing though the vapor. The data of Fig. 6 has been calibrated in terms of the cell length and alkali number density at room temperature to yield the absorption cross section: for the F_g=2 resonance $\sigma = 5.9\times10^{-12}$ cm^2. We also note that the two absorption resonances are in the ratio of the ground-state hyperfine level degeneracies (*i.e.*, 3/5) as expected. In addition, we calibrated the photodiode signal to laser power, P_{laser}, in the resonance cell, so that in combination with the optical absorption cross section we can make an independent assessment of the atoms' photon absorption rate, Γ_o.

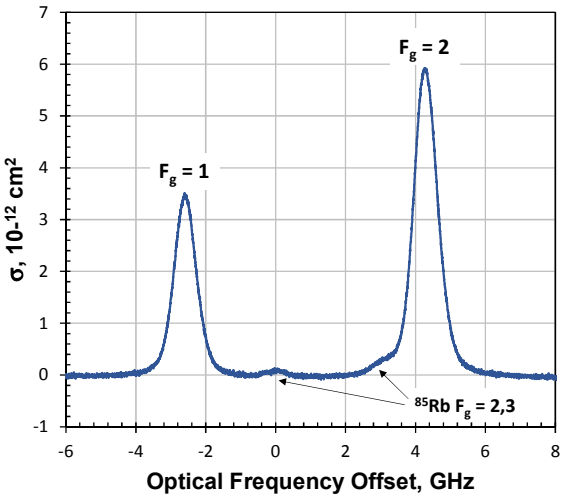
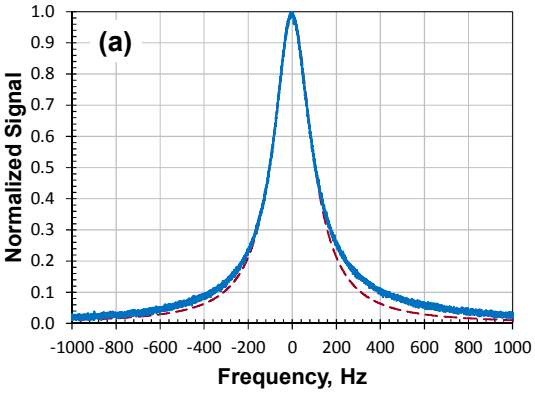


Figure 6: Optical absorption cross section for our ^{87}Rb resonance cell with 10 torr N_2.

In order to study the mesoscopic physics of light-broadening for the 0-0 transition, we set the light intensity to a specific value using neutral density filters, and then converted this to a photon absorption rate using our V_o-to-P_{laser} calibration along with the F_g=2 absorption cross section. We then measured the 0-0 transition lineshape as a function of microwave power, extrapolating to zero microwave power in order to infer the light-broadened linewidth, γ (HWHM). Microwave power was measured by examining the microwave signal prior to the horn with a spectrum analyzer. An example of a 0-0 transition lineshape is shown in Fig. 7a, and the microwave extrapolation for that particular light intensity is shown in Fig. 7b. Data were taken at T = 54 ºC with no temperature gradient (*i.e.*, $[Rb]\sigma L = 3.9 \pm 0.3$ for F_g=2). Consequently, these data correspond to a thick vapor under conditions of $R_{laser}/R_{cell} << 1$.

The primary result of the present work is shown in Fig. 8, where the light-broadened linewidth γ is plotted as a function of photon absorption rate Γ_o. Clearly, the most surprising result is the near independence of the light-broadened linewidth on photon absorption rate. Specifically, if we take $\gamma = \beta\Gamma_o+\gamma_o$, we find for the experimental data $\beta = (1.5 \pm 0.5)\times10^{-3}$ and γ_o = (75.9 ± 2.2) Hz. This slope is in severe disagreement with expectations based on the physics of microscopic atomic dynamics, where β is predicted to have the value ½ [33].



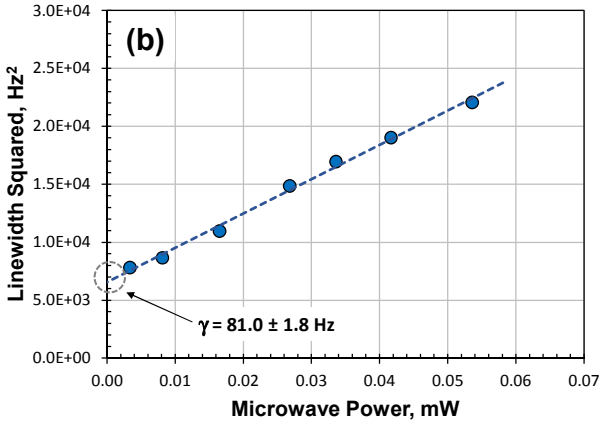


Figure 7: (a) Example of our measured 0-0 transition lineshape for $\Gamma_o \equiv (110 \pm 10)$ Hz; the solid line is the data, while the dashed line is a Lorentzian fit to the data considering that portion of the lineshape with normalized signal ≥ 0.5. (b) The linewidth squared plotted as a function of microwave power, showing a light-broadened linewidth of 81 Hz (HWHM). We measure the microwave signal power into the horn with a spectrum analyzer.

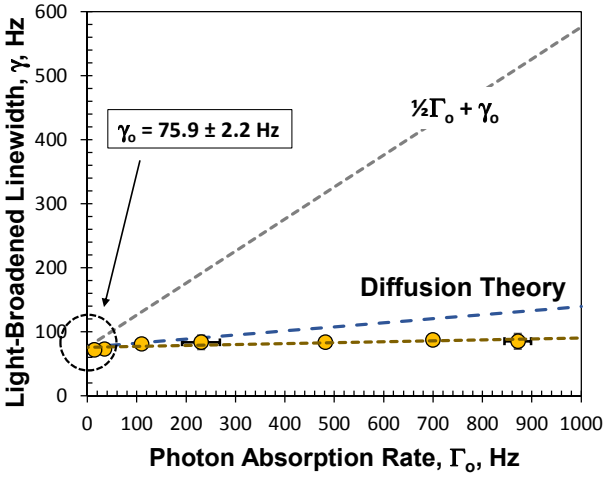


Figure 8: Light-broadened 0-0 transition linewidth vs. photon absorption rate, Γ_o. The slope of the data is significantly less than the microscopic quantum dynamic theory's prediction of $\Gamma_o/2$. The "Diffusion Theory" line considers the interplay between laser-beam and resonance-cell geometries on light-broadening.

C. Discussion

Recently, we developed a semi-quantitative theory of light-broadening for the 0-0 hyperfine transition considering the role of diffusional relaxation [34]. In brief, the optical pumping of vapor-phase systems is not a case of a few straight-forward rate equations; rather, one must carefully consider the role of diffusion in those equations [35,36]. In particular, when one has $R_{laser}/R_{cell} << 1$, a great many diffusion modes will contribute to the spatial variation of polarization in the resonance cell, and each of those modes will have its own longitudinal relaxation rate. Recognizing the interplay between laser beam geometry and cell geometry in the diffusion problem, the semi-quantitative theory defines a "vapor-wide" longitudinal relaxation rate, labeled as $1/T_1$:

$$\frac{1}{T_1} \equiv \frac{\sum_{\nu n} W_{\nu n}\, \gamma_{\nu n}}{\sum_{\nu n} W_{\nu n}}, \tag{5a}$$

$$W_{\nu n} = \left| \frac{A_{\nu n}}{J_1(x_{o\nu})} \right| e^{-\gamma_{\nu n}/\gamma_{11}}, \tag{5b}$$

In these expressions, $\gamma_{\nu n}$ is the relaxation rate for a specific diffusion mode, defined by two mode numbers ν and n, which are related to the radial and axial variation of the polarization for that mode, respectively. $W_{\nu n}$ is a weighting factor for the mode's contribution to vapor-wide longitudinal relaxation, and $A_{\nu n}$ is a diffusion mode amplitude related to Γ_o and the geometry of the situation.

To go from these vapor-wide longitudinal relaxation rates to a mesoscopic linewidth that incorporates laser-beam/resonance-cell geometry, we first note that under thin-vapor conditions and with $R_{laser}/R_{cell} >> 1$ we know that the 0-0 linewidth will be given by $\frac{1}{2}\Gamma_o+\gamma_o$ [33]. Thus, we can define a longitudinal/transverse relationship factor:

$$\kappa \equiv \frac{\frac{1}{2}\Gamma_o + \gamma_o}{1/T_{1,o}}, \tag{6}$$

where $1/T_{1,o}$ is the vapor-wide longitudinal relaxation rate computed from Eqs. (5) under thin-vapor and wide laser-beam conditions. Then, under all conditions we can write

$$\frac{1}{T_2} \equiv \frac{\kappa}{T_1}, \tag{7}$$

where $1/T_2$ is a vapor-wide transverse relaxation rate, which becomes an estimate of γ. In Fig. 8, the line labeled as "Diffusion Theory," shows $1/T_2$ vs. Γ_o, and we note that this theory is in quite good agreement with the measurements.

In these experiments, we have discovered another example of mesoscopic physics affecting the atomic clock signal in a vapor-phase system. Specifically, when high-order diffusion modes cannot be ignored in the physical situation, giving rise to spatial variations of clock signal (*i.e.*, hyperfine polarization) on scales smaller than the resonance cell diameter and length, the dependence of the hyperfine linewidth on physical parameters may be significantly different than that predicted from theories based on microscopic quantum dynamics.

IV. Outline of an Overarching Theory of Mesoscopic Vapor-Cell Physics

To date, our understanding of mesoscopic physics in the vapor-cell atomic clock has come from serendipitous phenomenological discoveries:

1. The position shift,
2. The pseudo light shift,
3. The temperature-gradient shift,
4. Inhomogeneous fields affecting saturation broadening, and (most recently)
5. Light-beam geometry affecting light-broadening.

Obviously, we could continue in this fashion, discovering one new phenomenon and then another, adding each time to a growing catalog of mesoscopic phenomena and their effects. However, while such a catalog will certainly be useful for understanding vapor-cell clock physics, it will not necessarily bring us closer to identifying an *optimum path* for vapor-cell clock improvement. What seems to be lacking is an overarching view of mesoscopic physics in vapor-phase systems. In this section, as an initial step in addressing that absence, we sketch a vision of an overarching mesoscopic-physics theory.

To begin, we consider microscopic quantum dynamics and consider the atom's evolution under a Hamiltonian $H(\vec{r},t)$:

$$H(\vec{r},t) = H_a + H_o(\vec{r}) + H_f(\vec{r},t). \tag{8}$$

Here, H_a is the atomic Hamiltonian describing the unperturbed atom's energy level structure, $H_f(\vec{r},t)$ describes the atom's interaction with light fields for optical pumping and microwave fields for magnetic resonance, and $H_o(\vec{r})$ describes "other" perturbations on the atom. These other perturbations would obviously include the quadratic Zeeman shift, but we also consider them as including collisional shifts and collisional broadening.

Describing the atom's dynamics in terms of the density matrix, ρ, and working in the Interaction Picture, the Louisville equation for ρ becomes [37].

$$\frac{\partial \rho(\vec{r},t)}{\partial t} = D\nabla^2\rho(\vec{r},t) - \frac{i}{\hbar}[V(\vec{r},t),\rho(\vec{r},t)] - R(\vec{r})[\rho(\vec{r},t)-\rho_o] \tag{8a}$$

where

$$V(\vec{r},t) \equiv e^{iH_a t/\hbar} H(\vec{r},t) e^{-iH_a t/\hbar}. \tag{8b}$$

In Eq. (8a), we have reformulated the density matrix equations in terms of a master equation [37], so that $V(\vec{r},t)$ not only includes the perturbations arising from all fields, but also the energy shift arising from (for example) collisions, while R is a tensor describing the relaxation (longitudinal and transverse) that comes from collisions; ρ_o is the density matrix for the

atom in the absence of all fields. Notice that diffusional relaxation has been explicitly included in the Louisville equation with D the diffusion coefficient.

To proceed, we now say that there is some "importance" function of position within the signal volume, $f(\vec{r})$:

$$\int_{\text{Sig.Vol.}} f(\vec{r})\,d^3\vec{r} = 1 \cdot \tag{9}$$

This function essentially gives a weight to regions in the signal volume with regard to their importance in defining the overall atomic signal of the clock. Then, averaging the Louisville equation with this importance function we have

$$\frac{\partial}{\partial t}\int_{\substack{\text{Sig.}\\ \text{Vol.}}} \rho(\vec{r},t) f(\vec{r})\,d^3\vec{r} = D\int_{\substack{\text{Sig.}\\ \text{Vol.}}} \left(\nabla^2\rho(\vec{r},t)\right) f(\vec{r})\,d^3\vec{r}$$

$$-\frac{i}{\hbar}\int_{\substack{\text{Sig.}\\ \text{Vol.}}} [V(\vec{r},t),\rho(\vec{r},t)] f(\vec{r})\,d^3\vec{r} \cdot$$

$$-\int_{\substack{\text{Sig.}\\ \text{Vol.}}} R(\vec{r})[\rho(\vec{r},t)-\rho_o] f(\vec{r})\,d^3\vec{r} \tag{10}$$

We now go a bit further and assume that as a consequence of this averaging, the density matrix at any location within the signal volume can be reasonably well approximated by the first few terms of a Taylor series expansion of the density matrix about some special location, $\vec{a}$. In other words, we assume that there is some location in the vapor that captures much of the atomic dynamics occurring at any location within the signal volume. The value of the hypothetical point $\vec{a}$, compared to any other point $\vec{b}$ within the vapor, is that for any location within the signal volume the Taylor series has the fewest expansion terms when the density matrix is expanded about $\vec{a}$. Thus, we write

$$\rho(\vec{r},t) = \rho(\vec{a},t) + (\vec{r}-\vec{a})\cdot\vec{\nabla}\rho(\vec{r},t)\Big|_{\vec{r}=\vec{a}}$$

$$+(\vec{r}-\vec{a})\cdot Q(\vec{a},t)\cdot(\vec{r}-\vec{a}) + \ldots, \tag{11}$$

where $Q(\vec{a},t)$ is the Hessian matrix of $\rho(\vec{r},t)$ evaluated at $\vec{a}$. Specifically, if we write the last term on the right-hand-side of Eq. (11) explicitly we have

$$(\vec{r}-\vec{a})\cdot Q(\vec{a},t)\cdot(\vec{r}-\vec{a}) = \sum_{i,j}(x_i-a_i)(x_j-a_j)\frac{\partial^2\rho(\vec{r},t)}{\partial x_i \partial x_j}\Big|_{\vec{r}=\vec{a}} \tag{12}$$

Expanding $\rho(\vec{r},t)$ in Eq. (10) with the Taylor series of Eq. (11), and retaining only lowest order terms in the expansion yields

$$\frac{\partial\rho(\vec{a},t)}{\partial t} = D\nabla^2\rho(\vec{r},t)\Big|_{\vec{r}=\vec{a}} - \frac{i}{\hbar}[\Lambda(t),\rho(\vec{a},t)],$$

$$-\langle R\rangle[\rho(\vec{a},t)-\rho_o] \tag{13a}$$

where

$$\Lambda(t) \equiv \int_{\text{Sig.Vol.}} V(\vec{r},t) f(\vec{r})\,d^3\vec{r} \cdot \tag{13b}$$

$$\langle R\rangle \equiv \int_{\text{Sig.Vol.}} R(\vec{r}) f(\vec{r})\,d^3\vec{r} \cdot \tag{13c}$$

Here, $\Lambda(t)$ and $\langle R\rangle$ are averages of the perturbations over the signal volume weighted by $f(\vec{r})$, and the lowest-order term that contributes to diffusion comes from the Hessian matrix $Q(\vec{a},t)$. In words, with Eq. (13a) we have reduced the problem of determining the density matrix's evolution over the entire signal volume *to a problem of determining the density matrix's evolution at a single point within the vapor*. Finally, recognizing that in some limit we expect

$$D\nabla^2\rho(\vec{r},t)\Big|_{\vec{r}=\vec{a}} \to D\frac{\rho(\vec{a},t)-\rho(\vec{R},t)}{\left|\vec{R}-\vec{a}\right|^2}, \tag{14}$$

where $\rho(\vec{R},t)$ is the density matrix evaluated at the vapor-cell boundaries, we make the ansatz that we can write Eq. (13a) in the form

$$\frac{\partial\rho(\vec{a},t)}{\partial t} = -\left(\langle R\rangle + \gamma_D(\vec{a})\right)[\rho(\vec{a},t)-\rho_o] - \frac{i}{\hbar}[\Lambda(t),\rho(\vec{a},t)]. \tag{15}$$

Here, $\gamma_D(\vec{a})$ is a diffusional relaxation rate that depends on the location $\vec{a}$ and diffusion coefficient D.

Thus, the mesoscopic theory of vapor-phase physics sketched here comes down to the determination of two functions: $f(\vec{r})$ and $\gamma_D(\vec{a})$. Finding (for example) universal scaling laws for these functions, and how the functions vary with regard to microwave power, optical-pumping light intensity, vapor temperature, etc. will form the crux of developing an overarching framework of mesoscopic physics… unfortunately, a not insignificant task.

V. SUMMARY

Contrary to pronouncements of vapor-cell clock stability limits in the early 1980s, the vapor-cell atomic clock today has broken those limits by orders-of-magnitude, and shows considerable promise for further improvement. It is our contention that realizing that promise will require a better understanding of mesoscopic physics in vapor-phase systems, a scale of phenomena larger than the microscopic scale of quantum dynamics, but smaller than the global scale of resonance-cell temperature and pressure.

In the present work, we cataloged a number of mesoscopic phenomena important to vapor-cell atomic clocks, and we added to that catalog by discussing the influence of laser-beam geometry on the light-broadening of 0-0 transition lineshapes. Additionally, we sketched an overarching theory of mesoscopic physics in vapor-phase systems that reduces the atomic dynamics averaged over the signal volume to atomic dynamics at one location within the vapor. The extent to which that theoretical sketch will prove of any value must depend on future investigations.

ACKNOWLEDGMENT

The authors thank Hunter Alexander for considerable assistance in performing the experiments.

REFERENCES

[1] T. Bandi, C. Affolderbach, C. Stefanucci, F. Merli, A. K. Skrivervik, and G. Mileti, "Compact high-performance continuous-wave double-resonance rubidium standard with 1.4×10^{-13} $\tau^{-1/2}$ stability," IEEE Trans. Ultrason. Ferroelec. & Freq. Control, vol. 61, pp. 1769-1778, 2014.

[2] I. Bablewski, J. Coffer, T. Driskell, and J. Camparo, "Progress in the development of a simple, laser-pumped, vapor-cell clock," in Proc. 43rd Annual Precise Time and Time Interval (PTTI) Systems and Application Meeting. US Naval Observatory: Washington, DC, 2011, pp. 483-488.

[3] F. K. Koide and D. J. Dederich, "Rubidium frequency standard test program for NAVSTAR GPS," in Proc. 10th Annual Precise Time and Time Interval (PTTI) Systems and Application Meeting. US Naval Observatory: Washington, DC, 1978, pp. 379-392.

[4] W. J. Riley, "Rubidium atomic frequency standards for GPS Block IIR," in Proc. 22nd Annual Precise Time and Time Interval (PTTI) Systems and Application Meeting. US Naval Observatory: Washington, DC, 1990, pp. 221-230.

[5] R. T. Dupuis, T. J. Lynch, and J. R. Vaccaro, "Rubidium frequency standard for the GPS IIF program and modifications for the RAFSMOD program," in Proc. 2008 IEEE Internat. Freq. Control Symp. IEEE Press: Piscataway, NJ, 2008, pp. 655-660.

[6] F. Levi, C. E. Calosso, A. Godone, and S. Micalizio," in Proc. 2013 Joint UFFC, EFTF and PFM Symposium. IEEE Press: Piscataway, N. J., 2013, pp. 599-605.

[7] J. C. Camparo and T. U. Driskell, "The mercury-ion clock and the pulsed-laser rubidium clock: Near-term candidates for future GPS deployment," Aerospace Report No. TOR-2015-03893, 5 October 2015. The Aerospace Corporation: El Segundo, CA, 2015.

[8] J. E. Lavery, "Operational stability of rubidium and cesium frequency standards," in Proc. 4th Annual Precise Time and Time Interval (PTTI) Systems and Application Meeting. US Naval Observatory: Washington, DC, 1972, pp. 168-181.

[9] D. E. Ringer, J. Gandy, and E. Jechart, "Spaceborne rubidium frequency standard for NAVSTAR GPS," in Proc. 7th Annual Precise Time and Time Interval (PTTI) Systems and Application Meeting. US Naval Observatory: Washington, DC, 1975, pp. 671-696.

[10] T. J. Lynch and W. J. Riley, "Test results for prototype GPS rubidium clocks," in Proc. 15th Annual Precise Time and Time Interval (PTTI) Systems and Application Meeting. US Naval Observatory: Washington, DC, 1983, pp. 269-280.

[11] H, Bethke, D. Ringer, and M. Van Melle, "Rubidium and cesium frequency standards status and performance on the GPS program," in Proc. 15th Annual Precise Time and Time Interval (PTTI) Systems and Application Meeting. US Naval Observatory: Washington, DC, 1984, pp. 127-141.

[12] F. Danzy and W. Riley, "Stability test results for GPS rubidium clocks," in Proc. 19th Annual Precise Time and Time Interval (PTTI) Systems and Application Meeting. US Naval Observatory: Washington, DC, 1987, pp. 267-274.

[13] Y. Ohuchi, H. Suga, M. Fujita, T. Suzuki, M. Uchino, K. Takahei, M. Tsuda, and Y. Saburi," in Proc. 2000 IEEE/EIA Internat. Freq. Control Symposium & Exhibition. IEEE Press: Piscataway, N. J., 2000, pp. 651-655.

[14] T. Bandi, C. Affolderbach, C. E. Calosso, and G. Mileti, "High-performance laser-pumped rubidium frequency standard for satellite navigation." Electron. Lett., vol. 47, pp. 698-699, 2011.

[15] G. Mei, D. Zhong, S. An, F. Zhao, F. Qi, F. Wang, G. Ming, W. Li, and P. Wang, "Main features of space rubidium atomic frequency standard for BeiDou satellites," in Proc. 2016 Eur. Freq. Time Forum. IEEE Press: Piscataway, N. J., DOI: 10.1109/EFTF.2016.7477803.

[16] T. R. Carver, "Rubidium oscillator experiments," in Proc. 11th Freq. Control Symp. IEEE Press: Piscataway, N. J. 1957, pp. 307-317.

[17] J. Camparo, "The rubidium atomic clock and basic research," Phys. Today, vol. 60, pp. 33-39, 2007.

[18] A. Risely and G. Busca, "Effect of line inhomogeneity on the frequency of passive Rb^{87} frequency standards," in Proc. 32nd Symp. Freq. Control. IEEE Press: Piscataway, NJ, 1978, pp. 506-513.

[19] A. Risley, S. Jarvis, Jr, and J. Vanier, "The dependence of frequency upon microwave power of wall-coated and buffer-gas-filled gas cell Rb^{87} frequency standards, J. Appl. Phys., vol. 51, pp. 4571-4576, 1980.

[20] J. C. Camparo and R. P. Frueholz, "A three-dimensional model of the gas cell atomic frequency standard," IEEE Trans. Ultrason. Ferroelec. and Freq. Control, vol. 36, pp. 185-190, 1989.

[21] L. Allen and J. H. Eberly, Optical Resonance and Two-Level Atoms,. Dover: New York, 1975, pp.47-50.

[22] E. Arimondo and G. Moruzzi, "Bloch-Siegert shift in optically oriented ^{199}Hg vapour," J. Phys. B: Atom. Molec. Phys., vol. 6, pp. 2382-2389, 1973.

[23] E. B. Sarosy, W. A. Johnson, S. K. Karuza, and F. J. Voit, "Measuring frequency changes due to microwave power variations as a function of C-field setting in a rubidium frequency standard," in Proc. 23rd Annual Precise Time and Time Interval (PTTI) Systems and Application Meeting. US Naval Observatory: Washington, DC, 1992, pp. 229-235.

[24] J. C. Camparo, R. P. Frueholz, and C. H. Volk, "Inhomogeneous light shift in alkali-metal atoms," Phys. Rev. A, vol. 27, pp. 1914-1924, 1983.

[25] B. S. Mathur, H. Tang, and W. Happer, "Light shifts in alkali atoms," Phys. Rev., vol. 171, pp. 11-19, 1968.

[26] F. Levi, J. Camparo, B. Francois, C. E. Calosso, S. Micalizio, and A. Godone, "Precision test of the ac Stark shift in rubidum atomic vapor," Phys. Rev. A, vol. 93, 023433, 2016.

[27] T. C. English, E. Jechart, and T. M. Kwon, "Elimination of the light shift in rubidium gas cell frequency standards using pulsed optical pumping," in Proc. 10th Annual Precise Time and Time Interval (PTTI) Systems and Application Meeting. US Naval Observatory: Washington, DC, 1978, pp. 147-168.

[28] S. Micalizio, A. Godone, F. Levi, and C. Calosso, "Pulsed optically pumped ^{87}Rb vapor cell frequency standard: A multilevel approach," Phys. Rev. A, vol. 79, 013403, 2009.

[29] P. J. Oreto, Y.-Y. Jau, A. B. Post, N. N. Kuzma, and W. Happer, "Buffer-gas-induced shift and broadening of hyperfine resonances in alkali-metal vapors," Phys. Rev. A, vol. 69, 042716, 2004.

[30] W. Happer, "Optical pumping," Rev. Mod. Phys., vol. 44, pp. 169-249, 1972.

[31] C. E. Calosso, A. Godone, F. Levi, and S. Micalizio, "Enhanced temperature sensitivity in vapor-cell frequency standards," IEEE Trans. Ultrason. Ferroelec. and Freq. Control, vol. 59, pp. 2646-2654, 2012.

[32] J. C. Camparo, "Saturation broadening by inhomogeneous fields," Phys. Rev. A, vol. 39, pp. 69-77, 1989.

[33] J. C. Camparo and R. P. Frueholz, "Linewidths of the 0-0 hyperfine transition in optically pumped alkali-metal vapors," Phys. Rev. A, vol. 31, pp. 1440-1448, 1985.

[34] J. C. Camparo, "The influence of diffusional relaxation on the clock signal in the laser-pumped rubidium atomic frequency standard," Aerospace Report No. TOR-2017-00316, 5 December 2016. The Aerospace Corporation: El Segundo, CA, 2015.

[35] P. Minguzzi, F. Strumia, and P. Violino, "Temperature effects in the relaxation of optically oriented alkali vapours," Il Nuovo Cimento, vol. 46B, pp. 145-162, 1966.

[36] F. A. Franz, "Relaxation at cell walls in optical-pumping experiments," Phys. Rev. A, vol. 6, pp. 1921-1925, 1972.

[37] K. Blum, Density Matrix Theory and Applications,. Plenum: New York, 1981.

Low-Power and Low-Profile Miniature Atomic Clock

Ceramic based flat form factor miniature atomic clock physics package (C-MAC)

Jacques Haesler, Laurent Balet, Sylvain Karlen,
Thomas Overstolz, Benjamin Gallinet,
Steve Lecomte and Fabien Droz
Systems, Time & Frequency
CSEM SA
Neuchâtel, Switzerland
jacques.haesler@csem.ch

Kari Kautio, Pentti Karioja and Markku Lahti
VTT Technical Research Center of Finland Ltd.
Oulu, Finland

Antti Määttänen, Ossi Lahtinen and Ville Hevonkorpi
Primoceler Oy
Tampere, Finland

***Abstract*—This paper presents the results of the ESA funded C-MAC activity, started mid-2015 and currently in the assembly and testing phase. The objective of the activity is to develop an innovative and low-cost ceramic-based physics package (PP) for ultra-low power miniature atomic clocks (MACs) with flat form factor for future portable devices (GNSS receiver, smartphone, tablet, laptop, etc.) and high-end demanding applications like on-board satellites.**

Keywords—Miniature atomic clock (MAC), chip-scale atomic clock (CSAC), low-temperature co-fired ceramics (LTCC), hermetic vacuum encapsulation, MEMS atomic vapor cell, thermal design.

I. INTRODUCTION

The capability to maintain accurate timing over extended period of time with compact and low power consumption devices is a key benefit for a number of applications.

In telecommunication and Telemetry, Tracking, and Command (TT&C) systems, a growing number of critical services require stringent integrity of the communication channel in all type of environment (in-door, intentional or unintentional jamming, spoofing…). Spread-spectrum techniques are being implemented, requiring excellent synchronization between the transmitter and the receiver. Miniature atomic clock (MAC) technology offers improved synchronization over extended period of time, thereby also improving user autonomy and system availability.

For GNSS applications and thanks to its superior timing accuracy over extended period of time, MAC guarantees fast re-acquisition of the signal and long coherence integration, thereby improving service availability in adverse environment.

Space-qualified atomic clock technology is available in Europe and is being successfully operated on-board the Galileo and GAIA spacecrafts. There is however no MAC technology available in Europe, the sole worldwide supplier being in the US (SA45.S by Microsemi Corporation). Over the last decade, efforts have been dedicated worldwide **Error! Reference source not found.** and also in Europe **Error! Reference source not found.Error! Reference source not found.** to the development of MACs at the system level, but they are limited in the size (cubic form factor) and production costs because of their technological approach. The cubic shape and high production costs are detrimental to their integration in compact portable devices and to their mass production.

This work is financed by the European Space Agency (ESA), Contract No. 4000114436/15INLIMM, "Ceramic Miniature Atomic Clock (C-MAC)".

II. OBJECTIVES

The objective of the C-MAC activity is to develop an innovative and low-cost ceramic based Physics Package (PP) for ultra-low power MACs with flat form factor for future portable devices (smartphone, tablet, laptop, GNSS receiver, etc.) and high-end demanding applications like on-board satellites.

III. PROJECT STATUS

The C-MAC activity started mid-2015 and it is currently in the manufacturing and assembly phase. We will start by presenting the detailed design of the 21 x 15 mm footprint C-MAC innovative physics package (Fig. 1) for a MAC with flat form factor (height < 5 mm), low power consumption (< 100 mW) and low production costs.

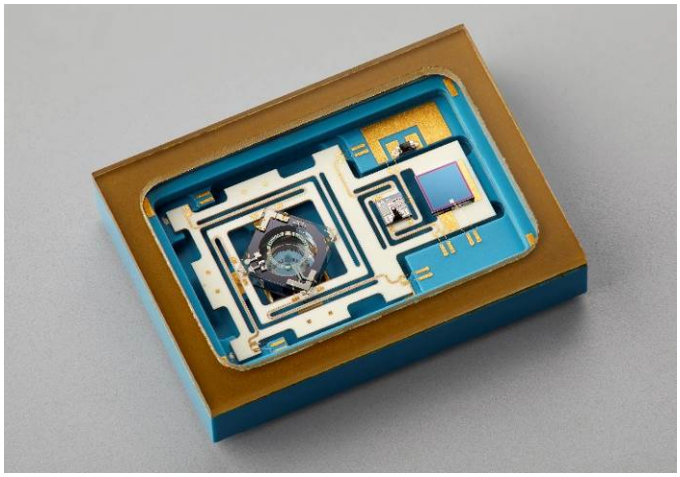


Fig. 1. Assembled C-MAC physics package without lid.

We will comment on the challenges faced during the design phase, which were tackled by implementing an innovative and

patent-pending design including low-temperature co-fired ceramic (LTCC) components, microelectromechanical system (MEMS) based atomic vapour cell (Fig. 2) and integrated diffractive optics. The low power consumption challenge will be emphasized by describing the implemented thermal design and by presenting the selected approach for low temperature and reliable vacuum encapsulation by a laser based technique.



Fig. 2. Picture of a MEMS atomic vapour cell after dicing (4 x 4 x 1.4 mm^3).

IV. Measured Power Consumption

The assembled C-MAC physics packages, prior to vacuum encapsulation, have been placed in a thermal vacuum chamber (TVC) in order to measure their power consumption as a function of pressure. The TVC temperature was set to 25°C. The VCSEL laser was biased and a self-heating corresponding to 2.5 mW was measured. The laser and the cell were then kept at 70°C and 95°C, respectively. The TVC pressure was varied from 10^{-6} to 10^{+3} mbar while the cell and laser heating powers were monitored. The heating power versus pressure curve illustrated in Fig. 3 defines the need for a vacuum level $<10^{-2}$ mbar in order to minimize the thermal losses by gaseous heat transfers. This value relaxes somehow the vacuum level constraints when compared to the 10^{-3} mbar value simulated in [4].

The overall measured C-MAC PP power consumption is in very good agreement with the thermal simulations, resulting in a measured low power consumption of 38 mW at 25°C ambient temperature. It has also been experimentally demonstrated that the maximum ambient operating temperature for the C-MAC PP is, as expected, 60°C.

V. Hermetic Vacuum Encapuslation Challenge

It has been shown above that a low-power consumption physics package can only be achieved thanks to hermetic vacuum encapsulation. Different encapsulation techniques have been evaluated and a laser based micro bonding solution has been selected. Preliminary results are very promising and we will comment on the latest results regarding the hermeticity and vacuum level achieved for the C-MAC physics packages with this technique.

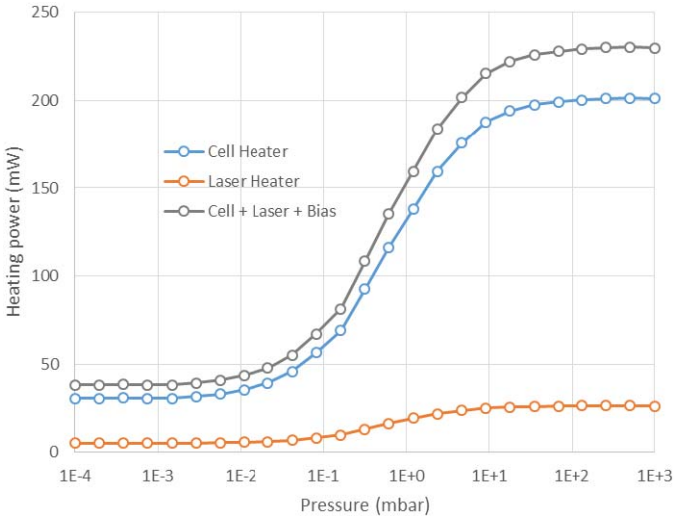


Fig. 3. C-MAC PP measured power consumption vs pressure at 25°C ambient temperature (cell at 95°C and laser at 70°C).

VI. Conclusion

The C-MAC activity targets the realization of an innovative and low-cost ceramic based physics package (PP) for ultra-low power MACs with flat form factor (height <5 mm). The project already allowed to validate the patent pending innovative design based on a planar waveguide with gratings couplers. The preliminary functional testing of the C-MAC PP as well as the low power consumption measurements in vacuum (< 40 mW) are all in line with the expectations. Hermetic vacuum encapsulation of the PP is on the good way but remains the most critical process in order to successfully reach the final objectives. State-of-the-art coherent population trapping (CPT) clock signals have been measured and will be presented.

Acknowledgment

The authors would like to thank the Swiss Confederation, the Canton of Neuchâtel, the Canton of Basel-Landschaft, the Cantons of Central Switzerland and CSEM Brazil for their collaboration and financial support for a similar and complementary development ongoing since years at CSEM. The authors would also like to thank the company Spectratime (Switzerland) for the C-MAC PP detailed design consultancy.

References

[1] S. Knappe et al., "A microfabricated atomic clock," Appl. Phys. Lett., vol. 85, pp. 1460–1462, 2004.

[2] C. Gorecki et al., "Towards the realization of the first European MEMS atomic clock", IEEE/LEOS International Conference on Optical MEMS and Nanophotonics, 2009.

[3] R. Chutani et al., "Laser light routing in an elongated micromachined vapor cell with diffraction gratings for atomic clock applications", Sci. Rep., vol. 5, p. 14001, 2015.

[4] R.K. Chutani et al., "Thermal management of fully LTCC-packaged Cs vapour cell for MEMS atomic clock", Sensors and Actuators A: Physical, vol. 174, pp. 58-68, February 2012.

[5] L. Balet et al., "Manufacturing and Functional Tests for a Flat Form Factor Miniature Atomic Clock", CSEM scientific and technical report, 2016

Impact of Static-Magnetic-Field-Gradients on Relaxation Times in a Rb Vapor Cell

Mohammadreza Gharavipour, Christoph Affolderbach, Florian Gruet and Gaetano Mileti
Laboratoire Temps-Fréquence (LTF), Institut de Physique
Université de Neuchâtel, Switzerland
Email: mohammadreza.gharavipour@unine.ch

Ivan S. Radojičić, Aleksandar J. Krmpot and Brana M. Jelenković
Institute of Physics
University of Belgrade, Serbia

***Abstract*—We apply an innovative method called Optically-Detected Spin-Echo to measure the intrinsic coherence relaxation time in the buffer-gas vapor cell of a Rb atomic clock [1]. This method suppresses the influence of static-magnetic-field-gradients across the cell which is a source of relaxation processes. Such studies are of interest for high-performance Rb atomic clocks, where both intrinsic population and coherence relaxation times (T_1 and T_2, respectively) of the "clock transition" ($5^2S_{1/2} \left| F_g = 1, m_F = 0\right\rangle \leftrightarrow \left| F_g = 2, m_F = 0\right\rangle$) are relevant.**

Keywords—Relaxation times; Spin-Echo; Rb atomic clock;

I. INTRODUCTION

Alkali vapor cells are used in precision measurements applications such as vapor cell atomic frequency standards, navigation systems, optical magnetometry and quantum information storage [2-6]. They rely on long-lived ground-state spin-polarization of the alkali vapor in the cell [7]. In a vapor-cell atomic clock, the clock stability is limited by the linewidth and contrast of the atomic resonance line, which both are influenced by the relaxation processes in the cell. Alkali atoms in a buffer-gas vapor cell may lose their polarizations due to collisions with the cell-walls, with the buffer-gas atoms, and among themselves (spin-exchange). These processes are well described by the relaxation theory in [2]. Based on this theory and above mentioned processes, we determine both intrinsic population and coherence relaxation times T_1 and T_2, respectively, approximately equal to 4.5 ms specifically for the "clock transition" ($5^2S_{1/2} \left| F_g = 1, m_F = 0\right\rangle \leftrightarrow \left| F_g = 2, m_F = 0\right\rangle$) of Rb atoms in our particular buffer-gas cell (see section II). The term "intrinsic" describes the relaxations that depend on the cell's properties only, such as cell temperature, pressure and the cell geometry, but do not depend on any external electro-magnetic field. In a vapor-cell atomic clock, a static magnetic field is applied to lift the Zeeman degeneracy. The alkali atoms may experience various static magnetic fields due to some residual static-magnetic-field-gradients (SMFG) across the cell. The SMFG may also give rise to an addition-*9nal relaxation source like in Nuclear Magnetic Resonance (NMR) [8]. In NMR experiments the total coherence relaxation time, conventionally denoted T_2*, is shorter than the intrinsic coherence relaxation time T_2 due to the static magnetic field inhomogeneity in the system that can be described by the local static magnetic field gradients, G. Then, the total coherence relaxation time is given by [9]:

$$T_2^{*-1} = T_2^{-1} + \eta\, G^2, \quad (1)$$

where η is a proportionality factor depending on atomic and experimental parameters.

In this article, we apply Optically-Detected Spin-Echo (ODSE) method demonstrated in [1] to suppress the impact of SMFG across a Rb vapor cell and measure T_2 time, while T_2* is accessed using Ramsey method [10].

II. EXPERIMENTAL SETUP

Our experimental setup is a Rb atomic clock, whose details were presented in [11]. It contains three main components: 1) a frequency-stabilized laser system, 2) the clock physics package (PP), and 3) a microwave synthesizer. The laser system [12] consists of a distributed-feedback laser diode that emits at 780 nm, an evacuated ^{87}Rb reference cell and an acousto-optical-modulator (AOM). The AOM is used as a fast switch to control the duration and intensity of the laser pulses. The PP is based on a compact magnetron-type microwave cavity [13]. It resonates at the ^{87}Rb clock transition frequency ≈ 6.835 GHz, with a TE_{011}-like field-mode geometry. The microwave cavity surrounds a cylindrical glass cell with both diameter and height of 25 mm. The cell is filled with ^{87}Rb atomic vapor and a mixture of Argon and Nitrogen buffer-gases with a partial pressure ratio of $P_{Ar}/P_{N2} = 1.6$. The microwave cavity is placed inside a C-field coil that generates a static magnetic field parallel to the cell's symmetry axis and the laser propagation vector. The microwave synthesizer is used to generate a ≈6.835 GHz radiation resonant with the ^{87}Rb clock transition [14].

III. EXPERIMENTAL RESULTS AND DISCUSSIONS

The ODSE method is inspired by the Ramsey method [10] combined with the NMR spin-echo method presented in [15]. The timing sequence of the ODSE scheme is shown in the inset of Fig. 1. First, an optical pumping laser pulse creates a

This work was supported by the Swiss National Science Foundation (SNSF grant no. 162346), the European Metrology Research Programme (EMRP project IND55-Mclocks), SNSF-Scopes project (152511) and Ministry of Education Science and Technological Development of Republic Serbia (III 45016 and OI 171038). The EMRP is jointly funded by EMRP participating countries within EURAMET and the European Union.

population imbalance by depopulating the ^{87}Rb $F_g = 2$ and filling the $F_g = 1$ ground state. Then, in absence of light, a $\pi/2$ microwave pulse creates a coherent superposition of the two hyperfine $m_F = 0$ states involved in the clock transition. The spins dephase at different rates and their coherences start to decay due to the SMFG across the cell. After a free evolution time, T_{SE} (dephasing time), a phase-reversal π microwave pulse flips the spins and inverts the dephasing effect. After an additional free evolution time equal to the initial dephasing time, T_{SE}, the dephased states are rephased at the instant of the second $\pi/2$ microwave pulse. The second $\pi/2$ pulse converts the accumulated atomic phase into a population difference between the hyperfine states. Finally, optical density (OD) is measured in the cell with a laser pulse on the transition from $F_g = 2$ by using a photodetector. OD is defined by:

$$\mathrm{OD} = -\ln (I_t/I_0), \tag{2}$$

where, I_0 and I_t are the incident and transmitted laser probe pulse intensities respectively.

In the ODSE method the detection of OD, i.e. of atomic population, is done with the laser. The Zeeman splitting in the $5S_{1/2}$ ground state is much smaller than the intrinsic optical and Doppler linewidths, thus laser detection delivers the population relaxation time, T_1', involving *all* the Zeeman levels in the ground states $F_g = 1$ and $F_g = 2$ *simultaneously* (and not the clock levels only). However, because the microwave radiation does resolve the different Zeeman sublevels *individually*, we can selectively access T_2 of the clock transition *alone*. We vary T_{SE} and record OD consequently when the microwave frequency is detuned from the clock transition by a fixed amount of δ [10]. The experimental data shown in Fig. 1 is fitted by the equation:

$$\mathrm{OD} = A + B\exp(-2T_{SE}/T_1'^{\mathrm{ODSE}}) + C\exp(-2T_{SE}/T_2^{ODSE})\sin(4\pi\delta T_{SE} + \varphi), \tag{3}$$

where A, B, C, $T_1'^{\mathrm{ODSE}}$, T_2^{ODSE}, δ and φ are the fitting parameters. The fit gives both the relaxation times of $T_1'^{\mathrm{ODSE}} = 3.21 \pm 0.05$ ms and $T_2^{\mathrm{ODSE}} = 4.30 \pm 0.85$ ms. $T_1'^{\mathrm{ODSE}}$ refers to the population relaxation time for the transitions between all m_F levels and T_2^{ODSE} is specific to the clock transition. The measured T_2^{ODSE} is in a good agreement with the predicted intrinsic coherence relaxation time T_2 (≈ 4.5 ms).

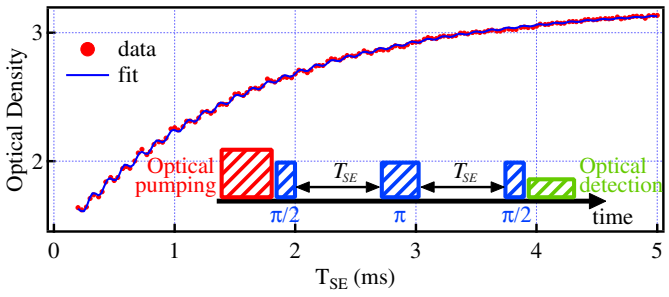


Fig. 1. Optical density of the vapor cell in the ODSE scheme. Solid red circles are the experimental data and blue curve is a fit based on equation (3). Inset: Timing sequences of ODSE scheme.

The relaxation times were also measured using the Ramsey method [10], in the same vapor cell and the same static magnetic field as used for the ODSE measurements. We found $T_1'^{\mathrm{Ramsey}} = 3.20 \pm 0.01$ ms and $T_2^{*\mathrm{Ramsey}} = 3.95 \pm 0.25$ ms. The obtained T_1' were consistent in both methods, while $T_2^{*\mathrm{Ramsey}}$ was shorter than T_2^{ODSE} (and also the predicted T_2) due to SFMG across the vapor cell. The measured relaxation times with ODSE method show higher uncertainties compared to the ones from Ramsey method. This can be attributed to the lower signal contrast due to the longer complete interrogation cycle in the case of ODSE.

IV. CONCLUSION

We have demonstrated that by using the ODSE method, the additional dephasing contributions arising from SMFG across a vapor cell can be suppressed. Such SMFG-induced dephasing can be considerable, even for our well-designed atomic clock PP with field gradients on the order of 2 – 4 % (obtained by measuring the broadening of the Zeeman linewidths and from [16]). Thus, the ODSE method allows measuring the intrinsic T_2, in good agreement with the relaxation theory. The current uncertainties in T_2^{ODSE} could be reduced by enhancing the signal contrast and by reducing the signal noise. The ODSE method is also of high interest to characterize T_2 in other quantum-optics systems, e.g. cold atoms or solid-state systems such as nitrogen-vacancy centres in diamond, for applications in quantum information, quantum memories, quantum sensing or quantum metrology [17-20].

ACKNOWLEDGMENT

We thank A. K. Skrivervik and A. Ivanov (both EPFL-LEMA) for their support on the microwave cavity, C. Calosso (INRIM) for providing the microwave LO, and M. Pellaton (LTF) for helpful discussions. We thank our former colleague S. Kang for his contributions to the early phases of the work.

REFERENCES

[1] M. Gharavipour, C. Affolderbach, F. Gruet, I. S. Radojičić, A. J. Krmpot, B. M. Jelenković. and G. Mileti, "Optically-Detected Spin-Echo method for relaxation times measurements in a Rb atomic vapor," New J. Phys., 19 063027, 2017.

[2] J. Vanier and C. Audoin, "The Quantum Physics of Atomic Frequency Standards". Bristol, U.K.: Adam Hilger, 1989.

[3] J.Camparo, "The Rb atomic clock and basic research," Phys. Today 60 33, 2007.

[4] F. X. Esnault *et al.* "HORACE: a compact cold atom clock for Galileo," J. Adv. Space Res. 47 (5), 854, 2011.

[5] D. Budker and M. Romalis, "Optical magnetometry," Nature Physics 3 227, 2007.

[6] B. Julsgaard, A. Kozhekin and E. S. Polzik, "Experimental long-lived entanglement of two macroscopic objects," Nature 413 400, 2001.

[7] D. Budker et al. "Resonant nonlinear magneto-optical effects in atoms," Rev. Mod. Phys. 74 115, 2002.

[8] H. Y. Carr and E. M. Purcell, "Effects of diffusion on free precession in NMR experiments," Phys. Rev., 94, no. 3, pp. 630, 1954.

[9] H. C. Torrey, "Bloch equations with diffusion terms," Phys. Rev., 104, 3, 563, 1956.

[10] A. Horsley, G.-X. Du, M. Pellaton, C. Affolderbach, G. Mileti, and P. Treutlein, "Imaging of relaxation times and microwave field strength in a microfabricated vapor cell," *Phys. Rev. A*, vol. 88, p. 063407, 2013.

[11] M. Gharavipour, C. Affolderbach, S. Kang, T. Bandi, F. Gruet, M. Pellaton and G. Mileti "High performance vapour-cell frequency standards," Jour. of Phys.: Conf. Series 723 012006, 2016.

[12] F. Gruet, M. Pellaton, C. Affolderbach, T. Bandi, R. Matthey and G. Mileti "Compact and frequency stabilized laser heads for Rubidium atomic clocks", Proc. ICSO- Ajaccio, Corsica, 9-12 Oct. 2012 no. 48.

[13] C. Stefanucci, T. Bandi, F. Merli, M. Pellaton, C. Affolderbach, G. Mileti and A. K. Skrivervik "Compact microwave cavity for high performance Rb frequency standards," Rev. Sci. Instrum. 83 104706, 2012.

[14] C. E. Calosso, S. Micalizio, A. Godone, E. K. Bertacco and F. Levi "Electronics for the pulsed Rb clock: design and characterization," IEEE Trans. Ultrason. Ferroelectr. Freq. Cont. 54 1731, 2007.

[15] E. L. Hahn "Spin echos," Phys. Rev. 80 580, 1950.

[16] C. Affolderbach, G. Du, T. Bandi, A. Horsley, P. Treutlein and G. Mileti "Imaging microwave and DC magnetic fields in vapour-cell Rb atomic clock," IEEE Trans. on Instrum. and Meas. 64, no 12, 3629, 2015.

[17] G. Wolfowicz, H. Maier-Flaig, R. Marino, A. Ferrier, H. Vezin, J. J. L. Morton and P. Goldner "Coherent Storage of Microwave Excitations in Rare-Earth Nuclear Spins," Phys. Rev. Lett. 114 170503, 2015.

[18] J. H. Shim, I. Niemeyer, J. Zhang and D. Suter "Robust dynamical decoupling for arbitrary quantum states of a single NV center in diamond," Europhysics Letters 99 4, 2012.

[19] M. Hosseini, B. M. Sparkes, G. Campbell, P. K. Lam and B. C. Buchler, "High efficiency coherent optical memory with warm rubidium vapour," Nature Comms. 2 174, 2011.

[20] W. Tittel, M. Afzelius, T. Chaneliére, R. L. Cone, S. Kröll, S. A. Moiseev and M. Sellars "Photon-echo quantum memory in solid state systems," Laser & Photon. Rev. 4 244, 2010.

Microfabrication of Cs-Filled MEMS Cell Using Sequential Plasma Activated Bonding

Kenta Terashima, Yoshikazu Hirai, Toshiyuki Tsuchiya, Osamu Tabata
Department of Micro Engineering
Kyoto University, Kyoto, Japan
Email: hirai@me.kyoto-u.ac.jp

***Abstract*—This paper report the microfabrication process of cesium (Cs) vapor cells using low-temperature wafer bonding process and its activation by a krypton fluoride (KrF) excimer laser. Low-temperature process with sequential plasma process for Si/glass anodic bonding enables to encapsulate cesium azide (CsN_3) in the cell below its melting point and reduce presence of impurities inside the cavities, leading good quality of spectroscopic measurement for MEMS atomic clocks. To obtain atomic Cs, a decomposition of CsN_3 was done by exposure with a KrF excimer laser. The short-term frequency stability demonstrated the potential of fabricated Cs-filled cell to be used in MEMS atomic clocks.**

Keywords—atomic clock; CSAC; vapor cell; CsN_3; sequential plasma activated bonding; KrF excimer laser

I. INTRODUCTION

Microfabricated atomic vapor cells (hereafter MEMS cell) containing alkali metal (Cs, Rb, or K) and buffer gas (typically, He, N_2, Ne, or Ar) are in common use for atomic-based instruments like chip scale atomic clocks (CSACs) [1], chip scale atomic magnetometers (CSAMs) [2], other quantum sensors [3], and International System (SI)-traceable set of references [4]. In recent years, CSACs that serve precise frequency and time references, has attracted a great attention to be used in applications such as sensor network synchronization, telecommunication systems, and global positioning systems. MEMS cells are generally fabricated by etching of a Si wafer and subsequent anodic bonding of a glass wafer to each side. Although this process becomes widespread in MEMS cell fabrication, difficulties are generally encountered in steps of the production of alkali metals and the filling of alkali metal into MEMS cells by wafer-level fabrication.

Among the different MEMS cell fabrication techniques, the UV decomposition of Cesium (or Rubidium) azide (CsN_3) into alkali metal is a promising approach for filling pure alkali metal in the cell and achieving a high frequency stability (Allan deviation) of the atomic clocks [5]. For this purpose, combinations of thermal evaporation in powder form under high vacuum conditions [6] or deposition of aqueous solution under normal atmospheric conditions [7] and following UV lamp radiation at 254 nm were used; however, long time UV exposure were necessary in order to observe azides decomposition. As an alternative method, a Raman laser activation of commercially available Cs-dispenser is one of a promising approach to produce Cs within an acceptable process time [8, 9]. However, the Cs-dispenser occupies half the cell volume. In order to reduce the cell footprint, the different approach using a Cs dispensable paste composed of cesium molybdate (Cs_2MoO_4), zirconium-aluminum (Zr–Al) powder, and a hybrid organic-inorganic binder was proposed [10]. Due to the high temperature involved in the anodic bonding to encapsulate Cs-dispensers or chemical precursors, there is still technological challenges in MEMS cell microfabrication to improve the frequency stability.

This paper aims to report a microfabrication of MEMS cell using low-temperature bonding technique to encapsulate alkali metal azides and a krypton fluoride (KrF) excimer laser for decomposition of the azides. This fabrication method differs from previous ones [5-10] in that a combination of surface activation treatment and anodic bonding via sequential plasma process [11] is employed for the process to improve the internal cell atmosphere purity. Furthermore the use of KrF ecimer laser enables to speed up a decomposition of azides compared with that of the UV light. The potential of the Cs-filled MEMS cell in atomic clocks applications is finally discussed.

II. ALKALI METAL PRODUCTION IN THE CELLS

Most of the currently reported wafer-level MEMS cell fabrications employ anodic bonding to seal the cell at ca. 400 °C, forming strong Si–O–Si bonds. This bonding process generates gaseous O_2 at the Si–glass interface during the bonding process [12], and increases degassing of water that remain in the cell after they are encapsulated. The oxidizing agents react with Cs, causing the atomic density to decrease over time. Additionally, when CsN_3 is heated above its melting point (310 °C) to under high vacuum conditions, the point at which CsN_3 can cause the splattering. Here, the generic reaction for the idealized decomposition of CsN_3 can be written as:

$$2CsN_3 \rightarrow 2Cs + 3N_2 \quad (1)$$

To solve these problems, the authors recently developed the microfabrication for MEMS cells, consisting of alkali-metal source tablet (AMST) technique as alkali metal dispensers [13, 14] and a combination of surface activation treatment and anodic bonding via sequential plasma process. In this bonding process, a O_2 reactive ion etching (RIE) plasma treatment followed by treatment with N_2 radicals are used for surface activation. The process of O_2 RIE plasma removes surface contaminants and oxidizes surfaces. Subsequent processing using N_2 radical generates chemically unstable silicon surfaces. The combined

effect of O_2 plasma and N_2 radical enhances bonding strength due to spontaneous reactions between the metastable surfaces. Consequently, the sequential plasma activated bonding is the low-temperature and chemical free plasma bonding process. This MEMS cells fabrication enabled (1) low-temperature anodic bonding to encapsulate the deposited CsN_3 and (2) production of Cs from CsN_3 at 295 °C by the short time heating, leading to an excellent quality of spectroscopic measurement for atomic clocks [15]. Therefore the low-temperature microfabrication using anodic bonding via sequential plasma process opens the door toward a development of high-performance MEMS cells.

III. Fabrication of Cs-Filled MEMS Cells

For the fabrication of MEMS cells, we employed a 4 inch Si wafer with a thickness of 1.5 mm and two glass wafers with a thickness of 0.3 mm. The cavity thickness (height) of 1.5 mm is sufficient to achieve a requirement of MEMS atomic clocks and suitable to compare a quality of the MEMS cells developed by others groups. In addition, to compare the quality of the MEMS cell with our previous study [15], the diameter of cavity for coherent population trapping (CPT) is 6 mm and the size of sample cavity was 8 mm × 8 mm as shown in Fig. 1. Two cavities were connected through microchannels to avoid the contamination from the CsN_3 during its decomposition [8].

Figure 2 shows a process of Cs-filled MEMS cell fabrication. First, an array of two cavities (through holes) and microchannels were fabricated by the optimized single-step of the deep reactive ion etching (DRIE) process [16]. After the DRIE process, KOH post-treatment was performed to smooth surface of Si. A glass wafer was then bonded on one side using conventional anodic bonding (heating to 400 °C and applying a potential of 400 V). Next, a quantity of the aqueous solution (0.3 mg of CsN_3) was filled into the sample cavities using a pipette. The sample cavities were then dried by removal of the water on the hotplate. Subsequently, the cavities were sealed by sequential plasma activated bonding (WAP-100, Bondtech Co., Ltd.) of a second glass substrate to the upper side of Si in high vacuum ($\approx 10^{-5}$ Pa) at a temperature of 250 °C and applying a potential of 250 V. It can be noted that this bonding technology enables the second bonding below the melting point of CsN_3 and avoids the conflict of bonding process with the decomposition of CsN_3. To obtain Cs from CsN_3, a decomposition was finally done by a KrF excimer laser of 248 nm wavelength (LAEX-1000, AOV Co., Ltd.) using a mask allowing an irradiation spot size of 2.5 mm × 2.5 mm, and its process time was about a few seconds.

Figure 3 shows a top view of the MEMS cell fabricated according to the described process. A metallic color of atomic Cs was visible in the sample cavity where an excessive amount of Cs was released by four times local heating with KrF laser. Cs production was observed in all fabricated five cells.

IV. Characterization

To demonstrate an ability of the Cs-filled MEMS cell to atomic clocks, spectroscopy measurement was carried out. A diode laser was tuned to the D1 transition in Cs at 894.6 nm. CPT resonance spectroscopy was realized by scanning the 4.596 GHz output frequency, one-half of the Cs ground-state hyper-

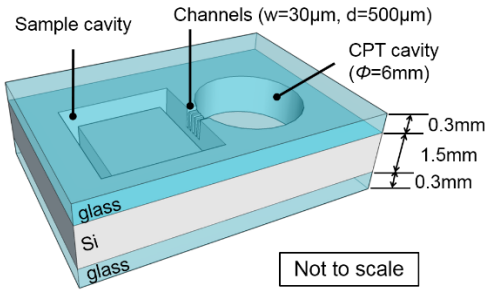


Fig. 1. Schematic illustration of a Cs-filled MEMS cell. The sample cavity is used for inserting AMST or depositing CsN_3. CsN_3 can produce Cs and N_2 buffer gas *in-situ* by thermal decomposition.

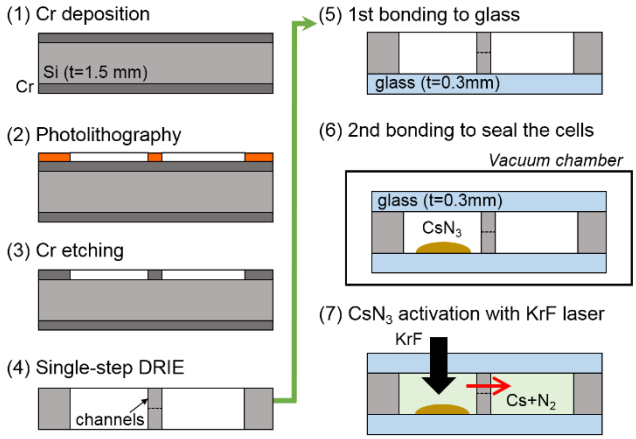


Fig. 2. Fabrication procedure of MEMS Cs–N_2 cell using sequential plasma activated Si/glass bonding and KrF excimer laser.

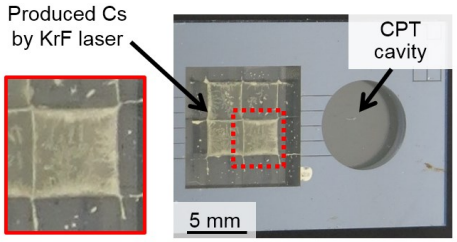


Fig. 3. Photograph of the MEMS Cs-N_2 cell afrer CsN_3 decomposition by KrF laser. The inset is the close-up view of Cs produced. For the Cs production, the deposited CsN_3 was locally heated by four times KrF laser activation.

fine oscillation frequency. The cell was placed in a magnetic shield and a magnetic field flux density value of 10 μT was applied using a solenoid in order to separate and discriminate correctly Doppler-broadened ground-state microwave Zeeman transitions. The CPT resonance was monitored by detecting the laser power transmitted through the cell using a photodiode.

Figure 4 shows a typical CPT resonance observed in the cell shown in Fig. 3. In the present case, the short-term frequency stability is measured to be 5×10^{-11} at an integration time of 1 sec. This short-term frequency stability compares well to the performance of previously reported alkali metal vapor cells for CSAC summarized in TABLE I [5, 7, 9, 17]. We expect an

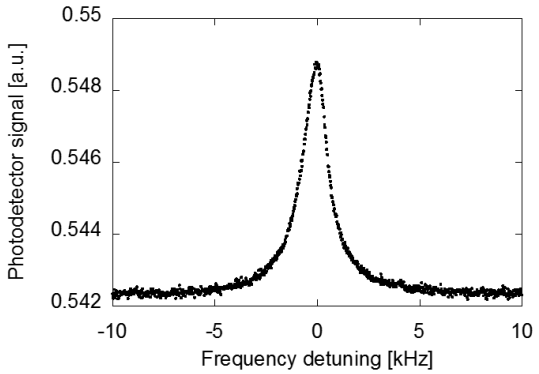


Fig. 4. CPT resonance obtained from the fabricaed Cs-N_2 cell.

TABLE I. COMPARISON OF MEMS CELLS PERFORMANCE OF THE ALLAN DEVIATION σ_y AT 1 SEC INTEGRATION TIME

References	Specifications		
	Alkali metal / *Buffer gas*	*Cavity height [mm]*	*Allan deviation*
Y. Pétremand *et al.* [17]	Rb / –	4.0	3×10^{-11}
R. Boudot *et al.* [9]	Cs / Ne	1.4	3.8×10^{-11}
S. Knappe *et al.* [5]	^{87}Rb / Ar, Ne	1.4	4×10^{-11}
T. Overstolz *et al.* [7]	^{87}Rb / Ar, N_2	1.6	7.7×10^{-11}
This paper	Cs / N_2	1.5	5×10^{-11}

improvement of this stability could be obtained by further optimizing the KrF excimer laser activation process conditions such as time and power, leading to control N_2 buffer gas pressure and amount of Cs atom in the cell.

V. CONCLUSIONS

We have presented the microfabrication of Cs vapor cell using the combination of surface activation treatment and anodic bonding via sequential plasma process and KrF excimer laser activation of CsN_3. The short-term frequency stability of the Cs-filled MEMS cell was found to be 5×10^{-11} at an integration time of 1 sec. Thus the MEMS cell made in the present microfabrication approach is applicable in MEMS atomic clocks. To confirm the long term suitability of this cell fabrication technology for atomic clocks, the evolution of the frequency stability along time (i.e., the frequency of the clock transition and degrade the aging performances) should be investigated.

ACKNOWLEDGMENTS

The present study was supported in part by the JSPS KAKENHI Grant Number 16K17502, the Innovative Techno-Hub for Integrated Medical Bio-imaging Project of the Special Coordination Funds for Promoting Science and Technology from the Ministry of Education, Culture, Sports, Science and Technology (MEXT), Japan, and the Nippon Sheet Glass Foundation for Materials Science and Engineering. Part of the present research was conducted at the Kyoto University Nano Technology Hub as part of the "Nanotechnology Platform Project" sponsored by MEXT, Japan.

REFERENCES

[1] S. Knappe, V. Shah, P.D.D. Schwindt, L. Hollberg, and J. Kitching, "A microfabricated atomic clock," Appl. Phys. Lett., vol. 85, pp. 1460–1462, 2004.

[2] P.D.D. Schwindt, S. Knappe, V. Shah, L. Hollberg, J. Kitching, L.-A. Liew, and J. Moreland, "Chip-scale atomic magnetometer," Appl. Phys. Lett., vol. 85, pp. 6409–6411, 2004.

[3] J. Kitching, S. Knappe, and E.A. Donley, "Atomic Sensors – A Review," IEEE Sens. J., vol. 11, pp. 1758–1749, 2011.

[4] J. Kitching, E.A. Donley, S. Knappe, M. Hummon, A.T. Dellis, J. Sherman, K. Srinivasan, V.A. Aksyuk, Q. Li, D. Westly, B. Roxworthy, and A. Lal, "NIST on a Chip: Realizing SI units with microfabricated alkali vapour cells," J. Phys.: Conf. Ser., vol. 723, 012056, 2016.

[5] S. Knappe, V. Gerginov, P.D.D. Schwindt, V. Shah, H. G. Robinson, L. Hollberg, and J. Kitching, "Atomic vapor cells for chip-scale atomic clocks with improved long-term frequency stability," Opt. Lett., vol. 29, pp. 2351–2353, 2005.

[6] L.-A. Liew, J. Moreland, and V. Gerginov, "Wafer-level filling of microfabricated atomic vapor cells based on thin-film deposition and photolysis of cesium azide," Appl. Phys. Lett., vol. 90, 114106, 2007.

[7] T. Overstolz, J. Haesler, G. Bergonzi, A. Pezous, P.-A. Clerc, S. Ischer, J. Kaufmann, and M. Despont, "Wafer scale fabrication of highly integrated rubidium vapor cells," in Proceeding of The 27th IEEE International Conference on Micro Electro Mechanical Systems (IEEE MEMS 2014), San Francisco, CA USA (January, 2014), pp. 552–555.

[8] M. Hasegawa, R.K. Chutani, C. Gorecki, R. Boudot, P. Dziuban, V. Giordano, S. Clatot, and L. Mauri, "Microfabrication of cesium vapor cells with buffer gas for MEMS atomic clocks," Sens. Actuator, A, vol. 167, pp. 594–601, 2011.

[9] R. Boudot, X. Liu, P. Abbé, R. Chutani, N. Passilly, S. Galliou, C. Gorecki, and V. Giordano, "A high-performance frequency stability compact CPT clock based on a Cs-Ne microcell," IEEE Trans. Ultrason. Ferroelectr. Freq. Control, vol. 59, pp. 2584–2587, 2012.

[10] V. Maurice, J. Rutkowski, E. Kroemer, S. Bargiel, N. Passilly, R. Boudot, C. Gorecki, L. Mauri, and M. Moraja, "Microfabricated vapor cells filled with a cesium dispensing paste for miniature atomic clocks," Appl. Phys. Lett., vol. 110, 164103, 2017.

[11] M.M.R. Howlade, S. Suehara, H. Takagi, T.H. Kim, R. Maeda, and T. Suga, "Room-temperature microfluidics packaging using sequential plasma activation process," IEEE Trans. Adv. Packag., vol 29, pp. 448–456, 2006.

[12] M. Esashi, "Wafer level packaging of MEMS," J. Micromech. Microeng., vol. 18, 073001, 2008.

[13] K. Tsujimoto, K. Ban, Y. Hirai, K. Sugano, T. Tsuchiya, N. Mizutani, and O. Tabata, "On-chip fabrication of alkali-metal vapor cells utilizing an alkali-metal source tablet," J. Micromech. Microeng., vol. 23, 115003, 2013.

[14] K. Ban, Y. Hirai, K. Tsujimoto, A. Terao, N. Mizutani, T. Kobayashi, and O. Tabata, "Characterization of alkali-metal vapor cells fabricated with an alkali-metal source tablet," J. Vac. Sci. Technol. A, vol. 34, 061601, 2016.

[15] Y. Hirai, K. Terashima, K. Nakamura, T. tsuchiya, and O. Tabata, "Low temperature, wafer-level process of alkali-metal vapor cells for micro-fabricated atomic clocks," in Proceeding of The 19th International Conference on Solid-State Sensors, Actuators and Microsystems (Transducers 2017), Kaohsiung, Taiwan (June 2017), pp. 431–434.

[16] R.K. Chutani, M. Hasegawa, V. Maurice∗, N. Passilly, and C. Gorecki, "Single-step deep reactive ion etching of ultra-deep silicon cavitieswith smooth sidewalls," Sens. Actuator, A, vol. 208, pp. 66–72, 2014.

[17] Y. Pétremand, C. Affolderbach, R. Straessle, M. Pellaton, D. Briand, G. Mileti, and N.F. de Rooij, "Microfabricated rubidium vapour cell with a thick glass core for small-scale atomic clock applications," J. Micromech. Microeng., vol. 22, 025013, 2012.

Cell-Based Stabilized Laser Sources and Light-Shifts in Pulsed Rb Atomic Clocks

Nil Almat, William Moreno, Matthieu Pellaton, Mohammadreza Gharavipour,
Florian Gruet, Christoph Affolderbach and Gaetano Mileti
Laboratoire Temps-Fréquence, Institut de Physique, Université de Neuchâtel
Neuchâtel, Switzerland
nil.almat@unine.ch

***Abstract*—We report on a narrow-linewidth diode laser source emitting at 780 nm, based on frequency doubling from 1.56 µm, which is frequency stabilized on the D2 transition line of Rubidium (Rb). This compact laser source shows a frequency stability of $2{\cdot}10^{-12}$ at 1 s and $< 5{\cdot}10^{-12}$ for τ up to 10^4 s. This laser source is evaluated in a modular four-laser setup to identify and locate the sources of instabilities. In view of the lasers' applications to vapor-cell Rb atomic clocks, we also studied the various light-shift coefficients in a pulsed optically-pumped Rb clock. Finally, we evaluate the impact of the frequency and intensity instabilities of the frequency-doubled optical sources on the clock stability.**

Keywords—Rubidium atomic clock; frequency doubling; frequency stabilization; light shift; optical pumping

I. INTRODUCTION

We have developed and evaluated several frequency-stabilized laser sources that use as references homemade evacuated alkali vapor cells with a volume < 2 cm^3. These laser sources make use of different types of laser diodes (LD) emitting either at 780 nm or 1.56 µm [1, 2]. Such laser sources have a variety of applications such as Differential Absorption Lidars for atmospheric research [3], interferometers [4], and atomic clocks [5].

In this communication, we report our studies on frequency-doubled (780 nm), stabilized laser sources (1.56 µm), in view of their applications in continuous-wave (CW) or pulsed optically pumped (POP) Rubidium clocks [5, 6]. In such clocks the laser is used for optical pumping and optical detection. Thus, the properties of the laser have a direct impact on the clock resonance line and consequently on the clock performances. In section II, we first describe our system to analyze the limits of our laser systems. We then report on our measurements of the relative frequency and optical power instabilities. In section III, we study the sensitivity of the Rb clock to these laser parameters through the light-shift (LS) effects. Combining the results of both studies allows to determine the potential performances of a clock based on frequency-doubled lasers. Clock configurations are optimized, taking into account more practical aspects such as volume, power consumption and reliability.

This work was supported by the Swiss National Science Foundation (SNSF grants no. 156621 and 162346) and the European Metrology Research Programme (EMRP project IND55-Mclocks). The EMRP is jointly funded by the EMRP participating countries within EURAMET and the European Union. We also acknowledge previous support from the European Space Agency (ESA) and the Swiss Space Office (Swiss Confederation).

II. FREQUENCY-STABILIZED LASER SYSTEMS

We evaluate the performance of our laser sources using the compact and modular system shown in Fig. 1. This system consists of four laser sources individually frequency stabilized to Rb atomic references. Two identical laser heads (LH 2.2 and 2.4), based on a 780 nm distributed feedback (DFB) LD (Eagleyard), include an evacuated Rb vapor cell in Doppler-free spectroscopy scheme and two photodetectors with their pre-amplification electronics. Each LH has a total volume of 0.63 dm^3 [1]. The other two optical sources under study consist of a pigtailed telecom LD emitting at 1.56 µm, with a linewidth of the order of 2 kHz for the Laser 1 (Rio) and of 2 MHz for the Laser 2 (Emcore). Both laser outputs are frequency doubled using fibered Second Harmonic Generators (SHG 1 and SHG 2) based on a periodically poled lithium niobate waveguide. The laser frequencies are stabilized to Rb D2 transition in compact (0.81 dm^3 volume) fiber-coupled Frequency Reference Units (FRU 1 and FRU 2). The spectroscopic setups are similar to the ones used in the LHs.

Two fibered beam splitters (BS) before and after (BS 1,2 and 3,4, resp.) the SHGs provide simultaneous generation of the two frequency stabilized wavelengths (1.56 µm and 780 nm) from a single optical source. The reference LHs' outputs (one at a time) are fiber-coupled which allows, by BS 6, simultaneous beat-note measurements with both lasers at 780 nm. Another advantage of our setup is the possibility to

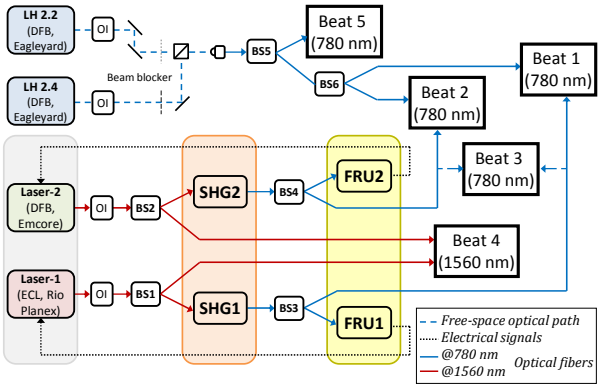


Fig. 1 Schema of the experimental setup based on two fibered 1.5 µm LDs, Laser 1 and Laser 2, and two reference laser heads, LH 2.2 and LH 2.4.

easily modify its configuration, thanks to the little optical alignment required in fibered systems, in order to identify the limits of the individual blocks.

The spectral properties and the frequency stabilities of the laser heads and Laser 2 were previously presented in [1] and [7], respectively. The frequency instability of the laser systems are measured by heterodyne beat-note technique at several points of the fibered system and at both wavelengths. The range of typical stabilities recorded is given by the colored bands shown in Fig. 2. Laser 1 demonstrates an excellent relative frequency stability, better than $5 \cdot 10^{-12}$ for τ up to 10^4 s. Thanks to its lower noise level, the estimated signal-to-noise limit of $2 \cdot 10^{-13}\, \tau^{-1/2}$ for Laser 1 is better by one order of magnitude compared to Laser 2 [7]. The measured instability of $2 \cdot 10^{-12}$ at 1 s for Laser 1 is currently limited by frequency instabilities of the reference LH. As for the mid-term, the thermal fluctuations in the laboratory are responsible for the instabilities. We suspect, in particular, the etalon effects in the fibered system and the optical feedback. Over longer time scales, the beat-note frequencies measured in the same configuration of our system over a period of time of several months are situated in an interval less than 100 kHz.

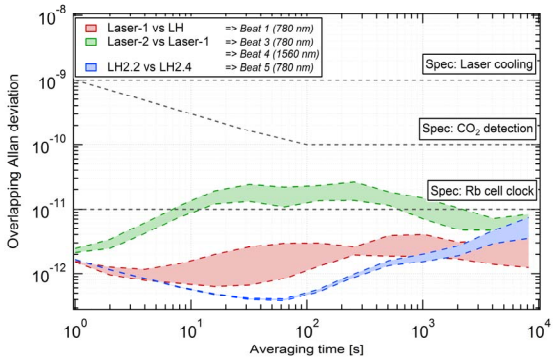


Fig. 2 Relative frequency fluctuations in terms of overlapping Allan deviation for the beat notes measured at Beat 1 in red, at Beat 3 and 4 in green, at Beat 5 in blue (for the beats cf. Fig. 1). Dashed lines indicate the specifications for diverse applications.

Preliminary measurements of the optical power fluctuations of the frequency-doubled laser systems at 10^4 s to 1 day timescales show one to two order of magnitude degradation of intensity stability compared to the reference LHs. A part of this degradation might be attributed to the higher thermal sensitivity of the fibered optics. To overcome this drawback, active optical power stabilization is being considered.

III. Light-Shift in Pulsed Rubidium Clocks

In a Rb atomic clock a laser source such as presented above can be used to prepare and interrogate the Rb atomic vapor. The atom-light interaction induces shifts of the atomic energy levels known as LS (or AC Stark shifts) [8]. Through this effect, the frequency instability and intensity fluctuations of the laser are among the main sources of long-term instability of the clock frequency (ν_{clock}) [5]. The impact of laser intensity (I_L) fluctuations on the clock frequency is described by the intensity LS coefficient, defined as $\alpha = \Delta\nu_{clock} / \Delta I_L$ for a fixed laser frequency f_L. By analogy, the frequency LS coefficient is defined as $\beta = \Delta\nu_{clock} / \Delta f_L$ for a fixed laser intensity I_L.

In a pulsed Rb clock, the sequences of optical pumping, microwave interrogation and the optical detection are separated in time [6], and the two optical pulses are defined with different duration and intensity. In previous studies, LSs were investigated by varying simultaneously the laser intensity during the whole POP scheme [5]. In this present study, we use the same Rb atomic clock as used in [5], but the shift of the clock frequency is recorded by varying the laser intensity during one of the two optical pulses only. The intensity and frequency LS coefficients for the pump pulse (α_{pump}, β_{pump}) and the detection pulse ($\alpha_{detection}$, $\beta_{detection}$) are determined from these data.

Fig. 3 shows the frequency bias of our Rb clock – i.e. the difference between ν_{clock} and the unperturbed hyperfine transition frequency of ^{87}Rb – as a function of laser power during the optical detection pulse. When the detection optical power is 1 mW and the laser is stabilized to the direct $|5S_{1/2}, F = 2\rangle \leftrightarrow |5P_{3/2}, F = 3\rangle$ transition (F2-3 in Fig. 3), the obtained coefficients are: $\alpha_{detection} = 4.4 \cdot 10^{-13}$ /% and $\beta_{detection} = -3 \cdot 10^{-14}$ /MHz. From a similar study for the optical pumping pulse, the lowest LS coefficients are obtained for a pump optical power of 12 mW and the laser stabilized to the same direct $|5S_{1/2}, F = 2\rangle \leftrightarrow |5P_{3/2}, F = 3\rangle$ transition. In this case we obtain $\alpha_{pump} = -4.4 \cdot 10^{-14}$ /% and $\beta_{pump} = -2.3 \cdot 10^{-14}$ /MHz.

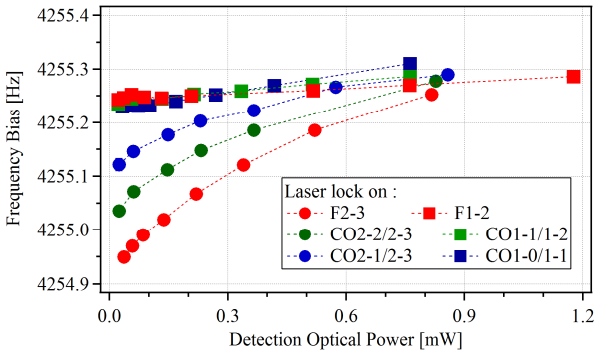


Fig. 3 POP Rb clock frequency bias measured as function of the optical power during the detection pulse for the six reference transitions in the laser head.

These LS coefficients are at the same order of magnitude as the LS coefficients obtained by varying simultaneously the laser intensity during the whole POP scheme [5]. For the direct $|5S_{1/2}, F = 2\rangle \leftrightarrow |5P_{3/2}, F = 3\rangle$ transition, we find global LS coefficients of $\alpha_{global} = 3 \cdot 10^{-13}$ /% and $\beta_{global} = -2 \cdot 10^{-15}$ /MHz. Combined with the frequency and intensity stability of the frequency-doubled laser, the contribution of the laser source to the clock stability can be estimated. With a frequency stability of $5 \cdot 10^{-12}$ (corresponding to 2 kHz at $\tau = 10^4$ s) and a laser intensity stability of $2 \cdot 10^{-3}$ at $\tau = 10^4$ s, the clock stability is estimated to $\sigma \approx 6 \cdot 10^{-14}$ at $\tau = 10^4$ s, where the main limitation is the intensity LS.

IV. Conclusion

We presented a compact and modular setup consisting of four laser sources frequency stabilized on Rb vapor cells in Doppler-free absorption spectroscopy schemes. The modularity

of the fiber-based setup allows identifying the sources limiting the frequency stability of the laser sources. The frequency stability of $2 \cdot 10^{-12}$ at 1 s and better than $5 \cdot 10^{-12}$ up to 10^4 s measured for the narrow linewidth Laser 1. This laser represents an excellent source for applications such as optically pumped Rb vapor-cell clocks using the CW or POP scheme. However, the optical power fluctuations present actually a limitation for their use in Rb clocks unless an active stabilization is implemented.

In view of such applications to compact atomic clocks, we studied the effects of the instabilities in the optical sources on POP Rb clock, through the evaluation of the frequency and intensity LS coefficients. The clock frequency shifts due to a variation in the light intensity were determined separately for the optical pump and detection sequences. These coefficients contribute to the global LS obtained by varying simultaneously the laser intensity during the whole POP scheme [5]. From the global LS coefficients, the clock instability induced by the laser frequency and intensity fluctuations is estimated to $\sigma \approx 6 \cdot 10^{-14}$ at $\tau = 10^4$ s. The main contribution to this instability is the intensity LS.

ACKNOWLEDGMENT

We thank our colleagues R. Matthey, S. Kang for their contributions to earlier phases of the studies and P. Scherler and M. Dürrenberger for their technical support. We also thank A. K. Skrivervik and A. Ivanov (both EPFL-LEMA, Switzerland) for their support on the microwave cavity, and C. Calosso (INRIM, Itlay) for providing the microwave LO.

REFERENCES

[1] F. Gruet, M. Pellaton, C. Affolderbach, T. Bandi, R. Matthey and G. Mileti, *Proc. of the Int..Conf. on Space Optics (ICSO)*, 2012.

[2] R. Matthey, F. Gruet, S. Schilt and G. Mileti, *Opt. Lett.* **40**(11), 2576-9, 2015.

[3] R. Matthey, W. Moreno, F. Gruet, P. Brochard, S. Schilt and G. Mileti, *J. of Phys. Conf. Ser.* **723** 012034, 2016.

[4] Y. Salvadé, F. Przygodda, M. Rohner, A. Polster, Y. Meyer, S. Monnerat, O. Gloriod, M. Llera, R. Matthey, J. Di Francesco, F. Gruet and G. Mileti, *Opt. Express* **24**(19), 21729-43, 2016.

[5] M. Gharavipour, C. Affolderbach, S. Kang, T. Bandi, F. Gruet, M. Pellaton and G. Mileti, *J. Phys. Conf. Ser.* **723** 012006, 2016.

[6] S. Micalizio,C.E. Calosso,A. Godone and F. Levi, *Metrologia* **49**, 425-436, 2012.

[7] W. Moreno, R. Matthey, F. Gruet, P. Brochard, S. Schilt and G. Mileti, *Proc. of the European Time and Frequency Forum (EFTF)*, 2016.

[8] B.S. Mathur,H. Tang and W. Happer, *Phys. Rev.* **171** 1, 1968.

SPINTRONIC based RF components

U. Ebels, J. Hem, A. Purbawati, A. Ruiz Calafora, C. Murapaka, L. Vila
SPINTEC, Univ. Grenoble Alpes, CEA-INAC, CNRS, Grenoble, France
K. Jaimes Merazzo, E. Jimenez and M.-C. Cyrille Univ. Grenoble Alpes, CEA-LETI, Grenoble France
R. Ferreira, International Iberian Nanotechnology Laboratory, Braga, Portugal
M. Kreissig, R. Ma and F. Ellinger, Technische Universität Dresden, Germany
R. Lebrun, S. Wittrock and V. Cros,
Unité Mixte de Physique CNRS, Thales, Univ. Paris-Sud, Université Paris-Saclay, Palaiseau, France
P. Bortolotti THALES TRT, Palaiseau France
(ursula.ebels@cea.fr)

Abstract— In the last two decades Spintronics has been an important driver for Information Technologies with the introduction in 1996 of magneto-resistive field sensors in data storage and in 2006 of magnetic random access memories. Spintronics can also bring alternative solutions for rf components used in Information-Communication Technologies. By virtue of their specific spin polarized transport properties spintronic devices become active, multifunctional, compact, low power, low cost, CMOS compatible rf components that combine functions of microwave signal generation (DC-to-RF converter), modulation and frequency selective microwave signal detection (RF-to-DC converter). In this presentation an overview will be provided for the realization of rf spintronic components and their corresponding rf properties with respect to different functions such as signal generation, modulation and detection. The results reported here were obtained in a collaborative effort within the FP7 project MOSAIC [1] including different laboratories SPINTEC-UGA/CEA/CNRS (F); CEA-LETI (F); INL, Braga (Pt); TUD (G); UMPhy CNRS/THALES (F); THALES TRT (F);

Keywords—Spintronics, magneto-resistance, spin torque oscillator, microwave signal generation, modulation

I. INTRODUCTION

There exist two important spintronic concepts: the magneto-resistance MR and the spin transfer torque STT [2]. When associating two ferromagnetic layers their relative magnetization orientation will define two resistance states upon passing a spin polarized current: low resistance for parallel and high resistance for antiparallel orientation. This *magneto-resistance MR* effect provides a readout of the magnetization state of the free layer. Magnetic tunnel junctions using MgO tunnel barriers provide a large resistance change.

The *spin transfer torque STT effect*, describes the transfer of spin angular momentum from conduction electrons to the local magnetization. By appropriate choice of the sign and amplitude of the spin polarized DC current, the spin transfer torque compensates the intrinsic losses, inducing steady state oscillations of the magnetization at constant precession amplitude [3]. These steady state magnetization oscillations are converted into a voltage signal via the magneto-resistance.

An important specific property of these DC-to-RF converters, called spin torque oscillators STO, is that the frequency depends on the precession amplitude that is set by the DC current. Increasing the current will therefore increase the amplitude and change the frequency. Hence the nanoscale magneto-resistive element represents a compact frequency tunable rf signal generator when loaded with a DC current, see Fig. 1 [4]. Multifunctional operation is provided when adding an additional rf signal source to the DC current. The STO can then either be injection locked (source frequency close to STO frequency or its harmonics) to an external source [5, 6] or its frequency and amplitude can be modulated (source frequency below the STO frequency) [7]. Finally, when the DC current is suppressed and only an rf current is supplied, then the device acts as an *rf signal rectifier* with frequency selectivity (*RF-to-DC converter*), see Fig. 1 [8, 9].

A strongpoint of spintronic devices is that they can cover a very large range of base frequencies 0.1-40GHz, defined by the different magnetic configurations. Here we distinguish (i) nanopillars with a magnetic vortex configuration suitable for signal emission and detection in the range of 0.1-2GHz, (ii) nanopillars with a uniform magnetization configuration suitable for emission and detection in the range of 2-20 GHz.



Fig. 1 Schematic for a micowave signal generator or DC-to-RF converter (left) and for a microwave signal detector or RF-to-DC converter (right).

II. SIGNAL GENERATION

A first challenge concerns the realization of spintronic devices of appropriate rf performances. For signal generation low linewidth and high output power are the two defining parameters. Output power is directly linked to the magneto-resistance and the quality of the magnetic tunnel junction devices. The devices presented here have TMR values of 100% a very low resistance area product of 1-2 Ωμm², while the barrier degradation threshold is higher than 500mV.

For vortex devices output power levels of P=1μW at linewidths of 100kHz-1MHz were obtained, while uniform devices show output power levels of 10-100nW at 10-20 MHz

linewidth. The main contributions to linewidth broadening are frequency- or equivalently phase-fluctuations. The corresponding phase noise, i.e. the PSD of the phase fluctuations, can be determined from the time traces of the magneto-resistive output signal. Appropriate signal analysis protocols were developed to extract via Hilbert transform the amplitude and phase fluctuations. A typical example of the corresponding phase- and amplitude noise PSDs of a uniform device is given in Fig. 2. The best values obtained are -50 to -60 dBc @1MHz offset frequencies for uniform devices [10] and -60 to -70 dBc @1MHz offset frequency for vortex devices [11]. Further reduction of phase noise can be obtained by (i) injection locking to an external source, (ii) locking and coupling between layers and devices (iii) phase locked loop operation.

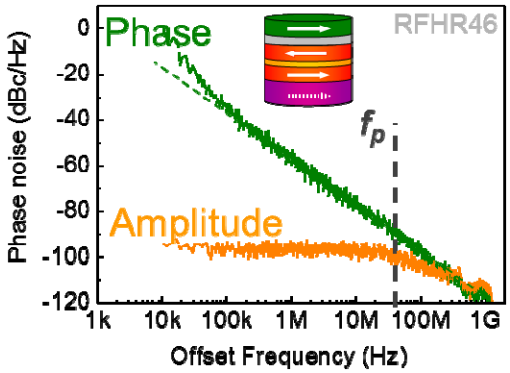


Fig. 2 Amplitude and phase noise plot for a uniform STO device.

III. Phase Locked Loop Operation

In order to realize stable signal sources, a common scheme for stabilization is to use a phase locked loop that compares the oscillator output signal to a stable reference signal generating a control signal proportional to the phase error to adjust the frequency. Within the FP7 project MOSAIC partner TU Dresden has custom designed a PLL circuit on 0.18µm CMOS technology. Successive iterations of the PLL design have shown measures that need to be taken to obtain stable locking, and most importantly how to increase the PLL bandwidth and with this to decrease the phase noise level [12]. For vortex devices, a phase noise reduction of 50 dB at 10kHz offset frequency was achieved, reaching phase noise levels of -85dBc within the PLL bandwidth of more than 2MHz. [13]

IV. Frequency Shift Keying

Spintronic devices provide a novel approach to signal mixing and modulation, where the same device can generate the signal via dc current injection and modulate it through an additional rf current at frequencies that are below the STO generation frequency, see Fig. 3. For uniform devices it was shown that under sinusoidal current modulation the maximum modulation rate for frequency and amplitude modulation is determined by the amplitude relaxation frequency f_p on the order of a few tens to a few hundred MHz. Experiments of digital frequency shift keying demonstrated data rates up to 60 Mbps for standalone devices as well as within specifically developed PCBs. These results will be of interest for wireless communication systems used in wireless sensor networks.

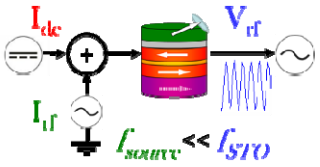


Fig. 3 Schematic for a micowave signal generator with rf input for modulation.

Acknowledgment

The work presented here is a summary of the FP7 project MOSAIC (317950) that provided financial support. The work results from a collaborative effort, and has equal contributions from the different partners. S. Wittrock acknowledges financial support from Labex First-TF, J. Hem acknowledges financial support from DGA and C. Murapaka acknowledges financial support from CNES. The devices were realized at the technological platform PTA at Grenoble. Further support by the ERC Advanced Grant Magical (N°669204) is acknowledged.

References

[1] www.fp7-Mosaic.eu

[2] IEEE Proceedings DOI:10.1109/ JPROC.2016.2554518.

[3] S. I Kiselev, J. C. Sankey, I. N. Krivorotov, N. C. Emley, R. J. Schoelkopf, R. A. Burhman, D. C. Ralph, Nautre **425**, 380 (2003).

[4] P. Villard et al., IEEE J. of Sol. State Circuits **45**, 214 (2010)

[5] B. Georges, J. Grollier, M. Darques, V. Cros, C. Deranlot, B. Marcilhac, G. Faini, and A. Fert, Phys. Rev. Lett. **101,** 017201 (2008)

[6] M. Quinsat et al. Appl. Phys. Lett.. **98**, 182503 (2011)

[7] M. Quinsat et al. Appl. Phys. Lett. **105**, 152401 (2014)

[8] A.S. Jenkins, E. Grimaldi, P. Bortolotti, R. Lebrun, H. Kubota, A. Fukushima, K. Yakushiji, G. de Loubens, O. Klein, S. Yuasa, V. Cros Appl. Phys. Lett. **105**, 172403 (2014)

[9] A.S. Jenkins, R. Lebrun, E. Grimaldi, S. Tsunegi, P. Bortolotti, H. Kubota, K. Yakushiji, A. Fukushima, G. de Loubens, O. Klein, S. Yuasa, V. Cros, Nature Nanotech **11**, 360-364 (2016)

[10] M. Quinsat et al. Appl. Phys. Lett. **97**, 182507 (2010)

[11] E. Grimaldi, A. Dussaux, P. Bortolotti, J. Grollier, G. Pillet, A. Fukushima, H. Kubota, K. Yakushiji, S. Yuasa, V. Cros, Phys. Rev. B **89** 104404 (2014)

[12] M. Kreißig, R. Lebrun, F. Protze, K. J. Merazzo, J. Hem, L. Vila, R. Ferreira, M.C-Cyrille, F. Ellinger, V. Cros, U. Ebels, and P. Bortolotti , AIP Advances 7, 056653 (2016)

[13] M. Kreißig, St. Wittrock, R. Lebrun, F. Protze, K. J. Merazzo, F. Ellinger, M.C-Cyrille, R. Ferreira, P. Bortolotti, U. Ebels and V. Cros, INTERMAG 2017 proceedings

A Fully Integrated Quartz MEMS VHF TCXO

R. L. Kubena[1], F. P. Stratton[1], H. D. Nguyen[1], D. J. Kirby[1], D. T. Chang[1], R. J. Joyce[1], Y. K. Yong[2], J. F. Garstecki[3], M. D. Cross[3], and S. E. Seman[3]

[1]Sensor and Materials Lab., HRL Laboratories, LLC., Malibu, Ca. 90265
[2]Dept. of Civil & Environmental Engineering, Rutgers University, Piscataway, NJ. 08854
[3]Johns Hopkins University Applied Physics Laboratory, Laurel, MD. 20723
Email: rlkubena@HRL.com

***Abstract* - We report on a 32-MHz quartz TCXO fully integrated with commercial CMOS electronics and vacuum packaged at wafer level using a low-temperature MEMS-after quartz process. The novel quartz resonator design provides for stress isolation from the CMOS substrate thereby yielding classical AT-cut f/T profiles and low hysteresis which can be compensated to < ± 0.2 ppm over temperature using on-chip third-order compensation circuity. The TCXO operates at low power of 2.5 mW and can be thinned to ≤ 300 µm as part of the wafer-level eutectic encapsulation. Full integration with large SOA CMOS wafers is possible using carrier wafer techniques.**

***Keywords* – Quartz MEMS, AT-cut TCXO oscillators, Stress isolation, CMOS integration, Temperature compensation, Wafer-level vacuum packaging.**

I. Introduction

Heterogeneous integration of quartz MEMS resonators on Si substrates has previously been demonstrated for UHF oscillators and filters [1], [2]. Although the previous work demonstrated the ability to integrate the resonators on Si substrates, no active electronics were included in the substrates for fully integrated quartz microsystems. This paper demonstrates for the first time the ability to fabricate and integrate VHF AT-cut quartz resonators on active commercial CMOS ASICs for fully integrated temperature compensated crystal oscillators (TCXOs). Wafer-level processing is utilized along with wafer-level vacuum packaging for producing miniaturized low-profile packages. Stress isolation features are etched directly into the quartz plate to isolate the resonator from the CTE mismatch between the resonator and the CMOS substrate. This is critical for obtaining predicted frequency versus temperature profiles and low hysteresis. COMSOL-based piezoelectric and thermal 3D finite element analysis (FEA) was used to design the resonators, and experimental correlation with the models was excellent.

II. VHF AT-cut Resonator Design

The resonator design was based on a trade-off between operating at low frequency for low power, high Q, and low Allan Deviation (ADEV) versus our quartz plasma etching capabilities for accurately defining thick quartz plates. For miniaturized VHF fundamental-mode shear-mode resonators, the sidewall profiles have been found to significantly affect the modal fidelity and the Q. Sidewall slopes defined by wet etching yield varying profiles versus crystallographic direction and result in undesirable acoustic reflections. Deep trench plasma etching provides much higher control on the sidewall profiles and dimensions allowing a more accurate match to the numerical models.

A 32-MHz fundamental-mode, shear-mode, AT-cut resonator bonded to a Si substrate was optimized within a custom piezoelectric COMSOL model [3] for high Q and low stress propagation from the mounts. The design is shown in Fig. 1. 200-nm-thick Au electrodes were used surrounded by a trench for modal confinement with an etch depth of 2.5 µm on each side of the quartz (5% of the plate thickness of 50 µm). The predicted admittance values are L_1 = 4.6 mH, C_1 = 5.5 fF, C_o = 0.85 pF, R_1 = 2.3 Ω, and Q = 400K.

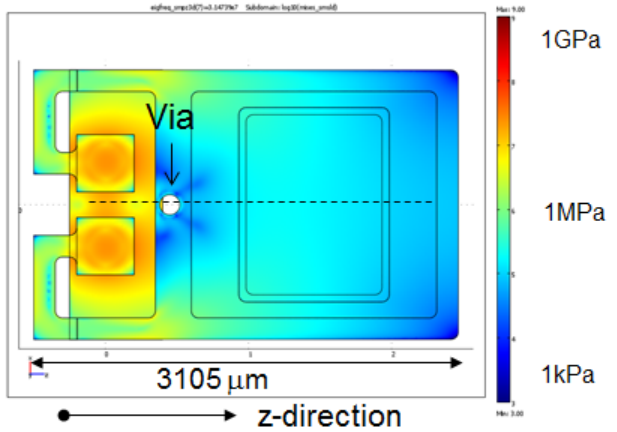


Fig 1. Layout of a 32-MHz AT-cut quartz MEMS resonator with integrated tethers for stress isolation from the CMOS ASIC. Von Mises stress distribution at 100° C relative to zero stress at RT is shown.

Spring tethers 150-um wide were formed between the resonators and the mounts to isolate the resonators from the stress variations over temperature. Assuming zero stress at room temperature, the calculated Von Mises stress distribution is shown in Fig. 1 at 100° C. At the Y-axis mid-plane of the quartz plate the stress was 71 kPa in the center of the electrodes for a hard mount to the Si substrate for a temperature increase of 75° C. The stress profile in the Z-axis direction is presented in Fig. 2 (along the dotted line in Fig. 1). We have noted [3] that stress levels below about 100 kPa are needed in order to maintain a predictable f/T profile within a few ppm. Thus, most all commercial quartz resonators are mounted with compliant epoxy in ceramic packages or with spring clips in metal packages. Our folded spring design provides for a compact resonator with many orders of magnitude of stress

isolation from the Si substrate. These springs are ideally fabricated with anisotropic plasma etching since wet etching produces highly asymmetric wide-wall profiles and poor dimensional control resulting in lower Q.

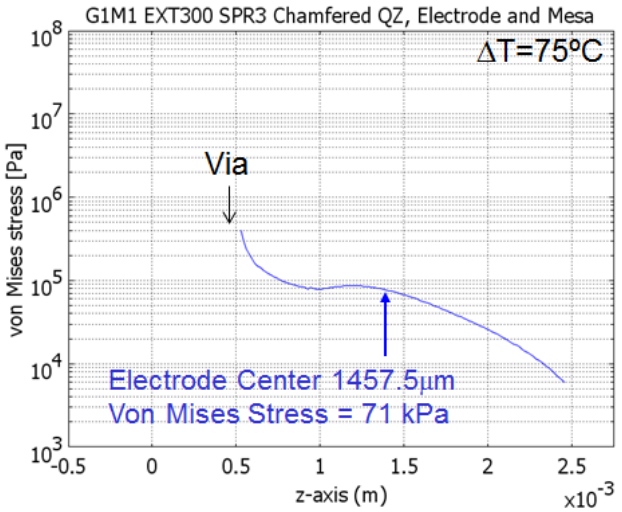


Fig. 2. Stress profile along the Z-axis at the mid-plane of the quartz plate in the Y direction.

III. Wafer-Level Fabrication

The fabrication process is shown in Figs. 3a and 3b. This fabrication of the AT-cut VHF resonators closely follows our UHF quartz MEMS process [1] with the following exceptions. First, the active quartz substrate was bonded to a quartz handle wafer using a wax adhesive after the front-side mesa plasma etch and metallization instead of using a fusion bond to a Si handle wafer. This reduces thermally-induced stress between the wafers and allows the use of thicker piezoelectric active layers during the resonator and via deep-trench, fluorine-based quartz plasma etch. Second, a 4-µm-thick Al mask was used instead of a resist mask during the 50-µm deep-trench etch.

The Pierce sustaining circuit and the cubic compensation electronics were designed into the IBM 7RF process and supplied in 8" wafer form. 3" cores were prepared using laser cutting to match the wafer size of the 3" AT-cut wafers. Vias were formed through the top passivation layer of the ASICs and an additional strap metal was added to the ASICs to connect the electronics to the bond pads of the resonator. Au seal ring metal shown in Fig. 3b, step 12, was also added to the ASIC to allow wafer-level vacuum encapsulation.

The quartz resonator/handle wafer pair was then bonded to the ASIC wafer using a 100º C Au/In eutectic bond and released in a tetrachloroethene (PCE) solution. Micrographs of a complete wafer and an individual oscillator are shown in Figs. 4 and 5, respectively. Next, the oscillators were vacuum encapsulated by wafer-level capping using a 340º C Au/Sn eutectic bond in a vacuum EVG bonding system. Independent vacuum testing using in-situ heaters showed that vacuum levels in the 500 mT range were achieved without getters. The back side of the ASICs and the capping wafer were then thinned to a total thickness of less than 300 µm. Openings to the ASIC control electronics for wire bonding were formed simultaneously in the capping Si wafer during thinning. A photograph of the completed TCXO is shown in Fig. 6 next to a US dime.

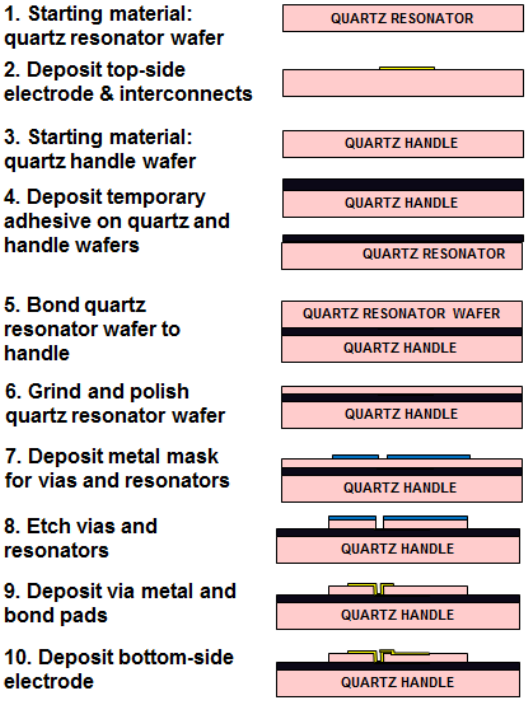


Fig. 3a. Fabrication process flow for VHF quartz MEMS resonators.

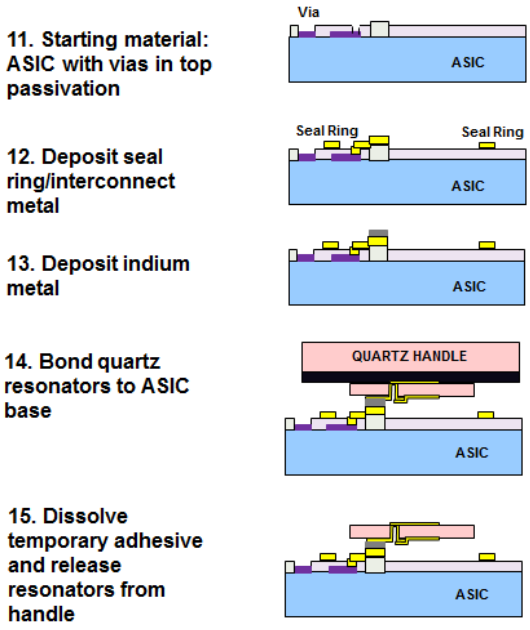


Fig. 3b. Integration of the quartz MEMS resonators with custom ASIC electronics.

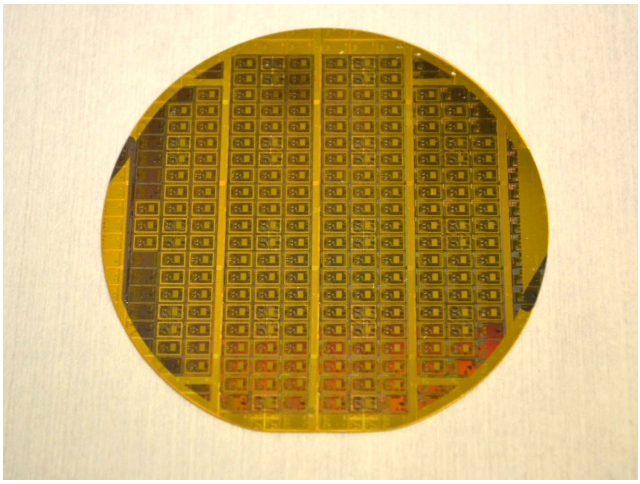


Fig. 4. Integrated TCXOs on a 3" Si ASIC after release from the handle wafer and prior to encapsulation.

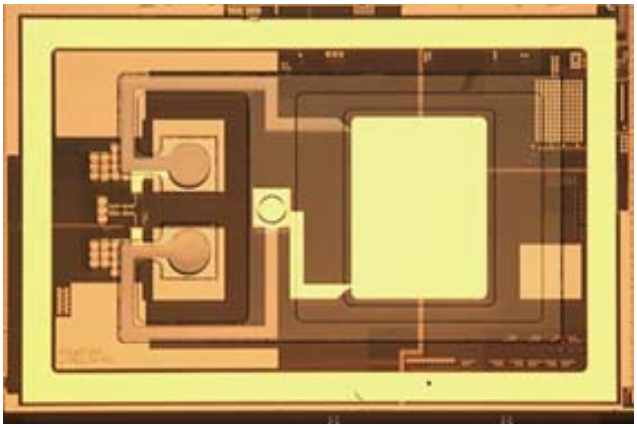


Fig. 5. A bonded AT-cut quartz resonator on a 7RF CMOS control ASIC. A Au rectangular seal ring surrounds the oscillator for wafer-level encapsulation.



Fig. 6. The wafer-level processed integrated TCXO after encapsulation and dicing shown next to a US dime.

IV. Oscillator Test Data

Test resonators were included on the mask to allow testing of the resonators after encapsulation. The admittance values matched those of the model except for the R_1. Separate tests showed that the interconnect resistance was about 6 Ω to the ASIC before Au/Sn sealing and increased 2 Ω after sealing due to Cr/Au interdiffusion in the trace metal. This resulted in a total measured R_1 after sealing of about 11 Ω and a Q of 90K. Controlling the metal interdiffusion and higher inherent R_1 designs will result in much higher measured unloaded Q.

The dependency of the Q on vacuum levels within the package was studied. Unpackaged oscillators were placed into a vacuum station, and the Qs were measured as a function of the background dry N_2 pressure. The Q reached a maximum below 10 T as shown in Fig. 7. Thus, packaged vacuums below 1 T are sufficient for yielding maximum Q.

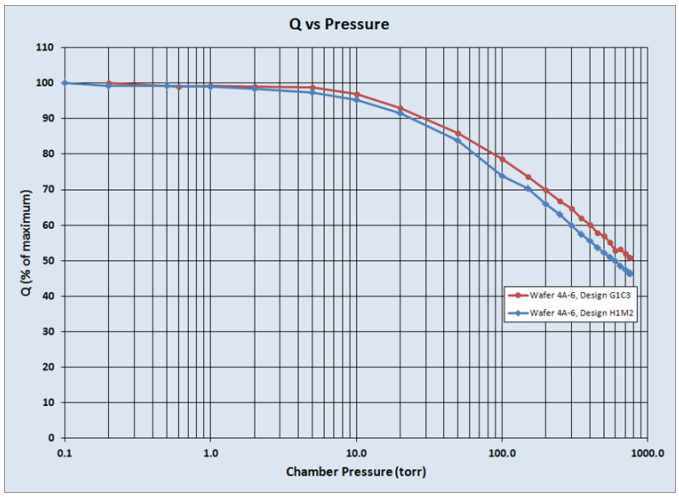


Fig. 7. Normalized Q relative to the maximum Q versus chamber pressure.

The temperature f/T profiles were measured in an oven and compared to the COMSOL models. A comparison is shown in Fig. 8. The measured data was taken both up and down in temperature and showed a hysteresis of about 74 ppb. After on-chip cubic compensation the temperature stability is shown in Fig. 9 and is stable to within ± 0.19 ppm with a hysteresis of 66 ppb over a temperature range of –17° to +70° C.

The ADEV of the TCXO was measured both without and with temperature compensation. The flicker floors were 3.0 x 10^{-11} (Fig. 10) and roughly 6 - 7 x 10^{-11} @ 1 sec., respectively. With improved low noise designs for the temperature compensation circuit and reduced interconnect resistance for higher Q, minimum ADEV values below 10^{-12} should be obtainable. The total power for the TCXO was measured to be 2.5 mW with temperature compensation.

V. Large Scale Fabrication

For future fabrication using large Si-based electronic wafers, the handle wafer can be sawed prior to the resonator release. Each resonator/handle wafer pair can then be placed on a larger Si carrier wafer with etch pockets using pick-and-place systems. The carrier wafer and the full-size electronic wafer can then be bonded wafer-to-wafer using metal-to-metal bonding. Finally, the quartz resonators can be released using the same techniques as described above. This allows one to 1) maximize the packaging density on the quartz wafer, 2) place

the resonators on arbitrary positions on the electronic wafer, 3) CTE match the carrier wafer to the electronic wafer over large areas, and 4) utilize full-size electronic wafers without cutting out smaller sections. This process is described in ref. 4. In-situ laser or ion-beam ablation can then be used to adjust the final frequency using a vacuum probe station prior to final wafer-level capping.

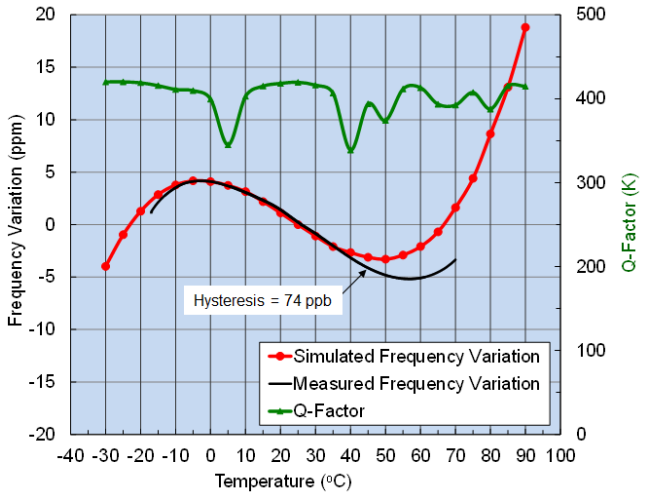


Fig. 8. COMSOL prediction of the Q (green curve) and frequency (red curve) versus temperature compared to measured f/T data (black curve).

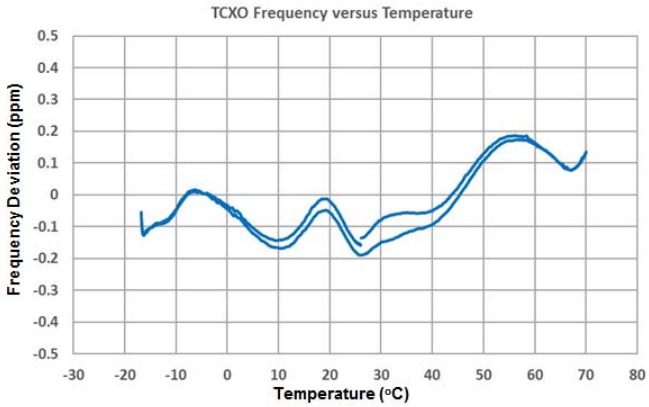


Fig. 9. f/T profile of the TCXO after a cubic temperature compensation showing a round-trip temperature cycle starting at 25° C.

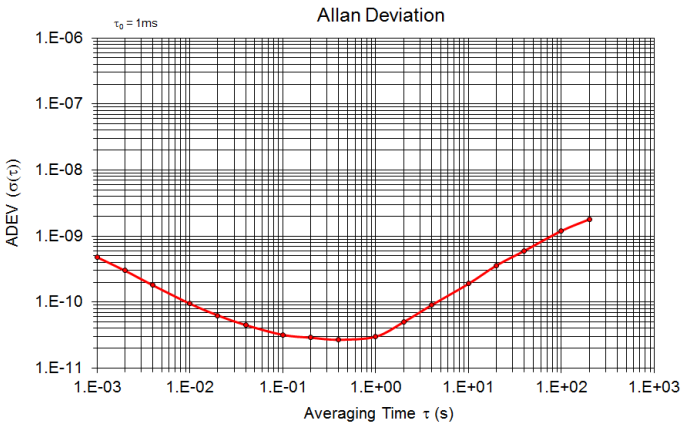


Fig. 10. Allan Deviation of the packaged oscillators before temperature compensation.

V. Summary

A chip-scale fully integrated quartz MEMS TCXO is reported for the first time. A 32-MHz fundamental shear-mode AT-cut quartz resonator was integrated with a commercial CMOS sustaining circuit with cubic temperature compensation electronics and vacuum encapsulated, all at wafer level. The TCXO showed temperature stability and hysteresis from -17° to +70° C of ± 0.19 ppm and 66 ppb, respectively, and required 2.5 mW of operating power. The results show that high performance quartz clocks can be directly integrated on advanced RF circuits using a low-temperature MEMS-after quartz process. Using Si wafer carrier techniques, this process can be extended to integration with full-size commercial ASIC wafers.

References

[1] R. L. Kubena et al., "Next generation quartz oscillators and filters for VHF-UHF systems," IEEE Int. Microw. Symp. Dig., San Francisco, CA., Jun. 2006, pp. 668-671.

[2] R. L. Kubena et al., "MEMS-based UHF monolithic crystal filters for integrated RF circuits," JMEMS, vol. 25, 2016, pp. 118 – 124.

[3] D. J. Kirby et al, "Optimizing UHF quartz MEMS resonators for high thermal stability, 2013 IEEE Int. Frequency Control Sym., Prague, Czech Republic, July 22 – 26, 2013.

[4] D. T. Chang and R. L. Kubena, "Large area integration of quartz resonators with electronics," US Patent # 7,555,824, issued 7/7/2009.

DORIS-class oscillator under radiations: the Jason family of satellites

Alexandre Belli and Pierre Exertier
Géoazur-CNRS
250 Rue Albert Einstein
06560 Valbonne
France
Email: belli@geoazur.unice.fr

Christian Jayles
Centre National d'Etudes Spatiales
18 Avenue Edouard Belin
31401 Toulouse
France

François Vernotte
UTINAM Observatory THTEA
Université de Franche Comté-CNRS
25000 Besançon
France

***Abstract*—The Jason family of satellites, which were launched in 2001, 2008 and 2016, embarked an ultra-stable-oscillator (USO) as the on-board frequency reference (short-term stability of a few 10^{-13} at 10-100 seconds) for the Doppler Orbitography and Radiopositioning Integrated on Satellite (DORIS) tracking system. All three satellites shared the same orbit (circular, 66°, 1335 km) and platform (PROTEUS) which is 3-axes stabilized. And all three oscillators have been perturbed by repetitive radiation exposures above the so-called South Atlantic Area, which implied deleterious frequency variations of various levels roughly from 10^{-12} to 10^{-11}.**

The primarily objective of this work is to compare the frequency response of these USOs to radiations. On the assumption that all environmental parameters (proton flux from the SAA, position, orientation of the platform, etc.) are identical, we demonstrate that the oscillators present the same behavior with a pseudo-periodic frequency variation at 59 days whilst enhancing a different sensitivity. From all the perturbation sources, a dedicated exposure to radiations is identified due to a very particular situation − platform and attitude law, orbit, satellite anisotropy.

I. Introduction

The Doppler Orbitography and Radiopositioning Integrated by Satellite (DORIS) tracking system has been used for years to control the orbitography of Earth observing satellites as Jason, SARAL, CryoSat, and Sentinel for the current missions. The short term stability of the on-board Ultra-Stable-Oscillator (USO) is a fundamental parameter of this Doppler geodetic space technique in order to maintain a very precise Doppler measurement during a given pass of the satellite above a ground beacon; it is of $3.5{\cdot}10^{-13}$ between 10 and 100 seconds. On the long term (1 day and beyond), the integrity of DORIS is based on a frequency accuracy of 10^{-12} in $\delta f/f_0$; due to the frequency drift of the oscillator of several 10^{-11}.d^{-1} generally, the monitoring is ensured by some ground beacons which are synchronized by an atomic frequency standard. Any inaccuracy or sudden change in the USO frequency greater than this level is reflected in the Doppler measurement and then in the geodetic products of DORIS as the precise orbit determination and the positioning [Tavernier et al., 2005].

The important perturbations which have affected the Jason-1 USO (launched in 2001) up to an instantaneous level of $6 \cdot 10^{-11}$ over several minutes were detected very early; their origin were fund in the South Atlantic Anomaly (SAA) where the satellite is passing regularly at an altitude of 1335 km, e.g. [Willis et al., 2004]. In order to reduce the sensibility of the oscillator to the high energetic proton flux occuring in this area, a pre-irradiation has been recommended leading to a new generation of oscillators from which the Jason-2 (launched in 2008) USO is the first one in space and Jason-3 (2016) the second [Auriol and Tourain, 2010].

As a result, the Jason-2 Doppler data have been extensively used to contribute to oceanography and space geodesy, e.g. [Zelensky et al., 2010]. But, the growing improvement of the precise orbit determination (POD) models together with the terrestrial reference frame paved the way of analyzing the Doppler data in even more detail. A model describing the frequency variations of the USO was established allowing to precisely determine the actual behavior of the quartz oscillator under temperature and radiation effects at a precision level of $5 - 6 \cdot 10^{-13}$ [Belli et al., 2015]. As a result, it has been demonstrated that the Jason-2 USO is actually affected by radiation (SAA) but at a much lower level (a few 10^{-12}) than its predecessor. After 8 years in space, Jason-2 was replaced by Jason-3; before changing its orbit however, both satellites have been placed on the same trajectory during the commissioning phase of the latter. Its USO revealed to be slightly more noisy than the former suggesting a higher sensitivity to radiation.

The present paper describes the common behavior of the USOs of the Jason family; it highlights their respective sensitivity to radiation effects. A frequency variation that occurs every 60 days at an amplitude of around $1 - 2 \cdot 10^{-10}$ is discussed; it affects all the three USOs and is phased with the attitude movements of the platform We propose a scenario following which the DORIS instrument would be more sensible to radiation towards the across track direction of the orbit, particularly when the attitude is fixed during 10 days, every 60 days. We show the results of our analysis and we conclude.

II. Jason family

A. Space segment

a) Orbit & attitude: The orbit of Jason satellites is circular, with 66 degrees of inclination, at an altitude of 1336

978-1-5386-2916-1/$31.00 ©2017 IEEE

km; it is the most elevated orbit of the DORIS-satellites. Due to the Earth flattening, the precession of the orbital plane is of $3^\circ \cdot d^{-1}$ with respect to the Sun position. Every 60 days, the orbital plane is thus aligned towards the Earth-Sun direction. The attitude laws of the PROTEUS platform are specific, because the solar panel rotation axis is the satellite Y axis and the pitch motion keeps the Z axis of the spacecraft always pointed towards the Earth, perpendicular to the reference ellipsoid − Jason-series being dedicated to the observation of the sea surface with a radar altimeter.

Concerning the yaw-motion (the yaw angle is Ψ), the nominal attitude law alternates yaw-steering and fixed-yaw regimes depending on the value of the angle between the Earth-Sun direction and the orbital plane (called: β' angle). In fixed-yaw regime ($|\beta'| < 15^\circ$), the satellite X axis is oriented towards the along track direction when the satellite is flying forward, and opposite to that when the satellite is flying backwards (before and after the flip).

The DORIS receivers have been placed behind the Y-wall of the platform; on the side ($-$Y). Thus every 60 days during the 10 days of fixed-yaw regime, the Y axis is oriented towards the across track direction. We will see in the following that a very special event in term of frequency variation occurs on each one of the USOs of the Jason family every 60 days; this event starts (and stops) during the yaw-fixed period.

b) Jason-2 passengers: Carmen-2 is an instrument dedicated to the measurement of the in-flight radiations [Bezerra et al., 2007]. The data consist in time series of particle flux observed at different energy levels (from 1 to 200 MeV) every 16 seconds. Its opening is located on the $-$Z axis of the platform. From 85 MeV which energy is the lower limit over which the oscillator may be corrupted, the integrated received dose has been established at around 230 rad (1 rad = 0.01 Gray SI) per month, from which we can deduce roughly an average dose of 0.31-0.35 rad for each pass of the satellite in the SAA area. This value has been measured in 2011 [Lemoine and Capdeville, 2006]; a geographical extension of the SAA was thus established from the data which is considered here as a constant. Obviously, some variations of the proton flux inside the SAA may appear both in time (i.e., over a 11-yr solar cycle) and in space; we did not take them into account.

In addition to Carmen-2, the T2L2 (Time Transfer by Laser Link) instrument has been of fundamental interest in order to help characterizing the on-board oscillator (DORIS USO) on the basis of the quality of its space segment [**?**]; the optics design, the detector and the picosecond (ps) event timer had led to an impressive stability of the ground-to-space link which was estimated at a level of a few ps over 100 s [Exertier et al., 2014]. From several laser stations equipped with an hydrogen maser (H-maser) as frequency standard, it has been possible to extract the reading of the on-board oscillator at a few parts in 10^{-13} ($\delta f/f0$); this unprecedented level of precision allowed detailed studies of its behavior in the space environment [Guillemot et al., 2009].

B. Oscillator

Among the physical effects that occur in low-Earth orbit on space oscillators as the temperature, magnetism, accelerations and vibrations, radiations are definitely the primary source of concern for the USO series dedicated to Jason satellites [Cibiel et al., 2006], [Galliou et al., 2007]. It is mainly due to the altitude and inclination of the chosen orbit, which means that the satellite crosses the SAA area once per revolution or a little less resulting in a very short dose exposure of the spacecraft electronic parts [Weaver et al., 2004]. The Table I summarizes the main coefficients which characterize the susceptibility of the Jason USOs to the aging, temperature and radiation effects; the values have been provided by CNES (the French Space Agency) and some manufacturers.

TABLE I
JASON USOS: EXPECTED COEFFICIENTS OF FREQUENCY SUSCEPTIBILITIES FOR BOTH GENERATIONS OF MATERIAL.

Satellite	Drift (d^{-1})	Temperature ($^\circ C^{-1}$)	Radiation (rad^{-1})
Jason-1	$\approx 10^{-10}$	$< 10^{-12}$	$6 - 0.5 \cdot 10^{-11}$
DGXX	$\approx 10^{-11}$	$6.5 \cdot 10^{-13}$	$2 - 7 \cdot 10^{-12}$

On Jason-1, the frequency signature of the SAA has reached an instantaneous level of $6 \cdot 10^{-11}$ followed by a short relaxation period. Due to this huge nonlinear change of the frequency over a short time period, some of the Doppler tracking data have been discarded by annalists despite the achievement of a dedicated model [Lemoine and Capdeville, 2006]. From this situation and other arguments in favor of an improvement of the DORIS on-board receiver, a new generation was developed, called DGXX [Auriol and Tourain, 2010], from which the first unit is flying on Jason-2 and the second on Jason-3. The new series of USOs has been systematically pre-irradiated at 30 krad over 1 hour, in order to decrease the quartz crystal sensibility as much as possible. As a result, the expected performance of the Jason-2 USO (short term stability) has been saved and, in the same time, its susceptibility has been decreased from $6 - 7$ to $2 - 3 \cdot 10^{-12}$/rad.

The characterization of the Jason-2 oscillator in its space environment has been assessed from the T2L2 data products essentially [Belli et al., 2015]. What reflects primarily is confirmation of its lower sensitivity and, above all, its long term stability combined with a slow decrease of the oscillator's drift by a factor of 10 over 8 years. The model which is strongly constrained by the Carmen-2 data uses an aging function ($\exp -(t/\tau)$ with τ=10 years) which drives the frequency response to radiation on the long term.

The study also shows the great influence of the attitude law of the platform under the form of regular abrupt changes in frequency; we observed the same situation for all Jason USOs. On the one hand, the temperature increases (or decreases) of 2-3°C over less than one day when the attitude moves in (and out) of the fixed-yaw regime. On the other, a pseudo-periodic effect (at around 60 days) appears in frequency under the form of a linear increase over 10 days followed be a relaxation period.

Jason-3, which USO is of the same generation has a much more important drift and a greater frequency response to radiation, what we describe in our analysis.

C. Data

The Precise Orbit Determination process (POD) which is systematically applied to all Earth observing mission is based on dynamical and geometrical models that were continuously improved for years. Local and above all global estimated geodetic parameters are determined on a regular basis [Zelensky et al., 2010]. The frequency bias of the on-board oscillator is estimated using the satellite passes over some dedicated time beacons [Tavernier et al., 2005]; time series of USO frequency biases are thus provided for each mission to a precision level of around $1 \cdot 10^{-12}$. This corresponds to a radial velocity of 0.3 mm.s^{-1} in term of Doppler effect what is roughly the actual limit of the DORIS space geodetic technique – orbit, measures and network.

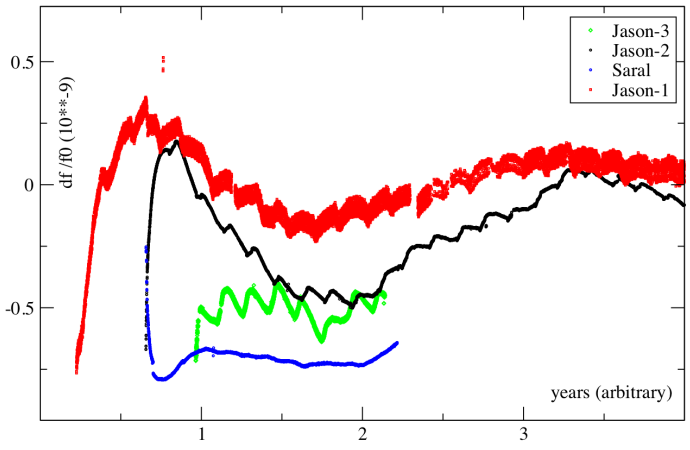


Fig. 1. DORIS USOs: relative frequency biases without drift; residuals (in 10^{-9}) with an arbitrary time scale (X-axis) in years.

Among the current DORIS missions, the Fig. 1 shows the behavior of some USOs without drift since the beginning of their launch. Obviously, each of these oscillators has its own drift, positive or negative; all exhibit a long term asymptotic behavior. What is of interest here, is a clear difference between SARAL (launched in 2013 on a polar orbit at 800 km altitude) and Jason's USOs, where the latter's exhibit a pseudo-periodic variation at around 60 days. While it is clearly correlated to the attitude law of the (common) platform, the question addressed here is to understand its origin. If it is due to radiation, what we believe actually, we propose a mechanism of modeling.

III. Analysis

Table II shows the value of the drifts we computed and then subtracted from the data at the beginning of each Jason mission and then 10 years later. We clearly see that the Jason-3 USO as a greater drift compared to Jason-2 (factor 4), whereas they must be comparable.

The current analysis was conducted in three steps corresponding to three time scales; the drift, the short term effects

TABLE II
Jason USOs: observed frequency drifts from relative frequency bias estimated throughout the Precise Orbit Determination process; at the beginning of the mission and then 10 yrs later.

Satellite	Drift (d^{-1})	id. after 10 yrs
Jason-1	$10.7 \cdot 10^{-11}$	10^{-11}
Jason-2	$1.9 \cdot 10^{-11}$	$0.2 \cdot 10^{-11}$
Jason-3	$8.1 \cdot 10^{-11}$	–

from temperature and SAA radiation, and then the 60-day period. All these phenomena were driven by the same sensibility coefficients actually (per satellite), which were considered as linear relative to the physical source: temperature ($T - < T >$) and particle flux F_p (in $p^+ cm^{-2} s^{-1} sr^{-1}$, for a given energy level E_p) both data series being provided by the respective space missions. This approach however cannot be valid for the Jason-1 USO after 2002, where the frequency response of the oscillator to the SAA exposures were clearly highly nonlinear; see [Lemoine and Capdeville, 2006].

A. Temperature & SAA

The temperature (T) of the USO box is measured regularly (from 0.5 to 5 min, depending on the mission; for Jason-2 & Jason-3). The initial model (with T^i, i=1,3) has been simplified to its linear term starting with the a priori sensitivity coefficient that was previously measured in a laboratory [Galliou et al., 2007]. Considering the very low signature of the frequency response to the temperature variation at the orbital period, the precision level of the data (frequency bias at $1 \cdot 10^{-12}$) and their time resolution (0.2 day), we estimated an average coefficient for successive periods of 60 days. We found an average value of $\pm 1 - 2 \cdot 10^{-12}$/°C per degree for both missions (of opposite sign, see Table III), which results in a frequency "jump" of $5 - 6 \cdot 10^{-12}$ occurring on less than one day for each attitude change.

The geographical map of the SAA area provided by the Carmen-2 data in addition to the orbit of each considered satellite have been significant supports in order to compute and integrate the received dose on-board the spacecraft along its trajectory (step of 1 minute). The model is based on a positive increase of the frequency with respect to the measured flux at each step of the orbit, and then on a relaxation period which is exponential over 10-7 minutes. A global coefficient (γ_Q), which was empirically estimated is used together with the sensibility $\gamma_1 = \delta f / f_0$ /rad^{-1} of the oscillator to convert the dose (1 Gray = 1 J . kg^{-1}) into the actual response $\delta f / f_0$. It is of great importance to constraint γ_Q by the previously determined value of 230 rad per month, while γ_1 is adjusted from the observed frequency biases.

During the formation flight of both Jason-2 & Jason-3 in 2016 (with a 1-minute interval), we assumed that the same dose which is measured by the former (Carmen-2) is received by the latter. Additionally, we assumed both platforms having an identical anisotropy (same γ_Q=0.05) but we considered the orbit and history of maneuvers provided by CNES for each

TABLE III
ONE YEAR OF DATA FOR JASON-2 (IN 2008-2009) & JASON-3 (IN 2016): AVERAGE VALUES OF ADJUSTED COEFFICIENTS OVER 60 DAY-PERIODS FOR THE FREQUENCY SENSITIVITY OF USOS TO TEMPERATURE (TEMP.) AND RADIATION (RAD.).

Satellite	Temperature (C^{-1})	Radiation (rad^{-1})
Jason-2	$-0.12 \pm 0.02\ 10^{-11}$	$+5.5 \pm 0.3\ 10^{-12}$
Jason-3	$+0.20 \pm 0.02\ 10^{-11}$	$+10.5 \pm 0.5\ 10^{-12}$

spacecraft independently. The Table III shows the average coefficients that were adjusted over successive 60-day periods. However, for the purpose of comparing both oscillators at the same age, and not at the same date, we computed here the coefficient of the Jason-2 USO for the period 2008-2009. Actually in 2016, the Jason-2 USO is 8 years old and thus has a sensitivity coefficient which has been dramatically reduced by the aging effect. As a result, the Jason-3 oscillator has a coefficient two times greater than the one of Jason-2 at the same age which result is in good agreement with the noise of their respective frequency bias time series.

The second step of our analysis highlights a 60-day period of $1 - 2 \cdot 10^{-10}$ relative amplitude for all Jason USOs. We saw that it is not possible to correlate this effect neither with the temperature (maximum $5 - 6 \cdot 10^{-12}$) nor the short term SAA radiation (maximum $1 - 3 \cdot 10^{-12}$). In addition, the frequency variations of the USOs under variations of the magnetic field, high energetic solar events, electronics discharges or accelerations were estimated at a much lower level [Cibiel et al., 2006].

B. The 60-day period

As it is seen in the data, each of the frequency ramp (increase) starts (and stops) when the spacecraft moves from yaw steering to yaw-fixed mode (and back). We saw that during this 10-day period the increasing is linear and is followed by a relaxation period of 45-50 days. The same event is regularly observed, the only change being the amplitude of this phenomenon which slowly reduces over the long term due to aging.

By looking at the orientation of the platform during this particular event, we know that the Y-satellite is aligned towards the across-track direction of the orbit. By taking into account the map of the declination $B_{declin.}$ of the magnetic field, we can see that both directions (Y axis and local declination) are strictly collinear when the satellite crosses the SAA area. By considering all the previously quoted parameters events, we hypothesized that the anisotropy of the platform is such as the DORIS electronic box is less protected in a given direction. Following this scenario, the USO might be a bit more affected by the SAA radiation (between 10 and 15%) during the yaw-fixed regime. The additional dose has been estimated at 15 rad for 10 days. Let us recall that the Carmen-2 instrument has its own aperture along the Z axis around which the spacecraft is moving. Thus, it is not possible to extract any signal from its data.

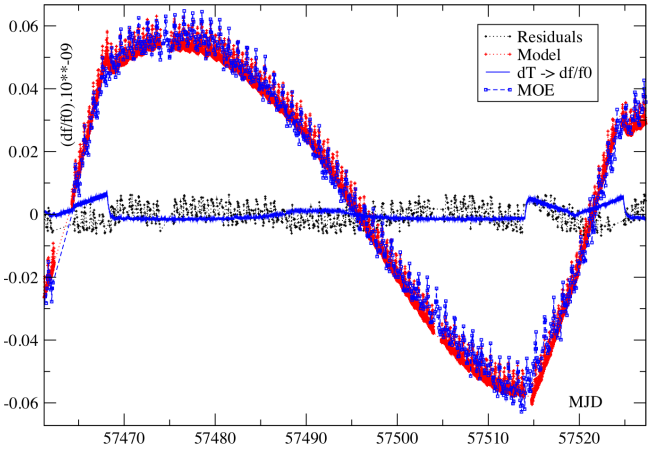


Fig. 2. Jason-3 USO: relative frequency bias without drift; data (blue), model (red) and residuals (black) in 10^{-9}, corresponding to the beginning of the mission (March 2016); the blue line shows the relative variations of the temperature (USO box) converted to frequency.

The modeling of this effect is similar to the one used to describe the SAA passes. But, as the current dose rate is weaker the corresponding relaxation period is longer [Weaver et al., 2004]. The following function has been adopted in order to describe the frequency response:

$$\begin{aligned} \delta\widetilde{\nu}_{YF} &= \gamma_1 \int_{t_0}^{t_{YF}} \gamma_Q \, D_{YF} \, dt \\ \delta\widetilde{\nu}(t > t_{YF}) &= \delta\widetilde{\nu}_{YF} \, (2 \exp^{-(t-t_{YF})/\tau} - 1) \end{aligned} \quad (1)$$

where:

t_0 and t_{YF}: dates (start and stop) of the yaw-fixed regime,
D_{YF}: dose exposure during the yaw-fixed regime (YF); this quantity is considered as a constant,
τ: empirical coefficient for the relaxation, fixed to 15 days.

The final analysis process consisted to add all the above mentioned effects – the long term drift, short term temperature and SAA radiation, and YF period – controlled by the common coefficients γ_1 and γ_Q and to adjust the quantity D_{YF}. The residuals, between each model and the corresponding time series of frequency bias, are of 1.5 10^{-12} and 3.4 10^{-12}, respectively for Jason-2 & -3 (see Fig. 2).

IV. CONCLUSION

The study of the behavior of the USO family of Jason satellites is of great interest for both improving the geodetic space technique and understanding the way to improve the long term stability of the reference oscillator. In addition to the first model that was developed earlier, the present study provides the main insights to accurately describe the frequency response to the temperature and radiation for several time scales. It compares the oscillator behaviors placed on the same type of orbit and spacecraft. The fact that both passenger instruments on Jason-2 (Carmen-2 and T2L2) provided data

to constraint the estimated parameters of its USO is of great importance, providing thus phenomenology and accuracy for the other oscillators.

A 60-day period appearing regularly as a frequency signal on each of the oscillators is assumed here to be of radiative origin with the assumption of a weakness of the platform (PROTEUS) when its Y axis is oriented towards the across direction of the orbit (yaw-fixed regime). Following this scenario, the radiation effect that affects the USOs should be increased by around 15% during 10 days for every fixed-yaw period. Inversely, this effect is used to help in characterizing the sensibility of the USOs to radiation. For Jason-2 and -3 USOs we show a two times greater effect on Jason-3 during its first year in space (both USOs at the same age). The proposed model achieved a RMS of the relative frequency residuals of $1 - 3 \cdot 10^{-12}$, which values are very close to the current limit of the overall DORIS system.

ACKNOWLEDGMENT

The authors would like to thank LABEX FIRST-TF which provides us financial support for this work. We thank also H. Capdeville (CLS - Toulouse) for providing us the MOE data, and the consortium DORIS (CNES) for helpful discussions.

REFERENCES

[Auriol and Tourain, 2010] Auriol, A. and Tourain, C. (2010). Doris system: The new age. *Advances in Space Research*, 46(12):1484 – 1496. DORIS: Precise Orbit Determination and Applications to Earth Sciences.

[Belli et al., 2015] Belli, A., Exertier, P., Samain, E., Courde, C., Vernotte, F., Jayles, C., and Auriol, A. (2015). Temperature, radiation and aging analysis of the doris ultra stable oscillator by means of the time transfer by laser link experiment on jason-2. *Advances in Space Research*, 58(12):–. Scientific Applications of DORIS in Space Geodesy.

[Bezerra et al., 2007] Bezerra, F., Lorfevre, E., Ecoffet, R., Falguere, D., and Bourdoux, P. (2007). Carmen/mex test board for the study of radiation effects on electronic components aboard jason-2 and sac-d satellites. In *Radiation and Its Effects on Components and Systems, 2007. RADECS 2007. 9th European Conference on*, pages 1–6.

[Cibiel et al., 2006] Cibiel, G., Boizot, B., j. Boy, J., f. Carlotti, J., Cambon, O., Devautour-Vinot, S., Candelier, V., Lamboley, J., Guibert, P., Largeteau, A., Inguimbert, C., and Piccheda, D. (2006). Ultra stable oscillators dedicated for space applications: oscillator and quartz material behaviors vs radiation. In *2006 IEEE International Frequency Control Symposium and Exposition*, pages 814–822.

[Exertier et al., 2014] Exertier, P., Samain, E., Martin, N., Courde, C., Laas-Bourez, M., Foussard, C., and Guillemot, P. (2014). Time transfer by laser link: Data analysis and validation to the ps level. *Advances in Space Research*, 54:2371–2385.

[Galliou et al., 2007] Galliou, S., Sthal, F., Vacheret, X., Brendel, R., Salzenstein, P., Rubiola, E., and Cibiel, G. (2007). A program to analyse the origin of noise in ultra-stable quartz crystal resonators. In *Frequency Control Symposium, 2007 Joint with the 21st European Frequency and Time Forum. IEEE International*, pages 1176–1181.

[Guillemot et al., 2009] Guillemot, P., Exertier, P., Samain, E., Jayles, C., Cibiel, G., and Leon, S. (2009). Fisrt application of the t2l2 ground to space time transfer : Characterisation of the doris uso. In *Frequency Control Symposium, 2009 Joint with the 22nd European Frequency and Time forum. IEEE International*, pages 711–714.

[Lemoine and Capdeville, 2006] Lemoine, J.-M. and Capdeville, H. (2006). A corrective model for jason-1 doris doppler data in relation to the south atlantic anomaly. *Journal of Geodesy*, 80(8):507–523.

[Tavernier et al., 2005] Tavernier, G., Fagard, H., Feissel-Vernier, M., Lemoine, F., Noll, C., Ries, J., Soudarin, L., and Willis, P. (2005). The international doris service. *Advances in Space Research*, 36(3):333 – 341. Satellite Dynamics in the Era of Interdisciplinary Space Geodesy.

[Weaver et al., 2004] Weaver, G. L., Reinhart, M. J., Sequeira, H. B., and Stapor, W. (2004). Examination of detailed frequency behavior of quartz resonators under low dose exposures to proton radiation. In *Frequency Control Symposium and Exposition, 2004. Proceedings of the 2004 IEEE International*, pages 356–364.

[Willis et al., 2004] Willis, P., Haines, B., Berthias, J.-P., Sengenes, P., and Mouël, J.-L. L. (2004). Comportement de l'oscillateur doris/jason au passage de l'anomalie sud-atlantique. *Comptes Rendus Geoscience*, 336(9):839 – 846.

[Zelensky et al., 2010] Zelensky, N. P., Lemoine, F. G., Ziebart, M., Sibthorpe, A., Willis, P., Beckley, B. D., Klosko, S. M., Chinn, D. S., Rowlands, D. D., Luthcke, S. B., Pavlis, D. E., and Luceri, V. (2010). Doris/slr pod modeling improvements for jason-1 and jason-2. *Advances in Space Research*, 46(12):1541 – 1558. DORIS: Precise Orbit Determination and Applications to Earth Sciences.

High Precision Time Measurement using a Self-timed Ring Oscillator based TDC

Assia El-Hadbi[1,2], Abdelkarim Cherkaoui[1], Oussama Elissati[2], and Laurent Fesquet[1]
[1]Univ. Grenoble-Alpes, CNRS, Lab. TIMA, F-38031 Grenoble, France
[2]Institut National des Postes et Télécommunications, Lab. STRS, Rabat, Morocco
Emails: {*assia.el-hadbi, abdelkarim.cherkaoui, laurent.fesquet*}*@univ-grenoble-alpes.fr*, *elissati@inpt.ac.ma*

***Abstract*—A new high resolution time-to-digital converter (TDC) based on a self-timed ring (STR) oscillator is presented. Thanks to the STR unique features, the time resolution of the proposed TDC can be tuned as fine as needed. In addition, on-the-fly time measurements can be carried out on fast non-periodic signals. To provide a proof of concept of this new technique, a design of a 5-stage STR-based TDC has been implemented and simulated using a 28 nm FDSOI CMOS technology.**

I. Introduction

Accurate time measurement is a necessity for a very large number of applications, such as high-energy physics, time-of-flight measurement, instrumentation and satellite positioning [1]. This can be carried out with devices called time-to-digital converters (TDCs) implemented mostly with digital elements. The accuracy of TDCs is related to the time resolution by which the measurement is performed. Thus, the time resolution is the most important characteristic of TDCs.

In many architectures, the resolution is bounded by the CMOS gate delay: it cannot be lower than the propagation delay of one logical gate [2], [3]. Other architectural techniques with a time resolution lower than the gate delay have been proposed [4]–[7]. For example, in the Vernier TDC, two events propagate in two delay lines having slightly different delays. The resulting effective resolution is the time difference between the two events which is smaller than the stage delay. However, it is very difficult to precisely adjust this time resolution without using complex calibration schemes [7].

In this paper, we present a new fully digital TDC architecture based on a self-timed ring (STR) oscillator. Its main features are:

- A time base generated by equidistant STR phases with a sub-gate phase resolution.
- An accurate time resolution which can be tuned as fine as needed, thanks to the STR characteristics.
- On-the-fly measurement on fast non-periodic signals.

II. Self-Timed Rings

A STR is the looped control circuit of a micropipeline [8]. Each ring stage is composed by a C-element (Muller gate) and an inverter as shown in Fig. 1. In this architecture, several events can propagate simultaneously without colliding thanks to a request/acknowledgement handshake protocol. The number of events is set at the ring initialization, and stays invariant.

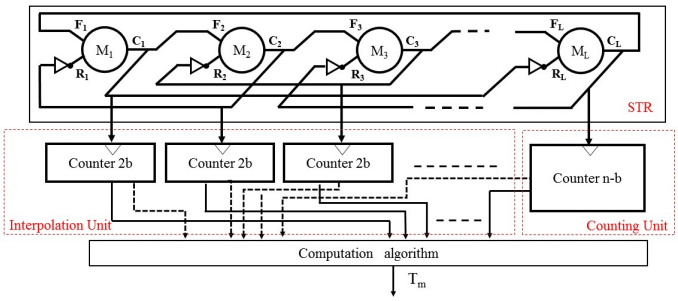


Figure 1. Proposed TDC architecture using a L-stage STR

The frequency does not depend on the number of stages, but rather on the occupancy ratio (number of events N over number of stages L) [9]. The ring exhibits a unique oscillation mode in which events propagate in the ring with a uniform time spacing (evenly-spaced oscillation mode) [9]. This unique behavior is due to the Charlie effect: the closer are the events at the inputs of a Muller gate, the longer is its propagation delay [10]. In the context of the STR, events push away from each other in time as they propagate in the ring. For a certain range of occupancies, this effect leads to a uniform event distribution (in time) at the ring outputs [10]. As a consequence, the STR can provide uniformly distributed events with a sub-gate time resolution. In practice, the time resolution is expressed as follows:

$$\Delta\varphi = \frac{T_{\mathrm{STR}} G}{2L} \tag{1}$$

where G is the greatest common divisor of N and L and T_{STR} is the oscillation period of the STR.

We can also notice that STRs are highly robust to PVT variations thanks to the Charlie effect [9]. Finally, STRs are configurable oscillators since they are able to provide different oscillation frequencies with a fixed number of stages by simply changing the number of events [11].

III. STR-based TDC

The principle of the STR-based TDC is presented in Fig. 2. An L-stage STR, with a number of events co-prime with L, provides L signals evenly distributed over its half oscillation period T_{STR}. The time interval T, which needs to be measured, is expressed as a function of $\Delta\varphi$ and T_{STR}. The idea is to firstly count the number of T_{STR} steps. Then, the remaining

978-1-5386-2916-1/$31.00 ©2017 IEEE

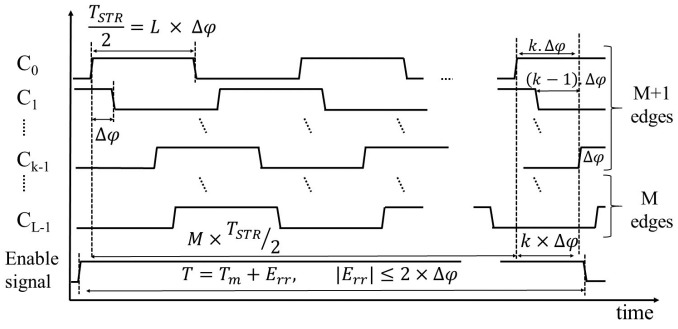


Figure 2. Time measurement diagram

Table I
SIMULATION RESULTS OF A 5-STAGE STR-BASED TDC USING 28 NM FDSOI CMOS TECHNOLOGY

T (ps)	50	500	1000	2000	3000
T_m (ps)	54	504	1008	1998	2988

time is quantified with a resolution of $\Delta\varphi$, as depicted in Fig. 2. The measured time value T_m is given by (2) using (1) for $G = 1$:

$$T_{\mathrm{m}} = M \cdot \frac{T_{\mathrm{STR}}}{2} + k \cdot \Delta\varphi = (M \cdot L + k) \cdot \Delta\varphi \qquad (2)$$

A simple architecture that derives from this equation is made by a double-edge counter at each STR output. k of these counters show the value $M + 1$ while $L - k$ other counters exhibit the value M. This information about M and $M+1$ is given by the two least significant bits of all counters. Therefore, only 2-bit counters are required in addition to one large counter in order to determine M and k (see Fig. 1).

IV. SIMULATION RESULTS

To validate the proposed method, we have used two different simulation flows: analog and high-level timed simulations. Analog simulations have been performed with Virtuoso analog design environment (ADE) in a 28 nm FDSOI technology. They served to validate the circuit functionality and measure technological parameters such as the propagation delays of the Muller gate. Then those parameters have been incorporated in high-level simulations. These simulations use custom libraries modeling jitter and analog effects in the C-elements (e.g. the Charlie effect) to evaluate the TDC in a noisy environment.

A proof of concept is presented using a 5-stage STR-based TDC.The propagation delay of the C-element is around 27.7 ps. The STR oscillation frequency is 5.56 GHz ($T_{\mathrm{STR}} = 180\,\mathrm{ps}$) with a time resolution of 18.0 ps. Table I shows analog simulation results for the architecture of Fig. 1. As it can be seen in the table, the measured interval T_m is equal to the interval T with an error which does not exceed $\Delta\varphi$ ($\mid E_{rr} \mid \leq \Delta\varphi$).

In a noisy environment, we have measured a 500 ps time interval 100 times for different resolutions $\Delta\varphi$ and for a fixed jitter standard deviation $\sigma = 1.0\,\mathrm{ps}$. All the measurements are correct ($\mid E_{rr} \mid \leq \Delta\varphi$) and the mean value T_{mean} from the 100 samples are equal to 501.1 ps. In fact, jitter does not affect the result since $\Delta\varphi = 18.0\,\mathrm{ps} \gg \sigma$. Consequently, on-the-fly measurements can be performed in this case. Conversely, for $\Delta\varphi \approx \sigma$, computing a mean value using several samples is required to filter the STR noise: on-the-fly measurement is not possible in this case. This sets the limits for on-the-fly measurement using this TDC for a resolution close to the jitter standard deviation.

V. CONCLUSION

A new architecture of a TDC based on STR with sub-gate time resolution is presented in this paper. We propose a proof of concept using analog and high-level simulations in a 28 nm FDSOI technology. The time resolution of this TDC can be adjusted as fine as desired by simply increasing the number of STR stages. Thanks to these features, on-the-fly time measurements can be carried out on fast non-periodic signals. Simulations show promising results in terms of measurement accuracy.

ACKNOWLEDGMENT

This work has been funded by "Région Rhône-Alpes" (France): ACCUEIL DOC grant n°15.005282.01 and COOPÉRA project n°17263.

REFERENCES

[1] C. N. M. Marins, P. Kaufmann, A. A. Ferreira, P. H. Lopes, M. C. de Paiva, R. M. Vilela, and A. C. da Silveira, "Precision clock and time transfer on a wireless telecommunication link," *IEEE Transactions on Instrumentation and Measurement*, vol. 59, no. 3, pp. 512–518, March 2010.

[2] Y. Arai, T. Matsumura, and K. I. Endo, "A CMOS four-channel times;1K time memory LSI with 1-ns/b resolution," *IEEE Journal of Solid-State Circuits*, vol. 27, no. 3, pp. 359–364, Mar 1992.

[3] Z. Cheng, X. Zheng, M. J. Deen, and H. Peng, "Recent developments and design challenges of high-performance ring oscillator CMOS time-to-digital converters," *IEEE Transactions on Electron Devices*, vol. 63, no. 1, pp. 235–251, Jan 2016.

[4] M. Z. Straayer and M. H. Perrott, "A multi-path gated ring oscillator TDC with first-order noise shaping," *IEEE Journal of Solid-State Circuits*, vol. 44, no. 4, pp. 1089–1098, April 2009.

[5] L. Vercesi, A. Liscidini, and R. Castello, "Two-dimensions vernier time-to-digital converter," *IEEE Journal of Solid-State Circuits*, vol. 45, no. 8, pp. 1504–1512, Aug 2010.

[6] M. Lee and A. A. Abidi, "A 9 b, 1.25 ps resolution coarse-fine time-to-digital converter in 90 nm CMOS that amplifies a time residue," *IEEE Journal of Solid-State Circuits*, vol. 43, no. 4, pp. 769–777, April 2008.

[7] P. Dudek, S. Szczepanski, and J. V. Hatfield, "A high-resolution CMOS time-to-digital converter utilizing a Vernier delay line," *IEEE Journal of Solid-State Circuits*, vol. 35, no. 2, pp. 240–247, Feb 2000.

[8] I. E. Sutherland, "Micropipelines," *Commun. ACM*, vol. 32, no. 6, pp. 720–738, Jun. 1989.

[9] J. Hamon, L. Fesquet, B. Miscopein, and M. Renaudin, "High-level time-accurate model for the design of self-timed ring oscillators," in *2008 14th IEEE International Symposium on Asynchronous Circuits and Systems*, April 2008, pp. 29–38.

[10] S. Fairbanks, "High precision timing using self-timed circuits," Computer laboratory, University of Cambridge, Tech. Rep., 2009. [Online]. Available: http://www.cl.cam.ac.uk/techreports/UCAM-CL-TR-738.pdf

[11] L. Fesquet, A. Cherkaoui, and O. Elissati, "Self-timed rings as low-phase noise programmable oscillators," in *New Circuits and Systems Conference, 2014 IEEE 12th International*, June 2014, pp. 409–412.

Measuring Thermodynamic Noise in Optical WGM Microresonators

Jinkang Lim and Che Wei Wong
Mesoscopic Optics and Quantum Electronics Laboratory,
University of California, Los Angeles
Los Angeles, CA 90095, U.S.A.
e-mail: jklim001@ucla.edu

Lute Maleki, Anatoliy A. Savchenkov, Elijah Dale, Wei Liang, Danny Eliyahu, Vladimir S. Ilchenko, and Andrey B. Matsko
OEwaves Inc., 465 N Halstead St.
Pasadena, CA 91107, U.S.A.
e-mail: andrey.matsko@oewaves.com

***Abstract*— We demonstrate the noise characteristics of crystalline whispering gallery mode (WGM) microresonators and the microresonator-stabilized lasers at the fundamental thermodynamic limit. We study environmental sensitivity of the microresonators, stabilize them, and demonstrate a WGM resonator stabilized laser characterized with 25 Hz linewidth and 32 Hz Allan deviation measured at 100 ms integration time.**

Keywords—Thermodynamic fluctuations, optical microresonator, whispering gallery modes, frequency noise

I. INTRODUCTION

Sub-Hz lasers have been demonstrated using high-finesse optical Fabry-Pérot (FP) cavities utilized for frequency stabilization. The stability of these cavities are achieved by taking advantage of ultra-low-expansion structures placed in vacuum and kept at the optimal temperature to operate at the zero thermal expansion point. Such cavity stabilized lasers exhibit fractional frequency instability at 10^{-15} level at 1-10 s integration times [1]. The unavoidable thermal motion of the cavity mirror's multilayer coating sets the limitation of the achievable stability. Nevertheless, high performance FP cavities are relatively bulky and their direct miniaturization to microscale size is technically challenging. A highly compact cavity with ability to stabilize laser frequency to a few Hz level is highly desirable for field applications, especially on mobile platforms.

High-*Q* whispering gallery mode microresonators (WGMR) have been implemented in low-noise lasers and clocks [2,3]. The WGMR host materials typically feature a broad transparency range leading to ultra-narrow resonances without any complex dielectric mirror-coatings. The resonators are also relatively immune to mechanical noise, owing to their miniature size and small mass at micro-gram level. Since early studies on fundamental thermal fluctuations in microspheres, theoretical predictions suggest that the thermodynamically bounded frequency instability of microresonators can be better than 10^{-13} in 1 s integration time, if proper material and stabilization technique are selected. However, in spite of significant progress, the existing WGMRs still experience large frequency instabilities and long-term frequency drifts hindering their application in precision metrology and timing.

Here we examine the noise characteristics of WGMRs and WGMR-stabilized lasers at the fundamental limit. We employ a thermally compensated WGMR design to reduce the thermal sensitivity of the resonator and reveal the residual environmental sensitivities at the thermodynamical noise limit. Subsequently we suppress the environmental perturbations using an evacuated rigid enclosure and demonstrate that a laser stabilized to the thermally compensated WGMR, working as an optical probe, shows a spectral linewidth of less than 25 Hz and a frequency instability of 1.67×10^{-13} (5.0×10^{-12}) on the 191 THz carrier at 0.1 (1) s integration time, which is the best among microresonators of this given size and morphology. Furthermore, we confirm that the center-shifted random walk noise, imposed by the correlation between the WGMR temperature and the ambient temperature or pressure change, triggers the long-term frequency instability and monotonic frequency drift of the laser stabilized to the WGMR at the thermodynamical noise limit [4].

II. THERMAL COMPENSATION OF A WGMR

Thermal expansion of the WGMR host material is one of the major reasons for frequency drift of its modes. This drift impacts phase noise at spectral frequencies lower than 100 Hz. To reduce the effect one needs to find a material with low thermal expansion coefficient, like Zerodur. Unfortunately, Zerodur is not optically transparent. We found, though, that sandwiching a thin magnesium fluoride resonator and Zerodur substrate results in a significant reduction of the resonator expansion. We performed numerical simulations and designed a compensated resonator. The resonator was successfully fabricated and tested (see Fig. 1).

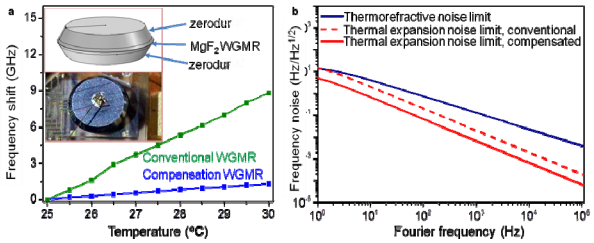


Figure 1 | Thermal-compensation MgF_2 WGMR. a, Measurement of the frequency shifts for the conventional MgF_2 WGMR (green) and thermal-

compensation WGMR (blue) respectively. The MgF_2 WGMR sandwiched by Zerodur in the packaged unit (Inset). MgF_2 resonator (middle) is glued in between two Zerodur blanks (top and bottom). The thickness of zerodur layer depends on thermo-mechanical properties of the resonator. **b,** Thermorefractive noise limit (blue) and thermal expansion noise limits (red) of the WGMR. The simulations show that the thermal expansion noise of the thermal-compensation WGMR (solid red line) has lower than the thermorefractive noise near the carrier frequency but the conventional one (dashed red line) has the similar noise. Therefore, the fundamental thermorefractive noise limit fluctuation can be reached with the thermal-compensation WGMR in this experiment.

III. Probing the WGM resonator noise

To probe a small environmental perturbation on the WGMR, we put the WGMR in a rigid vacuum chamber and stabilize a laser to the WGMR via the Pound-Drever-Hall (PDH) locking technique. The technical noise of the laser is compensated by two feedback loops: a piezoelectric transducer (PZT) onto a laser and an external acousto-optic modulator (AOM). The frequency noise power spectral density (PSD) and relative frequency instability of the stabilized laser are analyzed by heterodyne-beating against a Fabry-Pérot (FP) cavity reference laser, possessing 1 Hz linewidth and less than 0.1 Hz s^{-1} drift-rate. The PDH error signal is optimized for the best laser-WGM resonator stabilization.

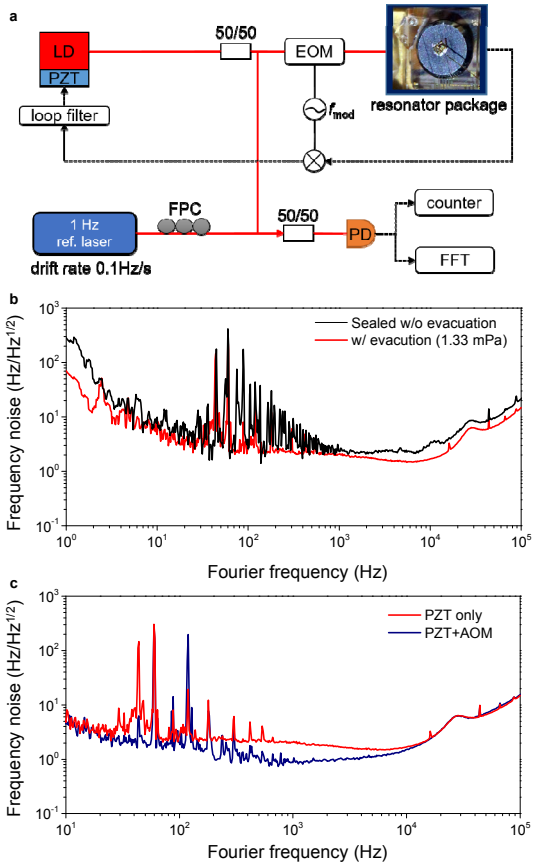


Figure 2 | Pound-Drever-Hall laser stabilization and frequency noise characterization. a. A self-injection locked WGM microlaser is coupled into a thermally-compensated WGM reference cavity in a vacuum chamber and stabilized via Pound-Drever-Hall (PDH) locking with both a piezoelectric transducer (PZT) and an acoustic-optical modulator (AOM). The spectral purity and relative frequency instability of the stabilized WGM laser are analyzed by heterodyne beating against a bulk Fabry-Pérot cavity laser that has a stabilized Hz-level linewidth and a drift rate of 0.1 Hz/s. LD: laser diode; EOM: electro-optic modulator; PD: photodetector; FPC: fiber polarization controller; SSA: signal source analyzer. **b.** Frequency noise in seal enclosure but no vacuum (black). The many spikes are observed in the acoustic noise frequency regime. Frequency noise at 10^{-5} torr (red). Most of the noise spikes are alleviated. The remaining spikes are mostly from harmonics of the 60 Hz electrical power-line noise. **c.** Frequency noise with PZT only feedback (red), and frequency noise with both PZT and AOM feedback (blue).

We modulate the laser frequency by applying a ramping voltage signal to either the PZT in the laser or the AOM to search a single WGM resonance near the reference laser frequency (191 THz). Figure 2**b** shows the frequency noise PSD curves for two different ambient pressure levels in the sealed chamber. We observe many noise spikes in the acoustic frequency regime originating from the laboratory environment when the WGMR is just sealed without evacuating the vacuum chamber (black). These spikes are suppressed by increasing the vacuum level to 1.33 mPa (red). The remaining spikes mostly come from the 60 Hz harmonics of the electrical power-line. In this measurement, we observed that the evacuated chamber substantially reduces acoustic noise peaks and provides further noise reduction near the carrier frequency. Since the PZT control loop has a limited feedback bandwidth, we added the second feedback loop using an external AOM to increase the feedback bandwidth for further technical noise suppression. With the AOM feedback loop, the bandwidth is extended to greater than 400 kHz. As a result, the noise over the 20 Hz offset frequencies is far more suppressed than only with the PZT feedback control in Figure 2**c**, which allows us to investigate the thermodynamical noise limit of the thermally compensated WGM resonator more clearly.

IV. Frequency noise of the stabilized laser

Figure 3a shows the comparative frequency noise power spectral density (FNPSD) curves of the laser stabilized to the thermally compensated resonator. For comparison, the theoretically estimated thermodynamical noise limit of the WGM resonator is also plotted. The frequency noise PSD of the free-running laser is shown by the black curve and the noise is substantially suppressed (30 dB at 10 Hz) as shown by the olive curve when the laser is stabilized to the WGM resonator. Below 30 Hz offset frequency, the stabilized laser frequency noise PSD curve falls off as $f^{-1.5}$ implying the thermorefractive noise limit of many thermal modes of the WGM resonator predicted by Matsko *et al*. From 30 Hz to 100 Hz, the frequency noise PSD curve falls off with f^{-1} implying the impact of flicker noise caused by the residual laser noise and electronic device noise. Two strong peaks originate from 60 Hz harmonics of the electrical power-line noise. The rising frequency noise above 1 kHz in the olive curve is due to the poles in the active feedback loops.

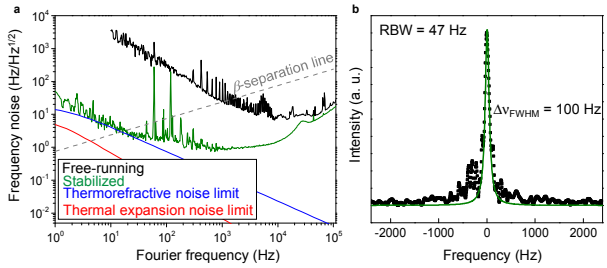


Figure 3 | Frequency noises of the stabilized laser oscillators, along with the linewidth estimates, in comparison with the thermodynamical limits. a. Frequency noise power spectral density measured by the beat signal between the microresonator-laser and the tabletop bulk 1 Hz FP laser. The frequency noise PSD of free-running self-injection locked laser used in our experiment (black), of the laser stabilized to the compensated reference cavity (olive). The theoretical thermodynamical frequency noise PSD predictions, from thermorefractive (blue) and thermal expansion (red) noise limits, are also illustrated for comparison. The effective linewidth evaluated from green curve by the phase noise method is 119 ± 2 Hz. Without the 60 Hz and 120 Hz power-line noise, the linewidth is determined to be ~ 25 ± 0.3 Hz. When the green curve is decomposed, the fundamental linewidth limit is 8.7 Hz. The β-separation line (dashed gray) method is also shown, with a linewidth estimate of ~ 30.6 ± 0.1 Hz, from the Gaussian linewidth approximation. **b.** The measured full-width at half-maximum linewidth on a spectrum analyzer with 47 Hz resolution bandwidth and 40 ms sweep time, giving a ≈ 100 Hz Lorentzian linewidth (olive) from fitting, which agrees with the integrated linewidth from the frequency noise PSD.

Characterizing the spectral linewidth of the resonator-stabilized laser from the PSD is not trivial due to the non-unified definition of linewidth of a flickering or drifting laser frequency, and therefore we estimated the spectral linewidth with two different methods. The integral linewidth is first calculated from the PSD with the phase noise method. An effective linewidth of 119 ± 2 Hz is deduced from the raw frequency noise PSD measurement from the olive curve in Figure 3b. We note that most of the residual noise and linewidth contribution arises from the 60 Hz and 120 Hz electrical power line frequency noise. When these two dominant noise peaks are excluded, an upper bound 25 ± 0.3 Hz is estimated. By fitting the frequency noise dependence using frequency decomposition method that removes the rest of spurious frequencies, we estimate the fundamental noise limited spectral purity and its resultant linewidth to be 8.7 Hz. The spectral linewidth is double-checked by the β-separation line method. The β-separation line is plotted in Figure 3**a** (dashed gray line). By integrating the frequency noise PSD up to 16 Hz offset frequency, which is the region above the β-separation line, we determine the linewidth of 30.6 ± 0.1 Hz. These measurements agree well with the linewidth measurement with a spectrum analyzer with 47 Hz resolution bandwidth (RBW) and 40 ms sweep time over the 5 kHz span. The resulting full-width at half-maximum linewidth is approximately 100 Hz, matching the frequency noise PSD measurement including the 60 Hz noise harmonic peaks.

V. PRESSURE DEPENDENCE OF A WGMR

WGMRs are impacted not only by temperature, but also by atmospheric pressure. There are two basic mechanisms related to change of the frequency of an open resonator due to change of the external pressure. Those include change of the ambient refractive index as well as deformation and stress of the resonator due to the pressure change. The first reason is related to the fact that the change of the atmospheric conditions leads to the change of the refractive index of the mode for the resonator in an open environment. It can be relatively small in larger device structures with a smaller inclusion factor. To characterize it we placed the packaged resonator into a vacuum chamber and observed the impact of the pressure change on the resonator frequency (Fig. 4). In what follows we provide a simple reasoning explaining the effect.

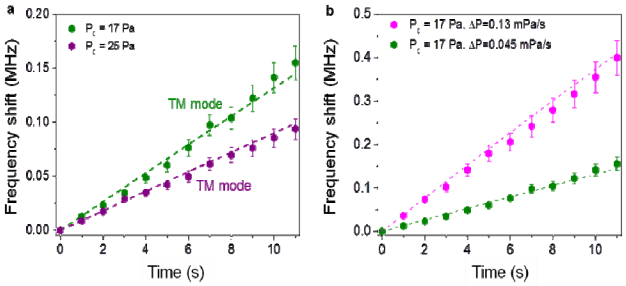


Figure 4 | Pressure dependence of the WGMR resonance frequency shift. a, The pressure in the vacuum chamber is slowly increased from 17 Pa (olive) and 25 Pa (purple) with 45 mPa/s. The frequency shift is measured by counting the beat frequency at every second while the micro-laser is stabilized to the WGMR by PDH locking. To confirm the frequency shift by the pressure change, the theoretically estimated lines for TM and TE modes are plotted together (dashed lines) with 10 % error bars of the measured data. **b,** The pressure in the vacuum chamber is increased from 17 Pa with 45 mPa s^{-1} (olive) and 130 mPa/s (magenta) respectively.

VI. ANALYTICAL MODEL OF THE PRESSURE DEPENDENCE

There are two basic mechanisms related to change of the frequency of an open resonator due to change of the external pressure. Those include change of the ambient refractive index mitigated by pressure change as well as deformation of the resonator. The first reason is related to the fact that the resonator is an open structure and that change of the atmospheric conditions leads to alteration of the refractive index of the mode.

It was shown that change of the refractive index of the medium surrounding a microsphere resonator results in relative frequency shift [5]:

$$\frac{\Delta\nu_{TM}}{\nu_0} \approx \frac{\Delta n_{air}}{(n_{TM}^2-1)^{3/2}}\frac{\lambda}{2\pi R};$$

$$\frac{\Delta\nu_{TE}}{\nu_0} \approx \frac{\Delta n_{air}}{(n_{TE}^2-1)^{3/2}}\left(2-\frac{1}{n_{TE}^2}\right)\frac{\lambda}{2\pi R};$$

where R is the radius of the resonator, n_{TE} and n_{TM} are the refractive indices of the resonator host material, λ is the wavelength, and Δn_{air} is the change of the index of refraction of air. We assume that TE mode has **E**||**Z**, so the evanescent field of TE mode is bigger as compared with one of the TM mode (the definition is opposite as compared with the definition given in [5] since we consider a more cylindrical

than spherical structure). While the frequency changes of the oppositely polarized modes are not identical, the difference between them is insignificant.

A. Fluctuation of index of refraction of the air

1) Fundamental limit due to particle fluctuations

The residual index of refraction of air given by the air itself is $n_0 \sim 3\times10^{-4}$. Fundamental change of the index of refraction of air is given by $\Delta n_{air} = n_0 N^{-1/2}$, where N is the number of particles interacting with the mode. Particle density in air is $\rho = N_a/V_{mol} = 2.4\times10^{19}$ cm^{-3}, where N_a is the Avogadro number, and V_{mol} is molar volume.

The physical volume of the evanescent field is $V \sim (\eta/d)V_{mode}$, where thickness of the evanescent field region is $\eta = \lambda/(2\pi(n_{TE}^2-1)^{1/2})$, and d is the thickness of field distribution in the mode. This volume value should not be mixed with the inclusion factor for the evanescent field, which is much smaller.

For a 35GHz resonator, for instance, $V_{mode} \sim 1.5\times10^{-7}$ cm^3, and d~3μm. The number of particles in the evanescent field is $N = 3\times10^{11}$ and $\Delta n_{air} \sim 5.4\times10^{-10}$. This gives $\Delta n_{TM}/n_0 \sim 1.5\times10^{-13}$. This is not a large value, and the spectral density of the noise is small since the characteristic frequency of the noise is 1MHz or higher.

2) Limit due to fluctuations of atmospheric pressure

The change of the refractive index of air associated with pressure and temperature change (if we assume the changes to be uncorrelated) is

$$\Delta n_{air} \approx n_0\left(\frac{\Delta P}{P} - \frac{\Delta T}{T}\right).$$

Taking into account $n_0 \sim 3\times10^{-4}$ at the atmospheric pressure and room temperature as well as the inclusion factor

$$\frac{1}{(n_{TM}^2-1)^{3/2}}\frac{\lambda}{2\pi R} \cong 3\times10^{-4}$$

for a MgF_2 resonator with 35 GHz FSR we find

$$\frac{\Delta\nu_{TM}}{\nu_0} \approx 9\times10^{-8}\left(\frac{\Delta P}{P} - \frac{\Delta T}{T}\right).$$

We need to know the spectral density of pressure and temperature noise to find the associated frequency and phase noise.

Using the database of the pressure measurements for Los Angeles taken from Jan. 1, 2001 to Oct. 20, 2013 (Fig. 5) we find the corresponding Allan deviation for the frequency of the modes of an open 35 GHz resonator (Fig. 6). It is clearly seen that the pressure variation can be important if we would like to achieve relative stability approaching 10^{-12} per 1s.

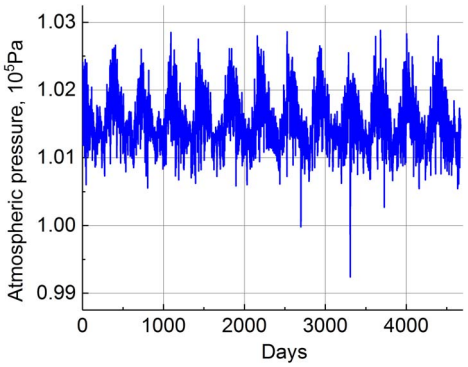


Figure 5 | Variation of atmospheric pressure in Los Angeles. Long term variations exceeding a percent are observed.

B. Deformation of the resonator due to variations of the atmospheric pressure

A change in the ambient pressure changes the volume of the resonator and the resonator radius, resulting in a frequency shift

$$\frac{\Delta\nu_{TM}}{\nu_0} \approx \frac{1}{3}\beta_T \Delta P$$

where $\beta_T = -(1/V)(dV/dP)]_T$ is the compressibility of the resonator host material (we assume that isothermal and adiabatic compressibility are approximately equal). The compressibility for MgF_2 is $\beta_T = 10^{-11}$ Pa^{-1}. The relative frequency changes by 3×10^{-9} if the pressure changes by 1 kPa (this is an approximate variation of the atmospheric pressure over a year, see Fig. 5). To compare, the relative mode frequency change due to the refractive index change occurring because of the relative pressure change by 1% is 9×10^{-10}. Therefore, the deformation of the resonator has higher impact on the pressure frequency shift of the resonator.

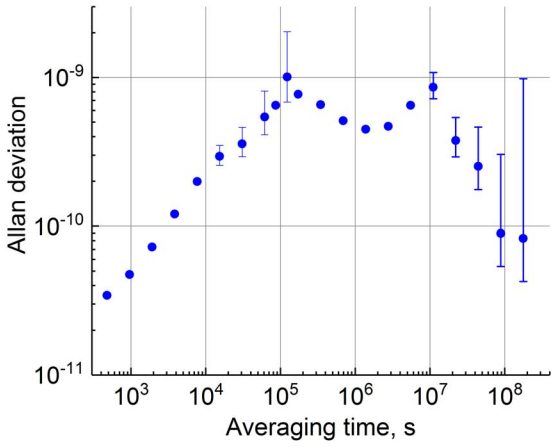


Figure 6 | Expected Allan deviation of the mode frequency due to the pressure variation. It is assumed that the resonator is not sealed**.** The long term data were taken from the Los Angeles pressure change database, while short term pressure data were taken at OEwaves lab.

There are a couple of observations we can make from this calculation. Firstly, a laser tightly locked to a WGM can be a good sensor for temperature and pressure variations. For

instance, if the mode of the WGMR has 100 kHz bandwidth and the laser is locked to the mode with 1 Hz accuracy, the relative temperature and pressure shift can be measured at 0.2 ppm level. Secondly, an increase in the resonator size results in the improvement of the environmental stability of the resonator, up to the limit given by the frequency shift due to mechanical deformation. Thirdly, the temperature and the pressure are two independent parameters that impact the resonator in comparable ways. Fourthly, a hermetic or semi-hermetic enclosure could improve the stability significantly.

VII. Frequency Stability

Using the thermally compensated resonator placed in a vacuum chamber we were able to achieve the thermorefractive noise limit for the resonator (Figure 7). To minimize the impact of the technical noise from the laboratory environment, the vacuum chamber was evacuated to the pressure of 1.33 mPa but the chamber temperature was not controlled. The residual thermo-mechanical fluctuations still exist near the carrier and cause the standard deviation in Allan deviation measurements. This measurement shows that the WGM resonator has relatively high noise sensitivity at low Fourier offset frequencies and therefore, further reduction of the thermal sensitivity via thermal compensation is desirable to reduce the measurement uncertainty.

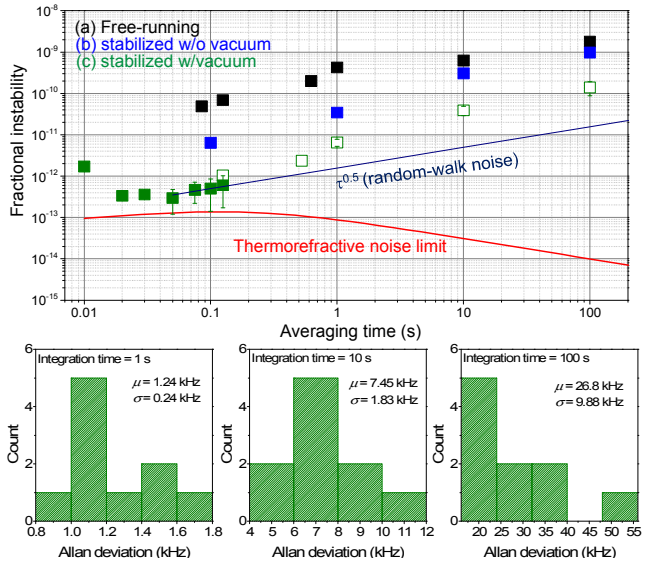


Figure 7 | Fractional frequency instability measurements. Measured fractional frequency instability of the beat frequency between the free-running laser and the 1 Hz FP reference laser is the black square in (a). The squares in (b)/(c) are the frequency stabilities of the beat signal between the laser referenced to the WGMR and the 1 Hz FP reference laser without/with vacuum respectively. The open red square in (c) is the mean (μ) and standard deviation (σ) of the frequency instability calculated from 10 sets of frequency counting data at 1 s averaging time, measured with a frequency counter. The filled red square in (c) is μ and σ of the frequency instability derived from the 74 measurement traces of the frequency noise PSD. Magenta area represents the possible Allan deviation bound limited by the random walk frequency noise. The lower panels show statistical measurements of the long-term stability at 1 s, 10 s and 100 s integration time respectively. Ten data sets for 10 minutes each have been taken by using a Λ-type counter at 1 s integration time, with the computed mean values and standard deviations shown.

VIII. Conclusion

We have shown that the impact of pereturbation from the surrounding medium is a major factor limiting the WGMR stability in the vicinity of the thermodynamic fluctuation limit. Placing a WGMR into an evacuated environment resulted in observation of the fundamental frequency noise. A laser locked to the resonator demonstrated 25 Hz linewidth but experienced the monotonic frequency drift due to the center shifted random walk probability distribution of the WGMR temperature, which is attributed to the limited temperature sensing accuracy and the correlation of the TEC controlled WGMR temperature change with the ambient temperature variation. We anticipate the long-term frequency drift could be mitigated by implementing a dual-mode temperature compensation technique and by tightly controlling the environmental temperature. WGMRs allow generating optical frequency combs with low input power, and it is reasonable to expect that stable microcombs excluding external references are feasible with a thermally compensated resonator placed in a proper environment. The stabilization technique is also promising for making the lasers suitable for interrogation of ultra-stable optical transitions utilized in optical clocks.

References

[1] M. Notcutt. et al., *Opt. Lett*. **30**, 1815-1817

[2] W. Liang et al., *Nat. Commun* **6**, 2468 (2015)

[3] A. A. Savchenkov et al, *Opt. Lett*. **38**, 2636 (2013)

[4] J. Lim et al., *Nat. Commun.* in press arXiv:1701.05285 (2017)

[5] I. Teraoka et al., *J. Opt. Soc. Am*. **20**, 1937 (2003)

In-Fibre Fabry-Pérot Microresonator with 100 Million Q-Factor

E. Obrzud[1,2], S. Lecomte[1], T. Herr[1]
[1]Time and Frequency Systems
Swiss Center for Electronics and Microtechnology
Neuchâtel, Switzerland

[2]Observatoire de Genève
Université de Genève
Versoix, Switzerland

***Abstract*—A single-mode, 100 million Q-factor, Kerr-nonlinear Fabry-Pérot microresonator with 10 GHz free-spectral range is fabricated. The resonator's group velocity dispersion, coupling ratio and nonlinearity can be engineered via choice of fibre and dielectric Bragg reflection coating.**

Keywords— microresonators, nonlinear optics, Fabry-Pérot

The field of ultra-high Q Kerr-nonlinear microresonators has developed significantly over the last few years. Ringtype and whispering-gallery mode microresonators combine strong light confinement with high optical nonlinearity to obtain high-Q performance for parametric frequency conversion processes, e.g. four-wave mixing (FWM). Due to these processes, new optical lines are generated giving rise to a Kerr frequency comb [1]. With a large span of achievable free spectral ranges (FSRs) (from 10 GHz to 1 THz), the microresonators find application in fields like astronomy [2, 3], optical communication [4], and microwave signal generation [5].

The novel Fabry-Pérot microresonator consists of a several mm long standard single-mode fibre (SMF) whose end facets are covered with a highly reflective dielectric coating (Fig.1a). For mechanical protection, direct compatibility with other fibre components (via the FC/PC connector) and for handling, the resonator is inserted into and glued to a standard ceramic ferrule (Fig.1c). The fabrication process is as follows. The SMF is fixed inside a ceramic fibre ferrule with an epoxy glue. The microresonator's end facets are precisely polished before being covered with a highly reflective, broadband dielectric coating via ion beam sputtering. A conceptually related resonator geometry with a FSR of 2 GHz and a finesse of >550 has been demonstrated in [6].

In this work, the standing-wave fiber cavities' FSR is approximately 9.7 GHz (Fig.2e) and their finesse is significantly higher than in previous work. The GVD is solely determined by the SMF as the dispersion of the dielectric coating is flat by design. The alignment-free, mechanically robust connection, and the compatibility and mode-matching with any fibre component give the fibre resonator a practical advantage over whispering-gallery mode and ring-type resonators. An important feature of the Fabry-Pérot microresonators is freedom of design of principal cavity parameters. First, the free-spectral range of the microresonator is defined by its length and can be adjusted by using standard fibre connector polishing techniques. Secondly, the dielectric coating allows for dispersion engineering by applying a non-zero group delay dispersion (GDD). This opens up new possibilities for dispersion engineering in microresonators such as frequency comb generation in the visible and mid-IR, dispersion flattening for broadband frequency comb spectra and ultra-short soliton pulse formation. Lastly, the resonator design enables the use of numerous types of optical fibres including highly nonlinear, dispersion engineered, mid-infrared or active gain fibres.

In order to measure the resonance width, a continuous-wave (CW) 1559 nm laser is coupled to the cavity and scanned across the resonance. The cavity is driven with a CW pump laser (Fig.1b) operating at 1559 nm wavelength. Sidebands generated by the intensity modulator enable frequency calibration for linewidth measurement (Fig.2a). Due to a weak birefringence induced by stress in the ferrule-mounted fibre, the polarisation modes are not frequency degenerate. With the right adjustment of the polarisation controller, only one

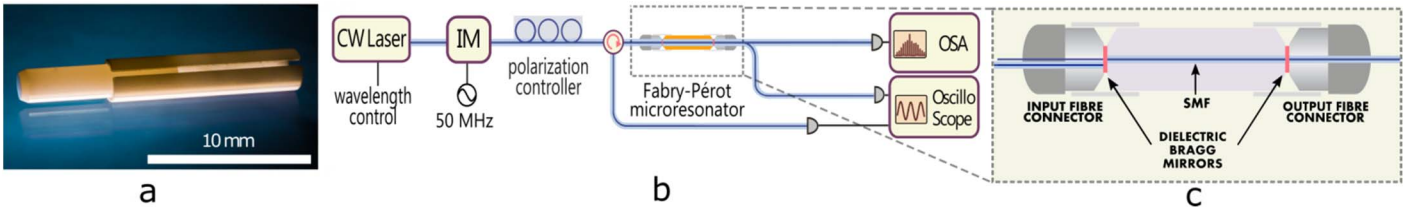


Fig. 1: **a**, Photograph of a Fabry-Pérot microresonator placed in a ceramic fibre mating sleeve. **b**, Experimental set-up linewidth measurement. IM, intensity modulator, OSA, optical spectrum analyser. **c**, Mounting scheme of a Fabry-Pérot microresonator.

978-1-5386-2916-1/$31.00 ©2017 IEEE

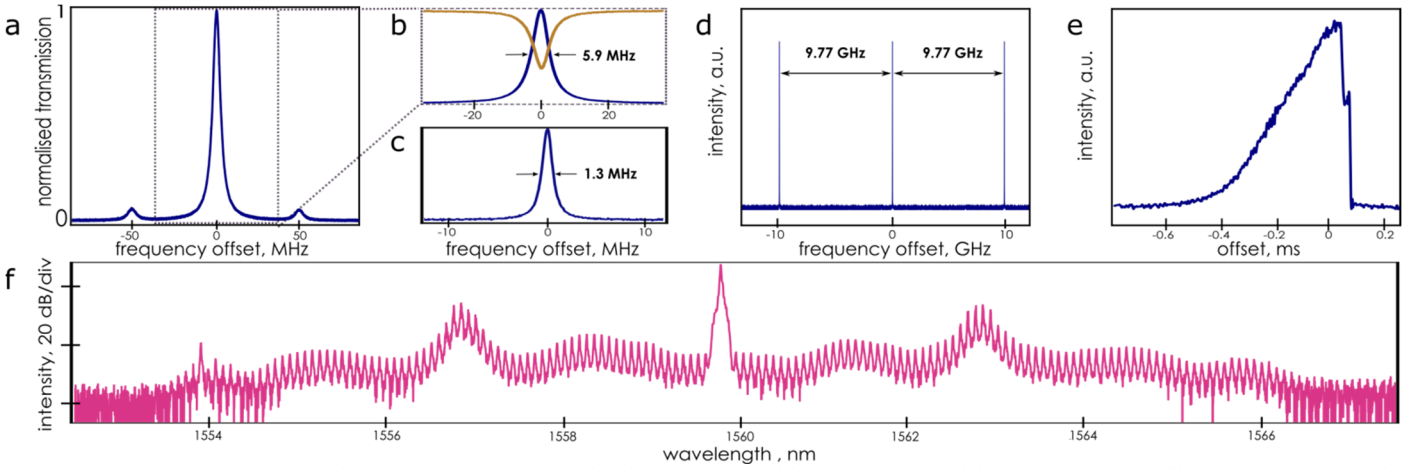


Fig. 2: **a**, Transmission signal of a Fabry-Pérot microresonator with sidebands generated by an intensity modulator for frequency calibration. **b**, Zoom into the resonance from **a**. The yellow line represents the reflected signal. **c**, Resonance of a Fabry-Pérot microresonator with mirror reflectivity of 99.997%. **d**, Wavelength scan over two FSR showing the existence of only one optical mode per free-spectral range of the cavity. e, Resonance of the 1.3 MHz Fabry-Péot cavity with 30 mW coupled power with evidence of soliton formation (”step-feature”). **f**, Kerr frequency comb generated in the 1.3 MHz sample.

polarisation mode is addressed, i.e. there is exactly one optical mode per one spectral range of the cavity (Fig.2d). This is another important feature not easily achievable in other microresonator platforms. Figure 2b presents the transmitted and reflected signal of a cavity characterised by a design mirror reflectivity of 99.95% and 99.997%. The resonance linewidth is 5.9 MHz (30 million Q factor) with a coupling at the level of 60%. Figure 2c shows a resonance of a Fabry-Pérot microresonator with symmetrical design mirror reflectivity of 99.997%. While the resonance linewidth is 1.3 MHz corresponding to a Q factor of 140 million, this resonator is strongly under-coupled (coupling of only 1%). The strong undercoupling is a result of additional cavity loss, likely resulting from scattering at the end facet interfaces and potentially absorption in the dielectric coating. It is expected that better surface and coating quality can further improve the Q factor and coupling. For a critically-coupled cavity, whose losses are dominated by the mirror coatings, a linewidth of 100 kHz and Q factor of 1.9×10^9 could theoretically be expected. With 30 mW coupled power, the resonance from Fig.2c reveals a soliton step (Fig.2e) and one can observe a Kerr frequency comb generation (Fig.2f). Applications include frequency comb generation for spectroscopy and low-noise microwave generation.

ACKNOWLEDGMENT

The authors acknowledge funding by the Swiss National Science Foundation (200021_166108) and the Canton of Neuchâtel.

REFERENCES

[1] P. DelHaye, A. Schliesser, O. Arcizet, T. Wilken, R. Holzwarth, T.J. Kippenberg, ”Optical frequency comb generation from a monolithic microresonator”, Nature 450, 1214-1217, 2007

[2] C.-H. Li, A.J. Benedick, P. Fendel, A.G. Glenday, F.X. K¨ artner, D.F. Phillips, D. Sasselov, A. Szentgyorgyi, R.L. Walsworth, ”A laser frequency comb that enables radial velocity measurements with a precision of 1 cm s−1”, Nature 452, 610-612, 2008

[3] T. Steinmetz, T. Wilken, C. Araujo-Hauck, R. Holzwarth, T.W. Hnsch, L. Pasquini, A. Manescau, S. D’Odorico, M.T. Murphy, T. Kentischer, W. Schmidt, T. Udem, ”Laser Frequency Combs for Astronomical Observations”, Science Vol. 321, Issue 5894, pp. 1335-1337, 2008

[4] J. Pfeifle, V. Brasch, M. Lauermann, Y. Yu, D. Wegner, T. Herr, K. Hartinger, P. Schindler, J. Li, D. Hillerkuss, R. Schmogrow, C. Weimann, R. Holzwarth, W. Freude, J. Leuthold, T.J. Kippenberg, C. Koos, ”Coherent terabit communications with microresonator Kerr frequency combs”, Nature Photonics 8, 375-380, 2014

[5] A.A. Savchenkov, A.B. Matsko, V.S. Ilchenko, I. Solomatine, D. Seidel, L. Maleki, ”Tunable Optical Frequency Comb with a Crystalline Whispering Gallery Mode Resonator”, Phys. Rev. Lett. 101, 093902, 2008

[6] D. Braje, L. Hollberg, S. Diddams, ”Brillouin-Enhanced Hyperparametric Generation of an Optical Frequency Comb in a Monolithic Highly Nonlinear Fiber Cavity Pumped by a cw Laser”, Phys.Rev.Lett.102,193902,2009

Time and frequency transfer over a 500 km cascaded White Rabbit network

Namneet Kaur, Florian Frank, Paul-Eric Pottie, Philip Tuckey
LNE-SYRTE, Observatoire de Paris, PSL Research University
CNRS, Sorbonne Universites, UPMC Univ. Paris 06
Paris 75014, France
Email: namneet.kaur@obspm.fr

***Abstract*—We perform experiments with White Rabbit for time and frequency dissemination over long distance optical fiber links. We consider a unidirectional link setup to ensure compatibility with active telecommunication networks and build the first four-span 500 km cascaded White Rabbit link, using commercial White Rabbit equipment and improved software parameters. We demonstrate a frequency transfer stability at the level of 2×10^{-15} at 200 000 s of integration time. The time transfer stability reaches a minimum of 1.2 ps at 20 seconds of integration time. Finally, we compare our results with infield applications and discuss the limitations of the performance.**

I. Introduction

Over the last few years, optical fiber links for frequency and time dissemination have evolved rapidly demonstrating frequency transfer with uncertainties (well) below 10^{-17} over several hundred km (see [1] and references therein). Currently, the most accurate way of comparing remotely located atomic clocks is by the means of optical frequency transfer by coherent fiber links [2]. Besides such highly demanding applications, there has been an increasing demand for fiber access to precise time and frequency standards in areas such as telecommunication, navigation, Internet, metrology for industry and some scientific applications with lower stability and accuracy requirements, and much larger scalability to many users. Indeed many methods for time and frequency transfer over optical fiber links have emerged as excellent alternatives to Global Navigation Satellite System (GNSS) based methods. Today, a very promising direction for time transfer over optical fiber links is the implementation of White Rabbit - Precision Time Protocol (WR - PTP) technology on long range networks [3], [4].

II. White Rabbit-Precision Time Protocol

A. White Rabbit for precise time and frequency transfer

Two time transfer experiments were performed on active telecommunication networks during the last two years. The first experiment by VTT is a 950 km link between Espoo and Kajaani in Finland, where WR is carried over an active Dense Wavelength Division Multiplexing (DWDM) network of the Finnish University Research network. They demonstrated time stability as low as 20 ps at 1000 seconds of integration time [3]. The second experiment is a 2×137 km link between VSL and Nikhef, The Netherlands. WR is carried by SURFnet on their active telecommunication network on a Coarse Wavelength Division Multiplexing band. They achieved a time stability of 10 ps at 1000 seconds of integration time [3]. These two experiments recently presented an accuracy budget below 8 ns using two different approaches for calibration.

Our work focuses on using WR for accurate long haul time and frequency dissemination, compatible with active telecommunication networks, targeting multiple users, with time accuracy in the range of one microsecond to about one nanosecond for achieving performances competitive with GPS time service.

III. Improving the White Rabbit Switch performance

We study first the performance of a White Rabbit Switch (WRS v3.3) in Grandmaster mode (in which the switch locks to an external reference). We observe suboptimal performance, shown by the phase noise spectral density (PSD) of the Grandmaster WR clock of -70 dBc/Hz at 1 Hz and an Allan Deviation of 1.3×10^{-11} at 1 second of integration time (NEQ BW=500 Hz), illustrated in Fig. 1 and 2 respectively, even if a very high quality signal is provided to the Grandmaster. This excess of noise is due to the phase and frequency lock of the local oscillator on the reference signal. This non optimal lock has repercussion on the whole frequency chain in a WR link. With the help of CERN, we implement a modified version of the configuration file, so that direct clocking of the multi-output clock distribution chip (AD9516-4) is enabled. In order to obtain the lowest relative frequency stability given that phase noise is constant, it is of interest to work at a higher frequency. For some practical reasons related to the frequency map inside the WR switch, we provided the WR switch with a 125 MHz input signal, generated by dividing a 1 GHz H-maser signal by 8. We also provided the switch with a 10 MHz input signal derived by coherent division from the same 1 GHz signal.

Fig. 1 shows the PSD of the WR clock for the default and the improved Grandmaster WRS. The PSD and Allan Deviation measurement are done with a Microsemi Phase test set 5120A. For the improved case, about 20 dB lower

978-1-5386-2916-1/$31.00 ©2017 IEEE

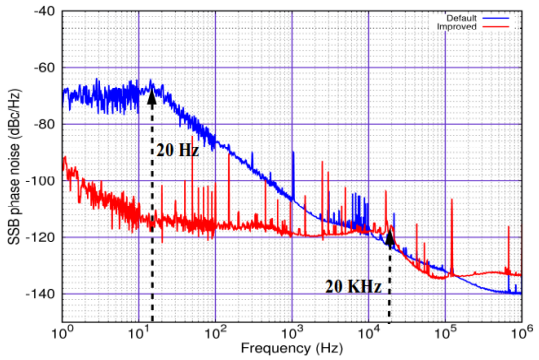


Fig. 1. Phase noise power spectral density for default and improved Grandmaster WR clock.

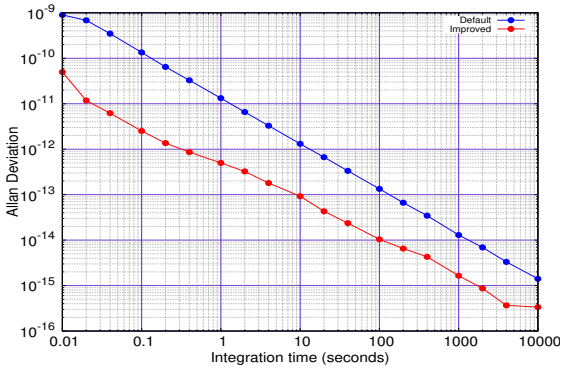


Fig. 2. Allan Deviation for default and Improved Grandmaster WR clock.

phase noise is obtained at 1 Hz and the bandwidth has been increased by a factor of a thousand. This improvement achieved an Allan deviation of 4.9×10^{-13} at 1 second of integration time (NEQ BW=500 Hz) as illustrated in Fig. 2. The performance limitation for the improved case is mainly due to the noise floor of the AD9516-4 used for the WR clock distribution as the external reference clock signal has even lower PSD (-110 dBc/Hz at 1 Hz).

For a Slave WRS synchronized to the Grandmaster WRS through a fiber link, we cannot use the same trick. The SoftPLL is used to lock the internal local oscillator to the clock recovered from the fiber link. The default servo bandwidth for the slave is about 20 Hz. To achieve better performance, the PLL bandwidth (BW) parameters are varied [5]. We consider a Slave WRS synchronized to the Grandmaster WRS by a 100 km uni-directional fiber link (i.e. utilizing dual fiber and the same wavelength of propagation in the two directions) at 1541 nm, with more than three times greater bandwidth of locking. Fig. 3 shows the relative frequency noise of the Slave clock with an increased bandwidth of 70 Hz. Fig. 3 also depicts the frequency noise of the free running local oscillator of the WRS and it is clear that a higher bandwidth should be used to lock the local oscillator, as the minimum of the relative frequency noise lies at about 200 Hz. We also record the error signal out of

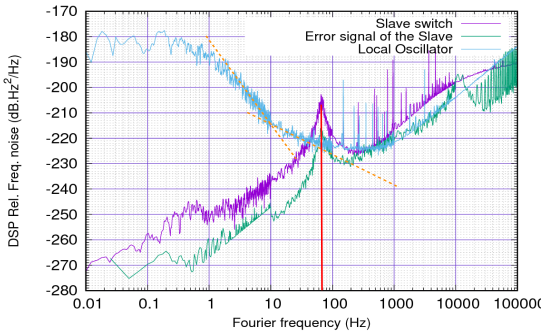


Fig. 3. Relative frequency noise for the Slave clock, the free running Local Oscillator and the error signal of the slave switch.

the SoftPLL of the slave WRS by an FFT analyser and the voltage noise is then converted to frequency noise which is also displayed in Fig. 3. By comparing the frequency noise of the Slave switch and the error signal out of the Slave PLL, we observe that the slave switch has an excess of noise of about 10 dB at low frequencies (less than 100 Hz). This shows that there is still room for improving the Slave switch performance.

Chromatic dispersion affects both the accuracy and the stability (short term) of time transfer as described in [6]. In a WR link, we use small form factor pluggable optical transceivers (SFP). We observed that the line-width is about 3 GHz in 0.25 Hz bandwidth of measurement for SFPs operated in the C-band. As chromatic dispersion scales linearly with the length of the link, it plays a significant and limiting role for long haul fiber links with SFPs, and the frequency stability of the emitters needs to be taken into account for links longer than 100 km. To tackle the limitation due to chromatic dispersion for long haul links, we employ a cascaded approach described in the following section, and tried a faster rate of communication between the master and the slave.

IV. A CASCADED 500 KM WHITE RABBIT LINK

We build the first four span 500 km uni-directional White Rabbit link using fiber spools, long range SFPs and dense wavelength division multiplexing technique. We describe the experimental setup and the results for the cascaded White Rabbit link in this section.

A. Experimental Setup

The experimental setup is illustrated in Fig. 4. We build a four span cascaded WR link of 500 km. Each span is 125 km long. We are using four White Rabbit switches and one WR-ZEN as end-receiver. All these equipments were manufactured by SevenSolutions [7]. The four 10 MHz outputs are recorded simultaneously by a dead-time free phase and frequency counter K+K, operated in Λ mode with 1-s gate time. For time transfer, the Grandmaster also receives a Pulse per second (PPS) generated (SDI PPS generator), amplified and distributed in the laboratory with a TimeTech PPS 16 channels amplifier. Time is transferred from the Grandmaster

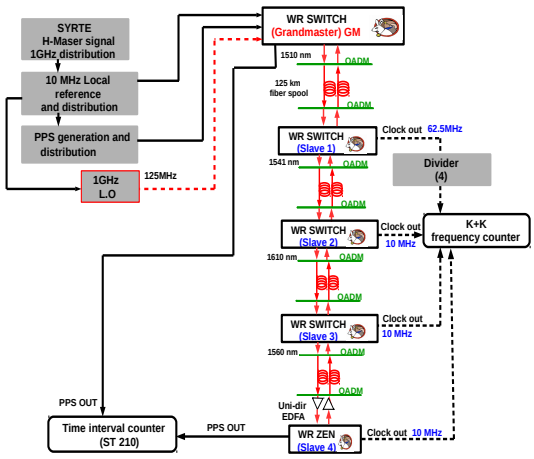


Fig. 4. Experimental Setup for the 500 km cascaded WR link.

to the Boundary Switches and finally the slave (end receiver) in a hierarchical manner using a cascaded approach. Each of the slaves outputs a PPS (Pulse per second) signal that may be compared with the PPS of the Grandmaster or with another output of the PPS amplifier using time interval counters. In the experimental data presented below, we were using a Physipus ST201 [8] to measure the time interval between the output PPS of the GM and the output PPS of the ZEN end-receiver. The ST201 is a high performance time interval counter with a single shot resolution of about 300 fs. The temperature of the experimental room was measured with a thermistance and recorded with a datalogger (Agilent 34972A). All the measurements were done simultaneously.

Regarding the optical layer, all the slave WRS utilize a 2×125 km uni-directional fiber link and long range SFPs in the C-band or OSC channels close to the C-Band. The first and the second span use 1510 nm and 1541 nm respectively. The third and the fourth span use 1610 nm and 1560 nm respectively. We are using OADMs (optical add drop multiplexer) to multiplex these four wavelengths. For the last stage, we use two uni-directional EDFAs to compensate for stronger losses.

In addition, we also modified configuration files of the switch to increase the PTP rate. We set the PTP rate to be 16 per seconds, but observe by logging an effective 14 packets per seconds rate. All the slave switches utilize increased bandwidth of locking of 60 Hz and the increased PTP rate.

B. Results

To show the impact of the PTP rate increase, we present the relative frequency deviation for the last slave WR-ZEN (clock out 10 MHz) at 500 km in the two situations, with standard PTP rate (Fig. 5) and the increased PTP rate (Fig. 6).With standard PTP rate we observe some spikes which are not

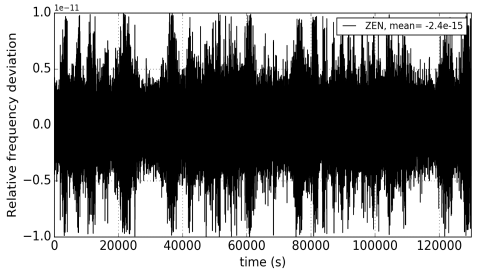


Fig. 5. Relative frequency deviations for WR-ZEN clock out with default PTP rate.

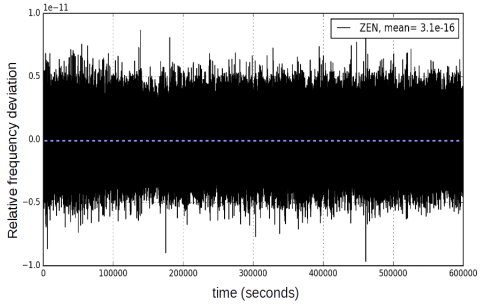


Fig. 6. Relative frequency deviations for WR-ZEN clock out with increased PTP rate.

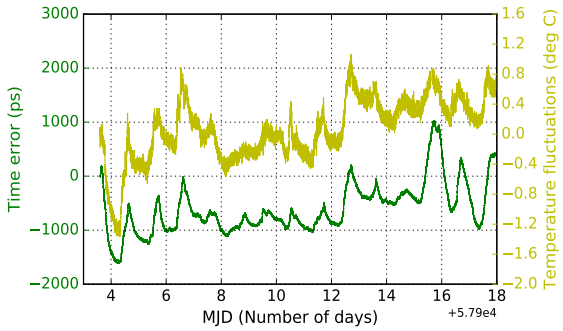


Fig. 7. Phase data for WR-ZEN and the temperature fluctuations of the experimental room (constant offset removed for both).

present with the increased PTP rate. With increased rate, peak to peak relative frequency deviations are at the level of 0.5×10^{-11}. The mean of the frequency data is 3×10^{-16}, which is below the statistical uncertainty of the data set. It is noticeable that the mean deviation to zero is about 7 times higher with the standard PTP rate.

Fig. 7. illustrates the time interval data for eighteen days of consecutive measurement for WR-ZEN. The peak to peak fluctuations are about 2.5 ns. These time fluctuations show some limitation for the accuracy and the frequency stability. Fig. 7 also shows the temperature fluctuations of about 0.8 K over the same eighteen days of measurement. We clearly see the correlation between the phase fluctuations and the temperature fluctuations. We observe a periodic modulation in the phase data, which is due to the temperature fluctuations

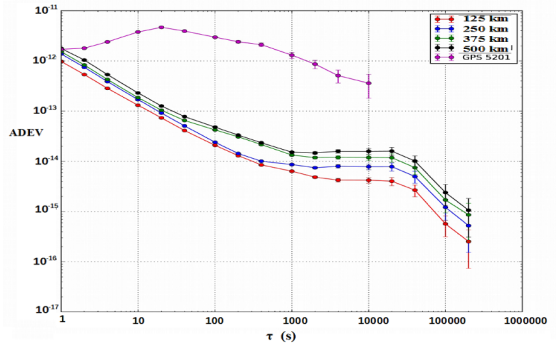


Fig. 8. Allan Deviation for the cascaded 500 km WR link and comparison with GPS Receiver.

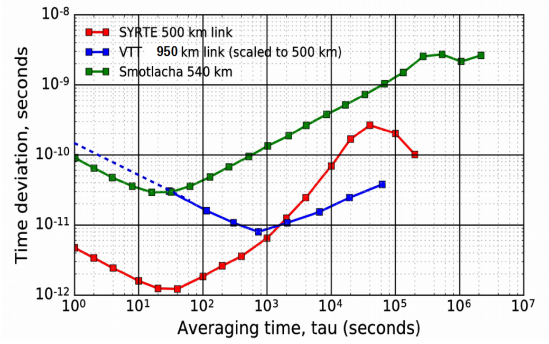


Fig. 9. Time Deviation for the 500 km White Rabbit link and comparison with infield applications.

acting on the optical length of the fiber. This periodic modulation adversely affects the stability at long integration time [9]. The wavelength variations were measured at 1541 nm, and were found to be 15 pm peak to peak. They are also correlated to the temperature fluctuations.

The Allan deviation (ADEV) for the cascaded stages of the 500 km link is presented in Fig. 8. For the first span at 125 km, we obtain a frequency stability of 1×10^{-12} at one second of integration time. The stability for each span degrades as the length of the link increases, and we attain a value of 2×10^{-12} at one second of integration time for the 500 km link. The stability degrades for each span by a factor a little smaller than $\sqrt{2}$. The stability scales down as τ^{-1} initially and then degrades showing a bump with a maximum at about 20000 seconds of integration time. The bump arises from the fiber thermal noise as the fiber is subject to temperature fluctuations with a sensitivity of 37 fs/(K.m) [10]. At 200 000 seconds of integration time, the frequency stability for 125 km span attains 8×10^{-16} and lies in the low region of 1×10^{-15} for the consecutive spans. This fiber noise bump is expected to be greatly reduced by a factor of five for the implementation on active telecommunication networks where the fiber is buried underground. We also compare the frequency stability of the cascaded 500 km WR link with a good quality GPS receiver 5201 and we observe similar short term stability of 2×10^{-12} at 1 second of integration time, but for long integration time (at 1 000 seconds) our cascaded WR link has better performance by almost two orders of magnitude.

The time deviation plot is presented in Fig. 9. We compare our lab experiment with two infield applications using the active telecommunication networks. The first one is a 950 km WR link by the Finnish metrology lab VTT between Espoo and Kajani in Finland [3], where the time stability has been scaled down to 500 km for easier comparison. The second one is a 540 km link by V. Smotlacha and co-workers for time transfer between the metrology labs of Prague and Vienna [11]. The time transfer stability for the 500 km cascaded link is 5.5 ps at one second of integration time and reaches a minimum of 1.2 ps at 20 seconds of integration time. The time stability degrades for long averaging times due to the thermal fiber noise but still remains below the ns level. The rapid increase of the TDEV is due to the common temperature excitation of all the cascaded stages. In comparison, we have improved the time stability at one second of integration by more than one order of magnitude. For longer averaging time, we expect to observe a similar behavior as in [3], [11] if implemented on active telecommunication networks.

V. Conclusion

We studied White Rabbit technology for long range time and frequency dissemination. We optimized the White Rabbit Switch operating conditions to achieve better performance. We improved the short term stability of the Grandmaster White Rabbit switch from 1.8×10^{-11} to 4.9×10^{-13} (NEQ BW=500 Hz) at one second of integration time. We utilized three times greater bandwidth of locking for the boundary WRS. We built the first four-span 500 km cascaded link using fiber spools and evaluated its performance for long range time and frequency dissemination. We demonstrated a frequency transfer stability at the level of 2×10^{-15} over one day of integration time. We do not observe any frequency shift within the statistical uncertainty. The time stability at one second of integration time is 5.5 ps and it reached a minimum of 1.2 ps at 20 seconds of integration time. The limitations for the performance are chromatic dispersion (optical emitter stability) at short integration time and fiber thermal noise for long integration time. In further work, we are studying practical solutions to be implemented in field for determining time accuracy.

Acknowledgment

The authors would like to thank Javier Dìaz, Rafa Rodriguez, J. Gabriel Ramìrez at Seven Solutions and Felipe Torres Gonzàlez at University of Granada for their collaboration and help. We would also like to thank people involved in the WR project for their continuous stimulations and sharing issues through the mailing list, and to thank especially Javier Serrano, Alessandro Rubini, T. Włostowski, and Mattia Rizzi at CERN for their help and support. This work was supported

by the LABEX Cluster of Excellence FIRST-TF (ANR-10-LABX-48-01), within the Program 'Investissements dAvenir' operated by the French National Research Agency (ANR) and by Bpifrance under the SCP Time project.

REFERENCES

[1] O. Lopez, F. Kéfélian, H. Jiang, A. Haboucha, A. Bercy, F. Stefani, B. Chanteau, A. Kanj, D. Rovera, J. Achkar, C. Chardonnet, P.-E. Pottie, A. Amy-Klein, G. Santarelli, "Frequency and time transfer for metrology and beyond using telecommunication network fibres", Comptes Rendus Physique, 16 (5), pp. 459-586 (2015).

[2] Lisdat, C. et al. "A clock network for geodesy and fundamental science", Nat. Commun. 7:12443 doi: 10.1038/ncomms12443 (2016).

[3] E.F. Dierikx, A.E. Wallin, T. Fordell, J. Myyry, P. Koponen, M.Merimaa, T.J.Pinkert, J.C.J. Koelemeij, H.Z. Peek and R. Smets, "White Rabbit Precision Time Protocol on Long Distance Fiber Links", IEEE Transactions on Ultrasonics, Ferroelectrics, and Frequency, DOI: 10.1109/TUFFC.2016.2518122 (2016).

[4] J. Serrano et al., "The White Rabbit project", IBIC2013, Oxford, UK, 2013.

[5] M.Rizzi talk,9th WR Workshop, talks available at http://www.ohwr.org/projects/white-rabbit/wiki/Mar2016Meeting

[6] N. Kaur, P. Tuckey and P. E. Pottie, "Time transfer over a White Rabbit network", 2016 European Frequency and Time Forum (EFTF), York, 2016, pp. 1-4.doi: 10.1109/EFTF.2016.7477793

[7] White Rabbit Switch http://www.ohwr.org/projects/white-rabbit/wiki/Switch, White Rabbit ZEN node http://sevensols.com/index.php/products/wr-zen-board/

[8] ST201,http://sigmatime.fr, Sigmatime, PHUSIPUS integration, 8 allée Bellevue, 06460 SAINT VALLIER DE THIEY, FRANCE

[9] Pierre Uhrich, Stabilité des Oscillateurs ultra-stables, Journées X-ENS-UPS de Physique 9 mai 2007, http://softs.polytechnique.fr/departements/physique/colloques/pdf/2007/Uhrich_Pierre_X-ENS-UPS2007.pdf

[10] L. G. Cohen and J. W. Fleming, Effect of temperature on transmission in lightguides, Bell Syst. Tech. J. 58, 945951 (1979).

[11] V. Smotlacha, A. Kuna and W. Mache, "Time transfer using fiber links", EFTF-2010 24th European Frequency and Time Forum, Noordwijk, 2010, pp. 1-8. DOI:10.1109/EFTF.2010.6533650.

A Novel Synchronization Method for WR System

X.Yuan, B.Wang
Department of Precision Instruments, Tsinghua University,
The state key lab of precision Measurement Technology and Instrument,
Beijing, P. R. China
yuanx15@mails.tsinghua.edu.cn, bo.wang@tsinghua.edu.cn

***Abstract*—White Rabbit precision time protocol (WR-PTP) implements sub-nanosecond synchronization of equipment in the fiber network within the range of 10km. For real applications, it needs additional auxiliary fiber link to calibration the asymmetry of the fiber link, because of the different wavelength of the uplink and downlink light. By implement only one wavelength light for both directions, we greatly simplified the calibration process and get one order time higher synchronization precision than the previous method. Without complex recalibration for each link, the new method would make the WR system much easier to be applied.**

Keywords—White Rabbit; Time Synchronization; Asymmetry; Calibration;

I. INTRODUCTION

White Rabbit (WR) project is a multi-laboratory, multi-company collaboration for the development of a new Ethernet-based technology which ensures sub-nanosecond synchronization between 1000 stations over a tree structure topology [1-2]. Initially, the WR system is used in the CERN Neutrino to Gran Sasso (CNGS) project to transfer the Coordinated Universal Time (UTC) from a Global Positioning System (GPS) receiver to the underground detection points [3], and now it has a wide range of application in cosmic particle detectors and timing distribution system [3-6]. A typical WR link consists of WR Master and WR salve [7]. Base on the Synchronous Ethernet [8], the WR slave locks their frequency of internal clock with that of clock recovered from data stream. So the phase difference between master and slave clock is fixed. To get the precise clock offset of master and slave, the precise time protocol (PTP) is performed and Digital Dual Mixer Time Difference (DDMTD) phase detector is used to enhance the accuracy of timestamp [9-11].

To keep the fiber cable length of uplink (slave to master) and downlink (master to slaver) equal, different wavelengths light are used to transmit the packets in a single mode fiber [12]. As WR is designed to be compatible to the Gigabit Ethernet standards, the bidirectional Small Form Factor Pluggable transceivers (SFPs) pair, operating at 1490/1310 nm, is adopted [13]. So the master transmits and receives laser light of 1490 nm and 1310 nm respectively. The salver transmits and receives laser light of 1310 nm and 1490 nm respectively.

However, as the effect of chromatic dispersion, the value of one-way transmission delay is not the half of the round trip delay, which can be obtained by PTP. To estimate the precise value of master to salve link delay, the asymmetry parameter α is defined to compensate the effect of chromatic dispersion [14].α is defined as

$$\alpha = \delta_{MS} / \delta_{SM} - 1 \tag{1}$$

Where δ_{MS} is the master to salve fiber propagation latency and δ_{SM} is the salve to master fiber propagation latency.

Theoretically, once the asymmetry parameter of one type fiber is calibrated correctly, the one-way link delay can be calculated precisely and the time difference will not change with the increase of fiber length. But in practical, the fiber link consists of fiber provided by different manufactures or different batches from same manufacture, the asymmetry parameter of each fiber section may be different. The difference will brings significant synchronization error for the long distance link and the asymmetry parameter value of whole fiber link is hard to be calibrated correctly ahead.

In this paper, we demonstrate a new synchronization method for the WR system. Two same wavelength light are used to transmit and receive packets in a single fiber. The proposed method simplifies the calibration procedure and brings significant improvement on the long distance synchronization accuracy. On a 50 km fiber link, constructed by different companies' fiber spool, the synchronization error maintains below 200 picosecond.

II. THE PROPOSED SYNCHRONIZATION METHOD

A. The synchronization model

The proposed synchronization method is shown in Fig. 1. two unidirectional Small Factor Pluggable transceivers (SFPs) modulate the Ethernet packets from the two WR device in same wavelength light, and two optical fiber circulators allow the optical signal transfer in a single fiber without mutual interference.

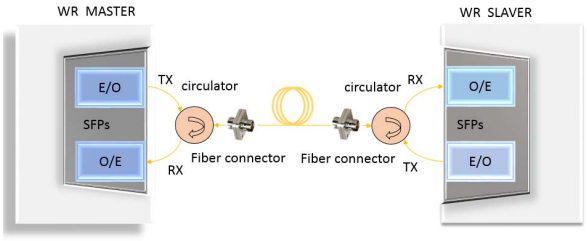


Fig. 1. The new synchronization method. E/O:electrical signal to optical signal; O/E:optical signal to electrical signal;

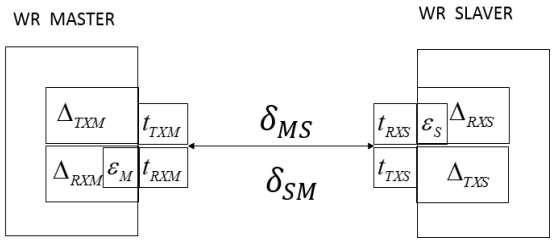


Fig. 2. WR link delay model. Δ_{TXM} , Δ_{RXM} are the transmission and reception delays of master device. Δ_{TXS} , Δ_{RXS} are the transmission and reception delays of slave device. ε_M , ε_S are the bitslide values while aligning the received data stream. δ_{MS}, δ_{SM} are the one-way propagation latencies in fiber; t_{TXM} , t_{RXM} , t_{TXS} and t_{RXS} are the transmission delays in fiber circulators.

The WR link delay model is characterized by the hardware delays and fiber propagation latencies presented in Fig. 2. The transmission and reception delays $(\Delta_{TXM}, \Delta_{RXM}, \Delta_{TXS}, \Delta_{RXS})$ are constant and unknown for each device. The bitslide values $(\varepsilon_M, \varepsilon_S)$ can be obtained from WR software [14]; the fiber propagation latencies $(\delta_{MS}, \delta_{SM})$ are the transmission time of light in both directions. The transmission delays in the fiber circulators $(t_{TXM}, t_{RXM}, t_{TXS}, t_{RXS})$ can be recognized as fixed values at the sub-nanosecond level synchronization for the same light wavelength.

Based on the delay link model above, the round trip $delay_{MM}$ is described as:

$$\begin{aligned} delay_{MM} &= \Delta_{TXM} + \Delta_{RXM} + \Delta_{TXS} + \Delta_{RXS} \\ &+ \delta_{MS} + \delta_{SM} + \varepsilon_M + \varepsilon_S + t_{TXM} + t_{RXM} + t_{TXS} + t_{RXS} \end{aligned} \quad (2)$$

Once the slave device synchronized with the master, $\varepsilon_M, \varepsilon_S$ are fixed and can be read by software. Hardware delays and transfer delays in fiber circulator can be recognized as constant at the sub-nanosecond level synchronization. The sum of them can be described as

$$\begin{aligned} \Delta'_{TXM} &= \Delta_{TXM} + t_{TXM} \\ \Delta'_{RXM} &= \Delta_{RXM} + t_{RXM} \\ \Delta'_{TXS} &= \Delta_{TXS} + t_{TXS} \\ \Delta'_{RXS} &= \Delta_{RXS} + t_{RXS} \end{aligned} \quad (3)$$

Since the light wavelength in uplink and downlink are same, the fiber latencies in the uplink and downlink are equal

$$\delta_{MS} = \delta_{SM} . \quad (4)$$

So the precise value of one-way delay is:

$$delay_{MS} = \Delta'_{TXM} + \Delta'_{RXS} + \delta_{MS} + \varepsilon_S . \quad (5)$$

B. The calibration of hardware delay

Before the one-way delay being calculated precisely, the hardware delay (Δ'_{TXS} , Δ'_{RXS}) of two WR devices need to be calibrated. Fig. 3 describes the schematic diagram of calibration experiment to get the accurate value of Δ'_{TXM} and Δ'_{RXS} for unknown WR device.

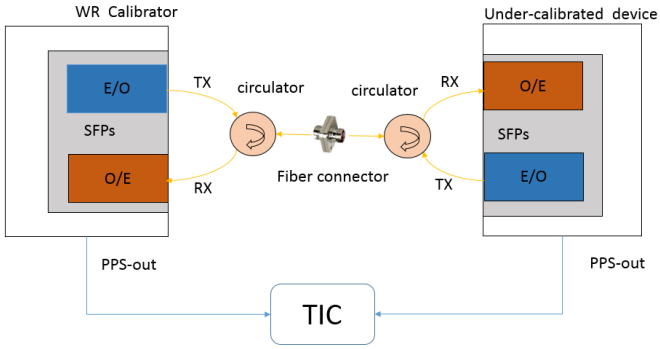


Fig. 3. The schematic diagram of calibration experiment. TIC: time interval counter;

The hardware delays value of under-calibrated device are configured to be zero before the unknown device synchronized with a calibrator (Δ'_{TXM} and Δ'_{RXM} values are known). So the average transmission and reception delays (Δ'_{TXS} , Δ'_{RXS}) of unknown slave device can be calculated as:

$$\Delta'_{TXS} = \Delta'_{RXS} = \left(delay_{MM} - \Delta'_{TXM} - \Delta'_{RXM} - \varepsilon_S - \varepsilon_M \right) / 2 \quad (6)$$

The correction value to compensate the slaver hardware delay asymmetry can be measured with the time interval counter (TIC) by comparing the 1PPS signals time deviation, represented as $skew_{PPS}$.

$$\Delta'_{TXS} = \left(delay_{MM} - \Delta'_{TXM} - \Delta'_{RXM} - \varepsilon_S - \varepsilon_M\right)/2 - skew_{PPS}$$
$$\Delta'_{RXS} = \left(delay_{MM} - \Delta'_{TXM} - \Delta'_{RXM} - \varepsilon_S - \varepsilon_M\right)/2 + skew_{PPS} \quad (7)$$

After the fixed delays of WR device calibrated precisely, the accurate one-way link delay $delay_{MS}$ can be transmitted to the slaver without the pre-calibration of α coefficient of fiber.

C. Test and result

To verify the synchronization performance of proposed method and the quality of hardware delay calibration, a 5km fiber (G652.D, manufactured by YOFC) is connected into the link. Fig. 4 shows the synchronization result of proposed scheme and conventional scheme. The red line is the result of proposed scheme, which has a mean synchronization error value of 50 ps and standard deviation of 30 ps. As a contrast, this 5km fiber is connected into the link in conventional scheme after the asymmetry parameter α is calibrated. The black line is the synchronization result, in which a mean synchronization error value of 172 ps and standard deviation of 32 ps is obtained. As the effect of asymmetry parameter is reduced, the proposed scheme has a better synchronization performance.

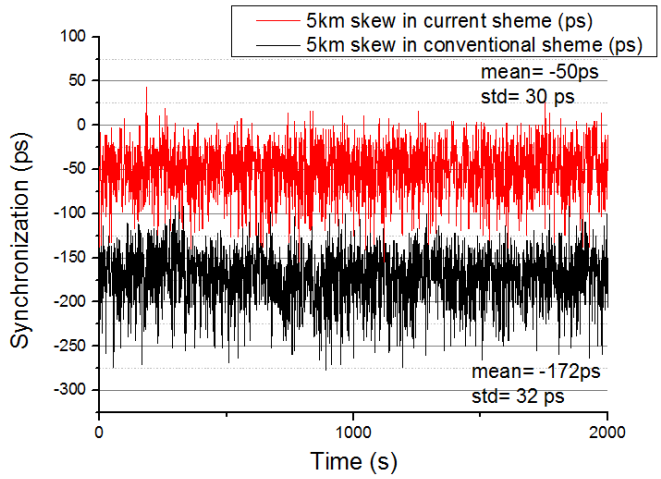


Fig. 4. Synchronization error of two scheme over 5km fiber.

Since the fiber, provided by different manufactures or different batches from same manufacture, has a different asymmetry parameter and the practical fiber link is usually connected section by section, we choose a 50 km G652.D fiber provided by another manufacture (CORNING) to simulate the performance of proposed scheme in practical situation. The result is described in Fig. 5.

The red line is the result of 50km fiber link in the proposed scheme, which has a mean synchronization error value of 132 ps and standard deviation of 28 ps. The result indicates that the proposed scheme can maintain high synchronization precision and it is available for the fiber link provided by different manufacture. In contrast, this 50km fiber is connected into conventional scheme. Keeping the value of α coefficient unchanged to simulate the case that the asymmetry parameter of fiber cannot be calibrated. The black line is the result of conventional scheme, which has a mean synchronization error value of 1574 ps and standard deviation of 38 ps. The result shows that the difference of fiber asymmetry parameter has a significant impact on the synchronization performance for the long fiber link in the conventional scheme.

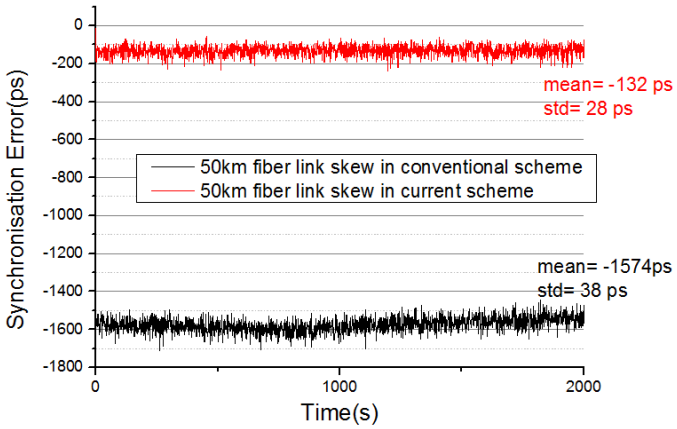


Fig. 5. Synchronization error of two scheme over 50km fiber.

III. CONCLUSION

We demonstrate a synchronization method for the White Rabbit system. With single wavelength lights transmitting in a single mode fiber, we achieve sub-nanosecond level synchronization performance for the 50 km fiber link without the calibration of asymmetry parameter. In addition, this scheme simplified calibration procedures of WR system and it's available for the deployed fiber link.

ACKNOWLEDGMENT

We acknowledge the financial support from the Program of International S&T Cooperation (No. 2016YFE0100200).

REFERENCES

[1] J. Serrano, M. Cattin, E. Gousio, E. van der Bij, T. Włostowski, G. Daniluk, and M. Lipi´nski, "THE WHITE RABBIT PROJECT", in IBIC, Oxford, UK, THBL2, pp.936—942, Sep 2013.

[2] Moreira, P, Serrano, J. Wlostowski, T. Loschmidt, P. Loschmidt and Gaderer, G. "White rabbit: Sub-nanosecond timing distribution over ethernet". IEEE, ISPCS, Brescia, Italy, pp. 1-5, Oct 2009.

[3] M. Lipinski, T. Wlostowski, J. Serrano, P. Alvarez, J. D. G. Cobas, A. Rubini, P. Moreira. "Performance results of the first White Rabbit installation for CNGS time transfer". IEEE, ISPCS, pp. 1-6 , Sep 2012.

[4] G. Gong, S. Chen, Q. Du, J. Li, Y. Liu, H. He. "Sub-nanosecond timing system design and development for LHAASO project". ICALEPCS, Grenoble, France, pp. WEBHMULT04, 2011.

[5] L. Sartini, F. Simeone, P. Pani, N. Lo Bue, G. Marinaro, A. Grubich, F. Gasparoni,"Nuclear Instruments and Methods in Physics Research Section A: Accelerators, Spectrometers, Detectors and Associated Equipment", Nuclear Instruments and Methods in Physics Research A , 2010.

[6] E. F. Dierikx, A. E. Wallin, T. Fordell, J. Myyry, P. Koponen, M. Merimaa, R. Smets. "White Rabbit Precision Time Protocol on Long-Distance Fiber Links". IEEE, UFFC, 63, 7 pp.945-952, Jan 2016.

[7] http://www.ohwr.org/projects/white-rabbit/wiki/, Mar, 2017

[8] T. Wlostowski. Precise time and frequency transfer in a white rabbit network. Master's thesis, Warsaw University of Technology, 2011.

[9] IEEE Standard for a Precision Clock Synchronization Protocol for Networked Measurement and Control Systems, IEEE 1588 (PTP), 2008.

[10] M. Lipiński, T. Włostowski, J. Serrano and P. Alvarez, "White rabbit: A PTP application for robust sub-nanosecond synchronization."IEEE, ISPCS, pp. 25-30, Sep 2011.

[11] P. Moriera, P. Alvarez, J. Serrano, I. Darwezeh and T. Wlostowski. "Digital dual mixer time difference for sub-nanosecond time synchronization in Ethernet", IEEE IFCS, pp. 449-453, Jun 2010.

[12] G.Daniluk, White Rabbit PTP Core: the sub-nanosecond time synchronization over Ethernet. Warsaw University of Technology, 2012.

[13] http://www.ohwr.org/projects/white-rabbit/wiki/SFP, Mar 2017.

[14] http://www.ohwr.org/projects/wr-calibration/wiki. White Rabbit calibration procedure, version 1.1. Nov 2015.

Ultra-low Phase Noise Synchronization of Microwave Sources with Fiber-Optic Timing System

Aram Kalaydzhyan[1,*], Ming Xin[1,2], Kemal Şafak[1,3], Michael Y. Peng[2], Kwangyun Jung[4,5], Wenting Wang[1], Jungwon Kim[4] and Franz X. Kärtner[1,2,3]

[1]Center for Free-Electron Laser Science, Deutsches Elektronen-Synchrotron DESY, Hamburg, Germany
[2]Research Laboratory of Electronics, Massachusetts Institute of Technology, Cambridge, USA
[3]Physics Department, University of Hamburg and the Hamburg Center for Ultrafast Imaging, Hamburg, Germany
[4]School of Mechanical and Aerospace Engineering, KAIST, Daejeon, South Korea
[5]Current address: Samsung Electro-Mechanics, Suwon, South Korea

*Email: aram.kalaydzhyan@desy.de

Abstract—We describe two different schemes for residual phase noise measurement of a dual-link optical-microwave timing system. The lengths of the fiber links are 1.2 km and 3.5 km. The residual single-sideband (SSB) phase noise of 10.833 GHz local oscillators lays below -135 dBc at 10 kHz offset. The RMS jitter integrated from 1 Hz to 10 MHz does not exceed 3 fs.

I. Introduction

Recently, fiber-optic timing systems that are based on femtosecond mode-locked lasers (MLLs) and balanced optical cross-correlators have demonstrated an ability to reach sub-fs precision of synchronization of remote laser and microwave sources [1,2]. Here, we shift our focus from the application of timing systems for future X-ray free electron laser sources to astronomical interferometry, where a timing system is required for the synchronization of a distributed array of radio telescopes. In these applications, a distributed network of antennas forms an interferometer array. An ultra-stable common reference signal should be distributed to each antenna to perform a phase locking between all local multi-GHz microwave oscillators [4]. Precision of the radio astronomical measurements depends directly on stability of the timing system. Since the target overall jitter of the system is in the range of few femtoseconds and below, phase noise measurements cannot be performed by commercially available signal source analyzers (SSAs), because their measurement noise floor is higher than the level of the measured signal. Conventional method of phase noise characterization of such timing systems is based on capturing amplitude spectral density of a phase error signal in the phase locked loops (PLLs) and calibration of the measured data with the phase detector transfer function. This method requires careful characterization of phase detectors of a timing system, because their sensitivity might depend non-linearly on frequency and amplitude of detected error signals. However, if the main purpose of the timing system is to provide stable phase locking of RF/microwave sources, one can simplify the task and utilize known interferometric techniques to measure phase noise between remotely locked local microwave oscillator within an approximation of identical timing links, local oscillators and PLLs.

II. Fiber-Optic Timing System

The fiber-based optical timing system that we focus on in this paper was described in details in [1,2]. Femtosecond optical pulsed of a 216.6 MHz MLL are fed into two polarization-maintaining dispersion-compensated fiber links with length of 1.2 km and 3.5 km. Pulses that are partially reflected from the ends of the fiber links are compared with fresh pulses from the MLL using optical cross-correlation to measure and compensate fiber length drifts using variable fiber delay lines. At the end of each link, a 10.8 GHz Sapphire Loaded Cavity Oscillator (SLCO) is referenced to incoming optical pulses using hybrid balanced optical-microwave phase detectors [3].

III. 180˚ Hybrid Coupler Based Phase Detector

An interferometric microwave phase detector, as originally described in [5], was assembled to characterize residual phase noise of the timing system. Its simplified scheme is shown in Fig. 1.

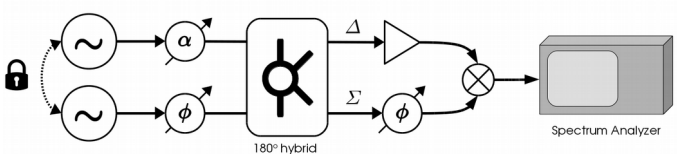


Fig. 1. Principle scheme of the phase detector system based on a 3dB 180˚ hybrid coupler.

About +10 dBm of microwave power from each remotely locked VCO goes to a corresponding arm of the phase detector through a phase shifter and a attenuator. These signals are combined in a 3-dB 180˚ hybrid. The attenuator is used to equalize the incoming signal powers. The phase shifter is adjusted such that the input signals to the 180˚ hybrid are in quadrature. Thus, a carrier-canceled signal on the Δ output of the coupler contains information about phase error between the input signals and modulated by carrier frequency. This signal is boosted by a low noise +30 dB gain amplifier and, afterwards, down-mixed using the signal from Σ output of the coupler the phase of which is tuned by another phase shifter to be in

quadrature with error signal on the double-balanced mixer. The down-mixed signal is then captured by a spectrum analyzer. Sensitivity of the phase detector can be measured by unlocking one of the oscillators from the reference frequency and measuring the amplitude of the oscillations on the Δ output of the coupler. Careful pre-tuning of the presented interferometric system suppresses the measurement noise floor down to -184 dBc, which is enough to characterize the timing system under test down to the 2.5 fs level. One can see the measured phase noise of the locked VCOs in Fig. 2. The residual single-sideband (SSB) phase noise of 10.833 GHz local oscillators lays below -135 dBc at 10 kHz offset.

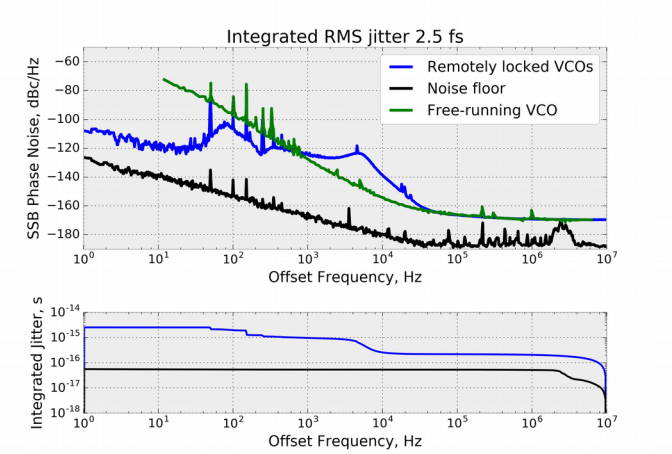


Fig. 2. Top: Residual phase noise performance of the remotely locked microwave sources (blue, 3 dB subtracted) measured by interferometric setup with the noise floor of -184 dBc (black) and compared with absolute phase noise of free-running VCOs. Bottom: Integrated RMS jitter.

Fig. 3.

IV. Cross-Correlated Phase Noise Measurement

Although this system exhibits very low phase noise shown above, it may suffer from mechanical and thermal drifts of phase shifters and cables, cross-talks and variation of input power. To eliminate these drifts effects from the measurement the, a well studied interferometric phase noise measurement setup [6] had been assembled. The scheme of the setup is shown in Fig. 3.

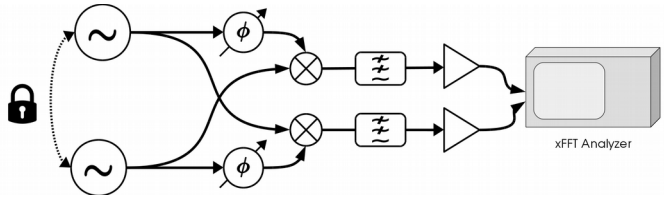


Fig. 4. Principle scheme of the cross-correlation phase noise measurement setup.

In this scheme, the signals from VCOs are split in two parts and mixed in quadrature in double-balanced mixers. Both arms of the setup are equal, except for the swapping of LO and RF signals on the phase detectors. The phase error signals are then amplified and captured by a cross-spectrum FFT analyzer. Thus, the uncorrelated noise created inside each arm of the measured setup is suppressed. The result of this measurement is shown in Fig. 4.

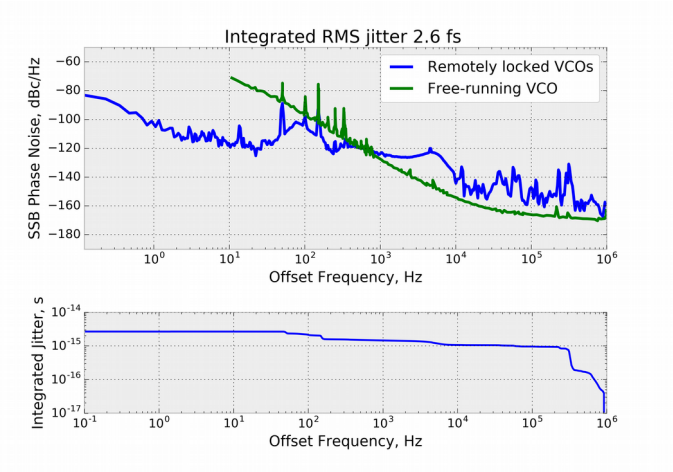


Fig. 5. Top: Residual phase noise performance of he remotely locked microwave sources (blue, 3 dB subtracted) measured by cross-correlating setup and compared with absolute phase noise of free-running VCOs. Bottom: Integrated RMS jitter.

The measured phase noise in the 1 Hz to 10 kHz range is in the good agreement with that in the previous section. This confirms that the calibration for both methods are accurate for fast time scales. The measurement is limited by the noise floor of the setup at offset frequencies higher than 10 kHz.

Conclusions

We have reported successful interferometric phase noise measurements of the dual-arm optical-microwave timing system with two different methods. Two 10.8 GHz microwave sources were referenced by the multi-km fiber timing system to the MLL with the repetition rate of 216 MHz using balanced optical-microwave phase detectors and optical cross-correlators. The referencing optical signal were received from the ends of two timing links with length of 1.2 km and 3.5 km. Both methods showed that the SLCOs were successfully synchronized and provided similar results. Measured relative timing jitter integrated from 1 Hz to 10 MHz was less than 3 fs.

References

[1] M. Xin, K. Şafak, M. Y. Peng, A. Kalaydzhyan, W. Wang, O. D. Mücke and F. X. Kärtner, "Attosecond precision multi-kilometer laser-microwave network," Light Sci. Appl. 6, e16187 (2017).

[2] M. Xin, K. Şafak, M. Y. Peng, A. Kalaydzhyan, P. T. Callahan, W. Wang, O. D. Mücke and F. X. Kärtner, "Breaking the femtosecond barrier in multi-kilometer timing synchronization systems," IEEE J. Sel. Top. Quantum Electron., 23, 3 (2017).

[3] M. Peng, A. Kalaydzhyan, F. X. Kärtner, "Balanced optical-microwave phase detector for sub-femtosecond optical-RF synchronization," Opt. Express 22, 27102 (2014).

[4] J. Cliche and B. Schillue, "Precision timing control for radioastronomy," IEEE Control Systems Magazine (2006).

[5] E. Ivanov, M. Edmund, R. Alec, "Phase noise detector", Patent EP0760954 B1.

[6] A. Hati, C.W. Nelson, C. Barnes, D. Lirette, T. Fortier, F.Quinlan, J.A. DeSalvo, A. Ludlow, T. Rosenband, S.A. Diddams, and D.A. Howe, “State-of-the-Art RF signal generation from optical frequency division,” IEEE T. Ultrason. Ferr. 60, (2013).

Multichannel Precision Time Delay Measurement in Optical Fibers

Jingwen Dong, Bo Wang, Hongwei Si, Lijun Wang
Department of Precision Instrument,
State Key Laboratory of Precision Measurement
Technology and Instruments, Tsinghua University
Beijing, China
bo.wang@tsinghua.edu.cn

Lijun Wang
Department of Physics, Tsinghua University
Beijing, China

***Abstract*—We report a novel method for multichannel transmission delay measurement in optical fibers. The fiber transfer delay measurement is converted into frequency measurement. As a key technique, a simple ambiguity resolving process based on phase discrimination and frequency locking is used to overcome the contradiction between measurement accuracy and system complexity. A real-time calibration method is employed to detect and eliminate system delay fluctuation. It achieves two-channel fiber transmission delay measurement with a high accuracy of 0.1 picosecond and dynamic range over tens of kilometers.**

Keywords—time delay; fiber transmission; multichannel measurement

I. INTRODUCTION

Optical fiber is one of transmission medium. With low loss, high capacity, high reliability and many other advantages, it is increasingly widely used in various fields. The fiber transfer delay (FTD) is an important parameter of the transmission characteristics for fiber transmission. For digital fiber-optic communications, the FTD measurement is used to estimate the transmission distance, the signal distortion caused by chromatic dispersion, etc. In wavelength-division multiplexing system, the FTD is closely related to the communication bandwidth, error rate and many other important characteristic parameters. For fiber based time and frequency distribution and synchronization, the accuracy of FTD measurement directly determines the time synchronization accuracy. In optically controlled phased array antenna, the FTD measurement is used to control the time delay of the transmitted signal for specified transmit direction angle. In distributed array system, FTD measurement plays a key role in beamforming [1-3].

Up to now, many techniques based on FTD measurement in time domain [4] or frequency domain [5] have been developed and successfully employed; while most of them either have drawbacks of low accuracy and existing dead zones, or require time-consuming ambiguity resolving process.

We reported a novel method for FTD measurement based on phase discrimination, dual-frequency locking and measurement [6]. Employing a real-time system delay calibration method, it achieves two-channel FTD measurement with a high accuracy of 0.1 picosecond and dynamic range over tens of kilometers. A good agreement in measurement results with the conventional pulsed method is obtained as well.

We acknowledge the financial support from the Program of International S&T Cooperation (No. 2016YFE0100200).

II. METHODS

The basic idea is transferring a laser light modulated by a microwave signal through the test fiber to make the frequency of the signal (f) locked onto the FTD (t). Thus, the FTD measurement is converted into the frequency measurement. Additionally, an optical switch is employed for multichannel FTD measurement. Figure 1 shows the principle of the two-channel FTD measurement system. A laser light, modulated by a microwave signal from a programmable frequency synthesizer, is transferred through the test fiber. After laser light detecting, microwave frequency mixing and filtering operations, an error signal $V_e \propto \cos(\phi_p)$ is obtained. Here, ϕ_p denotes the transmission induced phase delay, thus $\phi_p = 2\pi f \cdot t$. Using the error signal to control the frequency of the microwave signal (f), makes $V_e \propto \cos(\phi_p) = 0$, yielding:

$$t = \frac{(2N+1)}{4f}. \tag{1}$$

Here, f can be measured by a frequency counter. N is an integer and can be considered as an ambiguity of the FTD measurement. A course FTD measurement method is used to resolve this ambiguity. Through changing the frequency of microwave signal by frequency synthesizer and performing two frequency locking operations, we get two different frequencies f_1 and f_2, accompany with their ambiguities N_1 and N_2. FTD can be calculated by:

$$t_{\text{course}} = \frac{N_2 - N_1}{2(f_2 - f_1)}. \tag{2}$$

Here, $(N_2 - N_1)$ can be obtained from the zero-crossing detection of V_e during the microwave signal frequency scanning from f_1 to f_2. A 5-km fiber is inserted into the measurement loop for dead zone elimination. When no test fiber is connected, the laser light is reflected by the end surface of the optical switch. The system delay (including propagation delays of electronic circuits, cables, inserted fibers, etc.) is calibrated via the same method. Considering the temperature variation caused system delay fluctuation, real-time system delay measurement is necessary. Through transmission path switching, the real-time FTDs can be obtained by alternated measurement for each channel and system delay deduction.

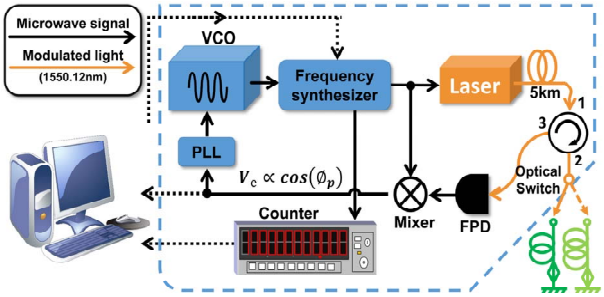


Fig. 1. Schematic of two-channel FTD measurement system. VCO, voltage control oscillator; FPD, fast photo detector; PLL, phase locked loop.

III. RESULTS

To verify the accuracy and the measurement range of the FTD measurement system, we used it to measure the FTD of 2-m fiber (Fig. 2), which can be considered as a constant, and 50-km fiber (Fig. 3). As a comparison, we also used a time interval counter (TIC) to measure the same fibers by transferring a pulse signal.

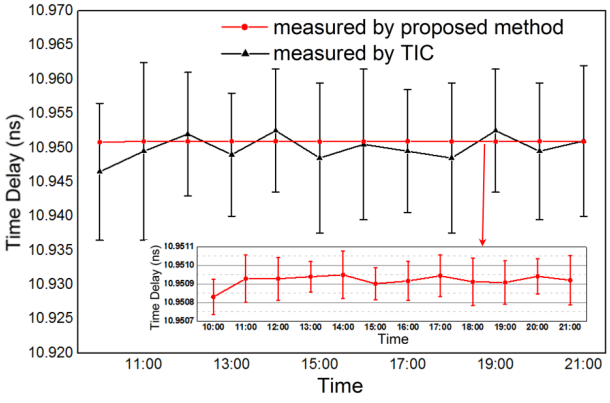


Fig. 2. FTD measurement results of 2-m fiber.

The means of all measured FTDs using two methods are well overlapped. For the 2-m fiber, the statistical error of the proposed method is below 0.2 ps and the long-term fluctuation of it is below ± 0.1 ps, whereas using pulse method, they increase to approximately 15 ps and ± 4 ps, respectively. For the 50-km long fiber, the long-term fluctuation increased to 1100 ps, which reflects the temperature fluctuation while taking measurement. Using the proposed method, the statistical error is 0.7 ps, whereas using pulse method, it increases to 140 ps. We also continuously and alternatively measured two ~10 km long fibers in door (Fig. 4). The results are closed to each other.

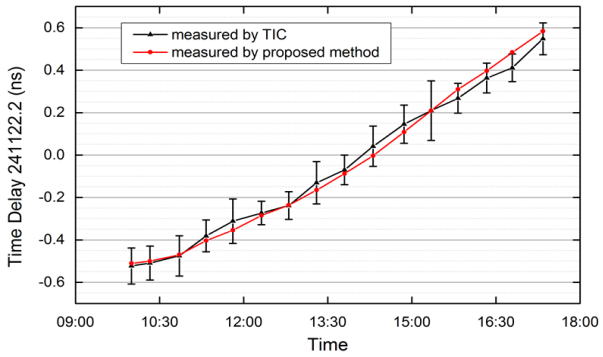


Fig. 3. FTD measurement results of 50-km fiber.

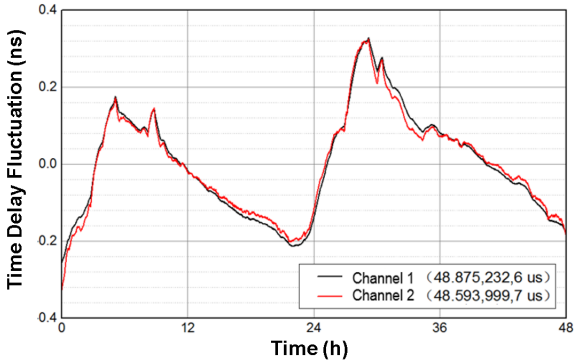


Fig. 4. FTD measurement results of two 10-km fibers.

The results indicate that the reported system could continuously measure at least two channel FTDs with accuracy of 0.1 ps and dynamic range over tens of kilometers.

ACKNOWLEDGMENT

We acknowledge the financial support from the Program of International S&T Cooperation (No. 2016YFE0100200).

REFERENCES

[1] I. Frigyes, et al., "Optically generated true-time delay in phased-array antennas," IEEE Trans. Microwave Treory Tech. vol. 43, pp. 2378–2386, 1995.

[2] R. -J. Essiambre, et al., "Capacity limits of optical fiber networks," J. Lightwave Technol. vol. 28, pp. 153902, 2010.

[3] B. Wang, et al., "Precise and continuous time and frequency synchronisation at the 5×10^{-19} level," Sci. Rep. vol. 2, pp. 556, 2012.

[4] D. L. Philen, et al., "Single-mode fiber OTDR: experiment and theory," IEEE Trans. Microwave Theory Tech. vol. 30, pp. 1487–1496, 1982.

[5] I. Fujima, et al., "High-resolution distance meter using optical intensity modulation at 28 GHz," Meas. Sci. Technol. vol. 9, pp. 1049–1052, 1998.

[6] J. W. Dong, et al., "Accurate and fast fiber transfer delay measurement based on phase discrimination and frequency measurement," Rev. Sci. Instru., vol. 87, pp. 662–701, 2016.

Experimental Constraint on Dark Matter-Standard Model Coupling with Optical Atomic Clocks

P. Wcisło, P. Morzyński, M. Bober, A. Cygan, D. Lisak, R. Ciuryło, and M. Zawada
Email: zawada@fizyka.umk.pl
Institute of Physics, Faculty of Physics, Astronomy and Informatics, Nicolaus Copernicus University,
Grudziądzka 5, PL-87-100 Toruń, Poland

***Abstract*—We have shown that a single optical atomic clock can be used as a detector for the hypothetical dark matter in the form of stable topological defects, for example, monopoles, strings or domain walls. We exploited differences in the susceptibilities to the fine-structure constant of essential parts of an optical atomic clock, i.e. the atoms and the cavity. We perform an experiment which constrained the strength of atomic coupling to hypothetical dark-matter cosmic objects. Under the conditions of our experiments, the degree of constraint was found to exceed the previously reported limits by more than three orders of magnitude [1].**

I. Introduction

The total mass density of the Universe appears to be dominated by dark matter. However, beyond its gravitational interactions at the galactic scale, little is known about its nature [2]. The general belief is that the dark matter is dominated by a non-baryonic component, which is likely composed of new fundamental particles or similar exotic states. To positively detect and define the constitution of the dark matter, the galactic scales has to be changed into laboratory scales. Unfortunately, searches for the most popular hypothetical particles that are thought to constitute the dark matter, supersymmetric Weakly Interacting Massive Particles (WIMPs), reported negative results. The most precise experiment up tu date, LUX, constrained the scattering cross section of the WIMPs on nucleons to below 10^{-45} cm^2 [3]. Recently, several proposals have emerged for validation of alternative theories explaining the origin of the dark matter [4]–[6]. In particular, a network of atomic clocks has been proposed to search for transient indicators of hypothetical dark matter [7] in the form of stable topological defects [8]. The clocks become desynchronized when a dark-matter object sweeps through the network. This pioneering approach, however, requires a comparison between at least two distant optical atomic clocks, e.g. over long phase-noise-compensated optical-fibre links [9].

By exploiting differences in the susceptibilities of the atoms and the cavity to the fine-structure constant [10], [11], we have recently shown that a single optical atomic clock [12] is already sensitive to dark-matter events [1]. We experimentally constrained the strength of atomic coupling to hypothetical dark-matter cosmic objects. Under the conditions of our experiments, the degree of constraint was found to exceed the previously reported limits [13] by more than three orders of magnitude.

Moreover, this implies that existing optical atomic clocks can serve as a global topological-defect dark-matter observatory, without any further developments in experimental apparatus or the need for long optical-fibre links.

II. Methods and results

The most important parts of the optical atomic clock are the local oscillator in the form of the clock laser and the prepared atomic sample. The frequency of the clock laser is tightly locked to the ultra-stable optical cavity. The beam, after passing through the frequency shifter, probes the trapped atoms. The shifter correction is actively controlled to keep the frequency of the beam locked to the clock transition. Therefore, the changes to the frequency correction reflect the changes to the frequency of the clock transition with respect to the cavity.

When the Earth traverses a dark matter (DM) object, for a nonzero DM-SM coupling, the presence of the DM will perturb the values of certain Standard Model (SM) parameters. In particular, we may expect a transient variation in the electromagnetic fine-structure constant α that can be expressed as $\delta\alpha/\alpha = \phi^2/\Lambda'^2_\alpha$, where ϕ is the DM field and Λ'_α is the energy scale (which inversely parametrizes the strength of the DM-SM coupling). This will shift the frequency of the electronic clock transition and the frequency of the chosen cavity mode. Different susceptibilities of these two frequencies to α variations ($\omega \propto \alpha^2$ for non-relativistic atoms and $\omega \propto \alpha$ for cavity) make a single optical atomic clock sensitive to a hypothetical dark matter and hence will directly manifest in the feedback signal.

In our measurement we used a system of two nearly identical optical-lattice clocks [14], [15] placed approximately 10 m apart. The common component in the feedback signals provides a constraint on the transient variation of α and on the magnitude of the DM-SM coupling. This common component can be extracted by cross-correlating the feedback signals. and on the magnitude of the DM-SM coupling. This common component can be extracted by cross-correlating the feedback signals. We can use our measurement to estimate a constraint on the energy scale Λ'_α under the assumption of the DM density of $\rho = 0.3$ GeV cm^{-3} [16]. The constraints on Λ'_α for the entire measurement duration, 45700 s, and for a small portion thereof, 100 s, are shown as functions of d as the grey and green lines, respectively, in Fig. 1.

978-1-5386-2916-1/$31.00 ©2017 IEEE

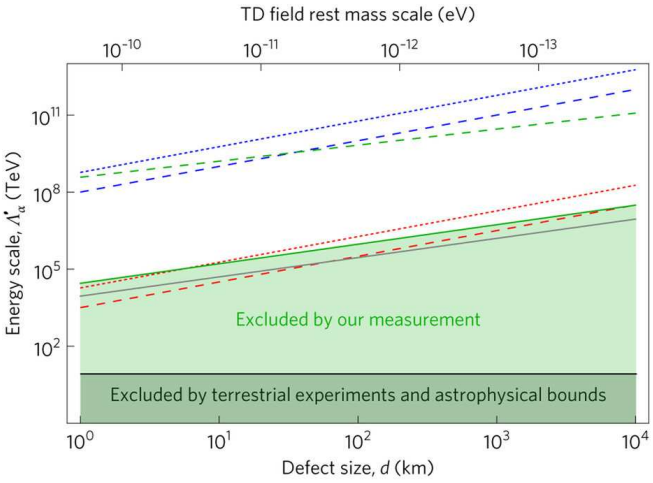


Fig. 1. **Constraint on the energy scale Λ'_α.** The grey and green lines represent the constraints we infer from the present measurement by cross-correlating the readouts in their entirety and by cross-correlating only a small portion of the readouts, respectively (see the text). The dashed blue and red lines, which are taken directly from Ref. [7], represent limits on the experimental constraints that could be achieved with a trans-continental network of Sr optical lattice clocks and a GPS constellation, respectively. However, these limits are underestimated. The dotted blue and red lines represent the corrected constraints (see the Methods section for details). The dashed green line represents the limit achievable using our approach under the same conditions considered in Ref. [7].

ACKNOWLEDGEMENTS

The reported measurements were performed at the National Laboratory FAMO in Toruń, Poland, and were supported by a subsidy from the Ministry of Science and Higher Education. Support has been received from the project EMPIR 15SIB03 OC18. This project has received funding from the EMPIR programme co-financed by the Participating States and from the European Unions Horizon 2020 research and innovation programme.

REFERENCES

[1] Wcisło P., *et al.*, Experimental constraint on dark matter detection with optical atomic clocks, *Nat. Astron.* **1**, 0009 (2016)
[2] Feng, J. L., Dark matter candidates from particle physics and methods of detection, *Ann. Rev. Astron. Astrophys.* **48**, 495, (2010)
[3] Akerib, D. S., *et al.*, First results from the LUX dark matter experiment at the Stanford Underground Research Facility, *Phys. Rev. Lett.* **112**, 091303 (2014)
[4] Budker, D., *et al.*, Proposal for a cosmic axion spin precession experiment (CASPEr), *Phys. Rev. X* **4**, 021030 (2014)
[5] Stadnik, Y. V., and Flambaum, V. V., Searching for topological defect dark matter via nongravitational signatures, *Phys. Rev. Lett.* **113**, 151301 (2014)
[6] Hees, A., *et al.*, Searching for an oscillating massive scalar field as a dark matter candidate using atomic hyperfine frequency comparisons, *Phys. Rev. Lett.* **117**, 061301 (2016)
[7] Derevianko, A., and Pospelov, M. Hunting for topological dark matter with atomic clocks, *Nat. Phys.* **10**, 933 (2014)
[8] Vilenkin, A., Cosmic strings and domain walls, *Phys. Rep.* **121** 263 (1985)
[9] Calonico, D., Inguscio, M., and Levi, F., Light and the distribution of time, *EPL-Europhys. Lett.* **110**, 1 (2015)
[10] Stadnik, Y. V., and Flambaum, V. V., Searching for dark matter and variation of fundamental constants with laser and maser interferometry, *Phys. Rev. Lett.* **114**, 161301 (2015)
[11] Stadnik, Y. V., and Flambaum, V. V., Enhanced effects of variation of the fundamental constants in laser interferometers and application to dark-matter detection, *Phys. Rev. A* **93**, 063630 (2016)
[12] Ludlow, A. D., *et al.*, Optical atomic clocks, *Rev. Mod. Phys.* **87**, 637 (2015)
[13] Olive, K. A., and Pospelov, M., Environmental dependence of masses and coupling constants *Phys. Rev. D* **77**, 043524 (2008)
[14] Bober, M., *et al.*, Strontium optical lattice clocks for practical realization of the metre and secondary representation of the second, *Meas. Sci. Technol.* **26**, 075201 (2015)
[15] Morzyński, P., *et al.*, Absolute measurement of the $^1S_0{}^3P_0$ clock transition in neutral ^{88}Sr over the 330 km-long stabilized fibre optic link *Sci. Rep.* **5**, 17495 (2015)
[16] Beringer, J., *et al.* Review of particle physics, *Phys. Rev. D* **86**, 010001 (2012)

Mass Defect Effects in Atomic Clocks

Valeriy I. Yudin and Alexey V. Taichenachev,
[1)] Novosibirsk State University, Novosibirsk 630090, Russia
[2)] Institute of Laser Physics SB RAS, Novosibirsk 630090, Russia
viyudin@mail.ru

***Abstract*—We consider some implications of the mass defect on the frequency of atomic transitions. We have found that some well-known frequency shifts (such as gravitational and quadratic Doppler shifts) can be interpreted as consequences of the mass defect, i.e., without the need for the concept of time dilation used in special and general relativity theories. Moreover, we show that the inclusion of the mass defect leads to previously unknown shifts for clocks based on trapped ions.**

Keywords—mass defect, atomic clocks, quantum metrology, special and general relativity

I. INTRODUCTION

At the present time, atomic clocks are most precise scientific devices. The principle of operation of these quantum instruments is based on modern methods of laser physics and high-precision spectroscopy. In this way, the unprecedented value of fractional instability and uncertainty at the level of 10^{-18} has already been achieved with the goal of 10^{-19} on the horizon [1]. Frequency measurements at such a level could have a huge influence on further developments in fundamental and applied physics. In particular, we can foresee tests of quantum electrodynamics and cosmological models, searches for drifts of the fundamental constants, new types of chronometric geodesy, and so on (see, for example, review [2]). However, this level of experimental accuracy requires a comparable level of theoretical support, which would account for systematic frequency shifts of atomic transitions due to different physical effects. Thus, modern atomic clocks are also at the point of interweaving different areas of theoretical physics.

In this paper we develop the mass defect concept with respect to atomic clocks. Historically, considerations of the mass defect have been connected with nuclear physics, where the mass defect explains the huge energy emitted due to different nuclear reactions. However, a quite unexpected result is that this effect has a direct relation to frequency standards, where it leads to shifts in the frequencies of atomic transitions.

II. MASS DEFECT PRODUCED SHIFTS IN ATOMIC CLOCKS

The main idea of our approach is following. Let us consider an arbitrary atomic transition between states $|g\rangle$ and $|e\rangle$ with unperturbed frequency $\omega_0 = (E_e^{(0)} - E_g^{(0)})/\hbar$, where $E_e^{(0)}$ and $E_g^{(0)}$ are the unperturbed energies of the corresponding states (see Fig.1). Using Einstein's famous formula, $E=Mc^2$, which links the mass M and energy E of a particle (c is the speed of light), we can find the rest masses of our particle, M_g and M_e, for the states $|g\rangle$ and $|e\rangle$, respectively: $E_g^{(0)} = M_g c^2$ and $E_e^{(0)} = M_e c^2$. The fact that $M_g \neq M_e$ is the essence of the so-called mass defect. In our case, the connection between M_g and M_e is the following:

$$M_e c^2 = M_g c^2 + \hbar\omega_0 \;\Rightarrow\; M_e = M_g + \hbar\omega_0 / c^2 . \quad (1)$$

We show that the relationship (1) allows us to reinterpret some well-known systematic frequency shifts (such as the so-called time dilation effects) [3,4]. Moreover, our approach actually predicts some new shifts previously unconsidered, to our knowledge, in the scientific literature.

A. Gravitational shift.

As the first example, let us show how the mass defect allows us to formulate a very simple explanation of the gravitational redshift even under a classical description of the gravitational field (as classical potential U_G). Indeed, because the potential energy of a particle in a classical gravitational field is equal to the product MU_G (where $U_G<0$), we can write the energy of j-th state $E_j(U_G)$ as:

$$E_j(U_G) = M_j c^2 + M_j U_G = M_j c^2 (1 + U_G / c^2), \; (j = g,e) \quad (2)$$

Using Eqs.(1) and (2), we find the frequency of the transition $|g\rangle \to |e\rangle$ in the gravitational field:

$$\omega = [E_e(U_G) - E_g(U_G)]/\hbar = \omega_0 (1 + U_G / c^2). \quad (3)$$

This expression coincides to the leading order of the well-known formula from general relativity theory:

$$\omega = \omega_0 \sqrt{1 + 2U_G / c^2} \approx \omega_0 (1 + U_G / c^2) \quad (4)$$

in the case of $|U_G|/c^2 \ll 1$.

We emphasize that the expression (3) was here derived without including the concept of time dilation, which is taken as a basis of Einstein's theory of relativity. Nevertheless, in deriving (3) we have used an equality of gravitational and inertial masses, $M_{grav}=M_{in}$, which is one of the cornerstones of general relativity.

B. Frequency shifts for atoms (ions) trapped in a confinement potential.

A second example concerns frequency shifts in the presence of a confinement potential $U(\mathbf{r})$, which we take to be the same for both states $|g\rangle$ and $|e\rangle$. Such a situation occurs both for clocks based on neutral atoms in optical lattice and those based on trapped ions. In this case, we have the standard task of quantizing the energy levels with translational degrees of freedom:

$$\hat{H}_j \left|\Psi_j(\mathbf{r})\right\rangle = \mathcal{E}_j \left|\Psi_j(\mathbf{r})\right\rangle,\ \hat{H}_j = \hat{\mathbf{p}}^2/2M_j + U(\mathbf{r}), \quad (5)$$

where Hamiltonian $\hat{H}_j$ and state $|\Psi_j(\mathbf{r})\rangle$ describe the translational motion of the particle in the j-th internal state $|j\rangle$ (j=g,e), and $\mathbf{r}$ is coordinate of atomic center-of-mass. Thus, taking into account the translational motion, the atomic wave function is described by the pair products $|j\rangle\otimes|\Psi_j(\mathbf{r})\rangle$. Because of the mass defect ($M_g \neq M_e$), the energy levels for the lower and upper states differ: $\mathcal{E}_g \neq \mathcal{E}_e$. Consequently, the frequency ω between corresponding levels of trapped particle is different from the unperturbed frequency, ω_0 (see Fig.1), with a value $\Delta\omega$: $\Delta\omega=\omega-\omega_0=(\mathcal{E}_e-\mathcal{E}_g)/\hbar$. Let us now estimate this value. For this purpose, we write the Hamiltonian for upper state $\hat{H}_e$ in the following form:

$$\hat{H}_e = \hat{H}_g + \Delta\hat{H};\ \Delta\hat{H} = \frac{\hat{\mathbf{p}}^2}{2M_e} - \frac{\hat{\mathbf{p}}^2}{2M_g} = -\frac{\hbar\omega_0\hat{\mathbf{p}}^2}{2M_e M_g c^2}, \quad (6)$$

where the operator $\Delta\hat{H}$ can be considered as a small perturbation. In this case, using the standard perturbation theory, energy $\mathcal{E}_e$ can be written as a series $\mathcal{E}_e=\mathcal{E}_e(0)+\Delta\mathcal{E}_e(1)+\Delta\mathcal{E}_e(2)+...$, where $\mathcal{E}_e(0)=\mathcal{E}_g$, and the first correction is determined as the average value $\Delta\mathcal{E}_e(1)=\langle\Psi_g|\Delta H|\Psi_g\rangle$. Using Eq. (6) and taking into account $M_g \approx M_e$, we obtain the following estimation of the relative value of shift:

$$\frac{\Delta\omega}{\omega_0} \approx -\frac{1}{2c^2}\frac{\left\langle\Psi_g\left|\hat{\mathbf{p}}^2\right|\Psi_g\right\rangle}{M_g^2}. \quad (7)$$

We note that this expression coincides with a well-known relativistic correction, which is the quadratic Doppler shift due to the time dilation effect for moving particle [4]. Indeed, at the present time the following explanation is conventionally used. In accordance with special relativity, the tick rate $\Delta t'$ in the moving (with velocity $\mathbf{v}$) coordinate system changes with respect to the tick rate Δt in motionless (laboratory) coordinate system by the law: $\Delta t'=\Delta t(1-\mathbf{v}^2/c^2)^{1/2}$. As a result, an atomic oscillation with eigenfrequency ω_0 is perceived by an external observer to be shifted to $\omega=\omega_0(1-\mathbf{v}^2/c^2)^{1/2}$. In the nonrelativistic limit, ($\mathbf{v}^2/c^2<<1$), we have:

$$\omega \approx \omega_0(1-\mathbf{v}^2/2c^2) = \omega_0(1-(\mathbf{p}/M)^2/2c^2),$$

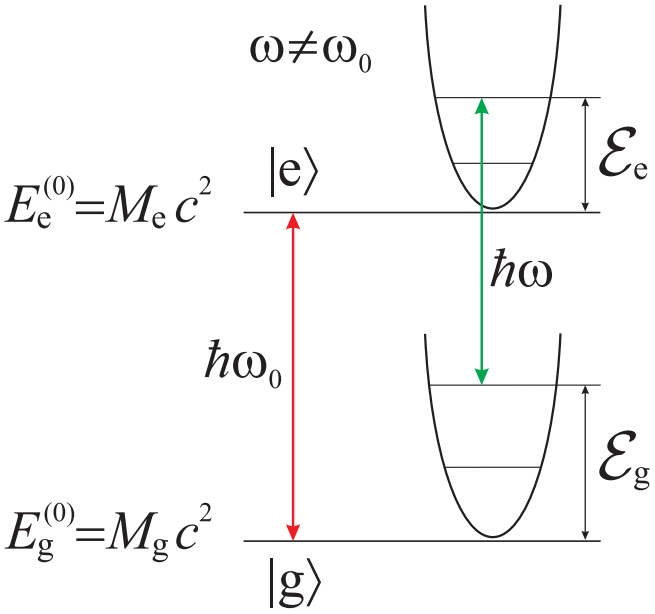


Fig. 1. Schemematic for an atomic transition $|g\rangle\rightarrow|e\rangle$. Also shown is the quantization of the energy levels for translational degrees of freedom in a confined potential, $U(\mathbf{r})$, where $\omega\neq\omega_0$ due to the mass defect.

where $\mathbf{p}$ is momentum of particle. Then, if we take into account quantum considerations through the replacement $\mathbf{p}\rightarrow\hat{\mathbf{p}}=-i\hbar\nabla$, we obtain the expression for motion-induced shift (7).

Thus, some well-known systematic shifts, previously interpreted as the time dilation effects in the frame of special and general relativity theories, can be considered as a consequence of the mass defect. Furthermore, our approach has predicted a series of previously unknown shifts (e.g., related to electric-field sensitivities) for ion clocks. These results could have importance for high-precision optical atomic clocks.

ACKNOWLEDGMENT

We thank C. Oates for useful discussions and comments.

This work was supported by the Russian Scientific Foundation (Project No. 16-12-00052). V.I.Yudin was also supported by Ministry of Education and Science of the Russian Federation (Project No. 3.1326.2017/4.6), and Russian Foundation for Basic Research (Project No. 17-02-00570).

REFERENCES

[1] M. Schioppo, R. C. Brown, W. F. McGrew, N. Hinkley, R. J. Fasano, K. Beloy, T. H. Yoon, G. Milani, D. Nicolodi, J. A. Sherman, N. B. Phillips, C. W. Oates, and A. D. Ludlow, "Ultrastable optical clock with two cold-atom ensembles", Nature Photonics vol. 11, pp.48–52 (2017).

[2] A. D. Ludlow, M. M. Boyd, J. Ye, E. Peik, and P. O. Schmidt, "Optical atomic clocks", Rev. Mod. Phys. vol. 87, pp.637-701 (2015).

[3] A. Einstein, Annal. Physik vol. 17, p.891 (1905).

[4] C. W. Chou, D. B. Hume, T. Rosenband, and D. J. Wineland, "Optical Clocks and Relativity", Science vol. 329, pp.1630-1633 (2010).

Improving Phonon Sector Tests of Lorentz Invariance

Maxim Goryachev, Eugene N. Ivanov, Michael E. Tobar
ARC Centre of Excellence for Engineered Quantum Systems, University of Western Australia
35 Stirling Hwy, Crawley WA, Australia
maxim.goryachev@uwa.edu.au

Philipp Haslinger, Holger Muller
Department of Physics,
University of California,
Berkeley, California, US

***Abstract*—An improved rotating experiment, which test Lorentz Invariance in the phonon sector is presented. The experiment utilises two rotating quartz Bulk Acoustic Wave Oscillators up to two orders of magnitude better than previous.**

Keywords— Bulk Acoustic Wave oscillators, low noise measurements, Lorentz Invariance violations, inertial mass

I. INTRODUCTION

One of the most important of axioms of modern physics is the assumption of anisotropy of space and time. Regardless of any philosophical meaning, whether it is true or not must be addressed by experiments the most well know of which is the classical Michelson-Morely experiment[1] testing anisotropy of the speed of light. Although such anisotropies may be a feature not only of photons but also of other particles. A general framework of how such experiments must be estimated and compared was introduced by Kosteleky[2] using a set of Lorentz violating coefficients and corresponding Lagrangian terms. Since then there has been a number of theoretical and experimental attempts to put bounds on the coefficients. Some of the experimental attempts are based on precision frequency metrology using various kinds of oscillators [3]. One of the most recent proposals involve quartz Bulk Acoustic Wave (BAW) oscillators to test anisotropies of inertial masses of ordinary matter particles, protons, neutrons and electrons[4,5]. The proposed approach proved to be reliable and sensitive enough to push the current limits on neutron coefficients by a few orders of magnitude comparing to modern laboratory tests and astrophysics observation.

II. PHYSICAL PRINCIPLES

BAW devices are mechanical resonators whose resonant frequency is a function of its effective mass. For this reason they have been used as precision mass sensors in many chemical and medical applications. The same idea may be employed to monitor resonator own inertial mass that is a combination inertial masses of composing particles. If the Lorentz invariance of these particles masses is violated, the total resonator mass and thus its frequency should be dependent on the direction in space. So, by rotating BAW resonators, one may get modulation of the resonance frequency at twice the rotation frequency that can be detected by phase noise measurements. In such approach, the sensitivity depends on the oscillator or resonator own phase noise as well as all kinds of systematics associated with the rotation.

The approach chosen at this stage of the experiment uses two room temperature voltage controlled 5MHz BAW oscillators. These oscillators are placed on a turn table and oriented in such a way that the displacement vectors are orthogonal to each other. This arrangement allows the setup to probe two directions in space in the same time. The frequency stability of the pair of oscillators is measured using the interferometer technique and a phased locked loop. The data of the frequency difference between two rotating oscillators is recorded for sufficient time to resolve sidebands associated with the turntable and Earth rotation. A photo of the two oscillators, with the rotating set up is shown in fig.1.

III. SENSITIVITY IMPROVEMENT

Comparing to the previous generation of the phonon sector Lorentz Invariance tests[4] the sensitivity is improved by the following means:

- using quartz oscillators with much better frequency stability (parts in 10^{-14} comparing to 10^{-12} for the previous stage in terms of Allan deviation at 1 second);
- using a turntable with smaller tilts and rotation instabilities;
- increasing measurement times by increasing overall reliability;
- improving data acquisition and noise measurement techniques by introducing an interferometer, improving long term stability of quartz oscillators.

The current design employs an air bearing turntable. This technology guarantees very low experiment vibration to which acoustic resonators are very susceptible. The optical range for the rotational frequency (1-3 Hz) was identified by injecting a test signal and calculating the signal to noise ratio by comparing to noise measurements. Orientation of oscillators is chosen based on results of g-sensitivity tests.

Data acquisition is built up on the rotating table as shown in fig. 1. The noise signal is amplified, filtered, digitised by a 24-bit analog-to-digital converter and transferred to the laboratory frame using a Wi-Fi acquisition system.

978-1-5386-2916-1/$31.00 ©2017 IEEE

Preliminary data have been collected over more than 100 days. The results suggest importance of systematics due to the magnetic field of the Earth. These systematic signals can be reduced by employing a set of magnetic shields. The measurements show stability of the phase locked loop and the interferometer over the whole span of the preliminary tests.

IV. PERSPECTIVES

Acoustic tests of Lorentz invariance can be further improved by the following approaches:

- employing crosscorrelation techniques by using more than two oscillators of arrays of oscillators;
- using quartz oscillators from space missions;
- adopting other phonon metrology technologies such as optomechanics or phonon lasers;
- developing cryogenic quartz oscillators[6].

. The latter approach includes perspectives of cryogenic implementation employing extremely high Quality factors of quartz BAW resonators at low temperatures [7,8]. Indeed, it has been demonstrated that the Q-factors of high overtone modes of electrode less plano-convex BAW resonators can exceed 10^9 that assuming the same noise level in the system potentially leads to 2-3 orders of magnitude improvement in frequency stability. With these further improvements in stability of quartz BAW oscillators, it will be possible to put limits on other Lorentz violating coefficients.

ACKNOWLEDGMENT

This work was supported by the Australian Research Council Grant No. CE110001013 and DP160100253 as well as the Austrian Science Fund (FWF) J3680.

REFERENCES

1. A. Michelson, E.W. Morley, “On the Relative Motion of the Earth and the Luminiferous Ether,” Amer. Jour. of Science, vol. 34, pp. 333-345, 1887.
2. D. Colladay and V. A. Kostelecký, “CPT Violation and the Standard Model,” Phys. Rev. D , vol. 55, p. 6760 (1997).
3. M. Nagel, S.R. Parker, E.V. Kovalchuk, P.L. Stanwix, J.G. Hartnett, E.N. Ivanov, A. Peters, M. E. Tobar, “Direct terrestrial test of Lorentz symmetry in electrodynamics to 10^{-18},” Nat. Commun., 6, 8174, 2015.
4. A. Lo, Ph. Haslinger, E. Mizrachi, L. Anderegg, H. Müller, M. Hohensee, M. Goryachev, M.E. Tobar, “Acoustic Tests of Lorentz Symmetry Using Quartz Oscillators,” Phys. Rev. X 6, 011018, 2016.
5. M. Goryachev, A. Lo, Ph. Haslinger, E. Mizrachi, L. Anderegg, H. Müller, M. Hohensee, M.E. Tobar, “Acoustic tests of Lorentz symmetry using Bulk Acoustic Wave quartz oscillators,” In A. Kostelecky, Seventh Meeting on CPT and Lorentz Symmetry, Bloomington, Indiana, 20-24 June 2016, 193-197, Singapore: World Scientific.
6. M. Goryachev, S. Galliou, J. Imbaud, Ph. Abbe, “Advances in development of quartz crystal oscillators at liquid helium temperatures,” Cryogenics, vol. 57, 104-112, 2013.
7. M. Goryachev, D.L. Creedon, S. Galliou, M.E. Tobar, “Observation of Rayleigh phonon scattering through excitation of extremely high overtones in low-loss cryogenic acoustic cavities for hybrid quantum systems,” Phys. Rev. Lett, vol. 111, 8, 085502, 2013.
8. M. Goryachev, D.L. Creedon, E.N. Ivanov, S. Galliou, R. Bourquin, M.E. Tobar, “Extremely low-loss acoustic phonons in a quartz bulk acoustic wave resonator at millikelvin temperature,” Appl. Phys. Lett. 100, 24, 243504, 2012.

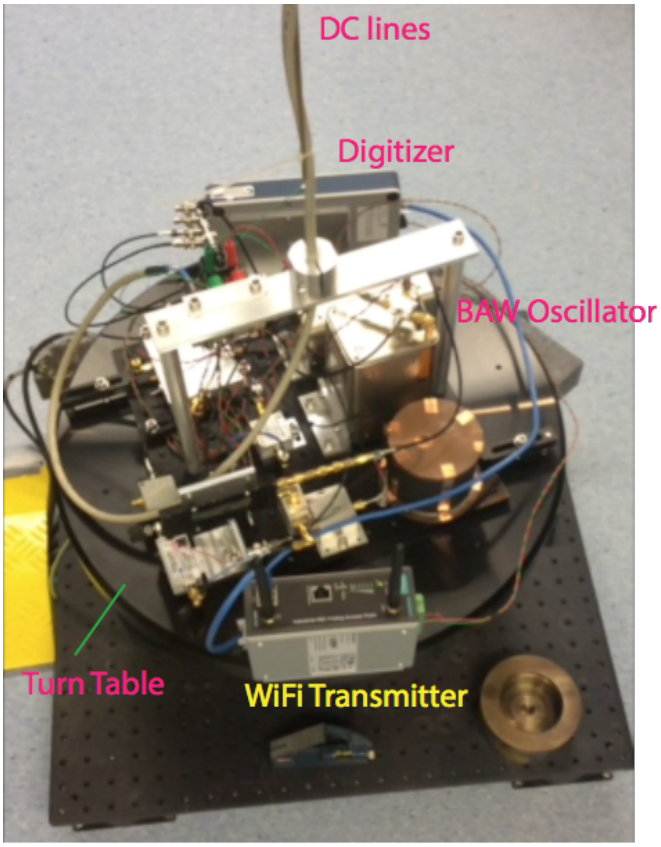


Fig. 1. Interferometer with two BAW oscillators on a rotating table.

Lorentz-symmetry test at Planck-scale suppression with a spin-polarized ^{133}Cs cold atom clock

H. Pihan-Le Bars*, C. Guerlin†, R.-D. Lasseri‡, J.-P. Ebran§, Q. G. Bailey¶, S. Bize*, E. Khan‡ and P. Wolf*
*SYRTE, Observatoire de Paris, PSL Research University, CNRS, Sorbonne Universités,
UPMC Univ. Paris 06, LNE, 75014 Paris, France
†Laboratoire Kastler Brossel, ENS-PSL Research University, CNRS,
UPMC-Sorbonne Universités, Collège de France, 75005 Paris, France
‡Institut de Physique Nucléaire, Université Paris-Sud, IN2P3-CNRS, F-91406 Orsay Cedex, France
§CEA, DAM, DIF, F-91297 Arpajon, France
¶Embry-Riddle Aeronautical University, 3700 Willow Creek Road, Prescott, Arizona 86301, USA

***Abstract*—We present an improved model relating the frequency shift between ^{133}Cs hyperfine Zeeman substates to the Lorentz-violating coefficients of the Standard-Model Extension (SME) framework. This model is based on a second order boost Lorentz transformation, which enables us to constrain the isotropic coefficient $\tilde{c}_{TT}$. It also takes into account the nuclear structure, beyond the usual Schmidt model, extending the scope of the analysis from purely proton to both proton and neutron coefficients. Applying this advanced model to FO2 ^{133}Cs cold atom fountain clock data, previously analyzed in [1], we improved by up to 13 orders of magnitude the present maximum sensitivities for laboratory tests, reaching the generally expected suppressions scale at which signatures of Lorentz violation could appear [2].**

***Index Terms*—Atomic clock, Lorentz invariance, Standard Model Extension.**

I. Introduction

The Lorentz invariance principle is a cornerstone of two major theories describing the modern physics : General Relativity and Standard Model. Despite their respective success, they fail to give a unified description of all the known physical interactions. To address this issue several alternative theories of unification have been developed over the last decades. Some of them, such as Loop Quantum Gravity, predict that Lorentz invariance could be violated at high energy scale. Although such energies far exceed our technological capacities, residual signatures of this Lorentz violation are expected to appear at low energy scale.

In the purpose of testing the limits of actual theories on the one hand and the predictions of alternative theories on the other hand, a large range of experimental set-ups have been used to search for these weak signatures on Earth. The low energy scale at which the effects are expected requires experiments with high precision and long term stability, such as atomic clocks.

We use the data obtained from the ^{133}Cs and ^{87}Rb dual fountain FO2 (see Fig.1), operated at the Paris Observatory, and previously analyzed in [1] to perform a Lorentz invariance test in the Standard Model Extension (SME) framework. The latter being a convenient and exhaustive framework including Standard Model and General Relativity fields along with additional terms describing Lorentz violation remnants parametrized by coefficients that must be experimentally measured. If some of these coefficients have non-zero values, it could result in a periodic variation of the clock frequency as both laboratory boost and orientation change with Earth's rotation and revolution.

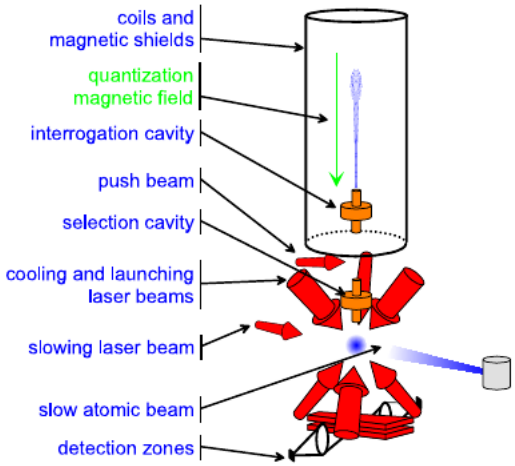


Fig. 1. Schematic view of an atomic fountain, from [4]. For further experimental details, see e.g. [5] and [6].

By improving the SME model used in [1] to set constraints on eight proton coefficients from the matter sector, we extend the scope of the analysis to nine coefficients for both proton and neutron, and we improve by up to 13 orders of magnitude the present constraints on several coefficients compared to the state-of-the-art laboratory limits [3].

II. Experimental setup, frequency shift measurement

The ^{133}Cs and ^{87}Rb double fountain was run in Cs mode on a combination of $|F=3, m_F> \longleftrightarrow |F=4, m_F>$ hyperfine transitions. In order to overcome a linear dependence on the magnetic field due to first order Zeeman effect, a combined observable ν_c is built by measuring quasi-simultaneously the clock frequency for $m_F = +3, -3, 0$ [1]. This combined

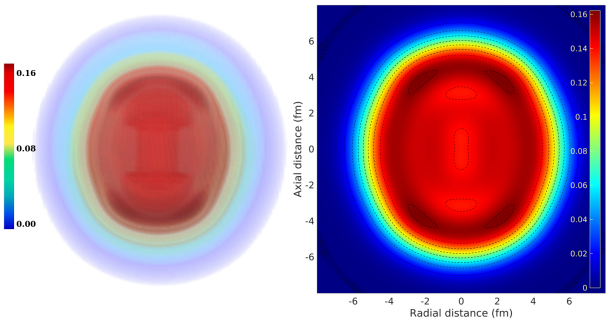


Fig. 2. Nucleonic density of ^{133}Cs in fm^{-3}, in the intrisic frame. Left: 3D representation. Right: 2D projection.

observable is related to the Lorentz violating $c_{\mu\nu}$ tensor through :

$$\nu_c = -\frac{9}{7h}\sum_{w=p,n}\gamma_w \tilde{c}_q^w - \frac{9}{8}K_z^{(2)}B^2 \qquad (1)$$

which corresponds to the minimal SME lab frame model for hyperfine transitions ([1], [7], [8]). The observable depends on a species dependent lab frame parameter $\tilde{c}_q^w$ (with w respectively p for proton and n for neutron), which contains the $c_{\mu\nu}$ tensor components characterizing a possible anisotropy of the nucleons dispersion relation. The second term in Eq.1 corresponds to the second order Zeeman correction.

The sensitivity on proton and neutron coefficients is controlled by the species dependent prefactor γ_w, whose values depend on the nuclear model considered.

III. Nuclear model dependence of the SME observable

The γ_w factor can be related to the matrix elements of the nucleus quadrupole moment operator, as described in [7].

In the case of the Schmidt shell model, used in the previous analysis [1], $\gamma_p = 1.1\times10^{-3}$ and $\gamma_n = 0$, meaning that the experiment is only sensitive to proton coefficients. As this model only takes into account a single nucleon contribution, it does not provide a realistic description of the nucleus for most atoms.

Recently, alternative nuclear models beyond the Schmidt model have been used to describe several atoms used in Lorentz invariance violation (LIV) experiments ([9], [10]). Here, we used Self-Consistent Relativistic Mean Field (SCRMF) theory to estimate both the neutron and proton contributions to the nuclear quadrupole moment involved in the SME LIV shift [2]. This leads to the following estimation of γ_w for the $^{133}_{55}$Cs nucleus: $\gamma_p = 8.32\times10^{-4}$ and $\gamma_n = 1.76\times10^{-5}$. The results are not much different from those obtained with the Shmidt model as γ_p remains a factor 45 greater than γ_n, however it makes us sensitive to the neutron SME coefficients.

The ^{133}Cs nucleus quadrupole moment arises from an anisotropic distribution of the nucleonic density, which can be easily seen by representing the nucleonic density in the intrisic frame (see Fig.2).

TABLE I

Limits on SME Lorentz violating parameters $\tilde{c}_{\mu\nu}^w$ for the proton and neutron, in GeV, when using SCRMF nuclear model. The last two columns show the maximal sensitivities on each nucleon as defined in [3]. In bold are the values which improve over the state-of-the-art laboratory limits published in [3], with in bracket the improvement in orders of magnitude.

Coefficient	Value and uncertainty(1σ) (GeV)	$\tilde{c}^p_{max}$ (GeV)	$\tilde{c}^n_{max}$ (GeV)
$\tilde{c}^p_Q + 0.021\ \tilde{c}^n_Q$	$(0.4\pm2.8)10^{-22}$	10^{-21}	$\mathbf{10^{-20(7)}}$
$\tilde{c}^p_- + 0.021\tilde{c}^n_-$	$(-0.2\pm1.2)10^{-23}$	10^{-23}	10^{-21}
$\tilde{c}^p_X + 0.021\tilde{c}^n_X$	$(2.0\pm7.0)10^{-24}$	10^{-23}	10^{-21}
$\tilde{c}^p_Y + 0.021\tilde{c}^n_Y$	$(-1.1\pm2.2)10^{-24}$	10^{-23}	10^{-22}
$\tilde{c}^p_Z + 0.021\tilde{c}^n_Z$	$(-1.3\pm5.2)10^{-24}$	10^{-23}	10^{-21}
$\tilde{c}^p_{TX} + 0.021\tilde{c}^n_{TX}$	$(2.0\pm7.6)10^{-20}$	10^{-19}	$\mathbf{10^{-17(12)}}$
$\tilde{c}^p_{TY} + 0.021\tilde{c}^n_{TY}$	$(-1.8\pm7.8)10^{-20}$	10^{-19}	$\mathbf{10^{-17(12)}}$
$\tilde{c}^p_{TZ} + 0.021\tilde{c}^n_{TZ}$	$(1.4\pm4.6)10^{-21}$	10^{-19}	$\mathbf{10^{-18(13)}}$
$\tilde{c}^p_{TT} + 0.021\tilde{c}^n_{TT}$	$(-2.2\pm9.1)10^{-16}$	$\mathbf{10^{-15(4)}}$	$\mathbf{10^{-13(2)}}$

IV. Second order boost model for time variation with respect to SCF coefficients

In order to search for a periodic modulation of the clock frequency, the results must be reported in a cosmological inertial frame taken by convention as the Sun Centered Frame (SCF), defined in [11]. The lab coefficients are thus expressed as functions of the SCF coefficients.

The transformation from the lab frame to the SCF is usually done via a first order boost $O(\beta)$ Lorentz transformation ([1], [7], [8]), but for the purpose of setting a limit on the isotropic coefficient $\tilde{c}_{TT}$, which appears suppressed by a factor β^2, we develop an improved model using a second order boost matrix. We also include the annual frequency, previously taken as a constant [1]. The model now exhibits in total 13 frequency components (25 quadratures), instead of 3 frequency components (5 quadratures) for the previous analysis.

V. Results and Conclusion

The bounds on $\tilde{c}_{\mu\nu}$ components obtained using the SCRMF model and the $O\left(\beta^2\right)$ model respectively introduced in Sec.III and Sec.IV are presented in Table I. We found no evidences for a Lorentz violation, but we improved the present bounds on $\tilde{c}_{\mu\nu}$ coefficients by 4 orders of magnitude for the proton coefficient $\tilde{c}^p_{TT}$ and by up to 13 orders of magnitude for several neutron coefficients compared to the state of the art [3]. These improvements bring the bounds for all proton and neutron $\tilde{c}_{\mu\nu}$ coefficients below or near one Planck scale suppression, i.e. 10^{-17} GeV, challenging the generally expected suppression.

References

[1] P. Wolf *et al.*, Phys. Rev. Lett. **96**, 060801 (2006).
[2] H. Pihan-Le Bars *et al.*, arXiv:1612.07390.
[3] V.A. Kostelecký and N. Russell, 2017 edition, arXiv:0801.0287v10.
[4] S. Bize *et al.*, Journal of Phy. B **38**, (2005)
[5] J. Guéna *et al.*, IEEE Trans. UFFC **59**, (2012)
[6] J. Guéna *et al.*, Metrologia **51**, (2014)
[7] V.A. Kostelecký and C.D. Lane, Phys. Rev. D **60**, 116010 (1999).
[8] R. Bluhm *et al.*, Phys. Rev. D **68**, 125008 (2003).
[9] V. V. Flambaum, Phys. Rev. Lett. **117**, 072501 (2016).
[10] B. Brown *et al.*, , arXiv:nucl-th/1604.08187.
[11] V.A. Kostelecký and M. Mewes, Phys. Rev. D 66, 056005 (2002).

An Additive Phase Noise Measurement Technique for Mixers with non-DC IF in Large Signal

Jason Breitbarth
CTO, Holzworth Instrumentation
Boulder, CO USA
support@holzworth.com

***Abstract*—Mixer phase noise with respect to system level performance is often assumed negligible, measured using small signal Y-factor noise figure measurements or in some cases measuring noise direct at DC. AC coupled IF port mixers, such as triple balanced mixers, cannot be measured directly at DC and Y factor methods do not show phase noise contributions in large signal or the effect of flicker noise. A method is demonstrated in this paper that allows for direct large signal additive phase noise measurements at arbitrary (non-DC) IF frequencies and compares phase noise measurement results to the more common DC coupled measurement in the case of the double balanced mixer.**

Keywords—phase noise, additive, residual, mixer, large signal, noise figure.

I. INTRODUCTION

Double balanced mixers used as phase detectors have been characterized extensively in both large and small signal. These mixers all have a DC-coupled IF port and the noise is down-converted from the same source and is centered at DC. High IP3 mixers often use a balun on the IF port, eliminating the DC component of the mixer and noise cannot be measured using the same method. The Y-Factor method may be used for these AC-coupled IF port mixers, however, mixer noise due to RF power levels will be neglected, as will the contribution of flicker noise. A new down-converting additive phase noise measurement method for quantifying phase noise in ac-coupled IF mixers in large signal is introduced and results are compared to traditional dc-coupled measurements.

Additive phase noise of components has been shown to be affected by power levels and frequency [1]. Y-factor noise figure measurements are only practical and accurate in small signal and far from the carrier and may be unrelated to actual use in large signal. The Y-factor does not measure flicker noise effects [2]. To measure AC-coupled IF port mixers, the traditional additive phase noise measurement is extended to utilize two incoherent and independent oscillators driving the RF and LO ports of a pair of DUT mixers. The IF frequency of the pair of mixers will be an identical sum and difference of the LO and RF frequencies except for the noise contributed by each mixer. The noise in each IF frequency path is measured as a traditional additive measurement. Common noise, the difference in noise between the LO and RF oscillators, will be cancelled while the unique noise, as a pair of DUT mixers, will be measured. Similar to frequency divider additive measurement and frequency multiplier additive, the mixer DUTs are measured as a pair. All data presented in this paper, except the cross-correlation result, is measured and shown as a pair.

The measurement can be extended to a three branch, one DUT, cross correlation system used for frequency multipliers [3] to directly measure the noise due to a single mixer. The single channel system will be verified by this method in the latter part of the paper. It has been shown that cross-correlation may have unintentional side effects [4] when measuring near the thermal floor and so the technique has been initially shown as a single channel system. Y-factor measurements of mixers have shown the noise figure due to passive diode based mixers to be that of the loss of the mixer itself. The white noise of the mixer in linear mode is expected to be near that of the thermal noise floor.

II. MEASUREMENT TECHNIQUE

The technique used to measure the additive phase noise of a mixer is like other frequency translation methods. Each path must be an identical frequency translation operation. Using two independent, incoherent oscillators as the LO and RF driver, the mixers each sum and difference the frequency of the LO and RF to the exact same IF frequency. An ideal mixer would multiply the LO and RF ideally, adding no noise. The two IF frequencies are identical, except noise added by the mixers. This method is applicable for up and down conversion. This paper focuses on the down-conversion measurement. All data is presented for a pair of devices.

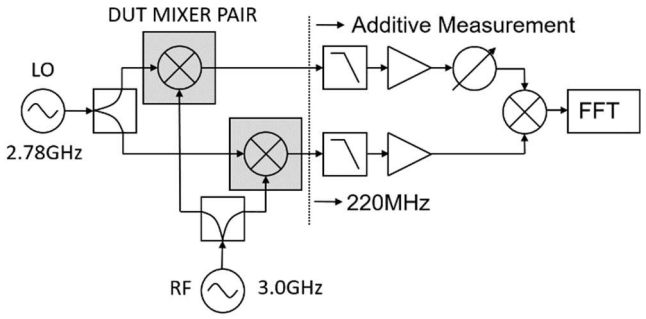


Fig. 1. The additive phase noise measurement system for non-DC IF mixer. The noise from the LO and RF is summed and differenced exactly in each mixer except the addition of added noise unique to each mixer. The phase noise at the IF port is measured as a traditional additive phase noise measurement. The resultant noise is due to the noise added by the pair of mixers.

A. Frequency Plan for Test

To test the measurement technique, three mixers and a frequency plan were chosen that would be relevant to industry. A down-conversion mixer scheme was selected. Low IF frequencies can be compared with less noise introduced than a high IF measurement. A low-side LO was adopted with frequencies selected to be mid S-band. An IF frequency that may be digitized directly, 220MHz was also selected. Very clean free running coaxial resonator oscillators powered by batteries were used to keep the signals as incoherent as possible with very low AM noise contribution. The oscillators were buffered with amplifiers (also on batteries) and attenuated appropriately. The LO is at 2.78GHz and the RF at 3.00GHz.

B. Devices and Operation for Test

Three mixers were selected that have been around for some time. A double balanced mixer and a triple balanced mixer with 13dBm drive and an active (type of gilbert cell) mixer with a 0dBm drive. RF drive levels were tested at two points, the P_{-1dB} compression point and 10dB below that in full linear operation.

A Marki Microave M1-02044MA double balanced mixer was used as the control group to compare DC coupled measurements with the AC coupled measurements. Tested at a P_{-1dB} point of 5dBm and linear operation at -5dB. 5dB conversion loss yields a test power at -1dBm at -10dBm.

The second device is a triple balanced mixer, a Minicircuits MCA-35MH. It has a non-DC IF port. The LO drive is 13dBm but has a higher IP3 at 20dBm. P_{-1dB} points are at 9dBm and linear operation tested at -1dBm. Conversion loss is about 7.5dB. Tested power levels were at 1dBm and -9dBm.

The last device is an active gilbert cell type mixer, a Linear Technology LTCC5510. The LO drive here is 0dBm but has the highest IP3 at 23dBm and a conversion gain of about 0dB after the IF baluns. P_{-1dB} was tested at 11dBm with linear operation at 1dBm.

All tests have a drive and IF tolerance of ±1dB. The drive levels of the sources were set with mechanical SMA attenuators in 1dB increments.

C. Noise Floor Characterization

The IF section of the measurement system used off the shelf parts. Two HX2400 RF amplifiers were used to amplify the IF output of the mixers to an HX3100 Phase detector as shown in Fig. 1. Attenuators were used after the amplifiers to maintain signal to noise ratio and drive the HX3100 at 9dBm on each port for optimal performance. The HX2400 amplifiers exhibit an approximate 4dB noise figure and this is consistent in the noise floor measurements in Fig 3.

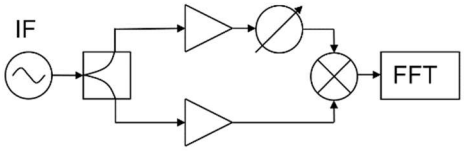


Fig. 2. Additive phase noise characterization of the IF portion of the measurement. Power levels from the 220MHz IF were varied corresponding to the mixer IF output drive levels.

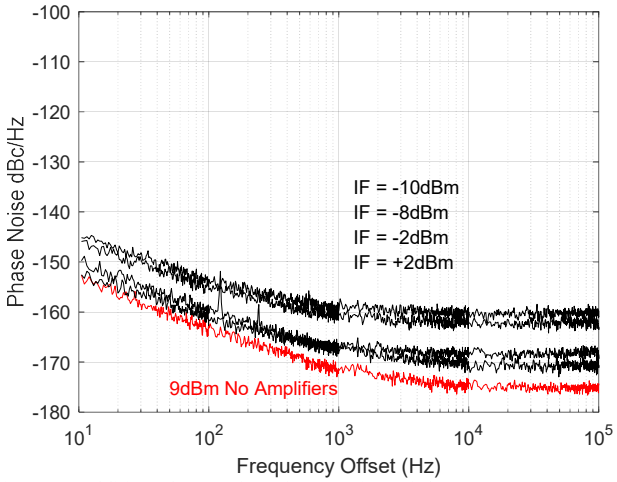


Fig. 3. Additive phase noise of IF portion of the measurement system at 220MHz. The power levels refer to the power going into each HX2400 amplifier. The red trace is the phase noise of the phase detector at 9dBm drive into each port without amplifiers.

III. Measurement Results

A control set of measurements comparing a DC coupled measurement with a 220MHz IF was completed first, verifying the measurement method. The M1-0204MA double balanced mixer was used for this measurement comparison.

A. Baseline DC coupled phase noise measurement

A baseline measurement of the additive noise of the M1-0204MA was completed using the setup show in Fig. 4. Data was taken at an LO power level of 13dBm and RF power levels of 5dBm and -5dBm. The results are shown in Fig. 5. A total of 3 mixers were measured to verify the test system and consistency of the devices.

To keep a consistent measurement, the mixer was terminated in 50Ω at the FFT, not a high impedance commonly used to optimize phase detectors. This was done so the measurements may be compared directly to the 220MHz IF measurement.

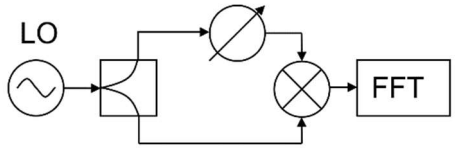


Fig. 4. DC coupled phase noise measurement setup to determine noise levels of the M1-0204MA. The DC coupled IF port is terminated into 50Ω in the FFT so results of the two measurements may be compared. The termination can affect flicker noise and the noise floor.

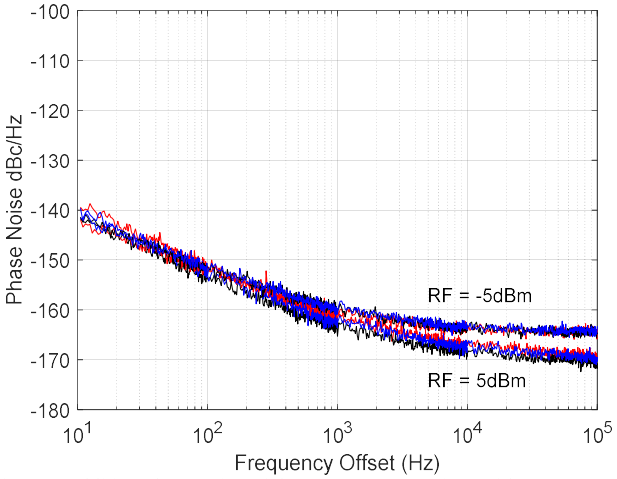


Fig. 5. Additive phase noise of the M1-0204MA mixer with a DC IF. Three mixers were measured with drive levels of +5dBm (P_{-1dB}) and -5dBm (linear) at the RF port. The LO drive level was at 13dBm. The mixers were measured at 2.78GHz.

B. Marki M1-0204MA at 220MHz IF

The results of the 220MHz IF measurement at P_{-1dB} compression are shown in Fig 6. The noise measured at the DC IF is shown in red for comparison. The blue is the noise floor of the IF section based on the output power of the mixer in that measurement, using the setup in Fig. 2. The far from the carrier noise of the mixer is about 3dB higher than that of the DC coupled measurement but is buried in the noise floor of the single channel measurement. The flicker noise is slightly higher close to the carrier for the DC coupled measurement.

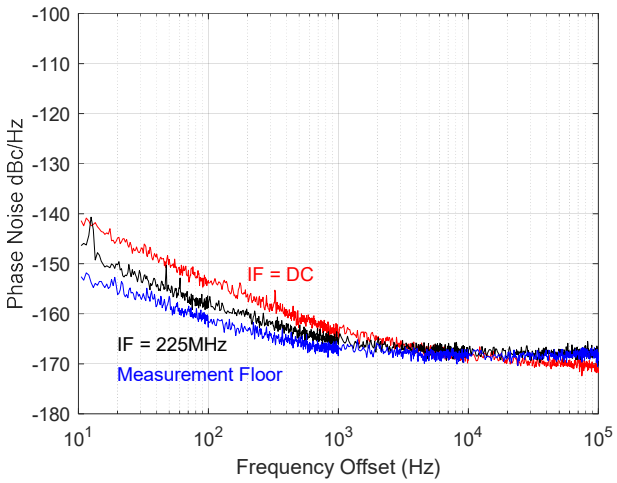


Fig. 6. Additive phase noise of the M1-0204MA mixer with an IF of 220MHz. LO at 2.78GHz and 13dBM. RF at 3.0GHz and 5dBm. Top trace (red) is the DC coupled mixer noise. The black trace is the mixer noise at 220MHz IF. Blue is the 220MHz IF noise floor for the power available at the output of the mixer (-1dBm).

The linear mode 220MHz IF measurement of the M1-0204MA is very consistent with the DC coupled measurement, as would be expected in Fig. 7. The noise floor is degraded by the 4dB noise figure of the HX2400 amplifiers before phase detection. This is a limitation of the single channel measurement system.

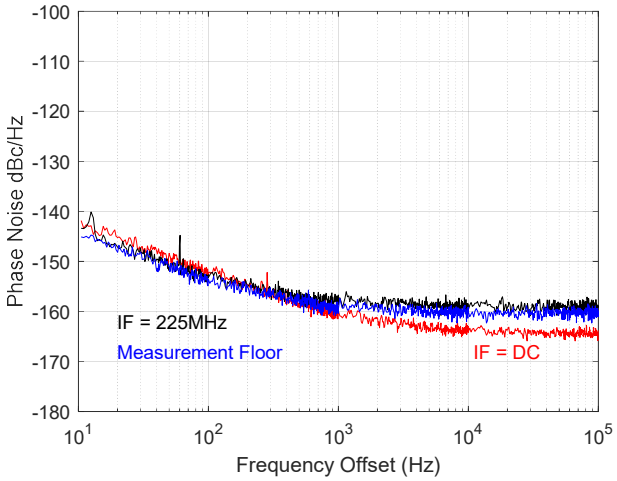


Fig. 7. Additive phase noise of the M1-0204MA mixer with an IF of 220MHz compared to a DC IF measurement. LO at 2.78GHz and 13dBm. RF at 3GHz and -5dBm. The DC IF measurement is in red. Center trace, blue, is the 220MHz IF measurement floor. The black is the M1-0204MA measurement at -5dBm.

C. Minicircuits MCA-35MH Triple Balanced Mixer at 220MHz IF

Triple balanced mixers have become more popular for their high IP3 and low spurious content. The MCA-35MH was selected because of the same 13dBm LO drive level as the double balanced mixer but has an IP3 of 20dBm and a conversion loss of 7.5dB. The balun on the IF port eliminates the ability to measure it as a phase detector direct at DC.

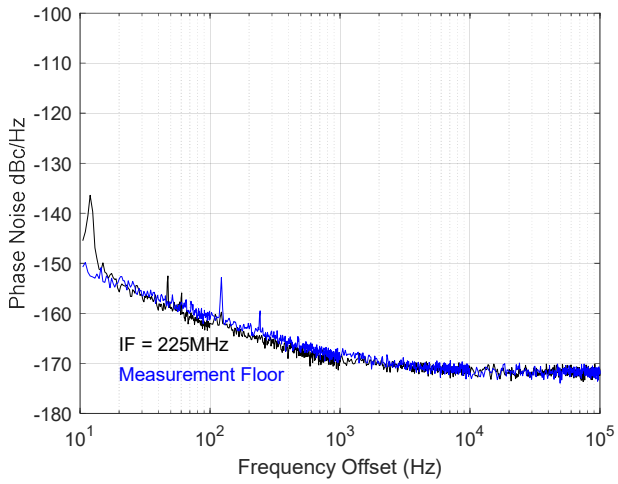


Fig. 8. Additive phase noise of the MCA-35MH mixer with an IF of 220MHz. LO at 2.78GHz and 13dBm. RF at 3GHz and 9dBm. Blue is the measurement of the MCA-35MH, black is the measurement floor. This mixer is below the noise floor of our single channel measurement.

The results of the P_{-1dB} measurement at 9dBm are shown in Fig. 8. The mixer is most likely thermally noise limited with a very low flicker corner that is nearly indistinguishable from the measurement floor. The measurement floor is dominated by the 4dB of the HX2400 amplifiers.

In linear mode, the noise for a pair is only about 3dB above the measurement noise floor shown in Fig. 9.

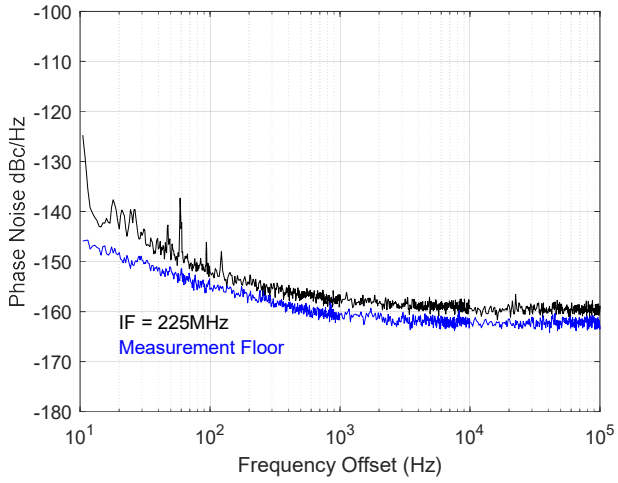


Fig. 9. Additive phase noise of the MCA-35MH mixer with an IF of 220MHz. LO at 2.78GHz and 13dBm. RF at 3GHz and -1dBm, linear mode of operation. Blue is the measurement of the MCA-35MH, black is the measurement floor. This mixer is still very close to the noise floor of the measurement system. It is measured as a pair and in an ideal case measure 3dB above a single mixer.

D. Linear Technology LTC5510

The LTC5510 represents a high IP3 active mixer. The low LO drive levels and high P_{-1dB} and IP3 make these attractive for use in many systems. The published noise floor is -152dBm/Hz, based on a spectrum analyzer measurement. The LTC5510 was power by a 3 cell and 4 cell battery at ~3.6V and ~5.0V respectively. The voltages are approximate as NiMh cells tend to start higher in voltage and then drop off as they discharge. Each mixer had a separate battery pack.

The LTC5510 exhibits a remarkable increase in flicker noise, shown in Fig. 10, compared to the linear mode of operation. Changing bias to 5V reduced it somewhat, but at 100kHz offset the floor of -152dBm/Hz could not be confirmed. In linear mode of operation, RF = 1dBm and 5V bias, the mixer has a much lower flicker corner and -158dBc/Hz floor for a pair. Assuming identical mixers (not verified) would yield a -161dBc/Hz or approximately -160dBm/Hz floor. The low bias voltage still exhibited high flicker noise in linear operation.

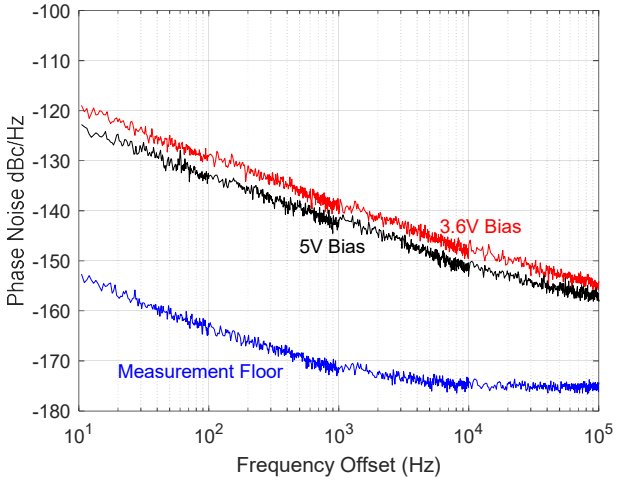


Fig. 10. Additive phase noise of the LTC5510 mixer with an IF of 220MHz. LO at 2.78GHz and 13dBm. RF at 3GHz and 11dBm, P-1dB mode of operation. Blue is the measurement of the noise floor. The HX2400 amplifiers were unnecessary. Both bias voltages exhibited high flicker noise corners in this mode of operation. The far from the carrier noise floor cannot be confirmed from this measurement.

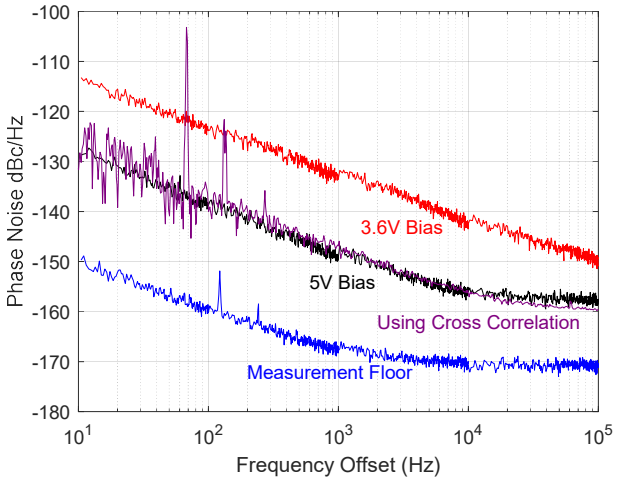


Fig. 11. Additive phase noise of the LTC5510 mixer in linear mode of operation. LO at 2.78GHz and 13dBm. RF at 3GHz and 1dBm. The blue trace is the noise floor of the measurement system. The LTC5510 exhibits much lower flicker noise at 5V bias than at 3.6V bias. Batteries were used in both to keep the measurement clean. The magenta trace is the results from a cross correlation measurement with LO = 3.0GHz and RF = 2.9GHz, derived from two unlocked HSX9001 synthesizers at 0dBm each.

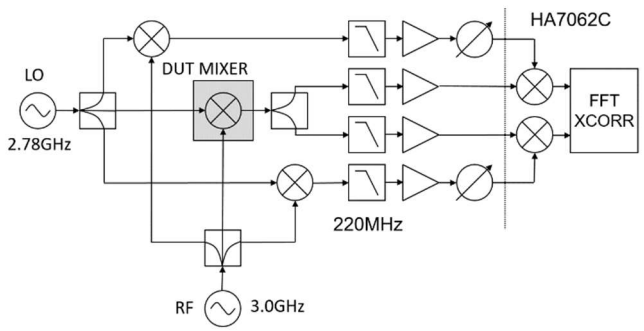


Fig. 12. Cross-correlation setup to measure a single DUT. All components are unique to each channel. In this case, only the noise due to a single device is measured. The devices do not need to be a matched set.

IV. Cross-correlation mixer measurements

The natural progression of this method is to extend it to cross correlation. To avoid possible noise limitations suggested in [4], the cross-correlation system was tested on the LTC5510 that exhibited much higher noise than the thermal limit. The cross-correlation version of the additive mixer method is shown in Fig. 12. Like any extension of a single channel to cross correlation, it requires twice as much hardware and an additional frequency translation device. The most useful part of the cross-correlation system in Fig. 12 is that the ch1 and ch2 mixers do not have to be identical to the DUT mixer and may be of an entirely different type altogether, provided they translate the frequency the same. In Fig. 12 only one mixer is measured, not a pair.

The results of the cross-correlated mixer measurement are shown in Fig. 11 next to the single channel measurements. These measurements were made at slightly different conditions with a 3.0GHz LO and 2.9GHz RF, both at 0dBm. The LO and RF frequencies were taken from HSX9001 synthesizers and the measurement done on a HA7062C with HX5100 phase shifters at a 100MHz IF. However, given the 1dB tolerance and slightly different conditions, they agree very closely in terms of measured noise.

V. Conclusions

A method for measuring the additive phase noise of a mixer with a non-DC IF has been presented. Three types of mixers and measurement results, representing different mixing technologies, have been presented. Although not completely conclusive, it can be suggested from the data that diode based mixers are indeed at or very close to thermal limits as measured by the Y-factor method. Active mixers may have a noise floor well above thermal, as indicated by their datasheets and spectrum analyzer measurements. The additional information of flicker noise and the exhibited response to RF power levels make these valuable measurements in low noise systems. The cross-correlation adaptation of this method demonstrates strong agreement to the single channel system.

Acknowledgment

Thank you to Christopher Marki at Marki Microwave for the mixer discussions and providing mixers to test.

References

[1] J. Breitbarth, “Additive Phase Noise Measurement of Amplifiers, Frequency Dividers and frequency multipliers,” Microwave Journal, June 2008.

[2] A. Hati, D. A. Howe, F. L. Walls, “Merits of PM noise measurement over noise figure: A study at microwave frequencies” IEEE Trans on UFFC, vol 53, no 10, pp 1889-1894. 2006.

[3] J. Breitbarth, ”Design and Characterization of Low Phase Noise Microwave Circuits,” *Ph.D. dissertation*, Department of Electrical Engineering, University of Colorado, Boulder, 2006.

[4] C. W. Nelson, A. Hati, D. A. Howe, “A collapse of the cross-spectral function in phase noise metrology,” Review of Scientific Instruments, Vol 85, 2014.

Next Generation 5G Radio Communication NW

Ulrich L. Rohde
BTU Cottbus, Munich, Germany

Ajay K. Poddar
Synergy Microwave NJ, USA

Ignaz Eisele
EMFT, Munich, Germany

Enrico Rubiola
FEMTO-ST Institute, France

***Abstract*—This paper discusses the expectations, challenges, and uncertainties of the next generation 5G radio communication networks. The acknowledged high expectations for new radios place challenges on designers and uncertainties on the selection of the frequency spectrum. Although, research community and industry leaders are engaged towards figuring out the dynamics of 5G (fifth generation), expectation continue high for the next-generation radio standard, which will require higher data rates, massive device connectivity, more system capacity, reduced latency, energy savings, and inexpensive solution. The transition from 4G to 5G can lead to significant augmentation in data rates and latency. Designers are engaged in cope with the needed dimension of time t in 5G, which aims at air latency of < 1 millisecond and cell throughput of > 10 Gbps at millimeter wave frequencies. Therefore, considerable design challenges stretch out ahead for system engineers to integrate novel technologies (CR, SDN, SDR), into interoperable platforms that intelligently connect to local and global NW and offers affordable solutions.**

Keywords— 5G, CR, MIMO, Radio, SDN, SDR

I. INTRODUCTION

The wireless NW (networks) have evolved from 1G to 4G networks, i.e., Frequency Division Multiple Access (FDMA) for 1G, Time Division Multiple Access (TDMA) for 2G, Code Division Multiple Access (CDMA) for 3G and Orthogonal Frequency Division Multiple Access (OFDMA) for 4G, allowing portable smart devices to become important electronic tools in daily life [1]. To meet the rising demand from user, industry and research communities spin out generations of new technology on roughly10-year basis (1G - 1981, 2G - 1992, 3G - 2001, and 4G - 2009). This decade-by-decade introduction of new generation technology has led to the general insight for fifth generation (5G) mobile to emerge around 2019-2020. Nevertheless, the subject matter is what 5G brings to users and at what cost and compromise? The critical parameters for next generation 5G technologies to beat the capability of prior generations: capacity and coverage, latency and reliability, energy consumption and cost, and improved access technology/infrastructure [1]-[4].

The 5G spectrum requirements are primarily driven by the expected increase in traffic capacity demands and the support for increasing users, however in author's view IoT (internet of things) and big data are leading driving force. Although, research community and industry leaders are engaged towards figuring out the dynamics of 5G (fifth generation), expectation continue high for the next-generation radio standard, which will require higher data rates, massive device connectivity, more system capacity, reduced latency, energy savings, and inexpensive solution. The transition from 4G to 5G can lead to significant augmentation in data rates and latency. Designers are engaged in cope with the needed dimension of time t in 5G, which aims at air latency of < 1ms (millisecond) and cell throughput of > 10 Gbps at millimeter wave frequencies. Therefore, considerable design challenges stretch out ahead for system engineers to integrate novel technologies: SDR (software defined radio), SDN (software defined network), and CR (cognitive radio) into interoperable platforms that intelligently connect to local and global NWs at reduced cost.

Table 1 describes the critical deviation between 4G and 5G. The challenge designer faces what changes are requisite to position next generation 5G radios. The possible change is envisaged in combination with 4G LTE, the anchor could be 4G LTE technology with 5G sub-6 GHz as an appendage. Uplink MIMO for 4G requires multiple separate data streams driving discrete antenna elements, identical to sub-6 GHz 5G. These antennas are adjusted for relative phase to beam-form as looked-for, but the lower frequency and lower number of antenna elements constrains the overall antenna gain and the narrowest beam cross-section. Figure (1) shows the typical 5G network, which can enable dual-connectivity between LTE operating within bands below 6GHz and the NX air interface in bands within the range 6 GHz to100 GHz.

Table 1: shows the critical deviation between 4G and 5G

Specifications	4G	5G
Full Form	Fourth Generation	Fifth Generation
Data Bandwidth	2Mbps to 1Gbps	1Gbps and higher
Frequency Band	2 to 8 GHz	3 to 300 GHz
Standards	AI access convergence including OFDMA, MC-CDMA, Network-LMPS	CDMA and BDMA
Technologies	Unified IP, seamless integration of broadband LAN/WAN/PAN/WLAN	Unified IP, seamless integration of broadband LAN/WAN/PAN/WLAN and advanced technologies based on OFDM modulation
Service	Dynamic information access, wearable devices, HD streaming, global roaming	Dynamic information access, wearable devices, HD streaming, any demand of users
Multiple Access	CDMA	CDMA, BDMA
Core Network	All IP Network	Flatter IP Network, 5G network interfacing
Handoff	Horizontal and vertical	Horizontal and vertical
Initiation from	Year 2010	Year 2015

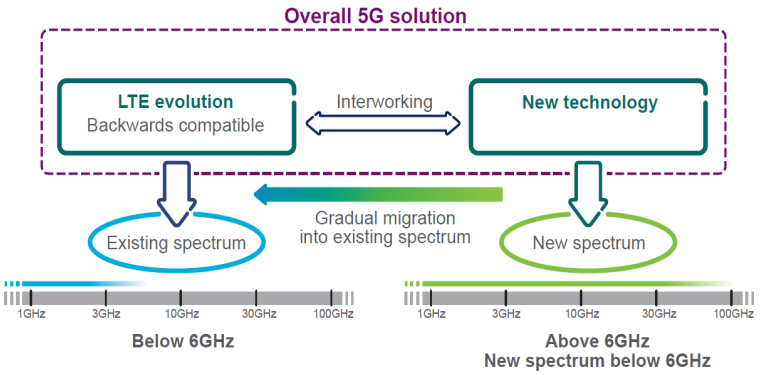


Fig.1: A typical 5G radio consisting of LTE inspired new technology

II. Millimeter Wave: Path to Next Generation

Historically, cellular networks have avoided millimeter ware frequency spectrum because of high propagation loss consequent in shorter transmission distance, reduced building penetration, and succumb absorption from atmospheric particles and rain drops. But short transmission paths due to high propagation losses allow for spectrum reuse application by limiting the amount of interference between adjacent cells. Furthermore, where longer paths are preferred, the shorter wavelengths of millimeter wave signals make it viable for small antennas to concentrate signals into extremely focused beams with adequate gain to surmount propagation losses. Also, the short wavelengths of millimeter wave signals formulate to construct multi-element, dynamic beamforming antennas that will be in compact size to fit into wireless handsets. For millimeter wave inspired next generation radio communication networks, a requirement is to characterize the propagation/attenuation dynamics at the specific frequencies and the relevant use-cases [3].

Figure (2) shows the typical atmospheric absorptions characteristics. It can be seen from Figure (2), 28 GHz and 38 GHz exhibit low absorption, can be suiatble candidate for 5G cellular systems. At these frequencies, the millimeter wave bands offer a massive amount of unlicensed spectrum. In fact, 28 and 38 GHz frequencies can be used to employ steerable directional antennas at base stations and mobile devices. At millimeter wave with their shorter wavelengths, make the realization of dense antenna arrays for massive MIMO systems practical as compared to lower-frequency systems [4].

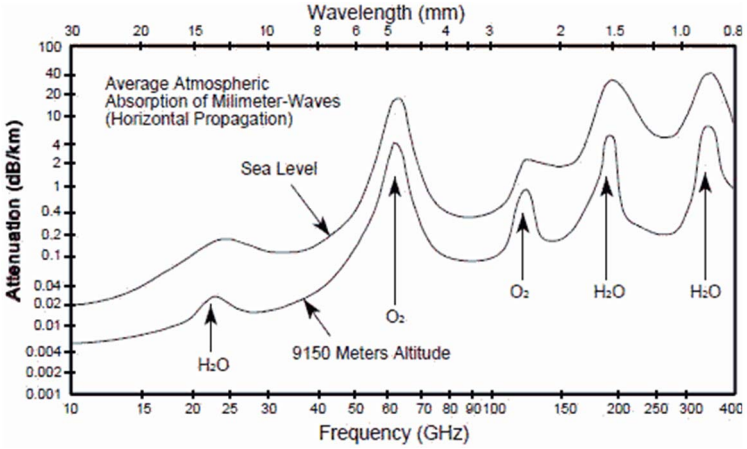


Fig.2: Shows the typical atmospheric absorptions characteristics

As depicted in Figure (2), the frequency window operating at millimeter wave spectrums permit opportunity of frequency spectrum reuse. And, supports advantaged frequency bands for point-to-point system such as local area network and vehicular radar system. Also, in the absorption resonance bands, for example 60 GHz, moderately secure communication network can be established, especially for high data rate systems where secure communications with a low probability of intercept is much sought-after [3]-[4]. These frequency bands are useful for services with a potentially high density of transmitters operating in proximity or for applications where unlicensed operations are desirable.

A. Millimeter Wave: Next Generation (5G) Radio Enbaler

Millimeter-wave is being considered as a key enabler of 5G by allocating more bandwidth to deliver faster, higher-quality video, and multimedia content and services. On the contrary, at lower frequencies, the same array of multiple antennas would render the large physical towers for cellular networks that are awfully impractical. The major confront in urban areas surrounded by tall buildings is desired signal penetrations. To support adequate coverage for users surrounded by tall buildings in big cities, base stations will necessitate being closer to improve capacity as well as should be cheaper to stay sustainable. For example, a typical 5G MIMO base station equipped with many more antennas would be able to serve more devices as envisioned by 5G and IoT applications. Figure (3) shows a comparison of a typical 4G MIMO cell to that of a 5G massive MIMO cell that is in principle equipped with many more base station antennas.

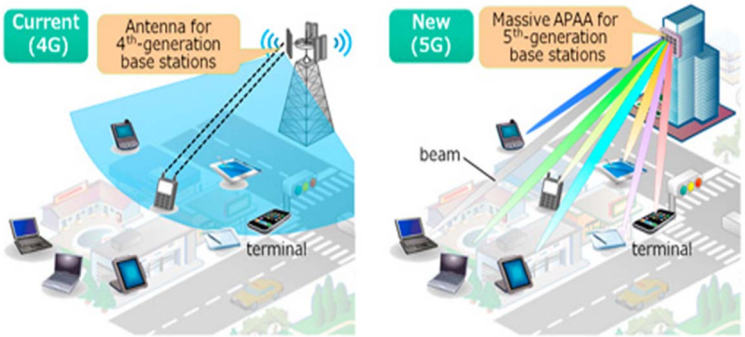


Fig. 3 Shows the typical antenna technology from 4G to 5G MIMO

B. Proposed 5G Millimeter Wave Frequency Standards

The proposed 5G millimeter wave frequency standard demands for following requirements: peak data rate >10Gbps, cell edge data rate of 100Mbps and 1msec latency end-to-end; could potentially be met in a variety of carrier frequencies. It is to note that peak data rate is empirically related to available spectrum as per Shannon-Hartley theorem, which states that capacity is a function of bandwidth and channel noise. For this reason, choice of high frequency in the millimeter wave range becomes necessary for 5G radio standard since it comes with large bandwidth. Recently, 3GPP (3rd Generation Partnership Projects) and ITU (International Telecommunication Union) have proposed two phase plan for 5G standards, Phase-1 (under 40 GHz), and Phase-2 (up to 100 GHz). ITU released a list of frequencies in millimeter wave ranges (between 24 GHz and 86 GHz): 24.25-27.5 GHz, 31.8-33.4 GHz, 37-40.5 GHz,

40.5-42.5 GHz, 45.5-50.2 GHz, 50.4-52.6 GHz, 66-76 GHz, and 81-86 GHz. FCC (Federal Communications Commission) in the USA (United States of America) issued a Notice of Proposed Rule Making (NPRM) that recommended new flexible service rules among the 28 GHz, 37 GHz, 39 GHz, and 64-71 GHz bands for next generation new 5G radios.

The proposed frequency spectrums that are gaining early momentum as a 5G new radio are: 28 GHz, 39 GHz, and 73 GHz. The leading runner is 28 GHz, the close follower is 39 GHz**,** and the real deal could be 73 GHz. Based on Shannon-Hartley theorem, more bandwidth equates to more data throughput, and that gives 73 GHz a big benefit over the other contenders. One key plus point of 73 GHz that sets it apart from 28 GHz and 39 GHz is the available contiguous bandwidth. For example, with 2 GHz of contiguous bandwidth for mobile communications, 73 GHz is the widest of the proposed frequency spectrum. By comparison, 28 GHz offers 850 MHz of bandwidth and for example in the USA; the two 39 GHz bands offer 1.6 GHz and 1.4 GHz bandwidth.

Down the line, ITU would play an important role in setting one frequency for mobile use with millimeter wave 5G wireless standards. This will provide a great financial support to handset makers and network infrastructure vendors if only one set of silicon instead of the multiple chips needed in 5G for global coverage. The verdict of a single band that can be agreed upon globally should be considered as an integrated task to strive for. Recently, 3GPP considers 3-bands for evaluation: sub-6 GHz (around 2 GHz or around 4 GHz), around 30 GHz, and around 70 GHz. The higher carrier frequencies are foremost linked with higher bandwidths but also exhibit lower channel coherence times, described by [2]

$$T_C = \sqrt{\frac{9}{16\pi v}}\frac{c}{f_c} \quad (1)$$

Where c is the speed of light in meter/second, v the speed of mobile in meter/second, T_c is the channel coherence time in seconds, and f_C the carrier frequency in hertz. From (1), the channel coherence time depends on the carrier frequency.

C. Millimeter Wave: Reservations and Road Map for 5G

There are reservations about the usage of millimeter wave frequency spectrum for 5G radio networks. Some argue that the desirability of millimeter wave spectrum is over-hyped for next generation radio communications. The fundamental basis for disagreement is millimeter wave signals do not propagate far and also unable to penetrate through numerous objects. This creates requirement of numerous base stations to cover a given region, for which site rental and backhaul expenses will become prohibitively pricey. They strongly believe that the usage of millimeter wave frequency spectrum will be limited to hotspots, in contention that sub-6GHz spectrum is likely to represent the "sweet-spot" for 5G radios. Despite above reservations, the support and momentum for millimeter wave to enable new 5G radios are ever growing strong. At any rate, high frequencies are preferred compared to the traditional lower frequency bands for two reasons: (i) larger bandwidth availability, and (ii) compact smaller antenna dimensions for a fixed gain, or higher gain for a given antenna size. It is well well-known that larger bandwidth is directly proportional to higher data transfer rates. Additionally, a larger bandwidth enables wideband spread-spectrum systems for reduced multipath and clutter, and systems with a soaring immunity to jamming and electromagnetic interferences.

The recent emerging trends in support of millimeter wave inspired spectrum roadmap for 5G lead to choice of several cellular-radio design schemes. One way forward on this roadmap would be to use cognitive-based SDR technology, allows communications via a variety of waveforms simply by reloading or reconfiguring the required software for the particular application. If integrated into 5G networks, cognitive SDR has the potential to help identify available frequencies and spectrums and reconfigure itself for the optimum performance. Stakeholders from all fronts (service providers, chipset and device manufacturers, and network infrastructure vendors) are unified towards defeating the challenges associated with millimeter wave frequency spectrum and move forward for cognitive SDR-SDN to meet data throughput requirement at lower cost [1]-[4].

III. RADIO CLASSIFICATIONS AND EVOLUTIONS

Conventional hardware based radio devices limit cross-functionality and can only be customized through physical intervention. This results in higher manufacture overhead and no flexibility in supporting multiple-waveform standards. The evolution and classification of radio (HR, SCR, SDR, ISR, and USR) is given in terms of capability and complexity.

- **Hardware Radio (HR)**
  - No changes to system can by done by software
- **Software-Controlled Radio (SCR)**
  - Control functionality implemented in software, but change of attributes (modulation and frequency band) cannot be done without changing hardware
- **Software-Defined Radio (SDR)**
  - Capable of covering substantial frequency range and executing software to support variation of modulation techniques, wide-band or narrow-band operation, enable security function, meet waveform performance requirements of legacy systems
  - Capable of storing large number of waveforms or air interfaces, adding new by software download
  - System software should be capable of applying new or replacement modules for added functionality or bug fixes without reloading entire set of software
  - Separate antenna system followed by some wideband filtering, amplification, and down conversion prior to receive A/D-conversion
  - The transmission chain provides reverse function of D/A-conversion, analog up-conversion, filtering and amplification
- **Ideal Software Radio (ISR)**
  - All capabilities of SDR, but eliminates analog amplification and heterodyne mixing prior to A/D-conversion and after D/A conversion
- **Ultimate Software Radio (USR)**
  - Ideal software radio in a chip, requires no external antenna and no restrictions on operating frequency
  - Can perform a wide ranges of adaptive services

The future is going to be USR in millimeter wave spectrum.

In this paper, high performance SDR inspired radio receiver is reported for applications in radio monitoring. The term SDR using DSP of sampled analog signals was coined by author in 1985, which is the first public software radio initiative reported with following characteristics [1]:

- Ease of design
  - Reduces design-cycle time, quicker iterations
- Ease of manufacture
  - Digital hardware reduces costs associated with manufacturing and testing radios
- Multimode operation
  - SR can change modes by loading appropriate software into memory
- Use of advanced signal processing techniques
  - Allows implementation of new receiver structures and signal processing techniques
- Fewer discrete components
  - DSP implement functions synchronization, demodulation, error correction, decryption, etc.
- Flexibility to incorporate additional functionality
  - Can be modified in the field to correct problems and to upgrade

From (1), technologies that enable SDR [1]:

- Antennas
  - Receive antennas are easier to achieve wide-band performance than transmit ones
  - New fractal & plasma antennas expected in smaller size and wideband capability
- Waveforms
  - Management and selection of multiple waveforms
  - Cancellation carriers and pulse shaping techniques
- Analog-to-digital converters
  - High ADC sampling speed
  - ADC bandwidth could be digitized instantaneously
- Digital signal processing/FPGAs
  - More specific purpose DSPs and FPGAs
- Batteries
  - More and more power needed (need to focus on more efficient use of power)
  - Fuel cell development for handhelds
- Terrain databases
  - Interference prediction, environment awareness
- Cognitive science
  - Know how multiple CRs work with each other

A fundamental challenge with SDR is how to achieve sufficient computational capacity, in particular for processing UWB high bit-rate waveforms, within acceptable size, power consumption, cost, and weight factors. SDR offers the flexibility of varying bandwidth and range, the ability to adapt to environmental parameters and employ optimal broadband pulse characteristics for channel equalization and robustness, and finally the capability to easily adapt to current and later generation communication infrastructures. The reported radio monitoring receiver (R&S ESMD) as shown in Figure (4), provides the SDR inspired UWB technology implementation for applications such as detecting unknown signals, identifying interference, spectrum monitoring, spectrum clearance, and signal search over wide frequency ranges, producing signal content and direction finding of identified signals. The dynamic range of active antennas plays an important role and is an interesting parameter for further investigation for ultra wideband (UWB) technology implementation on SDR platforms for next generation communication networks. Figure (5) shows the IEEE draft for "standards drive" development. As illustrated in Figure (5), CR will be the future for communication standard because of flexibility/intelligence lead to real time dynamically accessing the spectrum. Key components of next generation radios will include access-backhaul integration, flexible duplex, flexible spectrum usage, multi-antenna transmission, ultra-lean design, user/control separation, and device-to-device communication.

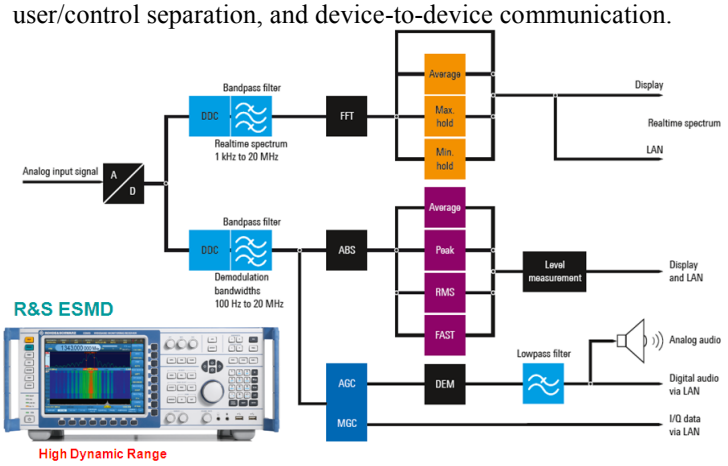


Fig. 4: SDR inspired next generation receiver (courtesy R&S)

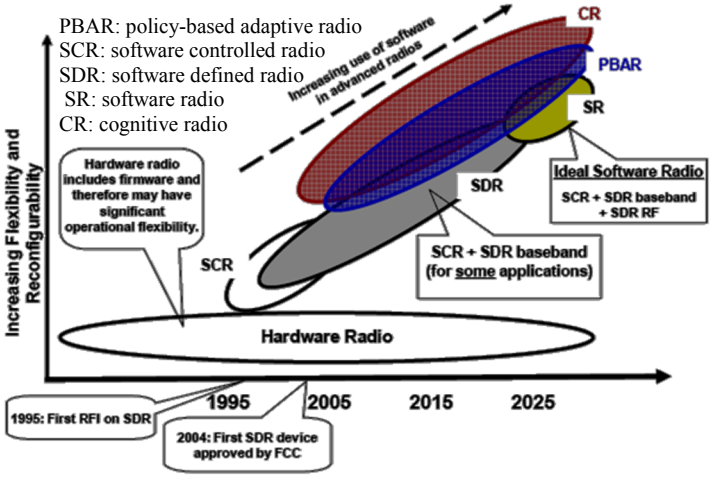


Fig.5: Shows the graph of "standards drive development"

IV. CONCLUSION

Next Generation Radios will be realized by the evolution of LTE for existing spectrum in combination with new radio technologies: SDR, SDN and CR, which target new spectrum.

REFERENCES

[1] Ulrich Rohde, Digital HF Radio: "A Sampling of Techniques, presented at the 3rd International Conf. on HF Communication Systems and Techniques", UK, Feb 26-28, 1985.

[2] Bartelt et al. "5G transport network requirements for the next generation fronthaul interface", EURASIP Journal on Wireless Communications and Networking, 2017

[3] Ulrich Rohde, Jerry Whitaker, "Communications Receivers: Principles and Design", 4th Edition, McGraw-Hill, March 2017

[4] Wei et al., "Software Defined Radio Implementation of a Non-Orthogonal Multiple Access System towards 5G", IEEE Access, *pp.*: 9604 - 9613, 2016.

The Two-Edge Anti-Jitter Circuit for Phase Noise Reduction on Received Frequency Standards

Michael J Underhill
Underhill Research Limited
Lingfield, UK
Email: mike@underhill.co.uk

***Abstract*—Measurements taken so far show that 'off-air' frequency-standards propagated by ground-waves can be used to set the frequency of a local rubidium oscillator to a few parts in a trillion (10^{12} =ppt). To achieve 1ppt with the AM broadcast frequency standard signal at 198kHz, R4 at Droitwich, over a path length of 200km to Lingfield in Surrey, the phase should not change by more than six degrees over 24 hours. However, a data signal phase modulates the R4 carrier observably by ± 22. 5°. To remove this unwanted modulation, a 'Two-Edge Anti-Jitter Circuit' has been devised using discrete CMOS, FET and Bipolar technology. The two-edge configuration removes time jitter from both the rising and falling edges of the waveform at the same time. Simulations in Simetrix (Spice equivalent) can compare with real circuit performance. The objective is to remove the data signal modulation so that weather, aircraft and night-time multi-path phase variations along the path may be revealed and measured.**

Keywords—phase noise reduction on frequenccy standards; propagation phase and frequency shifts; two-edge anti-jitter circuit

I. INTRODUCTION

Persistent ionospheric propagation frequency shifts of up to a Hz or so have previously been measured using Software Radio SDR receivers [1] and [2]. An accurate reference frequency source is required for the SDRs for accurate estimation of the absolute values of these frequency shifts. Currently a Spectratime LCR-900 Rubidium source is used. But whilst being very stable, its frequency needs to be set and occasionally checked against against a suitable more accurate stable external source. A GPS disciplined oscillator source could be be used for this, but we find that substantial weather induced propagation phase shifts occur at L-band frequencies in addition to any satellite orbit ephemeris, or ionospheric changes, and these are not fully predictable and cannot be adequately compensated.

There are low frequency 'off-air'sources available in the UK at 60kHz, 77.5kHz and 198kHz. At such low frequencies phase difference plots over several hours are necessary to achieve the desired accuracy. The SpectraVue software used with the measurement SDRs includes a phase difference plotting function which can be set to record the phase of a received carrier over time frames of minutes to several days.

The received signal-to-noise-ratio SNR, in Lingfield UK, for the carriers of the signals from 60kHz MSF in Rugby UK, 77.5kHz DCF-77 in Mainflingen Germany, are such that the observed phase jitter is too high for any useful carrier phase measurement. Substantial carrier phase noise reduction is required. Also MSF 60 kHz is on-off ampliude modulated, and DCF-77 is phase modulated by ±13° data signals.

II. THE DATA SIGNAL OFBBC RADIO 4 AT 198 KHZ

The 198kHz carrier signal from BBC R4 is phase modulated by a data signal with a phase deviation of ±22.5°. But apart from this, at 200km range the SNR appears good enough for phase measurements down to a degree or o.

Fig. 1 shows the data modulation over about a 20 second period.

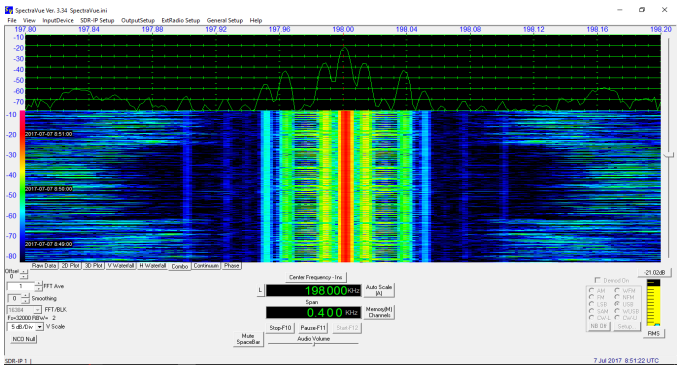


Fig. 1. Frequency Standard R4 198kHz spectrum/waterfall. Smart GPS locked. No phase jumps for transfer from one satellite to another. Span is 400 Hz and waterfall time markers are 60 sec apart. Data signal is 40 Hz bandwidth and has ~2 sec frames giving ~0.5 Hz lowest phase jitter frequency. Peak phase deviation is ± 22.5^0 50 Hz sidebands only 30dB down. Is this increase over the specification a non-linear effect over the path? .

III. OBJECTIVE

The objective is to use AJC technology on low frequency standard signals o remove data signal phase modulation and radio background noise down to the level at which so that weather, aircraft and night-time multi-path phase variations along the radio path may be revealed and measured.

As an example of magnitude of the problem, Fig, 2 shows a oneday (23hr 26min 6 sec = 84,406 sec) plot of the 198kHz carrier phase referenced to the 10MHz LCR-900 rubidium source being used as the reference source for the RFSpace SDR-IP receiver. The ± 22.5° phase modulation can be seen clearly. The vertical axis covers 360°. The upward drift of the mean of the plot can be estimated at about 30° over 24 hours This rate of phase change corresponds to a fractional frequency error $\delta f/f$ of

(30/360)/(198,000 ×24× 3600) = 4.9×10^{-12} or ~5 ppt. For 1 ppt the measured phase excursion should be less than 6°.

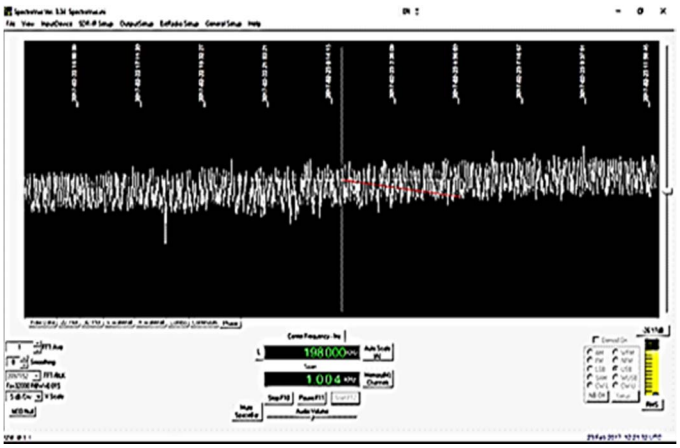


Fig. 2. Right to left plot of measured phase of 198 kHz BBC R4 carrier over 23.44 hours. Propagation path length is 200 km. Vertical scale is 360°. Carrier data phase modulation is ±22.5. Vertical phase range is 360^0. Phase deviation of data signal can be seen is ± 22.5^0 Mean phase < 3^0 over 60s gives error difference of < 7 in 10^{10}. One hour measurement gives 12 in 10^{12}. 12hrs gives 1 in 10^{12}

There are short-term variations in the phase but these are almost completely obscured by the 22.5^0 data modulation. The objective is to remove the data signal variations in phase by an Anti-Jitter Circuit [3].

The carrier phase plot in Fig. 3 shows the 22.5^0 modulation with practically no frequency error/drift over just over a minute after adustment of the LCR-900 prior to transfer to the Leo Bodmar GPS referenced clock.

IV. Discovery of Ground-Wave Red-Shift of Frequency?

The following measurements appear to have revealed a fundamental red-shift in the ground wave propagation of long-wave signals.

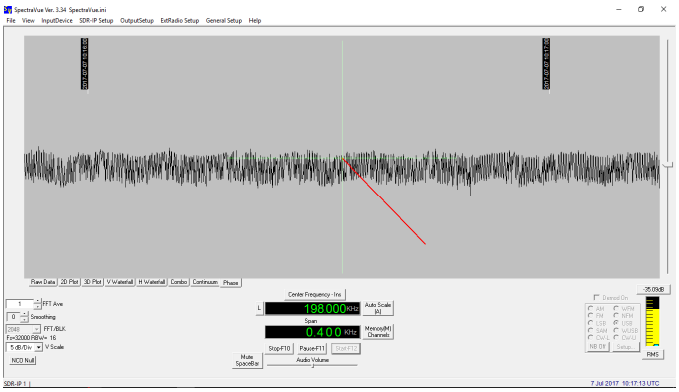


Fig. 3. Right to left plot of measured phase of 198 kHz BBC R4 carrier over about 1.3 minute after adustment of LCR-900 frequency. Horizontal time markers are 60 sec apart. . Spectratime LCR Rubidium Clock at 10MHz is fine tuned to give reference for RFSpace SDR-IP using SpectraVue to give phase plot of received 198 kHz signal. Propagation path length is 200 km. Vertical scale is 360°. Carrier data phase modulation is ±22.5°.

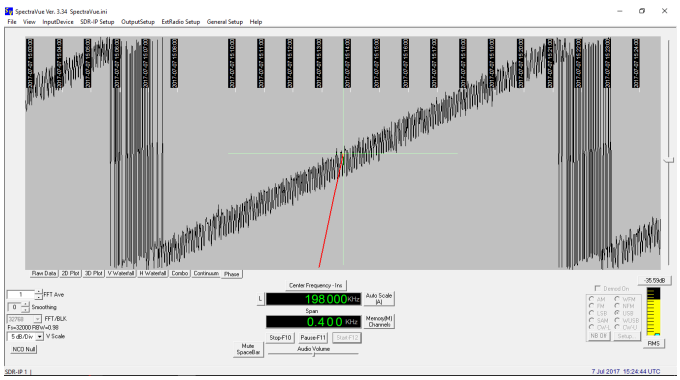


Fig. 4. Rubidium Clock is replaced by (Leo Bodmar) GPS referenced source at 10MHz. One cycle in ~15.5 minutes shows error of 5.4 in 10^9. Why? Both ends are referenced to the same GPS controlled clocks.



Fig. 5. Five cycles in ~15.5 minutes shows error of 5.4 in 10^9 now to accuracy that is 5 time greater. Why the error? Both ends are referenced to the same GPS controlled clocks. Path length is 200 km. To measure more accurately at various distances requires data phase jitter to be reduced by at least 10 times. How about an **Anti-Jitter Circuit (AJC)** to strip off the data signal? It should give at least ten times in speed/accuracy of measurement. °.

The 5.4 parts in 10^9 red-shiftof the BBC R4 standard frequency signal, shown by the measurements in Figs 3 to 5, is believed to be a new discovery' Further work will be undertaken to establish whether it is and artifact of the system or a fundamental discovery of a red-shift with distance or with curvature around the earth over 200 km?

If the data signal can be removed we can estimated that the measurements will measure this shift about ten times faster and with at least ten times more detail in the observed variations in carrier phase.

V. The Two-Edge Anti-Jitter Circuit

Various single-edge anf two-edge-AJC designs are available from a Toric Ltd archive. These all have been simulated in Simetrix simulation technology simulation. These will provide the basis for a new design suitable for operation on the LF frequency standard signals. The new design wil be simulated and optimised before a hardware model is made and tested for presentation at the cornference.

The Simetrix schematic in Fig. 2 shows the simple kind of discrete CMOS single-edge-AJC being developed into a two-

edge TE-AJC, for optimisation and then making into a discrete component CMOS circuit for testing on received signals.

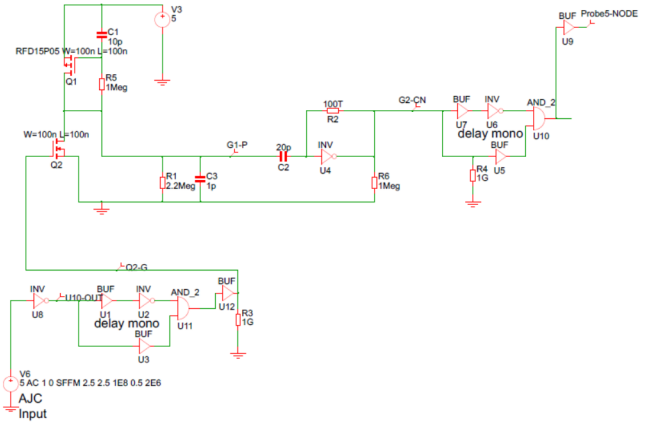


Fig. 6. Single-Edge AJC for development and upgrade to Two-Edge TE-AJC.

Fig. 7 shows a new simple design of a double AJC which operates to remove phase jitter on both the upward and downward transitions of a squared-off (saturated) input signal. It first doubles the frequency and so a divide-by -two arrangement of two D-fliops conveniently provides quadraure outputs at the input frequency, but with the phase jitter significantly redueced. At least 20 to 30db reduction of phase jitter is expected when the circuit is de-bugged and optimised

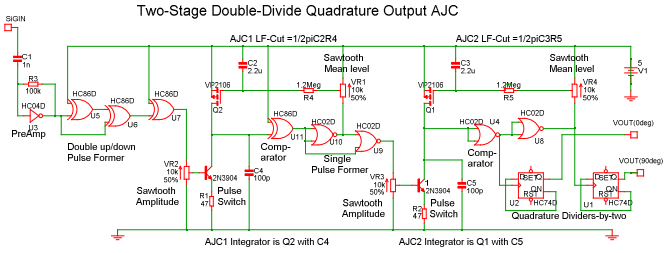


Fig. 7. The Two-Edge TE-AJC. Novelty is the Double Up/Down pulse-former using XOR gates to double the input frequency. The pulse length is one gate delay. Also two F/F dividers on right restore the frequency to its fundamental but one is delayed by quarter period to give quadrature outputs on original frequency.

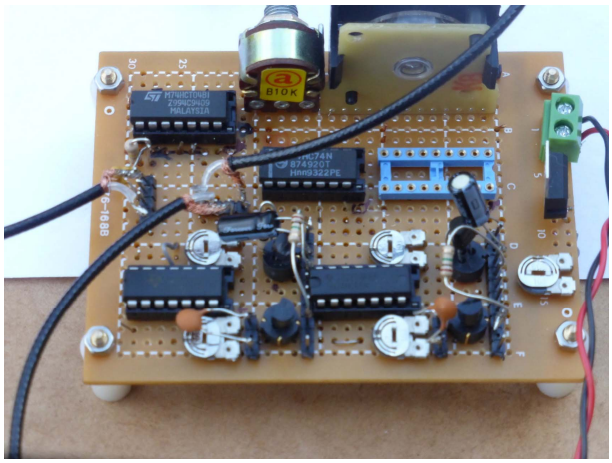


Fig. 8. New AJC breadboard illustrating its simplicity

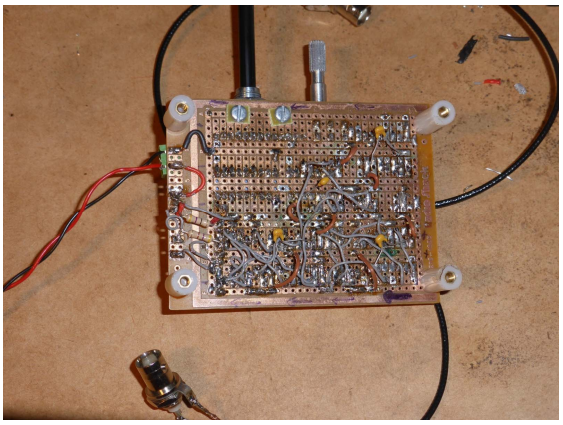


Fig. 9. Underside of NewAJC.

VI. Measurement Equipment

Figs 9 and 10 show the SDRs (Software Defined Radios) and GPS refeence souces used.

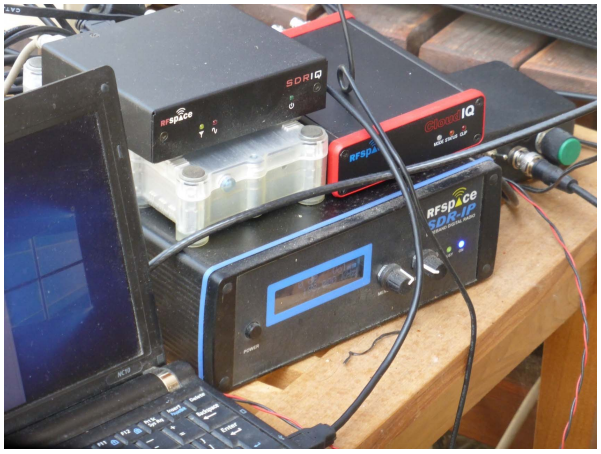


Fig. 10. Four SDR receivers and a 10MHz OCXO

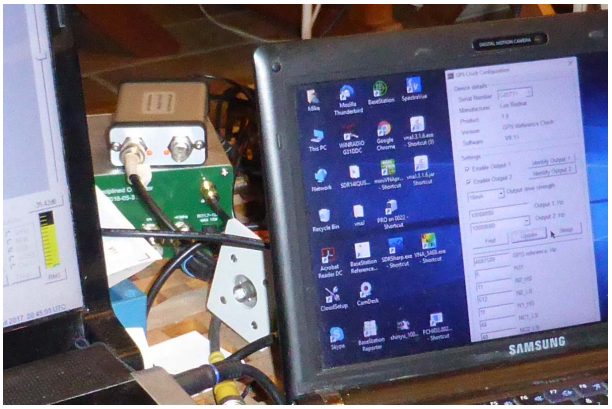


Fig. 11. Two GPS Clocks, ‘referenced’ on top with control menu on notebook on right, and ‘disciplined’ below.

VII. GPS Carrier Phase Measurements

Fig. 12 shows that the frequency-locked 'Disciplined' GPS source does not have adequate stability for use in carrier phase measurements. Whereas Fig 13 shows that the phase locked 'Referenced' GPS source has sufficient stability for carrier phase measurements and also can reveal some of the shorter term variations in carrier phase due to propagation path measurements. Both these are areas for future research.

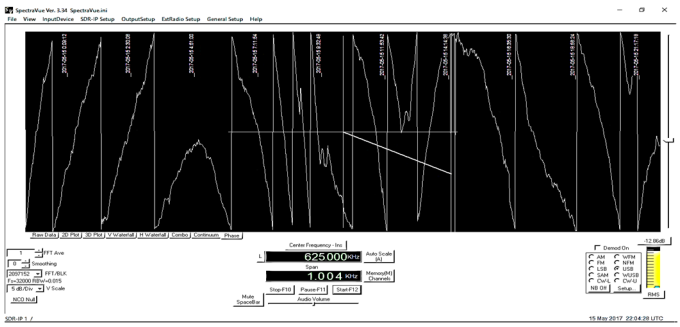


Fig. 12. Phase comparison of Disciplined and Referenced GPS clocks at 625kHz. The phase and frequency errors are found to be dominantly due to the the 'Disciplined' source, which is thus not usable for carrier phase measure ments

The truism "Frequency is the rate of change of phase" (in cycles per second) can be used to interpret the carrier phase plots shown in Fig. 13 ."

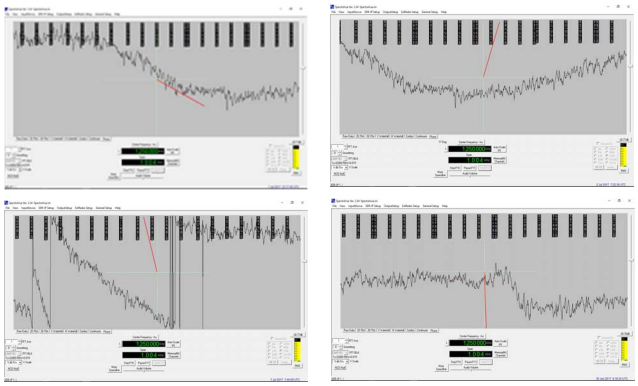


Fig. 13. Phase comparison of Disciplined and Referenced GPS clocks at 625k Hz over 24 hours.

VIII. Conclusion(s)

TE-AJC results are not yet available at the time of writing. On the basis of the measured results of similar past AJCs a conservative 20 to 30db rejection of the unwanted data modulation is expected. This should decrease measurement times for carrier phase and increase the accuracy both by about ten times.

An unexpected frequency red-shift of about 5 parts in 109 has been found for the transmission of the carrier of the BBC Radio 4 frequency standard at 198 kHz over a path length of 200km.

If confirmed by future measurements this 'discovery' could be considered to be of the deepest fundamental significance for physics.

An approach to the formulation of the theory backing such an effect is put forward in the companion conference paper [4].

References

[1] M. J. Underhill, "Propagation frequency shifts and impact on time and frequency transfer and gravity wave detection" IFCS 2016, May 9-12, New Orleans, Louisiana, pp. 1-5.

[2] M. J. Underhill, "Discovery of Persistent Ionospheric Frequency Shifts of a few Herz and Impact on Time and Frequency Transfer.", IFCS-EFTF 2015, April 12-16, Denver, Colorado, pp. 549-552.

[3] M. J. Underhill and J. Brodrick, "Chip implementation of AJC jitter reduction technology", 20th European Frequency and Time Forum (EFTF) 2006, pp. 133-138.

[4] M, J. Underhill, "Observed Propagation-Phase/Frequency-Shift Theory with Impact on Time/Frequency Transfer and GNSS", IFCS-EFTF 2017, July 9-13, Besancon, France.

Damped Sine Based Time Interval Counter

Nicolas Boucquey,*† Attila Kinali‡
*Institut Supérieur Industriel de Bruxelles, Belgium †CERN, Geneva, Switzerland
‡Max Planck Institute for Informatics, Saarland Informatics Campus, Germany

***Abstract*—Time interval counters based on the excitation of harmonic filters offer the promise of achieving sub-picosecond precision with seemingly simple systems. Unfortunately, the components used in such a system have very stringent requirements, making them both complex and expensive to build.**

We have investigated ways to relax the requirements on the components, simplify the circuitry, and the effects on the precision achieved.

I. Introduction

A. Background

Time interval counters or time-to-digital converters are one of the basic measurement instruments in a modern physics and engineering lab. Many methods were devised in the past (see e.g. [1]) and have achieved high resolution down to 1 ps (e.g. [2]). Besides tapped delay-line or ring-oscillator based ASICs, most of these methods result in relatively large and expensive circuits. In order to decrease cost and size while still achieving a high resolution, we have investigated damped sine based systems, pioneered by Panek and Prochazka [2], [3], [4], [5]. Even though the working principle is straightforward, their setup was quite involved with an SAW filter as interpolation element, and also required an elaborate frequency source to generate the 200 MHz sampling clock [6].

We report on our work-in-progress prototype of a similar system.

II. Simplification of the Design

The two obvious simplifications are replacing the SAW filter with a simple L-C tank and using an off the shelf quartz crystal oscillator.

Both of these simplifications were already tried by Ripamonti et al. [7] with some success and achieved a 4 ps RMS error. They used a simple amplitude mask to get the samples with the highest content of information, mapped the measured voltage amplitude to a phase and did a linear least-mean square fit over the phase data. Unfortunately, this measurement method relies on a well known frequency and damping of the L-C tank, both of which vary over time and temperature. Thus their design needed a special calibration step to measure the oscillation frequency of the L-C tank to compensate for temperature dependent frequency change of the reference curve used for the algorithm. They did this by sending, either before or after the measured pulse, a calibration pulse with well known timing. Without this calibration step there would be an additional measurement error that could be as large as 70 ps.

In order get a better estimate without the need of calibration, we choose to do a non-linear fit of the full wave damped sine. I.e using the prototype function $f(t) = A\sin(2\pi ft + \phi)e^{t/\tau}$ with the amplitude A, the frequency f, the phase ϕ and the damping τ being the free variables to be estimated.

The resulting block diagram can be seen in Figure 1. We used a 14 bit ADC with a 100MHz low noise crystal sampling clock. The ADC is pin-compatible with a 16 bit version, thus allowing a future upgrade path. Both ADCs are available as 125Msps variants, allowing high sample rates. If a lower noise sampling clock or a different sampling frequency is needed, this can be supplied using the external clock input.

As processor we choose an Xilinx Zynq 7 FPGA board, which allows us to do a lot of the processing in software on the board, or forward the data onto a PC for further processing. The non-linear fitting of the signal was done using a small python script running on the FPGA board directly, for simplicity reasons.

The input passes through an CMOS buffer gate in order to clean up the slew rate and obtain a well defined edge. After this, it passes through the exciter and the amplifier before going into the ADC board. The L-C tank we used for our experiments had an oscillation frequency of about 15 MHz and a Q of about 20. Both, the frequency and the Q, were rather low, and offer room for improvement.

III. Experimental Results

Even though our experimental was rather crude (Figure 2) and potentially added some additionally uncertainty the results we got were very promising. We measured the jitter using a random generated pulse, passing it through a splitter and feeding it to two of the input channels. The resulting plot Figure 3 shows a nice Gaussian distribution with a small RMS jitter of just 3.05 ps. The linearity was measured in a similar way, using only a single channel and measuring the delay versus the sampling clock. As can be seen in Figure 4 there is no obvious non-linearity visible. Unfortunately, due the number of samples are insufficient to exclude smaller non-linearities with high confidence.

IV. Future Work

As mentioned above, the excitation circuit and L-C tank can be further improved to give a lower measurement uncertainty. We believe that a factor of 2-3 should be possible and easy to achieve. The python script used for the non-linear fitting and thus for the estimation of the delay should be replaced by an

978-1-5386-2916-1/$31.00 ©2017 IEEE

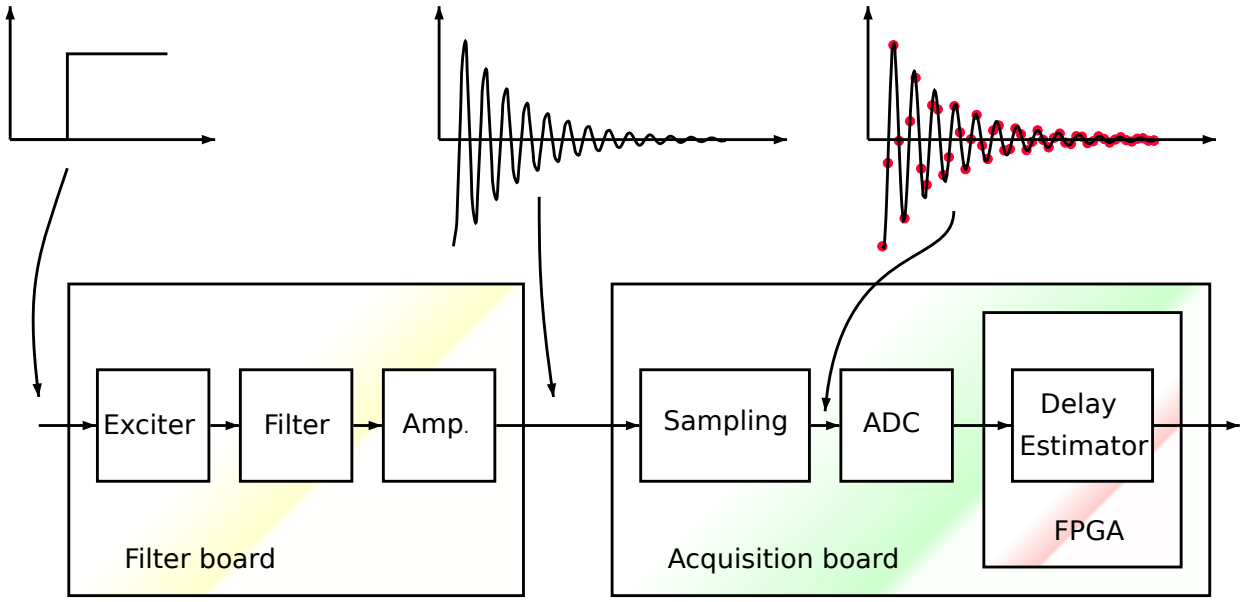


Figure 1. The overall block diagram of the time-interval counter design including the different signal forms at each stage. At the left enters the input edge, which is being filtered, amplified and then sampled by the ADC. The FPGA/CPU does the delay estimation.

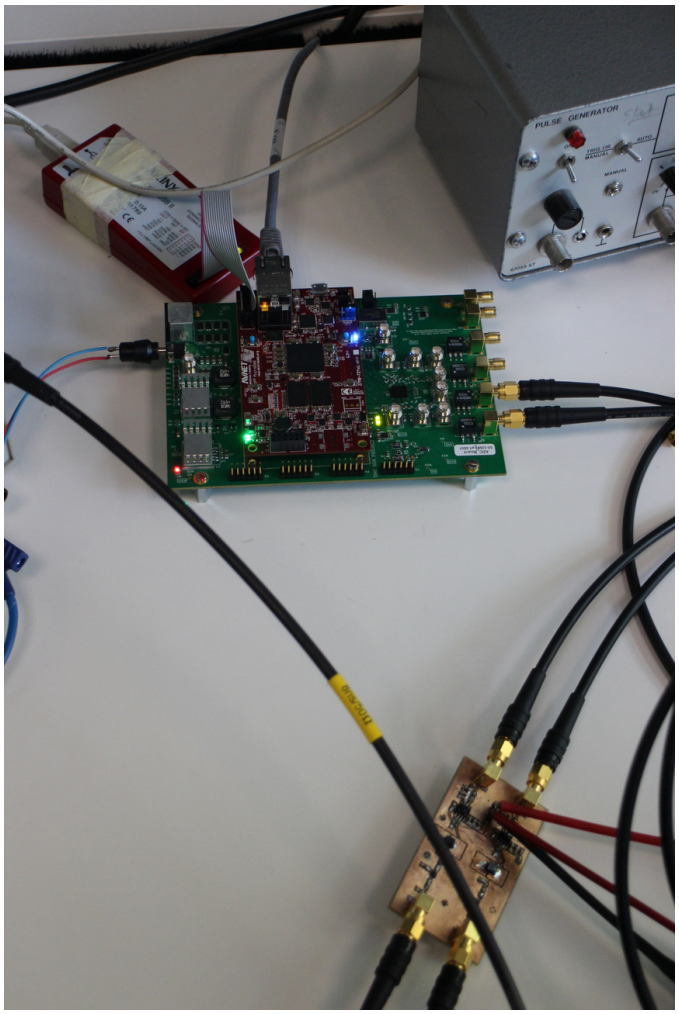


Figure 2. Experimental setup. Although being rather crude and potentially adding additionally uncertainty, our results were quite good.

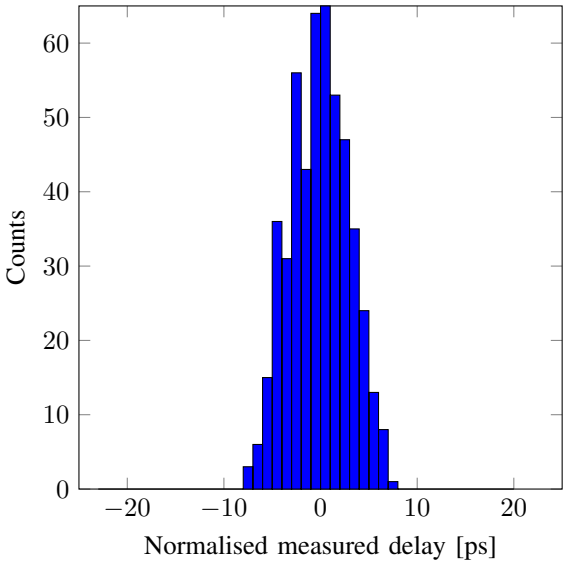


Figure 3. The jitter of a two channel, fixed delay measurement. RMS jitter is 3.05 ps

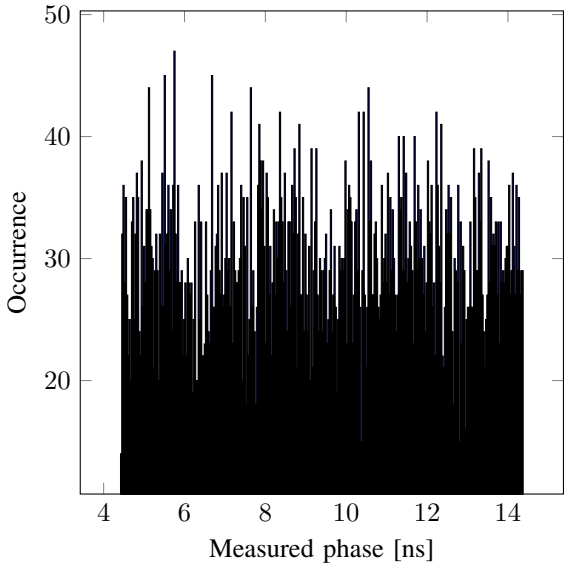


Figure 4. Linearity test using random pulses and measuring their delay versus the sampling clock. Even though there is no obvious non-linearity visible, the number of samples taken is too low for a proper evaluation.

appropriate algorithm and implemented in the FPGA to allow high rates of measurement.

V. Conclusion

We have simplified the design by Panek and improved on the results by Ripamonti et al. and achieved a low measurement uncertainty of 3 ps RMS without needing the complicated calibration procedure after each measurement.

References

[1] J. Kalisz, "Review of methods for time interval measurements with picosecond resolution," *Metrologia*, vol. 41, no. 1, pp. 17–32, dec 2003. [Online]. Available: http://dx.doi.org/10.1088/0026-1394/41/1/004

[2] P. Panek and I. Prochazka, "Time interval measurement device based on surface acoustic wave filter excitation, providing 1ps precision and stability," *Review of Scientific Instruments*, vol. 78, no. 9, 2007. [Online]. Available: http://scitation.aip.org/content/aip/journal/rsi/78/9/10.1063/1.2779217

[3] P. Panek, "Time-interval measurement based on saw filter excitation," *Instrumentation and Measurement, IEEE Transactions on*, vol. 57, no. 11, pp. 2582–2588, Nov 2008.

[4] I. Prochazka, J. Kodet, P. Panek, and U. Schreiber, "Novel concept of sub-picosecond timing system and its applications in fundamental metrology," in *Frequency Control and the European Frequency and Time Forum (FCS), 2011 Joint Conference of the IEEE International*, May 2011, pp. 1–4.

[5] P. Panek, J. Kodet, and I. Prochazka, "Event timing device providing subpicosecond precision," in *European Frequency and Time Forum International Frequency Control Symposium (EFTF/IFC), 2013 Joint*, July 2013, pp. 167–170.

[6] J. Kölbl, PeterSperber, and I. Prochazka, "Frequency source 200 MHz for time interval measurements, provididing sub-picosecond precision and stability," 200x.

[7] G. Ripamonti, A. Abba, and A. Geraci, "High frequency, high time resolution time-to-digital converter employing passive resonating circuits," *Review of Scientific Instruments*, vol. 81, no. 5, 2010. [Online]. Available: http://scitation.aip.org/content/aip/journal/rsi/81/5/10.1063/1.3432002

Analysis of the Carrier-Envelope Phase Noise of Passively Phase-Locked Er:Fiber Frequency Combs up to the Nyquist Frequency

Andreas Liehl, David Fehrenbacher, Philipp Sulzer, Denis V. Seletskiy, and Alfred Leitenstorfer
Department of Physics and Center for Applied Photonics
University of Konstanz
D-78457 Konstanz, Germany
E-Mail: Andreas.Liehl@uni-konstanz.de

We study the carrier-envelope phase noise of an Er:fiber frequency comb which is passively phase-locked at the full repetition rate of 100 MHz. A novel characterization method determines an out-of-loop phase jitter of only 250 mrad when integrated over 12 orders of magnitude: from 50 µHz up to the Nyquist frequency.

Optical frequency combs; Fiber lasers; Frequency metrology; Ultrafast technology

I. Introduction

Since the first demonstration of optical frequency synthesis using femtosecond frequency combs [1], these tools have become attractive in various applications such as microwave generation, optical atomic clocks, spectroscopy or attosecond science [2]. All these scenarios require the phase noise level to be as low as possible. Typically, stabilization of the carrier-envelope offset (CEO) frequency is achieved electronically via f-2f self-referencing techniques. However, such electronic feedback loops induce servo-bumps to the phase noise owing to their limited bandwidth. In an alternative, operating at full repetition rate of the comb, self-elimination of the CEO slippage by difference frequency generation (DFG) between two separate comb regions has been demonstrated [3,4]. The pulse-to-pulse stability of the electric field amplitude within a temporal wave packet is highly desirable for high-end scientific applications. However, no characterization of the carrier-envelope phase (CEP) noise performance of such sources has been demonstrated far into the MHz range. In this work, we present our novel detection scheme which allows for an out-of-loop measurement of the CEP noise up to the Nyquist frequency of 50 MHz. Although such analysis has been demonstrated for actively stabilized optical frequency combs based on Ti:Sa oscillators [5], we are not aware of any report concerning such a broadband noise characterization of fiber-based frequency combs.

II. Experimental Setup

In our study, we investigate the CEP noise performance of a passively phase-locked Er:fiber frequency comb with a repetition rate of 100 MHz (left part of Fig. 1a). The pulse energy and duration are 6 nJ and 105 fs, respectively, after re-amplification and compression of the phase-stable pulses that are generated via DFG [6]. The CEP noise is characterized by means of a spectrally-resolved output of an f-2f interferometer [7] (right part of Fig. 1a). Here, a red edge of an octave-spanning spectrum generated in a highly nonlinear fiber (HNF) is frequency-doubled in a type-I beta barium borate crystal (BBO) cut at 20°. A polarizer projects the frequency-doubled output onto the polarization of the fundamental comb modes, resulting in an interference which reveals the CEP. We employ two methods to analyze the CEP noise of our source.

III. Slow Fluctuations in the CEP

In the first branch of the interferometer, slow fluctuations of the CEP are detected by sequentially recording spectral interference by means of a CCD-based spectrometer. The

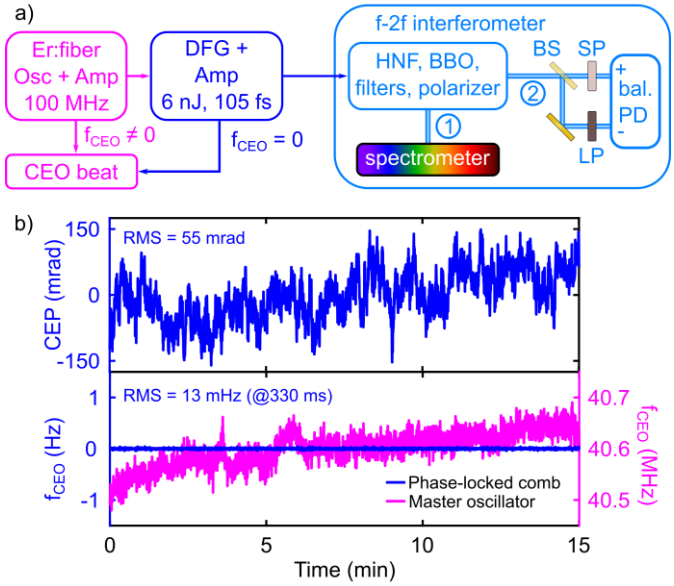


Fig. 1. a) Sketch of the experimental setup. Left: Er:fiber front-end, including master oscillator, DFG and amplifiers. Right: f-2f interferometer for detection of the CEP. BS, beam splitter; SP, shortpass filter; LP, longpass filter. b) Upper panel: Fluctuation of the CEP over 15 minutes. Lower panel: Resulting CEO frequency of the phase-locked comb (blue) in comparison to the free-running MO (pink) detected via CEO beat.

upper panel of Fig. 1b shows the stability of the CEP over a period of 15 minutes. Even over such a long period, only minor fluctuations with an RMS value of 55 mrad are observed, revealing an outstanding long-term stability of our Er:fiber frequency comb. This fact is further corroborated when the CEO frequency of the passively phase-locked comb is compared directly to the one of our free-running Er:fiber master oscillator (MO). The center frequency of their mutual beat note (CEO beat) is shown in Fig. 1. While the CEO frequency of the MO drifts by approximately 200 kHz, the CEO of the phase-locked comb remains centered around zero and shows only minute fluctuations with an RMS value of 13 mHz at an observation time of 330 ms (lower panel of Fig. 1b). This measurement reveals the impressive finding that the CEO drift of the phase-locked comb is passively suppressed by more than 7 orders of magnitude as compared to the MO.

IV. High Frequency Characterization of the CEP

The shot-to-shot evaluation of the CEP cannot be obtained by the measurement technique described above due its inherent limitation in data acquisition speed. Therefore, we developed a novel detection scheme (right side of Fig. 1a). Two adjacent spectral interference fringes are split about their center by division into two spatial branches with equal optical power and application of appropriate spectral filters in each branch (blue and red shaded regions in Fig. 2a). The low and high-frequency photons are directed to the two input channels of balanced differential photodetectors (bal. PD), respectively. The power in the red and blue wavelength band is maximum and minimum, respectively, when the CEP = -π/2 (solid graph in Fig. 2a). The conditions are reversed if the CEP is shifted by π (dotted graph). Sweeping the CEP over 2π results in a sinusoidal behavior of the difference signal (inset of Fig. 2a).

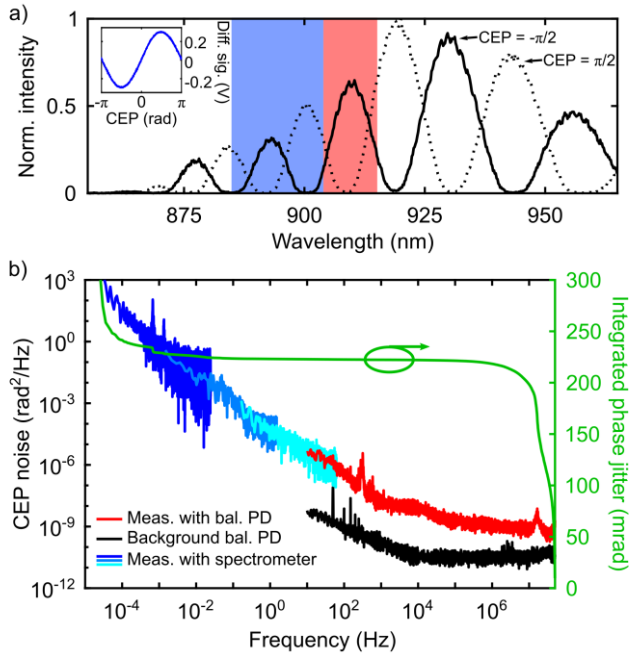


Fig. 2. a) Output spectra of the f-2f interferometer for CEP = -π/2 and π/2 (solid and dotted lines), blue/red bands denote the spectral windows used in the high-frequency noise characterization. Inset: Difference signal of the bal. PD when the CEP is swept over 2π. b) CEP noise density (left scale) and integrated phase jitter (right scale) as measured over 12 orders of magnitude.

Any fluctuations of the CEP translate to dynamic unbalance in the differential photocurrent of the bal. PD while its output is directly proportional to the CEP if set to zero or multiple integers of π.

V. Discussion

Owing to the large bandwidth of the balanced photodetectors, our technique allows a characterization of the CEP fluctuations up to the Nyquist frequency. Fig. 2b (left scale) shows the CEP noise density obtained from both the measurement using the balanced photodiodes (red) and the spectrometer (blue) as detector. The different blue shades correspond to different data acquisition times. We find two distinct noise characteristics. For low frequencies below 1 kHz, flicker noise builds up which is typical for out-of-loop measurements. In turn, the spectral noise density reaches a white noise floor at approximately 100 kHz. In between, there is a slight bump at 10 kHz which we attribute to amplitude-to-phase conversion mechanisms within our Er:fiber oscillator. Absence of any servo-bumps highlights the excellent performance of our passively phase-locked comb. These results constitute, to the best of our knowledge, the first demonstration of an out-of-loop detection of the CEP noise up to the Nyquist frequency in fiber-based frequency combs. We further calculated the total phase jitter (green line and right scale in Fig. 2b) which yields a record-low value of 250 mrad when integrated over 12 orders of magnitude in frequency, namely, from 50 µHz to 50 MHz. The drift of the CEP below 50 µHz is limited by thermal stability which could obviously be improved by active temperature stabilization or a slow feedback loop. In total, we believe that our Er:fiber frequency comb is highly suitable for applications in optical frequency metrology according to such an ultralow noise performance.

Acknowledgment

We thank D. Weise, Ch. Jentsch, H.-R. Schulte and U. Johann from Airbus DS GmbH, Friedrichshafen, Germany for their support.

References

[1] Th. Udem, R. Holzwarth, and T. W. Hänsch, "Optical frequency metrology," *Nature*, vol. 416, pp. 233-237, 2002.

[2] S. A. Diddams, "The evolving optical frequency comb [Invited]," *J. Opt. Soc. Am. B*, vol. 27, pp. B51-B62, 2010.

[3] R. Huber, A. Brodschelm, F. Tauser, and A. Leitenstorfer, "Generation and field-resolved detection of femtosecond electromagnetic pulses tunable up to 41 THz," *Appl. Phys. Lett.*, vol. 76, pp. 3191-3193, 2000.

[4] A. Baltuška, T. Fuji, and T. Kobayashi, "Controlling the Carrier-Envelope Phase of Ultrashort Light Pulses with Optical Parametric Amplifiers," *Phys. Rev. Lett.*, vol. 88, p. 133901, 2002.

[5] T. Fuji, J. Rauschenberger, C. Gohle, A. Apolonski, Th. Udem, V. S. Yakovlev, G. Tempea, T. W. Hänsch, and F. Krausz, "Attosecond control of optical waveforms," *New J. Phys.*, vol. 7, p. 116, 2005.

[6] D. Fehrenbacher, P. Sulzer, A. Liehl, T. Kälberer, C. Riek, D. V. Seletskiy, and A. Leitenstorfer, "Free-running performance and full control of a passively phase-stable Er:fiber frequency comb," *Optica*, vol. 2, pp. 917-923, 2015.

[7] M. Kakehata, H. Takada, Y. Kobayashi, K. Torizuka, Y. Fujihara, T. Homma, and H. Takahashi, "Single-shot measurement of carrier-envelope phase changes by spectral interferometry," *Opt. Lett.*, vol. 26, pp. 1436-1438, 2001.

Optical Frequency Comb Application in Time-delay Interferometer

Nan Yu*, Ivan Grudinin, and Massimo Tinto
Jet Propulsion Laboratory
California Institute of Technology
Pasadena, California, USA
*nan.yu@jpl.nasa.gov

***Abstract*— Time-delay interferometer (TDI) is well established as an effective technique to mitigate laser phase noises in laser interferometer gravitational wave detection. Just as important in the TDI scheme is the ability to suppress the rf local oscillator noises in the optical heterodyne measurements. We show that the local oscillator noises can be effectively and elegantly cancelled by employing optical frequency combs in which the rf signal phases are coherent with the optical phases. In addition, the deployment of optical combs eliminates the need for separate ultra-stable oscillators. This is a simpler and more reliable approach than the modulation scheme, and it can be applied to the most generalized TDI combinations.**

Keywords—Time-delay laser interferometer, microwave noise, optical frequency comb

I. INTRODUCTION

With the successful observations of gravitational wave signals in the ground LIGO observatory, there is renewed excitement about the laser interferometer space antenna (LISA) for low frequency cosmic gravitational wave sources. A space-based interferometer such as LISA measures relative frequency changes experienced by coherent laser beams exchanged by its three pairs of spacecraft. As the laser beams are received, they are made to interfere with the outgoing laser light. These heterodyne measurements are each down-converted with the use of an onboard local oscillator (LO), then digitized and numerically combined in order to cancel the lasers frequency fluctuations in the time-delay interferometer scheme [1]. The magnitude of the frequency fluctuation introduced by the LO into the heterodyne measurements contributes significantly to the overall measured laser phase noises by several orders of magnitude and the noises are not removed by TDI for cancellation of the optical phase noises. We describe a scheme to use self-referenced optical frequency combs (OFC) to suppress both optical and local oscillator noises in a modified time-delay interferometer scheme.

II. TIME-DELAY INTERFEROMTER

The space strain resulting from gravitational waves are very weak, on the order of 10^{-20} or weaker. Using laser interferometry for direct detection requires a similar fractional frequency stability of the laser in the signal frequency range of interest. At present, no lasers have a frequency noise performance that is even close to the requirement. In practice, laser interferometer gravitational wave detectors use two orthogonal arms of equal length. In this arrangement, a differential measurement between the two equal arms cancels out the common laser phase noise as in the case of LIGO. The successful gravitational wave signal detection demonstrates the power of such an approach.

In the space laser interferometer scheme, a similar approach is used with three spacecraft in a near equilateral triangle configuration. However, because of the spacecraft orbits, strict equilateral triangle is not possible, and consequently, the common mode laser noise cancellation is not as effective. To address this difficulty of unequal arm length measurements, the time-delay interferometer technique has been devised and became the baseline approach for the space laser interferometer for gravitational wave detection. The TDI can be thought of as a synthetic equal arm interferometer in the sense the laser phases in two arms are recorded separated and time stamped. The two laser fields are made to interferometer in signal processing by time-shift one laser signal relative to the other so that the laser noises are exactly aligned and hence cancelled.

III. SEF-REFERENCED OPTICAL FREQUENCY COMBS

An OFC consists of a set of narrow spectral lines equally spaced in the frequency domain. More importantly, when all the comb lines are phase coherent (i.e. have fixed phase relationship) the superposition of all comb lines manifest themselves as a periodical pulse train in the time domain. The pulse train propagates with a group velocity while the underlining optical carrier travels at the phase velocity. When the modes are exactly in phase, the peak of the carrier is aligned with the peak of the pulse envelope. In the absence of any dispersion, this relationship holds over time as the pulse propagates. In practice, dispersion changes the relative phases of the modes, and the peak of the carrier amplitude shifts from that of the pulse envelope. This offset is typically referred to as carrier envelope offset (CEO) phase shift and the rate of this offset phase change over a period gives the CEO frequency [2]. Like in a typical phase locking loop, the measured CEO phase can be used to stabilize the CEO itself, resulting in an OFC that has the well-defined relationship between the optical frequencies f_m in the modes and the rf frequency of the repetition rate f_{rep}, now referred to as self-referencing [3]. The striking property of the self-referenced OFC is the phase coherence between the optical carriers and their rf beat note signal. Recent studies have shown that the comb frequency precision can be at $1x10^{-18}$ while the CEO phase can be controlled down to the mrad level. Therefore, the stabilized OFC technique will provide an rf signal that can be significantly more stable than the current best space-qualified

ultra-stable oscillators (USO). Implementing OFC on board will eliminate all together the need for USOs.

IV. OPTICAL FRQUENCY COMB-TDI

Determined by spacecraft orbit dynamics, the relative distances between spacecraft are not constant. The heterodyne measurements will display resulting Doppler shifts, which is then removed from the data by using the onboard LO. The magnitude of the frequency fluctuations introduced by the LO into the heterodyne measurement depends linearly on the noises from the LO themselves and the inter-spacecraft relative velocities. Space-qualified, state of the art clocks are oven-stabilized crystal oscilaltors are estimated to have a "flicker noise" $S_y(f) = 8.0 \times 10^{-39}$ Hz^{-1} at the Fourier frequency of milli-hertz for a spacecraft relative velocity of 10 m/s. This is compared with the LISA noise level goal of $\sim 3 \times 10^{-44}$ Hz^{-1}, roughly five orders of magnitude smaller. This LO noise would degrade the LISA sensitivity to an unacceptable level. A technique involving modulated beams and additional side-bands to side-bands heterodyne measurements was formulated to calibrate out the clock noise [4]. This technique, however, considerably increases system complexity.

With a self-referenced optical frequency comb, it is possible to generate the heterodyne rf LO signal directly from the onboard laser. This results into a significant simplification of the onboard interferometer measurement subsystem as now the "clock" noise can be cancelled directly by applying a modified second-generation time-delay interferometric combination to the heterodyne phase measurements. This is because the optical frequency comb technique provides a rf frequency that is phase-coherent to the frequency of the highly stabilized onboard laser used for ranging. This approach avoids use of modulated laser beams and, as importantly, the need of any ultra-stable oscillator on board as mentioned before.

The technique of OFC-TDI can be understood in the following simplistic terms. In the orginal TDI scheme, the laser fields are detected through heterodyne measurements together with a local oscillator on each spacecraft. The recorded total phase noise then contains two parts, the laser phase noise from the received laser signal and that from LO for the heterodyne measuerments. By deriving the local oscillator signal from the laser signal, the total phase noise in the heterodyne measurement contains then only a single noise source, the laser noise, aside from a scaling factor of the optical to rf frequency ratio. In addition, the rf noise is effectively delayed by the same amount as that of the laser noise. Therefore, by cleverly combining the relationships of all the noises steming from the same laser source, we are able to show that both the laser phase noise and the local oscillator noise can be cancelled exactly and simultanwously while still maintaining gravitational wave signals [5]. We are conducting experiments to demonstrate the effectiveness of OFC-TDI for the LO noise suppression.

ACKNOWLEDGMENT

This research was carried out at the Jet Propulsion Laboratory, California Institute of Technology, under a contract with the National Aeronautics and Space Administration.

REFERENCES

[1] M. Tinto and J.W. Armstrong, Phys. Rev. D 59, 102003 (1999).

[2] Femtosecond Optical Frequency Comb: Principle, Operation, and Applications, J. Ye, S. Cundiff (Eds.), Kluwer Academic Publishing, Norwell, MA (2005).

[3] J. Reichert, M. Niering, R. Holzwarth, M. Weitz, T. Udem, and T. W. H¨ansch, Phys. Rev. Lett., 84, 3232 (2000).

[4] G. de Vine, B. Ware, K. McKenzie, R. E. Spero, W. M. Klipstein, and D.A. Shaddock, Phys. Rev. Lett. 104, 211103 (2010).

[5] Massimo Tinto and Nan Yu, Physical Review D 92, 042002 (2015).

Rapid electro-optic control of the carrier-envelope-offset frequency for ultra-low noise frequency combs

W. Hänsel[1], M. Giunta[1,2], M. Fischer[1], M. Lezius[1] and R. Holzwarth[1,2]

[1]Menlo Systems GmbH, Martinsried, Germany
[2]Max Planck Institute of Quantum Optics, Garching, Germany
w.haensel@menlosystems.com

***Abstract*—We report on a novel electro-optic modulator that acts on the carrier-envelope-offset frequency of a femtosecond pulsed laser with negligible cross-talk to the position of the optical carrier modes. The fast response on the nanosecond time scale allows to stabilize the carrier-envelope-offset frequency with a bandwidth in excess of 1 MHz while not perturbing a potential independent stabilization of a carrier mode to an optical reference. Out-of-loop verification of both optical and CEO frequency suggests a sub-Hz stability for all (partially virtual) spectral comb lines between 0 Hz and 400 THz.**

Keywords—carrier-envelope-offset frequency; frequency comb; precision metrology

I. INTRODUCTION

Since the first use of femtosecond pulsed lasers as "frequency comb", i.e. as a measurement device for the optical frequency of a well stabilized continuous-wave laser, femtosecond lasers have spread into an enormous variety of applications. Even only within metrology, their use has been largely diversified, covering applications like spectral purity transfer, phase locks across optical frequencies, direct frequency spectroscopy, spectrometer calibration in astrophysics, dual-frequency comb spectroscopy, and distance measurements, to name only a few. Many of the applications call for an increased stability of the involved lasers, notably with respect to the carrier-envelope-offset (CEO) frequency. Indeed, there is not yet a common tuning element which would serve a truly fast actuation of the CEO frequency across a variety of laser platforms. In many cases, a modulation of pump power or round-trip loss is used to indirectly influence the CEO frequency through nonlinear laser dynamics. However, the speed and even the sign of the actuation strongly depends on the laser type, it may even be of different sign for the same laser at different actuation frequencies.

Here we present a novel electro-optic actuator for the CEO frequency which works independent of the laser architecture and shows response times on the nanosecond time scale. It has the additional advantage that its actuation leaves a certain frequency in the laser spectrum unchanged, such that simultaneous optical referencing in vicinity to this fix point is achieved with negligible crosstalk.

II. ELECTRO-OPTIC CEO FREQUENCY CONTROL

The CEO actuator consists of a Mach-Zehnder-type interferometer (see Fig. 1a) which is tunable not in its relative path difference, but rather in the splitting ratio between the paths. The fixed path length difference is an integer multiple of a target wavelength close to the carrier wavelength of the laser, such that the phase of this target wave is independent of the distribution onto the paths. The path difference is chosen small with respect to the pulse width of the light travelling across, so that the pulse shape is not significantly changed upon redistribution of the light between the paths. However, the pulse center after the actuator changes continuously as the distribution onto the paths is changed, with the extreme points given when the light travels through a single path only. This behavior is illustrated in Fig. 1c and 1d. The actuator thus influences the group velocity of the transmitted light while it leaves the carrier-frequency unchanged. If placed inside a laser cavity, the group velocity change causes a stretching or compression of the mode spectrum while the chosen target frequency is left unchanged.

An environmentally stable path length difference as well as tuning of the splitting ratio is achieved with polarization optics, as shown in Fig. 1b. The combination of two quarter wave plates with an intermittent electro-optic tunable birefringent crystal (EOM) acts as polarization rotator for linear incident polarization and serves to adjust the distribution of the light amplitude onto the different Eigen-axes of the central integer wave plate. We have characterized the actuator performance by tracing the CEO frequency of a 250 MHz mode-locked Er-doped fiber laser [1] as a function of applied actuator voltage for modulation frequencies between 250 Hz and 3 MHz (see Fig. 2a). Within this range, the average response is approximately 400 kHz/V, showing a pronounced, but non-detrimental acoustic resonance around 750 kHz. The phase behavior is dominated by a simple delay (linear phase decrease) which is caused by the light propagation between the laser oscillator and the CEO frequency detection as well as by the electric signal delay. On top of this behavior, the imprint of the resonance is visible.

978-1-5386-2916-1/$31.00 ©2017 IEEE

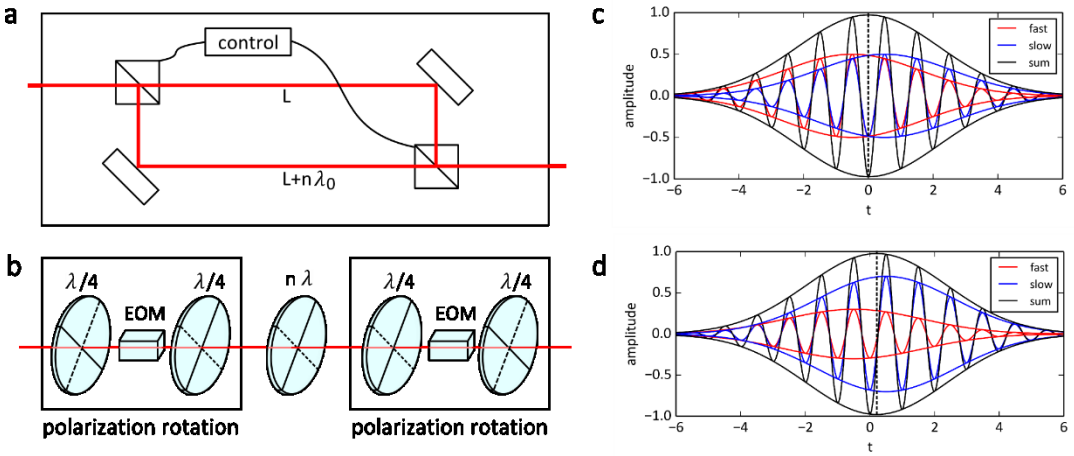


Fig. 1. a) Schematic of an integer-wavelength interferometer with adjustable splitting ratio at input and output port. The beam splitters (indicated as cubes) do not need to use polarization for the adjustment of the splitting ratio b) Implementation of the interferometer using electro-optically tunable birefringent crystals (EOM), c) Schematic of an outgoing pulse (black) as a sum of an advanced (red) and a delayed (blue) pulse with equal amplitude. The envelope of the outgoing pulse is centered at t=0, d) Schematic of an outgoing pulse (black) with advanced and delayed pulse having different amplitudes: the envelope maximum of the outgoing pulse is shifted away from t=0 without affecting the phase. In the subplots c) and d), the dashed line marks the envelope center of the outgoing pulse.

III. Frequency Comb Stabilization

The actuator described above has been used to stabilize the CEO frequency in a phase-lock loop (PLL). We observe the servo bump close to 2 MHz, suggesting a regulation bandwidth only slightly below this value. Fig. 2b shows the in-loop phase noise of the stabilized CEO frequency, featuring an integrated phase noise of less than 40 mrad (1 Hz – 10 MHz).

We have further stabilized an optical mode of this laser to an ultra-stable cw-laser at 1542nm, using an electro-optic modulator and a piezo-driven mirror, yielding similar noise performance. An out-of-loop verification of both the CEO frequency and the optical beat suggests that the ensemble of frequency comb lines (including the virtual comb lines down to 0 Hz) is stabilized to the sub-Hz level. The stability of virtual lines is assumed to stretch out to at least twice the carrier frequency.

Acknowledgment *(Heading 5)*

We gratefully acknowledge funding from the German space agency (DLR) under grants 50WM0934 and 50EE1223, the EU FP7 initial training network FACT, and the DARPA PULSE program (Project PµreComb under grant number W31P4Q-14-C-0050).

References

[1] W. Hänsel, H. Hoogland, M. Giunta, S. Schmid, T. Steinmetz, R. Doubek, P. Mayer, S. Dobner, C. Cleff, M. Fischer, and R. Holzwarth, "All polarization-maintaining fiber laser architecture for robust femtosecond pulse generation," Appl. Phys. B, vol. 123, p. 41

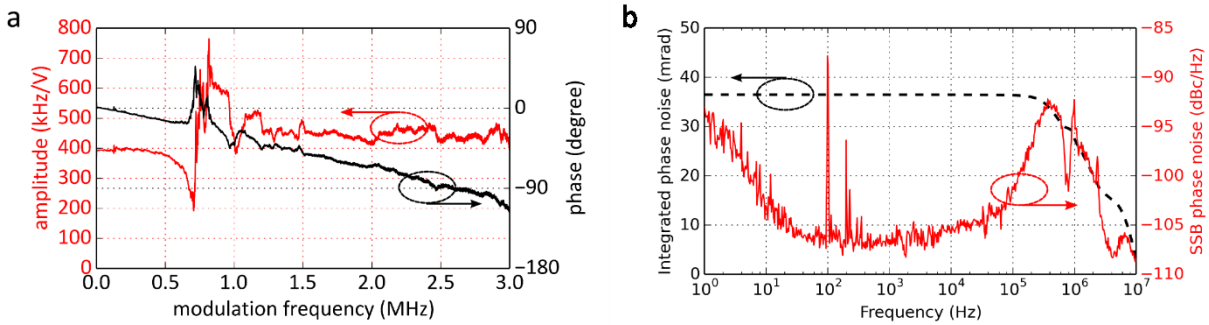


Fig. 2. a) Transfer function of the CEO actuator in the range of 250 Hz to 3 MHz. Left axis (red): amplitude response, right axis (black): phase response. b) Phase noise of the stabilized CEO frequency. Left axis: integrated phase noise (1Hz – 10 MHz), right axis: power spectral density of the single-sided phase noise.

Doppler-tolerant synchronization of clocks over free space at the femtosecond level

Hugo Bergeron, Jean-Daniel Deschênes
Center for Optics, Photonics and Lasers
Université Laval
Quebec City, QC, Canada
hugo.bergeron.3@ulaval.ca

Laura C. Sinclair, William C. Swann, Isaac Khader,
Esther Baumann, Nathan R. Newbury
Applied Physics Division
National Institute of Standards and Technology
Boulder, CO, USA

***Abstract*—We present a method of frequency comb-based two-way time transfer that allows sub-femtosecond synchronization even during motion with velocities of up to 24 m/s. To test synchronization under motion, a Doppler simulator based on a mobile retroreflector was added at one end of a 4-km free-space link. Using this simulator and Doppler-tolerant algorithms we demonstrate a time deviation which reaches a low of 100 attoseconds at 100 seconds averaging time and residual velocity-dependent bias which remains under 500 attoseconds.**

Work of the U.S. government not subject to copyright.

Keywords—Time and frequency transfer; Doppler effect; Frequency combs; Clock networks

I. INTRODUCTION

The extreme stability of optical clocks has motivated the development of new time and frequency transfer techniques. Those include frequency transfer over thousands of kilometers of fiber reaching 10^{-18} fractional stability [1,2] and femtosecond-level clock synchronization cross several kilometers of turbulent air [3-5]. In many cases, clock networks involve moving platforms such as aircraft and satellites [6]. Motion poses many challenges to time and frequency transfer, due in part to the finite speed of light. We present a method of frequency comb-based two-way time transfer based on the quasi-static work of Ref. [3] which allows sub-femtosecond synchronization despite 24 m/s motion. No stability degradation was observed and indeed the new Doppler-tolerant system supports a higher level of performance than Ref. [3].

II. EXPERIMENTAL SETUP

The physical system has been modified from that presented in Ref. [3] to include a moving retroreflector to induce Doppler effects. Fig. 1 shows the two sites that are part of the experiment: the master site (A) and the remote site (B). The setup includes master and remote optical clocks based on self-referenced frequency combs locked to C-band cavity-stabilized lasers. The frequency combs have a repetition rate of 200 MHz. A transfer comb with a 2-kHz repetition rate offset is added on site A to perform linear optical sampling (LOS) at both sites [7]. Pulses are transmitted over a 4-km folded free-space link. The folded path enables an out-of-loop comparison of the two clocks. To remove the 5-ns time ambiguity of the LOS signals, a two-way coarse timing system based on modulated CW carriers is multiplexed into the same free-space link. The clock offset, as computed on the remote site, is used to apply feedback to the remote clock. The servo loop has a 10-Hz bandwidth and features a Kalman filter that allows the system to operate when the free-space link fades.

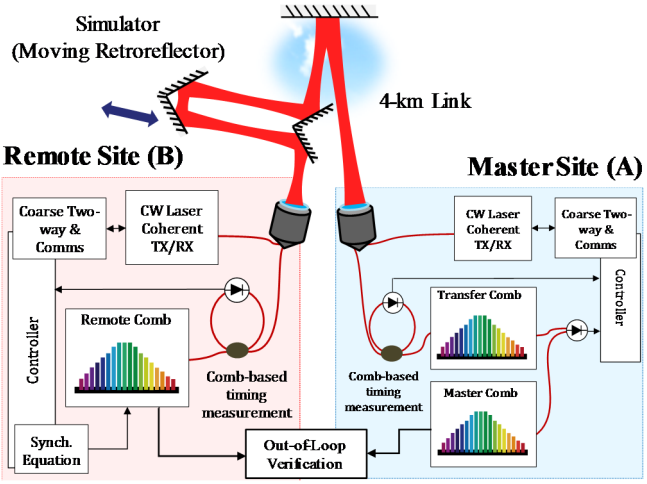


Fig. 1. Experimental setup. At each site, a frequency comb is phase-locked to a cavity stabilized laser (not shown here). CW lasers are used to gather coarse timing information and to transfer data across the link. On the master site (A), another comb is used to perform linear optical sampling. On the remote site (B), the clock offset is computed and is used to maintain synchronization between the clocks in site A's referential. To simulate clock motion, a Doppler simulator based on a retroreflector is added on site B. A separate out-of-loop measurement is performed to verify synchronization.

The setup was modified to simulate clock motion. Since the clocks used in this work are not yet fully portable, a "Doppler simulator" was built on one end of the free-space link. Its location is shown in Fig. 1. The simulator is based on a retroreflector mounted on a cart. The cart is moved along a 2-meter rail using a computer-controlled motor. Mirrors and other free-space optics were used to create effective displacements of 24 meters and velocities of up to 25 m/s.

The synchronization equations were rewritten to account for motion. Interpolation of the timing signals was used to account for the necessarily non-simultaneous LOS measurements. A velocity-dependent term was also added to address the fundamental non-reciprocity arising from to the finite speed of light. The final equation is

$$\Delta T_{AB} = \left(\frac{T_A - T_{A\to B} - T_B + T_{B\to A}}{2}\right) + \left(\frac{v}{c}\right)\left(\frac{T_A + T_{A\to B} - T_B - T_{B\to A}}{4}\right) \quad (1)$$

where ΔT_{AB} is the retrieved clock time offset. T_A is the departure time of a comb pulse from site A while $T_{A\to B}$ is the arrival time at site B of that same pulse. T_B and $T_{B\to A}$ have the same meaning but refer to a remote comb pulse departing from site B. These pulse departure and arrival times are derived from a combination of LOS and coarse timing signals. The first term in equation (1) is the classic two-way time transfer equation for static platforms. The velocity (v) relative to the speed of light (c) can be calculated from the Doppler-shifted repetition rates of the combs at the outputs of the free-space link.

III. Results

Using the setup and equation described above, we demonstrated successful synchronization across the 4-km link even during retroreflector motion. Fig. 2 shows a typical subset of the data for the velocity and out-of-loop time difference between the clocks during motion. The distance was varied between 4 km and 4 km + 24 m. The systematic time offset due to velocity is well below the loop residuals and is not visible on this scale. It is worth noting that using a non-Doppler-tolerant equation would lead picosecond-level clock time offsets. As in Ref. [3], long free-space dropouts were masked to make any underlying structure in the out-of-loop data more evident.

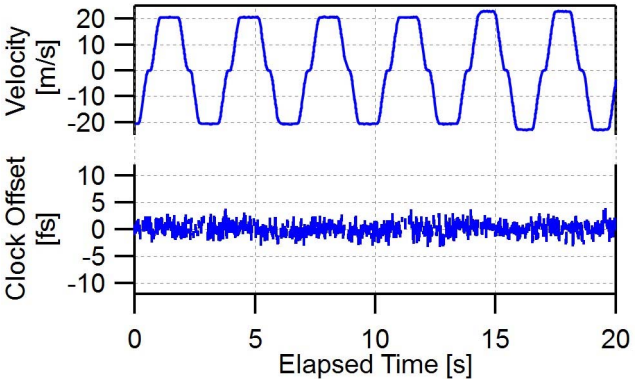


Fig. 2. Synchronization at the femtosecond level during motion. The clock offset has been averaged and re-sampled to a 10-Hz bandwidth, which the synchronization feedback bandwidth. The free-space link dropouts were masked to only show the results during active synchronization.

A small residual velocity dependence is found when performing a statistical analysis. For this analysis, the clock time offsets during constant-velocity segments were averaged and plotted against velocity. The results are shown in Fig. 3a. The residual bias remains below 500 as for velocities up to ±24 m/s with a slight statistically significant bias present at the highest velocities. For velocities beyond ±24 m/s, additional technical challenges will arise; however, equation (1) will remain valid to the first order. The time deviation, shown in Fig. 3b, stays below 1 fs from 0.1 to 200 seconds of averaging. Comparing these numbers with previous work reveals that no stability degradation occurs during motion. In fact, the time deviation is lower than before at all averaging times considered, dipping below 100 attoseconds at a hundred seconds of averaging.

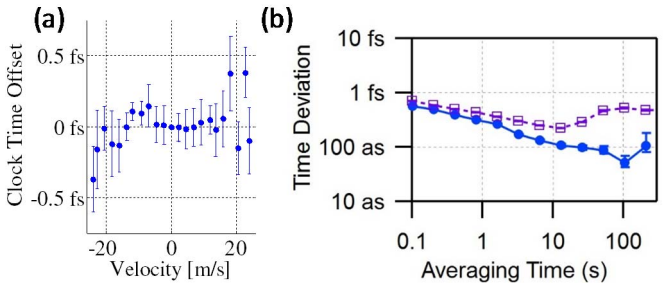


Fig. 3. (a) Constant-velocity averages of residual time offsets during synchronization. (b) Time deviation for a 4 km free-space link and ±24 m/s motion (blue circles) and for previous static results presented in Ref. [3] (purple squares).

IV. Conclusions

We demonstrate real-time synchronization of two optical clocks at the femtosecond level across a free-space link with a varying path length. We show that the velocity-dependent residuals are below 500 as for motion up to ±24m/s. No stability degradation is observed for ±24 m/s compared to a static link. The master synchronization equation presented here is valid for all velocities to first order although the implementation would need modifications to support even larger Doppler shifts. We believe that Doppler-tolerant optical two-way time and frequency transfer will be a crucial part of future clock networks.

References

[1] K. Predehl, G. Grosche, S. M. F. Raupach, S. Droste, O. Terra, J. Alnis, T. Legero, T. W. Hänsch, T. Udem, R. Holzwarth, and H. Schnatz, "A 920-Kilometer Optical Fiber Link for Frequency Metrology at the 19th Decimal Place," Science 336, 441–444 (2012).

[2] A. Bercy, F. Stefani, O. Lopez, C. Chardonnet, P.-E. Pottie, and A. Amy-Klein, "Two-way optical frequency comparisons at 5 × 10-21 relative stability over 100-km telecommunication network fibers," Phys. Rev. A 90, 061802 (2014).

[3] J.-D. Deschênes, L. C. Sinclair, F. R. Giorgetta, W. C. Swann, E. Baumann, H. Bergeron, M. Cermak, I. Coddington, and N. R. Newbury, "Synchronization of Distant Optical Clocks at the Femtosecond Level," Phys. Rev. X 6, 021016 (2016).

[4] H. Bergeron, L. C. Sinclair, W. C. Swann, C. W. Nelson, J.-D. Deschênes, E. Baumann, F. R. Giorgetta, I. Coddington, and N. R. Newbury, "Tight real-time synchronization of a microwave clock to an optical clock across a turbulent air path," Optica 3, 441 (2016).

[5] L. C. Sinclair, W. C. Swann, H. Bergeron, E. Baumann, M. Cermak, I. Coddington, J.-D. Deschênes, F. R. Giorgetta, J. C. Juarez, I. Khader, K. G. Petrillo, K. T. Souza, M. L. Dennis, and N. R. Newbury, "Synchronization of clocks through 12 km of strongly turbulent air over a city," Appl. Phys. Lett. 109, 151104 (2016).

[6] F. Riehle, "Optical clock networks," Nat. Photonics 11, 25–31 (2017).

[7] F. R. Giorgetta, W. C. Swann, L. C. Sinclair, E. Baumann, I. Coddington, and N. R. Newbury, Optical Two-Way Time and Frequency Transfer over Free Space, Nat. Photonics 7, 434 (2013).

Femtosecond Atmospheric Frequency Transfer Using Diode Laser with Electronic Phase Compensation

Shijun Chen, Dawei Chen, Qiang Chen
Zhongxing Telecommunication Equipment (ZTE) Corporation
Shenzhen, Guangdong
chen.shijun@zte.com.cn

Fuyu Sun, Jianguo Hu, Xianhe Huang, Dong Hou
School of Automation Engineering
University of Electronic Science and Technology of China
Chengdu, China
houdong@uestc.edu.cn

***Abstract*—We demonstrated an atmospheric radio-frequency transfer over a 50 m outdoor free-space link using a compact diode laser with an electronic phase compensation technique. With transferring a 1 GHz microwave signal in 5000 seconds, the total root-mean-square (RMS) timing fluctuation was measured to be about 560 fs, with fractional frequency instability on the order of 4×10^{-13} at 1 s, and order of 4×10^{-16} at 1000 s. This atmospheric frequency transfer scheme can be used to disseminate a commercial Rb or Cs clock via a free-space transmission link.**

Keywords—free-space communication; frequency dissemination; turbulence effect; phase compensation

I. INTRODUCTION

Timing and frequency transfer are important to precision scientific and engineering applications such as optical and microwave frequency standards, optical communication, radar, and navigation [1-4]. Over the past decades, many researches of highly stable frequency distribution were focused on the transfer technique via fiber link [5-10]. Recently, timing and frequency transfer based on optical laser over free-space links has begun to attract a remarkable attention as it can provide higher flexibility than fiber links [11]. This free-space frequency distribution can benefit the application for high-fidelity optical links in the future space-terrestrial networks [12] and alternative navigating schemes independent of the global positioning system [13]. In the last few years, there have been several important works in atmospheric free-space transfer of optical and microwave frequency information. Sprenger et al. have studied the frequency transmission of both optical-frequency and radio-frequency (RF) clock signals over 100 m atmospheric link using a continuous wave (CW) laser [14]. Gollapalli and Duan used a pulsed laser to achieve an atmospheric transfer of both RF and optical clock signals over 60 m free-space link [15, 16]. With two cavity stabilized optical frequency combs, Giorgetta et al. demonstrated an optical time-frequency transfer over kilometers free-space link via two-way exchange between coherent frequency combs with the timing resolution of femtosecond level [17, 18]. J. Miao et al. used microwave antennas to achieve a radio frequency dissemination scheme via free space link at different distances ranging from 10 to 640 m [19]. Recently, Kang et al. have reported a technique of timing jitter suppression for indoor atmospheric frequency comb transfer, which achieved few femtosecond timing fluctuation [20].

Although these works have demonstrated that the atmospheric free-space frequency transfers based on CW laser or optical frequency comb (OFC) achieve a high transmission precision of picosecond or femtosecond [14-21], the most of one-way outdoor atmospheric frequency transfer experiments have not reported the active suppression of timing fluctuations affected by air turbulence and temperature drift. In this case, the extra timing fluctuations would limit the application of laser-based atmospheric frequency transfer in the area where a higher precision synchronization system should be constructed.

In this paper, we present an outdoor atmospheric frequency transfer over free-space link using a compact diode laser with an electronic phase compensation technique. In our experiment, we loaded a 1 GHz microwave signal to a compact diode laser with a current amplitude modulation (AM) technique, and then transfer it over a 50 m free-space link. The timing fluctuation affected by turbulence was suppressed by an electronic phase compensation technique. The experiment result shows that the RMS timing fluctuation of the transferred 1 GHz microwave signal via a 50 m free-space link was ~560 fs within 5000 s in a normal outdoor environment.

II. SCHEMATIC AND EXPERIMENTAL SETUP

Figure 1 shows the schematic of our atmospheric frequency transfer using a CW laser with an electronic phase compensation technique. The optical carrier is provided by a CW diode laser. A microwave frequency source, is phase-shifted by a voltage-controlled phase shifter first, and then directly loaded onto the optical carrier via a current amplitude

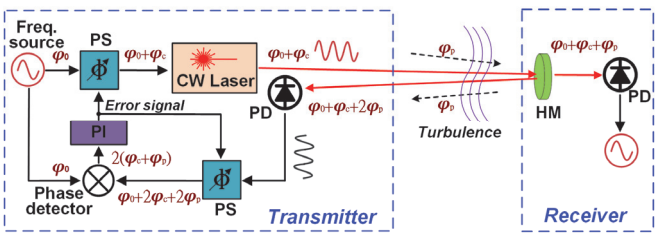


Fig. 1. Schematic of the atmospheric frequency transfer with an electronic phase compensation technique. PS: phase shifter, CW: Continuous-wave, PD: photodiode, HM: half-mirror, PI: Proportion-Integration controller.

modulation (AM) scheme. The modulated laser beam is launched into the free-space transmission link from the transmitter. On the receiver, half of the beam is reflected by a half-mirror, and the remaining half of beam is directly converted to a microwave signal via a high-speed photodiode for users. The returning beam which transmits the same optical path along the forward free-space transmission link, is detected by another high-speed photodiode on the transmitter. The detected microwave signal from the photodiode is phase-shifted by an identical electronic phase shifter, and then compared with the reference source signal on a phase detector, to generate a phase error signal which includes the information of timing fluctuations affected by air turbulence. This error signal is feed-backed to the two identical phase shifters via a PI servo controller, to adjust the phase delay on each phase shifter. When the servo loop is closed, the timing fluctuation affected by turbulence in the free-space frequency transmission can be corrected by the phase compensation technique. Note that, the phase shifters produce the same phase delays, because they are controlled by the same error signal simultaneously. The mechanism of the phase compensation will be explained in detail below.

As shown in Fig. 1, we assume that the frequency source generates a microwave signal with an initial phase φ_0. On the transmitter, this signal is phase-shifted with φ_c first, and then delivered to the receiver over a free-space link. Assuming the air turbulence introduces a phase fluctuation φ_p to the transmitted signal over an one-trip free-space link, the total phase delay of the recovered microwave signal on the receiver is given by $\varphi_{total}=\varphi_0+\varphi_c+\varphi_p$. With a half-mirror, half of beam is reflected to the transmitter along the almost same optical path, which will introduces a same turbulence-affected phase fluctuation φ_p. In this case, the returning microwave signal detected by the photodiode has a phase delay $\varphi_0+\varphi_c+2\varphi_p$ due to the twice turbulence effect. After passing through an identical phase-shifter, another phase delay φ_c is introduced to the returned microwave signal. Therefore, the phase delay of the returned microwave signal is given by $\varphi_{returned}=\varphi_0+2\varphi_c+2\varphi_p$. After eliminating the initial phase φ_0 by comparing with reference signal, we get an intermediate frequency signal with the phase error information $2(\varphi_c+\varphi_p)$. Here, this error signal is used to control the two identical phase shifters via a PI servo controller, for compensating the turbulence-affected phase φ_p.

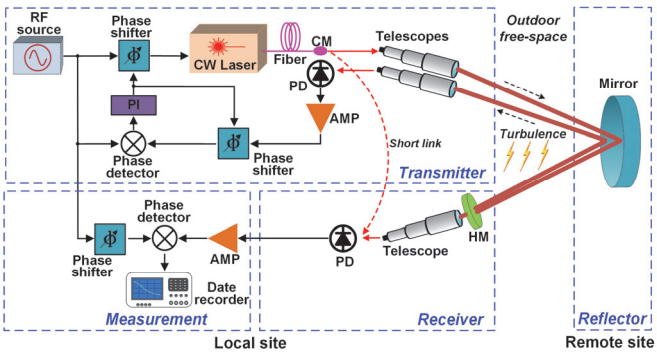


Fig. 2. Experimental setup of our atmospheric frequency transfer system using a compact diode laser with electronic phase compensation. PS: phase shifter, CM: collimator, PD: photodiode, AMP: amplifier, LPF: low-pass filter, HM: half-mirror, PI: Proportion-Integration controller.

When the servo loop is closed, the phase error $2(\varphi_c+\varphi_p)$ equals zero, and consequently, the timing fluctuation affected by air turbulence for the recovered microwave signal on receiver will be corrected as $\varphi_c=-\varphi_p$. With this electronic phase compensation technique, the timing fluctuation performance and stability of our atmospheric frequency transfer will be improved significantly, compared to the direct transmission link without phase compensation.

Figure 2 shows the experimental setup of our atmospheric frequency transfer system using a compact diode laser with electronic phase compensation. Our microwave transmission link was located on a long outdoor aisle in the engineering building of our university. At local site, an optical carrier was provided by a commercial Distributed Feedback Laser (DFB) laser diode centered at 1550 nm with a linewidth of about 3 MHz and an output power of 20 mW. A 1 GHz microwave signal with a power of ~20 mW, generated from a RF signal source (Agilent, E4421B), was phase-shifted first, and then loaded onto the optical carrier via a direct current AM scheme. The modulated laser beam was coupled to a telescope via a short fiber, and then launched into the free-space transmission link from the transmitter. At 25 m far away remote site, the beam was sent back to the receiver by a golden-coated two-inch reflector, which forms a total 50 m one-way transmission link in open air. At the receiver, half of the transmitted beam was reflected to transmitter along the same optical path by a half-mirror. The reflected beam with power of about 3 mW is collected by another telescope and tightly focused onto a high-speed photodiode on the transmitter. The converted 1 GHz microwave signal with twice phase fluctuations was amplified, phase shifted, and then mixed with the RF reference source signal to generate the phase error signal. This error signal was feed-backed to the two identical phase shifters (Mini-circuit, JSPHS-1000) via a fast PI servo controller, to compensate the phase fluctuations affected by the air turbulence. On the receiver, with another high-speed photodiode, the remaining beam with power of about 8 mW was also converted to a microwave signal. This recovered microwave signal, was also amplified, filtered and mixed with the frequency reference source, to produce a DC output. After low pass filtering, the DC signal was recorded on a digital voltage meter (Keysight, 34461A), for estimating the quality of the frequency transmission. Note that, our experimental setup was in an outdoor open air environment, the air turbulence and temperature drift could affect the phase of the transmission signal directly. In addition, we collected the optical light on the photodiode as much as possible to acquire the highest signal-to-noise ratio (SNR), and mounted the telescopes as strong as possible to cancel the influence from the beam wandering.

III. Experiment Results

The outdoor frequency transfer experiment was conducted in the midnight, and the most of windows and doors of our building were opened during the measuring time. Therefore, there were a strong wind and air flow around the aisle. The transfer experiment lasted for about 5000 s, and the timing fluctuations of the transferred microwave signal have been sampled with a voltage meter (Keysight, 34461A). In this experiment, the two telescopes were put as close as possible on

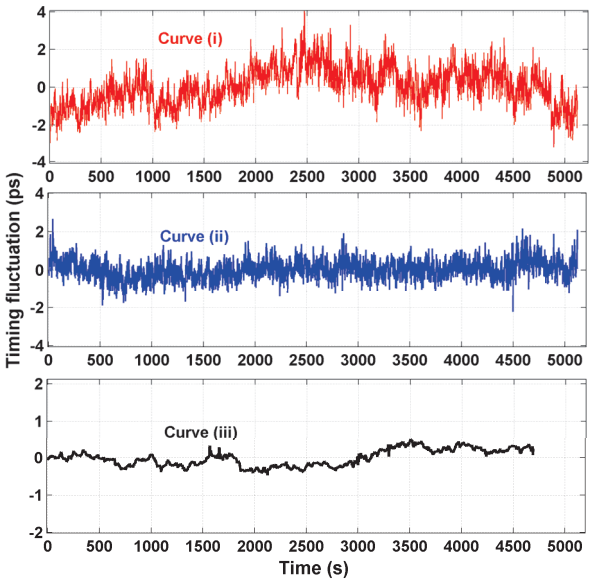


Fig. 3 Timing fluctuation results for the atmospheric microwave transfer. Curve (i): The result for 50 m free-space transmission link without phase compensation. Curve (ii): The result for 50 m free-space transmission link with phase compensation. Curve (iii): The result for a short link on local site as a measurement floor.

the transmitter, to get the identical turbulence effect over the bidirectional transmission links. Since the phase compensation can suppress the extra timing fluctuations affected by turbulence, we believe the quality of the frequency transfer could be improved distinctly, compared to the direct link.

The measured timing fluctuation results for the free-space transfer of 1 GHz microwave signal are shown in Fig. 3. Curve (i) shows the timing fluctuation of transmitted microwave signal without phase compensation, and its calculated RMS timing fluctuation is about 1.1 ps within 5000 s. Curve (ii) shows the timing fluctuations of transmitted microwave signal with phase compensation, and the RMS timing fluctuation is reduced to about 560 fs within 5000 s. Here, we also measured the timing fluctuations of frequency transfer with a short link (shown in Fig. 2) as the measurement floor, which is just attributed by the electronic noise of our photonic system. For this short link, its timing fluctuation is shown as curve (iii), and the RMS timing fluctuation is calculated out about 280 fs within 5000 s. With the comparison between the transmission link with and without phase compensation, we believe that the phase compensation technique suppressed the timing fluctuations effectively.

Figure 4 demonstrates the instability results for the transferred microwave signal. Curve (i) is the relative Allan Deviation result for the transferred signal without phase compensation, which is calculated out from the sampled data in Fig. 3. From Curve (i), it shows the 50 meters free-space frequency transmission link without phase compensation has a instability of 5×10^{-13} for 1 s and 8×10^{-16} for 1000 s. Curve (ii) is the relative Allan Deviation result for the transferred signal with phase compensation, and it shows the 50 meters free-space frequency transmission link with phase compensation has a instability of 4×10^{-13} for 1 s and 4×10^{-16} for 1000 s. Curve (iii) shows the measurement floor, which was obtained

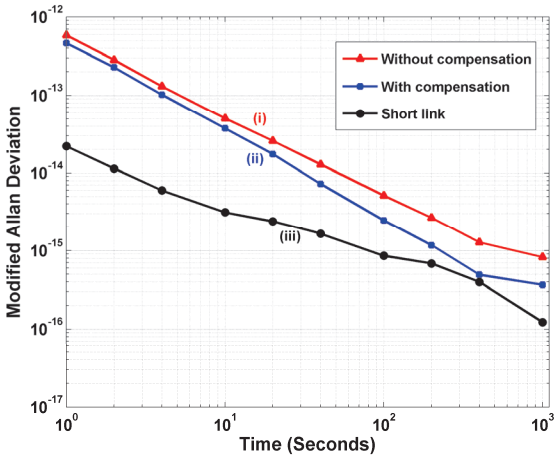


Fig. 4 Instability results for the atmospheric microwave transfer, (i) Relative Allan Deviation between the transferred microwave and reference signal without phase compensation; (ii) Relative Allan Deviation with phase compensation; (iii) Allan Deviation for a short link as Measurement floor.

via a short link (see Fig. 2). With comparison of these curves, we find that the instability of the transferred signal with phase compensation is improved greatly. Note that, curve (iii) is merely the lower bound of the instability incurred during atmospheric transfer of microwave signals. This is because it was measured only with the short link, and the most of turbulence effect was cancelled. This Allan Deviation measurement floor in our case is limited by the stability of the frequency source and the electronic noise on local site. With comparison of Curve (i) and (ii), we find that the long-term instability of the free-space transferred signal with phase compensation is reduced for about more than a half of order of magnitude at 1000 s due to the timing fluctuation suppression. The accuracy achieved by our atmospheric frequency transfer system with phase compensation may be quite adequate with some short distance free-space applications. With comparison with instability of our transfer result and a commercial Cs clock (5071A) [22], we can find that the instability of our transmission link is lower than the Cs clock. Therefore, we believe that disseminating a Cs or Rb clock signal over free-space link by using the proposed atmospheric frequency transfer scheme in this paper is feasible.

IV. Conclusion

We have demonstrated an outdoor atmospheric frequency transfer using a compact diode laser with a phase compensation technique. The RMS timing fluctuation for a 50 m transmission of a 1 GHz clock frequency was measured to be approximately 560 femtosecond within 5000 s, with fractional frequency instability on the order of 4×10^{-13} at 1 s, and order of 4×10^{-16} at 1000 s. The achieved instability demonstrates that such frequency transmission setup with phase compensation promises a high flexibility of timing and frequency dissemination in a practical application. For instance, transferring a Cs or Rb clock signal to remote users via a free-space transmission link. The outdoor atmospheric frequency transfer will suffer from the effect of environment, such as wind, temperature drift and vibration, resulting in the extra timing fluctuations. However, the most of these timing

fluctuations can be suppressed by the electronic phase compensation technique proposed in this paper. In the future, we will challenge in building an atmospheric frequency transmission link with lower timing fluctuation and longer distance using higher power laser, higher frequency microwave, and fast steering mirror which is used to cancel the beam vibration.

ACKNOWLEDGMENT

This work was supported by the National Key Research and Development Program of China (No. 2016YFB0502001, 2016YFB0502003), by Shenzhen strategic emerging industry special fund (No. JSGG20150330145709677), by the National Natural Science Foundation of China (No. 61601084), by State Key Laboratory of Advanced Optical Communication Systems and Networks, China, and by the ZTE Research Fund.

REFERENCES

1. J. Levine, "A review of time and frequency transfer methods," Metrologia, vol. 45, no. 6, pp. 162-174, December 2008.
2. B. H. Li, C. Rizos, H. K. Lee, and H. K. Lee, "A GPS-slaved time synchronization system for hybrid navigation," GPS Solut.,vol..10, no.3, pp. 207-217, July 2006.
3. W. Q. Wang, C. B. Ding, and X. D. Liang, "Time and phase synchronisation via direct-path signal for bistatic synthetic aperture radar systems," IET Radar Sonar. Nav., vol. 2, no. 1, pp. 1-11, February 2008.
4. S. Bregni, "A historical perspective on telecommunications network synchronization," IEEE Commun. Mag., vol. 36, no. 6, pp. 158-166, June 1998.
5. S. M. Foreman, K. W. Holman, D. D. Hudson, D. J. Jones, and J. Ye, "Remote transfer of ultrastable frequency references via fiber networks," Rev. Sci. Inst., vol. 78, no. 2, 021101, February 2007.
6. J. Kim, J. A. Cox, J. Chen, and F. X. Kärtner, "Drift-free femtosecond timing synchronization of remote optical and microwave sources," Nat. Photon., vol. 2, no. 12, pp. 733-736, December 2008.
7. D. Hou, P. Li, P. Xi, J. Zhao, and Z. Zhang, "Timing jitter reduction over 20-km urban fiber by compensating harmonic phase difference of locked femtosecond comb," Chin. Opt. Lett. vol. 8, no.10, pp. S993-S995, October 2010.
8. K. Predehl, G. Grosche, S. M. Raupach, S. Droste, O. Terra, J. Alnis, T. Legero, T. W. Hänsch, T. Udem, R. Holzwarth, and H. Schnatz, "A 920-kilometer optical fiber link for frequency metrology at the 19th decimal place," Science, vol. 336, no. 6080, pp. 441-444, April 2012.
9. X. Chen, J. Zhang, J. Lu, X. Lu, X. Tian, B. Liu, H. Wu, T. Tang, K. Shi, and Z. Zhang, "Feed-forward digital phase compensation for long-distance precise frequency dissemination via fiber network," Opt. Lett., vol. 40, no. 3, pp. 371-374, February 2015.
10. B. Wang, X. Zhu, C. Gao, Y. Bai, J. Dong, and L. Wang, "Square kilometre array telescope — precision reference frequency synchronisation via 1f-2f dissemination," Sci. Rep., vol. 5, September 2015.
11. T. Mao, Q. Chen, W. He, Y. Zou, H. Dai, and G. Gu, "Free-space optical communication using patterned modulation and bucket detection," Chin. Opt. Lett., vol. 14, no. 11, November 2016.
12. V. W. S. Chan, "Free-space optical communications," J. Lightwave Technol. vol. 24, no. 12, pp. 4750-4762, December 2006.
13. F. Pappalardi, S. J. Dunham, M. E. LeBlang, T. E. Jones, J. Bangert, and G. Kaplan, "Alternatives to GPS," in Proceedings of OCEANS 2001, MTS/IEEE Conference and Exhibition 2001.
14. B. Sprenger, J. Zhang, Z. Lu, and L. Wang, "Atmospheric transfer of optical and radio frequency clock signals," Opt. Lett., vol. 34, no. 7, pp. 965-967, April 2009.
15. R. P. Gollapalli and L. Duan, "Atmospheric timing transfer using a femtosecond frequency comb," IEEE Photon. J. vol. 2, no. 6, pp. 904-910, December 2010.
16. R. P. Gollapalli and L. Duan, "Multiheterodyne characterization of excess phase noise in atmospheric transfer of a femtosecond-laser frequency comb," J. Lightwave Technol. vol. 29, no.22, pp. 3401-3407, November 2011.
17. F. R. Giorgetta, W. C. Swann, L. C. Sinclair, E. Baumann, I. Coddington, and N. R. Newbury, "Optical two-way time and frequency transfer over free space," Nat. Photonics, vol. 7, no. 6, pp. 435-439, June 2013.
18. L. C. Sinclair, W. C. Swann, H. Bergeron, E. Baumann, M. Cermak, I. Coddington, J. D. Deschênes, F. R. Giorgetta, J. C. Juarez, I. Khader, K. G. Petrillo, K. T. Souza, M. L. Dennis, and N. R. Newbury, "Synchronization of clocks through 12 km of strongly turbulent air over a city," Appl. Phys. Lett., vol. 109, no. 15, October 2016.
19. J. Miao, B. Wang, Y. Bai, B. Y. Yuan, C. Gao, and L. J. Wang, "Portable microwave frequency dissemination in free space and implications on ground-to-satellite synchronization," Rev. Sci. Instrum., vol. 86, no. 5, May 2015.
20. J. Kang, J. Shin, C. Kim, K. Jung, S. Park, and J. Kim, "Few-femtosecond-resolution characterization and suppression of excess timing jitter and drift in indoor atmospheric frequency comb transfer," Opt. Express, vol. 22, no. 21, pp. 26023-26031, October 2014.
21. K. Djerroud, O. Acef, A. Clairon, P. Lemonde, C. N. Man, E. Samain, and P. Wolf, "Coherent optical link through the turbulent atmosphere," Opt. Lett., vol. 35, no. 9, pp. 1479-1481, May 2010.
22. Microsemi, "DS-5071a", http://www.microsemi.com/products /timing-synchronizationsystems/time-frequency-references/ cesium-frequency-standards/5071a , 2014.

Optically Pumped Cs Space Clock development

R.Schmeissner, P.Favard, A.Douahi,
P.Perez, N.Mestre, M.Baldy
Thales Electron Devices
Vélizy, France
Michel.Baldy@thalesgroup.com

A.Romer, F.Chastellain, W.W.Coppoolse
Thales Alenia Space,
Zurich, Switzerland

N. von Bandel, M.Garcia, M.Krakowski
III-V Lab
Palaiseau, France

S.Guérandel
LNE-SYRTE, Observatoire de Paris, CNRS, UPMC
Paris, France

Y.Folco
Thales Alenia Space
Cannes, France

W.Konrad
ARCOSIC Research e.U.
Mödling, Austria

Abstract **The Engineering Model design of the Optically pumped Space Cs Clock (OSCC) was completed in 2016 and is reported. The design describes a system of 12liters, 10kg, 30W power consumption and 12 years lifetime. It will be partially manufactured in 2017. In parallel, in depth analysis of the clock environment sensitivities was carried out and new laser sources were tested. The short-term stability of an existing Elegant Breadboard Clock was improved to below 2E-12$\tau^{-1/2}$ up to 10'000s.**

Keywords **GNSS, Optical Space Cs Clock (OSCC), DFB Laser**

I. Introduction

The optical pumping of the Cs hyperfine state was identified many years ago as a potential technology alternative to current clocks used in GNSS, and in particular in Galileo. Related industrial activities develop this technology also with focus on ground applications [1, 2]. Based on its heritage in the domains of Cs clock development, space system engineering and component qualification, Thales Group develops the Engineering Model (EM) of the Optically pumped Space Cs Clock (OSCC). The current project phase started in 2015 and will end in 2017.

II. Design of the Engineering Model

The OSCC engineering model was designed. Its mass and volume are in-line with the requirements of 12liters, 10kg 30W power consumption. The design lifetime is 12years. A visualization of the CAD model is shown in Figure 1. The system is composed of three sub-systems: an Atomic Resonator (AR) containing the thermal flux of Cs atoms, a Laser and Optics sub-system (L&O) and an Electronics Package (EP). The over-all housing concept relies on a specific stiffening structure. The AR is made of Titanium and the remaining housing parts of Aluminium. On the atomic resonator, sapphire optics are used. The latter are directly brazed to metal and the resulting junction remains hermetic under Cs tube bake-out temperature cycle.

The Cs clock development is supported by the European Space Agency under European GNSS Evolution Program (activity ID-98) and CNES under contract n° 150920. The DFB laser diode development project LAMA is supported by Euripides/CTI grant No. 14750.1 PFNM-NM

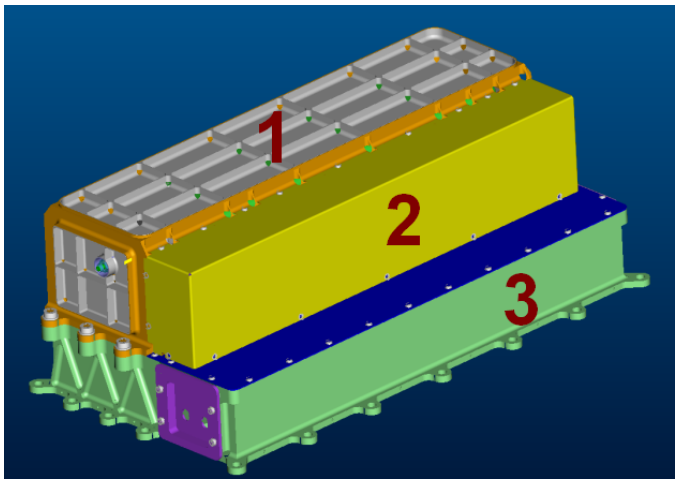


Fig. 1. Design of the OSCC Engineering Model, 1 Atomic Resonator, 2 Laser and Optics sub-system, 3 Electronics Package

Concerning space application and to withstand launch conditions, numerical analysis of the mechanical structure vibrational properties was implemented. The EP design was consolidated in terms of power consumption and signal properties. The entire system is controlled by a FPGA. High signal resolutions at low power consumption are achieved through the oversampling approach.

Based on the engineering model design, an EP and L&O sub-system are currently manufactured. They shall be tested in fall-2017.

III. Test of new Laser Diode Sources

An Elegant Breadboard (EBB) Prototype of the OSCC Clock was manufactured in 2013 and contained only the core functions of the Cs clock. This prototype was updated by so-called secondary loops actively stabilizing the physical environment of the Cs atoms: Optical Power, Magnetic Field and RF-Power. The improved setup is used to test different clock configurations and to de-risk the design files of the engineering model.

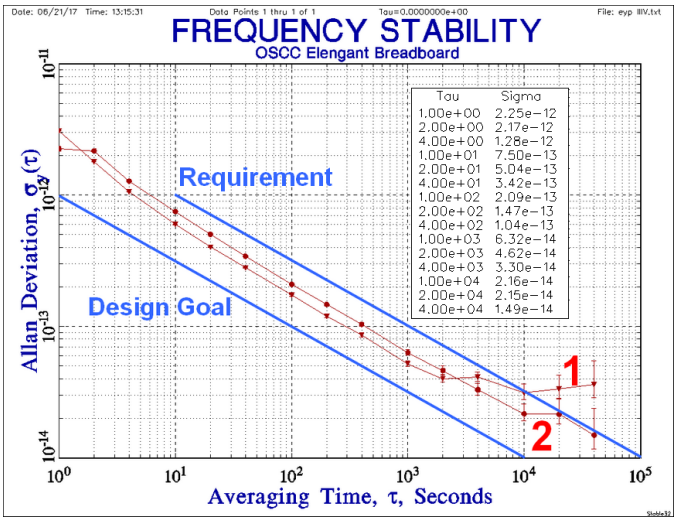


Fig. 2. OSCC stability performance measured against H-Maser at 100°C Cs oven temperature. Laser sources are: 1 III-V Lab, 2 eagleyard. The trace 1 was measured without, trace 2 with secondary lock-loops in operation.

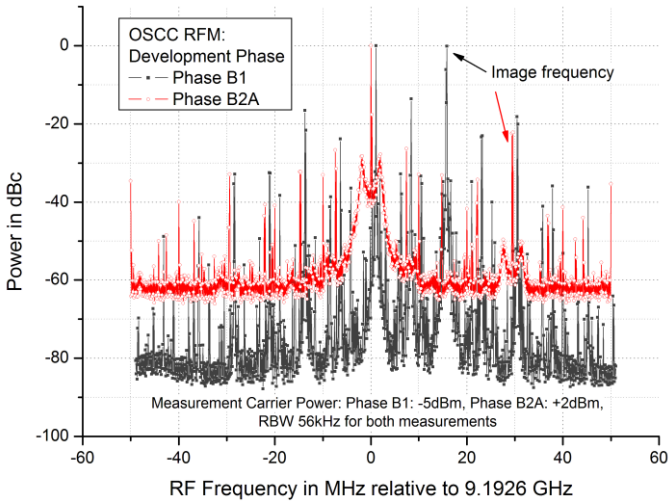


Fig. 3. Spectrum of the EM RF-Module. Phase B1 refers to the initial RF-Module design, phase B2A refers to the ongoing prototyping of Enigineering Model sub-systems.

A particular aspect of clock configuration concerns the laser source for optical hyperfine pumping and detection. TO3 packaged DFB laser diodes at the most suitable Cs D1 894nm transition became available from two suppliers in 2016 [4, 5, 6]. In the framework of OSCC project, these sources will undergo a space-evaluation in 2017.

Figure 2 shows the short-term stability of the improved EBB clock for two different laser diode sources and with/without secondary lock loops. Short-term stability of better than 2E-12$\tau^{-1/2}$ Allan Deviation was verified for the two laser diodes. The slightly better clock signal noise level for one of the two is most likely related to the smaller optical linewidth of this source. The observed clock short-term stability value is in-between the design-goal of 1E-12$\tau^{-1/2}$ and the requirement of 3E-12$\tau^{-1/2}$. The underlying clock SNR is limited by the shot noise of atomic fluorescence. The reproduced long-term stability floor at 1E5 seconds, measured on the OSCC Elegant Breadboard is better than 5E-14. Measurements indicate that the electronic flicker floor is well below this value. Hardware design improvements are expected to further improve the long-term stability.

IV. Hardware Development – RF Module

Compared to the EBB clock prototype, a new RF-Module was designed and already manufactured and tested. It links the 10MHz user signal to the 9.19GHz atomic interrogation signal. Key requirements concern low phase noise and the suppression of any image of the RF-carrier. Indeed, any additional frequency in the spectrum induces an RF-power dependent clock frequency shift, the Bloch-Siegert shift [7]. The phase noise requirements are reached through values as low as -90dBc at 1kHz from RF carrier. Figure 3 shows the suppression of any image frequency below -25dBc (non-optimized configuration). Space qualified equivalent components are available for the entire RF-Module design.

V. Summary of Development Activities

The design of the OSCC engineering model will be completed in 2017. A functually representative prototype is currenly manufactured. It shall demonstrate a long-term stability below 1E-14. The space evaluation of the optoelectronic components : low-noise, large area photodiode and DFB laser diode will start in fall 2017. The photodetector and the III-V Lab laser diode are specific developments for the OSCC application.

Acknowledgment

The authors acknowledge European Space Agency (ESA), the Centre National d'Etudes Spatiales (CNES), EURIPIDES and Thales Electron Devices for financial support of the project. The authors are grateful for helpful discussion and technical support to V.Hermann, G.Corridor and G.Gauthier at Thales Electron Devices, G.Baily and L.Morvan at Thales Research and Technology, Palaiseau, J.Delporte, F-X Esnault, O.Gilard and J.Mekki at CNES, Toulouse, C.Bringer and P.Waller at ESA-ESTEC, Noordwijk.

References

[1] Progress in the Development of Commercial Optically Pumped Cs Atomic Clock, Yuanhong Cao, et al., International Frequency Control Symposium , Proceedings of IFCS 2014

[2] Development of a transportable optically pumped atomic Cs beam clock, P.Berthoud et al., Proceedings of EFTF 2015

[3] The optical feedback spatial phase driving perturbations of DFB laser diodes in an optical clock, R.Schmeissner et al., Proceedings of EFTF 2016

[4] Towards an Engineering Model of Optical Space Cs Clock, R.Schmeissner et al., Proceedings of EFTF 2016

[5] DFB-ridge laser diodes at 894 nm for Cesium atomic clocks, N. Von Bandel, et al Photonics West 2016, OPTO-2016, Paper 9755-90

[6] eagleyard Part No. EYP-DFB-0852-00150-1500-TOC03-0005

[7] Vanier, J., & Audoin, C. (1989). The quantum physics of atomic frequency standards

GHz Ultrasonics for On Chip Delay Lines, Communications, Timing, Memory, and Sensing

Amit Lal
SonicMEMS Laboratory, School of Electrical and Computer Engineering
Cornell University
Ithaca, NY, USA
amit.lal@cornell.edu

***Abstract*—Integrated GHz ultrasonics on planar systems such as CMOS chips are enabled by integration of fast, deep sub-micron transistors and GHz thin film piezoelectric transducers. Precision and stability in a delay element block is one of the key specifications that directly impacts all the applications. We have implemented a pulse-echo transmit-receive ultrasonic delay element that is stable over time and has a novel diffraction based zero temperature coefficient of delay at two temperatures. The silicon bulk wave propagation leads to stable operation owing to low loss within silicon and large mode volume.**

Keywords— Integrated ultrasonics, delay lines, silicon bulk wave propagation

I. INTRODUCTION

Integrated GHz ultrasonics on planar systems such as CMOS chips are enabled by integration of fast, deep sub-micron transistors and GHz thin film piezoelectric transducers. Sonic wavelengths on the order of a few microns can generate wave packets with spatial extent that is less than the substrate thickness. The role of diffraction of wave packets, coupled with time-of flight have been used to form a useful set of devices. With integration with deeply scaled CMOS that provides GHz electronics, one can envision chip-scale microsystems that provide unprecedented manipulation of sonic energy. We have used these CMOS chips to demonstrate sensing biological ultrasonic impedance to extract fingerprints and tissue type [1,5], communicate on a chip using ultrasonic pulses [6, 7,8], and implemented ultrasonic memory [3,4]. A delay block is a circuit that shifts the input signal in time by a desired amount, and delivers a delayed output like the input signal. Delay elements can be used in wide range of applications including phase modulation in clocking systems as well as different digital systems. Furthermore, stable delay elements can be used as a timing reference in delay-locked-loops where the delay can be calibrated across different temperature and process variations. Precision and stability in a delay element block is one of the key specifications that directly impacts all the applications. We have implemented a pulse-echo transmit-receive ultrasonic delay element that is stable over time and has a novel diffraction based zero temperature coefficient of delay at two temperatures. The silicon bulk wave propagation leads to stable operation owing to low loss within silicon and large mode volume. The delay element achieves <6ppm stability and demonstrates zero temperature coefficient at 43C and 72C. A recently implemented oscillator using the delay element in an oscillator configuration achieved <1ppm stability [2].

REFERENCES

[1] J. Kuo, J. Hoople, M. Abdelmejeed, M. Abdel-moneum, and A. Lal, "64-Pixel Solid State CMOS Compatible Ultrasonic Fingerprint Reader," in 2017 IEEE International Conference on Micro Electro Mechanical Systems (MEMS), 22-26 Jan. 2017, 2017, p. 4 pp.

[2] Abdelmejeed, M., Kuo, J., Lal, A., "AlN GHz Ultrasonic Pulse Diffraction Based Transmit-Receive Oscillator with 1 Ppm Stability," The 19th International Conference on Solid State Sensors, Actuators, and Microsystems, Taiwan, pp. 106-109, June 2017

[3] J. Kuo, J. Hoople, S. Ardanuç, and A. Lal, "Towards ultrasonic through-silicon vias (UTSV)," in IEEE International Ultrasonics Symposium, IUS, 2014.

[4] J. Kuo, J. Hoople, and A. Lal, "Towards a CMOS compatible ultrasonic delay line memory," in 2015 IEEE International Ultrasonics Symposium, IUS 2015, 2015.

[5] J. Hoople, J. Kuo, M. Abdel-Moneum, and A. Lal, "Chipscale GHz ultrasonic channels for fingerprint scanning," in 2015 IEEE International Ultrasonics Symposium, IUS 2015, 2015.

[6] J. Hoople, J. Kuo, S. Ardanuc, and A. Lal, "Chip-scale reconfigurable phased-array sonic communication," in Ultrasonics Symposium (IUS), 2014 IEEE International, 2014, pp. 479–482.

[7] J. Hoople, J. Kuo, S. Ardanuc, and A. Lal, "Chip-scale sonic communication using AlN transducers," in Ultrasonics Symposium (IUS), 2013 IEEE International, 2013, pp. 1934–1937.

[8] J. Hoople, J. Kuo, J. Soon Bo Woon, N. Singh, and A. Lal, "Optimized response of AlN stack for chipscale GHz ultrasonics," in 2015 IEEE International Ultrasonics Symposium (IUS), 21-24 Oct. 2015, 2015, p. 4 pp.

Acoustic Delay Lines to Measure Piezoelectricity in 4H Silicon Carbide

Pen-Li Yu and Sunil A. Bhave
OxideMEMS Lab, Purdue University
West Lafayette, IN, 47907, USA
yu586@purdue.edu

This paper reports the first measurement of the electromechanical coupling coefficient (K^2) for the Rayleigh wave in 4H polytype of Silicon Carbide (SiC). We fabricate 18 acoustic delay lines on two 4H SiC chips. Transmitted acoustic signals are measured at 423 MHz and 676 MHz for devices with 16 μm and 10 μm wavelength, respectively. We post-process the transmitted signal in time-domain to isolate the surface acoustic wave transmission. From the filtered signals we extract K^2 to be (0.93±0.05) ×10^{-4} % and (0.66±0.02) ×10^{-4} % at 423 MHz and 676 MHz.

Keywords—Silicon Carbide; Piezoelectric coupling coefficient; Surface acoustic wave; Acoustic delay line; Time-domain analysis.

I. INTRODUCTION

Color centers in wide-bandgap semiconductor crystal have emerged as a promising quantum resource with applications in quantum computing and quantum sensing [1]. The localized electrons in the defects host room-temperature spin states with analogous properties to atoms trapped in vacuum. Interaction between these spin states and strain field open the prospects of control and readout these spin quantum bits (qubits) with resonant piezoelectric nano- and micro-electromechanical devices (NEMS and MEMS) [2]–[6]. MacQuarrie et al. [3] demonstrated that to control these defect spins in a non-piezoelectric semiconductor such as diamond, one can fabricate a piezoelectric transducer on the substrate to generate large oscillation stress [7]. In contrast to this approach, discovering a piezoelectric semiconductor crystal that hosts defect spins could add flexibility and scalability to the design of hybrid quantum devices.

A piezoelectric potential can be created in a binary crystal with non-inversion symmetry, such as zincblende and wurtzite crystal structures. In these crystals, ions are polarized under applied stress and strain. The wurtzite structure is commonly found to host the strongest piezoelectric semiconductors, such as GaN, AlN, and ZnO. Recently, 4H and 6H silicon carbide (SiC), SiC polytypes with wurtzite structure, were found to host coherent spin states in vacancy defects at room temperature [8]. 6H SiC has been reported to have weak piezoelectricity in 1965 [9] and 1989 [10]. In Ref. [10], the authors report the electromechanical coupling factor k_{31}^2 of 6H SiC to be k_{31}^2=9.8×10^{-2} % measured using a resonator. However, the electromechanical coupling factor for 4H SiC has not been characterized yet.

We report the first measurement on K^2 for the Rayleigh wave of 4H SiC using acoustic delay lines. We measure K^2 of (0.93±0.05) ×10^{-4} % and (0.66±0.02) ×10^{-4} % at 423 MHz and 676 MHz, respectively. This level of piezoelectricity, although relatively weak, together with its ultra-high Q-frequency product [7, 10], could allow mechanical control of the ground state spin triplet in 4H SiC [12].

II. DESIGN OF EXPERIMENT

We employ surface-acoustic-wave delay lines on a 4H SiC substrate to measure K^2 of the Rayleigh wave. The delay line consists of a pair of interdigital transducers (IDTs). It introduces a time delay to an applied signal through generation, propagation, and detection of the surface acoustic wave (SAW) on a piezoelectric substrate. The transmission scattering parameter S_{21} contains a term proportional to K^2 and is delayed by travel time of the SAW.

Along with the SAW transmission, there is also RF feedthrough due to capacitive coupling between the two ports. Ideally, the RF feedthrough should be minimized by optimizing the IDT which makes the feedthrough negligible. However, for weak piezoelectric substrate such as 4H SiC, the SAW contribution is smaller than the RF feedthrough background.

In this measurement, we perform inverse short-time Fourier transform (inverse STFT) to separate the RF feedthrough and SAW transmission in time-domain. This is feasible because the RF feedthrough travels close to the speed of light while the SAW travels at the Rayleigh wave speed. We filter out the RF feedthrough and convert the SAW signal back to frequency domain with STFT. K^2 can then be extracted from the filtered spectrum by the Mason model [13]

$$K^2 = \frac{1 + \left[R_g 2\pi f C_T\right]^2}{2\alpha\pi R_g C_T f_0 N_p} \widetilde{S_{21}}(f_0) \qquad (1)$$

Here, K^2 is defined by $2(V_{Sf} - V_{Sm})/V_{Sf}$, where V_{Sf} (V_{Sm}) is the velocity of the free surface (metalized surface), $\widetilde{S_{21}}(f_0)$ is the filtered signal S_{21}, $f_0 = V_{Sf}/\lambda = V_{Sf}/2p$ is the fundamental center frequency of the SAW, λ is the acoustic wavelength, p is the IDT pitch, α=2.87 for solid-electrode with 0.5 metallization ratio, N_p is the number of electrode pairs, C_T is the static total IDT capacitance. In equation (1), we assume that the acoustic attenuation in the delay length of interest is negligible for determining K^2.

We use a high-purity semi-insulating 4H SiC wafer with 4" diameter and 500 μm thickness from Cree Inc. The crystal is

<0001> oriented within 0.2°. The resistivity is 10^9 ohm-cm. The wafer is diced into 1 cm square chips. Based on the measurement scheme, we design IDTs with different apertures and delay lengths. The design parameters are summarized in Table I. We fabricate 18 delay lines with 8 µm and 12 µm pitches on two chips (Fig. 1) using contact photolithography and a lift off process. The IDTs have solid-electrodes with 190 nm/10 nm Aluminum/Titanium. Aluminum is chosen to avoid internal reflection between the IDT fingers.

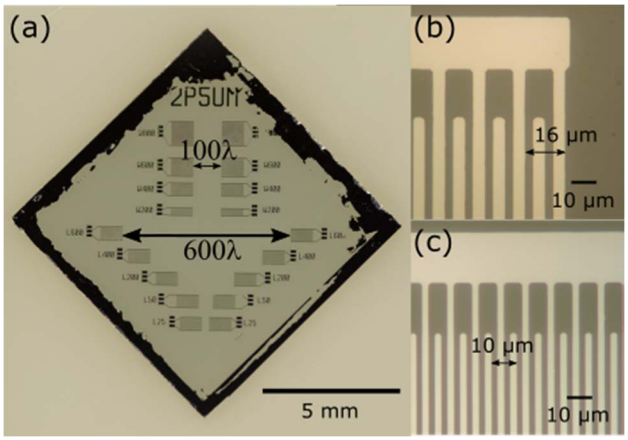


Fig. 1. Photographs of the fabricated acoustic delay lines on the 4H SiC substrates. (a) Nine delay lines with 5 µm pitch on a 1cm x 1cm SiC chip. The top four devices have a fixed IDT separation of 100 wavelength and four different apertures while the lower five devices have a fixed aperture of 400 µm and five different delay lengths. See Table I for the device parameters. The delay lines are 45° off from the chip edges to avoid reflected surface acoustic wave from the edges. (b)-(c) Photos of solid-electrode IDTs with 8 µm and 5 µm pitch, respectively.

TABLE I. DESIGN PARAMETERS OF THE SIC DELAY LINES

IDT pitch (p=λ/2)	8 µm, 5 µm
IDT pairs (N_p)	80
IDT aperture (W)	800, 600, 400, 200 µm
IDT separation (L_0)	600λ, 400λ, 200λ, 50λ, 25λ, 10λ

III. MEASUREMENT AND ANALYSIS

We measure the calibrated S parameters (S_{11}, S_{12}, S_{21}, and S_{22}) of all the acoustic delay lines using a network analyzer. The SAW velocity is reported to be 6832 m/s [14], and hence SAW signals for devices with 16 µm and 10 µm are expected to be at 427.0 MHz and 683 MHz, respectively. For each device, we analyze the amplitude and phase of S_{21}. In Fig. 2, we plot one of the measured S_{21} amplitude and phase spectrum (see Fig. 2 caption for device parameters). In Fig. 2 (a), we see a small peak with amplitude ripples at the expected frequency. On the other hand, the phase spectrum shown in Fig. 2 (b) has a cleaner SAW signature. We observe that the phase is linearly decreasing with frequency between 421 to 426 MHz, indicating the time delay due to SAW.

The device corresponding to the measurements in Fig. 2 has a delay length L, the distance between the centers of two IDTs:

$$L_0 + \frac{L_{\mathrm{IDT1}}}{2} + \frac{L_{\mathrm{IDT2}}}{2} = (400 + 40 + 40)16\ \mu\mathrm{m} = 7.68\ \mathrm{mm}$$

where L_0 is the IDT separation and $L_{\mathrm{IDT1(2)}}$ is the length of the first (second) IDT length. Hence the designed delay time is 7.68mm/(6832m/s) = 1.12 µs.

From the phase data between 421 MHz and 426 MHz, we extract a delay time by calculating the slope:

$$\tau = \frac{d\theta}{df}\frac{1}{360^o} = 1.15\ \mu s.$$

The number agrees well with the designed delay time. This proves that surface acoustic waves are generated and prorogated.

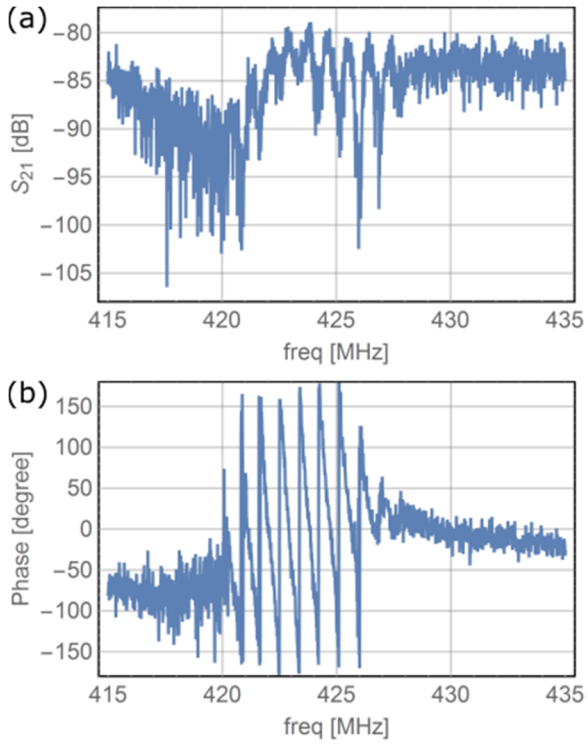


Fig. 2. Measured delay-line transmission signals. The device parameters are (p, N_p, W, L_0) = (8 µm, 80, 400 µm, 400 λ). (a) Magnitude of S_{21}. A small peak with amplitude fluctuation is visible in the 421-426 MHz range. (b) Phase of S_{21}. The negative slope of phase in the 421-426 MHz indicates a SAW delay time of 1.15 µs. This number is consistent with the expected 1.12 µs delay time.

We then perform the inverse STFT to convert the signal to time domain and plot two groups of data in Fig. 3. In Fig. 3 (a), we plot the S_{21} in time domain for devices with delay lengths (time) of 7.68 mm (1.12 µs), 4.48 mm (0.66 µs), 2.08 mm (0.30 µs), and 1.68mm (0.25 µs). For each data, we observe a RF feedthrough signal around 0s and a SAW signal at the expected delay time. In Fig. 3 (b), we plot the S_{21} in time domain for devices with the same delay length (time) of 2.88 mm (0.42 µs) and different apertures. We see that all SAW signals center at the expected delay time. Note that the SAW peaks at various delay time have the same amplitude. This verifies the assumption of Eq. 1 that the acoustic attention is negligible.

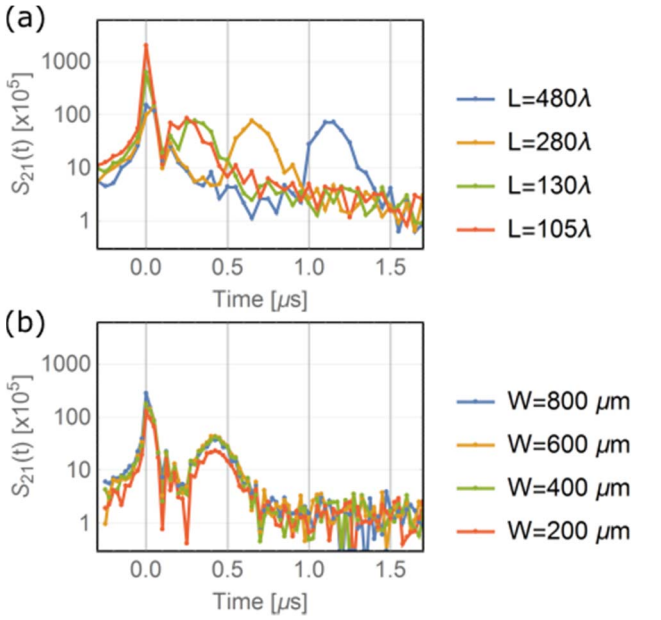


Fig. 3. Transmission signals in time domain [S_{21}(t)] for two groups of devices. For each data there are a RF feedthrough peaked around 0s and a second set of SAW signals peaked around their expected delay times. (a) Magnitude of S_{21}(t) as a function of time for four devices with different IDT separation L_0=400 λ, 200 λ, 50 λ, 25 λ. The fixed parameters are (p, N_p, W) = (8 μm, 80, 400 μm). The expected delay time for these devices are 1.12 μs, 0.66 μs, 0.30 μs, 0.25 μs, respectively. (b) Magnitude of S_{21}(t) for four devices with a common IDT separation L_0 = 100 λ, p = 8 μm, N_p = 80, and four different apertures W=800, 600, 400, 200 μm. The expected delay time is 0.42 μs. The SAW signals are relatively the same except for the W=200 μm device.

Since we can reliably detect the SAW in 4H SiC in time domain, we can filter out the RF feedthrough and isolate the SAW signals. We then perform STFT to transform time-domain SAW signals back to frequency domain. In Fig. 4, we plot two filtered signals in frequency domain. We can see that the background is greatly reduced (at least -20 dB reduction), and the remaining signals closely follow the shape of sinc function. As another check, we fit the filtered signals with the Mason model and find good agreement especially in the main lobe bandwidth. We then use Eq. 1 to extract K^2. We apply this time-domain filtering technique to all the data. The average K^2 is found to be (0.93±0.05)×10^{-4} and (0.66 ±0.02)×10^{-4} at 427 MHz and 676 MHz devices, respectively. The result is summarized in Table II.

TABLE II. SUMMARY OF THE MEASUREMENTS

Parameters	Measured values
Capacitance per finger pair (C_s)	1pF/cm
K^2 from data set with 8 μm pitch	$(0.93 \pm 0.05) \times 10^{-4}$%
K^2 from data set with 5 μm pitch	$(0.66 \pm 0.02) \times 10^{-4}$%

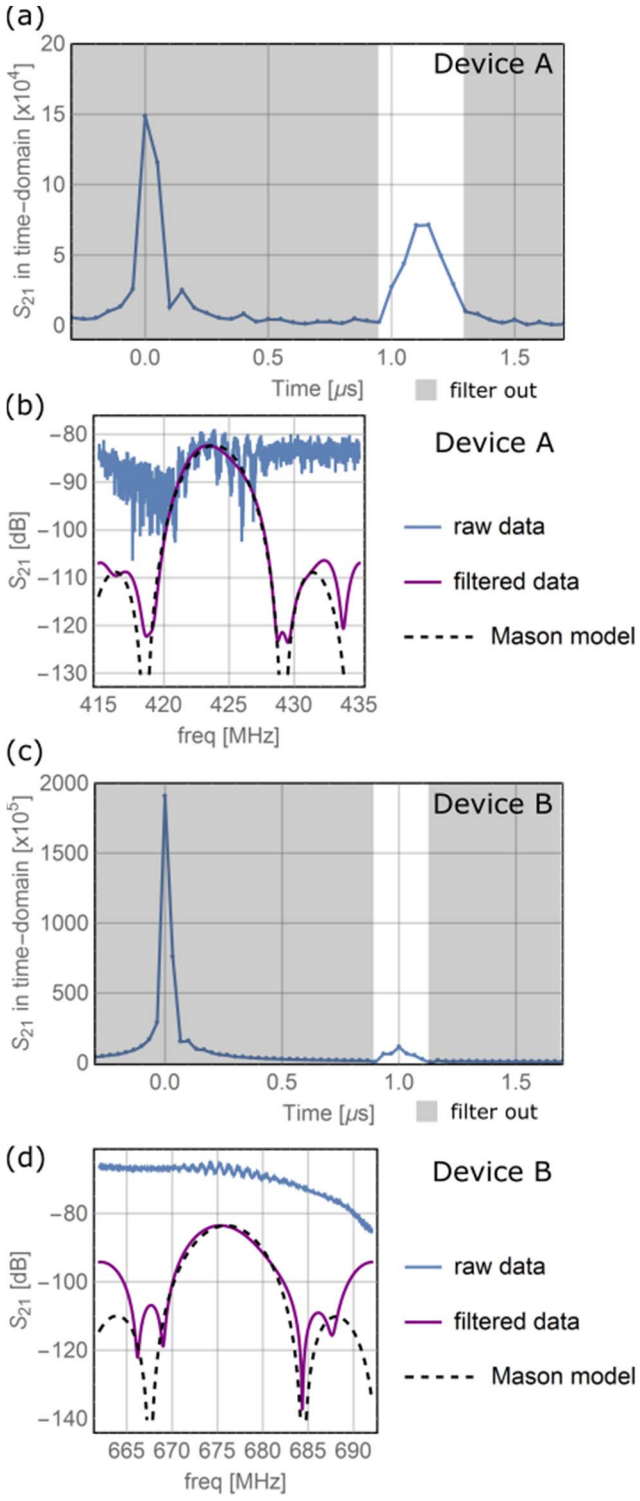


Fig. 4. Filtered signal by transforming to time domain. The plot shows the results for two devices A and B. The device parameters for A are (p, N_p, W, L_0) = (8 μm, 80, 400 μm, 400 λ). The device parameters for B are (p, N_p, W, L_0) = (5 μm, 80, 400 μm, 600 λ). (a) and (c) Time domain S_{21} for device A and B. The data in grey is filtered out. (b) and (d) Plots the raw data, filtered data, and the filtered curve based on the Mason model.

IV. DISCUSSION

We implement the measured Rayleigh wave speed, C_s, and K^2 into a 2D COMSOL simulation. We calculate that a 4H SiC delay line with a K^2 of 0.9×10^{-4} % can generate a stress of 0.5 MPa (equivalently a strain of 1×10^{-6}), and an in-plane displacement of 0.9 pm at +30 dBm RF power. A 4H SiC surface acoustic wave resonator with finesse of 100 can generate a stress of 50 MPa. This level of stress is sufficient to drive spin transition in the ground state triplet of the divacancy [12].

REFERENCES

[1] D. D. Awschalom, R. Epstein, and R. Hanson, "The diamond age of spintronics.," *Sci. Am.*, vol. 297, no. 4, pp. 84–91, 2007.

[2] S. Kolkowitz *et al.*, "Coherent sensing of a mechanical resonator with a single-spin qubit," *Science*, vol. 335, p. 1603, 2012.

[3] E. R. Macquarrie, T. A. Gosavi, N. R. Jungwirth, S. A. Bhave, and G. D. Fuchs, "Mechanical spin control of nitrogen-vacancy centers in diamond," *Phys. Rev. Lett.*, vol. 111, p. 227602, 2013.

[4] P. Ovartchaiyapong, K. W. Lee, B. A. Myers, and A. C. B. Jayich, "Dynamic strain-mediated coupling of a single diamond spin to a mechanical resonator," *Nat. Commun.*, vol. 5, p. 4429, 2014.

[5] P. Rabl, S. J. Kolkowitz, F. H. L. Koppens, J. G. E. Harris, P. Zoller, and M. D. Lukin, "A quantum spin transducer based on nanoelectromechanical resonator arrays," *Nat. Phys.*, vol. 6, no. 8, p. 602, 2010.

[6] M. J. A. Schuetz, E. M. Kessler, G. Giedke, L. M. K. Vandersypen, M. D. Lukin, and J. I. Cirac, "Universal quantum transducers based on surface acoustic waves," *Phys. Rev. X.*, vol. 5, no. 3, p. 31031, 2015.

[7] T. A. Gosavi, E. R. Macquarrie, G. D. Fuchs, and S. A. Bhave, "HBAR as a High Frequency High Stress Generator," in *Ultrasonics Symposium, 2015 IEEE*, 2015.

[8] W. F. Koehl, B. B. Buckley, F. J. Heremans, G. Calusine, and D. D. Awschalom, "Room temperature coherent control of defect spin qubits in silicon carbide," *Nat.*, vol. 479, no. 7371, p. 84, 2011.

[9] J. Van Daal, "No Title," *Philips Res. Reports*, vol. 3, p. 76, 1965.

[10] S. Karmann, R. Helbig, and R. A. Stein, "Piezoelectric properties and elastic constants of 4H and 6H SiC at temperatures 4-320 K," *J. Appl. Phys.*, vol. 66, no. 8, pp. 3922–3924, 1989.

[11] S. Ghaffari *et al.*, "Quantum Limit of Quality Factor in Silicon Micro and Nano Mechanical Resonators," *Sci. Rep.*, vol. 3, p. 3244, 2013.

[12] A. L. Falk *et al.*, "Electrically and mechanically tunable electron spins in silicon carbide color centers," *Phys. Rev. Lett.*, vol. 112, no. 18, p. 187601, 2014.

[13] S. Datta, *Surface acoustic wave devices*, 1986.

[14] Y. Takagaki, P. Santos, E. Wiebicke, O. Brandt, H.-P. Schönherr, and K. Ploog, "Guided propagation of surface acoustic waves in AlN and GaN films grown on 4H–SiC(0001) substrates," *Phys. Rev. B*, vol. 66, p. 155439, 2002.

An SH0 Lithium Niobate Correlator for Orthogonal Frequency Coded Spread Spectrum Communications

Tomás Manzaneque, Ruochen Lu, Yansong Yang and Songbin Gong
Department of Electrical and Computer Engineering
University of Illinois
Urbana-Champaign, USA

***Abstract*—This work presents the first demonstration of a frequency correlator based on shear horizontal waves in a suspended Lithium Niobate thin film. The device consists of symmetrically arranged input and output ports, each with five sections of transducers for five transmission bands over a wide frequency range from 154 to 297 MHz. The high electromechanical coupling of Lithium Niobate provides a fractional bandwidth over 60%, outperforming the state of the art surface acoustic wave correlators with a comparable insertion loss. The correlation has been verified with time-domain measurements, showing a voltage amplification factor of 2 for a correlated input, with respect to its time reversal.**

Keywords—frequency correlator; delay line; shear-horizontal waves; lithium niobate; piezoelectric; spread spectrum

I. INTRODUCTION

Spread Spectrum (SS) communication is a widely known radio frequency (RF) technique, with which each symbol in the data stream is represented with a code to improve security, enhance signal to noise ratio, and reject uncooperative interference. The coding spreads the signal spectrum over a bandwidth larger than what the data rate minimally requires. To share usage of the same bandwidth by many users, numerous sets of orthogonal codes can be employed. Among various coding schemes, the orthogonal frequency coding (OFC) provides the benefits of high time-bandwidth products and rich diversity in codes [1]. As shown in Fig. 1, OFC encodes each symbol with a train of chips at orthogonal frequencies. Acoustic correlators, also referred as matched filters, can be used to code the signal at the transmitter and recover the original data at the receiver by performing correlation directly at RF without consuming power. Their deployment can lead to circumvention of baseband correlation techniques that require complex digital signal processing and high power consumption. Conventionally, acoustic correlators have been implemented based on surface acoustic wave (SAW) devices on lithium niobate ($LiNbO_3$) and lithium tantalate substrates [2], which so far are limited in performance due to their moderate bandwidths (set by the electromechanical coupling k^2) and high propagation loss. Recent work has shown that thin-film waves in $LiNbO_3$ feature an electromechanical coupling in excess of 35% and propagation loss below 5 dB [3]-[7], greatly outperforming typical SAW devices. As a result, acoustic correlators using SH0 waves in suspended $LiNbO_3$ thin films are expected to offer superior performance, and further advance the state of the art for passive correlation. This work reports on the demonstration of the first OFC acoustic correlator based on SH0 waves in X-cut $LiNbO_3$ thin films.

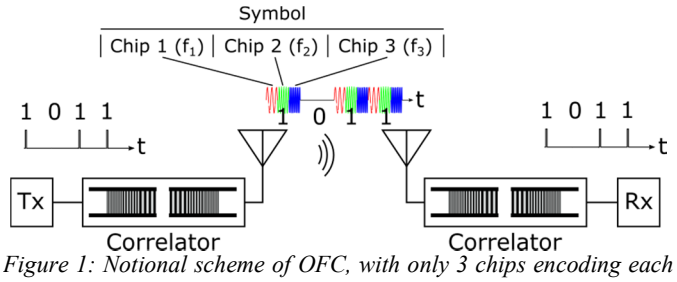


Figure 1: Notional scheme of OFC, with only 3 chips encoding each symbol. The correlator in the transmitter (Tx) converts a short pulse into a train of frequency chips. An identical correlator arranged in the reverse order must be used in the receiver (Rx) to recover the data.

II. DESIGN AND FABRICATION

The acoustic frequency correlator in this work consists of a delay line formed by two identical interdigital transducers (IDT) on a suspended X-cut $LiNbO_3$ thin film. The device is oriented -10° to -Y axis to provide optimal electromechanical coupling for the SH0 mode [8]. As depicted in Fig. 2, both IDTs are divided into n sections, with each section having a different electrode pitch W_i. Each transducer section can convert electrical signals into acoustic waves and vice versa within a frequency band centered at

$$f_i = \frac{v_p}{2W_i}, \tag{1}$$

where v_p is the phase velocity of SH0. The approximate bandwidth of each transducer section is

$$B_i = \frac{2f_i}{(N_i-1)}, \tag{2}$$

with N_i being the number of electrodes in Section i.

As seen in Fig. 2, the distance from Section i at the input IDT to Section i at the output IDT decreases with the section number, i. The device can establish correlation with an input symbol that is coded with a succession of chips consisting of sinusoids with frequencies, f_i, durations, $(N_i - 1)/2f_i$, and delays $(N_i - 1)/f_i$, in the same order as the sections in the input transducer of the device. When such a signal is received by the input IDT, the time differences between different chips in the signal are exactly compensated by the acoustic delays introduced by the device, resulting in all sinusoids to overlap in time at the output IDT. As a result, a compressed version of the input signal is produced at the output, with a shortened duration and magnified instantaneous power. The processing gain, defined as the magnification factor in terms of instantaneous power, is ap-

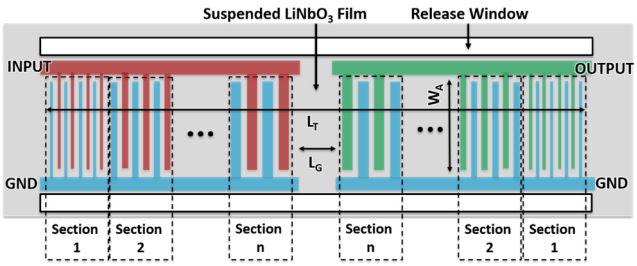
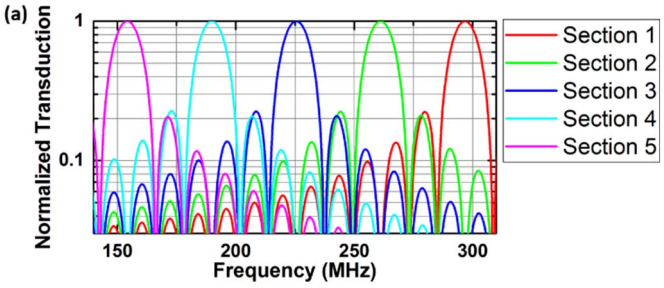


Figure 2: Schematic of the designed OFC frequency correlator. L_G is the separation between the input and output transducers for section n. L_T is the length of the correlator while W_A is the acoustic aperture size. The order of transducer sections referred throughout this work is defined from left to right.



(b)

Section	W_i (μm)	N_i	f_i (MHz)
1	6	51	296.9
2	6.818	45	261.2
3	7.895	39	225.6
4	9.375	33	190
5	11.539	27	154.4

Figure 3: (a) Frequency-domain responses of the individual transducer sections in the designed device, according to the impulse model. (b) Values of the electrode pitch and numbers of electrodes, chosen for the five chips to attain orthogonal responses for the transducers.

proximately the number of chips, n. To achieve the ideal processing gain of n, all sections in the transducers must be orthogonal to each other. In other words, each section must be maximally responsive to its own designated chip frequency (i.e. center frequencies of transducer sections are also the chip frequencies) while presenting transduction nulls at the center frequencies of any other transducer section.

In order to design a frequency correlator meeting the orthogonality condition, the impulse model was used to select the center frequencies [9]. This model considers the time-domain impulse response of an IDT. Specifically, the impulse response is modelled as a sinusoid with zero-crossings at the electrodes. In our case, the impulse response of each section in the IDTs is a sine function of frequency f_i and duration $(N_i - 1)/2f_i$. The frequency response of each section can be obtained by performing Fourier-transform on its impulse response. The result is a cardinal sine function (or sinc) centered at f_i and with zeros at

$$f_i^k = f_i\left(1 \pm \frac{4k}{N_i - 1}\right), \qquad k = 1, \ldots, \infty. \tag{3}$$

In order for all transducer sections to be orthogonal to each other, they must meet

$$(N_i - 1)W_i = (N_j - 1)W_j, \qquad \forall\, i, j, \tag{4}$$

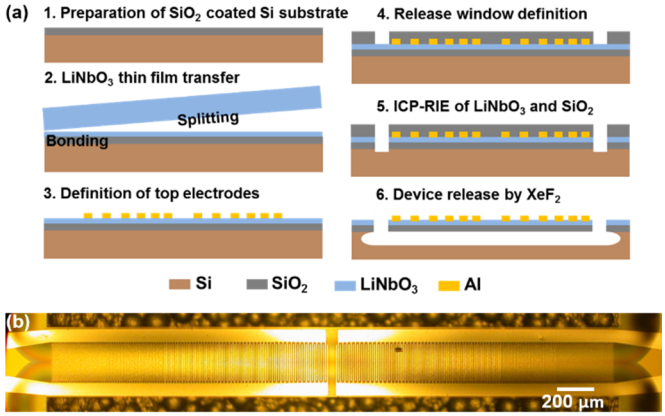


Figure 4: (a) Flow-chart of the fabrication process. (b) Optical microscope image of the fabricated device.

and $f_i \neq f_j$. This condition implies that all transducer sections in the device have the same length, and the chips in the signal have the same duration.

An OFC correlator was designed using 5 transducer sections, each with a length of 300 μm and corresponding to a chip in the signal. The smallest pitch, which defines the highest frequency, was chosen to be 6 μm. The successive sections were designed by choosing the numbers of electrodes as $N_j = N_i - 2k$ and calculating W_j according to (4). The number of zeros between the two center frequencies of adjacent sections is $k - 1$. In our design, k was set to 3, giving rise to two zeros between the center frequencies of adjacent sections, as illustrated in Fig. 3(a). The table in Fig. 3(b) lists the values of the electrode pitch, the number of electrodes in each section, and the center frequencies predicted by assuming a phase velocity of 3562 m/s. For all sections, the electrode width is set to half of the pitch. A separation between the input and output transducers for chip 5 (L_G) of 100 μm was chosen, resulting in a total device length (L_T) of 3.1 mm. The acoustic aperture (W_A) was fixed to 200 μm to attain a port impedance in the range of 100-500 Ω at all chip frequencies. The limitation imposed by Eq (4) makes it impractical to establish impedance matching to 50 Ω at all chip frequencies. Due to the differences in impedance for the set of center frequencies, designs with high fractional bandwidths are prone to suffer from a high insertion loss. Materials with high k^2 benefit from a lower insertion loss for a given bandwidth, as explained in [9].

The device was fabricated following the steps summarized in Fig. 4(a). The process starts with the transfer of an 800 nm-thick film of X-cut $LiNbO_3$ to a Si substrate using ion-implantation and thermally-induced slicing. An intermediate SiO_2 layer, with a thickness of 300 nm, is used to facilitate wafer to wafer bonding. Next, 80 nm-thick Al electrodes are defined by sputtering and lift-off. Then, a SiO_2 hard mask is first deposited using plasma-enhanced chemical vapor deposition (PECVD), and is subsequently pattered using fluorine-based reactive ion etching (RIE). This mask is used to define the release windows through the $LiNbO_3$ thin film with chlorine-based inductive coupled plasma (ICP)-RIE. Finally, the device is released by isotropic etching of the Si substrate with XeF_2. A top-view photograph of the fabricated device is shown in Fig. 4(b).

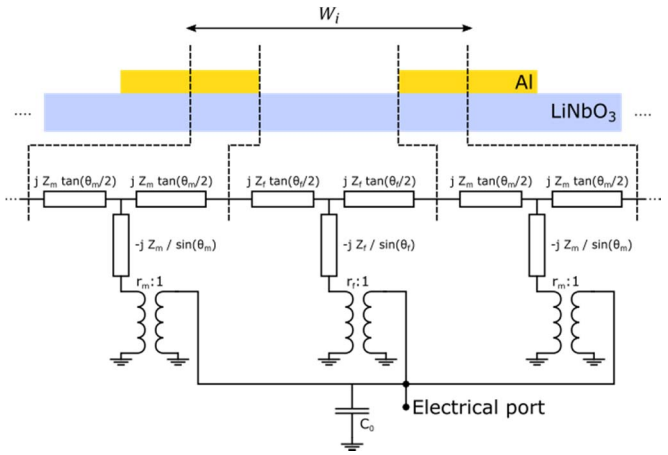


Figure 5: Sectional equivalent circuit of the acoustic transducer in the implemented Mason's model.

III. SIMULATION

The response of the fabricated 2-port OFC frequency correlator was simulated by using the aforementioned impulse model. The impulse responses of both the input and output transducers are calculated as the superposition of the impulse responses of the individual sections. Adequate time delays are employed to account for the spatial separation between sections for different frequencies. The acoustic radiation can be modelled by an admittance derived from the impulse response. A complete description of the procedure can be found in a previous publication of the authors [3].

Although the impulse model provides great flexibility and simplicity to simulate the response of large arrays of electrodes on piezoelectric substrates or thin films, it is inadequate in accounting for the discontinuities in the acoustic propagation medium induced by the succession of metallized and un-metallized areas. The presence of a metal on top of a piezoelectric material has the effect of short-circuiting the surface, reducing the electric field within the film. This translates into a difference between the phase velocities in the portions covered by an electrode (v_p^m) and those free of metalization (v_p^f), given by

$$v_p^f = v_p^m \left(1 + \frac{k^2}{2\left(1+(\epsilon_{11}\epsilon_{33}-\epsilon_{13}^2)^{-1/2}\right)}\right), \tag{5}$$

where ϵ_{11}, ϵ_{33} and ϵ_{31} are components of the relative permittivity tensor under constant stress, with 1 denoting the direction of wave propagation and 3 denoting the direction normal to the surface. For large values of k^2, as it is for SH0 waves in thin film $LiNbO_3$, this difference produces non-negligible reflections as the acoustic wave goes through the numerous portions of metalized and un-metalized thin film in the transducers. To account for this effect, the Mason's model was used. This method exploits a 1-D discretization of the delay line, in which each period of the transducer is modelled as a sectional equivalent circuit. Acoustic transmission line elements are introduced to model the wave propagation, while ideal transformers are included to account for the piezoelectric transduction. The model was modified as in [10] to include the aforementioned discontinuity in phase velocity. Fig. 5 shows the equivalent circuit used to represent each period of the transducer, with Z_f denoting the acoustic impedance of the free $LiNbO_3$ film and Z_m denoting the acoustic impedance of the metallized $LiNbO_3$ film. Z_f and Z_m are related by

$$\frac{Z_f}{Z_m} = \frac{v_f}{v_m}. \tag{6}$$

θ_m is the acoustic transit angle over half of an electrode for an acoustic wave at frequency ω. If the metallization factor, i.e. the ratio of the metallized to un-metallized area in each section, is denoted by m, θ_m is given by

$$\theta_m = m\frac{\omega W_i}{2v_p^m}. \tag{7}$$

Analogously, θ_f is the acoustic transit angle over the un-metalized portion between adjacent electrodes for an acoustic wave at frequency ω, given by

$$\theta_f = (1-m)\frac{\omega W_i}{v_p^f}. \tag{8}$$

The turn ratios of the ideal transformers are found as

$$r_m = \sqrt{2f_i C_0 k^2 Z_m}, \tag{9}$$

and

$$r_f = \sqrt{2f_i C_0 k^2 Z_f}. \tag{10}$$

In Mason's model, Eq (1) is no longer accurate in determining the transducer center frequency. Instead, the center frequency of each transducer Section can be obtained as

$$f_i = \frac{1}{2}\frac{1}{\left(m\frac{W_i}{v_p^m}+(1-m)\frac{W_i}{v_p^f}\right)}. \tag{11}$$

The entire input and output transducers are built by cascading the described blocks in series. The electrical terminals of all blocks in a transducer are connected in parallel, forming an electrical port. The correlator model is then constructed by cascading the models of the two IDTs in a symmetrical arrangement, and terminating the remaining acoustic edges with a resistance, Z_f, to represent a non-reflective boundary.

Both models described above were implemented for numerical calculation of the correlator response. The S11 and S21 parameters calculated with the impulse model, implemented in MATLAB, are shown in Fig. 6(a). A phase velocity of 3562 m/s was assumed for the SH0 mode. Mason's model was implemented with ADS and the results are plotted in Fig. 6(b). In this case, v_p^m = 3450 m/s and v_p^f = 4110 m/s. For both models, k^2 = 39 % was used. In addition, the transduction of the S0 mode, at higher frequencies, was considered in both models. To that end, an additional branch of cascaded sectional circuits with k^2 = 3.3 % was added in parallel to the intended SH0 branch. This S0 branch is modeled with a phase velocity of 6175 m/s in the impulse model, while v_p^m = 6200 m/s and v_p^f = 6300 m/s are used in Mason's model. Note that the disparity between Z_f and Z_m is signifant due to the high electromechanical coupling

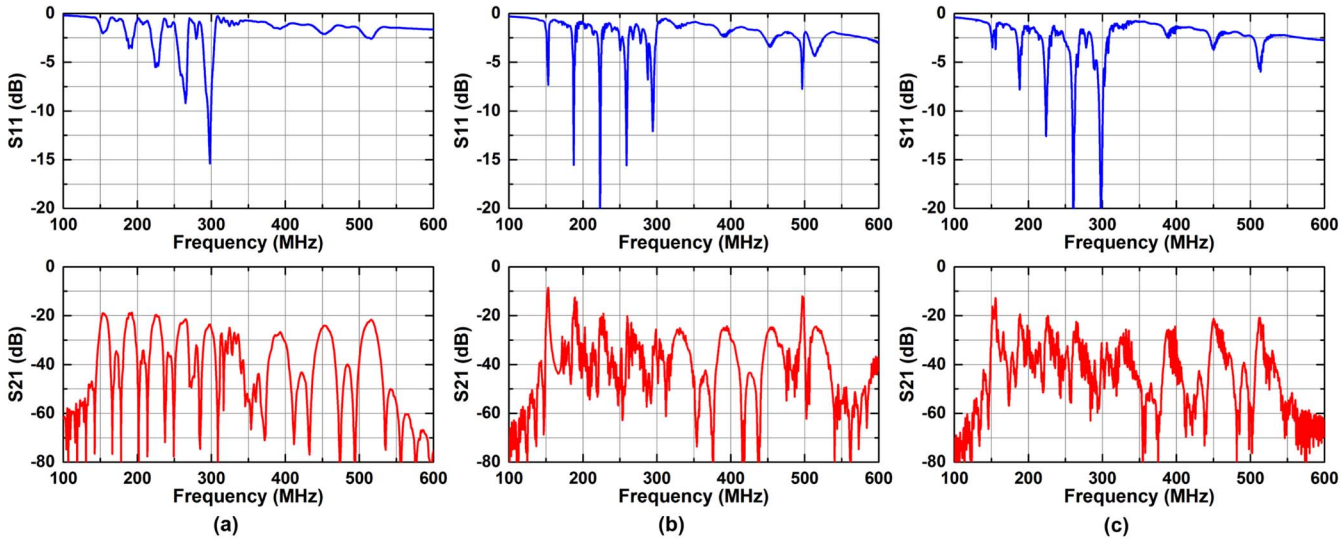


Figure 6: S-parameters of the designed OFC correlator. (a) Simulated with impulse response model. (b) Simulated with Mason's model. (c) Measurements.

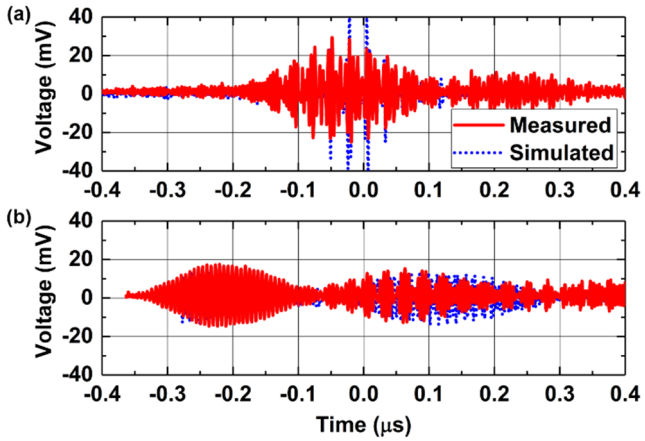


Figure 7: Measured and simulated correlator output signals for different inputs with an amplitude of 500 mV. (a) Correlated signal. (b) Uncorrelated signal. The simulated results are based on the impulse model.

of SH0 in $LiNbO_3$. As a result, acoustic wave propagation experiences non-negligible internal reflections within the IDTs. As predicted by Mason's model, this effect creates large ripples over the transmission bands, which are not present in the response predicted using the impulse model.

IV. Measurements

The S-parameters of the fabricated device were first measured with a vector network analyzer, and are shown in Fig. 6(c). With 50 Ω terminations at both ports, the insertion losses (IL) at the center frequencies of the first four chips (154, 190, 226, and 261 MHz) are around 20 dB. The chip with the highest frequency at 297 MHz endures a higher IL (30 dB) due to the response distortion from inadvertently excited S0 mode. Care must be taken in design in order to avoid any overlap between SH0 and S0 transmission bands that degrades the performance for higher frequency chips. In addition, our model shows an increasing IL for chips at higher frequencies. This is caused by the longer propagation distance in our design for the higher frequency chips, as well as the fact that propagation loss per unit distance is higher at higher frequencies. Future code design must take this effect into account to produce more constant IL at chip frequencies. Despite far from the optimal design, this demonstration shows a lower IL and a much larger fractional bandwidth (FBW=63%) than that reported for similar SAW correlators (IL≈35 dB, FBW=29%) [11].

The time-domain response was also measured to verify the correlation. The device was measured as a receiver correlator, to which an input signal coded with frequency chips and produced by an arbitrary wave generator was fed. The response at the output IDT was recorded by an oscilloscope. Fig. 7 shows the measured correlated signal, compared to the response for the time-reversal signal (uncorrelated). The amplitude for the correlated signal is found to be more than 2 times larger than that of the uncorrelated signal.

V. Conclusion

A frequency correlator based on SH0 waves in a suspended lithium niobate thin film has been demonstrated with higher bandwidth than previously reported SAW devices. An impulse model and a Mason's model have been used to simulate the response and design the device. The measurements show a much better agreement with Mason's model because Mason's model accounts for the acoustic reflections at the edges of the electrodes. The correlation response has been validated with time-domain measurements. This new class of devices have been demonstrated as a potential zero-power solution for performing correlation directly at RF.

References

[1] D. C. Malocha, D. Puccio and D. Gallagher, "Orthogonal frequency coding for SAW device applications," *IEEE Ultrasonics Symposium, 2004*, 2004, pp. 1082-1085 Vol.2.

[2] R. Brocato et al., "UWB communication using SAW correlators," Proceedings. 2004 IEEE Radio and Wireless Conference (IEEE Cat. No.04TH8746), 2004, pp. 267-270.

[3] T. Manzaneque, R. Lu, Y. Yang and S. Gong, “An SH0 Lithium Niobate Dispersive Delay Line for Chirp Compression-enabled Low Power Radios,” in *Micro Electro Mechanical Systems (MEMS), IEEE 29th International Conference on*, pp.111-114, Jan 2017.

[4] R. Wang, S. A. Bhave and K. Bhattacharjee, "Design and Fabrication of S0 Lamb-Wave Thin-Film Lithium Niobate Micromechanical Resonators," in *Journal of Microelectromechanical Systems*, vol. 24, no. 2, pp. 300-308, April 2015.

[5] S. Gong and G. Piazza, "Monolithic Multi-Frequency Wideband RF Filters Using Two-Port Laterally Vibrating Lithium Niobate MEMS Resonators," in *Journal of Microelectromechanical Systems*, vol. 23, no. 5, pp. 1188-1197, Oct. 2014.

[6] F. V. Pop, A. S. Kochhar, G. Vidal-Alvarez and G. Piazza, "Laterally vibrating lithium niobate MEMS resonators with 30% electromechanical coupling coefficient," *2017 IEEE 30th International Conference on Micro Electro Mechanical Systems (MEMS)*, Las Vegas, NV, 2017, pp. 966-969.

[7] R. H. Olsson, K. Hattar, S. J. Homeijer, M. Wiwi, M. Eichenfield, D. W. Branch, M. S. Baker, J. Nguyen, B. Clark, T. Bauer, T. A. Friedmann, "A high electromechanical coupling coefficient SH0 Lamb wave lithium niobate micromechanical resonator and a method for fabrication," *Sensors and Actuators A: Physical*, vol. 209, pp. 183-190, 2014.

[8] I. E. Kuznetsova et al., "Investigation of acoustic waves in thin plates of lithium niobate and lithium tantalate," *in IEEE Trans. on Ultrasonics, Ferroelectrics, and Frequency Control*, vol. 48, no. 1, pp. 322-328, 2001.

[9] C. S. Hartmann, D. T. Bell, and R. C. Rosenfeld. "Impulse model design of acoustic surface-wave filters." IEEE Transactions on Microwave Theory and Techniques 21, no. 4 (1973): 162-175.

[10] W. R. Smith, H. M. Gerard and W. R. Jones, "Analysis and Design of Dispersive Interdigital Surface-Wave Transducers," in *IEEE Transactions on Microwave Theory and Techniques*, vol. 20, no. 7, pp. 458-471, Jul 1972.

[11] D. R. Gallagher and D. C. Malocha, "Ultra wide band dual orthogonal frequency coded SAW correlators using harmonic operation," 2010 IEEE Int. Frequency Control Symp., Newport Beach, CA, 2010, pp. 301-306.

Observation of phononic frequency combs in a micromechanical resonator

Adarsh Ganesan*, Cuong Do and Ashwin Seshia
The Nanoscience Centre
University of Cambridge
Cambridge, UK
*ag815@cam.ac.uk

***Abstract*—Optical frequency combs have revolutionized the fields of time metrology, frequency synthesis and optical spectroscopy. Recently, we experimentally demonstrated the feasibility of its phononic analogue in a micromechanical resonator. The underlying nonlinear process for this generation was via parametric three-wave mixing. Now, in this paper, utilizing three nominally identical copies of this device, we show the emergence of three distinct regimes viz. 'Two-mode phononic frequency comb'; 'Two-mode non-phononic frequency comb'; 'Three-mode phononic frequency comb'.**

Keywords—MEMS, micromechanical resonator, frequency combs, acoustic phonons

I. Introduction

Optical frequency combs have enabled a wide variety of applications ranging from precision time metrology [1] to optical spectroscopy [2]. Recently, we experimentally demonstrated the feasibility of its phononic counterpart using a micromechanical resonator [3]. Such phononic frequency combs, complementary to the optical frequency combs, may potentially enable a further class of precision measurements and spectroscopic tools. These include ultra-precision micro- and nanoelectromechanical resonant sensors adapted for stable long-duration measurements, stabilization of ultrasound sources adapted for the accurate measurement of elastic properties of various media, and broadband multi-frequency acoustic spectroscopy. Quite apart from the application potential, the physical pathway underlying the phononic frequency comb is surprising and not well-studied. This pathway can also provide opportunities for more in-depth studies of the nonlinear phenomena operative in these systems.

The phononic frequency comb process, as reported in [3,4], is through the parametric interaction of phonon modes. While one phonon mode is directly driven, the other modes are excited through intrinsic parametric modulation. Specifically in [4], utilizing a micromechanical free-free beam AlN-on-Si resonator topology, the emergence of phononic frequency combs was evidenced in a system of two coupled phonon modes. Despite the possible existence of this nonlinear pathway in a given micromechanical device, the same phenomenon may not be observed in other nominally identical micromechanical devices demonstrating the potential sensitivity of such dynamics to precise fabrication tolerances and environmental conditions. In this paper, we show that three distinct nonlinear processes are observed in three separate nominally identical AlN-on-Si micromechanical resonators.

II. Experimental Method

A piezoelectric AlN coated Si based micromechanical resonator is considered for the demonstration of phononic frequency combs. This device is fabricated through a commercial foundry process (MEMSCAP). The experiments are carried out under ambient room temperature conditions. The geometry of the micromechanical resonator corresponds to a free-free beam topology of size $1100 \times 350 \times 11\ \mu m^3$ (Figure 1A). The device is driven using an external frequency synthesizer (Agilent 335ARB1U) and the resulting response is recorded using a Laser Doppler Vibrometer (Polytec MSA-400 Micro System Analyzer).

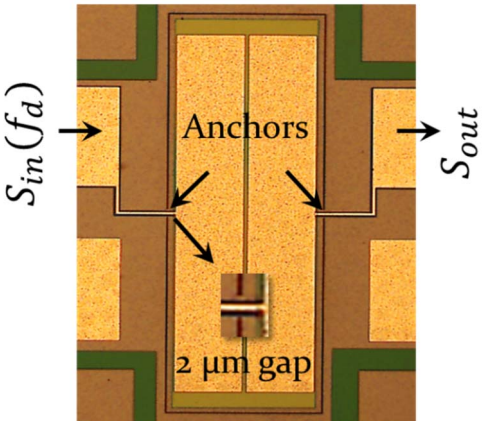


Figure 1: The electrical signal $S_{in}(f_d) = S_{in}\cos(2\pi f_d t)$ is applied to an AlN-on-Si micromechanical resonator of size $1100 \times 350 \times 11\ \mu m^3$ with a free-free beam topology.

III. Results

A. Two-Mode Phononic Frequency Comb (Device 1)

When the drive condition is adjusted to $S_{in}(f_d = 3.859\ MHz) = 20\ dBm$, the Laser Doppler Vibrometer (LDV) detected the excitation of frequency combs near $\frac{f_d}{2}$ and f_d respectively. The combs near f_d and $\frac{f_d}{2}$ correspond to the modes x and y respectively (Figure 2A). While the tone with frequency f_d is produced through the drive excitation of mode x (Figure 2A), the other tones are generated through an

intrinsic nonlinear mixing process. To further investigate this mechanism, the experiments were conducted at different drive frequencies f_d and power levels S_{in}. During this process, we observe three successive characteristic responses as the drive level is varied: $R1$: $\alpha\cos(2\pi f_d t)$; $R2$: $\alpha\cos(2\pi f_d t) + \beta\cos(\pi f_d t)$; $R3$: $\sum_{p\in Z}\alpha\cos\big(2\pi\big(f_0 + n(f_d - f_0)\big)t\big) + \sum_{p\in Z}\beta\cos\left(2\pi\left(\frac{f_0}{2} + n(f_d - f_0)\right)t\right)$. The response $R3$ relates to the excitation of frequency combs. Figure 2B plots the regions that constitute $R1, R2$ & $R3$ in the $S_{in} - f_d$ space.

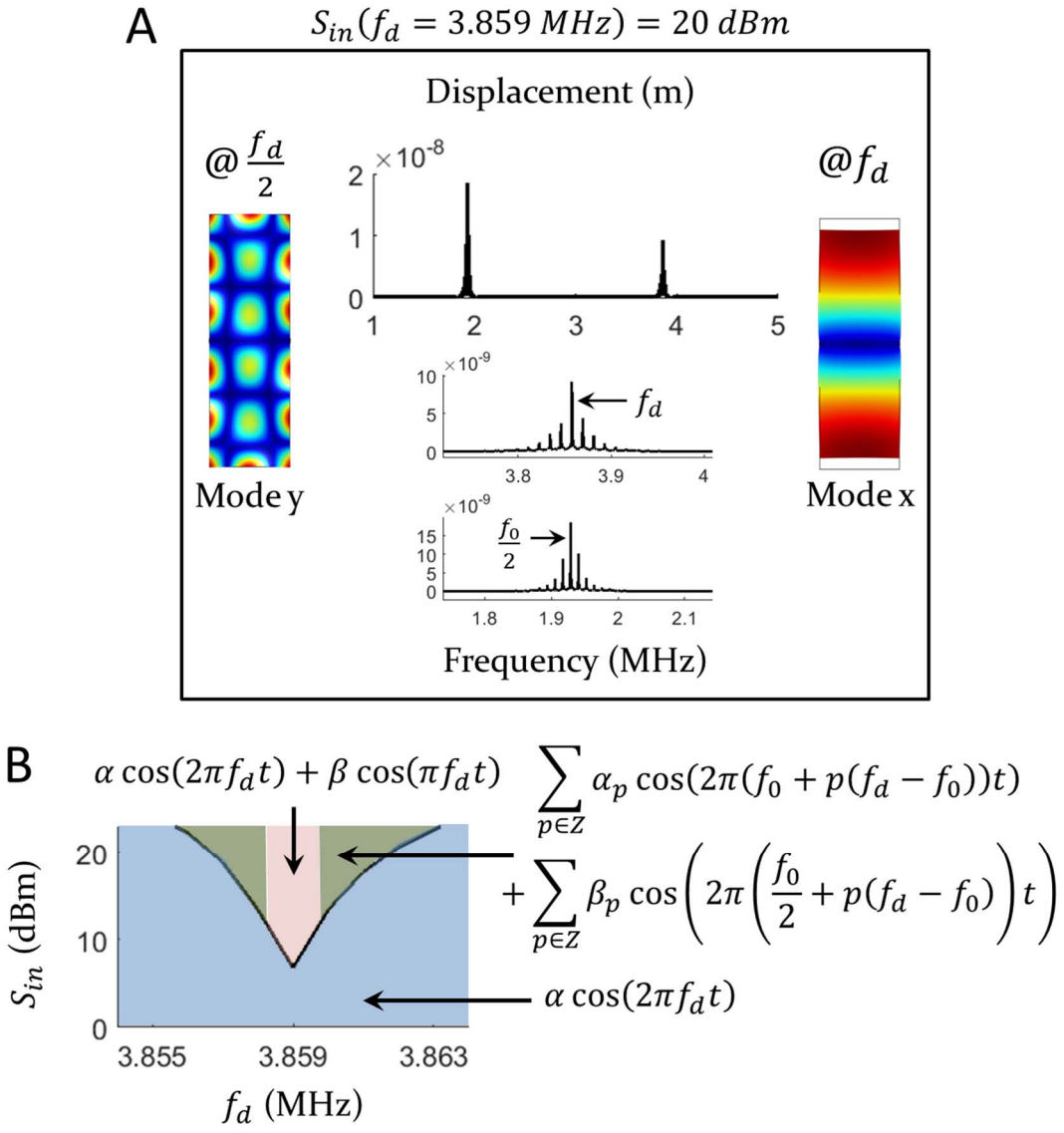


Figure 2: **Two-Mode Phononic Frequency Comb.** A: The frequency spectrum for the drive condition $S_{in}(f_d = 3.859\ MHz) = 20\ dBm$; B: $S_{in} - f_d$ map.

B. Two-Mode Non-Phononic Frequency Comb (Device 2)

When the drive condition is adjusted to $S_{in}(f_d = 3.852\ MHz) = 10\ dBm$, the Laser Doppler Vibrometer (LDV) detected the excitation of tones with frequencies $\frac{f_d}{2}$ and f_d which correspond to the modes x and y respectively (Figure 3A). While the tone with frequency f_d is produced through the drive excitation of mode x (Figure 3A), the tone with frequency $\frac{f_d}{2}$ is generated through autoparametric resonance. To further investigate this mechanism, the experiments were conducted at different drive frequencies f_d and power levels S_{in}. During this process, we had observed two characteristic responses: $R1$: $\alpha\cos(2\pi f_d t)$; $R2$: $\alpha\cos(2\pi f_d t) + \beta\cos(\pi f_d t)$. Figure 3B plots the regions that constitute $R1$& $R2$ in the $S_{in} - f_d$ space.

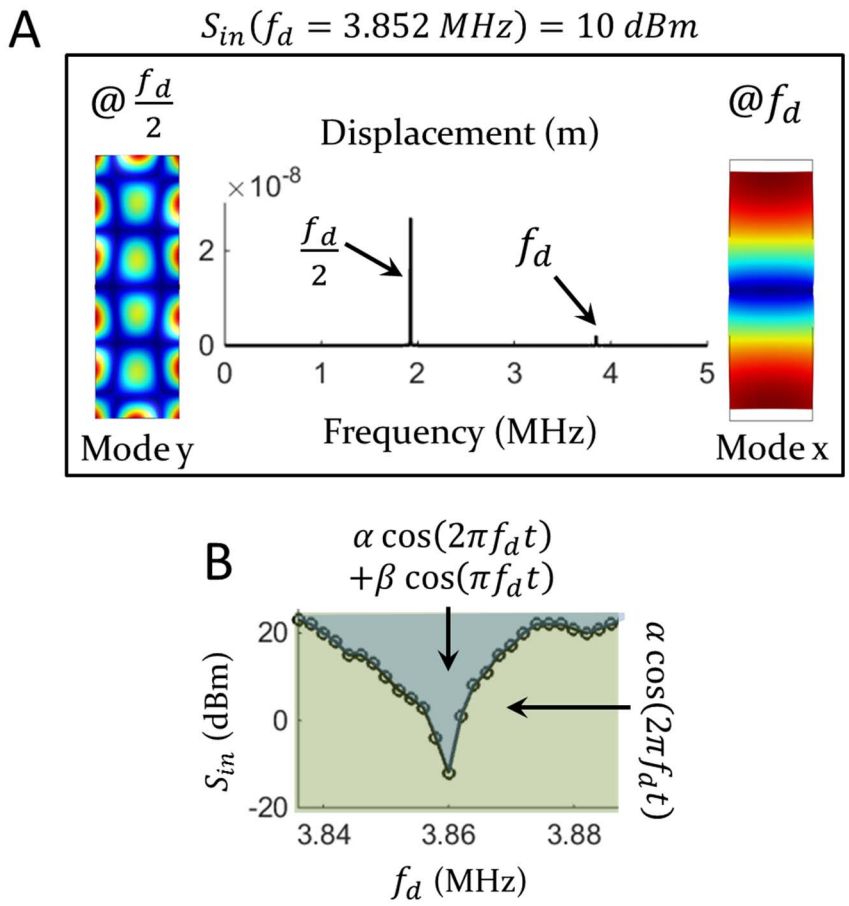


Figure 3: **Two-Mode Non-Phononic Frequency Comb.** A: The frequency spectrum for the drive condition $S_{in}(f_d = 3.852\ MHz) = 10\ dBm$; B: $S_{in} - f_d$ map.

C. Three-Mode Phononic Frequency Comb (Device 3)

For the third separate nominally identical device, when the drive condition is adjusted to $S_{in}(f_d = 3.857\ MHz) = 15\ dBm$, the electrical output S_{out} (Figure 1) corresponds to the excitation of frequency combs near f_d, f_m and f_n respectively. The combs near f_d, f_m and f_n correspond to the modes x, y and z respectively (Figure 4A). Modes y and z are parametrically excited as reported in [5]. While the tone with frequency f_d is produced through the drive excitation of mode x (Figure 4A), the other tones are generated through an intrinsic nonlinear process. To further investigate this mechanism, experiments were conducted at different drive frequencies f_d and power levels S_{in}. During this process, we observed three characteristic successive responses as the drive power is increased: $R1$: $\alpha\cos(2\pi f_d t)$; $R2$: $\alpha\cos(2\pi f_d t) + \beta\cos(2\pi f_m t) + \gamma\cos(2\pi f_n t)$; $R3$: $\sum_{p\in Z}\alpha\cos\big(2\pi\big(f_0 + n(f_d - f_0)\big)t\big) + \sum_{p\in Z}\beta\cos\big(2\pi\big(f_m + n(f_d - f_0)\big)t\big) + \sum_{p\in Z}\gamma\cos\big(2\pi\big(f_n + n(f_d - f_0)\big)t\big)$. The response $R3$ relates to the excitation of frequency combs. Figure 4B plots the regions that constitute $R1, R2$ & $R3$ in the $S_{in} - f_d$ space.

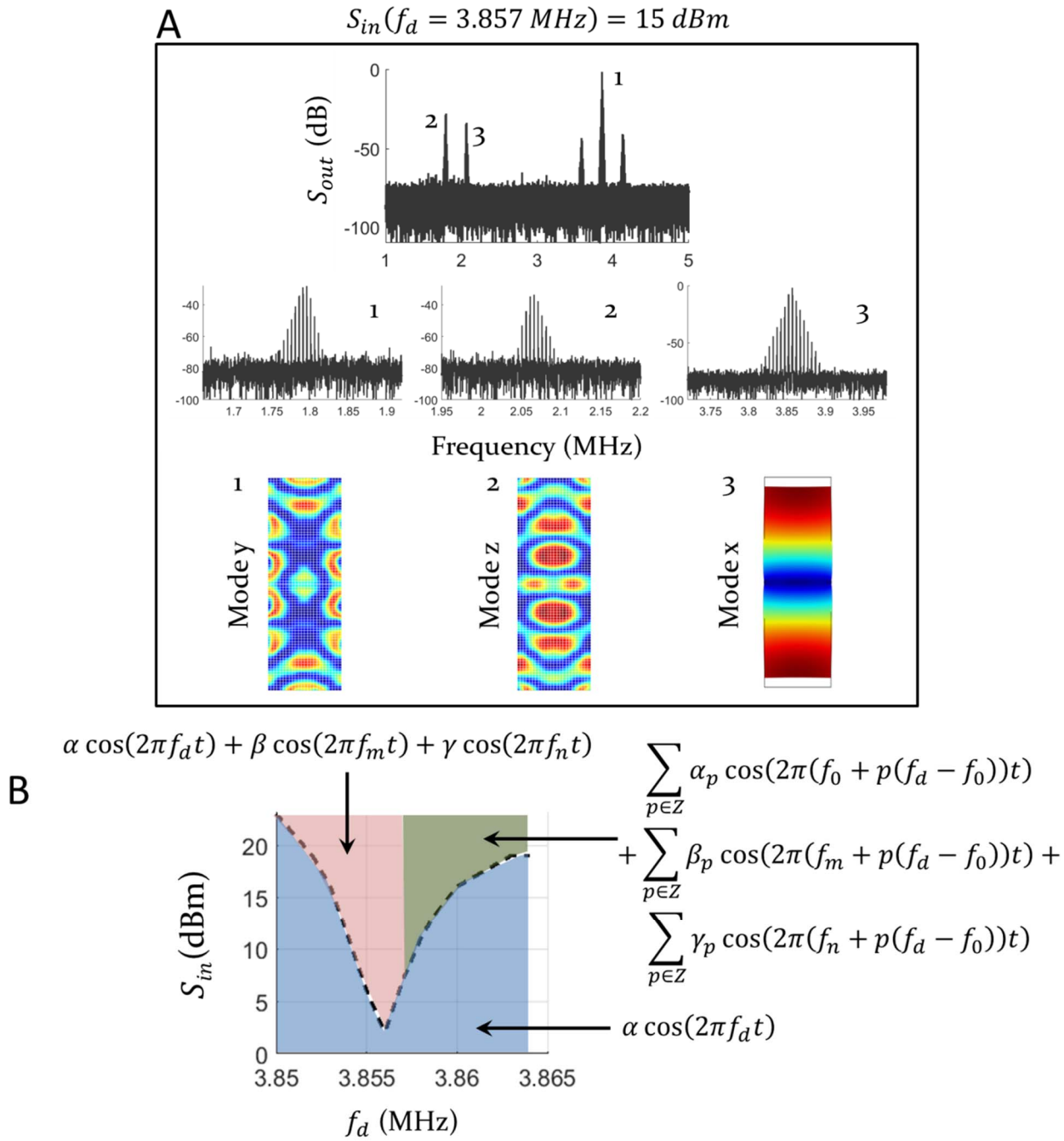


Figure 4: **Three-Mode Phononic Frequency Comb.** A: The frequency spectrum for the drive condition $S_{in}(f_d = 3.857\ MHz) = 15\ dBm$; B: $S_{in} - f_d$ map.

IV. Summary and Future Work

This paper demonstrates the variability of frequency comb processes across nominally identical copies of a micromechanical resonator. The three nominally identical devices demonstrate (1) generation of frequency combs following 2-mode parametric resonance, (2) absence of frequency comb formation following 2-mode parametric resonance, and (3) generation of frequency combs following 3-mode parametric resonance. This variability in behaviour across the three nominally identical device copies illustrates the potential sensitivity of the comb generation process to fabrication tolerances and environmental conditions that can impact on the specific system parameters, including the nature of non-linear modal coupling. Future work should address both experimental mapping of this behaviour across a range of device topologies and drive conditions, and predictive physical modelling underpinning device dynamics.

ACKNOWLEDGMENTS

Funding from the Cambridge Trusts is gratefully acknowledged.

REFERENCES

[1] T. Udem, R. Holzwarth, and T. W. Hansch, "Optical frequency metrology," *Nature,* vol. 416, pp. 233-237, 2002.

[2] J. Ye, *Femtosecond optical frequency comb: principle, operation and applications*: Springer Science & Business Media, 2005..

[3] A. Ganesan, C. Do, and A. A. Seshia, "Phononic Frequency Comb via Intrinsic Three-Wave Mixing," *Physical review letters,* vol. 118, p. 033903, 2017.

[4] L. S. Cao, D. X. Qi, R. W. Peng, M. Wang, and P. Schmelcher, "Phononic Frequency Combs through Nonlinear Resonances," *Physical Review Letters,* vol. 112, p. 075505, 2014.

[5] A. Ganesan, C. Do. And A. A. Seshia, "Observation of three-mode parametric instability in a micromechanical resonator", *Applied Physics Letters*, Vol. 109, No. 19, 193501, 2016.

The collisional frequency shift of a trapped-ion optical clock

Amar C. Vutha*, Tom Kirchner†, Pierre Dubé‡‡
*Department of Physics, University of Toronto, Toronto, Canada M5S 1A7
†Department of Physics and Astronomy, York University, Toronto, Canada M3J 1P3
‡National Research Council Canada, Ottawa, Canada K1A 0R6

As the performance of optical atomic clocks improves steadily, new sources of systematic errors need to be evaluated with increasingly higher accuracy. At present, the collisional frequency shift (CFS), due to interactions with background gas atoms in the environment of the clock ions, is in some cases the next-to-leading source of systematic uncertainty for trapped-ion optical clocks. Existing approaches towards evaluating the CFS have either assumed that only glancing-angle collisions are relevant [1], or assumed a worst-case scenario for the phase shift imparted to clock state superposition by a collision [2], [3]. The former approach, which was developed for laser-cooled cesium clocks, is not applicable to the deeply trapped atomic ions used in optical clocks, while the latter approach is likely to significantly overestimate the CFS.

To address this problem we have developed a framework, based on a non-perturbative quantum channel description of the collision process. Our method leads to a convenient master equation and a compact expression for the CFS [4]. In particular, this framework can be used to estimate the CFS in situations involving many partial waves and large collisional phase shifts, which is the case with thermal background gas atoms scattering off a clock ion. Our method lends itself to practical evaluations of the CFS, by using readily calculated molecular potential curves for the ion-background gas system to extract the collisional phase shifts which lead to the CFS. As an application of this method to a realistic and relevant situation, we have numerically estimated the frequency shift of the 674 nm clock transition in Sr^+ due to collisions with background helium gas. We find that the CFS is much smaller than the worst-case estimate provided in [3].

In this talk, we describe the theoretical background and motivate the steps that lead to our framework for calculating the CFS. Following this, we present our calculations for the Sr^+-He system as an example of the general method, and discuss possible extensions and improvements that will allow us to evaluate the CFS for the Sr^+ clock at the National Research Council Canada.

References

[1] K. Gibble, "Scattering of cold-atom coherences by hot atoms: Frequency shifts from background-gas collisions," *Phys. Rev. Lett.*, vol. 110, no. 18, pp. 1–5, 2013.

[2] T. Rosenband et al., "Frequency ratio of Al+ and Hg+ single-ion optical clocks; metrology at the 17th decimal place." *Science*, vol. 319, no. 5871, pp. 1808–12, mar 2008.

[3] P. Dubé, A. A. Madej, Z. Zhou, and J. E. Bernard, "Evaluation of systematic shifts of the $^{88}Sr^+$ single-ion optical frequency standard at the 10^{-17} level," *Phys. Rev. A*, vol. 87, p. 023806, Feb. 2013.

[4] A. Vutha, T. Kirchner, and P. Dubé, "The collisional frequency shift of a trapped-ion optical clock," *arXiv:1705.10019*, 2017.

978-1-5386-2916-1/$31.00 ©2017 IEEE

Rydberg Spectroscopy for DC Stark Shift Characterisation in Optical Lattice Clocks

Bowden*, William., Hobson, Richard., Gill, Patrick., Hill, Ian R.
Time and Frequency, National Physical Laboratory, Teddington, UK
*Clarendon Laboratory, Oxford University, Oxford, UK

Huillery, Paul H., Jones, Matthew. P. A
Department of Physics, Durham University
Durham, UK

***Abstract*—The DC Stark shift resulting from uncharacterized electric fields can compromise the accuracy of optical lattice clocks. We report on a new method to characterize these residual electric fields using Rydberg states. By performing electromagnetically induced transparency (EIT) spectroscopy to measure the quadratic Stark shifts of the 5s75d $^1D_2$ m_J = 0, ±1, ±2 states in strontium, we constrain the DC Stark shift of the clock transition to below 1 x 10^{-18}.**

Keywords— Rydberg; Stark shift; lattice clock; optical clock

I. INTRODUCTION

Uncharacterised DC electric fields can severely impact the accuracy of an atomic clock. For the $5s^2\ ^1S_0 \rightarrow 5s5p\ ^3P_0$ clock transition in strontium, an electric field of 570 V/m yields a DC Stark shift of 1 Hz [1] or 2 x 10^{-15} in fractional units, some three orders of magnitude above the lowest estimated total inaccuracy of a strontium optical lattice clock [2]. Where dielectric surface are close to the atoms, shifts as large as 1 x 10^{-13} have been observed [3]. While steps must be taken to reduce the residual electric field seen by the atoms, characterisation of the remaining field is necessary. This is typically done by direct spectroscopy of the clock transition with an externally applied electric field. With no residual electric field present, the quadratic nature of the perturbation implies the resulting induced frequency shift should be unchanged if the polarity of the applied field is reversed. This method relies on the ability to apply sufficiently large and stable electric fields at the atoms' position to induce a shift that can be quickly resolved during spectroscopy. For metallic vacuum chambers with minimal dielectric openings and no internal electrodes, resolving this shift can be problematic. Furthermore, the applied field can charge dielectric materials such as the vacuum viewports, resulting in a time dependence of the effective applied field.

We circumvent these challenges by performing electromagnetically induced transparency (EIT) spectroscopy to measure the quadratic Stark shifts of the 5s75d $^1D_2$ m_J = 0, ±1, ±2 Rydberg states to detect residual DC electric fields [4]. With a polarizability eight orders of magnitude larger than that of the clock transition, these states are well suited for electrometry. This work marks Rydberg states first use as a tool to characterize a systematic source of error affecting an atomic clock. Using this spectroscopic method, we reduce the fractional uncertainty of the DC Stark shift of the clock transition to below 1x10^{-18}.

II. RESULT

For the implementation of the EIT spectroscopy counter-propagating beams, one resonant with the $5s^2\ ^1S_0 \rightarrow 5s5p\ ^1P_1$ transition at 461 nm and the other with tuneable frequency at 413 nm, excite atoms to a chosen 5snd $^1D_2$ Rydberg state. The resulting EIT signal is measured using lock in detection of the 461 nm probe beam absorption via modulation of the 413 nm pump beam intensity by an optical chopper.

In the absence of an electric field, the Zeeman sub levels will split symmetrically with applied magnetic field. However, in the presence of an electric field, the resulting Stark shift will result in an asymmetry in the spectrum. To determine the residual electric field, we measure the splitting of EIT spectrum for various applied magnetic fields to extract the quadratic Stark shift. Figure 1 shows the relative energy splitting for various magnetic fields with and without an applied electric field.

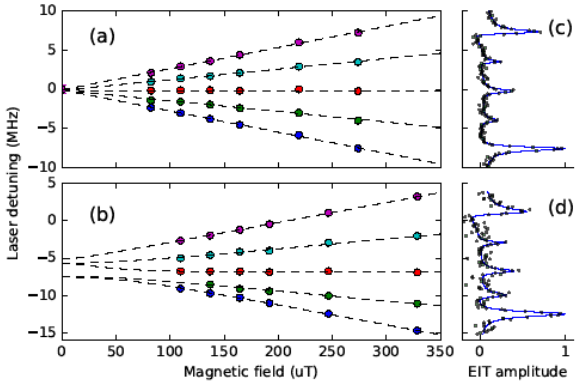


Figure 1: Inset *(a)* shows the Zeeman splitting without an applied electric field for the Rydberg state n = 75. The line centers are extracted from the EIT spectra, an example of which is shown in inset *(c)* for the highest B-field case. For the applied E-field case, insets *(b)* and *(d)*, the Stark shift is clearly visible.

REFERENCES

[1] T. Middelmann, S. Falke, C. Lisdat, and U. Sterr, "High Accuracy Correction of Blackbody

Radiation Shift in an Optical Lattice Clock," Phys. Rev. Lett. vol. 109, no. 263004, Dec. 2012.

[2] T. L. Nicholson, et al. "Systematic evaluation of an atomic clock at 2 x 10^{-18} total uncertainty," Nature Communications, vol. 6, no, 6896, April 2015.

[3] J. Lodewyck, M. Zawada, L. Lorini, M. Gurov, and P. Lemonde, "Observation and cancellation of a perturbing dc stark shift in strontium optical lattice clocks," IEEE Transactions on Ultrasonics, Ferroelectrics, and Frequency Control, vol. 59, no. 411, March 2012.

[4] S. Mauger, J. Millen and M. P. A. Jones, "Spectroscopy of strontium Rydberg states using electromagnetically induced transparency," Journal of Physics B: Atomic, Molecular and Optical Physics, vol. 40, no. 22, Nov. 2007.

The Italian Optical Link for Time and Frequency

Davide Calonico, Cecilia Clivati, Alberto Mura, Anna Tampellini and Filippo Levi
Physical Metrology Division
Istituto Nazionale di Ricerca Metrologica- INRIM
Turin, Italy
d.calonico@inrim.it

***Abstract*— The Italian Institute of Metrology (INRIM) developed an optical fibre backbone for the dissemination of accurate time and frequency standards to several research institutions of the Country. A network of research facilities, involved in areas ranging from atom and molecular spectroscopy to Very Long Baseline Interferometry (VLBI) for geodesy and radioastronomy, has been established. The time transfer over fibre has also been implemented for industrial users. We will describe the status of this 1800 km long facility, the most recent implementations and the research activities where fiber-based frequency dissemination is being exploited.**

Keywords—optical links, frequency metrology, VLBI, spectroscopy

I. INTRODUCTION

Optical fibre transfer is nowadays the best technique for the comparison of accurate clocks and for the dissemination of time and frequency standards [1]; in particular it is the only one suitable for optical frequency standards [1]. The Italian National Metrology Institute (INRIM) developed an optical fiber link for the dissemination of accurate time and frequency references to several research institutions across the Country [3]. First, the aim of this infrastructure is of boosting the experimental capabilities of the involved partner institutions and of allowing experiments which could not be performed using the previously available reference signals based on Global Positioning System (GPS) dissemination. In particular, the fibre-baseddissemination of an optical ultra-stable radiation referenced to the national primary frequency standard, which has an accuracy of $2x10^{-16}$ [4], encompasses by more than four orders of mangnitude GPS dissemination and has been exploited in several applications, ranging from high-resolution spectroscopy of atoms and molecules to geodesy and radio-astronomy based on Very Long Baseline Interferometry (VLBI). Second, we are investigating the possibilities offered by the fibre techniques to industrial users and new services based of time and frequency dissemination over fibre. For these targets, we implemented over our backbone the time transfer using the White Rabbit technique **Errore. L'origine riferimento non è stata trovata.**, that offers high robustness, high integrity levels and a very accurate traceability to UTC(IT), with sub-nanosecond accuracy.

In the following sections, we will illustrate the characteristics of the link and the present applications of this research infrastructure.

II. FIBRE LINK DESCRIPTION AND OPERATIONAL CONTROL

Currently, INRIM is connected with permanent links to several strategic locations: the financial district in Milano (279 km), the Institute for Radioastronomy in Medicina (514 km), the European Laboratory for Non-linear Spectroscopy, LENS, in Sesto Fiorentino (642 km), the Italian-French border in Modane, Frejus tunnel (150 km). The link has recently been extended to Roma (994 km) and during 2017, a further extension will reach the National Institute for Optics INO in Arcetri (682 km) and in Napoli (1306 km), the Galileo Precise Time Facility location in Fucino (1150 km), the Space Geodesy Center in Matera (1684 km). Using the cross-border connection in Modane, we plan to link to the French metrological institute LNE-SYRTE in Paris, another key step towards a network of European national metrological institutes.

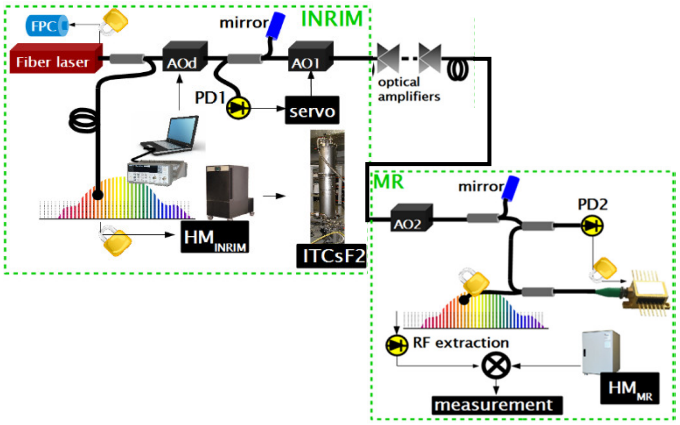


Figure 1. Experimental scheme of the traceability chain from INRIM to the HM of the radiotelescope in Medicina. In Florence, the signal of the link is the reference for an optical comb, and a local ultrastable laser is then locked on the referred comb. FPC: Fabry-Perot Cavity; AO: Acousto Optic Modulator; PD: Photo Diode.

The laser is then sent through the fiber, which is stabilised through the standard Doppler noise cancellation technique. The total loss experienced between INRIM and LENS (Florence) is 194 dB, partly compensated by a chain of 10 bidirectional Erbium Doped Fibre Amplifier (EDFA). The total number will amount to 30 for the whole project, and full optical regeneration is planned in Florence and Napoli. The amount of instrumentation placed along the fiber-haul poses the need of efficient remote monitoring and control capabilities. In particular, the EDFA gain proved to be extremely sensitive to the environmental temperature and has to be frequently

adjusted. Figure 1 reports the gain of some of the EDFAs located on the link from Torino to the radioantenna in Medicina. Such features result inup to 10 dB variations on the peak power of the beatnote used to phase-stabilize the optical link. The large fluctuations shown in Figure 1 cause the unlock of the active compensation, reducing the uptimes of the link. To overcome the problem, we have implemented a control using one of the amplifier as actuator, notably the first one of the chain that offers the largest gain dynamics. Figure 2 illustrates the result of a simple control loop on the EDFA actuator, in particular 7 days of continuous operation keeping the roundtrip beatnote amplitude constant within 1 dB. Few exception are shown, due to a clipping condition set on the minimum current of the amplifier, but they have not generated any unlock.

The remote control of the EDFA exploits the same fiber as the metrological dissemination for Ethernet-based communication to the devices. This approach guarantees reliable communication and short latency time, which are mandatory to enhance the infrastructure robustness. Figure 3 reports the cycle slips rate observed during the data taking, monitored with a double track oscillator technique. The total number of glitches was 377 and during the all 7 days, also the regeneration station at Medicina was continously locked to the signal incoming from the link, using a polarization control to compensate for the polarization rotation induced by the fibre.

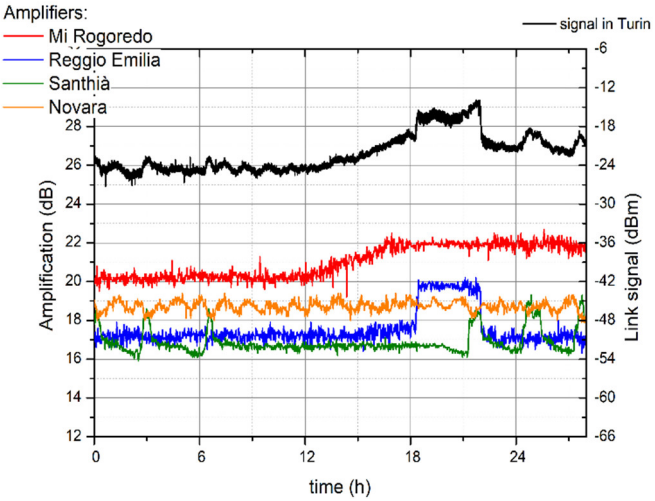


Figure 1: Monitor of the link before the implemntation of the active control of the amplifiers gain over one day: (upper black curve) Link signal reference, i.e. the amplitude of the beatnote between the ultrastable laser radiation and the roundtrip signal reflected back from the remote end of the fibre; (other lines) Gain of four main EDFAs along the fibre. The variation of the link signal due to the change of the gain for the EDFA in the sites of Mi-Rogoredo and Reggio Emilia is very close to the maximum dynamics of the active noise compensation electronics.

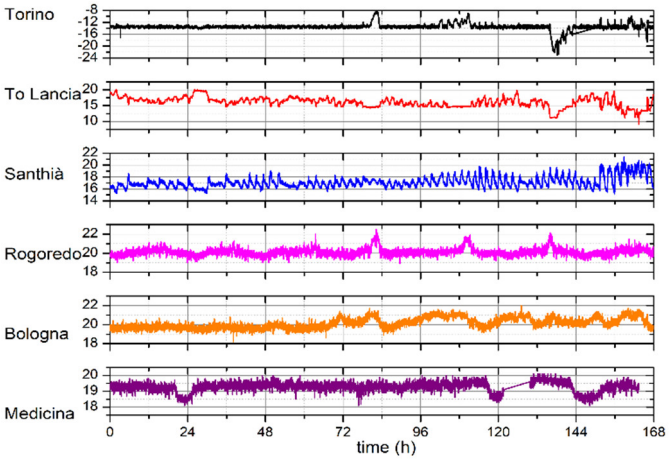


Figure 2: Link monitoring over 7 days of continuous operations, after the active control of the gain for the EDFA located in To-Lancia: (upper curve) amplitude of the beatnote between the laser and the radiation reflected back form the remote end of the link, exhibiting an overall stability at 1 dB level, with few exceptions; (second curve) gain of the EDFA located in To-Lancia, that acts as the actuator to control the link dynamics; (other curve) gain of amplifiers at selcted locations, where there are some relevant variations, in particular in Santhià.

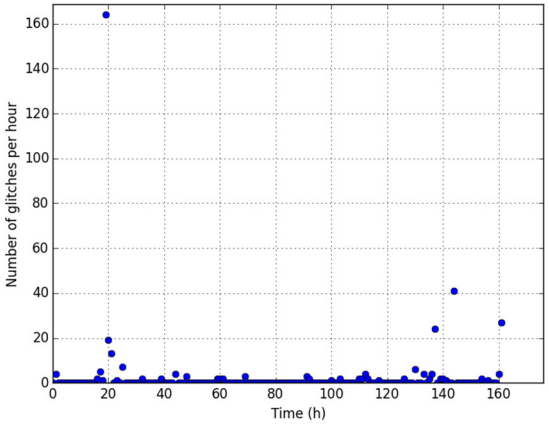


Figure 3: Cycle Slips per hour on the fibre link in 7 days of continous operations, measured with two Tracking Voltage Controlled Oscillators.

III. T/F Fiber Dissemination for Ultracold Atoms Spectroscopy, Molecular Spectroscopy and Quantum Simulation

At the Laboratory for Non Linear Spectroscopy, in Sesto Fiorentino, the traceability to the primary standard has been transferred to the visible domain around 578 nm and this allowed the currently most precise measurement of the clock transition of ^{173}Yb, at the 2×10^{-14} uncertainty level (limited by systematics), which could not be attained with the previously-available GPS-rferenced Rb oscillator [4]. This setup is also

enabling the simulation of quantum phenomena such as topological phases, through the measurement of Spin-Orbit Coupling on the cold Yb sample, continuously addressed by a fiber-link-referenced probe laser [7]. The long-term, resolved spectroscopy on the atom ensemble is performed through an extremely efficient interrogation scheme, which exploits the low frequency-instability (<10^{-14} on timescales of 10s of seconds) of the fiber-disseminated signal. The spectral purity of the fiber-disseminated radiation has also been transferred to a quantum cascade lasers emitting in the mid-infrared, the molecular fingerprint region, which is extremely interesting for some of the most challenging experiments, such as the search for variations of fundamental constants and the measurement of the electron dipole moment [8].

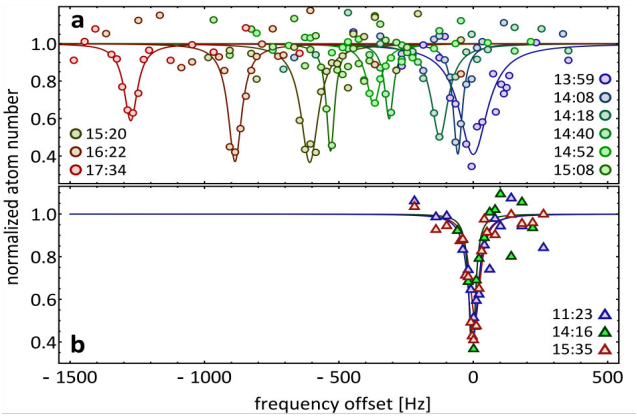


Figure 4: Fibre link dissemination at Florence, as reported in [6]. a) ultracold Ytterbium clock spectroscopic measured with the clock laser referred to a Rubidium clock signal (disciplined to GPS). Each line corresponds to a different epoch of the acquisition, within 4 ours of measurement: the data spread does not allow an average of the acquisitions. b) Spectroscopy within 4 hours locking the clock laser on the link reference signal. The data spread is now limited to few tens of Hz by the linewidth of the clock laser.

IV. T/F Remote reference for Radioastronomy

Another field of high relevance where state-of-the art frequency dissemination can be exploited is the investigation of the ultimate limits of spatial geodesy and radioastronomy based on VLBI. This technique is based on the correlation of measurements collected by a network of distant radiotelescopes, all equipped with high-quality local oscillators [9]. We are investigating the possibility of replacing the currently used H-masers with fiber-disseminated reference signals [10]. This allows the distribution of clock references of superior quality and opens completely new scenarios where the same clock can be delivered to multiple locations, thus allowing the full rejection of its contribution. We already exploited the fiber-based frequency dissemination in European VLBI campaigns involving the Medicina Radiotelescope [10], and we are now extending the link to the Space Geodesy Centre in Matera, southern Italy. Figure 5 shows a map of Italy with the indication of the main sites with radioastronomical or space facility. Figure 6 reports the first experimental fringes obtained in an international VLBI campaign involving 7 European observatories, among which Medicina used a remote HM reference transferred via a coherent fibre link. The fringes are the correlation of the radioastronomical signals measured at the radioantennas of Medicina and Wetzell, Germany. To fully benefit from the fibre link, the geodetic VLBI technique is high demanding in terms of the resilice of the frequency trasnfer. In fact, each geodetic campaign lasts 24 hours, and it is required an uptime of 100% for the frequency reference. The improvement on the link control has demonstrated to be adequate for this achievement, even if more test and mesurements have to be done.



Figure 5. Map and the fibre link, with the main locations for radioastronomical and space premises in Italy.

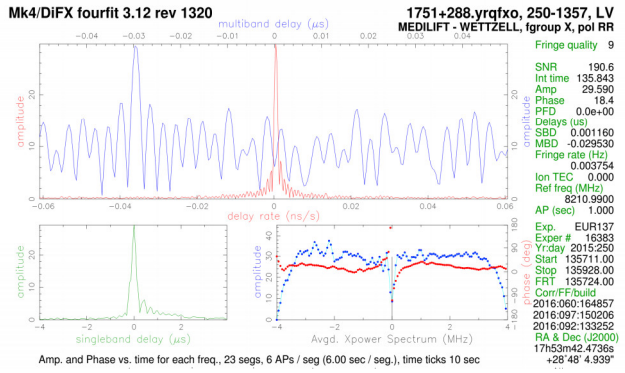


Figure 7: Interference fringes from a real VLBI campaign in 2015, whose results are reported in [11]. The fringes come from the interferometry beteen Medicina an the telescope in Wetzell, Germany. The Medicina radioantenna used the HM at INRIM disseminated by the fibre.(Courtesy of M. Negusini, INAF)

V. CHRONOMETRIC GEODESY

The Doppler-stabilised link to the Laboratoire Souterraine de Modane (LSM), inside the Frejus tunnel on the Italy-France border, has been used for a proof-of-principle experiment in relativistic geodesy, with the aim of demonstrating that optical clocks can be used as probes for the gravitational redshift [12, 13]. The ratio between a Yb clock and a transportable Sr clock was measured when they were co-located at INRIM and after one of them was transported to LSM, using the fiber-disseminated signal at 1.5 μm as a spectral bridge. This kind of experiments will significanlty change the paradigm in relativistic geodesy, allowing the investigation of changes of the gravitational potential at the cm level, and on timescales of hundreds of seconds, faster than those measured with classical instruments [12]. The connection to LSM is also the first span in the forthcoming link to the French Metrology Institute, planned for 2017.

VI. INDUSTRIAL USERS: THE FINANCIAL SECTOR USE CASE

Last, time transfer using White Rabbit is now permanently implemented on an independent link from INRIM to the financial district of Milano (279 km) [15]. This will be a suitable option for the UTC traceability of financial markets, as requested by a new regulation (2018) from the European Security and Markets Authority, named MiFIDII **Errore. L'origine riferimento non è stata trovata.**. The regulation asks for a traceability level depending on the financial activity, but in the most stringent case the required accuracy is 100 μs and sensibility 1 μs.

VII. CONCLUSION

We developed a national fiber backbone between several research institutions in Italy for the accurate dissemination of the national primary frequency standard: the present haul is 1800 km long and spans from the French border to Matera; 800 km are fully operational, disseminating our INRIM references, while the remainder will be implemented by 2017.

We are strongly focused on the exploitation of this facility in fields outside the core frequency metrology, and target the realization of distributed research facilities of continental scale, which could lead to novel, high-impact ways of doing research. The synchronization of the radiotelescopes in Medicina and Matera will build a thousand-km wide interferometer, whereas the connection of spectroscopy laboratories such as LENS and INO allows for the simultaneous monitoring of atomic and molecular transitions with unprecedented accuracy. The measurement capability of the single institute will be empowered, resulting in an extremely useful tool to probe Physics as we know it today. On the other hand, time transfer over fiber is a technique already mature for industrial user, and we started the implementation of permanent fibre links devoted to this target.

ACKNOWLEDGMENT

This research is funded by EMPIR-15SIB05-OFTEN, which has received funding from the EMPIR programme co-financed by the Participating States and from the European Union's Horizon 2020 research and innovation programme.

The authors thank Monia Negusini, Federico Perini, Matteo Stagni for the help in the elaboration of the interferometric fringes in the VLBI esperiment.

REFERENCES

[1] D. Calonico, M. Inguscio, F. Levi, Light and the distribution of time, 2015 *European Physics Letters* **110** 4000 (2015)

[2] C. Lisdat, *et al.*, A clock network for geodesy and fundamental science *Nature Com.* **7**, 12443 (2016)

[3] D. Calonico, *et al.* "High-accuracy coherent optical frequency transfer over a doubled 642-km fibre link," Appl. Phys. B 117, pp. 979–986, 2014.

[4] F. Levi, D. Calonico, C. E: Calosso, A. Godone, and G. A. Costanzo "Accuracy evaluation of ITCsF2: a nitrogen cooled caesium fountain," Metrologia 51, May 2014

[5] E. Dierikx, "White Rabbit Precision Time Protocol on Long-Distance Fiber Links" IEEE Tran. on UFFC, 63, 945 - 952, 2016.

[6] C. Clivati, et al., "Measuring absolute frequencies beyond the GPS limit via long-haul optical frequency dissemination," Opt. Express 24, pp. 11865-11875 (2016).

[7] L. F. Livi, G. Cappellini, M. Diem, L. Franchi, C. Clivati, M. Frittelli, F. Levi, D. Calonico, J. Catani, M. Inguscio, and L. Fallani, "Synthetic Dimensions and Spin-Orbit Coupling with an Optical Clock Transition," Phys. Rev. Lett. 117, p. 220401, Nov. 2016.

[8] S. Borri and G. Santambrogio, "Laser spectroscopy of cold molecules," Adv. In Physics: X, pp. 368-386 (2016).

[9] R. Thompson, J. M. Moran, and G. W. Swenson, Interferometry and Synthesis in Radio Astronomy, 2nd ed., Weinheim, Germany: Wiley-VCH, 2001.

[10] C. Clivati et al., "A Coherent Fiber Link for Very Long Baseline Interferometry," IEEE Trans. Ultrason. Ferroel. Freq. Contr. 62, pp. 1907-1911, Nov. 2015.

[11] C. Clivati et al., "A VLBI experiment using a remote atomic clock via a coherent fibre link," Sci. Rep. 7, 40992-8, Febr. 2017.

[12] T. Takano, M. Takamoto, I. Ushijima, N. Ohmae, T. Akatsuka, A. Yamaguchi, Y. Kuroishi, H. Munekane, B. Miyahara, H. Katori, Geopotential measurements with synchronously linked optical lattice clocks, *Nature Photonics* **10**, 662-666 (2016)

[13] J. Grotti et al. "Geodesy and metrology with a transportable optical clock", arXiv:1705.04089

[14] C. Clivati et al., "An optical fiber link for the remote comparison of optical clocks and geodesy experiments", proc. of the IFCS, Denver, p. 978, Apr. 2015.

[15] P. Tavella et al., "Time dissemination services: The experimental results of the European H2020 DEMETRA project ", 2016 IEEE International Frequency Control Symposium (IFCS), 1-5, 2016

Hybrid optical link for ultra-stable frequency comparison

D. Xu, W. K. Lee, F. Stefani, P. -E. Pottie
LNE-SYRTE
Observatoire de Paris, PSL Research University, CNRS,
Sorbonne Universites, UPMC
Paris, France

A. Amy-Klein, O. Lopez
Laboratoire de Physique des Lasers
Universite Paris 13, CNRS
Villetaneuse, France

***Abstract*—We present a hybrid fiber link to realize the local two-way optical frequency comparison with self-synchronization. It enables us to detect round-trip fiber noise and one-way fiber noise, and estimate the residuals. Moreover, we can check, to the best of our knowledge for the first time, the reciprocity of the accumulated noise forth and back over a bi-directional fiber, and also evaluate the noise correlation between two adjacent fibers with the hybrid setup.**

***Index Terms*—ultra-stable frequency comparison; hybrid optical link; local two-way**

I. Introduction

Optical fiber links have been developed rapidly for time dissemination and frequency transfer over the last decade. With the progress in the development of optical atomic clocks, the most demanding technique for distant comparisons of their performance is the optical frequency transfer using fiber links.

Optical frequency transfer via fiber networks has been performed with ever-increasing performance and fiber lengths. Meantime, different schemes of optical fiber links have been investigated: active noise compensation (ANC) method [1] and passive noise compensation methods called as Two-Way (TW) [2]. In ANC method, the phase noise added by the fiber links due to environmental fluctuation is actively compensated, whereas they are passively compensated for TWs: TW methods are based on post-processing data acquired independently at both ends of the link. The data must be synchronous for optimal noise rejection.

The two-way methods can be divided further into two types, referred in [3] as conventional two-way (CTW) and local two-way (LTW). In CTW method, optical frequency comparisons are obtained by post-processing the data, but efforts need to be paid to synchronize the acquisition of the data at the two ends of the link. Compared to LTW, the noise rejection gain in CTW method can be four times better. It is also possible to arrange the experimental setup at each end of the link, in addition to the classical data, one record another optical beat note between the laser and itself after a round-trip, which is the same signal as that detected in an ANC setup. From post-processing the data acquired locally only at one site, one can reject the propagation noise. In this case, the fiber noise could be suppressed in real-time, by measuring at one link end only, either at the local site or the remote site. The rejection is equivalent to an ANC setup. The advantage is that the data are self-synchronized and give the optimal rejection possible for an ideal synchronization.

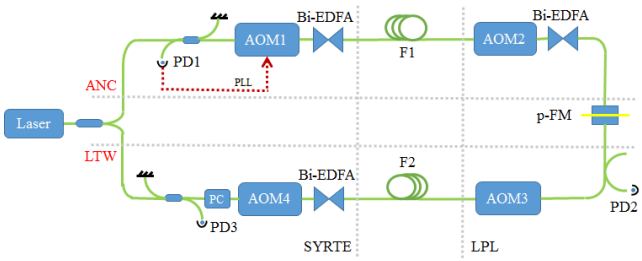


Fig. 1. Experimental scheme for the simultaneous optical frequency transfer and comparison. AOM, acousto-optic modulator; bi-EDFA, bi-directional erbium-doped fiber amplifier; PLL, phase-locked loop; PD, photodiode; PC, polarization controller; p-FM, partial Faraday mirror.

We investigate here a hybrid architecture, using active noise compensation on one of the fibers and using local two-way setup on the other fiber [3]. These fibers are used as a first span of the international optical link between NPL and SYRTE, and as a test bed for investigating the fundamental limits of fiber links. Compared to the above mentioned three schemes, the hybrid method has extra advantages that we will present at the conference.

II. Experimental scheme

The experimental scheme we implement for optical frequency transfer and comparison is shown in Fig. 1. The two fibers, denoted by F1 and F2, are urban fibers of length 43km connecting two laboratories, SYRTE and LPL. An active noise compensation (ANC) setup is built on F1; a local two-way (LTW) setup is built on F2. The ultra-stable laser is split into two parts. One part is injected into F1 for the ANC; the other part is injected into F2 for the LTW. A partial Faraday mirror (p-FM) is used at the LPL site, which makes a perfect fiber-length match in the remote setup as the uncommon fiber length is zero. After detection, electronic amplification and filtering, the beat notes are simultaneously recorded by two dead-time free frequency counters (K+K FXE) operated in Π-type and Λ-type with a gate time of 1 s.

978-1-5386-2916-1/$31.00 ©2017 IEEE

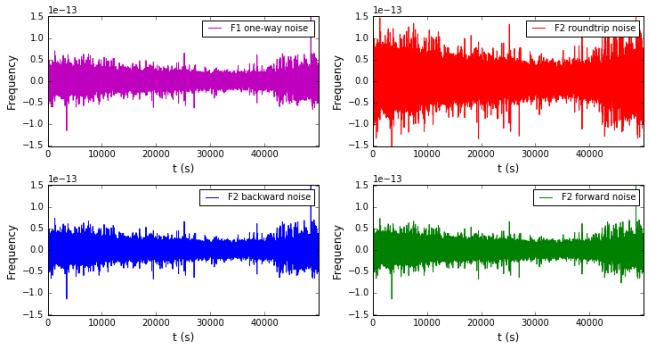


Fig. 2. Measurements of frequency data acquired only at SYRTE: one-way noise of F1, round-trip noise, one-way forward and backward noise of F2.

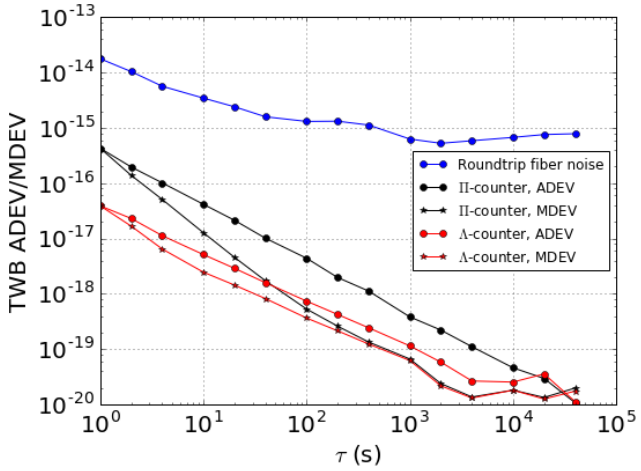


Fig. 3. Fractional frequency stabilities of bi-directional LTW method in terms of Allan deviation with Π-type counter and Λ-type counter.

III. Experimental results

At SYRTE site, we can simultaneously obtain four beat notes, containing abundant information about the two parallel fibers' noise: the one-way free running noise of F1, the round-trip noise, one-way forward noise, one-way backward noise of F2, shown in Fig. 2. The one-way noises of F1 and F2 are almost at the same level. The round-trip noise is twice of the forward and backward one-way noise on F2.

Based on the above four basic beat notes acquired only at SYRTE site, we can obtain a set of fractional frequency instabilities of uni-directional and bi-directional LTW methods [4]. For instance, the fractional frequency instabilities of bi-directional LTW method in terms of overlapping Allan deviation (ADEV) and the modified Allan deviation (MDEV) are shown in Fig. 3. The blue line is the free running round-trip fiber noise of F2. ADEV and MDEV calculated from the Π-type counter data start from 4×10^{-16} at 1 s integration time and decrease with the slope of -1 and -3/2, respectively. MDEVs of the data recorded with the Π-type counter and Λ-type counter converge to the same value.

These results show that the implementation of a very simple but robust and temperature insensitive interferometer at the end-user site enables extremely accurate frequency comparison, between NMIs and between advanced molecular spectroscopy experiment and primary frequency standards [5].

Beyond this very good performance, this hybrid setup enable us to assess the performance of optical frequency transfer in real time. This type of cascaded link gives us an independent method to measure the link stability and accuracy with improved resolution.

Finally, this hybrid setup enables us to detect round-trip noise and one-way noise, from which we can infer several perfectly synchronous observable of the free running fiber noise, compensated fiber noise, and estimate the residuals. In particular, we can discriminate events arising from the fiber and from the noise processing (default detection). Moreover, we can check, to the best of our knowledge for the first time, the reciprocity of the accumulated noise forth and back over a bidirectional fiber, and also evaluate the noise correlation between two adjacent fibers with the hybrid setup.

IV. Conclusion

We present here the latest experimental results of optical frequency comparison on a fiber link of 2×43 km connecting SYRTE to LPL through a dedicated pair of fibers over an urban area. The hybrid setup we have implemented enables us to transfer frequency with a relative frequency stability as low as 3.9×10^{-17} at 1 s integration time and ultimate resolution below 10^{-20}. Combined with another hybrid links between LPL and NPL (UK), this setup has already been used to perform optical frequency comparison between SYRTE and NPL Sr clocks with stability of 1×10^{-18} at 1000 s integration time [6].

References

[1] L. S. Ma, P. Jungner, J. Ye, and J. L. Hall, "Delivering the same optical frequency at two places: accurate cancellation of phase noise introduced by an optical fiber or other time-varying path," Opt. Lett., vol.19, pp. 1777-1779, November 1994.

[2] C. E. Calosso, E. Bertacco, D. Calonico, G. A. Costanzo, M. Frettelli, F. Levi, A. Mura, and A. Gonone, "Frequency transfer via a two-way optical phase comparison on a multiplexed fiber network," Opt. Lett., vol. 39, pp.1177-1180, March 2014.

[3] W. K. Lee, F. Stefani, A. Bercy, O. Lopez, A. Amy-Klein, and P. -E. Pottie, "Hybrid fiber link for accurate optical frequency comparisons," App. Phy. B, vol.123, pp. 161, May 2017.

[4] A. Bercy, F. Stefani, O. Lopez, Ch. Chardonnet, P. -E. Pottie, and A. Amy-Klein, "Two-way optical frequency comparison over 100 km telecommunication network fibers," Phy. Rev. A, vol. 90, pp. 061802, December 2014.

[5] B. Argence, B. Chanteau, O. Lopez, D. Nicolodi, M. Abgrall, Ch. Chardonnet, C. Dossy, B. Darqui, Y. L. Coq, and A. Amy-Klein, "Quantum cascade laser frequency stabilization at the sub-Hz level," Nat. Photon., pp.456-460, June 2015.

[6] P. Delva, J. Lodewyck, S.Bilicki, E. Bookjans, G. Vallet, R. Le Targat, P.-E. Pottie, C. Guerlin, F. Meynadier, C. Le Poncin-Lafitte, O. Lopez, A. Amy-Klein, W.-K. Lee, N. Quintin, C. Lisdat, A. Al-Masoudi, S. Drscher, C. Grebing, G. Grosche, A. Kuhl, S. Raupach, U. Sterr, I. R. Hill, R. Hobson, W. Bowden, J. Kronjger, G. Marra, A. Rolland, F. N. Baynes, H. S. Margolis, P. Gill, "Test of special relativity using a fiber network of optical clocks," Phys. Rev. Lett., vol. 118, pp. 221102, June 2017.

The Medium and Long Term Stability of the NAC Atomic Clock

Shemi Prazot, Avinoam Stern,Weiss Israel, Shlomo Marmor, Chagay Levi,Israel Yevilevich, Uriel Arad,Rony Man, Benny Levi
Miniature atomic clocks department
AccuBeat
Jerusalem, Israel
Shemi.prazot@accubeat.com

***Abstract*— The NAC1 ("Nano-Atomic-Clock") is a miniature, high reliability, CPT-based Rubidium Atomic clock. Its basic design and features were described in a previous paper. This paper provides further details and updates on the clock. In particular we focus on medium-term and long-term stability issues that are key parameters in commercial atomic clocks, as well as the wide temperature operational range and the high reliability feature of the NAC1.**

Keywords—NAC, NAC1, CPT; Atomic Clock; Medium Term Stability, Long Term Stability, Aging; Miniature Atomic clock;

I. INTRODUCTION

The Coherent Population Trapping (CPT) phenomenon has recently enabled the materialization of miniature low power atomic clocks [1] [2]. These clocks find a growing usage with new applications such as seismic sensing, underwater oil exploration, mobile radios, secure and enhanced performance GNSS receivers and more. Today the medium-term and the long-term stability (aging) of the clock are the key parameters of these miniature atomic clocks towards a wider use in numerous industrial applications. Compared to standard vapor-cell atomic clocks, CPT based atomic clocks are somewhat more complicated, hence handling the medium-term and the long-term issues requires a careful reduction of sensitivities as well as tight stabilization of many parameters of the clock. These requirements are challenging considering the limited space and the limited power allocated for the these miniature clocks.

Some new applications of miniature atomic clocks also require operation over the full industrial temperature range of -40℃ to 85℃ while still maintaining the reliability. Today other miniature clocks available in the market offer a limited temperature range. Some clocks offer wider temperature range but on the expense of increased size and power consumption. [2].

The NAC1 ("Nano-Atomic-Clock") is a miniature, high reliability, wide temperature range, CPT-based Rubidium Atomic clock. Its basic design and features were described in a previous paper [3]. The model which is discussed in the present paper is a first generation product named NAC1, now under serial production. It is depicted in in Fig. 1.



Fig. 1. Photograph of NAC1 with the dimensions of 41x35x22mm^3.

The main characteristics of NAC1 are summarized in Table 1 and Fig. 2 below. In the free-running mode NAC1 demonstrates a frequency stability (ADEV) of $8\cdot 10^{-12}$ at 1000s averaging time, and an aging (drift) of $3\cdot 10^{-10}$ per month.

Table 1: NAC1 Key Charteristics

Parameter	***Characteristic***
Output Frequency	10MHz
Dimensions	41x35x22mm3
Power Consumption	1.2W
ADEV	2E-10 @ 1 s 8E-12 @ 1000s
Phase Noise	-150dBc/√Hz @ Floor
Temp. Coefficient and Temp Range	±1E-9 over -20^{0}C to 65^{0}C (*)
Aging	3E-10/month

(*) Extended temperature range is further discussed below.

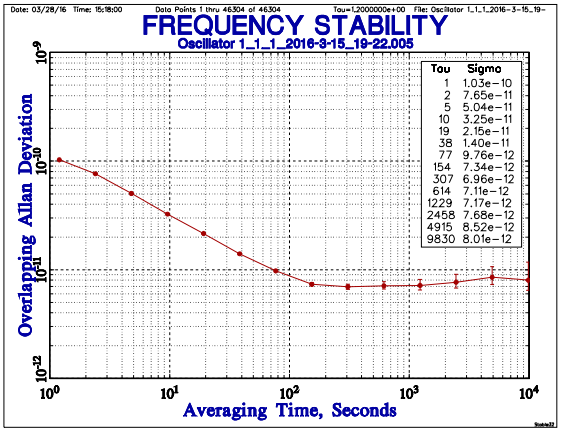


Fig. 2. NAC1 measured ADEV.

In this paper we focus on the important aspects of medium-term-stability and the long-term stability. In addition we discuss the clock design for high reliability and extended operating temperature range.

The paper is organized in six chapters. Chapter I is the introduction, chapter II provides a general design review of NAC1 and chapter III focuses on the glass technology used in NAC1 cell. Chapter IV discusses the medium-term-stability aspects of miniature CPT clock and the design concepts used in the NAC1 for improving the medium-term performance. Chapter V deals with long term stability, focusing on the vapor cell and its technology and chapter VI discusses the design for wide temperature rage of the clock.

II. NAC1 Design

For the completeness of reading we provide here a brief review of the design of NAC1 already given in [3].

The block diagram of the main frequency loop of the NAC1 is presented in Fig. 3. It is based on a TCXO which generates the 10MHz frequency. This frequency is multiplied by a synthesizer to 3.417… GHz and injected to a VCSEL laser diode included in the physics package. The RF frequency modulates the current of a VCSEL laser diode which operates at the wavelength of the D1 line (~795nm), thereby producing several sidebands. The laser beam is directed into the glass cell filled with ^{87}Rb and buffer gas after passing a λ/4 plate. The first two coherent sidebands excite the so called Λ transition in the Rubidium. When the separation of the two sidebands equals the Rubidium "clock frequency" a peak occurs in the vapor transmission. The transmission peak is then used to lock the TCXO to the CPT resonance line.

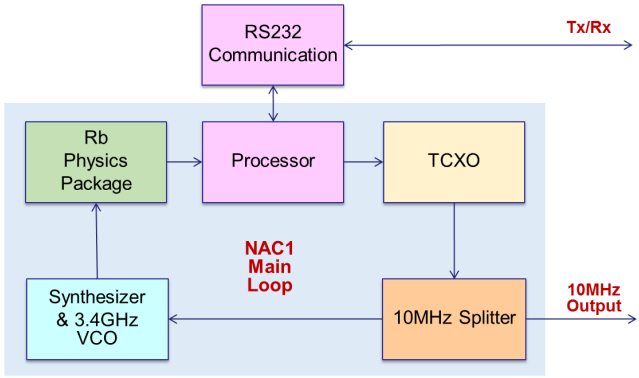


Fig. 3. Block Diagram of NAC1 showing the main frequency loop.

In addition to the main frequency loop described above, NAC1 uses six control loops to stabilize the different parameters of the clock. These loops are operating with a Time-Division-Multiplexing scheme (TDM) which separates the loops sensing and control in the time domain. These loops are described in the next chapters.

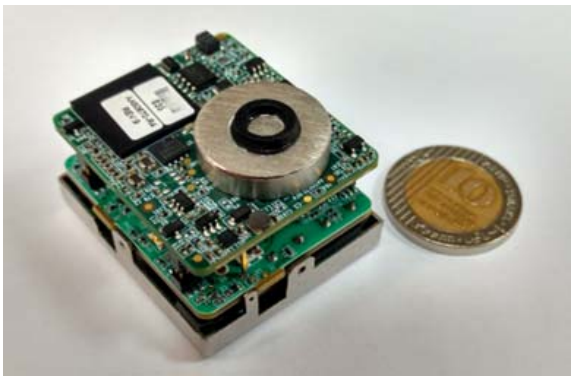


Fig. 4. Internal structure of NAC1 showing the physics package and electronic circuits.

III. Glass Technology

The Rubidium vapor cell in NAC1 is a simple miniature round glass ball filled with Rubidium87 and buffer gas a coated with partially transparent resistive coating. We make use of traditional glass and filling technology for the production of the cell, however still maintaining relatively very low power consumption. The use of traditional and mature glass technology prevents issues which are found in MEMS cells packaged under vacuum conditions, such as leaks and outgassing. Furthermore the glass manufacturing process is rather simple and its cost is low.



Fig. 5. Coated glass cells used in the NAC1 physics package

Vacuum issues of outgassing and leaks are critical in MEMS devices packaged under vacuum. While the use of vacuum packaging used for MEMS devices has the advantage of reducing the thermal conductivity and convection, it makes the vapor cell and the vacuum package susceptible to leaks and outgassing. These can degrade the performance of the clock dramatically, affect its temperature operating range and its long term stability. More important, these effects can harm the reliability. In our case, the NAC1 cell is mounted on the PCB, is exposed to the air and therefore has no leak issues. However this comes at the expense of somewhat higher power consumption

By using the glass cell technology and avoiding vacuum packaging we ensure high reliability and enable safe operation over a wide temperature range, which is not feasible today with clocks based on MEMS technologies.

IV. MEDIUM TERM STABILITY

Herein, we refer to the Allan Deviation at time constant around 1,000 to 10,000 seconds as the measure of the medium term stability. The key elements that impact the medium term stability are the vapor cell parameters, the laser parameters and magnetic field parameters. These are discussed in the following paragraphs.

A. Vapor Cell parameters

NAC1 contains a vapor cell made of a glass sphere filled with ^{87}Rb and buffer gas. The cell is coated with a partially transparent resistive heater where the heating is applied directly to the resistive coating. This heating method improves power efficiency and saves space.

As is well known, a ND filter is required in order to optimize the CPT signal with respect to power broadening [4]. The ND filter should be tuned to an optimal intensity which gives optimized SNR and CPT linewidth. In NAC1 the cell partially transparent coating serves as an ND filter, thus saving a separate ND filter component.

As can be seen in Fig. 5, the cell coating is composed of two layers: a thin coating layer covering the entire cell and another coating layer covering the cell's polar caps. The result of this structure is a partially transparent and higher resistance coating in the center part and an opaque lower resistant coating on the caps. The center coating determines the light attenuation and in turn the SNR and CPT linewidth, hence affecting the short-term-stability of the clock. The widths of the caps coating determines the maximum heating power for a given voltage supply. This maximum power limits the available heating power at the low temperature end, hence the minimum operational ambient temperature specified at -40℃ for NAC1. The combination of double layer coating enables meeting the low temperature end while optimizing thickness of central coating for SNR and linewidth.

The cell temperature stabilization is a key aspect of the medium-term-stability performance. In NAC1, the cell is thermally stabilized by inferring the temperature from the atomic vapor density rather than using a temperature sensor. The loop stabilizes the atoms density directly, not the temperature of a sensor which is not exactly equal to the rubidium temperature. The atomic vapor density (temperature) is then measured in a specific time slots using the optical absorption of the cell. This technique simplifies the cell structure, reduces production cost and improves the accuracy.

Another important parameter for the medium-term-stability is the buffer gas mixture inside the cell. The buffer gas mixture ratio is selected in order to minimize the sensitivity of the atomic vapor frequency to temperature. The main issue here is that during production of the cells we have to make sure that the ratio and pressure are not changed from the intended one. Therefore special care and methods are applied to ensure repeatable manufacturing conditions, in particular stable gases mixture and pressure.

B. Laser parameters

The light source used in the NAC1 is a 795nm VCSEL diode laser tuned and locked on the ^{87}Rb D1 line. The VCSEL key parameters that affect the short-term-stability and medium-term-stability of the clock are its wavelength, light intensity and modulation depth. These parameters affect short-term-stability via the CPT SNR and line width. They also determine medium-term-stability via the light shift effect (see below).

The controllable parameters which determine the VCSEL wavelength and light intensity during operation are the laser current and temperature. The light intensity increases with the laser current and decreases with the temperature, while the laser wavelength increases with both the current and temperature. In order to maintain both wavelength and intensity stable and constant, a nested double control loop is used. The nested double loop stabilizes the wavelength and the current by controlling the current and the temperature of the laser. The main advantage of this method, compared to temperature stabilization based on thermistor sensing, is a direct relation to the lasing media and better immunity to ambient temperature variations. In addition, it saves the conversion time required for VCSEL thermistor ADC readings.

NAC1 however also contains a thermistor located in close proximity to the laser chip which is used for fast initialization mode. In the fast initialization mode the temperature is controlled using the thermistor, which achieves a preliminary fast but coarse tuning of the temperature. During the steady state operation, the thermistor is disabled and the laser temperature stabilization is performed by the nested double loop as per above. This hybrid technique of nested double loop and thermistor provides the best tradeoff between fast startup and high stabilization of the laser parameters during a steady state operation.

As known, the laser parameters impact the clock frequency via the so called "light-shift". The light shift effect is an AC Stark shift where the energy levels of the atom are slightly shifted due to the presence of the resonant light (for semi classical treatment see [5]). In our case we deal with 4 transitions between the two ground hyperfine states ($5^2S_{1/2}$, F=1, F=2) and the two hyperfine excited states ($5^2S_{1/2}$, F'=1, F'=2) which are subject to a mixed AM-PM modulation of the laser light. This effect was analyzed in previous works [6]. We have performed our own similar analysis [3] which shows that light-shift is manifested through three parameters: 1) a direct light intensity change, 2) the wavelength detuning (so called δ) and 3) the RF modulation index change. The direct light intensity and the wavelength are well controlled using the nested double loop described above, so the most prominent effect is due to a change in the RF modulation index. The later effect is quite complicated and cannot be adjusted to zero due to the presence a mixed IM-PM laser modulation.

The RF modulation index depends on the VCSEL current and the RF power. The NAC1 is designed and calibrated to work with VCSEL current and RF power operating points that minimize the frequency variation due to RF power changes.

The VCSEL current determines the symmetry between the modulated sidebands of the VCSEL. The best operation point is where the VCSEL current ensures perfect sidebands symmetry and where variations in the RF power equally affect both first sidebands. On the other hand, optimizing the VCSEL current for sidebands symmetry increases the VCSEL linewidth, which degrades the short term frequency performance of the clock.

This trade-off in the VCSEL current is translated to a trade-off between the short-term and the medium-term stability. On this issue we decide to focus on the medium term stability, while still maintaining a reasonable short-term-stability around 1E-10/√tau.

The RF power determines the ratio between the carrier, first sidebands and higher sidebands. An optimum power which minimizes the light shift is found where the carrier and the first side bands are almost equal in intensity. Above this power the intensity of both the carrier and the first sidebands drop. This point is calculated during the integration step and is used as an initial operation point.

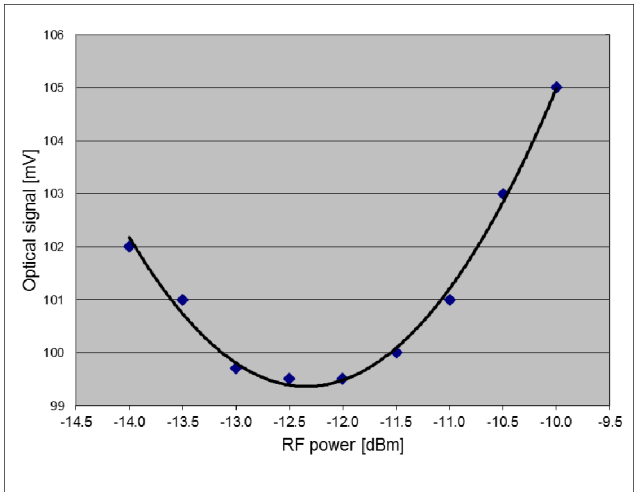


Fig. 6. Optical Signal level vs. RF power

In addition to the optimization in VCSEL current and RF power operation point, a dynamic control loop is added in order to stabilize the RF modulation index versus environmental (temperature) changes. This loop is based on the optical light measured by the photodetector. As can be seen in Figure 6, the signal measured by the photodetector against the RF power has a minimum at a specific RF power for any given VCSEL current (around the VCSEL current operation point as settled above). This minimum is determined by the Relaxation Oscillation parameter of the VCSEL. The RF power loop lock the RF power to this minimum, hence ensures operation in a well-defined RF power. In figure 7, the frequency dependency on the VCSEL current with and without the RF power loop is shown. As can be seen, the RF power loop compensates for variation in the current and ensure operation in a fixed point. This graph shows the advantages of this loop which determines constant modulation index even when the VCSEL parameters have been changed.

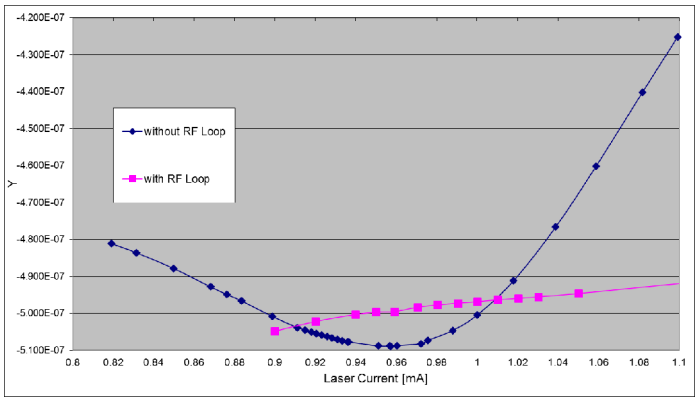


Fig. 7. Frequency dependency on the VCSEL current with and without the RF power loop

C. *Magnetic Field*

In order to reduce sensitivity to external magnetic fields(static and low frequency) , NAC1 uses the common structure of double mu-metal shielding. The physics package is placed in the inner shield, while the clock package is used as a second outer shield. The inner shield has a standard cylindrical structure. The cell assembly is mounted on a PCB which present a challenge for effective shielding due the gap that it introduces. In order to improve the shielding efficiency, the shield is created from top and bottom parts with overlapping teeth which penetrate the PCB from two sides. The teeth structure and locations were chosen after careful design, based on simulations and verified by actual testing.

A source of unwanted magnetic fields which are not protected by the shields are the heating currents. As mentioned, NAC1 is designed to operate over a wide temperature range and this requires a higher power at the low temperature end (-40□). Considering the low voltage supply (3.3V), the current needed for heating becomes significant. The main issue is with the cell heating current since the laser heater is shielded by the inner shield. As explained above, the cell is made of a glass sphere coated with a partially transparent resistive heater. The heating currents flows from pole to pole across the sphere maintaining axis symmetry. It can be shown that such a symmetry cancels the field induction within the sphere. In reality the symmetry is of course not perfect and small residual induction still remain within the sphere.

V. LONG TERM STABILITY ISSUES

This chapter discusses the issues of long-term-stability. Herein by long-term-stability we refer to the systematic frequency drift with respect to elapsing time, known as "aging".

Aging in traditional vapor cell atomic clocks (Rubidium or Cesium) is believed to be related to the following phenomena [7]:

a) Rubidium or Cesium migration inside the cell:
The alkali metal drops and metal film migrate from colder to hotter areas across the cell due to thermal gradients. An initial "aging" period is required to stabilize this process.

b) Rubidium or Cesium interaction with residual impurities inside the cell:
Again, an initial "aging" period is required to stabilize this process.

c) Stability of the buffer gas pressure and mixture in the cell:
The pressure shift is of the order of parts of 1E-11 (frequency) per mTorr (pressure). Diffusion of gases in and out the glass wall changes the pressure (density) and content of the buffer gas thereby changing the frequency.
Again, this effect requires an initial "aging" period for stabilization and reaching some steady state level.

d) Helium permeation in and out the cell.
About 4 mTorr of Helium exists in the earth atmosphere. The Helium permeates into the cell, changes the content of the buffer cell thereby changing the clock frequency. However, this effect is rather small, below 1E-11 per month[7]

e) Light shift effects:
"Light-shift" related shifts were discussed in the previous section since they are critical when dealing with the medium-term-stability. However, if for example, the RF power drifts in time, the clock's frequency shall drift as well due its sensitivity to the RF power.

As mentioned, NAC1 uses a conventional glass vapor cell. The glass technology used in NAC1 is based on our long experience and understanding of the aging processes in our non-CPT Rubidium clocks which helps in dealing with these effects. In fact we use the same proven procedures used in our standard vapor cell production to produce the vapor cells for NAC1.

The first four effects, a) thru c), are related to the vapor cell and to the vapor cell technology. Therefore they are controllable by the same methods and procedures we use in our glass cell manufacturing line. One of the basic methods to reduce the cell related long-term-stability issues is to subject the cells and the complete clock to an "aging" process, i.e., to operate it for a period of time in order to stabilize the effects a) thru c). For NAC1, each unit goes through a meticulous monitored aging process. The manufacturing stations include a cell pre-aging station, after pre-aging tests, full clock aging station and a final clock aging station where each clock is monitored until it reaches the specified aging rate.

The light shift effect, e), is manifested however in different ways when comparing a CPT clock to a conventional Rubidium Clock. In a conventional Rubidium clock one uses a Rubidium lamp and a microwave cavity while the CPT clock uses an RF modulated laser instead. As a result the frequency shifts mechanism are different as discussed above. Nevertheless, methods devised for the stabilization of "light shift" related shifts are valid for aging improvement as well. Furthermore, active loop stabilization of the light intensity and of the RF power, positions the NAC1 at a perhaps an advantageous place compare to the traditional vapor cell Rubidium clock.

A final note related to the outgassing. As mentioned above outgassing is a critical effect in MEMS devices packaged under vacuum. Such devices are very sensitive to outgassing inside the cell. Outgassing causes frequency drift as well as variation in the thermal conditions inside the cell. In addition, leaks in the physics package or in the vapor cell affect its long term stability by the same mechanism. In our case, the NAC1 cell is based on traditional glass technology and is exposed to the air. Therefore, it is immune to such effects, which are relevant for a cell in a vacuum environment.

VI. EXTENDED TEMPERATURE RANGE

NAC1 is designed to operate over temperature range of -40□ C to +75□ with a minimum frequency variation. For this end (a) all components should be operative over the full range, (b) various temperature sensitivities should be minimized and (c) active temperature stabilization loops are used for the critical components.

To start with, the temperature control of the VCSEL is of course essential as without it the wavelength can easily go out of range. The Laser temperature control loop is based on the hybrid method combining thermistor sensing for initialization and the nested double loop for steady state. The thermistor ensures fast initialization and the nested double loop provides for high precision and immunity to temperature changes (see above). The laser heating method uses resistive heating, which has the advantage of supporting wider temperature range compared to the use of a Thermoelectric Cooler based on Peltier effect (TEC) used in other works [8]. TEC elements are limited in cooling by the parasitic heating power generated inside the elements which limits the operational temperature range of the laser.

Next we refer to the electrical components. The key electrical components that affect the temperature steady-state and transient behavior of the NAC1 are the TCXO and the RF multiplication chain. The RF chain affects the clock stability through the RF power and the light shift effect as explained above. The RF chain power is sensitive to ambient temperature fluctuations. In order to reduce this sensitivity, the RF chain was designed with minimal number of components, where each component is carefully selected and designed for low temperature dependency. As part of this effort the 3.4GHz VCO is selected to provide a stable output power over the applicable wide temperature range. In addition, as explained above, NAC1 uses an RF power control loop to stabilize the RF power using the atomic vapor response.

Reducing the sensitivity of each part is not sufficient. One should make sure that the whole system behaves well during temperature changes. The output frequency vs. temperature of the whole system is dominated by three parameters: 1) the temperature dependency of the TCXO internal crystal and oscillator, 2) the internal compensation loop of the TCXO and 3) the Rubidium main control loop that locks the TCXO to the CPT resonance. If the dominant pole of the TCXO control loop and the dominant pole of the Rubidium frequency control loop are too close, instability may occur. This instability is manifested, for example, in the case of fast temperature changes when the disturbance is significant and the small signal linearity is not preserved. This results in a large transient frequency response which can exceed the steady state specifications. In order to prevent this issue the time constant of the main control loop was tuned to be ~100 ms, well below the TCXO time constant, hence separating the poles. This way the main control loop dominates the response of the crystal oscillator. The cost of using small time constant for the main loop is a somewhat degraded ADEV at 1 second averaging time where the Rubidium stability is worse than the TCXO stability.

As a final step to reduce the temperature sensitivity we use a temperature compensation algorithm built into the microprocessor. The algorithm compensates for remaining frequency shifts which are not dealt with by the other methods, and further reduces the temperature coefficient of the clock. For each unit we measure the frequency vs. temperature curve and apply a parabolic correction. The temperature compensation scheme is not based on direct ambient temperature measurement. Instead it is based on the measuring heating power which is inversely linear with the ambient temperature. This method saves extra components and ADC conversion time required for direct temperature reading.

The temperature dependency of NAC1 before temperature compensation is shown in figure 8. As can be seen it is parabolic. After applying the compensation algorithm the curve is almost flat.

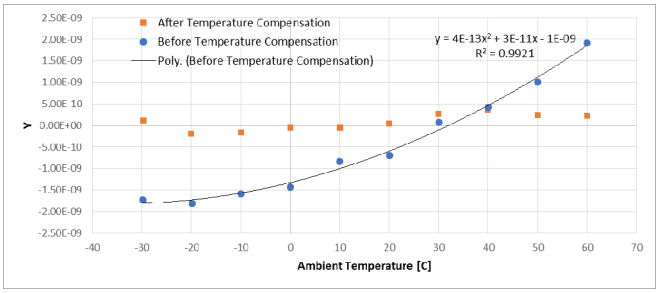


Fig. 8. Frequency dependancy on the ambient temperature

VII. . SUMMARY

This paper presented NAC1, AccuBeat's first generation of miniature atomic clock which is based on CPT in Rubidium87, now under serial production. The paper reviewed NAC1 design, with a focus on the glass technology used in its physics package, its heritage and reliability. We touched on the issues of medium-term and long-term-stability and discussed methods and algorithms used to cope with these issues. In particular the paper discussed the temperature sensitivity of the clock and the methods used to reduce or compensate for it.

REFERENCES

[1] Knappe, S., Schwindt, P. D. D., Shah, V., Hollberg, L., Kitching, J., Liew, L., & Moreland, J. (2005). A chip-scale atomic clock based on 87 Rb with improved frequency stability. Optics express, 13(4), 1249-1253.

[2] Maruyama, Y. Performance Results of a Miniature Cs D1 CPT Atomic Clock .Workshop on Synchronization and Timing Systems (WSTS) 2017

[3] Stern, A., Levy, B., Levy, C., Arad, U., Barash, Y., Mann, R., & Gorelik, A. (2016, April). The NAC1-a miniature CPT Rubidium clock. In European Frequency and Time Forum (EFTF), 2016 (pp. 1-4). IEEE.

[4] Vanier, J. (2005). Atomic clocks based on coherent population trapping: a review. Applied Physics B: Lasers and Optics, 81(4), 421-442.

[5] J. C. Camparo , " Light-shifts of an integrated filter-cell rubidium atomic clock," Aerospace Report No. TOR-2015-02236 (The Aerospace Corporation, El Segundo, CA, 2015).

[6] Levi, F., Godone, A., & Vanier, J. (2000). The light shift effect in the coherent population trapping cesium maser. IEEE transactions on ultrasonics, ferroelectrics, and frequency control, 47(2), 466-470.

[7] Camparo, J., & Klimcak, C. (2007). Influence of the atmosphere on a rubidium clock's frequency aging. AEROSPACE CORP LOS ANGELES CA.

[8] Deng, J., Vlitas, P., Taylor, D., Perletz, L., & Lutwak, R. (2008, April). A commercial CPT rubidium clock. In Proc. European Frequency and Time Forum (EFTF)(Toulouse, FR, 22–25 April 2008) (pp. E3B01-0099).

Towards miniaturization of a high performance coherent population trapping clock

P. Yun,
NTSC, Chinese Academy of Science
East Shuyuan Road, Lintong, Xi'an, 710600, Shaanxi,China
yunenxue@ntsc.ac.cn

F. Tricot, E. de Clercq, S. Guérandel
LNE-SYRTE, Observatoire de Paris, PSL Research University, CNRS, Sorbonne Universités, UPMC Univ. Paris 06
Paris, France

C. E. Calosso, S. Micalizio
Instituto Nazionale di Ricerca Metrologica, INRIM
Strada delle Cacce 91, 10135 Torino, Italy

M. Abdel Hafiz, R. Boudot
FEMTO-ST, CNRS, UBFC
26 chemin de l'Epitaphe, 25030 Besançon, France

***Abstract*—Atomic clocks based on coherent population trapping and constructive polarization modulation are promising for their high performance and compactness. Here we demonstrate the feasibility toward an even more compact atomic clock design.**

Keywords—atomic clock; coherent population trapping;DBR; high modulation efficiency;

I. INTRODUCTION

Atomic clocks based on coherent population trapping (CPT) are mostly known for the first chip scale atomic clock (CSAC) [1], which can be applied to the nano-satellite navigation, unmanned aerial vehicle, GPS receivers, etc. During the past years, great efforts have been made to boost the CPT clock performance while maintaining its advantages such as size, power, weight. A high performance coherent population trapping atomic clock [2] based on the constructive polarization modulation configuration [3,4], so called double modulation (DM) scheme, with fractional-frequency stability at the level of 3.2 x 10^{-13} $\tau^{-1/2}$ up to the averaging time of 100 seconds was demonstrated [5]. This prototype can be implemented with even more compact size by directly modulating a narrow linewidth laser diode with half ground states hyperfine splitting of alkali-metal atom to replace the electro-optic phase modulator used in our previous work. Here we choose ^{87}Rb just for demonstration, but it will also work for other alkali-metal atom, e.g. ^{85}Rb, ^{133}Cs.

II. COMPACT BICHROMATIC LASER

A. Main Setup

Our main setup is presented in Fig. 1. The main idea is to build a compact bichromatic laser source to replace the bulk fiber coupled electro-optic phase modulator (EOPM) used in [5], which is the bottleneck toward a highly compact high performance DM CPT clock. With the development of laser diode technology, a DBR laser diode with high modulation efficiency, narrow linewidth and high output power could be employed in our DM CPT clock.

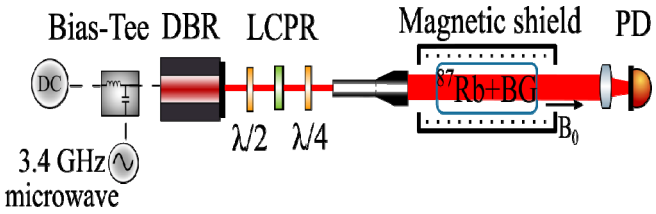


Fig. 1. The main setup for a CPT clock.

B. 3.4GHz microwave modulation efficiency measurement

To measure the modulation efficiency of our C-mount DBR laser chip (from Photodigm), we use the apparatus depicted in Fig. 2.

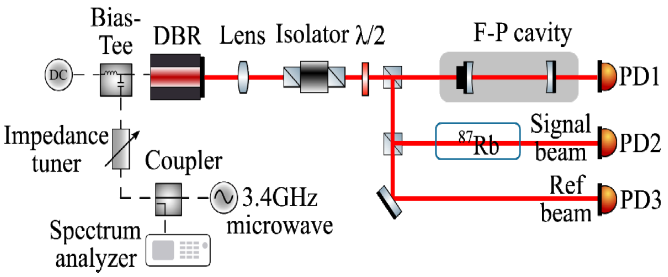


Fig. 2. Setup for modulation efficiency of DBR laser diode measurements.

To increase the microwave power coupled to the DBR chip, a triple-stub tuner is used to match the impedance between the source and the chip. A coupler and a spectrum analyzer (or microwave power meter) are used to monitor the chip microwave reflection. When the minimization of microwave reflection is observed, the impedance match is done, then we can investigate the sidebands ratio versus the DC current driving the DBR chip through a bias-tee.

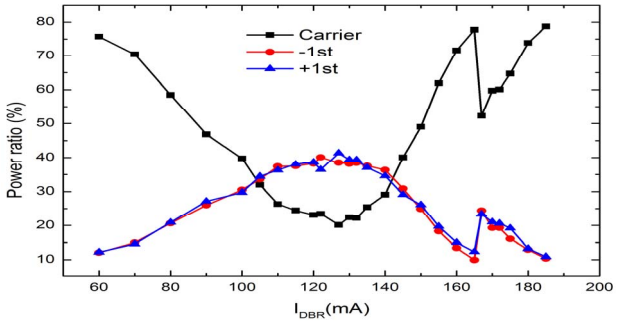


Fig. 3. Carrier and sidebands power ratio vs laser diode current. The laser diode is coupled with 23.12 dBm μwave with frequency at 3.417 GHz, and its temperature is stabilized at 20.2 °C.

A resonance behavior [6] of the modulation efficiency versus the current is clearly observed around 125 mA diode current in Fig. 3, with a high modulation efficiency range from 110 mA to 140 mA. This relative broad resonance peak is good for the atomic clock application, because the laser wavelength needs to be tuned to the D_1 line of ^{87}Rb, this can be realized by combining adjustment of the chip temperature, driven current and coupled microwave power. The discontinuity of modulation efficiency appearing at 167 mA is mainly due to the mode jump.

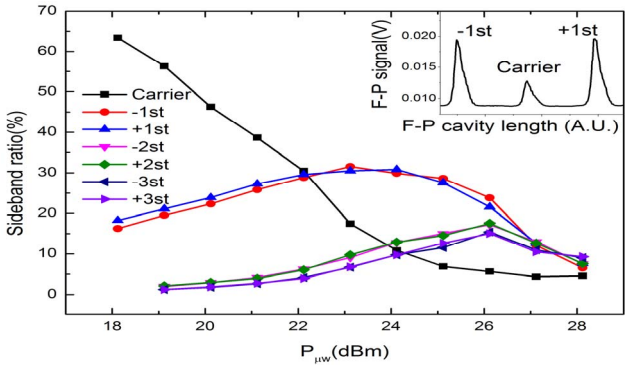


Fig. 4. Sidebands power ratio vs coupled 3.417 GHz μwave power. The laser diode is driven with 120 mA current, and its temperature is stabilized at 20.2 °C.

When the driving DC current is set to 120 mA, the sidebands power ratio versus microwave power is shown in Fig. 4, which is a typical behavior of Bessel modulation and the microwave power maximizing the ±1st sideband power is around 24.12 dBm. The sideband spectrum obtained from the F-P cavity is also drawn in the inset.

C. D_1 line spectrum of ^{87}Rb with multicolor laser

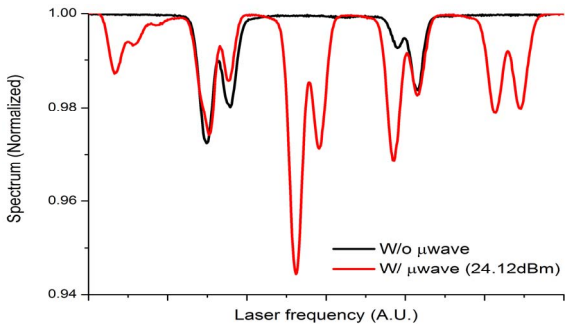


Fig. 5. D_1 line spectrum of ^{87}Rb in the vacuum cell with and without 3.417GHz μwave modulation, obtained by normalizing the signal beam to the reference beam without cell.

With this parameters: microwave power at 24.12 dBm, chip temperature at 20.2 °C, we scan the laser current around 120 mA and get the D_1 line spectrum of ^{87}Rb with microwave modulation as depicted in Fig. 5, which also shows the spectrum without the modulation. As the coupled microwave will induce a frequency shift for the carrier with respect to a uncoupled monochromatic light, i.e., about -3 GHz, the driving current for the D_1 line resonance peaks of ^{87}Rb in the modulation case is shifted of about -3mA compared to the case without modulation. This effect of the microwave modulation is similar to increase the chip temperature. It is not by coincidence that both the modulation resonance peak and D_1 line wavelength appeared around at 120 mA driven current, but rather with the optimization of the chip temperature. From the spectrum obtained by the modulated laser shown in Fig. 5, we conclude it is well suited for the DM CPT clock implementation.

III. SUMMARY

We have presented a new development of a high performance CPT clock towards miniaturization using a fast-modulated laser diode. It is similar to the effect of vertical cavity surface emitter laser (VCSEL), which speeds up the development of the miniature and chip scale CPT clock, the DBR laser with much narrower linewidth (~1 MHz), higher output power (>50 mW), and now with high enough modulation efficiency would bring a high performance CPT clock with very compact size into touch.

[1] J. Kitching, S. Knappe, and L. Hollberg, "Miniature vapor-cell atomic-frequency references," Applied physics letters 81, 553(2002)

[2] M. Abdel Hafiz, G. Coget, P. Yun, S. Guérandel, E. de Clercq, and R. Boudot, "A high-performance Raman-Ramsey Cs vapor cell atomic clock," Journal of Applied Physics 121, 104903 (2017)

[3] P. Yun, J.-M. Danet, D. Holleville, E. de Clercq, and S. Guérandel, "Constructive polari-zation modulation for coherent population trapping clock," Applied physics letters 105, 231106 (2014)

[4] P. Yun, E. de Clercq and S. Guérandel, "Coherent population trapping with polarization modulation," Journal of Applied Physics 119, 244502 (2016)

[5] P. Yun, F. Tricot, C. E. Calosso, S. Micalizio, B. Francois, R. Boudot, S. Guerandel, and E. de Clercq, "High-performance coherent population trapping clock with polarization modulation," Physical Review Applied 7, 01401 (2017)

[6] P. N. Melentiev, M. V. Subbotin, and V. I. Balykin, "Simple and Effective Modulation of Diode Lasers," Laser Physics 11, 1(2001)

Latest achievements on the pulsed CPT clock

F. Tricot, P. Yun*, E. de Clercq, S. Guerandel
LNE-SYRTE, Observatoire de Paris, PSL Research University, CNRS, Sorbonne Universités, UPMC Univ. Paris 06
61 avenue de l'Observatoire, 75014 Paris, France
*Now at NTSC, Chinese Academy of Science, East Shuyuan Road, Lintong, Xi'an, 710600, Shaanxi, China
francois.tricot@obspm.fr

***Abstract*— We report here the performance obtained with a laboratory compact caesium clock based on coherent population trapping (CPT). The clock is working with two orthogonal linear polarizations made by two phase-locked continuous lasers tuned to 895 nm and separated by 9192 MHz. Since the Local Oscillator (LO) noise and the laser relative intensity noise (RIN) are the two main noise source contributions important effort has been done to reduce their contributions and therefore improve the short-term frequency stability at the level of about 2.3×10^{-13} at 1 s. We present in this paper the results of these studies.**

Keywords—atomic clock, vapour cell, frequency stability, coherent population trapping, relative intensity noise.

I. INTRODUCTION

The next generations of compact atomic clock based on CPT phenomenon offer a good alternative and a promising candidate for on-board applications [1,2] since they have a simple scheme and a high performance stability. In this clock the atomic vapour cell is pumped and probed by two lasers separated by 9192 MHz.

Here we report investigations on the two main frequency noise sources of the SYRTE CPT clock prototype. In Section II we describe the experimental setup including the frequency synthesis chain. Our prototype combines a high signal contrast and a narrow resonance width by using a double Λ scheme and a Ramsey interrogation sequence [3]. It has been shown that the short-term frequency stability of our clock is limited by the LO noise and the RIN of the laser [4]. In Section III we present the reduction of the noise and their calculated stability contributions and the performance obtained.

II. EXPERIMENTAL SETUP

A. Phase noise

Two extended cavity diode lasers (ECDL) are tuned to the D1 line of the caesium at 895 nm. The inset in Fig.1 shows the energy levels involved for the double Λ interrogation. The laser beams are orthogonally linearly polarized in order to get simultaneous σ+ and σ- transitions. The Master laser is locked on the F = 4 → F' = 4 transition thanks to a saturated absorption scheme. The laser beams are superimposed through a polarizing beam splitter (PBS), one produces a beat-note at 9192 MHz used to phase-lock the slave laser to the master laser. The other path is sent to the atoms via the Ramsey acousto-optic modulator (AOM_R). The transmitted light signal is processed by the computer (PC) which drives simultaneously the AOM_R and a direct digital synthesizer (DDS) in the frequency synthesis chain. The frequency synthesis chain is referenced by our laboratory H-maser.

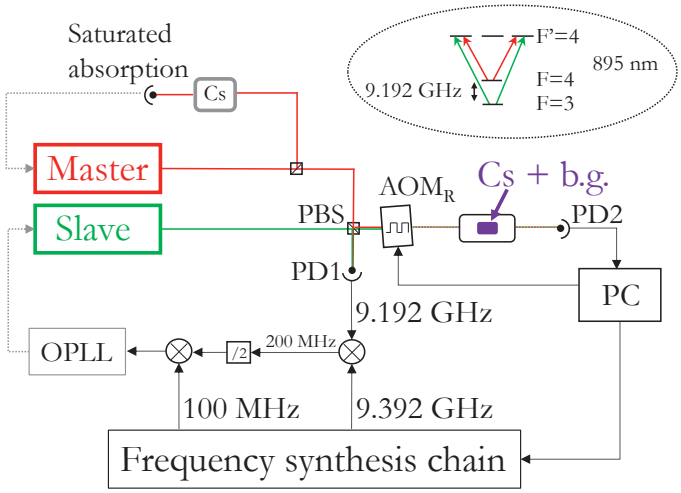


Fig. 1. Scheme of the experimental setup. The master laser is frequency locked by a saturated absorption scheme. The Slave laser is phase-locked on the master laser. PBS: polarizing beam splitter. PD1: fast photodiode. PD2: clock photodiode. OPLL: optical phase lock loop. AOM_R: the Ramsey acousto-optic modulator. The inset shows the Cs energy levels involved in the interrogation. The Cs cell, 5 cm long and 2 cm diameter, is filled with a buffer gas (b.g) mixture: N_2-Ar [5].

In Fig.2 we point out with red arrows the critical part of the chain to get a 9392 MHz signal with a very low phase noise. For more details, the synthesis chain is well explained in [6].

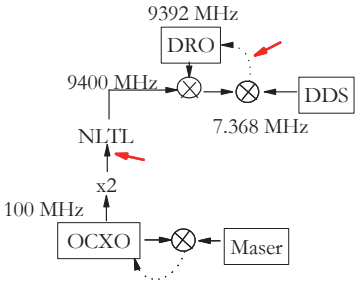


Fig. 2. Scheme of the frequency synthesis chain. The OCXO (Pascall, OCXOF-E-100) is phase-locked on the H-maser. The source is multiplied by a non-linear transmission line combe (NLTL) and used to phase-lock a dielectric resonator oscillator (DRO) at 9.392 GHz. Taking care of the signal power in the NLTL and of the phase lock-loop of the DRO [7] is the key to get a low phase noise contribution.

F. Tricot is supported by Thales Electron Devices and DGA

We improved again the injection of the source signal into the NLTL. In Fig.3 we see that the phase noise floor (>50 kHz Fourier frequency) of the 9400 MHz signal is depending on the signal power of the OCXO.

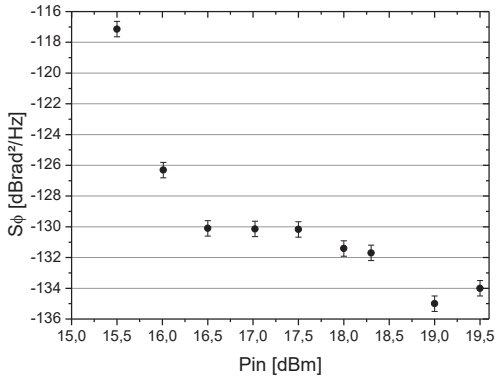


Fig. 3. The critical part is to find the power (Pin) of the OCXO signal injected in the NLTL [6]. We need at least 18 dBm of the OCXO signal to get a noise floor below -131 dBrad²/Hz and therefore to get a neglected contribution to the clock performance.

III. NOISE CONTRIBUTIONS

A. Phase noise

The down-conversion of the LO frequency noise at Fourier frequencies higher than the interrogation frequency known as Dick effect [8] is the main noise source contribution to the short-term stability of the SYRTE CPT clock. The DRO is phase locked with the same correction filter than it is used in ref [8] to get a low phase noise at 9392 MHz (Fig. 4).

The 9392 MHz signal issued from the frequency synthesis chain has a Dick effect contribution at the level of $\sigma_{yDick} = 6.5\times10^{-14}$ at 1 s [9]. The OPLL has also been improved by broadening the servo loop with optimization of the OPLL circuit. We finally get a total Dick effect contribution at 1.8×10^{-13} at 1 s.

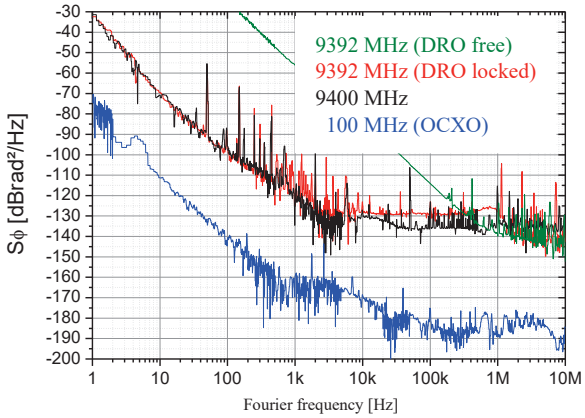


Fig. 4. Phase noise measurements of the different signals involved in the frequency synthesis chain. The phase noise of the OCXO signal (blue) is not degraded by the multiplication chain since the measured Sφ @ 9400 MHz (black) corresponds to the transposed Sφ @ 100 MHz (blue). The spectral purity of the 9400 MHz is transferred to the DRO (red) with a neglected degradation on the noise floor.

B. Intensity noise

The second main noise source for the pulsed lin-perp-lin CPT clock is the laser intensity noise. This noise is converted into a frequency noise through the clock frequency servo system. We implemented a new circuit in order to control the laser power (Fig. 5). The laser is passing through an AOM, a fraction of the zero order laser beam is detected by the photodiode in loop and compared to a precision voltage reference. The error signal is integrated to control the RF power which drives the AOM.

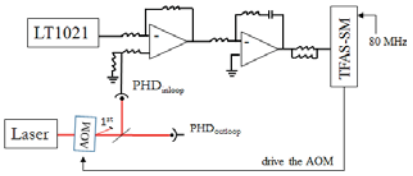


Fig. 5. Scheme of the set up and the circuit of the power lock. The photodiode (Thorlabs, PDA36A) in loop detects the laser beam and compares to a voltage precision reference (LT1021). The control is made by the attenuator (Mini-Circuit, TFAS-SM).

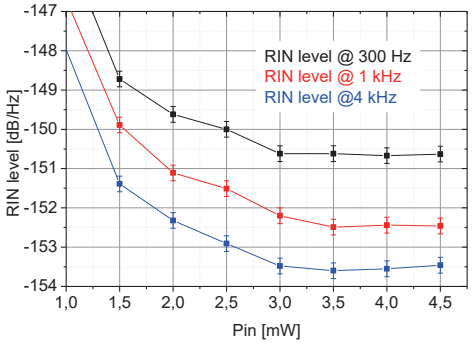


Fig. 6. RIN level measured out loop for different power laser in loop. At different Fourier frequency (300 Hz, 1 kHz, 4 kHz) we see that we reach a floor value of the RIN when there is at least 3 mW of the laser beam in the photo diode. Since we need power for the rest of the experiment we choose to send 3 mW for each photo diode.

To reject the photodetector noise, it came out that we need at least 3 mW of the laser beam into the photodiode in loop to get a low RIN for the laser beam (Fig. 6). The RIN contribution is calculated at the level of 0.7×10^{-13} and 1×10^{-13} at 1 s respectively measured before and after the AOM_R (Fig. 7).

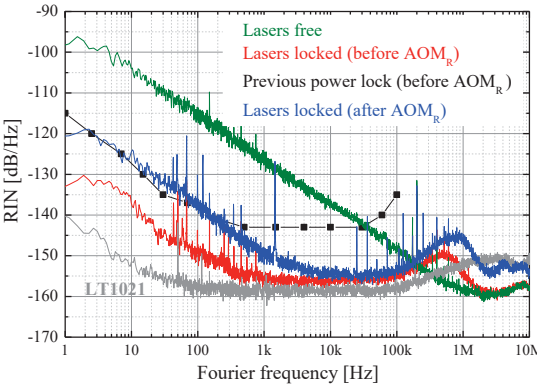


Fig. 7. RIN measured out loop when the laser is free (green), locked before the AOM_R (red, black) and after the AOM_R (blue). LT1021 noise is shown in grey. The RIN after AOM_R is now even better than our previous power locked measured before the AOM_R.

C. *Frequency stability*

The results of all the improvement are summarised in the TABLE I. We see that the Dick effect contribution is no longer dominated by the synthesis chain noise but only by the OPLL. The intensity noise contribution has been decreased as well.

TABLE I. FREQUENCY NOISE SOURCE AND ITS CONTRIBUTION

Frequency noise source		**Estimated σ_y (1 s) $\times 10^{13}$**
Dick effect	100 MHz + Frequency chain	0.65
	OPLL	1.7
Laser intensity		1.0
Total		**2.1**

These noise contributions improve the frequency stability at the level of about 2.3×10^{-13} at 1 s (Fig. 8.) among the best vapour cell clock [10-13]. This result is in a good agreement with the calculated total noise contribution. Further investigation still have to be addressed to understand and correct the deviation anomaly around 3 s and the residual drift after 100 s.

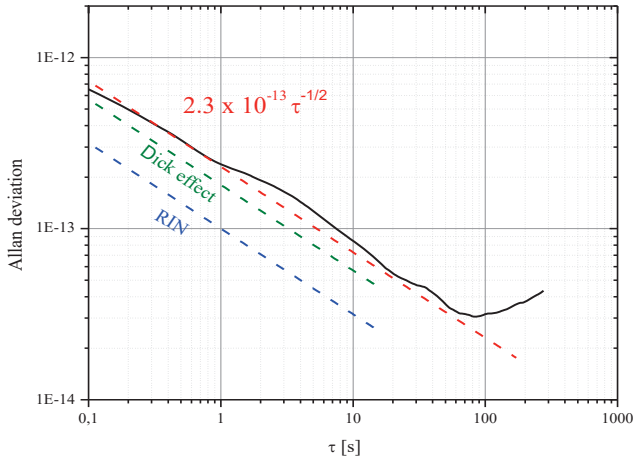


Fig. 8. Allan deviation of the clock frequency (black). The dashed lines are: the slope for the Allan deviation of the clock frequency (red), the Dick effect contribution (green) and the RIN contribution (blue). We see that the performance is mainly limited by the Dick effect.

The mid-term stability is limited by laser power drift and probable temperature effects on the Cs cell. We will study carefully the frequency variations due to the laser power, temperature and also magnetic field effects.

IV. CONCLUSION

We presented the pulsed CPT clock prototype and its improved short-term stability. We showed that the short-term stability is now mainly limited by the Dick Effect contribution of the OPLL. We are aiming to improve the long-term stability by taking into account the laser power drift.

ACKNOWLEDGMENT

We are very grateful for the electronic and mechanical assistance at SYRTE. We also thank Pierre Bonnay for manufacturing Cs cells at the glass workshop.

REFERENCES

[1] P. Waller *et al.*, "The in-orbit performances of GIOVE clocks", IEEE Trans. Ultrason., Ferroelect., Freq. Contr. **57**, 738 (2010)

[2] J. Vanier, "Atomic clocks based on coherente population trapping: a review", Appl. Phys. B **81**, 421-442 (2005)

[3] T. Zanon, S. Guérandel, E. de Clercq, D. Holleville, N. Dimarcq, and A. Clairon, "High Contrast Ramsey Fringes with Coherent Population Trapping Pulses in a Double Lambda Atomic System", Phys. Rev. Lett. **94**, 193002 (2005)

[4] J-M. Danet, M. Lours, S. Guerandel, E. de Clercq, "Dick effect in a pulsed atomic clock using Coherent Population Trapping", IEEE Trans. Ultrason., Ferroelect., Freq. Contr. **61**, 547 (2014)

[5] O. Kozlova, S. Guerandel, E. de Clercq, "Temperature and pressure shift of the Cs clock transition in the presence of buffer gases : Ne, N_2, Ar", Phys. Rev. A **83**, 062714 (2011)

[6] R. Boudot, S. Guerandel, E. de Clercq, "Simple-design low-noise NLTL-based frequency synthesizers for a CPT Cs Clock", IEEE Trans. Instrum. Meas. **58**, 3659 (2009)

[7] B. François, C. E. Calosso, J-M. Danet, R. Boudot, "A low phase noise microwave frequency synthesis for a high-performance cesium vapor cell atomic clock", Rev. Sci. Instrum. **85**, 094709 (2014)

[8] G. J. Dick, "Local oscillator induced instabilities in trapped ion frequency standards", 19th PTTI, 133 (1987)

[9] F. Tricot, P. Yun, B. François, S. Mejri, J-M. Danet, M. Lours, S. Guerandel, E de Clercq, "Progress on a pulsed CPT clock : Reduction of the main noise source contributions", IEEE, EFTF (2016)

[10] S. Micalizio, C. E. Calosso, A. Godone, F. Levi, "Metrological characterization of the pulsed Rb clock with optical detection", Metrologia **49**, 425 (2012)

[11] S. Kang, M. Gharavipour, C. Affolderbach, F. Gruet, G. Mileti, "*Demonstration of a high-performance pulsed optically pumped Rb clock based on a compact magnetron-type microwave cavity*", J. Appl. Phys. **177**, 104510 (2015)

[12] M. Abdel Hafiz and R. Boudot, "A coherent population trapping Cs vapor cell atomic clock base on push-pull optical pumping", J. Appl. Phys. **118**, 124903 (2015)

[13] P. Yun, F. Tricot, C. E. Calosso, S. Micalizio, B. François, R. Boudot, S. Guerandel, E. de Clercq, "High-performance coherent population trapping clock with polarization modulation", Phys. Rev. Appl. **7**, 014018 (2017)

Noise Sources Characterization and its Compact Modeling based on Physical Device simulations for Designing Low Phase Noise Oscillators

Jean-Christophe Nallatamby[1], Michel Prigent[1]
[1] Univ. Limoges, XLIM, UMR 7252,
F-19100 Brive-la-Gaillarde, France

David Cordeau[2], Jean-Marie Paillot[2],
[2] Univ. Poitiers, XLIM, UMR 7252, Angoulême, France

Invited paper

ABSTRACT

The modeling of microwave transistors in the field of RF and Microwave circuits design is an inevitable task. The developed model must be capable of predicting the non-linear characteristics of the active transistor which has a significant role in the design of RFPA and oscillators. This necessitates the measurement of low-frequency (LF) noise sources in order to model them electrically and thereby optimises the impact of noise in the case of oscillator design. A dedicated low-frequency noise measurement setup [1] has been developed at XLIM laboratory which allows the measurement of low-noise spectral densities at the ports of the device under both DC and large-signal operation regime. Furthermore, the experimentally measured noise characteristics of InGaP-GaAs heterojunction bipolar transistors (HBT) has been successfully incorporated into the commercially available physics-based device simulator (TCAD Sentaurus) in order to compute GR and diffusion noise through numerical simulation [2]. This concurrent experimental characterization and physical simulation of HBT device allows to accomplish cyclostationary electrical modeling of the LF noise sources. Indeed, it also helps to improve the phase noise of oscillator circuits and to understand the physical origin of these noise sources. The importance of cyclostationary noise in the design of oscillator circuits will be discussed. The knowledge of noise location and its physical origin is significantly important for oscillator designers in order to accurately predict the associated phase noise spectrum. The harmonic balance and the related technique, namely the conversion matrix method is used to calculate the phase fluctuations caused by the noise sources. Nowadays, the simulation methods of phase noise in oscillators are well established, particularly recent modern software allows handling of both linear and cyclostationary noise sources. Some experimental voltage controlled oscillator designs over the microwave frequency range of 2 GHz to 24 GHz will be presented [3-6].

REFERENCES

[1] A. A. L. De Souza, J.C. Nallatamby, and M. Prigent, "Low-frequency noise measurement of bipolar devices under high DC current density: wether transimpedance or voltage amplifiers," in *Proceedings of the European Microwave Integrated Circuits Conference*, 2006

[2] J.C Nallatamby et al., "Numerical simulation and characterization of trapping noise in InGaP-GaAs heterojunctions devices at high injection.," *IEEE Solid-State Electronics*, vol. 81, pp. 35-44, March 2013.

[3] D. Cordeau, D. Mellouli, J-M. Paillot, H. Mnif, and M. Loulou. " A Fully Monolithic 5.8 GHz Low Phase Noise Coupled VCO Network For Phased-Array Systems" *Analog Integrated Circuits and Signal Processing- Springer*, 2015, 82 (1), pp.335-340.

[4] Jérémy Hyvert, David Cordeau, Jean-Marie Paillo, Pascal Philippe, Bassem Fahs "A new class-C very low pahse-noise Ku-band VCO in 0.25 um SiGe BiCMOS technology". IMS 2015 – 17-22 May, Phoenix, Arizona

[5] E. Dupouy, J.-C. Nallatamby, M. Prigent and C. Laporte. "A Low Power, "Low Phase Noise 10 GHz MIC Oscillator" Proceedings of the 2008 IEEE International Frequency Control Symposium, Hawaii, USA, May 2008.

[6] "Fully Integrated and Plastic Packaged 24 GHz VCO for ISM and Automotive Applications", P. Cortese et al. European Microwave Conference Amsterdam, October 2004.

Investigation on flicker noise of overtones and anharmonic modes of ultra-stables quartz crystal resonators

Pokharel Alok, Sthal Fabrice, Imbaud Joel
FEMTO-ST Institute
Univ. Bourgogne Franche-Comté, CNRS, ENSMM
Besançon, France
fsthal@ens2m.fr

Esnault François-Xavier, Cibiel Gilles
Microwave and Time-Frequency
CNES
Toulouse, France

***Abstract*— In this paper, prototypes of SC-cut resonators with 5 MHz resonant frequency are presented. The resulting short-term stability of some resonators has been measured lower than $8{\cdot}10^{-14}$ in terms of Allan standard deviation. The results are compared according to the overtone behavior on different vibrating modes to find a correlation with the intrinsic noise of the resonators. The comparison of these resonators is given in terms of motional parameters and Q-factors measured at room temperature and at low temperature.**

Keywords—noise; SC-cut resonator; overtones; anharmonics; Q-factor

I. INTRODUCTION

The origin of noise in bulk acoustic wave resonators is studied following different ways by the FEMTO-ST Institute, Besançon, France and the Centre National d'Etudes Spatiales (CNES), Toulouse, France [1-3]. In this context, quartz crystal resonators have been achieved from a quartz crystal block supplied specifically for this study on $1/f$ noise. Several European manufacturers were involved in this partnership to achieve high quality resonators. The resulting flicker frequency floor of some resonators has been measured lower than $8{\cdot}10^{-14}$ in terms of Allan standard deviation. The results are compared according to the overtone behavior on different vibrating modes, harmonics and anharmonics, in order to find a correlation with the intrinsic noise of the resonators. A comparison of these resonators are given in terms of motional parameters and Q-factors measured at room temperature and at low temperature. The prototypes of these resonators are a typical 5 MHz SC-cut resonator. The diameter of the resonator is 14 mm for a thickness of 1.09 mm. A plano-convex shape allows the energy trapping for the 3rd overtone of the slowest thickness shear mode (C-mode). A radius of curvature of 130 mm has been chosen to optimize this energy trapping according to the Tiersten-Stevens model [4]. Electrodes diameter is 8 mm. The temperature turn over point of the resonator is chosen around 80°C (353 K) by adjusting the cutting angles.

II. RESONATOR MODELISATION

The resonator model is carried out using Tiersten's definitions as *e. g.* [4]. Because of the plano-convex shape, the thickness of the resonator $2h$ is given by the following expression (Fig. 1):

$$2h \cong 2h_0\left[1 - \frac{(x_1^2 + x_3^2)}{4Rh_0}\right] \qquad (1)$$

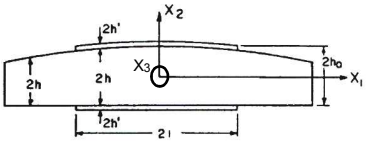


Fig. 1. Geomeric definition of a plano-convex resonator.

The amplitude of the mechanical displacement in the resonator is:

$$u_k^{(i)} = A_k^{(i)} \sin\frac{n\pi x_2}{2h} H_m\left(\sqrt{\alpha_n^{(i)}}x_1\right) H_p\left(\sqrt{\beta_n^{(i)}}x_3\right) \cdot e^{-\alpha_n^{(i)}\left(\frac{x_1^2}{2}\right)} e^{-\beta_n^{(i)}\left(\frac{x_3^2}{2}\right)} e^{j\omega_{nmp}t} \qquad (2)$$

with:

$$\alpha_n^{(i)2} = \frac{n^2\pi^2\hat{c}^{(i)}}{8Rh_0^3 M_n'^{(i)}} \quad \text{and} \quad \beta_n^{(i)2} = \frac{n^2\pi^2\hat{c}^{(i)}}{8Rh_0^3 P_n'^{(i)}} \qquad (3)$$

Where superscript *(i)* denotes the solution for the particular mode *A*, *B* or *C*, $n = 1, 3, 5, \ldots$ the overtone number, $m, p = 0, 0, 2, 4\ldots$, label the different mode shapes in the plane of the resonator, H_m and H_p are Hermit polynomials, R is the radius of curvature, $2h_0$ is the thickness of the resonator center, $M'^{(i)}_n$ and $P'^{(i)}_n$ are the dispersion constants. $A^{(i)}_k$ and $\hat{c}^{(i)}$ are the components of the eigenvectors and the eigenvalues of the Christoffel's tensor [5]. $\hat{c}^{(i)}$ corresponds with effective elastic constant associated to the propagation of the *(i)* mode. Resonant frequencies and motional capacitances are given by (4) and (5).

$$f_{nmp}^{(i)} = \sqrt{\frac{n^2\hat{c}^{(i)}}{16h_0^2\rho}\left[1 + \frac{1}{n\pi}\sqrt{\frac{2h_0}{R}}\left(\sqrt{\frac{M_n'^{(i)}}{\hat{c}^{(i)}}}(2m+1) + \sqrt{\frac{P_n'^{(i)}}{\hat{c}^{(i)}}}(2p+1)\right)\right]} \qquad (4)$$

$$C_{mot_nmp}^{(i)} = \frac{64\hat{e}_{26}^{(i)2}\left(\int_0^{\frac{D}{2}} e^{-\alpha_n^{(i)}\frac{x_1^2}{2}} H_m(\sqrt{\alpha_n^{(i)}}x_1)dx_1 \cdot \int_0^{\frac{D}{2}} e^{-\beta_n^{(i)}\frac{x_3^2}{2}} H_p(\sqrt{\beta_n^{(i)}}x_3)dx_3\right)^2 \sqrt{\alpha_n}\sqrt{\beta_n}}{n^2\pi^3 2^m m!2^p p! h_0 \hat{c}^{(i)}} \quad (5)$$

With D the electrode diameter, $\hat{e}^{(i)}_{26}$ the effective piezoelectric constant considers the direction of the vibration of the mode. Resolution of the Christoffel equations [5] gives the complex eigenvalue $\hat{c}^{(i)} + i\hat{\eta}^{(i)}$. An order of magnitude of the $Q^{(i)}$ factor can be obtained using the following equation:

$$Q^{(i)} = \frac{\hat{c}^{(i)}}{\hat{\eta}^{(i)} \cdot 2\pi f_{nmp}^{(i)}} \quad (6)$$

The energy trapping is quasi-independent of the electrodes dimension, in contoured resonators. It influences the motional resistance and the static capacitor. Consequently, we can compute the motional resistor R_{mot_nmp} from the motional capacitance C_{mot_nmp} using:

$$R_{mot_nmp} = \frac{1}{Q^{(i)} C_{mot_nmp}^{(i)} 2\pi f_{nmp}^{(i)}} = \frac{L_{mot_nmp}^{(i)} 2\pi f_{nmp}^{(i)}}{Q^{(i)}} \quad (7)$$

The static capacitor C_0 can also be computed with the following formula:

$$C_0 = \frac{\pi D^2}{4}\left(1 + \frac{(D/2)^2}{8Rh_0}\right)\frac{\varepsilon_{22} + \frac{\hat{e}_{26}^{(i)2}}{\hat{c}^{(i)}}}{2h_0} \quad (8)$$

With ε_{22} the permittivity constant in SC-cut.

III. EXPERIMENTAL MEASUREMENTS AT 353 K AND 4 K

Table I and II gives the expected theoretical resonant frequencies (given by (4)) for the prototype resonator at 353 K and 4 K.

TABLE I. RESONANT FREQUENCIES AT 4 K.

C Mode	C300	C320	C302	C340	C322	C304	C500	C700
Res. Freq. (MHz)	4.993	5.117	5.127	5.242	5.251	5.267	8.287	11.58
B Mode	**B300**	**B500**	**B700**	**B1100**	**B1300**	**B1500**		
Res. Freq. (MHz)	5.487	9.112	12.74	20.16	23.63	27.24		
A mode	**A300**	**A500**	**A900**	**A1100**	**A1300**	**A1500**		
Res. Freq. (MHz)	9.362	15.57	27.99	34.18	40.39	46.59		

TABLE II. RESONANT FREQUENCIES WITH Q-FACTORS AT 353 K

Mode 300	R_1 (Ω)	L_1(H)	C_1(fF)	C_0 (pF)	Q 10^6	$f_{res.(\|Zmin\|)}$ (MHz)
A	320	8.7	0.03	1.9	1.6	9.26
B	47	6.1	0.14	1.9	4.5	5.45
C	69	5.5	0.18	1.9	2.5	4.99

The experimental values are searched near the theoretical values on the network analyzer.

Table III shows overtones and anharmonics of mode C. Eight resonators were tested around 353 K and 4 K [6]. The resonators *a* to *h* were chosen for their different noise levels. The empty cells in Table III correspond to the modes that have not been found or without quality factor Q evaluation because of the failure in analyzer calibration.

This work was supported by "Région Bourgogne Franche-Comté" and the LABEX Cluster of Excellence FIRST-TF (ANR-10-LABX-48-01).

TABLE III. COMPARISON BETWEEN QUALITY FACTOR (MEASURED AT 4 K AND 353 K) AND THE SHORT-TERM STABILITY OF THE C300 MODE (MEASURED AT 353 K).

Q-factor (10^6)	res.	*a*	*b*	*c*	*d*	*e*	*f*	*g*	*h*
	σ_{y_floor}	6.26E-14	3.36E-13	1.81E-12	1.68E-13	6.25E-14	2.27E-12	2.30E-12	7.11E-14
	C300	33.52	29.05	21.79	43.57	23.78	1.74	43.57	43.57
4 K	C320	3.95	4.06	5.95	6.87	6.60	2.23	8.93	11.16
	C302	7.21	3.44	2.24	2.35	1.65	1.99	1.99	2.60
	C340			0.06	0.22	0.91		1.59	0.69
	C322	0.19	0.98		0.49	0.91		0.45	0.44
	C304	0.07			0.43			0.56	
	C500	48.22	12.05	36.16	72.33	31.51	0.44	48.22	36.16
	C700		20.22		67.40	39.67	10.11		40.43

Fig. 2 shows the quality factors Q measured not only at turnover temperature, but also at 4 K according to the noise level measured at 353 K. Q Measurement at 4K could highlight the effect of internal defects (if any) on Q. No clear trend seems to appear in the data plot. Each mode is represented by the best and worst resonators.

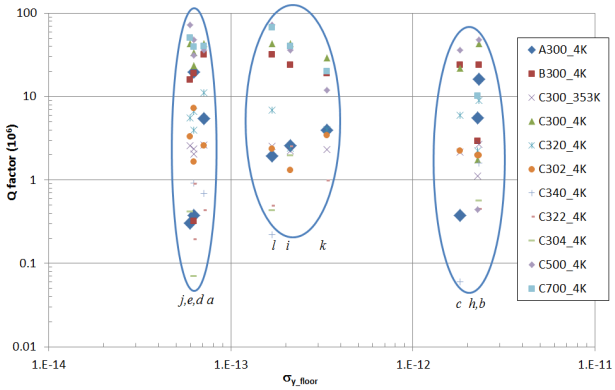


Fig. 2. Q factor measured at cryogenic temperature (4 K) and at turnover temperature according to the short-term stability of C300 mode (measured at 353 K).

Fig. 3 shows the quality factors Q measured at turnover temperature according to the frequency of anharmonic modes of 3rd overtone. Red dots represent the resonators that have a short-term stability up to 10^{-13}. Green dots the resonator with a short-term stability below 10^{-13}.

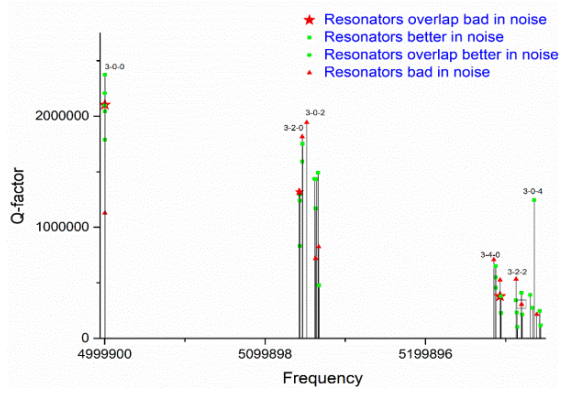


Fig. 3. Q factor measured at turnover temperature of anharmonic modes of C300 according their resonant frequency, the short-term stability is given by the color dots (Green ≤ 10^{-13} < Red).

No clear trend seems to appear in the data plot. Fig. 4 gives an example of resonators those are good and bad in noise performances. Resonators *e* and *f* have a short-term stability of $6.25 \cdot 10^{-14}$ and $2.27 \cdot 10^{-12}$ respectively. The Q-factor is represented according the frequency differences with the C300 mode. Overtones 500 and 700 are given for both resonators.

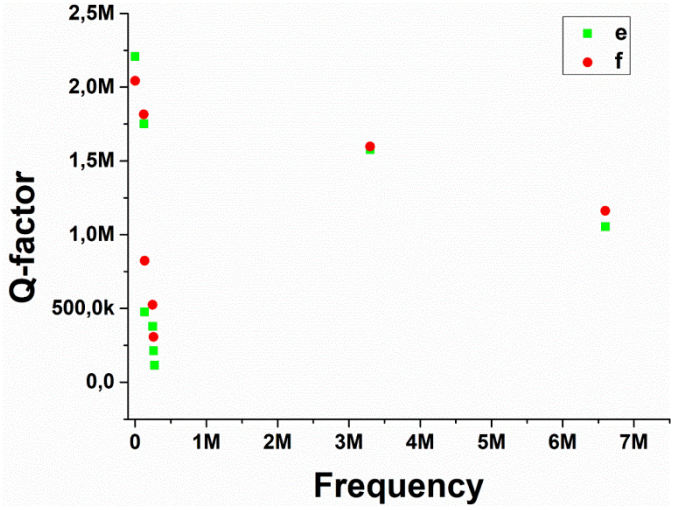


Fig. 4. The Q-factor of resonator *a* and *h* are presented acording the shift of frequency measured turnover temperature according to the short-term stability of C300 mode (measured also at turnover temperature).

Fig. 5 gives an example similar to Fig. 4 but with both bad resonators showing bad performances in noise. Anharmonic of C300 mode and overtones 500 and 700 are given. Resonators *c* and *g* have a short-term stability of $1.81 \cdot 10^{-12}$ and $2.30 \cdot 10^{-12}$ respectively. Similarly, Fig. 6 also gives an example similar to Fig. 5 but with one bad resonators and another average with performances in noise. Anharmonic of C300 mode and overtones 500 and 700 are given. Resonators *b* and *d* have a short-term stability of $3.36 \cdot 10^{-13}$ and $1.68 \cdot 10^{-13}$ respectively.

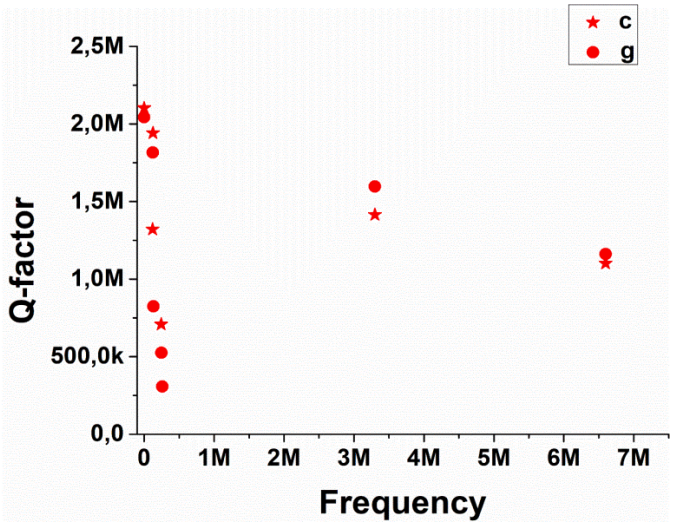


Fig. 5. The Q-factor of resonator *c* and *g* are presented acording the shift of frequency measured turnover temperature according to the short-term stability of C300 mode (measured also at turnover temperature).

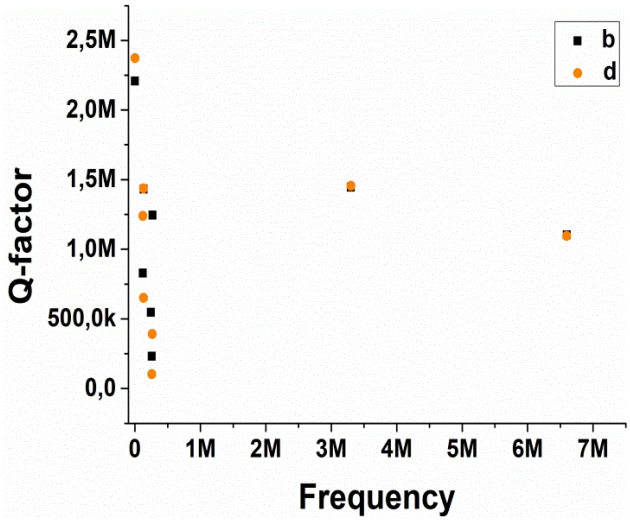


Fig. 6. The Q-factor of resonator *b* and *d* are presented acording the shift of frequency measured turnover temperature according to the short-term stability of C300 mode (measured also at turnover temperature).

IV. Conclusion

Quartz crystal resonators have been compared in terms of noise and quality factor of overtones and anharmonic modes. Measurements have been given according to turnover temperature (353 K) and at low temperature (4 K). There were no findings to show a relationship between the short-term stability of the C300 mode measured at turnover temperature and the behavior in terms of anharmonic modes and overtones. Therefore, we are continuously doing measurements on phase noise in anharmonic modes as well as in higher harmonic modes for several resonators.

Acknoledgement

This work was supported by the LABEX Cluster of Excellence FIRST-TF (ANR-10-LABX-48-01), within the Program "Investissements d'Avenir " operated by the French National Research Agency (ANR) and Region Bourgogne-Franche-Comté.

References

[1] F. Sthal, M. Devel, S. Ghosh, J. Imbaud, G. Cibiel, R. Bourquin, "Volume dependence in Handel's model of quartz crystal resonator noise", IEEE Transactions on Ultrasonics, Ferroelectrics and Frequency Control, vol. 60, no. 9, November, pp. 1971-1977, 2013.

[2] F. Sthal, M. Devel, J. Imbaud, R. Bourquin, G. Cibiel, "Fluctuation-dissipation theorem and 1/f noise of bulk acoustic wave cavities", Appl. Phys. Lett., vol. 107, 103502, pp. 1-4, 2015.

[3] F. Sthal, M. Devel, J. Imbaud, R. Bourquin, S. Ghosh, G. Cibiel, "Study on the origin of 1/f noise in quartz resonators", J. Stat. Mech., n° 6, May, 054025, 2016.

[4] D. S. Stevens, H. F. Tiersten, "An analysis of doubly rotated quartz resonators utilizing essentially thickness modes with transverse variation," J. Acous. Soc. Am., vol. 79, n° 6, pp. 1811-1826, 1986.

[5] R. Bourquin, B. Dulmet, J. J. Boy, "SC-cut resonator operating in anharmonic modes with B-mode reduction," Proc. European Frequency and Time Forum, Brighton, United Kingdom, March 1996, pp. 239-243.

[6] S. Galliou, J. Imbaud, M. Goryachev, R. Bourquin and P. Abbe, "Losses in high quality quartz crystal resonators at cryogenic temperatures," Appl.Phys. Lett., vol. 98, 091911, pp. 1–3, March 2011, DOI: 10.1063/1.3559611.

First Search for Axions of mass 110 μeV using milliKelvin cooled 26.6 GHz Microwave Resonator

Ben McAlister, Justin Kruger, Graeme Flower, Jeremey Bourhill, Maxim Goryachev, Stephen Parker, Eugene Ivanov, Michael Tobar

ARC Centre of Excellence for Engineered Quantum Systems, School of Physics
The University of Western Australia, 35 Stirling Highway
Crawley 6009, WA, Australia.
michael.tobar@uwa.edu.au

***Abstract*— We present the first search of axions at 110μeV by implementing a milliKelvin cooled 26.6 GHz Microwave Resonator with a low noise HEMT amplifier read out (aka the ORGAN Path finder experiment). Also, we consider the design of a haloscope experiment (ORGAN) to probe for axions over the 50 to 200 μev range. The motivation for this search is to perform the first direct test of a result, which claims a possible axion signal at these frequencies. There are many technical issues and optimizations that must be considered in the design of a high mass axion haloscope. We discuss the current status as well as its future.**

Keywords—dark matter, axion, high-Q cavity, low noise.

I. INTRODUCTION

Axions are a well known solution to the strong CP problem in QCD, proposed by Peccei and Quinn in 1977 [1]. In addition to providing an elegant solution to the strong CP problem, the axion is a compelling dark matter candidate [2]. Many searches for axions are currently underway, employing a variety of detection techniques. One such technique, known as a haloscope, exploits the axion two-photon coupling, in a process known as the inverse Primakoff effect. For an in depth discussion of haloscopes see [3,4]. The Frequency and Quantum Metrology group at the University of Western Australia is constructing a haloscope to scan for high mass axions, with corresponding photon frequencies around 26 GHz.

One motivation for this search is to perform the first direct test of an observed potential axion signal [5]. This work suggests that axions entering the weak link region of Josephson junctions are responsible for the anomalous Shapiro step-like features seen in a number of experiments. It is claimed that axions with a mass of roughly 110 μeV could create such an effect. This result is surprising, and has been considered potentially spurious, however, as the axion resides in a large and almost unbounded parameter space any candidate signals merit further investigation. Moreover, a recent extension of the Standard Model of Particle Physics, suggests the axion should exhibit a mass in the range 50-100 μeV [6]. Designing a haloscope at high mass presents many difficulties, which can be understood when one considers the expected power in a resonant cavity due to axion conversion [3].

II. ORGAN: STATUS AND FUTURE

The Cry**O**genic **R**esonant **G**roup **A**xion Co**N**verter (ORGAN) experiment has commenced its initial pathfinder experiment, with first results to be presented at the conference. Also, we have recently secured ARC funding through the Centre of Excellence for Engineered Quantum Systems, which will enable us to continue the path indicated here. The plan is to optimize our cavity to extract maximum signal through a series of steps, with performance predictions as as shown in figure 1. (but not dwelled upon here)

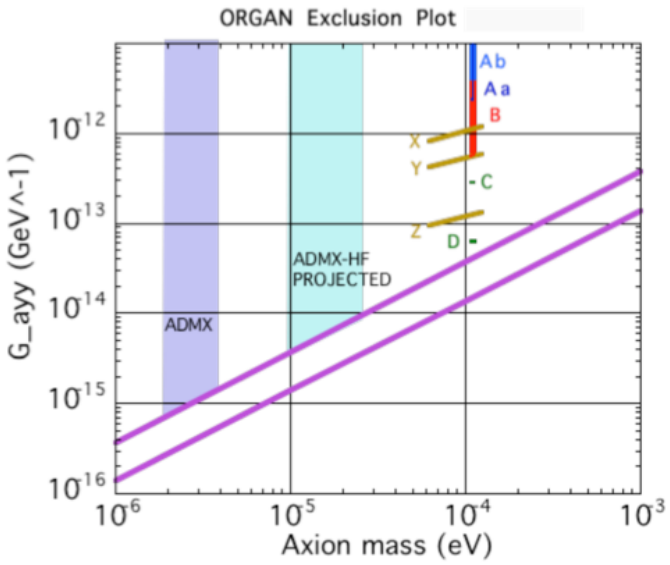


Fig. 1. Projected exclusion limits for ORGAN. Aa represents the first search we have just completed and Ab is a planned search for the Beck range with current technology and equipment, utilizing 2 cavities. B, C and D represent later phases. Changes include moving from 2 to 8 cavities, implementing a quantum limited JPA in place of the existing amplifier, upgrading the magnet from 7 T to 14 T and improving the quality factor of the cavity using lower loss materials. X, Y and Z represent larger searches at high frequency, with similar experimental scale-ups.

In order to achieve sensitive axion searches at high frequencies of 20 GHz and beyond, we have began our pathfinder experiment. This experiment explores a narrow

region around 26.6 GHz. For this initial run, a single copper resonant cavity was employed. This cavity has a radius of ~1 cm, and a length of 5 cm. The TM_{020} mode frequency of this cavity is 26.55 GHz at 20 mK. For future versions of this experiment a radially moving metallic rod will provide ~1 GHz of tuning, which is enough to cover the entire range of the Beck result [7]. The mode pattern density plot of our cavity is shown in fig. 2.

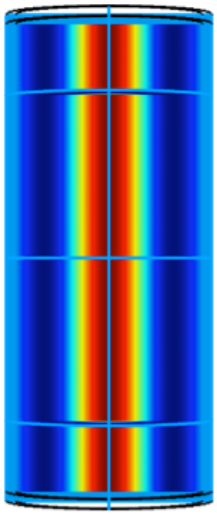


Fig. 2. Schematic of microwave cavity, with color density plot of the TM_{020} mode.

The cavity was cryogenically cooled initially to 4K for the first experimental run, and read out with a HEMT amplifier within a 7 Tesla magnet. The thermal noise of the cavity was measured with a two-channel digitizer, and was clearly observable. The initial run consisted of 10 days of continuous operation. The experiment was also run without the magnetic field to exclude potential spurious signals. No signals consistent with axion-like particle were observed, but a limit on detection sensitivity could be established. Further details will be presented at the conference.

ACKNOWLEDGMENT

This work was funded by the Australian Research Council Grant No. CE110001013.

REFERENCES

[1] R. D. Peccei and H. R. Quinn, Phys. Rev. D **16**, 1791 (1977). doi:10.1103/PhysRevD.16.1791

[2] J. Ipser and P. Sikivie, Phys. Rev. Lett. **50**, 925 (1983). doi:10.1103/PhysRevLett.50.925.

[3] P. Sikivie, Phys. Rev. Lett. **51**, 1415 (1983) Erratum: [Phys. Rev. Lett. **52**, 695 (1984)]. doi:10.1103/PhysRevLett.51.1415.

[4] P. Sikivie, Phys. Rev. D **32**, 2988 (1983) Erratum: [Phys. Rev. D **36**, 974 (1987)]. doi:10.1103/PhysRevD.32.2988.

[5] C. Beck, Phys. Rev. Lett. **111**, 231801 (2013) doi:10.1103/PhysRevLett.111.231801 [arXiv:1309.3790 [hep- ph]].

[6] G. Ballesteros, J. Redondo, A. Ringwald, C. Tamarit, Phys. Rev. Lett. **18**(7), 071802, 2017.

[7] C. Beck, Phys. Dark Univ. **7-8**, 6 (2015) doi:10.1016/j.dark.2015.03.002 [arXiv:1403.5676 [hep-ph]].

A Crystal-less Bluetooth Low Energy Radio Using a MEMS-based Frequency Reference System

Danielle Griffith[1], Ernest Ting-Ta Yen[2], Per Torstein Røine[1], Kaichien Tsai[2], Torjus Kallerud[1], and Brian Goodlin[3]
[1]Connected MCU, [2]Kilby Labs, [3]ATD
Texas Instruments
[1, 3]Dallas, USA / [2]Santa Clara, USA / [1]Oslo, Norway
ernest.ttyen@ti.com

***Abstract*—A system clock is implemented with a 2.52 GHz MEMS-based oscillator, divider, temperature sensor, digital PLL, and active temperature compensation to generate a 48 MHz frequency reference with ±10 ppm stability from –40°C to 105°C. An on-chip 32 kHz RC oscillator is also periodically calibrated by this reference clock to achieve ±500 ppm accuracy, allowing it to be used as the wireless node sleep timer. Additionally, the MEMS oscillator is advantaged in highly duty cycled protocols due to its 100× faster start-up time. This fully integrated reference system enables a crystal-less Bluetooth Low Energy compliant radio in 65 nm CMOS and could provide on-board design convenience to end users.**

Keywords—MEMS resonator; Bluetooth Low Energy (BLE); frequency reference; system-on-chip (SoC); crystal-less; oscillator

I. INTRODUCTION

Battery capacities of wearable devices and wireless nodes are often restricted by their form factors. To reduce power consumption for extended usage time, these systems are aggressively duty cycled to transmit short bursts of data at high data rates while put asleep (standby) for most of the time. The architecture of these systems usually requires two crystal oscillators. The high frequency one, running at 12 to 48 MHz, is used to synthesize radio frequencies for various protocols. For example, Bluetooth Low Energy (BLE) standard requires ±50 ppm stability for the transmitted frequency accuracy. This reference clock can also be re-used in MCU and other wireless node peripherals which require lower accuracy of about 1% (10,000 ppm). The other low frequency oscillator at 32.768 kHz is used to synchronize the data transmission between nodes. BLE protocol requires the accuracy of this synchronization clock to be within ±500 ppm. To enable small form-factor applications, it is desirable to implement low-power yet high accuracy system clocks without either crystal.

In [1], the 2.4 GHz ISM band transmitter uses a thin film-bulk acoustic wave resonator (FBAR) to replace the radio PLL and the high frequency crystal oscillator. This work achieves a 5 µs start-up time. However, a >3% tuning range in the FBAR DCO constrains the oscillator power consumption. More importantly from the system perspective, MCU and peripherals may not be able to share this clock due to the large frequency variation. Besides, a low frequency crystal is still needed for wireless node synchronization. In [2], an oscillator with a self-compensated LC tank achieves ±100 ppm frequency stability at 25 MHz using 23 mW power. Although the stability is good for most synchronization requirements, it is still insufficient for BLE radio standards. In [3], ±50 ppm frequency stability is demonstrated with an FBAR-based low-jitter reference clock at 628 MHz using 54.5 mW power. However remaining drift over temperature consumes the entire BLE transmitted frequency accuracy specification, leaving no margin for aging, packaging, or part-to-part variation. Also, the power consumption reported in [2] and [3] would be prohibitive in many battery powered systems. In [4], ±3 ppm frequency stability at 750 MHz is achieved with yet another FBAR-based oscillator. However, the 0.2°C-accurate temperature sensor and four-point trimming could significantly increase the die area and testing cost.

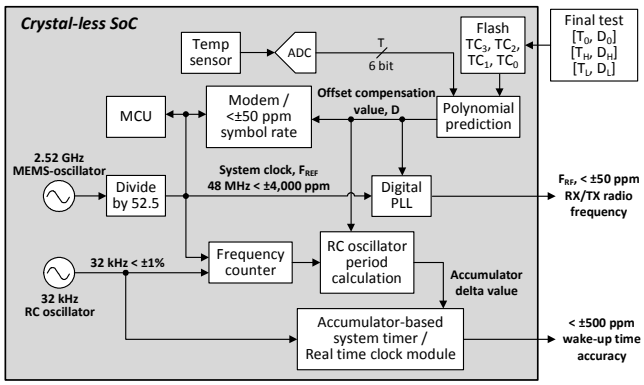


Fig. 1. Block diagram of the MEMS oscillator, divider, digital PLL, 32 kHz RC oscillator, and compensation method used to generate a crystal-less frequency reference system for a Bluetooth Low Energy radio.

The key to a successful product is to find a balance between performance, form factor, and power consumption. This paper will describe the architecture and design of a frequency reference system implemented with a MEMS-based oscillator to generate a 48 MHz system clock with ±10 ppm stability, compliant with BLE standards. Active compensation and power measurement results will also be discussed.

II. CRYSTAL-LESS FREQUENCY REFERENCE SYSTEM

Fig. 1 shows the frequency reference system that enables crystal-less BLE-compliant wireless nodes. A MEMS-based oscillator operating at 2.52 GHz is followed by a fixed divider to generate F_{REF} of 48 MHz with ±4,000 ppm (±0.4%) accuracy. Although this is sufficient for MCU system clock and other peripherals, the BLE standard would require further compensation to achieve the accuracy/stability specification.

Inside the digital PLL, F_{REF} is divided by 14 to generate a nominal PLL reference frequency of 3.429 MHz. Together with the 11-bit fractional frequency control word (FCW), it

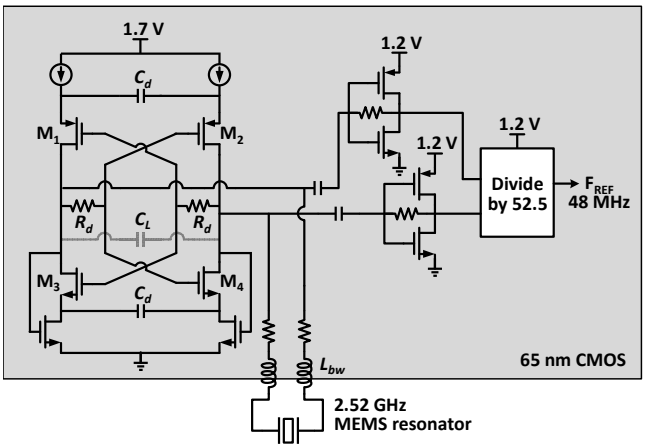


Fig. 2. An integrated complementary cross-coupled differential oscillator with buffer and divider to generate a 48 MHz reference clock.

gives a PLL step size of 48 MHz / (14×2^{11}) = 1.674 kHz, equivalent to a frequency step size of less than 0.7 ppm for the 2.4 GHz RF band. In other words, with saved calibration parameters and readings from the temperature sensor, a precise radio frequency F_{RF} for receiver (RX) and transmitter (TX) can be generated by adjusting the PLL's FCW as needed to calibrate the initial offset (±4,000 ppm) and to actively compensate the drift of the reference clock F_{REF} over temperature variation. On the other hand, the synchronization clock of accuracy better than ±500 ppm can be obtained by periodically calibrating the 32 kHz RC oscillator using the 48 MHz system clock mentioned above. The combination of these techniques removes the need of external quartz crystals while still generating *all* clock signals needed for a BLE compliant radio.

III. Circuit Implementation

A. MEMS-Based Oscillator and Divider

The oscillator core uses a fully differential complementary cross-coupled architecture due to its low power consumption [5-6]. As shown in Fig. 2, the 2.52 GHz output is buffered and sent to a fixed divide-by-52.5 divider to obtain a nominal frequency of 48 MHz. This signal can then be used as the reference clock for the synthesizer, the system clock for the MCU and peripherals, and to periodically calibrate the integrated 32 kHz RC oscillator to create the synchronization signal. In this work, no tuning capacitor is used in the oscillator core. Instead, all frequency tuning is done in the digital PLL as this allows a lower power and more flexible implementation for active temperature compensation. The oscillator is fabricated as a part of the wireless node SoC on a CMOS die, with the MEMS resonator die wire bonded to the SoC and co-packaged in a stacked-die configuration.

The oscillator's negative resistance R_n is given by

$$R_n \sim \frac{-g_m}{(2\pi f)^2 \cdot 4(C_0 + C_L)^2} \quad (1)$$

where g_m is the equivalent transconductance provided by transistors M_1 through M_4, C_0 is the equivalent shunt capacitance from the resonator, and C_L is the load capacitance from the oscillator core. The negative resistance must be kept higher than the loss in the resonator to sustain the oscillation. However increased load capacitance could lead to higher power. To achieve the lowest power consumption, C_L consists of only the transistor parasitic capacitance, with no switchable C_L to tune the oscillator frequency directly.

A parasitic resonance can occur between the bond wire inductance L_{bw} and the effective capacitance from the oscillator C_d in parallel with the shunt capacitance from the resonator C_0. This parasitic resonance can be expressed as

$$f_R = \frac{1}{2\pi\sqrt{L_{bw}\frac{C_d C_0}{C_d + C_0}}}. \quad (2)$$

The capacitance from the oscillator is a combination of ESD capacitance, bond pad capacitance, capacitance from the oscillator transistors, and any intentional tuning capacitance C_t. This parasitic resonance needs to be designed at a much higher frequency than the desired one to avoid wrong oscillation or frequency pulling which would degrade the oscillator frequency stability. In this study, f_R is designed 3× higher than the desired resonance frequency. Furthermore, a small damping resistor R_d is added to reduce the loop gain above 5 GHz. The bond wire length is also chosen to limit L_{bw} less than 0.5 nH, and the bond wires are spaced close to each other (average spacing of 100 μm) to create a mutual inductance that decreases the effective bond wire inductance.

B. Frequency Compensation over Temperature

Uncompensated MEMS resonators have a strong negative 1st-order temperature coefficient of frequency (TCF). Adding a SiO_2 compensation layer removes a large portion of the 1st-order TCF. However, the remaining 2nd-order term can still cause a large frequency drift over temperature variation. Therefore, active temperature compensation is often required for MEMS-based oscillators to match the performance of their quartz crystal counterparts. In this work, the frequency of packaged oscillators is measured at room temperature T_0 and two additional temperatures, T_H and T_L, to express the temperature characteristic as a 2nd-order polynomial

$$\frac{\Delta f}{f_0} = TC_2(T - T_0)^2 + TC_1(T - T_0) + TC_0, \quad (3)$$

where TC_2 is the curvature of the parabola, TC_1 describes the slope of the curve, and TC_0 is the initial accuracy offset due to process variation. After these three temperature tests, one can solve TC_2, TC_1, and TC_0 to interpolate any point on the curve for active temperature compensation [7].

The SoC contains a temperature sensor connected to a 6-bit ADC. During production testing, an on-chip frequency counter is used with an external frequency reference to accurately measure the MEMS oscillator frequency. Code on the tester reads out the temperature measured by the on-chip temperature sensor together with the measured frequency, and calculates the fractional offset D from the nominal 48 MHz at the divide-by-52.5 output. This D value is a signed integer with 22 fractional bits:

$$F_{REF} = 48\ \text{MHz} * \left(1 + \frac{D}{2^{22}}\right). \quad (4)$$

The three temperature and fractional offset pairs are used to calculate the coefficients TC_2, TC_1, and TC_0 of a 2nd-order polynomial that is used to predict the fractional frequency offset as a function of the temperature sensor output. These coefficients are then stored in the device flash.

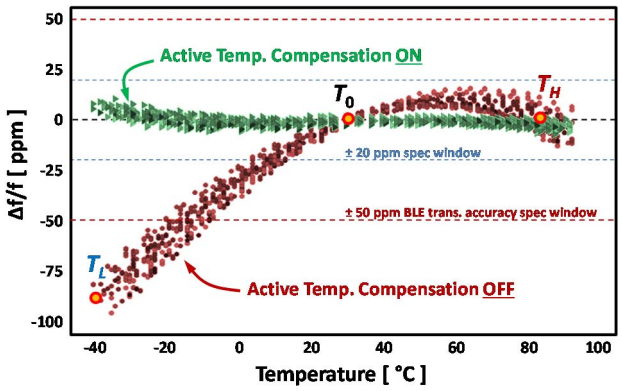


Fig. 3. Measured 48 MHz reference clock frequency stability as a function of temperature with active temperature compensation turned on and off.

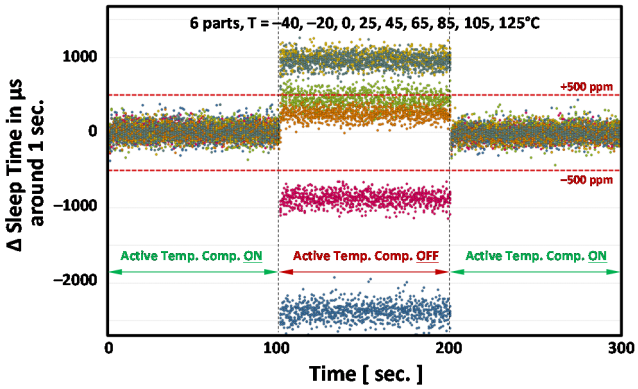


Fig. 4. Measured sleep time delta using an integrated 32 kHz RC oscillator with real time clock calibration from the MEMS-based reference clock.

During normal operation, firmware running on the SoC reads the temperature sensor before radio operation and calculates the predicted fractional frequency offset *D* value using the 2nd-order polynomial determined during production test. In addition, the modem uses internal numerically controlled oscillators and timers that can be compensated for the predicted fractional frequency offset to achieve accurate symbol rates.

C. Real Time Clock Calibration

In a low power wireless node, the real time clock module is required to keep track of the time and generate wake-up events with ±500 ppm accuracy. Typically this is done with an external 32 kHz crystal oscillator. In this frequency reference system, the 32 kHz crystal oscillator has been replaced by a fully integrated low power RC oscillator [8]. However this oscillator alone with frequency accuracy of ±0.21% (±2,100 ppm) is insufficient to generate the wake-up events. To meet the ±500 ppm specification, a frequency counter is used to measure the clock period of the 32 kHz RC oscillator against the MEMS oscillator period. This is done when the MEMS oscillator is already enabled for radio operation to have minimal impact on average power consumption. Firmware combines the frequency counter result with the predicted system clock frequency and calculates the fractional delta value to add to the accumulator-based timer in each RC oscillator period. In this way, the BLE synchronization clock requirements of ±500 ppm can be achieved with a fully integrated RC oscillator consuming less than 200 nW of power.

IV. Measurement Results

A. Frequency Stability

Fig. 3 shows the measurement results of the 48 MHz reference clock frequency stability from 40 packaged parts. The initial offset of the reference frequency F_{REF} has been calibrated with PLL FCW value. A tri-temperature insertion is also used to characterize their individual temperature response using a production VLCT (very-low-cost tester). When active temperature compensation is disabled, MEMS-oscillator and divider generate an F_{REF} that varies 125 ppm from –40°C to 105°C. This is the temperature characteristic inherited from passively compensated MEMS resonators. When active temperature compensation is enabled, the frequency stability is improved to better than ±10 ppm, leaving ample margin for aging and package stress induced frequency drift. Aging was measured on hundreds of units at various temperatures to calculate the activation energy. Extrapolation to a lifetime of 10-year continuous operation shows 11 ppm frequency drift. This is a pessimistic estimation as most applications involve highly duty-cycled, non-continuous operation. Combining the temperature compensation fitting error with device aging and packaging gives a frequency error less than ±50 ppm, meeting the BLE specification and other even more stringent requirements.

In Fig. 4, six different SoCs are operated with 1 second connection intervals for 300 seconds at temperatures between –40°C and 125°C. During the first and third 100-second intervals, active compensation of the 32 kHz oscillator is used, and all wake-up events occur within ±500 ppm of the ideal 1 second interval. The compensation is then disabled during the second 100-second interval, and the RC oscillator shows a native ±0.21% (±2,100 ppm) inaccuracy/instability.

B. Phase Noise and Power Consumption

Fig. 5 shows the phase noise measurement result at the transmitter output using a MEMS oscillator as the synthesizer reference clock. The measured phase noise is −79 dBc/Hz at 10 kHz offset from a 2.4 GHz carrier, and −123 dBc/Hz at 10 kHz offset from a 48 MHz carrier (not shown), both are sufficient to meet BLE radio requirements. The increase of noise slope below 1 kHz offset is due to the MEMS resonator's *Q* being lower than crystal *Q*, but it has only small impact on BLE modulation. Phase noise measurement above 1 kHz is almost identical to the quartz crystal, and rms jitter is measured 7.6 ps, meeting BLE performance needs (<12 ps from 1 kHz to 10 MHz).

Typical wireless communication protocols such as BLE or time-slotted channel hopping (TSCH) are duty cycle controlled in order to achieve low system power consumption. Often, a complete TX and RX packet contains pre-processing, oscillator start up, guard time, RX, RX to TX turnaround, TX, and post-processing, as shown in Fig. 6. The pre- and post-processing power consumption are determined by firmware execution time and peripherals used. Guard time is defined by the accuracy of low frequency timer and protocol requirement. Oscillator start-up represents the time required for an oscillator to be turned on and reach a stabilized state. Typical start-up time for a crystal oscillator is 400 µs which is longer compared to BLE single packet length of 80 to 328 µs. It implies that

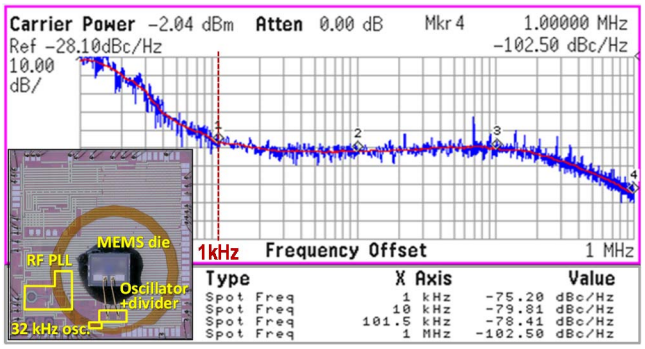


Fig. 5. Phase noise performance of the BLE radio chip synthesizer with 2.4 GHz carrier frequency. The inset shows the die photo of the MEMS-based frequency reference system in a stacked-die configuration.

oscillator's start-up time has a significant impact on the overall system power consumption. The start-up time of this integrated MEMS oscillator is only 4.8 µs, 100× faster than the case using an external quartz crystal, thus the start-up power can be reduced. Even though MEMS oscillator has higher steady state current, the averaged system power consumption remains the same compared to crystal oscillator.

When using a crystal oscillator, the measured average current for a typical BLE connectable advertisement and data packets are around 4.1 and 3.4 mA, respectively. When replacing the crystal oscillator with MEMS one, the measured current for both cases are about 4.4 and 3.4 mA. The 7% power increase during advertisement is because the radio remains active when transmitting in channels 37, 38, and 39. For data packets which are typically short, the average current remains the same. Power optimization to shorten pre-processing is on-going which will potentially further reduce the system power.

Inset of Fig. 5 shows the die photo of this crystal-less BLE radio fabricated with 65 nm CMOS. The area of the RF PLL, temperature sensor, and 32 kHz RC oscillator is 0.26 mm^2, which is needed in a radio regardless of the reference oscillator type. The area of the 2.52 GHz oscillator and divider is 0.05 mm^2 with a power consumption of only 1.4 mW. Table 1 summarizes further comparisons to previously published crystal-less reference clocks. This work meets both BLE transmit frequency accuracy and synchronization specification with minimum die size and testing effort.

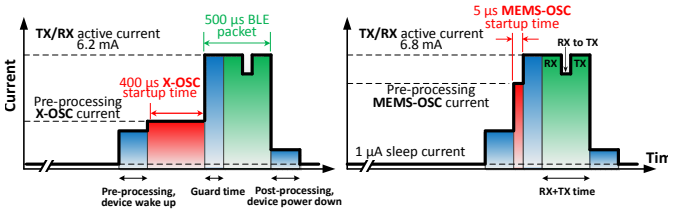


Fig. 6. Power (current) profile comparison using a crystal- and a MEMS-based oscillator.

V. Conclusion

A highly integrated radio chip could provide significant design convenience for end users. A crystal-less frequency reference system for wireless nodes has been demonstrated for this purpose by integrating a MEMS-based oscillator, divider, temperature sensor, digital PLL, and 32 kHz RC oscillator in a QFN package. Temperature stability of ±10 ppm from –40°C to 105°C is achieved with active compensation. The 32 kHz RC oscillator is also periodically calibrated by this reference clock to obtain stability better than ±500 ppm with only 200 nW of power. 100× faster start-up time could further advantage applications using highly duty-cycled protocols and enable a fully integrated low-power wireless connectivity.

References

[1] R. Thirunarayanan, et al., "Reducing energy dissipation in ULP systems: PLL-free FBAR-based fast startup transmitters," IEEE Trans. On Microwave Theory and Techniques, vol. 63, pp. 1100-1117, April 2015.

[2] N. Sinoussi, et al., "A single LC tank self-compensated CMOS oscillator with frequency stability of ±100ppm from −40°C to 85°C," IEEE Int. Freq. Control Symp., May 2012.

[3] S. Sridaran, et al., "Low jitter FBAR based chip scale precision oscillator", IEEE Int. Ultrasonics Symp, pp. 85-88, Sept. 2014.

[4] K. Sankaragomathi, et al., "A ±3ppm 1.1mW FBAR frequency reference with 750MHz output and 750mV supply" IEEE J. Solid State Circuits, pp. 454-455, 2015.

[5] R. Thirunarayanan, et al., "Complementary BAW oscillator for ultralow power consumption and low phase noise," IEEE New Circuits and Systems Conf, pp. 97-100, June 2011.

[6] D. Griffith, et al., "A ±10 ppm –40 to 125°C BAW-based frequency reference system for crystal-less wireless sensor nodes," in press, IEEE ISCAS, May 2017.

[7] E. T.-T. Yen et al., "A multi-tone testing technique for production characterization of micro-resonators" MEMS Conference, pp. 80-83, Jan. 2017.

[8] D. Griffith, et al., "A 190 nW 33 kHz RC oscillator with ±0.21% temperature stability and 4 ppm long term stability," ISSCC Dig. Tech. Papers, pp. 300-301, Feb. 2014.

TABLE I. Frequency Reference Performance Comparison

	IFCS '12 [2]	IUS '14 [3]	ISSCC '15 [4]	This Work
Process [µm]	0.18	0.6	0.065	0.065
Resonator Die Area [mm^2]	N/A	N/A	0.25	0.30
CMOS Area [mm^2]	N/A	<1	1.12	0.31 (2 osc. cores + divider + RF PLL + temp. sensor)
Oscillator Frequency [MHz]	1-133	628	750	2,520 (osc.) / 48 (divided)
Ref. Osc. Power Consumption [mW]	23.1 @ 25 MHz	54.5	1.1	1.4 (osc.+div.)
Number of Calibration Temp.	1 (on-chip heater)	-	4	3
Temp. Sensor Word	N/A	N/A	19 bit	6 bit
Freq. Tuning Technique	Switched capacitors	Switched capacitors	Switched capacitors	Digital PLL
Frequency Stability [ppm]	±100	±50	±3	±10
Meet BLE trans. freq. accuracy spec.	No	Yes[a]	Yes	Yes
Meet BLE sync. accuracy spec.	Yes	Yes	Yes	Yes

[a] No margin for aging

Mitigation of Lamplight-Induced Frequency Variations in Space Rubidium Clocks

Valerio Formichella, Patrizia Tavella
Department of Physical Metrology
Istituto Nazionale di Ricerca Metrologica
Torino, Italy
v.formichella@inrim.it

James Camparo
Physical Sciences Laboratories
The Aerospace Corporation
El Segundo, CA 90245, USA

***Abstract*—Rubidium clocks are currently the most common atomic clocks for space applications, playing a fundamental role in global navigation satellite systems. Their stability is affected by the light-shift effect, turning lamplight variations into frequency variations, e.g. lamplight jumps into frequency jumps. In our previous work, analyzing data from GPS rubidium (Rb) clocks, we uncovered the impact of the lamp on the in-orbit clock's performance. Specifically, the Rb clock's random walk of frequency seems to be driven by a compound Poisson process associated with lamplight intensity jumps. Moreover, large lamplight-induced frequency jumps could affect the validity of the navigation message. Here, we propose an active compensation scheme for lamplight-induced Rb clock frequency variations. We show how this could be implemented as an automated on-board process, and the potential improvements this scheme might yield in timekeeping/navigation performance.**

Keywords—rubidium clock; RAFS; light shift; random walk; long-term stability; frequency jumps; GNSS; GPS; navigation

I. INTRODUCTION

Rubidium atomic frequency standards (RAFS) are the most common atomic clocks for space applications, playing a fundamental role in global navigation satellite systems like GPS, Galileo and BeiDou. It is well known that their frequency is affected by the light-shift effect (LSE), due to the optical pumping light generated by the RAFS' rf-discharge lamp. The LSE translates lamplight variations into frequency variations, e.g. lamplight jumps into frequency jumps. In our previous work [1, 2, 3], we analyzed years of data from 10 GPS Block-IIR RAFS, and found evidence of this lamplight/frequency correlation. We proved that the long-term frequency stability of the RAFS is limited by the lamplight stability, and that the random walk frequency noise is likely driven by a compound Poisson process associated with lamplight intensity jumps. Moreover, a large lamplight-induced frequency jump could immediately affect the validity of the navigation message.

In order to mitigate these problems, we propose an active compensation scheme for the lamplight-induced frequency variations. An on-board software algorithm processes the lamplight data, and scans the data in real time with a jump detector. The amplitude of any detected lamplight intensity jump is multiplied by the RAFS' light-shift coefficient (LSC) to obtain the corresponding frequency jump amplitude, and a frequency correction is immediately applied to the clock's output. The aim is to improve the RAFS' long-term stability, and correct large lamplight-induced frequency jumps in a time smaller than the interval between consecutive navigation message upgrades. Of course, improper corrections could be a source of instability, and their quality and effectiveness will depend on the jump detection process and knowledge of the RAFS' LSC. Here, we study and simulate the complete detection/compensation procedure, determining the potential improvements of RAFS timekeeping, and the roadblocks that may impede its utility.

II. DETECTION AND CORRECTION

The jump detector takes as input averaged lamplight data. A tradeoff is necessary between the need to have a small false alarm probability and a small amplitude estimation error, and the delay in jump detection. The former are fundamental to avoid degrading the clock's output, the latter is necessary if the detection delay is to be smaller than the interval between consecutive navigation message upgrades. If the second requirement is not satisfied, the correction will not improve the validity of the navigation message in the case of large jumps. However, it would still be able to improve the RAFS' long-term frequency stability.

III. SIMULATION AND TEST

We simulate lamplight and frequency data series according to the results in [1, 2, 3], then apply the detection/compensation procedure, exploring different scenarios and trying to find the optimal settings to maximize the performance improvements. We also perform a test on real GPS data, which however is focused only on the long-term stability, since the available lamplight telemetry data correspond to a daily average.

REFERENCES

[1] V. Formichella, J. Camparo, I. Sesia, G. Signorile, L. Galleani, M. Huang, and P. Tavella, "The ac stark shift and space-borne rubidium atomic clocks," J. Appl. Phys., 120, 194501 (2016).

[2] V. Formichella, J. Camparo, and P. Tavella, "On-orbit GPS RAFS lamplight variations: statistics of lamplight jumps," to appear in Proc. 2017 PTTI.

[3] V. Formichella, J. Camparo, and P. Tavella, "Influence of the ac-Stark shift on GPS atomic clock timekeeping," Appl. Phys. Lett., 110, 043506 (2017).

Ethernet Time-Transfer Based On Low Frequency White Rabbit Solution

Francisco Girela-López, Felipe Torres-González, Javier Díaz
Dept. Computer Architecture and Technology
University of Granada, UGR
Granada, Spain
{girlop, felipetg, jda}@ugr.es

***Abstract*—White Rabbit (WR) [1] has become a feasible technology to develop advanced synchronization applications as wireless links. As a previous step to implement this application, the standard bandwidth has to be decreased. Due to the linear relation between bandwidth and frequency carrier in the WR architecture, we have modified an operational WR node to operate with a reference frequency of 12.5 MHz.**

In this paper we address the development of a low frequency carrier solution compatible with WR that allows the generation of Ethernet links with a low reference frequency and bandwidth capability on the White Rabbit Zynq Embedded Node (WR-ZEN).

Keywords— synchronization; time and frequency distribution; White Rabbit Technology; PTP; low-frequency;

I. INTRODUCTION

There are many applications which need high precision synchronization. In most cases, they are network applications which have remote nodes that share the same time reference. When the distance between nodes raises or the number of nodes is increased, wired networks become more expensive and difficult to deploy.

For this reason, wireless synchronization can be a good option to support advanced applications as wireless communications, local navigation systems or other future applications. Phasor Measurement Units (PMU) for Smart Grids or Remote Radio Heads for Telecom Synchronization are some examples of applications which globally require a dependable and accurate notion of time. Additionally, a future example is the next generation of mobile telecommunications, the 5G, where some applications would need few nanoseconds synchronization.

The lack of capable protocols was the reason to start working on the WR project, which led the development of an enhanced version of Precision Time Protocol (PTP) aiming to achieve sub-nanosecond time accuracy keeping the scalability of the system. Due to its improved performance, reliability and scalability [2] [3], a WR-based wireless synchronization could be able to enhance the time transfer accuracy.

Regarding this application, the linear relation between the reference frequency and the communication bandwidth involves the capability to adapt the transmission speed, which is a major requirement in wireless systems, due to bandwidth limitations. The study of the influence of system and link frequencies on synchronization accuracy is a key task to evaluate and correctly design future devices, which will be able to accomplish the strict timing requirements of WR technology.

II. WR-ZEN

The WR-ZEN [4] is a small stand-alone board that integrates the latest Xilinx Zynq Z-7015 device with a Dual ARM Cortex-A9 MPCore with CoreSight and containing an Artix Field Programmable Gate Array (FPGA) logic with 74K logic cells, 380KB of embedded memory and 160 Digital Signal Processor (DSP) blocks. Multiple interfaces have been included in this board, which are two optical small form-factor pluggable transceptor (SFP) Ethernet interfaces used to connect the different boards on WR, two copper Ethernet ports, a FPGA Mezzanine Card (FMC) expansion connector, Universal Serial Bus (USB) sockets and a SAMTEC connector. This SAMTEC connector has been used to replace the optical interface of WR in the low frequency design. The WR-ZEN node is provided with improved oscillators, Phase-Locked Loops (PLLs) and a clocking scheme that provides significant better short term stability than previous WR node designs. It also includes several SubMiniature version A (SMA) outputs that can be configured to generate signals from the FPGA and an input that allows the WR-ZEN to behave as grandmaster.

III. EXPERIMENTS AND RESULTS

In this paper we address the development of a low frequency carrier solution compatible with WR that allows the generation of Ethernet links with a low reference frequency and bandwidth capability. Our start point is the standard 1G Ethernet solution in the WR-ZEN, where the reference frequency is decreased by a factor of 10, operating at 12.5 MHz, to explore the impact on the synchronization accuracy. This way, the influence of this change can be characterized on the WR-core components.

Due to the frequency range of the transceiver logic used in the WR-ZEN, it is mandatory to replace this component in this experiment. For this reason, all the transmission and reception functionalities, as the encoding or the data serialization, and the clock data recovery procedure have been redesigned. Additionally, the optical interface has been replaced by a copper interface through the SAMTEC connector (figure 1).

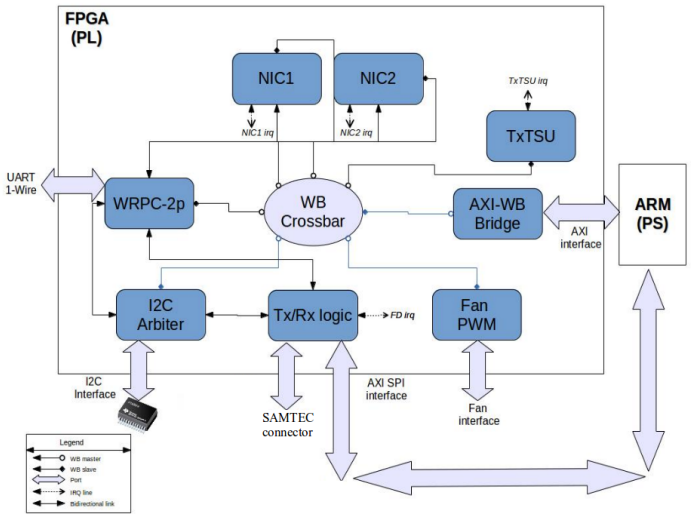


Fig. 1: Low frequency WR-ZEN block diagram

The equipment for the WR network is formed by two WR-ZENs, short coaxial cables connecting the boards and BNC-SMA cables used as probes to measure the clock output from the devices. Our measurement equipment has been the Microsemi 3120A Phase Noise Test and the Keysight 53230a counter, where the clock reference is provided by the master WR-ZEN.

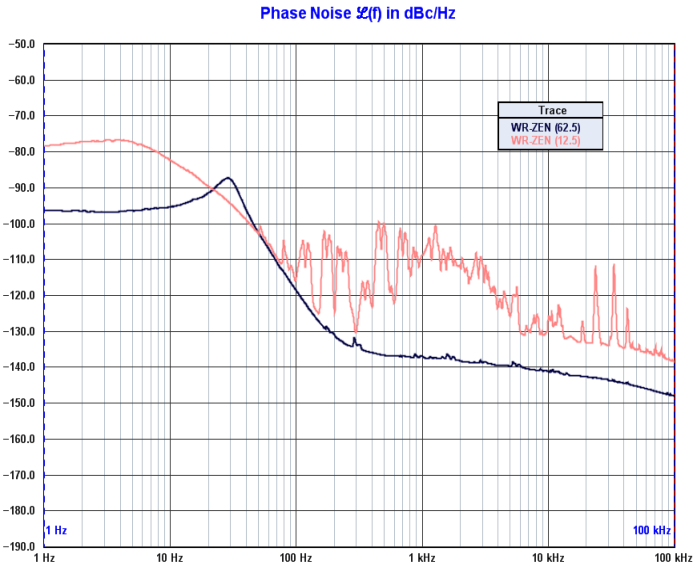


Fig. 2: Phase noise plot comparing the WR-ZEN (62.5 MHz) and the proposed version (12.5 MHz)

Figure 2 shows the phase noise on frequency transfer in the low frequency time-transfer. The blue line corresponds to a standard WR-ZEN with a reference frequency of 62.5 MHz. The red line presents the results for the WR-ZEN at 12.5 MHz.

As explained in [5], the SoftPLL tracks the reference frequency from the master and produces a control signal for tuning the frequency of the local oscillator. The SofPLL influence is shown in the low frequency offsets of the phase noise plot. Comparing with the standard WR-ZEN, there is a difference of 6.9 ps Root Mean Square (RMS) jitter integrated from 1Hz to 30Hz. This result suggests that a better parameterization of the PI control is needed in order to reject noise at low frequencies.

High frequency offsets reveal some undesired noise. The phase noise for these frequencies usually comes from the PLL included in the board, which is the same in both cases, and from the physical interface. Also the noise could be occasioned by the hand-made connector to join both devices and the physical routing to the SAMTEC connector.

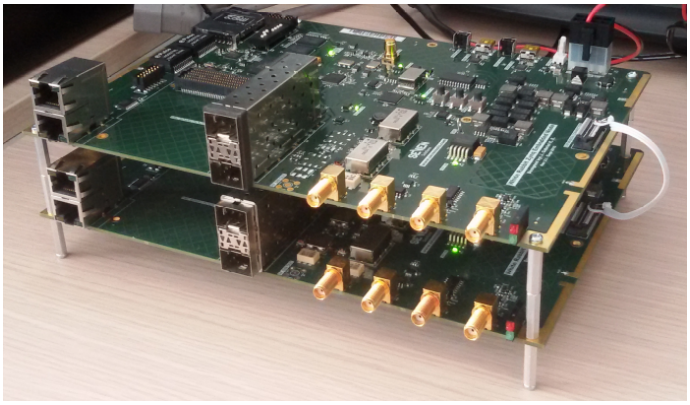


Fig. 3: WR-ZEN connected through SAMTEC connector

Table 1 provides the integrated RMS jitter in different regions of the spectrum.

Table 1: RMS jitter

Frequency	RMS jitter [ps]		
	1Hz-30Hz	1Hz-1kHz	1Hz-100kHz
62.5 MHz	3.3	3.9	3.9
12.5 MHz	9.2	9.7	11

In addition to the frequency-domain results, we have also obtained time-domain measurements. The Allan Deviation shows that the White Phase-Modulation (PM) noise is predominant.

Table 2: Allan Deviation measurements

Frequency	Allan Deviation (ADEV)			
	$\tau = 0.1$ s	$\tau = 1$ s	$\tau = 100$ s	$\tau = 1000$ s
62.5 MHz	5.85e-11	5.94e-12	6.05e-14	6.26e-15
12.5 MHz	1.65e-10	1.58e-11	1.78e-13	1.79e-14

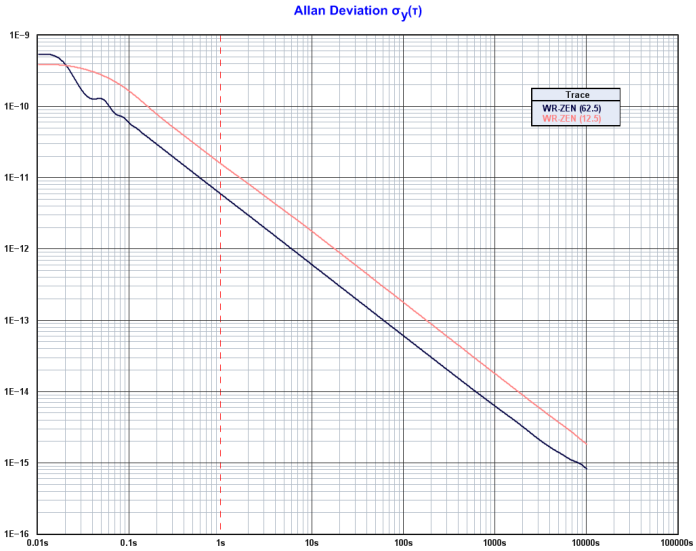


Fig. 4: ADEV plot comparing the WR-ZEN (62.5 MHz) and the proposed version (12.5 MHz)

Time Deviation plot highlights that the higher frequency noise shown in phase noise analysis of the 12.5 MHz version produces more instability in phase (time-domain).

Table 3: Time Deviation measurements

Frequency	Time Deviation (TDEV) [s]			
	$\tau = 0.1$ s	$\tau = 1$ s	$\tau = 100$ s	$\tau = 1000$ s
62.5 MHz	7.89e-13	3.42e-13	2.87e-13	3.9e-12
12.5 MHz	6.02e-12	2.38e-12	1.24e-12	1.1e-11

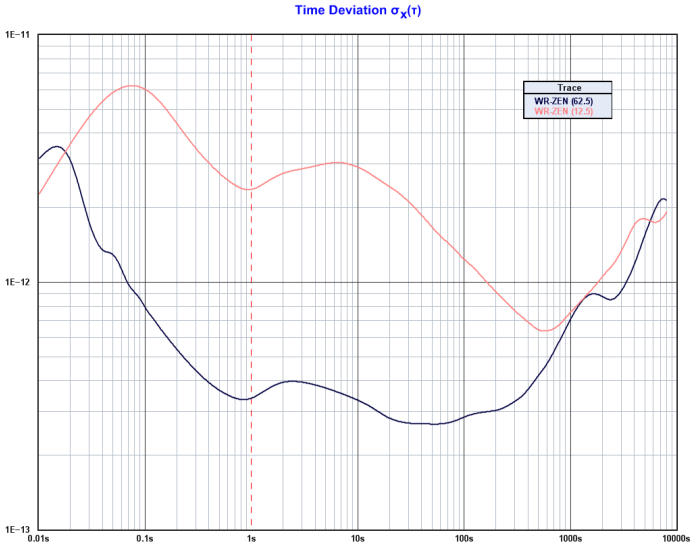


Fig. 5: TDEV plot comparing the WR-ZEN (62.5 MHz) and the proposed version (12.5 MHz)

Maximum time interval error (MTIE) is a measure of the worst case phase variation. It is useful to see if sub-nanosecond accuracy is ever lost.

In Figure 6 the green line shows the results for the presented version at 12.5 MHz. MTIE is compared against the standard version (blue line). The worst case values for the standard WR-ZEN stand around 100 ps while for the presented version there are around 600-700 ps. These values are significantly larger than in the normal version, but it still fulfills the sub-nanosecond accuracy requirements of WR.

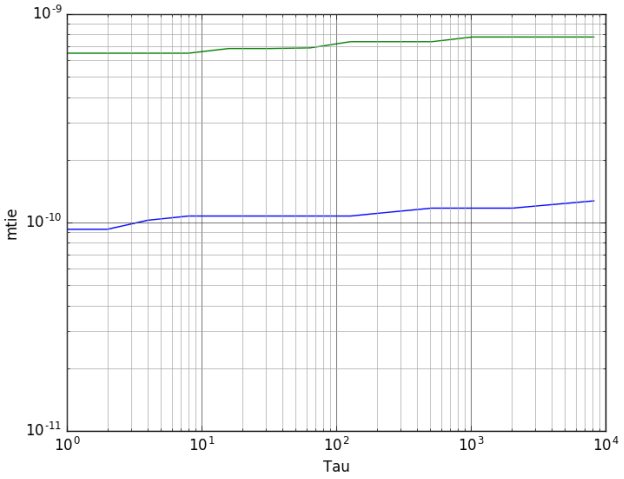


Fig. 6: MTIE plot comparing the WR-ZEN (62.5 MHz) and the proposed version (12.5 MHz)

IV. Conclusions

This paper proves that the low frequency White Rabbit addressed in this paper is functional. We have also measured our proposed solution and we have compared it to the standard WR-ZEN node. After this comparative, we can notice a significant degradation of performance, but we can confirm that it keeps the sub-nanosecond accuracy requirement of WR. Our goal has been to characterize a WR-based node using a reference frequency feasible to future wireless WR-links.

V. Future Work

The next step in our research work is to replace the physical interface used in this paper by a wireless interface. For this purpose, we will use additional hardware which will be integrated in the WR-ZEN node. Additionally, we will implement the needed control logic to manage the wireless communication.

Acknowledgment

We would like to acknowledge the BE-CO-HT CERN group, to the Timing Keepers research group at UGR, Seven Solutions, and the WR community for all the technical support. This Project has been partially supported by the Amiga-6 (AYA2015-65973-C3-2-R) and the H2020 ASTERICS EU (grant number 653477) projects.

REFERENCES

[1] J. Serrano, et al. The White Rabbit Project, in Proceedings of ICALEPCS TUC004, Kobe, Japan, 2009

[2] J. Díaz, R. Rodríguez-Gómez, E. Ros, *White Rabbit: When Every Nanosecond Counts*, Xcell Journal, Issue 91, pp. 18-25, Apr. 2015

[3] F. Torres González, J. Díaz, E. López Marín, R. Rodríguez, *Scalability analysis of the white-rabbit technology for cascade-chain networks*, 2016 IEEE International Symposium on Precision Clock Synchronization for Measurement, Control, and Communication (ISPCS), sept 2016, Stockholm, Sweden

[4] M. Jiménez López, J. L. Gutiérrez Rivas, J. Díaz, E. López Marín, R. Rodríguez, *WR-ZEN: Ultra-accurate synchronization SoC based on Zynq Technology,* European Frequency and Time Forum (EFTF), April 2016, York, United Kingdom

[5] G. Daniluk, *White Rabbit PTP Core the sub-nanosecond time synchronization over Ethernet*, M.S. thesis, Faculty of Electronics and Information Technologies, Warsaw, Poland, 2012.

In-situ Dispersion Measurement of a Coupled Optoelectronic Oscillator

O. Lelièvre, V. Crozatier, G. Baili, P. Nouchi, D. Dolfi, L. Morvan
Thales Research & Technology
1, avenue Augustin Fresnel
91700 Palaiseau, France

F. Goldfarb, F. Bretenaker
Laboratoire Aimé Cotton
CNRS, Univ. Paris-Sud, ENS
Cachan, Université Paris-Saclay,
Rue du Belvédère
91400 Orsay, France,

O. Llopis
Laboratoire d'Analyse et d'Architecture des Systèmes
LAAS, CNRS, Univ. de Toulouse
7, avenue du Colonel Roche
31031 Toulouse, France

***Abstract*— We present a direct measurement of the intra-cavity dispersion of a coupled optoelectronic oscillator (COEO). The measurement can be performed while the COEO is oscillating, taking into account the dispersion of the modulator and the saturated active medium, without any other component than the ones composing the oscillator. It eases the dispersion management before the detection stage for minimal amplitude-to-phase noise coupling.**

Keywords*— *Microwave photonic; Coupled Optoelectronic Oscillator; COEO

I. INTRODUCTION

Optical solutions for the generation of low phase noise RF oscillators at high frequency have been proposed within the last decades. Among them, the coupled optoelectronic oscillator (COEO) [1] is an architecture of primary interest (see Fig.1). It consists in two coupled loops. One combines optical and RF components, as in the optoelectronic oscillator (OEO) architecture [2]. The second loop, containing optical components only, is a harmonically actively mode-locked laser (HAMLL). Such lasers are known to provide low phase noise pulse trains at high repetition rate [3]. In a COEO, the two loops can be built with shorter fibers as compared to OEOs (typically hundreds of meters rather than kilometers).

However, because of the mode-locked regime of the laser, the laser cavity dispersion must be carefully optimized as it affects the phase noise of the pulse train [3]. Additionally, when the pulse is compressed on the detector, the RF gain on the optoelectronic loop is enhanced, and the amplitude-to-phase noise coupling is reduced [4]. Precise knowledge of the optical dispersion in both HAMLL and OEO loop is then a key for the phase noise optimization.

If the fiber dispersion can be conveniently shifted or compensated in the 1.5 µm region with precise characterizations from the suppliers, it is unfortunately not the case for the dispersion of the other components, especially the optical gain medium, and the intensity modulator. Optical amplifiers, either based on semi-conductor components or erbium-doped fibers, have a dispersion profile which depends on the resonant gain condition and the pumping power. Besides, in the particular case of semi-conductor gain medium, amplitude-to-phase coupling can enhance the dispersion effect through the Henry factor. Complete characterization of the component is a long task, which does not include non-linearities occurring in mode-locked regime. In the case of a Mach-Zehnder modulator (MZM), the dispersion depends on the bias point, which is blind-optimized as a function of the circulating RF power. In both cases, the setpoint reached when the COEO oscillates is not easily known, leaving uncertainty on the optical cavity dispersion.

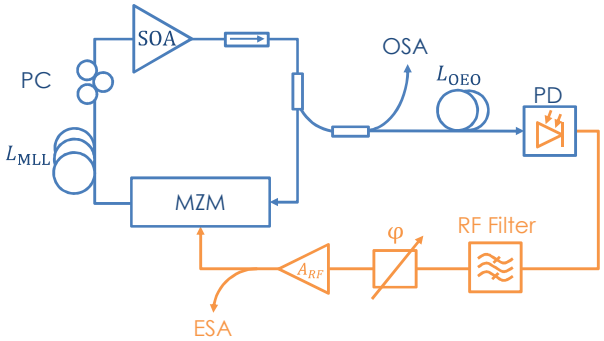


Fig. 1. Schematic setup of a COEO (SOA: Semiconductor Optical Amplifier, PC: Polarisation Controller, PD: Photodiode, MZM : Mach-Zehnder Modulator, A_{RF} : RF amplifier, φ: Phase Shifter, OSA: optical spectrum analyzer, ESA: electrical spectrum analyzer).

We present here an in-situ dispersion measurement of the dispersion in the optical cavity of a COEO, inspired by the method developed for passive mode-locked lasers [5]. This method does not need more components than required for the COEO itself. We test the method for different dispersion regimes (close to zero, normal or anormal).

II. PRINCIPLE

The COEO under investigation is depicted in Fig. 1. The HAMLL is built with a semiconductor optical amplifier (SOA) as the active medium. An optical isolator is added to ensure unidirectional oscillation. The cavity length and dispersion can be adjusted through the choice of optical fibers. The OEO loop is composed by an optical delay line, a fast photodiode, and RF components (bandpass filter, amplifier, and phase shifter). Both loops are coupled together through an optical coupler and a MZM. The COEO oscillation frequency is determined by the modes of the optical and optoelectronic cavities. In both cases,

978-1-5386-2916-1/$31.00 ©2017 IEEE

the mode frequencies are given by the resonant condition, i.e. the phase accumulated along the loop is an integer of 2π.

In the OEO loop, the accumulated RF phase φ_{RF} can be written

$$\varphi_{RF}(f) = 2\pi f\left(\tau_{RF} + \tau_{L_{OEO}}\right) + \varphi_{var}, \quad (1)$$

where f is the RF frequency, τ_{RF} and $\tau_{L_{OEO}}$ are the propagation delay experienced by the RF signal in the electrical and optical domains respectively, and φ_{var} is the phase shift introduced by the RF phase shifter. When the phase accumulation condition is fulfilled, i.e. $\varphi_{RF} = 2p\pi$, with p positive integer, the optoelectronic loop can oscillate at any frequency $f_p$defined as

$$f_p = \frac{p - \varphi_{var}/2\pi}{\tau_{RF} + \tau_{L_{OEO}}}, \quad (2)$$

Because of the RF bandpass filter, only few modes can oscillate around the filter central frequency. The RF frequency can be finely tuned within between consecutive modes thanks to the RF phase shifter.

In the optical loop, the accumulated optical phase can be written

$$\varphi_{opt}(\omega) = \frac{\omega}{c}\sum_i n_i(\omega)L_i, \quad (3)$$

where ω is the optical pulsation, c is the speed of light in vacuum and the sum term corresponds to all the optical components of physical length L_i and refractive index $n_i(\omega)$.

The cavity roundtrip time T_R is given by

$$T_R = \frac{\partial\varphi_{opt}}{\partial\omega} = \sum_i L_i \frac{\partial}{\partial\omega}\left(\frac{n_i(\omega)\omega}{c}\right). \quad (4)$$

The derivative term in the sum corresponds to the inverse of the group velocity V_{g_i}. This roundtrip time evolves with the wavelength as

$$\frac{\partial T_R}{\partial\lambda} = \sum_i L_i \frac{\partial}{\partial\lambda}\left(\frac{1}{V_{g_i}}\right) = \sum_i L_i D_i, \quad (5)$$

where D_i is the dispersion coefficient of the i^{th} optical component. Besides, in the case of most COEOs, the oscillation frequency seeded in the MZM is a harmonic of the fundamental repetition rate of the laser, i.e.

$$T_R = \frac{q}{f_{RF}}, \quad (6)$$

where q is a positive integer. One can finally write:

$$\frac{\partial f_{RF}}{\partial\lambda} = -\frac{f_{RF}^2}{q}\sum_i L_i D_i. \quad (7)$$

Because of the coupling of the two loops, the OEO loop sets the RF frequency, and thus the HAMLL optical spectrum shifts where the dispersion allows matching between the RF oscillation frequency and the HAMLL repetition rate. As f_{RF} can be tuned with the RF phase shifter, one can extract the cavity dispersion from the mutual shift of f_{RF} and the optical spectrum central wavelength of the HAMLL.

III. Experimental Results

The COEO is composed by the following components. A SOA provides gain at over a 80 nm optical band around 1.55 µm. The optical cavity can be independently adjusted in terms of length and dispersion with different types of optical fibers. The laser output is provided by a 3 dB optical coupler. In the OEO loop, we use a 50 m optical fiber delay line, and the RF components detailed in previous experiments [6], except for the RF phase shifter. In these conditions, the optical delay is much longer than the electrical delay, and the OEO mode spacing is in the MHz range. The band pass filter is centered at 10 GHz, so typical values of p of Eq. (2) are roughly 10000. These components are typical for COEOs, and no other components are required to measure the COEO dispersion.

We performed the measurement as follows. For different positions of the RF phase shifter, we measure the central wavelength of the HAMLL spectrum using a fraction of the optical output connected to an optical spectrum analyzer (OSA), and the COEO frequency using a fraction of the electrical output connected to an electrical spectrum analyzer (ESA).

First, the HAMLL includes a 500 m dispersion-compensating fiber, which is almost free from dispersion at 1.55 µm. The results are plotted in Fig. 2 (a), which show small variation of the RF frequency versus the optical spectrum position. The variation is quadratic, revealing third-order dispersion, as the group-velocity dispersion is small. The extracted value of the dispersion coefficient D is 0.437 ps/nm at 1560 nm. The quadratic fit shows a zero dispersion value at 1545 nm. Below 1555 nm, the COEO becomes unstable.

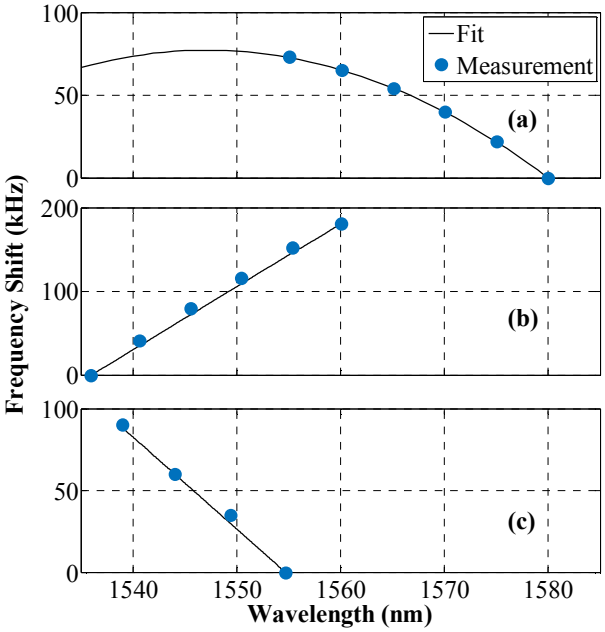


Fig. 2. COEO frequency shift versus HAMLL optical wavelength variation. Blue dots: experimental points, black line : linear (b), (c) and quadratic (a) fit. See text for details of HAMLL configurations.

Next, we added 50 m of dispersion-shifted fiber (-1.9 ps/nm), and 100 m of standard optical fiber (+1.7 ps/nm)

in the HAMLL. As can be seen in Fig. 2 (b) and (c) respectively, the RF frequency shifts faster and almost linearly, because of the dispersion added by the fibers. The extracted dispersion coefficient D are -1.99 ps/nm and 1.63 ps/nm, respectively, showing good agreement with the expected values. Measurement range is limited by stability and gain conditions, both in the optical and RF domains.

IV. CONCLUSION

We present a simple method for measuring the optical dispersion of a mode-locked laser in a COEO configuration, while it is its real operating conditions. The method does not require any other component than the ones composing the oscillator. This method can be used to perform the HAMLL dispersion measurement before compensating this dispersion in the OEO loop. This way, the optical pulse can be compressed at the detection stage, so as to optimize the phase noise performance of the COEO.

ACKNOWLEDGMENT

Authors would like to thanks the DGA (Direction Générale de l'Armement) for its financial support and fruitful discussions. The work of O. Lelièvre, V. Crozatier, G. Baili, P. Nouchi, D. Dolfi, L. Morvan, F. Goldfarb, and F. Bretenaker is performed in the framework of the joint research laboratory between Laboratoire Aimé Cotton and Thales Research & Technology.

REFERENCES

[1] X. S. Yao and L. Maleki, "Dual microwave and optical oscillator," Optics Letters, 1997.

[2] X. S. Yao and L. Maleki, "Converting light into spectrally pure microwave oscillation," Optics Letters, 1996.

[3] S. Gee, S. Ozharar, J.J. Plant, P.W. Juodawlkis, and J.P. Delfyett, "Intracavity dispersion effect on timing jitter of ultralow noise mode-locked semiconductor based external-cavity laser, " Optics Letters, 2009.

[4] A. B. Matsko, D. Eliyahu, and L. Maleki, "Theory of coupled optoelectronic microwave oscillator II: phase noise," Journal of Optical Society of America, B, 2013.

[5] W.H. Knox, "In situ measurement of complete intracavity dispersion in an operating Ti:sapphire femtosecond laser," Optics Letters, 1992.

[6] O. Lelièvre, V. Crozatier, G. Baili, P. Berger, G. Pillet, D. Dolfi, L. Morvan, F. Goldfarb, F. Bretenaker, and O. Llopis, " Ultra low noise 10 GHz dual loop optoelectronic oscillator: experimental results and simple model," Frequency Control Symposium : Proceedings, 2016.

Material Parameters of $Ca_3TaGa_3Si_2O_{14}$ (CTGS) Piezoelectric Single Crystal at Extreme Temperatures

A. Sotnikov, H. Schmidt, M.H. Haghighi
Institute for Solid State Research
IFW Dresden
Dresden, Germany

Yu. Suhak, H. Fritze
Institute of Energy research and Physical Technologies
Clausthal University of Technology
Goslar, Germany

M. Gorev
Kirensky Institute of Physics
Krasnoyarsk, Russia

S. Sakharov
JSC Fomos-Materials
Moscow, Russia

***Abstract*—The complete set of material parameters including elastic, dielectric and piezoelectric constants as well as thermal expansion were measured by different methods for the promising piezoelectric single crystal CTGS at extreme temperatures (4.2 – 1170 K).**

Keywords—CTGS; material parameters; extreme temperatures.

I. INTODUCTION

Single crystals of the langasite family are promising piezoelectric materials for various applications as ultrasonic transducers, bulk- and surface acoustic wave filters, resonators, actuators, and different kinds of sensors. Langasites have a trigonal structure (space group P321) as α-quartz but compared with piezoquartz they exhibit higher electromechanical coupling and absence of any phase transition below their melting point (1300…1500 °C). Specific features of the structure give the opportunity to synthesize more than hundred compounds with the structural formula $A_3BC_3D_2O_{14}$. Most crystals of the family (LGS, LGT, LGN) have a disordered structure resulting in increased dielectric and acoustic loss. Unlike crystals mentioned above, CTGS has an ordered structure resulting in better properties at elevated temperatures. In spite of many publications devoted to CTGS material parameters, its properties are still contradictory even at room temperature not to mention the elevated temperatures [1-6]. As for the cryogenic temperature range, there are no published data for now. To our best knowledge, data on the thermal expansion of CTGS are not available as well.

In this contribution, the full characterization of dielectric, piezoelectric and elastic constants as well as thermal expansion of CTGS single crystal is presented for a wide temperature range including cryogenic temperatures.

II. SAMPLES AND METHODS

CTGS single crystals used in this study were grown by the well-developed Czochralski technique by JSC Fomos-Materials (Moscow, Russia), and by Leibniz Institute for Crystal Growth, IKZ (Berlin, Germany). A set of rods and plates of different crystallographic orientations with the dimensions of 2x0.5x10 mm^3 and 10x10x0.5 mm^3, respectively, was prepared for electromechanical resonant method and dielectric spectroscopy. Crystal cubes of about 7x7x7 mm^3 size of the appropriate orientations were prepared for both ultrasonic pulse-echo and thermal expansion measurements. The resonant measurements were carried out with a network analyzer (Agilent E5100A). Sound velocity measurements were performed by a RITEC Advanced Ultrasonic Measurement System RAM-5000. Thermal expansion was determined using inductive Netzsch DIL-402C dilatometer and a homemade capacitive device. Additionally, piezoelectric coefficients were derived using laser Doppler vibrometry (Polytec OFV-505).

III. THERMAL EXPANSION

The thermal expansion coefficients were measured in the 2 K to 1200 K temperature range. The measurements were carried out on a cube sample with Y- and Z-cut faces (100 K – 1200 K) and on thin plates along Y- and Z directions (2 K – 100 K). Note that for the 32 class crystals, the X- and Y directions are equivalent from the point of view of the thermal expansion properties. The results obtained are shown in Figs. 1-2.

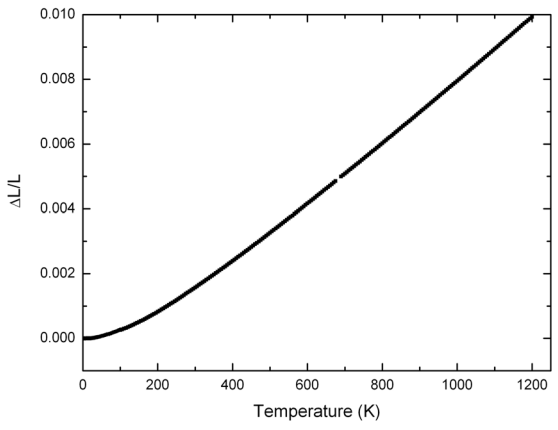


Figure 1. Relative length change versus temperature for the Y direction of CTGS single crystal.

Financial support from the German Research Foundation (DFG grants SO 1085/2-1 and FR 1301/21-1) as well as support from German BMBF (InnoProfile-Transfer 03IPT610Y) are gratefully acknowledged. Yu.S. and H.F. acknowledge the support of the Energie-Forschungszentrum Niedersachsen, Goslar, Germany

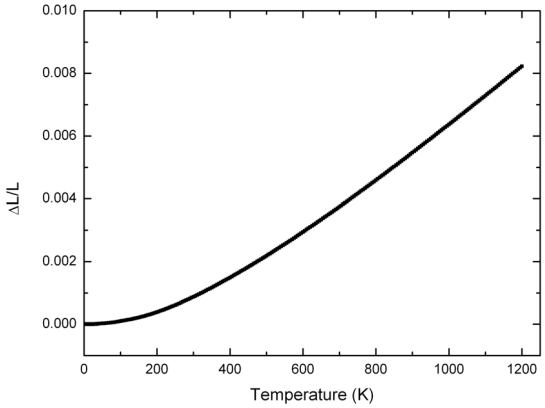


Figure 2. Relative length change versus temperature for the Z direction of CTGS single crystal

It is seen that at elevated and high temperatures ΔL/L for both Y- and Z directions vary almost lineary while at T ~ 200 K the slope changes and a plot saturates at cryogenic temperatures. Such behavior is qualitatively similar to that found in α-quartz crystal [7]. Thermal expansion data were used for the correct determination of the materials parameters at extreme temperatures.

IV. Dielectric Constants

The relative dielectric constants ε_{11} and ε_{33} were measured at a frequency of 10 kHz which is far below frequency position of any electromechanical resonance. Temperature dependences of the dielectric constants at temperatures between 4.2 and 300 K are depicted in Figs. 3, 4.

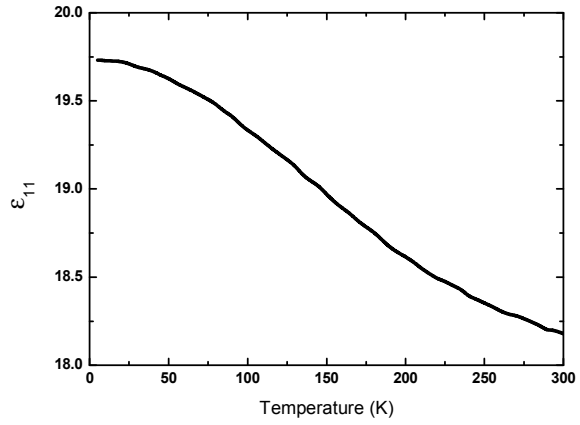


Figure 3. Relative dielectric constant ε_{11} versus temperature for CTGS single crystal

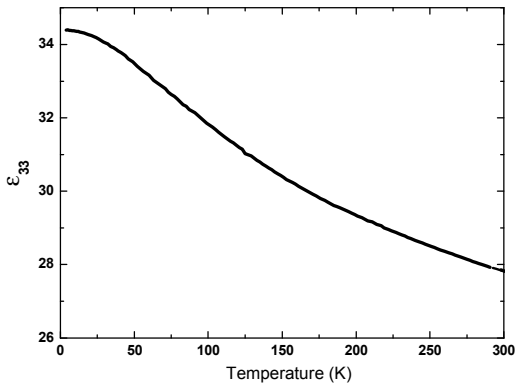


Figure 4. Relative dielectric constant ε_{33} versus temperature for CTGS single crystal

High temperature tails of the dielectric constants are presented in Ref. [6]. As is seen from Figs. 3, 4, both ε_{11} and ε_{33} increase with temperature decreasing followed by a saturation at low temperatures. Notice that this behavior is typical of so called incipient ferroelectrics and usually explained by quantum effects at cryogenic temperatures.

V. Elastic and Piezoelectric Constants at Extreme Temperatures

Piezoelectric response of CTGS was found to be strong in the whole measured temperature range including both very low (cryogenic) and very high temperatures confirming the successful operation of this crystal. As for acoustic attenuation, it was found to be very low at cryogenic temperatures while still reasonable at very high temperature. Figs. 5, 6 show ultrasonic pulse-echo patterns for Y-cut CTGS samples at

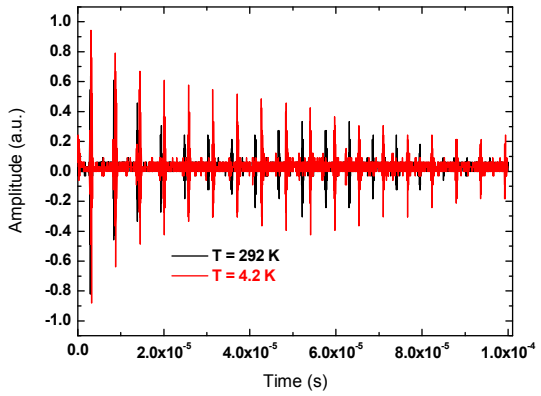


Figure 5. Pulse-echo pattern for the Y-cut CTGS single crystal at 292 K (black line) and 4.2 K (red line).

room temperature and at 4.2 K and 1125 K, respectively. Sound excitation and receiving were realized using the internal piezoelectric effect of the crystal.

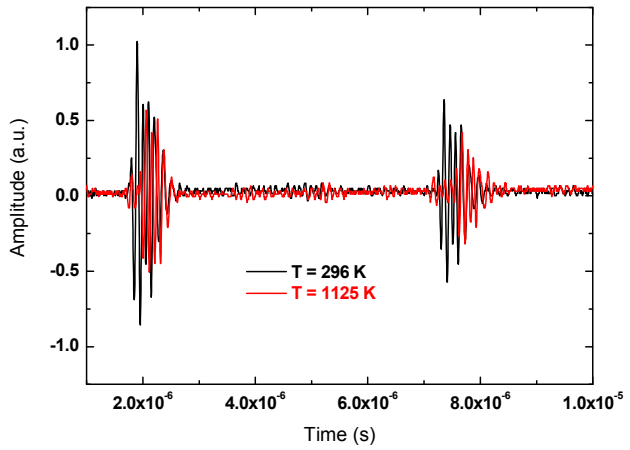


Figure 6. Pulse-echo pattern for the Y-cut CTGS single crystal at 296 K (black line) and 1125 K (red line).

The common feature of the temperature behavior of the elastic constants in CTGS is an increase with temperature decreasing followed by a saturation at cryogenic temperatures (the only exclusions are C_{44} and C_{66}). Figs. 7 and 8 show as examples temperature dependences of C_{11} and C_{44} elastic constants, respectively in the temperature range from 4.2 K to 1170 K.

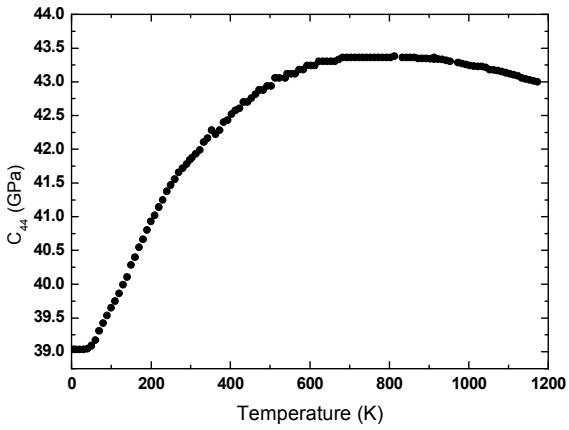


Figure 7. Temperature dependence of the elastic constant C_{44} for CTGS single crystal.

As examples, Figs. 9 and 10 represent temperature dependence of the elastic constants C_{33} and C_{12} in the low temperature range.

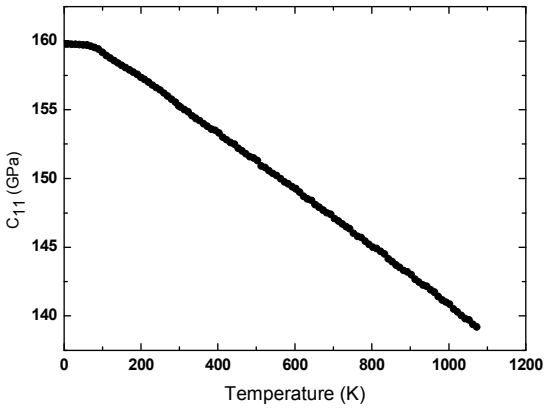


Figure 8. Temperature dependence of the elastic constant C_{11} for CTGS single crystal.

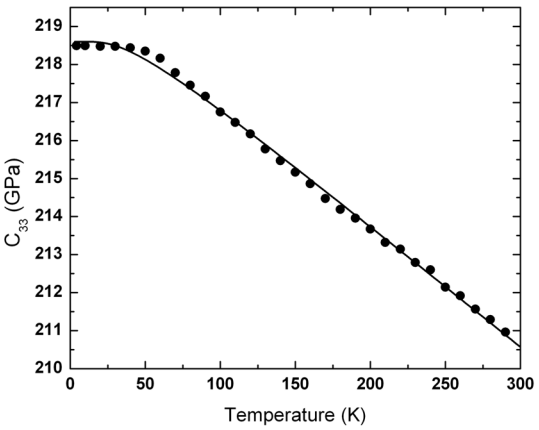


Figure 9. Temperature dependence of the elastic constant C_{33} for CTGS single crystal at temperatures between 4.2 and 300 K

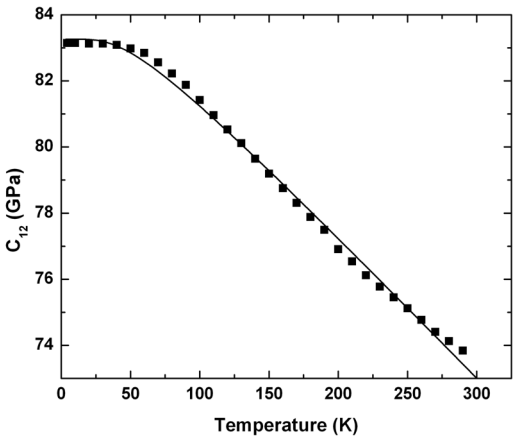


Figure 10. Temperature dependence of the elastic constant C_{12} for CTGS single crystal at temperatures between 4.2 and 300 K

The saturation of the elastic constants at cryogenic temperatures is connected with quantum effects; therefore C_{ij} versus T dependences can be fitted using the Varshni function developed on the base of Einstein oscillator model [8]:

$$C_{ij}(T) = C^0 - \frac{s}{\exp(t/T) - 1} \qquad (1)$$

where C^0 is the elastic constant at zero temperature, t relates to the Einstein temperature Θ_E, and s is the anharmonicity parameter of the lattice. The solid lines in Figs. 9 and 10 show least square fitting of the function (1) to the experimental points. The fitting parameters for different elastic constants are: C^0 =159.8 GPa, s = 4.08 GPa, t = 196 K for C_{11}; C^0 = 83.2 GPa, s = 5.9 GPa, t = 137 K for C_{12}; C^0 = 218.5 GPa, s = 3.28 GPa, t = 105.4 K for C_{33}. Finally, elastic, piezoelectric and dielectric constants of CTGS single crystal at extreme temperatures are presented in Table I. Notice that piezoelectric constant d_{11} at high temperatures was derived using different experimental techniques: pulse-echo method (PE), resonance method (R) and laser Doppler vibrometry (LDV).

TABLE I MATERIAL PARAMETERS OF CTGS SINGLE CRYSTAL AT EXTREME TEMPERATURES

Material constant	4.2 K	1073 K
C_{11} (GPa)	159.8	139.2
C_{12} (GPa)	83.15	60.1
C_{13} (GPa)	70.6	69.5
C_{14} (GPa)	1.2	0.57
C_{33} (GPa)	218.3	184.9
C_{44} (GPa)	39.02	43.1
C_{66} (GPa)	38.3	39.6
e_{11} (C/m^2)	-0.36	-0.43
e_{14} (C/m^2)	0.62	0.644
d_{11}(pm/V) (PE)	-4.81	-5.67
d_{11}(pm/V) (R)		-5.61
$\lvert d_{11} \rvert$ (pm/V) (LDV)		5.38
$\varepsilon_{11}/\varepsilon_0$	19.7	17.3
$\varepsilon_{33}/\varepsilon_0$	34.4	23.2

VI. HIGH TEMPERATURE STABILITY

The long-term properties of CTGS single crystals at high temperature (1000° C) were examined by measuring AC conductivity and resonance frequency of Y-cut shear thickness mode electromechanical resonators in air during 5250 hours. Fig. 11 shows electrical conductivity of two CTGS samples grown by JSC Fomos-Materials and IKZ, respectively. As it can be seen from the figure, the conductivity of both samples increases strongly within the first 500 hours of the thermal treatment and remains nearly stable during the next 1500 hours. Then, between 2000 – 5250 hours the conductivity of both samples decreases by about 20%. Fig. 12 represents the change of the resonance frequency of Y-cut resonator made from IKZ crystal. The change of the resonance frequency was about 0.25% during 5250 hours of the thermal treatment at 1000° C.

The Q-factor of the resonators at 1000° C was found to be about 3500.

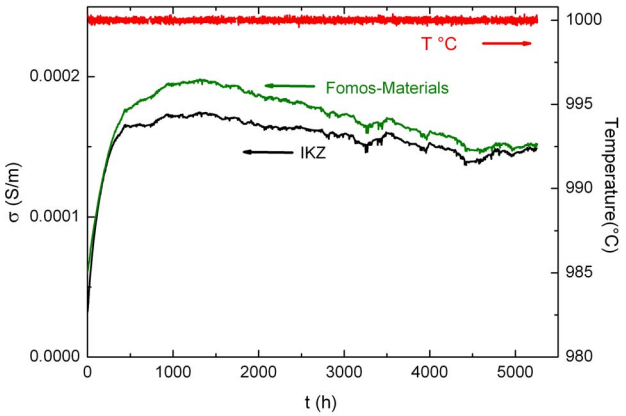


Figure 11. Electrical conductivity versus time for CTGS samples from two sources. Temperature is 1000°C.

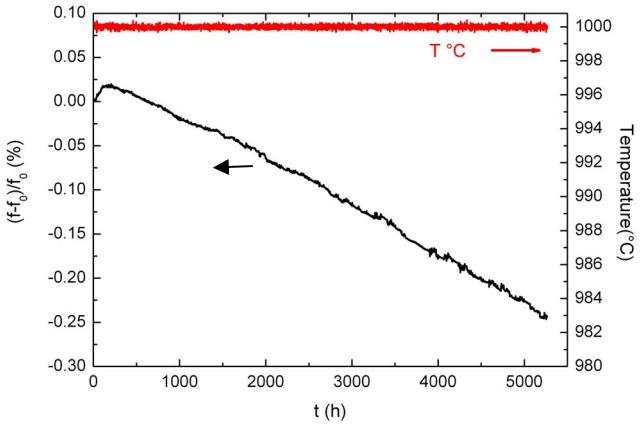


Figure 12. Relative change of the resonance frequency versus time for Y-cut CTGS resonator made from IKZ crystal. Temperature is 1000°C.

VII. CONCLUSIONS

The complete sets of material parameters were obtained for CTGS single crystals at extreme temperatures taking into account thermal expansion. Strong piezoelectric response as well as long-term stability at very high temperature predestine CTGS crystal as promising material for microacoustic and sensor applications for an extremely wide temperature range.

REFERENCES

[1] Yu.V. Pisarevsky, B.V. Mill, N.A. Moiseeva, A.V. Yakimov "Ordered $Ca_3TaGa_3Si_2O_{14}$ crystals: growth, electromechanical and optical properties", Proc. 18 Eur. Frequency and Time Forum, pp. 216-219, 2004.

[2] X. Shi, D. Yuan, X. Yin, A. Wei, S. Guo, F. Yu "Crystal growth and dielectric, piezoelectric and elastic properties of $Ca_3TaGa_3Si_2O_{14}$ single crystal", Solid State Comm., vol. 142, pp. 173-176, 2007.

[3] A. Sotnikov, H. Schmidt, M. Weihnacht, O. Buzanov, S. Sakharov "Material parameters of $Ca_3TaGa_3Si_2O_{14}$ single crystal revisited", Proc. IEEE International Ultrasonic Symposium, pp. 1688-1691, 2013.

[4] S.V. Biryukov, H. Schmidt, A. Sotnikov, M. Weihnacht, S. Sakharov, O. Buzanov "CTGS material parameters obtained by versatile SAW measurements", Proc. IEEE International Ultrasonic Symposium, pp. 882-885, 2014.

[5] H. Zu, Q. Lin, H. Wu, Y. Zheng, Q-M. Wang "Characterization of the dielectric, piezoelectric and elastic coefficients of $Ca_3TaGa_3Si_2O_{14}$ single crystal up to 800° C", IEEE Transactions on Ultrasonics, Ferroelectrics and Frequency Control", vol. 63, pp. 764-777, 2016.

[6] Y. Suhak, M. Schulz, A. Sotnikov, H. Schmidt, S. Ganschow, H. Fritze "Dielectric, piezoelectric and elastic constants of $Ca_3TaGa_3Si_2O_{14}$ single crystals at elevated temperatures", in press, Integrated Ferroelectrics.

[7] G.A. Lager, J.D. Jorgensen, F.J. Rotella "Crystal structure and thermal expansion of α-quartz SiO_2 at low temperatures", J. Appl. Phys., vol. 53, issue 10, pp. 6751-6756, 1982.

[8] Y.P. Varshni "Temperature dependence of the elastic constants", Phys. Rev. B, vol. 2, pp. 3952-3958, 1970.

Miniaturized VHF Quartz MEMs Resonator Design Methodology

D. J. Kirby[1], R. L. Kubena[1], Y. K. Yong[2], F. P. Stratton[1], H.D.Nguyen, R. J. Joyce[1], D. T. Chang[1], J. F. Garstecki[3]
[1]Sensor and Materials Lab., HRL Laboratories, LLC., Malibu, Ca. 90265
[2]Dept. of Civil & Environmental Engineering, Rutgers University, Piscataway, NJ. 08854
[3]Johns Hopkins University Applied Physics Laboratory, Laurel, MD. 20723
Email: djkirby@HRL.com

***Abstract* – The miniaturization of resonators for timing applications brings with it new challenges in terms of device optimization. As the device size is reduced, design intolerances lead to more significant differences between modeled and fabricated devices leading to poor performance. In this paper we present a methodology for improving resonator designs. A 32MHz AT-cut quartz thick VHF shear mode resonator is optimized for high Q and high thermal stability for integration on CMOS electronics. Uncompensated measured data agrees to within a few ppm of Comsol 3-d FEA simulations.**

***Keywords* – Quartz MEMS, AT-cut resonators, oscillators, frequency stability, stress isolation, CMOS integration.**

I. Introduction

Historically, 3-d FEA models have assumed quartz resonators with vertical side-walls. With most quartz resonators formed by wet-etching, the side-walls of a fabricated device are not vertical. It is no surprise then that the FEA results differ from measured data. With the development of dry etching fabrication techniques, quartz sidewalls are near vertical and reproducible. FEA models can therefore readily resemble realized devices more closely.

A methodology for resonator design is described in this paper. Not only is the fundamental resonator geometry important for high Q, but it is equally important to decouple the resonator from external perturbations that would otherwise disturb the *f-T* performance. In our case, spring tethers are used to decouple mechanical and thermally induced stresses between the CMOS substrate and the active resonator region, thus stabilizing the Q and frequency over temperature.

II. Methodology for VHF AT-cut Resonator Design

The frequency stability and total ppm excursion of a resonator *f/T* curve is determined by many factors including quartz angle of cut, resonator plate geometry, trench-mesa design, residual thermal stress gradients across the resonator, and resonator surface contamination. The methodology recommended here is to first ensure that the modeled resonator is close to realistic fabrication parameters including quartz sidewall angles. Key resonator features such as the quartz plate and electrode dimensions are then optimized using contour maps of Q and motional resistance versus resonator dimensions. Asymmetric trench mesas are implemented for improved confinement of the thickness shear mode. The mesas are modeled and optimized in X-, Y-and Z- directions. The stiffness of spring tethers are also geometrically optimized to minimize residual stress in the active electrode region.

Figure 1 presents a schematic of a resonator comprised of a quartz plate, electrodes on the top and bottom surfaces, tethers to the mounting regions, a through via and a trench mesa also on both top and bottom surfaces of the quartz. The edges of the quartz plate are sloped at 5° consistent with the angle obtained with dry etched components. The through quartz via allows for metal interconnect between the top and bottom sides of the quartz. Two mounts locate the bonding sites of the quartz wafer to the underlying substrate. A quartz mesa of width 'q' surrounds the active electrode region and is followed by a thinning or 'trench' in the quartz X- and Z- directions. The trench width is asymmetric between the X- and Z- directions. Beyond the trench, the quartz thickness returns to its original value. In this study, we use a quartz AT-cut angle θ = 35° 13.5' for the standalone resonator simulations.

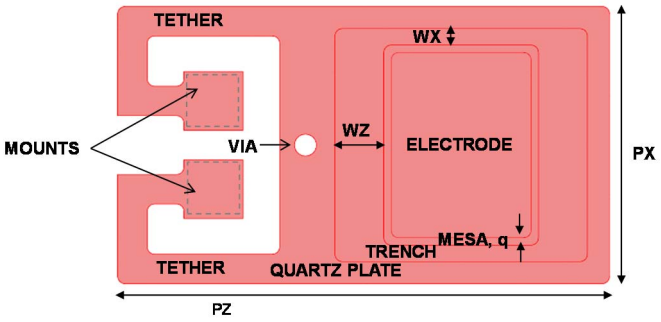


Fig. 1 Schematic of a resonator comprised of a quartz plate with sloped sidewalls, electrodes (top and bottom), tethers, mounting regions, a through via and a trench mesa (top and bottom).

Comsol 3-d FEA models are used to optimize key AT-cut quartz resonator dimensions such as the quartz plate (PX, PZ) in crystallographic X- and Z- axes in the form of a contour map. Over the contour map, the quartz plate dimensions are adjusted in PX and PZ, extending the resonator in the active electrode and mesa region. The quartz plate is varied in 10 µm increments along both X- (1855 µm to 1915 µm) and Z- (3310 µm to 3370 µm) axes. The contour plot (Fig. 2a), analyzing the device shown in Fig. 2b, reveals high Q regions free from interference by unwanted spurious modes. Spurious modes can drain energy from the desired shear mode. Simulated *f-T* performance confirms that improved stability is obtained in regions where

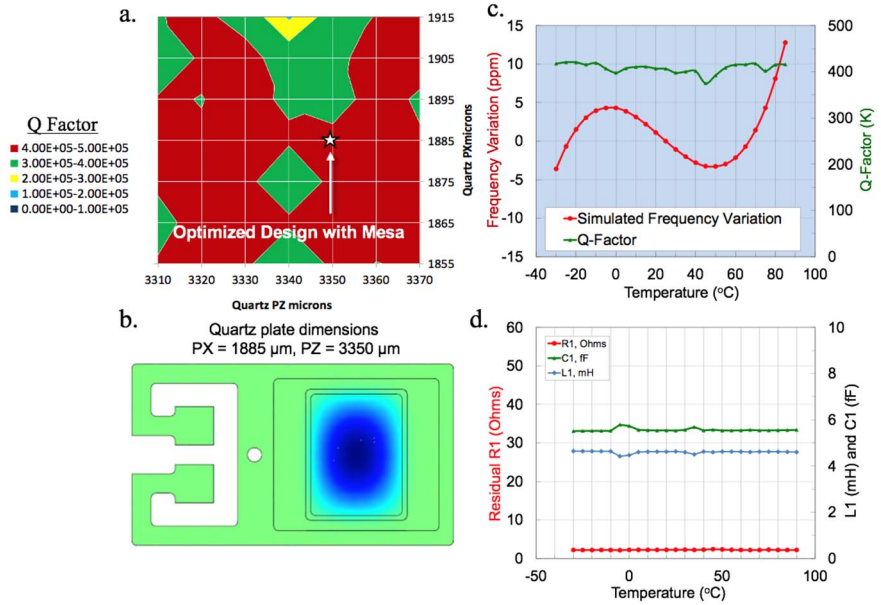


Fig 2. Optimized VHF resonator design with mesa. (a) Q-contour map used to determine optimum quartz plate dimensions. (b) Resonator configuration modelled. (c) Simulated *f-T* and *Q-T* profiles of spring resonator reveal stable performance. (d) Equivalent circuit parameters demonstrate highly stable performance.

the Q is higher over a broad region of parameter space, indicating that interference from spurious modes is minimized over that parameter space. Using the selected dimensions (PX = 1885 µm and PZ = =3350 µm), the *f-T* in Fig. 2c is generated from a region of high predicted Q, and demonstrates stable performance over the temperature range of interest (-35°C ≤ T ≤ +85°C). The corresponding predicted Q remains ~ 400K. The characteristic equivalent circuit parameters over temperature for the optimized are given in Fig. 2d in which we observe well-behaved RLC values from -30°C < T < 85°C. The equivalent RLC values at T = 25°C are summarized in Table 1.

Table 1. Equivalent circuit parameters for an optimized 32MHz design at T = 25°C.

Equivalent Circuit Parameters		
R1 (Ω)	*L1 (H)*	*C1 (F)*
2.25	4.63E-03	5.53E-15

The usefulness of the contour map analysis approach is evident if we consider an example of the same *f-T* and RLC analysis, but generated from a region of compromised Q, as indicated in Figure 3a) for quartz plate dimensions PX = 1915 µm and PZ = 3345 µm. In this case modal activity from spurious modes in close proximity with the thickness shear mode, degrade the frequency stability and the device Q. The corresponding *f-T* curve of Fig. 3c is observed to be noisy and contains activity dips. The equivalent circuit (RLC) values for this non-optimized device (Fig. 3d) are unstable over temperature, showing significant activity close to T=0°C and T=30°C. Therefore, we conclude that the Q contour maps are instrumental in optimizing new resonator designs.

It is also well known that the trench mesas are used to improve modal confinement and isolation from unwanted edge effects. FEA simulations were performed to optimize the resonator Q by varying the trench widths independently in the X- and Z- directions and also the trench depth. A contour plot for the same device as in Fig. 2 (PX=1885um, PZ=3350um), but *without* a trench mesa is presented in Fig 4a. We observe an activity dip (yellow) in the center of the plot causing the Q to drop to Q < 300K. We also observe a generally compromised Q over the contour plot dimensional parameter space. Figure 4c shows the predicted *f-T* and Q of this 'no-mesa' device. Significant modal activity appears at lower temperatures, centered at approximately T= -15°C. Clearly, performance is degraded compared with implementation of a trench mesa.

Residual thermal stress coupled into the device from the mounting regions also plays a prominent role in disturbing the well-designed *f-T* performance. To illustrate the significance of stress in the electrode region, we show in Fig. 5 the effect of increasing thermally induced stress on resonator thickness shear mode frequency for a resonator mounted to a silicon wafer. Assuming zero initial stress at 25°C, as the system temperature is increased incrementally to 100°C, the differential thermal expansion between quartz and silicon introduces thermal stress across the device. In order to simulate the coupling of stress between quartz and silicon, the mount rigidity between the quartz wafer and a silicon substrate is varied in the simulation. As the mounts are stiffened from E=2x10^6 Pa to E=2 x10^{15} Pa, the residual stress in the electrode region increases, and the *f-T* curves are artificially rotated counter-clockwise.

Measured data confirms this observation. In Fig. 6 the effect of thermally induced stress on the *f-T* curve of a resonator is demonstrated. The simulated (red) curve is the *f-T* response

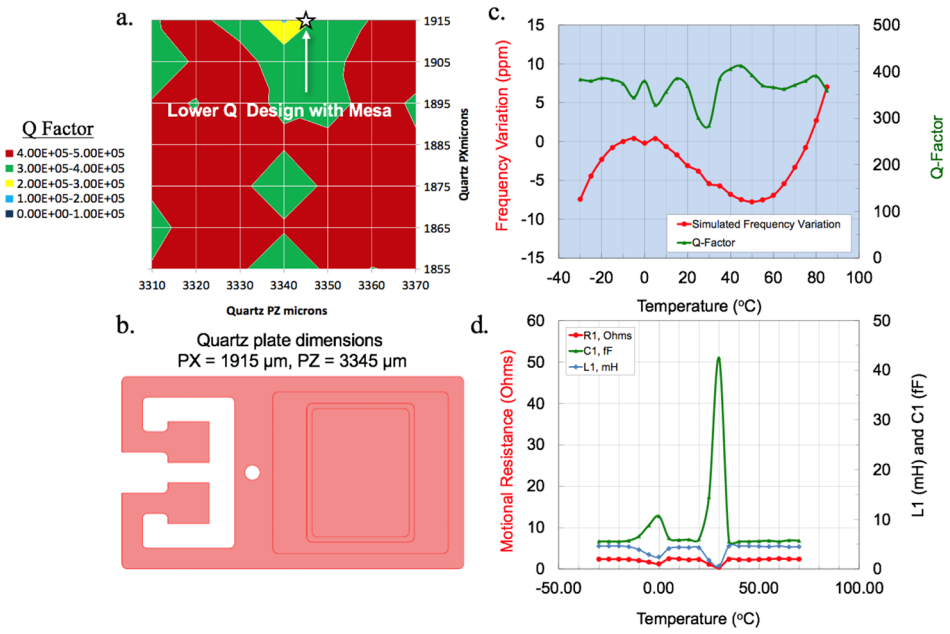


Fig 3. Non-optimized VHF resonator design with mesa. (a) Q-contour map showing lower Q for the selected quartz plate dimensions. (b) Resonator configuration modelled. (c) Simulated *f-T* and *Q-T* profiles of spring resonator show activity dips in the frequency *f-T* and *Q-T* profiles at approximately T=0°C and 30°C. (d) Equivalent circuit parameters demonstrate unstable performance.

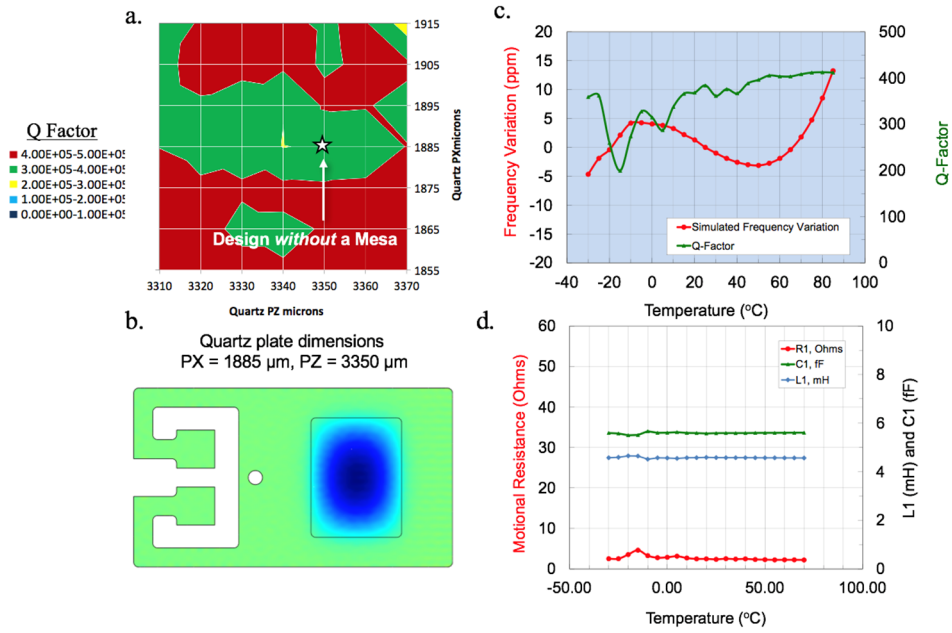


Fig 4. Simulation of VHF resonator design performed *without* a mesa. (a) Q-contour map showing lower Q for the previously optimized quartz plate dimensions. (b) Resonator configuration modelled. (c) Simulated *f-T* and *Q-T* profiles of spring resonator show activity dips in the frequency *f-T* and *Q-T* profiles, particularly for T < 0°C. (d) Equivalent circuit parameters demonstrate stable performance.

for a standalone resonator with perfectly absorbing mounts. This is compared with measured data (black) for a resonator, *without* stress relieving elements, bonded to a silicon substrate. The measured *f-T* data is rotated counter-clockwise due to the residual stress.

As previously noted [1, 2], stress in the active region should be reduced to levels < 100 kPa for stabilization of the *f-T* curve over temperature. Spring tethers between the active resonator region and the mounts, can efficiently mechanically decouple the resonator from the mounts and minimize residual stress. A comparison of residual stress in the electrode region for the device *with* and *without* mechanically decoupling tethers is shown in Fig 7. Assuming zero initial stress at 25°C, an elevated temperature of 100°C (ΔT=75°C) introduces thermally induced stress. In Fig. 7a, for a resonator design *without* spring tethers, the simulated Von Mises stress in the center of the electrodes is approximately 295 kPa. In contrast, stress

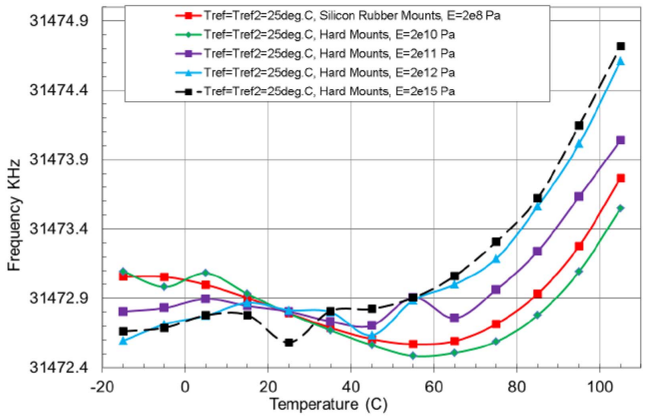


Fig 5. Simulation of the effect of varying thermally induced stresses accomplished by varying stiffness of the mounting material on the *f-T* curve of the AT-cut quartz resonator. For higher stiffness, the *f-T* curves rotate counter-clockwise. This simulates the effect of different thermal expansion coefficients between the quartz resonator and a silicon substrate. This effect can be minimized with the use of spring tethers.

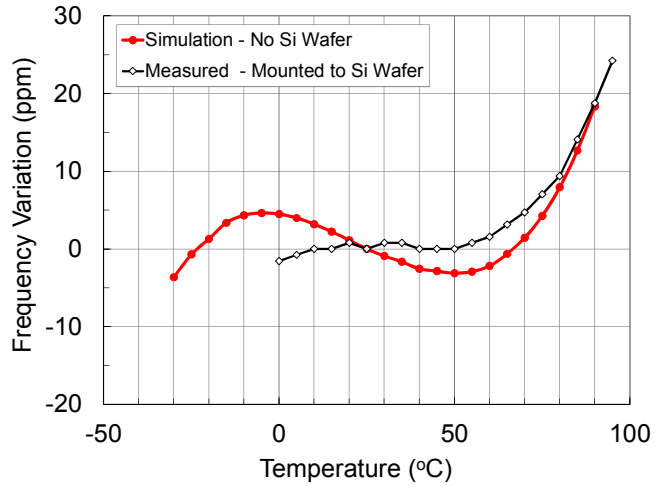


Figure 6. Effect of thermally induced stress on the *f-T* curve of a resonator. The simulated (red) curve is the *f-T* response for a standalone resonator with perfectly absorbing mounts. This is compared with measured data for a resonator *without* stress relief elements, bonded to a silicon substrate. The measured data is rotated counter-clockwise due to the residual stress.

relieving spring tethers, 200 µm wide, formed between the resonator and the mounts (Fig. 7b) provide mechanical isolation for the resonator from stress variations over temperature and prevent artificial rotation and de-stabilization of the *f-T* curve. The mounting locations exhibit high residual stress (100's kPa), however, the stress rapidly decays along the tethers such that stress in the electrode region is significantly reduced. For a design with spring tethers, the residual stress for a $\Delta T = 75°C$ is significantly reduced to approximately 78 kPa.

III. RESONATOR TEST DATA

Resonators were designed and fabricated with wafer level packaging techniques and integrated on CMOS electronics. A photograph of the completed resonator is presented in Fig. 8, showing the quartz plate electrodes, mesas, mounts and spring

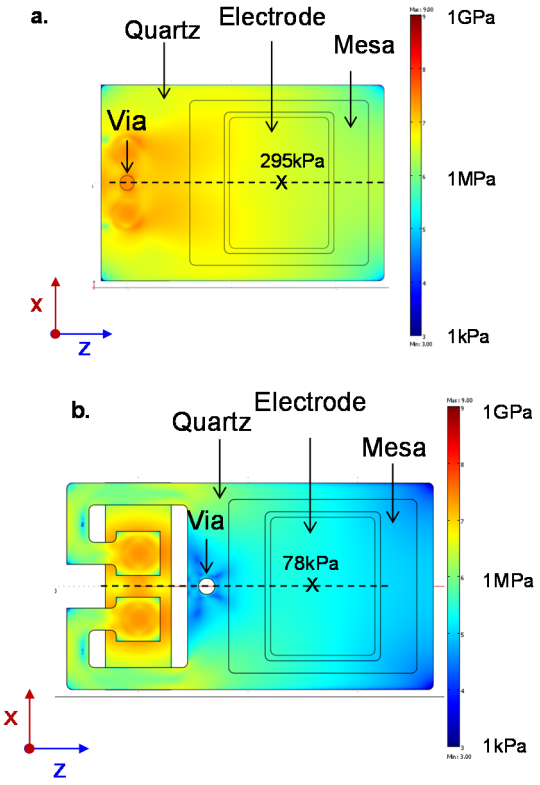


Figure 7. Residual thermal stress of VHF quartz resonators for an applied $\Delta T = 75°C$. (a) Residual stress in the electrode region for a device without tethers for mechanical decoupling of stresses from the mounting regions. (b) Reduced residual stress in the electrode region for a device with tethers to decouple stress in the mounting regions from the quartz active region under the electrodes.

tethers. The device uncompensated *f-T* profiles were tested in an oven for frequency stability. The measured data is overlayed with the simulation data in Fig. 9 for which the fabricated device exhibits an *f-T* performance that is stable over temperature and free from activity dips, as per the simulation

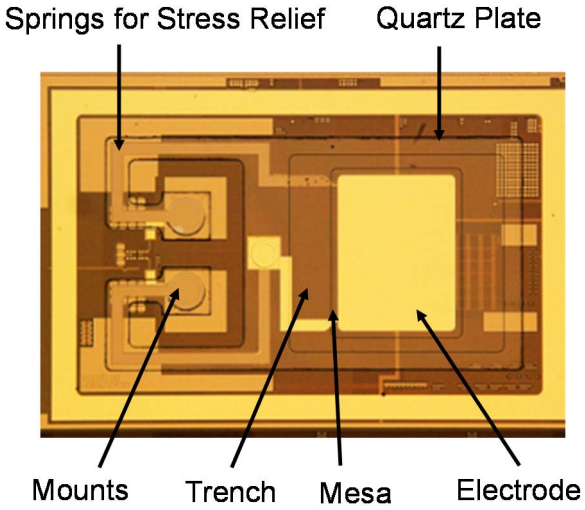


Fig. 8 Photograph of fabricated VHF quartz resonator with stress relieving springs, through vias, electrodes and trench mesa's.

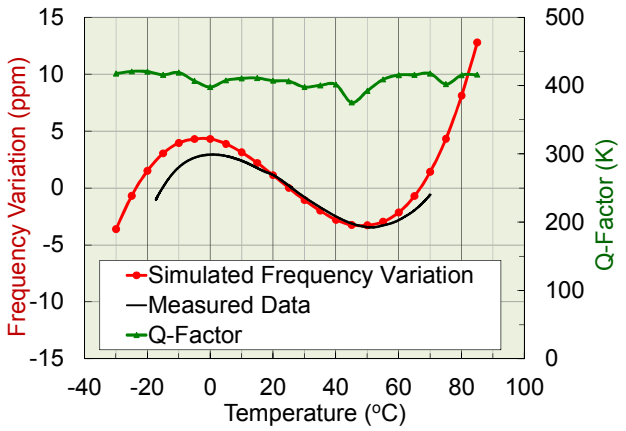


Fig. 9 The uncompensated *f-T* profile (black) and simulated *f-T* profile (red) for a G5S5 Gen 6-1 integrated oscillator. Measured data agrees to within a few ppm of simulated data.

result. Measured *f-T* data falls within a few ppm of the Comsol 3-d FEA *f-T* predictions over -20°C ≤ T ≤ +70°C.

IV. Summary

We have demonstrated a successful methodology for the design of miniaturized high Q VHF quartz AT-cut resonators integrated on a CMOS substrate with a high degree of frequency stability. Devices were optimized using accurate FEA models containing quartz dry etched side-wall angles, and lead to generation of contour maps for determination of regions of high frequency stability, high Q stability, and stable equivalent circuit parameters. Integrated devices were fabricated and tested over temperature. Introduction of the trench mesa provides improved predicted *f-T* and Q stability. Measured uncompensated device *f-T* performance agrees to within a few ppm of the Comsol 3-d FEA *f-T* predictions over the temperature range -35°C ≤ T ≤ +85°C.

References

[1] D. J. Kirby et al, "Optimizing UHF quartz MEMS resonators for high thermal stability", 2013 IEEE Int. Frequency Control Sym., Prague, Czech Republic, July 22 – 26, 2013, pp. 699 - 702.

[2] Yook-Kong Yong et al., "Modeling approach to analyze bonding stress in UHF quartz resonators", 2013 IEEE Int. Frequency Control Sym., Prague, Czech Republic, July 22 – 26, 2013, pp. 703 – 70

Capacitive Lamé Mode Resonator with Gap Closing Mechanism for Motional Resistance Reduction

Mohannad Y. Elsayed and Frederic Nabki
Electrical Engineering Department
École de Technologie Supérieure
Montreal, Canada
mohannad.elsayed@mail.mcgill.ca and frederic.nabki@etsmtl.ca

***Abstract*—This work presents a Lamé mode resonator featuring a novel gap closing mechanism which employs electrostatic force to reduce the capacitive transduction gaps to sub-micron values to overcome fabrication technology limitations. This leads to significant resonator loss and motional resistance reduction, which is highly advantageous as it simplifies the design of oscillation sustaining circuitry. Prototypes were fabricated in a commercial silicon-on-insulator technology, PiezoMUMPs from MEMSCAP. Upon the application of a DC voltage of 55 V between the resonator structure and electrodes, the gaps are reduced from 2.5 µm to 0.5 µm. A resonance frequency of 18 MHz with a quality factor of 120,000 was observed under 1 mTorr vacuum. A loss of 55 dB was measured at 55 V, which corresponds to a motional resistance of 56 kΩ, 5 times lower than that of a similar design without gap closers at the same voltage. The frequency tuning range is also increased significantly as a result of the gap reduction, which can be very useful for overcoming ambient conditions and fabrication variations.**

Keywords— Microelectromechanical systems (MEMS), micromachined resonators, bulk mode resonators, bulk micromachining, silicon-on-insulator (SOI), timing.

I. INTRODUCTION

Micromachined resonators have received continuously increasing attention due to their small sizes and their potential for integration with other MEMS resonators and circuits on the same chip. Bulk-mode devices typically exhibit high stiffness, and are consequently less prone to thermoelastic damping, compared to flexural devices, allowing them to achieve large quality factors (>10,000), even at atmospheric pressure, e.g. [1-8]. On the other hand, they exhibit relatively higher motional resistances due to their high stiffness, which often requires means of increasing the actuation forces and sensing signals in order to overcome this. In [1], relatively complex fabrication methods were used to realize sub-micron lateral gaps for capacitive actuation. In [2-5], high operating voltages were used to reduce the motional resistance. In [6-7], comb structures were added to the points of maximum vibration amplitudes in order to increase the drive forces and output signal pickup area at the expense of lowering the operating frequency and quality factor. In [8], piezoelectric actuation was used for bulk mode structures at the expense of the increased damping resulting from the different layers on top of the main resonating structure.

Gap closing structures have been introduced in [9-12] as an alternative method for transduction gap reduction by overcoming the fabrication technology limitations. In [9], a relatively complex gap closing and locking structure was presented, but no experimental results were reported. In [10-11], gap closing structures were employed in a width extensional resonator. In [12], gap closers were added to a wine-glass disk resonator. However, the gap closing structures suffered from break points which led to electrical contact between the electrodes and the resonator structure resulting in permanent failure.

In this work, a Lamé mode resonator with gap closing structures is presented. The gap closing mechanism relies on electrostatic pull-in between the resonator structure and the electrodes. Stopper structures were added in order to avoid electrical contact between the electrodes and resonator structure, and consequently ensure reliable operation. The minimum gap achievable using the presented structure is only limited by the mask grid size. This allows for realizing high quality factor and low loss bulk mode resonators without requiring excessive voltages or complex fabrication steps.

The paper begins with a description of the device design and FEM simulation results. The measurement results are then presented, followed by a conclusion.

II. RESONATOR DESIGN

The resonator is composed of a central square structure which is the main resonator structure. This square is anchored to the substrate through four support beams located at the corner nodal points. The resonator is surrounded by four electrodes as shown in Fig. 1. The resonator is separated from the electrodes by a capacitive gap (g_i), originally 2.5 µm in this design. Each of the electrodes is composed of a movable shuttle which is anchored through a folded suspension. Stopper structures are added which are initially separated for the movable shuttle by a certain gap (g_s), 2 µm in this design. Dimples are added to the structure in order to avoid stiction and ensure reversible pull-in. Alternatively, stiction forces and/or welding may be used to realize permanent pull-in. As a DC voltage is applied to the resonator, the movable electrodes move towards the resonator as a result of the electrostatic force generated. When the voltage exceeds the pull-in voltage, the

This work was supported in part by the Natural Sciences and Engineering Research Council of Canada, in part by the Quebec Fund for Research in Nature and Technology, in part by CMC Microsystems, in part by the Microsystems Strategic Alliance of Quebec, and in part by the Canada Foundation for Innovation.

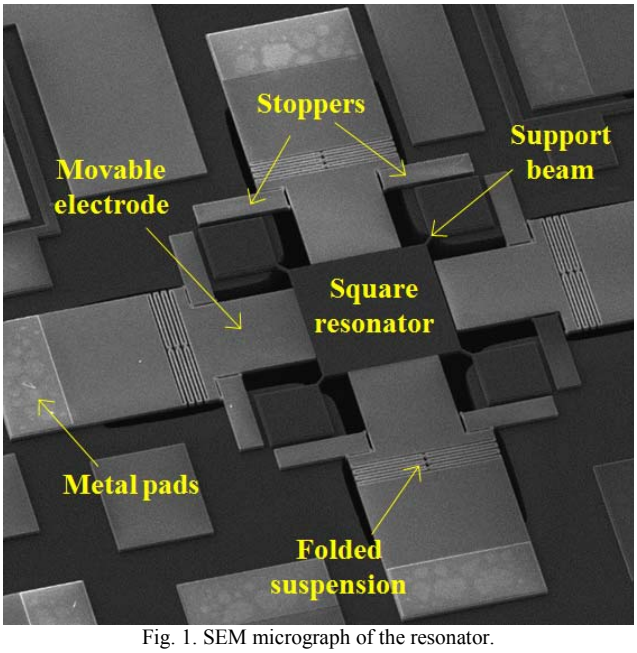


Fig. 1. SEM micrograph of the resonator.

electrodes are pulled-in stopping on the stoppers resulting in a final gap (g_f) of 0.5 µm, which is given by the difference as

$$g_f = g_i - g_s. \quad (1)$$

Fig. 2 shows FEM simulation results for the electrode displacement as a result of the applied DC voltage. As the voltage is lowered, the electrodes maintain the pulled-in position till a certain release voltage (V_r) at which the spring force becomes higher than the electrostatic voltage bringing the electrodes back to their original positions. This results in a hysteresis, as shown in Fig. 2. Simulation projects a pull-in voltage of ~61 V. The release voltage can be calculated based on force balance as

$$V_r = \sqrt{\frac{2k.g_s.g_f^2}{\varepsilon_0.A}} \quad (2)$$

where k is the equivalent spring constant of the suspension, ε_0 is the relative permittivity of free space, and A is the overlap area, to be ~28 V.

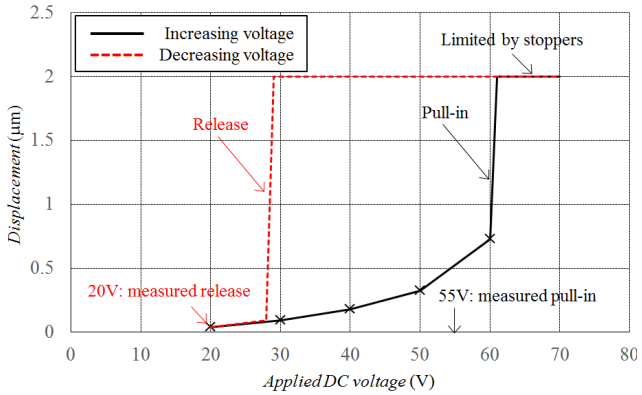
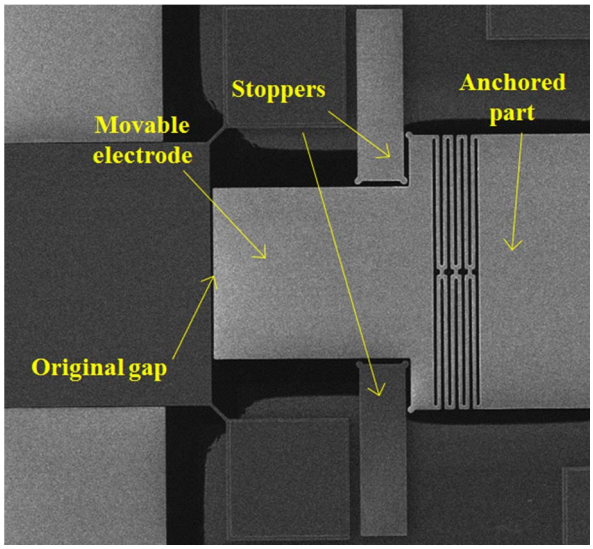
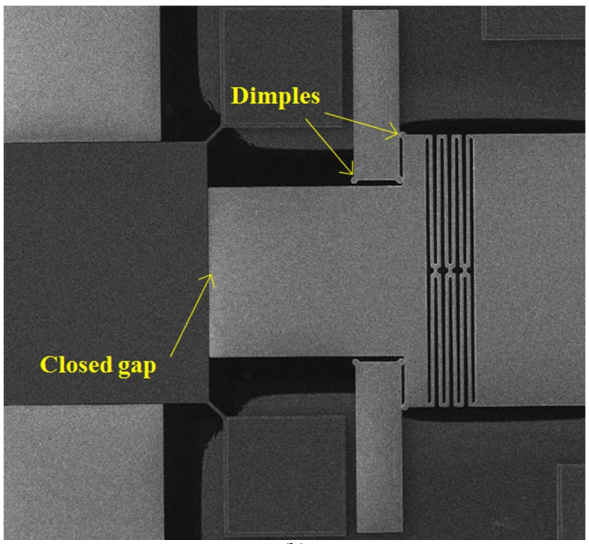


Fig. 2. FEM simulation for electrode displacement vs DC voltage.



(a)



(b)

Fig. 3. SEM micrographs of one electrode in: (a) original position, and (b) gap closed position due to SEM charging.

Figure 3 illustrates SEM micrographs of one of the electrodes in the original and gap closed positions, respectively.

III. Measurement Results

A pull-in voltage of 55 V and a release voltage of 20 V were observed. Figure 4 shows the resonator transmission curves in a differential setup in 1 mTorr vacuum and atmospheric pressure, respectively. No resonance peaks could be observed for DC voltages lower than the pull-in voltage. At a pull-in voltage of 55 V, resonance frequencies of ~17.97 MHz with quality factors of 15,600 in atmospheric pressure increasing to 120,230 in vacuum were observed. Transmission loss at resonance of 55 dB corresponding to a motional resistance of 56 kΩ was measured in 1 mTorr vacuum, which is 5 times lower than that reported in [2] for a similar resonator without gap closers, highlighting the

advantage of the design. The resonance frequency is tunable based on the electrostatic spring softening phenomenon. The tuning range is more than 10 times higher than the resonator presented in [2], as illustrated in Fig. 5.

IV. Conclusion

This work presents a Lame mode resonator featuring a novel gap closing mechanism which employs electrostatic force to reduce the capacitive transduction gaps to sub-micron values to overcome the fabrication technology limitations. This leads to significant resonator loss and motional resistance reduction, and tuning range increase.

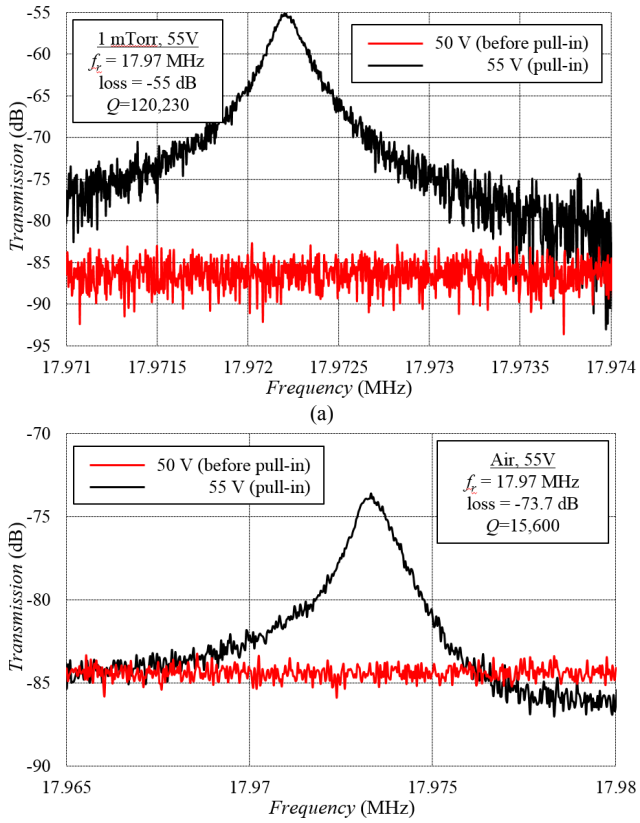


Fig. 4. Measured resonance characteristics at: (a) 1 mTorr vacuum, and (b) atmospheric pressure.

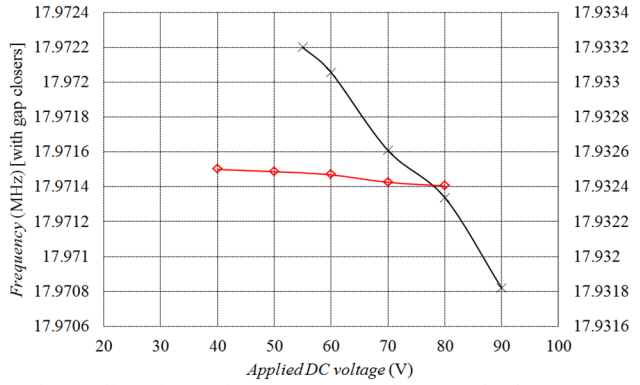


Fig. 5. Effect of DC voltage on resonance frequency for the resonator presented here (black) and a resonator without gap closers (red) [2].

References

[1] Y. Xie et al., "1.52-GHz micromechanical extensional wine-glass mode ring resonators," IEEE Trans. Ultrasonics, Ferroelectrics and Frequency Control, vol. 55, no. 4, pp. 890-907, May 2008.

[2] M. Elsayed and F. Nabki, "18-MHz silicon Lamé mode resonators with corner and central anchor architectures in a dual-wafer SOI technology," J. Microelectromech. Syst., vol. 26, no. 1, pp. 67-74, Feb. 2017.

[3] M. Elsayed, F. Nabki, and M. El-Gamal, "A 2000 °/sec dynamic range bulk mode dodecagon gyro for a commercial SOI technology," Proc. IEEE Conf. on Electronics, Circ., and Syst., Dec. 2011, pp. 264-267.

[4] L Khine and M. Palaniapan, "High-Q bulk-mode SOI square resonators with straight-beam anchors," J. Micromech. and Microeng., vol. 19, pp. 015017, 2009.

[5] G. Xereas and V. P. Chodavarapu, "Wafer-level vacuum-encapsulated Lamé mode resonator with f-Q Product of 2.23×10^{13} Hz," IEEE Electron Device Lett., vol. 36, no. 10, pp. 1079-1081, Oct. 2015.

[6] M. Elsayed, F. Nabki, and M. El-Gamal, "A combined comb/bulk mode gyroscope structure for enhanced sensitivity," Proc. IEEE Conf. MEMS, Jan. 2013, pp. 649-652.

[7] M. Elsayed, F. Nabki, and M. El-Gamal, "A novel comb architecture for enhancing the sensitivity of bulk mode gyroscopes," Sensors, vol. 13, pp. 16641-16656, Dec. 2013.

[8] M. Y. Elsayed et al, "Bulk mode disk resonator with transverse piezoelectric actuation and electrostatic tuning," J. Microelectromech. Syst., vol. 25, no. 2, pp. 252-261, April 2016.

[9] J.Jiang, J. Bao, Y. Du, and C. deng, "A novel movable electrode for realizing deep sub-micrometer gap in SOI-based MEMS square resonator," Microsyst. Technol., vol. 19, no. 5, pp. 793-772, May. 2013.

[10] E. Ng et al., "Stable pull-in electrodes for narrow gap actuation," Proc. IEEE Conf. MEMS, Jan. 2014, pp. 1281-1284.

[11] N. Toan and T. Ono, "Capacitive silicon resonator structure with movable electrodes to reduce capacitive gap widths based on electrostatic parallel plate actuation," Proc. IEEE Conf. MEMS, Jan. 2014, pp. 1245-1248.

[12] X. Li et al, "A 9.45 MHz micromechanical disk resonator with movable electrodes for gap reduction," Journal of Sensors and Actuators A: Physical, vol. 243, pp. 66-70, Jan. 2016.

HAL SAW Resonators Using $LiTaO_3$ Thin Plate on Quartz Substrate

Michio Kadota and Shuji Tanaka
Graduate School of Engineering, Tohoku University, Sendai, Miyagi, Japan
E-mail: mkadota@mems.mech.tohoku.ac.jp

***Abstract*— Surface acoustic wave (SAW) resonators with a moderate bandwidth and a large impedance ratio are obtained by Hetero Acoustic Layer (HAL) structure combing a $LiTaO_3$ (LT) thin plate and the substrate, which has a high velocity of leaky SAW and a small frequency temperature coefficient (TCF). In this study, a new type of HAL SAW resonators were fabricated using 0.5-1 μm thick 42°YX or 20°YX LT and 42°45'YX or 40°Y90°X quartz bonded together. An impedance ratio of 65 - 70 dB and a TCF of -26 ppm/°C were measured. Those impedance ratios are 13 - 21 dB better than that of a standard 42°YX LT SAW resonator fabricated in the same facility.**

Keywords— SAW resonator, $LiTaO_3$, quartz, impedance ratio, TCF, hetero acoustic layer

I. INTRODUCTION

In recent years, the mobile phone frequency range is busy with a lot of bands due to the wide spread of smart phones. Acoustic wave filters are being continuously required better steepness of passband and smaller temperature coefficient of frequency (TCF). Surface acoustic wave (SAW) duplexers with a small TCF of -10 ppm/°C were developed using a high density metal interdigital transducer (IDT) covered with a flattened SiO_2 film on $LiTaO_3$ (LT) or $LiNbO_3$ (LN) [1][2]. A Rayleigh SAW transversal filter and a longitudinally coupled resonator filter with zero TCF were developed by combining a ZnO film with negative TCF and a quartz substrate with a positive TCF [3][4][5]. Fundamental and higher modes of leaky SAW (LSAW) also showed a small TCF on a quartz substrate covered with ZnO [6].

Recently, Hetero Acoustic Layer (HAL) types of SAW devices were reported by different groups including us [7][8][9]. HAL SAW devices inherently have many variations of structure and a lot of potentials. Takai *et al.* reported an absolute TCF of 10 ppm/°C and a BosedQ factor of 4,000 using a HAL structure of rotated-YX LT plate/ SiO_2 film/ AlN film/ substrate [8]. Kakio *et al.* reported electromechanical coupling factors on 36°YX LT on c-sapphire and AT-90°X quartz [9]. In this study, the authors report the bandwidth (BW = (anti-resonant frequency f_a – resonant frequency f_r)/f_r) and impedance ratio (Z ratio = 20log(anti-resonant impedance Z_a/ resonant one Z_r) of different designs of HAL SAW resonators using a LT thin plate on a quartz substrates. In addition, the measured properties of the HAL SAW resonators on 42°YX LT/ 42°45'YX quartz and 20°YX LT/ 40°Y90°X were compared with those of a standard SAW resonator on 42°YX LT.

II. CALCULATION

FEM simulation was used to compare (a) standard SAW resonators on LT, and HAL SAW resonators using thin LT (0.15λ) on (b) Si and (c) quartz. Two different cut angles of LT, 42°YX LT (Euler angle: 0°, 132°, 0°) and 20°YX LT (Euler angle: 0°, 110°, 0°), were used for Figs. 1 and 2, respectively. In Fig. 1, the standard SAW resonator (a) shows a Z ratio of 65 dB, that well agrees with the reported values [9][11]. On the other hand, the HAL SAW resonators (b) and (c) show better Z ratios of 72 dB and 76 dB, respectively. In Fig. 2, the HAL SAW resonators (b) and (c) show further better Z ratios of 74 dB and 78 dB, respectively, while the standard SAW resonator (a) has a lot of ripples because of large leaky component. If the two cut angles are compared, 20°YX LT (Fig. 2) is preferable for LT/quartz HAL structure. A Z ratio of 78 dB and a BW of 6.1% are obtained.

Fig. 3 shows the calculated (a) BWs and (b) Z ratios of LT/quartz HAL SAW resonators. The cut angles of a LT plate (0.15λ) and a quartz plate were considered within (0°, 70-160°, 0°) and (0°, 110-165°, 90°), respectively. Large BW and Z ratio are obtained, when (0°, 107-125°, 0°) LT and (0°, 100-155°, 90°) quartz are combined. The maximum Z ratio reaches 78 dB, as mentioned above. A good performance is also obtained, when the propagation direction of quartz is rotated by 90° compared with 0°. Suitable Euler angles are (0°, 107-125°, 0°) for LT and (0°, 115-145°, 90°) for quartz.

Figs. 4 and 5 show LSAW phase velocities and TCFs on (0°, θ, 0°) and (0°, θ, 90°) quartz by solid lines and (0°, θ, 0°) LT by a broken line as a function of Euler angle θ. Around (0°, 90-150°, 0°) and (0°, 104-140°, 90°) quartzs shows LSAW velocity higher than 4,800 m/s, which have mainly a shear horizontal component.

LSAW on quartz has a positive TCF, when the Euler angle is (0°, 0-16°, 0°), (0°, 43-66°, 0°), (0°, 132-180°, 0°), (0°, 0-42°, 90°) and (0°, 125-180°, 90°) as shown by solid lines in Fig. 5. On the other hand, LSAW on LT has always a negative TCF as shown by a broken line in Fig. 5. A positive TCF of quartz can cancel a negative TCF of LT as our previous reports of the SAW filters combined a ZnO film with negative TCF and a quartz substrate with a ppositive TCF [3][4][5]. Taking account of Z ratio and TCF, a preferable Euler angle of quartz is found within (0°, 133-150°, 0°) and (0°, 126-140°, 90°) for (0°, 94-137°, 0°) LT.

This work was supported by the Strategic Information and Communications R & D Promotion Programme (SCOPE) from the Ministry of Internal Affairs and Communications of Japan.

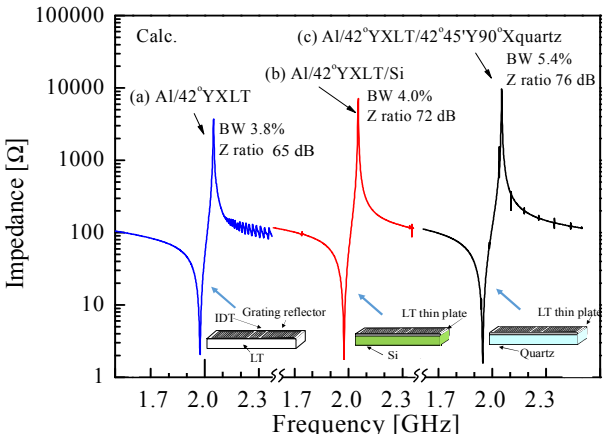


Fig.1 Frequency characteristics of resonators of (a) Al-IDT/42° YX-LT substrates, and Al-IDT/42° YX-LT thin plate on (b)Si and (c) 42°45'Y90°X quartz substrates.

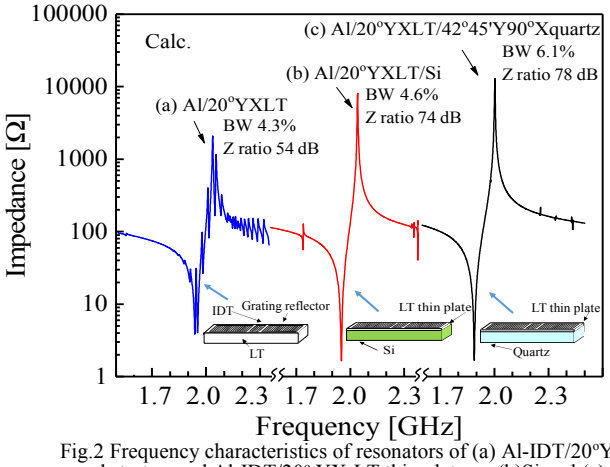


Fig.2 Frequency characteristics of resonators of (a) Al-IDT/20°YX-LT substrates, and Al-IDT/20° YX-LT thin plate on (b)Si and (c) 42°45'Y90°X quartz substrates.

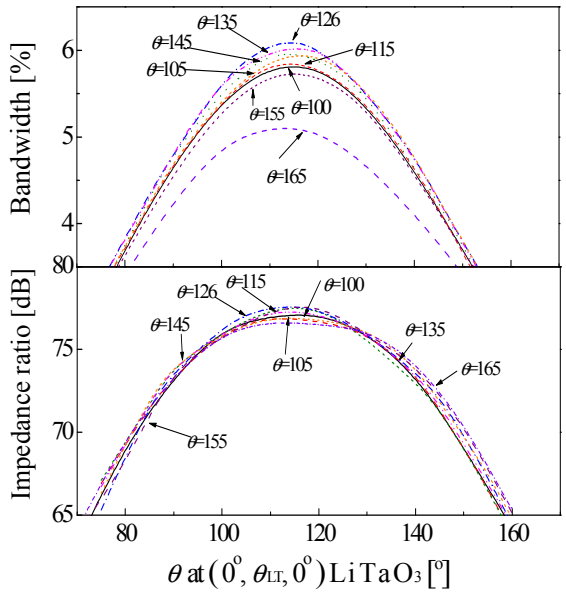


Fig.3 BWs and impedance ratios of resonators composed of on Al-IDT/ (0°, 70-160 °, 0°) LT thin plate on (0°, 115-165°, 90°) quartz.

Fig. 6 shows BWs and Z ratios on 20°YX LT/ 40°Y90°X-quartz as a function of LT thickness. The maximum BW and Z ratio are obtained at 0.18λ and 0.1λ (λ: wavelength), respectively. If the frequency is high, a thin LT plate is required accordingly.

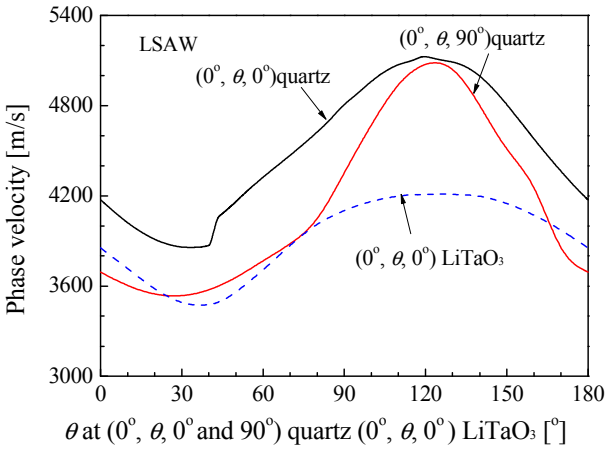


Fig.4 LSAW phase velocities on (0°, θ, 0°) and (0°, θ, 90°) quartz, and (0°, θ, 0°) LT as a function of θ.

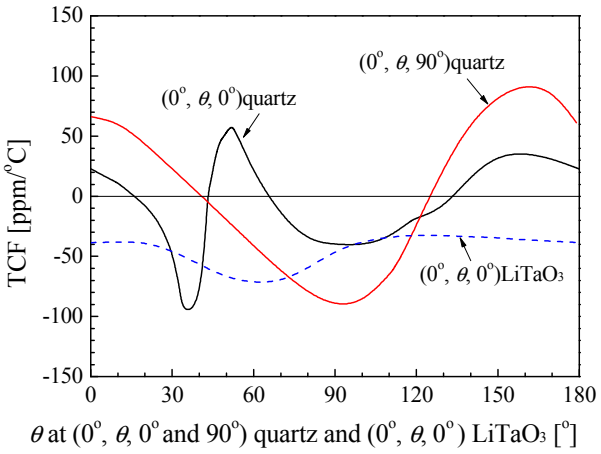


Fig.5 TCFs of LSAW on (0°, θ, 0°) and (0°, θ, 90°) quartz, and (0°, θ, 0°) LT as a function of θ.

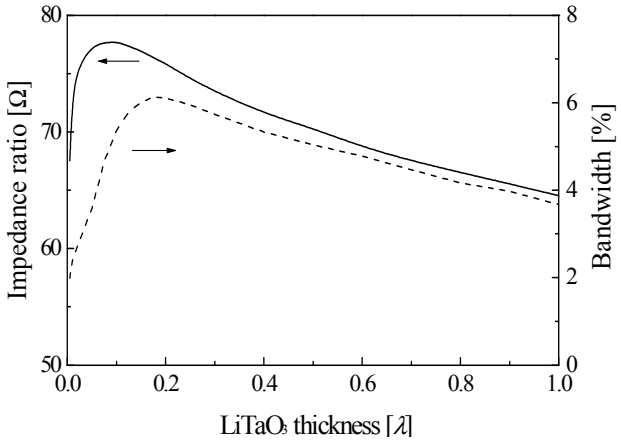


Fig.6 BWs (right axis) and Z ratios (left axis) on 20°YX-LT/ 40°Y90°X -quartz as a function of LT thickness.

Fig. 7 shows calculated (a) BWs and (b) Z ratios of LN/ quartz HAL SAW resonators using various Euler angles of LN thin plate (0.15λ. thickness) on quartz substrates. The HAL SAW resonator with LN thin plate/ quartz has also BW wider than 14% and Z ratio higher than 80 dB at (0°, 110-130°, 0°) LN and (0°, 115-135°, 90°) quartz.

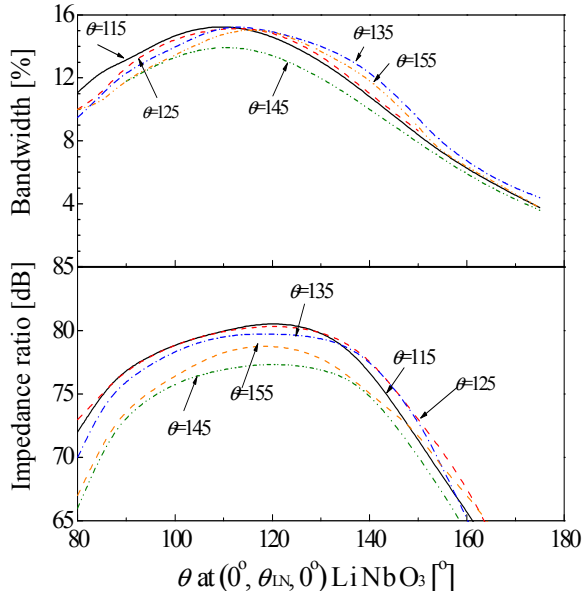


Fig.7 BWs and impedance ratios of resonators composed of on Al-IDT/ (0°, 80-170 °, 0°) LN thin plate on (0°, 115-1565°, 90°) quartz substrates.

III. FABRICATION OF RESONATOR

The HAL SAW resonators were fabricated by combining 42°YX LT/ 42°45'YX-quartz and 20°YX LT/ 40°Y90°X-quartz, that were not optimum in Euler angle. Fig. 8 shows the process. The thicknesses after bonding and polishing are 0.5±0.13 μm and 1.0±0.16 μm, respectively.

Cu electrodes with 0.23 μm thickness were formed on a 42°YX LT/ 42°45'YX-quartz and a 42°YX LT by photo-lithography. The Cu electrode is composed of an IDT with a wavelengths λ of 3.0 μm, an aperture of 40λ, and 60 finger pairs, and the grating reflectors with 50 fingers.

Au electrodes with 0.12 μm thickness were formed on 20°YX LT/ 40°Y90°X-quartz and 42°YX LT. The Au electrodes are composed of IDTs with wavelengths λ of 5.25 and 3.78 μm, apertures of 40λ and 50λ, and 60 finger pairs, and the grating reflectors have 30 and 50 fingers, respectively at each side of the IDT. Standard SAW resonators with Cu and Au IDT/ 42°YX LT structures were fabricated as a reference.

Fig. 9 shows the measured frequency characteristics of resonators composed of Cu/ 42°YX LT and Cu/ 42°YX LT/ 42°45'YX quartz. The HAL SAW resonator shows a BW of 4.9% and a Z ratio of 65 dB, both of which are 1.5 times wider and 13 dB higher than 3.3% and 52 dB for the standard SAW resonator, respectively. The resonance frequency is 110 MHz (9%) higher than that of the standard SAW resonator.

Fig. 10 shows frequency characteristics of resonators composed of Au/42°YX-LT and Au/ 20°YX LT/ 40°Y90°X-quartz. A 42°YX LT as a reference was used because a 20°YX LT has a lot of ripples between f_r and f_a due to a leaky component as shown in Fig.2. However, the 20°YX LT combined with a quartz substrate shows an excellent frequency characteristic without the ripples. The HAL SAW resonator shows a BW of 6.1% and a Z ratio of 70 dB, both of which are 1.5 times wider and 21 dB higher than 4.1% and 49 dB for the standard SAW resonator, respectively. Mechanical Q is proportion to a Z ratio/ BW, suggesting that the HAL SAW resonator 7.4 times higher Q than the standard SAW resonator.

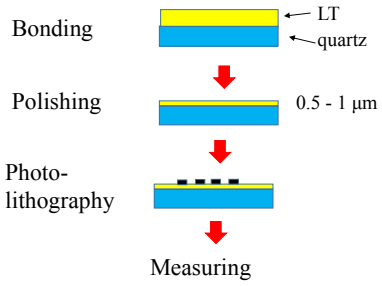


Fig.8 Fabrication process of HAL SAW.

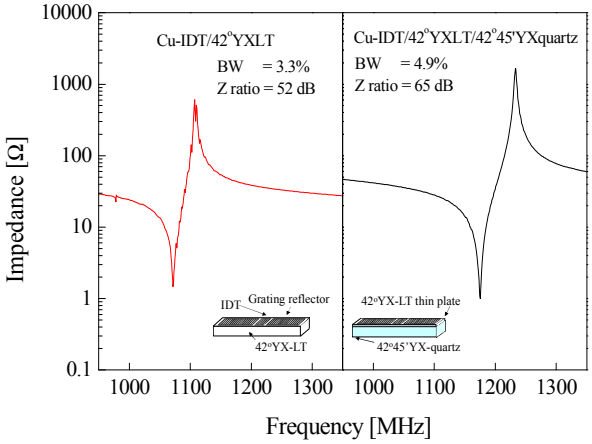


Fig.9 Measured frequency characteristic of Cu/42°YX-LT and Cu/42°YXLT thin plate/42°45'YXquartz.

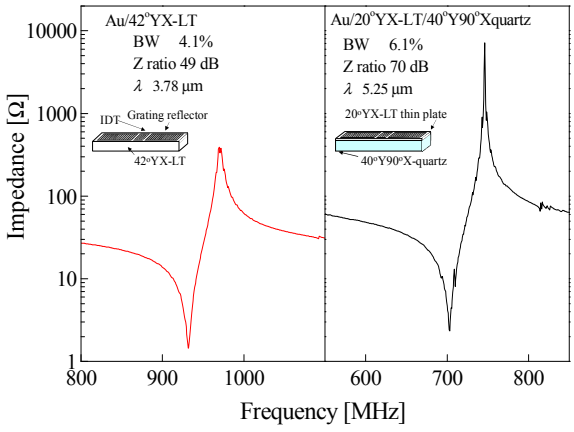


Fig.10 Measured frequency characteristic of Au/42°YX-LT and Au/20°YXLT thin plate/40°Y90°Xquartz.

The resonant peak is not sharp compared with the anti-resonant peak due to a limited IDT metal quality. If it is improved by using a better evaporation tool, a higher *Z* ratio could be obtained. Although small transverse ripples are observed in Figs. 9 and 10, they could be improved by optimizing the IDT thickness or apodizing the IDT.

Such a significant advantage in *Z* ratio clearly suggests high potential of LT/ quartz HAL SAW devices in comparison with the standard ones, but the achieved *Z* ratios are much smaller than the simulated values for both resonators. This may be because the fabrication process and the IDT quality and design were not optimized, as mentioned above.

The TCFs of three HAL SAW resonators with different λ were measured at temperatures of 25ºC, 35ºC and 45ºC. Fig. 11 shows the measured and calculated TCFs of resonance frequency versus normalized LT thickness. The measured and calculated TCFs do not match completely, but both show the trend that the TCF are improved with thinner LT. The best TCF is -26 ppm/ºC, which is about 3/5 of a standard Al IDT/ 42ºYX LT SAW device [11]. The relationship between the frequency and temperature of a SAW resonator on an Al-IDT/ ST-X quartz substrate is not linear but a quadratic curve, and the turn over temperature is at around 25ºC. Therefore, it is expected that the TCF of the HAL resonator from -20 to 80ºC is better than that from 25 to 45ºC. In addition, the TCF will be further improved at a suitable Euler angle of quartz.

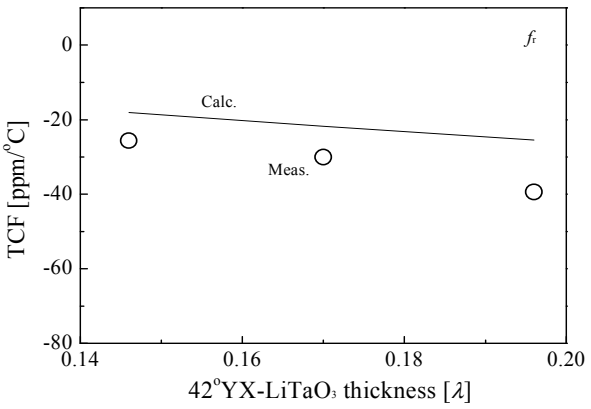


Fig.11 TCFs of fabricated resonators as a function of LT thickness.

IV. Conclusions

A HAL SAW resonator using a LT thin plate on a quartz substrate can achieve a large *Z* ratio and a small TCF simultaneously, because quartz shows a high LSAW velocity and a positive TCF in a suitable range of Euler angle. HAL SAW resonators with a structure of Cu/ 42ºYX LT thin plate/ 42º45'YX quartz and Au/ 20ºYX LT thin plate/ 40ºY90ºX quartz were fabricated and compared with standard Cu and Au/ 42ºYX LT SAW resonators. The HAL SAW resonators measured had 1.5 and 1.8 times wider BW, and 13 and 21 dB higher *Z* ratios than the standard ones, which correspond to 3 and 5.6 times higher Q. The measured TCF of the resonance frequency is as small as -26 ppm/ºC at a LT thickness of 0.15λ, which is about 3/5 compared with a conventional Al/ 42ºYX LT SAW device. The HAL SAW resonators fabricated in this study are still compromising on the cut angles of LT and quartz and IDT metal quality. Therefore, a better performance will be obtained with the optimized structure and fabrication process.

Acknowledgment

The authors would like to thank Dr. T. Yamamoto at NDK Co. Ltd. for supplying substrates.

References

[1] M. Kadota, T. Nakao, N. Taniguchi, E. Takata, M. Mimura, K. Nishiyama, T. Hada, and T. Komura, Jpn. J. Appl. Phys. vol.44, pp.4527-4530, 2005.

[2] M. Kadota, Takeshi Nakao, Kenji Nishiyama, Shunsuke Kido, Masanori Kato, Ryoichi Omote, Hiroshi Yonekura, Norihiko Takada, and Ryoichi Kita, Jpn. J. Appl. Phys., vol.46, pp.4714-4717, 2007.

[3] M.Kadota, Proc. IEEE Ultrason. Symp., pp.261-266, 1997.

[4] M. Kadota and H. Kando, IEEE trans. Ultrason. Ferroelec. Freq. Cont., vol.51, p.464-469, 2004.

[5] M.Kadota, Takeshi Nakao, Takaki Murata, and Kenji Matsuda, Jpn. J. Appl. Phys. vol.48, 07GG03-01-04, 2009.

[6] M. Kadota, IEICE, vol.J82-C-I, pp.706 714, 1999 [in Japanese].

[7] M. Kadota and S. Tanaka, Jpn. J. Appl. Phys., vol.54, 07HD09-01-04,2015.

[8] M. Kadota and S. Tanaka, Proc. IEEE Freq. Cont. Symp., pp.361-364, 2016.

[9] T. Takai, H. Iwamoto, Y. Tanamine, H. Yamazaki, T. Fuyutume, H. Kyoya, T. Nakao, H. Kando, M. Hiramoto, T. Toi, M. Koshino, and N. Nakajima, Proc. IEEE Ultrason. Symp., 6A2-01-04, 2016.

[10] M. Gomi, T. Kataoka, J. Hayashi, and S. Kakio, Proc. 37th Symp. Ultrason. Electronics, 1P3-2-01-02, 2016.

[11] T. Kimura, M.Kadota, and Y. Ida, ICE, vol.131-C, pp.1115-1119, 2011 [in Japanese].

[12] M. Miura, T. Matsuda, M. Ueda, Y. Satho, O, Ikata, Y. Ebata, and H. Takagi, Proc. IEEE Ultrason. Symp., pp.573-576, 2005.

Nonlinear Time domain-FFT study of the $f-2f$ frequency response of Lithium Niobate YX-127º SAW resonators

Yook-Kong Yong and Xiangnan Pang
Dept. of Civil and Environmental Engineering, Rutgers University. yyong@soe.rutgers.edu

***Abstract*—The nonlinear characteristics of SAW resonators have been of great interest recently. We present a new nonlinear solution algorithm for the f-2f nonlinear coupling phenomenon in SAW IDT resonators. Specifically we have applied our algorithm to obtain the f-2f frequency response of the lithium niobate YX-127º SAW IDT resonators. Lithium niobate was chosen because a complete set of its nonlinear material constants was known and published in the literature. The algorithm consisted of solving the nonlinear finite amplitude model in the time domain to obtain the time dependent response, and then performing a fast Fourier transform of the time dependent response. In order to minimize the transient response, the initial conditions for the time domain solution were obtained from the frequency response of the linear model. Results were presented for a one-electrode IDT SAW resonator at increasing drive voltages. The charge on the electrode IDT for the nonlinearly generated 2*f* mode increased with the square of the magnitude of *f* mode drive level voltage.**

Keywords—nonlinear vibrations, f-2f nonlinear coupling, nonlinear SAW IDT, lithium niobate YX-127º SAW IDT resonators

I. INTRODUCTION

There has been great interest in the nonlinear characteristics of SAW resonators and the methods of characterizing them [1, 2, 3, 4]. Due to the great number of eigenmodes and their complexities in a SAW resonator it is extremely difficult to determine apriori the nature of their interactions with the nonlinear SAW mode of interest. Also, there are few if any direct solution of the 2D and 3D nonlinear SAW IDT resonator employing the complete set of nonlinear piezoelectric equations. We present a nonlinear time dependent solution of the SAW IDT resonator to show the *f*-2*f* nonlinear coupling. A fast Fourier transform of the time domain solution yields the frequency response of the nonlinear model.

II. NONLINEAR PIEZOELECTRIC EQUATIONS.

Often in nonlinear models of vibrations the nonlinear material constants are not well known or measured. Assumptions were then made to simplify the nonlinear problem, and a one-dimensional version of the problem was modeled instead so that fewer values of the nonlinear material constants were needed. For the lithium niobate crystal a complete set of nonlinear material constants was available in the literature [5]. We present the complete set of nonlinear piezoelectric equations employed in our COMSOL finite element model.

A. Nonlinear stress equations of motion

$(T_{ij}+T_{jk}U_{i,k}),_j+\rho B_i=\rho\ddot{U}_i$ where T_{ij}, B_i, U_i, and ρ are respectively the Piola-Kirchhoff stress tensor of the 2nd kind, body force, finite displacement and mass density.

B. Charge equations of electrostatic, and electric field-electric potential relations

$D_{i,i}=0$ where D_i is the electric displacement.

$E_k=-\phi_{,k}$ where E_i and ϕ are the electric field and electric potential respectively.

C. Nonlinear strain-mechanical displacement relations

$$S_{ij}=\tfrac{1}{2}(U_{j,i}+U_{i,j}+U_{k,i}U_{k,j})$$

D. Nonlinear piezoelectric constitutive equations

$$T_{ij}=(C_{ijkl}+\tfrac{1}{2}C_{ijklmn}S_{mn})S_{kl}+\eta_{ijkl}\dot{S}_{kl}-(e_{kij}+e_{kijmn}S_{mn})E_k$$

$$D_i=(e_{ikl}+\tfrac{1}{2}e_{iklmn}S_{mn})S_{kl}+(\varepsilon_{ik}+\tfrac{1}{2}\varepsilon_{ijk}E_j)E_k$$

The nonlinear material constants C_{ijklmn}, e_{iklmn} and ε_{ijk} for lithium niobate are available [5].

III. TIME DOMAIN-FFT ALGORITHM

The time step Δt of the time domain solution was chosen to be sufficiently small $1/2\Delta t > 2f$ so that the fast Fourier transform of the time series would yield a frequency spectrum with the Nyquist frequency greater than the 2nd harmonic, 2*f*, mode. The time length T of solution was chosen to be sufficiently long so that $1/T = \Delta f$ was a frequency resolution sufficiently fine for capturing the modes of vibrations.

A. Time constant

Since we were interested in the steady state nonlinear solution of the SAW IDT resonator, the time length T should be comparable to the time constant of the fundamental SAW mode so that effects of the transient solution were dissipated.

This work was sponsored in part by Qorvo Inc. The views and conclusions contained in this document are those of the authors and should not be interpreted as representing the official policies, either expressly or implied, of Qorvo Inc.

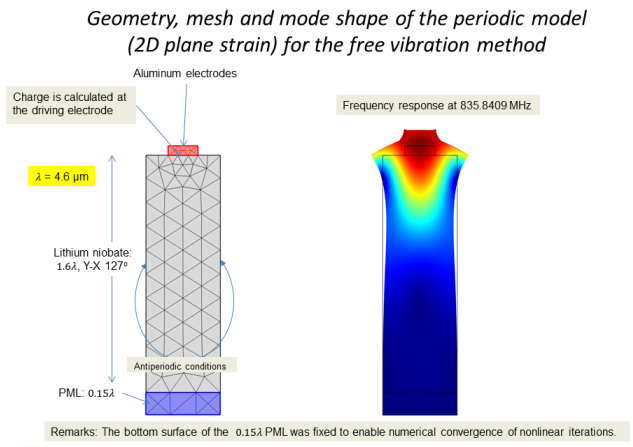


Fig. 1. 2D mesh model of the lithium niobate YX-127° SAW IDT resonator (left), and mode shape of the fundamental SAW mode. (right)

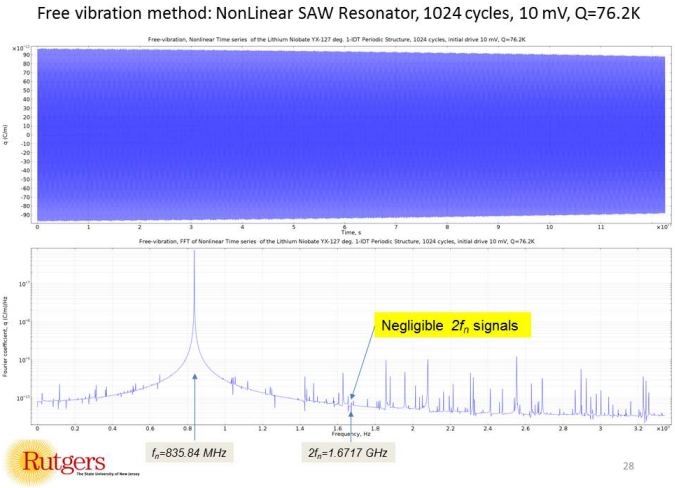


Fig. 2. Nonlinear time series (top) and its FFT (bottom) for a 10 mV *f* voltage drive

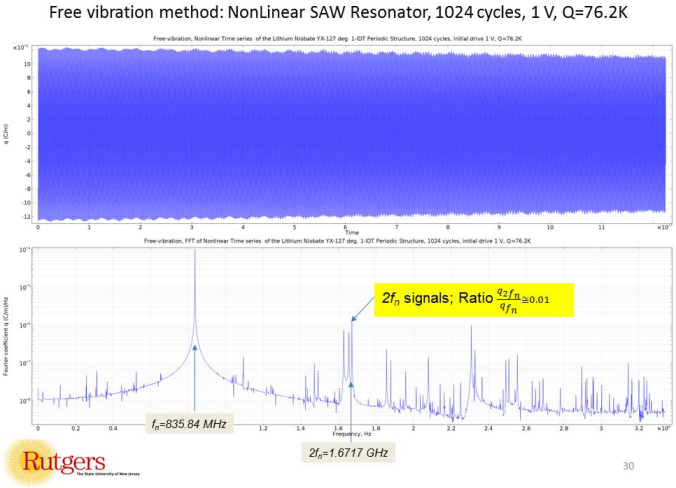


Fig. 3. Nonlinear time series (top) and its FFT (bottom) for a 1 V *f* voltage drive

The time constant $\tau = Q/(\pi f)$ was defined as the time required to reduce the amplitudes of the transient vibrations by a factor of $1/e$. Q was the quality factor of the resonator and f was the resonant frequency of the fundamental mode. The fundamental frequency of our lithium niobate resonator was 835.8409 MHz, and hence for a Q = 76,200, the time constant was 29.0 μs.

B. *Initial conditions for the time domain model*

Since the *f-2f* coupling in a lithium niobate SAW IDT resonator was weakly nonlinear, the frequency response of the linear solution at f was very nearly similar to its nonlinear solution at f. We could greatly minimize the magnitude of the transient solution by using initial conditions that were close to the nonlinear solution at f. Our COMSOL model has three steps: (Step 1) Linear frequency response at the drive voltage to obtain initial conditions for Step 2, (Step 2) free vibration nonlinear time dependent solution using initial conditions obtained from Step 1, and (Step 3) fast Fourier transform of the time series from Step 2 to obtain the frequency spectrum.

IV. Model and Results

We employed a 2D model of a one-electrode IDT SAW resonator as shown in Fig.1 in order to reduce the computation time and memory. The fundamental SAW mode is shown to the right of the mesh model. Figs. 2 and 3 show consecutively the effect of increasing the drive level voltage at f on the $2f$ coupling for 10 mV and 1 V respectively. For each figure, the top graph was the time series, and the bottom graph was the fast Fourier transform of the time series where a $2f$ mode was observed to be generated by the increase in voltage drive at f.

V. Summary

A new nonlinear solution algorithm for the *f-2f* nonlinear coupling phenomenon in SAW IDT resonators was presented. The results showed that the charge on the electrode IDT for the nonlinearly generated $2f$ mode increased with the square of the magnitude voltage drive level at f.

References

[1] "A nonlinear P matrix model to simulate intermodulation products in SAW devices", M. Solal, L. Chen J. Gratier, S. Hester, Proceedings of the 2012 IEEE Ultrasonics Symposium, Dresden, Germany, 2012, pp.62-66, DOI: 10.1109/ULTSYM.2012.0016

[2] "Study on generation mechanisms of second-order nonlinear signals in surface acoustic wave devices and their suppression, Ryo Nakagawa, Takanao Suzuki, Hiroshi Shimizu, Haruki Kyoya, and Ken-ya Hashimoto, Japanese Journal of Applied Physics 54, 07HD12 (2015) http://dx.doi.org/10.7567/JJAP.54.07HD12

[3] "Influence of electrode structure on generation of third-order nonlinearity in surface acoustic wave devices", Ryo Nakagawa, Takanao Suzuki, Hiroshi Shimizu, Haruki Kyoya, and Ken-ya Hashimoto, Japanese Journal of Applied Physics 54, 07HD11 (2015) http://dx.doi.org/10.7567/JJAP.54.07HD11

[4] "Full 2D-FEM calculations of third-order intermodulations in SAW devices", Andreas Mayer, Elena Mayer, Markus Mayer, Philipp J¨ager, Werner Ruile, Ingo Bleyl and Karl Wagner, Ultrasonics Symposium (IUS), 2016 IEEE International **DOI:** 10.1109/ULTSYM.2016.7728469

[5] "Nonlinear, elastic, piezoelectric, electrostrictive, and dielectric constants of lithium niobate", Yasuo Cho and Kazuhiko Yamanouchi, Journal of Applied Physics 61, 875 (1987); doi: 10.1063/1.338138

Buried Wave Devices

Victor Plessky, Julius Koskela
GVR Trade SA
Gorgier, Switzerland
victor.plessky@gmail.com

Bob Hammond
Resonant Inc.
Santa Barbara, CA, USA
bhammond@resonant.com

***Abstract*— A new type of acoustic wave device based on buried waves is proposed. Characteristic to the device is that wave guidance is achieved through the use of heavy metal electrodes buried deep inside a piezoelectric substrate. Such as a structure can be realized, for example, with wafer-wafer bonding techniques. In this work, simulations are used to characterize devices consisting of platinum electrodes buried inside lithium niobate substrate. Simulations imply extremely high coupling coefficient up to 25% and very good quality factor.**

Keywords—Acoustic wave devices; interfacial waves; buried waves; SAW filter; FEM

I. INTRODUCTION

The continuous demand for high-performance acoustic wave devices for mobile telecommunication market has led to the development of highly advanced surface-acoustic wave (SAW) and bulk-acoustic wave (BAW) devices, where approaches such as thin-film technology and advanced packaging are used to optimize losses, thermal stability, and electromechanical coupling coefficient [1-4]. Some specifications, such as for Band 41, demand extremely wide passband of the order of 10% and more which is very difficult to achieve using standard SAW substrates. Alternative can present the "interface waves" [5] when the IDT electrodes are surrounded by piezoelectric material and that increases the coupling. Here we consider a new acoustic wave type, which consists of heavy platinum electrodes buried deep inside a piezoelectric lithium niobate substrate. As localization of the wave is achieved mainly due to mass loading and slowing down of the wave, losses due to radiation of bulk-acoustic waves do not exist for periodic structure. The structure can be considered an interfacial wave device, where both substrates are of the same piezoelectric material; such a structure can be realized, we suppose, with wafer-wafer bonding techniques.

II. SIMULATIONS

Simulations with 2D finite-element method (FEM) [6] are used to characterize a periodic system of platinum electrodes buried inside rotated Y-cut $LiNbO_3$ substrate. The FEM computational mesh for a unit period is shown in Fig. 1. The substrate mesh continues to depth 2.5λ above and below the electrode; 1.0λ thick perfectly matched layers (PML) are used to suppress plate modes. Periodic boundary conditions are applied across the left and right boundary. The Kovacs materials parameters [7] are used for $LiNbO_3$. Platinum electrodes are assumed polycrystalline, and they are modeled as isotropic solid with density 21430 kg/m^3 and Lamé parameters $\lambda = 20.8 \cdot 10^{10}$ N/m^2 and $\mu = 5.6 \cdot 10^{10}$ N/m^2.

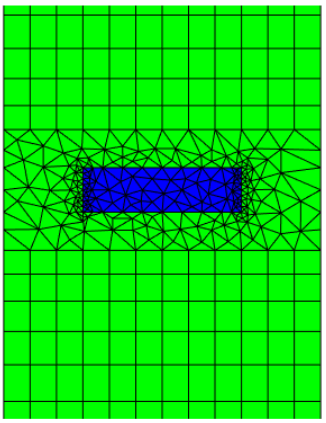


Fig. 1. Platinum (Pt) electrode buried in the bulk lithium niobate; part of FEM simulation mesh for a single period of the structure. The substrate continues across the top and bottom boundary; periodic boundary conditions are applied at the sides.

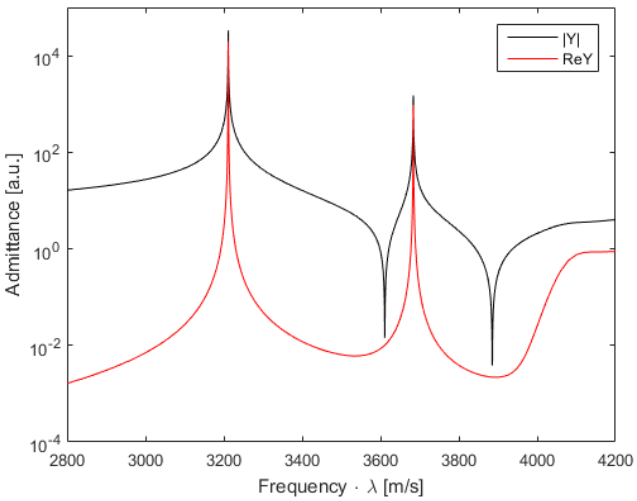


Fig. 2. Platinum thickness $h/\lambda = 7\%$ on 0°YX-cut $LiNbO_3$.

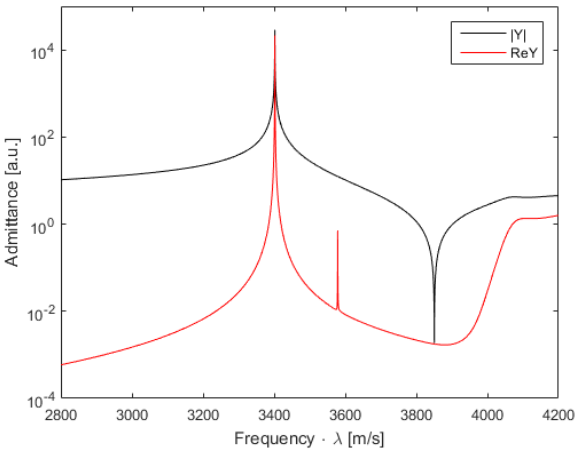


Fig. 3. Platinum thickness h/λ= 7% on 37°YX-cut $LiNbO_3$.

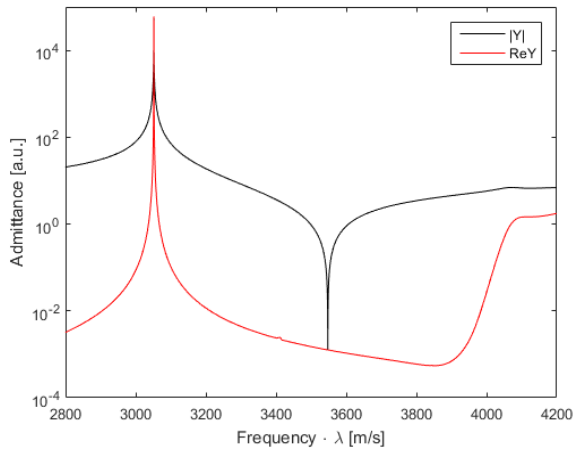


Fig. 4. Platinum thickness h/λ= 10% on 26°YX-cut $LiNbO_3$.

Figure 2 shows the harmonic admittance for 0°YX-cut $LiNbO_3$ with platinum thickness h/λ= 7%. The simulation reveals two resonances. The lower-frequency resonance has dominantly shear-horizontal polarization, whereas in the higher-frequency mode the dominant polarization is shear vertical. Both resonances have high Q-factor, shear-horizontal mode being better.

The higher-frequency mode can be suppressed by changing the cut angle. Fig. 3 shows the simulation for 37°YX-cut. The resonance-antiresonance distance of the main mode is about 448 m/s, corresponding roughly to coupling factor $k^2 \approx 25\%$.

For higher electrode thickness the situation is similar, but the cut angle must be optimized to suppress the higher-frequency mode. Figure 4 shows the simulation for h/λ= 10% electrodes on 26°YX-cut. The resonance-antiresonance distance is further slightly increased.

III. CONCLUSIONS

Simulated results are presented for a buried wave structure, where the localization of the acoustic waves is achieved with heavy platinum electrodes buried deep inside Y-cut lithium niobate substrate. To our knowledge this is the first time such a structure is reported. Such a buried wave device can have extremely high coupling coefficient and very good Q-factor. The crystal cut and the relative electrode thickness can be controlled to optimize the coupling factor.

Devices based from such structures could be used for filter design with relative bandwidths up to 10%-13%. Complete ladder filter could be buried. Such a filter needs no package.

A single resonator could also be suitable for sensor application, for example measurement of human body temperature. The antenna could be incorporated inside the substrate. Such a sensor would need no packaging or require external contacts.

REFERENCES

[1] T. Bauer, C. Eggs, K. Wagner, and P. Hagn, "A bright outlook for acoustic filtering: a new generation of low-profile SAW, TC SAW, and BAW devices for module integration", *IEEE Microw. Mag.*, vol. 16, no. 7, pp. 73-81, Aug. 2015.

[2] M. Miura, T. Nishizawa, T. Takahashi, O. Kawachi, S. Matsuda, T. Matsuda, M. Ueda, Y. Satoh, "Band3 duplexer using zero TCF Love wave device", in *2012 IEEE Ultrasonics Symposium*, Oct. 2012.

[3] B. Abbott, R. Aigner, A. Chen, K. Gamble, T. Kook, J. Kuypers, M. Solal, and K. Steiner, "High Q TCSAW", in *Sixth International Symposium on Acoustic Wave Devices for Future Mobile Communication Systems*, Chiba University, Japan, 2015.

[4] T. Takai, H. Iwamoto, Y. Takamine, H. Yamazaki, T. Fuyutsume, H. Kyoya, T. Nakao, H. Kando, M. Hiramoto, T. Toi, M. Koshino, and N. Nakajima, "Incredible high performance SAW resonator on novel multi-layered substrate", in *2016 IEEE International Ultrasonics Symposium,* Tours, France, 2016.J. Clerk Maxwell, A Treatise on Electricity and Magnetism, 3rd ed., vol. 2. Oxford: Clarendon, 1892, pp.68–73.

[5] V. Grigorievski, V. Plessky, and A. Grigorievskiy. "Interface Leaky Longitudinal Waves in Lithium Niobate and Lithium Tantalate." In 2007Ultrasonics Symposium , 2007. IEEE. pp. 1897-1900.

[6] J. Koskela, P. Maniadis, B.A.Willemsen, P.J.Turner, R.B.Hammond, N.O.Fenzi, and V. Plessky, "Hierarchical cascading in 2D FEM simulation of finite SAW devices with periodic block structure", in *2016 IEEE International Ultrasonics Symposium, 2016*.

[7] G. Kovacs, M. Anhorn, H. E. Engan, G. Visintini, and C. C. W. Ruppel, "Improved material constants for LiNbO3 and LiTaO3", Proc. 1990 IEEEE Ultrasonics Symp., pp. 435-438, 1990.

Periodically Poled $LiNbO_3$ transducer on (YX*l*)/128° cut for RF applications

Alexandre MATIC, Thomas BARON
Time-Frequency Dept.
FEMTO-ST, UBFC, UMR-CNRS 6174, ENSMM
26, chemin de l'Epitaphe, Besançon, FRANCE
alexandre.matic@femto-st.fr, thomas.baron@femto-st.fr

Florent BASSIGNOT
Femto-Engineering
15B, avenue des Montboucons, Besançon, FRANCE
florent.bassignot@femto-st.fr

Abstract* — *Previous studies have shown Periodically Poled Lithium Niobate structures on Z-cut $LiNbO_3$ could be used as acoustic transducers to generate acoustic waves. Investigations on Periodically Poled $LiNbO_3$ (YXl)/128° transducers have been conducted. Simulations have pointed out interesting electromechanical coupling from such transducers. Fabrication of Periodically Poled (YXl)/128° $LiNbO_3$ transducers bonded/thinned on Silicon is presented and confirm the possibilities of rotated cuts poling for new transducers.

Keywords* — *Periodically Poled Lithium Niobate, acousto-electric transducer, rotated cut, radio-frequency.

I. INTRODUCTION

Ferroelectric properties of Lithium Niobate ($LiNbO_3$) have been actively studied for almost 60 years due to excellent optical properties of this material. In 1980, Feng *et al*. have successfully realized a Periodically Poled Lithium Niobate (PPLN) device for optical purposes [1], consisting of Lithium Niobate domains with periodic reversal of its orientation. In late 90s – early 00s, it has been shown PPLN devices on Z-cut $LiNbO_3$ can be used as acoustic transducers; studies have been made on Z-cut to determine acoustic properties of these devices and to discuss about possible applications of PPLN acoustic devices [2]–[4]. Studies have demonstrated interesting properties of PPLN-based acoustic compared to standard SAW ones such as the robustness of the excitation versus defects or surface contamination, the opportunity to excite fundamental waves exhibiting an operating frequency twice as high for a same spatial period, and the possibility to excite waves of various polarizations. A functional acoustic resonator based on bulk and bonded/thinned Z-cut PPLN transducers operating at 131MHz have been demonstrated [5].

Nevertheless, actual state of art on Z-cut PPLN devices highlights low electromechanical coupling factors ($k^2 < 1\%$) and small quality factors (Q = 300-500) [6]. Ridge-shaped periodically poled acoustic transducers on Z-cut $LiNbO_3$ exhibits high coupling factors higher than 20% [7], but their performances are strongly dependent of edges verticality, and obtaining perfectly vertical ridges are a strong technological challenge.

As state of art on PPLN acoustic devices is limited to Z-cut Lithium Niobate, is it possible to get better figures of merit (k^2, Q factors) by using a different (YX*l*)/θ cut of Lithium Niobate?

In this paper, we actively studied a (YX*l*)/128° Lithium Niobate device bonded/thinned on Silicon; a schematic view of this structure is given by Fig.1. P is the acoustic period of the device, λ is the spatial period of the PPLN.

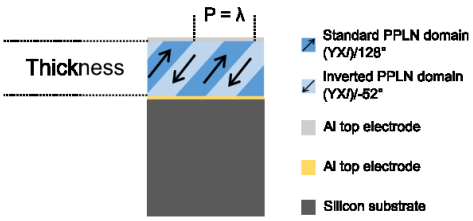


Fig. 1. Schematic profile view of a (YX*l*)/θ PPLN device bonded on Silicon

First of all, main acoustic properties from this device are identified through numerical simulations. Then, realization of (YX*l*)/128° Lithium Niobate bonded/thinned on Silicon resonators is described. Finally, electrical characterization of are made on two different resonators for validation of simulation results and extensive studies of experimental figures of merit of such devices.

II. NUMERICAL SIMULATIONS ON LITHIUM NIOBATE ROTATED CUTS

Numerical simulations have been made using a finite element/boundary integral method approach to compute harmonic admittance of PPLN device based on 45µm thick (YX*l*)/128° Lithium Niobate poled and bonded/thinned on Silicon. Simulation results on this device are given by Fig.2.

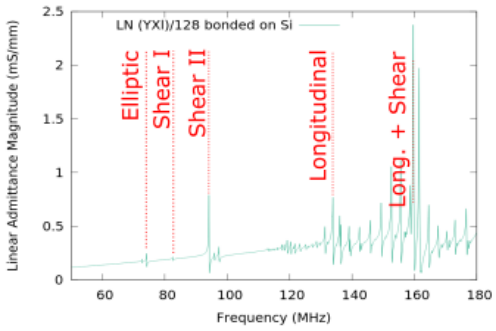


Fig. 2. Simulation on bonded/thinned Lithium Niobate (YX*l*)/*128*° at 45µm thickness and 50µm acoustic period. Modes listed in Table I are reported.

Simulation has been conducted on a 45µm thick Lithium Niobate (YX*l*)/*128°* cut bonded/thinned on silicon where the acoustic period is 50µm. Periodical boundary conditions have been considered on left and right side of our structure, while Dirichlet electric boundary conditions have been imposed on top (1 mV) and bottom (GND) side. Calculations are made considering a 1mm-width (along Y-axis) PPLN.

Numerical simulations have pointed out 5 different waves: an elliptic wave, a longitudinal wave and two shear waves and a longitudinal-shear wave. Pictures of some of these modes taken from numerical simulations can be seen on Fig.3.

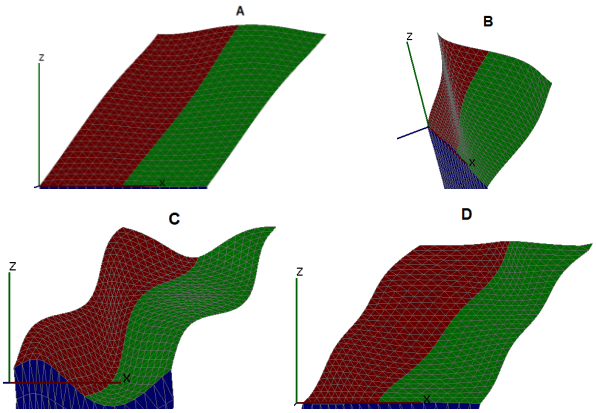


Fig. 3. Illustration of elliptic mode (**A**), shear-transverse mode (**B**), shear mode (**C**) and longitudinal modes (**D**) seen through numerical simulations

Dispersive effects can be observed between 120MHz and 200MHz, where the main longitudinal peaks are spitted into multiple peaks. Propagation through Silicon of these modes can be observed from numerical simulations, explaining such behavior on bonded devices. Results compilation and results on similar structure on Z-cut Lithium Niobate as comparison are given by Table I. As for longitudinal multiple modes, we only have reported the 2 most relevant peaks.

TABLE I. SIMULATED RESULTS ON (YX*L*)/128° AND Z-CUT PPLN BONDED ON SILICON

Structure	**Wave properties**		
	Mode behavior	***Velocity (m.s^{-1})***	***Coupling factor (%)***
45µm-thick $LiNbO_3$ (YX*l*)/*128°* on Si	Elliptic	3710	0.2
	Shear I (Transverse)	4120	0.15
	Shear II	4700	0.42
	Longitudinal	6700	0.31
	Longitudinal + Shear	7980	0.71
45µm-thick $LiNbO_3$ Z-cut on Si	Elliptic	3790	0.6
	Shear (Transverse)	4750	0.52
	Longitudinal	7860	0.23

It can be observed some similar modes can be both found in Z-cut and (YX*l*)/*128°* devices, but some other ones are only appearing on (YX*l*)/*128°* cut. Coupling factor of the elliptic wave is better on Z-cut, while longitudinal wave has a better coupling factor on (YX*l*)/*128°* cut.

III. FABRICATION OF PERIODICALLY POLED TRANSDUCERS ON (YXL)/128° LITHIUM NIOBATE

Domain reversal is made by applying a strong electric field to the material, which must be greater than coercive field of this material, equal to 21kV/mm for Z-cut congruent $LiNbO_3$. Common poling processes uses liquid electrolytes as electrodes and a photoresist mask to design periodically poled structures on the material, which allows to reach high voltage with reduced electric discharge issues [8].

Although, intrinsic properties of $LiNbO_3$ only allows orientation reversal along Z-axis of the material. Therefore, reverted domains will get tilted with an angle equal to the θ orientation of the material and coercive field will increase. The following formula then gives the coercive field according to the cut angle:

$$E_c(\theta) = E_c(\theta = 90°) / \cos(\theta - 90°) \quad (1)$$

For highly rotated cuts, poling process can become challenging as discharges will more likely happen at higher voltage. For this reason, poling on a 45µm thick (YX*l*)/128° bonded on Silicon has been investigated, as this cut is a good compromise between rise of acoustic performances and rise of coercive field, while the use of bonding/thinning technique allows to achieve very thin Lithium Niobate layers.

Bonding/thinning technique have been used for reducing thickness of a (YX*l*)/*128°* $LiNbO_3$ wafer to 45µm, using a process already validated for Z-cut $LiNbO_3$ PPLN with standard microfabrication processes such as photolithography for domain definition on photoresist mask and sputtering for electrode deposition [5]. Silicon back side is not polished to avoid bulk acoustic waves.



Fig. 4. Top Optical Microscope view and profile SEM picture of Periodically Poled Lithium Niobate Structures on (YX*l*)*128°* $LiNbO_3$ reported on Silicon wafer, with a 50µm period and 45 µm thickness

Fig.4 shows a successful on 45µm thick (YX*l*)/*128°* LiNbO3 wafer which has been bonded on Silicon wafer.

Tilting of inverted domains by the θ orientation of the material is observed. Similar period can be observed between profile SEM view and top optical microscope view.

Aluminum electrodes of two different dimensions (chip #1: 0.5 mm (*W*) x 2 mm (*L*) and chip #2: 2 mm (*W*) x 0.5 mm (*L*)) have been deposited on our devices to create resonators for characterization of our transducers. *W* and *L* correspond respectively to width and length of the electrode.

IV. Electrical Characterization of PPLN Transducers on (YXl)/128° Lithium Niobate

Characterizations have been made using a ZNB 8 Rohde-Schwarz Vector Network Analyzer with 500µm-gap GS Probe from Cascade Microtech. Results are given in terms of admittance and S-parameters for Chip #1 are given by Fig.5.

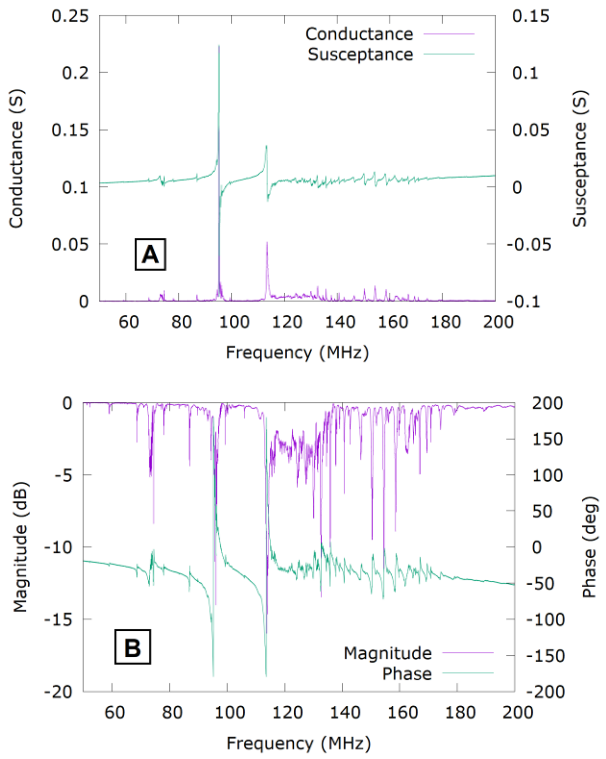


Fig. 5. Electrical characterizations of Chip #1 Lithium Niobate (YX*l*)/*128*° cut in terms of Admittance (A) and S-parameters (B)

Four different modes can be identified from both devices characterizations at 74.5, 86.8, 95.2 and 113.4MHz; the three first ones have been reported from simulations while 113.4MHz mode hasn't clearly been observed from simulations on bonded/thinned Lithium Niobate (YX*l*)/*128*° cut. Moreover, multiple peaks from 120 to 180MHz can also be observed from these electrical characterizations. Figures of merit associated to these modes is reported in Table II.

Comparison between theoretical results obtained from simulation (Table I) and experimental results of chip #1 (Table II) shows relative good correlation in terms of coupling factor for the elliptic mode (Fig.3A) at 74.4MHz (0.2% versus 0.25%) and Transverse-Shear I mode at 86.8MHz (0.15% versus 0.15%). Difference can be observed for chip #2. This difference can be due to the length of electrode and the number of periods of the device. Only ten periods are used on chip #2, while the simulation considers infinite number of periods.

TABLE II. Experimental results on bonded (YX*l*)\128° $LiNbO_3$

Structure	Wave properties			
	Frequency (MHz)	***Mode velocity ($m.s^{-1}$)***	***Q factor***	***Coupling factor (%)***
Chip 1	74.4	3720	1160	0.25
	86.8	4340	960	0.15
	95.2	4760	940	6.3
	113.4	5670	200	4
Chip 2	74.6	3730	3400	0.05
	86.8	4340	3100	0.05
	94.2	4710	< 50	8.3
	113.6	5680	< 50	3.4

Shear mode II at 95.2MHz shows a much higher coupling factor than expected. On the simulation, three sub-modes appear, while on experimental result only one exists.

One interface mode appear clearly at 113.4MHz on electrical measurements. On our simulation this mode exists, but presents low amplitude compare to other modes.

Finally, it appears bulk acoustic waves take place as expected between 120 and 180MHz. Amplitudes are much lower than simulation ones due to the roughness of the Silicon back side.

Coupling factor for modes at 95.2 and 113.4MHz are unprecedented on planar Z-cut PPLN devices, while ridge PPLN structures have reported very high coupling factor but with very poor *Q* factor [7]. These results shows the possibility of increasing the coupling factor when using Lithium Niobate rotated cuts with higher *Q* factor than ridge PPLN structures.

V. Conclusion

Numerical simulations have shown interesting results for coupling factor which is improved for some modes on Lithium Niobate (YX*l*)/*128*°.

Experimental poling of a (YX*l*)/128° $LiNbO_3$ using bonding/thinning technique has been achieved. Electric characterizations of resonators done on a Lithium Niobate (YX*l*)/*128*° cut bonded/thinned on Silicon have demonstrated a 6% coupling factor at 95MHz with a *Q* factor of 940.

These results give promising expectations for devices using rotated cut transducers of bulk and bonded/thinned Lithium Niobate. Filtering or wireless interrogation sensors applications could be addressed by such devices.

Transducers done on bulk material could bring smoother acoustic response and avoid wave dispersion, but it still represents a technological challenge due to coercive field rising. Other Lithium Niobate standard cut, such as (YX*l*)/*36*°

or *64°,* could also be explored for realization of PPLN devices to study wave behavior and evolution of figures of merit.

ACKNOWLEDGMENTS

This work has been developed under the support of the FEDER Research Grant No. FC0001257-11002 with SMART-INN project.

This work was also partly supported by the French RENATECH network and its FEMTO-ST technological facility.

REFERENCES

[1] D. Feng *et al.*, "Enhancement of second-harmonic generation in LiNbO3 crystals with periodic laminar ferroelectric domains," *Appl. Phys. Lett.*, vol. 37, no. 7, p. 607, Jul. 1980.

[2] S. Ballandras *et al.*, "A novel surface wave transducer based on periodically poled piezoelectric domain," in *IEEE International Frequency Control Sympposium and PDA Exhibition Jointly with the 17th European Frequency and Time Forum, 2003. Proceedings of the 2003*, pp. 893–896.

[3] A. K. Sarin Kumar *et al.*, "High-frequency surface acoustic wave device based on thin-film piezoelectric interdigital transducers," *Appl. Phys. Lett.*, vol. 85, no. 10, p. 1757, Sep. 2004.

[4] E. Courjon *et al.*, "Lamb wave transducers built on periodically poled Z-cut LiNbO3 wafers," *J. Appl. Phys.*, vol. 102, no. 11, p. 114107, Dec. 2007.

[5] F. Bassignot, E. Courjon, G. Ulliac, S. Ballandras, J. M. Lesage, and R. Petit, "Acoustic resonator based on periodically poled transducers: Fabrication and characterization," *J. Appl. Phys.*, vol. 112, no. 7, p. 74108, 2012.

[6] F. Bassignot, E. Courjon, G. Ulliac, S. Ballandras, J.-M. Lesage, and R. Petit, "Acoustic resonator based on periodically poled transducers: Concept and analysis," *J. Appl. Phys.*, vol. 111, no. 6, p. 64106, Mar. 2012.

[7] F. Henrot, F. Bassignot, J. Rauch, G. Ulliac, and S. Ballandras, "Ridge-shaped periodically poled transducer for wide band R- F filter," in *EFTF 2014*, 2014.

[8] M. Yamada, N. Nada, M. Saitoh, and K. Watanabe, "First-order quasi-phase matched LiNbO3 waveguide periodically poled by applying an external field for efficient blue second-harmonic generation," *Appl. Phys. Lett.*, vol. 62, no. 5, p. 435, Feb. 1993.

DRIE of high Q-factor length-extensional mode quartz micro-resonator

Paul Chapellier, Béatrice Verlhac, Pierre Lavenus
dept. DPhIEE/CMT
ONERA, The French Aerospace Lab
Châtillon, FRANCE

Bernard Dulmet
ENSMM
FEMTO-ST
Besançon, FRANCE

***Abstract*— A two dimensional (2D) length-extensional mode quartz micro-resonator has been designed and patented by ONERA. Thanks to a specific decoupling, this resonator is expected to show a very high Quality factor × Frequency product (Q.f) near the theoretical limit of 3.10^{13}. This design offers a range of frequencies between 1 MHz up to 10 MHz, thanks to homothetic geometries with thickness ranging from 210 to 30 µm. These very good characteristics and the small dimensions (final package is foreseen to be less than 10 mm^3) as well as the intrinsic qualities of quartz (high quality factor, piezoelectricity and good thermal stability) make this resonator capable of outperforming the MEMS silicon resonators of comparable size with performances comparable to Ultra Stable Oscillators.**

Nevertheless, the small dimensions at stake to achieve higher frequencies devices require specific manufacturing processes, such as Deep Reactive ion Etching of Quartz (DRIE). This paper focuses on the presentation of two proposed fabrication processes using Deep Reactive Ion Etching of quartz. It brings out critical factors for practical realizations and highlights the design adaptations necessary to enable the etching for depth comprised between 30 and 210 µm and to promote vertical etching walls. First realizations and characterizations are also reported.

Keywords—Quartz; resonator; DRIE; Time & Frequency; Ultra Stable Oscillators

I. INTRODUCTION

ONERA designed a 2D quartz resonator illustrated in Fig. 1 a) inspired by a previous quartz resonator developed to reach quantum ground state [1]. The vibration mode of interest is presented in Fig. 1 b) and c).

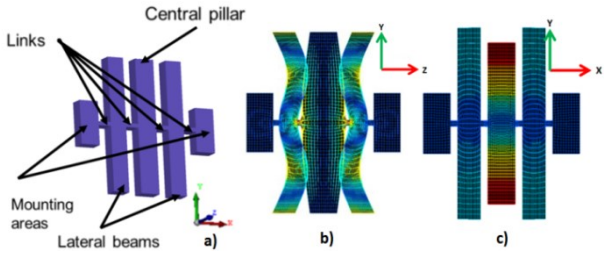


Fig. 1. a) sketch of the resonator; b) the X component of the magnified deformation showing the flexion in lateral beams; c) the Y predominant component of the deformation showing the out-of-phase length extension of pillar and lateral beams.

This new design was the object of thorough theoretical studies [3] and is expected to show a Q.f higher than 10^{13} which is very near the theoretical limit for quartz of 3.10^{13} [2] . Its small dimensions open the possibility of manufacturing this component at a wafer scale; making it a potential competitor to MEMS silicon based oscillators with better performances, in terms of noise and temperature sensitivity. The challenging part of the practical realization is to obtain deep etched depth from 30 to 210 µm with sidewalls as vertical as possible to ensure the best Q_{anchor}, defined as the ratio of the total strain energy and the energy lost in the mounting areas. Standard wet chemical etching is inadequate due to its high anisotropy [4]. DRIE of quartz was made possible thanks to the development of etching equipment with high density plasma but is not as mature as that of silicon.

II. PROCESS FLOW

An interesting feature of the resonator depicted in Fig. 1 is that its resonant frequency is inversely proportional to the length of the resonator as far as the whole geometry of the resonator is modified by a homothetic transformation to ensure the best decoupling. This can be used to adapt the resonant frequency of the 2D resonator for specific targeted applications. Two processes have been developed to fabricate the 2D resonators depending on their thickness.

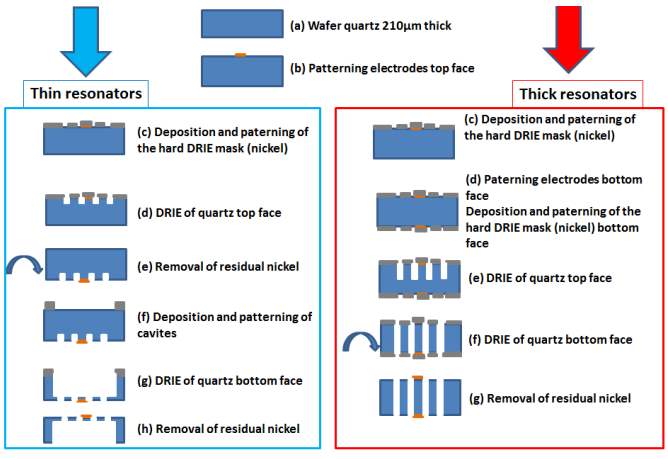


Fig. 2. Fabrication processes considered of the 2D resonator, on the left for the thinner ones, on the right for the thicker ones.

Wafers as thin as the thinner resonators (30 to 120 µm, 9.00 to 2.25 MHz) would be too fragile to be safely handled. Thus a process involving cavities machined in a thicker wafer has been considered (Fig. 2). However, for 120 µm up to 210 µm thick resonators (2.25 to 1.28 MHz) a quartz wafer as thick as the resonator is used and the DRIE is carried out on both sides to prevent an excessive decrease of the etch rate induced by high aspect ratio structure

III. Preliminary Experimental Results and Impact on the Expected Performances

A. Impact of ARDE

During the etching of resonators from the first generation design Fig. 3 a), it appeared that the trenches between the beams were etched at a slower rate that the others areas.

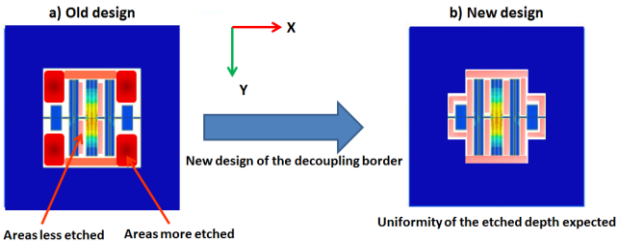


Fig. 3. a) old design of the decoupling border, b) new one.

The phenomenon is well known in the case of silicon and is called Aspect Ratio Dependent Etching (ARDE) which results in a decrease in the etching rate with the decrease in the apertures of the patterns. In our case, our observations have been successfully explained using the Knudsen model [5]. This is illustrated in Fig. 4, which shows the characteristic Apparent Etching rate versus lateral dimensions of the patterns for our DRIE process.

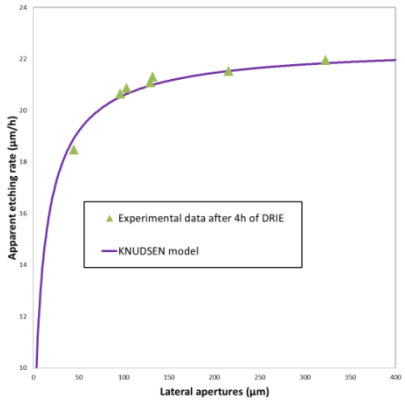


Fig. 4. Apparent etching rate versus lateral apertures of patterns after 4 etching hours and associated Knudsen model.

This suggests that a significant depletion of reactive plasma species (radicals) occurs at the bottom of the trenches, due to their random diffusion and partial sticking on the side-walls. The design of the resonator has been improved to take into account the ARDE phenomenon by unifying the final aspect ratio within the whole device (ratio of the etched depth over the aperture of the pattern) as shown in Fig. 3 b).

B. Impact of the edge profile

The profile of the edge is an important factor to ensure a high quality factor. However perfect sidewall verticality cannot be obtained with DRIE at the moment. Typical edges obtained with our DRIE process are about 87 to 89° as illustrated in Fig. 5.

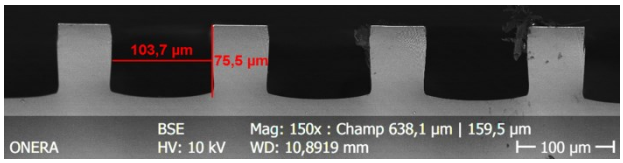


Fig. 5. Profil of trenches obtained after 3.5 hours of quartz DRIE

Finite elements simulations have been performed to estimate the impact of this angle on the quality factor and are shown in Fig. 6.

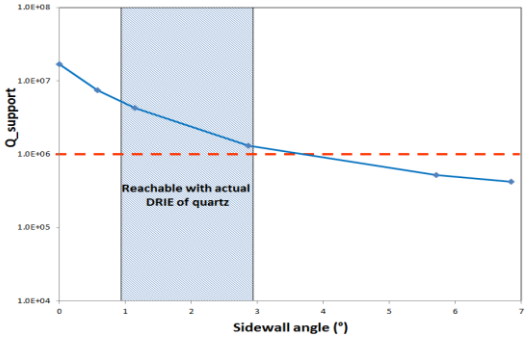


Fig. 6. Finite elements simulations of the characteristic $Q_{support}$ versus sidewall angle.

As expected, simulations predict a quick decrease of the quality factor as soon as the sidewall angle gets away from perfect verticality. With our actual DRIE of quartz process factor quality as high as 10^6 and Q.f product near 10^{13} can be expected. Further investigations must be done to improve the verticality of the profile, especially for the longer etching times.

IV. Resonator Fabrication

90 µm thick resonators have been manufactured using the thin resonator process with cavities. Gold electrodes are patterned, and then a thick layer of 3.0 µm sputtered nickel is deposited to make the hard mask. After a first etching step of 100 µm with the device patterns, wafer is flipped. A nickel layer is patterned to define cavities and DRIE of the cavities is performed to achieve the desired thickness of 90 µm. A device fabricated with this process is shown in Fig. 7. One should note that the design of the resonators differs slightly from the one presented in introduction but uses almost the same length extensional vibration mode. Similar quality factors are expected according to simulations. Resonators collectively etched with different lateral dimensions are illustrated in Fig. 8

and a tilted focused view of a 3.0 MHz resonator is presented in Fig. 9.

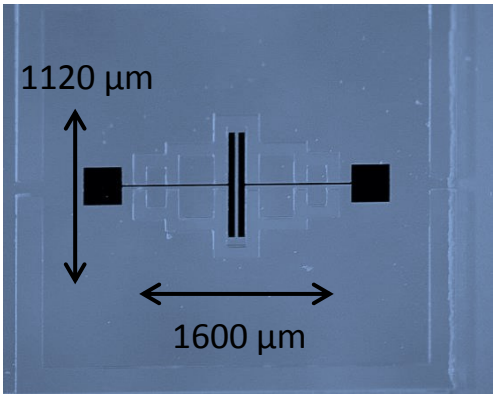


Fig. 7. Example of a 3.0 MHz resonator etched with the thin resonators process.

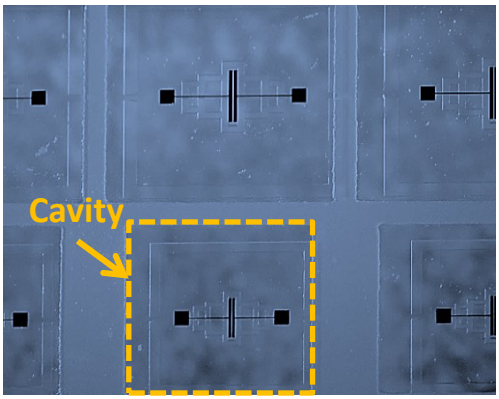


Fig. 8. Collective etching of resonators using thin resonator process. Top line: 2.25 MHz resonators, bottom line: 3.0 MHz resonators.

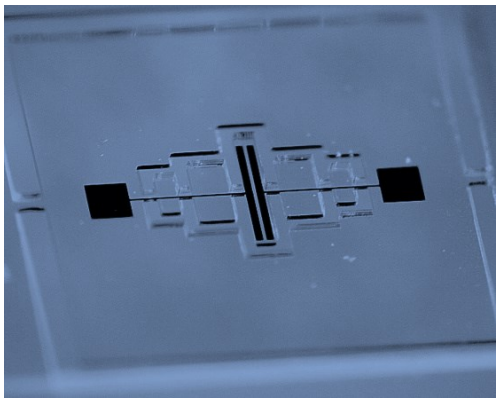


Fig. 9. Tilted view of a 3.0 MHz resonator.

On the backside of some resonators it remains some residual quartz at the links due to the bottling of the etching on the first step.

V. Resonator Characterizations

First characterizations of the resonator have been performed to measure the quality factor Q, the resonant frequency f and electrical parameters from the Butterworth Van Dyke (BVD) model (Fig. 10) for air pressure and under vacuum. Under 1 mbar the pressure threshold under which the losses due to air damping are neglected is reached.

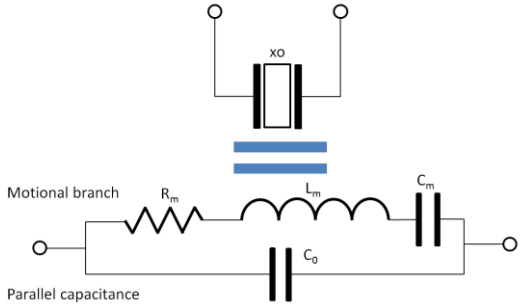


Fig. 10. Equivalent electrical circuit of the crystal resonator with BVD model.

Electrical equivalent variables are given in table 1 for air pressure and under vacuum for a 3.0 MHZ resonator.

Table 1 Equivalent electrical parameters of a 3.0 MHz resonator from measurements and simulations.

	Measurements		Simulated
P (mbar)	1013	1	0
R_m (kOhms)	139	11	1
C_m (aF)	57	56	-
L_m (H)	50	52	-
f_{res} (Hz)	**2 954 694**	**2 954 066**	**2 971 658**
Q	6750	**94 000**	**1 000 000** [6]

A resonant frequency of 2.956 MHz has been found under vacuum compared to the 2.971 MHz expected from the Finite Element Modelisation, a relative difference of less than 1%.

The quality factor Q goes from less than 7 000 under atmospheric pressure to almost 100 000 under vacuum, leading to a Q.f value (figure of merit of resonators for time frequency application) close to 3.1011, which is less than predicted by the simulations but near from the Q.f of some silicon based oscillators. The simulations took into account the anchor quality factor (expected to be as high as several millions [6]) as well as the viscous dissipation from the gold electrodes which would limit the overall quality factor of the resonator to a value around 1 000 000 making possible to reach a Q.f product of 1.10^{13} for higher frequencies and smaller resonators.

There are two possible reasons for the decrease of the Q factor. First, the defects in the geometry such as non-vertical sidewall and residual quartz between the links as it can be seen on the Fig.11, could limit the decoupling between the central and lateral beams and the decoupling structure. Also, on the back side, some micro-masking is present due to the absence of patterns of the resonators (black dots on Fig. 11) and could lead to a loss of symmetry and degrades the quality factor.

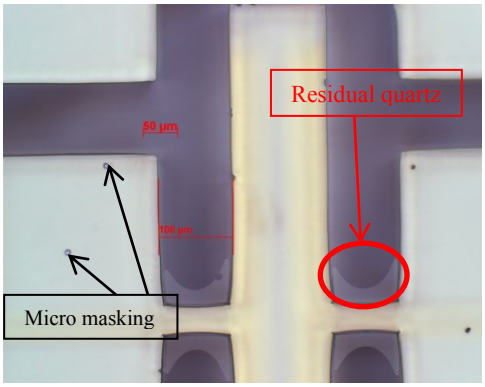


Fig. 11. Optical microscopy of the backside of a 3.0 MHz resonator, micro masking and residual quartz can be seen between the links.

Then the viscosity losses coming from the electrodes may have been theoretically underestimated because of the presence of residual surface contaminants probably oxide nickel which has not been totally removed during the cleaning steps. These possible two reasons need further investigations.

VI. Conclusion

Two processes have been developed in sight of the realization at a wafer level of 2D resonators for time & frequency applications. Improvement of the design was made to take into account the limitations of the actual process. Resonators using DRIE on both sides have been realized and first characterizations have been performed validating one of the processes and giving perspectives for process improvement. The proposed and validated process is particularly promising because it makes possible the choice of any quartz cut for the realization of resonators. This could make possible to choose quartz cuts with very low thermal sensitivity without the need of compensating layers. Further work will include phase noise and temperature stability of the resonator characterizations and integrating the resonator to a fully operational oscillator.

Acknowledgments

This work is founded by ONERA and CNES.

References

[1] M. Bahriz *et al.*, “A micromechanical resonator to reach the quantum regime,” *Proc. IEEE Sensors*, pp. 1991–1995, 2010.

[2] S. Ghaffari *et al.*, “Quantum limit of quality factor in silicon micro and nano mechanical resonators.,” *Sci. Rep.*, vol. 3, p. 3244, 2013.

[3] B. Bourgeteau *et al.*, “Quartz resonator for MEMS oscillator,” *2014 Eur. Freq. Time Forum, EFTF 2014*, pp. 286–289, 2015.

[4] R. Pelle, H. Christer, V. K. Ilia, and B. Ylva, “Etch rates of crystallographic planes in Z -cut quartz - experiments and simulation,” *J. Micromechanics Microengineering*, vol. 8, no. 1, p. 1, 1998.

[5] A. N. B. J.M.F.Zachariasse, “The dependence of nanostructure etch rates on feature size,” *Microelectron. Eng.*, vol. 30, pp. 349–352, 1996.

[6] B. Bourgeteau-Verlhac, R. Lévy, T. Perrier, P. Lavenus, J. Guérard, and O. Le Traon, “Gold Thin Film Viscoelastic Losses of a Length Extension Mode Resonator.”

[7] B. Bourgeteau, R. Levy, P. Lavenus, and O. Le Traon, “Multiphysical finite element modeling of a quartz micro-resonator thermal sensitivity,” *Symp. Des. Test, Integr. Packag. MEMS/MOEMS, DTIP 2015*, 2015.

Extraordinary OCXO solutions based on the IHR technology

Igor Abramzon, Vadim Tapkov, Alexey Kornilov
Magic Xtal Ltd.
Omsk, Russia
mxl@mxtal.ru

***Abstract*—The present paper reviews recent achievements in the Internally Heated Resonator (IHR) technology which has resulted in creation of advanced OCXO devices possessing extraordinary combination of performances.**

I. INTRODUCTION.

The IHR technology utilizes miniature oven control structure integrated with the crystal plate inside the TO-8 vacuum holder. Heating of only the crystal plate and excellent thermo-insulation from environment ensure very low power consumption and fast warming up of the OCXO as compared with the oscillators based on conventional external oven control concept. At the same time, extremely small sizes of the internal oven cause difficulty of uniform heating the crystal plate that makes for arising the thermal gradients contributing essential instability of the IHR frequency. Another constructive feature of the IHR oscillator (IHRO), arrangement of the sustaining circuitry outside the heated oven volume, makes its temperature sensitivity a serious source of frequency instability of the OCXO considerably exceeding this factor at the conventional oven designs. Thus, to provide radical reduction of frequency instability of the IHRO both shortcomings of its constructive concept should be overcome. The paper describes implementation of advanced techniques in the IHRO construction and circuitry which have enabled significant increase of their temperature frequency stability - to the level of the best conventional OCXO designs.

The long-term stability (aging) of a crystal resonator to a great extent depends on vacuum degree in its vacuum volume. For the IHR design sealed in miniature TO-8 holder and containing at the operation temperature various electronic and constructive materials preserving of perfect vacuum conditions during the OCXO lifetime is a serious problem. The paper presents long-time aging behavior of modern IHROs confirming low aging rate which earlier was a property only of high stability conventional OCXOs using ordinary crystal construction.

The short-term frequency stability (STS) of most OCXO designs at more than 1 s average time is noticeably influenced by thermal fluctuations of the oven control system. This influence becomes more evident in the IHRO designs for very low thermal inertia of the integrated oven and its strong thermal coupling with the crystal plate. The paper shows results of optimization of the internal oven and circuitry that has enabled for the IHR oscillator as low as $1x10^{-12}$/1s Allan variance combined with its utmost temperature stability.

Very low power consumption is most extraordinary property the IHROs providing them most important advantage over conventional OCXO concept. The paper displays ultimate figures of the power consumption of the developed IHRO designs measured for different ambient temperature ranges.

Short warm-up of the IHRO designs provides them another significant superiority over traditional OCXOs. The paper depicts warming-up processes of the indirect and direct heated IHR versions resuming the latter provide extremely fast warming-up combined with high temperature stability and STS.

Moreover there are considered in the work the ultra-durable and low g-sensitivity versions of the IHR designs providing operation of the OCXOs under severe mechanical shocks and vibration at high temperature stability, low power consumption and minimal degradation of the phase-noise level.

In conclusion the paper summarizes the basic performances of the new generation IHROs resuming the extraordinary combination of the characteristics makes the devices state-of-the-art solution for a frequency control and timing of various modern equipment.

II. CONSTRUCTION FEATURES OF THE IHROS AND ITS TEMPERATURE STABILITY.

Basic concept of modern IHR depicted schematically in Fig.1 was developed more than 10 year ago [1]. It contains inside the TO-8 vacuum holder the crystal plate with the film electrodes mounted on the ceramic substrate which bears the whole thermo-control circuitry and the metal screen covering the plate for better radiation insulation. The substrate, in turn, is fixed on the supporting mechanical structure which provides both thermal isolation of the internal oven from environment and proper mechanical durability of the construction. Excellent thermal isolation of the internal oven by deep vacuum degree inside the TO-8 holder and low thermal conductivity of the supporting structure ensure very small thermal losses resulting in extremely low power consumption of the IHR, about a tenth of the conventional OCXO consumption.

A structure of the OCXO based on the IHR concept is outlined in Fig. 2. In difference from traditional OCXO designs its sustaining circuitry is disposed on unheated outer PC board

978-1-5386-2916-1/$31.00 ©2017 IEEE

(fig.2) under ambient temperature conditions. Fig. 3 exhibits an exterior view of different OCXO models utilizing the IHR technology with the smallest one MXO37/8 approaching the sizes of the TO-8 holder.

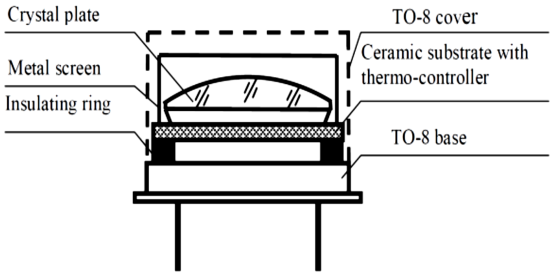


Fig. 1. Schematic drawing of the IHR structure.

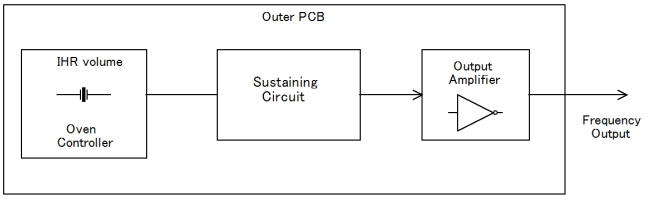
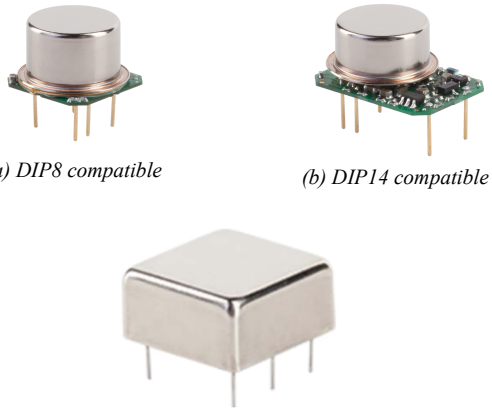


Fig. 2. Outline of the OCXO based on IHR concept



(a) DIP8 compatible *(b) DIP14 compatible*

(c) Hermetically sealed in 20x20 mm case

Fig. 3. Exterior view of the IHRO designs: DIP8 compatible (a), DIP14 compatible (b), hermetically sealed in 20x20 mm case (c)

As it follows from the IHRO structure its temperature instability of the frequency is contributed from two main sources: temperature instability of the IHR and of the sustaining circuitry. To improve temperature stability of the IHR its internal oven structure and circuitry have been essentially modified to ensure high accuracy and uniformity of heating the bulky high overtone crystal plate. That has yielded to increase of the temperature control accuracy 0.1- 0.2˚C with proportional reduction of the thermal gradients over the crystal.

The unheated sustaining circuitry of the IHRO along with the buffer amplifier and voltage regulator contribute into OCXO temperature instability through variation of the excitation level, changes of reference voltage on the corrector and other factors. Degree of the influence depending significantly on impedance of the crystal and sustaining circuitry varies from 20-30 ppb at 10 MHz operation frequency to 0.3-0.5 ppm at 100 MHz.

For minimization of the circuitry factor there has been utilized the analog compensation network correcting the oscillator frequency in accordance with ambient temperature changes (fig.4). The compensation signal is produced by the temperature sensor disposed on the unheated board and biases the electronic corrector to provide minimal frequency deviation of the oscillator [2].

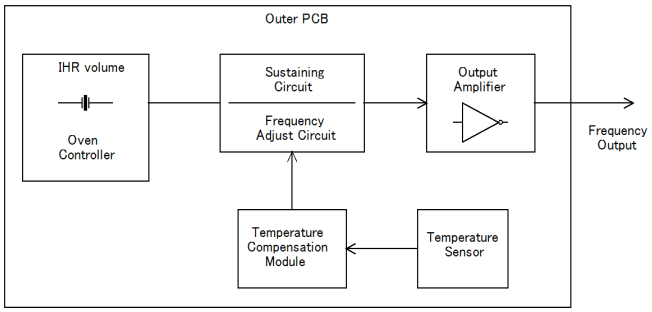


Fig. 4. The outline of temperature compensated IHRO structure.

The table below shows values of the temperature stability of modern OCXO models achieved with the improved IHR construction together with the effect of the temperature compensation technique.

TABLE I. TEMPERATURE STABILITY OF THE IHRO MODELS.

Type of the OCXO	Operational frequency, MHz	Utmost frequency stability, (-40 +85)^{0}C, ppb	
		No compensation	*Using compensation*
MXO37/8	10	10	2
	100	50	10
MXO37/14	10	5	1
	100	30	10
MXO37/R	10	5	0,5
	100	30	5

As it follows from the data the temperature stability of the DIP8 and DIP14 models is at the level of the high-end conventional OCXOs through attained at a few times smaller sizes and about one order lower power consumption. Meantime the MXO37/R oscillator exhibits superior frequency stability in wide temperature range attainable only with the double-oven OCXOs.

III. BASIC PERFORMANCES OF THE IHROS

The original construction features of IHRO concept determine essential difference of its basic performances from the conventional OCXO designs.

A. Power consumption

The power consumption providing most evident advantage of the IHROs over conventional OCXOs is almost entirely determined by thermal isolation of their internal oven structure from environment:

$P = (T_o - T_a)/ R_t$,

where P – the power consumption, T_o – IHR operation temperature, T_a – ambient temperature, R_t - thermal resistance between the integrated oven and environment characterizing thermal insulation of the IHR.

Owing to very small sizes of the internal oven and its excellent thermal insulation by the deep vacuum and low conductivity of the supporting structure the thermal resistance of the IHR can reach 1000 K/W. Power consumption of real IHR designs measured at 25^{0}C in dependence on ambient and operation temperatures is depicted in Fig.5.

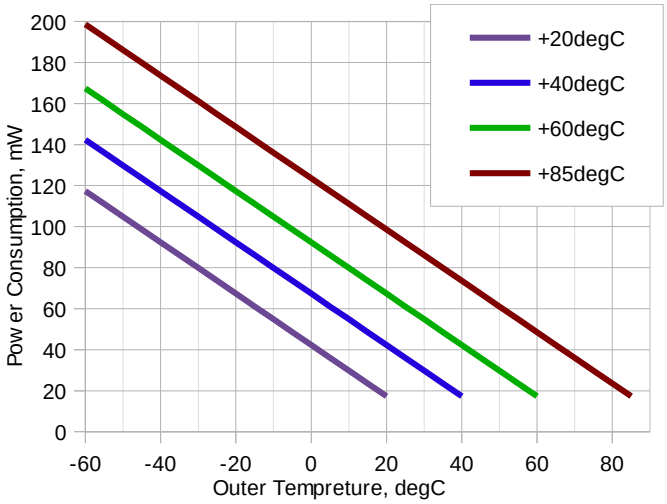


Fig. 5. Power consumption of the IHR at different operational temperature ranges.

As it follows from the plots very low power consumption is attained even at 90°C operation temperature used at wide operation temperature ranges while at narrow ranges the IHR devices ensure extremely low consumption values. That makes the IHROs a perfect solution for various battery supply devices, such as the high-end mobile radio or the underwater clocks. The latter operate in relatively stable sub-marine temperature conditions but are demanded for utmost frequency stability and the lowest power consumption.

B. *Warm-up time*

Very fast warming-up of the IHR construction (Fig.1) proceeds from very low thermal inertia of the internal heating system and its strong coupling with the crystal plate. Owing to these properties the IHR designs using the SC-cut plano-convex plates having low thermo-dynamic sensitivity ensure to 30 s warming-up to 0.1 ppm frequency accuracy that's at least three times faster than with conventional oven designs.

Significantly faster warming-up can be attained using *the composite heated IHR* version with the temperature sensor and the film heaters disposed directly on the crystal plate while the rest regulating elements are arranged on the supporting ceramic substrate [3].

The Fig.6 depicts warming-up curves for the indirect and composite IHRs utilizing the 10 MHz SC-cut crystal plate in dependence on the start-up power.

As it follows from the curves the composite IHR at 3W start power reaches utmost values of warm-up time: <15 s to 0.1 ppm accuracy and 20 s of 0.01 ppm accuracy operating at the room temperature. So fast warming up is result of almost "instant", within a few seconds, heating the SC-cut crystal plate to 90^{0}C operation point and its excellent thermo-dynamic properties.

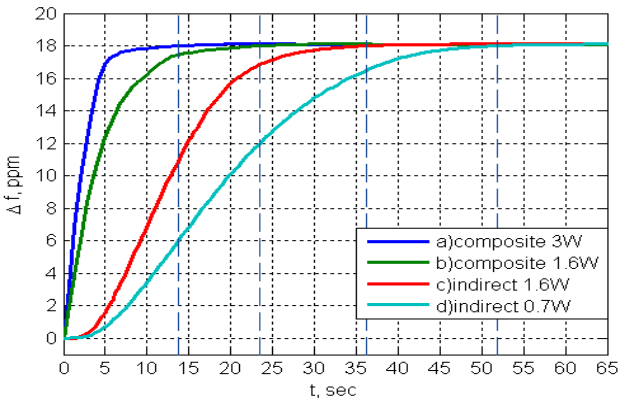


Fig. 6. Warming-up of the indirect (c, d) and composite heated (a, b) IHR versions vs. start-up power.

C. *Long-term stability*

The long-term frequency stability of a crystal resonator is a result of contribution of different intrinsic factors such as relaxation of the mechanical stresses in the crystal plate or sorption-desorption of residual substance on the film electrodes. The latter can be more significant factor in the IHR devices due to potential outgazing from different materials and components operating at high operation temperature in cold-weld sealed TO-8 holder.

The problem of preserving deep vacuum conditions inside the IHR volume has been resolved by choosing the "vacuum compatible" materials and effective vacuum cleaning the IHR structure before the cold-weld sealing. These measures along with utilizing high-overtone precision crystal plate have resulted in excellent aging performances of the IHROs, practically at the level of the high-end conventional OCXOs. The fig.7 displays the aging curves for a group of the 20 MHz oscillators built on the 5th overtone SC-cut IHR measured during one year operation time. The table 2 shows aging rate of these IHROs calculated after 1, 2, 3 months operation along with the first year total frequency shift.

Out of the data most of the IHRO units after 30 days operation provide 0.3 ppb/day rate and 0.15 ppb/day after 60 days. Total deviation of the frequency after the first year operation doesn't exceed 50 ppb that corresponds to the aging performances of the high stability conventional OCXOs.

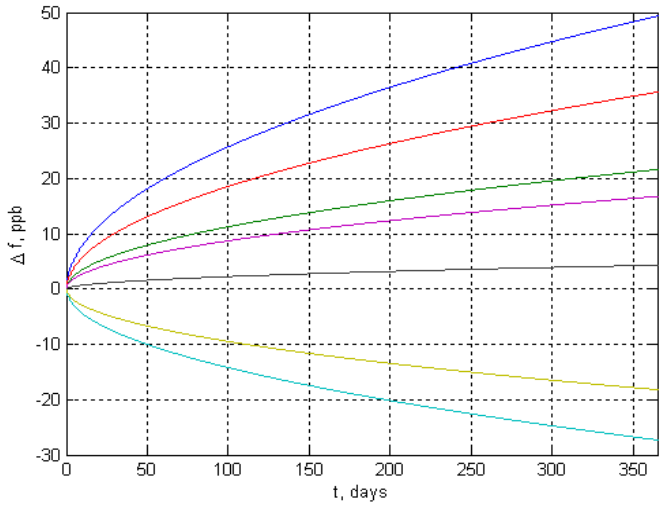


Fig. 7. Aging plots and statistic data for the IHROs.

TABLE II. AGING PARAMETERS OF THE 20 MHZ IHROS

Daily aging, 1x10^{-10}			First year shift, ppb
After 30 days	*After 60 days*	*After 90 days*	
-1,5..+ 2,5	-1..+1,5	-1..+1,5	-30..+50

D. Phase-noise and Allan variance

The phase-noise level of the IHROs in the middle and far offset from the carrier is close to that of the low-noise conventional OCXOs for utilizing common sustaining circuitry and parameters of the crystal plate. Meantime at 0.1-1 Hz region the phase-noise level becomes rather sensitive to temperature fluctuations of the oven control system which produces frequency fluctuations of the resonator through the thermo-dynamic effect. The influence is more noticeable in the IHR oscillators for much lower thermal inertia of the internal oven system having strong coupling with the crystal plate.

To reduce the phase-noise degradation of the IHROs the amplitude noise of the internal oven was minimized by optimal choice of parameters of the thermo-control circuitry without sacrificing the temperature control accuracy. Low thermo-dynamic sensitivity of the IHR was ensured by usage of the SC-cut crystal plate having optimal geometry and mounting structure. The fig.8 displays typical phase-noise patterns measured with the IHROs operating at 10 MHz and 100 MHz fundamental frequency which obviously are close to the level of low-noise conventional OCXOs.

The short-term instability of a crystal oscillator can be determined from the phase-noise plot and also is influenced by the oven fluctuations factor. The fig.9 depicts utmost values of Allan variance vs. average time attained with the high stability MXO37R model.

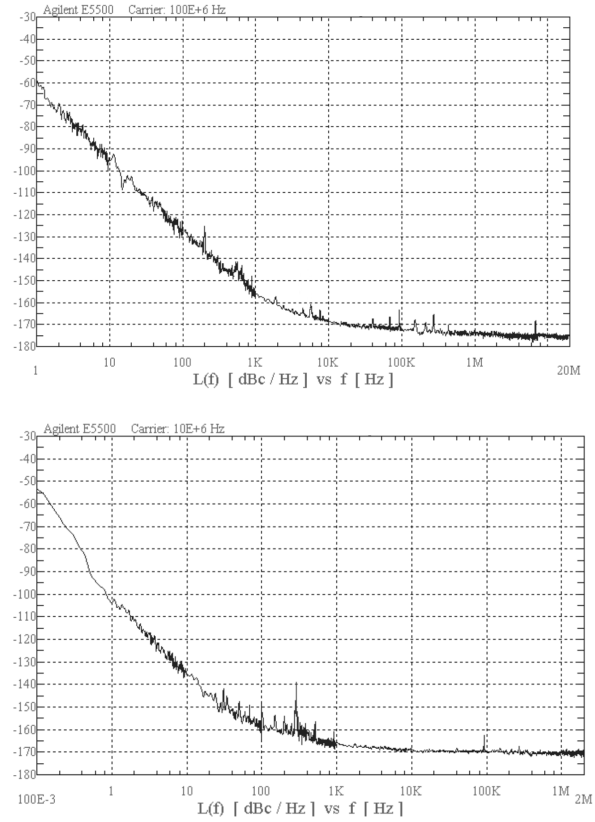


Fig. 8. Typical phase-noise level of 10 MHz and 100 MHz IHROs

As one can see the OCXO exhibits pretty good, to 1x10^{-12} / 1s, STS which is combined with 0.5 ppb in (-40 +85)^{o}C frequency stability and about 150 mW power consumption.

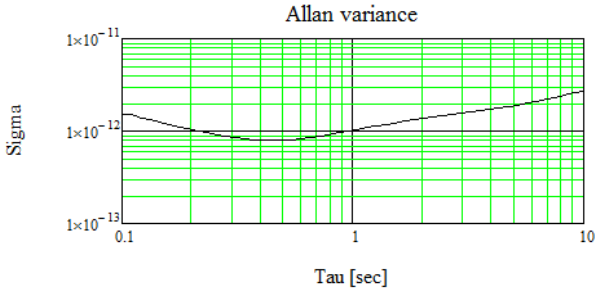


Fig. 9. Allan variance vs. average time for the MXO37/R model

E. Durability to mechanical factors

Portable and mobile radio-electronic equipment is often exploited in hard environmental conditions severe mechanical shocks and vibration. To withstand exposure to these factors the high durable MXO37D model has been created. Being implemented in the DIP8, DIP14 compatible sizes or 20x20 mm packaging the IHROs withstand up to 1000 g, 1 ms multiple shocks and 30 g, 0-2000 Hz vibration. In spite of robust IHR structure the OCXOs consume < 220 mW power and provide to 10 ppb frequency stability in (-40 +85)^{o}C range.

The acceleration or g-sensitivity of a crystal oscillator determines its phase-noise level under action of random or sine

vibration and therefore is crucial parameter for various mobile applications with high demands to purity of the reference signal. To reduce sensitivity of the IHROs to acceleration low g-sensitivity IHR construction with optimized geometry of the crystal plate and the mounted structure has been developed. The new IHR design has enabled considerable reduction of the g-sensitivity, to 0.2 ppb/g for the worst direction at 10 MHz operation frequency and to 0.3 ppb/g at 100 MHz.

Farther reduction of the acceleration sensitivity has been attained by installation of the IHRO module in the outer anti-vibration structure arranged in "europack" case. The phase-noise pattern of this device operating at 10MHz under 8g RMS vibration is depicted in fig. 10 for three orthogonal axes. Calculated from these data the g-sensitivity is less than 0.05 ppb/g at higher 100 Hz offset while at above 300 Hz offset the vibration produces negligible impact on the phase-noise level.

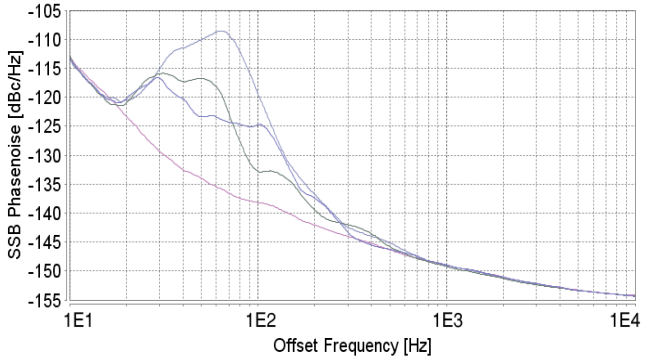


Fig. 10. Acceleration sensitivity vs. vibration frequency of the IHRO with outer anti-vibration protection.

F. Summary on basic performances of IHROs.

The basic performances of the OCXOs achievable with the up-to-the-date IHR technology are summarized in table 3.

TABLE III. UTMOST PERFORMANCES OF MODERN IHROS

Performances	Indirect heated IHRO	Composite heated IHRO
Operation frequency range, MHz	8-150	8-50
Temperature stability, (-40 +85)^{0}C	0.5 ppb	5 ppb
Aging per day (at 10 MHz), ppb/day	0.1	0.2
Allan variance, 1 s	$1x10^{-12}$	$5x10^{-12}$
Power consumption at 25 C, mW	130	
Warm up time to 0.1 ppm, s	30	15
G-sensitivity, worst direction, ppb/g	0.2	
Packaging	DIP8, DIP14, 20x20x12.6 mm	

Out of the data the modern IHROs provide for wide operation frequency range excellent frequency stability, low phase-noise level and high durability to mechanical factors, not yielding to the top level conventional OCXOs. At the same time, all the performances of the IHROs are combined with their extremely low power consumption, small sizes and very short warm-up time.

IV. CONCLUSION.

The many-years development work directed to improvement of the IHR technology has yielded a new generation of the OCXO devices combining very high frequency stability, low phase-noise level and high mechanical durability with extremely low power consumption, miniature sizes and very fast warming-up.

Owing to the extraordinary performances the modern IHROs are now a state-of-the-art solution for high precision timing and frequency control of various portable and/or battery supply systems which earlier had to compromise with usage of TCXOs, conventional OCXO or CSAC references.

[1] I. Abramzon, S. Baranushkin, A. Gubarev, O. Rotova, V. Tapkov, "High-Stability Miniature OCXOs Based on Advanced IHR Technology", Proceedings of the Joint 2007 European Frequency and Time Forum; 2007 IEEE Frequency Control Symposium., pp.242-245.

[2] Abramzon I. & Tapkov V. "Utmost OCXO Solutions Based on the IHR Technology", Microwae Journal, Vol. 57, No.4, April 2014.

[3] Igor Abramzon, "OCXO Designs Using Composite-Heating of the Crystal Resonator", IEEE Transactions on Ultrasonics, Ferroelectrinics and Frequency Control, V.41(2), pp. 284-287, April 1994.

The Design of a Novel Low Phase Noise Anti-Vibration OCXO

Songtao Jiang
Device department
Chengdu Spaceon Electronics Co., Ltd
Chengdu, China
Email: jsttao@163.com

Xu Wang
Device department
Chengdu Spaceon Electronics Co., Ltd
Chengdu, China
Email: wangxu1208@163.com

***Abstract*—Crystal Oscillators are widely used in many systems; and phase noise is one of the most important specifications of crystal oscillators. It is well known that crystal oscillators are acceleration sensitive devices. Vibration will degrade the phase noise of crystal oscillators used in many applications such as aircrafts, vehicles, and missiles, etc. This paper analyses the design of a novel low phase noise Anti-Vibration OCXO with emphasis on the influence of vibration on the phase noise. The solutions are analyzed in detail. Furthermore a low phase noise 100MHz anti-vibration OCXO has been designed based on the passive vibration isolation system combined with paired crystals compensation. The OCXO's SSB phase noise achieves -152dBc/Hz at 1 kHz offset frequency under random vibration condition.**

Keywords—OCXO; Anti-Vibration; Low Phase Noise

I. INTRODUCTION

As the stable standard frequency sources, crystal oscillators are widely used in different kinds of high speed moving equipment such as helicopters, air vehicles and missiles. However, crystal oscillators are very sensitive to vibration, acceleration and shock. These dynamic disturbances have the greatest influence on crystal oscillator's performance and can lead to producing frequency fluctuation and phase noise degradation. Therefore it is necessary to design the low phase noise anti-vibration crystal oscillator to improve its performance under dynamic environment.

The design methods of anti-vibration Oven Controlled Crystal Oscillator (OCXO) could be sorted into two categories: passive and active. Conventional passive methods usually require a large volume and have limitation to achieve a good vibration isolating effect below vibration frequency of 100Hz. Active methods such as using acceleration sensor and other feedback means usually effect at vibration frequency of 10Hz～200Hz [1,2]. In this paper, the causes and effects of crystal's acceleration sensitivity are reviewed and analyzed, and then a novel low phase noise 100MHz anti-vibration OCXO is designed based on the passive vibration isolation system combined with paired crystals compensation. The SSB phase noise of the designed anti-vibration OCXO achieves -152dBc/Hz@1kHz at the random vibration condition whose power spectral density is $0.04g^2$/Hz and frequency range is 50Hz～2000Hz. Meanwhile, the OCXO's package size is 38mm×38mm×20mm.

II. ANALYSIS AND SOLUTIONS

The acceleration sensitivity of quartz crystal resonators and oscillators as well as how vibrations modulate the frequency to degrade phase noise has been reported [3]. The resonant frequency of the quartz crystal resonator will bring tiny change under acceleration condition. The frequency $f(\vec{a})$ is given by

$$f(\vec{a}) = f_0(1 + \vec{\Gamma} \cdot \vec{a}) , \tag{1}$$

where f_0 is its frequency without acceleration, $\vec{\Gamma}$ refers to as the acceleration sensitivity vector, $\vec{a}$ means acceleration.

As $\vec{\Gamma}$ is a vector, the total magnitude of $\vec{\Gamma}$ is expressed as

$$\left|\vec{\Gamma}\right| = \sqrt{\Gamma_x^2 + \Gamma_y^2 + \Gamma_z^2} , \tag{2}$$

where Γ_x, Γ_y, Γ_z are the acceleration sensitivity vector of three axes at x, y, z.

When a crystal oscillator works under sinusoidal vibration at frequency $f_v$along a single axis, the single sideband level $L(f)$ of the oscillator's output is approximated by

$$L(f) = 20\log\left(\frac{(\vec{\Gamma}\cdot\vec{A})f_0}{2f_v}\right), \tag{3}$$

where $\vec{A}$ is the acceleration amplitude vector.

Usually, the crystal oscillator works under random vibration environment. For this case, we can approximate the single sideband level $L(f)$ by

$$L(f) = 10\log\left(\frac{(\vec{\Gamma}\cdot f_0)^2 G(f)}{2f^2}\right), \tag{4}$$

where $G(f)$ denotes the power spectral density of acceleration, f is the Fourier offset frequency in the spectral analysis of the phase noise.

In order to reduce the phase noise of the crystal oscillator in dynamic environment, we can decrease the $G(f)$ or $\vec{\Gamma}$ in formula (4). So we have two solutions. Firstly, a passive vibration isolation system is required to isolate the vibration, especially the high frequency vibration. Secondly, we can use some active

acceleration compensation methods to minimize the influence of $\vec{\Gamma}$, such as paired crystal resonators compensation.

III. ANTI-VIBRATION OCXO DESIGN

A. Vibration isolator design

We design a miniature vibration isolator inside the anti-vibration OCXO. This passive vibration isolation system is described in Fig.1.

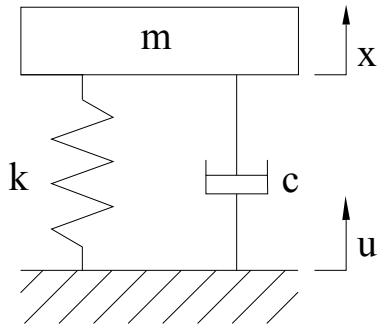


Fig.1. Model of vibration isolator

The transmission function of the vibration isolation model is given by

$$G(s) = \frac{x}{u} = \frac{cs+k}{ms^2+cs+k}, \quad (5)$$

where m is the weight, k is stiffness coefficient, c is damping coefficient, x and u are the displacement of the isolated object and the fixed substrate.

To conclude, the effect of the vibration isolation system is greatly related to the stiffness coefficient of material, the damping coefficient of structure, and the weight of the isolated object [4].

After comparing with many isolation material and structure, we have chosen the stretch stainless steel rope as the isolation material, and designed multi-underpropped isolation structure. The inside OCXO is suspended in the housing. The isolation structure sketch drawing is shown in Fig.2.

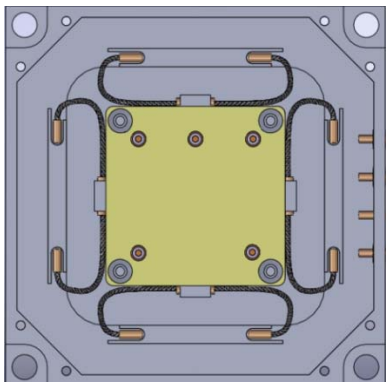


Fig.2. Sketch of vibration isolator

By adjusting the weight of the isolated object, the resonant frequency of the isolator is set below 50 Hz. The internal OCXO's electrical and signal cables should be soft and unrestricted. The foam fabric must then be affixed to the wall of the housing to avoid internal OCXO striking with the housing and partially isolating vibrating sound noise. The designed isolator can significantly attenuate the amplitude of the vibration upon the resonant frequency; especially the high frequency vibration close to 1 kHz.

B. Paired crystal resonators compensation design

In formula (1), when a crystal resonator numbered 1 receives acceleration, the resonant frequency will change in one direction. Suppose we have another crystal resonator numbered 2 which has the same magnitude of $\vec{\Gamma}$ and equal motional electric parameters, if the two crystals receive same direction acceleration ($\vec{\Gamma}_1 = \vec{\Gamma}_2$), the net acceleration is given by

$$\vec{\Gamma} = \frac{1}{2}(\vec{\Gamma}_1 + \vec{\Gamma}_2) = \vec{\Gamma}_1 . \quad (6)$$

If the two crystals receive the opposite direction acceleration ($\vec{\Gamma}_1 = -\vec{\Gamma}_2$), the net acceleration vector will be zero. The other crystal resonator will produce an equal resonant frequency change in the opposite direction. So the frequency change will be counteracted.

If the two crystals have different magnitude of $\vec{\Gamma}$ and receive the opposite direction acceleration, so that $\vec{\Gamma}_1 = -\vec{\Gamma}_2 + \vec{\gamma}$, the net acceleration is given by

$$\vec{\Gamma} = \frac{1}{2}(\vec{\Gamma}_1 + \vec{\Gamma}_2) = \frac{1}{2}\vec{\gamma} . \quad (7)$$

In order to compensate for three orientations' acceleration, it is necessary to mount four paired crystal resonators at least. The phase noise curve measured in Section IV shows that the vibration isolator designed in this paper has an excellent vibration isolation effect in the z direction (perpendicular to the paper's surface in Fig.2). So we adopt the dual crystal resonator horizontally to install the mirror to compensate for the x and y direction of the acceleration sensitivity. The double crystals' mounting mode is shown in Fig.3.

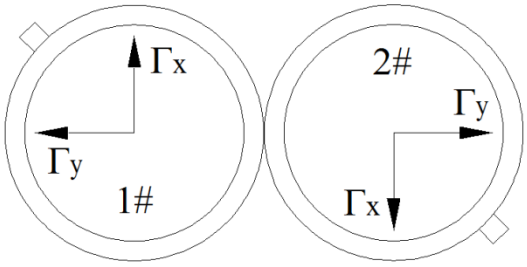


Fig.3. Double crystals' sensitivity direction

The oscillator circuit is shown in Fig.4, which is modified-Butler type circuit with the double paired crystals in series configuration. The drive level of this circuit should be higher

than adopting single crystal. The static phase noise and other performance of the dual crystal oscillator are similar to those of a single crystal oscillator through optimizing the circuit's parameters.

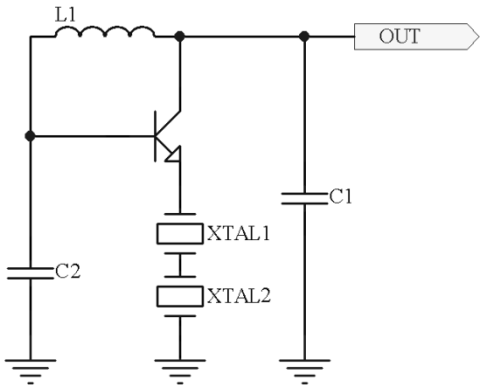


Fig.4. Functional schematic diagram

C. Crystal resonator selecting and pairing

There are many strict requirements on crystal resonators for paired crystals compensation. An important consideration is measuring and selecting the crystals' acceleration sensitivity $\vec{\Gamma}$ before assembling the crystals into oscillators. It's known that four-point mounting SC-cut crystal resonator has lower acceleration sensitivity [5]. So we chose the 5th overtone 100MHz SC-cut crystal resonator with HC-35/U cold weld holder in this paper. In addition, we designed the appropriative acceleration sensitivity measuring device that can fix the crystal resonator on an oscillator and measure the oscillator's dynamic phase noise and frequency change through vibration and overturning tests. The magnitude and polarity of $\vec{\Gamma}$ could be calculated by the measured dynamic phase noise and frequency change results. The photograph of the measuring device is shown in Fig.5. Since each crystal unit must be measured one by one; it's also a difficult and arduous task to measure $\vec{\Gamma}$ exactly.

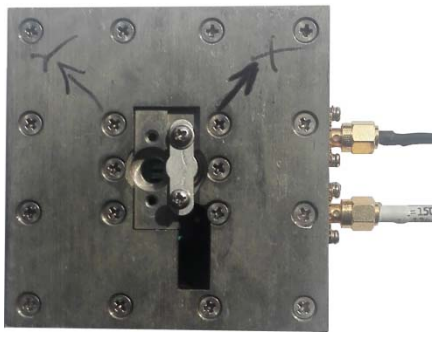


Fig.5. Crystals' acceleration sensitivity measuring device

The selected crystals' acceleration sensitivity should better be less than 0.3ppb/g at all three axes. Otherwise, the crystals' main motional electric parameters should be similar to ensure that the oscillator meets the specifications, such as motional resistances R, motional inductances L, motional capacitances C, series resonant frequencies f and temperature turn point TP. After measurement, the crystals which have matching parameters within the required tolerance will be selected and paired.

IV. MEASUREMENT

A. Measurement methods

In order to evaluate the effects of the vibration isolation system and paired crystals compensation, we measure the induced phase noise under vibration. The vibration measurement system is composed of a shake table, a vibration controller, an acceleration sensor and a signal source analyzer E5052B. The photograph of the measurement system is shown in Fig.6.



Fig.6. Vibration measurement system

Phase noise measurements are environmentally sensitive. When the shaking table is operating, the test results may be subject to single cable and power line jitter, electromagnetic interference and other interference, therefore it is important to consider the anti-interference and EMC.

The phase noise under random vibration condition is measured. The acceleration power spectral density is $0.04g^2/Hz$ and frequency range is 50Hz～2000Hz. The curve of the vibration condition is shown in Fig.7.

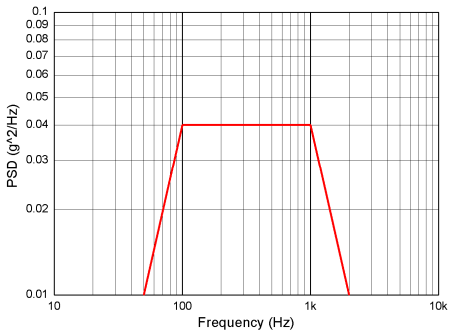


Fig.7. Random vibration condition

B. *Vibration testing results*

The designed 100MHz anti-vibration OCXO without paired crystals compensation is measured first. The phase noise curves under random vibration condition are shown in Fig.8. The worst dynamic phase noise in three axes is -149dBc/Hz at 1 kHz offset frequency. The results show that the isolator has a significant effect at about 1 kHz. But the vibration is amplified near the resonant frequency of the isolator itself, especially at x and y axes. The worst dynamic phase noise is -88dBc/Hz at 100 Hz offset frequency.

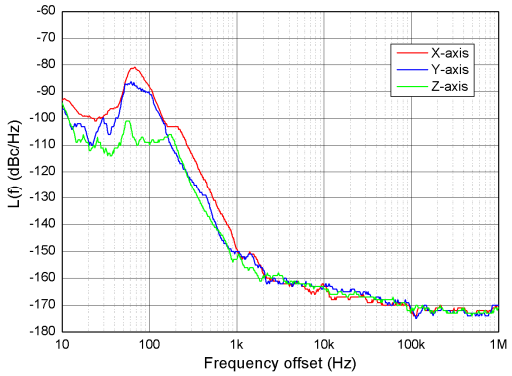


Fig.8. Phase noise of anti-vibration OCXO without paired crystals compensation

Then the anti-vibration OCXO with double paired crystals compensation is measured. The phase noise curves are shown in Fig.9. Comparing Fig.9 with Fig.8, it can be seen that the phase noise within 1 kHz is significantly optimized at the x and y axes. The phase noise under vibration achieves -107dBc/Hz@100Hz and -152dBc/Hz@1kHz at the worst axis.

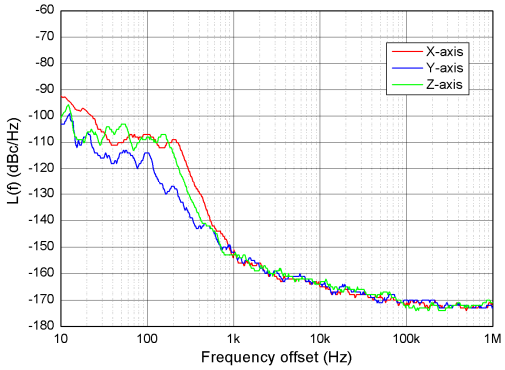


Fig.9. Phase noise of anti-vibration OCXO with paired crystals compensation

The measured results show that the anti-vibration OCXO with double paired crystals compensation has better dynamic phase noise performance. The photograph of the designed anti-vibration OCXO is shown in Fig.10 and its size is 38mm × 38mm × 20mm.

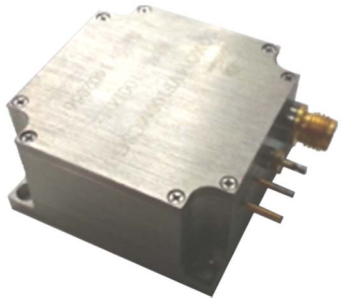


Fig.10. The designed anti-vibration OCXO.

V. CONCLUSION

In this paper, we have proposed, analyzed and designed a novel low phase anti-vibration OCXO, which is based on the passive vibration isolation system combined with paired crystals compensation. By means of selecting and pairing crystal resonators, as well as designing multi-underpropped isolator and double crystals oscillator circuit, the measured phase noise under vibration achieves -107dBc/Hz@100Hz and -152dBc/Hz@1kHz. In order to minimize the anti-vibration OCXO's package size, the small SMD SC-cut crystal resonators will be adopted in future work.

REFERENCES

[1] H. Fruehauf, "g-compensation, miniature, high performance quartz crystal oscillators", 38th Annual Precision Time and Time Interval(PTTI) Systems and Applications Meeting. pp. 251-258.

[2] M.Bloch, O. Mancini, T. McClelland, et al. "Acceleration G compensated quartz crystal oscillator", IEEE International Frequency Control Symposium. 2009, pp. 175-180.

[3] Steven J. Fry, Gregory A. Burnett, "Reducing the acceleration sensitivity of AT-strip quartz crystal oscillators", IEEE, 2010, pp. 25–30.

[4] Shu yi XU, Zhongping Chen. "Development of an anti-vibration crystal oscillator for reducing vibration-induced phase noise", Symposium on Piezoelectricity, Acoustic Waves and Device Applications, 2011, pp. 217–220.

[5] Larry D. Clayton, Errol P. Eernisse. "Four-point sc-cut crystal unit design calculations for reduced acceleration sensitivity", IEEE International Frequency Control Symposium. 1992, pp. 582-596.

High Stability Miniature Size OCXO

Using a SC-cut Crystal Resonator and Simultaneous Oscillations

Masato Ogawa, Manabu Ito , Kaoru Kobayashi, Manabu Ishikawa, Kazuo Akaike
Nihon Dempa Kogyo Co., Ltd
Saitama, Japan
ogawam@ndk.com

***Abstract*— This paper describes a high stability miniature size OCXO using a SC-cut crystal resonator with simultaneous oscillations as the method of taking two signals from one crystal, compared with the Twin-Crystal technology [2] which had the high accuracy temperature sensor by the two crystal units. This 9 x 7 mm size OCXO has satisfied around +/- 1 to 2 ppb in a range of ambient temperature from -40 to +85 °C by the ideal temperature sensor.**

Keywords—DSP; simultaneous oscillations;

I. INTRODUCTION

In recent years, 5G as a new generation communication specifications has been discussing actively, and higher densification of networks and improvement of communication quality have been studying intensively. Therefore, it will be expected that communication base stations will be more increasing. The typical requirements for the reference oscillators for these communication base stations are as follows:

(1) High frequency stability

(2) Low power consumption

(3) Small-sized package

(4) Wide temperature range

In the conventional 14 x 9 mm OCXO, the high accuracy temperature sensing had been applied using two AT-cut crystal resonators. [1] Furthermore, in this study, the 9 x 7 mm size OCXO have achieved higher stability and smaller size by the using one SC-cut crystal resonator and simultaneous oscillations as to get two oscillation modes. We had developed a 5.0 x 3.2 mm miniature size SC-cut crystal resonator for the use of simultaneous oscillations. The two oscillator circuits were connected from the SC-cut resonator.

II. HIGH-STABILITY TEMPERATURE SENSING CIRCUIT

As in the reference paper, the high accuracy temperature detection technology is applied as follows. [1] [2] Fig.1 shows a typical functional block diagram of high accuracy temperature detection circuit. The two crystal resonators, X1 and X2, have different frequency vs. temperature characteristics, and these crystal resonators should be very closely placed inside the same one ceramic package. For detecting internal temperature of the OCXO in the reference paper, an AT-cut crystal was used as a temperature sensor, instead of a thermistor. (We named this crystal unit Twin-Crystal because the two crystal resonators were built in one ceramic package.)

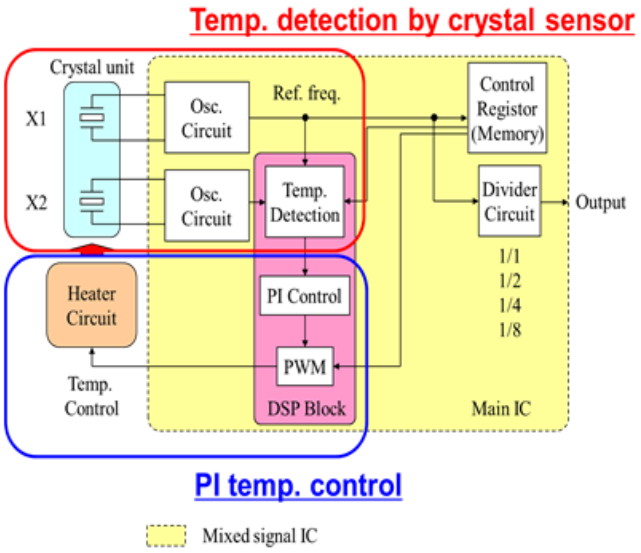


Fig. 1. A block diagram of high stability temperature detection circuit.

And regarding the both of the crystal resonators, the 3rd overtone oscillation mode was used, because it has higher frequency stability than the fundamental oscillation mode. Using Twin-Crystal and the two oscillation circuits, the differential clock signal is obtained by the undersampling X2 clock signal with respect to the X1 clock signal. The upper part of Fig.2 shows frequency-temperature characteristics of X1 and X2. By detecting the frequency difference between X1 and X2, the temperature characteristics of the first-order is obtained as shown in the lower part of Fig.2. This first-order line characteristics corresponds to ambient temperature detected by the crystals. Using such a temperature sensing technology, it is possible to directly obtain accurate temperature of the crystal unit. In this report, it had achieved that same temperature detection method had obtained by two oscillation mode signals from one crystal resonator, instead of two crystal resonators to make OCXO smaller and more stable. That is, the method of simultaneous oscillations had been achieved by one SC-cut resonator. It could make OCXO control higher accuracy of temperature than the conventional method which used two AT-cut crystal resonators.

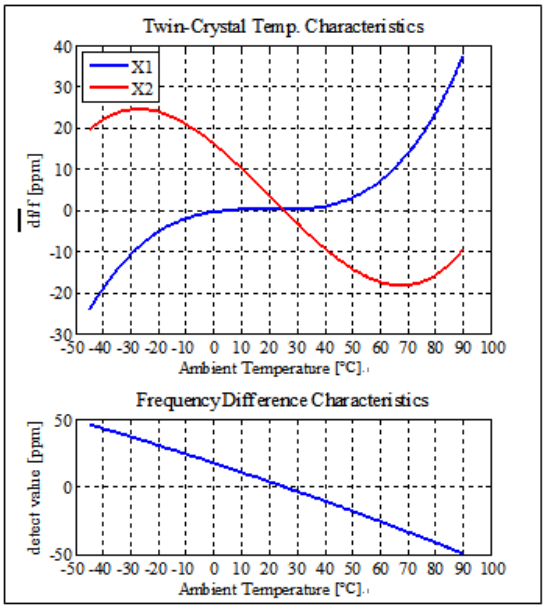


Fig. 2. Twin-Crystal's frequency vs. ambient temperature characteristics. (Top) is the frequency characteristics of Twin-Crystal. (Bottom) is the frequency difference characteristics between crystal resonators X1 and X2.

III. THE TECHNOLOGY OF SIMULTANEOUS OSCILLATIONS

We had developed a 5.0 x 3.2 mm miniature size SC-cut crystal resonator for the use of simultaneous oscillations. The two oscillator circuits were connected from the SC-cut resonator. The reference clock oscillator circuit (T1) was designed to oscillate C-mode 3rd over tone, The temperature sensing oscillator circuit (T2) was designed to oscillate C-mode fundamental. It was necessary that each oscillator circuits were designed to have sufficient negative resistance on the desired oscillation modes and no negative resistance on the other frequency area. Fig.3 shows a block diagram of simultaneous oscillations. We inserted the NDK original designed filters to achieve stable simultaneous oscillations and to prevent interference between each signals. Both filters, Filter 1 and Filter 2, reject unnecessary oscillation mode and keep isolation between the both oscillators.

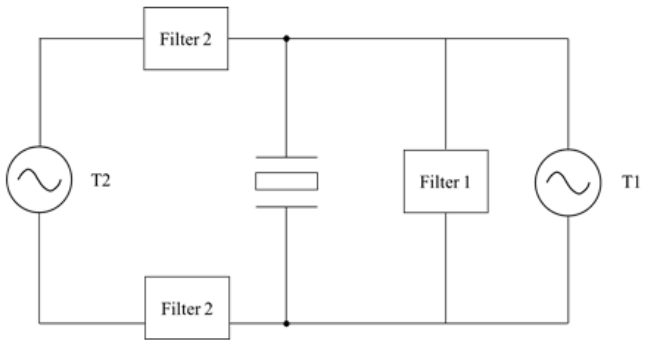


Fig. 3. A block diagram of simultaneous oscillations

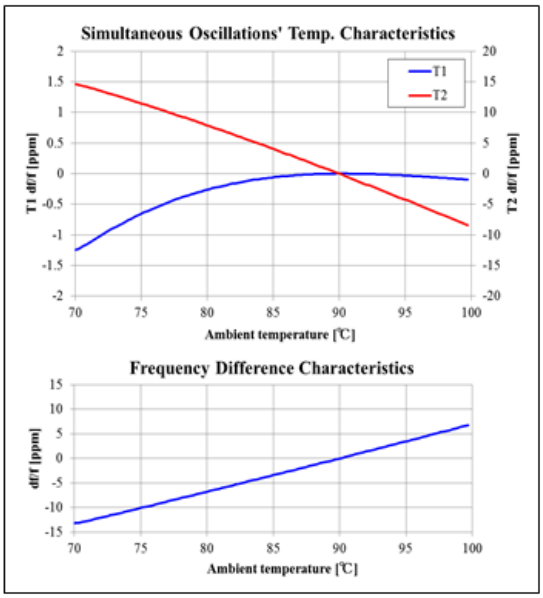


Fig. 4. The simultaneous oscillations' frequencies vs. ambient temperature characteristics. (Top) is the frequency characteristics of the reference clock oscillator T1 and the temperature sensing oscillator T2. (Bottom) is the frequency difference characteristics between T1 and T2.

In Fig.4, the upper part shows frequencies vs. ambient temperature characteristics of T1 and T2 of the simultaneous oscillations. The lower part shows the frequency difference characteristics between T1 and T2, and linear temperature characteristics was obtained by the difference data. Because we can take the appropriate gap of rotate angle between the 3rd over tone and fundamental by their original characteristics.

IV. THE DESIGN OF OSCILLATOR

We describe the design of the 9 x 7 mm size OCXO using simultaneous oscillations. A lot of circuits consist of a mixed signal IC including two oscillator circuits, a PLL circuit, a VCXO circuit in the output stage, a temperature detection circuit, a frequency compensation circuit, an A/D converter for frequency control by external voltage input. And we had obtained operating temperature range from -40 to +85 °C because the IC including DSP could achieve high speed processing of temperature control and other processes. Moreover, this IC has digital frequency control function using I^2C (Inter-Integrated Circuit) interface in addition to the conventional analog voltage frequency control function. The dotted line box of Fig.1 denotes the IC part.

Fig.5 shows the result of thermal analysis. In the PCB design, we considered parts locations to reduce the effect of IC self-heating on the resonator and to suppress temperature change of the IC, through the use of thermal analysis simulation. In other side, the 9 x 7 mm OCXO had so smaller internal space that maximum heater output power was quite limited. Therefore, it was necessary for resonator to warm efficiently and controlling. So, we optimized parts locations in consideration of these matters.

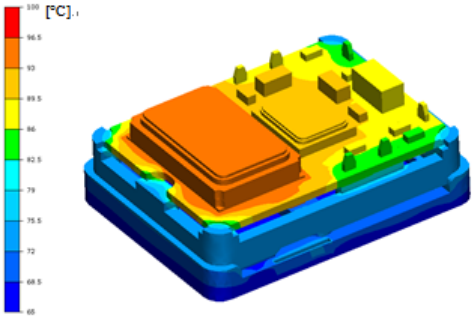


Fig. 5. The thermal analysis simulation.

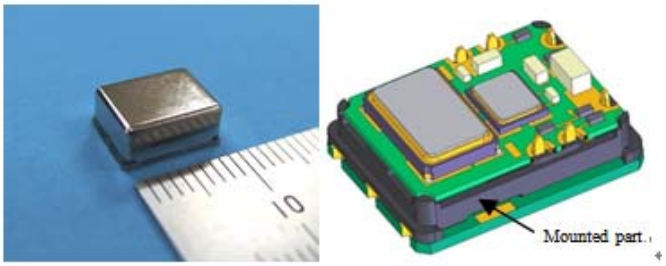


Fig. 6. The external appearance and the internal structure of tne 9 x 7 mm OCXO.

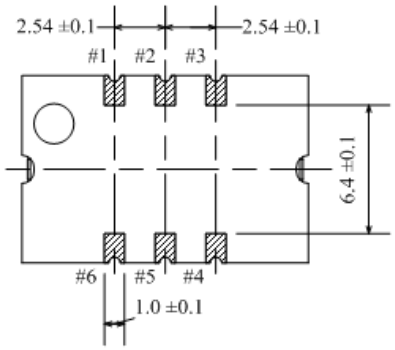


Fig. 7. The foot patterns of the 9 x 7 mm OCXO and the 14 x 9 mm OCXO.

Fig.6 shows the external appearance and the internal structure. The structure was chosen the method of docking by mounted part between the main multi-layer PCB and the double-sided base PCB. Therefore, we could use mounting spaces efficiently with the limited small size. Fig.7 shows the foot pattern of the 9 x 7 mm OCXO and the 14 x 9 mm OCXO. The 9 x 7 mm OCXO's foot pattern compatibles to the 14x9mm OCXO's one.

V. RESULTS

The features of the OCXO are as follows:

-Frequency stability (Tempco)

Max. ±3 ppb / -40 to +85 °C

-Nominal Frequency range: 5 MHz to 40 MHz

-Power supply voltage: 3.3 V ± 5 %

-Power consumption:

Max. 900 mW (During warm-up state)

Typ. 350 mW (at +25 °C, During steady state)

-Phase noise (fnom: 25 MHz)

Typ. -67 dBc / Hz (@1 Hz offset freq.)

Typ. -90 dBc / Hz (@10 Hz offset freq.)

Typ. -125 dBc / Hz (@100 Hz offset freq.)

Fig.8 shows the frequency vs. temperature characteristics of the OCXOs in reference to frequency at +25 °C. As the result, we had obtained around +/- 1 to 2 ppb in an ambient temperature range from -40 to +85 °C.

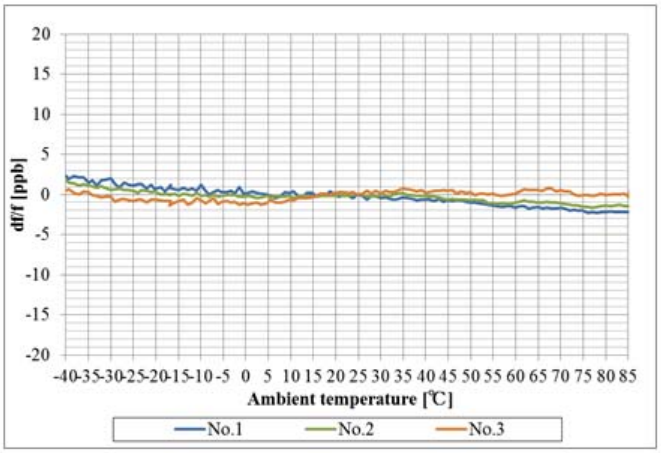


Fig. 8. The frequecy vs. temparture characteristics of the 9 x 7 mm OCXOs.

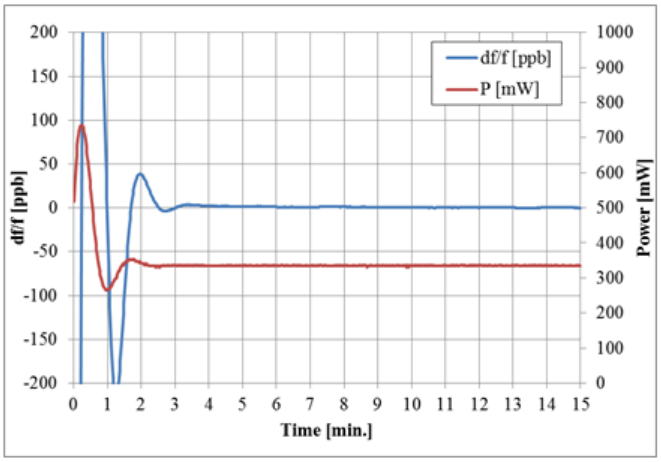


Fig. 9. The warm-up characteristics of the 9 x 7 mm OCXO.

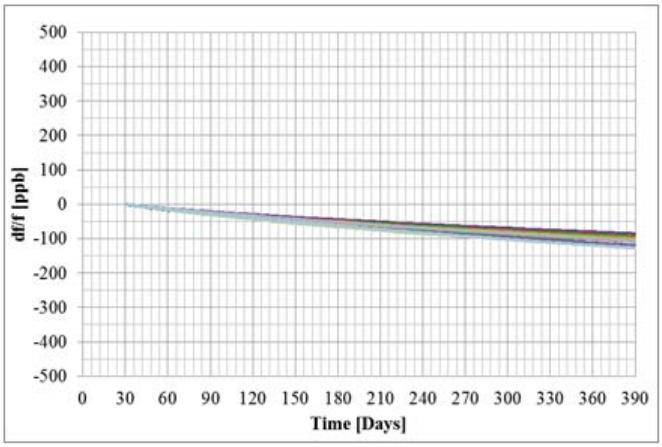


Fig. 10. The long term stability characteristics of the 9 x 7 mm OCXOs.

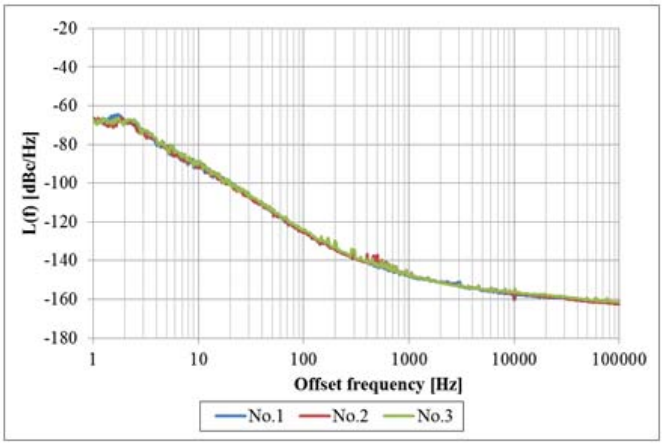


Fig. 11. The phase noise characteristics of the 9 x 7 mm OCXOs.

Fig.9 shows the warm-up characteristics of the OCXO at +25 °C state. Warm-up time is less than three minutes, and power consumption is achieved 350 mW during steady state. Fig.10 shows the long term stability characteristics of the OCXOs at +25 °C, Based on frequency after 30 days operation . These are the measurement data over one year. As the result, we had obtained typ. -100 ppb per year. Fig.11 shows the phase noise characteristics of the OCXOs. The phase noise characteristics of -67 dBc/Hz @ 1 Hz, -90 dBc/Hz @ 10 Hz, -125 dBc/Hz @ 100 Hz, -147 dBc/Hz @ 1 kHz, and -156 dBc/Hz @ 10 kHz offset frequencies were obtained.

VI. CONCLUSION

In this paper, we proposed the world's smallest and the best performance oscillator using the SC-cut crystal resonator and the simultaneous oscillations. As the result, the 9 x 7 mm OCXO had achieved around +/- 1 to 2 ppb in an ambient temperature range from -40 to +85 °C.

The technology of the simultaneous oscillations is the ultimate high stability temperature detection as crystal resonator can measure temperature itself. In the future, we will apply this technology to higher stability oscillators.

[1] Yasuto Ishii, Kaoru Kobayashi, Tsukasa Kobata, Manabu Ito, Shigenori Watanabe, Shinichi Sato, Kazuo Akaike "A New Generation DSPOCXO Using Crystal Temperature Sensor", International Frequency Control Symposium, IEEE, pp.341-344, 2012.

[2] Kaoru Kobayashi, Yoshiaki Mori, Tsukasa Kobata, Manabu Ito, Shigenori Watanabe, Shinichi Sato, Kazuo Akaike "High-Performance DSP-TCXO Using Twin-Crystal Oscillator", International Frequency Control Symposium, IEEE, pp.40-43, 2014.

A Novel Design of Voltage Controlled Temperature Compensated Crystal Oscillator

Jianguo Hu, Xianhe Huang, Qi Zhou, Dong Liu, and Wei Fu
School of Automation Engineering
University of Electronic Science and Technology of China
Chengdu, China
xianhehuang@uestc.edu.cn

***Abstract*—A novel design of voltage controlled temperature compensated crystal oscillator (VCTCXO) is presented. This design will consider the current temperature compensation and the voltage-controlled voltage of regulation of the central frequency as a whole. A variable capacitance diode is adopted to fit the function of two variables, which avoids the problem that the temperature of the crystal oscillator is decreased after the mutual interference between the load capacitance of the two varactor diodes and the change of the central frequency. On this basis, by the debug and work switch on the user control voltage of the output frequency control and microcontroller output voltage-controlled voltage switch, the voltage-controlled temperature compensation crystal oscillator can adapt to the user's output frequency control in the control voltage situation. This new approach provides a novel design of VCTCXO. The results show that this design achieve desired frequency temperature compensation effect.**

Keywords—frequency-temperature characteristics; temperature compensation; voltage controlled temperature compensated crystal oscillator (VCTCXO)

I. INTRODUCTION

With the rapid development of communication and measurement technology, a high stability of VCTCXO is increasingly in demand [1]. The VCTCXO is widely used for its temperature compensation, and its output frequency can be adjusted by a voltage signal. Usually, VCTCXO uses an AT-cut quartz crystal resonator. However, it requires frequency compensation when used in high-precision reference clocks that are exposed to changes in ambient temperature [2], and the relationship between the frequency and temperature was a cubic curve, as shown in Fig.1.

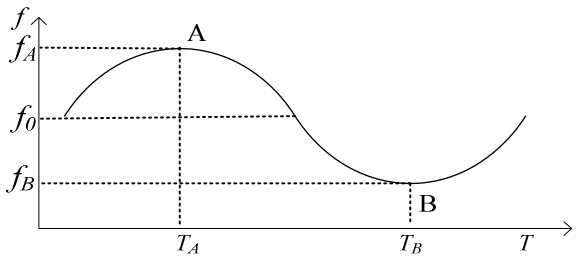


Fig.1. Frequency-temperature characteristic of AT-cut quartz resonator.

At present, the researchers use two parallel (or series) capacitors to form a VCTCXO [3], as shown in Fig. 2. A capacitor is used to compensate the temperature generated by the frequency drift, and another capacitor is used to control the VCTCXO at the voltage control central frequency. However, there are some deficiencies in this method. The crystal oscillator is connected in series with the load capacitance. Therefore, the output frequency is controlled by the nonlinear equation, which is not satisfied with the linear superposition principle [4]. In this case, when the output central frequency of the crystal oscillator changes, the frequency-temperature characteristic are also changes. The same set of temperature compensation data will cause the deterioration of the temperature stability of the crystal oscillator [5]. In view of the shortcomings above, this paper presents a new scheme which focus on the temperature compensation voltage and the voltage-controlled voltage of adjusting the central frequency as the whole to obtain better temperature compensation.

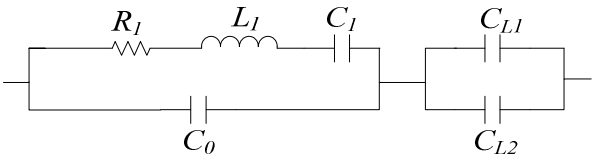


Fig.2. Equivalent circuit of the crystal resonator. C_0 and C_1 are equivalent shunt and series capacitance of quartz crystal, respectively; R_1 and L_1 are equivalent resistance and inductance; C_{L1} is the temperature dependent equivalent load capacitance required for TCXO; C_{L2} is the varactor diode equivalent load capacitance of the VCXO.

II. THE STRUCTURE OF THE NEW VCTCXO

We describe a novel design of VCTCXO. This design considers the current temperature compensation and the voltage-controlled voltage of regulation of the central frequency as a whole. The specific structure consists of a voltage-controlled crystal oscillator, a temperature sensor, a microcontroller, a D/A converter and a low-pass filter, as shown in Fig. 3.

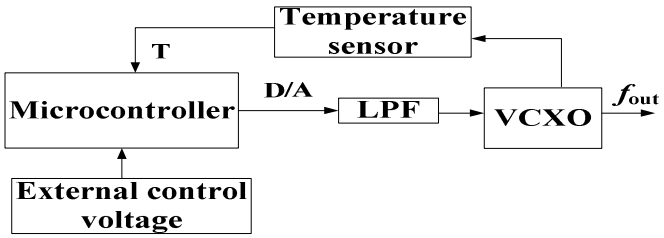


Fig.3. The block diagram of the new VCTCXO system.

A. The principle of temperature compensation for new voltage - controlled temperature compensation

According to Fig. 3, when the microcontroller reads the information measured by the temperature sensor in real time, it can control voltage of VCXO, and then to control the output frequency f_{out}. Finally, the system can realize temperature compensation.

B. Frequency-temperature characteristic of VCTCXO

The frequency stability of quartz crystals is often affected by temperature [6]. Our design considers the temperature compensation voltage and the voltage-controlled voltage of adjusting the center frequency as the whole. Construct the binary function relationship between the input environment temperature T, voltage control voltage V as input and the output frequency f_s, namely,

$$f_s = g(T, V) \tag{1}$$

Therefore, control the temperature box to the specific temperature point, then get the voltage control curve which show the relationship between output frequency f_s and voltage-controlled voltage V, as shown in Fig. 4 line segment. Then, change the temperature continuously and get the voltage control curve at the corresponding temperature to obtain a large number of the voltage control curves of different temperatures as shown in Fig. 4.

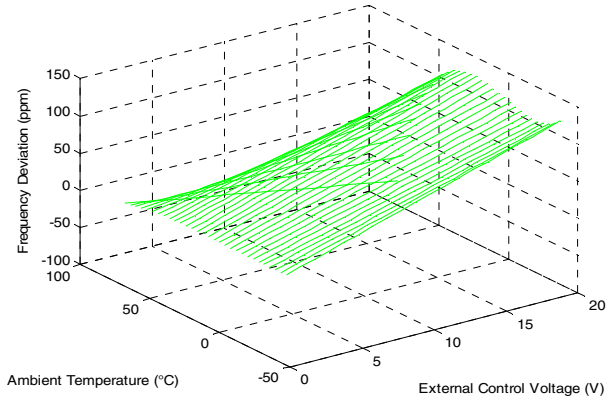


Fig.4. The output frequency deviation relationship of ambient temperature and external control voltage of VCTCXO.

III. THE IMPLEMENTATION OF THE NEW VCTCXO

In order to achieve the output frequency control into the output voltage control, and can achieve continuous frequency changes, there are two operating modes.

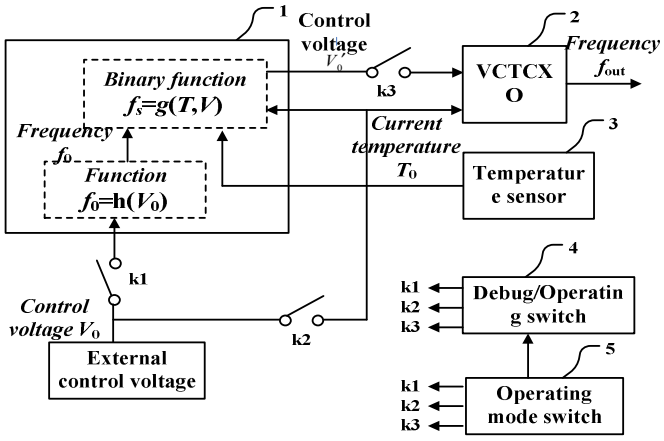


Fig.5. The operating mode structure of the new VCTCXO.

A. Operating mode of the new VCTCXO

Fig. 5 shows operating mode of the new VCTCXO. There are two modes working with different options for operating mode switches. The basic working principle is that the user continuously adjusts the control voltage V_0, so that the output frequency of the voltage controlled temperature compensated crystal oscillator is continuously changed, so as to achieve the required frequency. When the required frequency is reached, the voltage V_0 and the ambient temperature T_0 can be collected, f_0 is obtained by $f_s = g\ (T,\ V)$. At this time the microcontroller output voltage V'_0 is used as the oscillator voltage-controlled voltage, V'_0 is obtained by f_0 and current ambient temperature T'_0. When the current ambient temperature changes, the voltage-controlled voltage could be calculated by the formula f_s=$g(T,V)$,and the voltage-controlled voltage is loaded on the voltage-controlled crystal oscillator. The output frequency is f_{out} that the needs, finally temperature compensation are achieved.

B.Temperature compensation effect of VCTCXO

This design recovers the control voltage V_0 and the ambient temperature T_0 due to the debug state, and recalculates frequency$f_0$in the binary function, thus reducing the computational error of the voltage-controlled voltage caused by the fitting defect, and the accuracy of the output frequency f_{out} is improved, that is, the frequency deviation that the required is reduced. The temperature compensation effect is shown in Fig. 6, and the desired effect is achieved.

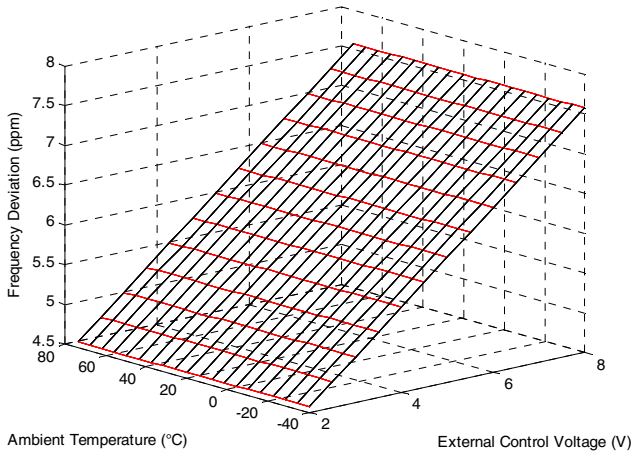


Fig.6. The output frequency relation curve after temperature compensation. The red lines describe the relationship between frequency deviation and ambient temperature, and the black lines depict the relationship between external control voltage and frequency deviation.

IV. CONCLUSIONS AND DISCUSSION

A novel design of voltage controlled temperature compensated crystal oscillator is presented. This design considers the temperature compensation voltage and the voltage-controlled voltage of adjusting the center frequency as a whole, to build the binary function relationship between the input ambient temperature T, voltage-controlled voltage V, and the output frequencyf_s. The results show that the program can achieve more effective temperature compensation.

REFERENCES

[1] M.Q.Li, X.H.Huang, F.Tan, Y.H.Fan, and X.Liang, "A novel microcomputer temperature-compensating methond for an overtone crystal oscillator," IEEE Trans. Ultrason. Freoelectr. Freq.Control, vol.52, pp.1919-1922, November 2005.

[2] J.Lim, H.Kim, T.N.Jackson, K.Choi, and D.Kenny, "An ultra-compact and low-power oven-controlled crystal oscillator design for precesion timing applications," IEEE Trans. Ultrason. Freoelectr. Freq.Control, vol.56, pp.1906-1914, Steptember 2010.

[3] X.H.Huang, D.Liu, Y.Wang, and Y.Chen, "Precise derivation for the equivalent circuit parameters of a crystal resonator with series capacitor," IEEE Transans. Ultrason. Ferroelectr. and Freq. Control, vol. 59, no. 6, pp.1316-1317, 2012.

[4] J. R. Vig, "Quartz crystal resonators and oscillators for frequency control and timing applications-a tutorial" [Online]. Available: http://www.ieee-uffc.org.

[5] X.H.Huang, D.Liu, Y.Wang, W.Fu, and J.J.Jiao, "The design of voltage controlled temperature compensate x'tal oscillator (VCTCXO)," Chinese Patent Application Number: 201410834197.9, December 2014.

[6] R.Achenbach, M.Feuerstack-Raible, F.Hiller, M.Keller, K.Meier, H.Rudolph, and R.Saur-Brosch, "A digitally temperature-compensated crystal osciallltor," IEEE J. Solid-St. Circ., vol.35, pp. 1502-1506, October 2000.

Limiting Factor for the Performance of High Stability Quartz Crystal Oscillators – The Residual Heat of Crystal Resonators

Xianhe Huang[1] Yuanlin Tang[1] Qi Zhou[1] Jianguo Hu[1] Wei Fu[1] Pingping Chen[2]
1 University of Electronic Science and Technology of China, Chengdu, China,
xianhehuang@uestc.edu.cn
2 Frequency control devices, Bowei Integrated Circuits Co.Ltd., Shijiazhuang, China,

***Abstract* — The high stability crystal oscillator has been playing the heart of modern electronic communication equipment for decades, because of its excellent performance and reasonable price. It has three most significant indexes, namely, the aging, the phase noise and the frequency temperature stability. We found that when investigating the frequency temperature stability of high stability quartz crystal oscillator, with the increase of the oven control accuracy, oscillator's frequency temperature characteristic is deteriorating instead of improving. This is considered as a result of the impact of the residual heat effect in crystal resonator. In this case, by reducing the drive level properly, the frequency temperature stability increases accordingly, achieving about 1ppb in the temperature range of -20~+70℃, which explains the validity of the residual heat effect. Furthermore, after reducing the drive level appropriately, the abatement of oscillator's aging and the improvement of close-to-carrier phase noise's performance signifies that the residual heat effect of crystal resonators may be the limiting factors for improving the performance of high stability quartz crystal oscillator.**

Keywords—crystal oscillator, frequency temperature stability, residual heat effect

I. INTRODUCTION

Owing to its low aging rate, low phase noise, miniaturization, excellent temperature performance and reasonable price, crystal oscillator has been play the core role in modern electronic communication equipment market for decades, which is verified by the production of thousands of crystal oscillators in the world every day. In recent decades, the processing technology of the crystal oscillator and its internal crystal resonator have benefited from considerable development of integrated circuitry and micro machining technology, making products lighter, thinner and smaller. However, in recent years, it is caught in squeeze between two sides' attack. At the high end of technical indicators, high stability crystal oscillator has been rocked by rubidium atomic clock which is miniaturized and cheaper than before. At the low side of technical indicators, MEMS oscillator impacts on ordinary crystal oscillator. Therefore, how to improve the aging rate, the close-to-carrier phase noise and the frequency temperature (f-T) stability index of high stability crystal oscillator becomes an important issue in the research of crystal oscillator.

II. PROBLEM STATEMENT

In the experiment, we design a 36*27mm oven-controlled SC-cut crystal oscillator. Its resonance frequency is 10MHz, and operating temperature range is from -20℃ to+70℃. The oven control precision is measured by the oscillation frequency of the same SC-cut crystal (B-mode). Its f-T characteristic's diagram is linear approximately. Fig. 1 shows the frequency temperature characteristic diagram of B-mode. It can be observed in Fig.1that the temperature variation in the range of -20 - +70℃ is about 0.021℃,

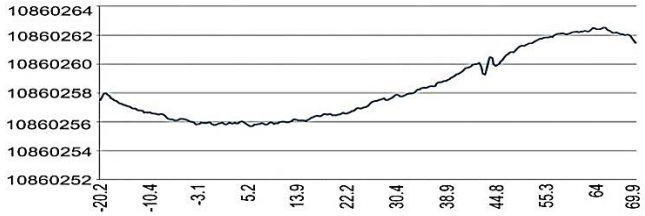


Fig 1. The temperature control precision measured with B-mode.

If C-mode is adopted, the temperature coefficient near zero temperature coefficient point is 5E-8/℃. which can make the temperature frequency accuracy of the 10MHz C-mode oscillator in full temperature range(-20—+70℃) is less than 1ppb. However, the tested f-T characteristic cannot meet the required 1ppb, as is shown in Fig. 2(a).

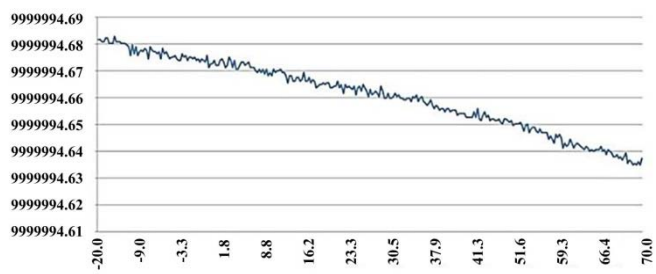


Fig. 2(a). The frequency temperature characteristic of C-mode

Through changing the resistance of the bridge, unexpectedly, the f-T characteristic of C-mode is similar to Fig. 2(b) ， having a minor variety by comparison. It has no change in trend as well, and the slope of every point is also negative. In fact, this makes it impossible for us to adjust the zero temperature coefficient point precisely to improve the index of f-T characteristic. Fig. 2(b) shows that the diagram after changing the resistance of the bridge is equivalent to the f-T characteristic curve (C-mode) after reducing the controlled temperature by 5℃.

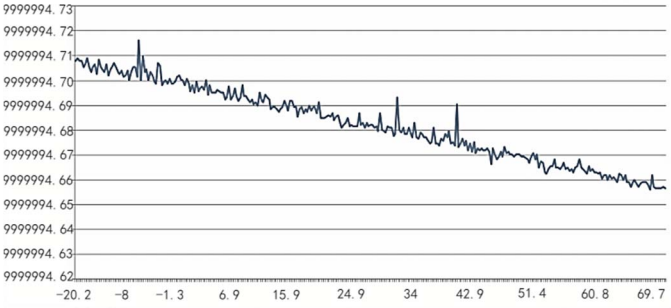


Fig. 2 (b). The C-mode frequency temperature characteristic (changing the resistance of the bridge is equivalent to reducing the controlled temperature by 5℃).

It is further found that when we intent to lower the temperature control precision, making the temperature changes over 0.04℃, the zero temperature coefficient point of C-mode can be observed clearly by adjusting bridge resistance.

III. Analysis and Experiment

If the temperature control's accuracy increases to a certain extent, the zero temperature coefficient point may disappear. It is not advisable to adjust this point precisely to improve the index of the f-T characteristic. Reducing the temperature control accuracy intentionally makes zero temperature coefficient point be able to be observed, but the increase of the f-T characteristic index is limited by inferior temperature control accuracy. This phenomenon is abnormal.

As we know, crystal resonator is based on piezoelectric effect. Mechanical vibration of the chip is driven by an alternating electric field in the oscillator circuit, and the energy of this vibration is transformed into a stable alternating electric field via piezoelectric effect. Due to the high Q value and the small electromechanical coupling coefficient, a large amount of energy would be transformed into thermal energy through the two energy conversions presented above. Part of the heat energy exists in the circuit element, which may cause the change of the temperature performance and the difference of oscillator's aging rate. Another part of thermal energy exists in the resonator, resulting in the variation of oscillator's temperature performance as well, which is called residual heat effect of crystal resonators. After improving the temperature control precision to a certain extent, this kind of effect could be observed and then become the main factor that affects accuracy.

Based on this, if the residual heat effect exists indeed, it is possible to decrease its influence and improve the f-T characteristic by reducing the drive level of oscillator properly. In Fig. 3, with the same control accuracy as Fig. 1, when the temperature changes about 0.02 ℃ in the range of -20—+70℃, the f-T characteristic of C-mode is shown under the premise that the drive power of oscillator in Fig2 is reduced to 70% (Other indicators may be effected, but this problem is prior to be verified regardless of others). It can be observed that the slope of f-T characteristic has been reversed, transformed into positive. Meanwhile, the purpose to improve the f-T characteristic index is achieved by adjusting the bridge resistance precisely. It confirms the theory that the impact of the residual heat effect does exist.

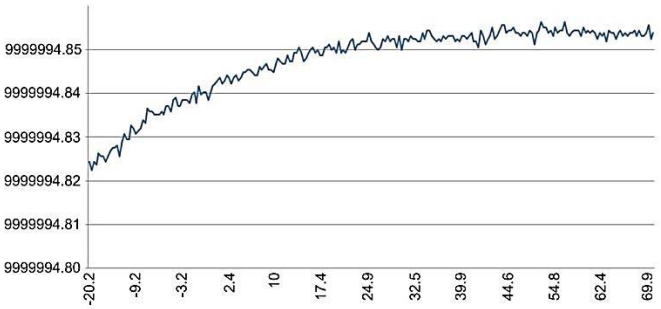


Fig. 3. The f-T characteristic after reducing the drive level of oscillator

IV. Experimental Result

After reducing the drive level of oscillator, residual heat effect of oscillator has been reduced. After adjusting the bridge resistance precisely, the f-T characteristic of a 10MHz SC-cut thermostatic oscillator can be obtained in the end (Fig 4). As it exhibits, the f-T characteristic achieves 1ppb approximately in the temperature range of -20—+70℃.

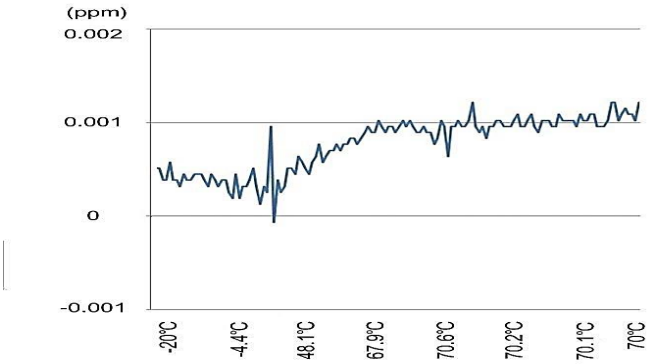


Fig. 4. The f-T characteristic in the end.

V. Conclusion

The existence of the residual heat effect of crystal resonator is resulted from two energy conversions in the crystal oscillator and small electromechanical coupling

coefficient of quartz crystal. If we lower the temperature control's precision, zero temperature coefficient point in the f-T characteristic curve may disappear, but further improvement of oscillator's f-T characteristic would be limited. To reduce the impact of this effect, the following three methods are feasible —absorbing and utilizing the residual heat, decreasing drive level in the oscillation circuit, or designing new resonator or new thermal oscillator.

Moreover, as is known to all, reducing the circuit's drive level is propitious to the improvement of the aging of crystal oscillator and the close-to-carrier (@1Hz, @0.1Hz) phase noise in the oscillator (However the noise floor would deteriorate). Yet the residual heat effect created by the energy conversion exists both in the resonator and in the circuit element, which illustrates that the residual heat effect may be the limiting factor of the high stability quartz crystal oscillator.

REFERENCES

[1] S. Houri, M. J. Geuze, and W. J. Venstra, "*Dynamic relaxation oscillations in a nonlinearly driven quartz crystal*" Appl. Phys. Lett. 107, 073502 (2015); doi: 10.1063/1.4928620.

[2] Maxim Goryachev and Serge Galliou, *" Precision Close-to-Carrier Phase Noise Simulation of BAW Oscillators "* IEEE Transactions on Ultrasonics, Ferroelectrics, and Frequency Control, vol. 58, no. 1, January 2011.

[3] Xianhe Huang, Pingping Chen, Wei Fu, and Junjie Jiao, "*Prediction, Simulation, and Verification of the Phase Noise in 80-MHz Low-Phase-Noise Crystal Oscillators*" IEEE TRANSACTIONS ON ULTRASONICS, FERROELECTRICS, AND FREQUENCY CONTROL, vol. 62, no. 9, september 2015.

[4] J. R. Vig, "*Quartz crystal resonators and oscillators for frequency control and timing applications—A tutorial*," [Online].Available:http://www.ieee-uffc.org/frequency-control/learning-vig-tut.asp.

[5] H. Brandenberger, "*High Quality Quartz Crystal Oscillators: Frequency Domain and Time Domain Stability*", 25th Annual Symposium on Frequency Control. 1971.

[6] M. M. Driscoll, "*Modeling phase noise in multifunction subassemblies*," IEEE Trans. Ultrason. Ferroelectr. Freq. Control, vol. 59, no.3, pp. 373–381, 2012.

[7] M. M. Driscoll, "*Low noise, VHF crystal-controlled oscillator utilizing dual, SC-cut resonators*," IEEE Trans. Ultrason. Ferroelectr. Freq. Control, vol. 33, no. 6, pp. 698–704, 1986.

[8] A. K. Poddar, U. L. Rohde, and A. M. Apte, "*How low can they go? Oscillator phase noise model, theoretical, experimental validation, and phase noise measurements*," IEEE Microw. Mag., vol. 14, no. 6, pp. 50–72, 2013.

[9] A. K. Poddar and U. L. Rohde, "*Crystal oscillators,*" in Wiley Encyclopedia of Electrical and Electronics Engineering. New York, NY, USA: Wiley, 2012, pp. 1–38.

[10] M. M. Driscoll, "*Oscillator AM-to-FM noise conversion due to the dynamic frequency-drive sensitivity of the crystal resonator,*" in Proc. IEEE Int. Frequency Control Symp., 2008, pp. 672–676.

Frequency stabilization of a quartz oscillator by using the method of delayed differentiation of ambient parameters

Rimantas Miškinis, Dmitrij Smirnov, Emilis Urba, Eglė Baniulienė
Time and Frequency Standard Laboratory
Center for Physical Sciences and Technology
Vilnius, Lithuania
E-mail: rimantas.miskinis@ftmc.

Albin Czubla
Time and Frequency Laboratory
Central Office of Measures
Warsaw, Poland
E-mail:a.czubla@gum.gov.pl

***Abstract*—A novel method for stabilization of a timing system based upon VCTCXO (Voltage Controlled, Temperature Compensated Oscillator) is proposed. A low-cost, low-power-consumption system developed features relative frequency stability as high as $5x10^{-9}$ as well as low sensitivity to instant jumps of temperature.**

Keywords— Voltage Controlled, Temperature Compensated Oscillator; timing system component

I. INTRODUCTION

The main drawback of temperature-compensated quartz oscillators (TCXOs) is their still insufficient temperature stability of frequency – even after decades of improvement. The main reason for that is a rather sophisticated influence of ambient temperature – thermal gradients varying with time affect the parameters of various oscillator components (quartz resonator, transistors, etc.) in different ways. While it is almost impossible to compensate for dynamic temperature effects using analogous circuitry, employing a microprocessor makes a solution possible.

We suggest a different approach based upon a novel technology – the method of delayed differentiation of ambient parameters. We have implemented such a system using commercially available components (a voltage-controlled TCXO with related circuitry, further referred to as VCTCXO) and a microprocessor-based control unit (CU), which is common for the entire system.

II. EXPERIMENTAL SYSTEM DESIGN

The system consists of the two main parts: the generator and the control unit (CU). The generator is made up by VCTCXO composed of a 10 MHz CFPT-126 type thermo-compensated rectangular signal oscillator and decoupling elements: a 74AXP1G06 type buffer and a HCPL9030 type high speed unidirectional digital isolator, and a DS18B20 type digital thermometer. The buffer features very low input capacitance – 0.5 pF. The operation of the digital isolator is based upon the giant magneto-resistance (GMR) effect. The both units are necessary to reduce the influence of external load on the operation of the system. CU consists of a version 2.0 Raspberry-Pi (RPi) single-board computer, a DAC8564 digital-to-analog converter, and an LTV-844 photocoupler.

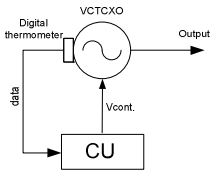


Fig. 1. Layout of the experimental system

The operating principle of the system is as follows. RPi receives temperature data from the digital thermometer, processes them, and sends them through the photocoupler to the DAC. Based upon the data received, the DAC forms the DC tuning voltage for the control of the oscillator frequency. The peak-to-peak stability of the DC tuning voltage is about ±30 μV per 24 hours, the voltage step is about 38 μV, which ensures that the deviation of the output frequency from the nominal value variation doesn't exceed 1·10-9 (0.01 Hz).

The system has two independent power supply units. The generator and the DAC are fed with high stability voltage of (3.3000 ± 0.0005) V from the dedicated power supply unit; those components are decoupled galvanically from the other components of the system, which are fed with voltage of 5.0 V from a standard power supply unit.

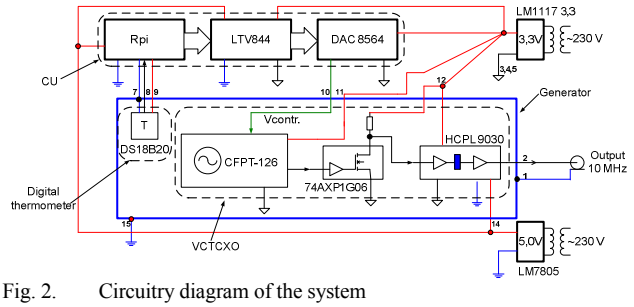


Fig. 2. Circuitry diagram of the system

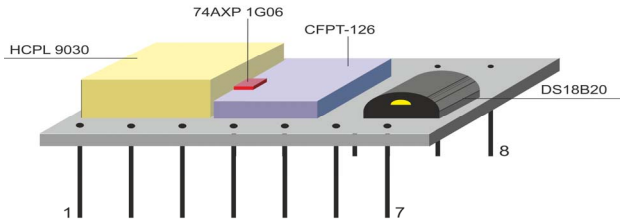


Fig. 3. The composition of the generator components

The main components of the generator are mounted in the metal-glass case 1203(151.15-2), which temperature is measured by the digital thermometer. The composition is depicted in Fig. 3.

III. IMPROVED ALGORITHM FOR TEMPERATURE COMPENSATION

Initially, we have intended the system for use at room temperature. Therefore, we have optimized the frequency stability parameters for the range of temperature of about (23 ± 10) °C.

At first, we have tested our system without thermo-compensation. The results imply that the system features temperature coefficient of frequency cannot be determined unambiguously: its value is about +0.032 Hz / °C when the temperature is constant or slowly varying; however, fast

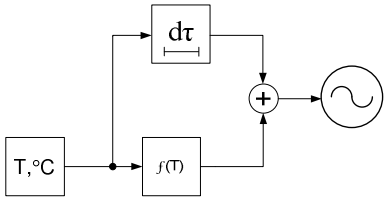


Fig. 4. Realization of generator thermo-compensation composition of the generator components

changes of case temperature (of the order of 1 °C / min) cause relative frequency offset of about $1.5 \cdot 10^{-8}$, which is too large for some applications. Frequency offsets caused by slowly varying temperature are easy to compensate, however, dynamic frequency compensation is problematic so far. Usually, such compensation requires a high resolution temperature sensor, or even several sensors, to evaluate thermal gradients inside the oscillator case. Sophisticated solutions with no temperature sensors as such are also used.

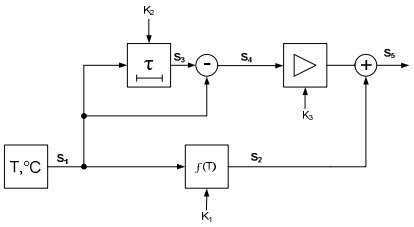


Fig. 5. The algorithm for the temperature compensation of frequency in detail

Temperature data from the digital thermometer are fed into CU, which forms the frequency correction signal proportional to the deviation of the case temperature from 23 °C. The frequency correction signal is generated by using a two-branch calculation model, where the first branch produces a linear correction (+0.032 Hz / °C) signal for constant or slow temperature changes, and the second branch produces a correction signal by means of our novel delayed differentiation algorithm (DDA) to compensate for fast changes of case temperature.

The essence of the delayed differentiation method proposed is the following: temperature data are differentiated not as usually (by subtracting the current value from the previous one) but by subtracting the current value from the value obtained some time ago. In other words, to control difficult to predict response of the system to fast temperature changes, we have not only to take into account the current value of temperature but also to evaluate the previous temperature data. We have arrived at the idea while analyzing the method of continuous control of chaos by self-controlling feedback. On the other hand, the control circuitry must have some properties of a band-pass filter because fast and large thermo-jumps are mitigated by the case of the generator (they turn into slow or small temperature changes inside the case), while very slow temperature variations are properly compensated by the f (T) branch. However, there is still some area of intermediate thermal effects difficult to compensate. Using a massive case would almost eliminate the problem but it wouldn't be the best solution for modern technology. The method of delayed differentiation of ambient parameters proposed by us allows using standard cases; it is intended for the abovementioned area of uncompensated thermal effects. In this paper, it is realized as described above; it has a delay element and features the properties of a band-pass filter (in our case, a combination of a high-pass filter and a group of rejection filters).

Fig. 5 outlines the algorithm for the temperature compensation of frequency in detail. The temperature data fed to the delayed differentiation branch of the algorithm are branched. The signal S1 in the first branch is delayed (the delay time is defined by setting the value of the coefficient K2) to produce the signal S3, which is subtracted from the non-delayed signal S1 in the second branch. The result of subtraction, the signal S4, is multiplied by the coefficient K3 and added to the signal S2 to produce the signal S5 used for adjusting the generator frequency. f (T) is the abovementioned linear correction function with the coefficient K1, which in our case is +0.032 Hz / °C. Generally, f (T) may be a more complex function, e.g., a polynomial, a multidimensional segmented polynomial array, or an artificial neural network.

IV. EXPERIMENTAL RESULTS

We have measured the frequency stability of the generator by means of the direct frequency measurement, using the standard methods. An SR-620 universal time interval counter operating in the frequency measurement mode is synchronized to the 10 MHz reference signal from the Lithuanian state time and frequency standard (a cesium atomic clock). The frequency value is registered every second.

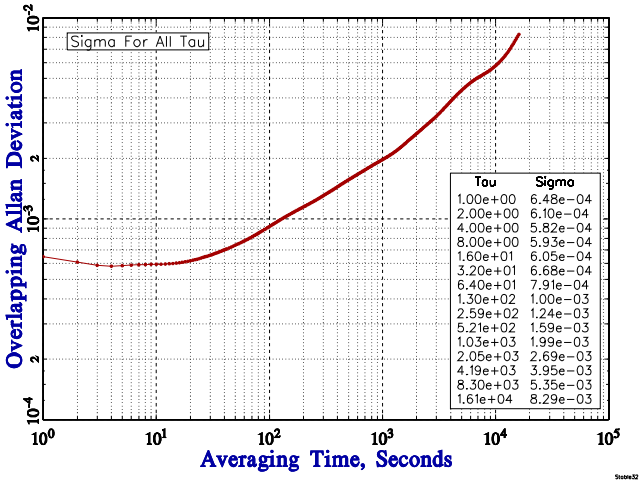


Fig. 6. Stability characteristic (in Hz) of the generator output frequency without software temperature compensation (the nominal frequency is 10 MHz)

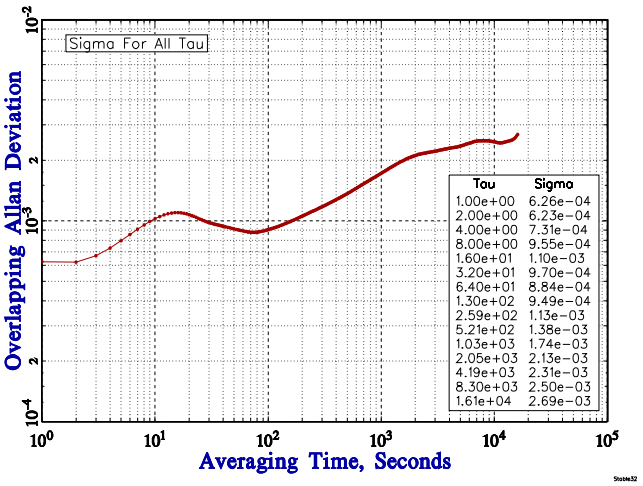


Fig. 7. Stability characteristic (in Hz) of the generator output frequency with software temperature compensation (the nominal frequency is 10 MHz)

Fig. 6 reveals a stability characteristic (the two-sample, or Allan, variance) of the output frequency of the generator without software-driven temperature compensation at normal operating conditions (without fast changes of temperature), while Fig. 7 reveals the same characteristic with the temperature compensation. The results of Fig. 7 imply that the temperature compensation algorithm improves the generator stability characteristics at long durations (starting with about 1 hour and longer), however, it slightly degrades them at short durations (10 to 20 s). Insignificant worsening of the stability characteristics is related to the rate and resolution of the data from the digital thermometer (in this case, sampling period is about 10 s, and the resolution is about 0.1 ºC).

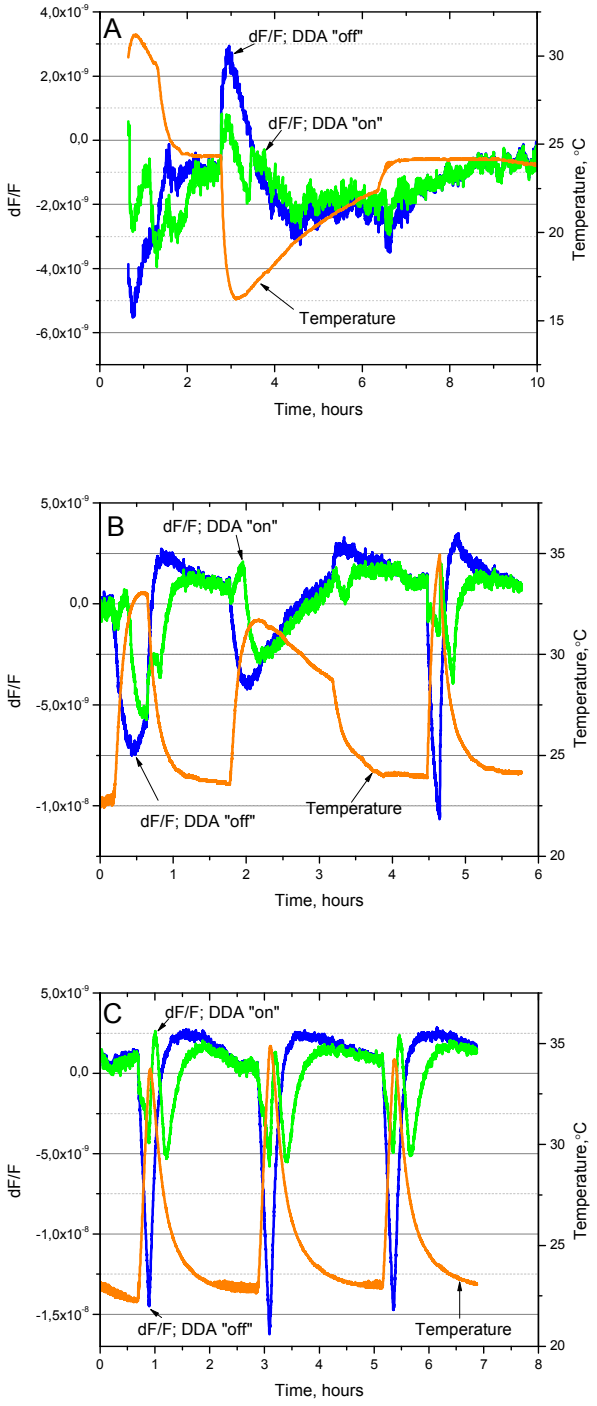


Fig. 8. The output frequency behavior of the generator operating in the two modes – with DDA on and off

Fig. 8 illustrates the impact of fast temperature changes on the generator output frequency. Here, the temperature is depicted by the orange lines, the output frequency when the software is compensating the temperature in a conventional mode, i. e., the linear temperature correction of frequency are

depicted by the blue lines, and the green lines show the output frequency when the algorithm for delayed differentiation of ambient parameters (DDA) is applied. It is seen from Fig. 8 A that a jump of temperature causes a sharp jump of frequency when the system is operating in the conventional mode, however the frequency jump is several times smaller when the DDA is on. To achieve a proper operation of the algorithm, it is necessary to fit the constants K_2 and K_3 taking into account the character of the most common or the most problematic temperature jumps, while the constant K_1 must be chosen for a concrete device regardless of the operating conditions. Fig. 8 B describes the frequency response with temperature changing more or less arbitrarily. Fig. 8 C reveals that the method is especially suitable for compensating periodical temperature jumps.

CONCLUSIONS

A relatively inexpensive realization of a generator with the stability increased by at least two times is possible.

Such a system requires commercially available components only and is flexible in the sense of programming; it allows employing external computing capabilities.

REFERENCES

[1] S. Fry, "Design and performance of precision miniature TCXOs", *RF Design*, pp. 44-50, Sept. 2006.

[2] K. Pyragas, „Continuous control of chaos by self-controlling feedback", *Phys. Lett. A*, vol. 170, no. 6, pp. 421-428, Nov. 1992.

Concept and main results for ultraprecise low noisy 10 MHz DOCXO ensuring Allan deviation of 1…2E-13 for 1…10 s.

Yakov Vorokhovsky, Arkady Nikonov, Aleksander Kotyukov, Alexey Kamochkin
Morion Inc., St.-Petersburg, Russia
morion@morion.com.ru

Abstract— A technical solution to combine the advantages of a new generation's DOCXO ensuring ~E-11 vs. temperature with ADEV of 1…2E-13 for 1…10 s has been created. It should be noted that a frequency stability vs. temperature change considerable improvement (up to 2…3E-11 for 55°C) allows reliable measurements of ADEV at 10 s (2E-13 as normal value) and considerably improves phase noise measurement for 0.1 Hz offset(up to -93…-96 dBc/Hz).

Keywords— OCXO, DOCXO, Phase noise, Allan Deviation

I. INTRO

Operation of modern telecom, navigation, control and measurement systems requires reference frequency sources. Their performance actually determines the systems' main characteristics. Frequency stability vs. temperature, long-term and short-term stabilities, and phase noise are the most important for many applications.

High-stability oven-controlled low-noisy crystal oscillators are one of those sources. Some examples of those oscillators' application are given below:

- 5 to 10 MHz crystal oscillators are being used in phase-lock loops of atomic frequency standards. Crystal oscillators in these systems determine phase noises at 0.1 Hz and higher and Allan deviation for 0.1 … 10 s;
- 5 to 40 MHz crystal oscillators are being used in synchronization modules for time base maintenance,

etc., etc.

Requirements for reference frequency sources are constantly tightened. Phase noise reduction with simultaneous improvement of frequency stability vs. temperature and long-term are often required [1].

The level of frequency stability vs. temperature change may directly influence Allan deviation (ADEV) for longer than 3 s intervals. It should be mentioned that even frequency stability vs. temperature up to 2…4E-10 could have a significant influence on the Allan Deviation. A task to create 10 MHz oscillators with frequency stability vs. temperature of 2…5E-11 combined with phase noise of -120 dBc/Hz at 1 Hz and ADEV of 1…2E-13 for 1…10 s is a real challenge.

II. FREQUENCY STABILITY VS. TEMPERATURE

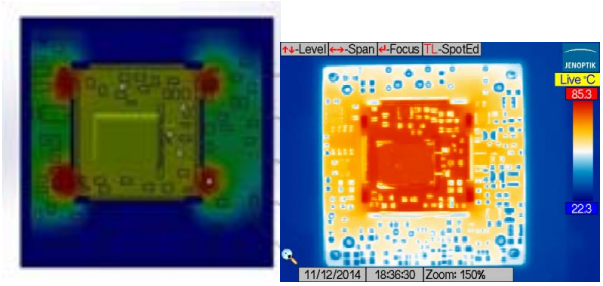
The achievement of excellent frequency stability vs. temperature requires the designers' considerable experience and attention to details in order to reject plenty of unsuitable solutions. Continuously growing requirements to the devices' dimensions make the oscillator's development task even more difficult.

To get frequency stability vs. temperature of about 1E-11 creating of double oven X-tal oscillator (DOCXO) is required.

To create a precise DOCXO we need to minimize temperature influence on the oscillator. The contribution of the crystal on the frequency stability vs. temperature of the oscillator is negligibly small, because the temperature of the crystal varies very little and double-rotated cuts of crystals with very little temperature coefficients are being used.

The frequency stability vs. temperature of the oscillator is caused by the temperature dependencies of the individual elements: capacitors, inductances, transistors, etc. Using thermal modelling for oscillators' designs, various circuitry and design solutions can significantly reduce the influence of various factors on the frequency stability vs. temperature [2], [3] and allow to achieve frequency stability up to 2…3E-11 vs. -20 ... +70°C.

The finite elements' method [4], [5] has been used for thermal modelling. Thermal modelling software allows to take into account such factors as: individually adjustable thermal conductivity of materials, the area of thermal contact between the material and the heating element, air convection and its influence on the heat transfer, dynamic thermal map of the design (i.e. during the warming or cooling of the structure). Registration of the above mentioned factors allows the building of the thermal model being very close to real conditions. This is shown on the Fig. 1, where the thermal model of the oscillator and its infrared camera picture can be seen.



a) Thermal model b) Infrared camera picture

Fig. 1. Comparison of the thermal model and infrared camera picture.

III. THERMAL MODEL OPTIMISATION

To get the excellent frequency vs. temperature stability we need to minimize heat transfer between crystal and most thermal sensitive elements, minimize temperature changes and thermal gradient on these elements. Heat transfer can be carried out in several ways: radiation, air convection and heat transfer through the design structure. The greatest contribution is made by heat transfer through the design structure, since the radiation and air convection heat transfer are much smaller. That means we need to have a good thermal isolation between crystal and most thermal sensitive elements and the rest of design.

You can see simplified DOCXO's thermal circuit on Fig.2

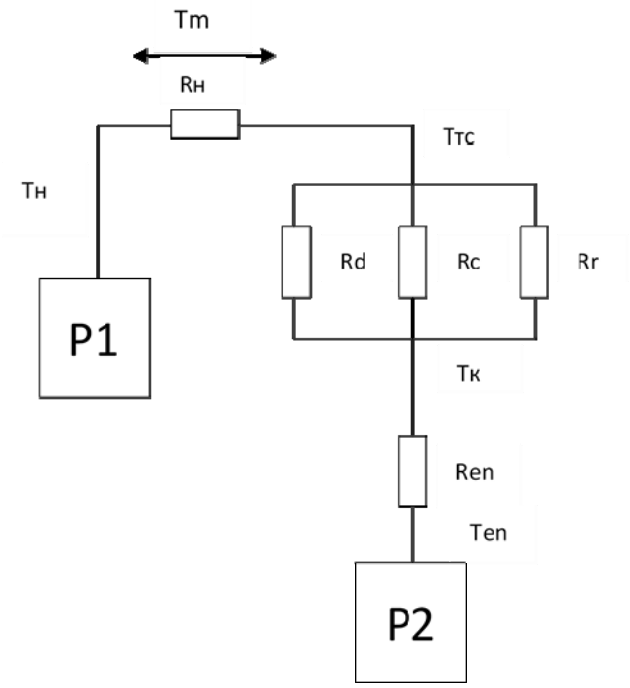


Fig. 2. Simplified thermal circuit of DOCXO: P1 - the source of heat flow, which sets the temperature T_H; P2 – the equivalent source of heat flow, which sets the temperature Ten; T_H – temperature near the heater of the oven; T_{TC} - crystal and most thermal sensitive elements' temperature; T_K – rest oscillator's design temperature; Ten – environmental temperature; R_H – thermal resistance between heater and crystal; Rd - thermal resistance because of the heat transfer through the design structure; Rc - thermal resistance because of the air convection; Rr - thermal resistance because of the radiation; Ren - thermal resistance between oscillator's design and environment.

Oven usage helps us drastically reduce fluctuations of T_{TC} when Ten changes.

P1 > P2 in normal operation mode. The heat flux can be represented as:

$$P = \Delta T / R_F$$

$$\Delta T = T_H - Ten ,$$

where R_F - thermal resistance between heater and environment that can be represented as:

$$R_F = (Rd \times Rc \times Rr)/([Rd \times Rc] + [Rc \times Rr] + [Rr \times Rd]) + Ren + R_H \quad (1)$$

In this case, the error temperature (Tm), which shows the quality of temperature maintenance on the crystal and most thermal sensitive elements, will be represented as:

$$Tm = P * R_H \quad (2)$$

As we can see from (2), we need to increase R_F and decrease R_H to reduce fluctuations of T_{TC} when Ten changes.

Increasing of the Ren is achieved by the thermal isolation between the internal stage and external case. Rr is much bigger than other thermal resistances. Rc can be drastically increased when internal oscillator's space is filled with the low thermal conductive material.

To increase Rd we need to reduce thermal connection between crystal and most thermal sensitive elements in the rest of the design.

Design optimization of DOCXO allows to achieve so good temperature stabilization of the crystal that its frequency vs. temperature stability becomes negligible for the corresponding stability of the oscillator.

New design DOCXO required resolution of several technical tasks, namely:

- internal stage design selection;
- provision of internal reference voltage high stability;
- provision of keeping high stability of the internal oven temperature;
- proper decoupling from loading.

IV. PHASE NOISE AND ALLAN DEVIATION

A. Circuitry

Circuitry solutions have a direct effect on phase noise and Allan Deviation [6].

In order to improve phase noise close to the carrier (0.1…10 Hz offsets), maximization of the systems quality factor is

require. I.e. it is necessary to choose such oscillator circuit that will allow to maximize loaded Q factor of a crystal resonator.

Maximal "clean" voltage shall be supplied to the oscillator's circuit and matching cascades as it considerably influences the phase noise close to the carrier.

A special attention shall be paid to oven-controlled low-noisy oscillator's PCB layout. All interferences caused by the oven's current may result in a considerable degradation of both the near and far zone noises and Allan Deviation for 1…10 s. Those fenomenas shall be minimized or completely excluded.

Quality of matching the buffer cascade to oscillator cascade and crystal circuit in particular, as well as the noise factor thereof, has a considerable influence on the far zone noises (1 kHz…1MHz offset). Optimization of the above described factors allows 10…20 dB improvement for the phase noises in the far zone.

B. Crystal

Design of low-noisy oscillators is impossible without a good crystal.

Significantly tight demands to the phase noise and Allan Deviation require a drastical improvement of crystals.

The measures below are aimed for the crystal parameters' considerable improvement with regard to phase noise and Allan Deviation:

- Special technology of crystal blank's surface treatment that enabled a higher yield according to most tight phase noise and Allan Deviation specification has been developed and implemented.
- Measuring system, enabling crystal testing at different power dissipations, has been developed. Use of this system caused the increase of the yield for the tightest phase noise close to the carrier.
- Studies to determine optimum power dissipation in a crystal with regard to the close to the carrier phase noises have been carried out [7], [8]. The experimental results are given in Table 1. The shown data enabled determination of a crystal type that will ensure high reliability within a long lifetime.

TABLE I. DEPENDENCE OF 10 MHZ OSCILLATOR PHASE NOISE AT 1 HZ OFFSET ON POWER DISSIPATED IN CRYSTALS.

Dissipated power, uW	**20**	**27**	**35**	**45**	**55**
Crystal, type 1	-119	-120	-120	-120	-119
Crystal, type 2	-116	-118	-120	-119	-117
Crystal, type 3	-115	-117	-118	-118	-117

The Table above shows that type 1 crystal is the least sensitive to the dissipated power.

C. Results

A new solution that combines a new generation's DOCXO ensuring ~E-11 vs. temperature with ADEV of 1…2E-13 for 1…10 s has been created. The obtained results are demonstrated on Fig. 3, 4.

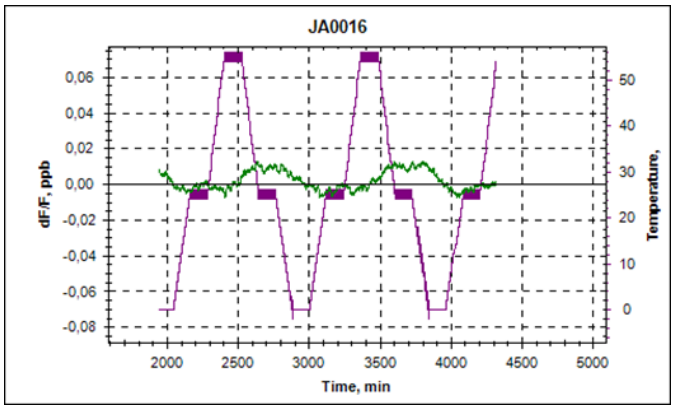
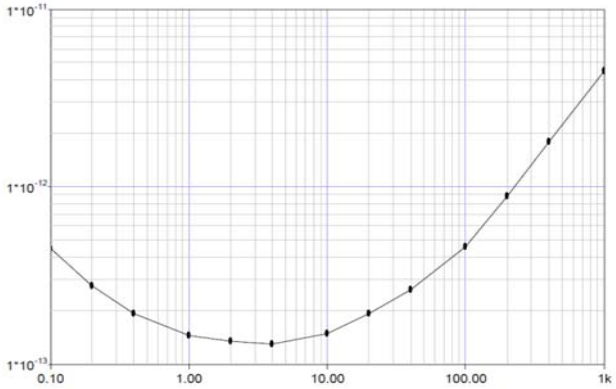
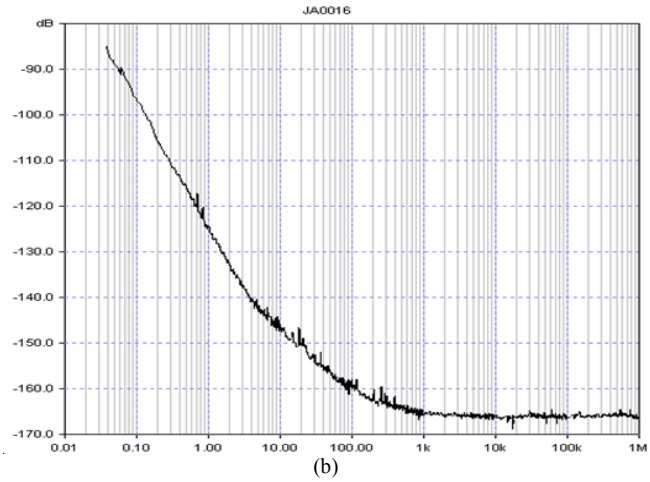


Fig. 3. Typical frequency stability vs. temperature for 10 MHz ultra low-noisy oscillators of the new generation.



(a)



(b)

Fig. 4. Typical Allan deviation (a) and phase noises (b) for ultra low-noisy oscillators of the new generation.

It should be noted that considerable improvement of frequency stability vs. temperature - up to 3…4E-11 for +70°C temperature change – allows to conduct reliable measurements of ADEV at 10 s (2E-13 as normal value) and considerably

improves phase noise measurement for 0.1 Hz offset (up to -93…-96 dBc/Hz). Package of ultra low-noisy oscillators of the new generation can be seen at Fig. 5.

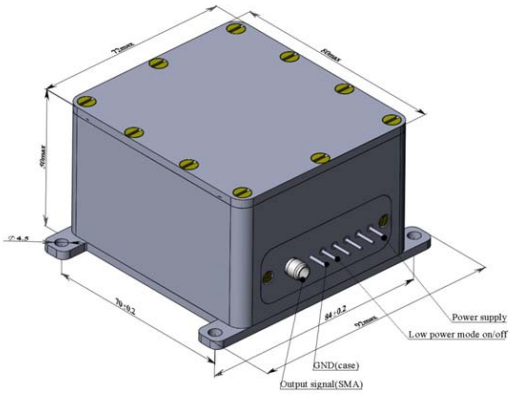


Fig. 5. Package of the ultra low-noisy oscillator of the new generation.

D. Allan Deviation vs. temperature measurement

ADEV of 1…2E-13 for 1…10 s could be degraded by the mechanical vibrations from standard thermal chambers with refrigerator inside it. In order to avoid mechanical effects, a thermal chamber with thermoelectric cooler has been developed (Fig. 6).



Fig. 6. Thermal chamber with thermoelectric cooler.

The results of the measurements can be seen at Fig. 7.

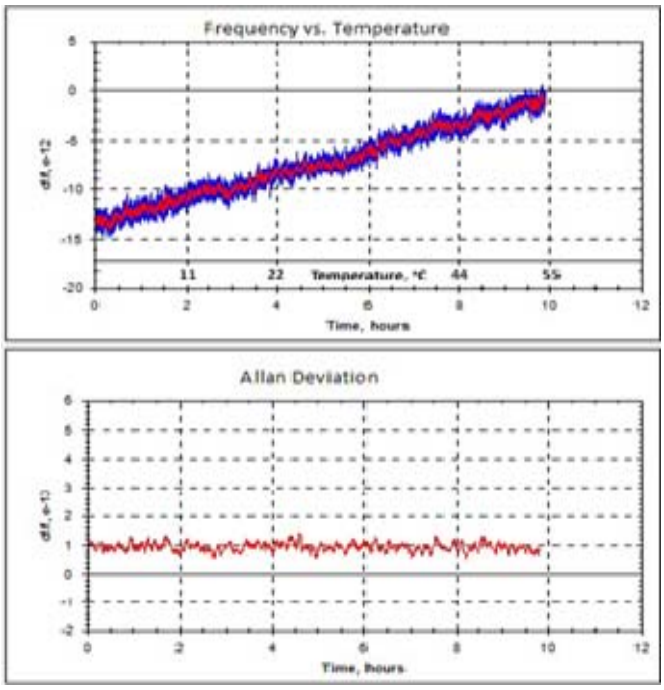


Fig. 7. Allan Deviation for 10 seconds vs. temperature changes from 0 to +55°C in 900 seconds window for ultra low-noisy oscillators of the new generation.

The continuous measurement of frequency difference between reference and measured oscillator per 10 seconds have been done. Allan deviation curve for Fig. 7 was obtained as follows: one counting was obtained as Allan Deviation calculation for 900 seconds segment, next, the computation window was moved at one step (10 seconds) and the calculation was repeated.

V. NEXT STEPS

1. Electrical digital tuning with the step 1…3E-14 is being implemented.
2. An oscillator in standard package 2”x2”x1”, meeting frequency stability up to 2…3E-11 vs. -20 to +70°C and ADEV of 1.5…2E-13 for 1…10 s is being designed.

REFERENCES

[1] Vorokhovsky Y., Nikonov A., Kotyukov A., Kamochkin A., “Current State of Precision Quartz Frequency Stabilization With Regard to Time-Frequency Support Tasks”, 8-th International Symposium "Metrology of Time and Space", 2016

[2] Nikonov A.G., Kotyukov A.V., Kamochkin A.S., Dyakonova N.I., “Recent achievements in performance of low profile ultra precision single oven quartz oscillators.”, EFTF2012

[3] Vorokhovsky Y., Nikonov A., Kotyukov A., Kamochkin A., “Efficiency of circuitry and design optimization in development of precision ovenized quartz oscillators”, PTTI2014

[4] Bastian Pentenrieder, “Finite element solutions of heat conduction problems in complicated 3D geometrics using the multigrid method.”, 2005, Technical University of Munich

[5] Nikishkov G.P., “Introduction to the Finite Element Method”, 2004, Lecture Notes, University of Aizu, Japan

[6] Kotyukov A., Nikonov A., Belyaev E., Kamochkin A., “Ultra-Precision Low-Noise Quartz Oscillators for Time Storage Tasks Solution in Telecommunication and Metrological Systems ”, 8-th International Symposium "Metrology of Time and Space", 2016

[7] Шитиков Г. Т., Цыганков П. Я., Орлов О. М., “Высокостабильные кварцевые автогенераторы”, «Советское радио», 1974

[8] Альтшуллер Г. Б., “Управление частотой кварцевых автогенераторов.”, «Связь», 1975

10 GHz Low Timing-Jitter and Broadband Optical Comb Generation Based on an Optoelectronic Oscillator

Huanfa Peng, Yongchi Xu, Xiaofeng Peng, Cheng Zhang, Lixin Zhu, Weiwei Hu and Zhangyuan Chen*
State Key Laboratory of Advanced Optical Communication Systems and Networks
School of Electronics Engineering and Computer Science, Peking University
Beijing 100871, P. R. China
Email: *chenzhy@pku.edu.cn

***Abstract*—10 GHz repetition rate, low timing-jitter and broadband optical comb generation based on a low phase noise optoelectronic oscillator is experimentally demonstrated. 10 GHz repetition rate optical comb and 10 GHz RF signal are obtained, simultaneously. A timing-jitter of 52.8 fs (integral range from 100 Hz to 1 MHz) for the optical comb and a phase noise of -132 dBc/Hz at 10 kHz offset for the RF signal are experimentally achieved. The influence of laser frequency noise on the timing-jitter of the optical comb is also investigated.**

Keywords—Optical comb; Optoelectronic oscillator; Timing-jitter; Phase noise

I. INTRODUCTION

Optical frequency comb (OFC) has attracted great attention for its many potential applications. Such as metrology, communication, and signal processing. In the past few decades, OFC plays a key role in the photonic analog-to-digital convertor (ADC) system [1]. Due to its lower timing-jitter than that of the electronic-based sampling clocks, the effective number of bits (ENOB) of the ADC can be brought to new levels [2]. With the development of photonic ADC towards high sampling-rate and better accuracy, an optical pulse source with high repetition-rate, low timing-jitter, and broadband is urgently required. Conventionally, some schemes are used to generate optical pulses [3]. One category is mode-locked laser (MLL), another utilizes the four-wavelength mixing in a high Q micro-resonator, and the other is based on the cascaded electro-optical modulators. The MLL can generate broadband OFC with low timing-jitter. Usually, the repetition-rate of the MLL is below 1 GHz. The second one can achieve an ultra-high repetition-rate and broadband OFC. The timing-jitter of the OFC based on the third one is limited by the phase noise of the external electronic oscillators. Recently, the combination of optical comb generator (OFCG) and optoelectronic oscillator (OEO) is a candidate to obtain an OFC with high repetition-rate, low timing-jitter, and broadband, simultaneously [3]. It has great potential in the application of photonic ADC [4].

In this paper, a 10 GHz low timing-jitter and broadband OFC generation system based on an OEO is proposed and experimentally demonstrated. Compared with [3], the optical bandpass filter (OBPF) is removed which improves the power efficiency of the system. Due to the narrow-bandwidth and high frequency stability of the transmission resonance of the high finesse Fabry-Perot (F-P) cavity inside the OFCG, the OFCG can serve as the oscillation mode selector instead of the narrow-bandwidth electrical bandpass filter (EBPF) [5,6]. Furthermore, a laser with low frequency noise, two optical isolators, and low phase noise amplifiers are utilized to reduce the timing-jitter of the optical pulses. A 10 GHz RF signal with single-sideband (SSB) phase noise of -132 dBc/Hz at 10 kHz offset and an OFC with timing-jitter of 52.8 fs (integral range from 100 Hz to 1 MHz) are obtained, simultaneously.

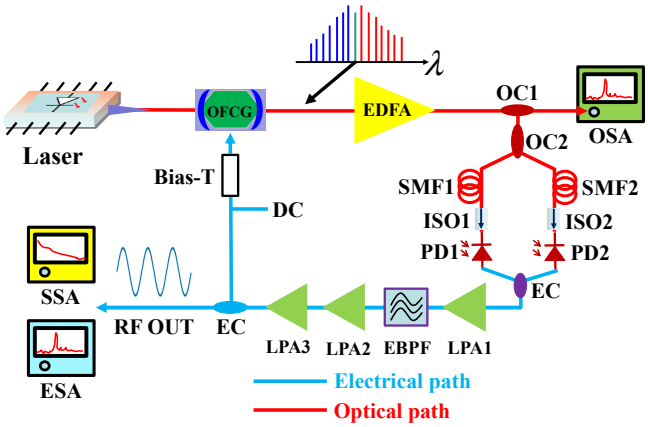


Fig. 1. Setup of the proposed 10 GHz OFC generation system based on an OEO. OFCG, optical comb generator; OC1, OC2, optical couplers; SMF1, SMF2, single-mode fibers; ISO1, ISO2, optical isolators; PD1, PD2, photodiodes; EC, electrical coupler; LPA1, LPA2, LPA3, low phase noise amplifiers; EBPF, electrical bandpass filter; ESA, electrical spectrum analyzer; SSA, signal source analyzer; OSA, optical spectrum analyzer.

II. PRINCIPLE AND EXPERIMENTAL SETUP

Fig. 1 shows the experimental setup of the proposed 10 GHz OFC generation system based on an OEO. The key component of the system is the OFCG. It is formed by a $LiNbO_3$ waveguide phase modulator inside a high finesse F-P cavity. The free-spectral range (FSR) and finesse of the F-P cavity are 2.5 GHz and 60, respectively [5]. Thus, the full width half maximum (FWHM) of the transmission resonance is about 42 MHz. The F-P cavity can be served as the mode selector instead of a narrow-bandwidth EBPF in the OEO loop. Due to the periodic transmission resonances of the F-P cavity, the frequency of the supported oscillation modes in the OEO

loop are integer multiples of the FSR. A 10 GHz EBPF with 3-dB bandwidth smaller than the FSR of the F-P cavity is utilized to suppress the unwanted transmission resonances of the F-P cavity. The temperature of the F-P cavity is stabilized by a temperature control system which improves the frequency stability of the OEO. The OFCG is driven by the feedback 10 GHz electrical signal through a Bias-T. Two single-mode fibers (2 km SMF1, 0.5 km SMF2) are used to suppress the oscillation side-modes. Due to the poor performance of the optical return loss (ORL) of the photodiodes (PD1, PD2), two optical isolators (ISO1, ISO2) are utilized to decrease the optical reflection induced phase noise. Three low phase noise amplifiers (LPA1, LPA2, and LPA3) with ultra-low flicker phase noise are intend to provide sufficient gain and improve the close-in phase noise performance of the OEO. The optical spectrum of the generated OFC is consisted by two sets of sidebands which correspond to two optical pulse trains. The repetition-rate of either of the two pulse trains is equal to the modulation frequency of the OFCG. By tuning the DC bias voltage applied on the OFCG, the two pulse trains can be merged to one single pulse train [5]. Thus, the OBPF used to select one pulse train to generate the feedback RF signal in [3] can be removed.

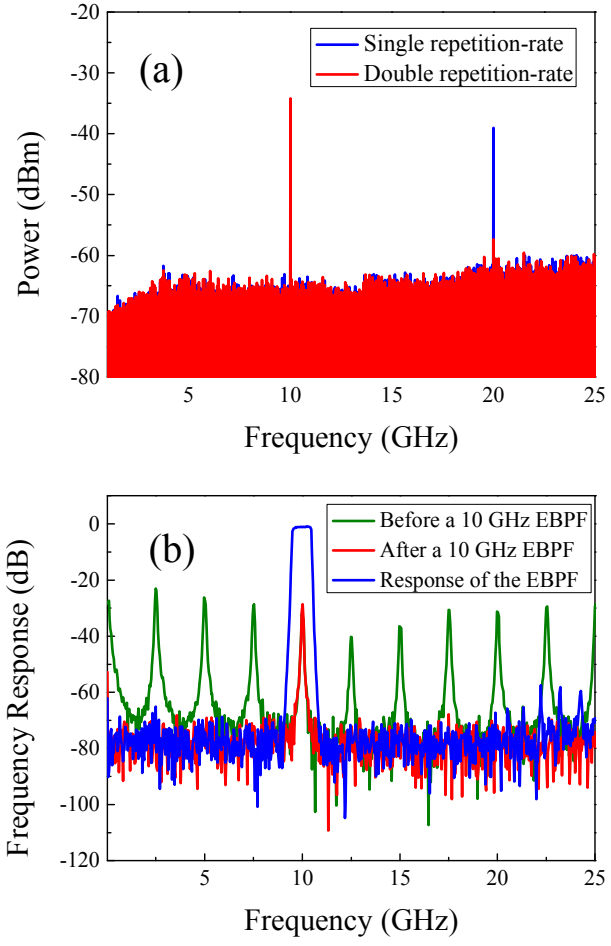


Fig. 2. (a) Photo-detection of the RF signal with 10 GHz modulation; (b) Frequency responses of the OFCG before and after the 10 GHz EBPF.

III. RESULTS AND DISCUSSION

An experiment based on the setup shown in Fig. 1 is implemented. Fig. 2(a) shows the photo-detected electrical signal from the output of OFCG with 10 GHz modulation frequency. By tuning the DC voltage applied on the Bias-T, a 10 GHz signal and a 20 GHz signal can be individually achieved. In order to obtain a feedback electrical signal whose frequency is equal to the modulation frequency to form a closed OEO loop, the DC bias voltage of the OFCG should be operated at the point which can generate 10 GHz signal. Fig. 2(b) shows the transmission responses of the OFCG measured by a vector network analyzer (VNA). The transmission resonances locate at integer multiples of FSR, as shown by the green curve in Fig. 2(b). In order to obtain single mode oscillation, a 10 GHz EBPF is employed to suppress the unwanted transmission resonances, as shown by the red curve.

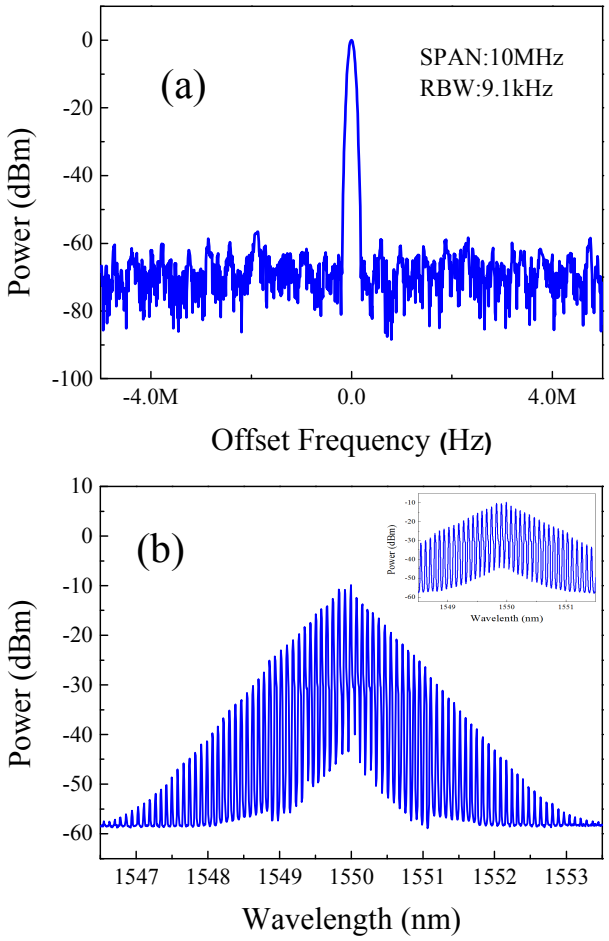


Fig. 3. (a) Electrical spectrum of the 10 GHz RF signal; (b) Optical spectrum of the generated OFC with observation span of 7 nm. (Inset: zoom in of the optical spectrum).

Fig. 3(a) shows the measured electrical spectrum of the generated 10 GHz RF signal by an electrical spectrum analyzer (ESA, Keysight N9030A). The observation span and resolution bandwidth are 10 MHz and 9.1 kHz, respectively. Correspondingly, a broadband OFC is achieved, as shown in Fig. 3(b). The optical spectrum consists of symmetrical sidebands. The frequency difference of the adjacent comb lines

is equal to 10 GHz, which is determined by the modulation frequency. The inset of Fig. 3(b) is the zoom in of the optical spectrum of the OFCG.

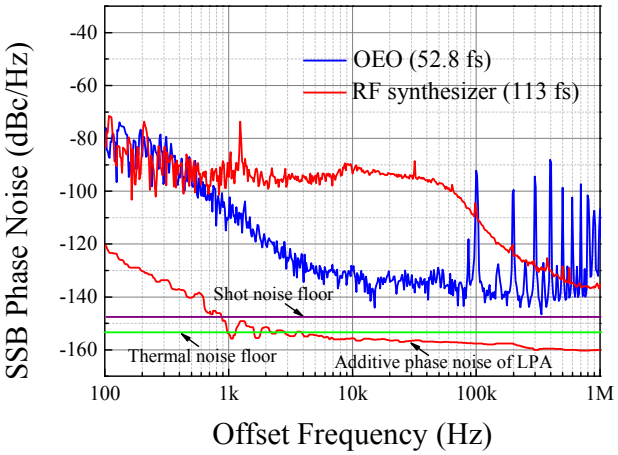


Fig. 4. SSB phase noise of the photo-detected 10 GHz RF signal from the optical pulses. For comparison, SSB phase noise of a 10 GHz RF synthesizer is also measured.

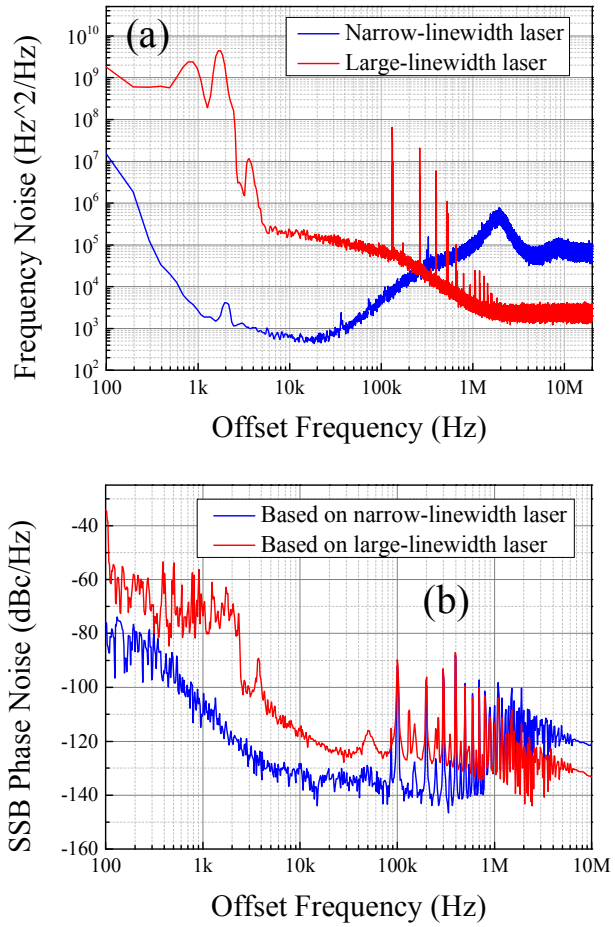


Fig. 5. (a) The measured frequency noise of the lasers used in the experiment; (b) Comparison of SSB phase noise for the OEOs by using different lasers.

The timing-jitter of the OFC is estimated by the phase noise of the photo-detected 10 GHz electrical signal, as shown in Fig. 4. The SSB phase noise of the oscillation 10 GHz signal is measured by a signal source analyzer (SSA, Keysight E5052B+E5053A down-convertor). The measured SSB phase noise of the 10 GHz RF signal is -132 dBc/Hz at 10 kHz offset. The timing-jitter of the optical pulse is calculated to be 52.8 fs with an integral range from 100 Hz to 1 MHz.

To investigate the frequency noise of the laser on the timing-jitter performance of the generated OFC, a narrow-linewidth and a large-linewidth lasers are utilized to perform a comparison. Fig. 5(a) shows the measured frequency noise of the two lasers by an optical noise analyzer (SYCATUS, A0040A). Correspondingly, the SSB phase noise of the 10 GHz OEOs by using the two lasers are shown in Fig. 5(b). It investigates that the OFC generation based on a narrow-linewidth laser achieves better timing-jitter performance than that of the large-linewidth laser. To achieve better timing-jitter performance of the OFC, a laser with lower frequency noise is preferred.

IV. Conclusion

In conclusion, a 10 GHz repetition-rate, low timing-jitter and broadband OFC generation based on an OEO is proposed and experimentally demonstrated. A timing-jitter of 52.8 fs is obtained with an integral range from 100 Hz to 1 MHz.

Acknowledgment

This work was supported in part by the National Natural Science foundation of China (Grant No. 61690194, Grant No. 61401005 and No. 61505002).

References

[1] G. C. Valley, “Photonic analog-to-digital converters,” Opt. Express 15, 1955-1982 (2008).

[2] A. Khilo, et. al., “Photonic ADC: overcoming the bottleneck of electronic jitter,” Opt. Express 20, 4454-4469 (2012).

[3] X. Xie, T. Sun, H. Peng, C. Zhang, P. Guo, L. Zhu, W. Hu, and Z. Chen, “Low-noise and broadband optical frequency comb generation based on an optoelectronic oscillator,” Opt. Lett. 39, 785-788 (2014).

[4] H. Peng, X. Peng, Y. Xu, C. Zhang, L. Zhu, W. Hu, and Z. Chen, “20 GS/s Photonic Analog-to-Digital Converter Using Optical Comb Based on an Optoelectronic Oscillator,” in proceedings of Conference on Lasers and Electro-optics, San Jose, CA (CLEO, 2016), paper SW3M. 4.

[5] S. Xiao, L. Hollberg, N. R. Newbury, and S. A. Diddams, “Toward a low-jitter 10 GHz pulsed source with an optical comb generator,” Opt. Express 16, 8498-8508 (2008).

[6] I. Ozdur, D. Mandridis, N. Hoghooghi, and P. J. Delfyett, J. Lightw, Technol., VOL. 28, NO. 21 3100-3106.

Effect of Joule Heating on the Performance of a Piezoresistive Micromechanical Oscillator

Liu Xu, Xueyong Wei*, Dong Pu, Zhuangde Jiang
State Key Laboratory for Manufacturing Systems Engineering, Xi'an Jiaotong University
Xi'an, 710049, China
*Email: seanwei@mail.xjtu.edu.cn

Juan Ren
School of Construction Machinery, Chang'an University
Xi'an, 710054, China
Email: juan.ren@chd.edu.cn

***Abstract*—Piezoresistive sensing has been regarded as an effective transduction method in MEMS resonator researches and piezoresistive micromechanical oscillators are therefore of great interests. The induced joule heating in the piezoresistive sensing, however, has a strong effect on the performance of the device. In this work, a micromechanical double ended tuning fork (DETF) based piezoresistive oscillator is studied. The results show the oscillation frequency drifts and the frequency stability decreases when the resonator body temperature increases due to the Joule heating. A linear trend between the minimum Allan deviation and the piezoresistive current is observed from the experiment.**

Keywords—Piezoresistive; Joule heating; micromechanical oscillator; frequency stability;

I. INTRODUCTION

Micro-and nano-electromechanical systems play more and more important roles in revolutionary technology. MEMS devices have superb applicability and offer fast-responding, low power consumption elements to many scientific disciplines such as telecommunications, transportation and healthcare. With the reduction in size, their frequency stability which is one of the most important features of oscillator is affected by their material, temperature stability, packaging and other factors reported in many academic studies. Frequency stability is one of the most principle problems to deal with over the past decades [1-3].

Piezoresistive effect, a phenomenon, has been seen in some crystalline or non-amorphous materials when mechanical strain is applied. The paper by C. S. Simth was one of the earliest reports highlighting the inherent piezoresistive effect in silicon. In contrast to the piezoelectric effect, the piezoresistive effect leads to a change only in the electrical resistance not in electric potential [4].

The piezoresistive and capacitive sensing methods have been widely used in the study of the micromechanical resonators. The capacitive method is commonly used to drive micromechanical resonators and to detect the mechanical motion, which is convenient to implement on chips. Instead of the capacitive sensing method, the piezoresistive sensing method shows an improved transduction characteristic and can be used to detect the mechanical motion of micro resonators due to the intrinsic piezoresistive effect of single-crystal silicon (SCS) [5-7]. However, the thermal effect induced by the Joule heating cannot be avoided and the increase of drain current may soften the beam due to the negative temperature coefficient of Young's modulus for SCS. When large currents flow through the narrow beam, Joule heating causes it to expand, soften and overshoot, thus the frequency drifts and the frequency stability will be degraded [8].

II. DESCRIPTION OF NEW SYSTEM

In this work, the effect of Joule heating on the performance of a piezoresistive micromechanical DETF oscillator is investigated. The DETF resonator with a length of 428μm, a width of 7μm and a thickness of 25μm is microfabricated based on the standard silicon on insulator (SOI) technology. After wire bonding, the device is placed in a vacuum environment for tests. The structure of the resonator is shown in Fig.1 and the in-phase lateral vibrational mode of the DETF resonator is discussed in this work. A schematic representation of the measurement setup for the open-loop measurement is shown in Fig. 1 [9].The DETF resonator is electrostatically actuated by combining a *DC* with an *AC* voltage on a unilateral moving electrode which is attached at the point of the largest displacement. The length of moving electrode is 140μm. A parallel capacitor is formed between the moving electrode and the fixed electrode. The beam is then excited by a periodical electrostatic force proportional to the product of V_{dc} and V_{ac}.

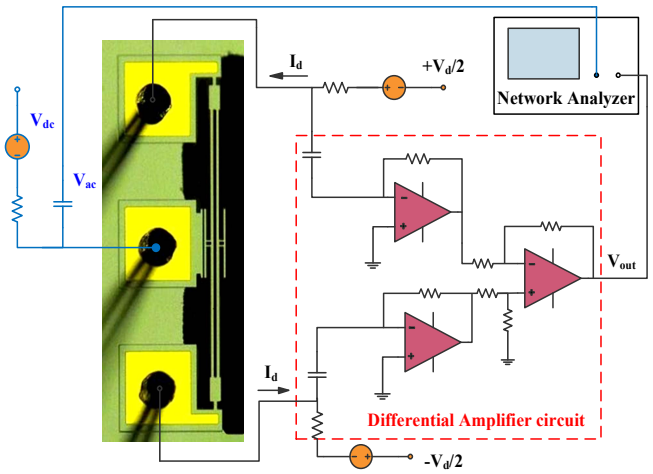


Fig. 1. Schematic representation of open-loop measurement setup for the double-ended tuning fork silicon micro-resonator.

The traditional configuration of piezoresistive sensing of capacitively actuated resonator may generate heavy feedthrough which hampers the accurate measurement of the resonance characteristics and changes the frequency response curve with an anti-resonance peak. This is particularly helpful when it is possible to use a differential sensing method which is employed to cancel the common-mode signals [10]. The transfer function of our system is expressed as:

$$H(\omega) = \frac{V_{out}}{V_{in}} = K_2 K_1 [2g_m + j\omega(C_{f_1} - C_{f_2})] \qquad (1)$$

Where K_1 is the gain of transimpedance amplifiers and K_2 is the gain of the differential amplifier. g_m is the trans-conductance of the system, and C_{f1}, C_{f2} are the feedthrough capacitance.

In this work, the in-phase vibration mode of DETF is studied and Fig.2a shows its mode shape. The first order frequency is 357.2 kHz obtained from the Finite Element Method simulation. Applying the differential piezoresistive sensing configuration to the DETF resonator, the complete cancellation of feedthrough is achieved, which could precisely measure the piezoresistive signal. In the course of measurements, the DETF resonator is fixed to the circuit board and placed in a vacuum at a pressure of 0.01 Pa and the room temperature of 25 ˚C. Using a trans-impedance amplifier to convert the output current of resonator to a voltage and amplified output power is collected and calculated by a network analyzer. The frequency response was measured while the drain current was decreased from 7 mA to 5 mA in step of 1 mA and the bias voltage was kept unchanged (V_{DC} of 13V and V_{AC} of -5dBm) as shown in Fig. 2b, which verifies that the frequency drift have a positive correlation to the drain currents.

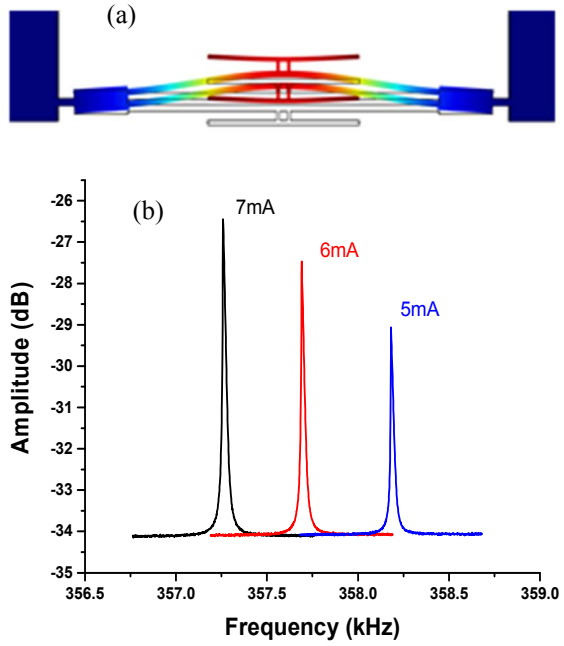


Fig. 2. (a) FEA simulated mode shape of in-phase mode in a DETF resonator. (b) Open-loop response of the DETF resonator at various drain currents.

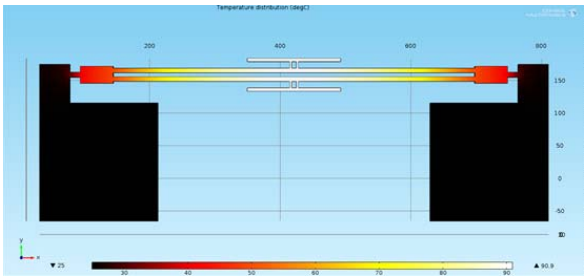


Fig. 3. Simulated temperature distribution in DETF at constant drain current.

The temperature of the bending beam rises, caused by the flow of large drain current thought it. FEM simulation of temperature distributions is shown in Fig. 3 when a constant drain current flows thought the beam. The silver color indicates higher temperature while the black is lower. The temperature distribution is symmetric about the center. Heat flows across the beam from hot to cold regions, dissipating thermal energy via the anchors. At the region of the beam close to the anchor whose dissipation area is large, the temperature dissipate faster, but the heat only dissipates through the surface of the middle region of the beam, which results in a higher temperature in the center. From Fig. 3, it can be seen that the temperature of the DETF ends is about to 25 ˚C which is in close proximity to the room temperature of the vacuum chamber and the temperature of the center is about to 91 ˚C, which is the highest temperature region of the DETF beam.

DETF resonator is embedded within the feedback loop of the oscillator circuit, which includes an amplifier, band-pass filter, phase shifter and gain controller. In this closed-loop oscillator, one signal of the comparator outputs is fed back to the driving electrode to excite the DETF resonator and the other one is fed into the frequency counter as shown in Fig. 4. According to the previous studies, we have known that the frequency stability is sensitive to the total phase shift of the closed-loop. The DETF is kept oscillation with the total phase of the loop close to zero. The resonant frequency of DETF drifts as the drain current varies and the total phase shift may fluctuate to some extent. The absolute value of the total phase shift caused by Joule heating is ignored in our experiment. The design parameters of band-pass filter are set to constant in the experiment.

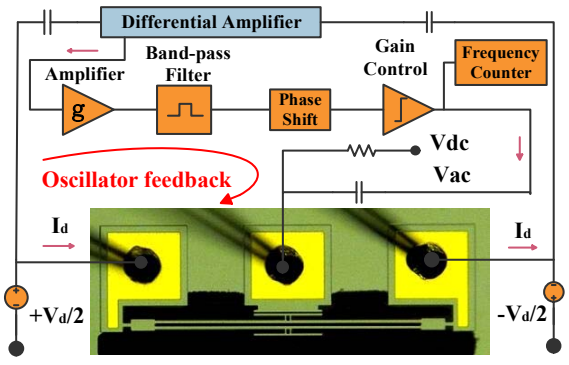


Fig. 4. Microscopic picture and schematic of the measurement setup of the piezoresistive DETF oscillator.

The output response of the oscillators is observed using a spectrum analyzer and the result is shown in Fig. 5. It is clear that a self-sustained oscillation is observed as only a single peak of 347 KHz appears in the spectrum, which is close to the resonant frequency and its magnitude can be controlled by V_{dc} and V_{ac}. The frequency outputs are logged by frequency counter with a sampling time of 1ms for 90s. Allan deviation is calculated to evaluate the frequency stability of the oscillator. The drain current I_d is voltage-controlled by V_d, while the amplitude V_{ac} is fixed at 237 mV, and the bias V_{dc} is set to 8V.

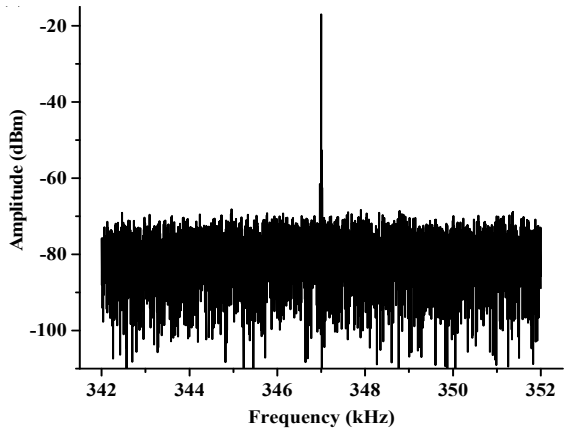


Fig. 5. Measured frequency spectrum of output signal of the piezoresistive DETF oscillator.

III. Experiment Results

Parameters f_0 and Q are the two significant performance metrics in the micro-resonator domain. For low enough energy dissipating, the system response shows tops at these particular frequencies. In addition, each resonator frequency equivalents to a particular mode of the motion known as a mode shape can be simulated by Finite Element Method. And the quality factor is defined as:

$$Q = 2\pi \frac{Average\ energy\ stored}{Energy\ lost\ per\ cycle} \tag{2}$$

We can estimate the resonant frequency of the system by locating the top in the frequency response while the quality factor can be calculated from:

$$Q = \frac{f_0}{\Delta f_{-3dB}} \tag{3}$$

Where, Δf_{-3dB} is the -3dB bandwidth around the resonator's frequency. From the data collected by the open-loop measurements, we calculate the quality factor by Eq. (3) which is 10000 when the drain current is 7mA.

The currents are forced through the beam throughout by the *DC* voltage source. Changing the voltage of the electrode plate at both ends of the beam cause to change the magnitude of drain currents which are through the beam. The drain current is increased from 6.6mA to 11.4mA with a step of 1.6mA and the bias voltages are constant. Four sets of time-domain frequency data are taken by the frequency counters and calculated by Allan deviation. The resultant Allan deviation σ is illustrated by the solid lines in Fig. 6 with different colors, for integration times covering five orders of magnitude.

The dashed line in Fig. 6 shows the thermal noise limit predicted, based on the *DR* formula expressed in the current domain [11-12].

$$\sigma_{A,exp} \approx \frac{1}{2Q}\frac{1}{SNR}\sqrt{\frac{1}{2\pi\tau}} \tag{4}$$

Where Q is the quality factor of the resonator, *SNR* is the signal-to-noise ratio, and τ is the integration time. We rescale the temperature to 300K and assume the *SNR* depends on temperature T and to scale like $\propto T^{-1/2}$. The calculated and extracted mechanical and electrical parameters are shown in Table I.

TABLE I. Design Parameters Of The DETF Resonator.

Parameter	*Source*	*Value*
Q	Measured	10000
SNR	Measured	50.6 dB
τ	Measured	1ms to 11s
σ	Eq. (4)	$1.18\times10^{-5} \rightarrow 8.34\times10^{-8}$

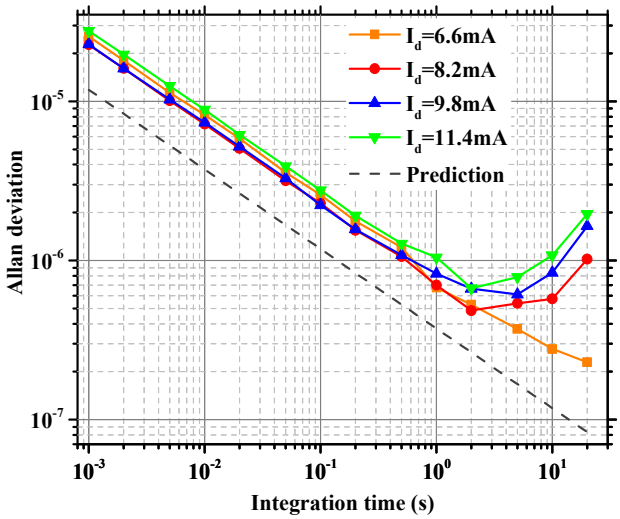


Fig. 6. Allan deviation of the DETF oscillator for integration time between 1ms and 20s with different drain current I_d.

Fig. 6 clearly shows that equation (4) accurately describes the frequency stability of our resonator for short integration times. This result suggests that, within this range, frequency stability of the oscillator drops as drain current increases which is attributed to thermal noise. The resonator body gains a higher temperature under larger drain current due to the Joule heating. Similarly, for longer integration times, the experimental observation significantly is in accordance with the expected behavior. The Allan deviation of green line whose drain current is 11.4mA is higher than the organ line whose drain current is 6.6mA in the whole integration times from 1ms to 11s. In the

other words, with increasing the drain currents, Joule heating cause a rise of the resonator's body temperature and make the magnitude of thermal nose higher than before.

It can be found that when integration time is above 2s, Allan deviation of each series at various drain currents can get the minimum value. The minimum Allan deviation of the measured oscillator as a function of drain current I_d is plotted in Fig. 7. A linear trend between the drain current and the Allan deviation is observed. The increase of Allan deviation implies that the frequency stability goes worse because of the piezoresistive transduction scheme induced self-heating.

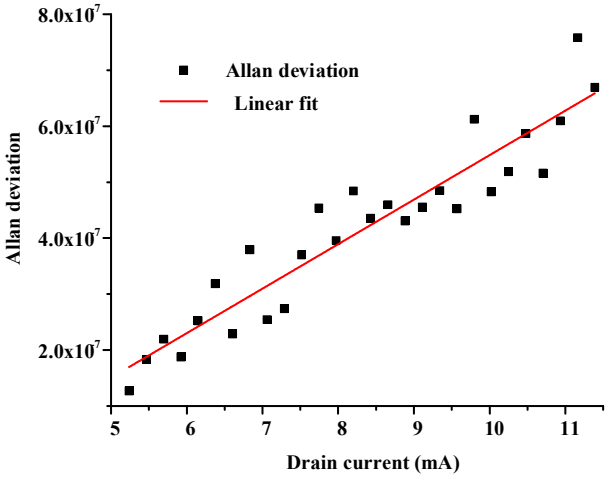


Fig. 7. Calculated Allan deviation ascends for a set of increasing drain current domain and the corresponding linear fit is given.

IV. CONCLUSIONS

Piezoresistive sensing has been regarded as an effective transduction method in MEMS research. In our system, the piezoresistive oscillator is implemented with a DETF resonator and a differential feedback circuit. The Allan deviation of the DETF oscillator with various drain currents is calculated for four sets of time-domain frequency data and the thermal noise limit line predicted by using DR formula. The results show the oscillation frequency drifts and the frequency stability decreases when the resonator body temperature increases due to Joule heating. A linear trend between the minimum Allan deviation and the piezoresistive current is observed.

ACKNOWLEDGMENT

This work is supported by the National Natural Science Foundation of China (51575439 and 51421004), Natural Science Foundation of Shaanxi Province (2014jm2-5054) and 111 project (B12016). We also appreciate the support from the Collaborative Innovation Center of High-End Manufacturing Equipment and International Joint Laboratory for Micro/Nano Manufacturing and Measurement Technologies.

REFERENCES

[1] Abdolvand, Reza, et al. "Micromachined Resonators: A Review." 7.9(2016):160.
[2] Craighead H G, "Nanoelectromechanical systems", Science, 2000, 290(5496): 1532-1535.
[3] Vanier J,"The Measurement of Time: Time, Frequency and the Atomic Clock", Physics Today, 2003, 56(2):45–67.
[4] Hopcroft, Matthew A. "Temperature-stabilized silicon resonators for frequency references." Vol. 68. No. 09. 2007.
[5] Sundaram, Subramanian, S.M. Massachusetts Institute of Technology. "Thermally-actuated piezoresistively-sensed mechanical silicon oscillator." Massachusetts Institute of Technology (2014).
[6] Zhang, Weiguan, H. Zhu, and E. Y. Lee. "Piezoresistive Transduction in a Double-Ended Tuning Fork SOI MEMS Resonator for Enhanced Linear Electrical Performance." IEEE Transactions on Electron Devices62.5 (2015):1596-1602.
[7] Lin T H, Lee E Y, Yan J, et al, "Methods for enhanced electrical transduction and characterization of micromechanical resonators", Sensors & Actuators A Physical, 2010, 158(2):263-272.
[8] Sundaram, S, and D. Weinstein. "Bulk mode piezoresistive thermal oscillators: time constants and scaling."Ultrasonics Ferroelectrics & Frequency Control IEEE Transactions on 62.8(2015):1554-1562.
[9] Wei X, Zhang T, Jiang Z, et al. "Frequency latching in nonlinear micromechanical resonators." Applied Physics Letters, 2017, 110 (14): 143506.
[10] Wei X, and Seshia A. A. "Differential piezoresistive sensing in a bulk-mode micromechanical resonator." Micro & Nano Letters, 8.2 (2013):107-110.
[11] Antonio D, Zanette D H, López D, "Frequency stabilization in nonlinear micromechanical oscillators", Nature Communications, 2012, 3(3):806-806.
[12] Sansa M, Sage E, Bullard E C, et al, "Frequency fluctuations in silicon nanoresonators", Nature Nanotechnology, 2016, 11(6):552-55

Quantum Theory of 1/f Frequency Fluctuations

Macroscopic Quantum Interference Present in Fundamental 1/f Noise Measured Since 1925

Peter H. Handel
Department of Physics and Astronomy & Center for Nanoscience
University of Missouri-St. Louis
Saint Louis, MO 63121, USA
handel@umsl.edu

***Abstract*— The conventional Quantum 1/f (Q1/f) Effect is present in any scattering cross section or process rate involving charged particles or current carriers. The present paper shows how bremsstrahlung and decoherence at all frequencies yield *macroscopic quantum interference*, resulting in probability density fluctuations at all frequencies in the outgoing scattered beam, that are observed as fundamental base-band 1/f noise and as 1/f frequency fluctuations, or phase noise close to carrier, in materials, devices, and resonant or non-resonant systems. We emphasize the role of the phenomenon of quantum decoherence showing that the fundamental, universal 1/f noise is both a phenomenon of decoherence and of the infrared divergence of quantum electrodynamics. This eliminates the last persisting misunderstandings of the Q1/f Theory and of this new field of Infra-quantum Physics. On this basis we give the first universal engineering formulas, applicable for the ultra-low noise optimization of all Hi-Tech applications, of the materials, devices and systems of modern industry, microelectronics, nanotechnology, highest stability resonators, oscillators and clocks, MEMS, and any resonant and non-resonant sensors. Q1/f noise, i.e, the coherent and conventional Q1/f Effects, is a new fundamental aspect of quantum physics, as basic as space and time. In resonators and oscillators, fundamental frequency fluctuations come usually from 1/f fluctuations in the dissipation.**

Keywords—electronic noise, phase noise close to carrier, fundamental 1/f noise, oscillators, resonators, quartz, MEMS, sensors.

I. INTRODUCTION

A. Conventional Quantum 1/f Effect Semiclassical Derivation

Consider scattering of a beam of charged particles, e.g., electrons, on a fixed force center. Part of the scattered wave function will have suffered bremsstrahlung energy losses. Decoherence [1] will randomize the phases of these bremsstrahlung loss components. They will then interfere with the main, non-bremsstrahlung part, giving additional 1/f noise currents in the scattered beam. The total outgoing scattered current per unit solid angle, divided by the incoming current density, is the scattering cross section $\sigma(\theta,\phi)$ *showing 1/f noise*.

To derive this quantum 1/f noise presnt in the scattering cross section, we start with the classical (Larmor) formula $2q^2\mathbf{a}^2/3c^3$, for the power radiated by a particle of charge e and acceleration **a**. The acceleration can be approximated by a delta function $\mathbf{a}(t) = \Delta\mathbf{v}\delta(t)$, whose Fourier transform $\Delta\mathbf{v}$ is constant and is the change in the velocity vector of the particle during the almost instantaneous scattering process. The one-sided spectral density of the emitted bremsstrahlung power $4e^2(\Delta\mathbf{v})^2/3c^3$ is therefore also constant. The number $4e^2(\Delta\mathbf{v})^2/3hfc^3$ of emitted photons per unit frequency interval is obtained by dividing with the energy hf of one photon. The probability amplitude of photon emission $[4e(\Delta\mathbf{v})^2/3hfc^3]^{1/2}e^{i\gamma}$ is given by the square root of this photon number spectrum, including also a phase factor $e^{i\gamma}$. Decoherence randomizes this phase [1]. Let ψ be the resulting Schrödinger wave function of the scattered outgoing charged particles, which is a single particle function. The beat term in the probability density $\rho=|\psi|^2$ is linear both in this bremsstrahlung photon emission amplitude and in the non-bremsstrahlung amplitude. Its spectral density will therefore be given by the product of the squared probability amplitude of photon emission (proportional to 1/f) with the squared non-bremsstrahlung amplitude (that is independent of f, because it represents the whole current, with negligible bremsstrahlung reductions, yielding only second-order terms). The resulting spectral density of fractional probability density fluctuations is obtained by dividing with $|\psi|^4$ and is therefore given by the conventiona Q1/f formula

$$|\psi|^{-4}S_{|\psi|^2}(f) = 8q^2(\Delta\mathbf{v})^2/3hfNc^3 = 2aA/fN = j^{-2}S_j(f) = S_{\delta\sigma/\sigma}, \quad (1)$$

where $\alpha = e^2/\hbar c = 1/137$ is the fine structure constant and $\alpha A = 4q^2(\Delta\mathbf{v})^2/3hc^3$ is known as the infrared exponent in quantum field theory. It will be called the quantum 1/f noise coefficient in electro-physics. The experimentally measured quantity also depends on some superposition or averaging processes and is often called, for historical reasons, a Hooge constant.

Eq. 1 seems to have been derived for just one particle. In fact, the derivation proceeds with a two-particle wave function, which is the product of two single-particle wave functions, or a slater determinant with two single, non-interacting, particle states. This leads to a bilinear result in the two-particle wave function, explaining the presence of products of four single-particle wave functions. Physically we understand this best through analogy with diffraction of non-interacting particles through a small opening. A single particle just gives an impact point on the screen, but the two-particle wave function already contains the information about the diffraction rings. The random phase of the 1/f noise current from each particle causes the 1/f noise power spectra to add, just as the currents add. The power spectrum is thus proportional to the number

N of particles used to define the current, just as the total current is. For the spectrum of fractional fluctuations we need to divide by the squared current, and this justifies the presence of N in the denominator of Eq. (1).

Eq. (1) was also derived in second quantization, using the commutation rules for boson field operators. For fermions one repeats the calculation replacing in the derivation the commutators of field operators by anticommutators, which yields

$$\rho^{-2}S_\rho(f) = j^{-2}S_j(f) = \sigma^{-2}S_\sigma(f) = 2\alpha A/f(N-1) \qquad (2)$$

This causes no difficulties, since $N \geq 2$ for particle correlations to be defined, and it is practically the same as Eq. (1), since usually $N >> 1$. Eqs. (1) and (2) suggest a new notion of "physical cross sections and process rates" which contain 1/f noise, and express with macro-quantum interference, a new law of physics, important in most high-technology fields.

B. Coherent Quantum 1/f Effect and General Q1/f Formula

In addition to the quantum 1/f effect (Q1/fE) just described, which I called "conventional" and which is present in the newly introduced notions of physical cross sections and process rates, there is also another type of Q1/fE. It is the "coherent Q1/fE," present in any current J, whether it was subject to a scattering process, or not. This one arises because of the coherent state of the electromagnetic field of any free physical particle, e.g., an electron. Indeed, if we consider the physical particle as being the bare particle plus its electromagnetic field, it will be described by a non-stationary state, because the field is not in an energy eigenstate. Such a non-stationary state always exhibits quantum fluctuations in time and space. Both the simple and the second-quantized calculations yield a simple universal 1/f noise power spectrum of a current of physical electrons or of any other charged particles. Specifically, the spectral density $S_{\delta J/J}(f)$ of fractional current fluctuations is [2]

$$S_{\delta J/J}(f) = 2\alpha/\pi fN. \qquad (3)$$

Here N is again the number of carriers used to define the current J. This is the coherent Q1/fE engineering formula.

The conventional Q1/fE in cross sections and process rates corresponds to the independent motion of particles, represented in the Hamiltonian by the kinetic energy of the particles' drift motion, $E_k = Nmv_d^2/2$. The coherent Q1/fE, on the other hand, comes from the coherent superposition of all vector potentials and magnetic fields generated by the particles, and from the coherent states in which the corresponding vector potential field oscillators are, which are not energy eigenstates. It is represented by the magnetic energy $E_m = 0.5LI^2$ in the hamiltonian. As a first approximation, we consider a superposition of the conventional and coherent quantum 1/f noise contributions proportional with the weight of the corresponding terms in the energy of a solid conductor or semiconductor carrying a current J with current density j. In very small samples or electronic devices, this magnetic energy

$$E_m = \int (B^2/8\pi)d^3x = [nevS/c]^2 \ln(R/r) \qquad (4)$$

is much smaller than the total kinetic energy E_k of the drift motion of the individual carriers

$$E_k = \sum_i m_i v^2/2 = nSmv^2/2 = E_m/s. \qquad (5)$$

Here we have introduced the magnetic field B, the carrier concentration n, the cross sectional area S and radius r of the cylindrical sample (e.g., a current carrying wire), the radius R of the electric circuit, and the "coherece ratio"

$$s = E_m/E_k = 2ne^2S/mc^2 \ln(R/r) = 2e^2N'/mc^2, \qquad (6)$$

where $N' = nS$ is the number of carriers per unit length of the sample and the natural logarithm ln(R/r) has been approximated by one in the last form. We expect the observed spectral density of the total fundamental Q1/f noise found in mobility fluctuations to be given by a relation of the form [2]

$$(1/\mu^2)S_\mu(f) = [1/(1+s)][2\alpha A/fN] + [s/(1+s)][2\alpha/\pi fN], \qquad (7)$$

which can be interpreted as an expression of the effective "Hooge constant" if the number N of carriers in the (homogeneous) sample and f are brought to the numerator of the left-hand side. *Only the conventional Q1/fE applies directly to the frequency fluctuations in resonators and oscillators.*

C. Past Misunderstandings

The Quantum Theory of 1/f Noise was misunderstood by some for many years, for many reasons, but finally for only one reason: In general, the bremsstrahlung energy loss components emerging from any scattering, or from other processes, are known *not to interfere with the main wave function*, (while we have claimed, interference usually happens. with random phases. As a special exception, I had also observed that decoherence happens only to 10% in beta radioactive decay!). The emergent bremsstrahlung energy loss components are indeed known to be orthogonal, with phases differing by 90 degrees in a certain quantum representation. *Therefore, some said that the Q1/f theory, based on such interference, was not valid.* But the experiment always verified my formulas in all domains, universally. *Their mistake was that they ignored the universal phenomenon of quantum decoherence,*. Indeed, soon after the superposition state with 90 degrees phase differences is created by brems-strahlung, decoherence scrambles the hases, *randomizing them*, as I always assumed in my theory of both the conventional and coherent quantum 1/f effects, which I introduced. This is why Schrödinger's cat is never found half dead and half alive, and why we don't have quantum computers yet!

This was finally understood by the scientific community, after a 2013 paper of mine [1], and there are no other logical objection left to my theory, and to my simple, practical, universal engineering formulas. They are applicable to all

high-tech fields, for anything existing in any do-main, in time and space. It's as basic as time and space, since it also happens with gravitons as infraquanta! I have all formulas for that quantum gravidynamic (QGD) 1/f noise also, including the "s' " parameters, combining the gravidynamic coherent and conventional contributions. It limits all existence in time and space, it sets fundamental limits to highest frequency stability, and to our knowledge of time and frequency. Our amply verified [2], universal, simple Q1/f engineering formulas allow us to reduce even these fundamental limits, by optimizing the system with Q1/f optimization.

Another sourse of misunderstandings was the frequency and temperature dependence of the Q1/fEs. Indees, quantum effects are generally known to occur at high frequencies and low temperature. Most critics verlooked that here Planck's constant appears in the denominator, which revrses these dependencies! The classical limit is thus not finite, is described by the earlier form of our theory, the turbulence theory of 1/f noise in an infinite, isotropically and homogeneously stirred plasma of charge sarriers. All are special forms of our "sufficient criterion" for 1/f noise at www.umsl.edu/~handel.

II. FREQUENY FLUCTUATIONS IN QUARTZ, MEMS, OR OTHER RSONATORS AND OSCILLATORS

A. Bulk Acoustic Wave (BAW) Quartz Resonators

The rate Γ of phonon interactions which remove phonons from the main quartz resonator mode is modulated by the conventional quantum 1/f effect, therefore exhibiting observable (macroscopic) quantum fluctuations, which causes Q1/f fluctuations in the resonance frequency $\omega=(\omega_0^2-\Gamma^2)^{1/2}$. Indeed, whenever a phonon is removed from the main resonator mode, the time-derivative of the polarization vector of the quartz crystal $d\mathbf{P}/dt=\dot{\mathbf{P}}$ is suddenly affected, suffering a step-like modification as a function of time. From Maxwell's equations we know, however, that $\dot{\mathbf{P}}$ is added to the current density **j** and that such a modification of the current causes radiation. Solving Maxwell's equations we find, like in the Introduction above, that as a result of the phonon removal there is a constant energy of $(1/4\pi\varepsilon_O)^4(\Delta\dot{\mathbf{P}})^2/3c^3$ radiated away per Hertz at any frequency f. Dividing this result by the energy of a photon hf, we find, as before, that there is thus a probability of $2\alpha(\Delta\dot{\mathbf{P}})^2/3\pi fe^2c^2$ for the emission (radiation) of a bremsstrahlung photon of frequency f. SI units were used here for a change instead of CGS.

Since there is a probability of $2\alpha(\Delta\dot{\mathbf{P}})^2/3\pi fe^2c^2 << 1$ for the emission of a bremsstrahlung photon of frequency f, the quartz crystal suffers a reaction, or a recoil in part of its quantum state. This causes the phonon-emission rate Γ to perform quantum oscillations with frequency f and with two-sided spectral density S' of fractional fluctuations given by the same expression, $S'_{\delta\Gamma/\Gamma}(f) = 2\alpha(\Delta\dot{\mathbf{P}})^2/3\pi fe^2c^2$. This is here the expression of the quantum 1/f effect. The one-sided spectrum of fractional fluctuations of the dissipation rate Γ is thus,

$$S_{\delta\Gamma/\Gamma}(f) = 4\alpha(\Delta\dot{\mathbf{P}})^2/3\pi fe^2c^2; \qquad (8)$$

This means that any radiation caused or implied by a quantum transition from one state to another comes with a price. It reacts back on the system, causing the rate of that transition to be modulated by exhibiting observable macroscopic quantum fluctuations. These have a spectral density of fractional rate fluctuations identical to the photon-numbers emitted in the transition considered. These calculated quantum fluctuations in the dissipation rate reveal the presence of macroscopic quantum interference with random phases caused by de-coherence. The interference is between the wave function of the crystal without QED bremsstrahlung losses (BL), and that of the crystal which suffered BL during the elementary act of dissipation, i.e., loss of a phonon from the main quartz (or MEMS [2], etc.) resonator mode. This is characteristic for the new field of infra-quantum physics (IQP) that is also realized in QGD with gravitons, in QLD with e.l.f. piezo-phonons, etc., with any kind of massless infra-quanta exhibiting infrared-divergent coupling to a current.

The vibrational energy of the crystal can be written in the form

$$W = n\hbar\omega = 2(Nm/2)(dx/dt)^2$$

$$=(Nm/e^2)(edx/dt)^2=(m/Ne^2)\varepsilon^2(\dot{\mathbf{P}}_i)^2; \qquad (9)$$

The factor two includes the potential energy contribution. We have denoted with ω an effective averaged phonon frequency for the solid considered, e.g., quartz, like in the Einstein model. Here m is the reduced mass of the elementary oscillating dipoles, e their charge, g a polarization constant of the order of the unity, and N their number in the resonator. Applying a variation Δn=1 in the number of phonons n,

$$\Delta n/n =2|\Delta\dot{\mathbf{P}}|/|\dot{\mathbf{P}}|, \text{ or } \Delta\dot{\mathbf{P}}=\dot{\mathbf{P}}/2n. \qquad (10)$$

Solving Eq. (9) for $\dot{\mathbf{P}}$ and substituting into (10), we obtain

$$|\Delta\dot{\mathbf{P}}| = (N\hbar\langle\omega\rangle/n)^{1/2}(e/2g). \qquad (11)$$

Substituting $\Delta\dot{\mathbf{P}}$ into Eq. (8), we get

$$\Gamma^{-2}S_\Gamma(f)=N\alpha\hbar\langle\omega\rangle/3n\pi mc^2fg^2\equiv\Lambda/f. \qquad (12)$$

This proves the presence of Q1/f fluctuations in Γ. The elementary dissipation process by loss of a phonon from the main resonator mode is likely to be a three-phonon process at room temperature, and a two-phonon process involving also a crystal defect, at low temperature. Considering room

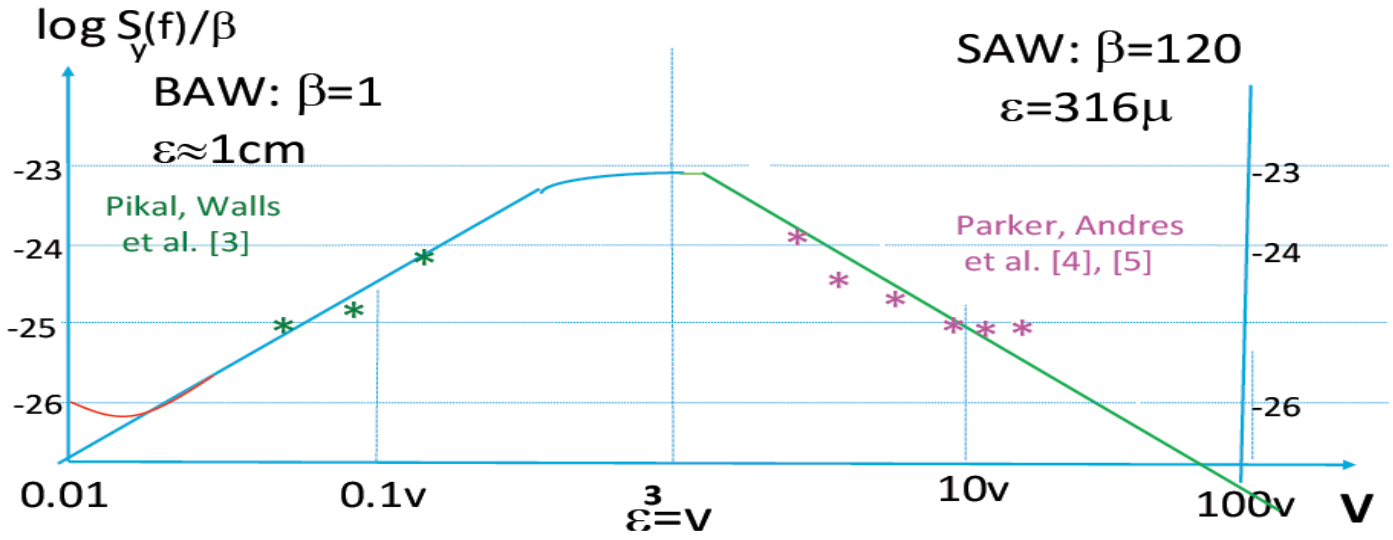


Fig. 1: FM noise in Si MEMS & quartz BAW, and SAW resonators: the red line adds the classical white noise at small volumes. The minimum on the red line corresponds to the Q1/f optimization point for ultra-low phase noise in BAW quartz, or MEMS.

temperature first, we realize that most of the bremsstrahlung associated with the three-phonon process could come from the loss of the participating thermal phonon, whose frequency we denote by $<\omega>$. Indeed, it is associated with a low phonon number $n=kT/<\omega>$. Using the harmonic oscillator relation

$$\omega^2 = \omega_o^2 - 2\Gamma^2, \quad \omega\delta\omega = -2\Gamma\delta\Gamma; \qquad (13)$$

between resonance frequency ω and dissipation Γ, we obtain

$$S_{\delta\omega/\omega}(f) = (1/4Q^4)S_{\delta\Gamma/\Gamma}(f) = (1/4Q^4)(\Lambda/f)$$
$$= N\alpha\hbar <\omega>/12n\pi mc^2 fg^2Q^4. \qquad (14)$$

Since N~V, is proportional to the volume, we get (Fig. 1)

$$S(f) = \beta'V/fQ^4, \text{ for } V\le\varepsilon^3. \quad \text{(Fig.1 left side, \& MEMS)} \quad (15)$$

Here, with a participating thermal phonon of $<\omega>=10^{10}$/s, with $n=kT/\hbar <\omega>$, T=300K and $kT=4\cdot10^{-21}$ J, we get

$$\beta' = (N/V)\alpha\hbar <\omega>/12n\pi g^2mc^2 = 10^{22}(1/137)$$
$$\cdot(10^{-27}10^8)^2/12kT\pi10^{-23}\ 9\ 10^{20} = 1. \qquad (16)$$

B. Surface Acoustic Wave (SAW) Quartz Resonators

For SAW, we consider many (V/ε^3) independent coherence volumes ε^3 that add their noise incoherently, and find

$$S(f) = \beta'\varepsilon^6/fVQ^4, \text{ for } V\ge\varepsilon^3. \quad \text{(Fig. 1 right side)} \quad (17)$$

C. The case of Defect Scattering: a two-phonon process

A phonon from the main resonator mode scatters on a defect and a phonon of similar frequency emerges into another mode with much smaller phonon occupation number $n_\omega=kT/\hbar\,\omega$. In this case we have to replace $<\omega>$ by ω and $n_{<\omega>}$ with n_ω. It gives a β-value which is $(<\omega>/\omega)^2$ smaller, i.e. 10^4-10^6 times smaller. Indeed, low-T phase noise is lower!

D. The General Case with Both Phonon Loss Processes

With $\Gamma=\Gamma' + \Gamma''$, we obtain for the combined phonon and defect scattering case, in general,

$$\beta=\beta'[\Gamma'^2 + (<\omega>/\omega)^2\Gamma''^2]/\Gamma^2. \qquad (18)$$

Although the defect scattering term is small at room temperature, it may become dominant at low temperatures, when the phonon scattering rate Γ' becomes much smaller than the defect scattering rate Γ''.

Since the 1/f noise level depends on the active volume, in the coherent regime one should use the lowest overtone and smallest diameter consistent with other circuit parameters. In the incoherent (low Q) case, the opposite should be considered. Q1/f phase noise was well verified! [6].

REFERENCES

[1] P. H. Handel:"Decoherence and Conventional Quantum 1/f Noise," Proc. ICNF'13, Montpellier, France, June 2013, pp. 1-4, DOI: [10.1109/ICNF.-2013.6578914].

[2] P. H. Handel, A. G. Tournier, "Nanoscale Engineering for Reducing Phase Noise in Electronic Devices," Proceedings of the IEEE Vol. **93**, pp. 1784-1814, October 2005; See Bibliography www.umsl.edu/~handel

[3] E. S. Ferre-Pikal, F. L. Walls et. al., Proc. 50th Freq. Control Sympos., 1996, pp. 844-851.

[4] T. E. Parker and D. Andres: "1/f Noise in surface acoustic wave resonators." Proc. 48th Ann. Freq. Contr. Symp., pp. 530-538, 1994.

[5] T.E. Parker, D. Andres, J.A. Greer and G.T. Montress: "1/f Noise in etched groove surface acoustic wave resonators." IEEE Transactions on Ultrasonics, Ferroelectrics and Frequency Control, 41, 853-862 (1994).

[6] F. Sthal, M. Devel, S. Ghosh, J. Imbaud, G. Cibiel# and R. Bourquin: "Volume dependence in Handel's model of quartz crystal resonator noise" IEEE Transactions on Ultrasonics, Ferroelectrics and Frequency Control, September 2013, Vol. 90, No. 9, pp. 1971-1977 (2013).

Spectral Performance and Noise Theory of Nonlinear Transmission Line Frequency Multipliers

Jason Breitbarth
Holzworth Instrumentation, CTO
Boulder, CO USA
support@holzworth.com

Zoya Popović
University of Colorado
Department of Electrical and Computer Engineering
Boulder, CO USA

***Abstract*— In this paper the theoretical and measured spectral performance of nonlinear transmission lines (NLTLs) and their applicability to frequency multiplication is presented. NLTLs, through nonlinear dispersion in large signal, create a sharp edge from a sinusoid that is rich in harmonics, making a very effective frequency multiplier. While the design of NLTLs has been widely published [1-2] for high harmonic content, prior to this work, the noise performance of NLTLs has only been published in [3]. The results presented in this paper demonstrate the near ideal $20 \cdot \log_{10} N$ phase noise multiplication as referenced to the additive phase noise of the fundamental with N being the multiplicative factor. Theoretical analysis of the noise properties of NLTLs show the effect of DC biasing and the overall change in phase shift of the NLTL in sum with AM source noise has the most dramatic influence in additive phase noise and is confirmed by measurement. An NLTL design with a -187dBc/Hz input referred phase noise is presented.**

Keywords—phase noise, NLTL, multiplier, additive, residual

I. INTRODUCTION

Low phase noise RF frequency generation is commonly accomplished through multiplication of a very high quality lower frequency source, typically a crystal oscillator. Frequency doubling, tripling and mixing are all utilized. Comb generation, or integer creation of harmonics, from the fundamental source is advantageous in many systems. Step recovery diodes have historically been used but the high drie levels and noise effects have been problematic at times. NLTLs, due to their passive nature in which they sharpen a wave, create high harmonics with potentially little added noise. The varactor is the key nonlinear component and has been shown to have negligible self noise in reverse bias [4]. This work develops both a theory to the dominant noise source and a measurement technique and results to confirm it. Design of a 100MHz input NLTL with measurements at the 10th harmonic is presented with an input referred phase noise of -187dBc/Hz.

Measurements and theory published in [3] were completed at the fundamental and 10th harmonic using a cross correlation system. Recent publications suggest cross-correlation measurements may be suspect at or near thermal limits [7]. This work is an extension of [3] with a new comb design and measurements at the 10th harmonic using a single channel phase noise system. A lower noise floor was achieved with this new design.

II. NLTL DESIGN AND OPERATION

NLTLs operate fundamentally different than step recovery diodes [5], frequency doublers or triplers [6]. Step recovery diodes use charge storage in the intrinsic region to generate a snap back effect, observed as a pulse and require high RF drive levels. Diode doublers and triplers operate via zero crossings, essentially a switch but cannot produce all integer harmonics. Nonlinear transmission lines operate on a large signal voltage variable delay. Line phase velocity decreases at higher voltages and increases at lower voltage. As a sinusoidal wave propagates along the line, the higher voltages travel faster relative to the lower voltages. The result is a sharp leading-edge rich in harmonics. The trailing edge has a gentler slope and a saw tooth wave is the best shape approximation. Additional filtering can manipulate the time domain saw tooth into an impulse, forming nearly equal integer harmonics.

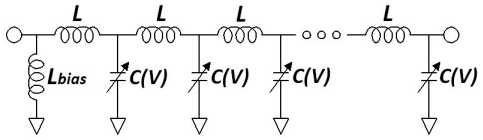


Fig. 1. Simplified NLTL model showing it acts like a variable phase shift delay line. A DC bias condition is added through an inductive bias.

A. Varctor Noise

An NLTL has only three fundamental components: inductors, varactors and some method to bias it. Air and ceramic core inductors (u_r=1) do not exhibit any significant voltage noise [4]. Voltage noise from a varactor in reverse bias was carefully measured by the system shown in Fig. 2 to be negligible in Fig. 3 consistent with [4]. In forward bias, when current is flowing, the noise becomes more significant. In this paper, the NLTL is biased almost completely out of forward conduction.

B. NLTL Design at 100MHz

The design of a uniform NLTL is relatively simple. The capacitance-voltage characteristics and size of available varactors determine the drive power and available harmonic power by the number of stages for a given input frequency. A capacitance range of approximately 4:1 has been found to be a good balance of compression vs source match and length of line. A 4:1 capacitance change yields a 2:1 input impedance change by Eqn 1. Optimized for 50Ω, the impedance varies from 35Ω to 70Ω or an S11 < -15dB. This design is for a 100MHz input

with harmonics to at least to 1GHz. A hyper-abrupt varactor (used as a pair), Toshiba 1SV285, was chosen for a 4:1 capacitance change over approximately 5V. An 18dBm drive power will reach full the full swing of varactor. The C-V characteristics of a varactor will continue down to forward conduction. To maximize the C-V characteristic a midpoint of 2V bias for 50ohms operation was selected.

Table 1 is the voltage vs capacitance relationship of the varactor as a pair of diodes. A midpoint bias of 2V required a 16nH inductor for 50Ω operation. The right-hand column of the table is the voltage vs delay per element by Eqn 2. The difference between the min and max voltages is the compression per stage. A 4:1 capacitance ratio yields a 2:1 compression per unit delay.

$$Z_0 = \sqrt{\frac{L}{C}} \quad (1)$$

$$\tau_{element} = \sqrt{C \cdot L} \quad (2)$$

An NLTL design of a 100MHz sinusoid input requires a certain amount of compression in time. The least amount of pulse compression is optimal, it will reduce the sensitivity to voltage noise on the line. The 20-80% rise time of the sinusoid, where most of the pulse compression will occur, happens over approximately 100 degrees, or about 2.8ns at 100MHz. Based on the table, 12 sections compress approximately 2.7ns over 5V. Fig. 4 is the complete schematic of the design and fabrication.

Voltage	Capacitance	Unit Delay
0	13pF	456ps
1	9.4pF	388ps
2	6.8pF	330ps
3	5.0pF	283ps
4	4.0pF	255ps
5	3.4pF	233ps

Table 1. Voltage vs Capacitance relationship vs unit delay (per L-D element) based on a 2V midpoint and 16nH inductor.

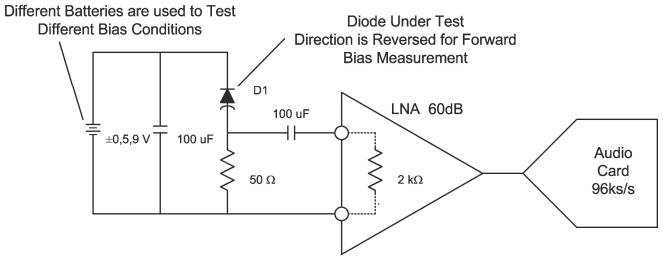


Fig. 2. Test apparatus to measure the noise due to a diode. The varactor diode was measured in both forward and reverse bias conditions. The measurements were all done on batteries

The NLT was modeled in spice, the time domain waveforms shown in Fig. 5 at the input, output and every 4 sections of line, showing the pulse compression along the way. Considerable ripple is always a problem with NLTLs. Inherently, they are unmatched somewhere along the line. Like a mixer, which is either a short circuit or an open circuit and a 'matched' condition is one in which each occurs about 50% of the time. A narrowband drive amplifier is not the best choice for an NLTL, broadband back match recommended.

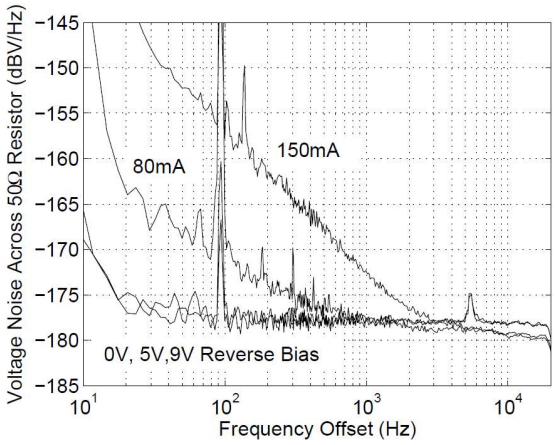


Fig. 3. Noise measurements of a PN junction varactor diode in forward and reverse bias. Current needs to be flowing for noise to be introduced. In reverse bias, the varactors exhibit no noise of their own.

The fabricated NLTL has a bias port and a bias-T with an option for loading a very clean bjt based 1.85V reference (close to the desired 2V) or being driven externally by a function generator or voltage source.

Fig. 6 is the measured harmonic output of the line when biased with 1.85V on-board. Input is 100MHz sinusoid at 18dBm.

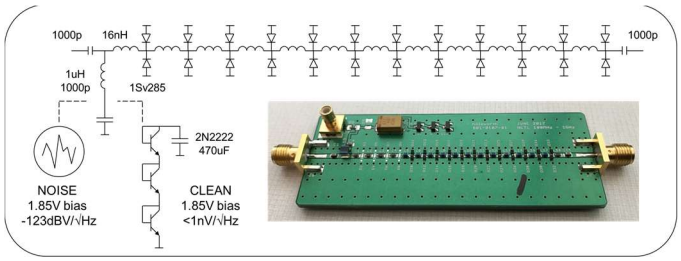


Fig. 4. Schematic and photo of the test NLTL. Two different bias conditions are shown. One uses three bypassed transistors powered by a battery through a current limiting resistor to create an extremely clean low noise 1.85V reference. The second is an external noise source for testing AM-PM conversion.

III. THEORETICAL NOISE

The NLTL operates as a voltage variable delay line. Provided it is biased out of heavy forward conduction, the dominant noise source is the voltage noise on the line itself. The NLTL operates opposite the function of a phase detector by introducing PM noise based on present AM noise by a rad/V constant in Eqn 3. The 3dB factor is for a single sideband measurement.

$$\mathcal{L}_{fm} = V_{rms\text{-}noise}\ (dBV / \sqrt{Hz}) + 20*\log_{10}(rad/V) - 3dB \quad (3)$$

The susceptibility to AM noise can be measured by introducing a DC change in the bias condition and measuring the phase output at the harmonic of interest. As a frequency multiplier, the AM-PM conversion of a harmonic may be higher or lower than others. This may be calculated from simulation or measurement.

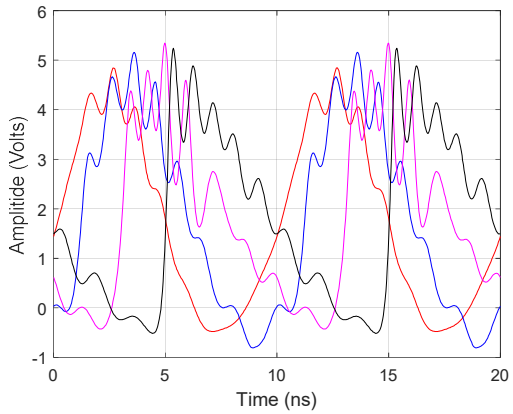


Fig. 5. Time domain analysis along the NLTL in simulation showing points at the beginning, end and every 4 elements. Simulation matches design at a nominal 4ns delay and 3ns of pulse compression.

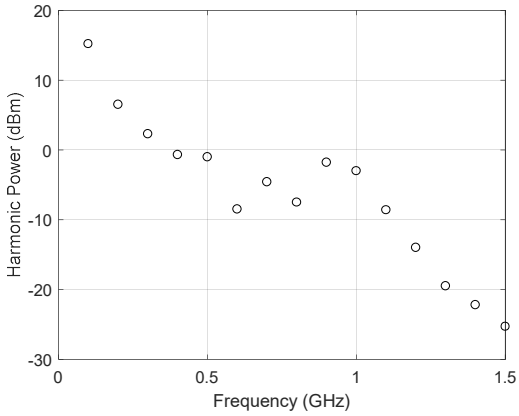


Fig. 6. Measured output harmonics of the fabricated NLTL using the on-board 1.85V bias. Input is a 100MHz sinusoid at 18dBm. The 1GHz comb at -2dBm is the measured harmonic.

IV. Single Channel Measurement

A basic diagram of the measurement of the NLTL at the 10th harmonic is shown in Fig. 7. The 100MHz source is an oven controlled crystal oscillator (OCXO) buffered by a medium power (25dBm) amplifier, both on batteries. The power splitter is broadband, extending well below and above 100MHz. The signal was attenuated to 18dBm after the power splitter, before the NLTL, to improve match and isolation between channels.

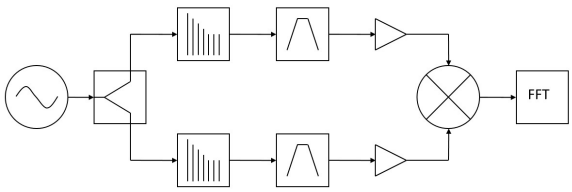


Fig. 7. Single channel measurement system to measure a pair of NLTLs. Diplexing and terminating lower frequencies out of the NLTL is important to maintain pulse compression and desired operation.

Filtering of the harmonic is the most critical part of the measurement system. The NLTL is a transmission line and a narrowband filter is typically reflective. If a filter is put directly behind the NLTL a majority of the propagating wave is reflected back, causing destructive interference. Prior to the 1GHz bandpass filter, a diplexer is used to terminate the first 5 harmonics of the NLTL. The amount of energy reflected from higher harmonics is not enough to disrupt the pulse forming of the NLTL.

The 1GHz filter reduced neighboring harmonics to at least 20dB below that of the desired harmonic. All other harmonics were considerably lower. The output power of the 1GHz harmonic was -3dBm after filtering.

Two HX2400 amplifiers were used to increase the power to the HX3100 phase detector. The amplifiers were attenuated prior to the phase detector to ensure 9dBm to each port, optimal for low phase noise measurements.

Fig. 8 is the results of the phase noise measurement and noise floor characterization of the system. The floor is limited by the power into the HX2400 amplifiers and their inherent 4dB noise figure. 3dB is added when measuring a pair of devices. It is thermally limited by Eqn 4. The calculated -167dBc/Hz is confirmed by measurement in Fig. 8.

$$-167\text{dBc/Hz} = -177\text{dBm}-(-3\text{dBm})+4\text{dB(NF)} +3\text{dB} \quad (4)$$

The NLTLs are measured at -164dBc/Hz, 3dB above the measurement limit. This measurement is consistent based on the AM-PM conversion of the NLTL and will be discussed in the following section.

A. AM-PM Conversion

The NLTL is inherently sensitive to AM-PM conversion. Phase noise is introduced as rad/V based on the compression of the line and frequency. Using the same setup as Fig. 7, the DC bias of the line was varied in one path and the phase shift measured. A 0.1V change resulted in a measured 0.72radian change at the phase detector, a 7.2rad/V AM-PM conversion. This is an extremely high susceptibility to AM-PM conversion. The additive phase noise measurements in Fig. 8 shows when one line is biased with a normal Agilent (Keysight) E3610A power supply and the resultant noise due to it as compared to a clean bias.

Fig. 9 is the result of biasing one of the lines with a noise generator with an offset of 1.85V (on-board 1.85V removed). Based on the theory the line is modulated by the bias voltage on the line at 7.2rad/V, the voltage noise is modulated into phase noise by:

$$\mathcal{L}_{fm} = V_{rms\text{-}noise}\ (\text{dBV} / \sqrt{\text{Hz}}) + 20*\log_{10}(\text{rad/V}) - 3\text{dB}$$

At 7.2rad/V, the measured phase noise will be 14dB higher in dBc/Hz than the voltage noise. The measured result in Fig. 9 confirms this at a measured phase noise of -109dBc/Hz for a voltage noise modulation of -123dBc/√Hz.

With a clean supply (sub 1nV/√Hz) the line still has broadband 50Ω noise around the carrier at -180.9dBV/√Hz. Applying the 14dB conversion would yield a phase noise of -167dBc/Hz each, or -164dBc/Hz, very close to what was measured.

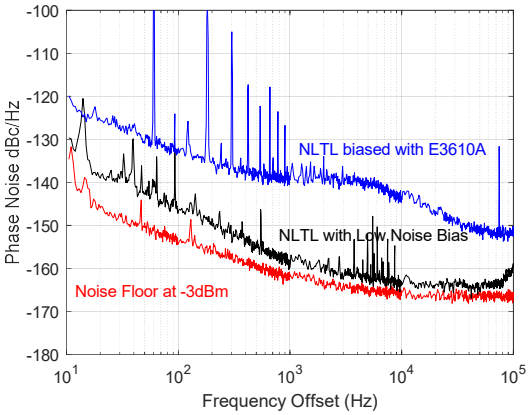


Fig. 8. Measured phase noise of a pair of NLTLs at 1GHz output. The red is the noise floor of the system at the same power. Black is using a very clean bias while the blue is using a bench power supply.

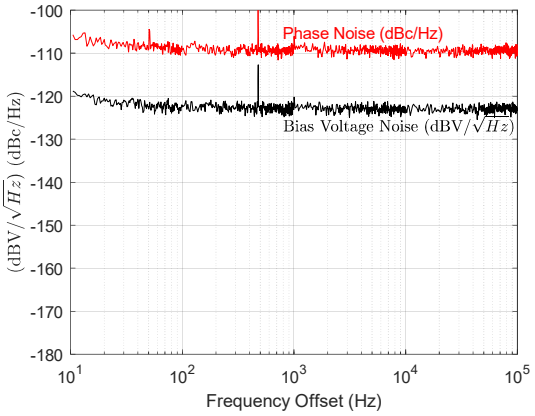


Fig. 9. Measured phase noise (red) when one line is modulated with voltage noise (black). The NLTL shows heavy influence on any voltage noise on the line.

B. System Verification of a multiplied crystal

It has been shown the NLTL is heavily dependent on the voltage noise on the line. It is similarly affected by the AM noise of the source. Fig. 10 is the results of multiplying a 100MHz OCXO with the NLTL and filtering at 1GHz. The drive level was 18dBm and shown in red. The light red plot would be an ideal x10 multiplication of the OCXO. The blue line, actual measurement, shows a deviation from this at offsets of 200Hz out past 1MHz. The additional noise correlates to the AM noise measured of the OCXO and amplifier pair. As the AM noise rolls off or is below the phase noise, the NLTL operates as a near ideal multiplier.

V. CONCLUSIONS

The NLTL is presented as a low phase noise frequency multiplier, limited by only by the voltage noise on the line. However, the NLTL is extremely susceptible to AM and bias voltage noise contributions and must be implemented carefully. An NLTL with an input referred noise of -187dBc/Hz, provided AM noise is not present, is demonstrated and is at the state of the art for clean frequency multiplication.

The AM-PM conversion does not show up in the additive measurements because it is an electrical property of the line and will be considered common mode in an identical pair of lines. Three identical NLTLs were measured to verify this.

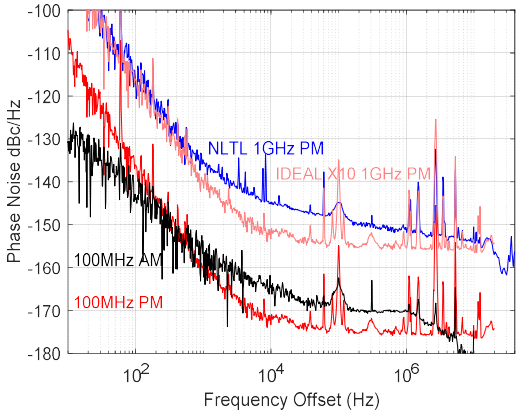


Fig. 10. Measured absolute phase noise of a x10 multiplied crystal oscillator. AM noise is converted to PM noise within the NLTL, degrading the multiplication.

ACKNOWLEDGMENT

A special thank you to Professor Zoya Popović for her hard work as my advisor and the patience for the relatively long period (11 years) it took me to publish.

REFERENCES

[1] M. J. W. Rodwell, M. Kamagawa, R. Yu, M. Chase, E. Carman, and K. S. Giboney, " GaAs Nonlinear Transmission Lines for Picosecond Pulse Generation and Millimeterwave Sampling," IEEE Trans. Microwave Theory Techn., vol. 39, no. 7, pp. 1194-1204, July 1991.

[2] M. G. Chase, "Nonlinear transmission lines picosecond pulse, impulse and millimeter-wave harmonic generation," Ph.D. dissertation, University of California, Santa Barbara, 1993.

[3] J. Breitbarth, "Design and Characterization of Low Phase Noise Microwave Circuits," *Ph.D. dissertation*, Department of Electrical Engineering, University of Colorado, Boulder, 2006.

[4] F. G. Ascarrunz, A. Zhang, E. S. Ferre, and F. L. Walls, "PM Noise Generated by Noisy Components," 1998 IEEE International Frequency Control Symposium, pp. 210-217.

[5] P. L. Ntake, "Frequency multiplication by a p-i-n diode when driven into avalanche breakdown," IEEE Trans. Microwave Theory Tech., vol. 23, no. 6, pp. 477–485, June 1975.

[6] M. M. Driscoll and T. D. Merrell, "Spectral performance of frequency multipliers and dividers," in IEEE Frequency Control Symposium, 1992, pp. 193–199.

[7] C. W. Nelson, A. Hati, D. A. Howe, "A collapse of the cross-spectral function in phase noise metrology," Review of Scientific Instruments, Vol 85, 2014.

[8] A. Haiti, D. A. Howe, F. L. Walls, D. Walker, "Noise Figure vs. PM Noise Measurements: A Study at Microwave Frequencies," *Proc. 2003 IEEE Int. Freq. Control Symp.*, pp.516-520, 2003.

Ultra-low phase-noise microwave oscillator based on electro-optical frequency division

Jiang Li
hQphotonics Inc
2500 E Colorado Blvd
Pasadena, CA, 91107, USA
Jiang.li@hqphotonics.net

Kerry Vahala
T. J Watson Laboratory of Applied Physics
California Institute of Technology
Pasadena, CA 91105, USA
vahala@caltech.edu

***Abstract*—We report the generation of ultra-low phase noise microwave signals using electro-optical frequency division. Two, independent 30 GHz eOFD oscillators are constructed and the measured phase noise for each oscillator is -151 dBc/Hz at 10 kHz offset and -109 dBc/Hz at 100 Hz offset. Phase locking to an external reference for long term synchronization is also demonstrated.**

Keywords—ultra-low phase noise; microwave oscillator; frequency comb;

I. INTRODUCTION

Optical frequency division has revolutionized precision time keeping and produced oscillators with ultra-high frequency stability [1-3]. In optical frequency division (OFD), a single, stable laser reference frequency (locked to a high stability Fabry-Perot cavity) is frequency divided to the microwave domain using an octave-spanning, mode-locked frequency comb. Associated with this process, the microwave signal is extracted by detection of the frequency-comb emission using highly-linear ultrafast photodetectors [4].

Recently, an alternative OFD approach (called electro-optical frequency division or eOFD) was demonstrated based on a dual-laser reference and electro-optical modulation (EOM) frequency combs [5]. A proof-of-principle demonstration was reported to show that the optical phase noise of the dual laser reference is divided by a factor of N-squared after division to the microwave domain where N is the frequency division factor [5]. Here, we report a significant advancement of the eOFD oscillator approach by demonstrating a 30 GHz oscillator having a single-sideband phase noise of -151 dBc/Hz at 10kHz offset (equivalent to -160 dBc/Hz when normalized to 10 GHz). Also, an external phase-lock-loop has been developed to synchronize the eOFD oscillator to external references for long term stability/synchronization.

II. EXPERIMENTAL RESULTS

Fig. 1a shows the concept of electro-optical frequency division. A dual-laser reference produces frequencies ν_1 and ν_2 with high relative frequency stability. These laser signals are sent to an EOM comb generator to create multiple comb lines. The EOM comb generator typically consists of phase modulators, intensity modulators, dispersion compensation and spectral broadeners [6,7]. The EOM comb generator is driven by a microwave voltage-controlled oscillator (VCO). The phase noise of the VCO is transferred into the line spacing noise of the EOM comb. Suppose that the $+N_1$-th order comb line of the EOM comb generated using ν_1 and the $-N_2$-th order comb line of the EOM comb generated using ν_2 are nearly overlapping at the spectral midpoint between ν_1 and ν_2. The beat note δf between these two comb lines is written as $\delta f = |\nu_2 - \nu_1 - N f_M|$ where $N = N_1 + N_2$. This beat note contains the free-running phase jitter of the microwave VCO multiplied by a factor N. If we null the jitter of this beat note by servo controlling the tuning port of the VCO, then in the closed loop case,

$$f_M = |\nu_2 - \nu_1 \pm \delta f| / N \qquad (1)$$

From Eq. (1) the comb line spacing (or equivalently the VCO frequency f_M) is locked to a small fraction (1/N) of the optical reference ($\nu_2 - \nu_1$). It can be further shown that the phase noise of the VCO is divided by a factor of N^2 relative to the dual optical references (within the servo lock bandwidth)[5]. Fig. 1b gives a more detailed functional diagram of the eOFD oscillator.

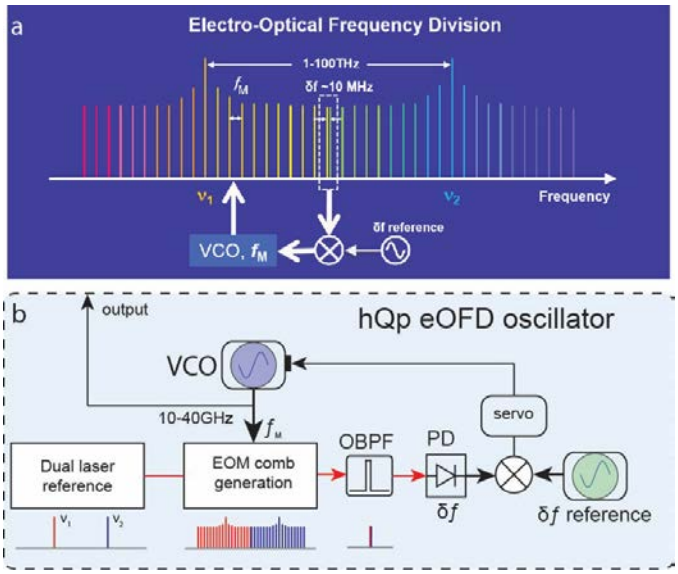


Fig. 1. (a) Conceptual diagram for Electro-Optical Frequency Divisioin (eOFD). (b). Functional diagram of the hQphotonics eOFD oscillator. A dual laser reference is sent to an EOM comb generator to create multiple comb lines. The spectral mid point of the EOM comb is filtered by an optical bandpass filter (OBPF) and detected at a photodetector (PD). The generated sideband beat note (δf) is compared with a low frequency reference to generate an error signal, which is used to servo control the microwave VCO.

This research was developed with funding from DARPA. The views, opinions, and/or findings expressed are those of the author(s) and should not be interpreted as representing the official views or policies of the Department of Defense or the U.S. Government.

From Eq. (1), it can be seen that increasing the division N as well as reducing the phase noise of the dual optical references will reduce the phase noise of the microwave VCO. Here we report measurements of phase noise using two, state-of-the-art 30 GHz eOFD oscillators. The output frequencies of the two oscillators were tuned to offset them by 20MHz. The equal amplitude oscillator signal outputs were mixed to generate an IF tone at 20MHz whose phase noise was measured by a phase noise analyzer (Rohde & Schwartz FSUP26). The phase noise of the IF tone is a sum of the phase noise of the two independent 30 GHz eOFD oscillators. Therefore, the phase noise of each 30 GHz eOFD oscillator can be obtained by substracting 3dB from that of the IF tone. The single-sideband phase noise of the 30 GHz eOFD oscillator is plotted in fig. 2. Note that spurs are not shown in the phase noise plot. As seen in fig. 2, the oscillator achieves -151 dBc/Hz at 10 kHz offset and -109 dBc/Hz at 100 Hz offset for the 30 GHz carrier.

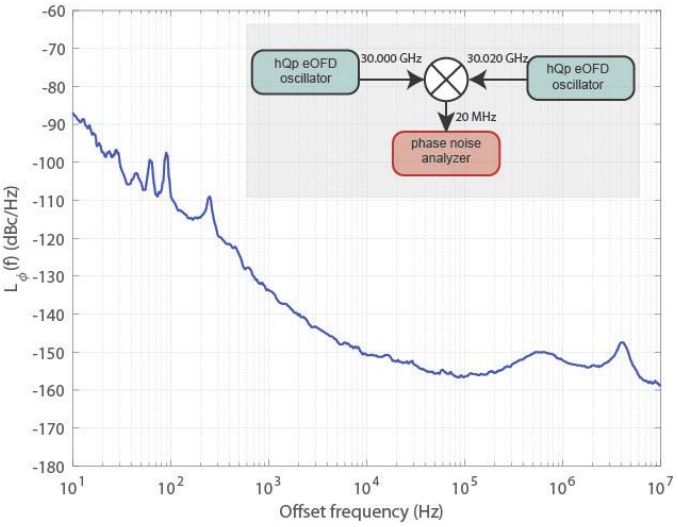


Fig. 2. Main panel shows the measured single-sideband phase noise of the hQphotonics eOFD oscillator at 30 GHz. Inset: two independent 30 GHz eOFD oscillators are mixed to generate an IF tone at 20 MHz for phase noise measurement.

We also demonstrated phase locking of the eOFD oscillator to external references for long term stability/synchoronization. Fig. 3 shows the measurement setup. The 30 GHz eOFD output is divided to 625 MHz by a chain of RF frequency prescalers. An external synthesizer is referenced to a 10MHz OCXO and generates an output at 625 MHz, which is compared against the divided output of the 30 GHz eOFD oscillator. The error signal is sent to a slow servo loop and then fed back to the external tuning port of the eOFD oscillator. The slow servo loop is designed to have a very low locking bandwidth of a few Hz so that the external phase lock loop would not affect the phase noise performance of the eOFD oscillator above ~10Hz offset.

The 30 GHz output is first divided to 10 GHz by an RF divider. Then the frequency of the 10 GHz signal is measured by a frequency counter (Tektronix FCA3120A), which uses as its reference the same 10MHz OCXO from the external reference synthesizer. Locking to the external reference for 24 hours was demonstrated as shown in Fig. 3b.

In conclusion, we have demonstrated a ultra-low phase noise microwave oscillator at 30 GHz based on electro-optical frequency division. The measured SSB phase noise of the 30 GHz oscillator is -151 dBc/Hz at 10 kHz offset and -109 dBc/Hz at 100 Hz. This is equivalent to -160 dBc/Hz at 10 kHz, and -118 dBc/Hz at 100 Hz when normalized to a 10 GHz carrier. Moreover, we have demonstrated external phase lock of the hQphotonics eOFD oscillator to an external reference for 24 hours.

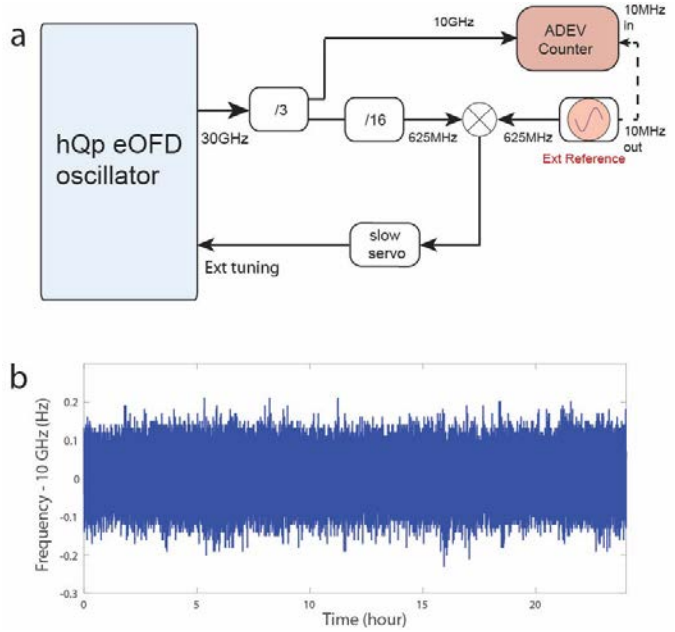


Fig. 3. (a) Measurement set up for phase lock of the hQp eOFD oscillator to an external reference. (b) Time series frequency counter data of the externally locked eOFD oscillator (30 GHz divided by 3 to produce a 10 GHz rate sent to the counter) measured over 24 hours.

ACKNOWLEDGMENT

The authors thank DARPA for support of this work.

REFERENCES

[1] Fortier, T. M., et al. "Generation of ultrastable microwaves via optical frequency division." *Nature Photonics* 5 (2011): 425-429.

[2] Quinlan, Franklyn, et al. "Optical amplification and pulse interleaving for low-noise photonic microwave generation." *Optics letters* 39.6 (2014): 1581-1584.

[3] Xie, Xiaopeng, et al. "Photonic microwave signals with zeptosecond-level absolute timing noise." *Nature Photonics* 11.1 (2017): 44-47.

[4] J. Taylor, S. Datta, A. Hati, C. Nelson, F. Quinlan, A. Joshi, S. Diddams, Characterization of Power-to-Phase Conversion in High-Speed P-I-N Photodiodes. *IEEE Photon. J.* **3**, 140–151 (2011).

[5] Li, Jiang, et al. "Electro-optical frequency division and stable microwave synthesis." *Science* 345 (2014): 309-313.

[6] M. Fujiwara, et al, "Flattened optical multicarrier generation of 12.5 GHz spaced 256 channels based on sinusoidal amplitude and phase hybrid modulation." *Electron. Lett.* **37**, 967–968 (2001).

[7] C. B. Huang, et al, Nonlinearly broadened phase-modulated continuous-wave laser frequency combs characterized using DPSK decoding. Opt.Express 16, 2520–2527 (2008).

Improving the frequency stability of atomic frequency standard basing on the noise asynchromism correction

Qian Wang*+, Rong Wei*, Richang Dong*+,Jinda Lin*, Wenli Wang*, Yuzhu Wang*
*Key Laboratory of Quantum Optics, Center for Cold Atom Physics, Shanghai Institute of Optics and Fine Mechanics, Chinese Academy of Science, Shanghai, 201800, China
+University of Chinese Academy of Sciences, Beijing, 100049, China
E-mail: weirong@siom.ac.cn

***Abstract*—We propose an improvement for increasing the performance of locked periodic atomic frequency standards(AFS), based on correcting the noise of the asynchronism of phase-detecting and feedback process. Theoretical analysis and numerical simulation show that the method can optimize the stability AFS which is related with d. And is the duty of phase-discriminating of AFS. If in-loop noise possesses white frequency noise characteristics, the stability will decrease following the coefficient of $\sqrt{(1-d)}$. Specially, when d approaches to 1, the stability will reach the limit of quantum project noise. Here we demonstrate three schemes to realize the idea in experiments and overlap-feedback is the most easily implemented one. Considering Dick effect in our method, the stability of our atomic fountain will be better than $1\times10^{-14}\tau^{-\frac{1}{2}}$ at d>0.93.**

Keywords—atomic frequency standard; noise correction; duty; digital simulation;

I. INTRODUCTION

Atomic frequency standard (AFS) has made great improvements recent years, such as the uncertainty and long-term stability of atomic fountain clock have been better than 2×10^{-16} [1] and 5×10^{-17} [2], respectively. Furthermore, the uncertainties of both optical lattice clock and optical ion clock have reached to small coefficients of 10^{-18} [3,4]. Based on suppressing noise, kinds of new methods have been pointed out to improve the performance of AFS by using new procedure. "zero-dead-time" is a well-known example, firstly demonstrated by Kasevich's group [5]. Straight after that, Bess' et.al have applied it to fountain interferometer [6]. Recently, Ludlow et.al of NIST have obtained ultrastable optical clock with two cold-atom ensembles by developing method of procedure controlling [7]. In the paper, we demonstrate an improvement of the frequency stability of AFS by correcting the asynchronism of phase-detecting and feedback process. Theoretical analysis and numerical model show that our method can increase the stability of AFS. Furthermore, the improvements become more and more obvious when increasing the duty.

Our method is applied to periodically-running AFS, i.e. the "prepare-phase detect-feedback" procedure. The local oscillator (LO) is locked to the spectrum of quantum system, and the output of LO represents the performance of the clock [8]. The stability of this type of AFS is mainly limited by the noises of quantum system, LO and frequency chain, which is expressed as:

$$\sigma_y^2(\tau)=\sigma_{y-Q}^2(\tau)+\sigma_{y-LO}^2(\tau) \tag{1}$$

Where $\sigma_{y-Q}^2(\tau)$ is contribution of quantum system dominated by quantum protection noise (QPN), while $\sigma_{y-LO}^2(\tau)$ represents frequency chain system's stability affected mainly by LO phase noise and Dick effect. For fountain clock (using commercial oscillator), optical clock, or similar AFS, $\sigma_{y-Q}^2(\tau)$ is far less than $\sigma_{y-LO}^2(\tau)$, therefore, people are focus on decreasing the value of $\sigma_{y-LO}^2(\tau)$ such as ZDT and our method.

II. THEORETICAL ANALYSIS AND SIMULATION

We study the affection of stability of AFS in terms of the relative delay between the feedback of atomic clock and noise detection. The relative frequency bias of output frequency of atomic clock is represented by $\bar{y}_i$. $\bar{y}_i$ is the average fractional frequency during the i^{th} clock cycle T_c (see Eq. (2) and Eq. (4). During every clock cycle T_c, we divide T_c into N portions (see Fig. 1), which correspond to the relative frequency bias of $y_{i,1},\cdots, y_{i,k}, \cdots, y_{i,N}$, respectively:

$$\bar{y}_i=\frac{1}{T_C}\int_{(i-1)T_C}^{T_C}\frac{\upsilon(t)-\upsilon_0}{\upsilon_0}dt \tag{2}$$

$$y_{i,k}=\frac{1}{NT_C}\int_{(i-1)T_C+(k-1)T_C/N}^{(i-1)T_C+kT_C/N}\frac{\upsilon(t)-\upsilon_0}{\upsilon_0}dt \tag{3}$$

$$\bar{y}_i=\frac{1}{N}\sum_{k=1}^{N}y_{i,k} \tag{4}$$

Where ν_0 is the frequency of atomic clock, $\nu(t)$ is the output frequency of LO system. Assuming the time interval of the first M portions is discriminating time T_R, and the other error introduced by discriminating process is $y_{i-other}$, so the error of measurement is:

$$y_{i-e}=\frac{1}{M}\sum_{k=1}^{M}y_{i,k}+y_{i-other} \tag{5}$$

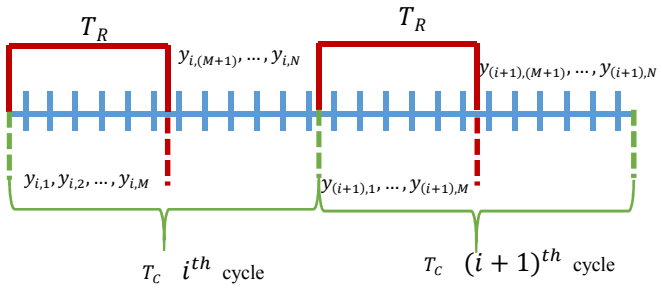


Fig.1. Noise data discretization in lock-in mode of atomic fountain clock.

The duty d can be defined as the ratio of phase-discriminating time T_R and atomic clock cycle T_c, see Eq. (6):

$$d = \frac{T_R}{T_C} = \frac{M}{N} \cdot \frac{T_C}{T_C} = \frac{M}{N} \tag{6}$$

We make three assumptions for the following discussions:

1. The short-term frequency stability of AFS is mainly reflected in the white frequency noise:

$$\sigma_y(\tau) = a\tau^{-1/2} \tag{7}$$

Where a is coefficient of white frequency noise. We ignore the contributions of flicker frequency noise and random walk noise, which mainly affect the long-term stability of the AFS.

2. The noise of LO system $\frac{1}{M}\sum_{k=1}^{M} y_{i,k}$ makes major contribution to error signal y_{i-e}, and defining the noise of LO and frequency chain in error signal is y_{i-LO}. Other noise $y_{i-other}$ is mainly dominated by the noise of quantum discrimination system y_{i-Q} which is much less than the LO system's noise:

$$y_{i-Q} \cong y_{i-other} \quad y_{i-LO} = \frac{1}{M}\sum_{k=1}^{M} y_{i,k} \tag{8}$$

$$\sigma_{y_{i-Q}} \ll \sigma_{y_{i-LO}} \tag{9}$$

3. The noise within lock-in bandwidth still has the property of white noise, which means it can be regarded as random noise whose average value is unequal to 0:

$$\bar{y}_{i,k} = c \quad \sigma_{y_{i,k}} = \frac{1}{\sqrt{N}}\sigma_{y_i} \tag{10}$$

Where c is corresponding the average periodic drift rate of LO.

In above three hypotheses, the first two agree with the practice, while the third is not necessarily coincide with real situation, and we will analyze the conditions at the end of the paper.

A. Direct correction of noise asynchronism

When AFS is in operation mode, its performance index is mainly described by $\bar{y}_i$, which can be measured directly when comparing the output of the AFS with a more precise frequency reference. The noise statistical property of Allan deviation (ADEV) of $\bar{y}_i$ embodies the stability of the AFS. Besides $\bar{y}_i$, the error y_{i-e} which is obtained by every phase-detecting process is also a measurable quantity, being acted as error signal feedback to LO, and it is abandoned after feedback process finishes. Furthermore from Eq. (4) and Eq. (5), we can see that there is a partial noise correlation between $\bar{y}_i$ and y_{i-e}, and it may offer ways to improve the stability of output signal. On the basis of the equations (4) (5) and (6), we can build new arrays $\langle Y_{i,k} \rangle$ and $\langle \bar{Y}_i \rangle$, expressed as:

$$Y_{i,k} = y_{i,k} - d \cdot y_{i-e} = y_{i,k} - \frac{1}{N}\sum_{k=1}^{M} y_{i,K} - d \cdot y_{i-Q} \tag{11}$$

$$\bar{Y}_i = \bar{y}_i - d \cdot y_{i-e} = \frac{1}{N}\left(\sum_{k=1}^{N} y_{i,K} - \sum_{k=1}^{M} y_{i,K}\right) - d \cdot y_{i-Q} \tag{12}$$

Where $\bar{Y}_i$ is average of $Y_{i,k}$ at T_c time interval, which is similar to the relationship of $y_{i,k}$ and $\bar{y}_i$. Considering the properties of white frequency noise of $y_{i,k}$ and y_{i-Q}, the stability of $\bar{Y}_i$ is derived as:

$$\begin{aligned} \sigma_{\bar{Y}}^2(\tau) &= (1-d)\sigma_y^2(\tau) + d \cdot \sigma_{y-Q}^2(\tau) \\ &= (1-d)a^2\tau^{-1} + d \cdot \sigma_{y-Q}^2(\tau) \end{aligned} \tag{13}$$

From Eq. (13), we know $\sigma_{\bar{Y}}^2(\tau)$ decreases with $\sigma_{\bar{y}}^2(\tau)$ by a coefficient of $(1-d)$, besides that, it contains another term $d \cdot \sigma_{y-Q}^2(\tau)$. $\sigma_{y-Q}^2(\tau)$ is far less than $\sigma_{\bar{y}}^2(\tau)$, $\sigma_{\bar{Y}}^2(\tau) < \sigma_{\bar{y}}^2(\tau)$, so Eq. (13) is effective. $\sigma_{\bar{Y}}^2(\tau)$ will vary from LO noise to QPN when d increases. For our ^{87}Rb atomic fountain clock, d is about 0.3, the stability may be raised to 0.83 times.

We perform the numerical simulation to verify noise asynchromism correction (NAC). Firstly, two white noise arrays $\langle y_{i,k} \rangle$ and $\langle y_{i-Q} \rangle$ representing the fractional frequency bias of LO system and quantum system, respectively, are built by software stable 32. Their array numbers are 2 million and 0.2 million which means locking period of AFS is 10 times of minimum interval. ADEV statistics fit:

$$\sigma_{y-LO}(\tau) = 2\times10^{-13}\tau^{-\frac{1}{2}}, \sigma_{y-Q}(\tau) = 4\times10^{-14}\tau^{-\frac{1}{2}} \tag{14}$$

We build arrays of $\langle Y_{i,k} \rangle$ by $\langle \bar{y}_i \rangle$ and $\langle y_{i-Q} \rangle$ following Eq. (11). Then we compute the stabilities of $\langle \bar{Y}_i \rangle$ with duty d ranging from 0 to 1 and changing step in 0.1. The ADEV statistics lines of $\langle Y_{i,k} \rangle s$ are shown in Fig. 2. From Fig. 2, we know that the stability of $\langle Y_{i,k} \rangle$ complies with the Eq. (1) when integration time is less than $T_c = 10$. whereas when integration time is larger than T_c, the stability trends to transit from Eq. (1) to Eq. (13), and it can be deemed as varying with τ^{-1} at some range. The law is most obvious in the case of $d = 1$, which is coincide with ZDT experiment [5]. The result of simulation quantificationally proves the validity of method.

In above discussion, we assume that the coefficient of $\sigma_{y-LO}(\tau)$ is invariant and neglect it is related to d by Dick effect. In fact, $\sigma_{y-LO}(\tau)$ is closely associated with the duty d described by Dick effect [9,10,11,12]. Taking account of the influence of Dick effect and the running parameters of our ^{87}Rb AFS [13,14], we come up with the method of NAC to deal with the $\sigma_{y-LO}(\tau)$. In Fig. 3 we show a sigma-d plot in two modes

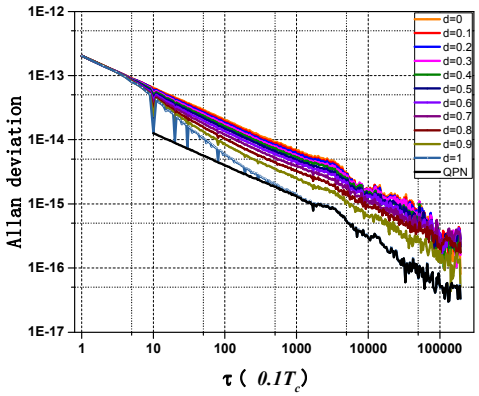


Fig.2. ADEV of the simulation on the basis of NAC. The stability is characterized in different duties d, which varies from 0 to1. Black curve shows the stability of QPN, orange curve shows stability when d=0.

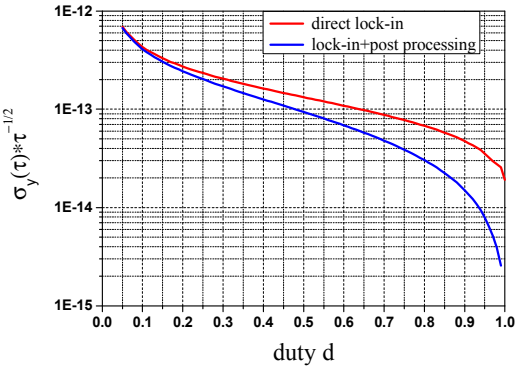


Fig.3. ADEV of considering the method of NAC. Red curve shows the normal operation mode without processing correction. On the contrary, blue curve represents the result based on NAC method.

with considering the Dick effect. The normal operation mode without NAC, is represented by red curve. while combining with NAC, stability curve is shown as the blue curve .The d-σ(τ) plot shows the contribution of the noise of LO system to stability decreases to E-14@1s when $d > 0.93$. Considering that d is increased by procedure of overlapping the period of the atomic fountain, it also decreases QPN's contribution to the stability to less than $1 \times 10^{-14}\tau^{-\frac{1}{2}}$. By controlling procedure and other related parameters, the stability of AFC is expected to reach the magnitude of $10^{-15}\tau^{-\frac{1}{2}}$.

Two ways are applied to realize the idea in experiments. One is post-processing. As following, recording $\langle y_{i-e}\rangle$ when AFS is running, then broadcasting the array $\langle y_{i-e}\rangle$ to the users of AFS, and finally using them to adjust the output of AFS ($\langle \bar{y}_i\rangle$) at the corresponding moment according to Eq. (11). It is a common method in time-frequency research field. The other way is letting the output of AFS passby a delay line (DL) and a phase modulator successively. y_{i-e} is acquired when i^{th} periodic signal passby the DL. Then giving corresponding modulation following Eq. (11) to the output of AFS. These two methods are feasible in theory, but difficult in practice. The post-processing method cannot be used directly and timely. DL scheme takes very strict requirement on DL. Its delay time must be larger than T_c on the scale of several seconds. While its precision needs to be far better than short-term stability of the AFS at corresponding time interval. It is difficult to fabricate the device. On account of the difficulties in implementation of above two methods, we put forward the third method: overlap feedback. This method gives an additional feedback to LO.

B. Overlap feedback

In order to overcome the shortages of post-processing and DL methods, we propose a new scheme: overlap feedback (OF). Considering Allan deviation is integration for time-span, we add an offset $-dy_{i-e}$ to $(i+1)^{th}$ cycle frequency signal, and it increases the extra noise for every cycle. Nevertheless this offset can counteract the last cycle error for many cycle integration and may result in decreasing of the total noise signal. To distinguish the correction signal $\bar{Y}_i$ of post-processing correction method, here we use $\bar{Y}_{r_i}$ to represent it:

$$\bar{Y}r_i = \bar{y}_i - d\cdot y_{(i-1)-e} = \frac{1}{N}\left(\sum_{k=1}^{N} y_{i,K} - \sum_{k=1}^{M} y_{i-1,K}\right) - d\cdot y_{(i-1)-Q} \tag{15}$$

Considering there is no relationship among all noise and integration time $\tau = LT_C$, stability can be described directly as:

$$\sigma^2_{\bar{Y}r}(\tau) = \sigma^2_{\bar{Y}}(\tau) + \frac{2d^2}{L^2}\sigma^2_y(T_c)\Big|_{L=\tau/T_c} = \sigma^2_{\bar{Y}}(\tau) + \frac{2d^2T_c^2}{\tau^2}\sigma^2_y(T_c) \tag{16}$$

It shows that it adds an additional term, $2d^2{T_C}^2{\sigma_y}^2(T_C)/\tau^2$, to the normal method, so it will deteriorate the short-term stability of AFS, but considering it converges fast with the integration time growing and varies with τ^{-1}, $\sigma_{Y_r}(\tau)$ will approach to $\sigma_Y(\tau)$ when $\tau \gg T_C$. The degree of stability deterioration become more and more obvious with the increase of d. $\sigma_{Y_r}(\tau)$ approaches to $\sigma_Y(\tau)$ with the increasing of integration time that is in keeping with theoretical expectation. Furthermore, the long-term stability comes up to the limit of QPN when duty is equal to 1.

The numerical simulation of $\langle \bar{Y}_{r_i}\rangle$ has also been used to verify the effectiveness of OF method, and the result has been shown in fig. 4. It is well coincident with Eq. (16). And comparing fig. 2 and fig. 4, we know OF method surely deteriorates the stability when $\tau < 2T_C$, but from then on, following the increase of the τ, the optimization of the stability become more and more obvious, and the line of $\sigma^2_{Yi}(\tau)$ is close to $\sigma^2_Y(\tau)$.

III. CONCLUSION

In this paper, we have shown an idea in increasing the stability of AFS, theoretical analysis and numerical simulation show that the idea is expected to improve the stability of periodic running AFS and the stability will decrease following the coefficient of $\sqrt{(1-d)}$. We also put forward that the methods of post-processing and DL will realize it in experiment,

but either of two methods has some shortages. So we improve it by OF method. It can also get the same improvement when

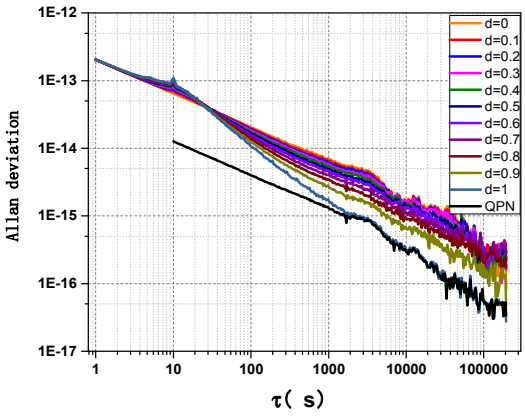


Fig.4. Using the overlap feedback (OF) method, the stability is described in different duties d which varies from 0 to1. Black curve shows QPN, orange curve shows stability when d=0.

$\tau \gg T_C$, but is at the price of deterioration of stability when $\tau < 2T_C$. For these ideas, d is a very important parameter, and it is similar for ZDT and so on[5-7]. But here the stability optimizes continuously with the increase of d, not requiring d rigorously equal to 1. The value of stability is better than $1 \times 10^{-14}\tau^{-\frac{1}{2}}$ for fountain AFS when d is close to 1.

At last, we discuss the case when the third assumption is false. We add the third assumption only in order to write the formula of stability expediently (from Eq. (12) to (13)). If it is false, equations about noise and all improvements of stability under the condition of d=1 are still right, but the suppressing of noise doesn't change with the $\sqrt{(1-d)}$. Besides that Eq. (13) and (16) will become more complex than their present formula. Considering that the idea reduces elements of the noise array, $\sigma_Y(\tau)$ still monotone decreases as duty increases. Hence this idea must be suitable, but here we don't discuss it in detail.

This work was supported by the Strategic Priority Research Program of the Chinese Academy of science under Grant No. XDB21030800.

REFERENCES

[1] F. Levi, et al. Accuracy evaluation of ITCsF2: A nitrogen cooled caesium fountain [J]. Metrologia, 51(3): 270 , 2014.

[2] T.L. Nicholson, M.J. Martin, J.R. Williams, B.J. Bloom, M. Bishof, M.D. Swallows, S.L. Campbell, and J. Ye, Phys. Rev. Lett. **109**, 230801, 2012.

[3] N. Huntemann, C. Sanner, B. Lipphardt, Chr. Tamm, E. Peik: Single-Ion Atomic Clock with 3x10-18 Systematic Uncertainty, Phys. Rev. Lett. **116**, 063001, 2016.

[4] B. J. Bloom, T. L. Nicholson, J. R. Williams, S. L. Campbell, M. Bishof, X. Zhang, S. L. Bromley, and J. Ye, Nature **506**, 71, 2014.

[5] G.W. Biedermann, K.Takase, X. Wu, L.Deslauriers, S.Roy, and M.A. Kasevich, Zero-Dead-Time Operation of Interleaved Atomic Clocks. Phys. Rev. Lett **111**,170802, 2013

[6] B. Fang, I. Dutta, D. Savoie, B. Venon, C. L. Garrido Alzar, R. Geiger and A. Landragin, Cold-atom Inertial Sensor without Deadtime. 2016 European Frequency and Time Forum (EFTF) , pp. 4, 2016.

[7] M. Schioppo, R. C. Brown, W. F. Mcgrew, N. Hinkley, R. J. Fasano, K. Beloy, T. H.Yoon, G. Milani, D. Nicolodi, J. A. Sherman, N. B. Phillips, C. W. Oates and A. D. Ludlow, Ultrastable optical clock with two cold-atom ensembles. nat. photonics **11,** 48-52, 2017.

[8] Yuanbo Du, Rong Wei, Richang Dong, Fan Zou, Jinda Lin, Wenli Wang , and Yuzhu Wang, Residual frequency drift in an atomic fountain clock, Chinese Optics Letters, 13(9), 091201, 2015.

[9] Y. N. Itano, J. C. Bergquist, J. J. Bollinger, J, M. Gilligan, D. J. Heinzen, F. L.Moore, M. G. Raizen and D. J. Wineland, Phys. Rev. A **47** 3554, 1993.

[10] Charles A. Greenhall, Member. IEEE TRANSAFSTIONS ON ULTRASONICS, FERROELECTRICS, AND FREQUENCY CONTROL, VOL. 45. NO. 4, JULY, 1998.

[11] Giorgio Santarelli, Claude Audoin, Ala'a Makdissi, Philippe Laurent, G. John Dick, and Andr é Clairon. IEEE TRANSAFSTIONS ON ULTRASONICS,FERROELECTRICS,AND FREQUENCY CONTROL, VOL. 45. NO. 4, JULY, 1998.

[12] Claude Audoin, Giorgio Santarelli, Ala'a Makdissi, and Andr é Clairon, IEEE TRANSAFSTIONS ON ULTRASONICS, FERROELECTRICS, AND FREQUENCY CONTROL, VOL. 45. NO. 4, JULY, 1998.

[13] Yuanbo Du, Rong Wei, Richang Dong, Fan Zou, Yuzhu Wang, Recent improvements on the atomic fountain clock at SIOM. Chin.Phys. B, **24**(7):070601, 2015.

[14] ChunYan Shi, Wei Rong, ZiChao Zhou, Progress in Rubidium Fountain Clock Research at SIOM. IEEE International Frequency Control Symposium. pp.559-563, 2011.

An Empirical Model of the Alkali rf-Discharge Lamp

James Camparo
Physical Sciences Laboratories
Mail Stop: M2/253
The Aerospace Corporation, PO Box 92957, Los Angeles, CA 90009
james.c.camparo@aero.org

Abstract — **The rubidium (Rb) atomic frequency standard (RAFS) is quite literally the workhorse of atomic timekeeping in space. Consequently, there is considerable interest in improving its frequency stability and reliability. Chief among the RAFS' components, the rf-discharge lamp is arguably the most problematic. The rf-discharge lamp not only determines the signal-to-noise ratio of the device, but fluctuations in its intensity and/or spectrum map onto the clock's output frequency via the light-shift effect. Understanding the rf-discharge lamp's operation and behavior would therefore seem important for understanding the limitations of a RAFS' frequency stability and reliability. It is surprising then to find that at present no well-articulated theory of the lamp's operation exists. To remedy that situation, we have begun a research project to develop a model of rf-discharge lamp operation, with the eventual goal of uncovering pathways for rf-discharge lamp, and thereby RAFS, improvement. In the present work, our purpose is to employ a semi-quantitative theory of the rf-discharge lamp to better understand the relation of electron number density and Rb light emission to lamp temperature.**

Keywords—Rb atomic clock, RAFS, rf-discharge lamp

I. INTRODUCTION

In the early 1980s, in an attempt to better understand rubidium (Rb) consumption by the alkali rf-discharge lamps used in Rb atomic frequency standards (RAFS) [1,2], Hans Eckert developed the first comprehensive theory of alkali rf-discharge lamp operation [3]. Briefly, his theory attempts to account for the spatial distribution of electron density in the discharge, the spatial distribution of rf-electric field strength in the discharge, and the discharge's power consumption. Eckert's main purpose was to develop a model of Rb concentration at the walls of the rf-discharge lamp, which could then be used as a boundary condition for calculations of Rb permeation into the glass material.

Here, we employ Eckert's theory as a starting point to address two coupled discharge lamp questions: 1) what is the relationship between electron density and lamp temperature (*i.e.*, Rb vapor pressure, p_{Rb}), and 2) how does the Rb lamplight emission depend on lamp temperature? On the surface, the questions would seem easily answered: as the Rb vapor pressure increases, more Rb atoms get ionized with a subsequent linear increase in electron density. Then, since the Rb lamplight is generated by e/Rb^+ recombination at the lamp's walls, the Rb lamplight emission would be nonlinear in vapor pressure (*i.e.*, lamplight ~ p_{Rb}^2). Unfortunately, this easy answer is at odds with experiment.

Clearly, some of the complication in answering these questions comes from the fact that the plasma physics of the discharge is complex, and indeed nonlinear [4]. It is therefore unlikely that a complete first-principles theory of rf-discharge lamp operation will ever be developed. In fact, it is unlikely that such a first-principles theory would hold much practical (*i.e.*, intuitive) value, since it would involve the numerical solution of a large system of simultaneous partial differential equations, involving parameters (*e.g.*, inelastic electron collision cross sections) that are poorly understood. Instead, the purpose here is to work towards a semi-quantitative conceptual model of the rf-discharge lamp that makes a fair attempt at capturing the important elements of the plasma physics, yet simultaneously offers a vehicle for developing an intuitive picture of the lamp's behavior.

In the next section we provide an overview of our rf-discharge theory, including multi-step ionization of Rb [5]. Of course, this leads to a nonlinear differential equation for the electron density, which requires approximation for its solution. In Section III we estimate the fraction of Rb that is ionized in the discharge from conservation of energy, and in Section IV we consider the density of Rb neutral atoms at the walls of the lamp, N_w. Since the Rb lamplight comes primarily from e/Rb^+ recombination at the lamp walls, N_w is a measure of the Rb light emitted by the lamp. Finally, in Section V we consider the radial distributions of electrons and Rb neutrals in the lamp.

II. RF-DISCHARGE LAMP THEORY OVERVIEW

Defining n_e and N_{Rb} as the number densities of free electrons and neutral Rb atoms in the discharge, we have in steady state

$$\frac{dn_e(\vec{r})}{dt} = 0 = k_{gi} n_e^m(\vec{r}) N_{Rb}(\vec{r}) + D_a \nabla^2 n_e(\vec{r}), \qquad (1)$$

where k_{gi} is a generalized rate constant for m-electron collisional ionization of Rb; D_a is the ambipolar diffusion coefficient for electrons in a several torr noble gas,[1] and we have assumed that the m-electron collisions necessary for Rb

[1] In order for the electrons to extract energy from the rf-field, the electrons must suffer scattering events. In the alkali rf-discharge lamp, the Rb vapor is enclosed with a Kr or Xe buffer gas at a several torr pressure (*i.e.*, a noble gas number density orders of magnitude larger than the alkali number density). Since the first excited state of the noble gas is much higher than the electron's average kinetic energy, the Kr/Xe atoms act as elastic scattering partners for the electrons.

ionization occur in the same localized region of the discharge (*i.e.*, we assume that the Rb atoms do not move significantly between multiple electron collisions).

Considering a cylindrical lamp with radius R and length L, and assuming that the electron density has no dependence on the azimuthal angle, we write ∇^2 as

$$\nabla^2 = \frac{1}{r}\frac{\partial}{\partial r}\left(r\frac{\partial}{\partial r}\right)+\frac{\partial^2}{\partial z^2}. \qquad (2)$$

Further, we assume that L >> R, so that to first-order we can ignore the dependence of n_e on z. Equation (1) then becomes

$$\frac{d^2 n_e(r)}{dr^2}+\frac{1}{r}\frac{dn_e(r)}{dr}+\left(\frac{k_{gi}}{D_a}\right)N_{Rb}(r)\,n_e^m(r) = 0. \qquad (3)$$

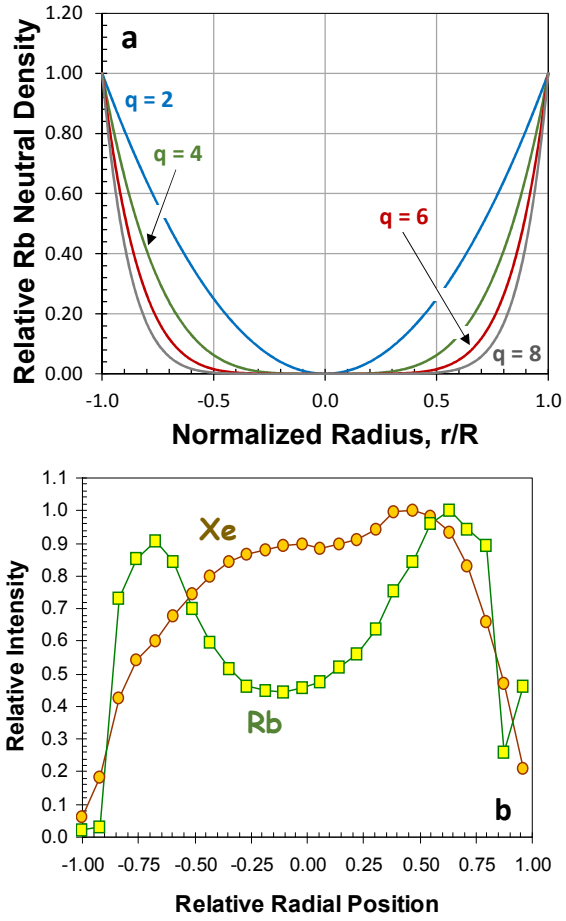


Figure 1: (a) $N_{Rb}(r)/N_w$ as a function of radial position for several different values of q. (b) Lamp spectra from Ref. 7, showing the radial variation of Rb light emission as a fiber connected to a spectrometer was scanned across the lamp's face.

To proceed, we recognize that there are two difficulties regarding Eq. (3): 1) the electrons' spatial distribution is coupled with that of the neutral Rb atoms, and 2) the equation is nonlinear in electron number density. To deal with the first, we follow Eckert [3] and write $N_{Rb}(r)$ as a power law in r:

$$N_{Rb}(r) = N_w\left(\frac{r}{R}\right)^q \qquad (4)$$

with q > 0. In effect, we are assuming that along the lamp axis only Rb^+ is present (*i.e.*, complete ionization), and that the neutral Rb number density increases towards the lamp's walls. This later assumption has been validated experimentally [6,7]. In particular, Fig. 1a shows $N_{Rb}(r)$ for several values of q, while Fig. 1b is a measurement of Rb lamp emission when a fiber was attached to a spectrometer and scanned across the face of an rf-discharge lamp [7]. Comparing the two figures, a reasonable range for likely q values would appear to be $2 \le q \le 4$.

For the second difficulty, we note that the electron density will likely be highest on axis, and that it will fall to near zero at the lamp's walls where fast e/Rb^+ recombination takes place. Further, we can reasonably expect that the greater the number of electron collisions required for ionization (*i.e.*, the greater m), the faster the electron density will fall as a function of lamp radius, r. Therefore, to linearize Eq. (3) we make the following replacement:

$$n_e^m(r) \rightarrow n_o^{m-1}\left(\frac{R}{r}\right)^{m-1} n_e(r), \qquad (5)$$

where n_o is an electron density parameter. Clearly, this replacement diverges at r = 0, and might therefore be considered problematic. However, note that $n_e^m(r)$ in Eq. (3) appears in combination with $N_{Rb}(r)$, which we have already taken as zero on axis. Thus, so long as $N_{Rb}(r)$ goes to zero faster at r = 0 then $n_e^m(r)$ goes to infinity, the replacement should not pose a problem. In other words, we require

$$2\beta \equiv q+1-m \ge 0. \qquad (6)$$

Notice that with $2 \le q \le 4$, and an expectation that m will likely lie between 2 and 6,[2] we anticipate 2β taking on values ranging from 0 to 3.

With these simplifying assumptions, and defining ρ as r/R, Eq. (3) becomes

$$\frac{d^2 n_e}{d\rho^2}+\frac{1}{\rho}\frac{dn_e}{d\rho}+\zeta^2\rho^{2\beta}n_e = 0 \qquad (7a)$$

with

[2] The lamp has an electron temperature around 5000 K, which implies an average electron energy of 0.65 eV. The first excited state of Rb is about 1.5 eV above the ground state, and the ionization potential of Rb is about 4 eV. We certainly need one electron collision to excite Rb to its first excited state, and then at least one more for ionization; thus $m \ge 2$. On average, however, we anticipate that with (m-1) collisions delivering 0.65 eV each to the atom, and a ladder of 2.5 eV to climb from Rb's 1st excited state, five more collisions will be necessary for ionization. Thus, a reasonable guess for the likely range of m values is 2 to 6.

$$\zeta^2 \equiv \left(\frac{k_{gi}R^2}{D_a}\right) N_w\, n_o^{m-1}. \qquad (7b)$$

Defining a new variable z: $z = \zeta\rho^{\beta+1}/(\beta+1)$, Eq. (7a) becomes

$$\frac{d^2 n_e}{dz^2} + \frac{1}{z}\frac{dn_e}{dz} + n_e = 0. \qquad (8)$$

This is just Bessel's equation of 0th-order, so that the radial variation of electron density across the lamp is given by

$$n_e(\rho) = n_e(0) J_o\left(\frac{R\rho^{\beta+1}}{\beta+1}\sqrt{\left(\frac{k_{gi}}{D_a}\right)N_w n_o^{m-1}}\right), \qquad (9)$$

where $n_e(0)$ is the electron density on axis.

If we now make the reasonable assumption that the first zero of $J_o(z)$ occurs at r = R (*i.e.*, that there are no nodes in the electron density distribution across the lamp radius), then

$$\frac{R}{\beta+1}\sqrt{\left(\frac{k_{gi}}{D_a}\right)N_w n_o^{m-1}} = 2.4048 = x_{01}.^{3} \qquad (10)$$

Equation (9) thus becomes

$$n_e(\rho) = n_e(0) J_o\left(x_{01}\rho^{\beta+1}\right). \qquad (11)$$

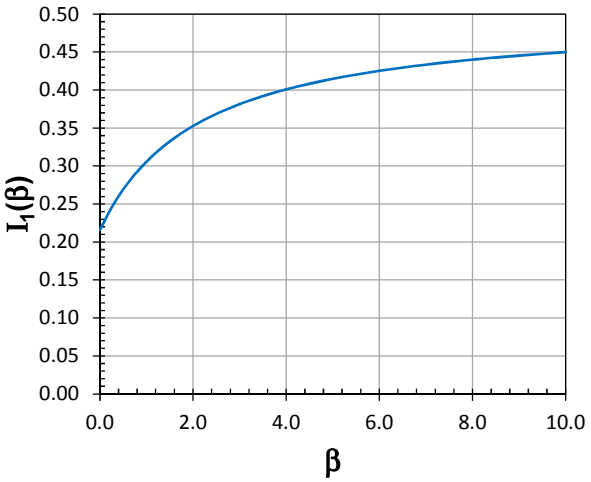


Figure 2: Graph of $I_1(\beta)$ for a range of possible β values. Given Eq. (6), and the likely values of q and m, we reasonably expect β to lie in the zero to 1.5 range. (The curve asymptotes to 0.5.)

We can go a bit further in clarifying Eq. (9) by relating $n_e(0)$ to the average fraction of Rb atoms that get ionized, η:

$$\eta[\mathrm{Rb}] = \frac{n_e(0)}{\pi}\int_0^1 J_o\left(x_{01}\rho^{\beta+1}\right)\rho\, d\rho\, d\theta, \qquad (12)$$

where [Rb] is the total rubidium number density in the vapor (neutrals and ions). As is well known, [Rb] is determined by the temperature of the Rb condensed phase via the Clausius-Clapeyron equation:

$$[\mathrm{Rb}] = \left(\frac{p_o}{kT_L}\right) e^{-\Delta G/kT_L}, \qquad (13)$$

where, T_L is the lamp base temperature, $p_o = 4.68\times10^7$ torr, and the heat of vaporization, ΔG, is 1.31×10^{-12} ergs [8]. Defining the integral over ρ in Eq. (12) as $I_1(\beta)$, we have

$$n_e(0) = \frac{\eta[\mathrm{Rb}]}{2\, I_1(\beta)}, \qquad (14)$$

which results in

$$n_e(\rho) = \frac{\eta[\mathrm{Rb}]}{2\, I_1(\beta)} J_o\left(x_{01}\rho^{\beta+1}\right). \qquad (15)$$

Figure 2 shows $I_1(\beta)$ for a range of potential β values. Note that with $\rho \le 1$, and in the limit $\beta \to \infty$, the argument of the Bessel function in the integral is zero so that the integral asymptotes to 0.5.

III. Estimation of Ionized Rb Fraction

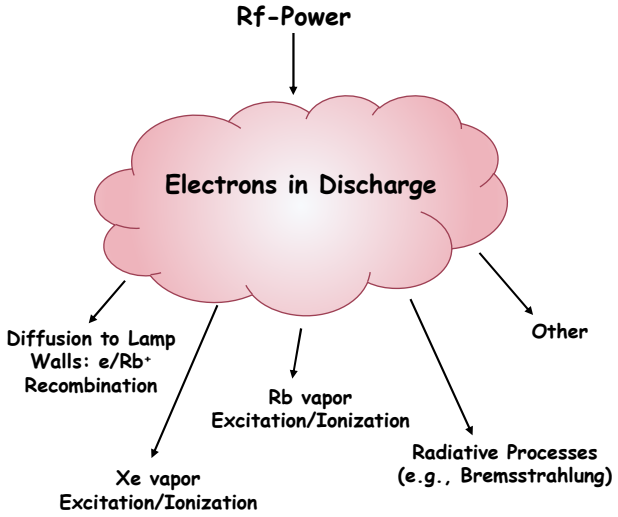


Figure 3: Illustration of energy-flow pathways in the plasma of an alkali rf-discharge lamp.

In order to estimate the fraction of Rb atoms that are ionized, η, we should first recognize that the rf-discharge lamps in atomic clocks are routinely powered by an rf-oscillator circuit (with a resonant frequency ν_o). Since the plasma frequency of the electrons is greater than ν_o under reasonable conditions, while the plasma frequency of the ions is less than ν_o, it is principally the electrons that oscillate in the field and extract energy from the field. Thus, we can imagine energy flow in the system as illustrated in Fig. 3: i) electromagnetic energy flows out of the rf-field at the rate P (*i.e.*, the oscillator circuit's input power), and into the electron

[3] This implies that

$$n_o^{m-1} = \frac{D_a}{k_{gi}N_w R^2}(\beta+1)^2 x_{01}^2.$$

ensemble;[4] ii) energy flows out of the electron ensemble in a multitude of ways, each of which may be very difficult to quantify.

Notwithstanding the myriad processes that cause the electrons to lose energy, in steady-state we have the condition:

$$\frac{dE_{electron}}{dt} \cong \frac{dE_{field}}{dt} \Rightarrow \frac{d\langle\varepsilon\rangle_{electron}}{dt} \cong \frac{d\langle\varepsilon\rangle_{field}}{dt}, \quad (16)$$

where $\langle\varepsilon\rangle_{electron}$ and $\langle\varepsilon\rangle_{field}$ are the lamp-volume averaged energy densities of the electrons and field, respectively, and where (for example) E_{field} is the total field energy in the resonant circuit's inductor:[5] $E_{field} = \pi R^2 L \langle\varepsilon\rangle_{field}$. Integrating Eq. (16), from t = 0 (where $E_{field} = E_{electrons} = 0$) to some time T when steady-state has been established, we find that the steady-state energy density of the rf-field equals the steady-state energy density of the discharge electrons: $\langle\varepsilon\rangle_{electron} = \langle\varepsilon\rangle_{field}$.

Defining P as the rf-power driving the discharge, we have

$$\langle\varepsilon\rangle_{field} = \frac{\tau_{osc} P}{\pi R^2 L} = \frac{PQ}{2\pi^2 \nu_o R^2 L}, \quad (17)$$

where τ_{osc} is the rf-oscillator circuit's time-constant (*i.e.*, the time scale over which energy is lost), which is related to the resonant circuit's loaded quality factor, Q. The energy density of the electrons in the discharge is

$$\langle\varepsilon\rangle_{field} = \frac{3}{2}\bar{n}_e k T_e = \frac{3}{2}\eta[Rb] k T_e, \quad (18)$$

where $\bar{n}_e$ is the average electron density in the discharge, from which η is defined, and T_e is the electron temperature. Equating Eqs. (17) and (18) then yields

$$\eta = \frac{PQ}{3\pi^2 \nu_o R^2 L k T_e [Rb]} = \frac{PQ}{\lambda_L \nu_o k T_e [Rb]}, \quad (19)$$

where λ_L is a lamp geometry factor that does not change with a specific RAFS design.

Typically, the rf-oscillator circuits that drive the rf-discharge lamps have $\nu_o \sim 10^2$ MHz and $Q \sim 10^2$ [9]. Further, the lamps routinely have a length of about one cm. Thus, considering an electron temperature of roughly 5000 K [10], and a typical millitorr Rb pressure for the discharge (*i.e.*, [Rb] $\sim 3\times10^{13}$ cm^{-3}), Fig. 3 shows η plotted as a function of P for several lamp radii. Figure 4 shows η as a function of lamp temperature, with [Rb] determined via Eq. 13, for several values of rf-power taking R = 0.4 cm.

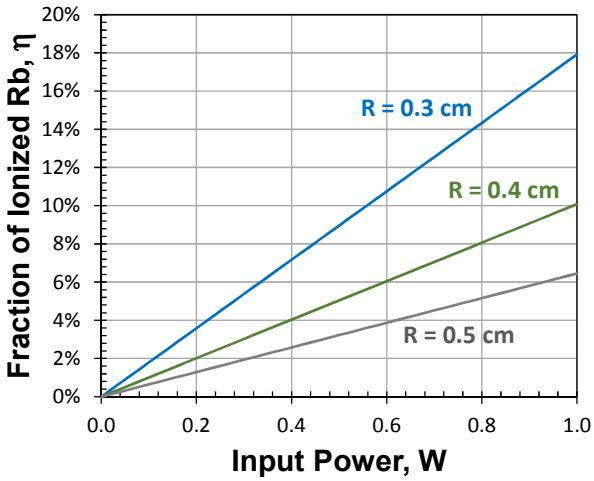


Figure 3: The fraction of ionized Rb in the vapor, η, as a function of rf-power for several values of lamp radii: $\nu_o = 10^2$ MHz, Q = 100, T_e = 5000 K, L = 1 cm, and [Rb] = 3×10^{13} cm^{-3}.

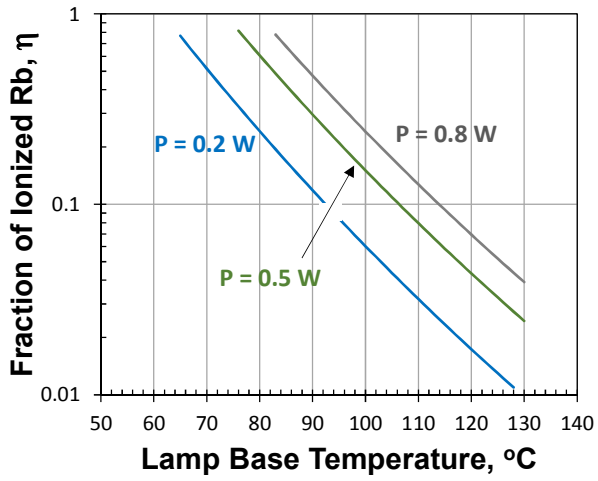


Figure 4: The fraction of ionized Rb in the vapor, η, as a function of lamp temperature for several values of the rf-power: $\nu_o = 10^2$ MHz, Q = 100, T_e = 5000 K, L = 1 cm, and R = 0.4 cm.

It is worth noting in Eq. (19) that the fraction of ionized Rb is inversely proportional to [Rb]. Thus, when combined with Eq. (14) for the electron density, we find that *$n_e(r)$ is independent of [Rb] (i.e., lamp base temperature)*. Further, since previous studies have found that $T_e \sim 1/\nu_o^2$ [11], Eq. (19) suggests that all other things being equal $\eta \sim \nu_o$.

IV. Estimation of the Rb Light Emission

To determine the Rb lamplight emission, we need to determine N_w. To this end, we note from charge neutrality that on average the number of electrons in the discharge must equal the number of Rb^+ in the discharge. Thus,

[4] We assume that the loaded-Q of the rf-oscillator circuit (*i.e.*, the quality factor of the circuit when the discharge is present) is significantly smaller than the unloaded-Q of the rf-oscillator circuit. Thus, we are assuming that radiative radiofrequency losses of rf-power are negligible while the lamp is in operation.

[5] Typically, the oscillator corresponds to either a Colpitts or Hartley oscillator circuit, and the windings of the circuit's inductor surround the lamp bulb's volume.

$$2\pi R^2\left\{\int_0^1 n_e(\rho)\rho d\rho + \int_0^1 N_{Rb}(\rho)\rho d\rho\right\} = \pi R^2[Rb]. \quad (20)$$

Substituting from Eqs. (4) and (15), this then yields

$$\eta[Rb] + 2N_w\int_0^1 \rho^{q+1}d\rho = [Rb] \quad (21a)$$

$$N_w = \tfrac{1}{2}(q+2)(1-\eta)[Rb]. \quad (21b)$$

Finally, substituting from Eq. (19) for η, we arrive at

$$N_w = \tfrac{1}{2}(q+2)[Rb] - \frac{(q+2)PQ}{2\lambda_L \nu_o kT_e}. \quad (22)$$

Since the Rb light emitted by the lamp will be proportional to N_w, Eq. (22) yields the observed result that Rb lamplight is proportional to [Rb]. Notice, however, that the intercept is negative, an unphysical condition. We interpret the negative intercept as defining a threshold condition on [Rb] for rf-discharge lamp operation:

$$[Rb]_{th} = \frac{PQ}{\lambda_L \nu_o kT_e}. \quad (23)$$

Specifically, for $[Rb] < [Rb]_{th}$, there are too few Rb atoms in the vapor for the discharge to light; the discharge only lights when $[Rb] > [Rb]_{th}$. Employing Eq. (13), we can convert Eq. (23) into a (transcendental) threshold condition on lamp temperature:

$$T_o e^{\Delta G/kT_o} = \frac{p_o \lambda_L \nu_o T_e}{PQ} \equiv \xi_{th}, \quad (24)$$

where T_o is the minimum lamp base temperature for rf-discharge lamp operation. Figure 5 shows the right and left portions of Eq. (24) plotted separately as a function of lamp base temperature, T_L. The location on the graph where the curves cross indicates the appropriate value of T_o. Clearly, the figure indicates that for reasonable lamp parameters, T_o lies in the range of 65 °C to 80 °C, which is consistent with observation.

V. Radial Distribution of Electrons

For completeness, Fig. 6 provides an illustrative example of the radial electron distribution for a range of likely 2β values. For the computations, we considered an rf-discharge lamp with the following parameters:

$P = 0.5$ W and $Q = 100$

$\nu_o = 10^2$ MHz

$R = 0.4$ cm and $L = 1$ cm

$T_e = 5000$ K

$T_{Rb} = 110$ °C $\Rightarrow$ $[Rb] = 1.9\times10^{13}$ cm^{-3}

These parameters yielded $\eta = 7.6\%$. From the figure, we see that increasing values of β tend to flatten the electron distribution for $\rho < 0.5$. Regardless of the different radial distribution shapes, however, integrating over these radial distributions in all cases yields the same average electron density across the lamp volume: 1.5×10^{12} cm^{-3}.

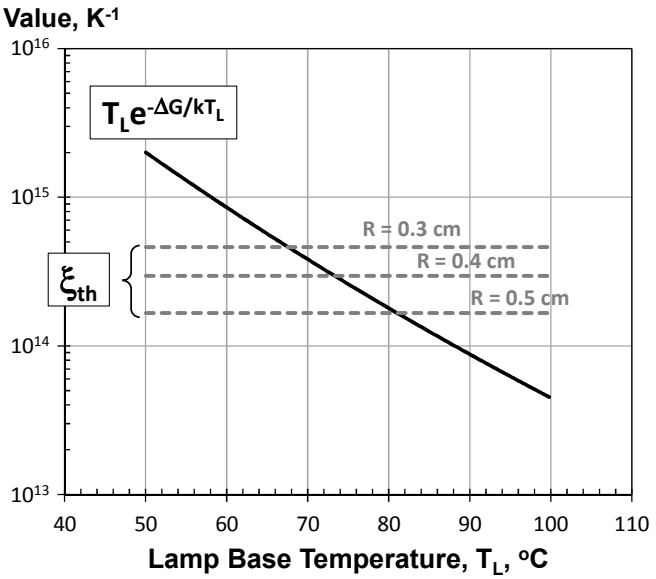


Figure 5: Indication of an rf-discharge lamp's threshold operating temperature, T_o: $L = 1$ cm, $\nu_o = 10^2$ MHz, $T_e = 5000$ K, $P = 0.5$ W, and $Q = 100$. The value of T_o is indicated by the abscissa value where the solid line crosses a dashed line.

For the same parameters, Fig. 7 shows the radial distribution of $N_{Rb}(r)$ for several values of q. As expected, operation of the discharge "piles up" alkali neutral atoms at the walls of the lamp. As q increases, the steepness of this pile-up also increases.

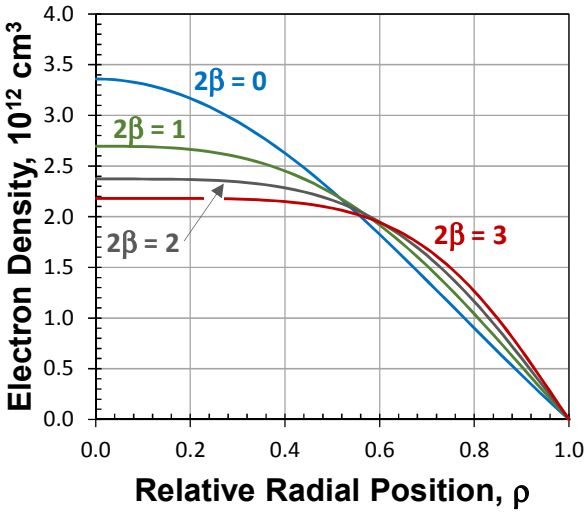


Figure 6: Radial electron distribution for a range of likely β values given reasonable rf-discharge lamp parameters.

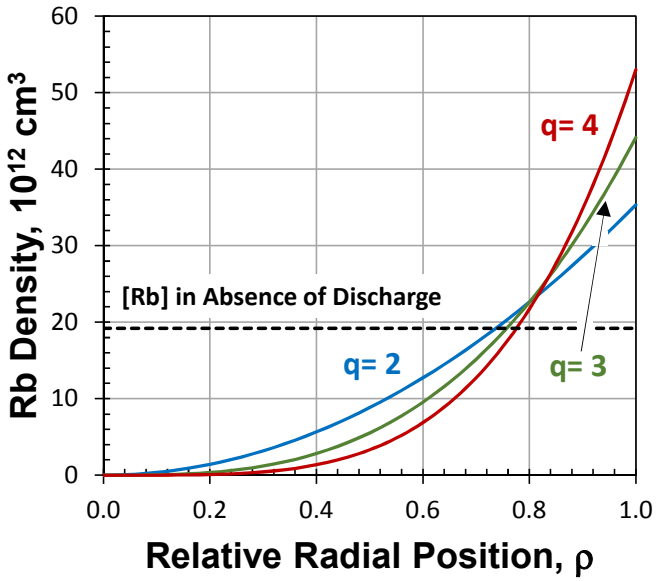


Figure 7: Radial Rb neutral distribution for a range of likely q values given reasonable rf-discharge lamp parameters.

VI. Summary

In this work, we have attempted to develop a semi-quantitative model of the rf-discharge lamp employed in rubidium (Rb) atomic frequency standards (RAFS). In particular, we have made a series of assumptions meant to lead us to closed form results regarding the lamp's characteristics. To the extent that our closed form results match observation, the assumptions are viable.

With our assumptions, the model is able to make several interesting predictions: 1) electron density in the discharge is effectively independent of alkali number density, 2) Rb light emission is linear in alkali number density (as observed experimentally), and 3) there is a threshold lamp temperature for lamp operation (consistent with experiment). In the future, we hope to use this model to better understand jumps in the light intensity of rf-discharge lamps employed in RAFS, which impact RAFS operation via the light-shift effect [12, 13].

Acknowledgment

The author thanks B. Jaduszliwer for a critical reading of this manuscript.

References

[1] R. P. Frueholz, M. Wun-Fogle, H. U. Eckert, C. H. Volk, and P. F. Jones, "Lamp reliability studies for improved satellite rubidium frequency standards," in Proc. 13th Annual Precise Time and Time Interval (PTTI) Systems and Application Meeting. US Naval Observatory: Washington, DC, 1981, pp. 767-790.

[2] C. H. Volk, R. P. Frueholz, T. C. English, T. J. Lynch, and W. J. Riley, "Lifetime and reliability of rubidium discharge lamps for use in atomic frequency standards," in Proc. 38th IEEE Internat. Freq. Control Symp. IEEE Press: Piscataway, NJ, 1984, pp. 387-400.

[3] H. U. Eckert, "An analytical model for rf inductive glow discharge columns in metal-gas mixtures and application to the Rb-Xe system," Aerospace Report No. TR-0082(2472-06)-1. The Aerospace Corporation: El Segundo CA, 1982.

[4] J. Camparo, F. Wang, W. Lybarger, and Y. Chan, "A complex permeability model of rf-discharge lamps," in Proc. 2013 Precise Time and Time Interval (PTTI) Systems and Applications Meeting, ION PTTI 2013. ION Press: Bellevue, WA, 2013, pp. 62-68.

[5] L. Vriens, "Multistep ionization in the positive column of low-pressure Na-Ne and Ne discharges," J. Appl. Phys., vol. 49, pp. 3814-3820, 1978.

[6] V. S. Zholnerov, I. M. Nekrylova, M. V. Spazheva, V. A. Trukhacheva, and V. I. Khutorshchikov, "Spatial distribution of atoms in electrodeless spectral lamps containing rubidium vapor," Opt. Spectrosc., vol. 56, pp. 148-149, 1984.

[7] J. C. Camparo and R. Mackay, "Spectral mode changes in an alkali rf discharge," J. Appl. Phys., vol. 101, 053303, 2007.

[8] T. J. Killian, "Thermionic phenomena caused by vapors of rubidium and potassium," Phys. Rev., vol. 27, pp. 578-587, 1926.

[9] J. C. Camparo and C. M. Klimcak, "Generation of ion-acoustic waves in an inductively coupled, low-pressure discharge lamp," J. Appl. Phys., vol. 99, 083306, 2006.

[10] H. van Tongeren, "Positive column of the Cs-Ar low-pressure discharge," J. Appl. Phys., vol. 45, pp. 89-96, 1974.

[11] N. L. Encalada, B. Jaduszliwer, W. E. Lybarger, and J. C. Camparo, "Noble-gas loss in alkali rf-discharge lamps and its possible dependence on electron temperature," IEEE Trans. Instrum. Meas., vol. 63, pp. 2642-2650, 2014.

[12] V. Formichella, J. Camparo, I. Sesia, G. Signorile, L. Galleani, M. Huang, and P. Tavella, "The ac Stark shift and space-borne rubidium atomic clocks," J. Appl. Phys., vol. 120, 194501, 2016.

[13] V. Formichella, J. Camparo, and P. Tavella, "Influence of the ac-Stark shift on GPS atomic clock timekeeping," Appl. Phys. Lett., vol. 110, 043506, 2017.

Theoretical and experimental study of Rb Coherent Population Trapping atomic clock with phase modulation detection

Yuichiro Yano, Motoaki Hara, Masatoshi Kajita, Tetsuya Ido
Space-Time Standards Laboratory
National Institute of Information and Communications Technology
4-2-1 Nukui-Kitamachi Koganei Tokyo, 184-8795 Japan
E-mail: y-yano@nict.go.jp

***Abstract*—We theoretically and experimentally study Coherent Population Trapping (CPT) resonance with phase modulation detection. We measured the time response behavior of CPT resonance using an ^{87}Rb gas cell and the D1-line vertical-cavity surface-emitting laser(VCSEL) and calculated the periodic behavior of the density matrix based on eigenvector algorithm. Experiment results are good agreement with calculation results.**

Keywords—Coherent Population Trapping atomic clock, Phase modulation,

Coherent population trapping (CPT) atomic clocks have been attractive for compact time keeping device because of its small and low-power consumption. Both of high signal to noise ratio and narrow linewidth of CPT resonance are required to improve short-term stability. However, narrower linewidth generally leads poor signal to noise ratio due to increasing in electrical noise because it leads to low frequency response. Previously, we theoretically show that high frequency response speed of CPT resonance can be obtained by phase modulation(PM) without degrading Q-value comparing conventional modulation (frequency modulation: FM)[1]. In this paper, we experimentally and theoretically study the modulation method to improve time response of CPT resonance. We measure the time response of CPT resonance using a ^{87}Rb gas cell and the D1-line VCSEL. We also calculate time evolution of density matrix element based on eigenvector algorithm in Ref. [2]. Experimental results are good agreement with calculation results.

Fig. 1 shows signal amplitude of CPT resonance as a function of repetition frequency f_{rep} that is number of measurement per unit time. For frequency modulation, transient phenomena are smaller when the repetition frequency is lower than resonance linewidth γ. When lower repetition frequency is set, the larger resonance signal can be obtained. When the repetition frequency larger than the resonance linewidth, the resonance signal decreases because CPT cannot keep up with the response of frequency variation. The slope of decrement of signal in $f_{rep} > \gamma$ is -20 dB/dec. It is shows that the response speed of CPT resonance is limited by relaxation of microwave transition. On the other hand, the time response of CPT resonance with PM is substantially different from that with FM. When the repetition frequency is small, the signal of CPT resonance is small. The signal of CPT resonance appears when repetition frequency is larger than γ. When the repetition frequency is set from γ to excitation relaxation ratio Γ, the signal is constant value and independent on f_{rep}. The signal decreases with increasing the repetition frequency larger than Γ. Thus, it is shown that the response speed of CPT resonance is limited by the relaxation of optical transition. Although the signal amplitude with PM is 0.6 times of that with FM, the better SNR will be obtained by PM detection because of avoiding low frequency noise.

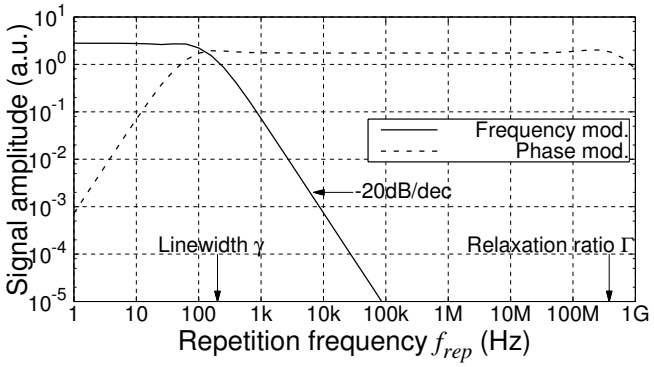


Fig. 1. Signal amplitude as a function of repetition frequency.

REFERENCES

[1] Y. Yano, M. Hara, M. Kajita, T. Ido, "Study of detection method of CPT reosonance for enhancing frequency stability of chip-scale atomic clocks", conference paper of The Institute of Electrical Engineers of Japan, no. ECT-16-061, Sep. 2016(in Japanese).

[2] Y. Yano, S. Goka and M. Kajita, "Estimation of the light shift in Ramsey-Coherent Population Trapping", in proceedings of 2015 IEEE IFCS & EFTF, 2015, pp.162-166.

Ultrahigh-Contrast Saturated-Absorption Resonance to Enhance Stability of CPT Atom Clocks

Denis Brazhnikov[1,2], Moustafa Abdel Hafiz[3], Grégoire Coget[3],
Alexei Taichenachev[1,2], Valeriy Yudin[1,2,4], Emeric de Clercq[5] and Rodolphe Boudot[3]

[1] Institute of Laser Physics SB RAS, Novosibirsk, Russia
[2] Novosibirsk State University, Novosibirsk, Russia
[3] Department of Time and Frequency Standards, FEMTO-ST, CNRS, UBFC, Besançon, France
[4] Novosibirsk State Technical University, Novosibirsk, Russia
[5] LNE-SYRTE, Observatoire de Paris, PSL Research University, CNRS,
Sorbonne Universités, UPMC Univ. Paris, France

Emails: brazhnikov@laser.nsc.ru, rodolphe.boudot@femto-st.fr, emeric.declercq@obspm.fr

***Abstract*—The results of detailed experimental and theoretical investigations of new nonlinear effect in the field of saturated-absorption spectroscopy of atom vapours are presented. The effect consists in observation of a high-contrast natural-linewidth absorption spike when ^{133}Cs atoms are being irradiated by the bichromatic counterpropagating laser beams. The results obtained can be useful in various fields of modern laser physics and applications where saturated-absorption resonances are used. For instance, the effect has been already implemented in the coherent-population-trapping atom clocks to enhance stabilization of optical frequencies and to improve stability of the clocks on the whole.**

Keywords—saturated-absorption resonance; microwave atom clocks; coherent population trapping; quantum metrology

I. INTRODUCTION

Saturated-absorption resonance (SAR) is a widely used tool in fundamental laser spectroscopy of atoms and molecules [1], and in many experiments with laser radiation. It plays an important role in quantum metrology for producing optical frequency standards including compact and mobile versions for ground and space-borne applications. For instance, many laboratories develop He-Ne, Nd:YAG, Yb:YAG, diode and other lasers frequency locked to optical transitions in iodine or methane molecules by means of SAR, including stabilization of optical frequency combs (for instance, see [2-4]). Besides the molecular vapours, the alkali-metal atoms are also used for the same purposes [5,6].

New bright feature of SAR has been discovered in the recent experiments [7,8]. It consists in observation of a high-contrast natural-linewidth absorption spike under linearly polarized counterpropagating laser beams (see an example of the signal on Fig. 1 and a part of experimental setup on Fig. 2). Each of the beams has two optical frequency components to simultaneously excite both hyperfine levels of the Cs ground state (Fig. 3). Such kind of the natural-linewidth absorption peaks were observed and studied before. Indeed, it is well-known that several physical reasons may cause a nonlinear absorption peak creation at the center of absorption profile. For instance, among these effects are the recoil effect [9,10], high-order spatial harmonics of atomic polarization [11], optical pumping effects [12–14] and magnetic-field-caused splitting [15]. Besides, Doppler-effect peculiarities for moving atom in a gas, whose open optical transition is being excited by two counterpropagating light waves, can also lead to the absorption peak observation [16,17].

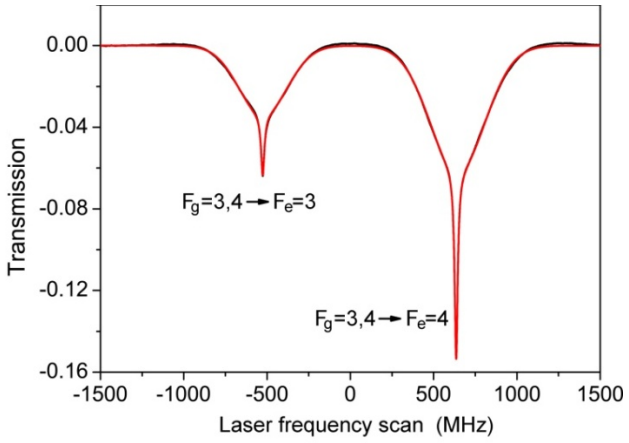


Fig. 1. Experimental resonance curves. The total laser power is 500 μW, polarizations of the counterpropagating light beams are perpendicular. F_g, F_e are the total angular momenta of the ground and excited energy levels of Cs.

Regularly, the contrast of SAR with respect to a wide background signal is not high in many studied configurations. However, the recent experiments [7,8] have revealed a saturated-absorption peak with ultrahigh contrast. In particular, under the appropriate conditions amplitude of the central

D.V. Brazhnikov was supported by RFBR (grant no. 15-02-08377) and MESRF (project no. 3.1326.2017), V.I. Yudin thanks RSF (project no. 16-12-10147), MESR (no. 3.1326.2017/4.6), and RFBR (grant no. 17-02-00570), Taichenachev was supported by RSF (project no. 16-12-00054). French authors thank LabeX FIRST-TF, Région de Franche-Comté, EURAMET (EMRP programm, MClocks project) and DGA. The EMRP is jointly funded by the EMRP participating countries within EURAMET and the European Union.

resonance could be twice bigger than amplitude of the Doppler-broadened background. Moreover, the SAR in the considered light-field configuration has been studied at first time.

The new effect has been already successfully implemented in the microwave coherent-population-trapping atom clocks in two laboratories (FEMTO-ST and LNE-SYRTE [18, 19]). It has appeared to be efficient for the optical frequency stabilization that improved stability of the clocks. At the same time, in spite of such the interest, physical reasons of the effect have not been understood and studied well enough yet. Therefore, our current research is devoted to comprehensive experimental and theoretical study of SAR under the light field composed of the bichromatic counterpropagating laser beams. The results help one to understand physical reasons for observation of the new effect as well as demonstrate influence of external magnetic field, Raman frequency detuning, laser beam polarizations and intensities on the properties of the nonlinear resonance. In this paper we just briefly discuss physical nature of the effect, while a full version of the study is going to be published soon [8].

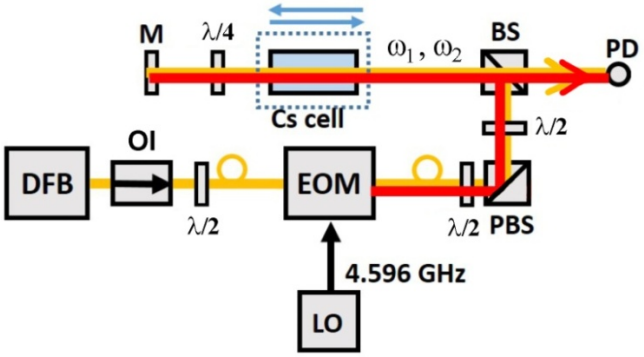


Fig. 2. Experimental setup: DFB – distributed feedback diode laser, OI – optical isolator, EOM – electro-optic modulator, LO – microwave frequency synthesizer, PBS – polarizing beam splitter, M – mirror, PD – photodiode.

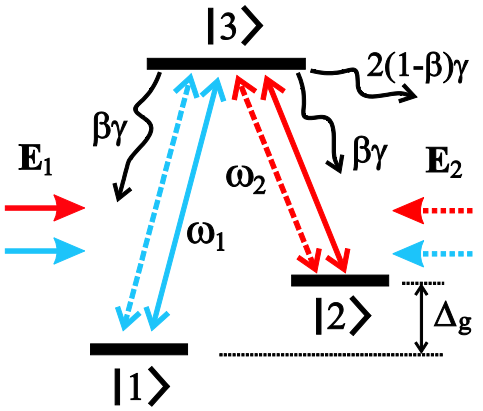


Fig. 3. Λ-scheme of atomic energy levels in ^{133}Cs: $|F_g=3\rangle \equiv |1\rangle$, $|F_g=4\rangle \equiv |2\rangle$, $|F_e=4\rangle \equiv |3\rangle$. Spontaneous relaxation rate of the excited state equals to 2γ. Branching ratio β governs the openness of the system.

II. PHYSICAL REASONS OF THE HIGH-CONTRAST SPIKE

The high-contrast-spike effect can be understood on the basis of the well-known Λ-scheme of atomic energy levels (see Fig. 3). In spite of the spectroscopic signal in our case is not the sub-natural linewidth resonance (as the "dark" resonance for instance), the effect is closely connected with the CPT phenomenon [20,21]. The effect can be also caused just by the population redistribution over the ground-state sublevels of an atom due to optical pumping. All these factors should be considered carefully.

A. HFS-CPT effect

If the one-photon frequency detuning Δ is much larger than the natural linewidth of an optical transition ($\Delta >> \gamma$), the counterpropagating beams act on the different velocity groups of atoms in a gas due to the Doppler effect (here the one-photon detuning $\Delta=\omega_1-\omega_{31}=\omega_2-\omega_{32}$ is assumed to be the same for both frequency components of the light field, and also the condition $\Delta=0$ means that two counterpropagating waves are both in resonance with the atoms at rest). In this case CPT ("dark" or non-coupled, NC) state can be created in each velocity group separately, embracing magnetic sublevels of the *different* hyperfine levels of the ground state ($F_g=3$ and $F_g=4$ for Cs). Therefore, level of absorption under $\Delta>>\gamma$ is low.

This effect can be explained on the basis of the Λ scheme depicted on Fig. 3 with $\Delta_g \approx 9.2$ GHz. The expression for the light field in a vapor cell is:

$$E(z,t) = E_1\left[e^{-i(\omega_1 t - k_1 z)} + e^{-i(\omega_2 t - k_2 z)}\right] + E_2\left[e^{-i(\omega_1 t + k_1 z - \phi + \phi_1)} + e^{-i(\omega_2 t + k_2 z + \phi + \phi_2)}\right] + c.c., \quad (1)$$

where the amplitudes $E_{1,2}$ are considered to be real values, while the relative phases of two frequency components of the counterpropagating beam are denoted as $\phi_{1,2}$. The angle ϕ corresponds to the mutual angle between linear polarizations of the counterpropagating waves in a real experiment.

So, each of two two-frequency waves from (1) pumps the atoms into the following non-coupled (CPT) states:

$$|NC_1\rangle = \left\{|1\rangle - e^{ik_{12}z}|2\rangle\right\}/\sqrt{2}\ , \quad (2)$$

$$|NC_2\rangle = \left\{|1\rangle - e^{-i(k_{12}z+\phi_{12}+2\phi)}|2\rangle\right\}/\sqrt{2}\ , \quad (3)$$

with $\phi_{12}=\phi_1-\phi_2$ and $k_{12}=k_1-k_2$. If the frequency detuning is not so large ($\Delta \sim \gamma$), the counterpropagating beams act on the same atoms in a gas and the result depends on the fact if two NC states (2) and (3) are the same or orthogonal to each other. In the latter case one can observe the increased absorption in vicinity of $\Delta \approx \gamma$ (see an example on Fig. 4). Also, as it is seen from (2) and (3), the HFS-CPT effect depends on position of the mirror "M" or position of the cell (see Fig. 2), polarizations of the beams (the angle ϕ in particular) as well as the cell length. Moreover, different points on the *z*-axis (along the cell) can exhibit the constructive (low level of absorption) or destructive (high level of absorption) action of the counterpropagating waves via the NC_1 and NC_2 states.

Apparently, the peak's effect does not depend essentially on the cell length when the length satisfies the condition $L>\pi/|k_{12}|\approx 1.6$ cm (in the case of Cs).

It should be noted that the qualitative analysis presented in this subsection has many in common with the one previously reported in [22], but for the counterpropagating light waves with σ^+ and σ^- polarizations.

B. Zeeman CPT effect

This effect has many in common with HFS-CPT and it can be treated with the help of Λ scheme too, taking $\Delta_g = 0$, $k_2 = -k_1$, $\omega_1 = \omega_2$. In this case the non-coupled states consist of the coherent superpositions of magnetic sublevels of *the same* hyperfine level (namely F_g=4 for the resonance on Fig. 1, right). In contrast to the HFS-CPT, the Zeeman CPT effect is insensitive to position of the mirror or the cell length, but its sign and magnitude strongly depend on the polarizations of the counterpropagating beams.

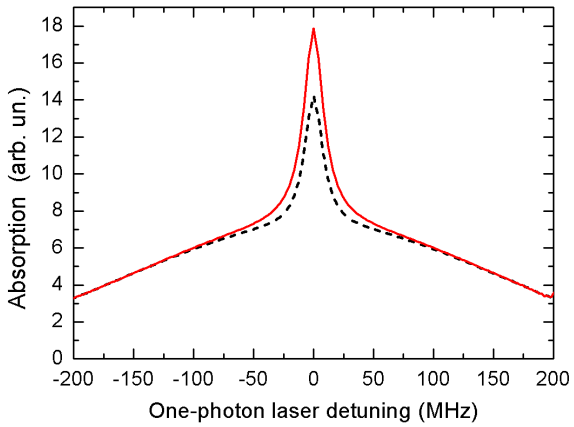


Fig. 4. High-contrast absorption spike calculated on the basis of the optical Bloch equations. Solid line for the orthogonal polarizations of the counterpropagating beams, while dashed one is for parallel polarizations. Cell length equals to 2 cm, Rabi frequencies are ~ γ. In this paper we consider the total population of the excited state $|3\rangle$ multiplied by the factor 10^3 (for convinience of presentation) as the theoretical spectroscopic signal.

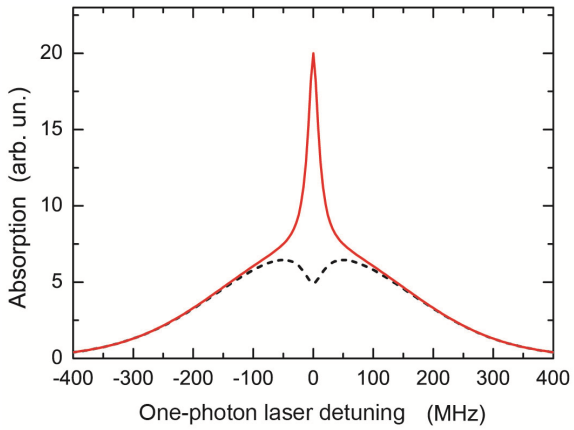


Fig. 5. Absorption curves for parallel (ϕ=0, dashed black line) and orthogonal (ϕ=π/2, solid red line) light wave polarizations. The static magnetic field is zero. The system of levels is assumed to be closed (i.e. the branching ratio β=1, see Fig. 3).

The similar theory was considered in [23] for the subnatural-linewidth resonance in the Hanle configuration under the two counterpropagating waves of equal frequency. The analysis was done for the general case of light wave polarizations. For reasons of a concise style, here we do not extend the theory for our case of the natural-linewidth saturated-absorption resonances (for instance, see [8]). Let us just provide a reader with an example of the absorption profile demonstrating the Zeeman CPT effect (Fig. 5). As one can see, the result of absorption at the center of the curve strongly depends on mutual orientations of the linear polarizations of the counterpropagating waves.

It is also obvious that the Zeeman CPT effect depends on an external magnetic field applied to the cell. For example, if the field is strong enough, it destroys the CPT states composed of magnetic sublevels of the same level (F_g=4 in the case of Cs) and the influence of the Zeeman CPT effect on a possibility of the peak's creation is significantly reduced. In this situation only the HFS-CPT or the optical pumping effect, which is mentioned in the next paragraph, can cause the absorption peak creation. And it is apparent that the magnitude of the peak effect is higher when all three reasons take place. Therefore, a magnetic shield is required to defend the spectroscopic cell from the external stray field and to activate the Zeeman CPT reason.

C. Optical pumping effect

It appears that absorption-peak effect can also result from just the optical pumping process, which redistributes populations of the ground sublevels $|1\rangle$ and $|2\rangle$. This effect is pretty simple and can be treated on the basis of rate equations, even without taking into account the low-frequency coherence between the sublevels.

To demonstrate a sense of the optical-pumping reason, let us briefly analyze the scheme on Fig. 3, but in the simplest case of two counterpropagating waves with the same frequencies ($\omega_1=\omega_2$). It means that we consider the Λ-scheme, which has degenerate ground state under the null magnetic field as in the subsection devoted to the Zeeman CPT effect (see paragraph B). However, now we take the splitting Δ_g is large enough to destroy the coherence between the $|1\rangle$ and $|2\rangle$ states. So, we can consider only the populations of the states.

If the detuning is large ($\Delta>>\gamma$) the counterpropagating light waves act on the separate resonance groups of atoms in a gas. Moreover, each group of atoms can be effectively described by the open two-level system ($\beta<1$), because one of two ground-state sublevels ($|1\rangle$ or $|2\rangle$) is not in resonance with the light wave and it accumulates the atomic population. The level of absorption in this situation is not so high due to the openness.

On the other hand, if the detuning Δ is swept near the center of the resonance curve ($\Delta\sim\gamma$), there are two symmetrical group of atoms with velocities $\upsilon_{1,2}=\pm\Delta_g/k$, which are resonant to both of the light waves (here we imply also $\Delta<<\Delta_g$). In this situation the Λ-scheme is closed ($\beta=1$), because no one ground-state sublevel accumulates the population. The level of light field absorption in the closed system is significantly higher than in the open system. It leads to the peak effect at the center of the

resonance profile ($\Delta \sim \gamma$). Note that the similar optical-pumping effect was also mentioned in [24] (potassium atoms were studied).

III. Conclusions

To conclude we can state that the high contrast of the nonlinear resonance observed is due to the simultaneous constructive action of several physical phenomena. Qualitative physical explanation has been provided with the help of a simple Λ scheme of atomic energy levels. However, to explain quantitatively the peak's amplitude and width observed in the real experiments one should consider a real structure of atomic energy levels when all peak-caused physical reasons considered here work together. We have also carried out such kind of calculations and the results are in agreement with the experimental data (to be published elsewhere).

Besides the new theoretical knowledge about the saturated-absorption resonances in a gas of atoms obtained during our investigations, the effect can be interesting and useful for modern quantum metrology, laser physics and high-resolution spectroscopy.

References

[1] V. S. Letokhov and V. P. Chebotaev, Nonlinear Laser Spectroscopy. Heidelberg, Germany: Springer-Verlag, 1977.

[2] N. Castagna et al., "Iodine stabilized IR laser sources", IEEE Xplore, January 2014 [Digest of the Joint UFFC, EFTF and PFM Symposium, Czech Republic, 21-25 July 2013, p. 405].

[3] S. M. Ignatovich et al., "Yb:YAG/I_2 optical frequency standard at 515 nm with instability at the level 10^{-15}", Journal of Physics: Conf. Series, vol. 793, 012010, February 2017.

[4] N. A. Koliada et al., "Stabilisation of a fibre frequency synthesiser using acousto-optical and electro-optical modulators", Quantum Electron., vol. 46, pp. 1110–1112, December 2016.

[5] D. C. Heinecke et al., "Optical frequency stabilization of a 10 GHz Ti:sapphire frequency comb by saturated absorption spectroscopy in ^{87}rubidium", Phys. Rev. A, vol. 80, 053806, November 2009.

[6] M. Lezius et al., "Space-borne frequency comb metrology", Optica, vol. 3, pp. 1381–1387, December 2016.

[7] M. Abdel Hafiz et al., "Doppler-free spectroscopy on the Cs D_1 line with a dual-frequency laser", Opt. Lett., vol. 41, pp. 2982–2985, July 2016.

[8] M. Abdel Hafiz et al., "High-contrast sub-Doppler absorption spikes in a hot atomic vapor cell exposed to a dual-frequency laser field", New J. Phys., in press, 2017.

[9] A.P. Kol'chenko, S.G. Rautian, and R.I. Sokolovskii, "Interaction of an atom with a strong electromagnetic field with the recoil effect taken into consideration", Sov. Phys. JETP, vol. 28, pp. 986–990, May 1969.

[10] J.L. Hall, C.J. Borde, and K. Uehara, "Direct optical resolution of the recoil effect using saturated absorption spectroscopy", Phys. Rev. Lett., vol. 37, pp. 1339–1342, 15 November 1976.

[11] J. Ishikawa et al., "Strong-field effects in coherent saturation spectroscopy of atomic beams", Phys. Rev. A, vol. 49, pp. 4794–4825, June 1994.

[12] P.G. Pappas et al., "Saturation spectroscopy with laser optical pumping in atomic barium", Phys. Rev. A, vol. 21, pp. 1955–1968, June 1980.

[13] E.G. Saprykin, A.A. Chernenko, and A.M. Shalagin, "Polarization phenomena in the transparency and adsorption effects induced by the field of counterpropagating waves", J. Exp. Theor. Phys., vol. 119, pp. 196–205, August 2014.

[14] D.B. Lazebnyi et al., "Electromagnetically induced absorption and electromagnetically induced transparency for optical transitions Fg→Fe in the field of elliptically polarized waves", J. Exp. Theor. Phys., vol. 121, pp. 934–949, December 2015.

[15] H.S. Lee et al., "Zeeman effect in the saturation spectroscopy of the ^{87}Rb D_2 line", J. Opt. Soc. Am. B, vol. 11, pp. 558–563, April 1994.

[16] V.V. Vasil'ev et al., "Dual structure of saturated absorption resonance at an open atomic transition", J. Exp. Theor. Phys., vol. 112, pp. 770–779, May 2011.

[17] D.V. Brazhnikov et al., "New polarisation effects in saturated absorption spectroscopy in the field of counterpropagating light waves", Quant. Electron., vol. 46, pp. 453–463, May 2016.

[18] M. Abdel Hafiz et al., "A CPT-based Cs vapor cell atomic clock with a short-term fractional frequency stability of $3\times10^{-13}\ \tau^{-1/2}$", Journal of Physics: Conf. Series, vol. 723, 012013, July 2016.

[19] P. Yun et al., "High-performance coherent population trapping clock with polarization modulation", Phys. Rev. Appl., vol. 7, 014018, January 2017.

[20] G. Alzetta et al., "An experimental method for the observation of r.f. transitions and laser beat resonances in oriented Na vapour", Nuovo Cimento B, vol. 36, pp. 5–20, 11 November 1976.

[21] E. Arimondo, "Coherent population trapping in laser spectroscopy", Progress in Optics, vol. 35, pp. 257–354, 1996.

[22] S.V. Kargapoltsev et al., "High-contrast dark resonance in $\sigma_+ - \sigma_-$ optical field", Laser Phys. Lett., vol. 1, pp. 495–499, 16 September 2004.

[23] D.V. Brazhnikov, A.V. Taichenachev, and V.I. Yudin, "Polarization method for controlling a sign of electromagnetically-induced transparency/absorption resonances", Eur. Phys. J.D, vol. 63, pp. 315–325, 23 June 2011.

[24] D. Bloch et al., "Doppler-free spectroscopy of the D_1 line of potassium", Laser Phys., vol. 6, pp. 670–678, August 1996.

A Caesium atomic beam microwave clock detected by distributed feedback laser diodes

Chang Liu, Shuhui Wang, Ziyu Chen, Yanhui Wang, Shimin Hou
Peking University,
Beijing, China
wangyanhui@pku.edu.cn, smhou@pku.edu.cn

Jinsheng Jia, Yong Sun, Bingqiang Zhang
China Building Materials Academy,
Beijing, China

***Abstract*—A compact caesium-atomic-beam microwave clock is investigated at Peking University. The atomic beam is prepared by magnetic state selection and detected, after microwave interrogation, by means of laser-induced fluorescence. Distributed feedback laser diodes are adopted for their large mode-hopping-free ranges, which ensure a care-free long-term operation. Besides, digital servo systems can automatically relock the laser's frequency when it is off-resonant. A 45-day continuous measurement of the output frequency is carried out. The 5-day frequency stability is $2.7 \cdot 10^{-14}$ and the short-term stability is as good as those of commercial cesium clocks.**

Keywords—microwave; quantum frequency standard; atomic clock; laser diode; caesium beam tube;

I. INTRODUCTION

Conventional caesium clocks, which take advantage of magnetic state selections, are widely adopted in time-keeping and communication systems, due to the outstanding long-term frequency stability of these clocks. The long-term frequency stability results from the less collision of the atoms than those of other compact microwave clocks such as rubidium vapor-cell clocks and H-masers. On the other hand, optically pumped caesium beam clocks demonstrate better short-term frequency stability because of their enhanced pumping efficiency [1-3].

The main difficulty of conventional caesium clocks stems from the time-dependent attenuation of the electron multiplier, which is the essential part for the detection of the atoms. Substituting optical detetion for the electron multiplier in a magnetic-state-selection caesium beam tube is a method that can solve this problem. Besides, as the atomic velocity distribution is largely determined by the state-preparation magnets, the optical detection method avoids microwave spectrum line broadening, which usually occurs in optically pumped caesium tubes because of their broadened atomic velocity distribution. In [4], an experiment system with external cavity diode laser (ECDL) as light source for the detection is established, and realized a short-term stability of $1.2\times10^{-11}\tau^{-1/2}$. The signal to noise ratio is compared between ECDLs and distributed-feedback lasers (DFB) [5]. Although the short-term stabilities are different when the atomic intensity is high, they are close at low oven temperature, when atomic shot noise is dominant. As DFB lasers show great advantages in reliability and size, we choose DFB lasers regarding the robustness and compactness of the clock. In [6], we report the preliminary results of the clock with DFB lasers as light source.

II. EXPERIMENTAL SET-UP

The overall system is shown in Fig.1. The caesium tube operates under a double-beam scheme, i.e. the oven has two outlets that point several-degree inward, and a two-pole magnet deflects the atoms so that the atoms on particular levels, including (F=3, m_F=0), one of the levels that participate the clock transition, can pass through certain apertures on the microwave cavity. A light collector, which is composed of a set of mirrors, on the atomic trajectory in the detection region focuses the fluorescence onto a photodiode mounted outside the tube.

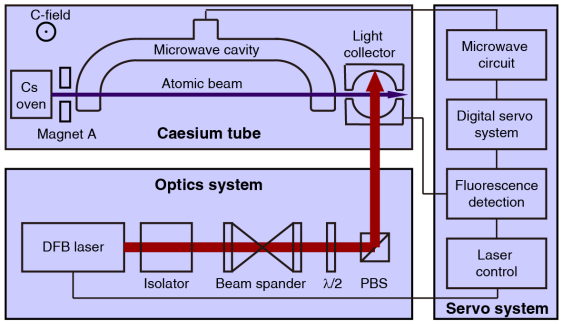


Fig. 1. Schematics of the clock.

The optics system equipped with an 852-nm DFB laser diode, whose linewidth is 2 MHz, provides the light beam for fluorescence generation. The laser diode and optical components are all sealed in a metal box mounted next to the caesium beam tube, for minimizing the fluctuations caused by air flow and mechanic vibration. The laser beam is first isolated then expanded. The output power can be adjusted by tuning the angle of the half-wave plate. Since the atomic beam shape is 6 mm in height and contrast of the signal saturates when light power is large, the typical size of the output beam is 6 mm in diameter and its power is 3 mW. The laser frequency is locked to the top of fluorescence spectrum of the atomic beam with synchronous detection method. Compared with the saturated absorption spectrum of an external atomic cell, the

fluorescence spectrum of the beam expels the crossover lines, while maintaining the Doppler-broadening-free linewidths. In order to detect the atoms which have undergone the clock transition, the frequency of the laser is locked to the ($6^2S_{1/2}$, F=4)-($6^2P_{3/2}$, F=5) cyclic transition, leading to much larger fluorescent photon number than those of 4-4 and 4-3 transitions, which further decreases the risk of frequency-lock to a wrong peak.

A digital servo system based on field-programmable gate arrays (FPGA), as shown in Fig. 2, locks the local oscillator's frequency to the central peak of microwave spectrum. In order to improve the long-term stability, the servo system also feedback controls the magnitude of the static magnetic field (C-field) and microwave power sequentially. Likewise, automatic laser frequency locking is accomplished by another servo circuit based on FPGA. It regularly checks whether the laser frequency is off-resonance according to the fluorescence signal, and relocks it when necessary.

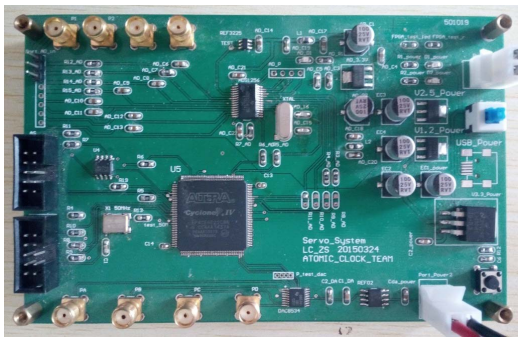
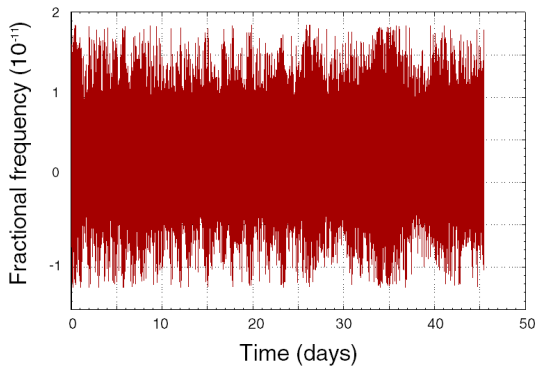


Fig. 2. The digital servo system.

III. RESULTS

The clock has been operated continuously for 45 days with surrounding temperature regulated within 1 K. Its frequency difference against an H-maser, which is continuously calibrated with TAI, is plotted in Fig. 3 with averaging time of 10 s. The corresponding frequency stability result is shown in Fig. 4. The short-term frequency stability is $1.1\times10^{-11}\tau^{-1/2}$, and 5-day frequency stability is $2.7\cdot10^{-14}$.



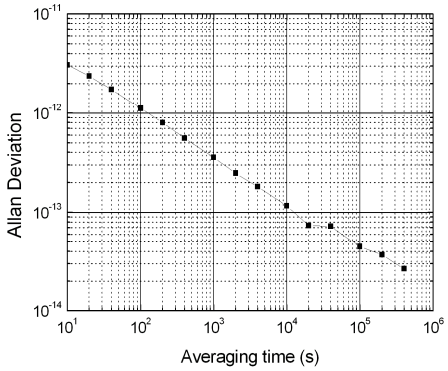


Fig. 3. Frational Frequency difference with sampling time of 10 s.

Fig. 4. Allan deviation of the fractional frequency difference during the 45-days measurement.

IV. LONG-TERM FREQUENCY STABILITY

The second-order Zeeman frequency shift of the clock is about $1.6\cdot10^{-10}$. The accurate measurement of second-order Zeeman frequency shift needs the knowledge of the average and the inhomogeneity of C-field. The inhomogeneity mainly stems from the structure of the coil and magnetic shield. Although not measured currently, the inhomogeneity is not likely to vary much during operation. The average of C-field along the atomic trajectory is feedback controlled, by measuring the frequency difference between (F=3, m_F=1)-(F=4, m_F=1) and (F=3, m_F=0)-(F=4, m_F=0) transitions and locking the difference to a preset value of 41 kHz. The frequency difference is measured for 1 s every 100 s and compensated by adjusting current through the C-field coil. Since 1-1 line has almost the same signal-to-noise ratio as 0-0 line, the relative uncertainty of each measurement is $6.0\cdot10^{-6}$, leading to $1.2\cdot10^{-5}$ relative uncertainty of second-order Zeeman frequency shift, i.e. $2.0\cdot10^{-15}$ with respect to the clock frequency. As a result, the second-order Zeeman shift is at present not a main limitation to the long-term stability.

Several frequency shifts are connected with microwave power, including end-to-end phase difference shift and cavity pulling. According to [7], we take advantage of the dependence of the detected signal's amplitude on the microwave power to feedback control the microwave power. The microwave power is also measured for 1 s with an interval of 100s. The estimated uncertainty of each measurement of microwave power is $3\cdot10^{-3}$ dBm. As we previously reports, the slope of the overall frequency shift to the microwave power is $2\cdot10^{-12}$ /dBm. Therefore, the instability depending on the microwave power variance is supposed to be lower than $1\cdot10^{-14}$ for averaging time longer than 100 s.

Light shift occurs when light near resonance exists in the microwave interrogation zone. Both fluorescence and scattered light contribute to this frequency shift. The overall dependence of frequency shift with respect to incident light power in our case is $1\cdot10^{-12}$ /mW as [4] shows. We find that the Allan deviation of the free-running light power varies proportional to

$\tau^{1/2}$, and is approximately 10^{-2} for averaging time of 10^5 s, indicating that the light shift is perhaps the reason that worsen the long-term stability. No servo control of the light power is implemented currently, which may be the cause of different long-term stability performances depending on the environmental temperature conditions.

V. CONCLUSION

The prototype of the optically-detected clock is built and tested at Peking University. With certain parameters servo-controlled, the 5-day frequency stability is $2.7 \cdot 10^{-14}$, which is obtained in a 45-day measurement, demonstrating that the clock is suitable for time-keeping and communication applications. Further improvement on light-shift control may improve the long-term stability to 10^{-15} level.

REFERENCES

[1] Y. Cao, X. Zhao, L. Yang, H. Chen, and S. Zhang, "Progress in the development of commercial optically pumped Cesium atomic clock," IEEE International Frequency Control Symposium, pp. 401-404, 2014.

[2] S. Lecomte, M. Haldimann, R. Ruffieux, and P. Berthoud, "Performance demonstration of a compact, single optical frequency Cesium beam clock for space applications," IEEE International Frequency Control Symposium Joint with the European Frequency and Time Forum, pp.1127-1131, 2007.

[3] V. Hermann, B. Leger, C. Vian, and J. F. Jarno, "Industrial development of an optically pumped Cs beam frequency standard for high performance applications," 2006 20th European Frequency and Time Forum, pp.432-435, 2006.

[4] C. Liu, R. Shi, Y. Wang, S. Liu, and T. Dong, "An optically detected cesium beam frequency standard with magnetic state selection," Proceedings of 2014 European Frequency and Time, pp. 175-177, 2014.

[5] C. Liu., S. Zhou, and Y. Wang, "Noise investigation on optical detection in a cesium beam clock with magnetic state selection," 2015 joint conference of the IEEE International Frequency Control Symposium and European Frequency and Time Forum, pp. 483-486, 2015.

[6] C. Liu, S. Zhou, J. Wan, S. Wang, and Y. Wang, "Recent progress in optically-pumped cesium beam clock at Peking University," Journal of Physics: Conference Series, vol. 723, p. S90, Oct. 2015.

[7] C. Audoin, F. Hamouda, L. Chassagne, and R. Barillet, "Controlling the microwave amplitude in optically pumped cesium beam frequency standards," IEEE Transactions on Ultrasonics Ferroelectrics and Frequency Control, vol. 46, pp. 407-413, March 1999.

Compact vapor cell cesium clock based on continuous wave optical pumping

Jianhong Wan, Chang Liu, Yanhui Wang
School of Electronics Engineering and Computer Science, Peking University,
Beijing, China
wangyanhui@pku.edu.cn

***Abstract*—A compact laser pumped vapor-cell cesium clock is introduced. The microwave cavity design is essential to the performance of the clock. In order to get a great homogeneity of the magnetic field, we use a compact magnetron cavity, which meanwhile reduces the size of physics package. Theoretical analysis shows the basic structure of the magnetron cavity, which is proved and further optimized by software simulation. Simulation results show that the magnetron cavity operates in the TE_{011} mode and has a high quality factor. The cesium clock with the magnetron cavity achieves a stability of $1.8\times10^{-12}\ \tau^{-1/2}$($1s\leqslant\tau\leqslant100s$).**

Keywords—cesium; laser diode; magnetron cavity; atomic clock;

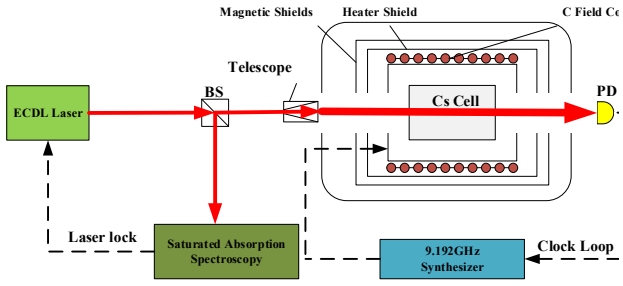
I. INTRODUCTION

Lamp-pumped rubidium clocks have been widely used in industrial and technical fields, such as telecommunications, space applications and navigation, where stable and reliable timing signals are required [1]. With the progress of single mode semiconductor laser diodes, much simpler system without the need of the hyperfine filter could be implemented in the cesium clocks. Several groups have done theoretical and experimental work about the continuous wave laser pumped double-resonance (DR) vapor-cell cesium clocks. Chantry et al. have developed a continues-wave Cs frequency standard with a short-term stability of $2\times10^{-11}\tau^{-1/2}$ [2,3]. Beverini et al. have undertaken theoretical analysis of the optical pumping process and the locking of the local oscillator to the reference transition [4]. Ohuchi et al. have proposed a mode-locked laser-type optical Cs frequency standards with a short-term stability of $1.2\times10^{-12}\tau^{-1/2}$ [5,6]. Actually, microwave cavity is an important part of the vapor-cell cesium frequency standards. In the frequency standard, the intensity of transition signal is closely related to the performance of microwave cavity. Usually cylindrical microwave cavities are used in the studies to apply the microwave field to the Cs atoms contained in vapor. In order to achieve a compact design and great homogeneity of the magnetic field, we select the magnetron cavity [7] as our model.

II. EXPERIMENTAL SETUP

The experimental setup is made up of three parts: laser system, physics package and local oscillator (LO) microwave synthesizer, as shown in Fig. 1. We use an ECDL laser diode as light source, of which the wavelength is 852 nm and the linewidth is 100 kHz. The laser beam enters the physics package via a telescope system for beam-expanding. A glass cell measuring 25 mm in diameter and 25 mm in length is inserted into the compact magnetron cavity. The cell is filled with ^{133}Cs and a mixture of $Ar+N_2$. A coil is used to generate the magnetic field, which is applied to lift the Zeeman degeneracy and isolate the clock transition. The Cs cell and magnetron cavity are temperature-stabilized by a heater. The cavity is surrounded by the magnetic shield to prevent the interference of external magnetic field. The microwave frequency is locked to the center of the DR line with the NI Labview system design software.

Fig. 1. Experimental schematic of CW laser-pumped DR Cs frequency



standard. ECDL, external cavity diode laser; BS, beam splitter; PD, photodetector.

The magnetron microwave cavity is actually a loop-gap resonator (LGR). According the LGR model, we estimated the resonance of the cavity by using the equation in [7],

$$\nu_{Cs}=\frac{1}{2\pi}\sqrt{\frac{n}{\pi r^2\varepsilon\mu}\frac{t}{w}}\sqrt{1+\frac{r^2}{R^2-(r+w)^2}}\sqrt{\frac{1}{1+2.5\frac{t}{w}}} \quad (1)$$

where ε is the dielectric constant, μ is the magnetic permeability, r is the inner loop radius, R is the shield radius, n is the number of supports, t is the thickness of gaps and w is the width. The simplified structure diagram is shown in Fig. 2.

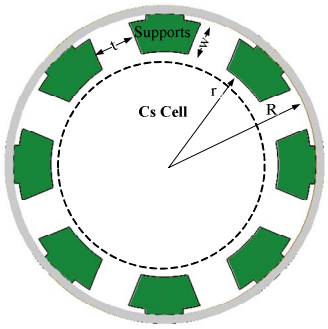


Fig. 2. The simplified structure diagram of the magnetron cross section.

We calculate the structure parameter by using the LGR model. A set of suitable values are r=13.6mm, R=18mm, n=8, t=5mm and w=3.9mm. More precise value of resonant frequency and quality factor should be determined by tuning the dimensions of the cavity. However, to adjust the dimensions of a manufactured cavity is not so easy. In order to facilitate the analysis and design, we compute the resonant frequency and quality factor of the cavity by using the ANSYS HFSS. The internal diameter of the cavity is 36 mm and the length is 34 mm. We show the simulation results of the distribution of magnetic field (H-field) in Fig. 3.

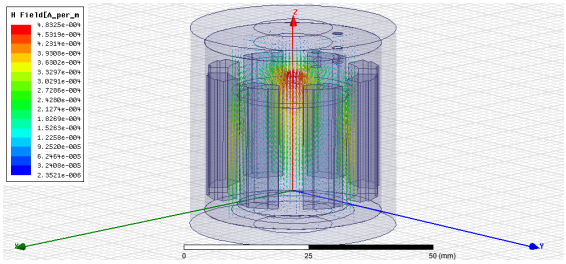


Fig. 3. The distribution of magnetic field (H-field).

As shown in Fig. 3, the H-field inside the cavity is uniform along the Z-axis. The simulation result indicates that the operation mode of the magnetron cavity is a TE_{011} mode and the magnetic field has a great homogeneity.

The manufactured magnetron cavity which is made of aluminum is shown in Fig. 4.



Fig. 4. The realized magnetron cavity.

In the experiment, we use a vector network analyzer (Agilent N5230A) to test the performance of cavity. The test result of cavity is reported in Fig. 5. To measure the loaded quality factor, the Cs cell is loaded into the magnetron cavity. From Fig. 5, the measured resonant frequency is about 9.193 GHz and quality factor is about 300. In addition, another resonating mode is about 9.317 GHz, which is not overlapping with the TE_{011} mode.

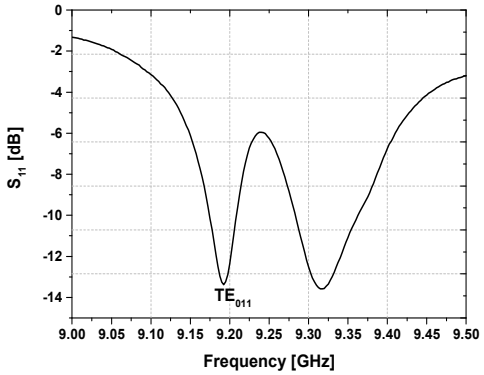


Fig. 5. The test result of magnetron cavity.The distribution of magnetic field (H-field).

III. RESULTS

In the experiment, the laser was locked to the F_g=4 to F_e=3, 5 cross-over transition of D_2 line, by using the saturated absorption spectroscopy. The spot diameter of laser beam incident to the Cs cell is about 15 mm and the power is 99.2 μW. The temperature of the cell was kept at 313 K. And the power of microwave signal which was injected into the cavity is about -14.7 dBm. Under these conditions, the full width at half maximum (FWHM) of DR signal is about 370 Hz and the contrast is about 12.5%. And the discriminator slope (D) is about 0.38 nA/Hz. The DR signal is shown in Fig. 6.

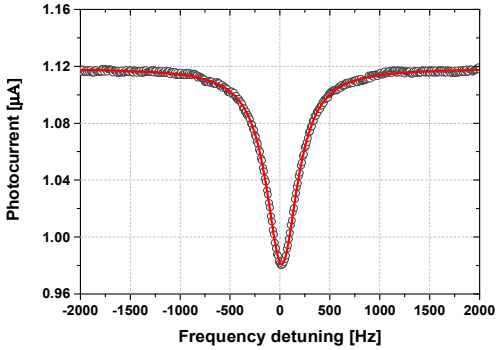


Fig. 6. Double resonance signal. The circle symbol is the experimental date of the DR signal. The red line is the fitting curve of the DR signal by a Lorentzian.

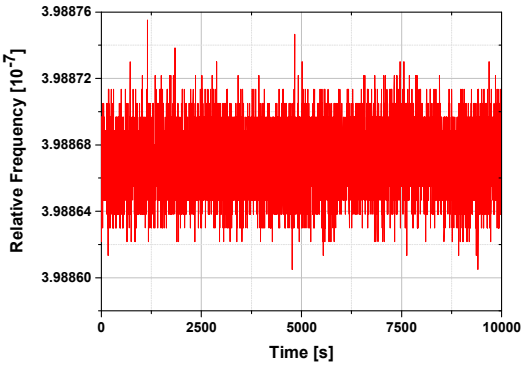


Fig. 7. The test results of relative frequency.

The short term stability of the Cs frequency standard can be predicted by the equation,

$$\sigma_y(\tau) = \frac{N}{\sqrt{2}D\nu_{Cs}}\tau^{-1/2} \qquad (2)$$

where N is the total detection noise power spectral density (1 Hz bandwidth), ν_{Cs} is Cs ground-state hyperfine frequency, D is the discriminator slope of the error signal close to the peak shown in Fig. 6. We estimate a shot-noise limit frequency standard stability of $1.1\times10^{-13}\,\tau^{-1/2}$. The limit due to the FM-to-AM conversion of laser FM noise, denoted by σ_{Laser}, is $2.3\times10^{-13}\,\tau^{-1/2}$. The signal-to-noise (S/N) limit of our Cs frequency standard is $1.5\times10^{-12}\,\tau^{-1/2}$, mainly due to the phase noise of the LO microwave synthesizer.

For measuring the stability of Cs clock, we use a passive hydrogen frequency standard (OSA 3700) as the reference. We calculate the frequency stability by using Hadamard deviation with the sample time of 1 second. The test results are shown in Fig. 7 and Fig. 8. The short term stability of our Cs frequency standard is $1.8\times10^{-12}\,\tau^{-1/2}$ ($1s\leq\tau\leq100s$). The measured short term stability of Cs frequency standard is quite in accordance with the estimated S/N limit. For longer averaging time, the stability rises can be explained by temperature shifts and light shift.

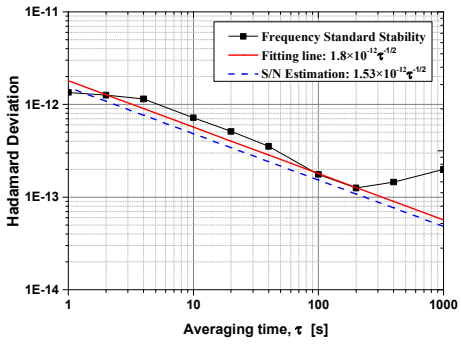


Fig. 8. The test result of Cs frequency standard. Solid line indicates the measured stability. Red line is the fitting line of the frequency stability. Dash line shows the S/N limit of the frequency standard.

IV. CONCLUSION

A compact CW laser pumped double-resonance vapor-cell Cs frequency standard is presented. To achieve the compact design and great homogeneity of the magnetic field, we use a compact magnetron cavity to replace the traditional cylindrical microwave cavity in the vapor-cell Cs frequency standard. In experiment, we find that the magnetron cavity operates in a TE_{011} mode and has a high quality factor. The performance test of Cs frequency standard indicates that the vapor-cell Cs frequency standard with magnetron cavity can achieve better frequency stability.

REFERENCES

[1] J. Camparo, "The rubidium atomic clock and basic research," Phys. Today, Vol. 60, pp. 33-39, 2007.

[2] P. J. Chantry, B. R. McAvoy, J. M. Zomp, I. Liberman, Towards a miniature laser-pumped cesium cell frequency standard, Proc. 46th. Ann. Freq. Control Symp. 1992 114-122.

[3] P. J. Chantry, I. Liberman, W. R. Verbanets, C. F. Petronio, R. L. Cather, W. D. Partlow, Miniature laser-pumped cesium cell atomic clock oscillator, Proc. 50th. Ann. Freq. Control Symp. 1996 1002-1010.

[4] N. Beverini, M. Ortolano, G. A. Costanzo, A. De Marchi, E. Maccioni, P. Marsili, V. Barychev, Cs cell atomic clock optically pumped by a diode laser, Laser Phys. 11 (2001) 1110-1116.

[5] Y. Ohuchi, H. Suga, M. Fujita, T. Suzuki, M. Uchino, K. Takahei, Y. Saburi, A high-stability laser-pumped Cs gas-cell frequency standard, Proc. IEEE Int. Freq. Control Symp. 2000 651-655.

[6] T. Hirayama, M. Yoshida, M. Nakazawa, K. Hagimoto, T. Ikegami, Mode-locked laser-type optical atomic clock with an optically pumped Cs gas cell, Opt. Lett., 32 (2007) 1241-1243.

[7] C. Stefanucci, T. Bandi, F. Merli, M. Pellaton, C. Affolderbach, G. Mileti, A. K. Skrivervik, "Compact microwave cavity for high performance rubidium frequency standards," Rev. Sci. Instrum., Vol. 83, 104706, 2012.

Simulation of the Ramsey cavity response

Fuyu Sun*, Xianhe Huang, Jianguo Hu, Qingsong Bai, and Dong Hou
School of Automation Engineering
University of Electronic Science and Technology of China
Chengdu, China
fysun1982@126.com

***Abstract*—Ceramic Sealing Window (CSW) and Frequency Tuning Rod (FTR) are two important components of the Ramsey cavity. Here, a complete electromagnetic model of the Ramsey cavity is built with Finite-element tool HFSS, and the effects of CSW and FTR on the cavity response are simulated and analyzed in detail. To achieve high coupling efficiency, the estimated parameter ranges of CSW and FTR are investigated. The results obtained here offer a helpful guide for Ramsey cavity design in Cs and Rb beam clocks.**

Keywords—Ramsey cavity; Ceramic Sealing Window (CSW); Frequency Tuning Rod (FTR)

I. INTRODUCTION

Microwave cavities are cores of physical packages for several frequency standards [1]-[10]. However, an analytical description of response characteristics of a real cavity based on Maxwell's equations remains unavailable [11]. Fortunately, with the help of an electromagnetic tool, people can simulate and analyze a very complex cavity structure. The validity of simulation method has been verified in cavity designs for different atomic clocks [12]-[17], including TE_{011} cavity for fountain clock [12,13] and vapor-cell clock [14], like-TE_{011} mode magnetron cavity [15]and Microloop-Gap Resonator for vapor-cell clock [16], and TE_{10p} mode U-shaped Ramsey cavity for beam-type clock [10,17]. Among these cavities, the latter has the most complex structure, in which more non-ideal factors are involved than others [18]. In particular, the uses of two important dielectric materials -- the Ceramic Sealing Window (CSW) and Frequency Tuning Rod (FTR) in cavity are significantly related to the cavity resonance. But very few analysis of the effects have been previously reported.

Here, a complete electromagnetic model is set up using Finite-element software HFSS with consideration of the presence of CSW and FTR. Then, the effects of the two dielectric materials on the cavity response are analyzed using Driven-mode of HFSS, and the corresponding design principles are also discussed.

II. CAVITY MODEL

Our cavity model is a structure of the Ramsey cavities typical of those used in traditional Cesium beam and Rubidium beam clocks, as shown in Fig. 1 [6,10]. The cavity can be divided into the cavity in vacuum providing separated oscillating fields which excite the clock transition and the coupler containing a FTR in air providing energy input. A thin CSW is located at the interface between vacuum and air, acting as a passage of energy coupling into the cavity. FTR is mainly used to adjust the resonance frequency slightly after processing.

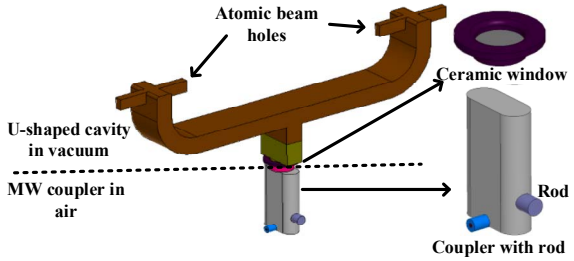


Fig. 1. Complete electromagnetic model of the Ramsey cavity.

Since the electromagnetic model of the cavity contains approximately thirty parameters, as a result, the obtainment of each set of satisfied cavity parameters needs a lot of optimizations. In Fig. 2, the response curves as functions of the length of FTR and L_{FTR} are given, where a CSW with thickness of L_{CSW} = 1.8 mm and dielectric constant of ε_{CSW} = 10.9, and a FTR with diameter of Φ_{FTR} = 5.4 mm and dielectric constant of ε_{FTR} = 5.5, are chosen for the simulation. Noting that Ramsey cavity is one-port cavity, people usually use the input VSWR or the Return loss (S_{11} parameter) to evaluate the coupling efficiency, the relationship between S_{11} and VSWR is defined by S_{11} = 20log((VSWR-1)/(VSWR+1)). From Fig. 2, the input VSWR and the resonance frequency are 1.0107 and 9.1926 GHz, respectively, while L_{FTR} = 8 mm, which meet the design requirements. A real cavity is manufactured, and tested, the measurement results show that the VSWR and the resonance frequency are about 1.126 and 9.1926 GHz, respectively, which are in agreement with simulations.

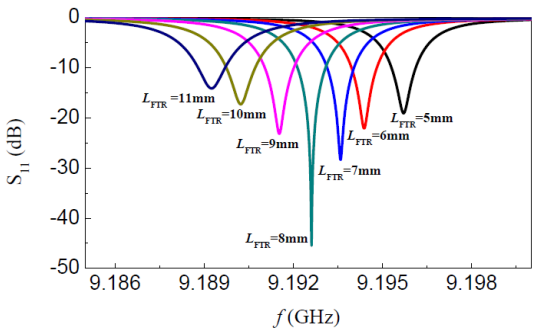


Fig. 2. S_{11} curves for different L_{FTR}.

III. SIMULATION AND ANALYSIS

A. The role of CSW

In order to eliminate the cavity pulling, the most important principle of the cavity design is to ensure that the cavity resonance frequency f is exactly resonated at the clock transition frequency $f_{(3,0)\leftrightarrow(4,0)}$. Following this principle, we sweep ε_{CSW} and record its value while keeping cavity-atom resonance ($f = f_{(3,0)\leftrightarrow(4,0)}$) at each value of L_{CSW} (0.4 mm, 0.6 mm,…4.8 mm), as indicated in Fig. 3, where a FTR with ε_{FTR} = 5.5 and Φ_{FTR} = 5.4mm is used. The upper and lower curves in Fig. 4 are ε_{Empty} and ε_{Full}, which corresponds to minimum (without FTR, L_{FTR} = 0 mm) and maximum length (full length of FTR, L_{FTR} = L_{Full}) of FTR, respectively. Because $f = f_{(3,0)\leftrightarrow(4,0)}$ when L_{FTR} = 0mm, $\varepsilon_{CSW} = \varepsilon_{Empty}$ and $L_{FTR} = L_{Full}$, $\varepsilon_{CSW} = \varepsilon_{Full}$, and f is inversely proportional to L_{FTR} and ε_{CSW}. The following conclusion is obtained: to guarantee $f = f_{(3,0)\leftrightarrow(4,0)}$ for a fixed CSW thickness, ε_{CSW} needs satisfy $\varepsilon_{Full} < \varepsilon_{CSW} < \varepsilon_{Empty}$. For instance, when L_{CSW} = 0.8 mm, 1.6 mm and 3.2 mm, the range of ε_{CSW} must satisfy $12.4 < \varepsilon_{CSW} < 23.9$, $6.2 < \varepsilon_{CSW} < 12.6$, and $3.1 < \varepsilon_{CSW} < 7.32$, respectively. The smaller the thickness and dielectric constant of FTR, the narrower the selectable range of dielectric constant of CSW.

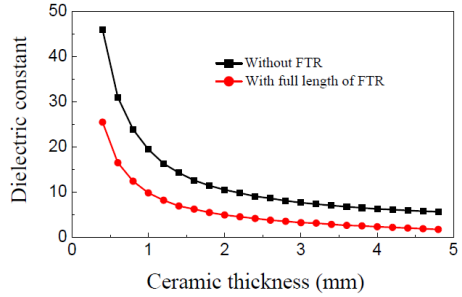


Fig. 3. ε_{CSW} versus L_{CSW} when $f = f_{(3,0)\leftrightarrow(4,0)}$.

Fig. 4 shows the cavity response at resonance as a function of ε_{CSW}. A rapid increase in VSWR is observed with increasing deviation from the optimum value (10.9 for our case). Comparing with thickness, the VSWR is more sensitive on the change of dielectric constant.

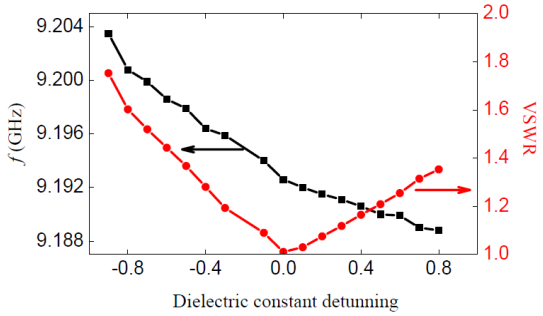


Fig. 4. Resonance characteristics versus ε_{CSW} detuning.

B. The role of FTR

Fig. 5 shows a series of response curves simulated at various FTR parameters, the resonance frequency f is inversely proportional to L_{FTR} and ε_{FTR}, no matter which FTR we choose.

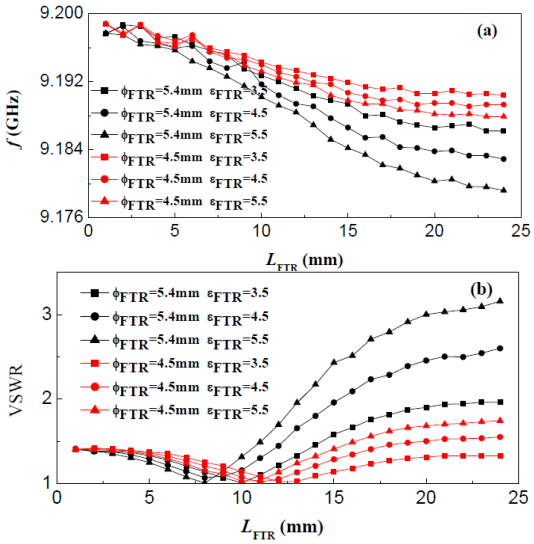


Fig. 5. (a) Resonance frequency f versus L_{FTR}. (b) VSWR versus L_{FTR}.

From Fig. 5, the larger the size and dielectric constant of FTR is, the wider the range of frequency-tuning will get, but it also makes the VSWR more sensitive to the change of length of FTR. It is apparently that the FTR with small values for both size and dielectric constant is more suitable to tune frequency, as long as the range of frequency-tuning can cover the clock frequency. For instance, the tuning range are about 8.4 MHz and 18.5 MHz for two different FTRs with Φ_{FTR} = 4.5 mm, ε_{FTR} = 3.5 and Φ_{FTR} = 5.4 mm, ε_{FTR} = 5.5, respectively. For the former, the VSWR is less than 1.43 in the whole frequency band. For the latter, the worst VSWR can reach up to 3.2.

IV. RESULTS AND DISCCUSION

As clearly shown in Fig. 4 and Fig. 5, the cavity resonance is quite sensitive to the changes in the parameters of the dielectric materials. Usually, L_{FTR} needs to be tuned to meet $f = f_{(3,0)\leftrightarrow(4,0)}$ while there exists cavity detuning, as a result of ε_{CSW} detuning to optimum value. Fig. 6 shows the variation of VSWR versus ε_{CSW} with ε_{FTR} = 5.5 and Φ_{FTR} = 5.4 mm, and L_{CSW} = 1.8mm. In Fig. 6, 4% deviation of the dielectric constant leads to VSWR of > 1.5, so that it is important to obtain the accurate value of ε_{CSW} during manufacturing.

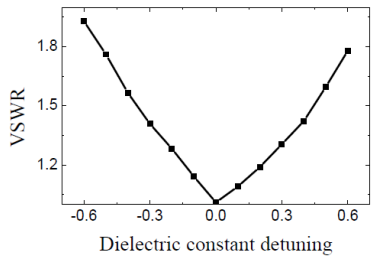


Fig. 6. VSWR versus ε_{CSW} detuning when $f = f_{(3,0)\leftrightarrow(4,0)}$ = 9.1926 GHz.

Similar to the mentioned purpose above, the effect of FTR on VSWR when $f = f_{(3,0)\leftrightarrow(4,0)}$ is also simulated. Six FTRs with various diameters (Φ_{FTR} = 4.5mm, 5.4mm) and dielectric constants (ε_{FTR} = 3.5, 4.5, 5.5) are used to tune resonance

frequency f. The VSWRs and the FTRs length are recorded when $f = f_{(3,0)\leftrightarrow(4,0)}$, the results are listed in Table I.

TABLE I. VSWRs for different FTR when $f = f_{(3,0)\leftrightarrow(4,0)}$

Φ_{FTR} /mm	4.5	4.5	4.5	5.4	5.4	5.4
ε_{FTR}	3.5	4.5	5.5	3.5	4.5	5.5
L_{FTR}/mm	13.4	12	10.7	10.2	9.1	8
VSWR	1.06	1.055	1.038	1.035	1.052	1.011

In Table I, the VSWRs of < 1.06 are presented with six different FTRs when $f = f_{(3,0)\leftrightarrow(4,0)}$. The simulation results here indicate that a high microwave coupling efficiency can be achieved using different FTRs, as long as the range of frequency-tuning can cover the clock transition frequency for a fixed CSW. So, again, we found that the VSWR at the clock frequency is mainly depends on the thickness and the dielectric constant of CSW.

V. CONCLUSION

In summary, a complete electromagnetic model of the Ramsey cavity is built and its resonance characteristics are analyzed with Finite-element method in this paper, where CSW for cavity sealing and power coupling, and FTR for frequency-tuning are both taken into account. All of analysis here are based on the Driven-mode, which is more accurate than that of the conventional Eigen-mode simulation. We demonstrated that the different FTRs can achieve similar coupling efficiency while keeping $f = f_{(3,0)\leftrightarrow(4,0)}$ (all VSWRs is less than 1.06) for a given CSW. The conclusions obtained here can help us to evaluate the effects of the two dielectric materials (CSW and FTR) on the cavity response. The method here demonstrated to estimate the optimum parameters of materials in cavity design can be extended to Rb beam clocks.

REFERENCES

[1] G. Busca, R. Brousseau, and J. Vanier, IEEE Trans. Instrum. Meas. IM-24, 291 (1975).

[2] J. Vanier, A. Godone, and F. Levi, Phys. Rev. A 58, 2345 (1998).

[3] J. G. Hartnett, M. E. Tobar, P. L. Stanwix, T. Morikawa, D. Cros, and O. Piquet, IEEE Trans. Ultrason. Ferroelectr. Freq. Control 52, 1638 (2005).

[4] B. Xia, D. Zhong, S. An, and G. Mei, IEEE Trans. Instrum.Meas. 55, 1000 (2006).

[5] S. Kang, M. Gharavipour, C. Affolderbach, and G. Mileti, J. Appl.Phys. 117, 104510 (2015).

[6] R. H. Kern, U.S. Patent 3967115 (29 Jun 1976).

[7] L. S. Cutler, Metrologia 42, S90 (2005).

[8] Y. Ovchinnikov, and G. Marra, Metrologia 48, 87 (2011).

[9] A. Bebeachibuli, M. S. Santos, D. V. Magalhaes, S. T. Muller, and V.S. Bagnato, Braz. J. Phys. 35, 4A (2005).

[10] C. Liu, and Y. Wang, Chin. Phys. B 24, 010602 (2015).

[11] A. G. Mungall, and H. Daams, Metrologia 6, 60 (1970).

[12] A. Khursheed, G. Vecchi, and A. De. Marchi, IEEE Trans. Ultrason. Ferroelectr. Freq. Control 43, 201 (1996).

[13] L. Devenoges, L. G. Bernier, J. Morel, G. Di. Domenico, A. Jallageas, and P. Thomann, in Proceedings of the European Frequency and Time Forum and IEEE Frequency Control Symposium (EFTF-IFCS Joint Meeting, Prague, 2013), p. 235.

[14] A. Godone, S. Micalizio, F. Levi, and C. Calosso, Rev. Sci. Instrum. 82, 074703 (2011).

[15] C. Stefanucci, T. Bandi, F. Merli, M. Pellaton, C. Affolderbach, G. Mileti, and A. K. Skrivervik, Rev. Sci. Instrum. 83, 104706 (2012).

[16] M. Violetti, M. Pellaton, C. Affolderbach, F. Merli, J. F. Zurcher, G. Mileti, and A. K. Skrivervik, IEEE Sensors J. 14, 3193 (2014).

[17] F. Sun and X. Huang, in Proceedings of the IEEE Frequency Control Symposium and European Frequency and Time Forum (IFCS-EFTF Joint Meeting, Denver, 2015), p. 487.

[18] J. Vanier and C. Audoin, The Quantum Physics of Atomic Frequency Standards (Bristol, U.K.: A. Hilger, 1989).

Study the phase transient of the RF Mach-Zehnder interferometric switch

Dandan Liu[1,2,3], Jun Ruan[1,3*], XinLiang Wang[1,2,3], Yong Guan[1,2,3], Fengxiang Yu[1,2,3], Junru Shi[1,3], Hui Zhang[1,3], Rui Lin[1,2,3], Jiang Chen[1,2,3], Xiaofei Zhang[1,3], Shougang Zhang[1,3]

1. National Time Service Center, Chinese Academy of Science, Xi'an, Shaanxi, 710600, China
2. University of Chinese Academy of Science, Beijing 100039, China
3. Key Laboratory of Time and Frequency Primary Standards, Chinese Academy of Science, Xi'an, Shaanxi, 710600, China
E-mail: liudandan@ntsc.ac.cn, *Ruanjun@ntsc.ac.cn

***Abstract*—The traditional switch exhibits phase discontinuity and transients in few hundreds microradian which will induce the larger microwave leakage shift in the atomic fountain clock. The RF Mach-Zehnder interferometric switch is developed in order to decrease the phase variations without inducing phase discontinuity. To detect the phase variations, the phase transient measurement system is also built and described in detail in this paper. The result shows the peak to peak phase variations of RF Mach-Zehnder interferometric is 10 microradians within the measurement resolution of a few microradians after five days averaging.**

Keywords—RF Mach-Zehnder interferometric switch; phase transient; atomic fountain;

I. INTRODUCTION

Nowdays, the most accurate caesium clocks are based on the fountain geometry. The atomic fountain primary frequency standards has a frequency uncertainty of 5×10^{-16} or less play an important role in calibrating the International Atomic Time (TAI) in the level of 10^{-16}, microwave leakage frequency shift will be the dominate term in the frequency uncertainty budget.

In fountain primary standard, the cold cesium samples are launch to interacted with the microwave field during the ascending and descending period. The resonant microwave field should be avoided along the atom trajectory. Otherwise, the resonant field introduce phase disturbances of the phase difference between the atoms and the interrogation field(during or between the two Ramsey interactions)$\Delta\phi$(rad), which leads to frequency shift $\Delta\nu=(\Delta\phi/(2\pi T)T$(Hz), where T is the Ramsey interrogation time (0.5 s typically).

The way to eliminate microwave leakage frequency shift is to used two time separate pulses to interrogate with cold atoms, However, a standard microwave switch exhibits strong phase transients on the order of several milliradian with a time constant of a few hundreds milliseconds. Mach–Zehnder-type interferometric RF switch can largely suppress phase transient, which is developed by different design[1-5].

Based on the above research, The paper introduce another MZ RF switch without phase noise and more stable temperature coefficient. The switch and phase transient measurement(PTM) system is designed and presented in section 2. followed by conclusions in section 3.

Much of the described work was supported by National Key R&D Program of China (2016YFF0200202)

II. THE DESIGN OF THE PTM SYSTEM

The PTM system consists of two direct digital synthesizer(DDS), data acquisition(DAQ) board and DSP Lock-in amplifier SR830. The scheme is depicted in Fig. 1. The two DDS are phase locked to the same H maser. The demodulator is realized by SR830, which requires two input signals, one is reference signal(REF) generated by one DDS. Another DDS with two channels output two signals with an offset 10 kHz. A switch is placed after the output of the 200 MHz signal. The device under test(DUT) signal is generated by mixing and low-pass filtering(LPF) two output signals. Assuming that the REF signal and DUT signal can be written as $V_{ref}\sin(\omega_{ref}t+\theta_{ref})$ and $V_{sig}\sin(\omega_r t+\theta_{sig})$, where V_{sig} and V_{ref} is the amplitude of the DUT and REF separately, θ_{sig} and θ_{ref} is the phase of the DUT and REF. SR830 amplifies DUT signal and multiplies REF signal using a phase-sensitive detector as shown in forum (1).

$$\begin{aligned} & V_{sig}\sin(\omega_r t+\theta_{sig})V_{ref}\sin(\omega_{ref}t+\theta_{ref}) \\ &= \frac{1}{2}V_{sig}V_{ref}\cos([\omega_r-\omega_{ref}]t+\theta_{sig}-\theta_{ref})- \\ & \quad \frac{1}{2}V_{sig}V_{ref}\cos([\omega_r+\omega_{ref}]t+\theta_{sig}+\theta_{ref}) \end{aligned} \tag{1}$$

Then the above output is passed through a low pass filter, the signal at higher frequency is removed. If $\omega_r=\omega_{ref}$, the filtered output will be $1/2V_{sig}V_{ref}\cos(\theta_{sig}-\theta_{ref})$, which is expressed as X. The DUT signal multiplies the REF signal shifted by 90° and then is passed through to a low pass filter, the output is $1/2V_{sig}V_{ref}\sin(\theta_{sig}-\theta_{ref})$, which is called Y. The parameters of low filtering can be set on the front panel of SR830.

The X and Y signals are acquired by the simultaneous sampling DAQ board(PCI-6122) with 16 bit resolution which is embedded in an industrial computer. Every input channel of PCI-6122 has its own ADC. The maximum sampling rate per channel can reach to 500 kS/s. The sampled X and Y signals are stored in the array and then are filtered with the function in Labwindows/CVI. The phase is obtained by calculating the inverse tangent quotient of X and Y. The phase variations is observed by long time averaging from cycle to cycle in order to

decrease the phase noise. The mean of phase at each cycle is saved to the file. The TTL trigger signal is provided both to the switch and acquisition. The acquisition can be started by rising or falling of the TTL signal and the acquisition data length can be set in the software.

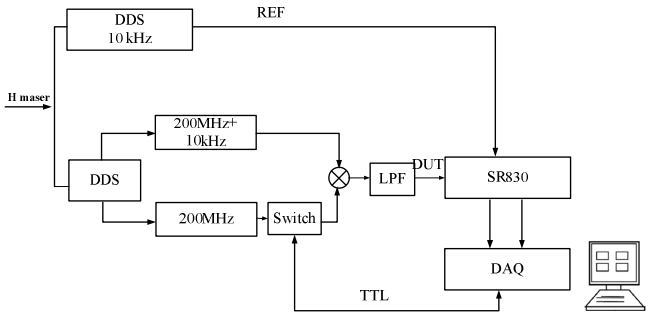


Fig. 1 Schematic of phase transient measurement setup

The design of switch is derive from optical Mach-Zehnder interferometer，which consist of two arms. One of the arms contain P-type, intrinsic, and N-type material (PIN) diode microwave switch and the other is free propagation. If the interferometer is exactly tuned to a dark fringe configuration, then, when the switch is on, the interferometer is attenuated by a destructive interference. In this way, the phase of RF signal is always unperturbed as atoms don't interact with the field propagating in a PIN switch. Fig. 2 shows the practical realization of this switch. The 200 MHz RF signal is split into two parts by a direction coupler, One of which is input to a fixed attenuator, another signal is first input to an controlled phase shifter and then to a controlled attenuator. The interferometer in phase is coarse tuned by cable length adjustment and finely tuned by mechanical phase shifter. A microwave high-attenuation(80 dB) and high speed (~ns)PIN diode switch is used in one arm. The Mach-Zehnder RF switch exhibit an extinction ratio of 60 to 75 dB.

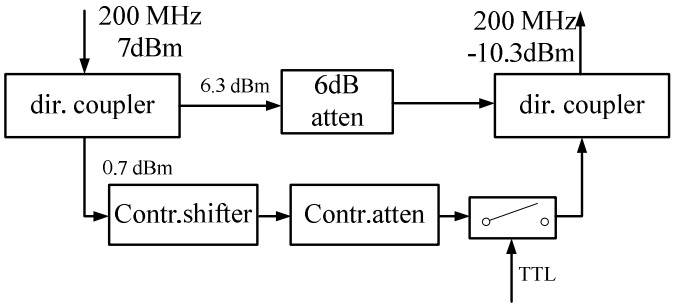


Fig. 2 Schematic of 200 MHz RF interferometric switch. dir. Coupler:direction coupler; Contr. shifter: Controlled phase shifter; Contr. atten: controlled attenuator.

III. RESULTS AND DISCUSSION

We investigated the phase transients of the switch and interferometric switch after five days measurement, From Fig. 3, the traditional switch shows large phase transients with few hundreds microradians in the hundreds of milliseconds, this large variations disappear after the switch is replaced by RF interferometric switch. The inset shows the enlargement of phase variations of RF interometric switch, which is 10 μrad at the peak to peak fluctuation. The allan variation of the averaging phase is 7 μrad at 100000 s as shown in Fig .4.

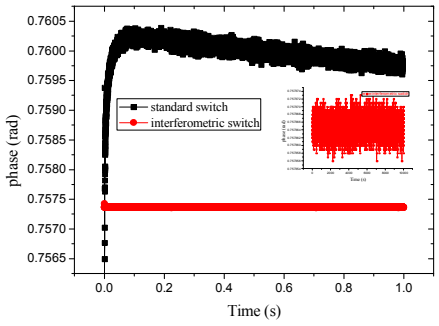


Fig. 3 Phase transient behavior of standard switch and interferometric switch

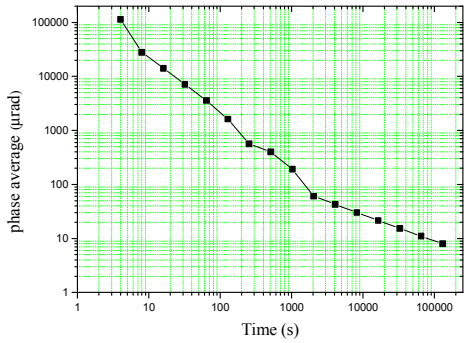


Fig .4 Allan variation of averaging phase

In the near future, we will apply the RF interferometric switch to the microwave synthesizer of the cesium atomic fountain clock and evaluate the microwave leakage shift.

REFERENCES

[1] G. Santarelli, G. Governatori, D. Chambon, M. Lours et al, "Switching atomic fountain clock microwave interrogation signal and high-resolution phase measurement," IEEE. Trans. Ultrason. Ferroelect. Freq, vol. 56, no. 7, pp. 1319–1326, July 2009.

[2] G. Santarelli, G. Governatori, M. Lours et al, "Phase transient measurement at the Micro radian level for atomic fountain clocks", IEEE Proceedings of the 20th European Frequency and Time Forum, pp. 166-172, 2006.

[3] M. Kazda, V. Gerginov, N. Huntemann, B. Lipphardt and S. Weyers, "Phase analysis for frequency standards in the microwave and optical domains", IEEE. Trans. Ultrason. Ferroelect. Freq, pp.2-6, 2015.

[4] Yu. Zhang, Kun. Liu, Fang. Fang et al, "Thermal effect of the microwave Mach-Zehnder interferometric switch", IEEE International Frequency Control Symposium(FCS), pp. 376-378, 2014.

[5] Kun. Liu, Fang. Fang, Nianfeng.Liu and Tianchu.Li, "phase transient measurement in vivo on microwave synthesizer of cesium atomic fountain clock" , China Time and Frequency Symposium, pp. 201-206, 2015.

Reduction of Dick effect in a pulsed CPT vapor cell clock by interleaving lock

Xiaolin Sun, Pengfei Cheng, Yani Zuo, Lijun Wang
Department of Physics, Tsinghua University
Beijing 100084, P. R. China

Jianwei Zhang, Lijun Wang
State Key Laboratory of Precision Measurement Technology and Instruments, Tsinghua University
Department of Precision Instrument, Tsinghua University
Beijing 100084, P. R. China
zhangjw@tsinghua.edu.cn

***Abstract*—The Dick effect is one of the main limits for a passive atomic frequency standard to reach its frequency instability limit due to quantum projection noise. In this paper, we report on the reduction of Dick effect of a Ramsey-CPT vapor cell clock using interleaving lock. Three parameters are investigated in the process of optimizing sensitivity function in details. By optimizing the sensitivity function, the Dick effect induced Allan deviation (DEAD) can be reduced to the level of 10^{-14}.**

Keywords—Ramsey-CPT; Dick effect; atomic clock

I. INTRODUCTION

Recently, atomic clocks based on vapor cells are drawing more and more attention, thanks to the potential of minimization, low power consumption and good performance of frequency instability. Several remarkable results of laboratory vapor cell clocks have been reported with a frequency instability reaching the level of 1~3E-13 [1-4], making them a promising solution to replace passive hydrogen masers. For Ramsey-CPT (coherence population trapping) atomic clocks, Dick effect is one of the main limits for instability improvement to the level of 1E-14. Dick effect was first introduced in 1987 [5], indicating that the down-conversion of the local oscillator's frequency noise at special Fourier frequencies degrades the atomic clocks' frequency stability. A lot of works have been done to minimize Dick effect in both of microwave [6-9] and optical atomic clocks [10,11]. However, how to minimize Dick effect in a Ramsey-CPT clock is seldom referred. In this paper, we report investigation of minimizing Dick effect of a Ramsey-CPT vapor cell clock by using interleaving lock. We theoretically demonstrate that the frequency stability can be improved from 6.11E-13/$\sqrt{\tau}$ to 1.64E-14/$\sqrt{\tau}$ for the same local oscillator (LO) by optimizing the sensitivity function to suppress the DEAD (Dick effect induced Allan deviation)

II. INVESTIAGTION OF OPTIMIZING SENSITIVITY FUCNTION FOR INTERLEAVING LOCK

Dick effect usually arises from dead time when the LO's frequency is not interrogated by the atoms. For the Ramsey-CPT clock, there are no obvious separation of dead time and interrogation time as in the fountain clock, ion trap clock or optical lattice clock. The probing process takes place directly in the leading part of one optical pulse, and atoms are then pumped to the dark states later. Besides, the theoretical calculation of sensitivity function of Ramsey-CPT is based on a three-level atomic model with a rather different form compared to the two-level atomic model, making the optimization more challenging.

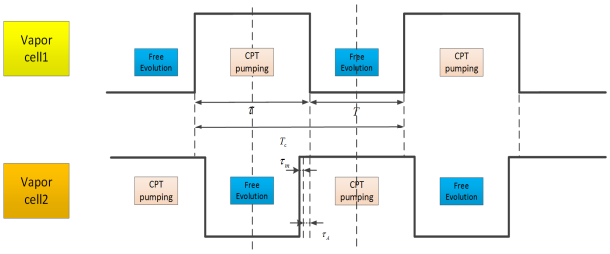


Fig. 1. Time sequence of an interleaved operating Ramsey-CPT clock.

The sensitivity function for Ramsey-CPT has been computed numerically and described by an effective function [12]. During the process of CPT pumping, the sensitivity function is equal to zero. This will cause sensitivity function's deviation from unity substantially. Two vapor cells can be applied to yield an interleaving-lock clock, and the time sequences are presented in Fig. 1. The composite sensitivity function of an interleaved operating Ramsey-CPT clock remains constant in most part of one cycle time, and thus provides a significantly reduced susceptibility to the frequency noise of LO at harmonics of $1/T_C$ [13].

Further reductions of DEAD could be realized by fine adjustment duty circle, average time and optical intensity in order to achieve an even more uniform composite sensitivity function. According to calculation, the DEAD is reduced to 1.64E-14/$\sqrt{\tau}$ from 6.11E-13/$\sqrt{\tau}$ for our current local oscillator (LO).

III. CONCLUSION

We have presented a method to greatly reduce Dick effect for Ramsey-CPT atomic clocks by interleaving lock. Due to the difference of the sensitivity function between Ramsey-CPT

This work is supported by the National Key Research and Development Program of China (No.2016YFA0302101), the National Natural Science Foundation of China (No.11304177), and the Initiative program of State Key Laboratory of Precision Measurement Technology and Instruments.

atomic clocks and other passive atomic clocks, duty circle, average time and optical intensity are optimized to obtain a more constant sensitivity function. Based on this results, a Dick-effect-free Ramsey-CPT atomic clock is in progress.

ACKNOWLEDGMENT

We would like to thank Chi Xu for helpful discussions. We are grateful to the Beijing Institute of Radio Metrology & Measurement (BIRMM) for manufacturing Cs cells.

REFERENCES

[1] S. Micalizio, C. E. Calosso, A. Godone, and F. Levi, "Metrological characterization of the pulsed Rb clock with optical detection," *Metrologia*, vol. 49, no. 4, p. 425, 2012.

[2] J.-M. Danet, O. Kozlova, P. Yun, S. Guérande, and E. de Clercq, "Compact atomic clock prototype based on coherent population trapping," *EPJ Web of Conferences*, vol. 77, p. 00017, 2014.

[3] M. A. Hafiz, X. Liu, S. Guérandel, E. D. Clercq, and R. Boudot, "A CPT-based Cs vapor cell atomic clock with a short-term fractional frequency stability of 3 x 10^{-13} $\tau^{-1/2}$," *J. Phys.: Conf. Ser.*, vol. 723, no. 1, p. 012013, 2016.

[4] G. Dong, J. Deng, J. Lin, S. Zhang, H. Lin, and Y. Wang, "Recent improvements on the pulsed optically pumped rubidium clock at SIOM," *Chin. Opt. Lett., COL*, vol. 15, no. 4, p. 040201, Apr. 2017.

[5] G. J. Dick, "Local oscillator induced instabilities in trapped ionfrequency standards," in *Proc. 19th Precise Time and Time Interval(PTTI) Applications and Planning Meeting*, 1987, pp. 133‑147.

[6] G. J. Dick, J. D. Prestage, C. A. Greenhall, and L. Maleki, "Local oscillator induced degradation of medium-term stability in passiveatomic frequency standards," in *Proc. 22nd Precise Time and Time Interval (PTTI) Applications and Planning Meeting*, 1990, pp.487‑508.

[7] C . Audoin, G. Santarelli, A. Makdissi, and A. Clairon, "Properties of an oscillator slaved to a periodically interrogated atomic resonator," *IEEE Trans. Ultrason. Ferroelectr. Freq. Control*, vol. 45, no. 4,pp. 877‑886, 1998.

[8] G. W. Biedermann, K. Takase, X. Wu, L. Deslauriers, S. Roy, and M. A. Kasevich, "Zero-Dead-Time Operation of Interleaved Atomic Clocks," *Phys. Rev. Lett.*, vol. 111, no. 17, p. 170802, Oct. 2013.

[9] Z. Jian-Wei, M. Kai, and W. Li-Jun, "Dick Effect in a Microwave Frequency Standard Based on Laser-Cooled $^{113}Cd^{+}$ Ions," *Chinese Phys. Lett.*, vol. 32, no. 1, p. 010601, 2015.

[10] A. Quessada, R. P. Kovacich, I. Courtillot, A. Clairon, G. Santarelli, and P. Lemonde, "The Dick effect for an optical frequency standard," *J. Opt. B: Quantum Semiclass. Opt.*, vol. 5, no. 2, p. S150, 2003.

[11] P. G. Westergaard, J. Lodewyck, and P. Lemonde, "Minimizing the dick effect in an optical lattice clock," *IEEE Transactions on Ultrasonics, Ferroelectrics, and Frequency Control*, vol. 57, no. 3, pp. 623–628, Mar. 2010.

[12] J. M. Danet, M. Lours, S. Guérandel, and E. D. Clercq, "Dick effect in a pulsed atomic clock using coherent population trapping," *IEEE Transactions on Ultrasonics, Ferroelectrics, and Frequency Control*, vol. 61, no. 4, pp. 567–574, Apr. 2014.

[13] M. Schioppo et al., "Ultrastable optical clock with two cold-atom ensembles," *Nat Photon*, vol. 11, no. 1, pp. 48–52, Jan. 2017.

Thermal management of microfabricated vapor cells for chip scale atomic clocks

Runqi Han, Zheng You[1], Fan Zhang and Yong Ruan[2]
Collaborative Innovation Center for Micro/Nano Fabrication, Device and System
State Key Laboratory of Precision Measurement Technology and Instrument
Department of Precision Instrument, Tsinghua University
Beijing 100084, China
Email: [1]yz-dpi@mail.tsinghua.edu.cn, [2]ruanyong@mail.tsinghua.edu.cn

***Abstract*—We investigated the thermal management design of microfabricated vapor cells by putting forward three wiring patterns. A theoretical model and a simulated analysis were implemented to optimize heating and temperature-measuring wiring patterns on the cell surface. The optimal pattern is able to maintain heating efficiency, optical transparence and weak additional electromagnetic field to ~nT level. Vapor cells with buffer gas based on the optimal design were microfabricated and tested by absorption spectroscopy at different temperatures. The results confirm cell performance in the appropriate temperature range and reveal potential for future applications of chip scale atomic clocks.**

Keywords—thermal management; vapor cell; microfabrication; spectroscopy; atomic clock

I. INTRODUCTION

The atomic clock, known as the atomic frequency standard, has been recognized as the most accurate time standard worldwide since invented, due to its high frequency stability and time accuracy. Thanks to the development of micro electro mechanical system (MEMS) technology and application of coherent population trapping (CPT) principle, all components of the atomic clocks are able to integrate together to a chip scale atomic clock (CSAC), which is absolutely more advantageous for the small size, low power consumption as well as high stability [1]. Because its power consumption is so low that it can be driven by a button battery and its size is up to cubic millimeter level, CSAC has played a significant role in fields of navigation, precision measurement and in particular the strategic defense field [2].

CPT principle is based on alkali metal atoms with certain electromagnetic fields, when observing electromagnetically induced transparency (EIT) phenomenon [3]. Fig. 1 shows the quantum part principle with three-energy level atoms, a simplified configuration sketch and CPT resonance peaks on absorption background [4]. CSAC operates with two closed loops, one for laser frequency stabilization on transition while the other for locking the high-frequency microwave oscillator on the clock resonance referred to alkali atom CPT phenomenon.

CSAC is composed of optical, physical and circuit systems [5], wherein the vapor cell is the core part of the physical system. The fabrication process of MEMS vapor cell has already been developed [6] and the glass-silicon-glass structure has taken full advantage of MEMS technology.

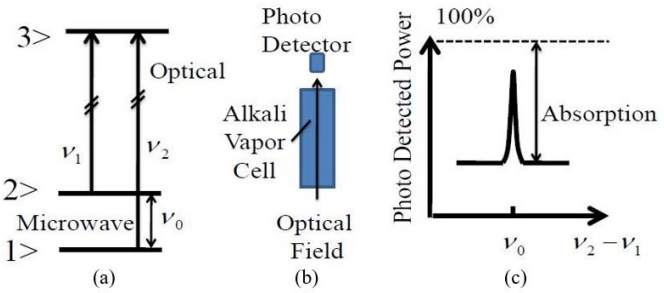


Fig. 1. (a) CPT principle sketch; (b) simplified configuration sketch; (c) CPT resonance peak on absorption background.

The light interacts with atoms in the vapor cell where it requires a certain operating temperature range, influencing CPT resonance and frequency stability [7]. The temperature affects saturation vapor pressure leading to the density of effective atoms [8]. Furthermore, since buffer gas and alkali atomic collisions have close relationship with the effective states of P level [9], the thermal factor has a significant influence on it.

The fundamental requirements for thermal management of vapor cells are not only high temperature accuracy and low power dissipation, but also high optical transparency, weak electromagnetic field and compatibility with MEMS technology. Besides, cell temperature gradients should be predictable and under control.

There have been several constructive designs to maintain the temperature of vapor cells. National Institute of Standards and Technology (NIST) implemented approaches including heaters based on square indium tin oxide (ITO) thin films attached to the glass substrate that were of high heating efficiency and little difficulty in microfabrication. Heaters with reduced electromagnetic fields using serpentine patterned ITO films glued via nonconductive epoxy achieved better performances [10]. Double layers of mirrored ITO patterns reduced the electromagnetic field caused by heating current. Moreover, NIST developed integrated in-situ heating based on boron-doped silicon as an alternative of ITO heaters [11]. It not only

occupied less space in no need of ITO layers and consumes lower power, but also had potential to working as temperature sensors due to conductive silicon heaters. Researchers from Stanford University and University of Colorado proposed another method to change thermal conduction switch from contact to separation in order to vary the whole thermal resistance [12,13]. An attempt to control temperature was to set an integrated chip (MAX1978) at the sealing of vapor cell because atoms easily condensed there and it maintained optical transparent [14]. The temperature coefficient of the alkali vapor cells were tested with folded heating electronic wires wound around the outer wall of vapor cells and wrapped by insulation material like cotton [15]. This method required preheating until predetermined temperature was reached and was inconvenient to apply in chip scale vapor cells. ITO thin films of flexible materials were fabricated and preliminary achievements were gained [16].

II. Design of Thermal Management

Thermal management design is to optimize heating and measuring wires on the glass substrate, with gold pads connected to the outer PID control closed loop. The cell cooling regime included heat convection and conduction with no specific active cooling system. High frequency alternating current far from operating bandwidth has less influence on the electromagnetic field, but it is more difficult to integrate in the chip scale atomic clock. In this article, only direct current situation is analyzed.

A. Three Wiring Pattern Designs

As far as the heating material is concerned, it can be divided into two categories according to optical transparency. Metal resistance is easy to fabricate but blocks the light. ITO thin films have combined electrical conductivity and optical transparency.

To calculate the resistance R_{ITO} of ITO in Equation (1), several factors are defined [17]. ρ represents a constant as 5×10^3 Ω·nm depending on fabrication technology and R_{ITO}* is defined as ITO thin film square resistance. d refers to the thickness of ITO thin film, L means the length along current direction and W stands for line width.

$$R_{ITO} = \frac{\rho L}{dW} = R^*_{ITO}\frac{L}{w}. \quad (1)$$

Considering materials for temperature measurement, the resistance of ITO as a function of temperature is still under investigation. Conventional platinum (Pt) metal is appropriate for high accuracy and a wide operating range.

In the whole design, ITO thin films and Pt metal are deposited on glass by MEMS technology. Three wiring patterns are designed and depicted in Fig. 2, which will be compared and optimized. In pattern A, ITO thin film consists of etched square cavities in order to reduce electromagnetic field and four rectangular gold pads are placed on either side. Pattern B has applied fin structures of ITO thin films and minimized the area of gold pads. Pattern C has enlarged the area of Pt metal resistance and folding lines of ITO are applied. With opposite current directions in heating wires on top and bottom surfaces of MEMS vapor cells, weaker electromagnetic field will be achieved by cancellation.

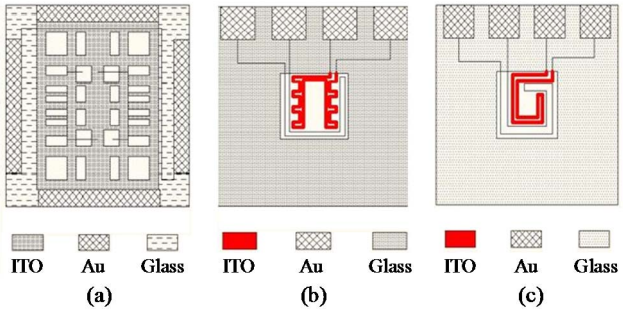


Fig. 2. Schematic of three wiring patterns,namely pattern A,b&c.

B. Theoretical Analysis of Steady State Thermal and Electromagnetic Fields

Based on the microfabricated vapor cells, Fig. 3 represents the built geometric model for theoretical analysis.

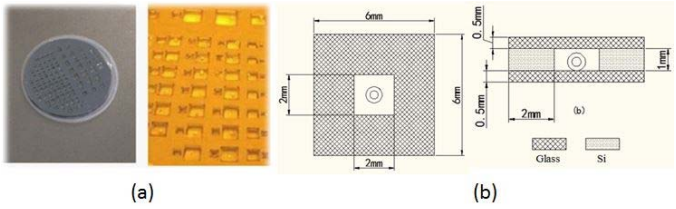


Fig. 3. (a) Photos of fabricated MEMS vapor cell; (b) geometric model of MEMS vapor cell.

In perspective of structure, the cell is like a sandwich, with silicon in the middle and two layers of glass on both sides with ITO and Pt. Silicon is etched with a cubic cavity in the center for light propagation and connected to glass by anodic bonding.

Because the vapor cell is composed of an irregular structure, methods of Squeeze Theorem are applied to calculate the range of heating power, shown in Fig. 4. Seen from the width of view, silicon layer is considered a full or through cavity.

$$R_{HEAT} = \frac{\delta_{glass}}{\lambda_{glass}A_{glass}} + \frac{\delta_{silicon}}{\lambda_{silicon}A_{silicon}}. \quad (2)$$

$$q = \frac{T_{cell}-T_{ambient}}{R_{HEAT}}. \quad (3)$$

Equation (2) and (3) calculate power consumption q with thermal resistance R_{HEAT}, area A, thickness δ, coefficient λ and temperature T. Considering the vapor cell operates around 90℃ and the ambient temperature is 25℃, heat convection and conduction are estimated by thermal resistance. The heating power figured out around 3W [18].

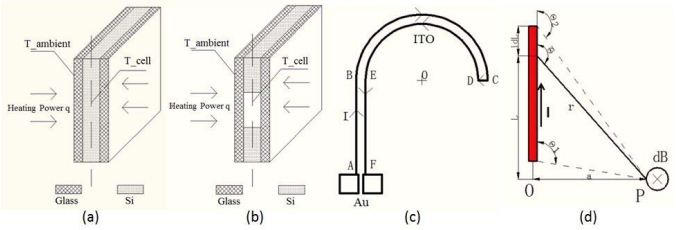


Fig. 4. (a)(b) Maximum and minimum heating power calculation model; (c) the simplified fold line model; (d) Biot Sava M's law schematic.

Electromagnetic field calculation is calculated by simplifying wiring structure to a semicircle fold line model, represented in Fig. 4. According to Bio Sva M's law, with input current less than 100 mA, the generated electromagnetic field intensity is between 10^{-6} and 10^{-8} T, acceptable for CPT resonance environment.

C. *Simulation Analysis of Steady State Thermal and Electromagnetic Fields*

The theoretical model has provided basic parameters for simulation. Considering the finite element analysis of thermal-electric and electromagnetic field in COMSOL software, approximations and linear transformations are made. For each wiring pattern, initial input current is the theoretically calculated value and then it is scanned to simulate. Afterwards the optimal current input is applied to calculate electromagnetic field.

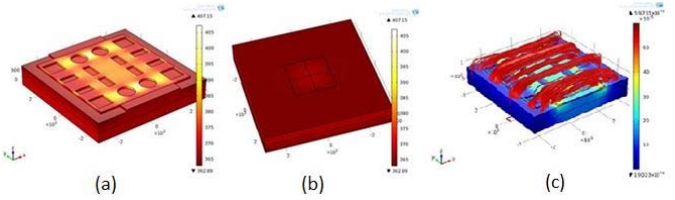


Fig. 5. (a)(b) Front and back surfaces of pattern A's thermal field; (c) optimal electromagnetic field distribution of pattern A.

Through simulation, pattern A has proved to require less input current than expected and its electromagnetic field intensity intends to be on the same order of geomagnetic field, shown in Fig. 5. Pattern B&C are simulated in the same way. They have weaker electromagnetic fields and shorter response time which is important because the conductive coefficient of glass is much lower than silicon. Moreover, the simulated input current value tends to be smaller than theoretical results because of the irregular structure.

Simulation results are listed in Table Ⅰ. Since the resistance of ITO film in pattern A is much smaller than those in the other two patterns, it requires larger input current and generates stronger electromagnetic field.

TABLE I. COMPARISON OF THREE WIRING PATTERN DESIGNS

Pattern	Comparison Category	
	Actual Input Current /mA	***Electromagnetic Field Intensity in the Center /nT***
a	37	99120
b	4	145.3
c	4	11.12

The comparison of simulation results with theoretical results is shown in Fig. 6. The conclusion is that pattern B&C have similar variation trends in the thermal field, but significantly differ in the electromagnetic field, where pattern B behaves irregularly, partly resulting from point effect.

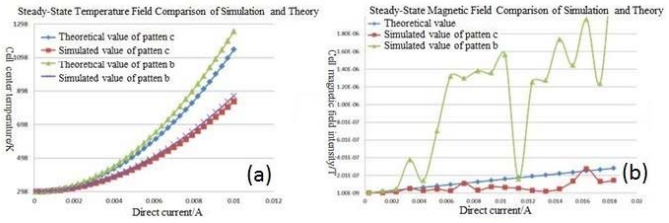


Fig. 6. Simulation and theoretical result comparison of pattern B&C in (a) thermal and (b) electromagnetic field.

In conclusion, pattern C is the optimal design and further fabrication is based on it.

III. MICROFABRICATION PROCESS

We fabricate thermal management wires on Pyrex glass substrate shown in Fig. 7. ITO of 0.1 μm thickness is ion sputtered by Explorer-14 on 500 μm thick, 150 mm diameter glass substrate and then photoresist is used as a mask layer for pattern C images. RIE etching of Oxford PlasmaPro 800Plus fabricated the ITO structure. Afterwards, Pt wiring pattern is transferred by lithography. Adhesion layer of Ti with Pt together is ion sputtered on the substrate. Then lift-off technology is used to form the temperature measurement wires.

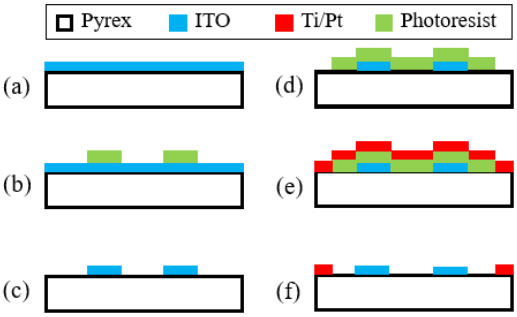


Fig. 7. Fabrication process of thermal management wires. (a) ITO ion sputtering on glass substrate; (b) lithography and photoresist as mask layers; (c) etching and photoresist removal; (d) lithography; (e) adhesion layer Ti and Pt ion sputtering; (f) lift off.

With preformed glass substrate, MEMS vapor cells are fabricated, represented in Fig. 8. 3000 Å SiO_2 and 10000 Å SiN are deposited by SPTS Delta LPX PECVD on <100> 900 μm thick silicon substrate as mask layers to protect silicon. Cell cavities are formed by RIE and KOH etching, followed by anodic bonding of AML AWB-04. Then we use wax to cover rubidium metal and introduce rubidium into the cell with the homemade working station. Surrounded by controlled buffer gas atmosphere, the second anodic bonding is operated and rubidium in the cell is activated at relatively high temperature when anodic bonded.

We obtained microfabricated cells with 150 mbar nitrogen buffer gas in less than 5 mm^3 volume. The leakage is less than 3×10^{-7} $Pa\cdot m^3/s$. Modification of this design can provide temperature gradient field of dual-cavity cells and prevent alkali metal condensation in the light path. Extended additional wires on the glass substrate of heating/measuring wires can actively

compensate the external field and operate as Helmholtz coils for CPT resonance.

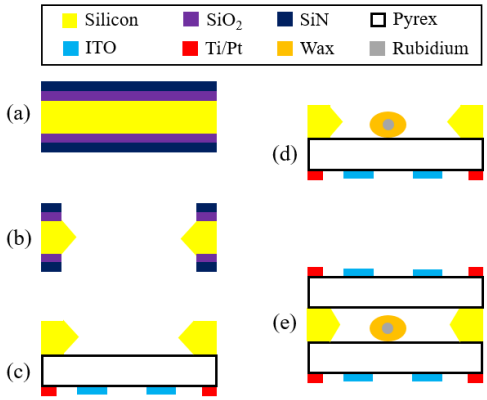


Fig. 8. Fabrication process of MEMS vapor cells. (a) PECVD SiO_2 and SiN as mask layers; (b) RIE etching of SiN and SiO_2, KOH etching of silicon to form through cell cavities; (c) removing mask layers and 1st anodic bonding with preformed glass substrate; (d) rubidium introduction through coverage of wax and filling with buffer gas; (e) 2nd anodic bonding and rubidium activation.

IV. Absorption Spectroscopy of Rubidium Microfabricated Cells

At different temperatures, we obtained natural abundance rubidium D1 line absorption spectroscopy of microfabricated vapor cells. Temperature is measured by a circuit, referred to thermal infrared imager (FLIR-T260, US). Absorption peaks are well observed at 90~120℃ shown in Fig. 9 and the temperature dependence is depicted.

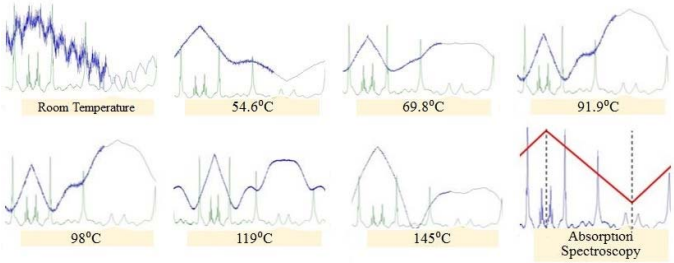


Fig. 9. Absorption spectroscopy of natural abundance rubidium cells at different temperatures. Blue curves represent measured spectroscopy, green curves are reference spectroscopy and the red line is the scanning ramp.

V. Conclusions

A study of thermal management design for microfabricated vapor cells has been analyzed by theory and simulation. Three wiring patterns are compared and the optimal design is able to keep heating efficient, optical transparent and negligible electromagnetic field generation. The vapor cells are microfabricated and tested by absorption spectroscopy experiments at different temperatures. The temperature dependence implies its importance and the appropriate temperature range is found. Further work includes wiring pattern improvement to provide temperature gradient field for dual-cavity cell, compensate external field and act as Helmholtz coils generating magnetic field in the cell.

Acknowledgment

This work was supported by the Independent Research Program of Tsinghua University (52300300917). The authors thank Zhengbo Wang and Zibo Guogao MEMS Research Institute for their help with the experiment.

References

[1] J. Kitching, S. Knappe, and L. Hollberg, "Miniature vapor-cell atomic-frequency references," Applied Physics Letters, vol. 81, pp. 553-555, 2002.

[2] P. D. Schwindt, S. Knappe, V. Shah, L. Hollberg, J. Kitching, L.-A. Liew, et al., "Chip-scale atomic magnetometer," Applied Physics Letters, vol. 85, pp. 6409-6411, 2004.

[3] L. Guo-Bin, D. Run-Chang, L. Chao-Yang, and G. Si-Hong, "CPT magnetometer with atomic energy level modulation," Chinese Physics Letters, vol. 25, p. 472, 2008.

[4] K. Deng, X. Chen, and Z. Wang, "Minimization of the temperature coefficient of resonance frequency shift in the coherent population trapping clock," Optics letters, vol. 36, pp. 1740-1742, 2011.

[5] S. Knappe, V. Shah, P. D. Schwindt, L. Hollberg, J. Kitching, L.-A. Liew, et al., "A microfabricated atomic clock," Applied Physics Letters, vol. 85, pp. 1460-1462, 2004.

[6] L.-A. Liew, S. Knappe, J. Moreland, H. Robinson, L. Hollberg, and J. Kitching, "Microfabricated alkali atom vapor cells," Applied Physics Letters, vol. 84, pp. 2694-2696, 2004.

[7] C. Schori, G. Mileti, B. Leuenbeger, and P. Rochat, "CPT atomic clock based on rubidium 85," in EFTF-2010 24th European Frequency and Time Forum, 2010, pp. 1-4.

[8] D. A. Steck, "Rubidium 87 D line data," ed, 2001.

[9] N. Allard and J. Kielkopf, "The effect of neutral nonresonant collisions on atomic spectral lines," Reviews of Modern Physics, vol. 54, p. 1103, 1982.

[10] P. D. Schwindt, B. Lindseth, S. Knappe, V. Shah, J. Kitching, and L.-A. Liew, "Chip-scale atomic magnetometer with improved sensitivity by use of the M x technique," Applied physics letters, vol. 90, p. 081102, 2007.

[11] L. Liew, J. Moreland, S. Knappe, V. Shah, P. Schwindt, V. Gerginov, et al., "Microfabricated alkali atom vapor cells with in-situ heating for atomic-based sensors," in Proc. 3rd Int. Symp. Sensor Science, Juelich, Germany, 2005, pp. 181-3.

[12] H.-S. Kim, H.-H. Liao, H. O. Song, and T. W. Kenny, "Variable thermal resistors (VTR) for thermal management of chip scale atomic clocks (CSAC)," in Micro Electro Mechanical Systems, 2008. MEMS 2008. IEEE 21st International Conference on, 2008, pp. 852-855.

[13] A. D. Laws, Y. Chang, V. M. Bright, and Y. Lee, "Thermal management of chip scale atomic clocks," vol. 68, ed, 2007.

[14] X. H. Qi, W. L. Chen, L. Yi, X. J. Zhou, and X. Z. Chen, "Modulation Transfer Spectroscopy of Coherent Population Trapping based on phase-coherent lasers," Optics express, vol. 17, pp. 6741-6746, 2009.

[15] K. Deng, X. Chen, and Z. Wang, "Minimization of the temperature coefficient of resonance frequency shift in the coherent population trapping clock," Optics letters, vol. 36, pp. 1740-1742, 2011.

[16] T. Zhang, Z. Gan, X. Zhao, H. Zhang, and S. Liu, "Fabrication of Hermetic Cell Using MEMS Technology," in Electronic Packaging Technology, 2006. ICEPT'06. 7th International Conference on, 2006, pp. 1-3.

[17] D. R. Cairns, R. P. Witte, D. K. Sparacin, S. M. Sachsman, D. C. Paine, G. P. Crawford, et al., "Strain-dependent electrical resistance of tin-doped indium oxide on polymer substrates," Applied Physics Letters, vol. 76, pp. 1425-1427, 2000.

[18] S. Knappe, P. Schwindt, V. Gerginov, V. Shah, L. Liew, J. Moreland, et al., "Microfabricated atomic clocks and magnetometers," Journal of Optics A: Pure and Applied Optics, vol. 8, p. S318, 2

High Sensitively Coherent Population Trapping Magnetometer with Optically Pumped Degenerate Atoms

Ryo Maeda
Ricoh Institute of Future Technology
Ricoh Co., Ltd.
Yokohama, Japan

Shigeyoshi Goka
Department of Electrical & Electronic Engineering
Tokyo Metropolitan University
Hachioji, Japan

***Abstract*— A high sensitive coherent population trapping (CPT) magnetometer with optically pumped degenerate state atoms has been developed. The CPT magnetometer in degenerate state, which does not require large magnetic field, has high sensitivity as a CPT magnetometer while keeping simple configuration. Our measurement system achieved magnetic sensitivity of 1pT/√Hz using this technique.**

Keywords—Coherent Population Trapping (CPT) resonance; atomic magnetometer; optical pumping;

I. INTRODUCTION

High sensitivity magnetometers using interactions between alkali metal atoms and light have many applications such as biomagnetism, MRI, geomagnetic anomalies, and magnetic monitoring of space [1]. There, the spin polarization of atoms due to the magnetic field is detected by a magneto-optical phenomenon such as Hanle effect, magnetic resonance, and CPT resonance [2-4]. Among them, the magnetometry by use of the coherent population trapping (CPT) resonance is a promising technology for realizing chip-scale magnetometers working at room temperature. However, the sensitivity of the conventional CPT magnetometry, which uses the splitted state of atoms, has a drawback that the magnetic field to be measured is affected by the fluctuation of the bias field for level splitting. In contrast, another approach by Pradhan et al., where the degenerate resonance [5] is employed, is able to overcome this limitation although their aim was on the vectorization of the measurement. In the present work, we experimentally demonstrate that improvement of the sensitivity of CPT magnetometer is possible to use the circularly polarized light.

II. MEASUREING PRINCIPLE

The principle for the magnetometry using of the degenerate CPT resonance is explained as follows. When the σ+ light is irradiated to the gas cell of ^{133}Cs atoms, the CPT resonances occur between the two ground states in Fig. 1. There, the shift of the resonance frequency from the clock transition is expressed by

$$\Delta f = \frac{2\mu_B B g}{h}\left(m_{g1} + m_{g2}\right), \qquad (1)$$

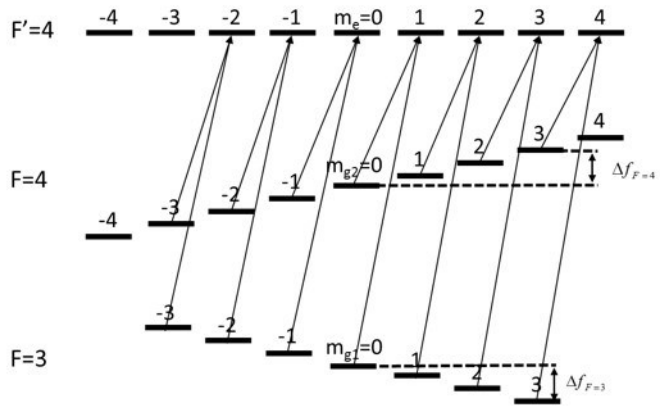


Fig. 1 Excitation Scheme with σ+ Transition in ^{133}Cs-D1 line

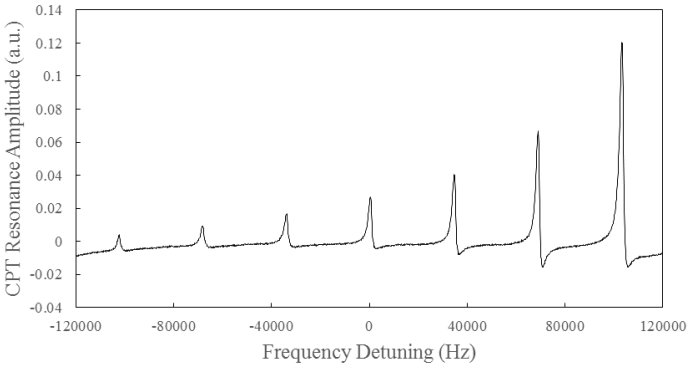


Fig. 2 CPT Resonance Spectrum in Zeeman Splitting State

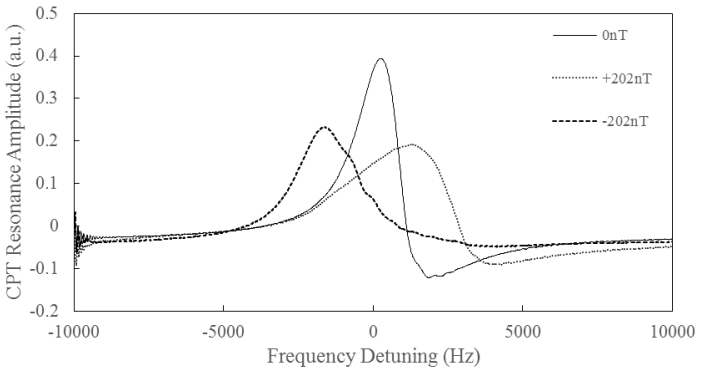


Fig. 3 CPT Resonance Spectrum in Optically Pumped Degenerate State

where μ_B is the Bohr magneton, h is the Planck constant, g and m is the g factor and the magnetic quantum number of the ground levels. According to Eq. 1, the shift of the frequency Δf is proportional to the magnetic quantum number m_{g1} (= m_{g2}). In addition, the amplitude of the resonance with highest magnetic quantum number would be significantly large as shown in Fig. 2. We pay special attention to the fact that this substantial dominance by a specific quantum number still holds when the magnetic field is so small that the degenerated state, where all spectral peaks overlapped and united into one, is realized as shown in Fig. 3. This approach offers a candidate of a high sensitivity magnetometer which gets rid of the fluctuation of the bias magnetic field.

III. SENSOR SETUP

A block diagram of the measurement system is shown in Fig. 4. The cesium vapor cell is a cylindrical shape, and N_2 is filled as buffer gas. In order to minimize the influence of ambient magnetic field, it was enclosed with a three-layer permalloy magnetic shield and heated by hot air. A vertical cavity surface emitting laser (VCSEL) was used as the light source, and the driving current was modulated at half the frequency of hyperfine structure frequency of cesium ground level. Also, in order to minimize laser noise, the driving current was modulated, and the laser wavelength was locked at the bottom of absorption line. Light power density was about 1.5mW/cm^2. The linearly polarized light output from the VCSEL was converted into the circularly polarized light by λ/4 plate, and after being transmitted through the cell, it was detected by a photodetector. The CPT signal was demodulated by a lock-in amplifier and becomes magnetic field signal.

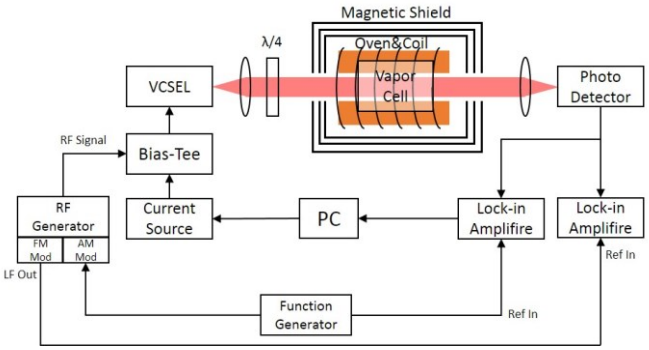


Fig. 4 Block Diagram of the Measurement System

IV. EXPERIMENT RESULT

The degenerate CPT resonance observed in this measurement system had high contrast of 55.6% and narrow linewidth of 482Hz. Figure 5 shows the output voltage of lock-in amplifier versus magnetic field characteristics. The voltage changed linearly within range of ±10nT, and its slope of around 0nT is -0.266nT/V. Figure 6 shows the sensitivity obtained from the voltage magnetic field conversion coefficient and the power spectral density of the output noise of the magnetometer. From this chart, the calculated sensitivity of the magnetometer near 10Hz is 1pT/√Hz.

V. CONCLUSION

A CPT magnetometer in optically pumped degenerate state was developed. We used optical pumping technique to increase the resonance amplitude of the Zeeman sublevel with highest magnetic quantum number. Thus, voltage magnetic field conversion coefficient of the resonance frequency in degenerate state becomes large. The experimental result showed sensitivity of 1pT/√Hz. We expect improvement of pumping rate will lead an increase of the shift of CPT resonance frequency in degenerate state resulting in further improvement of the sensitivity of the degenerate CPT magnetometer.

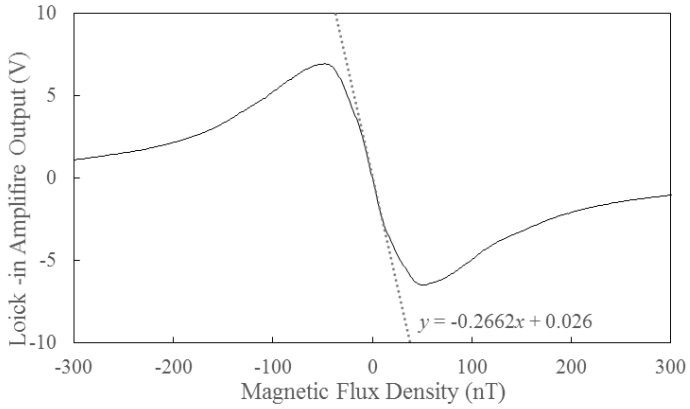


Fig. 5 Lock-in Amplifire Output vs. Magnetic Field

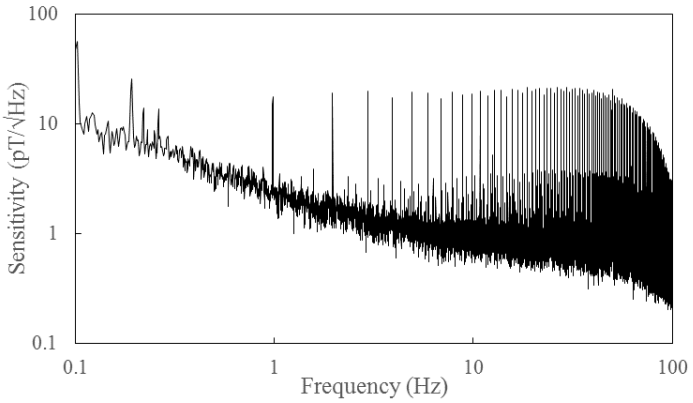


Fig. 6 Magnetometer Sensitivity

REFERENCES

[1] D. Budker, and M. Romalis, "Optical Magnetometry", Nat. Phys., Vol. 3, Iss. 4, pp. 227-234 (2007).

[2] D. Budker, D. F. Kimball, S. M. Rochester, V.V.Yashchuk, and M. Zolotorev, "Sensitive Magnetometry based on Nonlinear Magneto-Optical Rotation", Phys. Rev. A, Vol. 62, Iss. 4 (2000)

[3] P.D.D. Schwindt, B. Lindseth, S. Knappe, V. Shah, and J. Kitching, "Chip-scale atomic magnetometer with improved sensitivity by use of the Mx technique", Appl. Phys. Lett, Vol. 90, Iss. 8, 081102 (2007)

[4] J. Belfi, G. Bevilacqua, V. Biancalana, S. Cartaleva, Y. Dancheva, and L. Moi, "Cesium coherent population trapping magnetometer for cardiosignal detection in an unshielded environment", J. Opt. Soc. Am. B, Vol. 24, No. 9, pp. 2357-2362

[5] d A. K. Das, "Polarization rotation under two-photon Raman resonance for magnetometry", Appl. Phys. Lett., Vol. 100, Iss. 17, 173502 (2012)

The microwave down converted from ultra-stable laser by an optical frequency comb

Shaoyang Dai*, Fang Fang*, Shiying Cao, Nianfeng Liu, Rui Suo and Tianchu Li
National Institute of Metrology
Beijing, China
E-mail: daisy@nim.ac.cn, fangf@nim.ac.cn

***Abstract*—An ultra-stable microwave down converted from the ultra-stable laser directly by an optical frequency comb (OFC) is built at the National Institute of Metrology China. The repetition rate (f_r) of OFC is stabilized by stabilizing the sum of the carrier envelope offset frequency (f_{ceo}) of OFC and the beating frequency between the ultra-stable laser (USL) and OFC. A current feedback with 30 kHz bandwidth and a piezoelectric transducer with 1 kHz bandwidth are applied for the frequency stabilization. The frequency jitter of the stabilized sum frequency is about 4 Hz. Though the counting of locked f_r, the shifted frequency of the USL is about 2087 Hz/day. As the frequency jitter of the mixing frequency of f_{ceo} and the beating frequency between this OFC and another USL is about 10Hz, the short time stability of f_r is calculated to be about 5e-14. This ultra-stable microwave will be applied as the local oscillator for NIM5 Cs fountain to improve its shorter term instability.**

Keywords—Ultra-stable microwave, Ultra-stable laser, Optical frequency comb

I. INTRODUCTION

Ultra-stable microwave (USM) is of prime importance in various fields such as clocks [1], precision measurements [2], and other applications. At present, there are three kinds of USM sources, which are the quartz oscillator, cryogenic sapphire oscillator [3-4] and the optical microwave generation [5-7]. Every kind of USM has its own a dvantages and disadvantages.

Optical microwave generation is realized by transferring the stability of ultra-stable laser [8-9] (USL) to microwave using optical frequency comb [10-11] (OFC).

Since the 21st century, the line width of USL has been improved below 1 Hz [8], and the OFC was invented and has been robust [11]. These make the ultra-stable optical microwave generation possible.

In 2009, Physikalisch-Technische Bundesanstalt (PTB) stabilized their 9.6 GHz microwave oscillator to an optical clock laser at 344 THz by using a fiber-based OFC as a transfer oscillator [6]. The total fractional frequency instability of this optic-to-microwave and microwave-to-optic conversion resulted in 1.2×10^{-14} at 1 s averaging time. This microwave was applied in their Cs fountain CSF1. Finally, a reduced frequency instability of the clock below the 10^{-14} level at 100 s averaging time only limited by quantum projection noise was obtained [12].

Soon afterwards, LNE-SYRTE reported their 9.2 GHz low-noise microwave source down converted from the ultra-stable laser directly using an optical frequency comb [5]. The new microwave source exhibited a frequency stability of about 3×10^{-15} between 1 s and 10 s. In a further experiment, the new microwave source was applied to a Cesium fountain clock as the local oscillator; the resulting clock system exhibits a stability of $3.5\times10^{-14}\tau^{-1/2}$ [13].

In this letter, we reported our own USM source down converted from the self-made USL directly by a self-made Er-doped OFC. By stabilizing the sum frequency of the carrier envelope offset frequency (f_{ceo}) of the OFC and the beat frequency (f_b) of the USL and OFC, the repetition frequency (f_r) of OFC is stabilized. By measuring the sum frequency of f_{ceo} and f_b of the OFC and another USL, the stability of f_r is appraised. This USM is designed for the Cs fountain NIM5 [14].

II. EXPERIMENTAL SETUP

A. The ultra-stable laser

In the experiments, the 1542 nm fiber laser is stabilized by an ultra-stable reference cavity (shown in Fig.1) [15]. The Pound-Drever-Hall (PDH) locking system is applied to stabilize the laser. To verify the short term stability of this USL, a commercial USL (MenloSystems ORS1500) is used for the beating frequency signal. Shown in Fig.2, the frequency jitter of the beating frequency signal is below 2 Hz in one second which means that the second stability of the USL is better than 1×10^{-14}.

This work is supported by the Ministry of Science and Technology of China (Grants 2013YQ09094302).

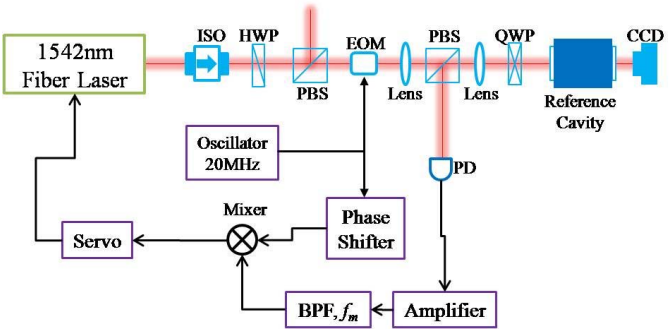


Fig. 1. The system structure of the ultra-stable laser. ISO, isolator. HWP, half wavelength plate. PBS, polarized beam splitter. EOM, acoustic optical modulator. QWP, quarter wave plate. PD, photon detector. CCD, charge coupled device. BPF, bandpass filter.

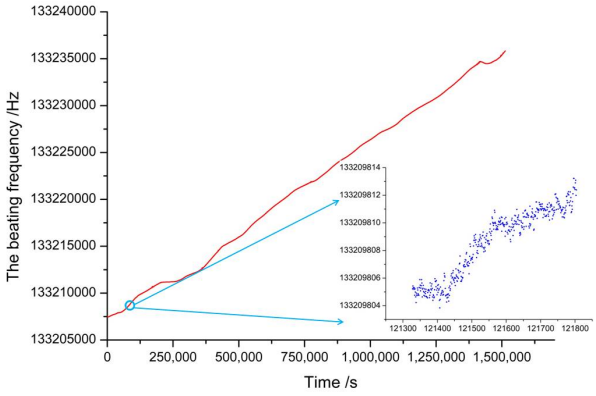


Fig. 2. The change curve of beating frequency signal between two ultra-stable lasers.

B. *The Er-doped fiber optical frequency comb [16]*

The Er-doped fiber OFC is shown in Fig.3. The f_r is obtained by detecting the light from the optical parametric oscillator. The f_{ceo} is obtained after power amplifying, spectrum spreading and "*f-to-2f*" frequency beating. The signal to noise ratio (SNR) of the f_{ceo} is about 40dB (resolution bandwidth (RBW) at 300 kHz).

The piezoelectric transducer (PZT) is used to controls the cavity length of the optical parametric oscillator. Through the current source of the optical parametric oscillator, the pumping power can be controlled.

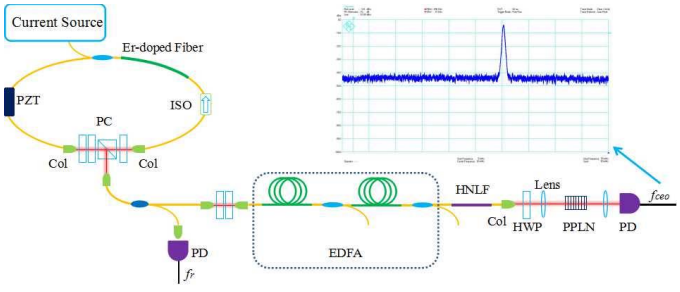


Fig. 3. The optical structure of the Er-doped fiber optical frequency comb. Inset. The frequency spectrum of f_{ceo}. ISO, isolator. HWP, half wavelength plate. PD, photon detector. PZT, piezoelectric transducer. PC, polarization control. Col, collimator. EDFA, erbium doped fiber amplifier. HNLF, high nonlinear fiber. PPLN, periodically poled lithium niobate.

C. *The ultra-stable microwave*

The light beams of the USL and OFC are coupled by a fiber coupler where the light powers are 3mW and 8mW. The coupled light is output by a collimator. Then, a half wave plate and a polarized beam splitter are applied for the optimal polarization light. A grating is used to separate the lights with different wavelengths in space. A photon detector is used to detect the targeted light and gains the beating frequency of USL and OFC. The light beam path is shown in Fig.4. By optimizing the light polarization and the adjusting the mirror before the PD, the f_b with SNR at 40 dB (RBW at 300 kHz) is obtained. The f_b is shown in Fig.5 (a).

Shown in Fig.4, the sum frequency of f_{ceo} and f_b is obtained by using a mixer. The SNR of the sum frequency is 35 dB (RBW at 300 kHz, shown in Fig5 (b)) which meets the requirements of the phase locked loop. The sum frequency is filtered by a band pass filter. The sum frequency is phase detected with the H master. Then, the error signals are fed back to the OFC in two ways, the current of the pumping source and the PZT in the cavity. By adjusting the parameters of the proportion integration, f_b+f_{ceo} is stabilized at 100 MHz.

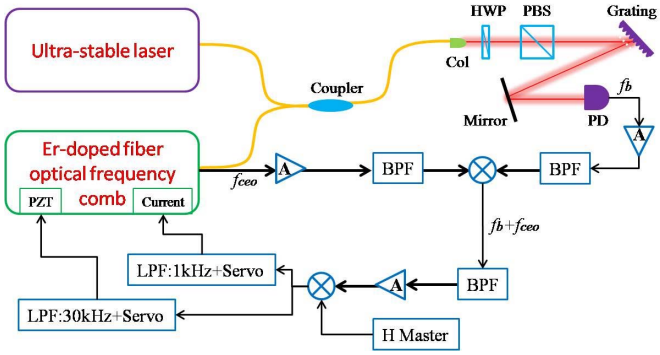


Fig. 4. The system structure diagram of the ultra-stable microwave. PC, polarization control. PBS, polarized beam splitter. Col, Collimator. PD, photon detector. HWP, half wavelength polarization. PZT, piezoelectric transducer. BPF, bandpass filter. A, amplifier. LPF, lowpass filter.

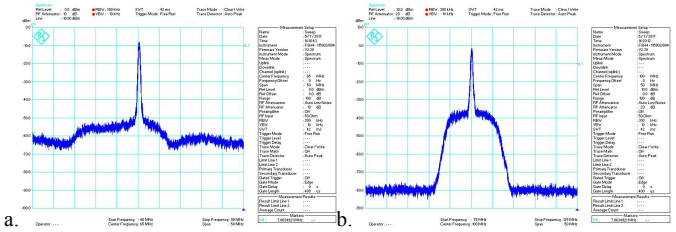


Fig. 5. a. The frequency spectrum of f_b. b. the frequency spectrum of f_b+f_{ceo}.

III. EXPERIMENTAL RESULTS

By measuring the sum frequency, the frequency jitter of f_b+f_{ceo} is about 4Hz which is shown in Fig.6 (a). The f_r is measured by a frequency counter and shown in Fig.6 (b). The measured frequency stability of f_r is limited by the stability of the frequency counter. However, the long term frequency shift of the USL is shown clearly. By fitting the counted frequency of f_r, the shifted frequency of USL is about 2087 Hz/day. To accurately obtain the short term stability of the ultra-stable microwave, we use the commercial USL.

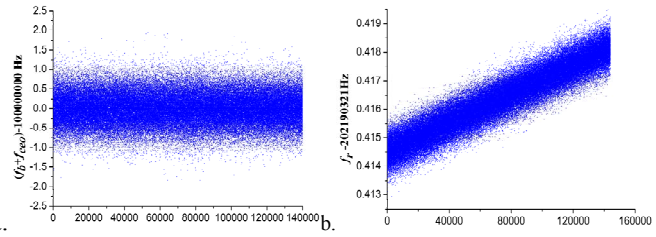


Fig. 6. a. The Frequency counter results for a 1-s gate time for the locked f_b+f_{ceo}. b. The Frequency counter results for a 1-s gate time for the locked f_r.

In Fig.7, the histograph among the optical frequency comb and both ultra-stable lasers is revealed clearly. When $f_{ceo}+f_b$ is stabilized, f_r will be stabilized. As f_{L2} is equal to $nf_r+f_{ceo}-f_{b2}$, the frequency jitter of $f_{ceo}-f_{b2}$ manifests the stability of f_r to some extent. Certainly, the precondition is that f_{L2} is stable enough. Shown in Fig.8, the second frequency jitter of $f_{ceo}-f_{b2}$ is about 10 Hz. Compared with the 194.4 THz laser frequency, the second stability of f_r is about 5×10^{-14}.

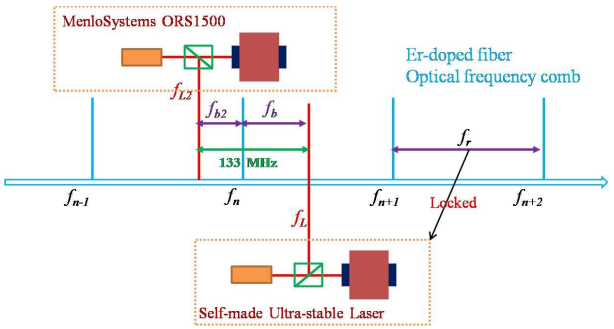


Fig. 7. The histograph among the optical frequency comb and both ultra-stable lasers.

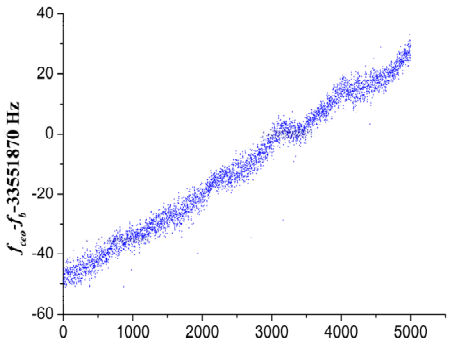


Fig. 8. The Frequency counter results for a 1-s gate time for $f_{ceo}-f_b$.

IV. CONCLUSION

In this paper, an 1542nm USL with shifted frequency at 2087 Hz/day and an Er-doped fiber OFC are self-made. The OFC is stabilized with the USL by stabilizing f_b+f_{ceo} with the H master. The stability of the USL is transferred to the f_r of the OFC. A commercial USL is applied to measure the stability of the USM. Through calculating the stability of f_r is about 5×10^{-14}. This stability is below the quantum projection noise limitation of NIM5. The further work is the application of the ultra-stable microwave in NIM5.

ACKNOWLEDGMENT

This work is supported by the Ministry of Science and Technology of China (Grants 2013YQ09094302).

REFERENCES

[1] R Wynands and S Weyers, Atomic fountain clocks, Metrologia, 42 (2005) S64 – S79.

[2] 1. R. J. Rafac, B. C. Young, J. A. Beall, W. M. Itano, D. J. Wineland, and J. C. Bergquist, Sub-dekahertz Ultraviolet Spectroscopy of $^{199}Hg^{+}$, Phys. Rev. Lett. 85, 2462, 2000.

[3] S.Grop, P. Y. Bourgeois, R. Boudot, Y. Kersale, E. Rubiola and V. Giordano, 10 GHz cryocooled sapphire oscillator with extremely low phase noise, Electron. Lett., 46(6), 420-422, 2010.

[4] J. G. Hartnett, N. R. Nand and C. Lu, Ultra-low-phase-noise cryo-cooled microwave dielectric-sapphire-resonator oscillators, Appl. Phys. Lett. 100, 183501, 2012..

[5] J. Millo, R. Boudot, M. Lours, P. Y. Bourgeois, A. N. Luiten, Y. Le Coq, Y. Kersalé, and G. Santarelli, Ultra-low-noise microwave extraction from fiber-based optical frequency comb, Optics Letters, 34 (23), 3707-3709, 2009.

[6] B. Lipphardt, G. Grosche, U. Sterr, C. Tamm, S. Weyers and H. Schnatz, The Stability of an Optical Clock Laser Transferred to the Interrogation Oscillator for a Cs Fountain, IEEE TRANSACTIONS ON INSTRUMENTATION AND MEASUREMENT, VOL. 58, NO. 4, APRIL 2009.

[7] W. Zhang, Z. Xu, M. Lours, R. Boudot, Y. Kersalé A. N. Luiten, Y. L. Coq and G. Santarelli, Advanced Noise Reduction Techniques for Ultra-Low Phase Noise Optical-to-Microwave Division With Femtosecond Fiber Combs, IEEE TRANSACTIONS ON ULTRASONICS, FERROELECTRICS, AND FREQUENCY CONTROL, vol. 58, no. 5, MAY 2011.

[8] A. D. Ludlow, X. Huang, M. Notcutt, T. Zanon-Willette, S. M. Foreman, M. M. Boyd, S. Blatt and J. Ye, Compact, thermal-noise-limited optical cavity for diode laser stabilization at $1*10^{-15}$, Optics Letters, 32(6), 641-643, 2007.

[9] M. Notcutt, L. S. Ma, J. Ye, and J. L. Hall, Simple and compact 1-Hz laser system via an improved mounting configuration of a reference cavity, Optics Letters, 30(14), 1815-1817, 2005.

[10] David J. Jones, Scott A. Diddams, Jinendra K. Ranka, Andrew Stentz, Robert S. Windeler, John L. Hall, Steven T. Cundiff, Carrier-Envelope Phase Control of Femtosecond Mode-Locked Lasers and Direct Optical Frequency Synthesis, Science, 635, 9, 2000.

[11] H. Inaba, Y. Daimon, F. L. Hong, A. Onae, K. Minoshima, T. R. Schibli, H. Matsumoto, M. Hirano, T. Okuno, M. Onishi and M. Nakazawa, Long-term measurement of optical frequencies using a simple, robust and low-noise fiber based frequency comb, Opt. Express, Vol. 14, Issue 12, pp. 5223-5231, 2006.

[12] S. Weyers, B. Lipphardt, and H. Schnatz, Reaching the quantum limit in a fountain clock using a microwave oscillator phase locked to an ultrastable laser, Phys. Rev. A, 79, 031803(R),2009.

[13] J. Millo, M. Abgrall, M. Lours, E.M.L. English, H. Jiang, J. Guéna, A. Clairon, S. Bize, Y. Le Coq and G. Santarelli, Ultra-low noise microwave generation with fiber-based optical frequency comb and application to atomic fountain clock, Applied Physics Letters, 94, 141105-141107, 2009.

[14] F. Fang, M. S. Li, P. W. Lin, W. L. Chen, N. F. Liu, Y. G. Lin, P.Wang, K. Liu, R. Suo and T. C. Li, NIM5 Cs fountain clock and its evaluation, Metrologia 52 (2015) 454 – 468.

[15] R. Suo, F. Fang and T. C. Li, Towards a 1542 nm laser stabilized to an optical cavity, Proc. of SPIE Vol. 8201, 820104, 2011.

[16] S. Y. Cao, F. Meng, B. K. Lin, Z. J. Fang and T. C. Li, Precise frequency control of an Er-doped fiber comb, Acta Phys. Sin., 61(13), 134205, 2012.

Design of Active All-optical Magnetometer

Duo Pan, Tiantian Shi, Xiang Peng, Jingbiao Chen, Hong Guo
State Key Laboratory of Advanced Optical Communication, System and Network,
School of Electronics Engineering and Computer Science, Peking University,
Beijing 100871, China
E-mail: panduo@pku.edu.cn

***Abstract*—We propose an active all-optical magnetometer based on Cesium four-level atomic system. The magnetometer is free of radio frequency antenna, thus has smaller measure volumes. With an theoretical milli Hertz linewidth of the four-level active optical clock, the magnetometer has a potential sensitivity of tens of fT $Hz^{-1/2}$.**

Keywords—active; all-optical; magnetometer; four-level.

I. INTRODUCTION

Since proposed [1], atomic magnetometers are widely used in biomedicine [2], geophysics [3], and space exploration [4], and the requirements of different application, highly sensitive, compact and low-cost AMs are preferred.

The active optical clock, first proposed in 2005[5, 6], has theoretically ultra-narrow linewidth due to the suppression of cavity pulling effect. And this unique characteristic also makes the active atomic system an excellent candidate for AMs. In reference [7], the magnetometer based on active mode has been demonstrated to be able to break the photon shot noise limitation.

In this paper, we propose an active all-optical magnetometer based on Cesium four-level atomic system. The magnetometer is free of radio frequency antenna, thus has smaller measure volumes. With an theoretical milli Hertz linewidth of the four-level active optical clock, the AM has the potential sensitivity of tens of fT $Hz^{-1/2}$.

II. METHODS

The AM described here operates in a similar manner to the four-level active optical clock reported in [8], and the stimulated emission is radiated between Cs $7S_{1/2}$ (F=4) and $6P_{3/2}$ (F=5) states. In the magnetic fields, energy levels' degeneracy is removed, as shown in Fig. 1. Hence with specific magnetic field direction, the output 1470 nm signal contains two series of optical spectrums, respectively resulting from σ^+ (green lines) and σ^- (purple lines) transitions. For the σ^+ transitions, the frequency differences between each other are quite small, compared with that between the σ^+ and σ^- transition series. The case in the σ^+ transitions is just the same. Therefore, when we detect the output signal with heterodyne method, the frequency value of the beating signal mainly reflects the frequency difference of the two series of transitions, which is determined by the applied magnetic field. By this method the magnetic field is measured.

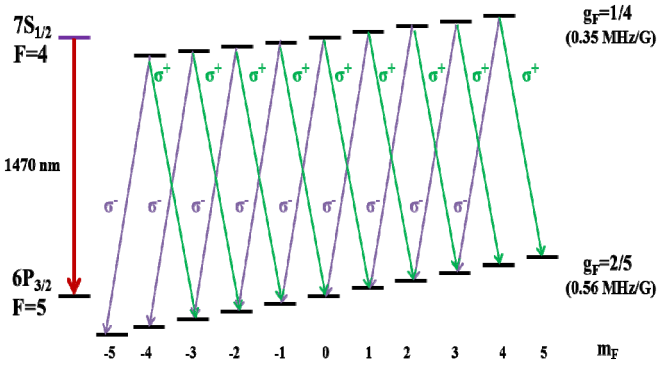


Fig. 1. Relevant energy level structure and transitions

Fig. 2 schematically shows the experimental setup of the active all-optical magnetometer. The cavity is composed of a concave mirror and a plane mirror. The former is coated with 459 nm high reflection and 1470 nm high-refection coating. The latter is coated with 459 nm high-reflection and the reflectivity of 1470 nm is 80%. The cavity mode linewidth is about 400 MHz, much wider than the atomic gain. The coils are utilized to produce magnetic field along the cavity axis. 1470 nm output signal is detected by a photo detector, and then the beating signal is measured by a frequency analyzer.

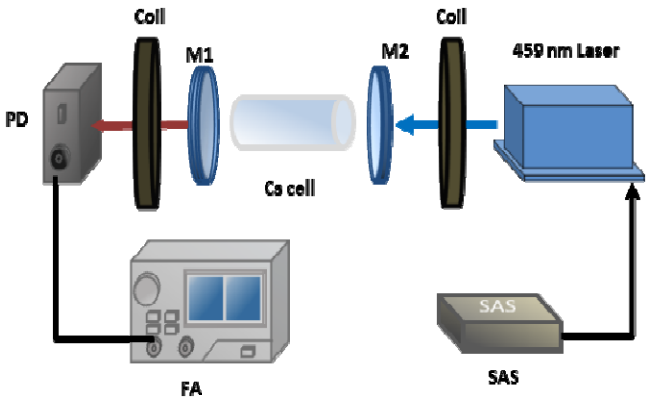


Fig. 2. Experimental setup of the active all-optical magnetometer. M: Mirror, SAS: Saturated absorption spectrum, PD: Photo detector. FA: Frequency analyzer.

III. RESULTS

When we apply a fixed magnetic field to separate the magnetic sublevels, a measurement of the beating signal is shown in Fig. 3, of which the linewidth is 3kHz. Hence the applied magnetic field is changed by changing the current of the coils, and the beating signal experiences corresponding frequency shifts. The frequency shifts under different applied magnetic fields are shown in Fig. 4. We see that the beating frequency changes linearly with the magnetic field, with a factor of 1.2 MHz/G, which meets well with the theoretical value of 1.12 MHz/G. By this method the magnetic field applied to the atomic cell is measured precisely.

In the next step, we will work on the suppression of the linewidth and the improvement of the signal to noise ratio. With an theoretical milli Hertz linewidth of the four-level active optical clock, the magnetometer has a potential sensitivity of tens of fT $Hz^{-1/2}$.

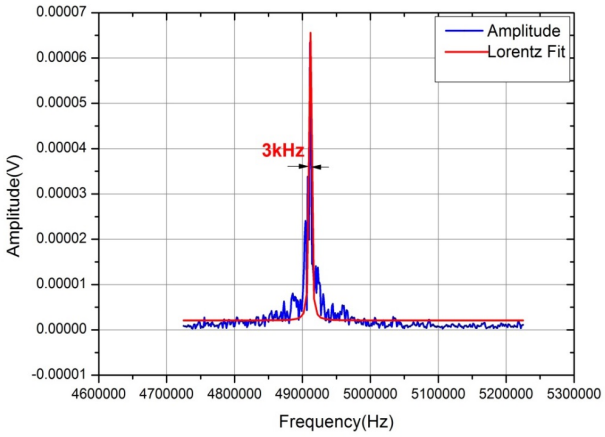


Fig. 3. Preliminary measurement of the beating signal.

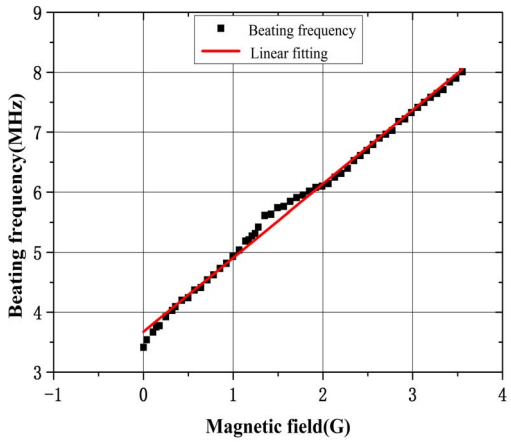


Fig. 4. The beating frequency under different applied magnetic fields.

IV. CONCLUSION

We propose an active all-optical magnetometer based on Cesium four-level atomic system. Theoretically, the active optical clock has a quantum limited linewidth of milli Hertz. With an non-deteriorated signal to noise ratio, the magnetometer based on this scheme has a potential sensitivity of tens of fT $Hz^{-1/2}$. In addition, the all-optical structure is free of radio frequency antenna, thus has smaller volume and lower cost compared with current systems.

ACKNOWLEDGMENT

This work is supported by the National Hi-Tech Research and Development (863) Program and the National Natural Science Foundation of China (Grant No. 91436210)

REFERENCES

[1] F. Bloch, W. Hansen, and M. Packard, "The nuclear induction experiment", Phys. Rev. 70, pp. 474-485 (1946).

[2] K. Enpuku, T. Minotani, T. Gima, Y. Kuroki, Y. Itoh, M. Yamashita, Y. Katakura, and S. Kuhara, "Detection of Magnetic Nanoparticles with Superconducting Quantum Interference Device (SQUID) Magnetometer and Application to Immunoassays", Jpn. J. Appl. Phys., 38, pp. 1102-1105 (1999).

[3] B. Sarma, B. Verma, and S. Satynanarayana, "Magnetic mapping of Majhgawan diamond pipe of central India", Geophysics, 64, pp. 1735-1739 (1999).

[4] J. M. Leger, F. Bertrand, T. Jager, M. Le Prado, I. Fratter, and J. C. Lalaurie, "Swarm absolute scalar and vector magnetometer based on Helium 4 optical pumping", Procedia Chemistry 1, pp. 634-637 (2009).

[5] J. Chen, X. Chen, "Optical Lattice Laser," Proceedings, 2005 IEEE Int. Frequency Control Symp., Vancouver, Canada, August 29-31, 2005, pp. 608-610

[6] J. Chen, "Active optical clock". Chin. Sci. Bull., 54 (3), pp. 348-352 (2009)

[7] J. Weiner, K. Cox, J. Bohnet, Z. Chen, and J. Thompson, "Superradiant Raman laser magnetometer", Appl. Phys. Lett. 101, 261107 (2012).

[8] D. Pan, Xiaobo Xue, and Jingbiao Chen, "Detailed problems in cesium active optical clock", Proceedings of 2016 IEEE Int. Frequency Control Symp, pp. 475-477.

Optimization of Frequency Modulation Parameters in Atomic Clocks Based on Coherent Population Trapping

V. I. Yudin, M. Yu. Basalaev, D. V. Kovalenko, A. V. Taichenachev
Novosibirsk State University, Novosibirsk, Russia
Institute of Laser Physics SB RAS, Novosibirsk, Russia
viyudin@mail.ru, mbasalaev@gmail.com

***Abstract*—Excitation of coherent population trapping resonances in dynamic regime is theoretically investigated. We formulate the criteria for quasistationary (adiabatic) and dynamic (non-adiabatic) responses of atomic system driven by bichromatic field. We optimize the parameters of frequency modulation of two-photon detuning, taking into account the low-frequency noise.**

Keywords—coherent population trapping, atomic clocks, dynamic regime, frequency stabilization, error signal

I. INTRODUCTION

Atomic clocks have a wide spectrum of applications in different areas of science (high precision measurements, testing of fundamental theories) and technology (navigation and telecommunication systems, geodesy, gravimetry, etc.) [1]. Main advantages of atomic clocks [2–4] based on coherent population trapping (CPT) consist of their low-power and compactness in combination with relatively high metrological characteristics (stability and accuracy) [5–7]. Therefore, these devices are greatly attractive for large consumer segment.

In the context of clock operation, determination of optimal regime of frequency stabilization is important task for CPT clocks. Experimental investigations of this question were done in papers [8–10]. However, detail theoretical consideration, where it is necessary to use the dynamic solution for atomic density matrix, was not done. To construct the exact periodic solution of density matrix equation we use recently developed method [11]. We calculate and optimize the error signal formed by the use of harmonic frequency modulation, which is usually applied for frequency stabilization in atomic clocks. Obtained theoretical results are in good qualitative agreement with different experiments [8-10].

II. GENERAL THEORY AND CALCULATIONS

As a model, we consider so-called dark resonance, which is formed in three-level Λ system under interaction with resonant bichromatic field

$$E(t) = E_1 e^{-i\omega_1 t} + E_2 e^{-i\omega_2 t} + \text{c.c.}\,. \qquad (1)$$

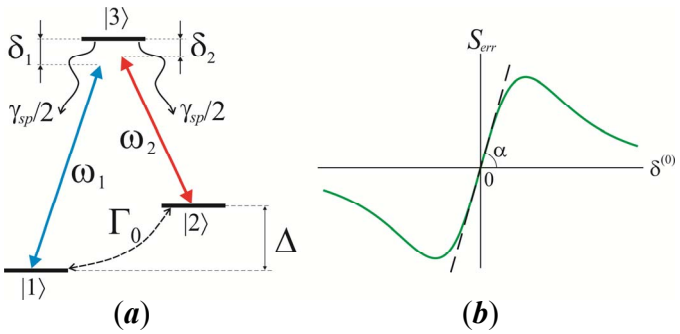


Fig. 1. (a) Scheme of atomic three-level Λ system. (b) Schematic view of error signal $S_{err}(\delta^{(0)})$.

CPT resonance is formed when the difference between optical frequencies $(\omega_1 - \omega_2)$ is varied near the low-frequency transition between lower energy levels $|1\rangle$ and $|2\rangle$: $(\omega_1 - \omega_2) \approx \Delta$ [see Fig. 1(a)]. The dynamics of the Λ system in the rotating wave approximation is described by the differential equation system for density matrix components

$$\begin{aligned}
&\left(\partial_t + \gamma_{opt} - i\delta_1\right)\rho_{31} = i\,\Omega_1(\rho_{11} - \rho_{33}) + i\,\Omega_2\rho_{21},\\
&\left(\partial_t + \gamma_{opt} - i\delta_2\right)\rho_{32} = i\,\Omega_2(\rho_{22} - \rho_{33}) + i\,\Omega_1\rho_{12},\\
&\left(\partial_t + \Gamma_0 + i\delta_r\right)\rho_{12} = i\left(\Omega_1^*\rho_{32} - \rho_{13}\Omega_2\right),\\
&\left(\partial_t + \Gamma_0\right)\rho_{11} = \frac{\gamma_{sp}}{2}\rho_{33} + \frac{\Gamma_0}{2}\mathrm{Tr}[\hat{\rho}] + i\left(\Omega_1^*\rho_{31} - \rho_{13}\Omega_1\right), \qquad (2)\\
&\left(\partial_t + \Gamma_0\right)\rho_{22} = \frac{\gamma_{sp}}{2}\rho_{33} + \frac{\Gamma_0}{2}\mathrm{Tr}[\hat{\rho}] + i\left(\Omega_2^*\rho_{32} - \rho_{23}\Omega_2\right),\\
&\left(\partial_t + \gamma_{sp} + \Gamma_0\right)\rho_{33} = i\left(\Omega_1\rho_{13} - \rho_{31}\Omega_1^*\right) + i\left(\Omega_2\rho_{23} - \rho_{32}\Omega_2^*\right),\\
&\rho_{21} = \rho_{12}^*, \quad \rho_{13} = \rho_{31}^*, \quad \rho_{23} = \rho_{32}^*, \ \mathrm{Tr}[\hat{\rho}] = \rho_{11} + \rho_{22} + \rho_{33} = 1.
\end{aligned}$$

Here $\delta_j = \omega_j - \omega_{3j}$ $(j = 1,2)$ is an one-photon detuning of frequency components ω_j on the resonant transition [see Fig. 1(a)]; $\delta_r = \omega_1 - \omega_2 - \Delta$ is two-photon (Raman) detuning; $\Omega_1 = d_{31}E_1/\hbar$ and $\Omega_2 = d_{32}E_2/\hbar$ are Rabi frequencies for the transitions $|1\rangle \leftrightarrow |3\rangle$ and $|2\rangle \leftrightarrow |3\rangle$ (d_{31} and d_{32} are reduced matrix

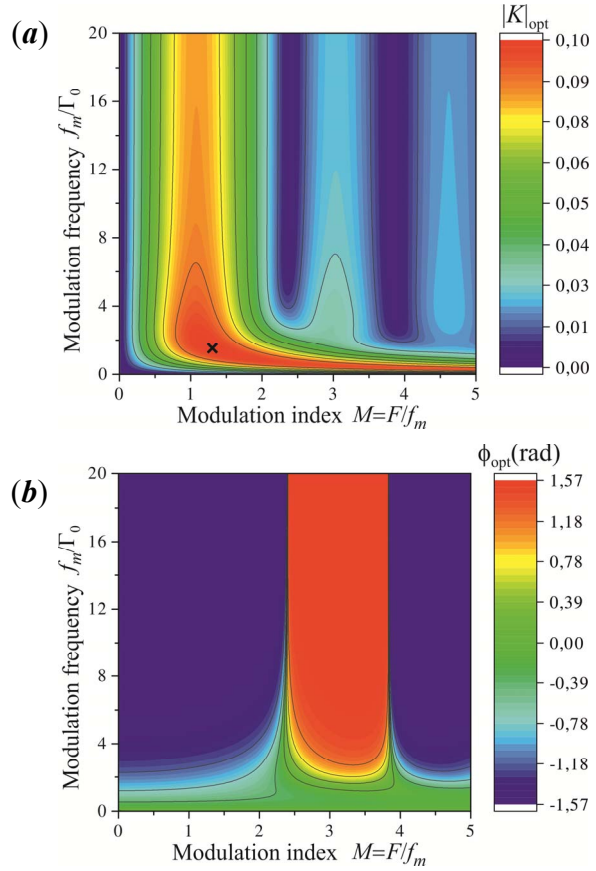


Fig. 2. Dependence of maximum slope $|K|_{opt}$ and optimal phase ϕ_{opt} on FM parameters of two-photon detuning (4). Plots are calculated under $\gamma_{opt} = 50\gamma_{sp}$, $\gamma_{sp} = 10^4\,\Gamma_0$, $\Omega_1 = \Omega_2 = 500\,\Gamma_0$, $\delta_1 = -\delta_2$.

elements of dipole moment for these transitions); γ_{sp} is spontaneous decay rate of upper level $|3\rangle$; γ_{opt} is rate of decoherence (spontaneous, collisional, etc.) of optical transitions $|1\rangle\leftrightarrow|3\rangle$ and $|2\rangle\leftrightarrow|3\rangle$; Γ_0 is relatively slow ($\Gamma_0 << \gamma_{sp}$, γ_{opt}) rate of relaxation to the equilibrium isotropic state: $\hat{\rho}_0 = \left(|1\rangle\langle 1| + |2\rangle\langle 2|\right)/2$.

As a detected signal we consider the output laser power from atomic cell. In our case of Λ system and for optically thin medium, the main spectroscopic information (per one atom) is contained in slowly varying value:

$$A(t) = -2\,\mathrm{Im}\{\Omega_1\rho_{13} + \Omega_2\rho_{23}\} = \left[\partial_t + \gamma + \Gamma_0\right]\rho_{33}\,. \qquad (3)$$

In atomic clocks the harmonic frequency modulation (FM) is usually applied, when the two-photon detuning depends on the time:

$$\delta_r(t) = \delta^{(0)} + F\cos(f_m t) = \delta^{(0)} + M\,f_m\cos(f_m t)\,, \qquad (4)$$

where $\delta^{(0)}$ is some constant term of two-photon detuning, F is amplitude of modulation, f_m is frequency of modulation, and $M = F/f_m$ is modulation index. The error signal is formed as a function on $\delta^{(0)}$:

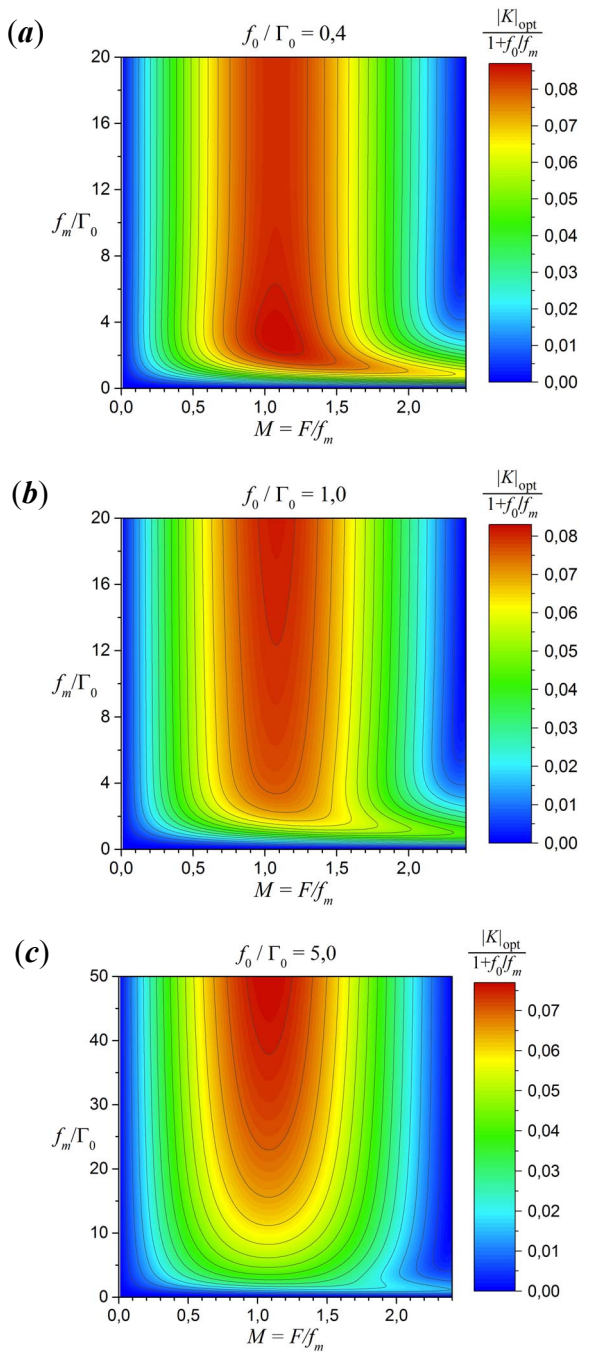


Fig. 3. Dependences of $|K|_{opt}/\left[1+(f_0/f_m)\right]$ on modulation parameters (index M and frequency f_m) for (*a*) $f_0 = 0.4\,\Gamma_0$, (*b*) $f_0 = \Gamma_0$, (*c*) $f_0 = 5\,\Gamma_0$. Numeric parameters of model (2) are following: $\gamma_{opt} = 50\gamma_{sp}$, $\gamma_{sp} = 10^4\,\Gamma_0$, $\Omega_1 = \Omega_2 = 500\,\Gamma_0$, $\delta_1 = -\delta_2$.

$$S_{err}(\delta_r^{(0)}) = \frac{1}{T}\int_0^T A(t)\cos\left(f_m t + \phi\right)dt\,, \qquad (5)$$

where $\cos(f_m t + \phi)$ is the reference signal, and ϕ is the phase of the reference signal relative to the harmonic dependence (4). A typical view of the functional dependence $S_{err}(\delta^{(0)})$ is shown

in Fig. 1(b), and it has a form of dispersion curve. One of key roles for clock stabilization plays the slope of the curve in the center of lineshape:

$$K = \tan(\alpha) = \left.\frac{\partial S_{err}}{\partial \delta_r^{(0)}}\right|_{\delta_r^{(0)}=0}. \quad (6)$$

The dependence of maximum slope (6) and corresponding optimal phase of reference signal on FM parameters of two-photon detuning (4) are shown in Fig. 2.

Other important parameter for clock stabilization is a noise spectral density $N(f_m)$. Indeed, the clock instability is proportional to the value $N(f_m)/|K|$, which should be minimized. As model of low-frequency noise we will consider the superposition of white and flicker noise (or $1/f$ noise):

$$N(f_m) = N_0\left(1 + f_0/f_m\right), \quad (7)$$

where $N_0 = N(f_m=\infty)$ is spectral density of white noise, frequency parameter f_0 is determined by the amplitude of flicker noise. To achieve good frequency stability in CPT clocks it is necessary to maximize the quantity

$$\sigma(f_m, F) = \frac{|K|_{\text{opt}}}{1+\left(f_0/f_m\right)}, \quad (8)$$

where $|K|_{\text{opt}}(f_m,F)$ is maximal slope of error signal for optimal phase ϕ_{opt} of reference signal (see Fig. 2). The calculated dependences of quantity (8) on modulation parameters for different values of frequency f_0 are shown in Fig. 3.

Our calculations show that the low-frequency noise (7) can lead to the displacement of optimum stabilization to the area of high modulation frequencies (f_m>10-100 kHz for typical atomic cells). This regime can be considered as CPT analog of Pound-Driver-Hall regime of frequency stabilization (i.e. when the modulation frequency is much greater than wide of CPT resonance in the steady-state condition).

ACKNOWLEDGMENT

The work was supported by the Russian Science Foundation (project No. 16-12-10147). M.Yu.B. was supported by the Russian Foundation for Basic Research (projects No. 16-32-60050 mol_a_dk, No. 16-32-00127 mol_a), by the Ministry of Education and Science of the Russian Federation (Project No. 3.1326.2017).

REFERENCES

[1] A. D. Ludlow, M. M. Boyd, J. Ye, E. Peik, and P. O. Schmidt, Rev. Mod. Phys., vol. 87, pp. 637–701, 2015.

[2] E. Arimondo, Prog. Opt., vol. 35, pp. 257–354, 1996.

[3] J. Vanier, Appl. Phys. B, vol. 81, pp. 421–442, 2005.

[4] V. Shah and J. Kitching, Adv. At. Mol. Opt. Phys., vol. 59, 21–74, 2010.

[5] S. Knappe, P. Schwindt, V. Shah, L. Hollberg, J. Kitching, L. Liew, and J. Moreland, Opt. Express, vol. 13, pp. 1249–1253, 2005.

[6] R. Lutwak, A. Rashed, M. Varghese, G. Tepolt, J. Leblanc, M. Mescher, D. K. Serkland, and G. M. Peake, Proc. IEEE International Frequency Control Symposium and European Frequency and Time Forum Geneva, Switzerland, pp. 1327-1333, 2007.

[7] Z.Wang, Chin. Phys. B, vol. 233, Art. 030601, 2014.

[8] I. Ben-Aroya, M. Kahanov, and G. Eisenstein, Opt. Express, vol. 15, pp. 15060–15065, 2007.

[9] M. Kahanov, I. Ben-Aroya, and G. Eisenstein, Opt. Lett., vol. 33, pp. 944–946, 2008.

[10] E. E. Mikhailov, T. Horrom, N. Belcher, and I. Novikova, J. Opt. Soc. Am. B, vol. 27, pp. 417–422, 2010.

[11] V. I. Yudin, A. V. Taichenachev, and M. Yu. Basalaev, Phys. Rev. A, vol. 93, Art. 013820, 2016.

Retrace and Disciplining Time Constant Effects on Holdover Clock Drifts in Chip-Scale Atomic Clock

Yoonkee Kim and Christopher P. Walter
U.S. Army Communications-Electronics Research, Development and Engineering Center (CERDEC)
Aberdeen Proving Ground, MD 21005

Abstract— **A GPS-disciplined oscillator (GPSDO) provides a cost-effective alternative to a primary clock such as a cesium-beam atomic clock. A rubidium (Rb) atomic oscillator is usually employed in a GPSDO as a holdover clock where maintaining the most accurate time is required during an extended absence of GPS signals. A commercially available Chip-Scale Atomic Clock (CSAC) offers a comparable long-term stability and is an attractive candidate for a holdover clock in certain applications especially where reduced Size, Weight, and Power (SWAP) is desirable. In this paper, the retrace effects on the holdover clock errors of CSAC from a cold start are characterized. The disciplining behaviors with various durations of the disciplining time are also characterized with short and long disciplining time constants in order to seek an optimal time constant.**

Keywords—Chip-Scale Atomic Clock (CSAC); retrace; disciplining time constant

I. INTRODUCTION

A GPS-disciplined oscillator (GPSDO) provides a cost-effective alternative to a primary clock such as a cesium-beam atomic clock [1]. A rubidium (Rb) atomic oscillator is usually employed in a GPSDO to maintain accurate time as a holdover clock in the absence of GPS signals. An oven-controlled crystal oscillator (OCXO) or a temperature-compensated crystal oscillator (TCXO) is also found in GPSDO's to reduce cost, size, weight, and power (CSWAP), although its stability is inferior to an atomic oscillator counterpart. A commercially available Chip-Scale Atomic Clock (CSAC) offers superior long-term stability to an OCXO or TCXO and is an attractive candidate for a holdover clock in certain applications especially where reduced SWAP is desirable [2]. The holdover clock error would be caused by a combination of the frequency offset, determined at the start of the holdover, and the drift of the clock. The clock error is also affected by environmental conditions; mainly temperature and others like vibration and shock. The author has reported the holdover clock errors in a GPS-disciplined CSAC as a function of disciplining time and temperature [3].

Retrace is defined as the change of frequency of an oscillator after exposure to on/off operations measured after the specified warm-up time [4]. Since the majority of GPSDO's in typical applications like network time servers are intended with continuous power, the retrace of the oscillator does not normally cause a problem. To take full advantage of its small SWAP, however, CSAC may be employed in the systems that would be powered during operation time only. The retrace of a CSAC needs to be characterized for its impact on holdover clock errors, especially when, after a long duration of being in a power-off state, a CSAC is cold-started and then loses a trustable clock input for disciplining while it still undergoes a retrace state. CSAC also offers a feature of internal disciplining capability from an external clock. The disciplining time constant is a user-settable parameter [5] and finding a proper time constant is another concern if this feature is utilized. In this paper, the retraces of CSAC samples from a cold start are measured. The retrace effects on the holdover clock errors are characterized. The disciplining behaviors with various durations of the disciplining time using a GPS are also measured with several disciplining time constants in order to seek an optimal time constant.

II. REGULAR CSAC VS. REDUCED-FORM-FACTOR CSAC

Fig. 1 shows a block diagram of the GPS-disciplined CSAC. The 1 PPS output of an external GPS receiver provides the clock input to discipline a CSAC. The 10 MHz and 1 pulse-per-second (PPS) outputs of a CSAC are measured at room temperature with a frequency/time interval counter or a phase noise analyzer connected to a high-performance cesium reference. To save time for the measurement of the long duration of clock drifts, the frequencies and clock pulses of multiple CSAC's were measured sequentially by employing RF switches. Samples of commercial-off-the-shelf regular CSAC's and reduced-form-factor CSAC's were randomly selected for the measurements. The reduced-form-factor CSAC was developed during the CSAC Manufacturing Technology Development executed by the Communications Electronics Research, Development and Engineering Center (CERDEC). The purpose was to improve the manufacturing processes and redesign components and electronics, including the physics package, for better manufacturability and higher yields, resulting in significant reduction of the manufacturing cost. Fig. 2 shows the comparison between the two CSAC types.

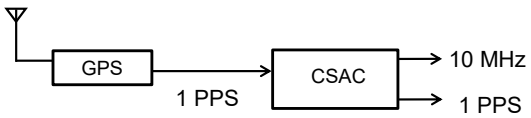


Figure 1. Block diagram of a GPS-disciplined CSAC.

U.S. Government work not protected by U.S. copyright

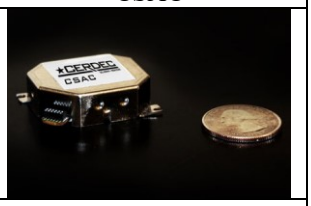
Regular CSAC	Reduced-form-factor CSAC
	
• 16cc/35g/125mW • Hermetically sealed • Thru-hole pins on bottom	• 12cc/23g/100mW • Non-hermetically sealed • Surface-mountable connector on side

Figure 2. Regular CSAC vs. reduced-form-factor CSAC.

III. CHARACTERIZATION

Fig. 3 shows measured stabilities of a regular CSAC and a reduced-form-factor CSAC. The other samples have similar stabilities to these two. The regular CSAC performs slightly better than the reduced-form-factor CSAC in short-term stability and phase noise. Long-term stability due to aging appear similar, reaching the flicker frequency floor of a few parts in 1E-12. Long-term stability is one of the main factors affecting holdover along with temperature, while short-term stability affects holdover insignificantly [3].

Fig. 4 shows the retrace of two CSACs (one regular CSAC and one reduced-form-factor CSAC) with the highest retrace and two CSACs with the lowest retrace. The regular CSACs show reduced noise as compared to the reduced-form-factor CSAC, which agrees with what was seen in the Allan deviation and phase noise data shown in Fig.3. The regular CSACs show a longer more gradual retrace in time than the reduced-form-factor CSACs, which reveal a smaller magnitude and shorter retrace curve in time.

Fig. 5 shows the holdover capability after a cold start of both the regular CSAC (solid lines) and the reduced-form-factor CSAC (dashed lines.) The definition of cold start is that CSAC's power is turned on after minimum 2 days of power-off. Disciplining starts immediately after the initial warm-up of less than 3 minutes. These plots demonstrate that a time constant (TC) of 30 seconds performs much better in terms of holdover than a TC of 120 minutes. Interestingly, the results also show that with a TC of 30 seconds and a relatively short disciplining time of five minutes, both the regular CSAC and the reduced-form-factor CSAC had significantly improved holdover performance over a TC of 120 minutes and a relatively longer disciplining time of 125 minutes. This is most likely due to the fact that in the case of a TC of 30 seconds and a disciplining time of 5 minutes, 10 averaging cycles were completed. In both cases where a TC of 120 minutes was used, less than one full cycle and just over one averaging cycle were completed respectively. Also observable in Fig. 5 is that the drift of the individual clocks seem to agree with the clock drift model [3]:

$$T(t) \cong y_0 t + \frac{1}{2} y' t^2 + \int_0^t y_{env}(t) dt$$

With the more rapid decay of clocks using a longer TC, the y_0 term of the estimated frequency offset from disciplining is dominant and the drifts appear linear. With a TC of 30 seconds, the quadratic effects of the y' term of the long-term drift due to aging can be seen in some of the data sets (i.e. TC=30 sec disciplining time = 125 min, clock M117.) The effect of retrace is also observable here in the results where TC = 30 seconds. As found in Fig. 4, the unit with the highest retrace was R297. This unit also demonstrates the worst holdover performance in both of the 30 second TC cases. This is due to the frequency of the clock still adjusting due to both the disciplining and retrace and corrupting the initial averaging cycles.

Fig. 6 shows the holdover capability after a warm start of both the regular CSAC and the reduced-form-factor CSAC. The definition of warm start is that CSAC's power is continuously on for at least two days before the start of disciplining. An unexplainable clock offset of 20 microseconds during disciplining is observed at a unit (R516) for TC = 30 sec and disciplining time = 5 min. Generally, the results agree with those from the cold start case. More apparent here is the benefit of the longer disciplining time. This can be observed in the comparison between disciplining times of 5 minutes versus 125 minutes, with a TC of 30 seconds. A longer disciplining time does indeed reduce the dispersion in the holdover, though it should be noted that the magnitude of these clock drifts is nearly the same in these two cases at < 20 µs. The benefit of a longer disciplining time is also apparent in the slope of the two 120 minute TC cases. As in the cold start data, some of the clocks in the 30 second TC sets seem to agree the clock drift model. In particular, the reduced-form-factor CSACs reveal an observable curvature indicative of the y' term beginning to dominate the y_0 term.

Fig. 7 shows the effect of TC on a single regular CSAC, with the red vertical lines signifying the removal of the disciplining clock PPS. The top row of plots show the raw frequency of the clock, and shows that with a 30 second TC, the short averaging time leads to higher frequency jitter during disciplining when compared to the 120 minute TC. The higher frequency jitter of a 30 second TC is understood probably because the CSAC frequency is adjusted more frequently from averaging the highly-jittered GPS 1 PPS's. This speculation becomes evident by observing this jitter is reduced and is roughly the same for both TC's during holdover because no more frequency adjustment occurs. The resolution of digital tuning of the frequency of CSAC is 1E-12 [2]. As expected with the shorter TC, when a 30 second TC is used, the frequency is quickly adjusted, and therefore the pulse-per-second is also relatively stable through disciplining. In contrast, because of the relatively slow frequency adjustment with a longer TC, the pulse-per-second goes through a saw-tooth like disciplining cycle. The frequency of the peaks in this pattern is directly correlated to the rate at which the frequency of the clock is being adjusted. These rates of frequency change, and therefore phase jumps, are inversely proportional to the length of the TC.

IV. CONCLUSION

GPS-disciplined CSAC were characterized for their retrace and the effect of disciplining time constant. These tests found the following: long-term drifts of regular CSAC and reduced-form-factor CSAC appear similar, although regular CSAC performs slightly better than reduced-form-factor CSAC in short-term stability and phase noise. Most of the CSAC's show no retrace or very small retrace if noticeable. Retrace seems less of a concern especially for reduced-form-factor CSAC. Short time constant (30 sec) significantly outperforms long time constant (120 min) for holdover in both short and long disciplining time. Longer disciplining time improves holdover. With the time constant of 30 sec, the clock errors of both CSAC types except one unit drift within twenty microseconds for three days at room temperature, regardless of cold or warm start and duration of disciplining time.

REFERENCES

[1] M. Lombardi, "The use of GPS disciplined oscillators as primary frequency standards for calibration and metrology laboratories," Measure, Vol. 3 No.3, pp. 56-65, 2008.

[2] Microsemi, Quantum SA.45s Chip-Scale Atomic Clock Specifications.

[3] Y. Kim, "Holdover Clock Errors In GPS-Disciplined Chip-Scale Atomic Clock," Proc. 2013 Precise Time and Time Interval Systems and Applications Meeting, pp. 101-106.

[4] J. Vanier, J.J.Gagnepain, .J.Riley, F.L.Walls, M.Granveaud, "Aging, Warm-up Time, and Retrace: Important Characteristics of Standard Frequency Generators," Proc. 1992 IEEE Freq. Contr. Symp., pp. 807-815.

[5] Microsemi, SA.45s Chip-Scale Atomic Clock User's Guide.

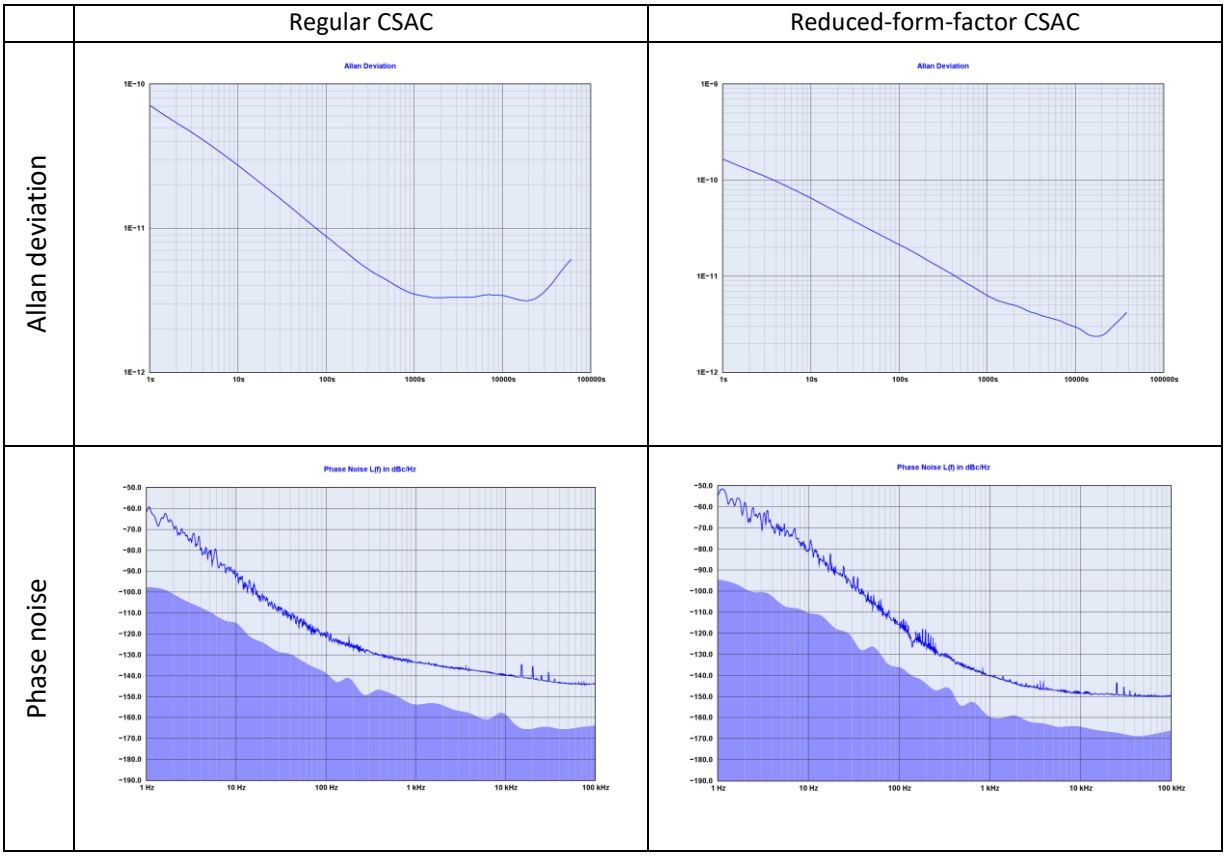


Figure 3. Allan deviation and phase noise of regular CSAC and reduced-form-factor CSAC.

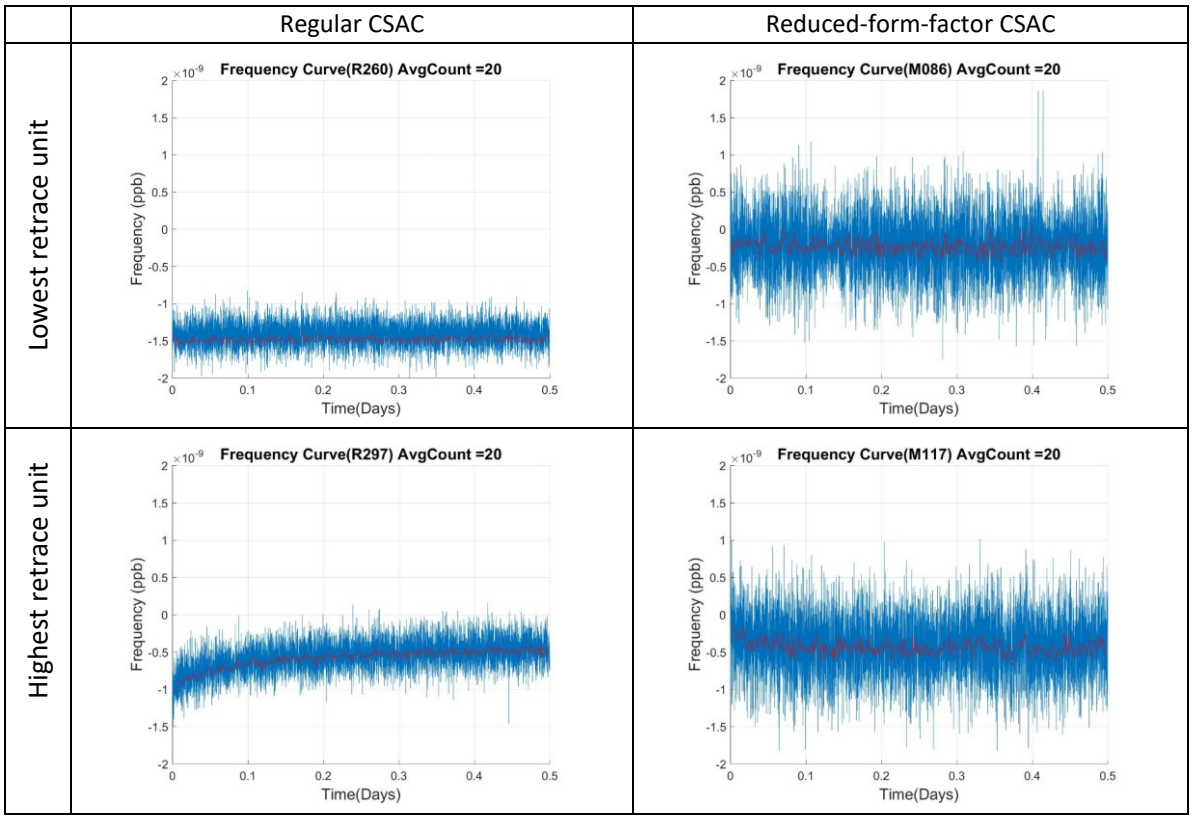


Figure 4. Cold start frequency retrace.

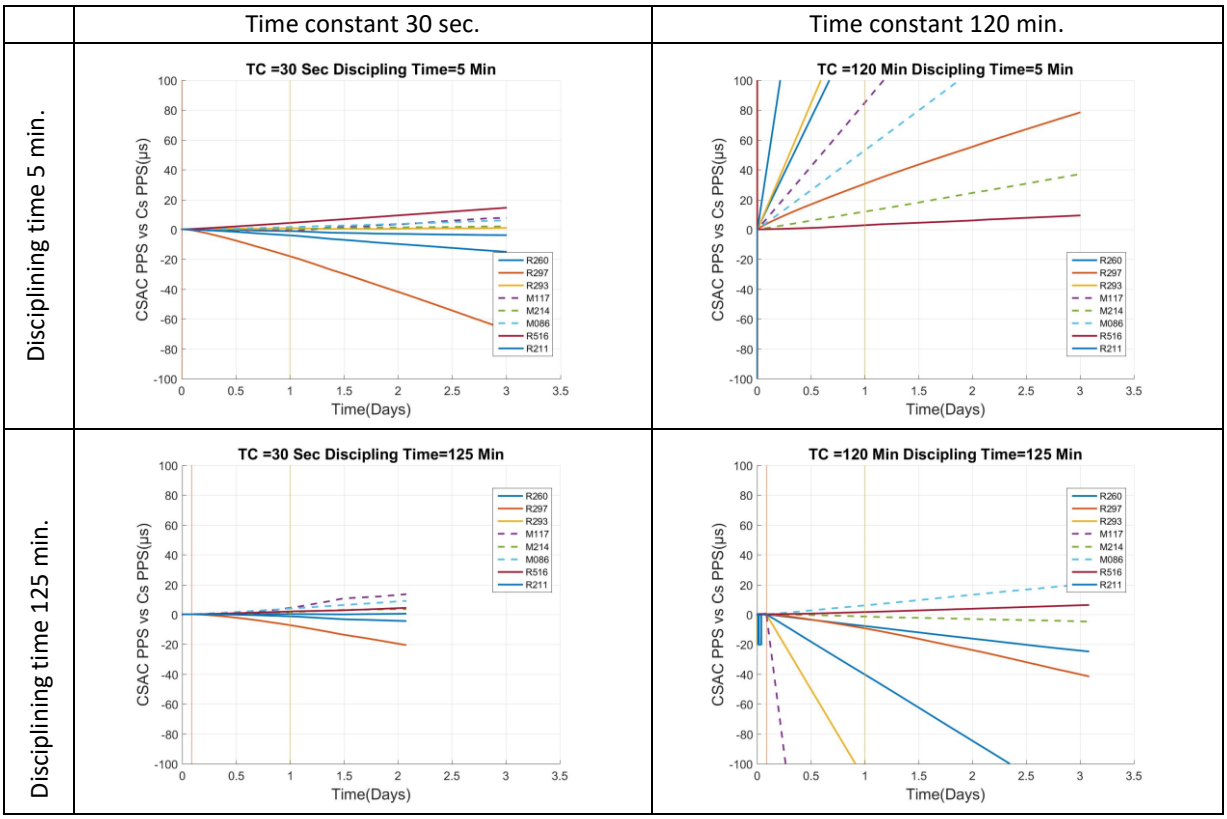


Figure 5. Cold start clock errors.

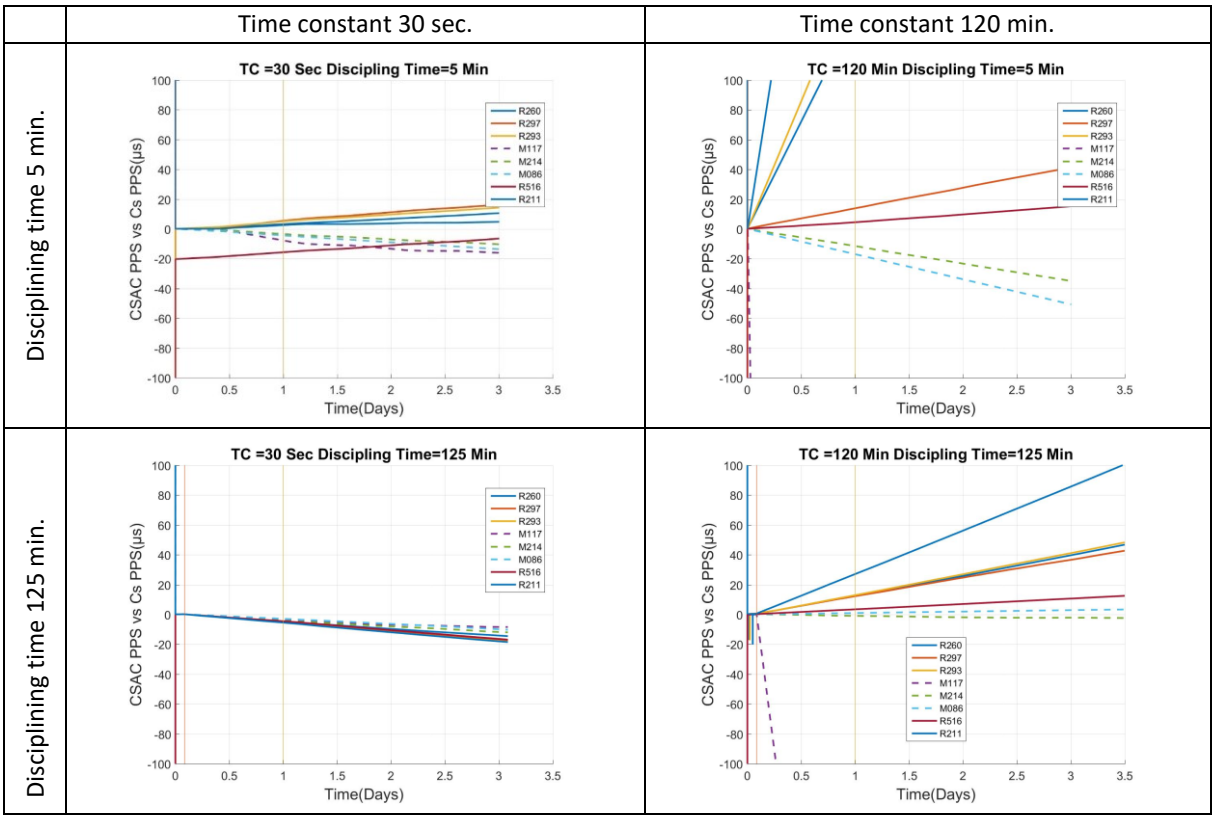


Figure 6. Warm start clock errors.

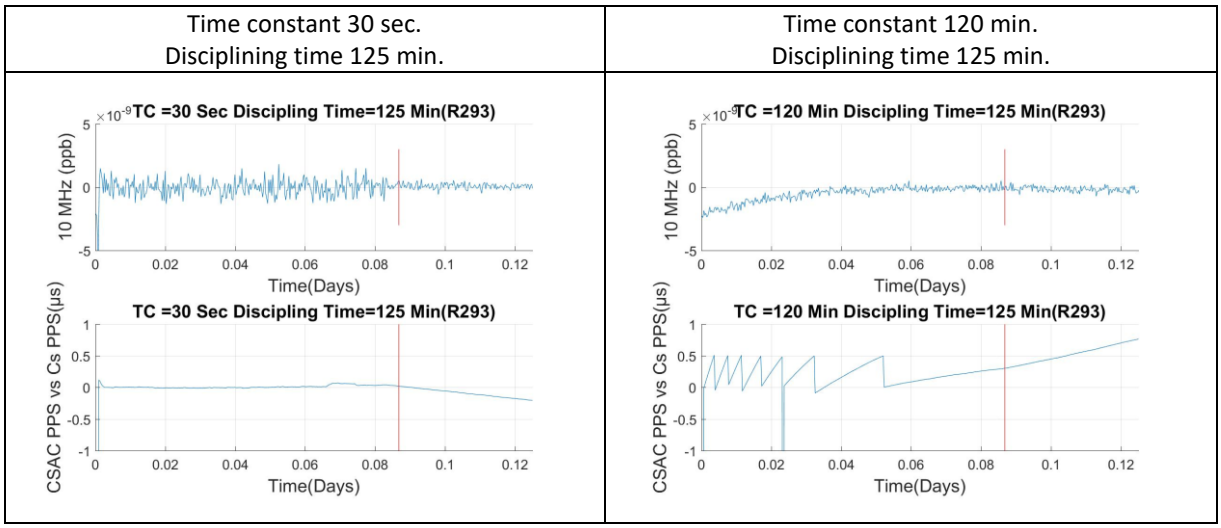


Figure 7. Frequency and phase changes during disciplining of short (30 sec) and long (120 min) time constant.

MEMS atomic vapor cells for gyroscope applications

Sylvain Karlen, Gilles Buchs, Thomas Overstolz, Nicolas Torcheboeuf, Emmanuel Onillon, Jacques Haesler and Dmitri Boiko
Systems, Time & Frequency
CSEM SA
Neuchâtel, Switzerland
dmitri.boiko@csem.ch

***Abstract*— MEMS cells filled with Rb and Xe atoms have been fabricated at CSEM for microgyroscope applications. Characterization of spin-polarized pumping efficiency and of the relaxation times of the Xe nuclear spins as a function of cell size and temperature will be presented and discussed, as well as preliminary results on a gyroscope configuration using non collinear pump and probe beams.**

Keywords—Nuclear magnetic resonance gyroscopes (NMRGs), MEMS atomic vapor cell.

I. INTRODUCTION

Important developments in the field of nuclear magnetic resonance gyroscopes (NMRGs) were carried out in the 1970s and 1980s before the concurrent ring laser gyroscopes technology started to prevail worldwide. In recent years, a renewed interest for atomic gyroscopes has appeared due to the synergies with developments realized on chip-scale atomic clocks (CSAC) [1] and chip-scale atomic magnetometers (CSAM) [2].

The typical operation of a NMRG is as follows: 1) a vapor cell contains one or more active NMR isotopes such as ^{129}Xe and ^{131}Xe, an alkali atom such as Rb, and some buffer gas such as N_2; 2) a circularly polarized pump beam resonant with an optical transition in the Rb atoms spin polarizes the alkali atoms; 3) the Rb polarization is transferred to the Xe nuclei through spin-exchange collisions, thereby creating a macroscopic nuclear spin polarization; 4) a magnetic field being applied to the cell, the Xe spins precess about the direction of the field at their Larmor frequency; 5) the Rb spins system functioning also as a magnetometer, the induced Xe polarization can be sensed and thus the rotation can be detected by measuring the Xe Larmor frequency shift [3-4].

II. MEMS CELLS MICROFABRICATION

The atomic vapor cell microfabrication process used at CSEM, shortly described in [1], is based on an RbN3 filling technique followed by UV-decomposition: 1) a 1mm thick silicon wafer is etched by DRIE with through-holes circular cavities of different sizes; 2) a first borofloat wafer is attached to the bottom of the wafer by anodic bonding; 3) an RbN_3 aqueous solution is then dispensed into the cavities by means of micro-dispensing; 4) after evaporation of the solvent, the cavities are sealed under a controlled Xe pressure and the wafer is diced into individual cells; 5) finally the cells are UV irradiated, giving rise to metallic Rb and gaseous nitrogen through the following reaction:

$$2RbN_3 \rightarrow 2Rb + 3N_2 \quad (1)$$

Fig. 1 shows an example of the microfabricated MEMS cells. The cells were filled with enriched Xe (50% 129Xe, 50% 131Xe) and N2.

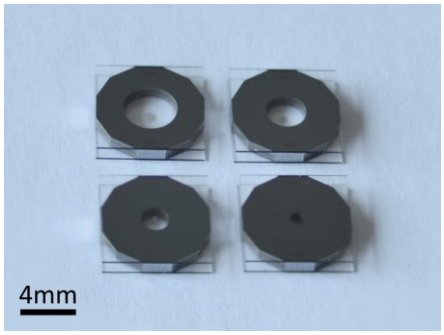


Fig. 1. 8 x 8 mm^2 MEMS atomic vapor cells for microgyroscope applications with cavities ranging from 1 to 4 mm in diameter.

III. EXPERIMENTAL SETUP

A MEMS atomic vapor cell is placed at the center of a three-axis Helmholtz coil system (see Fig. 2) mounted inside a three-layer shielding structure (not shown on the figure). The MEMS cell is heated at approximately 160°C with light from a laser diode emitting at 976 nm. Circularly polarized light obtained from a DFB laser radiating at 795 nm, i.e. resonant with the D1 transition of the Rb atoms, is used to polarize the Rb spins along the beam propagation direction. Different pump-probe beam configurations can be implemented either collinearly or non-collinearly with a Dehmelt detection scheme [3].

IV. RESULTS AND DISCUSSIONS

We will first present results on the characterization of our MEMS cells such as T_2^* measurements for the Xe nuclear spins as a function of cell size (see Fig. 1) and temperature. For this, we use a standard field switch technique as described in [6] with a single pump-probe beam aligned along the z-axis, an AC magnetic field aligned along the y axis and the switched DC magnetic field at a given angle in the x-z plane. An

example of the induced free-induction decay signal and its Fourier transform clearly shows the signatures of the two Xe isotopes.

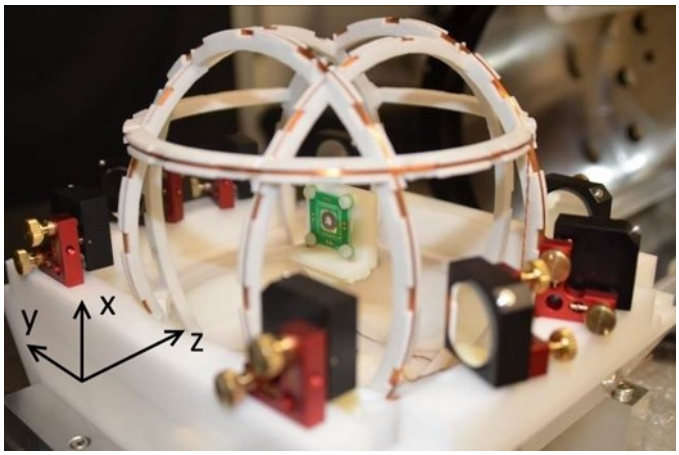


Fig. 2. Picture of the experimental setup: the MEMS cell is placed at the center of a set of three orthogonal magnetic coils (magnetic shielding not shown).

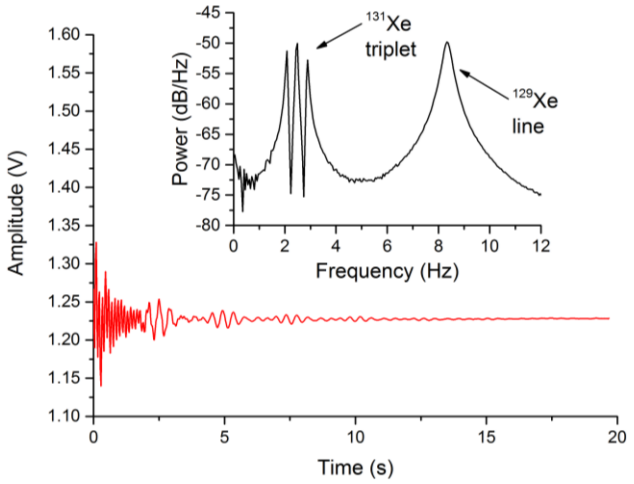


Fig. 3. Example of an experimental free induction decay signal: the insert shows the Fourier transform of the signal.

We will then present results for spin-polarized pumping efficiency in function of the pump and probe beam intensities in non-collinear beam configuration.

Finally, we will show preliminary results on a gyroscope configuration based on [7], using independent pump and probe beams. In particular, the observation of a minimum SNR pump and probe power ratio will be discussed.

ACKNOWLEDGMENT

This work is supported by European Union's Horizon 2020 research and innovation programme, Grant Agreement 699387 (NAVISAS) and CSEM's R&D activity financed by the canton of Neuchâtel.

REFERENCES

[1] S. Knappe, "MEMS atomic clocks," Compr. Microsystems, vol. 3, pp. 571–612, 2007.

[2] P. D. D. Schwindt, B. Lindseth, S. Knappe, V. Shah, J. Kitching, and L. A. Liew, "Chip-scale atomic magnetometer with improved sensitivity by use of the Mx technique," Appl. Phys. Lett., vol. 90, no. 8, p. 81102, 2007.

[3] E. A. Donley, "Nuclear magnetic resonance gyroscopes," in IEEE Sensors, 2010, pp. 17–22.

[4] C. Zhang, H. Yuan, Z. Tang, W. Quan, and J. C. Fang, "Inertial Rotation Measurement with Atomic Spins : From Angular Momentum Conservation to Quantum Phase Theory," Appl. Phys. Rev., vol. 3, no. 4, p. 41305, 2016.

[5] T. Overstolz, J. Haesler, G. Bergonzi, A. Pezous, P.-A. Clerc, S. Ischer, J. Kaufmann, and M. Despont, "Wafer scale fabrication of highly integrated rubidium vapor cells," in IEEE 27th International Conference on Micro Electro Mechanical Systems (MEMS), 2014, pp. 552–555.

[6] E. A. Donley, J. L. Long, T. C. Liebisch, E. R. Hodby, T. A. Fisher, and J. Kitching, "Nuclear quadrupole resonances in compact vapor cells: The crossover between the NMR and the nuclear quadrupole resonance interaction regimes," Phys. Rev. A, vol. 79, no. 1, p. 13420, 2009.

[7] E. J. Eklund, "Microgyroscope Based on Spin-Polarized Nuclei," Ph.D. disssertation, Universtity of California, Irvine, 2008.

Preliminary stability analysis of Rb fountains for timescale generation

L. Lorini*, K. Pavlenko‡, S. Bize*, B. Desruelle†, G. Stern†, I. Doronin‡, Yu. Pavlenko‡ and S. Donchenko§
*LNE-SYRTE, Observatoire de Paris, PSL Research University, CNRS,
Sorbonne Universités, UPMC Univ. Paris 06, 61 avenue de l'Observatoire, 75014 Paris, France
†MUQUANS, Institut d'Optique d'Aquitaine, rue François Mitterrand, 33400 Talence, France
‡JSC Vremya-CH, Russia, 603105, Nizhny Novgorod, Osharskaya str., 67
§FSUE VNIIFTRI, Russia, 141570, Moscow oblast', Solnechnogorski district, Mendeleevo

***Abstract*—Two Rb fountains for timekeeping have been manufactured in collaboration among JSC Vremya-CH, Russia, SYRTE laboratory and Muquans company, France and installed at FSUE VNIIFTRI, Russia. They have been designed to have compact footprint and autonomous operation for long periods. One of the fountain has a good short term stability, $1.17 \cdot 10^{-13}$ at 1 s, while the other one, which is running for longer time, is better than $5 \cdot 10^{-16}$ at 1 day.**

I. Introduction

A. Atomic fountains for timekeeping

Atomic fountains have been used as frequency standards for more than two decades, contributing to the progress in time and frequency metrology [1], [2], as well as providing some of the most stringent tests of fundamental physics theories [3], [4], [5]. Unlike the calibration activity, where the frequency of a stable oscillator can be measured by time to time with a fountain, timescale generation requires uninterrupted operation for extended periods of time. This operation has been proven to be technology challenging, and only recently some laboratories have started such an activity, either with the fountains they run as frequency standards [6], [7], or with fountains designed for that specific task [8]. When a fountain is specifically designed for timekeeping, it is not required to run it as a primary frequency standard: the choice of Rb atoms has then some advantages with respect to Cs, especially in terms of efficiency and reliability of laser sources.

B. Technical requirements

The increasing performance demanded to GNSSs (Global Navigation Satellite Systems) has set new and tighter requirements on time scale accuracy. For the Russian GLONASS, the difference between the Russian timescale UTC(SU) and the international timescale UTC shall not be larger than 3 ns by 2020. For this purpose, two cold rubidium fountains have been realized on request of the FSUE VNIIFTRI, the Russian federal laboratory generating UTC(SU). As the fountain main target is the realization of an accurate time scale, the two fountain most important feature is the medium-to-long term stability. The stability requirement established by VNIIFTRI is quite demanding: in term of Allan deviation it shall not exceed $4 \cdot 10^{-16}$ at 1 day integration time and $1 \cdot 10^{-16}$ at 16-days integration time.

C. Project collaboration

The design and realization of the two fountains has been the result of a scientific and commercial collaboration among JSC Vremya-CH, Russia, MuQuans company, France and SYRTE laboratory, France. SYRTE, which has long experience on atomic fountains [9], [10], has also provided to Vremya-CH the knowledge transfer they required and an extended people training program. The two fountains have been installed at VNIIFTRI, where they are currently running in their final operational conditions.

II. Design and realization

The fountains, realized and installed during the period 2014-2016, have been designed in two different versions, VerA and VerB.

A. Fountain design

The design and realization of the two fountains has been shared by the three involved partners. SYRTE has designed and realized the cold atom source, the detection subsystem and the fountain control system, MuQuans has realized the laser source and laser frequency control subsystem and JSC Vremya-CH has realized the rest of the system, including the atom interrogation subsystem and the fountain final integration. The design of the whole set-up has been aimed at a very compact footprint (fountain structure and two 19" racks), as demanded by the laboratory room constraints.

Following the customer requirements, the two fountains have been designed focusing on the stability performances; at the moment, none of the fountain has been evaluated for accuracy.

B. Realization of the laser system

The laser system realized by MuQuans is made in a compact 19" rack system with output beams delivered through optical fibers. It is based on frequency doubled telecom laser technology. Each laser frequency is referenced to a saturated absorption signal from a Rb cell; acousto-optical modulators and integrated splitters provide all the laser frequencies needed for the fountain operation. A programmable sequencer manages the laser frequencies during the different stages of the fountain cycle (molasses capture, launch, sub-Doppler cooling, detection).

978-1-5386-2916-1/$31.00 ©2017 IEEE

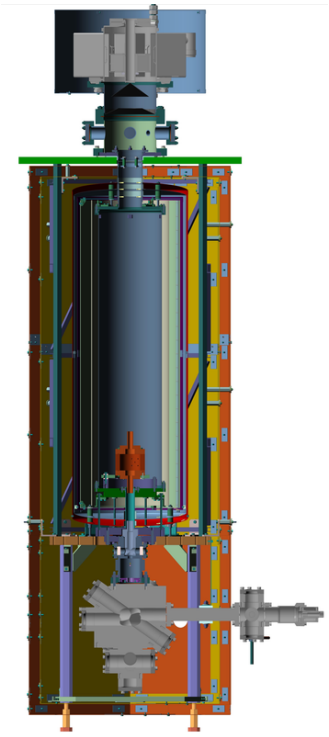


Fig. 1. Fountain structure drawing (VerA).

C. Realization of atom source

The atomic sources realized at SYRTE are different for the two fountain versions. In VerA, it is based on molasses capture from Rb hot vapor, in VerB the molasses is loaded from a slow beam of cold atoms generated in a 2D-MOT. The cold atom source of VerB provides higher molasses loading rates, at the cost of more complexity. The atom cooling, launching, detection and control systems, together with the laser system from MuQuans, have been characterized at SYRTE with before the final shipment to Russia.

D. Realization of the atom interrogation system

The cavity for atom interrogation, the state selection system and the atom flight vacuum chamber, together with magnetic field control and shielding system, have been realized by Vremya-CH with the support of the know-how transferred by SYRTE. A commercial, low noise synthesizer generates the microwave interrogation signal from a reference frequency distributed by VNIIFTRI.

E. Final integration and installation

The subsystems realized by MuQuans and SYRTE have been shipped to Russia by truck. Vremya-CH made the final integration at its plant and transported the fountain in its final shape at VNIIFTRI, where the installation has been made by Vremya-CH and SYRTE scientists. Installation of VerA has been finalized in the first half of 2016, while VerB has been installed at the end of 2016.

F. Autonomous operations for extended periods

The two fountains have been designed to run unattended for long periods of time. The laser system does not need to be relocked on a regular basis and the wide use of fibers and compact optical subsystems requires no alignment by the user. A wide set of diagnostic parameters (laser functional parameters, light levels for each fountain beam, many environmental parameters) are routinely logged to monitor the fountain operation. Remote access to the fountain control system allows the management of routine operations and the solution of minor issues.

III. Preliminary performance analysis

A. Fountain noise analysis

The stability of an atomic fountain can be expressed by the Allan variance as in the following formula:

$$\sigma_y(\tau) = \frac{2}{\pi Q_{at}} \sigma_{\delta P} \sqrt{\frac{T_c}{\tau}} \tag{1}$$

where Q_{at} is the quality factor of the atomic line, T_c is the fountain cycle time, $\sigma_{\delta P}$ is the measured noise of the transition probability between the two states of the clock transition (at $P = 1/2$ operation point). When the fountain is measuring the frequency of a local oscillator (LO), $\sigma_{\delta P}$, can be written as $\sqrt{\sigma_{Det}^2 + \sigma_{LO}^2}$: the σ_{Det} term is related to fountain detection noise properties, while σ_{LO} is the noise transferred by aliasing from the local oscillator [11] . This last term depends on the noise properties of the LO and on the details of the measurement cycle. The detection noise σ_{Det} can be described as a function of the detected atom number N_{at}:

$$\sigma_{Det} = \sqrt{\frac{1}{4N_{at}} + \frac{a}{N_{at}^2} + c} \tag{2}$$

where the first term describes the fundamental limit of quantum measurement (the quantum projection noise, QPN), while the second and third ones are related to technical limits of detection efficiency and laser noise, respectively.

An analysis of fountain detection noise is reported in Figure 2. Since the design of the detection area and detection efficiency very similar in both fountain versions, noise measurements can be fit by the same model. What is remarkable from Figure 2, is the capability of the fountains to operate in QPN limited regime for a quite large range of N_{at}, a result which is not easy to achieve.

From Equations 1 and 2, the detection noise does not limit the fountain stability above $5 \cdot 10^{-14}$ at 1 s, when $N_{at} \approx 10^6$.

B. Optimization of the fountain cycle

At VNIIFTRI, the local oscillator for VerA and VerB is an active Hydrogen maser filtered by a very low noise quartz (model VCH-1003M opt. L from Vremya-CH). With this architecture, the fountains operate in a regime where their stability is limited by the local oscillator aliased noise σ_{LO} and the limit given by the QPN cannot be approached. Given the

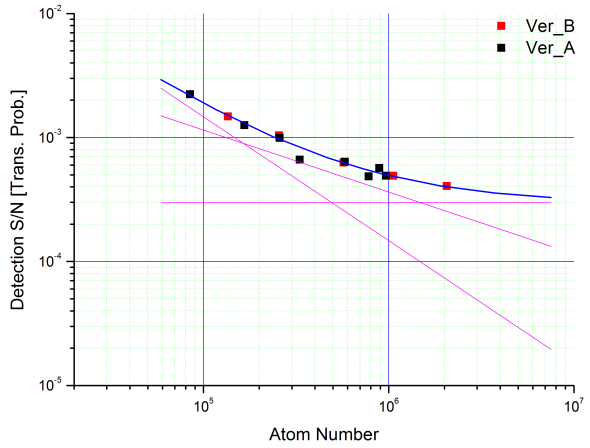


Fig. 2. Detection noise of the two fountains. The blue line is the noise model of Eq. 2, adapted to the data. Magenta lines show the three noise components of the model, pointing out the range where the fountain can run in the QPN limited regime

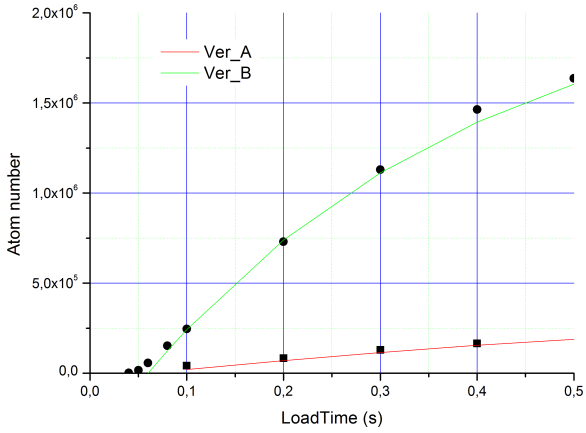


Fig. 3. Ver.A and Ver.B molasses loading rates. Ver.B has a molasses loading rate faster than Ver.A, which allows a better stability optimization

noise property of the local oscillator, the fountain stability can be optimized playing on the fountain duty cycle (T_R/T_c, where T_R is the duration of the Ramsey interrogation) [11]. In this respect, a low detection noise is important because it allows to extend the QPN limited regime towards the low atom number range, allowing shorter duty cycles. This optimization process is made shortening the fountain loading time until the number of atoms becomes too small, trading off between detection noise (σ_{Det}), aliased noise (σ_{LO}) and cycle time (T_c). When this optimization is made, the atom loading rate plays a chief role. With a given detection noise level, a fountain with a faster loading rate allows a shorter molasses loading time and a better duty cycle. VerA and VerB have similar detection noise levels, but VerB, thanks to the 2D-MOT Rb source, has a much faster loading rate and can operate at better stability.

Figure 4 shows a simulation of this optimization process for VerB, where the calculation of the stability with respect to molasses loading time has been made using Equation 1, and data from the noise (Figure 2) and loading models (Figure 3).

C. Short and medium term stability

After cycle optimization, the short term stability is found to be $1.32 \cdot 10^{-13}$ at 1 s for VerA (Fig.5) and $1.17 \cdot 10^{-13}$ at 1 s for VerB (Fig.6).

The VerA stability is worse than VerB one because the molasses loading rate limited the cycle optimization to a smaller duty cycle.

VerB stability already matches the requirement demanded by VNIIFTRI; VerA stability is close to the desired level and there is room for an improvement by optimizing the Rb hot vapor pressure, a process which can be made in the future.

D. Extended time operation and long term stability

Since their start, the fountains ran for several months with some interruptions due to different problems, or to tests and

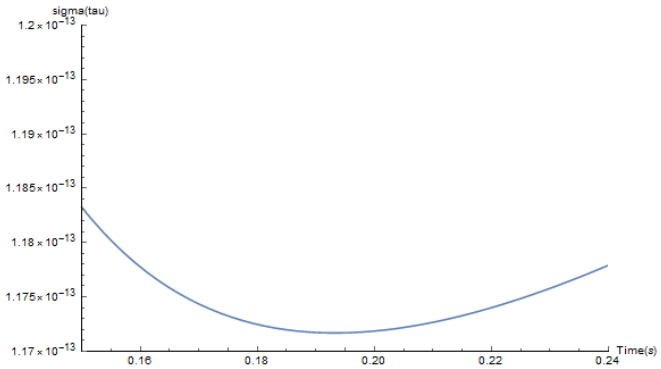


Fig. 4. Simulation of Ver.B stability ($\sigma_y(1s)$) vs. molasses loading time.

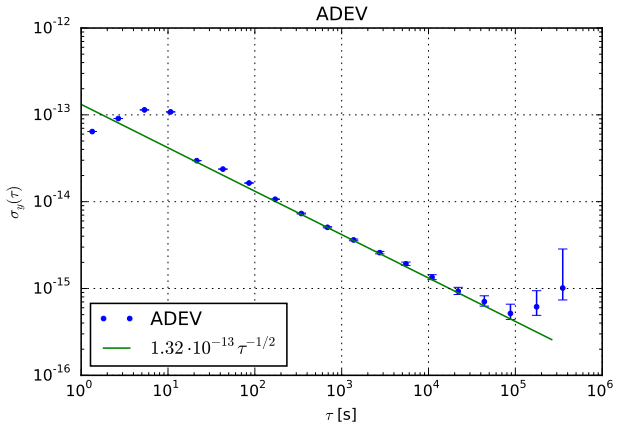


Fig. 5. Stability of VerA fountain vs. local oscillator (H-maser VCH-1003M opt. L).

adjustments. VerA fountain, which has started running first, has so far provided the longest dataset. Fig. 5 shows the stability plot of fountain VerA vs. H-maser VCH-1003M opt. L, after removal of a linear drift estimated as $1.27 \cdot 10^{-16}$/day.

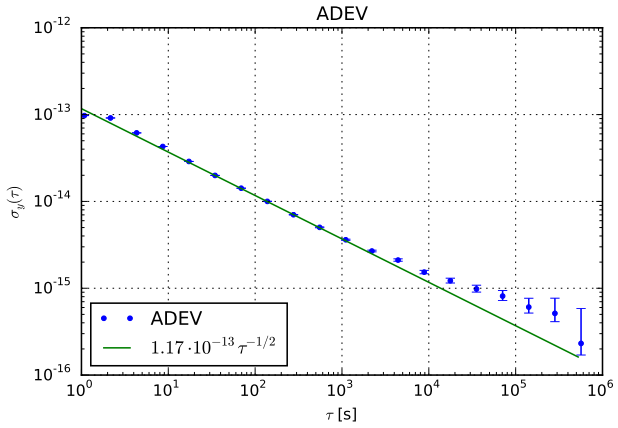


Fig. 6. Stability of VerB fountain vs. local oscillator (H-maser VCH-1003M opt. L).

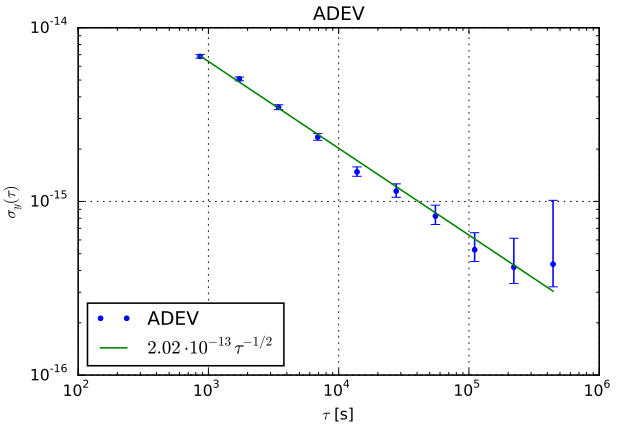


Fig. 8. Stability of VerB vs. VerA (local oscillator removed). These data have been collected before cycle optimization

The Allan deviation is better than $7 \cdot 10^{-16}$ at 1 day and approaches $2 \cdot 10^{-16}$ at 16 days. We point out that the data used for this analysis have been collected before cycle optimization. For longer integration periods, the stability is dominated by the H-maser. Fig.8 shows the stability of the frequency difference between VerA and VerB. As expected, the H-maser noise is removed and the $\tau^{-1/2}$ slope is well defined for integration intervals longer than 10^5 s.

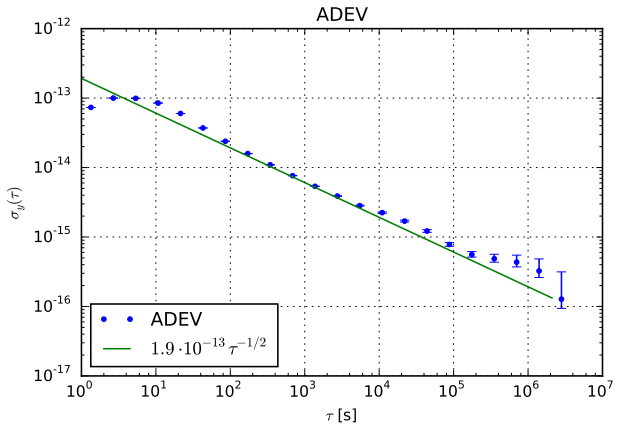


Fig. 7. Stability of VerA fountain vs. local oscillator (H-maser VCH-1003M opt. L) after removing the local oscillator drift $1.27 \cdot 10^{-16}$/day. These data have been collected before cycle optimization.

IV. Conclusions

Two Rb fountains with compact footprint and have been designed, realized and finally installed at VNIIFTRI within two years. Both the fountains have been designed to run unattended and to provide uninterrupted operation for extended periods of time. Fountain operation started recently and is already showing stability performances potentially in agreement with the project requirements. A noise analysis shows that both fountains have a very low detection noise, which does not limit the stability above $5 \cdot 10^{-14}$ at 1 s when a LO with state-of-art stability is used to interrogate the fountain. In the present situation, the fountain stability is limited by LO aliased noise: after cycle optimization VerB can run at $1.17 \cdot 10^{-13}$ at 1 s stability while VerA can run at $1.32 \cdot 10^{-13}$ at 1 s, with room for improvement. Until now, the fountains have accumulated several weeks of uninterrupted operation. Although some more data are required for a more reliable long term stability analysis, both fountains can provide stability performances well below $5 \cdot 10^{-16}$ at 1 day and a $\tau^{-1/2}$ slope behavior well defined for integration intervals longer than 10^5 s

References

[1] G. Petit and G. Panfilo. Comparison of frequency standards used for tai. *IEEE Transactions on Instrumentation and Measurement*, 62(99):1550, 2013.

[2] Gérard Petit, Felicitas Arias, and Gianna Panfilo. International atomic time: Status and future challenges. *Comptes Rendus Physique*, 16(5):480–488, June 2015.

[3] J. Guéna, M. Abgrall, D. Rovera, P. Rosenbusch, M. E. Tobar, Ph. Laurent, A. Clairon, and S. Bize. Improved tests of local position invariance using ^{87}Rb and ^{133}Cs fountains. *Phys. Rev. Lett.*, 109:080801, Aug 2012.

[4] Steven Peil, Scott Crane, James L. Hanssen, Thomas B. Swanson, and Christopher R. Ekstrom. Tests of local position invariance using continuously running atomic clocks. *Phys. Rev. A*, 87:010102, Jan 2013.

[5] A. Hees, J. Guéna, M. Abgrall, S. Bize, and P. Wolf. Searching for an oscillating massive scalar field as a dark matter candidate using atomic hyperfine frequency comparisons. *Phys. Rev. Lett.*, 117:061301, Aug 2016.

[6] A. Bauch, S. Weyers, D. Piester, E. Staliuniene, and W. Yang. Generation of UTC(PTB) as a fountain-clock based time scale. *Metrologia*, 49(3):180, June 2012.

[7] G. D. Rovera, M. Abgrall, S. Bize, B. Chupin, J. Guena, Ph Laurent, P. Rosenbusch, and P. Uhrich. The new UTC (OP) based on LNE-SYRTE atomic fountains. In *European Frequency and Time Forum & International Frequency Control Symposium (EFTF/IFCS), 2013*, pages 649–651. IEEE, 2013.

[8] Steven Peil, James L. Hanssen, Thomas B. Swanson, Jennifer Taylor, and Christopher R. Ekstrom. Evaluation of long term performance of continuously running atomic fountains. *Metrologia*, 51(3):263, June 2014.

[9] J. Guéna, P. Rosenbusch, P. Laurent, M. Abgrall, D. Rovera, G. Santarelli, M.E. Tobar, S. Bize, and A. Clairon. Demonstration of a dual alkali Rb/Cs fountain clock. *Ultrasonics, Ferroelectrics and Frequency Control, IEEE Transactions on*, 57(3):647, 2010.

[10] J. Guéna, M. Abgrall, D. Rovera, P. Laurent, B. Chupin, M. Lours, G. Santarelli, P. Rosenbusch, M.E. Tobar, R. Li, K. Gibble, A. Clairon, and S. Bize. Progress in atomic fountains at LNE-SYRTE. *Ultrasonics, Ferroelectrics and Frequency Control, IEEE Transactions on*, 59(3):391–410, march 2012.

[11] G. Santarelli, Claude Audoin, A. Makdissi, P. Laurent, G.J. Dick, and C. Clairon. Frequency stability degradation of an oscillator slaved to a periodically interrogated atomic resonator. *IEEE Transactions on Ultrasonics, Ferroelectrics and Frequency Control*, 45(4):887–894, July 1998.

Generalized Electronics for Compact Atomic Clocks

Claudio E. Calosso,
Michele Gozzelino,
Elio Bertacco,
Salvatore Micalizio
Instituto Nazionale di Ricerca Metrologica, INRIM
Strada delle Cacce 91, 10135 Torino, Italy
c.calosso@inrim.it

Bruno François,
Rodolphe Boudot
FEMTO-ST, CNRS, UBFC
26 chemin de l'Epitaphe, 25030 Besançon, France

LNE-SYRTE, Observatoire de Paris, PSL Research University, CNRS, Sorbonne Universités, UPMC Univ. Paris 06
61 Avenue de l'Observatoire,75014 Paris, France

Peter Yun

***Abstract*—We present the electronics we developed in the frame of IND55 EMRP project with the goal to support next generation sub-$10^{-13}/\sqrt{\tau}$ compact atomic clocks. In this regard, particular attention has been devoted to reduce the Dick/intermodulation effect in the low 10^{-14}, very close to the shot-noise limit. The scheme can adapt to Cs and Rb clocks with minimal modifications. The digital implementation guarantees a high degree of flexibility that allows to run very different clock typologies and to implement innovative schemes such as the frequency lock of the laser to the internal cell.**

Keywords—Dick effect, digital electronics, compact atomic clocks;

Recently, the European Metrology Research Programme (EMRP) has funded the IND55 Mclocks joint research project [1] to develop compact and high-performing microwave clocks for industrial applications such as navigation, telecommunication, defence and precision instruments. This project aims at taking full advantage of better performing laser and microwave sources and innovative techniques to prepare and detect the atoms. In this regard, several European national metrological institutes (NMIs) or research institutes, devised new cell-based prototypes that exhibit unprecedented frequency stability performances, of the order of 10^{-13} at 1 s with a medium long-term in the range of 10^{-14} or better. Three typologies have been selected: vapour-cell clock based on pulsed optical pumping (POP) [2], on cold atoms [3] and coherent population trapping (CPT) [4, 5, 6]. They are very different and allow matching many industrial applications having different levels of accuracy, stability, compactness, power consumption.

Despite their diversity, we decided to develop a generalized electronics able to run all of them with minimal modifications. This demanding task has been achieved by sharing the competences of the main NMIs involved in the project with the goal of obtaining a high-performing, flexible and simple platform. Particular attention has been devoted to generate a low phase noise and agile microwave [7], in order to interrogate the atoms with minimal Dick and intermodulation effect. The core is a module [8] that integrates an ultra-low

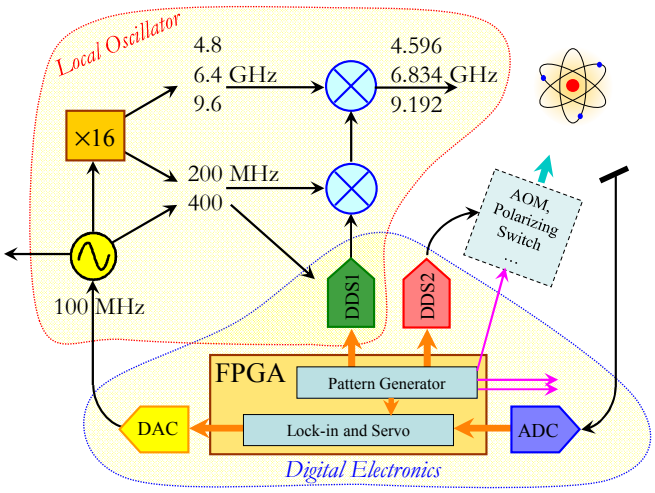
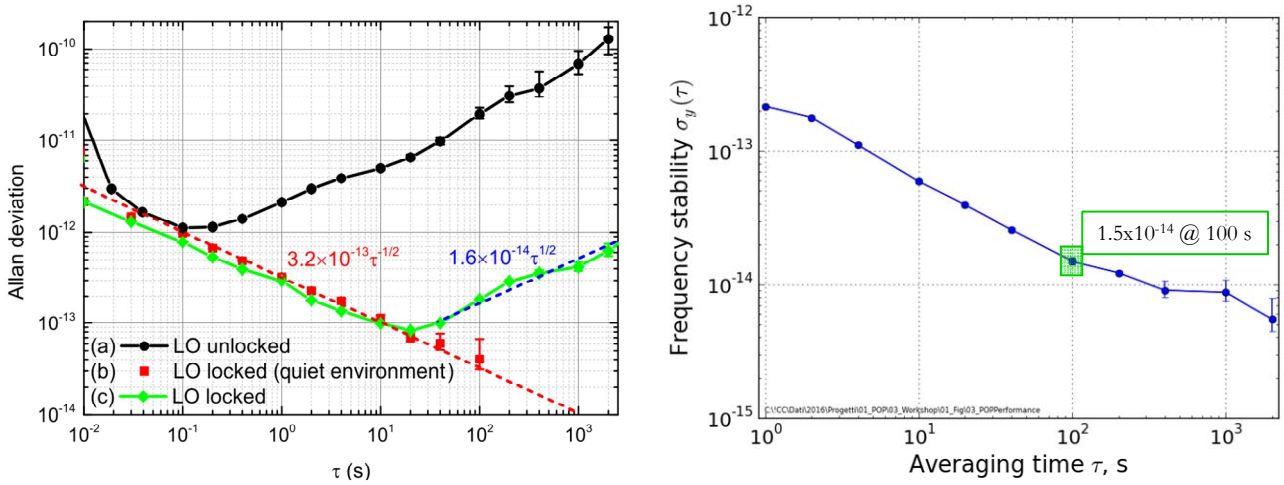


Fig. 1. Block diagram of the generalized electronics. It can subdivided into local oscillator and digital electronics. The dashed box contains the parts that are peculiar of each clock: acousto-optic modulator for POP, polarization switch for DMCPT…

noise 100 MHz oven controlled crystal oscillator (OCXO) and the first ×16 direct frequency multiplier stage. From its output at 1.6 GHz, three frequencies are generated by direct multiplication (1), programmable division (2) and direct digital synthesis (DDS) (3) and then mixed together. By changing the multiplier device (×3, ×4, ×6), the division factor and the numerical frequency of the DDS, we can obtain 4.596, 6.834 and 9.192 GHz as required by rubidium and caesium atoms. The DDS also provides simultaneous and fast phase, amplitude and frequency modulations and allows implementing the patterns required by these clocks typologies. During the development of this scheme, we faced with new criticalities: AM to PM cross-correlation collapse in the measurement of ultra-low noise sources; DDS spurs and residual phase noise; very-low noise voltage required by the



a) b)

Fig. 2. This platform has been used to run with two frequency standards: the Double Modulation Coherent Population Trapping at Syrte (a) and the Pulsed Optically Pumped clock at INRIM (b).

OCXO tuning. In order to provide compactness and flexibility, we integrated into a single board the low-frequency part of the scheme (two of the three arms) together with the electronics in charge of atomic signal detection and of frequency stabilization of the OCXO. This board is composed of DDSs, analog to digital converters (ADC) and digital to analog converters (DAC) driven by a field programmable gate array (FPGA) that provides synchronous operation at the level of 100 ns. The operational parameters are stored into the local memory and are used by a pattern generator to drive the DDSs (microwave and laser modulations) as well as several generalized loop controllers that process the atomic signals to extract the required information.

This platform has been tested with the double modulation coherent population trapping (DM-CPT) clock at SYRTE (Paris, France) and with the POP clock at INRIM (Torino, Italy), obtaining the fractional frequency stabilities reported respectively in Fig. 1.a and Fig. 2.b. For these clocks, the noise contribution to the short-term stability of each part has been evaluated and reported in Tab. 1. The total contribution is in the low 2.3×10^{-14} at 1 s, very close to the expected shot-noise limit of these clocks. In this regard, it was important to reduce the Dick effect down to 2×10^{-14}.

Besides clock characterization, the electronics, thanks to its flexibility, allowed the implementation of new schemes, like the laser frequency lock to the internal cell. In this regard, it's interesting to note the case of the POP clock, where, by simply processing the atomic signal from the internal cell, and without any additional hardware, we demonstrated the possibility to retrieve the frequency error and power level both of the microwave and of the laser. This information can be used to stabilize all these quantities at the same time. The result is a significant reduction of the clock setup, very important, for example, in the frame of compact atomic clocks.

Table 1. Noise budget for the DM CPT and POP clocks

Contribution to $\sigma_y(1s)$ due to:	**DM CPT**	**POP**
Intermodulation/Dick effect	2×10^{-14}	2×10^{-14}
OCXO frequency stability	7×10^{-15}	7×10^{-15}
Analog to digital converter	7×10^{-15}	7×10^{-15}
Signal conditioning	5×10^{-15}	6×10^{-15}
Total	2.3×10^{-14}	2.3×10^{-14}

REFERENCES

[1] www.inrim.it/Mclocks

[2] Micalizio S, Calosso CE, Godone A, Levi F. "Metrological characterization of the pulsed Rb clock with optical detection" Metrologia, vol. 49, p. 425-436, 2012, ISSN: 0026-1394, doi: 10.1088/0026-1394/49/4/425.

[3] De Sarlo, L and Langlois, M and Holleville, D and Lours, M and Dimarcq, N and Schaff, J-F and Bernon, S and Desruelle, B. "Preliminary Test of a Cold-Atom Based Clock Prototype on a Microgravity Platform". Proceedings of the 24th European Frequency and Time Forum

[4] P. Yun, F. Tricot, C. E. Calosso, S. Micalizio, B. François, R. Boudot, S. Guérandel, and E. de Clercq. "High-Performance Coherent Population Trapping Clock with Polarization Modulation". Phys. Rev. Applied, vol. 7, issue 1, 2017, doi: 10.1103/PhysRevApplied.7.014018

[5] M. Abdel Hafiz, R. Boudot. A coherent population trapping Cs vapour cell atomic clock based on push-pull optical pumping, Journal of Applied Physics, 118, 124903 (2015).

[6] J. M. Danet, M. Lours, S. Guérandel, E. De Clercq, Dick effect in a pulsed atomic clock using coherent population trapping, IEEE Trans. On UFFC 61, 4 (2014).

[7] Francois B, Calosso CE, Hafiz MA, Micalizio S, Boudot R. "Simple-design ultra-low phase noise microwave frequency synthesizers for high-performing Cs and Rb vapor-cell atomic clocks" Review of Scientific Instruments, vol. 86, issue 9, Sep-2015, DOI: 10.1063/1.4929384 .

[8] www.pascall.co.uk

PIN Photodiode Spurious Noise Characterization

R.Schmeissner, A.Maillard, P.Perez, M.Baldy
Department of Atomic Clocks
Thales Electron Devices
Vélizy, France
Roman.Schmeissner@thalesgroup.com

Abstract **The optical hyperfine pumping clock approach relies on the detection of a low level fluorescence. The clock stability is a function of the signal-to-noise ratio (SNR). This paper exhaustively analyzes the properties of spurious noise in the high-gain trans-impedance amplification of the low noise PIN photodiode signal. It is shown that long-term data acquisition and statistical analysis is an appropriate tool to characterize such phenomena. The few existing literature would attribute the spurious to the operational amplifiers. In contrast, it turns out that the photodiode itself is the source of the spurious.**

Keywords—PIN Photodiode, Spurious, Optical Clock

I. INTRODUCTION

Thales Electron Devices currently develops the Optical Space Cs Clock (OSCC) [1]. The latter is based on optical pumping of Cs ground-state hyperfine levels and fluorescence detection. In order to obtain the clock error signal, the photovoltaic output of a low noise, large area PIN photodiode is detected using trans-impedance amplification. The latter is based on a standard two-stage approach using low-noise operational amplifiers. The clock signal is synchronously detected at 40Hz. The PIN photodetector is either a Hamamatsu S1337-1010 or the equivalent one from First Sensor Company.

Although noise issues were considered during the circuit development, non-stationary spurious noise signals from the pre-amplification circuit were observed during clock operation. The frequency spectrum of these events is non-vanishing at the 40Hz frequency of synchronous detection of the clock signal. The spurious could consequently limit achievable SNR and clock stability. No interpretation of this spurious phenomenon was possible based on the few existing literature [2, 3].

The present paper studies the properties of the spurious noise exhaustively and identifies the noise origin. The characterization permits to estimate the impact of the spurious phenomenon on clock operation.

II. SPURIOUS NOISE TEMPORAL CHARACTERIZATION

Figure 1 shows a typical time-trace of the noise phenomenon. Typically measured temporal FWHM is 200 to 500µs (circuit bandwidth below 1kHz). The amplitude is not constant and varies up to tens of percent of the DC signal. Typical temporal spacing is of minutes. This type of noise is typically called "Popcorn" and attributed to charge accumulation at impurities in Op-Amp semiconductor.

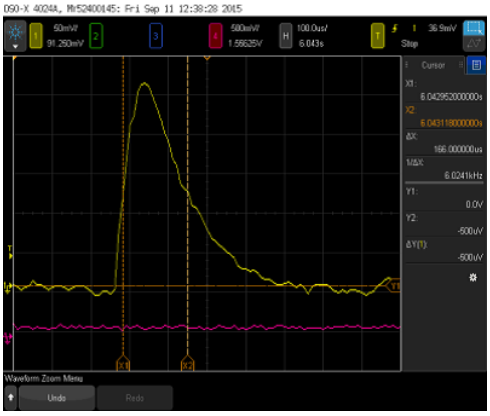


Fig. 1. Typical observation of a spurious event using an oszilloscope.

III. SPURIOUS NOISE STATISTICS

Although the noise phenomenon is non-stationary at short observation times, a time-invariant statistics is supposed to exist for longer measurement times. In order to characterize the noise phenomenon exhaustively a high data rate digital data acquisition is consequently set-up. The photodiode is illuminated using a DFB laser diode signal at 852nm highly attenuated to the order of 10nW. This optical signal leads to a DC output signal of the trans-impedance circuit of several volts.

After data acquisition of the DC signal over typically 15hours, only noise peaks with a higher than 5sgima deviations from Gaussian distribution are considered for statistics. Indeed, the existence of a time invariant statistics is verified.

In order to verify the hypothesis of the Op-Amp as noise origin, the two operational amplifiers of the trans-impedance amplification are replaced by equivalent ones of second sources (Texas Instruments or Analog Devices respectively). The spurious noise statistic is recorded for all combinations and shown in Figure 2. No difference is observed. As such, the hypothesis above appears to be unlikely.

The study was supported by Thales Electron Devices internal funding. Synergies are obtained with the OSCC Cs clock development supported by the European Space Agency under European GNSS Evolution Program (activity ID-98) and CNES under contract n° 150920.

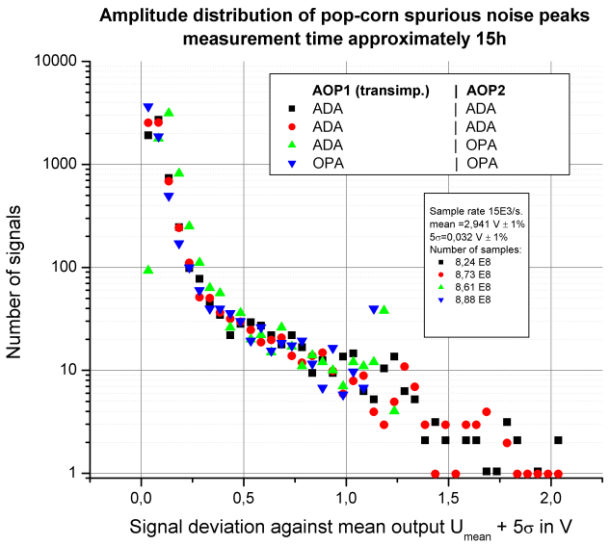


Fig. 2. Amplitude statistics of spurious for different types of equivalent operational amplifiers used in the trans-impedance circuit.

IV. Photodiode as Spurious Noise Source

Based on the conclusion from previous section, the only remaining root-cause of the spurious is the photodiode. In order to test this hypothesis, the typically used, low noise large area Hamamatsu S1337-1010BQ is replaced by the equivalent First Sensor PS-100-CER. The resulting spurious statistics is shown in the Figures 3 and 4 below.

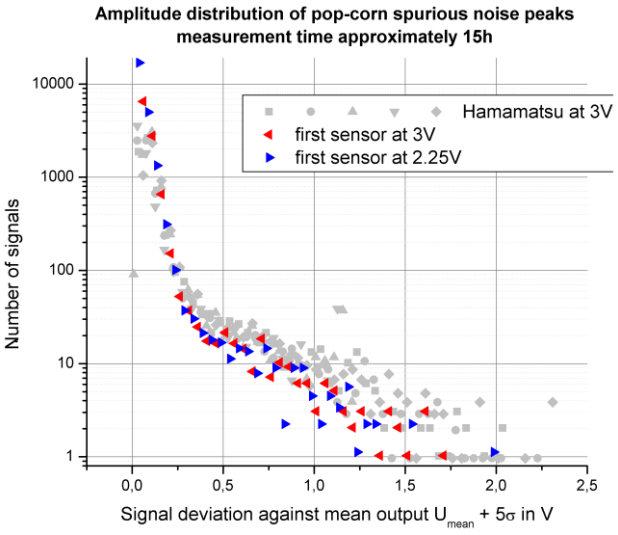


Fig. 3. Amplitude statistics of spurious for two PIN photodetectors of highly similar specification by from tow different sources. The indicated voltage (2.25V, 3V) is the DC output of the preamplification circuit/optical intensity.

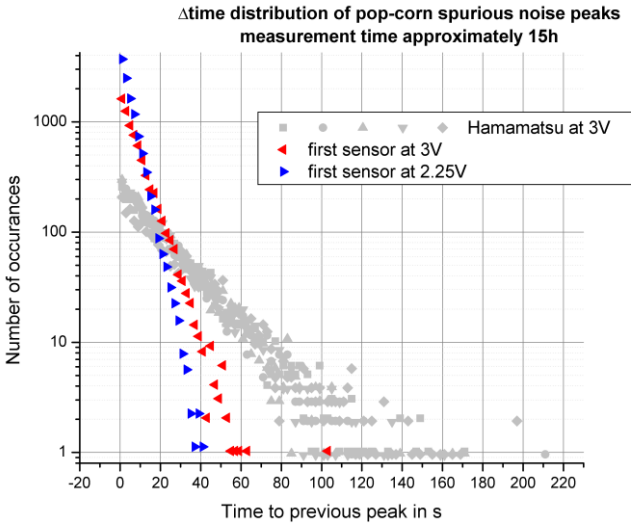


Fig. 4. Statistics of temporal occurance (time spacing) of spurious for two PIN photodetectors of highly similar specification by from tow different sources. The indicated voltage (2.25V, 3V) is the DC output of the preamplification circuit/optical intensity

V. Conclusions

Is is demonstrated that spurious (Popcorn) noise in trans-impedance photo-detection for optical clock application can be characterized by means of long-term data acquisition and statistical analysis. It turns out that the spurious amplitude and time-distribution depends on the used (equivalent) photo-detector and not on the (equivalent) operational amplifiers as described in the literature. No physical interpretation of the phenomenon is possible yet. Nevertheless and based on the here presented results, further investigations shall focus on the manufacturing processes of the photodetectors.

Acknowledgment

The study was carried out using hardware developed with support from European Space Agency (ESA) and the Centre National d'Etudes Spatiales (CNES). Thales Electron Devices provided internal financial support to the project. The authors are grateful for helpful discussion and technical support to G.Corridor at Thales Electron Devices and S. Guérandel at SYRTE, Observatoire de Paris. Technical support from the photodiode supplier First Sensor is acknowledged.

References

[1] Towards an Engineering Model of Optical Space Cs Clock, R.Schmeissner et al., Proceedings of EFTF 2016

[2] Operation Amplifier Noise Prediction, Application note AN519.1, November 1996, intersil

[3] Analysis and Measurement of Intrinsic Noise in Op Amp Circuits, Part VIII: Popcorn Noise, A.Kay, Texas Instruments

Progress in Mexican cesium atomic fountain-CsF1 using an Ultra-Stable Laser

C.A. Ortiz and J.M. López
Centro de Investigación y de Estudios Avanzados del Instituto Politécnico Nacional (IPN), CINVESTAV, Unidad Querétaro, Libramiento Norponiente No 2000, Fracc. Real de Juriquilla, Querétaro, Querétaro 76230, México. cortiz@cinvestav.mx

E. de Carlos López and C.A. Ortiz
Dirección de Tiempo y Frecuencia, Centro Nacional de Metrología, CENAM, km 4.5 carretera a los Cués, El Marqués, 76246, Querétaro, México.
cortiz@cenam.mx

***Abstract*— The Ramsey spectrum obtained with ultra high-resolution microwave spectroscopy of ^{133}Cs using the CENAM´s Cs fountain clock (CsF_1) is reported in this work. In addition, the renewed optical system is presented briefly. Ramsey fringes with an FWHM of 1.4 Hz were generated from the induced decay between two hyperfine levels of ^{133}Cs ground state. These preliminary results were obtained as an effort to test the functionality of all systems involved in the CsF_1 operation, specially an ultra-stable laser that operates as a master oscillator referenced to the D_2 line of ^{133}Cs using modulation transfer (MT) spectroscopy. The CsF_1 is now able to operate for extended periods (weeks) without making major adjustments. Evaluation of systematic effects is currently under way.**

Keywords— Microwave standards; Modulation transfer spectroscopy; Ramsey fringes; Ultra-stable laser.

I. INTRODUCTION

The Centro Nacional de Metrología, CENAM, is currently operating a cesium fountain clock, called CENAM CsF_1. This kind of clocks are the best experimental reproductions of the unit of time, reaching uncertainties about 3×10^{-16} of the International System of Units (SI), the second [1, 2]. The main objective of this work is present preliminary results of ultra high-resolution microwave spectroscopy of ^{133}Cs using an ultra-stable laser referenced to the D_2 line of ^{133}Cs using modulation transfer (MT) spectroscopy to manipulate the cesium atoms. Although the results are not definitive, they provide valuable information about optimum operating parameters and give us a clear direction in order to improve the experiment. Actually the atomic fountain is able to operate for extended periods (weeks) without making major adjustments.

II. ULTRA STABLE LASER

The master continuous wave laser is a commercial AlGaAs, Extended Cavity Diode Laser (ECDL) equipped with a low loss interference filter, 2 W maximum output power, 852 nm wavelength (near to Cs-133's D_2 line), and 20 kHz linewidth. The optical Ultra Low Expansion (ULE) cavity has a free spectral range of 1.49 GHz and a linewidth less than 2.3 kHz. To maintain their high quality thermal characteristics invariant, the housing of the cavity is kept in a high vacuum atmosphere (1 µPa) using an ionic vacuum pump. Temperature is controlled at 28.5 ± 0.0019 °C and the nearest resonance for that condition, is located 332 MHz towards higher frequencies respect to transition $|6^2s_{1/2}, F = 4\rangle \rightarrow |6^2p_{3/2}, F' = 5\rangle$ of ^{133}Cs. In order to stabilize the ECDL to the optical cavity, Pound-Drever Hall technique [3] was used. Once the servo loop filter (SLF) is activated, a reduced linewidth is obtained, becoming the coupled system laser and ULE optical cavity, an optical ultra-stable oscillator (USL).

III. EXPERIMENTAL DETAILS

The CENAM CsF_1´s MOT consists of a stainless steel sphere of 15 cm in diameter with 12 ports equipped with antireflection (T>99%) optical windows for 852 nm. For the cooling lasers and launching cycle (0, 0, 1) geometry was used, that is, four lasers are in the horizontal plane and two in the vertical axis. The pressure without Cs is around 10^{-8} Pa, and partial Cs pressure stays in the order of 10^{-6} Pa. The magnetic field gradient is produced using a pair of coils of 20 cm in diameter, positioned in the vertical axis, in anti-Helmholtz configuration. The maximum magnetic field gradient that can be obtained is around 6 G/cm. In order to minimize the impact of earth´s magnetic field in the MOT's center, the trap is surrounded by two permanent magnets strategically positioned.

In order to operate the CENAM cesium fountain clock based on an ultra-stable optical master oscillator, some improvements on the CsF_1 set up have been done. The USL is frequency prestabilized at the cooling transition of the ^{133}Cs $[|6^2s_{1/2}, F = 4\rangle \rightarrow |6^2p_{3/2}, F' = 5\rangle]$ using modulation transfer (MT) spectroscopy [4] and further stabilized to the resonance frequency of an ULE optical cavity. The laser's light is splitted to be modulated in four different acousto-optic modulators, which are arranged using cat's eye configuration [5] in order to control the frequency independently to carry out the cooling, launching and detection processes. The re-pumping laser is a DFB laser diode with characteristics as those used in the previous optical system. This laser is frequency stabilized at the $|6^2s_{1/2}, F = 3\rangle \rightarrow |6^2p_{3/2}, F' = 4\rangle$ cesium transition using polarization spectroscopy [6]. The vertical (upward and downward) and horizontal cooling beams are feed to the MOT using polarization maintaining (PM) optical fibers as well as the detection and re-pumping beams. With the intention of circularly polarized all beams, quarter-wave plates are disposed in the MOT's windows. The experimental setup of the CENAM CsF_1 is presented in figure 1.

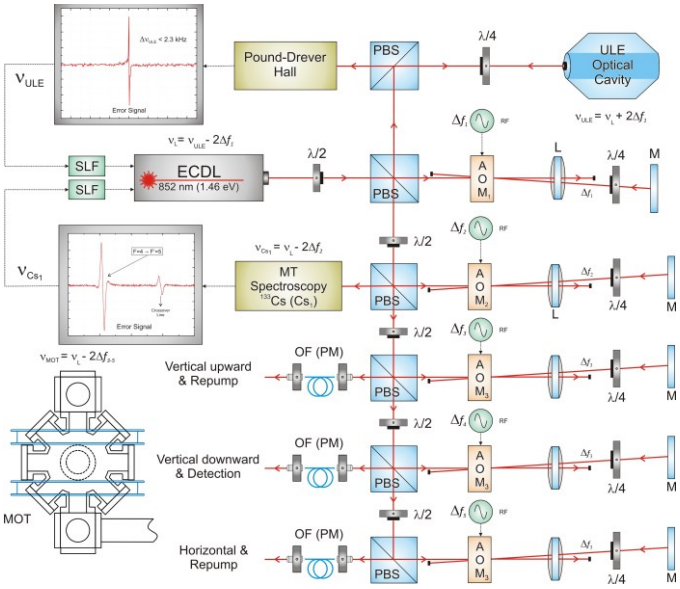


Fig. 1. Experimental setup of CENAM CsF_1. Red lines represent laser's light and black dashed lines represent electrical connections. PBS: polarizing beamsplitter; OF: optical fiber; λ/2: half-wave plate; λ/4: quarter-wave plate; L: lens; SLF: servo loop filter; AOM: acousto-optic modulator; M: mirror; PM: polarization maintaining.

IV. Ramsey Signal Detection

The results presented here were carried out launching the atomic cloud 44 cm above the center of the MOT, that is, about 4 cm over the lower microwave cavity, using $\delta = 3.4$ MHz. By virtue of no optical pumping stage was performed to populate the state $|6^2s_{1/2}, F = 3\rangle$, the atoms-microwaves interaction promotes the induced atomic decay $|6^2s_{1/2}, F = 4, m_F=0\rangle \rightarrow |6^2s_{1/2}, F = 3, m_F=0\rangle$. To detect the relative populations of the atomic states after the cloud interacts with the microwave field in double pass, two detectors placed on opposite windows of the detection zone were used. Each detector consists of a Si photodiode together with an ultra-low noise transimpedance amplifier (108 V/A gain) and an array of lenses to focus the center of the detection zone. The detectors are separated 2 cm relative each other in the vertical so the cloud can be detected in different places and times during its descent.

A probe beam tuned to the $|6^2s_{1/2}, F = 4\rangle \rightarrow |6^2p_{3/2}, F' = 5\rangle$ transition and a re-pumping beam were employed. Both beams travel the same path that the upward cooling beam. When the cloud falls and passes in front of the first detector, the detection beam is turned on during 10 ms, interacting with the atoms in the $|6^2s_{1/2}, F = 4\rangle$ state, at the same time they are removed from the cloud. The detection beam is then turned off for about 5 ms, while a re-pumping beam pulse is used to pump the remaining atoms from $|6^2s_{1/2}, F = 3\rangle$ state to the $|6^2s_{1/2}, F = 4\rangle$ state. After this, the detection beam is turned on again and the atomic population, previously in the $|6^2s_{1/2}, F = 3\rangle$ state, can be detected. The maximum values of the detected signals (respect to the background of the detection pulse) are used as a measure of the relative number of atoms in the $|6^2s_{1/2}, F = 3\rangle$ and $|6^2s_{1/2}, F = 4\rangle$ states. Dividing each value of the number of atoms by the total sum, the normalized atomic population in each state is obtained.

The microwaves were generated by a low noise frequency synthesizer (LNFS-100 Spectra Dynamics). The synthesizer was referenced to an active Hydrogen maser to ensure a good short time stability. This hydrogen maser has a frequency offset of about $1x10^{-13}$ relative to the UTC(CNM). The Ramsey pattern obtained with the CENAM´s Cs Fountain Clock is shown in figure 2, where each point represents one launch (no averaging). Figure 2. A) shows the full spectrum, using a window of 140 Hz around the central frequency (9192631770 Hz) and a step of 0.2 Hz between measurements. A detail of the central part of the spectrum is shown in figure 2. B), observing that the FWHM of the Ramsey fringes is about 1.4 Hz.

On the other hand, the central fringe of the Ramsey spectrum is blue shifted around 238 mHz from the central value, due mostly to the magnetic field. An estimate of the C-field can be carried out using the Breit-Rabi equation.

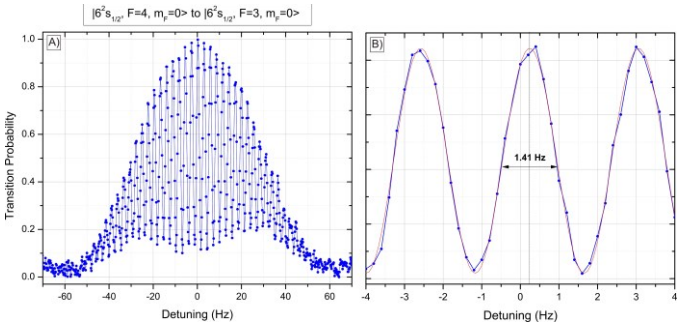


Fig. 2. Experimental Ramsey spectrum of the CENAM CsF_1 Fountain Clock (no averaging). A) 140 Hz window. B) 8 Hz window - Central fringe FWHM.

Acknowledgement

C. A. Ortiz thanks CONACYT for his Ph. D scholarship and CINVESTAV / CENAM for scientific and technical support.

References

[1] V. Gerginov, N. Nemitz, S. Weyers, R. Schröder, D. Griebsch and R. Wynands, "Uncertainty evaluation of the caesium fountain clock PTB-CSF2,"*Metrologia*, vol. 47, no. 1, pp. 65, December 2010.

[2] S. R. Jefferts, et. al., "Accuracy evaluation of NIST-F1," *Metrologia*, vol. 39, no. 4, pp. 321, 2002.

[3] E. D. Black, "An Introduction to Pound–Drever–Hall Laser Frequency Stabilization," *Am. J. Phys.*, vol 69, no. 1, pp. 79-87, January 2001.

[4] D. J. McCarron and S. A. King and S. L. Cornish, "Modulation transfer spectroscopy in atomic rubidium," *Measurement Science and Technology*, vol. 19, no. 10, pp. 105601, August 2008.

[5] E. A. Donley, T. P. Heavner, F. Levi, M. O. Tataw, and S. R. Jefferts, "Double-pass acousto-optic modulator system," *Review of Scientific Instruments*, vol. 76, no.6, pp. 063112, June 2005.

[6] A. Hernández-Hernández, E. Méndez-Martínez, A. Reyes-Reyes, J. Flores-Mijangos, J. Jiménez-Mier, M. López and E. de Carlos, "Polarized velocity selective spectroscopy of atomic rubidium using counterpropagating beams," *Optics Communications*, vol. 282, no. 5, pp. 887–891, March 2001.

Frequency Drift Detection Method Using Dual Alkali Gas for Coherent Population Trapping Atomic Clocks

Yota Furuse, Yuji Kase and Shigeyoshi Goka
Department of Electrical & Electronic Engineering
Tokyo Metropolitan University
Tokyo, Japan
goka@tmu.ac.jp

***Abstract*—We propose a frequency drift detection method for coherent population trapping (CPT) atomic clocks to improve their long-term frequency stability. One of the main reasons for frequency drift in gas-cell based atomic clocks is buffer gas pressure variations in the gas cells caused by leakage through the cell walls. In this work, the drift detection method is demonstrated experimentally using a dual alkali microelectromechanical system (MEMS) cell.**

Keywords—CPT; CSAC; gas cell; buffer gas; atomic clock

I. INTRODUCTION

Atomic clocks that are based on coherent population trapping (CPT) resonances, including chip-scale atomic clocks (CSACs) and miniature atomic clocks (MACs), contain alkali gas cells that are used to observe the CPT resonances. The long-term frequency stability of such atomic clocks is limited by pressure variations in the buffer gas enclosed inside the gas cells. Because the buffer gas pressure variations are caused by diffusion through the gas cell walls, it is theoretically impossible to remove a diffusion phenomenon.

However, CPT resonances can be excited without using microwave cavities, and it is thus possible to observe CPT resonances of other kinds of alkali gas when contained in the same gas cell[1-2]. In this paper, we propose a drift detection method using dual CPT resonances with a dual alkali gas cell.

II. FREQUENCY DRIFT DETECTION METHOD USING DUAL ALKALI GAS

The pressure shift that is caused by a buffer gas is generally given by the following equation[3-4]:

$$\Delta\nu = P\,[\,\beta + \delta\Delta T + \gamma\,(\Delta T)^2\,], \tag{1}$$

where P is the buffer gas pressure in the gas cell, β is the pressure coefficient, δ and γ are temperature coefficients, and ΔT is the temperature difference from a set temperature. Because typical atomic clocks keep the gas cell temperature constant, we can then assume that the average value of ΔT is constant over a long time scale; therefore, the CPT resonant frequency ν_{CPT} is given by the following equation:

$$\begin{aligned}\nu_{\mathrm{CPT}} &= \nu_0 + \Delta\nu \\ &= \nu_0 + P\beta',\end{aligned} \tag{2}$$

here ν_0 is the hyperfine splitting frequency and is a known constant. When two different types of alkali atoms are contained within the same gas cell, the frequency drift caused by the buffer gas pressure variation can be written as follows:

$$\Delta\nu_1 = \frac{\nu_{02} - \Delta\frac{\nu_{CPT2}}{\nu_{CPT1}}\nu_{01}}{\Delta\frac{\nu_{CPT2}}{\nu_{CPT1}} - \frac{\beta_2'}{\beta_1'}}, \tag{3}$$

where $\Delta\nu_r = \Delta(\nu_{\mathrm{CPT2}}/\nu_{\mathrm{CPT1}})$ is the variation of the frequency ratio between the two CPT resonances; this can be measured using the standalone atomic clock itself with the dual alkali gas, and β'_2/β'_1 can then be measured before use in the atomic clock. Therefore, an atomic clock with dual alkali gas can detect a frequency drift by monitoring $\Delta\nu_r$ and can then compensate the output frequency to improve its long-term frequency stability.

III. EXPERIMENTAL SETUP FOR MEASUREMENT OF THE DUAL CPT RESONANCES

The experimental setup is as shown in Fig. 1. Two similar sets of optical systems were prepared for Cs and Rb, and the orange color represents the optical systems related to Rb while the blue represents those related to Cs. The microelectromechanical system (MEMS) gas cell (shown in Fig. 2) has an optical length of 2 mm and contains a mixture of Cs, natural Rb, and 2.6 kPa of Ne buffer gas at a controlled temperature of 80°C. Because Ne has a smaller atomic radius than the other kinds of buffer gases, its leakage rate is relatively high[5], so the frequency variation can be measured over a shorter period of time.

795 and 894 nm single-mode vertical-cavity surface-emitting lasers (VCSELs) were used to excite ^{133}Cs and ^{85}Rb at the D1 line, and were modulated at 4.6 and 3.0 GHz by RF signal generators to generate first-order sidebands around the laser

carrier, respectively. Because the light wave difference between Cs and Rb lasers is more than 9 nm, they have little effect in terms of light shift (AC stark shift) on each other. The light beams from the VCSELs were σ+-polarized by the $\lambda/4$ wave plates, overlapped by the half-mirror and then transmitted through the same point in the gas cell. The transmitted light was split into two beams again by the half mirror, and any unnecessary signals were then cut out using band-pass filters (890 ± 5 nm for Cs and 800 ± 5 nm for Rb) and observed using photodiodes. These configurations were assumed to be applied to CSACs or MACs. Feedback loops were configured using lock-in amplifiers to stabilize the laser wavelength and maintain the CPT resonance frequency. The gas cell was covered by a double magnetic shield to block any external magnetic field effects.

In the experiments, a Global Positioning System (GPS)-based reference frequency source (NMIJ-DO) was connected to the RF signal generators, and the CPT resonance frequency was then measured by controlling the RF frequencies.

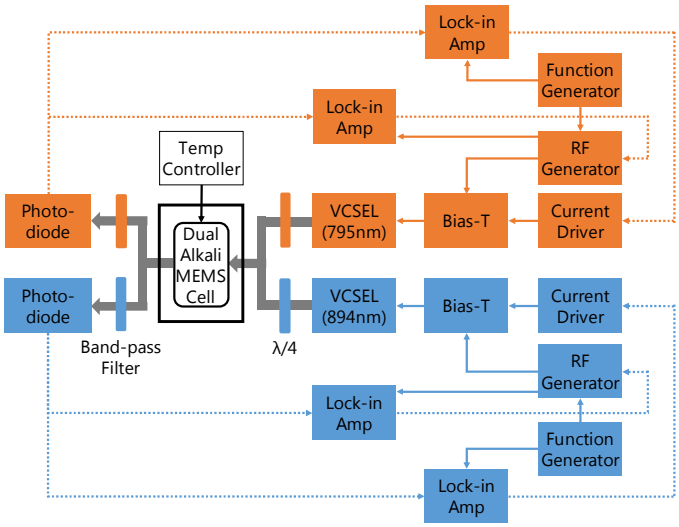


Fig. 1. Experimental setup used to measure the dual CPT resonances. Similar systems were prepared for Cs and Rb.

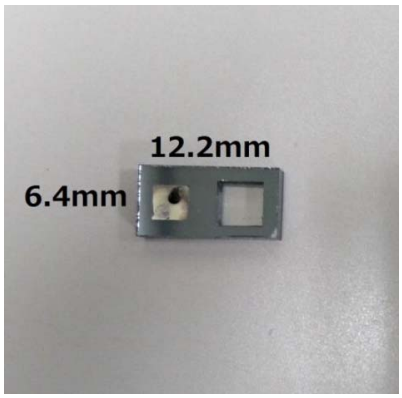


Fig. 2. Photograph showing the actual dual alkali microelectromechanical system (MEMS) gas cell.

IV. Experimental Results With Cs And Rb Microelectromechanical System Cell

Fig. 3 shows the ^{133}Cs and ^{85}Rb CPT resonances when measured simultaneously. It was confirmed that the dual CPT resonances could be observed at the same time.

First, to reduce the frequency shift with respect to small gas cell temperature changes during measurement of the long-term frequency variation, the temperature dependence of the CPT resonance frequency of Cs, which is assumed to be the clock resonance, was measured over the range from 60 to 100°C in which the CPT resonance could be observed. As a result, the frequency shift direction was reversed at approximately 80°C, which means that if the gas cell temperature was controlled around this temperature, then even if the gas cell temperature changed to some extent, it would be possible to suppress this change within a slight frequency shift range. We therefore decided to control the gas cell temperature at 80°C.

The CPT resonance frequencies of ^{133}Cs and ^{85}Rb were measured over one week. The frequency variations of Cs, Rb, and $\Delta\nu_r$ are shown in Fig. 4. The CPT frequency drift rate for Cs (ν_{CPT1}) was -2.7×10^{-12} per hour while that of Rb (ν_{CPT2}) was -3.4×10^{-11} per hour. We believe that the drift rate of Rb was larger than that of Cs because the temperature of the gas cell actually fluctuated. Fig. 5, 6 show the temperature dependence of CPT resonance frequency for Cs and Rb. The temperature coefficient of Cs around 80°C was −0.2 Hz/°C while that of Rb was −10.2 Hz/°C, so this difference would affect the results. The parameters for β'_2/β'_1 were estimated from the two days of data for $\Delta\nu_{CPT2}/\Delta\nu_{CPT1}$.

From equation (3), the measured $\Delta\nu_r$ of Fig. 4 (c), and the value of β'_2/β'_1, we estimated the drift-compensated frequency ν_{CPT1}, as shown in Fig. 7. The estimated drift rate is 2.3×10^{-13} per hour, which is one-tenth less than the value of the rate without compensation.

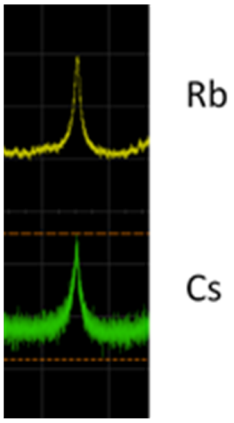
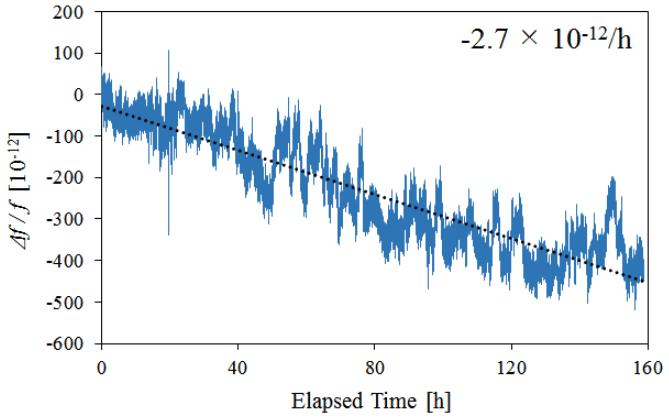
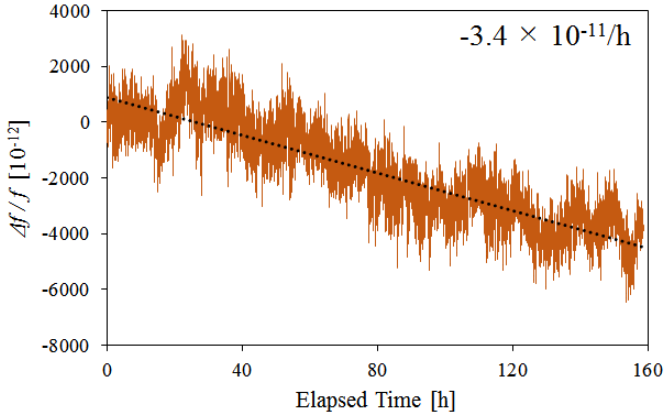


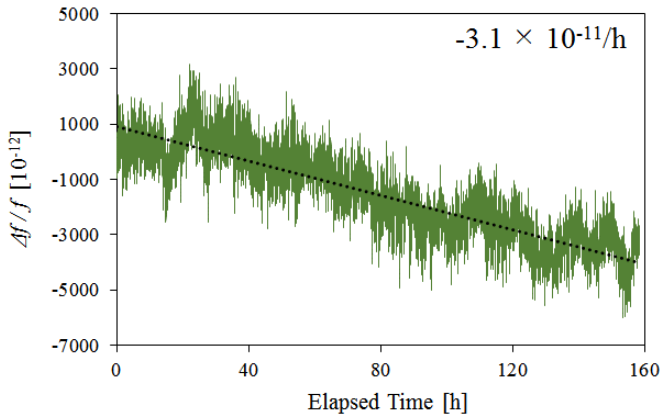
Fig. 3. CPT resonances observed simultaneously with the dual-alkali gas cell.



(a) CPT resonance frequency of Cs (ν_{CPT1}).



(b) CPT resonance frequency of Rb (ν_{CPT2}).



(c) $\Delta\nu_r$.

Fig. 4. Measured frequency variations of Cs, Rb, and $\Delta\nu_r$ over one week.

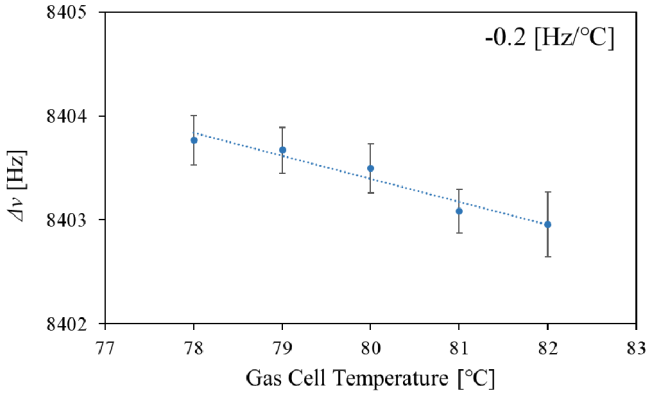


Fig. 5. Gas cell temperature dependence of CPT resonance frequency for Cs.

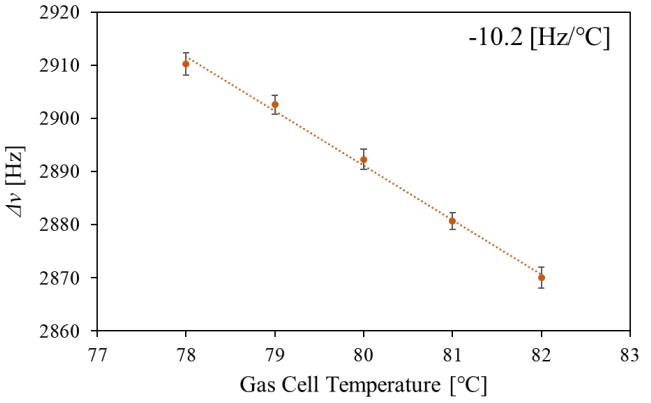


Fig. 6. Gas cell temperature dependence of CPT resonance frequency for Rb.

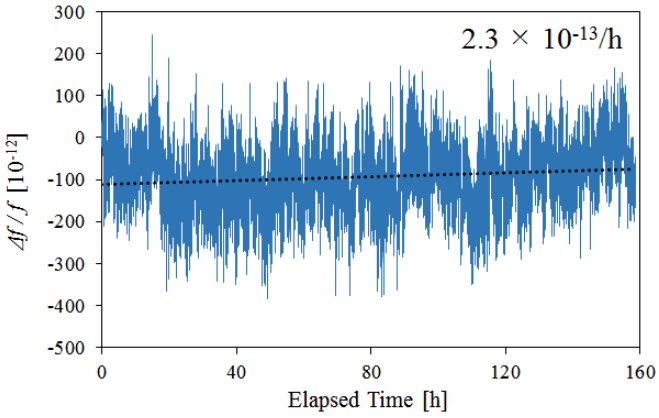


Fig. 7. Cs frequency compensation estimation using measured data (Fig. 4)

V. CONCLUSION

A frequency drift detection method for CPT atomic clocks was proposed for development of long-term frequency stability and frequency compensation using a dual alkali MEMS cell was demonstrated. Experiments showed that the compensated drift rate was ten times better than the value obtained without compensation. These results show that the proposed method can improve the long-term frequency stability of CPT-based atomic clocks.

ACKNOWLEDGMENT

The authors are grateful to Ricoh Company, Ltd. for providing us with the MEMS gas cell. This paper is based on part of the results obtained from a project subsidized by the New Energy and Industrial Technology Development Organization (NEDO).

REFERENCES

[1] S. Goka, "^{85}Rb Coherent-Population-Trapping Atomic Clock with Low Power Consumption," Jpn. J. Appl. Phys. **48** 082202, 2009.

[2] S. Goka, "^{85}Rb D1-Line Coherent-Population-Trapping Atomic Clock for Low-Power Operation," Jpn. J. Appl. Phys. **49** 062801, 2010.

[3] J. Vanier and C. Audoin "The quantum physics of atomic frequency standards," IOP Publishing, Bristol and Philadelphia, Ch. 3, 1989.

[4] O. Kozlova, R. Boudot, S. Guérandel, and E. Clercq, "Temperature Dependence Cancellation of the Cs Clock Frequency in the Presence of Ne Buffer Gas," IEEE Trans. Inst. Meas. **60**, 7, July 2011.

[5] S. Abdullah, C. Affolderbach, F. Gruet, and G. Mileti, "Aging studies on micro-fabricated alkali buffer-gas cells for miniature atomic clocks," Appl. Phys. Lett. **106**, 163505, 2015.

Magnetic field measurement by stimulated Raman transitions and smoothing by dynamical compensation in rubidium fountain clock

Wenli Wang[1], Richang Dong[1,2], Rong Wei[1,*], Tingting Chen[1,2], Qian Wang[1,2], and Yuzhu Wang[1]

[1] *Key Laboratory for Quantum Optics, Shanghai Institute of Optics and Fine Mechanics, Chinese Academy of Sciences, Shanghai 201800, People's Republic of China*

[2] *University of Chinese Academy of Sciences, Beijing 100049, People's Republic of China*

[*] Electronic address: weirong@siom.ac.cn

***Abstract*—We present a method for magnetic field measurement by the weak magnetic-sensitive Zeeman splitting and a method for measuring the magnetic field vector by probing the line strength of stimulated Raman transitions. Compared with the traditional measurement, the contrast of the weak magnetic-sensitive resonance signal is improved significantly for gradient field. We also present a dynamical compensation method to smooth the spatial fluctuation of the magnetic field in the fountain clock. A homogeneous field with a 0.4 nT peak-to-peak value is realized compared to 5nT under the static magnetic field.**

Keywords—magnetic field measurement; stimulated Raman transition; dynamical compensation; atomic fountain clock

I. INTRODUCTION

The Zeeman shift of atomic levels resulting from the applied static magnetic field plays a key role in the field of precision measurements, such as alkali-metal atomic gravimeters, atomic gyroscopes and atomic clocks [1-5]. To evaluate the systematic error caused by Zeeman effect, for example, the second-order Zeeman shift of atomic fountain clocks, the accurate information of both magnitude and orientation of magnetic field in the atomic flight region becomes particularly important. Several techniques like microwave radiating, stimulated Raman transition (SRT), resonant magneto-optic rotation, Larmor spin precession, and light mediated quantum interference effect have been applied to the precise measurement of magnetic field. Among these methods, SRT technique associated with the intervals and strengths of transition peaks is immune to the Doppler shift and the AC Stark shift. The method can be applied to measure the magnetic field intensity and angle, even with large gradient, along the whole space.

We study the stimulated Raman spectroscopy based on the ^{87}Rb D2 line for magnetic field measurement. Thirteen Λ Raman transitions are allowed by the two-photon electric-dipole selection rules, Δm=0, ±1, ±2, as shown in Fig. 1. For a given magnetic field B, the frequency difference in Fig. 1 can be deduced from the Breit-Rabi formula, where *a* and b are coefficients, $x=h\nu_0 (g_I+ g_J)\mu_B B /h\nu_0$. And seven transitions are used to measure the magnetic field intensity based on the first-

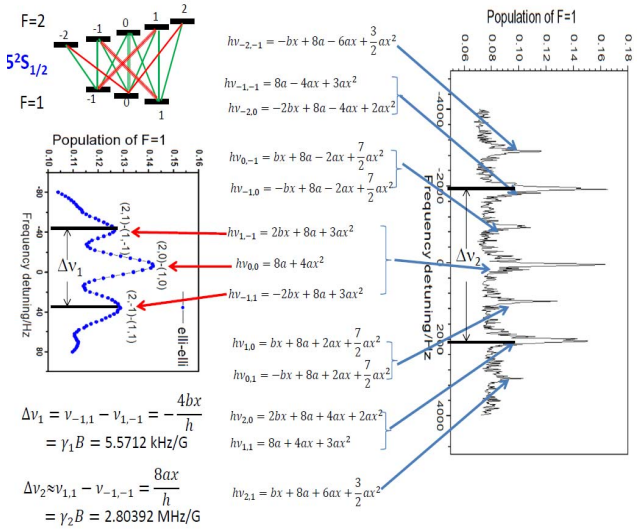


Fig. 1. (Color online) Stimulated Raman transition peaks as a function of frequency detuning based on the ^{87}Rb D2 line for magnetic field measurement.

order Zeeman effect in traditional SRT [6,7]. In this work, 1) we study the central three transitions, which are degenerate because of the small coefficients γ_2 and γ_3. When the two terms are taken into account, the degeneracy is relieved, and thus leads to the weak magnetic-sensitive Zeeman splitting (WMSZ). The WMSZ can be applied to measure the magnetic field with large gradient and enlarged range of SRT. 2) we present an alternative method for measuring the magnetic field vector, based on an irreducible tensor description of the interaction between the dichromatic light fields with the atomic levels, which are manifested by the relative line strengths. The direction of the magnetic field in our ^{87}Rb atomic fountain as a function of the height above the center of MOT is depicted. 3) based on the precision measurement of magnetic field, we put forward a dynamical compensation method to suppress the field spatial fluctuation along the atomic trajectory combined with the SRT method. Compared with the normal static method, the inhomogeneity of the magnetic field that the atoms interacted is reduced by one order of magnitude.

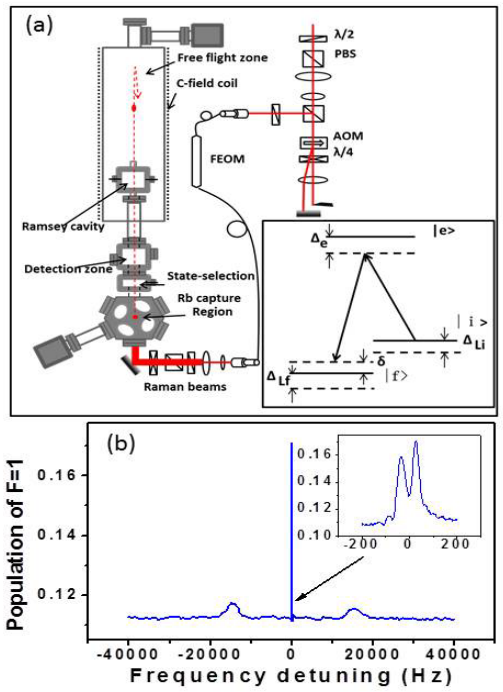


Fig. 2. (Color online) (a) Schematic setup for magnetic field measurement by stimulated Raman transition. FEOM—fiber electro-optical modulator, AOM—acoustic optical modulator. (Inset) Level scheme for stimulated Raman transition. (b)Simultaneous observation of the Raman transition peaks based on the weak magnetic-sensitive Zeeman splitting and the magnetic-sensitive Zeeman splitting.

II. WEAK MAGNETIC-SENSITIVE ZEEMAN SPLITTING (WMSZ)

The schematic of the experimental apparatus is shown in Fig. 2(a). In our cold atomic fountain, displayed in the left of Fig. 2(a), a magneto-optical trap (MOT) with a fold optical path is used to trap and launch atoms. As shown in the right side of Fig. 2(a), the Raman beams are produced by a fiber electro-optical modulator driven by a signal generator referred to the Hydrogen maser. The carrier and the +1st sideband modulated by the FEOM are used as the two Raman beams. In traditional SRT, with higher order terms neglected, the magnetic field B can be deduced by using the approximate formula $\Delta\nu=\gamma_1 B$, where γ_1 is about 1.4 MHz/G, $\Delta\nu$ is the frequency difference of these adjacent transition peaks. However, for measuring a magnetic field with large gradient G (=$\Delta B/\Delta z$), the high sensitivity will broaden the Raman resonance curves with $\delta\nu=\gamma_1\int G dz$. To overcome this obstacle, the splitting of two weak magnetic-sensitive resonances with lin || lin polarization configuration can be used. In theory, the frequency detuning of $|2, 1> \rightarrow |1, -1>$, $|2, 0> \rightarrow |1, 0>$ and $|2, -1> \rightarrow |1, 1>$ transitions under magnetic field from the unperturbed hyperfine transition are depicted by $\Delta\nu_{1,-1}=-\gamma_2 B+(3/4)\gamma_3 B^2$, $\Delta\nu_{0,0}=\gamma_3 B^2$ and $\Delta\nu_{-1,1}=\gamma_2 B+(3/4)\gamma_3 B^2$, respectively, where γ_2 is 2.7856 kHz/G, γ_3 is 575.15 Hz/G^2.

We present SRT with lin // lin optical fields to realize the Zeeman splitting of the weak magnetic-sensitive Raman transitions in the ^{87}Rb atomic fountain clock. The co-propagating Raman beams with the same polarization

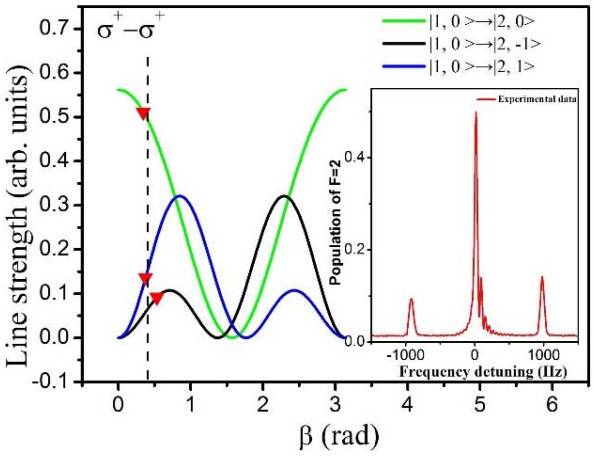


Fig. 3. (Color online) The dependences of SRT resonances on the angle β. The inset displays the SRT spectra versus the two-photon detuning δ with σ^+-σ^+ polarized beams for the launched height 527 mm. The red triangles indicate the experimental results of line strengths for each transition peaks with the total laser intensity is 1.7 μW/cm^2.

configuration are used to study the stimulated two-photon process. The frequency detuning of the Raman beams is increased progressively by a small increment and the process repeated. The interval of these splitting peaks can be used to measure magnetic field with large gradient. In this way a stimulated Raman spectrum as shown in Fig. 2(b) is generated [8], the line-width of the resonance curves of the weak magnetic-sensitive transitions is only 29.5Hz, compared to 3.38 kHz for the magnetic-sensitive transition curves, which leads to an increased contrast by 13 times. The calculated magnetic field intensity from the methods of MSZ and WMSZ are 10.433 mG and 10.381 mG, respectively, which are consistent with each other.

III. MAGNETIC FIELD VECTOR MEASUREMENT

In our fountain, the magnetic field vector is applied in the xoz plane at an angle β with respect to the propagation direction k of the Raman beams that is parallel to the direction of C-field Bc (z-axis). Figure 3 shows the dependences of SRT resonances on the angle β. The inset displays the SRT spectra versus the two-photon detuning δ with σ^+-σ^+ polarized beams for the launched height 527 mm. Three two-photon Λ transition peaks corresponding to 0→-1 (|1, 0> • |2, -1>), 0→0 and 0→1 between the individual magnetic sublevels are observed. In theory, based on an irreducible tensor description of the interaction between the dichromatic light fields with the atomic levels, the line strengths of the SRT resonance components can be calculated [9]. The effective Rabi frequency characterizing the stimulated two-photon Λ transition between the ground-state atoms has the formula as follows

$$\Omega_{eff}=\frac{\mu_0 d^2\sqrt{I_1 I_2}}{2\hbar^2\varepsilon_0}\sum_{p,q,F_s}\frac{a_p\cdot b_{-q}}{\Delta_s}G_1 G_2$$

where I_1 and I_2 are the Raman beam intensities, and α_p ($b=\alpha^*$) is the polarization tensor components of the two electric light fields. Three curves in Fig. 3 indicate the calculated values of relative transition probability of a two-photon process using above equation with the total laser intensity 1.7 μW/cm^2. The

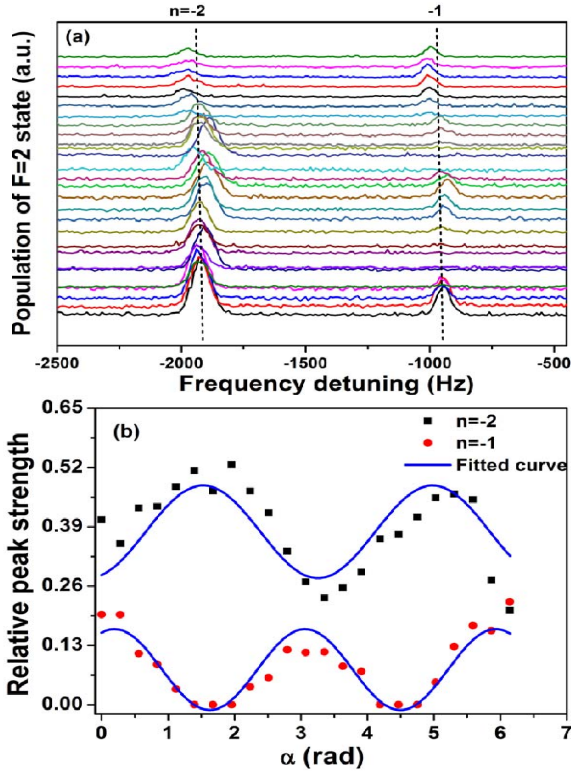


Fig. 4. (Color online) Angular dependence of the Raman transitions on the fixed laser polarization scheme.

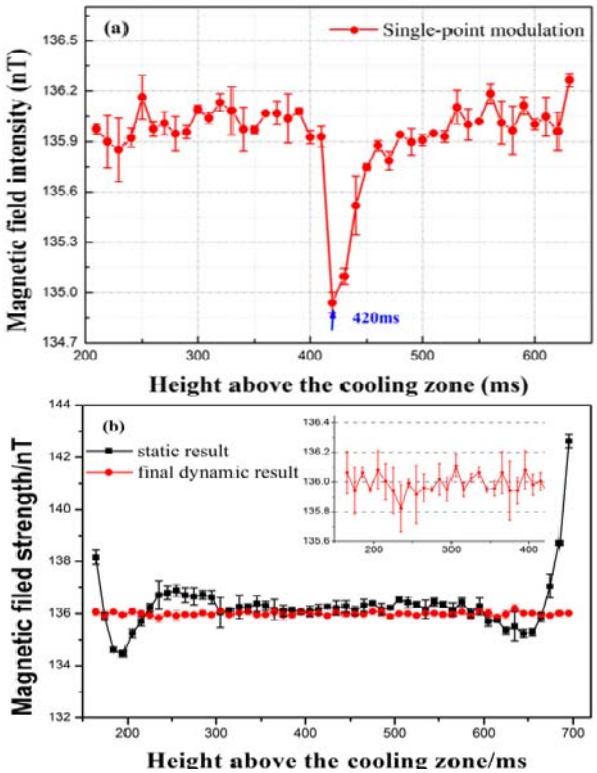


Fig.5. (Color online) (a)The dynamic response result of the corrected magnetic field strength above the cooling zone. (b) Mapping of the magnetic field strength via several repeated steps of dynamic correction process.

red triangles indicate experimental results of line strengths for each transition peaks. The angle between **B** and **k** at a launched height in the fountain can be calculated from every one of the three transitions with β=0.37 rad. An average value with a statistic standard deviation of 6.1 mrad is then obtained from the three transitions.

The electric field E travels in the xoy plane at a polarization angle α along the x direction. Stimulated Raman transition spectra for lin-lin excitation at different polarization angles α of the incident electric fields are also studied, as illustrated in Fig. 4(a). When the angle α increases, the odd-numbered resonance for 0→ -1 (+1) transitions gradually vanishes, while the even-numbered resonances for 0→ -2 (+2) transitions slowly grows; then, with the angle α continuing to increase, the odd-numbered resonance returns back and continually grows. In the special case considered here, for α=π/4, the odd-numbered peaks vanish; this implies that the projection direction of the magnetic field vector in the xoy plane is perpendicular to the polarization direction of Raman beams.

For a quantitative comparison with theory, the resonance strengths for the even-numbered peaks (black square) and the odd-numbered peaks (red circles) of Fig. 4(a), normalized to the total strength of all resonances, are measured for different polarization angle α as shown in Fig. 4(b), for linear polarization. The blue solid lines represent the best-fit theoretical curves. From the least square fit to the experimental SRT results, the angle α is obtained with a fitting error of 0.16 rad. There are systematic deviations mainly due to the power fluctuation (10% for peak to peak) of the incident Raman beams, which contributes to an uncertainty of less than 3%.

IV. DYNAMICAL COMPENSATION METHOD

We further study the dynamic response to the real time compensation process by means of single-point modulation [10]. At the location of launched height 420 ms, we alternate the coil voltage by 10 μA, denoted by the blue arrow as shown in Fig. 5(a). It is important to note that, the influence on the subsequent several points are observed since there exists 20 ms extension in our dynamic feedback process. The standard deviations associated with each point include the resonance curve center uncertainty and the positional uncertainty. After a number of repeated operation using our method, the full map of the magnetic field is generated, denoted by the red circle line as shown in Fig. 5(b), with the higher level of measured precision compared with the static result (black square line). The inset corresponds to the enlargement of red line region. It shows an inhomogeneity of the dynamic magnetic field 0.2 nT, and the error bars show the systematic uncertainty due to our measurement.

Besides the spatial inhomogeneity, the instability of the magnetic field accounting for temporal fluctuations creates a larger uncertainty in the correction value. We evaluated the temporal instability of the magnetic field measured by the SRT spectroscopy performed at a single point [11], not shown in this paper. We noticed that the temporal fluctuations in the magnetic field using our method did not deteriorate despite the additionally introduced variable I, which was the result we expected. Compared with the static method, the fluctuation of the magnetic field distribution was improved by one order of

magnitude, leading to an uncertainty of 4×10^{-17} associated with the second-order Zeeman shift, directly evaluated by calculating the time average of the square of the magnetic field over the atomic trajectory, and led to perfect homogeneity of the C-field.

ACKNOWLEDGMENT

This work was supported by Strategic Priority Research Program of the Chinese Academy of Sciences under Grant No. XDB21030800 and National Natural Science Foundation of China under Grant No. 11404353.

REFERENCES

[1] B. Canuel, F. Leduc, D. Holleville, A. Gauguet, J. Fils, A. Virdis, A. Clairon, N. Dimarcq, C. J. Borde, A. Landragin, "Six-axis inertial sensor using cold-atom interferometry," Phys. Rev. Lett., vol. 97, pp. 010402, 2006.

[2] A. Gauguet, B. Canuel, T. Lévèque, W. Chaibi, A. Landragin, "Characterization and limits of a cold-atom Sagnac interferometer," Phys. Rev. A, vol. 80, pp. 063604, 2009.

[3] A. Peters, K. Y. Chung, S. Chu, "High-precision gravity measurements using atom interferometry ," Metrologia., vol. 38, pp. 25, 2001.

[4] S. R. Jefferts, J. Shirley, T. E. Parker, T. P. Heavner, D. M. Meekhof, C. Nelson, F. Levi, G. Costanzo, A. De Marchi, R. Drullinger, L. Hollerg, W. K. Lee, F. L. Walls, "Accuracy evaluation of NIST-F1," Metrologia., vol. 39, pp. 321, 2002.

[5] V. Gerginov, N. Nemitz, S. Weyers, R. Schröder, D. Griebsch, R. Wynands, "Uncertainty evaluation of the caesium fountain clock PTB-CSF2," Metrologia., vol. 47, pp. 65-79, 2010.

[6] C. Y. Shi, R. Wei, Z. C. Zhou, D. S. Lv, T. Li, Y. Z. Wang, Chin. Opt. Lett., vol. 8, pp. 549, 2010.

[7] Z. C. Zhou, R. Wei, C. Y. Shi, T. Li, and Y. Z. Wang, Chin. Phys. B, vol. 20, pp. 034206, 2011.

[8] R. Dong, R. Wei, Y. Du, F. Zou, J. Lin, and Y. Wang, "Magnetic field measurement by weak magnetic-sensitive Zeeman splitting," Appl. Phys. Lett., vol. 106, pp. 152402, 2015.

[9] W. Wang, R. Dong, R. Wei, J. Lin, F. Zou, T. Chen, and Y. Wang, "Measuring magnetic field vector by stimulated Raman transitions," Appl. Phys. Lett., vol. 108, pp. 122401, 2016.

[10] W. Wang, R. Dong, R. Wei, T. Chen, Q, Wang, and Y. Wang, "C-field smoothing by trajectory dynamically tracing compensation in rubidium fountain clock," arxiv:1612.07469, 2016.

[11] J. Gu´ena, M. Abgrall, A. Clairon, and S Bize, "Contributing to TAI with a secondary representation of the SI second," *Metrologia.*, vol. 51, no. 1, pp. 108–120, Jan. 2014.

Impact of the environment on a hygrometry sensor response

Marianne SAGNARD*, Thierry LAROCHE†, Jean-Michel FRIEDT* and Sylvain BALLANDRAS†
* Femto-ST, Time and frequency department
15B av. des Montboucons 25000 BESANCON
Email: marianne.sagnard@frecnsys.fr, jmfriedt@femto-st.fr
†Frec'n'sys
18 rue Alain Savary 25000 BESANCON
Email: thierry.laroche@frecnsys.fr, sylvain.ballandras@frecnsys.fr

***Abstract*—The measure of hygrometry is a current approach for soil monitoring in geophysical applications. In that case, *in-situ* subsurface earth moisture control is tackled with the design of wireless and free from battery sensors interrogated from the surface. Since the most significant impact of humidity on ground physical properties is on the relative permittivity ε_r, the measurement is based on the capacitive pulling of an acoustic resonator. The connection of a variable capacitance in parallel with an antenna feeding the resonator with incoming power induces losses and hence, range losses through capacitive short circuit under strong moisture contents.**

Consequently, an alternative solution is considered. It consists in the design of a coupled resonator in which antenna and sensor (capacitive load) are electrically separated and linked by the acoustic field confined in the cavity between the electrodes forming the two ports. When probed by a Ground Penetrating RADAR, the echo delay, or in the case of a resonator, the frequency difference between the two modes is expected to depend on the humidity level.

Thus, this study is dedicated to the understanding of the impact of humidity on the different elements of sensor. This work also designs a surface acoustic wave resonator to convey the signal. In such a way, this work exhibits that under ideal load the set-up above mentioned indeed allows the measure of ε_r due to capacitive pulling, leading to a wired hygrometer. Then, the possibility to carry out wireless sensing using an antenna both as an antenna and as a sensitive area is explained.

I. Introduction

Passive sensors interrogated through a wireless link from the surface are ideally suited for subsurface physical and chemical sensing. Indeed, the lack of local energy source is consistent with the inaccessibility of the sensor once installed for any maintenance or battery replacement purpose. Acoustic transducers based on elastic waves guided in solids, used as intrinsic sensors, take advantage of the dependence of the parametric sensitivity on their physical characteristics (particularly the phase velocity) to environmental changes. More specifically, Surface Acoustic Wave (SAW) sensors based on this feature have been developed for temperature and stress remote sensing [1]. Such an approach however restricts the measured quantities to those impacting the acoustic wave characteristics, preventing the measurement of other specific properties. For example, to estimate the *in-situ* soil humidity, hygrometry sensors have to be developed. These zones are hard to access so wireless and remotely controlled sensors are preferably selected with respect to the classical time-domain reflectometry measurement (TDR) requiring an operator and the insertion of a probe in soil. Moreover, the SAW sensor can't be immersed in wet places. Consequently, innovative measurement means, such as the modification of electric boundary conditions using resistive or capacitive loads, must be elaborated.

Thus, a complementary approach consists in the use of an acoustic transducer as a radiofrequency transponder whose first port is connected to an antenna for wireless communication, and whose second port is connected to a load designed to change the basic operation mode of the device (for instance, mode coupling in longitudinally coupled resonator filter - LCRF) so that the returned signal conveys the load sensor environmental condition [2], [3]. If both of them are buried with the acoustic transducer, varying soil moisture will then affect both antenna and load impedance. Therefore, the arising question is how to separate both contributions and to prevent the symmetrical design of the transponder from being similarly affected on both ports by permittivity ε_r changes.

In addition, the use of an only coupled mode resonator allows a differential measurement while avoiding the use of several single port resonators that can couple one another and age in a different way along time, leading to the degradation of the sensor response.

In that purpose, this work focuses on the analysis of the response variations of a sensor composed of an antenna, a SAW LCRF and a sensitive zone, under the fluctuation of soil hygrometry as was experimentally adressed in [4]. In this way, a SAW device is designed and electrical equivalent circuits are used to represent the sensitive area and the antenna. The first step of this paper is to explain how antenna and sensing load parameters evolve under a change of ε_r. Indeed, the variation of soil humidity induces a fluctuation of ε_r. Consequently, the capacitive load used in the considered sensor changes too. Moreover, as mentioned above, antenna is also impacted by the soil moisture.

The first part of this paper then is dedicated to the study of the sensor component parameter variations with ε_r. Then, resonant frequency variations under the modification of electrical conditions (due to the presence of antenna and/or sensitive zone) is pointed out and discussed. Finally, the application presented in this work could be developed according to the sensitivity to the environment obtained on a specific SAW

978-1-5386-2916-1/$31.00 ©2017 IEEE

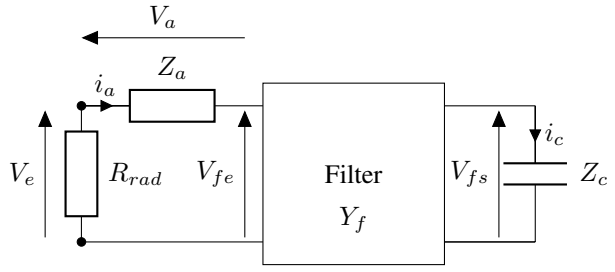


Figure 1. Illustration of an hygrometry sensor. It is composed of an antenna (Z_a and R_{rad}), of a SAW LCRF (Filter, Y_f) and of a capacitance (load, C_l). The output voltage V_e is measured at the terminals of R_{rad}.

design on Lithium Niobate.

II. Operating of a hygrometry sensor

This section explains the working principle of hygrometers based on surface acoustic waves. The sensor is at first sketched then its frequency response defined.

A. Basic diagram of the hygrometry sensor

Hygrometers that take advantage of guided waves in solids are composed of three parts:

1) A sensitive zone that measures the variation of soil humidity ;
2) A SAW filter, that conveys the signal ;
3) An antenna to communicate with an interrogator.

The sensitive zone is connected to the SAW device whose admittance is Y_f. The change in soil humidity affects the behavior of the sensor while the SAW transponder relays the signal to the antenna. The drawing of the system is represented figure 1.

The sensitive zone is, in first approach, assumed to be a pure capacitance C_l of impedance Z_c (also called "load" in this paper). However, it would be easy to consider an ***RLC*** circuit instead of a unique capacitance to take into account the inductive behavior of the component and also losses due to the wire bonding. The antenna is modeled by a impedance Z_a and a radiative resistance R_{rad} connected in series with the SAW filter. On figure 1, V_e (resp. V_a) is the voltage at the terminals of the radiative resistance (resp. antenna impedance) ; V_{fe} (resp. V_{fs}) is the input (resp. output) voltage of the filter. i_a and i_c are the currents that cross Z_a and the load C_l.

B. Frequency response of the sensor

Three cases are studied to understand the behavior of the sensor and to point out the contribution of each part of the device:

1) the system composed of the filter and of the capacitance. There is no antenna in this model (fig. 2(a));
2) the antenna and the filter are considered (fig. 2(b));
3) the behavior of the whole structure (antenna, filter and load) is investigated (fig. 1).

Each above mentioned items can be described by an equivalent electrical matrix which are described in the next sections. These matrices are cascaded to obtain the performance of the sensor [5].

1) Filter and capacitance (fig. 2(a)): The purpose is to find the link between V_{fe} and i_a taking into account Z_c and the components of $[Y_f]$.

The equations establishing the behavior of this first subsystem are :

$$\begin{cases} \begin{pmatrix} i_a \\ -i_c \end{pmatrix} = [Y_f] \begin{pmatrix} V_{fe} \\ V_{fs} \end{pmatrix} = \begin{bmatrix} Y_{f11} & Y_{f12} \\ Y_{f21} & Y_{f22} \end{bmatrix} \begin{pmatrix} V_{fe} \\ V_{fs} \end{pmatrix} & (1) \\ V_{fs} = Z_c i_c & (2) \end{cases}$$

From (1) and (2), i_a can be written as follow :

$$i_a = (Y_{f11} - Z_c \frac{Y_{f12}Y_{f21}}{1 + Z_c Y_{f22}}) V_{fe} \quad (3)$$

The term in brackets in (3) is the admittance at the input of the system.

2) Antenna and filter (fig. 2(a)): In the same way that in the previous paragraph, the behavior of the filter loaded by its antenna is determined. The system behaves following these equations:

$$\begin{cases} V_{fe} = V_e - V_a & (4) \\ V_a = i_a Z_a & (5) \\ i_a = Y_{f11} V_{fe} + Y_f 12 V_{fs} & (6) \\ i_s = -i_c = Y_{f21} V_{f21} + Y_{f22} V_{fs} & (7) \end{cases}$$

The injection of expressions of (4) and (5) in (6) leads to:

$$i_a = \frac{Y_{f11}}{1 + Z_a Y_{f11}} V_e + \frac{Y_{f12}}{1 + Z_a Y_{f11}} V_{fs} \quad (8)$$

Then, the previous equation is implemented in (7) :

$$i_s = \frac{Y_{f21}}{1 + Y_{f11} Z_a} V_e + (Y_{f22} - \frac{Y_{f12}Y_{f21}Z_a}{1 + Z_a Y_{f11}}) V_{fs} \quad (9)$$

The admittance matrix of the antenna-filter ensemble consequently reads:

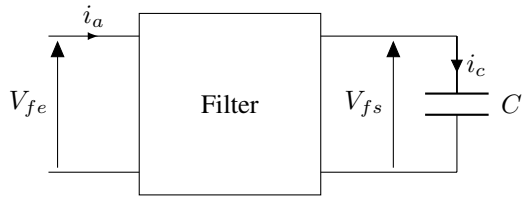
$$[Y_{AF}] = \begin{bmatrix} \frac{Y_{f11}}{1+Z_a Y_{f11}} & \frac{Y_{f12}}{1+Z_a Y_{f11}} \\ \frac{Y_{f21}}{1+Y_{f11} Z_a} & (Y_{f22} - \frac{Y_{f12}Y_{f21}Z_a}{1+Z_a Y_{f11}}) \end{bmatrix} \quad (10)$$

3) Whole system (antenna, filter and capacitance, fig. 1): If the previous results are gathered, the admittance at the input of the whole system is obtained:

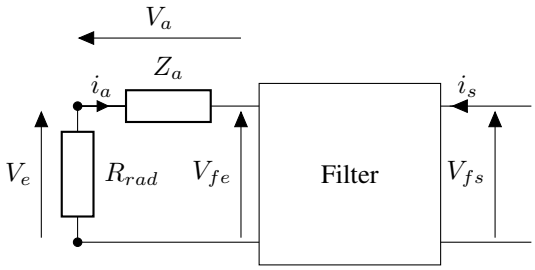
$$i_a = (Y_{AF11} - Z_c \frac{Y_{AF12}Y_{AF21}}{1 + Z_c Y_{AF22}}) V_e \quad (11)$$

where Y_{AFij} (subscripts i and $j \in [\![0, 1]\!]$) are the components of the admittance tensor Y_{AF}.

This admittance (in brackets) is the figure of merit of the system. From this quantity, we are able to know the behavior of the device and to draw, if needed, the S_{11} parameter (which is the effective value an electronic system will read).



(a) Filter and load impedance



(b) Antenna and LCRF

Figure 2. Diagram of the elements of the considered hygrometry sensor

The behavior of a passive and remotely controlled sensor based on the use of a unique SAW resonator is now defined considering (11). Consequently, the next section concentrates on the impact of soil humidity on both sensitive zone (which must be emphasized) and antenna (which should not have any influence on the device frequency response).

III. Variation of the electrical parameters of the load and of the antenna when soil humidity changes

As mentioned in Introduction, antenna and load are both submitted to the variation of humidity when dived in the ground. This section details their parameter dependence on soil hygrometry, and *de facto* the evolution of (11). Indeed, it is essential to understand how each part of the device reacts independently to allow for distinguishing the contribution of each element in the sensor response.

Moreover, soil humidity can be characterized through the relative permittivity ε_r. Actually, in air $\varepsilon_r = 1$ whereas it varies from 3 to 30 when the ground passes from dry to wet [6]. The following paragraph is devoted to the establishment of the link between ε_r and the elements of the antenna and the load.

A. Variation of the capacitance under hygrometry variations

The load C_l (of impedance $Z_c = \frac{1}{jC_l\omega}$, ω the angular frequency) is related to ε_r through the following equation:

$$C_l = \varepsilon_0 \varepsilon_r \times \frac{A}{d}\Big)_l \tag{12}$$

where $\varepsilon_0 = 8.854187 \times 10^{-12} F/m$ is the vacuum permittivity and $A/d)_l$ the ratio *area of the capacitor* on *width of the dielectric between the armatures*. In the previous equation, C_l only depends on ε_r ; $A/d)_l$ is fixed as a virtual geometric parameter and calculated below.

In dry earth, $\varepsilon_r = 3$ and C_l is arbitrarily dimensioned to be equal to 4 pF (this could be dealt in depth in further investigations). As a consequence, $A/d)_l$ is deduced as follows:

$$\frac{A}{d}\Big)_l = \frac{C_l}{\varepsilon_0 \varepsilon_r} = \frac{4 \times 10^{-12}}{8.854187 \times 10^{-12} \times 3} = 0.15059m \tag{13}$$

From (12) and (13), it is easy to determine that the capacitance is in the range [4pF ; 40pF] when buried in the ground.

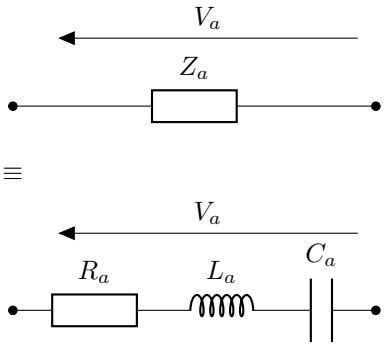


Figure 3. Equivalent circuit of the antenna without the radiative part

B. Antenna model and its variations versus soil humidity

A dipole antenna whose frequency resonance is 434 MHz (to interrogate in the industrial, scientific and medical ISM band) is used in this application. It is dimensioned to be a half wavelength antenna so the length of its wires is $l_w = 17.5cm$. Its quality factor Q is assumed to be around 10 and its radiative resistance is equal to $\simeq 73.5\Omega$ [7].

This kind of antenna can be modeled by an *RLC* circuit connected in series with the SAW filter (figure 3). As a consequence, Z_a reads:

$$Z_a = R_a + j(L_a\omega - \frac{1}{C_a\omega}) \tag{14}$$

where R_a represents the losses due to the Joule effect, L_a is the inductance due to the wires of the antenna and C_a its capacitance. The pulsation ω is equal to $2\pi f$ with f the current frequency. R_a and L_a are intrinsic parameters of the antenna.

Let us note that the geometric parameter $A/d)_a$ is, like in the previous section, a fixed parameter. At first, R_a, L_a and $A/d)_a$ are defined by studying the antenna in air. Then, the dependence of C_a (so, Z_a) on ε_r is examined.

1) Antenna inductance L_a: L_a directly stems from the geometry of the antenna :

$$L_a = \mu_0 \times 2l_w = 0.43\mu H \tag{15}$$

with $\mu_0 = 4\pi.10^{-7} H/m$ the permeability of the vacuum.

2) Loss resistance R_a: R_a is the resistance due to Joule effect in the wires of the antenna. Considering its material (Copper) and its dimensions, R_a is found equal to:

$$R_a = \frac{\rho \times 2l_w}{S} = 7.5m\Omega \tag{16}$$

assuming that $\rho = 1.7 \times 10^{-8}\Omega.m^{-1}$ the resistivity of Copper and S the section of the wire whose diameter is 1mm. It should be noticed that the skin effect could have been taken into account to adopt the point of view of antenna specialists. However, considering the resistance of a wire has got no impact on the conclusion of this work and makes easier the understanding of this paragraph.

3) Antenna capacitance C_a: The first step of the paragraph is to defined the virtual geometric constant $A/d)_a$ of the antenna capacitance. For that, the value of the antenna capacitance is at first defined in the air: $C_{a/air}$. Then, the relations governing the behavior of RLC circuit are used to calculate $A/d)_a$. Finally, the evolution of C_a versus ε_r is established.

In series RLC circuits, inductance and capacitance are derived from the resonance frequency f_r. Indeed, the magnitude of the impedance Z_a is minimum at f_r. Therefore:

$$L_a C_a \times (2\pi f_r)^2 = 1 \tag{17}$$

In air, the capacitance of the antenna $C_{a/air}$ is consequently equal to:

$$C_{a/air} = \frac{1}{L_a \times (2\pi f_r)^2} = 0.30576pF \tag{18}$$

From (12) and (18) :

$$\frac{A}{d}\Big)_a = \frac{C_{a/air}}{\varepsilon_0 \varepsilon_r} = 0.034533m \tag{19}$$

Finally, the evolution of C_a versus ε_r is the following :

$$C_a = \frac{A}{d}\Big)_a \varepsilon_0 \varepsilon_r = 0.034533\varepsilon_0 \varepsilon_r \tag{20}$$

4) Antenna response versus ε_r: All the antenna parameters are now known. Consequently, its frequency response can be plotted. Figure 4 points out the frequency shift of the antenna admittance Y_a when ε_r increases. Note that in this paragraph the behavior of the whole antenna (R_{rad} in series with Z_a) is examined. The dipole antenna used in this work is a half wavelength antenna, so its radiation resistance is equal to 73.5Ω [7]. The antenna resonance falls from 434 MHz to 79 MHz when the permittivity varies from 1 (air) to 30 (humid ground). As a consequence, the sensor will not operate above the antenna resonance but on its side. This could be an advantage to restrain the influence of the antenna on the system.

IV. Design of the filter

The choice to design a SAW LCRF (cf. fig 5) for this application was made to be close to the conditions described in reference [3]. Moreover, the coupling between the two modes is mandatory for the filter to act as a transponder and to transmit energy (so, information) from one port to another (i.e. from the load to the antenna).

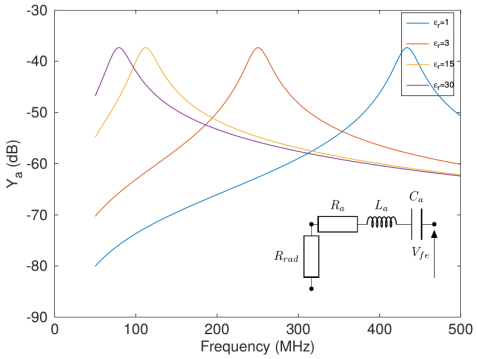


Figure 4. Evolution of the frequency response of the antenna when ground hygrometry varies

TABLE I. Summary of the dimensions of the SAW LCRF

	number of strips	p (μm)	a/p
Mirrors	480	4.42	0.5
Transducers	60	4.40	0.4
Coupler	100	4.42	0.5

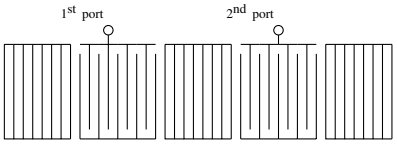


Figure 5. Diagram of a LCRF

Because of internal requirements, the device is made on (YXl)/128^o Lithium Niobate cut. A 350 nm thick Aluminum layer is deposited at the surface of the substrate to form the electrodes. The dimensions of this component are summarized in table I. The frequency response of the device can consequently be analyzed. s_{11} parameter and y_{11} admittance are then plotted on figure 6. They give several information. Firstly, the two modes are located at 433.546 MHz and at 434.188 MHz. Moreover, despite the high coupling factor of the Lithium Niobate and thanks to a source removal, a low coupling factor (resp. 0.08% and 0.171%) is achieved with spectral purity. Finally, the second resonance is perfectly adapted to 50Ω: the considered frequency corresponds to a real mode and the minimum of s_{11} is located at the resonance (for another configuration, this particular point could correspond to another impedance) whereas the first mode is lightly shifted from this working point.

In brief, the SAW transponder is now designed to operate in the considered ISM band.

V. Evolution of the frequency response of the device vs soil hygrometry

The behavior of each part of the system has just been studied. We now focus on the behavior of the antenna and/or the load connected to the filter.

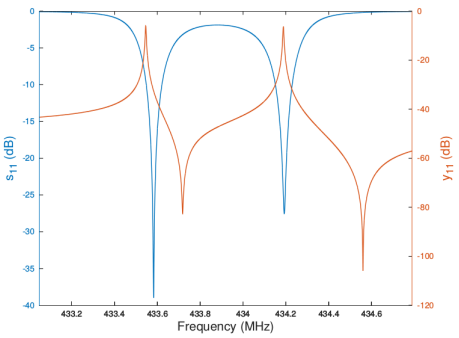


Figure 6. Frequency response of the SAW filter without the antenna or the capacitance. Its admittance Y_{11} and its parameter S_{11} are represented

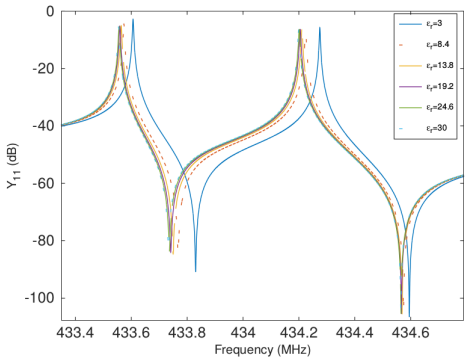


Figure 7. Evolution of the frequency response of the system represented fig. 2(a) when ε_r varies from 3 to 30

A. *Capacitance and filter for wired sensing*

At first, the case of figure 2(a) is examined. Knowing that the permittivity of the ground varies from 3 to 30, the response of the filter connected to the sensitive zone under this fluctuation is clarified. The results are reported on figure 7. The first observation that can be done is the decrease of the frequency resonances when C_l increases. Namely, the wetter the soil, the lower the frequency resonances. In fact, the first mode varies from 433.607 MHz to 433.555 MHz corresponding to a frequency shift of 52 kHz. As for the second mode, its resonance frequency experiences a 76 kHz shift (from 434.275 to 434.199 MHz). Moreover, figure 8 displays the evolution of each resonance frequency versus ε_r. Each mode has got its own behavior, so differential measurements can be done. This is also put forward on figure 9 that plots the frequency difference between the two modes (frequencies f_1 and f_2): when ε_r increases, the quantity $\Delta f = f_2 - f_1$ (in kHz) evolves according to:

$$\Delta f = 668.13 + 98.25 \times (\frac{1}{\varepsilon_r} - \frac{1}{3}) + 60.372 \times (\frac{1}{\varepsilon_r} - \frac{1}{3})^2 \quad (21)$$

Consequently, the *filter capacitance* system can already be used as a wired hygrometer.

Two remarks can be added:

- the results are consistent with the results of publication [3] ;
- it seems that the larger the mode coupling, the larger the frequency shift.

This paragraph confirmed that the evolution of soil humidity can be monitored using the system of figure 2(a). The next step is to focus on the influence of the hygrometry on the filter response when it is connected to the antenna. By this way, the design of a wireless hygrometer is getting closer.

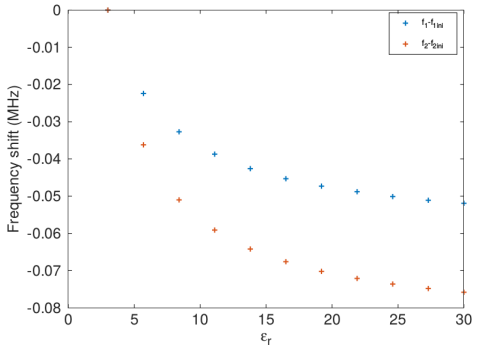


Figure 8. Evolution of the two resonance frequencies when the humidity of the soil varies. The second frequency (higher frequency) decreases faster than the first one (lower frequency)

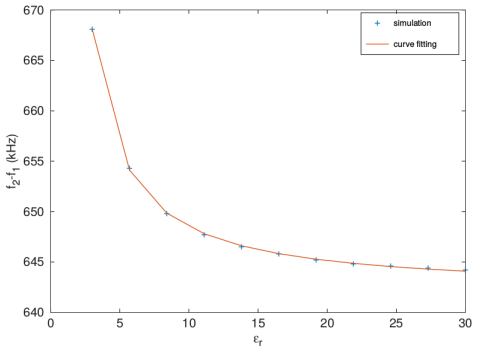


Figure 9. Evolution of the frequency difference $f_2 - f_1$ in the ground

B. *Antenna and filter system behavior*

We proceed using the same methodology than in the previous section to determine the behavior of the *antenna-filter* system when $\varepsilon_r \in [3; 30]$. The response of this structure is plotted on figure 10. The antiresonance seems to appear before the resonance, which is not possible if the different elements are correctly connected to each other (absence of short-circuit).

Hence, the studied frequency range is widened and the evolution of ε_r is restricted from 1 to 1.20. Actually, the lowering of the range of ε_r allows for the understanding of the behavior of the *antenna-filter* system along relative permittivity. Figure 11 displays a sizable decrease of the resonance frequencies. The frequency shift is high enough to make the first mode out of the mirror Bragg band, which leads to a loss of the first mode signature and to the location of the second mode just after the first antiresonance. No influence is seen on the antiresonances. At last, the resonances vary so much that we are no more able to determine the value of ε_r by monitoring the resonances, before even the flooding of the sensor into the ground.

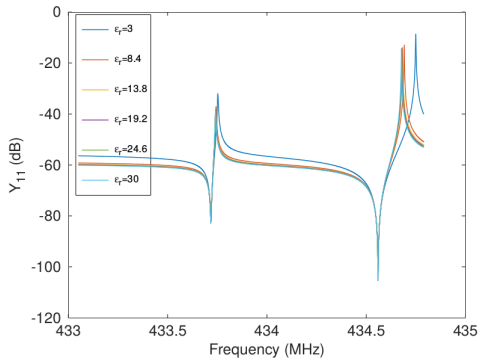


Figure 10. Evolution of the frequency response of the system represented fig. 2(b) when ε_r varies from 3 to 30

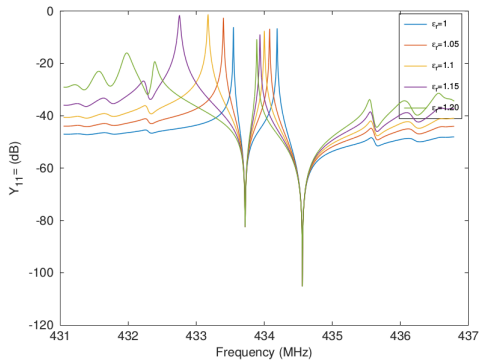


Figure 11. Evolution of the frequency response of the system represented fig. 2(b) when ε_r varies from 1 to 1.20

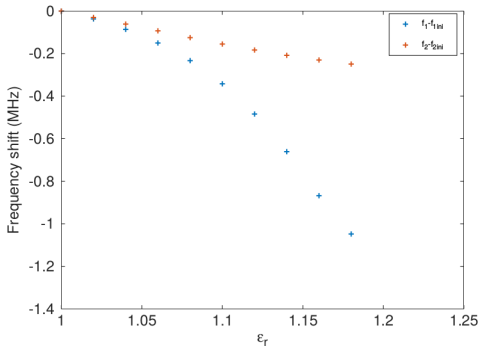


Figure 12. Evolution of the frequency shifts of the filter loaded by its antenna when relative permittivity varies from 1 to 1.20

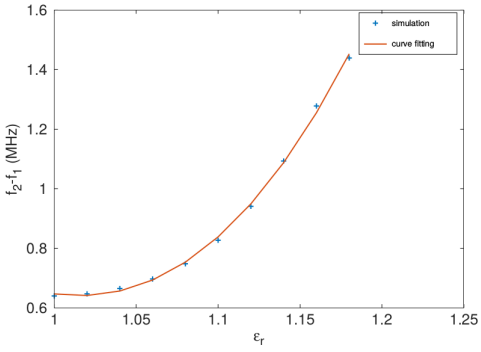


Figure 13. Evolution of the frequency difference $f_2 - f_1$ when relative permittivity varies from 1 to 1.20

However, in this narrow permittivity range, the different behaviors of the two modes versus ε_r are clearly visible: figure 11 shows a larger impact of ε_r on the first mode than on the second one. Next part is consequently dedicated to the exploiting of this particularity.

C. Antenna and filter as a wireless hygrometry sensor

The previous paragraphs pointed out the impact of humidity (through ε_r) on the response of the filter loaded by an antenna. Particularly, ε_r influences the value of the capacitance of the dipole antenna (see section II-B2). C_a modifications involve the shifting of the two resonances of the LCRF connected to the antenna with a larger impact on the first one than on the second mode (see section V-B).

Figure 12 shows the variation of both modes when $\varepsilon_r \in [1, 1.20]$: the first frequency resonance decreases of more than 1 MHz in this range whereas the second one is reduced of about only 200 kHz. Then, figure 13 makes visible the increase of the frequency difference $\Delta f = f_2 - f_1$ when relative permittivity increases too. This quantity can be estimated as follow:

$$\Delta f(MHz) = 0.64677 - 0.75019(\varepsilon_r - 1) + 23.6655(\varepsilon_r - 1)^2 + 29.91453(\varepsilon_r - 1)^3 \quad (22)$$

As a consequence, the possibility to conduct a differential measurement has been brought to light. Namely, the antenna forms both the interrogation part (emission and reception of the signal) and the sensitive area of the hygrometer.

VI. Conclusion

In order to develop a ground hygrometry sensor, the impact of humidity on the different elements of the system is studied. The sensor is in first instance composed of three parts :

- a sensitive zone to measure the variation of soil hygrometry ;
- a filter acting as a transponder ;
- an antenna.

This paper shows that the sensitive zone, modeled for now by a pure capacitance, varies from 4 to 40 pF linearly with ε_r (so, with the hygrometry). In further works, the load capacitance will be replaced by an impedance composed of fixed resistive and inductive parts that are distinctive features of the component, and of a capacitance whose value depends on earth hygrometry. As for the antenna, the large impact of ground ε_r on its frequency response is pointed out. Indeed, the dipole antenna, which can be modeled by an *RLC* circuit sees its frequency resonance collapse of 355 MHz with the increase of humidity. A SAW filter (LCRF type) is also designed on Lithium Niobate to work in the ISM band centered on 434 MHz.

Then, the effective impact of the humidity on the response of the *filter load* system is demonstrated: the variation of

several dozen of kHz on each mode is sufficient enough to calibrate the sensor and to measure the ground humidity. Actually, a wired hygrometer has been modeled. Regarding the influence of the antenna on the sensor, its huge sensitivity on environmental parameters is pointed out to the extent that a slight variation of ε_r make the signal out of the frequency range of interest. As a consequence, the study of this system is done for a variation of the permittivity comprised between 1 and 1.20 instead of from 3 to 30. This last point reveals that the two modes are impacted by the variation of antenna parameters (particularly, its capacitance due to ε_r changes) and that they behave differently. The shift of the frequency difference can be estimated with a third degree interpolation function. Consequently, a measure of relative permittivity can be carry out using the antenna, both to convey the signal and to be the sensor itself. By this way, a wireless hygrometry measurement can be conducted.

In future works, the SAW filter presented in this work will be manufactured to carry out calculation/test correlations and if needed, to adjust the model and to refine the design. The modification of the design of the SAW component is also considered to lower the impact of ε_r on the sensor response and consequently, to be able to measure soil humidity with the device presented in this article.

ACKNOWLEDGMENT

We are grateful to the DGA and to the ANRT for their financial backings.

REFERENCES

[1] A. Kawalec and M. Pasternak. A New High-Frequency Surface Acoustic Wave Sensor for Humidity Measurement. *IEEE Transactions on Instrumentation and Measurement*, 57(9):2019–2023, Sept 2008.

[2] L. Reindl, C. C. W. Ruppel, A. Kirmayr, N. Stockhausen, M. A. Hilhorst, and J. Balendonck. Radio-requestable passive SAW water-content sensor. *IEEE Transactions on Microwave Theory and Techniques*, 49(4):803–808, Apr 2001.

[3] T. Laroche, G. Martin, W. Daniau, S. Ballandras, J. M. Friedt, and J. F. Leguen. A coupled-mode filter structure for wireless transceiver-sensors using reactive loads. In *2012 IEEE International Frequency Control Symposium Proceedings*, pages 1–6, May 2012.

[4] J. M. Friedt. Passive cooperative targets for subsurface physical and chemical measurements. In *2016 16th International Conference on Ground Penetrating Radar (GPR)*, pages 1–6, June 2016.

[5] T. Laroche, J. Garcia, E. Courjon, S. Ballandras, and W. Daniau. A comprehensive model of the electrical response of SAW devices submitted to thermal perturbation. In *2014 European Frequency and Time Forum (EFTF)*, pages 71–74, June 2014.

[6] R.A van Overmeeren, S.V Sariowan, and J.C Gehrels. Ground penetrating radar for determining volumetric soil water content; results of comparative measurements at two test sites. *Journal of Hydrology*, 197(1–4):316–338, 1997.

[7] Constantine A. Balanis. *Antenna Theory: Analysis and Design*. John Wiley & Sons, February 2016.

Three-Parameter Liquid Sensor Based on Surface and Plate Acoustic Waves.

Voronova N.V.
IEEE member, post graduate student of the Kotelnikov' Institute of Radioengineering and Elrctronics Russian Academy of Sciences , the head of laboratory of the Acoustoelectronic and Piezokeramic ELPA Corporation
Moscow, Russia
e-mail: vonavl@mail.ru

Anisimkin V.I.
IEEE member, doctor of science, principal researcher, the Kotelnikov' Institute of Radioengineering and Elrctronics Russian Academy of Sciences
Moscow, Russia
e-mail: anis@cplire.ru

***Abstract*—This work deals with developing the sensor capable to detect viscosity, electric conductivity, and temperature of one and the same micro-liter liquid sample. The sensor is based on surface and plate acoustic waves propagating in LiNbO3 crystal. Properties of the waves and parameter of the sensor are measured and presented.**

Keywords—acoustic waves, piezoelectric plates, liquid sensors.

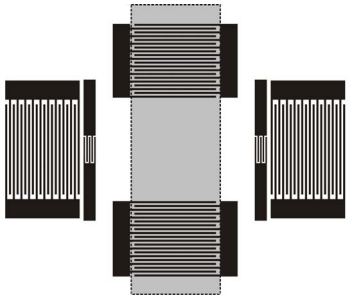
I. INTRODUCTION

Analysis of liquid substances is now required in many fields of science and technology. Usually, it is accomplished by means of individual sensors for each physical parameter [1]. The goal of the present paper is to develop three-parameter sensor measuring liquid viscosity η, electric conductivity σ, and temperature t for one and the same micro-liter sample simultaneously.

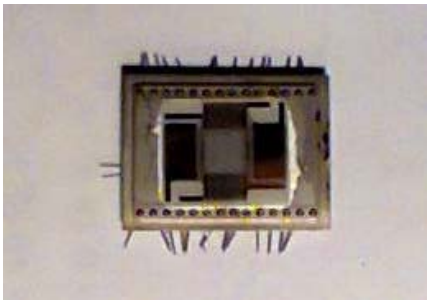
II. STRATEGY

The sensor is based on probing a liquid with 3 different acoustic waves propagating in same piezoelectric crystal. Elastic and electric fields of the waves penetrate to the liquid deposited on the crystal (the depth ~ 100 μm) and change the waves velocities (phases $\Delta\varphi$) and amplitudes (attenuations $\Delta\alpha$) depending on the liquid properties. The key point of this approach is to select the types of the waves and the forms of the wave responses properly. In order to do this, a mode family with large coupling constants (for efficient generation) together with small vertical displacements (for low radiation into a liquid) are found using common calculation procedure [2]. The best modes of the family are then selected using experimental approach detailed in [3].

The sensor was implemented on standard 128Y-LiNbO3 plate, 500 μm thick, with one polished, other grinded faces. A test liquid is deposited on the grinded (top) surface, while 3 pairs of interdigital transducers (IDTs) are located on the polished face (bottom) (Fig.1). The 1st (horizontal) IDTs pair with periodicity λ = 20 μm generates the surface acoustic wave (SAW). It is localized near the bottom surface and, thereby, does not "fill" the liquid viscosity η and conductivity σ. Instead, the wave measures the liquid temperature t translated from the top to the bottom thanks to thermal conductivity of the plate material. The form of the response for the SAW is taken to be the change in phase $\Delta\varphi$ as the most sensitive acoustic parameter.



(a)



(b)

Fig.1. Schematic view (a) and photo (b) of the three-parameter liquid sensor.

The 2nd (vertical) pair of IDTs with periodicity λ = 300 μm generates an acoustic Lamb mode selected purposely. The mode has direct physical contact with test liquid, but its propagation path on the top of the plate is totally metalized.

Thereby, it does not sense the liquid conductivity, but measures liquid viscosity. In order to reduce the temperature dependence of the mode the form of its response is taken to be the attenuation $\Delta\alpha$ as almost insensitive to temperature parameter.

Finally, the 3rd (horizontal) pair of IDTs with periodicity λ = 300 μm generates another Lamb mode whose propagation path is partially not metalized. This mode is selected purposely to have high sensitivity towards liquid conductivity σ, but low sensitivities to its viscosity and temperature. The form of the response is taken to be the phase $\Delta\varphi$ ensuring unique dependence on σ in contrast to the attenuation $\Delta\alpha$. Unwanted contributions from η and t are accounted in $\Delta\varphi$ by previous measurements.

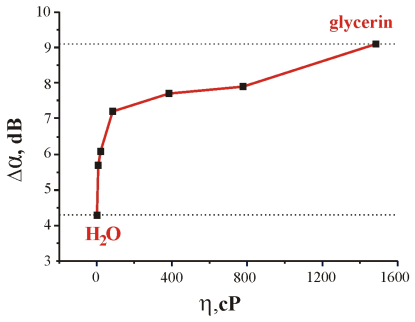
III. Results and Conclusions

Properties of the waves used in the sensor are listed in the Table1:

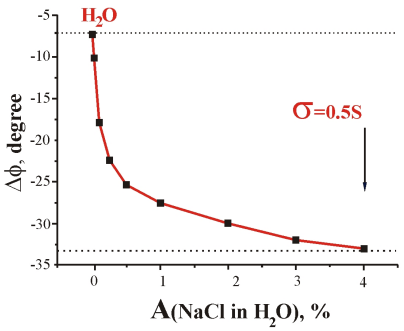
TABLE I. PROPERTIES OF THE WAWES

Channel №1 along X-axis (f = 185 MHz)		
$\Delta\varphi(\eta)$	$\Delta\varphi(\sigma)$	$\Delta\varphi(t)$
0	0	-11 degree/°C
Channel №2 perpendicular to X-axis (f = 29.77 MHz)		
$\Delta\alpha(\eta)$	$\Delta\alpha(\sigma)$	$\Delta\varphi(t)$
9.1 dB at η = 1500 cP	0	0
Channel №3 along X-axis (f = 23.90 MHz)		
$\Delta\varphi(\eta)$	$\Delta\varphi(\sigma)$	$\Delta\varphi(t)$
-6 degree at η = 1500 cP	-33 degree at σ = 0.5 S	-2.9 degree/°C

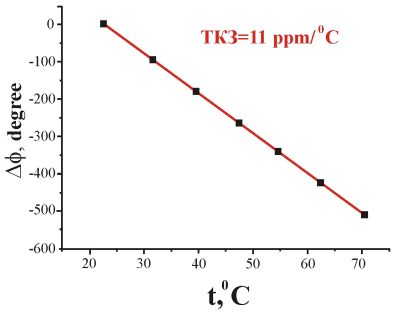
The calibration of the sensor is accomplished using water solutions of glycerin and NaCl [4] (Fig.2). The ranges of the measurements are from units to 1500 cP for viscosity, 0.005 to 0.5 S for conductivity, and 22 to 70 °C for temperature. Because of the forms of the dependences (Fig.2 a,b) precision of the measurements is decreased with increased η and σ. Typical volume of a test liquid is about 100 μl. The shape of the liquid is not critical as its thickness is much larger the penetration depth (~ 100 μm). On the other hand, the liquid zone should overlap the area between transducers for any measurement.



(a)



(b)



(c)

Fig.2. Calibration curves.

Acknowledgment

The work is supported by grant 15-07-00538 from Russian Foundation for Basic Research.

References

[1] O.L.Balashova. http://www.cplire.ru.

[2] E.L.Adler, J.K.Slaboszewics, G.W.Farnell, and C.K.Jen, "PC software for SAW propagation in anisotropic multi-layers", *IEEE Trans. Ultrason, Ferroelect., Freq. Contr.,* vol.37, pp.215-220, Sep.1990.

[3] I.V.Anisimkin, V.I.Anisimkin, "Attenuation of acoustic normal modes in piezoelectric plates loaded by viscous liquids", *IEEE Trans. Ultrason, Ferroelect., Freq. Contr.,* vol.53, pp.1487-1492, August 2006.

[4] R.C.Weast, ed. "Chemical Rubber Company Handbook of Chemistry and Physics", 66th ed. Chemical Rubber, Boca Raton, FL, 1985.

Elastic Properties of Graphene Oxide Films and Changes due to Gas Phase Adsorption.

E.Verona[1,4], IEEE member, I.E. Kuznetsova[1] IEEE member, V.I.Anisimkin[1] IEEE member,
S.P. Gubin[2], S.V.Tkachev[2], V.V. Kolesov[1], V.V. Kashin[1], B.D. Zaitsev[3] IEEE member,
A.M. Shikhabudinov[3]
[1]Kotelnikov Institute of Radio Engineering and Electronics of RAS, Moscow, 125009, Russia.
e-mail: kuziren@yandex.ru
[2]Kurnakov Institute of General and Inorganic Chemistry of RAS, Moscow, 119991, Russia
[3] Kotelnikov Institute of Radio Engineering and Electronics of RAS, Saratov, 410019, Russia.
[4]Institute for Photonics and Nanotechnologies, IFN-CNR, Via Cineto Romano 42, 00156 Rome, Italy

***Abstract*—This work deals with the characterization of Graphene Oxide (GO) films for application to acoustic gas sensors. The preparation of the GO dispersion and its deposition on the surface of SAW and BAW devices is reported. Measurements of the frequency dependence of the resistance and reactance for the different electro-acoustic structures tested, in the presence of dry air (reference) and of concentrations of different gases or vapors, allowed us to evaluate the elastic moduli and their dependence on the adsorbed gas. A negligible response to H_2, CO, CH_4, NO and O_2 has been demonstrated for GO, while exposure to humidity gives rise to high responses. The elastic modules of the film are 3 orders of value smaller than those of traditional sorbent materials, while the changes produced in the modules by humid air are 1 order of value larger.**

Keywords—BAW resonators, SAW delay lines, Graphene Oxide, elastic moduli, gas sensors.

I. INTRODUCTION

For a purposeful development of any gas sensor, the knowledge of the fundamental properties of the sorbent film is required. Last time attention of many researchers is concentrated on graphene oxide (GO) films as one of the most promising new candidate (see e.g. [1]). The goal of the present paper is to measure the elastic properties of GO films together with the changes produced by gas exposure. These data are suitable for both sensors based on bulk (BAW) and surface (SAW) wave propagation, including Lamb acoustic waves.

II. STRATEGY

The films were fabricated starting from China natural graphite (99.9% C). The material was grinded in a ball crusher (200-300 μm), oxidized, and dried for 6 hours at 50-60^{0}C. After that 0.4-0.5 g of graphite oxide was placed in a cylinder chamber (250 ml) together with distilled water (150 ml) and sonicated for 15 min. at 20.4 kHz and 0.1-1 W/sm^3. The GO-based dispersion was spry coated by an airgraph on the test devices: a langasite (4 MHz) and an AT-quartz (3 MHz) BAW resonators, as well as on a ST,x-quartz SAW delay line (29.9 MHz). After coating the samples were finally dried for 24 hours, at room temperature, before to be tested. The thickness of the films was measured by a mechanical profilometer.

Measurements have been taken in a gas tight chamber, 750 ml volume, and forced by a laminar gas flux (100 ml/min) of reference (dry air) or test (humid air, 1% H_2, 0.74 %CO, 1% CH_4, 0.44% NO, 100 % O_2) gases, at room temperature (22°C). At first, the elastic modules and their changes due to the gas adsorption have been evaluated by fitting the calculated frequency dependencies of the resistance and reactance to the values measured by a Network Analyzer (Keysight E5061B), as shown in Figure 1, while the density ρ was estimated as the ratio between the weight and volume of the film. After that, the density was measured more accurately by fitting the SAW response, calculated using the modules, and the response measured for the same substrate, film, and gas [2]. The results obtained at different values of relative humidity (RH) are reported in Table 1.

III. RESULTS AND CONCLUSIONS

Measurements have shown that the response of GO films to concentrations of H_2, CO, CH_4, NO and O2 is almost negligible, but is very large towards humidity. The elastic modules of the GO film are 3 orders of value smaller than those of traditional sorbent materials, such as SnO_2, CeO_2, Pd, Pt, etc., while the changes produced in the modules by humid air are 1 order of value larger.

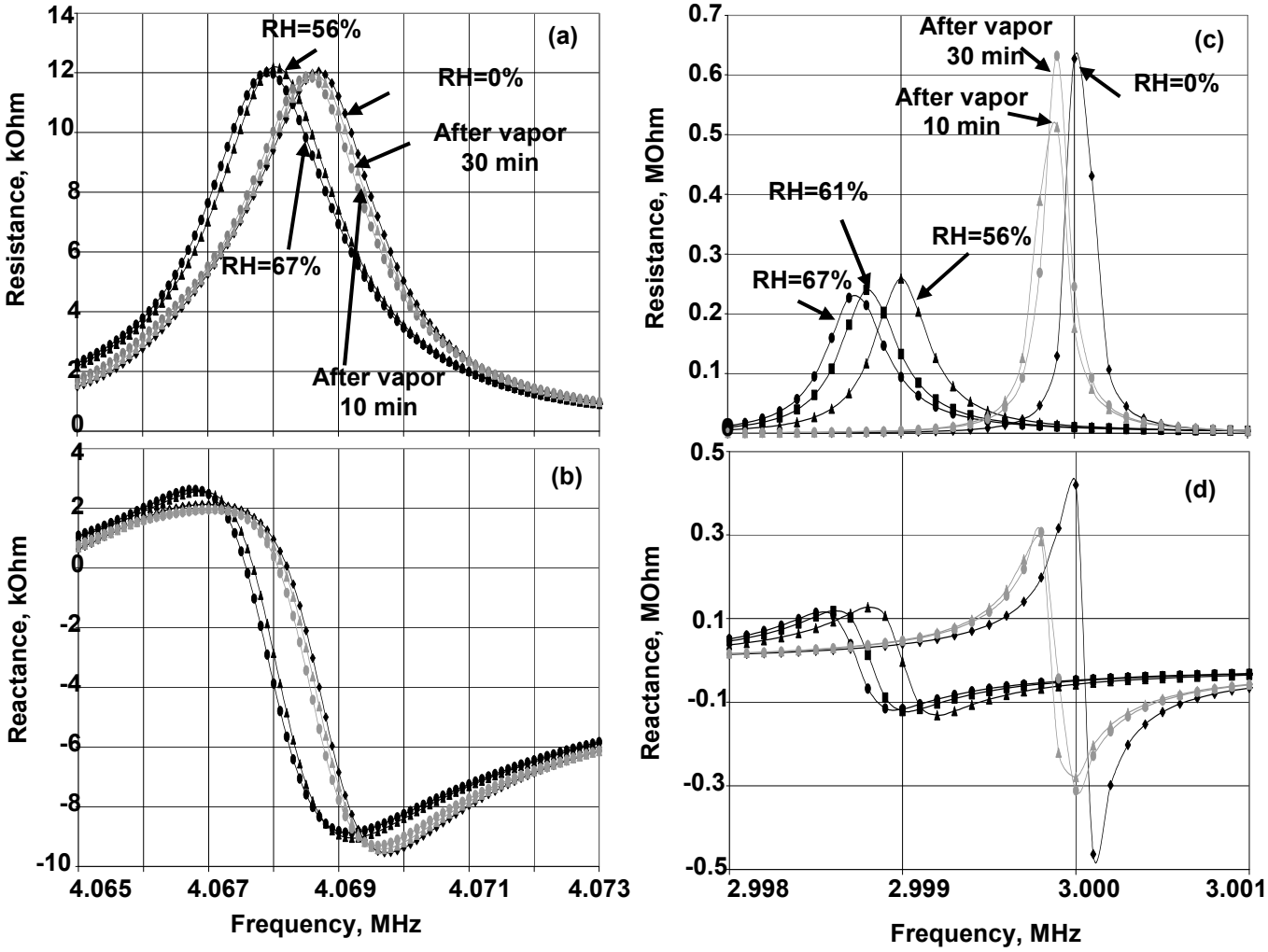


Fig. 1. Theoretical (solid line) and experimental (points) frequency dependencies of the resistance (a, c) and reactance (b, d) for the langasite (a,b) and quartz (c, d) based resonators, loaded by a GO film, 2 μm thick, for different water vapor concentrations.

TABLE I. PROPERTIES OF THE GO FILM EXPOSED TO DIFFERENT WATER VAPOR CONCENTRATIONS.

RH, (%)	ρ, (10^3 kg/m^3)	Δρ/ρ	C_{11}, (MPa)	$\Delta C_{11}/C_{11}$	C_{44}, (MPa)	$\Delta C_{44}/C_{44}$
0.47	0.85	0	18	0	4.5	0
56	0.8	- 0.06	12	- 0.33	2.7	-0.4
61	0.75	-0.12	13	- 0.28	2.0	-0.55
67	0.75	- 0.12	13	- 0.28	1.4	- 0.69

ACKNOWLEDGMENT

This work was supported by grant 15-19-20046 from Russian Science Foundation.

REFERENCES

[1] Z. Yuan, H. Tai, Z. Ye, C. Liu, G. Xie, X. Du, Y.Jiang, "Novel highly sensitive QCM humidity sensor with low hysteresis based on graphene oxide (GO)/poly(ethyleneimine) layered film", Sensors and Actuators B **234** 145 (2016).

[2] V.I. Anisimkin, E. Verona, "New capabilities for optimizing SAW gas sensors", IEEE Trans. on Ultrasonics, Ferroelectrics and Frequency Control, **UFFC 48**, 1413 (2001)..

SAW Torque Sensor for Marine Applications

Victor Kalinin, Arthur Leigh, Alexander Stopps
Transense Technologies plc
Bicester, Oxfordshire, UK
victor.kalinin@transense.co.uk

Stefan Blom Hanssen
Kongsberg Maritime
Trondheim, Norway

***Abstract*— Design of a torque sensor for aftermarket installation on marine propeller shafts is presented. The sensor is based on UHF SAW resonator sensing elements bonded to plate transducers that are clamped on the shaft and interrogated in a non-contact way through an easily installable RF coupler. A method of calibration of the transducers is described and the torque data logged during a one year period of testing on a ship are presented.**

Keywords—torque sensor; wireless SAW sensor; passive non-contact sensor; RF rotary coupler; sensor calibration

I. INTRODUCTION

Torque sensors based on different technologies are currently used for measuring torque applied to marine propeller shafts to monitor power transferred from main engines to propellers and torsional oscillations of the shafts. This information helps improve fuel efficiency, reduce CO_2 and NO_x emission, and avoid over-stressing of the engines. Some of the sensors employ traditional strain gauges with telemetry transmitters. Others are based on measuring a shaft twist angle by optical transducers with two slotted code wheels [1]. These systems imply expenditures up to €15-20 K, can be difficult in installation, or require a considerable axial length of the shaft.

Non-contact torque sensors based on SAW resonators could be an attractive alternative to the traditional solutions. Several of them have already been developed for automotive and industrial applications [2]. However, their design, assembly, and calibration methods are not suitable for aftermarket installation on big shafts with the diameter up to 400 mm. A more suitable approach was suggested in [3] for wind turbine gearboxes. It was proposed to install the resonant SAW shear strain sensing elements not directly on the shaft but on a plate transducer that could be easily clamped on the shaft and calibrated over the operational temperature range before installation. Calibration and preliminary test results proved to be promising but long-term field testing data were not available and were not reported in [3].

The aim of this paper is to present a design of the marine SAW torque sensor based on clamped plate transducers, design of an RF rotary coupler for their non-contact interrogation, a sensor calibration method, its installation on a solid 180-mm propeller shaft of a Norwegian passenger ship and results of more than one year testing in the real working environment.

II. PLATE TRANSDUCERS FOR THE SAW TORQUE SENSOR

The transducers employed two 4x6x0.35 mm SAW resonant sensing elements made on Y+34° cut quartz that were previously developed for automotive applications [2]. One of them, HFSAW, had three resonators working approximately at f_1 = 437 MHz, f_2 = 435 MHz, and f_3 = 433 MHz for measuring shear strain s and temperature T up to 500 με and 150°C. Simultaneous measurement of s and T was performed by measuring two difference frequencies, $F_{m1} = f_1 - f_2$ and $F_t = f_2 - f_3$ that depend in a different way on strain and temperature [4]. This was achieved by positioning the first two resonators at ±45° and the third one at 30° to the crystallographic X axis of the quartz substrate parallel to the shaft axis. The second sensing element, LFSAW, had only two resonators working at f_4 = 431 MHz, f_5 = 429 MHz for shear strain measurement using $F_{m2} = f_4 - f_5$. Since the propeller shaft may experience some bending, the two sensing elements needed to be installed on two opposite sides of the shaft and $F_m = (F_{m1} + F_{m2})/2$ was used to measure strain to achieve bending compensation.

The two plate transducers with SAW sensing elements bonded to them are shown in Fig. 1 before they were hermetically sealed by welded lids. The dimensions and the shape of the steel plates were designed by means of FEA to obtain the principal strain s_1 = 246 με on the underside surface of the plate when the maximum torque M_{max} = 56 kNm was applied to the propeller shaft. A perfect contact was assumed between the shaft and the stiff shoulders of the plate transducers having a curvature matching the shaft diameter. The shear modulus of the shaft was assumed to be equal to G =

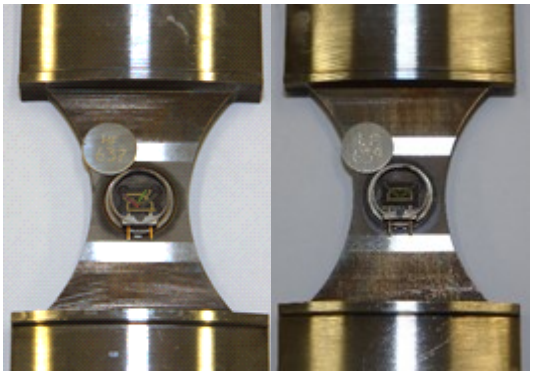


Fig. 1. Plate transducers with bonded HFSAW and LFSAW sensing elements.

82 GPa although its exact value was unknown. The simulated strain distribution on the plate and the solid propeller shaft are shown in Fig. 2 where the strain on the shaft surface is 298 με.

The stiff shoulders of the transducers were designed for clamping them to the shaft by means of heavy-duty flexible metal straps like those used in [3] on the 120-mm wind turbine gearbox shaft.

III. THE RF ROTARY COUPLER AND THE SAW READER

The RF coupler plays the role of the sensor antenna and the reader antenna coupled to each other by microstrip fringing fields. The coupler design was different from the one used in [3] for two reasons, (a) smaller radial and axial tolerances on the shaft movement that allowed using a planar rather than a coaxial cylindrical geometry and (b) ease of installation that required the rotor to consist of two detachable parts and the stator to be in the form of a 180° section. Both the stator and the rotor were made of FR4 PCB material and used 50Ω microstrips coupled back to back with the gap of 2 mm.

The stator antenna is shown in Fig. 3a and two halves of the rotor antenna are presented in Fig. 3b. One can see two coaxial cables for connection of the SAW sensing elements to the rotor. Mechanical design of the rotor allowed its quick assembly on the shaft by means of clamping simultaneously with the plate transducers bolted to the two halves.

Electrical design of the coupler was done by Microwave Office® and then the decoupling and loading components were optimized experimentally to reduce the standard deviation of the measured difference frequency σ_{Fm} down to 300 Hz and minimize the peak-to-peak variation of F_m with the rotation angle to 750 Hz (see Fig. 4). The obtained values were small enough for the application under consideration since the full scale (FS) variation of F_m due to torque was around 670 kHz. As a result, both random errors and the systematic error due to coupler rotation were below 0.13%FS.

The SAW reader used in the sensor for interrogation of the sensing elements is described in [2]. It excited the five SAW resonators sequentially with the frequency f_3 being measured only once every 500 interrogation cycles for temperature update. The peak power of the RF interrogation pulses was 2.4 dBm, their length was around 3 μs. Five SAW responses of each SAW resonator were coherently accumulated before estimating its frequency to reduce random errors. The torque and temperature readings were transmitted through the CAN

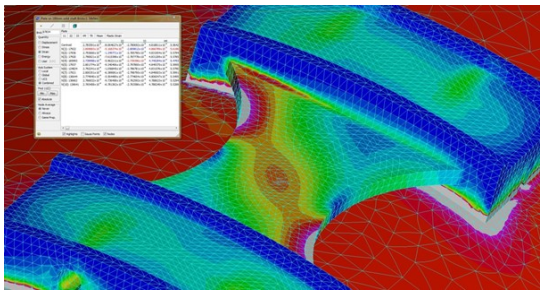
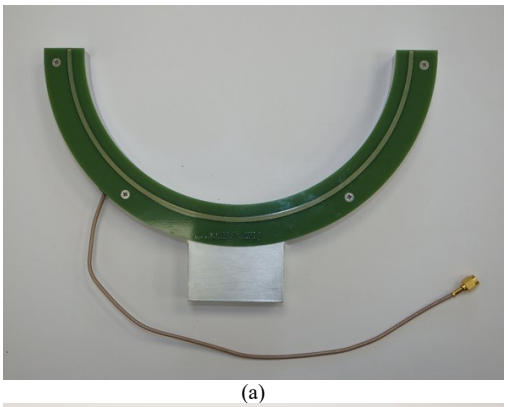
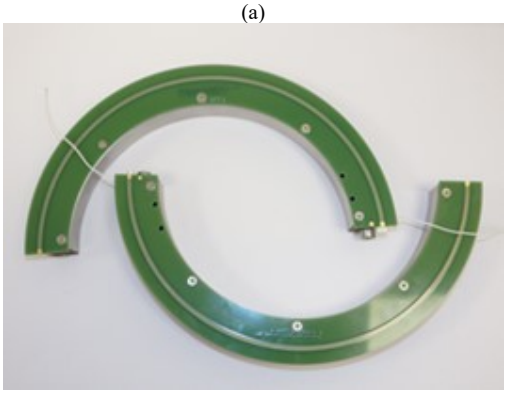


Fig. 2. Strain distribution on the plate transducer rigidly attached to the solid propeller shaft calculated by FEA.

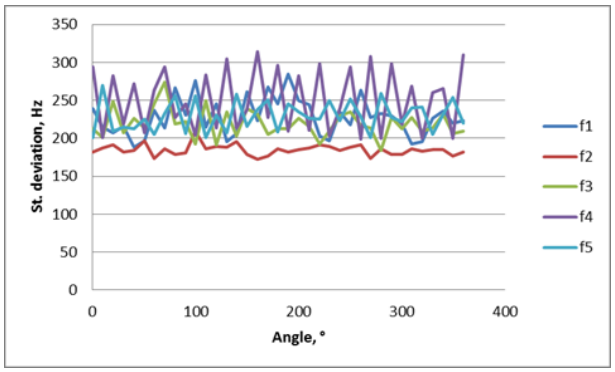


(a)

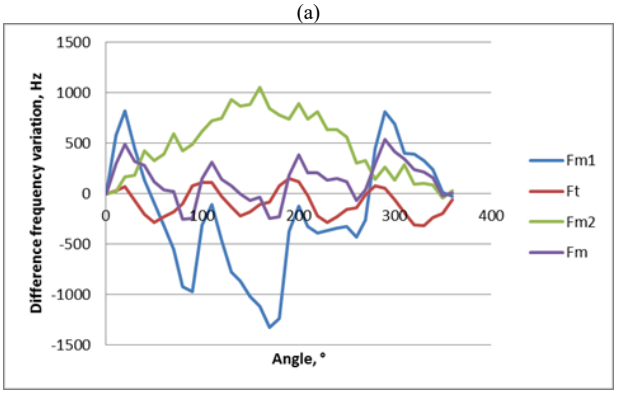


(b)

Fig. 3. The stator antenna (a) and the two halves of the rotor antenna (b) of the RF rotary coupler.



(a)



(b)

Fig. 4. Standard deviation of the measured resonant frequencies (a) and their differences (b) against the shaft rotation angle.

bus as signed 2 byte integers with the update rate of 2 kHz. Analogue torque output was also implemented to simplify interfacing with KONSBERG K-Chief data logging system.

IV. CALIBRATION

The aim of the calibration of the torque plate transducers was to find two functions, $F_m(M,T)$ and $F_t(M,T)$ from measurements performed on a special test shaft with the same diameter as the propeller shaft. The idea was to use a hollow test shaft with a reduced stiffness to achieve roughly the same level of shear strain on the plate as in the case of a solid propeller shaft but at a significantly lower calibration torque $M_{cal\,max}$ = 2 kNm that was achievable in the test rig.

The test shaft with a locally reduced diameter under the plate transducer was designed and analysed by FEA (see Fig. 5). The value of principle strain s_{2s} = 213 με on the plate underside surface was obtained by simulation assuming a perfect mechanical contact between the shaft surface and the transducer's shoulder. The test shaft was fabricated, the RF coupler was installed on it, the plate transducers were clamped by flexible straps and the whole assembly was installed in the oven of the torque calibration rig as shown in Fig. 6.

As a first step, the FEA result was validated by measuring the strain on the underside of the plate transducer by a strain gauge. The measured strain turned out to be somewhat lower, s_{2m} = 206.5 με, and it stayed almost constant over the operating temperature range. The 3.1% discrepancy between s_{2s} and s_{2m} might be due to inaccuracy of the FEA or wrong values of the stiffness modulus of the test shaft and the plate transducer or a strain gauge measurement error. However, a more significant source of discrepancy could be imperfect strain transfer from the shaft surface to the plate shoulders. Admitting this as the main cause of the discrepancy we assumed that the behavior of shaft/plate interface remained the same both for the test shaft and for the propeller shaft. Under this assumption, the scaling factor between the torque applied to the test shaft and the equivalent torque applied to the propeller shaft could be defined as

$$K = (s_{2s}/M_{cal\,max})/(s_1/M_{max}) = 24.244. \quad (1)$$

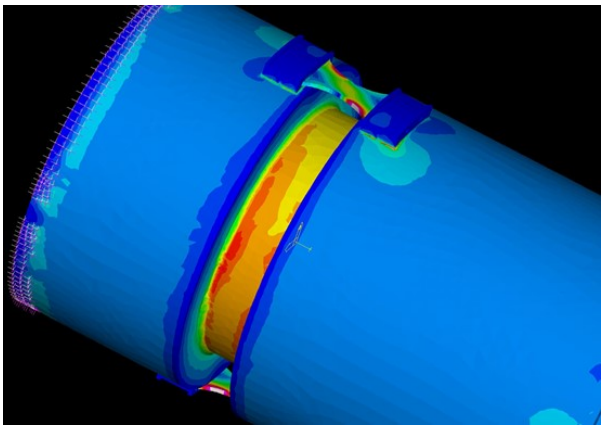


Fig. 5. Strain distribution on the plate transducer rigidly attached to the hollow test shaft calculated by FEA.

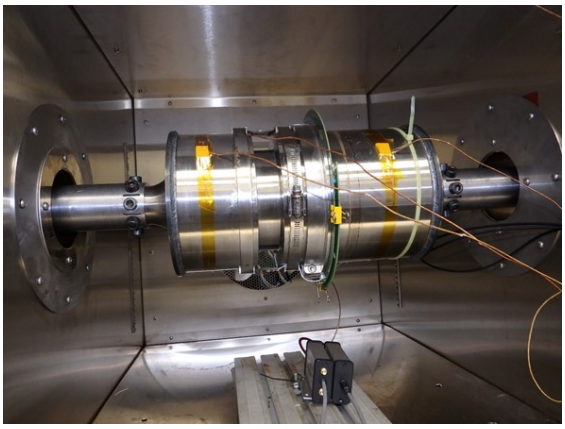


Fig. 6. The test shaft with the SAW plate transducers installed in the torque calibration rig.

Calibration of the plate transducers on the test shaft was performed within the temperature range from 10°C to 50°C after a certain amount of temperature cycling and mechanical exercising to stabilize the shaft/plate and the plate/sensing element interfaces. The calibration took into account unknown properties of the interfaces as well as the strain sensitivity of the HFSAW and LFSAW sensing elements. Calibration characteristics $F_m(M_{cal},T)$ and $F_t(M_{cal},T)$ are shown in Fig. 7. They were used to generate a calibration file for the test shaft that was loaded into the reader's memory.

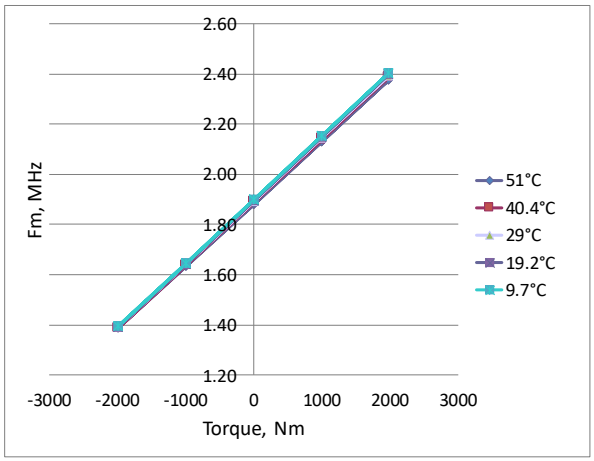
After calibration, the sensor performance was checked at several temperature and torque points. The difference between the indicated and the applied torque is shown in Fig. 8 where the indicated torque was averaged over 400 measurements to exclude random errors from consideration. One can see that the torque measurement errors were quite small, below 0.35%FS, at all temperatures below 40°C showing a good temperature compensation within this range. Hysteresis did not exceed 0.4%FS at these temperatures indicating quite a small amount of stick-slip in the shaft/plate interface on top of a visco-elastic creep-relaxation in the plate/sensing element glue bond.

After checking the torque measurement errors, the plate transducers were dismounted from the test shaft and the calibration file was adjusted for the solid propeller shaft by applying the scaling factor (1) to the output torque values.

V. INSTALLATION, TESTING AND DISCUSSION

The SAW torque sensor was transported to Trondheim, Norway, and installed on a 2-m section of the propeller shaft of a passenger ship next to the optical MetaPower® torque sensor [1] as shown in Fig. 9. The analogue output of the SAW reader was connected to the same KONGSBERG K-Chief® automation and alarm monitoring system as the optical sensor for data logging. The stator antenna was mounted next to the rotor on the base magnetically attached to the metal floor of the shaft compartment.

During clamping of the plate transducers to the shaft, variation of the difference frequencies F_{m1}, F_{m2}, and F_t was monitored by means of the reader. Fig. 10 shows this variation with the torque applied to the clamping screws of the metal



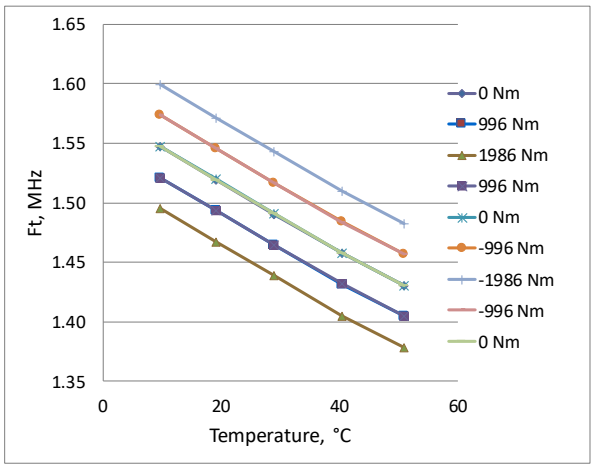


Fig. 7. Calibration characteristics of HFSAW and LFSAW plate transducers on the test shaft.

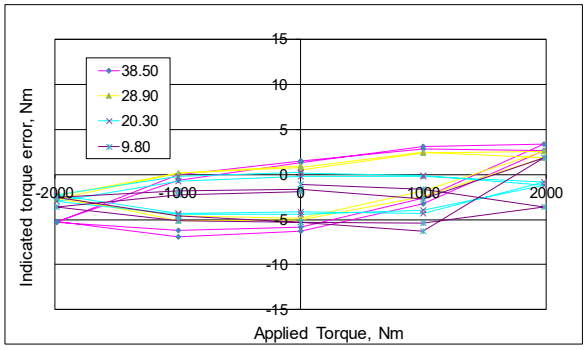


Fig. 8. Indicated torque error against applied torque measured on the test shaft at different temperatures.

bands. One can see that the clamping process did induce some bending and shear strain of the order of 10 με on the plates changing F_{m1} and F_{m2} predominantly in opposite directions. However, variation of the averaged difference frequency F_m did not exceed 14 kHz (2%FS) and remained stable after re-tightening the clamps 4 hours later. Unfortunately, no thermal cycling and mechanical exercising could be easily performed after the installation. It caused an increased instability and

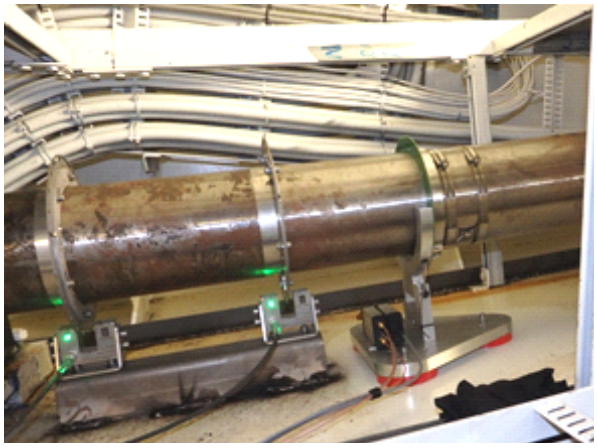


Fig. 9. SAW torque sensor (right) installed on the propeller shaft next to the optical torque sensor (left).

creep of the torque readings during some time needed for the shaft/plate interface to settle down.

After the installation, the SAW torque sensor was re-zeroed and then the engine started for the first time. The SAW torque sensor indicated an average torque of around 23 kNm while the expected value was 28 kNm. As it turned out later, the difference of 6 kNm was not due to the sensitivity being lower than needed but mostly due to a relatively fast creep of the reading caused by a slip in the plate/shaft interface. However, it was decided at that point to adjust the output of the SAW torque sensor by an extra factor of 1.3. The instantaneous torque logged for 15 s after this adjustment is shown in Fig. 11. One can see engine firing pulses with the peak-to-peak magnitude of around 10 kNm and the period corresponding to the shaft rotation speed of 612 rpm.

After 12 hours of running the engine was stopped for the first time. Fig. 12 shows the average SAW torque sensor and rpm value logged by KONGSBERG K-Chief® system. It is evident that the torque readings relaxed from -5 kNm back to zero during approximately 4 hours after removing the load.

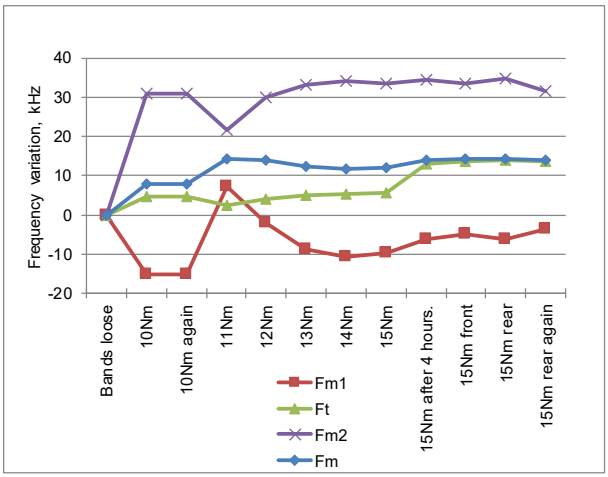


Fig. 10. Variation of the difference frequencies with the torque applied to the clamping screws of the metal straps during installation.

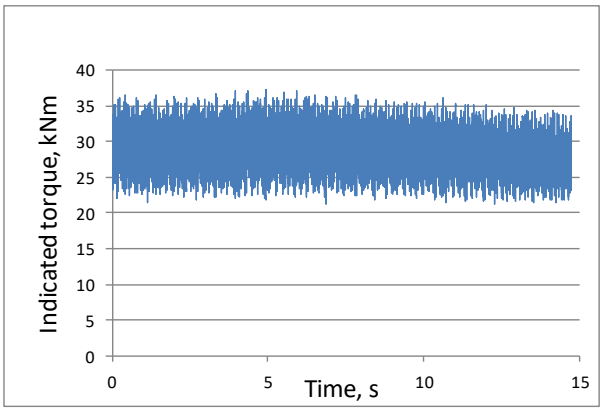


Fig. 11. Instantaneous torque output of the SAW sensor logged after the sensitivity adjustment by a factor of 1.3 during the first engine run.

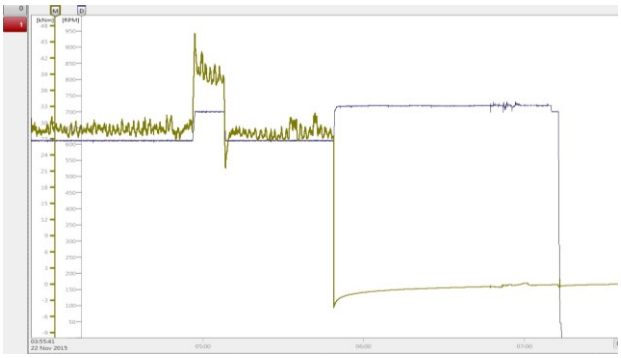


Fig. 12. Averaged torque output of the SAW sensor logged during the first stop of the engine.

This 17% creep and subsequent relaxation took place because of a stick-slip operation of the shaft/plate interface that had not reached the settled state yet.

Next day, during the second run of the engine, the extra scaling factor had to be reduced from 1.3 to 1.15 to achieve the SAW sensor reading similar to the optical sensor reading. After two weeks from the start of testing, it was further reduced to 1.0173 and remained constant till the end of the test period. The need for this sensitivity adjustment by 1.73% arose because of inaccuracies of FEA and the assumed stiffness modulus of the propeller shaft.

After the first 19 hours of operation, the SAW sensor creep and subsequent relaxation dropped to 4 kNm and this reduction continued because of a gradual settling of the shaft/plate interface. The averaged torque readings logged at the outputs of the SAW sensor and the optical sensor for 20 hours with the interval of 15 s after 26 days of testing are shown in Fig. 13. One can see that both sensors produced close torque readings apart from some offset between them. The amount of creep further dropped to approximately 2 kNm (6.6% of load).

The quality of the SAW torque sensor output did not deteriorate during the whole test period demonstrating a good stability of the sensor offset and torque sensitivity and durability of the SAW sensing elements. The averaged torque

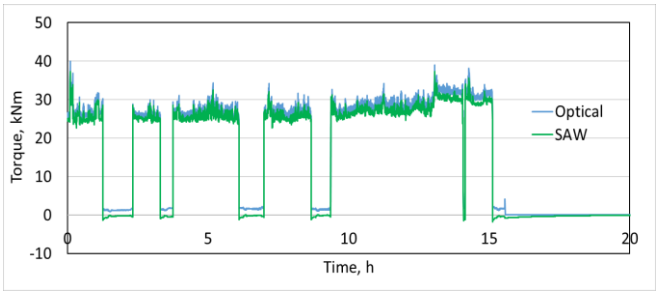


Fig. 13. Torque readings logged at the output of the SAW sensor (green) and the optical sensor (blue) after 26 days of testing.

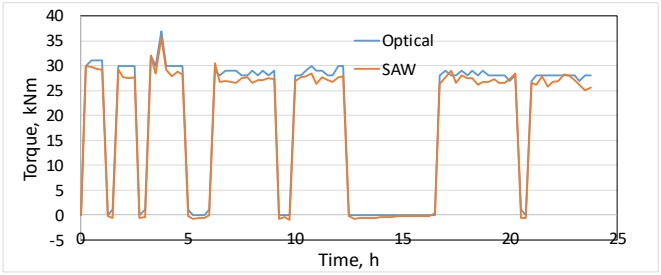


Fig. 14. Torque readings logged at the output of the SAW sensor (orange) and the optical sensor (blue) after 9 months of testing.

readings logged at the outputs of the SAW sensor and the optical sensor for 24 hours with the interval of 15 min after 9 months of testing are shown in Fig. 14. The creep was reduced to 0.6-0.8 kNm (2-3% of load) by that time. After 18 months of testing, the amount of creep dropped further to 1-2% of load.

The amount of creep achieved is still above a desired figure of 1%. It can be further reduced by increasing the clamping force which was limited by the design of the flexible metal straps used in the installation. As a result, the friction force between the shaft and the plate shoulders inversely proportional to the shaft diameter was 50% smaller for the 180-mm propeller shaft than for the 120-mm wind turbine gearbox shaft [3]. Stronger clamps will allow increasing the friction and reducing stick-slip in the shaft/plate interface.

Development of an after-installation burn-in procedure involving thermal cycling and mechanical exercising should help accelerate the process of settling the shaft/plate interface and possibly further reduce the amount of creep. Finally, further improvement could involve reduction of the plate transducer torsional stiffness.

Apart from the creep, another issue with the marine SAW torque sensor is a limited accuracy of the torque calibration. Since application of a known torque after installation of the sensor on the propeller shaft is problematic, we heavily relied on the accuracy of FEA and assumed values of Young's modulus and Poisson's ratio of the shaft to convert $s_2(M_{cal})$ into $s_1(M)$. In the future, more precise values of the shaft parameters should be used. Besides, a simpler geometry of the test shaft without a locally reduced diameter should help achieving a higher accuracy of FEA although it would require a higher value of the calibration torque.

VI. CONCLUSIONS

The SAW torque sensor suitable for aftermarket installation on marine propeller shafts was developed. It was based on two plate transducers with resonant SAW sensing elements that could be easily clamped on the shaft with flexible metal straps. It also employed an annular rotor antenna consisting of two halves that were also clamped on the shaft and the 180° stator antenna installed on the magnetic base. The SAW plate transducers were calibrated on a specially designed test shaft over the operating temperature range before installing them on the propeller shaft. After the installation, the sensor was tested for 18 months in marine environment on a passenger ship. It demonstrated a good stability of the torque sensitivity and the offset. However, it required a sensitivity adjustment by 1.73% and showed a 1-2% creep. Ways of reducing creep and improving the calibration accuracy were discussed.

REFERENCES

[1] https://www.km.kongsberg.com/ks/web/nokbg0397.nsf/AllWeb/225D7801DD799C9AC12575CC0030CB1F/$file/Metapower-Data-sheet.pdf?OpenElement

[2] V. Kalinin, "Wireless physical SAW sensors for automotive applications", Proceedings, 2011 IEEE Int. Ultrason. Symp., 18- 21 Oct. 2011, pp. 212 – 221.

[3] V. Kalinin, A. Leigh, A. Stopps, and E. Artigao, "Resonant SAW torque sensor for wind turbines", Proceedings, 2013 IEEE Int. Freq. Control Symp. and European Frequency and Time Forum, 21-25 July 2013, pp. 462-465.

[4] V. Kalinin, G. Bown, A. Leigh. Contactless torque and temperature sensor based on SAW resonators. Proceedings, 2006 IEEE Ultrason. Symp., 2006, pp. 1490-1493.

Direct integration of CNT forests on solidly mounted resonators and their influence on device performance

Teona Mirea, Jimena Olivares, Marta Clement, Jesús Sangrador, and Enrique Iborra
GMME-CEMDATIC-ETSIT
Universidad Politécnica de Madrid
Madrid, Spain
teona@etsit.upm.es

***Abstract*—Carbon nanotubes (CNTs) have been typically employed as active layers in sensors, however their vertically-aligned (forest) morphology has not been fully explored yet. Here we directly integrate CNT forests on AlN-based solidly mounted resonators and study their influence on the performance of the longitudinal and shear mode of operation. Results show that CNT forests induce quality factor degradation and that too tall forests lead to excessive degradation of the frequency response. A trade-off between device performance and surface area increase for better sensing can be found with forests of heights lower than ~ 10 µm. Additionally, we show that the shear mode is less degraded than the longitudinal mode and that multi-walled CNTs degrade in less extend the devices.**

Keywords—carbon nanotube forest; solidly mounted resonator; integration; performance influence.

I. INTRODUCTION

Carbon nanotubes (CNTs) have been thoroughly employed as active layers for sensing purposes, particularly in acoustic wave devices [1], [2]. Their high surface area and high chemical affinity make them suitable candidates for boosting the sensor selectivity through functionalization [3]. Typically CNTs have been employed in form of thin films of dispersed nanotubes deposited on the active area of the sensors. Recently, the authors have proposed the direct growth of vertically-aligned (forests) CNTs on AlN-based solidly mounted resonators (SMRs) [4]. Compared to dispersed CNTs, the vertically-aligned morphology offers greater surface areas for detection, selective growth of CNTs by patterning the catalyst, and the possibility of nm-size particle filtering by tuning the distances between the tubes[5], [6].

The direct growth of CNT forests on the top electrodes of SMRs (Fig. 1) required two previous studies: the development of SMRs sustaining high temperatures (CNT growth needs 650°C) [7], and the growth of CNT forests on pure metallic substrates [8]. In this work we discuss the influence of the CNT forests on the final performance of two types of device: (1) single mode devices working on the longitudinal mode, and (2) dual mode devices exciting both the shear and the longitudinal modes. While the longitudinal mode can be employed in gas sensing, the shear mode is needed if the CNT-based SMRs are to be used as biosensors in liquid media [9]. For both applications, the assessment of the forest influence on the device performance is crucial for the sensor optimization.

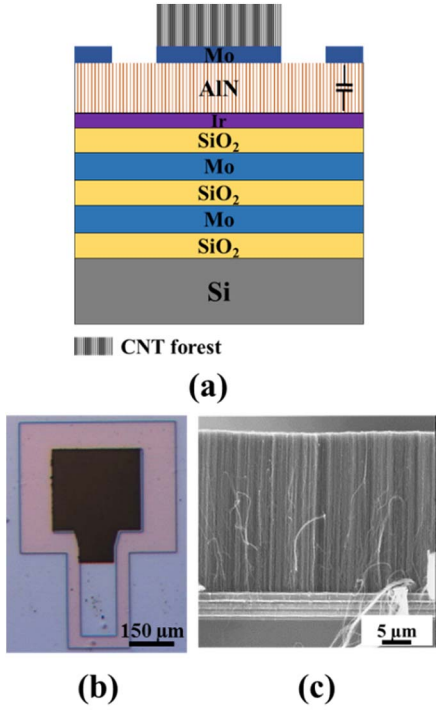


Fig. 1. SMR with integrated CNT forest on the active area of the top electrode. (a) Sketch, (b) optical top view image, and (c) scanning electron microscopy cross section image.

II. EXPERIMENTAL

The influence of CNT forest integration has been studied on the longitudinal and shear modes performances of AlN-based SMRs. These are composed of five alternating layers of SiO_2/Mo (620/629 nm-thick, respectively) as acoustic reflectors, a 120 nm-thick Ir bottom electrode, a 1 µm-thick AlN piezoelectric film and a 150 nm-thick Mo top electrode (Fig. 1(a)). For the single mode devices (longitudinal) the AlN layer was deposited with *c*-orientation, while for the dual mode devices (longitudinal and shear) the AlN layer was deposited with tilted grains [10]. CNT forests were grown using low pressure chemical vapor deposition (CVD) [11] and a catalytic system composed of a blocking layer (SiO_2 or Al) underneath a metallic catalyst (Fe) (Fig. 2). The blocking layer is crucial in this case to avoid bulk diffusion of the catalyst into the metallic top substrate [8]. The thicknesses of the catalytic systems were 50 nm for the SiO_2, 12 nm for the Al,

and different thicknesses for the Fe (1.5 nm, 2 nm and 6 nm). The catalytic bilayers were selectively deposited over the Mo top electrodes by a photolithographic lift-off process (Fig. 1). For the CVD process, NH_3 and C_2H_2 were used as reducing and carbon source gases, respectively. To be able to grow on metallic substrates, the temperature for the formation of the catalytic nanoparticles (NPs) was lowered (550°C/600°C) [6], compared to the one needed for CNT growth (650°C).

III. RESULTS AND DISCUSSION

The electrical characterization of the SMRs before and after CNT forest growth was performed to assess the influence of the forest on the device behavior. As mentioned, both longitudinal and shear modes have been studied. On one hand, for the integration of CNTs on single mode devices, the Al/Fe catalytic system was employed. On the other hand, the SiO_2/Fe catalytic system was the one used for the dual mode devices.

A. Integration on single mode devices

The CNT forests grown on the top electrodes of SMRs with *c*-oriented AlN were obtained by using the Al/Fe catalytic system with thicknesses of 12 nm and 1.5 nm, respectively (Fig. 2(a)). The obtained forests were composed of single-walled carbon nanotubes (SWCNTs). This is proved by their Raman spectrum (see Fig. 3), where we can observe strong RBM peaks, high G to D ratio, G band split, the presence of M and iTOLA peaks and the single component of the 2G peak [12]. The influence of the SWCNT forests on the SMR performance is shown by their electrical characterization in Fig. 4(a). It reveals that the forest induces degradation in both quality factors at resonance (Q_r) and anti-resonance (Q_a). The analysis of the SMRs frequency response at the different stages of the CNT growth demonstrates that Q_r degrades owing to the CVD process itself, probably due to the growth of a thin oxide film on the top electrode, while Q_a seems to be mainly affected by the presence of the forests. This last is demonstrated by the device electrical measurement after mechanically removing the CNTs which shows almost completely recover of Q_a (green curve in Fig. 4(a)).

Further, we also studied the influence of the forest height on the device behavior. By growing forests with different heights we observed that after a certain height value (~ 25 µm), the degradation induced starts to be prohibitive, i.e. *Q*-factors below 60 (Fig. 4 (b)).

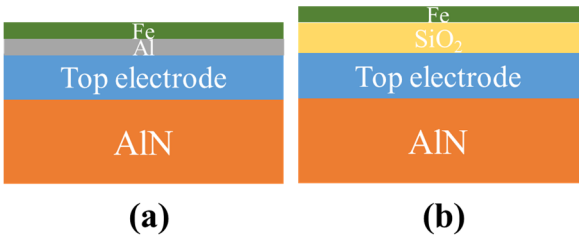


Fig. 2. Two types of catalytic systems used to grow CNT forest on the metallic top electrodes: (a) Al blocking layer and Fe catalyst, and (b) SiO_2 blocking layer and Fe.

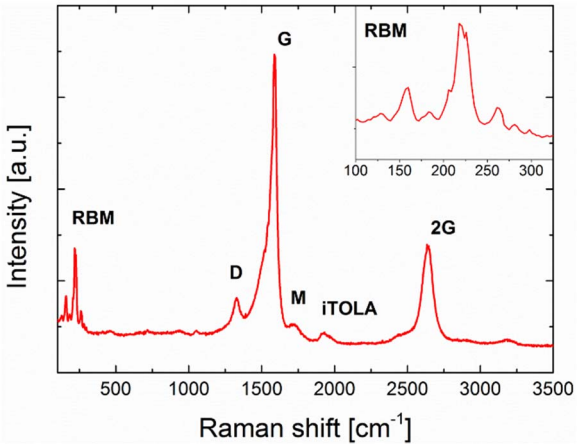


Fig. 3. Raman spectrum of the SWCNT forest grown with Al/Fe.

We hypothesize that this can be explained by several effects. Firstly, the presence of the CNT forest reduces the wave reflection at the top electrode/air interface compared with that of the uncovered device, since the acoustic impedance of the CNTs is larger than that of the air.

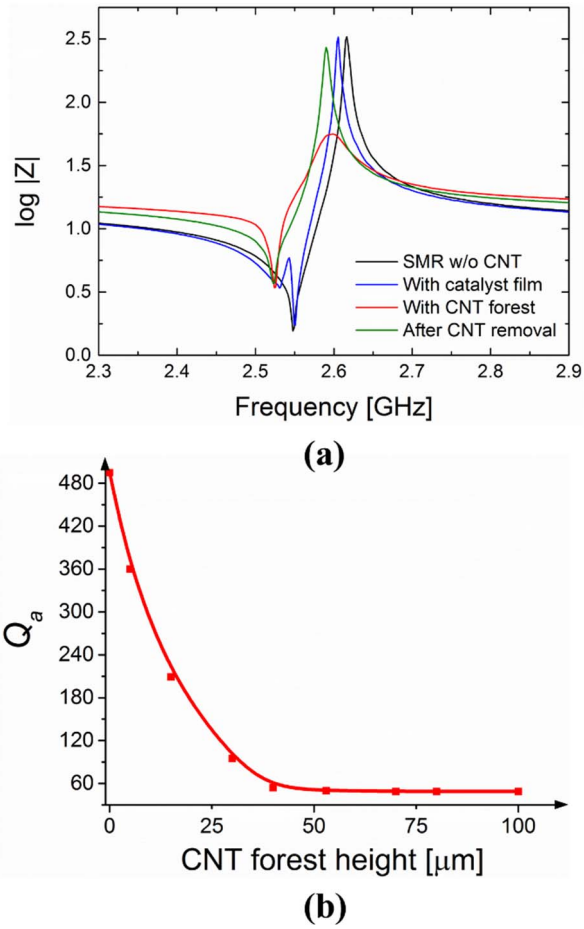


Fig. 4. SMR longitudinal mode peformance before and after CNT integration. (a) Electrical impedance of SMRs with and without CNTs, and (b) Q_a degradation with forest height.

In other words, some energy is radiated to the forest (Fig. 5(a)). Secondly, the reflection at the top CNT forest/air interface is poor due to low acoustic mismatch and loss of coherence owing to the heterogeneity of the forest (Fig. 5(b)). Finally, the CNT forest can be considered as a poroelastic film showing high viscous losses induced by the friction between tubes; the acoustic energy radiated to the forest may be rapidly lost before even reaching the top interface for backward reflection.

B. Integration on dual mode devices

The integration of CNT forests on SMRs with tilted AlN was obtained by using the SiO_2/Fe catalytic system. In this case, while the thickness of the blocking layer was set at 50 nm, two thickness of Fe were tested, i.e. 2 nm and 6 nm. By using these two thicknesses for the catalyst different forest morphologies were achieved. More particularly we grew SWCNTs with the lower thickness of Fe and multi-walled carbon nanotubes (MWCNTs) with the highest thickness of Fe (see Fig. 6). Both forests with the same height.

The electrical characterization of the dual mode devices, before and after CNTs integration, is presented in Fig. 7 and Table I. The results reveal that:

- Resonant and anti-resonant quality factors are degraded in both shear and longitudinal modes.
- The shear mode is slightly less degraded than the longitudinal mode in both cases, with SWCNTs and MWCNTs.
- MWCNTs induce less degradation than SWCNTs, proved by the higher quality factors after CNTs grown from 6 nm of Fe.

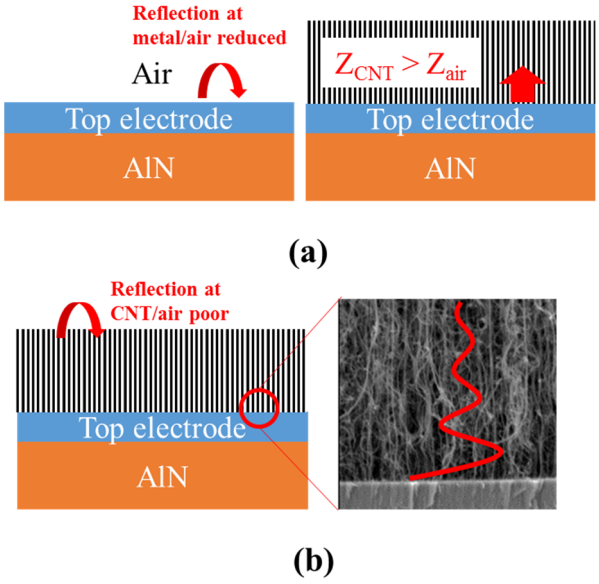


Fig. 5. Sketches explaining the degradation of Q_a due to the presence of the CNT forest on the top electrode.

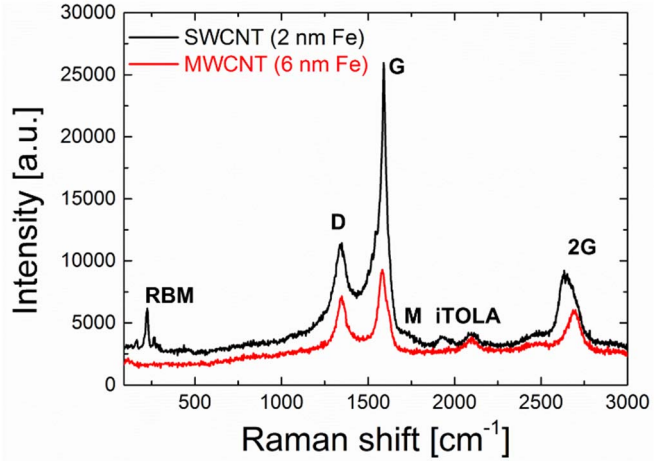
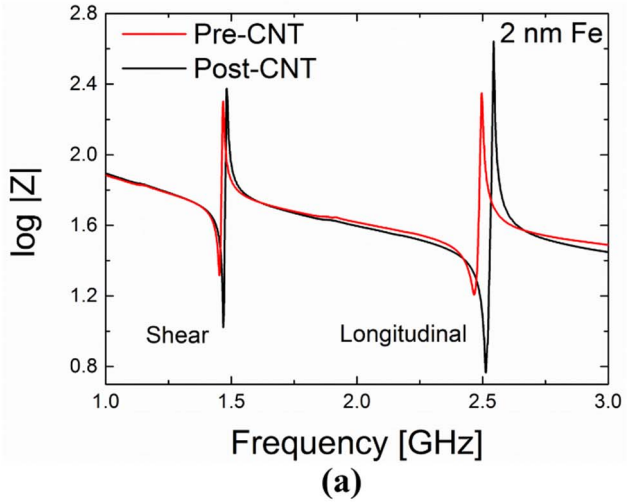


Fig. 6. Raman spectra of the forests obtained with the SiO_2/Fe catalyst on dual mode devices. SWCNT were grown with 2 nm of Fe and MWCNT with 6 nm of Fe.



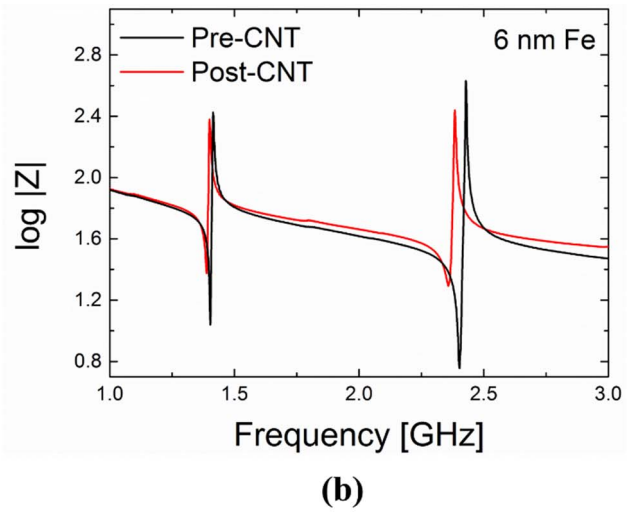


Fig. 7. Electrical impedances of the dual mode devices (showing the shear and longitudinal modes) before and after CNT integration for (a) 2 nm Fe and (b) 6 nm Fe.

TABLE I. QUALITY FACTORS OF THE SHEAR AND LONGITUDINAL MODES BEFORE AND AFTER CNT INTEGRATION

2 nm	Before CNT	After CNT
Shear	$Q_r = 268$	$Q_r = 145$
	$Q_a = 283$	$Q_a = 195$
Longitudinal	$Q_r = 230$	$Q_r = 109$
	$Q_a = 600$	$Q_a = 297$
6 nm	**Before CNT**	**After CNT**
Shear	$Q_r = 311$	$Q_r = 167$
	$Q_a = 289$	$Q_a = 252$
Longitudinal	$Q_r = 280$	$Q_r = 114$
	$Q_a = 564$	$Q_a = 341$

IV. CONCLUSIONS

SMRs with CNT forests directly integrated on their top electrode are envisaged for improving the application of these devices as both gas and biosensors. To optimize the sensors, the influence of the CNT direct integration on the device performance has to be previously known. In this work we investigated the influence of CNT forests on the longitudinal and shear modes operation of the devices, used for their gas and biosensing applications, respectively. By using and Al/Fe catalytic system to grow CNT forests on single mode devices (only longitudinal mode) we achieved SWCNTs and showed that they induce strong degradation on the anti-resonant quality factor as the height of the forest is increased. This suggests finding a trade-off between active surface area for sensing and performance degradation. We found that such trade-off could be by using forests with heights below 10 μm to prevent the resonator from excessive degradation, which is sufficient to increase the sensing surface area by several orders of magnitude. For the growth of dual mode devices (with shear and longitudinal modes) we used the SiO_2/Fe catalytic system and studied the influence of two forests morphologies, i.e. SWCNTs and MWCNTs. In dual mode devices we found that, on one hand, the shear mode is less degraded than the longitudinal mode with CNT integration, and, on the other hand, that MWCNTs are preferred since they induce slightly less degradation.

ACKNOWLEDGMENT

This work was partially supported by Ministerio de Economía y Competitividad del Gobierno de España through project MAT2013-45957-R.

REFERENCES

[1] M. Penza, P. Aversa, G. Cassano, D. Suriano, W. Wlodarski, M. Benetti, D. Cannatà, F. Di Pietrantonio, and E. Verona, "Thin-film bulk-acoustic-resonator gas sensor functionalized with a nanocomposite Langmuir-Blodgett layer of carbon nanotubes," *IEEE Trans. Electron Devices*, vol. 55, no. 5, pp. 1237–1243, 2008.

[2] M. Rinaldi, C. Zuniga, N. Sinha, M. Taheri, G. Piazza, S. M. Khamis, and A. T. Johnson, "Gravimetric chemical sensor based on the direct integration of SWNTS on AlN Contour-Mode MEMS resonators," in *2008 IEEE International Frequency Control Symposium*, 2008, pp. 443–448.

[3] K. Balasubramanian, M. Burghard, M. Burghard, and K. Balasubramanian, "Chemically Functionalized Carbon Nanotubes," *Small*, vol. 1, no. 2, pp. 180–192, 2005.

[4] T. Mirea, J. Olivares, M. DeMiguel-Ramos, M. Clement, J. Sangrador, E. Iborra, and S. Esconjauregui, "Carbon nanotube forests as top electrodes for AlN-based electroacoustic resonators," in *2014 IEEE International Ultrasonics Symposium*, 2014, pp. 1476–1479.

[5] Y.-T. Yeh, Y. Tang, A. Sebastian, A. Dasgupta, N. Perea-Lopez, I. Albert, H. Lu, M. Terrones, and S.-Y. Zheng, "Tunable and label-free virus enrichment for ultrasensitive virus detection using carbon nanotube arrays," *Sci. Adv.*, vol. 2, no. 10, pp. 1–13, 2016.

[6] A. L. Yost, S. Shahsavari, G. M. Bradwell, R. Polak, F. Fachin, R. E. Cohen, G. H. McKinley, M. Toner, M. F. Rubner, and B. L. Wardle, "Layer-by-layer functionalized nanotube arrays: A versatile microfluidic platform for biodetection," *Microsystems Nanoeng.*, vol. 1, p. 15037, Dec. 2015.

[7] T. Mirea, M. DeMiguel-Ramos, M. Clement, J. Olivares, E. Iborra, V. Yantchev, and I. Katardjiev, "AlN solidly mounted resonators for high temperature applications," in *2014 IEEE International Ultrasonics Symposium*, 2014, pp. 1524–1527.

[8] J. Olivares, T. Mirea, B. Díaz-Durán, M. Clement, M. DeMiguel-Ramos, J. Sangrador, J. de Frutos, and E. Iborra, "Growth of carbon nanotube forests on metallic thin films," *Carbon N. Y.*, vol. 90, pp. 9–15, 2015.

[9] J. Weber, W. M. Albers, J. Tuppurainen, M. Link, R. Gabl, W. Wersing, and M. Schreiter, "Shear mode FBARs as highly sensitive liquid biosensors," *Sensors Actuators, A Phys.*, vol. 128, no. 1, pp. 84–88, 2006.

[10] M. DeMiguel-Ramos, T. Mirea, M. Clement, J. Olivares, J. Sangrador, and E. Iborra, "Optimized tilted c-axis AlN films for improved operation of shear mode resonators," *Thin Solid Films*, vol. 590, pp. 219–223, 2015.

[11] J. Robertson, G. Zhong, S. Esconjauregui, C. Zhang, M. Fouquet, and S. Hofmann, "Chemical vapor deposition of carbon nanotube forests," *Phys. status solidi*, vol. 249, no. 12, pp. 2315–2322, Dec. 2012.

[12] W. Qian, T. Liu, F. Wei, and H. Yuan, "Quantitative Raman characterization of the mixed samples of the single and multi-wall carbon nanotubes," *Carbon N. Y.*, vol. 41, no. 9, pp. 1851–1854, 2003.

Satellite clock offset estimation and analysis based on arc-wise observation files

Meifang Wu
National Time Service Center, Chinese Academy of Sciences
University of Chinese Academy of Sciences
Xi'an, China
wumeifang@ntsc.ac.cn

Baoqi Sun
National Time Service Center, Chinese Academy of Sciences
University of Chinese Academy of Sciences
Xi'an, China
sunbaoqi@ntsc.ac.cn

Xuhai Yang
National Time Service Center, Chinese Academy of Sciences
University of Chinese Academy of Sciences
Xi'an, China
yyang@ntsc.ac.cn

Hang Su
National Time Service Center, Chinese Academy of Sciences
University of Chinese Academy of Sciences
Xi'an, China
suhang@ntsc.ac.c

***Abstract*—In order to meet the demand of GPS real/near real time (RT/NRT) application, it is proposed that a clock estimation algorithm with high reliability and adequate accuracy, which is based on arc-wise observation data gained by merging hourly files or 15-min files offered by IGS. It is analyzed emphatically that the critical influence factors of the algorithm, and account the efficacy of the algorithm. Test indicates that lengths of the observation arc, precision of the obit, ERP and station number are all the important influence factors of the novel algorithm. When the observation arc is set as 24h, 12h, 6h, 3h, 1h, 0.5h and the station number is 120, STD of the clock offset is 0.05ns, 0.11ns, 0.19ns, 0.22ns, 0.27ns, 0.29ns, while the STD of the clock offset decreases by 100%, 73%, 47%, 48%, 52%, 58% when the station number is reduced by half, what's more the STD of the clocks decreases by 120%, 27%, 5%, 4%, 4%, 7% as the precision of orbit decreases.**

***Keywords*—arc-wise observation data, clock offset estimation, undifferenced, real/near real time**

I. INTRODUCTION (*Heading 1*)

The development of GPS real/near real time (RT/NRT) application puts forward higher requirement in terms of reliability and timeliness on GPS products. Some certain geodetic missions, such as real time precise point positioning (RTPPP), GPS meteorology and atmospheric sounding, may require real/near real time GPS orbit and clock products within the desired time frame and with adequate accuracy.

IGS mature products include Final products, Rapid products, Ultra-rapid products and Real-time Service. The IGS Final and Rapid products are not suitable for any RT/NRT application because of their latency. The IGU product, which is of great interest, is update every six hours and with latency of three hours. It covers an interval of 48 hours where the first 24 hours are estimated from real observations and the last 24 hours are predicated orbit and clock information. RTS is correction data stream of broadcast ephemerides, published in RTCM-SSR (RTCM State Space Representation) format.

Taking into account the latency only the predicated part of the IGU product can be used for a RT/NRT processing, as well as the RTS and broadcast ephemeredes. Because of the deterministic behavior of clock, it is cannot be predicated over a long period of time, thus the precision of clock of IGU and broadcast ephemeredes is poor. And RTS acquisition heavily depends on network, resulting in low reliability.

Currently, many providers pay attention to the RT/NRT GPS orbit and clock products, such as CODE, JPL, Thales, BKG, GFZ[1-3]. And in our country, related work is also carried out. For example, Lou Yidong, Cai Hua and etc. use epoch-differenced method to estimate RT/NRT, Li Li, Xingxing Li and etc. adopt undifferenced method, and Xiaohong Zhang make use of mixed method[4-10]. But the three methods mentioned before are based on real-time data stream which has poor reliability. So RT/NRT GPS orbit and clock products with high reliability and adequate accuracy are desired.

The following list summarizes the available observation data within the IGS: daily file, hourly file, 15-min file and real-time data stream. It is proposed that a clock estimation algorithm with high reliability and adequate accuracy, which is based on arc-wise observation data gained by merging hourly files or 15-min files offered by IGS.

II. ALGORITHM FOR CLOCK OFFSET ESTIMATION BASED ON ARC-WISE OBSERVATION DATA

2.1 function model

Same as the traditional algorithm, clock offset estimation based on arc-wise observation data adopts undifferenced ionosphere-free phase and range combination observations, but the observation data is arc-wise, not only the daily file. The ionosphere-free liner combination based on undifferenced observations can be expressed as follows:

$$\begin{aligned} v^j_{k,\Phi}(i) = {} & \Delta t_k(i) - \Delta t^j(i) + \rho^j_k(i)/c + \delta\rho^j_{k,trop}/c \\ & + \lambda N^j_k/c + \varepsilon^j_{k,\Phi}(i) - \lambda\Phi^j_k(i)/c \end{aligned} \tag{1}$$

$$\begin{aligned} v^j_{k,p}(i) = {} & \Delta t_k(i) - \Delta t^j(i) + \rho^j_k(i)/c \\ & + \delta\rho^j_{k,trop}/c + \varepsilon^j_{k,p}(i) - p^j_k(i)/c \end{aligned} \tag{2}$$

where and are the residual errors of the pseudo range and carrier phase, respectively, is the receiver clock bias, is the satel-

lite clock bias, is the geometric distance between the satellite and receiver, is the tropospheric refraction, is the speed of the light in vacuum, is the wavelength of the linearly combined carrier phase observation, N is the phase ambiguity, is the ionosphere-free carrier phase combination, and is the ionosphere-free pseudo range combination.

Bernese GNSS software v5.2 developed by University of Bern is adopted in this article. The processing scheme for the clock offset estimation based on arc-wise observation data is shown in figure 1. Arc-wise observation data in RINEX format, Station coordinates (CRD), orbit and Earth rotation parameters (ERP) are input files for the clock offset estimation algorithm, while clock offset files in CLK format is output.

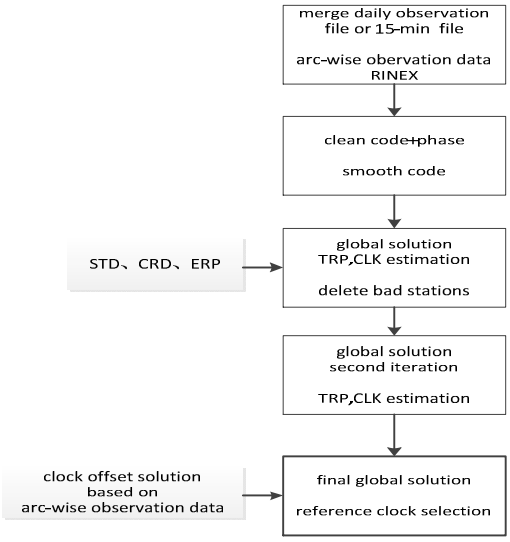


Fig. 1. Processing scheme for the clock offset estimation based on arc-wise observation data

A first data cleaning is done based on the Arc-wise observation data in RINEX format gained by merging hourly files or 15-min files applied by IGS. Data cleaning is done via an arc-wise consistency check of the four observation types using M-W linear combination and the difference between the ionosphere-free linear combination of code and phase measurement. In addition, the mean difference of code minus phase for an observation arc is computed and the code observations are replaced by the corresponding phase observations shifted by this code-minus-phase mean difference. The opposite effect of the ionosphere delay on the code and phase is taken into account in this case. The resultant product from this step is a smoothed code measurement.

In the next step we integrate the ORB, EPR and CRD into the procedure and clock synchronization between the receiver and the GPS broadcast time follows. The zero-difference processing in the first global solution involves the estimation of phase ambiguities, TRP for the stations, and clock parameters for the stations and satellites. A postfit residual screening is done to remove remaining outliers in the observations. The solution is repeated and normally converges in two iterations yielding reasonable postfit residuals. Stations with poor data quality are also deleted inn this process.

This type of "cleaned" code and phase observations is then used to obtain a final clock offset solution based on arc-wise observations and this time the TRP from previous step are held fixed in the clock estimation process. In order to get satellite clock corrections, which are both code and phase consistent, we have to use both observation types.

Table 1 Setting for parameters

	Parameters	**Processing strategies**
Observations	Measurements	LC/PC
	Elevation cutoff angle	5^o
	Phase windup	Model corrected
	Antenna phase center	IGS_08
	Tides	Model corrected
Error corrections	Satellite phase center	Absolute phase center
	Relativistic effects	Model corrected
	Reference clock	Fixed as a station clock
	Satellite orbits	IGU-P or CODE products
	Position of stations	Network solutions of CODE
	Tropospheric	GMF
Parameters estimation	Satellite clock offset	Estimated
	Receiver clock offset	Estimated
	Ambiguity	Float solution

2.2 Ground tracking network

Such a GPS clock generation concept based on arc-wise observation data is primarily dependent on the availability of ground tracking data. The stations from the IGS station network are delivering the data with different latencies and also at different sampling rates. The following list summarizes the available data streams within the IGS:

- daily files (sampling:30s),
- hourly files (30s),
- 15-min files (1s),
- near-time data stream (1s).

Since the reliability of real-time data stream is poor, and the latency of daily files is long, hourly files or 15-min files are merged to get arc-wise observation data.

III. EXPERIMENTS AND RESULTS ANALYSIS

It can be seen from formula (1) and (2), the influencing factors of clock estimation include the precision of orbit, ERP and the quality of observation data which means the number of tracking stations and the length of the observation arc. Thus, 3 experiment schemes are put forward.

1) Clocks are estimated based on arc observation data of different length, and the results are compared with IGS final products;

2) Changing the number of tracking station using in scheme 1), estimate the clocks and compare them with IGS final products;

3) Changing the orbit and ERP products using in scheme 1), estimate the clock and compare them with IGS final products.

Second Order Difference method is used to compare the clock gained by experiment schemes with IGS final products. Step 1, to select a reference satellite clock, then experiment results and IGS final products minus the reference clock separately to eliminate the effect of different reference clock when estimating clock. Step 2, compare the two results gained in step 1. Finally, the STD of result gained in step 2 is computed. The Second Order Difference method can be expressed as follows:

$$STD = \sqrt{\frac{\sum_{i=1}^{n}(\Delta_i - \overline{\Delta})(\Delta_i - \overline{\Delta})}{n}} \quad (3)$$

where is the result at epoch ingrained in step 2, and is the mean value of all the results gained in step 2.

3.1 Effect of the arc length on clock estimation based on arc observation data

About 120 global uniformly distributed IGS stations are used in the experiments scheme 1), as shown in figure 2. Data from days 178 to 207 of 2016 is used to estimate clocks. Orbit and ERP are fixed as CODE products, the length of arc observation data is set as 24h, 12h, 6h, 3h, 1h, or 0.5h. The sampling interval is 300s. GPS04 has no data, and GPS10 is the reference satellite. The result is shown in figure 3 and figure 4.

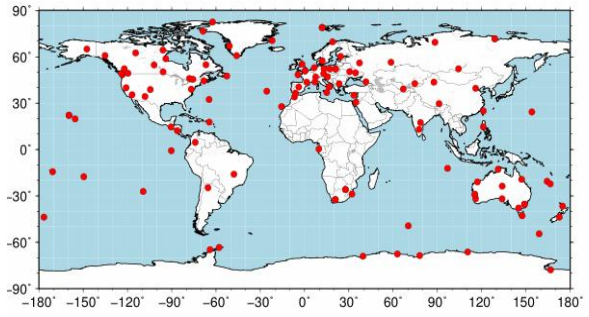


Fig. 2. Distribution of tracking stations in scheme 1)

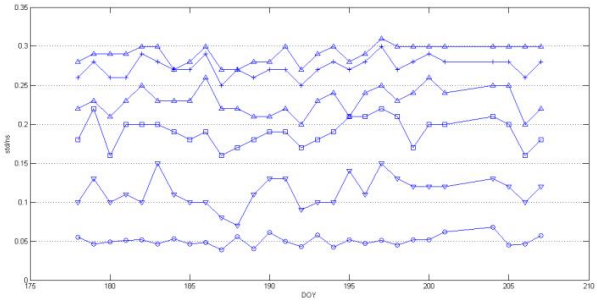


Fig. 3. STD (ns) of clocks estimated based on different length of arc observation data, the tracking station number is 120, ERP and orbit are fixed as CODE products.

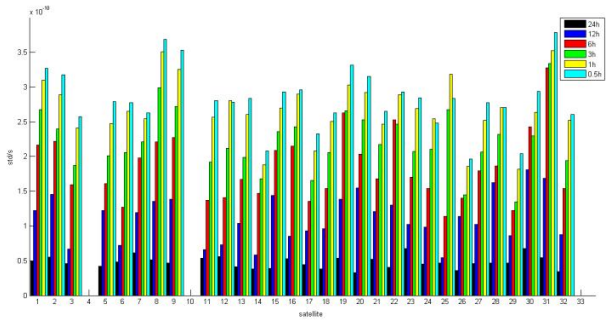


Fig. 4. STD (ns) of different satellites clocks estimated based on different length of arc observation data, the tracking station number is 120

As shown in figure 4, most of satellite clocks obey the rule that the shorter the observation arc, the poorer the precision of clocks. A few satellite clocks have poor accuracy, which is related to the satellite's own characteristics, such as the emission time, the type of satellite clocks or others. The relationship between the length of arc and the precision of clocks are expressed as bellows:

1)precision of the most satellite clocks is less than 0.05ns when observation arc is 24h;

2)precision of the most satellite clocks is less than 0.15ns when observation arc is 12h;

3)precision of the most satellite clocks is less than 0.20ns when observation arc is 6h;

4)precision of the most satellite clocks is less than 0.25ns when observation arc is 3h;

5)precision of the most satellite clocks is less than 0.28ns when observation arc is 1h;

6)precision of the most satellite clocks is less than 0.30ns when observation arc is 0.5h.

3.2 Effect of tracking station number on clock estimation based on arc observation data

In order to analyze the effect of tracking station number on clock estimation based on arc observation data, experiment scheme 2) has the same input parameters as scheme 1) except the number of tracking station. As shown in figure 5, about 60 tracking stations are used to estimate clocks, and the result is shown in figure 6.

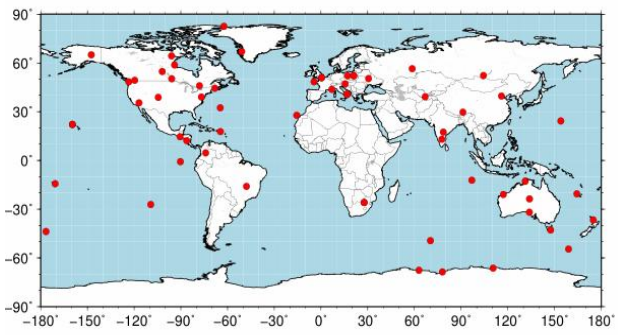


Fig. 5. Distribution of tracking stations in scheme 2)

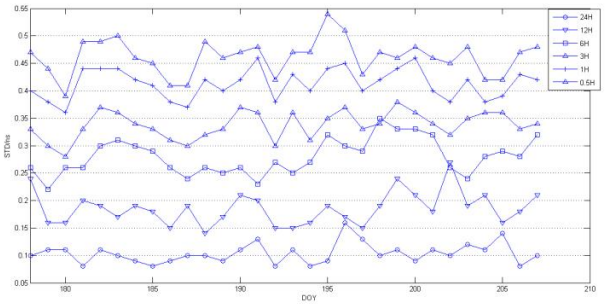


Fig. 6. STD (ns) of clocks estimated based on different length of arc observation data, the tracking station number is 60, ERP and orbit are fixed as CODE products.

It is can be seen from figure 6, when the station number is cut to half, most of satellite clocks obey the rule that the shorter the observation arc, the poorer the precision of clock, as well.

Compared scheme 1) with scheme 2), When the observation arc is set as 24h, 12h, 6h, 3h, 1h, 0.5h ,the STD of the clock offset decreases by 100%, 73%, 47%, 48%, 52%, 58% while the station number is reduced by half.

3.3 Effect of orbit and ERP precision on clock estimation based on arc observation data

In order to research the effect of orbit and ERP precision on clock estimation based on arc observation data, ERP and orbit are fixed as IGU-P products in scheme 3). And other parameters are set as same as in scheme 1). The result of scheme 3) is shown in figure 7. Besides, because of the poor precision of IGU-P orbit product on DOY 189-191, results of these days are excluded for statistics.

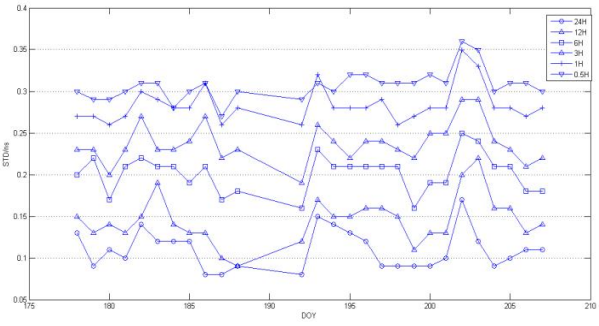


Fig. 7. STD (ns) of clocks estimated based on different length of arc observation data, the tracking station number is 120, ERP and orbit are fixed as IGU-P products.

It is can be seen from figure 7, when the orbit and ERP are fixed as different products, most of satellite clocks obey the rule that the shorter the observation arc, the poorer the precision of clock, as well.

Compared figure 3 with figure 7, it is can be known that the effect of the orbit decreases as the length of the observation arc decreases. When the observation arc is set as 24h, 12h, 6h, 3h, 1h, 0.5h, the STD of the clocks decreases by 120%, 27%, 5%, 4%, 4%, 7% as the orbit and ERP are fixed as IGU-P products.

3.4 Efficacy of the algorithm based on arc-wise observation data

As same as precision, computation time is a key problem of clock estimation. The computation time of clock estimation with different observation arc and station number is account, as shown in table 2. The hardware configuration of the computer is CPU: AMD Opteron Processor 6212.

Table 2 Computation time with different observation arc and station number (min)

observation arc / station number	55	120
24h	35	65
12h	15	38
6h	10	21
3h	9	12
1h	7	10
0.5h	5	9

As shown in table 2, the effect of station number on clock estimation based on arc-wise observation data is much larger than the effect of observation arc on it.

Test result shows that length of the observation arc, precision of the obit and station number is all the influence factors of clock offset estimation. Ambiguity parameter should be estimated when clock offset is calculated with undifferenced observations. If the observation arc is short, the ambiguity parameter cannot be estimated exactly. Thus, the shorter the observation arc, the worse the clock offset estimation result. Also, the orbit and ERP are the foundation of clock estimation using the novel algorithm, so, precision of the obit and ERP have certain influence on clock offset result.

IV. CONCLUSIONS

In summary, if the observation arc is set as a short interval (e.g. less than 3 hours), the NRT clock offset can be estimated using the algorithm based on arc-wise observation data, and the precision of result is better than that of broadcast ephemeris and IGU-P. Besides, the novel algorithm has high reliability because arc-wise observation data is gained by merging hourly files or 15-min files offered by IGS. What's more, RT clock offset may be estimated by using the novel algorithm combined with ultra-short term prediction of satellite clock offset.

In addition, there are more influence factors on clock offset estimation, such as sampling interval, station distribution, and et al. So, based on these factors, how to optimize the algorithm to improve the precision and speed of clock estimation is the questions to be further discussed.

REFERENCES

[1] H.Bock, R.Dach, et al. GPS clock correction estimation for near real-time orbit determination applications [J]. Aerospace Science and Technology 13(2009) 415-422.

[2] H.Bock, R.Dach, et al. High-rate GPS clock corrections from CODE: support of 1 Hz applications [J]. Journal of Geodesy, J Geod(2009)83:1083-1094.

[3] Maorong Ge, Junping Chen, et al. A computationally efficient approach for estimation high-rate satellite clock corrections in realtime [J]. GPS Solut, DOI 10.1007/s 10291-011-0206-Z.

[4] LOU Yidong. Research on Real-Time Precise GPS Orbit and Clock Offset Determination [D].Wuhan University, 2008.

[5] LOU Yidong, SHI Chuang, et al. Realization and Analysis of GPS Precise Clock Products [J]. Geomatics and Information Science of Wuhan University. 2009,34(1):88-91.

[6] CAI Hua, ZHAO Qile, et al. Implementation and Precision of GPS Precise Clock Estimation System [J]. Geomatics and Information Science of Wuhan University. 2009,(11):1293-1296.

[7] LI Xingxing, XU Yun, et al. Undifferenced Precise Satellite Clock Estimation and Precision Analysis [J]. Geomatics and Information Science of Wuhan University. 2010,35(6):661-664.

[8] Real-time Estimation of Precise Satellite Clock Bias Based on IGU Predicted Orbit [J].Journal of Geodesy and Geodynamics 2011, 33(2): 111-116.

[9] Xiaohong Zhang, Xingxing Li et al. Satellite clock estimation at 1 Hz for realtime kinematic PPP application [J]. GPS Solut. DOI 10.1007/s 10291-010-0191-7.

[10] Ding Wenwu. Research on Key Technologies of Real Time Precise Point Positioning System [D]. Institute of Geodesy and Geophysics, Chinese Academy of Science,2012.

[11] Rolf Dach, Simon Lutz, et al. Bernese GNSS Software Version 5.2 [M]. Astronomical Institute, University of Bern.

GPS All in View Time Comparison using Multi-receiver Ensemble

Shinn Yan Lin
National Standard Time and Frequency Laboratory,
TL, Chunghwa Telecom Co. Ltd.
Taoyuan, Taiwan ROC
sylin@cht.com.tw

Zhiheng Jiang
Bureau International des Poids et Mesures
Pavillon de Breteuil, F-92312, Sevres Cedex, France
zjiang@bipm.org

***Abstract*—we proposed a virtual GPS receiver model generated from a multi-receiver ensemble. The time difference between local reference and the realization GPS time (REFGPS) of the virtual receiver is the weighted REFGPS results of all calibrated receivers in ensemble. Depending on the numbers of receivers in ensemble, the measurements of the virtual GPS receiver in each epoch are got from different receivers and the quantity is several times than physical receivers. A long base line test showed the virtual receiver is more stable and robust and is potential to have better long term performance with respect to TWSTFT.**

Keywords—GPSTT, TWSTFT, long term discrepancy

I. MOTIVE AND INTRODUCTION

At present, the TWSTFT (Two-Way Satellite Time and Frequency Transfer) and GNSSTT (Global Navigation Satellite Systems time transfer) are the major long baseline time comparison technologies used as UTC (Coordinated Universal Time) links and for UTC computation. In last decades, accompany with the precision improvement and frequently calibration, many studies demonstrated that these two technologies exist long term discrepancy within the level of 1~5 ns [1][2][3][4][5].

The long term discrepancy between TWSTFT and GNSSTT can be contributed by multiple causes [5]. To improve the long term performance of long baseline time transfer, investigating the causes of the discrepancy and remove the known noise patterns are necessary.

This study is motivated from how to improve the long term performance of GNSSTT. Since GPSTT (Global Positing System time transfer) is the majority technology of GNSSTT, we focus on discussing the GPSTT in this paper.

In GPSTT, we set the GPS time or GPS satellite time to be the common clock, if the total electronic delay from GPS antennae center to the reference point of GPS stations, or the total delay [6], are accurately calibrated, the time difference between the reference time of stations can get from:

$$REF_{i,t}\text{-}REF_{j,t} = REFGPS_{i,t} - REFGPS_{i,t} \quad (1)$$

Where $REF_{i,t}$ and $REF_{j,t}$ are the reference time of stations I and j at epoch t, and the $REFGPS_{i,t}$ and $REFGPS_{i,t}$ are the time difference between GPS and reference time of station i and j at epoch t.

The tenability of equation (1) relies on:

a) The GPS time or GPS satellite time measured by all receivers at each epoch are identical.

b) The total delays of stations are kept stationary, or we know their exact values at each epoch.

Any violation of a) and b) would reduce the long term performance of GPSTT. If the baselines between each station are short, it's very reasonable to neglect the violation of condition a). We can focus on checking the long term variation of the total delay of GPS stations. We use the GPSP3 CCD (common clock difference) to observe the relative total delay variation between each GPS station in section II, and roughly discuss some of their possible causes.

The best way to improve the long term performance of GPSTT is to investigate all noise patterns of total delay and remove them, but before we fully understand the composition of the total delay variation, a compromise way is to use the multi receivers and their variations of total delay may be averaged out in long term. [2] proposed and tested a preliminary double-receiver system using the mean value of two receivers of each measurement epoch and the time transfer stability was considerably improved.

In section III, we propose a virtual ensemble receiver model which uses all measurements from multi receivers in ensemble. That the time difference between local reference point and the realization GPS time of the virtual receiver is the weighted averaging results of all calibrated receivers in ensemble. Since the measurements quantity of the virtual receiver is several times than a single receiver and got from different receivers, it's reasonable to expect the virtual receiver is more robust and stable than single receiver.

To verify the time transfer performance of virtual receivers, we test the DCD of GPSP3 AV and TWSTFT of NICT (National Institute of Information and Communications Technology)-TL(Telecommunication Laboratories) links in section IV. We test 9 GPS P3AV links including a virtual receiver link consisted of 2 virtual receivers from TL (4-receiver ensemble) and NICT (2-receiver ensemble) and

analyze the time deviation (TDev) of each DCD in short term and long term.

In 2017 CCTF (Consultative Committee for Time and Frequency) meeting, the working groups on TWSTFT and on GNSS jointly recommend the UTC laboratories to provide all data from redundant GNSS systems to the BIPM (Bureau international des poids et mesures); and recommend BIPM to study the use of redundant time transfer systems in UTC generation [7]. This is the major motivation of this study and we will discuss the redundancy in the virtual receiver ensemble in session V.

II. Very Short Baseline P3 CCD of GPS Receivers

We use the very short baseline CCD (common clock difference) to investigate the total delay variation of GPS stations. Due to the positions of receivers are very close, the common broadcast noises from GPS satellite will be averaged out in the CCD calculation, the residual variation of CCD of the 2 GPS time transfer results can be treated as the combination of their total delay variations.

The GPS stations in TL are chosen for long term CCDs comparison. TL owns 4 fixed GPS stations with different models of receivers (Table I), that we can avoid some common bias due to the model effects.

TABLE I. GPS Receivers in TL

Station	TLT0	TLT1	TLT2	TLT3
Antenna	ASH701945C_M SCIS	SEPCHOKE_B3E6 SPKE	JAV_RINGANT _G3T	SEPCHOKE_B3E 6 SPKE
Antenna Cable	FSJ1-50A	FSJ1-50A	FSJ1-50A	FSJ1-50A
Receiver	PolaRx4 Pro	Ashtech Z12T	TTS-4	GTR50
[a] Reference	[b] 5 MHz→10 MHz	[c] 5 MHz→20 MHz	5 MHz+1PPS	10 MHz+1PPS

[a.] All reference to the definition point of UTC(TL) (1 V rising edge of 1 PPS)
[b.] No 1 PPS reference input, TL monitor [UTC(TL)-1 PPS output] but no compensation
[c.] Latch point is not synced with 1 PPS input, TL monitor [20 MHz input-1 PPS input] and compensate

The latch points of 4 receivers are theoretically synced with the 1 PPS definition point of UTC(TL), and all their frequency references are also synced to the 5 MHz sine wave output of UTC(TL). For station TLT0 (PolaRx4 Pro), its latch point is synced with its 10 MHz frequency (5 MHz via a frequency doubler) input, not the definition point of UTC(TL). TL records the phase difference between its 1 PPS output and UTC(TL) for monitoring. The station TLT1 (Ashtech Z12T) is the primary GPS station of TL used for UTC link. Its latch point is not synced with the 1 PPS input but its 20 MHz reference frequency (5 MHz via a quadruple) input. TL redefine it latch points to let it synced with the definition point of UTC(TL) [8]. The latch points of TLT2 (Piktime TTS-4) are synced with a particular cycle of its external 5 MHz signal chosen by external 1 PPS input. [9]

The latch points of TLT3 (GTR50) are compensated according to their reference 1 PPS in measurement via their internal time interval counter, are designedly synced with their 1 PPS input.

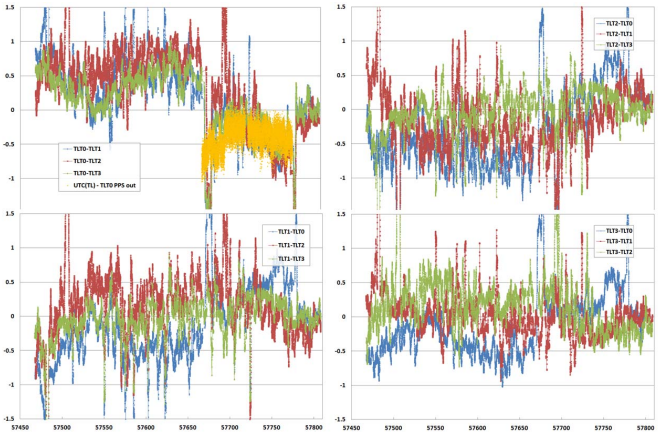


Fig. 1. The very short baseline GPSP3 CCDs of TL, 4 different types of receivers TLT0, TLT1, TLT2, and TLT3 are used. The phase difference between UTC(TL) and the PPS output of TLT0 are also graphed for comparison (yellow dots of upper left graph)

The GPSP3 CCD results are showed in Fig. 1. We find there are about ±0.5~±1.0 ns/year variation in each GPSP3 CCD, the stations TLT2 and TLT3 are relatively stable in long term, we note their latch points are designed to synced with their 1 PPS reference input.

The CCD variation of station TLT0 is larger than the other stations; we also note its latch points are phase locked to its reference frequency input and may migrate with respect to the reference points of UTC(TL). TL records the phase difference between its 1 PPS out and UTC(TL) over about 100 days (MJD 57650-57750), we find its variation is roughly match the CCD variation of TLT0 during that period. It implies that time transfer results of TLT0 will be more coincident with the other stations if we can compensate its latch point variation of TLT0.

III. Virtual Ensemble Receiver

In section II, we know that the total delay of a GPS station, at least the receivers in TL ensemble, is not stationary and exists up to ±1.0 ns/year variation. That means those variations will contribute ±1.0 ns/year discrepancy in GPSTT. In the case of TLT0 or PolaRx4 receiver, compensate the phase difference between its 1 PPS out and reference point may reduce the discrepancy. A long term observation is going on to verify it. For the other receiver models, we did not have clues yet how to remove their noise patterns to reduce the discrepancy of GPSTT.

The compromise way is to assemble the GPSTT results from multi receivers, if the number of measurement is large enough, we expect the different variation patterns will be averaged out and get a more stable result.

Here we propose a virtual ensemble receiver model which weighted from the REFGPS measurements of each station's CGGTTS (CCTF Group on GNSS Time Transfer Standards) [10] files. The REFGPS all in view values of our virtual ensemble receiver at each epoch is followed the steps below:

a) The zero point total delay value of each receiver in ensemble is the calibrated or aligned result of 2014 BIPM G1 calibration campaign (calibration ID 1001_2014) [11].

b) The REFGPS values of each GPS satellite at each epoch are the REFGPS values of all receivers in ensemble.

c) The all in view values of virtual receiver at each epoch are the equal weighting results after eliminating the outliers exceed 1 standard deviation.

d) Once new receivers introduced in ensemble or receivers in ensemble change setup, its total delay will be aligned according to the total delay of virtual receiver.

For TL 4-receiver ensemble, there are about 40-50 REFGPS measurement at each epoch. It's reasonable to expect the virtual receiver is more robust and redundant because the unreasonable measurement outliers will be removed automatically.

For b), it means the total delay of virtual receiver would close to the averaged total delay of all physical receivers in ensemble; for d), the total delay of virtual ensemble receiver will be kept in the value of the average of 2014 calibration results of all calibrated/aligned receivers. We will examine the total delay change for next calibration to check the repeatability in future study.

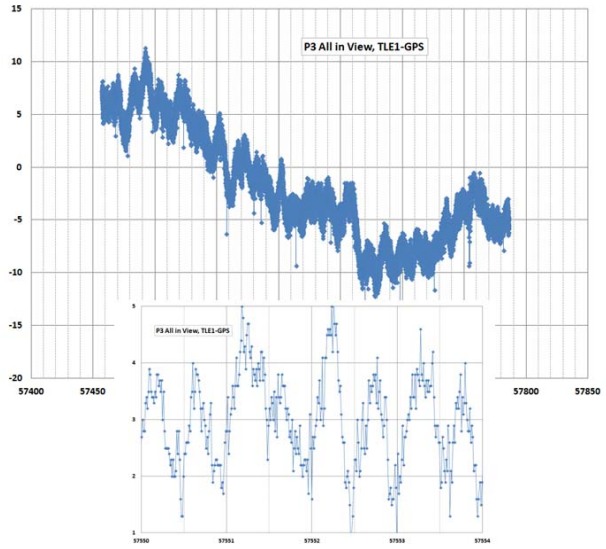


Fig. 2. The REFGPS (time difference between GPS time and the reference point of receiver) of TLE1. We note there are obvious half day cycle.

The GPSP3 all in view results of virtual ensemble receiver are showed in Fig. 2. The long baseline time comparison test will be described in section IV.

IV. Tested Example: TL/NICT Virtual Ensemble Receivers Link, TLE1-NCE1

We choose the GPS receiver ensembles in NICT and TL to test the long baseline GPSTT performance of our virtual ensemble receiver model.

The primary GPS stations of NICT and TL (NC01 and TLT1) are both calibrated at 2014 BIPM calibration tour, and the NICT-TL TWSTFT link was operated for many years, we can compare the virtual receiver link results with TWSTFT link's via DCD process.

The virtual receiver of TL, named as TLE1, is consisted of receivers TLT0, TLT1, TLT2, and TLT3. The virtual receiver of NICT, named as NCE1, is consisted of 2 receivers, NC01 (Septentrio PolaRx2 TR) is the primary receiver used for UTC link, and NC5G (Dicom GTR50) is the backup receiver for UTC link. The GPSP3 AV results of TLE1 and NCE1 are generated by using the steps of section III.

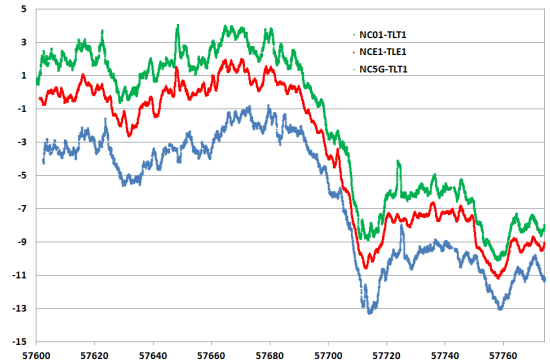


Fig. 3. The UTC(NICT)-UTC(TL) time transfer results measured by the primary receiver link NC01-TLT1 (green dots), backup receiver link NC5G-TLT1 (blue dots), and the virtual ensemble link NCE1-TLE1 (red dots).

Fig. 3 is the GPSP3 AV time comparison results of the virtual ensemble receiver link NCE1-TLE1, and 2 single physical receiver links, NC01-TLT1 and NC5G-TLT1. It's obvious that the time comparison results of 2 single physical receivers exits 2~4 ns discrepancy during MJD 57600~57780. The virtual ensemble receiver results are between these two.

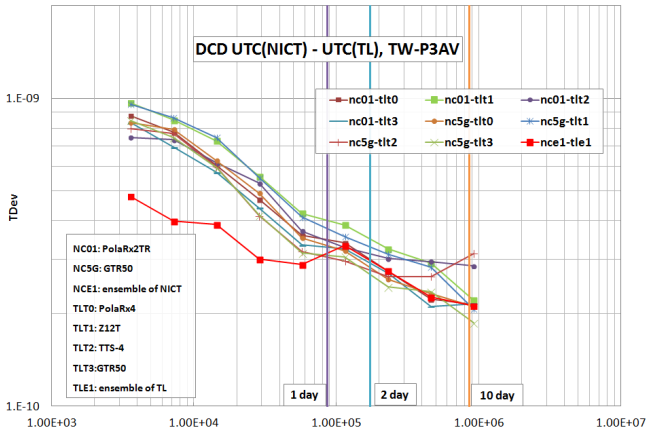


Fig. 4. The TDev of NICT-TL GPSP3TT and TWSTFT DCD, including virtual receivers link NCE1-TLE1 and other single-receiver links.

The time deviations (TDev) of UTC(NICT)-UTC(TL) GPSP3 AV links and TWSTFT link DCD is shown in Fig. 4. The GPSP3 AV links includes 8 single receiver links and one virtual receiver link, NCE1-TLE1. With respect to TWSTFT, the short term stability of the virtual receiver link (NCE1-TLE1) is much better than other single receiver links, and the long term performance of NCE1-TLE1 link is almost the most stable one of all GPSP3 AV links, and better than the primary receiver link NC01-TLT1.

V. CONCLUSION

From section II, we again demonstrate the total delay of a GPS station is not stationary; and, at least, in some receiver models, the latch points of receiver is not always synced with its external 1 PPS but slowly migrated. Measure and compensate the migration should improve the long term performance of GPSTT. Except the latch point migration, the GPSTT will achieve the most accurate if we can figure out all kinds of noise patterns of total delay and remove them.

In section IV, we demonstrated the GPSP3AV result of virtual ensemble receiver link is more stable than any single-physical receiver link. Due to its excellent short term performance, the virtual ensemble receiver can be used for precisely align or calibrate the total delay of other physical receivers.

Furthermore, the virtual ensemble receiver is definitely more robust and redundant because its total delay will keep stable even if any physical receiver in ensemble retreats or fails. In CCTF 2017 “Recommendation on the utilization and monitoring of redundant time transfer equipment in the timing laboratories contributing to UTC” [7], the working groups on TWSTFT and on GNSS jointly recommend the UTC laboratories to provide all data from redundant GNSS systems to the BIPM, and the BIPM to study the use of redundant time transfer systems in UTC generation. We expect there will be many receiver ensembles in UTC laboratories; our virtual ensemble receiver model can be the most potential way to perform a stable, robust, and redundant GNSS time transfer.

ACKNOWLEDGMENT

The authors would like to thank the colleagues in the BIPM and NICT for the cooperation of the time transfer experiments and sharing the data.

REFERENCES

[1] S. Y. Lin, W. H. Tseng, H. T. Lin, Y. J. Huang, and K. M. Feng, “Long-term Inconsistency between TWSTFT and GPS Time Transfer Results in PTB-TL and NICT-TL Time Links, Proc. EFTF 2010

[2] Z. Jiang, D. Matsakis, S. Mitchell, L. Breakiron, A. Bauch, D. Piester, H. Maeno and L. G. Bernier, “Long-term instability of GPS-based time transfer and proposals for improvements”, Proc. PTTI 2011

[3] Z. Jiang, L. Tisserand and G. Petit, “Tests of the BIPM portable calibration station - METODE: MEasurement of TOtal Delay”, Proc PTTI, 2012.

[4] Z. Jiang et al., BIPM Technology Memorandum TM263

[5] Z. Jiang, D. Matsakis and V. Zhang, “Long-term instability in UTC time links”, Proc. PTTI 2017.

[6] Z. Jiang, F. Arias, W. Lewandowski, G. Petit, "BIPM Calibration Scheme for UTC Time Links", Proc. EFTF 2011, pp 1064-1069

[7] CCTF 2017 Recommendation on the utilization and monitoring of redundant time transfer equipment in the timing laboratories contributing to UTC.

[8] S.Y. Lin et al., “A Modification of Z12T Metronome Time Transfer System”, Proc. EFTF 2014

[9] BIPM Guidelines for GNSS equipment calibration.

[10] D.W. Allan and C. Thomas, “Technical Directives for Standardization of GPS Time Receiver Software”, Metrologia, 1994, 31, pp. 69-79.

[11] ftp://ftp2.bipm.org/pub/tai/publication/gnss-calibration/group1/1001-2016/

Delay compensation of 1 PPS timetags in fiber-optic time distribution

P. Krehlik, M. Mazur and Ł. Śliwczyński
Faculty of Computer Science, Electronics and Telecommunications
AGH University of Science and Technology
Krakow, Poland

***Abstract*—In various fiber-optic time and frequency distribution systems the delay of 1 PPS timetags is stabilized and precisely calibrated. However in a case of long fiber path the 1 PPS signal is seriously delayed in respect to UTC, which is cumbersome in various applications. In this work we present an idea and experimental evaluation of a circuit designed for compensating this delay. The compensation up to 1 s may be introduced in 10 ns steps, and the standard uncertainty of the compensation is app. 550 fs.**

Keywords—time and frequency distribution; fiber optics; ELSTAB

I. INTRODUCTION

Fiber-optic systems for time and frequency (T&F) distribution become an alternative for standard satellite techniques, especially when the best stability and precise timescale calibration is needed [1, 2]. In previous papers the authors presented the so-called ELSTAB solution [2], in which the delay of the output 1 PPS signal is stabilized and calibrated with uncertainty of about 10 ... 50 ps [3]. However, the absolute value of this delay is proportional to the fiber length, and may reach milliseconds range. In this work we present a new module designed for compensating the delay introduced by the fiber, which may be used also in other similar T&F distributing systems. The schematic diagram of the ELSTAB system with added "1 PPS advancing" module is shown in Fig. 1.

The solution presented herein was practically implemented in the links connecting UTC(PTB) laboratory in Braunschweig and Deutsche Telekom center in Bremen, Germany [4].

II. THE CONCEPT OF 1 PPS ADVANCING MODULE

The apparent "advancing" of the 1 PPS signal reaching the remote terminal of the system is realized by extending this delay to a full second, in the circuit presented in Fig. 2. The 10 MHz signal is multiplied to 100 MHz to obtain better resolution of the 1 PPS signal positioning. 100 MHz signal enters the 28-bit digital down counter, and the incoming 1 PPS triggers the counting process, which decrements the counter output from 100 000 000 down to 0. The state of the counter is being compared with the reference value at the 28-bit comparator, and at certain instant the output of the comparator triggers the generation of the output 1 PPS pulse. The desired "advance" of 1 PPS (entered in tens of nanoseconds) should be entered into the register which provides the reference for the comparator. In our practical realization, the counter, comparator, register and 1 PPS pulse generator are implemented in a CPLD programmable digital circuit manufactured by Xilinx and a few additional components.

It should be mentioned that the total delay between 1 PPS signal entering the local terminal and outgoing the remote terminal may be set as "negative", thus the extra delays introduced by external cables, distributors etc. might be also taken into account and compensated.

III. EXPERIMENTAL VERIFICATION

The initial evaluation of the advancing module was performed with a time interval counter (TIC). We verified that the time difference between input and output 1 PPS pulses changes accordingly to the entered advance value for some hundreds of randomly generated numbers.

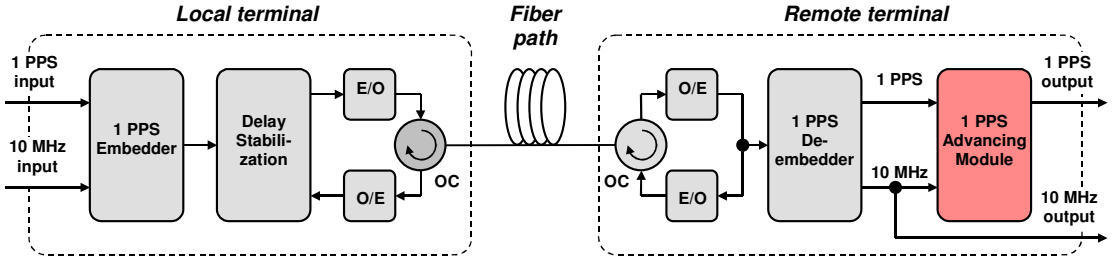


Fig. 1. The schematic diagram of the ELSTAB system with added "1PPS advancing" module. E/O stands for electro-optic converter, O/E - opto-electric converter, OC - optical circulator.

This work was supported by Polish National Science Center (NCN) under project no. 2015/17/B/ST7/03628.

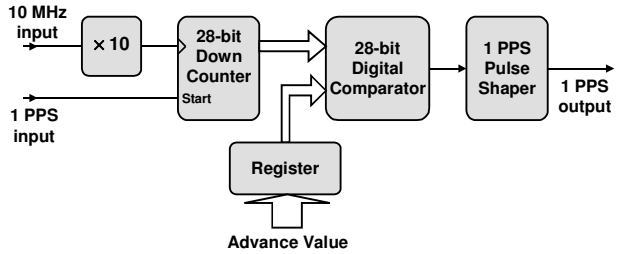


Fig. 2. Simplified schematic of the 1 PPS advancing module.

Next we measured the nonlinearity of the advancing module, i.e. the offset between the actual advance and the intended value, which is exactly N×10ns. Because it is unmanageable to measure nonlinearity for all possible advancing values, we focused on the range from zero to 5 ms, which corresponds to compensating the delay of up to 1000 km-long fiber route. We performed measurements both for 1000 randomly generated values of the advance (in the range 0 to 5 ms), and in some shorter periods also in a step-by-step manner. In the last stage we measured the phase noise (jitter) of the output 1 PPS pulses in respect to 10 MHz master signal, which is the timebase of the whole setup.

The measurements of nonlinearity (offset) and phase noise were performed with high-speed digital oscilloscope, in the setup similar as in our previous works [5].

The measured nonlinearity is presented in Fig. 3 a). For 1000 values of the advance spread over 5 ms range the standard deviation from expected N×10ns values is 550 fs, and peak-peak deviation is ±1.5 ps, which is negligible comparing to other sources of calibration uncertainty in our system [2, 5]. There is no visible trend in offset values over the investigated 5 ms range.

The phase noise of 1 PPS pulses is plotted in Fig. 3 b). As one may notice, the jitter is app. 2.5 ps, practically regardless of the absolute value of the advance. This value of the jitter is very closed to obtained in the older version of ELSTAB system with no 1 PPS advancing functionality, thus we may conclude that the added new feature does not affect the stability and calibration uncertainty of the entire system.

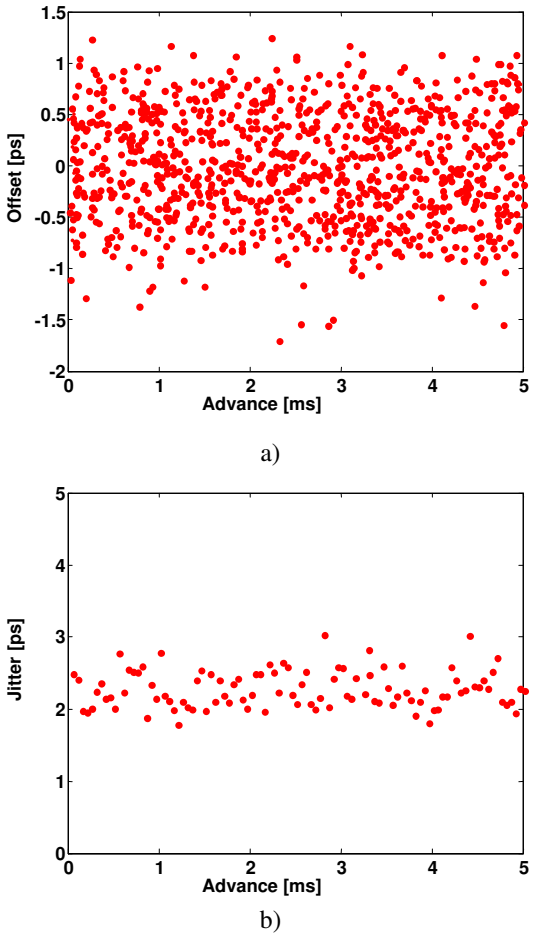


Fig. 3. Evaluation results: nonlinearity (offset) versus advancing value (a) and phase noise (jitter) versus advancing value (b).

IV. CONCLUSION AND FURTHER PLANS

In this work we proposed the solution for canceling the 1 PPS timetags delay introduced by the long-haul fiber transmission system. The idea was implemented in our ELSTAB technology, but may be used in similar systems dedicated for stabilized time and frequency transfer. The resolution of the proposed delay cancellation is 10 ns, and the nonlinearity (offset) is below ±1.5 ps (550 fs rms). Arbitrary value of 1 PPS „advancing" may be programmed.

In the next step we are going to add the further section of delay correction, with the resolution of 10 ps, covering the span between the current 10 ns steps. This way the input-to-output delay of the timetags would be adjusted to be very close to UTC reference.

REFERENCES

[1] M. Rost at al., "Time transfer through optical fibers over a distance of 73 km with an uncertainty below 100 ps," Metrologia, vol. 49, no. 6, 2012, pp. 772-778.

[2] P. Krehlik at al., "ELSTAB - fiber optic time and frequency distribution technology - a general characterization and fundamental limits," IEEE Trans. Ultrason., Ferroelect., Freq. Control, vol. 63, no. 7, 2016, pp. 993-1004.

[3] Ł. Śliwczyński at al., "Dissemination of time and RF frequency via a stabilized fibre optic link over a distance of 420 km," Metrologia, vol. 50, no. 2, 2013, pp. 133-145.

[4] Ł. Śliwczyński at al., "Fibre optic time transfer between PTB and Deutsche Telekom using multi-link redundant topology," in these proceedings.

[5] P. Krehlik at al., "Fiber optic joint time and frequency transfer with active stabilization of the propagation delay", IEEE Trans. Instrum. Meas., vol. 61, pp. 2844–2851, 2012.

Time and frequency transfer in modern DWDM telecommunication networks

Krzysztof Turza, Artur Binczewski, Wojbor Bogacki
Network Technology Division
Poznan Supercomputing and Networking Center (PSNC)
Poznań, Poland
kturza@man.poznan.pl, artur@man.poznan.pl,
wojbor@man.poznan.pl

Przemysław Krehlik, Łukasz Śliwczyński
Faculty of Computer Science, Electronics and Telecommunications
AGH University of Science and Technology
Kraków, Poland
krehlik@agh.edu.pl, sliwczyn@agh.edu.pl

***Abstract*—In the paper the authors present their experiments oriented on transferring time and frequency signals over modern telecommunication networks carrying 40/100 Gbps signals using coherent techniques. The experiments were performed in 1500 km-long loop arranged by PSNC in the PIONIER production network. We observed good stability of delivered signals: Modified Allan Deviation of 10^{-15} at 10^3 s averaging (for 10 MHz frequency signal), and Time Deviation below 10 ps for averaging up to 10^5 s for 1 PPS time signal.**

Keywords—DWDM, optical fiber, time and frequency transfer, coherent DWDM

I. BACKGROUND

In recent years, the authors have reported successful results of time and frequency (T&F) transfer via dark fiber links. In 2012, the first such link was established between Astrogeodynamical Observatory (AOS) in Borowiec near Poznan, and GUM in Warsaw [1]. In 2014, the next link using dark fiber was established between AOS and the National Laboratory for Atomic, Molecular and Optical Physics (KL FAMO) in Torun [2].

A commonly identified advantage of the dark fiber (i.e. a dedicated system operating on single fiber in both directions) over dense wavelength division multiplex (DWDM) transmission is that thanks to the great symmetry of propagation conditions it allows effective compensation of propagation delay fluctuations in optical fiber related e.g. to temperature changes [3], [4]. The DWDM network exploits two parallel, but separate optical fibers and optical networking components in the transmission path (like e.g. optical amplifiers, reconfigurable add-drop multiplexers (ROADMs), etc.). All these elements provided asymmetry in the optical path thus the fluctuations of the propagation delay could not be fully compensated.

DWDM networks, as being much affordable (because of high cost of dark fiber approach) and often the only (because of fiber availability) real option to connect two distant locations have already been investigated as a potential medium for precise T&F transfer (see e.g. [5]). In this paper we extend our investigations to the modern DWDM networks that appeared with the advent of coherent 100 Gbps technology (hereafter referred as coherent DWDM).

II. EXPERIMENTS

In our experiment, we measured stability of T&F signals transmitted as an "alien lambda" service in the DWDM network, carrying multichannel, coherent 100Gb/s data transmission. The T&F signals were actively stabilized using AGH-developed ELSTAB technology, but in contrary to a standard approach, which use single, dedicated fiber for both forward and backward signals transmission, the signals were spitted into two separated directions and transmitted via typical DWDM infrastructure. The optical path was arranged in the national PIONIER production network based on a newest version of ADVA FSP3000 equipment. The route had a form of 1500 km-long loop, with both local and remote ends located at PSNC PoP in Poznań - see Fig. 1. Stability of 10 MHz frequency signal was measured with VCH-314 frequency comparator (Vremya-Ch), and 1 PPS signal was analyzed with MTC108 precise time interval counter (developed by Military University of Technology) - see Fig 2.



Fig. 1. 15000 km-long testing loop in the national PIONIER network

This work was (partially) supported by the OFTEN 15SIB05 project. The project OFTEN has received funding from the EMPIR programme co-financed by the Participating States and from the European Union's Horizon 2020 research and innovation programme.

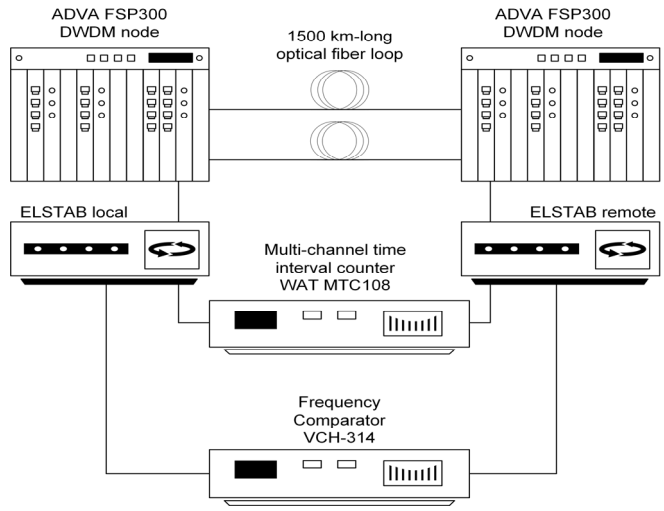


Fig. 2. Wiring diagram for experimental frequency transfer (ELSTAB system) in coherent DWDM system

III. RESULTS

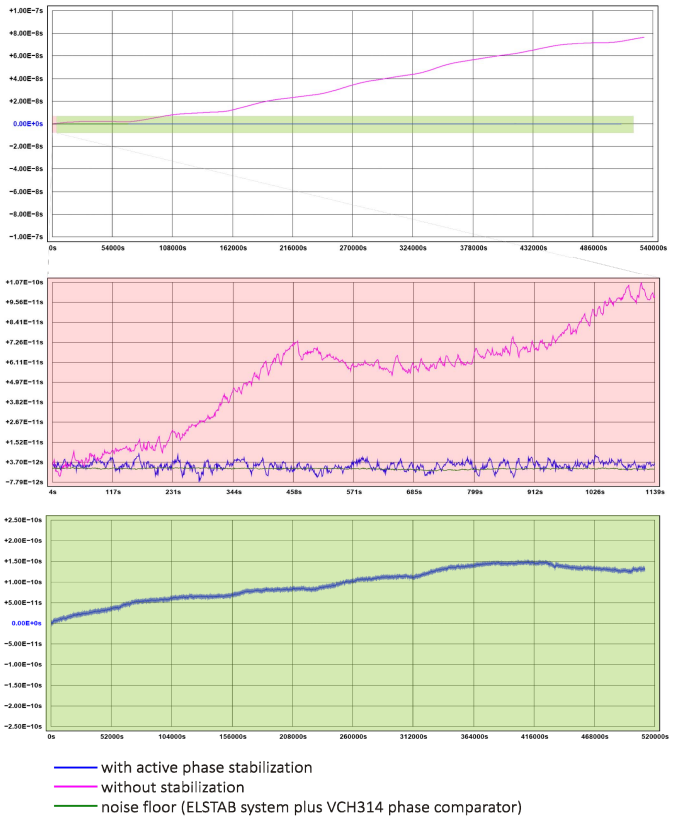


Fig. 3. Phase fluctuations of 10 MHz signal: general view of 6 days-long observations (top), short period enlarged (middle) and stabilized phase enlarged (bottom).

Stability of 10 MHz frequency transfer measured over 6-days period is illustrated in terms of time-domain phase fluctuations - Fig. 3, and Modified Allan Deviation (MDEV) - Fig. 4. The charts, are shown both the unstabilized (unidirectional) transmission in the DWDM network, stabilized transmission using forward-backward stabilizing loop (also transmitted in DWDM system), and a noise floor defined as the stability of the ELSTAB system measured with short patchcords (and attenuators) instead of the DWDM optical paths. For unstabilized transmission, one may observed the very pronounced phase drift related to the optical cable warm-up during the spring period, and additionally some diurnal oscillations. The mean relative frequency offset, related to this drift, was about $1.4*10^{-13}$, and The MDEV was limited to values not better than few times 10^{-14}. For stabilized transmission, the results are much better: the frequency offset do not exceed few times 10^{-16}, and ADEV goes down up to $2*10^{-16}$.

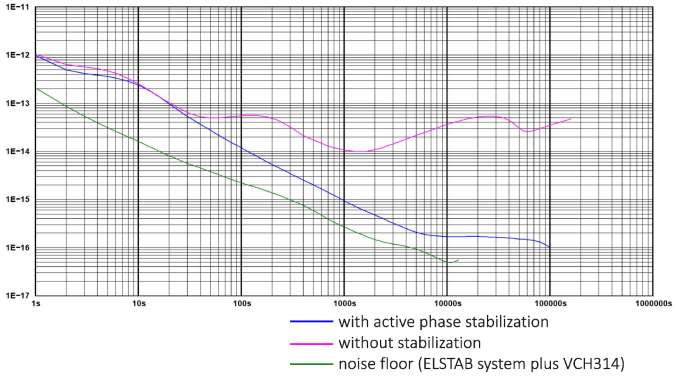


Fig. 4. Modified Allan Deviation of 10 MHz signals

Analyzing the frequency stability one can notice that the phase stabilization is not efficient for short averaging, but becomes quite effective for longer periods. This suggests that short-term phase fluctuations are not correlated for opposite directions, and probably should be attributed to the DWDM equipment, while long-term fluctuations, related to fibers temperature, are well correlated and thus can be suppressed in the stabilization system.

The results obtained for time transfer are similar: the stabilization is efficient mainly for longer averaging times (beyond 100 s), and offers two orders of magnitude improvement in terms of Time Deviation for 1 day averaging (Fig. 5). It should be stressed however, that absolute calibration of time transfer needs some external means, as the forward-backward delay asymmetry cannot be evaluated in a real DWDM network.

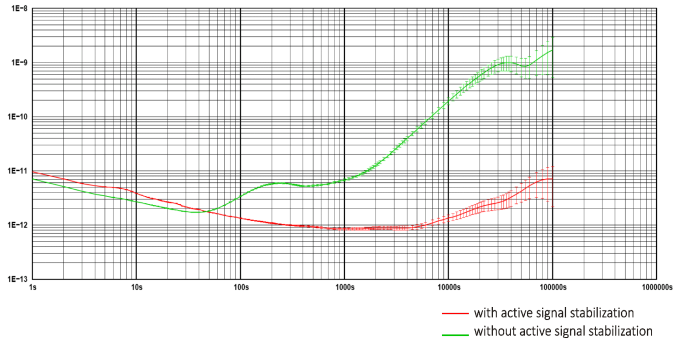


Fig. 5. Time Deviation of 1 PPS signals

IV. SUMMARY

This work presents the stabilized T&F transfer in the 100 Gb/s coherent DWDM network. The results are still noticeably worse than obtained in links based on dedicated single fiber transmission [1], but much more better than obtained in oldest generation of the DWDM network, reported previously in [5].

The significantly different results obtained in different types of DWDM networks calls for systematic research oriented on pointing out particular factors determining T&F transfer stability and accuracy.

ACKNOWLEDGMENT

We thank our colleagues from GUM for the technical and metrological support during non-coherent DWDM testing phase and our colleges from ORANGE Polska, who provided last mile fiber connections.

REFERENCES

[1] Ł. Śliwczyński, P. Krehlik, Ł. Buczek, M. Lipiński, A. Czubla, „Dissemination of time and RF frequency via a stabilized fibre optic link over a distance of 420 km", Metrologia, vol. 50, pp. 133–145, 2013.

[2] Ł. Buczek, J. Kołodziej, P. Krehlik, M. Lipiński, Ł. Śliwczyński, *at all*, "OPTIME - the system grows - a new 330 km line", Joint Conference of the IEEE International Frequency Control Symposium / European Frequency and Time Forum, Denver, CO, 2015, pp. 583-586.

[3] Ł. Śliwczyński, P. Krehlik, M. Lipiński, „Optical fibers in time and frequency transfer", Measurement Science and Technology, vol. 21, DOI 10.1088/0957-0233/21/7/075302, 2010.

[4] T. Pinkert, O. Böll, L. Willmann, G. Jansen, E. Dijck, B. Groeneveld *at all*, "Effect of soil temperature on optical frequency transfer through unidirectional dense-wavelength-division-multiplexing fiber-optic links", Appl Opt., vol. 54, pp728-38, 2015

[5] Ł. Śliwczyński, P. Krehlik, M. Lipiński, K. Turza, A. Binczewski, "Frequency distribution in delay-stabilized optical DWDM network over the distance of 3000 km", Joint Conference of the IEEE International Frequency Control Symposium / European Frequency and Time Forum, Denver, CO, 2015, pp. 280-283

A Novel Real time Cycle Slip Detection and Repair Method for a single Dual-frequency GNSS Receiver

Hang Yi, Hongbo Wang, Xueyun Wang, Shengkang Zhang, Haifeng Wang, Wenzhe Yang, Shuwei Wang
Beijing Institute of Radio Metrology and Measurement, Beijing China
Science and Technology on Metrology and Calibration Laboratory, Beijing China
E-mail: hang.yi@hotmail.com

***Abstract*—This paper develops a novel real time cycle slip detection and repair method for a single dual-frequency GNSS receiver. This method is based on several carrier-phase linear combinations, including WL (1, -1), Ultra-WL (-3, 4), NL (1, 1), GF (60,-77). First, we use the mean code range rate which is estimated by the former 10 code range data to detect and repair the big cycle slip. In this step, the big cycle slip is detected and repaired; however, some extra small cycle slip will be introduced into the carrier phase data. Second, the variation of the WL combination is used to detect the different cycle slip on L1 and L2 and the variation of the Ultra-WL combination is used to judge which frequency the cycle slip occurs on. With respect to the same cycle slip on L1 and L2, we use the variation of NL combination when the elevation of the satellite is low since it has lower noise than GF combination and the NL cycle slip is twice as L1 or L2 and use the variation of GF when the elevation of the satellite is high since the variation of the ionosphere delay is very smooth. After that, there are still some cycle slips with the same size and sign which occurs continually in every epoch on L1 or L2. For these cycle slips, we use the mean ionosphere residual method since the ionosphere residual is the same in all the 10 epochs. Finally, we can detect and repair all the cycle slip larger than 1 cycle in real time.**

Keywords—real time; cycle slip; dual-frequency; carrier-phase linear combination

I. INTRODUCTION

The carrier phase measurement is one of the most precise measurements at present for its accuracy to a millimeter level. By using carrier phase measurement, the post-processing precise point positioning (PPP) technique can provide accurate positioning globally with a single receiver [1]. However, real-time PPP cannot provide stable positioning solutions at the desired accuracy as well as post-process PPP do because of the cycle slip due to loss-of-lock in signal tracking. To achieve real time PPP, cycle slip must be correctly detected and repaired in real time [2].

Over the past decade, a number of methods have been developed to detect and repair cycle slips in carrier phase measurements. Many researchers use the double-differenced techniques since it can reduce most of the common errors; however, it is not suitable for our purpose of processing single GNSS receiver. Blewitt (1990) developed an automatic editing algorithm call TurboEdit which is suitable for single GNSS receiver [3]. In this method, Melbourne-Wübbena wide lane (MWWL) combination and geometry-free combination is used simultaneously to detect the cycle slip. The MWWL combination is very effective for cycle slip detection because of its low level of noise and insensitive to iononspheric changes. However it cannot detect the same cycle slip on L1 and L2 and it cannot judge which frequency the cycle slip occurs on. The geometry-free combination method is also called the ionospheric residual error method which relies on the slow variation of the ionospheric residual [4]. As a result, TurboEdit is suitable for satellites with a high elevation when the quality of the code data is very good and when the ionospheric residual is very stable. Liu (2011) developed a new cycle slip detection and repair approach based on the ionospheric total electron content (TEC) rate [5][6]. This method jointly uses the ionospheric total electron contents (TEC) rate (TECR) and Melbourne-Wübbena wide lane (MWWL) combination to uniquely determine the cycle slip on both L1 and L2 frequencies. In this method, the estimation of TECR is based on the measurements of the previous epochs and Liu (2011) suppose that all the epochs prior to the current epoch are free of cycle slips and if any, have been repaired. However, at the very beginning of the cycle slip detect, we do not know whether the cycle slip have been repaired and we should not make this supposition. Besides, according to the real data, we found that it is difficult to detect the cycle slip using the MWWL linear combination method when the elevation of the satellite is low because of the large noise of the code range.

In this paper, a novel real time cycle slip detection and repair method is proposed. In this method, only 10 epochs prior to the current epoch is needed and we do not care whether the cycle slip in these 10 epochs have been detected and repaired. Firstly, we use the mean code range rate which is estimated by the former 10 code range data to detect and repair the big cycle slip instead of the code-phase method. In the following steps, we do not use code measurement any more since the noise of the code measurement is too large. We selected several carrier phase linear combinations and use different combination to detected different cycle slips, including the different cycle slip on L1 and L2, the same cycle slip on L1 and L2, the same size and sign cycle slip occurs continually in every epoch on L1 or L2.

This paper is organized as below. The methodology of detecting and repairing cycle slip is developed in Sect. II. In

Sect. III, some cycle slip detection and repair experiment using this method is given. The conclusion is given in Sect. IV.

II. CYCLE SLIP DETECTION APPROACH

According to the general cycle slip detection methods such as TurboEdit method, phase-code comparison method, ionospheric residual method, we can see that,

- WL combination can detection the different cycle slip on L1 and L2 but cannot judge which frequency the cycle slip occurs on.
- GF combination can detect small cycle slip but cannot detect some special cycle slip pair such as (77N, 60N), N=0, ± 1, $\pm 2, \cdots$
- GF combination can detect and repair cycle slip smaller than 4 cycle. If the cycle slip is larger than 4 cycles, there may be some illegibility, for example, GF combination can detect cycle slip pair (-4,-3) and (5, 4), but cannot judge them.
- Phase-code comparison method can detect big cycle slip but cannot succeed in small slips

As a result, we should detect and repair the cycle slip larger than 4 cycles firstly. In this paper, the cycle slip is divided into four parts, the big cycle slip(larger than 4 cycles), the different cycle slip on L1 and L2, the same cycle slip on L1 and L2, the same size and sign cycle slip occurs continually in every epoch on L1 or L2. Fig.1 shows the process of this method.

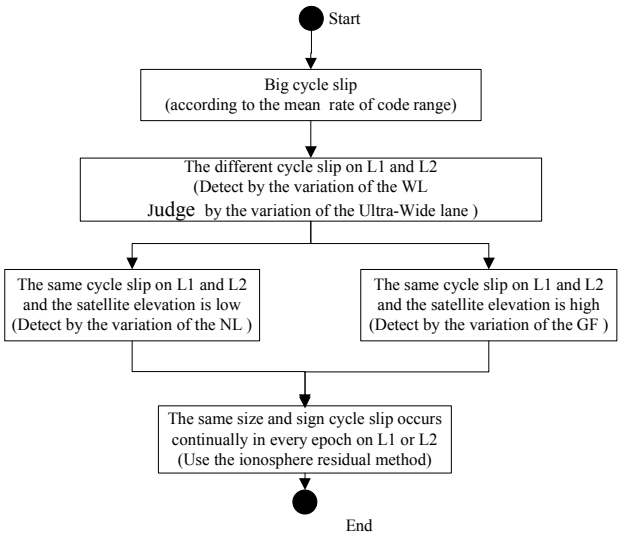


Fig. 1 The process of this method

A. The big cycle slip(>4cycles)

According to noise level of the code measurement, if we detect and repair the cycle slip using phase-code comparison method, there may be still some cycle slip larger than 4 cycles left. This paper purpose to detect and repair the rate of the cycle slips, that is, we compare the mean code range rate with the carrier phase rate and repair the carrier phase rate if its difference with the mean code range rate is larger than 0.5 cycles. The observation equations for dual-frequency carrier phase and pseudo range measurements can be written as:

$$\lambda_i \Phi_i = \rho + c\left(dt_s - dt_r\right) - I_i + T + \lambda_i N_i \quad (1)$$

$$P_i = \rho + c\left(dt_s - dt_r\right) + I_i + T \quad (2)$$

The code range and carrier phase rate can be written as:

$$\Delta(\lambda_i \Phi_i) = \Delta\rho + c\left(\Delta dt_s - \Delta dt_r\right) - \Delta I_i + \Delta T + \lambda_i \Delta N_i \quad (3)$$

$$\Delta(P) = \Delta\rho + c\left(\Delta dt_s - \Delta dt_r\right) + \Delta I_i + \Delta T \quad (4)$$

We can get,

$$\Delta(\lambda_i \Phi_i) - \Delta P = -2\Delta I_i + \lambda_i \Delta N_i \quad (5)$$

In Eq. (5), ΔI_i is close to zero, the cycle slip left will depend on the mean code range rate ΔP. In order to reduce the error of ΔP, the slope of the linear equation of code range is taken as ΔP. Since the noise level of slope is lower than that of code range by 10 times, the cycle slip left is less than 2 cycles. This step may introduce small cycle slip continually by epoch but it does not matter.

B. The different cycle slip on L1 and L2

The different cycle slip on L1 and L2 is easy to detect by WL combination method. In order to judge which frequency the cycle slip occurs on, we calculate the secondary difference of the Ultra-WL combination simultaneously. If the secondary difference of the Ultra-WL is the multiple of 3, then L1 occurs cycle slip and if the multiple of 4, then L2.

C. The same cycle slip on L1 and L2

We found that both the difference of GF combination and the secondary difference of the NL combination can be used to detect the same cycle slip on L1 and L2, however,

- The ionospheric residual changes rapidly when the elevation of the satellite is low and this may due to the failure of the cycle slip while using GF combination
- The quadratic term of the geometric distance for NL is twice that of L1 and L2 and the NL wavelength is very small, as a result, it is difficult to detect cycle slip using NL combination when the elevation of the satellite is high,

As an improvement, when the elevation of the satellite is low, we use NL combination to detect the same cycle slip on L1 and L2 since NL combination has lower noise than GF combination and the NL cycle slip is twice than that of L1 or L2; when the elevation of the satellite is high, we use GF combination to detect the same cycle slip on L1 and L2 since it is geometry-free and the ionospheric residual is stable.

D. The same size and sign cycle slip occurs continually in every epoch on L1 or L2

This part of cycle slips are introduced into the carrier phase data in step A. They have two characteristic as following.

- They are the same in every epoch;
- They are small cycle slips, less than 2 cycles, generally.

We can conclude that the inonspheric residual is the same in every epoch and we can calculate the mean inonspheric residual. By using inonspheric residual method, we can get the cycle slips from Table I.

TABLE I. THE CYCLE SLIPS AND INONSPHERIC RESIDUAL

Cycle slip on L1 (cycle)	Cycle slip on L2 (cycle)	Inonspheric residual (cycle)	Cycle slip on L1 (cycle)	Cycle slip on L2 (cycle)	Inonspheric residual (cycle)
-3	3	-411	-1	-1	17
-2	3	-351	3	2	26
-3	2	-334	-2	-2	34
-1	3	-291	2	1	43
-2	2	-274	-3	-3	51
-3	1	-257	1	0	60
0	3	-231	0	-1	77
-1	2	-214	-1	-2	94
-2	1	-197	3	1	103
-3	0	-180	-2	-3	111
1	3	-171	2	0	120
0	2	-154	1	-1	137
-1	1	-137	0	-2	154
-2	0	-120	-1	-3	171
2	3	-111	3	0	180
-3	-1	-103	2	-1	197
1	2	-94	1	-2	214
0	1	-77	0	-3	231
-1	0	-60	3	-1	257
3	3	-51	2	-2	274
-2	-1	-43	1	-3	291
2	2	-34	3	-2	334
-3	-2	-26	2	-3	351
1	1	-17	3	-3	411
0	0	0			

III. THE PROCESS OF THIS METHOD

The effectiveness of this method was tested using real code and carrier phase measurement data. Table II shows the original measurement data from our receiver. The MJD day is 57711, and MJD second is from 9 to 18. The PRN number is GPS PRN2 and the elevation is 24.25°. Since there is no cycle slip in the original data, some simulated cycle slips in Table III are added to the original data. Table IV~VIII is the cycle slip detected by our method.

In order to test the performance of our method, some special pairs of cycle slips are added to the original data, such as (-1,-1), (-9,-7), (-77,-60). In our test, cycle slip pair (x, y) means x cycles on L1 and y cycles on L2.

As shown in Table III, we made 3 experiments. In experiment 1, there are 2 pairs of cycle slips happened in MJD (57711, 12) and MJD (57711, 14), and the cycle slip pair is (-1, 0) and (-1,-1) separately. In experiment 2, there are 2 pairs of cycle slips happened in MJD (57711, 12) and MJD (57711, 14), and the cycle slip pair is (-9, 7) and (1, 1) separately. In experiment 3, there are 2 pairs of cycle slips happened in MJD (57711, 12) and MJD (57711, 14), and the cycle slip pair is (-77, -60) and (2, 2) separately.

TABLE II. THE ORIGINAL DATA FROM GNSS RECEIVER

Epoch	P1	L1	P2	L2
9	23377549.141	23377552.038	23377548.530	23377551.991
10	23377112.006	23377114.530	23377109.099	23377114.477
11	23376675.877	23376677.051	23376669.401	23376676.994
12	23376238.786	23376239.599	23376234.795	23376239.541
13	23375801.827	23375802.179	23375797.118	23375802.122
14	23375360.847	23375364.781	23375360.381	23375364.734
15	23374925.610	23374927.416	23374921.002	23374927.358
16	23374488.023	23374490.079	23374486.430	23374490.023
17	23374049.490	23374052.774	23374050.239	23374052.726
18	23373612.958	23373615.492	23373610.392	23373615.440

TABLE III. THE CYCLE SLIP PAIR ADDED IN THE ORIGINAL DATA

MJD		Experiment 1		Experiment 2		Experiment 3	
		L1	L2	L1	L2	L1	L2
57711	9	0	0	0	0	0	0
57711	10	0	0	-9	-7	0	0
57711	11	0	0	-9	-7	-77	-60
57711	12	-1	0	-9	-7	-77	-60
57711	13	-1	0	-9	-7	-77	-60
57711	14	-2	-1	-9	-7	-77	-60
57711	15	-2	-1	-9	-7	-75	-58
57711	16	-2	-1	-8	-6	-75	-58
57711	17	-2	-1	-8	-6	-75	-58
57711	18	-2	-1	-8	-6	-75	-58

In our method, the cycle slip is detected and repaired in 4 steps. The cycle slip detected by each step should be repaired before the next step. Table IV -Table VII show the cycle slip repair results in each step. The sum of these 4 tables is shown in Table VIII. We can see that Table VIII is the same with Table III which shows that the result is correct and our method is efficacious.

TABLE IV. THE BIG CYCLE REPAIR RESULTS

MJD		Cycle slip Pair 1		Cycle slip Pair 2		Cycle slip Pair 3	
		L1	L2	L1	L2	L1	L2
57711	9	0	0	0	0	0	0
57711	10	0	-1	-9	-8	0	-1
57711	11	0	-2	-9	-9	-77	-62
57711	12	-1	-3	-9	-10	-77	-63
57711	13	-1	-3	-9	-10	-77	-63
57711	14	-2	-4	-9	-10	-77	-63
57711	15	-1	-4	-8	-10	-74	-61
57711	16	0	-4	-6	-9	-73	-61
57711	17	1	-4	-5	-9	-72	-61
57711	18	2	-4	-4	-9	-71	-61

TABLE V. THE DIFFERENT CYCLE SLIP ON L1 AND L2

MJD		Cycle slip Pair 1		Cycle slip Pair 2		Cycle slip Pair 3	
		L1	L2	L1	L2	L1	L2
57711	9	0	0	0	0	0	0
57711	10	0	0	0	0	0	0
57711	11	0	0	0	0	0	0
57711	12	0	0	0	0	0	0
57711	13	0	-1	0	-1	0	-1
57711	14	0	-2	0	-2	0	-2
57711	15	-1	-3	-1	-3	-1	-3
57711	16	-2	-4	-2	-4	-2	-4
57711	17	-3	-5	-3	-5	-3	-5
57711	18	-4	-6	-4	-6	-4	-6

TABLE VI. THE SAME CYCLE SLIP ON L1 AND L2

MJD		Cycle slip Pair 1		Cycle slip Pair 2		Cycle slip Pair 3	
		L1	L2	L1	L2	L1	L2
57711	9	0	0	0	0	0	0
57711	10	0	0	0	0	0	0
57711	11	0	0	0	0	0	0
57711	12	0	0	0	0	0	0
57711	13	0	0	0	0	0	0
57711	14	0	0	0	0	0	0
57711	15	0	0	0	0	0	0
57711	16	0	0	0	0	0	0
57711	17	0	0	0	0	0	0
57711	18	0	0	0	0	0	0

TABLE VII. THE SAME SIZE AND SIGN CYCLE SLIP OCCURS CONTINUALLY IN EVERY EPOCH ON L1 OR L2

MJD		Cycle slip Pair 1		Cycle slip Pair 2		Cycle slip Pair 3	
		L1	L2	L1	L2	L1	L2
57711	9	0	0	0	0	0	0
57711	10	0	1	0	1	0	1
57711	11	0	2	0	2	0	2
57711	12	0	3	0	3	0	3
57711	13	0	4	0	4	0	4
57711	14	0	5	0	5	0	5
57711	15	0	6	0	6	0	6
57711	16	0	7	0	7	0	7
57711	17	0	8	0	8	0	8
57711	18	0	9	0	9	0	9

TABLE VIII. TOTAL CYCLE SLIP(SUM OF TABLE.IV~TABLE VII)

MJD		Cycle slip Pair 1		Cycle slip Pair 2		Cycle slip Pair 3	
		L1	L2	L1	L2	L1	L2
57711	9	0	0	0	0	0	0
57711	10	0	0	-9	-7	0	0
57711	11	0	0	-9	-7	-77	-60
57711	12	-1	0	-9	-7	-77	-60
57711	13	-1	0	-9	-7	-77	-60
57711	14	-2	-1	-9	-7	-77	-60
57711	15	-2	-1	-9	-7	-75	-58
57711	16	-2	-1	-8	-6	-75	-58
57711	17	-2	-1	-8	-6	-75	-58
57711	18	-2	-1	-8	-6	-75	-58

IV. CONCLUSION

This paper develops a novel real time cycle slip detection and repair method for a single dual-frequency GNSS receiver. In this method, the slope of code range is used to detect the big cycle slip on L1 and L2, the WL combination and Ultra-WL combination is used to detect the difference cycle slip on L1 and L2, the NL combination and GF combination is used to detect the same cycle slip on L1 and L2, the ionospheric residual method is used to detect the same size and sign cycle slip occurs continually in every epoch on L1 or L2. This method is suitable for the dual- or multi-frequency GNSS receiver. It has been proofed to be effective to detect and repair all the cycle slip larger than 1 cycle in real time.

REFERENCES

[1] Zumberge JF, Heflin MB, Jefferson DC, Watkins MM, Webb FH (1997) Precise point positioning for the efficient and robust analysis of GPS data from large networks. J Geophys Res 102(B3):5005–5017 .

[2] Rongxin Fang, Chuang Shi, Yidong Lou, Qile Zhao, Real-time Cycle-slip Detection of GPS Undifferenced Carrier-phase Measurements, International Conference on Earth Observation Data Processing and Analysis (ICEODPA), Proc. of SPIE Vol. 7285 72851U-1.

[3] Blewitt G (1990) An automatic editing algorithm for GPS data, Geophys Res Lett 17(3):199–202 .

[4] Hui Hu, Lian Fang, GPS Cycle Slip Detection and Correction Based on High Order Difference and Lagrange Interpolation, 2nd International Conference on Power Electronics and Intelligent Transportation System, 2009, pp.384-387.

[5] Zhizhao Liu, A new automated cycle slip detection and repair method for a single dual-frequency GPS receiver, J Geod (2011) 85:171–183.

[6] Changsheng Cai, Zhizhao Liu, Pengfei Xia, Wujiao Dai, Cycle slip detection and repair for undifferenced GPS observations under high ionospheric activity, GPS Solut (2013) 17:247–260.

Three Loops - A Method for Tracking A New TWSTFT Signal FBOC

Haifeng Wang, Xueyun Wang, Hongbo Wang, Hang Yi, Shuwei Wang, Wenzhe Yang, Shengkang Zhang
Science and Technology on Metrology and Calibration Laboratory
Beijing Institute of Radio Metrology and Measurement, Beijing, China
Email:haifengwang203@163.com

***Abstract*—In this paper, a new defined modem with Flexible Binary Offset Carrier (FBOC) signal has been developed by the Beijing Institute of Radio Metrology and Measurement (BIRMM), we demonstrate our work details on receiving the FBOC signal. We realize it based on the FPGA and DSP hardware platform. A structure of three loops to solve the tracking ambiguous problem is also demonstrated. To evaluate the performance of the tracking algorithm in our modem, a local 70MHz IF TWSTFT experiment was done, and the results show that the new signal and the tracking algorithm meets our expectations.**

Keywords—TWSTFT; FBOC; modem;

I. INTRODUCTION

Conventional TWSTFT provides a few 10^{-10} level of frequency stability at time of 1s. With the higher performance of the TWSTFT technology that people are looking for as well as decreasing the satellite link fee and making the frequency band of satellite occupation flexible, a new defined modem with Flexible Binary Offset Carrier (FBOC) signal has been developed by the Beijing Institute of Radio Metrology and Measurement (BIRMM).

In this paper, we demonstrate our work details on receiving the FBOC signal, and based on the FPGA and DSP hardware platform we realize it. Since the concept of FBOC signal is similar to BOC signal in GNSS, its self-correlation function contain many peaks which induces more than one zero-cross point that result in the discriminator ambiguous and make it difficult to decide which point to track. So this ambiguous problem of receiving FBOC signal is the main issue of our work. To solve this problem we developed a new tracking structure which is made up of three loops, the code loop, the sub-carrier loop and the carrier loop. It is similar to the GNSS BOC[1] signal tracking structure, but the difference is that the sub-carrier is a sine wave instead of square wave and the discriminator is PLL instead of DLL[2].

To evaluate the performance of the tracking algorithm in our modem, a local 70MHz IF TWSTFT experiment was done. In the process of the experiment, our modem worked in self-transmit and self-receive mode, the transmitter and the receiver use the same 10MHz external reference from a cesium atomic clock and we also use a short coaxial-cable to connect the transmitter and the receiver, so that we can wipe off the errors caused by different clocks. The measurement results show that the performance of the time and frequency transfer meets our expectations, with a standard deviation (1σ) of 2.43ps and the frequency stability 4.20×10^{-12}@1s.

II. THEORY SIMULATION OF FBOC

A. Time Domain of FBOC

The generation of FBOC signal is adding a subcarrier which is a periodical rectangle signal to a BPSK signal, so that the power spectral density (PSD) is split into two sidebands and the span between them is determined by the frequency of the subcarrier. The bandwidth of the signal can be changed when we control the frequency of the subcarrier. The IF BPSK and FBOC signal are described by the following:

$$s_{BPSK}(t) = D(t)c(t)\sin(2\pi f_{70MHz}t) \tag{1}$$

$$s_{FBOC}(t) = D(t)c(t)s_c(t)\sin(2\pi f_{70MHz}t) \tag{2}$$

Where D(t) is the information data, c(t) is the spreading code and $s_c(t)$ is the subcarrier, it is obvious that the difference of the BPSK and FBOC signal is the subcarrier modulation in the time domain.

B. Self-Correlation Function of FBOC

The principle of TWSTFT system is the self-correlation receiving of the spreading code, therefore the characteristic of self-correlation function of the signal in use is the crucial point of the ranging performance of TWSTFT system. The self-correlation function of FBOC signal is described by the following:

$$R(\tau) = \int_{-\infty}^{\infty} s_{FBOC}(t)s_{FBOC}(t+\tau)e^{-j2\pi ft}dt \tag{3}$$

The self-correlation function (SCF) of BPSK and FBOC are shown in Fig.1, where frequency of the code and subcarrier are 125 kHz and 10 MHz in FBOC signal, and the frequency of the code is 2.5MHz in BPSK signal. As can be seen from Fig.1, the SCF of the FBOC is more complex than BPSK, but the first peak of its SCF is sharper, the ranging performance must be much better. Its self-correlation function contains many peaks which induces more than one zero-cross point that result in the discriminator ambiguous. In chapter IV, the receiving method will be discussed in details.

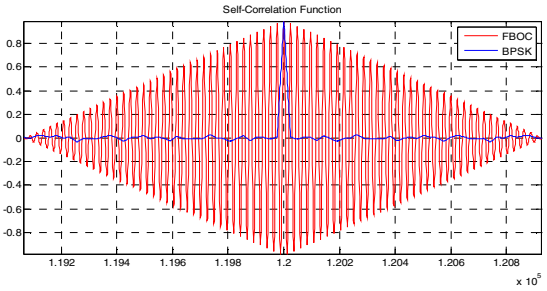


Fig. 1. SCF of BPSK and FBOC

C. *Frequency Domain of FBOC*

The TWSTFT system operates by renting the commercial communication satellite transponder to exchange the ranging data. The signal bandwidth is the main factor which determines the cost of TWSTFT system. Usually, the frequency of the subcarrier is much higher than the frequency of spreading code, the bandwidth of sideband signal is quite narrow, which is the real bandwidth we refund. The ranging performance could be benefited from the broad equivalent bandwidth. The power spectral density of BPSK and FBOC is shown in Fig.2, where frequency of the code and subcarrier are 125 kHz and 10 MHz in FBOC signal, and the frequency of the code is 2.5MHz in BPSK signal.

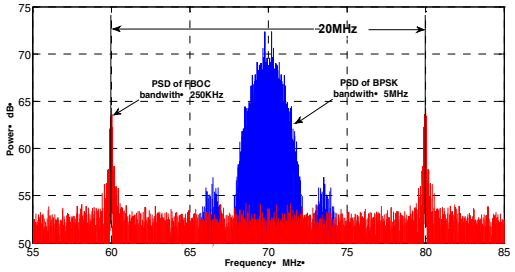


Fig. 2. PSD of BPSK and FBOC

III. HARDWARE ARCHITECTURE

Currently, there are two main popular ways to realize a receiver in the field of TWSTFT, one is base on GPU[3] card and another is based on logic chips[4]. To facilitate our design, we develop our work based on our previous version modem. The core parts of the FBOC receiver are FPGA, high-speed DSP, DAC and ADC chips. The modulation, demodulation units are highly synchronized to an external 10MHz frequency signal input. The architecture of the modulation and the demodulation unit are digital. The processing procedure of intermediate frequency (IF) signal is shown in Fig.3.

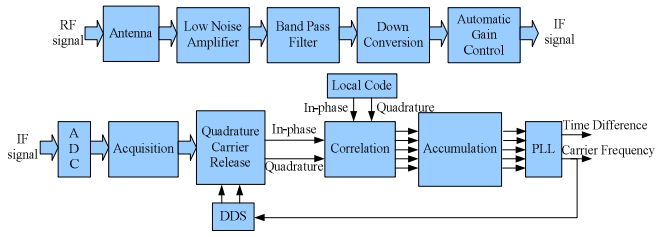


Fig. 3. Procedure of IF Data

The RF signal is converted into IF signal by a low noise amplifier (LNA), a band pass filter (BPF) and a down convertor. IF signal is digitized through an analog to digital convertor (ADC). Acquisition module makes coarse synchronization to the signal, and the initial code phase and carrier frequency are supplied to the tracking module. The signal is quadrature down converted in quadrature carrier release module. Five correlation values are supplied to the integral summation module. PLL module tracks the code and carrier in real-time and the error signal is fed back to the local code and carrier generator. The measure value of the time difference is framed for transmission in the host computer.

IV. TRACKING APPROACH

As can be seen from Fig.4, when shift both the code and subcarrier by small steps, we find that the SCF of FBOC is Three-Dimensional, it contains only one peak from the code chip dimension and many equal peaks from subcarrier chip dimension, this inspires our idea of tracking FBOC signal.

The SCF is still the product of a matching code function and a subcarrier, but now independent shifts are assigned to the code and sub-carrier components so that the two can be tracked respectively as long as the code tracking is precise enough to resolve the ambiguity of the subcarrier. In fact this can be achieved because of the high carrier-to-noise ratio in TWSTFT links. Take the frequency of code and subcarrier are 125 kHz and 10 MHz for example, one period of subcarrier is 100ns, and the tracking precision of less than 100ns in code dimension with the frequency of 125 kHz is so easy achieved in our daily TWSTFT links with the carrier-to-noise ratio 50dBHz above.

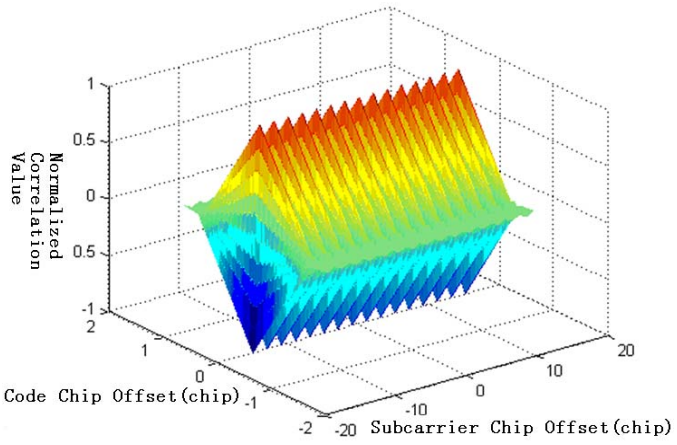


Fig. 4. Three-Dimensional Correlation for FBOC

The proposed Three-Loops tracking architecture is shown in Fig.5, it is made up of three main parts, the carrier loop, the subcarrier loop and the code loop. As we know that traditional tracking loop use three square waveforms as the local module to correlate with the received signal, but the phase of periodic square waveform generated in logic processor has big jitter because of the NCO mechanism, especially when the frequency of the sampling clock to the frequency of the square waveform ratio is not big. In contrast, the generation of the sine waveform is more stable than the square waveform in logic

processor when use NCO mechanism. Meanwhile, considering the IF signal is always band-limited because all the high frequency components are filtered out by the RF device and down convertor. So using sine waveform as the local module to track the FBOC signal is reasonable and consistent with the theory.

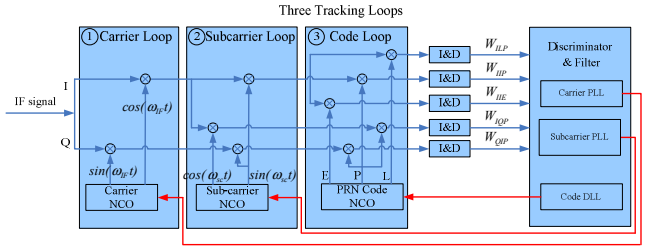


Fig. 5. Three Loops for Tracking FBOC Signal

V. EXPERIMENT

To evaluate the performance of the tracking algorithm and our system, a local 70MHz IF TWSTFT experiment was done, as shown in Fig.6. In the process of the experiment, our modem worked in self-transmit and self-receive mode, the transmitter and the receiver use the same 10MHz external reference from a cesium atomic clock and we also use a short coaxial-cable to connect the transmitter and the receiver, so that we can wipe off the errors caused by different clocks. A time interval counter with high resolution works to measure the time offset between the transmitter and the receiver. The measure value of the time interval and ranging data are framed for transmission in the host computer finally.

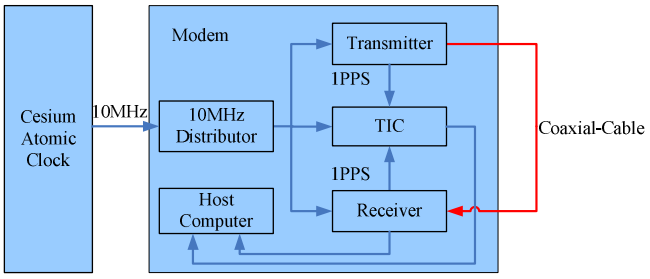


Fig. 6. Connection Diagram of Experiment

The signal is successfully generated and acquired with carrier-to-noise ratio of 85dBHz. Fig.7 shows the frequency spectrum of the generated FBOC signal. The frequency of the code and subcarrier are 125 kHz and 10 MHz. The left picture shows that the whole bandwidth is about 20MHz and the right picture shows the bandwidth of sideband is about 250 kHz.

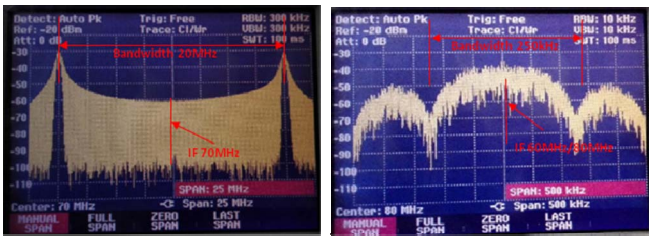


Fig. 7. Frequency Spectrum of FBOC

The time of the IF experiment is about 3 days, Fig.8 shows that the time stability and the frequency stability using the Stable32 software, during this period the modem operates steadily. The time and frequency measurement result shows that the deviation (1σ) is equal to 2.43ps and the frequency stability is 4.20×10^{-12}@1s.

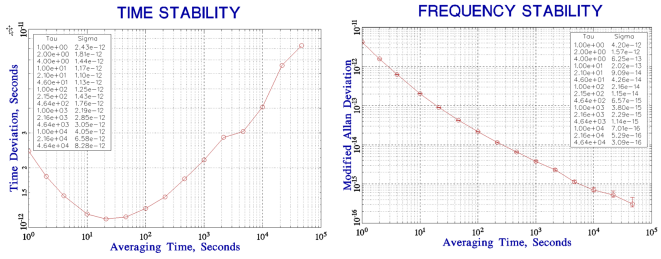


Fig. 8. Time Stability and Frequency Stability

VI. CONCLUSION

A FBOC based modem is developed by BIRMM, and the IF performance of the tracking algorithm and our modem has been validated. To solve the problem of ambiguity, we have developed a new tracking structure which is made up of three loops, and it works steadily during the whole experiment period about 3 days. The measurement precision of the FBOC signal is quite good because of high carrier-to-noise ratio in IF experiment, zero-baseline and long baseline experiment based on GEO will be the focus of future work.

REFERENCES

[1] Betz, J.W., 'Binary offset carrier modulations for radio navigation', Navig., J. Inst. Navig., 2001, 48, (4), pp. 227–286.

[2] Hodgart, M., Blunt, P., 'Dual estimate receiver of binary offset carrier modulated signals for global navigation satellite systems', Electron. Lett., 2007, 43, (16), pp. 877–878. ISSN 0013-5194.

[3] Tadahiro Gotoh, Jun Amagai, Thomas Hobiger, Miho Fujieda, and Masanori Aida, 'Development of a GPU-Based Two-Way Time Transfer Modem', IEEE Transactions On Instrumentation and Measurement, vol. 60, no. 7, July 2011.

[4] Shengkang Zhang, Xueyun Wang, Haifeng Wang, 'A New Modem for Two Way Satellite Time and Frequency Transfer', 2015 Joint Conference of the IEEE International Frequency Control Symposium & the European Frequency and Time Forum, pp.250-253, 2015.

Progress on the REFIMEVE+ Project for Optical Frequency Standard Dissemination

E. Cantin, N. Quintin, F. Wiotte, C. Chardonnet, A. Amy-Klein, O. Lopez
Laboratoire de Physique des Lasers, LPL
Université Paris 13, CNRS,
Villetaneuse, France
etienne.cantin@univ-paris13.fr

G. Santarelli
Laboratoire Photonique, Numérique et Nanoscience, LP2N
Institut d'Optique d'Aquitaine, Université de Bordeaux,
Talence, France

E. Camisard
RENATER
Paris, France

P.-E. Pottie
LNE- SYRTE,
PSL Research University, CNRS, Sorbonne Universites,
UPMC Univ. Paris 06, France

***Abstract*—High-resolution time and frequency transfer between remote laboratories are of major interest for many fundamentals applications, such as tests of general relativity or temporal variation of fundamental constants performed by comparing clocks signals. We report on the progress of a metrological fiber network on the French territory, with extensions to Europe, which aims to provide an ultra-stable frequency signal to around 20 laboratories. This network is based on the dissemination of an ultra-stable signal using optical links through the academic fiber internet network. As a first step, we have demonstrated robust links of up to 1480 km with stability at 10^4 s and accuracy below 10^{-19}.**

Keywords—optical fiber link; ultra-stable frequency dissemination; clocks comparison;

I. INTRODUCTION

The REFIMEVE project (a french acronym for Réseau Fibré Métrologique à Vocation Européenne) will use a standard telecommunication fiber network to transfer an ultra-stable optical signal to 20 laboratories all over France, with extensions to National Metrological Institutes in Europe. The ultra-stable signal arises from a laser stabilized to an ultra-stable cavity itself referenced to a fountain clock or a hydrogen maser via a frequency comb located in SYRTE. On each fiber link, the round-trip propagation noise is detected in order to implement an active compensation of the noise arising from the signal propagation. This requires using a bidirectional technology, instead of a unidirectional one as commonly used by telecommunication network. Compared to frequency transfers by satellite means, limited to a few 10^{-16} after several days of integration, fiber links allow a comparison of current atomic clocks with stability as low as a few $10^{-20}@10^4$s. It is thus a promising technology for clocks comparison, time and frequency transfer in general and also for other applications as geodesy for example [1]. The two main limitations come first from the propagation delay through the fiber which limits the correction bandwidth and amplitude and secondly from the interferometric noise from the short reference fiber paths which are not compensated.

We will report on the current progress of the metrological fiber network REFIMEVE. A contract and knowledge transfer with the company MuQuans leads to the development and the deployment of industrial instruments to propagate the signal on the French territory.

II. A NATIONAL FREQUENCY REFERENCE DISSEMINATION

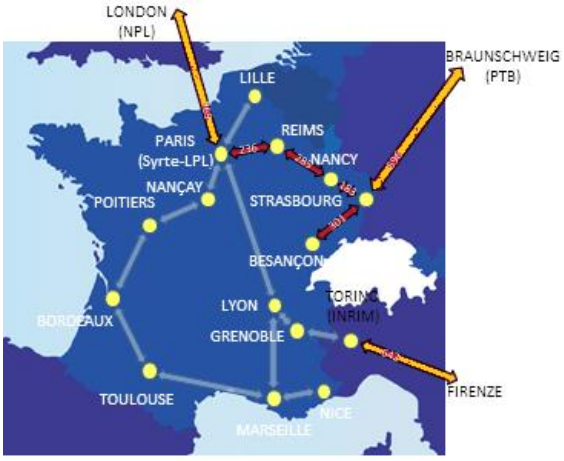


Fig. 1. Map of the REFIMEVE network. Red fiber links are achieved or under deployment (with the distance between two cities in km), blue fiber links concern the future deployment and yellow links are european links.

A. Implementation of a fiber link

Fig. 1. shows a map of the planned fiber network in France. To implement a link between two cities, we use a cascaded fiber link with a compensation of the noise accumulated on each fiber segments. After hundreds of kilometers of fiber, the signal is attenuated (with an average loss of 0.25dB/km depending on the fiber link) and the signal to noise ratio reduces. We then need to amplify the optical signal and to regenerate it, that is to track and copy the signal on a laser

source used to propagate the signal on the following fiber segment. Vibrations, thermal fluctuations or mechanical constraints lead to a dephasing of the ultra-stable signal which degrades its stability and accuracy. To actively cancel this noise, we compare the initial signal (injected in the fiber link) with the signal after a back and forth propagation in the fiber in order to detect the round-trip phase noise, which is then compensated with an optoelectronical actuator [8].

An optical link of the REFIMEVE project can then be described as a cascaded link composed of bidirectional amplifiers and repeater laser stations (RLS) as depicted in Fig. 2 [2][3]. RLSs enable us both to regenerate the signal and to compensate the noise on the link. Furthermore, this technique is implemented in the channel #44 (at 1542.12 nm) of the Internet fiber telecommunication network RENATER (french acronym for REseau NAtional de télécommunications pour la Technologie l'Enseignement et la Recherche). It can be applied to any fiber network using Wavelength Division Multiplexing technique. A remote control on each instrument is needed to improve and optimize the stability of the link. A global supervision of the REFIMEVE fiber network is in development to control and optimize all the instruments on each link.

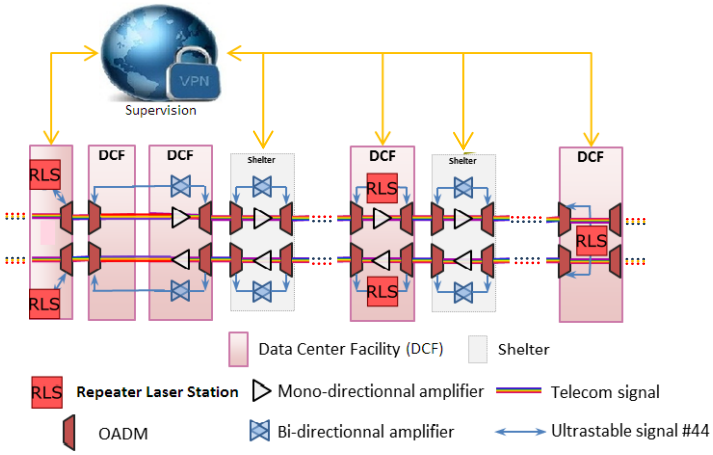


Fig. 2. Scheme of a cascaded link composed of Optical Add Drop Multiplexers (OADM), bidirectionnal amplifiers and repeater laser stations in a Dense WDM network. The signal goes back and forth in each fiber for an active compensation of the noise. A remote control of each instrument is achieved via a ssh protocol.

B. *Results*

Such cascaded fiber links have already demonstrated unique performance in metrology for clocks comparison [1][4] or frequency and time transfer [3]. Moreover, these results have been shown through standard telecommunication fiber network in continual evolution, with different architectures and equipments, which demonstrates the robustness and reliability of this technique. For example, we have recently demonstrated the compatibility with Raman amplifiers installed on the RENATER network.

The performance of the cascaded links is assessed using an auxiliary output of the RLSs. They enable us to perform two-way frequency transfer between the end stations of the link or between two stations of different links. On the Paris-Strasbourg link of 1420 km, we obtained a relative stability at 1 s of a few 10^{-16} which reaches 10^{-19} after a few 10^4 s [2][3], as shown in Fig. 3. Accuracy was demonstrated to be of the order of 10^{-19}.

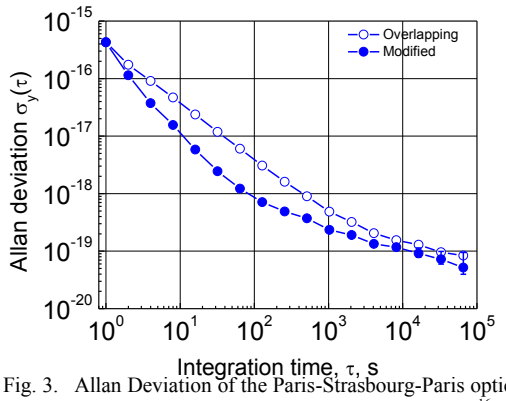


Fig. 3. Allan Deviation of the Paris-Strasbourg-Paris optical fiber link during a clock campaign. The relative stability at 1 s is 4. 10^{-16} and 10^{-19} after a few 10^4 s [2][3]. Accuracy was demonstrated to be of the order of 10^{-19}.

C. *To the end users*

The REFIMEVE project aims to serve the ultra-stable signal to different laboratories and companies. For the users of the project, we have developed two different modules depending on the configuration. The ultra-stable signal can either be extracted along a main link, using an extraction station [5][6] (first proposed by G. Grosche, patent 2010), or it can be distributed using the RLS user output and a dedicated user module. These modules can be associated to a frequency comb to transfer the stability of the optical signal to other frequency domains [7].

D. *Knowledge Transfer*

As a vital necessity for the extension and viability of a network of optical fiber links, the collaboration with companies is at the center of the REFIMEVE project. For that purpose we organized knowledge transfer to SMEs. A major advance in the project is the realization of an industrialization-grade prototype of RLS developed by the companies MuQuans and SYRLINKS and which will be commercialized by the company MuQuans. The test of the station has been a success and a deployment in the field is ongoing.

Knowledge transfer to EDFA manufacturer Keopsys leads to a new bi-directional amplifier on the market, with reliable remote abilities and very low noise factor even at very low input power. These new amplifiers were set up on our international links and recent results will be shown.

III. PERSPECTIVES

Thanks to the validation and the industrialization of the different equipments of the project, the dissemination of the ultra-stable signal is currently in progress. The next deployment will link Strasbourg and Besançon, Paris and Lille, and Paris to Lyon and Grenoble (see Fig. 1.). This network will pave the way to new applications as for instance test of satellite based frequency transfer, high resolution atomic or molecular spectroscopy and chronometric geodesy.

ACKNOWLEDGMENT

This work would not have been possible without the support of the GIP RENATER. The authors are deeply grateful to L. Gydé, T. Bono and E. Camisard from GIP RENATER. We acknowledge funding support from the Agence Nationale de la Recherche the Agence Nationale de la Recherche (ANR blanc LIOM 2011-BS04-009-01, Labex First-TF ANR 10 LABX 48 01, Equipex REFIMEVE+ ANR-11-EQPX-0039), the European Metrology Research Programm (contract SIB-02 NEAT-FT), IFRAF-Conseil Régional Ile-de-France, CNRS with Action Spécifique Gravitation, Références, Astronomie, Métrologie (GRAM).

REFERENCES

[1] C. Lisdat et al, "A clock network for geodesy and fundamental Science," Nat. Com. 7, 12443 (2016).

[2] N. Chiodo et al, "Cascaded optical fiber link using the internet network for remote clocks comparaison," Opt. Exp., vol. 23, issue 26, p. 33927-33937, 2015.

[3] O. Lopez et al, "Frequency and time transfer for metrology and beyond using telecommunication network fibres," Comptes Rendus Physique 16, p. 531-539, 2015.

[4] J. Guéna, et al., "First international comparison of fountain primary frequency standards via a long distance optical fiber link", Metrologia, Volume 54, Number 3, 2017.

[5] A. Bercy et al., "In-line extraction of an ultra-stable frequency signal over an optical fiber link," JOSA B, 2014.

[6] A. Bercy et al., "Ultrastable optical frequency dissemination on a multi-access fibre network", Appl. Phys. B, 2016.

[7] B. Argence et al., "Quantum cascade laser frequency stabilization at the sub-Hz level", Nature Photonics 9, 456–460 (2015)

[8] L. S. Ma et al., "Delivering the same optical frequency at two places, accurate cancellation of phase noise introduced by an optical fiber or other time-varying path," Opt. Lett. 19, 1777–1779 (1994)

A atomic time algorithm based on predictable weighting and wavelet multi-scale threshold denoising

Huijie Song[*&+], ShaoWu Dong[*&#], Jun Ruan[*&], Tao Liu[*&], LiLi Qu[*&], YanPing Wang[*&], Yi Qi[*&], Xiang Wang[*&], Juan Hou[*&]

[*]National Time Service Center， Chinese Academy of Sciences, Xi'an, China
[&]Key Laboratory of Time and Frequency Primary Standards, National Time Service Center, CAS, Xi'an, China
[+]University of Chinese Academy of Science, Beijing, China
[#]School of Astronomy and Space Sciences, University of Chinese Academy of Science, Beijing 100049
E-mail: songhuijie@ntsc.ac.cn

***Abstract*—The principle of predictable weighting algorithm is that a good clock is a predictable clock, we observed that deterministic signature such as frequency drift and ageing do not affect time scale stability if well predicted in studies of the algorithm. The clock difference is a non-stationary random process, in order to reduce noises of atomic clock, improve the stability of time scale, wavelet muti-scale threshold is studyed to reduce the effects of atomic clock noise, in this paper, the influence of different threshold function for atomic clocks noise reduction is studyed. The advantage of this algorithm is that the predictable weighting is made full use to produce time scale, at the same time, atomic clock noises are reduced, it improve the stability of time scale in many aspects and is an optimizable algorithm of atomic time scale.**

Keywords—atomic time scale; predictable weighting algorithm; wavelet; threshold denoising

I. INTRODUCTION

In the generation of a time scale, prediction of atomic clock behaviour plays an important role and it is inserted in all time scale algorithms. Many papers have already dealt with the prediction problem[1-6]. In the establishment of Coordinated Universal Time(UTC) and International Atomic Time(TAI), the prediction algorithm is useful to avoid or minimize the time and frequency jumps of the time scale when a clock is added or removed from the ensemble. on the other hand, the predictable weighting algorithm is also critical to the generation of a time scale.

The algorithm based on predictable weighting was that a clock with strong signature such as frequency drift or aging can nevertheless be correctly used in the timescale ensemble if its behaviour is well predicted. In the predictability weighting algorithm the difference between the predicted and the real frequency of the atomic clocks was evaluated[7].

This work is supported by Nature Science Foundation of China under Grant No.11473029.

wavelet is a mathematical tool that can be used to analyze data, which have become more and more widely used in the field of signal denoising. Atomic clock noises had different analytical methods[8-9], The threshold denoising method is a simple, effective wavelet denoising method. The idea of threshold denoising method is that the coefficients of the magnitude greater than and below a certain threshold are respectively processed by the coefficients of each layer after the wavelet decomposition. Then the processed wavelet coefficients were inversely transformed, and the signal was reconstructed.

Atomic clock signal is a typical nonlinear and nonstationary process. In theory, standard deviation can be used for evaluating frequency stability of atomic clock. When

measurement interval is variant, standard deviation is divergent but convergent. we may evaluate the stability of time scale by using Allan variance.

In this paper, a algorithm based on predictability weighting and wavelet multi-scale threshold denoising is put forward. Comparing to the predictable weighting algorithm, the algorithm proposed in this paper is more stable for generation time scale.

II THE PREDICTABLE ATOMIC TIME ALGORITHM

A Prediction algorithm[10]

Considering two successive intervals of TA(atomic time) calculation, $I_{k-1}\left(t_{k-1},t_k\right)$ and $I_k\left(t_k,t_{k+1}\right)$, the prediction term $h_i^{'}\left(t\right)$ can be expressed as the following quadratic form to describe the frequency drift of H-masers or the ageing of the caesium clocks:

$$h_i^{'}\left(t\right)=a_{i,I_k}\left(t_k\right)+B_{ip,I_k}\left(t_k\right)\left(t-t_k\right)+\frac{1}{2}C_{ip,I_k}\left(t\right)\left(t-t_k\right)^2 \quad (1)$$

The estimation of the parameters of (1) leads to this formula:

$$\hat{h}_i^{'}(t) = \hat{a}_{i,I_k}(t_k) + \hat{B}_{ip,I_k}(t-t_k) + \frac{1}{2}\hat{C}_{ip,I_k}(t_k - t_{k-1})(t-t_k)$$

$$+\frac{1}{2}\hat{C}_{ip,I_k}(t-t_k)^2 \quad (2)$$

Where the symbol ^ indicates the estimate of the parameters reported in (1). The physical meanings of the terms in (2) are

$\hat{a}_{i,I_k}$ is the estimation of the time correction relative to EAL of the clock H_i at the date t_k

$\hat{B}_{ip,I_k}$ is the estimation of the frequency of clock H_i, relative to EAL, predicted for the period $[t_k, t]$

$\hat{C}_{ip,I_k}$ is the estimation of the frequency drift of the clock H_i, relative to a frequency reference, predicted for the period $[t_k, t]$

Relationship (2) describing the correction applied to atomic clocks includes three parameters: the phase, the frequency and the frequency drift. The estimation of the time correction $a_i(t_k)$, added to avoid time jumps, is given by the last known difference between EAL and each clock and is expressed as

$$\hat{a}_{i,I_k}(t_k) = \left[EAL(t_k) - h_i(t_k)\right] = x_i(t_k) \quad (3)$$

From a theoretical point of view the best estimation of the mean frequency B_{ip,I_k} for any interval is the difference with respect to EAL between the first and the last clock data points for that interval as expressed by the following relationship:

$$\hat{B}_{ip,I_k} = \frac{x_i(t_{k+1}) - x(t_k)}{t_{k+1} - t_k} \quad (4)$$

For simplicity of notation the frequency of the clock H_i with respect to EAL and obtained by the relationship (4) will be indicated thereafter by y_{i,I_k}. To estimate the frequency drift of the clocks under the hypothesis that this drift remains constant over a one-month interval, the frequency data y_{TT-h_i} of the clock with respect to Terrestrial Time(TT) are used to estimate the drift.

B. Predictable weighting algorithm[7]

In predictable weighting algorithm, we maintain the four-iteration process used previously by changing the method used to evaluated the weight and the value of the maximum weight. The differences between the predicted and the real frequencies are evaluated for each one-month interval over one year and these values are used to define the weight. Using one year of data we maintain the long-term stability of EAL and UTC. Each iteration runs as follows

(1) The values $[\mathrm{EAL} - h_i]$ are found using a given set of relative weights. In the first iteration, the weights are those obtained in the previous computation interval after normalization. In the following iterations, they are those obtained from the previous iteration.

(2) The absolute value of the difference between the frequency y_{i,I_k} as defined in (4) and the predicted frequency $\hat{y}_{i,I_k}$ obtained by the relationship (2) corresponds to

$$\in_{i,I_k} = \left| y_{i,I_k} - \hat{y}_{i,I_k} \right| \quad (5)$$

Where the index i identifies the clock and I_k the time interval.

(3) The square of (5) is evaluated for each clock.

(4) One year of $\in_{i,I_k}$ is considered to ensure long-term stability of EAL and UTC.

(5) A filter has been implemented to give a more predominant role to more recent measurements with respect to older ones, considering that new measurements have most reliable statistics:

$$\sigma_i^2 = \frac{\sum_{j=1}^{M}\left(\frac{M+1-j}{M}\right)\in_{i,j}^2}{\sum_{j=1}^{M}\left(\frac{M+1-j}{M}\right)} \quad (6)$$

Where i identifies the clocks, j the calculation interval and M the number of available measurements(which can vary from 5 to 12 given that 5 is the minimum number of months requested to observe the behaviour of a clock prior to its introduction into the UTC calculation and one year is the standard period of observation).

(6) The relative weight of clock H_i is computed theoretically using a temporary value given by

$$\omega_{i,.temp} = \frac{1/\sigma_i^2}{\sum_{i=1}^{N} 1/\sigma_i^2} \quad (7)$$

The new weight ω_i of clock H_i is equal to $\omega_{i,.temp}$ except in two cases.

(1) Clock H_i satisfies the requirement set for the limitation of weight as for the current algorithm.

(2) Clock H_i shows abnormal behavior during the interval of computation so it cannot contribute.

III THE THRESHOLD FUNCTION AND THRESHOLD ESTIMATE

In this paper, the hard threshold function and the soft threshold function were used. The hard threshold function was expressed as follow:

$$\eta(\omega)=\omega I\left(|\omega|>T\right) \tag{8}$$

Where ω is the original wavelet coefficients of the signal, η is the wavelet coefficients of the threshold. I is sign function . The soft threshold function was expressed as follow:

$$\eta(\omega)=(\omega-\mathrm{sgn}(\omega)T)I\left(|\omega|>T\right) \tag{9}$$

The meaning of the parameters are the same as the expression(8).

On the basis of the soft threshold, it can be improved to higher order. There is a smooth transition between noise and useful signals. Its expression as follow[11]

$$\eta(\omega)=\begin{cases}\omega+T-\dfrac{T}{2k+1} & \omega<-T\\ \dfrac{1}{(2k+1)T^{2k}}\omega^{2k+1} & |\omega|\le T\\ \omega-T+\dfrac{T}{2k+1} & \omega>T\end{cases} \tag{10}$$

Where T is threshold. For a joint distribution of the multidimensional independent normal variable, the optimal threshold was obtained by the minimum maximum estimate, the conclusion was drawn when the dimension was going to infinity. Threshold selection satisfied:

$$T=\sigma_n\sqrt{2\ln N} \tag{11}$$

Where σ_n was noise standard deviation, N was the length of the signal. The ideal estimate of noise reduction in the large number of risk function was obtained, The definition of risk function was $R(t)=\frac{1}{N}\left\|\hat{f}-f\right\|^2$. Because of the orthogonality of the wavelet transform, the risk function can also be written in wavelet domain.

$$R(t)=\frac{1}{N}\left\|\eta_t(Y)-X\right\|^2 \tag{12}$$

the optimal threshold selection can be obtained by minimizing the risk function

$$t^*=\arg\min_{t>0} ER(t) \tag{13}$$

IV EXPERIMENTAL RESULT

By using atomic clock data of UTC(NTSC)-clock(NTSC, i), the algorithm was used in the test computation for evaluating the effect. The atomic clocks involved in the calculation included hydrogen masers: HM226, HM227, HM296, HM297 and caesium atomic clocks: Cs2959, Cs2962, Cs1011, Cs1016, Cs2964, Cs1018, Cs2573.The sampling interval was one hour. Data sampling time period was January 1,2016 to July 30,2016(MJD：57388~57599). The first six months of the data were used to estimate weights, Four months of data were used to estimate frequency drift, the period of timescale computation was 30 day. The atomic time algorithm based on predictable weighting, predictable weighting and wavelet multi-scale threshold denoising were discussed respectively. The complete flow chart of predictability weighting and wavelet multi-scale threshold denoising is reported in figure 1.

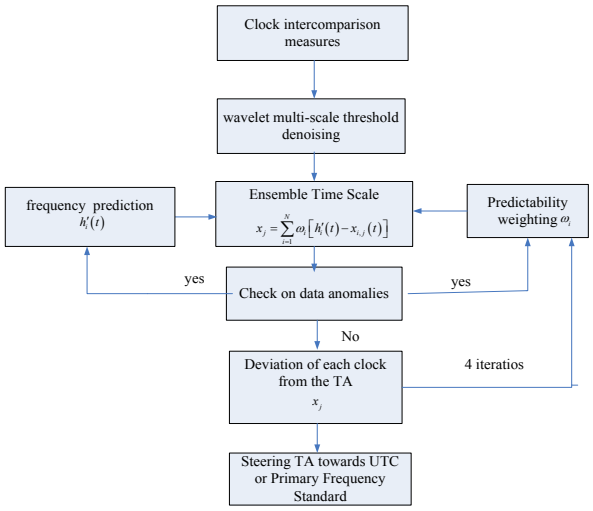


Fig. 1. Complete flow chart of an example of ensemble time scale realization

The timescales generated by two algorithms were shown in figure 2. The algorithm1 was calculated by using predictability weighting, the algorithm2 was calculated by using predictability weighting and wavelet three-scale threshold denoising. The ADEV of the timescale of two algorithms were showed in figure 3 and table 1 in detail.

Compare two algorithms, the stability of time scale produced by the algorithm2 did benefit short-term stability, especially short-term stability in previous 8 hours. We cannot find any significant difference between algorithm 2 and algorithm 1 in long-term stability. The reason of the analysis was that the effect of the noise of atomic clocks on different scales was reduced by the threshold denoising. Analyzing the Allan deviation diagram, the white frequency noise and flicker frequency noise of timescale were mainly reduced by the algorithm 2. For the long-term stability of time scales, both algorithm are based on the predictability weighting of atomic clocks. the influence of different threshold function for atomic clocks noise reduction was studyed, four threshold functions were used to generate the timescales. In order to clear, the produced time scale of the different threshold function was added two, four and six nanoseconds respectively in figure 4. Analyzing these timescales and their Allan deviations, the timescales generated by different threshold function had not changed at all.

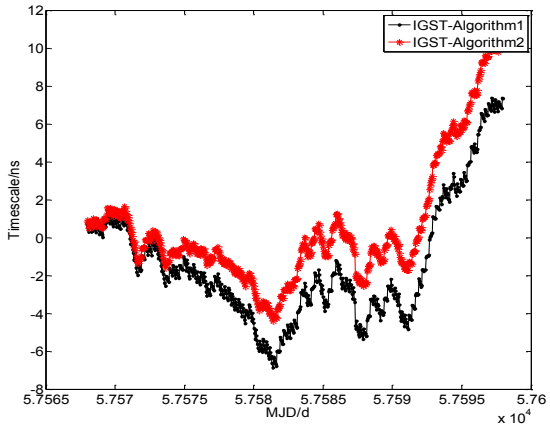


Fig. 2. The timescales generated by two algorithms

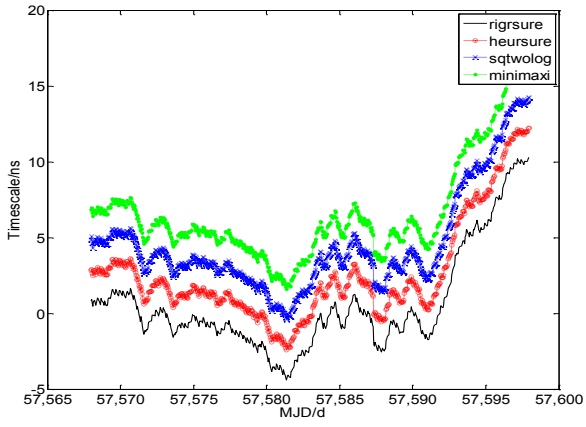


Fig. 4. Time scales based on different threshold function

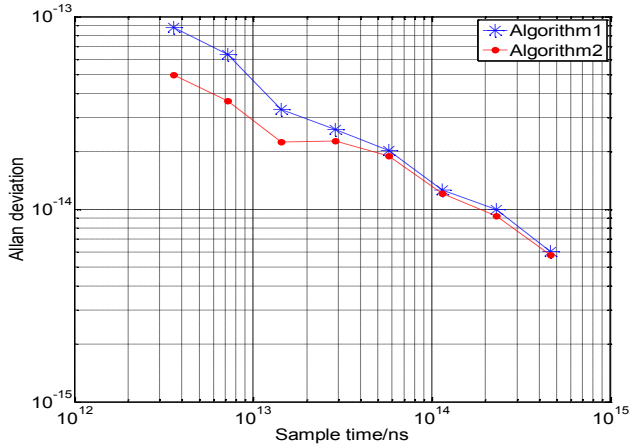


Fig. 3. The ADEV of the timescale of two algorithms

TABLE I. THE ADEV OF THE TIMESCALE OF TWO ALGORITHMS

Sample time/hour	***A*lgorithm1**	**Algorithm2**
1	8.77e-14	4.98e-14
2	6.35e-14	3.64e-14
4	3.29e-14	2.23e-14
8	2.60e-14	2.26e-14
16	2.02e-14	1.89e-14
32	1.26e-14	1.21e-14
64	1.00e-14	9.20e-15
128	6.02e-15	5.79e-15

V CONCLUSION

The atomic time algorithm based on predictability and wavelet multi-scale threshold denoising ensured the long-term stability of atomic clocks. By multi-scale threshold denoising , noises were reduced, the short-term stability of the timescale was improved. The selection of threshold functions had little effect on the scale stability.

REFERENCES

[1] Panfilo G and Tavella P, "Atomic clock prediction based on stochastic differential equations," Metrologia, vol.45, 2008, pp.108-116.

[2] Bauch A, Sen Gupta A and Staliunene E, "ime scale prediction using information from external sources, "19th European Frequency and Time Forum(Besancon, France) pp442-448,2005.

[3] Busca G and Wang Q, "Time prediction accuracy for a space clock," Metrologia, vol.40 , 2003, pp. 265-269.

[4] Tavella P and Gotta M, "Uncertainty and prediction of clock errors in space and ground applications ,"Proc. 14thEuropean Frequency and Time Forum(Becancon, France)pp. 90-95, 2000.

[5] Brown K R, "The theory of the GPS composite clock," proc. ION-GPS(Albuquerque, NM) pp. 223-241, 1991.

[6] Panfilo G, Harmegnies A and Tisserrand L, " A new prediction algorithm for EAL," proc. EFTF-IFCS,(San Francisco,CA), 2011.

[7] G Panfilo, A Harmegnies and L Tisserand, "A new weighting procedure for UTC, " Metrologia, vol.51, 2014, pp. 285-292.

[8] SONG Hui-jie, DONG Shao-wu, WANG Zheng-ming, "An Analysis of NTSC's Timekeeping Hydrogen Masers," Chinese Astronomy and Astrophysics, vol.40, pp. 569-577, 2016.

[9] SONG Hui-jie, DONG Shao-wu, LI Wei, " Research on the Method of Noise Error Estimation of Atomic Clocks," Acta Astronomica Sinica, vol.58, pp. 1-10,2017.

[10] G Panfilo, Aurelie Harmegnies and Laurent Tisserand, A new prediction algorithm for the generation of International Atomic Time, Metrologia51 (2012) 49-56

[11] Wei Zhou, Wavelet analysis application based on MATLAB, 2nd ed., Xi An: Xidian University, 2010.

EGNSS Based Robust Synchronization Service

E. Dierikx
VSL, Dutch Metrology Institute, Delft, Netherlands
edierikx@vsl.nl

M. Kirkko-Jaakkola
NLS / Finnish Geospatial Research Institute (FGI)
Helsinki, Finland

A. Wallin, M. Merimaa
VTT/MIKES, Espoo, Finland

V. Catalano
European GNSS Agency (GSA), Prague, Czech Republic

R. Bauernfeind
NavCert, Braunschweig, Germany

K.A. Aarmo
European Commission (EC), Brussels, Belgium

D. Borio
Joint Research Centre (JRC), Ispra, Italy

***Abstract*—This paper describes the development of a concept for a European GNSS based robust synchronization service. The service concept is designed upon the infrastructure of the Galileo and EGNOS systems and includes specific features for establishing a robust service suitable for critical infrastructures.**

Keywords—GNSS, timing, synchronization

I. INTRODUCTION

Time determination capabilities are inherent to global navigation satellite systems (GNSS). In this sense, both EGNOS and Galileo provide time determination capabilities within the current portfolio of positioning services that they offer. However, no GNSS currently offers time determination as a service per se, and therefore, no performance specifications for this time service are available.

As a matter of fact, time determination capabilities have the particularity to be exploited by sectors which are critical for the functioning of the modern society, such as the telecom, management of power grids and finance sectors.

While timing represents by itself a small market if only timing receivers are taken into account, it is an enabler of critical infrastructures, including the European economic infrastructure. Failure of these critical infrastructures would have significant impact on vital societal functions such as health, safety, security, economic or social well-being of people. Research and development on timing service has been done extensively in several others projects [1-3]. For extra focus on robustness of GNSS based timing services, the EC has initiated, under the EU Horizon 2020 Framework Programme, a call for research and development for robust European GNSS (EGNSS) Timing Services [4]. In response to this call, a project has been started with the following objectives:

1) the definition of a Timing Service for both Galileo and EGNOS, with a strong emphasis on the 'robustness' and well-defined performance specifications.

2) the development of a Standardization roadmap and of Certification schemes supporting applications using the Galileo and EGNOS Timing Service.

3) the development of a synchronization service using the robust timing features developed under objective 1).

II. DEFINING USER SEGMENTS

Three user segments have been defined, depending on the required level of timing accuracy.

A. User Segment 1: ms-level accuracy

Applications requiring an uncertainty of 1 ms or more can be found in time stamping applications for government bodies and some economic transactions. Also synchronization for public applications like clocks on church towers, railway stations, public buildings, home computers, mobile phones and tablets can be included in this segment. The number of potential users is large, (millions), but the price must be low (€-range). A paid synchronization service in this segment is acceptable only for the cases where an audit trail is needed for legal purposes or to comply with national or international regulations; e.g. "Markets in Financial Instruments Directive II" (MiFID II) [6].

B. User Segment 2: µs-level accuracy

Synchronization at the level of microseconds is required for operating telecommunication networks, monitoring the stability of electric power grids, time stamping in electronic algorithmic financial trading, digital video broadcasting services and calibration services. The number of potential users is much smaller than in User Segment 1, but still in the order of thousands while the price can be in the k€ -range.

978-1-5386-2916-1/$31.00 ©2017 IEEE

C. User Segment 3: ns-level accuracy

Synchronization requirements at the nanosecond level are typically found in scientific applications such as radio astronomy, observatories, particle detectors and other academic research. Furthermore national metrology institutes, timing laboratories and the best calibration laboratories require timing with this level accuracy. Although current requirements from telecommunication networks and electric power grids are at the µs-level, it is expected that, in the near future, the requirements for these applications will be tightened to the ns-level. Therefore, the number of potential users, which is presently limited to <100, is growing. The price level in this segment is at the level of tens of k€.

III. Synchronization Service Description

The basic idea of a synchronization service is that the clock of a time user is synchronized in time and frequency to the clock of a reference time facility (Fig.1). In this concept, the synchronization service provider (SSP) has an active role in providing clock steering parameters to the user. These clock steering parameters are computed from GNSS time observations of both the user and the reference with respect to their local clocks.

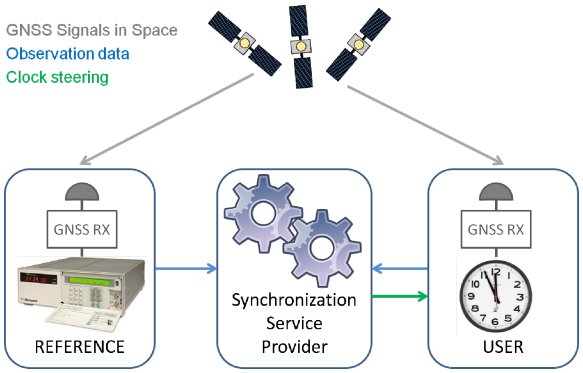


Fig. 1. Basic concept of the EGNSS based synchronization service.

To guarantee the robustness of the service, it will include one or more of the following robustness features developed and tested in the project [5]:

- Interference Detection
- Ionosphere mitigation
- T-RAIM: (Time - Receiver Autonomous Integrity Monitoring) identification and exclusion of outliers in the measurement set
- Multi-GNSS constellation processing
- Exploitation of the known properties of local oscillator
- Exploitation of EGNOS integrity information

The architecture of the proposed synchronization service is shown below Fig. 2. The synchronization service provider (SSP) is shown as a separate entity, however, it can be a timing reference laboratory or a UTC(k) laboratory, or alternatively it can be combined with the Time Service Provider (TSP) in the Galileo ground mission segment (GMS).

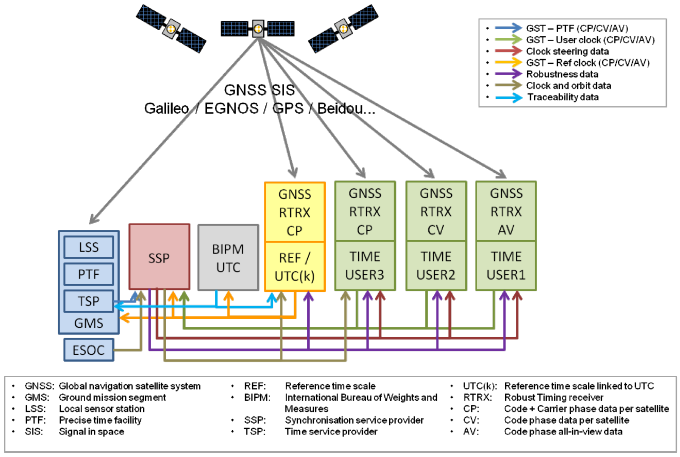


Fig. 2. Schematic diagram of an EGNSS based robust synchronization service.

The service concept aims at capabilities to serve all three user profiles mentioned in Section II. The SSP provider is proposed to be implemented in a flexible way that allows services at different levels of accuracy. Therefore, in term of time transfer techniques, it should support both common-view (CV) and all-in-view (AV) observation data, and both code-phase measurements and carrier-phase (CP) measurement data. For processing of the CP data, the SSP requires access to accurate orbit and clock prediction of the satellite, e.g. provide by ESOC.

Although it is not a strict requirement for all applications, it is strongly recommended that reference time facility (REF) is a UTC(k) laboratory or operate a time scale that is traceable to UTC.

IV. Synchronization Service Demonstrator Specification

As a next step in the project, specification and requirements for a demonstrator of the synchronization service are being defined. This includes specifications for the users, the REF, the SSP and for the service as a whole.

A. Time User

A list of specifications for three types of different users to be implemented in the demonstrator is given in Table I.

Table I. Specifications for three different types of users to be implemented in the demonstrator.

	USER1	**USER2**	**USER3**
Local clock	Rb OCXO TCXO	Cs Rb OCXO	H-maser Cs Rb
Timescale steering	soft- or hardware on the clock	software on the clock	phase/frequency offset generator
GNSS receiver	Single-frequency, cheap	Single or Dual frequency	Dual-freq timing, expensive
GNSS receiver processing	Robust concepts	Robust concepts	Robust concepts
GNSS post-processing	Code phase All-in-view	Code phase Common-view	Code + Carrier phase PPP

	USER1	USER2	USER3
SIS Orbit + Clock data	Broadcast/ EGNOS	Broadcast orbits	ESOC orbit products
Ionosphere corrections	Broadcast/ EGNOS	EGNOS/ SSP-estimate?	Dual-frequency iono-free
Troposhpere corrections			PPP estimate
Reporting data format	ASCII: timestamp, [GST - local clock]	CGGTTS	RINEX
Performance level	> 1 ms	< 1 ms, > 1 µs	< 1 µs, > 5 ns

B. *Reference Time Facility*

The requirements on the Reference laboratory are identical to the requirement on USER3 in the previous slide, except that:

- The local clock is either a high-performance Cs clock or an active H-maser.
- The uncertainty of the REF data shall be < 5 ns (95% probability interval)
- The reference laboratory in the demonstrator shall have a timescale traceable to UTC or have a UTC realization on its own.

C. *Synchronization Service Provider*

It is proposed that the Synchronization Service Provider for the demonstrator shall be developed and implemented according to the model shown in Fig. 3.

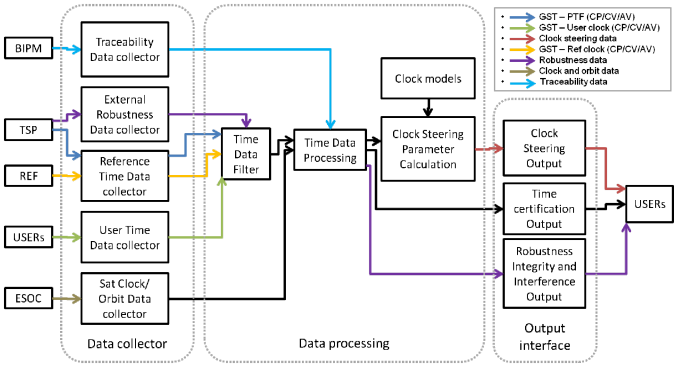


Fig. 3. Schematic lay-out for the synchronization service provider

The SSP in the demonstrator consists of the following sub-components:

- Input interfaces for automated data collection from the REF, the users, the Galileo TSP, BIPM and ESOC. The input interfaces shall operate over secured internet connections.
- A time data filter unit for detecting and marking obvious outliers, suspicious and erroneous time data from the REF, the users and the PTF.
- A time data processing unit for calculating clock difference between the REF and the user.
- A unit for calculating clock steering parameters, based on available clock models.
- Output interfaces for:
  - communicating clock steering parameters to the user or directly to the user clock.
  - providing periodic time certification reports to the user.
  - robustness, integrity and interference data to users or user clocks.

  The output interfaces shall operate over secured internet connections

D. *The Synchronization Service*

- The Synchronization Service demonstrator shall be developed in a way that allows scaling to larger numbers of users. The level of scalability shall meet the expected number of users mentioned in Section II.
- The Synchronization Service shall demonstrate that performance requirements for the users as mentioned in table 1 are met.
- The Synchronization Service shall be implemented with commercial off-the-shelf equipment.
- The Synchronization Service shall take advantage of the robustness features developed and tested in the project, as much as possible, within the limitations of available equipment, and within the limitation of the operation of the Galileo system. Provisions shall be implemented for evaluating the level of robustness of the service.
- The Synchronization Service shall be developed such that estimations can be made of the long-term availability of the service, the mean time between failure and the mean time to repair.

V. NEXT STEPS

The synchronization service and the demonstrator specification are being verified with relevant stakeholders. These stakeholders can be potential users of the service, potential service providers or any other relevant party. The feedback of these stakeholders will be used to further fine-tune the synchronization service concept description and the demonstrator specification. A cost/benefit analysis is under preparation to support the business model for this synchronization service concept.

REFERENCES

[1] http://rime.inrim.it/H2020-Demetra/

[2] F. Gottifredi, M. Gotta, E. Varriale, D. Cretoni, "Synchronet – an innovative system", Coordinates, Jul. 2008.

[3] M.A. Lombardi, "A NIST disciplined oscillator delivering UTC(NIST) to the calibration laboratory", NCSLi Measure, vol. 5, no. 4, Dec. 2010, pp. 46-54.

[4] "COUNCIL DIRECTIVE 2008/114/EC of 8 December 2008 on the identification and designation of European critical infrastructures and the assessment of the need to improve their protection", Official Journal of the European Union, 23 Dec. 2008, L 345, pp. 75-82.

[5] M. Kirkko-Jaakkola, H. Kuusniemi, S. Söderholm, S. Kaasalainen, H. Zelle, E. Dierikx, M. Grzebellus, M. Merimaa, "Concepts for a Robust GNSS Timing Service", submitted for ENC 2017.

[6] ESMA, "Final Report, Draft Regulatory and Implementing Technical Standards MiFID II/MiFIR", 2015.

Clock Stability for Low Frequency Radar Tomography of Asteroids

Ricardo Granados*, Alain Herique, Etienne Le-Coarer, Sylvain Rochat
Univ. Grenoble Alpes
CNRS, IPAG
F-38000 Grenoble, France
Email: *ricardo.granados-alfaro@univ-grenoble-alpes.fr

***Abstract*—The actual knowledge of internal structure in asteroids is based on indirect and theoretical modeling approaches. Bi-static Radar tomography between a lander on the asteroid surface and a spacecraft orbiting around can provide a better understanding of it based on the measurement of wave propagation delay (i.e. dielectric permittivity). The constraints over a space mission instrument are demanding, frequency stability and time synchronization is one of the main limitations for measurement accuracy and can induce operational constraints. In this paper we perform a time analysis to understand the impact of the frequency stability of the clocks in propagation delay detection in order to propose calibration and synchronization schemes that can improve science and instrument design.**

***Keywords*—bi-static; radar; synchronization; calibration; OCXO; asteroid; tomography.**

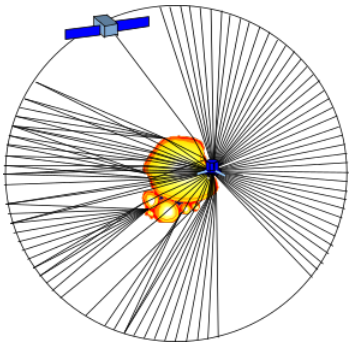


Fig. 1. Radio-wave propagation through asteroid for different Orbiter positions.

I. Introduction

The internal structure of asteroids is poorly known. Remote sensing cannot give enough details. Instead, direct study can give valuable information. Therefore the primary objective of this radar is to measure the propagation delay of a radio-wave through an asteroid to deduce the dielectric permittivity. This property relates to the mineralogy and porosity of the material. The secondary objective is to measure the signal scattering to deduce internal structural homogeneity, to discriminate monolithic structure against building blocks [1]. The information coming from this measurements will give insight about the formation of the asteroid and how to model its evolution. In consequence, will give insight of the history of the Solar System itself. Another relevant objective of studying mechanical and electrical properties of the body is to help in the design of technologies that can deal with hazardous asteroids and for future human exploration [2].

The Low Frequency Radar (LFR) counts with the heritage of CONSERT, an instrument aboard Rosetta mission which studied the comet 67P/Churyumov-Gerasimenko [3], [4]. As CONSERT, the LFR, is a bi-static radar. It consists in two separate electronics. One aboard the Orbiter, flying around the asteroid and the other in the Lander, placed in the asteroid's surface. Each electronic will have its own clock, this means an asynchronous system and a calendar drift. The LFR propagates electromagnetic waves from the Orbiter to the Lander through the asteroid to measure the propagation delay (see Fig. 1). In this paper we study the impact of clock stability in the measurement of propagation delay of the radio-wave. It is of interest to know the effect of the clock drift at different time scales during the asteroid characterization. To follow the phase and time correlations during a complete measurement a long term simulation is performed. This time analysis on the clock drift will help to improve electronic design, to establish a synchronization and calibration process and to propose on-board or/and on-ground methods to compensate the drift.

The instrument has been specified to resolve a variation of 10% in the mean porosity along a path of 150m. The time accuracy on the propagation delay measurement has to be better than the code symbol time of 50ns (BW=20 MHz). A 60MHz carrier has been selected to limit scattering loses.

II. Transponder Concept and Operation

Within the given space constraints of mass and power consumption it was not possible to get sufficiently stable clocks. To preserve the Lander to Orbiter synchronization during the whole experiment duration without resynchronization process it was required a stability of $\Delta f/f \approx 10^{-12}$ [5] . The in-time transponder structure used in CONSERT/Rosetta Fig. 2, allows to reduce the synchronization constraint with a clock stability requirement of $\Delta f/f \approx 10^{-7}$. This is achievable with an Oven Controlled Crystal Oscillator (OCXO).

The in-time transponder structure is a two way wave propagation named Ping-Pong. First the Orbiter sends a coded signal (Binary Phase Shift Key BPSK) through the asteroid to the Lander. The Lander receives the signal and pulse compress it to find the peak. This peak represents the propagation delay. Then the Lander sends the same coded signal through the asteroid back to the Orbiter but synchronized to the peak detected Fig. 3.

978-1-5386-2916-1/$31.00 ©2017 IEEE

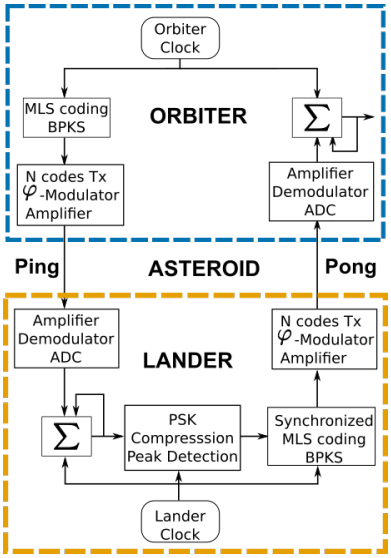


Fig. 2. Block diagram transponder concept.

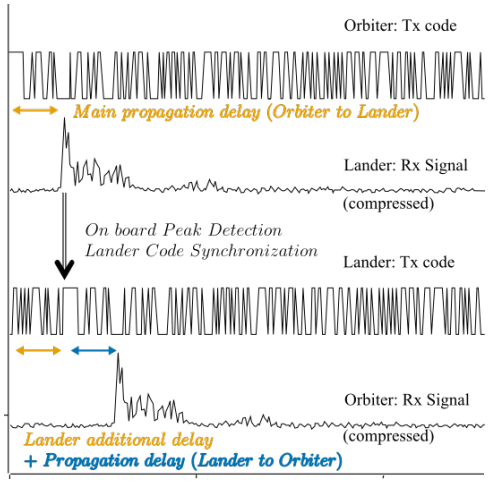


Fig. 3. Ping Pong synchronization process.

The first transmission Orbiter to Lander is used for synchronization, called Ping. The second transmission Lander to Orbiter is the science signal, called Pong. This Ping-Pong sequence receives the name of a Sounding. During one orbit several Soundings are performed for different Orbiter positions, this process is called a Scan. In Table I all of this definitions of elements are condensed with observations about the operation of the instrument for each one.

During the mission there will be no direct way to recover the carrier due to the negative Signal to Noise Ratio (SNR), result of sending the signal through the asteroid. Therefore the instrument relies in its ability to keep the frequency and time synchronization without sharing carrier or time. As stated in Table I LFR will perform a time synchronization each Scan, in order to synchronize calendars. This synchronization scheme is not in the scope of this paper. But the accuracy coming from it is taken into account for all the time analysis and simulations.

TABLE I. ELEMENTS FORMING THE ASTEROID CHARACTERIZATION

Element	Composed by	Observations
Tx Window	N codes	Composed of a carrier signal modulated in phase by a Maximum length Sequence (MLS) code
Ping and Pong	Tx and Rx windows	When Orbiter is in Tx mode Lander should be in Rx mode and vice versa
Sounding	A Ping Pong	Frequency difference is considered constant.
Scan	Several Soundings	Frequency difference is variable at this time scale
Asteroid Characterization	Various scans	Instrument is turned off between Scans, Spacecraft/Lander are in charge. LFR Synchronization after turning on

III. FREQUENCY STABILITY REQUIREMENTS FOR EACH TIME SCALE

As mentioned before, LFR transponder consists in two separate electronics (Orbiter and Lander) running an automat in an FPGA. Each one will have its own clock, because of the clock instabilities, both clocks will have slightly different frequencies, causing a phase rotation effect and a calendar drift. Therefore the synchronization must be preserved during the whole experiment. For this project there are two types of constraints on clocks. One type is related to the frequency accuracy when the frequency difference needs to be lower than a given maximum. The other is related to the frequency stability when accurate knowledge of the difference allows on-board or on-ground compensation.

In this project we recognize 4 different time scales: coherent accumulation, Ping to Pong, Sounding to Sounding, Transmission (Tx) Reception (Rx) scheduling. The constraints in frequency and time are different for each one and also the reference of interest. Each one will be explained in the following sections.

A. Coherent Addition

In order to improve the low SNR at the reception, an accumulation of N codes is performed. This accumulation depends completely in the frequency accuracy between both clocks. Therefore the length of the accumulation time is limited by the drift between clocks and also by physical properties (i.e. movement of Orbiter against Lander). It is a well known effect that accumulation magnitude varies in function of the clock drift, see Fig. 4. For this project it is required to have a drift less than 60° of the carrier phase during coherent accumulation (∼12 ms). No possible post-processing to correct errors.

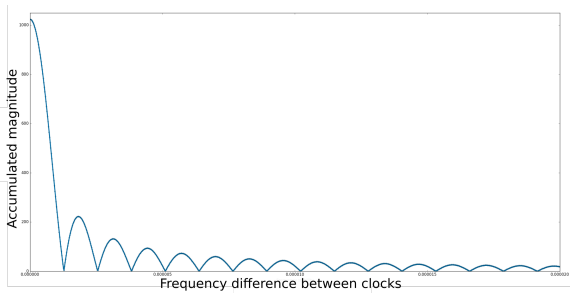


Fig. 4. Effect of clock drift in coherent addition magnitude.

B. Ping to Pong

1) Time Reference: From Ping to Pong the Lander has to preserve calendar versus Orbiter. This means having accurate time stamps from the Rx start time and Tx start time. Error in this time scale introduces error in the propagation delay measurement. This constraint involves the follow up of the stability of the clock. This constraint limits the error to be smaller than the symbol code resolution (50ns) over 20.

We will introduce a time analysis of the Ping-Pong. The time diagram for one Sounding is shown in Fig. 5 and the times for Orbiter and Lander references in Table II. For the Ping transmission: the transmitted signal from Orbiter will have a delay after reaching the Lander. The propagation delay is obtained by the difference between the arrival time and the Lander reception time. In Table II Orbiter is considered the reference, so only the Lander presents the clock drift and initial time error. The process is analogous from Lander to Orbiter in the Pong transmission.

$$(t_{O,T_c} + \tau_0) - t_{l,R_c} = -T_0 - \Delta Ping(\Delta f/f) + \tau_0 \quad (1)$$

$$(t_{l,T_c} + \tau_0) - t_{O,R_c} = T_0 + (\Delta f/f)(\Delta Ping + \Delta Pong) + \tau_0 \quad (2)$$

Where t_{O,T_c} is the Transmission of the Orbiter referred to the clock in the Orbiter. t_{l,R_c} is the Reception in the Lander referred to the clock in the Lander. T_0 is the initial time error coming from the synchronization process of the LFR. $\Delta Ping$ is the time, in clock ticks, between the start time of the Sounding and the Orbiter transmission. $\Delta Pong$ is the time between Orbiter transmission and Orbiter reception, also in clock ticks. $\Delta f/f$ is the fractional frequency, the normalized difference between both clock frequencies. τ_0 is the propagation delay. $(t_{O,T_c} + \tau_0)$ is the Arrival time of the signal to the Lander and $(t_{l,T_c} + \tau_0)$ the Arrival time of the signal to the Orbiter.

2) Phase Reference: Phase will present a rotation effect due to the clock drift. The difference between transmission and reception times give the information of the phase movement for one way, Ping or Pong.

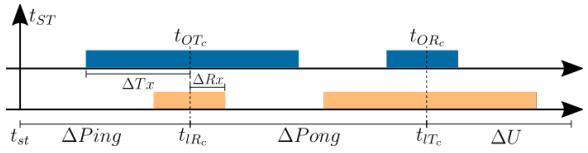


Fig. 5. Ping Pong time diagram. In blue Orbiter, in orange Lander. In this diagram is not depicted the initial error T_0. The first sub index in times, the Capital letters denote Orbiter reference and minuscule letters Lander reference. The second sub index denotes the action, Transmission or Reception.

TABLE II. TIMES REFERENCED TO ORBITER AND LANDER FOR A SOUNDING

Orbiter	Lander
$t_{ST} = 0$	$t_{st} = t_{ST} + T_0$
$t_{OT_c} = t_{ST} + \Delta Ping$	$t_{lR_c} = t_{st} + \Delta Ping(1 + \Delta f/f)$
$t_{OR_c} = t_{OT_c} + \Delta Pong$	$t_{lT_c} = t_{lR_c} + \Delta Pong(1 + \Delta f/f)$
$t_{ST_2} = t_{OR_c} + \Delta U$	$t_{lR_c} = t_{lT_c} + \Delta U(1 + \Delta f/f)$

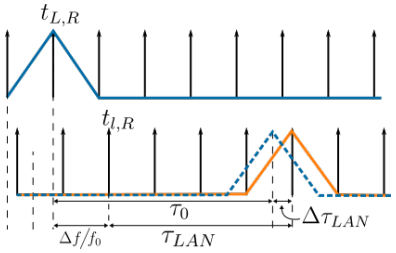


Fig. 6. Sampling effect, the real peak will be moved to the nearest sampling point. In blue the Orbiter transmission, in dotted blue the peak arrival to the Lander coming from the Orbiter, in orange the lander peak detected.

The peak detection is done at the sampling frequency (100MHz) inducing a jitter on the measured delay [6]. The jitter comes from the movement of the real peak to the nearest sampling position Fig. 6. This change introduce an error in time and in amplitude of the peak detected. To calculate the jitter $\Delta\tau_{LAN} = ((t_{O,T_c} + \tau_0) - t_{l,R_c}) mod(1/Fs)$ the sign comes from which sampling point is the nearest. From the asynchronous system the time reference is lost from Sounding to Sounding which leads to a uniform distribution of the jitter through a sampling period. So the propagation delay measured in the lander sets as $\tau_{LAN} = (t_{O,T_c} + \tau_0) - t_{l,R_c} + \Delta\tau_{LAN}$ for the Orbiter $\tau_{ORB} = ((t_{l,T_c} + \tau_0) - t_{O,R_c} + \tau_{LAN})/2$. Notice that the propagation in the Orbiter includes the propagation measured in the Lander and is divided by 2, this because of the two way propagation of the signal (See Fig.3). Also the propagation in the Orbiter is expected to be measured on-ground therefore it does not have the jitter treatment as in Lander. Is also important to remark that all this times are constrained into modulo one code length, due to the coherent accumulation.

From the way the automat is implemented, an extra jitter will appear coming from the use of 100MHz clock for the reception and the need of 120MHz clock for the transmission. This effect remains under study.

C. Sounding to Sounding

The starting time for each Sounding in the Lander will be different to the Orbiter, for the first Sounding in a Scan coming from the T_0 of the accuracy in synchronization and for the rest will add the clock drift.

1) Time reference: The time reference from Sounding to Sounding will be affected by the calendar drift. In case there is a miss peak-detection, knowing how the time reference changes from Sounding to Sounding will allow to correct the transponder time. With this is possible to increase the radar sensitivity and reduce the SNR margins. Time reference preservation over few pulses is typically 10ns in 10 minutes.

2) Phase reference: Phase will present a rotation effect, if we can correct phase from Sounding to Sounding, is possible to have coherent processing which increases the science return. The phase should not change more than 60° over 1 hour typically.

For both references this can be corrected on-board or on-ground.

D. Tx - Rx window schedule

Orbiter has to be in Tx mode while Lander is in Rx mode and vice versa. For this the Tx window should be sufficiently larger than the Rx window to avoid that the difference between calendars make the Rx window be outside of the Tx window. The synchronization error and clock drift should not put this windows outside the margins. This is a constraint of accuracy between clocks. No possible post processing to correct.

A resume of the requirements of each times scale is presented in Table III. Notice that the ones at the extreme left and extreme right are accuracy type and the ones in the middle are the stability type constraints.

IV. Long term simulations

A long term simulation is proposed to understand the correlations in phase and time that exists from one Sounding to another during a complete Scan, also it will help to understand how different clock characteristics (e.g. temperature, frequency offset) will affect the measurements. This simulations will give information needed to improve electronic design, to propose a synchronization scheme, and to come with on-ground or on-board processing to compensate this changes.

For the simulations we use a model for the oscillator [6] where we can introduce temperature changes, voltage supply changes, and initial frequency offset. For this simulations we will not consider the random phase noise.

A. Time error $E(t)$ clock model

The model used for the simulation is

$$E(t) = T_0 + y_0 t + (A \cdot log(B \cdot t) + C) + \int_0^t T(t)\,\mathrm{d}t + \int_0^t V(t)\,\mathrm{d}t \tag{3}$$

Where T_0 is the initial time error coming from the synchronization process, y_0 is the initial frequency offset, $(A \cdot log(B \cdot t) + C)$ is the logarithmic model of aging, the values for A, B and C were chosen to represent real measured clocks, $\int_0^t T(t)\,\mathrm{d}t$ represents the accumulation over time of the error produced by the time variable temperature, the function of temperature is based in a sinusoid wave and also in results from preliminary thermal analysis of the Lander, and $\int_0^t V(t)\,\mathrm{d}t$ is the accumulation of error of the time variable voltage.

B. Method

From the Ping Pong analysis we have each time for Orbiter and Lander operations. The clock stability is updated at the start of each Sounding and considered constant for the rest of that Sounding. This is an expected behaviour due that temperature changes are slower than the Sounding to Sounding time and temperature is the main source of stability change. Also is taken into account the jitter coming from the sampling points positions.

TABLE III. Requirements for each time scale

	Coherent Addition	Ping to Pong	Sounding to Sounding	Scan
Carrier Phase	10^{-7}	x	10^{-11}	x
Time Symbol	x	10^{-8}	10^{-12}	x
Few codes	x	x	x	10^{-7}

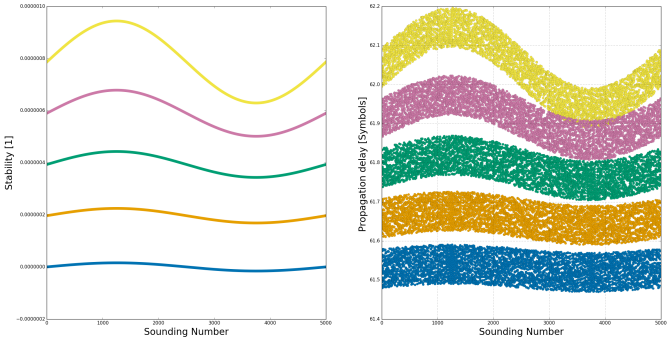


Fig. 7. Left: Stability curves for 5 different cases, changing frequency offset and temperature wave amplitude. Right: The propagation delay measured in the Orbiter. Initial frequency difference gives an offset to the value expected and temperature makes the propagation delay follow the same shape, the spread in the curves is of 0.1 Symbols. Propagation delay was fixed to 61.5 Symbols.

C. Preeliminary results

1) Initial frequency offset: The initial frequency difference y_0 generates an offset error for the propagation delay. Fig. 7.

2) Temperature effect: Propagation delay follows the thermal evolution. The spread for few soundings is half of a sampling period, from the time analysis we observed that the jitter covers one sampling period but to find the propagation delay in the Orbiter it is needed to divide by 2. Fig. 7. Temperature is the main parameter driving the stability of the clock.

3) Aging effect: Aging is of importance at the separation of LFR due that aging continues even if clocks are off. So a calibration is needed before separation to adjust aging. During a Scan time aging is not the main parameter driving stability, although the model is a logarithmic one $(A \cdot log(B \cdot t) + C)$ for a scan time the behaviour is almost constant. So the effect is the same as a frequency offset.

4) Voltage effect: The changes coming from the voltage supply $\int_0^t V(t)\,\mathrm{d}t$ are two orders of magnitude smaller than the temperature, so are not included in the simulation plot.

V. Ping Pong Pong

A way to follow the clock drift is proposed by implementing the Ping-Pong-Pong sequence, which is the transmission of one Ping and two Pong windows consequently, see Fig. 8. It is necessary to assure that the geometry between Orbiter and Lander is the same for both Pongs, so the radio-wave takes the same path. By knowing the time between Pongs, ΔPP, the difference measured in the propagation delays comes only from the clock drift. This is limited on-board by the sampling rate and SNR, and limited physically by the movement of Lander with respect to the Orbiter.

$$\Delta f/f = (\tau_{ORB_1} - \tau_{ORB_2})/\Delta PP \tag{4}$$

To have an on-board clock drift follow it is necessary to include in the Orbiter propagation delay the jitter coming from the sampling points $\Delta\tau_{ORB}$ just as it was explained in the Lander. This limits the clock drift resolution Fig 9.

VI. Clock Specifications

From the Analysis some specifications of the clock and the instrument are possible to determine.

A. Voltage supply

For the simulations a change of 1% of the power supply was used, this is compliant with the power supply to be used. The effect coming from power supply is negligible and will not affect the measurement. Now the stability in the control voltage pin is under study to check if variations of the power supply over the DAC, that feeds the voltage control pin has no impact in the stability.

B. Tx window size

The Tx window needs margins to allow the Rx window to be inside during the whole experiment. The Tx window has a direct impact in the power budget of the instrument, and is critical for the science return.

$$\Delta T_x > \tau_0 + \int_0^{tScan} \Delta f/f \, \mathrm{d}t + T_0 + \Delta R_x \qquad (5)$$

Where τ_0 is a range of the propagation delay, T_0 is the synchronization error at the beginning of the Scan, R_x is the size of the Rx window, and last the integral represents the accumulated time error coming from all the stability changes

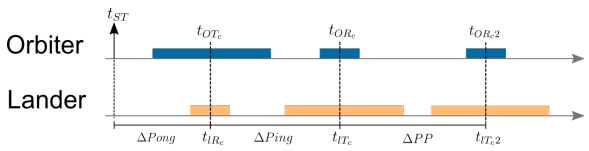


Fig. 8. Ping Pong Pong time diagram.

of the clock. This result gives the minimum Tx window size. T_0 is the only variable to be specified yet.

VII. Conclusion

The results of the time analysis give us valuable information to understand how each clock parameter will affect the propagation delay measurement. This work also helps to improve the physical design and operation of the instrument, i.e. the aperture time of the transmission window. By reducing to the minimum this window the power consumption of the instrument reduces too, making changes in the heating design and power consumption budget. Also gives us the possibility to think in correction methods for the clock drift on-board or on-ground. With the information coming from the housekeeping and the follow of the drift in the Ping Pong Pong is possible to do the phase reconstruction and have a coherent process for several Soundings. This work will serve as a base to propose the complete synchronization and calibration scheme used for the whole mission. And also for all the post processing analysis of the data.

References

[1] A. Herique, et al., *Radar Tomography of Asteroids*, IAAA Planetary Defense Conference, Bucharest, Rumania, 2011.

[2] P. Michel, et al., *Science case for the Asteroid Impact Mission (AIM): A component of the Asteroid Impact & Deflection Assessment (AIDA) mission*, Advances in Space Research, vol. 57, no. 112, pp. 2529-2547,2016.

[3] W. Kofman, et al., *The Comet Nucleus Sounding Experiment by Radiowave Transmission (CONSERT): A short Description of the Instrument and of the Commissioning Stages*, Space Science Reviews, vol. 128, pp. 413-432, 2007.

[4] W. Kofman, et al., *Propierties of the 67P/Chryumov-Gerasimenko interior revealed by CONSERT radar*, Science Magazine, vol. 349, no.16247, 2015.

[5] W. Kofman, et al., *Comet nucleus sounding experiment by radiowave transmission*, Adv. Space Res., vol. 21, pp. 1589-1598, 1998.

[6] O. Pasquero, A. Hrique, W. Kofman, *Oversampled Pulse Compression Based on Signal Modeling: Application to CONSERT/Rosetta Radar*, IEEE Trans. Geosci. Remote Sens., vol. 55,no. 4 pp. 2225-2238, 2017.

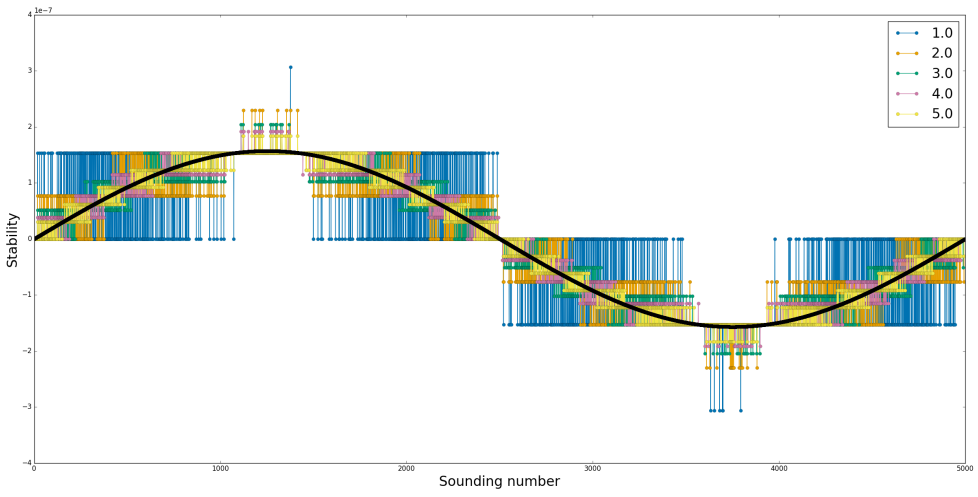


Fig. 9. Follow of the clock drift using Pong Pong technique. In colors the clock drift deduction changing the ratio between $\Delta PP/\Delta Pong$. In black is the real stability used for the simulation. Is possible to see that by increasing the time between Pongs the accuracy improves.

A New TWSTFT Station in Warsaw

Michał Marszalec, Tomasz Kossek, Marzenna Lusawa
Laboratory of Electrical, Electronic & Optoelectronic Metrology
National Institute of Telecommunications
Warsaw, Poland
m.marszalec@itl.waw.pl

Albin Czubla, Piotr Szterk, Roman Osmyk
Time and Frequency Laboratory
Central Office of Measures
Warsaw, Poland
a.czubla@gum.gov.pl

Przemysław Krehlik, Łukasz Śliwczyński, Marcin Lipiński
Faculty of Computer Science, Electronics and Telecommunications
AGH University of Science and Technology
Krakow, Poland
krehlik@agh.edu.pl

***Abstract*—This year, the final works on launching two-way satellite time and frequency transfer (TWSTFT) station in Warsaw are going to be completed. The facility of Central Office of Measures (GUM), organization responsible for maintaining the Polish realization of the international Universal Coordinated Time (UTC(PL)) is located in the center of city and is surrounded by a number of high buildings. Therefore it was difficult to establish in GUM directly TWSTFT station. Based on many years of close cooperation between National Institute of Telecommunications (NIT) and GUM the decision of placing TWSTFT station at NIT has been made, because NIT is located outside of strict city center and the antenna view is much better. The optical time transfer system (OTTS) to connect GUM and NIT is used. The length of the fiber optic line is about 28 km. Until now, the line was used for the purpose of continuous time comparison between the two organizations, so the entire fiber optic part of time transfer had to be redesigned to support two parallel transmissions. This paper aims to outline the status of the new TWSTFT station in Warsaw (at NIT-GUM) and the methods used to resolve some of the problems encountered.**

Keywords—time transfer, remote station, two way, satellite, optical fibre

I. INTRODUCTION

GUM and NIT together with other organizations for almost 20-ty the years cooperate in the field of time and frequency metrology. Most of the equipped with precise cesium and hydrogen clocks Polish laboratories have exchange their measurements results from GPS-CV time transfer systems [1]. Last years the Optical Fiber Time and Frequency Transfer network was built for a few laboratories [2, 3]. This enables the connection between UTC(AOS), realized by Astrogeodynamic Observatory in Borowiec (AOS) near Poznan, and UTC(PL), maintained by GUM in Warsaw, through 420 km fiber optic line. AOS is also equipped with TWSTFT [4] station. Building a second TWSTFT station in Poland (in Warsaw) opens up many possibilities to investigate the TWSTFT links with reference to the optical fiber links and to join Europe-Asia and/or Europe-Europe TWSTFT links.

II. SATTELITE COMPONENET OF THE SYSTEM

A. Localization

As it was mentioned in the Abstract, GUM is located in the center of city and is surrounded by a number of high buildings. The 'western' and 'eastern' satellites used for TWSTFT links are in view from Warsaw, but at the very low elevation: about 10º.



Fig. 1. TWSTFT Antenna system installed on the roof of the main buiding of National Institute of Telecommunications

The distance between GUM and NIT is about 16 km in straight line and the fiber optic link is about 28 km. The main building of NIT is located among buildings and trees, however with similar height (in both directions: to the 'western' and 'eastern' satellites).

The SATRE modem was installed with calibrated cables supplied by manufacturer (TimeTech).



Fig. 2. SATRE modem from TimeTech installed in NIT's Timestandard Chamber.

After settling all official matters, the satellite part of the system has been started. Fig. 3 shows measurement session of SATRE modem in LOCK state to PTB signal.

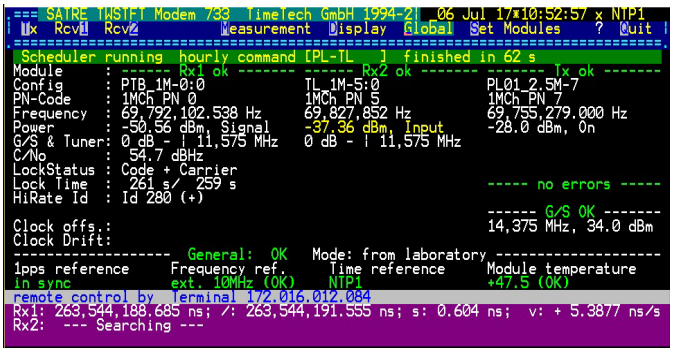


Fig. 3. Measurement session of SATRE modem

B. *Operational tests*

The test of the new TWSTFT station were done in June and the first week of July.

The Europe-Asia group of TWSTFT contains the following stations: France (OP), Germany (PTB), Poland (PL-NIT/GUM), Russia (SU,KM), India (NPLI), China (NTSC, NIM), Taiwan (TL), Korea (KRISS), Japan (NICT).

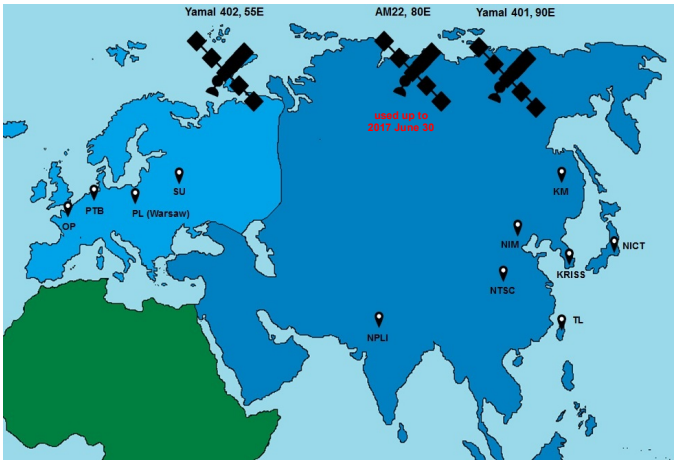


Fig. 4. The Europe-Asia TWSTFT scheme

After the end of usage of AM22 satellite the constellation of two satellites (Yamal 402 and 401) is now tested (Yamal 401 at the end of July). Fig. 5 and Fig. 6 show clean carrier sessions results for AM22 and Yamal-402 constellations.

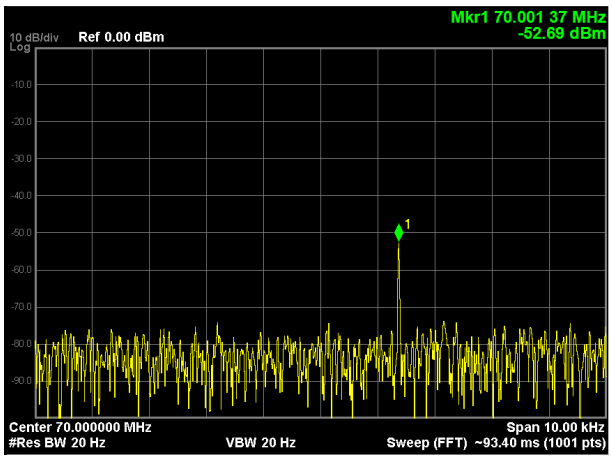


Fig. 5. Clean carrier session results for AM22, Satellite (up to June 2017)

On the above figure standalone clean carrier signal for NIT/GUM station has been caught (Warsaw-AM22-Warsaw).

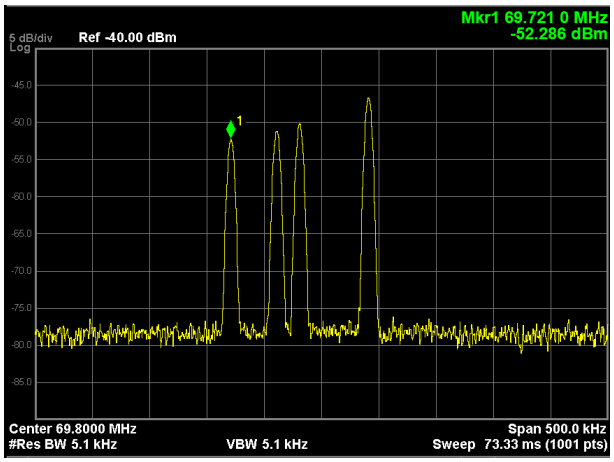


Fig. 6. Clean carrier session results for Yamal-402, Satellite (July 2017)

Transmission for Yamal-402 has been tested in first week of July. (Fig 6.) Clean carrier session results:

- PL01 – 69.721 MHz
- NIM02 – 69.761 MHz
- PTB04 – 69.781 MHz
- SU01 – 69.841 MHz

III. FIBRE-OPTICAL TIME TRANSFER COMPONENET OF THE SYSTEM

As it was mentioned before, optical part of time-transfer system had to be redesigned to transmit to NIT not only 1PPS of UTC(PL) but also the 10 MHz reference frequency signal with fixed phase relative to UTC(PL) signal. Before installation of TWSTFT only one optical time transfer system (OTTS 2) system consisted of two 1 PPS transmitter-receiver pairs working simultaneously on close wavelengths (DWDM channels) was used to make direct comparisons between GUM and NIT.

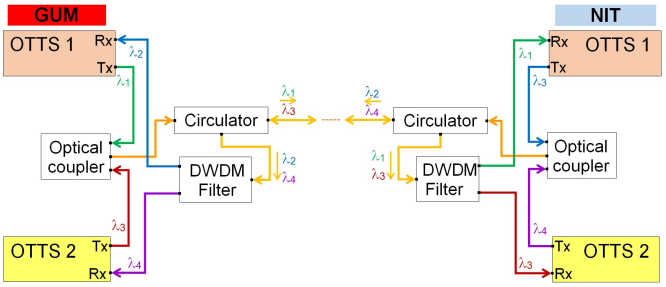


Fig. 7. Scheme of redesigned optical part of time-transfer system

Currently, the system has been changed to make possible operation of two optical time transfer systems using the same fiber link. The standard optical filters designed for Dense Wavelength Division Multiplexing (DWDM) technology have been applied in order to separate transmission of this two systems. The UTC(PL) transfer from GUM to NIT is realized using the more advanced system build by AGH (University of Science and Technology, Krakow, Poland), with stabilization of propagation delay of the reference 10 MHz signal (one of the earliest versions – prior to ELSTAB system), and by in-direct 1PPS signal generation with help of Femtostepper. The second part of the optical fiber system is used to determine and apply the proper phase-shift of 1 PPS into Femtostepper.

Also calibration of all delays was very important issue. After the experience of participation in the pilot comparison of time interval measurements with high speed oscilloscopes [6] the uncertainty budget was determined with optimal accuracy.

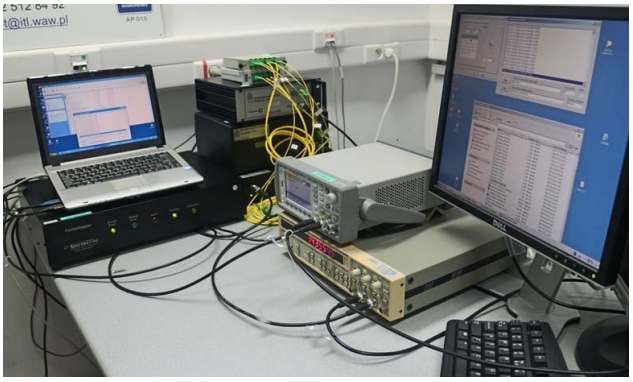


Fig. 8. Equipement for optical part of time-transfer system installed in NIT

IV. AUTOMATION

All measurements from the optical part of the transfer system and also TWSTFT are automated. The processing data from TWSTFT modem demands:

- acquire raw data from SATRE modem (TCP/IP port 2001),
- filtration data according to official schedule of comparisons,
- calculation data and conversion to the final version file conforming to Recommendation ITU-R [7],
- uploading data on BIPM FTP server.

All above operation will be completed on virtualized server within computing center of NIT after starting the comparison of the Europe-Asia group by the BIPM.

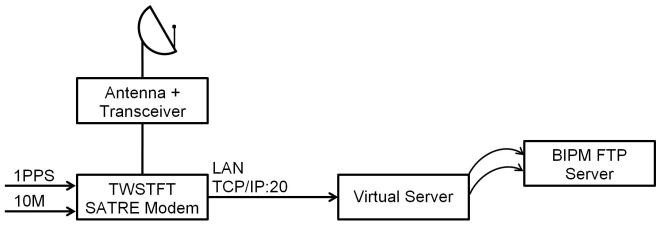


Fig. 9. Scheme of TWSTFT dataflow

V. CONCLUSIONS

The works are still ongoing. Precise calibration of all delays used in the UTC(PL) transfer to the SATRE modem (NIT's location) has been started. It is planned to use time interval measurements and also phase comparison methods. The team is planning to complete automation process of measurement data flow. This process will contain integration of all reference time and frequency comparisons systems in the NIT lab into a single database for faster and instant analysis of results. The TWSTFT is now directed to the 'eastern' satellite. The interesting issue is to investigate the influence of relatively long distant location of two Polish TWSTFT stations (the second station, located in AOS in Borowiec is distant from Warsaw of about 270 km) on comparison results by reference to the results obtained from the long fiber connection between

GUM and AOS. The other actions are to apply algorithms and methods on decoding signals by using SDR technique (Software Defined Radioreceiver) and calibration of PL01 station with the moving calibration TW station.

ACKNOWLEDGMENT

The authors are deeply indebted to all co-authors of papers quoted, which testify many fruitful long-lasting cooperations The authors specially acknowledges Mr. P. Dudek from Diomar company for technical support and telecommunication operator Orange Polska for research support.

REFERENCES

[1] W. Lewandowski, J. Azoubib, W.J. Klepczynski, "GPS: primary tool for time transfer," Proceedings of the IEEE, vol. 87, pp. 163-172, 1999.

[2] L. Sliwczynski, P. Krehlik, M. Lipinski, L. Buczek, J. Kolodziej, A. Binczewski, J. Nawrocki, J. Pieczerak, "Remote synchronization of atomic clocks," 2016 21st International Conference on Microwave, Radar and Wireless Communications (MIKON), 2016, pp.68–73.

[3] A. Czubla, R. Osmyk, P. Szterk, W. Adamowicz, M. Marszalec, and Ł. Sliwczyński, "Optical Fiber Time and Frequency Transfer inside Urban Telecom Network in Warsaw – Results of Initial Tests," 2012 European Frequency and Time Forum, 2012, pp.1–3.

[4] W. Schafer, "Two-Way Time Transfer - A Universal Tool for Metrology and Wide-Area Time Synchronisation," NPL, Teddington, UK, 17 September 2002

[5] P. Krehlik, L. Sliwczynski, L. Buczek, and M. Lipinski, "Fiber-Optic Joint Time and Frequency Transfer With Active Stabilization of the Propagation Delay," in IEEE Transactions on instrumentation and measurement, vol. 61, NO. 10, OCTOBER 2012, pp. 2844–2851.

[6] A. Czubla, P. Szterk, P. Krehlik, L. Sliwczynski, M. Yogun, R. Hamid, K. AlDawood, F. Almuhlaki, A. Aljawan, I. Alboraih, B. Pinter, M. Marszalec, M. Lusawa, "Pilot Comparison of Time Interval Measurements with High Speed Oscilloscopes – initial results", poster on EFTF 2016.

[7] Recommendation ITU-R TF.1153-4 "The operational use of two-way satellite time and frequency transfer employing pseudorandom noise codes"

Time Delay Measurements: Estimation of the Error Budget

Marco Siccardi
SKK Electronics
Cuneo, Italy
Email: siccardi@skk.it

Giovanni Daniele Rovera
LNE-SYRTE, Observatoire de Paris, PSL Research University,
CNRS, Sorbonne Universités, UPMC Univ. Paris 06, Paris, France
Email: daniele.rovera@obspm.fr

I. Introduction

The measurement of the time difference between two events consists in estimating, quite often with a Time Interval Counter (TIC), how much time elapses between two time markers. A time marker is defined here as the instant when a "two level" pulsed electrical signal crosses a certain threshold. In this paper we will restrict the estimation of the error budget to the case, usually encountered in a time laboratory, of the measurement of the time difference between two coherent series of regularly spaced time markers. Other uncertainty components must be taken into account when a single event is compared to a time scale. Two series of time markers, usually One Pulse Per Second (1PPS), are coherent when issued from the same clock, or from two similar low noise clocks with a small and predictable drift. In this later case the evaluation of the time delay at a given time is a little bit more complicate, but the uncertainty budget will be similar to the common clock configuration, with the statistical part taking into account also the short term noise of the clock difference instead of the noise of the measuring system alone.

II. Definition of the Measurand

The first step for an accurate measurement is the definition of the measurand, since a poor definition of the measurand can lead to inconsistent results. An example of badly defined measurand can be the Allan standard deviation of signal affected by white phase noise without specification of the analysis bandwidth. For the purpose of this paper we will define as a time marker the time when the rising front of a pulsed electrical signal, in a well defined reference plane, crosses a given threshold level. Typically the reference plane is chosen at the output connector of the timescale generating equipment, when properly terminated (on a $50\,\Omega$ load). In many laboratory the threshold level is defined at $1\,\mathrm{V}$ but other laboratories prefers $1.25\,\mathrm{V}$ and in some cases the level must be adapted to the level effectively available at the output connector of the equipment under test. Considering the speed of light the definition of the reference plane of the output connector is not a big issue for accuracy targets in tenths of ps, but can become critical when a better accuracy is expected. In this case "symmetrical" connectors like the APC7 will allow a better definition of the reference plane. By using this definition of the measurand one must be aware that the instrument used to measure the signal above defined can in some mode perturb the measurement and therefore the perturbation must be evaluated and taken in account in the computation.

Ideally the time difference should be measured directly at the physical location where the pulsed signals are defined, because when the signal travels in space the associated time marker shifts. In most cases this is not possible and so the signals are transferred to the TIC by using transmission lines, and the measurement is subsequently corrected for the delays introduced by the test setup. This operation, which is in turn a calibration, is obtained combining algebraically constant quantities called "Cable Delay" and "Internal Delay" of the TIC. These delays are affected by Type-B uncertainty of significant magnitude, possibly of the order of $1\,\mathrm{ns}$. The use of indirect comparison techniques to mitigate uncertainty by elision helps up to a certain points, but it fails when there are inhomogeneities in the apparatus, as it happens during calibration campaign of UTC links between laboratories.

The amount of the Type-B uncertainty is strongly related to the real shape of the pulsed signals under measurement, which are quite often generically called 1PPS due to their repetition rate [1], and in particular to their rise or fall time. The signals, traveling from source to the comparator of the TIC, are subject to distortion due to the bandwidth limitation of cables, as well as to the bandwidth limitation of the TIC front end [2]. In fact, the effect of the multiple low-pass filtering on the input pulse is to increase its rise-time, as described by time domain convolution, and consequently to change the delay of the time-stamp. This occurs either by changing the length and the quality of the cables, as well as the TIC. Other sources of Type-B uncertainty are due to inaccurate matching along the path of the pulsed signal path, up to the TIC input termination. This leads to change of amplitude at the TIC comparator, and so to a time-shift of the marker, which increases with slower rising time.

The objective of this work is to provide a way forward in the estimation of this Type-B uncertainty, considering that a $100\,\mathrm{ps}$ is already good results. The paper will also discuss how the overall uncertainty can be limited by applying certain measurement techniques and by having a good definition of the signal under measurement.

III. Delay measurement with the Pivot method.

The pivot method was developed to perform accurate measurement by rejecting the error introduced by the asymmetries of the setup. In this case there is no need to calibrate the delay of all the components of the measurement setup because they are supposed constant (at first approach). The time difference between the signal at connector A and an auxiliary coherent

978-1-5386-2916-1/$31.00 ©2017 IEEE

TABLE I. ERROR BUDGET (ALL VALUES IN PS)

	bias A	u_A	bias B	u_B	u(A-B) raw	u(A-B) corr
Standard deviation	0	10	0	10	14	14
Quantization error	0	4	0	4	6	6
Time-base error	0	0	0	0	0	0
Trigger error	0	5	0	5	1	1
Impedance mismatch	0	10	0	10	14	10
Probe cable delay	40006	6	40006	6	1	1
TIC input filter	800	80	800	80	8	8
TIC non linearity	0	50	0	50	70	70
Quadratic sum					73	72

signal C is measured by a TIC by using cables of unknown delay. The same setup is then used to measure B-C, by simply moving the probe cable from A to B. When necessary the measurement A-C is repeated to check the stability of the system. With this measurement technique many of the biases due to cable delays, TIC channels asymmetry. etc... are eluded because are expected identical in both measurements, nevertheless some of the delays depend on the shape of the PPS signal or on the delay effectively measured in each individual measurement and therefore are only partially compensated. In a realistic uncertainty budget of a time delay measurement at least the following components must be considered:

- Statistical uncertainty
- Quantization error
- Time-base error
- Trigger error
- Impedance mismatch error
- Probe cable delay
- TIC input filter
- TIC non linearity

As the measurement is performed 2 times, one in A and one in B the uncorrelated uncertainties must be quadratic summed, while some bias can be totally or partially compensated because constant in each measurement.

IV. EXAMPLES OF UNCERTAINTY BUDGET TYPICALLY ENCOUNTERED.

For the examples reported here we only consider the Stanford Research SR620 because is widely diffused in time laboratories and, in despite of the old design, is still between the most suited for this type of measurement, where the resolution cannot be enhanced by numerical interpolation based on statistic. We start with the simple case of the measurement of the time difference between two 1 PPS signals issued from two almost identical devices with a rise time of about $500\,\mathrm{ps}$.

The numerical values reported here are representative of the case of a measurement between the output of two 1PPS generator/distributor driven by the same low noise clock that also serves as reference of the TIC. The delay of the probe cable of about $10\,\mathrm{m}$ has been chosen to put in evidence that the propagation delay of the pulse ($1\,\mathrm{V}$ trigger level) is due to the theoretical cable delay of $40\,\mathrm{ns}$ plus the additional delay of about $6\,\mathrm{ps}$; more details in additional delays due to signal propagation can be found in [2]. For the TIC non linearity we use a value that can be found in the TIC operating manual. We did verify that this value is realistic when the TIC reads delays bigger than $20\,\mathrm{ns}$, but is widely underestimated when the TIC reads values lower than $10\,\mathrm{ns}$.

To stress the problem encountered when the measurement is performed between two 1PPS signals of different shapes we consider the case when the signal A has a rising time as in the above example and the signal B has a rise time of $4\,\mathrm{ns}$.

TABLE II. ERROR BUDGET (ALL VALUES IN PS)

	bias A	u_A	bias B	u_B	u(A-B) raw	u(A-B) corr
Standard deviation	0	10	0	10	14	14
Quantization error	0	4	0	4	6	6
Time-base error	0	0	0	0	0	0
Trigger error	0	5	0	40	35	35
Impedance mismatch	0	10	0	100	100	30
Probe cable delay	40006	6	40200	50	200	50
TIC input filter	800	80	1250	100	450	90
TIC non linearity	0	50	0	50	70	70
Quadratic sum					508	133

In this second example the trigger error of $20\,\mathrm{mV}$ is no longer compensated by the two identical shapes of the 1PPS signals. The trigger error due to impedance mismatch is evaluated by considering a mismatch of about 10 % in the output impedance of the PPS sources versus the input impedance of the TIC. Although it is possible to evaluate the additional cable delay for each individual pulse shape and take this value into account we consider that this bias is not removed from the measurement and therefore we consider the expected value [2] as uncertainty. Similar consideration is done for the additional delay due to the input low pass filter of the TIC.

V. CONCLUSION

The uncertainty of the time differences between two coherent signals is one of the components that has to be taken into account for the calibration of time links used for TAI calculation. The uncertainty budget reported here can be used as rule of thumb to estimate the uncertainty of a delay measurement in the frame of a TAI link calibration. When the uncertainty of $500\,\mathrm{ps}$ reported in the specification of the SR620 is sufficient there is no need to analyze this component in details. With an optimized setup using cables of appropriate lengths and only measuring PPS signals of rise time lower than $2\,\mathrm{ns}$ an uncertainty of $200\,\mathrm{ps}$ without applying any delay correction. When the target is below $100\,\mathrm{ps}$ a detailed analysis is required and the use of a TIC with lower non-linearity and a wider input bandwidth is recommended.

REFERENCES

[1] M. Siccardi, M. Abgrall, and G. Rovera, "About time measurements," in *European Frequency and Time Forum (EFTF), 2012*, pp. 379–382, April 2012.

[2] M. Siccardi, D. Rovera, and S. Romisch, "Delay measurements of pps signals in timing systems," in *2016 IEEE International Frequency Control Symposium (IFCS)*, pp. 1–6, May 2016.

Some Approximated Methods of Calculation Sagnac Correction For Optical Fiber Time Transfer

Albin Czubla
Time and Frequency Laboratory
Central Office of Measures
Warsaw, Poland
a.czubla@gum.gov.pl

Przemysław Krehlik, Łukasz Śliwczyński, Jacek Kołodziej
Faculty of Computer Science, Electronics and Telecommunications
AGH University of Science and Technology
Krakow, Poland
krehlik@agh.edu.pl

Artur Binczewski, Krzysztof Turza,Wojbor Bogacki, Piotr Rydlichowski
Poznan Supercomputing and Networking Center (PSNC)
Poznań, Poland
artur@man.poznan.pl

***Abstract*—In this paper we present simply algorithms for calculation of Sagnac correction for optical fiber time transfer based on limited knowledge of the fiber route and using the more detailed but confidential data known by network operator only. The considered methods are quite easy for implementation and can make the calculation of Sagnac correction more friendly for time and frequency community.**

Keywords—calculation Sagnac correction; optical fiber link, time transfer

I. INTRODUCTION

The optical fiber time transfer links can achieve a sub-nanosecond accuracy and precision at picoseconds level [1, 2]. Because of Earth rotation, the light travelling along the fiber root is subjected to shortened or elongated distance according to direction of travelling and the time of travelling in onward and backward directions can be different. This effect, called Sagnac effect, is very well known in TWSTFT and optical fiber time transfer [1-4], however the calculation of the value of Sagnac correction for optical fiber link can be difficult in practice. The real coordinates of fiber route are often not known exactly or confidential for internal use of optical network operator only. In this paper we present some practical methods of evaluation value of Sagnac correction, typically based on the limited knowledge of the coordinates of some nodes along fiber route only, and compare the results to the more precise calculation based on more detailed data managed by the optical fiber link network operator.

II. THE BASE FORMULAS

Sagnac correction $\Delta\tau_{Sagnac}$ can be determined according to the general formula [5]:

$$\Delta\tau_{Sagnac} = \pm 2\,\omega A_E / c^2 \qquad (1)$$

where ω – is the rotation speed of the Earth, A_E – is the area of equatorial projection of the surface swept by the vector extending from the centre of the Earth and moving along the fiber, and c – is the speed of light in vacuum. The graph illustration of the A_E component is shown in Fig. 1.

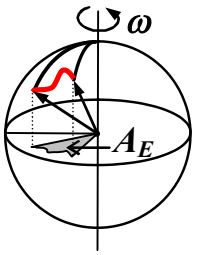


Fig. 1. Illustration of the A_E component in the formula for Sagnac correction (the red curve represents an exemplary fiber route).

In the above formula (1), the positive sign '+' should be applied for the movement in East direction, and the negative sign '-' for the movement in West direction.

Consequently, if the fiber route crosses the same meridian several times, some parts of the area A_E would take positive signs and other parts would take negative signs. And theoretically, if the fiber route runs along the meridian, the Sagnac correction would take the zero value. It is a very useful feature, especially for considering the range of the possible values of the Sagnac correction if the knowledge of the given fiber route is limited to the coordinated of the nodes and to the lengths of fibers between nodes.

So, the problem of calculation of Sagnac correction is mainly reduced to calculation the area A_E, if we omit the other much smaller factors as e.g. variation in the Earth rotation speed and tidal movements, then the Cartesian equatorial coordinate system is the most convenient. Because of the

This work was supported by Polish National Science Center (NCN) under project no. 2015/17/B/ST7/03628.

details of fiber route are given rather in geographical coordinates only, there should be used the formulas to convert geographical coordinates (λ, φ, h) referred to an ellipsoid into Cartesian equatorial coordinates (x, y, z), as follows:

$$\begin{aligned} x &= \left(R_N + h\right)\cdot\cos\varphi\cdot\cos\lambda \\ y &= \left(R_N + h\right)\cdot\cos\varphi\cdot\sin\lambda \\ z &= \left(R_N\cdot b^2/a^2 + h\right)\cdot\sin\varphi \end{aligned} \tag{2}$$

where: $R_N = a^2/\sqrt{a^2\cdot\cos^2\varphi + b^2\cdot\sin^2\varphi}$, and a and b are the semi-major and semi-minor axes of Earth ellipsoid respectively. The values of a and b parameters can differ slightly between different adopted Earth reference ellipsoid systems used on maps and when determining the geographical coordinates.

There are also useful the simplified formulas for calculation of the arc length l and the area A of a skew circular sector formed by two radius (r_1 and r_2):

$$\begin{aligned} l &= \frac{1}{2}\left(r_1 + r_2\right)\cdot\beta \\ A &= \frac{1}{2}r_1\cdot r_2\cdot\beta \end{aligned} \tag{3}$$

where: β is the measure of the angle between the radius vectors r_1 and r_2 expressed in radians.

III. The Considered Methods

Very often, the knowledge of the fiber route is limited to coordinates of the end points or to known position of the some nodes along the fiber route. It is enough for rough estimation of the value of Sagnac correction. In the first approximation (Method I), we can assume that the real fiber route is between the meridians and the parallels (the circles of latitudes) which cross the consecutive or end nodes. The equatorial projection of a such case is shown in Fig. 2.

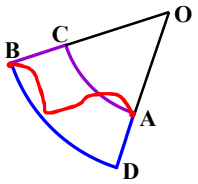


Fig. 2. Illustration of equatorial projection of an exemplary fiber route (the red curve AB) with projection of the meridians and parallels crossing the nodes of the fiber route (the violet and blue lines correspond to the considered projection of hypothetical fiber routes, the point O represents the centre of Earth).

Even though the real fiber route runs partly beyond the region between the meridians and parallels crossing its nodes, the areas of the circular sectors (AOC and BOD) created by the equatorial projections of these meridians and parallels seem to be a good approximation of the A_E area and are easy to calculate.

The above method was used for estimation Sagnac correction for the link GUM-AOS [2]. However, a network operator can easily complete the information about nodes with the lengths of fiber of particular segments of the route. In a such case, we can estimate the value of Sagnac corrrection analysing the possible fiber routes between the fixed nodes and with the fixed lengths (Method II), similarly as it was done in the paper [3]. There are possible two different sub-cases (Fig. 3.): the first sub-case when the length of the fiber is sufficient for a hypothetical fiber route between the nodes along the meridians crossing these nodes and along the single parallel (Fig. 3a), and the second sub-case when the length of the fiber is to short for a hypothetical fiber route between the nodes along the meridians and the single parallel (Fig. 3b). The other sub-case, when nodes of the fiber route are located nearly at the same meridians, is not considered here.

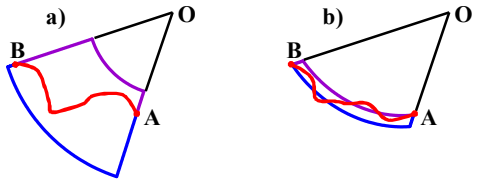


Fig. 3. Illustration of equatorial projection of exemplary fiber routes (the red curves AB) and projection of the extreme hypothetical routes with fixed lengths of fibers (the violet lines for the possible smallest A_E areas and the blue ones for the possible largest A_E areas, a) and b) correspond to long and short fiber lengths respectively, the point O represents the centre of Earth).

In the both sub-cases shown in Fig. 3, the possible smallest and largest A_E areas are quite easy to calculate, but should be followed by a bit more complicated determination of the extreme hypothetical routes on the curved Earth ellipsoid.

Finally, there is also possible the very accurate calculation of Sagnac correction, when the more detailed coordination of the real fiber routes are known (Method III). Because a direct access to a such data is typically not allowed due to confidentiality reasons, the calculation of Sagnac correction can be performed by network operator according to the appropriate formulas and algorithm. The detailed results obtained by network operator can be a very good reference for validation of accuracy and uncertainty estimation of the other less accurate methods.

IV. Exemplary Results

Together with network operator, there were performed calculation of Sagnac corrections for three real fiber routes in Poland (Fig. 4). The chosen fiber links represent different cases of geographical positions and are very useful for validation of the considered methods.



Fig. 4. The schematic traces of three real fiber routes chosen for calculation Sagnac correction: Poznan – Warsaw (c.360 km fiber link) – the red line, Poznan-Gdansk (c. 530 km fiber link) – the green line, and Poznan-Wroclaw (c. 345 km fiber link) – the blue line.

TABLE I. EXEMPLARY RESULTS OF CALCULATION SAGNAC CORRECTIONS

The applied methods	**Obtained values of Sagnac corrrection**		
	Poznan-Warsow	***Poznan-Gdansk***	***Poznan-Wroclaw***
Method I – 2 end nodes	885 ps (881 ÷888) ps	350 ps (334 ÷366) ps	31 ps (30 ÷32) ps
Method II – 2 end nodes	884 ps (865 ÷903) ps	350 ps (315 ÷385) ps	31 ps (29 ÷33) ps
Method III (nr of points)	885 ps (2458)	369 ps (7488)	48 ps (7292)
max. differ.	<2 ps	19 ps	17 ps

The obtained results of calculation are shown in the Table 1. All calculations were performed by optical network operator because only the coordinates of the end points and main nodes can be available public (are not confidentional). All results agree within 20 ps, however in the case of Poznan-Wroclaw the Methods I and II do not cover the reference value (the value taken from Method III). Better results would be obtained allowing for the knowledge of coordinates of more nodes along the fiber routes as e.g. regeneration points.

V. CONCLUSIONS

Presented briefly above, the methods of calculation of Sagnac correction can be quite easy applied for the real optical fiber time and frequency transfer links. Together with involvement of the network operator, as in our case, it is possible to obtain an enhanced accuracy of calculation of Sagnac correction, sufficient also for more demanding users.

The crucial is the knowledge of the end nodes coordinates and the Method III should be improve to cover the sub-case with nodes at the same or close meridians. The uncertainty analysis is required, too.

REFERENCES

[1] P. Krehlik at al., "ELSTAB - fiber optic time and frequency distribution technology - a general characterization and fundamental limits," IEEE Trans. Ultrason., Ferroelect., Freq. Control, vol. 63, no. 7, 2016, pp. 993-1004

[2] Ł. Śliwczyński at al., "Dissemination of time and RF frequency via a stabilised fibre optic link over a distance of 420 km". Metrologia, vol. 50 (2013), pp. 133-145.

[3] J. Geršl, P. Delva and P. Wolf, "Relativistic corrections for time and frequency transfer in optical fibers", Metrologia, vol. 52 (2015), pp. 552-564

[4] D. W. Hanson, "Fundamentals of Two-Way Time Transfer by Sattelite", in Proc.of 43rd Annual Symposium on Frequency Control, 1989, pp. 174-178.

[5] A. Dobrogowski, Signal of time (*in Polish:* Sygnał czasu), Wydawnictwo Politechniki Poznańskiej, Poznań, 2003.

Analysis of Uncertainty in Time Traceability links Using GPS Common View and Optical Fiber Techniques

Lingda Meng[1,2], Ya Liu[2], Feng Zhu[2], Xiaohui Li[2]
1. University of Chinese Academy of Sciences, Beijing China
2. National Time Service Center, Chinese Academy of Sciences, Xi'an China
e-mail: menglingda@ntsc.ac.cn

***Abstract*—In a test field of satellite navigation system, two different time traceability links were built base on the GPS common-view (GPS CV) and optical fibers time transfer techniques. Both techniques are utilized to compare the test field time (TFT) with UTC(NTSC). A time traceability link must be calibrated and detection to assure the system time traceability accuracy and stability. In many cases, calibration campaigns have been very infrequent due to the expense and lack of suitable equipment. The paper is devoted to study the uncertainty of the test field's both traceability links which are under real environmental conditions and without influencing of the normal operation of the time traceability inks. Our results show that the uncertainty of GPS common-view traceability link results is estimated as 3ns and optical fiber link(57km) is better than 0.2ns. The results can be used for the traceability links inter calibrated, abnormal detection and studying the two techniques fusion time traceability method.**

Keywords—time and frequency transfer; GPS common-view; optical fiber; time transfer link calibration; Type A and Type B time and frequency transfer uncertainty

I. INTRODUCTION

Time and Frequency transfer is used to compare remote clocks or frequency standards. The technique of GPS CV has the advantages of continuity, mature technology and easy to realize, that make it widely used in remote clocks or frequency comparison. It is also used in the computation of International Atomic Time (TAI) and UTC. Optical fiber time transfer is a high-precision time and frequency transfer methods. In recent years, we can observe rapid progress in the field of time and frequency transfer via optical fibers. Compared with the GPS CV that transmit through the atmosphere, transmission through optical fiber has less error cause, which allows for precise transfer. In the test field (Xi'an), we employ both techniques for comparing the TFT with UTC(NTSC).

In the test field, satellite navigation system time traceability links were built by GPS CV comparison and optical fibers time transfer techniques. Both traceability links are utilized to improve the stability and accuracy. In order to assure the time transfer accuracy, time traceability links must be calibrated. The uncertainty of each link is a combination of the Type A and Type B uncertainties. The Type A uncertainty is mainly introduced by the stability of the time and frequency transfer technique used, and the Type B uncertainty is a measure of the time transfer accuracy. The Type B uncertainty of a time transfer link is dominated by the uncertainty of link delay calibration. The Type B uncertainty of a time transfer link is also associated with effects other than calibration uncertainty. After a calibration, any change in the link, such as the delay change due to equipment aging or malfunction, will change the calibration result and increase the uncertainty. Therefore, it is necessary to have frequent calibrations in order to keep the Type B uncertainty of a time transfer link as close to the calibration uncertainty as possible. However, we lack suitable equipment and higher precision time transfer technique to calibrate the optical fiber link. In lieu of analysis the optical fiber link uncertainty, we employed the comparisons between mobile two-way satellite time and frequency (TWSTFT) station link ($Link_{TW}$) and optical fiber link ($Link_{OF}$) to obtain some information. Because the $Link_{TW}$ and $Link_{OF}$ between the test field and NTSC compares the same pair of removes clocks, the double difference removes the clock difference, and reveals the combined relative change between the two links. Although it is impossible to tell the instabilities originate, the uncertainty of $Link_{OF}$ can be estimate. As the same, we use double difference to study the GPS CV traceability link ($Link_{GPS}$) uncertainty, because the precise of optical fiber time transfer is well above GPS CV time transfer.

In this paper we use the double difference technique to study the uncertainty in $Link_{GPS}$ and $Link_{OF}$ between the test field in Xi'an and the NTSC in Lintong. The time traceability link uncertainty analysis method shows in section 2. The uncertainty of $Link_{GPS}$ and $Link_{OF}$ shows in section 3. Section 4 summarize the study.

II. TRACEABILITY LINK UNCERTAINTY ANALYSIS METHOD

A. Time Traceability Data

The GPS CV technique currently is the best operational means for comparing remote time scales. For distances up to about 1000km, GPS CV time transfer can be realized with a precision and accuracy of about 2ns.The formula for calculation GPS CV time traceability data is as in (1).

$$T_{GPS} = T_A - T_B = T_A - (Link_{GPS} + T_{clock}) \quad (1)$$

Where T_{GPS} is GPS CV time traceability data and $Link_{GPS}$ is GPS CV time traceability link delay.

TWSTFT using spread-spectrum techniques is capable of 100ps precision, but requires transmit and receive satellite terminals at both stations, which must work together in pairs. The formula for calculation GPS CV time traceability data is as in (2).

$$T_{TW} = T_A - T_B = T_A - (Link_{TW} + T_{clock}) \quad (2)$$

Where T_{TW} is TWSTFT time traceability data and $Link_{TW}$ is TWSTFT time traceability link delay.

In recent years, we can observe rapid progress in the field of time and frequency transfer via optical fibers. Notable results have been already achieved even with relatively long optical links. Some of these projects are dealing with a high performance optical frequency transfer, which is typically used for comparing optical frequency standards. The formula for calculation optical fibers time traceability data is as in (3).

$$T_{OF} = T_A - T_B = T_A - (Link_{OF} + T_{clock}) \quad (3)$$

Where T_{OF} is optical fibers time traceability data and $Link_{OP}$ is optical fibers time traceability link delay.

The variations of local clocks and remove clocks are the same for the $Link_{TW}$, $Link_{GPS}$ and $Link_{OF}$ in the formulas. We have to remove them when we compute the time traceability link uncertainty by time traceability data. The double difference removes the clock difference and reveals the combined relative change between two links.

B. Double Difference Data and Uncertainty Analysis Method

We use the standard deviation(STD) to estimate the Type A uncertainty, the standard uncertainty calculated according to equation (4).

$$\sigma = \sqrt{\frac{1}{n}\sum_{i=1}^{n}(x_i - \bar{x}_i)^2} \quad (4)$$

Currently optical fibers time frequency transfer technique provides the best precision for comparing remote time scales under real environmental conditions. We lack suitable equipment and higher precision time transfer technique to calibrate the optical fiber link. In this paper, we employed the comparisons between mobile two-way satellite time and frequency (TWSTFT) station link ($Link_{TW}$) and optical fiber link ($Link_{OF}$) to obtain some information. As the same, we use double difference to study the GPS CV traceability link ($Link_{GPS}$) uncertainty.

The formula as in (5) can be used to obtain the double difference data between $Link_{TW}$ and $Link_{OF}$.

$$T_{OP} - T_{TW} = Link_{TW} - Link_{OP} \quad (5)$$

The double difference data between $Link_{OF}$ and $Link_{GPS}$ can be calculated by the equation (6).

$$T_{OP} - T_{GPS} = Link_{GPS} - Link_{OP} \quad (6)$$

The double difference data can be added into equation (4), we find the following equation of calculation the $Link_{OF}$ and $Link_{GPS}$ uncertainty.

$$\sigma_{OP} = \sqrt{\frac{1}{n}\sum_{i=1}^{n}\left[(Link_{TW} - Link_{OP}) - \overline{(Link_{TW} - Link_{OP})}\right]^2} \quad (7)$$

$$\sigma_{GPS} = \sqrt{\frac{1}{n}\sum_{i=1}^{n}\left[(Link_{GPS} - Link_{OP}) - \overline{(Link_{GPS} - Link_{OP})}\right]^2} \quad (8)$$

The Type B uncertainty of $Link_{OF}$ is associated with signal delay in both setups and the delay of the transmission link. Besides the Type B uncertainty of $Link_{GPS}$ among the delay of equipment or the delay of a time transfer link in both sites. The combined standard uncertainty of the estimate time transfer link is denoted by $u_c(L)$ and the formula is as in (9).

$$u_c(L) = \sqrt{u_a(L)^2 + u_b(L)^2} \quad (9)$$

III. UNCERTAINTY OF TIME TRACEABILITY LINKS

We use the double difference of $Link_{OF} - Link_{TW}$ to study the uncertainty in $Link_{OF}$, and $Link_{GPS}$ - $Link_{OF}$ to $Link_{GPS}$. The double difference data *mean* value and *RMS* value of both residual series were calculated. The formula for calculation is as in (10) and (11).

$$Mean = \frac{1}{n}\sum_{i=1}^{n}(L_A - L_B) \quad (10)$$

$$RMS = \sqrt{\frac{1}{n-1}\sum_{i=1}^{n}(L_A - L_B)^2} \quad (11)$$

A. Uncertainty in Optical Fiber Time Traceability Link

We present a direct comparison between UTC(NTSC) in Lintong and TFT in Xi'an by using the mobile TWSTFT station and optical fiber time transfer technique. Two different techniques were used to obtain the time traceability data at the same time. The reference signals for both $Link_{TW}$ and $Link_{OF}$ at Xi'an and Lintong are derived from UTC(NTSC) and TFT. Each of the hardware delay correction is available for comparisons. The double difference of the NTSC/TFT comparison covers the period of UTC from Jul 10, 2016 to Jul 17, 2016.

Figure 1 shows [UTC (NTSC) - TFT] via TWSTFT and via optical fiber measurements for a period of seven days after applying the corrections. The blue point for the computation of the difference between [UTC (NTSC) - TFT] obtained by two-way measurements and the red point obtained by optical fiber measurements, two methods data agree well with each other.

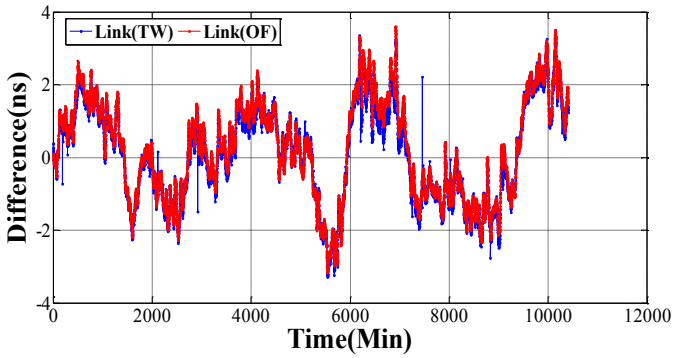


Fig. 1. Time difference of the TFT-UTC(NTSC) by using $Link_{OF}$ and $Link_{TW}$

The double difference of TWSTFT and optical fiber reflects the larger dispersion between the two method. Fig. 2 show double difference of TWSTFT and optical fiber comparison links.

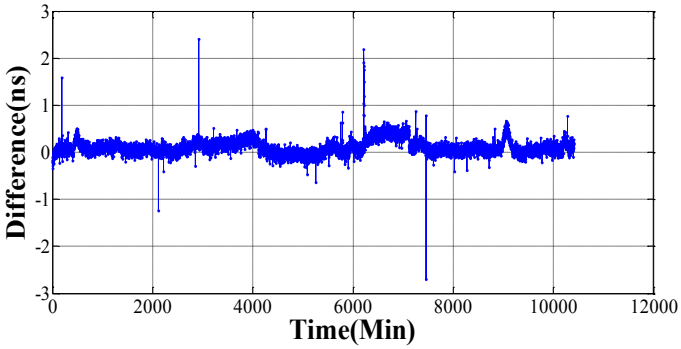


Fig. 2. Double difference of $Link_{OF}$ - $Link_{TW}$ for the TFT-UTC(NTSC)

Table 1 shows the double difference data period, mean value, RMS value and standard deviation. These results reflect the larger dispersion between TWSTFT and optical fiber time transfer, the performance of optical fiber time transfer method is better than these results.

TABLE I. OPTICAL FIBER RESULTS

Data period	*mean*	*RMS*	*STD*
Jul. 10th to Jul. 17th , 2016(UTC)	0.10ns	0.16ns	0.14ns

The Type B uncertainty of optical fiber time traceability link mainly comes from time delay device, signal receiver and transmitter error. In the test field, the Type B uncertainty of optical fiber time traceability link (u_B=0.10ns) estimate by the information of hardware parameter. Therefore the combined standard uncertainty of the optical fiber time transfer link in the test field calculate as follow:

$u_C = \sqrt{u_A^2 + u_B^2} = \sqrt{0.14^2+0.10^2}$=0.17ns , and it is better than 0.2ns.

B. *Uncertainty in GPS CV Time Traceability Link*

In this section, we analyze the $Link_{OF}$ and $Link_{GPS}$ double difference for comparisons of NTSC/TFT. The double difference of the NTSC/TFT comparison covers the period of UTC from Dec. 23, 2016 to Feb. 28, 2017.

Figure 3 shows [UTC (NTSC) - UTC (TFT)] via GPS CV and via optical fiber measurements for a period of three months after applying all the corrections. The blue point for the hourly averaged time difference between [UTC (NTSC) - TFT] obtained by GPS CV measurements and the red point obtained by optical fiber measurements. The optical fiber time difference data is more smoothly than the GPS CV time-transfer results. Although there is a system difference between GPS CV time traceability data and optical fiber time traceability data, two methods of time transfer results have the same change tendency.

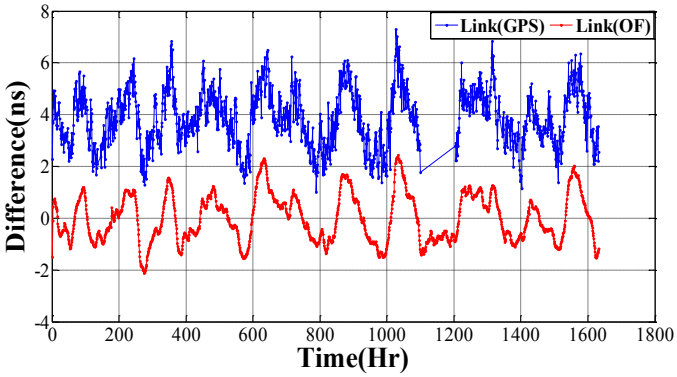


Fig. 3. Hourly averaged time difference of the TFT-UTC(NTSC) by using $Link_{OF}$ and $Link_{GPS}$.

The double difference data without systematic difference of GPS CV and optical fiber hourly averaged time traceability data is shown in figure 4. The precision of optical fiber time transfer technique is higher than the GPS CV time comparison, so the double difference data reflect the performance of GPS CV time comparison link.

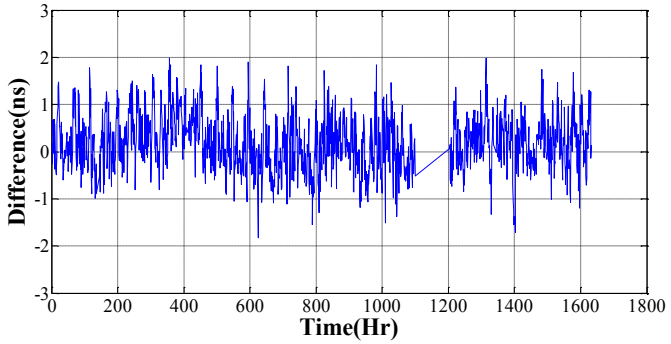


Fig. 4. Double difference of the hourly averaged $Link_{GPS}$ – $Link_{OF}$ for the TFT-UTC(NTSC).

Table 2 shows the data period, *mean* value, *RMS* value and standard deviation. The results reflect the performance of GPS CV time traceability link in this test field.

TABLE II. GPS CV RESULTS

Data period	*mean*	*RMS*	*STD*
Dec. 23th, 2016 to Feb. 28th,2017	0.21ns	1.42ns	1.39ns

The Type B uncertainty of GPS CV time traceability link mainly comes from receiver calibration, antenna coordinates, satellite ephemeris and ionosphere errors. In the test field, the Type B uncertainty of GPS CV time traceability link(u_B=2.24ns) obtained by delay calibration and related information. Therefore the combined standard uncertainty of the GPS CV time comparison link calculate as follow:

$u_C = \sqrt{u_A^2 + u_B^2} = \sqrt{1.39^2+2.24^2}$=2.64ns, and it is better than 3ns.

IV. CONCLUSIONS

In a test field of satellite navigation system, the system time is traceable to UTC(NTSC) by using two different time traceability links. The time traceability links were built base on the GPS common-view (GPS CV) comparison and optical fibers time transfer techniques, both techniques are utilized to compare the test field time (TFT) with UTC(NTSC). We obtained the same variations of time traceability data both GPS CV and optical fiber by analysis the time comparison principle. We used the double difference to remove the same changes and study the time traceability links uncertainty of GPS CV and optical fiber in the test field. Our results show that the uncertainty of GPS CV traceability link results is estimated as 3.0ns and optical fiber link is better than 0.2ns. The results can be used for the traceability links inter calibrated, abnormal detection and studying the two techniques fusion time traceability method.

REFERENCES

[1] S.C. Ebenhag, P.O. Hedekvist, P. Jarlemark, R. Emardson, K. Jaldehag, C. Rieck and P. Löthberg, "Measurements and Error Sources in Time Transfer Using Asynchronous Fiber Network", IEEE Trans. Instr. Meas., vol. 59, 2010, pp. 1918–1924.

[2] G. D. Rovera, J-M Torre, R. Sherwood, M. Abgrall, C. Courde, M. Laas-Bourez, and P. Uhrich, "Link Calibration against Receiver Calibration: an Assessment of GPS Time Transfer Uncertainty," Metrologia, Vol. 51, 2014, pp. 476-490.

[3] S.C. Ebenhag, C. Wingqvist and P.O. Hedekvist, "Real-time Phase Stable One-way Frequency Transfer over Optical Fiber", European Frequency and Time Forum (EFTF) , 2012, pp. 206–210.

[4] Z. Jiang and W. Lewandowski, "An Approach to the Uncertainty Estimation of [UTC − UTC(k)]," Proc. 2014 ION PTTI Meeting, 2014, pp. 7985.

[5] Piester D, Rost M, Fujieda M, Feldmann T and Bauch A 2011 Remote atomic clock synchronization via satellites and optical fibers Adv. Radio Sci. 9 1-7.

Global Time Synchronization Mechanism for Radio Interferometer Network

EH. Ait Mansour, B. Da Silva, S. Bosse
Electronics, Station de Radioastronomie de Nançay
Observatoire de Paris, OBSPM
Nançay, France
eaitmansour, Bruno.Da_Silva, stephane.bosse@obspm.fr

Karl-Ludwig Klein
Pôle de physique solaire, LESIA, Meudon
Observatoire de Paris, OBSPM
Nançay, France
ludwig.klein @obspm.fr

***Abstract*—In both wired and wireless networks, synchronization is an important service for a wide range of applications in distributed systems. This includes radio interferometry. However, literature researches show that many distributed protocols cannot satisfy sub-ns time synchronization accuracy due to asymmetric delay errors, accumulated jitters and because of the strategy used to adjust offsets. This paper proposes a global time synchronization algorithm in distributed networks. The algorithm allows us to minimize asymmetric delays with sub-ns accuracy better than 10ps and achieved global time synchronization. The theory of the algorithm used is presented and analyzed.**

Keywords—Time Synchronization; Algorithm; Asymmetric Delay; Adjustment; Sub-ns; Accuracy

I. INTRODUCTION

Time synchronization is a critical problem of infrastructure for any distributed networks including radio interferometer [1]. Many global time synchronization algorithms were developed previously, but few of them can reach sub-ns accuracy in the distributed networks [3, 4, 7]. Additionally, several system challenges limit the accuracy, such as asymmetric delays, long propagation delays, number of nodes and other sources of delay causes by measurement method. The main objective of this paper is to reach a sub-ns global time synchronization of a radio interferometer array as the Nançay Radioheliograph [2]. This work is presented in the following steps: Firstly, we propose an algorithm based on the computation of global delay offsets and the theory of how to adjust global time synchronization in a distributed network (section III.A). Secondly, we present iterative algorithm with generic implementation and compensate random asymmetric delays between master and slaves based on error estimation and minimization (section III.B). Finally, we test the algorithm using measurements from the previous work on a distributed network with cables of lengths up to 3.2km with asymmetric delays assumptions. The performance and limitations of the algorithm are discussed in section IV.

II. SYNCHRONIZATION PROTOCOLS AND LIMITATIONS

In distributed networks, physical clock drifts, temperature changing and measurements errors reduced synchronization accuracy [5]. Identically, networks topology affects slightly synchronization accuracy. However, mean errors increase rapidly with number of nodes [7]. The biggest source of offset and jitter errors in synchronization algorithm stems from random delays between master slaves [7]. Offset delays estimation accuracy is important issue in time synchronization system [3]. Most time synchronization protocols proved global time synchronization over Ethernet. They estimated and calibrated non deterministic sources delays, mean offsets and jitters estimation increased PTP accuracy to sub-us [3]. Using precision PHTER, PTP protocol achieved sub-ns with PPS [6].

III. FULL SYNCHRONIZATION ALGORITHM

A. Offset delays compensation

In this section we present the main contributions of this paper. We describe the proposed algorithm for global time synchronization based on the previous researches in distributed networks. Consider an interferometer array with N antennas ($1 \leq i \leq N$). Where each slave has round trip delay ($d^i_{MM} = d^i_{MS} + d^i_{SM}$). Consider two slaves (i, i+1). Here we make assumptions; we neglected asymmetric delays between master and slave. Additionally, d^i_{MM} delays are assumed different for each slave.

$$d^i_{MS} = d^i_{SM} \; ; \; d^i_{MM} \neq d^{i+1}_{MM} \qquad (1)$$

For global synchronization, it is necessary to set to zero time difference between each slave pair, the synchronization condition is: $\Delta T_{i,i+1} = 0$. The offsets compensation vector for N antennas is given in :

$$\begin{bmatrix} \delta_{x1} \\ \delta_{x2} \\ \dots \\ \delta_{x(N-1)} \end{bmatrix} = \begin{bmatrix} \Delta T_{1,2} \\ \Delta T_{3,4} \\ \dots \\ \Delta T_{N-1,N} \end{bmatrix} + \begin{bmatrix} \delta_{x2} \\ \delta_{x3} \\ \dots \\ \delta_{xN} \end{bmatrix} \qquad (2)$$

In the offset delays compensation process, we introduced $\frac{\delta_{xi}}{2}$ in the path of slave clocks. According to the assumption (symmetric delays), all clocks arrive simultaneously at the slave side ($\delta_{xi} + d^i_{MM} = \delta_{x(i+1)} + d^{i+1}_{MM}, \; 1 \leq i \leq N$).

B. Asymmetric delay error minimisation

In this section we present an iterative algorithm to compute offsets vector (δ_{xi}). This algorithm enables us to reach global time synchronization in distributed networks. Here we make assumptions; we considered asymmetric delays between master and slave.

$$d^i_{MS} \neq d^i_{SM} \; ; \; d^i_{MM} \neq d^{i+1}_{MM} \qquad (3)$$

Let μ and *Min* are the adjustable algorithm parameters. Let *Min* define synchronization accuracy and μ define algorithm step-size. Values of the two factors affect directly the convergence or divergence and synchronization period (T_{Sync})

to achieve the required accuracy (time convergence). For each iteration, the proposed algorithm estimate global mean error for all slaves after offsets calibration (μ_e) in (4). This error due to asymmetric delays between master and slaves. When required accuracy is not reached, algorithm updates d_{MM}^i according to (4).

$$\begin{cases} \mu_e = \frac{1}{N}\sum_{i=1}^{N}(d_{MS}^{A(i)} - d_{MS}^i) \\ d_{MM}^{i+1} = d_{MM}^i - sign(\mu_e) * \mu * d_{SM}^{A(i)} \end{cases} \quad (4)$$

IV. RESULTS AND DISCUSSIONS

In this section we proceed to evaluate the performance of proposed algorithm and limitations in radio interferometer array. Algorithm delay parameters had chosen according the [8]. Consider an interferometer network with N antennas sketched in star topology. The 1550ns and 1390ns fiber optics link used between master and slave. Let L^i be length of fiber link between master and slave (i). The linear approximation for average can be presented in (5). Let e_{Ad}^i define asymmetric delay error after offsets adjustment between master and slave ($e_{Ad}^i = d_{MS}^i - d_{SM}^i$). Assumed $mean(e_{Ad}^i)(\text{ns}) = -7.8 * 10^{-5} * L^i$). Consider random jitter due to repeatability of master to slave delay measurement with 50ps and 30ps of standard deviation (Tab. 2 in [8]). Then global error is sum of jitter error and asymmetric delay error. Assumed the linear approximation for link delay (d_{MS}^i) can be presented in (5).

$$\begin{cases} \text{Average(ns)}^i \approx -7.8 * 10^{-5} * L^i + 16 \\ d_{MS}^i\ (ns) \approx 9.8 * L^i + 470 \end{cases} \quad (5)$$

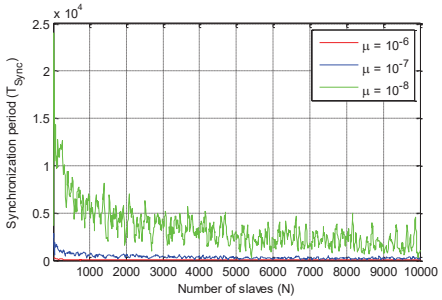


Fig. 1. Synchronization period (T_{Sync}) vs. number of slaves (N) for different values of algorithm parameter μ.

Quite surprisingly, the synchronization period (T_{Sync}) decreased rapidly with increasing number of slaves (Fig. 1). This may be introduced by the varying length of the error estimation vector (N) (Fig. 1). The bigger N, the better is the mean error estimation. This means that the time synchronization period is minimal in widely distributed arrays. After simulations analysis, algorithm accuracy μ_e it can be presented as follows: $\mu_e \approx \mu_0 \pm \frac{e_{pp}}{2}$, $e_{pp} = \mu_0$. The proposed algorithm may achieve a required accuracy *Min.* It depends on step-size parameter μ and number of slaves N (Tab. 1). However, in order to obtain algorithm convergence, *Min* have to be chosen great than $|\mu_e|$. According to these results, we concluded that we may control global algorithm accuracy by adjusting the parameters *Min* and μ. The above evaluation shows that global time synchronization can affectively achieved with sub-ns accuracy in distributed networks. The proposed algorithm can compensate offset asymmetric delays with adjustable accuracy bellow 10ps. Our algorithm performed better then [8, 6]. Therefore, accuracy may reduce in real hardware implementation.

TABLE I. OFFSET MEAN ERROR $\mu_0(ps)$ AFTER CALIBRATION VERSUS NUMBER OF SLAVES N

u	$\mu_0(N = 10)$	$\mu_0(N = 10^2)$	$\mu_0(N = 10^3)$
10^{-3}	14.11	79.74	98.64
10^{-5}	1.17	1.15	0.65
10^{-7}	$1.112*10^{-2}$	$1.19*10^{-2}$	$1.01*10^{-3}$

V. CONCLUSIONS AND FUTURE WORK

Overall, in this paper we suggested global time synchronization algorithm in distributed network such as a radio interferometer array with sub-ns accuracy. The main result of this research is an iterative algorithm for asymmetric offset delays error compensation and minimization. We illustrate that the synchronization period and accuracy can be controlled with algorithm parameters. The proposed algorithm can achieved accuracy better than 10ps. Besides, algorithm hardware implementation may be possible and computational complexity is reduced comparing with algorithms developed previously. Master Hardware architecture for global time synchronization algorithm implementation and testing in radio interferometer networks of 4 slaves is ongoing. This board is based on quad channel time measurement device TDC (THS788) with 8ps accuracy and 13ps of jitter, and programmable delay chips DTC (MC100EP195FAG) for offsets delay adjustment with 10ps accuracy. Finally, Virtex-6 FPGA board (ML605) will be used for offset delays computation and adjustment.

ACKNOWLEDGMENT

The authors would like to thank Exploration Spatiale des Environnements Plantaires (ESEP), for thesis funding.

REFERENCES

[1] A. T. Sutinjo, T. M. Colegate, R. B. Wayth, "Characterization of a Low-Frequency Radio Astronomy Prototype Array in Western Australia," IEEE Transactions on Antennas and Propagation, Oct 2015.

[2] K.-L. Klein, A. Kerdraon, "Solar Physics at Nanc¸ay Radio Observatory: Recent Developments," IEEE General Assembly and Scientific Symposium, 2011.

[3] I. Freire, I. Sousa, A. Klautau, " Analysis and Evaluation of Endto- End PTP Synchronization for Ethernet-based Fronthaul," Dec. 2016 Global Communications Conference (GLOBECOM), 2016 IEEE.

[4] A. Mahmood, R. Exel, T. Sauter, "Delay and Jitter Characterizationfor Software-Based Clock Synchronization Over WLAN Using PTP," IEEE Trans. Industrial Informatics 10 (2): 1198-1206, 2014.

[5] A. Elsts , S. Duquennoy, "Microsecond Accuracy Time Synchronization Using the IEEE 802.15.4 TSCH Protocol," Local Computer Networks Workshops (LCN Workshops), 2016 IEEE 41st Conference on, 2016. 7-10 Nov. 2016.

[6] Texas Instrument, "AN-1728 IEEE 1588 Precision Time Protocol Time Synchronization Performance," Application Report , April 2013.

[7] K. S. Lee, H. Wang, V. Shrivastav, H. Weatherspoon, "Globally Synchronized Time via Datacenter Networks," SIGCOMM, Florianopolis, Brazil, August 2016.

[8] G. Gong, S. Chen, Q. Du, J. Li, Y. Liu, "Sub-nanosecond Timing System Design and Development for LHAASO Project," ICALEPCS2011, Grenoble, France, October 2011

Fractional Brownian Motion and its Application in the Simulation of Noise in Atomic Clocks

Attila Kinali,*
*Max Planck Institute for Informatics, Saarland Informatics Campus, Germany

***Abstract*—Proper generation of power law ($1/f^\alpha$) noise for the simulation of atomic clocks has been a topic of research for a long time. Yet one important class of algorithms, namely fractional Brownian motion, has seen very little attention in the time and frequency control community. We aim here to review the current state of research in fractional Brownian motion, how it can be applied to atomic clocks and where there are open problems.**

I. Introduction

The simulation of power law noise ($1/f^\alpha$) has been a topic for a long time. Generally speaking, there are three categories of generation algorithms:

(1) Using Gaussian white noise source, transforming the signal into the frequency space using the Fast-Fourier-Transform (FFT) and filtering in frequency space, and finally using the inverse-FFT to transform the signal back [1].
(2) Filtering a Gaussian white noise source using a chain of linear filters [2].
(3) Using a Levy process and generating the samples directly [3].

When looking at stochastic clock models, like in Tavella [4] there is an obvious fourth choice: integrating the signal of a Gaussian white noise source. Unfortunately, this process is only able to generate $1/f^\alpha$ noise with even exponents α, as an integration step causes the power spectral density to be multiplied by $1/f^2$.

To gain access to smaller steps of α fractional integration would be required. This class of noise is called fractional Brownian motion or fractional Gaussian noise, and offers a broad class of algorithms to efficiently generate noise as well as rich mathematics for analysis. Even though the use of fractional integration to generate noise for simulation of atomic clock has been proposed by Barnes and Allan [5] in 1966, to the best knowledge of the author this has not been used in the context of atomic clocks ever since.

II. Fractional Brownian Motion

A. Barnes and Allan's Noise Model

Barnes and Allan have analyzed in [5] flicker noise and came to a few important conclusions:

- Integration of noise cannot guarantee that the resulting noise is stationary. In general, Gaussian noise with a PSD of $1/f^\alpha$ with $\alpha \geq 1$ is not stationary anymore.
- Integration of noise multiplies the PSD by $1/f^2$
- To achieve PSDs with steps smaller than $\alpha = 2m$ one must apply fractional integration.

An intuitive fractional integral of a Bownian motion process $B(t)$ to achieve $1/f$-noise was defined by Barnes and Allan [5]:

$$B_\lambda(t,\omega) = \frac{1}{\Gamma(\lambda)} \int_0^t (t-u)^{\lambda-1} \,\mathrm{d}B(u,\omega)$$

This is the application of the Rieman-Liouville integral, based on Cauchy's formula for repeated integration. With $\lambda > 0$ being the integration factor. Using a $\lambda = \frac{1}{2}$ the integral will generate $1/f$-noise with Gaussian distribution. Please note that one cannot directly integrate over Gaussian noise as Barnes and Allan did in [5] as Gaussian noise is not continuous. Instead one has to use a Brownian motion process and use it to create continuous increments (c.f. [6]).

B. Mandelbrot and van Ness' Model

One problem of the above equation is, that it is not time-translation invariant and thus not stationary. Mandelbrot and van Ness reformulated in [7] the process as:

$$\begin{aligned} B_H(t,\omega) =& \frac{1}{\Gamma(H+\frac{1}{2})} \int_0^t (t-u)^{H-\frac{1}{2}} \,\mathrm{d}B(u,\omega) \\ &+ \int_{-\infty}^0 \left((t-u)^{H-\frac{1}{2}} - (-u)^{H-\frac{1}{2}} \right) \mathrm{d}B(u,\omega) \end{aligned}$$

with $H = \lambda + \frac{1}{2}$ being the Hurst exponent. To the best knowledge of the author, all mathematical treatments deal with $0 < H < 1$, because for $H \geq 0$ the fractional Brownian Motion is mean square continuous and for $H < 1$, the fractional Brownian Motion has stationary increments ([7, Proposition 3.7]). Additionally, the explicit formula for the covariance function as given by Mandelbrot and van Ness ([7])

$$\begin{aligned} \rho(s,t) &= \mathbb{E}\left[B_H(s) B_H(t)\right] \\ &= \frac{1}{2}\left(t^{2H} + s^{2H} + (t-s)^{2H} \right) \end{aligned}$$

breaks down for $H \notin (0,1)$. Due to B_H with $0 < H < 1$ having nice mathematical properties, the other class of fractional Brownian motion outside this range is not being studied. Unfortunately, this restriction to $H > 0$ excludes the important $1/f$-noise.

C. Simulation of Fractional Brownian Motion

The evaluation of the integrals for fractional Brownian motion is computationally intensive and scales with $\mathrm{O}(n)$, n being the number of samples generated. There exist a few algorithms with a lower time complexity and Dieker

978-1-5386-2916-1/$31.00 ©2017 IEEE

gives a short overview of the available algorithms and their characteristics in [8]. Most of these are based on having an explicit formula for the covariance function. As we have seen above, for fractional Brownian motion, the covariance function is only defined for $0 < H < 1$, and thus excludes $\frac{1}{f}$-noise. As such, it is not clear how to efficiently simulate the whole range of noises seen in atomic clocks using fractional Brownian motion.

III. Open Questions

A. Physical Meaning

Noise in atomic clocks are usually analyzed using the Allan deviation and its variants or using the power spectral density. While the Allan deviation family has been invented to analyze $1/f^{\alpha}$-noises, they are not suited to distinquish different kind of influences, especially differentiating between systematic and stochastic components is difficult at best. Simlilarly, the PSD cannot distinguish between e.g. true white noise and a signal whose PSD just happens to be white, but has a fixed phase relation between frequencies.

Thus, the existence of different mathematical describtions of frational Brownian motion raise the question of what the differences between those mean for a physical system and what kind of mathematical model describes the noise seen in physical systems best.

B. Mathematical Description of Fractional Brownian Motion with $H \notin (0, 1)$

While the mathematical description breaks down for $H \notin (0, 1)$ it is easy to extend the description beyond $H = 1$ by (integer) integration of fractional Brownian motion. The cases of $H = 1$ and $H \leq 0$ remain an open problem though. Although (integer) differentiation readily leads to noises with $H < 0$, the numerical accuracy of this method needs to be evaluated. Using fractional integration or fractional differentiation would also fill the gabs of $H = 0$ and $H = 1$, but has the aformentioned drawback of large computational complexity and numerical instability.

C. Efficient Simulation Algorithms for $H \notin (0, 1)$

With the lack of mathematical description of fractional Brownian motion for $H \notin (0, 1)$ it is also difficult to come up with fast simulation algorithms. Especially such, that operate incrementatlly and allow the change of the noise parameters over time, as seen in real atomic clocks.

References

[1] N. J. Kasdin and T. Walter, "Discrete simulation of power law noise [for oscillator stability evaluation]," in *Proceedings of the 1992 IEEE Frequency Control Symposium*, May 1992, pp. 274–283.

[2] J. Park, K. Muhammad, and K. Roy, "Efficient modeling of $1/f^{\alpha}$ noise using multirate process," *IEEE Transactions on Computer-Aided Design of Integrated Circuits and Systems*, vol. 25, no. 7, pp. 1247–1256, July 2006.

[3] E. Milotti, "Exact numerical simulation of power-law noises," *Phys. Rev. E*, vol. 72, p. 056701, Nov 2005. [Online]. Available: http://link.aps.org/doi/10.1103/PhysRevE.72.056701

[4] L. Galleani, L. Sacerdote, P. Tavella, and C. Zucca, "A mathematical model for the atomic clock error," *Metrologia*, vol. 40, no. 3, p. S257, 2003. [Online]. Available: http://stacks.iop.org/0026-1394/40/i=3/a=305

[5] J. A. Barnes and D. W. Allan, "A statistical model of flicker noise," *Proceedings of the IEEE*, vol. 54, no. 2, pp. 176–178, Feb 1966.

[6] F. Biagini, Y. Hu, B. Oksendal, and T. Zang, *Stochastic Calculus for Fractional Brownian Motion and Applications*. Springer, 2008.

[7] B. B. Mandelbrot and J. W. V. Ness, "Fractional brownian motions, fractional noises and applications," *SIAM Review*, vol. 10, no. 4, pp. 422–437, 1968. [Online]. Available: http://dx.doi.org/10.1137/1010093

[8] T. Dieker, "Simulation of fractional Brownian motion, revised version," Master's thesis, University of Twente, the Netherlands, 2004.

White-Rabbit-enabled Data Acquisition System

José López-Jiménez, Miguel Jiménez-López, Javier Díaz
University of Granada
Granada, Spain
{joselj, klyone, jda}@ugr.es

José Luis Gutiérrez-Rivas
Seven Solutions
Granada, Spain
jlgutierrez@sevensols.com

***Abstract*— This work examines the feasibility of using Ethernet-based time transfer methods based on White Rabbit technology to discipline all the clock domains of a networked data acquisition system (DAQ). Existing systems provide synchronization capabilities, albeit the performance achieved is often not accurate enough for scientific infrastructures and Smart Grid applications requiring frequency coherent and simultaneous trigger of ADC devices across the facility. White Rabbit networks are known for their sub-nanosecond accuracy attained with fiber-optic Ethernet links. By integrating a data acquisition solution into White Rabbit nodes and distributing over long distances, we show that it is possible to tag the acquired data in a deterministic manner similarly to what is done in a local DAQ. This result can be the first step towards a multi-device, remotely operated synchronized data acquisition system for the aforementioned fields of application being capable of building distributed DAQ systems scattered across tens of kilometers with an accuracy equivalent to that of a locally deployed DAQ.**

Keywords—White Rabbit; data acquisition; daq; time synchronization; adc

I. INTRODUCTION

During the recent years, there has been a boost in the performance of synchronization networks. This is due to increasing demands from fields such as next-generation communication networks (5G) [4], energy generation and distribution (Smart grid and particularly their Wide-Area Measurements Systems or WAMS) [1][2],[3] and a variety of scientific infrastructures like CERN, CTA or SKA [20][22][23]. All these fields share the necessity to keep distant data acquisition equipment synchronized in order to operate properly, requiring the same sampling frequency and also the same trigger signals to properly operate. All these data acquisition systems (or DAQs) are only possible by means of providing a synchronization mechanism that allows to capture data simultaneously on different locations of the infrastructure [5]. To this day, there are proposed solutions that provide the network architecture needed for a distributed data acquisition system, although they fall short of providing accurately phase-aligned timing along the whole system [24]. The White Rabbit (WR) project provides the possibility of deploying a Gigabit Ethernet fiber network expanding along kilometers and keeping sub-nanosecond accuracy for time and frequency dissemination [9].

Time synchronization and accuracy is an essential requirement in data acquisition. It is clear to see that all the data generated along the system must share a common time reference so that the succession of events captured can be recovered and chronologically sorted.

One fundamental part of data acquisition systems are analog-to-digital converters (ADC). Due to the need of precisely matching components, these are usually implemented as integrated circuits that quantize analog electrical inputs sampled in regular periods as dictated by an oscillator that, in a distributed system, is highly challenging to disseminate across the different locations.

In this paper we make use of WR network equipment and an open hardware data acquisition FMC (FPGA Mezzanine Card) ADC (FMC-ADC-100m14b4cha) to develop an instrument capable of capturing reliably time-tagged data in any facility that provides a WR-capable link and distribute the system over tens of Km with minimum penalty of the DAQ system performance.

Next section II introduces the WR technology and its properties. Section III focuses on the development of the data acquisition system developed by the authors in terms of hardware, gateware and software. Finally, sections IV and V present the results and conclusions of the evaluation of this system in three different scenarios.

II. THE WHITE RABBIT TECHNOLOGY

The White Rabbit project [11] was initiated by the European Organization for Nuclear Research (CERN) [20], GSI Helmholtz Centre for Heavy Ion Research [21] and several private companies as a collaboration aiming to achieve synchronization accuracy better than one nanosecond and precision of tens of picoseconds over a fiber-optic Ethernet network that can span thousands of nodes and links of up to 10 km each. Its development is open for both hardware and software components.

A White Rabbit network is generally implemented as a hierarchical structure in which every link is seen as a master-slave pair. The nodes use two-step message exchange to send its current time to the slave.

WR performance is achieved as a combination of three technologies spread along several layers of the OSI reference model:

978-1-5386-2916-1/$31.00 ©2017 IEEE

- Synchronous Ethernet (Sync-E) [7]. The master encodes its clock in the Ethernet line and the slave can recover it and create its own phase-aligned copy. This means that all WR-capable devices share the same physical clock domain in the entire network.
- WR-PTP message exchange. In standard Precise Time Protocol (PTP) [8], master and slave exchange messages containing timestamps of departure and arrival of previous frames. An estimation of the link delay can be made assuming the two one-way delays are identical. WR implements an extension for PTP that accounts for compensation of asymmetries in the link, provides granularity and serves as Sync-E signaling. The software project supporting this, PPSi, is open source and supports several architectures [9].
- Digital Dual Mixed Time Difference, implemented as a FPGA module, measures the phase difference between the master clock and the slave clock. The phase measurement is used as feedback to fine-tune the slave clock frequency and phase.

III. IMPLEMENTATION

In order to develop our DAQ, we use ADC sampling cards synchronized by WR and commanded using a simple API to trigger the acquisition and operation. For this purpose, the FMC-ADC-100m14b4cha project [12] hosted at the Open Hardware Repository has been chosen as the starting point of this work. It provides a stable working design in which a FPGA Mezzanine Card analog-to-digital converter (FMC ADC) card is inserted into a SPEC board. The SPEC is a PCI board that acts as both a carrier for a FMC card and a node that provides WR capabilities.

However, the SPEC FMC ADC samples data using a free running clock. As a consequence, the acquired data is not accurately time-tagged since there is always an unknown drift between the sampling clock and the WR one. Even if the epoch was corrected every time an acquisition is launched, the error between the acquisition start and the acquisition end is not negligible. In addition, the SPEC card needs to be hosted in a GNU/Linux-running full-size PC [10].

Our design aims to solve both of these problems by integrating the FMC design into the WR clock domain, thus sharing the same sampling clock among potentially a large amount of FMC ADC cards in distant locations. The proposed design also has the advantage of being implemented in a new development board that features an embedded GNU/Linux system. Its components are introduced in the lines below.

A. Hardware elements

The hardware concerning this development is based on three elements: a FMC ADC card to convert the analog input signals into digital samples, a Zynq-based development board and the WR switch that provides a common time reference.

1) FMC-ADC 100m14b4cha

The mezzanine card used for this work supports up to 4 input analog channels and an additional one as an external trigger source. The ADC chip used is a Linear Technologies LTC2174-14, with serial LVDS output and 14-bit resolution. This card design and its related software and HDL code are published under open licenses [10].

There is a slight modification to the FMC ADC hardware card from its original configuration to feed the ADC chip with a clock routed from the White Rabbit Core via a differential pair going through the FMC socket. For the sake of simplicity, the sampling rate has been reduced to 62.5 MHz which is the highest rate supported by the ADC chip that is also derived from directly dividing the 125 MHz clock.

2) Development board

The selected development board WR-ZEN [13] is a standalone WR node that features a Xilinx Zynq-7015 SoC. This chip includes a 7-series Artix FPGA plus a dual-core ARM CPU. The CPU runs Linux 3.19. The board also contains a FMC high pin count (HPC) socket that eases the process of carrying the WR clock to the ADC chip. Regarding high performance I/O, the Zynq provides two GTX transceivers which are used for each of the two fiber-optic Gigabit Ethernet ports of the board

3) WR Switch

White Rabbit switches are devices that provide accurate timing to other devices through its 18 Ethernet ports. It can act as a grandmaster device or as a slave/master in a per port basis. It features a Virtex-6 FPGA and an ARM CPU running GNU/Linux. In this work, it is only involved as the primary timing source for all the WR-ZEN ADC cards deployed across the network.

B. FPGA Gateware

The FPGA gateware (VHDL code) is comprised of two main IP cores: the White Rabbit PTP Core and the FMC ADC one. The FPGA components are interconnected using Wishbone buses [14], but there is the need to introduce Wishbone-AXI bridges to communicate with the CPU. Fig. 1 presents the general modular view of the system.

While the White Rabbit PTP Core is used without significant adaptations, there are some relevant modifications that have been made to the components of the original FMC ADC core [10].

One of the fundamental modules of the FMC ADC core is the time tagging core. This is responsible for assigning a timestamp to events such as the start and the end of an acquisition and the sample in which the trigger condition is met. The time tagging module has been modified with the result that the time counters are now controlled inside the WR clock domain.

Also, originally raw data coming from the FMC card, after being deserialized, was written into a dedicated DDR3 memory that featured its own Spartan 6 memory controller. This is no longer the case since the WR-ZEN has a single RAM chip that is essential for the operation of the OS. The memory in the board is divided into two equal parts: the lower half of the memory is dedicated for the OS, while the upper half is reserved as a bare metal memory that accommodates the 4 Gbit/s data stream generated by the ADC card.

In term of resources utilization, the implemented design reports by Xilinx Vivado 2015.4.2 show that the design requires

less than one third of the available resources for look-up tables (LUT) and flip-flops (FF). In contrast, due to the high rate data generation of the ADC chip, a very high proportion of the block RAM (BRAM) present in the device are allocated for buffering purposes. Table I. shows the summary of this report as stated by the Vivado design suite for the chosen SoC (xc7z015clg485-1).

TABLE I. FPGA RESOURCE UTILIZATION

Resource	Utilization	Available	Util. %
LUT	15679	46200	33.94
LUTRAM	268	14400	1.86
FF	15129	92400	16.37
BRAM	80	95	84.21
DSP	7	160	4.38
IO	115	150	76.67
GT	2	4	50
BUFG	7	32	21.88
MMCM	2	3	66.67

C. *Software*

The modifications made to the software part are centered on the driver side. Nonetheless, part of the development has been dedicated to the creation of a web-based tool and minor modifications to the acquisition software.

On the driver side, there are five Linux kernel modules that are briefly described in the following lines:

- FMC bus driver: it is a generic FMC bus driver that allows registering different FMC devices in the system. It was developed by the OHWR community and it is used without any important modifications.
- ZIO bus driver: this is a generic I/O bus driver that allows reading/writing information from different devices in the system via sysfs in a faster and optimal way. It was developed by the OHWR community, too, and it is used without any important modifications.
- ZEN driver: it is the main module for the WR-ZEN board. It is responsible for the FPGA accesses in order to perform initialization and configuration tasks. Moreover, it also takes care of the interrupt management.
- FMC ADC driver: based on SPEC FMC ADC module from OHWR, its main goal is to retrieve all data from the input channels of the FMC ADC board and save it in the system RAM memory. During normal operation of the ADC, while a capture has been started but the trigger has not yet been shot, the raw data stream from all four channels is written to a reserved region of th RAM as a buffer, preventing Linux from using it. This stream needs to store a huge amount of data in a very short time period (4 gigabit per second) and therefore the system must include a DMA controller to guarantee a high bandwidth in data transfers. The FMC ADC driver uses the DMAengine layer of the Linux kernel to configure the embedded PL330 DMA controller inside the Zynq device in order to transfer data from the FMC ADC input channels to the RAM buffer.
- PL330 DMA driver: it manages the PL330 DMA controller and exports the DMAengine function set to ease the interaction between different kernel modules. It is part of the Linux kernel source but some minor modifications were needed to fix the scatter-gather mechanism and work properly along the rest of the system.

In addition to the drivers, some user-space tools are provided to get data from the FMC ADC card. These use the system call through the filesystem to call kernel functions. Thanks to the ZIO support of the FMC ADC driver, the user-space tools only have to read/write some files from the sysfs filesystem to get all the information and the data from the kernel.

Again in the userspace side, a web-based acquisition manager has been implemented in PHP running on a Lighttpd web server [17] in order to monitor and control the acquisition of data remotely.

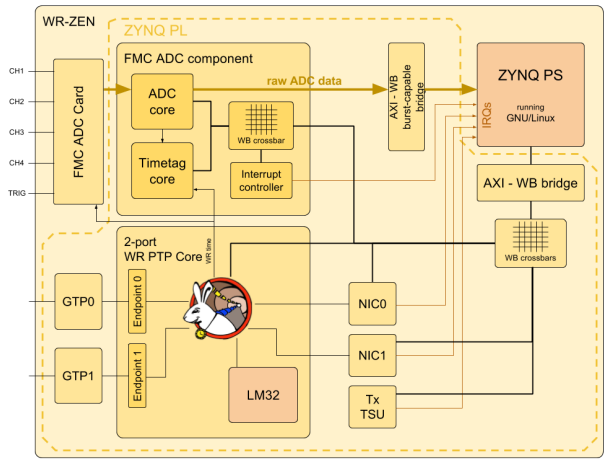


Fig. 1. Project design overview. The diagram emphasizes the relevance of the two most important components in the FPGA logic: the WR PTP core provides precise timing and acts as a the network equipment termination for the fiber-optic ports. The FMC ADC compoment acquires the raw data and places it in a region of the RAM memory via a bridge. The CPU governs all the FPGA modules through the Wishbone bus structure.

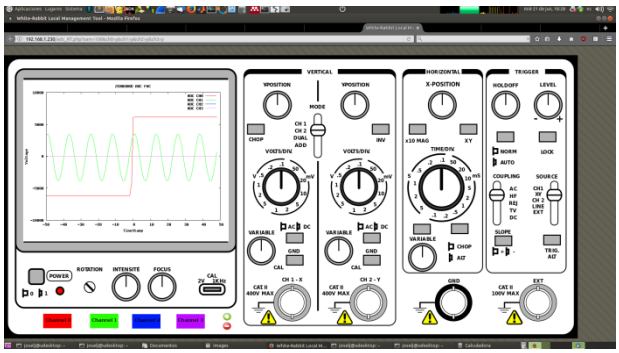


Fig. 2. Remote data acquisition manager screenshot. Developed in PHP and running on a Lighttpd web server, it eases monitoring the data acquisition from the four analog inputs of the ADC FMC card remotely.

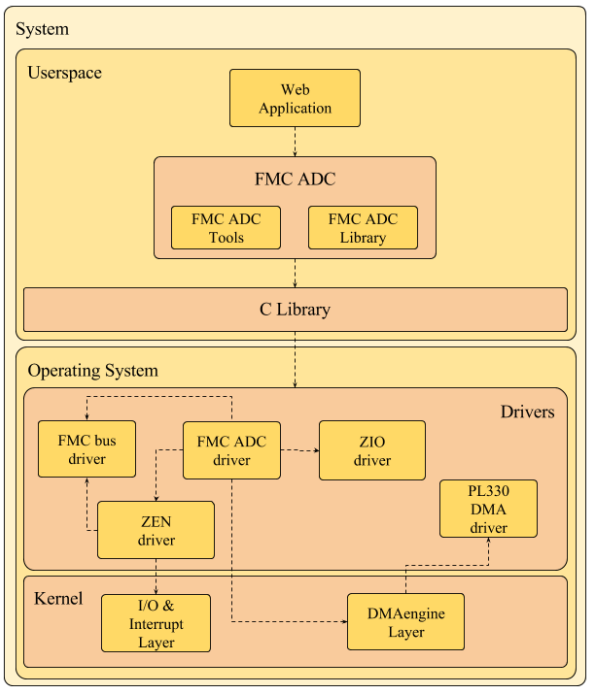


Fig. 3. Software overview. This picture shows all the software components that act in the current design. In the top half of the picture, the user-space side, there is a web application that displays the FMC ADC captured data. To retrieve all the information, the web application uses tools known as FMC ADC tools. They are implemented in C code, allows to get the raw data from different input channels. In the bottom half of the picture, the kernel side is introduced. It includes several Linux drivers that govern the control of the WR-ZEN and the FMC ADC boards. These modules expose a public API through the filesystem of the kernel allowing the user-space applications to call different driver functions. The FMC and ZIO bus drivers do not depend on other modules but they are needed by the ZEN and FMC ADC ones (see the arrows in the picture). The FMC ADC driver needs to configure the PL330 DMA kernel module and it is performed via the DMAengine layer. It isolates from the specific implementation of the DMA and allows to re-use the current code with other DMA controller without performing notable changes.

IV. Methods and Results

In order to test the performance of the new design, three experiments have been carried out in which different levels of synchronization can be compared and characterized. In the first of them, two WR-ZEN hosting FMC ADC cards are synchronized using industry standard PTP. For the second experiment the two WR-ZEN are connected to a White Rabbit switch that provides a common clock and time reference. The third experiment shows the drift that the free running ADC cards endure when frequency adjustments are no longer applied.

The performance of the synchronization is evaluated by comparing the difference between the timestamps in which the trigger is shot in both WR-ZEN ADCs and how this metric evolves with time. It is considered that the trigger is shot when a rising edge is detected and voltage crosses 0 V.

All three experiments share most of the material, which is summarized in the following list:

- 2x WR-ZEN boards,
- 2x FMC-ADC 100m14b4ch cards,
- 1x White Rabbit Switch,
- 1x General purpose Ethernet switch,
- 1x General purpose PC as a PTP master,
- 1x Iso-tech AFG-21225 function generator,
- 1x BNC T-adapter splitter,
- 2x BNC-LEMO adapters,
- 2x LEMO cables, same length,
- 1x 5 km optical fiber reel,
- SFPs, auxiliary Ethernet cables and optical fibers.

A. *PTP synchronization*

The first experiment is set up to show the performance that can be achieved synchronizing both WR-ZEN FMC ADC using general purpose network equipment. The detailed arrangement can be found in Fig. 4. In it, one of the channels of the function generator is used to distribute a 2.5-pulse per second (PPS) 10-Vpp pulse train to both FMC ADC cards via a BNC splitter and two cables of the same length. The synchronization source for this setup is a general purpose PC running an implementation of PTP (*ptp4l*, [19]) as a master. PTP timestamps are generated in software on the PC side.

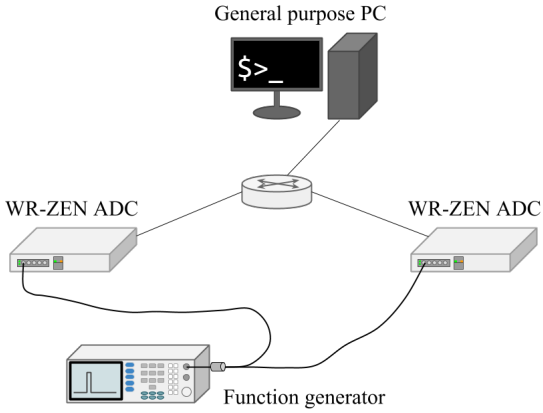


Fig. 4. PTP synchronization setup. Two WR-ZENs are synchronized to a PTPv2 general purpose PC using software timestamps. An arbitrary function generator distributes a 2.5-PPS signal to both FMC ADC cards.

For this scenario, a period of 320 seconds of the taken measurements is shown in Fig. 5 and the results are summarized in table II. Along the 5-minute sampling period, the 800 corresponding pulses have been tagged with an average measured error of 98 microseconds. This value is higher than a typical LAN setup of PTP, but it can be explained considering that the master PTP PC of the setup is not dedicated exclusively for that purpose, and an unknown amount of other running processes can be acting as sources of jitter in the form of a high CPU load.

Please note that in this setup the sampling clocks are not locked to any common reference. As a result, even though the clock offset is corrected once per second, the real frequency of

TABLE II. PTPV2 (SOFTWARE IMPLEMENTATION) SYNCHRONIZATION SUMMARY

Number of samples (N)	800
Average error	98 µs
Standard deviation	38 µs

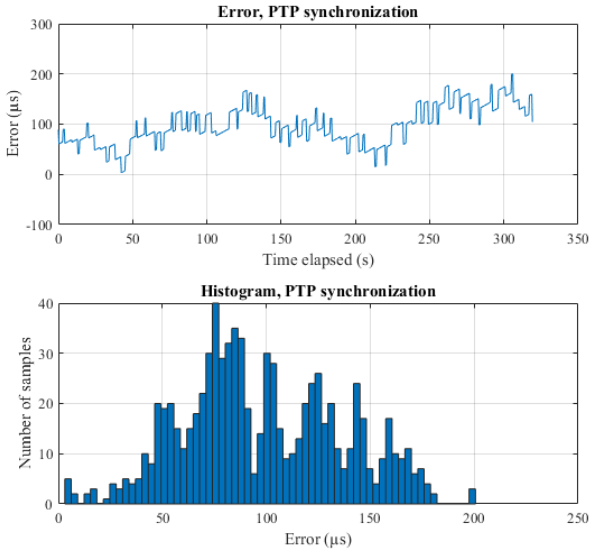


Fig. 5. Difference between the trigger timestamps measured in both WR-ZEN ADCs and histogram representation of the same magnitude.

the oscillators is not changed and therefore drift is never compensated.

B. White Rabbit synchronization

This test reveals the capabilities of the White-Rabbit-enabled ADC card by having a lab setup in which we simulate having two remote WR-ZEN ADC cards capturing the same physical signal. A schematic view is seen in Fig. 6. A White Rabbit Switch provides precise synchronization to both WR-ZEN. One of the WR-ZENs is connected to the switch via a short (i.e. 2 meter) fiber, while the second one is connected to the switch via a 5 km optical fiber reel. Please note that this added length of fiber equals to over 24 microseconds of asymmetry in the link compared to the closer WR-ZEN.

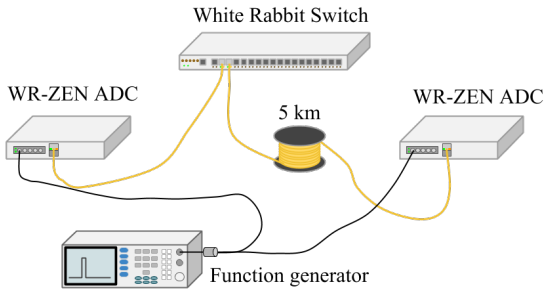


Fig. 6. White Rabbit synchronization setup. Both WR-ZENs are connected to a WR switch with different fiber lengths using WR to synchronize their clocks. An arbitrary function gnerator distributes a 2.5-PPS signal to both FMC ADC cards.

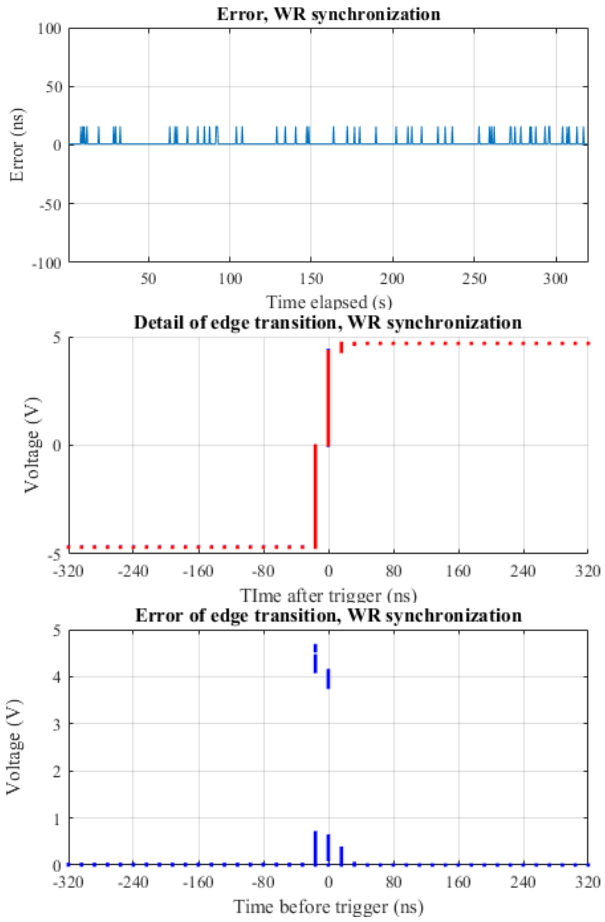


Fig. 7. WR synchronization results. The first graph shows the difference between the trigger timstamps measured in both WR-ZEN ADCs, bound between 0 and 16 ns. The second graph shows a detailed view of the rising edge of all 800 pulses captured in the two WR-ZEN ADCs in the setup for this experiment, in red for the "close" one and blue for the remote one. Note that the equal results for both cards make it difficult to tell the two data series. The third graph shows the voltage measured error for every sample of the captured 800 pulses. Note that when capturing a 10 Vpp signal, a voltage error below 5 Vpp cannot guarantee that a trigger event has taken place.

In the same manner as the previous PTP experiment, both ADCs are fed with the same 2.5-PPS 10-Vpp pulse train and the same cables. The results for a 320 second period are shown in Fig. 7 and summarized in table III. Of the 800 pulses captured over the measurement lapse, 91 % of all the trigger events are capture within the same clock period and, therefore, share the exact trigger timestamp. The remaining 9 % of the pulses are capture within a one clock cycle difference. This equals to a 1,437 nanosecond mean difference over the whole interval. The following lines are dedicated to discussing the reasons for this behavior.

Considering that the sampling period of the ADC chip is limited to 16 ns, the majority of the measured errors between the two cards is shown as 0 ns. This is, of course, not the case when working with real world equipment. When the measured error is reported as zero, there is still an accuracy limit from WR synchronization, which for this simple setup can be expected to be well below 250 picoseconds [13].

Furthermore, when measuring an analog signal there is always the uncertainty added by inherent aspects such as thermal noise, interference, and limitations such as the rise time of the function generator. Thus, a few millivolts difference between the measurement in the two ADC chips translates to a different moment for which the trigger is shot. All these factors explain the one-clock-period step that is sometimes observed in the results for this section.

C. *Free running clocks*

The last test reveals the effect of lack of synchronization when the starting conditions are the same for both WR-ZEN ADC boards. The initial conditions for this test are the same as for the White Rabbit experiment. While the two cards are synchronized and both WR-ZEN are showing an error bound between 0 and 16 ns and the aforementioned 2.5-PPS pulse train is being continuously time-tagged, the optical fibers are disconnected and the WR-ZENs lose their ability to have their clock locked to the common reference of the WR switch. Accordingly, the drift is clearly noticeable in just a few seconds.

This effect is visible in the graphs in Fig. 8. The measured drift between both ADCs is of 152 parts per billion in this period. This result is perfectly acceptable, inside the manufacturing accuracy at shipment and accounting for the aging of the oscillators.

As a result, these tests entail that capturing data from remote locations in a distributed approach can only be accomplished if the sampling clock is phase-locked across the entire network. Since the moment this lock is lost, an unknown and variable drift is introduced to the measurement. This drift, moreover, depends on environmental conditions such as temperature and the physical condition and age of the oscillators.

V. CONCLUSIONS

It has been proven that is possible to build a distributed DAQ based on WR technology. A new design has been done using SoC-based architecture that keeps complying with WR timing requirements: the synchronization is held with an accuracy below 1 ns. The resulting system is capable of acquiring up to four analog signals within a single clock domain across remote locations thanks to WR phase-compensating techniques. The maximum time uncertainty of the sampled test signal is of one clock period (16 ns at the current sampling rate) with an average of 1.437 ns of error over time. This result is superior to that of the starting design or synchronizing via software PTP (with average error in the range of 100 µs) due to the frequency drift suffered by oscillators. The proposed design can thus be used in to accurately timestamp and monitor analog signals in large scientific facilities or intrinsically distributed Smart Grid applications.

In addition to this, the user-oriented remote monitoring and control interface has been successfully integrated in the system, facilitating the remote management of data acquisition.

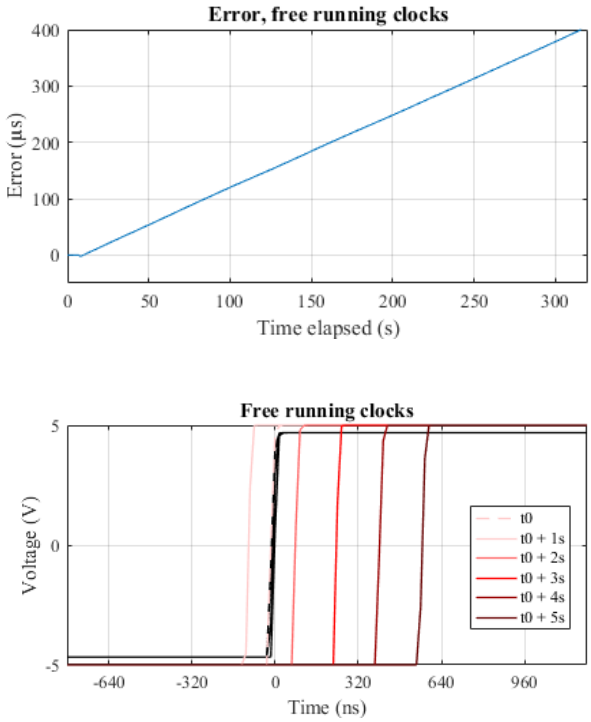


Fig. 8. Free running clocks results. The first graph shows the difference between the trigger timestamps measured in both WR-ZEN ADCs. Initially, both WR-ZENs are WR-synchronized. After 10 seconds, the WR switch is turned off (this is called *t0*) and the clocks start steadily diverging. The second graph shows the increasing disalingment of the free running WR-ZEN ADCs by taking five snapshots of the five seconds following *t0*.

TABLE III. WR SYNCHRONIZATION SUMMARY

Number of samples (N)	800
Average error	1.437 ns
Standard deviation	4.575 ns

ACKNOWLEDGEMENT

This work was supported by the project AYA2015-65973-C3-2-R: "AMIGA6: gas in and around galaxies. Preparation for SKA science and contribution to the design of the SKA data flow. Signal and Data Transmission (SaDT)".

We would also like to show our gratitude to the BE-CO-HT CERN section and to the Seven Solutions staff for their support and assistance.

REFERENCES

[1] J.L. Gutierrez-Rivas et al., Sub-nanosecond synchronization accuracy for time-sensitive applications on industrial networks, European Frequency and Time Forum - EFTF, 2016.

[2] J. Díaz Javier, J.L. Gutiérrez, R. Rodríguez, B. Rat Benoi, "Industrial White-Rabbit Solutions", Poster at "The 2015 Joint Conference of the IEEE Int'l Frequency Control Symposium & European Frequency & Time Forum, IFCS-EFTF, Denver, Colorado USA April 12-16, 2015.

[3] International Electrotechnical Commission. IEC 61850 Communication networks and systems for power utility automation.

[4] Li, H., Han, L., Duan, R., & Garner, G. M. (2017). Analysis of the Synchronization Requirements of 5g and Corresponding Solutions. *IEEE Communications Standards Magazine*, 1(1), 52–58. https://doi.org/10.1109/MCOMSTD.2017.1600768ST

[5] White Rabbit: When Every Second Counts [Online]. *Xcell Journal, Issue 91, Q2 2015.* Available: https://www.xilinx.com/publications/archives/xcell/Xcell91.pdf

[6] Franco, S. (2002). *Design With Operational Amplifiers And Analog Integrated Circuits.* McGraw-Hill.

[7] *Timing and synchronization aspects in packet networks*. ITU-T Recommendation G.8261, 2014.

[8] *1588-2008 - IEEE Standard for a Precision Clock Synchronization Protocol for Networked Measurement and Control Systems*. IEEE, 2008. doi:10.1109/IEEESTD.2008.4579760

[9] *PPSi: PTP Ported to Silicon.* The Open Hardware Repository. [Online] Available: http://www.ohwr.org/projects/ppsi/wiki

[10] *Cattin, M.*, *Lampridis, D.*, FmcAdc100m14b4cha Gateware guide, Release 4.1, 2016. [Online] Available: http://www.ohwr.org/attachments/4435/fmcadc100m14b4cha_gateware_manual_v4.1.pdf

[11] J. Serrano *et al*., "The White Rabbit project," in *Proc. ICALEPCS TUC004*, Kobe, Japan, 2009, pp. 93-95 [Online]. Available: http://accelconf.web.cern.ch/AccelConf/icalepcs2009/papers/tuc004.pdf

[12] OHWR, "FMC ADC 100M 14b 4cha - Open Hardware Repository", *Ohwr.org*. [Online]. Available: http://www.ohwr.org/projects/fmc-adc-100m14b4cha.

[13] M. Jiménez-López, J. L. Gutiérrez-Rivas, J. Díaz, E. López-Marín and R. Rodríguez, "WR-ZEN: Ultra-accurate synchronization SoC based on Zynq technology," *2016 European Frequency and Time Forum (EFTF)*, York, 2016, pp. 1-4.

[14] Open Cores, Wishbone B4, Available: https://opencores.org/cdn/downloads/wbspec_b4.pdf, Wishbone, 2010 [Accessed: 03- Mar- 2017].

[15] Gonzalez Cobas, J. D., Nellaga, S., Vaga, F., Rubini, A., & Wlostowski, T. (2013). *ZIO: The Ultimate Linux I/O Framework* (No. CERN-ACC-2013-0242).

[16] Moreira P., Serrano J, Wlostowski T., Loschmidt P. and Gaderer G. White rabbit: Sub-nanosecond timing distribution over ethernet. ISBN 978-1-4244-4391-8. International Symposium on Precision Clock Synchronization for Measurement, Control and Communication, 2009. ISPCS 2009

[17] Lighttpd Web Server. https://www.lighttpd.net/.

[18] IEEE Instrumentation and Measurement Society. IEEE 1588 Standard for a Precision Clock Synchronization Protocol for Networked Measurement and Control Systems.

[19] The Linux PTP Project. [Online] Available: http://linuxptp.sourceforge.net/

[20] CERN. European Organization for Nuclear Research. https://home.cern

[21] GSI Helmholtzzentrum für Schwerionenforschung. http://www.gsi.de

[22] CTA. Cherenkov Telescope Array. https://www.cta-observatory.org

[23] SKA Square Kilometer Array Project [Online] Available: http://skatelescope.org/project/

[24] Carroll, M. D., & Hadzic, I. "Network-distributed oscilloscope and method of operation thereof". US Patent number US20100117624 A1. May 13, 2010

System of Comparison of Time Scales of Distant Objects via Optical Fiber

Kolmogorov O.V., Donchenko S.S., Prokhorov D.V.
Russian metrological institute of technical physics and radio engineering
FSUE "VNIIFTRI"
Mendeleevo, Moscow region, Russia
e-mail: kolmogorov@vniiftri.ru

***Abstract* — In this paper, we describe Time Scales Comparison System (TSCS) for distant clock synchronization via optical fiber.**

Keywords* — *time scale; comparison; synchronization; optical fiber.

I. INTRODUCTION

One of the fundamental problems in the creation of instruments for metrological assurance of the GLONASS global navigation system has been the development of precision instruments for comparing and synchronizing the time scales of distant objects. The modern requirements imposed on instruments for metrological assurance of the GLONASS system includes synchronization of the time scales of distant objects in real time with instrumental error not greater than 100 psec. The highest degree of precision of synchronization of the time scales of distant objects is achieved through the use of fiber-optic communication lines [1]. Through use of different methods of synchronization, it is possible to achieve errors of synchronization from 50 ps for ranges up to 5 km and up to 100–120 ps for ranges on the order of 100 km. However, the drawbacks of existing methods of synchronization of time scales with the use of fiber-optic communication lines limits the precision and capabilities gained with the use of global navigation systems [2]. Among the drawbacks is the fact that the delays of a signal that has traversed an optical fiber cannot be calculated with sufficient precision and that it is difficult to achieve equality between the lengths of two optical fibers in the cable of a fiber-optic communication line. This has made it necessary to develop a system for synchronization of time scales that utilizes only a single optical fiber and is independent of the delay of the signal at the current moment of time.

II. METHODOLOGY AND MEASUREMENT SETUP

TSCS consists of two modules, placed at remote objects, connected via optical fiber, where two clocks form a time scale of the first object (TS 1) and a time scale of the second object (TS 2). Principle of TSCS operation is based on the measurement of moments of emission and reception of laser pulses, propagating in optical fiber.

Pulse generator (PG) forms a sequence of pulses (timestamps), which are converted by the laser transmitting module (LTM) into optical pulses. Each optical timestamp pulse passes through the splitter-combiner block (SCB); a small part of the optical pulse goes to the optical receiver module (ORM), the main part of the optical pulse goes to the fiber optic link (FOL). The electrical signal from the photodetector module passes through the broadband amplifier (BA) and arrives to event timer (ET), which measures the moment of pulse transmittance in timescale of first object (TS1).

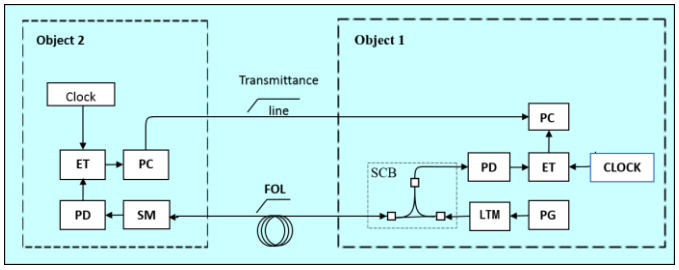


Fig.1. TSCS scheme

The optical pulse comes via fiber optic link to object 2 with a certain time delay τ_d. Part of optical pulse passes through the semitransparent mirror to the photodetector module of the object 2, which converts it to an electrical signal, moment of registration is measured by ET of second object in timescale of second object (TS2).

Part of the optical pulse, reflected from the semitransparent mirror is going back to fiber line. With a time delay strictly equal to the delay τ_d in the line during the direct passage, the reflected pulse arrives to ET of first object.

The measurement information from the point B ET is transmitted via a dedicated fiber-optic line to object A, where is postprocessed and the time difference between two remote clocks is defined as:

$$\Delta T = T_I - (T_{T1} + T_{T2})/2 + \tau_{dh}, \quad (1)$$

where T_{II} – moment of pulse registration in TS 2; T_{T1} – moment of pulse emission in TS 1; T_{T2} – moment of reflected pulse registration in TS 1; τ_{dh} – correction for delay hardware.

The time diagram of the device operation is shown in Fig. 2, where A and B are the time scale of the first and second objects, respectively, t_A and t_B are the second PPS timestamps of points A and B, respectively. Calibrated delays in the

transmitting laser and photodetector modules, broadband amplifiers, and timing devices are not shown.

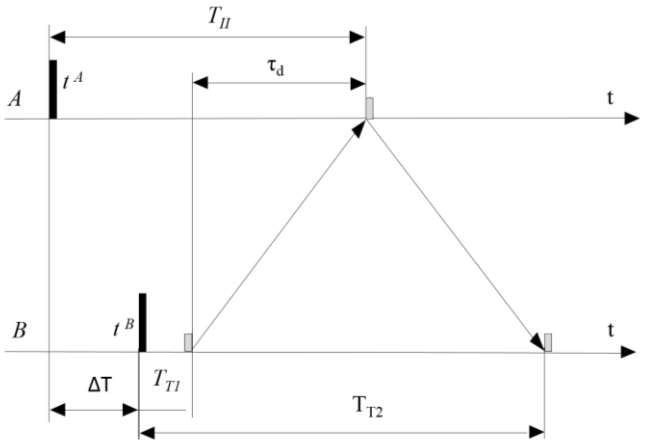


Fig.2. Time diagram of TSCS work

TSCS calculates difference between time scales, according to the obtained data. Measurements can be performed with repetition rate up to several thousand per second for averaging of results.

III. MEASUREMENT RESULTS

During experimental researches hardware delay of system was measured. Two TSCS modules were placed in one object, connected by optical fiber. 1 PPS signal, formed by clock, was given to both modules (corresponding to TS 1 and TS 2) by the splitter. Results of measurement were used for compensation hardware delay (fig.3).

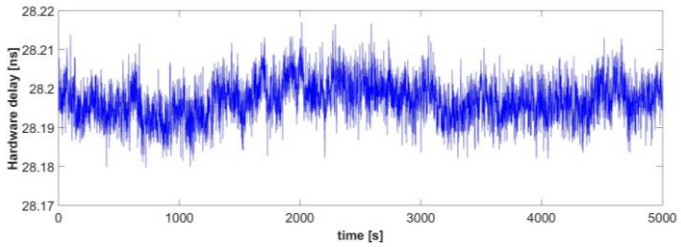


Fig.3. Results of hardware delay measurement

Two modules TSCS are placed at two objects, connected by an optical link length of 1.3 km. Each object has clock, which forms object time scale. Experimental researches have proved system workability. Measurement results are shown in Fig. 4.

Accuracy of TSCS is characterized by following values: standard uncertainty obtained from Type A evaluation is 10 – 20 ps; standard uncertainty obtained from Type B evaluation is 50 ps (provided the temperature stability of ± 1 °C in objects, where TSCS modules are located)[3].

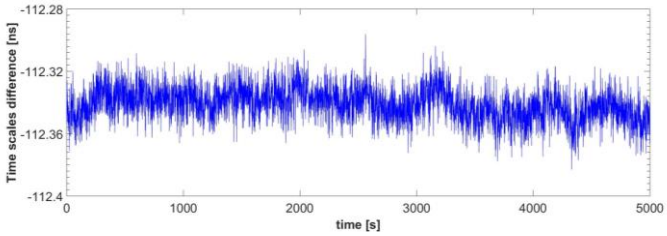


Fig.4. Results of TCSC measurements

IV. CONCLUSION

Thus, the possibility of synchronization of spatially remote objects time scales with total uncertainly not greater than 60 ps for objects up to 30 km apart. Synchronization precision is increased with usage of more precise measuring instruments, the execution of a set of measurements in the second cycle, and integration of the results of measurements together with averaging of the measurement results.

REFERENCES

[1] M. Rost, D. Piester, W. Yang, et al., "Time transfer through optical fi bers over a distance of 73 km with an uncertaintybelow 100 psec," *Metrologia*, **49**, No. 6, 772–779 (2012).

[2] S. S. Donchenko, O. V. Kolmogorov, and D. V. Prokhorov, "A system of unilateral and bilateral comparisons of time scales," *Izmer. Tekhn.*, No. 1, 14–17 (2015).

[3] S.S. Donchenko, O.V. Kolmogorov, D.V. Prokhorov. Results of experimental research of one - and two way time scales comparisons system. Metrology of time and space. VIII International Symposium. Symposium materials. Saint Petersburg, Russia, 14 – 16 September, 2016, pp 228 – 230.

Characterization of the phase-noise induced by an optical frequency doubler

Marion Delehaye, Jacques Millo, Pierre-Yves Bourgeois, Lucas Groult, Ahmed Bakir, Rodolphe Boudot, Enrico Rubiola, Vincent Giordano, Emmanuel Bigler, Yann Kersalé and Clément Lacroûte
FEMTO-ST institute, univ. Bourgogne Franche-Comté, CNRS
ENSMM Time and frequency dept. 26 Rue de l'Épitaphe 25030 Besançon cedex
clement.lacroute@femto-st.fr

***Abstract*— We report on the characterization, including residual phase noise and fractional frequency instability, of second harmonic generation fiber-coupled periodically poled LiNbO3 (PPLN) waveguides. We observe a residual phase noise as low as -35 dBrad^2/Hz at 1 Hz, which makes them compatible with the best up-to-date optical clocks and ultra-stable cavities.**

Keywords*— *optical atomic clocks; second harmonic generation; phase noise; frequency metrology

State-of-the-art optical atomic clocks have attained short-term fractional frequency stabilities in the low 10^{-16} range [1,2]. This has been made possible thanks to improved performances of the clock lasers, which are pre-stabilized using ultra-stable Fabry-Perot (FP) resonators [3]. Many of the last-generation optical atomic clocks rely on frequency doubling via second harmonic generation (SHG) to produce the laser clock frequency [4,5], where the pump laser used for SHG is stabilized to the ultra-stable FP resonator. It is therefore necessary to ensure that the SHG setup does not degrade the beam fractional frequency stability.

Bulk crystals and periodically poled (PP) crystals have been used and characterized, and it has been shown that they introduce very low phase noise, at the price of a poor SHG efficiency [6-8].

In this study, we employ fiber-coupled PPLN waveguides to perform the frequency doubling from an extended cavity diode laser at a wavelength λ = 871 nm to the electric quadrupole transition clock frequency of Yb^+ at λ = 435.5 nm. These modules are both compact, highly-efficient, and avoid the use of an enhancement cavity. We report SHG efficiencies up to 117.5 % /W.

We measure the phase noise induced by the SHG with a Mach-Zehnder interferometer and a novel noise rejection technique and observe a residual phase noise as low as -35 dBrad^2/Hz at 1 Hz (see Fig. 1), which makes them compatible with the best up-to-date optical clocks and ultra-stable cavities.

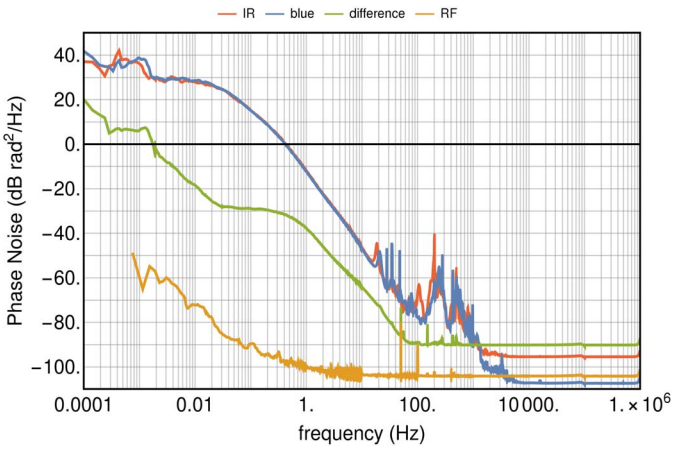


Fig. 1. Optical phase noise measured using a Mach-Zehnder interferometer. Red: pump laser phase noise at 871 nm. Blue: second harmonic phase noise at 435.5 nm , scaled to 871 nm. Green: phase noise obtained when mixing the pump and second harmonic signals, allowing an estimation of the residual phase noise of the second harmonic beam. Orange: noise floor of the electronic measurement setup.

REFERENCES

[1] B. J. Bloom, T. L. Nicholson, J. R. Williams, S. L. Campbell, M. Bishof, X. Zhang, W. Zhang, S. L. Bromley, and J. Ye, "An Optical Lattice Clock with Accuracy and Stability at the 10^{-18} Level", Nature, vol. 506, pp. 71-75, 2014.

[2] I. Ushijima, M. Takamoto, M. Das, T. Ohkubo, and H. Katori, "Cryogenic Optical Lattice Clocks", Nat. Phot., vol. 9, pp. 185-189, 2015.

[3] Y. Y. Jiang, A. D. Ludlow, N. D. Lemke, R. W. Fox, J. A. Sherman, L.-S. Ma, and C. W. Oates, "Making Optical Atomic Clocks more stable with 10^{-16}-Level Laser Stabilization", Nat. Phot., vol. 5, pp. 158-161, 2011.

[4] C. W. Chou, D. B. Hume, J. C. J. Koelemeij, D. J. Wineland, and T. Rosenband, "Frequency Comparison of Two High-Accuracy Al^+ Optical Clocks", Phys. Rev. Lett., vol. 104, pp. 070802, 2010.

[5] R. Tyumenev, M. Favier, S. Bilicki, E. Bookjans, R. Le Targat, J. Lodewyck, D. Nicolodi, Y. Le Coq, M. Abgrall, J Guéna, L. De Sarlo, and S. Bize, "Comparing a Mercury Optical Lattice Clock with Microwave and Optical Frequency Standards", New Jour. Phys., vol. 18, pp. 113002, 2016.

[6] R. Wynands, O. Coste, C. Rembe, and D. Meschede, "How Accurate is Optical Second-Harmonic Generation?", Opt. Lett., vol. 20, pp. 1095–1097, 1995.

[7] Jörn Stenger, Harald Schnatz, Christian Tamm, and Harald R. Telle, "Ultraprecise Measurement of Optical Frequency Ratios", Phys. Rev. Lett., vol. 88, pp. 073601, 2002.

[8] D. Yeaton-Massey and R. X. Adhikari, "A New Bound on Excess Frequency Noise in Second Harmonic Generation in PPKTP at the 10^{-19} Level", Opt. Expr., vol. 20, pp. 21019–21024, 2012.

Inverted crossover resonances with ΔF=0 or 1

Inverted crossover resonances with the intercombination line of ^{171}Yb

John McFerran
School of Physics
University of Western Australia
Crawley, 6009, Australia
john.mcferran@uwa.edu.au

Emeric de Clercq
LNE-SYRTE, Observatoire de Paris, PSL Research University, CNRS, Sorbonne Universités, UPMC Univ. Paris VI, 61 avenue de l'Observatoire, 75014 Paris, France
emeric.declercq@obspm.fr

***Abstract*—We demonstrate the presence of inverted crossover resonances (ICRs) in the intercombination line of ^{171}Yb (I=1/2) with the use of saturated fluorescence spectroscopy on an atomic beam. The principal lines involved in the crossover are symmetrically separated Zeeman transitions. The signals are observed for both the hyperfine lines of the ^{171}Yb $^1S_0$-$^3P_1$ line. We use a four-level rate equation model to help validate the nature of the resonance. In the case of F'=3/2 (upper state) the resonance can be used to frequency stabilize laser light for laser cooling of ^{171}Yb. While that of the F'=1/2 ICR acts as a rather robust frequency reference with an overall fractional frequency uncertainty in the low 10^{-11} range.**

Keywords—ytterbium; crossover resonance; saturated fluorescence spectroscopy; four level rate equation.

I. Introduction

Saturated fluorescence (or absorption) spectroscopy on an atomic beam normally yields a saturation dip at the centre of a Doppler profile. In the case of the $^1S_0$-$^3P_1$ line in ^{171}Yb with an applied magnetic bias, one observes enhanced absorption (and fluorescence) rather than suppressed absorption. The behaviour occurs because the nuclear spin-1/2 isotope generates a four level system with a pair of Zeeman transitions forming the principal lines of a crossover resonance. The paired ground states implies that the usual saturation associated with two-level, or V-, schemes no longer prevails. Crossover resonances are not commonly observed on atomic beams because the natural linewidth of the transition needs to be below a few megahertz (for a sufficiently collimated atomic beam). The ICR in ^{171}Yb is apparent when the separation of the principal lines ranges from ~1 MHz to tens of megahertz, which is unlike the case of ICRs in gas cells where the separation is typically hundreds of MHz [1,2]. The ICR is present for both hyperfine lines of ^{171}Yb, where ΔF=0 (F'=1/2) or ΔF=1 (F'=3/2).

II. Experiment and Model

The saturated fluorescence spectroscopy (SFS) scheme is performed with a retroreflected laser beam (556nm) at right angles to a low-divergence atomic beam. A small dc magnetic field is a applied vertically that sets the quantisation axis. Fluorescence is detected by a photomultiplier cell (which lies approximately along the quantisation axis). Modulation and signal recovery is performed with a lock-in amplifier. The first harmonic gives stronger SNR and therefore improved frequency instability for the laser cooling. Whereas the third harmonic is more important for the absolute frequency measurements (minimising the influence of the Doppler background).

An example of the ICR is shown in Fig. 1 for the F'=1/2 hyperfine line and a bias B-field of 0.10 mT. The amplitude of the FM was 0.4MHz and the intensity 53 I_{sat}. Here first harmonic detection was used and the time taken to sweep across the central discriminator was 1.1 s. An optical beat between the sub-harmonic of the 556 nm light and an element of a frequency comb was used to calibrate the frequency scale.

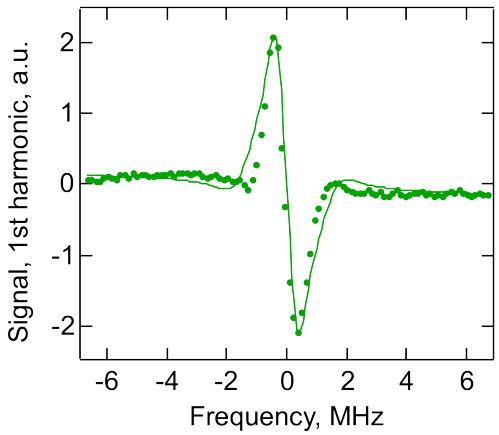


Fig. 1. The ICR resonance for the $^1S_0$-$^3P_1$ (F'=1/2) line with first harmonic signal detection. Overlaid is a curve generated with a four level rate equation model based on the experimental parameters (see text).

To model the ICR a set of rate equations is solved describing population changes in a four-level system [3]. The model incorporates the Zeeman and Doppler shifts, which for non-zero B involves two subsets of slightly divergent atoms (see Fig. 2). The model also incorporates the artificial broadening generated by the frequency modulation [4]. The applied amplitude of FM is relatively strong to enhance the SNR, but with the consequence of broadening the lines beyond the intensity broadened linewidth (more so in the case of third harmonic detection). Fig. 3 shows the relevant energy levels for the F=1/2-F'=1/2 hyperfine line. The upper state magnetic sublevels shift with a g_F factor of 28 MHz/mT. The branching ratios from the upper states are denoted alongside the

respective transitions. The model successfully describes the behaviour as the level structure transforms from a degenerate two-level scheme (B=0) to a four-level system ($B\neq0$); i.e., a saturation dip converts to an inverted crossover resonance. In Fig. 1, the slight discrepancy between experimental data and model (beyond the main discriminator) may be due to the fastest atoms not having time to reach the steady state regime.

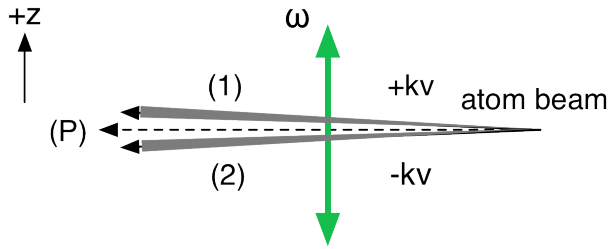


Fig. 2. The ICR is created by two subsets of atoms within the atomic beam, each with equal but opposite transverse velocity. *P* represents those atoms traveling exactly at right angles to the overlapped laser beams (and responsible for the principal lines). Note, this image should not be taken too literally, because the subsets are in velocity space, rather than position.

One aspect of the experiment that the model does not reproduce is the relative strengths of the ICRs between the two hyperfine lines. The F'=1/2 ICR is approximately 40% stronger than that for the F'=3/2 when measured, while the model suggests that the latter should be ~10% stronger. A likely explanation for this is that the model does not take into account the spatial dependence of fluorescence with polarisation. With different branching ratios (and the orientation of the incident light's polarisation along B), the two hyperfine lines have different spatial distributions of fluorescence intensity.

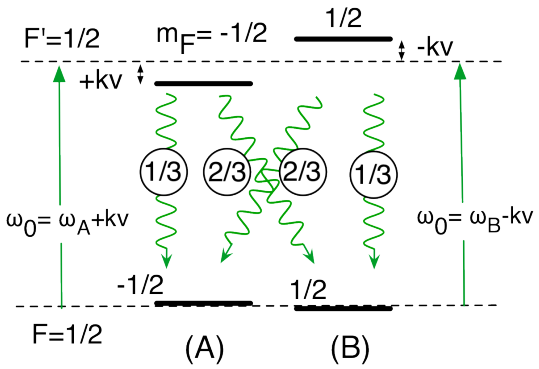


Fig. 3. Relevant energy levels of the $^1S_0$-$^3P_1$ line in ^{171}Yb (for F'=1/2). Shown encircled are the relaxation branching ratios for this particular hyperfine line (the coefficients are reversed for the F'=3/2 line). For sufficiently small B there exists a subsets of atoms with transverse velocity v that matches the Zeeman shift.

The derivative signals of the ICRs (1st or 3rd) are used to stabilize the 556 nm laser frequency. In the case of the F'=1/2 hyperfine line, the centre frequency is insensitive to first-order Zeeman shifts and is equal to the two-level resonance frequency in the absence of a magnetic field. Repeated measurements of the absolute frequency against a H-maser over the course of two months produced a statistical uncertainty of 2×10^{-11} (1σ standard deviation). An assessment of relevant systematic shifts reveals a systematic uncertainty of 4.3×10^{-11}. The $^1S_0$-$^3P_0$ transition in ^{171}Yb was used as an accuracy check of the H-maser frequency [6]. The absolute frequency of the $^1S_0$-$^3P_1$ (F'=1/2) ^{171}Yb line centre is reported in [5]. The absolute frequency of the F'=3/2 line can also be deduced based on the hyperfine line frequency separation [7] (and with reduced uncertainty compared to previous measurements).

The ICR associated with the F'=3/2 hyperfine line is suited to frequency stabilisation for the purpose of laser cooling of ^{171}Yb atoms. The frequency instability at 1s is 10 kHz and falls to ~0.5kHz at 600s with an atomic flow rate of $\sim4\times10^{10}$ s^{-1} intersecting the 556 nm beams. Compare this to the natural linewidth of 184 kHz. Atomic cloud temperatures of 15 μK are reached with a dual-wavelength magneto-optical trap. By varying the atom flow rate the laser frequency instability is changed via the ICR lock. In doing so we do *not* observe a cloud temperature dependence on frequency instability (suggesting that other factors are limiting the temperature).

Similar inverted crossover resonances are expected to occur whenever the atom has a nuclear spin of 1/2 and the transition has a sufficiently narrow natural linewidth; other examples include the intercombination lines in ^{199}Hg ($\Gamma/2\pi$=1.3 MHz), ^{111}Cd and ^{113}Cd ($\Gamma/2\pi$ =65 kHz). In the case of ^{173}Yb where I=5/2 we see that the ICR is extremely weak. This is understandable given that three different (absolute) velocity sub-groups are involved (instead of one). Modelling an eight-level scheme associated with I=3/2 (and S=0) may yield further insights (e.g. for ^{201}Hg).

Acknowledgment

We are thankful for the assistance from Nils Nemitz, Frédéric du Burck and Stefan Weyers. This work was supported by the Australian Research Council (grant LE110100054 and Future Fellowship FT110100392).

References

[1] T.W. Hänsch, I.S. Shahin, and A.L. Schawlow, "High-resolution saturation spectroscopy of the sodium *D* lines with a pulsed tunable dye laser," Phys. Rev. Lett., 27, 707, 1971.

[2] O. Schmidt, K.-M. Knaak, R. Wynands, and D. Meschede, "Cesium saturation spectroscopy revisited: How to reverse peaks and observe narrow resonances," Appl. Phys. B, 59, 167, 1994.

[3] P.G. Pappas, M.M. Burns, D.D. Hinshelwood, M.S. Feld, and D.E. Murnick, "Saturation spectroscopy with laser optical pumping in atomic barium," Phys. Rev. A, 21, 1955, 1980.

[4] G.V.H. Wilson, "Modulation broadening of NMR and ESR line shapes," J. Applied Physics, 34, 3276, 1963.

[5] L.A. Salter, E. de Clercq and J.J. McFerran, "Inverted crossover resonance within one Zeeman manifold", arXiv,physics.atom-ph 1611.03249v2.

[6] L. Nenadović and J.J. McFerran, "Clock and inter-combination line frequency separation in ^{171}Yb," J. Phys. B, 49, 065004, 2016.

[7] J.J. McFerran, "An inverted crossover resonance aiding laser cooling of ^{171}Yb, " J. Opt. Soc. Am. B, 33, 1278, 2016.

Towards Doppler-free spectroscopy of O_3 isotopes at 28 THz with a Quantum Cascade Laser locked to a stabilized frequency comb reference.

T. Zanon-Willette, Marco Minissale, H. Elandaloussi, Pascal Jeseck, C. Rouillé, Corinne Boursier, Christof Janssen
LERMA, Observatoire de Paris, PSL Research University, CNRS, Sorbonne Universités, UPMC Univ. Paris 06, F-75005, Paris, France
Email: thomas.zanon@upmc.fr

***Abstract*—Quantum Cascade Lasers (QCLs) in the mid-IR range have become now suitable devices for ultra-high resolution laser spectroscopy, molecular trace gas sensors and the study of the possible time dependence of fundamental physical constants. We present here systematic studies of ozone molecular lines using Doppler absorption spectroscopy over a 1.6 cm^{-1} mode-hop free tuning frequency range of a DFB-QCL centered around 1049 cm^{-1}. We apply controllable non-linear corrections on the current waveform driving the laser frequency. The resulting effect is a very efficient linearization of molecular spectra over the full current ramp, leading to a residual error in frequency below 2×10^{-4} cm^{-1} over the entire spectrum ($< 2 \times 10^{-7}$). The free running laser spectrometer is coupled to two single pass absorption cells, arranged in a parallel setup, which allows for the study of pressure induced line shifts. First experimental pressure shift measurements for individual ozone absorption lines are reported. We also present our emerging project to stabilize the QCL source on an optical frequency-comb using experimental techniques for efficient non linear frequency conversion between IR and Telecom wavelengths.**

I. Free-running QCL experiment: first experimental pressure-shift measurements of ozone molecular lines at 9.54 μm

The advent of QCLs in the Mid-IR offers new avenues for high precision molecular spectroscopy, in particular when combined with novel techniques concerning the transfer of time and frequency references via optical fibers. The project aims at developing this new technology in the 10 μm (1000 cm^{-1}) region for applications in atmospheric physics, planetology and fundamental physics. We are actually developing a new ultra-high resolution molecular laser spectrometer to study ozone O_3 and its isotopomers ($^{16}O^{17}O^{16}O$, $^{16}O^{16}O^{17}O$ or $^{16}O^{18}O^{16}O$ for example). We plan to realize accurate measurements of various molecular parameters of O_3 isotopomers in the IR spectrum (absolute intensities, frequency position, pressure shift of molecular lines by others species, etc...). These data will thus strongly improve atmospheric molecular databases such as HITRAN [1]. Preliminary results of our new laser spectrometer in free running mode already allow for first observations of molecular line frequency shifts due to collisions with noble gas molecules like He, Ar and Xe. These are consistent with previous measurements based on FTIR techniques [2]. The planned investigations will also help understanding a potential effect of nuclear origin in anomalous mass independent isotope fractionation [3]. The anomalous fractionation of ozone (non mass independent) arises from the formation reaction. Some theoretical studies have proposed its

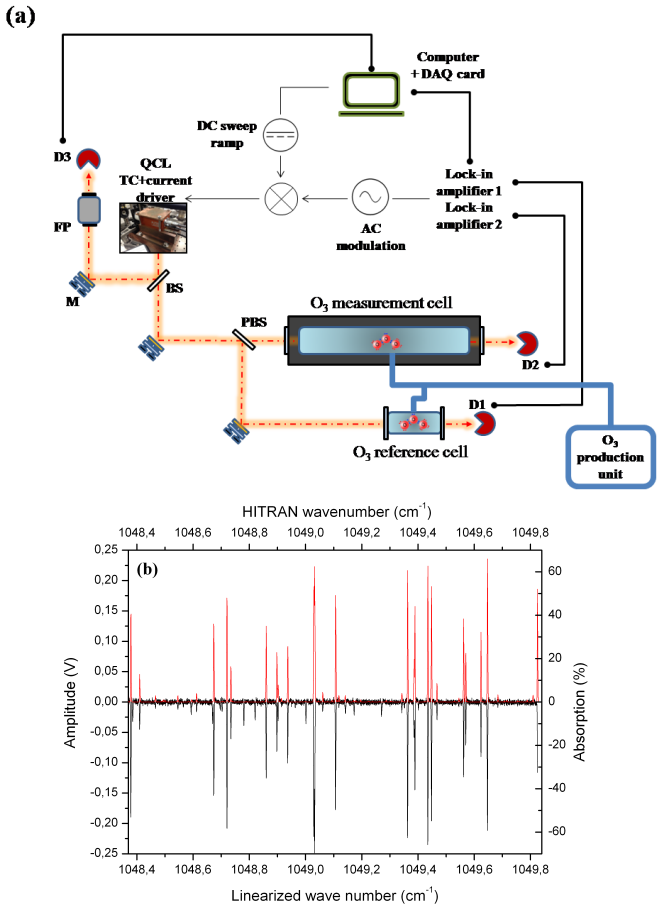


Fig. 1. (a) Schematic of the molecular line Doppler spectroscopy with a free running laser source: QCL, distributed feedback quantum cascade laser; BS, beam splitter; PBS, polarizing beam splitter; FP, Fabry-Pérot étalon; D, detector; DAQ card, data acquisition card; TC, temperature controller. (b) Synthetic (up) and experimental (down) O_3 molecular lines spectra recorded over 1.6 cm^{-1} at 28 THz.

978-1-5386-2916-1/$31.00 ©2017 IEEE

Line (cm^{-1})	Pressure shift 10^{-2}·MHz·hPa^{-1} Xenon	Argon	Helium
1049.36312	-8.4±0.2	-5.3±0.2	–
1049.62425	-8.2±0.2	-6.2±0.2	–
1052.04284	-9.8±0.2	-7.2±0.2	-1.3±0.5
1052.19324	-11.4±0.3	-9.2±0.3	-1.1±0.4

TABLE I
MEASURED PRESSURE SHIFT. FOR EACH GAS (XE, AR, AND HE) AND LINE, CORRESPONDING PRESSURE-SHIFT IS REPORTED WITH ASSOCIATED ERROR.

origin from a symmetry breaking when atomic oxygen ^{16}O is replaced by ^{17}O or ^{18}O in the main ozone isotopomers. In order to study these isotopic effects at the interface between fundamental molecular physics and quantum chemistry, a new molecular laser spectrometer will be realized based on a DFB-Quantum Cascade Laser (QCL) in the 9.5 μm (1050 cm^{-1}) spectral range (see Fig. 1(a) and (b)).

II. TOWARDS A QUANTUM CASCADE LASER STABILIZATION SCHEME ON A REFERENCED FREQUENCY COMB

We have started recently a new project for QCL stabilization on a frequency-comb. These frequency stabilization techniques require some nonlinear optical mixing processes by realizing a frequency sum generation (SFG) between the QCL (Alpes laser) and a frequency-shifted comb (FC-1500 MenloSystems) inside a $AgGaSe_2$ crystal (see Fig. 2) [4], [5]. The QCL frequency locked to a tooth of the optical comb by an electronic servo loop system will offer a first robust frequency stabilization scheme to demonstrate high resolution molecular spectroscopy of ozone for atmospheric sciences applications. We will then test our laser frequency stabilization technique by realizing the first demonstration of high resolution spectroscopy using a saturated absorption technique on ozone molecular lines, as shown in Fig. 3. This will allow to improve the accuracy of pressure-shifts measurements by several orders of magnitude working at lower gas pressure. A semi-classical density matrix treatment of a Doppler-free saturation spectroscopy including various effects of laser parameters like collision broadening, laser line width, saturation intensity and pressure shifts will be implemented in parallel with the experiment for quantitative comparisons.

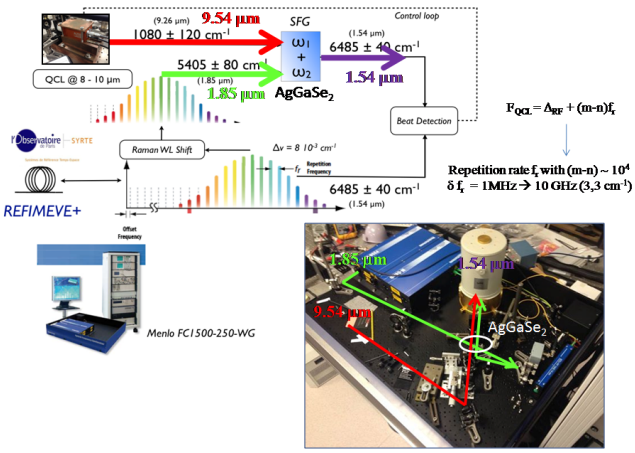


Fig. 2. Experimental setup for non linear sum frequency conversion between the QCL at 9.5 μm and a frequency-shifted comb (FC-1500 MenloSystems) inside a $AgGaSe_2$ crystal.

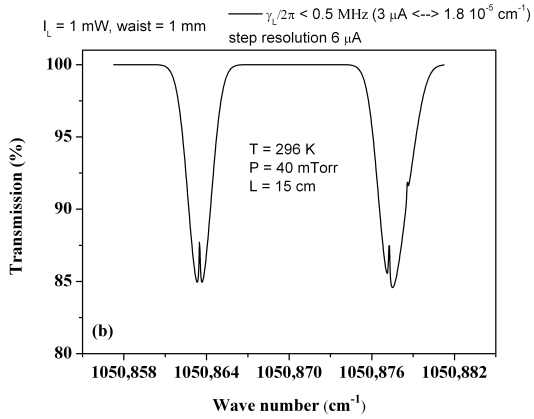


Fig. 3. Synthetic Doppler-free spectrum of O_3 molecular line expected with saturated absorption spectroscopy in 15 cm long cell.

ACKNOWLEDGMENT

This experimental project is financially supported by CNRS, the île de France DIM-ACAV, the French equipex RE-FIMEVE+ and labex FIRST-TF.

REFERENCES

[1] D. Chris Benner, P.F. Bernath, M. Birk, L. Bizzocchi, V. Boudon, L.R. Brown, A. Campargue, K. Chance, E.A. Cohen, L.H. Coudert, V.M. Devi, B.J. Drouin, A. Fayt, J.M. Flaud, R.R. Gamache, J.J. Harrison, J.M. Hartmann, C. Hill, J.T. Hodges, D. Jacquemart, A. Jolly, J. Lamouroux, R.J. Le Roy, G. Li, D.A. Long, O.M. Lyulin, C.J. Mackie, S.T. Massie, S. Mikhailenko, H. S. P. Müller, O.V. Naumenko, A.V. Nikitin, J. Orphal, V. Perevalov, A. Perrin, E.R. Polovtseva, C. Richard, M.A.H. Smith, E. Starikova, K. Sung, S. Tashkun, J. Tennyson, G.C. Toon, Vl.G. Tyuterev and G. Wagner, *The HITRAN 2012 molecular spectroscopic database*, J. Quant. Spectrosc. Radiat. Trans., **130** 4, (2013).

[2] M.A.H. Smith, C.P. Rinsland, V.M. Devi, D.Chris Benner, and K.B. Thakur, *Measurements of air-broadened and nitrogenbroadened half-widths and shifts of ozone lines near 9 µm*, J. Opt. Soc. Am. B, **5**, 585, (1988).

[3] C.A.M. Renninkmeijer, C. Janssen, J. Kaiser, T. Röckmann, T.S. Rhee and S.S. Assonov, *Isotope effects in the chemistry of atmospheric trace compounds*, Chem. Rev. **103**, 5125 (2003).

[4] B. Chanteau, O. Lopez, W. Zhang, D. Nicolodi, B. Argence, F. Auguste, M. Abgrall, C. Chardonnet, G. Santarelli, B. Darquié, Y. Le Coq and A. Amy-Klein, *Mid-infrared laser phase-locking to a remote near-infrared frequency reference for high-precision molecular spectroscopy*, New J. Phys. **15**, 073003 (2013).

[5] B. Argence, B. Chanteau, O. Lopez, D. Nicolodi, M. Abgrall, C. Chardonnet, C. Daussy, B. Darquié, Y. Le Coq and A. Amy-Klein, *Quantum cascade laser frequency stabilization at the sub-Hz level*, Nature Photonics **9**, 456 (2015).

Short-length homodyne interferometer for self-stabilization of an optical frequency comb

James P. Cahill and Weimin Zhou
U.S. Army Research Laboratory
Adelphi, MD, USA 20783
Email: james.p.cahill15.civ@mail.mil

Curtis R. Menyuk
University of Maryland: Baltimore County
Baltimore, MD, USA 21250

***Abstract*—We stabilized the repetition rate of an optical frequency comb with a self-referenced phase-locked loop that used a short-path-length fiber-optic interferometer to generate its error signal. In this work, we used a homodyne interferometer instead of a heterodyne interferometer, so that the architecture of the phase-locked loop was simpler than our previous implementation. We used the stabilized repetition rate to generate a 10-GHz signal with a phase noise of −120 dBc/Hz at an offset frequency of 1 kHz. The simplified architecture and the short path length imbalance of the interferometer would allow it to be fabricated on an all-passive silicon chip and may lead to a chip-scale optical frequency comb with an ultra-low-noise repetition rate.**

I. Introduction

An optical frequency comb (OFC) with a low-noise repetition rate can be used to generate ultra-low-phase-noise microwaves. A low-noise repetition rate is also important in other applications such as optical time and frequency transfer and dual comb spectroscopy. However, the size, weight, power-consumption, and cost (SWAP-C) of an OFC make its inclusion in many scenarios outside of the laboratory a challenge. Microresonator-based Kerr combs are one technology that promises to reduce the SWAP-C of OFCs [1]. However, the challenge of creating a low-SWAP-C system does not end with the OFC itself. In order to achieve a low-noise repetition rate, an OFC is typically locked to a single-frequency laser that is, in turn, locked to an optical cavity, such as a ULE glass Fabry-Pérot resonator [2]. Such cavities are generally manufactured by hand and require bulky environmental isolation; so, cavity-stabilization is another barrier for applications that require low SWAP-C.

Instead of being referenced to an external cavity-stabilized laser, the repetition rate of an OFC can be self-stabilized with a phase-locked loop (PLL) that uses a delay-line interferometer to generate its error signal [3], [4], [5]. This technique is attractive, because it eliminates the need for a second optical source and the external optical cavity. Moreover, short-path-length interferometers can be fabricated on a photonic-integrated chip using only passive components, so that they can be much smaller and more readily mass-produced than, for example, a crystalline optical cavity. In combination with the rapidly-advancing field of microresonator-based optical frequency comb generation, delay-line-interferometer-based self-stabilization could lead to a chip-scale OFC with an ultra-low-noise repetition rate.

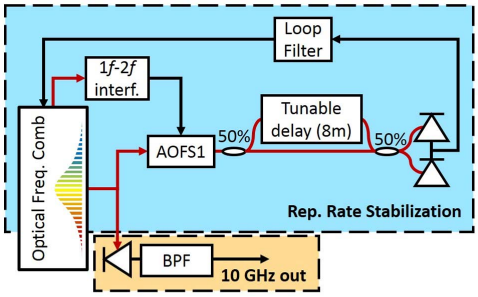


Fig. 1. Experimental setup for stabilizing the repetition rate and generating the 10-GHz signal.

We experimentally demonstrated that the repetition rate of an OFC can be stabilized using an interferometer with an 8-m path-length difference, which is sufficiently short that the interferometer could be realized on an integrated chip [5]. However, in that manuscript, we used a heterodyne interferometer to generate the error signal in the PLL. Heterodyne interferometers are frequently used in delay-line PLLs in the literature [6] and can take advantage of the AM-noise suppression and relatively high phase-to-voltage gain of microwave double-balanced mixers. However, in [5], we used an acousto-optic frequency shifter to induce the heterodyne frequency shift, and this component increased the complexity and power-consumption of the stabilization circuit and raised the difficulty of realizing the interferometer on-chip. These issues would appear even if the acousto-optic frequency shifter were replaced with other common frequency-shifting elements, such as a single-sideband modulator. Hence, it is advantageous to demonstrate a homodyne interferometer that eliminates the frequency-shifting element from the interferometer.

In the work presented here, we stabilized an OFC with a homodyne fiber-optic interferometer that had a path length difference of approximately 8 m. We used the repetition rate to generate a 10-GHz signal with phase noise of −120 dBc/Hz at 1-kHz offset frequency. This level is equal to the level that we achieved with the heterodyne interferometer and was limited by environmental and shot noise—not by the performance of the interferometer or the PLL.

U.S. Government work not protected by U.S. copyright

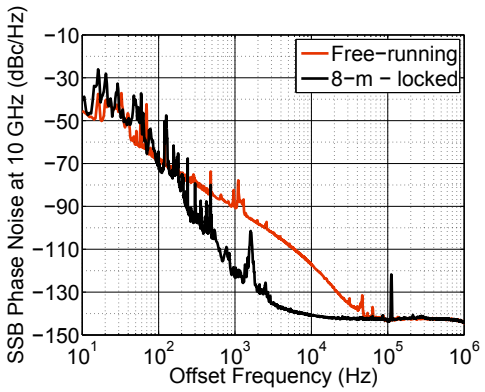


Fig. 2. Single-sideband phase noise of the 10-GHz signals generated by the OFC when it was free-running (red) and when it was locked using the 8-m homodyne interferometer (black).

II. Results

We stabilized the OFC using the circuit shown in Fig. 1. The $1f$–$2f$ interferometer measured the carrier-envelope offset frequency of the OFC; the acousto-optic frequency shifter (AOFS1) used this measurement to cancel the carrier-envelope offset frequency and mitigate its noise contribution. This partially stabilized light was sent through an asymmetric fiber-optic Mach-Zehnder interferometer with a tunable path-delay difference of approximately 40 ± 1.5 ns, which corresponds to approximately 8 m of optical fiber. The path-delay was tuned with a resolution of at least 1 ps in order to ensure that the delayed and non-delayed pulses temporally overlapped at the output of the interferometer. We used a commercially-available balanced photodiode pair (BPD) with an integrated transimpedance amplifier to detect the phase difference between the delayed and non-delayed light. This signal was sent through a loop filter and fed back to control the OFC repetition rate via an intra-cavity electro-optic modulator.

Figure 2 compares the single-sideband (SSB) phase noise of the 10-GHz signal generated by the OFC when the repetition rate was free-running (red) to the SSB phase noise of the signal generated when the OFC was stabilized using the 8-m homodyne interferometer. When the OFC was locked, the phase noise of 10-GHz signal reached approximately -120 dBc/Hz at an offset frequency of 1 kHz. The phase noise levels at all offset frequencies match the results obtained with the heterodyne interferometer. Hence, as we showed for the heterodyne interferometer in [5], we expect that the phase noise at offset frequencies below approximately 10 kHz is dominated by environmental noise, while the phase noise at offset frequencies above approximately 10 kHz is dominated by shot noise.

III. Conclusion

In conclusion, we used a homodyne interferometer to stabilize the repetition rate of an OFC. We generated a 10-GHz signal with the stabilized repetition rate that had a SSB phase noise of -120 dBc/Hz at an offset frequency of 1 kHz. The short path length and simplified homodyne architecture of the interferometer indicate that it could be realized on a fully-passive photonic integrated chip. In combination with miniature OFC technologies, such as microresonator Kerr combs, these results may lead to a fully-integrated, low SWAP-C OFC with an ultra-low-noise repetition rate.

References

[1] P. Del'Haye, A. Schliesser, O. Arcizet, T. Wilken, R. Holzwarth, and T. J. Kippenberg, "Optical frequency comb generation from a monolithic microresonator," *Nature*, vol. 450, pp. 1214–1217, December 2007.

[2] T. M. Fortier, F. Quinlan, A. Hati, C. Nelson, J. A. Taylor, Y. Fu, J. Campbell, and S. A. Diddams, "Photonic microwave generation with high-power photodiodes," *Opt. Lett.*, vol. 38, no. 10, pp. 1712–1714, May 2013.

[3] K. Jung and J. Kim, "All-fibre photonic signal generator for attosecond timing and ultralow-noise microwave," *Sci. Rep.*, vol. 5, p. 16250, November 2015.

[4] J. P. Cahill, W. Zhou, and C. R. Menyuk, "Self-delay-line-referenced optical frequency comb for low-phase noise microwave generation," in *Proceedings of IEEE International Frequency Control Symposium*, 2016.

[5] ——, "Self-stabilization of an optical frequency comb using a short-path-length interferometer," submitted for publication.

[6] F. Kéfélian, H. Jiang, P. Lemonde, and G. Santarelli, "Ultralow-frequency-noise stabilization of a laser by locking to an optical fiber-delay line," *Opt. Lett.*, vol. 34, no. 7, pp. 914–916, Apr 2009.

Resent Progresses of Dual-wavelength Good-bad Cavity Active Optical Clock

Duo Pan, Tiantian Shi, Biao Xue, Jingbiao Chen
State Key Laboratory of Advanced Optical Communication, System and Network,
School of Electronics Engineering and Computer Science, Peking University,
Beijing 100871, China
E-mail: jbchen@pku.edu.cn

***Abstract*—We propose a dual-wavelength good-bad cavity active optical clock, of which the two output signals with different wavelength share the same cavity, and work in good cavity and bad cavity regime, respectively. The good cavity signal is locked to a super cavity by the PDH technique, and thus the main cavity length of the active optical clock is stabilized. The frequency stability of the clock signal is expected to be improved by 2 orders of magnitude than that of the PDH stabilized signal, due to the suppression of cavity pulling effect in the bad cavity. Experimentally, we take the Nd: YAG 1064 nm transition as good-cavity gain medium, and the bad-cavity signal works on Cs 1470 nm transition. The dual-wavelength output of the active optical clock is realized, and the power and linewidth characteristics are preliminarily studied.**

Keywords—active optical clock; dual-wavelength; good-bad cavity;

I. INTRODUCTION

The stability of optical clocks is currently limited by the linewidth of the local oscillator [1], which is hard to improve, due to the cavity-length noise of the super cavity induced by the thermal Brownian-motion. The active optical clock, first proposed in 2005[2, 3], has dramatically reduced the sensibility of the output frequency to the cavity-length noise, nevertheless, the stability is still limited by the residual cavity pulling effect.

As optical cavity technology continues to develop, the linewidth cavity- stabilized laser through PDH method has already achieved tens of mHz [4]. To combine the cavity technology together with the active optical clock, in this paper, we propose a dual-wavelength good-bad cavity active optical clock, of which the two output signals with different wavelength share the same cavity, and work in good cavity and bad cavity regime, respectively. The good cavity signal is locked to a super cavity by the PDH technique, and thus the main cavity length of the active optical clock is stabilized. The frequency stability of the clock signal is expected to be improved by 2 orders of magnitude than that of the PDH stabilized signal, due to the suppression of cavity pulling effect in the bad cavity.

Experimentally, we take the Nd: YAG 1064 nm transition as good-cavity gain medium, and the bad-cavity signal works on Cs 1470 nm transition. The dual-wavelength output of the active optical clock is realized, and the power and linewidth characteristics are preliminarily studied.

This work is supported by the National Natural Science Foundation of China (Grant Nos. 91436210).

II. EXPERIMENTAL SETUP

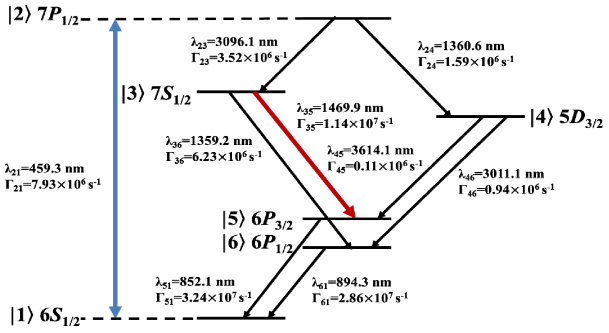
The basic experimental structure of Cs 4-level active atomic clock has already been reported in [5]. On this base, we put the Nd: YAG crystal into the cavity and pump it with the 808nm laser, the experimental setup is shown in Fig. 1. Cavity mirror M1 is coated with 808nm anti-reflection, and 1064nm &1470nm high-reflection. M2 is coated with 459nm anti-reflection, and the reflectivity of 1064nm and 1470nm is 95% and 70, respectively. The cavity is bad for 1064nm, with the laser gain linewidth being 132 GHz and the cavity mode linewidth being 13.5 MHz, while for 1470nm, the system works in deep bad-cavity regime [5]. M3 is used to guide the output signals, with anti-reflection for 459nm and high reflection for 1064&1470nm. M4 is to distinguish the good and bad cavity signals, with high-reflection for 1064nm and anti-reflection for 1470nm.

We built the integrated experimental structure of the dual-wavelength active optical clock, which is shown in fig. 2. With two cavity mirrors semi-fixed on a invar cavity body, the structure significantly reduced the noise introduced by the environment.

In the future, the good cavity signal will be stabilized by PDH technique, thus realizing stabilization of the main cavity and suppression of the linewidth of bad-cavity signal.

III. EXPERIMENTAL RESULTS

We experimentally realized the single longitude mode output of both good and bad cavity signal, the output power is measured as shown in Fig. 3, where the red line represents for the 1470nm laser, and the black line for the 1064 laser.



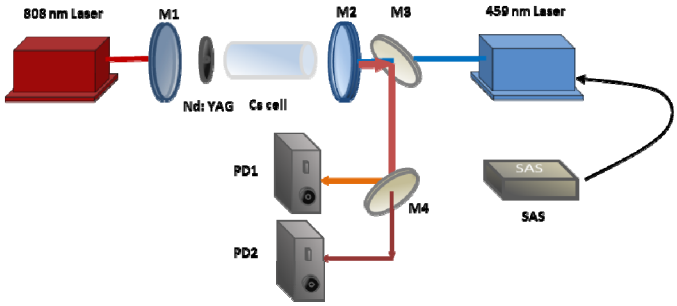


Fig. 1. Relevant energy levels of Cs and experimental setup of dual-wavelength good-bad cavity active optical clock. M: Mirror, SAS: Saturated absorption spectrum, PD: Photon diode.

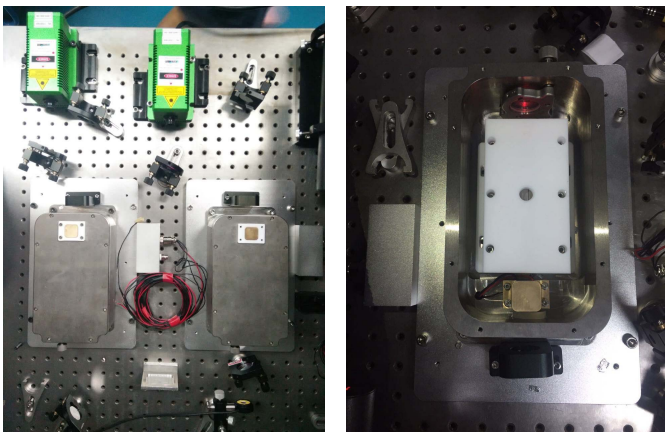


Fig. 2. The integrated experimental structure of the dual-wavelength active optical clock.

The linewidth of the output signals is measured through heterodyning between two similar systems. The beating signal of the 1064 nm good cavity and 1470 nm bad cavity are shown respectively in fig. 4 and fig. 5. For 1064 nm, the beating signal has a linewidth of 15.4 kHz, thus the linewidth of a single system is 10.9 kHz. The 1470 nm clock signal has a linewidth of 331 Hz, which is much narrower than the good cavity signal, because of the decreased influence of cavity length noise in deep bad cavity regime.

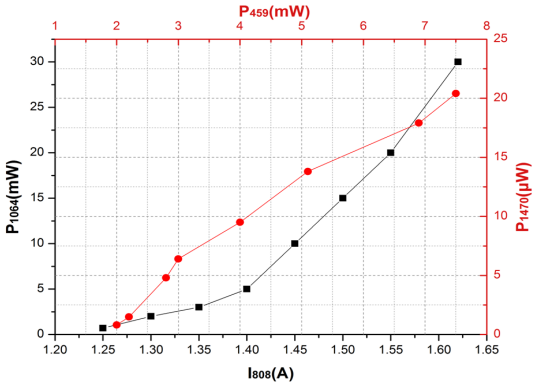


Fig. 3. Output power of the 1064 good-cavity signal and 1470 bad-cavity signal vary with the pumping power.

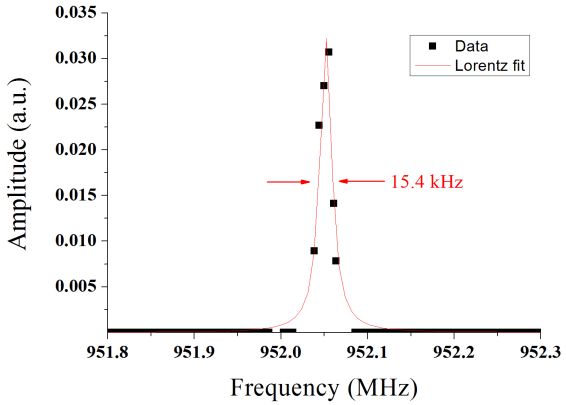


Fig. 4. Beating signal of 1064 nm good cavity laser.

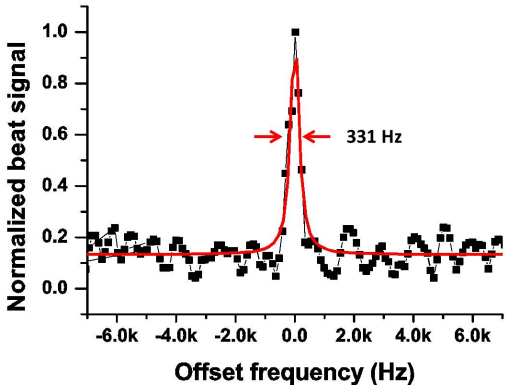


Fig. 5. Beating signal of 1470 nm bad cavity laser.

To measure the cavity pulling effect of the dual-wavelength, we mannually changed the volage applied to the piezoceramics (PZT) of the cavity, thus changing the resonance frequency of the cavity. The frequency detuning of the output signal is expressed by the frequency variation of the beating signal. When the cavity frequency changes for 112 MHz, the frequency of 1064 nm good cavity signal changed exactly with

the cavity, while the 1470 nm bad cavity signal just have a frequency variation of 1 MHz, which experimentally proved the suppression of cavity pulling effect in bad cavity regime.

In the future, we will work on the PDH stabilization, in which the good cavity signal is locked to a super cavity by the PDH technique, and thus the main cavity length of the active optical clock is stabilized. The frequency stability of the clock signal is expected to be improved by 2 orders of magnitude than that of the PDH stabilized signal, due to the suppression of cavity pulling effect in the bad cavity.

IV. CONCLUSION

In this paper, we propose a dual-wavelength good-bad cavity active optical clock, which combine the PDH technique and bad cavity together, and is expected to suppress the linewidth of clock signal by 2 orders of magnitude than that of the PDH stabilization.

Experimentally, The dual-wavelength output of the active optical clock is realized, and the power and linewidth characteristics are preliminarily studied. In the future, we will work on the PDH stabilization of the good cavity signal.

ACKNOWLEDGMENT

This work is supported by the National Natural Science Foundation of China (Grant Nos. 91436210)

REFERENCES

[1] Y. Jiang, A. Ludlow, N. Lemke, R. Fox, J. Sherman, L. Ma and C. Oates, "Making optical atomic clocks more stable with 10^{-16}-level laser stabilization". Nature Photonics, 5(3), pp. 158-161 (2011).

[2] J. Chen, X. Chen, "Optical Lattice Laser," Proceedings, 2005 IEEE Int. Frequency Control Symp., Vancouver, Canada, August 29-31, pp. 608-610 (2005).

[3] J. Chen, "Active optical clock". Chin. Sci. Bull., 54 (3), pp. 348-352 (2009)..

[4] T. Kessler, C. Hagemann, C. Grebing, T. Legero, U. Sterr, F. Riehle, "A sub-40-mHz-linewidth laser based on a silicon single-crystal optical cavity", Nature Photonics, 6(10), 687-692 (2011).

[5] D. Pan, Z. Xu, X. Xue, W. Zhuang and J. Chen, "Lasing of CesiumActive Optical Clock with 459 nm Laser Pumping", Proceedings of 2014 IEEE Int. Frequency Control Symp, May 19-22, Taipei, 242-245.

Prospects for an active optical clock using forbidden transition in trapped ions

Georgy A. Kazakov, Thorsten Schumm
Institute of Atomic and Subatomic Physics
Vienna University of Technology
Stadionallee 2, 1020 Vienna, Austria
Email: kazakov.george@gmail.com

***Abstract*—The concept of an active optical frequency standard was proposed about 10 years ago. The idea was to use optically trapped alkaline-earth atoms as a gain medium to built an extremely narrow-line laser, whose frequency would be robust against fluctuations of the cavity length. The main challenge in the realization of this concept is the short trap lifetime of the atoms. Recently we showed, that in such a laser, neutral atoms may be replaced by charged ions in a radio-frequency (RF) Paul trap with much longer lifetime. This idea rests on two pillars: the effect of synchronization of radiating dipoles with moderate inhomogeneous broadening, and the possibility to compensate (in leading orders) micromotion-induced shifts for some ion species in specially designed traps.**

I. Introduction

In modern optical clocks the frequency of a stable narrow-line *clock laser* is feedback-stabilized to some narrow and robust *etalon transition* in trapped atoms or ions (*quantum discriminator*). The clock laser (*local oscillator*) is pre-stabilized to some macroscopic cavity; its stability is limited by mechanical and thermal noise [1]. In the most advanced, specially designed high-precision systems, this stability (Allan variance) may attain a level of 4×10^{-17} on the timescale $1 - 100$ s [2]. At the same time, the linewidth of the clock transition in modern optical clocks may be significantly narrower than the linewidth of the local oscillator. In other words, the laser probes a transition that is much narrower than the laser itself. Therefore, instability of the local oscillator is currently the limiting factor in the performance of optical clocks. A breakthrough in this field would allow to drastically reduce the averaging time necessary to measure some frequency with the desired precision. This progress would advance a broad range of applications in fundamental and applied science, including relativistic relativistic geodesy [3], study of the variation of fundamental constants [4], searches for dark matter [5], stabilization of quantum networks [6], etc.

The stability of the clock laser can be improved by *locking it to another reference, more stable than the macroscopic cavity*. In the last decade, two approaches towards such a reference have been proposed, based on *continuous interrogation* of an atomic ensemble coupled to an optical cavity. The first one, an *active optical clock* [7], [8], is based on the idea to build a laser, where the gain medium is formed by atoms with a narrow and robust lasing transition. Operation in the *bad cavity regime*, where the linewidth of the cavity mode significantly exceeds the gain profile, makes the frequency of such a laser robust to fluctuations of the cavity length. The second (*passive*) approach, *direct cavity-enhanced non-linear spectroscopy*, is based on the strong non-linear response of an atomic ensemble to the driving laser light, which allows continuous adjustment of the laser, in contrast with "pulsed" interrogation in conventional optical clocks [9].

Up to now, most activities towards the realization of these approaches exploited the idea to use neutral atoms confined to the Lamb-Dicke regime in an optical lattice potential as a gain medium. A series of proof-of-principle experiments, including lasing on the metrology-relevant $^3P_0 \rightarrow {}^1S_0$ transition in trapped ^{87}Sr atoms in a pulsed regime [10], have been recently performed in the group of J. K. Thompson in JILA, USA (active approach), and in the group of J. Thomsen in University of Copenhagen [11] (passive approach). A serious obstacle for the creation of a continuously operating device is the limited trap lifetime of the atoms. In [12], [13] we showed how these problems can be overcome using special methods to compensate the atom losses, which are currently being implemented in the group of F. Schreck, University of Amsterdam. This way is however technically challenging.

II. Trapped ions approach: a concept

In contrast to neutral atoms, charged ions may be trapped in RF Paul traps for hours and days, without the need for sophisticated methods to compensate for ion losses. Such a traps may contain large ensembles of trapped ions, which at low temperatures forms a regular structure, a so-called *Coulomb crystal*. Large Coulomb crystals are not used in present *passive optical clocks*, because of inhomogeneous broadening caused by the micromotion-related shifts and quadrupole interactions between the ions. However, in *bad cavity lasers* the radiating dipoles synchronize and generate a stable radiation, if the inhomogeneous broadening is not too large [14]. Also, micromotion-induced second-order Doppler and Stark shifts may be mutually compensated for ions with negative differential polarizability of the clock states in the RF Paul trap at a specially chosen *magic frequency* of the trapping field [15]. Some of these ions, such as Ca^+, Sr^+, Ba^+ and Ra^+ have clock transitions in the visible or near-infrared range, where a high-finesse optical cavity may be constructed.

III. $^{176}Lu^+$ as a possible active ion

In [16] we studied the possibility to build an active optical clock with $^{176}Lu^+$. Such an ion is an interesting candidate for the role of the gain element: the transition $^3D_2 \rightarrow {}^1S_0$ has a

978-1-5386-2916-1/$31.00 ©2017 IEEE

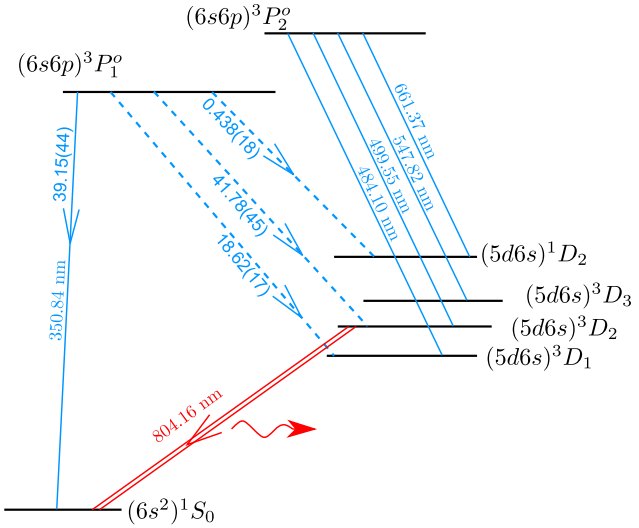


Fig. 1. General pumping scheme for a 804 nm bad cavity laser on $^{176}Lu^+$ ions. Dashed lines denote the most relevant spontaneous decays, solid lines correspond to both spontaneous and laser-induced transitions; wavelengths (in nm) and experimental branching ratios (in % according [17], uncertainties are given in parenthesis) are indicated.

convenient 804 nm wavelength and negative differential scalar polarizability, according recent results [17]. The upper state can be efficiently pumped via the $^3P_1^o$ level (see figure 1). Supposing that the ions form a spherical Coulomb crystal in a linear Paul trap, where all the motion except the micromotion is frozen out, we found that about 0.5 pW of output laser power can be produced, if the Paul trap has a confinement frequency of about 1 MHz, contains 10^5 ions coupled to a single circularly polarized Gaussian standing wave mode of the cavity with finesse $\mathcal{F} = 10^5$. This should be enough to lock the phase of a slave laser with a few Hz linewidth (which may be attained with the help of pre-locking to a commercially available macroscopic cavity), providing relative frequency instability well below the 10^{-17} level on the timescale of one second. An order-of-magnitude estimation of the linewidth of the output laser radiation performed on the basis of a theory for the bad-cavity laser with two-level active atoms without inhomogeneous effects [8] gives a value of a few mHz; the linewidth may be further reduced by decreasing of the confinement frequency.

On the other hand, $^{176}Lu^+$ has a complex hyperfine structure determined by its large nuclear angular moment ($I = 7$). Therefore, many multi-frequency lasers should be used for pumping population into the upper lasing state. An alternative option is to implement the *passive scheme* based on non-linear cavity-enhanced spectroscopy. Also, the micromotion will heat the ion ensemble, and direct or sympathetic cooling has to be applied.

IV. Conclusion

We conclude that creation of active optical frequency standard with large Coulomb crystals of trapped ions seems to be challenging but feasible idea. The ion species $^{176}Lu^+$ is a promising candidate, altough another ions with negative differential polarizability of the clock state, such as Ca^+, Sr^+, Ba^+ and Ra^+, also may be used in such a standard.

Acknowledgment

The authors would like to thank Murray Douglas Barrett, John Bollinger, Justin Bohnet and Athreya Shankar for useful discussion. The study has been supported by the EU FET-Open project 664732 NuClock.

References

[1] K. Numata, A. Kemery, J. Camp, *Thermal-Noise Limit in the Frequency Stabilization of Lasers with Rigid Cavities*. Phys. Rev. Lett. **93**, p. 250602, 2004

[2] D.G. Matei, T. Legero, S. Häfner, C. Grebing, R. Weyrich, W. Zhang, L. Sonderhouse, J.M. Robinson, J. Ye, F. Riehle, U. Sterr, *1.5 μm lasers with sub 10 mHz linewidth*. Phys. Rev. Lett. **118**, p. 263202, 2017

[3] C. W. Chou, D. B. Hume, J. C. J. Koelemeij, D. J. Wineland, T. Rosenband. *Frequency Comparison of Two High-Accuracy Al^+ Optical Clocks.* Phys. Rev. Lett. 104, p. 070802, 2010

[4] R. M. Godun, P. B. R. Nisbet-Jones, J. M. Jones, S. A. King, L. A. M. Johnson, H. S. Margolis, K. Szymaniec, S. N. Lea, K. Bongs, and P. Gill, *Frequency Ratio of Two Optical Clock Transitions in $^{171}Yb^+$ and Constraints on the Time Variation of Fundamental Constants* Phys. Rev. Lett. **113**, p. 210801, 2014

[5] A. Arvanitaki, J. Huang, K. Van Tilburg, *Searching for dilaton dark matter with atomic clocks*. Phys. Rev. D **91**, p. 015015, 2015

[6] P. Kómár, E. M. Kessler, M. Bishof, L. Jiang, A. S. Sørensen, J. Ye, M. D. Lukin,*A quantum network of clocks.* Nature Physics **10**, p. 582, 2014

[7] J. Chen, X. Chen, *Optical Lattice Laser*. Proceedings of the 2005 IEEE IFCS and Exposition, p. 608

[8] D. Meiser, J. Ye, D. R. Carlson, and M. J. Holland, *Prospects for a Millihertz-Linewidth Laser*. Phys. Rev. Lett. **102**, p. 163601, 2009

[9] M. J. Martin, D. Meiser, J. W. Thomsen, Jun Ye, and M. J. Holland, *Extreme nonlinear response of ultranarrow optical transitions in cavity QED for laser stabilization*. Phys. Rev. A **84**, p. 063813, 2011

[10] M. A. Norcia, M. N. Winchester, J. R. K. Cline, J. K. Thompson, *Superradiance on the milliHertz linewidth strontium clock transition.* Science Advances **2**, p. e1601231, 2016

[11] P. G. Westergaard, B. T. R. Christensen, D. Tieri, R. Matin, J. Cooper, M. Holland, Jun Ye, and Jan W. Thomsen, *Observation of motion-dependent nonlinear dispersion with narrow-linewidth atoms in an optical cavity*. Phys. Rev. Lett. **114**, p. 093002, 2015

[12] G. Kazakov, T. Schumm, *Active optical frequency standard using cold atoms: perspectives and challenges*. Proceedings of EFTF-2014, p. 411, 2014

[13] G. Kazakov, T. Schumm, *Active optical frequency standard using sequential coupling of atomic ensembles*. Phys. Rev. A **87**, p. 013821, 2013

[14] G. Kazakov, T. Schumm, *Stability analysis for bad cavity lasers using inhomogeneously broadened spin-1/2 atoms as a gain medium.* Phys. Rev. A **95**, p. 023839, 2017

[15] K. Arnold, E. Hajiyev, E. Paez, C. H. Lee, M. D. Barrett, J. Bollinger, *Prospects for atomic clocks based on large ion crystals.* Phys. Rev. A **92**, p 032108, 2015

[16] G. Kazakov, J. Bohnet, T. Schumm, *Prospect for bad cavity laser on large ion crystal.* arXiv:1704.08318 (2017)

[17] E. Paez, K. J. Arnold, E. Hajiyev, M. D. Barrett, S. G. Porsev, V. A. Dzuba, U. I. Safronova, M. S. Safronova, M. D. Barrett, *Atomic Properties of Lu^+*. Phys. Rev. A **93**, p. 042112, 2016

Deep laser cooling of Mg in dipole trap for frequency standard

O.N. Prudnikov, A.V. Taichenachev, V.I. Yudin
Institute of Laser Physics, 630090, Novosibirsk, Russia
Novosibirsk State University, 630090, Novosibirsk, Russia

E.M. Rasel
Institutur Quantenoptik, Universitat Hannover,
Welfengarten 1, D-30167 Hannover, Germany

***Abstract*—We study deep laser cooling of ^{24}Mg atoms in dipole optical trap with pumping field resonant to narrow $(3s3s)^1S_0 \rightarrow (3s3p)^3P_1$ (λ = 457nm) optical transition. We consider two quantum models: the first one based on direct numerical solution of quantum kinetic equation for atom density matrix and the second one is simplified model based on decomposition of atom density matrix on vibration states in dipole trap. Both models shows close results. We search pumping field intensity and detuning for minimum laser cooling energy of atoms and fast laser cooling.**

Keywords— laser cooling; optical lattices; dipole trap

I. INTRODUCTION

Nowadays deep laser cooling of neutral atoms is routinely used for broad range of modern quantum physics researches including metrology, atom optics, and quantum degeneracy studies. The well-known techniques for laser cooling below the Doppler limit, like sub-Doppler polarization gradient cooling [1], velocity selective coherent population trapping [2,3] or Raman cooling [4,5] are restricted to atoms with degenerated over angular momentum energy levels or hyperfine structure. However, for atoms with single ground state ^{24}Mg, ^{40}Ca, ^{88}Sr, ^{174}Yb are of interest for developing optical time standard these well-known techniques can not be applied. For example, for ^{24}Mg atoms with the ground state $^1S_0$ the Doppler cooling temperature ($k_B T_D \approx \hbar\gamma/2$) can be reached on closed singlet transition $^1S_0 \rightarrow {}^1P_1$ (λ = 285.3 nm). For lower temperature additional cooling on $^3P_2 \rightarrow {}^3D_3$ optical transition with degenerated over angular momentum energy levels can be applied [6,7]. However, the experimental realization of laser cooling on $^3P_2 \rightarrow {}^3D_3$ optical transition do not results significant progress. The atoms were cooled to temperature T≈1 mK is about Doppler limit only [7].

One of the way for deep laser cooling of such elements is using narrow lines and "quenching" techniques of narrow-line laser cooling [8-10] successfully applied for ^{40}Ca atoms, the recent progress on cooling ^{88}Sr on narrow line in dipole trap was also reported in [11], but, to our knowledge, still do not show significant progress for ^{24}Mg atoms.

In the following paper we study application of this cooling scheme for ^{24}Mg atom on narrow $(3s3s)^1S_0 \rightarrow (3s3p)^3P_1$ (λ_1 = 457 nm, γ_1 = 196 s^{-1}) optical transition. Additional light field resonant to $(3s3p)^3P_1 \rightarrow (3s4s)^1S_0$ optical transition λ_2 = 462 nm, γ_{21} = 109 s^{-1} and $\gamma_{23} = 2.1\cdot10^7$ s^{-1}) is applied for optical quenching (see Fig.1), i.e. increasing effective linewidth of optical transition [10].

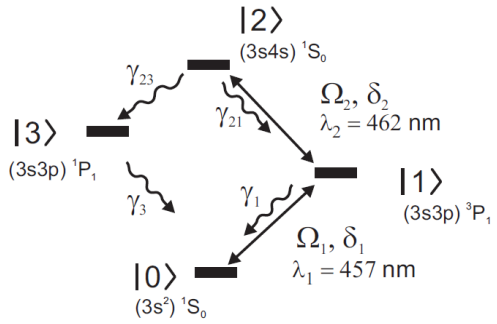


Fig. 1. Relevant energy levels for optical quenching and cooling of ^{24}Mg.

We find the semiclassical description of laser cooling of Mg atom with narrow optical transition can't be used here because of main requirements for semiclasical description are not fulfilled [1,12,14]. For description of laser cooling we use quantum approaches that allow to take into account optical pumping and photon recoil effects in laser cooling. In the paper we point attention to minimum laser cooling temperature for described scheme and cooling time as well.

II. DESCRIPTION OF THE MODEL

We consider motion of ^{24}Mg atom in the dipole optical trap with λ_D = 1064 nm that provide higher polarizability of the atom in excited state $(3s3p)\ ^3P_1$ that in the ground state $(3s3s)^1S_0$. In the following paper we restrict our consideration by two level model only assuming the quenching field results to increasing effective linewidth of optical transition to γ_{eff} that is function of on intensity of quenching field [10]:

$$\gamma_{eff} = \gamma_1 + \gamma_2 \frac{\Omega_2^2}{\gamma_2^2 + 4\delta_2^2} \qquad (1)$$

with Ω_2 is Rabi and δ_2 is detuning of quench field. Thus, for example, to reach γ_{eff} = 100 γ_1 at δ_2 = 0 one have to apply quench field intensity I_q≈1.6 W/cm^2. The simulated

polarizability difference for the optical dipole trap wavelength is about $\alpha_e/\alpha_g = 1.46$. In the trap (Fig.2) the quantum nature of atomic motion becomes essential. For considered optical trap depth for the ground state Ug = 200 μK vibration energy separation for the lowest states $\hbar\omega_g \approx 16.6\,\mu K$ and for excited state optical potential depth Ue = 292 μK the lowest states separation $\hbar\omega_e \approx 20.1\,\mu K$. This strong energy levels separation require quantum model for description of laser cooling dynamics of atoms in the trap.

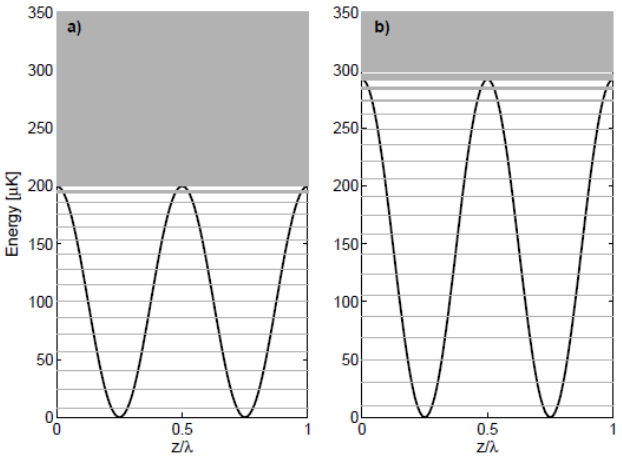


Fig. 2. Ac Shtark shift and vibration energy levels for ground $^1S_0$ (a) and excited $^3P_1$ (b) states of ^{24}Mg atoms in dipole optical trap with λ_D = 1064nm.

We consider two quantum approaches. The first based on decomposition of atom wave function on optical potential vibration level states. Restricting the limited number of lowest vibration states we find atoms stationary distribution over the vibration levels in the trap, as well as the laser cooling dynamics to these stationary states. This approach is similar to method was described in [13]. However, our model we also take into account the optical coherence of vibration states, i.e. do not limit consideration by well-resolved vibration levels separation.

The second method we consider is based on direct numerical solution of quantum equation for atomic density matrix that allows to take into account not only the fixed number of the lowest vibration level states but whole atoms in the trap, including tunneling effects and above barrier motion. However, in this method, due to high complicity of the problem we omit the recoil effects from the pumping field that is equivalent to orthogonal orientation of wave vectors of pumping and optical trap light waves in considered one-dimensional model.

A. *Two-level model: exact numerical solution of quantum density matrix equation*

We consider the motion of Mg atom in optical dipole trap is standing light wave propagating along *z* direction with linear polarization along *x*. The pumping light field wave also linear polarized along *x* propagated along *z* or *y*. The quantum equation for atomic density matrix describes evolution of internal and external states of atoms

$$\frac{\partial}{\partial t}\hat{\rho} = -\frac{i}{\hbar}\left[\hat{H}_0 + \hat{V}_p, \hat{\rho}\right] + \hat{\Gamma}\{\hat{\rho}\} \qquad (2)$$

with $\hat{H}_0$ is Hamiltonian, $\hat{V}_p$ describes interaction with pumping field and $\hat{\Gamma}\{\hat{\rho}\}$ describes relaxation due to spontaneous decay.

In the following we restrict our consideration by effective two-level model with $(3s3s)^1S_0$ is the ground (g) and $(3s3p)^3P_1$ is excited state (e) with effective linewidth γ_{eff} defined by the quench field (1). Further, in considered two-level model we omit parameters indexes Ω_1, δ_1 and γ_1 by writing Ω, δ and γ instead.

Hamiltonian of atom in the trap has the following form:

$$\hat{H}_0 = \frac{\hat{p}^2}{2M} + U_g \cos^2(kz)|g\rangle\langle g| + \left[U_e \cos^2(kz) + \hbar\omega_0\right]|e\rangle\langle e| \qquad (3)$$

with optical potentials depth in the ground Ug and Ue in excited states, $\hbar\omega_0$ is energy difference of unperturbed ground and excited states. The wavevector $k=2\pi/\lambda_D$ is defined by the dipole optical trap.

The following equation (2) for atomic density matrix $\hat{\rho}$ can be solved numerically with total account of quantum recoil effects of atom-light interaction by methods we suggest in [15,16]. This method allows to get steady-state solution taking into account kinetics of atoms in the dipole trap and atoms with above barrier motion.

B. *Decomposition on vibration states model*

The second method use simplification and based on decomposition of atomic wave function on vibration states in the trap.

$$\begin{aligned} \rho^{ee}_{nm} &= \langle e,n|\hat{\rho}|e,m\rangle \quad \rho^{eg}_{nm} = \langle e,n|\hat{\rho}|g,m\rangle \\ \rho^{ge}_{nm} &= \langle g,n|\hat{\rho}|e,m\rangle \quad \rho^{gg}_{nm} = \langle g,n|\hat{\rho}|g,m\rangle \end{aligned} \qquad (4)$$

It well describes the cooling of atoms localized on the lowest vibration levels in the trap. The equation for these components has similar to (2) form:

$$\begin{aligned} &\frac{\partial}{\partial t}\rho^{ee}_{nm} = -\gamma_{eff}\rho^{ee}_{nm} - i\left(\omega^{(e)}_n - \omega^{(e)}_n\right)\rho^{ee}_{nm} - i\sum_k\left(\Omega_{nk}\rho^{ge}_{km} - \rho^{eg}_{nk}\Omega^+_{km}\right) \\ &\frac{\partial}{\partial t}\rho^{eg}_{nm} + \left[\frac{\gamma_{eff}}{2} - i\delta\right]\rho^{eg}_{nm} = -i\left(\omega^{(e)}_n - \omega^{(g)}_n\right)\rho^{eg}_{nm} - i\sum_k\left(\Omega_{nk}\rho^{gg}_{km} - \rho^{ee}_{nk}\Omega_{km}\right) \\ &\frac{\partial}{\partial t}\rho^{ge}_{nm} + \left[\frac{\gamma_{eff}}{2} + i\delta\right]\rho^{ge}_{nm} = -i\left(\omega^{(g)}_n - \omega^{(e)}_n\right)\rho^{ge}_{nm} - i\sum_k\left(\Omega^+_{nk}\rho^{gg}_{km} - \rho^{ee}_{nk}\Omega^+_{km}\right) \\ &\frac{\partial}{\partial t}\rho^{gg}_{nm} = \hat{\gamma}\left\{\rho^{ee}_{nm}\right\} - i\left(\omega^{(g)}_n - \omega^{(g)}_n\right)\rho^{gg}_{nm} - i\sum_k\left(\Omega^+_{nk}\rho^{eg}_{km} - \rho^{ge}_{nk}\Omega_{km}\right) \end{aligned} \qquad (5)$$

where $\hbar\omega^{(e)}_n$, $\hbar\omega^{(g)}_n$ are vibration energy of excited and ground states, matrix elements Ω_{nm} defines coupling of ground and excited vibration states

$$\Omega_{nm} = \langle e,n|\Omega/2\ \exp(ik_s z\cos\theta)|g,m\rangle = \frac{\Omega}{2}\int \psi_n^{*(e)}(z)e^{ik_s z\cos\theta}\psi_m^{(g)}(z)dz \quad (6)$$

The income to the ground sate due spontaneous relaxation described by $\hat{\gamma}\{\rho_{nm}^{ee}\} = \gamma_{eff}\sum_{\nu\mu}\Gamma_{nm}^{\nu\mu}\rho_{\nu\mu}^{ee}$

$$\Gamma_{nm}^{\nu\mu} = \iint \psi_n^{*(g)}(z_1)\psi_\nu^{(e)}(z_1)\tilde{\gamma}(z_1-z_2)\psi_\mu^{*(e)}(z_2)\psi_m^{(g)}(z_2)\,dz_1dz_2$$

$$\tilde{\gamma}(q) = 3\left(\frac{\sin(k_s q)}{(k_s q)^3} - \frac{\cos(k_s q)}{(k_s q)^2}\right)$$

with $k_s = 2\pi/\lambda$ (λ = 457nm) is wave vector of spontaneously emitted photons.

For better physical insight we additionally to exact numerical solution of density matrix equation (2) of section A and to numerical solution of equations (5) for density matrix in vibration states basis will consider one more simplification that neglect the optical coherence of vibration states ρ_{nm}^{ee}, ρ_{nm}^{gg}. This simplification allows to write simple balance equations for the populations of excited and ground states:

$$\frac{\partial}{\partial t}\rho_{nn}^{ee} = -\gamma_{eff}\left(1+\sum_{m=1}^{Ng}S_{nm}\right)\rho_{nn}^{ee} + \gamma_{eff}\sum_{m=1}^{Ng}S_{nm}\rho_{mm}^{gg},\ n=1..Ne$$
$$\frac{\partial}{\partial t}\rho_{mm}^{gg} = \gamma_{eff}\sum_{n=1}^{Ne}\left(\Gamma_{mm}^{nn}+S_{nm}\right)\rho_{nn}^{ee} - \gamma_{eff}\left(\sum_{n=1}^{Ne}S_{nm}\right)\rho_{mm}^{gg},\ m=1..Ng \quad (7)$$

with saturation parameters

$$S_{nm} = \frac{|\Omega_{nm}|^2}{\gamma_{eff}^2/4 + \left[\delta - (\omega_n^{(e)} - \omega_m^{(g)})\right]^2}$$

for the fixed number of excited (*Ne*) and ground (*Ng*) vibration states are taken into account. The equation (7) can be solved analytically. For the low intensity of pumping field Ω, restricting by two lowest vibration levels on the ground state the solution of (7) takes the following form for ρ_{00}^{gg} and ρ_{11}^{gg}

$$\rho_{00}^{gg} = \left[1 + \frac{\Gamma_{11}^{00}S_{00} + \Gamma_{11}^{11}S_{10}}{(1-\Gamma_{11}^{00})S_{01} + (1-\Gamma_{11}^{11})S_{11}}\right]^{-1}$$
$$\rho_{11}^{gg} = \left[1 + \frac{(1-\Gamma_{11}^{00})S_{01} + (1-\Gamma_{11}^{11})S_{11}}{\Gamma_{11}^{00}S_{00} + \Gamma_{11}^{11}S_{10}}\right]^{-1}$$

describe for ρ_{00}^{gg} smooth curve on detuning with minimums determined by $\omega_0^{(e)} \to \omega_0^{(g)}$ and $\omega_1^{(e)} \to \omega_0^{(g)}$ resonances (i.e. for detuning $\delta = \omega_0^{(e)} - \omega_0^{(g)}$ and $\delta = \omega_1^{(e)} - \omega_0^{(g)}$) and maximum for detuning close to $\delta = \omega_0^{(e)} - \omega_1^{(g)}$ and $\delta = \omega_1^{(e)} - \omega_1^{(g)}$.

III. Results

The fugure 3 shows the energy of cooled Mg atoms in the dipole trap obtained and population of the ground state vibration levels obtained by both described above methods (section A and section B).

Both methods demonstrates close results with the differences far from the minimum cooling energy when the populations of the top vibration levels are not negligible and tunneling effects and above barrier motion of atoms can not be neglected. Nevertheless, the simplified model eq.(5) well describe the laser cooling near the minimum of energy and allows to estimate the cooling time.

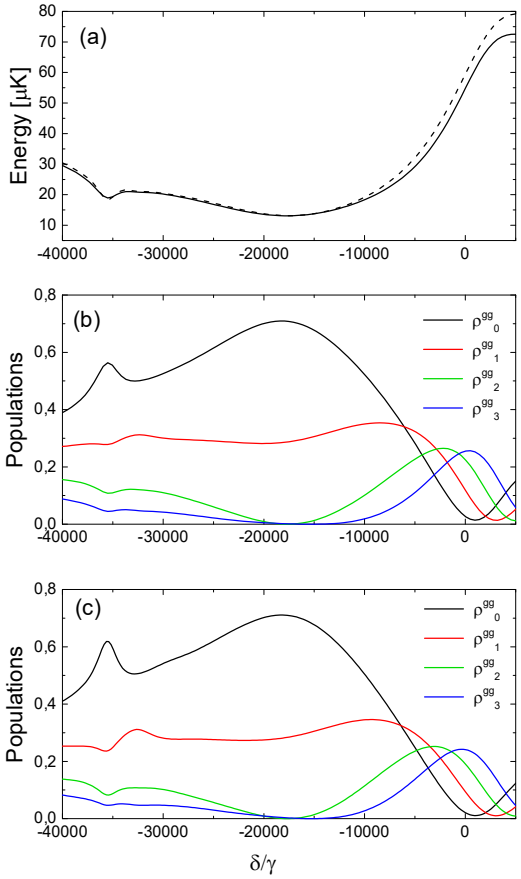


Fig. 3. Energy of cooled ^{24}Mg atoms in the tipole trap (a) as function of pumping filed detuning obtained by exact numerical solution of eq.(2) (solid line) and by decomposition of vibration state method (dashed line). Populations of the ground state vibration levels (g) as function of detuning for exact numerical solution (b) and decomposition on vibration state model (c). Pumping field Rabi Ω = 2000γ (I = 0.34 W/cm^2), γ_{eff} = 100γ. Orthogonal orientation of pumping field and the trap θ = π/2.

As well the populations and energy of ^{24}Mg atoms in dipole trap and coplanar geometry of pumping field is shown on figure 4. We see the balance equations (7) well describe atom behavior in the trap for low intensity of pumping field. The modulations of population and total energy on detuning corresponds to resonances $\omega_0^{(e)} \to \omega_1^{(g)}$, $\omega_0^{(e)} \to \omega_2^{(g)}$, $\omega_0^{(e)} \to \omega_3^{(g)}$, and $\omega_0^{(e)} \to \omega_4^{(g)}$. With increasing the pumping field intensity the balance equation approach (7) violates. Additionally, we see the field shift of the resonances (Fig. 4(b) and 4(d)).

For solution of dynamical problem we assume the atom populates the highest vibration energy state of the ground state optical potential at t = 0.

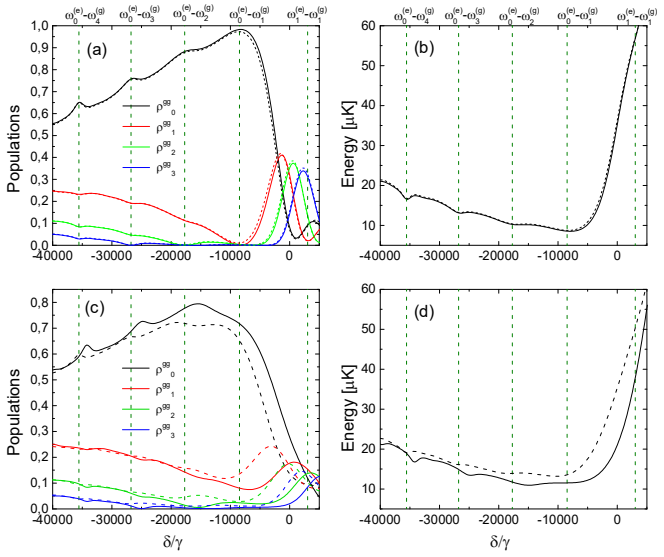


Fig. 4. Populations and energy of cooled ^{24}Mg atoms in the tipole trap for different intensity of pumping field ((a) and (b) for Rabi Ω=2000γ and (c) and (d) for Ω=10000γ) as function of pumping filed detuning obtained by exact numerical solution of eq.(5) - solid lines and by balance equations (7) - dashed lines. Coplanar geometry of pumping field and the trap θ = 0.

The time evolution of vibration levels population has a complex dependence. To find the cooling time we fit $\rho^{gg}_{00}(t)$ by exponential function of the form $\rho^{gg}_{00}(t) = a - b\exp(-t/\tau)$ with τ describes the cooling time. We find the energy of cooled atoms do not depends on parameter γ_{eff} (i.e. on quenching field intensity) in the range of our simulations $\gamma < \gamma_{eff} < 100\gamma$, while the cooling time τ is inversely proportional to γ_{eff} in considered model. This allow us to represent the cooling time τ in basic form through dimensionless value $\tilde{\tau}$ ($\tau = \tilde{\tau}/\gamma_{eff}$).

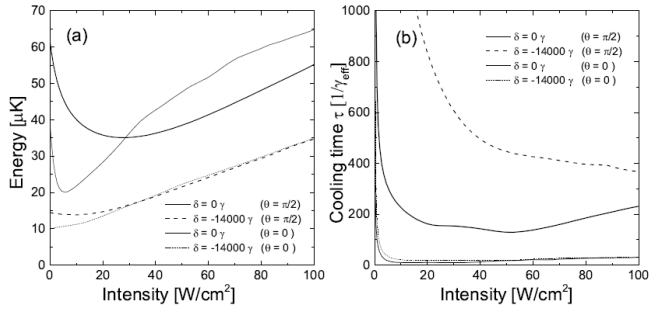


Fig. 5. Energy of cooled ^{24}Mg atoms in the dipole trap (a) and cooling time $\tilde{\tau}$ (b) in considered optical dipole trap for different orientation of pumping wave and dipole trap difined by angle θ and different detunings obtained by solution based on decomposition on vibration state model as function of pumping field intensity.

IV. Conclusion

We study laser cooling of ^{24}Mg atoms in the dipole trap with pumping field resonant to narrow $(3s3s)^1S_0 \rightarrow (3s3p)^3P_1$ (λ = 457nm) optical transition and quench field resonant to $(3s3p)^3P_1 \rightarrow (3s4s)^1S_0$ optical transition λ_2 = 462 nm. The effect of quenching field we consider here is in widening of optical transition to γ_{eff} only. We consider two quantum models. The first one is based on direct numerical solution of quantum kinetic equation for atom density matrix and the second one is simplified model based on decomposition of atom density matrix on vibration states in dipole trap. Additionally to vibration state model we consider simplified balance equations that allow clarify modulations on detuning the atom energy and population of vibration levels.

Both considered models describe cooling of atoms on the lowest vibration levels with difference appears for high intensity of pumping field (above 50 W/cm^2 or Rabi above 25000γ) when the populations of the top vibration levels are not negligible and tunneling effects and above barrier motion of atoms can not be neglected. Nevertheless, the vibration state model well describe the laser cooling to minimum of cooling energy (about 10μK). Additionally this model allows to estimate the cooling time. The parameters of pumping field for cooling to minimum energy do not coincide with conditions for fast cooling. We find parameters that allow cooling the atoms for reasonable cooling time $\tau \approx 10/\gamma_{eff}$ ($\tau \approx 0.5$ ms for $\gamma_{eff} = 100\gamma$) to energy E ≈ 12μK.

Finally we note the important assumption we used for accounting the quench field (1) might not be enough adequate the real situation and demands more detailed consideration on a base of three level scheme in dipole trap. We hope to finish this consideration in the near future.

The work was supported by Russian Science Foundation (project N16-12-00054). V.I.Yudin acknowledges the support of the Ministry of Education and Science (3.1326.2017/4.6) and RFBR (grant 17-02-00570).

References

[1] J. Dalibard and C. Cohen-Tannoudji, J. Opt. Soc. Am. B v.6, pp.2023-2045 (1989)

[2] J. Lawall, F. Bardou, B. Saubamea, K. Shimizu, M. Leduc, A.Aspect, and C. Cohen-Tannoudji, Phys. Rev. Lett. vol. 73, p.1915 (1994).

[3] C. S. Adams, H. J. Lee, N. Davidson, M. Kasevich, and S. Chu, Phys. Rev. Lett. vol. 74, pp.3577–3580 (1995).

[4] M. Kasevich and S. Chu, Phys. Rev. Lett. v.69, p.1741 (1992).

[5] J. Reichel, F. Bardou, M. Ben Dahan, E. Peik, S. Rand, C. Salomon, and C. Cohen-Tannoudji, Phys. Rev. Lett. v. 75, p. 4575 (1995).

[6] A.P. Kulosa, D. Fim, K.H. Zipfel, S. Ruhmann, S. Sauer, N. Jha, K. Gibble, W. Ertmer, E.M. Rasel, M.S. Safronova, U.I. Safronova, S.G. Porsev, arXiv: 1508.01118v1, physics.atom-ph, 5 Aug 2015.

[7] M. Riedmann, H. Kelkar, T. Wubbena, A. Pape, A. Kulosa, K. Zipfel, D. Fim, S. Ruhmann, J. Friebe, W. Ertmer, and E.Rasel, Phys. Rev. A v. 86, 043416 (2012).

[8] E.A. Curtis, C.W. Oates, and L.Holberg Phys. Rev. A v. 64, 031403 (2001)

[9] T. Binnewies, G. Wilpers, U. Sterr, J. Helmcke,T.E. Mehlstabler, E.M. Rasel, and W. Ertmer Phys. Rev. Lett. v. 87, 123002 (2001)

[10] T.E. Mehlstabler, J. Keupp, A.Douillet, N. Rehbein, E.M. Rasel J.Opt.B: Quantum Semiclass. Opt. v. 5, S183 (2003)

[11] M.Chalony, A.Kastberg, B.Klappauf and D.Wilkowski, PRL v.107, 243002 (2011)

[12] J. Javanainen PRA v. 44, pp. 5857-5880 (1990)

[13] Y. Castin and J. Dalibard Europhys. Lett., v. 14, pp. 761-766 (1991)

[14] O.N. Prudnikov, A. V. Taichenachev, A. M. Tumaikin and V. I. Yudin, JETP v. 98, pp. 438-454 (2004)

[15] O.N. Prudnikov, A.V. Taichenachev, A.V. Tumaikin, V.I. Yudin, Phys. Rev. A v.75, 023413 (2007)

[16] O. N. Prudnikov, R.Ya. Ilenkov, A. V. Taichenachev, A. M. Tumaikin, and V. I. Yudin, JETP v.112, pp.939-945 (2011)

Towards black body radiation shift uncertainty in optical lattice clocks at 10^{-18} level at room temperatures

Piotr Ablewski, Marcin Bober and Michał Zawada
Institute of Physics, Faculty of Physics, Astronomy and Informatics
Nicolaus Copernicus University
Grudziadzka 5, 87-100 Toruń, Poland

E-mail: piotra@fizyka.umk.pl

***Abstract*—We present current status of work on blackbody radiation impact on ultra-narrow optical resonances. The emissivities of the most popular materials, which are used for construction of vacuum chambers, have been measured in the temperatures close to the room temperature. We have developed a new vacuum system designed exclusively for the emissivity measurements. We have measured the emissivity of samples made from different materials and with different finishing. This data has been also used to perform numerical simulation of temperature distribution of an optical clock vacuum set-up.**

I. Introduction

Optical atomic clocks have already achieved uncertainty of 10^{-18} [1]. At this level the blackbody radiation (BBR) shift gives one of the main contribution to the error budget, especially in case of strontium atoms [2], [3]. Calculations exploiting configuration interaction (CI) and many-body perturbation theory (MBPT) [4]–[8] show that ultra-narrow transition at 698 nm is very sensitive to blackbody radiation. To evaluate the shift of atomic resonance induced by thermal radiation of environment, the temperature of vacuum system parts visible by trapped atoms has to be known.

One of the possible ways to achieve that goal is to perform a direct measurement of temperature in the exact place where cold atoms are stored [1]. Another method is to cover the inner surface of vacuum chamber parts with material of high emissivity, such as Acktar or Vantablack [9], [10]. The shift can be also greatly minimised by loading the atoms into a tube made from material with high emissivity and cool this tube down to a cryogenic temperature [5], [9].

All these methods share one serious disadvantage they are not easily applicable in the existing operating optical clocks systems due to the necessity of major changes in chamber construction or complete redesign of the optical clock system. In that case, a simulation of temperature distribution of the optical clock set-up can be the best solution. High precision data from the simulation can be used to calculate BBR shift of clock transition with the smallest possible numerical error.

II. Emissivity measurements at room temperatures

We have developed the vacuum system to measure the emissivities of different materials in room temperatures. Samples made of cooper (CU-ETP), stainless steel (1.4301), titanium (grade 5 6Al-4V) and aluminium (PA38) with different types of finishing have been checked. Our measurement setup is shown on Fig. 1.

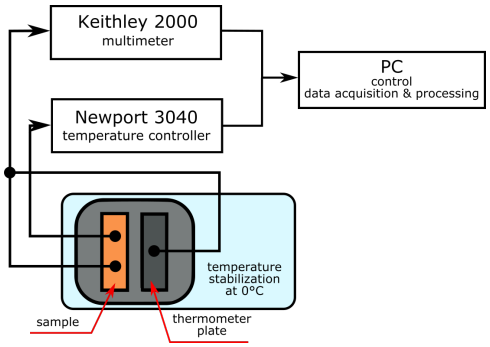


Fig. 1. Scheme of emissivity measurement set-up

All surfaces of chamber and the thermometer have been covered with KRYLON Ultra-Flat Black painting to provide high emissivity in wide spectra range [11]. The chamber temperature has been stabilized at 0°C, temperature of the sample has been stabilized at the room temperature and temperature of thermometer plate has been measured. This data have been used to feed the numerical simulation supported by analytical calculations to extract the emissivities of the samples. Thermometers used for the measurements were calibrated at the level of 10mK.

III. Numerical simulation of the heat transfer in an optical atomic clock system

The results of our thermal measurements and emissivity calculations have been used as an input data for the numerical simulation of thermal distribution of a strontium optical clock system. The numerical code for finite elements method (FEM)

978-1-5386-2916-1/$31.00 ©2017 IEEE

simulation has been written and optimized. The output of the simulation has been compared with the output of simulation from SolidWorks ThermalAnalysis module, which was our previous method to estimate the BBR shifts [2], [3].

Our code includes analytical solutions of view factors coefficients between typical surfaces and shapes which can be commonly found in optical clock systems. The code for the calculations has been optimised for modern multicore and multithreaded processors, and graphics cards. This will allow calculating the thermal distribution of clock systems and BRR shifts in real time, without need to use computational power of supercomputers.

ACKNOWLEDGMENT

The reported measurements were performed at the National Laboratory FAMO in Toruń, Poland, and were supported by a subsidy from the Ministry of Science and Higher Education.

Support has been received from the project EMPIR 15SIB03 OC18. This project has received funding from the EMPIR programme co-financed by the Participating States and from the European Unions Horizon 2020 research and innovation programme.

The research was part of the grant for PhD students founded by Faculty of Physics, Astronomy and Informatics, Nicolaus Copernicus University in Toruń (grant No 2712-F).

REFERENCES

[1] T. L. Nicholson, S. L. Campbell, R. B. Hutson, G. E. Marti, B. J. Bloom, R. L. McNally, W. Zhang, M. D. Barrett, M. S. Safronova, G. F. Strouse, W. L. Tew and J. Ye, "Systematic evaluation of an atomic clock at 2×10^{18} total uncertainty", Nat. Commun., vol. 6, pp. 6896, April 2015.

[2] M. Bober, P. Morzyński, A. Cygan, D. Lisak, P. Masłowski, M. Prymaczek, P. Wcisłło, P. Ablewski, M. Piwiński, Sz. Wójtewicz, K. Bielska, D. Bartoszek-Bober, R. S. Trawiński, M. Zawada, R. Ciuryło, J. Zachorowski, M. Piotrowski, W. Gawlik, F. Ozimek and Cz. Radzewicz, "Strontium optical lattice clocks for practical realization of the metre and secondary representation of the second", Meas. Sci. Technol., vol. 26, pp. 075201, June 2015.

[3] Cz. Radzewicz, M. Bober, P. Morzyński, A. Cygan, D. Lisak, D. Bartoszek-Bober, P. Masłowski, P. Ablewski, J. Zachorowski, W. Gawlik, R. Ciuryło and M. Zawada, "Accuracy budget of the ^{88}Sr optical atomic clocks at KL FAMO", Phys. Scr., vol. 91, pp. 084003, July 2016.

[4] T. Middelmann, C. Lisdat, S. Falke, J. S. R. Vellore Winfred, F. Riehle and U. Sterr, "Tackling the blackbody shift in a strontium optical lattice clock", IEEE Trans. Instrum. Meas., vol. 60, pp. 2550-2557, January 2011.

[5] Th. Middelmann, S. Falke, Ch. Lisdat and U. Sterr, "High Accuracy Correction of Blackbody Radiation Shift in an Optical Lattice Clock", Phys. Rev. Lett., vol. 109, pp. 263004, December 2012.

[6] M. S. Safronova, D. Jiang, B. Arora, Ch. W. Clark, M. G. Kozlov, U. I. Safronova and W. R. Johnson, "Blackbody Radiation Shifts and Theoretical Contributions to Atomic Clock Research", IEEE Trans. Ultrason., Ferroelect., Freq. Control, vol. 57, pp. 94-105, January 2010

[7] M. S. Safronova, S. G. Porsev, U. I. Safronova, M. G. Kozlov and Ch. W. Clark, "Blackbody-radiation shift in the Sr optical atomic clock", Phys. Rev. A, vol. 87, pp. 1-9, January 2013.

[8] V. V. Flambaum, S. G. Porsev and M. S. Safronova, "Energy shift due to anisotropic black body radiation", Phys. Rev. A., vol. 93, pp. 2-5, August 2015.

[9] I. Ushijima, M. Takamoto, M. Das, T. Ohkubo and H. Katori, "Cryogenic optical lattice clocks", Nat. Photon., vol. 9, pp. 1-5, February 2015.

[10] K. Beloy, N. Hinkley, N. B. Phillips, J. A. Sherman, M. Schioppo, J. Lehman, A. Feldman, L. M. Hanssen, C. W. Oates, and A. D. Ludlow, "Atomic Clock with 1×10^{-18} Room-Temperature Blackbody Stark Uncertainty", Phys. Rev. Lett., vol. 113, pp. 260801, December 2014.

[11] https://masterweb.jpl.nasa.gov/reference/paints.html

Recent progress of neutral mercury lattice clock in SIOM

X H Fu[1,2,3], S Fang[1,2], R C Zhao[1,2,3], J F Sun[1,2], Z Xu[1,2,4], and Y Z Wang[1,2,4]
1, Key Laboratory of Quantum Optics, Chinese Academy of Sciences, Shanghai 201800, China
2, Shanghai Institute of Optics and Fine Mechanics, Chinese Academy of Sciences, Shanghai 201800, China
3, University of Chinese Academy of Sciences, Beijing 100049, China
4, Center of Cold atom physics, Chinese Academy of Sciences, Shanghai 201800, China
E-mail: xuzhen@siom.ac.cn

Abstract — **The optical lattice clock develops fast in recent years, and its stability and accuracy has already surpassed the microwave fountain clock and the optical clock based on ion trap. The mercury (Hg) lattice clock has the possibility to make a breakthrough in the limitation of blackbody radiation shift for strontium (Sr) and ytterbium (Yb) lattice clock, and reach the uncertainty in E-18 level at room temperature. For the purposes of laser cooling of mercury atoms and interrogating of the clock transition from $^1S_0$ state to $^3P_0$ state, a high-power cooling laser at 253.7 nm and an ultra-stable Hz-level linewidth laser at 265.6 nm are required, respectively. Here, we report our development of these laser sources for a neutral Hg lattice clock.**

Keywords—optical lattice clock; mercury atom; high power laser.

I. INTRODUCTION

The optical lattice clock develops fast in recent years [1,2,3,4], and its stability and accuracy has already surpassed the microwave fountain clock [5] and the optical clock based on ion trap [6]. Due to the obstacle of blackbody radiation, the fractional uncertainties of strontium (Sr) and ytterbium (Yb) lattice clock is very hard to reduce to E-18 level, unless to reduce the temperature uncertainty to mK level [2] or cool the ambient temperature to below 100 K [3]. The mercury (Hg) lattice clock has the possibility to make a breakthrough in the limitation of blackbody radiation shift [7], and reach the uncertainty in E-18 level at room temperature. To demonstrate a mercury lattice clock, a high-power cooling laser at 253.7 nm and an ultra-stable Hz-level linewidth laser at 265.6 nm are required, for the purposes of laser cooling of mercury atoms and interrogating of the clock transition from $^1S_0$ state to $^3P_0$ state, respectively.

It's very challenge to realize more than 100 mW output power at 253.7 nm. The only possible way is frequency quadrupled from a high power 1014.8 nm infrared laser, which can generate from optical pumped semiconductor laser [9], ECDL seeded fiber amplifier [10] and optical pumped Yb:YAG thin disk laser [11],optical pumped semiconductor laser, and liquid nitrogen cooled Yb-doped fiber laser amplifier [12]. We developed a kind of room temperature 1014.8 nm high power fiber laser amplifier [13], which can generate 8 W output power with one stage, and 20 W with two stage. Based on this high power and also robust operation technique, 75 mW of 253.7 nm UV laser was generated with two commercial frequency doubling cavity. But the conversion efficiency and operation stability was still not good. Here, we report a series development on this UV laser system, including a home-made ECDL laser, two high efficient frequency doubling cavity, and the other works for long term operation and stability.

The linewidth of clock transition is about 100 mHz for ^{199}Hg. To interrogate this transition, an ultra-stable Hz-level linewidth 265.6 nm laser is required. It has to be frequency quadrupled from an ultra-stable high power 1062.5 nm laser, which is frequency stabilized on a high-finesse reference cavity. Ultra-low drift and ultra-low noise are important characteristics of the reference cavity. Another key point is how to suppress the additional noise during fiber transferring. Fiber noise cancellation technique can sufficiently reduce the noise from transfer fiber. Now we are establishing our ultra-stable clock laser system for 265.6 nm clock transition.

In this paper, we report our development of these laser sources for a neutral Hg lattice clock. With these laser systems, we expect to find the clock transition of ^{199}Hg atoms in MOT.

II. THE COOLING LASER SYSTEM

As mentioned above, to establish a neutral mercury optical lattice clock, the most challenging thing is to generate a high power deep UV laser at 253.7 nm for laser cooling of neutral mercury atom. In our previous work, we developed a room temperature 1014.8 nm fiber laser amplifier with a short polarization-maintaining Yb-doped fiber. But only 75 mW UV laser is generated at 4 W input power of IR laser with two commercial doubling cavities. Here we present our recent improvement of cooling laser system.

A home-made external cavity diode laser (ECDL) works as seed laser for the 1014.8 nm fiber laser amplifier. After a single stage of fiber laser amplifier, the IR laser power can reach about 7 W. Two cascaded high efficient doubling cavities with LBO crystal and BBO crystal was completely demonstrated. The first-stage doubling cavity is locked by Pound-Drever-Hall (PDH) technique with a 5 MHz current modulation on seed laser, while the second stage is locked by Hansch-Couillaud (HC) method.

This work is supported by the Strategic Priority Research Program of the Chinese Academy of Sciences (XDB21030800); National Natural Science Foundation of China (Grant NO. 91436105).

A. *Home-made ECDL and fiber laser amplification*

A home-made external cavity diode laser (ECDL) at 1014.8 nm is home made as seed laser. The ECDL adopted Littrow configuration with an AR-coated laser diode (Eagleyard, EYP-RWE-1060) and 1800 lines/mm grating with 30% diffraction efficiency around 1014.8 nm. The output power is about 45 mW. And the ASE suppression ratio is about 55 dB which is even better than our used commercial laser (Toptica, DL pro), as shown in Fig 1. It guarantees the safe running and high ASE suppression ratio of single-stage fiber laser amplifier. Moreover, driven by a home-made current source with noise of 20.5 nA (RMS, 1-100 kHz, measured at 100 mA with 50 Ohm load), the linewidth of the ECDL is as narrow as below 100 kHz. The result is measured by self-heterodyne detection with 5 km fiber delay and 92.5 MHz frequency shift. The measured spectra is shown in Fig 2 (black dots), fitted with Voigt function (red line) which includes Lorentz item (white noise) and Gaussian item (1/*f* noise)[14]. As a result, the linewidth is 65 kHz, neglecting the Gaussian linewidth 0.28 kHz. This is suitable for the $^1S_0$-$^3P_1$ cooling transition with a natural linewidth of 1.27 MHz.

After an optical isolator, the laser is further filtered by a low pass filter (Semrock, FF01-935/170-25) which has 30 dB ASE suppression at 1030 nm and transmission of more than 95% at 1014.8 nm. Then the laser is coupled into a PM single mode fiber (PM 980) with laser power of 20 mW, which is sufficient for the 1014.8 nm single-stage fiber laser amplifier. Finally, the maximal output power is about 7 W achieved and the ASE suppression ratio is about 45 dB.

B. *Two cascaded high efficient doubling cavities*

The high conversion efficiency and stability from IR fundamental laser (1014.8 nm) to UV laser (253.7 nm) is crucial to generate high power cooling laser in UV. In our new cooling laser system, two bow-tie ring cavities are adopted to enhance the conversion efficiency.

In the first doubling cavity with a 20 mm long AR-coated LBO crystal, the beam waist of IR TEM_{00} mode is about 45μm at the center of LBO crystal, and the transmissivity of input coupler is about 3% around 1014.8 nm. Two lenses are used to match the laser beam from fiber laser amplifier to doubling cavity with a high efficiency of about 97.5%. The doubling cavity is locked by PDH technique with a 5 MHz current modulation on seed laser. The output power of green laser is about 3.0 W at 4.9 W input power of IR laser with conversion efficiency of 61%, as shown in Fig 3.

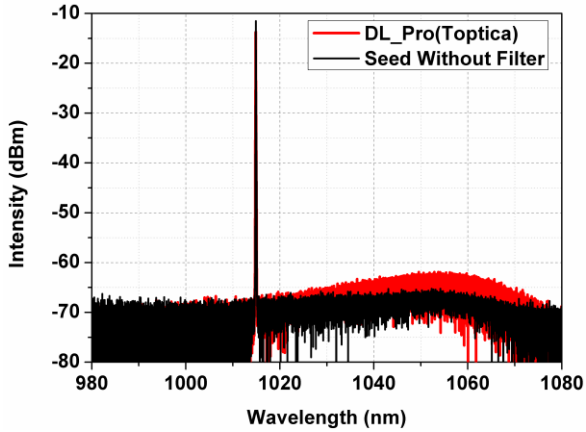


Fig. 1. The comparison of ASE between the home-made ECDL (black) and the commercial ECDL (red). The ASE of the home-made ECDL is about 7 dB lower than the commercial ECDL at 1050 nm.

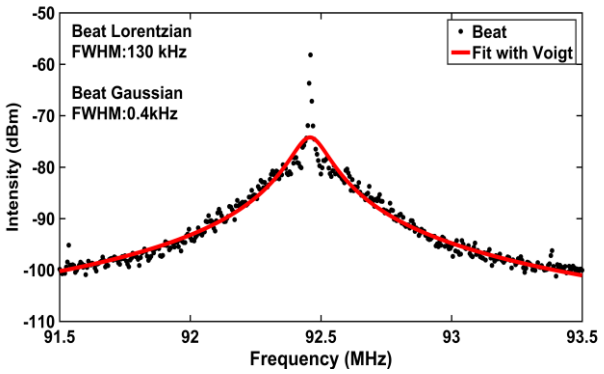


Fig. 2. The beat spectra of the self-heterodyne detection measured by the signal analyser N9020A (Keysight). Black dots are mesured result and the red line is the fitted result with Voigt function including Lorentzian item and Gaussian item. The peak in the spectra is resulted from the low white noise. The resolution bandwidth of the analyser is 3 kHz, and avarag times 100, sweep time 2 s.

In the second doubling cavity with a 7 mm long Brewster-angle incident BBO crystal, a beam splitter is used as an output coupler immediately after BBO crystal to split the UV light from the green light. This method can avoid the UV damage on the cavity mirrors. The beam waist of green laser is about 35 μm in the center of BBO crystal, and the transmissivity of input coupler is about 2% around 507.4 nm. Two cylindrical lenses and two spherical lenses are used to mode match the output green laser from the first doubling cavity and the fundamental mode of second doubling cavity with high efficiency of about 92%. The doubling cavity is locked by Hansch-Couillaud method. The highest output power of UV laser is about 770 mW at 2.7 W

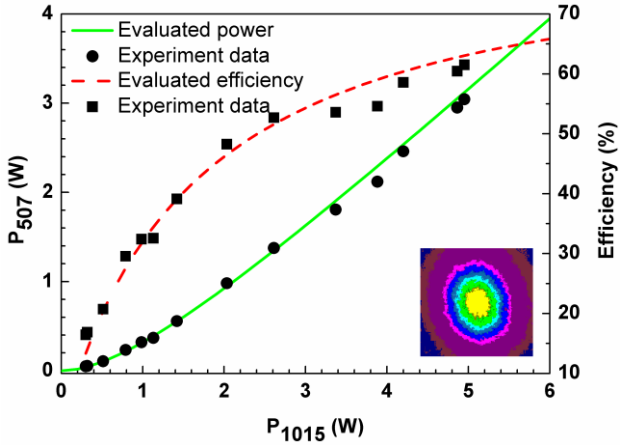


Fig. 3. The performance of first doubling cavity. (a) The output power of green laser versus the input power of IR laser. (b) The conversion efficiency versus the input power of IR laser. The green (red) line is given by theoretical calculation.

input power of green laser with conversion efficiency of 28.5%, and then the power decreases with time to a stable value of 520 mW shown in Fig 4(a). The performances of these two doubling cavities are well agreed with our design and calculation.

Running at the stable power of 100 mW, the saturated absorption spectroscopy (SAS) of ^{202}Hg with high signal to noise ratio is detected, as shown in Fig 4(b).

III. The Development Of The Clock Laser System

To probe the spectroscopy of clock transition of ^{199}Hg atom, an Hz-level linewidth laser at 265.6 nm is under construction. The configuration is as following:

A commercial fiber laser (NKT, Basik-Y10) at 1062.5 nm with power of 20 mW and linewidth of 3 kHz is locked to a 100 mm-long ULE ultra-stable cavity (ATFilm). Then, the stabilized laser is amplified by a 2 W 1064 nm fiber laser amplifier. To remove the linewidth broadening induced from the amplification, the amplified laser is phase-locked to the stabilized laser before the amplifier. This decreases the requirement of the low relative intensity noise (RIN) for the laser amplifier. After that, with a single passed PPLN crystal and a frequency doubling cavity, the few mW of 265.6 nm ultra-stable UV laser will be generated. The optical design of whole clock laser system is shown in Fig 5. Since the ultra-stable cavity is located on a passive vibration-damped platform, but the laser system is on an

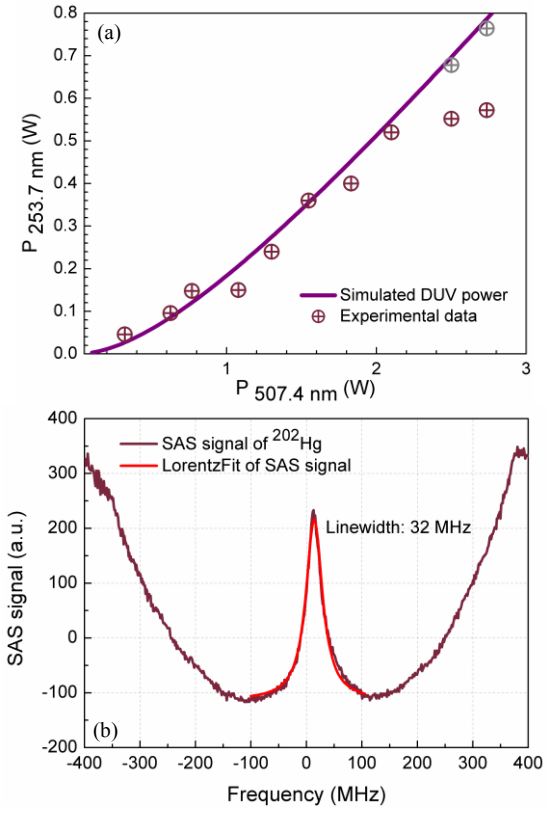


Fig. 4. The performance of second doubling cavity at different input power. (a) The output power of UV laser versus the input power of green laser. (b) SAS of 202Hg detected with our developed cooling laser system.

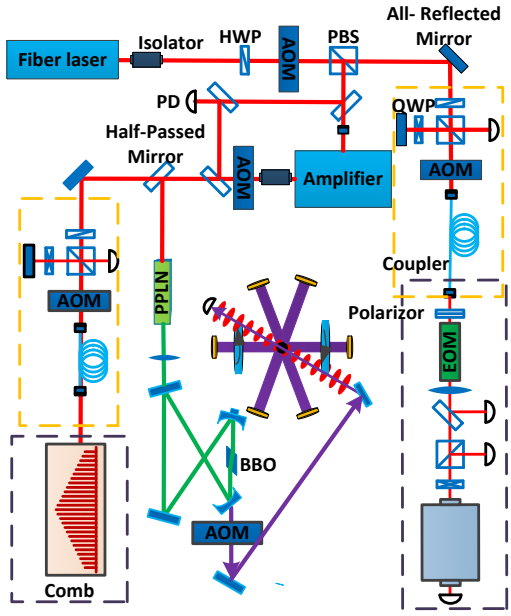


Fig. 5. The optical schematic of the clock laser system. HWP: half-wave plate, QWP:quater-wave plate, PBS:polareized beam splitter, PD:Photo diode. The Half-Passed Mirror is acually consisted of a HWP and a PBS. And the configuration in the yellow dashed box is fiber cancellator.

optical table, a noise-cancelled fiber link is adopted. And the fiber-noise-cancellation (FNC) method is also used to connect our stabilized laser to the fiber frequency comb, which is about 50 m far away from our lab and is locked to a Hydrogen clock or another fiber-stabilized laser[15].

A. The development of ultra stable laser system

In order to remove the influence of the pressure floating induced air index change and increase the heat transfer time from outside to the cavity, the ultra-stable cavity is located in a carefully designed vacuum system shown in Fig 6.

The vacuum system contains four layers from ULE cavity to outside: the cavity support, the gold-coated shield,

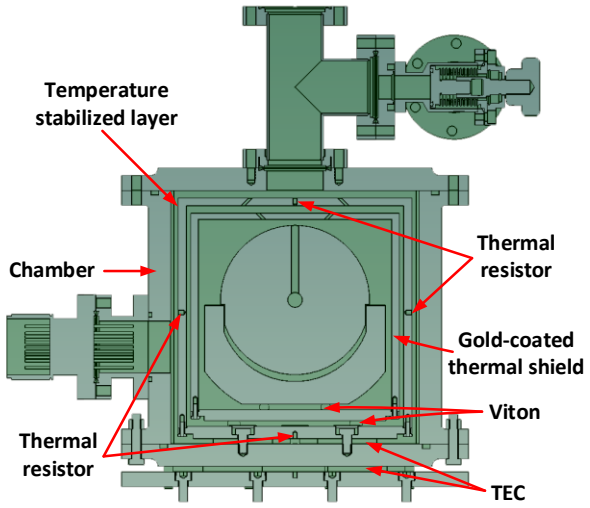


Fig. 6. A sectioned view of the ultra-stable cavity assembly.

the temperature stabilized layer, and the vacuum chamber. The vacuum pressure reaches 1x10-7 Torr now.

There are four TECs installed inside the vacuum and another four are located outside to achieve two-stage temperature stabilization. And four NTC thermal resistors are glued on the surfaces of thermal-stabilized layer: one is at the bottom, one is at the top, and two are at the side which avoids the optical windows. The one at the side surface is adopted as the control point, and the left three are used to monitor the temperature. Fig 7 shows a 11-days continuous measurement of temperature. The temperature fluctuations of three test points are all less than 0.8 mK (peak to peak), and two of which are within 0.4 mK (peak to peak). The short-term temperature drift is even better. Considered that the system would be located in an acoustic-isolation enclosure, the temperature fluctuation could be reduced further.

For the purpose of detecting μW-level fast modulated optical signal, a detector is designed with high gain of 100 kv/A and DC output, based on a single-stage transimpedance amplifier. The output voltage noise density of the detector in the dark is shown in Fig 8. Thus the equivalent input current noise is as low as 0.8 pA/sqrt (Hz) at 20 MHz (center frequency of EOM) and it is smaller than the most of commercial optical detectors. The bandwidth is around 50 MHz which is sufficient for 20 MHz signal detection. Taking these advantages, the noise floor of PDH error signal is about 200 mVpp without any extra amplification and with 15 μW laser input. Moreover, we have also designed other circuites like the cavity locking servo, the fiber noise cansellation servo.

B. Results.

The 1062.5 nm fiber laser has been roughly locked to the cavity. Here, we report some current results including finesse measurement and the evaluation of some factors' influences on the ultra-stable laser.

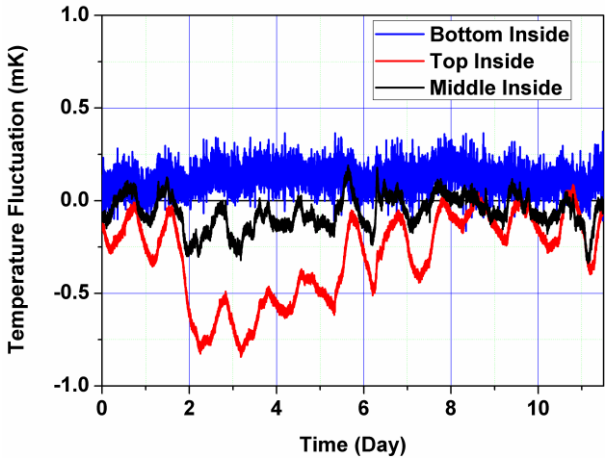


Fig. 7. The temperature shift of the stabilized layer in vacuum chamber in 11 days. The temperature of sensers at the top, in the middle, at the bottom are 24.9944 °C, 24.9385 °C and 25.025 °C, respectively.

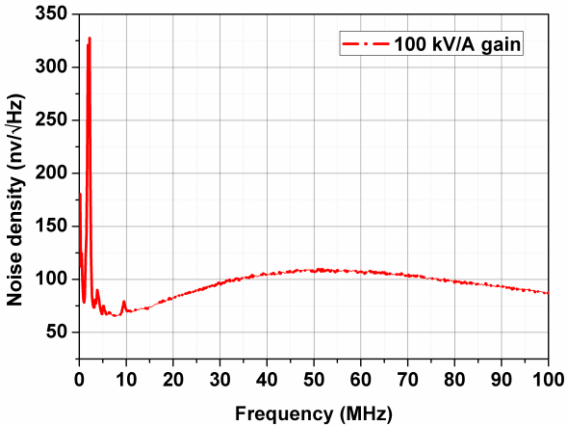


Fig. 8. The noise density spectrum of the output voltage from the detector measured by the signal analyser (Keysight, N9020A).

The finesse of the cavity is measured by the cavity-ring-down spectroscopy from the transmission signal. Fig 9 shows the transmission signal fitted with the formula in [16] (page 120, formula 4.23). The finesse turns out to be 460,000.

We have also tested the influence of the vibration and the residual amplitude modulation (RAM) on the frequency of the stabilized laser. Fig 10 shows the tested results with Brown thermal noise. Among the curves, the vibration (1-20 Hz) and the RAM induced frequency noise are both under the thermal noise limit. It should be mentioned that during the calculation the vibration sensitivity is estimated as 1.4 $x10^{-10}$/g in reference with [17]. And the vibration induced frequency noise above 20 Hz is resulted from the sound noise which is not shielded currently.

We are now working on the two-stage frequency doubling system after a 1062.5 nm fiber laser amplification. Eventually we would measure the clock frequency of the ^{199}Hg in the MOT which is a key step to pursue the Hg optical lattice clock.

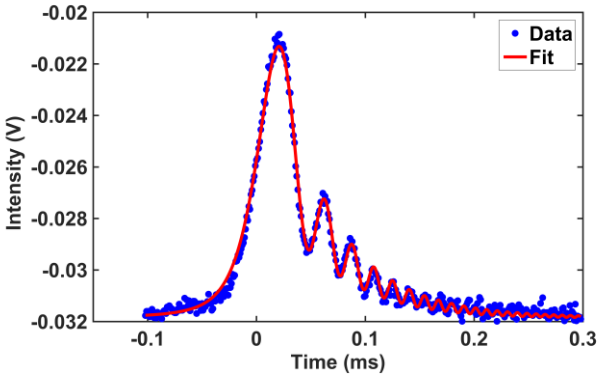


Fig. 9. The transmission cavity-ring-down spectroscopy (blue dots), and the fitting line (red line).

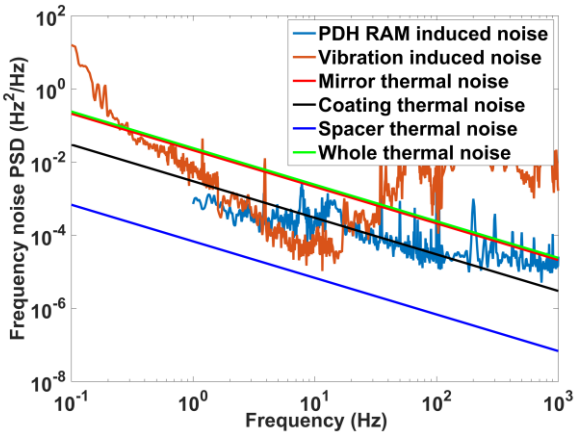


Fig. 10. The Frequency noise power spectral density (PSD) induced by RAM, vibration, and cavity thermal noise. Vibration induced noise below 0.5 Hz is resulted from the electronics noise of the vibration detector.

ACKNOWLEDGMENT

We thank Tang Li, Junchao Huang and Lingke Wang, for the help on the application of the frequency comb.

REFERENCE

[1]. J. J. McFerran, L. Yi, S. Mejri, S. D. Manno, W. Zhang, J. Guéna, Y. Le Coq, and S. Bize, "Neutral atom frequency reference in the deep ultraviolet with fractional uncertainty = 5.7×10^{-15}," Phys. Rev. Lett., vol. 108, pp. 103004, May 2012.

[2]. T. L. Nicholson, S. L. Campbell, R. B. Hutson, G. E. Marti, B. J. Bloom, R. L. McNally, W. Zhang, M. D. Barrett, M. S. Safronova, G. F. Strouse, W. L. Tew, and J. Ye, "Systematic evaluation of an atomic clock at 2×10^{-18} total uncertainty," Nature Communications, vol 6, pp. 6896, April 2015.

[3]. I. Ushijima, M. Takamoto, M. Das, T. Ohkubo, and H. Katori, "Cryogenic optical lattice clocks," Nature Photonics, vol. 9, pp. 185-189, February 2015.

[4]. M. Abgrall, B. Chupin, L. De Sarlo, J. Guena, P. Laurent, Y. Le Coq, R. Le Targat, J. Lodewyck, M. Lours, P. Rosenbusch, G. D. Rovera, and S. Bize, "Atomic fountains and optical clocks at SYRTE: Status and perspectives," C. R. Physique, vol. 5, pp. 461-470, May 2015.

[5]. S. Peil, J. L. Hanssen, T. B. Swanson, J. Taylor, and C. R. Ekstrom, "Evaluation of long term performance of continuously running atomic fountains," Metrologia, vol. 51, pp. 263-269, May 2014.

[6]. N. Huntemann, C. Sanner, B. Lipphardt, C. Tam, and E. Peik, "Single-ion Atomic clock with 3×10^{-18} systematic uncertainty," Phys. Rev. Lett., vol. 116, pp. 063001, February 2016.

[7]. S. G. Porsev, and A. Derevianko, "Multipolar theory of blackbody radiation shift of atomic energy levels and its implications for optical lattice clocks," Phys. Rev. A, vol. 74, pp. 020502, August 2006.

[8]. J. Hu, L. Zhang, H. Liu, K. Liu, Z. Xu, and Y. Feng, "High power room temperature 1014.8 nm Yb fiber amplifier and frequency quadrupling to 253.7 nm for laser cooling of mercury atoms," Optics Express, Vol. 21, pp. 30958-30963, December 2013.

[9]. J. Paul, et al., "Doppler-free spectroscopy of mercury at 253.7 nm using a high-power frequency-quadrupled optically pumped external-cavity semiconductor laser", Optics Letters, vol. 36, pp. 61-63, 2011.

[10]. H. Hachisu, K. Miyagishi, S.G. Porsev, A. Derevianko, V.D. Ovsiannikov, V.G. Pal'chikov, M. Takamoto, and H. Katori, "Trapping of neutral mercury atoms and prospects for optical lattice clocks", Physical Review Letters, vol. 100, pp. 053001, 2008.

[11]. M. Scheid, et al., "750 mW continuous-wave solid-state deep ultraviolet laser source at the 253.7 nm transition in mercur," Optics Letters, vol. 32, pp. 955, 2007.

[12]. A. Serfert, et al., "Narrow-linewidth multi-Watt Yb-doped fiber amplifier at 1014.8 nm", Applied Optics, vol. 45, pp. 7908, 2006.

[13]. J. Hu, L. Zhang, H. Liu, K. Liu, Z. Xu, and Y. Feng, "High power room temperature 1014.8 nm Yb fiber amplifier and frequency quadrupling to 253.7 nm for laser cooling of mercury atoms," Optics Express, Vol. 21, pp. 30958-30963, December 2013.

[14]. A. Canagasabey, A. Michie, J. Canning, J. Holdsworth, S. Fleming, H.C. Wang, M.L. Aslund, "A comparision of delayed self-heterodyne interference measurement of laser linewidth using Mach-Zehnder and Michelson interferometers", Sensors, vol. 11, pp. 9233-9241, 2011.

[15]. Jing Dong, Yongqi Hu, Junchao Huang, Meifeng Ye, Qiuzhi QU, Tang Li, and Liang Liu, "Subhertz linewidth laser by locking to a fiber delay line", vol 54,pp 1152-1156 , February 2015.

[16]. M.J. Martin, "Quantum metrology and many-body physics:pushing the frontier of the optical lattice clock", PHD, University of Colorado, 2013.

[17]. J. Milo, D.V. Maglhaes, C. Mandache. Y.L. Coq, E.M.L. English, P.G. Westergaard, J. Lodewyck, S. Bize, P. Lemonde, and G. Santarelli, "Ultrastable lasers based on vibration insensitive cavities", Physical Review A, vol. 79, pp. 053829-053835, 2009.

Thermal noise limited ultra-stable laser at 1555 nm

Zhaoyang Tai[1,2], Lulu Yan[1,2], Yanyan Zhang[1,2], Wenyu Zhao[1], Xiaofei Zhang[1,2], Shougang Zhang[1,2] and Haifeng Jiang[1,2*]

[1] Key Laboratory of Time and Frequency Primary Standards, National Time Service Center, Xi'an 710600, China
[2] School of Astronomy and Space Science, University of Chinese Academy of Sciences, Beijing 100049, China
haifeng.jiang@ntsc.ac.cn

***Abstract*—We present the designs and performances of cavity-stabilized lasers at 1555 nm, which are built as the frequency source for a transportable photonic microwave generation system. The frequency instability reaches the thermal noise limit of 10 cm-long vertically held cavity of 7×10^{-16} at 1 s averaging time, and the beat signal of the two lasers reveals a remarkable linewidth of 185 mHz.**

Keywords—Fabry-Perot; Optical resonator; Laser stabilization; Frequency standard

I. INTRODUCTION

The State-of-the-art ultra-stable lasers based on high finesse optical reference cavity have reached the frequency stability of 1×10^{-16} at 1s averaging time [1]. The lasers have therefore become the frequency sources for the most precision applications, such as gravitational wave detection [2], optical atomic clocks [3], quantum optomechanics [4], and photonic ultra-low phase noise microwave generation [5].

II. DESIGNS AND EXPERIMENTS

The ultra-stable cavities are designed based on the ideas of symmetry and balance to minimize acceleration sensitivity. Our Fabry-Pérot (F-P) reference cavity is a 100 mm-long, 110-mm-diameter cylinder, with a 7 mm-thick flange in its mid-plane, on which the cavity is vertically mounted rigidly. Based on the finite element modeling (FEM), the vibration sensitivity is calculated to be 2×10^{-11} /ms^{-2} in the length direction. Since the thermal noise is the fundamental limitation for an ultra-stable cavity, our cavity is made of Ultralow expansion (ULE) glass, with a pair of plano-concave (radius of curvature of 1000 mm) mirrors, and coated at 1555 nm. Due to the big radius of curvature of the concave mirror of the cavity, the thermal noise limit of such a 100 mm-long ULE glass cavity is calculated to be at a rather low level of 6.2×10^{-16} [6].

A commercial fiber laser (NKT Photonics Koheras Adjustik-E15) is locked to the reference cavity by using the Pound–Drever–Hall (PDH) frequency stabilization method [6], in which the residual amplitude modulation is reduced by a free space electro-optic modulator (EOM) cut at Brewster's angle [7] . To evaluate the performance of the ultra-stable laser, two identical laser systems are built independently, and linked by a 80 m-long fiber applying fiber noise cancellation technique [8].

III. RESULTS

Figure 1. shows the frequency instability of one laser from the beat-note of the lasers (1 Hz/s linear drift removed). The beatnote signal is recorded by a dead time free Π type counter (K+K Messtechnik, model FXQE80) in phase averaging mode, and the modified Allan deviation is employed to indicate frequency instability. The frequency instability is 7×10^{-16} at 1-10 s averaging time, and the instability rises to 1×10^{-15} at 100 s due to the temperature fluctuation of the two laser system placed in two different labs without active thermal control.

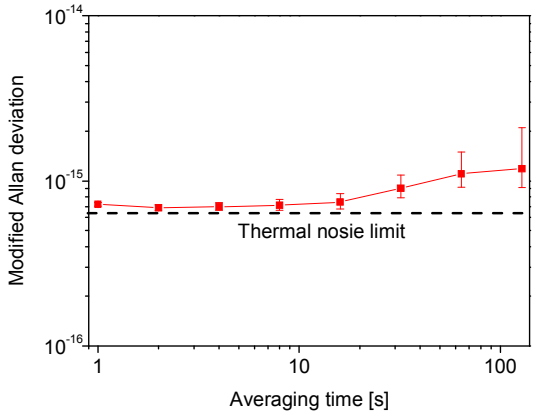


Fig. 1. Fractional frequency instability of one stabilized laser. Black dashed line: thermal-noise-limited frequency instability, 6.2×10^{-16}.

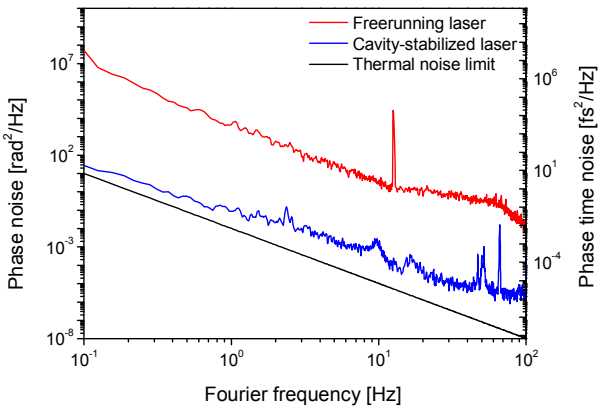


Fig. 2. Phase and time noise power spectral density of the laser. Blue line: phase noise of a stabilized laser; red line: phase noise of a free running laser; and black line: thermal noise limit.

The phase noise spectrum $S_\phi(f)$ of the laser is shown in Fig. 2. We convert the beatnote between the two lasers into a voltage fluctuation using a home-made frequency-to-voltage converter, and analyze the noise level with a fast Fourier transform (FFT) analyzer (SR 785, Stanford). The phase noise of the free running laser is suppressed by more than 50 dB for low frequencies. The right axis shows the corresponding phase time noise of the laser, and the time jitter from 1 Hz to 100 kHz is integrated to be approximately 360 attoseconds.

Figure 3 demonstrates the linewidth of the laser beatnote measured with an FFT analyzer (SR 785, Stanford) at a resolution bandwidth (RBW) of 125 mHz. From the fit with the Lorentz line shape, the full-width at half-maximum (FWHM) is 185 mHz, which is very narrow for a 10-cm long entire ULE cavity-stabilized one. The measurement noise floor (123 mHz) is obtained by measuring the beatnote of two stable RF signals under the same RBW; this result is consistent with the setting value of 125 mHz..

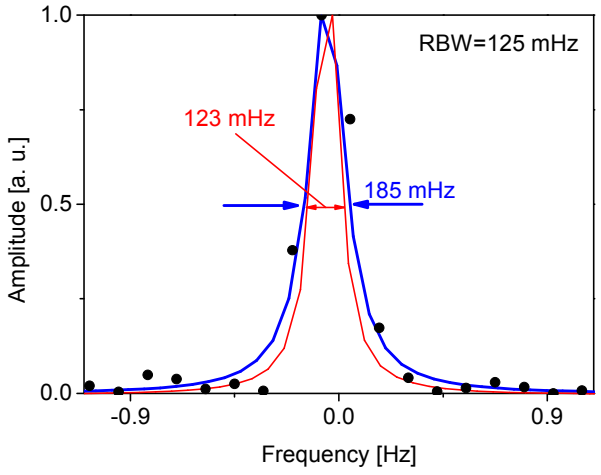


Fig. 3. Linewidth of beatnote between two stabilized lasers. Black dots: beatnote of two stabilized lasers, blue thick line: Lorentz fit of two stabilized lasers, red thin line: Lorentz fit of the beatnote of two microwave signal at same RBW of 125 mHz.

IV. CONCLUTION AND DISCUSSION

In conclusion, we report a cavity-stabilized ultra-stable laser at 1555 nm based on a commercially available cavity made entirely of ULE glass. Frequency instability is measured to be 7×10^{-16} from 1 to 10 s. The beatnote between the two systems exhibits a linewidth of about 0.185 Hz; the real linewidth of one laser should be narrower as a function of the noise contribution of the second laser and the measurement system. Both laser systems are built in our laboratory, and due to the good structural stability, one has been successfully moved to the cesium fountain clock lab at the National Time Service Center of Chinese Academy of Sciences. It is combine d with a compact Er-dropped-fiber-based optical frequency comb to realize ultra-low phase noise 9.2 GHz microwave generation as the local oscillator [10]. Since the frequency instability of the laser is well below that of the best fountain clocks, we can conclude that the laser system is competent for this task.

ACKNOWLEDGMENT

This work is supported by the National Natural Science Foundation of China under Grant No 91536217, the West Light Foundation of the Chinese Academy of Sciences under Grant No 2013ZD02, and the Youth Innovation Promotion Association of CAS under Grant No 2015334.

REFERENCES

[1] T. Kessler, C. Hagemann, C. Grebing, T. Legero, U. Sterr, F. Riehle, M. J. Martin, L. Chen, and J. Ye, "A sub-40-mHz-linewidth laser based on a silicon single-crystal optical cavity," Nat. Photonics, vol. 6, pp. 687-692, 2012.

[2] B. P. Abbott, et al., "Observation of Gravitational Waves from a Binary Black Hole Merger," Phys. Rev. Lett., vol. 116, pp. 061102, 2016.

[3] Y. Y. Jiang, A. D. Ludlow, N. D. Lemke, R. W. Fox, J. A. Sherman, L.-S. Ma, and C. W. Oates, "Making optical atomic clocks more stable with 10 −16-level laser stabilization," Nat. Photonics vol. 5, pp. 158–161, 2011.

[4] W. Marshall, C. Simon, R.Penrose, and D. Bouwmeester, "Towards quantum superpositions of a mirror," Phys. Rev. Lett., vol. 91, pp. 130401, 2003.

[5] T. M. Fortier, M. S. Kirchner, F. Quinlan, J. Taylor, J. C. Bergquist, T. Rosenband, N. Lemke, A. Ludlow, Y. Jiang, C. W. Oates, and S. A. Diddams, "Generation of ultrastable microwaves via optical frequency division," Nat. Photonics, vol. 5, pp. 425-429, 2011.

[6] K. Numata, A. Kemery, and J. Camp, "Thermal-noise limit in the frequency stabilization of lasers with rigid cavities," Phys. Rev. Lett., vol. 93, pp. 250602, 2004

[7] R. W. P. Drever, J. L. Hall, F. V. Kowalski, J. Hough, G. M. Ford, A. J. Munley, and H. Ward, "Laser phase and frequency stabilization using an optical resonator," Appl. Phys. B, vol. 31, pp. 97-105, 1983.

[8] Z. Tai, L. Yan, Y. Zhang, X. Zhang, W. Guo, S. Zhang, and H. Jiang, "Electro-optic modulator with ultra-low residual amplitude modulation for frequency modulation and laser stabilization," Opt. Lett., vol. 41, pp. 5584-5587, 2016

[9] L. S. Ma, P. Jungner, J. Ye, and J. L. Hall, "Delivering the same optical frequency at two places: accurate cancellation of phase noise introduced by an optical fiber or other time-varying path," Opt. Lett., vol. 19, pp. 1777–1779, 1994.

[10] Y. Zhang, W. Zhao, S. Meng, L. Yan, W. Guo, S. Zhang and H. Jiang, "A long-term frequency-stabilized erbium-fiber-laser-based optical frequency comb with an intra-cavity electro-optic modulator," Chin. Phys. B, vol. 24, pp. 064209, 2015.

Multiple lasers stabilization on a single three color optical cavity

Gianmaria Milani*†, Benjamin Rauf*†, Piero Barbieri*†, Filippo Bregolin*†,
Marco Pizzocaro*, Pierre Thoumany*, Filippo Levi* and Davide Calonico*
*Istituto Nazionale di Ricerca Metrologica, Strada delle Cacce 91, 10135 Torino, Italy
† Politecnico di Torino, Corso Duca degli Abruzzi 24, 10129 Torino, Italy

Email: g.milani@inrim.it

***Abstract*—We designed and implemented a simple and robust optical system for the frequency stabilization of lasers at different wavelength, used for the cooling and trapping of atoms in a Yb optical lattice clock. We used a single ultra-stable cavity to lock the frequency of three different lasers at $399\,\mathrm{nm}$, $556\,\mathrm{nm}$ and $759\,\mathrm{nm}$ exploiting the offset sideband locking technique, derived from the common Pound-Drever-Hall method. A linewidth of less than $300\,\mathrm{Hz}$ is obtained at $556\,\mathrm{nm}$ with a fractional frequency stability of 3×10^{-14} at $1\,\mathrm{s}$. At $759\,\mathrm{nm}$ we measured a long term drift less than $20\,\mathrm{kHz}$ per day, which is sufficient to keep the lattice light shift fractional uncertainty under 1×10^{-18}. The system was tested by simultaneously locking the three lasers to the cavity and operating the clock without any significant reduction in number of atoms.**

I. Introduction

We realized the frequency stabilization of different lasers radiations on the same optical cavity using the offset sideband locking technique [1] that constitutes a simple, robust as well as compact solution for atom trapping and spectroscopy experiments. The offset sideband locking technique is derived from the Pound-Drever-Hall (PDH) method [2] in which a single electro optic phase modulator (EOM) is used to stabilize and to bridge the frequency of the laser to the cavity resonance. A phase-modulated RF signal is provided to the EOM in order to generate sidebands at Ω_{gap} (RF frequency) and an additional set of sidebands around them spaced by Ω_{PDH} (modulation frequency). These are used to tune the frequency of the laser in order to match the cavity resonance and to obtain the usual PDH error signal by demodulating the cavity's reflected light signal at Ω_{PDH}. This approach has been exploited in a previous work [3] where different lasers are stabilized on three optical cavities contained in a single ultra-low expansion glass (ULE) block. Our system uses a single optical cavity [4], which does not require a custom manufactured piece of equipment, to stabilize the magneto optical trap (MOT) lasers and the lattice laser of the INRIM Yb optical lattice clock [5]. The atomic transitions involved are: the first stage MOT ($^1\mathrm{S}_0 \rightarrow ^1\mathrm{P}_1$, $\lambda = 399\,\mathrm{nm}$, natural linewidth $\Gamma = 29\,\mathrm{MHz}$) and the second stage MOT ($^1\mathrm{S}_0 \rightarrow ^3\mathrm{P}_1$, $\lambda = 556\,\mathrm{nm}$, $\Gamma = 184\,\mathrm{kHz}$). The clock operation demands a laser linewidth and daily frequency drift of less than $1\,\mathrm{MHz}$ and $100\,\mathrm{kHz}$ for the first and the second stage MOT laser respectively. The optical lattice is operated at the magic wavelength ($759\,\mathrm{nm}$) where the ac Stark shift for the two clock states is equal, yielding to an unperturbed clock transition at first order [6]. The fractional uncertainty introduced by the lattice laser light shifts has to be kept less than 1×10^{-18}. Considering a first-order clock-transition sensitivity of $21.6\,\mathrm{E_r\,mHz/GHz}$ [5] and a lattice trap depth of 200 recoil energies ($\mathrm{E_r}$) the required total lattice frequency shift accumulated in a typical day of measure ($\simeq 10\,\mathrm{h}$) is below $120\,\mathrm{kHz}$.

II. Experimental setup

The multi-wavelengths cavity consists of a commercial $10\,\mathrm{cm}$ ($\Delta\nu_{FSR} = 1.5$ GHz) horizontal cylindrical ULE spacer with two fused silica mirrors (hemispherical resonator) featuring triple-v coating for $399\,\mathrm{nm}$, $556\,\mathrm{nm}$ and $759\,\mathrm{nm}$ light [4]. The cavity is made by Advanced Thin Films and is kept inside a temperature-stabilized vacuum-housing. The $399\,\mathrm{nm}$ light is generated by cavity-enhanced second harmonic generation (SHG) from a tapered amplified diode laser at $798\,\mathrm{nm}$ [7] while the $556\,\mathrm{nm}$ radiation is produced by SHG of an amplified $1112\,\mathrm{nm}$ fiber laser in single pass through a non linear crystal. The lattice laser is a commercial titanium sapphire at $759\,\mathrm{nm}$. The frequency stabilization of the $556\,\mathrm{nm}$ laser acts on an acusto-optic modulator (AOM) and on the laser's piezo for the fast and slow lock respectively. The $399\,\mathrm{nm}$ ($798\,\mathrm{nm}$) and $759\,\mathrm{nm}$ radiations are locked to the cavity using the respective laser's piezo only. The $399\,\mathrm{nm}$ laser can also be stabilized locking the $798\,\mathrm{nm}$ laser to the cavity. We successfully implemented and tested this other scheme by extracting the $798\,\mathrm{nm}$ laser beam before the duplication cavity and sending it through an optical fiber to the EOM and then to the cavity bench where it is overlapped with the $759\,\mathrm{nm}$ line using a 50/50 beamsplitter. We used Jenoptik fiber-based broadband EOMs for the 759 and $556\,\mathrm{nm}$ lines and a QBIG EOM with two resonance frequencies for the $399\,\mathrm{nm}$ laser. In addition to the cavity, the optical bench accommodates the fiber output couplers, all the mode-matching telescopes as well as three photodiodes which detect the reflected light coming from the cavity. The reflected signals of the $759\,\mathrm{nm}$ and $798\,\mathrm{nm}$ beams are collected by the same photodetector while the electronic signal is splitted and then independently filtered to feed two distinct servo locks. The cavity breadboard can be easily moved, ensuring transportability.

978-1-5386-2916-1/$31.00 ©2017 IEEE

TABLE I
MEASURED CAVITY PROPERTIES.

λ/nm	Finesse		Throughput/%
	declared	measured	
399	1000-3000	550 ± 60	3
556	15 000	13900 ± 600	20
759	1000-3000	1660 ± 150	65
798	/	1200 ± 150	69

III. RESULTS

The measured optical properties of the cavity are reported in Tab. I. We measured a temperature where the coefficient of thermal expansion vanishes (zero CTE) of 30.4 ± 0.3 °C. At $556\,\mathrm{nm}$ we observed a linewidth smaller than $300\,\mathrm{Hz}$ and a fractional frequency stability at $1\,\mathrm{s}$ of 3×10^{-14}. We measured the frequency of the $759\,\mathrm{nm}$ laser locked to the cavity using a fiber-based frequency comb referenced to a hydrogen maser. The assessed drift is less than $2\,\mathrm{kHz/h}$. We noticed a higher frequency drift when the $399\,\mathrm{nm}$ light is present inside the cavity caused by the higher optical absorption at this wavelength (see. Tab. I). To overcome this issue we lock the $798\,\mathrm{nm}$ diode laser before the doubling cavity, thus avoiding the presence of $399\,\mathrm{nm}$ radiation inside the multi-wavelength cavity.

We have successfully tested this system during the typical working condition locking the $399\,\mathrm{nm}$ (or $798\,\mathrm{nm}$), $556\,\mathrm{nm}$ and $759\,\mathrm{nm}$ lasers at the same time. Observing the two stage MOT as well as the atoms trapped in the lattice we did not measured a significant reduction in the number of atoms.

REFERENCES

[1] J. I. Thorpe, K. Numata, and J. Livas, "Laser frequency stabilization and control through offset sideband locking to optical cavities," *Opt. Express*, vol. 16, no. 20, pp. 15 980–15 990, Sep 2008. [Online]. Available: http://www.opticsexpress.org/abstract.cfm?URI=oe-16-20-15980

[2] R. W. P. Drever, J. L. Hall, F. V. Kowalski, J. Hough, G. M. Ford, A. J. Munley, and H. Ward, "Laser phase and frequency stabilization using an optical resonator," *Appl. Phys. B*, vol. 31, no. 2, pp. 97–105, Jun. 1983. [Online]. Available: http://www.springerlink.com/content/rgg2823656435593/

[3] A. Nevsky, S. Alighanbari, Q.-F. Chen, I. Ernsting, S. Vasilyev, S. Schiller, G. Barwood, P. Gill, N. Poli, and G. M. Tino, "Robust frequency stabilization of multiple spectroscopy lasers with large and tunable offset frequencies," *Opt. Lett.*, vol. 38, no. 22, pp. 4903–4906, Nov 2013. [Online]. Available: http://ol.osa.org/abstract.cfm?URI=ol-38-22-4903

[4] G. Milani, B. Rauf, P. Barbieri, F. Bregolin, M. Pizzocaro, P. Thoumany, F. Levi, and D. Calonico, "Multiple wavelength stabilization on a single optical cavity using the offset sideband locking technique," *Opt. Lett.*, vol. 42, no. 10, pp. 1970–1973, May 2017.

[5] M. Pizzocaro, P. Thoumany, B. Rauf, F. Bregolin, G. Milani, C. Clivati, G. A. Costanzo, F. Levi, and D. Calonico, "Absolute frequency measurement of the ${}^1S_0 - {}^3P_0$ transition of ${}^{171}\mathrm{Yb}$," *Metrologia*, vol. 54, p. 102, Feb. 2017.

[6] H. Katori, M. Takamoto, V. G. Pal'chikov, and V. D. Ovsiannikov, "Ultrastable optical clock with neutral atoms in an engineered light shift trap," *Phys. Rev. Lett.*, vol. 91, p. 173005, Oct 2003. [Online]. Available: http://link.aps.org/doi/10.1103/PhysRevLett.91.173005

[7] M. Pizzocaro, D. Calonico, P. C. Pastor, J. Catani, G. A. Costanzo, F. Levi, and L. Lorini, "Efficient frequency doubling at 399 nm," *Appl. Opt.*, vol. 53, no. 16, pp. 3388–3392, Jun 2014. [Online]. Available: http://ao.osa.org/abstract.cfm?URI=ao-53-16-3388

Progress towards a two-photon clock based on laser-cooled calcium

Shreyas Potnis, Shira Jackson and Amar C. Vutha
Department of Physics, University of Toronto, Toronto, Canada M5S 1A7,
Email: vutha@physics.utoronto.ca

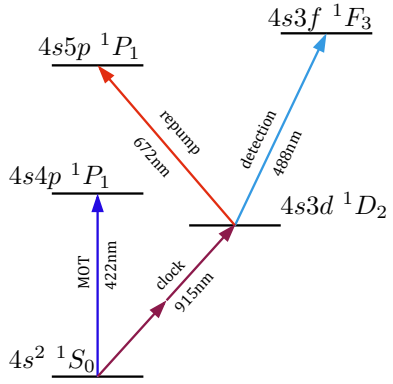
The remarkable and steady improvements in the accuracy of optical clocks have greatly advanced the state of the art in time and frequency metrology. In addition to the accuracy of these clocks, the high precision available from them can open up new classes of measurements. In particular, optical clocks with high signal-to-noise ratios (SNR) can be used as components of sensitive antennae for micro-hertz-band gravitational waves [1], [2]. Such clocks could also be useful for field applications such as geodesy [3], and as transportable secondary frequency standards to enable comparisons between distant primary standards [4].

For such applications of optical clocks, optical frequency references based on two-photon transitions are attractive due to the technological simplicity offered by the operation of a single-stage magneto-optical trap (MOT). The 40-Hz-wide two-photon transition in calcium (Fig. 1(a)) is a convenient optical frequency reference [5]. In a MOT, this transition can be measured with a high SNR that could allow it to rapidly average down to a frequency instability $< 10^{-16}$ [1].

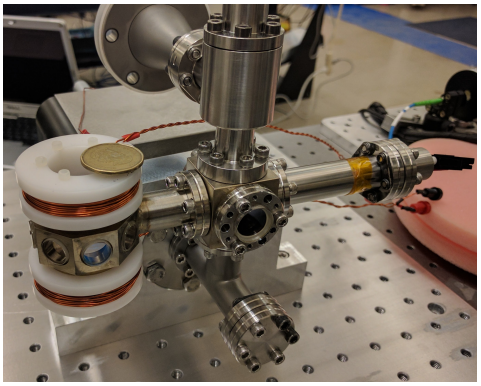
We have developed a compact apparatus in which calcium atoms are captured in a MOT directly from an atomic beam (Fig. 1(b)), and subsequently interrogated by a pair of counter-propagating clock laser beams. The 915 nm clock laser uses an improved variant of the interference-filter-based external cavity diode laser design, and is stabilized to a single high-finesse cavity. We have constructed two such clock lasers, and observed laser linewidths that are narrow enough to interrogate the calcium two-photon clock transition (Fig. 1(c) shows a beatnote linewidth of ∼80 Hz measured between two nominally identical lasers).

In this poster, we present the motivation for developing the calcium two-photon clock, and describe our experimental progress towards the observation of the two-photon clock transition.

(a)



(b)



(c)

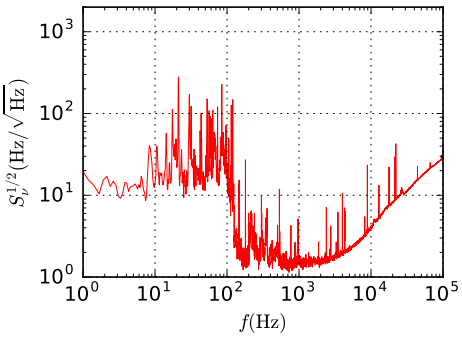


Fig. 1. (a) Level structure of ^{40}Ca showing the relevant energy levels and lasers. (b) Compact vacuum chamber for a calcium MOT. (c) Spectral density of frequency fluctuations of the beatnote between two clock lasers locked to independent cavities.

978-1-5386-2916-1/$31.00 ©2017 IEEE

REFERENCES

[1] A. C. Vutha, "Optical frequency standards for gravitational wave detection using satellite doppler velocimetry," *New Journal of Physics*, vol. 17, no. 6, p. 063030, 2015.

[2] S. Kolkowitz, I. Pikovski, N. Langellier, M. D. Lukin, R. L. Walsworth, and J. Ye, "Gravitational wave detection with optical lattice atomic clocks," *Phys. Rev. D*, vol. 94, p. 124043, 2016.

[3] T. Takano, M. Takamoto, I. Ushijima, N. Ohmae, T. Akatsuka, A. Yamaguchi, Y. Kuroishi, H. Munekane, B. Miyahara, and H. Katori, "Geopotential measurements with synchronously linked optical lattice clocks," *Nature Photonics*, vol. 10, no. 10, pp. 662–666, 2016.

[4] S. B. Koller, J. Grotti, S. Vogt, A. Al-Masoudi, S. Dörscher, S. Häfner, U. Sterr, and C. Lisdat, "Transportable optical lattice clock with 7×10^{-17} uncertainty," *Phys. Rev. Lett.*, vol. 118, p. 073601, 2017.

[5] J. Hall, M. Zhu, and P. Buch, "Prospects for using laser-prepared atomic fountains for optical frequency standards applications," *JOSA B*, vol. 6, no. 11, pp. 2194–2205, 1989.

A Spectrograph to Characterize Comb Spectra

Rafael A. Probst [1,2]*, Tilo Steinmetz [2], Yuanjie Wu [1,2], Frank Grupp [3], Thomas Udem [1], Ronald Holzwarth [1,2]

[1] Max-Planck-Institut für Quantenoptik, Garching, Germany
[2] Menlo Systems GmbH, Martinsried, Germany
[3] Universitätssternwarte München, Munich, Germany
* r.probst@menlosystems.com

***Abstract*—We present a compact echelle spectrograph for characterizing properties of laser frequency combs with large mode spacing, e.g. for astronomical purposes (astro-combs). The spectrograph is inexpensive and easy to build thanks to the use of standard optical components and photographic equipment. Despite its compact dimensions, it features the same resolution as many full-sized spectrographs at astronomical observatories. This is accomplished through the use of a single-mode fiber as a spectrograph input, through which we can conveniently inject the light of an astro-comb.**

Keywords—frequency combs; echelle spectrographs

I. INTRODUCTION

Laser frequency combs (LFCs) have become widely used tools for precision measurements of optical frequencies [1]. In the past ten years, applications in astronomy have been developed, where the LFC is used to calibrate an echelle spectrograph [2–4]. Boosting its precision, this is anticipated to provide great benefits to the fields of exoplanet hunting [3], cosmic dynamics [5], and the search for cosmic variability of fundamental constants [6].

A key characteristic of astronomical frequency combs (astro-combs) is the large mode spacing adapted to the spectrograph's resolution, allowing it to resolve the comb structure. Further, an astro-comb needs to cover a wide spectral range, usually in the visible, with a flat spectrum. This allows covering the range of a spectrograph with calibration lines of good signal quality, without any over- or underexposed lines.

The mode spacing of an astro-comb can easily be characterized with a photodetector and an RF-spectrum analyzer. The spectral coverage can be monitored with a small CCD spectrometer. For characterizing some other properties, however, there is hardly an alternative to using an echelle spectrograph. Judging the spectral flatness on a line-by-line basis requires resolving individual lines over a wide range. Further, the astro-comb spectrum can contain a continuum background, which is observed when the signal level between the modes does not fall to zero. In the past, such properties were studied in campaigns at observatories [4]. Such time-consuming trips could be spared with a lab-based spectrograph. The spectrograph could also be used to characterize structured spectra from other coherent sources such as microresonators, or to perform absorption spectroscopy measurements.

II. SPECTROGRAPH DESIGN

A. General considerations

Astronomical spectrographs are usually fed with multimode optical fibers. Earth's atmosphere makes it hard to inject star light efficiently into single-mode fibers, as the image of a star is blurred into a non-diffraction-limited seeing disk. At near-infrared wavelengths, adaptive optics starts to enable single-mode fiber coupling with reasonable efficiency, but the visible range is of primary interest for spectroscopy. With the spectrograph entrance slit being the output of a multimode fiber, the spectrograph is unable to reach a diffraction-limited resolution. For high-resolution spectroscopy, a big echelle grating with a large number of grooves needs to be illuminated. The spectrographs are, therefore, of significant cost and size.

A spectrograph that is solely built for astro-comb characterization, on the other hand, profits from the single-mode nature of the laser beam, and can easily reach a diffraction-limited resolution. Hence, our spectrograph can be much smaller, and built from cost-efficient standard optics with 1 inch diameter.

Similarly, astronomical spectrographs have to deal with extremely faint targets, which is why they use back-thinned CCDs with very high quantum efficiency. In addition, the CCDs need to be cooled, often down to –120°C, to suppress dark current. This is because of the very long exposure times. Cooling of the image sensor has to be done in a dry atmosphere to prevent condensation of water. Fortunately, none of this is needed with the amount of light delivered by the astro-comb. We can thus employ a much more inexpensive camera.

B. Optical layout

Fig. 1 shows the layout of our spectrograph. The light enters through a single-mode fiber for 400–680 nm. It is collimated into a beam of 9.5 mm FWHM through a 90° off-axis parabolic mirror (OAP) with a 101.6 mm effective focal length (EFL). This is followed by an echelle grating (31.6 grooves/mm, 63° blaze angle), which reflects the beam back to the first OAP. The 1.5° tilt of the grating shifts the beam upwards and allows the light to pass above the input fiber without getting obstructed. The beam is re-collimated by another OAP with a 50.8 mm EFL. The shorter EFL of this OAP reduces the beam diameter, while at the same time

978-1-5386-2916-1/$31.00 ©2017 IEEE

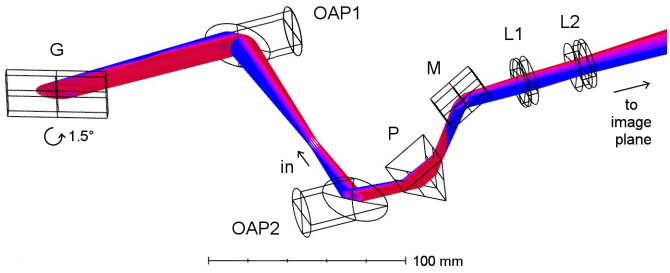


Fig. 1. Optical design of the spectrograph. G: grating (turned by 1.5° around its surface normal). OAP1/OAP2: 90° off-axis parabolic mirror with 101.6/50.8 mm effective focal length. P: N-SF11 equilateral prism. M: fold mirror. L1/L2: achromatic lens with 125/–100 mm focal length.

increasing its angular dispersion, which magnifies the image. Next, the light passes through an equilateral N-SF11 prism, which induces angular dispersion perpendicular to that of the grating, to separate the diffraction orders from one another. Finally, we project the image on a screen with a system of two lenses with variable distance. This serves as a visual demonstration for our lab visitors. For measurements, we replace the lens telescope with a camera lens.

C. Camera

In order to try the simplest possible solution, we explore the use of a photographic camera (Canon EOS M3) for our spectrograph. We give it a lens with a 200 mm fixed focal length, which roughly matches the image size to the 22.3×14.9 mm² (6000×4000 px²) CMOS image sensor. The camera can be remotely controlled and read out via Wi-Fi and USB, respectively. The setup with camera is shown in Fig. 2.

III. Results & Outlook

Fig. 3 shows a part of the echellogram recorded with the spectrograph, using an astro-comb with 18 GHz mode spacing as a light source. From the image we determine the spectrograph resolution to be of 124 000, which however declines towards the borders of the echelle orders to about half

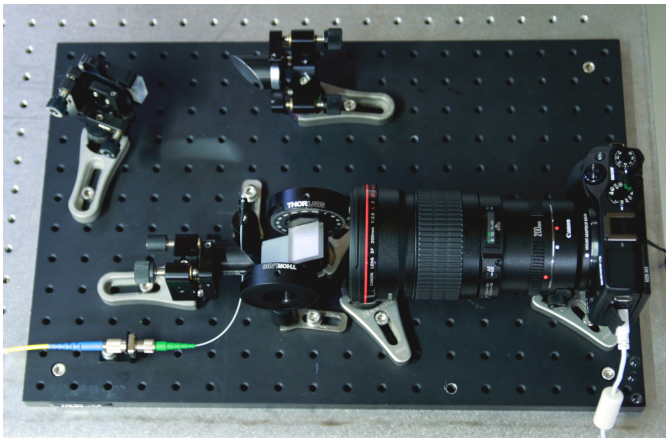


Fig. 2. Photo of the echelle spectrograph. The dimensions of the black base plate are 30 x 45 cm².

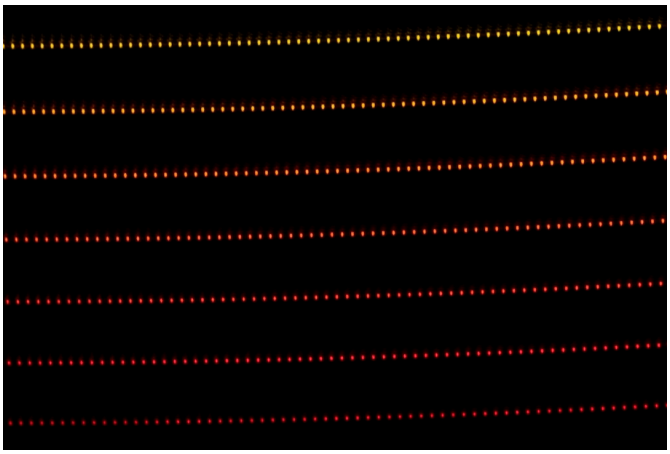


Fig. 3. Part of the echellogram recorded with the spectrograph. Each dot represents a mode of an 18 GHz frequency comb. The color is as recorded by the RGB image sensor and replicates the perception of the human eye.

this value. This is because the image plane is curved cylindrically. In total, we can accommodate 33 echelle orders (grating diffraction order 87–120) on the image sensor, covering a spectral range of 477–658 nm.

Applications of our spectrograph have successfully been demonstrated [7]. This includes the characterization of the continuum background of an astro-comb, which can have a significant impact on spectrograph calibration. Upgrades of the spectrograph such as the addition of a second fiber channel, as well as temperature and pressure stabilization, might allow characterizing the calibration precision provided by the astro-comb [7].

Acknowledgment

We want to thank Florian Kerber, Gaspare Lo Curto, Gerardo Avila, Luca Pasquini and Antonio Manescau from the European Southern Observatory, and Hanna Kellermann from the University Observatory Munich, for helpful discussions and advice.

References

[1] Th. Udem, R. Holzwarth, and T. W. Hänsch, "Optical frequency metrology," Nature, vol. 416, pp. 233–237, 2002.

[2] M. T. Murphy *et al.*, "High-precision wavelength calibration of astronomical spectrographs with laser frequency combs," Mon. Not. R. Astron. Soc., vol. 380, pp. 839–847, 2007.

[3] T. Wilken *et al.*, "A spectrograph for exoplanet observations calibrated at the centimetre-per-second level," Nature, vol. 485, pp. 611–614, 2012

[4] R. A. Probst *et al.*, "Relative stability of two laser frequency combs for routine operation on HARPS and FOCES," Proc. SPIE, vol. 9908, pp. 990864, 2016.

[5] J. Liske *et al.*, "Cosmic dynamics in the era of extremely large telescopes," Mon. Not. R. Astron. Soc., vol. 386, pp. 1192–1218, 2008.

[6] J. K. Webb, J. A. King, M. T. Murphy, V. V. Flambaum, R. F. Carswell, and M. B. Bainbridge, "Indications of a Spatial Variation of the Fine Structure Constant," Phys. Rev. Lett., vol. 107, pp. 191101, 2011.

[7] R. A. Probst *et al.*, "A compact echelle spectrograph for characterization of astro‑combs," Appl. Phys. B, vol. 123, pp. 76, 2017.

Methane Based Microwave Reference Oscillator

M.A. Gubin
P.N. Lebedev Physical Institute, Russian Academy of Sciences
N.E. Bauman Moscow State Technical University
National Research Nuclear University 'MEPhI'
Moscow, Russia
gubin@sci.lebedev.ru

A.N. Kireev[1], D.A. Tyurikov[1], A.S. Shelkovnikov[1], A.V. Tausenev[1,2], D.S. Chernykh[1], D.V. Shepelev[2], A.V.Konyashchenko[1, 2]
1. P.N. Lebedev Physical Institute, Russian Academy of Sciences
Moscow, Russia

2. Avesta Ltd., Moscow, Russia

***Abstract*—Two microwave reference oscillators based on a He-Ne/CH_4 optical frequency standard ($\lambda = 3.39$ μm) and femtosecond Er fiber laser ($\lambda = 1.55$ μm) optical-to-microwave frequency divider were created. The measurements have demonstrated short term frequency instability (Allan deviation) of the output microwave signal at 1.5 GHz at the level of 1×10^{-14} ($\tau = 1$ s). Interrogative oscillator with such stability is attractive for application in Cs and Rb atomic fountains.**

Keywords—femtosecond optical to microwave frequency divider, fiber laser, He-Ne/CH_4 frequency standard, ultra-low phase noise microwave generator, interrogative oscillator

I. INTRODUCTION

Compact and reliable microwave reference oscillators with $(1\text{-}5)\times10^{-15}$ (for averaging times $\tau = 1 - 1000$ s) instability and low phase noise are needed for variety of applications - atomic fountains, radio astronomy, radars, etc [1 and references therein]. Common approach to their development is based on stabilized lasers and further optical-to-microwave frequency division [2]. Typically a laser is locked to high finesse Fabri – Perot (FP) optical cavity using Pound - Drever - Hall technique and an optical frequency comb based on a mode-locked femtosecond (fs) laser serves as a frequency divider. In present investigation we follow the above mentioned optical-to-microwave division scheme but as an optical reference a He-Ne/CH_4 laser ($\lambda = 3.39$ μm) stabilized over narrow saturated dispersion resonance in CH_4 is used.

Our approach has some advantages. He-Ne/CH_4 optical frequency standard (OFS) potentially has considerably less frequency drifts as compared to FP cavity fringes at averaging times $\tau > 10$ s because output frequency of the He-Ne/CH_4 OFS is determined by the CH_4 spectral line and not by the length of the resonator. The direct influence of vibrations, temperature instability, Brownian fluctuations (in the mirror surfaces, substrates and resonator body) is suppressed by an electronic feedback loop in the frequency range of the loop bandwidth. Thus the demands on temperature stability, mechanical isolation are less strict especially if the OFS has a compact and rigid construction.

Additionally the optical-to-microwave frequency division scheme for the He-Ne/CH_4 laser is relatively simple. It includes an optical frequency comb based on a fs Er fiber laser and difference frequency generation (DFG) in a nonlinear crystal and only one parameter of the comb - pulse repetition rate (f_{rep}) - should be stabilized [3,4].

The main goal of this work is to develop a microwave reference oscillator based on the methane OFS and fs optical frequency divider (OFD) with the instability 1×10^{-14} ($\tau = 1$ s) in the microwave range of spectrum.

The interrogative oscillator with above mentioned instability would be useful in atomic fountains (Cs/Rb) where the oscillator frequency instability is a crucial parameter because of the "Dick effect" [5]. Decrease of the instability at 9.2/6.8 GHz for example from 1×10^{-13} to 1×10^{-14} ($\tau = 1$ s) allows to reduce the time needed for reaching Cs fountain nominal accuracy ~ 2×10^{-16} from 10 days to one day [6].

II. THE MAIN COMPONENTS OF THE OSCILLATOR

A. He-Ne/CH_4 OFS

Our He-Ne/CH_4 OFS ($\lambda = 3.39$ μm) is a new version of the system previously used as a frequency reference in molecular optical clock [3, 4]. It consists of two continuous wave lasers: a two-mode "Reference" He-Ne/CH_4 laser and a single-mode "Heterodyne" He-Ne laser. The Reference laser generates two linear orthogonally polarized modes. The saturated dispersion (SD) sub-Doppler resonance in methane is detected in the inter-mode beat frequency and is used for the laser stabilization.

The Reference laser resonator is a folding six mirror cavity made of zerodur with dimensions 20 cm × 20 cm × 5 cm. The resonator optical length is about 1 m with ~ 40 cm of active (He-Ne) and ~ 60 cm of passive (CH_4) media (Fig. 1). All optical elements are attached directly to zerodur block and have no any mechanical adjustments. This results in 1-2 orders better passive frequency stability as compared to previous invar made laser resonators [7, 8]. One of the intermediate mirrors is a mirror with specified phase shift providing 5 MHz frequency difference between two generating modes.

Such laser design and replacement of previously used liquid nitrogen cooled InSb photodetector by room temperature InAs detector made a whole device more compact and convenient for next improvements such as temperature stabilization and vibration isolation.

978-1-5386-2916-1/$31.00 ©2017 IEEE

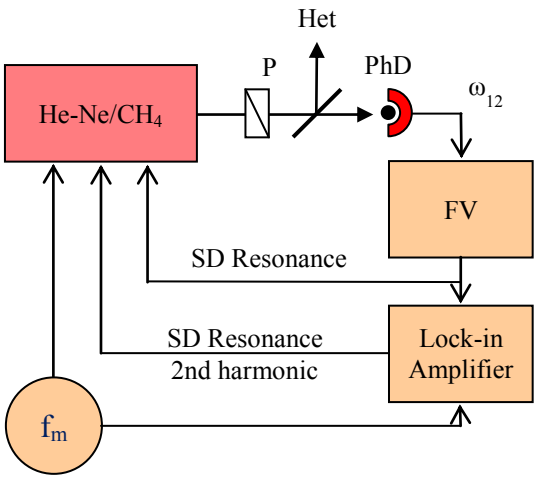


Fig. 1. Scheme of the Reference He-Ne/CH_4 laser with zerodur made resonator, P - polarizer, PhD - InAs photodetector (300 K), FV - frequency to voltage converter, f_m - modulation frequency. Het - output beam for phase locking of the He-Ne Heterodyne laser (not shown).

The signal of SD resonance in the Reference laser is used for a "fast" feedback loop and a signal of the 2nd harmonic of modulation frequency is used for a "slow" feedback loop.

Frequency instability of the Reference laser is determined by noise of the inter-mode beat frequency ω_{12}. There are three main sources of noise - technical fluctuations of the laser resonator optical length, additive noise of the photodetector and laser spontaneous emission (Shawlow-Townes noise). Shawlow-Townes noise of ω_{12} is fundamental limit of the laser stability and in the Reference laser it's spectral density has a typical value of $\delta\omega_{12} \approx 0.2$ Hz/Hz$^{1/2}$ at the 2nd harmonic of modulation frequency (24 kHz).

The SD resonance has FWHM $2\gamma \approx 450$ kHz (magnetic hyperfine structure is not resolved) and peak-to-peak amplitude $\Delta\omega_{12} \approx 120$ kHz (Fig. 2). With this parameters the slope of the SD resonance is $S = \Delta\omega_{12}/\gamma \approx 0.5$. So the noise spectral density of laser frequency under stabilization can be estimated by the value $\delta\omega_{12}/S \approx 0.4$ Hz/Hz$^{1/2}$ which gives lower limit for Allan deviation 3×10^{-15} at 1 s averaging time.

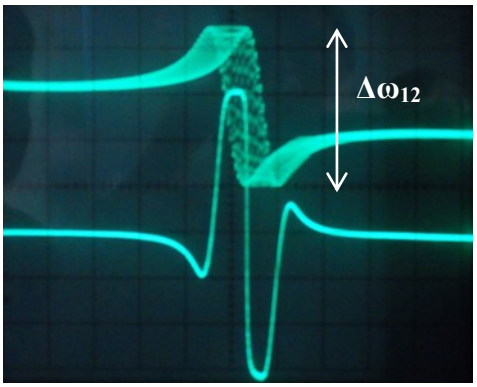


Fig. 2. Saturation dispersion signals of CH_4 line used for He-Ne/CH_4 OFS frequency stabilization. Upper trace – output of Frequency-to-Voltage Converter, lower trace – output of Lock-in-Amplifier ("2nd" harmonic of SD resonance). Modulation frequency is 12 kHz.

This work was supported by the Russian Science Foundation (Project No. 16-19-10694).

The Allan deviation of two independent zerodur He-Ne/CH_4 Reference lasers for $\tau = 0.01$ - 1000 s is shown in Fig. 3. The stability equal to 7×10^{-15} at $\tau = 1$ s was reached [9]. Recalculation for one device gives the value 5×10^{-15} which is not far from estimated. The Allan deviation of the previous version of He-Ne/CH_4 Reference laser (with invar resonator and liquid nitrogen cooled photodetector) stabilized over saturated absorption resonances (SA) is also shown in Fig. 3 for comparison with the present version.

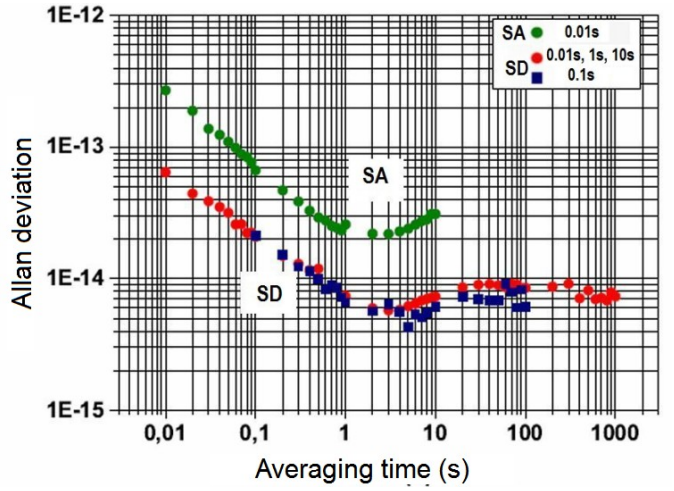


Fig. 3. Allan deviation: green circles - invar cavity laser, SA resonances, InSb photodetector at 77K, 0.01s counter gate time [8]; red circles / blue squares – zerodur cavity laser, SD resonances, InAs photodetector at room temperature, counter gate time: 0.01s, 1s and 10s (red circles) and 0.1s (blue squares).

Further stability improvement to 1×10^{-15} at 1 s seems feasible for a Reference laser.

The Heterodyne He-Ne laser which is a part of the OFS is also a zerodur block of 20 cm × 10 cm × 5 cm. The Heterodyne laser frequency is phase locked to the Reference laser with fixed 2 MHz offset. The Heterodyne laser operating in the single-mode regime has an output power ~2 mW and about 80% of it is used for stabilization of the DFG IR comb in the 3400 nm spectral region [4].

B. Femtosecond Er fiber laser OFD

Two identical OFD based on fs Er fiber lasers with Kerr nonlinearity as mode locking mechanism were created (Fig. 4). The lasers are based on polarization maintained (PM) optical fibers for increasing of the temporal stability of fs operation. The pulse repetition rates of both lasers are close to each other - $f_{rep} \approx 60$ MHz and $\Delta f_{rep} \approx 400$ Hz. This small frequency difference can be measured with high accuracy by a frequency counter.

The beat signal of the He-Ne Heterodyne laser radiation and the nearest DFG comb component is used for phase locking of the Er laser repetition frequency f_{rep} to the methane OFS frequency. There are three channels of active control of the repetition frequency: electro optic modulator, piezoelectric transducer and thermoelectric controller (Fig. 4). Realized phase lock loop (PLL) bandwidth is about 130 kHz (Fig. 5).

The output power of the fs Er oscillators is ~ 10 mW. It is amplified up to 120 mW and broadened in a highly nonlinear

fiber into the range 1000-2200 nm. An optical scheme of both OFD is similar to that described in [4] and is based on difference frequency generation in a periodically polarized lithium niobate crystal. The DFG comb covers the spectral range 3200 – 3500 nm and has a total power ~ 60 μW.

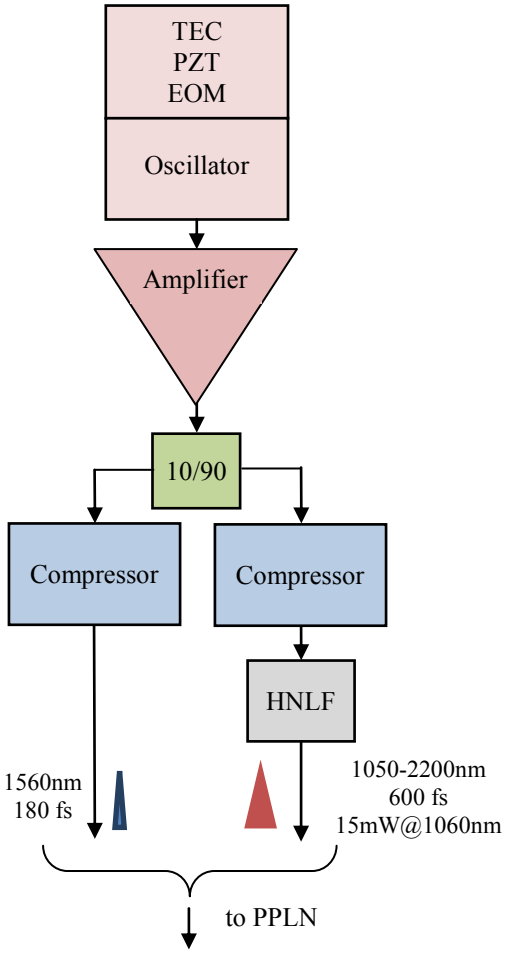


Fig. 4. Femtosecond part of the optical frequency divider. TEC - thermoelectric controller, PZT - piezoelectric transducer, EOM - electro optic modulator, HNLF - highly nonlinear fiber, PPLN - periodically polarized lithium niobate.

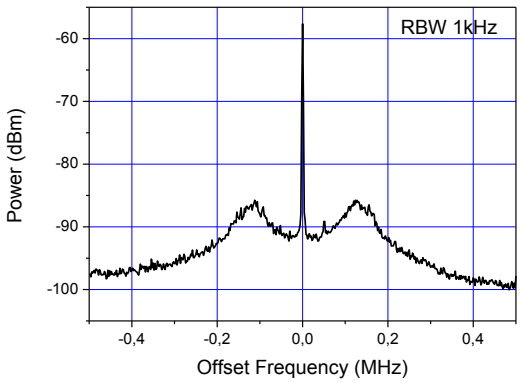


Fig. 5. The phase-locked beat signal between the DFG comb component and the single-mode He-Ne Heterodyne laser (RBW – resolution bandwidth).

III. RESULTS

The scheme of experiment with two independent microwave reference oscillators is shown in Fig. 6. The output signal of the OFD represents a comb of harmonics of f_{rep}. The relative frequency instability of harmonics decreases with harmonic's number but the signal/noise ratio of the detected comb harmonics falls with frequency and for 10 GHz region is 20 dB lower than at 1 GHz. To avoid an increase of frequency instability due to lack of the signal we used in our measurements harmonics with N = 26 (1550 MHz). These components were filtered from the spectrum of each oscillator, mixed and counted at 10 kHz difference frequency.

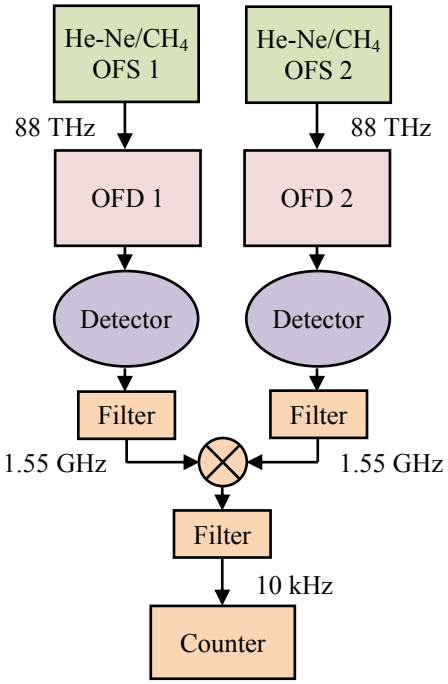


Fig. 6. Scheme of the experiment with two methane based microwave oscillators.

Earlier [10] the contribution of the OFD frequency instability was estimated using a scheme similar to the scheme in Fig. 6 but with one significant difference - two OFDs were locked to one He-Ne/CH_4 OFS. The OFD showed the relative instability about 1×10^{-14} for averaging time $\tau = 1$ s that decreased reaching 1×10^{-16} for $\tau = 100$ s.

In the present work two OFDs are locked to two independent He-Ne/CH_4 OFSs and the result of their comparison is shown in Fig. 7. Frequency counters of "Λ" and "Π" type were used for evaluation of the frequency instability of the created methane based microwave oscillator. A 100 Hz-band filter was placed at the input of Π-type counter.

Behaviour of the curves reflects two sources of instability. At short averaging times ($\tau < 1$ s) it corresponds to Allan deviation characterizing the fs OFD [10] and reflects the white phase noise spectral density of fluctuations with a slope $1/\tau$ (Fig. 7, blue squares). For longer averaging times ($\tau > 1$ s) the instability is determined by the frequency fluctuations of the He-Ne/CH_4 OFS (see Fig. 3).

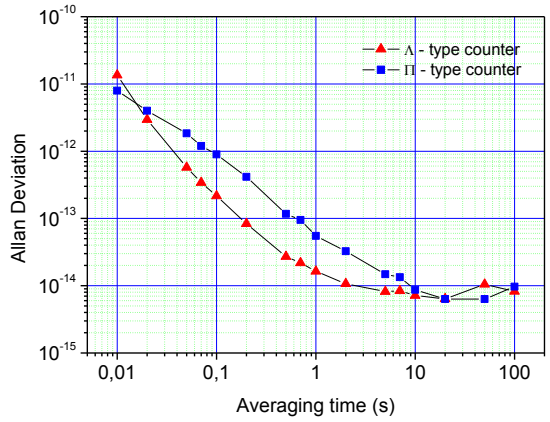


Fig. 7. Relative instability of the output signals at 1550 MHz for two independent methane referenced oscillators. Red triangles - data obtained with Λ-type counter; blue squares - data obtained with Π-type counter and 100 Hz-band filter at the counter input.

The contribution of white phase noise into the measured instability depends on the transmission bandwidth of a channel at the frequency counter input. H-masers are usually tested with a 3 Hz-band filter. Recalculation of the data from Fig. 7 for the 3 Hz-band filter gives the value of frequency instability related to one system 1×10^{-14} for $\tau = 1$ s.

In conclusion. Microwave oscillator with frequency instability 1×10^{-14} at $\tau = 1$ s is created. The oscillator is based on the compact methane stabilized He-Ne/CH_4 standard with zerodur resonator and PM Er fiber femtosecond laser. The frequency instability of the OFD determines the instability of the device for $\tau < 1$ s whereas the OFS determines the instability for $\tau > 1$ s. The obtained level of the instability meets the requirements of interrogative oscillators for Cs/Rb atomic fountains.

REFERENCES

[1] A. Hati, C.W. Nelson, C. Barnes, D. Lirette, T. Fortier, F. Quinlan, J.A. Desalvo, A. Ludlow, S.A. Diddams, and D.A. Howe, "State-of-the-Art RF Signal Generation From Optical Frequency Division", IEEE Trans. Ultrason. Ferroelectr. Freq. Control, vol. 60, pp. 1796–1803, 2013.

[2] T.M.Fortier, M.S.Kirchner, F.Quinlan, J.Taylor, J.C.Bergquist, T.Rosenband, N.Lemke, A.Ludlow, Y.Jiang, C.W.Oates and S.A.Diddams, "Generation of ultrastable microwaves via optical frequency division", Nat. Photonics, vol. 5, pp. 425-429, 2011.

[3] S.Foreman, A.Marian, J.Ye, E. Petrukhin, M. Gubin, O.Mücke, F.Wong, E.Ippen, F.Kaertner, «Demonstration of a HeNe/CH_4-Based Optical Molecular Clock», «Optics Letters», vol. 30, No 5, , March 1, 2005, p.570.

[4] M.A. Gubin, A.N. Kireev, A.V. Konyashchenko, P.G. Kryukov, A.S. Shelkovnikov, A.V. Tausenev, D.A. Tyurikov, "Femtosecond fiber laser based methane optical clock", Appl. Phys. B, vol. 95, pp.661-666, 2009.

[5] G. Santarelli, C. Audoin, A. Makdissi, P. Laurent, G.J. Dick, and A. Clairon, "Frequency stability degradation of an oscillator slaved to a periodically interrogated atomic resonator", IEEE Trans. Ultrason. Ferroelectr. Freq. Control, vol. 45, pp. 887–894, 1998.

[6] B. Lipphardt, V. Gerginov, and S. Weyers, "Optical Stabilization of a Microwave Oscillator for Fountain Clock Interrogation", IEEE Trans. Ultrason. Ferroelectr. Freq. Control, vol. 64, pp. 761–766, 2017.

[7] M. A. Gubin, D. A. Tyurikov, A. S. Shelkovnikov, E. V. Koval'chuk, G. Kramer, and B. Lipphardt, "Transportable He-Ne/CH_4 Optical Frequency Stasndard and Absolute Measurements of its Frequency", IEEE J. Quantum Electron. **31,** 2177 (1995).

[8] M. Gubin, A. Shelkovnikov, E.Kovalchuk, D.Krylova, E.Petrukhin, D. Tyurikov, "Present performance of the transportable He-Ne/CH_4 optical frequency standards", in Proceedings of the 1999 Joint Meeting of the EFTF and of the IEEE IFCS, 13-16 April 1999, Besancon, France, Volume 2, p.710. IEEE Catalog No.99CH36313.

[9] A.N. Kireev, A.S. Shelkovnikov, D.A. Tyurikov, V.A. Lazarev, and M.A. Gubin, "Monoblock He-Ne/CH_4 laser with the short-term and long-term frequency stability better than 1×10^{-14} ", in Frontiers in Optics 2016, OSA Technical Digest (online) (Optical Society of America, 2016), paper JW4A.180.

[10] A. Kireev, A. Tausenev, D. Tyurikov, A. Shelkovnikov, D. Shepelev, A. Konyashchenko, and M. Gubin, "Femtosecond optical-to-microwave frequency divider with a relative instability of 10^{-14} - 10^{-16} ($\tau = 1$ – 100 s)", Quantum Electronics, vol. 46,pp. 1139-1141, 2016.

Revisiting the Relation between Laser Spectrum and Phase Noise Spectral Density with New Outcomes

Pierre Brochard, Stéphane Schilt, Thomas Südmeyer
Laboratoire Temps-Fréquence, Université de Neuchâtel, Neuchâtel, Suisse
email : pierre.brochard@unine.ch

***Abstract*—We revisit an expansion series introduced a long time ago by D. Middleton to link the phase noise power spectral density (PN-PSD) of an oscillator to its power spectrum, which is poorly known and used in the laser community. In contrast, a different approach proposed by D. Elliott is widely used to compute the spectrum of a laser from its PN-PSD. We show some benefits brought by the use of Middleton's series both on the conceptual and quantitative points of view and we introduce a simple guideline to implement this approach with an arbitrary PN-PSD. We illustrate these considerations with several experimental examples.**

Keywords— *Laser noise, Phase noise, Spectral analysis*

I. INTRODUCTION

Stable and low-noise optical or microwave oscillators are used in many scientific areas today. Therefore, it is primordial to properly understand and characterize their spectral and noise properties, such as their frequency or phase noise, their power spectrum, or their linewidth, which are all related to each other to some extent. Of particular interest in this context is the relationship that links the phase noise power spectral density (PN-PSD) $S_\phi(f)$ and the power spectrum $S_E(\nu-\nu_0)$ of an oscillator of frequency ν_0, where f is the Fourier frequency.

This relationship has been studied for the first time several decades ago by D. Middleton in the context of modulated electrical oscillators for communications signals [1]. Middleton introduced the mathematical expression (1) in the form of an infinite series of convolution products, known as Middleton's expansion series:

$$S_E(\nu-\nu_0) = E_0^2\, e^{-\phi_{rms}^2}\, \delta(\nu) + E_0^2\, e^{-\phi_{rms}^2}\, S_\phi(f) + E_0^2\, e^{-\phi_{rms}^2} \sum_{n=2}^{\infty} \frac{1}{n!} S_\phi(f) *^{n-1} S_\phi(f) \quad (1)$$

where E_0 is the amplitude of the signal and ϕ_{rms} its integrated phase noise. Since this expression is made of an infinite sum of self-convolution terms of the PN-PSD (denoted $*^{n-1}$), its use has been essentially restricted so far to the particular case of low phase noise, where only the first two terms (n = 0 and n = 1) have a significant contribution to the power spectrum.

Three decades after Middleton, D. Elliott and co-authors discussed the same relationship in a different form (2) made of a Fourier transform $\mathcal{F}$ of the exponential function of the autocorrelation function of the oscillator phase [2], which they specifically applied in the field of lasers:

$$S_E(\nu-\nu_0) = E_0^2\, e^{-\phi_{rms}^2}\, \delta(\nu) * \mathcal{F}\left[e^{\int_0^{+\infty} S_\phi(f)\cdot\cos(2\pi f\tau)df}\right] \quad (2)$$

With the universalization of the fast Fourier transform (FFT) algorithm that was unknown at the time of Middleton's initial work, Elliott's formula has been much widely used than Middleton's approach, especially in the field of lasers where the latter has remained fairly unknown. However, Middleton's approach presents several advantages over the use of Elliott's formula to compute the power spectrum corresponding to a given PN-PSD. In this paper, we revisit Middleton's expansion with the aim of demonstrating its interest, both on the conceptual and quantitative points of view, to compute the power spectrum for an arbitrary PN-PSD. We show that the computation is easier to implement and provides more accurate results compared to Elliott's formula. We illustrate our considerations with several experimental examples and show how Middleton's series can be used in all different regimes of low, intermediate, and high integrated phase noise.

II. MIDDLETON'S EXPANSION COMPUTATION

The mathematical details of this work can be found in our recently submitted work [3]. We have shown that only a limited number N of terms of Middleton's infinite expansion have to be taken into account to compute the power spectrum. An important outcome is that this number can be unambiguously determined prior to the calculation for any physical type of noise spectrum and depends only on the integrated phase noise of the signal:

$$N = \phi_{\mathrm{rms}}^2 + 3\phi_{\mathrm{rms}}\,. \quad (3)$$

The first component of this expression (ϕ_{rms}^2) corresponds to the term of the series (1) that has the maximum amplitude, whereas additional terms ($3\phi_{\mathrm{rms}}$) must be considered to obtain a sufficient accuracy on the computed spectrum. Elliott's general formula is more difficult to implement in practice as it involves the double integration process (2), where the first integral has to be computed a large number of times for different values of the correlation time τ. Great care is required in the choice of these values (proper sampling of the autocorrelation function) to retrieve a correct spectral lineshape, but these parameters are not known *a priori* before the computation is performed. An improper choice of these parameters may lead to numerical artifacts, resulting in an incorrect spectrum as illustrated in Fig. 1a for an experimental PN-PSD. In contrast, the computation of Middleton's series with the number of terms given by (3) is straightforward and in excellent agreement with the spectrum that we experimentally measured (not shown in the figure).

III. EXAMPLES AND EXPERIMENTAL DEMONSTRATION

In the following, we present some examples of application of Middleton's series computed using our simple criterion (3).

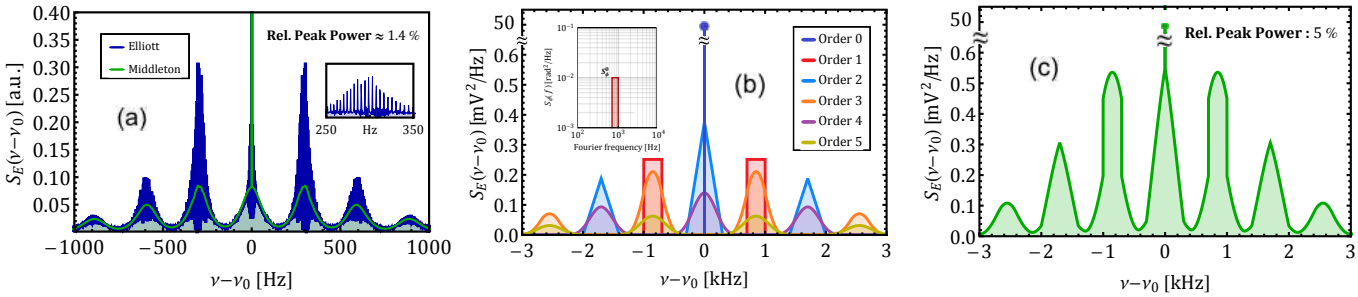


Fig 1. (a) Example of artifact that can occur in the power spectrum computed using Elliott's formula (blue) in comparison with the use of Middleton's expansion (green line). Inset: Zoom on the discrepancy. (b-c) Quantitative explanation of the power spectrum computed using Middleton's series for a rectangular PN-PSD with $\phi_{\mathrm{rms}} = 1.73$ rad (Inset). (b) Individual terms of orders 1-5 of Middleton's series. (c) Complete power spectrum.

A. *Qualitative power spectrum description*

Middleton's expansion gives a qualitative understanding of the power spectrum corresponding to an arbitrary PN-PSD, as shown in Fig. 1(b-c) for a narrow-band PN-PSD. The resulting spectrum is the sum of many self-convolution products of the double sideband PN-PSD. The 0th-order term corresponds to a coherent peak at ν_0; the 1st-order term is the double sideband PN-PSD located on each side of the coherent peak; higher order terms are successive self-convolution products of the PN-PSD, leading to sidebands of different shapes that tend to a Gaussian shape at increasing order number (Fig. 1b).

Another case that can be qualitatively understood from Middleton's series is the high integrated phase noise regime. A high number of terms need to be taken into account in this case according to (3). From the central limit theorem, a high-order multiple self-convolution of any PN-PSD tends towards a Gaussian distribution, explaining why the spectrum is Gaussian at high ϕ_{rms} independently of the shape of the FN-PSD.

B. *Power spectra in the different phase noise regimes*

From our investigations, we defined three different regimes of phase noise that lead to different characteristic features in the corresponding power spectra. We give a more precise limits between these regimes than the two extreme cases generally considered (low noise for $\phi_{\mathrm{rms}} \ll 1$ and high noise for $\phi_{\mathrm{rms}} \gg 1$). In the low phase noise regime, the power spectrum consists of a coherent peak surrounded by the PN-PSD $S_\phi(f)$, therefore only the terms $n = 0$ and 1 of Middleton's series contribute to the spectrum, leading to a limit of $\phi_{\mathrm{rms}} < \pi/8$. For intermediate phase noise $\pi/8 < \phi_{\mathrm{rms}} < \pi$, up to 20 terms must be considered to accurately compute the power spectrum. Finally, the large noise regime occurs when $\phi_{\mathrm{rms}} > \pi$, where the spectrum tends to a Gaussian shape. These different cases are experimentally illustrated in Fig. 2. In each case the power spectrum computed from the experimental PN-PSD using Middleton's series is in excellent agreement with the measured spectrum.

C. *Exact mathematical expression for the spectral width*

Different approximations have been proposed to estimate the linewidth of an oscillator directly from its PN-PSD [4] without computing Elliott's complete power spectrum. These approaches are widely used in the laser community and give fairly good estimations, but they apply only to the high integrated phase noise regime. Using Middleton's expansion and considering the central limit theorem, we provide an exact mathematical link between the widths (standard dev.) of the power spectrum σ_{RF} and of the double sideband PN-PSD σ_ϕ: $\sigma_{\mathrm{RF}} = \phi_{\mathrm{rms}} \cdot \sigma_\phi$. Applied to the experimental data of Fig. 2, the observed spectral widths σ_{RF}= 478, 11'197 and 23'593 Hz, respectively, are in excellent agreement with the calculated values of $\phi_{\mathrm{rms}} \cdot \sigma_\phi$ = 474, 11'280 and 23'621 Hz.

IV. Conclusion and Outlook

By revisiting an old formula describing the relationship between the PN-PSD and the power spectrum of an oscillator, we have shown its benefit and simplicity. We have introduced a simple guideline to determine the number of terms to be considered in the computation and have shown the advantage of this approach in several simulations and experimental results compared to Elliott's formula commonly used in the laser community. Based on these investigations, we believe that the use of Middleton's series should be advertised and used in the laser community.

References

[1] D. Middleton, Mag. J. Sci. **42**(330), 689–707, 1951.
[2] D. S. Elliott, R. Roy, and S. J. Smith, Phys. Rev. A **26**(1), 12-18, 1982
[3] P. Brochard, T. Südmeyer, and S. Schilt, submitted to IEEE TUFFC
[4] G. Di Domenico, S. Schilt, and P. Thomann, Appl. Opt. **49**, 4801, 2010

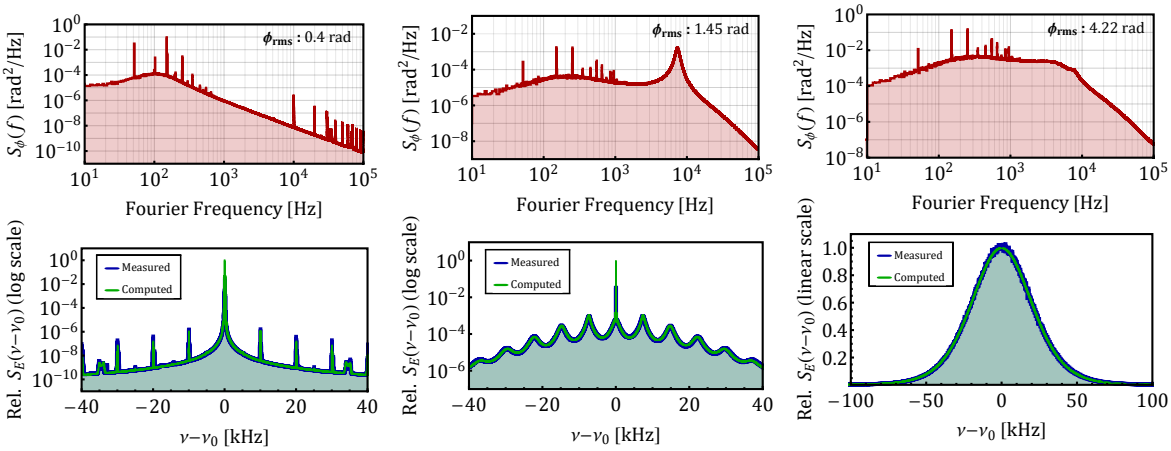


Fig 2. Comparison of the power spectra computed using Middleton's series with experimental spectra. Top: experimental PN-PSD measured for different signals: low (left), intermediate (middle) and high (right) integrated phase noise. Bottom: Corresponding power spectra experimentally measured (blue) and computed (green).

Photonic Microwave generation at NTSC

Lulu Yan[1,2]， Wenyu Zhao[1], Yanyan Zhang[1,2], Zhaoyang Tai[1,2], Pan Zhang[1], Xiaofei Zhang[1,2], Wenge Guo[1], Shougang Zhang[1,2], Haifeng Jiang[1,2,*]

[1] Key Laboratory of Time and Frequency Primary Standards, National Time Service Center, Xi'an 710600, China
[2] School of Astronomy and Space Science, University of Chinese Academy of Sciences, Beijing 100049, China
*haifeng.jiang@ntsc.ac.cn

Abstract—We report photonic microwave generation based on Er:fiber-based optical frequency combs and 1.55 μm ultra-stable lasers. The frequency instability of the 9.6 GHz microwave signals is 3×10^{-15}@ 1s, and the synthesized tunable 9.192 GHz signal exhibits an instability of 6.7×10^{-15} @1s. Further improvement of the photonic oscillators is undergoing.

Keywords—microwave sources; optical frequency comb; ultra-stable laser;

I. INTRODUCTION

Atom fountain clocks provide the most accurate realization of the International System of Unit (SI) second and define the accuracy of the widely used international atomic time. Highly performed fountain clocks reach frequency uncertainty at low 10^{-16} level, exhibiting $1\sim3\times10^{-14}/\tau^{1/2}$ for short term stabilities, limited only by quantum project noise. However, most of the fountain clocks shows $10^{-13}/\tau^{1/2}$ frequency instabilities due to the Dick effect of local oscillator noise[1], which can be eliminated by using the Ultra-stable photonic microwave. Ultra-stable photonic microwave is one solution for eliminating Dick effect.

In this paper, we report on the progress of ultra-stable photonic microwave generation developed at NTSC. Preliminary results show that the microwave generators exhibit a frequency instability of well below 1×10^{-14}@ 1s, which is enough for suppressing the Dick effect[2].

II. EXPERIMENTAL SETUP

The scheme of experimental setup is shown in Fig. 1. The photonic microwave generation follows standard optical-comb-based approaches[3], where we stabilize the repetition rate (f_r) of optical comb to a continuous wavelength (CW) laser. The reference CW laser is made by ourselves [4]. Our experimental setup comprises 3 part: the first one is a low-noise CW laser at 1555 nm. (We will talk little about CW laser as to the correlation work has been submitted to EFTF); the second one is photonic microwave generation by two Er:fiber-based optical frequency combs and measurement system by using down conversion technique; and the third one is the specially designed ultra-low phase noise frequency synthesizers, which is used to realize microwave signals output at about 9.192 GHz and the instability measurement system.

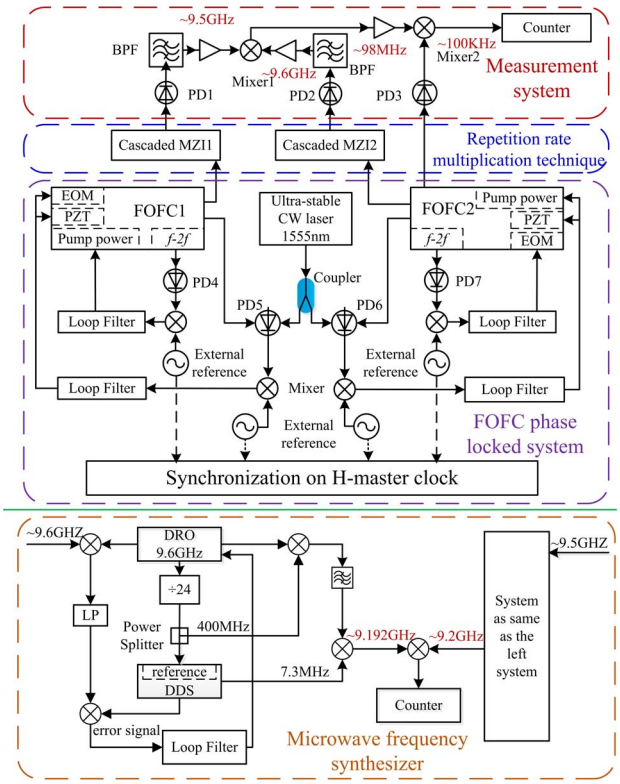


Fig.1 Scheme of experiment setup. At the top of the green solid line is optical generation microwave signal system and measurement system. The bottom is the microwave frequency synthesizer and measurement system. FOFC: Er:doped fiber optical frequency comb.

The upper part of Fig. 1 shows the scheme of the photonics microwave generation and measurement system. First of all, both of these two Erbium doped fiber optical frequency combs are phase locked to a ultra-stable CW laser at the same time. Furthermore we synchronously phase locked the f_{ceo} to two external signal generators with an H-master clock reference (10 MHz). The f_r of these two optical frequency combs are about 196 MHz and 232 MHz, respectively. Then two low-noise and high bandwidth InGaAs photo detectors (Discovery model DSC30S) are used to extract microwave signals near 9.6 GHz and 9.5 GHz from the pulse trains of these two optical frequency combs. Further, an approach of repetition rate multiplication based on a series of cascaded Mach-Zehnder interferometer (MZI)[5] is employed to get a higher signal output power (about -23 dBm) at the higher harmonic signals.

We employ the down conversion technique to measure the instability of the microwave sources (see the red dotted frame at the top of Fig. 1) Two microwave signals which output from

two independent fiber optical frequency combs (FOFC) are detected by PD1 and PD2, respectively, and then they are input to a mixer (Marki model M1-0412LA) to get an IF frequency near 98 MHz. We can't get an actual result by measuring the 98 MHz signal directly, because it is limited by the frequency instability of H-master clock reference signal with a level of 10^{-13} @ 1s. The 98 MHz signal is further down mixed to near 100 kHz. Therefore, the reference noise effect is reduced by a factor of about 1000. Figs. 2 shows the frequency spectrum of microwave signal near 9.5 GHz, and the insert is frequency fluctuations of beatnote (recorded by Agilent 53230A) between two microwave signals.

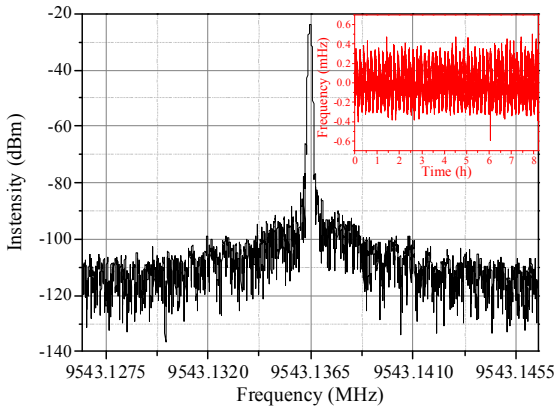


Fig. 2 (a): residual frequency fluctuations of photonic microwave generator; (b) ~9.5 GHz microwave signal extract from one microwave source.

We design a ultra-low phase noise frequency synthesizer to shift the 9.5~9.6 GHz signal to 9.192 GHz signal. As shown in the lower part of Fig. 1, the 9.6 GHz local oscillator is phase-locked on a high order harmonics (~9.6 GHz) of the repetition rate of an optical frequency comb. First, the 9.6 GHz signal is 24 times frequency-divided to produce 400 MHz reference frequency for two direct digital synthesizers (DDS); 400 MHz signal is also used at down frequency conversion part of generating 9.2 GHz signal. One DDS is used to compensate the frequency difference of the high order harmonics from 9.6 GHz. The other DDS (7.3 MHz) is to produce a tunable 9.192 GHz for atomic transition interrogation. We develop two identical systems to evaluate the frequency instability of the produced microwave by comparing their phases.

The black squares in Fig. 3 shows that the instability of ultra-stable microwave signal at ~ 9.6 GHz is about 3×10^{-15} @ 1 s. The instability of our home-made ultra-stable CW laser indicated by the red circles is 7×10^{-16} at 1 s, please find Tai `s paper [4] in this proceeding for details. The instability of microwave synthesizer from ~9.5 GHz (~9.6 GHz) to 9.192 GHz is about 6.7×10^{-15} @ 1 s. Assuming the noise of CW laser, OFOC and microwave synthesizer are not correlated, the relative frequency instability of the microwave generator would be about 7×10^{-15} @ 1 s.

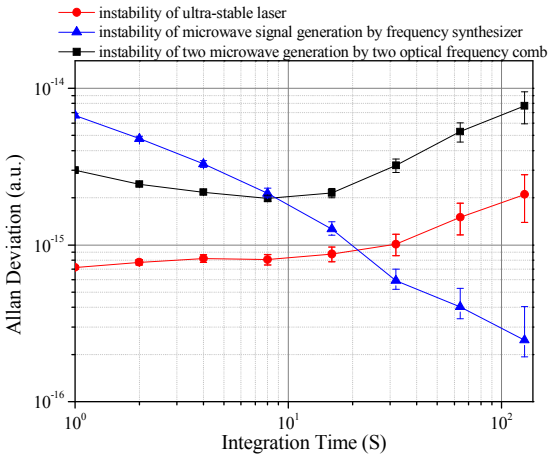


Fig. 3 Circles: fractional frequency instability of ultra-stable CW laser (characterized by the allan standard deviation). Squares: fractional frequency instability of the microwave signal generated by the fiber-based optical frequency combs at 9.6 GHz. Triangles: fractional frequency instability of 9.192GHz shifting by frequency synthesizer.

III. CURRENT RESULTS

We have demonstrated a photonic microwave generation experiment, where an Er:fiber-based optical frequency comb is phase locked to a ultra-stable CW laser. The instability of 9.6 GHz microwave signals is 3×10^{-15}@ 1s, and the instability of synthesized 9.192 GHz signal is about 7×10^{-15} @ 1s. The measurement of additional phase noise is undergoing.

ACKNOWLEDGMENT

This work is supported by National Natural Science Foundation of China under Grant No 91536217, and the West Light Foundation of the Chinese Academy of Sciences under Grant No 2013ZD02, and the Youth Innovation Promotion Association of CAS under Grant No 2015334.

REFERENCES

[1] G.Santarelli, C. Audoin, A. Makdissi, P. Laurent, G. J. Dick, and A. Clairon, "Properties of an oscillator slaved to a periodically interrogated atomic resonator," IEEE Trans. Ultrason. Ferroelectr. Freq. Control, vol. 45, pp.887-886,1998.

[2] J. Millo, M. Abgrall, M. Lours, E. M. L. English, H. Jiang, J.Guena, A. Clairon, S.Bize, Y. Le Coq, G. Santarelli and M. E. Tobar, "Ultralow noise microwave generation with fiber-based optical frequency comb and application to atomic fountain clock," App. Phy. Lett., America, vol.94, pp. 141105, April 2009.

[3] X. Xie, R. Bouchand, D. Nicolodi, M. Giunta, W. Hamsel, M. Lezius, A. Joshi, S. Datta, C. Alexandre, M. Lours, P. Tremblin, G. Santarelli, R. Holzwarth and Y. Le Coq, "Photonic microwave signals with zaptosecond-level absolute timing noise," nature photonics, vol. 11, pp. 44-47, 2016.

[4] Z. Tai, L. Yan, Y. Zhang, X. Zhang, W. Guo, S. Zhang and H. Jiang, "Thermal noise limited ultra-stable laser at 1555 nm,"in this proceeding (the paper ID is 1189)

[5] H. Jiang, J. Taylor, F. Quinlan, T. Fortier and S. A. Diddams, "Noise floor reduction of an Er:fiber laser-based photonic," IEEE Photon. Journal, America, vol. 3,pp. 1004-1012, December 2011.

High-temperature Calcium Vapor Cell Construction and Spectroscopy

Nathan Lemke,
Christopher Erickson
Air Force Research Laboratory
Space Vehicles Directorate
Kirtland Air Force Base, United States

Kyle W. Martin,
Jordan Armstrong
Applied Technology Associates
Albuquerque, NM

Jarom Jackson,
Dallin Durfee
Department of Physics and Astronomy
Brigham Young University
Provo, UT

Abstract— **We describe the construction, operation, and resulting spectroscopy of a high-temperature calcium vapor cell using the 657 nm intercombination transition in neutral calcium. Alkali contaminants inside the cell resulted in the emission of off-resonant fluorescence. The resulting lifetime of the $^3P_1$ state in calcium atoms subjected to collisions with the contaminant vapor is quantified.**

Keywords— high-temperature vapor cell; calcium; spectroscopy

I. INTRODUCTION

The narrow natural linewidth (375 Hz) of the 657 nm $^1S_0$ - $^3P_1$ transition of neutral calcium makes it an attractive candidate to provide fractional frequency instabilities of less than 10^{-14} at one second [1-2]. Vapor cells containing a small amount of the alkaline earth metal are an appealing atomic source that could provide high vapor density with reduced system size compared to existing clocks. Due to the low vapor pressure of calcium, the temperature required to achieve sufficient vapor density (ca. 500 °C) yields additional materials and manufacturing challenges compared to vapor cells commonly used for alkali metal atoms [3-5]. We investigate a new option for a calcium vapor cell that is simple in design.

II. CALCIUM VAPOR CELL AND HEATING PACKAGE DESIGN

Europium doped calcium fluoride (Eu:CaF_2) promises to be a viable option for a calcium vapor cell due to its low chemical reactivity and machinability [4]. The vapor cell consists of a 2”x 1”x1” crystal with a blind ¾” diameter core milled from the center. The surface containing the opening is highly polished, and a 1”x1”x1/4” lid is optically contacted to the open face in atmosphere in a laboratory environment. After the contact bond is verified, the bond is mechanically broken, and the opened cell is placed in a vacuum chamber outfitted for optical contact bonding. A 0.5 g ingot of 99% pure calcium metal is placed inside the cell. Finally, the chamber is evacuated to a background pressure of 10^{-6} Torr, and the cell lid is again optically contacted using a linear motion feedthrough to seal the cell.

We designed a heating package which allows sufficient optical access on all sides for laser cooling and trapping. The package consists of heaters made from a tungsten filament embedded in aluminum nitride, with a cut-out in the central region for optical access. Transparent sapphire plates are used as heat spreaders, and a copper housing holds together all the components to complete the heating package.

Low conductivity mounting springs are used to thermally and mechanically isolate the vapor cell inside of a high vacuum chamber. Compared to previous reports [5, 6], this cell manufacturing technique is superior in that no calcium atoms have been observed to leak out of the cell.

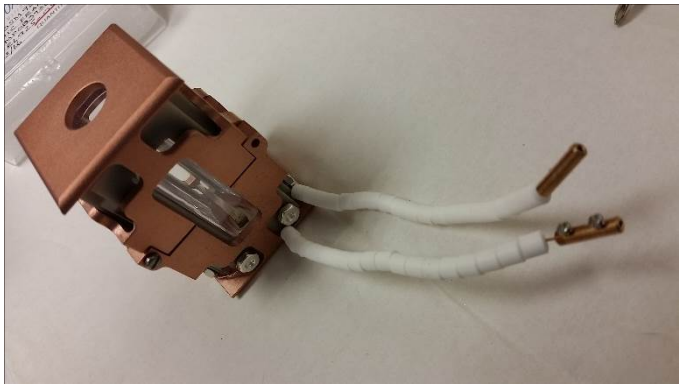


Fig. 1. The completed calcium vapor cell inside the heating package.

III. EXPERIMENTAL RESULTS

After heating the cell to ~ 480 °C, we observed that 657 nm light was absorbed by the calcium vapor in the cell as expected, but the fluorescent light scattered out of the cell was yellow. A grating spectrometer identified the wavelength of the fluoresced light to be 589 nm, very near to the wavelength of the well-known sodium doublet. In addition to the yellow fluorescence, spectral lines corresponding to D1 and D2 transitions in Rb, Li, and K were observed.

Upon reducing the temperature of the calcium vapor, we also observed fluorescence and absorption of light on the 657

nm calcium transition at temperatures far lower than expected, including significant absorption with temperatures as cool as 300 °C. At this temperature, bright red fluorescence was seen where there should have been unperceivable red scattering, which also suggests an impurity with significantly higher vapor pressure than calcium was present inside the cell.

An electron microscope-based elemental detection system was used to search for alkali impurities in a sample of Eu:CaF_2 and a Ca ingot similar to the one in the vapor cell, but did not find evidence of any alkali atoms. This indicates that while the contaminants seem to produce a robust vapor, the vapor is coming from very small amounts of solid material. If there were enough of the alkalis to create a saturated vapor, their vapor pressures would be quite high at the cell operating temperatures.

We performed lifetime measurements of the excited $^3P_1$ state of calcium in the vapor cell and found the state to be quenched relative to the vacuum lifetime (0.4 ms). The state remains long-lived nonetheless, with a lifetime (ca. 0.1 ms) that depends only weakly on the vapor cell temperature.

Future plans to mitigate the vapor cell impurities include vacuum baking the Eu:CaF_2 crystal prior to filling it with calcium metal; inclusion of a non-evaporable getter pump inside the cell that is suited for high-temperature operation; and using higher a purity calcium ingot. We hope that these additional features could result in a background vapor pressure low enough to support the formation of a magneto-optical trap inside the vapor cell.

ACKNOWLEDGMENT

The authors would like to thank Gretchen Phelps, Michael Bishop, Mayer Landau, and John Burke for many useful discussions. We acknowledge support from CINT User Proposal #U2015A0063.

REFERENCES

[1] U. Sterr et al., C. R. Physique 5 (2004)

[2] R. Fox, J. Sherman, W. Douglas, J. Olson, A. Ludlow, and C.W. Oates, Proc. 2012 IEEE Intl. Freq. Cont. Symp. 404-406 (2012).

[3] K. Vogel, Ph.D. Dissertation

[4] C. Erickson, B. Neyenhuis, and D. Durfee, Rev. Sci. Inst. 76, 123 110 (2005).

[5] J. Armstrong, N. Lemke, K. Martin, and C. Erickson, Proc. of the 48th Annual PTTI Meeting, p. 147-149 (2016).

[6] J. Armstrong, N. Lemke, K. Martin, and C. Erickson, Proc. SPIE 9763, Slow Light, Fast Light, and Opto-Atomic Precision Metrology IX, 976303

G-LAS

A Ring Laser Goniometer for Angular Metrology

Jacopo Belfi*, Nicolò Beverini*†, Giorgio Carelli*†, Angela Di Virgilio*, Umberto Giacomelli*†, Enrico Maccioni*†, Milena Astrua‡, Marco Pisani‡, Marco Santiano‡

*INFN, sezione di Pisa, Pisa, Italy

†Department of Physics, University of Pisa, Pisa, Italy

‡Istituto Nazionale di Ricerca Metrologica, INRIM, Torino, Italy

e-mail: {jacopo.belfi,angela.divirgilio}@pi.infn.it ; {nicolo.beverini, enrico.maccioni}@unipi.it , umberto.giacomelli@df.unipi.it ; {m.astrua,m.pisani,m.santiano}@inrim.it

Abstract*—Accurate measurement of angles down to the nanoradian level is required in precision mechanical industry, as well in geodesy, astronomy and experimental physics. G-LAS (GyroLaser Angular Standard) is the new transportable prototype of goniometer, based on a ring laser gyroscope mounted on a precision turntable, that is presently under test in a collaboration between INRIM and INFN. The target is to achieve an accuracy of the order of 10 nrad, being the accuracy of the most precise existing angular encoders at the level of some 100 nrad.

Keywords—angular metrology; laser gyroscopes; Sagnac effect

I. INTRODUCTION

A joint project between the Italian Metrologic Institute (INRIM) and the Italian Nuclear Physics Institute (INFN) has the target of building a prototype of ring laser goniometer with accuracy of the order of 10 nrad [1]. This kind of goniometer exploits the Sagnac effect: a ring laser (RL) in rotational motion with respect to an inertial frame sees a differential length of the effective optical path of the two oppositely travelling beams. This produces a relative frequency shift (Sagnac frequency) between them, which is proportional to the RL angular speed. The scale factor that links the Sagnac frequency f_{Sagnac} and the RL cavity angular speed Ω is given by a simple geometrical relation:

$$f_{Sagnac} = \frac{4A}{\lambda P}\vec{\Omega}\cdot\hat{n} = k\,\Omega\cos\vartheta \qquad (1)$$

where P is the cavity length, A is the area enclosed by the optical path, λ is the laser wavelength, and ϑ is the angle between the rotation axis and the area versor $\hat{n}$. In the case of a square optical cavity with side L, the value of the scale factor k is simply L/λ.

Applications of RLs in angular metrology have been foreseen since the end '60s [2], just after the invention of the laser. The basic idea is to use the interference fringes by the two counter-propagating modes as an ultra-fine angular scale dividing the full 2π angle. The value of the angle ϕ can be evaluated as $\phi = 2\pi\, N_\phi / N_{2\pi}$, where

$$N_\phi = \frac{1}{2\pi}\int_{t_0}^{t_1} f(t)dt = \frac{k}{2\pi}\int_{t_0}^{t_1}\Omega(t)dt = \frac{k}{2\pi}\phi \qquad (2)$$

is the number of fringes counted in the time $t_1 - t_0$, while the number of fringes counted in one full period T:

$$N_{2\pi} = \frac{1}{2\pi}\int_{t_0}^{t_0+T} f(t)dt = \frac{k}{2\pi}\int_{t_0}^{t_0+T}\Omega(t)dt = k \qquad (3)$$

gives the self-calibration of the scale factor.

The most effective realization is given by the apparatus developed by Yu. V. Filatov and collaborators since the end of '70s. It makes use of a monolithic RL, 11 cm in side-length, mounted on a turntable [3]. The typical accuracy of this instrument is at the level of 100 nrad, limited by the errors due to the influence of environmental parameters on the ring laser dynamics.

II. THE APPARATUS

Fig. 1 shows the present state of G-LAS (GyroLaser Angular Standard). The RL consists in a square optical cavity (Fig. 2) closed by two flat and two concave (R= 4m) high-quality mirrors (reflectivity larger than 99.99%). The cavity is contained inside a vacuum chamber composed by four angular towers connected through steel pipes.

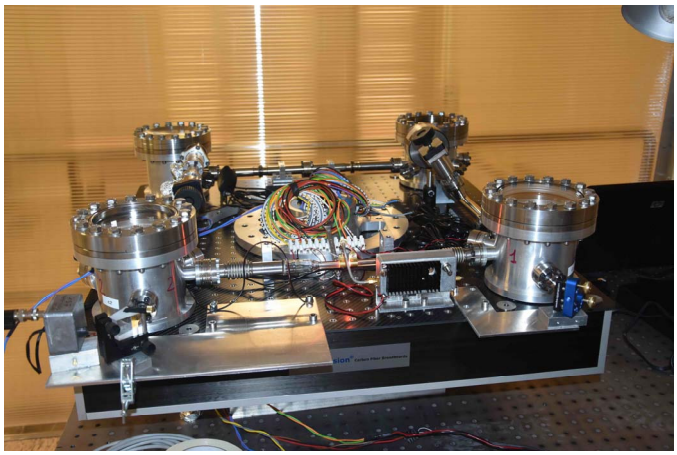


Fig. 1. The vacuum chamber homing the RL optical cavity.

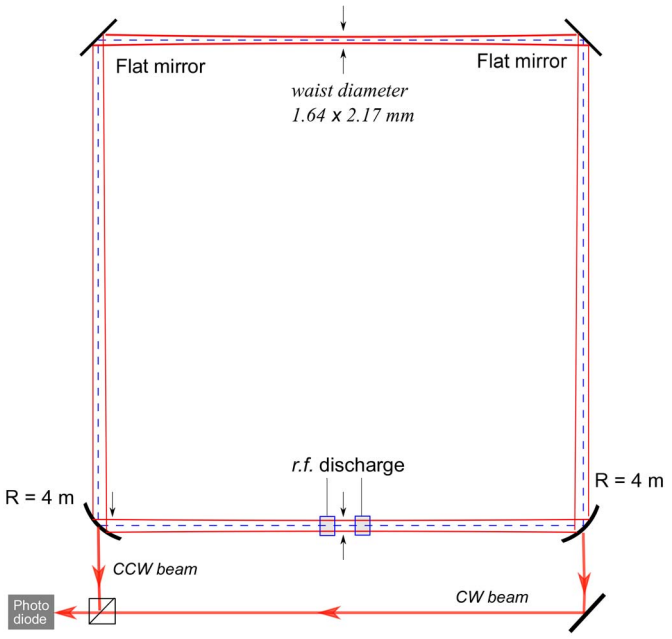


Fig. 2. Scheme of the optical cavity.

The towers are screwed on a 70×70 cm^2 board realized by a carbon fibre honeycomb, closed between two layers of carbon fibre panels. Board material had chosen for its properties of stiffness and lightness and for its moderate thermal expansion coefficient ($2.5 \cdot 10^{-6}$ K^{-1}). The mirrors close a square optical cavity with the side of 500 mm. The four mirrors (two flat and two concave with R=4 m) are mounted on high-quality mounting with piezoelectric drives.

The whole cavity is filled with He-Ne mixture; no window is inserted in the optical path. Active medium is excited by external electrodes through a RF discharge on a glass capillary sealed in the middle of one side.

The beams escaping from the two mirrors adjacent to the discharge are extracted through vacuum windows and combined together on a photodiode. The interference signal is digitized by an ADC and recorded on a computer. In the next future, a specially designed combining prism will be put in position inside the vacuum chamber, immediately behind one of the flat mirrors, in order to reduce the perturbation induced by the asymmetry between the paths.

The board is mounted on a high-precision turntable Airtech (model ABRS-300MP), with integrated direct driving motor and high accuracy optical encoder. By the high accuracy manufacturing it claims a sub-microradian rotation errors and a resolution in angle position better than 0.2 µrad. Moreover, a sophisticate control system should provide a constant speed rotating rate Ω, with a relative error ΔΩ/Ω lower than 10^{-5}.

III. Ring Laser Operation

First of all, we tested the RL operation. The requirement is to work in a regime of stable single mode operation. The FSR of the laser cavity is 150 MHz, while the gain profile of He-Ne laser is inhomogeneously broadened with a typical width FWHM of 1500 MHz. In these condition single longitudinal mode operation can be obtained by operating near threshold at a He density larger than the typical one of shortest laser, thus increasing the homogeneous width. Moreover, the use of 50%-50% ^{20}Ne/^{22}Ne isotope mixture avoids cross-saturation between the two counter-rotating laser beams [4]. Transversal TEM00 mode is selected by the diameter of the discharge capillary. In this way we were obtained RL single mode operation with an emission power of 0.4 µW by using a mixture of 25 Pa of Ne in 300 Pa of He.

Measuring the decay ring-down time of the laser radiation switching off quickly the plasma discharge, around 17 µs, we tested the quality factor of the optical cavity. This gives a cavity finesse of 16000 and a total losses of 400 ppm, which is consistent with the specification of mirror reflectivity >99.99%.

IV. Rotation Tests

We operated the gyroscope at different angular speeds of the turntable in both directions. As expected, at lowest rotational speed, the coupling between the two counter-propagating beams, due to the radiation back scattering on the mirrors, distorts the Sagnac signal, and eventually locks the two laser frequencies together, nulling f_{Sagnac} [4]. We observed the threshold of locking around 200 Hz, which corresponds to a rotation speed of $2.5 \cdot 10^{-4}$ rad/s that is a factor 5 larger than the local vertical component of the Earth rotation rate.

We have performed runs in both directions at nominal rotating rate of 1°/s, 1,5°/s, and 2°/s. The acquisition speed of our ADC card presently used does not allow faster rotation rates.

A difference between the Sagnac frequencies for two rotation direction at a same nominal speed is produced primary by the composition of the table rotation vector with the Earth rotation vector, keeping into account the possible orienting errors. In the following, we will indicate with γ the local geodetic co-latitude value, and with ϑ and φ the misalignment angle of the turntable axis, respectively, with the local vertical direction and with the normal to the optical path. The instantaneous Sagnac frequency for the CW and CCW rotation of the turntable is given by:

$$f^{\pm}_{Sagnac} = k\left(\Omega \hat{n}_t \pm \Omega_E \hat{n}_E\right) \cdot \hat{n}_o \qquad (4)$$

where Ω and Ω_E are respectively the turntable and the Earth rotational speed, and the "+"and the "-" stand respectively for the CCW and CW table rotation. $\hat{n}_t, \hat{n}_E, \hat{n}_o$ are respectively the versors of the table axis, of the Earth axis, and the normal to the surface enclosed by the optical path.

Developing (4) up to the 2nd order, with φ, ϑ ≪ 1 and $\Omega_E \ll \Omega$, we obtain:

$$f^{\pm}_{Sagnac} = k\left\{\Omega\left(1-\varphi^2/2\right) \pm \Omega_E\left[\cos\left(\gamma+\vartheta_{NS}\right) - \varphi \sin\gamma \cos\left(\Omega t+\delta\right)\right]\right\} \qquad (5)$$

Here, ϑ_{NS} is the projection of ϑ on the meridian plane (Nord-South direction) and δ is the initial phase.

Equation (4) neglects the frequency shift due to back-scattering, This can be modelled [5] by adding a term that is proportional to Ω^{-1}:

$$\Delta f_{bs} = -\left(l^2/k\right)\Omega^{-1} \ , \qquad (6)$$

where l is the locking threshold frequency. The actual value of l is defined by the interference of the radiation back scattered from the four mirrors. Thus, it can fluctuate in the time, following the variations optical cavity geometry. By using for l the measured value of ~200 Hz, we can estimate for our system at a rotation rate of 1°/s an inaccuracy over f_{Sagnac} of the order of 3 Hz (that is 200 ppm), which decreases to 50 ppm at 2°s. We must consider, however, that the goniometer in its operating condition should work at a rotational speed at least a factor 10 larger, reducing by more than two orders of magnitude the size of Δf_{bs}. Moreover, changes in the geometry (primary, due to thermal dilatations) should occur only on long term, and a shorter turn period allows a more frequent self-calibration. Finally, back scattering is important in present runs, but does not appear to be a limiting factor of the goniometric accuracy.

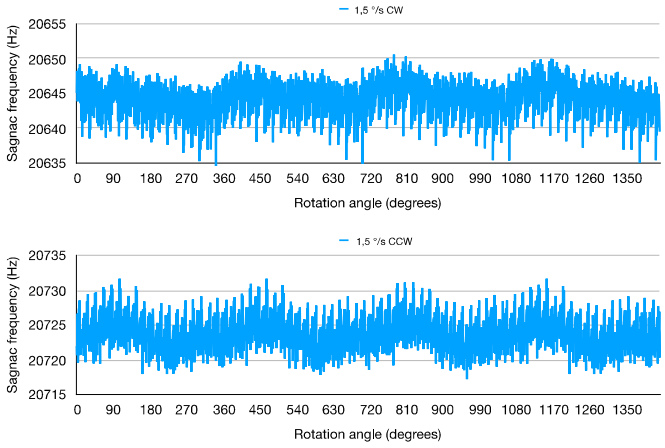


Fig. 3. Plot of the instantaneous Sagnac frequency as a function of the angular rotation for a turntable speed of 1.5°/s. Upper plot: CW rotation; lower plot: CCW rotation.

The raw data acquired by the ADC are processed through Hilbert transform in order to obtain the phase $\psi(t)$ and the instantaneous frequency $f_{Sagnac}(t)$ of the Sagnac signal. The mean value of f_{Sagnac} over a full nominal period is during each run self-consistent $\pm 10^{-5}$. In Fig. 3 we present the plot of the f_{Sagnac} as a function of the rotation angle of the turntable for a speed of 1,5°/s. Fig. 4 plots the deviation of the phase $\psi(t)$ from the linear behavior, that is the function $\psi(t) - \langle f_{Sagnac} \rangle t$, where the angular parenthesis indicate the average over a period.

In Fig. 3 and Fig. 4 is evident an oscillation of the instantaneous Sagnac frequency and of the phase with the period of the table 2π rotation. This oscillation, especially evident on the phase evolution, can be observed in all the runs. The amplitude of the frequency oscillation is almost constant at the different rotation rate and, following (4), could be consistent with a value of the misalignment angle φ of the optical beam plane with the turntable axis of the order of 30 mrad.

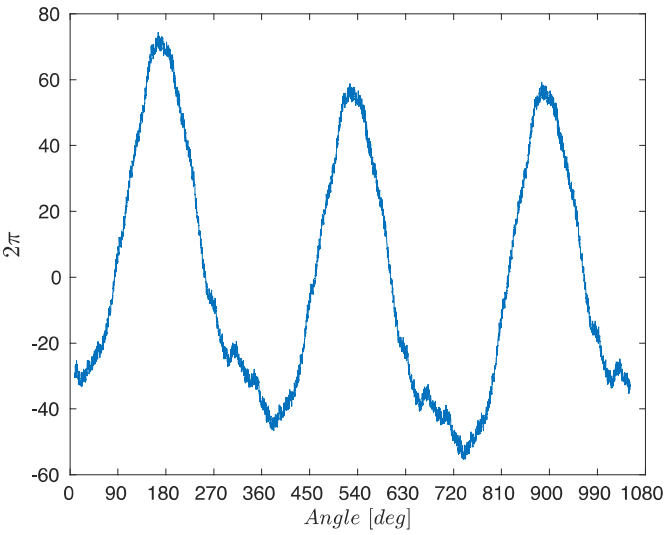


Fig. 4. Plot of the deviation of the phase $\psi(t)$ of the Sagnac signal from linearity. The turntable speed is 1.5°/s CCW. The units of y-axis are phase periods.

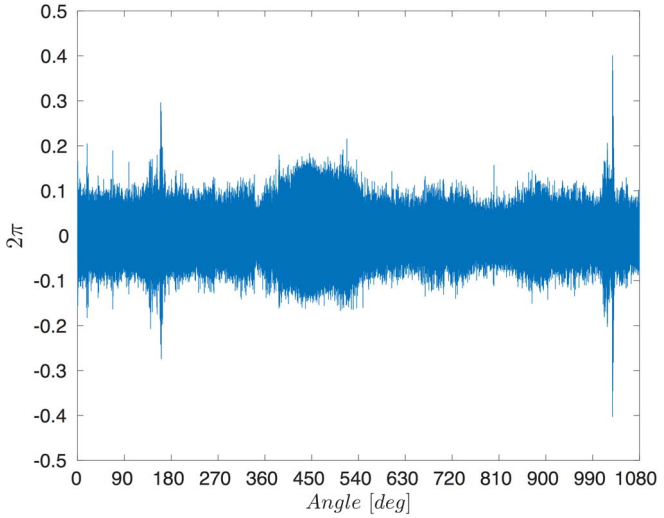


Fig. 5. Plot of the deviation of the phase $\psi(t)$ of the Sagnac signal from linearity. The turntable speed is 2°/s CW The units of y-axis are phase periods. Data are high-pass filtered at 1 Hz.

Filtering out the low frequencies, as shown in Fig.5 for the 1 Hz high-pass data of clockwise run at 2°/s, shows that the evolution of the phase comes in regular way, with a noise always lower than 1/5 of 2π. This noise is primary in the vibrational bandwidth and is probably connected to the non optimized setting of the turntable control parameters: on the data high-pass filtered at 100 Hz (Fig. 6) the noise is reduced to less than $2\pi/100$ with a small residual modulation at f_{Sagnac}. This suggests that the resolution on the full table rotation can reach $0.01/N_{2\pi} \approx 2 \cdot 10^{-9}$, equivalent to ~15 nrad (0.003").

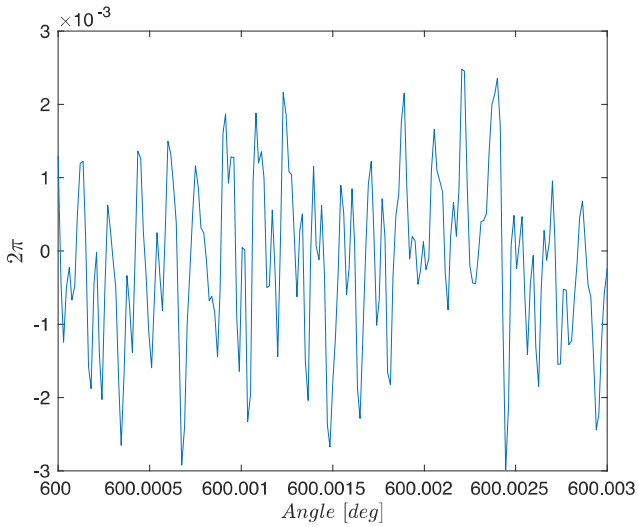


Fig. 6. Plot of the deviation of the phase ψ(t) of the Sagnac signal from linearity. The turntable speed is 1.5°/s CCW The units of y-axis are phase periods. Data are high-pass filtered at 100 Hz.

V. CONCLUSION

We have tested the operation of the first prototype of G-LAS. We were able to observe the Sagnac interference signal with good resolution at different speed of the turntable. At present, the angular resolution appears to satisfy the project requirements. Work is in progress in order to reduce the sources of noise that presently limit the performances and to ensure the accuracy. The optimization of the control parameter of the turntable and the implementation of its encoder will be necessary in order to reduce the mechanical noise and to provide the self-calibration of the instrument. A custom combination prism positioned close to a mirror inside the vacuum chamber will replace the present external combination of the two counter-propagating beams, which use two different output mirrors, eliminating an important noise source.

The position of the spot on the mirrors and the observed periodic fluctuation of the Sagnac frequency signal indicates that the capillary is not sufficiently straight; in the near future a new improved capillary will be implemented. Moreover, new electronics will be used in order to operate at higher rotation regime.

REFERENCES

[1] Belfi, J., Beverini, N., Di Virgilio, A., Maccioni, E., Astrua, M., Pisani, M., Santiano, M., "Planar angle metrology: G-LAS, the INRIM - INFN ring laser goniometer", 2016 European Frequency and Time Forum, EFTF 2016, art. no. 7477837

[2] Catherin J. M., Dessus B., French Patent No. 1511089; granted 26.01.68.

[3] Yu. V. Filatov, D. P. Loukianov and R. Probst, "Dynamic angle measurement by means of a ring laser ", Metrologia vol. 34 pp. 343-351, 1997.

[4] Schreiber K.U., and Wells, J-P. R., "Large ring lasers for rotation sensing", Rev. Sci. Instrum. 84, 041101 (2013)

[5] Primalov and Filatov, Sov. J. QE **7** 802 (1977)

The Optical Rubidium Atomic Frequency Standard at AFRL

Nathan D. Lemke, Gretchen Phelps, John H. Burke
Air Force Research Laboratory
Space Vehicles Directorate
Kirtland Air Force Base, United States

Kyle Martin, Matthew S. Bigelow
Applied Technology Associates
Albuquerque, United States

***Abstract*—We present a compact optical frequency standard based on two-photon spectroscopy at 778 nm in a rubidium vapor cell. We demonstrate fractional instability of 3e-13/$\sqrt{\tau/s}$ for timescales up to 10,000 s. Additionally, we describe a secondary system operation in which the short-term stability is improved (though at the expense of the long-term stability) using increased laser power, resulting in 1 s instability < 1e-13. The system has been designed as an advanced atomic frequency standard for GNSS applications, and is currently being investigated for demonstration on AFRL's Navigation Technology Satellite 3 (NTS-3), an upcoming space flight experiment to middle earth orbit scheduled for launch in 2022.**

Keywords—optical frequency standard; two-photon spectroscopy

I. INTRODUCTION

Space-based atomic frequency standards are critical to the operation of global navigation satellite systems. Current space-qualified atomic clocks, while generally meeting mission needs, have several undesirable features including a reliance on specialized parts and manufacturing processes, significant frequency drift, and occasional on-orbit frequency anomalies that lead to increased user range error. For these reasons, the Air Force Research Laboratory has been investigating potential advanced atomic frequency standards that have a path toward space qualification. Specific program goals include improving the stability over current GPS clocks by approximately one order of magnitude and employing only commercially available components and/or standard manufacturing protocols, all while avoiding significant increases to the size, weight, and power compared to current technology.

While many appealing atomic systems could in principle meet these goals, we choose to investigate an optical clock based on the 778 nm two-photon transition ($5S_{1/2}\rightarrow5D_{5/2}$, see Fig. 1) in a rubidium vapor cell [1-4] for several reasons. First, the relatively large atomic linewidth ($\Delta\nu \approx 330$ kHz, $Q \approx 10^9$) eliminates the need for pre-stabilization of the clock laser and enables high-bandwidth feedback from the atomic signal to the clock laser. Second, the two-photon architecture provides a simple method for overcoming Doppler broadening without the need to implement laser cooling, as in most optical clocks, or the buffer gases used in many RF clocks. Finally, the recent advances in compact fiber frequency combs [5-6] enable both the required optical clockwork as well as the possibility for space-based spectroscopy and time-transfer protocols.

II. EXPERIMENT AND RESULTS

Figure 1 shows the relevant atomic states in Rb that form the Optical Rubidium Atomic Frequency Standard (O-RAFS). The relatively small 2 nm detuning between the two-photon virtual intermediate state and the $5P_{3/2}$ state enables significant laser excitation of the vapor at modest optical intensity (typically 500/s per atom for 30 mW of laser power and a 0.6 mm intensity radius). Detection of the excitation rate is accomplished by monitoring the atomic fluorescence at 420 nm, corresponding to the $6P_{3/2}\rightarrow5S_{1/2}$ decay channel. Stray 778 nm light is rejected by a spectral filter, enabling a high signal-to-noise ratio measurement. Coupled with a high vapor density (10^{18}-10^{19}/m^3), the system allows for detection rates of 10^{10}/s.

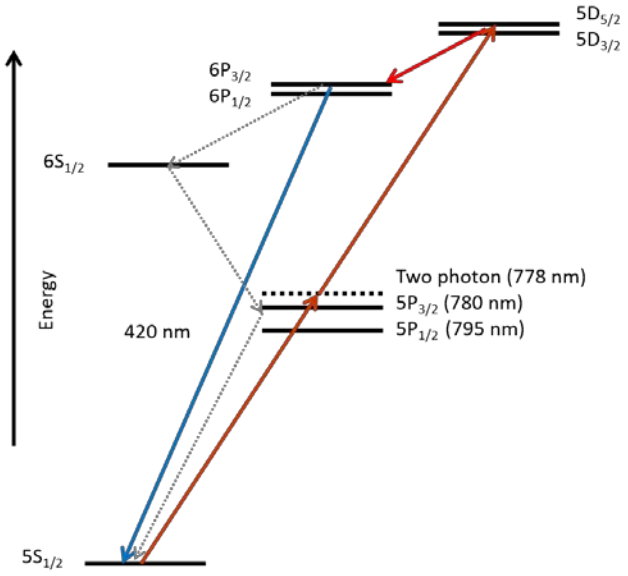


Fig. 1. The relevant energy levels in rubidium. An optical frequency standard is obtained through driving the two-photon transition ($5S_{1/2}$ to $5D_{5/2}$) with subsequent detection of the 420 nm fluorescence.

The clock's local oscillator is a free-running C-band telecom laser that produces light at 1556 nm. A portion of the seed light is taken to form an optical beat note with a fiber frequency comb, based on the NIST design [5], and whose repetition rate output will ultimately be compared to a hydrogen maser to determine the clock stability (Fig. 2) using a phase measurement test device. The remaining portion of the seed laser

output enters a low V_π waveguide electro-optic modulator (EOM) for phase modulation. We mitigate residual amplitude modulation (RAM) in the EOM using a single point of feedback to the bias voltage applied to the EOM, resulting in > 30 dB suppression of the RAM signal [7].

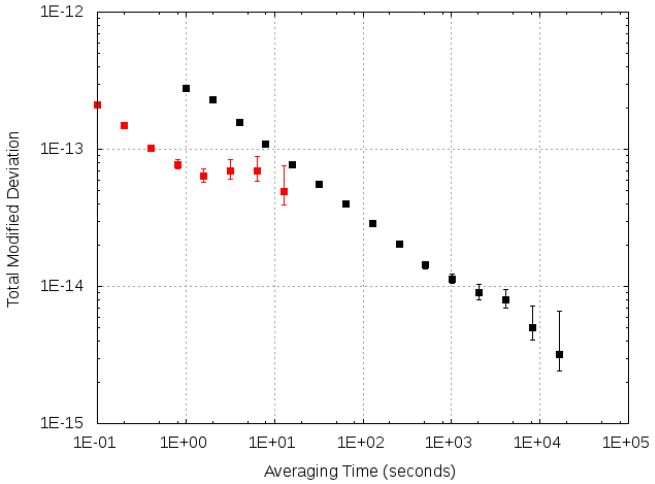


Fig. 2. Total Modified Deviation of O-RAFS under standard conditions (black markers) and when optimized for short-term stability only (red markers). The latter data is most likely limited by the H-maser reference.

After the EOM, the modulated light is frequency doubled in a waveguide-based second harmonic generating crystal and subsequently amplified. The resulting 778 nm light enters a variable optical attenuator (VOA) that is used to stabilize the optical power incident upon the atomic vapor, after which the light is collimated and enters the Rb vapor cell, which is heated to 100 °C. The generated fluorescence signal at 420 nm is then detected with a photomultiplier tube, the output of which is demodulated, generating an error signal for locking the laser to the atomic resonance. The laser system design described above offers an all-fiber solution, and the only free space optics are the fiber launcher and cat's eye retroreflector around the vapor cell. The small form factor provided by these optical components, coupled with the inclusion of digital control electronics, allows for a prototype system design that will occupy a volume < 30 L.

The clock performance is limited on short-time scales by photon shot noise, which can be readily overcome by increasing either the vapor density (via the cell temperature) or the laser intensity. The red markers in Fig. 2 show data with reduced photon shot noise, although this comes at the expense of the long-term stability by increasing the ac Stark shift associated with the excitation laser. We observe a fractional instability at 1 s of 7×10^{-14}, which is consistent with the expected limit imposed by the hydrogen maser reference. Measurements of the fluorescence signal noise properties (away from the modulation frequency of 500 kHz) suggest clock instabilities $<5\times10^{-14}$ at 1 s should be feasible.

To observe the best long-term clock performance, we reduce the laser power by a factor of 4 (Fig. 2, black markers) and observe the instability to be $3 \times 10^{-13}/\sqrt{\tau/\mathrm{s}}$ for τ up to 10,000 s, which exceeds the typical performance of the current RF clocks for use in GPS by a factor of ~3 [8]. Furthermore, O-RAFS, constructed primarily from commercially available components, offers a high potential for system manufacturability as compared to other RF solutions. Therefore, O-RAFS remains an attractive candidate for future space operation. AFRL is currently working to determine the viability of placing a prototype version of O-RAFS on the upcoming NTS-3 flight experiment to MEO in the 2022 timeframe.

ACKNOWLEDGMENT

The authors would like to thank Ian Coddington, Laura Sinclair, Nate Newbury, Mike Wojcik, Mike Holt, Ben Stuhl, Jordan Armstrong, Michael Bishop, Brian Kasch, Spencer Olson, and Matt Squires for many useful discussions.

REFERENCES

[1] F. Nez, F. Biraben, R. Felder, and Y. Millerioux, Opt. Commun. **102**, 432-438 (1993).

[2] D. Touahri, O. Acef, A. Clairon, J. J. Zondy, R. Felder, L. Hilco, B. de Beauvoir, F. Birabem, and F. Nez, Opt. Commun. **133**, 471-478 (1997).

[3] N. D. Zameroski, G. D. Hager, C. J. Erickson, and J. H. Burke, J. Phys. B At. Mol. Opt. Phys. **47**, 22 (2014).

[4] Y. Millerioux, D. Touahri, L. Hilico, A. Clairon, R. Felder, F. Birabem, and B. de Beauvoir, Opt. Commun. **108**, 91-96 (1994).

[5] L. C. Sinclair, I. Coddington, W. C. Swann, G. B . Rieker, A. Hati, K. Iwakuni, and N. R. Newbury, Opt. Exp. **22**, (2014).

[6] S. A. Diddams, J. Opt. Soc. Am. B **27**, (2010).

[7] M. Zhu and J. L. Hall, J. Opt. Soc. Am. B **10**, (1992).

[8] http://www.excelitas.com/Pages/Product/Space-Qualified-Rubidium-Frequency-Standards.aspx

Frequency comb-assisted QCL stabilization for high resolution molecular spectroscopy

R. Santagata*, D.B.A. Tran, O. Lopez, B. Argence,
S.K. Tokunaga, B. Darquié, A. Amy-Klein
Laboratoire de Physique des Lasers,
Université Paris 13, Sorbonne Paris Cité, CNRS
Villetaneuse, France
rosa.santagata@univ-paris13.fr *: also at LNE-SYRTE

D. Nicolodi, M. Abgrall, Y. Le Coq, R. Le Targat, D. Xu,
W.-K. Lee, P.-E. Pottie
LNE-SYRTE,
Observatoire de Paris, PSL Research University, CNRS,
Sorbonne Universités, UPMC,
Paris, France

***Abstract*— We present a frequency comb-assisted experimental setup which enables us to both coherently transfer the stability and accuracy of a remote near-infrared (NIR) ultrastable laser to a mid-infrared (MIR) quantum cascade laser (QCL), and widely tune the QCL frequency for spectroscopic applications. The QCL is stabilized at the level of 2×10^{-15} from 1 to 100 s, with an accuracy of 10^{-14} after 100 s. The achievable frequency tuning paves the way for high-resolution saturated absorption spectroscopy of molecular transitions, in particular in spectral regions that were previously inaccessible with standard stabilized MIR lasers. Preliminary results show a sensitivity at the kHz level on transition center frequencies.**

Keywords: optical frequency comb; frequency stabilization; frequency transfer; high resolution molecular spectroscopy; quantum cascade lasers.

I. INTRODUCTION

The optical frequency comb (OFC) technology is a unique tool for high accuracy measurements. It allows us to transfer the spectral properties from one laser source to another, which opens the way for precision tests in several fields of physics. Ultra-high resolution molecular spectroscopy can strongly benefit from this tool in terms of improvements in precision and sensitivity, especially in the MIR "fingerprint" region which exhibits intense and narrow rovibrational molecular transitions. In the last years, this has prompted several efforts in order to extend the frequency comb techniques from the NIR and visible domains to the MIR region, as well as to develop efficient MIR laser sources. It is however very challenging to develop frequency stabilization schemes in the MIR because in this region tools commonly available in the visible and NIR domains are scarce.

In recent years, an OFC has been used to transfer the spectral features of a NIR ultrastable laser emitting at 1.54 µm to a QCL emitting in the MIR at 10.3 µm [1]. Following this work, we present here an experimental setup that allows us to tune the frequency of the QCL by scanning the OFC repetition rate f_{rep}. This provides a laser source that copies the stability and accuracy of the NIR reference laser, and is at the same time tuneable, allowing high resolution molecular spectroscopy experiments. We also report preliminary results of spectroscopic investigations conducted on methanol.

II. QCL STABILIZATION

The experimental setup is shown in figure 1. The MIR laser source is a room temperature distributed-feedback QCL (Alpes Lasers) emitting at ν_{QCL}=10.3 µm, with a tuning range of 180 GHz. It is phase-locked to a OFC consisting of an erbium-doped fibre mode-locked laser emitting around 1.54 µm. The comb repetition rate of $f_{rep} \approx 250$ MHz is stabilized by phase-locking one tooth of the OFC onto a local optical oscillator (LO) itself phase-locked to a NIR frequency reference generated at SYRTE laboratory and transferred to LPL laboratory through a 43-km long optical-fibre link [2]. This NIR reference ν_{ref}=1.54 µm exhibits a relative frequency stability lower than 2×10^{-15} between 1 and 100 s [3]. Its absolute frequency is known with an uncertainty of 10^{-14} at this timescale when referenced to an H-maser via a local OFC at SYRTE. At LPL, the frequency reference is used to phase-lock a local laser diode of frequency ν_{LO}, acting as a LO. To achieve a broad frequency tuning at LPL, tuneable sidebands are generated in the LO signal by phase modulating the LO laser diode using a fibered electro-optic modulator (EOM) the frequency f_{EOM}, of which can be tuned over 8.5 GHz. One of the LO sidebands is phase-locked to the NIR reference (using PLL1, figure 1) enabling both frequency stabilization and tuning of the LO carrier frequency ν_{LO}. The OFC repetition rate f_{rep} is in turn phase-locked to the LO carrier frequency (using PLL2) after removal of the comb carrier-envelope offset frequency. The QCL is finally phase-locked to the stabilized OFC. To bridge the gap between the NIR and MIR domains a sum-frequency generation process is used. We overlap the QCL beam and an OFC output at 1.81 µm in an AgGaSe2 crystal. The resulting shifted comb centered at 1.54 µm is then combined with the main comb output enabling the detection of the beat note between the QCL frequency and the n^{th} harmonic of f_{rep} which is used to phase-lock the QCL (using PLL3). The developed frequency chain allows us therefore to copy to the QCL the stability and accuracy of the tuneable LO. The QCL can be tuned on a range given by the EOM tuning range after scaling from the NIR to the MIR. It is currently limited by the course of the piezo actuator acting on the OFC optical cavity.

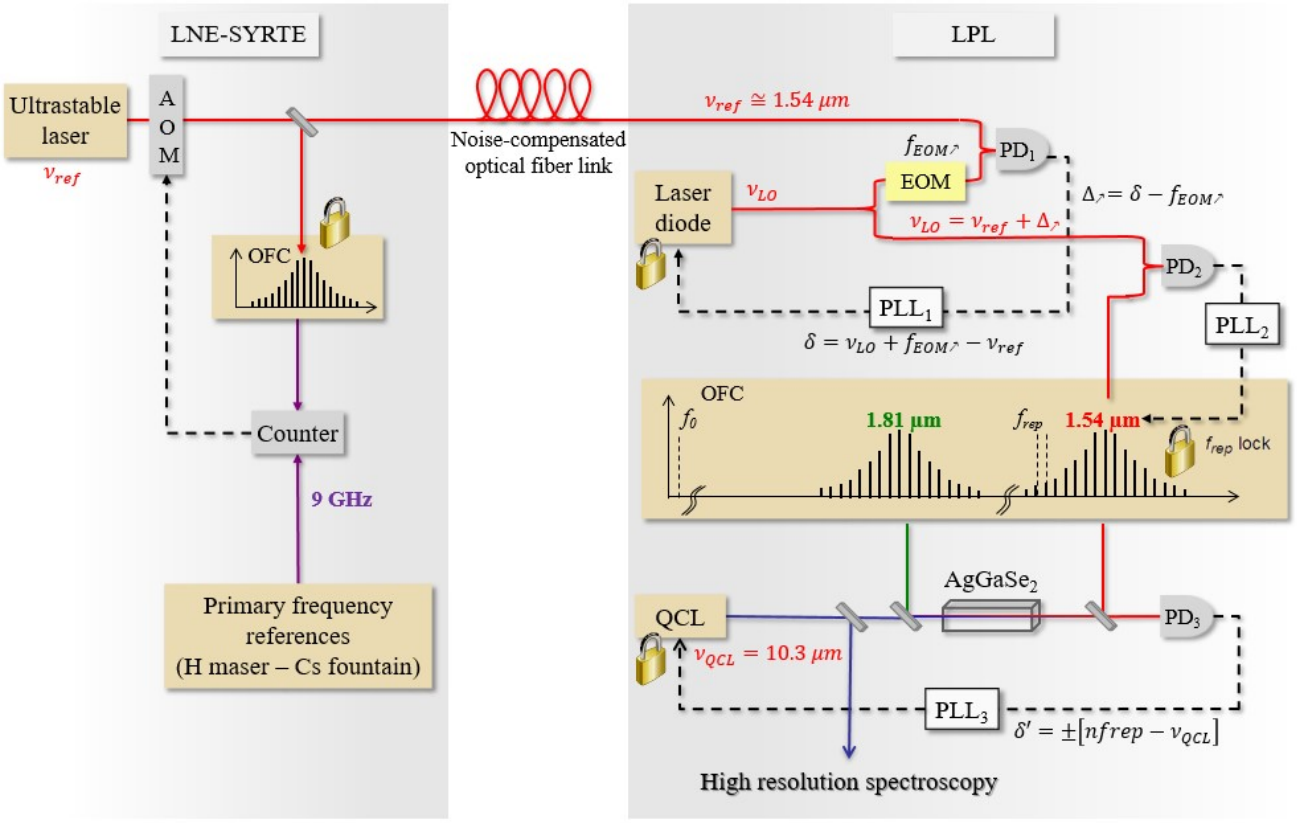


Fig. 1. Experimental setup. The NIR frequency reference ν_{ref} generated at SYRTE is transferred to LPL through a 43-km-long optical-fibre link. At SYRTE, its absolute frequency is measured against primary frequency standards by the use of an OFC. At LPL, the comb repetition rate f_{rep} of a local OFC is phase-locked onto this reference, through a tuneable diode laser used as an optical local oscillator. By phase-locking the QCL onto a high harmonic of f_{rep}, the stability and accuracy of the NIR reference signal, as well as the tuneability of the local oscillator, are copied to the MIR domain. AOM: acousto-optic modulator, OFC: optical frequency comb, LO: local oscillator, EOM: electro-optic modulator, PLL: phase-lock loop, PD: photodetector.

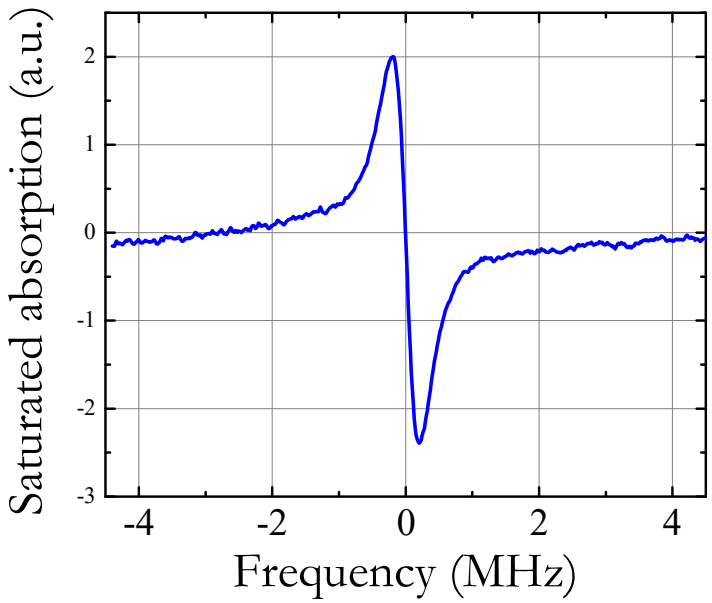


FIG. 2. Frequency-modulated saturated absorption spectrum of a methanol line located at ~971.9443 cm^{-1}. Pressure: 7 µbar. Average of 5 up and down spectra. Lock-in amplifier time constant of 100 ms per point. Frequency step: 15 kHz.

III. METHANOL SPECTROSCOPY

The main purpose of this work is to use the developed QCL laser source for high resolution rotational-vibrational spectroscopy. We currently aim to measure absorption frequencies of methanol around 10.3 μm and their pressure shifts and broadenings. In our setup, we perform frequency modulation saturated absorption spectroscopy through a multipass cell (Aerodyne Research). The effective absorption length of 36.4 m allows us to obtain high enough signal-to-noise ratios at pressures down to a few Pa, thus reducing pressure broadening and shift effects.

Preliminary measurements have been performed on a few absorption lines of methanol (see figure 2). We observe a pressure broadening of ~150 kHz/Pa and a pressure shift of around –4 kHz/Pa, in agreement with the literature. These transitions frequencies were previously measured with uncertainties of around 15 MHz [4] and can be found in the HITRAN database [5]. The sensitivity of our setup in determining the central frequency of the transitions is around 1 kHz, most probably limited by a combination of the limited signal-to-noise ratio and pressure effects. The methanol molecule is a promising candidate to test the possible time variation of the proton-to-electron mass ratio, given its extremely sensitive torsion–rotation transitions.

CONCLUSION AND PERSPECTIVES

We have presented an experimental setup that allows a precise and tuneable frequency control of a MIR QCL referenced to an OFC on a wide spectral range. The capability of the system has been tested by performing saturated absorption spectroscopy of methanol. Preliminary results show a sensitivity in determining the central frequency of ~ 1 kHz (10^4 better than the results reported, to date, in literature).

In the long term, we plan to perform ultra-high resolution spectroscopy of chiral molecules in order to measure for the first time an effect of parity violation [6]. Parity violation caused by the weak interaction has been already observed in high energy physics and atoms, but never seen in molecules. It is expected to induce frequency differences of the order of 10^{-13} in the rovibrational spectra of the enantiomers of well chosen organo-metallic chiral species. Our setup which allows a very precise tuning of a QCL frequency at a level of 10^{-14} is a step towards this goal.

ACKNOWLEDGMENT

This work was partly funded from the European Metrology Research Programme EMRP/EMPIR under 15SIB05 OFTEN. We acknowledge funding support from the Agence Nationale de la Recherche (ANR blanc LIOM 2011-BS04-009-01, ANR-15-CE30-0005-01 and Labex First-TF ANR 10 LABX 48 01), Région Ile-de-France (DIM Nano-K), CNRS and Université Paris 13.

REFERENCES

[1] B. Argence et al., "Quantum cascade laser frequency stabilization at the sub-Hz level", *Nature Photon.* **9**, 456-460 (2015).

[2] W.-K. Lee et al., "Hybrid fiber links for accurate optical frequency comparisons", *Appl. Phys. B* **123**, 161-172 (2017).

[3] J. Guéna et al., "Progress in atomic fountains at LNE-SYRTE", *IEEE. Trans. Ultrason. Ferroelec. Freq. Control* **59**, 391-409 (2012).

[4] L.-H. Xu et al., "New assignments, line intensities, and HITRAN database for CH_3OH at 10 μm", *J. Mol. Spectroscop.* **228**, 453-470 (2004).

[5] L.S. Rothman et al., "The HITRAN2012 molecular spectroscopic database", *J. Quant. Spectrosc. Radiat. Transf.* **130**, 4-50 (2013)

[6] S. Tokunaga et al., "Probing weak force-induced parity violation by high-resolution mid-infrared molecular spectroscopy", *Mol. Phys.* **111**, 2363-2373 (2013).

1.5 µm - optical frequency standard iodine stabilized in the 10^{-15} range for space applications

C. Philippe, J. Gillot, D. Holleville, M. Lours,
R. Le Targat, P. Wolf and O. Acef
LNE-SYRTE, Observatoire de Paris, PSL Research Univ.,
CNRS, Sorbonne Univ., UPMC Univ. Paris 06, 61, Av. de
l'Observatoire, 75014 Paris, France
charles.philippe@obspm.fr

T. Lévèque
Centre National d'Etudes Spatiales CNES,
18 Av. Edouard Belin, 31401 Toulouse, France

R. Le Goff
SODERN (Airbus-Safran Launchers Group),
20 Av. Descartes, F-94451 Limeil-Brévannes, France

Summary— **We lead the development of an optical frequency standard (OFS) operating in the C-band of Telecom domain, with demonstrated residual frequency instability of 4.8 x 10^{-14} $\tau^{-1/2}$ and a minimum value of 6 x 10^{-15} from 50 s to 100 s. The frequency stabilization is fulfilled using Doppler free spectroscopy of $^{127}I_2$ iodine vapor, associated to modulation transfer spectroscopy technique. The iodine hyperfine line used to stabilize the 1542 nm laser diode exhibits a quality factor at 514 nm (Q ~10^9).**
An efficient third harmonic generation (THG) process is developed to bridge the frequency gap between IR and visible ranges of the optical domain. The efficiency of the THG operation is P_{3w}/P_w > 36 %.
A more compact-fully fibered OFS is under development, using frequency modulation technique associated to third harmonic of the iodine saturation line. This approach could meet the needs of various space projects requiring high precision length measurement between independent spacecrafts, or stabilization of the long distance optical links.

Keywords—Optical frequency standard, metrology, laser stabilization, harmonic generation, modulation transfer technique, high resolution spectroscopy, iodine, space.

I. INTRODUCTION

Various space missions requiring accurate length measurement between independent spacecrafts, or stabilization of the long distance between them, need ultrastable optical frequency standards (OFS), emitting high optical power, and operating in a very compact configuration. This inter-satellites laser interferometry is involved in space projects such as Next Generation Gravity Missions (NGGM), Gravitational Wave Detection (LISA), Earth Gravity Mapping (GRACE FO), precise Space Geodesy based on cold atoms (GRICE), etc.[1-3]. Our project is based on a C-band Telecom laser diode, frequency tripled in order to interrogate an iodine hyperfine transition among thousands lines existing in the green range of the visible domain.

This approach makes possible the establishment of a very compact OFS, with low electrical power consumption, in fibered configuration and benefiting from high technological maturity of various Telecom components suitable for space applications. The targeted technological readiness level is TRL 4.

Our OFS could be optimized -and frequency stabilized- to operate at any wavelength in the C-Telecom band (1530 nm – 1565 nm). Moreover, the 1.5 µm technology units offer an opportunity to realize high speed and efficient optical communications between spacecrafts (LEO-LEO or LEO-GEO), using numerous efficient components to fulfill phase or amplitude modulation of the optical beam. Furthermore, our approach promotes efficient ground to space optical links through the existing atmospheric transparency windows around both 1.5 µm and 0.5 µm ranges.

II. EXPERIMENT AND RESULTS

The third harmonic generation (THG) process is carried out using a combination of two Lithium Niobate nonlinear waveguided crystals, arranged in an original optical architecture. The whole optical arrangement reported in this work is fibered. We have generated up to ~ 290 mW continuous wave (CW) of optical power at 514 nm from only 800 mW of infrared power at 1542 nm. To our knowledge, the corresponding optical conversion efficiency ($\eta = P_{3\omega}/P_{\omega} > 36$ %), has never been demonstrated in case of CW-THG process [4]. The total electrical consumption of the THG process is only 20 Watts, which will be drastically reduced for space application, knowing that less than 10 mW of green power is

978-1-5386-2916-1/$31.00 ©2017 IEEE

needed for the Doppler free iodine spectroscopy. As a first step, we have associated to this fibered frequency tripled laser, a free space optical bench dedicated to the iodine vapor spectroscopy, allowing us to perform the frequency stabilization purpose. We have used the well-known frequency modulation transfer technique for the iodine hyperfine line detection (Fig. 1.).

The pump beam (4 mW) is modulated (f_{mod} = 220 kHz) with a free space electro-optic phase modulator, while the unmodulated probe beam (~ 400 µW) is split into two parts: a reference beam and an interrogating beam coupled to a 20 cm long sealed quartz cell. The iodine saturation signal is extracted with a balanced silicon photodiode (Fig. 1). Two acousto-optic modulators (AOM) are used to stabilize the pump and probe optical powers, to minimize light shifts effect. The interaction length in the 20 cm sealed quartz cell, is extended to 1.2 m thanks to 6 successive passes. The iodine pressure is about ~ 1 Pa using a temperature control of the cold cell finger around -15 °C, within few mK. In this regime, the experimental iodine linewidth is measured as ~ 587 kHz.

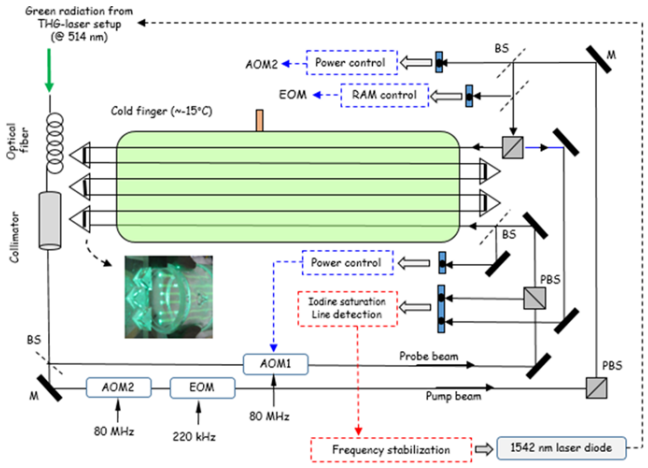


Fig. 1. Scheme of the optical bench dedicated to the Doppler free iodine spectroscopy using modulation transfer technique.

The first derivative of the a_1 hyperfine component of the R34 (44-0) $^{127}I_2$ line at 514.017 nm is used to stabilized the laser diode emitting at 1542 nm used in this work. The frequency instabilities corrections are added to the laser diode injection current.

Figure 2 shows the residual frequency instabilities of the locked IR laser diode, measured at the level of 4.8 x10^{-14} $\tau^{-1/2}$ with a minimum value of 6 x10^{-15} from 50 s to 100 s. This Allan standard deviation is associated to the optical beat note between the iodine stabilized laser diode and an independent frequency reference based on a similar laser diode locked to an ultrastable optical cavity [6]. This reference setup is located in an independent building of SYRTE Laboratory. A 200 m long optical fiber is used to fulfill this frequency comparison. This architecture imposes the use of a particular iodine line (R34 (44-0) $^{127}I_2$ line at 514.017 nm) in coincidence with that reference laser.

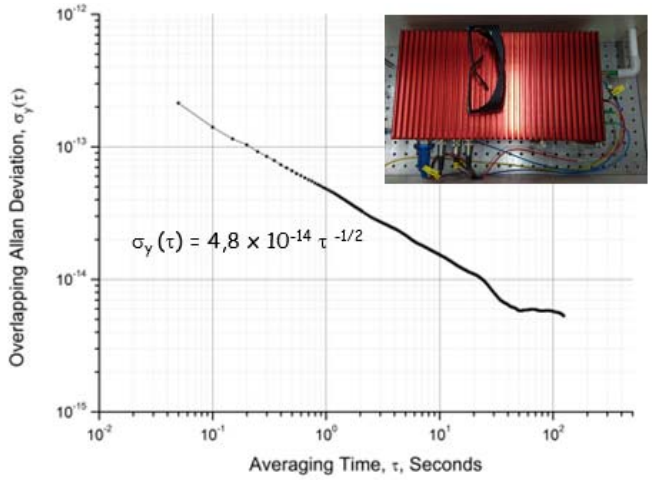


Fig. 2. Fractional Allan standard deviation of the iodine stabilized Telecom laser diode at ~ 1542 nm. The insert shows the home-made frequency tripled laser diode.

The short term frequency stability reported on Fig.2 is limited by the signal to noise ratio of the particular iodine saturation signal used in this work. The new development described below utilizes on another hyperfine line located around 514. 6 nm, with higher S/N and narrow linewidth (Q > 10^9).

For the long term frequency stability, we have observed an unexpected high sensitivity of the iodine center line (at 514 nm), to the magnetic field fluctuations in the lab, induced by the metropolitan traffic, during our day measurements. Frequency shifts due to Zeeman effect have been studied by several groups [7, 8] and estimated at the 10^{-15} level around 514 nm, in term of relative frequency instabilities if the polarization of the involved optical beams is rigorously linear [8].

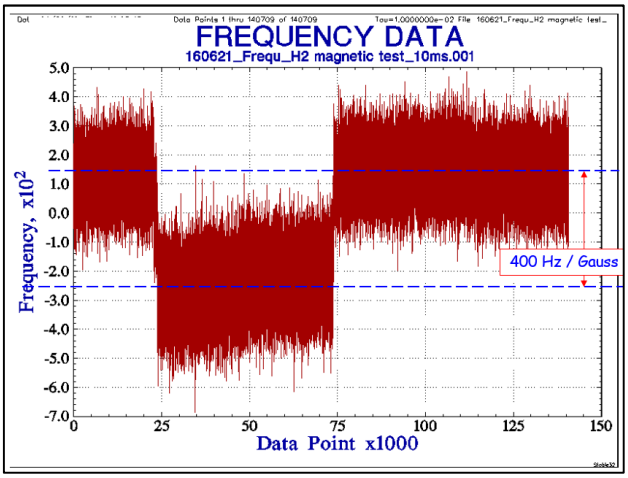


Fig. 3. Frequency shift of the iodine center line due to 1 Gauss external DC magnetic. The sensitivity is evaluated as ~ 2 x 10^{-12} / gauss

We take into account this strict condition (Fig. 1), but we observe a frequency shift of about 400 Hz when we apply a 1 Gauss external DC magnetic field (Fig. 3)

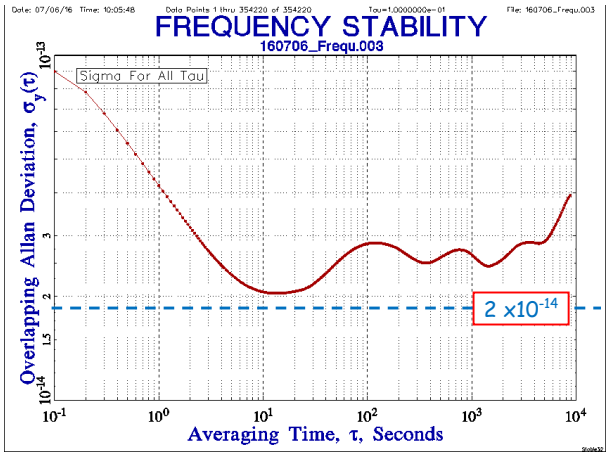


Fig. 4 Typical fractional Allan standard deviation of the iodine stabilized laser diode in presence of metropolitan traffic magnetic perturbations.

The magnetic field fluctuations due to the metropolitan traffic during the day, recorded in the vicinity of the iodine cell, were measured to be up to 35 mG (Fig. 5). Our previous frequency stability measurement reported on Fig. 2, was obtained during the night, when the metropolitan traffic was stopped. The typical frequency stability evaluated during the day is reported on Fig. 4. The noise floor shown at the $2x10^{-14}$ level corresponds to the day magnetic field fluctuation measured in the lab and reported on Fig. 5.

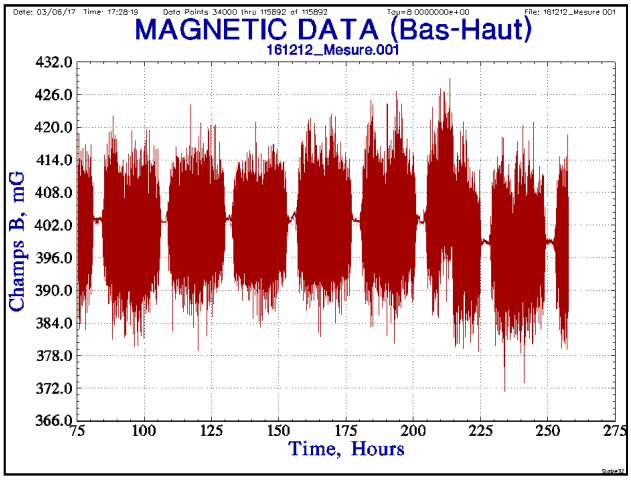


Fig. 5. Diurnal magnetic field fluctuations, in the vicinity of the iodine cell, recorded continuously over ~ 10 days.

III. NEW COMPACT OPTICAL FREQUENCY STANDARD UNDER DEVELOPEMENT

We start a new development in order to match as well as possible space mission's requirements, especially in terms of compactness. This target leads us to operate in a different way the frequency modulation spectroscopy. In this case, the frequency modulation is applied in the infrared part (at 1544 nm) thanks to the use of compact and efficient fibered acousto-optic and/or electro-optic devices. The frequency modulation is operated before the THG process. The frequency-modulated green radiation is extracted from the new frequency tripled laser using a mode optical fiber optimized at 514 nm. In this way, the frequency tripled laser will be directly connected through this fiber to a new sealed iodine cell as shown on Fig. 6. The iodine cell is surrounded in this case by a magnetic shield, in order to insure a residual magnetic field less than 1 mG. The targeted total optical volume (laser + cell) is less than 10 liters.

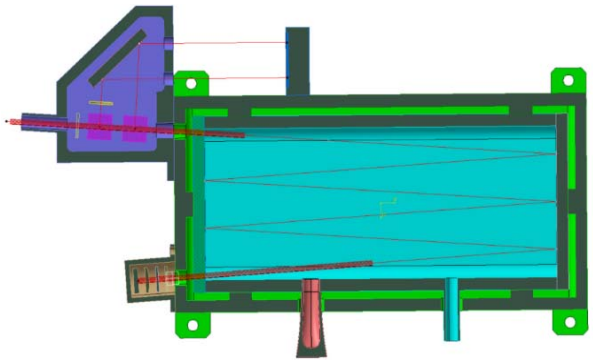


Fig. 6. Design of the new optical bench, including the iodine cell.

We have tested this new approach by implementing the frequency modulation, using a fibered acousto-optic modulator (AOM) operating at 1.5 µm. In this case, we use the third harmonic signal of the iodine saturation line to stabilize the IR laser. We have measured a preliminary residual frequency instability at level of $2.2\ x10^{-13}\ \tau^{-1/2}$ with a minimum value of $5\ x10^{-14}$ between 400 s and 1000 s (Fig 7.).

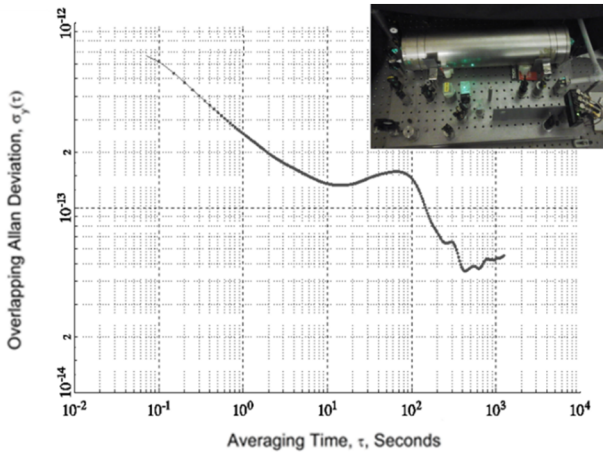


Fig. 7. Fractional Allan standard deviation of the iodine stabilized Telecom laser diode at ~ 1542 nm with the frequency modulation spectroscopy technique. The insert shows preliminary optical setup realized to test the IR modulation scheme.

The Doppler free iodine spectroscopy in the vicinity of 1544 nm brought to light new promising hyperfine lines that show a greater quality factor. Theses hyperfine lines, assigned to the

R46 (44-0) at 514.6 nm, exhibits linewidth of 300 kHz that is two times narrower than previous iodine lines (Fig. 8.).

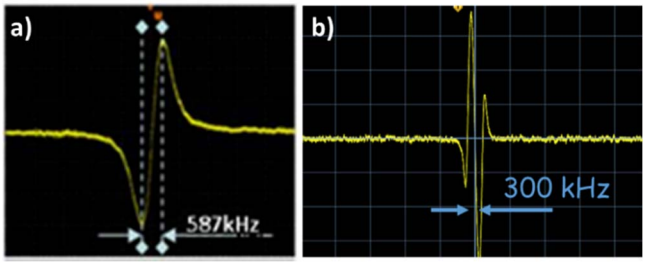


Fig. 8. Linewidth comparison of two iodine hyperfine lines recorded around 514.0 nm (a) and 514.6 nm (b).

IV. CONCLUSION

We have reported on the development of a compact optical frequency standard, based on a third harmonic generation (THG) process of a Telecom laser diode at 1542 nm, frequency stabilized to a hyperfine iodine line at 514 nm. The THG operation yields to a harmonic power of 290 mW in the green domain, generated from 800 mW of IR fundamental power. Furthermore, we have shown the possibility of using narrow transitions of molecular iodine in the green domain, to stabilize the laser diode frequency in the 10^{-15} range using only 5% of that harmonic power. These results bring us to develop a new fully fibered and compact frequency stabilized system with less than 10 l of total optical volume.

The feasibility of this new approach was tested and a preliminary frequency stability at the level of 2.2 $x10^{-13}$ $\tau^{-1/2}$ was already demonstrated.

REFERENCES

[1] P. L. Bender, J. L. Hall, J. Ye, W.M. Klipstein, " Satellite-Satellite Laser Links for Future Gravity missions", Space Science Reviews July 2003, Volume 108, Issue 1, pp 377-384.

[2] M. Shao and D. H. Staelin, "Long- baseline optical interferometer for astrometry", Journal of the Optical Society of America Vol. 67, Issue 1, pp. 81-86 (1977).

[3] K. Doringshoff, K. Mohle, M. Nagel, E. V. Kovalchuk, A. Peters, "High performance iodine frequency reference for tests of the LISA laser system," in Proceedings of EFTF-2010 24th European Frequency and Time Forum pp.1-6, 13-16 April 2010,

[4] Ch. Philippe, E. Chea, Y. Nishida, F. Du Burch and O. Acef, « Efficient third harmonic generation of a CW-fibered 1.5 µm laser diode », Appl. Physics B., Vol. 22, N°10, Oct 2016

[5] S. Gerstenkorn, and P. Luc, Atlas du spectre d'absorption de la molécule d'iode, Editions du C.N.R.S., Paris, France, 1978.

[6] B. Argence, E. Prevost, T. Leveque, R. Le Goff, P. Lemonde, S. Bize and G. Santarelli, "Prototype of an ultra-stable optical cavity for space applications » Optics Express 20 (23) pp. 25409-25420 (2012).

[7] J. Vigué, M. Broyer and J.C. Lehmann, « Natural and magnetic predissociation of iodine B state", Journal de Phys. Vol. 42, 1981, pp. 937-947.

[8] A. N. Goncharov, S.V. Gateva-Kosteva, M.N. Skvortsov, and V.P. Chebotayev, " direct observation of the anomalous Zeeman effect at the X-B transition of molecular iodine by the method of nonlinear spectroscopy", Appl. Phys. B 52, 311 314 (1991).

The H2020 European Project DEMETRA:

Experimental Time Services based on European GNSS Signals

P. Tavella, I. Sesia, G. Cerretto, G. Signorile, D. Calonico, R. Costa, C. Clivati, E. Cantoni, C. De Stefano, M. Frittelli, V. Formichella
INRIM, Italy

E. Biserni, V. Leone, E. Zarroli, D. Sormani
ANTARES, Italy

P. Defraigne, Q.Baire
Observatoire Royal de Belgique, ORB, Belgium

M. Gandara, V. Hamoniaux
Thales Alenia Space France, TAS-F, France

E. Varriale, Q. Morante
Thales Alenia Space Italy, TAS-I, Italy

T. Widomski, J. Kaczmarek, J. Uzycki, K. Borgulski, P. Olbrysz, J. Kowalski, K.Gliwka
ELPROMA, Poland

A. Cernigliaro, F. Fiasca, A.Perucca, M.Facca
AIZOON, Italy

V. Dhiri,
Telespazio VEGA UK Ltd, United Kingdom

M.T. Veiga, T. Suárez, J.Diaz
DEIMOS, Spain

M.Mangiantini
METEC, Italy

A.E. Wallin
MIKES Metrology, VTT Technical Research Centre of Finland Ltd, Finland

L. Galleani
Politecnico di Torino, Italy

P. Whibberly, D. Hindley
National Physical Laboratory, NPL, United Kingdom

***Abstract*—DEMETRA, the "DEMonstrator of Egnss services based on Time Reference Architecture", is an European Project funded by the European Union in the Horizon 2020 program. The main aim of the project was to develop and test a prototype of Time Service Provider based the European Global Navigation Satellite System (GNSS) providing innovative or improved time services based on different technologies and embedded in a modular architecture. The main innovative features are time certification, non-repudiation, integrity, reliability, resilience. The demonstrator has been developed and tested during the years 2015-2016. Nine different time services were developed and tested also in real environment at users premises. The paper reports the results of the experimental campaigns and the main lesson learned also by the trials with potential users.**

Keywords— EGNSS; time dissemination; time services;

I. INTRODUCTION

The GNSSs are disseminating time at 10-20 ns accuracy and the signal is worldwide available. Nevertheless some users are not completely satisfied with the GNSS time service as the GNSS receivers can fail, the signal can be disrupted, anomalies are not identified, and particularly the clock at user level is not certified or validated by the time service provider. We started thinking to the possible features to be added to the European GNSS time dissemination service, and also to independent time dissemination subsystem to be used in parallel with the GNSS receiver to increase the resilience and reliability of the time information.

In parallel, a User Needs Analysis and a Business Plan was carried out during the project, by entering in contact with possible market segments trying to identify their needs. The market analysis of the European GNSS Agency in 2015 [1] reported for the first the European time timing and synchronisation service available from GNSS and the main strategic markets were deemed to be energy, telecom, and finance.

II. THE DEMETRA SET UP

The concept of DEMETRA Architecture and the nine time services are described in [1] [3] The demonstrator has been assembled and integrated at INRIM premises in Turin by the end of February 2016. After the integration, it has been tested for six months with two experimentation test campaigns:

- Closed Loop Test (March-May 2016) where the User Terminal (UT) was placed in the same location of the Reference Time Generator.

End to End Test (July-October 2016) where the User Terminal was located in a real user environment, integrated into the user application to test the real advantages and feasibility of

the new time services. In Fig 1. the demonstrator fully assembled in the DEMETRA laboratory is shown.



Fig. 1: Demonstrator integrated in the DEMETRA Laboratory at INRIM, Italy.

The demonstrator was based on a Common Infrastructure and on 9 time services, five of which based on the European GNSS:
Service 1: Time broadcasting over TV/Radio links
Service 2: Certified Trusted Time Distribution using NTP
Service 3:Time and Frequency Distribution over Optical link
Service 4: Time and Frequency Distribution via GEO Satellite
Service 5: User GNSS Receiver Calibration
Service 6: Certified Time Steering
Service 7: Time Monitoring and Steering
Service 8: Time Integrity
Service 9: All-in-one Time Synchronization Solution.

III. The DEMETRA Experimental Results

Some experimental results are here reported, the full experimentation campaign will be reported in the paper. In Fig. 2 we show the frequency offset of the service "Trusted Time Distribution", where the dissemination of UTC time and frequency is carried out over the Internet using an enhanced NTP (Network Time Protocol). The Service demonstrated an accuracy of 1 ms for LAN application and 10 ms on the internet for time dissemination

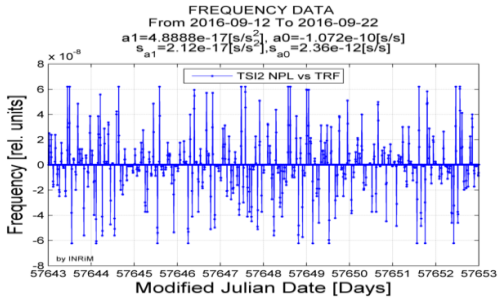


Fig. 2: Trusted Time Distribution: Frequency offset of the clocks in the User Terminals versus the Reference signal

The service "Time and Frequency Distribution via GEO Satellite" has been developed to back-up traditional synchronization systems based on GNSS and it allows to synchronize user clocks in each user terminal of a network by using a geostationary satellite. As shown in Fig. 3 the User Time offset was stably remaining in a range narrower than +/- 100 ns.
Regarding the feature of integrity, a Time Integrity service was developed with the aim to check possible anomalies in the Galileo transmission of GGTO and UTC and possible frequency jump on the Galileo clocks (Fig. 4).

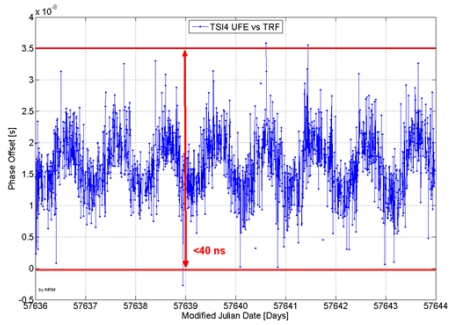
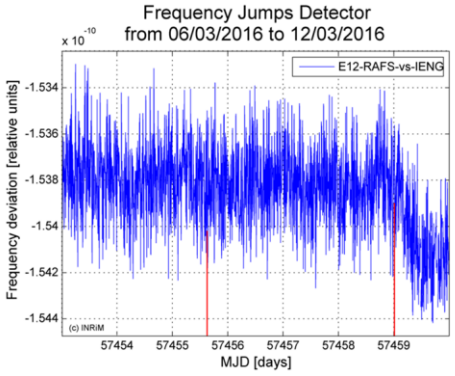


Fig. 3: Time and Frequency Distribution via GEO Satellite: phase/time offset of the UT with respect to the reference time



###SVN###	####MJD####	#########DATE#########	###AMPLITUDE###	###UNITS###	###DETECTED ANOMALY##
E12	57455.6285	2016-03-08 15:05:00	4.72e-13	[rel.units]	Frequency Jump
E12	57459.0035	2016-03-12 00:05:00	4.86e-13	[rel.units]	Frequency Jump
E19	57456.0000	2016-03-09 00:00:00	3.22e-09	[seconds]	Phase Jump

Fig. 4: Time Integrity: Space clock jumps detection and list of not usable satellites

IV. Conclusions

The time service demonstrator, funded by the European project DEMETRA, has been designed, developed, qualified, and integrated at INRIM. All the test campaign has been carried out in March-October 2016 and monitored on the website www.demetratime.eu.

ACKNOWLEDGEMENTS

This project has received funding from the European GNSS Agency under the European Union's Horizon 2020 research and innovation programme under grant agreement No 640658.

REFERENCES

[1] http://www.gsa.europa.eu/2015-gnss-market-report
[2] P. Tavella and DEMETRA consortium, "The Horizon 2020 DEMETRA project: DEMonstrator of EGNSS services based on Time Reference Architecture", Metrology for Aerospace (MetroAeroSpace), 2015 IEEE Benevento 2015, http://ieeexplore.ieee.org/xpl/articleDetails.jsp?arnumber=7180634.
[3] P. Tavella and DEMETRA consortium "The European Project DEMETRA: Demonstrating Time Dissemination Services", in proc ION PTTI Precise Time and Time Interval meeting, Monterey CA, Jan 2016
[4] P.Tavella and DEMETRA Consortium "Time Dissemination Services:The Experimental Results of the European H2020 DEMETRA", paper presented at the IEEE International Frequency Control Symposium, May 2016, New Orleans (Louisiana). May 2016 https://doi.org/10.1109/FCS.2016.7563585

Design and performance of Cs fountain frequency standards constructed for metrology laboratories

R.J. Hendricks, F. Ozimek and K. Szymaniec
National Physical Laboratory
Teddington, U.K.

S. Beattie and B. Jian
National Research Council
Ottawa, Canada

P. Dunst, B. Nagorny and J. Nawrocki
Astrogeodynamical Observatory
Space Research Centre
Borowiec, Poland

W. Chen
National Institute of Metrology
Beijing, China

K. Gibble
Pennsylvania State University
University Park, USA

***Abstract*— Following a refined NPL design, we have constructed several Cs fountain primary frequency standards for use in different metrology laboratories. In this paper we describe the design of these new systems and present measurements of their performance.**

I. INTRODUCTION

Laser-cooled Cs fountain clocks were developed as metrological instruments in the early 1990s. Two decades later they have become indispensable for the calibration and steering of UTC/TAI as well as for improving the stability of local realisations of UTC [1]. They have set limits on the variation of fundamental constants and underpinned the development of a new generation of atomic frequency standards. The construction and operation of all of the existing primary standards has involved significant development effort by individual laboratories. Here we report the design and construction of several Cs fountain frequency standards at NPL for operation at other laboratories. Taking advantage of NPL's experience has shortened the development process and enabled the delivery of fully functioning systems. In this paper we describe the design and performance of these new systems.

II. SYSTEM DESIGN

A cold-atom primary fountain frequency-standard consists of a physics package (a vacuum vessel with cooling, detection and flight chambers, and microwave cavities), an optical assembly producing light for atom cooling and detection, microwave sources, and an electronic control system. The physics package of the new systems is largely based on the approach first developed with NPL-CsF2 – a single-stage magneto-optical trap as the cold atom source, optical pumping into the $m_F = 0$ clock state, and a cancellation of the collisional shift to enable high accuracy [2]. This approach provides a relatively compact transportable device that offers robust operation with minimal maintenance without compromising performance. Differences from NPL-CsF2 include the reduction of the overall size of the structure, rigid fixing of the vacuum vessel to a supporting frame, and pre-aligned optics for cooling and detection, which attach directly to the vessel. Ramsey interrogation is performed in a state-of-the-art microwave cavity that minimises the distributed cavity phase frequency shift [3], using a design first implemented in the NPL-CsF3 fountain. The new optical assembly has a small footprint and excellent stability. It is modular, with commercially-available laser heads, a separate saturated spectroscopy module and a beam distribution module. These modules are connected by optical fibres to ease transportation and maintenance.

III. PERFORMANCE

Two complete primary-standard systems and one standalone physics package have been built, with more anticipated in the near future. One system has been installed at CBK-AOS in Borowiec, Poland and is fully functional. The standalone physics package has been delivered to the NRC lab in Ottawa. The assembly work was carried out at NPL in the UK with participation of staff from the recipient labs. Prior to shipment, the instruments were tested to demonstrate the signal-to-noise ratio and short-term stability against one of the NPL hydrogen masers. We measured a short-term stability of $\sigma_y(\tau)=1.7\times10^{-13}$ (1s), almost entirely limited by local oscillator phase noise. This is typical for a Cs fountain standard using microwaves synthesized from a high-quality room-temperature quartz crystal. We also carried out a preliminary evaluation of key systematic effects, including frequency shifts due to the 2nd order Zeeman effect, blackbody radiation and cold collisions. The results suggest that the systems are capable of achieving an accuracy at the low 10^{-16} level – similar to that of

978-1-5386-2916-1/$31.00 ©2017 IEEE

the best established primary standards. Full accuracy evaluations of the delivered systems are underway.

REFERENCES

[1] J. Guena, M. Abgrall, D. Rovera, P. Laurent, B, Chupin, M. Lours, G. Santarelli, P. Rosenbusch, M. E. Tobar, R. Li, K. Gibble, A. Clairon, and S. Bize, "Progress in atomic fountains at LNE-SYRTE", IEEE Trans. Ultrason., Ferroelect., Freq. Control, vol. 59, pp. 391–410, 2012.

[2] K. Szymaniec, S. N. Lea, K. Gibble, S. E. Park, K. Liu and P. Glowacki, "NPL Cs fountain frequency standards and the quest for the ultimate accuracy", Journal of Physics: Conference series, vol. 723, 012003, 2016.

[3] K. Gibble, S. N. Lea, and K. Szymaniec, "A microwave cavity designed to minimize distributed cavity phase errors in a primary caesium frequency standard", Conference on Precision Electromagnetic Measurement, 2012.

Cold-atom-based commercial microwave clock at the 10^{-15} level

Bruno Pelle and Bruno Desruelle
Time and Frequency division
Muquans
Bordeaux, France
bruno.pelle@muquans.com

Ramon Szmuk and David Holleville
LNE-SYRTE
Observatoire de Paris
Paris, France

***Abstract*—Laser cooled atomic clocks allow to both extend spectroscopy duration and better control the systematics. We present a commercial microwave clock that achieve an extreme stability and accuracy in the 10^{-15} range within a day, with a turnkey product dedicated for continuous long-term operation.**

Keywords—Microwave clocks, cold atoms, isotropic cooling

I. INTRODUCTION

Microwave clocks have reached their best short-term [1] and long-term stabilities [2], as well as their best accuracy [1], with cold atoms based fountain clocks. So far, these results have required laboratory-size experiments, but current efforts are underway to develop more compact and fully autonomous setups for space [3] or civil applications.

In a first attempt to develop such a more compact atomic clock with performances close to the ones of atomic fountains, a project named Horace and based on isotropic cooling of caesium atoms in a copper cavity started in SYRTE in 2001 [4]. It reached a best short-term fractional frequency uncertainty of 2.2×10^{-13} at 1 s [5] and a best long-term frequency instability of 3.2×10^{-15} in 20 000 s [6]. In a perspective of technological transfer, a second project was initiated in 2011 from a collaboration between SYRTE, LP2N (Bordeaux), and Muquans. The physics package design is similar, but using rubidium instead of caesium atoms. They are expected to have a cold collisions shift lower than caesium atoms and can be cooled down with frequency doubled telecom lasers [7] which have shown extreme robustness and reliability. This prototype demonstrated similar short-term and long-term stabilities, and could be operated in both micro-gravity and airborne noisy environment [8].

Our objective is to propose the first commercially available atomic clock that can reach the 10^{-15} level. A detailed technical analysis is ongoing to improve the performances of our prototype and several improvements are in progress to demonstrate with a second generation prototype a short-term instability close to 3×10^{-13} at 1 s with a long-term instability close to 1×10^{-15}. An accuracy budget is under preparation with a targeted accuracy in the 5×10^{-15} range.

II. WORKING PRINCIPLE AND RESULTS

To the contrary to all existing commercial atomic clocks, our MuClock is based on laser cooled atoms which allow to extend the duration of the spectroscopy compared to other technologies, therefore narrowing the clock transition linewidth. This long interrogation time leads to short-term instabilities in the low 10^{-13} at 1 s. As the atoms are also better temporally and spatially localized, it allows us to reach an estimated accuracy in the 10^{-15} range.

A. Temporal Sequence

The apparatus is based on a copper cavity, which is first used as an integrating sphere for isotropic cooling where 10^7 atoms are cooled to sub-Doppler temperatures in optical molasses. We then interrogate the free-falling atoms with microwave pulses delivered by the resonant cavity in a so-called Ramsey sequence with T_R = 40 ms. Eventually, we detect the atoms in one of the hyperfine state in an absorption column. By the mean of atom recapture, we increase the cycle time to repetition rates of the order of 5-20 Hz.

B. Expected noise sources

The frequency stability performance of the MuClock can be explained by three fundamental noise sources that cannot be overcome in this setup: the statistical shot-noise from thermodynamics (SN) [9] and quantum projection noise (QPN) [10] in the detection, in addition to the phase noise introduced by the local oscillator through the Dick effect [11].

C. Results

A first frequency stability measurement of our first generation prototype has been achieved. We compared it with an ultra-stable frequency reference at SYRTE (1×10^{-13} at 1 s and reaching few 10^{-16} in the long-term). We obtained a short-term instability of 3.7×10^{-13} at 1 s and a long-term Flicker floor at 3×10^{-15} reached after 25 000 s. These limitations on the short and long-term instability are currently under investigation.

978-1-5386-2916-1/$31.00 ©2017 IEEE

D. Short-term instability estimation

The short-term instability of our clock can be approximated by [12]:

$$\frac{\sigma_{\delta\nu}}{\nu_0} = \frac{1}{\pi}\frac{1}{Q_{at}}\frac{1}{C \times SNR}\sqrt{\frac{T_C}{\tau}}, \qquad (1)$$

where $Q_{at} = \nu_0/\Delta\nu$ is the quality factor of the atomic resonance, with $\Delta\nu = 1/(2T_R)$ for a Ramsey interrogation and $\nu_0 = \nu_{HFS}$ in absence of any bias, C is the fringe contrast, SNR = $N/\delta N$ is ultimately limited by the atom number N and its noise δN including the SN, QPN, and Dick effect, T_C is the cycle duration, and τ is the integration time.

With our experimental parameters, we obtain a short-term instability of $\sigma_{\delta\nu}/\nu_0 = 3.9\times10^{-13}$ at $\tau = 1$ s, in agreement with our experimental characterization.

III. Conclusion

To conclude, we have developed a first cold atoms based microwave clock which is compatible with airborne operation [8]. We reached a short-term instability of 3.7×10^{-13} at 1 s and a long-term Flicker floor at 3×10^{-15} after 25 000 s. We are limited by both the fundamental atomic noise and the Dick effect. With our second generation product, we intend to reach soon a short-term instability close to 3×10^{-13} with a long-term instability close to 1×10^{-15}. We target an accuracy in the 5×10^{-15} range with an accuracy budget under preparation.

Acknowledgment

The authors would like to thank the former contributors on the Horace and Rubiclock projects, as well as the work that has been achieved so far. Helpful discussions with A. Landragin, and M. Abgrall are gratefully acknowledged. We also acknowledge the support from CNES, BPI and ESA.

References

[1] J. Guéna, M. Abgrall, D. Rovera, P. Laurent, B. Chupin, M. Lours, G. Santarelli, P. Rosen-busch, M.E. Tobar, R. Li, K. Gibble, A. Clairon, and S. Bize, "Progress in atomic fountains at LNE-SYRTE," IEEE Transactions on Ultrasonics, Ferroelectrics, and Frequency Control, vol. 59, no. 3, pp. 391-409, 2012.

[2] S. Peil, J. L. Hanssen, T. B. Swanson, J. Taylor, and C. R. Ekstrom, "Evaluation of long term performance of continuously running atomic fountains," Metrologia, vol. 51, no. 3, pp. 263-269, 2014.

[3] P. Laurent, D. Massonnet, L. Cacciapuoti, and C. Salomon, "The ACES/PHARAO space mission", Comptes Rendus Physique, Vol. 16, no. 5, pp. 540-552, 2015.

[4] E. Guillot, P. Pottie, and N. Dimarcq, "Three-dimensional cooling of cesium atoms in a reflecting copper cylinder," Optics Letters, vol. 26, no. 21, pp. 1639-1641, 2001.

[5] F.-X. Esnault, D. Holleville, N. Rossetto, S. Guerandel, and N. Dimarcq, "High-stability compact atomic clock based on isotropic laser cooling," Phys. Rev. A, vol. 82, no. 3, pp. 033436, 2010.

[6] F.-X. Esnault, N. Rossetto, D. Holleville, J. Delporte, N. Dimarcq, "HORACE: A compact cold atom clock for Galileo," Advances in Space Research, vol. 47, no. 5, pp. 854-858, 2011.

[7] V. Ménoret, R. Geiger, G. Stern, N. Zahzam, B. Battelier, A. Bresson, A. Landragin, and P. Bouyer, "Dual-wavelength laser source for onboard atom interferometry," Optics Letters, vol. 36, no. 21, pp. 4128-4130, 2011.

[8] L. De Sarlo, M. Langlois, J.-F. Schaff, M. Lours, D. Holleville, and N. Dimarcq, "Rubiclock, cold-atom based clock prototype on a microgravity platform: results of the second flight campaign", Proc. 2014 European Frequency and Time Forum (EFTF 2014), 2015.

[9] R.K Pathria and P. D. Beale, Statistical Mechanics, 3rd ed., Eds. Boston: Academic Press, 2011.

[10] W. M. Itano, J. C. Bergquist, J. J. Bollinger, J. M. Gilligan, D. J. Heinzen, F. L. Moore, M. G. Raizen, and D. J. Wineland, "Quantum projection noise: Population fluctuations in two-level systems," Phys. Rev. A, vol. 47, no. 5, pp. 3554-3570, 1993.

[11] G. J. Dick, "Local oscillator induced instabilities in trapped ion frequency standards," Proc. 19th Annu. Precise Time and Time Interval Conference, vol. 40, pp. 133-147, 1987.

[12] G. Santarelli, Ph. Laurent, P. Lemonde, A. Clairon, A. G. Mann, S. Chang, A. N. Luiten, and C. Salomon, "Quantum Projection Noise in an Atomic Fountain: A High Stability Cesium Frequency Standard," Phys. Rev. Lett., vol. 82, no. 23, pp. 4619-4622, 1999.

Investigation of dual species ions cloud by molecular-dynamics simulation for microwave clocks

Y. N. Zuo, P. F. Cheng, X. L. Sun, L. J. Wang
Department of Physics, Tsinghua University
Beijing 100084, P. R. China

J. W. Zhang, L. J. Wang
State Key Laboratory of Precision Measurement Technology and Instruments
Department of Precision Instruments, Tsinghua University
Beijing 100084, P. R. China
E-mail: zhangjw@tsinghua.edu.cn

***Abstract*—A microwave atomic clock based on $^{113}Cd^{+}$ ions at Tsinghua University is carried out for seven years. To further improve the performance of the clock, a new experimental setup with dual traps and dual species ions was proposed. To investigate the efficiency of sympathetic cooling and the dynamic process of ions, numerical simulation study of the dual-species ion ensembles by the Molecular-dynamics simulation is applied.**

Keywords—molecular dynamics; dual species ions; microwave clocks

I. INTRODUCTION

The laser cooling makes it possible to obtain cold atomic/ion ensembles at ultra-low temperature, which was widely applied in many areas, for instance, quantum frequency standard[1], quantum information processing[2], and plasma physics[3]. However, due to the unavailability of lasers at some wavelength, a part of ions cannot be Doppler cooled by lasers directly. As an alternative, sympathetic cooling by the long-range Coulomb interaction among ions has attracted a wide spread attention. By means of sympathetic cooling, one can prepare ultracold ion ensembles even down to mK temperature level[4]. Sympathetic cooling is also applied to cool a kind of ions even though it can be laser-cooled directly to avoid the unwanted influences by the cooling laser, like light shift, even though the ions have available cooling lasers.

At Tsinghua University, a microwave atomic clock based on laser cooled $^{113}Cd^{+}$ ions was initiated in 2010. So far, the frequency of the clock transition was obtained to be 15 199 862 855.019 2(10) Hz with a fractional uncertainty of 6.6×10^{-14}, and the frequency instability was measured to be $6.1\times10^{-13}\tau^{-1/2}$ [5]. In order to improve frequency stability and reduce the Dick effect, the researches of a new system based on sympathetic cooling and interleaving lock were carried out [6,7]. In the new system, the $^{113}Cd^{+}$ ions are continuously sympathetically cooled by Doppler laser-cooled $^{24}Mg^{+}$ ions with a red-shifted 280 nm laser.

In order to improve the signal-to-noise ratio (SNR), a large ion cloud has to be trapped for the microwave frequency standard. Obviously, the efficiency of sympathetic cooling strongly depends on the number of ions, the mass ratio between the sympathetically cooled ions and laser-cooled ions, and the number ratio of the two species ions. Therefore, it is vital to study the dynamic process of the dual species ion systems in linear ion traps to improve the performance of frequency standard based on sympathetic cooling. This paper report the numerical simulation study of the dual-species ion ensembles using the Molecular-dynamics simulation method[8].

II. EXPERIMENTAL SETUP

In our experiments, $^{113}Cd^{+}$ and $^{24}Mg^{+}$ ions will be confined in the identical linear Paul trap at the same time. The sketches and setup of the trap is shown in Fig.1, and more detailed description of the experimental setup can be found in Ref. [6,7].

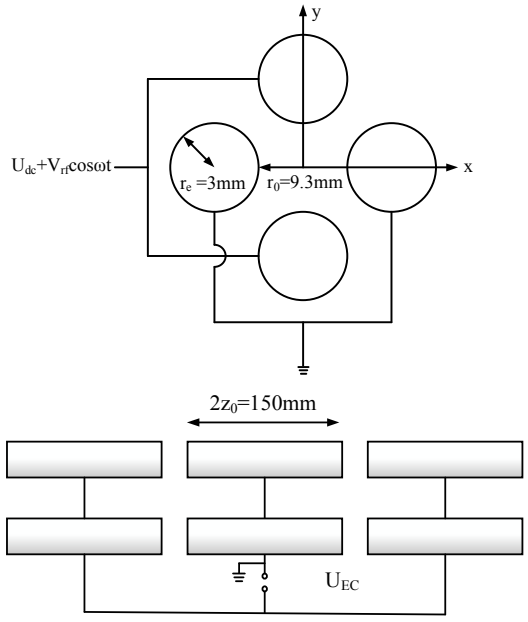


Fig. 1. RF potential and the sketch of one of the linear Paul trap (not to scale).

The confinement of the ions in the radial plane is obtained by applying an radio frequency(RF) field $V_{rf}\cos\omega t$ to the diagonal electrode rods. The RF frequency is 2 MHz, and the amplitude V_{rf} can be adjusted in the range from 50V to 1000 V. The confinement of the ions in the axial direction is obtained by applying DC voltage to the endcap electrodes.

This work is supported by the National Key Research and Development Program of China (No.2016YFA0302101), the National Natural Science Foundation of China (No.11304177), and the Initiative program of State Key Laboratory of Precision Measurement Technology and Instruments.

The motion of ions in a Paul trap is described by the Mathieu equation. The solution of the ions' motion equation is determined by the values of q and a, called *stability parameters*:

$$q=\frac{2QV_{rf}}{mr_0^2\Omega^2},\quad a=\frac{4QU_{dc}}{mr_0^2\Omega^2},$$

where Ω is the angular frequency of RF, m is the mass of ions, Q is the charge of ions, r_0 is the nearest distance from the center to any electrode surfaces. In Fig. 2, the lowest order of stability regions for both Cd^+ and Mg^+ ions are shown. For our trap, q and a are marked out, too.

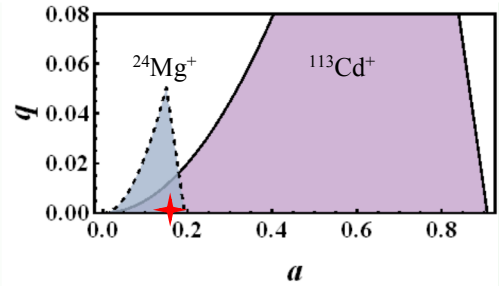


Fig. 2. The lowest stability region for both x and y directions, where a and q are present in the charge-mass ratio of $^{113}Cd^+$. Blue part is the lowest stability region for $^{24}Mg^+$; pink part is for $^{113}Cd^+$.

The $^{24}Mg^+$ ions subsequently Doppler laser cooled by a 280 nm laser. The energy levels of $^{24}Mg^+$ and $^{113}Cd^+$ for laser cooling, pumping and detection are shown in Fig. 3.

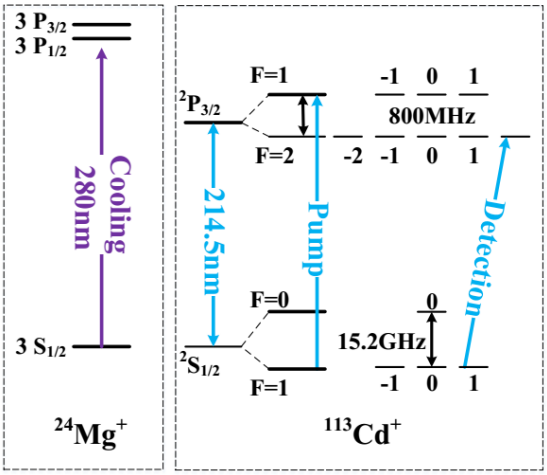


Fig. 3. Energy level diagram of the lowest relevant energy levels for $^{24}Mg^+$ and $^{113}Cd^+$ (not to scale) .

III. MD SIMULATION

Simulations of dual-species ion crystals in linear Paul traps are based on solving Newton's equations of motion[8] for all laser-cooled and sympathetically cooled ions as

$$m_i\ddot{r}_i=\mathbf{F}_i\left(r_1,...r_{LC+SC},v_1,...v_{LC+SC},t\right)$$
$$=\mathbf{F}_i^{trap}+\mathbf{F}_i^{Cloulomb}+\mathbf{F}_i^{stochastic}+\mathbf{F}_i^{laser},$$

where $i=1,...,N_{LC}+N_{SC}$ (N_{LC} and N_{SC} are the number of the laser-cooled and sympathetically cooled ions), m_i, r_i and v_i are the ion's mass, positon and velocity vectors, $\mathbf{F}_i\left(r_1,...r_{LC+SC},v_1,...v_{LC+SC},t\right)$ is the force acting on ion i. Particularly, $\mathbf{F}_i^{trap}$ is the trapping potential force, which can be given by

$$\mathbf{F}_i^{trap}=Q_i\nabla\varphi(x,y,z,t),$$

where Q_i is the charge and $\varphi(x,y,z,t)$ is the trapping potential of the ions. In consideration of the RF micromotion, the potential near the center of the trap can be illustrated easily by using the pseudopotential as

$$\varphi(x,y,z,t)=\frac{2V_{rf}}{r_0^2}\left(x^2-y^2\right)\cos(\Omega t)$$
$$+\kappa\frac{U_{EC}}{2z_0^2}\left(2z^2-x^2-y^2\right),$$

where Ω is the frequency of the RF field(with amplitude V_{rf}), U_{EC} is the DC potential, κ is an dimensionless parameter that takes into the particular end cap geometry chosen, z_0 is half the distance between the two end caps, r_0 is the minimum distance from the trap axis to each of the electrodes . The Coulomb interaction force $\mathbf{F}_i^{Cloulomb}$ on ion i from all other ions can be express as follows:

$$\mathbf{F}_i^{Cloulomb}=\frac{Q_i}{4\pi\varepsilon_0}\nabla\sum_{j\neq i}\frac{Q_j\mathbf{r}_{ij}}{\left|\mathbf{r}_{ij}\right|^2},$$

where $\mathbf{r}_{ij}$ is the distance vector between the ions i and j, ε_0 is the vacuum permittivity. The stochastic force $\mathbf{F}_i^{stochastic}$ can heat up the ion ensemble due to the uncertainty of the actions, like residual gas components and stray potential, and it cannot be described by a unified formula. The laser cooling force $\mathbf{F}_i^{laser}$ can be considered as a linear viscous damping force plus a constant light pressure force in the direction of laser:

$$\mathbf{F}_i^{laser}=-\alpha_i\dot{r}_i+F_i^{lp}$$
$$=-\hbar k^2\frac{s}{(s+1)^2}\frac{\Delta\omega\Gamma}{\Delta\omega^2+\Gamma^2/4}\dot{r}_i-\hbar k\frac{\Gamma}{2}\frac{s}{s+1},$$

where α_i is the damping coefficient related to the laser power density and frequency detuning, F_i^{lp} is the laser radiation force related to the direction of propagation and power density

of the laser, k is the wavevector of the laser, $s = \frac{\Omega_R^2/2}{\Delta\omega^2 + \Gamma^2/4}$ is the saturation parameter, $\Delta\omega = \omega - \omega_0$ is the frequency difference between the center transition frequency, Γ is the natural linewidth of the ion's transition. The light pressure force F_i^{lp} pushes the laser-cooled ion ensemble in the laser beam direction and gives a spatial offset from the potential well center.

Based on the model, The MD simulation is always used to track the temporal evolutions of position and velocity vectors of all ions, and they are developed from the numerical solution of the classical dynamic equations.

IV. PRELIMINARY RESULTS AND DISSCUSION

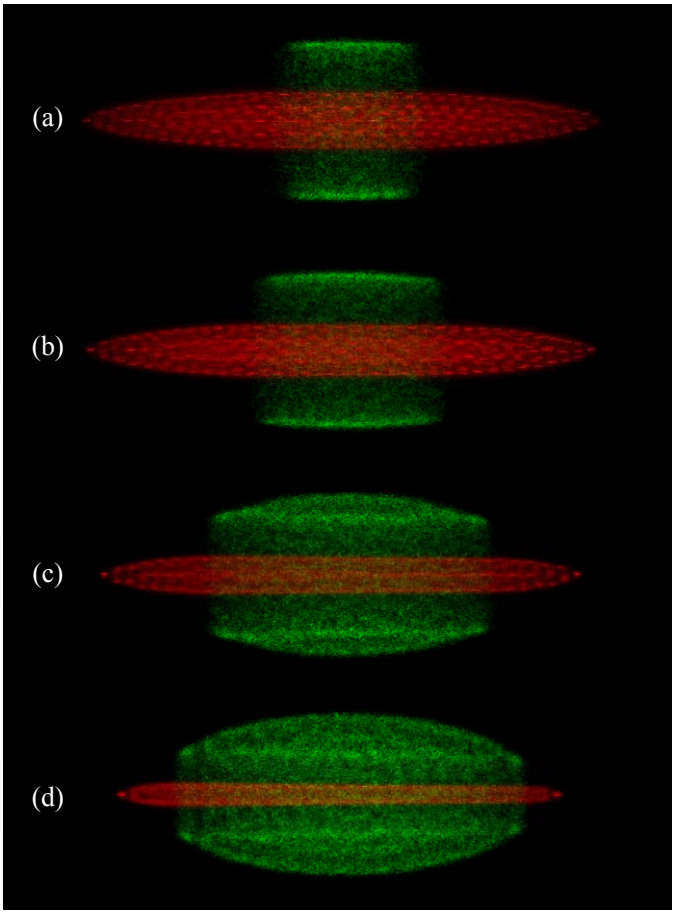


Fig. 4. Simulated CCD images of increasing numbers of Cd^+ ions(green) sympathetically cooled by Mg^+(red). Each image consists of 500 ions totally, where the percent of Cd^+ are 10%, 20%, 50%, and 80% respectivly.

The MD simulation is carried out based on the IonMD[9,10], an open source MD simulation software for multi-component Coulomb crystals. IonMD simulations were implemented in C++ with a front end Python script. Numerical integration is performed using the leapfrog integration technique. Ion trajectories, three-dimensional renderings of ion crystals and CCD images can be simulated. With the parameters of the experimental setupsome preliminary results are obtained and shown in Fig. 4. So far, an ions assemble of 500 ions in total is simulated. As we can see, the cadmium ions can be sympathetically cooled by magnesium ions, even the ratio of the magnesium ions is low. The simulation of the efficiency of sympathetic cooling of large number ions to 10^5 needs rather powerful computing ability. So, these works are still undergoing.

ACKNOWLEDGMENT

We thank M. DePalatis, J.Q. Huang and Z.B. Wang for the greatest help on MD program coding.

REFERENCES

[1] Huntemann N, Okhapkin M, Lipphardt B, et al. "High-Accuracy Optical Clock Based on the Octupole Transition in $^{171}Yb^{+}$". *Phys. Rev. Lett*, Vol. 108, pp. 090801, March 2012.

[2] Häffner H, Roos C F, Blatt R. "Quantum computing with trapped ions". *Phys. Rep*, Vol. 469(4), pp. 155-203. December 2008.

[3] Schiffer J P. "Layered structure in condensed, cold, one-component plasmas confined in external fields". *Phys. Rev. Lett*, Vol. 61, pp. 1843-18485. October 1988,

[4] Ostendorf A, Zhang C B, Wilson M A, et al. "Sympathetic cooling of complex molecular ions to millikelvin temperatures". *Phys. Rev. Lett*, Vol. 97, pp. 243005, December 2006

[5] Miao K, Zhang J W, Sun X L, et al. "High accuracy measurement of the ground-state hyperfine splitting in a $^{113}Cd^{+}$ microwave clock", *Opt. Lett.*, Vol. 40, pp. 4249-4252, August 2015,

[6] J. Zhang, K. Miao, L. Wang, X. Sun and L. Wang, "Towards a high-performance microwave frequency standard based on $^{113}Cd^{+}$ ions," *2015 Joint Conference of the IEEE International Frequency Control Symposium & the European Frequency and Time Forum*, Denver, CO, 2015, pp. 758-760.

[7] Y. N. Zuo, K. Miao, C. Gao, J. W. Zhang and L. J. Wang, "Progress of the dual-traps microwave frequency standard based on $^{113}Cd^{+}$ ions," *2016 IEEE International Frequency Control Symposium (IFCS)*, New Orleans, LA, 2016, pp. 1-4.

[8] Zhang C B, Offenberg D, Roth B, et al. "Molecular-dynamics simulations of cold single-species and multispecies ion ensembles in a linear Paul trap", *Phys. Rev. A,* Vol. 76, pp. 012719, July 2007.

[9] https://github.com/mivade/IonMD/tree/thesis

[10] De Palatis M V. Production of cold barium monohalide ions[D]. Georgia Institute of Technology, 2013.

High-Resolution Frequency Synthesizers over X-band using SILPLL Opto-Electronic Oscillators

Tianchi Sun, and Afshin S. Daryoush
Department of ECE, Drexel University
Philadelphia, PA 19104 USA
daryoush@ece.drexel.edu

Ajay Poddar, Li Zhang, and Ulrich Rohde
Synergy Microwave Corp.
201 Mclean Blvd
Paterson, NJ 07504 USA

***Abstract*—Opto-electronic oscillators with their demonstrated low phase noise are popular due to the increasing demand of very clean local oscillator and clock signal sources. Forced techniques are applied on an OEO system reducing the phase noise and suppresses side mode observed in standard OEO with long delays. A frequency synthesizer working at X-band is demonstrated using dispersive optical transversal filter cascaded with YIG filter to electronically fine and coarse tune the oscillation frequency of the synthesized frequency, as a replacement for fixed frequency high Q metallic filter. Close-in to carrier phase noise of -135 dBc/Hz at 10 kHz are reported by $V_{\pi/2}$ operation of a Mach-Zehnder (MZM) over 9 GHz to 11 GHz with frequency tuning step as small as 10 kHz/pm.**

Keywords*—opto-electronic oscillator, self-injection locked phase locked loop, YIG filter, optical transversal filter, chirped fiber Bragg grating.*

I. Introduction

High frequency microwave oscillators become popular with the increasing need for high speed data transmission. Opto-electronics oscillators [1] used as promising way for creating high frequency RF signal with great purity perfectly meet this demand. The self-injection locking phase locking SILDPLL OEO set-up is described in Fig. 1. The low RIN fiber laser (TWL-C-HP-M) is used to provide wavelength tunable laser signal. The signal transmits through optical fiber to create the delay line and then received by photodetector (DSC50S) to set signal pass through narrow band filter. Narrow band filter is the core of the OEO, which is use to select the oscillation frequency. High Q metallic filter is the classic design in use but it needs mechanical adjusting which is not suitable for computer control system based OEO described in Fig. 1. YIG [2] filter will be introduced in this paper to replace the role of high Q metallic filter. Meantime, in order to compensate for poorer frequency selectivity of a widely tunable YIG filter, a narrowband optical transversal filter [3][4] realized by using chirped fiber Bragg grating (CFBG).

Except the optical frequency selectivity, self-injection locking [5], self-phase locking [6] and their combination SILPLL [7] is also applied to provide reduction for synthesizer phase noise in both close in and far away to the carrier frequency. The block diagram depicts SIL and DSPLL [8][9] simultaneously. There are two paths for modulated signal after MZM, one transmits the main loop of OEO and the other loop is split into two using as 3 km and 8 km dual phase locking signal. The combined phase locking signal is then inputted to a custom design 'Mixer+LPFA' board. A double balanced mixer is integrated on this board with a low pass filter amplifier (using Op-Amp circuits) to work as phase detector and low pass portion of the PLL. The phase error of the OEO main loop is compared with the dual delay lines of the phase locking loop and the phase error signal is fed back to the bias port of MZM. Self-Injection locking signal takes the advantage of phase lock loop path and share the same 3km fiber using in SPLL path.

The novelty of this paper is design and testing of high frequency resolution X-band synthesizer using SILPLL OEO. The high resolution and wavelength sensitive tuning is due to fine tuning of an optical transversal filter using a chirped fiber Bragg grating (CFBG) as dispersive component for narrowband filtering.

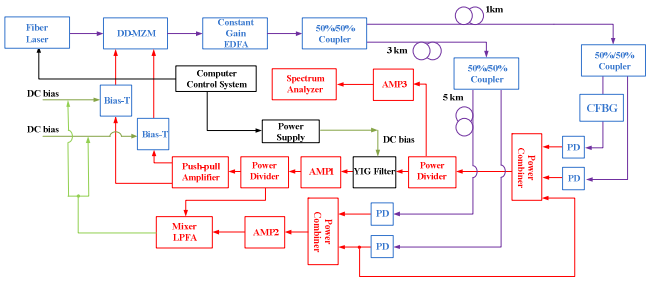


Fig. 1 Block diagram of experimentally demonstrated SILDPLL OEO system.

II. Frequency Tuning Techniques and Its Performance

A. Coarse Tunability Using YIG Filter

YIG filter is attractive in its very broad tuning range and its easily computer control set-up. Using system depicted in Fig. 1, with the tuning of YIG filter, the coarse tuning of synthesizer is achieved as 25 MHz/mA in Fig. 2. The highest resolution for power supply Agilent E3631A working at constant current mode is 1 mA. A higher frequency tuning resolution and narrowband filtering is achieved by dispersive CFBG based transversal filter as opposed to fiber based [10].

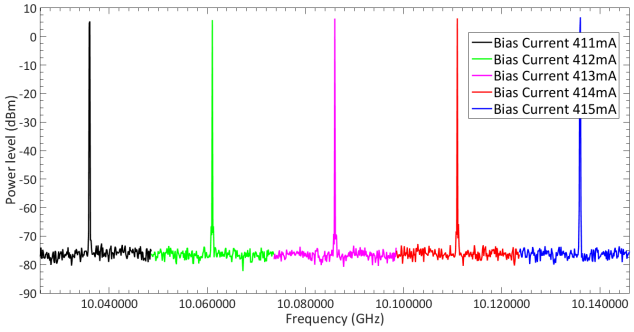


Fig. 2 Synthesizer output frequency versus YIG filter current tuning.

B. Fine Tunability Using Transversal Filter

An optical transversal filter, as reported in [4] could provide a narrowband filtering of microwave signals. For the first order transversal filter depicted in Fig. 3, one path is using short SMF-28 fiber as the reference path, while the other is delayed using dispersive chirped fiber Bragg grating.

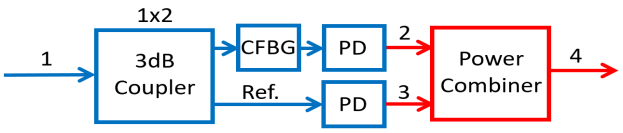


Fig. 3. 1st Order optical transversal filter using 3dB couplers and CFBG.

Transfer function of this filter at RF frequency is:

$$H(\omega)=|1+\cos[\omega(\tau_d+\tau_D)]|/2 \quad (1)$$

where τ_d is the delay difference at fiber laser wavelength. It's related to delay of the chirped fiber Bragg grating at wavelength λo. Parameter τ_D is due to wavelength dispersion characteristics of the CFBG and is expressed as:

$$\tau_D=D(\Delta\lambda) \quad (2)$$

In equation (2), D is the dispersion parameter of CFBG in unit of ps/nm, while $\Delta\lambda$ is difference between the optical source wavelength and the original wavelength λo. The tuning performance of transversal optical filter cascaded with a commercially available YIG filter (Tektronix 183-60) is depicted in Fig. 4. Using fiber Bragg grating module (DCM-20A/SCA Motorola), the dispersion D is -150 ps/nm and delay τ_d is about 20 ns. This delay creates 40 MHz null to null passing band, which is too wide compared with high Q transversal filter needed; therefore, a 30 m of SMF-28 fiber added to reduce passband filter and achieve a null to null bandwidth to around 4.5 MHz. Meanwhile, because of power imbalance introduced by CFBG, RF attenuator and amplifier is required to balance output signal level in the two photodetected arms. The achieved tuning sensitivity is 10 kHz/pm using pico-meter resolution of the fiber laser (TWL-C-HP-M). The wavelength tuning range is 40 nm, which results in an overall tuning range reaches up to 400 MHz. This fine tuning range is much larger than 30 m SMF-28 transversal filter tuning range (1 MHz maximum) [10] and can easily cover the tuning gap that exist due to the coarse tuning of 25 MHz/mA using YIG filter.

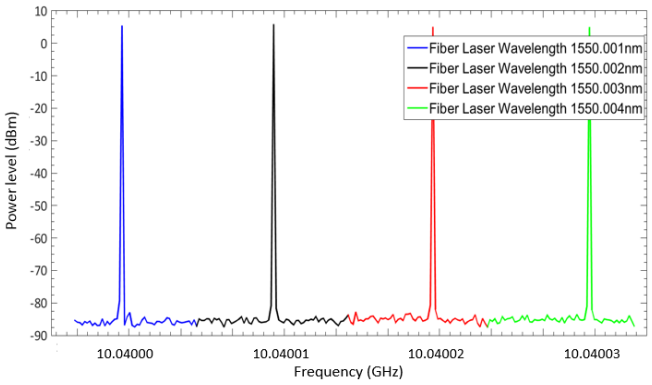


Fig. 4 Synthesizer output frequency VS optical wavelength tuning.

III. Phase Noise Performance Test

A. Phase Noise Performance of X-band Synthesizer

The phase noise performance is important to show the cleanness of this OEO based system. With the helping of forced techniques SILDSPLL, both close in to the carrier and far to the carrier phase noise get reduction. The phase noise is -109 dBc/Hz at offset frequency 1kHz and -135 dBc/Hz at offset frequency 10 kHz in Fig. 5. The side mode peak is also successfully suppressed using narrow band filter and phase locking system for this OEO.

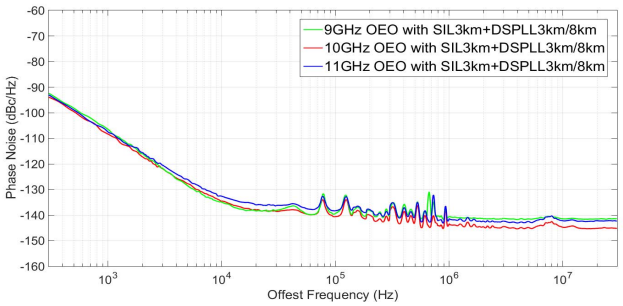


Fig. 5 X-band synthesizer phase noise performance at different frequency.

IV. Conclusion

This paper reports on realization of a SILPLL OEO frequency synthesizer over X-band. Phase noise reach -135 dBc/Hz at offset frequency 10 kHz over 9-11 GHz with the smallest tuning step of 10 kHz/pm achieved as the fiber laser wavelength is tuned in a highly dispersive CFBG of the optical transversal filter. Coarse tuning is achieved using YIG filter over 9-11GHz.

References

[1] X. S. Yao and L. Maleki, "Optoelectronic microwave oscillator," J. Opt. Soc. Am. B 13, 1725-1735 (1996)

[2] M. Aigle, G. Hechtfischer, W. Hohenester, R. Jünemann, and C. Evers, "A systematic way to YIG-filter-design," in 37th European Microwave Conference, Munich, 2007.

[3] Y. Jiang et al., "A selectable multiband bandpass microwave photonic filter," IEEE Photonics Journal, vol. 5, no. 3, p. 3, June 2013.

[4] J. Mora et al., "Photonic microwave tunable single-bandpass filter based on a Mach-Zehnder interferometer," J. Lightwave Tech., vol. 24, no. 7, July 2006.

[5] L. Zhang et al., "Analytical and experimental evaluation of SSB phase noise reduction in self-injection locked oscillators using optical delay loops," IEEE Photonics J., vol. 5, no. 6, Dec. 2013.

[6] L. Zhang et al., "Comparison of optical self-phase locked loop techniques for frequency stabilization of oscillators," IEEE Photonics J., vol. 6, no. 5, Oct. 2014.

[7] Zhang Li, Ajay K. Poddar, Ulrich L. Rohde, and Afshin S. Daryoush. "Self-ILPLL Using Optical Feedback for Phase Noise Reduction in Microwave Oscillators." Photonics Technology Letters, IEEE 27, no. 6 (2015): 624-627.

[8] A. Poddar, A. Daryoush, and U. Rohde, "Self-injection locked phase locked loop optoelectronic oscillator," US Patent US9088369B2, 2012.

[9] A. Poddar, A. Daryoush, and U. Rohde, "Integrated production of self-injection locked self-phase locked opto-electronic oscillators," US Patent US9094133B2, 2013.

[10] T. Sun et al., "Forced SILPLL Oscillation of X- and K-Band Frequency Synthesized Opto-electronic Oscillators," 2016 IEEE Microwave Photonics (MWP), Long Beach, USA, 2016.

A Highly Stable OEO Using a Multi-Purpose Optical-Delay Stabilization System

Luka Bogataj, Jurij Tratnik, Bostjan Batagelj
Faculty of Electrical Engineering
University of Ljubljana
Ljubljana, Slovenia
luka.bogataj@fe.uni-lj.si

Jurij Tratnik, Luka Bogataj, Uros Dragonja
InLambda BDT d.o.o.
Ajdovscina, Slovenia
jurij.tratnik@inlambda.com

***Abstract*— This paper presents the implementation of an active fiber optical-delay stabilization system in an opto-electronic oscillator. The primary use of the system is to stabilize optical point-to-point fiber links for synchronization purposes; however, the system can also be efficiently used as a stable optical delay line in an opto-electronic oscillator. By using a multi-purpose optical delay stabilization system with an opto-electronic oscillator, a frequency drift of 0.02 ppm/K was achieved.**

Keywords*— *delay, stabilization, long-term stability, frequency drift, CWDM, oscillator, compensation, temperature

I. INTRODUCTION

The fiber optic delay line is a key element in any opto-electronic oscillator (OEO). Its low insertion loss enables the realization of a long delay time and therefore a low phase noise of the oscillator. The problem is that the delay time is temperature dependent and that it causes a frequency drift in the OEO. This delay time depends greatly on the temperature sensitivity of the optical fiber's refractive index.

To eliminate the frequency drift of an OEO, different methods were proposed in the literature. The most straightforward method is thermal stabilization of the optical fiber [1]. To avoid fiber stabilization, the use of a photonic crystal fiber [2] or Fabry-Perot etalon [3] was proposed. If the use of specialized components is unwanted, monitoring signal [4] or the phase-locked loop [5] can be used. Recently, a method with no monitoring signal and no external oscillator [6] was presented by the authors of this paper. It is based on a frequency discriminator and the laser's wavelength alterations.

In this paper an OEO with an optical-delay stabilization system (ODSS) is presented. The stabilization of the group delay is achieved with a group delay measurement and the temperature variations of the ODSS's internal optical fiber, as presented in [7]. A monitoring signal is used to measure the group delay.

Delay stabilization systems are primarily intended for synchronization applications [8,9] and can achieve a femtosecond delay stability [10]. In our experimental OEO, an ODSS was used to stabilize the optical delay of the OEO fiber spool. We used an ODSS composed of two rack units and based on CWDM technology [7].

This work was supported by the Slovenian Research Agency (ARRS) as part of the "Algorithms and optimization procedures in telecommunications" programme.

In the following section the experimental setup of the OEO with an ODSS is described. The ODSS is explained and the experimental results are presented. In the last section the experimental results are compared to other known methods for reducing the frequency drift.

II. EXPERIMENTAL SETUP

Our experimental 3-GHz OEO consisted of a directly modulated semiconductor laser diode (with a wavelength of 1290 nm) in a coaxial package and a PIN photodetector with an inbuilt preamplifier. The laser diode and photodetector were thermally stabilized at 30°C. The OEO's electrical part consisted of a microwave amplifier, a narrowband filter (with a quality factor of 8300), a wideband filter and a power divider. The narrowband filter was thermally stabilized. The wideband filter was located in the OEO's loop to prevent oscillations at higher modes.

The two-unit ODSS was located between the laser output and the photodetector input. A 3-km-long, single-mode optical fiber connected the two units of the ODSS. A block diagram of the OEO and the measurement is shown in Fig. 1.

The OEO's frequency was measured with a spectrum analyzer, which was locked to the external reference, provided by a GPS-disciplined oscillator (GPSDO).

A photograph of the complete device (OEO with ODSS) is shown in Fig. 2. The top rack unit is an optical receiver and a transmitter. The second unit from the top is an electrical part of the OEO loop. The third unit from the top is the ODSS unit A and the bottom rack is the ODSS unit B. The ODSS units A and B are different in terms of construction and function, but they are interchangeable in the OEO loop (and in fiber-link delay-stabilization applications).

A. Optical-Delay Stabilization System

The block diagram of the ODSS units is shown in Fig. 3. Unit A consists of a delay-compensation module (DCM), a coarse wavelength-division (CWD) multiplexer and a compensation fiber spool (CF) with 1100 m of optical fiber. Unit B consists of a CWD de-multiplexer and a Faraday mirror (FRM). The DCM, multiplexer, de-multiplexer and FRM are thermally stabilized to a constant temperature.

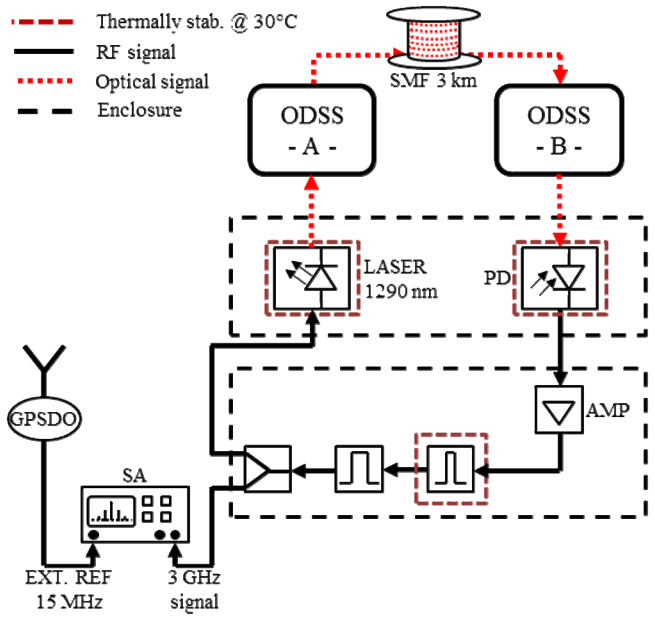


Fig. 1. A block diagram of the OEO with a two-unit ODSS.



Fig. 2. Photograph of the device (OEO with ODSS) used in the experiment.

As shown in Fig. 3, one of the CWDM channels (labeled as λ_{comp} in Fig. 3) is used to measure the group delay through the optical fiber, connecting units A and B. In a device, used in the experiment, a 1330-nm channel was used for monitoring the group delay. The remaining CWDM channels (user channels λ_1, λ_2, λ_3 and λ_4 in Fig. 3) can be used freely. The channel wavelengths were 1290 nm, 1310 nm, 1350 nm and 1370 nm. The number of channels depends on the wavelength-division multiplexer and can be increased.

The group delay is stabilized for all channels and its drift was measured to be less than 1 ps/K/km with this particular system. The system is designed to transfer arbitrary user signals independently from unit A to unit B and vice versa with a constant group delay.

The measurement of the group delay is performed using the DCM. The latter also controls the temperature of the CF to hold the measured group delay constant. The group delay is measured by comparing the phase of the internal UHF oscillator with its reflection from unit B [7]. The internal oscillator was not locked to the external reference. The electro-optical and opto-electrical conversions for the monitoring signal are also performed in the DCM.

In our experimental OEO, a user channel of 1290 nm (λ_1 in Fig. 3) was employed for the OEO's delay line. The measurements that are presented in the following section therefore reflect the stability of the ODSS itself. The group delay of the optical part is constant, even if the OEO does not oscillate. The total length of the optical delay line in our experimental OEO was 4100 m. In addition, the external, 3-km-long, optical fiber and the 1.1-km-long, internal compensation fiber are added to the total length of the optical path in the OEO.

The length of the external optical fiber (connecting unit A and B) affects the maximum temperature span of the environment. In our experiment, the operating environment's temperature span was 15 K. If the length of the external optical fiber were to be doubled, the temperature span would be halved.

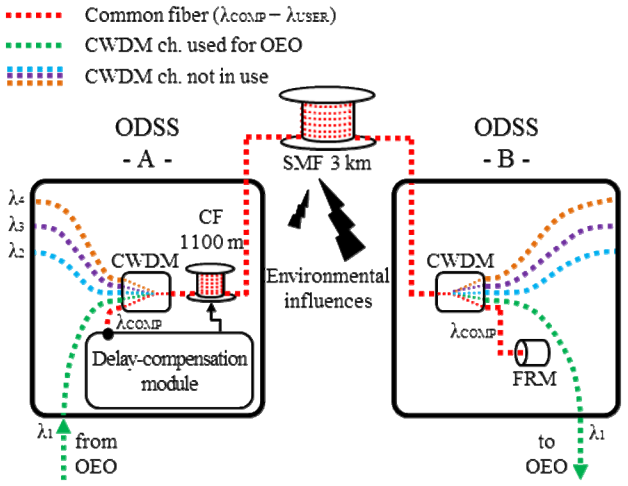


Fig. 3. Block diagram of a multi-purpose ODSS used for fiber-link delay stabilization or OEO frequency stabilization.

B. *Measurement Results*

In our experiment the OEO's frequency was measured over a period of 40 hours in a non-controlled laboratory environment. During the measurement, the temperature of the environment changed by 5.5 K. The maximum frequency change during the time period of 40 hours was 350 Hz. The temperature coefficient of the OEO's frequency was 64 Hz/K or 0.02 ppm/K. The measurement results are shown in Fig. 4. If the stabilization system was turned off, the frequency drift of the OEO was approximately 16 kHz/K.

The single side-band phase-noise spectrum was measured with a two-channel, cross-correlation, signal-source analyzer. The purpose of the phase-noise measurement was not to minimize the oscillator's noise, but to provide a control measurement.

At a 10-Hz frequency offset, the measured phase noise was -58 dBc/Hz. At a 10-kHz frequency offset, the measured phase noise was -123 dBc/Hz. The phase noise spectrum is shown in Fig. 5. The oscillator's output signal power was -11 dBm. The same power level was also at the modulation input of the laser diode. A low power level in the OEO loop enables a wide choice of the appropriate components. However, this is not the optimum situation for phase-noise performance.

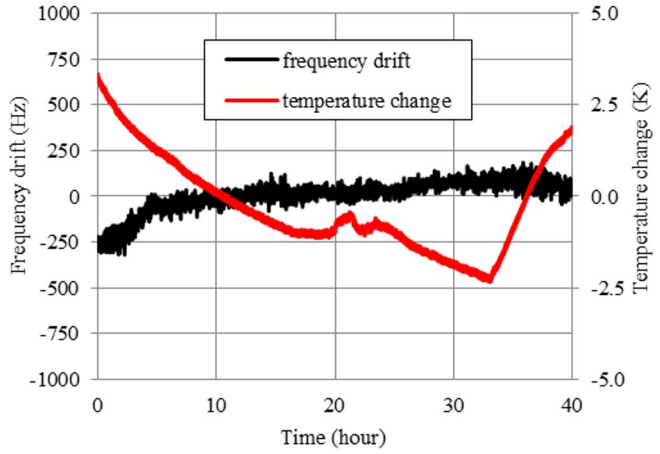


Fig. 4. Measurement of frequency stability during the period of 40 hours.

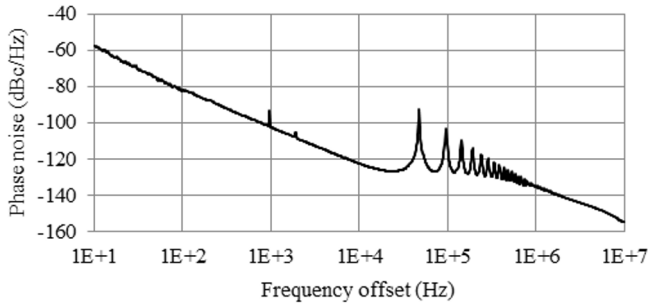


Fig. 5. Single side-band phase-noise spectrum of an experimental OEO with ODSS at 3 GHz.

III. SUMMARY

Our measurements confirm that it is possible to reduce the frequency drift of an OEO with a delay stabilization system, based on CWDM technology and intended for a constant group delay signal transfer.

The frequency drift of an OEO with an ODSS is lower than the method with a frequency discriminator [6]. With a frequency discriminator, a frequency drift of 0.05 ppm/K was achieved. Our experimental OEO also had a lower frequency drift than the method with thermal stabilization [1], where a frequency drift of 0.1 ppm/K was achieved. With the implementation of the ODSS into the OEO, the frequency drift was improved by a factor of 2.5 compared to a frequency-discriminator method. As with these methods, no external reference is needed to achieve the result of 0.02 ppm/K.

Compared to a frequency discriminator [6], an ODSS is convenient and easily operated. The main operating advantage is that no tuning of the oscillator's loop parameters is needed to implement the ODSS into the OEO. The ODSS is very convenient to use since its implementation into the OEO is no different from the connection of a fiber spool only. The length of the total optical path in an OEO with an ODSS is also optional. The length of the optical path only affects the maximum temperature span of the operating environment.

REFERENCES

[1] D. Eliyahu, K. Sariri, M. Kamran, and M. Tokhmakhian, "Improving short and long term frequency stability of the opto-electronic oscillator," in *Proc. IEEE Int. Freq. Control Symp. PDA Exhib.,* 2002, pp. 580-583.

[2] A. S. Daryoush, H. W. Li, G. Bouwmans, D. Decoster, J. Chazelas, and F. Deborgies, "Performance Evaluation of Opto-electronic Oscillators Employing Photonic Crystal Fibers," 2006 European Microwave Conference, Manchester, 2006, pp. 1111-1114.

[3] M. Bagnell, J. Davila-Rodriguez, and P. J. Delfyett, "Millimeter-Wave Generation in an Optoelectronic Oscillator Using an Ultrahigh Finesse Etalon as a Photonic Filter," in *Journal of Lightwave Technology*, vol. 32, no. 6, pp. 1063-1067, March 15, 2014.

[4] K. Xu, Z. Wu, J. Zheng, J. Dai, Y. Dai, F. Yin, J. Li, Y. Zhou, and J. Lin, "Long-term stability improvement of tunable optoelectronic oscillator using dynamic feedback compensation," in *Optics Express*, vol. 23, no. 10, 12935-12941, 2015.

[5] A. Bluestone, D. T. Spencer, S. Srinivasan, D. Guerra, J. E. Bowers, and L. Theogarajan, "An Ultra-Low Phase-Noise 20-GHz PLL Utilizing an Optoelectronic Voltage-Controlled Oscillator," in *IEEE Transactions on Microwave Theory and Techniques*, vol. 63, no. 3, pp. 1046-1052, March 2015.

[6] L. Bogataj, M. Vidmar, and B. Batagelj, "Improving the side-mode suppression ratio and reducing frequency drift in an opto-electronic oscillator with a feedback control loop and additional phase modulation,« in *J. Lightw. Technol.*, vol. 34, no. 3, pp. 885-890, Dec. 2015.

[7] J. Tratnik, U. Dragonja, and B. Batagelj, "Multi-purpose constant-delay optical link," EFTF 2014, pp. 333-335, June 2014.

[8] W. Shillue, "Fiber distribution of local oscillator for Atacama Large Millimeter Array," 2008 OSA Optical Fib. Comm. Conf. and Expo - OFC/NFOEC, OthP6, Feb. 2008.

[9] M. Ferianis, "State of the art in high-stability timing, phase reference distribution and synchronization systems," 2009 Particle Accelerator Conf. – PAC09, WE3GRI02, May 2009.

[10] M. Amemiya, K. Watabe, T. Suzuyama, T. Naito, and H. Tsuchida, "Optical timing distribution system with femtosecond stability," in *IEEJ Trans. on El. and Electronic Eng.*, vol. 7, no. 1, pp. 187-189, Dec. 2012.

COEO Phase locking and performance optimisation

R. Khayatzadeh, V. Auroux, A. Fernandez, O. Llopis

LAAS-CNRS, Université de Toulouse, CNRS, UPS, Toulouse, France
7 avenue du Colonel Roche, 31031, Toulouse, France
rkhayatz@laas.fr

***Abstract*—In this paper, a coupled optoelectronic oscillator (COEO) is phase locked to a low noise RF oscillator in order to reduce the phase noise close to the carrier. Biasing current of the optical semiconductor amplifier (SOA) and a varactor diode in the RF part of the COEO are used as two different actuators to perform phase locking. The lock on the optical device is finally simpler and more efficient than the lock on the RF loop. In the second part of this paper, phase noise of the COEO is reduced by more than 15 dB using a chirped Bragg filter that compensates the dispersion of the optical loop.**

Keywords*— *Microwave oscillator; microwave optics; optoelectronic oscillator; phase noise; phase locking

I. INTRODUCTION

The significant advance in telecommunication and signal processing systems in the past decades has increased the requirement for high spectral purity microwave and millimeter wave oscillators. Frequency multiplication from highly stable sources, such as quartz sources, is limited by the increase of the noise floor, which is often prohibitive at millimeter wave frequencies. On the other side, convergence of microwave and photonics techniques become very popular to generate highly stable signals in this frequency range [1-3]. Coupled optoelectronic oscillator (COEO) is one of the well-known microwave-photonics techniques able to produce spectrally pure radio frequency and millimeter-wave signals [4], [5]. The main idea behind the COEO is based on the optoelectronic oscillator (OEO) which uses optical storage energy element to achive high spectral purity [3] and [6]. However, in the COEO approach, the laser source and the resonator become the same device. The advantages are the following: no locking circuit is required and a very high equivalent Q factor and efficient spurious mode suppresion can be achieved [4], [5] and [7-9]. The COEO behaves as a resonator based OEO, because the optical signal is going through an optical loop (which increases the effective Q factor) but with an optical source which is part of the system and which intimately depends on the RF signal it generates.

If the devices included in the COEO loops are well chosen, and particularly the active devices (optical and microwave amplifiers), and if the fiber length and dispersion parameters are optimized, low phase noise operation can be achieved. The design of our 10 GHz OEO has already been described elsewhere [10], and thus only the key elements are given here. The phase noise obtained with this set-up is good, but the oscillator remains sensitive at very low offset frequencies to vibrations or thermal fluctuations. Therefore, it is interesting to investigate on the stabilization of the COEO frequency using small bandwidth loops and a quartz-referenced source.

In this work, the 10 GHz COEO is phase locked to a low noise local oscillator in order to reduce the close-in phase noise value. In this approach, two different actuators, one in the RF part and one in the optical part, are tested. The first actuator is the bias current of the semiconductor optical amplifier (SOA) included in the mode-locked laser. The bias current is modulated by the command signal from the servo loop. Recently, there have been some publications on RF phase shifters based on current control of an SOA in a microwave photonic system [11], [14]. This approach relies on Coherent Population Oscillations (CPO) in semiconductor structures [12], [13]. The basic working principle of this approach is to change the group velocity using a sharp variation of the refractive index. This variation of the refractive index originates from the population oscillation induced by the pump and probe signals in a two level system. Based on this approach, biasing current of an SOA allows one to control the delay and phase shift of the RF output signal.

The second actuator is a varactor diode that is placed into the RF part of the COEO. This voltage controlled capacitance is connected in series and changes the phase of the RF signal before the electro optical modulator.

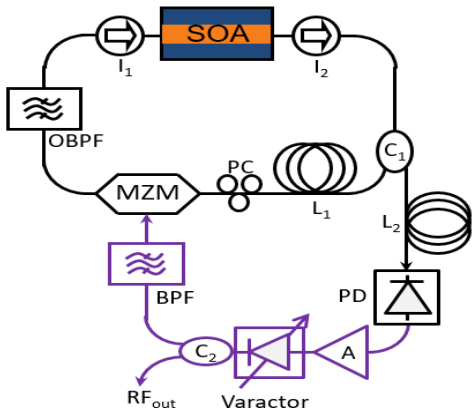


Fig. 1. Experimental setup. SOA: Semiconductor optical amplifier, MZM: Mach-Zehnder modulator, PD: Photodiode, PC: Polarization controller, OBPF: Optical Band-pass filter, BPF: Band-pass filter , C1: optical coupler, C2: RF coupler.

Using this phase locking approach, the phase noise value at 10 Hz offset frequency is reduced by a factor of more than 20 dB and 30 dB for the RF actuator (varactor) and optical

actuator (biasing current of SOA), respectively. In the first step, a simulation on MATLAB Simulink is presented in order to model the phase locking conditions of the COEO from a system point of view.

In the second part of this paper, a dispersion compensation technique using a chirped Bragg filter is presented. Using this technique, the phase noise of the COEO is reduced by 10 dB at 10 kHz offset frequency. The advantage of using a Bragg filter is that the group velocity dispersion of the optical fiber can be compensated independently without changing the optical cavity length. Whereas in the techniques based on dispersion compensating fibers (DCF), one needs to add some meters of DCF fiber in the optical loop. Therefore, the free spectral range (FSR) of the optical cavity will be changed.

II. SIMULATION OF LONG TERM STABILIZATION

The schematic diagram of the system is presented in Fig. 2. The coupled optoelectronic oscillator (COEO) system is considered as a first order system with the response time of one millisecond. The gain of this system is measured and is equal to 50 Hz/mA (current actuator). The output frequency of the COEO is set to an arbitrary value (for example 9.9 GHz) and the aim is to reach to the frequency of the Quartz (for example 10 GHz). An integrator is placed just after the COEO frequency in order to transform frequency to phase. An integrator is also used for the Quartz to transform the output frequency to phase. We need to mention that these integrators are not needed in real experimental realization. However, since in real experiments we use phase detector to phase lock the two oscillators we need to transform frequency to phase. The phase detector constant is 200 mV/rad.

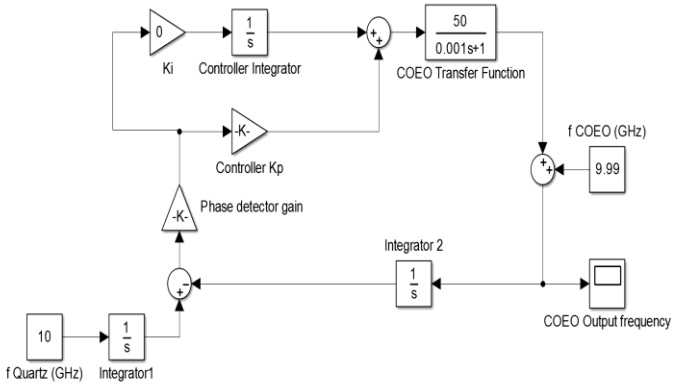


Fig. 2. Schematic diagram of COEO phase locking simulation MATLAB Simulink.

The simulation results for different proportional gain values (Kp) are presented in Fig. 2. In this simulation the integrator gain is set to zero. As can be seen in this figure, the COEO oscillator frequency reaches 10 GHz, which means that it is smoothly locked to the quartz.

III. EXPERIMENTAL SETUP OF LONG TERM STABILIZATION

Fig.1 presents the architecture of the COEO. In this figure, the optical parts and the RF parts are shown by black lines and violet lines, respectively. The SOA is chosen because of its

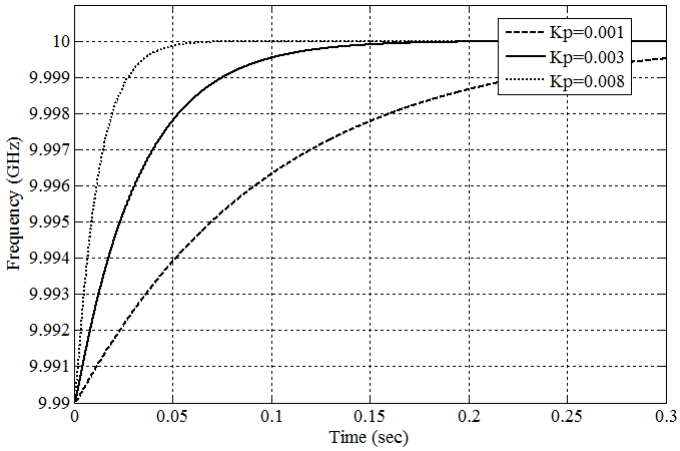


Fig. 3. COEO phase locking simulation MATLAB Simulink results.

compact size and low close to carrier phase noise. The SOA features an output saturation power of 16 dBm and a 30 dB small signal gain. In order to reduce the spontaneous emission of the SOA a 2 nm optical filter is placed in the optical loop. The optical delay line (L1) is a dispersion compensating fiber (DCF) of 100 m combined with 400 m standard single mode fiber (SMF). The optical delay line (L2) is a single mode fiber of 150 m. The second fiber delay (L2) before the fast photodiode enables both the filtering of side modes through Vernier effect and the increase of the optoelectronic loop quality factor. A polarization controller is placed before the modulator to control the polarization of the light at the input of the 40 GHz bandwidth MZM. The RF beat note is amplified, filtered and sent back to the MZM using the RF feedback part. The filter used in this work is a dielectric resonator centered at 10 GHz and features a loaded quality factor of 2500. The varactor placed in the RF part can be used either to adjust the RF phase with a DC voltage (compensation of a drift) or to phase lock the COEO.

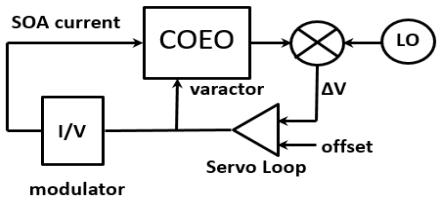


Fig. 4. Schematic diagram of the phase locking system. LO: Local oscillator.

Fig. 4 shows the schematic diagram of the COEO phase locking system. The local oscillator (LO) is a low phase noise Anritsu signal generator. The error signal (ΔV) at the output of the mixer (phase detector) is added to an offset signal and sent to a variable gain servo loop ($0 < G < 40$ dB) and the control signal at the output of the servo loop is sent to one of the two actuators. In case of using current actuator, the command signal is sent to the current modulator of the current controller module (ILX LDC3900). The COEO tuning coefficient obtained with the current is measured and is equal to 50 Hz/mA. The tuning coefficient obtained with the varactor

diode is not linear. It is of 450 Hz/V near 0 V, and drops at 150 Hz/V near 4 V offset.

IV. Results and Discussion

Fig. 5 depicts the measured phase noise for three different scenarios. The black curve presents the phase noise of the free running COEO. The grey curve shows the measured phase noise of the COEO locked on low noise LO using current modulation of the SOA and the brown curve shows the phase noise results for the COEO locked on LO using varactor. As it is shown in this figure, the phase noise value for the locking scenarios at close-in offset frequencies are hugely reduced. This phase noise reduction at 10 Hz offset frequency for the scenario in which the current is used as the actuator is more than 30 dB and for the scenario in which the varactor is used is more than 20 dB. The locking bandwidth for the current actuator is around 500 Hz and around 100 Hz for the varactor approach. In any case, the locking bandwidth is limited by the Q factor of the COEO. The measured microwave Q of this system is in the range of 2 10^6, which corresponds to a half-bandwidth of 2.6 kHz.

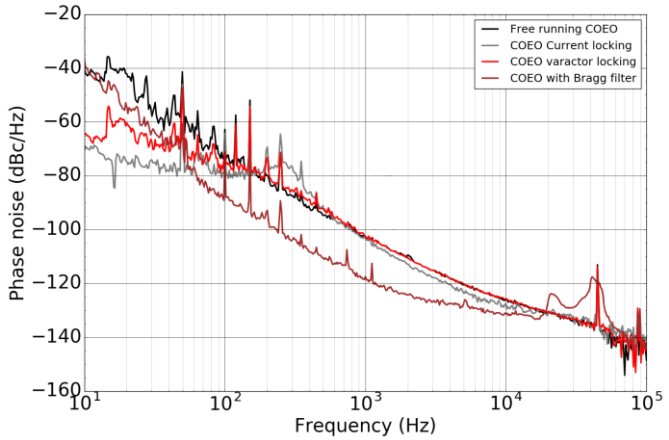


Fig. 5. Phase noise measurement results: free running COEO (black curve), COEO phase locked on LO using current modulation of SOA (gray curve), COEO phase locked on LO using varactor (red curve) and COEO using Bragg filter (brown curve).

V. Dispersion Optimization

Fig. 6 presents the schematic diagram of the experimental COEO based on chirped Bragg filter. As can be seen in this figure, the OBPF and DCF are replaced by a chirped fiber Bragg grating (CFBG) filter with chromatic dispersion of -7 ps/nm and . Considering 400 m SMF fiber with chromatic dispersion of 17 ps/(nm. km) in the optical cavity, we can compensate the GVD utilizing the mentioned CFBG. Another advantage of using a CFBG is that one can remove the spontaneous emission of the SOA which is a large band amplifier.

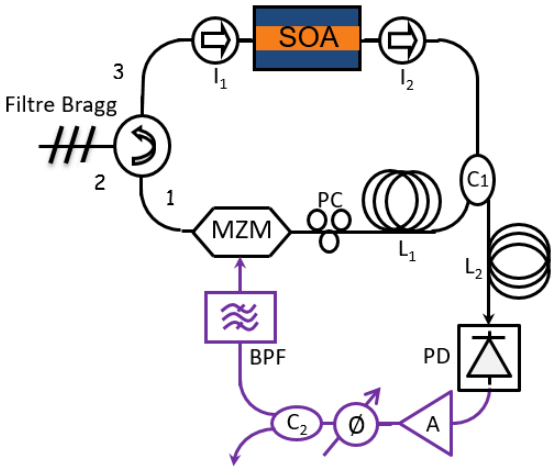


Fig. 6 Experimental setup of the COEO with a chirped Bragg filter.

The phase noise measurement result for the COEO based on Bragg filter is presented in Fig. 5 (brown curve). As can be seen in this figure, the phase noise PSD close to the carrier is hugely reduced. For example at 1 kHz offset frequency the phase noise value of -120 dBc/ Hz is obtained which is 15 dB better than the previous results.

VI. Conclusion

In this work, a 10 GHz COEO is phase locked to a low noise RF oscillator using two different actuators from optical and RF parts of the COEO. The optical actuator is the bias current of the SOA and the RF actuator is a varactor that is placed in the RF feedback part of the COEO. The optical actuator approach appears to be the more efficient one. It is also readily available on any system of this type, and thus very easy to set-up. A dispersion compensation technique utilizing a chirped Bragg filter is also presented in order to optimize the performance of the COEO. Using this technique, a phase noise reduction of more than 15 dB at 1 kHz off-set frequency is observed.

VII. References

[1] J. Yao, «Microwave Photonics,» J. Lightw. Technol., vol. 27, n. 13, pp. 314-335, 2009.

[2] L. Maleki, «The optoelectronic oscillator,» Nature Photonics, vol. 5, pp. 728-730, 2011.

[3] S. Yao and L. Maleki, «Optoelectronic microwave oscillator,» J. Opt. Soc. B, vol. 13, pp. 1725-1735, 1996.

[4] S. Yao and L. Maleki, «Dual microwave and optical oscillator,» Opt. Lett., vol. 22, pp. 1867-1869, 1997.

[5] E. Salik, N. Yu and L. Maleki, «An ultralow phase noise coupled optoelectronic oscillator,» IEEE Photon. Technol. Lett., vol. 19, n. 16, pp. 444-446, 2007.

[6] K. Saleh, P. H. Merrer, O. Llopis and G. Cibiel, «Optoelectronic Oscillator Based on fiber Ring Resonator: Overall System Optimization and Phase Noise Reduction,» in IEEE-Int. Frequency Control Symposium, Baltimore, 2012.

[7] N. Yu, E. Salik and L. Maleki, «Ultralow-noise mode-locked laser with coupled optoelectronic oscillator configuration,» Opt. Lett., vol. 30, n. 110, pp. 1231-1233, 2005.

This work is supported in part by the Direction Générale de l'Arrmement (French MoD) and by Région Occitanie.

[8] F. Quinlan, C. Williams, S. Ozharar, S. Gee and P. Delfyett, «Self-stabilization of the optical frequencies and the pulserepetition rate in a coupled optoelectronic oscillator,» J. Lightw. Technol., vol. 26, n. 115, pp. 2571-2577, 2008.

[9] S. Yao, L. Davis, and L. Maleki, «Coupled optoelectronic oscillator for generating both RF signal and optical pulses,» J. Lightw. Technol., vol. 18, n. 1, pp. 73-78, 2000.

[10] V. Auroux, A. Fernandez, O. Llopis, P. Beaure d'Augères and A. Vouzellaud, «Coupled optoelectronic oscillators: design and performance comparison at 10 GHz and 30 GHz» in IEEE-Int. Frequency Control Symposium, New Orleans, 2016.

[11] P. Berger, M. Alouini, J. Bourderionnet, F. Bretenaker and D. Dolfi « Slow light using semiconductor optical amplifiers: model and noise characteristics,» C. R. Physique, vol. 10, pp. 991-999, 2009.

[12] P.-C. Ku, et al., «Slow light in semiconductor quantum wells,» Opt. Lett. , vol. 29, pp. 2291–2293, 2004.

[13] J. Mørk, et al., «Slow light in a semiconductor waveguide at gigahertz frequencies,» Opt. Express, vol. 13, pp. 8136–8145, 2005.

[14] P. Berger et al., «intermodulation distortion in microwave phase shifters based on slow and fast light propagation in semiconductor optical amplifiers,» Opt. Lett., vol. 35, pp. 2762-2764, 2010.

Low Phase Noise 10 GHz Coupled Optoelectronic Oscillator

O. Lelièvre, V. Crozatier, G. Baili, P. Nouchi, D. Dolfi, L. Morvan
Thales Research & Technology
1, avenue Augustin Fresnel
91700 Palaiseau, France

F. Goldfarb, F. Bretenaker
Laboratoire Aimé Cotton
CNRS, Univ. Paris-Sud, ENS
Cachan, Université Paris-Saclay,
Rue du Belvédère
91400 Orsay, France,

O. Llopis
Laboratoire d'Analyse et d'Architecture des Systèmes
LAAS, CNRS, Univ. de Toulouse
7, avenue du Colonel Roche
31031 Toulouse, France

***Abstract*— We present our recent results on a 10 GHz coupled optoelectronic oscillator (COEO). With a total of 550 m of fiber, the COEO exhibits phase noise level of -140 dBc/Hz at 10 kHz and -137 dBc/Hz for the first spur.**

Keywords*— *Microwave photonic; Coupled Optoelectronic Oscillator; COEO; Optoelectronic Oscillator

I. INTRODUCTION

High purity microwave signals at high frequency (above 1 GHz) are of primary interest for various applications, including telecommunication, navigation, and RADAR systems. The usual way to provide GHz range oscillators consists in multiplying the output of ultra-stable low frequency quartz oscillators. However the multiplication process inherently degrades the phase noise performances of the oscillator.

Optics can provide elegant and competitive alternative solutions for low phase noise high frequency oscillators. One of them is the optoelectronic oscillator (OEO) [1] which uses long optical fibers with low propagation losses as the high-Q element on the oscillator. However, as the fiber is made longer to reach a lower phase noise, the rejection of the non-oscillating side modes of the optoelectronic cavity becomes poorer. Introducing a second loop with a different optical delay leads to a reduction of the level of these spurs [2], at the expense of complexity. Moreover, the laser used to carry the RF signal can set a limit to the phase noise performances, both at low offset frequency (because of its frequency noise) and high offset frequency (because of its relative intensity noise) [3].

Another alternative lies in coupled OEOs (COEO) [4] where the CW laser is replaced by a high-Q optical loop (see Fig. 1). This optical loop corresponds to a harmonically active mode-locked laser (MLL), which provides low phase noise and high repetition rate pulse trains. Moreover, the coupling of the MLL with the optoelectronic loop leads to a high rejection of cavity spurs. Both loops can be made with rather short fibers, which can ease the further integration of the device [5]. In this paper, we present our recent results on the phase noise optimization of low-phase noise 10 GHz COEOs at 1.5 µm.

II. EXPERIMENTAL RESULTS

The COEO under study is pictured in Fig. 1. The MLL is built with an optical fiber and a semiconductor optical amplifier (SOA) as active medium. An optical isolator ensure unidirectional oscillation, while the the optical fiber can be adjusted in terms of length and dispersion. The optoelectronic loop is composed by an optical fiber delay line, a fast photodiode, and RF components imposing a sufficient RF gain for the loop to oscillate (RF amplifier) at 10 GHz (RF filter). The two loops are coupled together through an optical coupler and a Mach-Zehnder intensity modulator (MZM). Finally, a RF phase shifter is used to match the resonances of both cavities at the oscillation frequency.

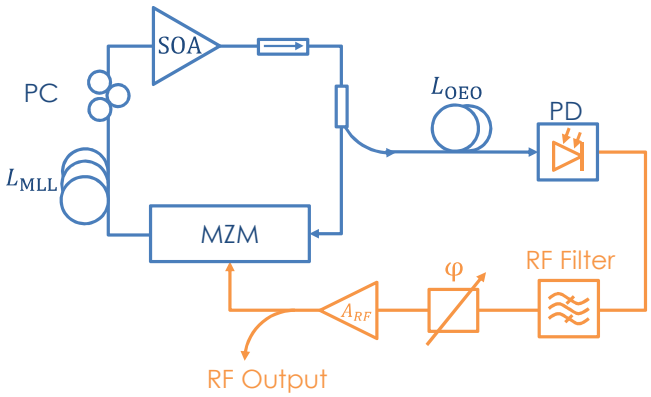


Fig. 1. Schematic setup of a COEO (SOA: Semiconductor Optical Amplifier, PC: Polarisation Controller, PD: Photodiode MZM : Mach Zehnder Modulator, A_{RF} : RF amplifier, φ: Phase Shifter)

As in the case of a classical OEO, the optical fibers properties must be carefully chosen. Longer fibers in both optoelectronic and laser cavities will induces a better filtering of the circulating RF signal, but may also induce a large spur level due to the non-oscillating side modes. Because of the phase-locking in the MLL, the dispersion of the laser cavity must also be taken into account. Indeed, the phase noise of harmonically actively mode-locked laser depends on the cavity dispersion [6]. Moreover, the RF gain on the optoelectronic loop is enhanced when the pulse is compressed on the detector, provided it is not saturated [7]. Hopefully, in the 1.55 µm telecom window region, it is easy to adjust independently the

length and the dispersion of the cavities by using a combination of commercial standard, dispersion-shifted or dispersion compensating fibers.

For the optical loop, we selected a 500-m long dispersion-compensating fiber (DCF), to limit the net dispersion of the cavity, and benefit from short pulses at the detection without the need for large dispersion management. Consequently, only 50 m of dispersion-shifted fiber (DSF) is used in the optoelectronic loop. The RF components (filter, amplifier) detailed in previous experiments [3] are used in this work.

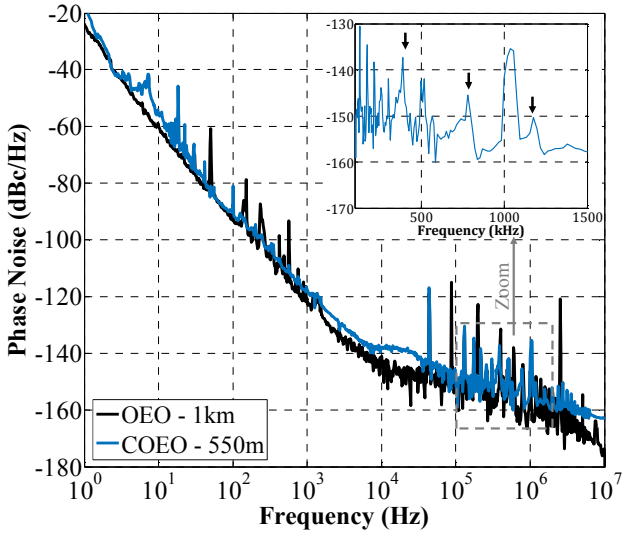


Fig. 2. Phase Noise of the COEO at 10 GHz with 500 m of DCF in the MLL, and 50 m of DSF in the optoelectronic loop (blue). Comparison with the OEO of reference [3] based on 1 km fiber. In the inset, the black arrows indicates the position of the COEO spurs.

The COEO phase noise performances are characterized using a Keysight E5052B signal-source analyzer. The cross correlation number was set to 100 at 1 Hz in order to reach a low noise floor. The results are shown in Fig. 2. Phase noise levels of -118 dBc/Hz at 1 kHz and -140 dBc/Hz at 10 kHz are achieved. The first spurious peak corresponding to the COEO parasitic mode is located at 388 kHz as expected from the laser cavity length, with a noise level of -137 dBc/Hz. The sharp peaks close to it are measurement spurious. These results are comparable to the state-of-the-art of dual-loop OEOs [3], but are obtained with shorter fibers, and close to the state-of-the-art of COEOs [5].

Ongoing work will focus on the modeling and further optimization of the COEO. Because of the use of DCF in the laser cavity, the intra-cavity pulses are short and may lead to non-linearities in the SOA. Dividing the cavity length in two fibers, with opposite dispersion signs could circumvent the problem.

III. Conclusion

We implemented a low phase-noise COEO based on a DCF optical loop, and DSF optoelectronic loop exhibiting a phase noise equal below -140 dBc/Hz at 10 kHz and above. Optimization of the COEO is on the way.

Acknowledgment

Authors would like to thanks the DGA (Direction Générale de l'Armement) for its financial support and fruitful discussions. The work of O. Lelièvre, V. Crozatier, G. Baili, P. Nouchi, D. Dolfi, L. Morvan, F. Goldfarb, and F. Bretenaker is performed in the framework of the joint research laboratory between Laboratoire Aimé Cotton and Thales Research & Technology.

References

[1] X. S. Yao and L. Maleki, "Converting light into spectrally pure microwave oscillation," Optics Letters, 1996.

[2] D. Eliyahu and L. Maleki, " Low phase noise and spurious level in multi-loop opto-electronic oscillators," Frequency Control Symposium : Proceedings, 2003.

[3] O. Lelièvre, V. Crozatier, G. Baili, P. Berger, G. Pillet, D. Dolfi, L. Morvan, F. Goldfarb, F. Bretenaker, and O. Llopis, " Ultra low noise 10 GHz dual loop optoelectronic oscillator: experimental results and simple model," Frequency Control Symposium : Proceedings, 2016.

[4] X. S. Yao and L. Maleki, "Dual microwave and optical oscillator," Optics Letters, 1997.

[5] E. Salik, N. Yu, and L. Maleki, "An Ultralow Phase Noise Coupled Optoelectronic Oscillator," IEEE Photonics Technology Letters, 2007.

[6] S. Gee, S. Ozharar, J.J. Plant, P.W. Juodawlkis, and J.P. Delfyett, "Intracavity dispersion effect on timing jitter of ultralow noise mode-locked semiconductor based external-cavity laser, " Optics Letters, 2009.

[7] A. B. Matsko, D. Eliyahu, and L. Maleki, "Theory of coupled optoelectronic microwave oscillator II: phase noise," Journal of Optical Society of America, B, 2013.

Towards magnesium optical lattice clock: Spectroscopy with 40 Hz linewidth

N. Jha, S. Rühmann, D. Fim, K. Zipfel, S. Sauer, W. Friesen, W. Ertmer, and E. M. Rasel
Institut für Quantenoptik
Leibniz Universität Hannover
Hannover, Germany
jha@iqo.uni-hannover.de

***Abstract*— We present the progress towards the first realization of an optical lattice clock based on the Bosonic ^{24}Mg $^1S_0 - {}^3P_0$ optical transition. We achieve the highest Q-factor for Mg with linewidths below 50 Hz which allows a precise determination of the systematic shifts.**

Keywords—Optical lattice clock, Magnesium, Frequency standard

I. INTRODUCTION

Optical lattice clocks utilizing the high-Q transitions of alkaline earth (-like) elements have surpassed the current state of the art fountain clocks in both stability and uncertainty. Being one of the alkaline earth elements, magnesium also possesses all the qualities relevant for an optical frequency standard. The demonstration of Mg optical lattice clock has so far not been possible due to a rather large tunneling induced broadening in the optical lattice trap. In the present work, we report on the improvements in the optical lattice setup to suppress the tunneling induced linewidth broadening to below 50 Hz allowing us to achieve the highest Q-value of 1.6×10^{-13} for the Bosonic Mg.

II. CLOCK TRANSITION SPECTROSCOPY

In the Mg optical lattice clock experiment at IQ Hannover, we interrogate the bosonic atoms trapped in an optical lattice in the Lamb-Dicke regime. The interrogation laser is stabilized to a high finesse ULE cavity, reaching frequency stability of 4×10^{-16} in 1 second. Building on our previous work [1] on measuring the magic wavelength for the magnetic field induced [2] ^{24}Mg $^1S_0 - {}^3P_0$ clock transition, we further improve the optical lattice setup that allows us to reach trap depths of 50 E_{Recoil}. Such a deep optical lattice created within an enhancement cavity intertwining the vacuum chamber allowed us to reduce the tunneling induced line broadening as well as to more precisely measure the lattice induced AC-Stark shifts. Having suppressed the lattice contributions to the linewidth, we could observe the influence of the probe laser intensity as well as the homogeneous magnetic field on the measured clock transition linewidth. Improvements in the atom loading efficiency to the optical lattice, and an improved normalized detection scheme with higher S/N ratio allowed us to perform spectroscopy at low magnetic and probe laser fields. Following these improvements, we could reduce the linewidth to below 50 Hz. This reduced linewidth allows us to perform more precise determination of various systematic shifts influencing our frequency measurements. We will present these improved systematic shift measurements and the progress towards a frequency measurement against the available frequency standards at PTB via the 73 km long optical fibre link [3].

This work was supported in part by Deutsche Forschungsgemeinschaft (DFG) within QUEST, Center for Quantum Engineering and Space-Time Research. Moreover we acknowledge financial support from DFG Research Training Group (Graduiertenkolleg) 1729, the Marie Curie Initial Training Network FACT (ITN-FACT) Program, call FP7-PEOPLE-2013-ITN and the DLR BOOST project.

ACKNOWLEDGMENT

We acknowledge K. Gibble, M. Safranova, U. I. Safranova and S.G. Porsev for the theoretically support. We are immensely grateful to A. Bauch from Physikalisch Technische Bundesanstalt (PTB) for providing the passive H-maser. We also thank O. Prudnikov for helpful discussions.

REFERENCES

[1] A. P. Kulosa, D. Fim, K. H. Zipfel, S. Rühmann, S. Sauer, N. Jha, K. Gibble, W. Ertmer, E. M. Rasel, M. S. Safronova, U. I. Safronova, and S. G. Porsev, Phys. Rev. Lett. **115**, 240801 (2015).

[2] A. V. Taichenachev, V. I. Yudin, C. W. Oates, C. W. Hoyt, Z. W. Barber, and L. Hollberg, Phys. Rev. Lett. **96**, 083001 (2006).

[3] A. Pape, O. Terra, J. Friebe, M. Riedmann, T. Wübbena, E. M. Rasel, K. Predehl, T. Legero, B. Lipphardt, H. Schnatz, and G. Grosche, Opt. Exp. **18**, 21477 (2010).

Optical-clock local-oscillator universal interrogation protocol for zero probe-field-induced frequency-shifts

T. Zanon-Willette
and R. Lefevre
LERMA, Observatoire de Paris,
PSL Research University,
CNRS, Sorbonne Universités,
UPMC Univ. Paris 06, F-75005,
Paris, France
Email: thomas.zanon@upmc.fr

A.V. Taichenachev
and V.I. Yudin
Novosibirsk State University,
ul. Pirogova 2, Novosibirsk 630090, Russia
Institute of Laser Physics, SB RAS,
pr. Akademika Lavrent'eva 13/3,
Novosibirsk 630090, Russia

***Abstract*—Optical clock interrogation protocols, based on laser-pulse spectroscopy, are suffering from probe-induced frequency-shifts and their variations induced by laser power. Original Hyper-Ramsey probing scheme, which was proposed to alleviate those issues, does not apply below fractional frequency changes of 10^{-18} when decoherence and relaxation by spontaneous emission or collisions are present. We present a universal interrogation protocol based on composite laser-pulses spectroscopy with phase-modulation for both fermionic and bosonic optical clocks, eliminating probe-induced frequency-shifts at all orders even in presence of various dissipative processes. This scheme, using a magic combination of $\pm\pi/4$ and $\pm 3\pi/4$ phase-modulated generalized Hyper-Ramsey resonances, extremely robust to errors in laser parameters, can be applied to atomic, molecular and nuclear frequency metrology, mass spectrometry and precision spectroscopy.**

I. Composite optical-pulses spectroscopy, decoherence and relaxation

A new class of optical clocks is now developed based on very narrow atomic transitions interrogated by composite pulses spectroscopy for robust compensation of laser probe-induced frequency-shifts [1]. But in presence of radiative corrections due to decoherence and relaxation by spontaneous emission, the search for an absolute interrogation protocol where these probe-induced frequency-shifts are totally canceled, even for relatively important variations of experimental parameters, still remains open. However, it has been pointed out that the reliability of interrogation schemes against uncompensated probe frequency-shifts and laser power variations might be severely limited by decoherence due to the finite line-width of laser probes being pre-stabilized on high-finesse optical resonators [2], compromising the improvements of further metrological performances [3].

II. Universal elimination protocol of probe-field-induced frequency-shifts

We manage to overcome such a fundamental obstacle by realizing an ultra-robust clock-laser stabilization scheme taking into account atomic decoherence and relaxation by both spontaneous emission and weak collisions as shown in Fig. 1. The error signal is synthesized by repeating and combining several atomic population excitation fraction measurements based on laser phase-modulation [4] of generalized Hyper-Ramsey resonances [5]. A universal interrogation scheme for fermionic and bosonic clock resonances is proposed to eliminate laser probe-induced frequency-shifts at all orders using a combination of $\pm\pi/4$ and $\pm 3\pi/4$ phase-modulated GHR resonances [6] even in presence of various dissipative processes as reported in Fig. 2. The error signal is absolutely protected against probe-induced frequency-shifts at all orders as shown in Fig. 3(a). Note that this ultra-stable error signal is remarkable over a few additional features. It produces a zero crossing point with enhanced immunity to residual offset fluctuations (see Fig. 3(b) with solid dots), insensitive to large pulse area variation, also absolutely independent of a perfect quantum state initialization. It exhibits the same dispersive

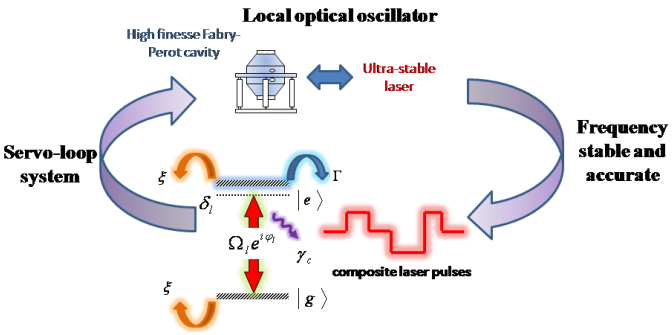


Fig. 1. Optical-clock local-oscillator stabilization scheme based on composite laser pulse spectroscopy probing a fermionic or a bosonic atomic transition perturbed by dissipative processes. The laser induced decoherence is called γ_c, relaxation by spontaneous emission is labeled Γ and ξ is the relaxation rate of the population difference due to collisions.

978-1-5386-2916-1/$31.00 ©2017 IEEE

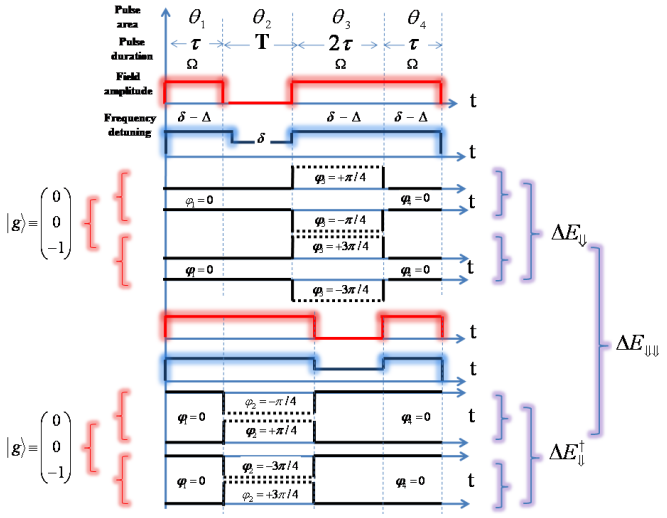


Fig. 2. Universal laser probe interrogation protocol to generate a dispersive error signal free from residual laser probe-induced frequency-shifts when dissipative processes are present. The dispersive error signal is generated by combining two sequences of composite pulses which are reversed in time ordering. Optical pulses are defined by a generalized area θ_l (l = 1,2..,k,..,n), the frequency detuning δ_l, the field amplitude $\Omega_l e^{i\varphi_l}$ including a phase-step modulation φ_l, a pulse duration τ_l and a single free evolution time T applied somewhere at the desired l = k pulse. The general clock frequency detuning is defined by $\delta_l = \delta - \Delta$ where a residual error in pre-compensation of laser probe induced frequency-shift is Δ.

line-shape locked at the unperturbed clock frequency even for non vanishing real and imaginary parts of any optical coherence which may interfered with the laser probe during the composite pulse spectroscopy [7].

III. Conclusion

We have been able to achieve a universal and very robust composite laser-pulses interrogation scheme which exhibits an ultra-stable laser frequency locking-point impervious to any variation of experimental parameters. Our universal scheme has been implemented by combining two sequences of composite laser-pulses that are reversed in pulse order. The probe-induced frequency-shifts are perfectly eliminated at all orders in laser power regardless of the two-level radiative configuration. This new optical-clock local oscillator stabilization scheme, extremely robust to errors in laser parameters, can be applied to stabilize local oscillators in optical clocks based on neutral atoms or single ions [8] and precision spectroscopy.

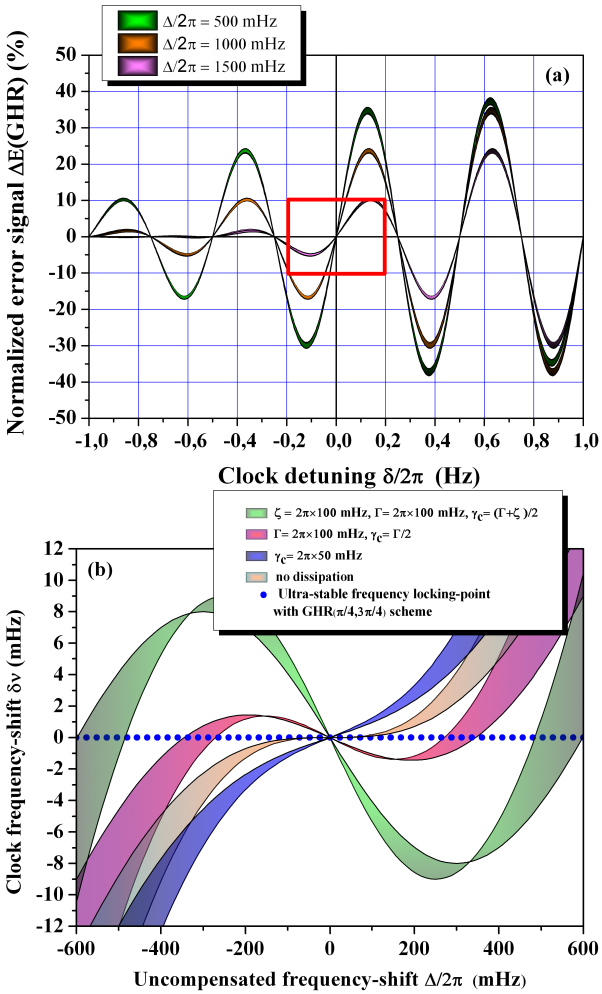


Fig. 3. (a) Typical dispersive error signal versus clock frequency detuning $\delta/2\pi$ used to stabilize the optical-clock local-oscillator. The ultra-stable laser frequency locking-point is delimited by a bounding box around $\delta \mapsto 0$. Resilience of the frequency locking-point to various uncompensated probe-induced frequency-shifts $\Delta/2\pi$ is demonstrated. (b) Robustness of frequency locking-points bsed on HR and GHR$(\pi/4, 3\pi/4)$ protocols versus uncompensated probe-shifts $\Delta/2\pi$ when decoherence, relaxation by spontaneous emission and collisions are toggled on or off. Pulse area variation is set to $\Delta\theta/\theta = \pm 10\%$ (shadow regions). Dissipative parameters of the two-level system used as an atomic frequency reference are fixed to $\gamma_c = 2\pi \times 50$ mHz, $\Gamma = 2\pi \times 100$ mHz and $\xi/2\pi = 100$ mHz. The standard Rabi frequency for all pulses is $\Omega = \pi/2\tau$ where τ is the pulse duration reference. Pulse duration is $\tau = 3/16$ s with free evolution time T = 2 s.

Acknowledgment

V.I.Yudin was supported by the Ministry of Education and Science of the Russian Federation (Project No. 3.1326.2017). A.V. Taichenachev was supported by the Russian Scientific Foundation (Project No. 16-12-00052).

References

[1] T. Zanon-Willette, M. Minissale, V.I. Yudin and A.V. Taichenachev, *Composite pulses in Hyper-Ramsey spectroscopy for the next generation of atomic clocks*, J. Phys.: Conf. Ser. **723** 012057 (2016).

[2] T. Kessler, C. Hagemann, C. Grebing, T. Legero, U. Sterr, F. Riehle, M.J. Martin, L. Chen and J. Ye, *A sub-40-mHz-linewidth laser based on a silicon single-crystal optical cavity*, Nature Photon. **6**, 687 (2012).

[3] V.I. Yudin, A.V. Taichenachev, M.Yu. Basaleev and T. Zanon-Willette, *Synthetic Frequency Protocol in the Ramsey Spectroscopy of Clock Transitions*, Phys. Rev. A **94**, 052505 (2016).

[4] V. Letchumanan, P. Gill, A. G. Sinclair and E. Riis, *Optical-clock local-oscillator stabilization scheme*, J. Opt. Soc. Am. B **23**, 714 (2006).

[5] T. Zanon-Willette, E. de Clercq and E. Arimondo, *Probe light-shift elimination in generalized hyper-Ramsey quantum clocks*, Phys. Rev. A **93**, 042506 (2016).

[6] T. Zanon-Willette, R. Lefevre, A.V. Taichenachev and V.I. Yudin, *Universal interrogation protocol for zero probe-field-induced frequency-shift in high-accuracy quantum clocks*, ArXiv **arXiv:1702.06433** (2017).

[7] J.D. Prestage and S.K. Chung, *Repetitive interrogation of 2-level quantum systems*, Frequency Control Symposium (FCS), IEEE, 220 (2010).

[8] A.D. Ludlow, M.M. Boyd, J. Ye, E. Peik and P.O. Schmidt, *Optical atomic clocks*, Rev. Mod. Phys. **87**, 637 (2015).

A Mercury Optical Lattice Clock with Improved Magic Wavelength Control

Guo C., Favier M., Calvert J., Cambier V., Galland N., De Sarlo L., and Bize S.
LNE-SYRTE, Observatoire de Paris
PSL Research University, CNRS, Sorbonne Universits, UPMC Univ. Paris 06
Paris, France
Email: sebastien.bize@obspm.fr

***Abstract*—We report on the recent improvements of the optical lattice frequency standard at $1.1\,$PHz based on ^{199}Hg operating at LNE-SYRTE. In particular we describe a frequency locking scheme that allows us to trace the frequency of the optical lattice trapping frequency to the SI second down to an accuracy of $100\,$kHz, pushing the limit of the corresponding term in the clock error budget below 1×10^{-18}. Furthermore we will detail preliminary results obtained with a pre-cooling stage giving a bright flux of cold mercury atoms. We finally discuss the impact of the mercury clock for present and future optical frequency comparisons.**

I. Introduction

Comparison between different atomic clock, in the microwave and optical domain, is a cornerstone of time and frequency metrology and a fundamental requirement for the future definition of the SI second based on an optical transition [1], [2].

The value of these comparisons is augmented by the diversity of atomic species that can be nowadays compared. This diversity, as it has always been the case, transcends the realm of pure metrology and leads to important applications in fundamental science [3] and, more recently, in geodesy [4].

In this respect, frequency references based on the ultranarrow $^1S_0$ - $^3P_0$ transition of neutral mercury, at a frequency of $1.1\,$PHz, offer many opportunities for clock comparisons as it was recently demonstrated [5], [6]. This opportunities are naturally further enhanced by taking advantage of the recent availability of long-haul coherent fiber links.

The mercury frequency standard operating at LNE-SYRTE, the only one so far in Europe has a relative uncertainty budget of 1.7×10^{-16}, confirmed by frequency comparison with ^{87}Sr down to a statistical uncertainty of 5×10^{-17} [6]. The main contribution to this uncertainty comes from the linear component of the light shift associated to the optical lattice or linear lattice light shift (LLS).

In this presentation we report on a frequency locking scheme that traces the frequency of the optical lattice trapping frequency to the SI second down to an accuracy of $100\,$kHz which eliminates one important contribution to the uncertainty of the linear LLS.

Furthermore, we will also report on the set-up and characterization of a pre-cooling stage that will allow to improve the operating condition of the mercury frequency standard by providing a bright flux of cold atoms. This will lead to a reduction of the cycle time of the clock, an improvement of the lifetime of the atoms in the lattice, and therefore to a significant reduction of the Dick effect, which is the present limit to the short-term stability of our mercury clock.

After reminding the existing experimental setup, we will briefly summarize the content of the presentation.

II. A Mercury Optical Lattice Clock

Neutral mercury is a promising candidate to build an extremely performing optical lattice clock thanks to several favorable atomic properties. The clock transition is very weakly coupled to static and thermal radiation fields. These two characteristics greatly reduce the efforts needed to control the blackbody radiation shift, one of the limiting factors in almost all the other optical clocks. Additionally, ^{199}Hg has a simple structure with spin for which tensor component of light shift is null and vector component can be exactly canceled when alternatively interrogating the two Zeeman components of the clock transition. Finally, the $^3P_1$ state used for laser cooling has a $1.3\,$MHz linewidth yielding Doppler limited temperatures as low as $30\,$K. This allows for direct loading in the magic wavelength optical lattice from a single stage magneto-optical trap (MOT). Finally, mercury high vapor pressure at room temperature suppresses the need for an oven and thus reduces temperature gradients on the experimental setup and simplifies the MOT loading process.

The experimental clock sequence is as follows. Atoms are directly loaded from a mercury vapor into a MOT. Light for the MOT at $254\,$nm is provided by fourth harmonic generation from a fiber-amplified extended cavity diode laser (ECDL). The MOT is loaded in presence of the optical lattice which is realized by a Fabry-Perot cavity loaded by the second harmonic of a Ti:Sa laser operating at $725\,$nm. After turning off the MOT fields roughly 5% of the atoms are left in the lattice. We then perform a state selection sequence that leaves in $20\,$ms several 10^3 atoms in a single Zeeman component of the $^3P_0$ state. This atomic sample is then interrogated by a Rabi pulse of a duration of typically $80\,$ms of a light source at the clock frequency of $1.13\,$PHz. This frequency is generated, similarly to the cooling light, by the fourth harmonic of a fiber-amplified fiber laser operating at 1062.5nm. In order to probe the narrow clock transition, the laser is stabilized on a $10\,$cm-long Fabry-Perot cavity with a finesse of ~ 850000 and a

978-1-5386-2916-1/$31.00 ©2017 IEEE

thermal relative frequency flicker noise floor of 4×10^{-16}. The population of atoms transferred to the ${}^1S_0$ state is then detected and the frequency of the clock light is steered according to this information.

III. Locking the lattice frequency to a frequency comb

The magic wavelength for the mercury clock transition lies around $362.5\,\mathrm{nm}$. As pointed out in the previous section, we obtain this wavelength by frequency doubling the light of a Ti:Sa laser at $725\,\mathrm{nm}$.

Unfortunately this wavelenth is too short for our optical frequency comb to count it with a significant SNR. We therefore devised and implement the following scheme. A commercial ECDL emitting at $1450\,\mathrm{nm}$ is sent via an uncompensated optical fiber to the optical frequency comb facility at SYRTE. A beatnote is sent back consisting of the frequency difference between the ECDL light and the closest integer multiple of the comb repetition frequency. The beatnote frequency is stabilised by applying feedback to the extended cavity length. The stabilized ECDL output is then frequency doubled to $725\,\mathrm{nm}$ and a second beatnote is realized with the output of the Ti:Sa laser. This beatnote is offset-locked in frequency by applying feedback to the Ti:Sa laser. When both feedback loops are closed the frequency difference between the Ti:Sa can be traced to the repetition rate of the comb, which is continuously compared to the SYRTE primary frequency reference.

In order to realize a flexible and compliant locking scheme, we implemented a mixed digital and analog chain that will be described in detail in the presentation. The state of both loops can be monitored on-line and adjusted dynamically in order, for instance, to realize a cycle-to-cycle modulation of the lattice frequency during clock operation.

Acknowledgment

This work is funded by the ERC grant AdOC.

References

[1] International Committee for Weights and Measures (BIPM), "Proceedings of session ii of the 104^{th} meeting (15-16 october 2015)," BIPM, Tech. Rep., 2015.

[2] H. S. Margolis and P. Gill, "Least-squares analysis of clock frequency comparison data to deduce optimized frequency and frequency ratio values," *Metrologia*, vol. 52, no. 5, p. 628, 2015.

[3] R. M. Godun, P. B. R. Nisbet-Jones, J. M. Jones, S. A. King, L. A. M. Johnson, H. S. Margolis, K. Szymaniec, S. N. Lea, K. Bongs, and P. Gill, "Frequency ratio of two optical clock transitions in ${}^{171}\mathrm{yb}^{+}$ and constraints on the time variation of fundamental constants," *Phys. Rev. Lett.*, vol. 113, p. 210801, Nov 2014.

[4] C. Lisdat, G. Grosche, N. Quintin, C. Shi, S. M. F. Raupach, C. Grebing, D. Nicolodi, F. Stefani, A. Al-Masoudi, S. Dörscher, S. Häfner, J. L. Robyr, N. Chiodo, S. Bilicki, E. Bookjans, A. Koczwara, S. Koke, A. Kuhl, F. Wiotte, F. Meynadier, E. Camisard, M. Abgrall, M. Lours, T. Legero, H. Schnatz, U. Sterr, H. Denker, C. Chardonnet, Y. Le Coq, G. Santarelli, A. Amy-Klein, R. Le Targat, J. Lodewyck, O. Lopez, and P. E. Pottie, "A clock network for geodesy and fundamental science," *Nature Communications*, vol. 7, pp. 12 443 EP –, 08 2016.

[5] K. Yamanaka, N. Ohmae, I. Ushijima, M. Takamoto, and H. Katori, "Frequency ratio of ${}^{199}\mathrm{Hg}$ and ${}^{87}\mathrm{Sr}$ optical lattice clocks beyond the si limit," *Phys. Rev. Lett.*, vol. 114, p. 230801, 2015.

[6] R. Tyumenev, M. Favier, S. Bilicki, E. Bookjans, R. L. Targat, J. Lodewyck, D. Nicolodi, Y. L. Coq, M. Abgrall, J. Guna, L. D. Sarlo, and S. Bize, "Comparing a mercury optical lattice clock with microwave and optical frequency standards," *New Journal of Physics*, vol. 18, no. 11, p. 113002, 2016. [Online]. Available: http://stacks.iop.org/1367-2630/18/i=11/a=113002

[7] M. Petersen, J. Millo, D. V. Magalhaes, C. Mandache, S. T. Dawkins, R. Chicireanu, Y. Lecoq, O. Acef, G. Santarelli, A. Clairon, and S. Bize, "Magneto-optical trap of neutral mercury for an optical lattice clock," in *2008 IEEE International Frequency Control Symposium*, May 2008, pp. 451–454.

NEMS Infrared Detectors based on High Quality Factor 50 nm Thick AlN Nano-Plate Resonators

Zhenyun Qian, Vageeswar Rajaram, Sungho Kang and Matteo Rinaldi
Electrical and Computer Engineering
Northeastern University
Boston, USA
qian@ece.neu.edu; rinaldi@ece.neu.edu

***Abstract*—This paper reports on the first demonstration of ultra-fast (thermal time constant, τ ~80μs) and high resolution (noise equivalent power, *NEP ~656 pW/Hz$^{1/2}$*) infrared detectors based on high quality factor *50-nm* thick aluminum nitride (AlN) piezoelectric resonant nano-plates. For the first time, we show that by employing nanoscale (*30 nm*) aluminum anchors, both high thermal resistance (R_{th} ~9.2×10^5 *K/W*) and high quality factor (*Q ~1000*) can be achieved in greatly scaled AlN nano-plate resonators. Furthermore, we experimentally demonstrate that the resonant structures are capable of efficiently absorbing short- to mid- wavelength infrared (absorption, η ~47%, for blackbody radiation at *625 °C*) without any additional absorber. These unique features are exploited for the first experimental demonstration of AlN NEMS resonant infrared detectors with highly reduced area (down to *20×22 μm^2*, comparable to the ones of state-of-the-art microbolometers) and over *4*× improved figure of merit (*FoM=1/(NEP·τ)*) compared to what previously achieved by the same technology.**

Keywords—Infrared Detector; Uncooled; Aluminum Nitride; Nano-Plate Resonator; Scaling; Quality factor

I. INTRODUCTION

Nano-electromechanical system (NEMS) infrared (IR) detectors based on AlN nano-plate resonators (NPRs) have shown great potential to replace conventional microbolometers for the next-generation high-performance uncooled IR detectors [1]. The performance of such resonant IR detectors in terms of thermal sensitivity, noise equivalent power (*NEP*) and response time (τ) can be improved by scaling the device volume and simultaneously maintaining high values of quality factor (Q) and transduction efficiency [2]. In fact, thermal detectors based on 50 nm thick AlN NPRs have been reported by our group [3] showing two orders of magnitude improvement in figure of merit compared to previous demonstrations ($FoM=1/(NEP\cdot\tau)\propto\eta\cdot C_0\cdot TCF\cdot Q/t^2$, where η, C_0, TCF and t are the IR absorption coefficient, static electrical capacitance, temperature coefficient of frequency and thickness of the resonant structure, respectively). However, the smallest devices (*28×30 μm^2*) in [3] show limited Q values below *300* (*~1/4* of the ones of larger devices), making them less capable in applications that require high resolution (due to the increased noise). This issue is addressed in this work by mitigating anchor loss in such greatly scaled 50 nm thick AlN NPRs. Nanoscale metal anchors are employed instead of conventional AlN and metal anchors used in [3] to introduce higher acoustic impedance mismatch between the resonant body and the anchors, and therefore reducing the energy loss through the anchors. Such optimization in anchors not only boosts the Q from less than *300* to *1157* for the same design of resonant body in [3], but also increases the thermal resistance (R_{th}) by ~*2* orders of magnitude (due to smaller cross-sectional area of the anchors), resulting in a high-performance IR detector with both high resolution (*NEP ~466 pW/Hz$^{1/2}$*) and fast detection speed (τ ~*164 μs*). Moreover, a record small detector (*20×22 μm^2*, comparable to the ones of state-of-the-art microbolometers) with *NEP ~656 pW/Hz$^{1/2}$* and τ ~*80μs* is experimentally demonstrated thanks to the high Q (*~902*) preserved by the new anchoring scheme and the ultra-thin AlN employed. It is worth noting that the capability of trading response time ($\tau=R_{th}\cdot C_{th}$, where C_{th} is the thermal capacitance of the detector) for higher resolution ($NEP=f_n/\eta\cdot R_{th}\cdot TCF\cdot f_0$, where f_n and f_0 are the frequency noise spectral density and the center frequency of the resonant detector, respectively) by increasing the R_{th} is particularly important for such small-pixel devices due to the higher requirement in resolution (less delivered IR power for a smaller pixel area given a fixed power density). Furthermore, we experimentally demonstrate that the resonant structures are capable of efficiently absorbing short- to mid- wavelength IR (η ~*47%*, for blackbody radiation at *625 °C*) without any additional absorber. These experimental results suggest great potential of the AlN NEMS IR detectors for the implementation of high performance IR cameras.

II. DEVICE DESIGN

In this work, the resonant body of lateral-extensional mode resonators is composed of a *50 nm* thick AlN piezoelectric layer sandwiched by a *30 nm* thick Al interdigitated electrode (IDE) and a *20 nm* thick platinum plate (Fig. 1). The freestanding vibrating structure is supported by two narrow Al anchors from each side (Fig.1 and 2). The thermal isolation of the devices is mainly determined by the anchors as they connect the resonant body to the heat sink (substrate). By completely removing the AlN on the anchors, the heat transfer through the AlN layer is eliminated. On the other hand, such design also increases the acoustic impedance mismatch between the resonant body and anchors hence reduces the energy loss through the device anchors, which is a major source of Q degradation in piezoelectric MEMS resonators operating below 1 GHz. Two different sizes of the AlN NPRs with same anchor dimensions are designed (Fig. 2).

This work was partially supported by NSF CAREER Award: ECCS-1350114.

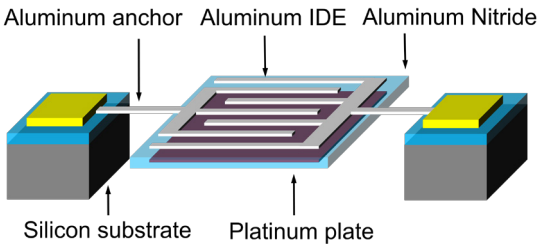


Fig. 1. (a) 3D schematic representation of the AlN nano-plate resonator with nanoscale metallic (Al) anchors.

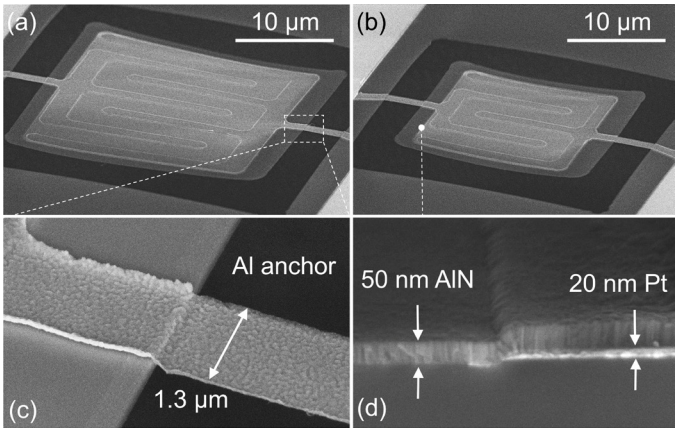


Fig. 2. SEM images of fabricated 50 nm AlN NPRs with lateral dimensions of (a) 28×30 μm² and (b) 20×22 μm². (c) A close-up view of the Al anchor. (d) A cross sectional view highlighting the 20 nm platinum (Pt) and 50 nm AlN thin films deposited on the silicon substrate.

III. Experimental Results

The electromechanical performance of the fabricated devices was measured in a vacuum probe station (Fig. 3), showing that despite the significantly reduced device area, a reasonably high quality factor (*Q ~902*) was achieved for the *20×22 μm²* device (the smallest volume laterally vibrating NEMS resonators reported to date). It is worth noting that the *Q* of the *28×30 μm²* device is *4* times higher compared to the one shown in [3] thanks to the improved anchor design.

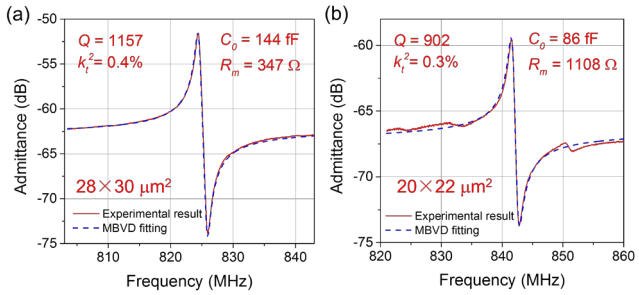


Fig. 3. Measured admittance curves and MBVD fitting of the (a) 28×30 μm² and (b) 20×22 μm² devices.

The *TCF* of the devices were then characterized and found to be ~ *-63 ppm/°C* (Fig. 4). The thermal properties of the two different size devices were estimated based on their geometry and material properties (Table. 1) showing an ultra-low thermal time constant *τ*~ *80μs* for the smaller device. The estimated thermal resistances of the devices (*~2* orders of magnitude higher than the ones in [3]) were confirmed by the self-heating measurement described in [1], showing a reasonable agreement (Table 1). The frequency responses to broadband IR radiation of the devices were also measured in vacuum with a blackbody source (Fig. 5). The IR powers delivered to the devices were estimated based on the device areas and the calibrated power density and found to be *983 nW* and *515 nW* for the *28×30 μm²* and *20×22 μm²* devices respectively. The absorbed powers of the two devices were back calculated based on their frequency responses, measured *TCF* and R_{th}, and found to be *~47%* of the delivered powers for both devices. The frequency noise spectral densities, f_n, of the two devices were extracted by monitoring the short-term (*0.25 ms*) frequency instability and the *NEP* values were calculated to be *~466 pW/Hz^1/2* and *~656 pW/Hz^1/2* for the large and small devices respectively.

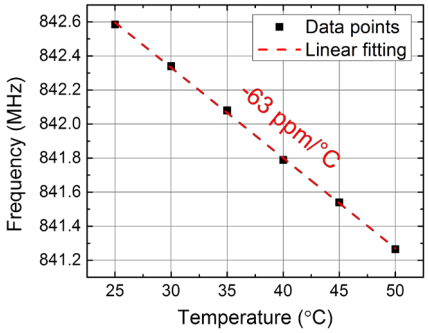


Fig. 4. Measured TCF of the 20×22 μm² device. The high TCF is due to the relatively large temperature coefficient of Young's modulus of the metal electrodes.

TABLE I. Thermal Properties of the IR Detectors

Detector Size (μm²)	Thermal Properties			
	Estimated Rth (K/W)	*Measured Rth (K/W)*	*Estimated Cth (J/K)*	*Estimated τ (μs)*
28 × 30	9.8×10^5	9.1×10^5	1.7×10^{-10}	164
20 × 22	9.8×10^5	9.2×10^5	0.82×10^{-10}	80

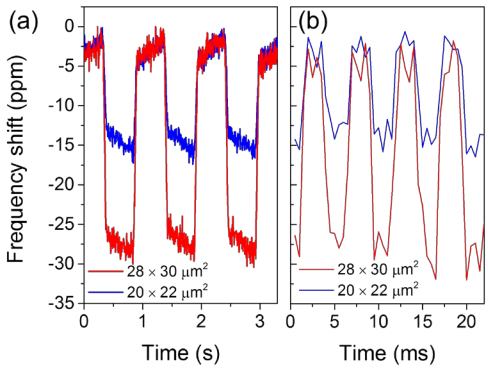


Fig. 5. Measured frequency responses of the two different size devices when exposed to a 625 °C blackbody radiation modulated at (a) 1 Hz and (b) 200 Hz by a mechanical chopper. The unchanged frequency shift with higher chopping frequency (chopper limit) suggests a response time shorter than 5 ms.

References

[1] Y. Hui *et al.*, *Nat. Commun. 7:11249*, doi:10.1038/ncomms11249, 2016.
[2] Z. Qian *et al.*, *IFCS 2016*, pp. 1–3, doi: 10.1109/FCS.2016.7563552.
[3] Z. Qian *et al.*, *Proc. Hilton Head 2016*, pp. 58–59.

An Ultra-Sensitive Piezoelectric-on-Silicon Flapping Mode MEMS Lateral Field Magnetometer

Sagnik Ghosh, *Student Member, IEEE*
Department of Electronic Engineering
City University of Hong Kong
Kowloon, Hong Kong
sghosh5-c@my.cityu.edu.hk

Joshua E.-Y. Lee, *Senior Member*
State Key Laboratory of Millimeter Waves, Department of Electronic Engineering, City University of Hong Kong
Kowloon, Hong Kong
josh.lee@cityu.edu.hk

***Abstract*—We experimentally demonstrate the sensing of lateral magnetic fields using the piezoelectric effect in a resonant MEMS thin-film piezoelectric-on-silicon (TPoS) CMOS-compatible magnetometer. The proposed out-of-plane flapping resonant mode offers strong electromechanical coupling through the piezoelectric Aluminum Nitride (AlN) transducer to enhance the responsivity of the device while operating at atmospheric pressure. The responsivity is here defined as the ratio of output motional current to the external magnetic field strength, normalized over the input excitation current of the device. We have experimentally measured a responsivity of 12156 ppm/T while operating the device at a resonant frequency of 159 kHz, despite even an air-damped quality factor of 526 under ambient conditions.**

Keywords—Lorentz force MEMS magnetometer; thin-film piezoelectric-on-silicon (TPoS); responsivity; flapping mode.

I. INTRODUCTION

Electronic compasses have been ubiquitously incorporated into the latest smartphones in the form of Hall-effect sensors or magnetoresistive (MR) sensors [1]. Lorentz force magnetic field sensors based on MEMS technology have emerged as a promising alternative owing to their lower power consumption, commendable resolution, small form factor, and compatibility with CMOS fabrication processes [1].

We have previously presented a Lorentz force magnetic field sensor based on thin-film piezoelectric-on-silicon (TPoS) resonators to detect out-of-plane (*z*-axis) fields [2]. Piezoelectric transduction in TPoS magnetometers offer notably stronger electromechanical coupling efficiency compared to capacitive magnetometers which have been extensively reported to date [1,3]. The stronger coupling from the piezoelectric transducer is exploited to enhance sensitivity to compensate for a lower quality (Q) factor expected when the device is operated at atmospheric pressure. In addition, piezoelectric sensing does not require a DC biasing current as with the case of piezoresistive sensing which increases power consumption and thermal noise [4]. Furthermore, piezoelectric-AlN is also CMOS-compatible [5]. Table 1 compares the responsivity of our device with previously reported Lorentz force magnetic field sensors for detection of lateral (*x*-*y* plane) magnetic fields.

This work was supported by a grant from the Research Grants Council of Hong Kong under project number CityU 11211116.

The responsivity of a magnetic field sensor is defined here as the ratio of the output modulated current from the device over the applied external magnetic field density, normalized with respect to the input excitation current. Given that the Lorentz force applied to the device scales proportionally with the input excitation current, normalizing over the excitation current provides a more direct comparison of the sensor's scale factor, and is expressed as ppm/T (μA/T.A).

TABLE I. SUMMARY OF PREVIOUSLY REPORTED LORENTZ FORCE MAGNETIC FIELD SENSORS (FOR DETECTING LATERAL MAGNETIC FIELDS)

Publications	Transduction	Responsivity (ppm/T)	Condition	Q-factor
This work	Piezoelectric	12156	Air	526
M. Li et al. [1]	Capacitive	1417	Vacuum (0.75 Torr)	10000
V. Rouf et al. [3]	Capacitive	138.7	Vacuum (15 Torr)	300

Pursuant to realizing the capability of detecting fields in all three axes ultimately on a single chip, we here report a TPoS Lorentz force magnetometer for detecting fields in the plane of fabrication (*x*-*y* plane). We here experimentally demonstrate a responsivity of 12156 ppm/T at atmospheric pressure (i.e. no vacuum packaging) by exciting a unique out-of-plane (*z*-axis) flapping resonant mode through Lorentz forces.

II. SENSOR DESIGN AND MODELLING

A schematic of our proposed device is depicted in Fig. 1a. The device comprises an 800 μm wide suspended square plate, which is supported by two tethers on two opposite sides of the square plate. The square plate functions as the resonator to be mechanically actuated by Lorentz forces resulting from the cross product of a line current running along the sides of the plate and a lateral magnetic field. This excitation current is routed through the supporting tethers. As shown in Fig. 1a, an output patch electrode of a piezoelectric transducer stack is placed at the center of the square plate, while the input tracks are routed along the perimeter of the square plate. A pair of AC drive currents (I_{AC}) are applied along the input metal tracks via a pair of differential AC input voltages ($+V_{in}/2$ and $-V_{in}/2$). Applying an external magnetic field along the *y*-axis (B_y) results in a pair of Lorentz forces (F_L) acting normal to plane of

the device along the two free (i.e. unclamped) sides of the square plate. Individual component (F_L) among such a pair of Lorentz forces can, therefore, be mathematically expressed as,

$$F_L = LI_{AC} \times B_y \tag{1}$$

where L denotes the effective length of the current carrying input metal trace.

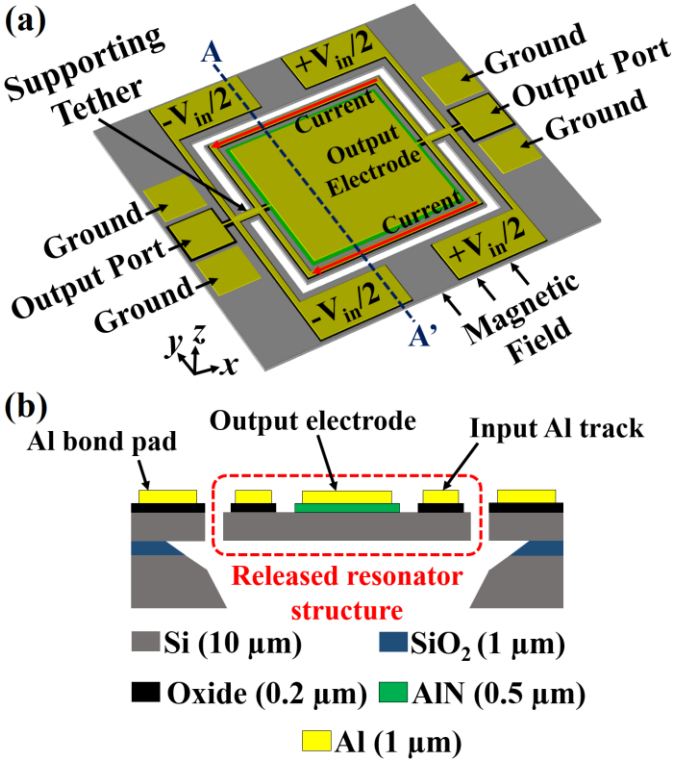


Fig. 1. (a) Perspective view schematic of the flapping mode based resonating TPoS magnetometer with required biasing configuration. (b) Cross-sectional view of the released resonator structure as seen across the line section AA' drawn on the schematic of our proposed device (thicknesses of respective layers are quoted inside the brackets).

The currents (I_{AC}) are applied around the resonant frequency of the intended resonant mode (which is depicted in Fig. 2) to maximize the displacement amplitude of the device as determined by the quality (Q) factor [3]. Fig. 2 shows that the vibration mode can be described by a square plate that flaps along its free edges with the largest displacements at its corners. Based on the displacement profile of the vibration mode shape, we refer this vibration mode as the flapping mode. The flapping mode can be suitably actuated through a set of Lorentz forces applied normal to the plane of the device along the free (i.e. unclamped) edges of the square plate where most of the displacement occurs. At resonance, the displacement amplitude of the resonator is amplified by the Q-factor associated with the flapping mode relative to the off-resonance displacement amplitude. The resulting z-axis displacement (u_m) taken at the corners of the square plate at resonance is given by,

$$u_m = \frac{2F_L}{k}Q \tag{2}$$

where k and Q denote the spring constant and mechanical Q-factor of the device respectively. As shown in Fig. 2, the region where the sum of lateral stresses is maximum is around the center of the square plate where the z-axis displacement is minimal. Conversely, along the edges of the square plate, the sum of lateral stresses is nearly zero. Placing the piezoelectric transducer over the center of the square plate (as shown in Fig. 1a) to coincide with the region of maximum lateral stresses is beneficial to enhancing the electromechanical coupling in the transducer. In the piezoelectric transducer, the surface stress on the resonator is coupled into charges on the top metal electrode through the direct piezoelectric effect. The spatially-dependent charge density (ρ) developed on the piezoelectric transducer resulting from the direct piezoelectric effect is given by [2],

$$\rho = d_{31}T_x + d_{32}T_y \tag{3}$$

where T_x and T_y represent the stress components along x- and y-directions respectively, while d_{31} and d_{32} denote the piezoelectric coefficients that relate the vertical electric displacement (i.e. across the thickness of the transducer film) to the x- and y-axis stresses (i.e. within the lateral plane of the transducer film) respectively. It should be noted that the bottom silicon layer (which has a thickness of 10 µm) serves as the ground electrode for the device. Hence, the total charge (q) induced on the output patch electrode on the top of the Al-AlN-Si piezoelectric transducer stack can be computed by integrating the charge density (ρ) over the surface area of the output patch electrode. To determine the coupling efficiency of the piezoelectric transducer, we have here defined the electromechanical coupling factor (η) as the ratio of the induced total output charge (q) over the displacement amplitude (u_m) of the device at the resonance [6]:

$$\eta = \frac{q}{u_m} \tag{4}$$

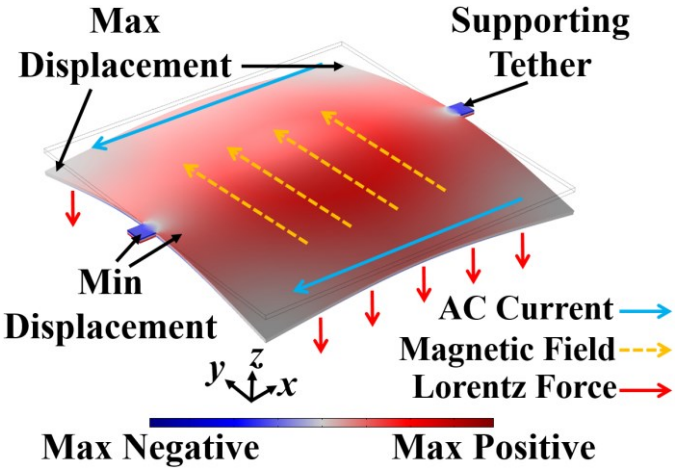


Fig. 2. Lateral plane stress profile (given by sum of stress components in the x and y axes) associated with the out-of-plane flapping mode of the resonant MEMS magnetometer obtained by FEA simulation using COMSOL. Note that maximum z-axis displacement occurs at the corners of the plate, while displacement at the supporting tethers is minimal. A simulated resonant frequency of 159.35 kHz was obtained for a 800 µm wide square plate.

The total output charge stored on the output electrode is modulated at the resonant frequency, yielding an output modulated current (I_{out}) given by the product of the resonant radian frequency (ω_n) of the device and the total output charge (q). From equation (4), I_{out} is therefore a function of the electromechanical coupling factor (η) and the displacement amplitude (u_m) of the resonator:

$$I_{out} = \omega_n \eta u_m = (2\pi f_n)\eta \frac{2F_L}{k} Q \qquad (5)$$

where f_n is the resonant frequency (represented in Hz) of the device. Using equation (1) and (5), the responsivity (R) of the device can be expressed as a ratio of I_{out} over the external lateral magnetic flux density (B_y), normalized against the input excitation AC current (I_{AC}):

$$R = \frac{I_{out}}{I_{AC} B_y} = (2\pi f_n)\eta \frac{2L}{k} Q \qquad (6)$$

We have formulated a finite-element (FE) model in COMSOL multiphysics to simulate the responsivity (R) of our proposed device. The first step of our FE simulation involves an eigenfrequency analysis to determine the resonant frequency of the flapping mode, which was found to be 159.35 kHz. In the second step, we have performed a frequency domain analysis, where the device was loaded with a uniformly distributed line force (acting normal to the plane of the device) along the two unclamped edges to mimic the action of the Lorentz force. In the frequency domain analysis, the excitation frequency was swept around the resonant frequency (obtained previously from the eigenfrequency analysis). The FE model yields a responsivity (R) of 10238 ppm/T.

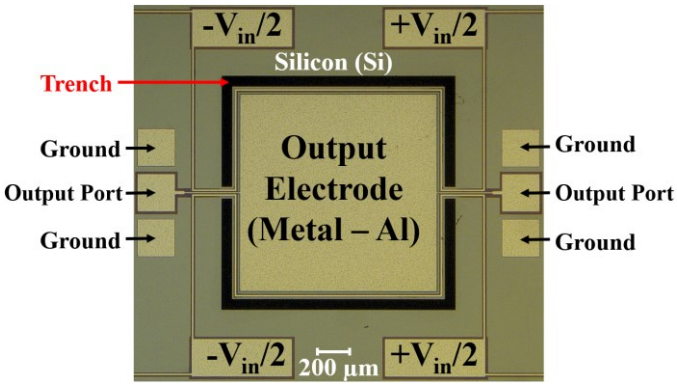


Fig. 3. Optical micrograph of the fabricated flapping mode based resonant MEMS magnetometer.

The device was fabricated using a standard AlN-on-SOI MEMS process. An optical micrograph of our fabricated device is depicted in Fig. 3, while Fig. 1b shows the layer-by-layer structure of the released MEMS magnetic field sensor along with the metal (Al) bond pads. The Al tracks for routing the input excitation current and Al bond pads (located on the unreleased portions of the device) are isolated from the bottom silicon layer using a 0.2 µm thick thermally grown oxide layer, while the output patch electrode is placed on top of a 0.5 µm thick piezoelectric-AlN layer.

III. Measurement Results and Discussions

The fabricated device was packaged on a custom-designed printed circuit board with wire bonds as interconnects for testing. We measured the electrical transmission (S_{21}) of our fabricated device in atmospheric pressure using a Bode 100 network analyzer, where the frequency of AC drive currents was swept around the resonant frequency of the device with a span of 5 kHz. A transimpedance amplifier (TIA) with a gain of 4.7 kΩ was connected between the output port of the device and the network analyzer. We first measured the transmission S_{21} of the device with no magnetic field applied to obtain a baseline reading, which we refer to here as the offset. We then measured the S_{21} at increasing field densities. Fig. 4 illustrates a notable amplitude change (by 28 dB) when the device was exposed to an external lateral magnetic field of 2.85 mT relative to having no external magnetic field applied. From the measured S_{21}, we have extracted a mechanical Q-factor of 526 using a model curve fit based on the commonly used LRC equivalent circuit [7].

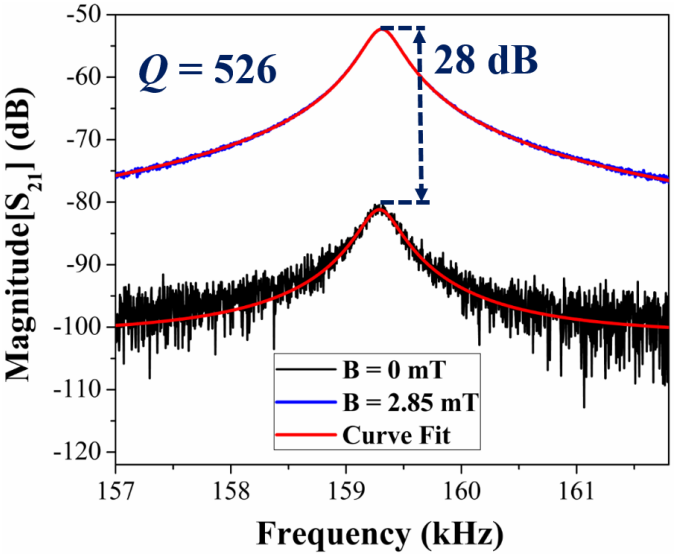


Fig. 4. Measured electrical transmission magnitude of the flapping mode TPoS MEMS magnetometer with and without magnetic field applied.

From equation (1), we see that that the direction of the applied Lorentz force is determined by the direction of the input AC excitation current as well as the polarity of the external magnetic field. Fig. 5 shows that the device is capable of distinguishing between fields where the polarity is reversed using the phase component of the S_{21}. Fig. 5 shows that the S_{21} phase component shifts by 180° when we separately applied fields of the same magnetic field strength (2.85 mT) but with polarities reversed while the biasing configuration for the AC excitation current was kept unchanged.

From the S_{21} curves measured at different magnetic field inputs, we deduced the voltage output at resonance given that the input voltage level is known. The calibration curve in Fig. 6 plots the output voltage for different magnetic field inputs minus the offset voltage (derived from the initial baseline measurement). The negative sign denotes a reverse in the field polarity. The slope of the best fit line defines the sensitivity of the device, which was found to be 0.28 V/T.

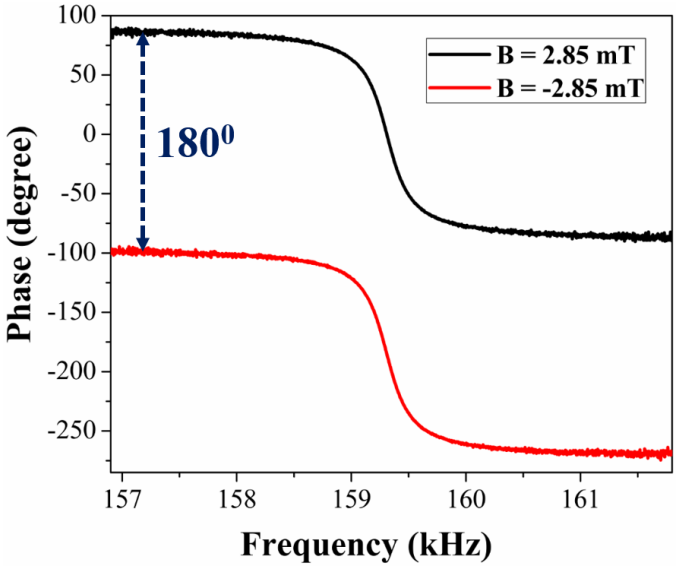


Fig. 5. Measured 180° phase shift in the electrical transmission response when the polarity of the external magnetic field is reversed.

It should be noted that an input AC current of 5 mA was applied during the measurements. Using the responsivity relation in equation (6), and taking into account the gain of the TIA, we obtain a measured responsivity of 12156 ppm/T for our proposed device. This measured responsivity value agrees well with our FE simulated responsivity value of 10238 ppm/T.

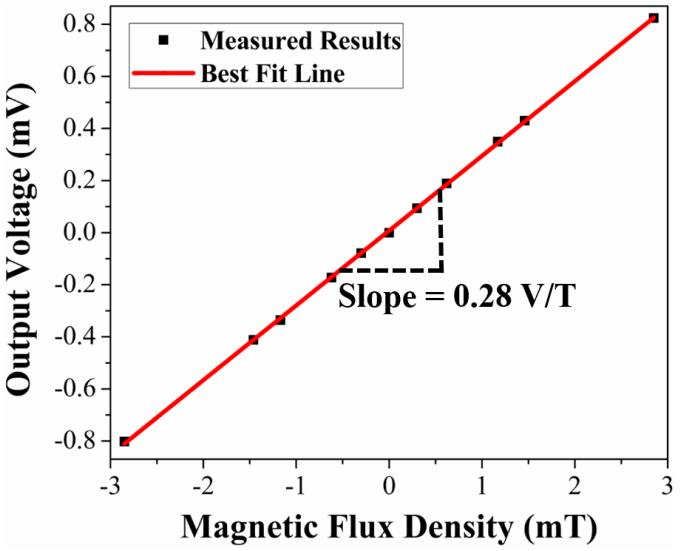


Fig. 6. Measured amplified output voltage as a function of external magnetic field strengths; the slope of the best fit line defines the sensitivity of the device.

A look at the effect of vacuum pressure on the performance of capacitive magnetometers (summarized in Table 1) reveals that the level of vacuum has a notable effect on the Q-factor of the device and thus also the responsivity. By extrapolation, we can expect Q-factors lower than 100 in atmospheric pressure when no vacuum encapsulation is employed. As the readout transducer is based on vertical parallel plate, the benefits from increasing the area of the plate to improve responsivity is counteracted by the increase in squeezed-film damping. As such, vacuum encapsulation is critical for capacitive magnetic sensors. In comparison, the Q-factor of our device measured at atmospheric pressure is much larger than for capacitive vertical plate magnetometers due to the absence of parallel plates. And despite this Q-factor in air being only 5.5% of the high Q-factor for the capacitive magnetometer in vacuum reported in [1], the proposed device still records a net increase in responsivity by 8.5 times compared to the vacuum encapsulated device in [1] due to significantly stronger electromechanical coupling.

IV. Conclusions

In this work, we have successfully designed, fabricated and characterized a resonant micromachined TPoS lateral field MEMS magnetometer with a high responsivity of 12156 ppm/T even in atmospheric pressure. The high responsivity obtained even in atmospheric pressure stems from the strong electromechanical coupling of the piezoelectric transducer that is well matched to the associated strain profile of the unique flapping vibration mode proposed herein.

References

[1] M. Li, V. T. Rouf, M. J. Thompson, et al., "Three-axis Lorentz force magnetic sensor for electronic compass applications," IEEE J. Microelectromech. Syst., vol. 21, no. 4, pp. 1002-1010, August 2012.

[2] S. Ghosh, J. E. Y. Lee "A Lorentz force magnetometer based on a piezoelectric-on-silicon square-extensional mode micromechanical resonator," Appl. Phys. Lett., vol. 110, no. 25, pp. 253507, June 2017.

[3] V. T. Rouf, M. Li, D. A. Horsley, "Area-efficient three axis mems lorentz force magnetometer," IEEE Sensors, vol. 13, no. 11, pp. 4474-4481, November 2013.

[4] E. Mehdizadeh, V. Kumar, S. Pourkamali, "Sensitivity enhancement of Lorentz force MEMS resonant magnetometers via internal thermal-piezoresistive amplification," IEEE Electron Device Lett., vol. 35, no. 2, pp. 268-270, February 2014.

[5] R. H. Olsson, K. E. Wojciechowski, M. Baker, et al., "Post-CMOS-compatible aluminum nitride resonant MEMS accelerometers," IEEE J. Microelectromech. Syst., vol. 18, no. 3, pp. 671-678, October 2009.

[6] G. K. Ho, R. Abdolvand, A. Sivapurapu, et al., "Piezoelectric-on-silicon lateral bulk acoustic wave micromechanical resonators," IEEE J. Microelectromech. Syst., vol. 17, no. 2, pp. 512-520, April 2008.

[7] J. E.-Y. Lee, A. A. Seshia, "Direct parameter extraction in feedthrough-embedded capacitive MEMS resonators," Sens. Actuators A: Phys., vol. 167, no. 2, pp. 237-244, February 2011.

Impact of output metric on the resolution of mode-localized MEMS resonant sensors

J. Juillard, P. Prache, P. Maris Ferreira
GEEPS – UMR 8507 – CNRS, CentraleSupélec, U. Paris-Sud, U. Pierre et Marie Curie
Gif-sur-Yvette, France
jerome.juillard@supelec.fr

N. Barniol
Dpt. of Electronic Engineering
U. Autonoma de Barcelona
Barcelona, Spain

***Abstract*—In this paper, we investigate how additive noise, e.g. thermomechanical noise, impacts the resolution of mode-localized resonant sensing architectures based on two weakly-coupled resonators. Existing work suggests that the resolution of these sensors can be improved by decreasing the coupling coefficient of the resonators. The present work gives an analytical proof that this result does not hold when the ratio of the motional amplitudes of the resonators is used as an output metric, and that, in this case, the sensor resolution is actually independent of the coupling strength. We then extend our proof, supported by transient simulations of a simple model, to other output metrics.**

Keywords— resonant sensors; coupled resonators; thermomechanical noise.

I. INTRODUCTION

Resonant sensing based on coupled MEMS resonators has received considerable interest in the past 5 years [1-5]. The "mode-localization" approach proposed in [1] relies on two (or more) matched resonators coupled through a "weak" restoring force (weak with respect to each resonator's own restoring force). It can be shown that, when the system is stimulated close to one of its resonance frequencies, the ratio of the motional amplitudes of the resonators is highly sensitive to any mismatch of their - uncoupled - natural frequencies (Fig. 1). Other output metrics, such as the relative shift in eigenstate, as in [1], have also been proposed [2]. The sensitivity of such measurements is inversely proportional to the coupling strength (i.e. the ratio of the coupling stiffness to each resonator's stiffness). One may use amplitude ratio measurements for high-sensitivity differential sensing, where one resonator is used as a reference, the other as a sensing cell, to detect infinitesimal changes of its stiffness or mass. In [3], it is reported that the resolution of these sensors is linearly proportional to the coupling strength and that it may consequently surpass that of "conventional" sensors based on a single resonator.

An alternative approach to differential resonant sensing consists in using mutually injection-locked oscillators (MILOs) based on matched MEMS resonators [4-5]. In this closed-loop approach, an electronic mixer is used to enforce the resonators into a synchronized oscillation state, in which the phase difference between the resonators becomes highly sensitive to any stiffness or mass mismatch and can thus provide a differential measurement of a physical quantity of interest [5]. An interesting result in [4] is that, in a MILO, decreasing the coupling strength (in that case, the ratio of the injection signal to each resonator's own feedback signal) results in an increase of the sensor sensitivity, as in mode-localized approaches, but does not improve its resolution.

In spite of many conceptual differences (reactive vs. non-reactive coupling, closed-loop vs. open-loop, etc.), the MILO-based and mode-localized approaches have several similarities. In this paper, we prove that mode-localized sensors based on the amplitude ratio output metric provide measurements whose resolution is independent on coupling strength. Thus, the gain in sensitivity made by decreasing the coupling strength is in fact compensated by an amplification of the additive noise in the system (e.g. thermomechanical), as in the MILO-based approach, and the resolution obtained with this output metric is in fact comparable to that of conventional resonant sensors. We also show that this result is valid for other output metrics such as their phase difference.

In section II, we set the framework and the notations used in our proof. In section III, we study the equations governing the steady-state of the system, and establish the sensitivity of the amplitude ratio and of the phase difference output metrics. In section IV, we study the case when the system is perturbed by additive noise sources Our analytical results are validated with transient simulations of the system. In section V, we compare the results obtained in this paper to prior work, and discuss the relative merits of MILOs, mode-localized approaches, and single-oscillator approaches, in terms of sensitivity and resolution.

II. NOTATIONS AND FRAMEWORK

Consider two nearly-identical coupled linear resonators described by the following non-dimensional model:

$$\begin{aligned} x+\frac{1}{Q}\frac{dx}{dt}+\frac{d^2x}{dt^2}&=\kappa(y-x)+f_x(t)+n_x(t)\\ (1+\varepsilon)y+\frac{1}{Q}\frac{dy}{dt}+\frac{d^2y}{dt^2}&=\kappa(x-y)+n_y(t)\end{aligned} \quad (1)$$

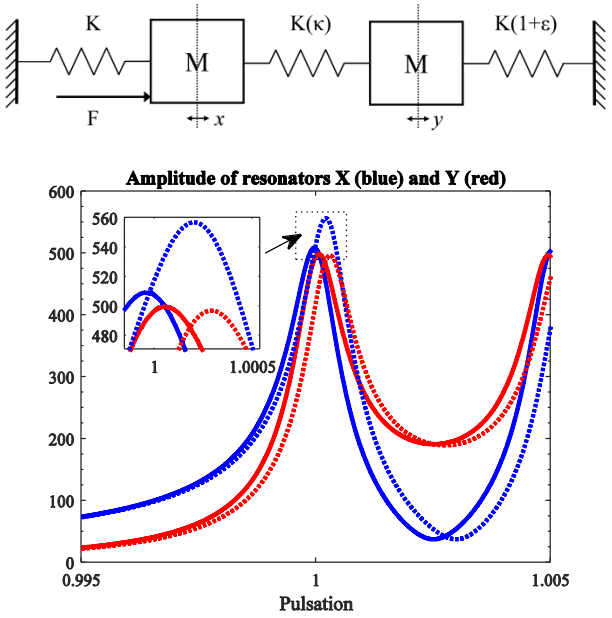


Fig. 1. Top: symbolic representation of a mode-localized sensor as a mass-spring system. Bottom: simulated amplitude responses for varying pulsation, in the case Q =1000, $\kappa = 5\times10^{-3}$, $\varepsilon = 0$ (solid line) $\varepsilon = 10^{-3}$ (dotted line).

where x and y denote the (non-dimensional) position of each resonator, Q >>1 is their quality factor, κ <<1 is the relative coupling strength (i.e. the ratio of the coupling stiffness to the nominal stiffness of the resonators), ε <<1 is the relative stiffness mismatch, $f_x = F\sin\omega t$ is an external force, and n_x and n_y are additive perturbations. These may for example represent the contributions of thermomechanical or electronic noise in the system.

When ε=0 and $\omega \approx 1$, the two resonators oscillate in phase, with the same amplitude. A small variation of ε results in a comparatively large change of the oscillation amplitudes of the resonators (as depicted in Fig. 1), and also in their phase difference. The sensitivity of these output metrics is studied in section III.

III. Sensitivity of Mode-Localized Resonant Sensors

In the absence of perturbations ($n_x = n_y = 0$), the steady-state solution of (1):

$$\begin{aligned} x(t) &= X_\varepsilon \sin(\omega t + \phi_\varepsilon) \\ y(t) &= Y_\varepsilon \sin(\omega t + \phi_\varepsilon + \psi_\varepsilon) \end{aligned} \tag{2}$$

is given by a nonlinear set of equations $\underline{\mathbf{g}}(X_\varepsilon, Y_\varepsilon, \phi_\varepsilon, \psi_\varepsilon) = \underline{\mathbf{0}}$:

$$\begin{cases} \left(1+\kappa-\omega^2\right)X_\varepsilon - \kappa Y_\varepsilon\cos\psi_\varepsilon - F\cos\phi_\varepsilon = 0 \\ \dfrac{\omega}{Q}X_\varepsilon - \kappa Y_\varepsilon\sin\psi_\varepsilon + F\sin\phi_\varepsilon = 0 \\ \left(1+\kappa+\varepsilon-\omega^2\right)Y_\varepsilon - \kappa X_\varepsilon\cos\psi_\varepsilon = 0 \\ \dfrac{\omega}{Q}Y_\varepsilon + \kappa X_\varepsilon\sin\psi_\varepsilon = 0 \end{cases} \tag{3}$$

From (3), it is trivial to establish that:

$$\begin{cases} \tan\psi_\varepsilon = -\dfrac{\omega}{Q\left(1+\kappa+\varepsilon-\omega^2\right)} \\ \dfrac{X_\varepsilon}{Y_\varepsilon} = \dfrac{1}{\kappa}\left(\left(1+\kappa+\varepsilon-\omega^2\right)^2 + \dfrac{\omega^2}{Q^2}\right)^{1/2} \end{cases}, \tag{4}$$

For a given value of the pulsation ω, the sensitivity to mismatch of the phase difference or of the amplitude ratio can be derived from (4) by differentiation with respect to ε. In particular, when ε=0 and ω=1, we find:

$$\begin{cases} S_{\psi_0} = \dfrac{Q}{1+Q^2\kappa^2} \approx \dfrac{1}{Q\kappa^2} \\ S_{X_0/Y_0} = \dfrac{Q}{\left(1+Q^2\kappa^2\right)^{1/2}} \approx \dfrac{1}{\kappa} \end{cases}, \tag{5}$$

where the approximations hold provided κQ >>1, i.e. the two peaks in the frequency response of either of the resonators are well-resolved.

IV. Resolution of Mode-Localized Resonant Sensors

When the system is perturbed by additive noise sources n_x and n_y, one may look for a solution of (1) of the form:

$$\begin{aligned} x(t) &= \left(X_0 + \delta X(t)\right)\sin\left(\omega t + \phi_0 + \delta\phi(t)\right) \\ y(t) &= \left(Y_0 + \delta Y(t)\right)\sin\left(\omega t + \phi_0 + \psi_0 + \delta\psi(t)\right) \end{aligned}, \tag{6}$$

where the amplitude and phase fluctuations are assumed to be small and slowly-varying. Differential equations governing the slow dynamics (hence the spectra) of these fluctuations may be derived using a number of perturbation methods, as in [4]. However, in the present paper, our interest lies in the near-DC terms of these fluctuations (corresponding to close to the carrier fluctuations of x and y), from which the "ultimate" resolution of the different output metrics may be derived. These near-DC terms are governed by a linear set of equations:

$$\underline{\underline{\mathbf{J}}} \times \begin{bmatrix} \delta X & \delta Y & \delta\phi & \delta\psi \end{bmatrix}^T = \begin{bmatrix} n_x^s & n_x^c & n_y^s & n_y^c \end{bmatrix}^T, \tag{7}$$

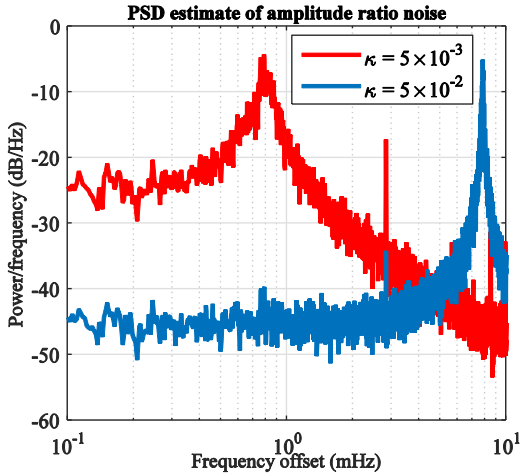


Fig. 2. Spectrum of amplitude ratio fluctuations. Simulation parameters are ω=1, Q =1000, $\varepsilon = 0$. The peak in the response corresponds to the resonance of the out-of-phase mode at frequency offset $\Delta f = \kappa / \pi$.

where $\underline{\underline{\mathbf{J}}}$ is the Jacobian of $\underline{\mathbf{g}}$ at steady-state $\left(X_\varepsilon, Y_\varepsilon, \phi_\varepsilon, \psi_\varepsilon\right)$, and the right-hand term corresponds to the projections of the additive noise on sin(ωt) and cos(ωt). This linear system can be solved analytically. The resolution of each output metric can then be obtained as the ratio of the magnitude of its fluctuations on a (near-DC) frequency band to its sensitivity.

For example, close to in-phase resonance and supposing $\kappa Q >> 1$, we find, when ε=0:

$$\begin{cases} \delta\psi \approx \dfrac{1}{\kappa Q}\dfrac{2n_y^c}{F} \\ \dfrac{\delta X - \delta Y}{X_0} \approx -\dfrac{1}{\kappa Q}\dfrac{2n_y^s}{F} \end{cases}, \tag{8}$$

where the first line corresponds to the phase difference fluctuations, and the second line to the amplitude ratio fluctuations. Both quantities are inversely proportional to κ, as confirmed by transient simulations of (1): for example, Fig. 2 shows the spectrum of the amplitude ratio fluctuations obtained by simulation for two values of κ. The power of the near-DC fluctuations is multiplied by 100 when κ is divided by 10, as predicted by (8). The simulations also show that the spectrum of the phase difference fluctuations is superposed to that of the amplitude ratio fluctuations.

From (5) and (8), the resolution of the amplitude ratio output metric in a frequency band Δf may be expressed as:

$$R_{X_0/Y_0} = \frac{2}{Q}\frac{N}{F}\Delta f^{1/2}, \tag{9}$$

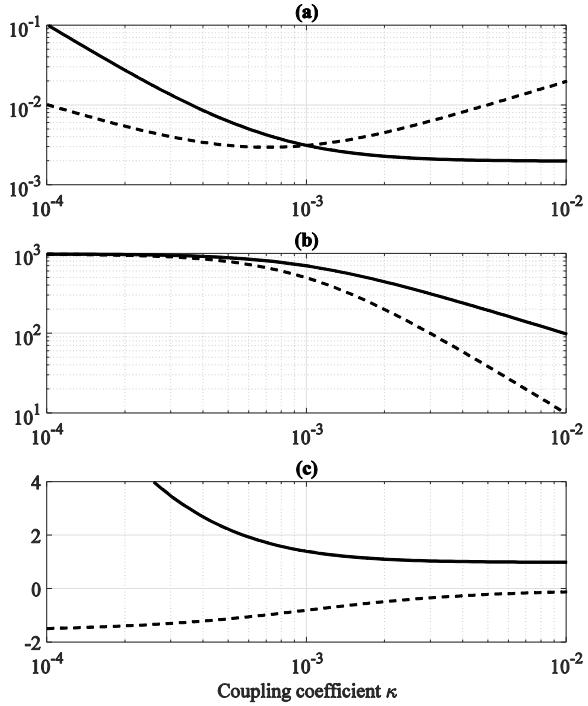


Fig. 3. Resolution (a), sensitivity (b) and value (c) of the amplitude ratio (full lines) and phase difference (dashed lines) output metrics vs. coupling coefficient κ, resulting from the analytical solution of (7). Calculation parameters are ω=1, Q =1000, $\varepsilon = 0$, F =1. The resolution is calculated for a unit noise magnitude and frequency band (N =1, Δf =1).

where N corresponds to the magnitude of the additive perturbations. Hence, the resolution of this output metric is independent of κ. Likewise, the resolution of phase difference measurements can be expressed as:

$$R_{\psi_0} = 2\kappa\frac{N}{F}\Delta f^{1/2}. \tag{10}$$

Thus, the resolution of this output metric is proportional to κ. However, note that (8-10) are established under the assumption that $\kappa Q \gg$. Consequently, as far as metrological performance is considered and provided the assumption is verified, the amplitude ratio is a better output metric than the phase difference.

We show in Fig. 3 how both output metrics behave in terms of resolution and sensitivity for different values of κ. These results are obtained by solving (3) and (7) without any simplifying assumption. It is remarkable that, when $\kappa Q \le 1$, the phase difference becomes a better output metric than the amplitude ratio. One should also stress that the resolution in Fig. 3-a is plotted for a unit frequency band, regardless of the value of κ, even though our simulations (Fig. 2) show that the bandwidth of amplitude ratio or phase difference fluctuations is clearly dependent of κ.

V. DISCUSSION

It may seem surprising that the above results, in particular equation (9), are in contradiction with those in [3], which predict that the resolution of the amplitude ratio output metric is proportional to κ (is, in fact, on the order of κ times the resolution we predict). However, upon close reading, there seems to be a mistake in the derivation of equation (21) in [3]: the authors are clearly interested in determining thermomechanically-induced "close to the carrier" fluctuations of the modal coordinates of the weakly-coupled system. Yet, they integrate the corresponding spectral densities in an angular frequency band $\Delta\omega$ close to ω=0, instead of ω=1 (so that near-DC modal coordinate fluctuations are estimated, rather than close-to-the-carrier ones or near-DC amplitude fluctuations). Consequently, the noise in the system is underestimated by a factor Q. This error, combined with other approximations, leads to an erroneous prediction, in [3], of the resolution of mode-localized sensors.

Within the limits of the framework of the present paper, it appears that mode-localized sensors do not provide any particular advantage in terms of resolution compared to classical resonant sensors based on the measurement of the oscillation frequency of a single resonator [6], [7]. As a basis for comparison, consider an oscillator governed by:

$$(1+\varepsilon)x+\frac{1}{Q}\frac{dx}{dt}+\frac{d^2x}{dt^2}=f_x(t)+n_x(t)\,, \tag{11}$$

where f_x is a feedback-generated (harmonic) force in quadrature with x. With our notations, the sensitivity to ε and the resolution of the angular frequency of such a system are:

$$S_{\omega_0}=\frac{1}{2}\,, \tag{12}$$

$$\delta\omega=\frac{1}{Q}\frac{n_s^x}{F}\Rightarrow R_{\omega_0}=\frac{1}{Q}\frac{N}{F}\Delta f^{1/2}\,. \tag{13}$$

Likewise, consider a MILO-based sensor relying on active "strong" coupling of two resonators through two actuation forces generated with a nonlinear mixer [4] (Fig. 4). With the digital mixing scheme studied in [4-5], the sensitivity to ε and the resolution of the phase difference are:

$$S_{\psi_0}=Q\,, \tag{14}$$

$$\delta\psi=\frac{1}{Q}\frac{n_s^y-n_s^x}{F}\Rightarrow R_{\psi_0}=\frac{\sqrt{2}}{Q}\frac{N}{F}\Delta f^{1/2}\,. \tag{15}$$

Thus, all these architectures have output metrics with comparable resolutions (9) (13) (15), even though their sensitivities (5) (12) (14) differ vastly. In fact, one may design "weakly-coupled" MILO architectures with sensitivities much larger than (14): however, as mentioned in the introduction, this does not improve the resolution of the system, and raises several realization issues (implementation of accurate analog gains, for example) and metrological issues as well (reduction of the locking range of the MILO, and increase of the sensor response time) [4].

In fact, it should be noted that the increase in sensitivity of (mode-localized or MILO-based) coupled sensors usually comes at the cost of a decrease of the range of the measurement, compared to the single resonator case. However, this drawback may be compensated for with proper feedback control techniques (e.g. adjusting the stiffness of resonator x by changing its bias voltage to keep track of the variations of ε), but entails added complexity to the system.

It is our opinion that, more than their large sensitivity, the main interest of sensors based on (actively or passively) coupled resonators is that they can provide differential measurements (i.e. that are insensitive to drift at first order) of the physical quantity of interest. On the other hand, the design of differential architectures based on two nominally-identical, *uncoupled* oscillator loops is quite challenging. In fact, the closer the oscillators are to each other (in order to better eliminate drift), the more likely it becomes that unwanted, parasitic couplings (electrical, mechanical, etc.) affect the normal behavior of the system (through modulation, frequency pulling and locking, etc.). As we have shown in this paper, MILOs and mode-localized approaches are two solutions to this issue with comparable metrological performance.

To be complete, our analysis of mode-localized sensor output metrics should be expanded with a study of their dynamic characteristics. Other application- and context-dependent issues (ease of implementation, compatibility of these approaches with VLSI) should also be considered.

REFERENCES

[1] P. Thiruvenkatanathan, J. Yan, J. Woodhouse , A. A. Seshia, "Enhancing Parametric Sensitivity in Electrically Coupled MEMS Resonators", IEEE Journal of Microelectromechanical Systems, vol. 18, 2009.

[2] C. Zhao et al., "A review on coupled MEMS resonators for sensing applications utilizing mode localization", Sensors and Actuators A, vol. 249, pp. 93-111, 2016.

[3] P. Thiruvenkatanathan, J. Woodhouse, J. Yan, A. A. Seshia, "Limits to mode-localized sensing using micro- and nanomechanical resonator arrays", Journal of Applied Physics, vol. 109, 104903, 2011.

[4] J. Juillard, P. Prache, N. Barniol, "Analysis of mutually injection-locked oscillators for differential resonant sensing", IEEE Transactions on Circuits and Systems – I : regular papers, vol. 63, pp. 1055-1066, 2016.

[5] P. Prache, N. Barniol, A. Uranga, and J. Juillard, "Temperature-drift rejection and sensitivity to mismatch of synchronized strongly-coupled M/NEMS resonators", IEEE MEMS Conference, pp. 1054-1057, 2016.

[6] G. Stemme, "Resonant silicon sensors", Journal of Micromechanics and Microengineering, vol. 1, pp. 113-125, 1991.

[7] A. N. Cleland, M. L. Roukes, "Noise processes in nanomechanical resonators", Journal of Applied Physics, vol. 92, pp. 2758-2769, 2002.

Closed-loop tracking of amplitude and frequency in a mode-localized resonant MEMS sensor

Milind Pandit, Chun Zhao, Guillermo Sobreviela, Aref Mustafazade and Ashwin A Seshia
Nanoscience Centre, Department of Engineering, University of Cambridge,
11 JJ Thomson Avenue , Cambridge CB3 0FF

***Abstract*—In this paper, the amplitude and frequency stability of a mode-localized sensor are characterized in a closed loop setup. The system describes an absolute amplitude ratio sensitivity of 5250 to stiffness perturbations in linear operation. A stability of 432ppm at 500s integration time is observed for amplitude ratio measurements. A resolution of 85ppb corresponding to normalised stiffness perturbations in amplitude ratio measurements is thus demonstrated at 500s integration time. Comparisons to frequency shift sensing within the same device shows that amplitude ratio sensing provides higher accuracies for long term measurements due to intrinsic common mode rejection properties in a mode-localized system.**

I. Introduction

Mode localization in a configuration of Weakly Coupled Resonators (WCRs) have been shown to provide orders of magnitude higher sensitivity in Amplitude Ratio (AR) measurements as compared to conventional single resonator frequency shift measurements [1] [2]. The intrinsic common mode rejection of parametric noise in the amplitude ratio has been credited for its use in long term measurements as a sensor [3] [4] [5].

However, until recently, measurements of the resolution of a mode localised resonant sensor have all been characterised in an open loop configuration, where the resolution is significantly limited by the swept frequency network analyzer measurements. By measuring the minimum observable shift in amplitude ratio through a network analyzer, the resolution of the amplitude ratio of a coupled 2-DOF system was shown to be 0.0096 [6]. Using a similar approach, an open loop experiment on a mode localised accelerometer previously demonstrated a resolution of $619\mu g$ [7].

The oscillator system is adapted from the preliminary designs of the direct feedback oscillator for WCRs that have been shown previously through theoretical calculation and experimental validation[8] [9]. Although, an oscillator design was presented in this work [8], no further stability or resolutions were measured to fully establish the advantages of amplitude ratio measurements over conventional frequency shift measurements.

In this work, the stability, sensitivity and resolution of a prototype mode-localised sensor has been successfully characterized in a closed loop configuration. The paper also compares the resolution of the frequency shift and amplitude ratio as output metrics over a range of integration times, showing an improvement of up to 10x when using amplitude ratio as the readout metric over long integration times ($\tau > 500s$).

II. Experiment

A. Device Description

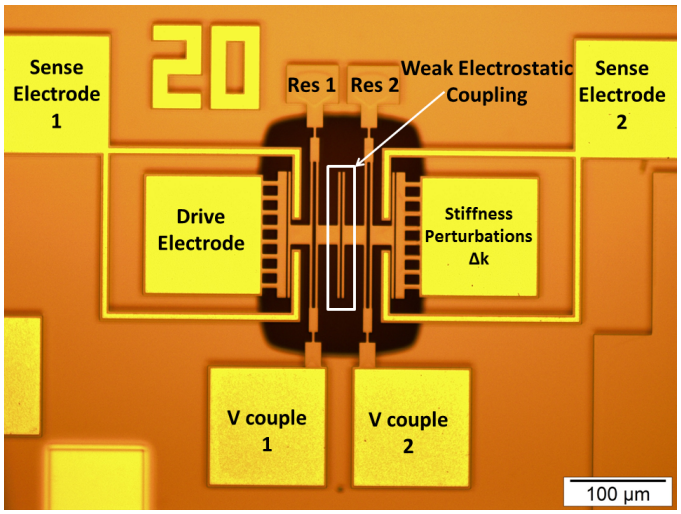


Fig. 1: Optical Micrograph of the device.

Two identical, coupled double ended tuning fork (DETF) resonators were used for this experiment. An optical micrograph of the device is shown in Fig. 1. The structural parameters of the device are provided in Table I. The device was fabricated by MEMSCAP Inc. using SOIMUMPS, a commercial process that uses silicon-on-insulator (SOI) wafers.

TABLE I: Device Parameters

Parameter	Dimensions
Beam Length	350 μm
Beam Width	6 μm
Electrode Length	260 μm
Electrode Width	6 μm
Device Layer Thickness	25 μm
Proof Mass (2 for each DETF)	40 μm $\times$ 40 μm
Electrode Gaps	2 μm

B. Measurement setup

All the experiments were conducted in a custom vacuum chamber at a pressure of 10mTorr without any temperature regulation in the chamber. The two resonators are weakly coupled by an electrostatic spring created by applying a voltage

978-1-5386-2916-1/$31.00 ©2017 IEEE

difference across an air gap electrode arrangement situated between the resonators. The drive electrode is used to drive resonator 1 with a combination of a DC polarization voltage and an AC excitation voltage. The two sense electrodes are biased at the same sense DC voltage and are used to sense the amplitude of vibration of both the resonators. The perturbation electrode is used to apply a DC voltage to introduce a negative stiffness perturbations on resonator 2 for characterization of device sensitivity. The loop is closed using the output current of resonator 1 that is first converted to a voltage through a Transimpedance Amplifier (TIA), then passed through a soft limiter for amplitude control and finally through phase shifters to satisfy the Barkhausen criteria. The experimental setup including the oscillator topology is illustrated in Fig. 2.

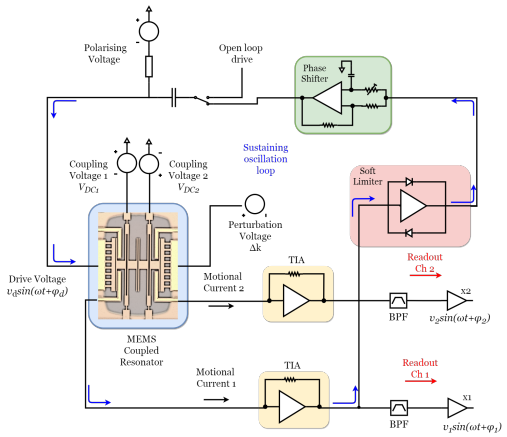


Fig. 2: Experimental Setup.

III. Results and Discussion

A. Stability Analysis

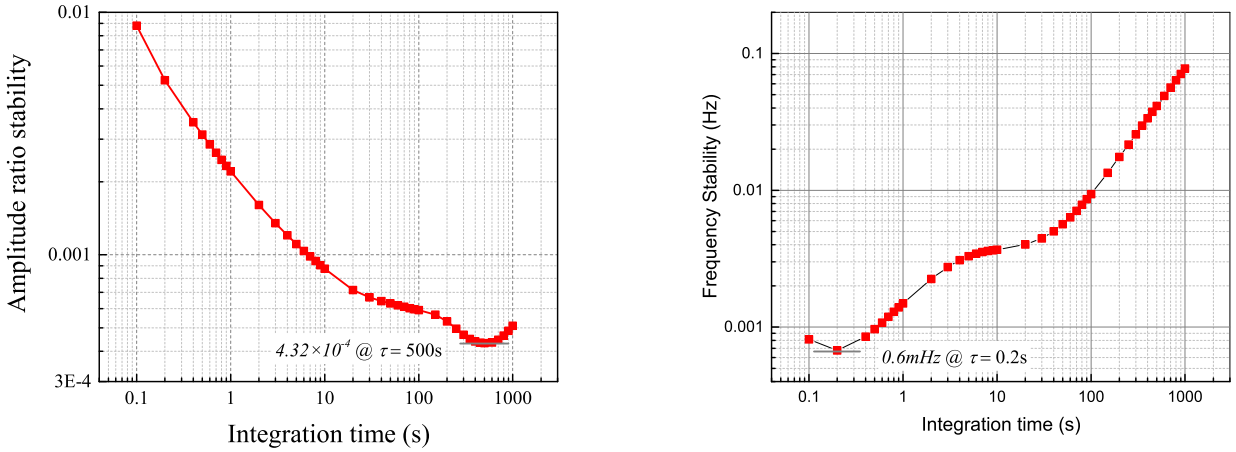
For stability analysis, the coupling voltage was set to 5V to achieve high sensitivity while ensuring that no modal overlap was observed. Furthermore, the resonators were biased to have an amplitude ratio of 10 based on an analysis of the operating range[10]. The loop was then closed in the anti-phase mode and the amplitudes of the respective resonators and the frequencies were measured for 16 hours in order to obtain their long-term stabilities. The stabilities of the frequency and amplitude ratio were characterized by the normalized Allan Deviation and presented for relative comparison in Fig. 3. A best stability of 432ppm in amplitude ratio was observed at $\tau = 500s$ while the frequency stability of 0.6mHz was achieved at $\tau = 0.2s$.

B. Sensitivity Analysis

Next, a sensitivity experiment was performed by applying stiffness perturbations on Resonator 2 while measuring the shift in amplitude ratio as well as frequency. The results are shown in Fig. 4. The results of the closed loop sensitivities of the two resonator amplitudes, the amplitude ratio and the frequency are compared to their open loop counterparts. Due to biasing the system away from the *veering zone*, the amplitude of resonator 1 (X_1) remains relatively constant while that of resonator 2 (X_2) changes with stiffness perturbations. Consequently, there is a a linear shift in amplitude ratio with the application of stiffness perturbations. Thus the amplitude ratio sensitivity to stiffness perturbations can be derived as:

$$S_{AR} = \frac{\partial AR}{\partial(\Delta k/k)} = -5250/(\Delta k/k) \quad (1)$$

The operating region of the oscillator is limited to the anti-phase mode where the modal frequency is insensitive to stiffness perturbations. Therefore, the frequency sensitivity presented in Fig. 4(d), where the closed loop frequency changes by only 2 Hz over the range of the stiffness perturbations, does not represent the maximum sensitivity achieved with frequency shift sensing in this device. In this particular operating region, the in-phase mode has the maximum frequency sensitivity. Due to the symmetry of in-phase mode and anti-phase mode, it is assumed that the frequency stability of in-phase mode is



(a) (b)

Fig. 3: Stability of the amplitude ratio (a), and frequency (b) shown in terms of modified Allan deviation plots

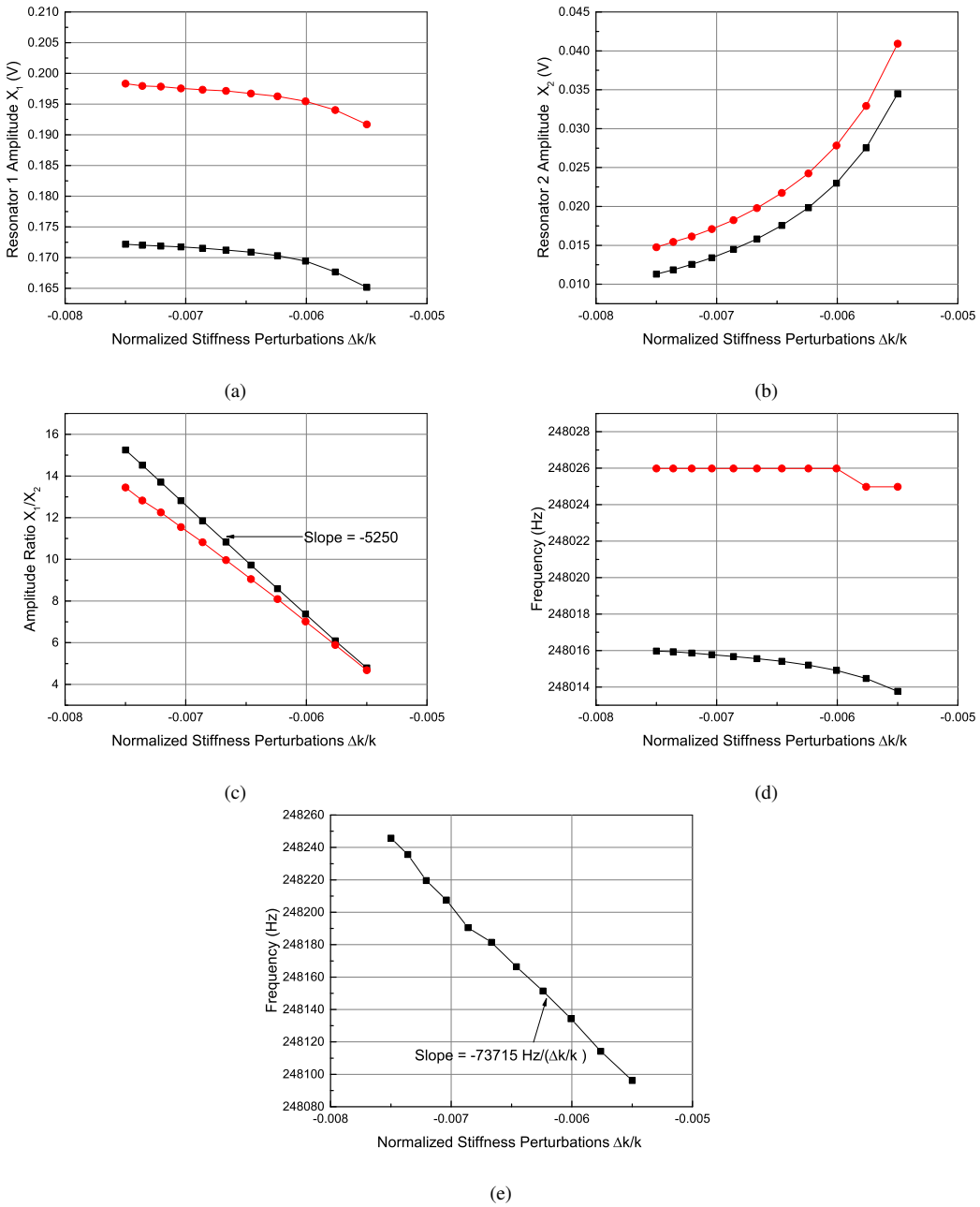


Fig. 4: Sensitivity of amplitude of resonator 1 (a) and resonator 2 (b), amplitude ratio (c), and frequency (d) in open loop (Red) and closed loop (Black) configuration .

similar to the anti-phase mode. To achieve the highest input referred resolution for the frequency shift sensitivity, frequency shifts in the in-phase mode, as shown in Fig. 4(e) are used [9]. With these two assumptions, the open loop frequency sensitivity of in-phase mode can be used as the approximate frequency sensitivity of the device. The sensitivity of the frequency shift output is found to be:

$$S_f = \frac{\partial f}{\partial(\Delta k/k)} = 73715 Hz/(\Delta k/k) \tag{2}$$

C. *Input-referred Stability*

Using the stability and the sensitivity calculated previously, the input-referred stability can be estimated for both amplitude ratio output and frequency shift output from the same device. The input referred stability signifies the minimum normalized perturbation $\langle \frac{\Delta k}{k} \rangle$ that can be sensed by the mode localized system. This can be calculated for amplitude ratio and frequency as follows:

$$\langle \frac{\Delta k}{k} \rangle_{AR} = \frac{\langle AR \rangle}{S_{AR}} \tag{3}$$

$$\langle \frac{\Delta k}{k} \rangle_f = \frac{\langle f \rangle}{S_f} \tag{4}$$

Equation 3 and Equation 4 are used to create the input-referred resolution curves for both amplitude ratio and frequency. These are superimposed upon each other to compare their input-referred stability at a range of integration times ($0.1s \leq \tau \leq 1000s$) in Fig. 5.

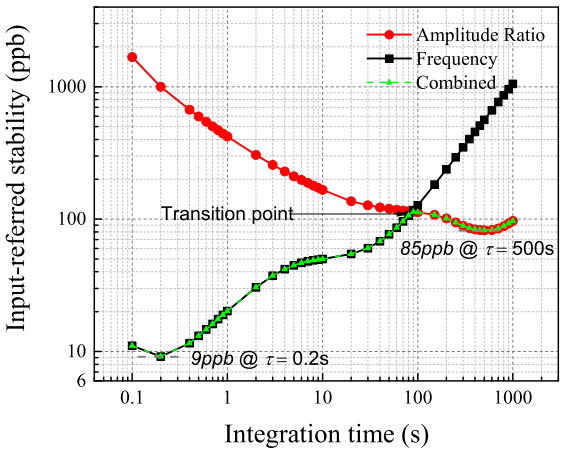


Fig. 5: Input-referred Resolution of frequency shift and amplitude ratio output

A minimum of 9ppb is estimated in the input-referred frequency stability at $\tau = 0.2s$ while a minimum of 85ppb is achieved in the input-referred amplitude ratio stability at $\tau = 500s$. The two curves intersect at $\tau \approx 100s$ after which, the resolution of amplitude ratio sensing is better than that of frequency shift sensing.

The results show that for short integration times (below 100s), frequency shift sensing provides a better measurement resolution. However, for longer integration times, amplitude ratio sensing allows for improved resolution due to the absence of common mode random variations, i.e. first order temperature dependent drifts, that are predominant in frequency shift sensing at larger integration times. The results thus demonstrate the potential benefits of using amplitude ratio shift sensing for applications that require high resolution for long term measurements. Additionally, combining both measurements within a single device could allow for both short-term and long duration high-resolution measurements to be conducted within the same device. Further improvements in amplitude-based readout techniques to reduce the impact of interface circuit noise will also enable measurements requiring both very high resolution and high stability to be conducted within the same MEMS device.

IV. Conclusion and Future Work

This work presents the first characterization of the input-referred resolution for both amplitude ratio and frequency shift output of the mode localized sensor operated in a closed loop setup. The results show that the input-referred stability for frequency shift sensing in the mode localized sensor is better at lower integration times while that of the amplitude ratio sensing is better at higher integration times. This behaviour is attributed to the rejection of common mode variations in amplitude ratio sensing that is predominantly present in frequency shift sensing.

This work also demonstrates the potential practical benefits of the amplitude ratio sensing over the conventional frequency shift sensing. However, there are many parameters that affect the stability of the measured amplitude and those need to be studied thoroughly to improve the stability of the system in both short and long integration times. Studies are being conducted currently to better understand the factors limiting the resolution of the amplitude ratio with the aim to improve the resolution of mode-localized sensing.

V. Acknowledgement

This work is supported by funding from Innovate UK and Natural Environment Research Council.

References

[1] P. Thiruvenkatanathan, J. Yan, J. Woodhouse, and A. A. Seshia,, "Enhancing Parametric Sensitivity in Electrically Coupled MEMS Resonators," *J. Microelectromechanical Syst.*, vol. 18. no. 5, pp. 1077-1086, Oct. 2009

[2] C. Zhao, G. .S Wood, J. Xie, H. Chang, S. H. Pu and M. Kraft, "Comparative study of different output metrics for a three weakly coupled resonator sensor," in *J. Microelectromechanical Syst.*, vol. 25, no. 4, pp. 626-636, 2016.

[3] P. Thiruvenkatanathan, J. Yan, and A. A. Seshia, "Differential amplification of structural perturbations in weakly coupled MEMS resonators," *IEEE Trans. Ultrason. Ferroelectr. Freq. Control*, vol. 57. no. 3,pp. 690-697, Mar. 2009

[4] M. Spletzer, A. Raman, A. Q. Wu, X. Xu, and R. Reifenberger, "Ultrasensitive mass sensing using mode localization in coupled microcantilevers," *Appl. Phys. Lett.*, vol. 88. no. 25,p.254102, Nov. 2015

[5] P. Thiruvenkatanathan, and A. A. Seshia,, "Mode-Localized Displacement Sensing," *J. Microelectromechanical Syst.*, vol. 21. no. 5, pp. 1016-1018, Oct. 2012

[6] P. Thiruvenkatanathan, J. Woodhouse, J. Yan, and A. A. Seshia, "Limits to mode-localized sensing using micro- and nanomechanical resonator arrays," *J. Appl. Phys*, vol. 109. no. 10,p.104903, May. 2011

[7] H. Zhang, B. Li, W. Yuan, M. Kraft and H. Chang, "An Acceleration Sensing Method Based on the Mode Localization of Weakly Coupled Resonators," *J. Microelectromechanical Syst.*, vol. 25. no. 2,pp. 286-296, Apr. 2016.

[8] C. Zhao, M. Pandit, B. Sun, G. Sobreviela, X. Zou and A. A. Seshia, "A Closed-Loop Readout Configuration for Mode-Localized Resonant MEMS Sensors," in *J. Microelectromechanical Syst.*, vol. 26, no. 3, pp. 501-503, Jun. 2017.

[9] C. Zhao, G. .S Wood, S. H. Pu, and M. Kraft, "A Feasibility Study for a Self-oscillating Loop for a Three Degree-of-Freedom Coupled MEMS Resonator Force Sensor," in *Procedia Eng.*, vol. 120, pp. 887-891, 2015.

[10] C. Zhao, G. .S Wood, J. Xie, H. Chang, S. H. Pu and M. Kraft, "A Three Degree-of-Freedom Weakly Coupled Resonator Sensor With Enhanced Stiffness Sensitivity," in *J. Microelectromechanical Syst.*, vol. 25, no. 1, pp. 38-51, Feb. 2016.

Transparent Piezoelectric Transducers for Large Area Ultrasonic Actuators

Daniele Sette, Sebastjan Glinsek, Stéphanie Girod, Nicolas Godard and Emmanuel Defay
Department of Materials Research and Technology
Luxembourg Institute of Science and Technology
Luxembourg
sebastjan.glinsek@list.lu

***Abstract*— This work focuses on the fabrication of transparent piezoelectric transducers on glass substrates for ultrasonic actuation. Transparent Lead Titanate Zirconate (PZT) thin films are grown on glass following a sol-gel route and InterDigital Electrodes (IDE) are patterned by photolithography. The electrodes design aims to optimize the volume of active piezoelectric material together with the transparency of the actuator stack. The actuator is used in d_{33} mode offering high transduction capabilities, while the IDE design allows for increasing the area of the actuator in the cm² range. The results demonstrate that fully transparent actuators with ultrasonic range resonant frequency (~100 kHz) can be fabricated on glass substrates and peak-to-peak displacement of 300 nm is demonstrated. Direct applications of these actuators are haptic devices for tactile sensation of surface roughness.**

Keywords—piezoelectric transducer, transparent electronics, haptic devices

I. AIM OF THE STUDY

Piezoelectric thin films have been extensively deployed in MEMS components [1, 2]. Moreover, recent works have demonstrated the fabrication of PZT thin films on glass substrates exhibiting well-crystallized perovskite phase and transmittance in the visible range higher than 60 % [3, 4].

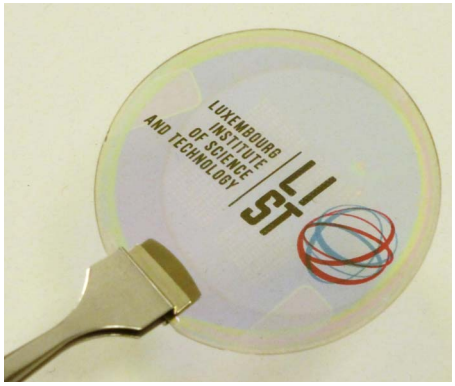


Fig. 1. Fused silica substrate with 20 nm-thick buffer layer, 200 nm-thick crystallized PZT, and aluminum-doped ZnO (AZO) top IDE.

In this work, we aim to develop large area ultrasonic transducers based on thin piezoelectric films that can be integrated on glass. Although piezoelectric haptic prototypes on glass substrates have been realized before [5], the structures employ parallel plates metallic electrodes (PPE), preventing a uniform positioning of the actuators on glass. The choice of transparent IDE opens up numerous design options while keeping transmittance high (cf. Fig. 1, 2).

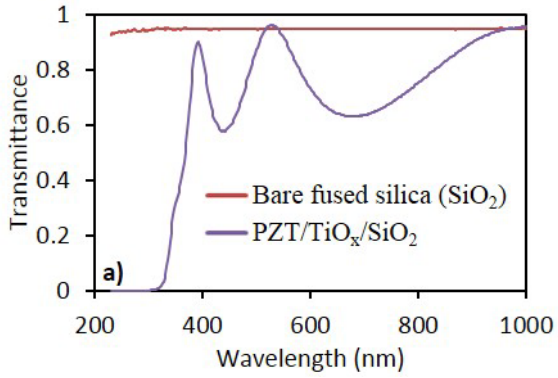


Fig. 2. Optical transmittance of buffered PZT thin film on fused silica substrate.

II. EXPERIMENTAL APPROACH

$Pb(Zr_{0.53}Ti_{0.47})O_3$ films are deposited on fused silica substrates on which ~20 nm-thick buffer layer, i.e., TiO_2 or HfO_2, has been processed. A sol-gel process is used to grow up to 1 µm-thick PZT. A circular IDE design (Fig. 3) is patterned by lift-off lithography with different lateral gaps and electrodes width (2 to 20 µm). Indium tin oxide (ITO) and aluminum-doped ZnO (AZO) were tested as transparent electrodes materials, while Pt and Ti/Au where used as the references. The design allows optimization of the volume of the active piezoelectric material and the capacitance per unit surface. The mechanical resonance is characterized with laser vibrometer (Polytec). Moreover, a specific design was developed to measure an effective d_{33} piezo-coefficient (Aixacct).

III. MAIN RESULTS

The Fig. 1 shows a 2” fused silica wafer (500 µm-thick) with buffer layer, 200 nm-thick PZT and patterned transparent AZO electrodes. Light transmittance, measured in the visible

range, is higher than 60 % (Fig. 2), enabling enough transparency for display utilization. X-ray diffraction and scanning electron microscopy characterization revealed that PZT films with thicknesses up to 1 µm are single-phase polycrystalline perovskites with dense microstructure and no cracks have been detected. Converse piezoelectric measurements on a cantilever-like structure with 200 nm-thick PZT layer yields effective d_{33} value of 140 pm/V.

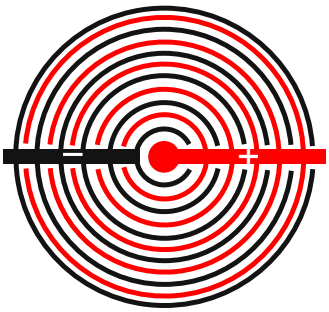


Fig. 3. IDE large area transducer design.

The electrical characterization of an 8 mm-diameter circular actuator with Ti/Au electrodes exhibits at 1 kHz a capacitance $C_0 = 1.1$ nF, with dielectric losses tanσ below 5 % (Fig. 4). It corresponds to a capacitance per unit surface of 2.2 nF/cm², despite the fact that 50 % of the piezoelectric material in the actuator is not active due to zero-field underneath the electrodes. As shown in Fig. 5, the remanent polarization P_r of the 8-mm diameter actuator with 5 µm gap between the electrodes is 20 µC/cm², while coercive voltage is 27 V.

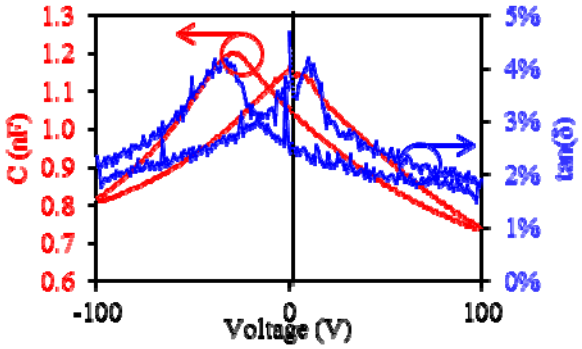


Fig. 4. The 1 kHz capacitance C and dielectric losses tanσ as functions of applied voltage of an 8 mm diameter IDE capacitor on 800 nm-thick PZT layer.

The mechanical resonance of this device, measured with a laser vibrometer, is plotted in Fig. 6. At resonant frequency $f_0 = 104$ kHz peak-to-peak displacement is 32 nm when actuated with a 10 $V_{p\text{-}p}$ sinusoidal voltage, corresponding to a quality factor $Q = 109$ in air. Increase of the actuation voltage to 200 $V_{p\text{-}p}$ and optimization of the impedance LC matching circuit lead to a peak-to-peak displacement of 300 nm at resonance. These results on functional large area and transparent thin films piezo-actuators demonstrate the potential for ultrasonic and haptic applications.

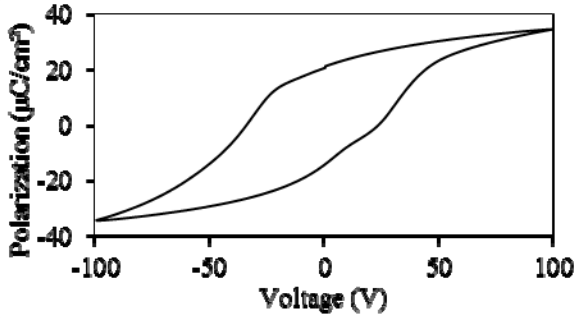


Fig. 5. Polarization P – voltage V hysteresis loop of an 8 mm-diameter IDE capacitor on 800 nm-thick PZT film. Gap between the electrodes is 5 µm.

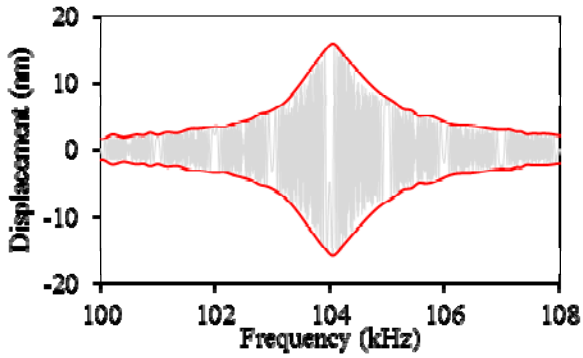


Fig. 6. Resonance of an 8 mm diameter IDE capacitor on 800 nm thick PZT films (10 $V_{p\text{-}p}$ actuation).

REFERENCES

[1] F. Akasheh, T. Myers, J. D. Fraser, S. Bose, and A. Bandyopahyay, "Development of piezoelectric micromachined ultrasonic transducers", Sensor. Actuat. A-Phys., vol. 111, pp. 275-287, 2004.

[2] M. Cueff, E. Defay, P. Rey, G. Le Rhun, F. Perruchot, C. Ferrandon, D. Mercier, F. Domingue, A. Suhm, M. Aïd, L. Liu, S. Pacheco, M. Miller, "A fully packaged piezoelectric switch with low voltage actuation and electrostatic hold", Micro Electro Mechanical Systems (MEMS), 2010 IEEE 23rd International Conference on, Wanchai, Hong Kong, pp. 212-215, 2010.

[3] K. K. Uprety, L. E. Ocola, and O. Auicello, "Growth and characterization of transparent Pb(Zr,Ti)O_3 capacitor on glass substrate", J. Appl. Phys., vol. 102, pp. 084107, 2007.

[4] R.H.T. Wilke, S. Trolier-McKinstry, P.B. Reid, and D.A. Schwartz, "PZT Piezoelectric Films on Glass for Gen-X Imaging", Adaptive X-Ray Optics, Proc. of SPIE, vol. 7803, pp. 780300, 2010.

[5] F. Bernard, F. Casset, J.S. Danel, C. Chappaz, S. Basrour, "Characterization of a smartphone size haptic rendering system based on thin-film AlN actuators on glass substrates", J. Micromech. Microeng., vol. 26, pp. 084007, 2016.

Characterization of Single-Port SAW Resonators at 3.7 GHz Based on Epitaxial $LiNbO_3$ Layers

Alexandre Clairet, Stefania Oliveri, Anthony Almirall, Thomas Baron, William Daniau, and Ausrine Bartasyte
FEMTO-ST Institute, UBFC, CNRS, ENSMM
Time and Frequency department
Besançon, France
Email: alexandre.clairet@femto-st.fr

***Abstract*—The performance of single-port surface acoustic wave resonators based on 150 nm thick Z-axis oriented $LiNbO_3$ films on C-sapphire was studied by means of simulations. The resonance frequencies close to 3.7 GHz were targeted. The dependence of wave velocity and electromechanical coupling on the propagation direction was determined. Effects of a presence of 60° growth domains in films, or changes in Li composition in $LiNbO_3$ layers and thicknesses of piezoelectric film and electrodes on the SAW properties was evaluated theoretically, as well.**

Keywords— $LiNbO_3$; thin films; SAW; high frequency;

I. INTRODUCTION

$LiNbO_3$ (LN) single crystals are widely used for the surface acoustic wave (SAW) devices such as radio frequency (RF) filters and sensors due especially its high electromechanical coupling factor, k^2. Its k^2 is around 5 % for a Rayleigh wave and higher than 10 % for a pseudo-SAW (PSAW), also known as Leaky SAW [1]. To be applied, SAW devices must have low insertion losses and a pure spectral signature. In the case of RF filters, low temperature coefficient of frequency (TCF) and high electromechanical coupling count, as well. So far the frequency of SAW devices based on single crystal technology is limited to the 3.5 GHz. Next generation applications of SAW devices demands operational frequencies at least up to 6 GHz. There are two possibilities to increase the SAW frequency: a creation of guided acoustic waves in the heterostructures and/or a reduction of the period of interdigital transducers (IDTs). However, deep UV lithography is already used at its resolution limits. The possibility to accelerate SAW have been demonstrated theoretically and experimentally for LN films on sapphire or diamond substrates, in which propagation velocities are higher than in LN single crystals [2-4]. In literature, Z-axis oriented epitaxial growth of LN films is the most frequently studied one. The propagation velocities and electromechanical coupling along X- and Y- axis as a function of thickness of Z-LN films on C-sapphire substrates have been estimated by means of simulations and have been confirmed experimentally. It has been shown that these two propagation directions presented different acoustic responses. Little is known about acoustical propagation along other directions in this heterostructure. The as-grown films usually present 60° oriented growth domains, which can be eliminated by growing or annealing films at high-temperature (around 800 °C) [2]. However, at these temperatures Li_2O volatility from films is considerable. The acoustic velocity in $LiNbO_3$ depends on the Li nonstoichiometry, as well. Thus, uncontrolled Li_2O volatility may result in difficulties to reproduce the operational frequencies of acoustical devices based on LN films. In order to optimize the acoustical performance of grown of Z-LN films, it is worth knowing in advance if the presence of 180° domains impacts the propagation properties and if the change of Li nonstoichiometry induces significant modification of frequency.

In this work the complete angular dispersions of propagation velocities and electromechanical coupling were determined numerically for Z-LN films on C-sapphire substrates in order to evaluate the possible effect of the presence of 60 ° growth domains in films. Finite element analysis was used to estimate the effect of Li nonstoichiometry on the acoustical response (frequency, k^2, and TCF) of single-port SAW resonator operating at 3.7 GHz and to compare the compositional effect to the possible fabrication imprecisions (variations in the thicknesses of the piezoelectric film and IDTs).

II. EXPERIMENTAL DETAILS

The main epitaxial relationship of Z-LN films with C-sapphire (Sapp) substrate is $(0001)_{film}||(0001)_{Al2O3}$ and $[11\bar{2}0]_{film}||[11\bar{2}0]_{Al2O3}$ (matrix) and the 60° growth domains present $[11\bar{2}0]_{film}||[\bar{1}\bar{1}20]_{Al2O3}$. According to IEEE convention [5], these two orientations can be named as LN(ZXt)/ψ//Sapp(ZXt)/ψ and LN(ZXt)/ψ+60° // Sapp(ZXt)/ψ. The heterostructure composed of 150 nm thick Z-LN film on C-sapphire substrate was considered in this study. In order to find out theoretically k^2, TCF and resonant frequencies of single-port SAW resonators, 1D and 2D simulations were performed by combined finite element (FEM)/boundary element analysis [5]. The single-port resonator consisted of sixty aluminum IDT pairs and twenty aluminum mirrors on each side of resonator. The thickness of Al and the SAW wavelength were set to 100 nm and 1.4 µm, respectively. Four propagation directions, ψ, in LN films were considered: (ZXt)/0°, (ZXt)/30°, (ZXt)/60°, and (ZXt)/90°. The elastic, piezoelectric and dielectric constants of congruent LN were taken from Kovacs et al. [6] and the equivalent constants for stoichiometric LN were estimated from Kushibiki et al. data

This work was supported by French National Research Agency fundings ANR LiLit (ANR-16-CE24-0022-011), ANR JCJC LiLa (ANR-12-JS04-0008-01), Labex ACTION program (ANR-11-LABX-0001-01), the French RENATECH network, and FEDER Research Grant No. FC0001257-11002 with SMART-INN project.

[7]. The possible variations in thicknesses of electrodes and piezoelectric film were assumed to be ± 5 nm.

III. RESULTS

A. 1D simulations

The dependence of effective permittivity, ε_{eff}, on propagation velocity in Al/LN(ZXt)/0°/Sapp(ZXt)/0° stack (propagation direction is along X-axis), obtained by 1D simulations, is presented in Fig.1. There were observed two SAW modes with v = 4845 m/s (wave ♯1) and v = 5256 m/s (wave ♯2) with purely real effective permittivity. The frequencies of these modes were 3.46 GHz and 3.75 GHz, respectively. These two surface acoustic waves with v = 4906 m/s (f = 3.50 GHz) and v = 5174 m/s (f = 3.70 GHz) were also observed for the LN(ZXt)/60°/Sapp(ZXt)/0° configuration. The change of the wave velocity of these two modes in LN(ZXt)/0°/Sapp(ZXt)/0° and LN(ZXt)/60°/ Sapp(ZXt)/0° heterostructures as a function of propagation direction ($0° \leq \psi \leq 360°$) is illustrated in Fig. 2 a. In the case of LN film matrix and 180° growth domains the angular dispersions of wave velocities and k^2 presented six-fold symmetry. This indicated that the propagation properties along X (Y) and –X (-Y) axes were equivalent. In the case of both growth orientations, the wave ♯2 vanished and wave ♯1 accelerated when propagation direction was parallel to Y or –Y axes ($\psi = 30 + 60n$, where n is integer). The velocity of the wave ♯2 was highest when it propagated along X or –X axes ($\psi = 0 + 60n$). The angular dispersion of velocities of both waves was reduced in LN(ZXt)/60°/Sapp(ZXt)/0° growth domains compared to that of LN(ZXt)/0°/Sapp(ZXt)/0° matrix. In the case of wave ♯1, the minimum value of the velocity was increased from 4845 m/s to 4907 m/s in the 60 °- domains while its maximum value was similar for the both growth orientations. Accordingly, the maximum velocity of wave ♯2 changed from 5280 m/s to 5175 m/s in the secondary orientation.

The change of the electromechanical coupling factor of wave ♯1 and wave ♯2 in LN(ZXt)/0°/Sapp(ZXt)/0° and LN(ZXt)/60°/Sapp(ZXt)/0° heterostructures as a function of propagation direction ($0° \leq \psi \leq 360°$) is presented in Fig. 2 b. In the case of wave ♯2, k^2 was increased by more than a factor of two in 60°-domains (4.25 %) compared to that in the film matrix (1.9 %). The highest k^2 of this wave was observed at $\psi = 0 + 60n$ in both growth orientations. The wave ♯1

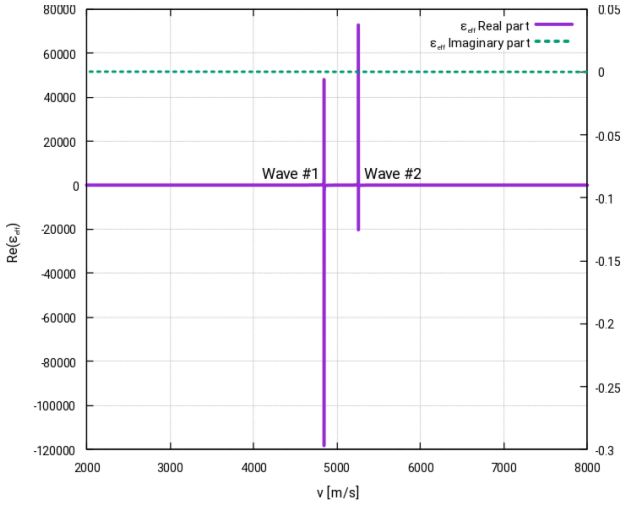


Fig. 1. Real and imaginary parts of the effective permittivity as a function of wave velocity, determined for the stack of 100 nm Al/150 nm $LiNbO_3$ /sapphire.

propagating in LN(ZXt)/0°/Sapp(ZXt)/0° and LN(ZXt)/60°/ Sapp(ZXt)/0° heterostructures presented maxima of k^2 at $\psi = 0 + 60n$ and $\psi = 30 + 60n$, respectively.

B. 2D simulations

2D simulations by using the FEM/boundary element analysis were done for two main propagation directions, ψ = 0° and 90°, and two growth orientations: LN(ZXt)/0°// Sapp(ZXt)/0°, LN(ZXt)/90°//Sapp(ZXt)/90°, LN(ZXt)/60°// Sapp(ZXt)/0°, and LN(ZXt)/150°//Sapp(ZXt)/90°. The frequency dependence of complex admittance of the studied single-port resonator was determined for each configuration. The Fig. 3 shows frequency function of the real part of the admittance – conductance, G. One can note that SAW velocity was considerably modified when wave propagated along X-axis in 60°- domains compared to the propagation in the matrix, while the SAW propagating along Y-axis was not affected (identical conductance) by the 60 ° rotation of the LN lattice with respect to the sapphire one. The SAW resonator based on LN(ZXt)/0°// Sapp(ZXt)/0° presented single resonant frequency at 3.49 GHz (v = 4884 m/s). This velocity was close

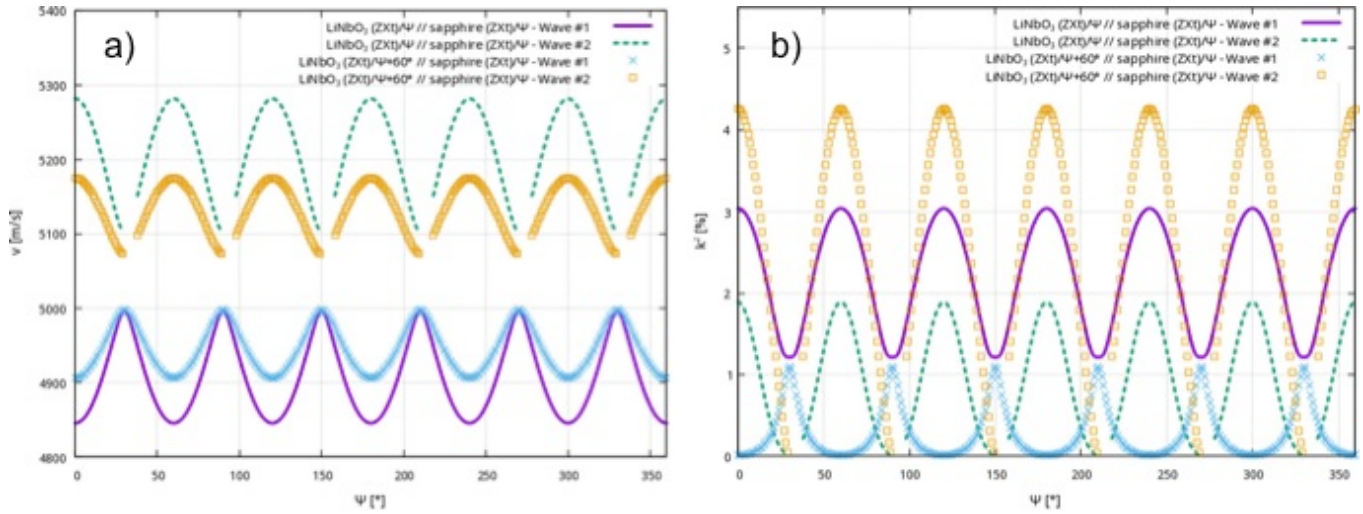


Fig. 2. Wave velocity, v, (a) and electromechanical coupling factor, k^2, (b) as a function of propagation direction, ψ, of wave ♯1 and wave ♯2 for the two crystalline growth orientations: $LiNbO_3$ (ZXt)/ψ // sapphire (ZXt)/ψ (solid and dashed lines) and $LiNbO_3$ (ZXt)/ψ + 60◦ // sapphire (ZXt)/ψ (curves with crosses and squares).

to that of the wave #1 (v = 4845 m/s), predicted by means of 1D simulations. In the case of both LN(ZXt)/90°// Sapp(ZXt)/90° and LN(ZXt)/150°// Sapp(ZXt)/90° (matrix and 60°-domains, respectively) structures, the wave #1 was observed with frequency of 3.58 GHz (v = 5015 m/s) while the wave #2 was not present again. Finally, the SAW frequency response simulated for the LN(ZXt)/60°// Sapp(ZXt)/0° configuration showed a resonance at 3.638 GHz (v = 5093 m/s) which could correspond to the wave #2 according to 1D analysis.

To summarize, the presence of 60° growth domains may significantly affect operational frequency and electromechanical coupling of SAW devices based on epitaxial Z-LN layers on C-sapphire. It is important to note that this theoretical analysis was not able to predict the frequency response of the mixture of the two growth orientations.

We would like to stress that the difference in the theoretical and experimental frequencies of SAW devices based on LN films may have different origin than the presence of growth domains and might be related to: (i) imprecision in thicknesses of piezoelectric and/or electrode layers; (ii) difference in Li nonstoichiometry; (iii) presence of residual stresses; (iv) etc. The effect of change in thickness of LN (hLN) and Al (hAl) layers on the propagation velocity, electromechanical coupling and TCF is summarized in the Table I. In general, the wave velocity decreased and k^2 increased with the increase of LN thickness. The thicker Al electrodes (+ 5 nm) resulted in the faster propagation and ameliorated coupling of SAW resonators. The drift of frequency with temperature increased for thicker Al and LN layers. Li nonstoichiometry effect on the propagation velocity seemed to be minor as velocity in stoichiometric LN/sapphire heterostructure was calculated to be lower only by 10 m/s than in the congruent LN/sapphire.

TABLE I. EVOLUTION OF THE WAVE VELOCITY, COUPLING FACTOR, AND TCF AS A FUNCTION OF LN AND Al FILM THICKNESSES

SAW configuration	Parameter	v [m/s]	k^2 [%]	TCF [ppm/°C]
0° // 0°	Reference	4884	3.65	-72.7
	$LiNbO_3$ - 5 nm	4900	3.47	-72.0
	$LiNbO_3$ + 5 nm	4864	3.81	-73.2
	Al - 5 nm	4913	3.48	-70.3
	Al + 5 nm	4848	3.74	-74.6
90° // 90°	Reference	5015	5.51e-2	
	$LiNbO_3$ - 5 nm	5037	4.80e-2	
	$LiNbO_3$ + 5 nm	4985	6.23e-2	
	Al - 5 nm	5064	5.46e-2	
	Al + 5 nm	4963	5.57e-2	
60° // 0°	Reference	5093	2.03e-2	-73.9
	$LiNbO_3$ - 5 nm	5110	1.35e-2	-73.3
	$LiNbO_3$ + 5 nm	5075	2.04e-2	-74.5
	Al - 5 nm	5127	0.67e-2	-71.3
	Al + 5 nm	5054	3.42e-2	-76.0
150° // 90°	Reference	5015	4.82e-2	
	$LiNbO_3$ - 5 nm	5037	4.11e-2	
	$LiNbO_3$ + 5 nm	4990	5.54e-2	
	Al - 5 nm	5064	5.45e-2	
	Al + 5 nm	4963	5.57e-2	

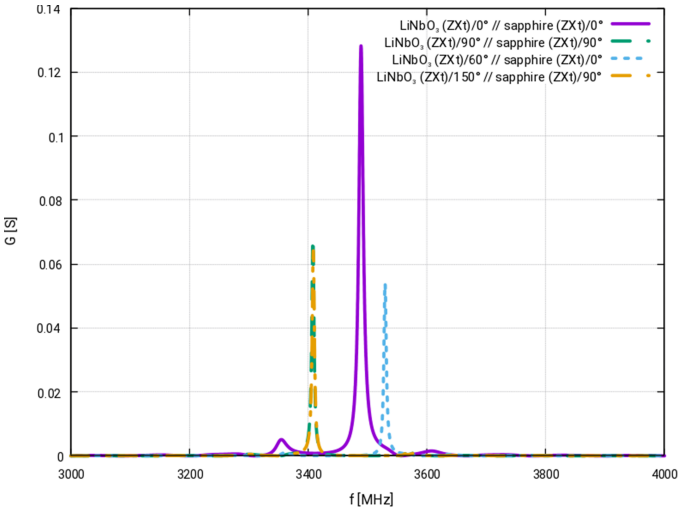


Fig. 3. Conductance, G, as a function of frequency for the four SAW configurations: LN(ZXt)/0°// Sapp(ZXt)/0°, LN(ZXt)/90°//Sapp(ZXt)/90°, LN(ZXt)/60°// Sapp(ZXt)/0°, and LN(ZXt)/150°//Sapp(ZXt)/90°.

IV. CONCLUDING REMARKS

It was shown by 1D and 2D FEM/boundary element analysis that the presence of 60° growth domains might significantly affect operational frequency and electromechanical coupling of SAW devices based on epitaxial Z-LN layers on C-sapphire. Li nontsoichiometry effect on the acoustic propagation properties (k^2, TCF and frequency) seemed to be negligible as compared to the possible imprecisions and inhomogeneity of the thicknesses of piezoelectric layer and IDTs.

ACKNOWLEDGMENT

We are grateful to S. Ballandras for the fruitful discussions and design of the single-port resonator.

REFERENCES

[1] P. Defranould and P. Wright, Filtres à ondes de surface, Techniques de lingénieur - Matériaux pour l'électronique et dispositifs associés, Editions T.I., E2200, 2000.

[2] A. Bartasyte, S. Margueron, T. Baron, S. Oliveri, and P. Boulet, Toward high-quality epitaxial $LiNbO_3$ and $LiTaO_3$ thin films for acoustic and optical applications, Adv. Mater. Interfaces 2017, 1600998 and references wherein.

[3] Y. Shibata, K. Kaya, K. Akashi, M. Kanai, T. Kawai, and S. Kawai, "Epitaxial growth and surface acoustic wave properties of lithium niobate films grown by pulsed laser deposition", J. Appl. Phys., vol. 77, p. 1498, .1995

[4] H.K. Lam, J.Y.Dai, and H.L.W Chan, J. Cryst. Growth, vol. 268, p. 144, 2004.

[5] IEEE Standard on Piezoelectricity, ANSI/IEEE Std 176-1987, 1988.

[6] G. Kovacs, M. Anhorn, H.E. Engan, G. Visintini, and C.C.W. Ruppel, "Improved Material Constants for $LiNbO_3$ and $LiTaO_3$" , IEEE IUS, p. 435, 1990

[7] J. Kushibiki, I. Takanaga, S. Komatsuzaki, and T. Ujiie, "Chemical composition dependences of the acoustical physical constants of $LiNbO_3$ and $LiTaO_3$ single crystals," J. Appl. Phys., vol. 91, no. 10, pp. 6341–6349, May 2002.

AlN-Solidly mounted resonators sustaining up to 1000°C with TCF compensation

Teona Mirea, Jimena Olivares, Marta Clement, José Luis Olivera, Jesús Sangrador, and Enrique Iborra
GMME-CEMDATIC-ETSIT
Universidad Politécnica de Madrid
Madrid, Spain
teona@etsit.upm.es

***Abstract*—Surface acoustic wave (SAW) devices are currently the most exploited acoustic wave devices for high temperature applications due to their straightforward fabrication (few photolithographic steps) and ability for wireless interrogation. However they have some drawbacks like the destructive agglomeration of their electrodes, leading to low power handling, or their low operating frequencies (MHz range). In this work we present AlN-based solidly mounted resonators (SMRs) as an alternative to SAWs for high temperature applications. They offer the advantages of simplicity, high power handling and high operating frequencies. We prove that, with a proper design, SMRs can sustain temperatures as high as 1000°C with temperature coefficients of frequency significantly lower than SAW devices, which is crucial for sensing applications at high temperatures.**

Keywords—AlN-based SMR; high temperature; TCF compensation.

I. INTRODUCTION

Surface acoustic wave (SAW) devices employing langasite (LGS) substrates are the most frequently acoustic devices used for sensing applications in harsh environments. Particularly, they have been proven to operate at temperatures above 1000°C [1]. Their success for this particular application lies on the fact that LGS is one of the most stable piezoelectric substrates at such high temperatures and on the possibility of the wireless interrogation of SAW devices, mainly in the form of delay lines. Recently, AlN-based SAW devices employing sapphire substrates have been demonstrated for operation at 1050°C [2]. AlN retains its piezoelectricity up to 1150°C [3], being chemically stable up to 1040°C [4]. Compared with LGS-based SAWs, AlN-based SAW devices can reach higher frequencies, at which LGS presents propagation losses. AlN-based SAW devices showed temperature coefficients of frequency (TCF) of -68 ppm/°C at 20°C and -80 ppm/°C at 500°C.

Although SAW-based devices are the preferred choice for high temperature applications due to the wireless interrogation possibility, they still present the drawback of the destructive agglomeration suffered by the long, thin and narrow strips of the interdigital transducers (IDTs) at such high temperatures. Many efforts have been devoted to the development of suitable metals for IDTs, being Pt and Ir alloys the best choice [5], [6]. Nevertheless, metal destruction at high temperatures still limits the power handling capabilities of such devices.

In this work we present an alternative to SAW-based devices, based on thin film bulk acoustic wave resonators (FBARs), namely AlN-based solidly mounted resonators (SMRs). As suggested by Aubert *et al.* [2], AlN-based SAW devices can be a promising alternative to LGS-based ones. Likewise, we propose to use AlN films but in this case in SMRs, to offer a solution to the power handling limitation in SAW devices and the possibility of operating at frequencies of several GHz. In FBARs the destructive agglomeration of the electrodes can be minimized by increasing their thickness at expenses of reducing that of the AlN film in order to keep the resonant frequency constant. This approach cannot be envisaged in SAW-based devices, since their resonant frequency is set by the IDTs pitch. The metal/AlN/metal sandwiched structure of FBARs allows then for high power handling. Additionally, if sensing applications others than temperature sensing are pursued, FBARs appear as the potential choice owing to the low TCF that can be achieved (< -10 ppm/°C).

In a previous work we presented 2.5 GHz AlN-based SMRs particularly designed to sustain temperatures as high as 700°C [7]. In this work we extend that study by testing two types of acoustic reflectors: (1) made of SiO_2/Mo, and (2) fully insulating reflectors made of SiO_2/AlN, and proving that these devices can sustain temperatures up to 1000°C.

II. METHODS

As mentioned, two types of acoustic reflectors have been used to fabricate the SMRs (Fig. 1). A partially conductive reflector composed of five alternating layers of SiO_2/Mo (620/629 nm-thick, respectively) (Fig. 1(b)), and a fully insulating one made of seven alternating layers of SiO_2/AlN (516/916 nm-thick, respectively) (Fig. 1(c)). The structure of the SiO_2/AlN reflector was, in some cases, modified to achieve a better TCF compensation by modifying the thickness of the outermost films. Since these structures are multilayered, special attention was paid to the sputtering deposition conditions of the materials. These were tuned to improve adhesion between layers and reduce stress to values below < 200 MPa. In this context, the first SiO_2 layer of both types of reflectors was thermally grown to improve adhesion with the underlying Si substrate. With the same purpose, a thin (15 nm-thick) sputtered Ti film was placed between each layer of the SiO_2/Mo reflector.

978-1-5386-2916-1/$31.00 ©2017 IEEE

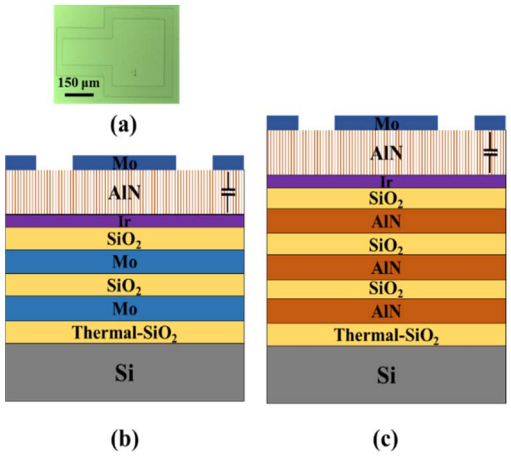


Fig. 1. Structure of the SMRs. (a) Optical top view of an actual device, (b) sketch of a device using a five layers SiO_2/Mo acoustic reflector and (c) sketch of a device using a seven layers SiO_2/AlN acoustic reflector.

To preserve the fully insulating nature of the SiO_2/AlN reflector the Ti interlayer was not employed in this case; this is crucial if SMRs with electrical extensions are needed [8]. On both types of reflectors we mounted a piezoelectric sandwich composed of a 120 nm-thick Ir bottom electrode, a 1 µm-thick AlN piezoelectric, and a 150 nm-thick Mo top electrode (Fig. 1). A thin Ti layer (15 nm-thick was added underneath the Ir bottom electrode). The piezoelectric AlN was deposited in an UHV sputtering system and its stress was controlled by lowering the bias applied to the substrate [9].

The finished SMRs were annealed at 1000 ºC for in HV (10^{-6} Torr) for two hours. The frequency response of the devices was measured before and after the heat treatment. The electrical response of some SMRs made of partially conductive reflectors was also in-situ monitored during annealing, in this case at atmospheric pressure and temperatures up to 550°C.

In order to check whether the films had experienced any inter-diffusion during the high temperature treatments, several SMRs, some of them as-grown and others subjected to the heat treatment, were assessed by Rutherford Backscattering Spectrometry (RBS) using a 5 MeV tandem accelerator. Since the technique only gives information of the first surface layers (around 3 to 5 µm, depending on the experimental conditions), in some cases several layers were removed before the measurement in order to assess deeper layers. The RBS spectra were measured using a 4He beam at 2 MeV impinging normally on the samples and detecting the backscattering ions with the surface barrier detector set at 170.5 º. The spectra were fitted with a model to obtain the composition, atomic ratio and depth distribution of the layers composing the SMRs (SiO_2, AlN, Ir, Mo, Ti).

III. RESULTS AND DISCUSSION

A. TCF characterization of as-deposited SMRs

In a first step, we assessed the TCF of the fabricated devices at low temperatures (25°C to 100°C) by monitoring the real part of their electrical admittance, Re(Y) (i.e. the maximum of the peak). Table I shows the measured TCF values of devices with the regular SiO_2/Mo and SiO_2/AlN reflectors, and additionally that a TCF-compensated SiO_2/AlN reflector. In the latter the thicknesses of the first and second layers of the reflector were set to 1.3 µm for the SiO_2 and 700 nm for the AlN. The obtained values show that regular SiO_2/AlN reflectors display lower values of the TCF than SiO_2/Mo reflectors, due to the lower coefficient of thermal expansion of AlN ($4.5 \cdot 10^{-6}$/°C), compared to that of Mo ($4.8 \cdot 10^{-6}$/°C). Additionally, the TCF of the SMRs can be further reduced to -10 ppm/°C by using compensated SiO_2/AlN reflectors, without drastically worsening the device frequency performance.

TABLE I. MEASURED TCF AT LOW TEMPERATURES (25°C TO 100°C) USING DIFFERENT ACOUSTIC REFLECTORS

Acoustic Reflector	Compensation	TCF [ppm/°C]
SiO_2/Mo	NO	-19 ± 1
SiO_2/AlN	NO	-16 ± 0.9
SiO_2/AlN	YES	-10 ± 1

B. Effects of the heat treatments

The electrical response of devices made with regular SiO_2/Mo and SiO_2/AlN reflectors, before and after annealing them in vacuum at 1000°C for two hours, are presented in Fig. 2. These results clearly prove that the electrical performance of the devices is not significantly affected after the high temperature treatment. Their quality factors are preserved as well as the piezoelectric activity of the AlN films (their electromechanical coupling coefficient barely varies).

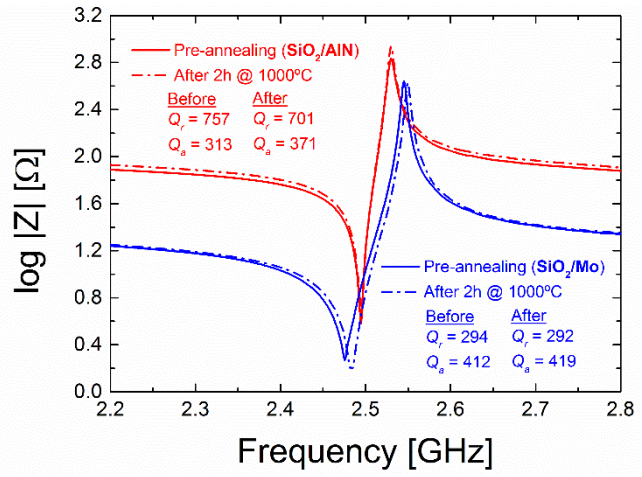


Fig. 2. Electrical impedances before and after 2h annealing at 1000°C of the SMRs made of (a) the SiO_2/Mo reflector and (b) the SiO_2/AlN reflector.

The RBS spectra of three types of structures, with and without annealing treatment, are presented in Fig. 3. These structures are: the entire SiO_2/Mo reflector (Fig. 3(a)), the entire SiO_2/AlN reflector (Fig. 3(b)), and a complete device on a SiO_2/AlN reflector after having removed the Mo top electrode (Fig. 3(c)). By comparing the spectra of the acoustic reflectors (Fig. 3(a) and (b)) we can only detect inter-diffusion in the SiO_2/Mo reflector (Fig. 3(a)). These is evinced by the

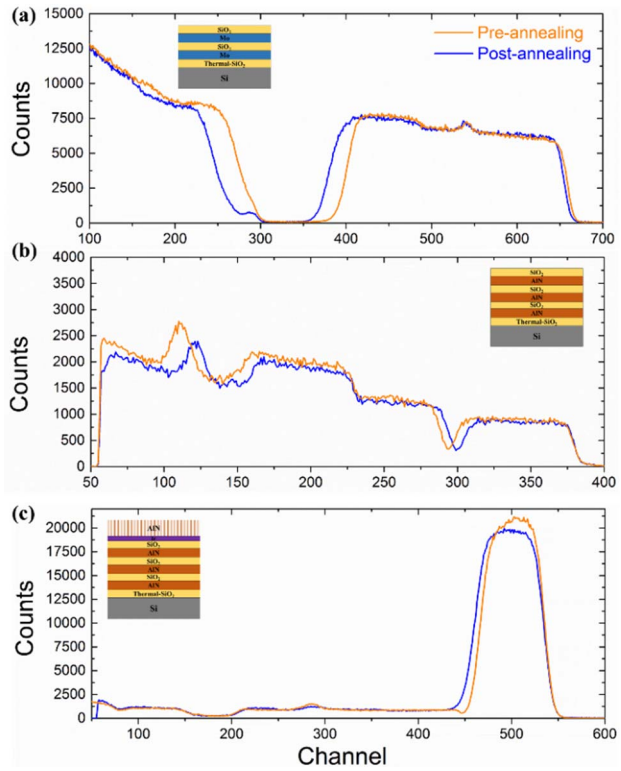


Fig. 3. RBS spectra of three different samples (insets): (a) a complete SiO_2/Mo reflector, (b) a complete SiO_2/AlN reflector, and (c) a device without the Mo top electrode made of the SiO_2/AlN reflector.

tiny change in the slope of the Mo signal appearing around channel 400 and corresponding to the first SiO_2/Mo interface. Adjusting the spectra yields interfaces widths of around 30 nm. In the case of the sample containing the Ir bottom electrode of Fig. 3(c), intermixing between the Ir bottom electrode and the Ti and SiO_2 underneath layers is clearly noticeable.

It is important to remind that the as-deposited and heat-treated samples assessed by RBS are actually different dices taken from the same silicon wafer. The different widths displayed by some signals in the spectra cannot be attributed to inter-diffusion effects arising from the thermal treatments, but rather to inhomogeneity in the thickness of the different films across the 100 mm silicon wafer resulting from the sputtering process.

Both, the lack of homogeneity and the inter-diffusion effects in the acoustic reflectors do not significantly affect the performance of the SMRs after the high temperature treatments.

C. In-situ characterization at high temperatures

The in-situ electrical characterization of SMRs is performed at atmospheric pressure, hence the devices being passivated with a thin SiO_2 capping layer, and it requires a specific set-up since regular RF cables cannot be used. In this work we present a first home-made set-up for this scope (Fig. 4). It is composed of:

- An open oven with a thermocouple temperature controller (Fig. 4(a)).
- A home-made rigid 50 ohms coaxial RF cable made of a 1.5 mm in diameter Cu core, a quartz tube forming the dielectric filling, and a 4 mm inner diameter stainless steel external tube (Fig. 4(b)). The Cu core and the exterior tube were welded to a 1 mm in diameter Au probes for the signal and ground contacts, respectively. The contact to the device was achieved by bonding the device to a 50 ohms Au co-planar micro strip. The device was placed on a 5 mm-thick ceramic support (Figs. 4(c) and (d)).
- A portable NA (Keysight Fieldfox N9912A) connected to the rigid RF cable through a regular low loss flexible one (Fig. 4(a)). It offers a simple calibration option for non-standard adapters (in this case the home-made RF cable) to connect the device under test.

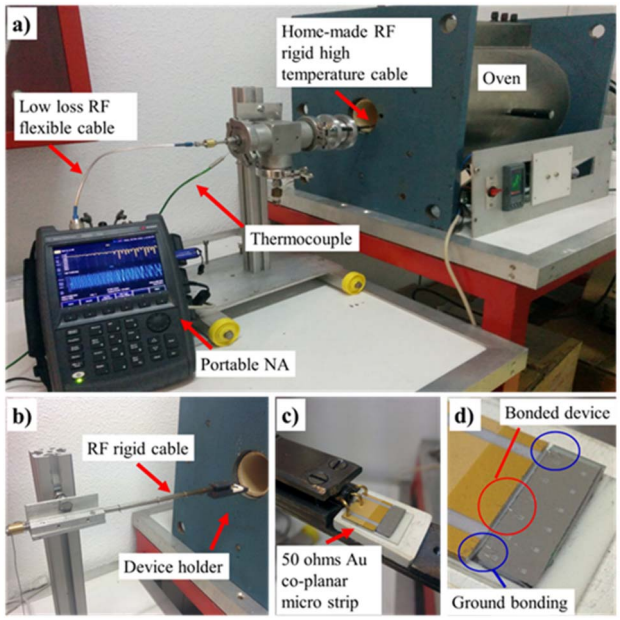


Fig. 4. Measurement set-up for the high temperature in-situ characterization of SMRs: (a) whole set-up composed of the open oven, the home-made rigid RF cable connected to the low loss flexible one, and the portable NA; (b) close view of the rigid RF cable; (c) rigid cable holder where its Au probes are connected to an Au coplanar micro-strip to which the device is bonded, and (d) close view of the bonded devices where the SiO_2 capping layer is observed.

Fig. 5 shows the in-situ frequency response of SMRs using SiO_2/Mo reflectors up to 550ºC. While increasing the temperature, parasitic effects, which we attribute to variations of the rigid cable and set-up materials properties, appear. These parasitic effects can be cleaned by employing the port-extensions compensation option of the portable NA. Parasitic effects are, to a certain extent , cleaned in these measurements, however, above 450ºC the signal starts suffering severe degradation. This is attributed to the contact loss that appears at those temperatures between the Al wire

of the ultrasonic bonding we needed to use and the top electrode of the device. The best wire materials found in the literature for high temperature bonding are Pt or Inconel [30], [32], however we did not have the means for using them in this work. In all cases, a good adhesion between these metal wires and the top electrode should be guaranteed.

Despite the signal degradation above 450ºC, the extracted shifts in resonant frequency (Fig. 6) are in good agreement with the TCF calculated for this type of device at low temperatures (Table I).

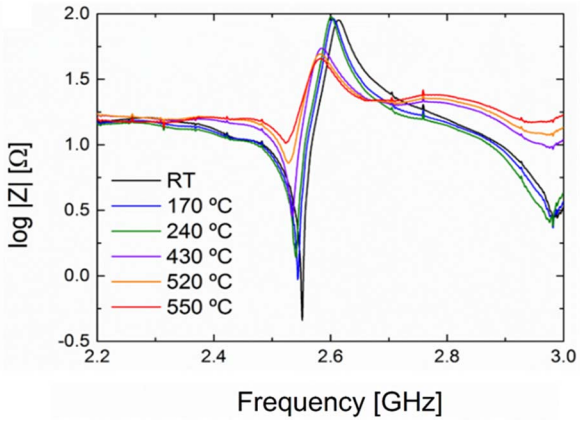


Fig. 5. In-situ electrical impedance of an SMR with SiO_2/Mo acoustic reflector at several temperatures. Parasitic effects arising from possible properties variations of the materials composing the set-up, are compensated by adapting the port extensions during measurements.

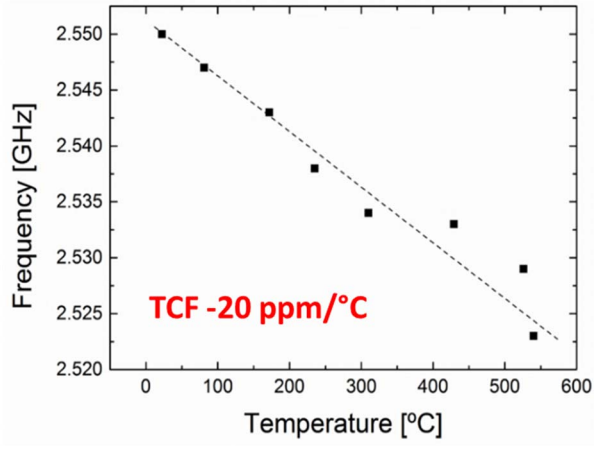


Fig. 6. Frequency shifts at high temperatures of an SMR with SiO_2/Mo acoustic reflector, and its calculated TCF.

IV. CONCLUSIONS

We have designed AlN-based SMRs with both, SiO_2/Mo and SiO_2/AlN reflectors, for operation at very high temperatures and proved that they can sustain up to 1000°C. Their electrical characterization before and after annealing them for 2h proved that their integrity and performance is maintained. RBS characterization proved that inter-diffusion between the device layers only occurs in SiO_2/Mo reflectors and between the Ir bottom electrode and the thin Ti layer underneath. Both SiO_2/Mo and SiO_2/AlN reflectors provide the devices with TCF of -19 ppm/°C and -16 ppm/°C, respectively. These can be improved by TCF compensation to a value of -10 ppm/°C without drastically compromising the device performance.

Additionaly, we have performed in-situ electrical characterization of SMRs composed of SiO_2/Mo reflectors up to a temperature of 550°C. This temperature limitation was imposed by our home made measurement set-up, whose improvements are ongoing. Nevertheles, we have proved that the TCF of this devices is preserved also at very high temperatures.

ACKNOWLEDGMENT

This work was partially supported by Ministerio de Economía y Competitividad del Gobierno de España through project MAT2013-45957-R.

REFERENCES

[1] M. Pereira da Cunha *et al.*, "Recent advances in harsh environment acoustic wave sensors for contemporary applications," in *2011 IEEE SENSORS Proceedings*, 2011, pp. 614–617.

[2] T. Aubert *et al.*, "*In situ* high-temperature characterization of AlN-based surface acoustic wave devices," *J. Appl. Phys.*, vol. 114, no. 1, p. 14505, Jul. 2013.

[3] N. D. Patel and P. S. Nicholson, "High frequency, high temperature ultrasonic transducers," *NDT Int.*, vol. 23, no. 5, pp. 262–266, Oct. 1990.

[4] O. Ambacher, M. S. Brandt, R. Dimitrov, T. Metzger, and M. Stutzman, "Thermal stability and desorption of Group III nitrides prepared by metal organic chemical vapor deposition," *J. Vac. Sci. Technol. B Microelectron. Nanom. Struct.*, vol. 14, no. 6, p. 3532, 1996.

[5] M. Pereira da Cunha *et al.*, "Pt-Ni / Pt-Zr electrodes for stable SAW resonator operation during repeated temperature cycling up to 1000ºC," in *2015 IEEE International Ultrasonics Symposium*, 2015, pp. 1–4.

[6] T. Aubert, J. Bardong, O. Elmazria, G. Bruckner, and B. Assouar, "Iridium interdigital transducers for high-temperature surface acoustic wave applications," *IEEE Trans. Ultrason. Ferroelectr. Freq. Control*, vol. 59, no. 2, pp. 194–197, Feb. 2012.

[7] T. Mirea *et al.*, "AlN solidly mounted resonators for high temperature applications," in *2014 IEEE International Ultrasonics Symposium*, 2014, pp. 1524–1527.

[8] M. DeMiguel-Ramos *et al.*, "Influence of the electrical extensions in AlN-BAW resonators for in-liquid biosensors," in *2014 European Frequency and Time Forum (EFTF)*, 2014, pp. 301–304.

[9] M.-A. Dubois and P. Muralt, "Stress and piezoelectric properties of aluminum nitride thin films deposited onto metal electrodes by pulsed direct current reactive sputtering," *J. Appl. Phys.*, vol. 89, no. 11, pp. 6389–6395, Jun. 2001.

Brillouin and Kerr-based Whispering Gallery Mode crystalline fluoride-type resonators for low noise microwave source

Jean-Pierre Aubry, Souleymane Diallo, Romain Martinenghi, Yanne Chembo
Institut Femto-st, département optique PM Duffieux
Université Bourgogne Franche-Comté
15B Avenue des Montboucons, 25000 Besançon France
Jp.aubry@femto.st.fr; Souleymane.diallo@femto-st.fr

Abstract: **we report on Whispering Gallery mode resonators based on fluoride materials, MgF_2, BaF_2, CaF_2 and LiF, under Stimulated Brillouin Scattering (SBS). We have simulated various fluoride material under various disc orientation. We have identified the specific orientation [111] in BaF2 as providing a low longitudinal wave velocity variation over the disc periphery, leading to a narrow line Brillouin frequency. Material influence is also pointed out under these configurations.**

Key words – WGM optical resonators, Stimulated Brillouin Scattering, material characterization

I - INTRODUCTION

Since couple of decades, Whispering Gallery Mode (WGM) resonators are acknowledged for their potential applications in microwave generation, single frequency source or Comb generator. Materials for WGM include a lot of Infra-Red (IR) transparent devices from silica to fluoride-type single crystal. Various oscillator topologies based on linear and non-linear selective excitation have been described. A balance should be identified between a low threshold / high power non-linear resonance and the simplification of the oscillator design, to minimize potential source of noise and reduce the oscillator size [1]. Various methods are known to couple an optical signal to a resonant WGM disc, such as ”taper” or “prism” coupling. The former exhibits a minimum coupling loss but is not adequate for operational application, the latter is more dedicated to rigid and stable mounted coupling as shown in figure 1.

One topic will be to adjust SBS frequency and the FSR /Free Spectral range), to “enhance” backward Brillouin scattering. Resonators were built at the proper dimension to get Brillouin frequency and FSR frequency very close.

OEO (Opto-Electronic Oscillators) have been widely studied during the last decades, based on fiber or micro resonator, either in linear regime , where a Mach Zehnder Modulator (MZM) is used to convey RF onto optical, disc provide selectivity, and high speed photodiode reverts to RF domain , or in nonlinear regime or lasing configuration based on Kerr or Brillouin effect. Today’s best configuration in RF range, seems to be a fiber based COEO (Coupled Opto Electronic Oscillator) providing RF signal in the 30 GHz range with phase noise performances as low as -150 dBc/Hz on floor and # -120 dBc/Hz@1kHz [9]. Synthesizer based on Silica on-chip Brillouin oscillator are demonstrated as low as -160 dBc/Hz on floor [14]. The aim of our work is to reach similar target with crystalline resonators and prism coupling for size, consumption and transportability.

II- PRISM COUPLING AND SBS ON [XYZ] DIRECTION ON XF_2

Because of transportability issue, we will focus only on prism coupling for final device, while fiber taper will be used for testing when possible with a regular telecom fiber. In SBS-prism scheme, we have compared fluoride materials with various crystallographic orientations.

The conservation of energy law drives the Brillouin scattering:

$$\mathbf{K_p = K_s + K_B}$$

$$\nu_p = \nu_s + \nu_B$$

where p denotes the pump optical wavelength, S denotes the scattered light and B denotes the acoustic media, bold **K** denotes the wave vector and ν is the frequency. SBS involves electrostriction coupling acoustic wave to the pump and scattered optical field in the propagation direction, and appears above a threshold optical power.

The experimental set up of prism coupling is shown on fig.1. The disc optical resonances are characterized by the coupling efficiency and their intrinsic quality factor Q and coupled Q by the cavity ring down technique. Intrinsic Q versus material properties will be discussed in §5.

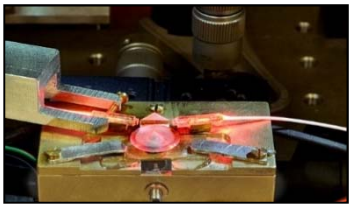


Figure 1: Prism resonator coupling set-up under visible light.

Experiments on taper and prism coupling and SBS tests will be compared, along with Brillouin threshold, between CaF_2,BaF_2, LiF. SBS threshold is also tested versus “crystalline” qualities, characterized by the IR and UV spectra and X-ray analysis. Conditions for selection of material and crystalline orientation for a proper integration in a Brillouin-based low noise microwave oscillator are discussed in conclusion.

III – SIMULATION SBS ON FLURORIDE MATERIAL

Stimulated Brillouin Scattering is a diffraction by the longitudinal acoustic wave generated through electrostriction, coupling pump light radiation and acoustic wave. In fact , rather than the wave vector of the longitudinal acoustic wave, we show that we should consider the longitudinal polarization, the Poynting vector, slightly angle-offseted from the acoustic wave propagation vector.

III-1 Azimuthal longitudinal acoustic waves

In most of works reported on Brillouin scattering of fluoride-type crystals, acoustic wave velocities are erroneously reported as $V_a = [(C_{11}+C_{12}+2.C_{24})/(2\rho)]^{1/2}$ or $V_a = [(C_{11}/(2\rho)]^{1/2}$ These values are only valid on the [110] or [100] direction of propagation of a longitudinal wave, as shown in Kittel and Dieulesaint-Royer books [4]. We develop here a more complete formulation of details of velocity and polarization of longitudinal acoustic waves propagating at the periphery of a crystalline disc, over 2π. In fact the acoustic wave must be recalculated on every position Ψ over periphery, and simple expression as given above occurs only at specific propagation direction along natural axis.

Acoustic waves over the disc periphery obey to the Christoffel equation, rewriting the plane wave equation:

$$\rho.V^2.U_i = C_{ijkl}.n_j.n_k.U_l,$$

Introducing the Christoffel tensor:

$$\Gamma_{il} = C_{ijkl}.n_j.n_k$$

the propagation equation becomes

$$\Gamma_{il} \,.\, U_l = \rho.V^2.U_i$$

where U_i, U_l are the polarization vectors of acoustic waves propagating along a direction $\vec{n}$ (n_i, n_j, n_k), all varying with Ψ.
Our calculation first expresses the elastic coefficient matrix C_{ij} in the rotated plane, given by the disc orientation **n**, following the process given in [3], by $[C']=[M].[C].[M]^T$, where [C] is the original elastic matrix, and [M] the rotation matrix defined by Bond in [3] from the guiding cosine. We then solve the propagation equation with a wave vector $\mathbf{K_B}(\Psi)$, around the disc, by getting the eigenvalue and eigenvector of the Christoffel equation, giving velocity and polarization of the acoustic waves, by solving:

$$|\Gamma_{il} - \rho.V^2.\delta_{il}| = 0$$

for each Ψ value. This leads to the longitudinal velocity $V_a(\Psi)$ in XZ rotated plane, and two transversal waves, not active in Brillouin scattering. This generalizes the result given in [5] for CaF_2, for any direction in any material.

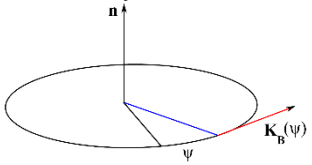


Figure 2: disc and acoustic propagation orientation

Figures 3a and 3b gives an example of the longitudinal acoustic wave frequency for BaF_2 in disc orientation [100], exhibiting a periodicity $\pi/4$, and for BaF_2 in disc orientation [111], showing a periodicity $2\pi/3$, as expected from a cubic crystal observed along its cube diagonal (fig.9). While in [100] disc orientation, the longitudinal acoustic wave velocity varies by more than 11 m/s over disc periphery (0.25%), the velocity variation is only 0.015 m/s (3.4 ppm) in the [111] disc orientation. The Brillouin frequency deviation will follow the same anisotropy.
Table 1a and 1b provides average values and amplitude of variation of Brillouin frequency generated by longitudinal acoustic (using $\nu_B=2.n.V_a/\lambda_p$) on various fluoride type materials with orientation [100] and [111], or X-, Y-, Z-cut in $LiNbO_3$.

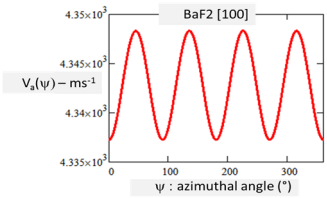


Figure 3a: BaF2 [100] Brillouin LA acoustic wave velocity dispersion

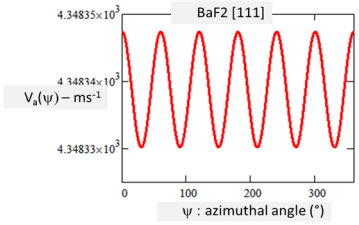


Figure 3b: BaF2 [111] Brillouin LA acoustic wave velocity dispersion

The acoustic simulations show that a proper Barium Fluoride disc -[111] oriented- exhibits a minimum dispersion of the "longitudinal" acoustic wave velocity, responsible of Brillouin scattering of the optical signal at the disc periphery.
In fact, $[111]-BaF_2$ offers a minimal dispersion of longitudinal acoustic wave velocity, very close to the behavior of an isotropic media. We can then have the advantage of a low loss crystal (ie very high Q) and of isotopic media in determination of power in the Brillouin frequency.

Numerical simulations at a laser wavelength of 1550 nm give a Brillouin frequency of 8.2 GHz in $[111]-BaF_2$ with a dispersion over 2π of few tens of kHz, while in CaF_2, SrF_2, LiF, MgF_2, whatever the chosen orientation is, (table 1a and 1b) , the Brillouin frequencies (from 10 to 13 GHz) exhibit spread over periphery in the range of 10's to 100's of MHz.

Following [4] we define the standard deviation of the Brillouin frequency, $v(Hz) = \sqrt{\frac{1}{360}\int_0^{360}(\vartheta_B(\Psi)-<\vartheta_B>)^2}$, defining a rms bandwidth of Brillouin Scattering. BaF_2 rms value is as low as 12 kHz, other material of interest (CaF_2, MgF_2, LiF…), even if they have their own optical quality, do not present such an "ideal" longitudinal wave velocity stability. Compared to other fluoride-type materials, BaF2 exhibits a very specific narrow Brillouin frequency dispersion.

III-2 Polarization of longitudinal acoustic waves

The longitudinal wave propagating around the periphery of a disc are so called "pseudo longitudinal" which means that at any point of the disc periphery the propagation vector and the polarization of "quasi-longitudinal" acoustic wave, the acoustic Poynting vector, form a small angle ρ(Ψ), less than few milli-radians over 2π.

Therefore, the Brillouin scattering frequency:

$$\nu_B = \frac{2\,n\,V_a}{\lambda_p}\sin(\theta/2),$$

assuming θ = π in ideal geometry of isotropic SBS, can be developed around the small "pseudo longitudinal" angle ρ, replacing θ = π by θ(Ψ) = π-ρ(Ψ). This provides some additional selection criteria for the energy and momentum conservation that drives the SBS process.

This angle ρ(Ψ) might be computed between the propagation vector $k_p(\Psi)$ and the polarization vector LA(Ψ) on every point of the disc periphery, after resolution of propagation of acoustic waves, given in III-1.
The scattering process is generated by "thermal" acoustic wave's, electrostriction and pump power. In ideal condition (ie when propagation is along a main crystallographic direction) acoustic wave energy propagates parallel to the k_B wave vector. In other angle Ψ of propagation, the scattering process is generated by the energy vector (Poynting vector) rather than by the propagation vector k_B. This situation is depicted on following graph. The green hash simulates acoustic polarisation non-colinear with k_B.

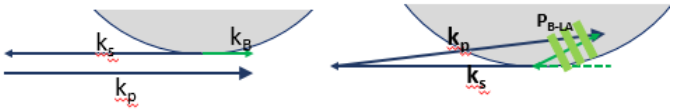


Figure 4: light scattering by acoustic wave left: collinear, right non collinear acoustic wave vector and Poynting vector

Table 1a and 1b give the maximum value of the out of plane angle ρ(Ψ)= $\left(\overrightarrow{k_p(\Psi)}, \overrightarrow{\mathrm{LA}(\Psi)}\right)$.
In CaF_2 the out of plane component of the longitudinal wave unit vector is as high as 8° , (3° in SrF_2) while this out of plane component is as low as 0.2° in BaF_2. The Y component of the longitudinal acoustic wave in BaF_2 and CaF_2 [111] are given on fig.4. The Longitudinal acoustic wave is well in plane in BaF_2 and is strongly out of plane in CaF_2 and SrF_2.

Then, the optical-acoustic interaction, due to the acoustic plate deformation, via electrostriction, is not collinear with acoustic wave propagation over the all periphery. The coupling must be considered between optical propagation and the acoustic energy flow. Fig. 5 gives the simulation of Brillouin frequency over the disc periphery, taking into account the variation of the longitudinal acoustic velocity (Va(Ψ)) and the misalignment ρ(Ψ) between the propagation vector $\mathbf{K_B}$ and the LA wave polarization. KB is the Brillouin factor, KB=2*n/λ_p.

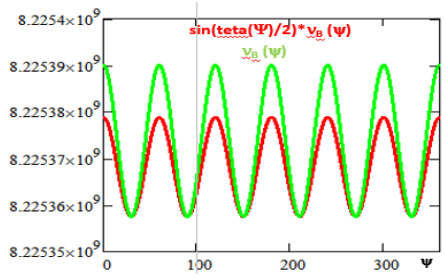


Figure 5: Impact of Poynting vector misalignment between propagation vector and polarization vector on Brillouin Frequency

Then BaF_2 [111] appears to be very specific in terms of longitudinal acoustic wave on disc periphery: low longitudinal acoustic velocity variation, quasi ideal longitudinal polarization, low out of plane acoustic polarization. Table 1 gives main characteristic of acoustic behavior and Brillouin frequency for [111] orientation in major fluoride materials.
Such characteristics are strongly orientation dependent. Fig.6 gives the BaF2 [111] Brillouin frequency under small misalignment of the disc normal **n** versus the ideal [111] direction, given by a tilt angle δ.

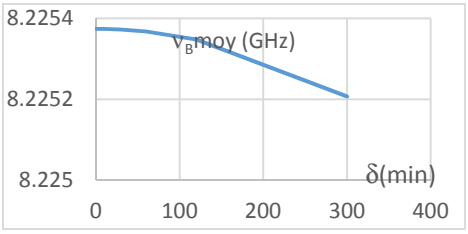


Figure 6: Brillouin frequency evolution vs [111] misorientation (in ')

δ is the angle between the ideal orientation [111] and the orientation of the normal **n** of the device

Our simulation allows to estimate the influence of the δ mismatch angle on the amplitude of variation of ν_B frequency over the disc periphery. The angle accuracy of the [111] disc orientation is required to be in some minutes of angle to maintain peak to peak variation at a minimum, and then expect to benefit of a highly stable Brillouin frequency.

Following tables summarize the average Brillouin frequency, its peak-peak variation and its rms value, along with the out of plane angle of acoustic polarization Δρ, over 2π, for various material and orientation.

material in [111]	ref	Brillouin frequency	Δ ν_B	Std dev	Δρ (°)
CaF_2 @ 1064 nm	[4]	17.7 GHz	112 MHz	40 MHz	
CaF_2 @ 1064 nm	this work	17.74 GHz	112.2 MHz	40 MHz	8°
CaF_2 @ 1550 nm	this work	12.15 GHz	70 MHz	27 MHz	8°
SrF_2 @ 1550 nm	this work	9.67 GHz	7 MHz	2.5 MHz	2.7°
BaF2 @ 1550 nm	this work	8.2254 GHz	32 kHz	11.5 kHz	0.19°

Table 1a: Brillouin computation in CaF2, SrF2 and BaF2 [111]

material/1550nm	Brillouin frequency	$\Delta \nu_B$	Std dev	$\Delta\rho$ (°)
CaF_2 [100]	12.71 GHz	389 MHz	138 MHz	7
BaF_2 [100]	8.2149 GHz	7.4 MHz	2.6 MHz	0.2 °
SrF_2 [100]	9.787 GHz	129 MHz	46 MHz	3 °
LiF [100]	12.520 GHz	512 MHz	180 MHz	10 °
LiF [111]	13.2 GHz	32 MHz	11 MHz	8 °
MgF_2 [100]	12.374 GHz	758 MHz	260 MHz	8 °
MgF_2 [111]	13.087 GHz	478 MHz	170 MHz	13 °
$LiNbO_3$ [100]	20.509 GHz	640 MHz	230 MHz	9 °
$LiNbO_3$ [010]	20.267 GHz	700 MHz	250 MHz	10 °
$LiNbO_3$ [001]	19.259 GHz	320 MHz	110 MHz	8 °

Table 1b: Brillouin behavior in various material/direction

BaF_2 exhibits a very stable Brillouin frequency, with peak to peak variation less than 30 kHz, and rms value of 11.5 kHz.
The angle between the energy flow (Poynting vector) and the propagation vector is as small as 0.19° in BaF_2, compared to 8° in CaF_2, 13° in MgF_2. BaF_2 shows a narrower variation than other fluorides. Then we can expect to take benefit of the stable longitudinal acoustic wave to provide a highly stable narrow band Brillouin interaction. This might be explained by the ionic radius (next table) and the $2\pi/3$ symmetry of a cubic material observed around the [111] diagonal direction of the cube. In CaF_2, both ions have similar size, then the (111) Ca^{++} plane is distorted by F^- ions, while in BaF_2, the size of Ba^{++} ions make the (111) plane more a Barium plane, less distorted by F^- ions.

ionic radii	Li^+	Mg^{2+}	Ca^{2+}	Sr^{2+}	Ba^{2+}	F^-
(pm)	90	86	114	132	149	119

Table 2: ionic radii of ions

Fig. 7 gives a view of fluoride crystal along the [111] direction, showing the $2\pi/3$ symmetry around this direction.

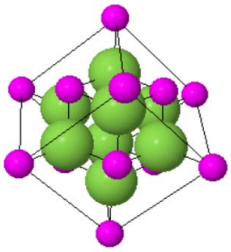


Figure 7: XF_2 showing $2\pi/3$ symmetry along [111]
(green: F^-, pink: Ca^{2+}) (visual from Wikipedia)

IV-FSR FREQUENCY AND BRILLOUIN FREQUENCY

The FSR frequency of a crystalline fluoride type material, given by $\frac{c}{\pi.n.d}$, defines the primary set of resonances.
Adjusting Brillouin frequency at FSR frequency needs to get:

$$\vartheta_B = \frac{2.n\,V_a}{\lambda_p} = FSR = \frac{c}{\pi.n.d}$$

Where c is light velocity in vacuum, n is material index, d is disc diameter, λ_p the wavelength.
The diameter of the fluoride disc will be taught to adjust at the exact dimension and tolerance to overlap both Brillouin and FSR frequencies. We may have two parameters to perform this adjustment. The first one might be the temperature (V_a varies linearly with temperature, while FSR varies as 1/d(T) because of the linear expansion – not exactly isotropic – of the fluoride material), the second one will be the wavelength λ_p. If ν_B falls exactly in the middle between two adjacent FSR line, the requested total adjustment range should be the FSR value.

Willing to take benefit of low variation of V_a and ν_B in BaF_2 [111] and to get FSR spacing superposition to Brillouin frequency, to tentatively perform a narrow band injection locking, we design a BaF_2 resonator, orientation [111] with 7.92 mm in diameter after surface preparation for high Q resonator. The Koheras laser used in our experiment has a tuning range of +/- 1 nm around 1550 nm. The disc diameter tolerance should be less than 5.10^{-3} mm.

IV-1 Brillouin scattering Bandwidth

The natural linewidth of any WGM of a good high Q resonator is in the range of some 10's to 100's of kHz. Table 1 shows that Brillouin frequencies (rms), varies by +/- 11 kHz on BaF_2, +/- 2.5 MHz on SrF_2, and +/- 27 MHz on CaF_2. Then it is clear that, for an ideally tuned $\nu_{WGM} = \langle\nu_B\rangle$ configuration, coupling between light and acoustic waves will not take place on all of the periphery, but only at location where both ν_{WGM} and $\nu_B(\Psi)$ frequencies are really equal.
As ν_B varies over Ψ, the SBS frequency might couple with a gallery mode only in limited area of the periphery. We can then introduced an efficiency coefficient, as the arear of periphery where $\nu_B(\Psi)$-rms $\leq \nu_{WGM} \leq \nu_B(\Psi)$+rms, the overlap area of natural BW of the WGM and the BW of the Brillouin gain.
The overlap factor introduced in eq.1 in Ref.12 will be strongly affected by the sensitivity of Brillouin RF over Ψ. As $\nu_B(\Psi)$ varies more than the BW of any gallery mode , SBS will occur on a fragment of periphery, reducing drastically its efficiency.

V- RAW MATERIAL CHARACTERIZATION & INFLUENCE

Fluoride material are commercially available under various grades (VUV, IR, KX,…).
Disc resonators have been qualified by X Ray orientation to identify large crystalline defects, HR XRD (high resolution X ray diffraction) to identify local crystalline perturbation, IR and UV spectra, and by chemical analysis. Efficiency of our polishing process [5] is also correlated with the nonlinear optics behavior, Kerr and Brillouin.
Acoustic wave velocity is dependent of C_r and density ρ, by $V \approx \sqrt{\frac{C_r}{\rho}}$, where C_r is the rotated elastic coefficient, ρ the density. Any "local" perturbation on C_r or ρ will affect the acoustic wave velocity, energy dissipation, energy scattering.
Crystalline perfection can be estimated through classical X-ray diffraction (multiple pics in diffraction area) or by HR-XRD, [15]. HR-XRD provides information regarding the crystal disorder by observing the FWMH (full width mean height) of a diffraction pic, focusing on a specific plane family.

Impurities, either interstitial or substitutional may be present in IR, dislocations and even structural disorder might be present in IR material, without significant impact on typical optical performance in IR range (ie for optical window..) while exhibiting strong UV signature. UV spectra of two typical BaF2 materials are presented below:

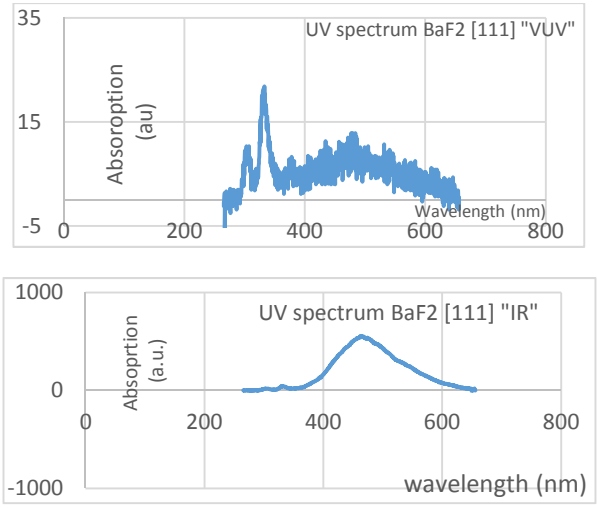


Figure 8: UV absorption spectra of BaF_2 [111] units. a) "VUV" material, b) "IR" material (at scale)

The UV and X-ray spectra then reflect structural defects, which may impact either the local density ρ and local elastic constant, driving a significant impact on acoustic wave velocity.

High resolution X-Ray diffraction have been tested on samples VUV-CaF_2[100] and VUV-CaF_2[111], IR-BaF_2[111] and VUV-BaF_2[111]. The following graphs summarize the results of HR-XRD investigation.
For CaF_2, main diffraction is obtained on [022], [111] and [004] atomic plane, because of the factor of structure. The [004] and [111] orientation were choosen for Rocking Curve measurement to determine crystalline quality. The key information if the FWHM, Full Width at Half Maximum. In these data, FWHM is # 0.0127° for sample [100] and # 0.017° for sample [111]. Such value is very high, compared to defect-free cristalline known references (such as defect free Si : FHWM # 0.003°). This indicates that both CaF2 samples contain a significant density of defect.

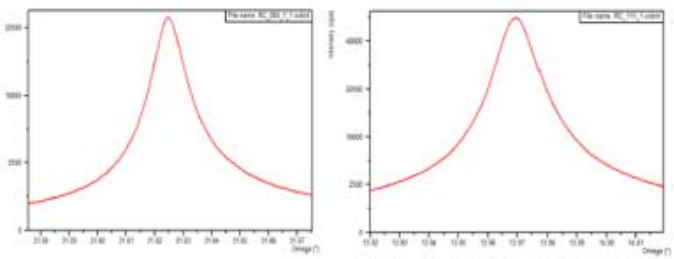


Figure 9: XRD rocking curve – [004] peak
left: CaF_2[100]VUV right: CaF_2 [111] VUV

For BaF_2, under the same X-ray diffraction condition, even if the IR and VUV crystal appear to be single crystals, the Rocking Curve experiment reveals also high defect density.
The Rocking Curve of the VUV-BaF2 [111] sample (next graph) provides a FWHM # 0.323°, which is huge compared to classical single crystal, confirming that these VUV samples contain high concentration of defects.

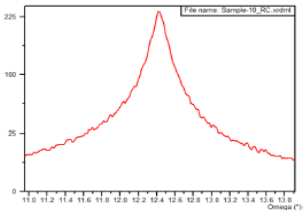


Figure 10: Rocking Curve BaF2 [111] VUV- FWHM#0.323°

The Rocking Curve of BaF2 111-IR is even more surprising (next graph). Rocking Curve average FWHM # 0.121 ° (high) and moreover, shows "splitting of peaks", appearing of various regions of the disc, revealing an-isotropic material .

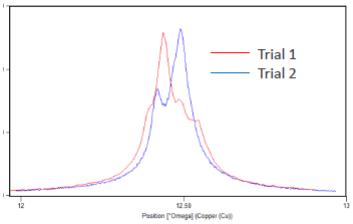


Figure 11: Rocking Curve of BaF_2 [111]-IR, showing peak splitting

From experts (Ref.15), the peak splitting could be explained by lattice strain gradient (in agreement with large FWHM) or by system of pseudo-planes, associated to twinning. In any case, that indicates that both BaF_2 grade, IR and VUV, contain high density of defects. UV spectrum analysis and HR.-XRD both confirm that BaF2 –IR contain high density of defects. This will need to be investigated further, before making any attempts of disc polishing, high Q measurement and even high Q Brillouin oscillator testing, as all potential crystalline defect may have an impact on acoustic waves.

VI- EXPERIEMNTAL

Various materials configuration are compared in this study.

Table 3 provides material grades and crystalline orientation covered by our experimental work. Not all of the experimental results are available as by today, and will be reported later

material	orientation	mat grade
BaF2	[111]	IR
BaF2	[111]	VUV
BaF2	[111]	KX
CaF2	[111]	IR
CaF2	[100]	IR
LiF	[100]	IR

Table 3: material grade and orientation tested

VI-A Q CHARACRERIZATION

The various material and material grades along with crystalline orientation [001] and [111] have been tested to characterize

intrinsic Q performance via taper coupling (LiF, CaF2, MgF2) or via optimized prism coupling (BaF2, CaF2, MgF2,…).

We are still on the process of material characterization under Kerr and Stimulated Brillouin Scattering. Issues are expected in SBS, because of the dissipation of acoustic energy provided by high acoustic losses material, acoustic Q and decay enhanced by material losses, absorption and dissipation generated from local impurities, and some impact on Brillouin threshold.

VI-B BRILLOUIN CHARACTERIZATION

The experimental spectra, Kerr and Brillouin, obtained with CaF_2, BaF_2 MgF_2 and LiF, among various orientation, are obtained using the set up fig. 12, recording simultaneously forward and backward signals.

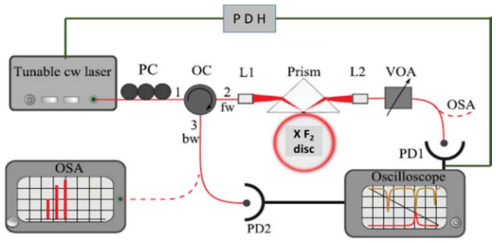


Figure 12: experimental set up

PC is the polarization control, OC is the optical circulator, L1 and L2 are input and output lens, PD are photodiodes, OSA is optical Spectrum analyzer. A PDH loop might be added between PD1 and tunable laser to stabilize the measurement conditions.

A typical example, for LiF is given below:

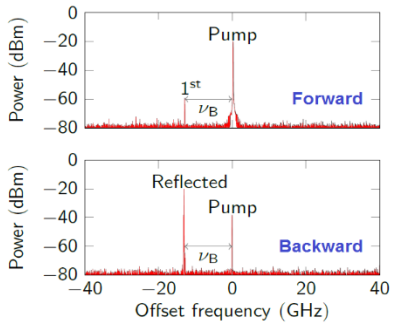


Figure 13: forward and backward scattering in LiF, from ref.

The forward signal is a scattered "residual" Brillouin, while the interesting signal is reflected (backward).
Computation as in §3 provides $<\nu_B>$ # 13.2 GHz and ν_B variation over 2π disc periphery $\Delta\nu_B$= 32 MHz, for LiF[111], and ($<\nu_B>$ # 12.52 GHz, $\Delta\nu_B$= 512 MHz for LiF [100]. In both case the fluctuation of ν_B over the periphery is too wide to allow selective coupling with specific optical resonances using FSR.

Fig.14 gives the forward and backward response of CaF_2 [111] VUV material. The absorption in the forward signal is providing a backward signal

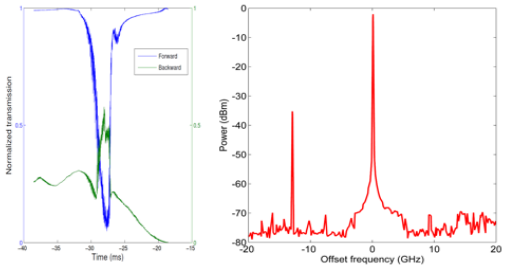


Figure 14: CaF_2 [111] VUV forward & backward

The amplitude of the backward signal is close to be high enough to be exploited in a Brillouin oscillator set up.

VI-C FSR BRILLOUIN INJECTION & STABILIZATION

The attempt of adjusting Brillouin frequency (by a small variation of the laser wavelength) on the FSR interval, on a PDH (Pound Drever Hall) stabilized lock loop.

In most of the case reported here (CaF2, MgF2, SrF2 of any orientation, BaF2 [100], the Brillouin frequency varies along the periphery of the disc by value ranging from +/- 2.5 MHz (SrF2) to 40 MHz (CaF2) and even 500 MHz for LiF.
For a high Q microdisc resonator, Q value greater than 10^9 are accessible with a properly polished resonator, providing line width in the 100's kHz range.

One target of this work will be to fine tune the FSR frequency and the Brillouin frequency in BaF2 [111] to benefit from a quasi-constant Brillouin frequency over 2π of disc periphery, and from the high energy in the main WGM mode, or any over WGM mode with cascaded Brillouin.

VI-D BRILLOUIN OSCILLATOR

Before defining a dedicated or ideal topology, we need to define a fixture maintaining prism and disc in close and stable coupling conditions. The difficulty, is to get an efficient coupling distance between prism and disc, being rigid and stable enough under normal environmental conditions.
After a classical "hand made" preparation of micro resonator disc (V-shaping, grinding, polishing,..) of the disc placed on an axis-symmetric stub, disc are positioned on the test jig, and adjustment will be carried by manipulating the stub support, in a friction-controlled plate to the basis.
After adjustment of the prism position and the related grin-lenses, a visual approach bring disc to a reference position, then visual coupling is optimized under red light, then IR coupling adjustment is optimized, based on optical scope observation.

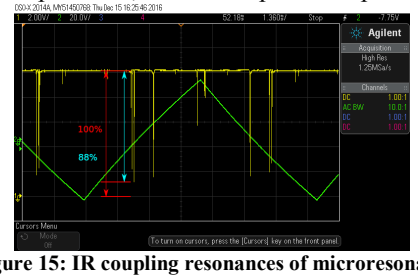


Figure 15: IR coupling resonances of microresonator

The key is to be able to then « fix » the positions disc/prism, without perturbing these coupling conditions, and in a way rigid and stable enough to maintain these coupling conditions for a while. Next picture presents a configuration where resonances survive to the manipulation.

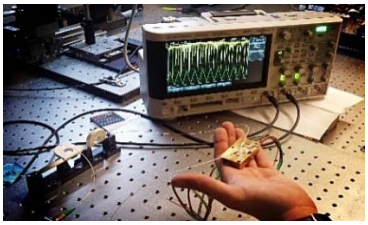


Figure 16: IR coupling robustness of test jig

VII- CONCLUSION

The aim of our work is to explore feasibility and performance of microwave sources using basic and the simplest oscillator's configuration, using Stimulated Brillouin Scattering in fluoride resonators. This work allows us to point out the criticality of the raw material (crystalline orientation, crystalline defects, chemical defects,..) further than the polishing process.

Demonstration of injection capabilities by fine tuning (PDH lock) of the superposition of Brillouin frequency over a FSR spacing provides interesting scheme for microwave source.
Among the various family of fluoride-type material, of various possible simple orientations [100], [110] [111], the most attractive combination if BaF_2 [111], for which it seems to be possible to get a superposition of the Brillouin frequency ν_B, with an expected bandwidth less than 12 kHz rms for a reasonably high Q (10^9) resonators, and the FSR, within a reduced bandwidth (less than 50 kHz) providing an opportunity of having stimulated Brillouin scattering on the full periphery of the disc, thus providing high enough output power.
SBS combines optical and acoustic difficulties. SBS integrates optical issue (polishing, optical dissipation, losses, Q,..) and the acoustic properties of the material, including polarization, amplitude, amplitude decay, dissipation, acoustic Q, and dissipation / velocity scattering / polarization scattering due to local crystalline defects (impurities, dislocations [, …). We are still working on optimization of polishing and identification of the "best" material for our application. Next step will be to integrate such SBS BaF_2 resonator in a simple OEO, where the optical to RF conversion and the RF selection are integrated in the resonator, avoiding MZM, high gain amplifier or DRO's lock (9) in the RF loop.
In short, Stimulated Brillouin Scattering, might be a powerful tool to provide low noise microwave source, sensors, etc.
Because of very specific acoustic wave behavior, BaF_2, is a very attractive candidate to build Brillouin- based devices.
The key point is that Brillouin is based on acoustic wave behavior, and acoustic behavior is highly sensitive to crystalline characteristics of the disc. It means that it might be useless to develop Brillouin- based devices without a proper in-depth analysis of material properties, and deploying tools and mean to improve these materials. Low temperature (1K) IR and FIR might be a tool to identify impurities in fluoride materials [16].

VIII- ACKNOWLEDGEMENT

This work was supported by University of Bourgogne Franche Comté, the Labex First-TF, Labex Action and by Interreg funds /Ignition project / Collégium SMYLE.

REFERENCES

[1] J.Li, H.Lee & K.Vahala,.Low-noise Brilloouin laser on a chip at 1064n nm, OPTICS LETTERS, Vol.30, N°1, Jan.15, 2014

[2] W.Loh, A.S.Grenn, F.N.Baynes, D.C.Cole, F.J.Quinlan, H.S.Lee, K.J.Vahala, S.B.Papp & S.A.Diddams, Dual-microcavity narrow-linewidth Brillouin Laser, Optica, 2015

[3] B.A Auld, Acoustic fields ans waves in solids, vol.2, RE Krieger, 1990

[4] E.Dieulesaint, D.Royer, Ondes elastiques dans les solides, Dunod, 1978, and C.Kittel, Solid State Physics, 8th edition, Wiley

[5] I.S.Grudinin, A.B.Matsko and L.Maleki. Brillouin lasing with a CaF2 whispering gallery mode resonator, Physical Review letters, 102(4); 043902, 2009

[6] S.Diallo, Utilisation des non linéarités Kerr et Brillouin dans les résonateurs à mode de galerie cristallins pour la synthèse de micro-ondes, PHD Thesis, Unisersité Bourgogne Franche Comté, Femto-st, 2016

[7] G.Lin, S.Diallo, K.Saleh, R.Martinenghi, J-C.Beugnot, T.Sylvestre, and Y.K.Chembo, Cascaded Brillouin lasing in monolithic barium fluoride whispering gallery mode resonators, Applied Physics Letters 105, 231103 (2014)

[8] T.Sonehara, Y.Konno, H.Kaminaga and S.Saikan, Frequency-modulated stimulated Brillouin Spectroscopy in crystals, J.Opt.Soc.Am. B, vol.24, N°5, May 2007

[9] O.Llopis, P.H.Merrer, A.Bouchier, K.Saleh, G.Cibiel, High-Q optical resonators: characterization and application to stabilization of lasers and high spectral purity microwave oscillators, SPIE Photonics West, San Francisco, 2010, 75791B-1, hal-00483200

[10] G.Lin and Y.Chembo, Opto-acoustic phenomena in whispering gallery mode resonators, Int'l Journal o Optomechatronics, Vol.10, N°1, p32-39, 2016

[11] G.Lin, S.Diallo, J:m:Dudley and Y.Chembo, Universsal nonlinear scattering in ultra-high Q whispering gallery mode resonators, Optics Express, Vol24, N°13, 2016

[12] G.Lin, S.Diallo, K.Saleh, R.Martinenghi, J-C. Beugnot, T,Sylvestre and Y.Chembo, Cascaded Brillouin lasing in monolithic barium fluoride whispering gallery mode resonators, Appl. Phys. Lett, 105, 231103 (2014)

[13] W.G. Kleppmann, High-temperature disorder and the elastic constants in fluorite crystals, J.Phys.C: Solid State Phys., Vol.11, 1978

[14] J.Li, H.Lee and K.Vahala, Microwave synthesizer using on-chip Brillouin oscillator, Nat. Commun. 4:2097, doi:10.1038/ncomms3097, (2013)

[15] K.Vaideeswaran, Private communication, XRD results 2017-06-22, CSEM-Neuchâtel, CR projet Interreg / Ignition / Smyle, 2017

[16] J.P.Aubry, G.Morlot, G.Villermain-Lecolier, and A.Hadni, FIR spectra of Strontium flooride doped with Rare Earth, Infared physics, 1978, Vol.18, pp 901-908

Soliton-Based Optical Kerr Frequency Comb for Low-Noise Microwave Generation

Erwan Lucas, John D. Jost, Tobias J. Kippenberg
Ecole Polytechnique Fédérale de Lausanne (EPFL)
1015 Lausanne, Switzerland
Email: tobias.kippenberg@epfl.ch.

Katja Beha, Matthias Lezius , Ronald Holzwarth
Menlo Systems GmbH
82152 Martinsried, Germany

***Abstract*— Photonic generation of microwaves has shown record level low-noise performance, using optical frequency combs. We demonstrate direct low-noise microwaves with optical microresonator frequency combs via dissipative Kerr temporal soliton formation.**

Keywords*— *microwave photonic oscillator; Kerr frequency comb; dissipative Kerr soliton; nonlinear optics; microresonator

I. Introduction

Optical frequency combs provide an equidistant grid of optical frequency components, enabling a wide array of diverse and new technologies [1]. One such application is photonic microwave generation where optical frequency combs provide unprecedented low-noise performance via optical frequency division [2], [3]. Although providing excellent performance, it comes at the expense of size and complexity. In this work, we pursue a different route to provide both a compact and low-noise microwave source by direct microwave generation with microresonator based optical Kerr frequency combs (KFC) [4] that are formed via dissipative Kerr temporal solitons (DKS) in the microresonators [5]. A unique aspect of KFCs is their wide comb spacing (10 GHz - 1THz) due to the small dimensions of the resonator. This enables a wide range of applications including optical communication, spectroscopy and direct generation of microwave signals. For this latter application, crystalline resonators are appealing over other microresonator platforms, as their narrow Raman gain and low thermorefractive coefficient imply that the noise introduced by the resonator will be very low.

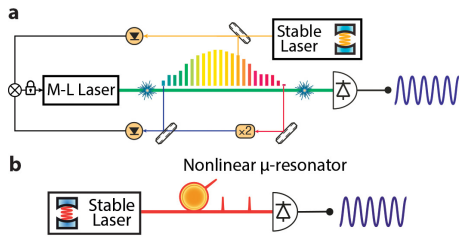


Fig. 1. Principle of photonic low noise microwave generation. (a) Optical frequency division. The optical frequency comb spectrum – typically derived from a mode locked laser (M-L Laser) – is stabilized by phase-locking the nth comb element to an optical reference after offset subtraction. (b) For the direct microwave synthesis employed here, the pulse train is derived via nonlinear frequency conversion directly from the optical reference, which is part of the resulting Kerr frequency comb.

II. Ultrastable Laser Pumping

Here we demonstrate low-noise microwaves using DKS generated in a crystalline magnesium fluoride (MgF_2) microresonator (14.09 GHz repetition rate) with the pump laser (1553 nm) phase-locked to a sub-Hz reference cavity stabilized laser (MENLO ORS1500).

A. Experimental setup, soliton generation

In a microresonator with appropriate dispersion, solitons emerge when the continuous wave pump laser is scanned from short to long wavelengths across a high-Q resonance [5]. Single or multiple solitons can be formed in the cavity using a controlled frequency scan of the laser. This requires pump laser tunability, which not typically possible for an ultra-stable laser locked to a high-finesse reference cavity. We circumvent this problem by implementing a high frequency offset lock of a pump diode laser to the reference ultra-stable laser. After the generation of the soliton state, we enable the lock with the appropriate offset frequency to preserve it. The optical spectrum corresponding to a single soliton in the microresonator is presented in Fig. 2b. We observed no noticeable change in the optical spectrum of the KFC after enabling the offset locking, implying that the soliton has not significantly changed.

The experimental setup is shown in Fig. 2a. The pump laser is an external cavity diode laser (Toptica CTL) at 1553 nm. The heterodyne beat with the reference laser is photo-detected, amplified, then down mixed to 70 MHz with a tunable RF synthesizer and compared to a commercial atomic clock via a phase comparator. A servo is used to implement a slow feedback on the laser piezo and a fast feedback on the diode laser current allowing a 1 MHz actuation bandwidth. This approach enables an offset lock ranging from 1 to 10 GHz. The pump laser is amplified to ~ 250 mW and coupled to the microresonator using a tapered optical fiber. The remaining pump light at the output is suppressed using a narrow fiber Bragg grating notch filter and the resulting pulse train is amplified and send to a high-power handling photodiode (Discovery DSC40S). The generated microwave spectrum and phase noise are measured with electronic spectrum and phase noise analyzer (Rohde & Schwarz FSW and FSUP).

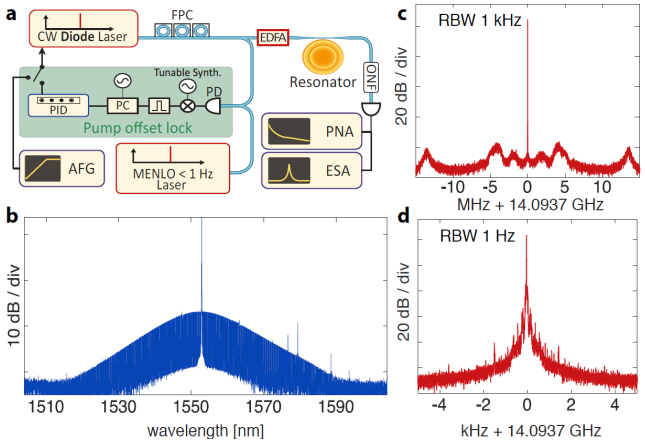


Fig. 2. a.) The experimental setup for generating low noise microwaves. The components are: continuous wave (CW) diode laser, fiber polarization controller (FPC), Optical notch filter (ONF), Phase comparator (PC), Phase Noise Analyzer (PNA), Arbitrary function generator (AFG), and Electronic Spectrum Analyzer (ESA). b.) Optical spectrum of a single DKS. c.) and d.) Show the microwave signal measured on the ESA with two different spans and resolution bandwidths (RBW)

B. Spectral purity and stability of the RF signal

Fig. 2c,d shows a typical RF spectrum of the signal generated by the DKS comb detection. A very pure microwave tone is measured on the electronic spectrum analyzer with over 80 dB signal to noise ratio on a 1 kHz resolution bandwidth. On a span of 30 MHz, the RF background reveals several broad spikes, which we attribute on one hand to the servo bump (around 1 MHz), while the others (4, 13 MHz) are corresponding to specific resonances of the DKS [6], [7]. The modulation sidebands visible on a narrower span for 1 Hz resolution bandwidth are possibly resulting from the voltage supply and driving electronics. The phase noise of the signal is measured with two different phase noise measurement devices for comparison one with cross correlations (FSW) and one without (FSUP) a cross correlation technique (Fig. 3). The phase noise performance obtained between 51 kHz to 100 kHz approach the FSUP limitations at -130 dBc/Hz, although 10^5 cross-correlations were applied. The shot noise floor of -157 dBc/Hz is reached at 1 MHz offset. At higher offsets, we are limited by the servo bump and the two DKS resonances. The limitations at low offset Fourier frequencies, possibly originate from the thermal fluctuations in the resonator due to the intensity noise of the laser and temperature drifts. The Allan deviation is bellow 10^{-10} for averaging times between 10^{-2} to 10 s. The thermal drift is shown to dominate starting from 0.1 s. The phase locked nature of the laser is also verified as the Allan deviation of the inloop stabilized laser beatnote averages down as τ^{-1}.

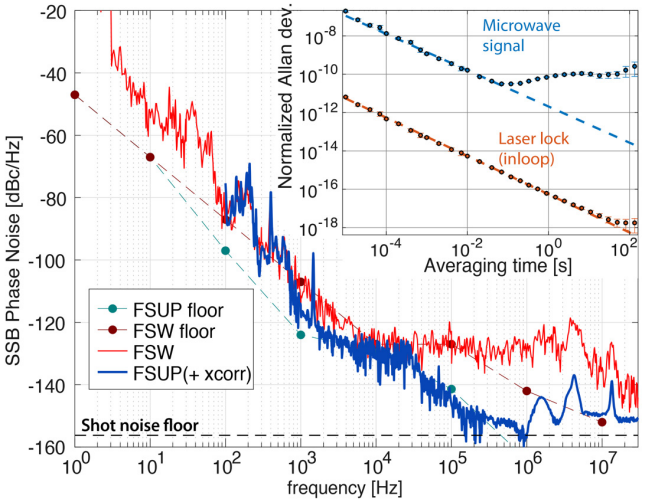


Fig. 3. Phase noise measurement with two different devices: Rhode and Schwarz FSUP and FSW. The FSUP uses a cross correlation technique providing a lower noise floor. The solid lines show measured data and the dotted lines the device noise floor. The inset figure shows the normalized overlapping Allan deviation of the counted microwave signal and the counted in-loop signal of the heterodyned signal of the locked lasers.

C. Noise transduction process

Our experimental setup enables the study of how pump laser frequency noise couples to the soliton repetition rate noise, as locking the laser effectively narrows its linewidth. After generation of a soliton state, we record the phase noise of the microwave signal before and after enabling the laser lock. In some case, locking the laser improved drastically the phase noise close to carrier, with more than 40 dB reduction at 100 Hz offset. Interestingly, when repeating this measurement in various soliton states and at different laser detuning, some soliton states present inherently a low phase noise and no significant improvement is observed when enabling the laser lock. Such behavior can originate from local disruptions in the microresonator dispersion, caused by linear coupling between mode families (avoided mode crossings) [8]. We studied the properties of the soliton as function of detuning and revealed that, these mode crossings induce detuning-dependent spikes to appear in the comb spectrum [9], [10] (as seen in Fig. 2b). The associated modification of the spectral center of mass (soliton recoil) produces a change of the group velocity and thus an increased sensitivity to pump laser noise, similar to the Gordon-Haus effect in mode locked lasers [11], [12]. Thus, at some detuning values, the conversion of pump laser frequency noise into RF frequency noise is stronger, explaining why narrowing the laser linewidth has a large impact. Conversely, this observation reveals that in the proper detuning range, the coupling from frequency noise of the pump laser into repetition rate phase noise can be minimized.

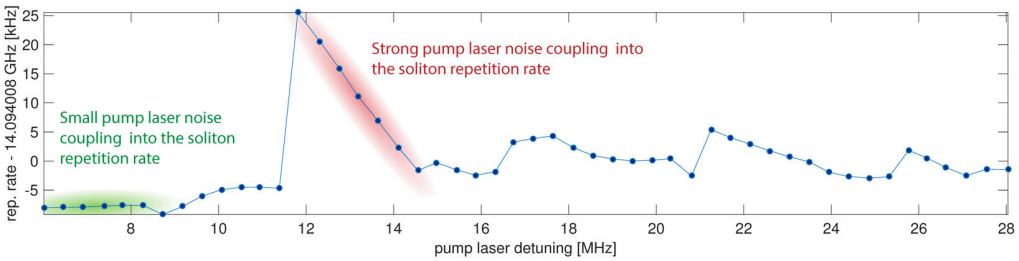


Fig. 4. Measurement of the soliton repetition rate versus the laser – cavity detuning. The detuning-dependent excitation of mode crossing cause changes in the soliton repetition rate and increased coupling from pump frequency noise to repetition rate noise.

III. Locking the Pump Laser to the Microcavity

We further investigate how the high-quality factor of the microcavity can be leveraged to directly narrow the pump laser linewidth using the Pound-Drever-Hall (PHD) method. The working principle is illustrated in Fig. 5a. A diode laser is used as a pump and phase modulated before coupling to the cavity. The filtered pump light in the transmission from the resonator is then used to derive the PDH error signal, which is fed-back on the laser. When a soliton is generated in the cavity, the laser is effectively detuned from the resonance [9], such that the PDH locking is done on one of the sidebands. In this method, the detuning corresponds to the PDH local oscillator (LO) frequency and can be precisely set and maintained.

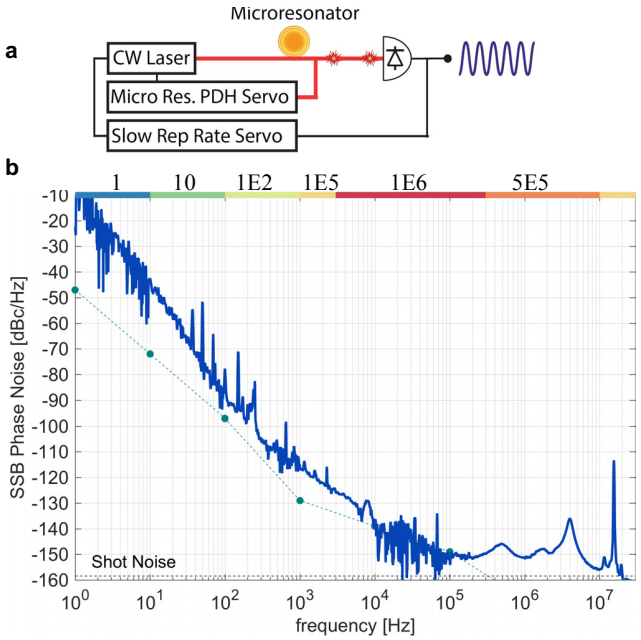


Fig. 5. (a) Experimental scheme employed for offset locking the laser to the microresoantor while producing a soliton. The microwave frequency is slowly stabilized to the common RF clock, to avoid longterm drifts, by feedback on the pump power. (b) Phase noise of the 14 GHz tone measured on the FSUP when applying the offset PDH locking. The modulation tone at the PDH LO frequency is visible around 18 MHz. The colored bars and number at the top indicate the amount of cross-correlations applied in each band. The dotted line indicate the device noise floor, accounting for the number of cross-correlations.

We observed a drastic reduction of the microwave phase noise when enabling the lock. In order to mitigate the effects of the drift on the phase noise measurement, we added a slow phase lock loop that stabilized the repetition rate to the common clock of the FSUP via a feedback on the pump power. This eliminated the long term drift that prevented a larger number of cross-correlations to be implemented and allowed the number of cross correlations to be increased to 1 million for some offset frequencies. (measurement time ~3 hours), reaching ~ -140 dBc/Hz at 10 kHz.

IV. Conclusion

We have shown that the photonic generation of low noise microwaves with soliton Kerr frequency comb is possible. The advances toward the realization of a compact RF photonic oscillator and a description of the noise processes in Kerr frequency combs were presented. In addition the high level of control demonstrated over the pump laser enbales detailed studies of the internal soltion dynamics. It is anticipated that by improving the environmental control and improvement of the pump laser intensity stabilization will help in further reducing the phase noise of the generated microwave tone, especially its long-term stability. In the future, a robust packaging of the system will enable better stability and a smaller footprint.

References

[1] S. Cundiff and J. Ye, "Colloquium: Femtosecond optical frequency combs," *Rev. Mod. Phys.*, vol. 75, no. 1, pp. 325–342, Mar. 2003.

[2] X. Xie *et al.*, "Photonic microwave signals with zeptosecond-level absolute timing noise," *Nat Phot.*, vol. 11, no. 1, pp. 44–47, Jan. 2017.

[3] T. M. Fortier *et al.*, "Generation of ultrastable microwaves via optical frequency division," *Nat. Photon.*, vol. 5, no. 7, pp. 425–429, Jun. 2011.

[4] W. Liang *et al.*, "High spectral purity Kerr frequency comb radio frequency photonic oscillator.," *Nat. Commun.*, vol. 6, p. 7957, Jan. 2015.

[5] T. Herr *et al.*, "Temporal solitons in optical microresonators," *Nat. Photon.*, vol. 8, no. 2, pp. 145–152, Dec. 2013.

[6] H. Guo *et al.*, "Universal dynamics and deterministic switching of dissipative Kerr solitons in optical microresonators," *Nat. Phys.*, vol. 13, no. 1, pp. 94–102, Jan. 2017.

[7] A. B. Matsko and L. Maleki, "Noise conversion in Kerr comb RF photonic oscillators," *J. Opt. Soc. Am. B*, vol. 32, no. 2, pp. 232–240, Oct. 2015.

[8] T. Herr *et al.*, "Mode spectrum and temporal soliton formation in optical microresonators," *Phys. Rev. Lett.*, vol. 113, no. 12, p. 123901, Nov. 2014.

[9] E. Lucas, H. Guo, J. D. Jost, M. Karpov, and T. J. Kippenberg, "Detuning-dependent properties and dispersion-induced instabilities of temporal dissipative Kerr solitons in optical microresonators," *Phys. Rev. A*, vol. 95, no. 4, p. 43822, Apr. 2017.

[10] X. Yi, Q.-F. Yang, X. Zhang, K. Y. Yang, X. Li, and K. Vahala, "Single-mode dispersive waves and soliton microcomb dynamics," *Nat. Commun.*, vol. 8, p. 14869, Mar. 2017.

[11] J. P. Gordon and H. A. Haus, "Random walk of coherently amplified solitons in optical fiber transmission," *Opt. Lett.*, vol. 11, no. 10, pp. 665–667, 1986.

[12] R. Paschotta, "Noise of mode-locked lasers (Part II): timing jitter and other fluctuations," *Appl. Phys. B*, vol. 79, no. 2, pp. 163–173, May 2004.

ACKNOWLEDGMENTS

This work was supported by Contract W31P4Q-14-C-0050 from the Defense Advanced Research Projects Agency (DARPA), Defense Sciences Office (DSO) and from the Swiss National Science Foundation under grant agreement No. 161573. E.L. acknowledges support by the European Space Technology Centre with ESA Contract No.: 4000118777/16/NL/GM.

Optical Synthesis Using Kerr Frequency Combs

Shamsul Arafin, Arda Simsek, Seong-Kyun Kim, Mark J. Rodwell and Larry A. Coldren

Department of Electrical and Computer Engineering, University of California, Santa Barbara, CA, 93106, U.S.A.
e-mail: sarafin@ece.ucsb.edu

Lute Maleki, Wei Liang, Vladimir Ilchenko, Anatoliy Savchenkov, Danny Eliyahu, and Andrey Matsko

OEwaves Inc., 465 N Halstead St. Pasadena, CA 91107, U.S.A.
e-mail: andrey.matsko@oewaves.com

Gordon Morrison, Milan Mashanovitch, and Leif Johansson

Freedom Photonics LLC, 41 Aero Camino, Santa Barbara, CA 93117, U.S.A.

***Abstract*— An InP-based photonic integrated circuit was demonstrated for offset locking an on-chip broadly tunable laser to a heterogeneously integrated optical frequency comb oscillator based on a crystalline whispering gallery mode resonator. Optical tuning within 60nm band is demonstrated. The locked laser has excellent spectral purity, sub-kHz linewidth, and good frequency stability.**

Keywords*— *photonic integrated circuits, integrated optics, optical phase-locked loop, heterodyne, optical frequency comb, optical microresonator, whispering gallery mode, self-injection locked semiconductor laser

I. INTRODUCTION

Synthesizers are key capabilities in time and frequency applications. The advent of optical techniques in these fields has made a number of important applications possible, so optical synthesis supporting optical frequency control is under intense development in several laboratories around the world. Many coherent optical systems can be realized by using optical phase lock loops (OPLLs) as key elements of optical synthesis. These include optical atomic clocks, light detection and ranging (LiDAR), fiber optic sensing, optical tomography and terahertz wave generation. High-performance, low-power and compact photonic integrated circuits (PICs) -based OPLLs are important for enabling these applications and have been actively studied recently [1,2]. These demonstrated PICs consumed as high as ≥0.5 W [3] of power and their footprint exceeded 2.3 mm^2 [4]. Further improvement of these parameters is needed in designing compact and low-power systems.

In this paper we report on an experimental realization of an OPLL-based optical synthesizer. The device includes a compact, low-power coherent optical system involving a 60-nm-tunable LO laser, couplers and photodetectors monolithically integrated on a standard InP/InGaAsP material platform, as well as an integrated Kerr optical frequency comb (OFC) generator operating as a frequency reference. The heterodyne OPLL transfers the phase noise of a reference frequency comb to the generally noisy LO laser, within the loop bandwidth. Therefore, having an excellent LO is a prerequisite for success in realization of a high performance OPLL. We demonstrate the offset locking of an on-chip Y-branch laser to the OFC unit, making this an important step forward towards the future demonstration of a chip-scale, low-power, ultra-stable optical frequency synthesizer.

We found that the geometrical size and the electrical power consumption for the PICs can be improved significantly with a careful design [5,6]. The inherent advantages of chip integration can be enhanced in this way, and the system can be made much smaller. This is attractive since the small-sized PICs enable a short OPLL loop delay, which results in a larger loop bandwidth.

To create the optical synthesizer we utilized an OPLL involving commercial-off-the-shelf parts. This loop required usage of an optical amplifier to achieve locking to low power frequency comb lines. To show that the entire system can be placed on a chip we designed an OPLL with a trans-impedance amplifier (TIA) increasing the sensitivity of the system significantly. No optical amplification is needed when TIAs provides high electrical gain with minimal noise.

II. EXPERIMENT

Schematic of the experimental setup is shown in Fig. 1. It included two separate integrated components: an optical receiver chip and a frequency comb.

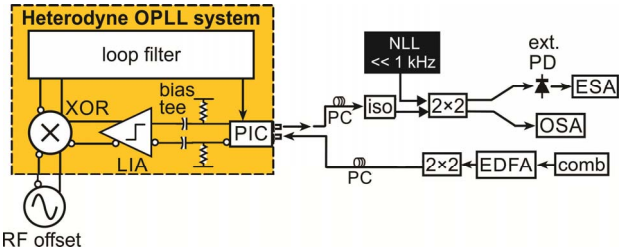


Figure 1: Experimental setup. The heterodyne OPLL system monitors the performance of the Y-branch laser. (ESA: electrical spectrum analyzer, OSA: optical spectrum analyzer, PC: polarization controller, iso: isolator and ext. PD: external photodiode, and EDFA: erbium-doped fiber amplifier, LIA: limiting amplifier, PIC: photonic integrated circuit

A. Broadly tunable laser and the receiver

This work was supported in part by DARPA MTO

The Y-branch laser in the full back-end PIC has a three times smaller cavity compared to standard sampled-grating distributed Bragg reflector. With short gain and mirror sections as well as a highly reflective back cleaved/HR-coated mirror, the device requires low current, and therefore lower drive power. The short cavity design was made by shortening the gain section and introducing zero-length back mirror through high-reflection coating, replacing the standard long back mirror. The emission wavelength is tuned via Vernier effect and was designed for high efficiency at 30º C ambient. The tuning range of the laser is measured to be 60 nm without changing the temperature, covering the entire C-band of optical communication. The laser shows good single-mode working performance with a side-mode suppression ratio of > 45 dB across the entire tuning range. No long absorber section or integrated booster preamplifier was included in this design so that the power consumption and chip-size could be reduced further. The output and input waveguide cleaved facets were coated with anti-reflection coating to suppress parasitic reflection. The laser is integrated into the receiver depicted in Figure 2.

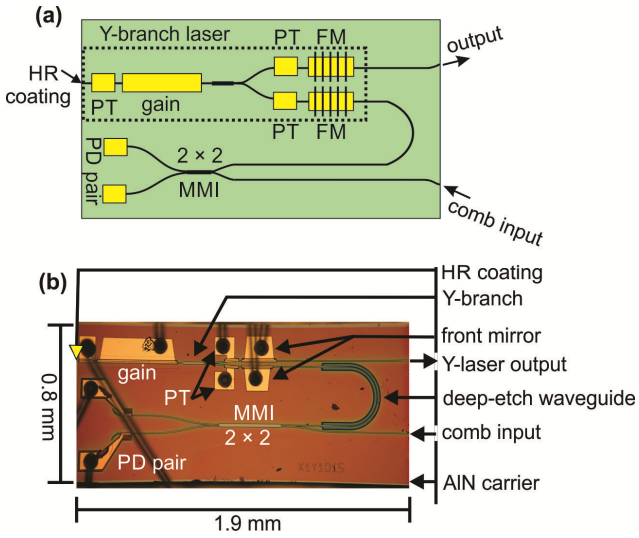


Figure 2: (a) Functional schematic of the photonic integrated receiver circuit composed of a Y-branch laser, two MMI couplers, and a balanced photodetector pair, (b) microscope image of the PIC mounted on a separate aluminium-nitride (AlN) carrier and wirebonded. (HR: high reflection, MMI: multimode interference, PT: phase tuner, FM: front mirror, PD: photodetector), (c) Schematic of the Kerr frequency comb generator.

B. *Kerr frequency comb oscillator*

We used an OFC generator consisting of a semiconductor laser pumping a crystalline MgF_2 resonator with a mode spacing of 25.5 GHz. The unit was packaged in a 12 cc form factor and its fiber-coupled output was sent to an optical spectrum analyzer (OSA). The measured optical spectrum with a 50-dB span of 23nm is shown in Fig. 3(a). The strongest central line at 1555.27nm is the residual light from the pump laser. The RF signal generated by the beat frequency of the comb lines on a fast PD integrated in the packaged unit was measured to distinguish between chaotic and coherent regimes of the frequency comb. An exceptionally high spectrally pure RF line was observed. The 3-dB bandwidth of the RF beat tone at 25.7 GHz is <100 Hz, limited by the resolution bandwidth (RBW) of the electronic spectrum analyzer, ESA. The phase noise of the repetition rate of the OFC, as well as the pump light, is shown at Fig. 3d.

Depending on the initial conditions, the OFC unit produces frequency combs varying in shape (see Fig. 4). The variations can be linked to the different number of optical pulses within the WGMR. While all the realized solutions are intrinsically stable and suitable for LO stabilization, the solution corresponding to the single pulse localized in the resonator is advantageous, as it does not have any envelope structure. Changing of the power of the comb lines makes the offset locking to some of the modes of the OFC a difficult task. We utilized the frequency combs with the smoothest envelope.

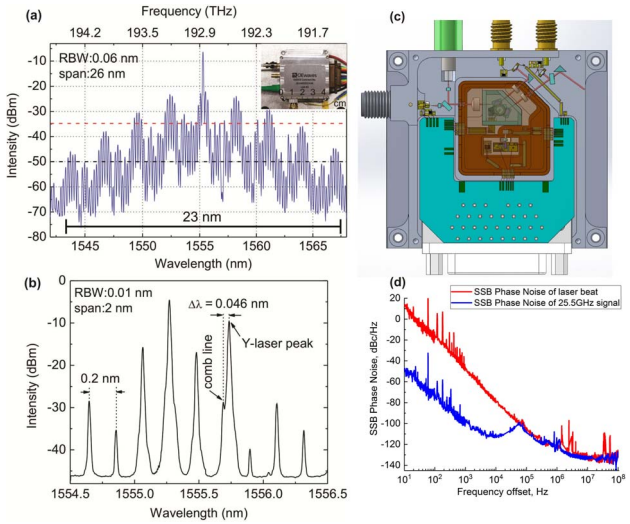


Figure 3: (a) Optical spectrum of a stabilized Kerr frequency comb generated by the OFC generator, as shown as inset. The comb spans 23 nm defined as the width where the intensity ≥ -50 dBm (black dotted line) and has a line spacing of 0.2 nm, yielding more than 115 lines. The optical output comb power exiting the fiber is 100 µW obtained after subtracting the pump laser power, meaning only ~0.5 µW per comb line is achieved in the wavelength range of 1542 nm-1568 nm. The horizontal (red) dashed line denotes the 0.5 µW per comb line power level, and (b) optical spectrum when Y-branch laser is offset--locked to the comb at 1555.69 nm with a wavelength difference of 0.046 nm. (c) Schematic of the frequency comb unit. (d) Single sideband phase noise of the laser and the comb repetition rate of the comb unit. The laser phase noise is measured by beating the laser with a similar device at a fast photodiode.

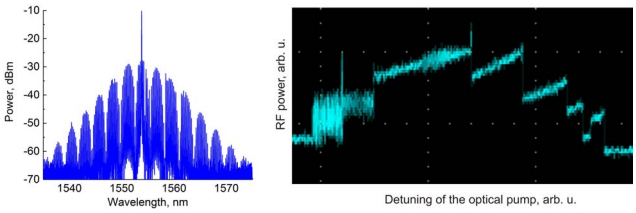


Figure 4: Illustration of the multi-stability of the Kerr frequency comb (compare with the spectrum in Fig. 3a). Left: Another type of Kerr comb frequency spectrum emitted by the oscillator. Right: An oscilloscope trace illustrating the RF power generated by the frequency combs emitted by the oscillator on a fast photodiode. The observed power jumps correspond to different comb regimes.

C. Heterodyne OPLL System

In the OPLL system reported here, a SiGe based commercial-off-the-shelf (COTS) limiting amplifier with 30-dB differential gain was used (Fig. 5). This gain is equal to 31.6 in linear units, indicating that offset phase-locking can be achieved using error signals with a peak to peak magnitude of approximately 10 mV. This corresponds to 0.2 mA required beat current in 50 Ω common mode logic system. In fact, this beat current is produced by beating optical comb-line power of 10 µW with the given 1 mW LO power. Please note that the responsivity of the on-chip PDs is assumed to be 1 A/W. The beat current I_{beat} can be calculated by the following expression:

$$I_{beat} = 2\sqrt{I_{REF} I_{LO}}$$
$$I_{beat} = 2\sqrt{0.01(mA)\times 1(mA)}$$
$$I_{beat} = 0.2mA$$

.

where, I_{REF} and I_{LO} are the photocurrents in the on-chip PD resulting from the optical power of the reference comb line and on-chip LO, respectively.

Hence, the minimum input optical comb line power required for the offset locking is experimentally measured to be about 10 µW.

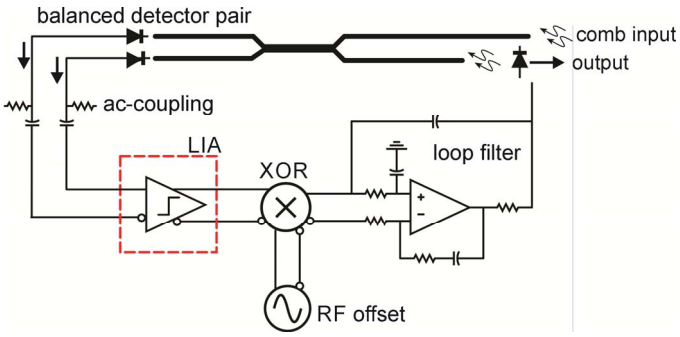


Figure 5: Schematic of the OPLL utilized in the optical synthesizer.

D. OPLL with improved sensitivity

Since the comb output power is not high for offset locking, an amplifier (the EDFA) is necessary to obtain adequate optical power levels in our presented OFS (see Fig. 1). For a fully chip-scale OFS, however, it is important to eliminate the EDFA and replace it with an on-chip semiconductor optical amplifiers. Furthermore, there is also an alternative way by which we could get rid of the EDFA. Instead of amplifying the power in the optical domain, we can increase the sensitivity of our electronic ICs so that the weak error signal generated by beating of the on-chip laser and low-power comb line on the balanced photodiodes can be handled by the feedback electronics. Specifically, the sensitivity of our OPLL system will be increased by using high-gain amplifiers with low noise figure so that on-chip lasers can be phase locked to a comb line without an EDFA. This also helps in reducing the OFS system power consumption further.

For this, we have designed a TIA with low noise, high gain and wide bandwidth using 130 nm SiGe HBT process (Fig. 6). This chip is designed for 80 dB voltage gain and 120 dBohm transimpedance gain with 30GHz bandwidth. It has less than 10 pA/Hz$^{1/2}$ input referred noise current up to 20 GHz with respect to 50 fF photodiode capacitance. These are the features that makes this application specific IC suitable for the frequency synthesis system.

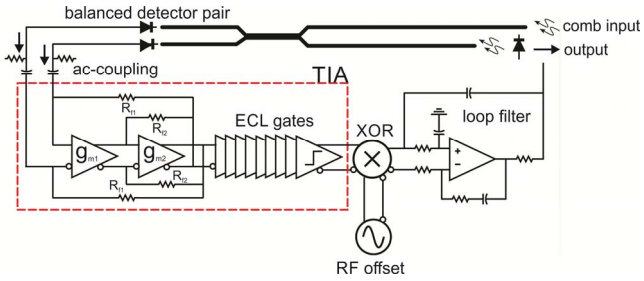


Figure 6: Schematic of the sensitive OPLL with low noise transimpedance amplifier.

As mentioned previously, each single harmonic of the optical frequency comb has only 0.5 µW of power. After considering the fiber coupling loss of 6 dB and optical power splitting by 2 x 2 MMI, the on-chip comb power available for beating is about 60 nW, whereas the local oscillator's power is about 1 mW. Given the responsivity of the on-chip PDs is 1 A/W, the beat current resulting from between on-chip-laser and one of the comb lines is approximately 15 µA in each PD, as shown in the following:

$$I_{beat} = 2\sqrt{I_{LO} I_{REF}}$$
$$I_{beat} = 2\sqrt{60(nA)\times 1(mA)}$$
$$I_{beat} = 15\mu A$$

This current needs to be amplified by the TIA and produce a logic output of 300 mV, which will drive the digital XOR gate. Thus, TIA should have at least the following gain.

$$Gain = \frac{300mV}{15\mu A} = 20k\Omega$$

$$Gain(dB\Omega) = 20\log_{10} 20000 = 86$$

Our TIA has more than enough gain to lock the local oscillator to the optical frequency comb lines. Functional test of the TIA demonstrates 60 dB differential gain, with a proper DC restoration loop this gain can be as high as 80 dB as simulated.

This sensitivity can be improved to as low as 60 nW using the novel TIA design discussed here. When this is achieved, EDFA is no longer needed and the OFS system total power consumption will be much lower as well as it will be more compact and will be closer to a true chip scale OFS system with much less than 2 Watts of power consumption. Implementation of the compact structure is our current goal.

III. CONCLUSION

A miniature and low power photonic coherent synthesizer with an integrated broadly tunable laser and an integrated Kerr

frequency comb oscillator are developed. Low noise optical tone is produced on demand by tuning the laser across the comb span and phase locking it to any of the comb lines. In this way, the higher power laser reproduces the high spectral purity of the frequency comb. The demonstrated PIC synthesizer is promising for reduction of the total power consumption to watt-level in a highly integrated package.

REFERENCES

[1] S. Ristic, A. Bhardwaj, M. J. Rodwell, L. A. Coldren, and L. A. Johansson, "An Optical Phase-Locked Loop Photonic Integrated Circuit," *Journal of Lightwave Technology,* vol. 28, no. 4, pp. 526-538, 2010

[2] R. J. Steed, F. Pozzi, M. J. Fice, C. C. Renaud, D. C. Rogers, I. F. Lealman, D. G. Moodie, P. J. Cannard, C. Lynch, L. Johnston, M. J. Robertson, R. Cronin, L. Pavlovic, L. Naglic, M. Vidmar, and A. J. Seeds, "Monolithically integrated heterodyne optical phase-lock loop with RF XOR phase detector " *Optics Express* vol. 19, no. 21, pp. 20048-20053, 2011.

[3] H.-C. Park, M. Lu, E. Bloch, T. Reed, Z. Griffith, L. Johansson, L. Coldren, and M. Rodwell, "40Gbit/s coherent optical receiver using a Costas loop," *Optics Express,* vol. 20, no. 26, pp. B197-B203, 2012.

[4] M. Lu, H.-C. Park, A. Sivananthan, J. S. Parker, E. Bloch, L. A. Johansson, M. J. W. Rodwell, and L. A. Coldren, "Monolithic Integration of a High-Speed Widely Tunable Optical Coherent Receiver," *IEEE Photonics Technology Letters,* vol. 25, no. 11, pp. 1077-1080, 2013.

[5] Shamsul Arafin, Arda Simsek, Seong-Kyun Kim, Sarvagya Dwivedi, Wei Liang, Danny Eliyahu, Jonathan Klamkin, Andrey Matsko, Leif Johansson, Lute Maleki, Mark Rodwell, and Larry Coldren, "Towards chip-scale optical frequency synthesis based on optical heterodyne phase-locked loop," Opt. Express vol. 25, no. 2, pp. 681-695, 2017.

[6] S. Arafin, A. Simsek, S.-K. Kim, W. Liang, D. Eliyahu, G. Morrison, M. Mashanovitch, A. Matsko, L. Johansson, L. Maleki, M. J. Rodwell, and L. A. Coldren, "Power-efficient Kerr frequency comb based tunable optical source," IEEE Photonics Journal vol. 9, no. 3, art. no. 6600814, 2017.

Perturbation Analysis of Nonlinear Signal Generation in Radio Frequency Bulk Acoustic Wave Resonators

[1]Ken-ya Hashimoto, [2,1]Xinyi Li, and [2]Jingfu Bao
[1]*Graduate School of Engineering, Chiba University, Inage-ku, Chiba 263-8522 Japan*
[2]School of Electronic Engineering, University of Electronic Science and Technology of China, Chengdu 611731, China
k.hashimoto@ieee.org, kimilee56@gmail.com

***Abstract*—This paper describes perturbation analysis of nonlinear signal generation in radio frequency (RF) bulk acoustic wave (BAW) devices. Nonlinear constitutive equations with the *h* form are used where the electric flux density is an independent variable. In conventional ones with the *e* form, the electric flux density is a dependent variable. This choice makes generated nonlinear fields satisfy Gauss' law for electricity automatically. It is shown that non-linear characteristics of RF BAW devices can be simulated well by the simple first order perturbation analysis, and the harmonic balance analysis is not necessary. Origin of the nonlinearity is also discussed.**

I. Introduction

Recent advance in mobile communication technologies requests ultimate suppression of nonlinear signal generation in radio frequency (RF) surface and bulk acoustic wave (SAW/BAW) devices. For the purpose, accurate and fast simulation tools are demanded.

Shim and Feld demonstrated that nonlinear behavior of RF BAW devices is simulated well by the use of one-dimensional (1D) nonlinear Mason model[1]. In the analysis, the piezoelectric layer is subdivided into certain number of thin layers, and total fields are calculated by the harmonic balance (HB) method[2] where generation of multiple harmonics and inter-modulation distortions (IMDs) are taken into account simultaneously.

The authors understand that the HB method is required only when the nonlinearity is large. Since nonlinearity under concern is extremely weak, the lower-order perturbation analysis should be applicable in principle, and its validity was demonstrated for RF SAW devices[3].

Why is the HB analysis necessary for RF BAW devices? The authors thinks that this is due to use of nonlinear constitutive equations with the *e* form where the electric flux density *D* is a dependent variable, and thus resulting nonlinear *D* field will be spatially non-uniform in the first-order perturbation analysis. This non-uniformity violates Gauss' law for electricity which requests *D* to be uniform in the 1D analysis for the thickness extensional (TE) mode.

This paper describes the perturbation analysis of RF BAW devices using nonlinear constitutive equations with the *h* form. This choice makes generated nonlinear fields satisfy Gauss' law for electricity automatically even for higher-order perturbed solutions.

It is shown that non-linear characteristics are simulated well by the simple first order perturbation analysis.

Origin of the nonlinearity is also discussed.

II. Perturbation Analysis

Let us consider a configuration shown in Fig. 1. C-axis of the 6mm piezoelectric film with the thickness L is aligned to the x axis, and the surface area A (y-z plane) is very wide.

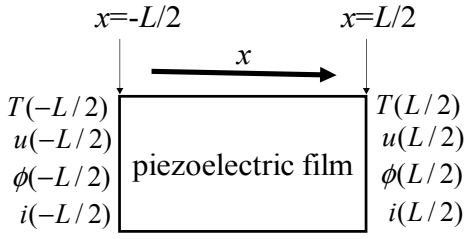


Fig.1 Configuration under consideration.

The 1D analysis of RF BAW devices starts from the equation of motion and Gauss' law for electricity:

$$\rho ii = \frac{\partial T}{\partial x}, \tag{1}$$

$$\frac{\partial D}{\partial x} = 0, \tag{2}$$

where ρ is the mass density, u, T and D are the displacement, stress and electric flux density, respectively. Eq. (2) requests that D is uniform throughout the structure.

Here the nonlinear constitutive equations are expressed in the following *h*-form:

$$T = c^{\mathrm{D}}S - hD + T_{\mathrm{N}}(S,D) \ , \tag{3}$$

$$E = \beta^{\mathrm{S}}D - hS + E_{\mathrm{N}}(S,D), \tag{4}$$

where c^D, h and β^S are stiffness at constant D, piezoelectric constant, and inverse permittivity at constant S, respectively, and T_N and E_N are higher order terms generating nonlinear responses. In Eq. (4), E is the electric field, and is related to the electric potential ϕ as

$$E = -\frac{\partial \phi}{\partial x} \tag{5}$$

under the quasi-static approximation. In Eqs. (3) and (4), S is the strain, which is related to u as

$$S = \frac{\partial u}{\partial x}. \tag{6}$$

Substitution of Eqs. (3) and (6) into Eq. (1) gives

$$c^{\mathrm{D}} \frac{\partial^2 u}{\partial x^2} - \rho \ddot{u} = -\frac{\partial T_{\mathrm{N}}}{\partial x}. \tag{7}$$

For the derivation, the relation of Eq. (2) is used. Substitution of Eq. (4) into Eq. (5) and its integration gives

$$\begin{aligned} \phi(+L/2) - \phi(-L/2) &= -\int_{-L/2}^{+L/2} E dx \\ &= -\beta^{\mathrm{S}} DL + h\{u(+L/2) - u(-L/2)\} - \int_{-L/2}^{+L/2} E_{\mathrm{N}}(x) dx \end{aligned}. \tag{8}$$

The current I is given by

$$I = -\dot{D}A \cdot \tag{9}$$

Following to the thermo-dynamic analysis[4],[5], nonlinear constitutive equations are derived by expanding the Helmhortz energy to the fourth-order of S and D. Then T_{N} and E_{N} in Eqs. (3) and (4) are given in the following forms:

$$\begin{aligned} T_{\mathrm{N}} = &-\frac{1}{2}\chi_{20}^{\mathrm{T}} S^2 - \chi_{11}^{\mathrm{T}} DS - \frac{1}{2}\chi_{02}^{\mathrm{T}} D^2 \\ &-\frac{1}{6}\chi_{30}^{\mathrm{T}} S^3 - \frac{1}{2}\chi_{21}^{\mathrm{T}} S^2 D - \frac{1}{2}\chi_{12}^{\mathrm{T}} SD^2 - \frac{1}{6}\chi_{03}^{\mathrm{T}} D^3 \end{aligned}, \tag{10}$$

$$\begin{aligned} E_{\mathrm{N}} = &-\frac{1}{2}\chi_{11}^{\mathrm{T}} S^2 - \chi_{02}^{\mathrm{T}} SD - \frac{1}{2}\chi_{02}^{\mathrm{E}} D^2 \\ &-\frac{1}{6}\chi_{21}^{\mathrm{T}} S^3 - \frac{1}{2}\chi_{12}^{\mathrm{T}} S^2 D - \frac{1}{2}\chi_{03}^{\mathrm{T}} SD^2 - \frac{1}{6}\chi_{03}^{\mathrm{E}} D^3 \end{aligned}. \tag{11}$$

The perturbation analysis starts from derivation of the linear responses at the driving frequency. When we ignore T_{N} and E_{N} in Eqs. (3) and (4) and the peripheral circuit conditions are specified, we can calculate linear responses of S and D in the RF BAW resonator under concern using the present model with setting T_{N}=E_{N}=0. Of course, it is equivalent to traditional 1D linear analyses such as the Mason model.

Using these zero-th order solutions, we can calculate T_{N} and E_{N} in Eqs. (3) and (4). Their calculation procedure will be detailed in the next section.

When T_{N} and E_{N} are given, Eq. (7) can be regarded as a second-order linear partial differential equation with a force oscillation term -$\partial T_{\mathrm{N}}/\partial x$.

It should be noted that since Eq. (7) is linear, responses caused by multiple frequency components appearing T_{N} and E_{N} can be calculated separately.

The general solution of Eq. (7) is given by

$$\begin{aligned} u(x) = &B_+ \exp(-jk_{\mathrm{B}}x) + B_- \exp(+jk_{\mathrm{B}}x) \\ &-\frac{1}{2c^{\mathrm{D}}} \int_{-L/2}^{+L/2} s(x-x') T_N(x') \exp(-jk_{\mathrm{B}}|x-x'|) dx' \end{aligned}, \tag{12}$$

where $k_{\mathrm{B}} = \omega\sqrt{\rho/c^{\mathrm{D}}}$, ω is the radial frequency of generated nonlinear signal, $B_\pm$ are coefficients to be determined by the boundary conditions, and

$$s(x) = \begin{cases} -1 & x < 0 \\ 1 & x > 0 \end{cases}. \tag{13}$$

When we select $T(\pm L/2)$, $u(\pm L/2)$, $\phi(\pm L/2)$, and I as variables, substitution of Eq. (12) into Eq. (3)-(6) and (8)-(9) gives their relations in a following form:

$$\begin{pmatrix} T(-L/2) \\ u(-L/2) \\ \phi(-L/2) \\ i \end{pmatrix} = \begin{pmatrix} H_{11} & H_{12} & 0 & H_{14} \\ H_{21} & H_{11} & 0 & H_{24} \\ H_{31} & H_{32} & 1 & H_{34} \\ 0 & 0 & 0 & 1 \end{pmatrix} \begin{pmatrix} T(L/2) \\ u(L/2) \\ \phi(L/2) \\ i \end{pmatrix} + \begin{pmatrix} G_1 \\ G_2 \\ G_3 \\ 0 \end{pmatrix}, \tag{14}$$

where

$$H_{11} = \cos(k_{\mathrm{B}}L),\ H_{12} = k_{\mathrm{B}}c^{\mathrm{D}} \sin(k_{\mathrm{B}}L),\ H_{21} = -\frac{1}{k_{\mathrm{B}}c^{\mathrm{D}}} \sin(k_{\mathrm{B}}L),$$

$$H_{14} = -\frac{h}{j\omega A}\{\cos(k_{\mathrm{B}}L) - 1\},\ H_{24} = \frac{h}{j\omega A k_{\mathrm{B}}c^{\mathrm{D}}} \sin(k_{\mathrm{B}}L),$$

$$H_{31} = -\frac{h}{k_{\mathrm{B}}c^{\mathrm{D}}} \sin(k_{\mathrm{B}}L),\ H_{32} = h\{\cos(k_{\mathrm{B}}L) - 1\},$$

$$H_{34} = -\frac{\beta^S L}{j\omega A} + \frac{h^2}{j\omega A k_{\mathrm{B}}c^{\mathrm{D}}} \sin(k_{\mathrm{B}}L),$$

$$G_1 = -j\frac{k_{\mathrm{B}}}{2} F_+ \exp(jk_{\mathrm{B}}L/2) + j\frac{k_{\mathrm{B}}}{2} F_- \exp(-jk_{\mathrm{B}}L/2),$$

$$G_2 = \frac{1}{2c^{\mathrm{D}}} F_+ \exp(jk_{\mathrm{B}}L/2) + \frac{1}{2c^{\mathrm{D}}} F_- \exp(-jk_{\mathrm{B}}L/2),$$

$$G_3 = hG_2 + F_0,$$

$$F_0 = \int_{-L/2}^{+L/2} E_{\mathrm{N}}(x') dx' \tag{15}$$

$$F_\pm = \int_{-L/2}^{+L/2} T_{\mathrm{N}}(x') \exp(\pm jk_{\mathrm{B}}x') dx'. \tag{16}$$

Calculation procedure of F_0 and $F_\pm$ will be discussed later.

Next, let us consider the case where the device under concern is composed of multiple (N) layers. It is clear that linear and nonlinear behaviors of all layers are expressed in the same form as Eq. (14). Note that h=0 for dielectric materials while the term including β^{S} in H_{34} should be replaced by -RL/A for metals with resistivity R.

Let us denote [H] and [G] matrices of the n-th layer as [H_n] and [G_n], respectively. Since T, u, ϕ, and I are continuous at boundaries, the [H] and [G] matrices [$\mathrm{H_t}$] and [$\mathrm{G_t}$] of the total structure are given by

$$[\mathrm{H_t}] = [\mathrm{H_1}][\mathrm{H_2}] \cdots [\mathrm{H_N}] \tag{17}$$

$$[Gt]=[H_1]\{[H_2](- -([H_{N-1}][G_N]+[G_{N-1}])- -)+[G_2]\}+[G_1] \quad (18)$$

Since $[H_t]$ and $[Gt]$ will possess the same forms as those given in Eq.(14), and T=0 at the top and bottom surfaces, mathematical manipulation of Eq. (14) gives the voltage drop v across the whole structure as

$$v = Zi + v_N \quad (19)$$

where

$$Z = H_{32}^t H_{14}^t / H_{12}^t - H_{34}^t \quad (20)$$

is the input impedance of the resonator, and

$$v_N = G_1^t H_{32}^t / H_{12}^t - G_3^t \quad (21)$$

is the open-circuited voltage for the nonlinear output.

Applying the peripheral circuit conditions to Eq. (19), we can then calculate the nonlinear response in the circuit level.

III. Calculation Procedure

It is clear that the equations derived for the first-order perturbed calculation is identical with those for the zero-th order calculation when we ignore G_1, G_2 and G_3, and the driving frequency is used for ω. When the linear analysis is performed in this way, input impedance of the resonator under concern is given by Eq, (20), and thus we can determine v and i by taking the peripheral circuit conditions are specified.

Since T=0 and $u = -H_{12}^{t-1} H_{14}^t i$ at the top surface, u and T at the the bottom surface of the first layer can be calculated by using the following relations derived from Eq. (14):

$$u(-L/2) = H_{21}T(L/2) + H_{11}u(L/2) + H_{24}i \quad (22)$$

$$T(-L/2) = H_{11}T(L/2) + H_{12}u(L/2) + H_{14}i \quad (23)$$

Since T and u at the top surface of the next layer are equal to those at the bottom surface of the preceding layer, we can calculate T and u at every boundaries by applying the relations of Eqs. (22) and (23) recursively from the top layer to the bottom.

Using thus calculated T and u at the top surface of each layer, we can calculate F_0 and $F_\pm$ defined in Eqs. (15) and (16), respectively. For second harmonics (H2), they are given by

$$F_0 = \frac{1}{2}k_B^2\chi_{11}^T\left[(B_+^2 + B_-^2)P_2 - 2B_+B_-L\right] + jk_B\chi_{02}^T D(B_+ - B_-)P_1 - \frac{1}{2}\chi_{02}^E D^2 L, \quad (24)$$

$$F_\pm = \frac{1}{2}k_B^2\chi_{20}^T\left[B_\pm^2 L - 2B_+B_-P_2 + B_\mp^2 P_4\right] + jk_B\chi_{11}^T D\left[B_\pm P_1 - B_\mp P_3\right] - \frac{1}{2}\chi_{02}^T D^2 P_2, \quad (25)$$

where $P_n = L\mathrm{sinc}(nk_BL/2)$ and

$$B_\pm = \exp(\pm jk_BL/2)\left[-\frac{T(L/2)+hD}{2jk_Bc^D} + \frac{1}{2}u(L/2)\right]. \quad (26)$$

IV. Experimental Verification

The present method was applied for the H2 analysis of an air-gap type FBAR with the Ru/AlN/Ru structure[6]. In the analysis, nonlinear signals were assumed to be generated in the AlN layer predominantly, and their generation in the Ru layers was ignored.

Fig. 2 shows measured input admittance Y_a of the resonator with the simulated one. Their agreement is well. For the fitting, the AlN thickness was adjusted and parasitic capacitance was added in parallel. In the figure, the simulated input admittance Y_{2a} at the H2 frequencies is also shown. No acoustic resonance exists in Y_{2a} in this frequency range.

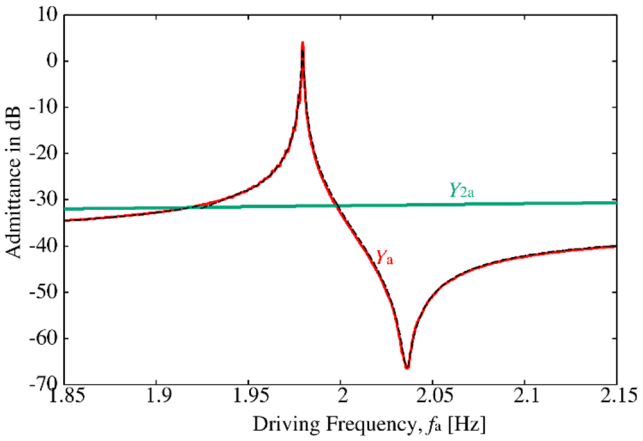


Fig. 2 Measured and simulated input admittance

Fig. 3 shows calculated and measured H2 at the input power of +26 dBm. Two calculations are shown: (a) only χ_{20}^T is considered, and (b) only χ_{11}^T is considered. The agreement is well for both cases, and validity of the present analysis is confirmed. Discrepancies is expected to be due to inaccuracy of the parameter adjustment given at the fitting to Y_a.

It should be noted that inclusion of nonzero χ_{02}^T or χ_{02}^E creates a dip in the H2 response at the anti-resonance frequency[1]. This is because in Eqs. (24) and (25), terms including χ_{02}^T or χ_{02}^E depend on D, and D is close to zero at the frequency. Since the dip is not seen in the experimental H2, we can conclude their contributions are negligible.

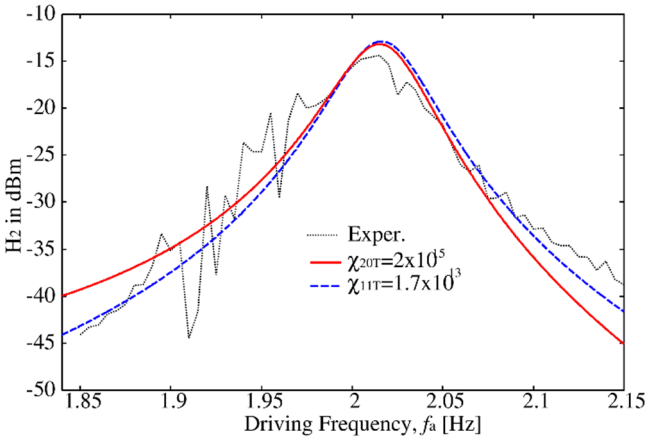


Fig. 3 Measured and simulated H2 responses

V. VOLTAGE COEFFICIENT OF FREQUENCY

Let us discuss variation of resonance frequencies with the superimposed DC bias voltage V_{DC}, which is called voltage coefficient of frequency (VCF)[7].

V_{DC} was applied to the device used for the H2 measurement, and variation of resonance and anti-resonance frequencies were measured. These frequencies changed linearly with V_{DC}; measured VCFs were +31 ppm/V and +26 ppm/V for the resonance and anti-resonance frequencies, respectively.

We express $D=D_{RF}+D_{DC}$ and assume $|D_{RF}|<<|D_{DC}|$. Then the nonlinear constitutive equations given in Eqs. (3), (4), (10) and (11) can be linearized as

$$T_{RF} \sim \left(c^D - \chi_{20}^T S_{DC} - \chi_{11}^T D_{DC}\right) S_{RF} - \left(h + \chi_{11}^T S_{DC} + \chi_{02}^T D_{DC}\right) D_{RF} \tag{27}$$

$$E_{RF} \sim \left(\beta^S - \chi_{02}^T S_{DC} - \chi_{02}^E D_{DC}\right) D_{RF} - \left(h + \chi_{11}^T S_{DC} + \chi_{02}^T D_{DC}\right) S_{RF} \tag{28}$$

Third-order terms proportional to D_{DC}^2 were ignored in these equations because the experiment exhibited only linear variation.

Since T~0 for DC, Eqs. (3), (4), (10) and (11) also give

$$D_{DC} = \frac{1}{L_p\left(\beta^S - h^2/c^D\right)} V_{DC} \tag{29}$$

$$S_{DC} = \frac{h}{c^D} D_{DC} = \frac{h/c^D}{L_p\left(\beta^S - h^2/c^D\right)} V_{DC} \tag{30}$$

where L_p is the thickness of the piezoelectric layer.

It should be noted that since D_{RF}~0 at the anti-resonance, VCF at the anti-resonance VCF_a is given by

$$VCF_a = \frac{1}{V_{DC}} \frac{df}{f} = -\frac{\chi_{11}^T + \chi_{20}^T h/c^D}{L_p\left(\beta^S c^D - h^2\right)} \left(\frac{c^D}{f} \frac{df}{dc^D} \right) . \tag{31}$$

The last term corresponds to sensitivity of the anti-resonance frequency with c^D, and its value is close to 0.5. It can be estimated numerically for the present structure by the linear analysis described above, and substitution of its value and the experimental VCF to Eq. (31) gives $\chi_{11}^T+\chi_{20}^T h/c^D=5\times10^{11}$ V/m. Let us assume χ_{11}^T is responsible and χ_{20}^T is negligible for VCF. Then this value of χ_{11}^T is 35 times smaller than the value required for explaining the measured H2 shown in Fig. 2. From this, it is concluded that χ_{20}^T is responsible for generation of the H2 generation at least for the device used for the discussion. This result is consistent with that given in [8].

On the other hand, since E_{RF}~0 at the resonance, VCF at the resonance VCF_r is given by

$$\frac{VCF_r}{VCF_a} \sim 1 + \frac{2\chi_{11}^T (h^2/\beta^S c^D) + \chi_{02}^T (2 + h^2/\beta^S c^D) + \chi_{02}^E (h/\beta^S)^2}{\chi_{11}^T + \chi_{20}^T h/c^D} . \tag{32}$$

In this case, not only χ_{11}^T and χ_{20}^T but also χ_{02}^T and χ_{02}^E contribute to VCF. Since experimental VCF at the resonance is somewhat different from that at the anti-resonance, it is concluded that contribution of χ_{02}^T and χ_{02}^E is not negligible for VCF occurrence.

VI. CONCLUSIONS

This paper dealt with the perturbation analysis of RF BAW devices using nonlinear constitutive equations with the h form. This choice makes generated nonlinear fields satisfy Gauss' law for electricity automatically. Non-linear characteristics are simulated well by the present analysis.

Since no iterative calculation is necessary and most of all necessary calculations can be completed analytically in advance, the simulation execution is extremely fast.

The calculation procedure described in this paper is also applicable to non-linear analyses of third harmonics and second and third intermodulation distortions (IMD2 and IMD3). For the case, formulas for F_0 and $F_\pm$ must be used, but they can be derived in closed forms with small efforts.

ACKNOWLEDGMENT

The authors thank Dr. M.Ueda and Mr. T.Nishihara of Taiyo Yuden, Co. Ltd. for supplying measured data used in this paper and their fruitful discussions. Xinyi Li also acknowledges the support of the Japanese Government (MEXT) for the scholarship through the Super Global University Project.

REFERENCES

[1] D.S.Shim, and D.A.Feld, "A General Nonlinear Mason Model and Its Application to Piezoelectric Resonators," International Journal of RF and Microwave Computer-Aided Engineering, **21**, 5 (2011) pp. 486-495

[2] H.G.Brachtendorf, G.Welsch, and R.Laur, "Fast Simulation of the Steady-State of Circuits by the Harmonic Balance Technique," Proc. International Symp. on Circuits and Systems (1995) 1388-1391.

[3] R.Nakagawa, T.Suzuki, H.Shimizu, H.Kyoya, K.Nako, and K.Hashimoto, "Discussion about Generation Mechanisms of Third-Order Nonlinear Signals in Surface Acoustic Wave Resonators on the Basis of Simulation," Jpn. J. Appl. Phys., **55**, 7 (2016) 07KD02-1~7

[4] B.A.Auld, "Thermodynamics of Solids," in Acoustic Fields and Waves in Solids, Second Edition, Vol. 1 (Klinger, Malabar, FL, USA, 1990) pp. 275-280.

[5] S.Tashiro, K.Ishii, and K.Nagata, "Measurement of the Nonlinear Coefficient of a Third-Higher Term in Lead Zirconate Titanate Piezoelectric Ceramics," J. Ceram. Soc. Jpn., **110**, 7 (2002) pp. 649–655.

[6] S.Taniguchi, T.Yokoyama, M.Iwaki, T.Nishihara, M.Ueda and Y.Satoh, "An Air-Gap Type FBAR Filter Fabricated Using a Thin Sacrificed Layer on a Flat Substrate," Proc. IEEE Ultrason. Symp. (2007) pp. 600-603

[7] R.Aigner, N.H.Huynh, M.Handtmann, and S.Marksteiner, "Behavior of BAW Devices at High Power Levels," Tech. Digest, IEEE International Microwave Symp. (2005) pp. 429-432

[8] D.A.Feld, "One-Parameter Nonlinear Mason Model for Predicting 2nd & 3rd Order Nonlinearities in BAW Devices," Proc. IEEE Ultrason. Symp. (2009) pp. 1082-1087

Improving coupling coefficient distribution on BAW filters manufactured on 200mm wafers

Sergey Mishin
Advanced Modular Systems, Inc
Goleta, CA/USA
smishin@amssb.com

Yury Oshmyansky
Advanced Modular Systems, Inc
Goleta, CA/USA
yoshmyansky@amssb.com

***Abstract*— In the past, most BAW and FBAR filters were produced on 150mm wafers. Typical yield on 150mm wafers was >90% [1], [2]. In the last few years, most filter manufacturers started migrating to 200mm wafers in order to reduce the cost of manufacturing. Unfortunately, due to variation of coupling coefficient (kt^2) [3], [4], [5], yields on 200mm wafers were significantly lower than on 150mm wafers. Stress in the piezoelectric material is the largest variable that changes coupling coefficient [6]. Figure 1. Shows how coupling coefficient varies with stress for devices that use piezoelectric aluminum nitride (AlN) and molybdenum (Mo) electrodes. Depending on the exact processing involved in making a filter, the same AlN deposition process will produce a completely different stress/kt^2 variation across the wafer. Figure 2 illustrates a difference coupling coefficient variation across wafer, using tungsten (W) vs. Mo electrode material while leaving everything else the same. In order to be able to obtain the best coupling coefficient with different processing on 200mm wafer, it is critical to have independent control of film stress across wafer. In this paper, we will demonstrate a method of controlling coupling coefficient across wafer within less than +/- 1% (total range) of the target.**

Keywords—film stress; coupling coefficient; AlN; aluminum nitride; stress control

Figure 1. Coupling coefficient as a function of average stress in AlN films.

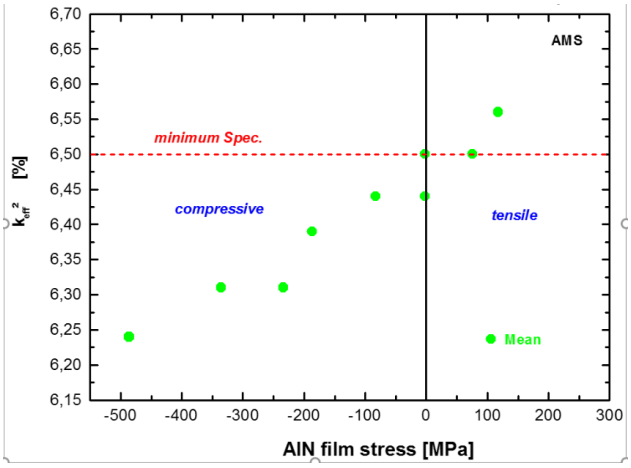
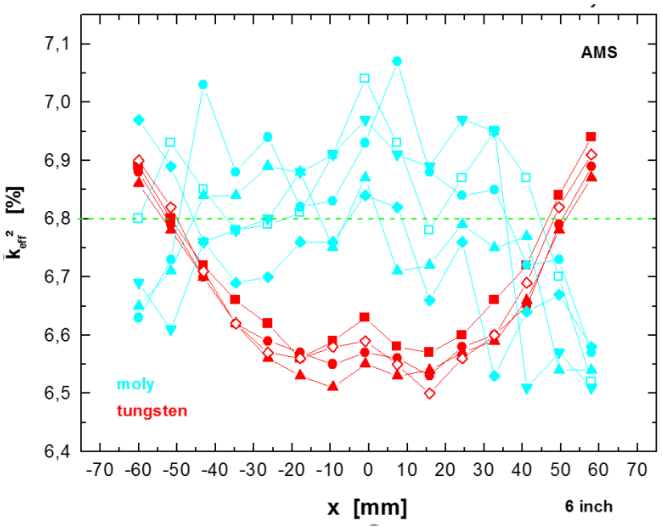


Figure 2. Coupling coefficient variation across wafer on Mo vs. W electrodes



I. INTRODUCTION

As most of the high volume manufacturers of FBAR/BAW filters are moving to 200mm wafer from 150mm wafer, new challenges emerged. One of the most critical is significantly higher variation of kt^2 across 200mm wafer. As can be seen in Figure 3, area of the 200mm wafer that can meet the kt^2 specifications is almost the same as on the 150mm wafer. In order to meet the same or even tighter specifications of the new filter products, it is important to be able to produce highly uniform kt^2 across wafer. For different processes it means ability to control stress across wafer.

Considering the importance of AlN film sterss and film thickness uniformity, it is necessary to have independent film stress and thickness control.

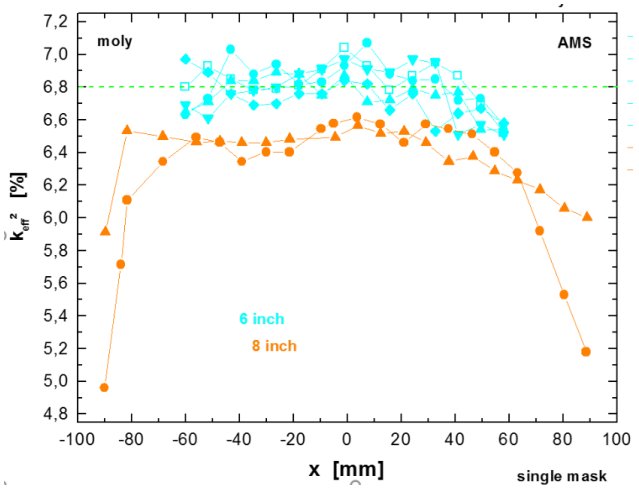
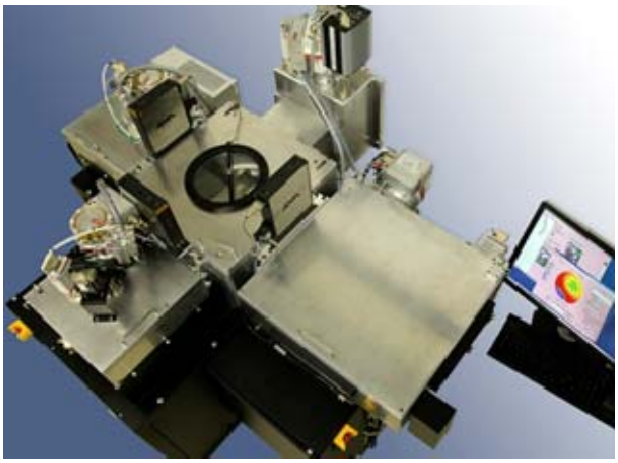


Figure 3. Typical results from 150mm wafer compared to 200mm wafer

II. EQUIPMEMT

In this investigation, we used Advanced Modular Systems cluster tool with three process modules: AlN deposition chamber, electrode deposition chamber and focus ion beam trimming module (shown in Figure 4).


Figure 4. AMSystems cluster tool with three modules (AlN deposition, Mo deposition and pre-clean/trimming)

AlN deposition process uses a high-volume production dual magnetron system with positive plasma column and with AC power applied between targets (magnetrons). Frequency of AC power is 40 kHz and power may vary from 3 to 10 kW.

It is a reactive deposition process in deep poison mode using pure Al targets. High purity research grade 99.9999% argon and nitrogen process gasses we used for all depositions.

Substrate rotation is used to reduce variation of non-uniformity of deposited film properties across the substrate. Integrated Laser interferometer is used to control average deposition thickness of the AlN films during process.

The trimming module uses DC focused ion beam source with argon process gas to improve thickness/uniformity of deposited films. Film thickness trimming/tuning is processing based on ion beam scanning across a wafer with power variation based on film thickness map. Use of the trimming process opens up a much wider process window for stress and other film properties control, because it allows avoiding of spending too much effort on controlling thickness uniformity during the deposition.

Figure 5. Focus Ion Beam Profile



Unlike back-sputter etch module in the traditional cluster tools, AMS trimming module can be used to both, cleaning the surface before deposition, as well as improving thickness uniformity after the deposition. It is very cost effective solution, because it doesn't cost any more than RF sputter etch chamber, but does a double duty as a pre-clean chamber and trimming chamber.

III. SYSTEM DESIGN FOR STRESS CONTROL IN ALUMINUM NITRIDE DEPOSITION

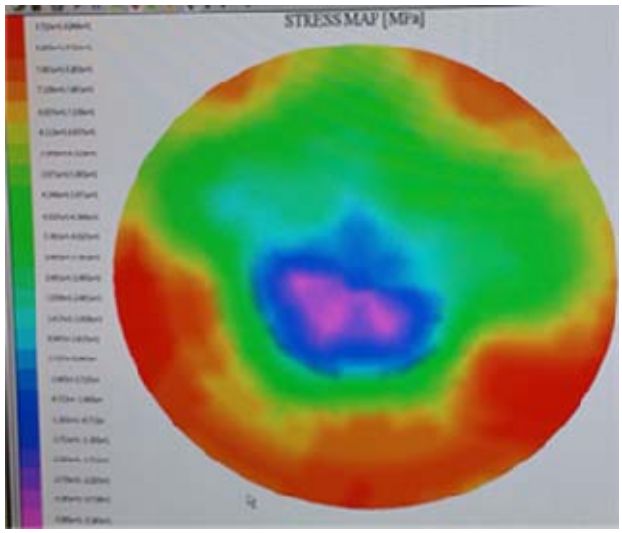
When using a standard rotary magnetron deposition system for the piezolectric AlN on 200mm wafer, stress variation across wafer is typically greater than 350MPa. In most designs, it also produces more tensile films in the center of the wafer. This is partially due to the inherent geometric limitations of the single target system, as well as the location of the racetracks on the target and the distance between racetracks and the anode or chamber wall. As a result, it produces high density plasma with positive column in the center of the target and low density plasma (due to elimination of positive plasma column) at the edge of the target. Since more material on the center of the wafer is deposited from the center of the target, and more material on the edge of the wafer is deposited from the target edge, it produces highly non-uniform center-to-edge AlN film properties (such as stress and coupling coefficient). It is very hard to optimize rotary magnetron system to give both, good thickness uniformity and good stress variation across wafer.

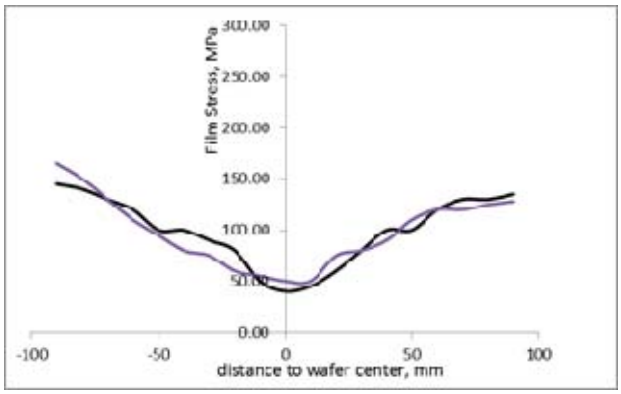
It is much easier to obtain good stress control and thickness uniformity of deposited film in a system with two independent magnetrons (targets), that allow fairly easy geometric manipulation of the target surface, as well

as independent magnetic field control on each target surface.

The AlN film, deposited mostly from the inner target produces largest effects on film properties near the center of the wafer. The AlN film, deposited on the wafer edge, mostly come from the outer target. Since, the AC power is applied between two targets (shields do not participated in plasma discharge) it creates symmetrical discharge and the positive plasma columns that are equal for the discharges. During the deposition, each target acts alternatively as an anode or cathode for the half of the cycle. Due to the same length of plasma discharge and plasma density, AlN film properties (stress for example) on the center of the wafer and on the wafer edge are the same. As result, the stress uniformity across the wafer is less than +/- 75 MPa for 200mm wafers, see Figure 6.

Figure 6. Typical AMS AlN film cross wafer stress for 200mm



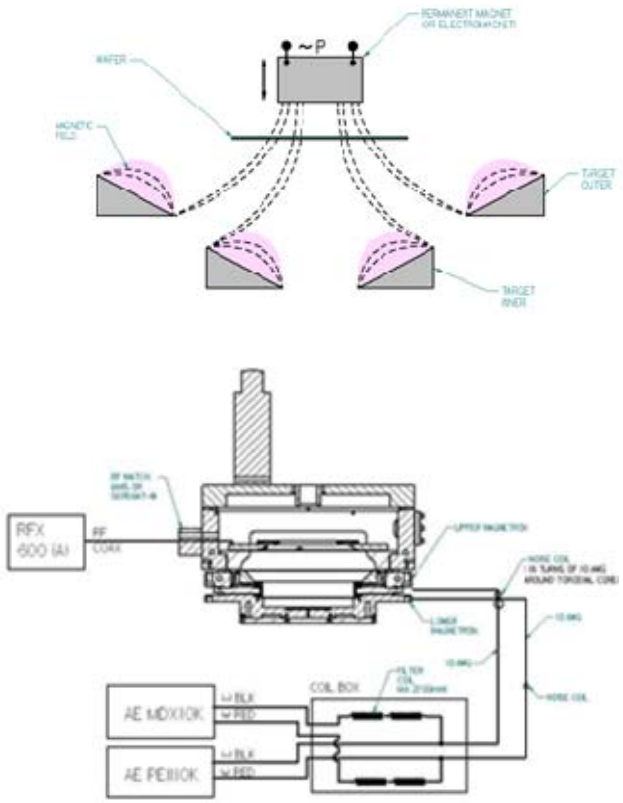


Additional DC power supply, in parallel with AC power supply, allows to shift reference point for AC power and precisely control center-to-edge thickness uniformity.

Wafer rotation is also used to improve both thickness uniformity and stress variation across wafer.

Figure 7 below shows a typical configurations (magnetic and electrical) used for the 200mm wafers.

Figure 7. Typical configuration used for the 200mm wafers.



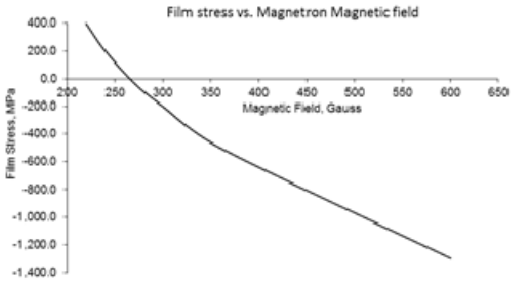
IV. CONTROLLING COUPLING COEFFICIENT FOR DIFFERENT PROCESSES

Depending on the processing used in manufacturing a particular filter technology, it is sometimes required to have a non-uniform stress distribution on a wafer. For example, when a film, that has perfectly uniform stress distribution on a prime silicon wafer, is deposited on a product wafer, stress is much more compressive in the center than on the edge of the wafer. This typically results in lower coupling coefficient in the center of the wafer. There are three potential ways of addressing this problem through AlN deposition:

1. Dis-balancing magnetons magnetic field (inner or outer) with supplemental magnetic fields located above the wafer.
2. Adjusting magnetic field on the magnetrons to purposely unbalance the stress across the wafer.
3. Increasing/decreasing the ratio of the deposition coming from outer vs. inner target.

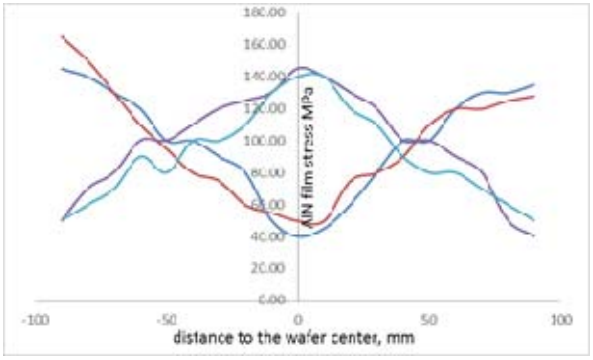
Since magnetron magnetic field has significant impact on film stress (see figure 8), it would be reasonable to spend significant amount of effort to control the magnetron magnetic field.

Figure 8. AlN film stress depeds on Magnetorn magnetic field



The easiest way to adjust the stress across wafer is to adjust magnetic field by dis-ballancing magnetic field by changing the magnetic field strength behing the wafer. This requires either a simple change of the permanent magnets or adjusting current to the electromagnet located behind the wafer. This methode allows to sputter more compressive or more tensile stress from inner target to the center of the wafer and can provide up to 300MPa stress change from the center to the edge of the wafer. It has a small impact on thickness uniformity that is easily corrected by the trimming process.

Figure 9. AlN film stress distribution across 200mm wafer



If a more significant change is required, it may be necessary to change the magnetic field ratio between inner and outer magnetrons. This requires much more extensive hardware modificaton and process re-carechterization. Figure 10 shows how adjustment of the magnetic field on two magnetrons can change stress across wafer.

If the magnetron ratio is already changed to have significantly different stress material coming from each magnetron on a different part of the wafer, changing the amount of material coming from each target will result in even bigger change in stress between the center and the edge. Typically, this kind of change will impact thickness uniformity the most and will require most trimming to compensate for thickness non-uniformity.

After making all of the above adjustments to the system, we were able to obtain excellent coupling coefficient uniformity over a ten wafer lot of BAW filter 200mm wafers.

Figure 10. Impact of the magnetron magnetic field ratio on stress across wafer.

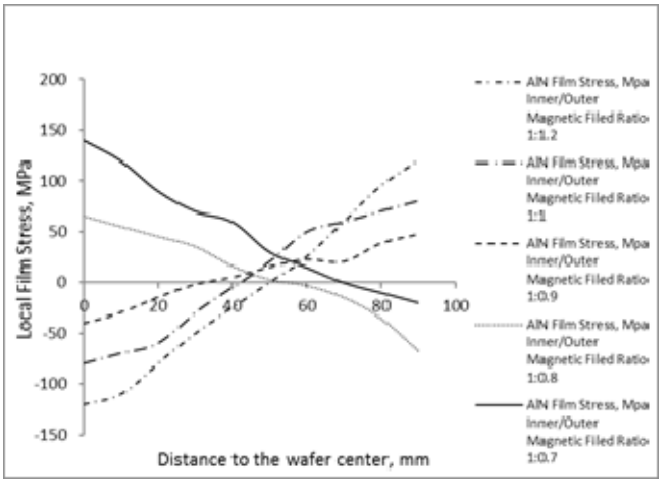
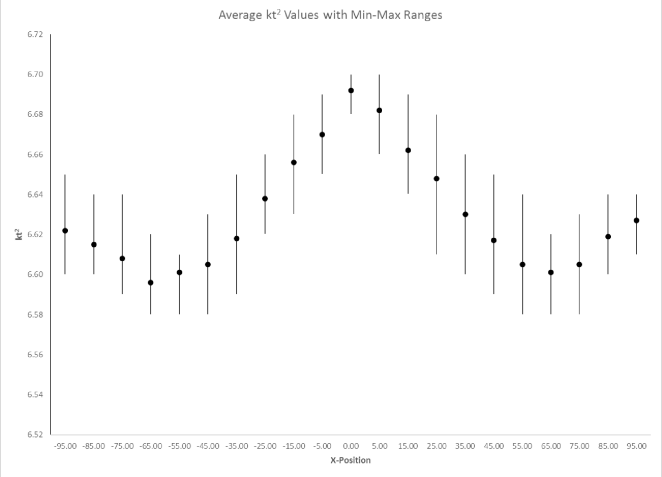


Figure 11. Coupling coefficient across 200mm wafers.



V. SUMMARY

We were able to demonstrate highly uniform coupling coefficient across 200mm BAW/FBAR wafers using AlN deposition on a dual magnetron deposition system with integrated pre-clean/trimming module. Stress and kt^2 uniformity across wafer was achieved without compromising thickness uniformity or crystal orientation of the deposited AlN film.

REFERENCES

[1] Mishin Sergey, et al. "Sputtering Processes for Bulk Acoustic Wave Filters". Semiconductor International, 3/1/2003

[2] Frank Z. Bi and Bradley P. Barber "Bulk Acoustic wave RF Technology", 2008 IEEE

[3] Sergey Mishin, Brian Sylvia and Daniel R. Marx "Improving Manufacturability of AlN Deposition Used in Making Bulk Acoustic Wave Devices", 2005 IEEE ULTRASONICS SYMPOSIUM
[4] K. Hashimoto "RF BULK ACOUSTIC WAVE FILTERS FOR COMMUNICATIONS", pp.173-195
[5] Robert Aigner "Corrective Actions to Meet Extreme Tolerance Requirements for Thin Films" 2007 Octagon Communication Inc. DBA MPDigest
[6] Sergey Mishin, Yury Oshmyansky and Frank Bi "Thickness Control by Ion Beam Milling in Acoustic Resonator Devices", 2010 IEEE FREQUENCY CONTROL SYMPOSIUM

Use of Double-Raised-Border Structure for Quality Factor Enhancement of Type II Piston Mode FBAR

Xinyi Li*†, Jingfu Bao*, Yulin Huang*†, Benfeng Zhang†‡ Gongbin Tang†‡
Tatsuya Omori† and Ken-ya Hashimoto†‡
*School of Electronic Engineering, University of Electronic Science and Technology of China, Chengdu, 611731, China
†Graduate School of Engineering, Chiba University, Inage-ku, Chiba, 263-8522, Japan
‡School of Electronic Information and Electrical Engineering, Shanghai Jiao Tong University, Shanghai 200240, China
Email: kimilee56@gmail.com

***Abstract*—This paper investigates applicability of double raised borders to the piston mode film bulk acoustic resonator (FBAR). It is shown that it offers significant improvement of the quality factor at the antiresonance without sacrificing the spurious level when the structure is designed appropriately. This enhancement is attributed to the reduction of the mode-conversion and the increase of the reflection coefficient at the border region.**

***Keywords*—FBAR; piston mode; Bragg reflector; quality factor**

I. Introduction

The mobile phone market grew rapidly in the last decade. Film bulk acoustic resonators (FBARs) are one of the most important devices in modern communication systems, and are widely used as frontend filters and duplexers [1]–[6].

The main resonance of FBARs is caused by the first-order thickness extension (TE1) vibration of the piezoelectric film sandwiched between two metal layers. Owing to finite lateral size, the TE1 mode will be reflected or converted to other Lamb modes at the side rims. It may cause spurious resonances and/or energy leakage to surroundings, which are the biggest concerns in the FBAR design. In the past decade, several strategies have been proposed for the purpose [7]–[10]. Among them, the most important advance is the so-called the piston mode operation, which was first proposed by Kaitila, et al. [11].

Its core concept is designing border regions to behave as if mechanically free boundaries so that spurious lateral modes are not sensed in the center active region. Comparing with other techniques such as apodization [12], the piston mode design offers higher quality factor for the main resonance.

In contrast to solidly mounted resonator (SMR) structures [13], [14], FBAR structures using AlN need to place a recessed frame at the inner side of the raised one for the piston mode operation [15]. This is due to so called the type-II dispersion where the first-order symmetric (S1) Lamb mode is evanescent at frequencies above the main resonance [11], [16].

It is clear that power leakage will be prominent when the raised frame height is not enough. On the other hand, when the height is too large, mode-conversion to the other Lamb modes will be significant, and they will be leaked away from surroundings. Thus achievable reflectivity for the S1 mode is expected to be limited when the single raised frame is used.

This paper discusses applicability of the double raised border to type II piston mode FBAR structures. Comparing with the single raised border, the double one offers higher reflection coefficient for the S1 mode, which results in enhancement of the Q factor. Although the reflection coefficient increases with the number of raised elements, it also causes reduction of the effective K^2 due to enlargement of the non-active area.

The difference in mode-conversion and reflection between single one and double one is also analyzed.

II. Resonator Design

Fig. 1 shows the double-raised-border (DRB) structure discussed in this paper. In the active region, the Ru thicknesses $h_{\rm t}$ and $h_{\rm b}$ are set identical so that only symmetric Lamb modes are electrically active. $h_{\rm p}$ and $h_{\rm t}$ were set at 1.0 μm and 0.3 μm, respectively, so that the effective electromechanical coupling factor K^2 is large and the resonance occurs at 2 GHz. The whole length of center active area L was chosen as 100 μm so that the impedance given by the shunt capacitance C_0 is close to 50 Ω.

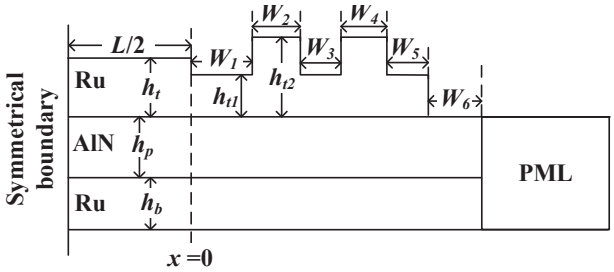


Fig. 1. Schematic structure of piston mode FBAR

In the following designs, W_2 and W_3 were fixed equal to W_4 and W_5, respectively, so that the border serves as the Bragg reflector (see Fig. 2).

This structure was analyzed and designed by the two-dimensional finite element method (FEM) software COMSOL. The maximum grid size was set as 200 nm to ensure the accuracy of FEM results [17]. The perfectly matched Layer (PML) was given to the right side edge to eliminate the reflection while the symmetrical condition was given at the

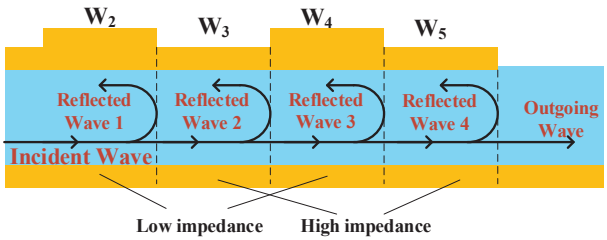


Fig. 2. Mechanism of the double raised border

left side edge. It should be noted that acoustic damping and ohmic loss were not included in the following calculation.

Fig. 3 shows the dispersion curves of Lamb modes in the active region (blue curve). The lateral axis is the lateral wavenumber. The main resonance occurs near the cutoff frequency f_0 of the S1 mode, and transverse mode resonances occur in the frequency range between the bifurcation point f_b and f_0.

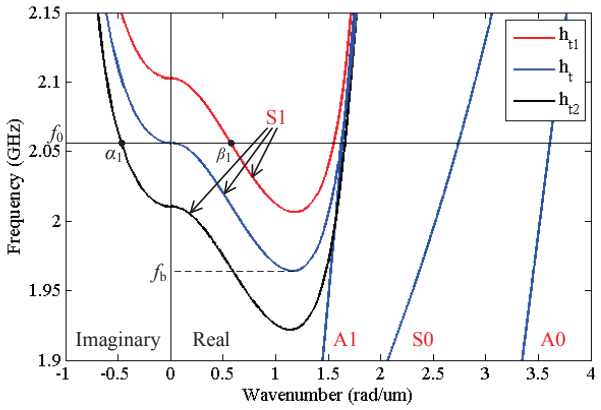


Fig. 3. Dispersion curves

The thickness h_{t2} in the raised region was set so that the S1 mode is evanescent in the frequency range as shown in the black line. In contrast, the thickness h_{t1} in the recessed region was set so that the lateral wavenumber of S1 mode is somewhat large as shown in the red line.

The widths W_1, W_2 and W_3 were optimized to maximize the anti-resonance Q under the piston mode operation [11].

In addition to the double raised structure, the single raised one (SRB) and that without the recessed border (WRB) were also designed for comparison. Table I shows designed structural parameters for these three cases.

III. Simulation Results

Fig. 4 shows calculated S_{11} for these three designs in the Smith chart. The double raised border exhibits almost ideal S_{11} between the resonance and antiresonance frequencies. This is owed to almost 100% reflection of incident Lamb modes at the border region.

TABLE I
THE PARAMETERS OF RESONATORS FOR SIMULATION

Parameter	Value (μm)		
	WRB	SRB	DRB
h_{t1}	0.3	0.274	0.274
h_{t2}	0.3	0.3285	0.3285
W_1	1.23	1.23	1.23
W_2	4.0	4.0	2.0
W_3	0.96	0.96	0.7
W_4	0	0	2.0
W_5	0	0	0.7

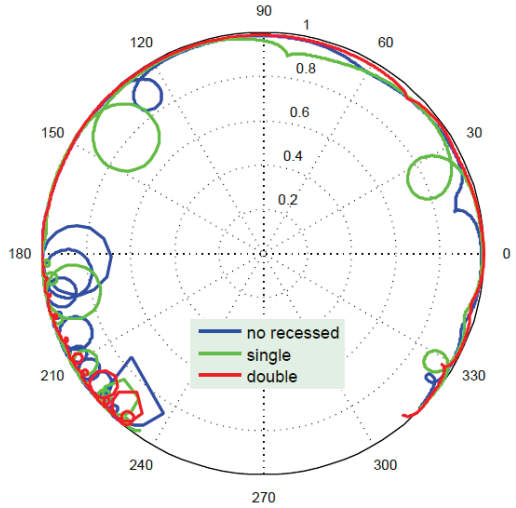


Fig. 4. S_{11} of three structures in the Smith chart

Transverse mode resonances can be clearly seen below the main resonance. This is because no additional loss mechanism is included in the analysis and Q is extremely high also for these resonances. The piston mode operation is frequency dependent, and perfect cancellation is possible only at one frequency.

Table II shows estimated Bode Q factors at the resonance and antiresonance frequencies [18]. Although the piston mode operation causes slight Q deterioration at the resonance, the anti-resonance Q is enhanced. Especially, the enhancement is prominent for the double raised border structure.

TABLE II
SIMULATION RESULT OF THREE CASES

Case	Q_r	Q_a	K_e^2
WRB	900,000	3,780	6.46 %
SRB	40,000	4,640	6.39 %
DRB	300,000	10,300	6.33 %

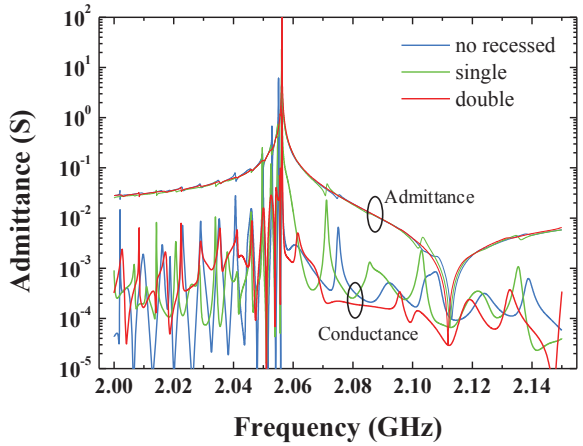
The table also shows the effective coupling coefficient K_e^2 calculated by [6]

$$K_e^2 = \frac{\pi}{2}\frac{f_r}{f_a}\cot\left(\frac{\pi}{2}\frac{f_r}{f_a}\right). \quad (1)$$

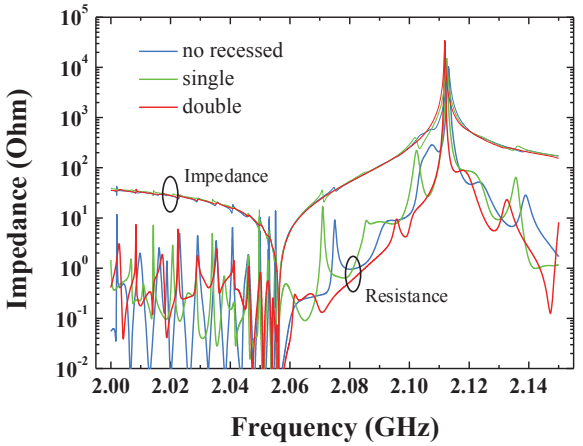
It is obvious that due to the introduction of non-active border region, the shunt capacitance C_0 is enlarged while the motional

one is unchanged. The whole length of the DRB structure is 0.44 μm longer than that of the SRB. It results in slight decrease (6.32% $\rightarrow$ 6.26%) in K_{e}^2. It is clear that the triple raised border will improve Q further, but achievable Q will be limited by other loss mechanisms. The double raised structure seems most appropriate from the tradeoff with the K_{e}^2 reduction.

Fig. 5 shows the conductance and resistance curves of these three structures with the admittance and impedance curves. It is seen that the double-raised-border structure gives the lowest conductance around f_{a} while keeping resistance around f_{r} low. Spurious resonances are also seen between the resonance and antiresonance, and are well suppressed for the double-raised-border structure. Detailed discussion on this will be given in the following section.



(a) Admittance



(b) Impedance

Fig. 5. Impedance and Admittance curves of three structures

IV. Reflectivity at Borders

The frequency domain analysis method [19], [20] was applied for these three structures, and the reflectivity at the border region was calculated. The estimated the power reflection coefficients for the S1- mode incidence are 94.0%, 74.2% and 98.7% for DRB, SRB and WRB cases, respectively, at the resonance frequency. This result explains variation of Q_{r} shown in with Table II.

Impact of the border design is further investigated by the fast Fourier transform (FFT) of the out-of-plane displacement $U_z(x)$ at f_{r}. All the data given below are normalized by amplitude of the incident S1- mode.

Fig. 6 shows the result at the tether region. DRB offers much smaller amplitude than SRB. Namely, less power passes through the tether. Nevertheless the power loss is minimal for WRB. This is related to the highest resonance Q of the structure.

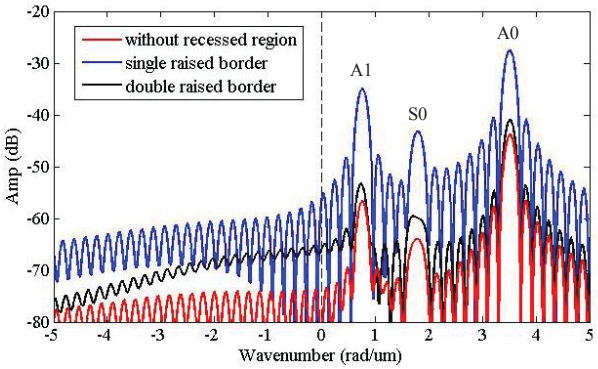


Fig. 6. Spectrum of U_z at the tether region.

Fig. 7 shows the results at the active region. It is clear that the mode conversion is weakest in WRB. For the S0, A0 and S1 modes, DRB offers weaker mode conversion than SRB. However, it is stronger for the A1 mode. Since it is not excitable in the active region, it is considered to be generated by the mode conversion from the incident S1 mode at the border region. Stronger A0 generation may be due to increased number of the structural discontinuities.

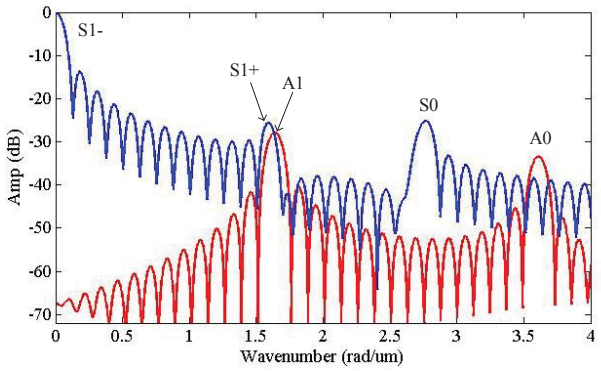
In the total reflected energy, the energy proportion of A1 mode is 10.2% for the double one and 2.68% for the single one. These results agree well with the qualitative analysis based on Fig. 7.

V. Conclusion

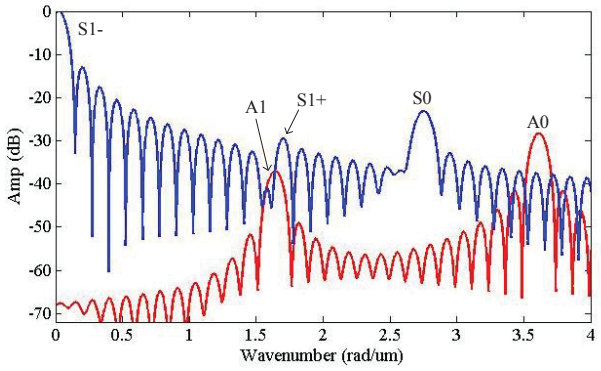
It was shown that the double-raised-border offers better Q factor than the single-raised-border case while keeping the piston mode operation. The Q enhancement is significant both for the resonance and anti-resonance frequencies compared with the single raised structure when the border is designed appropriately. By analysing the spectrum of U_z in wavenumber domain, it is verified that the novel structure owns higher reflection coefficient than original type-II piston mode structure.

Acknowledgment

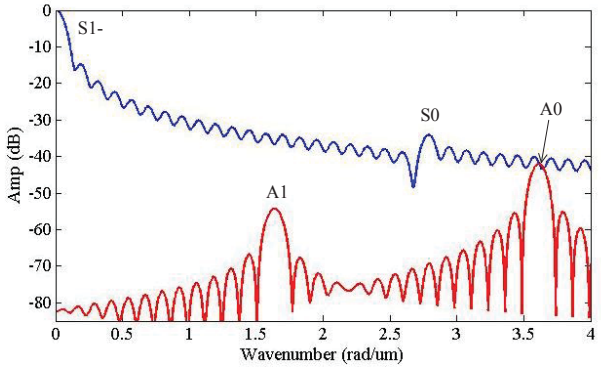
Xinyi Li and Gongbin Tang acknowledge the support of the Japanese Government (MEXT) for the scholarship through the Super Global University Project.



(a) Active area of double-raised-border



(b) Active area of single-raised-border



(c) Active area without raised-border

Fig. 7. Spectrum of U_z of single and double raised border structure

REFERENCES

[1] C. Lam, "A review of the timing and filtering technologies in smartphones," in *2016 IEEE International Frequency Control Symposium*. IEEE, 2016, pp. 1–6.

[2] J. Kaitila, "Review of wave propagation in baw thin film devices-progress and prospects," in *2007 IEEE Ultrasonics Symposium*. IEEE, 2007, pp. 120–129.

[3] R. Ruby, M. Small, F. Bi, D. Lee, L. Callaghan, R. Parker, and S. Ortiz, "Positioning fbar technology in the frequency and timing domain," *IEEE transactions on ultrasonics, ferroelectrics, and frequency control*, vol. 59, no. 3, pp. 334–345, 2012.

[4] R. Ruby, "A decade of fbar success and what is needed for another successful decade," in *2011 Symposium on Piezoelectricity, Acoustic Waves and Device Applications (SPAWDA)*. IEEE, 2011, pp. 365–369.

[5] H. Bhugra and G. Piazza, *Piezoelectric MEMS Resonators*. Springer, 2017.

[6] K.-Y. Hashimoto, *RF bulk acoustic wave filters for communications*. Artech House, 2009.

[7] A. Link, E. Schmidhammer, H. Heinze, M. Mayer, B. Bader, and R. Weigel, "Appropriate methods to suppress spurious fbar modes in volume production," in *Microwave Symposium Digest, 2006. IEEE MTT-S International*. IEEE, 2006, pp. 394–397.

[8] H. Park, I. Song, J.-S. Shin, M.-C. Lee, S. U. Son, C.-S. Kim, D.-H. Kim, and J. Cui, "Advanced lateral structures of baw resonator for spurious mode suppression," in *2012 42nd European Microwave Conference*. IEEE, 2012, pp. 104–107.

[9] J. Kaitila and J. D. Larson, "Complex peripheral lamb modes in fbars," in *European Frequency and Time Forum 2013*. IEEE, 2013, pp. 757–760.

[10] J. Liu, T. Omori, C. Ahn, and K.-y. Hashimoto, "Impact of surface periodic grating on fbar structures to spurious transverse resonances," in *European Frequency and Time Forum 2013*. IEEE, 2013, pp. 1957–1960.

[11] J. Kaitila, M. Ylilammi, J. Ella, and R. Aigner, "Spurious resonance free bulk acoustic wave resonators," in *IEEE International Ultrasonics Symposium 2003*, vol. 1. IEEE, 2003, pp. 84–87.

[12] A. Link, E. Schmidhammer, H. Heinze, M. Schmiedgen, B. Bader, K. Wagner, and R. Weige, "Suppression of spurious modes in mirror-type thin film baw resonators using an appropriate shape of the active area," in *2005 IEEE Ultrasonics Symposium*. IEEE, 2005, pp. 1179–1182.

[13] G. Fattinger, S. Marksteiner, J. Kaitila, and R. Aigner, "Optimization of acoustic dispersion for high performance thin film baw resonators," in *2005 IEEE International Ultrasonics Symposium*, vol. 2. IEEE, 2005, pp. 1175–1178.

[14] C. Zhou, D. Zhang, W. Pang, and H. Zhang, "Spurious free and temperature stable giga-hertz acoustic wave resonators with enhanced quality factor," in *Microwave Conference Proceedings (APMC), 2012 Asia-Pacific*. IEEE, 2012, pp. 1286–1288.

[15] R. Thalhammer, J. Kaitila, S. Zieglmeier, and L. Elbrecht, "Spurious mode suppression in baw resonators," in *2006 IEEE International Ultrasonics Symposium*. IEEE, 2006, pp. 456–459.

[16] B. Auld, *Acoustic waves and fields in solids*. New York: Wileyand, Sons, 1973.

[17] R. Thalhammer and J. D. Larson, "Finite element analysis of baw devices: Principles and perspectives," in *2015 IEEE International Ultrasonics Symposium*. IEEE, 2015.

[18] D. A. Feld, R. Parker, R. Ruby, P. Bradley, and S. Dong, "After 60 years: A new formula for computing quality factor is warranted," in *IEEE International Ultrasonics Symposium 2008*. IEEE, 2008, pp. 431–436.

[19] F. Thalmayr, K.-y. Hashimoto, T. Omori, and M. Yamaguchi, "Frequency domain analysis of lamb wave scattering and application to film bulk acoustic wave resonators," *IEEE transactions on ultrasonics, ferroelectrics, and frequency control*, vol. 57, no. 7, 2010.

[20] F. Thalmayr, K.-Y. Hashimoto, T. Omori, and M. Yamaguchi, "Power deduction from surface fields in multilayer waveguides," *IEEE transactions on ultrasonics, ferroelectrics, and frequency control*, vol. 57, no. 2, 2010.

An Apodized 3-GHz Thin Film Piezoelectric on Substrate FBAR

Gayathri Pillai[1], Anurag A. Zope[1], Julius Ming-Lin Tsai[2], and Sheng-Shian Li[1]
[1]Institute of NanoEngineering and MicroSystems, National Tsing Hua University, Hsinchu, Taiwan
[2]InvenSense Inc., San Jose, CA, USA

***Abstract*— An apodization method is illustrated in this work to enable displacement and strain energy confinement at the central section of the composite thin Film Bulk Acoustic wave Resonator (c-FBAR) while in operation at the resonance mode. The device is excited at a higher order thickness extensional mode. The proposed resonator is designed in *sinc* shape to attain high degree of energy localization. Here, the thin film piezoelectric on substrate (TPoS) configuration implemented by the Aluminum Nitride (AlN) MEMS-CMOS InvenSense Inc. platform is used to realize the resonators. The c-FBAR performance parameters are extracted through de-embedding the CMOS+MEMS measured data. An equivalent electrical modeling for c-FBAR operating in the Super High Frequency (SHF) is demonstrated. We successfully report a sinc c-FBAR resonator operating at 3.264 GHz with an electromechanical coupling coefficient >2.12%, an unloaded *Q* >2,500, and Figure of Merit of 53.**

Keywords—apodization; c-FBAR; TPoS; super high frequency; electromechanical coupling; quality factor, Figure of Merit.

I. INTRODUCTION

Thin Piezo on Substrate (TPoS) technology has been an attractive approach to realize telecommunication systems as it effectively combines the electromechanical coupling property of the piezoelectric material and the excellent mechanical characteristics of device layer substrate such as Single Crystal Silicon (SCS) [1]. The high acoustic velocity and relatively low dielectric constant of Aluminum Nitride (AlN) makes it an optimum choice for the Super High Frequency (SHF) device realization. In this work, asymmetric or composite thin Film Bulk Acoustic wave Resonator (c-FBAR) is discussed owing to the composite-structure feature of the platform.

The resonator in this work is operated in higher order thickness extensional mode so as to support a standing wave across the piezoelectric layer as illustrated in [2]. The target mode also has the highest stress concentration in the piezoelectric material ensuring the highest electromechanical coupling among the other higher order modes.

In this work, apodization or resonator shaping technique is used to improve the Bulk Acoustic Wave device performance. The idea is validated by modeling and measurement techniques.

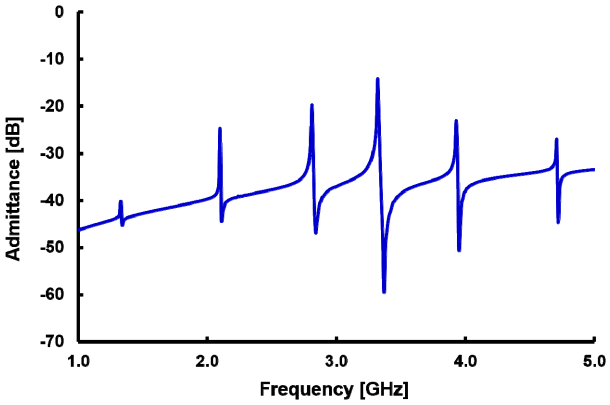


Fig. 1: Admittance plot for c-FBAR from 1 to 5 GHz.

2. RESNOATOR DESIGN

Thin Piezo on Silicon topology based resonators have odd and even harmonic mode generation due to the non-cancellation of strain for even modes unlike the symmetric FBARs. Figure 1 presents a wide range frequency response carried out in COMSOL to see the generation of multiple thickness extension modes. To select the target mode for the resonator design, electromechanical coupling coefficient (k_{teff}^2) was computed for each of the dominant peaks of the c-FBAR. The electromechanical coupling coefficients for the higher order thickness extension modes at 2.8 GHz, 3.33 GHz, and 3.8 GHz were computed to be 2.6%, 3.6% and 1.9%, respectively, using

$$k_{teff}^2 = \frac{\pi f_r}{2 f_a} \frac{1}{\tan(\frac{\pi f_r}{2 f_a})} \quad (1)$$

where f_a and f_r are the anti-resonance and resonance frequencies, respectively.

The concept of apodization is utilized to engineer the device geometry such that the energy can be accumulated in specific regions of the resonating body. For the resonator structure discussed here, the device geometry is modified into a sinc shape to attain energy confinement. The sinc function can be mathematically defined as

$$\sin c(x) = \frac{\sin(\pi x)}{\pi x} \quad (2)$$

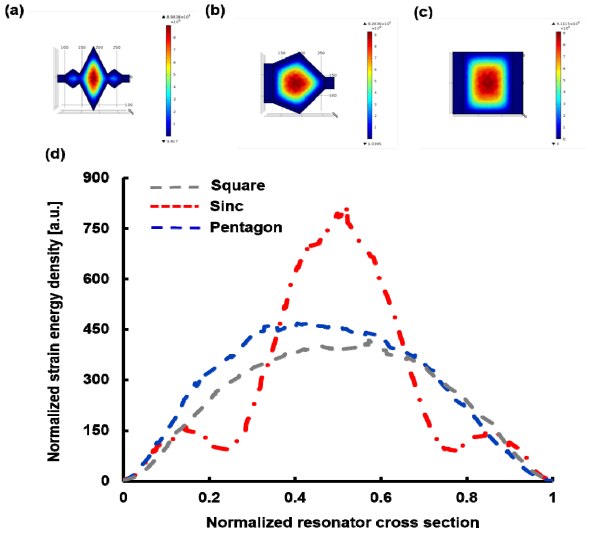


Fig. 2: (a), (b), and (c) show the COMSOL Finite Element Analysis strain energy density profiles at resonance frequency for sinc, pentagon, and square c-FBARs, respectively. (d) Normalized strain energy density spread along the resonator cross-section.

where the value at $x = 0$ is defined as the limit as $x \to 0$ to be sinc(0) = 1. For a sinc function, more than 90% of the total energy is confined within the main lobe of the sinc function, i.e., between -π to π [3]. The TPoS resonator designed here is modeled to a sinc shape within an interval of -2π to 2π, i.e., the resonator has a main lobe and two side lobes. The main lobe of the sinc function extends from -π to π and its side lobes are from -2π to -π and π to 2π. To verify the energy confinement nature, COMSOL Finite Element Method was used. Figure 2 illustrates strain energy density study for different c-FBAR designs. Figure 2(a) asserts the energy concentration idea of sinc c-FBAR. Energy profiles for pentagon and square c-FBARs are also plotted in Figure 2(b) and (c) for comparison.

The resonator is realized using the InvenSense Inc. platform. The fabrication process starts with a device wafer made of single crystal silicon. Controlled thin layers of bottom electrode molybdenum, piezoelectric aluminum nitride layer, and top electrode aluminum are deposited on the silicon

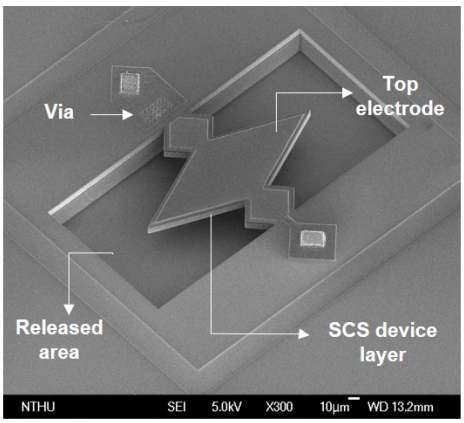


Fig. 3: SEM of a one-port sinc c-FBAR fabricated using the InvenSense Inc. platform.

device layer. The quality of the aluminum nitride can be enhanced by depositing seed layer of AlN on low-roughness Si wafers. Finally eutectic bonding is used to create both a hermetic seal around the MEMS structure as well as low-parasitic electrical interconnects between the MEMS structures and CMOS circuits. The SEM of the resonator is provided in Figure 3.

3. MEASUREMENT RESULTS

The c-FBAR resonator is driven into resonance by applying an AC input signal using a Network Analyzer. Since the device operates in the GHz range, Ground-Signal-Ground (GSG) probes are used. One-port GSG measurement of the c-FBAR resonator was carried out at 0 dBm power level. The measurement plane was transferred to the GSG tip by carrying out calibration using the CS-5 calibration kit. The measured raw data however consist of parasitic capacitance from the device package, interconnect resistances, etc. These parasitic elements heavily impede the c-FBAR performance and hence it is required to remove them by de-embedding procedure. The de-embedding formula is shown in equation (3) [4].

$$Z_{de-embedded} = \frac{1}{Y_{device} - Y_{open}} - \frac{1}{Y_{short} - Y_{open}} \quad (3)$$

Electrical equivalent circuit of the c-FBAR depicted in Figure 4 is used to fit its response to the de-embedded data, thereby enabling an efficient parameter extraction. Making use of the mBVD model with series inductor (L_s) and parallel resistance (R_p) as explained in [2], values of the motional arm (R_m, L_m, and C_m), static arm (R_o and C_o), and the series loss resistor and inductor (R_s and L_s) are computed. The equations used for parameter extraction are given in equations (4) to (6). The extracted parameters of mBVD model for the resonator are R_m = 1.15 Ω, L_m = 0.142 μH, C_m = 16.71 fF, C_o = 970 fF, and R_s = 2.5 Ω. The importance of de-embedding for the data analysis is evident in Figure 5. There is no clear resonance peak in the admittance plot depicted in Figure 5(a). The phase plot in Figure 5(b) also indicates that the c-FBAR resonator is severely loaded by the capacitive parasitics contributed by the CMOS unit and also the CMOS-MEMS bond pads.

$$R_m = \frac{\pi^2}{8\omega_r C_o k_{teff}^2 Q} \quad (4)$$

$$L_m = \frac{\pi^2}{8\omega_r^2 C_o k_{teff}^2} \quad (5)$$

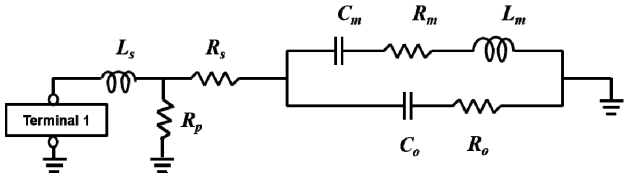


Fig. 4. Schematic of a one-port mBVD model with parasitic components.

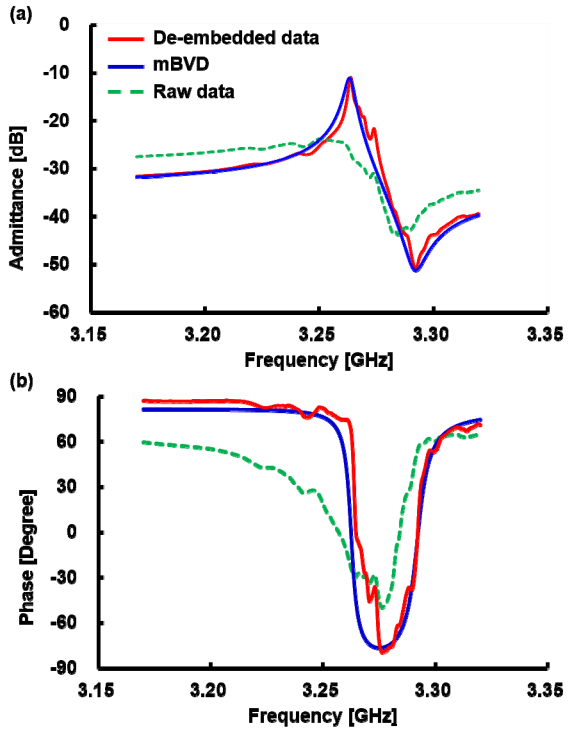


Fig. 5. Illustration of (a) admittance and (b) phase plot comparison among de-embedded data, raw measurement results, and fitted modified mBVD model for the proposed sinc c-FBAR.

$$C_m = \frac{8}{\pi^2} C_o k_{teff}^2 \tag{6}$$

$$Q_u = Q_l \left(1 + \frac{R_s}{R_m}\right) \tag{7}$$

Owing to the extremely low R_m, R_s severely loads the Q at resonance. The unloaded quality factor is computed using Equation (7) [5]. Loaded quality factor (Q_l) and unloaded quality factor (Q_u) of the resonator are found to be 790 and 2507, respectively, at the device resonance frequency of 3.264 GHz. Figure of Merit (*FoM*), i.e., $k_t^2 * Q$, of the resonator is computed to be 53.1. Table 1 compares this work with ZnO-based c-FBAR [6]. Sinc c-FBAR has a higher FoM_1 and FoM_2 compared to ZnO based asymmetric FBAR.

From Figure 5(a), it can be studied that the 3dB bandwidth of real measurement is narrower than the equivalent electrical fitted model. To authenticate it, the loaded Q (Q_l) values of mBVD model and de-embedded measurement data are compared. The Q_l at resonance for measured data is around 1,100 whereas as the fitted model's Q_l is 790. Based on the aforementioned fact, it is anticipated that the device's actual unloaded quality factor would be much higher than the Q_u computed using the mBVD model.

TABLE I: PERFORMANCE COMPARISON WITH THE STATE OF THE ART COMSPOSITE FBAR.

REFERENCES	JMM 2010 [6]	THIS WORK
Piezoelectric Material	ZnO	AlN
f_r (GHz)	5.04	3.26
k_t^2 (%)	3.88	2.12
FoM_1 ($f_r * Q_u$)	3424	8182
FoM_2 ($k_t^2 * Q_u$)	26.4	53.1

4. CONCLUSION

A resonator design using apodization principle is realized in this work on a TPoS topology. Here, the concept of apodization is used to design AlN on Si-based c-FBAR. The resonator is designed in a sinc shape so as to attain the energy confinement away from the device anchor while operating at resonance frequency. COMSOL is used to study the above-mentioned hypothesis. To incorporate the parasitic elements impeding the intrinsic resonator performance, additional inductance and resistances are added to the traditional mBVD model to fit the measurement data. Upon performing de-embedding, the device performance parameters are extracted. A Q_u of 2,507 and a Figure of Merit (FoM_1) of 53.14 was achieved for sinc c-FBARs.

ACKNOWLEDGMENT

The authors would like to thank the financial support from the Ministry of Science and Technology (MOST) of Taiwan under grant of MOST-103-2221-E-007-113-MY3 and the Toward World-Class University Project, and also thank InvenSense Inc. for providing the fabrication platform.

REFERENCES

[1] R. Abdolvand, H. M. Lavasani, G. K. Ho, and F. Ayazi, "Thin-film piezoelectric-on-silicon resonators for high-frequency reference oscillator applications," *IEEE Transactions on Ultrasonics, Ferroelectrics, and Frequency Control*, vol. 55, no. 12, pp. 2596-2606, Dec. 2008.

[2] G. Pillai, A. A. Zope, J. M.-L. Tsai, and S.-S. Li, "3-GHz BAW composite resonators integrated with CMOS in a single-chip configuration," *Proceedings*, 2016 IEEE Int. Frequency Control Symp., New Orleans, LA, May 9-12, 2016.

[3] J. G. Proakis and D. G. Manolakis, *Digital Signal Processing*. 4th ed. New Jersey: Prentice Hall, 2007. Print.

[4] K. Hashimoto, "Fundamentals of RF acoustic resonators and their characterization," *Tutorial, IEEE Frequency Control Symposium,* 2015.

[5] J. Larson, P. Bradley, S. Wartenberg, and R. Ruby, "Modified Butterworth - Van Dyke circuit for FBAR resonators and automated measurement system," *Proceedings*, IEEE Ultrasonics Symposium, San Juan, Puerto Rico, Oct. 22-25, 2000, pp. 863-868, vol. 1.

[6] W. Pang, H. Zhang, R. C. Ruby, H. Yu, and E.S. Kim, "Analytical and experimental study on the second harmonic mode response of a bulk acoustic wave resonator," *J. Micromech. Microeng.*, vol. 20, no. 11, pp. 115-125, Oct. 2010.

Analytical Modeling of Low-Loss Disk Flexure Resonators

Jonathan M. Puder
OxideMEMS Lab
Cornell University
Ithaca, USA

Jeffrey S. Pulskamp, Ryan Q. Rudy, and Ronald G. Polcawich
Sensors and Electron Devices Directorate
US Army Research Laboratory
Adelphi, USA

Sunil A. Bhave
OxideMEMS Lab
Purdue University
West Lafayette, IN

***Abstract*—This paper presents for the first time a closed form analytical solution for the motional resistance, R_m, of the transverse (1,1) mode of two port disk flexure resonators (DFRs), enabling rapid performance prediction and device optimization. This work is motivated by a recently reported -1 dB peak S_{21} and 9 Ω motional resistance DFR that has demonstrated the viability of non-traditional flexure based modes as high-performance, low frequency MEMS resonators. Modeled R_m values are validated using on-wafer extracted e_{31} piezoelectric stress constants, measured layer thicknesses, independently measured elastic moduli, and analytical mode shapes**

Keywords— Motional resistance, piezoelectricity, resonator

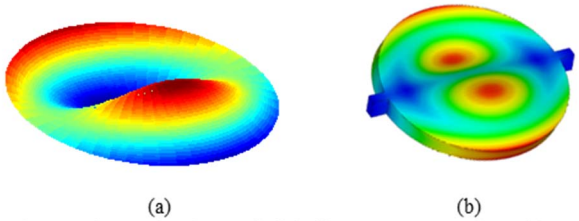
I. Introduction

Military communications systems, such as SINCGARS, continue to rely on sub-100 MHz filters, and require IF filters with narrow bandwidth, exceptional stop-band rejection, and frequency trimming capabilities. While early literature focused on flexure-based devices to meet these needs, in recent years research efforts have moved towards other modes. However, recently published resonator performance of -1 dB peak S_{21} and 9 Ω motional resistance (R_m) for six parallel (1,1) PZT-on-silicon [1,2,3,4] disk flexure resonators terminated directly to 50 Ω highlights the potential of flexure-based devices as high-performance resonators at low frequencies [5]. To provide insight into the performance of these modes, this work will present an analytical expression for R_m, an important modeling parameter. This analytical expression is validated by fitting only the mechanical quality factor (Q_m), and using independently measured or extracted parameters, including e_{31}.

II. Theory

A. Motional Resistance

Modal analysis was used to model the (1,1) mode (Fig. 1) of the continuous disk as a driven, lumped mass-spring system by comparing the elastic energies of the two systems as well as the work done by the modal force and piezoelectric stress. Analytical mode shapes of the (1,1) mode of disk flexure consisting of modified and ordinary Bessel functions of the first kind [6], were used to obtain modal stresses and strains. The modal force and equivalent stiffness were used to derive a quasi-static displacement. Then, using extracted mechanical quality factor (Q_m), the frequency response of the predicted real displacement was calculated. Displacement was converted to a frequency- and time-dependent charge on the output port via the direct piezoelectric effect. The application of a time derivative and rearrangement returns the closed-form expression for R_m in Equation (1),



(a) (b)

Fig. 1. The mode shape of disk flexure resonator from (a) FEA Eigen frequency analysis (b) analytical mode shapes expressions.

$$R_m = \frac{4\pi\gamma\lambda^2 t_{tot}^2\sqrt{Y_c\rho_c}}{Q_m\sqrt{3(1-\nu^2)}\left(k\, e_{31} h \int_{A_{el}} \beta\, r\, dr d\theta\right)^2} \quad (1)$$

β in (1) is given by,

$$\beta = \cos(\theta)\left(J_1(kr) - I_1(kr)\right) \quad (2)$$

where γ is the ratio of modal mass to total mass, λ is a frequency constant, k is the wavenumber, t_{tot} is the total disk thickness, Y_c and ρ_c are the composite elastic moduli and density, υ is Poisson's ratio, h is the distance from the neutral axis to the mid-plane of the piezoelectric layer, and J_1 and I_1 are the ordinary and modified Bessel functions of the first kind [6]. The model predicts high coupling due to energy transduction through both the e_{31} and e_{32} (e_{31}=e_{32} for PZT and AlN) constants, and motional resistance to be independent of radius.

B. Comparison to Other Low Frequency Modes

To understand the advantages of disk resonators, they are compared and contrasted with two other common modes found at low frequencies. Beam resonators are often designed to excite length extension (LE) modes, and have spurious modes of beam

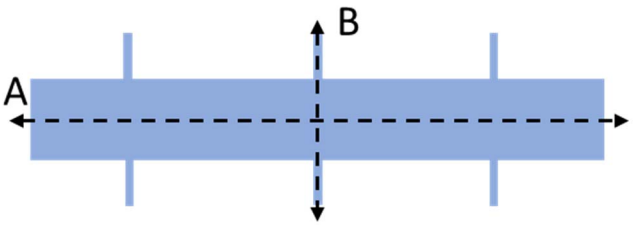


Fig. 2. A top view of the resonator with planes of symmetry marked. Recetangular electrodes are either symmetric about A or symmetric/antisymmetric about B.

flexure (BF). Equations for the motional resistance of these modes are given by [7]

$$R_{m_{Beam\ Flexure}} = \frac{\sqrt{Y_c I \rho_c w_{tot} t_{tot}}}{4LQ_m \left[e_{31} h \int_L \frac{d^2 u_n}{dx^2} w_{el}(x) dx\right]^2} \quad (3)$$

$$R_{m_{Beam\ Extension}} = \frac{n\pi w_{tot} t_{tot} \sqrt{Y_c \rho_c}}{2Q_m \left[e_{31} \int_L \frac{du_n}{dx} w_{el}(x) dx\right]^2} \quad (4)$$

Where the w_{tot} is the total width of the resonator, I is the area moment of inertia, u_n is the unity normalized mode shape of the n^{th} mode, L is the length of the resonator, and w_{el} is the width of the rectangular electrodes. For these expressions, the electrodes are assumed to symmetric or anti symmetric about the planes shown in the schematic of Fig. 2.

Comparing first to beam flexure, both modes are inversely proportional to h^2 and $e_{31}{}^2$. However, the R_m of BF modes scale linearly with L and inversely with w_{tot}, while the disk is not expected to scale with R. However, if L and w_{tot} are changed at the same rate, then the BF R_m is not affected. This approximate relationship would occur as a device is scaled to higher frequencies. Therefore, both modes will have consistent R_m across R and L/w_{tot} ratios. Since R and L are the primary frequency determining dimension in both modes, consistent R_m across a wide range of frequencies should be expected, if t_{tot} is held constant and the L/w_{tot} ratio is maintained. This principle is confirmed in [8], where parameterized simulations of disk resonators with varied widths and silicon thicknesses are run. For both modes, a thicker device with the piezoelectric material far from the neutral axis will result in lower R_m due the scaling with h, assuming that Q_m is not affected by layer thicknesses. However, very thick devices will violate the assumptions used to derive the analytical mode shapes and invalidate the derived R_m expressions. Finally, for both modes, it is possible to have infinite R_m if the neutral axis and midplane of the piezoelectric layer are coincident, since h would be zero. The R_m of BF and DFRs show very similar behavior, which is expected due to both modes being characterized by out of plane flexure.

Comparing DFR R_m and LE R_m, first it is apparent that the LE mode cannot scale with h since this parameter is only defined for flexure resonators. Additionally, the R_m for LE modes can never be infinite in a non-trivial case. The LE mode R_m is expected to scale directly with t_{tot}, while that of the DFR will not have such a clear relation, since h and t_{tot} share a complex relationship. The LE mode R_m is not expected to scale with the primary frequency determining dimension, L, nor is the DFR R_m. However, the LE R_m does scale inversely with the other in plane dimension, w_{el}. Therefore, by maintaining a constant width and changing the length, devices with the same R_m may be fabricated across a wide range of frequencies for LE resonators.

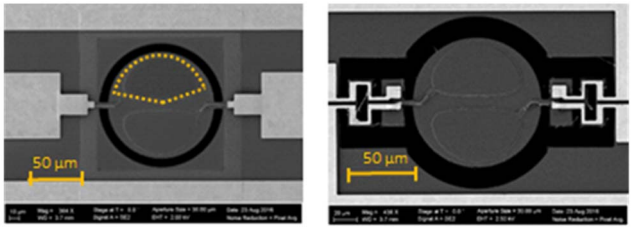


Fig. 3. Micrographs of fabricated devices with both types of anchors. The radius of the disks was 56 µm. The approximated electrode shape used in modeling is traced over Fig. 3a.

III. Experimental Validation

A. Device Details

To validate the derived R_m of the DFRs, devices were fabricated in a PZT on silicon stack [1]. The devices consisted of a 1 µm buried SiO_2 layer, a 10 µm silicon device layer, 300 nm of SiO_2, 125 nm of platinum for the bottom electrode, 0.5 µm of PZT, and 50 nm of platinum for the top electrode. The disks were designed to have a 56 µm radius. Additionally, the disks were fabricated with two types of anchors, which may be seen in Fig 3.

B. e_{31} Piezoelectric Coefficients

Cantilever test structures were used to independently extract the electric-field dependent piezoelectric e_{31} constants under quasi-static conditions [9,10,11]. This field dependence arises directly from the fact that PZT is a ferroelectric material. At 0.5 µm PZT film thickness, the coercive voltage of PZT is less than 2 V. This allows for more rigorous model validation at various operating points due to the fact that the piezoelectric stress constants of PZT can vary between 3-10 C/m^2. The e_{31} were found to vary widely across the wafer, and three examples of extracted coefficients may be seen in Fig. 4.

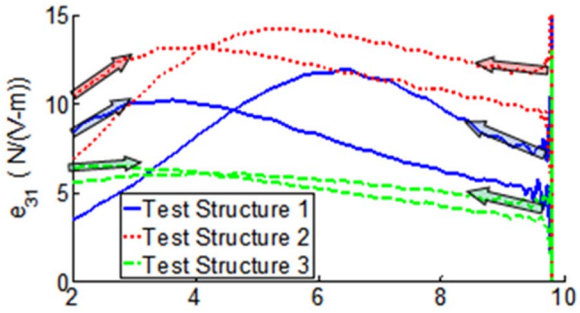


Fig. 4. The e_{31} constants extracted from cantilever test structures. The widely varying cross-wafer values partially explain the variation seen in R_m. The discontinuity at 10V is due to data processing artifacts. Arrows indicate the direction of the unipolar voltage sweep start from 0V up to 10 V and returning to 0V.

The coefficients were extracted using a 90 Hz sine wave with minimum and maximum values of 0 and 10 V, respectively.

Actual devices are operated in a small-AC-on-large-DC signal condition at much higher frequencies. This discrepancy in testing conditions likely contributed to agreement discrepancies in subsequent R_m validation.

C. Measurement and Model Comparison

The scattering parameters of the PZT-on-silicon resonators were measured on a Rhode & Schwarz ZVB8 network analyzer terminated to 50 Ω and calibrated using short, open, load, and through standards (GGB CS-5) with varied superimposed DC biases on both ports. The experimental R_m was extracted by fitting to the well-known modified Butterworth van-Dyke (mBVD) model, and Q_m was extracted via fitting. Tether resistances were obtained via resistivity test structures and combined designed and measured geometries. Using extracted properties, independently measured mechanical material properties [10], and only one fitted parameter (Q_m), values of R_m were calculated (Fig. 5). Frequencies varied from 22.2 to 22.6 MHz at 10V. The extracted R_m varied from 48Ω to 335Ω, which may be attributed to the widely varying e_{31} (Fig. 4) and Q_m. Both e_{31} and Q_m vary cross-wafer and tune with voltage. Although there is a large spread in R_m, the model still matches well without fitting e_{31}. The average error across all voltages was 23%.

D. Predicting High Performance

Fig. 6 plots the predicted S_{21} of device 2 of Fig 5. when placed in parallel six times along with the measured performance of the device from [5] at 8 V. Device 2 was located on the same die as the device from [5]. Since the frequency and shunt capacitance are related to the radius, it is necessary to array the resonators to obtain the desired shunt impedance. This agreement illustrates the ability of this model to accurately predict the behavior of low loss and low R_m devices.

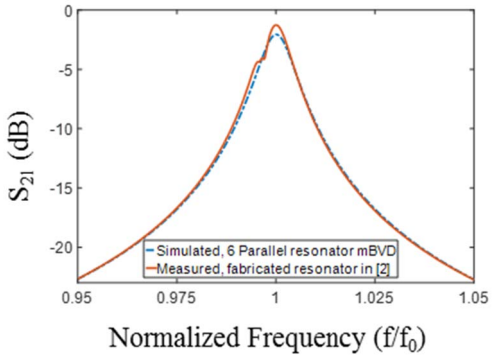


Fig. 6. Simulated S_{21} for Device 2 of Figure 5 in parallel six times, and measured resonator data from the device in [2] at 8V. Both devices were located on the same die. Discrepancies arise from unknown individual disk Q_m, varying e_{31} and center frequency misalignment.

IV. Conclusion

The R_m model presented and validated has provided insight into the design of disk resonators, and has been able to predict the high performance demonstrated in [5]. They are expected to maintain consistent motional resistance across a wide range of frequencies, so long as the device thickness does not approach the radius. Thicker devices with the piezoelectric layer far from the neutral axis are predicted to have a lower R_m as a general trend if Q_m is not affected by relative layer thicknesses. These insights, along with the demonstrated low loss in fabricated devices, warrant a more thorough investigation into the scaling of this family of modes to higher frequencies.

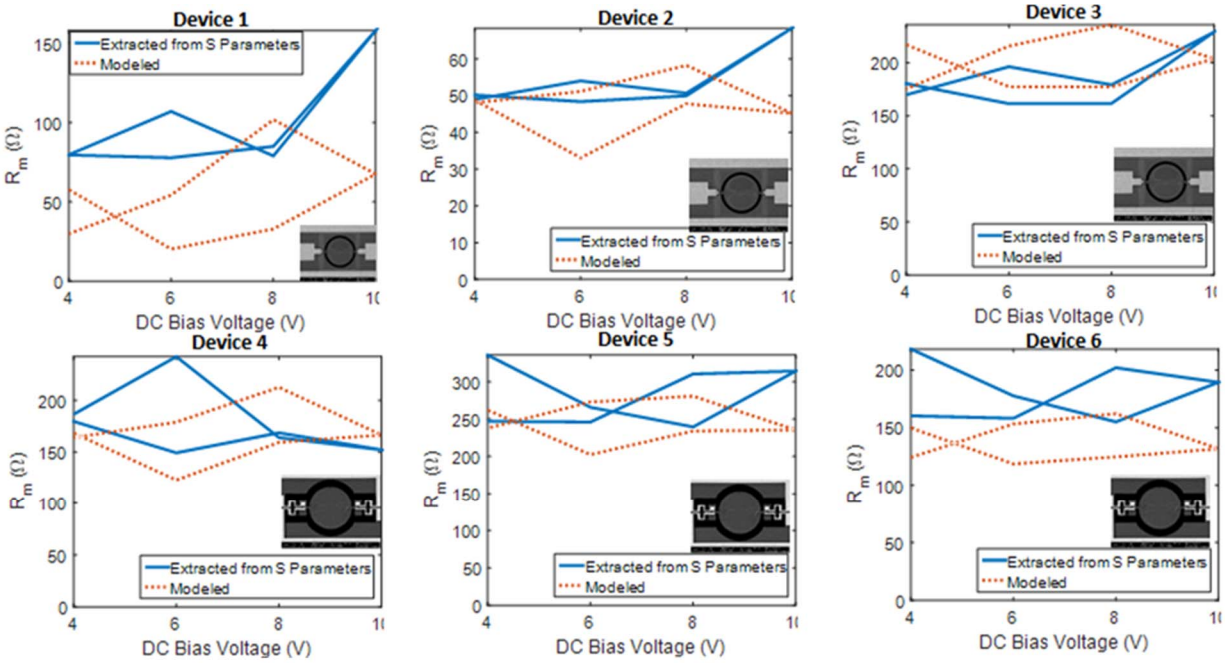


Fig 5. Extracted (solid) and modeled (dashed) R_m. Modeled R_m used extracted e_{31} and Q_m (Fig. 2). Discrepancies in curve shapes is attributed to differences in e_{31} extraction conditions (quasi-static) and RF testing conditions. Overall average error was 23%.

REFERENCES

[1] Pulskamp, J.S., et. al. (2012). “Electrode-shaping for the excitation and detection of permitted arbitrary modes in arbitrary geometries in piezoelectric resonators.” *IEEE Trans. Ultrason., Ferroelect., Freq. Contr., 59*(5), 1043-1060.

[2] S. S. Bedair, J. S. Pulskamp, R. G. Polcawich, R. Q. Rudy and J. Puder, "Thin-film piezoelectric transformers operating in harmonics of out-of-plane flexure modes," *2015 Transducers - 2015 18th International Conference on Solid-State Sensors, Actuators and Microsystems (TRANSDUCERS)*, Anchorage, AK, 2015, pp. 714-717.

[3] J. S. Pulskamp, R. Q. Rudy, S. S. Bedair, J. M. Puder, M. G. Breen and R. G. Polcawich, "Ferroelectric PZT MEMS HF/VHF resonators/filters," *2016 IEEE International Frequency Control Symposium (IFCS)*, New Orleans, LA, 2016, pp. 1-4.

[4] J. S. Pulskamp, S. S. Bedair, G. Ronald and S. A. Bhave, "Ferroelectric PZT RF MEMS resonators," *2011 Joint Conference of the IEEE International Frequency Control and the European Frequency and Time Forum (FCS) Proceedings*, San Fransisco, CA, 2011, pp. 1-6.

[5] Rudy, R.Q, et al.. “Piezoelectric Disk Flexure Resonator with 1 dB Loss.” *2016 IEEE International Frequency Control Symposium*.

[6] T.B. Gabrielson. "Frequency Constants for Transverse Vibration Of Annular Disks". *The J. of the Acoust. Soc. of Amer.*, vol. 105, no. 6, pp. 3311-3317, June 1999.

[7] Puder, J.M., et al. (2017). “A General Analytical Formulation for the Motional Parameters of Acoustic Resonators.” *Transactions on Ultrasonics, Ferroelectrics, and Frequency Control*, submitted.

[8] Puder, J. M., et.al., “Fundamental Limits of Disk Flexure Resonators,” *2017 IEEE Intl. Fre. Cont. Symp*, accepted.

[9] Puder, J.M., et al. (2016). “Modeling of High-Electric Bias Field Induced Piezoelectric Nonlinearity.” *2016 International Workshop on Acoustic Transduction Materials and Devices*.

[10] Yagnamurthy, S., et. al. (2011). “Mechanical and Ferroelectric Behavior of PZT-Based Thin Films.” *J. Microelectromech. Syst., 20*(6), 1250-1258.

[11] Polcawich, Ronald G., and Jeffrey S. Pulskamp. "Additive processes for piezoelectric materials: Piezoelectric MEMS." MEMS materials and Processes Handbook (2011): 273-353.

Fundamental Limits of Disk Flexure Resonators

Jonathan M. Puder
OxideMEMS Lab
Cornell University
Ithaca, USA

Jeffrey S. Pulskamp, Ryan Q. Rudy, and Ronald G. Polcawich
Sensors and Electron Devices Directorate
US Army Research Laboratory
Adelphi, USA

Sunil A. Bhave
OxideMEMS Lab
Purdue University
West Lafayette, IN

***Abstract*— High performance PZT-on-silicon disk flexure resonators were recently demonstrated with peak $|S_{21}|$ of -1 dB with direct 50 Ω termination, high bandwidth tunability, and high coupling at 22 MHz. This paper explores the performance limits and design optimization of this new resonator in the space of radius and silicon thickness of the (1,1) disk flexure mode. This effort is enabled by the Rapid Analytical/FEA Technique, a novel method for expedited acoustic resonator simulation. Simulations indicate that monolithic integration of disk resonators with -0.5 dB max$|S_{21}|$ may be achieved across a wide range of HF and low-VHF frequencies without the need for external impedance matching.**

Keywords—component; formatting; style; styling; insert (*key words****)***

I. Introduction

Piezoelectric MEMS contour resonators and filters promise frequency agility in an increasingly crowded and dynamic electromagnetic environment. The center frequencies of these devices are lithographically defined, enabling the monolithic integration of filter banks on a single chip. While recent research has focused on commercial interests in the UHF to S bands, military applications still demand high performance devices below 500 MHz.

Recently a PZT-on-silicon [1,2,3,4] device consisting of six electrically parallel disk flexure resonators (DFR) terminated directly to 50 Ω demonstrated a peak $|S_{21}|$ of -1 dB at 22 MHz, and insertion loss, *IL*, of 0.92 dB [5]. The motional resistance, R_m, was 9 Ω, and high electromechanical coupling (k_{eff}^2) and bandwidth tuning were demonstrated. To understand if this performance may be realized at higher frequencies, this paper investigates the fundamental performance and frequency limits of piezoelectric-on-silicon DFRs supported by the novel Rapid Analytical/FEA Technique (RAFT) [6]. This modeling technique enables designers to accurately simulate the scattering (S) parameters of piezoelectrically transduced resonators with full 3D models orders of magnitude faster than commercially available FEA packages. With the help of the RAFT, the results of a parametric study of the scaling of R_m, max $|S_{21}|$, k_{eff}^2, f_r, and figure of merit (*FOM*) with disk radius (r_{disk}) and the silicon thickness (t_{Si}) are presented.

II. Ease of Use

The RAFT requires the same parameters (moduli, density, piezoelectric coefficients, etc.) as standard FEA. To address the fact that mechanical quality factor is often not known before fabrication and testing, a "volumetric" material quality factor (Q_{mat}) was derived dependent on material loss, thickness, and stress profile and is given by

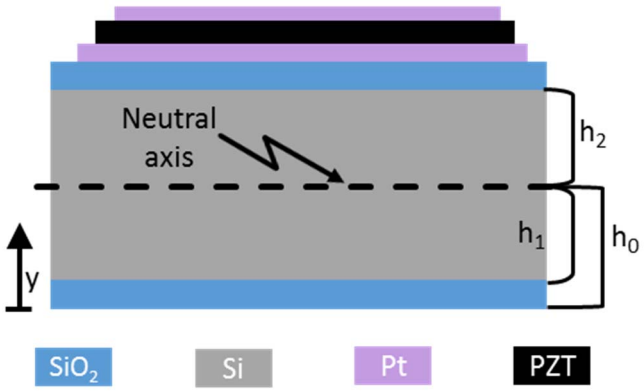


Fig. 1. A schematic of the PZT on silicon resonator with the definition of y and h_n denoted.

$$Q_{mat} = \frac{Y_1\, y^3|_{h_0}^{h_1} + Y_2\, y^3|_{h_1}^{h_2} + \cdots + Y_n\, y^3|_{h_{n-1}}^{h_n}}{\frac{Y_1}{Q_1}\, y^3|_{h_0}^{h_1} + \frac{Y_1}{Q_2}\, y^3|_{h_1}^{h_2} + \cdots + \frac{Y_n}{Q_n}\, y^3|_{h_{n-1}}^{h_n}} \quad (1)$$

Where Y is the elastic modulus, y is the distance from the neutral axis, h is the distance of the top of the n^{th} layer from the neutral axis, and Q_n is the material quality factor of the n^{th} layer. A schematic of the geometric parameters for a PZT on silicon stack may be seen in Fig 1. Assigned material quality factors for silicon dioxide, silicon, platinum and PZT in that order were: 100, 100,000, 100, and 200. In addition, a "limiting" Q_{lim} of 750 was added to the resonator to avoid abnormally high Q_m.

$$Q_m = \frac{Q_{mat} \cdot Q_{lim}}{Q_{mat} + Q_{lim}} \quad (2)$$

For accurate and realistic simulation, required parameters were measured, extracted from test structures, or taken from design. The elastic moduli of the material stack were independently measured [7], and densities were taken from bulk measurements. Piezoelectric coefficients were set to 10 C/m^2, a value within the range extracted from on-wafer cantilever test structures. Tether resistances were derived from designed dimensions and resistivity test structures, and permittivity was extracted from fabricated devices. Lateral dimensions for model

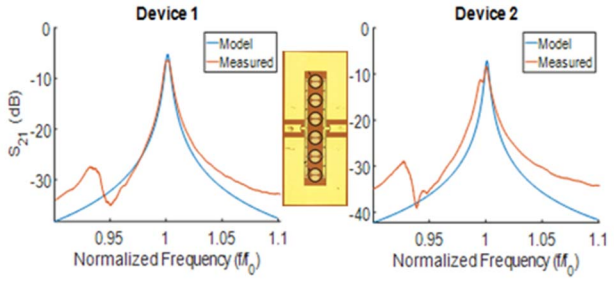


Fig. 2. Agreement between model and experiment. Fabricated devices consist of six 77 MHz resonators in parallel. Sources of discrepancy are nearby spurious modes and frequency misalignment of individual resonators. See inset for image of fabricated resonators.

validation were taken from design, and layer thicknesses were taken from nominal deposition thicknesses.

To parametrically explore the design space of DFRs, 250 simulations to generate S parameters were run at various r_{disk} and t_{Si} for a total simulation time of 27 hours, or 6.5 minutes per simulation. This low simulation time was enabled by the RAFT, in which rapid Eigen frequency simulations are run first. These are then processed in an analytical software package utilizing a generalized expression for R_m. r_{disk} varied from 12 to 60 µm, and t_{Si} varied from 1 to 10 µm.

III. Results

A. Validation

The model was validated against measurements of devices consisting of six electrically parallel DFRs using measured Q_m and extracted on-wafer e_{31} (Fig. 2). Since this paper is only concerned with the (1,1) disk flexure mode, spurious modes were not modeled in these measurements, and are the largest source of discrepancy.

B. Simulation Results

Contour plots of the performance parameters extracted from the simulations versus t_{Si} and r_{disk} may be seen in Figs. 3, 4, 5 and 5. The performance of the device from [5] is marked by a star in these figures Figs. 3-6. Fig. 3, 4, and 5 indicate that max|S21|, R_m, k_{eff}^2, and *FOM* are all primarily determined by the t_{Si}, and nearly constant across r_{disk}. This agrees with the result from [8], in which an analytical expression for the R_m of the (1,1) mode of disk flexure is presented. Given this, devices with similar performance parameters may be designed across a wide range of frequencies by adjusting r_{disk} (Fig 6). Fig. 3 and 4a indicate that for single resonators, the lowest R_m and max|S21| that may be obtained are at higher t_{Si}. However, when disks are placed electrically in parallel to obtain approximately 50 Ω shunt reactance, the lowest loss of ~0.5 dB occurs at ~2.5 µm t_{Si} across all r_{disk} (Fig. 4b). This region coincides with the region of optimal *FOM* in Fig. 5b. This result stems from properties of the PZT-on-silicon stack and flexure based resonators. By adding silicon, a high Q_m material, to PZT, a low Q_m material, the resonator coupling is reduced, while the overall resonator Q_m. increases. At zero t_{Si}, there should be no coupling since the neutral axis would coincide with the mid-plane of the piezoelectric layer, and no bending moment would exist. At large t_{Si}, most of resonator would be a non-piezoelectric, and coupling would be minimized. Therefore, there must be an optimal t_{Si} for maximized *FOM*, which simulations suggest are ~2.5 µm and 35, respectively, with a Q_m of 580.

The upper frequency limit for high performance disks occurs around 100 MHz. At this frequencies, the r_{disk} is less than 2.5 times t_{Si}. The mode transforms and begins to store more energy in in-plane shear, which is not directly transduced by PZT. The effects of this may be seen in the upper left hand corner of Fig. 3, 4, and 5, where the performance metrics sharply dip. A comparison of the displacements of a mode with favorable and unfavorable r_{disk}/t_{Si} is shown in Fig 7.

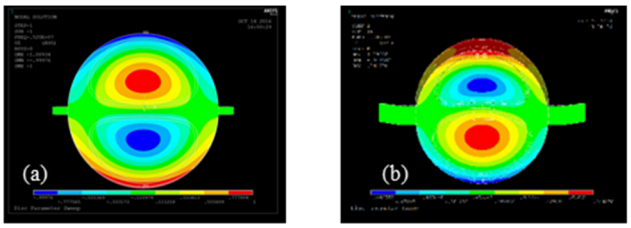


Fig. 7. Top view of simulated disks' out of plane displacement. (a) has a favorable r_{disk}/t_{Si} ratio, while (b) exhibit high shear, noticeable along the top edge, which creates a significant displacement of the anchors.

C. Comparison to -1 dB Device

The RAFT accurately predicted the performance of the device from [5] despite using a nominal e_{31} of 10 C/m^2 and an

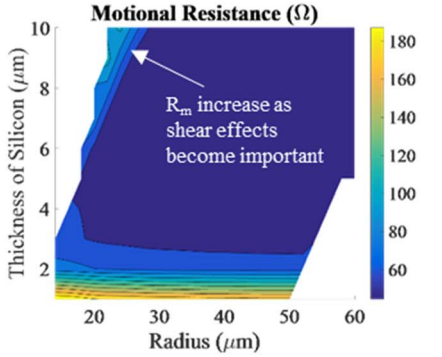


Fig. 3. Modeled R_m of a single resonator as a function of r_{disk} and t_{Si}. Note at r_{disk}/t_{Si} and as r_{disk} approaches t_{Si}, R_m begins to increase.

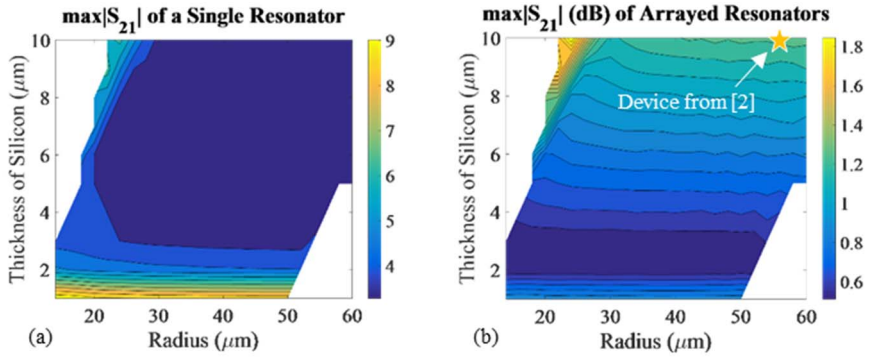


Fig. 4. Maximum $|S_{21}|$ for (a) a single resonator (b) resonators cascaded for 50 Ω shunt impedance. Note loss increasing with low r_{disk}/t_{Si} ratios. Optimal designs are predicted to have loss ~ -0.5 dB.

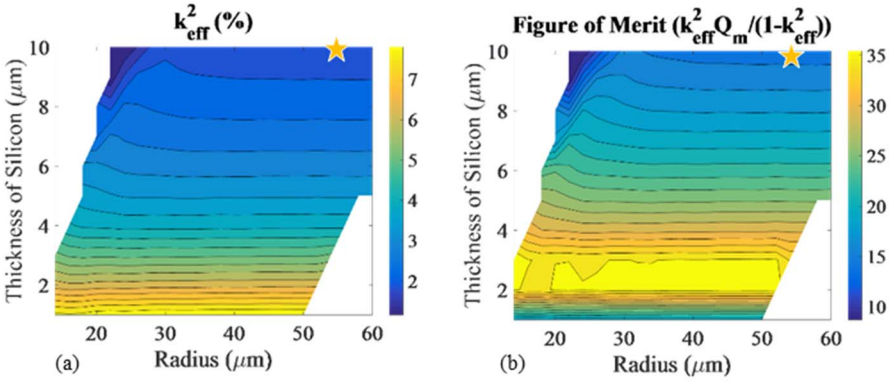


Fig. 5. The (a) electromechanical coupling and (b) Figure of Merit (*FOM*) predicted. Ratios of shunt and motional capacitances were used to arrive at k_{eff}^2 and volumetric Q_m was used to arrive at the *FOM*.

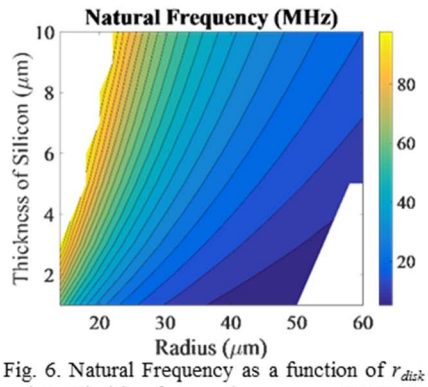


Fig. 6. Natural Frequency as a function of r_{disk} and t_{Si}. Limiting frequencies are near 100 MHz before shear starts to degrade the mode.

analytically modeled Q_m, with an included limiting Q, to predict R_m. The relative permittivity was also set to a typical value of 440. Resonator performance parameters for the simulated and fabricated device may be seen in Table 1. This shows that the RAFT can effectively predict the performance of low loss devices, even without properties extracted from test structures.

TABLE I. COMPARISON OF SIMULATION AND MEASUREMENT

	Fabricated Device	***Simulated Device***
Maximum S_{21} (dB)	-1	-1.28
k_{eff}^2(%)	2.09	1.95
Q_m	815	741
Figure of Merit ($k_{eff}^2 \cdot Q_m$)	16.9	14.73
R_m (Ω)	9	7.5

IV. CONCLUSION

Monolithically integrated disk resonators terminated directly to 50 Ω have been predicted to have low losses of -0.5 dB max|S_{21}| across a wide range of frequencies when placed in parallel electrically. The model, which used typical values for material properties and Q_m, was compared to the fabricated -1 dB device and was able to accurately predict performance parameters. The upper limit for sub-1 dB loss occurs around 90 MHz, when the mode beings to store more energy in in-plane shear. The model also predicts a point of maximum *FOM*, which coincides with optimal max|S_{21}|, where added silicon enhances Q_m more than it decreases k_{eff}^2. These results suggest that general out-of-plane flexure devices have potential to be high performance devices at low frequencies.

[1] Pulskamp, J.S., et. al. (2012). "Electrode-shaping for the excitation and detection of permitted arbitrary modes in arbitrary geometries in piezoelectric resonators." *IEEE Trans. Ultrason., Ferroelect., Freq. Cont.*

[2] S. S. Bedair, J. S. Pulskamp, R. G. Polcawich, R. Q. Rudy and J. Puder, "Thin-film piezoelectric transformers operating in harmonics of out-of-plane flexure modes," *2015 Transducers - 2015 18th International Conference on Solid-State Sensors, Actuators and Microsystems (TRANSDUCERS)*, Anchorage, AK, 2015, pp. 714-717.

[3] J. S. Pulskamp, R. Q. Rudy, S. S. Bedair, J. M. Puder, M. G. Breen and R. G. Polcawich, "Ferroelectric PZT MEMS HF/VHF resonators/filters," *2016 IEEE International Frequency Control Symposium (IFCS)*, New Orleans, LA, 2016, pp. 1-4.

[4] J. S. Pulskamp, S. S. Bedair, G. Ronald and S. A. Bhave, "Ferroelectric PZT RF MEMS resonators," *2011 Joint Conference of the IEEE International Frequency Control and the European Frequency and Time Forum (FCS) Proceedings*, San Fransisco, CA, 2011, pp. 1-6.

[5] Rudy, R.Q, et al.(2016). "Piezoelectric Disk Flexure Resonator with 1 dB Loss." *2016 Proc. IEEE Intl. Freq. Cont. Symp*.

[6] Puder, J.M.. et al. "Orders of Magnitude Reduction in Acoustic Resonator Simulation Times via the Wide-Band Rapid Analytical-FEA Technique." *2017 IEEE Intl. Fre. Cont. Symp*, accepted.

[7] Yagnamurthy, S., et. al. (2011). "Mechanical and Ferroelectric Behavior of PZT-Based Thin Films." *J. of Microelectromech Syst.,* vol. 20, no. 6.

[8] Puder, J.M.. et al. "Analytical Modeling of Low Loss Disk Flexure Resonators." *2017 IEEE Intl. Fre. Cont. Symp*, accepted.

Substrate texturing for homogeneous deposition of tilted c-axis AlN films for shear mode operation

M. Sierra-Zapata, M. Clement, T. Mirea, J. Olivares, and E. Iborra
GMME-CEMDATIC-ETSIT. Universidad Politécnica de Madrid
Madrid, Spain
eiborra@etsit.upm.es

***Abstract*—We propose two methods to improve the growth process of AlN films displaying the c-axis uniformly tilted, intended for the excitation of shear modes in acoustic resonators. The two methods aim at modifying the surface topography of the substrates in order to produce a family of parallel planes offering a suitable orientation for the subsequent growth of uniformly tilted AlN microcrystals. The first method is based on an ion milling process over rough substrates. Rough substrates, obtained by depositing a W layer on sputtered porous silicon oxide layers, are bombarded with a wide beam of Ar ions impinging on the sample surface at an angle of 65º. All treated surfaces lead to increased mean tilt angles of the subsequently grown AlN films, which in turn improves the coupling factor of the shear mode resonators. The second method consists in transferring the topography of a blazed diffraction grating to a photoresist layer spun over metal substrates. The photoresist pattern is then transferred to the substrates by a non- selective directional reactive ion etching process with SF_6.**

Keywords— BAW resonators; shear mode resonator; tilted grains AlN

I. INTRODUCTION

Gravimetric sensors based on electroacoustic resonators with surfaces functionalized to promote the binding of targeted species are good candidates for biological sensing in liquid environments. Compared with quartz crystal microbalances (QCMs), resonators based on AlN thin films offer the possibility of achieving greater sensitivities, since they can be operated at frequencies in the range of GHz by reducing the thickness of the piezoelectric film [1].

For in-liquid applications, it is advisable that gravimetric sensors based in bulk acoustic wave (BAW) resonators operate in the shear mode, which radiates less acoustic energy to the liquid medium than the longitudinal mode. To excite shear modes in piezoelectric AlN films a component of the electric field must be normal to the c-axis, to produce shear displacements by virtue of the d_{15} piezoelectric coefficient. Two electrical configurations have been envisaged to achieve such excitation. The first one, called lateral excitation, is achieved by applying an electric field between two coplanar electrodes defined on top of a highly c-axis oriented film. This geometric arrangement would provide, according to previously reported works [2,3], a straightforward excitation of the shear mode. The second configuration is based on the conventional excitation of AlN films using two electrodes placed on each side of the piezoelectric layer, but in this case, the AlN is made of microcrystals uniformly tilted with respect to the normal of the film, and this to the electric field [4]. This solution has proven to be far more effective than the lateral excitation [5]. It has been reported that tilt angles ranging from 20º to 45º provide the greatest values of the electromechanical coupling factor for the shear mode (k_S^2) [6]. Among the different techniques developed to achieve AlN films with tilted grains [7-9], off-axis sputter deposition over rough under-layers turns out to be the most effective [8]. In these kind of substrates, when the flux of atoms impinging on the different inclines is uniform, AlN grains tend to grow normally to the slopes in equal number in all directions, giving rise to a randomly-oriented AlN layer with averaged null piezoelectric response. However, if an impinging direction is encouraged (e.g. by displacing the substrate with respect to the target axis), the crystals will grow faster on the inclines most exposed to the atom flux and their mean tilt angle, normal to those planes, will be more uniform [9].

Two possible approaches can be used for controlling the uniformity and characteristics of these inclines. The first consists in carefully controlling the roughness of layers of the device that are closer to the active AlN film, either the bottom electrode or the uppermost layer of the acoustic reflector, in the case of solidly mounted resonators (SMRs). The second method involves the addition of a polycrystalline seed layer showing a controlled preferred orientation and exhibiting facets with the desired tilt angle [4, 10]. Both methods suffer from a significant lack of homogeneity in the basal orientation of the inclines, leading to some dispersion in the direction of the AlN microcrystals.

The aim of this paper is investigate new procedures to homogenizing the orientation of the substrate inclines for the subsequent growth of AlN films with homogenously tilted grains. We propose two approaches to achieve this goal. The first one, hereafter "sculpturing", consist in pre-treating the substrates by Ar-ion milling at incident angles close to 65º in order to sculpture the roughness of their surface before AlN deposition. The second approach, hereafter "nanoimprinting", involves nanoimprinting a photoresist layer spun over the bottom electrode of the SMR and etching it subsequently

through a directional and poorly selective reactive ion etch (RIE) process, in order to transfer a saw-tooth-like profile to the substrate surface.

II. METHODS

The test substrates were 2×2 cm^2 silicon dies covered with a λ/4 acoustic reflectors made of alternating SiO_2 and Mo films as low and high acoustic impedance layers, respectively. The targeted resonant frequency was around 2.5 GHz for the longitudinal mode and 1.4 GHz for shear mode. The uppermost SiO_2 layer of the reflector consisted in a sputtered porous layer displaying a mean roughness of around 4 nm. As bottom electrode we used sputtered tungsten (W) films or evaporated iridium (Ir) films.

Before AlN deposition, some samples were subjected to a roughness sculpturing process. These samples were bombarded by ion milling with an extended 100 mm in-diameter Ar-ion beam produced by a Gencoa IM75 ion gun of variable ion energy and current. Other samples were subjected to the nanoimprinting process. First, they were covered with a photoresist layer, which was subsequently nanoimprinted on the center with a PDMS replica of a 12x12 mm^2, 1200 lines/mm diffraction grating having a blaze angle of 26º. The samples were then etched by CHF_3/SF_6-based reactive ion etching (RIE) process adjusted to reduce the etch selectivity between the photoresist and the underlying substrate. This method allowed us to transfer the imprinted profile to the W bottom electrode or the SiO_2 uppermost layer of the SMR.

The AlN layers films were then sputtered in ultra-high vacuum system from a 150 mm in-diameter Al target in Ar/N_2 (40:60) mixtures. The substrates were displaced 5 cm from the center of the substrate holder, placed 5.8 cm apart from the target. The tilt angle of AlN grains was routinely derived from the position of the quasi-LO IR mode in the infrared reflectance spectra measured by Fourier transform IR spectroscopy (FTIR), using the method described in [11, 12]. Some samples were also assessed by measuring the XRD pole figure of the (00·2) reflection. Both measuring methods yielded similar values of the c-axis tilt angle.

BAW resonators were produced by adding a Mo top electrode to the whole structure. They were characterized by deriving their electrical impedance from the measurement of the reflection coefficient (S_{11}) performed with a network analyzer between 100 MHz and 5 GHz.

III. RESULTS AND DISCUSSION

A. *Texturing the roughness of the substrate*

Opposite to the growth of highly *c*-axis oriented AlN films, which requires polishing the surface of the acoustic mirrors, tilted AlN films can be achieved by taking advantage of the native roughness of the substrates combined with an off-axis sputter deposition. However, if this surface is not previously conditioned, the resulting AlN film displays a significant dispersion in the tilt angle. Trying to improve the uniformity of the inherently rough surface of an acoustic mirror, resulting from the successive growth of the different composing layers, we decided sculpture the surface of the W bottom electrodes of several devices by ion milling them at 65º with respect to the surface normal at different ion energies and currents. During the process a part of each sample was intentionally masked with a glass plate so that the subsequent AlN film grew simultaneously on treated and not-treated areas. After the ion milling the samples were immediately loaded in the sputtering chamber for the off-axis AlN sputter process. The position of the A1-LO peak in the IR reflectance spectra measured in the sculptured part of the samples was systematically shifted toward greater wavenumbers, revealing that the sculpturing process tended to increase the tilt angle of the samples, to a greater or lesser extent.

Figure 1 shows the tilt angle derived from FTIR measurements of AlN films grown on W electrodes sculpted for 20 minutes under different experimental conditions. It is important to note that the data of figure 1 correspond to sample dies coming from the same 100 mm silicon wafer covered with a five-layer SiO_2/Mo-based acoustic reflector. This is so because samples coming from different substrates give rise to strong variations in the tilt angle, due to the uncontrolled roughness profiles of the acoustic reflectors from run to run. Results of figure 1 reveal that there is a threshold voltage (1050 V) above which the ion-milling process has a significant effect in the surface conditioning that promotes the growth of more tilted AlN films. Additionally, for voltages values above the threshold, lower ion currents induce greater tilt angles, which suggests that a too high bombardment may produce a smoothing of the rough surface.

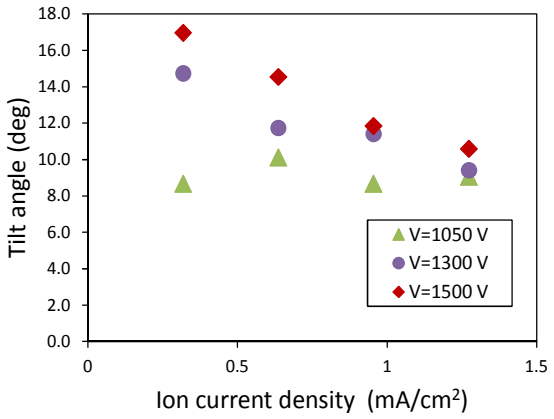


Fig. 1. Tilt angle of AlN films grown over ion milled W substrates as a function of the ion current density and the Ar ion acelerating voltage

However, despite the evident increase of the tilt angle, the electric characterization of the resonators did not show a clear improvement in the performance of the shear modes, being impossible to find a trend between tilt angle and electro-mechanical coupling factor k^2_s. All the results obtained in a large number of samples treated under different conditions suggested that the uncontrolled roughness profiles of the reflectors are hardly homogenized by an ion-milling process. Moreover, the lower values of k^2_s obtained in some samples after the ion milling treatment pointed out that, in some cases, the latter might even induce damage in the sample, leading to AlN films of lower piezoelectric activity.

B. Transfer of slopes by nanoimprint and RIE

To achieve greater tilt angles and improve uniformity and reproducibility of the engineered surfaces, we developed a two-step profile transfer method based on, first, nanoimprinting a saw-tooth profile on a thin photoresist layer (400 nm thick) using a stamp made of PDMS, and then transferring the profile to the substrate. The actual master for the stamp was a 1200 lines/mm ruled diffraction grating with a blaze angle of 26º. The transfer method was a RIE process based on an SF_6 plasma for W layers and on CHF_3 and SF_6 mixtures for SiO_2 layers. The etching processes were tuned to obtain the same etch rate for the resist and the layer underneath. Figure 2 shows a scheme of the etching process at different moments.

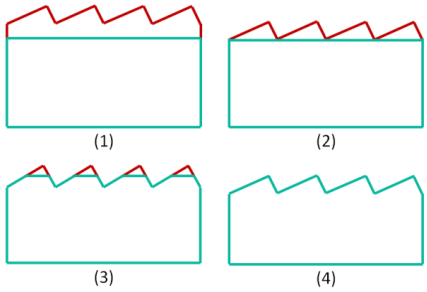


Fig. 2. Scheme of the transfer etching process. (1) starting profile; (2) moment just before starting substarte etching; (3) same etch rate for resist and substrate maintain the geometry; (4) end of the process.

Similar profiles of the surface topography were obtained when transferring the pattern directly to the W bottom electrode or when transferring the pattern to the SiO_2 outermost layer of the acoustic reflector before the growth of the W electrode. Fig. 3 shows two AFM 3D images of the topography of the W top electrode. Picture a) corresponds to a W substrate directly subjected to the profile transfer process and picture b) to a W layer grown on top of a nanoimprinted SiO_2 layer.

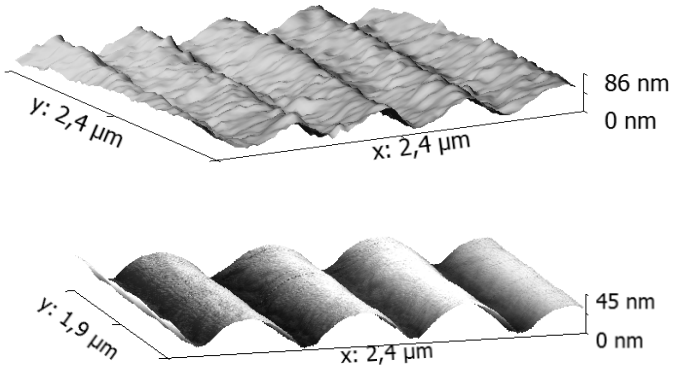


Fig. 3. AFM image of the surface of a) W film patterned through the two-step nanoimprinting process and b) W film deposited on a textured SiO_2 layer.

AlN films grown of top of W films textured through the nano-imprinting process tended to grow normal to the substrates, regardless of the surface topography. This is due to the fact that AlN microcrystals grow with the (00·2) planes parallel to the (110) planes of the W grains, which always grow parallel to the surface when deposited by sputtering, regardless of the sputtering conditions. In fact, we varied the W sputter parameters and sample position in the substrate holder to investigate the effect of the directionality of the sputter process but we achieved always the same results. To solve this problem, we had to introduce a decoupling layer to prevent AlN grains from growing with the c-axis normal to the (110) planes of W. We tried with SiO_2 (without success) and with AlN thin layers sputtered under low energy conditions -low power (600 W) and high pressure (5 mTorr) - to promote the growth of randomly oriented AlN microcrystals. This way we succeed in "erasing" the memory of the surface and growing AlN films with the c-axis normal to the W layer inclines, as shown in the sketches of figure 4. The thickness of this AlN thin layer played an important role on the tilt angle of the subsequent AlN films as shown in figure 5.

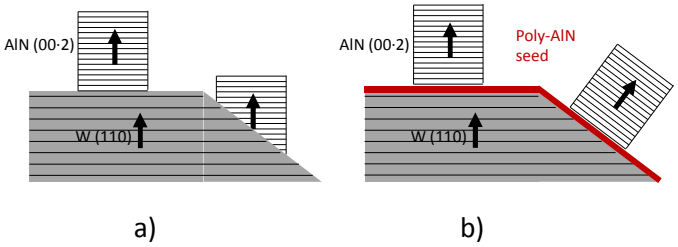


Fig. 4. Sketch showing the mechanism that prevents the AlN grains from growing normally to the surface on engineered W films. a) normal growth on W inclines and b) growth on W slopes afer erasing the surface memory via a poly-AlN layer

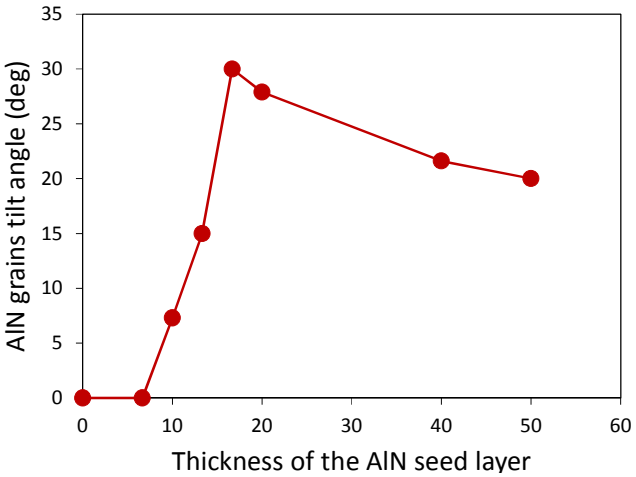


Fig. 5. Tilt angle of the piezoelectrc AlN films grown of top of engineered surfaces as a funtion of the thickness of the poly-Aln film.

With the help of the poly-AlN decoupling layer we were able to produce AlN films with uniformly inclined microcrystals with mean tilt angles close to 30º from the normal, as shown in the XRD pole measurements of figure 6. These plots reveal that there is clear improvement in the uniformity of the tilt angle after the conditioning of the surface topography, which is additionally shifted to higher values (around 30º).

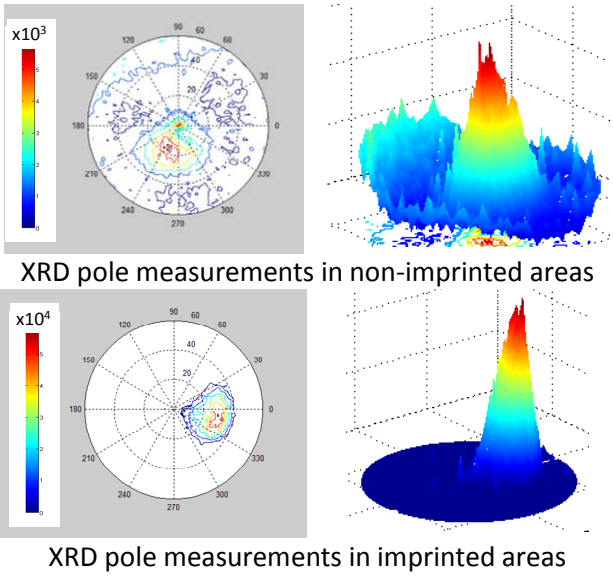


Fig. 6. Pole figure of the (00·2) AlN XRD reflection in non-imprinted and imprinted areas of a same sample.

Finally, we show in figure 7 the values of the electromechanical coupling factors achieved in the resonators subjected to surface conditioning. The shear mode resonators achieved by the two methods have coupling factors greater than those displayed by non-conditioned SMRs, reaching values close to 3%, similar to those obtained only by adding a miss-oriented thicker AlN seed layer on smooth substrates [10].

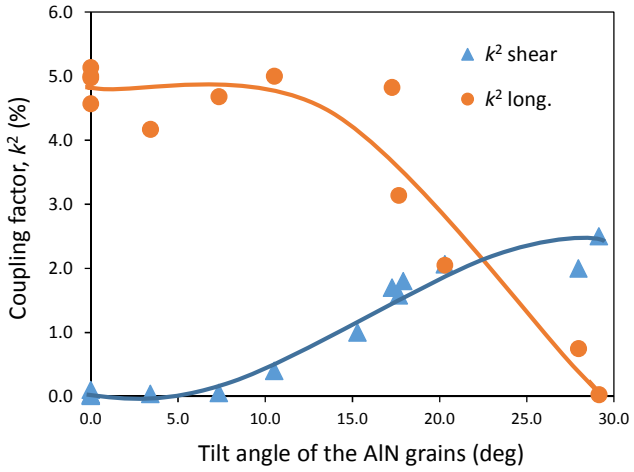


Fig. 7. Variation of the coupling factor of longitudinal and shear modes as a function of the AlN grain tilt angle.

IV. CONCLUSIOTNS

We investigate two new methods to engineer the bottom electrodes of SMRs in order to achieve tooth saw-like profiles that promote the growth of tilted AlN films. The first method, based in texturing the inherent roughness of the acoustic mirror surface by ion milling it at high angles (65º), leads to an increase in the tilt angle of the grains of the subsequently grown AlN films, but does not improve their piezoelectric activity. The second method, based on sculpturing the surface of the bottom electrodes in a saw-tooth pattern throw a two-step nanoimprinting-RIE process does not promote by itself the growth of tilted films. The influence of the metal substrate crystallinity prevails over that of the substrate topography. A randomly oriented AlN seed layer prevents the AlN films from growing along the preferred orientation of the metallic surfaces. Films grown of imprinted samples display improved uniformity of the tilt angle, which reaches values of 30°.

ACKNOWLEDGMENT

This work was partially supported by Ministerio de Economía y Competitividad del Gobierno de España through project MAT2013-45957-R.

REFERENCES

[1] Mario DeMiguel-Ramos, Bárbara Díaz-Durán, José-Miguel Escolano, Mariano Barba, Teona Mirea, Jimena Olivares, Marta Clement, Enrique Iborra, "Gravimetric biosensor based on a 1.3 GHz AlN shear-mode solidly mounted resonator". Sensors and Actuators B 239 (2017) 1282–1288. DOI: 10.1016/j.snb.2016.09.079.

[2] E. Milyutin, S. Gentil, P. Muralt, Shear mode bulk acoustic wave resonator based on c-axis oriented AlN thin film, J. Appl. Phys. 104 (2008) 084508.

[3] Da Chen, J. Wang, D. Li, Y. Xu, Z. Li, Solidly mounted resonators operated inthickness shear mode based on c-axis oriented AlN films, Sens. Actuators A 165 (2011) 379–384.

[4] G. Wingqvist, J. Bjurstr€om, A. Hellgren, and I. Katardjiev, Sens. Actuators, B 127(1), 248 (2007).

[5] M. Clement, E. Iborra, J. Olivares, M. DeMiguel-Ramos, T. Mirea, J. Sangrador. "On the effectiveness of lateral excitation of shear modes in AlN layered resonators" Ultrasonics 54 (2014) pp. 1504-1508; DOI: 10.1016/j.ultras.2014.04.014

[6] J. Bjurström, D. Rosén, I. Katardjiev, V. Yantchev, I. Petrov, Dependence of the Electromechanical Coupling on the Degree of Orientation of c-Textured Thin AlN Films, T. Ultrason. Ferr. Freq. Control 51(10) (2004) 1–7.

[7] T. Yanagitani and M Kiuchi, Control of in-plane and out-of-plane texture in shear mode piezoelectric ZnO films by ion-beam irradiation, Journal of Applied Physics 102 (2007) 044115.

[8] M. Moreira and J. Bjurström, Synthesis of c-tilted AlN films with a good tilt and thickness uniformity, Proceedings of IEEE Ultrasonics Symposium (2012) 1238–1241.

[9] J. Bjurstrom, G. Wingqvist and I. Katardjiev, Synthesis of textured thin piezoelectric AlN films with a nonzero C-axis mean tilt for the fabrication of shear mode resonators, Transactions on Ultrasonics, Ferroelectrics and Frequency Control (2006) 2095-2100.

[10] M. DeMiguel-Ramos, T. Mirea, M. Clement, J. Olivares, J. Sangrador and E. Iborra, "Optimized tilted c-axis AlN films for improved operation of shear mode resonators" Thin Solid Films 590 (2015) 219-223.

[11] E. Iborra, M. Clement, L. Vergara, A. Sanz-Hervás, J. Olivares, J. Sangrador "Dependence of the IR reflectance LO absorption bands on the crystalline texture of AlN films" Applied Physics Letters 88 (2006) pp. 231901.1-3

[12] J. Olivares, S. González-Castilla, M. Clement, A. Sanz-Hervás, L. Vergara, J. Sangrador, E. Iborra "Combined assessment of piezoelectric AlN films using X-ray diffraction, infrared absorption and atomic force microscopy" Diamond and Related Materials. Vol. 16 (2007) pp.1421-1424.

Properties of AlScN thin films for hybrid BAW/SAW resonator fabrication

V. Pashchenko, S. Mertin, F. Parsapour, J. Li, P. Muralt
Electroceramic Thin Films Group
Ecole Polytechnique Fédérale de Lausanne
Lausanne, Switzerland

S. Ballandras
Frec|N|Sys
Besançon, France

***Abstract*—New hybrid bulk-surface acoustic wave resonators using scandium doped aluminium nitride thin films were simulated, using material constants from piezoelectric measurement techniques for thin films. Afterwards they were fabricated and an electromechanical coupling of 4.3% was achieved.**

Keywords—aluminium scandium nitride; bulk acoustic wave; surface acoustic wave; thin-film resonators; piezoelectric properties; electromechanical coupling

I. INTRODUCTION

Nowadays, thin-film bulk acoustic wave resonators (FBAR) are widely used in the area of telecommunication systems. The great advances in aluminium nitride (AlN) piezoelectric film sputtering technology contributed to the evolution of this type of devices. The main advantages of TFBARs firstly are the ideal excitation mode based on the highest possible piezoelectric coupling in the material (longitudinal), and secondly the high achievable quality factor of the fundamental thickness-mode resonance. The main disadvantage of FBARs is their mono-frequency characteristics, which complicates design freedom and device flexibility. Normally, only one AlN thickness is available on a wafer. There are different papers dedicated to multi-frequency devices such as Lamb Wave [1], or Cross-Sectional Lamé mode resonators [2]. These devices are challenging in fabrication and possess only a low Q-factor. A new type of so-called 3rd type FBAR based on the bulk acoustic wave (BAW) excitation in the AlN pillars and transformation to surface acoustic wave (SAW) on non-piezoelectric substrates was proposed and theoretically proven in [3]. The advantages of this resonator type are high achievable effective electromechanical coupling k^2, operational frequency dependence by the interdigitated transducer (IDT) pitch and the absence of the acoustic multilayer mirror, which complicates the device fabrication. First experimental results of the hybrid BAW/SAW resonator based on AlN thin film were reported [4]. Experimentally observed k^2 of those resonators based on AlN film were not more than 1%. However, high k^2 could be achieve with AlN films doped with Sc. Unfortunately, not all material constants of such AlScN films are known, which makes the calculation of the device characteristics less reliable. In this work, we report the experimental result of the piezoelectric measurements and extraction technics for of $Al_{85}Sc_{15}N$ films. Based on the extracted data the $Al_{85}Sc_{15}N$ BAW/SAW hybrid resonators were first simulated, then fabricated and characterized.

II. ALSCN SPUTTER DEPOSITION

C-axis textured $Al_{85}Sc_{15}N$ films were deposited by reactive magnetron sputtering in a Spider 600 cluster tool of *Pfeiffer Vacuum*. The 200-mm $Al_{85}Sc_{15}$ alloy target was operated with 1500 W pulsed DC power. The substrate was heated to 300 °C and subjected to an RF bias. Prior to deposition, the system was pumped down to a base pressure $2x10^{-7}$ mbar. The substrates were 100-mm-diameter Si wafers with a 200-nm-thick wet-oxide SiO_2 layer, and sapphire wafers. 200 nm of Pt layers were deposited at 350°C as bottom electrodes, on which AlScN grows with preferential (0001) or c-axis orientation *[5,6]*. Finally, 200 nm thick Pt top electrodes were deposited.

III. MEASUREMENT OF PIEZOELCTRIC PROPERTIES

A. Piezoelectric constants $e_{31,f}$ and $d_{33,f}$

The transversal piezoelectric coefficient $e_{31,f}$ of the AlScN films was determined with a four-point bending setup of *aixACCT Systems* [7], using Si(100) cantilevers along [110] direction with a Poisson ratio of 0.064. The measurement of an AlN sample was used as reference. By bending the cantilever, a charge difference is produced between top and bottom electrode due to the in-plane strain S_1. Its displacement at the centre is measured with a laser interferometer. From the measured charge and displacement the $e_{31,f}$ value can be derived.

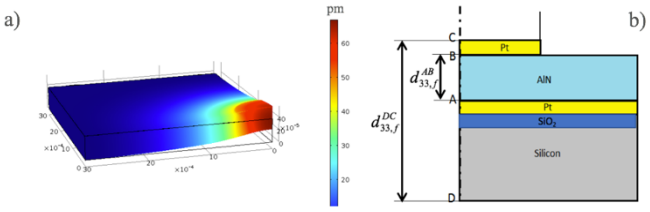


Fig. 1. a) Finite element simulation of the sample for $d_{33,f}$ measurements. Simulation performed for the film thicknesses: AlN 0.5 µm; SiO_2 0.2 µm and Pt 0.1 µm. b) Schematic drawing of the $d_{33,f}$ device with substrate, Pt top and bottom electrodes, and AlN film.

To determine the longitudinal piezoelectric coefficient $d_{33,f}$ a double-beam interferometer is used, which eliminates the contribution of the bended sample to the measured piezoelectric response of the film [8]. Applying an electric potential V on the piezoelectric material induces strain which is proportional to the $d_{33,f}$ coefficient of film. Finite element modeling (FEM, see Fig. 1) of a known AlN film with $d_{33,f}$ = 3.9 pm/V was performed, since the displacement of the thin films is not identical with the measured values for all electrode sizes. The same electrode size of 525 µm was then applied to

extract $d_{33,f}$ of the $Al_{85}Sc_{15}N$ films. Fig. 2 depicts the meausred and simulated $d_{33,f}$ values for different electrode sizes.

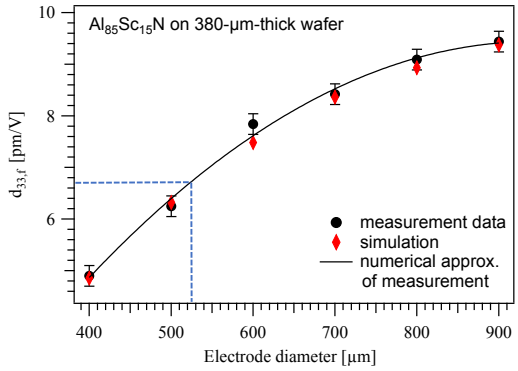


Fig. 2. Electrode size effect on the measured $d_{33,f}$ value. Comparison of measured and simulated $d_{33,f}$ of $Al_{85}Sc_{15}N$.

B. Extraction of Electromechanical Coupling k^2

For effective k^2 measurement high-overtone bulk acoustic wave test resonators (HBAR) were fabricated with the structure Pt/AlScN/Pt/Si. After that S_{11} measurements using an HP 8720D Vector Network Analyzer and manual probe station was implemented. For extracting k^2 multiple reflections of the wave were taken into account by applying modified Butterworth–van Dyke equivalent circuit.

IV. Results

A. BAW/SAW resonator fabrication

A hybrid BAW/SAW resonator is basically a SAW device in which each electrode finger is replaced by a thickness-extensional BAW resonator based on AlScN. The substrate material is not piezoelectric e.g. silicon or sapphire. The FBAR elements are repeated with a period of λ_{SAW}. The piezoelectric film thickness typically ranges from $\lambda_{BAW}/2$ to $\lambda_{BAW}/4$. SAW and BAW wavelengths corresponding to the same frequency lead to an efficient transformation of BAWs into SAWs on the substrate surface. A hybrid resonator design was calculated using the values e_{31} and e_{33} extracted from the measured coefficients $e_{31,f}$ and $d_{33,f}$. Piezoelectric coefficient e_{15} and the stiffness constant c_{ij} were taken from ab-initio calculations [9].

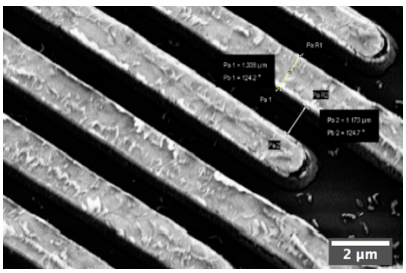


Fig. 3. SEM image of the patterned AlScN film by ICP etching, grown on sapphire.

New hybrid AlScN based resonators were fabricated on sapphire (0001) substrates. SAW wavelength is 5 µm, AlScN film thickness 3 µm. Test device sets were fabricated, consisting of the resonators with different wavelength λ, fingers aperture W, number of IDT fingers pairs N_p and number of fingers in reflectors N_r. More details of the resonators fabrication are described in Ref. [4]. The AlScN pillars were fabricated by Inductively Coupled Plasma etching (ICP). Microphotography of the ~1 µm depth AlScN fingers is shown in Fig. 3.

B. BAW/SAW resonator characterization

Microwave characterization was carried out with an HP 8720D Vector Network Analyzer. Device characteristics are depicted in Fig. 3. The first resonance peak at 642 MHz shows the SAW velocity of AlScN and is mainly localized in the pillar structure, and the second peak at 796 MHz shows the SAW velocity of sapphire, and is confined by the interface. The first resonance exhibits a k^2 of 1.1% and the second of 4.3%, which is about 3 time higher than for AlN/sapphire SAW device.

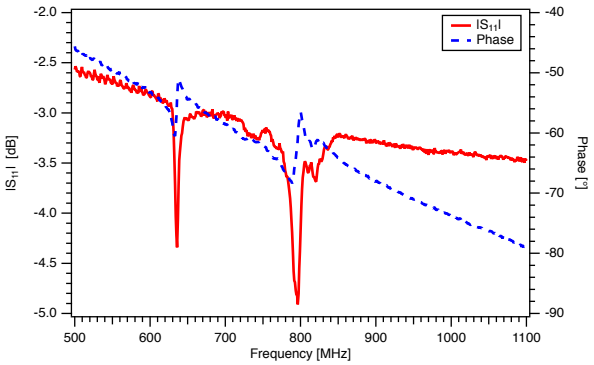


Fig. 4. Typical measured data of hybrid BAW/SAW resonator based on AlScN film on sapphire.

Acknowledgment

Micromachining and electron microscopy were performed at EPFL-CMi. The work was funded by the Swiss Commission of Technology and Innovation (CTI).

References

[1] J. Zou and C. S. Lam, "Electrode design of AlN Lamb wave resonators" in *2016 IEEE International Frequency Control Symposium (IFCS)*, 2016

[2] C. Cassella, Z. Qian, G. Hummel, and M. Rinaldi, "1.02 GHz crosssectional Lamé mode resonator with high KT2 exceeding 4.6%" in MEMS 2016, Shanghai, CHINA, 24-28 January 2016, pp. 659–662

[3] V. Plessky, S. Ballandras, V. Grigorievsky, and V. Yantchev, "3rd type of FBARs?" in *2013 Joint UFFC, EFTF and PFM Symposium*, pp. 239–242

[4] V. Pashchenko, R. Matloub, F. Parsapourkolour, P. Muralt, S. Ballandras, K. Haffner. "Hybrid BAW/SAW AlN and AlScN thin film resonator" in *2016 IEEE International Ultrasonics Symposium Proceedings*, 2016

[5] M.-A. Dubois, P. Muralt. "Properties of aluminum nitride thin films for piezoelectric transducers and microwave filter applications", *Applied Physics Letters* 74, 3032–3034 (1999)

[6] R. Matloub, M. Hadad, A. Mazzalai, N. Chidambaram, G. Moulard, C. S. Sandu, Th . Metzger, P. Muralt. "Piezoelectric Al1-xScxN thin films: A semiconductor compatible solution for mechanical energy harvesting and sensors." *Applied Physics Letters* 102, 152903 (2013).

[7] K. Prume, P. Muralt, F. Calame, T. Schmitz-Kempen, and S. Tiedke, "Extensive electromechanical characterization of PZT thin films for MEMS applications by electrical and mechanical excitation signals", *Journal of Electroceramics*, Vol. 19, No. 4, pp. 407–411, Mar. 2007

[8] A. L. Kholkin, C. Wütchrich, D. V. Taylor, and N. Setter, "Interferometric measurements of electric field-induced displacements in piezoelectric thin films," Review of Scientific Instruments, Vol. 67, No. 5, pp. 1935–1941, May 1996

[9] M. A. Caro, S. Zhang, T. Riekkinen, M. Ylilammi, M. A. Moram, O. Lopez-Acevedo, J. Molarius, and T. Laurila, J. Phys: Condens. Matter 27 (2015) 245901.

Temperature Coefficients of Quartz at Cryogenic Temperature

Jérémy Bon, Roger Bourquin, Philippe Abbé, Xavier Vacheret, Serge Galliou
FEMTO-ST, Time and Frequency dept.
Univ. Bourgogne Franche-Comté, CNRS, ENSMM
Besançon, France
Jeremy.bon@femto-st.fr, serge.galliou@femto-st.fr

***Abstract*—The temperature coefficients of the elastic coefficients of quartz within [4 K, 15 K], the operating range of conventional cryocoolers, are predicted from experimental data. Raw data consist of a set of frequency-temperature curves recorded from bulk acoustic wave resonators made in different plates cut according to various angles relative to the crystallographic axes. Raw data are then processed as described in the paper in order to provide the 1st, 2nd, and 3rd order temperature coefficients of the seven elastic coefficients of quartz crystal.**

Keywords—quartz; elastic coefficients; temperature coefficients; liquid-helium temperature; low mechanical loss; high quality factor.

I. INTRODUCTION

Usually temperature sensitivity cannot be neglected when designing a quartz resonator-based device. Even at temperatures lower than 6 K, where the material properties are less sensitive to temperature than at room temperature, the remaining sensitivity has to be considered. The resonant frequency of a quartz crystal resonator is not an exception to this rule: the remaining fractional frequency change versus temperature is typically a few 10^{-9} K^{-1} close to 4 K [1-2]. This is still too much to realize a stable frequency source even with a temperature control exhibiting a typical gain of 1000: definitely, such an application would need a temperature compensated cut. It should be reminded that quartz resonators look very attractive around 4 K because of their very high quality factor that can be greater than one billion [3]. Conversely, quartz resonators could also be used as temperature sensors provided they are made in an appropriate cut, i.e. a very temperature-sensitive one. In both cases, to design a frequency reference or a temperature sensor the knowledge of the temperature coefficients of the elastic constants of the material is mandatory, the resonance frequency depending on these elastic constants. A set of coefficient values already exists for the quartz crystal since 1975 [4] but it covers the very wide range [4K, 400 K], and consequently becomes irrelevant inside the shorter operating range of conventional cryorefrigerators. These are the main reasons why we carried out a campaign of measurements to determine the 1st, 2nd and 3rd order temperature coefficients of the elastic constants of quartz within [4 K, 15 K].

This work is supported by Conseil Régional de Franche-Comté, Grant No. 2013-F05497-0000. J.B. is thankful to Ministère de l'Enseignement Supérieur et de la Recherche, for his grant.

II. METHOD OF CALCULATION

The thermal coefficients can be determine from various experimental principles. It can be from resonant ultrasound spectroscopy, phase velocity measurements by pulse echo overlap methods, laser ultrasonic techniques or combined resonance techniques. Nevertheless, their implementation at cryogenic temperatures arises technical difficulties. The selected alternative consists in probing the temperature sensitivity of resonance frequencies of dedicated quartz devices.

A. Theoretical principle

Basically, a flat plate exhibits bulk acoustic waves (BAW) resonance frequencies derived from $f_n = \frac{n}{2h}\sqrt{\frac{C_e}{\rho}}$ where n is the overtone order, $2h$ the plate thickness, ρ its density, and C_e an elastic coefficient that looks like a combination of the material elastic constants C_{ijkl} depending on the cut orientation with respect to the crystallographic axis in case of quartz because of its anisotropy. All these parameters are temperature dependent yielding to a temperature-dependent frequency. Usually, the frequency-temperature characteristic can be fitted effectively by a 3rd order polynomial approximation, and this operation can be applied to each parameter. Once experimental frequency-temperature records processed this way, the three corresponding temperature coefficients of the elastic coefficient(s) can be extracted accordingly. The calculation is just somewhat complicated by the fact that there are seven coefficients C_{ijkl} for the quartz crystal. A set of combinations should therefore be considered involving a set of resonator cuts to be tested.

B. Relationships and assumptions

Actually, the tested devices are not flat plates but plano-convex disks, a shape commonly used to trap efficiently the acoustic energy. This is one way to preserve the resonator against disturbances from its environment (i.e. parasitic stresses and then frequency changes), and consequently a kind of guarantee to qualify the material regardless of the device structure. However, the modelling is complicated and the resulting frequency is as follows, according to the Stevens-Tiersten model [5], one of the most accurate theories:

$$f_{nmp}^2 = f_n^2\left[1+\frac{1}{n\pi}\sqrt{\frac{2h}{R_0}}\left(\sqrt{\frac{M_n}{C_e}}(2m+1)+\sqrt{\frac{P_n}{C_e}}(2p+1)\right)\right] \quad (1)$$

Where f_n are the eigenfrequencies of the corresponding infinite flat plate, R_0 the curvature radius of the convex face, m, p the number of modal lines in the resonator plane, M_n and P_n the dispersion constants.

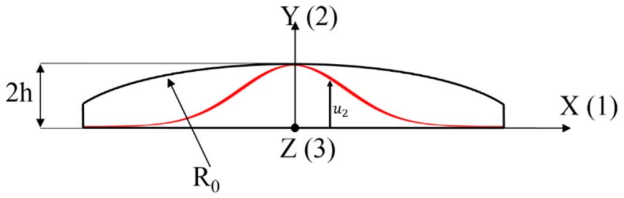


Fig. 1. Plano-convex resonators. In such trapped-energy devices, the vibration displacement u_2 along the Y-axis exhibits a Gaussian distribution.

Fig. 2 gives the frequency deviation as a function of temperature from experimental data for the 1st, 13th and 15th overtones of the (quasi)longitudinal mode, the A mode, of a X-cut. It can be notice that the behaviour of these three plots are rather similar, and sufficiently close together to neglect as a first approximation the dispersion constants M_n and P_n related to the energy trapping.

When taking into account this last assumption, the calculation of the temperature coefficients of the elastic constants can just be drawn from the expression of eigenfrequencies of the infinite flat plate given by:

$$f_n^{\xi 2}(T) = \frac{n^2}{16h^2(T)}\frac{\overline{c_e^{\xi}}(T)}{\rho(T)}\left(1-\frac{8k_\alpha^2(T)}{n^2\pi^2}-r\right), \quad (2)$$

where ξ stands for the A, B or C mode (the extensional and both thickness shear modes respectively), k_α^2 is the coupling electromechanical coefficient, and r the ratio of electrode and resonator masses.

Nevertheless, some additional assumptions can still be made in equation (2) by considering some orders of magnitude. First, the last term within parentheses, r, typically in the order of 10^{-3}, can be considered as a constant over the small temperature range used in this study. Consequently, it is not temperature dependent and then not involved in the following calculation. Moreover, the electromechanical coefficient has a small value, and decreases significantly for high overtones: thus, it can also be neglected. Furthermore, it can be shown that the effective elastic coefficients $\overline{Ce}$ take values close to their version without piezoelectricity (without the top bar) which are the eigenvalues of the Christoffel tensor [6]. As a result, the issue becomes a pure mechanical one.

The cubic shape of the frequency-temperature characteristics observed experimentally implies that the thermal coefficients of the elastic constants should be provided up to the third order as well. The thermal coefficient of elastic constants TC_{ij} are link to the thermal sensitivities of effective elastic constants which can be obtained by differentiating equation (2) with respected to temperature

$$T^{(1)}C_e \approx 2T^{(1)}f + T^{(1)}\rho + 2T^{(1)}h$$

$$T^{(2)}C_e \approx \frac{1}{2}(TC_e)^2 - \left(T^{(1)}f\right)^2 - \frac{1}{2}\left(T^{(1)}\rho\right)^2 - \left(T^{(1)}h\right)^2 + 2T^{(2)}f + T^{(2)}\rho + 2T^{(2)}h$$

$$T^{(3)}C_e \approx 2T^{(3)}f - 2T^{(1)}fT^{(2)}f + \frac{2}{3}T^{(1)}f + \frac{1}{3}\left(T^{(1)}\rho\right)^3 - \frac{1}{3}\left(T^{(1)}C_e\right)^3 + \frac{2}{3}\left(T^{(1)}h\right)^3 - T^{(1)}\rho T^{(2)}\rho - 2T^{(1)}hT^{(2)}h + 2T^{(3)}h + T^{(1)}C_eT^{(2)}C_e + T^{(3)}\rho, \quad (3)$$

where T^qC_e, T^qf, T^qh and $T^q\rho$ are q-order thermal sensitivities of the effective elastic coefficients, frequency thickness and mass density respectively.

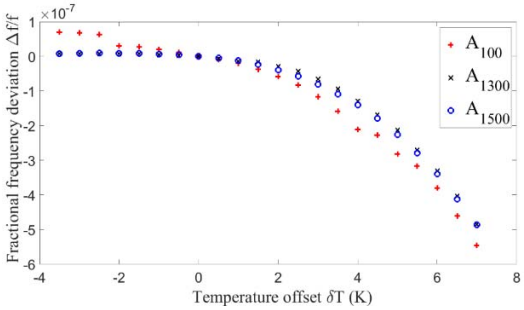


Fig.2. Resonance fractional frequency shift $\frac{f(T)-f(T_{ref})}{f(T_{ref})}$ versus temperature offset $\delta T = T - T_{ref}$, where $T_{ref} = 8K$. These experimental measurements are for a 600 µm thick X-cut with a radius of curvature $R_0 = 250\ mm$

The thermal coefficients of frequency given in Table I are obtained by fitting frequency-temperature characteristics from measurements of five quartz cuts and averaged on several overtone numbers of each tested cut in order to determine the seven elements of the elastic-coefficient tensor for a trigonal 32 material. The thermal coefficients of thickness and mass density are determined [7] by interpolating over [4K-15K] the expansion coefficients given in [8] for quartz material.

III. EXPERIMENT

A. Experimental set-up

Resonators have been tested in a conventional pulse tube cryorefrigerator SRP082B. The resonators are embedded inside an oxygen-free cooper block screwed on its cold stage. The operating temperature is controlled at ±3 mK within [4 K, 15 K] by a Lakeshore 335 probing a cernox sensor and actuating a heater embedded inside the copper block. For a given temperature, the resonator admittance around the frequency of the overtone/mode to be investigated is recorded by means of a network analyzer locked on a hydrogen maser in order to take advantage of the frequency stability and accuracy of the latter. The analyzer provides a 0.001 dB and 0.01° resolution in magnitude and phase respectively with a frequency resolution that can reach 1 mHz. A calibration procedure should be followed before recording, to cancel the influence of the coaxial cable feeding the resonator inside the vacuum chamber and the network analyzer. This calibration involves three coaxial cables ended respectively by a standard 50 Ω, an open circuit and a short circuit.

B. Devices under test

As mentioned above, a set of dedicated BAW energy-trapped resonators with gold electrodes, as shown in Fig. 3, has been made and tested. The realization of 13 mm diameter plano-convex resonators follows a conventional process: plate orientation with respect to the crystal axis, plate cutting, rounding, lapping, polishing and gold-electrode coating for piezoelectric actuation and readout. Depending on the cut angle of the tested device as well as the targeted mode, the electrical field has to be normal or parallel to the y-axis (see Fig. 1). In the latter case, two half electrodes are coated on each side of the resonator instead of both full electrodes (see Fig. 3).

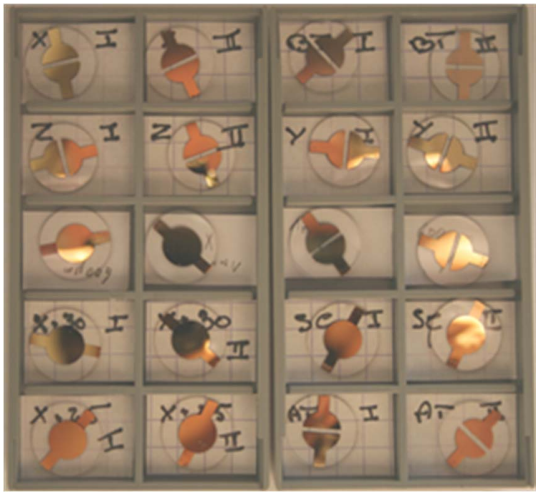


Fig. 3. Set of plano-convex resonators tested for determining the temperature coefficients of the elastic constants of quartz at 4 K.

Table I shows, from left to right, from which cut and modes each experimental frequency-temperature characteristic is taken from, the corresponding frequency coefficients of the polynomial fit, and the targeted elastic coefficient. Quartz-cuts summarized in Table I comply with the IEEE-standard 176-1978: AT (0°, -35.3°), SC (22°, -34°), X (30°, 0°), Y (0°, 0°) and Z (0°, 90°).

TABLE I. TARGETED ELASTIC COEFFICIENTS

Cut	From experimental data				Target
	Mode	$T^{(1)}f$ *In* 10^{-7}	$T^{(2)}f$ *In* 10^{-8}	$T^{(3)}f$ *In* 10^{-9}	
AT	C_{300}, C_{500}	0.769	0.748	0.105	C_{14}
SC	A_{300}, A_{500}	-1.178	-2.189	-2.747	C_{13}, C_{33}
SC	B_{300}, B_{302} B_{320}, B_{500}	-0.879	-1.672	-1.832	C_{13}, C_{33}
X	A_{100}, A_{1300}, A_{1500}	-0.143	-0.451	-0.581	C_{11}, (C_{12}[a])
Y	C_{300}, C_{500}	1.339	1.869	1.289	C_{66}
Z	C_{300}, C_{500}	-1.465	-2.662	-3.571	C_{44}

[a.] Calculated from C_{11} and C_{66}

IV. RESULTS

Table II shows the resulting 1st, 2nd and 3rd order temperature coefficients of the *Cij*'s, for quartz, with T_{ref} = 8 K.

TABLE II. RESULTING COEFFICIENTS

C_{ij}	$T^{(1)}C_{ijkl}$ in 10^{-7}	$T^{(2)}C_{ijkl}$ in 10^{-8}	$T^{(3)}C_{ijkl}$ in 10^{-9}
C_{11}	-0.235 (20 %)[b]	1.28 (20 %)	-3.25 (21 %)
C_{12}[c]	-6.39 (31 %)	-10.56 (29 %)	-4.22 (202 %)
C_{13}	-7.18 (88 %)	-7.42 (22 %)	-0.877 (187 %)
C_{14}	-1.35 (51 %)	-1.31 (49 %)	-7.93 (141 %)
C_{33}	-4.62 (35 %)	-5.65 (20 %)	-7.62 (255 %)
C_{44}	-3.17 (24 %)	-4.37 (20 %)	-11.6 (86 %)
C_{66}	3.08 (23 %)	5.92 (20 %)	0.486 (201 %)

[b.] Uncertainties mainly come from possible cut-angle deviations especially during the lapping and polishing process.

[c.] Calculated from C_{11} and C_{66}

V. CONCLUSION

Resulting data will be used to identify temperature compensated cuts in the very useful range [4 K, 15 K], where quartz resonators exhibit Q-factors of about one billion. Anyway, it is important to keep in mind that there is always a more practical remaining uncertainty in addition to the unavoidable uncertainty due to any theoretical modelling. Indeed, the main uncertainty results from the final cut-angle values after lapping and polishing in the plano-convex shaping process, in addition to the uncertainty about the blank plate angle. Thus, although data given in table II have to be used as the basis of a theoretical guideline, an additional series of tests cannot be skipped.

REFERENCES

[1] S. Galliou, J. Imbaud, R. Bourquin, N. Bazin, Ph. Abbé, "Outstanding quality factors of bulk acoustic wave resonators at cryogenic temperature", proc. 22nd EFTF, Toulouse, France, 5 pages (in DVD Toulouse Space Show), 22-25 April 2008.

[2] M. Goryachev, S. Galliou, J. Imbaud, R. Bourquin, Ph. Abbé, "Recent Investigations on BAW Resonators at Cryogenic Temperatures," IEEE IFCS-EFTF 2011, San Francisco, Ca, USA, May 2011.

[3] S. Galliou, M. Goryachev, R. Bourquin, Ph. Abbé, J. P. Aubry, and M. E. Tobar, "Extremely Low Loss Phonon-Trapping Cryogenic Acoustic Cavities for Future Physical Experiments," Nature: Scientific Reports, Sci. Rep. 3, 2132, 2013.

[4] A. G. Smagin, "Frequency-temperature characteristics of quartz crystal units of different cuts operating over a wide temperature range including helium temperatures" Proc. 49th IEEE IFCS, 31 May- 2 June 1995.

[5] D. S. Stevens, H. F. Tiersten, "An analysis of doubly rotated quartz resonators utilizing essential thickness modes with transverse variation," J. Acoust. Soc. Am. Vol.79, N°6, pp. 1811-1826, June 1986.

[6] D. Royer and E. Dieulsaint, "Elastic Waves in Solids I, Free and Guided Propagation", Springer, 2000.

[7] J. Bon, S. Galliou, R. Bourquin, "Temperature coefficients of crystalline-quartz elastic constants over the cryogenic range [4 K, 15 K]", Appl. Phys. Lett., 109, 231902, 2016.

[8] T. H. K. Baron, J. F. Collins, T. W. Smith, and G. K. White, "Thermal expansion, Grüneisen functions and static lattice properties of quartz", J. Phys. C 15, 3311-3326, 1982.

Anti-Symmetric Shear-Extensional AlN Lamb-Wave Resonators with $k_t^2 > 4\%$

Bumkyung Jo, Mayur Ghatge, and Roozbeh Tabrizian
Electrical and Computer Engineering
University of Florida
Gainesville, USA
edwardjo6317@ufl.edu, ruyam@ufl.edu, rtabrizian@ece.ufl.edu

Abstract—**This paper presents a waveguide-based aluminum nitride resonator that simultaneously exploit transverse (d_{31}) and shear (d_{15}) piezoelectric constants to realize a large electromechanical coupling factor (k_t^2), while having a frequency defined by lateral dimensions. An anti-symmetric Lamb wave with co-existing in-plane extensional and thickness-shear elastic energy distribution is used along with proper dispersive energy trapping to simultaneously exploit transverse and shear electromechanical coupling of AlN film. Specifically, the shear transduction ($k_{t,15}^2$) benefits from the large d_{15} constant (due to the columnar single crystallinity) as well as low in-plane relative permittivity (due to the in-plane poly crystallinity) of the AlN film, and hence significantly improves the overall k_t^2. A proof-of-concept device operating at 733MHz with a Q of ~1400 and k_t^2 of ~4.4% is demonstrated.**

Keywords—aluminum nitride resonator, transverse-extensional (d31) piezoelectric constant, thickness-shear (d_{15}) piezoelectric constants, lateral frequency scalability.

I. Introduction and Background

Simultaneous realization of large k_t^2 and lithographical frequency definition is essential for implementation of wide-band filter arrays, with frequencies extended over the wide UHF spectrum. FBARs benefit from large longitudinal piezoelectric coefficient (i.e. d_{33}), but have a frequency tied to their uniform thickness. In-plane extensional resonators, on the other hand, provide the desired lateral frequency definition; however, their k_t^2 is limited by small transverse (i.e. d_{31}) piezoelectric constant. Various techniques have been devised to improve the transduction efficiency of in-plane AlN-transduced resonators including introduction of dopants [1], integration of AlN films on the sidewall of silicon structures [2], and most recently acoustic coupling of in-plane and out-of-plane extensional modes (i.e. cross-sectional Lamé mode) [3]. These techniques either impose fabrication processing challenges, or suffer from significant k_t^2 drop / inconsistency with variation of cross-sectional aspect ratio, which is inevitable for frequency scaling of the resonators.

II. Anti-Symmetric Lamb-Wave AlN Resonator

Symmetric Lamb waves have been conventionally used for realization of high Q resonators as they provide nodal points for low-loss anchoring of the device. Furthermore, symmetric Lamb waves can be excited by application of vertical electric fields across the thickness (i.e. C-axis) direction of the piezo film and through d_{31} and / or d_{33} piezoelectric constants. ***Unlike conventional approach, in this work we utilize a anti-symmetric wave that has a considerable fraction of acoustic energy stored in thickness-shear elastic field, and hence can be excited through d_{15} piezoelectric constant.*** In the absence of nodal points in the vibration mode shape, we have used dispersive energy trapping technique to realize low anchoring loss through coupling propagating Lamb waves in active region with evanescent waves in flanks (Fig. 1). Fig. 2 shows the cross-sectional mode shape of the anti-symmetric Lamb wave, highlighting both extensional and shear volumetric energy

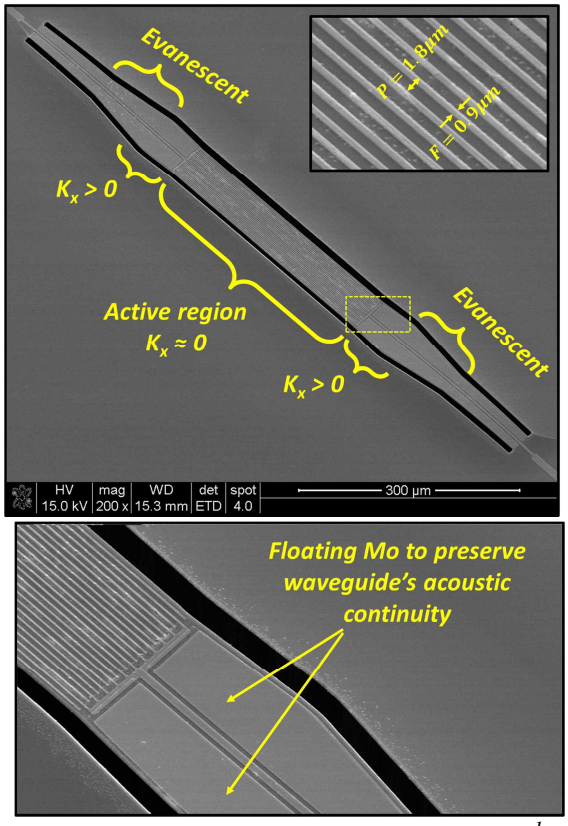


Fig. 1: SEM image of the acoustically engineered 23rd shear-extensional anti-symmetric AlN Lamb-wave resonator.

distribution. Excitation of these elastic fields requires simultaneous application of vertical (parallel to C-axis) and lateral (perpendicular to C-axis) electric field. This is achieved through the configuration shown in Fig. 3. Such a transduction scheme benefit from cumulative effects of $k^2_{t,31}$ and $k^2_{t,15}$.

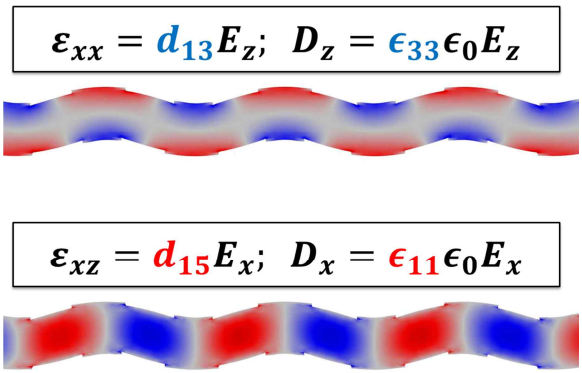


Fig. 2: cross-sectional mode shape of the anti-symmetric shear-extensional Lamb wave, highlighting both extensional (top) and shear (bottom) volumetric elastic energy distribution. Corresponding electromechanical coupling relation for each field is also demonstrated.

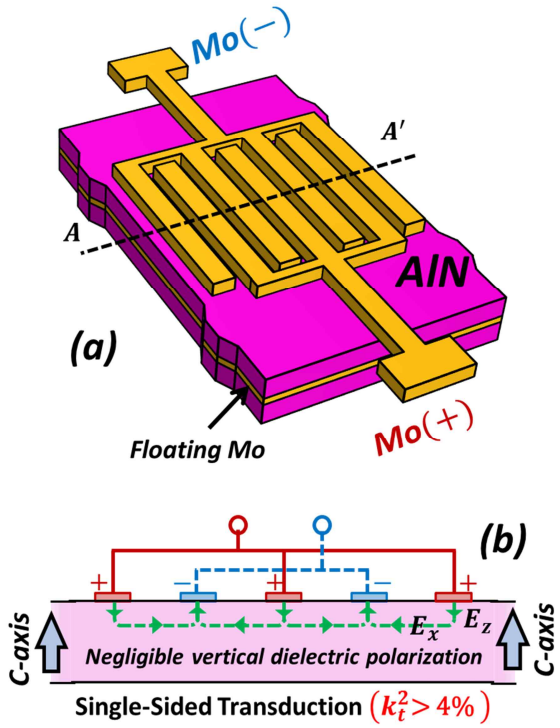


Fig. 3: Schematic of device concept (a). The d_{15}-enhanced electromechanical transduction concept; resulting in excitation of lateral (E_x) and vertical (E_z) electric fields in film bulk and surface respectively (b).

III. Resonator Characterization

Fig. 4 shows the measured admittance of the resonator shown in Fig.1, operating at 733MHz, with a Q of ~1400 and k_t^2 of 4.4%. Such a high k_t^2, along with the high Q, of the device make it highly suitable for realization of wide-band filters with a frequency defined by in-plane dimensions of the resonators.

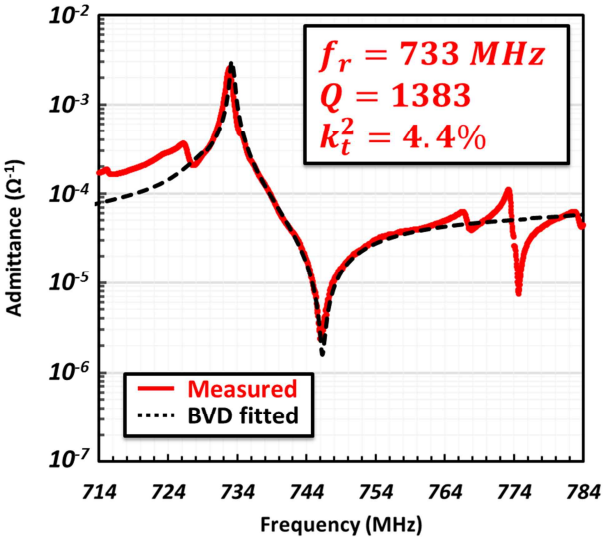


Fig. 4: Measured admittance of the device shown in Fig. 1 in comparison with BVD model fitted to the response.

Acknowledgment

The authors thank the staff at Nanoscale Research Facility at the University of Florida for their help with the device fabrication.

References

[1] S. Mishin, et. al. (2013). *IEEE EFTF/IFC 2013*, pp. 126-128.
[2] R. Tabrizian, et. al. (2011). *IEEE Transducers 2011*, pp. 1520-1523.
[3] C. Cassella, et. al. (2016). *IEEE JMEMS*, 25 (2), 275- 285.

Wideband and low phase noise up-converted direct frequency synthesis using high frequency DAC and Oscillator

Jean-marc LESAGE, Jean-François PENN
DGA – Information Superiority
DGA French MoD
Bruz, France
Email: jean-marc.lesage@intradef.gouv.fr

***Abstract*— This article demonstrates that up-converted direct frequency synthesizer using low phase noise local oscillator and high speed DAC (Digital to Analog Converter) allows reaching simultaneously high spectral purity and wide frequency agility. A multiplied-frequency OCSO (Oven Controlled SAW Oscillator) or an OEO (Opto-Electronic Oscillator) is used to provide the clock to the DAC and also to up-convert the output frequency DAC in any microwave frequency band of interest. Within our experiments operating in S or X frequency band, we obtain more than 500 MHz bandwidth, showing a high Spurious Free Dynamic Range (SFDR) about 70 to 80 dBc and a very low phase noise level (lower than -140 dBc/Hz).**

Keywords*— *Saw Oscillator; OEO (Opto-Electronic Oscillator); low phase noise and agile microwave frequency synthesis

I. INTRODUCTION

Electronic warfare sub-systems always need wider frequency band agile synthesizer. This one must also show low noise and low spurious level. One can design indirect frequency synthesizer as phase locked loop (PLL) but it is difficult to reach in the same time fine frequency resolution and low spurious level. Moreover, there is a limitation of phase noise by the phase detector in the loopband of the PLL.

Up to recently, Direct Digital Synthesizer (DDS) was not dedicated to this topic because DAC with improved noise performances required working at low frequency. We have shown [1] that it was no more a reality since, on the first hand, few GHz clock DAC with low spurious and low noise performances [2] and on the other hand, low phase noise local oscillator [3] are available on commercial market. So by combining ULN (Ultra Low Noise) high frequency local oscillator (LO) and high frequency DAC, one can achieve state of the art frequency synthesis, outperforming then current established limits.

A new high frequency DAC has been designed by E2V in the frame of DGA founded project in order to increase the frequency clock up to 6 GSps [2], [5]. Simultaneously, the phase noise and SFDR have been improved in comparison of the previous DAC. In order to benefit of these new performances, a new multiplied OCSO [3] has been developed by Rakon around 5 GHz. This LO frequency gives the best frequency plan in the same time for different output frequency bands.

We demonstrate firstly the synthesis performance that we can reach in S band with new high frequency components, in comparison with the previous results [1]. Secondly, X-band synthesis is realized and comparison is done between multiplied OCSO and OEO for the local oscillator (LO).

II. UP-CONVERTED DIRECT DIGITAL FREQUENCY AGILE SYNTHESIS SCHEME

Fig. 1 shows the scheme of synthesis. The multiplied OCSO provides the DAC's clock without any added jitter on the frequency output and also perform the up-conversion of the output frequency DAC in any microwave frequency band of interest.

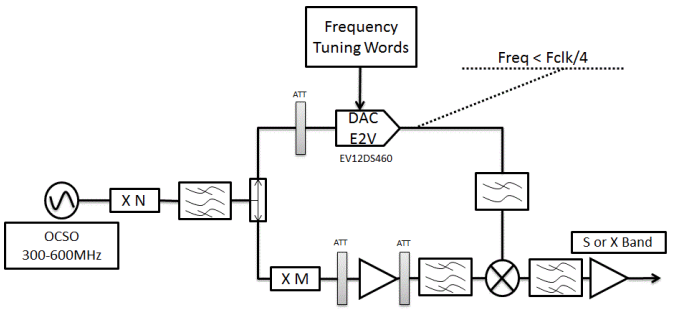


Fig. 1. Scheme of the proposed up-converted direct frequency synthesis

As explained in [1], the DAC output frequency must be chosen between *Fclk/8* and *Fclk/4* (with *Fclk* the DAC clock frequency) in order to prevent spurs in the desired output frequency band (simple harmonic or folding). Another reason is that the parallel data multiplexer speed can product spurious at *n.Fclk/4* in Mux 2 or *n Fclk/8* in Mux 4 mode. Finally, we remind that specific DAC mode NRTZ (Narrow Return To zero) [4], [5] is chosen because it offers the best compromise between low phase noise and SFDR (Spurious Free Dynamic Range) in the first Nyquist band.

As the frequency clock has been improved from around 3 GSps in [1] up to around 5 GSps in this work, the maximal output frequency bandwidth is increased up to 625 MHz,

depending of the Spurious Free Dynamic Range (SFDR) that is needed.

The DAC clock is provided by a multiplied OCSO with a low noise frequency multiplier-by-10 [3]. In order to reach the S band, the same 5 GHz LO is used to up-convert the DAC output (M=1).

The fig. 2 shows the DAC with the ddigital pattern generator board and the OCSO. The power consumption of the DAC is inferior to 2,5 W. For the OCSO with the low noise multiplier, it is inferior to 5 W after warm-up.

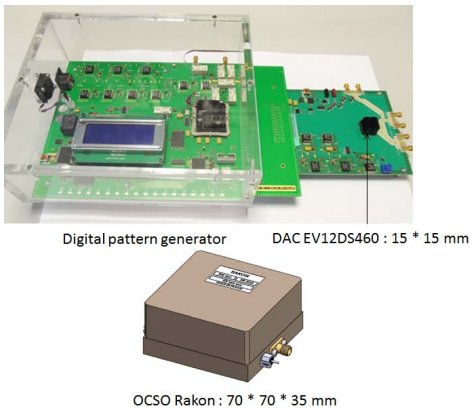


Fig. 2. Pictures of DAC and OCSO

Concerning the X band scheme, a frequency multiplier-by-2 is used (M=2), as described in figure 1. For comparison, we realize another synthesis in X band using a microwave oscillator at the direct frequency of 10 GHz. We choose state of the art and off-the-shelf OEO [6]. A frequency divider-by-2 is used to provide the clock of the DAC, as described below.

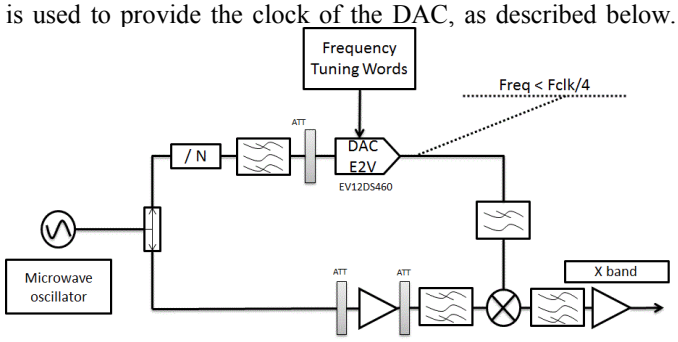


Fig. 3. Scheme of the high frequency proposed up-converted direct frequency synthesis with a low noise divider

III. PERFORMANCE OF THE PROPOSED S-BAND SYNTHESIS

A. S-Band phase noise results

Phase noise floor level better than -143 dBc/Hz is reached. Fig. 4 shows the worst results in the frequency output band in comparison with the previous results [1] where a phase noise level floor of -135 dBc/Hz was obtained. This is the worst case because the lower output frequency of the synthesis is the upper output frequency of the DAC. The DAC phase noise is not limited by thermal, quantification or clock induced noise but by technical noise, that increase with the ratio *Fout/Fclk*.

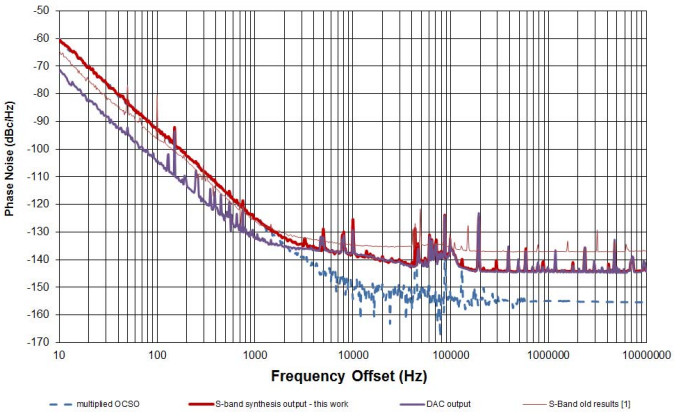


Fig. 4. S-Band synthesis phase noise

At the same time, there is a slight degradation of the close-to-the-carrier phase noise that is explained by the slight higher frequency of the reference OCSO in comparison with the previous work. The Q factors of the SAW resonator at the two frequencies are equals. If better close-to-the-carrier phase noise is needed, only the Q factor of the SAW resonator should be improved because the limitation doesn't come from the DAC.

B. S-band SFDR results

Fig. 5 shows an example of obtained spectrum in S-Band. The overall SFDR is resumed in Table I. This is given over a 500 MHz fixed frequency span for a given frequency output band.

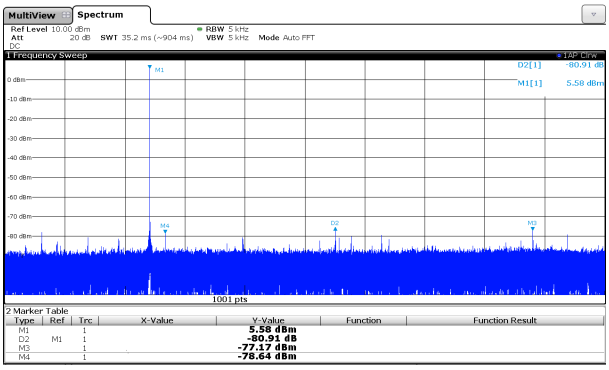


Fig. 5. SFDR of S-Band synthesis (example of spectrum)

TABLE I. SFDR OF S BAND SYNTHESIS

	Previous work [1]	***This work***
SFDR over 500 MHz fixed span	69 dBc for output frequency in 200 MHz	76 dBc for output frequency in 300 MHz
SFDR over 500 MHz fixed span	55 dBc for every output frequency in the span	63 dBc for every output frequency in the span

These results show that the DAC frequency clock increase allows wider frequency span and easier frequency plan to avoid mixing spurs. The DAC harmonics that the frequency

plan can't avoid have also been reduced. Given these points, the overall SFDR of the S-Band synthesis has been improved in comparison with [1] and is better than 70 dBc over a 500 MHz span for 60 % of the output frequencies.

C. *Perspectives*

In order to improve SFDR, the DAC frequency clock should be increased. Consequently, the maximum DAC output frequency will increase. On the other side, the DAC maximum frequency should be kept as low as possible in order to give the lowest phase noise floor. Given these points, the best compromise may be the DAC technical noise floor reduction when DAC frequency output increases.

IV. PERFORMANCE OF THE PROPOSED X-BAND SYNTHESIS

A. *X-band phase noise results*

The phase noise results are quite similar in S (Fig. 4) and X band (Fig. 6), when using OCSO. As the phase noise floor is determined mainly by the DAC noise floor, there is no more than 1 dB of difference in the two frequency bands.

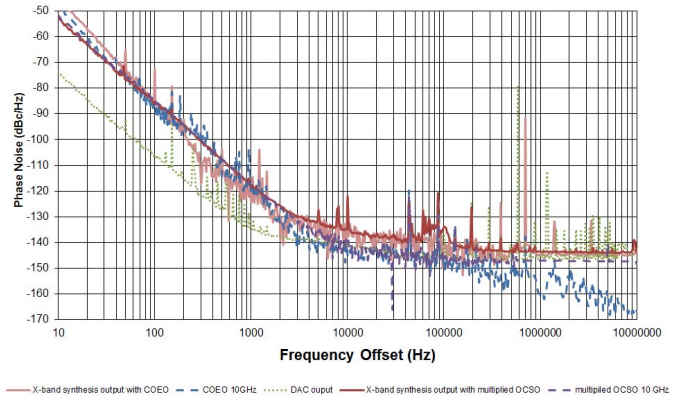


Fig. 6. X-Band synthesis phase noise

Concerning the close to the carrier phase noise, there is a degradation of 6 dB in X-band caused by the multiplier-by-2.

For frequency offset of 10 kHz, the phase noise is higher for the X-band (-136 dBc/Hz) than S-band (-139 dBc/Hz) because the contribution of the multiplier-by-2 begins to appear.

The use of OEO combined with low noise frequency divider show the same level of phase noise than multiplied OCSO for X-band synthesis, as shown in Fig. 6.

Contrary to the S-Band, the DAC noise floor reduction only is not enough to improve the synthesis noise floor. The LO phase noise floor reduction is also needed. Moreover, as the OEO phase noise should be kept when increasing his frequency and if it is possible to reduce the phase noise floor of OEO without degradation of the close-to-the-carrier phase noise, OEO will be advantageous for desired frequency synthesis output up or equal to X-band.

B. *X-band SFDR results*

Fig. 7 shows an example of obtained spectrum in X-band. The SFDR is better than 70 dBc for 500 MHz bandwidth. This is a better result than in S-band because there is a better rejection of the intermodulation spurs with higher frequency difference between OL and DAC output.

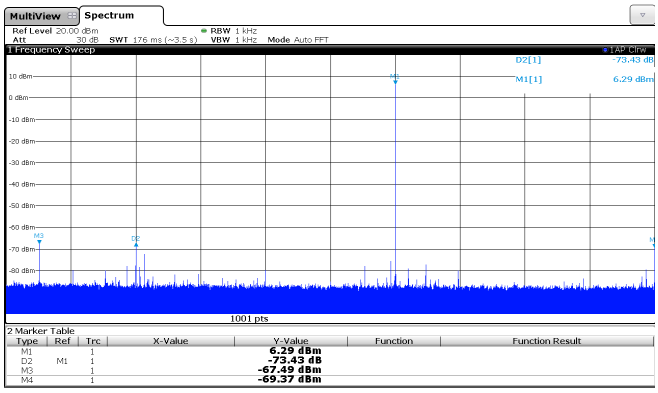


Fig. 7. SFDR of X-Band synthesis (example of spectrum)

The main limitation to SFDR improvement comes from the data multiplexing of the DAC because of the low speed of FPGA of the digital pattern generator. The mixing between frequency output, harmonics and folding with the Fclk/4 and Flck/8 spurs are the highest level spurs. Future main development will consist in reducing this spurs level or cancelling the data multiplex.

V. CONCLUSION

We demonstrate that a simple up-converted direct frequency synthesis can reach large frequency bandwidth with high SFDR (about 70 to 80 dBc over 500 MHz) and a very low phase noise level (lower than -140 dBc/Hz), thanks to the availability of high frequency LO and DAC.

In order to improve the performances, the DAC phase noise floor (technical noise) and multiplex spurs level should be reduced.

Concerning frequency synthesis output up or equal to X-band, OEO will be well dedicated to play the role of LO.

REFERENCES

[1] Wideband, low noise and low spurious agile direct frequency synthesis based on combination of SAW Oscillator and high speed DAC, Jean-Marc LESAGE, Adrien CAPAINE, Jean-François PENN, Guy JESTIN

[2] http://www.e2v.com/products/semiconductors/dac

[3] http://www.rakon.com/products/families/ocxo-ocso#cat_149

[4] F.Bore, M. Wigender, A. Glascott-Jones,E. Dumaine, C.Lambert and S. Calais, "3 GS/s 7 GHz BW 12 Bit MuxDAC for direct microwave signal generation over L, S or C bands" , IEEE International Conference on Microwaves, Communications, Antennas and Electronics Systems (COMCAS), 7-9 Nov. 2011

[5] Direct conversion to X band using a 4.5 GSps SiGe Digital to Analog Converter, IEEE radar 2014 Lille

[6] Danny Eliyahu, David Seidel, and Lute Maleki , "Phase Noise of a High Performance OEO and an Ultra Low Noise Floor Cross-Correlation Microwave Photonic Homodyne System", OEwaves Inc, IEEE International Frequency Control 2000

Dynamic Phase Shifting Method Utilized in the Enhanced Frequency Controlled Clock System

Vladimir Stofanik[1], Adam Fibich[1], Tomas Bagala[1], Peter Kubinec[1]
[1]Institute of Electronics and Photonics, Slovak University of Technology
Bratislava, Slovak Republic
vladimir.stofanik@stuba.sk, adam.fibich@stuba.sk, tomas.bagala@stuba.sk, peter.kubinec@stuba.sk

***Abstract*— In this paper, we describe low-noise clock system based on combination of the chip-scale atomic clock CSAC SA.45s and the low-noise OCXO. We introduce here a new approach of frequency comparison resolution enhancement, which is based on continuous dynamic phase shifting of the evaluated signal. We have efficiently utilized fine-resolution phase shifter, which is embedded in DCM (Digital Clock Manager) blocks within widely used FPGAs from XILINX, Inc. The maximum residual frequency instabilities of the developed clock system were measured below ±0.02 ppb.**

Keywords*— *CSAC, OCXO, DCM, FPGA, DAC, phase shifter, frequency stability, phase-noise

I. INTRODUCTION

The chip-scale atomic clocks (CSACs) give today great potential for wide range of commercial, industrial and especially military and aerospace systems requiring superior long-term frequency stability. Moreover, the CSACs are characterized with much lower power consumption and much faster warm-up compared to oven-controlled crystal oscillators (OCXOs). On the other hand, a good OCXO can exhibit much lower phase noise levels compared to the CSAC [1], [2], [3].

There are several motivations to implement built-in time-to-digital converters in an FPGA, like system integration, commercial availability, low cost or fast design cycles. Precise phase shifting of a clock signal is that can be exploited for time interval measurement with resolution smaller than the period of this clock signal [4]. Utilization of dynamic fine-resolution phase shifter modules within the FPGA, as base element for high resolution frequency measurements, greatly simplifies physical design; and eliminates the need of an external calibration process.

For the developed clock system, we required comparison of two frequencies with high resolution. It was achieved thanks to utilization of dynamic phase shifter module within the XC3S200 FPGA (the Spartan-3 family of XILINX, Inc.) [5].

II. ENHANCED FREQUENCY CONTROLLED CLOCK SYSTEM WITH DYNAMIC PHASE SHIFTING

We implemented closed loop system for short-term frequency stability improvement of the CSAC SA.45s that incorporates the tunable 10-MHz OCXO MTI 230-0827, the low power consumption microcontroller MSP430G2553, the low-noise 16-bit digital-to-analog converter LTC2601 and digital circuits implemented in the FPGA XC3S200 (Fig.1).

This research was supported by the Ministry of Education of Slovak Republic under the grant VEGA No. 1/0664/14.

Principle of the system operation is based on periodical evaluation of an actual OCXO frequency during defined integration interval, followed with the OCXO frequency tuning to eliminate the slow frequency deviations of the OCXO. The integration interval determines the resolution of the evaluated OCXO frequency, as well as the system reaction time. It is important to choose the integration time as a compromise between the resolution and the system reaction time [3].

If there is request for the low phase noise sinusoidal signal generation, then the OCXO is switched on; and it is rapidly locking using the feedback control loop to the CSAC reference frequency. The CSAC ensures excellent long-term stability of the system; while consuming relatively low power. On the other hand, the OCXO serves excellent short term stability, i.e. the very low phase noise level, however consumes much more power.

The novel closed loop clock system, shown in Fig. 1, incorporates two DCM (digital clock manager) blocks DCM1 and DCM2 within the FPGA XC3S200, which multiply measured frequency from OCXO and reference frequency from CSAC, respectively by factor 12. Resulting frequencies at the DCM1 and DCM2 block outputs differ only little; and both are close to 120 MHz; that is the nominal value in our case.

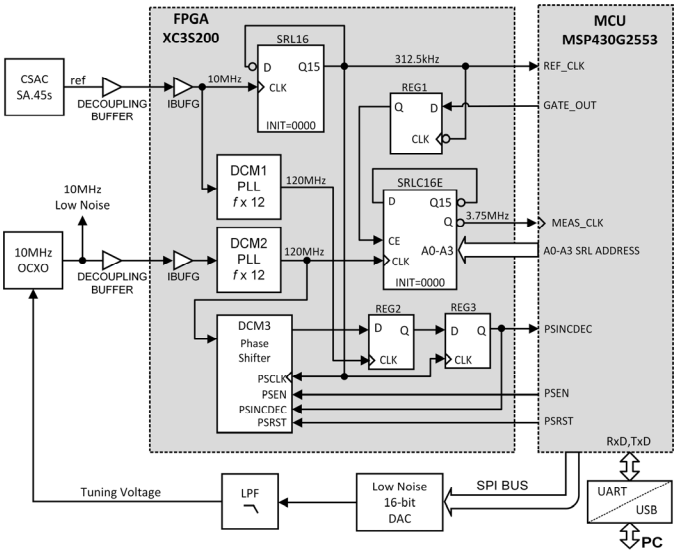


Fig. 1. Simplified block diagram of developed low-noise clock system.

The coarse counter can be implemented efficiently in the FPGA using two basic building blocks; one simplest sixteen stage shift register SRL16; and one sixteen stage shift register with clock enable input SRLC16E. The SRL16 divides the frequency of the reference signal from CSAC by 32; resulting periodic reference signal with frequency 312 500 Hz is connected to the MCU input REF_CLK. The integration interval for coarse frequency measurement is formed by integer number of REF_CLK signal periods.

Algorithm implemented in MCU dynamically select the appropriate integration interval to balance between the two opposite criteria: required high frequency measurement resolution vs. required rapid system reactions; usually if we consider the frequency controlled closed loop clock systems.

The second important part of our implementation is the fine frequency resolution measurement circuit utilizing additional DCM block configured as dynamic phase shifter enhancing the overall frequency measurement resolution dramatically. The novel idea, we implemented here, is the continuous comparison of phase shift between measured clock frequency (the OCXO) and reference signals frequency (the CSAC) during whole integration interval; rather than only at the beginning and at the end of the interval.

We utilized here the manipulation of dynamic phase shift of measured signal within the DCM3 block operating in dynamic phase shifter mode. The resolution of the phase shifter is represented by smallest delay step equals to ±40 ps approximately [5], [6].

Moreover, in the locked closed-loop frequency controlled systems, the fluctuations of the phase of measured signal are directly related to the dynamic phase shifter manipulation. In our implementation; these variations are related to regular switching between two possible states of the PSINCDEC control signal of the phase shifter (within the DCM3 block).

If the PSINCDEC=1, increase of the delay is requested next; one step equals to +40 ps approximately. If the PSINCDEC=0, decrease of the delay is requested next; one step equals to –40 ps approximately. The phase shifter block (DCM3) requires for dynamic phase shift switching two additional signals: PSCLK and PSEN. The PSCLK is connected to REF_CLK signal to ensure synchronization together with clock enable signal PSEN and PSRST signals controlled by MCU. Signal PSRST presets the phase shifter block to its predefined initial value (e.g. to zero phase shift).

Phase relation between measured and reference signal is sampled regularly using REG2 and REG3 registers during whole integration interval; in our implementation, the maximum phase sampling and manipulation frequency was selected to 78 125 Hz; that is the frequency of REF_CLK signal divided by four.

When the frequency of OCXO differs too much from the reference frequency derived from the CSAC (e.g. shortly after OCXO switching on), coarse frequency measurement is used only to control frequency of the OCXO; and the results from fine phase shifter circuit is informative only.

III. Experimental Results

Figure 2 shows measured frequency instability of the enhanced stability clock system measured at the OCXO output over 30-minute time interval after warm-up. All measurements in time domain were performed with assistance of the CNT-91 timer/counter/analyzer (Pendulum, Inc.), for which external reference frequency (10 MHz) was derived directly from the CSAC SA.45s.

The OCXO´s frequency changes evidently in the case when the feedback control is disabled; it was caused due to small ambient temperature variations in the room. On the other hand, in the case when the control loop is enabled, the output frequency becomes evidently much more stable. Figure 3 illustrates that the maximum residual frequency variations were measured below ±0.02 ppb.

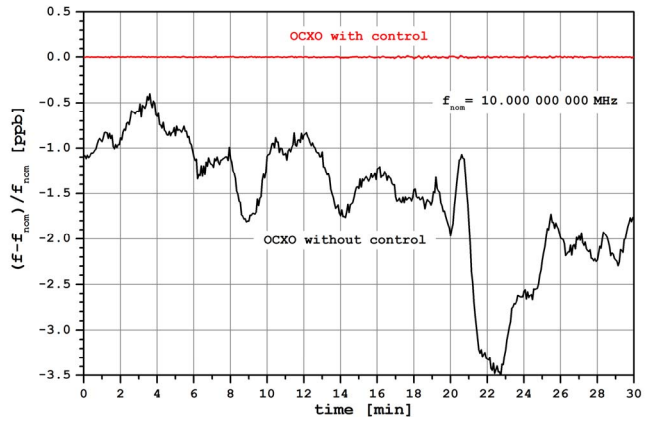


Fig. 2. Comparison of measured frequency instabilities of the OCXO MTI 230-0827 in developed clock system with feedback control loop enabled (red) and with feedback control loop disabled (black).

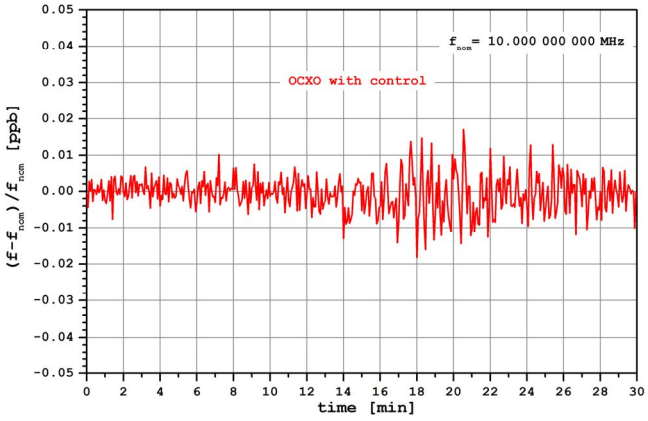


Fig. 3. Measured frequency instability of the OCXO MTI 230-0827 in developed clock system with feedback control loop enabled.

Allan deviations of the CSAC SA.45s and of the OCXO MTI 230-0827 without feedback control are compared in Fig. 4. The Allan deviation curves crossed at the averaging time approximately twenty seconds; i.e. the long-term stability of the CSAC was better above the twenty second averaging period; and short term stability of the OCXO was better up to twenty seconds [3].

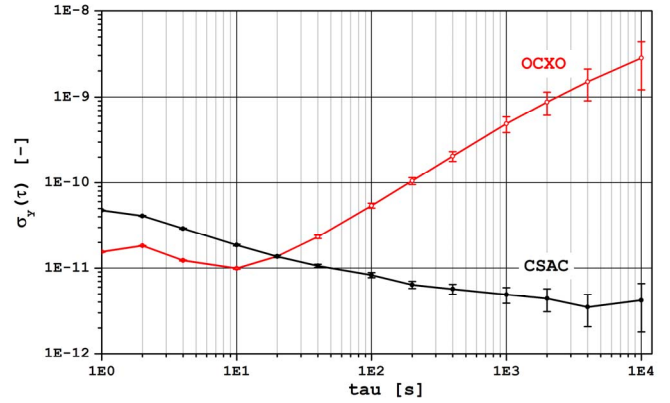


Fig. 4. Comparison of measured Allan deviation of the CSAC SA.45s (black) and of the OCXO MTI 230-0827 without feedback control (red); for τ_0 = 1 s, NEQ BW = 0.5 Hz [3].

Finally, measured phase noise distributions of the CSAC and of the OCXO without control loop and with control are compared in Fig.5. The phase noise level of controlled OCXO in the closed loop system is below the phase noise level of the CSAC SA.45s for all offset frequencies above 2 Hz. The lowest phase noise levels were measured when the OCXO was without the feedback control loop; however, the long-term stability is inferior, of course (as it is shown in Fig. 3). All phase noise measurements were performed with assistance of the 5115A Phase Noise Test Set (Symmetricom, Inc.) and with rubidium frequency standard GPS-12R (Pendulum, Inc.) forming the low-noise 10-MHz reference signal. Experimental setup of the developed enhanced clock system used during measurements is illustrated in Fig. 6.

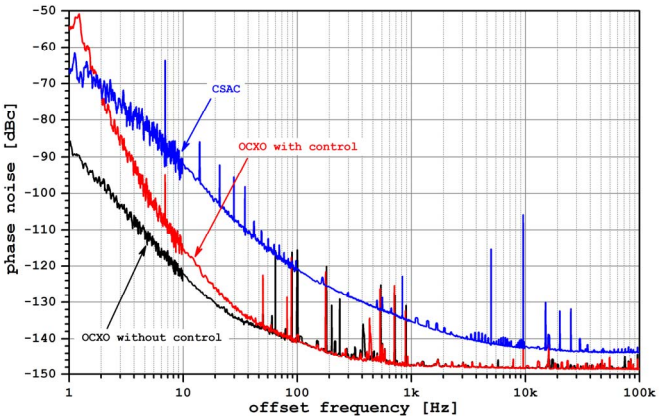


Fig. 5. Comparison of measured phase noise distributions of the CSAC SA.45s (blue) and of the OCXO MTI 230-0827 in developed clock system; with feedback control loop enabled (red) and with feedback control loop disabled (black).

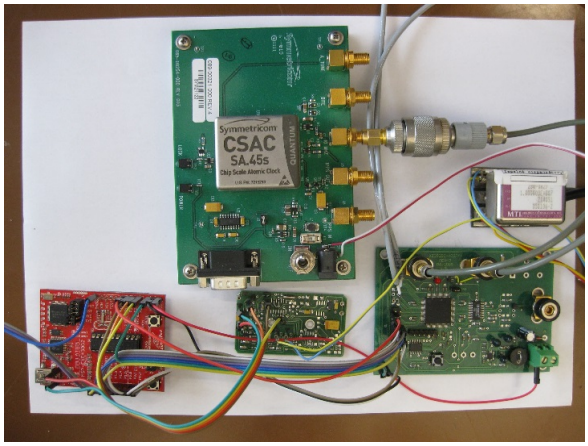


Fig. 6. Illustration of the experimental setup of the developed clock system used during the measurements.

IV. Conclusions

The enhanced low-noise clock system, based on combination of the chip scale atomic clock CSAC SA.45s and the low-noise OCXO, with the residual frequency instabilities below ±0.02 ppb, has been developed. Required high frequency resolution of the system was achieved thanks to utilization of the dynamic phase shifter embedded within different families of FPGAs from XILINX, Inc. The system time uncertainty is theoretically limited by single elementary delay step of the used phase shifter; which is ±40 ps approximately, in the case of used XC3S200 FPGA [5], [6].

References

[1] QUANTUM SA.45s Chip Scale Atomic Clock (Microsemi, Inc.): http://www.microsemi.com/document-portal/doc_download/133305-quantum-sa-45s-csac.

[2] 230 SERIES OCXO specifications (MTI-Milliren Technologies Inc.): www.mti-milliren.com/pdfs/230.pdf.

[3] T. Bagala, A. Fibich, V. Stofanik "Improvement of short-term frequency stability of the Chip Scale Atomic Clock," Proc. of the 2016 IEEE IFCS, 4 pp., DOI: 10.1109/ FCS.2016.7546746.

[4] A. Quiros-Olozabal, M.A. Cifredo-Chacon, J.M. Guerrero-Rodriguez, "Accurate Time-to-Digital Converter based on Xilinx's Digital Clock Managers," Proc. Of the 2010 International Conference on Field Programmable Logic and Applications, pp. 502–507, DOI: 10.1109/FPL.2010.100.

[5] Using Digital Clock Managers (DCMs) in Spartan-3 FPGAs XAPP462 (v1.1) January 5, 2006, Xilinx, Inc. https://www.xilinx.com/support/documentation/application_notes/xapp462.pdf

[6] Spartan-3 FPGA Family Data Sheet: DC and Switching Characteristics, DS099 (v3.1) June 27, 2013, Xilinx, Inc. https://www.xilinx.com/support/documentation/data_sheets/ds099.pdf

A Fully-Digital Realtime SoC FPGA based Phase Noise Analyzer with Cross-Correlation

P.-Y. Bourgeois, G. Goavec-Merou, J.-M. Friedt and E. Rubiola

Department of Time & Frequency
FEMTO-ST Institute, CNRS, Université de Bourgogne - Franche-Comté
Besançon, France
pyb2@femto-st.fr

***Abstract*—We report on a fully-digital and realtime operation of a phase noise analyzer using modern digital techniques with cross-correlation. With the advent of system on chip field-programmable gate arrays (SoC FPGAs) embedding hard core central processing unit, coprocessor and FPGA onto a single integrated circuit, the building of sensitive analysis devices for Time & Frequency research is made accessible at virtually no cost and benefits from reconfigurability. Used with high-speed digitizers we have successfully implemented a four-channel system whose preliminary results at 10 MHz shows a residual white noise floor $<$ -185 dBrad^2/Hz up to 5 MHz off the carrier, and flicker $<$ -127 dBrad^2/Hz using cross-correlation.**

I. Introduction

In the field of Time and Frequency metrology, precise phase estimation is essential for the building and qualification of ultrastable clocks and oscillators with low-jitter. [1].

For more than a decade, with the democratization of Field-Progammable Gate Arrays (FPGAs) used with high-speed digitizers, digital signal processing techniques inherited from telecommunication systems and Software Defined Radio (SDR) [2]–[7] enable to rethink spectral measurements with higher dynamic ranges than traditional coherent demodulation techniques using saturated mixers. Eventually cross-correlation techniques push these limits downwards at a rate of $1/\sqrt{m}$ with m the number of realizations [8], only limited by the storage area and processing power. Also, such digital devices can be useful in understanding collapse effects on cross-spectral estimations [9].

After a short insight on noise spectrum analysis based on digital down conversion and on design workflow, we describe some preliminary measurements on two different platforms.

II. DDC-based noise spectrum analysis

A. Principle of operation

A typical digital down-converter (DDC) based noise analyzer is sketched in Figure 1.

The phase modulated noise degrading a perfect sinusoid is downconverted to DC after sampling thanks to a numerically controlled oscillator (NCO) set up at the carrier frequency. Successive filtering/decimation stages allow to focus on lower decades off the carrier or examine the spectral measure at lower sampling rates by filtering out aliased noise while reducing the measurement bandwidth. Phase estimation is done by calculating the arctangent function of the in-phase and quadrature components of the demodulated and filtered signal. Eventually the amplitude is also estimated. From the phase time series (amplitude time series), the Fourier transform is computed after proper windowing. Ultimately the cross-spectrum is returned.

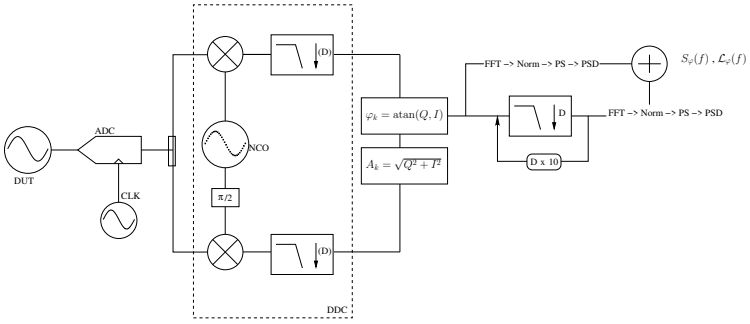


Fig. 1. Principle of a digital phase noise measurement system

B. Design workflow

As we target profound knowledge of digital techniques for metrology, all algorithms and building blocks (except some First In First Out (FIFO) structures) have been developped from scratch at FEMTO-ST. Therefore we have developped a complete EcoSystem from front-end (digitizers) to user space (final user) in order to guarantee code sanity and circular design workflow. C-C++-based libraries enable digital blocks to either match the performances and requirements of the hardware implementation or to be used as threaded double-precision blocks when used at low data rates within the CPU or deported CPU-side. All data transfers from FPGA to CPU or deported host are managed using multi-threaded direct memory access DMA (or ethernet sockets) techniques. Additionally, a Qt-based graphical user interface allows realtime evaluation of the embedded solution with saving features for data inspection.

Experimentations have been mainly performed on Xilinx Zynq-ZC706 coupled to 2 pairs of AD9652 RF digitizers, 16 bits, 250 Msps, under full control. We have also investigated on "out-of-the-box" SDR platform from Ettus Research

978-1-5386-2916-1/$31.00 ©2017 IEEE

(USRP X310). Concerning the latter, the provided DDC and first filtering/decimation stage was used as it.

III. Measurement chain

Some key elements of the signal path according to Fig. 1 are resumed in this section.

A. Offset compensation

The collected samples usually suffer from remaining offsets of the A/D converters leading to gain mismatch in the spectrum that is sometimes observed in analyzers (Fig. 2).

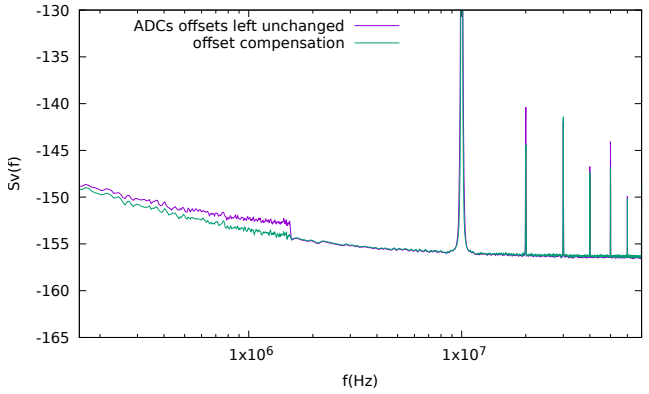


Fig. 2. Distorded spectrum in presence of gain mismatch.

B. NCO

The numerically controlled oscillator is designed with a 32 bit accumulator and lookup table (LUT) size of 2^{12} addresses. It is cadenced to the operating ADC clock (250 Msps) and provides two 16-bits synthetized frequencies in quadrature. No extra algorithm or weighting function such as Taylor series correction were employed and lead to matching results of the Xilinx IP core.

Both NCO output are mixed with the A/D data to provide in-phase and quadrature (IQ) components of the demodulated signal.

C. Filtering/decimation

An FIR (finite impulse response) filter with 128 coefficients acts as a sinc filter. Such a situation may quickly end up consuming a lot of ressources (namely DSP48, highly efficient Multiply-Accumulate slices). As decimation is usually desirable, the required ressources are then lowered as number of operations are useless. They are even lowered for the lower stages, where the data rate becomes decimated compared to the system clock, through judicious reuse of idle slices. It is embedded in a complex form to ensure providing the required filtered I/Q components.

While the full bit width remains unchanged for the first stage, no extra quantization noise is induced by the chain: all the operations that where performed in fixed point thus produce matching results when casted to double precision.

D. Phase extraction

The arctangent function is implemented using a CORDIC (COordinate Rotation Digital Computer) algorithm known to be robust and efficient to quickly converge to the desired angle. Thanks to a 25 iterations process, the phase resolution is in principle $r = \tan^{-1}(2^{-24}) \sim 6 \cdot 10^{-8}$ radians. It is designed to provide a 4-quadrant as would provide the `atan2` function.

The output phase flow is constrained within $\pm\pi$ rotations. An additional block to unwrap phases enable to reconstruct the linear progression of the phase. At high speed, side effects may lead to wrong interpretation of the phase series and produce jumps that need to be detected and circumvent.

Also the linear slope is coupled to the detuning of the analyzed frequency, the NCO frequency, and clock or reference frequency. In order to recover the true phase fluctuations, a linear regression algorithm is thus necessary [10].

Unlike several implementations where linear slopes are removed over long data sets (e.g. [2]), it has been chosen to extract the phase after the I/Q filtering/decimation processes.

The phase time series are windowed (Hanning) and finally processed through a standard radix-2 FFT algorithm to qualify the noise power spectral densities.

IV. Fully digital realtime ADC characterization

In order to qualify the high-speed digitizers, we reproduced the technique developped in [6]. Two pairs of ADCs are analyzed simultaneously in realtime (Figure 3).

The four upper decades are fully performed within the FPGA. Data are transfered to CPU for averaging and display. The I/Q data stream of the fourth filtering stage is directly transfered to CPU at a rate of 25 ksps per channel where spectrum estimation is done continuously for lower decades.

For the AD9652 characterized in this measurement, we deduce from the white voltage noise of -153 dBV^2 an equivalent number of bits (ENOB) of 11.3, in perfect agreement with the datasheet.

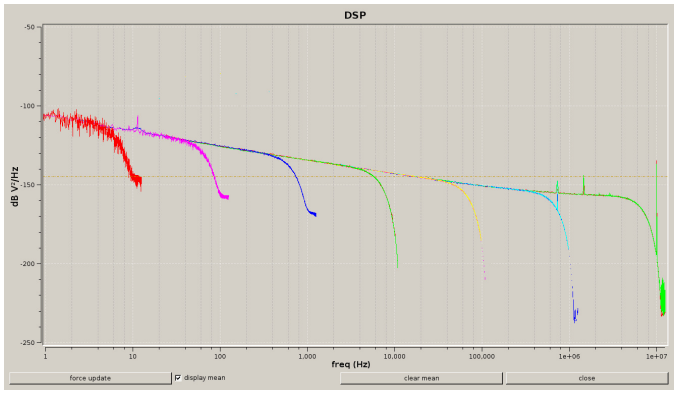


Fig. 3. Snapshot of a user interface with simultaneous measurement of 2 pairs of ADCs (in dBV^2/Hz), 4 min. of averaging

V. Fully digital realtime 4-channel noise floor

A four-channel system has been developped enabling suppression of ADC noises and clocks noise while cross-correlation is operating.

The noise floor was measured by feeding the same synthesizer 10 MHz, 12 dBm signal into the four ADCs.

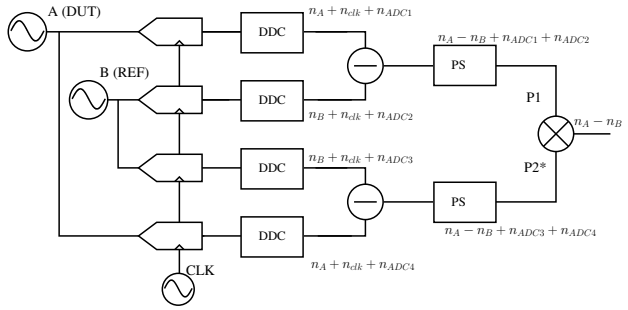


Fig. 4. Principle of a 4-channels phase noise analyzer with cross-correlation.

A. Noise rejection capability

The correct operation of the cross-correlations may be checked by performing the first decade (DDC + phase recovery) within the FPGA. The 25 Msps 4 complex channels are transfered to the CPU via DMA, where the windowing, and cross-spectrum are calculated. Eventually all spectrums (frames) are stored into an external hard drive for data inspection.

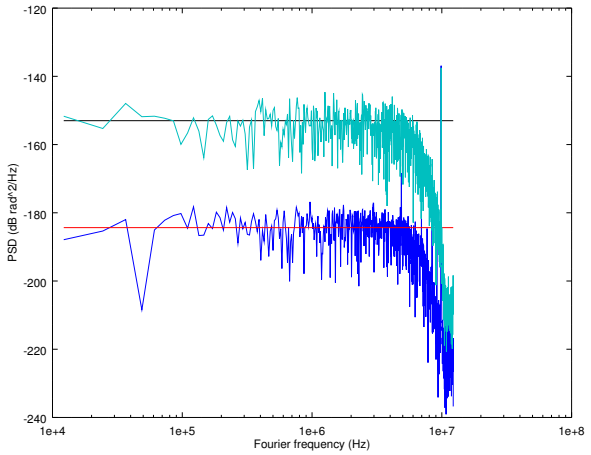


Fig. 5. Straight line (up) : ADC noise fit. Spectrum (up) : First frame (m=1) showing the ADC noise limit. Straight line (down) : Estimated spectrum for 1,863,000 averages. Spectrum (down) : Measured spectrum @frame 1,863,000

The first frame corresponds to a cross-correlation factor (m=1) and is reprensented on Fig. 5. A straight line fit gives the limitation of the measurement (~ -153 dBrad^2/Hz, white) due to the ADC noise. As one selects the frame number 1,863,000, the expected noise rejection would be represented by the estimated line down on the graph, hence $5{\cdot}\log_{10}(m) \simeq 31.3$ dB lower. The corresponding spectrum is also represented. The overall process took $\sim$ 130 min to accomplish (stotage takes time).

B. Noise floor evaluation

Preliminary results of a fully digital realtime implementation are presented in Figure 6. In these proceedings but also to prove the reconfiguration ability, we have chosen to glue two different runs done independently. The two higher decades (10 kHz – 1 MHz) have been computed while the lower decades analysis was disabled in order to gain data transfer bandwidth. This enables a much faster convergence of the noise floor in several hours (43,918.976 averages). The four lower decades were obtained by running the phasemeter continuously for approximately three days (2,859 averages for the 1 Hz – 10 Hz decade).

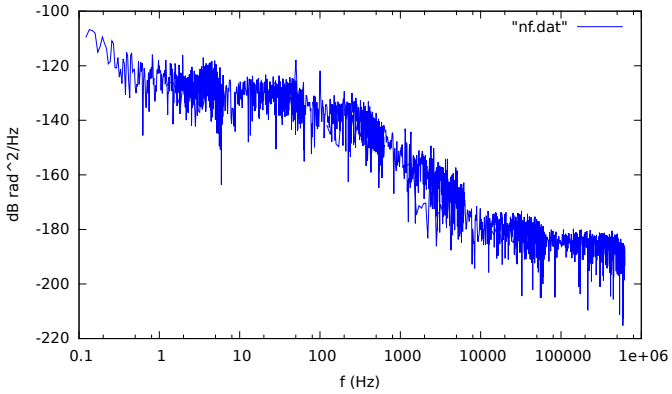


Fig. 6. Fully digital realtime 4-channel noise floor measurement with reconfiguration

.

C. Issues

During our experiments we have observed that from time to time the 2 pairs of A/D converters could experience synchronization problems when a measurement process starts (otherwise when the samples are aligned, they keep their alignment during the whole measure). A 1-sample misalignement lead to dramatic results and spectral measure cannot be trusted. Indeed, an extra-rejection of flicker noise is expected. We also experience problems with commercial devices for which we report here an erratum (Fig. 9 in [6]). A detector of misalignment can be implemented to restart the measurement in case of failure. These kind of issues are known and new techniques based on the JESD protocol should avoid this. This situation is mainly encouraged by the use of developpment platforms where the signal lengths are hardly matched (we have for example observed such effects when 2 different signals clocks are not synchronized at the ns level).

D. SDR equipment as an alternative study

Modern Software Defined Radio equipment embed high-speed digitizers suitable to the development of sensitive phase measurement systems. The tested platform concerns specifically here the Ettus Research USRP X310, an attractive

solution for T&F research also because they are open-source / open-hardware solutions. Other groups like [7] have presented interesting results for time deviation purpuses. Eventually such a system was tested "out of the box" providing its dedicated Digital Down Converter.

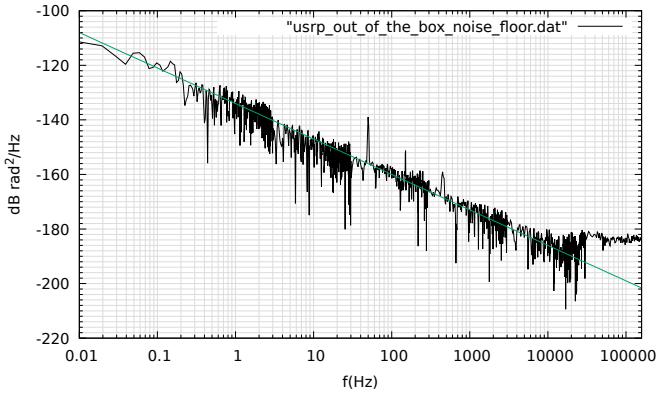


Fig. 7. usrp noise floor.

The white noise floor clearly shows some extra quantization noise due to the DDC we have no control of yet. A significant amount of this noise is folded back to lower frequencies leading to the presented uncommon spectrum.

VI. Application to the measurement of low noise RF synthesizer

The SDR solution has been tested to the measurement of a low noise RF synthesizer (R&S SMA100A used in our experiments) and compared to a commercial high-end 90 k$ instrument (Fig. 8).

For the short term, the limitation is probably due to the SDR device, although we should have observed the spikes revealed by the commercial analyzer. Indeed in [6] we observed similar behaviour.

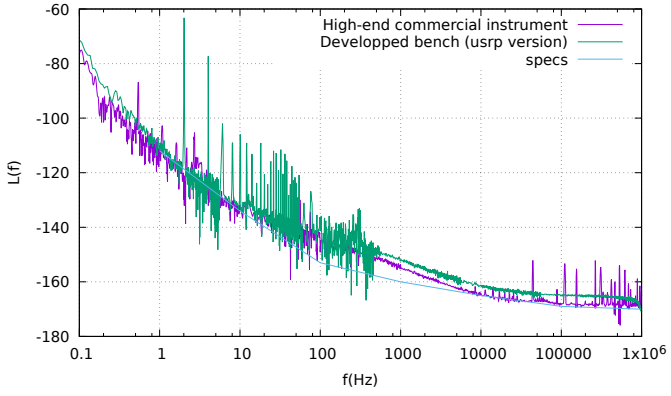


Fig. 8. Measurement of a low noise synthesizer : comparison between High-end instrument and SDR platform @ 10 MHz, 10 dBm.

From 1 Hz – 1kHz, we observe a dense area of spikes, regularly spaced and folded by the main 2 Hz spike. Interestingly, for this frequency, the commercial analyzer shows anti-correlation.

A close up of the 10 Hz – 100 Hz area is analyzed in the following figure. Although not recommended, we removed the 'outliers', and both curves look similar, with a bit more resolution as compared to the smoothed version of the high-end analyzer.

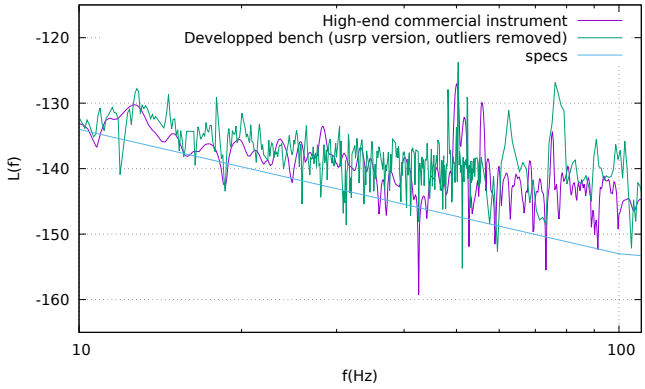


Fig. 9. close up of the Fig.8, with removed outliers

.

VII. Conclusion

We have successfully developped a reconfigurable fully-digital phase noise analyzer with realtime operation. White noise floor of $<$ -185 dbrad^2/Hz and flicker $<$ -127 dBrad^2/Hz in a preliminary experiment have been measured.

Acknowledgment

This work is supported by the ANR Programme d'Investissement d'Avenir in progress at the Time and Frequency Departments of FEMTO-ST Institute (Oscillator IMP, First-TF and Refimeve+), and by the Région de Franche-Comté. The authors would like to thank F. Vernotte for fruitful discussions.

References

[1] F. Walls, S. Stein, J. E. Gray, and D. J. Glaze, "Design considerations in state-of-the-art signal processing and phase noise measurement systems," in *Proc. 30th Ann. SFC*, 1976, p. 271.

[2] L. Angrisani, M. D'Apuzzo, and M. D'Arco, "A digital signal-processing approach for phase noise measurement," *IEEE Transactions on instrumentation and measurement*, vol. 50, no. 4, pp. 930–935, 2001.

[3] G. P. Landis, I. Galysh, and T. Petsopoulos, "A new digital phase measurement system," in *33rd Annual Precise Time and Time Interval (PTTI) Meeting*, 2001, pp. 543–552.

[4] J. Grove, J. Hein, J. Retta, P. Schweiger, W. Solbrig, and S. Stein, "Direct-digital phase-noise measurement," in *Frequency Control Symposium and Exposition, 2004. Proceedings of the 2004 IEEE International*. IEEE, 2004, pp. 287–291.

[5] C. W. Nelson and D. A. Howe, "A sub-sampling digital pm/am noise measurement system," *NCSLI Measure*, vol. 7, no. 3, pp. 70–73, 2012.

[6] P.-Y. Bourgeois, T. Imaike, G. Goavec-Merou, and E. Rubiola, "Noise in high-speed digital-to-analog converters," in *Frequency Control Symposium & the European Frequency and Time Forum (FCS), 2015 Joint Conference of the IEEE International*. IEEE, 2015, pp. 672–675.

[7] J. A. Sherman and R. Jördens, "Oscillator metrology with software defined radio," *Review of Scientific Instruments*, vol. 87, no. 5, p. 054711, 2016.

[8] E. Rubiola and F. Vernotte, "The cross-spectrum experimental method," *arXiv preprint arXiv:1003.0113*, 2010.
[9] C. Nelson, A. Hati, and D. Howe, "A collapse of the cross-spectral function in phase noise metrology," *Review of Scientific Instruments*, vol. 85, no. 2, p. 024705, 2014.
[10] E. Rubiola, M. Lenczner, P.-Y. Bourgeois, and F. Vernotte, "The Ω counter, a frequency counter based on the linear regression," *IEEE transactions on ultrasonics, ferroelectrics, and frequency control*, vol. 63, no. 7, pp. 961–969, 2016.

Full Digital Phase Noise Measurement by using Two Reference Oscillators and Multichannel ADCs

Takeshi IMAIKE
College of Science and Technology
Nihon University
Chiba, Japan
imaike.takeshi@nihon-u.ac.jp

***Abstract*— It is realized that full digital phase noise measurement system which computes phase noise spectrum after sampling oscillator's signal using analog to digital converter directly. However, in these reports oscillator pairs are used; i.e. DUT oscillator and reference oscillator pairs are needed. These method needs low phase noise characteristics less than DUT oscillator for reference oscillator, or an oscillator of the same specification is required. On the other hand, in traditional (analog and digital mixed) phase noise measurement, it can measure the DUT's phase noise by using two reference oscillators with calculation of cross-correlation, even if the phase noise of the reference oscillator is greater than the DUT. However, there is no report that two reference oscillators are used in full digital phase noise measurement. In this paper we discuss about full digital phase noise measurement system using two reference oscillator. As a result, it was able to measure the DUT phase noise using two reference oscillators which phase noise were greater than DUT.**

Keywords—digital phase noise measurement; cross-spectrum method; cross-correlation; digital down conversion

I. INTRODUCTION

In recent years, the development of broadband wireless communication technology has been advanced for the purpose of increasing the wireless communication traffic, and it is important to highly accurately evaluate the phase noise characteristic of the local oscillator serving as the reference of the carrier signal in the higher frequency band. It is realized that full digital phase noise measurement system which computes phase noise spectrum after sampling oscillator's signal using analog to digital converter directly for high precision phase noise measurement[1],[2],[3]. However, in these reports oscillator pairs are used; i.e. DUT oscillator and reference oscillator pairs are needed. These method needs low phase noise characteristics less than DUT oscillator for reference oscillator, or an oscillator of the same specification is required. On the other hand, in traditional (analog or analog and digital mixed) phase noise measurement, it can measure the phase noise of DUT by using two reference oscillators with calculation of cross-spectrum, even if the phase noise of the reference oscillator is larger than the DUT[4]. Figure 1 shows conventional phase noise measurement system using two reference oscillator based on phase locked loop. In this method, it is necessary to calculate the transfer function of the PLL, and the phase detection sensitivity of the mixer varies depending on the input signal power, therefore calibration is required every time the measurement is performed. On the other hand, it is unnecessary to design PLL in fully digital phase noise measurement system and calibrate phase detection sensitivity because analog mixer is not used. However, there is no report that two reference oscillators are used in full digital phase noise measurement. In this paper we discuss about full digital phase noise measurement system using two reference oscillator and the phase noise measurement result of the frequency synthesizer is shown.

II. PRINCIPLE OF FULL DIGITAL PHASE NOISE MEASUREMENT

Figure 2 shows the configuration of the principle to realize the digital phase noise measurement method. The DUT signal sampled by analog to digital converter is orthogonal demodulated by the numerical controlled oscillator(NCO) at the same frequency of the DUT. After divided into in-phase component (I) and quadrature component (Q), it is converted into phase ϕ by $\tan^{-1}(Q/I)$ calculation. Finally, the phase noise spectrum S_ϕ is obtained by FFT. However, phase noise of clock driving ADC is mixed to measured result in this method. Furthermore, a dynamic range is limited by the effective number of bits (ENOB) of ADC and Nyquist frequency, so it needs cross-correlation calculation using multichannel ADCs to extend the dynamic range[3],[4],[5].

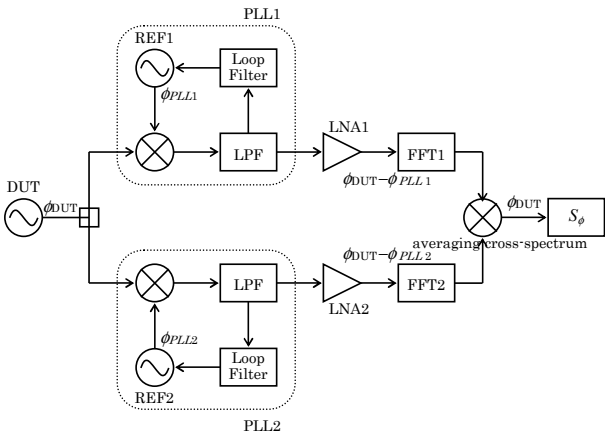


Fig. 1. Schematic diagram of conventional phase noise analyzer using cross-spectrum.

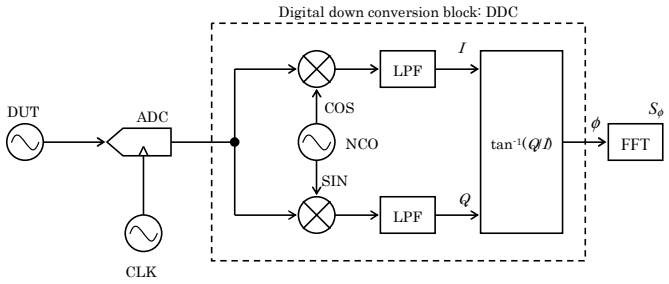


Fig. 2. Schematic diagram of full digital phase noise mesurement system[5].

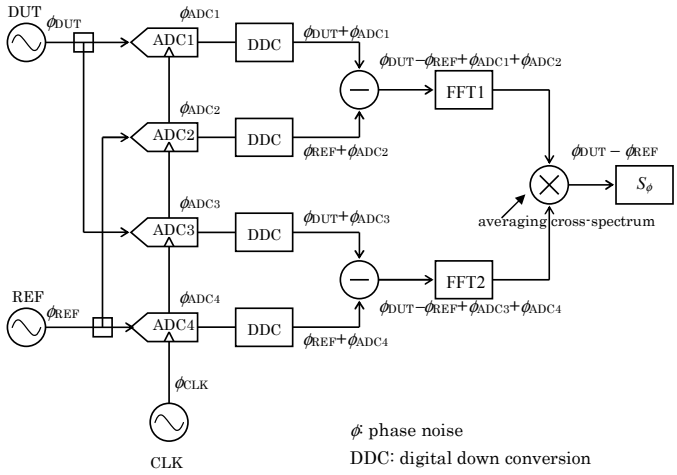


Fig. 3. Schematic diagram of 4 channel full digital phase noise measurement using single reference oscillator[3].

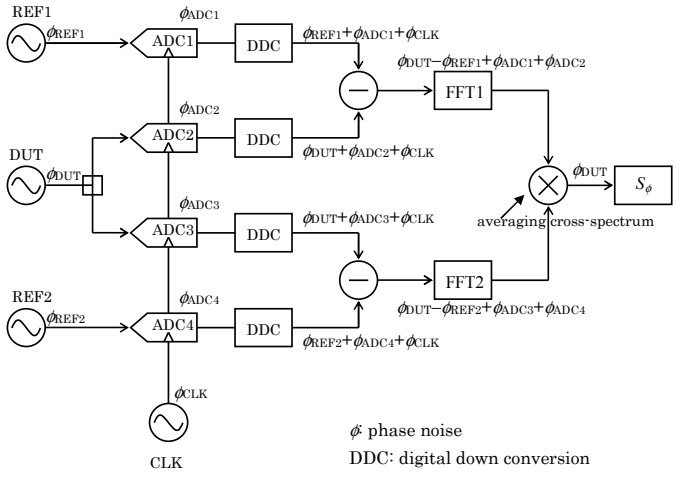


Fig. 4. Schematic diagram of 4 channel full digital phase noise measurement using two reference oscillator.

Figure 3 shows the schematic of 4 channel full digital phase noise measurement system using single reference oscillator. The output of the DUT is divided into two by a power splitter and input to channels 1 and 3 of the ADC, respectively. Also the signal of the reference oscillator is similarly input to the channels 2 and 4. The phase noise of the DUT is ϕ_{DUT}, the phase noise of the reference oscillator is ϕ_{REF}, the phase noise of the clock ϕ_{CLK}, and the phase noise of the ADCs are ϕ_{ADC1} to ϕ_{ADC4}, respectively. ϕ_{CLK}, and ϕ_{ADC} are mixed on the down-conversion output of each channel, but ϕ_{CLK} is canceled by subtraction. Furthermore, when there is no correlation between the phase noise of the four ADCs, ϕ_{ADC1} to ϕ_{ADC4} are reduced by averaging the cross-spectrum of the FFT results. Here, when the average number of cross-spectrum is M, the noise power level decreases $10\log\sqrt{M}$[2].

Figure 4 shows the schematic of 4 channel full digital phase noise measurement system using two reference oscillator we proposed this time. The signal of the DUT is branched into two by a power splitter and input to ADC 2 and ADC 3. The REF1 signal and the REF2 signal are input to ADC1 and ADC4, respectively. Except for the connection of the analog portion, it is the same as the block diagram shown in Fig. 3. In this method, even if the phase noise of the reference oscillators 1 and 2 is larger than the DUT, it is possible to extract only the phase noise of the DUT by averaging the cross-spectrum unlike Figure 3 configuration.

III. Experiment

Figure 5 shows the experimental set up. All ADCs were driven at 160Msamples/s, 16bit(ENOB: 12.1bit). After sampling, it transferred to Windows® based PC by optical fiber link and sampled data is stored in HDD. The phase noise was calculated with double precision in C language. The oscillation frequency of DUT and REF was used 12.8MHz. The clock signal of ADC was generated by on-board PLL from 10MHz OCXO and frequency synthesizers ware used for all oscillators (DUT: SG-6221, REF1: N5172B, REF2: WF1974). The DUT with phase noise less than REF was used ($\phi_{DUT} \leq \phi_{REF1}, \phi_{REF2}$) in the region where the offset frequency is lower than 1 kHz

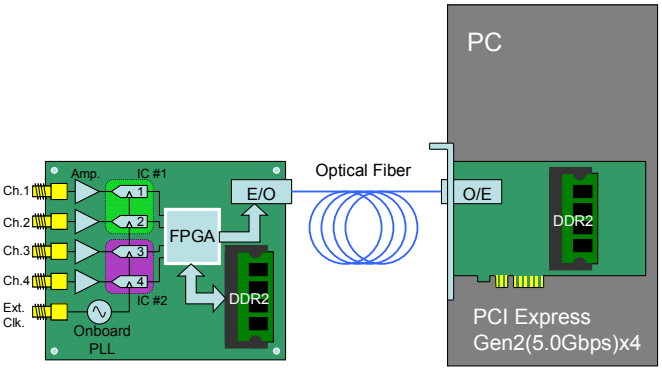


Fig. 5. Experimental setup for sampled data acquisition and transfer to computer.

IV. RESULTS

Figure 6 shows the measurement results of phase noise. The green line is the true $S_{\phi DUT}$, the red line shows the phase noise spectrum of FFT1($\phi_{DUT}-\phi_{REF1}+\phi_{ADC1}+\phi_{ADC2}$), the ash line shows the spectrum of FFT2($\phi_{DUT}-\phi_{REF2}+\phi_{ADC3}+\phi_{ADC4}$), the black lien shows cross-spectrum between FFT1 and FFT2. Since ϕ_{REF1}, $\phi_{REF2} \geq \phi_{DUT}$, the phase noise spectrum FFT1 and FFT2 cannot accurately measure ϕ_{DUT}. On the other hand, the method based on cross-spectrum, it was obtained that the result agreed with the true phase noise characteristic. From this result, we cleared that phase noise measurement using two reference oscillators is effective even in full digital phase noise measurement.

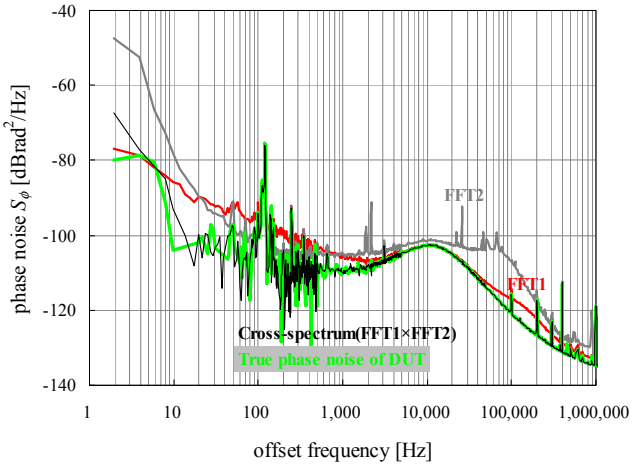


Fig. 6. Phase noise characteristics measured with configuration of Figure 4 (DUT: SG - 6221, REF1: N 5172 B, REF2: WF 1972).

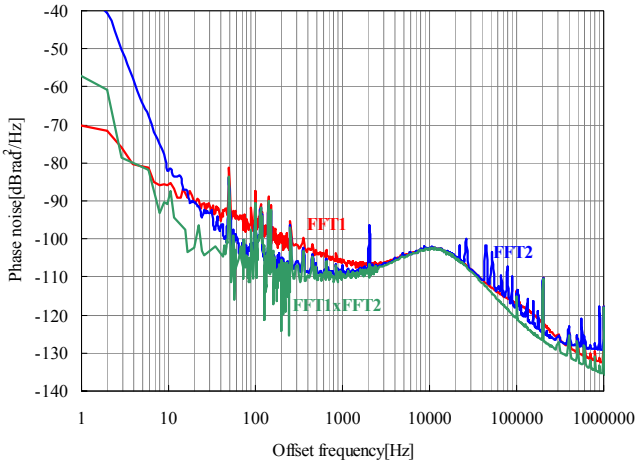


Fig. 7. Phase noise measurement result (DUT: SG - 6221, REF1: N 5172 B, REF2: WF 1972).

Figures 7 to 10 show the results of measurements on another day. Figure 7 shows the result when SG - 6221 is used for DUT, N 5172 B for REF 1, and WF 1972 for REF 2. Figure 8 shows the result when N5172B is used for DUT, SG - 6221 for REF 1, and WF 1972 for REF 2. Figure 9 shows the result when WF1972 is used for DUT, SG - 6221 for REF 1, and WF 1972 for REF 2. Figure 10 compares the phase noise of the three synthesizers measured with the new method proposed this time. It can see that the results of FFT 1 or FFT 2 in Figures 7 to 9 match the trend of phase noise when selecting two synthesizers out of the three.

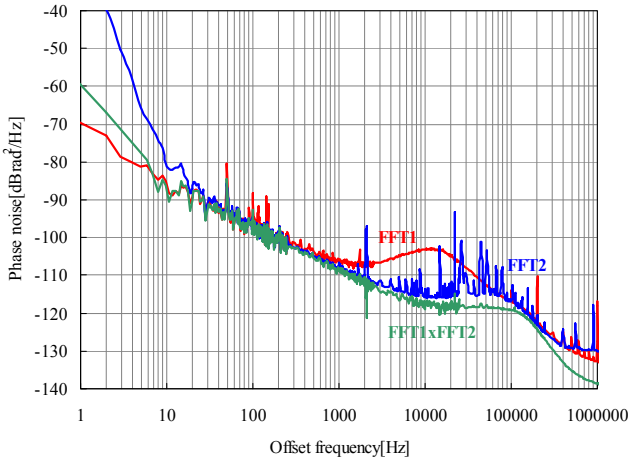


Fig. 8. Phase noise measurement result (DUT: N 5172 B, REF1: SG - 6221, REF2: WF 1972).

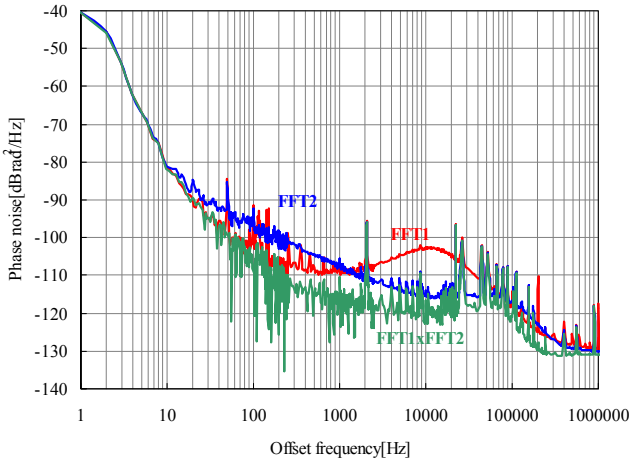


Fig. 9. Phase noise measurement result (DUT: WF1972, REF1: SG - 6221, REF2: N5172B).

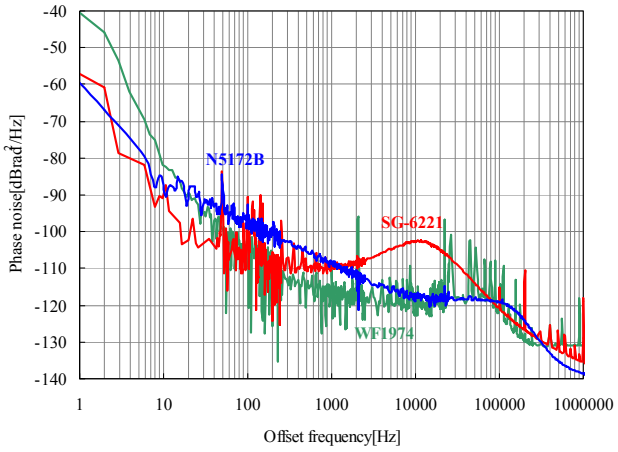


Fig. 10. Comparison of phase noise characteristics of three synthesizers.

V. CONCLUSION

In this paper we discuss full digital phase noise measurement system using two reference oscillator based on using multichannel ADC and cross-spectrum. As a result, it can measure the DUT phase noise using two reference oscillators which phase noise are greater than DUT. In the future we have to demonstrate with extremely low phase noise oscillator.

ACKNOWLEDGMENT

I would like to thank both Dr. Enrico Rubiola and Dr. Pierre-Yves Bourgeois (FEMTO-ST, France) who gave valuable discussion and advice in advancing this research.

REFERENCES

[1] Grove, et al.: “Direct-Digital Phase-Noise Measurement”, Proc. of the IEEE UFFC, pp.288-291, 2004.

[2] D.A. Howe, A. Hati, C.W. Nelson, and D. Lirette: “PM-AM Correlation Measurements and Analysis”, Proc. of 2012 IFCS, pp.16-20, 2012.

[3] P.-Y. Bourgeois, T. Imaike, G. Goavec-Merou, and E. Rubiola: “Noise in High-Speed Digital-to-Analog Converters”, Proc. of 2015 Joint Conference of the IEEE IFCS & the EFTF, pp.672-675, 2015.

[4] K. Gheen, “Phase Noise Measurement Methods and Techniques”, PhaseNoise_webcast19Jul12.pdf, Agilent Technologies, 2012.

[5] T. Imaike, and Y. Sakuta: “Full Digital Phase Noise Measurement System based on Under Sampling Technique”, Trans. on Fundamentals and Materials IEEJ, Vol.137, No.1, pp.71-77, 2017.

Frequency Synthesis Using Low-Pass Single-Bit Multi-Step Look-Ahead Sigma-Delta Modulators in Quadrature Upconversion Scheme

Charis Basetas, Paul Peter Sotiriadis
Department of Electrical and Computer Engineering
National Technical University of Athens
Athens, Greece
E-mail: chbasetas@gmail.com, pps@ieee.org

Nikos Temenos
Department of Informatics and Telecommunications
National and Kapodistrian University of Athens
Athens, Greece
E-mail: ntemenos@gmail.com

***Abstract*—All-digital frequency synthesis using two low-pass single-bit Multi-Step Look-Ahead sigma-delta modultors (MSLA SDMs) is presented. MSLA SDMs provide better noise shaping characteristics, i.e. SNDR and bandwidth, than conventional SDMs at the cost of higher hardware complexity. The balance between complexity and performance is adjusted by the number of look-ahead steps, which is an additional design parameter. The frequency synthesizer system is comprised of two identical low-pass single-bit MSLA SDMs. Their inputs are orthogonal sinusoidals generated by a direct digital synthesizer (DDS). The frequency range of the synthesizer using a single clock signal is determined by the oversampling ratio (OSR) of the SDMs. A lower OSR results in a wider frequency range, but reduces the output SNDR. System-level simulation results of the frequency synthesizer are presented, showcasing the performance advantage of using MSLA SDMs instead of conventional ones.**

***Index Terms*—Sigma-delta, noise shaping, single-bit quantization, modulator, all-digital, quadrature, low-pass, synthesizer, look-ahead**

I. Introduction

Accurate and finely controled frequency synthesis is crucial for many modern applications. Digital frequency synthesizers have many advantages over mixed-signal and analog ones. They exhibit excellent digital accuracy, high resolution frequency control and fast frequency hopping. Furthermore, they inherit all the advantages of digital circuits, such as immunity to process, voltage and temperature variations, portability, scalability, reconfigurability, faster design cycle and smaller chip area.

Direct digital synthesizers (DDS) [1] are digital circuits capable of generating a large number of frequencies using a single reference clock. However, they require a DAC for their operation, which is a mixed-signal component. All-digital alternatives such as the PDDS (Pulse DDS) have been proposed, but they introduce frequency spurs or a high noise floor [2]. Another approach is the use of a digital single-bit band-pass sigma-delta modulator (SDM) to shape the quantization noise out of the desired frequency band [3]. This requires that the operating frequency of the SDM is at least twice that of the maximum synthesizable frequency. Thus, the SDM speed is the limiting factor.

Arbitrary maximum synthesizable frequencies, limited only by the speed of a digital miltiplexer, can be achieved using two low-pass SDMs in quadrature configuration. The two low-pass SDMs can be clocked at a lower frequency, while their outputs are upconverted and interleaved by three digital multiplexers. A fourth multiplexer running at a much higher frequency can be used to generate an even higher output frequency. This work replaces conventional SDMs in the aforementioned configuration with single-bit Multi-Step Look-Ahead (MSLA) SDMs [4]. They are digital SDMs that improve upon the noise shaping characteristics and stability of conventional SDMs by considering current and future quantization errors for the determination of their output. Conventional SDMs only take into account the instantaneous quantization error. This enables the use of more aggressive NTFs (noise transfer functions) leading to increased bandwidth, i.e. lower oversampling ratio (OSR), while retaining higher signal-to-noise-and-distortion ratio (SNDR) than conventional single-bit SDMs.

In the next section the proposed architecture is presented. In section III system-level simultion results are shown, demonstrating the performance advantage of using MSLA SDMs over conventional ones. Section IV concludes the discussion.

II. Frequency Synthesis Using Low-Pass MSLA SDMs in Quadrature Upconversion Scheme

In this section we first describe the proposed frequency synthesizer arcitecture, followed by a brief discussion about MSLA SDMs.

A. The Proposed Frequency Synthesizer Architecture

The proposed set-up is shown Fig. 1. Two DDSs are used to generate two orthogonal sinusoidals with frequency

$$f_{BB} = \left(w/2^N\right) f_{clk}.$$

To avoid an image in the final signal spectrum, a $\pi/2$ phase difference is required between the I and Q components. This is the reason why the initial value of the sine look-up table (LUT) phase accumulator is $w_0 = 0.5w$, whereas the initial value of the cosine LUT phase accumulator is $w_0 = 0$. The

978-1-5386-2916-1/$31.00 ©2017 IEEE

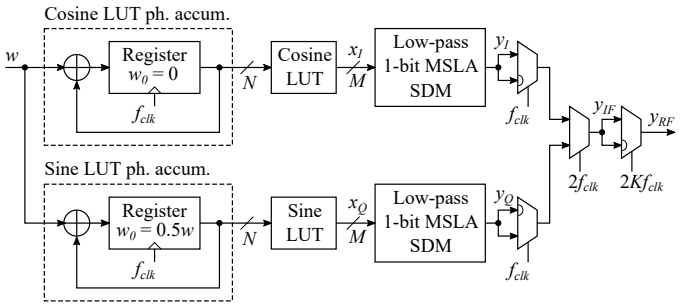


Fig. 1. All-digital frequency synthesizer using two 1-bit low-pass MSLA SDMs in quadrature configuration.

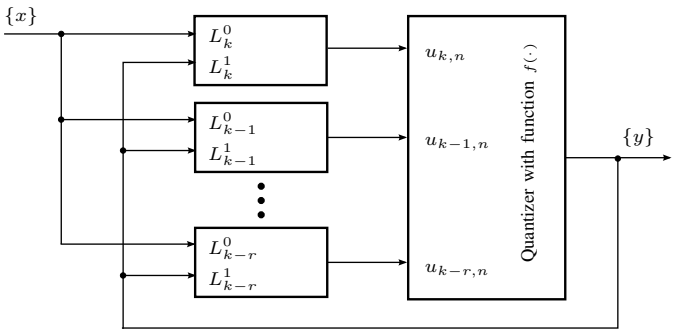


Fig. 2. The MSLA SDM system diagram.

two sinusoidal I and Q components x_I and x_Q are fed to two identical single-bit low-pass MSLA SDMs. They convert their multi-bit inputs to two single-bit bitstreams. These are then passed through a number of multiplexers that upconvert and interleave them. The sampling frequency of each multiplexer in Fig. 1 is shown under the multiplexer. The multiplexers processing the MSLA SDM output signals toggle between their inputs (normal and inverted) at a rate f_{clk}, whereas the next multiplexer toggles between the output of the I path multiplexer and the output of the Q path multiplexer at a rate $2f_{clk}$. This process results in an intermediate single-bit signal y_{IF} (Fig. 1) with frequency

$$f_{IF} = (f_{clk}/2) + f_{BB}. \tag{1}$$

This might actually be the frequency to be generated, but in the case that a higher frequency is desired another multiplexer running at frequency $2Kf_{clk}$ can be used. The resulting signal is single-bit and has frequencies given by

$$f_{RF,i} = mf_{clk} \mp (f_{IF}/2)\,,\ 0 \le m \le K,\ m \in \mathbb{N}^+ \tag{2}$$

as long as $0 \le f_{RF,i} < Kf_{clk}$.

Since the generated signal is single-bit, no DAC is required and therefore the synthesizer is all-digital. However, an analog bandpass filter is required in some applications to remove the out-of-band quantization noise generated by the MSLA SDMs.

The bandwidth of the frequency synthesizer is determined by the MSLA SDM OSR. The frequency range of the generated intermediate signal, i.e. the bandwidth of the frequency synthesizer for the output signal y_{IF}, for a given OSR is

$$\mathrm{BW}_{IF} = \left[\frac{f_{clk}}{2} - \frac{f_{clk}}{2 \cdot \mathrm{OSR}}, \frac{f_{clk}}{2} + \frac{f_{clk}}{2 \cdot \mathrm{OSR}}\right]. \tag{3}$$

The bandwidth of the y_{RF} signal is split into many frequency bands. Each frequency given by (2) lies inside such a frequency band. The frequency bands of the signal y_{RF} are given by

$$\mathrm{BW}_{RF} = \left[mf_{clk} \mp \frac{f_{clk}}{4} - \frac{f_{clk}}{2 \cdot \mathrm{OSR}}, mf_{clk} \mp \frac{f_{clk}}{4} + \frac{f_{clk}}{2 \cdot \mathrm{OSR}}\right] \tag{4}$$

for the values of m valid in (2).

B. The Role of the MSLA SDM Design Choices

The MSLA SDM system diagram is shown in Fig. 2. It is comprised of $r+1$ two-input digital IIR filters (L_j^0, L_j^1), $k - r \le j \le k$, and an $(r+1)$-input quantizer. The number of look-ahead steps k adjusts the trade-off between hardware complexity and performance. Typical values allowing for improved performance with moderate complexity increase are $r = k$, $k \in [3, 8]$. For a more detailed presentation the reader is referred to [4].

The in-band noise and the SNDR are determined by the MSLA SDM NTF order, the OSR and the NTF out-of-band gain $||NTF||_\infty$. A higher OSR results in higher SNDR at the cost of a smaller in-band frequency range. The stability limits of the sigma-delta loop manifest themselves as a type of gain-bandwidth product. More specifically, in a conventional single-bit SDM the NTF out-of-band-gain (gain) and 1/OSR (bandwidth) product cannot exceed a certain value for the loop to remain stable. In MSLA SDMs, as the number of look-ahead steps k increases, so does the $||NTF||_\infty$-1/OSR product. Thus, for a certain OSR value, more look-ahead steps k result in higher NTF out-of-band gain and in-band SNDR. However, in order to achieve the in-band noise floor dictated by the MSLA SDM NTF, a clock signal with low enough phase noise should be used. Therefore, the clock signal spectral purity is also of great importance.

C. The Noise Frequency Response of the Synthesizer

The NTF at the position of the y_{IF} signal in Fig. 1 is easily derived from that of the low-pass MSLA SDMs using the well-known transformation $z \to -z^2$ for the NTF of bandpass SDMs [5], i.e.

$$NTF_{BP}(z) = NTF_{LP}(z)|_{z=-z^2}. \tag{5}$$

The NTF at the position of the y_{RF} signal is derived from NTF_{BP} by observing that the final multiplexer essentially multiplies a possibly upsampled version of y_{IF} using zero-order hold (ZOH) with a cosine wave having frequency $\omega = \pi$ or $f = Kf_{clk}$. The upsampled by $2(K-1)$ version of

y_{IF}, converted to continuous time representation and assuming $y_{IF}[n] = 0,\ n < 0$, is

$$y_{ZOH,IF}(t) = \sum_{n=0}^{\infty} y_{IF}[n] \cdot \text{rect}\left(\frac{t - \frac{1}{2}nT_{clk}}{\frac{1}{2}T_{clk}} - \frac{1}{2}\right) \quad (6)$$

where $T_{clk} = 1/f_{clk}$. So, the y_{RF} signal in continuous time representation is

$$y_{RF}(t) = y_{ZOH,IF}(t) \cdot \cos(2\pi K f_{clk} t). \quad (7)$$

Taking the Fourier transforms of (6) we can write

$$Y_{ZOH,IF}(f) = H_{ZOH}(f) \cdot Y_{IF}(f) \quad (8)$$

where

$$H_{ZOH}(f) = e^{-j\pi f \frac{T_{clk}}{2}} \frac{\sin(\pi f \frac{T_{clk}}{2})}{\pi f \frac{T_{clk}}{2}}. \quad (9)$$

The Fourier transform of (7) is the convolution of the Fourier transforms of $y_{RF}(t)$ and $\cos(2\pi K f_{clk} t)$, i.e.

$$Y_{RF}(f) = Y_{ZOH,IF}(f) * \frac{\delta(f - Kf_{clk}) + \delta(f + Kf_{clk})}{2}. \quad (10)$$

Combining (8), (9) and (10) we get the following relation

$$Y_{RF}(f) = \left[e^{-j\pi f \frac{T_{clk}}{2}} \frac{\sin(\pi f \frac{T_{clk}}{2})}{\pi f \frac{T_{clk}}{2}} \cdot Y_{IF}(f)\right] * \frac{\delta(f - Kf_{clk}) + \delta(f + Kf_{clk})}{2}. \quad (11)$$

Therefore, NTF_{BP} is transformed by first shaping it by the transfer function of the ZOH including upsampling and then convolving it with the spectrum of a cosine signal with frequency $f = Kf_{clk}$ which is composed of two delta functions at frequencies $f - Kf_{clk}$ and $f + Kf_{clk}$. To avoid confusion, in the remainder of the paper the term NTF applies to the NTF of the low-pass MSLA SDMs.

III. Simulation Results

The performance of the proposed architecture is highlighted in Fig. 3 where the power spectrum of the y_{IF} signal is shown. The I and Q inputs are $x_I = 0.4\cos(2\pi \cdot 0.01n)$ and $x_Q = 0.4\sin(2\pi \cdot 0.01(n + 0.5))$ respectively. The MSLA SDMs are configured with 7-th order low-pass filters, OSR $= 32$ and $r = k = 6$. Assuming the clock frequency is $f_{clk} = 250$ MHz, and thus the sampling frequency for signal y_{IF} is $f_s = 2f_{clk} = 500$ MHz, the resolution bandwidth is RBW $= 333.33$ Hz, resulting in a spurious-free dynamic range (SFDR) of DR $= -137\,\text{dB} - 10\log_{10}(\text{RBW}) = -162$ dBc/Hz. The SNDR is calculated at 104.5 dB. So high SNDR with that OSR value is not achievable with conventional single-bit SDMs. This is due to the more aggressive NTFs, i.e. NTFs with higher out-of-band gain, possible with single-bit MSLA SDMs in comparison with conventional single-bit SDMs.

The power spectra of the two low-pass MSLA SDM outputs, y_I and y_Q, are identical. The one for output x_I is shown in Fig. 4. Note that the sampling frequency for signal y_I is half

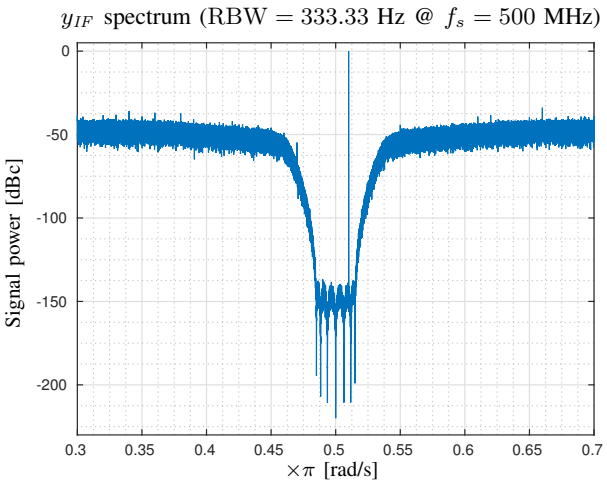


Fig. 3. Spectrum of the frequency synthesizer output y_{IF}.

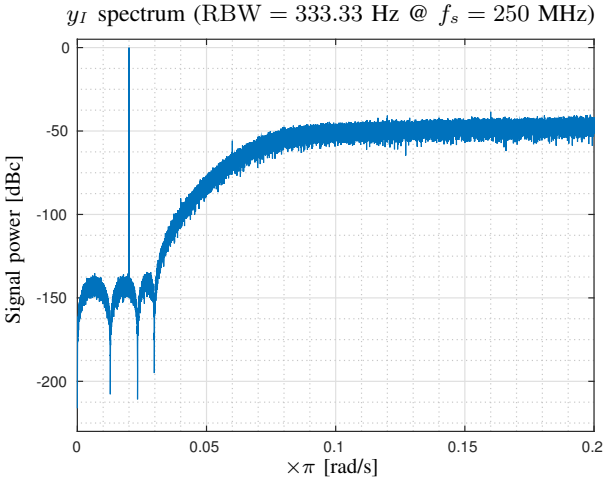


Fig. 4. Spectrum of the MSLA SDM output y_I.

of that used for signal y_{IF}, namely $f_s = f_{clk} = 250$ MHz. This is because for the interleaving process, both signals y_I and y_Q are used alternately as seen in Fig. 1.

In the case that a higher output frequency than y_{IF} is needed, one can use the output y_{RF} provided by the final multiplexer in Fig. 1. Using a value of $K = 2$, i.e. having a sampling frequency $f_s = 4f_{clk} = 1$ GHz, results in the power spectrum shown in Fig. 5. The generated frequencies are given by (2). A zoomed-in version of this plot for $m = 2$ and the minus sign in (2) is depicted in Fig. 6. In our test case we have $f_{BB} = 0.01f_{clk} = 2.5$ MHz. From (1), the intermediate frequency is $f_{IF} = 125 + 2.5$ MHz $= 127.5$ MHz. Thus, the generated frequencies for $K = 2$ are

$$f_{RF,1} = 0 \cdot 250 + 63.75 \text{ MHz} = 63.75 \text{ MHz}$$
$$f_{RF,2} = 1 \cdot 250 - 63.75 \text{ MHz} = 186.25 \text{ MHz}$$
$$f_{RF,3} = 1 \cdot 250 + 63.75 \text{ MHz} = 313.75 \text{ MHz}$$
$$f_{RF,4} = 2 \cdot 250 - 63.75 \text{ MHz} = 436.25 \text{ MHz}.$$

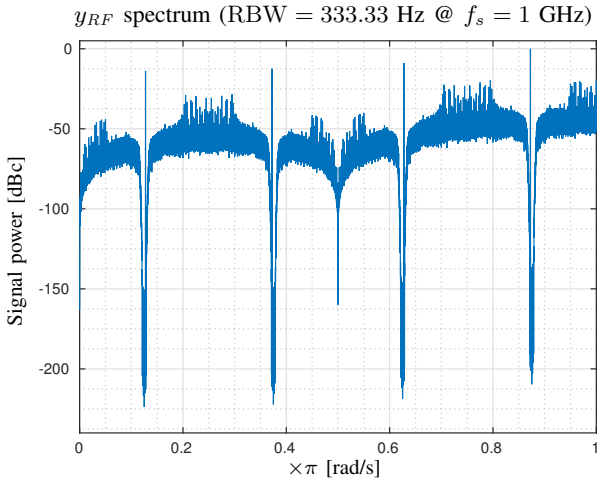


Fig. 5. Spectrum of the the frequency synthesizer output y_{RF} for $K = 2$.

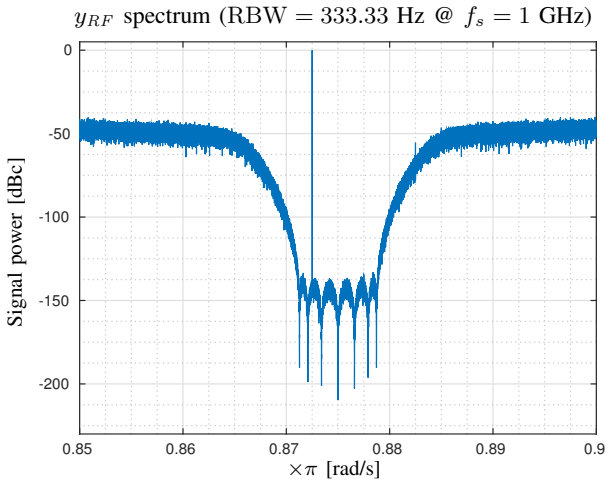


Fig. 6. Zoomed-in spectrum of the the frequency synthesizer output y_{RF}.

Since the OSR is 32, the passband of signal y_I in Fig. 4 is from DC to $f_{clk}/(2 \cdot 32) = 3.90625$ MHz. The bandwidth of the quadrature upconverted signal y_{IF} as given by (3) is 7.8125 MHz, twice that of the y_I signal, with generated frequencies ranging from 121.09375 MHz to 128.90625 MHz. For the frequency range of the zoomed-in y_{RF} signal spectrum in Fig. 6, we refer to (4) using $m = 2$ and the minus sign. This gives a frequency band ranging from 433.59375 MHz to 441.40625 MHz. The resulting bandwidth is 7.8125 MHz, the same as that of the y_{IF} signal.

In Table I the SNDR and SFDR of various MSLA SDM based frequency synthesizers are displayed for the y_{IF} output signal. The I and Q inputs are the same as those of the previous paragraph. For $k = 0$ the MSLA SDM reduces to a conventional SDM. The NTFs are designed using the highest out-of-band gain possible for the specific values of the OSR and the number of look-ahead steps k. For the determination of stability $3 \cdot 10^6$ output samples for each MSLA SDM are considered. The performance improvements over conventional

TABLE I
SNDR AND SFDR COMPARISON

OSR	r, k [a]	$\|\|NTF\|\|_\infty$ [b]	**SNDR [dB]**	**SFDR** [c] **[dBc/Hz]**
32	0	1.62	98.9	−142
32	3	1.68	102.0	−150
32	5	1.71	104.9	−161
64	0	1.57	140.6	−194
64	3	1.60	142.0	−182
64	5	1.65	147.4	−196
128	0	1.57	188.6	−233
128	3	1.61	193.9	−234
128	5	1.64	198.4	−242

[a] $r = k = 0$ corresponds to a conventional single-bit SDM.
[b] The NTF out-of-band gain.
[c] Assuming sampling rate $f_s = 500$ MHz.

SDMs are significant even for small values of k. The SFDR is calculated assuming sampling rate $f_s = 500$ MHz.

IV. CONCLUSION

Frequency synthesis using two low-pass single-bit MSLA SDMs in quadrature upconversion scheme was presented. It was shown that the performance advantages of using single-bit MSLA SDMs over conventional single-bit SDMs are significant. The proposed frequency synthesizer architecture is purely digital apart from a bandpass analog filter required for the attenuation of the out-of-band quantization noise in some applications. The highest possible generated frequency is only limited by the final multiplexer operating frequency. This allows the proposed frequency synthesizer to be used for synthesizing frequencies well in the GHz range.

REFERENCES

[1] J. Vankka, M. Waltari, M. Kosunen, and K. A. I. Halonen, "A direct digital synthesizer with an on-chip D/A-converter," *IEEE J. Solid-State Circuits*, vol. 33, no. 2, pp. 218–227, Feb. 1998.
[2] P. P. Sotiriadis and K. Galanopoulos, "Direct all-digital frequency synthesis techniques, spurs suppression, and deterministic jitter correction," *IEEE Trans. Circuits Syst. I*, vol. 59, no. 5, pp. 958–968, May 2012.
[3] C. Basetas and P. P. Sotiriadis, "Single-bit-output all-digital frequency synthesis using multi-step look-ahead bandpass Σ-Δ modulator-like quantization processing," in *IEEE Int. Freq. Contr. Symp. & Europ. Freq. and Time Forum*, Denver, Colorado, Apr. 12–16, 2015, pp. 448–451.
[4] C. Basetas, T. Orfanos, and P. P. Sotiriadis, "A class of 1-bit multi-step look-ahead Σ-Δ modulators," *IEEE Trans. Circuits Syst. I*, vol. 64, no. 1, pp. 24–37, Jan. 2017.
[5] R. Schreier and G. C. Temes, *Understanding Delta-Sigma Data Converters*, S. V. Kartalopoulos, Ed. John Wiley & Sons, Inc., 2005.

Wide-Band Frequency Synthesis Using Hardware-Efficient Band-Pass Single-Bit Multi-Step Look-Ahead Sigma-Delta Modulators

Charis Basetas, Paul Peter Sotiriadis
Department of Electrical and Computer Engineering
National Technical University of Athens
Athens, Greece
E-mail: chbasetas@gmail.com, pps@ieee.org

Nikos Temenos
Department of Informatics and Telecommunications
National and Kapodistrian University of Athens
Athens, Greece
E-mail: ntemenos@gmail.com

***Abstract*—Band-pass sigma-delta modulators (SDMs) can be used for all-digital frequency synthesis with low noise in the SDM passband. To avoid mixed-signal components such as DACs, a single-bit output is required. The noise shaping characteristics of single-bit sigma-delta modulators are limited by stability requirements. Look-ahead SDMs have been proposed to increase the bandwidth and signal-to-noise-and-distortion ratio (SNDR) of conventional single-bit ones. The cost is increased hardware complexity, but Multi-Step Look-Ahead sigma-delta modulators (MSLA SDMs) can significantly reduce the required hardware complexity, while retaining the advantages of look-ahead SDMs. This work demonstrates the hardware requirements of MSLA SDMs and proposes an all-digital frequency synthesizer architecture based on band-pass MSLA SDMs. The performance of the poposed synthesizer architecture is investigated for various configurations. Finally, the advantages of using MSLA SDMs instead of conventional single-bit ones in terms of bandwidth and SNDR are quantified.**

***Index Terms*—Sigma-delta, noise shaping, single-bit quantization, modulator, all-digital, band-pass, synthesizer, look-ahead**

I. Introduction

All-digital frequency synthesis has been proposed [1] to avoid the use of analog or mixed-signal components. Some of the advantages of purely digital circuits are immunity to thermal noise, process and power supply variations, and fast design cycle due to the availability of many design automation tools. All-digital frequency synthesizers also facilitate the generation of a wide range of frequencies using a single reference clock. For true all-digital designs, a single-bit output should be used, so that no multi-bit digital-to-analog converter (DAC) is required. Furthermore, single-bit quantization allows for inherently linear output since there are only two output signal levels. Therefore, there are only gain and offset errors which do not impact the output spectrum and can be easily corrected using digital calibration techniques. However, traditional single-bit output synthesizers such as the PDDS (Pulse Direct Digital Synthesizer) suffer from frequency spurs and/or a high noise floor [2]. Digital single-bit sigma-delta modulators (SDMs) [3] can be used to shape the quantization noise out of the desired frequency band.

Single-bit SDMs have limited noise shaping capabilities due to stability restrictions. Multi-bit SDMs exhibit increased stability, but they require a DAC for the conversion of their digital multi-bit output to analog. Look-ahead SDMs [4] can offer increased bandwidth, signal-to-noise-and-distortion ratio (SNDR) and spurious-free dynamic range (SFDR) than conventional single-bit SDMs. The cost is increased hardware complexity which makes their implementation for real-time applications especially difficult. Multi-Step Look-Ahead sigma-delta modulators (MSLA SDMs) were proposed in [5] to enable hardware-efficient implementation of look-ahead SDMs.

In the next section the MSLA SDM system is briefly described. In section III its hardware complexity is investigated and shown to be low enough for real-time frequency synthesis. Section IV provides simulation results showcasing the advantages of using MSLA SDMs for frequency synthesis over conventional ones. Finally, section V concludes the discussion.

II. MSLA SDM Basics

Conventional SDMs consider only the current quantization error for the determination of their output. Look-ahead SDMs [4] improve upon the stability and noise shaping characteristics of conventional SDMs by taking into account current and future quantization errors. This is accomplished by formulating an appropriate cost function including costs associated with future quantization errors. The decision on the next output is based on the minimization of the cost function. The term "look-ahead" does not imply that the input is predicted. Instead, the output is delayed by a number of samples equal to the look-ahead steps used. A higher number of look-ahead steps results in higher SNDR, SFDR and bandwidth, due to the possibility to use more aggressive noise transfer functions (NTFs), i.e. NTFs with higher out-of-band gain and thus lower in-band noise.

The MSLA SDM is a type of look-ahead SDM proposed in [5] that has lower hardware complexity compared to other types of look-ahead SDMs. Its system diagram is shown in Fig. 1. The modulator input sequence is denoted $\{x\}$, while

978-1-5386-2916-1/$31.00 ©2017 IEEE

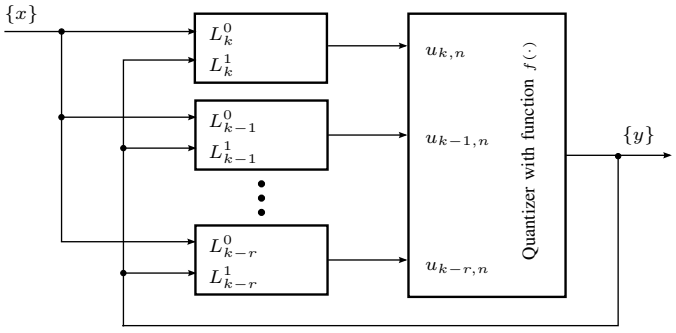


Fig. 1. The MSLA SDM system diagram.

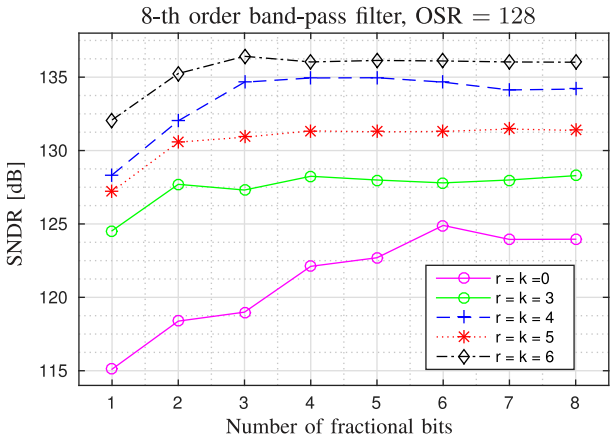


Fig. 2. SNDR vs. number of quantizer input fractional bits of the MSLA SDM frequency synthesizer with 8-th order band-pass filter and OSR = 128.

$\{y\}$ is the output sequence. The system is comprised of $r+1$ two-input digital IIR filters $\{L_j^0, L_j^1\}$ yielding $r+1$ outputs u_j, $k-r \le j \le k$, where k is the number of look-ahead steps and $r+1$ is the number of partial quantization error costs taken into account. The order of each IIR filter $\{L_j^0, L_j^1\}$ is $j+k$ whereas its coefficients are determined by the chosen NTF. The output of the modulator is given by a $(r+1)$-input quantizer described by a function $f(\mathbf{u}) : \Re^{r+1} \to \{\pm 1\}$, $\mathbf{u} = [u_{k-r,n}, u_{k-r+1,n}, \ldots, u_{k,n}]$, where n is the discrete time index. The quantizer input vector u is composed of the outputs of the IIR filters as shown in Fig. 1. The details of the quantizer function and the IIR filter coefficients are discussed thoroughly in [5].

III. MSLA SDM Hardware Implemention Investigation

As already mentioned the hardware implementation of a MSLA SDM is based on $r+1$ digital IIR filters and an $(r+1)$-input quantizer. Typical configurations are $r = k$ with $k \in [3, 8]$. For each two-input IIR filter of order m, $3m$ multiply and accumulate operations are needed for the calculation of its next output. The implementation of IIR filters has been thoroughly described in literature [6] and is not discussed here.

System-level simulations of MSLA SDMs have shown that 2-3 fractional bits and 4-5 integer bits for the representation of the quantizer input signals are enough to guarantee stable and accurate operation. This claim is justified in Fig. 2 where the SNDR of a MSLA SDM with an 8-th order band-pass filter and oversampling ratio OSR = 128 is shown for various fractional bits with look-ahead steps k as a parameter. The NTF has a central frequency $\omega_0 = 2\pi \cdot 0.38$ and the sinusoidal input signal has amplitude $A = 0.2$. Use of more than 3 fractional bits has no observable impact on the SNDR. Notice also how the SNDR improves as k is increased. This happens due to the higher out-of-band gain possible for the deisgn of the NTF while also retaining stability when using more look-ahead steps. For the simulation we have designed the NTFs using the Delta Sigma Toolbox in Matlab [7]. For each number of look-ahead steps k we have selected the highest possible NTF out-of-band gain.

For moderate values of k a look-up table (LUT) implementation of the MSLA SDM quantizer is viable. The quantizer function $f(\mathbf{u})$ is an odd function, meaning that the LUT size can be halved. As an example consider the case of $r = k = 3$ using 6 bits for each of the 4 quantizer inputs. This means that there are $(4 \cdot 6) = 24$ input bits. For each input combination the LUT stores 1 bit. Therefore, exploiting odd symmetry, a total of $2^{24-1} = 8.389$ Mbits of data need to be stored. Using logic optimization during synthesis this number is typically reduced by one to two orders of magnitude. This is well within the capabilities of modern digital circuits and FPGAs.

TABLE I
MSLA SDM Quantizer Synthesis Results

Primitive	Description	Used	Utilization
LUT6	6-input LUT	4244	2.58%
LUT5	5-input LUT	390	
LUT4	4-input LUT	310	
LUT3	3-input LUT	802	
LUT2	2-input LUT	462	
MUXF7	16:1 multiplexer	10	$< 0.01\%$

For the MSLA SDM configuration used in Fig. 2 with $r = k = 3$ and 6 bits (3 fractional bits, 2 integer bits and 1 sign bit) for each quantizer input, we have synthesized the resulting MSLA SDM quantizer for a Xilinx Kintex-7 FPGA KC705 Evaluation Kit target device. The final implementation report mentions the following primitives: 4244 6-input LUTs, 390 5-input LUTs, 310 4-input LUTs, 802 3-input LUTs, 462 2-input LUTs and 10 16:1 multiplexers. This is just 2.58% of the FPGA resources. These results are summarized in Table I.

IV. Band-pass MSLA SDM Based Frequency Synthesizer

A band-pass MSLA SDM can be used as part of an all-digital frequency synthesizer as shown in Fig. 3. A DDS (Direct Digital Synthesizer) [8] is used to generate a high-resolution digital sinusoidal signal which is then quantized to 1 bit by the MSLA SDM. The frequency control word w

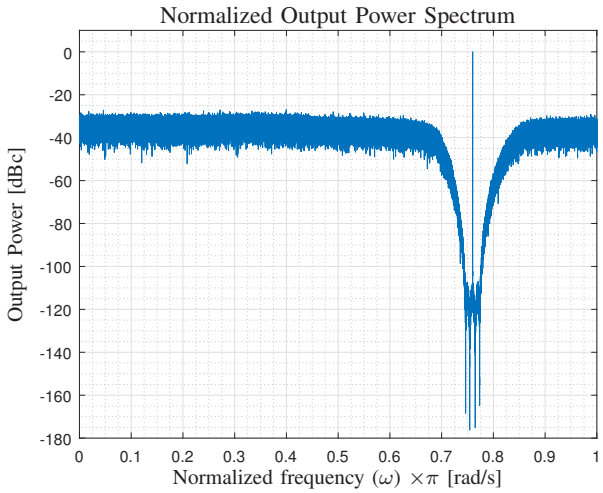


Fig. 5. Output power spectrum of the 8-th order band-pass MSLA SDM based synthesizer for OSR $= 32$ and $r = k = 4$.

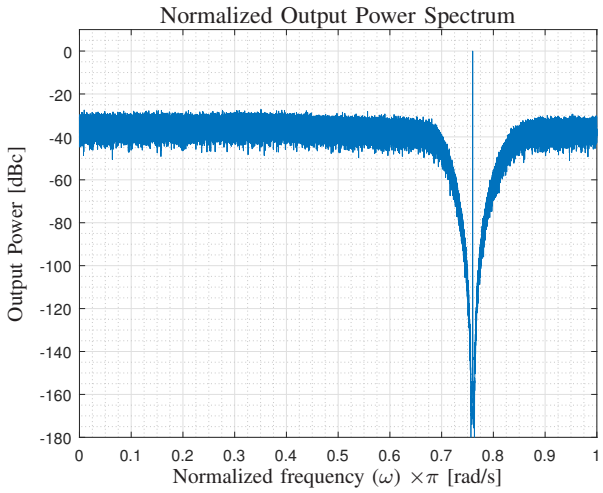


Fig. 6. Output power spectrum of the 8-th order band-pass MSLA SDM based synthesizer for OSR $= 128$ and $r = k = 4$.

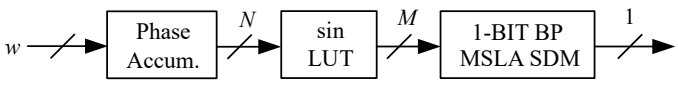


Fig. 3. All-digital frequency synthesizer using a 1-bit band-pass MSLA SDM.

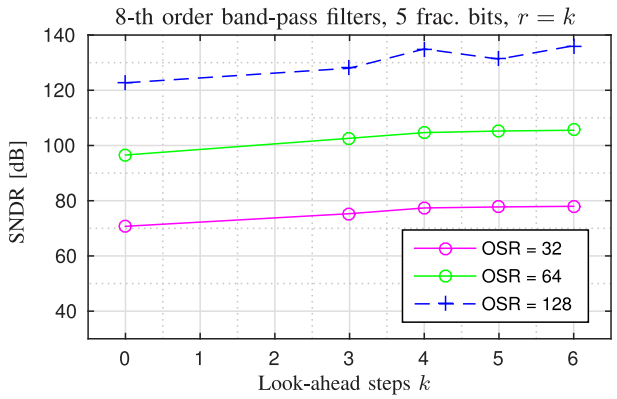


Fig. 4. SNDR vs. look-ahead steps k of the 8-th order band-pass MSLA SDM frequency synthesizer with OSR as a parameter.

selects the output frequency as $f_{\text{synth}} = (w/2^N) f_{\text{clk}}$, where N is the bit-width of the phase accumulator.

The in-band SNDR of 8-th order band-pass MSLA SDM frequency synthesizers for different values of OSR and look-ahead steps k is depicted in Fig. 4. For $k = 0$ the MSLA SDM reduces to a conventional SDM. The sinusoidal input has amplitude $A = 0.2$ while the central frequency of the NTFs is $\omega_0 = 2\pi \cdot 0.38$. The SNDR improvement over conventional SDMs ($k = 0$) is 10 dB or more for $k > 3$. The range of the synthesizable frequencies is determined by the NTF central frequency and the OSR and is given by

$$f_{\text{synth}} \in [f_0 - \frac{1}{4 \cdot \text{OSR}} f_{\text{clk}}, f_0 + \frac{1}{4 \cdot \text{OSR}} f_{\text{clk}}] \qquad (1)$$

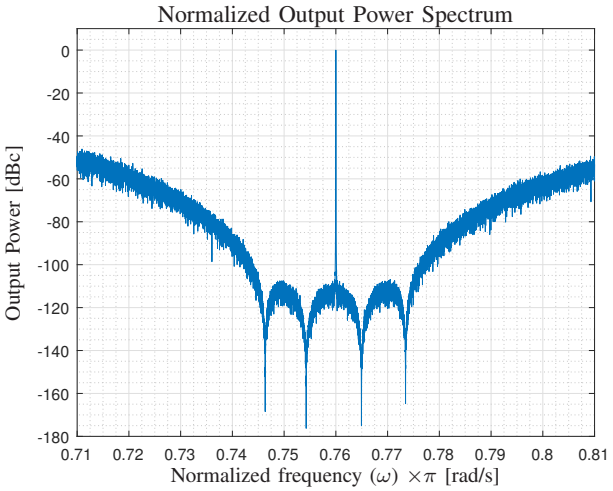


Fig. 7. Zoom-in of Fig. 5.

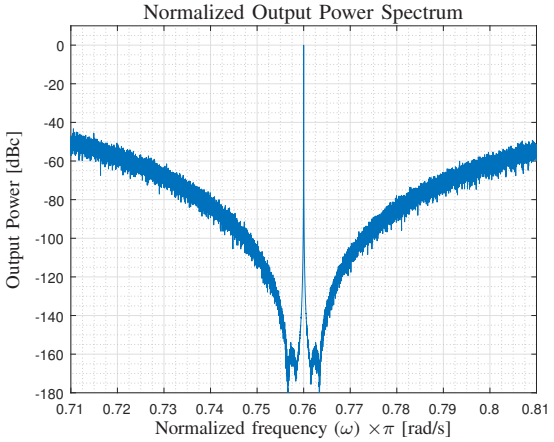


Fig. 8. Zoom-in of Fig. 6.

where f_0 is the central frequency of the NTF. Therefore, the synthesizable frequency bandwidth is

$$\mathrm{BW}_{\mathrm{synth}} = f_{\mathrm{clk}}/(2 \cdot \mathrm{OSR}). \quad (2)$$

Wideband frequency synthesis with low in-band noise is possible using a lower value for the OSR and exploiting the higher SNDR of MSLA SDMs over conventional single-bit ones.

For two of the aforementioned cases, namely for $r = k = 4$ and $\mathrm{OSR} = 32$ and $\mathrm{OSR} = 128$, the resulting output power spectra are plotted in Fig. 5 and Fig. 6 respectively. The output power is normalized with respect to the carrier. Zoomed-in versions of the previous plots are shown in Fig. 7 and 8 for the cases of $\mathrm{OSR} = 32$ and $\mathrm{OSR} = 128$ respectively. Notice that using a lower OSR results in increased synthesizable frequency bandwidth as indicated by (1) and (2), but the in-band noise gets higher. This is a typical design trade-off.

V. Conclusion

All-digital frequency synthesis using a DDS followed by a single-bit band-pass MSLA SDM was presented. The hardware requirements of the MSLA SDM $(r+1)$-input quantizer and IIR filters where analyzed and it was shown that the hardware overhead of using MSLA SDMs is not prohibitive for real-time operation. The performance advantage of MSLA SDMs over conventional single-bit ones in terms of SNDR was quantified for various cases via simulation and it was found to be significant.

References

[1] P. P. Sotiriadis and K. Galanopoulos, "Direct all-digital frequency synthesis techniques, spurs suppression, and deterministic jitter correction," *IEEE Trans. Circuits Syst. I*, vol. 59, no. 5, pp. 958–968, May 2012.

[2] P. P. Sotiriadis, "Spurs-free single-bit-output all-digital frequency synthesizers with forward and feedback spurs and noise cancellation," *IEEE Trans. Circuits Syst. I*, vol. 63, no. 5, pp. 567–576, May 2016.

[3] R. Schreier and G. C. Temes, *Understanding Delta-Sigma Data Converters*, S. V. Kartalopoulos, Ed. John Wiley & Sons, Inc., 2005.

[4] E. Janssen and A. van Roermund, *Look-Ahead Based Sigma-Delta Modulation*. Springer, 2011.

[5] C. Basetas, T. Orfanos, and P. P. Sotiriadis, "A class of 1-bit multi-step look-ahead Σ-Δ modulators," *IEEE Trans. Circuits Syst. I*, vol. 64, no. 1, pp. 24–37, Jan. 2017.

[6] A. V. Oppenheim and R. W. Schafer, *Discrete-Time Signal Processing*, 2nd ed. Prentice-Hall, 1999.

[7] R. Schreier. (2011, Dec.) Delta sigma toolbox. [Online]. Available: http://www.mathworks.com/matlabcentral/fileexchange/19-delta-sigma-toolbox

[8] J. Vankka, M. Waltari, M. Kosunen, and K. A. I. Halonen, "A direct digital synthesizer with an on-chip D/A-converter," *IEEE J. Solid-State Circuits*, vol. 33, no. 2, pp. 218–227, Feb. 1998.

Phase Noise Measurements of Surface Acoustic Wave Resonators at 2.4 GHz

E. Vaillant, J. Imbaud, F. Sthal
FEMTO-ST Institute
Time and frequency dept.
Univ. Bourgogne Franche-Comté, CNRS, ENSMM
Besançon, France
etienne.vaillant@femto-st.fr

F-X. Esnault*, G. Cibiel*
*Microwave and Time-Frequency Department, CNES,
Toulouse, France

***Abstract*—In this paper, a passive measurement system is used to explore the phase noise of surface acoustic wave resonators. This method is based on the carrier suppression technique. The resonant frequency is around 2.4 GHz and the power dissipated through the resonators around 500 µW. The 1/*f* noise is measured and the Allan standard deviation σ_{y_floor} of an oscillator containing the test resonator is estimated.**

Keywords—1/f noise; resonator; SAW; MEMS; phase noise; carrier suppression.

I. INTRODUCTION

The contribution in terms of noise of resonating devices in oscillators is not well-known one of the most generic methods of expressing frequency instability. MEMS technologies could be perturbed by the inherent noise of the resonator which limits performances. The FEMTO-ST Institute, Besancon, France and the French space agency (CNES), Toulouse, France investigate the origins of noise in resonators for several years [1]. Numerous micro-resonators dedicated to time bases are now developed by many laboratories [2-4]. Many resonating devices can be used to stabilize oscillators and their frequency stability is a condition for a low generated noise. As a matter of fact, noise in resonators used as frequency sources will affect system performance [5]. The 1/*f* noise in a surface acoustic wave (SAW) resonator is a parameter of great importance since it limits the close-to-carrier phase noise of an oscillator using the resonator [6-8].

In this paper, we measure the inherent noise of SAW resonators without the associated oscillator. First of all, a characterization of SAW electrical parameters has been done to evaluate the quality factor at resonant frequency. Then, the phase noise measurement has been measured with a passive method using carrier suppression technique [9], at 2 439 MHz. The driving source of the system comes from a frequency synthesizer N51B1B from Keysight.

II. RESONATOR CHARACTERISTICS AND CONDITIONING

A. SAW features

The S parameters of four similar resonators have been measured in order to get their Q factor. S_{21} parameters, presented in Fig. 1 leads to the unloaded Q factor of these resonators by use of the slope of the phase at the resonant frequency. Results are shown in table I.

The slope of the phase curve at the resonant frequency f_{res} leads to the Leeson frequency f_L, according to (1):

$$f_L = \frac{1}{\frac{\Delta\emptyset}{\Delta f}_{\pm 1^\circ}} \quad (1)$$

The Q factor is then calculated using $Q_L = \frac{f_{res}}{2.f_L}$.

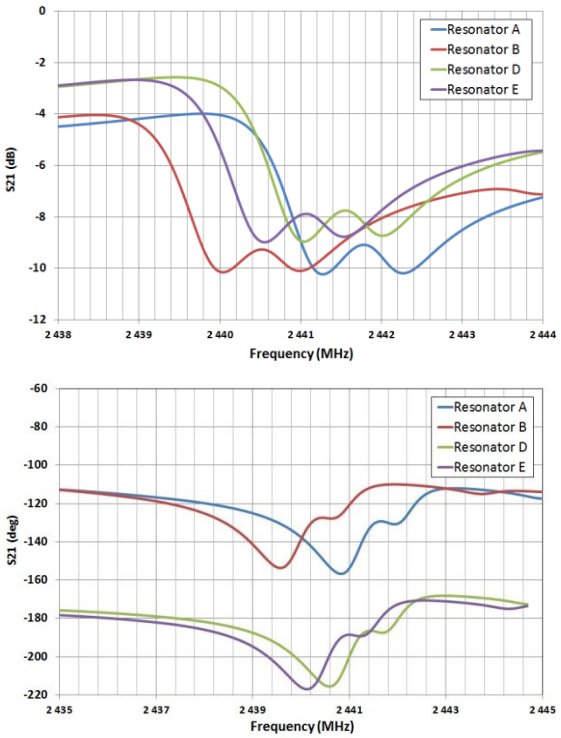


Fig. 1. Electrical response S_{21} of SAW resonators on a VNA around 2.4 GHz.

The loaded Q has been evaluated around 300. A quite important ratio between the loaded and unloaded Q factor is noticeable. The loaded Q has been measured using a vector network analyzer but it also can be estimated through the following formula:

$$IL = 20 * \log(1 - \frac{Q_L}{Q_U}) \quad (2)$$

where IL represents the insertion loss, Q_L and Q_U are respectively the loaded and unloaded quality factor.

TABLE I. UNLOADED Q FACTOR AND LOSS AT RESONANCE OF SAW RESONATORS

Res. n°	Loss (dB)	Q_U	f_{res} *(MHz)*
A	-3.98	873	2 439.7
B	-4,03	952	2 438.4
D	-2.56	1 439	2 439.4
E	-1.95	1 138	2 438.9

Resonators are directly melted on a PCB with two SMA connectors, as shown in Fig. 2.

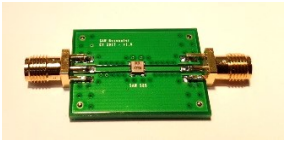


Fig. 2. Assembly of SAW resonator on PCB.

This PCB has been inserted into an aluminum case that has been thermally controlled, so as to avoid fluctuations of the room temperature.

III. PHASE NOISE MEASUREMENTS

The phase noise measurement of the SAW resonator has been done using a carrier suppression system. The principle of this method is to reduce the noise from the source leaving the noise coming from the measured resonator. A block diagram of the principle is shown in Fig. 3. The input power of the system comes from the N51B1B synthesizer. The carrier signal of the driving source is split into two equal parts to drive the two arms of the system, on one of which the Device Under Test (DUT) is set-up. On the other one an attenuator and a phase shifter are used in order to equilibrate the system. The carrier of the driving source is then canceled when the two signals are combined 180° out of phase.

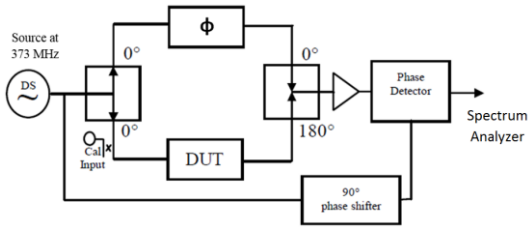


Fig. 3. Block diagram of the carrier suppression principle.

When the carrier suppression is achieved (around -85 dBm for these measurements), the resulting signal only made up of the noise coming from the resonator is strongly amplified and mixed with the source signal to be shifted down to the low frequency domain and processed by the fast Fourier transform spectrum analyzer.

The measurement setup is shown on Fig. 4. Each resonator has been measured by the carrier suppression system in single arm (with an attenuator plus a phase shifter on the second arm to compensate, as shown in Fig. 3). Indeed phase noise of the driving source was low enough to clearly distinguish the noise of the DUT (Fig. 5).

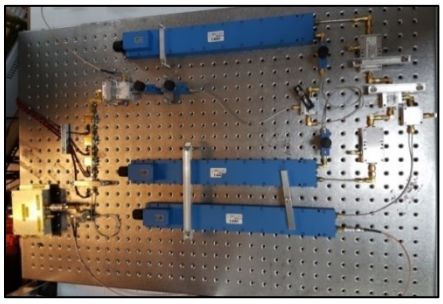


Fig. 4. Block diagram of the carrier suppression principle.

Calibration of the measurement system is obtained by injecting a known amount of phase noise (simulated by a sideband) on the arm containing the DUT. The measurement is corrected using a calibration factor determined from the sideband.

The noise floor of the measurement system has been measured to be at -160 dBc/Hz at 1 kHz offset from the carrier, and -150 dBc/Hz at 1 Hz offset. This result is shown in Fig. 5. In order to do this measurement, resonators have been replaced by simple attenuators and phase shifters reproducing an equivalent electrical behavior, at 2 439 MHz.

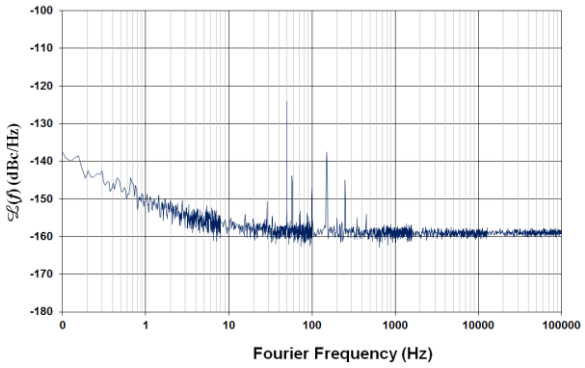


Fig. 5. Phase noise floor of the measurement system at 2 438 MHz.

IV. RESULTS

Fig. 6 and 7 present the single side band power spectral density (PSD) of the phase fluctuations, $\mathscr{L}(f)$. The drive level power dissipated by resonators is about 500 µW. The close-to-carrier phase noise level of the measurement system is at least 15 to 20 dB below the noise of resonators.

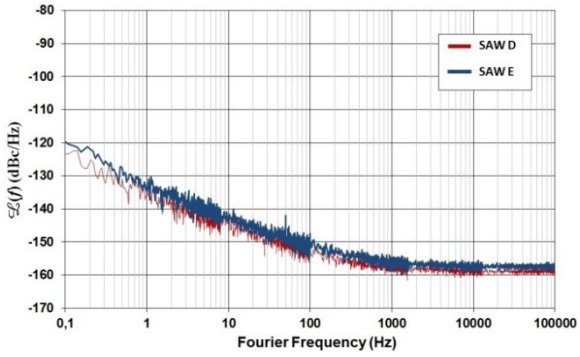


Fig. 6. Single Side Band phase noise of the resonator at 2 438 MHz, with a driving power equal to 500 µW.

Two resonators (*A* and *B*) have also been measured together so as to be sure that the noise of the carrier coming from the synthesizer is well removed by the system. In this configuration the contribution of the driving source noise to the total noise is rejected. The result is 3 dB lower, as expected, due to the equal amount of noise coming from both resonators. Result is shown in Fig. 7.

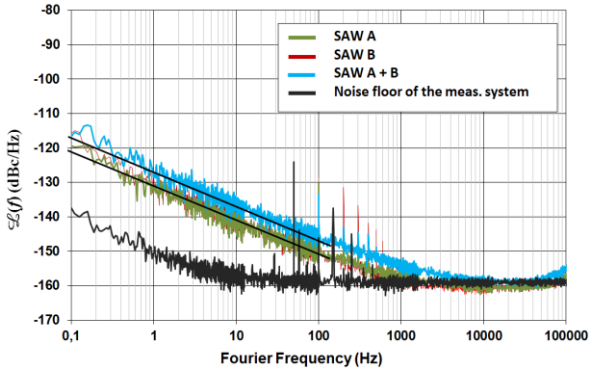


Fig. 7. Single Side Band phase noise of the resonator at 2 438 MHz, with a driving power equal to 500 µW.

The measured noise given by the passive measurement can be transformed into equivalent oscillator noise *(dBrad²/Hz)* and into Allan standard deviation (σ_{y_floor} *(10⁻⁹))* [10]. Considering the 1/*f* noise slope and the noise value obtained at 1 Hz in Fig. 6 and Fig. 7, the Allan standard deviation σ_{y_floor} of an oscillator containing the test resonator in which the only source of flicker frequency noise is the test resonator can be computed as follows [9]:

$$\sigma_{y_floor} = \sqrt{2 \cdot ln2 \cdot S_y(1Hz)} \qquad (1)$$

The relationship between S_φ and S_y is given by:

$$S_y(1\ Hz) \approx \frac{f_L^2}{f_{res}^2} S_\varphi(1Hz) \qquad (2)$$

The flicker floor of the Allan standard deviation turns out to be around a few 10^{-9}. A summary of phase noise measurement results is given in Table II. The corresponding σ_{y_floor} is also included in the Table. The measurement has been obtained at a temperature fixed at 25°C.

TABLE II. NOISE RESULTS OF SEVERAL SAW RESONATORS

Power	***500 µW***			
Res.	*A*	*B*	*D*	*E*
Q_L	332	318	300	289
ℒ(1 Hz) dBc/Hz	-130	-130	-135	-134
S_φ***(1Hz) (dBrad²/Hz)***	-127	-127	-132	-131
σ_{y_floor} ***(10⁻⁹)***	0.79	0.83	0.49	0.58

In this set of experiment a relation between the intrinsic Q factor of the resonator and the phase noise does not appear to be relevant. Even though, both *D* and *E* resonators show a phase noise level at least 4 dB below the noise of *A* and *B*. More measurements will be carried out with many other SAW resonators in order to compare results and to look for a Q_U^{-4} dependence for $S_y(f)$, the power spectral density of fractional frequency fluctuations [6].

Measurements according to driving power will be discussed and compared to other kinds of acoustic resonators.

V. CONCLUSION

Single Sideband phase noise of surface acoustic wave resonators has been investigated at a microwave frequency, around 2.4 GHz. The four SAW resonators measured show a short-term stability around few 10^{-9}. Measurements of phase noise against high input power will be further investigated. If enough power is provided, a significant reduction of close-to-carrier phase noise can be expected [11].

ACKNOWLEDGMENT

Authors thank the "Région Franche-Comté" and CNES, for the founding support.

REFERENCES

[1] F. Sthal, M. Devel, J. Imbaud, R. Bourquin, A. Bakir, C. Vuillemin, G. Santunu, P. Abbe, D. Vernier, G. Cibiel, "1/*f* noise of quartz resonators: Measurements, modelization and comparison studies", Proc. IEEE Joint UFFC, EFTF and PFM Symp., Denver, Colorado, 12-16 April, pp. 158-161, 2015.

[2] G. Piazza, A. Tazzoli, N. Miller, J. Segovia, C. Cassella, J. Koo, B. Otis, K. McNaul, B. Gibson, K. Turner, T. Palmer, "Dynamics of Microscale Thin Film AlN Piezoelectric Resonators Enables Low Phase Noise UHF Frequency Sources", in Proc. IEEE Int. Freq. Contr. Symp., pp. 555-558, 2013.

[3] M. E. Ivan, B. Dulmet, G. Martin, P. Abbe, L. Robert, S. Ballandras, "New electrostatically-excited single crystal silicon resonator vibrating in a Thickness-Extensional mode", in Proc. IEEE Int. Freq. Contr. Symp., pp. 743-748, 2012.

[4] T. Barron, D. Gachon, G. Martin, S. Alzuaga, D. Hermelin, J. P. Romand, S. Ballandras, "Temperature Compensated Radio-Frequency Harmonic Bulk Acoustic Resonators", in Proc. IEEE Int. Freq. Contr. Symp., pp. 652-655, 2012.

[5] J. R. Vig, Y. Kim, "Noise in Microelectromechanical System Resonators", IEEE TUFFC, vol. 46, no. 6, November 1999.

[6] T. E. Parker, "1/*f* frequency fluctuations in quartz acoustic resonators", in Appl. Phys. Lett. 46, n° 3, pp. 246-248, February 1985.

[7] T. E. Parker, D. Andres, "Dependance of SAW resonators 1/*f* noise on device size", in Proc IEEE Int. Freq. Contr. Symp., pp.178-185, 1993.

[8] T. E. Parker, D. Andres, J. A. Greer, G. K. Montress, "l/*f* Noise in Etched Groove Surface Acoustic Wave (SAW) Resonators", IEEE TUFFC, vol 41, no. 6, pp. 853-862, November 1994.

[9] F. Sthal, J. Imbaud, X. Vacheret, P. Salzenstein, G. Cibiel, S. Galliou, "Computation method for the short-term stability of quartz crystal resonators obtained from passive phase noise measures", IEEE Trans. on Ultrason., Ferroelect. and Freq. Contr., vol. 60, no. 7, July, pp. 1530-1532, 2013.

[10] E. Rubiola, "Phase noise and frequency stability in oscillators", Cambridge University Press, 2009.

[11] M. J. Loboda, T. E. Parker, J. A. Greer and G. K. Montress, "Reduction of Close-to-carrier phase noise in surface acoustic wave resonators", in Proc. IEEE Ultrasonics Symposium, pp. 43-46, 1987.

Software Defined Radio Platform for Time and Frequency Metrology

Nicolas Boucquey,*† Attila Kinali‡
*Institut Supérieur Industriel de Bruxelles, Belgium †CERN, Geneva, Switzerland
‡Max Planck Institute for Informatics, Saarland Informatics Campus, Germany

***Abstract*—Using software defined radio (SDR) systems for time and frequency metrology offers the possibility to perform measurements with high precision. Common off the shelf SDR systems are not always a good match for metrological applications as they do not generally offer ways to lock the local sampling clock to an external source or have lax noise requirements. We have built a flexible platform for SDR based time and frequency metrology based on a high-speed, multi-channel ADC and FPGA with integrated CPU.**

I. Introduction

A. Background

Sherman and Jördens [1] demonstrated the advantages of an SDR based time and frequency metrology system and achieved very good results at a quite low cost. Unfortunately, there are several issues with commercial SDR systems. As they are primarily optimized for communication applications, they have relatively low requirements for ADC input noise, jitter/noise of the sampling clock, and seldom offer the possibility to lock the sampling clock to an external reference without extensive modifications to the electronics.

II. The ADC board

For our experiments with damped sine based time-to-digital converters we required an low-noise ADC platform for the evaluation of the method employed. As none of the available board did fit our needs, we have designed an SDR platform specifically with time and frequency metrology in mind, based on a 4 channel, 14 bit, 125 Msps ADC which interfaces directly with an Zynq 7 FPGA with an integrated ARM Cortex-A9 processor. The ADC is pin and interface compatible with a 16 bit version and can be simply replaced. The sampling clock is provided by a low noise on board crystal oscillator, but can be switched to an external source. Special care was taken to design the power supply to isolate the noisy DC/DC converters from the ADC. To achieve this, two linear converters were used back-to back to ensure a high damping of the ripple produced by the DC/DC converter and the FPGA board. The use of an FPGA with integrated processor allows preprocessing the data before sending it over the "slow" Gigabit Ethernet interface. The current board achieves an SNR or 75 dBFS, i.e. without degradation of the specified performance of the ADC. The SNR translates to 12.2 bit ENOB.

The complete design files are available as open hardware under the CERN Open Hardware License (COHL) on the CERN project homepage [2].

References

[1] J. A. Sherman and R. Jördens, "Oscillator metrology with software defined radio," *Review of Scientific Instruments*, vol. 87, no. 5, p. 054711, 2016. [Online]. Available: http://dx.doi.org/10.1063/1.4950898

[2] N. Boucquey, A. Kinali, J. Serano, and T. Wlostowski, "Multi-channel time interval counter and fine delay generator." [Online]. Available: http://www.ohwr.org/projects/r19-tdc-del-a

978-1-5386-2916-1/$31.00 ©2017 IEEE

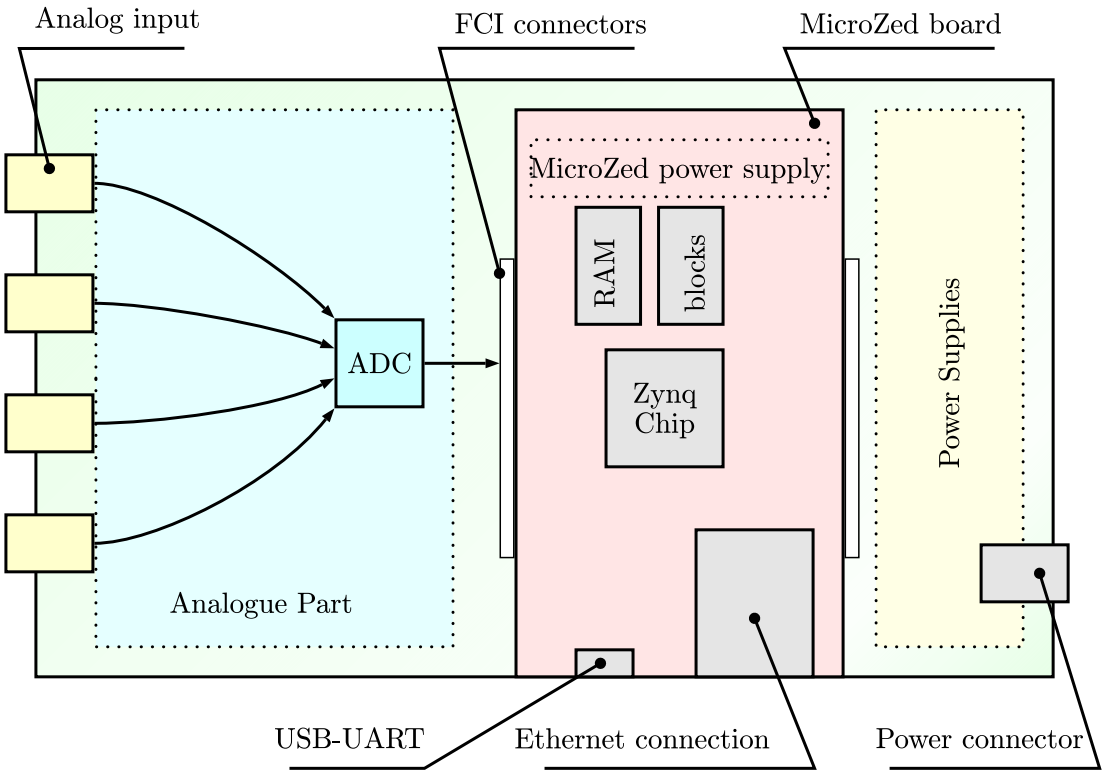


Figure 1. The overall layout of the ADC board

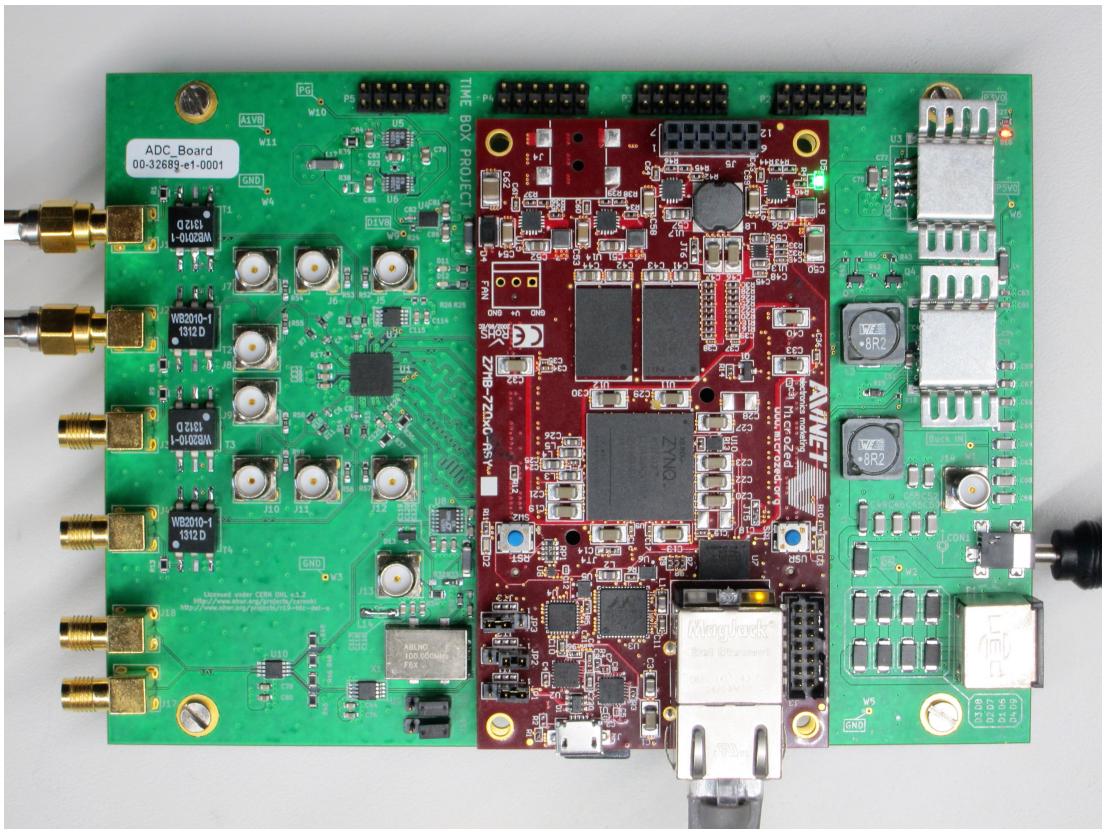


Figure 2. The final board

Noise interaction with time quantization of TIC

Magnus Danielson
R&D System Design
Net Insight AB
Stockholm, Sweden
Email: magda@netinsight.net

***Abstract*—This article investigates the interaction of white noise and the systematic noise of a time quantization that occurs in a time-interval counter (TIC). By buildiing a theoretical model, do analysis and simulatiion, understanding of quantization effect and noise interaction is achieved.**

***Index Terms*—noise, quantization**

I. Introduction

This article studies the effect of time-interval counters quantization of phase into countable time measures, and how this quantization behaves under the effect of noise.

When measuring oscillators, time-interval counters and frequency counters is used. The main principle of a frequency counter is to measure the amount of cycles and then the time that elapses from the start of the first cycle and the end of the last cycle, these being known as the start and stop events. This time-difference is expressed in forms of counts of the time-base clock cycles. For time interval counters, two different inputs is used for the start and stop events to measure the time-difference.

In modern counters, time interpolators will interpolate the start and stop events to be a fractional of the time-base period, and the time resolution is often denoted the single-shot resolution. Through averaging, the resolution can be increased below the single-shot resolution, and such averaging is often assumed to improve precision by $\sqrt{N}$.

When using such data in Allan deviation (ADEV) processing [1], it follows a $1/\tau$ curve, similar to that of White Phase Modulation Noise, such that it is often assumed to be the white noise, this does however not follow the expected $\sqrt{N}$ property, which derives from white noise assumption and standard deviation. However, depending on the filtering such as Modified Allan Deviation (MDEV) or Parabolic Deviation (PDEV) it does not behave exactly as white noise.

The single-shot resolution noise, is in fact a systematic effect and not a random noise effect. It's treatment depends requires attention to other details. This paper is dedicated to illustrate some of these effects.

II. Waiting jitter

Consider a signal of frequency f_1 as being measured and quantized against a reference signal f_0. Often the reference signal is 10 MHz and then interpolated to achieve a higher resolution, as the 100 ns resolution is a bit coarse for most uses today. By using an interpolation mechanism the resolution can be improved with a factor of N_I then the apparent reference rate will be $f_{0I} = N_I f_0$ and the resulting time resolution becomes $\Delta t_{0I} = 1/(N_I f_0)$. This is often denoted the single-shot resolution of the counter, as it is the time-resolution of a single event.

The basic frequency relationship it takes E event counts in the f_1 clock and T time counts in the f_{0I}, forming the relation of $E/f_1 \hat{=} T/f_{0I}$ resolving for $f_1 \hat{=} f_{oI} E/T$ which is the traditional Π-estimator of frequency. However, whenever the frequency is slightly off, for instance when both clocks derive from atomic clocks, such a rational number will not make the same number of interpolator bins at all times, the phase difference between the clocks will differ a little for each cycle, but it is only when it is large enough compared to Δt_{01} that we measure, as it goes beoynd the quanitzation step of the counter and the phase difference falls to zero. This forms a sawtooth jitter known as waiting jitter [2].

Waiting jitter is the phase errors we experience in DDS systems, behaving as aliasing components of a sampled system as the sawtooth overtones wraps around the Nyquist multiples. A similar pattern can be observed in counters.

The initial case of a very close frequency can occur with other ratios, just that the next phase is far from the previous, but as you look at the full beating pattern before it re-occurs you will notice that it is the same sweeping range of of phases, that just have been temporally re-arranged. This temporal re-arrangement is in play when you have long enough observation interval for it to occur.

On short observation interval, the phase can be seemingly captured by the quantiszation such that none or only a fraction of the average phase is reflected since the quantization hides the actual phase error.

This waiting jitter is a systematic component disturbing the measurement.

III. Random noise and waiting jitter

A. Analysis

The waiting jitter sawtooth shaped phase error, that is the difference between actual and quantized phase, is however not the only signals. Since both the input signal and the reference signal present noise, and in particular phase noise we need to look at the interaction of noise with the quantization process. While we know we have white and flicker phase modulation noises, as well as white and flicker frequency modulation noises, this initial analysis will be done for white

phase modulation noise only, under the assumption that it dominates for short tau analysis.

The white phase modulation noise, being Gaussian i.i.d. noise, has the classical Gaussian bell-shape distribution around it's mean scalled by its variance σ^2. As the mean is shifted by the phase error, some fraction of this bell-shape will be at or beyond the quantization border, and thus when the mean of the bell is precisely on the quantization border, half the time it will be below and half the time it will be above the border, thus creating randomly alternating quantization decisions. The cumulative probability distribution of the gaussian probability distribution is that of the error-function erf. As we observe a number of these decisions for the same phase-relationship, as we average these decisions we get the average phase as mesured. The phase error of the averages phase compared to actual phase, will now resemble the sawtooth shape, but as the amount of noise is increased, the better average is achieved and thus the low phase error parts will smooth out of the error.

Thus, as the amount of noise increases, the waiting jitter effect reduces.

B. Simulation of quantization

In order to simulate this effect, we need to model the quantization. Since we assume a uniform quantization step q for an offsets $x(n)$, a simple model of quantization is to establish the number of quantization steps $l(n)$. Then the quantized level $x_q(n)$ as well as the resulting quantization error $e_q(x,n)$ can be expressed:

$$l(n) = \left\lfloor \frac{x(n)}{q} \right\rfloor \quad (1)$$

$$x_q(n) = ql(n) \quad (2)$$

$$e_q(x,n) = x_q(n) - x(n) \quad (3)$$

The average estimated phase $\hat{x}$ as estimated over N samples can be expressed as a sequence $x_q(n)$ of quantized values, where the sequence is based on the noise level σ giving:

$$x(n) = x + \sigma rand(n) \quad (4)$$

$$x_q(n) = q\left\lfloor \frac{x(n)}{q} \right\rfloor \quad (5)$$

$$\hat{x}(x) = \frac{1}{N}\sum_{n=0}^{N-1} x_q(n) \quad (6)$$

$$e_{q,avg}(x) = \hat{x}(x) - x \quad (7)$$

In the following, dBq is dB in reference to the quantization step, which for these plots is 10 ns.

In Fig 1 the effect of averaging is apparent. With noise power being -50 dBq (green dots) only wth very small remaining error to the next level the noise is able to start smoothing out the step.

The next level is the -40 dBq (red) in which the noise s reaching further into the quantization error. As we add noise to -30 dBq (yellow) and -20 dBq (orange) it is apparent that

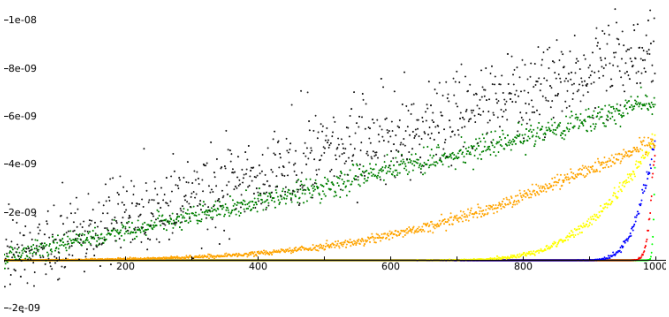


Fig. 1. Average phase with -50 dBq (green), -40 dBq (red), -30 dBq (blue), -20 dBq (yellow), -10 dBq (orange), 0 dBq (dark green) and +10 dBq (black) for 0-9.99 ns (scale is 1/1000 of a cycle.

the noise is starting to really average out, but only with 0 dBq (green) a linear line approximating the expected line 0 to 9.99 ns. With +10 dBq, much of the expected line has occured, but it is now apparent that it has close to averaged out the quantization step, but the variance is now much more apparent, thus the noise is significantly adding.

The deviation of the quantized values and the deviation of the averaged quantized values is two diffent values. In order to get a good understanding of the behaviour, we need to sweep over the full set of phase relationships in order to estimate the effect of quantization and noise. The average error for a phase value over N samples then becomes:

$$\hat{e}_q(x) = \frac{1}{N}\sum_{n=0}^{N-1} e_q(x,n) \quad (8)$$

The resulting variance for M different phases and N samples of each phase becomes:

$$\hat{\sigma}_q^2 = \frac{1}{NM-1}\sum_{m=0}^{M-1}\sum_{n=0}^{N-1}\left[e_q(m\frac{q}{M},n) - \hat{e}_q(m\frac{q}{M})\right]^2 \quad (9)$$

Similarly, if N samples is averaged for each sample, we then evaluate the

$$\hat{e}_{q,avg} = \frac{1}{M}\sum_{m=0}^{M-1} e_{q,avg}(m\frac{q}{M}) \quad (10)$$

$$\hat{\sigma}_{q,avg} = \sqrt{\frac{1}{M-1}\sum_{m=0}^{M-1}(e_{q,avg}(m\frac{q}{M}) - \hat{e}_{q,avg})^2} \quad (11)$$

In Fig 2 the overall effect of noise and quantization is investigated as the noise is swept from -50 dBq to +30 dBq.

The average error (red), starts of at -6 dB N drops with added noise. It is apparent that from +15 dBq and upwards, the simulation would need to be trimmed for better result.

The RMS error relating to quantization (blue) starts of at -6 dB and slopes down to have a minimum of -19.21 dB at +8 dBq, to then raise proportional with the increasing gain.

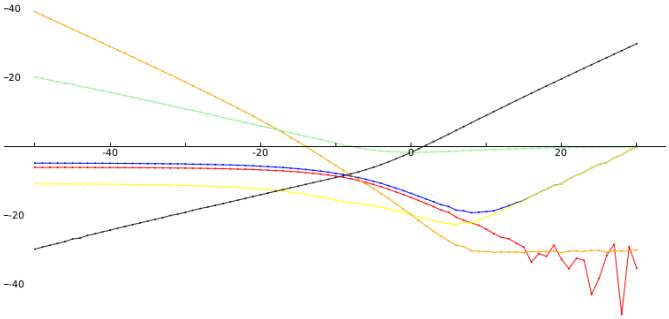


Fig. 2. The plot, in db, is done by sweeping from -50 dBq to +30 dBq, the overall average error (red), RMS error (blue), RMS compared to quantization step (yellow), RMS compard to noise (orange), total averge RMS relative quantization (black) and total average RMS relatiive to noise (bright green).

The RMS relating to quantization (yellow) starts of at -10 dB and slopes down to have a minimum of -22.66 dB at +6 dBq, to the raise proportional with the increasing gain, aligning to the RMS error curve.

The RMS relating to noise (orange) starts of at +39.17 dB and slopes down to reach a minimum -30.74 dB at +11 dBq to then flatten out.

The overall RMS compared to quantization step (black) shows the noise slowly increasing in the noise compression region up to about -8 dBq at which the compression stops and the noise increases. This is better seen in the overall RMS compared to the noise (bright green) which starts with 20 dB higher noise than actual present due to the noise compression of the quantization step. As noise increases, it experience less compression and at about -8 dBq the compression stops and it aligns up to the actual noise level.

IV. Conclusion

Inspried by the old HP5328A counter, noise interaction with time quantization and effect of averaging has been simulated. It has been found that for low noise-levels, as compared to the quantization step, noise is excagerated and the amplitude relates to that of the quantization step. This aligns with the rule of thumb that the $1/\tau$ in ADEV correspons at $\tau = 1s$ to the single-shot resolution of the counter, i.e. the TIC time quantization step.

By adjusting the noise level the normal variance, as also being expereinced by ADEV can be minimized by letting the noise level be at +8 dBq. However, the average error can be seen continue going down.

The noise experience compression by the interaction, as illustrated by the simulations and the plots, as noise increase significantly above the quantization step, the compression effect disappears,

The average noise, as experienced by MDEV and PDEV can use the higher resolution achieved by the noise de-modulating the quantization step. The slope seems consistent with a 1/N behavior.

References

[1] D. W. Allan, “Statistics of atomic frequency standards,” *Proceeedings of the IEEE, Vol. 54, No. 2*, February, 1966.

[2] P. R. Trischitta and E. L. Varma, *Jitter in Digital Transmission Systems*, 1989.

32-QAM All-Digital RF Signal Generator Based on a Homodyne Sigma-Delta Modulation Scheme

Paul Peter Sotiriadis, Charis Basetas
Department of Electrical and Computer Engineering
National Technical University of Athens
Athens, Greece
E-mail: chbasetas@gmail.com, pps@ieee.org

Nikos Temenos
Department of Informatics and Telecommunications
National and Kapodistrian University of Athens
Athens, Greece
E-mail: ntemenos@gmail.com

***Abstract*—An all-digital sigma-delta modulator (SDM) based RF synthesizer is presented. A multiplier-less architecture for the implementation of the band-pass SDM loop filter is proposed. Furthermore, this architecture enables the adjustment of the loop filter central frequency by exploiting homodyne up- and down-conversion. The RF synthesizer is comprised of a direct digital synthesizer (DDS) and the proposed multiplier-less single-bit band-pass SDM. Due to the simplicity of the synthesizer building blocks very high generated frequencies are possible. Modualtion is easily incorporated and as a test case its performance in a 32-QAM modulation scheme is presented.**

***Index Terms*—Sigma-delta, noise shaping, single-bit quantization, multiplier-less, all-digital, homodyne, synthesizer, RF, QAM**

I. Introduction

Sigma-delta modulators (SDMs) have been proposed for all-digital frequency synthesis in a limited bandwidth dependent on the SDM oversampling ratio (OSR). Analog blocks suffer from thermal noise, dependence on the power source quality, non-linearities due to component mismatches, lack of design tool automation and increased concept-to-market time when a circuit is migrated to another IC technology. On the contrary, digital circuits do not exhibit these problems. Therefore, all-digital frequency synthesizers offer significant advantages over analog or mixed-signal designs. Single-bit representation of the output signal is crucial for the omission of mixed-signal components such as DACs.

A typical all-digital SDM-based frequency synthesizer is shown in Fig. 1. The adder and the register work as a phase accumulator generating $kw \mod 2^n$ on the k-th rising clock edge, where w is the frequency control word (FCW) [1]. Its output is fed to the cosine look-up table (LUT) whose output is $\cos(2\pi kw/2^n)$ where n is the bit-width of the accumulator's register. The LUT output is passed through a single-bit band-pass sigma-delta modulator which shapes the quantization noise outside the band of interest. Random dithering may be added to remove any frequency spurs.

II. Single-bit SDM with Quadrature Homodyne Filter

The single-bit SDM is depicted in Fig. 2. The loop filter $F(z)$ determines the OSR and the noise shaping characteristics

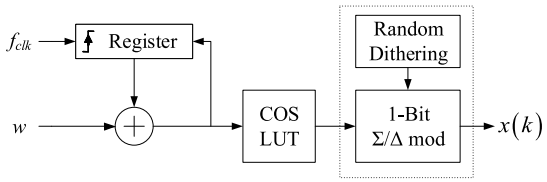


Fig. 1. Pulse DDS (PDDS) with sigma-delta noise shaping.

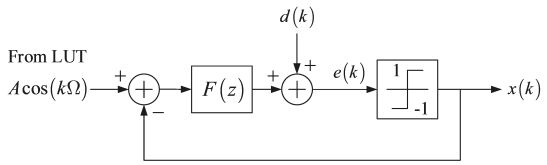


Fig. 2. The single-bit band-pass SDM.

of the SDM. A typical digital filter requires different coefficients if a change in its passband is needed. This is the case if different bands of frequencies are to be generated. Therefore, any optimizations in a programmable filter implementation would be difficult. The quadrature homodyne filter (QHF) architecture [2] can address this issue.

A. The Quadrature Homodyne Filter Architecture

The QHF architecture, shown in Fig. 3, implements the band-pass filter $F(z)$ using two fixed identical low-pass filters $H(z)$ and quadrature homodyne down- and up-conversion to achieve band-pass frequency response centered at the carrier angular frequency Ω. The QHF architecture in Fig. 3 requires

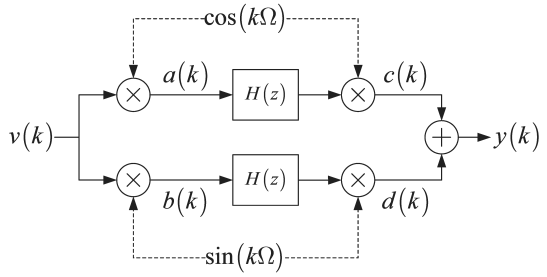


Fig. 3. The quadrature homodyne filter architecture.

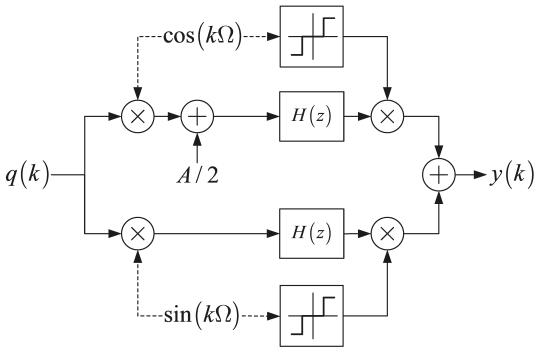


Fig. 4. QHF multiplier-free architecture; $q(k) = -x(k)$.

four multiplications, an addition and two identical low-pass filters. It is shown next that the multiplications can be eliminated.

B. The Multiplier-less Quadrature Homodyne Filter

The low-pass filters $H(z)$ of the QHF architecture can be chosen to have coefficients which are powers of 2 or sums of two or three powers of 2. This way the required multiplications are reduced to additions and shift operations.

The other four multiplications can be eliminated by exploiting first-order approximation of the QHF input and 3-level quantization of the sine and cosine signals in Fig. 3. The former eliminates the left hand side multipliers while the latter eliminates the right hand side ones. The final multiplier-less QHF architecture is shown in Fig. 4.

III. The Multiplier-less RF Synthesizer

Using the multiplier-less QHF architecture for the implementation of the SDM loop filter, the PDDS with sigma-delta noise shaping in Fig. 1 can be used for the generation of a wide range of radio frequencies by adjusting the central frequency of the QHF. Amplitude modulation can be added by varying A in Fig. 4, whereas frequency or phase modulation can be included by adding an appropriate value to w or just before the cosine LUT (Fig. 1).

A. 32-QAM Modulation Simulation Results

The aforementioned RF synthesizer architecture has been simulated in Matlab for the generation of a 32-QAM modulated RF signal. The 32-QAM modulation-demodulation simulation setup is shown in Fig. 5. The square-root raised cosine filters are used for the reduction of inter-symbol interference (ISI).

In our test-case an OSR of 1024 is used. The square-root, raised cosine filters are designed to span 10 symbols with roll-off factor $\beta = 0.25$. Using the aforementioned system parameters, the near-in spectrum in Fig. 6 was obtained for 10,000 symbols. Notice that the bandwidth of the RF synthesizer (noise suppressed frequency range), determined by the OSR, is selected according to the signal bandwidth to minimize the required OSR while retaining stability. Channel

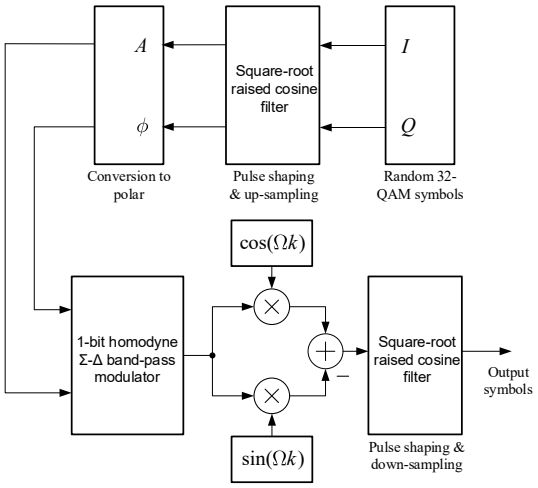


Fig. 5. 32-QAM modulation-demodulation simulation setup.

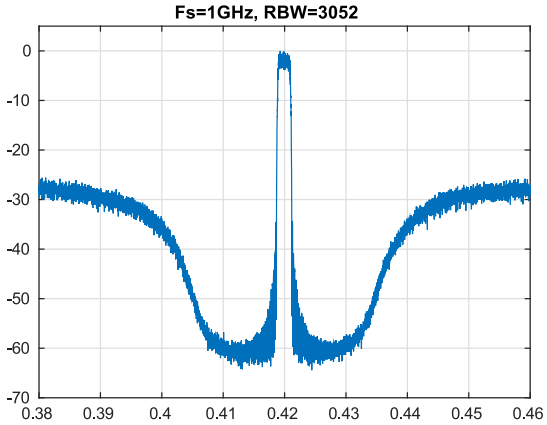


Fig. 6. Spectrum with 32-QAM modulation and OSR $= 1024$. Y-axis in dB, X-axis: Discrete-Time Frequency

selection is accomplished by adjusting the central frequency of the SDM.

After demodulation, the constellation diagram of the demodulated signal was attained, resulting in an RMS EVM of 0.956%. Assuming a clock frequency of 1 GHz, the proposed all-digital transmitter is capable of achieving a symbol rate of 976.56 Ksymbols/s. For 32-QAM modulation this is translated to a data rate of 4.882 Mbits/s.

References

[1] V. S. Reinhardt, "Direct digital synthesizers," *Technical Report, Hughes Aircraft Co, Space and Communications Group, L.A., CA*, Dec. 1985.

[2] P. P. Sotiriadis, "Single-bit all digital frequency synthesis using homodyne sigma-delta modulation," *IEEE Trans. Ultrason., Ferroelectr., Freq. Control*, to appear.

The Portable CPT Atomic Clocks - Recent Developments

Zhenwei Zhang, Renfu Yang, Xueyun Wang
Science and Technology on Metrology and Calibration Laboratory,
Beijing Institute of Radio Metrology and Measurement, Beijing, China

Email: zhangzhenwei1314@126.com

***Abstract*—The authors are developing a portable CPT atomic clock, trying to refine the firmware to reduce power, improve performance, and ensure reliable operation over the expected range of environmental conditions. The overall volume of the physics package is less than 2 cm^3, with resonance cell size of φ3mm×3mm, filled with Rb atomics and buffer gases. The portable CPT atomic clock is a complete packaged atomic clock, with overall size of 20 cm^3, power consumption about 750mW, and short-term stability of 3-5x10^{-12}/100s. The magnitude and power is smaller than previous prototype. The portable CPT atomic clock itself may find applications in broadband, secure communications, and precise location and navigation systems.**

Keywords—CPT atomic clock; physics packag; eshort-term stability

I. INTRODUCTION

Our research group at the Beijing Institute of Radio Metrology and Measurement (BIRMM), has been developing CPT atomic clock technology since 2012. At 2015 China Time & Frequency Symposium(CTFS), we presented our first demonstration of CPT atomic clock with power consumption of ≈3 W and short-term stability of 8×10^{-12}/100s[1]. At the 2016 IFCS, we presented our first demonstration of a fully integrated Portable CPT Atomic Clocks with power consumption <2W and short-term stability 4-5$\times10^{-12}$/100s[2].

Since our previous report, we have continued the development of Portable CPT Atomic Clocks to improve performance and manufacturability. In particular, the power consumption has been reduced to 725 mW.

II. CPT ATOMIC CLOCK OVERVIEW

The essential elements of the physics package are the resonance cell, shown in Figure 1, we are developing a portable CPT atomic clock, trying to refine the firmware to reduce power, improve performance, and ensure reliable operation over the expected range of environmental conditions. The overall volume of the physics package is less than 2 cm^3, with resonance cell size of φ3mm×3mm, filled with Rb atomics and buffer gases. The physics package operates at 85°C in 25°C ambient temperature with <0.6W of heater power.

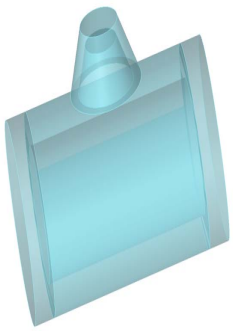


Fig.1. The resonance cell

Iterative improvements include high-performing MCU for digital signal processes, analog signal amplifier, current source for stable homogeneous magnetic field, and other minor improvements to reduce power consumption and improve performance. The portable CPT atomic clock is a complete packaged atomic clock, with overall size of 20 cm3, power consumption < 750mW, and short-term stability < 5x10^{-12}/100s. The magnitude and power is smaller than previous prototype.

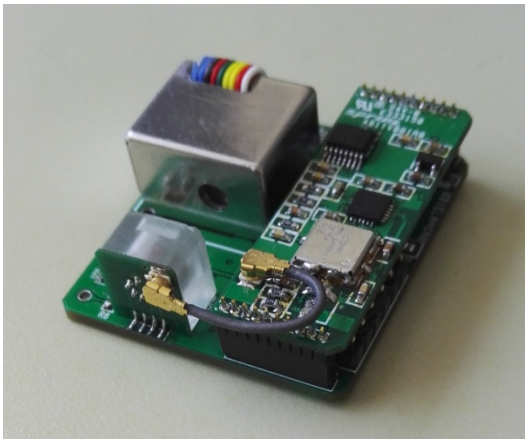


Fig.2. CPT atomic clock prototype photograph

III. CPT ATOMIC CLOCK PERFORMANCE

The overall power consumption of the CPT atomic clock has been reduced to 725mW, illustrated in Table 1 below. The majority of the power consumption is physics package heater.

Improvements in the efficiency of the physics heater are our major effort now.

Table 1: CPT atomic clock power consumption

System	Component	Power
Digital-analog board	MCU	30mW
	ADC,DAC	30mW
	Analog	5mW
Microwave synthesizer	3.4GHz VCO	15mW
	PLL	10mW
	10MHz TCXO	10mW
	Power splitter	10mW
Physics package	Heater power	500mW
	TEC power	100mW
	VCSEL power	5mW
	C-field	10mW
other		5mW
Total		725 mW

In 2016 we reported that the short-term stability of the CPT atomic clock was 4-5$\times 10^{-12}$/100s. With improved electronics and firmware, CPT atomic clock has improved over previous results. Figure 3 shows the stability data for 10 pre-production prototypes. All units exhibit $<5\times 10^{-12}$ in intervals of $\tau < 100$s. Nonetheless, the long-term stability of the deliverable units diverges from ideal behavior at longer averaging times, principally due to early non-linear aging effects.

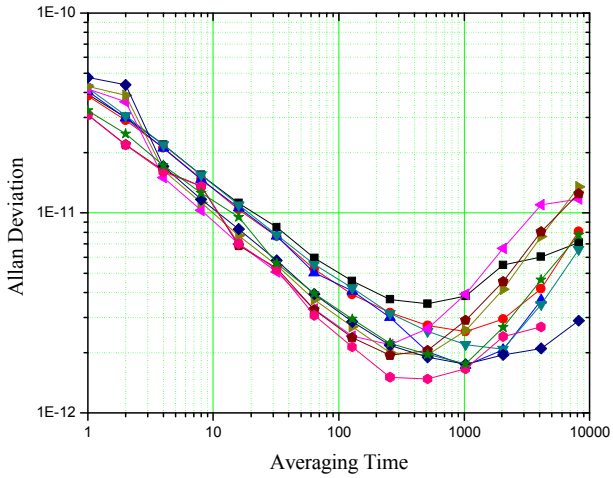


Fig.3: Allan deviation for 10 prototypes

IV. CONCLUSION

We have built and tested 10 prototype portable atomic clocks, with volume 20 cm3 and power consumption 750 mW. All 10 devices exhibit excellent short-term stability of 3-5$\times 10^{-12}$/100s. Following effort will be spent refining the firmware to reduce power, improve performance, and ensure reliable operation over the expected range of environmental conditions.

REFERENCES

[1] Zhang Zhenwei, Yang Renfu. Design On Miniature CPT Atomic Clock. 2015 China Time & Frequency Symposium . Beijing:P229-233.

[2] Yang Renfu, Zhang Zhenwei, The Recent Progress of Portable CPT Atomic Clocks in BIRMM. 2016 IEEE International Frequency Control Symposium(IFCS).

Characteristics of Space Mini Passive Hydrogen maser in Shanghai Astronomical Observatory

Xie Yonghui, Shuai Tao, Chen Pengfei, Pei Yuxian, Shen Chao, Pan Xiaoyan, Zhao yang, and Lin Chuanfu
Shanghai Astronomical Observatory
Chinese Academy of Sciences
Shanghai, China
xyh@shao.ac.cn

***Abstract*—Shanghai Astronomical Observatory is developing space mini passive hydrogen maser for future application in satellite navigation system. Study on key technologies, including miniatured cavity-bulb assembly, absorption pump and magnetic state selection system, have been carried out. Weight of physical package is controlled within 10kg and atomic signal is up to 2dB. Miniatured electronic package weight of 5Kg is developed while keeping system framework as conventional time-separated control method. Engineering model weighting 14.5Kg has been developed. Frequency stability of $1.2\times10^{-12}t^{-1/2}$(1s≤t≤10000s) and temperature coefficient of 5×10^{-14}/℃ are measured. Engineering modification and environmental test are carried out.**

Keywords—passive; mini; hydrogen maser;

I. INTRODUCTION

Passive hydrogen maser (PHM) has the best frequency stability performance, typically less than 5E-15/day, currently available for Global Navigation System (GNSS), and its frequency drift is in the order of E-15, much better than widely used rubidium clock. Dozens of PHM have been employed in CALILEO since 2008[1] and Beidou system since 2015, and have shown remarkable performance advantage and capacity of long term operation in space. Weight and volume much exceeding that of rubidium clock are main shortage of PHM, this is strictly restricted in space application. Some research institutes have devoted in development of mini PHM[2] and have achieved progress. Shanghai Astronomical Observatory has long history of research on PHM and study on Mini PHM had been carried out since 2010. Key components of physics package, which contains 2/3 of total weight, have been redesigned, while parameters are kept as conventional PHM. Mechanical structure of the PHM, especially microwave cavity, absorption pump and ion pump, are optimized to keep the mechanical strength. Thermal design is another focus for its importance in temperature coefficient and long-term performance. Performance tests, including temperature coefficient, vibration and magnetic test, are also carried out.

II. PHYSICS PACKAGE

In Physics package of mini PHM, hydrogen atoms make transition and emitting microwave signal with precise frequency, by which the VCXO is locked and high performance output is realised. Key component of Physics package is cavity-bulb assembly, where hydrogen atoms take transition and microwave energy collected. Parameters of cavity-bulb assembly, such as cavity Q factor, filling factor, storage time and relaxation rate directly determine system performance [3]. Absorption pump and ion pump form vacuum system are employed to keep the vacuum environment in storage bulb. Hydrogen is supplied by hydrogen source, purified by nickel tube and dissociated into atoms in discharge bulb. Atoms in high state is selected and focused into storage bulb by quadripole state selector. Magnetic shields surround the cavity-bulb assembly prevent influence from ambient magnetic field.

Comparing to widely used magnetron cavity, novel electrode microwave cavity has advantage in Q factor and weight, and has been applied successfully in our 23kg space PHM. Its mechanical property and reliability have been proved to satisfy space application by dozens of vibration test and years of practical operation in space. So it is still adapted in mini space PHM.

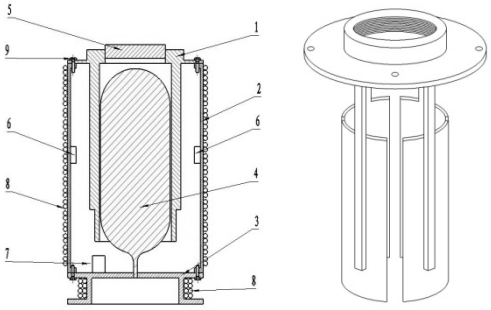


Fig. 1. structure of novel kind of electrode cavity(left) and electrode tube(right). 1 : electrode tube ; 2 : cylinder cavity ; 3 : base plate ; 4 : storage bulb ; 5 : frequency adjust knob ; 6 : coupling loop ; 7 : varactor diode loop ; 8 : thermal control coil

Redesign of the cavity-bulb assembly especially reduction of cavity diameter and length is key factor of mini PHM design. Cavity resonance frequency and filling factor must be maintained; because of this structure parameters such as bulb size, diameter and gaps of electrode are optimized. Cavity Q factor at about 6000 is realized by silver plating of the cavity surface and properly reduction of antennas of varactor and microwave coupling loop. Cavity tuning range of varactor is

set up to 200KHz to ensure cavity resonance frequency in control in the whole life time.

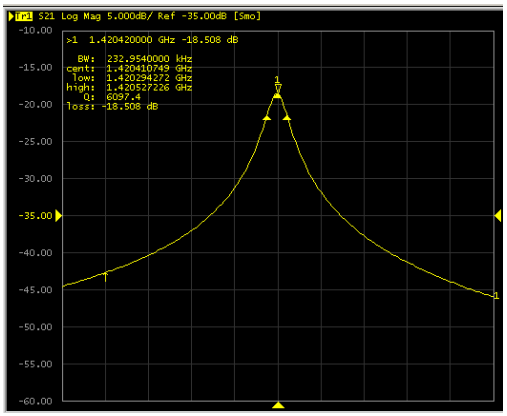


Fig. 2. Cavity resonance characteristics

Getter material is changed from traditional titanium getter to new getter material with lower activation temperature of 500 ℃, and Getter package is transformed from thin plate to small piece of 25mm in diameter, totally 400g of getter pieces are filled in the pump and String together by heater strip. Smaller piece of getter provides more absorption area and coinciding higher pumping speed while absorption ability of 40bar*L H2 is ensured. Ion pump is put far away from the cavity-bulb assembly to prevent influence from the pump magnetic field, and a smaller ion pump of 1L is equipped in the vacuum system to eliminate residual gases. Operating current of the ion pump is greatly reduced to less than 0.5uA under new pump structure design, which is sufficient for 12 years operation.

Magnetic shielding system is composed of 4 layers of 1J85 cylinders. Diameters of the shielding are reduced following the cavity miniature and shielding effect is improved accordingly.

Other major parts of redesign for physics package of mini PHM are listed below:

- Ion pump for outer vacuum system is omitted and vacuum valve is employed temporarily at ground test stage.
- Redesign of thermal control layers and thermal structure.
- Size of hydrogen supply is compressed to install into physics package with 40L of H2 reserved.
- Miniature of dissociator with discharge power maintained.

Weight of physics package is finally controlled within 9.5Kg, and atomic signal is up to 3dBm at -80dBm input and 4Hz in width. Theoretical frequency stability is better than $7\times 10^{-13}/t^{-1/2}$ [4].



Fig. 3. Physics package of mini PHM

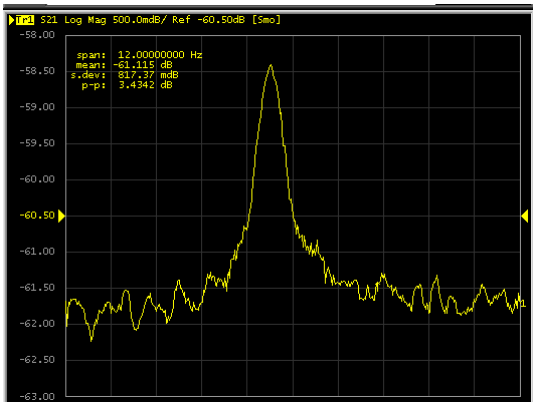


Fig. 4. Atomic signal of physics package of mini PHM, microwave input is -80dBm, span is 50Hz

We have carried out vibration test of the physics package. Structures of key components including cavity-bulb assembly, magnetic shielding system and the getter are proved to be firm enough for 14grms of vibration. Parameters and performance of these components are stable after the test.

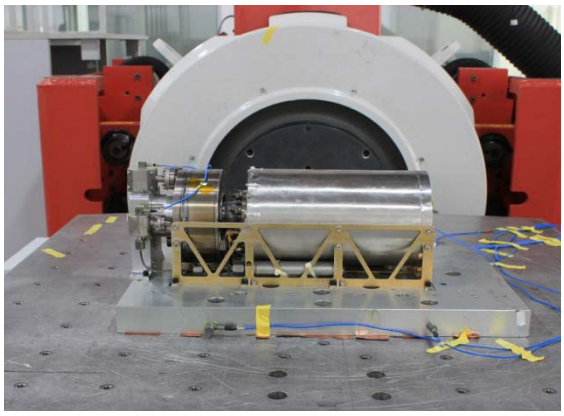


Fig. 5. Vibration test for key components of the physics package

III. ELECTRONICS PACKAGE

Time-separated control method for the two control loop is still employed in electronics package of mini PHM. This scheme has been studied for a long period in our laboratory and is proved to have advantage in long term frequency stability and drift. Its performance and reliability are verified by Application in our 23kg space PHM.

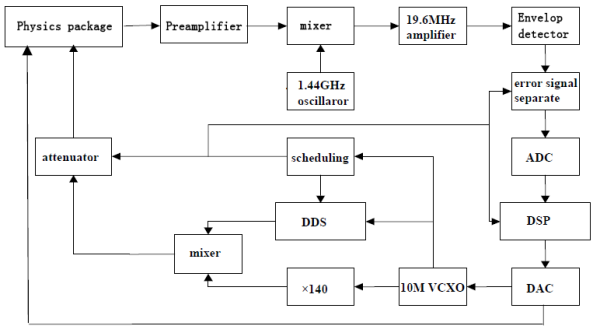


Fig. 6. Block-diagram of electronics package

Major works of miniaturization and optimization for electronics package of mini PHM are listed below:

- Modules of electronics package are rearranged and modules with similar function are integrated.
- Single operational amplifiers are replaced by dual operational amplifiers.
- Thickness of outside shell is decreased while fulfilling anti irradiation demand.
- DA converter in servo unit is upgraded to 16 bits to further diminish additional noise.
- Loop parameters of servo unit modified according to atomic signal of mini PHM.

In the end 30% of volume reduction and 25% of weight reduction are achieved in electronics package.

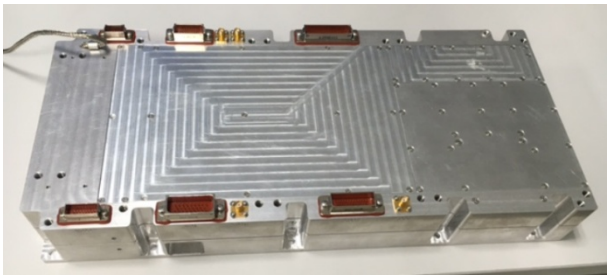


Fig. 7. Structure of electronics package

IV. PERFORMANCE TEST

Mini PHM is developed based on above-mentioned physics package and electronics package.

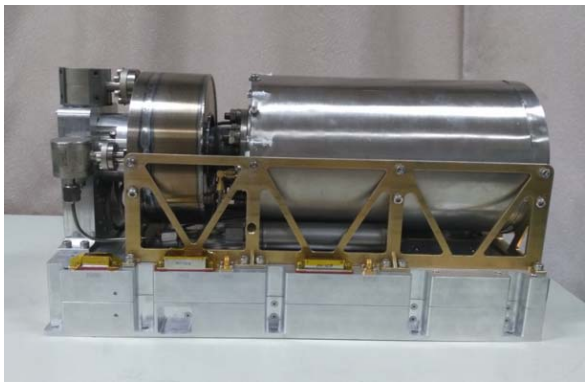


Fig. 8. Structure of mini PHM

After optimization of loop parameters such as input microwave power, demodulation phase, amplification factor of error signal, etc. we carried out performance test includes temperature coefficient, magnetic coefficient, frequency drift and frequency stability.

Temperature coefficient in atmosphere environment is test between temperature from 20℃ to 36℃. Frequency shift is 1.2×10^{-13} and corresponding temperature coefficient is 7.5×10^{-14}/℃. Temperature coefficient in vacuum is expected to be less for better thermal control efficiency of physics package;

Magnetic coefficient is benefit from 4 layer of magnetic shield and low magnitude of C field, and has been measured by 2Gauss of environment magnetic change produce by Helmholtz coil. Frequency shift less than 6×10^{-13} is measured, which means magnetic coefficient less than 3×10^{-13}/Guass.

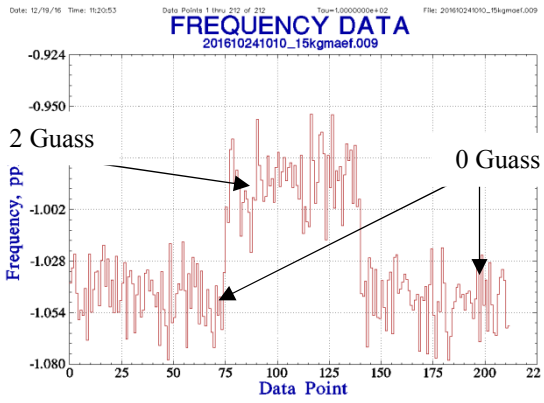


Fig. 9. Result of magnetic coefficient test, averaged by 100s

With benefit of modification in physics package, electrical package and loop parameters, frequency stability performance of the space mini passive hydrogen maser has achieved continues improvement. Long-term performance test is carried out in temperature controlled environment for more than 17days. Frequency drift is measured to be 5.8×10^{-15}/day and frequency stability is $1.2\times10^{-12}/t^{-1/2}$(1S～10000S),$7.6\times10^{-15}$/1day with drift not removed. Better frequency stability result is expected in vacuum environment with less temperature fluctuation.

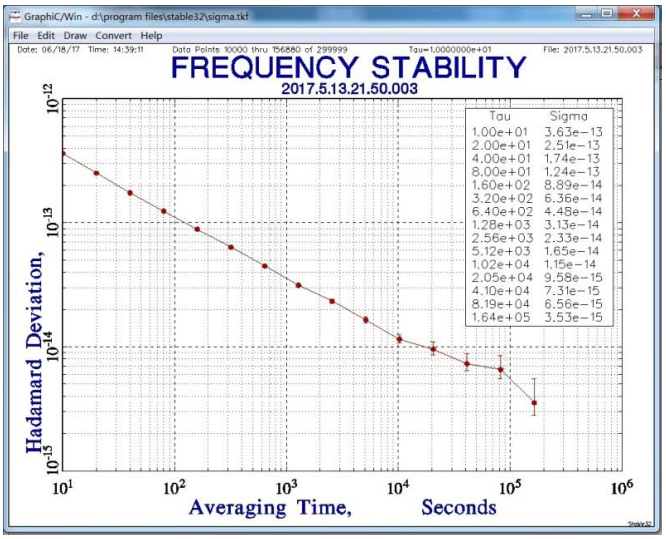


Fig. 10. Hadamard deviation of 17 days test

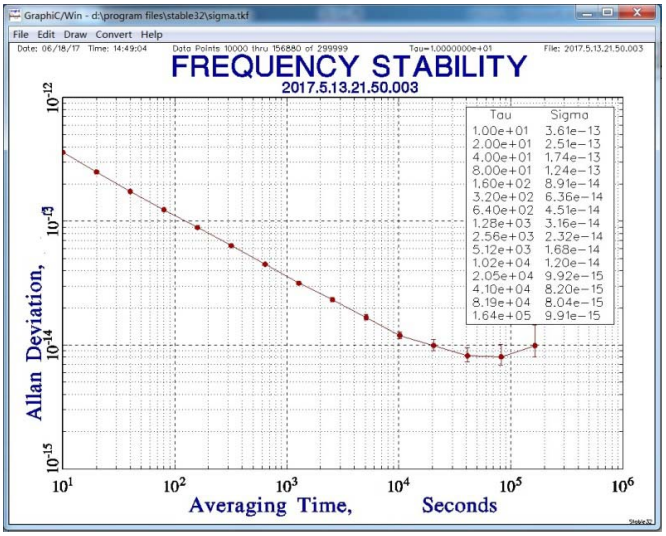


Fig. 11. Allan deviation of 17 days test (drift not removed).

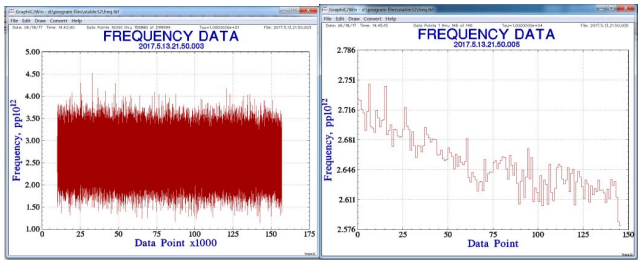


Fig. 12. Fractional frequency offset of 17 days test, sampling by 1s at left and average by 10000s at right.

V. CONCLUSIONS

Prototype of mini PHM is developed in Shanghai Astronomical Observatory. Comparing to previous PHM, Mini PHM has 35% of weight reduction and corresponding size and power consumption compression, while its performance, such as frequency stability and drift, is maintained, which contribute to wider application of PHM. Development of engineering models is now in progress.

REFERENCES

[1] Qinghua Wang, Pierre Mosset, and Fabien Droz, "Life time of space passive hydrogen maser," European Frequency & Time Forum & international Frequency Control Symposium, 2014;973-976

[2] Marco Belloni, Marina Gioia, Simone Beretta and Giovanni Busca, "Space mini passive hydrogen maser for space applications," Frequency Control and the Eruopean Frequency and Time Forum, 2011 joint coference of IEEE international, San Francisco.

[3] N.A.Demidov, A.A.Belyaev, B.A.Sakharov, and A.A.Uljanov, "Passive hydrogen maser frequency stability and accuracy investigation," 7th EFTF Meeting, Neuchatel, 1993.

[4] Qinghua Wang, Pierre Mosset, Fabien Droz, and Pascal Rochat, "Verification and ptimization of the physics parameters of the onboard galileo passive hydrogen maser," 38th PTTI Meeting, Washington, pp.1-13, 2006.

Progress towards Chip-Scale Atomic Clock in Peking University

Jianye Zhao*, Ruiyuan Liu, Hongling Meng, Ermeng Hu, Canbin He, Zhong Wang
School of Electronics Engineering and Computer Science
Peking University
Beijing, China
zhaojianye@pku.edu.cn

***Abstract*—In this papar we reported our progress toward chip-scale atomic clock (CPT) based on the ^{87}Rb coherent population trapping (CPT) transition. During last year, we did great work in improving the performance of our CSAC, especially in frequency drift and long-term frequency stability. It is a remarkable achievement that the amplitude of the drift is around 7.0×10^{-12}/day and long-term stability is around 6.7×10^{-12} at 10^5s.**

Keywords—CSAC; CPT; Atomic clocks; Long-term stability

I. INTRODUCTION

Atomic clocks play an essential role in the timing and synchronization of modern communications and navigation systems. Since the idea of chip-scale atomic clocks (CSACs) based on coherent population trapping (CPT) transition was proposed in [1] , application value of CSACs has been increasingly emerged awing to its portability, battery-powered consumption and potential excellent performance. Micro-Electro-Mechanical System (MEMS) alkali atom vapor cell developed in CSAC more than ten years ago [2] pushed forward lots of work on the lower power consumption and smaller volume in world wide [3,4]. However, for an atomic clock, accurate and stable frequency output is also critical. Buffer gas control, temperature accuracy, magnetic field stability [5] and alternating electric field of the laser have noticeable impact on frequency output. In addition, modulation method, laser intensity, frequency and microwave power are crucial causes of frequency instability due to light shift. For these reasons, poor long-term stability and significant frequency shift of such an atomic clock have been preventing its practical application in the rapid emergence of broadband and secure communications.

In order to improve outputting performance of CSACs, our group dedicated to demonstrate a simple implementation of ^{87}Rb CSAC with a reduced frequency drift rate and a moderate long-term stability.

II. ATOMIC CLOCK PHYSICS

In CSACs, kinds of negative factors (buffer gas, external field and light field) of frequency shift and frequency instability stem from physics package components. Therefore, our research was carried out based on physics package. Fig.1 detailed exploded view of a typical physics package, including a Vertical-Cavity Surface Emitting Laser (VCSEL) with an operating wavelength 794.9nm(+/-0.5nm), an attenuator, a λ/4 wave plate, a ^{87}Rb vapor cell with a solenoid, a heater and a photodetector (PD). Physics package is assembled and integrated by a thermal conductive frame and connects to servo circuit through a leadless chip carrier (LCC). The linearly polarized light emitted from VCSEL is converted to circularly polarized light by a quarter waveplate and passes through a moderate attenuator. A heater is used to warm up VCSEL and Alkali vapor cell with 5mK temperature accuracy. After passing through the cell, the light is collected by a photodetector (PD) and light intensity is converted to electrical signal. A solenoid is used to generate constant magnetic field to lift up degeneracy of Zeeman levels and a shield is used to protect physics package from spurious environmental magnetic fields.

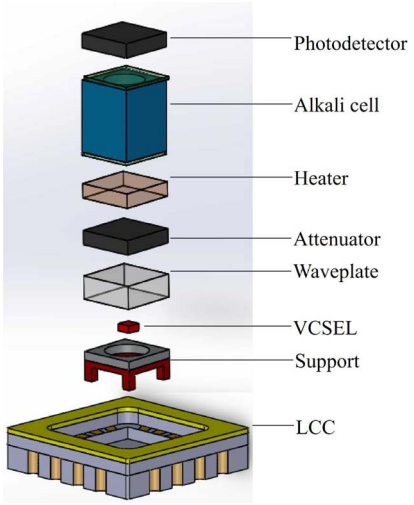


Fig.1. Physics package architecture

^{87}Rb atom can be simplified as a three-level Λ-type system. As illustrated in Fig.2, both hyperfine components of the ground state $S_{1/2}$ of an alkali atom are coupled to a common excited state by two coherent laser fields ω1, ω2. If the frequency difference of laser fields gets close to the atomic hyperfine splitting of the two ground states, quantum coherence between the two hyperfine components will be effectively generated. In our clock, VCSEL modulated by 3.4GHz radio frequency emits linearly polarized dichromatic ~795 nm light, which serves as coherent laser fields.

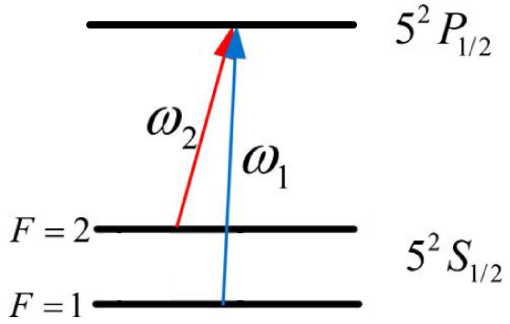


Fig. 2. Simplified representation of three levels of the ^{87}Rb atoms.

III. ELECTRONICS DESIGN

In our work, combination of electronics and physics ensures good performance of a CSAC. Once powered on, the clock can autonomously starts up and locks into the central frequency of CPT. Fig.3 is the Skematic of our CSACs. Microcontroller MSP 430 is the core of the processing. Initially, a given temperature and magnetic field keep the clock in proper working condition. After that, a direct current source controlled by MSP430 drives VCSEL and locked by absorption-locking loop. In CPT-locking loop, a temperature compensated crystal oscillator (TCXO) outputs 10MHz frequency which is multiplied around 340 times and a 3.4 GHz RF source is synthesized. These two current source are modulated and injected into VCSEL[6]. Signals are taken by photodetector and separated by two operational amplifiers. Also, the error signals obtained by a lock-in amplifier are used to provide feedback to the driven current and thus to lock the laser's wavelength to the absorption line. Then, the servo sequences to scan the microwave frequency with an FM modulation rate, and the error signal taken by another lock-in amplifier aims to provide feedback for the frequency of the microwave. The digital error signals in MSP430 are filtered and demodulated by a servo algorithm, based on discrete Fourier transformation (DFT) algorithm. As a result, the frequency of the crystal oscillator is stabilized to the CPT atomic resonance and stabilized 10MHz frequency is output.

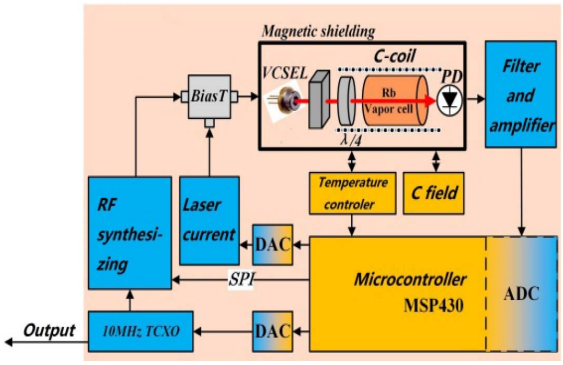


Fig.3. Block diagram of chip-scale atomic clock

IV. EXPERIMENTAL RESULTS

Light shift in the clock is viewed as a combined effect between the atomic energy level and multi-frequency laser fields. In view of the effect, we propose two optimization schemes to improve long-term stability. 1) Relative low light intensity. It aims to reduce frequency shift sensitivity to light intensity[7]. 2) Relative high modulation index of RF power. It aims to reduce light shift factor and disperse laser power to more multi-frequency sidebands and reduce frequency shift sensitivity to laser frequency detuning[8]. Fig.4 indicates CPT resonance frequency shift as a function of the light intensity with different microwave powers. The dashed guide line is fitted for same microwave power. The different light intensities are realized by attenuators with three different attenuation coefficients, 97%, 95% and 90%, and generate three group of data A, B, and C. In each light intensity, CPT resonance frequency is locked at six different microwave powers. From Fig. 4, it clearly shows that the frequency shift changes linearly with the light intensity and microwave power of −0.35 dBm is well fitted for a low frequency sensitivity to the light intensity.

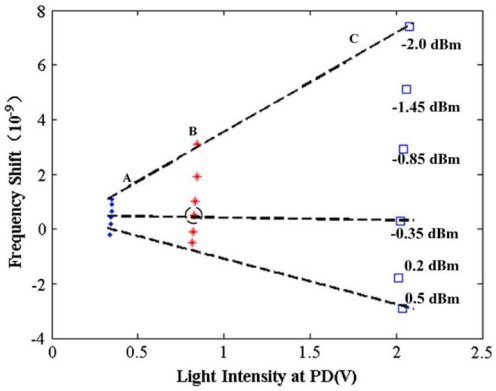


Fig.4. Frequency shift as a function of the light intensity and microwave power in the CSAC.

Considering a demanding for SNR (signal to noise ratio) and frequency stability, we use a moderate 95% attenuator and microwave power of −0.35 dBm. SNR is guaranteed to achieve good short-term stability and long-term stability is optimized by proper microwave power. Results are shown in Fig.5 as Allan Deviation vs averaging time. Although volume and power are limited in 16cm^3 and 200mW, our CSACs' long-term frequency stability is improved to 6.7×10^{-12} at 10^5 s and the frequency drift is reduced to 7.0×10^{-12}/day.

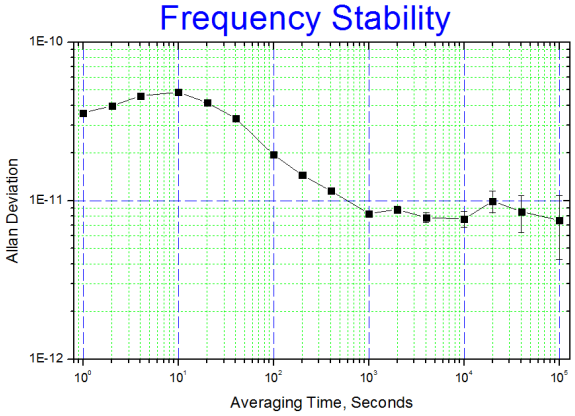


Fig.5. Long-term stability of CSAC

ACKNOWLEDGMENT

This work was supported by the National Natural Science Foundations of China under Grant 61535001.

REFERENCES

[1] J. Kitching, S. Knappe, and L. Hollberg, "Miniature vapor-cell atomic-frequency references," Appl. Phys. Lett. **81**, 553 (2002).

[2] L. Liew, S. Knappe, J. Moreland, H. Robinson, L. Hollberg, and J. kitching, "Microfabricated alkali atom vapor cells," Appl. Phys. Lett, **84**, 2694 (2004).

[3] R. Lutwak, P. Vlitas, M. Varghese, M. Mescher, D. K. Serkland, and G. M. Peake, "The MAC – a miniature atomic clock," in Proceedings of the 2005 IEEE International Frequency Control Symposium and Exposition, 752 (2005).

[4] R. Lutwak, A. Rashed, M. Varghese, G. Tepolt, J. LeBlanc, M. Mescher, D. K. Serkland, K. M. Geib, G. M. Peake, and S. Römisch, "The chip-scale atomic clock – prototype evaluation," in the 39th Annual Precise Time and Time Interval (PTTI) Meeting, 269 (2008).

[5] K. Shenoi, Synchronization and Timing in Telecommunications (BookSurge Publishing, Charleston, 2009).

[6] Xing, Cheng, et al. "Low power chip-scale CPT atomic clock with new microwave frequency modulation technique." IEEE International Frequency Control Symposium 2014:1-3.

[7] C. Affolderbach, C. Andreeva, S. Cartaleva, T. Karaulanov, G. Mileti, D. Slavov, "Light-shift suppression in laser optically pumped vapour-cell atomic frequency standards," Appl. Phys. B **80**, 841 (2005).

[8] V. Shah, P. D. D. Schwindt, V. Gerginov, S. Knappe, L. Hollberg, J. Kitching, "Active light shift stabilization in modulated CPT clocks," in Proceedings of 2006 IEEE International Frequency Control Symposium and Exposition, pp.699-701, 2006.

Analytical Expressions for Parameters of the Dark Resonance in a Vacuum Vapour Cell

Denis V. Brazhnikov
Institute of Laser Physics SB RAS,
Novosibirsk, Russia
&
Novosibirsk State University,
Novosibirsk, Russia
brazhnikov@laser.nsc.ru

Moustafa Abdel Hafiz,
Grégoire Coget,
Rodolphe Boudot
Department of Time and Frequency Standards,
FEMTO-ST, CNRS, UBFC
Besançon, France
rodolphe.boudot@femto-st.fr

***Abstract*—In spite of great number of papers devoted to theoretical and experimental study of the coherent population trapping phenomenon (CPT), still there is a lack of analytical results for the properties of the CPT-caused dark resonance in some principal cases. We will present the results of our study for single and double Λ schemes of atomic energy levels, which are of great importance for various applications of CPT (atom clocks, magnetometers, etc.). Analytical expressions for width and amplitude of the dark resonances have been obtained, which are valid for wide range of light wave intensities. The results concern closed as well as open Λ schemes. We will also discuss the difference between the two Λ schemes and state the condition when a double scheme can be effectively treated as a single Λ scheme. The analytical approximate formulas obtained have been compared with exact numerical solutions based on the optical Bloch equations as well as experimental.**

Keywords—coherent population trapping; dark resonance; vapour cell; density matrix; quantum metrology

I. INTRODUCTION

Coherent population trapping phenomenon (CPT) has been attracting great interest during long time since its discovery in 1976 [1]. It has found numerous applications in laser physics and spectroscopy, nonlinear optics, laser cooling of atoms, quantum metrology and quantum informatics. The basic model underlying the description of CPT is a single Λ scheme of atomic energy levels [2, 3] (Fig. 1a). Also there is a double Λ scheme (Fig. 1b), which is relevant for some applications too, especially for atom clocks.

Dark resonance is the main spectroscopic manifestation of CPT. It can be observed as a narrow dip in absorption (or fluorescence) property of a vapour cell, when it is being irradiated by the resonant light waves. One of the main conditions is that the two-photon (Raman) frequency detuning must be close to zero [2, 3]. The brilliant feature of the dark resonance consists in its potentially small width, which can be much smaller than the natural linewidth γ of optical transition.

In spite of a really huge number of papers in the direction of CPT and its applications, none of them gives any clear analytical expression for the width and amplitude of the dark resonance in the case of a vacuum vapour cell beyond the perturbation theory limits. Several works contain such kind of analytical expressions only for electromagnetically-induced transparency (EIT) regime, when one of the laser waves is much weaker than the other, i.e. $I_p << I_c$ [4, 5]. At the same time, there are a lot of experimental data as well as numerical calculations for the parameters of dark resonances under the CPT regime ($I_p \approx I_c$) in vacuum cells (e.g., see [6-8]). Only analytical expressions valid for wide range of intensities, which can be found in the literature, are some phenomenological approximate formulas to fit experimental curves, which do not follow directly from any theoretical analysis.

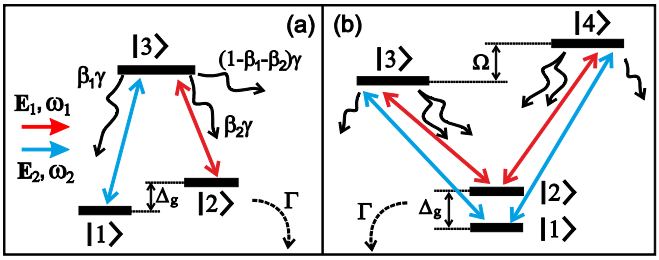


Fig. 1. Single (a) and double (b) Λ schemes of atomic energy levels.

Here, due to the lack of space, we briefly present the results of analytical study of the single Λ scheme only. Analytical expressions for the dark resonance parameters have been derived under several assumptions. In particular, we assume power broadening is the main source of the dark resonance broadening, without taking into account time-of-flight relaxation or residual Doppler broadening (due to difference of absolute values of the wave vectors). The Λ scheme is also assumed to be closed system of levels. These conditions allow us obtaining explicit and relatively simple analytical formulas for the dark resonance parameters, which are valid for wide range of the light wave intensities until Doppler width $k\upsilon_0$ (with υ_0 the most probable thermal velocity in a gas) is much larger than the Rabi frequencies of optical transitions. The latter condition is regularly satisfied in experiments with CPT in a thermal gas. In this abstract we take one-photon frequency

The authors thank LabeX FIRST-TF and Région de Franche-Comté. D.V.B. also thanks RFBR for the support (grant no. 15-02-08377).

detuning equal to zero, just for shortness. Our analytical results have been compared with the experimental data obtained with a cesium vapour cell (to be presented during the Conference).

II. SINGLE Λ SCHEME

Here, for shortness, we focus only on a closed scheme of levels (Γ=0) and assume branching ratios to be equal: $\beta_1=\beta_2=1/2$, as well as the Rabi frequencies: $R_1=R_2=R$ (see Fig. 1a). Then, using the density matrix formalism, we come to the expression for the excited state population:

$$W_\Lambda = \frac{4R^2\Delta^2}{4\Delta^2 x^2 + 16R^4 + \Delta^2\left(\gamma^2+\Delta^2\right)+4\Delta^2R^2} \qquad (1)$$

Here $\Delta=\omega_1-\omega_2-\Delta_g$ is the two-photon (Raman) detuning with Δ_g the frequency difference between ground-state levels, $x=k\upsilon$ is the Doppler frequency shift for a moving atom. Spontaneous relaxation rate of the excited state is equal to γ.

The spectroscopic signal is proportional to $\langle W_\Lambda\rangle_\upsilon$:

$$\left\langle W_\Lambda\right\rangle_\upsilon = \frac{1}{\sqrt{\pi}\upsilon_0}\int_{-\infty}^{+\infty} W_\Lambda\, e^{-\upsilon^2/\upsilon_0^2}\, d\upsilon \qquad (2)$$

Inserting (1) to (2) one can easily obtain the exact solution expressed through the error function [4]. However, it is not convenient for our theoretical analysis, because in general it cannot provide us with some relatively simple expression for width and amplitude of the resonance. Therefore, the main problem consists in finding the most convenient approximation for (2). Also it would be very useful, if this approximation is valid for wide range of light wave intensities.

Let us write the final approximate formula for the dark resonance width in a vacuum vapour cell:

$$\mathrm{FWHM} \approx \frac{8R^2}{k\upsilon_0\,\xi_1(R)} \qquad (3)$$

with the dimensionless functions of R:

$$\xi_1(R) = \sqrt{\frac{2}{\pi}\left[1+\xi_0(R)-\sqrt{1+2\xi_0(R)}\right]}$$

$$\xi_0(R) = 4\eta\left(1+\eta\right)\ , \qquad \eta = \frac{\sqrt{\pi}}{2k\upsilon_0}\sqrt{\gamma^2+12R^2}$$

Fig. 2 shows the expression (3) is quite good approximation for wide range of intensities (compare solid blue and dashed black curves). If condition $R\lesssim\gamma$ is satisfied, expression (3) can be reduced to the following:

$$\mathrm{FWHM}\Big|_{R\le\gamma} \approx \frac{4R^2}{\sqrt{\gamma^2+12R^2}} \qquad (4)$$

One can see that under the weak-field regime the width is linearly proportional to the intensity (as far as $I \sim R^2$). An expression for the resonance amplitude can be obtained analogically, see exp. (5).

It may seem that the closed double Λ scheme is equivalent to the closed single Λ scheme, if the coherence between $|3\rangle$ and $|4\rangle$ upper-state levels is neglected (see Fig. 1b). Indeed, the single Λ scheme does not have this type of coherence (see Fig. 1a). However, it will be shown that only the coherence taken into account makes two closed Λ schemes equivalent (with the effective substitution $R_\Lambda=\sqrt{2}\,R_{\Lambda-\Lambda}$).

$$A_0 \approx \frac{4\pi R^2}{(k\upsilon_0)^2\,\xi_0(R)} \qquad (5)$$

The other theoretical and experimental results will be presented and discussed in details during the poster session.

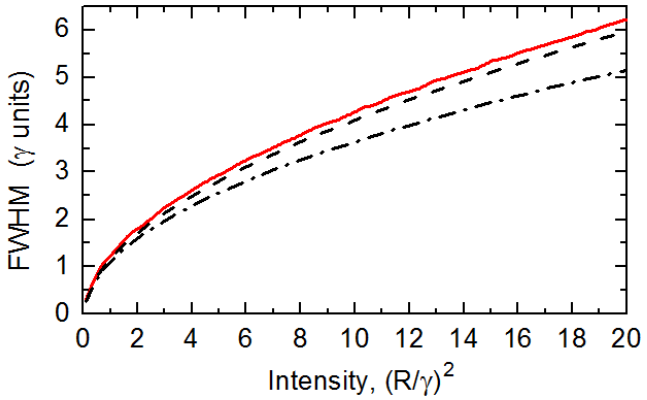


Fig. 2. Width of the dark resonance in a vacuum vapour cell for a single Λ scheme versus the light-wave intensity. Doppler width $k\upsilon_0$ equals to 50γ (typical for the experiments with thermal alkali-metal atoms). Solid line corresponds to the numerical calculations on the basis of the accurate expression (2), while dashed line corresponds to the approximate formula (3). The dashed-dotted line is explained by the simple expression (4), which is valid for the weak and moderate light fields ($R\lesssim\gamma$).

ACKNOWLEDGMENT

D.V.B. thanks Dr. Emeric de Clercq (LNE-SYRTE, Paris) and Prof. Alexey V. Taichenachev (ILP SB RAS, Novosibirsk) for stimulating discussions.

REFERENCES

[1] G. Alzetta et al., "An experimental method for the observation of r.f. transitions and laser beat resonances in oriented Na vapour", Nuovo Cimento B, vol. 36, pp.5–20, November 1976.

[2] E. Arimondo and G. Orriols, "Nonabsorbing atomic coherences by coherent two-photon transitions in a three-level optical pumping", Lett. Nuovo Cimento, vol. 17, pp.333–338, November 1976.

[3] H. R. Gray, R. M. Whitley, and C. R. Stroud, Jr., "Coherent trapping of atomic populations", Opt. Lett., vol. 3, pp. 218–220, December 1978.

[4] A. V. Taichenachev, A. M. Tumaikin, and V. I. Yudin, "Influence of atomic motion on the shape of two-photon resonance in gas", JETP Lett., vol. 72, pp. 119–122, August 2000.

[5] A. Javan et al., "Narrowing of electromagnetically induced transparency resonance in a Doppler-broadened medium", Phys. Rev. A, vol. 66, 013805, July 2002.

[6] C. Y. Ye and A. S. Zibrov, "Width of the electromagnetically induced transparency resonance in atomic vapor", Phys. Rev. A, vol. 65, 023806, January 2002.

[7] S. Khan et al., "Coherent population trapping (CPT) versus electromagnetically induced transparency (EIT)", Eur. Phys. J. D, vol. 71, art. no. 38, February 2017.

[8] R. A. Malitskiy et al., "Magneto-optical CPT resonances in rubidium excited by femtosecond laser comb", Proc. of SPIE, vol. 7993, 799312, January 2011.

An electronic controller based on FPGA for the Ramsey-CPT Atomic Clock

Pengfei Cheng*†, Xiaolin Sun*†, Fengwei Liu*‡, Daonong Zhang¶, Jianwei Zhang†‡, Lijun Wang*†‡
*Department of Physics, Tsinghua University, Beijing 100084, P. R. China
†State Key Laboratory of Precision Measurement Technology and Instruments, Tsinghua University
‡Department of Precision Instrument, Tsinghua University, Beijing 100084, P. R. China
¶North China Power Engineering CO.，LTD, Beijing 100084, P. R. China
zhangjw@tsinghua.edu.cn

***Abstract*—**High performance compact microwave atomic clocks are on great demand in many areas. Different schemes are proposed to improve the performance and minimize the size of an atomic clock. Vapor cell atomic clocks based on Ramsey-CPT (coherent population trapping) are very promising due to its simple all optical configuration. In this paper, we report an integrated electronic controller based on a FPGA (Field Programmable Gate Array) for our Ramsey-CPT clock.

Keywords—FPGA; Data acquisition systems; Ramsey-CPT; atomic clock

Atomic clocks based on Ramsey-CPT are compact with relative high performance[1],[2], which can be used in the areas of satellite navigation, high-speed communication, power grid, and so on. We demonstrated a Ramsey-CPT clock with lin-par-lin CPT configuration and dispersion detection[3], which has the protential to be miniaturized for its simple architecture. Due to the high speed and powerful parallel processing, FPGA are introduced as the electronic controller.

In order to the implement the Ramsey-CPT technique, the coherent dichromatic laser are pulse-modulated at 1 kHz. The clock signal is sampled at every rising edge of the transmitted laser pulses with a delay of approximate 10 microseconds, and the sampling lasts several microseconds. Thus, the speed of data acquisition, processing and the controlling of the time sequense are crucial for the electronic controller to success the task of acquiring data and generat the feedback to lock the local oscillator. Traditional PC-based data acquisition cards cannot satisfied this demand of real time processing. A sample-and-hold amplifier was introduced previously to overcome this difficulty, which turned out to be unsuccessful[4]. Data acquisition systems based on FPGAs (DASF) have stable time-base and the ability of real-time data processing. For our Ramsey-CPT clock, a commercial DASF is applied to handle all the controlling tasks, including the feedback loop for the local oscillator, the controlling of the microwave phase shifting, the temperature of vapor cell, the actively stabilization of the pulsed laser power, and the generation of controlling time sequences. Furthermore, thanks to the powerful multitask performance of the DASF, some complex signal processing methods, such as the self-correlation and digital filters, can be implement in real-time data processing.

The schematic diagram of the Ramsey-CPT clock with the DASF is shown in Fig. 1. The commercial DASF (NI USB-

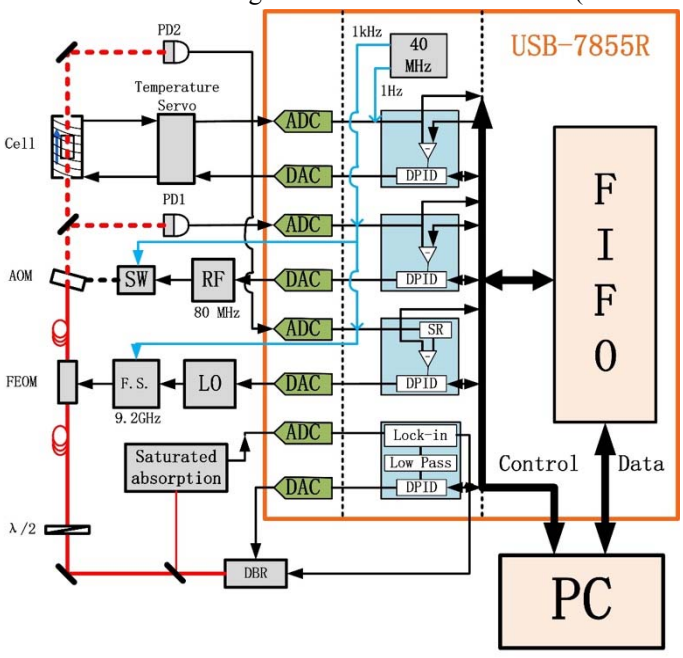


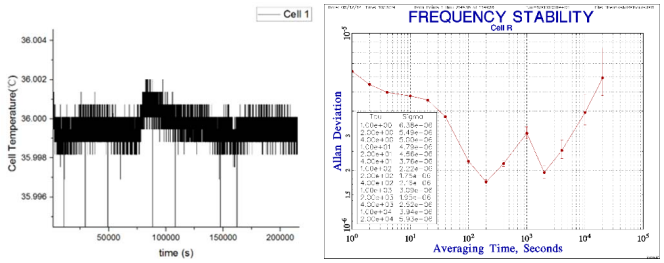
Fig. 1. Schematic diagram of the experimental setup. PD: photo detector; SW:switch; F.S.: frequency synthesizer; LO: local oscillator; DPID: digital proportional–integral–derivative controller; SR: shifting register; FIFO: first-in-first-out buffer; PC: personal computor; RF: radio frequency signal generator. Blue lines are the trigger signals to the phase modulator, the RF switch (SW), and the sampling trigger of ADCs. All of the DPIDs and operation parameters are controlled and set via the user interface program on PC.

This work is supported by the National Key Research and Development Program of China (No.2016YFA0302101), the National Natural Science Foundation of China (No.11304177), and the Initiative program of State Key Laboratory of Precision Measurement Technology and Instruments.

7855R with Kintex-7) has 8 channels of both 16-bits analog-to-digital-converters (ADCs) and 16-bits digital-to-analog-converters (DACs) with 1 MS/s sampling rate, and a 48-bits digital input/output (DIO) port. This DASF can be programmed using LabVIEW FPGA modules to shortened the development cycle. A distributed Bragg reflector (DBR) diode laser at 894 nm is used to excite ^{133}Cs D_1 lines. A fiber electro-optic modulator (FEOM) is used to generate the two coherent optical field, which is then pulsed by an acoustic-optic modulator (AOM).

The onboard resources of the DASF are sufficient to realize all of the controlling in the Ramsey-CPT clock. The operation parameters are monitored and set via a user interface program on PC developed using LabView.

The FPGA-LabVIEW programs, including the user interface on PC and the high-speed data acquisition and processing have been finished and tested. For the temperature stabilization of atomic cells, the output current of AD 590 is converted to a voltage signal by a transimpedance amplifier, and the voltage signal is sampled via on board 16-bits ADC in 1 kHz and averaged every 1000 samples to obtain the temperature error data. The theoretical temperature resolution is 0.6 mK. The test results of temperature stabilization are shown in Fig.2. As we can see in Fig. 2, the long-term temperature fluctuation is in a range of several mK, and the Allan devition of temperature is less than 10^{-5} from 1s to 10000s.

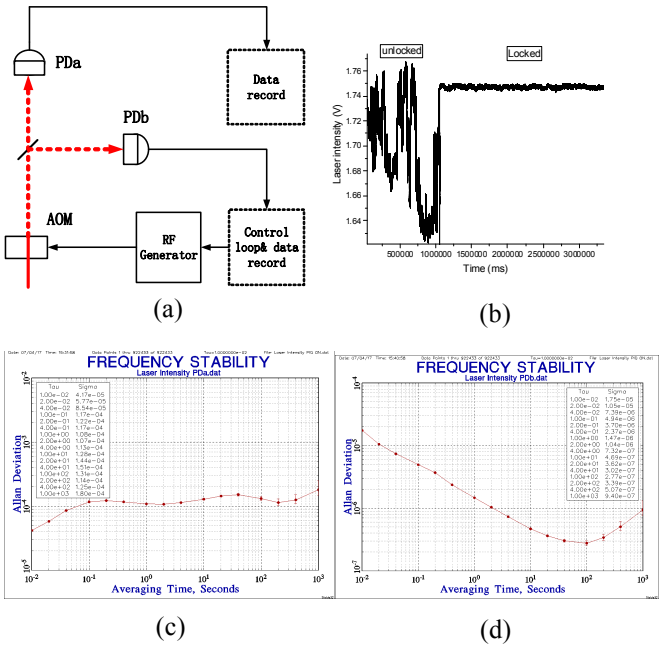


(a) (b)

Fig. 2. Temperature stabilization test results. (a) the temperature fluctions in 60 hours, (b) the Allan devitaion of relative stabilization.

The pulsed laser is generated by switching driving signal of the AOM. For the power stabilization of the pulsed laser, the power of the laser is detected by a photodiode (PD), and the power of the driving rf (radio frequency) signal is controlled by the DASF in real time. Figure 3 (a) is the schematic diagram of the laser power stabilization. Two identical fast PDs (PDA-36A, Thorlabs) are applied to detect the power of the pulsed laser simultaneously in and out of the feedback loop. The detected signals are digitalized with 1 MHz sampling rate. As shown in Fig. 3 (b), the laser power fluctuation with the feedback control is suppressed more than 20 times than free running. Since the laser pulse is splited by a BK7 window, the relative fluctuation of the laser power detected by two PD should be the same. However, the Allan deviations of the laser power detected by PDa and PDb are significant different, as shown in Fig. 3 (c) and (d). Laser power stabilization detected by PDb shows 1.75×10^{-5} @0.01s, and 2.77×10^{-7} @100s in Allan devition, which is a fantastic result. But the results detected by PDa are 4.17×10^{-5}@0.01s and 1.33×10^{-4} @100s , respectively. The reason for these difference is still under investigation.

In summary, based on the preliminary results of cell temperature and pulsed laser power stabilization, FPGA shows its superiority in the applications of atomic clocks for its high speed data acquisition, processing capacity and the variety convenience for digital processing. The digital controller for the LO frequency lock and the laser frequency stabilization are also going to be tested soon. In the next phase, a customer designed FPGA board will be developed to replace the current commercial one, which will further reduce the size of electronic controller for our Ramsey-CPT atomic clock.



(a) (b)

(c) (d)

Fig. 3. Pulsed laser power stabilization test scheme and results. (a) a scheme of pulsed laser intensity setup; (b) fluctuation of laser intensity detected by PDa; (c) (d) ralative laser intensity Allan devition detected by PDa and PDb.

REFERENCES

[1] J. Vanier, "Atomic clocks based on coherent population trapping: a review", Appl. Phys. B Lasers Opt. **81**, 421-442 (2005).

[2] A. V. Taichenachev, V. I. Yudin, V. L. Velichansky and S. A. Zibrov, "On the unique possibility of significantly increasing the contrast of dark resonances on the D1 line of ^{87}Rb," JETP Lett. **82**, 398-403 (2005).

[3] X. L. Sun, J. W. Zhang, P.F. Cheng, C. Xu, L. Zhao, and L. J. Wang, "Investigation of Ramsey spectroscopy in a lin-par-lin Ramsey coherent population trapping clock with dispersion detection," Opt. Express 24, 4532-4541 (2016).

[4] P. F. Cheng et al., "A vapor cell atomic clock of ^{87}Rb based on Ramsey-CPT with dispersion detection," 2016 IEEE International Frequency Control Symposium (IFCS), New Orleans, LA, 2016, pp. 1-3.

A merchandized optically pumped Cesium atomic clock

Yuanhong Cao, Xingwen Zhao, Wei Xie, Qiang Wei, Lin Yang,
Haijun Chen*, Shougang Zhang +
Chendu Spaceon Electronics CO., LTD., Chengdu, China
*CETC-12 institute, Beijng, China
+National Time Service Center, Chinese Academy of Sciences, Xi'an, China
E-mail: sccyh@163.com

***Abstract*—A merchandized optically pumped Cesium atomic clock has been realized in China recently. This clock was studied and designed under the support from Chinese National Key Scientific Instrument and Equipment Development Project. Experiencing the two steps of principal and engineering prototype, the clock starts to produce in small scale and comprehensively application tests by users. The tests show the performance of the clock can satisfy for applications' requirements and the producing procedure of the clock can qualify for massively manufacture according to manufacturing a common merchandise, which means the work of the project resolve the matter of Chinese localization Cesium atomic clock.**

Keywords—optically pumped; Cesium atomic clock; 5 G network; merchandized

I. INTRODUCTION (*Heading 1*)

In virtue of the high frequency accuracy, Cesium atomic clock has been popularly used as primary frequency standard to generate AT (atomic time) in national time laboratories in the world over 50 years[1]. Unfortunately, this traditional Cesium atomic clock based magnetic technique can not widely be applied in the industry areas such as telecom, power grid synchronization, being enslaved of complicated manufacture procession and high costs and controlled by few companies. Alternatively, the new Cesium clock based optically pumped technique cesium can remove the magnetic parts and electronic multiplier in the traditional clock and has achieved the combination of excellent accuracy and low cost. To make that clock as satellite atomic clock, there is Optically-pumped cesium beam frequency standard for GPS-III satellite in USA[2]; by OSCC project control, a space Cs beam optically pumped atomic clock prototype was made for Galileo as the frequency standard in the satellite system. Meanwhile, there are several optically Cesium atomic clock prototypes for civil application completed by France and Swiss. Although the formal products has never been available to buy, optically-pumped Cesium atomic clock is the representative of Cesium atomic clock technology at least[2]~[5]. Moreover, the telecom network including 5 G demands more accuracy of frequency standard in their Primary Reference Clock(PRC), which means Cesium atomic clock will necessary to develop to qualify for the applications in the future

In China, there is no own Cesium atomic clock product and industry, although several schematic prototypes were designed[6], which blocks Chinese accurate timing applications such as telecom network and power synchronization. Aiming to this market demanding and being supported by Chinese National Key Scientific Instrument and Equipment Development Project, Spaceon has been started up the optically pumped Cesium atomic clock project in 2009, and has fabricated the first industrial prototype has been realized in the end of 2014, and has made it merchandized in 2016 finally.

II. FINAL DESIGN IMPROVEMENTS

In our configuration of the clock at the final design, an elaborated Laser module locked by Cesium absorption spectrum line is used as the pumped source to upset the population of Cesium beam in the pumped area of Cesium beam; simultaneously, the partial one split from the Laser brunch and followingly shifted 251MHz is to probe atomic transition in the checking area of Cesium beam. Whereas, the atomic discriminated signal from checking area can lock the OCXO and the atomic frequency standard will be offered to users at last. According to stimulation and trial, the Cesium oven was redesigned to prevent Cesium leakage in movement and at high temperature condition. The Cesium mass was added properly, and the lifetime will be enhanced to 12 years. In Laser module, two layers shielded the saturation absorption cell and some optical devices were integrated, which will keep the wavelength and Laser intensity stable than before. Laser electronics samples the discrimination signal from the saturation absorption cell and synchronously discriminates the frequency with Cesium atoms. In addition, this Laser electronics can automatically find the saturation absorption spectrum line and go into the locked point. Especially, the Laser will be relocked while unlocked incident occurs. All the electronics including OCXO servo, RF circuits and temperature controller have been updated, and the clock's work parameters can be adjusted and recorded by PC locally or remotely. In order to cover the applications in telecom, a universal E1 module has be designed in the clock. To be conveniently used by costumers, we have designed a touch screen to show the clock status and operate the clock. The clock frame and other mechanics have been reinforced and the panel has been relocated simultaneously to work normally in

engineering rigorous condition. The main modifications made finally are show below in details.

A. Technical Design

All margins, column widths, line spaces, and text fonts are prescribed; please do not alter them. You may note peculiarities. For example, the head margin in this template measures proportionately large. This measurement and others are deliberate, please do not revise the values.

1) C-field Stability

As is known, microwave cavity is the key part for interaction between electric-magnetic field and Cesium, whereas C-field is generate the quantum direction by constant current. In that way, C-field is one of main elements to affect the long-term frequency stability and shall be elaborated in its design. Firstly, C-field uniformity is considered at 180 degrade of phase shift between the two interaction areas with complementary coils separately used to generate C-field and enhance the uniformity. Secondly, Cesium oven must be heated at a constant temperature point, and a heated controller is necessary. The same as the inside design, a digital PID is employed in the circuits, and ensures temperature stability below 0.003℃ by a very stable constant current source to regulate. According to the design, 1E-4 in non-uniformity and instability has been realized and can satisfy the beam requirements to keep the standard stability.

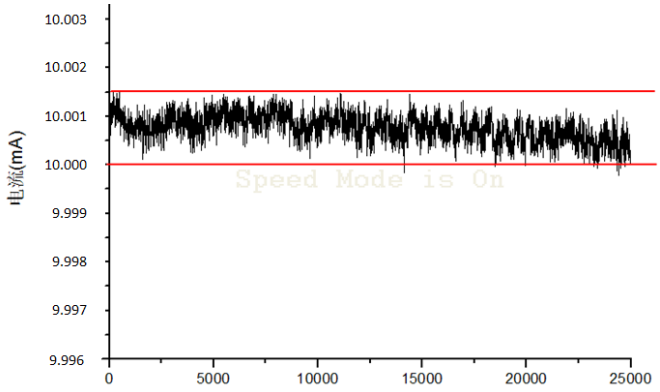


Fig. 1. C- field stability arives 1E-4 on 10mA by design a constant current circuit.

2) Modifying Lasr Control Electronics

In the clock, the Laser is to pump Cesium atom and check the clock transition simultaneously. It has two parts: Laser optical system and Laser electronics. In the optical system, a DFB Laser is used as the pumped source, which is locked at 852.1187nm of Cesium atom in a saturation absorption cell. In other side, part of the light is shifted 251MHz by an AOM to match the spectrum of F=4→F’ =5 transition in order to check the atom in the probe area. Laser optical system must be skillfully designed, finely fabricated and carefully adjusted so as to reduce the affection from vibration and temperature sensitivity. In our Laser optical system, an integrated design method has been adopted, and which could resolve above problem. Furthermore, all the optical devices will be mounted on a same plate by slots and reinforced by epoxy. In this way, electronic and magnetic interference from external surrounds can be isolated in an extent. The function of the laser electronics includes constant current power supply for Laser and locked circuit which control Laser frequency at Cesium D2 line by a Cesium saturation absorption cell. The Laser performance decides Cesium’s frequency standard stability. Moreover, this electronics cannot ensure Laser system locked in a long time, and sometimes the unlocked phenomena would occur. In our design, the automatic circuits have been used, and the dynamic course of the circuits which will scan the Laser current and locked on the Cesium saturation absorption point. Especially, the relocked status will be realized in two minutes if the Laser unlocked, which could help the Cesium clock satisfy kinds of applications such as Telecom. Therefore, a stable Laser is necessary to prepare. In the clock, a special structure for Cesium saturation absorption cell and Laser diode has been definitely designed and the 10^{-10}/s accuracy of the Laser is obtained finally, which is shown in figure 2.

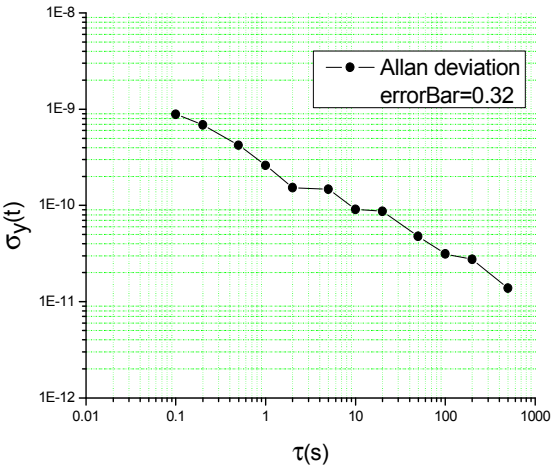


Fig. 2. The Laser frequency stablity is 2E-10/s by testing beat frequency.

3) Heat Sinking Simulation and Design

In the clock, Laser must work in very table temperature environment and heat sinking design is necessary to deliberate definitely. In the early design, some deficiency is exited and bring low efficiency in the heat sinking in side of the clock, and there a high10 degrade inward than outward.

In order to eliminate this deficiency, simulation has been applied to calculate the heat sinking parameters at the definite boundary condition. While simulating air streaming, the outcome shows that air streaming was blocked nearby wind fun and bring heat accumulation in the air routine. Basing on the heat sinking simulation, the modification for structure has resigned. Whereas, the heat sinking has completely changed and the inside temperature shows the improvement. That is, while the outside temperature is 50 degrade, the temperature close to Laser is 54.53 degrade shown in figure 3, and the clock works normally at more wide range of environment

This project was supported by Chinese National Key Scientific Instrument and Equipment Development Project (*No.2012YQ200183*).

temperature.

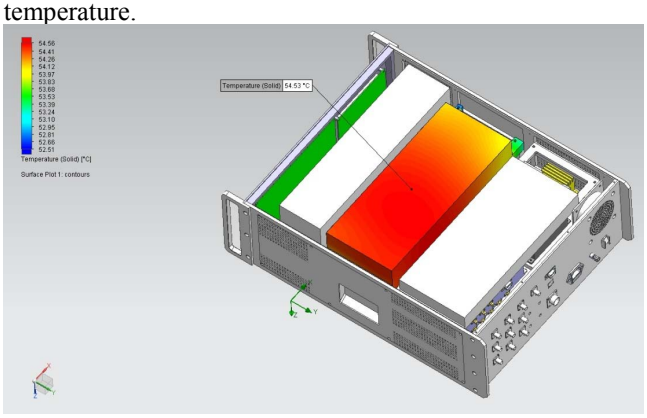


Fig. 3. Simulation of the side structure at 50 degrade and shows the temperature change.

B. Completing and Testing the Clock

By the above-mentioned modifications, the final version of the clock has been finished, and the clock names for TA1000, The size is 446×177×550(mm^3), and the height is 4U.



Fig. 4. The final vervsion of the Cesium atomic clock TA1000 with modern and formal surface.

The typical testing data of frequency stability of the clock is 1.2E-12/100s， 2.5E-13/1000s， 7.4E-14/10000s， 2.5E-14/100000s.

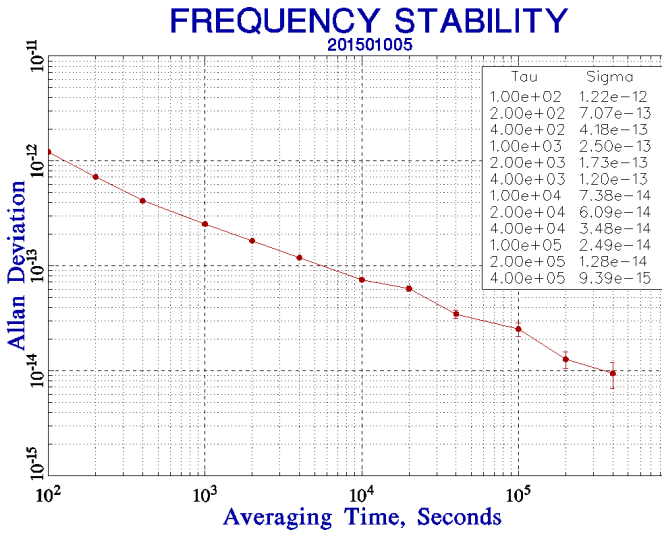


Fig. 5. The Allan deviation of the clock repsents great potentiality to arrive the high-performance model.

Qualifying for customers' demanding, the standard model of the clock has been manufactured firstly. The Allan deviation data of the 8 clocks finished last year are shown in figure 6, which improve the standard clock producing procedure is very mature by the good data uniformity.

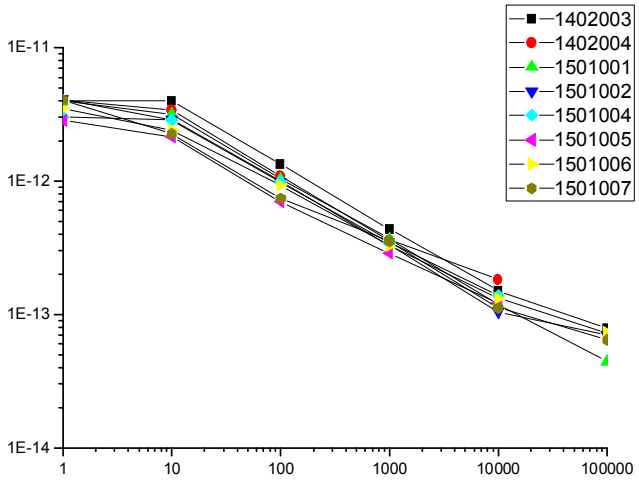


Fig. 6. The data of Allan show good uniformity in the producing processs.

Before being as formal product, the clock has gone through different tests including high-low temperature test and storage, low atmospheric pressure, magnetic sensibility, EMC etc. Especially, vibration and shock test has passed the exam by test criteria of road transport shown in in figure 7, which means the clock can be moved in long distance.



Fig. 7. Vibration and shock test under the criteria of emulation for road transport.

III. APPLICATIONS TESTS

Application test is crucial while expanding the clock to customers, therefore three representative tests in applying areas have been finished.

A. PRC Test in Telecom Network

In telecom network, Primary Reference Clock (PRC) is the highest time and frequency standard and all of the network equipment must be kept timing synchronization with PRC. In

this test, the clock TA1000 is installed in telecom customer's time-Lab to monitor the Time Interval Error (TIE). TIE Time interval error is the data type used for these statistics and is very important to be as the basement for analyzing ADEV,MDEV,TDEV and MTIE.

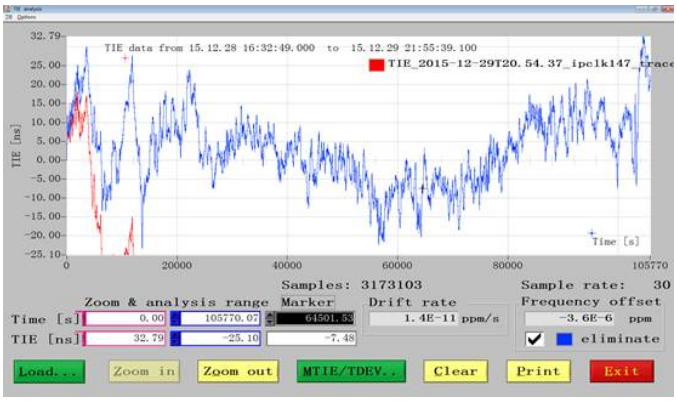


Fig. 8. TIE of the clock shows the qualification for 5G as PRC.

In figure 8, the TIE is in the ±30ns which qualify the requirement to PRC in the future telecom such as 5G.

B. Time-Keeping Atomic Clock in Clocks Group

In national time and frequency center, Cesium clock can be added in the atomic clocks group to keep the national Atomic Time (AT). In this application, the requirement is extremely high and demands high-performance model to hold the post. TA1000 provide to the center and tests in a long term, and the test data show in figure 9.

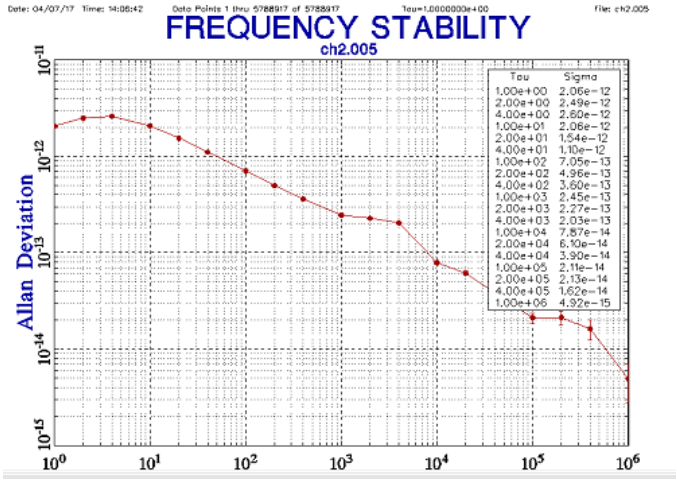


Fig. 9. Example of a figure caption. Note that color is okay in this format, the on-line publication will keep colors. (*figure caption*)

According the test data, the Allan deviation is 2.06E-12/10s ， 7.05E-12/100s ， 2.45E-13/1000s ， 7.87E-14/10000s ， 2.11E-14/100000s， 4.92E-15/1000000s, which arrive high-performance level and can be received to use in atomic clocks group to keep national time and frequency standard.

C. PRC in Grid Nework Synchronization

Grid network demands timing synchronization to automatically check wrong occurred at random, and atomic clock is necessary to use. According to the criterion of REC-G.811-199709, there is a requirement about frequency accuracy is 1*E-11. According the customer request, TA1000 was as its PRC and installed in their network and has tested. Outcome shows TA1000 passes the test easily, which proves the clock can be used in power synchronization area.

IV. CONCLUSION

The optically-pumped Cesium atomic clock TA1000 has experienced 10 years to research and develop in our team. In the course, core technique and technology has been resolved and the necessary steps have been gone through under the reiteration to make sure technical and environment specifications. Finally, TA1000 is completed and nominated as first merchandized Cesium atomic clock in China.

ACKNOWLEDGMENT

The whole work of the clock is supported by Chinese National Key Scientific Instrument and Equipment Development Project from Chinese MOST (Ministry of Science and Technology) as first project in atomic clock field in China. The course is organized by CETC (China Electronics Technology Group Corporation). UTSC (National Time Service Center) and CETC-12 institute are the cooperation units and respond for providing Laser system and Cesium Beam. The above support give us enough confidence to complete the works. Also, except paper authors, many thanks to Jie Ma, Xiaofeng Li, Shunlu Xiao, Miao Liu, Lianshi Wang, Chunmei Lu, Xiaogang Xu, Zhengzhong Wang, Wei xie, Tianyu Xie, Lan Zhang, Leiji Liu, Jun Zhou. Especially, we shall give much respect to Song Liu, Hao Li, ChunHao Han, Yuxiang Shi, Yingjun Chu, who work hard to take the clock's application tests. In a word, thanks to your excellent endeavors and contributions, our Cesium atomic clock can be reached to a formal product.

REFERENCES

[1] KALRA, S. N., R. BAILEY, and H. DAAMs: Cesium beam standard of frequency. Can. J. Phys. 36, 1442 (1958).

[2] R. Lutwak et al., "Optically-pumped cesium beam frequency standard for GPS-III", 33rd Annual Precise Time and Time Interval (PTTI) Meeting, 2001, Long Beach, CA, USA.

[3] S. Guérandel et al., "Compact cesium beam frequency standard: improvements of the frequency stability towards the 10-12 t-1/2 level", 16th European Time and Frequency Forum, 2002, St-Petersburg, Russia.

[4] Lecomte, Steve, et al. "Performance demonstration of a compact, single optical frequency Cesium beam clock for space applications." Frequency Control Symposium, 2007 Joint with the 21st European Frequency and Time Forum. IEEE International. IEEE, 2007.

[5] V. Hermann et al., "OSCC project: a space Cs beam optically pumped atomic clock for Galileo", 21th European Time and Frequency Forum, 2007, Geneva, Switzerland, in these proceedings.

[6] CHEN Jing-biao, WANG Feng-zhi, WANG Yi-qiu, YANG Donhai (Dept. of Electronics; TProgress and Minimization of Optically Pumped Cesium Beam Frequency Standard[J]; Journal of Optoelectronics. laser; 2000-05.

Increasement of effective number of detected atoms in KRISS-F1(Cs) fountain clock by optical pumping

Sangmin Lee[1,2], Myoung-Sun Heo[1], Taeg Youg Kwon[1], Hyun-Gue Hong[1], Sang-Bum Lee, and Sang Eon Park[1,2]
[1]Center for Time and Frequency, Korea Research Institute of Standards and Science (KRISS),
Daejeon 305-340, South Korea
[2]Science of Measurement, University of Science and Technology (UST), Daejeon 305-350, South Korea
*e-mail: parkse@kriss.re.kr

***Abstract*—We have performed optical pumping (OP) technique to increase the effective number of detected atoms in the KRISS-F1 (Cs) fountain clock using two laser frequencies. The maximum gain of detected signal is 3.5. We anticipate the short-term stability of KRISS-F1(Cs) will be improved with OP.**

Keywords—fountain clock; spin polarization; optical pumping; short-term stability

It is important to improve the short-term stability in the atomic clock, since the statistical uncertainty is directly proportional to the short-term stability. The measurement time can be reduced for the atomic clock with the better short-term stability. Normally the short-term stability of the KRISS-F1(Cs) fountain clock is $3.5\times10^{-14}/\tau^{1/2}$ using a cryogenic sapphire oscillator (CSO) with an ultra-low-vibration pulse-tube cryocooler for a magneto-optical trap (MOT) operation [1,2]. The short-term stability of the Yb lattice clock at KRISS is currently few $10^{-15}/\tau^{1/2}$ [3]. Therefore the short-term stability improvement of the KRISS-F1(Cs) is desirable to make a quick measurement of the absolute frequency between two clocks. The short-term stability of the atomic clock is determined by several effects, such as an atomic quality factor, a noise of local oscillator, and a quantum projection noise (QPN) etc [1]. The QPN is related to the total number of the detected atoms. In order to improve short-term stability of the KRISS-F1(Cs) further, we need more number of Cs atoms. The longer the period of atomic cooling, the longer the sampling time. Therefore we won't get much gain in the short-term stability. The 2D+ MOT or low-velocity-intense-source of atom (LVIS) apparatus generating high flux slow atomic beam has been used in few Cs atomic fountain clocks operating with optical molasses (OM) [4]. However additional vacuum chamber and high power cooling lasers make the system complicated. NPL Cs fountain clock, NPL-CsF2 has been introduced an spin polarization technique by OP to accumulate ground state population in F=4, m_F=0 [5]. We also performed same technique to increase the number of detected atoms of the KRISS-F1(Cs).

We use two DBR lasers (852 nm) and one tapered amplifier for the fountain operation. A portion of cooling laser beam is used for OP laser tuned to the F=4 to F′=4 with a detuning of 17 MHz, And a part of repumping laser beam is used for second OP laser tuned to the F=3 to F′=4. Two laser beams are combined and coupled into single polarization maintained (PM) optical fiber and delivered to the physics package. High degree of film polarizer is installed at the end of fiber output collimator. Intensity of both laser beams are approximately 1.3 mW/cm^2 each. The optimum OP duration is 0.4 ms. The maximum gain of detected signal is 3.5. We are currently performing optimization of the gain factor. The detailed results will be presented at the conference.

ACKNOWLEDGMENT

This work was supported partly by the Korea Research Institute of Standards and Science under the project "Research on Time and Space Measurements," Grant No. 17011005.

REFERENCES

[1] S. Lee, M.-S. Heo, T. Y. Kwon, H.-G. Hong, S.-B. Lee, A. P. Hilton, A. N. Luiten, J. G. Hartnett, and S. E. Park, "Operating atomic fountain clock using robust DBR laser: Short-term stability analysis, IEEE Trans. Instrum. Meas. Vol. 66, pp. 1349-1354, 2017.

[2] M.-S. Heo, S. E. Park, W.-K. Lee, S.-B. Lee, H.-G. Hong, T. Y. Kwon, C. Y. Park, D.-H. Yu, G. Santarelli, A. P. Hilton, A. N. Luiten, and J. G. Hartnett, "Drift-compensated low-noise frequency synthesis based on a cryoCSO for the KRISS-F1," IEEE Trans. Instrum. Meas. Vol. 66, pp. 1343-1348, 2017.

[3] H. Kim, M.-S. Heo, W.-K. Lee, C. Y. Park, H.-G. Hong, S.-W. Hwang, and D.-H. Yu, "Improved absolute frequency measurement of the ^{171}Yb optical lattice clock at KRISS relative to the SI second," accepted in Jpn. J. Appl. Phys., available at arXiv 1701.04534.

[4] J. Guéna, M. Abgrall, D. Rovera, P. Laurent, B. Chupin, M. Lours, G. Santarelli, P. Rosenbusch, M. E. Tobar, R. Li, K. Gibble, A. Clairon, and S. Bize, "Progress in atomic fountains at LNE-SYRTE." IEEE Trans. Ultrason. Ferroelectr. Freq. Control, vol. 59, pp. 391–409, March 2012.

[5] K. Szymaniec, J.-R. Noh, S. E. Park, and A. Takamizawa, "Spin polarization in a freely evolving sample of cold atoms," Appl. Phys. B, vol. 111, pp.527–535, March 2013.

Design of a Space Atomic Clock with Intracavity Cooling

Desheng Lü, Xiangkai Peng, Wei Ren, Qiuzhi Qu, Tang Li and Liang Liu
Key Laboratory of Quantum Optics and Center of Cold Atom Physics
Shanghai Institute of Optics and Fine Mechanics, Chinese Academy of Science (SIOM, CSA)
Shanghai 201800, China
dslv@siom.ac.cn

***Abstract*— We present the design of a space atomic clock with intracavity cooling of atoms (SACIC). Combined with a 2D MOT, the rubidium atoms are cooled, state-selected, interrogated and then detected in a cylindrical microwave cavity. This design can largely reduce the dead time in the clock cycle. Furthermore, in benefit of its compact structure, we can lay out two same microwave cavity in the space clock to cancel the Dick effect with a zero dead time.**

Keywords—cold atom clock; microwave cavity; Dick effect.

I. INTRODUCTION

In recent years, laser cooling techniques combined with microgravity environment allow the development of cold atom clocks in space [1, 2, 3]. China's cold atom clock was launched with Tiangong-2 last year and has been working smoothly in orbit since then [4].

In general, the configuration of a space cold atom clock is reconstructed from the fountain clock with the modification of a traditional Ramsey microwave cavity [1, 4]. In space microgravity, the cold atoms can be launched with a much lower speed to travel the interrogation microwave cavity than on the ground. The longer interrogation time can narrow the Ramsey linewidth. However, different from on the ground, the constant travelling speed of the cold atoms in microgravity will extend the dead time at the same time. This will degrade the performance of the clock due to the Dick effect [5].

In order to improve the performance of the clock. We present a new design of a space atomic clock with intracavity cooling (SACIC). The cold rubidium atom beam are pushed by a two-dimensional magneto-optical trap to a cylindrical microwave cavity. And then the rubidium atoms are captured, cooled, state-selected, interrogated and then detected in cavity [6]. This can largely reduce the dead time in the clock cycle.

II. SACIC PHYSICAL PACKAGE CONFIGURATION

Figure 1 shows the schematic of physical package of the SACIC. A TE011 cylindrical cavity is placed into a low pressure vacuum chamber. Around the cavity and at the end caps of cavity, there are six orthogonal apertures to allow the cooling laser beams passing through to forming an optical molasses. The vacuum chamber is enclosed by three layers μ metal magnetic shields. Inside the outer magnetic shield, a 2D MOT is designed to generate the slow rubidium atoms beam.

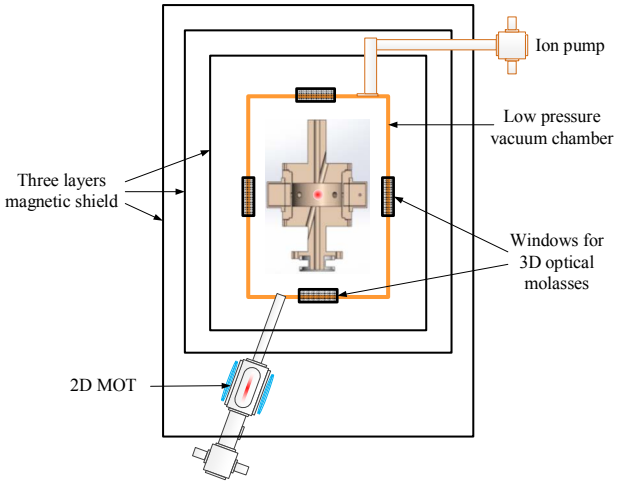


Fig. 1. Physical package of the SACIC.

III. MICROWAVE CAVITY DESIGN AND LASER ARRANGEMENT

Figure 2 shows the structure of the microwave cavity for 87 rubidium atoms. It is a TE011 cylindrical cavity which be usually used in atomic fountain clock. There are four microwave feeds around the cavity to minimize the distributed cavity phase variation [7]. The six orthogonal apertures in diameter of 10 mm allow the laser beams to pass through. The other two declining apertures allow the cold rubidium atom beam to incident and the fluorescence signal to output.

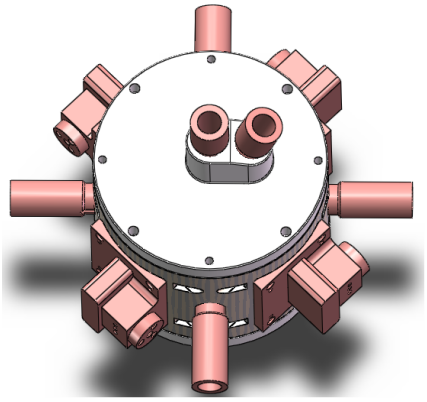


Fig. 2 The structure of the microwave cavity

Figure 3 shows the laser beams arrangement for the procedure of cooling, state selection and detection. Most of the beams will be reused in a clock cycle.

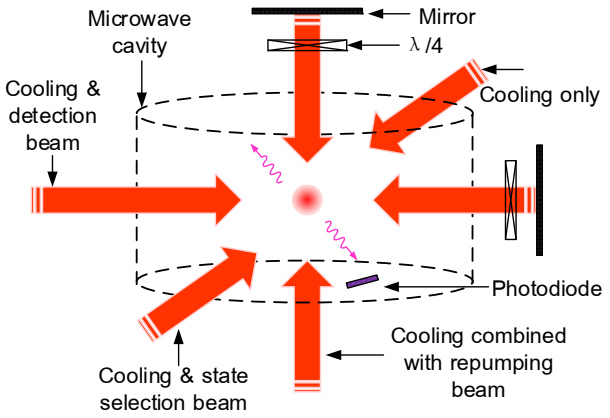


Fig. 3 Laser beams arrangement

IV. STABILITY OF THE SACIC

In the operation of the SACIC, it is a trade-off between the interrogation time and the detected atoms. For an compromise, interrogation time T=1s and detected atoms 10^6 is reasonable. This implies we can get a 0. 5Hz Ramsey linewidth and a 1000 signal to noise ratio (S/N).

Figure 4 shows one clock cycle in the SACIC sequence. We can see the dead time is much less than the interrogation time in the cycle.

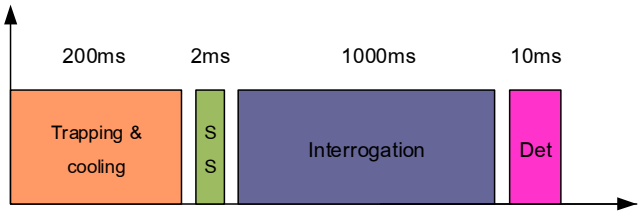


Fig. 4 Time consuming of the four clock steps in one cycle. SS-state selection, Det-detection

Equation (1) shows the stability of the space cold atom clock. For the rubidium atoms, in case of the trapping, state-selecting and detecting time is 212 ms as showed in Fig. 4, we can get a clock stability $2.6\times10^{-14}\tau^{-1/2}$.

$$\sigma_y(\tau) = \frac{1}{\pi \cdot S/N \cdot Q_{at}} \cdot \sqrt{\frac{T_c}{\tau}} \quad (1)$$

Furthermore, in benefit of SACIC's compact structure, we can lay out two same microwave cavity in the space clock to cancel the Dick effect with a zero dead time operation mode [8]. At this operation mode, the clock will reduce the requirement for the phase noise of the local oscillator. The stability of the clock will follow the equation (2) in a short time. Operation with a 0.5Hz Ramsey linewidth and a S/N 1000, the clock stability will be $2.3\times10^{-14}\tau^{-1}$.

$$\sigma_y(\tau) = \frac{1}{\pi \cdot S/N \cdot Q_{at}} \cdot \frac{1}{\tau} \quad (2)$$

V. CONCLUSIONS

In conclusion, we proposed a design of a compact space atomic clock. In the space microgravity environment, the cold atoms will stay in the microwave cavity after being captured until the next clock cycle. This reduces the time interval between two clock steps in one clock cycle and largely reduces the Dick effect. If assemble two same microwave cavity in the space, the clock can operate with a zero dead time mode. Operation with a 0.5Hz Ramsey linewidth and a S/N 1000, the clock stability will be $2.3\times10^{-14}\tau^{-1}$.

ACKNOWLEDGMENT

The authors would like to acknowledge Yuanci Gao for the discusses of cavity EM field simulation. We acknowledge Zhiqiao Long for the design of the vacuum chamber.

REFERENCES

[1] Laurent PH, Abgrall M, Jentsch CH, Lemonde P, Santarelli G, Clairon A, Maksimovic I, Bize S, Salomon CH, Blonde D, Vega J F, Grosjean O, Pocard F, Saccoccio M, Chaubet M, Ladiette N, Guillet L,. Zenone I, Delaroche CH, Sirmain CH 2006 Applied Physics B **84** 683

[2] Laurent PH, Massonnet D, Cacciapuoti L, Salomon CH 2015 Comptes Rendus Physique **16** 540

[3] Lin Li, Qiuzhi Qu, Bin Wang, Tang Li, Jianbo Zhao, Jingwei Ji, Wei Ren, Xin Zhao, Meifeng Ye, Yuanyuan Yao, Desheng Lü, Liang Liu, "Initail test of a rubidium space cold atom clock", 2016 CHIN. PHYS. LETT. Vol 3, No. 6

[4] Liang Liu, Desheng Lü, Tang Li, Qiuzhi Qu, Bin Wang, Lin Li, Wei Ren, Jianbo Zhao, Test of cold atom clock in orbit, EFTF 2017

[5] Santarelli G, Audoin C, Makdissi A, Laurent PH, Dick G J, Clairon A 1998 IEEE Trans. Ultrason. Ferroelectr. Freq. Control, **45** 895

[6] Stella Torres Muler, Daniel Varela Magalhaes, Renato Ferracini Alves, and Vanderlei Salvador Bagnato, Compact frequency standard based on an intracavity sample of cold cesium atoms, 2011, J. Opt. Soc. Am. B, Vol. 28, No. 11

[7] Ruoxin Li, Kurt Gibble, Evaluating and minimizing distributed cavity phase errors in atomic clocks, Metrologia 47 (2010) 534–551

[8] G.W. Biedermann, K. Takase, X. Wu, L. Deslauriers, S. Roy, and M. A. Kasevich, Zero-Dead-Time Operation of Interleaved Atomic Clocks, PRL 111, 170802 (2013)

MEMS atomic vapor cells sealed by Cu-Cu thermocompression bonding

Sylvain Karlen, Jacques Haesler , Thomas Overstolz, Giovanni Bergonzi and Steve Lecomte
Systems, Time & Frequency
CSEM SA
Neuchâtel, Switzerland
sylvain.karlen@csem.ch

***Abstract*— MEMS atomic vapor cells have a large variety of applications in atomic devices such as chip-scale atomic clocks (CSACs), atomic magnetometers and atomic gyroscopes. We report here on the successful wafer-level hermetic sealing of such cells by Cu-Cu thermocompression bonding. This innovative method is used as an alternative to anodic bonding and allows to overcome some of its limitations. In particular, it enables a lower oxygen contamination inside the sealed volume and makes possible the use of alternative materials as substrates. These results pave the way to an improvement of the CSACs performances regarding long term frequency drift and lifetime.**

Keywords—MEMS atomic vapor cells, chip-scale atomic clock (CSAC), buffer gas, Cu-Cu thermocompression bonding

I. Introduction

MEMS atomic vapor cells have a large variety of applications in atomic devices such as chip-scale atomic clocks (CSACs) [1], atomic magnetometers [2] and atomic gyroscopes [3]. They consist of hermetically sealed cavities, filled with a metallic alkali and a buffer gas and having an optical access. Most of MEMS cells reported in literature are sealed by anodic bonding of a borosilicate glass wafer to silicon. Despite its multiple advantages, this bonding method suffers from a few limitations : it is first known to produce residual oxygen inside the sealed cavity [4]. This oxygen rapidly reacts with alkali metals, thus reducing the available amount and can, in certain cases, limit the cell lifetime [5]. Secondly, due to the requirement of mobile ions, anodic bonding is limited to a few combinations of materials such as glass and silicon. Glass was even shown to have limitation for CSACs long term frequency stability [6].

As an alternative, we report here on the successful use of Cu-Cu thermocompression bonding as a wafer-level compatible bonding technique for the fabrication of MEMS atomic vapor cells. In contrary to anodic bonding, this method relies on an intermediate layer. It is based on the diffusion of two identical metals into the lattice of each-other under heat and pressure [4]. As compared to anodic bonding, this alternative sealing method enables a lower oxygen contamination of the cell volume as well as the use of any CTE-matching combination of substrates.

II. Microfabrication process

Our atomic vapor cell design is based on the two-cavity cell design of [7]. The microfabrication process is described in Fig. 1: A 1 mm thick Si wafer is microstructured with through-holes cavities joint by microchannels. A Cu sealing layer is then deposited above a Ta adhesion layer onto the silicon surface. Cu and Ta are chosen for the absence of intermetallic phase in the Cu-Rb and Ta-Rb systems and for their extremely small (if not absent) inter-miscibility with Rb [8], [9]. Sealing rings are then structured with the same combination of layers on two Borosilicate wafers.

The first Borosilicate wafer is bonded to the bottom of the silicon cavity under vacuum. Prior to the bonding, a forming gas treatment is realized in order to remove the copper oxide [10]. The cells are then filled with dispensing micropills and, after a second forming gas treatment, the sealing is realized by bonding of the second glass wafer under the desired atmosphere (buffer gas or vacuum). This process being realized at a wafer level, the cells are finally diced into individual pieces and the dispensing pill is activated with a laser. A picture of the final device is presented in Fig. 2.

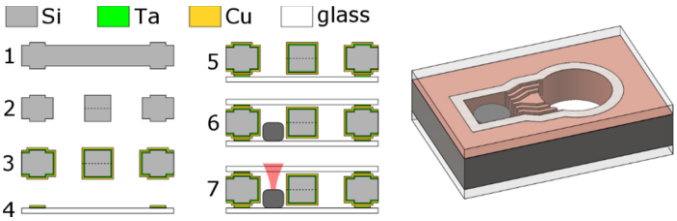


Fig. 1. [left]: Microfabrication process of Cu-Cu thermocompression cells: (1) DRIE etching of TTV release structures; (2) DRIE etching of cavities and microchannels; (3) Ta and Cu deposition on silicon; (4) Lift-off structuration of Ta and Cu on Borosilicate; (5) Bonding of the first window; (6) Filling with rubidium dispensing pill and bonding of the second window; (7) Laser activation of the dispensing pill [right]: 3D model of the cell design.

Most of buffered Rb cells reported in literature use a mixture of Ar-N_2. However, the cells presented here are filled with natural Rb dispensing pills and in that case, N_2 cannot be used as it is absorbed by the Zirconium present in the pill [11]. Therefore, we used of a mixture of Ar and Ne, as those two gases have an opposite temperature dependence in term of frequency shift [12].

978-1-5386-2916-1/$31.00 ©2017 IEEE

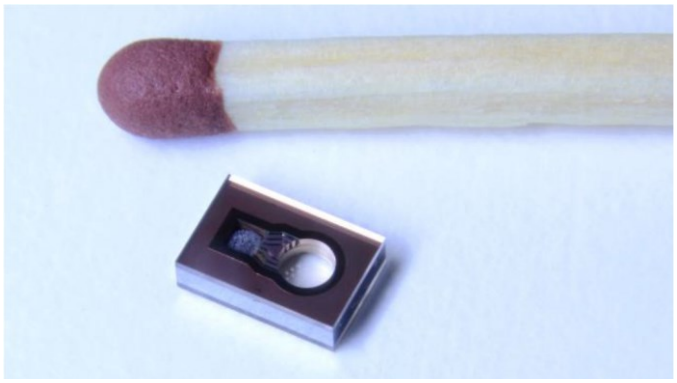


Fig. 2. Image of the device: 4 x 6 mm cell after dicing.

III. Preliminary spectroscopic validation

The suitability for atomic clocks applications of Cu-Cu thermocompresison cells filled with Ar-Ne mixture was tested in a CPT spectroscopy setup. The cell is placed in a thermo-regulated double magnetic shielding with optical access. A VCSEL is used as a laser source emitting at 795 nm and the MEMS cell absorption is measured by a photodiode. The laser frequency is locked to the ^{85}Rb D1 absorption line. Its injection current, and thus its frequency, is modulated at ~3.035 GHz. The laser carrier frequency and one of its first-order modulation sidebands are therefore brought in resonance with the ^{85}Rb D1 ground states hyperfine frequency creating the CPT effect. A small magnetic field is applied inside the shielding in order to split the sub-Zeeman levels and access the 0-0 clock transition. Fig. 3 shows an example of a CPT signal recorded from this setup. At a temperature of 95°C and a laser power of 16 µW, a contrast of 0.85% and a lorentzian FWHM of 3.5 kHz were observed. A more specific study of this clock signal will be realized in the future. Such a CPT signal is nevertheless similar at first sight to signals measured with anodic bonded MEMS atomic cells filled with natural rubidium and with Ar and N_2 buffer gas.

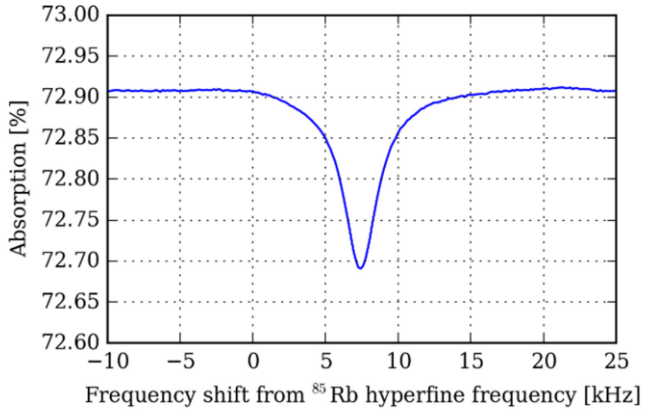


Fig. 3. CPT signal measured with a Cu-Cu thermocompression cell filled with buffer gas. (temperature: 95°C; incident laser power: 16 µW; signal contrast: 0.85% (absorption contrast: 0.31%); FWHM: 3.5 kHz.

IV. Conclusion

The potential of Cu-Cu thermocompression for the microfabrication of MEMS atomic vapor cells was demonstrated. Rubidium dispensing micropills were used to fill the cells and a novel Ar-Ne buffer gas mixture was developed for this filling method. Preliminary spectroscopic characterizations were made and showed CPT spectroscopic properties potentially in agreement with CSACs applications.
The application of this bonding technology to MEMS atomic vapor cells potentially enables the fabrication of cells with a lower contamination level as compared to anodic bonding as well as the bonding of alternative materials to silicon and glass. This novel technique could therefore lead to an improved cell lifetime and long term frequency stability and an improvement of overall CSACs long-term performances.

Acknowledgments

We gratefully acknowledge G. Mileti (Université de Neuchâtel, Switzerland), for the fruitful discussions on atomic vapor cells, F. Gruet (Université de Neuchâtel, Switzerland) for his help with the saturated absorption spectroscopy measurements, S. Biselli and K. Vaideeswaran (CSEM SA) for the FIB samples preparation and SEM analysis as well as A. Bionaz, M. Amine, and P.-A. Clerc (CSEM SA) for their participation in the MEMS cell manufacturing.

This work was funded by the European Space Agency (ESA) under the Networking and Partnering Initiative (NPI) (ESA Contract No. 4000112650/14/NL/GLC) and CSEM's R&D activity financed by the canton of Neuchâtel.

References

[1] L. A. Liew, S. Knappe, J. Moreland, H. Robinson, L. Hollberg, and J. Kitching, "Microfabricated alkali atom vapor cells," Appl. Phys. Lett., vol. 84, no. 14, pp. 2694–2696, 2004.

[2] P. D. D. Schwindt, S. Knappe, V. Shah, L. Hollberg, J. Kitching, L.-A. A. Liew, and J. Moreland, "Chip-scale atomic magnetometer," Appl. Phys. Lett., vol. 85, no. 26, pp. 6409–6411, 2004.

[3] E. a. Donley, "Nuclear magnetic resonance gyroscopes," in IEEE Sensors, 2010, pp. 17–22.

[4] P. Ramm, J. J. Q. Lu, and M. M. V. Taklo, Handbook of Wafer Bonding. John Wiley & Sons, 2012.

[5] S. Karlen, J. Gobet, T. Overstolz, H. Jacques, and L. Steve, "Lifetime assessment of RbN3-filled MEMS atomic vapor cells with Al2O3 coating," Opt. Express, vol. 25, no. 3, pp. 2187–2194, 2017.

[6] S. Abdullah, C. Affolderbach, F. Gruet, and G. Mileti, "Aging studies on micro-fabricated alkali buffer-gas cells for miniature atomic clocks," Appl. Phys. Lett., vol. 106, no. 16, p. 163505, 2015.

[7] M. Hasegawa, R. K. Chutani, C. Gorecki, R. Boudot, P. Dziuban, V. Giordano, S. Clatot, and L. Mauri, "Microfabrication of cesium vapor cells with buffer gas for MEMS atomic clocks," Sensors Actuators A Phys., vol. 167, no. 2, pp. 594–601, 2011.

[8] C. Addison, "The chemistry of the liquid alkali metals," 1984.

[9] A. D. Pelton, "The Cu-Rb (Copper-Rubidium) System," Bull. Alloy Phase Diagrams, vol. 7, no. 1, 1986.

[10] C. S. Tan, K. N. Chen, A. Fan, and R. Reif, "The Effect of Forming Gas Anneal on the Oxygen Content in Bonded Copper Layer," J. Electron. Mater., vol. 34, no. 12, pp. 1598–1602, 2005.

[11] E. Kroemer, M. Abdel Hafiz, V. Maurice, B. Fouilland, C. Gorecki, and R. Boudot, “Cs vapor microcells with Ne-He buffer gas mixture for high operation-temperature miniature atomic clocks,” Opt. Express, vol. 23, no. 14, p. 18373, 2015.

[12] B. L. Bean and R. H. Lambert, “Temperature dependence of hyperfine density shifts. IV. Na23, K39, and Rb85 in He, Ne, Ar, and N2 at low temperatures,” Phys. Rev. A, vol. 13, no. 1, pp. 492–494, Jan. 1976.

Preliminary evaluation of the AOS-CsF1 primary frequency standard

P. Dunst, B. Nagórny, D. Lemański, P. Nogaś, J. Nawrocki
Astrogeodynamical Observatory
Space Research Centre
Borowiec, Poland
pdunst@cbk.poznan.pl

R.J. Hendricks, F. Ozimek, K. Szymaniec
National Physical Laboratory
Teddington, U.K.

***Abstract*— We report on operation of a new caesium fountain primary frequency standard at the Astrogeodynamical Observatory of the Polish Space Research Centre. The device was assembled and tested at the National Physical Laboratory in Teddington and subsequently transported to Borowiec where it was fully commissioned in December 2016. We demonstrate its performance in terms of stability in short- and long-term and report preliminary measurements of the systematics effects.**

I. INTRODUCTION

The Time Section of the Astrogeodynamical Observatory (AOS) is one of the UTC laboratories in Poland. In addition, it provides absolute and traceable frequency reference for Polish research institutes via a growing network of fibre links [1]. In order to enhance its capability, AOS is acquiring two primary frequency standards based on the cold atom fountain technology. The standards are being built by National Physical Laboratory following a proven physics package design of NPL-CsF2 and CsF3 [2]. Improvements of the design include reduction the overall size and higher rigidity of the structure, small footprint optical assembly and upgraded electronic control system.

II. PRELIMIANRY PERFORMANCE AND UNCERTAINTY

The first fountain standard AOS-CsF1 was completed in 2016 and fully tested at NPL prior to shipment. A 15-day run demonstrated agreement with the rate of the TT timescale. The system was then transported to the AOS premises and re-integrated. It demonstrates signal-to-noise ratio of 1600 and short-term stability of 1.1×10^{-13} in 1s which are the same as these achieved during tests at NPL. Full evaluation of the systematic effects is underway. The major systematic effects which contribute the largest frequency corrections are 2nd order Zeeman effect, black body radiation, cold collisions and gravitational redshift due to position of the standard above the geoid. We will also present details of the setup and plans to integrate the new primary standard to the local timescale at AOS.

III. FUTURE WORKS

It is envisaged that upon completion of the accuracy evaluation, AOS-CsF1 will regularly contribute data to the TAI calibrations by BIPM. The second fountain, AOS-CsF2 is expected to be delivered in summer 2017; it will operate at a remote location linked to the AOS clocks by an optical fibre link with electronically stabilized delay.

ACKNOWLEDGMENT

This project is funded by Polish Ministry of Science and Higher Education decision no. 6436/IA/SP/2015.

REFERENCES

[1] Piotr Morzyński et al. „Absolute measurement of the 1S0 − 3P0 clock transition in neutral 88Sr over the 330 km-long stabilized fibre optic link”, Scientific Reports 5, 17495, 2015.

[2] K Szymaniec, S N Lea, K Gibble, S E Park, K Liu and P Głowacki „NPL Cs fountain frequency standards and the quest for the ultimate accuracy”, Journal of Physics: Conference Series, vol. 723, 2016.

Continuous Cold Atomic Beam in a Zerodur Chamber for Atom Interferometry

Myoung-Sun Heo, Taeg Yong Kwon, Sang Eon Park, Sang-Bum Lee, Hyun-Gue Hong
Center for Time and Frequency
Korea Research Institute of Standards and Science
Daejeon, 34113 Rep. of Korea

Sin Hyuk Yim, Kyu Min Shim
Agency for Defense Development
Daejeon, 34186 Rep. of Korea

***Abstract*—We generated a continuous cold atomic beam using a two-dimensional magneto-optical trap for atom interferometry. The vacuum system is made of Zerodur glass with a large optical access for a compact system.**

Keywords—atomic beam; Zerodur; atom interferometer; 2D MOT; 2D$^+$ MOT

I. INTRODUCTION

Interferometry using cold atoms interacting with light has been widely used for a highly sensitive sensor having many potential applications such as gravimeter [1], inertial sensors [2-4] and tests of fundamental physics [5]. Here we report a continuous atomic beam source using two-dimensional magneto-optical trap (2D MOT) inside a Zerodur vacuum chamber.

II. EXPERIMENTAL SETUP AND RESULTS

A. Zerodur Vacuum Chamber

Fig. 1 shows the schematic view of the beam machine. The vacuum chamber was made of 15-mm-thick Zerodur blocks which were polished and directly bonded using optical contact. It consists of two vacuum chambers connected by a Zerodur block which has a 1-mm diameter hole for differential pumping and atomic beam channel. There is a mirror-coated 45°-cut Zerodur block (inset of Fig. 1) attached to this connecting block for a retarding beam. A rubidium (Rb) dispenser and a getter pump was installed in the trap chamber. The second chamber has been continuously pumped out using an ion pump, so its pressure has been maintained below 1×10^{-9} hPa.

B. 2D$^+$ MOT

A pair of 25-mW circularly polarized cooling lasers which are perpendicular to each other are retroreflected for a 2D MOT. They have elliptical cross sections (10 mm × 30 mm) elongated along the atomic beam (axial) direction using cylindrical lenses to ensure a large cooling volume. A continuous atomic beam was extracted from the 2D MOT using a linearly polarized pushing laser. An additional laser beam with the same laser frequency as those of cooling lasers was introduced in the axial direction propagating against the pushing laser beam using reflection on the mirror coated on 45°-cut Zerodur block. This configuration, called a 2D$^+$ MOT, helps to reduce the mean and the width of the longitudinal velocity of the atomic beam further than those of the 2D MOT without a retarding beam [6].

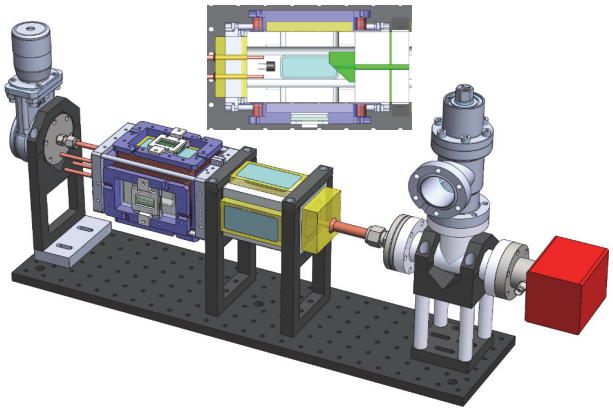


Fig. 1. Schematic drawing of the atomic beam machine without optics. Inset shows the horizontal cross section of the trap chamber.

The transverse magnetic field gradient of ~21 G/cm was produced with two pairs of anti-Helmholtz coils. Additional two pairs of Helmholtz coils were used for compensation of external fields, transverse alignment of zero-field line and shutoff of the atomic beam for a beam characterization.

Characteristic of an atomic beam was investigated by observing fluorescence after cutting off the atomic beam using a magnetic field, assuming a Gaussian velocity distribution. The atomic flux more than 10^{10}/s is observed. Fig.2 shows that the the mean and the full width half maximum (FWHM) of the longitudinal velocity of the atomic beam increase with power of the pushing laser. Note that for the weakest pushing laser, the FWHM width could go down to 2.4 m/s.

Identify applicable sponsor/s here. If no sponsors, delete this text box (*sponsors*).

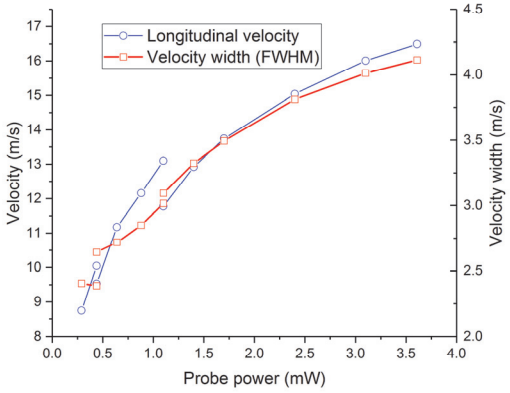


Fig. 2. The mean and the width of the longitudinal velocity of the atomic beam as a function of power of the pushing laser

III. SUMMARY

A continuous atomic beam from $2D^+$ MOT was produced inside a Zerodur chamber. The typical atomic flux was 10^9/s to 10^{10}/s. The mean and the width of the longitudinal velocity was highly dependent on power of the pushing laser. We plan to make this system more compact by replacing large expansion optics with gratings.

REFERENCES

[1] P Gillot, O. Francis, A. Landragin, F. Pereira Dos Santos, and S. Merlet, "Stability comparison of two absolute gravimeters: optical versus atomic interferometers," Metrologia, vol. 51, pp. L15-L17, June 2014.

[2] B. Canuel, F. Leduc, D. Holleville, A. Gauguet, J. Fils, A. Virdis, A. Clairon, N. Dimarcq, Ch. J. Bordé, A. Landragin, and P. Bouyer, "Six-Axis Inertial Sensor Using Cold-Atom Interferometry," Phys. Rev. Lett., vol. 97, p. 010402, July 2006.

[3] D. S. Durfee, Y. K. Shaham, and M. A. Kasevich, "Long-Term Stability of an Area-Reversible Atom-Interferometer Sagnac Gyroscope," Phys. Rev. Lett, vol. 97, p. 240801, December 2006.

[4] Saijun Wu, Edward Su, and Mara Prentiss, "Demonstration of an Area-Enclosing Guided-Atom Interferometer for Rotation Sensing," Phys. Rev. Lett. Vol. 99, p. 173201, October 2007.

[5] Holger Müller, Achim Peters, and Steven Chu, "A precision measurement of the gravitational redshift by the interference of matter waves," Nature, vol. 463, pp. 926-929, Feb. 2010.

[6] K. Dieckmann, R.J.C. Spreeuw, M. Weidemüller, and J.T.M. Walraven, "Two-dimensional magneto-optical trap as a source of slow atoms," Phys. Rev. A, vol 58, pp. 3891-3895, November 1998.

A low phase noise Raman lasers system based on optical injection and an optical phase-lock loop

C. F. Wu*†, X. S. Yan†‡, J.H. Tu※, P.X. Miao※, P. Ma※, J.W. Zhang†‡, L. J. Wang*†‡

*Department of Physics, Tsinghua University, Beijing 100084, People's Republic of China

†State Key Laboratory of Precision Measurement Technology and Instruments, Beijing 100084, People's Republic of China

‡Department of Precision Instruments, Tsinghua University, Beijing 100084, People's Republic of China

※Lanzhou Institute of Physics, Lanzhou, People's Republic of China

E-mail: zhangjw@tsinghua.edu.cn

***Abstract*— Raman lasers with a frequency difference equal to the hyperfine splitting of ground state have been widely used in quantum precision measurements. In this paper, we report a hybrid Raman lasers system combined with the optical injection and optical phase-lock loop. This design not only offers us the convenience to independently adjust the intensity and polarization of Raman lasers, but also suppress the phase noise caused by the air turbulence and vibration of mirrors.**

Keywords—Raman lasers; optical phase-lock loop; optical injection

I. INTRODUCTION

Raman lasers with a frequency difference equal to the hyperfine splitting of ground state have been widely used in atom interferometers[1], atomic clock[2, 3], and other quantum precision measurements. The phase coherence of Raman lasers is crucial in those experiments [4]. There are several ways to get Raman lasers. One can phase lock a laser to another laser by an optical phase-lock loops (OPLL). Another way is to directly generate Raman lasers by a modulator, for instance, an acousto-optic modulator (AOM)[5], an electro-optic modulator (EOM), or a current-modulated vertical-cavity surface-emitting laser (VCSEL) with radio frequency (rf) signal [6,7].

At Tsinghua University, a coherent population trapping (CPT) microwave clock based on cold cesium beam is initiated in 2013, where Raman lasers at 852 nm with 9.2 GHz frequency difference are applied to detect the CPT signal. The schematic diagram of the Raman lasers is shown in Fig. 1. A part of the master laser output is phase modulated by a fiber EOM (FEOM) to generate the phase coherent sideband by a 9.2 GHz signal. The sideband and the master laser are power amplified by two slave lasers (Slave2 and Slave1) via optical injection lock, respectively. This design offers us the convenience to independently adjust the intensity and polarization of Raman lasers. However, the phase coherence of the Raman lasers is found degraded seriously after several mirrors which are used to direct the lasers onto Cs beam. Because the Raman lasers are spatially separated, the air turbulence and vibration of mirrors cause unavoidable phase noise.

II. EXPERIMENTAL SETUP

In this paper, we report a hybrid Raman lasers system combined with the optical injection and optical phase-lock loop. At the end part of the Raman laser beams close to the detection zone, the beat-note of two color components of the Raman lasers is detected by a fast photodetector, then it is mixed with a 9.2 GHz microwave signal referenced to a hydrogen clock. Thus, the phase noise is obtained from the IF output of the mixer, which is used to generate feedback to correct the phase of the FEOM driving signal.

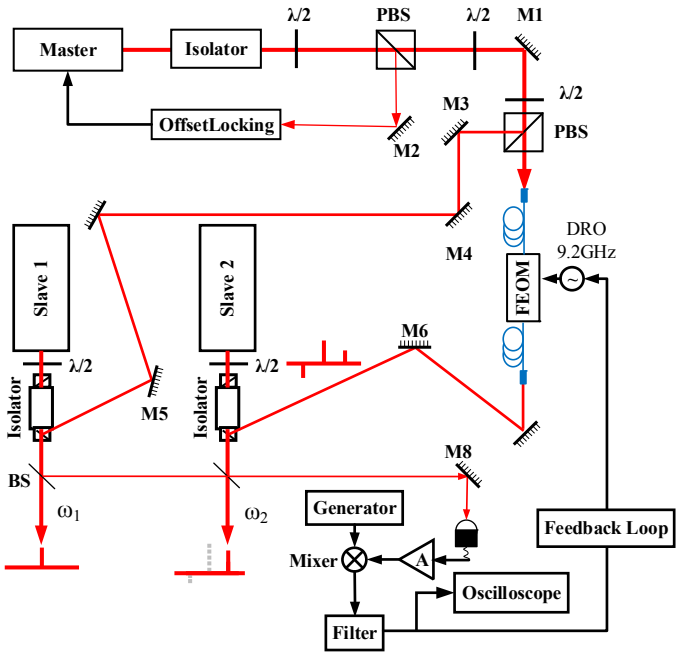


Fig. 1. Experimental setup of hybrid Raman lasers system. M: mirror; DRO: dielectric resonator oscillator; BS: beam splitter; A: amplifier.

This work is supported by the National Key Research and Development Program of China (No.2016YFA0302101), the foundation of China Academy of Space Technology, and the Initiative program of State Key Laboratory of Precision Measurement Technology and Instruments.

III. RESULTS

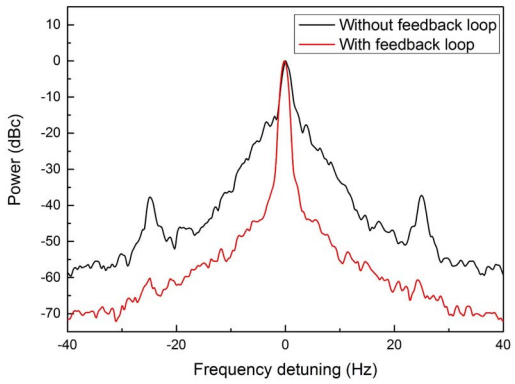


Fig. 2. Beat note signal between two slave lasers with center frequency at 9.192631770 GHz.

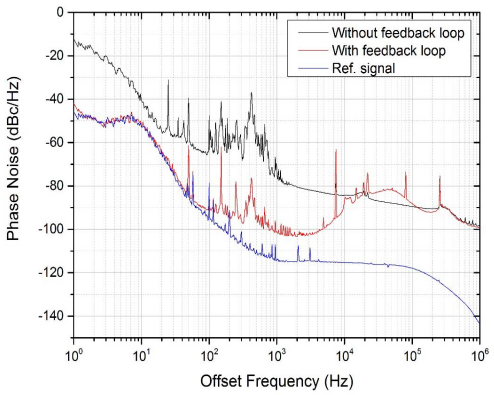


Fig. 3. Phase noise spectral density of the lasers from 1Hz to 1MHz for the case that OPLL is on (red) and off (black curve), respectively. The blue curve is the phase noise of the reference signal.

As shown in Fig. 2, beat note signal of two slave lasers is measured to characterize the phase coherence with feedback loop and without feedback loop, respectively. The 3-dB linewidths of these curves are 1 Hz, which are limited by the resolution of the spectrum analyzer.

The phase noise spectral density (PSD) of the lasers is shown in Fig. 3, as a reference, the Ref signal is also measured. Compared with the condition of without feedback loop, phase noise is suppressed caused by the air turbulence and vibration of mirrors.

IV. CONCLUSION

In conclusion, we demonstrate a low phase noise Raman lasers system based on optical injection and an optical phase-lock loop, which take the advantage of convenience to independently adjust the intensity and polarization of Raman lasers and suppressing the phase noises caused by the air turbulence, vibration of mirrors.

REFERENCES

[1] M. Kasevich and S. Chu, "Atomic interferometry using stimulated Raman transitions," Phys Rev Lett, vol. 67, pp. 181-184, Jul 08 1991.

[2] D. Höckel, M. Scholz, and O. Benson, "A robust phase-locked diode laser system for EIT experiments in cesium," Applied Physics B, vol. 94, pp. 429-435, 2008.

[3] J. Vanier, "Atomic clocks based on coherent population trapping: a review," Applied Physics B, vol. 81, pp. 421-442, 2005.

[4] M. J. Snadden, R. B. M. Clarke, and E. Riis, "Injection-locking technique for heterodyne optical phase locking of a diode laser," Optics Letters, vol. 22, p. 892, 1997.

[5] P. Yun, B. Tan, W. Deng, and S. Gu, "High coherent bi-chromatic laser with gigahertz splitting produced by the high diffraction orders of acousto-optic modulator used for coherent population trapping experiments," Rev Sci Instrum, vol. 82, p. 123104, Dec 2011.

[6] W. Chen, X. Qi, L. Yi, K. Deng, Z. Wang, J. Chen, et al., "Optical phase locking with a large and tunable frequency difference based on a vertical-cavity surface-emitting laser," Optics Letters, vol. 33, p. 357, 2008.

[7] H. B. Xue, Y. Y. Feng, X. J. Wang, S. Chen, and Z. Y. Zhou, "Note: Generation of Raman laser beams based on a sideband injection-locking technique using a fiber electro-optical modulator," Rev Sci Instrum, vol. 84, p. 046104, Apr 2013.

First Results on Rb Fountain Rb304 Frequency Standard Developed at VNIIFTRI

D.S. Kupalov, V.N. Baryshev, I.Y. Blinov, A.I. Boiko, Y.S. Domnin, L.N. Kopilov, M.N. Khromov, O.V. Kupalova, A.V. Novoselov

VNIIFTRI
Mendeleevo, Russia
kupalov@vniiftri.ru

***Abstract*— The design, operating parameters and the preliminarily evaluation of the main systematic frequency shifts of the Rb fountain type frequency standard, developed at VNIIFTRI, are presented.**

***Keywords*— metrology, time and frequency standard, atomic fountain, cold atoms.**

I. INTRODUCTION

In 2004, the Consultative Committee for Time and Frequency (CCTF) proposed a first secondary representation of the second, which was then adopted by the Comit's International des Poids et Mesures (CIPM) [1, 2]. Frequency of ^{87}Rb hyperfine transition is one of contenders for the representation of the SI second. The project on Rb fountains has been started in VNIIFTRI four years ago. Two Rb fountains (Rb1 and Rb2) with fractional instability at the level of $(1\div2)\times10^{-16}$ after 16 days of averaging have been developed for use in time keeping service of VNIIFTRI. Another goal was the precision measurement of the absolute frequency of the Rb hyperfine transition. In this paper, we report the estimation of the main systematic frequency shifts of Rb304 fountain frequency standard.

II. THE PHYSICAL PACKAGE

The Rb304 vacuum system is made of titanium, except the microwave cavity and flight tube. The system is pumped by ion pump (20 l/s) and two getter pumps, which are placed in the bottom of physical package. The vacuum pressure is lower than 3×10^{-10} mbar. Rubidium atoms are collected directly from background vapor in the (1, 1, 1) configuration optical molasses. Atomic source with valve and 1 g isotope ^{87}Rb is placed behind the two layers bottom magnetic shields. To form six cooling laser beams with proper lin _|_ lin polarization and diameter 25 mm at the $1/e^2$ intensity level, adjustable collimators are mounted on the trapping chamber. There are two additional windows for the repump beam and CCD camera for monitoring the atomic cloud.

A state-selection cavity with a Q factor ~ 850 is located above the trapping chamber. The microwave cavity and the flight tube are surrounded by C-field cylinder made of aluminum alloy and five layers of μ-metal magnetic shields. The total shield factor is about 2×10^5.

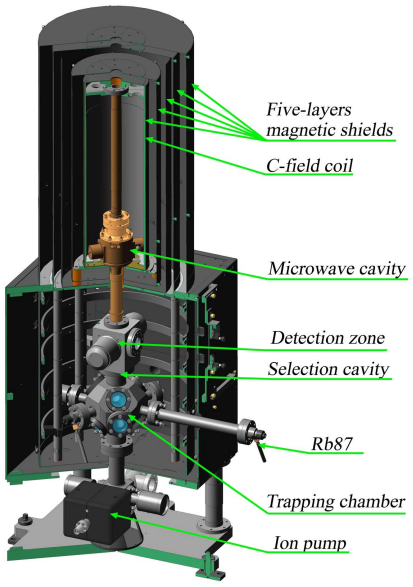


Fig. 1. Schematic of Rb304 physical package.

The cylindrical TE_{011} microwave cavity, made of oxygen-free copper, is located at the height of 0.48 m above the trapping chamber center. Two symmetrical rectangular TE_{101} waveguides excite microwave field inside cavity. Waveguides are weakly coupled to the cavity through two round holes, positioned on opposite sides of the cavity cylindrical body. The cavity loaded quality factor is $Q_c \sim 28\,600$.

III. THE LASER SYSTEM

The laser system of Rb304 consists of two lasers. The light for cooling and detection beams is provided by a Toptica TA pro diode laser with a tapered amplifier and a total output power of about 1 W. The laser frequency is locked to the $F = 2 \rightarrow F' = 3$ optical cycling transition of ^{87}Rb D_2 line by modulation transfer spectroscopy. The output laser beam is split into three parts: the first is used to form the detection beams, the second and the third are used to form up-going and down-going beams of the optical trap. The frequencies and intensities of the all light beams are controlled with acousto-optic modulators (AOM) in double-pass cat`s eye configuration.

The repump light is provided by Toptica DL 100 pro design diode laser. The laser frequency is locked to the $F = 1 \rightarrow F' = 1, 2$ crossover transition by frequency modulation (FM) spectroscopy and shifted to frequency of $F = 1 \rightarrow F' = 2$ transition by double-pass AOM. The output laser beam is split into two parts: repump beam for optical trap and beam for detection. Mechanical shutters with stepper motors are used in laser system to prevent any penetration of laser radiation into the fountain during interrogation of the atoms. The light from optical bench is coupled to the vacuum system with polarization maintaining optical fibers and collimators.

IV. THE MICROWAVE SYNTHESIZER

The commercial synthesizer RB-1 (SpectraDynamics, Inc.) with frequencies locked to the reference H-maser (Vremya-Ch) forms microwave signals for state selection and Ramsey interrogation. There are splitter, phase shifter and attenuator for symmetrical exciting the microwave field inside the cavity.

V. OPERATING OF THE FOUNTAIN

The duration of one full fountain cycle is 1.5 second. At first, the atoms are collected in the optical molasses directly from ^{87}Rb background vapor for 600 ms and TA pro laser frequency is red detuned from $F = 2 \rightarrow F' = 3$ cycling transition. Then the atoms are accelerated for 1 ms in a moving molasses, and are further cooled for another 1 ms by reducing adiabatically the cooling beams intensities and detuning their frequencies by −41 MHz. The initial velocity of atomic cloud is 4 m/s. Calculated from the time of flight (TOF) signal, the temperature of the atoms after post-cooling phase is about 4 μK. After that, the atoms pass the cylindrical state selection cavity and interrogate with TE_{011} microwave field resonant to the $|F = 2, m = 0\rangle \rightarrow |F = 1, m = 0\rangle$ hyperfine transition. The amplitude and duration of the microwave field correspond to a π- pulse for transition between two hyperfine states. Atoms with other magnetic sub-states $|F = 2, m = -2, -1, 1, 2\rangle$ are deflected from the atomic beam by resonant light. For this purpose, a part of upper detection beam is used. As a result, all atoms in state $|F = 1, m = 0\rangle$ enter the microwave cavity, where the clock transition $|F = 1, m = 0\rangle \rightarrow |F = 2, m = 0\rangle$ is excited. The numbers N_1 and N_2 of atoms in the $F = 1$ and $F = 2$ states are measured by two detectors consisting of low-noise photodiodes and pair of aspherical lenses. This measurement derives the relative population of the $|F = 2, m = 0\rangle$ state $P_2 = N_2/(N_1 + N_2)$, which is insensitive to the total number of atoms $N_1 + N_2$ fluctuations.

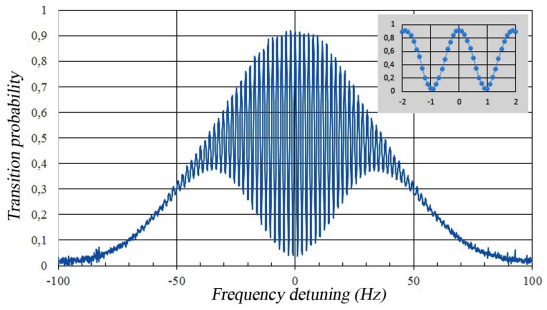


Fig. 2. The Ramsey fringes of Rb304.

A Ramsey fringes (transition probabilities as a function of detuning) pattern is shown in Fig. 2, with a frequency-scanning step of 0.1 Hz without averaging. The width of central Ramsey fringe (FWHM) is 0.96 Hz.

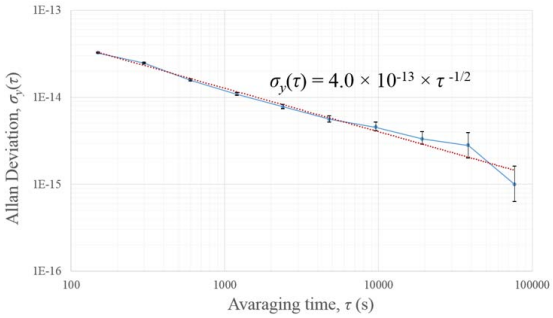


Fig. 3. Allan deviation of Rb304 vs H-maser.

Fig. 3 shows the Allan deviation $\sigma_y(\tau)$ of the frequency measured by comparing the frequency of Rb304 fountain vs H-maser, as a function of the averaging time τ. This measurement shows that the frequency stability of the Rb304 after one day of averaging is 1.4×10^{-15}. The fit line $\sigma_y(\tau) = 4.0\times10^{-13} \times \tau^{-1/2}$ in the graph corresponds to the white frequency noise model.

VI. CHARACTERIZATION OF SYSTEMATIC FREQUENCY SHIFTS

Currently, the budget uncertainty of rubidium frequency standard is under investigation. Below, we present the evaluation of the main factors leading to frequency offsets and their uncertainties.

A. Blackbody radiation shift

The blackbody radiation (BBR) shift is one of the largest systematic corrections and a significant source of uncertainty in atomic fountains. While in the interrogation region, the atoms are exposed to the thermal electromagnetic radiation emitted by the walls of the vacuum chamber, what leads to a frequency shift of the Rb clock transition. The relative frequency shift of the Rb clock transition can be calculated from the formula [3]:

$$\frac{\Delta f_{BBR}}{f_0} = \beta \left(\frac{T}{300K}\right)^4 \left[1 + \varepsilon \left(\frac{T}{300K}\right)^2\right] \quad (1)$$

Here, f_0 is the frequency of the ^{87}Rb ground state hyperfine transition, T is the temperature, constant coefficients $\beta = -1.256(4)\times10^{-14}$ and $\varepsilon = 0.011$ which correspond to a fractional frequency uncertainty of 4×10^{-17} are taken from [4, 5]. Rb304 is located in a room with temperature maintained at (299.4±0.5) K, and temperature of the flight tube is the same. Three PT100 calibrate thermometers (two on the top and bottom of flight tube and one on the outer layer of the shield) control the temperatures continuously. The measured gradient along the flight tube is below 0.15 K. The average temperature difference between the flight tube and the magnetic shield is less than 0.1 K. The operating temperature of the fountain is 299.4 K and the BBR frequency shift is equal to -126×10^{-16} with combined uncertainty of 1×10^{-16}:

$$\frac{\Delta f_{BBR}}{f_0} = (-12.6 \pm 0.1) \cdot 10^{-15}$$

.

B. Quadratic Zeeman shift

The relative shift in the clock transition frequency due to the constant magnetic field is calculated by the Breit-Rabi formula [6]. According to this the quadratic Zeeman shift of the clock transition $|F = 1,\ m = 0\rangle \rightarrow |F = 2,\ m = 0\rangle$ in the magnetic field B is defined as

$$\frac{\Delta f_{Z2}}{f_0} = \frac{(g_J - g_I)^2 \mu_B^2}{2h^2 f_0^2} \cdot B^2 \quad (2)$$

Here $g_J = 2.00233113$ and $g_I = -0.0009951414$ are electron and nuclear g-factors for ^{87}Rb [7] respectively, μ_B is the Bohr magnetron and h is the Planck constant. The average amplitude of the magnetic C-field experienced by the launched atoms was measured from a linear Zeeman frequency shift of the magnetically sensitive transition $|F = 1, m=1\rangle \rightarrow |F= 2, m=1\rangle$ on different heights, which is equal to

$$\Delta f_{Z1} = \frac{(g_J - g_I)\mu_B}{2h} B \quad (3)$$

To restore the magnetic field map, we used the deconvolution of the averaged magnetic fields,

$$\langle B \rangle_i = \frac{\sum_{j=1}^{i} B_j t_j}{\sum_{j=1}^{i} t_j}, \langle B \rangle_1 = B_1 \quad (4)$$

Here B_j is calculated from $\langle B \rangle_i$ and t_j, where t_j is the duration time that atoms spend between the j point and the $(j+1)$ point during free-fall [8].

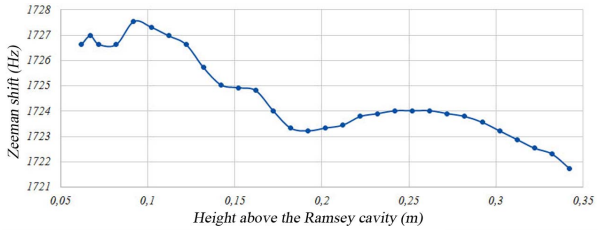


Fig. 4. Frequency of the central Ramsey fringe of the magnetically sensitive transition as a function of the height

Based on these data the variance of the magnetic field standard deviation of the magnetic field $\sigma = \sqrt{\langle B(z)^2 \rangle - \langle B(z) \rangle^2} = 0.17$ nT gives the magnitude of the quadratic Zeeman fractional frequency shift less than 1×10^{-18}. For the C-field of 123.03 nT, the linear Zeeman shift of the magnetically sensitive transition $|F = 1, m=1\rangle \rightarrow |F = 2, m=1\rangle$ is equal to 1724.8 Hz. This value did not change by more than ±0.5 Hz during the measurement period about half a year. It means that the uncertainty of the quadratic Zeeman shift is less than 1×10^{-16}. As a result, the relative frequency shift due to the second-order Zeeman effect is:

$$\frac{\Delta f_Z}{f_0} = (127.4 \pm 0.1) \cdot 10^{-15}$$

.

C. Gravitational redshift

The gravitational frequency shift of the ground frequency standard is defined by the height of its position with respect to the geoid sea level. The gravitational red shift is given by the equation [9]:

$$\frac{\Delta f_G}{f_0} = \frac{g}{c^2} \cdot h \quad (5)$$

where g is the local gravitational acceleration, c is the speed of light and h is the orthometric height of the standard.

The orthometric height of the time-averaged trajectories of atoms in Rb304 fountain was measured by means of known reference point located on laboratory building downstairs. The value of this reference point is (212.01±0.03) m. Taking into account that the fountain locates on the third floor, the height of the time-averaged trajectories of atoms in Rb304 is (222.3±0.5) m. According to (5), the relative frequency shift due to the gravitational potential is:

$$\frac{\Delta f_G}{f_0} = (24.3 \pm 0.1) \cdot 10^{-15}$$

VII. Summary

The Rb fountain frequency standard prototype Rb304 has been developed at VNIIFTRI. In this paper, we have reported design, operation, performance and preliminary evaluation of Rb304. The other uncertainties due to collisional shift, microwave leakage, DCP, cavity pulling, collisions with background gases will be evaluated after modification of the detection zone.

To improve Rb304 short-term stability and decrease its frequency measurements uncertainty, a high performance H-maser will be used as reference maser. It belongs to the ensemble of H-masers generating real-time time scale which is used to produce UTC(SU).

References

[1] 2007 International Committee for Weights and Measures 2006, Recommendations adopted by the CIPM, Proc`es-Verbaux des S´eances du Comit´e International des Poids et Mesures, 95th meeting (2006) p 249.

[2] J. Gu´ena, M. Abgrall, A. Clairon and S. Bize, “Contributing to TAI with a Secondary Representation of the SI Second”, Metrologia, vol. 51, 2014, pp. 108-120.

[3] V. G. Pal’chikov, Yu. S. Domnin, and A. V. Novoselov “Black-body radiation effects and light shifts in atomic frequency standards”, J. Opt. B: Quantum and Semiclass. Opt. 5, s131–s135 (2003).

[4] Angstmann E. J., Dzuba V. A. and Flambaum V. V. 2006 *Phys. Rev.* A 74 023405.

[5] Safronova M. S., Jiand D. and Safronova U. I. 2010, arXiv:physics.atom- ph/1007.0462.

[6] Breit G. and Rabi I. I., 1931 *Phys. Rev.* 38 2082–3.

[7] Arimondo E., Inguscio M. and Violino P. 1977 Rev. Mod. Phys. 49 31–75.

[8] Fang Fang, Mingshou Li, Pingwei Lin, Weiliang Chen, Nianfeng Liu, Yige Lin, Ping Wang, Kun Liu, Rui Suo and Tianchu Li “NIM5 Cs fountain clock and its evaluation”, Metrologia 52 (2015) 454–468.

[9] Vanier J. and Audoin C. 1989 The Quantum Physics of Atomic Frequency Standards (Bristol: Hilger) p 785.

Microfabricated vapor cells for miniature atomic clocks based on post-sealing activated cesium dispensers

V. Maurice, J. Rutkowski, E. Kroemer, S. Bargiel, N. Passilly, R. Boudot, R. Chutani, S. Galliou and C. Gorecki
Institut FEMTO-ST
(UMR CNRS 6174, Université Bourgogne Franche-Comté, ENSMM)
Besançon, France

L. Mauri and M. Moraja
SAES Getters
Lainate, Italy

***Abstract*—We report techniques based on cesium dispensers to fill microfabricated vapor cells for miniature atomic clocks applications. Two main types of dispensers are considered, which take the form of pills or paste. Whereas the pill contains a large quantity of Cs, the paste is more compatible with wafer-level fabrication. In both cases, the main advantage is the release of the cesium vapor only once the cell has been sealed, ensuring an optimal cell fabrication. Activation is thus performed through local heating of the dispenser with a laser. Cells using both dispenser types are shown to be compatible with atomic clocks requirements, namely a clock frequency instability below 1 x 10^{-11} at one day integration time.**

Keywords—alkali vapor cells; alkali vapor dispensing; miniature atomic clocks

I. INTRODUCTION

Microfabricated alkali vapor cells are one of the main components of miniature atomic clocks. The advent of such miniaturized clocks has been partly allowed by microelectromechanical systems fabrications means, providing small and low-cost cells [1]. The latter are often based on silicon, in which cavities are etched, and glass, used to sandwich and thereby seal the cavities. Although this architecture is now being used by several actors, main differences still lie in the cell filling of alkali metals and buffer gas, for which various solutions have been proposed.

In early attempts, barium azide and cesium chloride were introduced in the cells before sealing, but it led to atmosphere instability because of recombination of nitrogen with barium [2]. Then, another solution consisted in pipetting elemental cesium in the cells, in order to avoid trapping any precursor after sealing. This approach yielded a much more stable atmosphere [3]. Nevertheless, the cells were filled one by one, and it was consequently later proposed to employ an array of micromachined nozzles aligned with the cell one [4].

A technique, more compatible with wafer-level fabrication, is based on cesium azide (CsN_3) [5]. In this case, the compound, is deposited by evaporation through a shadow mask, over the entire cell wafer. After anodic bonding, UV radiation is used to decompose the compound into elemental alkali metal and nitrogen. An alternative to deposit Cs azide is to dilute it in deionized water and pipetted it into the cells [6, 7]. Yet, the quantities of Cs and N_2 being linked, the consumption of Cs during cell passivation might not be compensated for the nominal N_2 pressures.

Our approach was thus to insert a Cs dispenser in the cells. Such dispenser has the main advantage to remain inert at the temperature of anodic bonding (typically 350°C) ensuring an optimal and hermetic sealing. Hence, once the cells are closed, a high power laser diode is used to locally heat the dispenser above 600°C, temperature at which the reduction reaction of the precursors starts and releases pure Cs vapor [8, 9]. Another advantage is that Cs quantity is not linked with buffer gas pressure as, e.g., in the cesium azide based solution.

In this framework, two different types of dispensers have been tested. On the one hand, we used a solid cesium dispenser (trade name Cs/AMAX/Pill/1-0.6 from SAES Getters) taking the form of a pill. It is composed of a zirconium-aluminum alloy powder mixed to chromium-free cesium precursor. This type of dispenser provides robustness and cell batches filled by this manner have already shown reliability over several years. Nevertheless, pills dispensers still presents several drawbacks. First of all, their insertion in the cell preform is a slow process and can be impeded by the tendency of pills to pick up ambient humidity and to disaggregate after a while. Secondly, pills are relatively cumbersome and the cavity hosting them is quite large. It typically occupies half the cell volume [10] and prevents decreasing the cell size.

On the second hand, we employed more recently a cesium dispensable paste [11]. This paste can more conveniently be deposited using conventional liquid dispensing techniques such

978-1-5386-2916-1/$31.00 ©2017 IEEE

as screen or stencil printing, spray coating, micro-drop dispensing, stamping or inkjet printing. Such deposition techniques are more suitable for wafer-level production than pick and place solutions. Unlike dispenser pills, the paste can be patterned at the desired size so that the cell volume can be reduced. The paste was specifically developed and provided by SAES Getters. It is a proprietary chromate-free formulation composed of an organic-inorganic mixture of cesium molybdate (Cs_2MoO_4, Zr-Al alloy powder, a stabilizer and a binder). Once deposited and dried at room temperature, the paste can be consolidated through a heat treatment (typically at 200°C for 1 hour). Like for dispenser pills, a high-power laser can be used to decompose cesium molybdate and produce elemental cesium.

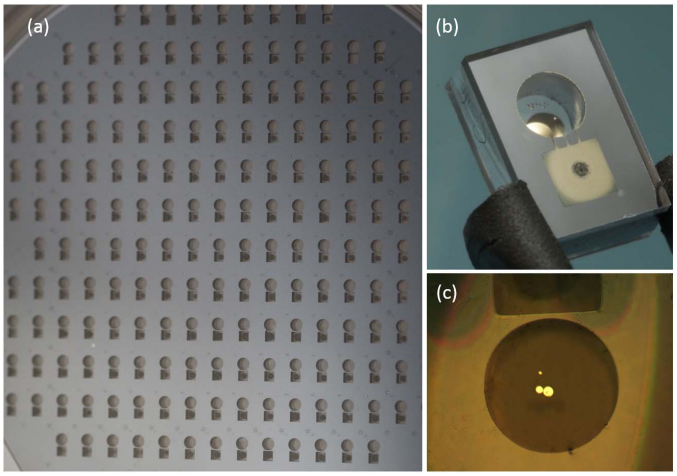


Fig. 1. Examples of (a) a 4" wafer including about 200 cells before dicing, (b) a cell with a high quantity of condensed Cs resulting from laser activation of a dispenser pill and (c) a reasonable quantity of condensed Cs.

II. CHARACTERIZATION & RESULTS

The fabricated cells have been characterized with a linear absorption spectroscopy setup where several cells can be measured in parallel over long period of time as well as with a bench-top clock prototype based on coherent population trapping (CPT).

Absorption spectroscopy shows that a cesium saturated vapor can be maintained within the cells for more than a year at 85°C. When using dispensers made of paste, a limited amount should be deposited within the cell. It is interesting to notice that cells containing a larger quantity of paste (which was then in contact with the Si sidewalls) did not show cesium absorption after a few weeks.

The cells were later on placed on a CPT based clock prototype, which includes a vertical-cavity surface-emitting laser (VCSEL) resonant with the Cs D_1 line and frequency-modulated at 4.596 GHz. In this case, the tested cells are filled with a neon buffer gas, in order to get a narrower resonance signal and a better frequency measurement resolution.

For the measurement of one cell filled with paste, the contribution of the AC Stark shift to the clock frequency has been discarded by measuring the clock frequency as a function of the optical power in order to extrapolate it at null laser power. Variations of such frequency over time are expected to partly correspond to the inner atmosphere variations of the cell. The fractional frequency drift rate recorded during nearly 2 weeks is estimated at around $-4.4.\ 10^{-12}$ per day, and thus makes the cell compliant with a clock fractional frequency stability objective at the level of $1.\ 10^{-11}$ at one day integration time.

ACKNOWLEDGMENT

This work was supported by the Direction Générale de l'Armement (DGA), Région Franche-Comté, Labex FIRST-TF and Bpifrance. This work was also partly supported by the French RENATECH network and its FEMTO-ST technological facility.

The authors gratefully acknowledge the help from C. Rocher, P. Abbé, M. Abdel Hafiz, R. Vicarini and L. Gauthier-Manuel (FEMTO-ST).

REFERENCES

[1] J. Kitching, S. Knappe, and L. Hollberg, "Miniature vapor-cell atomic-frequency references," Appl. Phys. Lett., vol. 81, pp. 553-555 (2002).

[2] L.-A. Liew, S. Knappe, J. Moreland, H. G. Robinson, L. Hollberg, and J. Kitching, "Microfabricated alkali atom vapor cells," Appl. Phys. Lett., vol. 84, pp. 2694-2696 (2004).

[3] S. Knappe, V. Gerginov, P. D. D. Schwindt, V. Shah, H. G. Robinson, L. Hollberg, and J. Kitching, "Atomic vapor cells for chip-scale atomic clocks with improved long-term frequency stability," Opt. Lett., vol. 30, pp. 2351-2353 (2005).

[4] M. A. Perez, S. Knappe, and J. Kitching, "MEMS techniques for the parallel fabrication of Chip Scale Atomic Devices," 2010 IEEE Sensors, Kona, HI, 2010, pp. 2155-2158.

[5] L.-A. Liew, J. Moreland, and V. Gerginov, "Wafer-level filling of microfabricated atomic vapor cells based on thin-film deposition and photolysis of cesium azide", Appl. Phys. Lett., vol. 90, p. 114106 (2007).

[6] S. Woetzel, V. Schultze, R. IJsselsteijn, T. Schulz, S. Anders, R. Stolz, and H.-G. Meyer, "Microfabricated atomic vapor cell arrays for magnetic field measurements", Review of Scientific Instruments, vol. 82, 033111 (2011).

[7] T. Overstolz, J. Haesler, G. Bergonzi, A. Pezous, P.-A. Clerc, S. Ischer, J. Kaufmann, and M. Despont, "Wafer scale fabrication of highly integrated rubidium vapor cells", in 27th International Conference on Micro Electro Mechanical Systems (MEMS) (IEEE, 2014) pp. 552–555.

[8] A. Douahi, L. Nieradko, J.-C. Beugnot, J. Dziuban, H. Maillote, S. Guérandel, M. Moraja, C. Gorecki, and V. Giordano, "Vapour microcell for chip scale atomic frequency standard", Electronics Letters vol. 43, p. 34 (2007).

[9] M. Hasegawa, R. K. Chutani, C. Gorecki, R. Boudot, P. Dziuban, V. Giordano, S. Clatot, and L. Mauri, "Microfabrication of cesium vapor cells with buffer gas for MEMS atomic clocks", Sens. Actuat. A: Phys., vol. 167, p. 594 (2011).

[10] R. K. Chutani, M. Hasegawa, V. Maurice, N. Passilly, C. Gorecki, "Single-step deep reactive ion etching of ultra-deep silicon cavities with smooth sidewalls", Sens. Actuat. A: Phys., vol. 208, pp. 66-72 (2014).

[11] V. Maurice, J. Rutkowski, E. Kroemer, S. Bargiel, N. Passilly, R. Boudot, C. Gorecki, L. Mauri, M. Moraja, "Microfabricated vapor cells filled with a cesium dispensing paste for miniature atomic clocks", under revision in Appl. Phys. Lett., Feb. 2017.

Laser intensity noise transfer for pulsed vapor-cell clocks with optical detection

Michele Gozzelino
Dept. of Physical Metrology
INRIM
Dept. of Electronics and Telecommunications
Politecnico di Torino
Torino, Italy
Email: m.gozzelino@inrim.it

Salvatore Micalizio, Filippo Levi, Aldo Godone and Claudio E. Calosso
Dept. of Physical Metrology
INRIM
Torino, Italy
Email: c.calosso@inrim.it
Email: s.micalizio@inrim.it
Email: f.levi@inrim.it

***Abstract*—We propose a signal-theory approach to estimate the contribution from laser intensity noise to the short-term stability of compact atomic clocks based on optical detection. We remove the approximation of white intensity noise, which is usually found in literature, and propose a method for a more faithful estimate, given an arbitrary noise spectrum at the input. This is of fundamental importance, since laser intensity noise is currently one of the main limiting factors of vapor-cell clocks.**

I. Introduction

Vapor-cell clocks with optical detection have recently reached very good performances in terms of frequency stability [1–5], especially in the short term, reaching the 10^{-13} level of fractional frequency stability at one second.
It is common practice to use optical detection by monitoring the absorption profile of a laser after the passage through the cell [6]. Laser amplitude noise at the output of the cell is thus directly added to the error signal, degrading the clock performances (laser AM-AM transfer). Typically the optical probing is performed using diode lasers. Even though this kind of lasers show amplitude noise levels near the shot noise (or even below when implementing amplitude squeezing [7]), other effects can amplify it. In particular, the passage through a resonant vapor gives rise to amplitude noise degradation, a mechanism known as FM-AM conversion [8,9]). In the end, the resulting relative intensity noise (RIN) of the laser impinging the photo-detector gives a contribution to the clock short-term stability of few parts in 10^{-13}.

Indeed, since other stability contributions (e.g. from shot-noise and Dick-effect from the local oscillator) are kept in the low 10^{-14} [10], laser amplitude noise is the main limiting factor of most of the state-of-the-art prototypes.

A full comprehension of the transfer mechanism from a given amplitude-noise level to the clock's stability is then needed. This would provide a better characterization of the clock's stability contributions. Moreover, from an operational point of view, it can provide strategies to mitigate the unwanted performance degradation. Finally, it allows to make precise constraints on the kind of source needed to reach a certain target.

II. Noise-transfer model

Existing estimates of the laser AM-AM and FM-AM contributions to the clock stability make use of some approximations. Typically white noise is assumed as input [11,12]. This assumption is not always valid, especially in pulsed operation where the main stability contribution comes from Fourier frequencies in the interval between 100 and 200 Hz (around the clock cycle frequency). The proposed model aims to calculate the contribution to the stability $\sigma_y(\tau)$ given the laser relative intensity noise (RIN) for a clock in pulsed operation. The experimental set-up is pictorially depicted in fig. 1. We neglect laser noise during the pumping pulse, since its effect is mitigated by saturation, and consider only the laser intensity noise during the detection phase.

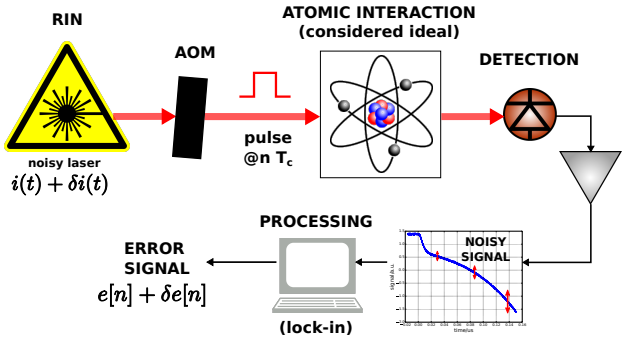


Figure 1. Pictorial representation of the scheme and of the quantities involved. Typical timings for the pulsed operations are $\tau_d = 200$ μs and $T_c = 5$ ms

In figure 2 the relative signal theory model is presented in time domain.
The first block shows how the clock operation processes the laser intensity noise $\delta i(t)$ during the optical detection phase. $h_a(t)$ is the impulse response describing the laser probing of the atoms; $h_\Delta(t)$ represents the lock-in differentiation performed to obtain the error signal. The latter is available as a sequence of samples $e[n] + \delta e[n]$, each every $2T_c$, after both sides of the atomic resonance are probed. Finally, the

978-1-5386-2916-1/$31.00 ©2017 IEEE

output is scaled to fractional frequency[1] and the Allan variance algorithm is performed.

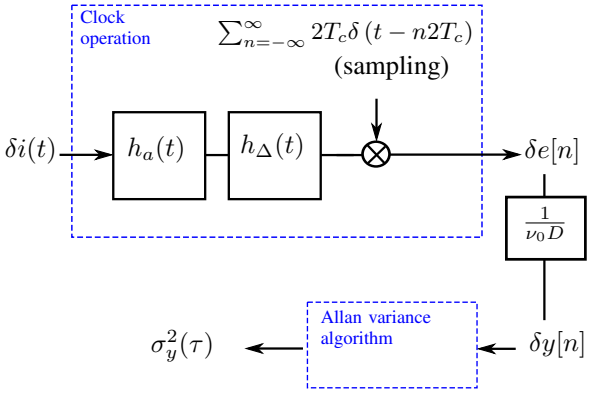


Figure 2. Block scheme of the model predicting the clock stability, with a given laser intensity noise $i(t)$ as input, in time domain.

We have developed the model by means of the Fourier formalism as in [13]. $h_a(t)$, $h_\Delta(t)$ and $h_A(t)$ (the Allan variance impulse response) are translated into their respective Fourier transforms: $H_a(f)$, $H_\Delta(f)$ and $H_A(f)$. We can define also the total transfer function of the clock as $H(f) = H_a(f)H_\Delta(f)$. This leads to the sequent formula to predict the clock fractional frequency stability [14]:

$$\sigma_y^2(\tau) = \frac{1}{D^2\nu_0^2}\int_{-f_c/2}^{f_c/2} |H_A(f,\tau)|^2 S_{E'}(f)df \qquad (1)$$

where ν_0 is the mean resonance frequency, D the signal/frequency discriminant, and $S_{E'}$ the Power Spectral Density of the error signal (considering only the contribution from the laser RIN) including the aliased part:

$$S_{E'}(f) = \sum_{k=-\infty}^{\infty} |H(f+kf_c/2)|^2 S_I(f+kf_c/2) \qquad (2)$$

Equations (1) and (2) are useful relations, which directly link the laser intensity noise (usually experimentally available as a Power Spectral Density), to its contribution to the total clock stability.

III. CONCLUSION

We have analysed in detail how laser intensity noise affects the short-term stability of a clock (in pulsed operation with optical detection), making use of signal-theory formalism. This allows for a reliable estimation, starting from a given arbitrary intensity noise spectrum at the input. The model also gives more insight into the origin of the noise transfer, which is basically, as in the Dick-effect case, an aliasing process. A precise estimation can lead to a clear discrimination between the noise sources or to a proper choice of the laser source during the design process. It is to be noted that, concerning the long-term stability, the Fourier frequencies of interest in the aliasing process are the odd multiples of $f_c/2$, due to the periodicity of the lock-in transfer function ($H_\Delta = 4sin^2(\pi f T_c)$). This is in agreement with the intuitive reasoning that a sinusoidal noise will not interfere with the lock-in if its periodicity is equal to an even multiple of the lock-in differentiating cycle time (T_c). Finally, to give an order of magnitude of the impact of aliasing to the short term stability, we can apply the model back to the simplified case of white noise. In this case, the noise level is degraded by a factor $4T_c/\tau_d$, which is greater than 100 for the typical timing sequence of compact vapor-cell clocks, resulting in a degradation of a factor 10 in the stability.

[1]The model, as stated above, predicts the stability of the clock in open-loop condition. We can assume its validity also in closed-loop operation, given the high-gain of the loop integrator. Thus (at least for long averages times, i.e. $\tau >> T_c$) the error signal noise is directly translated into frequency noise given the slope of the signal/frequency discriminant D.

REFERENCES

[1] S. Kang, M. Gharavipour, C. Affolderbach, F. Gruet, and G. Mileti, "Demonstration of a high-performance pulsed optically pumped Rb clock based on a compact magnetron-type microwave cavity," *Journal of Applied Physics*, vol. 117, no. 10, p. 104510, 2015.

[2] M. A. Hafiz and R. Boudot, "A coherent population trapping Cs vapor cell atomic clock based on push-pull optical pumping," *Journal of Applied Physics*, vol. 118, no. 12, p. 124903, 2015.

[3] G. Dong, J. Deng, J. Lin, S. Zhang, H. Lin, and Y. Wang, "Recent improvements on the pulsed optically pumped rubidium clock at SIOM," *Chin. Opt. Lett.*, vol. 15, p. 040201, Apr 2017.

[4] P. Yun, F. Tricot, C. E. Calosso, S. Micalizio, B. François, R. Boudot, S. Guérandel, and E. de Clercq, "High-performance coherent population trapping clock with polarization modulation," *Phys. Rev. Applied*, vol. 7, p. 014018, Jan 2017.

[5] T. Bandi, C. Affolderbach, C. Stefanucci, F. Merli, A. K. Skrivervik, and G. Mileti, "Compact high-performance continuous-wave double-resonance rubidium standard with $1.4 \times 10^{-13} \cdot \tau^{-1/2}$ stability," *IEEE Transactions on Ultrasonics, Ferroelectrics, and Frequency Control*, vol. 61, pp. 1769–1778, November 2014.

[6] S. Micalizio, C. E. Calosso, A. Godone, and F. Levi, "Metrological characterization of the pulsed Rb clock with optical detection," *Metrologia*, vol. 49, no. 4, p. 425, 2012.

[7] S. Machida, Y. Yamamoto, and Y. Itaya, "Observation of amplitude squeezing in a constant-current-driven semiconductor laser," *Phys. Rev. Lett.*, vol. 58, pp. 1000–1003, Mar 1987.

[8] J. C. Camparo, "Conversion of laser phase noise to amplitude noise in an optically thick vapor," *J. Opt. Soc. Am. B*, vol. 15, pp. 1177–1186, Mar 1998.

[9] J. C. Camparo and J. G. Coffer, "Conversion of laser phase noise to amplitude noise in a resonant atomic vapor: The role of laser linewidth," *Phys. Rev. A*, vol. 59, pp. 728–735, Jan 1999.

[10] B. Franois, C. E. Calosso, M. A. Hafiz, S. Micalizio, and R. Boudot, "Simple-design ultra-low phase noise microwave frequency synthesizers for high-performing Cs and Rb vapor-cell atomic clocks," *Review of Scientific Instruments*, vol. 86, no. 9, p. 094707, 2015.

[11] C. Audoin, G. Santarelli, A. Makdissi, and A. Clairon, "Properties of an oscillator slaved to a periodically interrogated atomic resonator," *IEEE Transactions on Ultrasonics, Ferroelectrics, and Frequency Control*, vol. 45, pp. 877–886, July 1998.

[12] G. Santarelli, P. Laurent, P. Lemonde, A. Clairon, A. G. Mann, S. Chang, A. N. Luiten, and C. Salomon, "Quantum projection noise in an atomic fountain: A high stability Cesium frequency standard," *Phys. Rev. Lett.*, vol. 82, pp. 4619–4622, Jun 1999.

[13] C. E. Calosso, C. Clivati, and S. Micalizio, "Avoiding aliasing in allan variance: An application to fiber link data analysis," *IEEE Transactions on Ultrasonics, Ferroelectrics, and Frequency Control*, vol. 63, pp. 646–655, April 2016.

[14] F. Vernotte, G. Zalamansky, and E. Lantz, "Time stability characterization and spectral aliasing. Part II: a frequency-domain approach," *Metrologia*, vol. 35, no. 5, p. 731, 1998.

The NRC-FCs2 primary frequency standard at the National Research Council Canada

Scott Beattie, Bin Jian, A. John Alcock, John Bernard, and Marina Gertsvolf
National Research Council Canada
Ottawa, Canada

Rich Hendricks, Filip Ozimek, and Krzysztof Szymaniec
National Physical Laboratory
Teddington, UK

Kurt Gibble
Department of Physics
The Pennsylvania State University
State Park, USA

***Abstract*—At the National Research Council Canada, we are performing final assembly and initial testing of our new atomic fountain clock, NRC-FCs2. This fountain clock incorporates several improvements in the optical, microwave, and computer systems from our previous generation clock, NRC-FCs1, as well as a new physics package designed at the National Physical Laboratory (UK). With these changes, NRC-FCs2 is expected to reach uncertainties < 5×10^{-16}. We will discuss the recent improvements made in the various subsystems of NRC-FCs2 and present preliminary results in its evaluation.**

Keywords—Primary frequency standard, clock, atom cooling and trapping

I. INTRODUCTION

Caesium fountain clock primary frequency standards provide the most accurate realization of the SI second. Through continued advances, fountain clocks have reached fractional uncertainties approaching 10^{-16}. Primary frequency standards hold particular importance in the world of metrology as in addition to serving as the reference for frequency and time, the SI second is fundamental in the definitions and practical realizations of the SI metre and candela, as well as in the volt and the future kilogram and kelvin.

At the National Research Council (NRC), we are currently integrating a new physics package into our system for our new primary frequency standard, NRC-FCs2, and beginning initial testing of its performance. This fountain clock utilizes several refurbished subsystems of our previous generation fountain, NRC-FCs1. In addition, the physics package of NRC-FCs2 was designed and assembled at the National Physical Laboratory (NPL) in the UK. We will discuss our recent improvements and our preliminary results from testing and evaluation.

II. APPARATUS

Many systems have been improved from NRC-FCs1. This includes the laser and optical system, where the laser lock bandwidth and stability have been improved by adding fast current feedback to the cooling laser diode. The optical layout has been modified to improve stability and efficiency. In addition, improved servos to the AOM powers have yielded higher stability and control of the laser intensities. The computer system has been modified to give improved flexibility and control of the experimental sequence. We have also improved our microwave local oscillator to the system which will allow us to reach short term stabilities of $\sigma_y(1\ \mathrm{s}) \sim 2 \times 10^{-13}$, an improvement of more than a factor of two over the previous performance.

The physics package of NRC-FCs2 was built at NPL (UK) and was based on the proven design of NPL-CsF2 fountain clock. The physics package includes a vacuum system containing atom trapping and detection regions, a magnetically shielded drift region with a water cooling jacket for temperature stabilization, and microwave cavities for Ramsey and state selection interactions. The system design allows for the cancellation of the collisional shift and includes a Ramsey cavity design which minimizes the distributed cavity phase shift, one of the main contributors to the systematic uncertainty in state of the art fountain clocks [1, 2, 3].

III. INITIAL TESTING

The physics package for NRC-FCs2 was shipped to Canada from the UK and arrived in late January, 2017. The vacuum system was still under ultra-high vacuum upon its arrival after a door-to-door shipping time of about 20 days. Caesium

ampoules were added to the system, and after two weeks, the entire system (with Cs) was at a pressure of ~10^{-10} mbar.

Within a month of its arrival at the NRC, the physics package had been integrated with our other systems such that we observed the laser-cooled atoms in a magneto optical trap, and detected atoms after a launch to 30 cm above the Ramsey cavity. The microwave local oscillator and magnetic shielding will soon be added to the system, at which point Ramsey fringes can be detected.

IV. CONCLUSION

The expected type-B uncertainty for NRC-FCs2 after full evaluation is at the level of a few parts in 10^{16}, at which point it is expected that it will contribute to the steering of UTC/TAI. We are currently working to test the performance of NRC-FCs2 and evaluate the frequency shifts and associated uncertainties of several systematic effects. We will present results from our measurements of shifts associated with the second order Zeeman effect, cold atomic collisions, microwave leakage, and blackbody radiation. We will also present our progress on evaluating the distributed cavity phase and microwave lensing shifts of NRC-FCs2.

REFERENCES

[1] K. Szymaniec, S. E. Park, G. Marra, and W. Chalupczak, "First accuracy evaluation of the NPL-CsF2 primary frequency standard," *Metrologia*, **47**, 4, June 2010, pp. 363-376, doi:10.1088/0026-1394/47/4/003.

[2] R. Li, K. Gibble, and K. Szymaniec, "Improved accuracy of the NPL-CsF2 primary frequency standard: evaluation of distributed cavity phase and microwave lensing frequency shifts," *Metrologia*, **48**, 5, August 2011, pp. 283-289, doi:10.1088/0026-1394/48/5/007.

[3] R. Li and K. Gibble, "Evaluating and minimizing distributed cavity phase errors in atomic clocks," *Metrologia*, **47**, 5, August 2010, pp. 534-551, doi:10.1088/0026-1394/47/5/004.

Closed-Loop Characterization of Cesium Magnetometers Operating at Ambient Temperature

Janet W. Lou and Geoffrey A. Cranch
Optical Sciences Division
U.S. Naval Research Laboratory
Washington, DC 20375 USA
janet.lou@nrl.navy.mil

***Abstract*—Closed-loop characterizations of optically-pumped Cs vapor-based magnetometers operating at ambient temperature are presented. The optical power is shown to play a critical role in defining the magnetic field sensitivity due to its effect on signal-to-noise ratio and dephasing lifetime. A closed-loop characterization reveals additional factors such as the uniformity of the magnetic field and oscillator noise that influence the performance of a practical magnetometer, which do not arise in an open-loop characterization.**

Keywords—atomic vapor magnetometer; vapor cell

I. INTRODUCTION

Optically-pumped atomic vapor magnetometers are of interest for a range of applications from medicine to geological and military surveying [1]. Remote underwater applications require high sensitivity and high reliability with long-term stability. We have previously reported a magnetometer specifically aimed at meeting the challenges of a remote system operating without thermal control, which eliminates the need for electronics in the water [2].

A practical magnetometer is typically operated in a closed-loop configuration to provide a large dynamic range. However, this may effect the measurement resolution compared with an open-loop configuration. Typical open-loop measurements, such as dephasing time (T_2) and signal-to-noise ratio (SNR), can indicate the *potential* magnetic field sensitivity but those results can be misleading. They do not take into account the combined effects, nor do they account for magnetic field uniformity or oscillator noise. Our measurements illustrate the important role of optical power on SNR and T_2, in the context of a practical, closed-loop magnetometer.

II. EXPERIMENTAL SETUP

The magnetometer setup is a dual-laser system as shown in Fig. 1. Two lasers are frequency locked using the DAVLL technique [3]. The pump laser is locked to the D2 transition and amplitude modulated by a VCO-driven fast switch. The probe laser is locked to the D1 transition. The pump and probe are spatially overlapped and pass through the length of the Cs vapor cell. At the output, the pump is removed with a bandpass filter. Following the NMOR technique [4], the probe signal is sent through a Wollaston prism and the two orthogonal polarizations

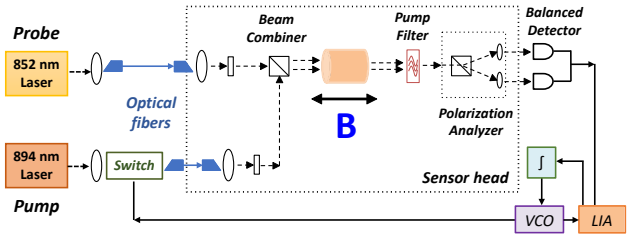


Fig. 1: Closed-loop magnetometer setup. VCO = voltage-controlled oscillator. LIA = lock-in amplifier.

are detected by a balanced amplified detector. We compare two cylindrical cells with: (1) 7.5 mm diameter, 2 cm length, and 200 Torr Ne buffer gas, and (2) 15 mm diameter, 7.5 cm length, and 50 Torr Ne buffer gas.

The vapor cells are characterized inside three layers of magnetic shielding, which reduces the ambient magnetic field to ~150 nT. A solenoid coil inside the chamber generates a controlled magnetic field parallel to the direction of beam propagation.

A. Upper state lifetimes

The upper state lifetimes of the vapor cells are characterized with the modified Franzen method [5]. The individual detector outputs as well as the balanced output are recorded by an oscilloscope. The ratio of the measured difference signal to the sum of the individual signals is numerically fit to the sum of two exponentials to obtain the relaxation time, T_2.

B. Signal-to-noise ratio

The SNR of the difference signal from the balanced detector is measured using a spectrum analyzer. For this measurement, the modulation frequency is set to twice the Larmor frequency corresponding to the magnetic field set by the solenoid. Note that in this case the VCO driving the switch is operating as a fixed frequency oscillator (*i.e.*, without a feedback signal).

C. Closed-loop noise floor

The LIA measures the in-phase and out-of-phase components of the balanced detector signal, referenced to the VCO output frequency. We send the out-of-phase (dispersive) signal into an integrator and feed back the error signal to the

This work was supported by the Office of Naval Research.

U.S. Government work not protected by U.S. copyright

VCO. Thus, the VCO output frequency is locked to the detected Larmor frequency. The integration time is set to achieve a loop bandwidth of ~20 Hz.

III. Results

Each vapor cell is characterized as a function of optical power. Using the results of the open-loop T_2 and SNR measurements, expected noise floors are derived. Finally, measurements of the error signal in a closed-loop configuration demonstrate the true measurement resolution.

A. Lifetime and SNR

Fig. 2 shows the measured T_2 for each of the vapor cells. Fig. 3 shows the measured SNR at 50 Hz from the carrier. In both cases, data is shown as a function of probe power for average pump powers (50% duty cycle) ranging from ~0.1 to ~1.8 mW. Note that it is necessary to keep the probe power below the peak pump power in all cases in order to maintain a good dispersive signal. There is a strong exponential dependence of the SNR and only a relatively weak dependence of T_2 on probe power. For both cells, the SNR becomes limited by the intrinsic noise of the VCO at high powers.

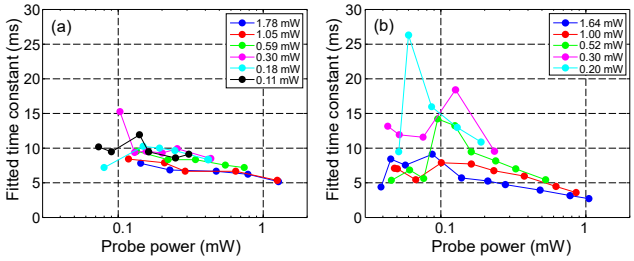


Fig. 2. Measured lifetimes. (a) 50 Torr cell. (b) 200 Torr cell.

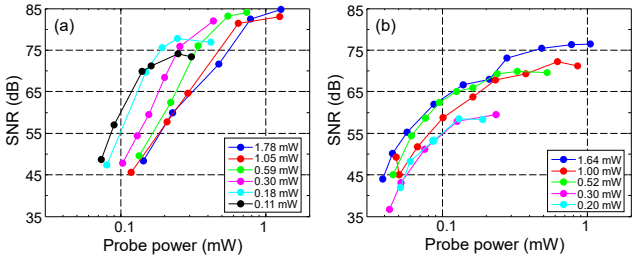


Fig. 3. Measured SNRs. (a) 50 Torr cell. (b) 200 Torr cell.

B. Closed-loop noise floor

The true noise floor of the closed-loop magnetometer is given by the error signal voltage applied to the VCO expressed in term of magnetic field strength. The noise spectral density at 10 Hz is shown in Fig. 4. Also shown is the theoretical magnetic field resolution applicable for the corresponding open-loop configuration [6], given by $dB = h/(g_s*\mu_B*SNR*T_2*\tau^{1/2})$, where h is Planck's constant, g_s is the electron Lande factor, μ_B is the Bohr magneton, and τ is the measurement time.

IV. Discussion and Summary

The measured closed-loop magnetic field sensitivity results are more than an order of magnitude higher than open-loop measurements suggest. The SNR at 10 Hz, which is lower by a factor of 2 to 4 compared to that at 50 Hz due to the VCO noise,

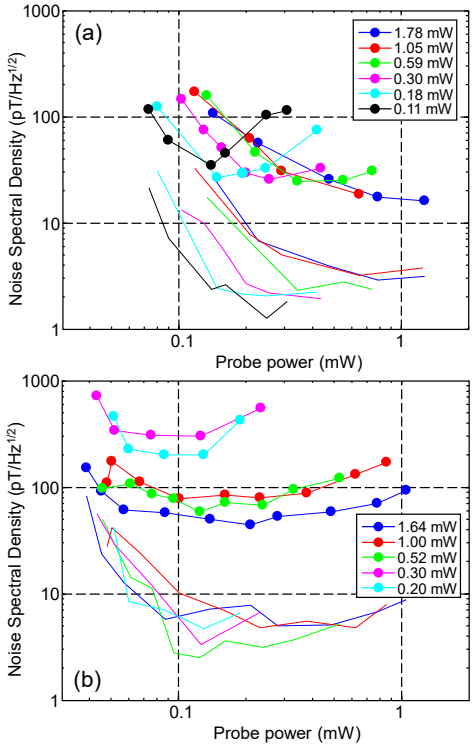


Fig. 4. Measured @ 10 Hz (x and dotted lines) and calculated (solid lines) noise spectral density. (a) 50 Torr cell. (b) 200 Torr cell.

accounts for part of that degradation. Linewidth broadening also contributes to an increased noise floor when operating closed-loop. In the case of the 200 Torr cell, this broadening is due to the buffer gas. In the case of the 50 Torr cell, the non-uniformity of the magnetic field over its relatively long length also leads to broadening.

In summary, optically-pumped Cs vapor cell magnetometers operating at ambient temperature are characterized in a closed-loop system. These results reveal necessary trade-offs for implementing a practical magnetometer that are not obvious using open-loop characterizations. We show that decreasing the optical probe power can increase the T_2, but with a significant degradation to the SNR. To optimize the magnetometer sensitivity, the pump and probe powers should be carefully selected to yield the highest SNR×T_2 product.

References

[1] D. Budker and M. Romalis, "Optical magnetometry," Nat. Phys., vol. 3, no. 4, pp. 227-234, Apr. 2007.

[2] J. W. Lou, F. K. Fatemi, and G. A. Cranch, "Remote Atomic Vapor Magnetometer with Sub-pT Resolution Operating at Ambient Temperature," 2015 Joint Conf. IEEE Intern. Freq. Contr. Symp. & Europ. Freq. Time Forum, Denver, CO, A2L-B4, 2015.

[3] K. L. Corwin, Z.-T. Lu, C. F. Hand, R. J. Epstein, and C. E. Wieman, "Frequency-stabilized diode laser with the Zeeman shift in an atomic vapor," Appl. Opt., vol. 37, no. 15, pp. 3295-3298, May 1998.

[4] D. Budker, D. F. Kimball, S. M. Rochester, V. V. Yashchuk, and M. Zolotorev, "Sensitive magnetometry based on nonlinear magneto-optical rotation," Phys. Rev. A, vol. 62, no. 4, 043403, Sep. 2000.

[5] F. A. Franz and E. Luscher, "Spin Relaxation of Optically Pumped Cesium," Phys. Rev., vol. 135, no. 3A, pp. A582-A588, Aug. 1964.

[6] D. Budker and D. F. J. Kimball, ed., Optical Magnetometry, New York: Cambridge, 2013.

Compact Atom Interferometer Using a Single Laser

Sheng-wey Chiow and Nan Yu*
Jet Propulsion Laboratory, California Institute of Technology
Pasadena, California, USA
*nan.yu@jpl.nasa.gov

***Abstract*—A laser system for a light-pulse atom interferometer typically includes a number of laser sources for cooling and for atom optics to meet different frequency detuning requirements at different stages of a measurement sequence. The number of laser units required makes the achievable minimum size and power of the instrument challenging, especially for space applications. We demonstrate a compact cesium atom interferometer operated by only a single laser. This is achieved by dynamically changing the laser output frequency while maintaining spectroscopic reference to an atomic transition. We are able to generate cold atoms and obtain atom interferometer fringes all with the same laser.**

Keywords—atom interferometer, Cs atoms, cold atom

I. INTRODUCTION

Atom interferometer (AI) based sensors exhibit precision and accuracy unattainable with classical sensors, thanks to the inherent stability of atomic properties. Efforts focusing on miniaturizing and mobilizing atomic sensors for field applications have been active worldwide. The complexity of required laser system and the size of vacuum chamber driven by optical access requirement limit the applicability of such technology in size, weight, and power (SWaP) challenging environments, such as in space. For instance, a typical physics package of AI includes six viewports for laser cooling and trapping, two viewports for AI beams, and two more access paths for detection and a vacuum pump. Similarly, a typical laser system for an AI includes two lasers for cooling and repumping, and two for Raman transitions as the AI beam splitters. In this paper, we report our efforts in developing a miniaturized atomic accelerometer for planetary exploration. We describe a physics package configuration having minimum needed optical access (thus small volume), and a laser optics system utilizing a single laser for the entire sensor operation.

II. LASER SYSTEM

In cold atom experiments, a common laser configuration is to have one or more master lasers locked to atomic transitions, and the frequency of light to the atoms is shifted by acousto-optic modulators (AOMs) and/or phase-locking of additional lasers. However, different frequency components are never applied at full power simultaneously. We develop a laser locking architecture that maximally utilizes the output power of a diode laser for atomic manipulations. In this configuration, ~10% of the laser output (at frequency f_0) is picked up for spectroscopy and laser frequency stabilization while the rest is directed to a frequency and amplitude modulation subsystem and then distributed to the atoms.

In the spectroscopy subsystem, instead of locking the light to an atomic transition directly, a frequency sideband (at frequency f_0+f_M) induced by a fiber-coupled phase modulator (PM) is used for error signal generation in the subsequent frequency modulation spectroscopy around an atomic transition at f_a. When the feedback loop is closed, the laser lases at $f_0=f_a-f_M$. Due to the huge bandwidth > 10 GHz of the PM, and an agile microwave direct digital synthesizer, f_0 can be rapidly tuned to provide a full coverage of cooling and atom optics, typically on the order of few GHz for Cs, with a proper choice of the atomic transition f_a. This scheme is similar to the configuration demonstrated in [1]. However, there is no stable isotope other than ^{133}Cs for spectroscopy, thus a complicated spectroscopy pattern emerges and depends on f_M, due to the phase-modulated sidebands. A lookup table of microwave power to the PM is developed and employed to minimize other resonant frequency sidebands, and an etalon of ~1 GHz bandwidth is inserted before the spectroscopy detector to eliminate their residual contributions. We achieve arbitrary frequency hopping pattern with a 1.5 GHz span, with settling time of < 5 ms per step, which is limited by the mechanical resonance of the extended cavity diode laser.

III. COMPACT PHYSICS PACKAGE

Large viewports are demanded for both laser cooling and atom optics. The minimum vacuum chamber dimension is limited by the number of optical accesses, which is larger than eight for six cooling beams and two atom optics beams. We reduce this critical number by two by utilizing one of the cooling beam paths for atom optics. While the frequency difference for the two purposes is mitigated by the above mentioned laser system, the different requirements for light polarization combination need to be addressed. We adapt liquid crystal variable retarders (LCVRs) for dynamic switching of polarization combination from σ^+-σ^- for cooling to lin⊥lin for two-photon Raman transitions in one path, thus enabling the beam path sharing. As opposed to high voltage needed for Pockels cells, LCVRs are effectively capacitors driven by 2 kHz square waves with up to 10 V rms, contributing marginally to the control system. In fact, we drive the LCVRs directly with 10 V analog output channels of a multifunction I/O board. A quarter-wave switching time of ~ 3 ms is achieved, which is sufficient for this demonstration.

With the functioning of the laser system, we demonstrated a Mach-Zehnder atom interferometer using two-photon Raman transitions on Cs. A fringe contrast of ~20% for 10 ms interrogation time is achieved, which is limited by the thermal width of the cloud.

IV. CONCLUSION

We demonstrate two approaches to reduce SWaP of future atomic sensors in a compact setup. A frequency agile single laser system is developed to support the entire frequency range for cooling and atom optics. An Mach-Zehnder AI fringe is obtained by using a beam path sharing configuration between cooling and atom interferometry. These approaches will significantly reduce the SWaP of future atomic sensors for space applications.

ACKNOWLEDGMENT

Authors gratefully acknowledge valuable discussions with Holger Mueller. This research was carried out at the Jet Propulsion Laboratory, California Institute of Technology, under a contract with the National Aeronautics and Space Administration.

REFERENCES

[1] Theron, Fabien, Olivier Carraz, Geoffrey Renon, Nassim Zahzam, Yannick Bidel, Malo Cadoret, and Alexandre Bresson. "Narrow linewidth single laser source system for onboard atom interferometry." *Applied Physics B* 118, no. 1 (2015): 1-5.

A large mode optical resonator for enhanced atom interferometry

Sapam Ranjita Chanu, Nicolas Mielec, David Holleville, Bess Fang, Arnaud Landragin, and Remi Geiger
LNE-SYRTE, Observatoire de Paris, PSL University,
CNRS, Sorbonne Universités, UPMC Univ.
Paris, France

Isabelle Riou and Benjamin Canuel
LP2N, Laboratoire Photonique, Numérique et Nanosciences
Université Bordeaux-IOGS-CNRS : UMR 5298
Talence, France.

Abstract— The development of atom interferometry in the last few decades has led to high precision measurements of inertial effects and tests of fundamental physics. New methods for higher sensitivity atom interferometers (AIs) are being explored, particularly the interrogation of atoms with optical cavities [1]. Its benefits would be higher optical power allowing large momentum transfer beam splitters, and possibly cleaner and controlled phase profiles. However high sensitivity AIs require long interrogation times, which combined with cold atom expansion, bring the challenges of large waists in cavities.

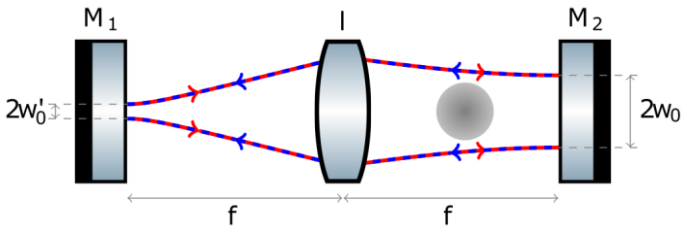


Fig. 1 Marginally stable resonator able to support a large diameter Gaussian beam suited for large momentum beam splitters in atom interferometry. The grey disc shows the area where atoms will be interrogated.

We propose an optical resonator composed of a convergent lens with two flat mirrors at its focal planes as shown on figure 1. When perfectly aligned any input field can be resonating inside. Especially, when a Gaussian beam, with waist w_0' on the first mirror, is inputted to the cavity, the lens conjugates it to the second mirror with waist $w_0 = \chi f/\pi\, w_0'$. This cavity is marginally stable and exhibits a half degenerate behaviour: all modes resonate at the same frequencies, odd and even modes being separated by half a free spectral range. Thus it does not have strong mode cleaning properties but it is able to magnify any input field. When misaligned, this cavity goes out of its degenerate behaviour and the circulating field begins to degrade due to mode filtering**.** A numerical study of the cavity behaviour, using an ABCD transfer matrix formalism, showed that typical controllable misalignments of a few micrometres would not be critical for atom interrogation. Further degradations due to surface defects and tilts are being investigated.

We realise this cavity with a 20 cm lens and an 8 µm input waist Gaussian beam which allows for a 7 mm waist inside the cavity. Atom interferometry in Raman configuration is done with two pulsed counter-propagating laser beams at 852 nm separated by a few GHz. The control of the cavity length cannot be realized using these beams since they are pulsed. We send a 771 nm laser derived from an ultrastable link to control the length of the cavity with a Pound-Drever-Hall scheme.

Keywords— Degenerate optical cavity; atom interferometer

REFERENCES

[1] P. Hamilton, M. Jaffe, J .M. Brown, L. Maisenbacher, B. Estey and H. Muller, "Atom Interferometry in an Optical Cavity ." Phys. Rev. Lett, vol. 114, p. 100405, 2015 .

[2] I . Riou, N. Mielec G. Lefevre, M. Prevedelli, A. Landragin, P. Bouyer, A. Bertoldi, R. Geiger , and B. Canuel, arXiv 1701.01473, 2017.

- FIRST-TF (ANR-10-LABX-48-01), and Equipex MIGA (ANR-11-EQPX-0028), city of Paris (Emergence project HSENS-MWGRAV), l'Observatoire de Paris, CNRS GRAM (Gravitation, Références, Astronomie, Métrologie) and H2020 - Marie Curie fellowship (Grant agreement 660081- MWGRAV).

Liquid-Level Sensing by a Cylindrical Piezoelectric Resonator Operating in a Trapped-Energy Mode

Ken Yamada and Koki Watanabe
Department of Electronic Engineering
Tohoku Gakuin University
Tagajo 985-8537, Japan

***Abstract*— A new configuration is presented for detecting a small-scale variation in liquid level. Here, a piezoelectric cylindrical resonator operating in a trapped-energy mode is employed instead of the plate-type resonators such as used in the former studies. It has been confirmed that steep variations in *G* on the dipping depth *d* is observed in the evanescent-field range.**

Keywords—liquid-level sensing; trapped-energy mode; cylindrical piezoelectric resonator

I. INTRODUCTION

A new method for detecting a small-scale variation in liquid level has been presented by the authors' group [1]-[8]. The method employs a piezoelectric thickness-wave resonator operating in a trapped-energy mode. In the trapped-energy vibration mode, an evanescent field is created in the unelectroded surrounding region of the vibrator. When this evanescent-wave region is dipped in a liquid, a small leakage of vibration energy occurs depending on the dipping depth. Therefore, small variations in liquid level are detected by observing the changes in the resonance characteristics of the vibrators, such as quality factor Q_m and the electric conductance G.

In this paper, a new attempt is presented to detect the liquid level using a cylindrical-type piezoelectric resonator operating in a trapped-energy mode.

II. RESONATOR CONFIGURATION AND EXPERIMENTAL SETUP

The trapped-energy resonator was made of a PZT cylinder (TOKIN NEPEC-6) of 10.0 mm outer diameter, 30.0 mm length, and 0.85 mm thickness, and polarized in the thickness direction, as shown in Fig. 1. A stripe electrode of 4.0 mm width was put around the center of the outer surface, and the inner surface was covered entirely with an electrode. The electric admittance characteristic observed in the air is shown in Fig. 2. The resonance frequency f_R was 3.722 MHz, and the quality factor Q_{mR} at f_R was about 300. Spurious-free response peculiar to the trapped-energy resonator is obtained around the resonance point.

The resonator was supported vertically by clamping its one end without affecting the main mode of vibration. Then, the cylinder was dipped in the liquids to be tested from its bottom (lower) end, as shown in Fig. 3. The clamping of the resonator in this manner would be applicable only to trapped-energy vibrators because conventional vibrators with full electrodes on both surfaces will degrade the quality factor and therefore deteriorate the sensitivity.

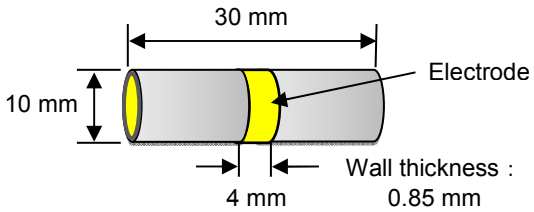


Fig. 1. Configuration of the cylindrical trapped-energy resonator.

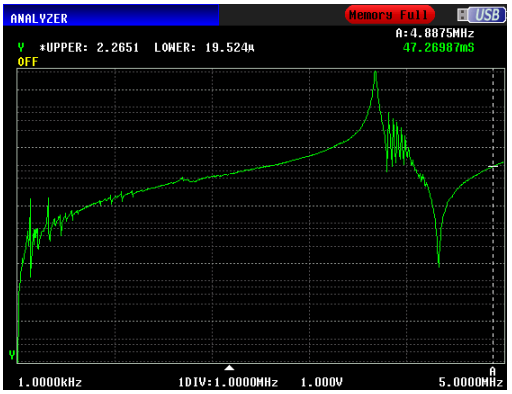


Fig. 2. Electric admittance characteristic of the trapped-energy resonator observed in the air.

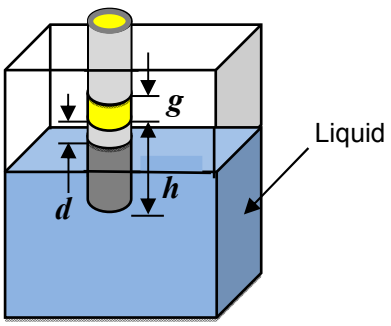


Fig. 3. Experimental setup for detecting the liquid-level variation.

The sample liquids employed were water, glycerin, olive oil, and honey. The dipping depth d was varied step by step using a pulse-motor stage moved in the vertical direction. Instead of Q_{mR}, the variation in G against d at the resonance point was measured using an impedance analyzer (IM3570, HIOKI E.E. Corp., Japan) because it corresponds to the variation in Q_{mR} as long as Q_{mR} is large. The measurements were conducted at room temperature.

III. Experimental Results and Discussion

Fig. 4 shows the frequency responses of the conductance G for several values of the dipping depth d in water. Here, d is measured from the lower end of the electrode, h denotes the length from the electrode to the bottom end of the resonator, and g is the electrode width. When the water level is at the bottom of the resonator ($d=h$) and at $d=h/2$, the conductance curves are almost the same and not affected by the water loading. However, the resonance curve gradually loses its height by increasing the dipping depth.

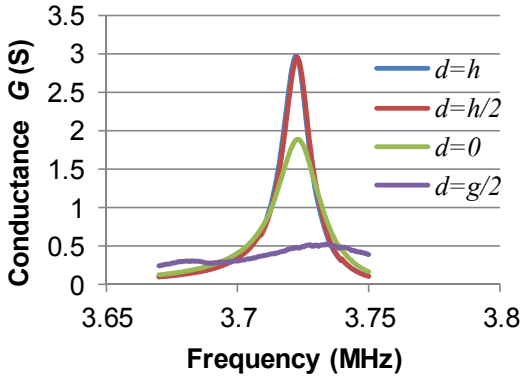


Fig. 4. Frequency responses of conductance G around f_R for several values of liquid level d.

Some examples of the variation in G on the depth d at f_R obtained for water (a), glycerin (b), olive oil (c), and honey (d), are shown in Fig. 5 . It is noted that G decreases gradually according to the increment of liquid level. The variations in G becomes steep when the liquid level is at the evanescent-wave region, i.e., around the electrode edge of the trapped-energy resonator. It is shown that the variation of the G values are slightly different for the four kinds of the liquid.

In summary, feasibility of liquid-level detection using a cylindrical resonator operating in a trapped-energy mode has been confirmed. Steep variations in G on the dipping depth d have been observed in the evanescent-field range. Further investigations are required for clarifying the effect of viscosity, acoustic impedance, and dielectric properties of liquids on measurement results.

References

[1] K. Yamada, H. Honda, S. Horiuchi, and T. Kinai: Jpn. J. Appl. Phys. **48** (2009) 07GB08.

[2] K. Yamada, S. Horiuchi, H. Honda, and T. Kinai: Proc. 2009 IEEE Ultrassonic Symp., p.2508.

[3] S. Seto, S. Horiuchi, and K. Yamada: Jpn. J. Appl. Phys. **49** (2010) 07HC05.

[4] K. Yamada and S. Seto: Proc. 2010 IEEE Ultrassonic Symp., p.1439

[5] K. Yamada, S. Seto, and S. Horiuchi: Proc. 2011 IEEE Ultrasonic Symp., p.1522.

[6] K. Yamada, T. Koyama, and S. Seto: Jpn. J. Appl. Phys. **51** (2012) 07GC04.

[7] K. Yamada, T. Ishioka, and N. Aita: Proc. 2013 Joint UFFC, EFTF and PFM Symp., p.282.

[8] K. Yamada and Y. Kunii: Proc. 2016 IEEE Frequency Control Symp.

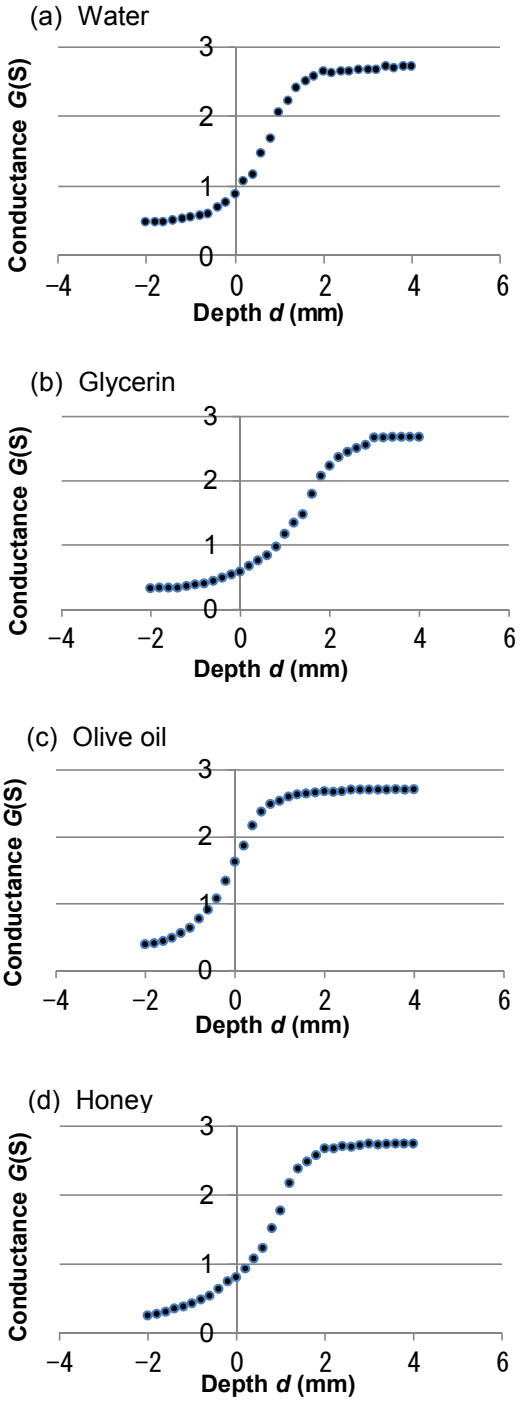


Fig. 5. Variations in G with dipping depth d. Sample liquids are water (a), glycerin (b), olive oil (c), and honey (d).

A new method for measuring properties of liquid by using a single quartz crystal microbalance

Feng Tan*, Peng Ye, Duyu Qiu, Lianping Guo, Wuhuang Huang,Hao Zeng and Dong Hou
School of Automation Engineering
University of Electronic Science and Technology of China
Chengdu, China
tanfeng@uestc.edu.cn

***Abstract*—As an ultra-sensitive mass sensing device, quartz crystal microbalance (QCM) can also be used to detect a variety of analytes in liquid environment. Previous works reported separate density and viscosity measurements of liquid by using dual QCMs. In this work, we present a novel theoretical model and a new method to separate density and viscosity measurements of liquid only using a single QCM, based on the frequency response analysis. Experimental results demonstrate the merit of the single QCM setup in determining the physical properties of liquid is an exciting new solvent.**

Keywords—Quartz crystal microbalance, density, viscosity, liquid

I. INTRODUCTION

As an ultra-sensitive sensing device, Quartz crystal microbalance (QCM) is a novel and powerful analytical tool in liquid applications. In 1980s，QCM was proved that it can work in a liquid[1]. Kanazawa and Gordon [2,3] found that the frequency shift of the QCM in contact with a liquid depends on the product of the density and viscosity of this liquid. A few years later, Ward, M. D *et al.* reported that the mass of the liquid on the surface of the QCM sensor can also shift the frequency[4]. After that, Schumacher groups[5] and A. R. Loveday group[6] further verified the validity of the conclusion.

Researchers tried to discriminate the density and viscosity of liquid. Martin and coworkers report a continuum model that describes the QCM simultaneously loaded by a thin surface mass layer and a semi-infinite Newtonian liquid[7], but they concluded that with only one QCM sensor, the viscosity and density of liquid cannot be extracted. With such assumption they designed a measurement method with dual QCM sensors and applied for a patent in 1993. In 2009, N.Doy *et al.* made further research based on the previous work of Martin[8]. They came up with the explicit expression of liquid viscosity and density based on the dual QCM sensors measurement method.

In 2011, Atsushi Itoh *et al.* simultaneously measured the frequency shift and the conductance shift of QCM sensors, and established equations to solve the density and viscosity of the liquid. Although this method only applied single QCM sensor[9], but the measurement process is more complex and the accuracy of the result needs to be improved. They did not give the explicit expressions for liquid viscosity and density.

In this work, a new theoretical model is presented and a new method is described by using single QCM sensor based on frequency response analysis. The article is aimed to provide a new and simple way to separate the density and viscosity of liquid, and to discriminate the frequency shift caused by mass loading and that caused by properties of liquid.

II. THEORETICAL MODEL

When the upper surface of a QCM is loaded with a liquid, the frequency of the QCM sensor would be changed. There is clear evidence that both stress and pressure contribute to the measured frequency shifts. Obviously, the QCM operating in fluid is not only sensitive to the liquid loading, but also to the properties of the liquid. Theoretical expressions of the density and the viscosity are derived and shown as follows[10,11]:

$$\rho_L = \frac{\Delta f_2 - \Delta f_1}{K_{Pf} \cdot C_{Pf} \cdot V_{L2} \cdot f_0} \tag{1}$$

$$\eta_L = \frac{K_{Pf} \cdot C_{Pf}}{(\Delta f_2 - \Delta f_1) \cdot V_{L2} \cdot f_0} \cdot \left[\frac{\Delta f_1 \cdot V_{L2} - V_{L1} \cdot (\Delta f_2 - \Delta f_1)}{K_{Tf} \cdot C_{Lf}} \right]^2 \tag{2}$$

where Δf_1 and Δf_2 are frequency shift caused by V_{L1} and V_{L2} , respectively; K_{Pf} is the pressure sensitivity coefficient of the sensor, $K_{Pf} = f_0 \cdot K_f / nD$, and $K_f = -23.3 \times 10^{-15} (msN^{-1})$, K_f is defined as force-frequency coefficient, K_{Tf} is the stress sensitivity coefficient, $K_{Tf} = -2.75 \times 10^{-11} (m^2 / N)$, C_{Pf} is a pressure-frequency coefficient, C_{Lf} is a stress-frequency coefficient of QCM in the liquid phase, and f_0 is the natural (reference) frequency of QCM; ρ_L and η_L are the density and viscosity of liquid, V_{L1} is the volume of liquid added to the QCM at the first time, V_{L2} is the volume of liquid added to the QCM at the second time, respectively.

III. EXPERIMENT

In this work, an AT-cut QCM with 3rd overtone at 10 MHz and conventional thermally evaporated gold electrodes is used (Tongfang Guoxin Electronics co., LTD.). The diameter of the gold electrodes is 5mm. Figure 1 shows the schematic of the experimental setup consisting of a micropipet (Model EpT.I.P.S®10uL, Eppendorf), a Universal Counter (Model 53132A, Agilent) and a QCM sensor driving circuit.

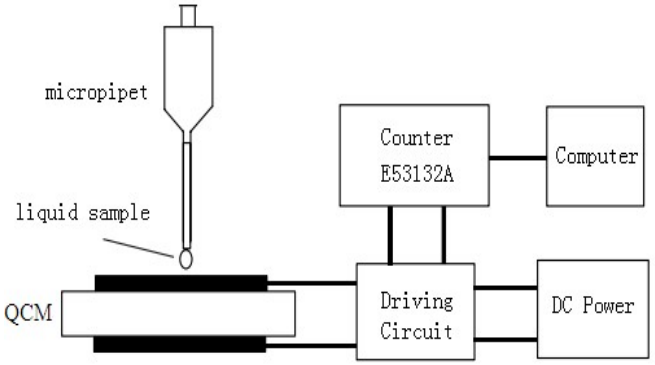


Fig. 1. Measuring Schematic of liquid properties with QCM

Firstly, Pure water is chosen as the reference sample and $\rho_W = 1.0\times10^3\,\mathrm{Kg/m^3}$ and $\eta_w = 8.949\times10^{-4}\,\mathrm{Pa\cdot s}$ denote its density and the viscosity, respectively. We first experimentally determine $C_{Pf} = 7.3903\times10^4\,\mathrm{m\cdot Hz^2}$ and $C_{Lf} = -1.2877\times10^6\,\mathrm{m\cdot\sqrt{Hz^3}}$ in equations (1)and (2).

NaCl, KCl is obtained from Sigma Aldrich and diluted with DI water. In this work, Aqueous solutions with NaCl, KCl concentrations of 10%, 20%, and 30% are prepared as target samples. Measurements are performed at room of 25℃. and frequency shifts are recorded.

IV. RESULTS AND DISCUSION

Fig. 2 and Fig. 3. show the fitting plots of the frequency shifts of QCM for NaCl and KCl solutions with different volumes.

In this work, we find that if the electrode of the QCM is not covered completely, the frequency shift varies nonlinearly as the liquid volume changes. Only when the liquid covers the electrode completely, there exists a linear relationship between the frequency shift and the added liquids in some volume ranges.

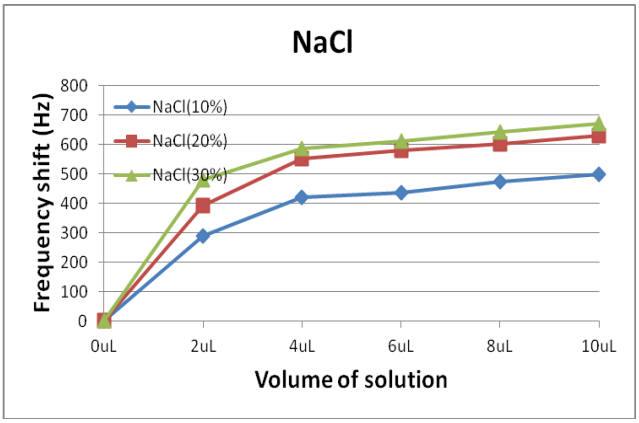


Fig. 2. Frequency shifts measured of NaCl samples

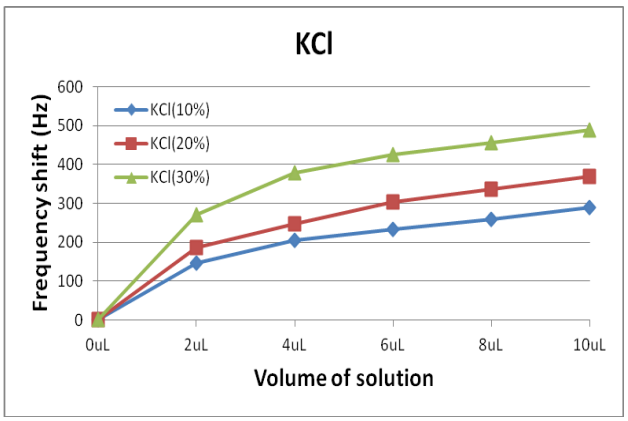


Fig. 3. Frequency shifts measured of KCl samples

During the experiment, the volume of the added liquid was varied 2 μL each time. Obviously, we can see that there has an nonlinearly relationship between loaded liquid and frequency shifts when the volume of the liquid is less than 4 μL according to Fig. 2 and Fig. 3, the pressure exerted on the upper surface of QCM arising from the added liquid and its viscosity together caused the frequency shift. We also can see that there has a linearly relationship between loaded liquid and frequency shifts when the volume of the loaded liquid is from 4 μL to 10 μL , at this time, only the pressure exerted on the upper surface of QCM arising from the added liquid played a role. Frequency shifts in different volumes of liquid samples are shown in Table. I.

TABLE I. Frequency shifts in different volumes of liquid samples

Solution Concentration(*wt*%) Volulme	NaCl			KCl		
	10	20	30	10	20	30
4 μL	-419	-545	-588	-418	-449	-488
6 μL	-437	-569	-614	-445	-477	-522
8 μL	-473-	-601	-643	-478	-516	-557
10 μL	498	-623	-675	-506	-549	-589

With these frequency shifts, density and viscosity of the NaCl and KCl solutions with different concentrations can be calculated by using Eq(1) and Eq(2). The density and viscosity of the NaCl and KCl solutions with different concentrations is given in TABLE II.

TABLE II. Measured Density and viscosity of NaCl and KCl solutions at 25℃

Solution	NaCl			KCl		
Concentration(*wt*%)	10	20	30	10	20	30
Density(g/cm^3)	1.068	1.156	1.22	1.28	1.40	1.51
Viscosity(mPa.s)	1.1	1.7	1.9	0.86	0.90	0.98

There are several factors influence the test precision as follows: (1) Cleanness of the QCM sensor surface. (2) The work state of the driving circuit of QCM sensor. (3) Environment. Putting the sensor and the driving circuit in a thermostatic chamber can lower the error. (4) The stability and

accuracy of reference source of the frequency meter.

V. CONCLUSION

In conclusion, this paper presents a new model and a novel method to separate density and viscosity measurements of liquids based on the frequency response analysis of QCM, and the experimental results demonstrate its feasibility.

REFERENCES

[1] P.L. Konash, G.J. Bastiaans, Piezoelectric crystals as detectors in liquid chromatography, Anal. Chem. 52 (1980) 1929–1931.

[2] K.K. Kanazawa, J.G. Gordon, Frequency of a quartz microbalance in contact with liquid, Anal. Chem. 57 (1985) 1770–1771.

[3] C.E. Reed, K.K. Kanazawa, and J.H. Kaufmann,1990, "Physical description of a viscoelastically loaded AT-cut quartz resonator" J. Appl. Phys.68:1993-2001.

[4] Schumacher, R. Angew. Chem. Int. Ed. Engl. 1990, 29,329-343.

[5] Ward, M. D.; Buttry, D. A. Science 1990, 249, 1000-1007.

[6] Hillman, A. R.; Loveday, D. C.; Swam, M. J. J. Chem.Soc. Faraday Trans. 1991, 87, 2047-2053.

[7] Stephen J. Martin,* Victoria Edwards Granstaff, and Gregory C. Frye, Characterization of a Quartz Crystal Microbalance with Simultaneous Mass and Liquid Loading, Anal. Chem. 1091, 63, 2272-2281.

[8] Martin S J, Wessendorf K O, Gebert C T, Frye G C, Cernosek R W, Casaus L and Mitchell M A 1993,Measuring liquid properties with smooth- and textured-surface resonators Proc. IEEE Frequency Control Symp. (Salt Lake City, UT) pp 603–608.

[9] Atsushi Itoh and Motoko Ichihashi, Separate measurement of the density and viscosity of a liquid using a quartz crystal microbalance based on admittance analysis (QCM-A), Meas. Sci. Technol. 22 (2011) 015402 (6pp).

[10] Tan F, Qiu D Y, Guo L P, et al. Separate density and viscosity measurements of unknown liquid using quartz crystal microbalance[J]. Aip Advances, 2016, 6(9):206-49.

[11] A METHOD FOR MEASURING THE PROPERTIES OF LIQUID BASED ON A QUARTZ CRYSTAL MICROBALANCE SENSOR，US Patent: 14/933,648.

ACKNOWLEDGMENT

This work was financially supported by the Fundamental Research Funds for the Central Universities (ZYGX2015J077).

Design and Characterization of Surface Acoustic Wave Resonance (SAR) System for In-liquid Sensing

K. Kustanovich, V. Yantchev* and A. Jesorka
Biophysical Technology Laboratory, Department of Chemistry & Chemical Engineering
Chalmers University of Technology
Göteborg, Sweden
*E-mail: ventsi.yantchev@gmail.com

***Abstract*—Sensors capable of in-liquid operation are of primary importance not only for biosensors applications, but also for liquid monitoring. Surface acoustic waves (SAW) have been employed for long time in various in-liquid sensors at relatively high frequencies. Unlike their QCM counterparts, SAW in-liquid sensors employ delay-line topology. Here, for the first time, we discuss a new concept for building a SAW in-liquid sensor employing surface acoustic wave resonance (SAR) in a one-port configuration. To demonstrate its utility, a SAR technological platform embedded in a polydimethylsiloxane (PDMS) microfluidic device was fabricated and characterized. Designs with suppressed spurious content were identified. Initial measurements in a liquid environment are performed. In comparison to a delay-line topology, the SAR concept features comparable sensitivity, while offering better electrical performance and smaller size.**

Keywords—Sensor; SH-SAW; Resonance; Microfluidics

I. INTRODUCTION

Electroacoustic (EA) technology has gained considerable attention in the sensors field during the last decades. One of the most explored sensing concepts is related to gravimetric sensing, with potential application in both gas-chemical and biochemical sensors. For the latter, the sensor must be able to retain its functionality when immersed in liquid, and reliably sense mass depositions on the sensing surface resulting from a specific biochemical reaction. There has been substantial, sustained effort in the area of microfluidics-integrated sensing technology to develop highly sensitive, label free, real time devices based on the thin-film electroacoustic technology. These efforts have been going on for more than 20 years, however, with limited practical success. A wide range of thin film piezoelectric transducers has been developed and studied, and their potential demonstrated [1, 2]. However, much of the practical developments are still remaining in their early stages. Moreover, their true potential should be still demonstrated. Thickness excited quasi-shear transducers (shear-FBAR) have shown so far the best performance in terms of sensitivity, resolution, manufacturability and cost, and are currently the only device type that reached the stage of commercial prototypes [3]. Thin-film S0-Lamb waves and their equivalent extensional plate modes are also showing promise, since they use established technology originally developed for commercial RF filter production. However, practical considerations comprising process uniformity, device fragility, and strong local pressure and temperature sensitivity, are limiting these approaches.

On the other hand, QCM [4] and SH-SAW (e.g., Love wave and LSAW) approaches have already demonstrated their utility. Currently, the SAW field enters its third stage of development, initiated by the invention of the incredibly high performance (IHP) [5] and hetero-acoustic layer (HAL) [6] substrates. These substrates enable great confinement of the SH-SAW near the surface as well as robust temperature compensation, while exhibiting high electromechanical couplings needed for sensors with large dynamic range. The new SAW substrates have strong potential for commercialization, driven by the fabrication technology established by the RF filter industry.

For in-liquid operation, however, the acoustic wave employed must not radiate into the liquid. This demand has limited the choice of acoustic waves. SH-SAWs have generated considerable interest because of the robust technology and their facile integration with microfluidics [7-10]. Unlike the other EA concepts, SH-SAW is employed only in two-port delay-line configurations. For in-liquid operation the SH-SAW delay line biosensors are characterized with strong signal loss in transmission emanating from the significant SH-SAW damping in the liquid substrate along the delay path between the two SAW transducers.

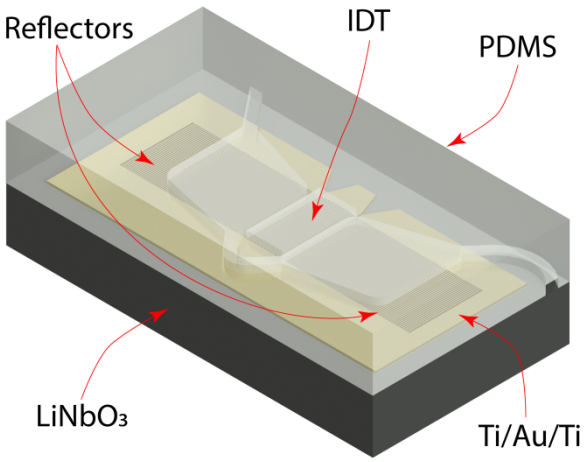


Fig. 1. 3D render of the surface acoustic wave resonance (SAR) topology. Two interconnected microfluidic containers are overlaping with the reflective SAW gratings, while the IDT in between is protected by an air-gap cavity.

We acknowledge the European Union (Horizon 2020 FET Open research grant, Project ID: 664786); the Swedish Strategic Research Foundation (SSF).

Development of resonant SAW devices, as alternative to delay line geometries, has remained insufficiently explored. Only few works have been attempting this development so far. It has been initially recognized that two-port SAW resonant devices are useful for in-liquid sensing and compatible with fluorescent microscopy, owing to the high substrate transparency [11]. Further development of two-port resonant sensors was spearheaded by the Karlsruhe Institute of Technology [12], where a 2-port resonant device was fabricated on a $LiTaO_3$ substrate. These promising initial studies highlighted the potential of the SH-SAW resonant approach for achieving lower losses along with the ability to provide some complementary information during monitoring of protein films [12]. A disadvantage of these state of the art SH-SAW resonant sensor designs is that both the reflectors and the transducers are part of the sensing cavity, thus providing a complex sensor signal determined by the perturbations in both SAW propagation and SAW excitation characteristics. Accordingly, the devices are also to some extent susceptible to electrical short circuiting effects when immersed in conductive liquids.

We initiated a new direction for the development in this clearly insufficiently explored domain of resonant SAW bio-sensors. To alleviate the above difficulties, we introduce a new concept for in-liquid sensing, employing a surface acoustic wave resonance (SAR) in a one-port configuration integrated with microfluidic sample delivery to form a novel lab-on-a-chip building block (Fig. 1). The sensor has a small footprint of < 1 mm^2, operates at ~185 MHz and demonstrates figures of merit comparable to other SAW in-liquid sensors, while offering a quality factor (Q) value in water of about 250, low impedance and sustained performance in conductive liquids.

The proposed liquid phase sensor design employs a 1-port SH-SAW resonant topology, in which the transduction part is electrically and mechanically isolated from the sensed analytes. The proposed topology further enables direct integration with microfluidics and low-frequency impedance spectroscopy [13]. Hence, the potential to develop a versatile lab-on-a-chip sensor, integrating the functionalities of SAW resonance, impedance spectroscopy and fluorescent microscopy.

II. Design and Fabrication of the SAR sensor

The fundamental idea is to use the reflective gratings of the one-port SAW resonator as sensing elements, while the transducer is a wide-band interdigital transducer (IDT) placed in-between the reflectors and protected from the liquid.

Thus, the frequency shifts of the SAW resonance will be determined by the changes in SAW propagation characteristics (phase velocity and reflectivity), when propagating under the reflective gratings subjected to mass or electrical load. A PDMS layer containing the microfluidic containers and interconnecting channels is bonded on top of a one-port SAW resonator such that the containers overlap with the reflective gratings, while IDT remains protected from the measurement environment.

We employ a high-coupling SH-SAW, guided along the X-direction of Y-cut $LiNbO_3$ by means of an Au periodic strip grating (Fig. 1). Both the IDT and the reflective gratings are formed by a periodical array of 270 nm thick Au strips with pitch $p_0 = 10$ µm and strip width of about $p_0/2$. Number of strips in IDT is $N_t = 21$, number of strips in each reflector is $N_r = 69$, from which 49 are overlapping with a microfluidic container, while the device aperture is $W = 40*p_0$. After electrode deposition, a 100 nm thick SiO_2 layer is deposited on top for passivation as well as to promote O_2 plasma-bonding to the PDMS microfluidic structure.

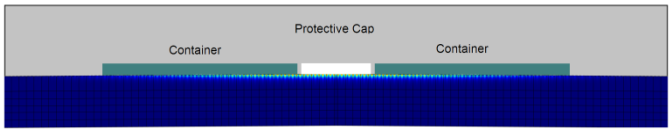


Fig. 2. Operation principle of the SAR sensor demonstrated by finite element method (FEM) frequency response analysis. The SAW energy is emitted out of the IDT in both directions, being reflected by the reflective grating loaded with the aquous analyte being sensed. The sensitivity is determined by the SAW energy confined in the reflective gratings.

In Fig. 2, the principle of operation of the SAR liquid-phase sensor is demonstrated. COMSOL Multiphysics® (version 5.2) frequency response analysis was used to simulate the SAW displacement magnitude along the 1-port SAW resonator. The sensing ability of the SAR sensor is determined solely by the propagation characteristics of the SAW under the reflective gratings.

Our integration concept for the SAW resonator and the microfluidic sample delivery has brought additional complexity to the resonator design. To identify designs with clearly pronounced resonances, we performed series of experiments where we integrated four basic types of SAW resonator designs with microfluidics. These SAW resonator designs were as follows:

1. **Regular design**: A SAW resonator as described above where the reflective gratings are synchronously placed around the IDT;
2. **Piston mode design**: A synchronous SAW resonator with design suppressing the transverse modes in the structure;
3. Synchronous design with IDT **apodization**;
4. **Hiccup design**: A design with $-p_0/10$ break in periodicity at the center of the IDT.

In Fig. 3, the hiccup, the piston mode, and the apodized resonators are shown as fabricated. The regular resonator looks like the hiccup resonator but with synchronous design. Initially, the SAW resonators were characterized in air (Fig. 4). All of them have demonstrated a Q of about 1000. The regular design expectedly exhibited few transversal modes near the resonance. The piston mode design has led to effective suppression of these transversal modes. The hiccup and apodized designs show responses with significantly suppressed side-lobes as compared to synchronous designs.

When the thick PDMS layer is placed and bonded over the SAW resonators, all of them have exhibited performance degradation due to damping (Fig. 5). Still, the device performance was retained, since SH-SAWs are sufficiently sustainable in the visco-elastic PDMS material. All devices

demonstrate a Q of about 60, and 20 – 30 Ohm impedance at resonance. All spurious resonances have been sufficiently suppressed by the damping.

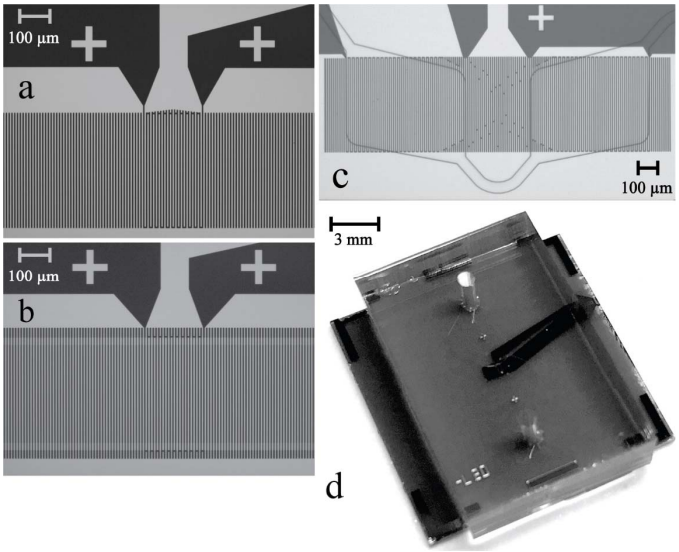


Fig. 3. (a) Inspection microscope image of the fabricated hiccup design SAR device. The crosses outside the electrode areas are alignment marks. (b) Inspection microscope image of the fabricated piston mode design SAR device. (c) Microscopy image of the assembled microfluidic sensor device with apodized IDT. Here the reflective gratings are arranged in an interdigitated fashion forming a capacitor that eventually allows for electrochemical impedance spectroscopy to be integrated directly into the topology. (d) Photograph of the SAR sensor-integrated microfluidic device. The sensor contact pads (right side) are sized appropriately for contacting with measurement probes.

When a PDMS channel layer with microfluidic cavities, but without air cavity above the IDT, was bonded over the SAW resonator (see Fig. 3 (c), (d)), unwanted concurrent ripples near the main resonance appeared for both the regular and the piston mode designs.

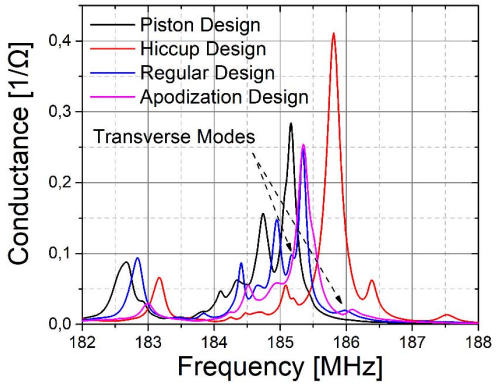


Fig. 4. Close-in resonance conductance of the SAW resonators in air.

Only the hiccup and the apodized designs have shown susceptibility to these ripples. In Figure 6, the conductance close to resonance is shown as measured for the SAW device with water in the microfluidic-containers. The presence of liquid in the containers led to a split resonance performance of the regular and piston-mode resonator designs, which makes these types of design unpractical for sensing applications.

This design iteration pointed out that hiccup and apodized resonators can tolerate the spurious content introduced by the microfluidic system. Thus, subsequent designs are focused on the use of a hiccup and apodized resonators along with an air cavity above the IDT.

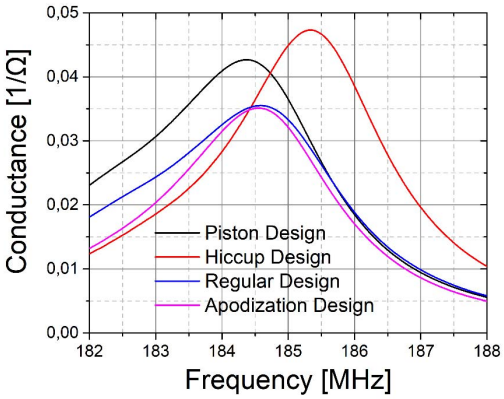


Fig. 5. Close-in resonance conductance of SAW resonators bonded with 1 cm thick PDMS piece.

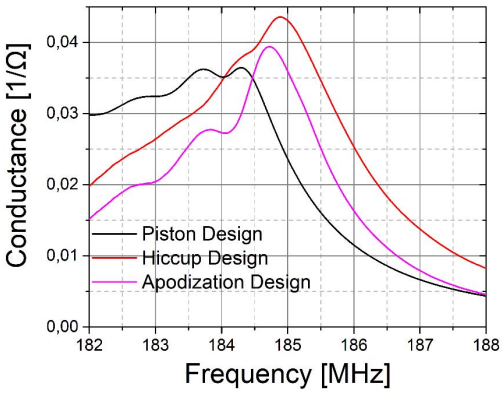


Fig. 6. Close-in resonance conductance of SAW resonators bonded to the PDMS sample delivery system consisiting of two microfluidic containers overlapping with the SAW reflectors (Fig. 3 (c)).

III. SAR Sensor Characterisation

Here we report on the performance measurements on our latest SAR sensor iteration. The sensor employs sample delivery by means of a PDMS device, with a protective air cavity bonded onto the main SAW resonator with hiccup design. In Fig. 7, the close-in resonance responses of the as-fabricated SAR biosensor is shown, measured in containers filled with air and water, respectively. The resonance frequency is about 185 MHz. A frequency shift of the conductance peak and the zero of the admittance phase of about 915 ppm could be observed upon water loading, also accompanied by a 10% decrease of the magnitude of the conductance peak. The device quality factor dropped from 300 to 250 under water loading. The phase of the admittance signal demonstrates sufficient linearity in the vicinity of its zero point. It is noted that the measured

conductance of about 0.125 1/Ω indicates low sensor impedance of about 8 Ohms at resonance. This allows for a simplified sensor design with a further reduction in number of strips in the IDT and improved sensitivity, while keeping impedance at resonance close to 50 Ohm.

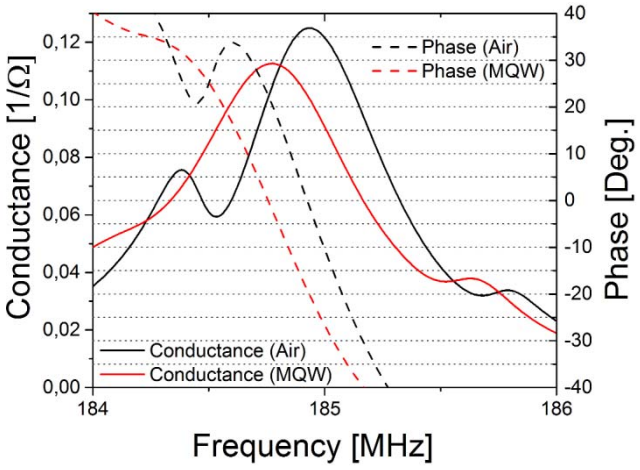


Fig. 7. Close-in resonance conductance of the SAR sensor. SAR sensor consits of a SAW resonator with hiccup design, bonded to a PDMS sample delivery device, consisting of two microfluidic containers and a protective air-cavity above the IDT.

For comparison, the apodized design demonstrated frequency shift of about 1220 ppm due to the larger amount of energy confined in the sensing reflectors. In supplementary experiment, a delay line geometry employing the same substrate and Au periodic strip gratings (simultaneously fabricated on the same wafer) was characterized in air and water, respectively. A frequency shift of the S21 phase of 1450 ppm was measured upon water loading. The minimum insertion loss was about -20 dB. Thus, the SAR sensor in our very first iteration demonstrates about 60% of the sensitivity of the delay line. Further comparison (not presented here) with state of art electroacoustic technology demonstrated that the achieved SAR sensitivity to viscous load (scaled with respect to frequency) is comparable to the 900 MHz FBAR [14] and 100 MHz SAW delay line [15], which were reported earlier in the literature. During these viscous-load measurements, the SAR sensor demonstrated only marginal damping on the order of 2%, compared to 30% in the case of an FBAR.

It is also noted that sensitivity improvements are feasible and will be pursued in future designs. Currently we pursue the concept of designing an energy trap into the SAW reflectors, with the goal of enhancing SAR sensitivity.

IV. Conclusions

A new concept of the surface acoustic resonance (SAR) for in-liquid sensors has been demonstrated for the first time. The chip layout allows for successful integration with an appropriately defined PDMS sample delivery system. The device sensitivity was found to be comparable to other electro-acoustic technologies, with further improvements through refined design possible. Inherent to the SAR sensing platform are its low impedance at resonance, retained Q when immersed in liquid, low susceptibility to viscous damping and small dimensions. With respect to conventional SAW delay lines, the SAR sensor inherits the ruggedness of the SAW technology, while demonstrating low-loss and low-impedance performance. We conclude that the SAR approach shows high potential in view of the possibility to develop a versatile lab-on-a-chip sensing platform technology, which allows for integration of the functionalities of SAW resonance, impedance spectroscopy and optical techniques.

References

[1] I. Katardjiev and V. Yantchev, "Recent developments in thin film electro-acoustic technology for biosensor applications," (in English), *Vacuum,* vol. 86, no. 5, pp. 520-531, Jan 5 2012.

[2] M. DeMiguel-Ramos *et al.*, "Gravimetric biosensor based on a 1.3 GHz AlN shear-mode solidly mounted resonator," (in English), *Sensors and Actuators B-Chemical,* vol. 239, pp. 1282-1288, Feb 2017.

[3] M. Nirschl *et al.*, "CMOS-Integrated Film Bulk Acoustic Resonators for Label-Free Biosensing," (in English), *Sensors,* vol. 10, no. 5, pp. 4180-4193, May 2010.

[4] J. Auge, P. Hauptmann, J. Hartmann, S. Rosler, and R. Lucklum, "New Design for Qcm Sensors in Liquids," (in English), *Sensors and Actuators B-Chemical,* vol. 24, no. 1-3, pp. 43-48, Mar 1995.

[5] T. Takai *et al.*, "Incredible High Performance SAW resonator on Novel Multi-layerd Substrate," (in English), *2016 Ieee International Ultrasonics Symposium (Ius),* 2016.

[6] M. Kadota and S. Tanaka, "HAL SAW Resonators Using 42°YX-LiTaO3 Thin Plate on Quartz Substrate," (in English), *2017 European Frequency and Time Forum (Eftf),* Conference Proceedings July 2017.

[7] K. Lange, B. E. Rapp, and M. Rapp, "Surface acoustic wave biosensors: a review," (in English), *Analytical and Bioanalytical Chemistry,* vol. 391, no. 5, pp. 1509-1519, Jul 2008.

[8] J. Kondoh, Y. Matsui, and S. Shiokawa, "New Biosensor Using Shear Horizontal Surface-Acoustic-Wave Device," (in English), *Japanese Journal of Applied Physics Part 1-Regular Papers Short Notes & Review Papers,* vol. 32, no. 5b, pp. 2376-2379, May 1993.

[9] J. Kondoh, "A liquid-phase sensor using shear horizontal surface acoustic wave devices," (in English), *Electronics and Communications in Japan,* vol. 96, no. 2, pp. 41-49, Feb 2013.

[10] K. Mitsakakis, A. Tserepi, and E. Gizeli, "SAW device integrated with microfluidics for array-type biosensing," (in English), *Microelectronic Engineering,* vol. 86, no. 4-6, pp. 1416-1418, Apr-Jun 2009.

[11] D. D. Stubbs, S. H. Lee, and W. D. Hunt, "Molecular Recognition for Electronic Noses Using Surface Acoustic Wave Immunoassay Sensors," (in English), *Ieee Sensors Journal,* vol. 2, no. 4, pp. 294-300, Aug 2002.

[12] S. Hohmann *et al.*, "Surface Acoustic Wave (SAW) Resonators for Monitoring Conditioning Film Formation," (in English), *Sensors,* vol. 15, no. 5, pp. 11873-11888, May 2015.

[13] A. Jesorka, K. Kustanovich, and V. Yantchev, "A Surface Acoustic Wave Resonant Sensor," (in English), *Swedish Patent and Registration Office,* Patent no. 200697SE, May 2017.

[14] T. Mirea, E. Iborra, and V. Yantchev, "S-0 Lamb wave resonators for in-liquid sensing: promising alternative to shear bulk acoustic wave devices," (in English), *2016 European Frequency and Time Forum (Eftf),* 2016.

[15] T. Morita, M. Sugimoto, and J. Kondoh, "Measurements of Standard-Viscosity Liquids Using Shear Horizontal Surface Acoustic Wave Sensors," (in English), *Japanese Journal of Applied Physics,* vol. 48, no. 7, Jul 2009.

A micromechanical resonant optical power meter

Xuan Chen[1], Dong Pu[1], Tianyi Zhang[1], Zhuangde Jiang[1] and Xueyong Wei[1, 2,*]
1. State Key Laboratory for Manufacturing Systems Engineering, Xi'an Jiaotong University, Xi'an, 710049, China
2. State Key Laboratory of Applied Optics, Changchun Institute of Optics, Fine Mechanics and Physics, Chinese Academy of Sciences, Changchun 130033, China
*Corresponding Email: seanwei@mail.xjtu.edu.cn

***Abstract*—This paper presents a new kind of micromechanical optical power meter using a micro disk resonator. With the change of laser power irradiated on the surface of resonator, the resonant frequency of the micromechanical resonator drifts because of its body temperature change. The simulation result is verified by the experimental data. A linear relationship between the laser power and the resonant frequency is obtained by both open-loop and closed-loop experiments. The minimum detectable optical power is found to be 0.98μW. The response time of the detector is less than 0.3s when the optical power changes.**

Keywords—Optical power meter; Micromechanical resonator; resonant frequency;

I. INTRODUCTION

Photo-detection techniques have been developed for many years, and play an important role in various area such as bioluminescence, astronomical photometry and military. At present, the most mature methods for detecting laser power are photoelectric detection and thermal detection. Those optical power meters using photoelectric method, like photomultiplier tubes (PMT) and single-photon avalanche diodes (SPAD) [1-2], can achieve high precision, but the range of wavelength to be detected is limited by the nature of the photoelectric material. Besides, those optical power meters using photoelectric method usually requires cooling environment, which limits their application. Those optical power meters based on thermal effect of laser include the pyroelectric type [3] and the calorimetry type [4-5]. They absorb the radiation of optical power, resulting in an increase of temperature in the sensitive components [6]. This kind of power meter can work in room temperature, and have no limitations in working wavelength. However, generally they have difficulties in improving precision or response time, and are usually quite complex in structure [7-8].

Due to the increased demanding for micro-machined optical power meter in many different areas, such as spectrometer, gas detector and remote temperature detector, MEMS-based optical power meter has drawn growing attention [9]. A new kind of optical power meter using a silicon disk resonator is proposed in this paper. It is based on the frequency fluctuations caused by laser induced heating. The temperature of the laser heated silicon is mainly determined by the intrinsic absorption of the semiconductor and the absorption of the thermal generated electron-hole pairs [10]. Thus, this new kind of optical power meter is expected to be used in any range of optical spectrum. Besides, the good thermal conductance of silicon ensures a quick response time of our optical power meter.

II. PRINCIPLE OF OPERATION

The new kind of optical power meter proposed by this paper is composed of three parts including the sensitive components, the frequency tracking oscillator circuits and a monitor (Fig.1). The sensitive components of our detector is a single crystal silicon (SCS) disk resonator and additive absorption materials can be applied on the surface of micromechanical resonator depending on the capability of microfabrication process. The optical power meter utilizes the frequency fluctuations of the disk resonator in different laser power irradiation. The frequency tracking oscillator circuits include the open-loop circuit and the closed-loop circuit, showing the drift of the resonant frequency caused by temperature effect. And the monitor shows the power of laser irradiation according to the correspondence between the resonant frequency and laser power.

III. DESIGN AND SIMULATION

The single crystal silicon (SCS) disk resonator with a radius of 750μm and a thickness of 10μm is microfabricated based on the standard silicon on insulator (SOI) technology. After wire bonding, the device is placed in a vacuum environment in this work. The structure of the resonator is shown in Fig.2 (a).

Comsol Multiphysics® is used to simulate the relationship between the resonant frequency and the irradiated laser power. The simulation process is divided into two steps. Firstly, the temperature distribution of the resonator is obtained according to the laser power and the structure of resonator. Secondly, the resonant frequencies of different modes are obtained according to the temperature distribution of the resonator. The laser irradiation is simplified as a Gaussian distribution thermal source in this simulation. The support of the disk is set to be a constant temperature, which is 273K. The temperature of the disk resonator increases when a laser irradiated on the surface of it, and thus the resonant frequency decreases due to the decrease of the equivalent stiffness. The formula of resonant frequency f is as bellow.

$$f = \frac{k}{2\pi R}\sqrt{\frac{E}{\rho(1-\nu^2)}} \quad (1)$$

Where k is the dimensionless frequency parameter, R is the disk radius, E, ν and ρ are Young's modulus, Poisson's ratio and density of the disk material.

The temperature distribution and the relationship between laser power and center temperature of the disk resonator are simulated as shown in Fig.2 (b). The temperature of resonator

body increases almost 2K when the laser power increases 1mW. The resonant frequency is then simulated based on different temperature distributions.

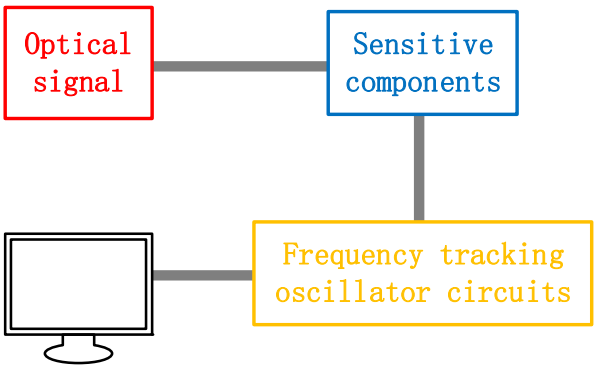


Fig. 1. The principle sketch of the proposed micromechanical resonant optical power meter.

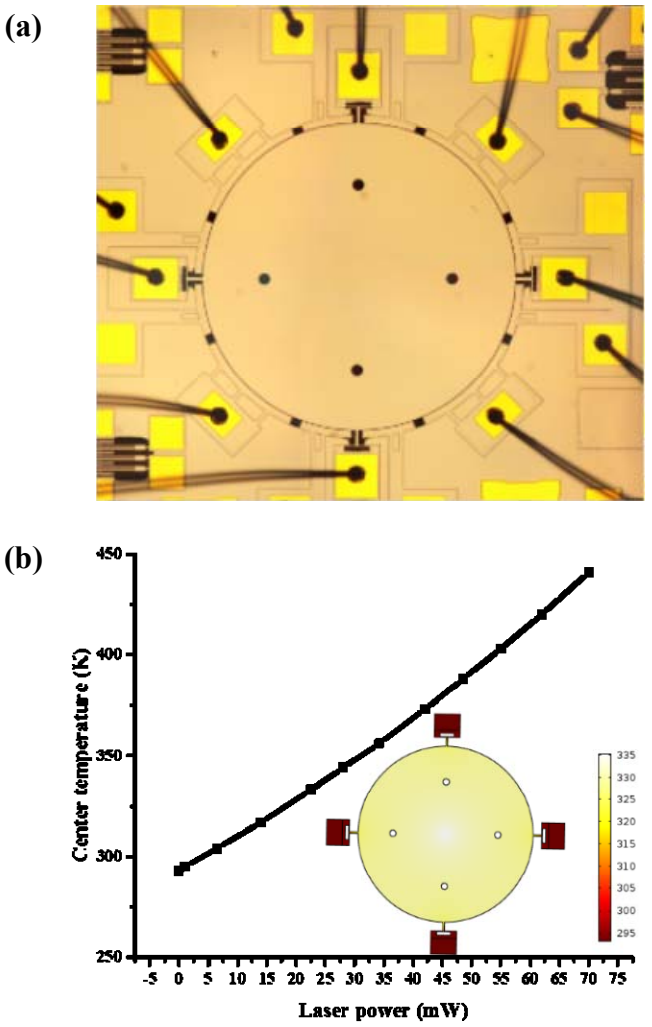


Fig. 2. (a) Microscopic picture of the SCS disk resonator. (b) Computing the center temperature of the disk resonator at different laser power, an almost linear relationship is obtained (with a tiny quadratic term). The simulation of temperature distribution with the laser power of 22.5mW is inserted.

IV. Experimental Results and Analysis

The device temperature is influenced by the laser power irradiated on the center of the disk. The fibers used for the transmission of laser are 600nm in diameter. The wavelength of the laser used in our experiment is 488nm.

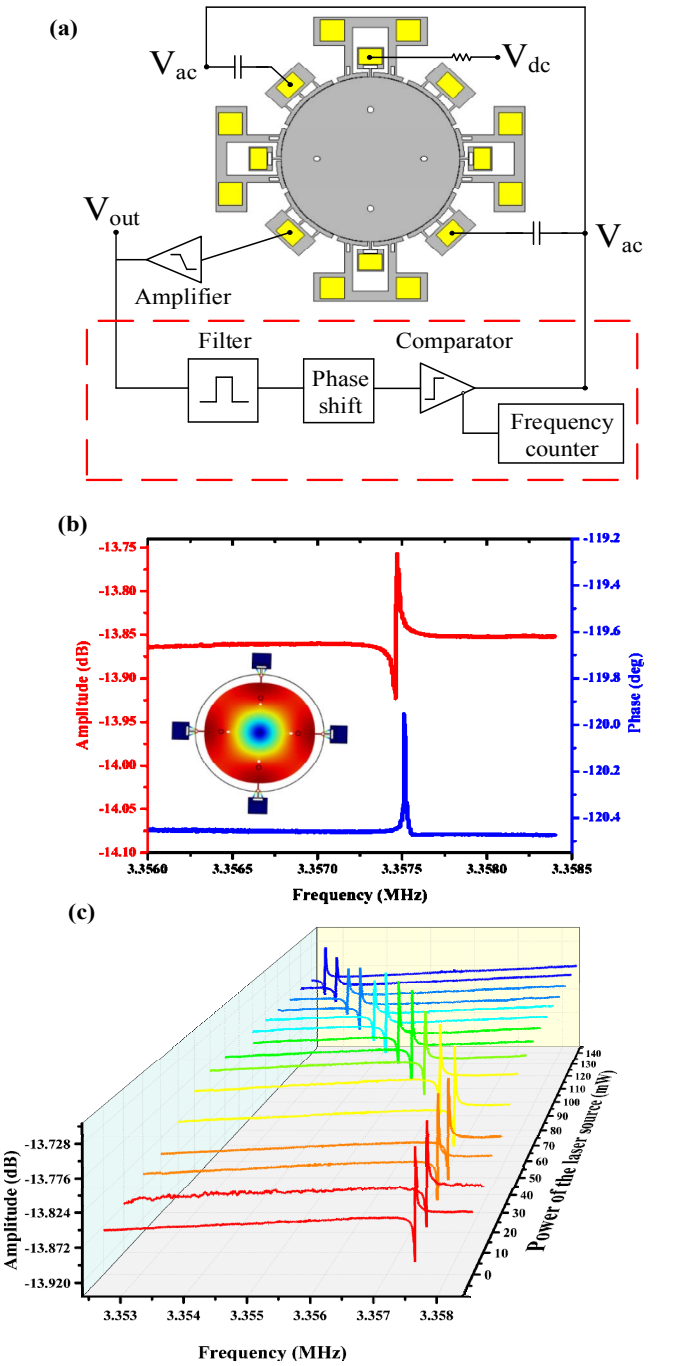


Fig. 3. (a) The schematic of the experiment. The closed-loop circuit is in the red dotted rectangle. (b) The amplitude and phase response of the bulk mode of SCS disk resonator without laser irradiation. And the bulk mode shape of the resonator from Comsol Multiphysics® is inserted. (c) Frequency fluctuations are recorded when the power of laser source is set from 0mW to 140mW. The fluctuations of frequency in the first four curves are quite small because of the loss of energy in the laser transmission.

Capacitive transduction method is used to excite and detect the frequency response of the disk resonator, which is easy to conduct and will not be influenced by the increase of temperature. Electrostatic excitation with both a DC voltage and an AC voltage is applied on the disk resonator.

A. Open-loop circuit method

The schematic of the open-loop circuit is the part outside the red dotted rectangle in Fig.3 (a). In the open-loop circuit method, the AC voltage is provided by vector network analyzer.

The resonant frequency of the bulk-mode is firstly tested without the laser irradiation in the open-loop circuit (Fig.3 (b)). The resonant frequency in the experiment is quite close to that from the simulation.

As the laser power increases in the experiment, temperature of the disk resonator increases, while the resonant frequency observed in the experiment decreases as shown in Fig.3 (c).

B. Closed-loop circuit method

The part of schematic in the red dotted rectangle in Fig.3 (a) shows the closed-loop circuit, which contains an amplifier, a band pass filter, a phase shift and a comparator. The comparator output is fed back to activate the resonator. The oscillation signal is measured by a spectrum analyzer, and the frequency outputs are recorded by a frequency counter.

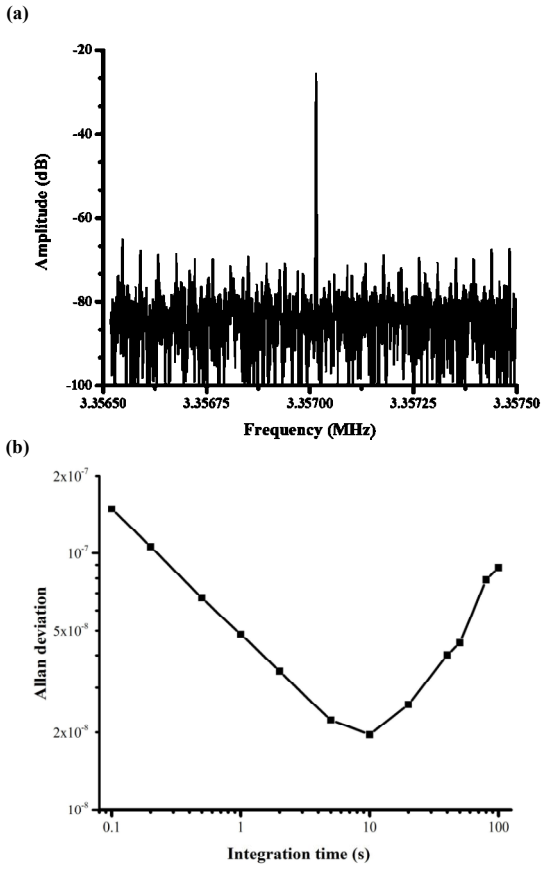


Fig. 4. (a) Frequency spectrum of the output signal measured by a spectrum analyzer. (b) Allan deviation of the bulk mode of the disk resonator is calculated.

In the closed-loop testing, the frequency response of the resonator measured by the spectrum analyzer is shown in Fig.4 (a). Allan deviation is calculated with the frequency outputs recorded by the frequency counter to evaluate the stability of the closed-loop oscillation as shown in Fig.4 (b). The short-term frequency stability floor of the resonator is approximately 20ppb for an averaging time of 10s. According to the Allan deviation, the minimum frequency fluctuation that our detector can detect is 0.068Hz, thus the resolution of our optical power meter is approximately 0.98μW.

In this experiment, when the laser power output is increased, the shift of resonant frequency is logged by the frequency counter as shown in Fig.5 (a). The slope of the frequency vs laser power line from the closed-loop experiment is quite close to that of the open-loop experiment. In order to know the response time of our detector, a quick laser power increase about 0.3mW is set. The result shows that the resonant frequency is back to be stable within 0.3s as shown in Fig.5 (b). Considering the time of manual operation and the response time of the laser power, the response time of our optical power meter is far less than 0.3s.

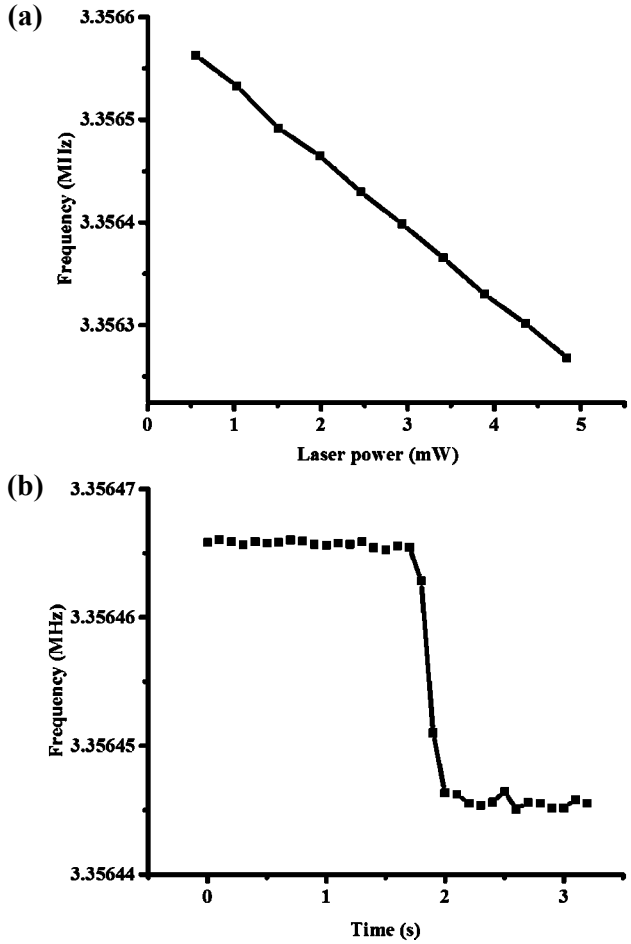


Fig. 5. (a) Resonant frequency of the disk resonator logged by the frequency counter in the closed-loop experiment. (b) The time sequence curve read by the frequency counter. The resonant frequency is back to stable in less than 0.3s after the laser irradiation power is changed.

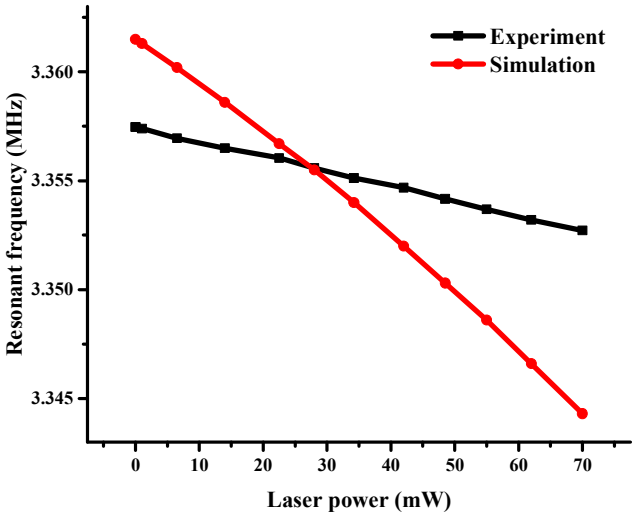


Fig. 6. The frequency vs laser power data from simulation and exprimental results are plotted. The slope of the simulation result is larger.

TABLE I. SPECIFICATIONS OF THE OPTICAL POWER METER

Characteristics	**Value**
Device materials	Single Crystal silicon
Thickness	10μm
Diameter	1.5mm
Working frequency	3.35MHz
Scale Factor	-6.8×10^4 Hz/W
Working wavelength	full-wave band
Resolution	0.98μW
Response time	Less than 0.3s

C. Analysis

Comparing the results from simulation and the open-loop experiment, the slope of the simulation line is -2.46×10^5 Hz/W, while the slope of the open-loop experiment line is -6.8×10^4 Hz/W, which means as laser power increases 1mW, the resonant frequency in simulation reduces 246Hz while the experiment one reduces 68Hz. The slope of the simulation line is much larger than the one of the experiment line, which is possibly caused by the loss of laser power in the experiment, such as reflection of silicon and thermal radiation in the vacuum environment. The output of laser is about 5mm away from the disk. The divergence angle of the optical fiber is another cause of the loss of laser power. According to the differences in result between simulation and experiment, the utilization rate of the laser power in our experiment is around 27.6%.

V. CONCLUSION

In summary, this work presents a new resonant type optical power meter based on micromechanical disk resonator. The resonant frequency fluctuates when the laser irradiation changes. Effective methods including the open-loop and the closed-loop methods are employed to detect the resonant frequency. The minimum frequency fluctuation that our detector can detect is about 0.068Hz, which is corresponding to a detectable laser power of 0.98μW. Full specifications of our optical power meter is given in Table I. Higher sensitivity can be reached by using frequency detection method with higher resolution or higher power absorption rate.

ACKNOWLEDGMENT

This work is supported by the National Natural Science Foundation of China (51575439 and 51421004), Natural Science Foundation of Shaanxi Province (2014jm2-5054) and 111 project (B12016). We also appreciate the support from the Collaborative Innovation Center of High-End Manufacturing Equipment and International Joint Laboratory for Micro/Nano Manufacturing and Measurement Technologies.

REFERENCES

[1] Brown R G W, Jones R, Rarity J G, et al. Characterization of silicon avalanche photodiodes for photon correlation measurements. 2: Active quenching, Applied Optics, 1987, 26(12):2383.

[2] Cova S, Ghioni M, Lacaita A, et al. Avalanche photodiodes and quenching circuits for single-photon detection, Applied Optics, 1996, 35(12):1956.

[3] Hammerich M, Olafsson A. A versatile, low-cost pyroelectric laser power monitor for the 1 mW to 50 W range[J]. Journal of Physics E Scientific Instruments, 1988, 21(1):80.

[4] Edwards J G. A standard calorimeter for pulsed lasers[J]. Journal of Physics E Scientific Instruments, 1975, 8(8):663.

[5] Birky M M. Calorimeter for laser energy measurements.[J]. Applied Optics, 1971, 10(1):132-5.

[6] Rogalski A. Infrared detectors: an overview[J]. Infrared Physics & Technology, 2002, 43(3–5):187-210.

[7] Razeghi M. Current status and future trends of infrared detectors[J]. Opto-Electronics Review, 1998, 1998(3):155-194.

[8] Graf A, Arndt M, Sauer M, et al. REVIEW ARTICLE:, Review of micromachined thermopiles for infrared detection[J]. Measurement Science & Technology, 2007, 18(7):R59-R75.

[9] Graf A, Arndt M, Sauer M, et al. REVIEW ARTICLE:, Review of micromachined thermopiles for infrared detection[J]. Measurement Science & Technology, 2007, 18(7):R59-R75.

[10] Ferrieu F, Auvert G. "Temperature evolutions in silicon induced by a scanned cw laser, pulsed laser, or an electron beam," 1983, 54(5):2646-2649.

Piezoelectric harvester scavenges energy from cavity of phononic crystal

Hongping Hu[1,2], Yajun Zheng[1], Shan Jiang[1,2], Yuantai Hu[1], Vincent Laude[2]
[1] Department of Mechanics, Huazhong University of Science and Technology, Wuhan 430074, P. R. China
[2] Institute of FEMTO-ST, CNRS UMR 6174, Université de Bourgogne Franche-Comté, Besançon 25030, France
huhp@hust.edu.cn

***Abstract*—We propose a model of a piezoelectric power harvester that scavenges energy from the cavity of a phononic crystal (PnC). The band structure of the PnC with a cavity is calculated by super-cell technique. The energy is collected in the cavity when the frequency of the cavity defect mode appears inside the band gap. As a result, the harvester can transform mechanical energy into electric energy efficiently.**

Keywords—Power harvester; cavity; phononic crystal

I. INTRODUCTION

Energy supplied sensor networks have become an urgent problem to solve. Wireless energy supply is necessary for microelectronics located away from a fixed power source, especially for portable or implantable electronics.

Extracting energy from the operating environment of electronics is a viable method for wireless energy supply. Vibration and noise exist extensively in the surrounding environment. Piezoelectric material is a natural candidate for designing power harvesters because of its high electromechanical coupling coefficient. Piezoelectric power harvesters can extract most efficiently power at resonance. The following characteristics can further improve the performance of the harvester. The harvesters can store energy at low resonance frequencies because energy of ambient vibrations is abundant in the low frequency range [1]. A harvester with broad frequency band is more efficient while working in an environment with wideband and/or variable frequency vibration [2, 3]. Furthermore, the applicability of the harvester can be improved if it has an adjustable natural frequency because different vibration sources may have different frequencies, and the frequency of even a single environmental vibration source may sometimes fluctuate [4].

As an artificial periodic structure, metamaterial and PnCs with broad band gaps were developed as power harvesters [5, 6]. The concepts of wave focusing, localization, and funneling was leveraged to establish energy harvester configurations [7].

II. THEORETICAL MODEL

As depicted in Fig. 1, the piezoelectric harvester consists of a beam PnC with a cavity. To the cavity is attached a piezoelectric unimorph. The PnC is composed of a metal beam arrayed periodically with masses. The unimorph is connected to a circuit whose impedance is simplified to Z. The beam is driven by a harmonic excitation $A\sin(\omega t)$ on the bottom of the cavity.

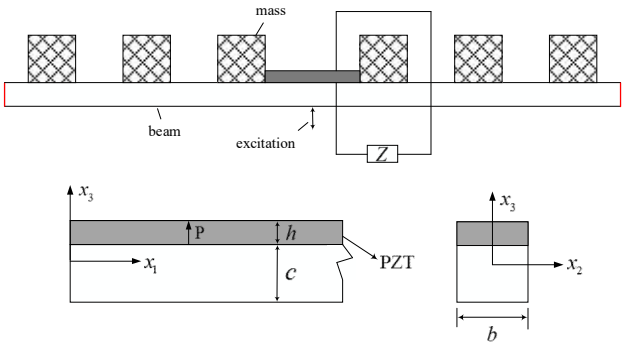


Fig. 1. A piezoelectric harvester model by PnC with cavity

The harvester is analysed by the finite element method with Comsol Multiphysics with a plane-stress assumption. The output power can be written as

$$P = \frac{1}{4}\left(VI^* + IV^*\right). \tag{1}$$

Output voltage V and current I are related by Ohm's law as $V = IZ$.

III. RESULTS AND DISCUSSION

Aluminum, steel, and PZT-5H are selected as the materials for beam, mass, and piezoelectric layer, respectively. The length of unit cell is l_0=20mm and the width of the mass is l_m=10mm. Thickness c and width b of the beam are 1mm and 20 mm.

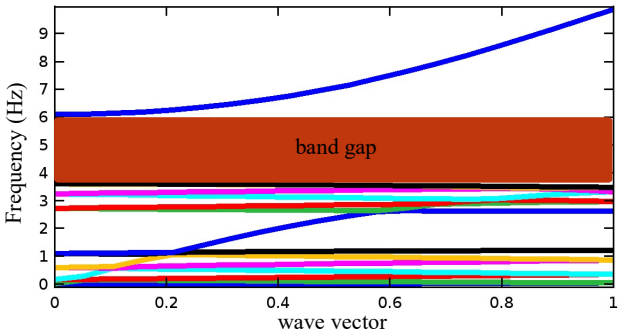


Fig. 2. Band structure of the PnC without cavity.

Firstly, we calculate the band structure of the PnC without cavity by use of the Bloch theorem. Fig. 2 shows that a band gap appears between 3591.5 and 6087.7 Hz.

We then compute the band structure by the super-cell technique. The length of the cavity is chosen as l_c=1.2l_0 to locate the frequency of cavity defect mode inside the band gap. A band of the defect mode spans from 4683.9 to 4692.7 Hz, as shown in Fig. 3.

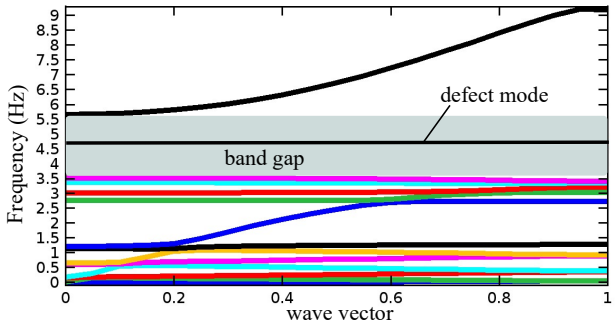


Fig. 3. Band structure of the PnC with cavity.

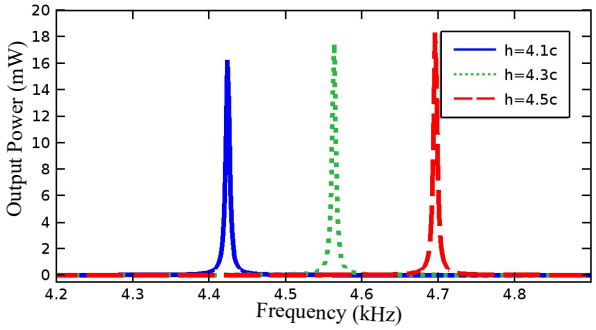


Fig. 4. Output power of the harvester versues frequency for different thicknesses of the piezoelectric layer.

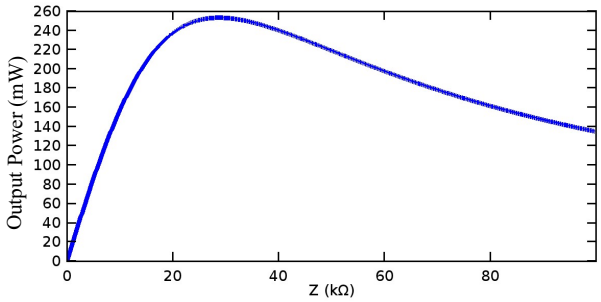


Fig. 5. Output power of the harvester versus circuit resistance.

Furthermore, we introduce a piezoelectric layer inside the cavity of the PnC. The length of PZT is l_p=1.6l_0. Acceleration of the excitation is set to $A\omega^2$=1. As shown in Fig. 4, large output powers are obtained around the frequency of the defect mode by harvesters with different thickness of PZT. The maximum output power appears at a higher frequency for the harvester with a thicker PZT layer.

Finally, Fig. 5 illustrates the output power of the harvester versus external circuit resistance. The output power increases monotonously at first, then decreases gradually with increasing circuit resistance. Therefore, an optimal circuit resistance exists to get a maximal output power.

IV. Conclusion

A piezoelectric power harvester was proposed to scavenge energy from the cavity of a phononic crystal. The frequency of defect mode appears within the band gap by design of the phononic crystal and its cavity. A piezoelectric layer is introduced into the cavity. The dependence of the output power with the geometric parameters of the harvester and circuit resistance has been investigated. The frequencies of the band gap and the defect mode could be further lowered in future research.

Acknowledgment

This work was supported by the National Natural Science Foundation of China (grants 11272126 and 11672113). Hu and Jiang also acknowledge support from China Scholarship Council (Grants Nos. 201606165026 and 201606160045).

References

[1] H. P. Hu, H. Xue, and Y. T. Hu, "A spiral-shaped harvester with an improved harvesting element and an adaptive storage circuit," *IEEE Transactions on Ultrasonics Ferroelectrics and Frequency Control,* vol. 54, no. 6, pp. 1177-1187, 2007.

[2] H. Xue, Y. T. Hu, and Q. M. Wang, "Broadband piezoelectric energy harvesting devices using multiple bimorphs with different operating frequencies," *IEEE Transactions on Ultrasonics Ferroelectrics and Frequency Control,* vol. 55, no. 9, pp. 2104-2108, , 2008.

[3] H. Xue, and H. P. Hu, "Nonlinear characteristics of a circular plate piezoelectric harvester with relatively large deflection near resonance," *IEEE Transactions on Ultrasonics Ferroelectrics and Frequency Control,* vol. 55, no. 9, pp. 2092-2096, 2008.

[4] Y. T. Hu, H. Xue, and H. P. Hu, "A piezoelectric power harvester with adjustable frequency through axial preloads," *Smart Materials & Structures,* vol. 16, pp. 1961, 2007.

[5] Z. S. Chen, Y. M. Yang, Z. M. Lu, and Y. T. Luo, "Broadband characteristics of vibration energy harvesting using one-dimensional phononic piezoelectric cantilever beams," *Physica B: Condensed Matter,* vol. 410, pp. 5-12, 2013.

[6] S. Tol, F. Degertekin, and A. Erturk, "Gradient-index phononic crystal lens-based enhancement of elastic wave energy harvesting," *Applied Physics Letters,* vol. 109, no. 6, pp. 063902, 2016.

[7] M. Carrara, M. Cacan, J. Toussaint, M. Leamy, M. Ruzzene, and A. Erturk, "Metamaterial-inspired structures and concepts for elastoacoustic wave energy harvesting," *Smart Materials & Structures,* vol. 22, no. 6, pp. 065004, 2013.

Integration of multilayered graphene on AlN based resonators as a functionalization platform for biosensors

L. Gordillo-Dagallier, J. Olivares, B. Marco-Dufort, J.L. Olivera, J.M. Escolano, T. Mirea, M. Clement, and E. Iborra
GMME-CEMDATIC-ETSIT. Universidad Politécnica de Madrid
Madrid, Spain
eiborra@etsit.upm.es

***Abstract*—In this communication we present the integration of graphene on the top electrode of solidly mounted resonators based on piezoelectric AlN thin films for gravimetric sensor applications. Because its particular chemical structure, graphene shows great potential as a bio-functionalization platform. However, in order to be commercially viable, direct deposition on the resonators is preferred to transfer techniques. The high temperatures involved in graphene chemical vapor deposition make this integration complex. Specially developed acoustic resonators, which can withstand high temperatures, combined with the use of multi-layered top electrodes for AlN resonators, allow a successful integration of graphene. Finally, oxygen plasma treatments to optimize the creation of defects on the graphene layer can be used to firmly bond receptors on its surface.**

Keywords—Graphene integration; BAW resonators; gravimetric sensors; surface functionalization

I. INTRODUCTION

Applications for graphene are studied in a variety of fields; for sensors, graphene is demonstrating very good possibilities. For instance, in the field of chemical sensors, the particular chemical structure of graphene makes it especially interesting for the surface functionalization of biosensors [1]. Graphene layers on top of devices can be obtained by several means, which include the direct transfer of already synthesized graphene layers as well as chemical vapor deposition (CVD) techniques. Transfer methods allow obtaining a graphene layer on virtually any surface. However, the existing transfer methods are usually complex and not reproducible. Additionally, the binding of transferred graphene to the surface is not always tight enough to withstand a subsequent functionalization process, for which several incubations and rinsing stages are usually needed. CVD graphene has the advantage of better adhesion. However, it needs a particular (catalytic) surface to grow. Transition metals such as Ni, Co, Ir, Mo or W have been the object of study. The graphene growth process depends on the nature of the catalyst, concretely on the competition between C-C bonding and C-metal bonding [2]. For the particular applications, bio-functionalization, graphene should have some particular features that are not the commonly pursued ones. First, the adherence of graphene to the top electrode should be as tight as possible because the basis of gravimetric detection needs the added mass to coherently vibrate with the resonator. Besides, acoustic energy could detach the layer. Secondly, during the functionalization process, several reagents are used to covalently bind the receptor species to the surface. Therefore, some chemical reactions that debilitate the graphene structure might occur. To ensure that this does not detach the graphene film, it is better to have two or even three graphene layers instead of the always-pursued monolayer structure. The control of the deposition process, including the choice of the particular catalyst metal, is very important in this case, as it determines the characteristics of the whole structure. Another issue to take into consideration is that, usually, temperatures as high as 1000ºC are needed for high quality mono-layered graphene deposition, although lower temperatures (down to 600ºC) can be used if the appropriate catalyst and process conditions are chosen, but, even in these last cases, temperatures are still very high. The devices on which the graphene layer is deposited must withstand these temperatures without losing their performances. For instance, metals can be oxidized, semiconductors can be doped, and compounds can be decomposed. Additionally, the changes in sizes due to dilatation can generate stress between layers of different materials, which can create defects or even delamination if the adherence is not very good. In the particular case of solidly mounted resonators (SMRs), which are composed of a piezoelectric AlN capacitor deposited on a layered acoustic reflector containing five or more piled layers, the main issue is to preserve the mechanical integrity of the whole structure, and he its functionality. Due to the different thermal expansion coefficients of the materials involved in the multi-layered structure, in-plane stress develops during CVD-graphene deposition, which may lead to the delamination of the multi-layered structure. It is important to choose adequately the materials and their deposition conditions to minimize the thermal expansion and improve the adhesion between layers.

In this paper, we present the integration of graphene on AlN-based SMRs as a functionalization platform for chemical sensors. We describe a procedure to manufacture SMRs containing acoustic reflectors specifically designed to be withstand the high temperatures (up to 1000ºC) to which the samples are subjected during the CVD growth of graphene. We describe the process for obtaining low-defect and few-layer graphene on top of the SMR.

978-1-5386-2916-1/$31.00 ©2017 IEEE

II. EXPERIMENTAL

SMRs are composed of Ir/AlN/Mo piezoelectric stacks deposited on acoustic Bragg reflectors made of nine alternate SiO_2 and AlN layers a quarter-wavelength thick (see Fig. 1). All the films were deposited by sputtering. The deposition conditions of the high impedance (AlN) and low impedance (SiO_2) layers of the reflector were adjusted to minimize the residual stress of each film. After deposition, the reflectors were subjected to heat-treatments under vacuum at different temperatures to assess their temperature resistance. Then, the piezoelectric stack was deposited with both *c*-axis oriented and tilted-*c*-axis AlN films. A proper design combined with low-stress materials yielded SMRs capable of sustaining temperatures as high as 1000ºC without losing their performance.

SMRs with a W top electrode were also used because this material has a high acoustic impedance and is commonly used in resonators. Moreover, a Ti thin film under and over the top electrode was tested, as Ti is a typical adhesion between metals.

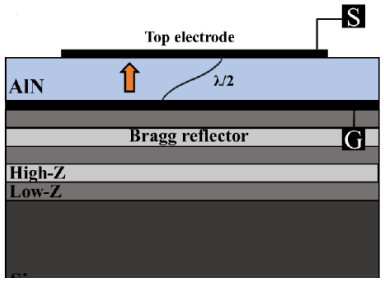


Fig. 1. AlN-based SMR

A thin film of catalyst polycrystalline nickel (50-120 nm) was thermally evaporated over the Mo top electrode for subsequent graphene deposition. The use of polycrystalline Ni is attractive due to its low cost compared to single crystalline Ni, and therefore more suitable for industrial commercialization. Ni films had to be thin enough not to interfere with the resonator performance, but thick enough to avoid the formation of Ni droplets on the surface during heating due to dewetting [3], which could deteriorate graphene quality or promote CNT growth if nanoparticles are formed. Figure 2 shows an AFM image showing the surface of a representative sample after graphene deposition on a 100 nm-thick Ni layer.

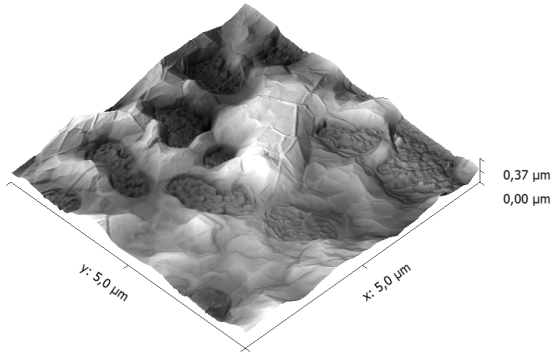


Fig. 2. 3D-AFM image of the droplets formed in Ni surface due to Ni dewetting from the substrate. Observe the fold structure of the graphene on the Ni surface.

Graphene was grown in a high vacuum custom-made CVD chamber on top of the Ni catalyst deposited on the SMRs. The chamber was pumped down to a pressure of 10^{-6} Torr with a turbo-molecular pump before starting the depositions. A pyrolytic carbon heater was used as a substrate holder to decompose diluted C_2H_2 gas (acetylene) at a low temperature (650 °C). The total pressure in the chamber was kept relatively high and constant (~10 mTorr). The SMRs were first heated in argon at a rate of 50°C/min up to 650 °C, in order to minimize the height of the Ni droplets formed. They were then annealed for 4 min in a mixture of Ar and C_2H_2 (18 % by volume). Finally, the SMRs were slowly cooled down at a rate of 15 °C/min in pure Ar from 650 to 600 °C and then rapidly cooled to room temperature (Fig. 3). The graphene obtained on Ni-Mo and Ni-W top electrodes was compared with the graphene grown on Ni-SiO_2 samples, in order to determine the influence of the under-layer in the characteristics of the obtained graphene.

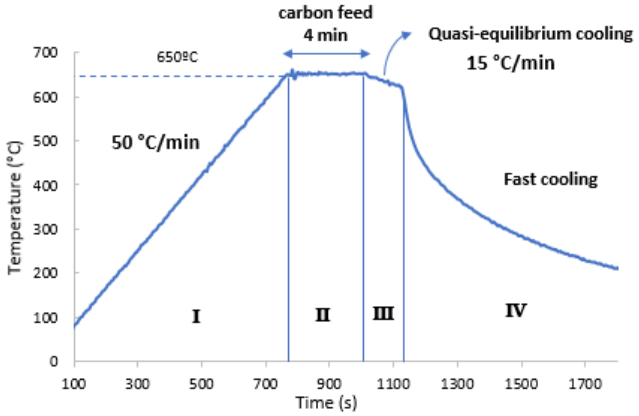


Fig. 3. Temperature evolution during the graphene growth process. Four stages are represented, corresponding to the sample heating (I), the C_2H_2 supply (II), the slow cooling (III), and the fast cooling (IV) stages.

The CVD-grown graphene obtained on top of the SMRs was characterized using Raman spectroscopy with an excitation light of 532 nm wavelength. Multiple measurements were taken throughout the samples to assess the uniformity and quality of the coverage. Then, the SMRs performance was determined by deriving the electrical impedance spectrum from the reflection coefficient (S_{11}) measured with a network analyzer.

Finally, as a first step for surface functionalization, a low damage oxygen radical plasma treatment was used to generate controlled defect in graphene. The optimal parameters of operation were 30 W of RF power, a pressure of 25 mTorr and an O_2 flow of 25 sccm. In order to protect the sample from the energetic ions associated with plasmas, a glass shield was placed on top of the samples, only allowing thermalized reactive oxygen radicals to reach the surface and thus protecting the graphene from heavy damage [4]. The samples were characterized using Raman spectroscopy before and after each plasma treatments (of different durations) for monitoring the amount of defects and the integrity of the graphene layer.

III. RESULTS AND DISCUSSION

The main characteristics of the CVD-grown graphene are the low level of defects and the presence of two or three layers

weakly coupled. A typical Raman spectrum is shown in Fig.4 in blue, with the characteristic D peak (~1350 cm^{-1}), which is related with defects in the graphene structure, G peak (~1580 cm^{-1}) and 2D peak (~2700 cm^{-1}). The number of graphene layers can be inferred from the I_{2D}/I_G ratio, which is $I_{2D}/I_G > 1$, and the analysis of the 2D peak, which is well fitted with a single Lorentzian peak and has a FWHM of around 40 cm^{-1} [5]. Moreover, this fitting suggests that the interlayer coupling is weak [6].

Higher C_2H_2 flow rates and lower overall pressures, as well as quick variations of total pressure, result in an increased D peak (see Fig. 4a). Thus, given a C_2H_2-Ar flow ratio, raising the total pressure and keeping it constant during the growth process show to be an effective method to control the number of defects in the as-grown graphene. However, when the overall pressure is raised over a threshold, no graphene grows. Furthermore, slowing the cooling rate until reaching 600°C delivers graphene with better quality, greater coverage and uniformity, and fewer layers, as can be deduced from the increased I_{2D}/I_G ratio in Fig. 4b. Nevertheless, if the cooling rate is slowed until lower temperatures (<500ºC), no graphene growth is observed.

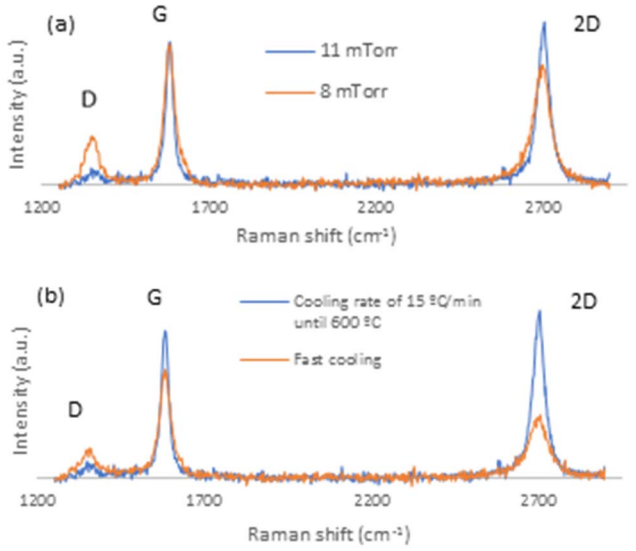


Fig. 4. (a) Comparison of the Raman spectra of graphene grown upon fast cooling and with a cooling rate of 15 °C/min from 650 to 600 °C. (b) Influence of overall pressure during growth process.

The nature of the under-layer of the Ni catalyst was found to have a major influence on the quality of the as-grown graphene. The results shown above correspond to Ni deposited directly on the Mo top electrode. With a W top the graphene quality obtained is similar. However, when introducing even a very thin Ti film between the Ni and the Mo, graphite and nickel carbides were grown. An explanation to this results is proposed below. The hydrocarbon gas precursor (C_2H_2) is decomposed at 650ºC catalytically on the Ni surface (see stage II in Fig. 3) and carbon diffuses into the Ni bulk. It is believed that graphene then grows following a combination of two mechanisms: carbon segregation from the Ni bulk under thermal equilibrium conditions at carbon concentrations below the solubility limit, and direct surface non-equilibrium carbon precipitation during quenching [7] (see Fig. 3). The surface curvature associated with the presence of grain boundaries and defects on the polycrystalline Ni substrate act as active sites for multilayer graphene nucleation [8]. Once a particular nucleation site is activated, it fulfils the carbon atoms for the growing graphene from the surrounding grains. The graphene layers then grow laterally from the nucleation site and cover the Ni surface [7]. Due to these phenomena, there is an equilibrium between carbon diffusion into the Ni bulk and carbon segregation through the active nucleation points (graphene construction and destruction). By acting upon this equilibrium (stages II and III in Fig. 3) and controlling carbon precipitation during fast cooling (stage IV in Fig. 3), it is possible to obtain high quality few-layered graphene even on polycrystalline Ni. While the equilibrium can be controlled by regulating the C_2H_2 flow rate, the duration of the C_2H_2 supply, and the overall pressure and temperature process; the carbon precipitation upon rapid cooling can be limited if an adequate substrate is chosen.

On one hand, by keeping the pressure constant during the whole growth process, disturbances in the equilibrium are minimized and low number of defects are induced during the graphene crystallization. Higher overall pressures may slow carbon segregation, resulting in a more controlled process, and thus obtaining graphene with lower defects and higher quality. On the other hand, by decreasing the cooling rate, this equilibrium segregated phase is kept until 600 ºC. As reported by Reina et al. [9], decreasing the cooling rate reduces the number of multi-layer graphene nucleation sites, and therefore increases the Ni surface covered by few-layers. Moreover, by diluting the C_2H_2 in Ar, the amount of carbon in solution into the Ni bulk is controlled, and therefore the amount of carbon precipitation upon cooling. Once 600ºC was reached, fast cooling allows to freeze the graphene structure resulting in a full few-layered graphene coverage. Regarding the influence of the under-layer, a Mo layer under the Ni acts as a carbon sink, retaining dissolved excess carbon species in the form of molybdenum carbides, as suggested in [10]. However, a Ti layer acts as a diffusion barrier. As the carbon is retained near the surface by the diffusion barrier, it can segregate easier back to it, resulting in multi-layer graphene.

The theory exposed above has been proven to be valid for different catalysts as graphene has been grown successfully on Fe and Co. In order to extrapolate the growth process parameters to obtain similar graphene quality, the solubility of carbon in the catalyst must be taken into account. If the solubility in the new catalyst is lower than in Ni, growth times and C_2H_2 flow rates must be increased.

To check whether the performance of the SMRs was affected by the integration of the graphene, the electrical impedance spectra of the SMRs before and after graphene deposition was measured, as shown in Fig. 5. The slight variation in frequency, also observed after a heat treatment without graphene deposition, is due to variations of thicknesses of the different layers, which became more compact. The quality factor and the electromechanical coupling coefficient do not substantially vary. Therefore, it was concluded that the integration of the graphene does not significantly modify the performance of the SMRs.

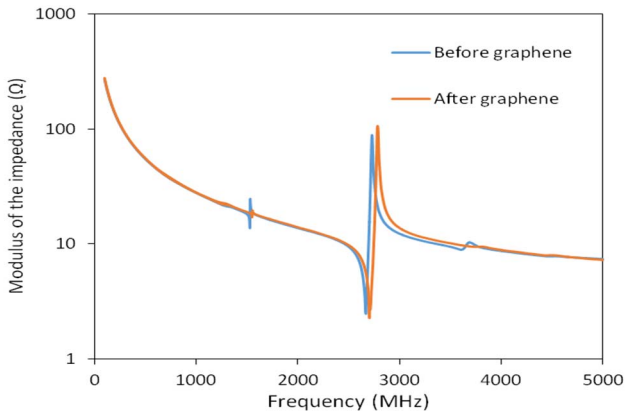


Fig. 5. Modulus of the impedance spectra of a device before and after the deposition of graphene on the top electrode.

After successful integration of the graphene on the SMRs, its surface was functionalized for bio-detecting demonstration. To do this, shear mode resonators made with tilted AlN grains were used for in liquid operation [11]. Functionalization starts with surface exposition to an O_2 plasma used to create oxygen-containing defects on the graphene surface. This is evidenced in Fig. 6, which shows Raman spectra before and after a plasma treatment. After the plasma treatment, the D peak – or defect peak – appears at around 1350 cm^{-1}. The intensities of the G and 2D peaks are unaffected by the plasma treatment, thus, we can conclude that the plasma treatment successfully introduced defects in the graphene while maintaining its structural integrity.

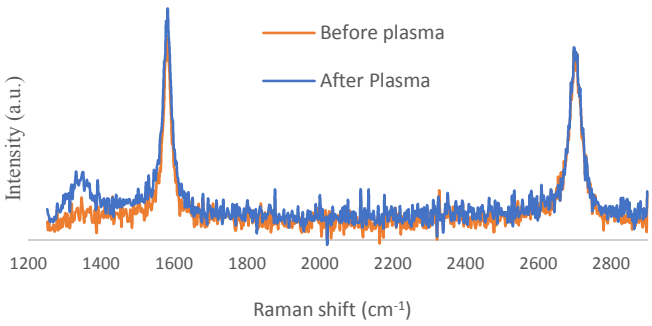


Fig. 6. Raman spectra of the few-layered graphene surface of an SMR before and after the low damage O_2 treatmen. Note the appearance of the defect D peak at around 1350 cm^{-1} after the plasma treatment.

After the plasma treatment, streptavidin was bonded to the surface of the graphene on top of the SMRs. A protocol was developed to covalently bond Streptavidin to oxygen-containing defects on the surface of the graphene, using standard EDC/NHS (1-ethyl-3-(3-dimethylaminopropyl) carbodiimide hydro-chloride/N-Hydroxysuccinimide) chemistry. To characterize this union, streptavidin conjugated to Qdot® 655v was used and fluorescence microscopy was employed to see the fluorescence signal. The red signal shown in Fig. 7(a) evidences the uniform distribution of streptavidin-Qdot on top of a graphene sample (positive control). Figure 7(b) shows a negative control in which EDC/NHS was omitted.

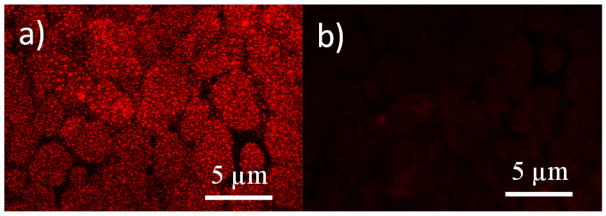


Fig. 7. Fluorescence microscopy images of the surface of graphene incubated with streptavidin conjugated to Qdot® 655, a) positive and b) negative controls. The underlying texture of the graphene is visualized.

IV. CONCLUSIONS

Graphene directly grown by CVD was integrated on SMR as a functionalization platform for chemical sensing. After developing devices able to withstand the high process temperature, few-layered graphene was grown on them. A model of the graphene growth, which can be extended to other catalysts, is proposed. The performance of resonators is not degraded by graphene growth. O_2 plasma treatment allows control of defect formation on the graphene layer. The viability of SMR with graphene was demonstrated.

ACKNOWLEDGMENT

This work was partially supported by MICINN del Gobierno de España through project MAT2013-45957-R.

REFERENCES

[1] D.J. Joe, et al., "Surface Functionalized Graphene Biosensor on Sapphire for Cancer Cell Detection", J Nanosci Nanotechnol. 16(1) (2016) pp. 144-151.

[2] H. Chen et al., "Contrasting Behavior of Carbon Nucleation in the Initial Stages of Graphene Epitaxial Growth on Stepped Metal Surfaces", Phys. Rev. Lett. 104 (2010), 186101.

[3] R.G. Golik, et al., "Analysis of Structural Transformations and Fluctuation Effects in the Nanosized Nickel Films in the Vicinity of the Melting Point", Journal of Communications Technology and Electronics 57(6) (2012) pp. 629-633.

[4] C-H Huang, et al., "Ultra low-damage radical treatment for the highly controllable oxidation of large-scale graphene sheets", Carbon 73 (2014) pp.244-251.

[5] A. C. Ferrari, "Raman Spectroscopy of graphene and graphite", Solid State Communications 143 (2007) pp. 47–57.

[6] Z. Luo, et al., "Large-Scale Synthesis of Bi-Layer Graphene in Strongly Coupled Stacking Order", Adv. Funct. Mater. 21 (2011) pp. 911-917.

[7] L. Baraton, et al., "On the mechanisms of precipitation of graphene on nickel thin films", Europhysics Letters 96(4) (2011).

[8] Y. Zhang et al., "Comparison of Graphene Growth on Single-Crystalline and Polycrystalline Ni by Chemical Vapor Deposition", J. Phys. Chem. Lett. 1 (2010) pp. 3101-3107.

[9] A. Reina et al., "Growth of Large-Area Single- and Bi-Layer Graphene by Controlled Carbon Precipitation on Polycrystalline Ni Surfaces", Nano Res 2 (2009) pp. 509-516.

[10] B. Dai, et al., "Rational design of a binary metal alloy for chemical vapour deposition growth of uniform single-layer graphene", Nature Communications 2 (2011).

[11] Mario DeMiguel-Ramos, Bárbara Díaz-Durán, José-Miguel Escolano, Mariano Barba, Teona Mirea, Jimena Olivares, Marta Clement, Enrique Iborra, "Gravimetric biosensor based on a 1.3 GHz AlN shear-mode solidly mounted resonator". Sensors and Actuators B 239 (2017) 1282–1288.

Kalman Filter Approaches for a Mixed Clock Ensemble

Marion Gödel, Tobias D. Schmidt and Johann Furthner
Institute of Communication and Navigation
German Aerospace Center (DLR)
Oberpfaffenhofen, Germany
Email: marion.goedel@dlr.de

***Abstract*—Clock ensembling is a promising concept for future time scale generation as robustness and stability can be considerably improved compared to master clock approaches. While ensembles consisting of the same clock types were already demonstrated to improve robustness of the generated time scale, ensembles using different clock types can clearly benefit from the advantages of the individual single clocks contributing to the time generation process. In particular, the performance of the ensemble time can be improved over a wide range of averaging times by combining clocks exhibiting superior stabilities for distinct time scales. In future, this approach could be used to integrate newly developed clock types such as e.g. optical clocks into a clock ensemble.**

***Keywords*—clock ensembling, Kalman filter, time scale, clock model, simulation, Implicit Ensemble Mean.**

I. Introduction

Various research fields such as navigation, geodesy applications, and financial trading demand a robust and stable time scale. Clock ensembling is a promising concept ensuring this requirement by combining a set of clocks instead of using an individual clock output. Approaches using Kalman filters [1] as time scale algorithms seem to provide the best prospects, since they were developed and designed to estimate quantities from a noisy signal. Recently, we were able to present first experimental results based on real measurements of a laboratory hardware demonstrator consisting of three identical Rubidium frequency standards controlled by a Kalman filter [2]. A stable ensemble time reference is generated even in the presence of significant artificial jumps on the clocks' output signals.

As strength lies in unity, the goal of clock ensembling is to provide a time scale which is better than the sum of its parts. This means that the ensemble time is both more robust and more stable than the single clock contributions.

In order to enhance the robustness of the system, the ensembling algorithms use individual clocks as sensors to identify and respond to anomalies. Examples of a frequency and phase jump detection algorithm using the Kalman filter is given in [3] and [2], respectively. More detection algorithms for different kinds of anomalies are given in [4] [5] [6]. To improve stability, the ensembling approach provides different options. An ensemble of n identical clocks directly results in a decrease in overlapping Allan deviation by a factor of $\sqrt{n}$ [7]. However, a considerably better option is to combine different types of clocks. This allows the ensemble to use the superior performance of individual clocks for arbitrary times. Considering the latest clock developments, it is of high interest to combine long-term stable clocks such as e. g. classical hydrogen masers with modern optical clocks (cavities as well as atomic/molecular transitions) which provide an extremely high stability for short averaging times. An overview of the achievements in optical clock technologies was provided e. g. by Poli *et al.* [8] and Ludlow *et al.* [9]. However, numerous new promising investigations were presented the community within the last few years (refer to the respective scientific journals).

II. State of the Art

Unfortunately, there is no absolute information about the behavior of a single clock. Instead, only the phase difference between two clocks is accessible by direct observations using common measurement techniques. This is one of the main challenges for clock ensembling algorithms. Estimating the individual clock states from relative measurement yields an underdetermined and therefore overall unobservable system. Consequently, the estimation errors of the clock state estimates are growing without bound over time. The ensembling community has tackled this challenge with two different Kalman filter approaches. One solution implements the so called basic time scale equation (BTSE) to resolve the unobservability [10]. However, the BTSE imposes assumptions that are only fulfilled in a sufficiently large ensemble. Therefore, an alternative technique was developed that uses the pure Kalman filter, trying to minimize the influence of the unobservability on the estimation process [11] [12].

The error covariance matrix in the Kalman filter provides information about the quality of the state estimation. In an unobservable system, the matrix entries grow without limit which may result in numerical instability. Therefore, Brown proposed a covariance reduction which is transparent to the estimation process [7]. Moreover, Greenhall developed another reduction method which additionally improves stability aimed for a scenario of distributed clocks with different stabilities [13]. The generated paper time scale by both methods is called the Implicit Ensemble Mean (IEM).

978-1-5386-2916-1/$31.00 ©2017 IEEE

The hardware demonstrator used for the previous publication of the authors [2] features a clock ensemble composed of three identical Rubidium clocks and a micro phase stepper (MPS) featuring an oven controlled crystal oscillator (OCXO). The ensemble time was formed using the pure Kalman filter approach utilizing Brown's reduction method. The IEM was realized by applying control values on the micro phase stepper. By adding a simple jump detection algorithm, an enhanced robustness of the IEM realization compared to the individual clocks was successfully demonstrated.

III. Methods

In this work we focus on the stability aspect. Throughout this publication we are considering a single-laboratory scenario with a small measurement noise. The performance of the ensemble time can be further improved by accounting for the imperfections of the system. Therefore, we pursue two different topics that impact on the stability of the IEM realization:

First, we want to model the ensemble clocks as closely as possible. For example, an OCXO typically experiences flicker frequency noise which is not represented in the typically used two- or three-state clock model [14] [15]. In addition, newly developed clock types, as optical clocks, show a different behavior than the classical clock types (Cesium, Maser, etc.). Their stability characteristics cannot be modeled sufficiently by the common three-state model. Davis *et al.* proposed an extension by Markov processes which account for the flicker frequency noise [16]. We have used this model to incorporate the noise types that are not covered in the three-state model.

Secondly, we address the stability of the Implicit Ensemble Mean generated from a fictional mixed clock ensemble. The reduction method proposed by Brown tends to follow one clock in the ensemble in scenarios without measurement noise [13]. Consequently, the advantage of clock ensembling - the performance of the ensemble should be better than the individual contributions for all times - is not ensured. Greenhall's reduction overcomes this issue, but due to matrix inversions it is numerically unstable if the measurement noise is negligible. Davis *et al.* proposed a covariance reduction for scenarios without measurement noise. This seems to be a suitable approach for our scenario as we are looking at a single-laboratory scenario with an insignificant measurement noise. However, this reduction does not provide a method to obtain the IEM. Therefore, we combine the formulas proposed by Greenhall and Davis to benefit from both concepts in order to generate a stable IEM for a mixed clock ensemble.

A. Modeling of Clocks

Davis *et al.* proposed to extend the classical three-state model with a set of Gauss-Markov processes to model flicker frequency noise. These processes appear in an Allan deviation plot as negative parabolas. Thus, the Markov processes can also be used to adjust the slope of the clocks' Allan deviation in certain regions. Each Markov process can be described by the differential equations

$$\frac{dx}{dt} = y(t), \frac{dy}{dt} = -Ry(t) + n(t)$$

with the white noise process $n(t)$. For each Gauss-Markov process, $y(t)$ is a new state in the clock model in which the Markov process operates and $x(t)$ is the associated time offset that is added to the first state of the classical three-state model. There exists a stationary solution for $y(t)$ with variance $U = \frac{\sigma_M^2}{2R}$, where $1/R$ is the time constant. The Markov process can also be described in an iterative fashion by a first order difference equation of the form

$$\begin{pmatrix} x(t_k) \\ y(t_k) \end{pmatrix} = \begin{pmatrix} 1 & \frac{-1+\exp(R\tau_0)}{R} \\ 0 & \exp(-R\tau_0) \end{pmatrix} \begin{pmatrix} x(t_{k-1}) \\ y(t_{k-1}) \end{pmatrix} + \begin{pmatrix} w_x(t_k) \\ w_y(t_k) \end{pmatrix}$$

with discretization time $\tau_0 = t_k - t_{k-1}$ [17]. The process noise vector $w = \begin{pmatrix} w_x(t) & w_y(t) \end{pmatrix}^{\mathrm{T}}$ has mean zero and covariance matrix

$$Q_m(\tau_0, j) = \sigma_{Mj}^2 \begin{pmatrix} \tau_0^3 a_{11}(R_j\tau_0) & \tau_0^2 a_{12}(R_j\tau_0) \\ \tau_0^2 a_{21}(R_j\tau_0) & \tau_0 a_{22}(R_j\tau_0) \end{pmatrix}.$$

The therein used subterms are given by

$$a_{11}(x) = \frac{-\frac{3}{2} + x + 2\exp(-x) - \frac{1}{2}\exp(-2x)}{x^3}$$
$$a_{12}(x) = \frac{\frac{1}{2} - \exp(-x) + \frac{1}{2}\exp(-2x)}{x^2} = a_{21}(x)$$
$$a_{22}(x) = \frac{1 - \exp(-2x)}{2x}.$$

The Allan deviation of a single Markov process is given by

$$\sigma_y^2(\tau) = U \frac{-3 + 4\exp(-R\tau) - \exp(-2R\tau) + 2R\tau}{R^2\tau^2}.$$

One can numerically find the maximum of each process at $\tau \approx 1.8926/R$. Using this information, we can place the Markov process on the x-axis of an Allan deviation plot by adjusting R and on the y-axis by changing U. A variable amount of Markov processes can be added to the classical clock model to account for arbitrary behaviors of noise contributions.

B. Combination Greenhall & Davis

Greenhall [13] defined the Implicit Ensemble Mean as

$$\tilde{x}_0 = \sum_{i=1}^{n} a_{ri}\tilde{x}_i = a_r^T\tilde{x}$$

with $\tilde{x} = x - \hat{x}$, the difference between the true clock state x and its estimate $\hat{x}$, as well as the IEM weights a_{ri}. The reading of clock i is denoted as x_i. This definition of the IEM is used throughout this paper.

Furthermore, Greenhall points out that due to small measurement noise R, the error covariance matrix of the filter may become (close to) singular. In a scenario of clocks in distributed labs, this can be resolved by using only one clock per lab. As a result, only measurement links with a

higher noise will remain in the system, as the links between stations will always be worse than between clocks in the same laboratory. Since we are considering a scenario in which all clocks are in one laboratory, this approach can not be utilized. As a consequence, we observe numerical problems with the two inversions (first, for calculating the Kalman gain and second, for solving the linear system for the implicit weights) in our scenario.

Considering the properties of the different reduction methods and IEM formulas, we combine the reduction proposed by Davis *et al.* with the IEM formula of Greenhall [13] even though the reduction was developed for scenarios without measurement noise. In the best case, the reduction would be numerically stable and the IEM formula would provide an ensemble mean that follows the best performance of the ensemble at every averaging time.

We implement the reduction proposed in [16] with the S-matrix of the shape

$$S = \begin{pmatrix} 0 & 0 & \cdots & 0 \\ 0 & 1 & & \\ \vdots & & \ddots & \\ 0 & & & 1 \end{pmatrix}.$$

For the reduction, S is applied on both sides to the error covariance matrix $\hat{P}^+$ from the Kalman filter

$$\hat{P}^+ \leftarrow S\hat{P}^+S^T$$

Unfortunately, Davis *et al.* do not calculate the ensemble mean. Thus, we apply the Greenhall formula for the IEM, as it utilizes the performances of all clocks in the ensemble. Applying the selection matrix A all components associated with the phase offsets of the ensemble clocks are extracted from $\hat{P}^+$ to form

$$P_{rxx} = A\hat{P}^+A^T.$$

Subsequently, the linear system

$$\begin{pmatrix} P_{rxx} & 1_N \\ p \cdot 1_N & 0 \end{pmatrix} \begin{pmatrix} a_r \\ \theta \end{pmatrix} = \begin{pmatrix} 0_N \\ p \end{pmatrix}$$

is solved in order to obtain the weights a_r. The system is scaled by p to avoid a large imbalance among the parts of the matrix. As suggested in [13],

$$p = \max(\mathrm{diag}(P_{rxx}))$$

was chosen. In addition, we assure that the covariance matrix is symmetric by

$$\hat{P}^+ \leftarrow \frac{1}{2}\left(\hat{P}^+ + (\hat{P}^+)^T\right).$$

It is noted, that it is not yet clarified how the reduction proposed by Davis *et al.* affects the covariance matrix in a scenario with measurement noise.

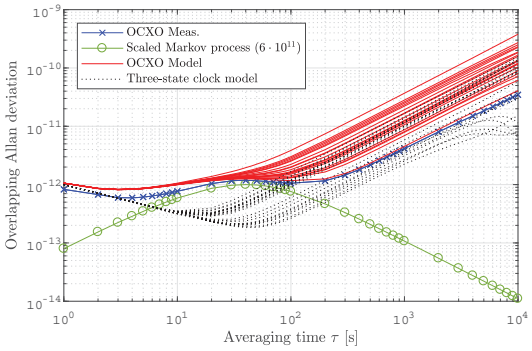


Fig. 1. Measurement of the OCXO (blue crosses) against the AHM and 20 simulations of the OCXO model (red solid lines) using one Markov process. In addition, the overlapping Allan deviation of the scaled Markov process (green circles) and 20 simulations of the classical three state model (black dotted lines) are shown.

IV. Simulation Results

A. Modeling of real clock behaviors

We are using the approach proposed by Davis *et al.* in which flicker frequency noise of clocks is modeled by adding Markov processes to the classical three-state model. The parameter set for clock models and the Markov processes of the in the following presented real clock types are listed in table I and II, respectively.

1) Micro Phase Stepper (Lange-Electronic KL-3382): In the authors' previous publication [2], a micro phase stepper was used for the realization of the Implicit Ensemble Mean. The OCXO (Morion MV180) built in the MPS was fitted with the classical clock model. As a consequence, we observed a significant discrepancy between simulations and measurements. Now, we account for the difference by adding a single Markov process with peak at an averaging time of 40 s in the OADEV. The measurement was performed relative to one of our active hydrogen masers (AHM) which shows a higher stability over all measured averaging times presented in this study. The measurement of the OCXO, together with the stability of simulated clocks using Markov processes is shown in figure 1. As an example, for this device the (scaled) shape of the Markov process as well as the stability of a clock simulated with the classical three-state model is depicted. There is a significant variation among the simulations of both OCXO models due to the realization of the random run component.

2) Hydrogen Maser (Kvarz CH1-75): In our laboratory there are three active hydrogen masers. Their phase offsets were measured using a frequency comparator (VCH-314, Vremya) and the individual stabilities are obtained applying the three-corner-hat method [18]. The measurements are used as a base for the model. We add one Markov process to adjust the slope of the long-term behavior (compare figure 2).

3) High Performance Cesium (Microsemi 5071A): The Cesium clock 5071A is a high precision frequency normal

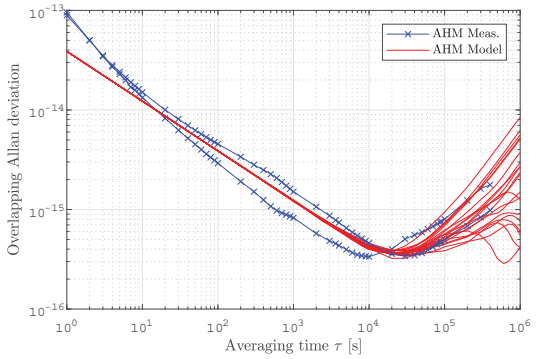


Fig. 2. Measurements of two AHM obtained by the three-corner-hat method (blue crosses) and 20 simulations (red solid lines) of the AHM model incorporating one Markov process.

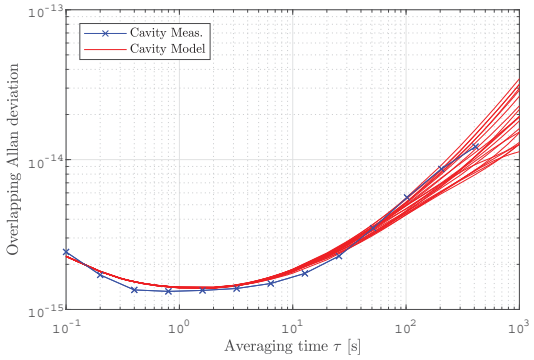


Fig. 4. Measurement (blue crosses) of the cavity and 20 simulations (red solid lines) of its model including five Markov processes.

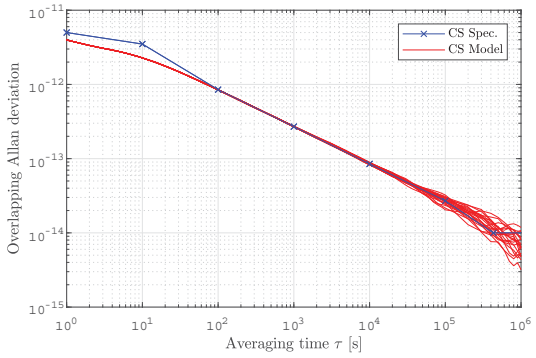


Fig. 3. Specification (blue crosses) of the Cesium frequency normal and 20 simulations (red solid lines) of its model featuring two Markov processes.

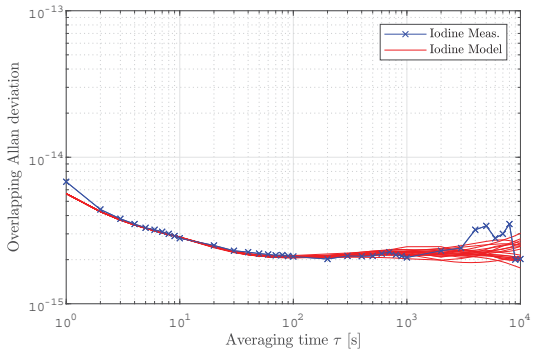


Fig. 5. Measurement (blue crosses) of the Iodine clock and 20 simulations (red solid lines) of its model comprising four Markov processes.

for which the manufacturer (Microsemi) provides the Allan deviation in the specifications over a wide range of averaging times. These values are used to model this specific Cesium clock. We place two Markov processes with maxima at $\tau = 1\,\mathrm{s}$ and $\tau = 5\,\mathrm{s}$ with equal intensity to adapt the behavior in the short-term regime. Several simulations obtained with the resulting clock model are depicted in figure 3 together with the specification of the device.

4) Cavity stabilized near-infrared laser (Menlo Systems ORS1064): The optical reference system (ORS) consists of a continuous wave fiber laser emitting with sub-Hz linewidth at 1064 nm locked to a stable high-finesse cavity. It was measured against an ultra low noise optical frequency comb (FC1500-250-ULN, Menlo Systems) which in turn is locked to an ORS1500 (cavity stabilized laser emitting at 1500 nm, Menlo Systems). The authors note that the measurements of the OSR1064 were performed by Menlo Systems and were kindly provided for this study.

The clock experiences a strong FFM noise which we model by four Markov processes in similar size (similar U) in the short-term regime. In addition, one Markov process is used to adjust the behavior around 1000 s. The resulting model is used to simulate several cavities. Their stabilities are presented in figure 4 along with the measurement.

5) Optical clock based on molecular Iodine (DLR RY, Bremen): Schuldt *et al.* [19] have developed a frequency reference based on the hyperfine component a_1 of the molecular iodine transition R(56)32-0. We use the performance of the 'elegant bread-board' (EBB) model measured against an non-planar-ring-oscillator type Nd:YAG laser (Coherent Inc., Prometheus) with a fundamental wavelength of 1064 nm and the second harmonic at 532 nm. For a detailed description of the measurement setup and and the clock design it is referred to [19]. The clock experiences mainly flicker floor frequency modulation noise. This behavior was modeled by adding four Markov processes in similar size (similar U) over most averaging times. Figure 5 shows the measurement of the Iodine in comparison to a set of simulations of the chosen model.

B. Generating an ensemble time from a fictional simulated clock ensemble

We want to demonstrate a successful ensemble time generation using the clock model extended by Markov processes.

TABLE I
PROCESS NOISE (q-) PARAMETERS FOR THE THREE-STATE CLOCK MODELS

Clock type	q-Parameters q_1	q_2	q_3
Oven Controlled Crystal Oscillator	10^{-24}	$5 \cdot 10^{-32}$	10^{-32}
Active Hydrogen Maser	$1.5 \cdot 10^{-27}$	10^{-45}	10^{-47}
High Performance Cesium	10^{-23}	10^{-50}	10^{-52}
Optical reference system OSR1064	10^{-31}	10^{-33}	$5 \cdot 10^{-38}$
Optical Iodine clock	$3 \cdot 10^{-29}$	10^{-31}	10^{-43}

TABLE II
PARAMETERS FOR THE MARKOV PROCESSES IN THE CLOCK MODELS

Clock type	R	U
Oven Controlled Crystal Oscillator	$1.89/40$	$4 \cdot 10^{-24}$
Active Hydrogen Maser	$1.89/(7 \cdot 10^5)$	$1.5 \cdot 10^{-30}$
High Performance Cesium	$1.89/1$	10^{-23}
	$1.89/5$	10^{-23}
Optical reference system OSR1064	$1.89/0.02$	$2 \cdot 10^{-29}$
	$1.89/0.675$	$2 \cdot 10^{-30}$
	$1.89/2.7$	10^{-30}
	$1.89/10.8$	$2 \cdot 10^{-30}$
	$1.89/2407$	$4 \cdot 10^{-28}$
Optical Iodine clock	$1.89/7$	$1.2 \cdot 10^{-29}$
	$1.89/100$	$5 \cdot 10^{-30}$
	$1.89/700$	$8 \cdot 10^{-30}$
	$1.89/7000$	10^{-29}

Davis *et al.* have not generated an ensemble mean with their extension of the classical three-state model. In our work, we choose a fictional scenario of three clocks each exhibiting a different performance characteristic. Clock 3 has an excellent short term stability ($\tau \in [1, 10]$ s), clock 2 performs best around an averaging time of 40 seconds and clock 1 outperforms the other two for averaging times greater than 200 seconds. The q-parameters for these fictional clocks can be found in table III.

The relative phase measurements to the first clock are used as inputs to the Kalman filter. A measurement noise of 10^{-35} impacts both measurements. The scenario is simulated for roughly 83 hours.

In figure 6 a single simulation run of the specified scenario is shown. As expected, the stability of the phase difference measurements is at every averaging time close to the clock with the inferior stability. The estimates produced by the Kalman filter match closely the actual phase states of all three clocks. Consequently, the Greenhall IEM outperforms the individual clocks for all averaging times.

In order to test the used algorithm for clock models exhibiting Markov processes, we added one process to each clock in the ensemble (refer to table IV for the parameters). In

TABLE III
q-PARAMETERS FOR THE CLOCK MODELS OF THE FICTIONAL ENSEMBLE

Clock	q-Parameters q_1	q_2	q_3
#1	10^{-37}	10^{-38}	10^{-40}
#2	10^{-33}	10^{-37}	10^{-42}
#3	10^{-31}	10^{-43}	10^{-45}

TABLE IV
PARAMETERS FOR THE MARKOV PROCESSES IN THE CLOCK MODELS IN THE FICTIONAL ENSEMBLE

Clock	R	U
#1	$1.89/1$	$2 \cdot 10^{-33}$
#2	$1.89/30$	10^{-31}
#3	$1.89/1000$	10^{-32}

figure 7 the OADEV of a single simulation of the clock models with and without Markov process are compared. Besides the impact of the Markov process, there are also differences due to the different noise realizations of the random run. Clock 3 is only minimally impacted by a single Markov process with maximum at 1000 s, whereas clock 2 is significantly altered by a Markov process with its maximum at 40 s resulting in a performance degradation of roughly half an order of magnitude for averaging times between 1 s and 100 s. A Markov process with peak at 1 s was added to clock 1 that impacts only the short-term performance (less than 10 s averaging time). The results of the simulations are shown in figure 8.

The Kalman filter inputs such as the transition matrix and the process noise covariance matrix were adapted as outlined in [16] to estimate the Markov processes. The resulting estimates are for most averaging time aligned with the actual phase states. One can observe a degradation of the estimate compared to the actual phase state for short averaging times (below 10 s) in clock 3. Nevertheless, after adding in the Markov processes the resulting ensemble time outperforms the individual clocks of the ensemble. Thus, the proof-of-concept of a mixed ensemble IEM is successfully demonstrated.

However, we observe a high sensitivity of the ensembling algorithm with respect to a variation of the input parameters (q-parameters, Markov process parameters). As a result, the generation of an ensemble time for a clock ensemble featuring the real clocks modeled in this paper that maintains the desired properties of the IEM was not sufficiently reproducible. This challenge will be tackled in future investigations.

V. CONCLUSION & OUTLOOK

All together, we successfully demonstrated that the classical three-state clock model extended by Markov processes can be used to model various clock types. In addition, we have shown a fictional scenario - with and without Markov processes -

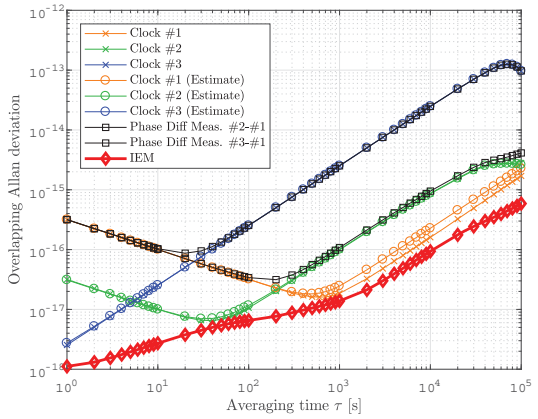


Fig. 6. Performance of the Implicit Ensemble Mean (red diamonds) using the Davis-Greenhall-combination obtained from a simulated fictional clock ensemble (classical three-state clock model). In addition, the stability of the individual clock phase offset (orange / green / blue crosses) compared to their estimates (orange / green / blue circles) as well as the phase difference measurements (black squares) are shown.

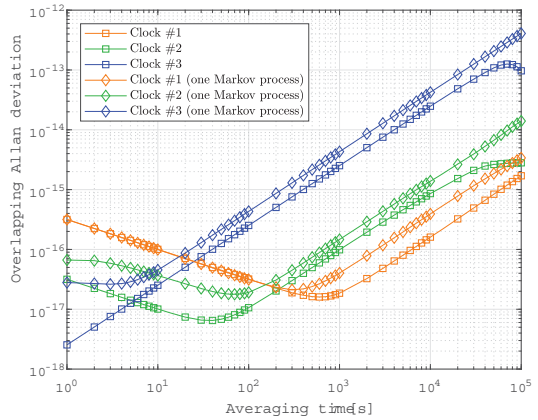


Fig. 7. Single simulation of the clock model used for the fictional ensemble with (diamonds) and without (squares) Markov processes.

in which we obtain an IEM that performed better than each individual ensemble clock for most averaging times.

As a next step, we want to include the real clocks' behavior modeled in this publication in the clock ensemble. In particular, we want to address the numerical instabilities that we have observed performing the simulations. There are several possible ways to stabilize the filter: One option is applying a scaling method that transforms the states to a similar, higher size. Another option, that may be used as addition or alternative are robust filter implementations such as the square root filter proposed by Potter and Stern [20].

Nevertheless, the covariance reduction of Davis *et al.* was developed for scenarios without measurement noise. For this reason, we subsequently want to mathematically derive the implications resulting from this discrepancy. The same holds for the combination of the reduction with the Greenhall

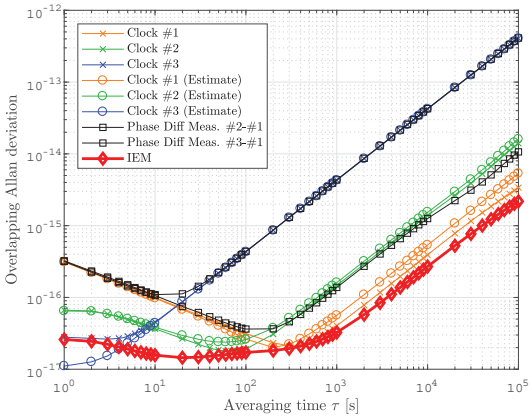


Fig. 8. Performance of the Implicit Ensemble Mean (red diamonds) obtained with the Davis-Greenhall-combination of a simulated fictional clock ensemble. Each clocks performance (orange / green / blue crosses) was altered by a single Markov process. Besides the stability of the phase difference measurements (black squares) passed to the Kalman filter and the resulting individual clock estimates (orange / green / blue circles) are presented.

formulas in order to obtain an IEM.

Acknowledgment

The authors would like to thank Dr. Judah Levine, Dr. Patrizia Tavella and Valerio Formichella for their valuable comments and suggestions. Furthermore, the provided measurement data of the cavity stabilized laser by Menlo Systems is gratefully acknowledged. Moreover, the authors thank their partners at DLR-RY in Bremen for providing the measurement results of the optical Iodine clock used for this study.

References

[1] R. E. Kalman, "A new approach to linear filtering and prediction problems," *Transactions of the ASME–Journal of Basic Engineering*, vol. 82, no. Series D, pp. 35–45, 1960.

[2] M. Gödel and J. Furthner, "Robust ensemble time onboard a satellite," in *Proceedings of the 2017 International Technical Meeting of The Institute of Navigation*, Monterey, California, January 2017, pp. 26–43.

[3] L. Galleani and P. Tavella, "Using the Kalman filter to detect frequency jumps in atomic clocks," in *2011 Joint Conference of the IEEE International Frequency Control and the European Frequency and Time Forum (FCS) Proceedings*, May 2011, pp. 1–3.

[4] ——, "Detection and identification of atomic clock anomalies," *Metrologia*, vol. 45, no. 6, pp. 127–133, 2008.

[5] E. Nunzi, L. Galleani, P. Tavella, and P. Carbone, "Detection of anomalies in the behavior of atomic clocks," *IEEE Transactions on Instrumentation and Measurement*, vol. 56, no. 2, pp. 523–528, April 2007.

[6] W. J. Riley, "Frequency jump detection and analysis," in *Proceedings of the 40th Annual Precise Time and Time Interval Systems and Applications Meeting*, Reston, VA, Dec 2008, pp. 241–254.

[7] K. R. Brown, "The theory of the GPS Composite Clock," *Proceedings of the 4th International Technical Meeting of the Satellite Division of The Institute of Navigation (ION GPS 1991)*, pp. 223–242, September 1991.

[8] N. Poli, C. W. Oates, P. Gill, and G. M. Tino, "Optical atomic clocks," *Italian Physical Society*, vol. 36, no. 12, pp. 555–624, 2013.

[9] A. D. Ludlow, M. M. Boyd, J. Ye, E. Peik, and P. O. Schmidt, "Optical atomic clocks," *Rev. Mod. Phys.*, vol. 87, pp. 637–701, Jun 2015.

[10] S. R. Stein, "Advances in time-scale algorithms," in *The 24th Annual Precise Time and Time Interval (PTTI) Applications and Planning Meeting*, 1993, pp. 289–302.
[11] C. A. Greenhall, "Reduced Kalman filters for clock ensembles," *Joint Conference of the IEEE International Frequency Control Symposium and European Frequency and Time Forum, San Francisco, California, USA*, 2011.
[12] ——, "A review of reduced Kalman filters for clock ensembles," *Ultrasonics, Ferroelectrics, and Frequency Control, IEEE Transactions on*, vol. 59, no. 3, pp. 491–496, March 2012.
[13] ——, "A Kalman filter clock ensemble algorithm that admits measurement noise: corrections and update," *Metrologia*, vol. 44, no. 6, p. 311321, 2006.
[14] L. Galleani, L. Sacerdote, P. Tavella, and C. Zucca, "A mathematical model for the atomic clock error," *Metrologia*, vol. 40, pp. 257–264, 2003.
[15] C. Zucca and P. Tavella, "The clock model and its relationship with the Allan and related variances," *IEEE Transactions on Ultrasonics, Ferroelectrics, and Frequency Control*, vol. 52, no. 2, pp. 289–296, Feb 2005.
[16] J. A. Davis, C. A. Greenhall, and P. W. Stacey, "A Kalman filter clock algorithm for use in the presence of flicker frequency modulation noise," *Metrologia*, vol. 42, no. 1, pp. 1–10, 2005.
[17] R. G. Brown and P. Y. Hwang, *Introduction to random signals and applied Kalman filtering: with MATLAB exercises and solutions*, 4th ed. Wiley, 1997, vol. 1.
[18] F. Vernotte, M. Addouche, J. Delporte, and M. Brunet, "The three cornered hat method: An attempt to identify some clock correlations," in *IEEE International Ultrasonics, Ferroelectrics, and Frequency Control Joint 50th Anniversary Conference*, 2004.
[19] T. Schuldt, K. Döringshoff, E. V. Kovalchuk, A. Keetman, J. Pahl, A. Peters, and C. Braxmaier, "Development of a compact optical absolute frequency reference for space with 10^{-15} instability," *Appl. Opt.*, vol. 56, no. 4, pp. 1101–1106, Feb 2017.
[20] J. E. Potter and R. G. Stern, "Statistical filtering of space navigation measurements," Massachusetts Institute of Technology, Cambridge, MA, United States, Tech. Rep. 19630010877, Jan 1963.

Two way time comparison via optical fiber at BIRMM

Xueyun WANG, Wenzhe YANG, Hongbo WANG, Haifeng WANG, Hang YI, Shuwei WANG, Shengkang ZHANG, Zhenwei ZHANG

Science and Technology on Metrology and Calibration Laboratory,
Beijing Institute of Radio Metrology and Measurement, Beijing, China

Email: wxy203_3@126.com

***Abstract*—Nowadays time and frequency transfer through optical fiber become more important with its further reduction of uncertainty. A two-way time comparison via optical fiber experiment that utilizes the carrier phase of the transmitted signal has been done at Beijing Institute of Radio Metrology and Measurement (BIRMM) laboratory. The principle and equipments are similar to the well-known two-way satellite time and frequency transfer (TWSTFT), but all equipments needed to lock to the external 5MHz reference which provided by H-maser. In the experiment a 1.75GHz carrier frequency is used, and the pseudo-random noise (PRN) code rate is set to 20Mchip/s. The measurement results (common clock difference, CCD) show that the method of carrier phase has uncertainty with the standard deviation (1 σ) less than 21ps.**

Keywords—Two way time comparison; optical fiber; carrier phase

I. INTRODUCTION (*Heading 1*)

Time and Frequency transfer through optical fibers which has shown low instabilities has been used for remote optical frequency standards comparison and many other ground synchronization stations[1]. Optical fiber links for time and frequency transfer have been established among a lot of institutes located in the same region [2] [3].

Currently, two-way optical time and frequency transfer methods are widely used, referring to the two-way satellite time and frequency transfer (TWSTFT), we could use the optical fiber links instead of satellite to realize the two-way optical time and frequency transfer. Generally, two way time transfer through optical fiber is based on spread spectrum and pseudo code ranging. Several institutes has done experiments with this scheme and got a lot of valuable results.

In this paper, we propose a twoway time comparison through optical fiber scheme based on the carrier phase technology. An experiment has been done in our laboratory using this method. The principle and equipments in our experiment is similar to the well-known two-way satellite time and frequency transfer (TWSTFT), but all equipments must lock to the external frequency reference. A 1.75GHz carrier frequency is used, and the pseudo-random noise (PRN) code rate is set to 20Mchip/s. Theoretically, it would get better results utilized the carrier phase scheme than the 20Mchip/s pseudo code ranging scheme.

In the following Section 2, we introduce the basic experimental setup. Following in Section 3, we report and discuss the testing results. Finally a summary will be given in Section 4.

II. EXPERIMENTAL SETUP

The time comparison system is set up as shown in Fig.1. Here the H-maser clock provided the 5MHz signal and the 1PPS signal to the devices of the two sites such as TWSTFT modem and Up/Down Converter, so the carrier phase data is effective. The TWSTFT modem is used to transmit and receive the 70MHz BPSK signal modulated by 20Mchip/s PRN code. The Up/Down Converter was used to up convert the 70MHz signal to 1.75GHz signal and down convert the 1.75GHz signal to 70MHz IF signal. The increased carrier frequency can improve the CCD results which are calculated with carrier frequency values measured by the TWSTFT modems. The signals from the Up/Down Converter are transformed by using electro-optical converter (E/O) and opto-electrical converter (O/E) with laser wavelengths of nominally 1550 nm. In this experiment the forward and back optical links are two different optical fiber Rolls and both the length is 2.2km. At the same time, we also measure the temperature variation in our laboratory. Fig.2 shows the experimental system image in our laboratory.

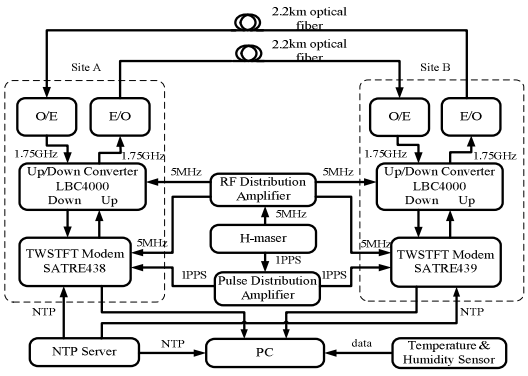


Fig.1 . The block diagram of two-way time comparison via optical fiber experiment.



Fig.2. The experimental system image in our laboratory.

III. EXPERIMENT AND DISCUSS

In this experiment, we can get two kinds of data: the delay values based on pseudo code ranging and the carrier frequency values. Firstly, in terms of the equation of TWSTFT, we can calculate the CCD with the delay values obtained by the two sites. The Fig.3 shows the time delay values which measured by modem and we can find that there is some fluctuation. Fig.4 and Fig.5 are extremely demonstrated the reason for the fluctuation, note that the trend of the delay variation is mostly consistent with the trend of temperature variation. The temperature variation has induced to the delay variation of the optical fibers.

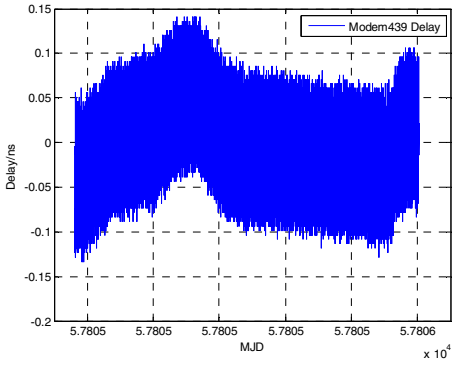


Fig.3. The time delay data measured by modem,which has been subtract a mean value.

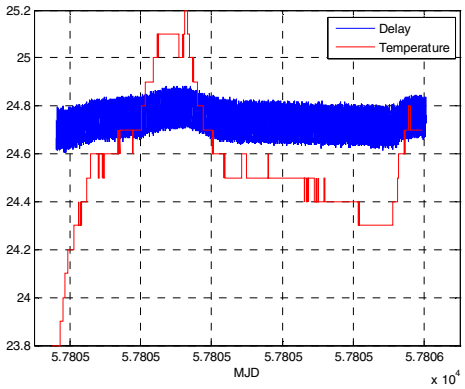


Fig.4. The temperature impact on the delay measured.The red line is the temperature variation, the blue line is the delay subtracted a constant.

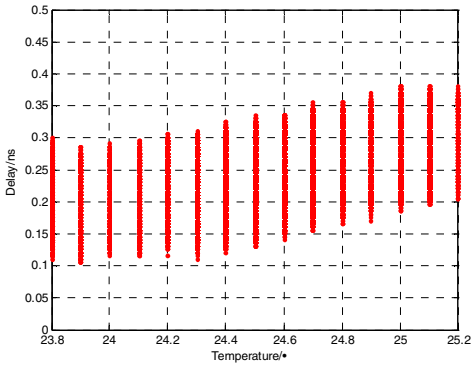


Fig.5. The relationship of temperature and delay.

Secondly, we try to calculate the CCD utilizes the algorithm of carrier phase with the carrier frequency values measured by modem. We can get the results according to following equation:

$$d\phi_k = -\int_{t_0}^{t_k} f_d(t)dt \tag{1}$$

In this equation, the term in left hand side $d\phi_k$ is the integral Doppler, which is the variation of the carrier phase, and the unit is period. The term in right hand side $f_d(t)$ is the Doppler shift. To get the delay value $D_{cp} = T * d\phi_k$ whose unit is second, we should multiply the carrier period T. So the delay value D_{cp} can be described by following equation:

$$D_{cp} = T * d\phi_k \tag{2}$$

Where T is the reciprocal of 1.75 GHz.

The Doppler shift $f_d(t)$ can be calculated by the carrier frequency which is measured by modem per second subtracting the IF center carrier frequency. The Fig.6 shows the time delay values calculated by the frequency values. The blue points are the delay measured by modem and the red points are the delay calculated by the carrier phase. Because we can only get the relative delay variation with carrier phase, for easy to compare, the PRN results has been subtracted a constant.

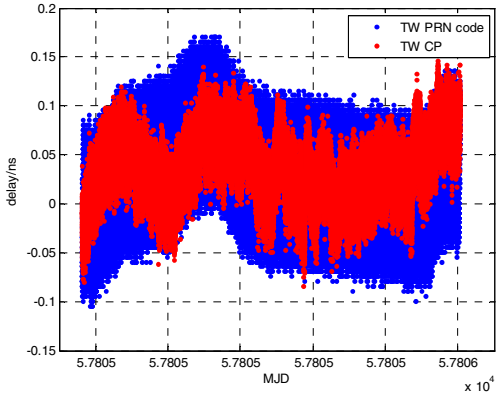


Fig.6. The comparison with the two methods

Thirdly, according to above methods, we can calculate separately the delay of the forward and back optical fiber links utilized the carrier frequency values. After that, we can calculate the CCD. The results are shown in the Fig.7. In terms of the raw data, we can calculate the uncertainty with standard deviation (1 σ) less than 24ps with the PRN method and 21ps with the carrier phase method.

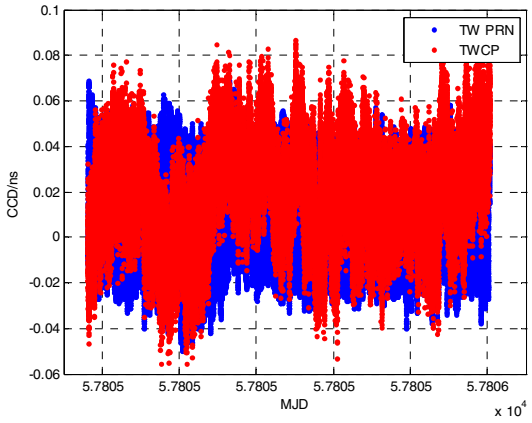


Fig.7. The CCD calculated with the two methods

IV. CONCLUSION

This is the first time that the two way time comparison through optical fiber experiment based on the carrier phase is implemented in our laboratory. According to theory, the results based on the carrier phase should be much better than based on the pseudo code, but the preliminary test results have show that the method base on the carrier phase with the L band carrier has the same level uncertainty to the method based on the 20Mchip/s PRN through the optical fiber link. It may be caused by the equipment noise and we would do further investigation in next step work.

REFERENCES

[1] D. Piester, M. Fujieda, M. Rost, A. Bauch. "Time Transfer Through Optical Fibers.(TTTOF): First Results of Calibrated Clock Comparisons", 41st Precise Time and Time Interval(PTTI) Meeting, 16-19 Nov 2009, Santa Ana Pueblo, New Mexico, USA.

[2] H. Schnatz et al., 2009, "Phase-Coherent Frequency Comparison of Optical Clocks Using a Telecom Fiber Link," in Proceedings of the European Frequency and Time Forum (EFTF) and IEEE Frequency Control Symposium (FCS), 20-24 April 2009, Besançon, France (IEEE CFP09FRE), pp.807-812.

[3] Fujieda, Mihu, et al. "Ultrastable frequency dissemination via optical fiber at NICT." Instrumentation and Measurement, IEEE Transactions on 58.4 (2009): 1223-1228.

Fully and optimally use the redundancy in a TWSTFT network for accurate time transfer

Zhiheng JIANG
Time Department
Bureau International des Poids et Mesures (BIPM)
SEVRES CEDEX, France
zjiang@bipm.org

Shinn-Yan LIN Wen-Hung TSENG
National Standard Time and Frequency Laboratry
Telecommunication and Laboratories (TL)
Chinese Taipei
sylin@cht.com.tw, whtseng@cht.com.tw

***Abstract*— Two-way Satellite Time and Frequency transfer (TWSTFT) is a primary technique for UTC generation [1]. Only the direct link, the so called UTC link between a Lab(*k*) and PTB, is used for UTC generation. The numerous redundant links are measured but never used. The concept of the TWSTFT network time transfer has been discussed by several authors [2,3,4,10]. [5,6] are examples of the very first use of redundancy (Triangle Closure Calibration) in the TW network for the time link calibrations. It is based on using all the direct UTC and redundant links (Fig. 1) and the hypothesis that the TWSTFT measurement errors obey the normal distribution with an homogeneous distribution over the whole network. However [7,8] proved that the hypothesis may not be held. Considerable biases exist, such as the diurnals, which cannot be fully averaged out by increasing the measurement quantity or eliminated in a simple least square (LSQ) network adjustment [3]. The maximised gains in uncertainty depend on the optimal use of the redundancy in the TWSTFT network but the maximum number of the measurements to be used. We first discussed the weak points of the equal-weight network time transfer and then proposed our solutions: (1) Weighting each link according to its uncertainty estimate; (2) Using the GPSPPP to strengthen or replace the errored TWSTFT links in the network adjustment. Obviously, unequal weighting is necessary; (3) The above solutions can be extended to use all types of observations, such as the TWOTFT (Two-Way Optical fibre Time and Frequency Transfer) etc. The global network adjustment takes the link measurement to establish its observation equation. Therefore, there are theoretically not limits in the types and the numbers of the observations (GPS, GLONASS, GALILEO, BEIDOU, TWOTFT, TWSTFT/SDR [13] etc.) on any baseline in the network T/F transfer. Such all the redundancy is used. This is called the multi-technique network T/F transfer [9].**

Keywords—TWSTFT, redundancy, time transfer, link transfer, network transfer, diurnal, uncertainty

I. INTRODUCTION

The worldwide UTC time and frequency (T/F) network is highly redundant. First the GNSS and TW (Two Way Satellite Time and Frequency Transfer or TWSTFT) are each other redundant and then both of them have each a large scale of redundant observations. In addition, new techniques are coming such as the TWOTFT (Two-Way Optical fibre Time and Frequency Transfer) etc. The redundancy is becoming a challenge for the UTC data processing. That is why the CCTF (Comité Consultatif du Temps et des Fréquences) 2017 has made two recommendations for GNSS and TW in which a key issue is how to fully use the redundant measurement data [11], in particular, recommended BIPM to "support studies of improving TWSTFT with redundant measurements in the TWSTFT network". This is the major motivation of this study.

In this paper, we discuss the redundancy in view of the TW network because the redundancy created by all the T/F transfer techniques is coinciding with the TW network.

TW is a major technique used in UTC generation. More than two third of UTC clocks and almost all the primary frequency standards are transferred using TW [1]. As discussed in [2,3,4,10] and shown in Figure 1, TW measurement data are rich of redundancy: all the links in the network are measured but only the red links are used for UTC computation.

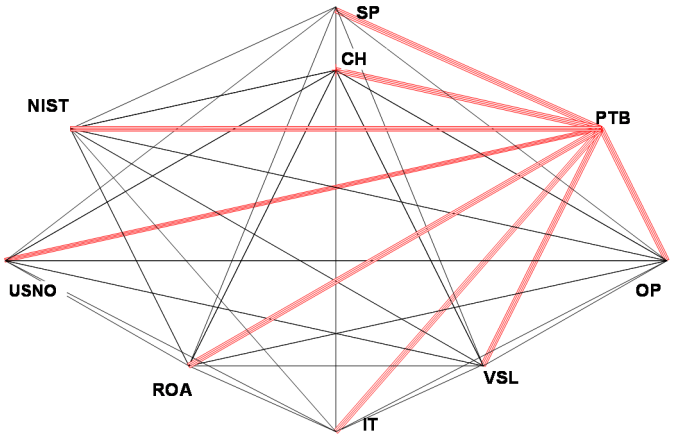


Fig. 1. A TW network with 9 TW laboratories in Europe and America. The 8 red lines are the UTC links and the rest 27 black lines are the redundant links

The redundancy has been studied by serval authors since 10 years and the TW network T/F transfer has been proposed. There are some limited progresses since then. Among them, a typical example is the approval of the triangle closure calibration (TCC) for UTC links [5,6]. The early studies hypnotised that the uncertainty sources were of normal distribution with the white noise coming from the measurement errors. They can be averaged out by increasing the measurement numbers, that is, the fully use of the redundant measurements in an LSQ network adjustment. However, the latest studies show that the uncertainty of the redundant data is not always of normal and homogeneous distribution [7,8].

Some of the links may be biased and the ratio of the total uncertainty may vary by factors of 2 to 4 from one link to an adjacent one. That is, not all the redundant links will improve the uncertainty and some may decrease stability of the TWSTFT. In fact, the quality of some UTC links is worse than that of relevant redundant links.

We will discuss below how to fully and optimally use the rich redundancy in the TW network. The method and the conclusion are also suitable for the TWSTFT SDR network.

We outline the future development towards the multi-technique network time and frequency transfer using all available measurements [9]: TWSTFT, GNSS and TWOTFT etc. We discuss a simple case, the TW+GPSPPP network.

II. TWSTFT NETWORK TIME-FREQUENCY TRANSFER: METHOD, THEORY AND TESTS

If we use one sentence to describe the *redundancy* in the TWSTFT, it is, *TWSTFT is measured as a network but used as single-links* (Figure 1). For a N-point network, there are N(N-1)/2 independently measured links. Among them, only the N-1 Lab(k)-PTB links are for UTC generation. Other $(N^2-3N+2)/2$ links are redundant and never used. As a function of N, the redundancy increases quickly. The ratio of the redundant links over the UTC links is 0 for N=2; 2.5 for N=7; 6.5 for N=15 and 9 for N=20. This suggests that for TW network of N=20, for every nine measured links, only one is used for UTC computation. In the European-American network N=13. For Asia-Pacific region, N=8. If the whole Europe-America-Asia TW network becomes fully operational, the waste redundancy increases 90%. Accordingly, more TW laboratories there are, more redundancy are wasted.

In metrology practices, increasing redundancy is the major method to improve the measurement uncertainty. In Figure 1 (N=9), every UTC baseline (Lab-PTB) is independently, directly or indirectly, measured 8 times. An indirect or redundant link is measured through an intermediate laboratory, e.g. the direct link OP-PTB is also measured with the indirect/redundant links OP-CH-PTB, OP-NIST-PTB, OP-SP-PTB etc. Here CH, NIST and USNO are relaying labs. By averaging, in the hypothesis of normal distribution, the measurement errors can be reduced by a factor of about $\sqrt{(m)}$, m is number of the redundant links.

Rigorous mathematic model was developed in [2] for a global network adjustment which allows optimally using the entire geometric constraints comprised in the network. Here is a quick recall of the simplified LSQ model under the normal error distribution condition:

Instead of setting up directly one by one the triangle closure condition, we establish the observation equation at a measurement epoch as:

$$w_{ij}: V_{ij} = (X_i - X_j) - L_{ij} \qquad (2.1)$$

$$X_{PTB} = 0 \qquad (2.2)$$

here i and j are two laboratories; X_i and X_j are the estimations of the true clock readings at i and j with X_i-X_j the adjusted time link; L_{ij} is the measured time link; w_{ij} the weight and V_{ij} on the left is the residual, which is called also the correction to the measured link. For every observation epoch and for every pair of TW link observation, there is an observation equation. We have then a linear equation system. This system will have unique and the most optimal solution in the least square sense when an arbitrary clock is fixed to an arbitrary constant. Note here that, although the unknowns here are X, what we are really interested in is the correction V_{ij} to the measured link L_{ij}. Therefore fixing any clock in the network will not change the corrections. We set $X_{PTB} = 0$. The LSQ solution gives not only a correction for every measured link on its measuring epoch but also its uncertainty estimation.

It is easy to prove that the corrections such obtained satisfy all the triangle closure conditions supplied by the redundant measurements and in consequence any arbitrary n-side ($n \le N$) polygon closure equals zero. Assuming we have a triangle closure of three laboratories 1, 2 and 3, the closure equals:

$$\begin{aligned}\Delta &= L_{12} + L_{23} - L_{13} \\ &= [(X_1-X_2)-V_{12}]+[(X_2-X_3)-V_{23}]-[(X_1-X_3)-V_{13}] \\ &= -V_{12} -V_{23} +V_{13}\end{aligned} \qquad (2.3)$$

Equation (2.3) gives the relationship between a closure and its related LSQ corrections.

Because any n-side polygon can be decomposed into sub-triangles, the independent triangles are the basic elements of our study. In fact, if the independent triangle conditions are satisfied, any n-side ($n \le N$) closures must be zero. This implies that in a network, a time transfer between any two points, through any link(s) gives exactly the same result with the same uncertainty. This is the TW *network transfer*. The result of a T/F transfer and its uncertainty between any points does not depend on the trajectories going through. Obviously, compared to a single-link, T/F transfer through a network will greatly increase the robustness of the whole system and reduce the measurement uncertainty.

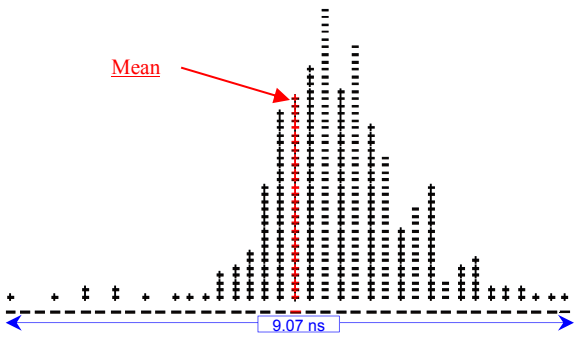


Fig. 2. Histogram of the 338 triangle closures for the triangle CH-OP-VSL of a UTC month. Outliers should be removed for the final adjustment.

Figure 2 is the histogram of the 338 triangle closures for CH-OP-VSL of a UTC month: the total variation is about 9 ns (with outliers) with mean=0.653ns and the root of mean squares RMS=1.972ns.

Before further discussion, we define the term 'Dif' of B versus A: Dif=(A-B)/A. The Dif is a relative value describing how differ A from B. A and B represents respectively the diurnal-biased and the diurnal-free observations. Obviously,

the bigger a +Dif, the more importance the affection of the bias in A. A Dif may be positive or negative.

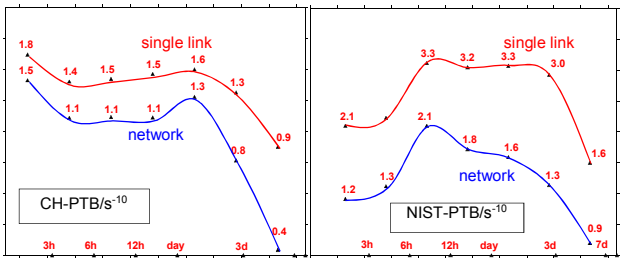


Fig. 3. TDev of the single-link (red) and network (blue). Time stabilities are considerably improved over all the terms. The Difs are 45% and 85% respectively for CH-PTB and NIST-PTB (cf. Table 1)

Figure 3 illustrates the TDev comparisons between single-link and network transfers for the two official UTC links: CH-PTB and NIST-PTB. The first is an inner-European short baseline and the latter is a trans-Atlantic long baseline. Red curves are the single-link TDev and blue curves the network TDev. In network solutions, Time stabilities are considerably improved over all the terms of the averaging time. The Difs are 45% and 85% respectively for these two baselines.

Table I presents the TDev comparisons of the 8 UTC links over different terms of averaging time: 2, 4, 8, 16, 32 and 64 hours. The Dif is the average of the 6 terms, listed in the decreasing order of the Difs. Measurement errors are significantly reduced for most of the links.

TABLE I. DIFS IN TDEV (UNIT IN 0.1 NS) OVER THE 6 TERMS FROM 2 TO 64 HOURS. FOR EACH LINK, THE UPPER-LINE VALUES ARE THE TDEV OF SINGLE-LINK AND THE LOWER-LINE VALUES ARE THAT OF NETWORK. THE DIF IS THE AVERAGE OF THE 6 TERMS

Link	2h	4h	8h	16h	32h	64h	Dif
	.21	.22	.33	.32	.33	.30	
NIST-PTB	.12	.13	.21	.18	.16	.13	**+85%**
	.15	.18	.31	.27	.23	.17	
USNO-PTB	.11	.12	.19	.14	.13	.09	**+55%**
	.18	.14	.15	.15	.16	.13	
CH-PTB	.15	.11	.11	.11	.13	.08	**+45%**
	.28	.27	.26	.19	.16	.12	
SP-PTB	.18	.16	.15	.13	.12	.15	**+40%**
	.24	.31	.39	.43	.49	.34	
IT-PTB	.19	.25	.35	.31	.34	.30	**+25%**
	.48	.38	.47	.49	.54	.61	
VSL-PTB	.34	.30	.34	.35	.50	.78	**+20%**
	.31	.31	.38	.29	.29	.41	
ROA-PTB	.26	.25	.30	.21	.29	.48	**+10%**
	.28	.25	.29	.31	.37	.26	
OP-PTB	.24	.23	.27	.29	.33	.25	**+5%**
Average							**+36%**

III. BIASES IN THE TW NETWORK

The TW network adjustment is based on the hypothesis that the normal uncertainty. Is it always true ?

In Table I, the link to link comparisons of the TDev of the UTC vs. the redundant links are listed in the order of the decreasing Dif values. Usually, the longer a link distance, the worse the uncertainty and the biggr the +Difs. However, as can be seen, the smallest TDev at 2h are of 12 ps and 11 ps belonging to the longest trans-Atlantic links USNO-PTB and NIST-PTB. However all the shorter inner-European links have bigger TDev and smaller +Difs. The latter suggests that the LSQ network adjustment does not work. The smallest Dif is +5% belonging to one of the shortest link OP-PTB. This implys that inner-European links may be affected by not only the white noise but also certain biases in the measurement. In contrast, the very long inter-continental links, e.g., NIST-PTB, USNO-PTB, over Atlantic are not. It is important to emphasise that the bias exists in most of the inner-European UTC links (Figures 1 and 4) and special measures should be taken.

In the following, we discuss the affections of the biases using the Dif values. It is enough to prove that the *redundant* links are sometime considerably more stable than the UTC links. Further TDev analysis shows that the bias is dominated by the diurnal signals in the TW links.

Let A-B denotes a UTC link of the baseline between laboratories A and B, as shown in Figure 4, the baseline between PTB and Lab(*k*). A *redundant* link between A and B is the link involving an intermediate laboratory C (Lab(*i*) in Figure 4): $(A\text{-}B)^C = A - C + (C\text{-}B)$. For example, using NIST as the intermediate lab, we can obtain the *redundant* link between PTB and OP, i.e. $(PTB\text{-}OP)^{NIST} = PTB - NIST + (NIST\text{-}OP)$.

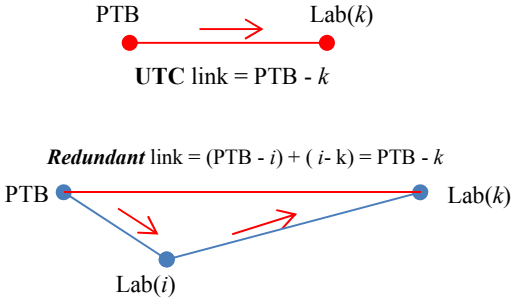


Fig. 4. The UTC and *redundant* links between PTB and lab(*k*). To date, all the UTC links are direct therefore the shortest.

We assess the existences of the bias and its influence to the link stability through the UTC links vs. the *redundant* links. Three Dif values are used as the indicators:

1. Dif of the TW UTC and redundant links referring to GPSPPP, that is, to analyse the double clock difference (DCD). GPSPPP is a completely independent from TW. It is more precise and diurnal-free. Obviously, the smaller the Dif (obtained by the standard deviation σ of the DCD) the better;
2. Dif of the Time deviation on different averaging times of UTC and the redundant links;
3. Dif of the TW SATRE UTC and redundant links refereeing to the TW SDR links which are more stable with a u_A of about 0.2 ns and almost diurnal-free [13].

3.1) Referring to GPSPPP

Table II lists the Difs, w.r.t. GPSPPP, for the six inner-European UTC links versus the redundant links relaying on the corresponding intermediate laboratory NIST. The Dif on average is +48.7 %. This implies the existence of the bias in the UTC links but in the redundant links via NIST.

TABLE II. COMPARING GPSPPP TO THE TW UTC LINKS AND THE REDUNDANT LINKS VIA NIST

link	N	UTC link ± σ /ns	Redundant ± σ_N/ via NIST/ns	Dif = (σ - σ_N)/σ via NIST %
CHPTB	335	1.785 ± 0.610	1.476 ± 0.227	63 %
ITPTB	365	-4.720 ± 0.812	-4.515 ± 0.425	48 %
OPPTB	355	-1.619 ± 0.427	-1.559 ± 0.196	54 %
ROAPTB	335	2.111 ± 0.831	1.832 ± 0.412	50 %
SPPTB	360	2.047 ± 0.536	1.811 ± 0.251	53 %
VSLPTB	370	0.431 ± 0.558	0.862 ± 0.425	24 %
Mean				**48.7 %**

3.2) Referring to the Time Deviations

We can analyse the Difs of the TDev on different averaging times to study how reduced the diurnal and the instability in the redundant links. Figure 5 is the TDev of the UTC (blue) and redundant (red) links for the baseline between OP and PTB. The TDev is obtained by using 3 years of continuous data [7]. We observe that the diurnal is greatly reduced and stability is significantly improved in the redundant links.

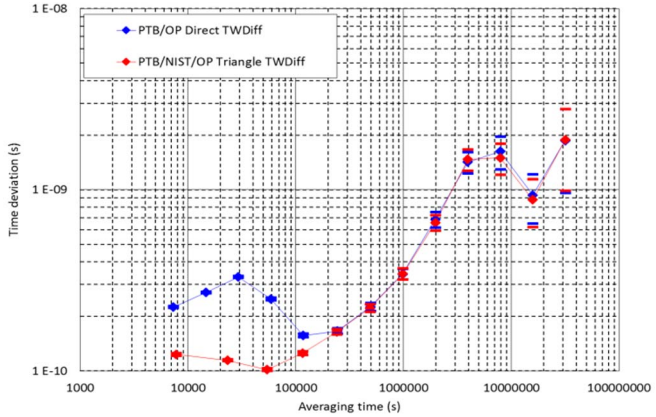


Fig. 5. TDevs of the UTC link (blue) and redundant (red) link for the baseline between OP and PTB [7]

TABLE III. DIF IN TDEV OF THE TW UTC LINK (**OP–PTB**) VERSUS THE REDUNDANT LINKS VIA NIST

Averaging Time	UTC link±σ /ns	Redundant ±σ_{Xn} via NIST/ns	Dif = (σ - σ_{Xn})/σ via NIST %
2 hours	0.326	0.125	62 %
4 hours	0.361	0.117	68 %
8 hours	0.191	0.062	68 %
16 hours	0.135	0.071	47 %
32 hours	0.125	0.066	47 %
Mean			**58 %**

As the Figure 5, Table III is the link between OP and PTB. Here the Difs on each averaging time of 2, 4, 6, 8, 16 and 32 hours are given. The Dif on the link OP and PTB is +60 % for the redundant link via NIST. Again we showed the existence of bias in UTC links.

3.3) Referring to the TWSTFT SDR

The Software-Defined Radio (SDR) Receiver for TWSTFT is a newly developed technique, characterized by a significant reduction in the diurnal and the measurement noise in e.g. the UTC TW links. Compared to the results using TW SATRE modem, the SDR can improve the stability by a factor two or three. Hens we use the SDR TW as a precise reference to compute the Difs.

Figure 6 is the comparison of the Time deviations of the UTC and redundant (via NIST) links for the baseline between OP and PTB. In the order of the stability from the most stable stable to the most instable, we have the indirect/redundant SDR (green), the indirect/redundant SATRE (violet), the links of SDR UTC (blue) and the SATRE UTC (red). It is interesting to notice that the redundant (indirect) SATRE link is more stable than the SDR UTC link and that the performance of SDR UTC link can be improved further with the corresponding redundant/indirect link.

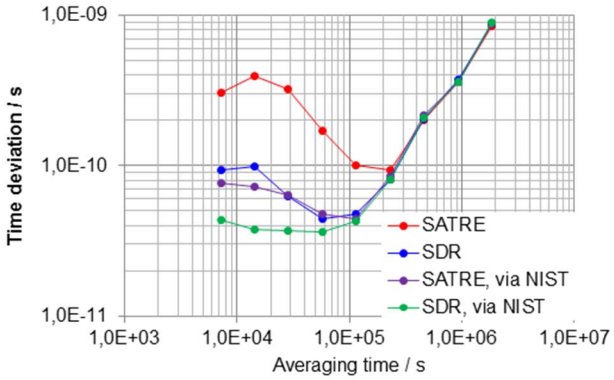


Fig. 6. Comparison of the Time deviations of UTC and redundant (via NIST) links for the baseline between OP and PTB. The UTC link is biased while the redundant link is not.

By above, we proved that in the inner-European TW links there are significant bias in some UTC links which is mainly presented as the diurnals and the corresponding redundant links are rather diurnal-free and more stable. At present, none of the redundant links are used in the UTC computation.

As discussed in the beginning of the chapter, these inner-European diurnals might not be fully eliminated in the global equal-weighting TW network adjustment. However, by composing the redundant link via a relaying laboratory, the diurnal can be greatly reduced. It should be reasonable to heavily weight the good redundant links in the LSQ network adjustment.

The SDR can also effectively reduce the diurnals but there seem still the residuals. The latter however, can be visibly reduced by using the redundant SDR links.

It is noted here that not all the labs can be served as relaying lab to reduce the diurnals. [8] gives example, if an European lab, e.g. , SP, is used as the relaying, all the Difs in the Tables II and III become negative.

More discussions were made in [7,8] where the UTC link is termed as the *direct* link and the redundant link as *indirect* link.

IV. THE REDUNDANCY IN A TW+GPSPPP NETWORK

TW is the primary technique in UTC time and frequency transfers, prior to GPS for a long time. However, its major uncertainty source, the diurnal, affects the UTC links. This is in

particular the case in Europe. The affections cannot be completely eliminated by the SDR or by a network adjustment.

Fortunately, the UTC network is highly redundant with not only the TW links but also the GNSS links.

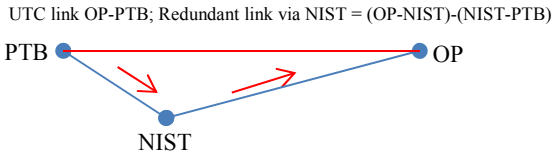


Fig. 7. UTC and redundant links in the triangle OP-NIST-PTB

We propose two solutions.

4.1) Network solution 1: using only the TW data

As the uncertainty of the links in the TW network does not distribute homogenously, certain of them may be suffered more by the measurement errors or the diurnals than the others. We can make an optimal adjustment by unequally weighting the links according to the link uncertainties. The most used ruler is to assignee the weight of a link as 1 over the square of its uncertainty. For example, in Figure 7, as we know that the UTC link OP-PTB is strongly affected by a bias, its weight can be as weaker as necessary. And as proven in the chapter III, the Dif factor of 2 to 3 is expected. This weighting philosophy can be extended to the whole network, as shown in Figure 1, because the inner-European UTC links are affected by the diurnals more than the other redundant links relayed by NIST and USNO, we can heavily weight the latter based on the quality of the link on question. An iteration of the LSQ network adjustment may need to find the optimal weighting assignment for all the links. The weighting method and its effects will be discussed in a separate paper. The extreme case is the weights of UTC links approximating to zero and the network solution becomes a group of redundant links of the network.

4.2) Network solution 2: using the mixed TW and PPP data

As we know, the GPSPPP does not suffer the diurnals and is very precise thanks to the GPS carrier phase information. In Figure 7, we may improve or even replace the diurnal affected UTC links by the GPSPPP links. Because these two types of observations of GPS and TW are independent, the most optimal LSQ solution exists in the network adjustment.

The above two solutions can be used identically for the TW SDR network adjustment.

V. CONCLUSION

We proved the TW link uncertainty is not homogeneous in the TW network and may not obey strictly the normal distribution. Some UTC links are suffered the bias, in particular the diurnals. However, many redundant links, including the indirect TW links and GPSPPP links, are not. Full use of this redundancy will greatly improve the stability of the UTC time transfer. Two solutions are proposed: 1) Reasonably weighting the direct and the indirect/redundant TW links in the TW network adjustment; 2) Introducing the GPSPPP link and perform a combined TW and GPS network adjustment. Note here that it is not a TW+PPP *link* combination [12] but a global TW+PPP combined *network* adjustment.

This principle can be extended to the multi-technique network time and frequency transfer to fully use the integer high redundancy in the UTC linking network.

The ceaseless increased redundancy created by the TWSTFT, GNSS and the TWOTFT (Two-Way Optical-fibre Time and Frequency Transfer) observables in the UTC network is a challenge for the worldwide accurate time and frequency comparisons.

With the same principle of the TW network T/F transfer, all the types of the observations may be used to establish the observation equation (Equation 2.1) in the LSQ adjustment. For a same baseline, different links of TWTFT, GPSPPP and TWOTFT etc. can be used in a single adjustment.

A data processing procedure for the network time and frequency transfers has been developed at BIPM and installed in the UTC/TAI computation software package Tsoft.

REFERENCES

[1] BIPM Circular T 349, ftp://ftp2.bipm.org/pub/tai//Circular-T/cirthtm/cirt.349.html, Feb. 2017

[2] Z Jiang. and G. Petit (2006): Redundancy in the TAI TWSTFT time transfer network, Proc. EFTF 2006, pp. 468-475

[3] Z. Jiang (2008) "Towards a TWSTFT network time transfer", Metrologia, IOP Publishing Ltd, vol. 45, pp. 6–11, 2008, doi:10.1088/0026-1394/45/6/S02

[4] W. H. Tseng, S. Y. Lin, K. M. Feng, M. Fujieda, and H. Maeno (2010) Improving TWSTFT Short-Term Stability by Network Time Transfer, IEEE Trans. Ultrason. Ferroelectr. Freq. Control, vol. 57, pp. 161-167, 2010

[5] TWSTFT Calibration Guidelines for UTC Time Links V2016 ftp://tai.bipm.org/TFG/TWSTFT-Calibration/Guidelines

[6] Z. Jiang, D. Piester, C. Schlunegger, E. Dierikx, V. Zhang, J. Galindo, D. Matsakis (2016) The 2015 TWSTFT calibration for UTC and related time links, Proc. EFTF2016

[7] V Zhang, T Parker, S Zhang (2016) A Study on Reducing the Diurnal in the Europe-to-Europe TWSTFT Links, Proc. EFTF2016

[8] Z Jiang, V Zhang, T E Parker, J Yao, Y. Huang and S. Lin (2017) Accurate TWSTFT time transfer with indirect links, Proc. PTTI2017

[9] Z Jiang (2008) Accurate Time and Frequency Transfer Strategy--from Single-Technique-Single-Link to Multi-Techniques-Network, IN. Proc. Asia-Pacific Workshop on Time and Frequency, Jakarta, Oct. 2008

[10] W. H. Tseng, S. Y. Lin, K. M. Feng (2008) Analysis of the Asia-Pacific TWSTFT network, Proc. IFCS, pp. 487-492, 2008

[11] Recommendation of the 2017 CCTF, On improving Two-Way Satellite Time and Frequency Transfer (TWSTFT) for UTC Generation, http://www.bipm.org/en/committees/cc/cctf/publications-cc.html

[12] Jiang Z, Petit G, Combination of TWSTFT and GNSS for accurate UTC time transfer, Metrologia 46 (2009) 305-314

[13] Huang Y.J., Tseng W. H., Lin S.Y., Yang S. H. and Fujieda M. (2016) TWSTFT Results by using Software-Defined Receiver Data, Proc. EFTF2016 pp 1-4

Fiber optic time transfer between PTB and Deutsche Telekom using multi-link redundant topology

Ł. Śliwczyński, P. Krehlik, J. Kołodziej
Faculty of Computer Science, Electronics and Telecommunications
AGH University of Science and Technology
Krakow, Poland

H. Imlau, H. Ender
Deutsche Telekom Technik GmbH
Bremen, Germany

H. Schnatz, D. Piester, A. Bauch
Physikalisch-Technische Bundesanstalt (PTB)
Braunschweig, Germany

***Abstract*—We report on the upgrade of a fiber optic network for time and frequency transfer between PTB in Braunschweig and the test center of Deutsche Telekom in Bremen, Germany. The network provides 10 MHz and 1 PPS signals at remote locations intended for the supervision of the mobile telecommunication network of Deutsche Telekom. Here we present the results of the time transfer calibration of the link.**

Keywords—time transfer; fiber optic; dark fiber; bi-directional link; ELSTAB

I. INTRODUCTION

The cooperation between Deutsche Telekom, PTB and AGH in the field of fiber optic time and frequency has started in 2015, when a link connecting PTB in Braunschweig with Deutsche Telekom test center in Bremen was established for an experimental proof of concept (PoC) [1], [2]. This about 446 km long PoC link was arranged as a loop having both ends at PTB, where the main part of the measurements was undertaken. Along the link seven single-path bi-directional optical amplifiers (SPBA) were installed to compensate the attenuation of the fiber. At PTB local and remote modules of the ELSTAB optical time transfer system were installed. In Bremen, a special tapping module extracting stabilized 1 PPS and 10 MHz signals from the bi-directional fiber link was used.

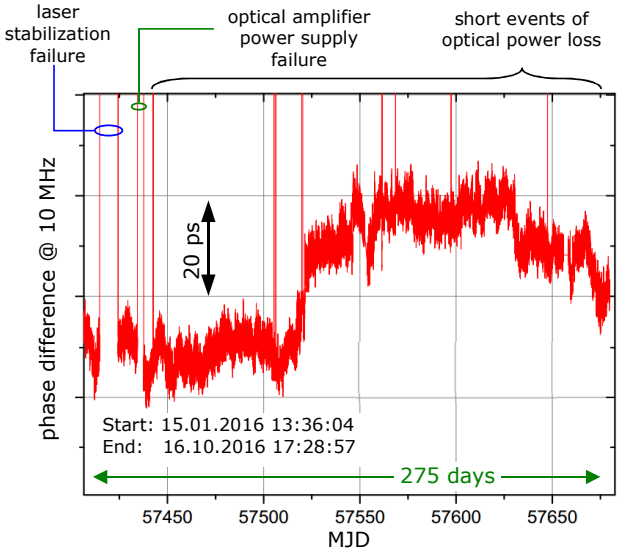


Fig. 1. Measured difference between fluctuations of the input 10 MHz phase and the signal after the 446 km round trip loop in the PoC link PTB-Deutsche Telekom over almost one year.

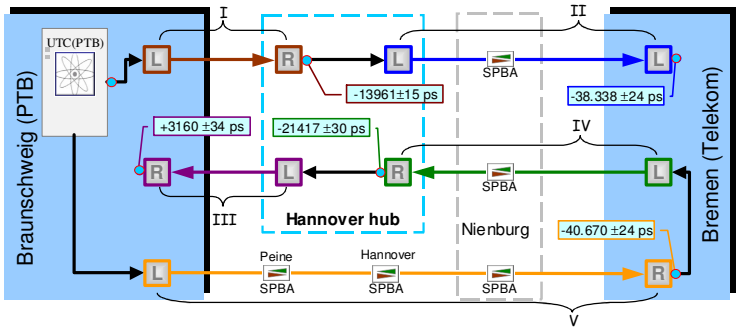
This work was partially supported by the EMPIR initiative co-funded by the European Union's Horizon 2020 research and innovation programme and the Participating States via project 15SIB05. Support was also received from the Faculty of Computer Science, Electronics and Telecommunications, AGH University of Science and Technology, Krakow, Poland.

II. TOWARDS THE OPERATIONAL PTB-DEUTSCHE TELEKOM LINK

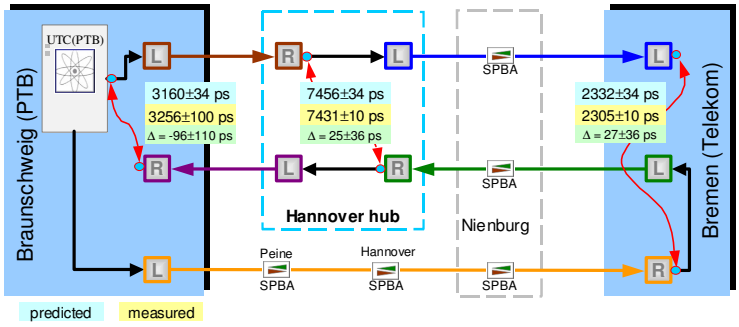
The operation of the PoC link was terminated in November 2016 (see Fig. 1 showing a 275-day record of data) and work was started to migrate it to a second phase, where an adequate redundancy necessary for telecom infrastructure had to be achieved.

In this PoC phase 2 four sets of ELSTAB equipment with two SPBAs were installed, establishing two new and independent connections between PTB and Deutsche Telekom, running in opposite directions. In addition, a "hub" was incorporated at a Deutsche Telekom site in Hannover to provide access to the 1 PPS and 10 MHz signals there. The fiber path connecting the end points was deliberately chosen different to those used in the first phase of the PoC link. Thanks to that part of the "old" PoC link could still be used for verification purposes.

The sketch of the entire infrastructure is presented in Fig. 2a. In its current configuration one of the links is supplying synchronization signals from PTB to Deutsche Telekom, whereas the "old" link is connected in series with one of the "new" links, forming this way a loop that starts and ends at PTB. At the Hannover "hub" signals sent from PTB are available via two different routes - one directly from Braunschweig and the second one via Bremen.



(a)



(b)

Fig. 2. Sketch of the link connecting PTB and Deutsche Telekom, showing: the results of the calibration of 1 PPS signal relative to UTC(PTB) (a) and the results of calibration cross-checking (b).

III. Calibration of Time Transfer

To calibrate the time transfer in such a multi-link architecture (Fig. 2), where several links are connected in series, it was necessary to calibrate each link separately and to measure the propagation delay between the source of UTC signal and the reference point of the local module. Thanks to the features of the ELSTAB system, the time transfer calibration of each individual link may be performed at the place where the local module is operated. Thus, the calibration of links I and V were performed at PTB, that of links II and III in Hannover and that of link IV in Bremen. The results together with the estimated uncertainties are inserted in Fig. 2a close to the output of each remote module. The 1 PPS pulses at the outputs of the remote modules are roughly aligned to compensate for the propagation delay induced by the transfer system [3].

IV. Verification of the Time Transfer Calibration

The redundant and cross-connected topology of the entire system made it possible to validate the calibration by direct comparisons of the phases of 1 PPS signals at PTB, Bremen and Hannover, respectively.

The results of such measurements are given in Fig. 2b. The measurements at Hannover and Bremen were carried out using an Agilent DSO81004A real-time digital oscilloscope, whereas at PTB a Stanford Research SR620 Time Interval Counter was used. The agreement between the measured values and the result of calibration (denoted as Δ in Fig. 2b) is better than 100 ps and is within the uncertainty of the measurement.

V. Conclusion

In this paper, we have shown the evolution of the PoC fiber link connecting PTB and Deutsche Telekom sites in Hannover and Bremen. The redundant topology of PoC phase 2 link allowed to cross-check the calibration of time dissemination in different locations. This was the first time when such cross-check was possible in a real telecom network. Obtained results proved the correctness of methods used to calibrate the links.

Acknowledgment

We acknowledge the support of Jürgen Becker, Thomas Polewka and Holger Seifert of PTB and of Marvin Barasi, Christiane Feldmann, Uwe Habighorst, Olaf Kappner and André Krüger of Deutsche Telekom during the installation and supervision of operations.

References

[1] Ł. Śliwczyński, P. Krehlik, J. Kołodziej, H. Imlau, H. Ender, H. Schnatz, D. Piester, A. Bauch, "Towards Sub-Nanosecond Synchronization of a Telecom Network by Fiber Optic Distribution of UTC(k)," Proc. Euro. Frequency and Time Forum, 4–7 Apr. 2016, York, U.K., DOI 10.1109/EFTF.2016.7477772.

[2] Ł. Śliwczyński, P. Krehlik, J. Kołodziej, H. Imlau, H. Ender, H. Schnatz, D. Piester, A. Bauch, "Fiber optic time transfer for UTC-traceable synchronization for telecom networks," IEEE Communications Standards Magazine, DOI 10.1109/MCOMSTD.2017.1600766ST, vol. 1, no. 1, pp. 66-73, 2017.

[3] P. Krehlik, M. Mazur, Ł. Śliwczyński, "Delay compensation of 1 PPS timetags in fiber-optic time distribution," in these proceedings.

A Cost-Efficient Regional Synchronization System

R. Píriz, P. Roldán, D. Sanz
GMV
Tres Cantos, Spain
rpiriz@gmv.com

J. Díaz, A. González
Seven Solutions
Granada, Spain

T. Polewka, A. Bauch
Physikalisch-Technische Bundesanstalt (PTB)
38116 Braunschweig, Germany

***Abstract*— GNSS timing is currently used worldwide in critical real-time systems that require precise synchronization or time-stamping at geographically dispersed sites, such as wireless telecom stations, electrical power grids, and financial services. For applications where multiple equipment needs to be deployed, it is desirable to use low-cost, single-frequency receivers. Increasing demands in cost-saving and accuracy will make the availability of precise single-frequency solutions more and more interesting. In the space operations domain, an application example of GNSS-based synchronization is passive ranging for geostationary satellites. This paper analyzes the application of low-cost GNSS receivers to multi-site synchronization for geostationary satellite orbit determination based of Time Difference of Arrival (TDOA) measurements. The receiver timing signals are measured at the Physikalisch-Technische Bundesanstalt (PTB) in Braunschweig, Germany. By comparing the receiver output timepulse with the reference UTC(PTB) timescale clock using a Time Interval Counter (TIC), one can fully characterize the behavior of the GNSS-derived time solution, and also calibrate the average receiver chain delay. It is expected that the largest contribution to the GNSS timepulse error will be the ionosphere.**

Keywords— synchronization; low-cost; GNSS; GPS; calibration; geostationary; satellite; orbit determination; regional; ionosphere

I. MOTIVATION

Passive ranging for geostationary telecom satellites is a new technique based on the Time Difference Of Arrival (TDOA) of the satellite TV signal to two or more dedicated ground stations [1]. The principle is depicted in Fig. 1. This concept eliminates the need of dedicated transmissions for ranging and collects tracking data, silently in the background, without need of coordination with satellite operations. Good signal synchronization between ground stations is key to calculate the TDOA accurately and therefore to reduce the final ranging and orbit determination error.

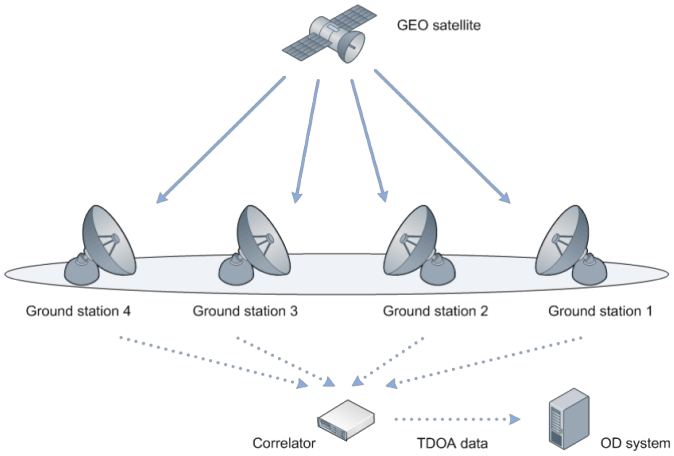


Fig. 1. Principle of geostationary satellite tracking based on passive ranging (Image: SES Astra).

II. THE LEA-M8F GNSS RECEIVER

The LEA-M8F receiver from u-blox is a low-cost single-frequency multi-GNSS module optimized for time and frequency applications. The output timepulse jitter (or digital resolution) specified by the manufacturer is ±2 ns. The receiver allows to input a precise antenna position calculated offline by the user. It is also possible to enter by configuration the total receiver chain delay in order to generate a calibrated timepulse.

The LEA-M8F can generate GNSS raw data including pseudorange and carrier-phase measurements, and navigation messages. Raw data allows the calculation of a precise antenna position offline using PPP/RTK.

We have integrated the LEA-M8F into a prototype board providing 1PPS and 10 MHz output signals. The unit can be powered and configured by USB, connected to the user computer, or powered autonomously by a DC source. The GNSS board is shown in Fig. 2.

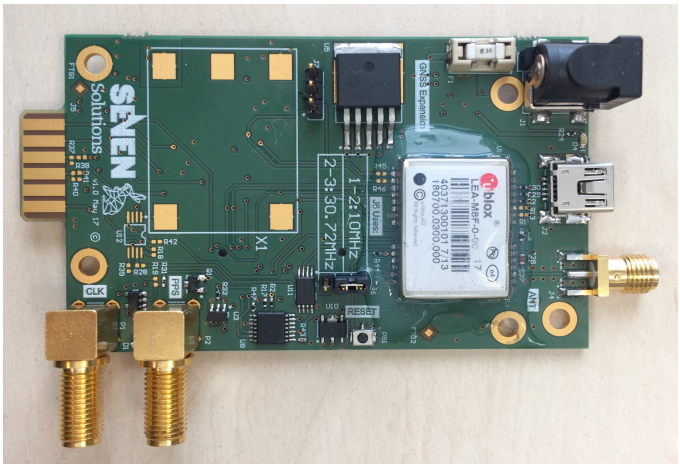


Fig. 2. The GNSS board integrating the LEA-M8F receiver from u-blox.

III. CALIBRATION AT PTB

Two test units have travelled to PTB for calibration, measuring the 1PPS difference between the UTC(PTB) master clock and the GNSS board, using a Time Interval Counter (TIC). The GNSS boards are configured to use GPS-only and to generate a 1PPS aligned to UTC(USNO) derived from the GPS signals. The antenna installation is shown in Fig. 3.



Fig. 3. GNSS antenna installation at PTB.

The two antenna cables have a length of 20 m each, and a measured delay of 81 ns. This value was entered into the LEA-M8F for 1PPS compensation. TIC results were recorded for almost 42 hours in June 2017. Room temperature was maintained at 24°C. The calibration results are shown in Fig. 4.

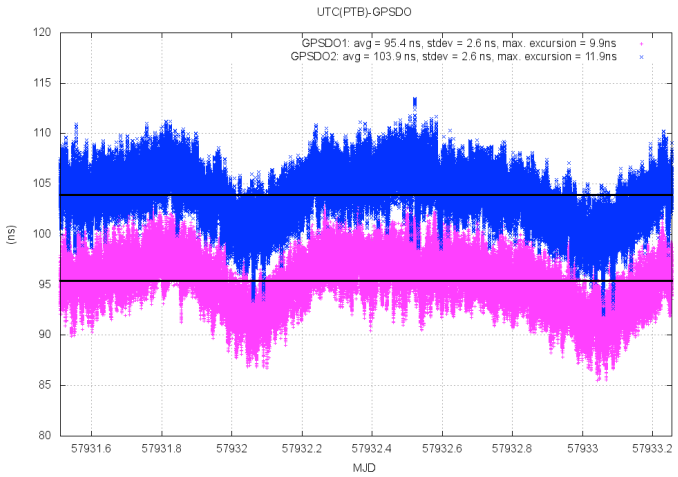


Fig. 4. Calibration results of the two GNSS boards.

The average difference between the two receiver chains is 8.5 ns. The instantaneous differences are shown in Fig. 5 and Fig. 6. The green lines around the average indicate ±4 ns (twice the nominal 1PPS jitter).

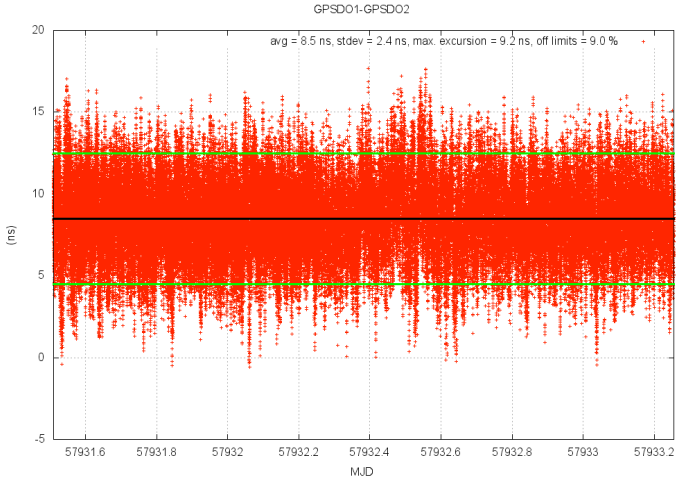


Fig. 5. Calibration difference between the two GNSS boards (as time series).

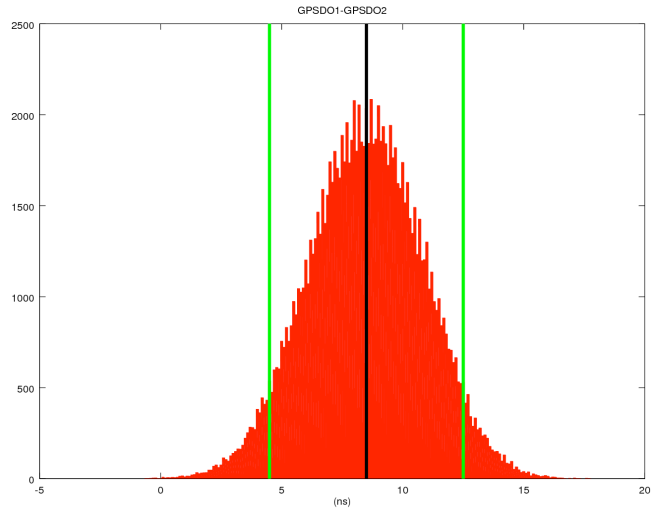


Fig. 6. Calibration difference between the two GNSS boards (as histogram).

As can be seen from Fig. 5, the instantaneous synchronization excursions can reach up to almost 10 ns, but the standard deviation over the 42 hours is 2.4 ns only. This figure can be brought down to around 1 ns (1-σ) by filtering TDOA measurements over a few minutes. Table 1 shows the noise reduction after filtering the raw measurements from Fig. 5 in consecutive intervals of 1, 5, and 10 minutes.

TABLE I. SYNCHRONIZATION NOISE REDUCTION AFTER FILTERING

Fitting Interval	Standard Deviation (ns)
Unfiltered (raw)	2.4
1 min	1.5
5 min	1.0
10 min	0.7

IV. IONOSPHERIC ERROR

We have compared the single-frequency clock solution, corrected by the Klobuchar iono model, against the dual-frequency solution ("truth"), processing RINEX data from receivers at four timing laboratories in Europe: NPL in the UK, PTB in Germany, ROA in Spain, and SP in Sweden. The locations are representative of a European TDOA tracking network. The results are shown in Fig. 7.

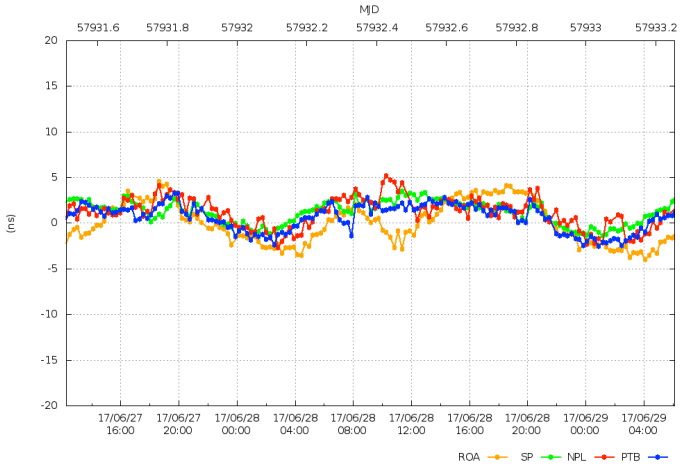


Fig. 7. Timing performance of the Klobuchar iono model at four European timing labs.

As can be seen, the iono error is highly correlated among stations, but differences can reach up to 5 ns. The resulting synchronization error in TDOA measurements cannot in general be filtered out.

CONCLUSIONS

A systematic bias of 8.5 ns has been found between two receivers of the same model (LEA-M8F). This bias can be calibrated in factory using a TIC, with an uncertainty better than 1 ns. After calibration, synchronization errors between two co-located receivers (mainly due to the relative clock jitter) can be reduced to 1 ns (1-σ) after TDOA filtering.

For separate receivers, the iono error is in general highly correlated over wide regions, but local synchronization errors of up to 5 ns over continental Europe are currently possible using the Klobuchar model.

ACKNOWLEDGMENT

We are grateful to the following timing laboratories for contributing to this paper with RINEX observation files from their GNSS receivers: NPL in the UK, PTB in Germany, ROA in Spain, and SP in Sweden.

REFERENCES

[1] L. Rodríguez et al., "Passive Ranging for Geostationary Satellites: On a Novel System and Operational Benefits", 13th International Conference on Space Operations 2014, 5-9 May 2014, Pasadena, CA.

Research on Autonomous High-precision Time Synchronization Method of UAVs Based on Side-tone Signal

Tao Liu
National Time Service Center, Chinese Academy of Sciences
University of Chinese Academy of Sciences
Xi'an, China
liutao@ntsc.ac.cn

Yonghui Hu
National Time Service Center, Chinese Academy of Sciences
University of Chinese Academy of Sciences
Xi'an, China
huyonghui@ntsc.ac.cn

Yu Hua
National Time Service Center, Chinese Academy of Sciences
University of Chinese Academy of Sciences
Xi'an, China
hy@ntsc.ac.cn

Meifang Wu
National Time Service Center, Chinese Academy of Sciences
University of Chinese Academy of Sciences
Xi'an, China
wumeifang@ntsc.ac.c

***Abstract*—Based on the existing communication links between UAVs, a short wave side tone ranging signal for UAV platform is constructed, based on the phase characteristic of side tone signal and the principle of bidirectional time comparison, this paper proposed a high-precision time synchronization method which can achieve the high-precision time synchronization for formation UAVs independently without GNSS navigation system and ground control station. The simulation results show that the synchronization accuracy can reach μs level for formation UAVs in the autonomous mode.**

Keywords—UAVs, Time synchronization, Side tone signal, Autonomous mode

I. INTRODUCTION (*Heading 1*)

The pattern of UAV formation and autonomous operation will be the main direction of its future application development, especially in the case of out of the ground monitoring and control system, to complete tasks of the coordination control, formation to maintain, joint reconnaissance and combat, and to improve the capacity of the autonomous survival and self-management for the unmanned aerial vehicles(UAVs), an important premise is to achieve the high-precision relative ranging and time synchronization between the UAVs.

The traditional "master-slave" time synchronization method, the core idea is the use of channel symmetry, through the signal of the two-way transmission, the signal transmission delay measurement, for the formation of the group of unmanned aerial vehicles (UAVs), on the one hand, because of the uncertainty of the communication link and the dynamic change of the network topology, makes the channel have serious asymmetry. Therefore, the traditional time synchronization algorithm is no longer applicable. On the other hand, the traditional time synchronization method needs to send the time synchronization signal frequently, which will greatly improve the enemy's passive detection system to combat our unit discovery probability, that will increase risk of our formation suffered by enemy anti-radiation attack weapons, therefore, need using low spectral density signal for time synchronization, improve the concealment of the time synchronization system signal.

Learned from the idea of side tone ranging in the areas of satellite monitoring and control, based on the study of existing communication links between UAVs, this paper constructs a short-wave side tone ranging signal for the formation of UAV platform, and proposes a kind of the method of directly measuring the transmission delay by using the phase relationship of the multi-side audio signal carrier, and the frequency of the side tone signal is designed to realize the unidirectional correction of the signal transmission delay. The relative measurement can make the UAV independent of the ground monitoring and control equipment, relying solely on their own tracking and measurement equipment to complete high-precision time synchronization, out of the GNSS satellite navigation system and ground monitoring and control system to rely on to improve the synchronization accuracy between UAVs, and because the algorithm has higher robustness and survivability, and thus improve the autonomy of the entire fleet survivability.

II. DESIGN OF SIDE TONE SIGNAL IN TIME SYNCHRONIZATION SYSTEM

For the non-dispersive channels with delay of τ , if the side tone signal is used, because of the transmission phase of multiple frequency side tones in the channel is different, and make use of the characteristic, the transmission phase of the receiver can be accurately measured , and the transmission delay also can be measured.

The carrier with the frequency of f is transmitted in the channel with delay of τ , the phase change caused by the carrier frequency is:

$$\Delta\theta = 2\pi f\tau \tag{1}$$

If the two carriers with frequency of f_1 and f_2 are transmitted simultaneously in the channel, the instantaneous phase of the receiving terminal is:

$$\theta_1 = 2\pi f_1 \tau + \theta_{10} \tag{2}$$

$$\theta_2 = 2\pi f_2 \tau + \theta_{20} \tag{3}$$

Among them, θ_{10} and θ_{20} is the initial phase of the sending end. The translation delay is:

$$\tau = (\Delta\theta_{rec} - \Delta\theta_0)/2\pi\Delta f \tag{4}$$

$\Delta\theta_{rec} = \theta_1 - \theta_2$ is the phase difference of the carrier frequency in the receiver side, $\Delta\theta_0 = \theta_{10} - \theta_{20}$ is the phase difference of the carrier frequency in the sending side, $\Delta f = f_1 - f_2$ is the frequency difference of the carrier frequency.

Derivative to the above formula:

$$\delta_\tau = \delta_{\Delta\theta}/2\pi\Delta f \tag{5}$$

That shows, the propagation delay estimation accuracy is inversely proportional to the difference frequency, and the frequency difference detection accuracy is proportional to the difference frequency.

However, in practical applications, due to the periodic nature of the carrier frequency signal, there is a problem of phase blur in the instantaneous phase of the receiver, thus, there is a question of how to solve the phase ambiguity. In this paper, make use of the characteristics of the side tone signal, for different ranging ambiguity of the side tone signal, the ambiguity is calculated using the frequency relationship between the signals.

In the design of the side tone signal, any ranging signal system in order to meet and meet the ranging accuracy and maximum distance index, and to correctly select the upper and lower limits of the maximum and minimum frequency of the upper and lower frequencies. In order to meet the maximum measurement distance, the selected side tone frequency should not exceed one whole cycle of the round trip phase delay, the highest frequency should meet its ranging accuracy requirements.

The maximum transmission distance of the transceiver should be less than the minimum difference frequency:

$$\Delta f_L \le c / R_{\max} \tag{6}$$

The maximum difference frequency should meet the requirement of delay detection accuracy:

$$\Delta f_H \ge \frac{\delta_\theta}{2\pi\delta_x} \tag{7}$$

δx represents for the accuracy of the delay estimation, and δ_θ represents for the detection accuracy of the difference frequency phase.

The design of the side tone signal:

(1)The detection accuracy of the differential frequency: $\delta_\theta = 28.8^\circ$;

(2)The accuracy of the time delay estimation: $\delta_x = 100ns$;

(3) The error of the Distance measurement: $\delta_R = 30m$;

(4)The Maximum no blur distance: $R_{\max} = 375km$;

So, the side tone frequency is designed as follows:

$$\Delta f_1 = 800kHz \tag{8}$$

$$\Delta f_2 = 100kHz \tag{9}$$

$$\Delta f_3 = 20kHz \tag{10}$$

$$\Delta f_4 = 4kHz \tag{11}$$

$$\Delta f_5 = 800Hz \tag{12}$$

There are two kinds of modes to transmit the side tone signal that is concurrent mode and rotation mode. This paper uses concurrency model, multiple side tone is sending at the same time, after receiving the demodulator signal of the receiver, the delay measuring equipment performs orthogonal correlation processing to extract the phase information of the difference frequency side tone, solves the ambiguity to obtain the delay information. This requires that each side of the tone signal at the same time to send, while receiving, and can obtain the initial phase information when it was sending, thereby correcting the phase information of the difference frequency delay.

In order to reduce the bandwidth occupied by the side tone signal, normally the lower frequency side tone signal is folded over a higher frequency; the folded side tone signal is called a folding sound. For the signal designed in this paper, fold all frequencies to 100 KHz, the transmitter transmits a folded signal of 900 kHz, 100 kHz, 120 kHz, 104 kHz, 100.8 kHz, the channel transmits a superposition of five frequencies.

III. MULTI-SIDE TONE RECEPTION AND PHASE SEEK

The system block diagram for using the side tone to obtain the channel transmission delay is showed in Figure 1, including the generation of the side tone signal, the transmission of the side tone signal, and the receiving of the side tone signal, the solution of phase information for difference frequency, phase matching and solution ambiguity, and the calculation of the transmission delay.

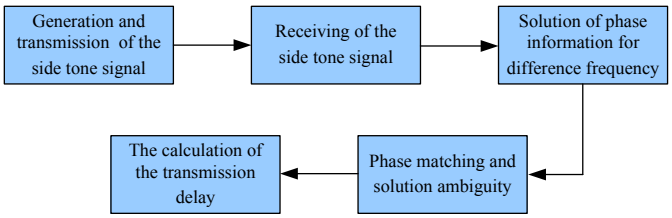


Fig. 1. The system block diagram for using the side tone to obtain the channel transmission delay

The system for obtaining the channel transmission delay by using the side tone includes the generation and transmission of the side tone, the reception of the side tone signal, the determination of the difference frequency phase information, the phase matching solution and the transmission delay of the search.

The received side tone signal is a superimposed signal of a plurality of different frequencies, in order to detect the phase information of each difference frequency, this paper adopted the method of the orthogonal correlation to obtain the phase information.

The transmitted signal is $b(t)=\cos(2\pi f_1 t+\theta_0)$, f_1 is the Carrier frequency, θ_0 is initial phase, when the signal is transmitted through a channel with delay of τ, the received signal is $s(t)=A\cos[2\pi f_1(t+\tau)+\theta_0]=A\cos(2\pi f_1 t+\theta_1)$.

The received signal is orthogonal correlation method, the local generation of the same frequency orthogonal signal are respectively related to the received signal:

$$I_1=s(t)\cos(2\pi f_1 t)=A\cos(2\pi f_1 t+\theta_1)\cos(2\pi f_1 t)=\frac{A}{2}[\cos(4\pi f_1 t+\theta_1)+\cos(\theta_1)]$$

$$Q_1=s(t)\sin(2\pi f_1 t)=A\cos(2\pi f_1 t+\theta_1)\sin(2\pi f_1 t)=\frac{A}{2}[\sin(4\pi f_1 t+\theta_1)-\sin(\theta_1)]$$

Through the low-pass filter, after filtering the high frequency signal, there is

$$I_1=\frac{A}{2}\cos(\theta_1) \tag{13}$$

$$Q_1=-\frac{A}{2}\sin(\theta_1) \tag{14}$$

For the signal with the carrier frequency f_2, there is:

$$I_2=\frac{A}{2}\cos(\theta_2) \tag{15}$$

$$Q_2=-\frac{A}{2}\sin(\theta_2) \tag{16}$$

At the same time, according to the triangular formula, there is:

$$\sin(\theta_1-\theta_2)=\sin\theta_1\cos\theta_2-\cos\theta_2\sin\theta_1 \tag{17}$$

$$\cos(\theta_2-\theta_1)=\cos\theta_2\cos\theta_1-\sin\theta_2\sin\theta_1 \tag{18}$$

After the calculation, the phase error which brought by the transmission delay is:

$$\Delta\theta=\theta_2-\theta_1=\arctan(\frac{\sin(\theta_2-\theta_1)}{\cos(\theta_2-\theta_1)})=\arctan(\frac{I_2Q_1-I_1Q_2}{I_2I_1-Q_2Q_1}) \tag{19}$$

After measuring the transmission delay phase difference of each difference frequency, the phase can be solved by software.

The calculation results are as follows:

$$\begin{cases}N_{800Hz}=0, & \Delta\theta_{800Hz}>0\\ N_{800Hz}=1, & \Delta\theta_{800Hz}<0\end{cases} \tag{20}$$

$$N_{4kHz}=\Delta f_4\tau_{800Hz}-\frac{\Delta\theta_4}{2\pi} \tag{21}$$

$$\tau_{4kHz}=(N_{4kHz}+\frac{\Delta\theta_4}{2\pi})/4000 \tag{22}$$

$$\tau_{20kHz}=(N_{20kHz}+\frac{\Delta\theta_3}{2\pi})/20000 \tag{23}$$

$$\tau_{100kHz}=(N_{100kHz}+\frac{\Delta\theta_2}{2\pi})/100000 \tag{24}$$

$$\tau_{800kHz}=(N_{800kHz}+\frac{\Delta\theta_1}{2\pi})/800000 \tag{25}$$

IV. SIMULATION VERIFICATION

In order to verify the correctness of the method, in this paper, also did some simulation of the above system.

The side tone frequency is:

$f_1=900kHz$、$f_2=100kHz$、

$f_3=120kHz$、$f_4=104kHz$、$f_5=100.8kHz$;

The sampling frequency is: $f_s=10MHz$;

The transmission delay is: $\tau=[0.3us \quad 0.5us \quad 1us \quad 5us]$

The simulation results are as follows:

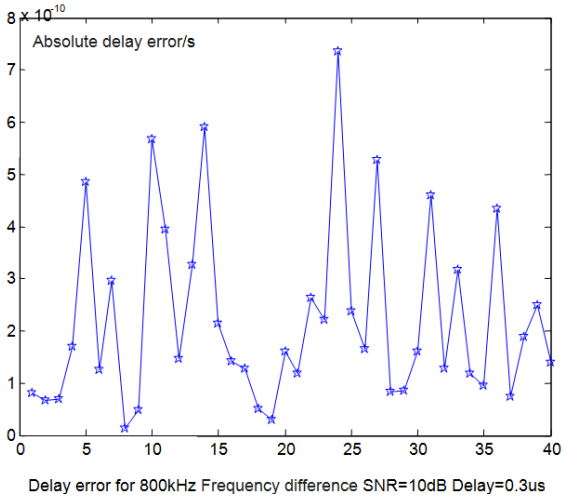


Fig. 2. Delay error for 800kHz Frequency difference，Delay=0.3μs

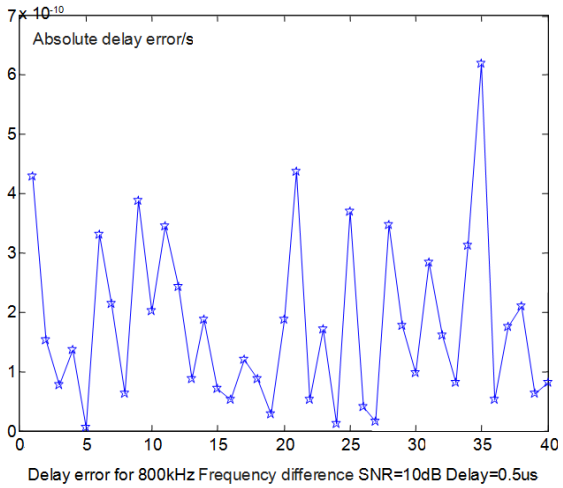


Fig. 3. Delay error for 800kHz Frequency difference，Delay=0.5μs

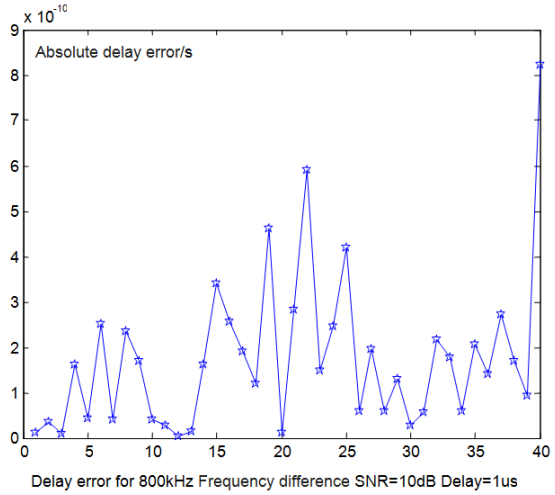


Fig. 4. Delay error for 800kHz Frequency difference，Delay=1μs

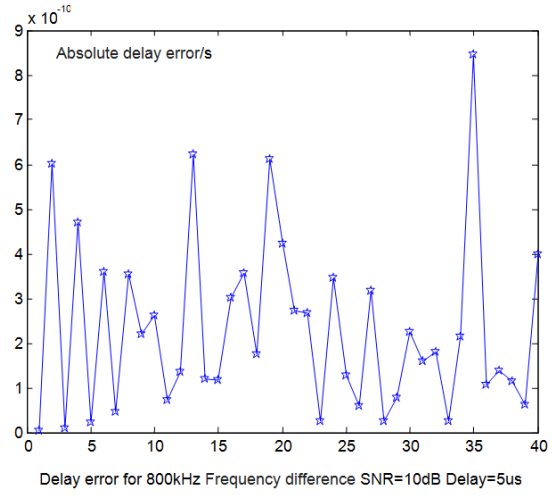


Fig. 5. Delay error for 800kHz Frequency difference，Delay=5μs

V. CONCLUSIONS

In summary, in this paper, the method of measuring the transmission delay by using the side tone carrier phase relationship directly can measure the phase difference directly at the signal receiving end. The signal transmission delay can be obtained by solving the ambiguity without considering the symmetry of the link. The one-way measurement and correction, to achieve both sides of the high precision of time synchronization, the simulation proved that the method is feasible and feasible, formation UAV in the autonomous mode, the synchronization accuracy can reach us level.

VI. ACKNOWLEDGEMENTS

The research work was supported by National Natural Science Foundation of China under Grant No. 11403033.

REFERENCES

[1] Daniel Gonzales, John Hollywood, Gina Kingston. Network-Centric Operations Case Study: Air-to-Air Combat With and Without Link 16. National Defense Research Institute, 2005. 88-91.

[2] Leitgeb E, Zettl K, and Sheikh M S, et al.. Investigation in free space optical communication links between Unmanned Aerial Vehicles (UAVs) [C]. International Conference on Transparent Optical Networks, Rome, Italy, 2007: 152-155.

[3] [2] P. W. Kinman and J. B. Berner, “Two-Way Ranging During Early Mission Phase,” 2003 IEEE Aerospace Conference, March 8-15, 2003, Big Sky, MT.

[4] S. Bryant, “Using Digital Signal Processor Technology to Simplify Deep Space Ranging,” 2001 IEEE Aerospace Conference, March 10-17, 2001, Big Sky, MT.

[5] Hui Zhou, Wei Zhou. A Time and Frequency Measurement technique Based on Length Vernier. Proceedings of the 2006 IEEE International Frequency Control Symposium, 2006. 267-272.

[6] Ruggier C J. Delta differential one-way ranging. [J] DSMS Telecommunications Link Design Handbook,2004. 35-37.

[7] Leungs. High precision real time navigat ion for spacecraft formati on f lying. Institute of Navigati on . ION GPS 2003[C] . Port land: ION publ ication department , 2003: 2 182-2 193.

[8] Ding W D, Wang J L. Time sunchronization design for integrated positioning and georeferencing systems. Proceedings of SSC Spatial Intelligence, Innovation and Praxis. Melbourne,2005.

[9] Zhong Xing-wang, Chen Hao. The analysis and correct ion techniques of movement influence on inter-satellite two-way time transfer [J] . Chinese Space Science and Technology, 2007, 34(2) : 182 -187.]

[10] Jin Shi, Zhang Xiao-lin, and Zhou Qi. A statistical model for the UAV communication channel[J]. Acta Aeronautica et Astronautica Sinica, 2005, 25(1): 62-65.

Accurate time transfer based on communication satellite

Longxia Xu
National Time Service Center
CAS
Xi'an, China
xulongxia@ntsc.ac.cn

Jingya Chen
Key lab of Precision Navigation and Timing Technology
CAS
Xi'an, China

Xiaohui Li
Key lab of Precision Navigation and Timing Technology
CAS
Xi'an, China

FengZhu
Key lab of Precision Navigation and Timing Technology
CAS
Xi'an, China

Abstract—**As we all known, the accuracy of time that provided by navigation systems is about tens of nanoseconds. Some applications, such as the time synchronization between ground stations in VLBI, need several nanoseconds or better accuracy of time. This paper provides a possible way for accurate time transfer via communication satellites. Users with simple receive devices can achieve time equivalent to that of common view time transfer. The transponder on the communication satellite is used to transmit the navigation signal generated and uploaded by the ground station. This method makes full use of the function of navigation and communication of GEO satellites. It is a possible way for accurate time transfer via communication satellite based on the principle of common-view time transfer. Test results indicate this method can provide time information with the accuracy of better than 5ns.**

Keywords—GNSS; common view time transfer; communication satellite; transponder;

I. INTRODUCTION

At present, the accuracy of one-way timing method provided by GNSS is about tens of nanoseconds [1,2]. This method is mainly influenced by broadcast ephemeris error and ionosphere correction error. It can't meet the requirements of users of several nanoseconds time accuracy. This paper provides a possible way for accurate time transfer via communication satellites [3,4,5,6]. The principle is similar to that of common-view time transfer. However, differently from the traditional common view method, users only with a simple receiving device can realize time synchronization of several nanoseconds.

II. PRINCIPLE OF THE TIMING METHOD

This method is implemented based on the Chinese area positioning system. The over-life-operation communication satellites are used to transmit the C band navigation signal generated by the ground master station with on-board transponders in this system. The ground master station keeps the system time scale with assemble atomic clocks and provides the time and frequency signals to the other parts of the system. The system time of this system is steered to the national time scale UTC(NTSC) in real time by optical time and frequency transfer link and common view time transfer link.

Each monitor station keep local time with a free running atomic clock. Several monitor stations observe one communication satellite at the same time to determine the orbit parameters which will be broadcasted in the navigation message. As the byproduct, the time offsets between each monitor station and the master station are also obtained.

The Chinese area positioning system not only can provide positions but also accurate time information.

The monitor receivers are set up on the monitor stations to receive the C band navigation signals transmitted by communication satellites. The pseudo-ranges from ground master station to transponders, and then to receivers are measured.

The virtual clock biases represent the time delay from master station to transponders are deducted from the pseudo-ranges. And then the down geometrical distance are also deducted with the orbit parameters in navigation messages. At last, The precise cumulative time offsets obtained from orbit determination are also deducted to exclude the effect of atomic clocks. Finally, the time biases between the local time of monitor stations and the system time kept by master station are calculated with receivers.

Then the time biases are modeled and compiled into the navigation message of communication satellites and broadcast to users for their applications.

Users receive the C band navigation signal and get the pseudo-ranges. After the same corrections as that of time biases , one can get the time offsets between use's local time and the system time, that is the one-way timing result. The time biases broadcasted in navigation message are applied to correct users' one-way timing result. This equivalents users carry out once common-view time transfer via communication satellite with the master station.

This paper is sponsored by national natural science foundation of China (11503030) and national defense innovation foundation (CXJJ-16M205).

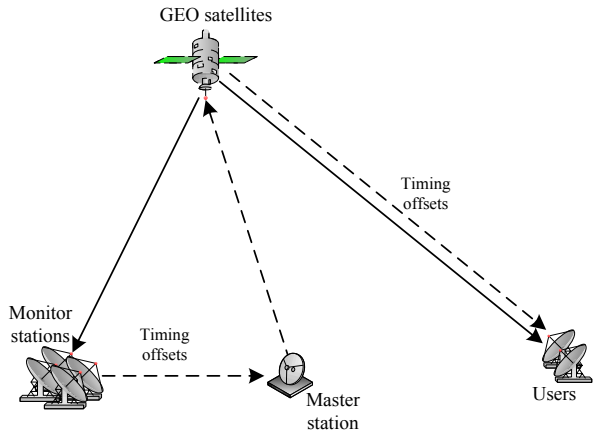


Fig1. Principle of the timing method based on communication satellite

It is obviously that this method has several advantages. First of all, the orbital plane of the communication satellite is about 1.5 times higher than that of MEO satellites and is visible 24-hours a day in its coverage area. Secondly, the atmosphere delay of C band signal contributed by ionosphere is only one in seven parts of that of L band signal. Thirdly, users applied with the broadcasted time corrections equally implement once common-view time transfer with the master station which is obviously superior than traditional one-way timing method of GNSS. All of these benefits insured the accuracy of this method.

III. TEST RESULTS

This paper has implemented some experiments between the monitor stations to test the accuracy of this method. As shown in Figure 2, the TWSTFT results of the same pair monitor stations are used to evaluate the result of this method.

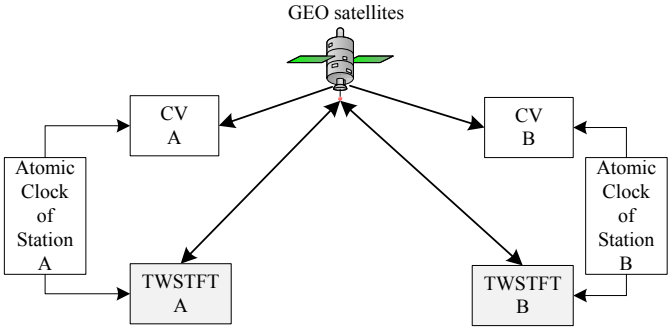


Fig2. Experiment and evaluation method of test result

Three experiments have been carried out respectively on the baselines of XA-KS (3000km), XA-SY (1800km) and KS-SY (2000km). Figure 3 gives the one-way timing result of the master station XA. It can be seen that the result performs good stability. That's because the high stability of reference signal for receivers and the accurate satellite virtual atomic clock correction which is determined according to the uplink delay from master station to transponders[7].

Figure 4~6 provide the test results of the three baselines of XA-KS (3000km), XA-SY (1800km) and KS-SY (3900km) reference to the result of TWSTFT[8, 9, 10]. It is obviously that the three baselines results behaves periodical variations. There is a long-term trend performing each day. Besides, there are many regulated spikes in one day which can be seen from figure 5~6.

The primary contributor of the results is the ephemeris error of communication satellites. It performs more obviously with the increase of distance from master station to monitor station. The essence is that the satellite virtual clock correction almost counteract the influence of ephemeris error in master station. However, it is not the truth at the monitor station. And the spikes appeared in one day are mainly due to the update period of ephemeris parameters. It presents a peak between two adjacent ephemeris parameters.

Despite the above problems, the instability of the test results are better than 5ns. The systematic delay that affect the accuracy of timing results can be measured through relative delay calibration with a common reference receiver.

The timing transfer method that based on communication satellites has to consider the problem of maneuvers. Figure 7 shows the one-way timing result of two monitor stations in the period of maneuvering. It can be seen that the two monitor stations' one-way timing results appear thousands of nanoseconds fluctuation at the same time. The time transfer result of the two stations is partially affected.

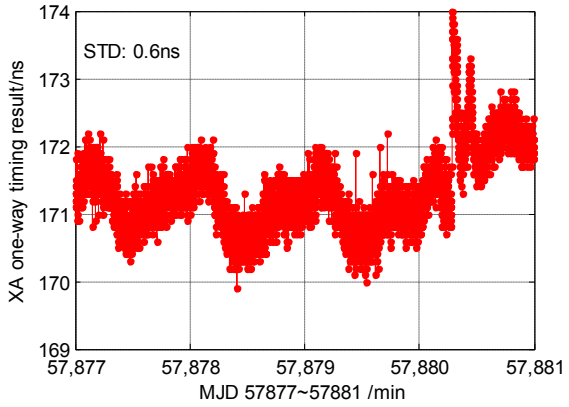


Fig3. One-way timing result of XA (master station, STD: 0.6ns)

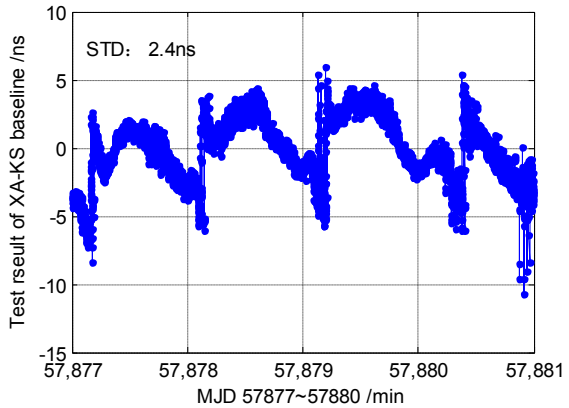


Fig4. Test result of XA-KS baseline (STD: 2.4ns) via communication satellites

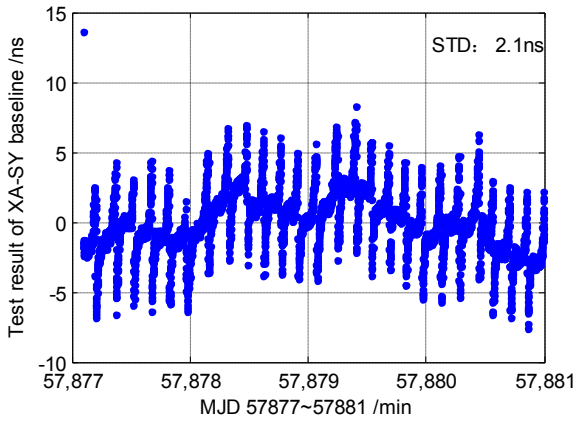


Fig5. Test result of XA-SY baseline (STD: 2.1ns) via communication satellites

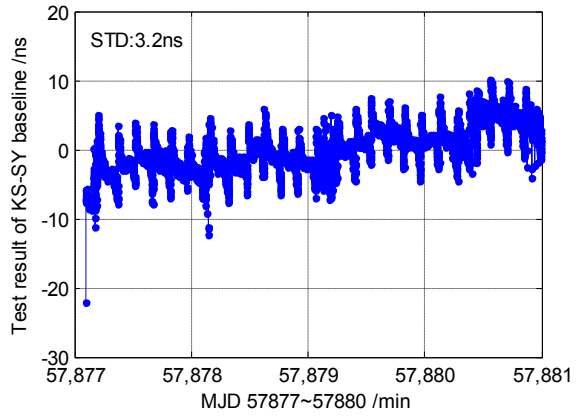


Fig6. Test result of KS-SY baseline (STD: 3.2ns) via communication satellites

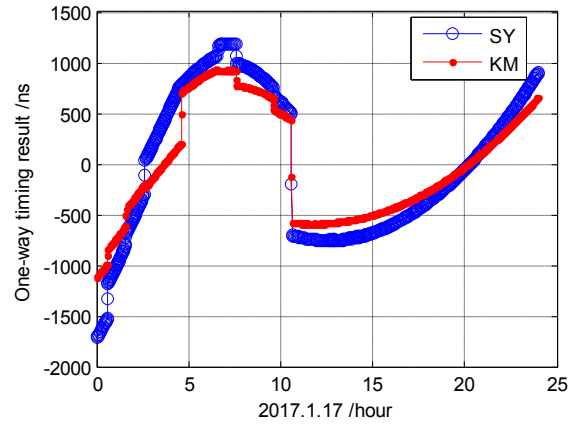


Fig7. One-way timing result of SY and KM monitor stations under communication satellite maneuvers

IV. CONCLUSIONS

A new timing method is proposed based on the Chinese area positioning system. Experiment test result indicate this method can provide timing instability of better than 5ns time transfer service. This can meet the requirements of many applications.

However, there is a intractable problem that must be taken into account. The communication satellites that near or already retired perform frequent maneuvers to maintain its orbit. The predicted positions of the communication satellites in the period of maneuvers and after are affected obviously by the maneuvers. Therefore, the rapid orbit recovery method requires study to guarantee the precise prediction of satellite position when occur maneuvers.

REFERENCES

[1] Rose, J. A. R., Tong, J. R., and Allain, D. J., “The use of ionospheric tomography and elevation masks to reduce the overall error in singlefrequency GPS timing applications,” Advances in Space Research. vol. 47, pp. 276-288, 2011.

[2] Levine, J, “A review of time and frequency transfer methods,” Metrologia. vol. 45, pp. S162-S174, 2008.

[3] Longxia Xu, Xiaohui Li, Yanrong Xue, Chenglin Cai and Meijun Guo. Study of a new one-way timing method, Sci of China, 2012, 55(12), pp: 2476-2481.

[4] Xu Longxia, Li Xiaohui, Xue Yanrong. A new timing method based on common-view[C], 2012 IEEE International Frequency Control Symposium, 2012.5.21-24, Baltimore, MD, United States. 2012 IFCS Proceedings, 181-184.

[5] David W. Allan and Marc A.Weiss. Accurate time and frequency transfer during common-view of a GPS satellite[C]. Proc 34th Annual Freq Control Symposium, 334-346, 1980.

[6] XU Longxia, LI Xiaohui, CHEN Jingya. Realization of the GNSS Oneway Timing Method, Journal of time and frequency,2016, 39(4),pp: 290-300.

[7] LI XiaoHui, WU HaiTao, BIAN YuJing, WANG DanNi, Satellite Virtual Atomic Clock with Pseudorange Difference Function, Science in China Series G: Physics, Mechanics & Astronomy, 2009, 52(1), in press.

[8] Li B D, Liu L, and Ju X M, “Precision analysis of satellite two-way timing,” Journal of Time and Frequency. vol. 33, pp. 129-133,2010.

[9] Zhou S S, Hu X G, Wu B, et al. Orbit determination and time synchronization for a GEO/IGSO satellite navigation constellation with regional tracking network. Sci China Phys Mech Astron, 2011, 54: 1089-1097.

[10] Liu L, Han C H, Tang B. Method and Test Analysis of Geostationary Satellite Two-way Common View Time Transfer. ACTA

The Study of Near Real-time GPS/BDS Time Transfer

Hongbo Wang, Hang Yi, Shengkang Zhang, Haifeng Wang, Xueyun Wang, Wenzhe Yang, Shuwei Wang
Science and Technology on Metrology and Calibration Laboratory
Beijing Institute of Radio Metrology and Measurement (BIRMM), Beijing, China
Email: wanghomeboy@139.com

***Abstract*—This paper introduces the design of a near real-time BDS/GPS time transfer method. A Beidou data communication module is assembled into a time transfer receiver. The clock difference computation procedure is modified and a customized protocol is designed for comparison data exchange. The time difference of zero-baseline common-clock by GPS and BDS is compared. The performance of this method is almost the same level as CGGTTS standard with an uncertainty below 2 ns. The uncertainty by BDS is a little better than GPS.**

Keywords—Time Transfer; Beidou; RDSS; Near Real-Time

I. INTRODUCTION

In order to adapt the emerging navigation systems like Galileo, BeiDou, QZSS, the standard for GNSS time transfer was revised in 2015. The extended standard is called CGGTTS-Version 2E [1]. In this standard, the conventional observation schedule is remained, so it could be compatible with the old version. Still, the final time difference result between labs could be calculated after the exchange and post-process of CGGTTS files. So the GNSS time transfer based on V2E is not real-time. The latency is about one day. Therefore, it is not adapted for real and quasi-real time applications. Nowadays, there are many applications of rapid remote time comparison. It was recognized that a more rapid GNSS time transfer technique would benefit. In China and western countries, there are some studies and experiments on rapid GNSS time transfer. Using PPP and IGS real-time products is a way to compare atomic clocks near real-time, with latency down to some minutes [2].

This paper introduces a near real-time BDS/GPS time transfer method. In our design, the data fit period is reduced and a new comparison schedule is defined. With 1-second calculated time differences from each satellite, a customized time transfer protocol based on Beidou RDSS communication is designed. By assemble a Beidou RDSS module in a time transfer receiver, the generated data could be exchanged within 3min, so that the near real-time atomic time comparison could be realized.

II. THE TIME TRANSFER PRINCIPLE

The basis of our design is CGGTTS standard and GNSS common-view. But the comparison schedule is different from the definition in CGGTTS. The data fit period is shortened to meet the needs of near real-time applications. The conventional time transfer receiver is assembled with a communication module to realize data exchange rapidly. Here, we have chosen a Beidou Radio Determination Satellite Service (RDSS) communication module to implement the function because it is convenient and flexible, only need to be covered by a Beidou GEO satellite. Fig.1 shows the design of our time transfer system.

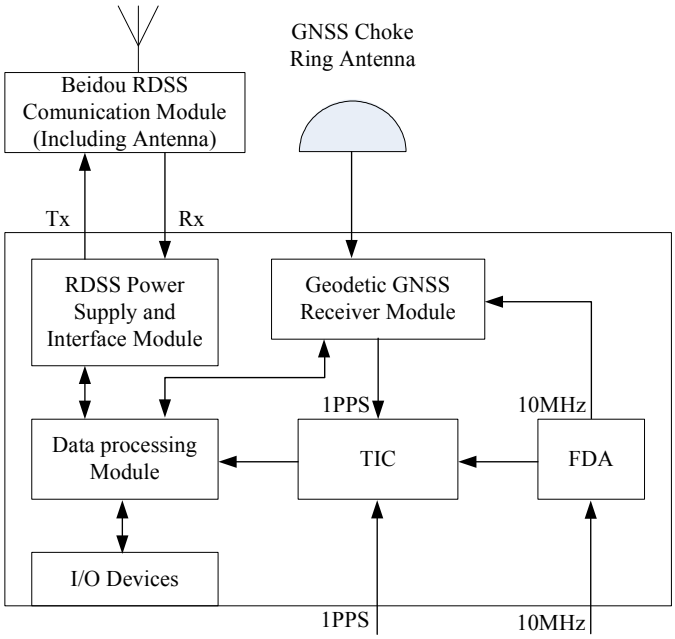


Fig. 1. The design of near real-time GPS/BDS time transfer system

And a specialized protocol is designed for time comparison data exchange between local lab and remote lab. With this protocol, each station could calculate the time difference between the two labs.

A. Receiver Calibration

To get the accurate time difference between local time and GPS or Beidou System time, the delay calibration of the receiver is a critical work. The calibration values would be contained by the exchanged messages between labs. The calibrations of GPS and BDS were implemented separately. The GPS receiver was calibrated by a simulator, and the result is validated by the BIPM's APMP campaign [3].

The calibration of B1 and B2 receiver delays was done by a BDS simulator [4]. The delay difference between B1 and B2 is much larger than that of GPS. But the result of our chosen receiver is consistent with the data published in [5], and with the B1 and B2 receiver delays obtained, the ionospheic delays are almost the same of GPS.

B. The generation of local time difference

For a single station, the time differences between local time and each satellite are calculated once per second. The corrections for these 1-second time differences follow the definition in [1]. Since the receiver is a dual-frequency instrument for both GPS and BDS, the ionosphere-free combinations are formed with P1 and P2 for GPS, and B1I and B2I for BDS. The tropospheric delays are calculated by empirical model. The procedure of the time difference calculation is introduced in [6]. Using these 1-second time differences, the CGGTTS files for GPS and BDS could be generated, as well as the RINEX files [7].

C. Observation Schedule

Though CGGTTS V2E is compatible with the old version, the start time for each observation period is changed because of the 4-minutes offset every day. It is complicated to know which period the current observation belongs to. In our design, the conventional CGGTTS schedule is modified. For convenience, we divide every hour into 20 periods, with the start time of the first period is 0':00''. Thus, there are 480 observation periods in a whole day, and the start time of each period does not change every day. It is easy to figure out which period the observation is in. The data from a SV is used only when the effective data is more than 100 during a 180s-period. Thus, big errors could be detected and removed, and the noise could be averaged to a relative low level. Besides, 3 minutes is a proper toleration time for most near real-time applications.

III. OVERVIEW OF BEIDOU RDSS COMMUNICATION

The GEO satellites of Beidou System could provide Radio Determination Satellite Service (RDSS) which supports data communication. There are several different levels of communication priority. The highest priority of Beidou RDSS could transmit data every second, with 1680 bits in a message. It must be authorized and supported by Chinese military organizations. With a common civil SIM card and device, users could send short messages with a period no less than one minute, with 616 bits in a message. Table I and Table II show the transmitting and receiving data format of Beidou RDSS.

TABLE I. TRANSMITTING DATA FORMAT OF BEIDOU RDSS

Head	Length	Tx Address	Class	Rx Address	Message Length	Response Status	Message	Check sum
$TXSQ	16bit	24bit	8bit	24bit	16bit	8bit	Up to 1680bit	8bit

TABLE II. RECEIVING DATA FORMAT OF BEIDOU RDSS

Head	Length	Rx Addr	Class	Tx Addr	Tx Time		Message Length	Message	CRC indicator	Check sum
					h	min				
$TXXX	16bit	24bit	8bit	24bit	8bit	8bit	16bit	Up to 1680bit	8bit	8bit

A. RDSS communication latency test

A test was done to validate the latency of Beidou RDSS. Fig. 2 shows the latency statistics. From the result, we could see that most messages could be received in 3s. However, several messages are delayed obviously, even up to over 10s.

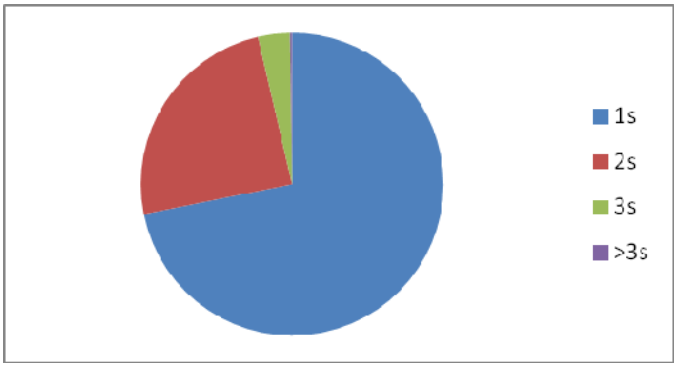


Fig. 2. The Beidou RDSS latency statistics

B. RDSS communication instrument

Using civil Beidou RDSS, BIRMM (Beijing Institute of Radio Metrology and Measurement) has put forward a method, allowing the comparison of atomic clocks near real-time. Fig.3 shows the civil SIM card, module and antenna for Beidou RDSS communication.

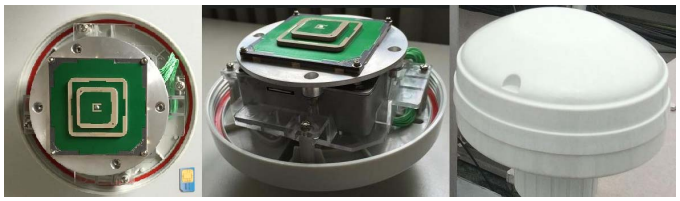


Fig. 3. The Beidou RDSS communication module and Antenna

The instantaneous power assumption of the communication module could reach 50W when transmitting data, so it is assembled in the antenna. Also the power supply must be guaranteed; otherwise the possibility of data lost would be increase. Fig.4 shows the power supply and interface unit of Beidou RDSS.

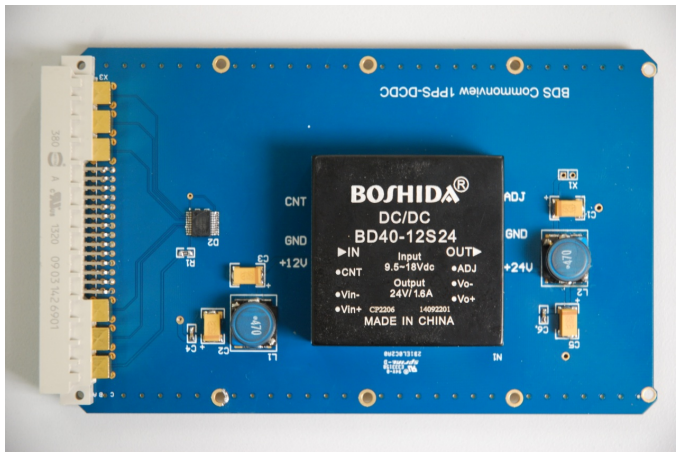


Fig. 4. The power supply and interface unit of Beidou RDSS

IV. BEIDOU RDSS TIME TRANSFER PROTOCOL

For most users, it is difficult to apply a military RDSS authorization. So the protocol is based on the general civil communication standard, with limited 616 bits in a message. Since there is possibility of large latency up to 10s and the civil RDSS communication period is no less than 1 minute, the period of our time transfer protocol is defined 90s.

A. Lab Information

The "Lab Information" in our protocol is similar as the CGGTTS file header, with some parameters omitted, contains some basic and important information of the labs, including:

HEADER: the header of "Lab Information", 4 bytes;

LAB_ID: acronym of the laboratory, 4 bytes;

COORDINATE: coordinate X, Y, Z, in the ITRF of the antenna phase center for GPS L3 and BDS B3 (combination of B1 and B2), in 0.01m, 24 bytes in total;

REFDELAY: time delay between the local 1PPS reference point and the receiver 1PPS input, in 0.1ns, 2 bytes;

INTDELAY: receiver hardware delay, there are 4 values for our instrument, GPS P1/P2 and BDS B1I/B2I, in 0.1ns, 8 bytes in total;

CABDELAY: delays from the antenna to the main unit, in 0.1ns, 2 bytes;

CKSUM: The checksum of the "Lab Information", 1byte.

"Lab Information" is exchanged right after the communication link established. One station sends the local information to the remote station. When the remote station receives this information, it replies a confirmation message, and vice versa.

During the time comparison, any station could send "Lab Information" request at the message transmitting time, the request has the highest priority and would occupy the chance of data exchange. And the remote station needs to reply the request first. For efficiency, the local site needs not to confirm.

B. Comparison Data

Because of the limited civil RDSS communication capacity, our protocol only contains the basic data for time comparison which has to be compressed in binary. For a time comparison format, the necessary parameters include number of tracked SV, the start time of each observation (MJD and time), calculated time differences for the specified observation types of each SV. Table III and Table IV describe the comparison data format and the definition of observation types.

For a GNSS system, the microsecond parts of the time differences between local time and the GNSS system time from different SVs are almost the same, so we use "REFSYS_us" in our protocol to represent the common microsecond part. The nanosecond parts are different from different SVs, so we define "REFSYS_ns" to represent this part. The combination of these two part forms the final time difference result. Thus, more bits could be saved to transfer more observations.

TABLE III. TIME TRANSFER MESSAGE BY BEIDOU RDSS

Index	Field	Description		Number of Bit
1	Header	The header of the message		32
2	Num	The number of observations N		8
3	MJD	Start Time of the Observation	Day in MJD	16
4	STTIME		Time in second of day	20
5	REFSYS_us	The microsecond part of time difference between local time and GNSS time		20
6	PRN	The GNSS observation (Repeated N times)	PRN of the satellite	8
	REFSYS_ns		The nanosecond part of time difference between local time and GNSS time	13
	FRC		Observation types (See Table II)	3
7	CRC	The checksum of the message		8

TABLE IV. BINARY CODE FOR DIFFERENT OBSERVATION TYPES

Observation Types	L1C	L1P	L2P	L3P	L5P	B1C	B2C	B3P
Binary Code	000	001	010	011	100	101	110	111

In a message of 616 bits, up to 21 observations could be transferred to the remote site. To improve the time transfer performance, the L3P and B3P combination observations are the prior exchanged data. Other observation types also could be transferred if there are enough spare bits.

In a 180s observation period, the time comparison data could be exchanged twice, one for GPS and the other for BDS. The GPS and BDS data are transferred separately. The satellite system could be distinguished from the header and PRN in the message.

After the message from the remote site is received, it is decoded according to the protocol. The data of a common SV from both sites are picked out to calculate a time difference. Since there may be several common-view SVs, the time differences from all common-view SVs are averaged to synthesize a final time difference between the two labs. If the common-view SVs are less than 4, a result would be synthesized from the observations from a single site, and then the time difference between the two labs could be obtained. There are two time comparison results, one from GPS, and the other from BDS.

V. EXPERIMENT

A zero-baseline common-clock experiment has been done with the near real-time GPS/BDS time transfer instruments, as shown in Fig.5. The two devices use the same GNSS antenna signal distributed by a GNSS amplifier and distribution unit. The external reference frequency signals are from a same hydrogen maser, while the 1PPS signals are from the UTC distribution unit. The REFDELAY of the two cables are calibrated by a TIC and all the calibration parameters are preset in the system.

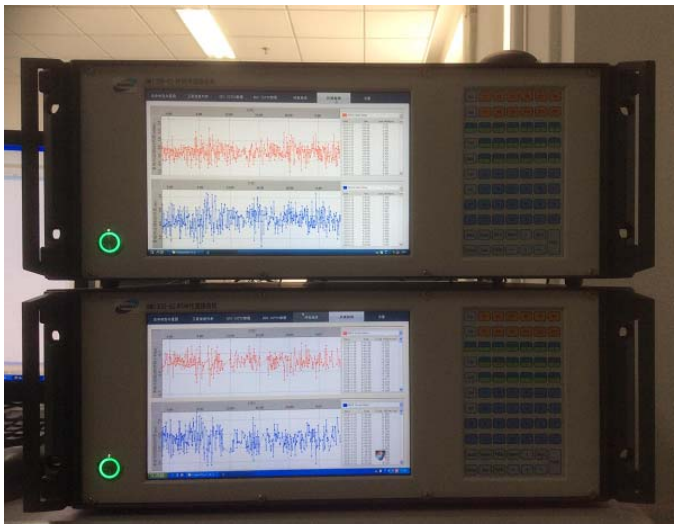


Fig. 5. The zero-baseline common-clock experiment

Fig.6 is the 24h test results, red for GPS and blue for BDS. The standard deviation from GPS is 1.5ns, while it is 1.1ns from BDS.

Some exchanged data between local and remote sites might be lost during the communication. Generally, the availability could exceed 95%.

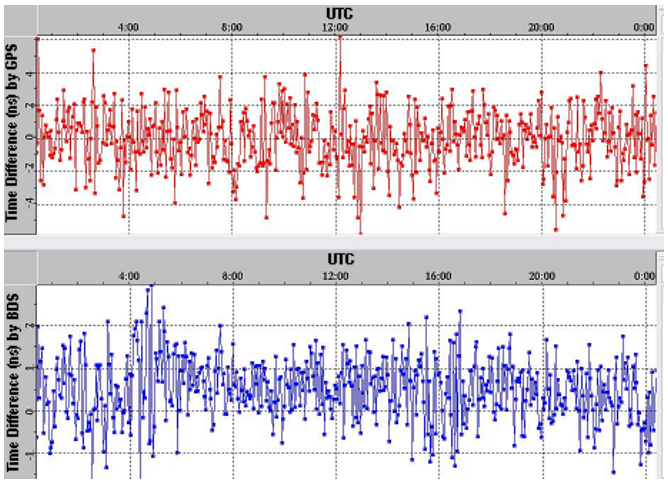


Fig. 6. The results of near real-time GPS/BDS time transfer

Fig.7 shows the result of zero-baseline common clock experiment from CGGTTS GPS L3 observations post-processing. The standard deviation is 0.93ns. The jumps may worsen the result.

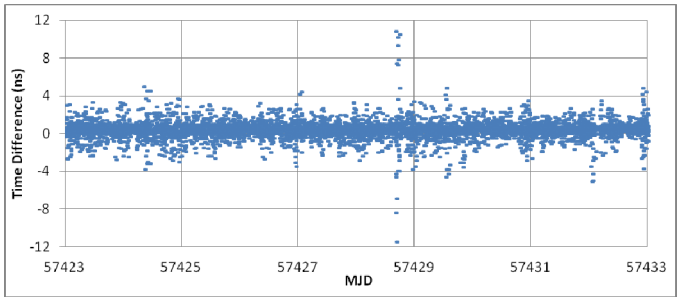


Fig. 7. The zero-baseline common clock result from CGGTTS GPS L3

By comparing our proposed method and conventional CGGTTS standard, it could be seen that the performances are at the same level for zero-baseline common clock. More tests should be done to verify the performance of our method for longer base-line.

VI. SUMMARY AND DISCUSSION

The quasi real-time time transfer technique is needed in many industrial applications. GNSS is still the best way to realize it. With the development of communication technology and equipment, the combination of traditional time transfer receiver and communication module is the future development trend. Our design has verified this preliminary feasibility. By proper definition, the near real-time GNSS time transfer could reach the performance of conventional way.

There are many ways that could implement GNSS time data exchange. The access of mobile Internet for a time transfer receiver could be flexible. With an unlimited communication capacity, all the information could be exchanged even without coding and compressing. Our protocol could be expanded and modified. In the future, the Beidou RDSS communication module may be instead by a LTE module.

REFERENCES

[1] P. Defraigne, G. Petit, “CGGTTS-Version 2E: an extended standard for GNSS Time Transfer,” Metrologia 2015, 52, G1.

[2] P. Defraigne, W. Aerts, E. Pottiaux, “Monitoring of UTC(k)’s using PPP and IGS real-time products,” GPS Solution, 2015, vol. 19, pp.165–172.

[3] K. Liang, A. Zhang, “UTC time link calibration in the frame of APMP-Campaigns in 2014-2016 ,” unpublished.

[4] H. Wang, H. Yi, S. Zhang, “The study of Beidou timing receiver delay calibration,” Proceedings of 2015 Joint Conference of IFCS & EFTF, pp.541-544.

[5] O. Montenbruck, A. Hauschild, P. Steigenberger, “Differential code bias estimation using multi-gnss observations and global ionosphere maps,” Proceedings of ION ITM 2014, San Diego, USA, 26–28 Jan.

[6] H. Yi, H. Wang, S. Zhang, “Research on time and frequency transfer based on BeiDou Common View,” Proceedings of 2015 Joint Conference of IFCS & EFTF, pp.553-556.

[7] H. Wang, H. Yi, S. Zhang, “The development of GPS/BDS time transfer system,” Proceedings of 2016 EFTF.

CLONETS – Clock Network Services

Strategy and innovation for clock services over optical-fibre networks

Przemysław Krehlik, Łukasz Śliwczyński
AGH University of Science and Technology
Cracow, Poland

Jiri Dostal, Jan Radil, Vladimir Smotlacha, Radek Velc, Josef Vojtěch
CESNET
Prague, Czech Republic

Mauro Campanella
Consortium GARR
Rome, Italy

Davide Calonico, Cecilia Clivati, Filippo Levi
Istituto Nazionale di Ricerca Metrologica
Turin, Italy

Ondřej Číp, Simon Rerucha
Institute of Scientific Instruments of the ASCR, v.v.i. (ISI)
Brno, Czech Republic

Ronald Holzwarth, Maurice Lessing
Menlo Systems
Martinsried, Germany

Fabiola Camargo, Bruno Desruelle, Jean Lautier-Gaud
Muquans
Talence, France

Elizabeth Laier English, Jochen Kronjäger, Peter Whibberley
National Physical Laboratory
Teddington, United Kingdom

Paul-Eric Pottie, Richard Tavares, Philip Tuckey
LNE-SYRTE, Observatoire de Paris, PSL Research University, CNRS, Sorbonne Universités, UPMC
Paris, France
contact@clonets.eu

František John, Milan Šnajder, Jiří Štefl
OPTOKON a.s.
Jihlava, Czech Republic

Paweł Nogaś, Robert Urbaniak
Piktime Systems sp. z o.o.
Poznan, Poland

Artur Binczewski, Wojbor Bogacki, Krzysztof Turza
Poznan Supercomputing and Networking Center
Poznan, Poland

Gesine Grosche, Harald Schnatz
Physikalisch-Technische Bundesanstalt
Braunschweig, Germany

Emilie Camisard, Nicolas Quintin
Réseau National de Télécommunications pour la Technologie, l'Enseignement et la Recherche
Paris, France

Javier Diaz, Trinidad García, Eduardo Ros
Seven Solutions S.L.
Granada, Spain

Alessandro Galardini
Conzorzio Torino Piemont Internet Exchange
Turin, Italy

Alwyn Seeds, Zhen Yang
University College London
London, United Kingdom

Anne Amy-Klein
LPL, Université Paris 13, CNRS
Villetaneuse, France

This project receives funding from the European Union's Horizon 2020 research and innovation programme under grant agreement no. 731107.

***Abstract*—Methods for long-distance time and frequency transfer over optical fibres have demonstrated excellent performances and are evolving rapidly. CLONETS is a new European Union-funded coordination and support action intended to accelerate the transfer of these technologies to industry and to strengthen the coordination between research infrastructures and research and education network providers, in order to prepare the deployment of this technology for a sustainable, pan-European fibre network, providing high-performance clock services to European research infrastructures and supporting wider services to industry and society.**

Keywords—optical fibre, network, clock, time, dissemination, service

I. INTRODUCTION

As is well-known, long-distance time and frequency transfer methods based on optical fibre links have evolved rapidly in recent years, demonstrating excellent performance for frequency transfer and considerable promise for accurate time transfer. They are attractive both for very high-performance applications such as optical clock comparisons, and for many industrial and societal applications, as an alternative and complement to radio- and satellite-based methods.

Such high-performance links have been developed and are operating in several countries in Europe, including a small number of cross-border connections. These developments have attracted a wide range of financial support, at both the national and European Union levels, for example through the European metrology research programmes EMRP and EMPIR. Nevertheless, the high cost of optical fibre rental can be a challenge to the perenniality of these links.

CLONETS is a new, European Union-funded project which aims to prepare the transition from the present situation toward a permanent, pan-European, optical fibre-based network providing time and frequency comparisons and distribution at the highest performance levels for research infrastructures, as well as support to a wide range of services for industry and society.

II. CLONETS ACTIVITIES AND OBJECTIVES

CLONETS brings together a diversified group of actors: National Metrology Institutes (NMIs), academic research groups, National Research and Education Network providers (NRENs), an internet exchange and small and medium-sized high-technology companies. Although it does not, for practical reasons, include the totality of the leading European contributors, its participants concentrate a very wide range of expertise and activities in this area.

CLONETS is a coordination and support action, whose function is to identify scenarios and prepare strategies for the future evolution of optical fibre-based time and frequency networks. Its main objectives may be summarized as follows:

a) collect information on future needs of research infrastructures and on key optical fibre telecommunications and time and frequency transfer technologies expected to have a growing impact;

b) study industrial and societal applications beyond research infrastructures, identifying stakeholders and their needs and estimating the potential economic and societal impacts of possible developments;

c) define strategies to support future work, including scenarios for the implementation and management of a core pan-European network and roadmaps for the industrial transfer of the corresponding technology and the development of new commercial products to support the network;

d) contribute to the training of highly-skilled specialists needed to support these developments and to the policy processeses necessary for their realisation;

e) study the possible contractual and commercial arrangements necessary for the running of such services.

CLONETS will consult widely among research infrastructures including NMIs, and industrial and societal user groups, in order to anticipate the future needs and opportunities for optical fibre-based time and frequency distribution.

CLONETS is an action under the Horizon 2020 European Research Infrastructures work programme. As such it is anticipated that its findings and propositions feed into later stages of this work programme and lead to further EU-supported actions, with the aim of implementing a pan-European optical fibre time and frequency network.

III. INITIAL WORK

The CLONETS project started at the beginning of 2017. Information about the project may be found at the website www.clonets.eu. Work has started on a number of subjects. One theme concerns scientific and technical reviews of central subjects including methods developed for high-performance time and frequency transfer over optical fibre; current installed telecommunications equipment, particularly in the national research and education networks; trends and evolutions in telecommunications methods and technology, and the interplay between these subjects.

Another direction of work is the preparation of comprehensive surveys of needs and applications for time and frequency transfer over optical fibre. Two surveys will be carried out, one aimed at research infrastructures and the second for a wide range of other application areas including government, industry, societal, etc. The survey results will help to define the contours of the future optical fibre network for time and frequency and the services it will support. Information about these surveys and how to participate in them is available at the address www.clonets.eu/clonets-news.html.

A Masters programme and short training courses are also in development.

Influence of UTC Parameters Generating Method on BDS Positioning Accuracy

Dandan Li[1,2,3], Longxia Xu[1,2], Xiaohui Li[1,2], Bo Li[1,2,3]
1National Time Service Center, Chinese Academy of Sciences, Xi'an, Shaanxi, China
2Key Laboratory of Precision Navigation and Timing Technology, Chinese Academy of Sciences, Xi'an, Shaanxi, China
3University of Chinese Academy of Sciences, Beijing, China
e-mail: leedanvip@163.com

***Abstract*—Based on analysis of existing UTC parameters generating method, a new method for generating UTC parameters is proposed. Only changing the way of generating UTC parameters, the timing precision is improved from the level of tens of nanoseconds to nanoseconds when using the proposed method. And the positioning accuracy is also improved. In the paper, influence of the proposed method on BDS positioning accuracy is analyzed in theory and then the experiment platform is built and the improvement of user positioning accuracy is verified by the short baseline and long baseline experiment. Results show that the positioning accuracy of Lintong and Sanya users is improved after using the traceability method proposed in this paper.**

Keywords—BeiDou Satellite Navigation System; Time Bias; UTC Parameters; Positioning Accuracy

I. INTRODUCTION

At present, the timing accuracy of satellite navigation system is the highest and it is tens of nanoseconds when providing broadcast timing service. For users requiring timing accuracy of nanoseconds, there is no timing system meeting their demands. So they can only rely on the common-view time transfer and two-way satellite time frequency transfer[1][2]. But these methods are high cost, limited real-time and user capability[3][4].

In 2016, the author proposed a new method of generating BDS UTC parameters. The principle is introduced and comparison test is carried out to verify the timing accuracy of the method[5].

At present, the positioning accuracy of BeiDou satellite navigation system is better than 8 meters. In this paper, influence of the proposed method on BDS positioning accuracy is analyzed in theory and the experiment platform is built and then the short baseline and long baseline experiments are carried out which verify the improvement of user positioning accuracy by using the proposed method.

II. POSITIONING PRINCIPLE

Fig. 1 shows the principle of BDS UTC parameters generating method. Station A represents National Time Service Center, Chinese Academy of Sciences and station B represents the user.

ρ_m is the pseudo-range of BeiDou satellite which is measured at National Time Service Center. Its expression is shown in formula (1). The reference of base station receiver is UTC(NTSC).

$$\rho_m = r_m + c\cdot(\delta t_m - \delta t^s) + I_m + T_m + c\cdot\varepsilon_m \tag{1}$$

r_m is the geometric range between the BeiDou satellite and the base station receiver. δt_m is receiver clock offset. δt^s is satellite clock offset. I_m is ionospheric delay. T_m is tropospheric delay. ε_{m} is other errors.

After correcting for these effects, we can get the time bias between UTC(NTSC) and the system time broadcast by BeiDou satellite and then the UTC parameters are generated[5]. $\Delta\rho_{\mathrm{m}}$ is the value after correction.

$$\Delta\rho_m / c = UTC(NTSC) - BDT_{svi} + \varepsilon_m^{'} \tag{2}$$

$\varepsilon_m^{'}$ includes satellite clock errors, satellite ephemeris errors, ionospheric delay correction errors, tropospheric delay correction errors and other errors.

The user obtains pseudo-range observations of visual BeiDou satellites and then using the satellite clock offset, the ionospheric delay, the tropospheric delay and the Sagnac effect for correction, ρ_i' is obtained.

$$\begin{cases} \rho_1' = D_1 + c\cdot\left(b_B - BDT_{sv1}\right) + \varepsilon_1^B \\ \rho_2' = D_2 + c\cdot\left(b_B - BDT_{sv2}\right) + \varepsilon_2^B \\ \rho_3' = D_3 + c\cdot\left(b_B - BDT_{sv3}\right) + \varepsilon_3^B \\ \rho_4' = D_4 + c\cdot\left(b_B - BDT_{sv4}\right) + \varepsilon_4^B \end{cases} \tag{3}$$

D_i is the geometric range between BeiDou satellite and the user. b_B is user's local time. BDT_{svi} is the system time broadcast by BeiDou satellite i . ε_i^B includes satellite ephemeris and satellite clock errors, ionospheric delay correction errors, tropospheric delay correction errors and other errors.

Fund project：The National Natural Science Foundation of China(Grant No.11503030); The National Defense Innovation Foundation of China (Grant No.CXJJ-16M205)

According to equation (3), user's positioning results can be obtained.

The time bias can be predicted using the UTC parameters corresponding to each BeiDou satellite which is generated though the proposed method. Equation (4) shows the predicting time bias. The user can carry out the second correction which is shown in equation (5). According to equation (5), we can obtain the positioning result using the proposed method.

$$\begin{cases} \Delta T_1 = UTC(NTSC) - BDT_{sv1} + \varepsilon_1^A / c \\ \Delta T_2 = UTC(NTSC) - BDT_{sv2} + \varepsilon_2^A / c \\ \Delta T_3 = UTC(NTSC) - BDT_{sv3} + \varepsilon_3^A / c \\ \Delta T_4 = UTC(NTSC) - BDT_{sv4} + \varepsilon_4^A / c \end{cases} \tag{4}$$

$$\begin{cases} \rho_1'' = \rho_1' - c \cdot \Delta T_1 = D_1 + c \cdot (b_B - UTC(NTSC)) + \varepsilon_1^B - \varepsilon_1^A \\ \rho_2'' = \rho_2' - c \cdot \Delta T_2 = D_2 + c \cdot (b_B - UTC(NTSC)) + \varepsilon_2^B - \varepsilon_2^A \\ \rho_3'' = \rho_3' - c \cdot \Delta T_3 = D_3 + c \cdot (b_B - UTC(NTSC)) + \varepsilon_3^B - \varepsilon_3^A \\ \rho_4'' = \rho_4' - c \cdot \Delta T_4 = D_4 + c \cdot (b_B - UTC(NTSC)) + \varepsilon_4^B - \varepsilon_4^A \end{cases} \tag{5}$$

Comparing equation (3) and (5), it is found that the pseudo-range is corrected again after using the new model parameters. With the second correction, the satellite clock errors are completely counteracted and the satellite ephemeris errors and the errors in the transmission path are partly counteracted further, so that the positioning accuracy can be further improved.

By comparing the positioning results before and after using the proposed method with the precise coordinates of station B, improvement of the positioning accuracy is analyzed.

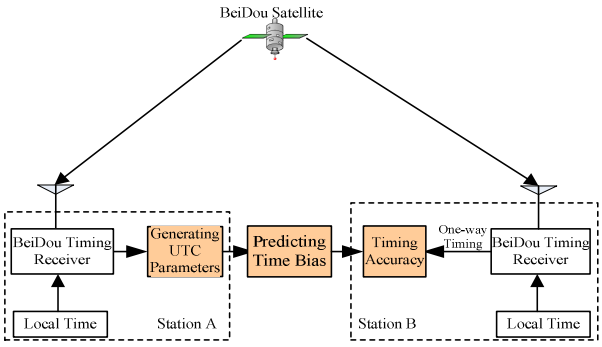


Fig. 1. Principle of BDS UTC parameters generating method

III. THE POSITIONING RESULTS OF LINTONG USER

According to equation (3), user's position can be calculated. Comparing the calculated result with user's precise position, positioning errors are obtained which is shown in Fig. 2.

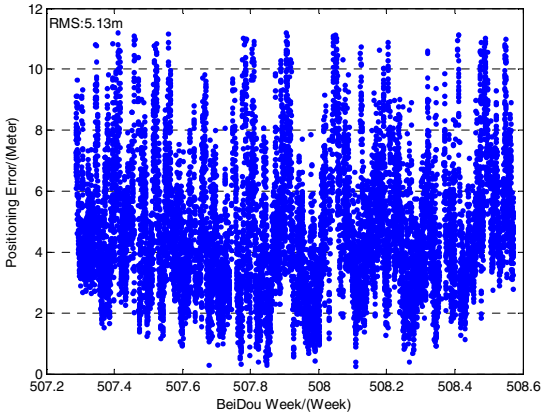


Fig. 2. Positioning errors of Lintong user

As can be seen from Fig. 2, the positioning error of Lintong user is 5.13 meters.

According to equation (5), user's position after using predicting time bias can be obtained. The root mean square of the Lintong users' positioning errors are shown in Table 1. S_len is the smoothing data length and P_len is the predicting data length and their unit are both minute.

As can be seen from Table 1:

1.When the smoothing data length is constant, with the increase of the predicting data length, the positioning errors of Lintong users are increased except few cases.

2.When the predicting data length is constant, with the increase of the smoothing data length, the positioning errors of Lintong users are gradually reduced. However, there are some individual cases.

3. When the smoothing data length and predicting data length are within a certain range, the positioning errors of the Lintong users calculated according to equation (5) are smaller than that calculated by equation (3).

IV. THE POSITIONING RESULTS OF SANYA USER

Using the same analysis method, positioning errors of Sanya user are obtained. Results calculated by equation (3) are shown in Fig. 3. Results calculated by equation (5) are shown in Table 2.

As can be seen from Fig. 3, the positioning error of Sanya user is 4.98 meters.

The meaning and unit of parameters in Table 2 are the same as that in Table 1.

As can be seen from Table 2:

1. With the increase of the predicting data length, the positioning errors of Sanya users are increased except few cases when the smoothing data length is constant.

2.When the predicting data length is constant, with the increase of the smoothing data length, the positioning errors of Sanya users are gradually reduced.

3. Only the smoothing data length and predicting data length are within a certain range, the positioning errors of Sanya users calculated according to equation (5) are smaller than that calculated by equation (3).

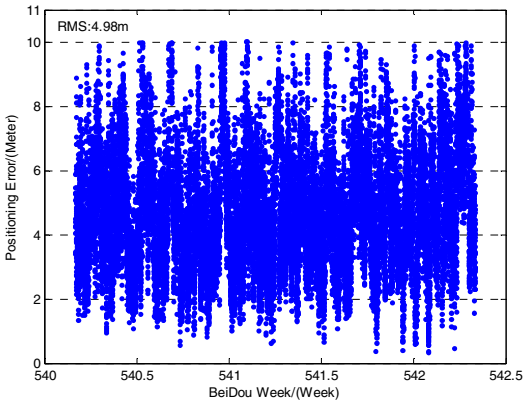


Fig. 3. Positioning errors of Sanya user

V. CONCLUSION

At present, the positioning accuracy of BeiDou satellite navigation system is better than 8 meters. After using the UTC parameters generated by the proposed method, pseudo-range is corrected again. So that the satellite clock errors are completely counteracted and the satellite ephemeris errors and the errors in the transmission path are partly counteracted further, and then the positioning accuracy can be further improved. In addition, since there is no change in the navigation message, it has no effect on the user receiver.

REFERENCES

[1] Mi I. Review of two-way satellite time and frequency transfer[J]. MAPAN-Journal of Metrology Society of India, 2006, 21 (4): 243-248.

[2] Ju L. A review of time and frequency transfer methods[J]. Metrologia, 2008, 45 (6): 162-174.

[3] Xu Longxia, Li Xiaohui, Xue Yanrong, et al. Study of a new one-way timing method[J]. Science China Physics Mechanics & Astronomy, 2012, 55 (55): 2476-2481.

[4] Xu Longxia, Li Xiaohui, Xue Yanrong, et al. A new timing method based on common-view[C]. 2012 IEEE International Frequency Control Symposium, Baltimore, MD, United States, May 21-24, 2012.

[5] Li Dandan, Xu Longxia, Zhu Feng, et al. A New Method of Generating UTC Parameters for BeiDou Navigation Satellite System[J]. Journal of Astronautics, 2017, 38(4):367-374.

TABLE I. ROOT MEAN SQUARE OF LINTONG USER' POSITIONING ERRORS (UNIT: METER)

P_len / S_len	5	10	15	20	25	30	35	40	45	50	55	60
10	4.97	5.33	5.64	6.30	6.99	7.07	7.92	8.93	8.77	9.85	11	10.9
20	4.97	5.21	5.48	5.92	6.25	6.77	6.67	7.39	8.18	7.88	8.53	9.41
30	5.10	5.36	5.68	5.87	6.13	6.66	6.16	6.59	7.64	7.31	7.22	8.39
40	5.16	5.39	5.56	5.89	5.92	5.86	6.34	6.40	6.87	7	6.89	7.20
50	5.18	5.36	5.58	5.66	5.94	6	6.49	6.40	6.94	6.84	6.9	6.72
60	5.14	5.28	5.41	5.53	5.76	6	6.38	6.56	6.18	6.41	6.58	6.29
120	4.72	4.80	4.87	4.90	5.05	5.20	5.1	5.41	5.36	5.52	5.78	6.01
180	4.70	4.74	4.79	4.83	4.93	5.02	4.94	4.87	5.04	5.01	5.08	5.04
240	4.51	4.57	4.63	4.55	4.64	4.76	4.69	4.76	4.79	4.78	4.76	4.78
300	4.28	4.31	4.33	4.34	4.37	4.41	4.34	4.40	4.26	4.36	4.27	4.35
360	4.11	4.13	4.16	4.08	4.11	4.23	4.22	4.18	4.21	4.25	4.25	4.08
420	4.07	4.11	4.14	4.18	4.13	4.23	4.26	4.17	4.36	4.15	4.03	4.34
480	3.89	3.90	3.9	3.81	3.94	3.92	3.73	3.77	3.69	3.92	3.86	3.79

TABLE II. ROOT MEAN SQUARE OF SANYA USER' POSITIONING ERRORS (UNIT: METER)

P_len / S_len	5	10	15	20	25	30	35	40	45	50	55	60
10	5.09	5.5	6.06	6.38	7.05	7.81	8.39	8.53	9.26	9.98	10	11
20	5.02	5.26	5.48	5.88	6.01	6.38	6.75	6.89	7.35	7.51	8.12	8.13
30	4.96	5.13	5.3	5.55	5.73	5.99	6.19	6.58	6.62	7.01	7.4	7.07
40	4.87	5.01	5.17	5.36	5.58	5.62	5.98	6.24	6.06	6.6	6.75	6.49
50	4.83	4.95	5.08	5.25	5.41	5.51	5.69	5.98	5.89	6.18	6.15	6.37
60	4.81	4.93	5.04	5.18	5.27	5.39	5.57	5.7	5.76	5.96	6.02	6.12

Monitoring of Time Signals Broadcast by EFR Long-Wave Transmitters at PTB

Bernhard Sbick
EFR Europäische Funk-Rundsteuerung GmbH
80335 München, Germany
sbick@efr.de

Klaus Katzmann
HKW-Elektronik GmbH
99848 Wutha-Farnroda, Germany

Egle Staliuniene, Dirk Piester, and Andreas Bauch
Physikalisch-Technische Bundesanstalt (PTB)
Bundesallee 100, 38116 Braunschweig, Germany
Andreas.bauch@ptb.de

***Abstract*—We report on a new means for obtaining time information via long-wave signals, provided by Europäische Funkrundsteuerung GmbH (EFR) via three transmitters located at Mainflingen, Germany (129.1 KHz), Burg, Germany (139.0 kHz), and Lakihegy, Hungary (135.6 kHz), respectively. The signals are received and continuously monitored by Physikalisch-Technische Bundesanstalt, PTB, in Braunschweig.**

Keywords—time dissemination, long-wave transmitter, legal time

I. SUMMARY

Time-of-day information is needed in many applications in the fields of power network management, smart metering, traffic monitoring and control. In Germany, the Units and Time Act prescribes the use of legal units in official and commercial transactions, and the date and the time must be used in accordance with legal time as realized and disseminated by Physikalisch-Technische Bundesanstalt (PTB).

For over 20 years in Europe, the Europäische Funkrundsteuerung GmbH (EFR) has been using three long wave transmitters for the encrypted transmission of various data services. Originally these stations were used exclusively for the transmission of control commands and tariff information in service of utilities to support tariff, load and generation management in the electricity sector. HKW-Elektronik GmbH (HKW in short) has been engaged in developing receive technology for the service in order to support wider applications of the existing infrastructure since a few years.

At present the following three long-wave transmitters are involved:

DCF49, Location Mainflingen (near Frankfurt / Main), Germany, carrier frequency: 129.1kHz, operated on the same campus as the well-known German standard frequency and time-signal transmitter DCF77 for which PTB is providing the signals [1],

DCF39, Location Burg (near Magdeburg), Germany, carrier frequency: 139.0kHz,

HGA22, Location Lakihegy (near Budapest), Hungary, carrier frequency: 135.6kHz.

The three transmitters, each with a range of about 500 km, give reliable coverage over a large part of Central Europe. They use a "Frequency-Shift Keying" (FSK) modulation to embed the information of the different data services in the respective carrier frequency. With a transmission capacity of 200 baud these transmitters enable much faster data transmission than the "classic" technique of the AM modulated time signal transmitter, such as DCF77. The EFR transmitters now also broadcast time-of-day information derived locally and autonomously using GPS receivers at the transmitter sites and meteorological information. The time information is provided in two kinds of proprietary “telegrams”: (high-accuracy (HA) and low-accuracy (LA). The signals from the three transmitters share a common schedule regarding their transmission: A HA telegram is transmitted every two minutes, a LA telegram every 10 seconds.

EFR and PTB agreed to install a monitoring system for the EFR signals received at PTB which provides comparison of the timing information obtained with legal time as realized in the PTB time laboratory. To this end, an "EFR time-signal monitor" EZM-01 was developed by HKW under contract with EFR and installed in PTB, shown in Figure 1. It receives the signals from the three transmitters via an active loop antenna. The telegrams are extracted and compared with a DCF77 time-code signal representing legal time generated locally. This signal is in parallel used to monitor the DCF77 signals received in PTB. As a result, one obtains the time difference between time of reception of the telegram (including the time information contained) with respect to the time reference. The resolution of the measurement is 0.1 ms. To achieve this kind of accuracy, it is necessary to take into account the correct distance between PTB and the three transmitters, assuming that the signals received propagate via ground-wave.

EFR and PTB contractually agreed to provide the results of this monitoring in a dedicated bulletin which is publicly available at ftp.ptb.de/pub/time/bulletin/EFR. Supervision routines alert PTB and EFR staff via e-mail in case of missing signals as well as outliers in the received time information above an agreed threshold.

During February 2017, the time information contained in the LA telegrams of the three transmitters had a characteristic offset from the PTB reference time of about 50 ms for DCF39 and 100 ms for the DCF49 and HGA22, respectively. Much better agreement is found for the HA telegrams, where the mean offset is less than 0.1 ms and the about 710 values obtained during a day scatter between ±0.2 ms only. The number of erroneous LA results with an offset exceeding 0.5 s was 4 during the first three weeks of February for each signal and zero for the HA results.

On a regular basis PTB checks the proper function of the EFR time-signal monitor by intentionally introducing a time offset in the reference signal and watching the offset reported in the evaluation of the received telegrams.

Making use of these signals and its documentation provided by PTB, users in Germany and neighboring countries have one more means to relate their local clocks to German legal time. German legal time, on the other hand, is by construction very close to Coordinated Universal Time, except of the one or two hour(s) offset, depending on the time of the year.



Figure 1 EFR time-signal monitor and its host computer operated in PTB under the auspice of PTB's time dissemination working group.

REFERENCES

[1] D. Piester, A. Bauch, J. Becker, and A. Hoppmann, "Time and frequency broadcast with DCF77", Proc. 43rd Annual Time and Time Interval (PTTI) Systems and Applications Meeting, 14-17 Nov 2011, Long Beach, California, USA, pp. 185-196, 2012.

Calibration Method of TWSTFT Stations Equipped With SDR receivers

Tung Thanh Thai, Alberto Mura, Ilaria Sesia
INRiM
Istituto Nazionale di Ricerca Metrologica, Turin, Italy
Email: i.sesia@inrim.it

Joseph Achkar, Giovanni Daniele Rovera
LNE-SYRTE, Observatoire de Paris
- LNE - CNRS - UPMC, Paris, France
Email: daniele.rovera@obspm.fr

Following a pilot study initiated by the CCTF WG on TWSTFT and coordinated by the BIPM, since the summer of 2016 several laboratories have been testing a new type of TWSTFT receiving equipment based on a Software Defined Radio. This type of receiver has been developed with the aim of mitigate some of the time transfer instabilities observed in the TWSTFT links based on SATRE modem. One of the major feature of the SDR receiver is the low AM-PM conversion, thank to the particular design of the software correlator [1]. At present the SDR system is only used as a receiver in parallel with the regular TWSTFT SATRE system and the investigation is mainly focused on the instability improvement. Nevertheless, considering that in the frame of the TAI network the TWSTFT links are mostly used for their accuracy, it is useful to develop a calibration method for such devices to allow a direct comparison with the traditional links, and to investigate the long term instability.

In the ITU TWSTFT files [2] three variables are used to take in account the hardware delays. The REFDELAY parameter takes into account the delay between the internal timebase of a TWSTFT station and the local timescale. The CALR parameter, specific to each link (i. e. a couple of stations), considers all the delays of the links that are not compensated by the symmetry of the link. A third parameter, the ESDVAR, can be used in some case to include a voluntary change in the hardware of a station.

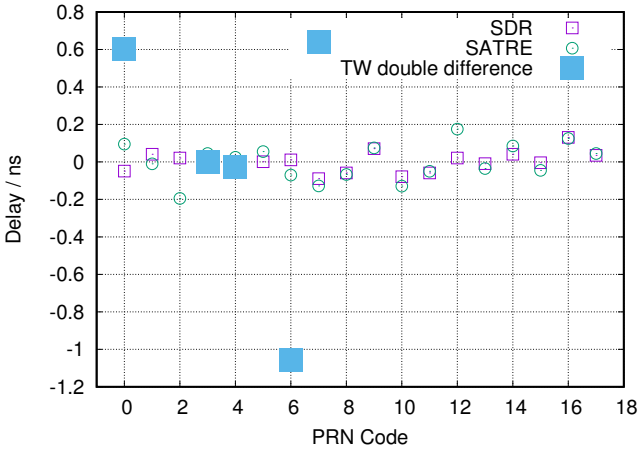
Within a station equipped with a SATRE modem the internal time base is generally materialized by the raising edge of a pulse generated by the modem itself, named PPS-TX. The REFDELAY is therefore easily measured by measuring the time difference between the PPS-TX and the reference point materializing the local time scale. For the SDR receiver such a signal representing the internal timebase is not available; therefore, it is necessary to find an indirect measurement of REFDELAY. The CALR, specific to each link, can be evaluated by a calibration campaign employing a mobile TWSTFT station, or by comparison with other time transfer techniques. In our analysis we build ITU TWSTFT/SDR files by using the same CALR of the nominal ITU TWSTFT/SATRE files and we take into account the delay due to the replacement of SATRE modem by the SDR receiver in the REFDELAY parameter.

This “virtual” REFDELAY is evaluated in two steps. The first step is to create ITU TWSTFT/SDR files with the CALR coefficient that are used in the nominal TWSTFT operation, by letting the REFDELAY value be 0. In the second step the difference between the nominal and SDR ITU files is performed for a given link. As a result we obtain the value to be inserted in the REFDELAY field of ITU TWSTFT/SDR file for the considered local TWSTFT SDR station. Such value should be valid for all the links for that station.

Applying the estimated REFDELAY parameter to perform data analysis, we noticed some differences of about 1 ns can be observed when comparing the time differences obtained for the nominal link and the ones obtained by using the SDR receiver at the local station. Such difference can be possibly due to the different delays of the modems corresponding to the different PRN codes, specific for each link. We thus measured the delay differences between the SATRE modem and the SDR receiver, for the PRN codes currently used in the TWSTFT.

Figure 1 shows the time difference between TWSTFT equipped with SATRE modem on both sides and with an SDR receiver on IT side, when the REFDELAY has been aligned on the IT-PTB link as previously described (blue squares). On the same figure are also displayed, with an arbitrary offset, the delays of PRN codes generated by a SATRE modem (circles) and received at the same time by a SATRE modem and SDR receiver(empty squares).

Fig. 1. Time delay of different PRN codes



978-1-5386-2916-1/$31.00 ©2017 IEEE

From this figure it is evident that both SATRE and SDR does not suffer from internal delay depending on PRN code, at least at the 100 ps level. We are currently investigating other possible causes of the observed time differences between SDR links calibrated as proposed in this paper. With this method the REFDELAY must be evaluated at every reset of the receiver, but once the first calibration has been performed in this way, the REFDELAY change can be easily monitored and corrected by measuring in a closed loop the code emitted by the local SATRE modem during the odd hour.

REFERENCES

[1] Y. J. Huang and H. W. Tsao, "Design and Evaluation of an Open-Loop Receiver for TWSTFT Applications," *IEEE Transactions on Instrumentation and Measurement*, vol. 64, pp. 1553–1558, June 2015.

[2] "ITU-R Recommendation TF.1153-4: The operational use of two-way satellite time and frequency transfer employing pseudorandom noise codes," tech. rep., ITU, 2015. Available at: https://www.itu.int/rec/R-REC-TF.1153-4-201508-I/en.

Reference signal distribution for the ACES microwave link ground terminal at SYRTE

M. Abgrall*, Ph. Laurent*, D. G. Rovera*
*LNE-SYRTE, Observatoire de Paris, PSL Research University, CNRS, Sorbonne Universités, UPMC Univ. Paris 06, France
Email: michel.abgrall@obspm.fr

***Abstract*—This paper presents the distribution system providing the UTC(OP) time and frequency reference signals to the microwave time transfer ground terminal (MWL-GT) of the Atomic Clock Ensemble in Space mission (ACES) at SYRTE. UTC(OP) is generated in the first floor of the building B. The MWL-GT will be installed on the top of the building A inside the campus of Observatoire de Paris, which offers the clearest field of view of the ISS passes. An ensemble of 6 optical fibers and coaxial cables installed between the two locations allows to transmit and monitor the reference signals and to calibrate the delays.**

I. Introduction

The ACES mission is based on the comparison of the on board time and frequency references made of the cold atom clock PHARAO [1] and the space hydrogen maser SHM, to state of the art atomic fountains and optical clocks located on ground in different laboratories, to perform experiments in metrology and fundamental physics. The payload will fly on board the International Space Station (ISS) with a launch scheduled in 2018. One of the two time transfer techniques developed for the mission is the two way microwave link MWL. The second technique is the laser time transfer ELT. The MWL performances should reach a time stability remaining below 10 ps over averaging periods of several days and an accuracy of 100 ps. Different ground terminals are being deployed at PTB in Germany, SYRTE in France, NPL in UK, NIST and JPL in USA, NICT in Japan.

II. Description of the System

At SYRTE, the reference signal distributed to the MWL-GT will be based on UTC(OP), that is generated from a hydrogen maser steered using atomic fountain calibrations [1], [2]. The UTC(OP) signal generation and distribution were completely rebuilt in 2015 with new equipments [3] specially designed to operate at 100 MHz in order to present a noise level compliant with ACES specifications. This system is in operation in the first floor of the building B inside the campus of Observatoire de Paris. The MWL-GT will be installed on the top of the building A, which offers the clearest field of view of the ISS passes. An ensemble of 6 optical fibers and coaxial cables installed between the two locations allows to transmit and monitor the reference signals and to calibrate the delays.

An overview of the system is given in Figure 1. The main 100 MHz signal is transmitted via a two way stabilized optical fiber link (fiber 5, uplink). This link is a simplified version of similar long-distance links [4]. The reference signal modulates the current of a 1.55 μm diode laser that is coupled to the fiber. At the remote end, a fast photodiode detects the intensity modulation and delivers the signal to the MWL-GT distribution system. A fraction of this recovered signal is used to modulate a second diode laser that is coupled back to the fiber. At the emission site, the returned signal is detected by another fast photodiode and then mixed with the reference signal to detect the phase variations imposed by the two propagation passes through the fiber. A temperature-controlled fiber spool of $\sim$ 200 m is inserted to control the length of the link to cancel these phase variations with a computer operated servo-loop that drives the current applied to a Peltier (time constant $\sim$ 10 s). At the remote site, the 100 MHz output is frequency divided to produce a 10 MHz signal for the clock of a 1 PPS generator. The system includes RF and 1 PPS distributor in order to provide the reference signals for two MWL-GT (the main station and a second similar one that will be installed for several weeks for relative calibration). A second stabilized fiber link (fiber 6, downlink), that sends back the 100 MHz signal from the MWL-GT distribution system to the UTC(OP) generation location, is operated to verify the operation consistency. Additional fibers and coaxial cables connecting the two sites are also available for 1 PPS signal synchronization and for delay calibrations.

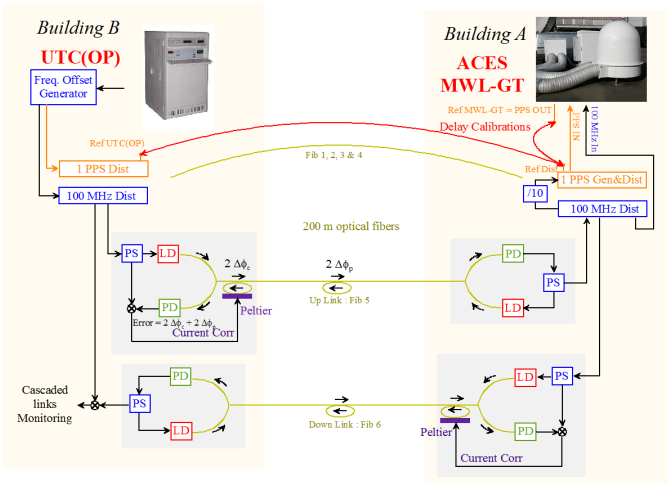


Fig. 1. Schematic view of the reference signal distribution to the MWL-GT at SYRTE

III. Stabilized Link Operation

Figure 2 shows the inloop phase error and the Peltier current correction of the up and down links respectively over

[1]Projet d'Horloge Atomique à Refroidissement d'Atomes en Orbite

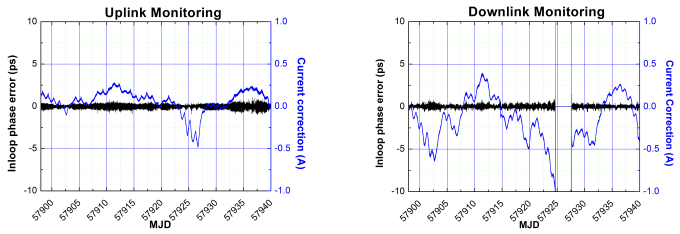


Fig. 2. Inloop error (black line) and Peltier current correction (blue line) for the uplink (left) and downlink (right), respectively.

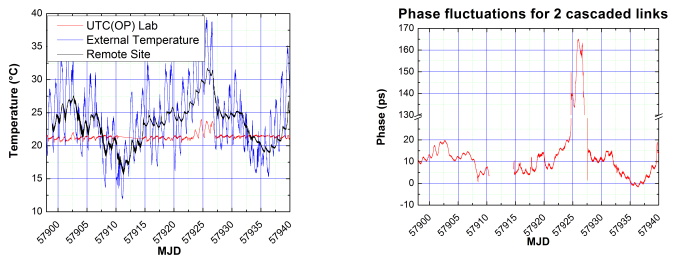


Fig. 3. Left : temperature measured in different locations; right: phase fluctuations of the two cascaded links.

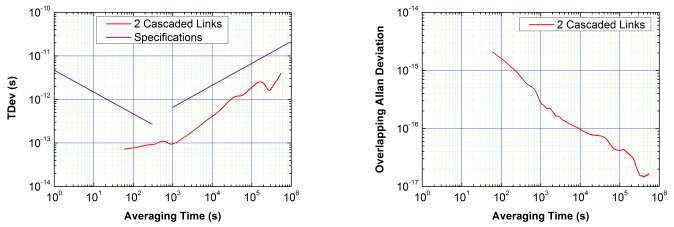


Fig. 4. Time deviation (left) and overlapping Allan deviation of the phase fluctuations of the two cascaded links.

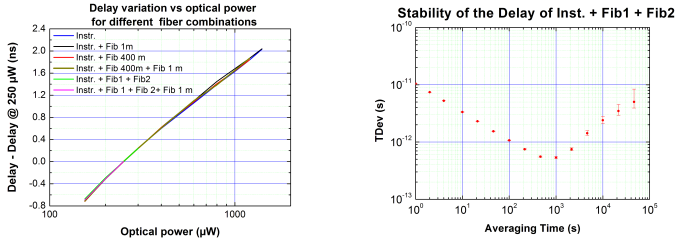


Fig. 5. Left: variation of the TimeLink Rx module as a function of the received optical power; right: stability of the transmitted 1 PPS signal via two unstabilized fibers.

a period of 40 d. The links have been designed to provide a phase correction range of ± 300 ps for an applied current of ± 1 A. The main link (uplink) remained continuously locked over the period whereas the monitoring link (downlink) went out of range between MJD 57925 and 57927, due to exceptionally hot weather. Indeed, the ambient temperature was not stabilized at the remote site and reached more than 30°C (Figure 3, left), which affected the fiber spool used for the stabilization of the downlink. The right part of Figure 3 shows that the phase fluctuations of the two cascaded links remained below ± 10 ps around an average value of 10 ps, if we except the two days period when the down link was not locked. This corresponds to an average frequency error in the 10^{-18} range. After the hot weather period, the downlink loop was closed again, without any phase adjustment, and the phase at the output of the two cascaded links recovered the same value. This was also tested in case of a power supply shut-down.

Figure 4 shows a stability analysis the two cascades links in terms of time deviation (left) and Allan deviation (right). The time stability is below 0.1 ps for averaging periods up to 1000 s and remains below 10 ps for averaging time of ~ 10 d, which is compliant with ACES specifications. The frequency stability reaches the 10^{-17} range for averaging periods larger than 10^4 s.

IV. Delay Calibration

The delay calibration aims at measuring the time difference between UTC(OP) reference point and that of the MWL-GT. For that purpose, we used 4 additional fibers connecting the two locations. To demonstrate the procedure before the MWL-GT installation, we present the results of the measurements between UTC(OP) and one of the 1 PPS outputs of the signal distribution at the remote site. The use of 1 PPS signals transmitted via coaxial cables for that purpose would lead to a significant uncertainty due to the distortion of the pulse rising time during propagation. This can only be used for resynchronization of the 1 PPS generation (rising time of several tens of ns after propagation in a ~ 200 m long cable). For the delay calibration, we used TimeLink laser modules (Tx and Rx) from Linear Photonics that allow transmitting 1 PPS signals via optical fibers. The jitter of these devices is of the order of 10 ps (see Figure 5, right). The 1 PPS output of the receiver presents a rising time of ~ 1 ns. The pulse is generated internally if the average input power is larger than a threshold of ~ 200 μW. We have characterized the sensitivity of the receiver delay as a function of the input optical power (Figure 5, left) using a fiber variable attenuator. The delay evolves in a ~ 3 ns range for the full range of attenuation. This was done using different fibers. We also verified that the variations of the delay introduced by the variable attenuator used for the measurement is lower than 20 ps (test using a laser diode with a 1 GHz amplitude modulation and a fast photodiode). Hence, the delay measurement system is composed of the Rx module, a variable attenuator, an optical power splitter with one output connected to the Rx module and the other arm connected to a power meter. Different combinations of fibers are inserted between the emitter output and the variable attenuator input, as shown in Figure 6. The attenuator is adjusted to get the same optical power level of 250μW to better than 1 μW thus compensating for the fiber attenuation and for the losses at the fiber connections. This ensures a reproducibility of the measurements of the order of a few tens of ps.

We used a differential calibration method composed of two steps as described in Figure 6. A first series of measurements is performed at the emitter site with different combination of fibers. For some of them a 1.5 m long fiber is used at the MWL-GT distribution site to connect two fibers. For this measurement series A, the Tx module is fed by an arbitrary 1 PPS output X of UTC(OP) distribution system. The output of the Rx module is connected to one channel of a high resolution

event timer (bandwidth 25 GHz, accuracy better than 1 ps, linearity error $<$ 300 fs rms), while the other one is connected to UTC(OP). All the measurements are performed at a trigger level of 1 V. The low uncertainty of the measurement is ensured by the use of short cables and high bandwidth event timer [5]. The results are given in Figure 7. The instrumental delay corresponds to the measurement with the variable attenuator directly connected to the emitter. Although only 3 different fibers are necessary for the method, the measurement was carried out with 4 fibers and also tested adding a 400 m long spool to verify the consistency of the results. Simple calculations provide de delay of each fiber. A standard deviation was also calculated confirming the repeatability of the measurements. Figure 5 (right) presents the delay stability for one of the fiber configurations. It remains well below 10 ps for averaging periods of 1 d even thought these fibers are not stabilized. This means that the calibration process can be done within a few hours with a negligible impact of the fiber thermal fluctuations.

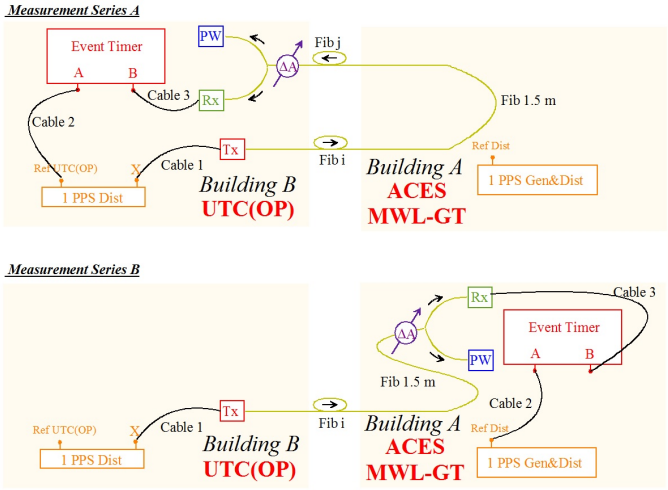


Fig. 6. Delay calibration procedure

Fiber combination	Delay (ns)
Inst	82.087
Inst +1.5 m	89.302
Inst + Fib1 +Fib 2 +1.5m	2021.195
Inst +Fib1 + Fib3 +1.5m	2024.173
Inst +Fib1 + Fib4 +1.5m	2021.424
Inst +Fib2 + Fib3 +1.5m	2023.021
Inst +Fib2 +Fib 3 +1.5m	2023.017
Inst +Fib2 + Fib4 +1.5m	2020.292
Inst +Fib3 + Fib4 +1.5m	2023.257
Inst +Fib1 +Fib 4 +1.5m + 400m	4004.431
Inst +Fib2 + Fib4 +1.5m + 400m	4003.29
Inst +Fib3 +Fib 4 +1.5m + 400m	4006.277

Fiber	Delay (ns)	std dev (ps)
1.5 m	7.215	N/A
400m	1983.008	11
Fib 1	966.518	5
Fib 2	965.376	5
Fib 3	968.3475	5
Fib 4	965.608	5

Fig. 7. Measurement series A results

In a second measurement series, the measurement system (starting from the variable attenuator) is transported and operated at the MWL-GT distribution system site with the same cable configuration, except that the second input of the event timer is connected to the 1 PPS distribution reference point. The raw measurement results for the different fibers are listed in Figure 8. Simple calculations provide the value of 2688.98 ns for delay between the 1 PPS distribution reference point and that of UTC(OP), with a standard deviation of 19 ps and pic to pic differences with respect to the average lower than ± 40 ps. Moreover, the calibration was repeated three weeks later. The same value was obtained within 20 ps.

This shows that with this calibration procedure, a goal of 100 ps for the combined uncertainty on the delay between UTC(OP) and that of the MWL-GT can be achieved.

Fiber combination	Delay(ns)
Inst + Fib3 +1.5 m	3746.647
Inst + Fib3 +1.5 m +400	5729.674
Inst + Fib1 +1.5 m +400	5727.806
Inst + Fib1 +1.5 m	3744.783
Inst + Fib2 +1.5 m	3743.666
Inst + Fib2 +1.5 m +400	5726.654
Inst + Fib2 +1.5 m +400 (connector test)	5726.638
Inst + Fib4 +1.5 m +400	5726.908
Inst + Fib4 +1.5 m	3743.878

Fig. 8. Measurement series B results

V. Conclusion

This paper describes the system implemented at SYRTE to provide the time and frequency reference UTC(OP) to the ACES MWL-GT. It is based on a simple and robust stabilized optical fiber link operating with laser diodes modulated at 100 MHz. The operation of a downlink demonstrates that the residual phase fluctuations are compliant with ACES specifications leading to frequency instability in the 10^{-17} range for averaging periods larger than 10^4 s. We also describe a procedure based on measurements with 1 PPS signals transmitted via additional fibers using TimeLink modules to calibrate the delay between the reference points of UTC(OP) and that of the ACES MWL-GT, that fulfils the goal of a 100 ps combined uncertainty.

References

[1] Rovera G D, Bize S, Chupin B, Guéna J, Laurent Ph, Rosenbusch P, Uhrich P and Abgrall M, "UTC(OP) based on LNE-SYRTE atomic fountain primary frequency standards," 2016 *Metrologia* **53** S81-S88

[2] Guéna J., Abgrall M., Rovera D., Laurent Ph., Chupin B., Lours M., Santarelli G., Rosenbusch, P., Tobar M., Li R., Gibble K., Clairon A. and Bize S., "Progress in atomic fountains at LNE-SYRTE," *IEEE Transactions on Ultrasonics, Ferroelectrics, and Frequency Control*, **59**, 2012, 391-409

[3] Rovera G., Abgrall M. and Siccardi M., "Characterization of an auxiliary offset generator for steering of H Masers," *Proc. of the 26th European Frequency and Time Forum (EFTF)*, 2012, 14-15.

[4] Daussy C., Lopez O., Amy-Klein A., Goncharov A., Guinet M., Chardonnet C., Narbonneau F., Lours M., Chambon D., Bize S., Clairon A., Santarelli G., Tobar M. E., and Luiten A. N., Long-distance frequency dissemination with a resolution of 1017, *Phys. Rev. Lett.*, vol. 94, no. 20, art. no. 203904, 2005

[5] Siccardi M., Rovera G. D., Römish S., "Time Delay Measurements: Estimation of the Error Budget," to be published in *Proc. of Joint Conf. IEEE Int. Frequency Control Symp. and European Frequency and Time Forum*, 2017.

Modeling time and frequency fiber links with bi-directional amplifiers using transmission matrixes

Ł. Śliwczyński, P. Krehlik, K. Salwik
Faculty of Computer Science, Electronics and Telecommunications
AGH University of Science and Technology
Krakow, Poland

***Abstract*—In the paper we present a method intended to use for optimization of the signal-to-noise ratio in fiber optic links for time and RF frequency transfer exploiting bi-directional amplifiers. The method is based on transmission matrixes and its main intention is to take into account the asymmetry of the propagation conditions of backscattered signals that is lacking in previously published models. Such asymmetry may be intentionally introduced in the link by adding wavelength-selective isolators to have additional level of control on the propagation of backscattered signals.**

Keywords—fiber optic link; bi-directional optical amplifier; frequency transfer; time transfer; Rayleigh backscattering

I. INTRODUCTION

Optical fibers, thanks to a very good symmetry when operated bi-directionally, are very well suited for precise time and frequency transfer. For covering distances greater than about 100 km optical amplifiers are necessary to compensate loss of the fibers. To preserve the symmetry of the link the optical amplifiers must be operated bi-directionally [1] that results, however, in amplification of undesired signals occurring mostly due to Rayleigh backscattering (see Fig. 1a) and amplified spontaneous emission (ASE) occurring in optical amplifiers. These are a source of noise when received by the photodiode, degrading the stability of the transmitted time/frequency signals or even causing malfunctioning of the link.

The signal to noise ratio (SNR) of the link may be optimized judiciously choosing the gains of the optical bi-directional amplifiers (OBA) [2], [3]. In the links with relatively long inter-amplifier spans it may be, however, difficult to obtain satisfactory results. In such cases the effective solution may be to apply a wavelength selective isolator (WSI, see Fig. 1b) that blocks the propagation of backscattered signals by introducing the asymmetry in the propagation of undesired forward and backward signals. Because any asymmetry inevitably increases the influence of temperature changes on the stability of the time/frequency signals (e.g. by affecting the chromatic dispersion of optical filters) the number of WSIs used should be limited to minimum and their position along the link should be determined.

This requires a model of the link, describing the propagation of the backscattered signals. The models of bi-directional link proposed in [2] and [3] and based on direct summation of various scattered powers have a drawback that they can not take into account the asymmetry of the propagation of signals in both directions.

II. MODEL BASED ON TRANSMISSION MATRIXES

The propagation of signals in the bi-directional fiber link may be conveniently described using the concept of transmission matrixes. In its basic form this formalism [4] ascribes a 2x2 matrix to each component of some system, where the propagation of forward and backward signals occurs. In case of the fiber link under discussion the matrix size have to be increased to 6 because the number of signals to be analyzed is greater, namely the main forward and backward signals, odd-scattered forward and backward signals and even-scattered forward and backward signals (see Fig. 1 for examples).

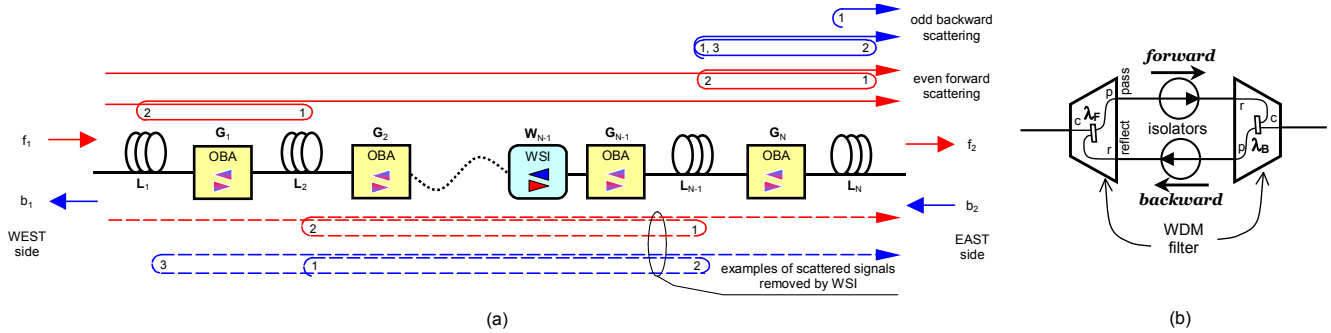


Fig. 1. Illustration of a bi-directional chain of optical amplifiers, showing propagation of backscattered signals (a) and internal structure of a WSI (b). Digits used on the lines showing various scattered signals are used to designate the number of each consecutive backscattering event.

This work was supported by Polish National Science Center under the decision DEC-2014/15/B/ST7/00471.

The transfer matrix **T** relates the west and eastside of the bi-directional fiber link accordingly to the relation:

$$\begin{bmatrix} f_1 \\ b_1 \\ f_1^o \\ b_1^o \\ f_1^e \\ b_1^e \end{bmatrix} = \mathbf{T} \begin{bmatrix} f_2 \\ b_2 \\ f_2^o \\ b_2^o \\ f_2^e \\ b_2^e \end{bmatrix}, \tag{1}$$

where symbols f and b denotes the main forward and backward signals, the subscripts '1' and '2' denote the west and east side of particular link component and the superscripts 'o' and 'e' are for the odd and even scattered signals, respectively. The resulting transmission matrix for the entire link is obtained by multiplying the matrixes of all individual components, starting from the most left component:

$$\mathbf{T} = \mathbf{L}_1 \cdot \mathbf{G}_1 \cdot \mathbf{L}_2 \cdot \mathbf{G}_2 \cdot \ldots \cdot \mathbf{W}_{N-1} \cdot \mathbf{G}_{N-1} \cdot \mathbf{L}_{N-1} \cdot \mathbf{G}_N \cdot \mathbf{L}_N , \tag{2}$$

where $\mathbf{L}$, $\mathbf{G}$ and $\mathbf{W}$ are the transmission matrixes for a fiber span, OBA and WSI, respectively. As an example, the form of the transfer matrix for a fiber span is presented in equation 3:

$$\mathbf{L} = \begin{bmatrix} 1/L & 0 & 0 & 0 & 0 & 0 \\ 0 & L & 0 & 0 & 0 & 0 \\ R/L & 0 & L & 0 & 0 & 0 \\ 0 & -R/L & 0 & 1/L & 0 & 0 \\ 0 & 0 & -R/L & 0 & 1/L & 0 \\ 0 & -R^2/L & 0 & R/L & 0 & L \end{bmatrix}, \tag{3}$$

where L and R denotes the loss of the span and the Rayleigh backscattering coefficient. This form was derived by analyzing equations relating various main and scattered signals.

III. Numerical Results

As an example a simulation of the link composed of 9 fiber spans with total attenuation of 117 dB and including 8 OBAs was performed (losses of the spans were assumed the same as in the fiber optic link connecting two Polish time laboratories, namely GUM in Warsaw and AOS in Borowiec). Using the model outlined in the abstract the optimal value of SNR without incorporating any WSI was estimated as 25.6 dB. Next the SNR was estimated assuming various numbers of WSIs distributed along the link (only some of all possible configurations were analyzed). The results are presented in Fig. 2. It may be observed that in our particular case single WSI improves SNR up to 2.2 dB, two WSIs up to 3.4 dB and three WSIs up to 4.4 dB. The conclusion that may be drawn is that in presented example using just a single WSI seems to be not sufficient and using of two of them is reasonable compromise. The best places for installation of WSIs are next OBAs number 3 and 6.

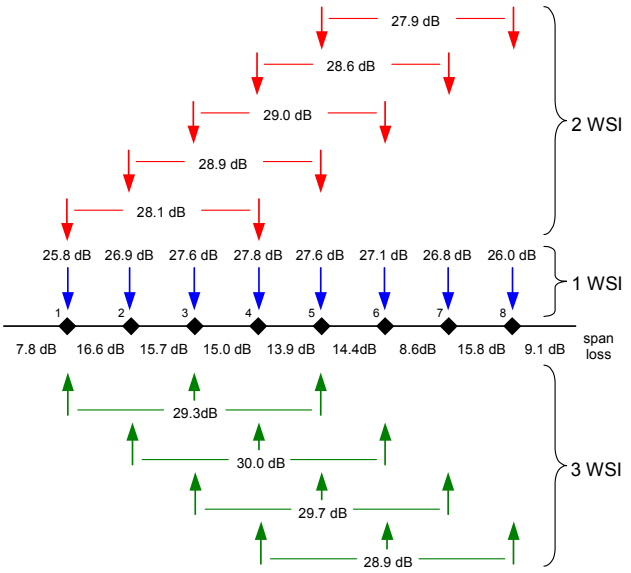


Fig. 2. SNR calculated at the ends of example link using various number of WSI distributed along the link.

IV. Summary

The proposed method is able to simulate the impact of asymmetry in propagation of various backscattered signals in bi-directional fiber optic link for time and frequency transfer on SNR. This is a useful tool for finding optimal gain settings of OBAs and analyzing the impact of WSIs for theirs various localizations. In this abstract only the outline of the model was presented to illustrate the general idea of applying transmission matrixes to model bi-directional fiber optic link. The full model that was used in presented numerical example includes also other effects, like e.g. propagation of ASE and conversion of laser phase noise into amplitude noise via fiber's chromatic dispersion, similarly as it was discussed in [3].

References

[1] Ł. Śliwczyński, P. Krehlik, Ł. Buczek, M. Lipiński, "Frequency transfer in electronically stabilized fiber optic link exploiting bidirectional optical amplifiers", IEEE Trans. Instr. and Meas., vol. 61, pp. 2573-2580, 2012.

[2] C. Delisle, J. Conradi, "Model of bidirectional transmission in an open cascade of optical amplifiers", J. Light. Techn., vol 15, pp. 749-757, 1997

[3] Ł. Śliwczyński, J. Kołodziej: „Bidirectional optical amplification in long-distance two-way fiber optic time and frequency transfer systems", IEEE Trans. Instr. and Meas., vol. 62, pp. 253-262, 2013.

[4] L. Coldren, S. Corzine, M. Mašanović, "Diode lasers and photonic integrated circuits", Hoboken, New Yersey, Willey, 2011.

Further results of time transfer through the optical fiber at NIM

Kun LIANG, Aimin ZHANG, Zhiqiang YANG
National Institute of Metrology
NIM
Beijing, China
Liangk@nim.ac.cn

Ye WANG, Jian WANG
Beijing Jiaotong University
BJTU
Beijing, China

Xiangwei ZHU, Huaming CHEN
National University of Defense Technology
NUDT
Changsha, China

***Abstract*—The performance analysis of TWOTFT with the two terminal equipments at the two remotes sites has been implemented and one way time transfer through optical fiber has been designed and the performance evaluation, demonstration, and verification experiments in short distance have been realized and its uncertainty has been evaluated as roughly 2.1 ns.**

Keywords—component; formatting; style; styling; insert (key words)

I. INTRODUCTION

Since 2015, the first results of time transfer in two ways through the optical fiber (TWOTFT) at NIM (National Institute of Metrology, Beijing, China) have been demonstrated [1]. The experiments in the real optical path of 109 km distance at most with two terminal equipments at one site and in the laboratory optical fiber roll have been implemented. The uncertainty of time transfer has been evaluated as less then 200 ps.

After that, we planned to use TWOTFT for one of time transfer links between the two campuses (Chanping campus and Hepingli campus, about 40 km away from each other) of NIM, thus the more experiments with the two terminal equipments separately at these two remote sites for verifying the further effectiveness of remote time transfer. The results by TWOTFT reference to the two different time and frequency sources could agree with those by GPS carrier phase time transfer as figure 1-3 shows.

Moreover, at NIM, the facilities of the timekeeping system have been distributed into three parts. The main part for generation of UTC(NIM) is operated at the Changping campus. And the facility for calibration and test service and some experimental facility for research and developing for new methods are separately located in the second floor and the fourth floor of one building at the Hepingli campus. Thus, it is needed for us to transfer the time signal of UTC(NIM) at the Changping campus to the other sites since UTC(NIM) is very accurate and stable as the national time and frequency primary metrological standard.

II. FURTHER STUDY ON TWOTFT

As figure 1 shows, the similar principle to that of TWSTFT is followed in TWOTFT, and we use the intermediate-frequency signal modems and the O/E converters and E/O converters for the experiments, and thus compared with TWSTFT we can omit some delays such as sagnac delay, satellite path delay through the satellite transponder, ionospheric delay and other delays due to the satellite and free space.

A. Experiment Setups for Remote Comparison in Different Sites

We have implemented the CCD experiments between two stations with the same time and frequency sources and the comparison between the two stations with the different time and frequency sources. As we describe above, in the former experiments, we have always put the two stations including one modem and one O/E or E/O converter in the same sites. However, in real application of remote comparison, we should use the two stations in the two remote sites. For this target and the further verification of performances of TWOTFT, the remote comparison in the different sites should be implemented as the experiment setup in figure 2.

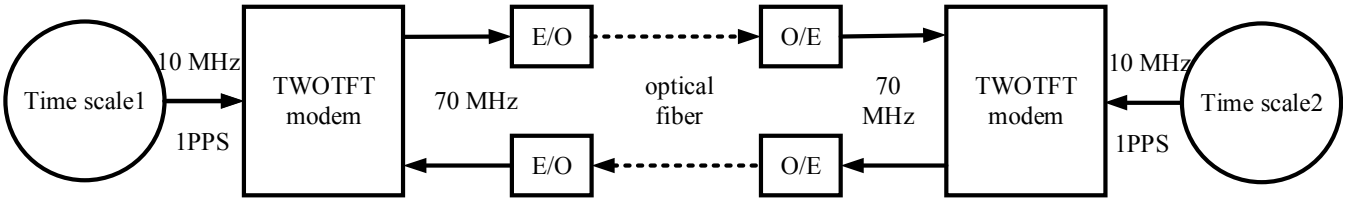


Fig. 1. TWOTFT principle

Supported by Chinese NSFC program 11303024 and the key research program of Chinese MST 2017YFF0212000

One optical link between NIM two campuses (Changping campus and Hepingli campus) has been selected and the baseline is about 53 kilometers. We have the two GNSS time transfer receivers IM2P (Septentrio PolaRx2eTR) and IM06 (Dicom GTR50) on this link so that TWSTFT referenced to the same time scales can be compared with the GPS carrier phase link. IM06 is the master GPS time and frequency transfer receiver of NIM for TAI contribution, and it has been always connected to UTC(NIM). Modem 3 and modem 4 (Timetech Satre products) have been used for the realization of TWOTFT (see more details in [1]) at this time.

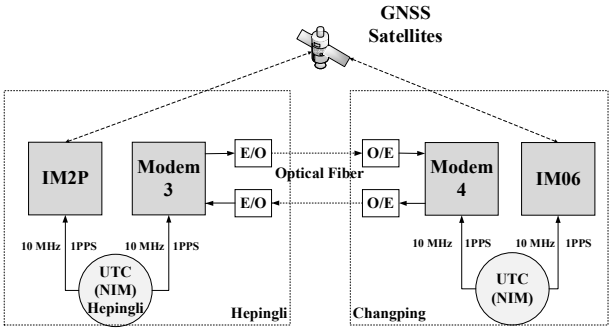


Fig. 2. Setups for remote comparison in different sites

B. *Numerical Results*

We got the results of TWOTFT and GPS carrier phase time transfer for comparison as figure 3 and 4 show. GPS carrier phase results are acquired by PPP processing and the consistence has been got from the ones by TWOTFT in terms of both accuracy and trend. From figure 5 and 6, the time and frequency stability for the results by the two methods is similar, hereinto TWOTFT has 1-s data processing interval much finer than that of GPS carrier phase time transfer, which is 5 minutes.

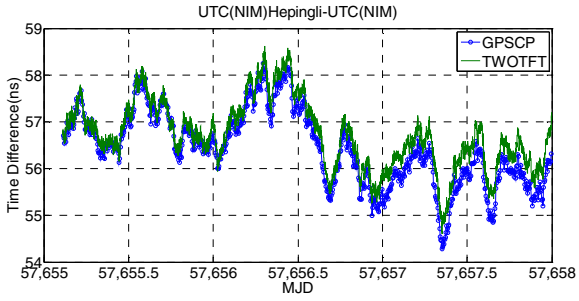


Fig. 3. Comparison of time differences by two methods

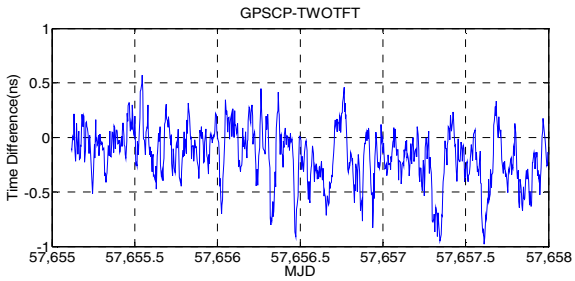


Fig. 4. Double difference between the two methods

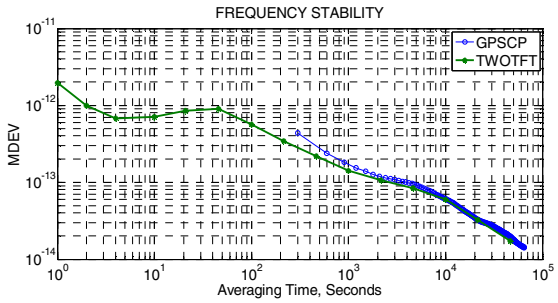


Fig. 5. Comparison of frequency stability by two methods

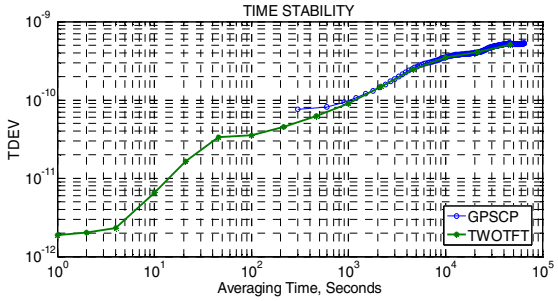


Fig. 6. Comparison of time stability by two methods

TABLE I. STATISTICS FOR THE RESLUTS BY THE DIFFERENT METHODS

Methods	Mean value (ns)	Stand deviation (ns)
TWOTFT	56.7	0.7
IM2P-IM06 GPSP3	57.4	1.0
IM2P-IM06 GPSCP	56.5	0.8

III. ONE WAY TIME TRANSFER BY OPTICAL FIBER

Since the construction of one time scale costs much resource and manpower, and it is complicated enough for any user to keep the time scale accurate and stable, and we have several real optical fiber links, it might be useful to transmit the time signal to other places by them so that the user can easily acquire one high-performance time scale remotely with nearly few resources.

A. Principles

The realization principle is quite direct. Firstly, we modulate the frequency signal (5 MHz and 10 MHz) on the optical carrier via one E/O converter and through the optical fiber the modulated signal could be sent to the remote site and be demodulated to the microwave frequency signal from the optical carrier. Meanwhile, at the remote site, we constructed the time generation system by one micro-stepper with the reference to the frequency signal transmitted from the local site via one piece of optical fiber, one O/E converter and calibrate the time link with some link calibration methods and finally we can transfer the time from the local site to the remote site in fact. In the implementation, the E/O and O/E converters should be the relatively cheap commercial products in wide application, and for the time transfer link calibration, two calibrated GNSS time transfer receivers could be used for this time transfer link calibration, necessarily the two calibrated receivers are separately referenced to the local time scale and the remote time scale, and then this calibrated GPS time transfer link is used to calibrated the time transfer link of one way time transfer by optical fiber. Thus, we might image that the link calibration uncertainty of one way time transfer could be mainly from calibration of this GNSS time transfer link. That is to say, the accuracy of one way time transfer by optical fiber mainly could inherit that of the GNSS time link calibration, and the stability of time transfer by optical fiber might depend on the signal transmission through the optical fiber.

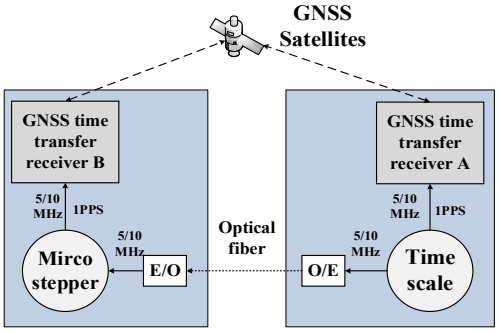


Fig. 7. Principle scheme of one way time transfer by optical fiber

B. Performance Evaluation of the Elements in the System

There are several main elements in the one way time transfer system via optical fiber. In this part, the evaluation of their performances by the specific experiments has been described. Because the frequency signal with 10 MHz or 5 MHz is sent for the final construction of one time scale, the frequency stability could be the most significant interest for us.

Firstly, the performance of E/O and O/E converters has been evaluated. The experiment setup is shown in figure 8. The signal of Hydrogen maser is sent to remote site via one piece of 1.8-m optical fiber by E/O and O/E converters and the sent back to the local site, finally acquired and analyzed by the time interval analyzer (Symmetricom 5120A) by Allan Deviation (ADEV).

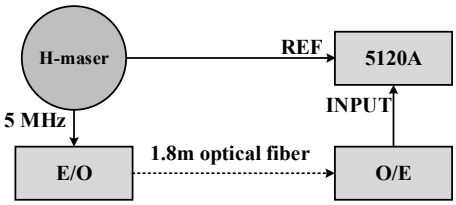


Fig. 8. E/O and O/E test setup

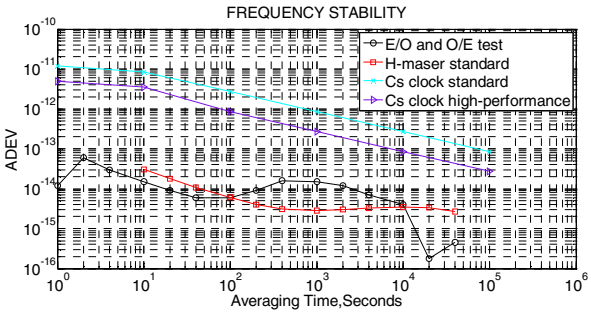


Fig. 9. E/O and O/E test results

Furtherly, the instability of the performance of E/O and O/E converters combined with the 100-m optical fiber has been evaluated by the same time interval analyzer. The 100-m optical fiber link has been built by doubling the single trip between the labs located separately in the second floor and the fourth floor with the connection of one flange. This link between the second floor and the fourth floor is just the link which we finally want to apply the one way time transfer through optical fiber in.

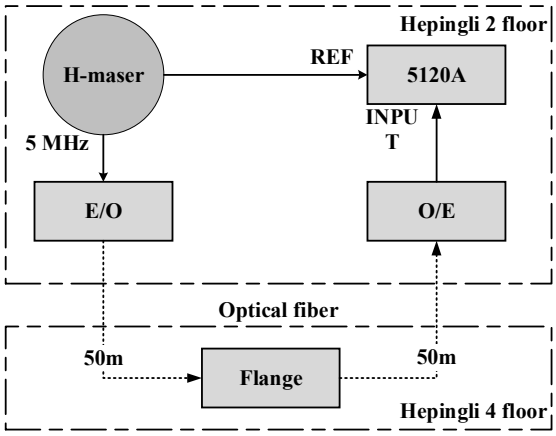


Fig. 10. E/O and O/E test setup with the real optical link

From figure 9 and 11, it could be seen that not only E/O and O/E convertes and them with the destinate optical fiber might provide the enough frequency stability level for the frequency signal transfer of the cesium clock; however, for frequency signal transfer of the hydrogen maser, until several thousands of seconds of averaging time, the ability in stability for them to provide could be in the edge, and this stability is roughly the similar to the one of the hydrogen maser, so it has been not clear for this exact ability for hydrogen maser's

transfer yet. In the experiments of section III C, it will be discussed as well.

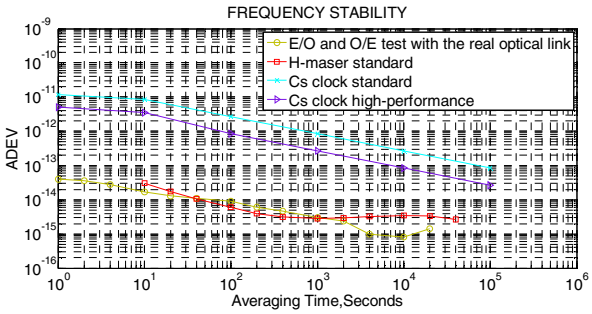


Fig. 11. Results of E/O and O/E test with the real optical link

Finally, the performance of the micro-steppers has been evaluated by analyzing the instability between its input signal and its output signal. The signal is from one frequency source with low noise (LNFR-100). The two micro-steppers (SDI HROG-5 and Symmetricom AOG110) that are the most used for the time community have been selected for our later realization purpose. During the test, frequency and phase deviations are set as 0 in the micro-steppers.

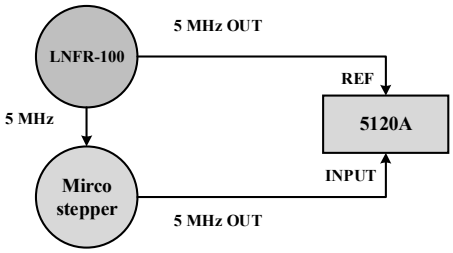


Fig. 12. Micro-stepper test

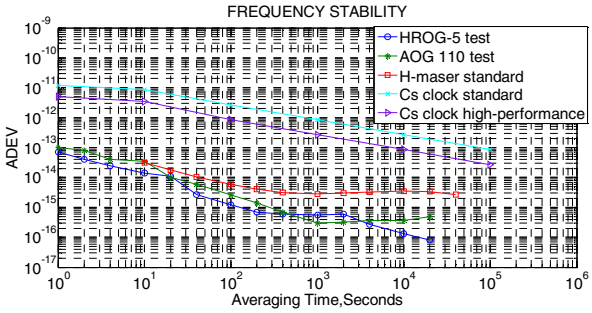


Fig. 13. Results of micro-stepper test

From figure 13, it is shown that HROG-5 and AOG110 have the similar time instability level. Both HROG-5 and AOG110 could provide the eligible stability ability for the hydrogen maser and the cesium clock frequency signal transfer. Furthermore, another closed loop experiment including the E/O and O/E converters, optical fiber and the micro-stepper have been implemented for the further investigation, which setup is shown in figure 14. Thus, from the results in figure 15 for this experiment, we also see the obvious ability in cesium clock transfer and roughly near stability until ten thousands of seconds of averaging time between the experiment results and hydrogen maser.

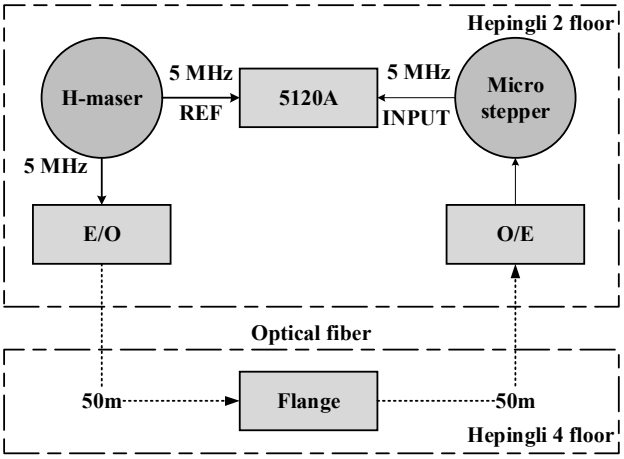


Fig. 14. O/E and E/O with Mrico stepper test

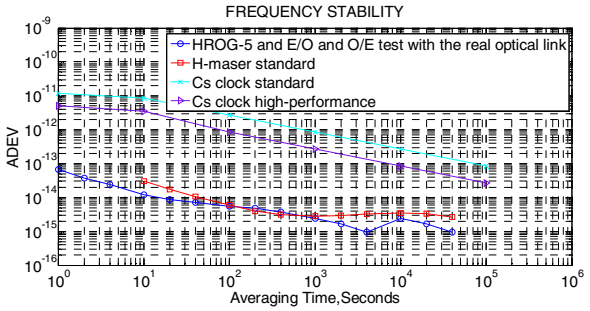


Fig. 15. Results of the closed loop experiment

C. *Experiment Setups*

At present, the related tests to get the experimental results for performances verification of the one way time transfer in the path length of tens of meters (at present 50 meters) have been implemented and the experiments in the longer baseline of several kilometers will be planed. Base on this optical link, the verification experiments have been divided into three phases.

First, in figure 16, the $UTC(NIM)_{Hepingli}$ is used as the local reference for one way time transfer, which is one time scale based on one Cesium clock located in second floor, building 18, Hepingli campus and steered to UTC(NIM) located in Changping campus by remote calibration by GPS time and frequency transfer. The target time scale that the reference time scale will be transferred to is located in the fourth floor, Building 18, Hepingli campus. For the time transfer link calibration, IM2P receiver and IM20 (NIM-TF-GNSS-2J) receiver have been used, which are separately referenced to $UTC(NIM)_{Hepingli}$ and the target time scale. And another receiver IM06 referenced to UTC(NIM) is used for the construction of time comparison link with separately IM2P and IM20. Hereinto from MJD 57655 to MJD 57657, the experiment setup in figure 15 was the same as that in figure 2,

modem 3 and modem 4 have been used for the realization of TWOTFT in figure 2. Thus, in this experimental setup, the general consistence of the target time scale with the reference time scale could be investigated from the comparison results separately between IM20 and IM06 and between IM2P and IM06 and between modem 3 and modem 4. In this experiment, later IM20 is replaced by IM07 (NIM-TF-GNSS-1) and there was one data gap in-between because of the other use of IM20 at that time.

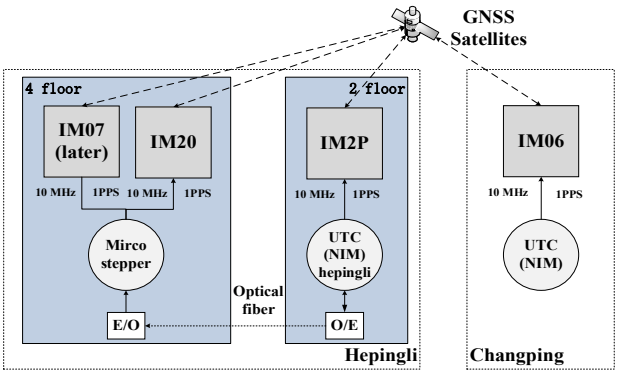


Fig. 16. Experiment setup for time transfer of Cesium clock

Secondly, certainly moving clock is also one method for the time transfer link calibration. And for the verification of the accuracy for one way time transfer, the experiment setup in figure 17 has been built. One time scale (we call this TC-HH) based on one steered hydrogen maser is used as the local reference, which is one time scale based on one hydrogen maser located in second floor, Building 18, Hepingli campus. The target time scale is in the same location as the first verification experiment. IM13 (NIM-TF-GNSS-3) has been used, which is referenced to the target time scale. At the same time, UTC(NIM) and TC-HH is compared with the two way optical fiber time transfer. The time link calibration value between TC-HH and the target time scale was got from the moving method with one Cesium clock. Thus, in this experimental setup, the accuracy could be investigated with the combined results of TWOTFT, GPS time transfer and moving clock.

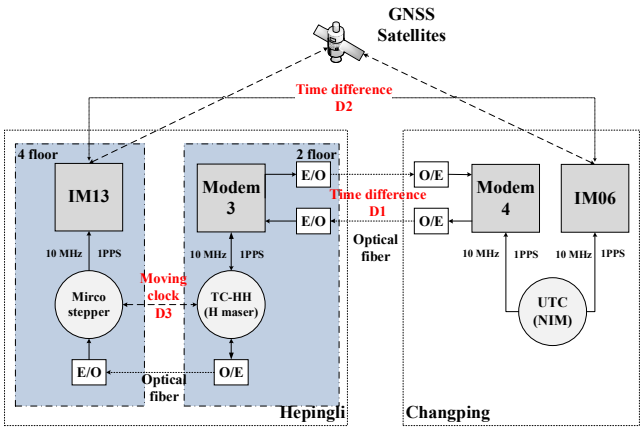


Fig. 17. Experiment setup for time transfer of Hydrogen maser

Finally, the evaluation experiment for the comprehensive performances of one way and two way optical fiber time transfer including the accuracy and stability has been designed, and the setup is shown in figure 18. Here, one time scale (we call this TC-HC) based on one steered hydrogen maser is used as the local reference, and the hydrogen maser located in Changping campus, Building 18, Hepingli campus and its frequency signal (5 MHz) has been sent to the lab in the second floor, Hepingli campus through the specific method and equipments developed by NIM (see details in [3]). The target time scale that the reference time scale will be transferred to is located in the fourth floor, Building 18, Hepingli campus. For the time transfer link calibration, IM07 receiver and IM13 receiver have been used, which are separately referenced to the reference time scale and the target time scale. At the same time, UTC(NIM) and TC-HC is compared with TWOTFT.

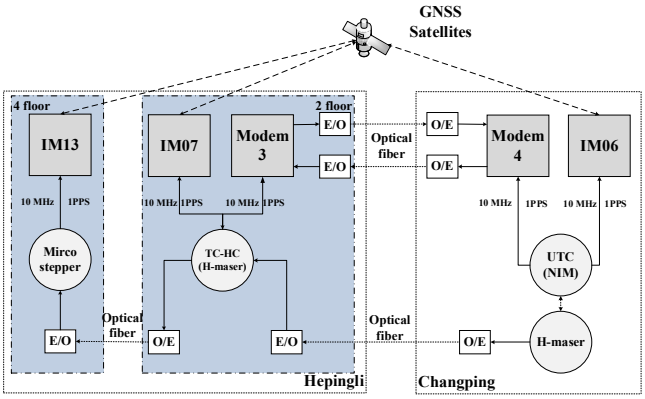


Fig. 18. Experiment setup for time transfer of remote Hydrogen maser

D. *Numerical Results*

According to the experiment setups shown in figure 16, the results from figure 19 and table II roughly describe the consistence between the reference time scale and the target time scale in one way time transfer via optical fiber. TWOTFT-P3 in table II shows the time difference between modem3-modem4 and IM2P-IM06(P3). IM2P-IM20/IM07 in table II shows the time difference between UTC(NIM)$_{\text{Hepingli}}$ and 1PPS (pulse per second) out of the micro-stepper in the 4$^{\text{th}}$ floor which is the reference point of the IM20/IM07.

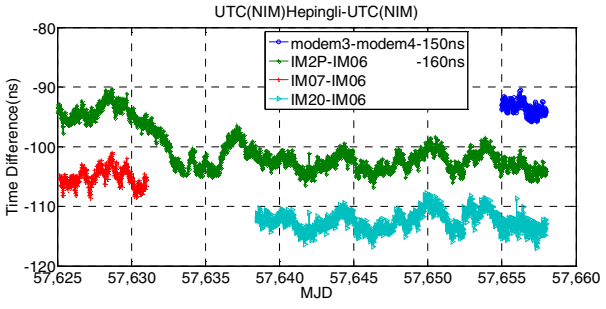


Fig. 19. Time results for time transfer of Cesium clock

TABLE II. STATISTICS FOR THE RESLUTS BY THE DIFFERENT METHODS

	MJD57625-MJD57630	MJD57638-MJD57654	MJD57655-MJD57657
modem3-modem4	-	-	56.7ns
IM2P-IM06(P3)	65.8 ns	57.5 ns	57.4ns
TWOTFT-P3	-	-	-0.7 ns
IM07-IM06(P3)	-	-113.4 ns	-113.5 ns
IM20-IM06(P3)	-105.1 ns	-	-
IM2P –IM20/IM07(P3)	170.9 ns	170.9 ns	170.9 ns

For the experiment in terms of figure 17, the results in figure 20 and table III could show the final agreement in accuracy among one way time transfer via optical fiber with the link calibration of GPS, TWOTFT and moving clock. For moving clock, there is just the result for one time, anyway it is also the mean difference of the measurements between the reference time scale and the target time scale for about two hours.

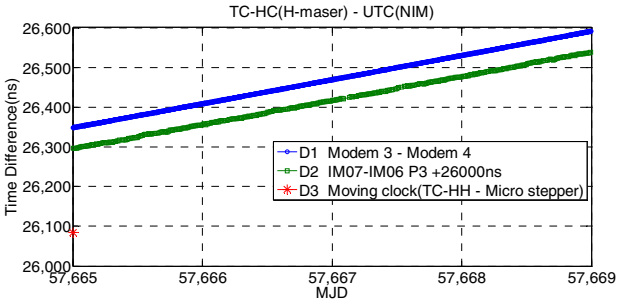


Fig. 20. Time results 1 for time transfer of Hydrogen maser

TABLE III. STATISTICS FOR THE RESLUTS BY THE DIFFERENT METHODS

	Mean (ns)	Frequency deviation
D1	26468.8	6.984 e-13
D2	384.9	6.948 e-13
D3	26084.6	/
D1-D2-D3	-0.7	3.612 e-15

In the experiment as figure 18 described, the results in figure 21 and table IV, depicted the consistence between the time difference trends and the frequency transfer results. TWOTFT-CP and TWOTFT-P3 in table IV show the time differences by separately carrier phase measurements and P3 code between modem3-modem4 and IM07-IM06. However, the reference delays of modem 3 and modem 4 weren't calibrated at that time, we cannot just compare time transfer results of TWOTFT.

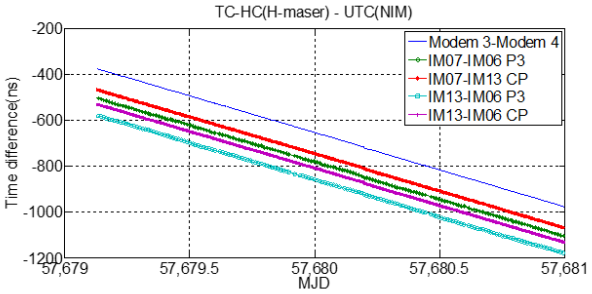


Fig. 21. Time results 2 for time transfer of Hydrogen maser

TABLE IV. STATISTICS FOR THE RESLUTS BY THE DIFFERENT METHODS

	Mean (ns)	Frequency deviation
modem3-modem4	-476.4	-3.689 e-12
IM07-IM06 P3	-576.4	-3.687 e-12
IM13-IM06 P3	-1680.3	-3.691 e-12
IM07-IM06 CP	-576.9	-3.691 e-12
IM13-IM06 CP	-1681.1	-3.692 e-12
IM07-IM13(CP)	1104.2	1.175 e-15
IM07-IM13(P3)	1103.9	6.973 e-16
TWOTFT-CP	100.5	1.132 e-15
TWOTFT-P3	100.0	1.646 e-15

IV. UNCERTAINTY EVALUATION

The uncertainty for one way and two way time transfer are evaluated for their necessity in application.

A. One Way Time Transfer

The system of one way time transfer through optical fiber is composed of one pair of E/O and O/E converters, optical fiber and one micro-stepper. The uncertainty sources could include statistical part and the systematical part. The statistical part could include the contribution of the optical fiber link consisting of E/O, O/E and optical fiber link, and the uncertainty due to their statistical elements might be evaluated with the whole optical fiber link as shown in figure 22. With the difference references of the cesium clock and the hydrogen maser, we got the difference results. Here, we may choose the worse one at the shortest term for the uncertainty contribution. And the uncertainty due to the systematic effects mainly involves the contribution from the calibration of optical fiber time transfer link. According to our experiences, GPS time link calibration would be less than 2 ns if it is implemented strictly in terms of the principle of BIPM calibration guideline [2]. Thus, the uncertainty budget could be simply got in table V. Obviously, the unbalanced uncertainty contribution has been seen and the final combine standard uncertainty is 2.1 ns.

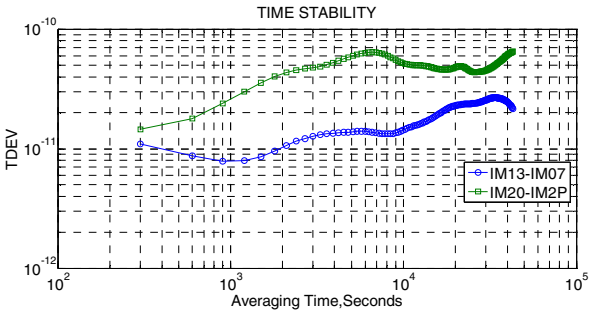


Fig. 22. Time results 2 for time transfer of Hydrogen maser

TABLE V. UNCERTAINTY BUDGET

Uncertainty Source	Type	Value
Measurement stability (IM13 and IM07 in figure 17 or IM20 and IM2P in figure 15)	A	20 ps
Time transfer link calibration	B	2 ns
Total standard combined uncertainty		2.1 ns

B. Remote Camparison by Optical Fiber in Different Sites

Evaluation of the uncertainty for TWOTFT has been done in the former study [1], and the experiments implemented here should be follow its rules because the realization of the method is not so different at present.

V. SUMMARY AND PROSPECTIVES

The further performance analysis of TWOTFT with the two terminal equipments at the two remotes sites has been designed and implemented. The one way time transfer through optical fiber that is using low-cost commercial products has been designed and the performance evaluation, demonstration for the time transfer of both cesium clock and the hydrogen maser, and verification experiments in short distance have been realized and its uncertainty has been evaluated as roughly 2.1 ns. In the future, the more investigation may be focused on the transfer in the longer distance and the more precise E/O and O/E converters for the long-distance application.

ACKNOWLEDGMENT

We thank NRCan for support of the NRCan_PPP software.

REFERENCES

[1]. LIANG Kun, ZHANG Aimin, YANG Zhiqiang, CHEN Weiliang, WANG Weibo, BAI Long, FU Guitao. Preliminary time transfer through optical fiber at NIM. Proceedings of IFCS&EFTF2015.

[2]. BIPM. BIPM guidelines for GNSS equipment calibration V2.0. 2014

[3]. Chen Weiliang, et cl., Research report of NIM project “AKY1301”, 2014.

Enhanced Predictability of Hydrogen Maser Using Random Pursuit Strategy

Yuzhuo Wang, Yuan Gao, Aimin Zhang, Weibo Wang, Yige Lin
National Institute of Metrology (NIM)
Beijing, China
wangyzh@nim.ac.cn; zhangam@nim.ac.cn

***Abstract*—The predictability of atomic clock is generally used to characterize its overall performance. Anomalous clock behaviors lead to greater prediction error in traditional prediction method, such as polynomial fitting predictor and Kalman filter predictor. Our previous work developed random pursuit strategy (RPS) to avoid or minimize above the problem. It was further applied to real data of three Hydrogen masers to verify its effectiveness. Compared to Kalman filter predictor worked on suitable condition, the RPS showed a certain advantage, particularly for clock data with phase or frequency jumps. It could be helpful for steering and weighting algorithms in time keeping.**

Keywords—time scale; atomic clock; frequency prediction; Kalman filter

I. INTRODUCTION

Hydrogen maser (H-maser) has been widely used as master clock in time keeping system due to its better predictability [1-3]. In generation of UTC, the relative weight attributed to each participated clock is arranged according to its predictability [4, 5]. It become gradually a key evaluation standard of atomic clock, which is based on the saying 'a good clock is a predictable clock' [6, 7]. It is usually accepted that hydrogen maser shows the characteristics of frequency shift and stochastic phase (or frequency) jump. This stochastic jumps may case a serious impact on clock predictability [8]. Nevertheless, it is not easy to detect accurately the anomalous clock behavior, such as minor phase or frequency jump.

Some methods about atomic clock prediction have been reported in recent years, including stochastic differential equations [8], optimal strategy to deal with non-stationary behavior[9], etc. In addition, our previous work developed random pursuit strategy(RPS) [10], a novel atomic clock prediction algorithm. In this work, we applied RPS to the measured data of three Hydrogen masers at National Institute of Metrology (NIM). The RPS showed an ability to reduce prediction error for Hydrogen maser in some cases.

II. ENHANCED RELIABILITY OF PREDICTION

A. Comparisons between two kinds of past data

RPS was described in detail in our previous work [10]. In this algorithm, the past data used to prediction are randomly divided into several non-overlaping subspace. Each subspace is corresponding to a predictor. An predictor ensemble consists of these predictors. Each predictor operating a subspace represents a possible prediction. The final prediction result is weighted average of all possible predictions, which are obtained by polynomial fitting method in subspaces.

In this work, the linear model with frequency and frequency shift parameters was used to estimate the further trend of H-maser. It is written as $y_i = a_i + b_i t$ where y_i represents the prediction value of linear predictor-i; a_i and b_i are estimated values of frequency and frequency shift of linear predictor-i; t is the epoch. Fig. 1 shows the frequency of the H-maser and it has a frequency jump point. The point is considered as anomalous behavior of the H-maser. In Fig. 1, two segments (A: MJD 57197 to 57245 and B: MJD 57301 to 57349) of data are selected as past data. Every segment includes 49 data points. The number of data points in a segment is an experienced parameter according to the characteristics of atomic clocks. The next point's prediction is performed using segment A and the segment B as past data.

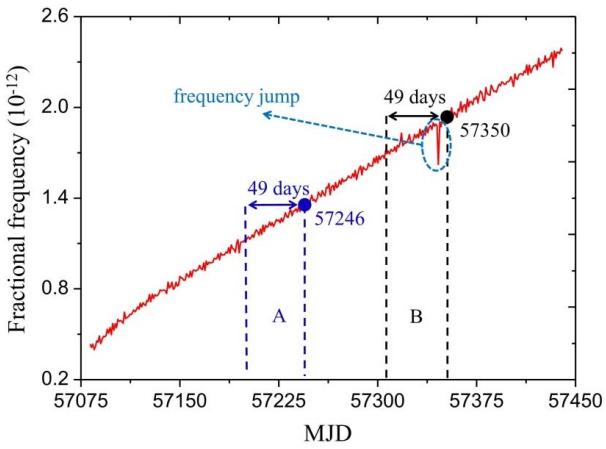


Fig. 1. Measured frequency of UTC(NIM) - H-maser.

The 49 past data points of segment A were randomly grouped as 7 groups in Table 1. For convenience of expression, these points were numbered from 1 to 49. Every group includes 7 data points, which are as one random sample. The parameters a_i and b_i of predictor-i were estimated using the least square method, since the next point's prediction value y_{ip} (MJD 57246) originated from each predictor can be calculated. The measured frequency value of the H-maser is 1.3594×10^{-12} at MJD 57246. The each of 7 predictors represents one possible trend of the H-maser, so that the weighted average of these prediction values originated from all predictors is as the prediction value of the predictor ensemble. In this work, the weight of each predictor

was refined by the average absolute deviation. Fig. 2 shows the relative weights of all predictors. The weight represents a possibility. The trend of the predictor with bigger weight is recognized as much possibility. In other words, the past data points attributed to the predictor with bigger weight more likely represent the characteristic of H-maser.

Table 1. A randomized grouping solution in segment A.

Predictor-*i*	Random sample	Parameters (a_i, b_i)	Prediction value y_{ip}
1	{ 10, 15, 20, 35, 37, 42, 48}	$(5.4450\times10^{-15}, 1.0981\times10^{-12})$	1.3703×10^{-12}
2	{ 1, 2, 16, 27, 28, 30, 31}	$(5.1764\times10^{-15}, 1.0092\times10^{-12})$	1.3581×10^{-12}
3	{ 4, 11, 21, 23, 39, 40, 49}	$(5.0607\times10^{-15}, 1.1039\times10^{-12})$	1.3569×10^{-12}
4	{ 3, 8, 12, 17, 24, 25, 36}	$(4.4297\times10^{-15}, 1.1203\times10^{-12})$	1.3418×10^{-12}
5	{ 13, 18, 32, 41, 43, 44, 46}	$(5.5049\times10^{-15}, 1.0883\times10^{-12})$	1.3635×10^{-12}
6	{ 6, 7, 9, 14, 19, 26, 47}	$(5.1251\times10^{-15}, 1.1040\times10^{-12})$	1.3603×10^{-12}
7	{ 5, 22, 29, 33, 34, 38, 45}	$(4.7602\times10^{-15}, 1.1235\times10^{-12})$	1.3615×10^{-12}

Table 2. A randomized grouping solution in segment B.

Predictor-*i*	Random sample	Parameters (a_i, b_i)	Prediction value y_{ip}
1	{ 20, 22, 24, 26, 28, 42, 44}	$(5.5546\times10^{-15}, 4.3853\times10^{-13})$	1.9272×10^{-12}
2	{ 9, 11, 15, 16, 17, 25, 43}	$(5.0092\times10^{-15}, 5.6360\times10^{-13})$	1.9061×10^{-12}
3	{ 4, 6, 8, 38, 41, 48, 49}	$(4.5975\times10^{-15}, 6.6568\times10^{-13})$	1.8978×10^{-12}
4	{ 1, 7, 18, 27, 37, 39, 40}	$(5.0532\times10^{-15}, 5.7210\times10^{-13})$	1.9264×10^{-12}
5	{ 2, 10, 19, 29, 31, 32, 45}	$(5.1930\times10^{-15}, 5.1736\times10^{-13})$	1.9091×10^{-12}
6	{ 5, 14, 21, 34, 35, 36, ***46***}	$(1.5571\times10^{-15}, 1.3660\times10^{-12})$	1.7833×10^{-12}
7	{ 3, 12, 13, 23, 30, 33, 47}	$(5.0854\times10^{-15}, 5.4877\times10^{-13})$	1.9117×10^{-12}

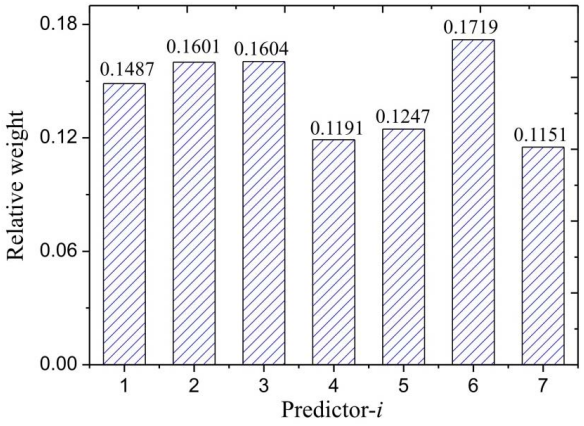


Fig. 2. Relative weight of 7 predictors in segment A.

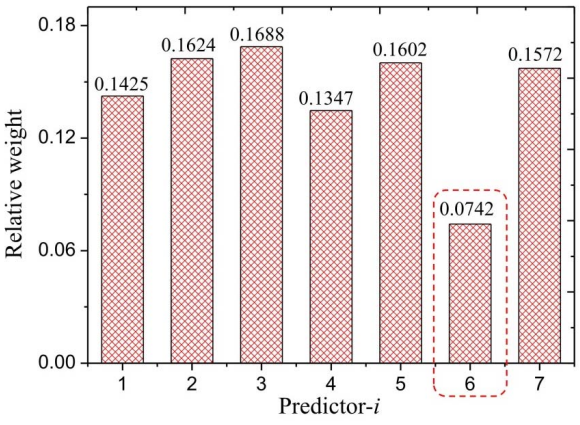


Fig. 3. Relative weight of 7 predictors in segment B.

Similarly, the one randomized grouping solution was performed using the segment B in Fig. 1 as the past data (see Table 2). The data points of the segment B were also numbered from 1 to 49 and the segment B had a frequency jump on the 46th point. The measured frequency value of the H-maser on MJD 57350 is 1.9132×10^{-12}. The bigger deviation 0.1299×10^{-12}, originated from predictor-6 was found due to frequency jump on the 46th point. Other predictor have a similar prediction trend, since their prediction values are relatively close. Fig. 3 shows the weights of 7 predictor and the weight of line-6 is minimum, which is less than 50% of the weight maximum. The data points attributed to the predictor-6 have smaller contribution to further prediction. It is helpful to improve the predictability of H-maser.

Apart from obvious jump points, some points with high noise are less easy to identify. They also affect the further prediction. In RPS, these points are also considered as smaller contribution to further prediction.

B. Reliability of prediction

Due to the presence of random noise, there are always some errors between predicted and measured values. A single of prediction errors does not reasonably evaluate the performance of prediction algorithm, because the measured value maybe have higher noise, even jump. The average value of prediction errors during long-term may be better choice.

In RPS, each prediction value generated from one randomized grouping solution represents a possibility of further measured value. To enhance reliability of prediction, 100 randomized grouping solutions were built to implement prediction using the 49 past data points in this work. Fig. 4 shows the statistical results of the prediction errors during MJD 57245 to 57285. Every point in Fig. 4 represents average prediction error of 100 randomized grouping solutions on

certain MJD. The histogram of prediction error distribution on MJD 57246, 57256, 57277, and 57284 are shown in Fig. 5. It may be related to noise type. Furthermore, H-maser has the stationary random noise, therefore it represents Gauss distribution. The curves of probability density distribution were also shown in Fig. 5. The prediction value with maximum possible is as final prediction result.

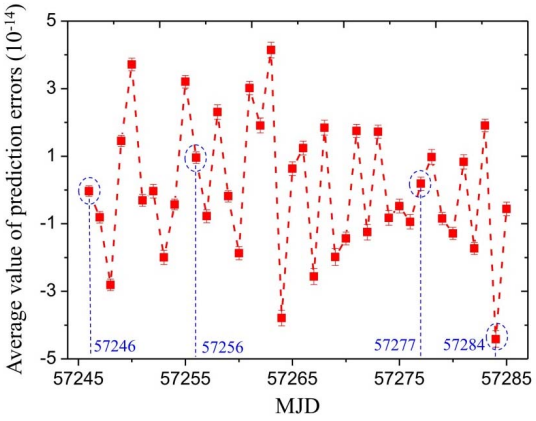


Fig. 4. Average value of 100 random prediction errors.

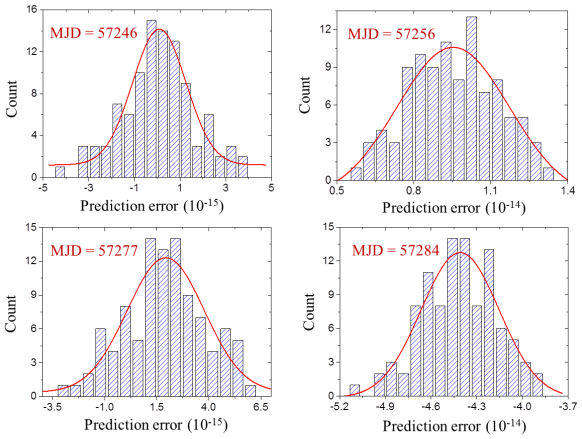


Fig. 5. Prediction error distribution.

III. Application to Three Hydrogen Masers

We applied RPS to the daily readings of three H-masers (Hm-1, Hm-2 and Hm-3) over approximately one year, which are compared to time reference UTC(NIM), the real-time local time and frequency standard in China. In order to investigate the performance of RPS, the outliers in H-maser data are not removed before performing prediction.

Compared to the Kalman filter predictor worked on suitable condition, the RPS could improve the predictability of atomic clocks. The frequency stability (Allan deviation (1 d)) of Hm-1 , Hm-2 and Hm-3 was 2.7236×10^{-14}, 2.5564×10^{-15}, and 1.3311×10^{-15} respectively. The prediction results of the three H-masers are shown in Fig. 6 to Fig. 11. When applied to Hm-1, the RPS showed great advantage (~19.35%) due to Hm-1 having high noise and bigger frequency jumps. It was further verified that the effect of high noise or jump points on prediction could be reduced by using RPS. Consistent results were seen, when applied to Hm-2, which has no bigger jumps (more than 3σ). Nevertheless, the prediction results of Hm-3 were not consistent with Hm-1 and Hm-2. The prediction capability of the random pursuit strategy only exceeds ~1.12% of Kalman filter predictor's (See Fig. 11). It is probably because the theoretical linear model is not suitable for some time segments with frequency fluctuations in the Hm-3 data. The inset map of Fig. 6 shows this phenomenon. In addition, the improvement of prediction capability is also limited for a clock with high performance.

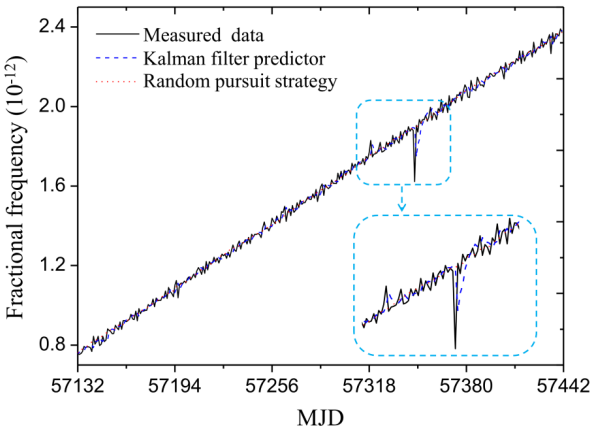


Fig. 6. Prediction frequency of H-maser (Hm-1) with Allan deviaton 2.7236×10^{-14} (1 d).

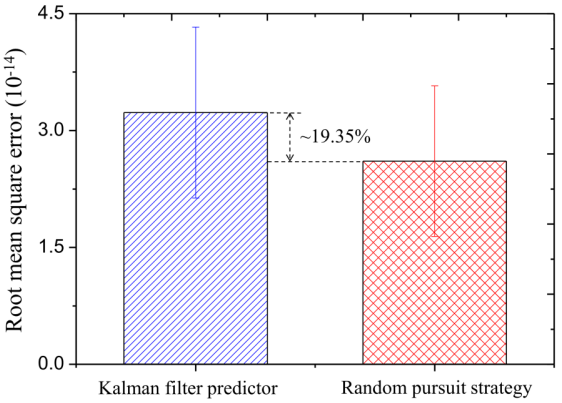


Fig. 7. Prediction errors of H-maser (Hm-1).

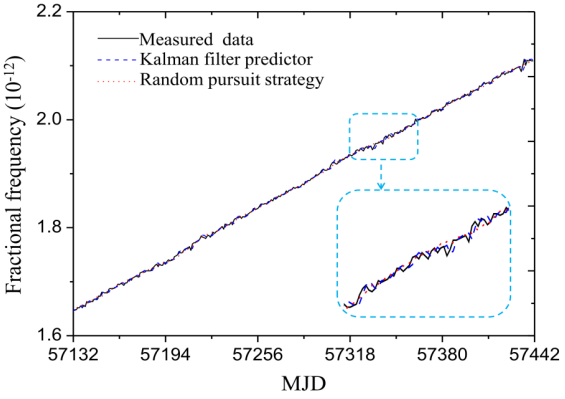


Fig. 8. Prediction frequency of H-maser (Hm-2) with Allan deviation 2.5564×10^{-15} (1 d).

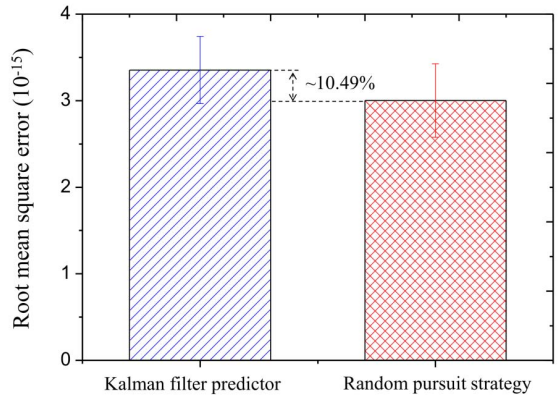


Fig. 9. Prediction errors of H-maser (Hm-2).

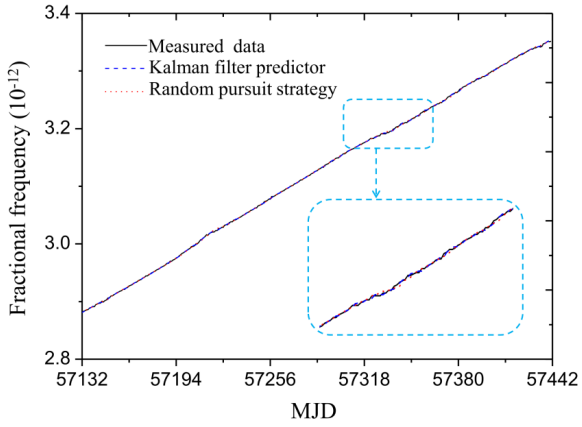


Fig. 10. Prediction frequency of H-maser (Hm-3) with Allan deviaton 1.3311×10^{-15} (1 d).

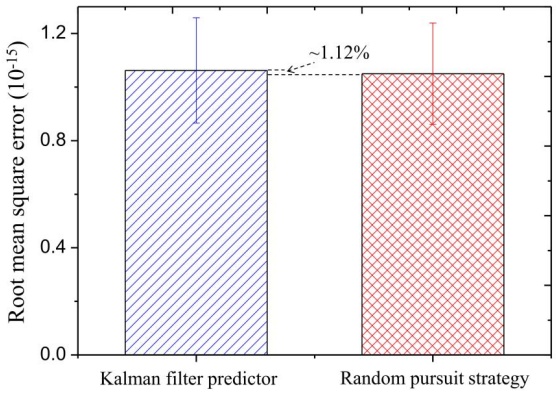


Fig. 11. Prediction errors of H-maser (Hm-3).

IV. CONCLUSION

In polynomial fitting predictor and Kalman filter predictor, some assistant methods are used to removed outliers in the past data, and then remainder data have equal contribution to future prediction. Nevertheless, some points with minor jump or high noise still exist in remainder data. The RPS arranges different contributions for past data by random grouping solution. In other words, the data with high noise will be arranged minor contributions to future prediction; the data with high qualify will obtain larger contributions to future prediction. The main idea of RPS was further verified by real measured data of three Hydrogen masers at NIM. Compared to Kalman filter predictor worked on suitable condition, it showed an enhanced predictability of H-maser.

ACKNOWLEDGMENT

This work was supported by the National Key R&D Program of China with grant no. 2016YFF0200203.

REFERENCES

[1] Z. Aimin, G. Yuan, L. Kun, Y. Zhiqiang, W. Weibo, N. Dayu, Z. Kejia and Z. Yue, Research on Time Keeping at NIM. Journal of Metrology Society of India, 2012. **27**(1): p. 55-61.

[2] Peter B Whibberley, John A Davis and Setnam L Shemar, Local representations of UTC in national laboratories. Metrologia, 2011. **48**(48): p. S154.

[3] Tavella Patrizia, Statistical and mathematical tools for atomic clocks. Metrologia, 2008. **45**(6): p. S183.

[4] G. Panfilo, A. Harmegnies and L. Tisserand, A new weighting procedure for UTC. Metrologia, 2014. **51**(3): p. 285-292.

[5] Federica Parisi and Gianna Panfilo, A new approach to UTC calculation by means of the Kalman filter. 2016. **53**(5): p. 1185-1192.

[6] G. Panfilo, A. Harmegnies and L. Tisserand. A new prediction algorithm for EAL. in Frequency Control and the European Frequency and Time Forum (FCS), 2011 Joint Conference of the IEEE International. 2011.

[7] Judah Levine, Introduction to time and frequency metrology. Review of Scientific Instruments, 1999. **70**(6): p. 2567-2596.

[8] C. Zucca and P. Tavella, A mathematical model for the atomic clock error in case of jumps. Metrologia, 2015. **52**(4): p. 514-521.

[9] C Zucca, P Tavella and G Peskir, Detecting atomic clock frequency trends using an optimal stopping method. Metrologia, 2016. **53**(3): p. S89-S95.

[10] W. Yuzhuo, C. Yu, G. Yuan, X. Qinghua and Z. Aimin, Atomic clock prediction algorithm: random pursuit strategy. Metrologia, 2017. **54**(3): p. 381.

The possibility of testing the Einstein Equivalence Principle (EEP) using Two Way Satellite Time and Frequency Transfer (TW) and a Software Defined Receiver (SDR)

Wen-Hung Tseng
Telecommunication Laboratories,
Chunghwa Telecom Co., Ltd.,
Taiwan

Demetrios Matsakis
U.S. Naval Observatory,
USA

***Abstract*—The Einstein Equivalence Principle (EEP) requires that clocks in free fall, when observed by other clocks in free fall, show no frequency variations. To some approximation, clocks on the surface of the Earth can be considered freely falling in the solar gravitational potential, and one would expect to find no frequency variations between the clocks as the Earth's rotation modulates the potential experienced by each clock. A previous study [1] using GPS satellites yielded an upper limit to an EEP violation of $<10^{-3}$, parameterized as a fraction of the expected differential gravitational redshift of a clock pair not in free fall. Upper limits were also found using TW, but these were much higher than with GPS. We investigate the attainable limits of a search for EEP-violation using SDR-enhanced TW, and find a three-sigma uncertainty slightly higher than 10^{-4} may be achievable, using optimistic assumptions.**

Keywords—General Relativity, Equivalence Principle, Software Defined Receiver, Two Way Satellite Time Transfer, TWSTT, TWSTFT

I. INTRODUCTION

Tests of Local Position Invariance (LPI), one of the tenets of the Einstein Equivalence Principle (EEP), typically rely on measurements of relativistic frequency shifts in clocks. The most common LPI tests are null measurements, looking for non-cancellation of gravitational and motional time dilation in the frequency comparison of two different types of clocks in the same local inertial frame. A fundamentally different null test can be carried out by looking for a non-cancellation of the relativistic frequency effects between two freely-falling clocks at different gravitational potentials (note that a clock on the ground is not freely falling with respect to the Earth). This cancellation is routinely observed in GPS satellite clocks, and explained in [2] as due to the gravitational and Doppler effects having equal magnitude but opposite sign. Because the local inertial frame varies over the orbit, the authors of [3] argue for an approach based directly on the relativity of simultaneity.

Searches for EEP violations have tested relativity in many ways, often reporting upper limits in the range 10^{-8} to $2\ 10^{-13}$ [4-7]. Except for the "3-sigma" upper limit of 10^{-3} reported in the first phase of this work [1] (and based upon the limitations inferred from diurnals whose phase did not stay in synch with that expected from an EEP violation), the most comparable attained limits to our approach may be the 1% results from Voyager and Galileo data [6,7], if not Gravity Probe A, whose measurement uncertainty was $2\ 10^{-4}$ (3-sigma) [8]. According to Schiff's conjecture, the validity of the Weak Equivalence Principle (WEP) necessarily implies the validity of the strong EEP, along with its two other components LPI and Local Lorentz Invariance [4,5]. We search for a possible violation in the form of frequency differences between pairs of clocks that would vary diurnally, as the Earth's rotation modulates the solar potential experienced by each clock. The obstacle to carrying out such a test is the technology for frequency comparison of remote clocks. Our simulated search for LPI violations employs TW frequency-transfer data obtained from geostationary satellites; more precise comparisons via optical fibers are expected in the near future [9,10].

For this work, TW can be briefly described as a technique in which timing information from a site's reference clock (better termed frequency information if the system is not fully calibrated) is superimposed upon a microwave carrier signal and transmitted to a geostationary satellite, from which it is re-transmited to a second site. The second site also transmits a signal synchronized with its reference clock to the satellite, and this signal is retransmitted so as to be received by the first site. By differencing the transmit and receive times recorded at the two sites, the path delay can be largely removed and the actual time or frequency difference between the two sites' reference clocks estimated. The chief limitation in the use of historical TW data is the existence of artificial 24-hour diurnals, whose period, phase, and amplitude are variable on all baselines [11]. Due to the obscuration of these diurnals, in

[1] the use of TW frequency data taken between the USNO and the Alternate Master Clock, yielded only very coarse upper limits for EEP variations, of order 10^{-2}. However, since diurnals have been largely eliminated on some baselines through the use of SDR's [12, 13], it is conceivable that lower limits can be achieved in the future. In this work, we employ optimistic assumptions about the removal of the artificial diurnals to explore the attainable limits.

II. Methodology and Results

In order to search for a diurnal frequency shift in ground clocks that would be in synchrony with the solar potential, we first simulate a 1-day set of hourly-averaged frequency transfer data between pairs of sites, characterized by white frequency noise. The justification for ignoring non-white noise is that the analysis is based upon independent daily solutions, which are insensitive to subhourly and superdaily noise. Daily solutions for the expected diurnals due to an EEP-violating parameter and its orthogonal "quadrature" parameter, which peaks six hours later, would be obtained from daily fits over only non-redundant site pairs, because the assumption that the hourly noise is site-based requires that for any three labs only two baselines are retained. The EEP-violating parameter was the frequency shift due to the gravitational potential expected from a clock at given latitude and longitude on the surface of the Earth at that time, using the following formulae:

$$\Delta f/f = -GM_{Sun}\cos(\delta)/(c^2 D_{Sun}) \quad (1)$$

$$= -GM_{Sun}\, r_{earth}\cos(\theta)\cos(\lambda)\cos(\delta)/(c^2 D^2_{Sun,0}) \quad (2)$$

$$= -4.2\ 10^{-13}\cos(\theta)\cos(\lambda)\cos(\delta)/(D_{Sun,0}/D_{Sun})^2 \quad (3)$$

$$= -36\cos(\theta)\cos(\lambda)\cos(\delta)/(D_{Sun,0}/D_{Sun})^2 \text{ ns/day} \quad (4)$$

where G is the gravitational constant, M_{Sun} is the solar mass, $D_{Sun,0}$ is one astronomical unit (nominal distance of the Sun from the center of the Earth), D_{Sun} is the distance of the Sun from the clock at the time of observation, r_{earth} is the nominal radius of the Earth, θ is the solar hour angle, δ is the Sun's declination, and λ is the site latitude [14]. The position and distance of the Sun were computed using the low-precision formulae provided in the Astronomical Almanac [15], and its declination was fixed over a day. The peak frequency variation would be doubled to 72 ns/day for clocks on opposite sides of the equator on the equinox.

As outlined in Appendix I, correlations between observations of site pairs that include a common site were taken into account using standard mathematical formulae that invoke the covariance matrix of the observations. For baselines (site pairs) that share a common site, the data are assumed correlated through that site's clock as well as its receive system. However the effect of uncorrelated noise in real data would be to attain better precision than estimated in this work.

Quantitatively, the data noise was assumed to be site-based and white with the RMS frequency noise contributed by any one site to be 0.1 ns/day. These values correspond to about 60 ps variation between hourly points on any one baseline, but would be considered conservative if data were taken continuously over the hour in the absence of diurnals. Consistent with the data noise models, solutions were carried out using a covariance model with identical values for all observations. The measurement covariances were set to zero for pairs of baselines without a common site, and to +/-0.1 $(\text{ns/day})^2$ for each baseline pair that included one common site. The assumed autocorrelations (between identical baselines) were twice these values. Note that the derived upper limits can be simply scaled to any desired assumption for the white noise level.

Thermal and other effects unrelated to relativity that could cause a diurnal signature [11] were ignored, among them satellite motion [16] and thermal effects. Ignoring thermal effects cannot be completely justified by the fact that any thermally-caused diurnals would be expected to attain their maximum/minimum several hours after noon/midnight, as opposed to the exact times expected for EEP-violating diurnals. However, improved techniques will result in lower thermal diurnals as well as higher signal to noise.

We have also ignored the effects of solar tides, and the lunar potential, which would mostly lead to frequency variations with approximately half-day periodicity. The rigidity of the Earth's response to the shifting potentials would result in a deviation from free-fall that we do not fully evaluate here. The maximum solar tide can be estimated as

$$r_{earth}\, M_{Sun}/\, M_{Earth}/(D_{Sun,0}/r_{Earth})^3 = 0.16 \text{ m} \quad (5)$$

and its net frequency variation due to the Earth's field is

$$GM_{Earth}/(c^2 r^2_{Earth})(0.16\text{ m}) = (1.1\ 10^{-16}/\text{m})(0.16\text{ m}) = 1.8\ 10^{-16} \quad (6)$$

and so the maximum effect as a fraction of the EEP-violating parameter would be $5\ 10^{-4}$.

Lunar effects would average out due to the 24.8-hour average time between meridian crossings, and in any case their associated EEP-violation would be weaker by the solar/lunar mass ratio divided by their distance squared, or

$$(2.0*10^{30}\text{kg}/7.3*10^{22}\text{ kg}) / (1.5*10^{8}\text{ km}/3.8*10^{5}\text{ km})^2 = 420 \quad (7)$$

Another consideration is that we have ignored deterministic diurnals that may be caused by the "solar Sagnac effect" [17]. In analogy to the well-known Sagnac correction for the Earth's rotational velocity [18], a classical analysis that ignores higher-order terms indicates that there may be a diurnal signature inferred from the second term in the numerator of the following formula:

$$\Delta t_{Sagnac} = \pm \frac{2(\omega_E A + \omega_\odot A')}{c^2} \quad (8)$$

where ω_E is the Earth's rotational velocity, $\omega_\odot$ is the angular velocity of the Earth's orbit around the Sun, A is the perpendicular projection of the area to the equatorial plane, and A' is the perpendicular projection of the area to the plane of the ecliptic. Note that in equation (8), the first term in the numerator is the Sagnac effect as currently applied to TW phase data. It is a constant, and therefore makes no contribution to the frequency data, but we include it here to show that it is different from the contribution due to the Earth's motion about the Sun.

A final consideration would be possible effects due to other violations of relativity [19]. For example, in [10] a violation of Lorentz invariance is parameterized in such a manner as to result in "sidereal-diurnals", relevant to the Earth's rotation about an axis defined using the observed Doppler shift of the Cosmic Microwave Background. This effect would be washed out in a one-year averaging against true 24-hour diurnals, however we note that once the EEP is violated, none of the fundamental precepts of special or general relativity would be assured.

The results of this process are provided in Table 1. To generate the table, several possible TW networks were modeled using the parameterization developed in this section, and the formulas provided in Appendix I. Assuming each day's data was independently processed, the attainable precision after 100 days was assumed to be 10 times better. If one were to reduce operational data taken for a few minutes every two hours for this purpose, the amount of data needed to attain this precision would be larger by a factor of 2 or 3, depending upon the actual noise of this system. However, as noted above, residual diurnals may also be a limiting factor.

The precisions shown in Table 1 are consistent with the idea that a 36 ns/day diurnal of known phase would be observable against 0.14 ns/day white noise with an SNR of approximately 1000 to 1, and the most geographically distant site pairs at 45 degrees latitude would have an SNR of 1400 to 1, all of which is mitigated by the fact that the improvements resulting from having N nearby sites are less than expected from $\sqrt{N}$.

III. Conclusions

Although fiber-optic links, coupled with optical frequency standards, should be able to provide lower upper limits, we suggest that operational SDR data be at some point employed to confirm any reported violations.

References

[1] D. Matsakis, "Investigating a Null Test of the Einstein Equivalence Principle with Clocks at Different Solar Gravitational Potentials", 2016 IEEE International Frequency Control Symposium (IFCS), New Orleans, LA, 2016, pp. 1-6.

[2] B. Hoffman, "Noon-Midnight Red Shift", Phys. Rev. 121, 1961, p 337

[3] N. Ashby and M. Weiss, "Why there is no noon-midnight shift in the GPS", http://arXiv [gr-qc]:1307.6525, 2013

[4] C. Will, "The Confrontation between General Relativity and Experiment", Living Rev. Relativity 17, 4, 2014

[5] S. Kopeikin, M. Efroimsky, and G. Kaplan, "Relativistic Celestial Mechanics of the Solar System", Wiley Press, 2011

[6] T.P. Krisher, J.D. Anderson, and J.K. Campbell, "Test of the gravitational redshift effect at Saturn", Phys. Rev. Lett, 64, 1332-1335,1990

[7] T.P. Krisher, D.D. Morabito, and J.D. Anderson, "The Galileo solar redshift experiment", Phys. Rev. Lett., 70, 2213-2216, 1993

[8] R.F.C.Vessot, M.W. Levine, E.M Mattison, E.L. Blomberg, T.E. Hoffman, G.U. Nystrom, B.F. Farrel, R. Decher, P.B. Eby, C.R. Baugher, J.W. Watts, D.L.Teuber, and F.O. Wills, "Test of relativistic gravitation with a space-born hydrogen maser", Phys. Rev. Lett. 5, 1980, pp. 2081-4.

[9] E-M Rasel, "Quantum tests of the Einstein Equivalence Principle on Ground and in Space", IFCS-EFTF, Denver, Co., 2015

[10] P. Delva et al., "Test of Special Relativity Using a Fiber Network of Optical Clocks", Phys. Rev. Lett. 118, 221102, 2 June 2017.

[11] D. Matsakis, "Characterizing the Diurnal Signature in Two Way Satellite Time Transfer (TWSTT) Data with a Kalman Filter", ION-PTTI, Monetery, Ca, 2016.

[12] Y-J Huang, M. Fujieda, H Takiguchi, W-H Tseng, and H-W Tsao, "Stability improvement of an operational two-way satellite time and frequency transfer system", Metrologia 53, 2016, pp. 881-890

[13] V. Zhang, J. Achkar, Y-J Huang, Z. Jiang, S-Y Lin, T. Parker, and D. Piester, "A Study on Using SDR Receivers for the Europe-Europe and Transatlantic TWSTFT Links," in Proc. 2017 Precise Time and Time Interval Meeting (PTTI), Monterey, CA, Jan 30-Feb. 2, 2017.

[14] E.E. Mamajek, A. Prsa, G. Torres, P. Harmanec, M. Asplund, P. D. Bennett, N. Capitaine, J. Christensen-Dalsgaard, E. Depagne, W. M. Folkner, M. Haberreiter, S. Hekker, J. L. Hilton, V. Kostov, D. W. Kurtz, J. Laskar, B. D. Mason, E. F. Milone, M. M. Montgomery, M. T. Richards, J. Schou, S. G. Stewart, "IAU 2015 Resolution B3 on Recommended Nominal Conversion Constants for Selected Solar and Planetary Properties", http://arXiv.org/abs/1510.07674, 2015

[15] The Astronomical Almanac is an official publication of the US Naval Observatory. Information is available on www.usno.navy.mil/usno/AA.

[16] W-H Tseng, K-M Feng, S-Y Lin, H-T Lin, Y-J Huang, and C-S Liao, "Sagnac effect and diurnal correction on two-way satellite time transfer," *IEEE Trans. Instrum. Meas.*,, vol. 60, no. 7, pp. 2298-2303, Jul. 2011.

[17] W-H Tseng and D. Matsakis, 2017, "Correcting for the Sagnac Effect in Satellite Based Time Transfer", in prep.

[18] G. Sagnac, "L'ether lumineux demontre par l'effet du vent relatif d'aether dans un interometre en rotation uniforme", 1913, Comptes Rendus, 157, pp. 708-710.

[19] W-H Tseng, "Propagation time correction on Earth's orbital motion for two-way satellite time and frequency transfer", Proceedings of the ION 2017 Pacific PNT Meeting, Honolulu, Hawaii, May 2017, pp. 978-987.

[20] The BIPM's acronyms for laboratories is downloadable as table 3 from here: http://www.bipm.org/en/bipm/tai/annual-report.html

[21] G.J. Beirman, Factorization methods for discrete sequential estimation, Academic Press, 1977, pp 47-49.

Table 1 Uncertainty of EEP-violating parameter expected from five networks after averaging 100 daily batches, in which data are assumed to be taken continuously and characterized by 0.1 ns/day white site-based frequency noise among hourly averages. These networks contain different subsets of laboratories currently participating in TW. As expected, the attainable accuracy under these very optimistic assumptions improves with geographic distribution.

Asian Labs	European Labs	North American Labs	EEP-violation uncertainty
Acronym [20]	Acronym [20]	Acronym [20]	1 σ
-	AOS, CH, IPQ, IT, NPL, PTB, ROA, SP, VSL	NIST, USNO	$7.6\ 10^{-5}$
KRIS, NICT, NIM, NTSC, TL	PTB, SU	-	$7.6\ 10^{-5}$
NTSC, NICT, NIM, KRIS, TL	PTB, SU	USNO	$5.1\ 10^{-5}$
NICT, NTSC, TL	AOS, IPQ, IT, NPL, SP, SU	NIST, USNO	$4.3\ 10^{-5}$
KRIS, NICT, NTSC, TL	AOS, IPQ, IT, SP, SU	NIST, USNO	$4.3\ 10^{-5}$

Appendix I. Generalized Least Squares Parameter Fitting

Assume there are N pairs of sites (baselines) in the solution for a given day, and 24 hourly points available for each baseline in that solution. The average value of the 24 daily points from each baseline is subtracted out; in any case it is orthogonal to the two sinusoidal parameters fitted below.

Let S be the 24Nx24N covariance matrix of the observations. It can be determined by the monthly average of data, or set to a pre-determined value. Each baseline pair is composed of up to four sites, written as (A-B) and (C-D). If sites A, B, C, and D are four different sites, then the correlation is taken to be exactly zero. If sites A and C are identical, or if B and D are identical, then the correlation will be positive and related to the noise associated in the common site. If sites A and D are identical, or if sites B and C are identical, the correlation will be negative but again related to the noise of the common site. If site A is identical to site C site and site B is identical to site D, then the covariance is related to the root sum square (RSS) of the noise associated with site A and B. In all cases, it doesn't matter whether the "noise" is due to a variation of the clock associated with any given site or is due to the time transfer noise of that site's receive system. However, one criterion for the choice of sites was the quality of its clock.

We write $P=S^{-1}$, and define a solution design matrix A with 24*N rows and 2 columns. The elements of A are defined by dependence of the data on the EEP-violating and quadrature parameters. The two components of the parameter vector X are the EEP-violating term and its quadrature term. The data form a column vector Z, with 24*N components. The 24Nx24N covariance matrix of the observations, S, is computed using the geometrical considerations described in section II. Those elements of S whose corresponding baseline pairs are expected to have zero covariance are set to zero, the others are determined monthly using the observed covariances of mean-removed 12-hour frequencies.

The problem reduces to finding a 2-component column vector X, given data vector Z and design matrix A: $Z = A*X$, with known correlations S. It can be shown [21], that if $P=S^{-1}$, then X = final parameter values = $(A^T S^{-1}A)^{-1} *A^T S^{-1}*Z = (A^T PA)^{-1} *A^T*P*Z$, and the squared statistical uncertainties of the two parameters of X are the corresponding diagonal elements of $(A^T PA)^{-1}$.

Anchor Stations for Inter-satellite Link and Design for its Time Synchronization

Bai Yan, Lu Xiaochun, Jing Wenfang, Zhang Ke
Dept. of Navigation and Communication National Time Service Center, Chinese Academy of Science
Xi'an, China
by@ntsc.ac.cn

Bai Yan, Lu Xiaochun, Jing Wngfang
Key Laboratory for Precise Navigation Positioning and Timing of Chinese Academy of Science
Xi'an, China

***Abstract*—Inter-satellite link technology is one of hot issues in current satellite navigation field and construction of inter-satellite link system cannot be completed without the cooperation and supports of ground anchor stations. In this paper, with respect to time synchronization issue which is of great importance in the construction of anchor stations for inter-satellite link, key technological issues such as time system design for anchor station, method of synchronization with standard time, clock error of anchor station and the determination of its precision have been deeply discussed and studied. On the base of relevant studies, a complete design method and solution of time synchronization system for anchor station has been proposed herein, thereby offering solution ideas and technological supports for resolving key problems encountered during the construction of anchor stations for inter-satellite link in China. The anchor station time system proposed in this paper can better ensure the time difference between ground station and BDT is less than 1us and the time synchronization precision of anchor station is less than 5ns, thereby guaranteeing the reliability of anchor station acting as Pseudolite being connected to inter-satellite link while offering further reference for subsequent testings and development of inter-satellite link.**

Keywords—inter-satellite link; anchor station; time synchronization; clock error; precision;

I. INTRODUCTION

Inter-satellite link is an important component of Global Navigation Satellite System (GNSS), which, under the supports from measuring and communication functions offered by inter-satellite link, can perform autonomous navigation, which not only has effectively reduced the number of ground stations, lowered systemic cost and maintenance cost, but also has shorten the upgrading period of ephemeris and enhanced the performance of whole system. In war times, when ground system is destructed or fails, satellite navigation system can achieve autonomous operation depending on inter-satellite link, thereby improving the viability of the whole system. In normal cases, with inter-satellite measurements, ground system can determine the navigation satellite orbit accurately, further improving and enhancing positioning accuracy of system. Therefore, inter-satellite link is one crucial technology in construction of modernized high precision GNSS[1].

Construction of inter-satellite link system cannot be successful without the cooperation and supports of ground anchor stations. First, in the early period of inter-satellite link system construction, anchor stations are needed to complete various testings and experiments in order to ensure that various functions and performances of inter-satellite link system are in compliance with designed indexes. In addition, although inter-satellite link can accurately determine relative positions of different satellites, the whole constellation as a rigid body, whose overall rotation relative to the earth is unobservable. In other words, it is impossible to determine absolute position of a satellite only by autonomous orbit determination using inter-satellite measurements because of the equation coefficient matrix rank deficiency. In order to deal with the influence of constellation rotation on orbit determination and solve rank deficiency problem, J.A.Rajan has studied satellite autonomous orbit determination of based on ground anchor station, and pointing this problem can be settled by building the ground anchor stations and increasing the ground-satellite measurements. Since the position of anchor station are known, this leading into the position reference to satellite constellation through satellite-ground link and therefore it is possible to improve autonomous orbit determination precision effectively [2].

It can be seen from the above two points that anchor station of inter-satellite link is not only a ground equipment used to test satellite, but also a pseudolite, which will participate in the whole consternation network operation and improve satellite autonomous orbit determination precision, thereby being of very great significance for the guarantee and improvement of whole inter-satellite link system in terms of its performance and function. Hence, higher requirements should be imposed on the construction of anchor stations to ensure of function completeness and performance stability, which is the foundation for anchor station to serve the inter-satellite link.

This work is supported by a grant from the National Nature Science Foundation of China(No.11203027)。

In the process of construction of anchor station, one of very important aspects needed to be considered is time synchronization issue in anchor station. Only when the anchor station clock is strictly synchronized to the standard time reference for Beidou System, could correct link between satellite and the ground be ensured, and could precision of satellite-ground distance measuring and the satellite autonomous orbit determination be ensured.

In this paper, time synchronization issue in anchor station has been mainly studied. The key technological issues such as time system design for anchor station, method of synchronization with standard time, clock error of anchor station and the determination of its precision have been deeply discussed and studied. On the base of relevant studies, a complete design method and solution of time synchronization system for anchor station has been proposed herein, thereby offering solution ideas and technological supports for resolving key problems encountered during the construction of anchor stations for inter-satellite link in China.

II. OVERALL STRUCTURE DESIGN OF ANCHOR STATION

In the process of designing anchor station, what should be firstly considered is that as a ground station, anchor station should satisfy requirements related to in-orbit testings and experiments for inter-satellite link; In the meanwhile, the anchor station should act as a pseudolite which is connected to the constellation network. Taking as many as factors into consideration, index argument, station distribution, function allocation into different parts, system interface allocation and system reconfigurability among others should be optimized with a view to adapt to the further development of this system to the largest extent. At the same time, matured, advanced and reliable technologies should be used as many as possible to ensure the stability and reliability of the equipment.

The anchor station consists of several modules including antenna, transceiver, comprehensive baseband, time-frequency and signal acquisition analysis, in which, the active phased array antenna is used to build a point to point link of satellite-ground for high-precision pseudo-range measurement and high speed data transmission, thereby offering high-precision observations and data switching channels for precise orbit determination, time synchronization, autonomous operation and testings and experiments of inter-satellite link and satellite-ground link. In the meanwhile, with highly flexible directing feature of phased array antenna, it is possible to allocate corresponding time interval and build a satellite-ground link for measuring and communication, providing a good physical channel for autonomous operation, absolute zero-value calibration and uplink injection in emergency, and achieving inter-satellite and satellite-ground integrated operation management mode.

The transceiver module can realize up-converter for sent signals and down-converter for received signals, having the functions of controllable RF frequency, controlled receiving and transmitting gain, channel cold backup and multi-channel switching, etc.

Comprehensive baseband module consists of multi-functional digital baseband and upper computer, and is an important unit for inter-satellite link measuring and communication and the core part of whole system. It can realize the pseduo code two-way ranging, receive orders from upper computer, control work mode and work parameters of active phased antenna array, create control orders for transceiver and time-frequency module, etc. while transmitting measurements and communication information generated by baseband by framing to upper computer.

Signal acquisition analysis module is mainly composed of acquisition and playback device, and spectrum analyzer, mainly used for signals real-time monitoring and offline exact management, in order to help users find and analyze problems during testing ad experimental process.

Time-frequency module contains frequency synthesis and allocation device as well as reference time input and time difference monitoring equipment. This module is also the key part designed in this study and whose design principle and method to realize time synchronization will be detailed in the following section 3 and section 4.

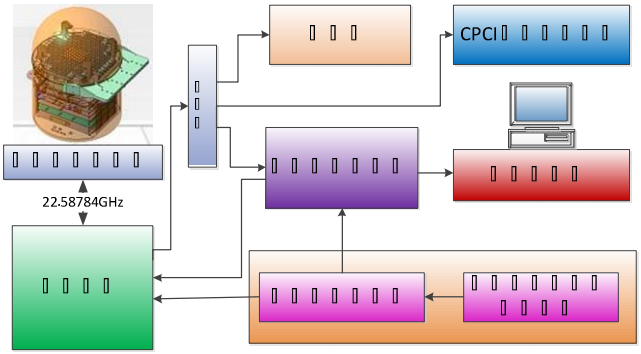


Figure 1 Modules of Anchor Station of Inter-satellite Link

Specific structure of anchor station for inter-satellite link is shown in Figure 1.

III. TIME SYNCHRONIZATION FOR ANCHOR STATION

National Time Service Center, China Academy of Sciences (NTSC) is the organization to create and release time-frequency standard in China, having high-precision time-frequency standards which can provide high-precision time-frequency signals, whose time service system is very important fundamental project and public welfare facilities. The coordinated universal time(UTC) kept by NTSC master station ranks in the first places globally, with time difference between UTC and BDT (Beidou Time) less than 150ns. Therefore, when designing anchor station time system, it is better to trace the anchor station time to UTC (NTSC) as much as possible in order to keep the anchor station time consistent with UTC. Specific time synchronization system can be designed through two methods.

A. Direct Connection to UTC(NTSC) Reference

If the anchor station can obtained the system time offered by NTSC, then 1PPS and 10MHz source from NTSC could be directly adopted. For example, when anchor station is located in NTSC master station, then 1PPS and 10MHz

signals from outlets of time-frequency sub system in NTSC master station may be directly sent to frequency synthesis and allocation equipment in anchor station through cable. Next, 10MHz signal will be synthesized by such frequency synthesis and allocation equipment to generate various low noise frequency signals of 10.23MHz, 50MHz and 80Mhz, which, after being shunted, isolation driven and amplified, will be sent to many other equipment such as transceiver channel, multi-functional digital baseband, and signal monitoring and acquisition equipment. At the same time, frequency synthesis and allocation equipment will conduct level-conversion for UTC 1PPS to obtain differential 1PPS signal of LVDS and RS422, which will be sent to other parts for time synchronization after being shunted and driven.

In addition, although the UTC(NTSC) is highly synchronized with BDT, in order to ensure the precision of satellite autonomous orbit determination in inter-satellite link, it is required to obtain precise anchor station clock error (namely, the time difference between anchor station and BD),which could be achieved by using forecast model of time difference between UTC and BDT offered by NTSC time difference monitoring system. This forecast model, through special equipment, monitor the time different between UTC(NTSC) and BDT. With the original time difference observations, in combination with BD time assessment data and IGS precise orbit, clock error and data of ionosphere and troposphere, this model will correct the real-time data observed previously and then integrate the corrected data with existing monitoring data, which will be served as the forecast of long time or short-time system time difference. The forecast uncertainty per day resulted from this model is less than 3ns (1σ).

Principle for direct connection to UTC time system is shown in Figure 2.

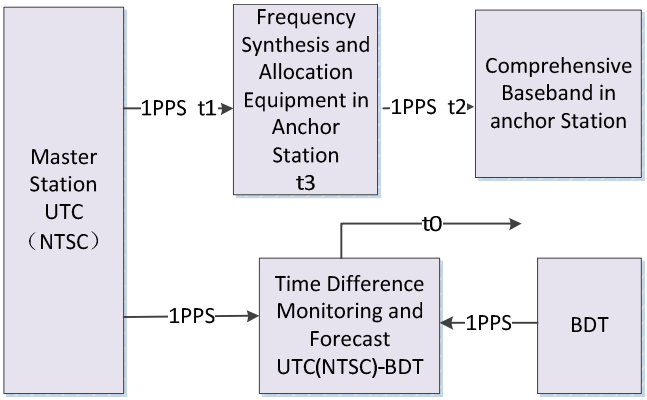


Figure 2 Principle of Direct Connection to UTC

B. *Tracing to UTC through Two-Way Transfer*

When anchor station is located in wildfield, direct connection to external standard time is therefore impossible, some distant calibration and comparison approaches may be adopted to trace the existing time to UTC(NTSC). For instance, two-way satellite time transfer(TWSTT) could be used to synchronize time between wildfield station and NTSC master station. Specifically, assume there is one satellite that can be observed both by wildfield station and NTSC master station, such wildfield station and NTSC master station can mutually transmit time signals, which, after being transmitted through satellite, will be received by each other. In this way, the time difference between wildfield station and NTSC master station could be attained. Next, wildfield station time could be corrected and synchronized with UTC(NTSC) in master station . Then, wildfield station can transmit its time through cable to anchor station, thereby achieving the time synchronization between anchor station and NTSC master station. TWSTT could eliminate public errors including satellite orbit error, satellite clock error, anchor station location error and troposphere delay error, and weaken ionosphere delay error. Through TWSTT, the precision of time synchronization between wildfield station and NTSC master station could be as high as 3ns.

Specific principle of time tracing to UTC(NTSC) through TWSTT is described in Figure 3.

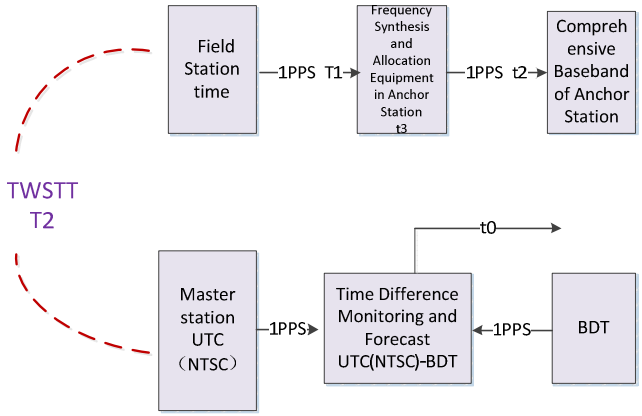


Figure 3 Principle of Time Tracing to UTC (NTSC) through TWSTT

C. *Analysis of Clock Error and its Precision for Anchor Station*

As a pseudolite, anchor station must ensure that time difference between anchor station time and BDT is less than 1us in order to guarantee a normal satellite-ground link. At the same time, to achieve autonomous orbit determination and time synchronization functions of inter-satellite link, precise satellite clock error and ground station clock error are further required, so as to ensure the normal working of the whole inter-satellite link system. As for BeiDou Navigation Satellite system(BDS), BeiDou Operation Control System is responsible for satellite time synchronization with BDT, also it forecast the time difference between satellite time and BDT. About satellite clock error will not be discussed in this paper. Only anchor station clock error is analyzed herein.

Regarding about anchor station, its time could be synchronized with BDT using the solution mentioned in the previous section. However, what is the anchor station clock error after synchronization and what is the precision of time synchronization? These problems are required to be solved if anchor station is connected to satellite-ground network as a pseudoite. Only when the clock error is determined, could error of range measurement caused by clock error of anchor station be reduced to the largest extent.

With respect to the two time system design solutions mentioned in the previous section, in this section, how to accurately determine clock error of anchor station and the precision of time synchronization will be detailed.

As for the first solution, namely, anchor station time is directly provided by UTC(NTSC). In this case, 1PPS and 10MHz signals from outlets of time-frequency sub-system equipment in NTSC master station are transmitted to frequency synthesis and allocation equipment of anchor station through cable. In the meanwhile, frequency synthesis and allocation equipment transmits 1PPS signal through cable to inlet of comprehensive baseband. In this way, the 1PPS signal from time-frequency sub-system to anchor station baseband, have been experienced two time delays caused by cables and the time delay of frequency synthesis and allocation equipment itself. The so-called clock error of anchor station means time difference between 1PPS from inlet of comprehensive baseband and the 1PPS of BDT. Therefore, such time difference actually contains four parts, such as, the cable time delay t1 from NTSC master station to frequency synthesis and allocation equipment in anchor station, the cable time delay t2 from frequency synthesis and allocation equipment to comprehensive baseband, time delay t3 of frequency synthesis and allocation equipment itself, as well as the time difference t0 between master station UTC (NTSC) and BDT.

First, the two cable time delays, t1 and t2, and time delay of frequency synthesis and allocation equipment, t3, could be calibrated through Vector Network Analyzer. The time difference t0 could be obtained through special time difference monitoring and forecast system. Then the final clock error of anchor station, Δt is obtained through the following formula:

$$\Delta t = (t1 + t2 + t3) + t0 \qquad (1)$$

Generally, The time difference between UTC(NTSC) and BDT, t0 is less than 150ns. Time delay t1 caused by 100m cable is no more than 400ns. The cable time delay t2 is calculated as the maximum value, namely 3ns. The time delay t3 is no more than 2ns. Then clock error between anchor station and BDT, Δt is less than 555ns, which can satisfy the requirement that time synchronization between anchor station time and BDT is less than 1us.

Precision of anchor station time synchronization could be obtained through calibration precision or forecast precision of various time delays forming the clock error. Forecast precision of t0, namely, UTC(NTSC)-BDT, is 3ns. Calibration precision of two cable time delays t1 and t2 are 1.5ns and 1.5ns, respectively. Calibration precision of frequency synthesis and allocation equipment itself, t3, is 1.5ns. Therefore, the precision of anchor station time synchronization is:

$$\sigma = \sqrt{3^2 + 1.5^2 + 1.5^2 + 1.5^2} = 3.97\text{ns}$$

In other words, precision of time synchronization is 3.97ns when UTC(NTSC) time reference from is directly adopted by anchor station.

As for the second solution, namely, field station adopts TWSTT to synchronize its time with NTSC master station UTC, time difference between field station and UTC(NTSC) after TWSTT is applied is T2. Similarly, time difference between UTC(NTSC) and BDT provided by time difference monitoring and forecast system is t0. In addition, field station time standard is sent to frequency synthesis and allocation equipment in anchor station through cable, the time delay of such cable after calibration is T1. The cable time delay between frequency synthesis and allocation equipment and comprehensive baseband is t2. The time delay of frequency allocation and amplification equipment itself is t3. Finally, clock error of anchor station, Δt could be obtained through the following formula:

$$\Delta t = (T2 + T1 + t2 + t3) + t0 \qquad (2)$$

Time difference between field station and UTC(NTSC) after TWSFF, i.e., T2, is less than 10ns. In the same principle, time difference between UTC(NTSC) and BDT, i.e., t0, is less than 150ns. Time delay T1 caused by 100m cable is no more than 400ns. The cable time delay t2 is estimated as the maximum value, namely 3ns. The time delay t3 is no more than 2ns. Then clock error of anchor station，Δt is less than 565ns, which can satisfy the requirement that time synchronization between anchor station and BDT is less than 1us.

Similarly, forecast precision of time difference between UTC(NTSC) and BDT, i.e., t0, is 3ns. Precision of T2, namely, is 3ns. Calibration precision of cable time delays T1 and t2 are 1.5ns and 1.5ns respectively. Calibration precision of time delay for t3 is 1.5ns.

Therefore, the precision of anchor station time synchronization is obtained through the following formula:

$$\sigma = \sqrt{3^2 + 3^2 + 1.5^2 + 1.5^2 + 1.5^2} = 4.96\text{ns}$$

In other worlds, the precision of anchor station time synchronization after TWSTT approach is 4.96ns.

Based the first kind of time synchronization method, a ground anchor station is built in Xi'an. Figure 4 is the monitoring results about clock error in anchor station. The curve show the changes of the time difference between the anchor station 1PPS and master station UTC(NTSC) 1PPS within 86 hours, and its precision is better than 3ns. This result is accordance with the previous analysis.

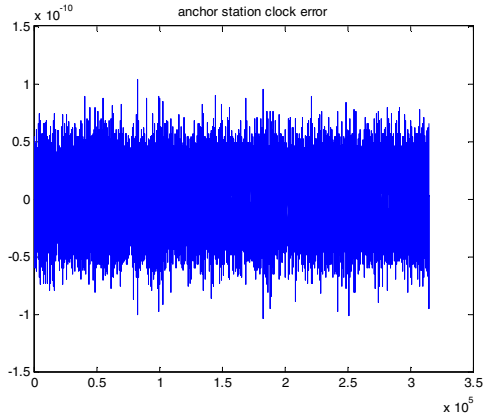


Figure 4 the monitoring results about clock error

IV. CONCLUSION

With respect to inter-satellite link technology, one of hot issues related to satellite navigation, a method to construct anchor stations for inter-satellite link is proposed in this paper. Furthermore, time synchronization system and synchronization methods are designed, clock error of anchor station and its precision are analyzed. It can be indicated from the findings that time system for anchor station designed herein can keep the time difference between anchor station and BDT within 1us with the precision of anchor station time synchronization is better than 5ns, thereby offering more reliable approach for anchor station to be connected to inter-satellite link network as a pseudo-lite and providing reference for subsequent testing and further development of inter-satellite link.

REFERENCES

[1] Chen Zhonggui. Key Technologies of Autonomous Operation for Navigation Satellite Constellations Using Inter-satellite Tracking Data. The Doctoral Dissertation in National University of Defense Technology, 2012, 5

[2] J.A.Rajan，Peter Brodie，Dr.Harris Rawicz．Modernizing GPS Autonomous Navigation with Anchor Capability，ION GPS/GNSS 2003,9：1534-1542

[3] Liu Li、Han Chunhao. Two Way Satellite Time Transfer and Its Error Analysis. Progress in Astronomy，2004,9，vol.22, No.3

[4] XU Yong，CHANG Qing，YU Zhijian. On new measurement and communication techniques of GNSS inter－satellite links. Science China:Technology Science. 2012，42(2):230 －240

[5] Maine K P, Anderson P, Langer J. Crosslink for the next-generation GPS. In: Proceedings of the 2003 IEEE Aerospace Conference. IEEE. 2003. 1–8

[6] Sanchez M, Pulido J A. The ESA “GNSS+” Project Inter-satellite ranging and communication links in the frame of the GNSS infrastructure evolutions. In: Proceedings of the 21st International Technical Meeting of the Satellite Division of the Institute of Navigation. Georgia: The Institute of Navigation, 2008. 2538–2546

[7] Zhu Jun. Research on Orbit Determination and Time Synchronizing of Navigation Satellite Based on Crosslinks. The Doctoral Dissertation in National University of Defense Technology. 2011. 4

Observed Propagation-Phase/Frequency-Shift Theory with Impact on Time/Frequency Transfer and GNSS

Michael J Underhill
Underhill Research Ltd
Lingfield, UK
e-mail: mike@underhill.co.uk

***Abstract*—More observations and measurements have been made of propagation phase and frequency shifts of L-band GNSS signals and carriers and standard frequency signals between 60kHz and 20MHz. Fluctuations have been observed which may or may not be attributable to weather, winds, clouds aircraft, ionospheric states, tides, etc. This paper presents new electromagnetic theory and multipath splitting of short-wave Standard Frequency Signals into components with persistent frequency shifts of up to a Hertz over paths of 500km to 11000km. These discoveries were made using SDR receivers with milliHertz resolution. Further data has been collected over the past year for frequencies between ~1MHz and 25MHz. The focus here is on categorizing and explaining the several significant effects that have been observed. The theory so far developed is based on extending and second order 'Landau damping' as seen in plasmas (as in the ionosphere) to newly discovered properties of free-space. The objective of the theory is to be able to extrapolate the observed short wave ionospheric and surface wave effects to GHz frequencies to enable estimation of the magnitude of any possible effects on any existing satellite navigation systems. Small short term, diurnal and seasonal frequency variations continue to be investigated as a possible method of detecting gravity waves. A Rubidium source is now installed for better future estimates of the absolute frequency shifts of observed trans-Atlantic surface waves between 1 and 5MHz. The new Propagation-Phase/Frequency-Shift (PPFS) theory is based on the 'Filamentary Model of Electromagnetism' originally announced in 2011. It also supports the concept of EM detection and generation of gravity-potential-waves.**

Keywords— Time and Frequency Transfer; new ionospheric and spatial propagation effects; SDR milliHz measurements

I. INTRODUCTION AND AIM

The objective is theoretical explanations for all observed and measured effects seen in electromagnetic and gravity wave propagation. As an example, Fig. 1 shows several ionospheric propagation effects for a 5400km path between Canada and the UK over about 24 hours and these all need explanations.

In Figs 1 to 3the following carrier frequency shift effects can be seen and need explaining:

1. Positive and negative Doppler shifts from Ionospheric layers rising, descending or altering in slope.
2. Oscillations in ionospheric heights and path lengths have periods of typically 1.5 hours. This is as yet unexplained. Ionospheric tidal oscillations?
3. A diurnal (daily) saw-tooth variation of mean frequency of up to ± 1 Hz. This severely limits the use of CHU or similar as reliably accurate frequency sources when ionospheric propagation is used.
4. Smooth dispersion from continuous multi-path spreading of wave energy.
5. Occasional distinct splitting into distinct multiple ground bounce reflections.
6. A small redshift ~25 to 75 mHz of the frequency average taken over 24 hours. (This is larger and more obvious from measurements taken over longer ionospheric paths at higher frequencies.)
7. The presence of low dispersion surface-wave (?) signals at the onset and cessation of ionospheric propagation
8. An apparent diurnal variation in the red-shift of the surface wave signals of about 50 mHz. This would imply that the redshift is varying depending on the motion of the path relative to the earth's surface spin velocity and its orbital velocity around the sun. This would appear to be a new fundamental discovery.

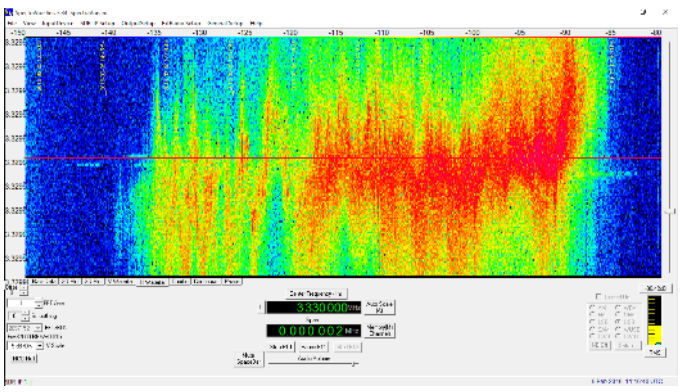


Fig. 1. The carrier frequency of CHU in Ottawa, Canada on 3330kHz at 5400km received in Lingfield, UK with 2Hz vertical bandwidth over one day to 1117 UTC on 6 Feb 2016, with 15mHz resolution. A Spectratime LCR-900 rubidium reference was used, but uncalibrated with a possible frqency error of<10 to15 mHz. Several propagation frequency shift effects can be seen. Particularly the red-shift (downshift) mechanisms seen need explanation.

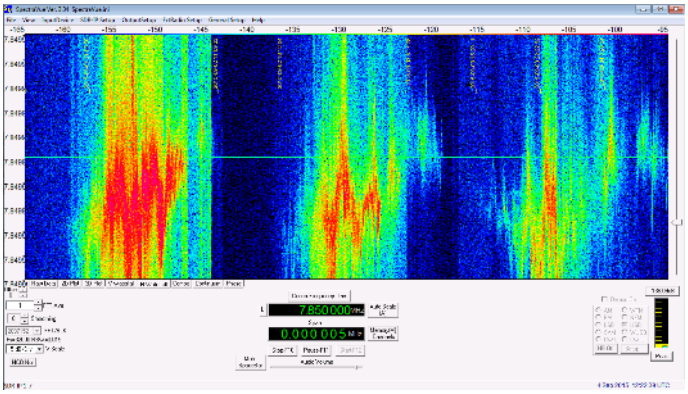


Fig. 2. Three day plot of CHU in Ottawa, Canada on 7850kHz at 5400km received in Lingfield, UK with 5Hz vertical bandwidth to 1117 UTC on 4 Sept 2015, with 15mHz resolution. A Spectratime LCR-900 rubidium reference was used, but uncalibrated with a possible freqency error of ~100 mHz.

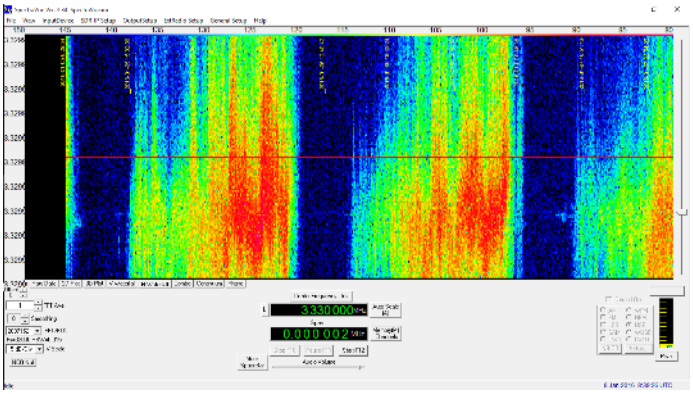


Fig. 3. Three day plot of CHU in Ottawa, Canada on 3332kHz at 5400km received in Lingfield, UK with 2Hz vertical bandwidth to 1117 UTC on 8 Jan 2016, with 15mHz resolution. A Spectratime LCR-900 rubidium reference was used, but uncalibrated with a possible freqency error of ~100 mHz.

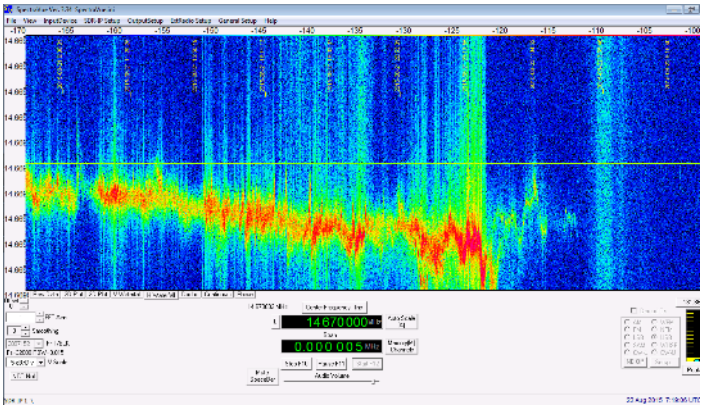


Fig. 4. One day plot of CHU in Ottawa, Canada on 14670kHz at 5400km received in Lingfield, UK with 5Hz vertical bandwidth to 0719 UTC on 22 Aug 2015, with 15mHz resolution. The local reference used had a possible freqency error of<50 to 100 mHz.

II. Propagation-Phase/Frequency-Shift (PPFS) Concept and Theory

The new Propagation-Phase/Frequency-Shift (PPFS) theory presented here is a development from the concept of *coupling* in the 2011 Filamentary-Model-of-Electromagnetism (FME) [1] and in [2]. It is also based on and validated by the many measurements of propagated waves and the measurement techniques used as reported in the references [3-9]. The only related theory found so far found is the 1936 Landau Damping Theory of Lev Landau [10]. This deals with frequency shifts in electron plasmas. The ionosphere is an electron-plasma. Pulsar signals act as if free-space were a very weak electron plasma.

The basic PPFS concept is that *delayed-self-coupling* in electromagnetic waves in a homogenous medium such as free-space or a plasma, albeit small, cases a continuous and progressive red-shift in frequency accompanied by a proportional loss in energy.

The new theory proposes that the lost energy is converted into a gravity wave at twice the electromagnetic wave frequency together with a dc gravity component. At sufficient distance from an electromagnetic source the relative amplitudes of the electromagnetic waves reach an asymptotic equilibrium.

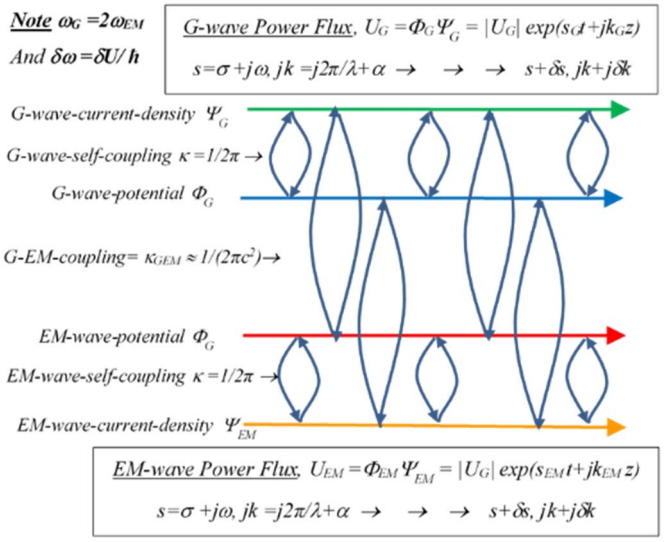


Fig. 5. **The Model for PPFS Theory** consists of Electromagnetic (EM-) and Gravitational (G-) waves travelling from left to right, both mildly self-coupled, with coupling coefficient $\kappa = 1/2\pi$, and weakly coupled to each other, with parametric inter-coupling coefficient $\kappa_{GEM} \approx 1/2\pi c^2$. The G-wave is at twice the frequency of the EM-wave and has a quarter-power dc component. All coupling has a fixed fundamental time delay which is a function of root frequency $\tau(\sqrt{f})$ where $f = \omega/2\pi$. Because of this, energy is progressively lost from the EM-wave and transferred to the G-wave until equilibrium is reached. A discovery is that the frequency red-shift δf is proportional to the loss of energy δU with Planck's Constant h as the constant of proportionality. We have $\delta f = \delta U/h$.

This model provides the basis for more detailed for the PPFS mathemeatics which is currentlybeing developed.

III. Measured GPS Phase/Frequency Fluctuations

One useful example measured so far is shown in Fig. 3. It shws phase fluctuations of the GPS locked source over 24 hours.

A future objective is to use this to measure any ContinuousRed-Shifts with distance of the 198 kHz standard frequency signal at Droitwich, UK. So far the GPS frequency errors appear small enough to be able to do this.

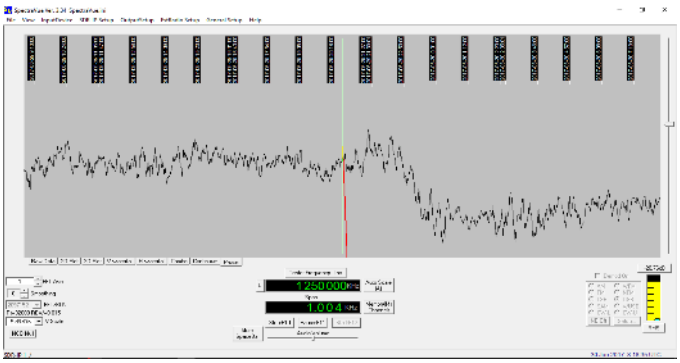


Fig. 6. GPS disciplined oscillator soure right-to-left time record of received phase compared with Spectratime LCR-900 rubidium oscillator over 44 minutes. Vertical scale is 0 to 360° measured at divided down frequeny of 1.25 MHz, so that the total scale represents a distance measurement variation of 240 metres. (Weather conditions were cloudy and overcast throuhout the record.) RFSpace SDR-IP receiver was locked to the LCR-900 source Steady state peak-to-peak error seen to be ~50 metres. Frequency is rate of change of phase, so we can calulate that the three hour step-down in freuqncy, right of centre, is a steady frequency error of 25 parts in 10^{12} or ~-40mHz at the 1575 MHz GPS refernce frequency. (One satellite off-frequency by 40mHz, relative to others?)

I. Conclusion

From observations on a series of measured results of frequency shifts a model has been produced as a basis of the PPFS theory aimed at explaining most if not all the observed effects. Further development of supporting mathematics and equations is under development.

References

[1] M. J. Underhill, "A Physical Model of Electro-magnetism for a Theory of Everything", *PIERS Online*, Vol.7, No. 2, 2011, pp. 196 -200. Also in *Proc. PIERS 2011*, March 20-23, Marrakesh, Morocco, pp. 1665 – 1669.

[2] M. J. Underhill, "Coupled Electromagnetic Wave Propagation in Space and around Surfaces and Interfaces", *Proc. PIERS 2013*, August 12-15, Stockholm, Sweden, pp. 394 – 398.

[3] M. J. Underhill, "Anomalous Ground-Wave Tilt Measured Over Wet Ground", *IET Conf. on Ionospheric Radio Systems and Techniques 2012*, 15-17 May 2012,| Royal York Hotel, York, UK

[4] M. J. Underhill, "Estimation of Ionospheric layer heights and velocities using available DRM signals", *IET IRST 2012 Conf. Proc.*, 15-17 May, 2012, pp. 1 - 5.

[5] M. J. Underhill, "Coupled Electromagnetic Wave Propagation in Space and around Surfaces and Interfaces", Proc. PIERS 2013, August 12-15, Stockholm, Sweden, pp. 394 – 398.

[6] M. J. Underhill, "Discovery of Persistent Ionospheric Frequency Shifts of a few Herz and Impact on Time and Frequency Transfer.", IFCS-EFTF 2015, April 12-16, Denver, Colorado, pp. 549-552.

[7] M. J. Underhill, "SDR and Self-Focusing Radar Techniques for milliHerz Measurement of Multi-Component Phase Noise Spectra?" IFCS-EFTF 2015, April 12-16, Denver, Colorado.

[8] M. J. Underhill, "Discovery of Ionospheric 'Hubble' Frequency Shifts and Impact on Gravity Wave Detection and the Age of the Universe?," *Proc. PIERS 2015*, Prague, 6-9 July 2015, pp. 2885-2889

[9] M. J. Underhill., "Propagation frequency shifts and impact on time and frequency transfer and gravity wave detection" IFCS 2016, May 9-12, New Orleans, Louisiana, pp. 1-5.

[10] Lev Landau (in 1946) https://en.wikipedia.org/wiki/Landau_damping

Initial Use of Galileo Signals in PTB

Andreas Bauch, Julia Leute, Thomas Polewka, Dirk Piester, Egle Staliuniene
Physikalisch-Technische Bundesanstalt (PTB)
Bundesallee 100, 38116 Braunschweig, Germany
Andreas.Bauch@ptb.de

Weijin Qin
National Time Service Center (NTSC)
Chinese Academy of Science
Lintong, Shaanxi Province, 710600 P. R. China

***Abstract*—We report on the initial use of Galileo signals in the Time and Frequency Department of Physikalisch-Technische Bundeanstalt (PTB). To this end PTB operated five GNSS receivers capable of receiving Galileo Open Service signals with calibrated signal delays for the two frequencies E1 and E5a.**

Keywords—GNSS, Galileo, time and frequency metrology

I. SUMMARY

By law, PTB is entrusted with the realization and dissemination of legal time for Germany. PTB offers the "classical" and well-known dissemination services, via long wave, telephone and the public internet. Many users in Germany and elsewhere use in lieu thereof GPS signals as reference for the local realization of time unit, frequency and time-of-day. There is an ongoing debate about the status of measurements and time information generated in this way. Since a couple of years PTB publishes the results of GPS observations with respect to the local reference time scale UTC(PTB) using a GPS receiver whose calibration has been ensured by BIPM, recently in particular through the campaigns that involve the so called G1 laboratories. In addition, the standard files in CGGTTS and RINEX format of several receivers are published on the public ftp site of PTB for the experienced user.

Following the declaration of Galileo initial services by the European Commission we see a need to provide similar service involving Galileo signals. Currently PTB operates five GNSS receivers that provide also Galileo observation data. Two of them autonomously generate "CGGTTS-like" files (MESIT GTR51), in case of the three others the r2cggtts (V71b) software, recently made available by ORB, is used to generate standard files. Starting April 2017, the PTB Time Service Bulletin will also contain daily mean values of Galileo System Time (GST) minus UTC(PTB) from one receiver. In addition, we are going to report the GST to GPS time difference as reported in the Galileo Signal-in-Space and retrieved from the header of RINEX Navigation files. The user may himself compare this value with the difference obtained locally in PTB from the same receiver on a daily basis. At the moment this difference is of order 2-3 ns.

The critical issue of course is the calibration of Galileo signal delays in the receivers. The recipe how to determine the delay for the Galileo E5a signals was published in [1] and a script was built thereon by GMV, Tres Cantos, Spain [2] and used to determine the internal delays for the Galileo Sensor Station receiver at PTB whose GPS signal delays had before been determined with respect to the PTB reference receiver. Based thereon the internal Galileo delays of the other four receivers were determined. The uncertainty for the delay values is obviously larger than for the GPS delays, but we consider that as a first step to go. One of us (W.Q.) is currently engaged to develop a procedure on her own so that we may in the future study the delay values obtained for PTB receivers as a function of the parameters in the processing as well as of time. This should give a better confidence, even if the need for an absolute calibration of the receiver delays remains an open issue at the moment.

Code-based ionosphere-free time comparisons using Galileo signals have been established with Institute of Photonics and Electronics, Czech Academy of Sciences, CZ (UFE), since more than a year and between a secondary realization of UTC(PTB) at the DCF77 long-wave transmitter facility in Mainflingen, Germany, and PTB Braunschweig since Summer 2016 [3]. Results will be presented.

ACKNOWLEDGMENT

We acknowledge the continuous support of Pascale Defraigne and colleagues involved in providing the r2cggtts software, Alexander Kuna and Petr Panek of UFE for their support in operation of our different MESIT receivers, and we thank Ricardo Piriz of GMV for providing the Galileo receiver delay calibration. W. Q. acknowledges funding of her stay in PTB by Chinese National Science Council.

REFERENCES

[1] P. Defraigne, W. Aerts, G. Cerretto, E. Cantoni, J.-M. Sleewaegen, "Calibration of Galileo signals for time metrology", IEEE Trans. Ultrason. Ferroelect. Freq. Contr., vol. 61, no. 12, pp. 1967-1975, 2014.

[2] R. Piriz, D. Rodriguez, P. Roldan, A. Mudrak, A. Bauch, J. Leute, P. Pánek, A. Kuna, "Relative Calibration of Galileo Receivers within the Time Validation Facility (TVF)", Proc. 2015 Joint Conference of the IEEE International Frequency Control Symposium & European Frequency and Time Forum, 12-16 Apr 2015, Denver, Colorado, USA, pp. 245-249, 2015.

[3] D. Piester, A. Bauch, J. Becker, J. Leute, T. Polewka, F. Riedel, D. Sibold, E. Staliuniene, S. Weyers, "PTB's Time and Frequency Services 2015 – 2016", Proc. 2017 Precise Time and Time Interval Meeting – ION PTTI 2017, 30 Jan - 2 Feb 2017, Monterey, CA, USA, 2017.

Experimental study of a miniaturized calcium atomic beam tube for small optical frequency standard

Haijun Chen, Zhongzheng Liu, Shunlu Xiao
National Key Laboratory of Science and Technology on Vacuum Electronics
Beijing Vacuum Electronics Research Institute
Beijing 100015, China
E-mail: e1412225@163.com

Haosen Shang, Shengnan Zhang, Jingbiao Chen
State Key Laboratory of Advanced Optical Communication System and Network
School of Electronics Engineering and Computer Science,
Peking University
Beijing 100871, China

***Abstract*—With the advantage of relatively simple structure, the optical frequency standard based on calcium thermal atomic beam has the potential to be miniaturized and engineered. We develop a new fully vacuum-sealed calcium atomic beam tube, which divergence angle of calcium atomic beam is narrower and background noise of 423 nm laser-induced fluorescence is much lower than its predecessor. This paper describes experimental study of this new tube using the 657 nm clock transition laser and 423 nm detection laser.**

Keywords—optical frequency standard; Calcium atomic beam tube; miniaturization; frequency stability;

I. INTRODUCTION

Currently the frequency stability and uncertainty of optical clock have reached 10^{-16} level at 1 s and 10^{-18} level respectively in the laboratory [1-4], much better than that of the microwave frequency standard. This greatly promotes the development of fundamental physics and metrology. However, in order to obtain better performance, these optical clocks usually adopt cold atomic scheme, which makes the system very complex and is not feasible to practical general application.

With the advantage of relatively simple structure, the optical frequency standard based on calcium thermal atomic beam was realized by PTB [5] and NIST [6]. For improving the signal-to-noise ratio of the 657 nm clock transition spectroscopy, Peking University proposed the application of the electron-shelving detection method [7, 8], which uses the fast $^1S_0$-$^1P_1$ 423nm transition to detect the narrow $^1S_0$-$^3P_1$ 657 nm clock transition. Based on this technology, McFerran et al.[9] built an optical frequency standard using a calcium atomic beam vacuum device in a flange-sealed structure and achieved a stability of 9 x 10^{-14}/1s, while the one developed at Peking university obtained an increased stability of 3 x 10^{-14}/1s[10].

To further reduce the volume of calcium optical frequency standard, we previously developed a fully vacuum-sealed calcium beam tube with no flanges [11], which has operated for more than 24 months. Based on this device, we recently developed a new fully vacuum-sealed calcium atomic beam tube. Though this tube has a similar structure to the previous one, it has an improved divergence beam angle and background noise of 423 nm laser-induced fluorescence. We have carried out a series of experimental studies on the newly fabricated calcium atomic beam tube. This paper presents some latest results of our studies on the fully vacuum-sealed calcium beam tubes for compact Ca beam optical clocks.

II. DESIGN AND FABRICATION

A photograph of the newly fabricated tube is shown in Figure 1. This tube has the same modular structure as its predecessor, mainly consisting of a calcium oven, a saturation absorption section, an optical Ramsey interaction section, a fluorescence detector, and a small ion pump.

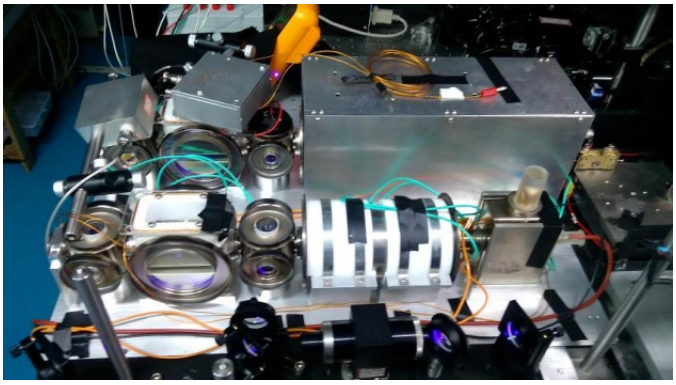


Fig. 1. A photograph of a fully vacuum-sealed Calcium beam tube for compact Ca beam optical clock.

It is desirable to have smaller divergence angle of atomic beam so as to improve the utilization rate of calcium atoms and reduce the Doppler line width of the 423nm laser-induced fluorescence of the Ca $4s^2\ ^1S_0 \rightarrow 4s4p\ ^1P_1$ transition. On the other hand, stronger fluorescence signal can be detected to improve the short-term stability of calcium optical frequency standard under the same oven temperature. Therefore, we optimized the manufacturing process of the micro-hole array used for ejecting Calcium atomic beam and achieved more uniform diameters and Angles of the micro-holes, this effectively reduced the divergence angle of the beam.

The signal-to-noise ratio of the clock transition signal and the short-term frequency stability can be improved by

reducing the scattering light background of the 423nm fluorescence detection zone. Previous experiments show that, the laser windows of fluorescence detector which sealed by metallization technique and the metal cylinder of detector are the major sources of high light background. Due to current technological constrains, there is no way to further improve the laser window. Therefore, in the design of this tube, we extended the distance between the laser window and the atomic interaction area, and used a light trap instead of the emergent light window. In order to absorb stray light, we blacked the interior surface of the fluorescence detector as shown in figure 2. These measures result in the light background reduction by about one order of magnitude.

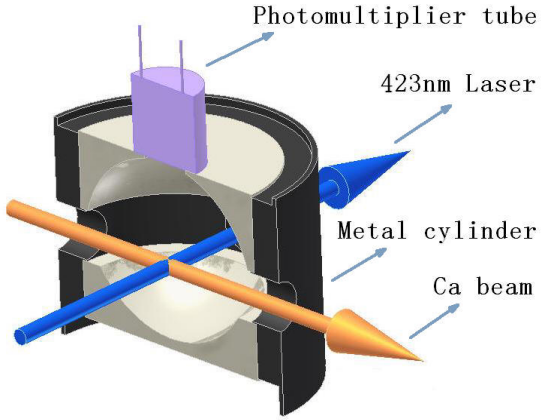


Fig. 2. "Blacked" Fluorescence collecting detector

III. EXPERIMENTAL RESULTS AND DISCUSSION

Figure 3 gives the experimental scheme of the calcium atomic beam tube. First, the frequency of the 423 nm laser is locked by calcium atom fluorescence spectrum. Then, the calcium atomic clock transitions are excited by the 657 nm laser interrogation. Finally, the calcium atoms are detected by the locked 423nm laser with electron-shelving detection method [7, 8].

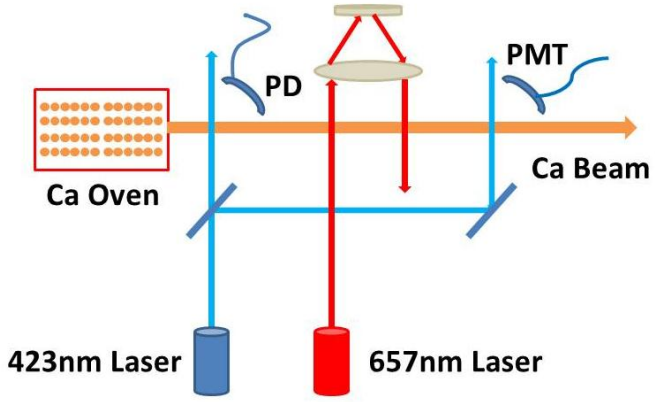


Fig. 3. Experimental scheme of the calcium atomic beam tube

Figure 4 shows the 423nm laser-induced fluorescence of the Ca $4s2\ ^1S_0 \rightarrow 4s4p\ ^1P_1$ transition in the detection zone without 657nm laser. According to the isotope shift [12], the Doppler line width of ^{40}Ca can be calculated, which is about 60MHz, reduced by 40% compared to the previous one. This result indicates that our measures taken to reduce the divergence angle are valid.

In addition, the temperature of the calcium oven required to provide the same fluorescence signals is lower as compared to previous tubes. That means the annual consumption of atoms is lower while the life of the tube becomes longer. These features are very beneficial to the practical applications.

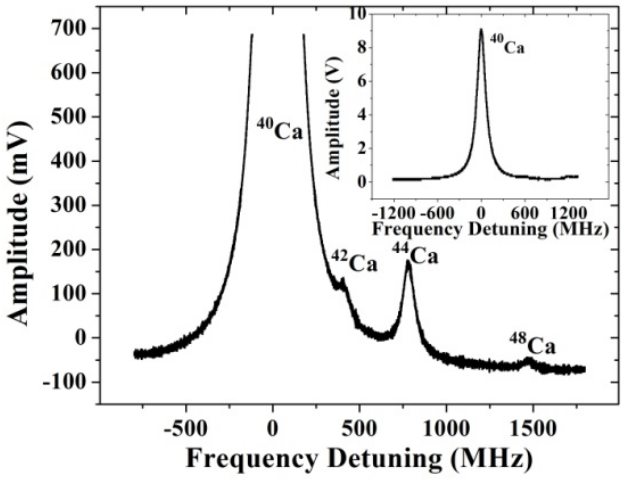


Fig. 4. The 423nm laser-induced fluorescence of the Ca $4s2\ ^1S_0 \rightarrow 4s4p\ ^1P_1$ transition

The Ca clock transition spectroscopy can be measured when the 423 nm laser is locked and the frequency of 657 nm laser is scanning. The line width was found to be 500 kHz. After locking the 657 nm laser frequency to the center of the 657 nm clock saturation spectroscopy, the frequency stability reached 8×10^{-14}/1s and decreased to 2×10^{-14} at 100 s, as was measured by residual error amplitude. To obtain more accurate data, we estimated the instability by comparing with the system in a flange-sealed design whose fractional instability is 3.0×10^{-14}[10]. Finally, a stability of 6.8×10^{-14}/1s and 1.8×10^{-15} after 1000 s was achieved, as shown in the figure 5.

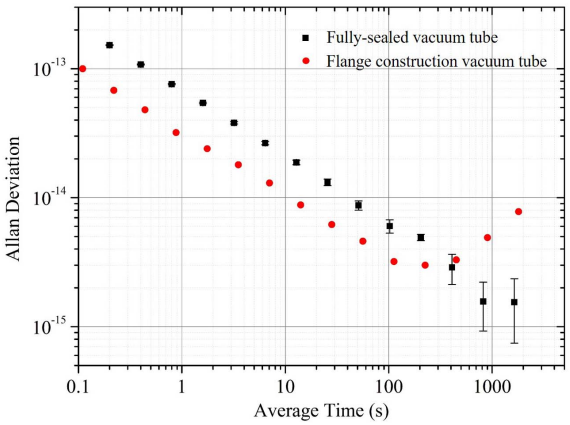


Fig. 5. Allan deviation of Ca beam optical clock with the new full-sealed vacuum tube versus the system in a flange-sealed design

IV. CONCLUSION

In conclusion, we have developed a new miniaturized fully vacuum-sealed calcium atomic beam tube with narrower divergence angle of the calcium atomic beam and much lower background noise of 423 nm laser-induced fluorescence as compared to the previous. The frequency stability of the small optical frequency standard with this new tube has reached 6.8 $\times 10^{-14}/\sqrt{\tau}$. We believe this work has laid a foundation for the engineering application of small calcium beam optical clock.

ACKNOWLEDGMENT

This work is supported by the National Hi-tech Research and Development (863) Program and the authors appreciate the support of the Peking University.

REFERENCES

[1] N. Hinkley, J. A. Sherman, N. B. Phillips, et al., "An atomic clock with 10^{-18} instability," Science, vol. 341, pp.1215-1218, 2013.

[2] B. J. Bloom, T. L. Nicholson, J. R. Williams, et al., "An optical lattice clock with accuracy and stability at the 10^{-18} level," Nature, vol. 506, pp.71-75, 2014.

[3] T. L. Nicholson, S. L. Campbell, R. B. Hutson, et al., "Systematic evaluation of an atomic clock at 2×10^{-18} total uncertainty," Nature Communications, vol. 6, pp. 6896, 2015.

[4] Ichiro Ushijima, Masao Takamoto, Manoj Das, et al., "Cryogenic optical lattice clock," Nature Photonics, vol. 9, pp. 185-189, 2015.

[5] P. Kersten, F. Mensing, U. Sterr, F. Riehle, "A transportable optical calcium frequency standard," Applied Physics B, vol. 68, pp. 27-38, 1999.

[6] Fox R. W, Sherman J. A., Douglas W., et al., "A high stability optical frequency reference based on thermal calcium at-oms," 2012 IEEE International Frequency Control Symposium (IFCS), Baltimore, 21-24 May, 2012.

[7] Huang Kaikai, Zhang Jianwei, Yu Deshui, Chen Zhenhui, Zhuang Wei, Chen, Jingbiao. Application of electron-shelving detection via 423 nm transition in Calcium-beam optical frequency standard, Chin. Phys. Lett., 2006, 23(12):3198-3201.

[8] Kaikai Huang, Donghai Yang, Jingbiao Chen, Small compact Calcium-beam optical frequency standard in Peking university and its new scheme, Proc. of 20th EFTF, Braunschweig Germany, 2006:376-378.

[9] John J. McFerran, Andre N. Luiten, "Fractional frequency instability in the 10-14 range with a thermal beam optical fre-quency reference," J. Opt. Soc. Am. B, vol. 27, pp. 277-285, 2010.

[10] Xiaogang Zhang, Shengnan Zhang, Zhaojie Jiang, et al., "A Transportable Calcium Atomic Beam OpticalClock" 2016 IEEE International Frequency Control Symposium (IFCS), New Orleans, 478-481 May, 2016.

[11] Haijun Chen, Xiaogang Zhang, Youhuan Liang, et al., "Study of a fully vacuum-sealed calcium atomic beam tube for optical frequency standard" 2016 IEEE International Frequency Control Symposium (IFCS), New Orleans, 482-485 May, 2016.

[12] E. J. Salumbides, V. Maslinskas, I. M. Dildar, "High-precision frequency measurement of the 423-nm Ca I line" Physical Review A 83, 012502 (2011)

A Small Calcium Beam Optical Frequency Standard with Fully-sealed Vacuum Tube

Haosen Shang, Xiaogang Zhang, Shengnan Zhang, Jingbiao Chen
State Key Laboratory of Advanced Optical Communication, System and Network,
School of Electronics Engineering and Computer Science,
Peking University, Beijing 100871, China
E-mail: jbchen@pku.edu.cn

Haijun Chen
National Key Laboratory of Science and Technology on Vacuum Electronics,
Beijing Vacuum Electronics Research Institute,
Beijing 100015, China
E-mail: e1412225@163.com

***Abstract*—In this paper a small Calcium beam optical frequency standard utilizing fully-sealed Calcium beam vacuum tube owning smaller size compared with vacuum system with flanges is demonstrated. Adopting the electron shelving detection method, we detect the clock transition 657 nm saturation absorbing spectroscopy whose linewidth is 500 kHz. The instability of this small optical frequency standard is 6.8×10^{-14} at 1 second and 1.8×10^{-15} after 1000 seconds of averaging by comparing with another small Calcium beam optical frequency standard whose reported instability is 3.0×10^{-14} at 1 second. The optical part of the whole system is specially designed for robustness and miniaturization.**

Keywords—small Calcium beam optical frequency standard; fully-sealed Calcium beam vacuum tube; electron-shelving detection method;

I. INTRODUCTION

Achievements of optical clock [1, 2] push the pace of the research in geopotential measurements [3], gravitational wave detection [4], or other fundamental physics. However the size and complexity limit its further application into the conditions where a transportable one is much more needed.

Till now, the research of small optical frequency standard mainly focuses on the Calcium [5-10] and Strontium [11].Thanks to the development of the optical lattice technology and laser cooling technology, the PTB has realized a transportable Strontium optical clock with 10^{-17} uncertainty [11], nevertheless, the size which is 2.2 m × 3 m × 2.2 m and the power consumption of the whole system is still relatively large.

Optical frequency standard based on atomic beam owns much more simple construction compared with optical lattice clock or ion clock. The relevant work of Calcium atomic beam clock has been reported in [5-10]. The PTB detected the Ca clock transition directly, and is limited by the signal-to-noise ratio of the clock transition spectroscopy [5]. It is difficult to ensure good short-term or medium-term instability [5]. To solve this problem, we put forward the application of the electron-shelving detection method into Calcium beam optical frequency standard for the first time [6, 7] to greatly improve the signal-to-noise ratio. In that case, Mcferran J. J. et al. followed this idea and realized an instability of 9.2×10^{-14} at 1s [8]. After that, we propose a dispersion detection of clock transition to realize a Calcium beam optical frequency standard [9]. Till now, we realize a small Calcium beam optical frequency standard with vacuum tube sealed by flanges, the instability is 3×10^{-14} at 1s [10].

Besides, in conventional atomic beam optical frequency standard, an atomic beam vacuum system sealed by flanges is used as the quantum reference source. It is well known that large vacuum systems with flange typically require bulky ion pumps to maintain vacuum, this kind vacuum system generally occupies larger volume in the whole system, which is not good for the miniaturization of the optical clock, and thereby a fully-sealed vacuum system without flanges is implemented in our work.

Here we use a fully-sealed Calcium beam vacuum tube without flanges whose size is 55 cm×16 cm×15 cm [12,13]. Its structure is specially designed to meet with our scheme. In this Calcium beam optical frequency standard, a 423 nm external cavity diode laser which has been locked to detect the 657 nm clock transition spectroscopy, namely the electron shelving detection method [14]. The 657 nm laser is pre-locked to an ultrahigh finesse FP cavity by Pound-Drever-Hall technique [15, 16]. A 500 kHz saturation absorbing spectroscopy of 657 nm is used to lock the driver of AOM (acoustic optic modulator). To estimate the instability of this small Calcium beam optical frequency standard, we compared this one with another Calcium beam optical frequency standard whose reported instability at 1s is 3.0×10^{-14} [10]. The beating signal of the two optical frequency standard gives an instability of 6.8×10^{-14} at 1s and 1.8×10^{-15} after 1000 s of averaging.

II. EXPERIMENT

The experimental setup of Calcium beam optical frequency standard utilizing fully-sealed vacuum tube is basically demonstrated in figure 1. Compared with conventional vacuum tube sealed by flanges, a new fully-sealed vacuum tube is designed to minimize the total size of the whole system.

This work is supported by the National Hi-tech Research and Development (863) Program and National Natural Science Foundation of China (Grant Nos.91436210).

Besides, a fully-sealed one is much more robust in the fluctuations for the sake of the mechanical vibrations.

The Calcium granules are placed in a small oven which is surrounded by heating wire. A thermistor is put beside the oven to sense the temperature. A high-precision servo circuit is utilized to control the temperature and the actual temperature will fluctuate below $\pm$ 30 mK. Sieve-like holes on the body of the oven are helpful to form directional atomic beam flow, three apertures are put in the direction of the flow in turn to minimize the divergence of the atomic beam.

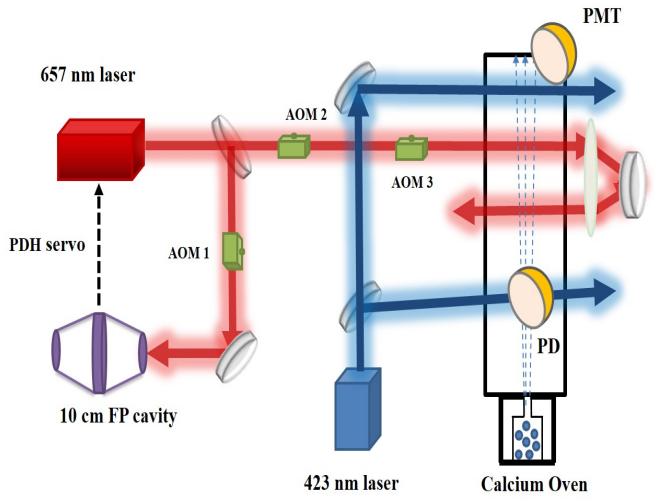


Fig 1. Setup of the small Calcium optical frequency standard. AOM, acoustic optics modulator. PMT, photomultiplier tube. PD, photodetector. A 657 nm external cavity diode laser is pre-locked to the 10 cm FP cavity using Pound-Drever-Hall technique, and the 657 nm laser is delivered to the vacuum tube using the polarization maintaining fiber which is not showed in the figure. A PMT is placed in the latter window to collect the 423 nm fluorescence. And a PD is placed in the former window to collect the 423 nm fluorescence used to lock the 423 nm external cavity diode laser. The half wave plates placed before 423 nm or 657 nm laser interacts with the atoms are not showed in the figure. The isolators and relevant electronic device are not showed in the figure but will be described in the paper.

Electron shelving detection method is adopted in our scheme to improve the signal-to-noise ratio of the 657 nm clock transition. We made a small 423 nm external cavity diode laser with a single laser diode provided by Nichia Corporation. The maximum power output of this blue laser is approximate 40 mW which is abundant for our experiments. As have been showed in figure 1, The 423 nm laser interacts with the Calcium atoms and 423 nm fluorescence will be collected in the former and latter window, respectively. The fluorescence of the former window is detected by a PD and the fluorescence of the latter window is detected by a PMT. In the latter window, the laser is orthogonal with the atomic beam. In that case the Doppler shift can be eliminated. Whereas the laser interacts with the atomic beam in an acute angle in the former window, hence a fluorescence with a Doppler shift can be directly used as the servo signal to lock the 423 nm laser. No additional modulation and demodulation circuits are needed in our scheme and thus much less noise will be introduced into the system. Besides, we find that the Hanle effect influence the spatial intensity distribution of the 423 nm resonance fluorescence, the intensity of the fluorescence is related with the direction of the magnetic field and the 423 nm laser polarization [17]. In the plane which is perpendicular to the polarization direction of laser the maximum intensity of fluorescence can be acquired, at the same time the polarization direction of laser is parallel to the magnetic field direction [17]. This can improve the fluorescence intensity for almost one order and is helpful to improve the signal-to-noise ratio of the whole system.

The 657 nm external cavity diode laser is pre-locked to an optical cavity whose length is 10 cm using the Pound-Drever-Hall technique [15, 16] and the finesse is about 250,000. The cavity is put inside a small vacuum chamber and the temperature is set at zero crossing temperature. For the sake of the deviation of the cavity mode and the clock transition frequency, three acoustic optics modulators (AOM) are used to compensate the frequency deviation. The AOM 2 and AOM 3 are double passed. The 657 nm laser is delivered by a polarization maintaining fiber to the vacuum tube. And the 657 nm saturation absorbing spectroscopy is implemented by cat eye configuration to eliminate the first order Doppler shift. A 5 G magnetic field applied into the zone where the 657 nm laser interacts with the atoms is used to split the magnetic sublevels. A 500 kHz linewidth 657 nm saturation absorbing spectroscopy can be acquired when the laser is detuning by sweep the frequency of driver of the AOM in 100 ms sweeping time, as demonstrated in figure 2. The signal-to-noise ratio of the clock transition spectroscopy proved to surpass 10000[10]. And a 6 kHz sinusoidal signal applied into the driver of the AOM is used to modulate the clock transition spectroscopy, and the optimal dispersive error signal is acquired to feed back to the driver of the AOM 3.

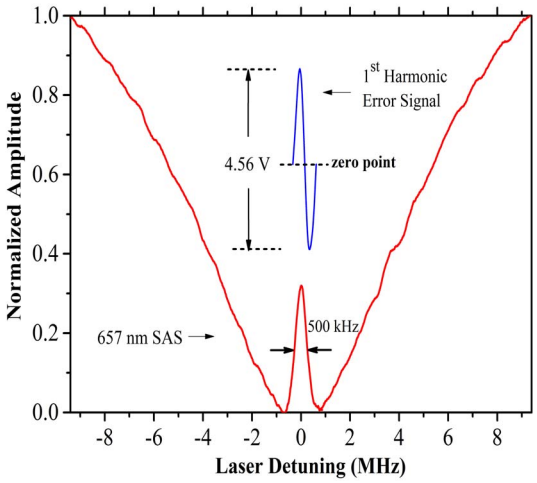


Fig 2. The clock transition spectroscopy and error signal. The red-solid line is the 657 nm clock transition saturation absorbing spectroscopy whose linewidth is 500 kHz in 100 ms sweeping time. And the blue-solid line is the first-order harmonic error signal used to lock the clock transition signal, the intensity of which is approximately 4.56 V.

After locking, we firstly estimate the instability of the optical frequency standard system by self-estimation and the instability is at the same level compared with [10] whose fractional instability is 3.0×10^{-14}. And then the beating frequency signal of the two optical frequency standards is

recorded by the frequency counter. We assume that the Allan deviation of the beating signal shows the instability of the small calcium beam optical frequency standard using fully-sealed vacuum tube, because the instability of each system has been self-estimated preliminarily and the instability of the system with flanges is better than the system using fully-sealed vacuum tube.

III. RESULT

To analyze the property of the Calcium beam optical frequency standard using fully-sealed vacuum tube, the influence of the temperature of the oven on the instability have been investigated. We only change the temperature of the oven of the fully-sealed vacuum tube from 773 K to 793 K and any other parameter keeps unchanged. The beating frequency signal is recorded for approximate five minutes to acquire the instability at 1s and 10s of averaging. As what have been depicted in the figure 3, we find that the 1s instability at 773 K is 1.2×10^{-12}. When the temperature is rising to 793 K, instability of 6.5×10^{-14} at 1s is achieved. It indicates that the rising of the temperature of the oven can acquire better instability. It is because of the improving of the signal to noise ratio of the clock transition spectroscopy. Besides, judging from the data in the figure 3, we infer that the instability can be further improved when the temperature goes on rising, but the lifetime of the oven should be considered at the same time.

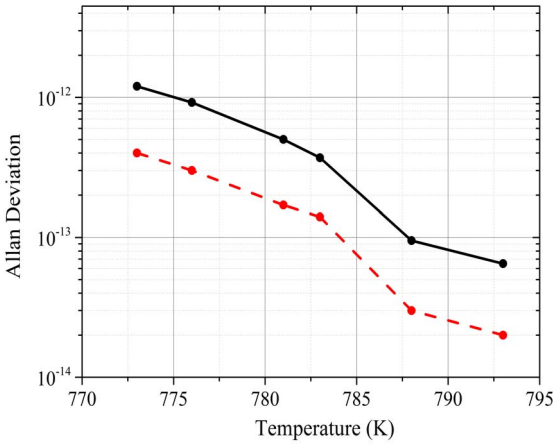


Fig 3. The influence of the temperature of the oven on the instability. The black solid line is the instability at 1s, and the red dash line is the instability at 10 s.

In that case, we record the beating signal of the two systems at 793 K for more than 3 hours although one servo unlocks occurred, we acquire the instability of the system and depicted in figure 5. The instability of the small Calcium beam optical frequency standard with fully-sealed vacuum system at 1s is 6.8×10^{-14}, and is 1.8×10^{-15} after 1000 s of averaging. The data in the figure 4 fits with the $6.8 \times 10^{-14}/\sqrt{\tau}$.

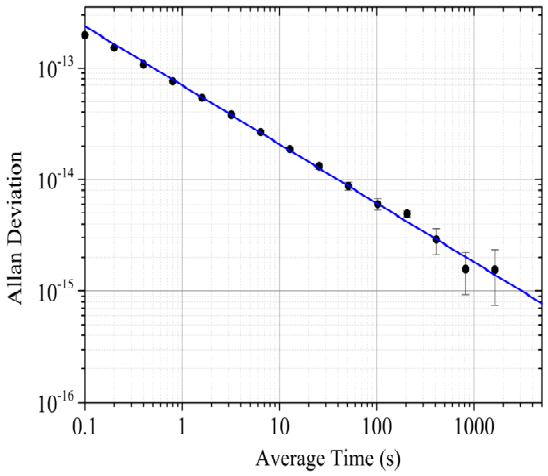


Fig 4.Total Allan deviation of the small Calcium optical frequency standard. The blue-solid line indicates an instability of $6.8 \times 10^{-14}/\sqrt{\tau}$. A servo unlocks occurred about 200 s of averaging.

IV. CONCLUSION

In this paper, we realize a small Calcium beam optical frequency standard utilizing fully-sealed vacuum system, it broadens the practical application of the optical clocks whose instability and uncertainty have surpassed the commercial microwave atomic clock. The influence of the temperature of the oven on the instability has been investigated. And the system has an instability of $6.8 \times 10^{-14}/\sqrt{\tau}$ beating with another small Calcium optical frequency standard whose reported instability at 1s is 3×10^{-14}, what's more an instability of 1.8×10^{-15} after 1000 seconds of averaging is acquired. The mechanical structure is designed for transportability. And the instability is potential to enter the 10^{-15} level at 1s when adopting the Ramsey scheme. In that case the work of this paper can be applied into the condition where demands for the instability of the atomic clock and small size.

ACKNOWLEDGMENT

This work is supported by the National Hi-tech Research and Development (863) Program and National Natural Science Foundation of China (Grant No.91436210).

REFERENCES

[1] B.J. Bloom, T.L. Nicholson, J.R. Williams, et al., "An optical lattice clock with accuracy and stability at the 10^{-18} level," Nature, 2014, 506:71-75.

[2] Schioppo M, Brown R.C., Mcgrew W.F., et al., "Ultrastable optical clock with two cold-atom ensembles," Nature Photon., 2017, 11(1): 48-52.

[3] Takano T., Takamoto M., Ushijima I., et al., "Geopotential measurements with synchronously linked optical lattice clocks," Nature Photon., 2016, 10.

[4] Kolkowitz S., Langellier N., Pikovski I., et al., "Gravitational wave detection with optical lattice clocks," Phys. Rev. D, 2016, 94(12): 124043.

[5] Kersten P., Mensing F., Sterr U., et al., “A transportable optical calcium frequency standard,” Appl. Phys. B, 1999, 68(1):27-38.

[6] Kaikai Huang, et al., “Application of electron-shelving detection via 423 nm transition in Calcium beam optical frequency standard,” Chin. Phys. Lett., 2006, 23(12):3198

[7] Huang K., Yang D., Chen J., “Small compact Calcium-beam optical frequency standard in Peking University and its new scheme,” Frequency and Time Forum (EFTF), 2006 20th European. IEEE, 2006: 376-378.

[8] Mcferran J.J., Hartnett J.G., Luiten A.N., “Fractional frequency instability in the 10^{-14} range with a thermal beam optical frequency reference,” J. Opt. Soc. Am. B, 2010, 27(2):277-285.

[9] Zhang X., Xue X., Pan D., et al., “Dispersion detection of optical clock transition in thermal atomic beam,” European Frequency and Time Forum & International Frequency Control Symposium (EFTF/IFCS), 2013 Joint. IEEE, 2013: 399-401.

[10] Xiaogang Zhang et al., “A transportable Calcium atomic beam optical clock,” 2016 IEEE International Frequency Control Symposium (IFCS), New Orleans, 9-12May,2016:1-4.

[11] Koller S.B., Grotti J., Vogt S., et al., “Transportable optical lattice clock with 10^{-17} uncertainty,” Phys. Rev. Lett., 2017, 118(7): 073601.

[12] Haijun Chen, Xiaogang Zhang, Youhuang Liang, et al., “Study of a fully vacuum-sealed Calcium atomic beam tube for optical frequency standard,” 2016 IEEE International Frequency Control Symposium (IFCS), New Orleans, 482-485, May, 2016.

[13] Haijun Chen, Haosen Shang, Zhongzheng Liu, et al., “Experimental study of a miniaturized calcium atomic beam tube for small optical frequency standard,” 2017 IEEE International Frequency Control Symposium (IFCS), Besancon, France, 10-13July, 2017.

[14] Nagourney W., Sandberg J., Dehmelt H., “Shelved optical electron amplifier: Observation of quantum jumps,” Phys. Rev. Lett., 1986, 56(26): 2797.

[15] Drever R.W.P., Hall J.L., Kowalski F.V., et al., “Laser phase and frequency stabilization using an optical resonator,” Appl. Phys. B, 1983, 31(2): 97-105.

[16] Pound R.V., “Electronic frequency stabilization of microwave oscillators,” Rev. Sci. Instrum., 1946, 17(11): 490-505.

[17] Xiaogang Zhang, Shengnan Zhang, Duo Pan, et al., “Hanle detection for optical clocks,” The Scientific World J., 2015, 2015: 1-6.

New Clock Laser System for the Second Yb Optical Lattice Clock at KRISS

Won-Kyu Lee,* Chang Yong Park, Myoung-Sun Heo, Huidong Kim, Sang Eon Park, and Dai-Hyuk Yu
Center for Time and Frequency, Korea Research Institute of Standards and Science (KRISS),
Daejeon 34113, South Korea
*e-mail: oneqlee@kriss.re.kr

***Abstract*—We design and develop a new clock laser system for the second Yb optical lattice clock (OLC) at KRISS with the targeted uncertainty of 10^{-18} level. With a longer ULE cavity, the fused silica substrates, and the crystalline mirror coatings, the overall thermal limit is expected to be 4.3×10^{-17}. The rapid evaluation of the systematic uncertainties of the second OLC will be possible with this new clock laser system.**

Keywords—clock laser, optical lattice clock, cavity, uncertainty evaluation, crystalline coating

The absolute frequency and the systematic uncertainty of the Yb optical lattice clock (OLC) at KRISS (Korea Research Institute of Standards and Science) were first measured in 2013 [1]. Since then, the systematic uncertainty has been significantly improved [2,3]. Recently, we have reported the absolute frequency of the Yb OLC at KRISS relative to the SI second with a relative uncertainty of 1.1×10^{-15} [4]. The systematic uncertainty of the Yb OLC only was 1.8×10^{-16} and is on the way of improvement. In evaluating the systematic uncertainties, we utilized the stability of the clock laser by interleaved measurements with the stability of $7.5\times10^{-15}/\tau^{1/2}$ and the statistical uncertainty reached 1×10^{-16} at 5,800 s [4]. The clock laser at 578 nm was generated by sum frequency generation (SFG) of a 1319-nm Nd:YAG laser and a 1030-nm Yb-doped fiber laser, and was stabilized to a 10-cm-long horizontal high-finesse cavity made of ultra-low-expansion glass (ULE) [2]. The mirror substrates were also made of ULE, so that the thermal noise limit was expected to be $1\sim2\times10^{-15}$.

At the time of the submission of this abstract, the systematic uncertainty has been reduced to 1.1×10^{-16} approaching the expected optimal value of 5×10^{-17}, which is limited mainly by the black-body radiation shift. To obtain better accuracy, we are now developing a new Yb OLC at KRISS targeting the frequency uncertainty level of 10^{-18}. For the evaluation of the uncertainties at this level, a new clock laser system with the frequency stability close to or even below 10^{-16} is greatly required to decrease the statistical uncertainty in reasonably short time, thus, a cuboid-shaped longer cavity (50 mm × 50 mm × 300 mm) was designed [5,6]. The cavity spacer material is ULE with the zero-crossing temperature for thermal expansion around room temperature. Two mirror substrates (one is planar and the other has a radius of curvature of 1 m) are made of fused silica to reduce the thermal noise. Additional ULE rings are adopted at the outer surface of the fused silica mirror substrates to compensate for the deformation due to thermal expansion mismatch [7]. Crystalline coatings were transferred to the substrates to reduce the thermal noise from the mirror coatings [8]. The overall thermal limit is expected to be 4.3×10^{-17} (3.5×10^{-17} from the spacer, 8.5×10^{-18} from the substrates, and 2.3×10^{-17} from the mirror coatings). The finesse of the cavity of this new clock laser was measured to be 2.56×10^{5} by the cavity ring-down time and is shown in Fig. 1 with the cavity (0,0) mode profile in the inset. As the crystalline coating at 578 nm is not available, the reflective coating has been designed to be centered around 1156.8 nm. The 578 nm clock laser will be obtained by the second harmonic generation (SHG) of a laser diode at 1156 nm using a ridge-type waveguide periodically-poled-lithium-niobate (WG-PPLN) crystal [9,10]. Compared with the SFG system, the new system is much simpler with only one laser involved.

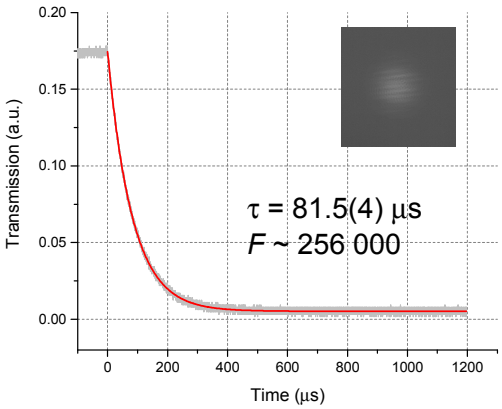


Fig. 1. The measured finesse of the high-finesse cavity of the new clock laser system. The cavity mode profile is shown in the inset.

The new cavity is horizontally mounted at the optimal support points to reduce the vibration sensitivity. The vertical, longitudinal, and transverse vibration sensitivities are calculated by finite element analysis to determine the optimum support position [5]. The photo of the new clock laser system for the second Yb OLC at KRISS including the high-finesse cavity, the cavity mount, the thermal shield, and the vacuum chamber is shown in Fig. 2. The temperature of the cavity is stabilized at the value for the zero thermal expansion within 10

mK accuracy. One active aluminum layer and two passive aluminum layers were used for the temperature stabilization. With the help of the stainless steel vacuum chamber, the thermal time constant is expected to be more than one day. The vacuum chamber is placed on an active vibration isolation table, which is enclosed by an acoustic shield with a 20-dB isolation. A preliminary result of the performance of the new clock laser system will be presented at the conference of EFTF2017.

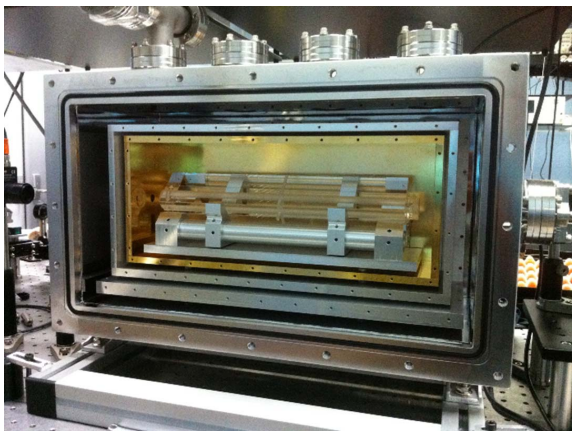


Fig. 2. Photo of the new clock laser system for the second Yb OLC at KRISS including the high-finesse cavity, the cavity mount, the thermal shield, and the vacuum chamber.

ACKNOWLEDGMENT

This work was supported partly by the Korea Research Institute of Standards and Science under the project "Research on Time and Space Measurements," Grant No. 17011005, and also partly by the R&D Convergence Program of NST (National Research Council of Science and Technology) of Republic of Korea (Grant No. CAP-15-08-KRISS).

REFERENCES

[1] C. Y. Park, D.-H. Yu, W.-K. Lee, S. E. Park, E. B. Kim, S. K. Lee, J. W. Cho, T. H. Yoon, J. Mun, S. J. Park, T. Y. Kwon, and S.-B. Lee, "Absolute frequency measurement of $^{1}S_{0}(F=1/2)$–$^{3}P_{0}(F=1/2)$ transition of ^{171}Yb atoms in a one-dimensional optical lattice at KRISS," Metrologia, vol. 50, pp. 119–128, February 2013.

[2] D.-H. Yu, C. Y. Park, W.-K. Lee, S. Lee, S. E. Park, J. Mun, S.-B. Lee, and T. Y. Kwon, "An Yb optical lattice clock: current status at KRISS," J. Kor. Phys. Soc., vol. 63, pp. 883–889, April 2013.

[3] S. Lee, C. Y. Park, W.-K. Lee, and D.-H. Yu, "Cancellation of collisional frequency shifts in optical lattice clocks with Rabi spectroscopy," New J. Phys., vol. 18, pp. 033030, March 2016.

[4] H. Kim, M.-S. Heo, W.-K. Lee, C. Y. Park, H.-G. Hong, S.-W. Hwang, and D.-H. Yu, "Improved absolute frequency measurement of the ^{171}Yb optical lattice clock at KRISS relative to the SI second," accepted in Jpn. J. Appl. Phys., available at arXiv 1701.04534.

[5] W.-K. Lee, C. Y. Park, S. E. Park, M.-S. Heo, H. Kim, and D.-H. Yu, "Design of clock laser with 10^{-16} frequency stability for rapid uncertainty evaluation of Yb lattice clock," presented at European Frequency and Time Forum (EFTF), 2016.

[6] J. Keller, S. Ignatovich, S. A. Webster, T. E. Mehlstäubler, "Simple vibration-insensitive cavity for laser stabilization at the 10^{-16} level," Appl. Phys. B, vol. 116, pp. 203–210, October 2013.

[7] T. Legero, T. Kessler, and U. Sterr, "Tuning the thermal expansion properties of optical reference cavities with fused silica mirrors", J. Opt. Soc. Am. B, vol. 27, pp. 914-919, May 2010.

[8] G. D. Cole, W. Zhang, B. J. Bjork, D. Follman, P. Heu, C. Deutsch, L. Sonderhouse, J. Robinson, C. Franz, A. Alexandrovski, M. Notcutt, O. H. Heckl, J. Ye, and M. Aspelmeyer, "High-performance near- and mid-infrared crystalline coatings," Optica, vol. 3, pp. 647–656, June 2016.

[9] W.-K. Lee, C. Y. Park, D.-H. Yu, S. E. Park, S.-B. Lee, and T. Y. Kwon, "Generation of 578-nm yellow light over 10 mW by second harmonic generation of an 1156-nm external-cavity diode laser," Opt. Express, vol. 19, pp. 17453–17461, August 2011.

[10] E. B. Kim, W.-K. Lee, C. Y. Park, D.-H. Yu, and S. E. Park, "Narrow linewidth 578 nm light generation using frequency-doubling with a waveguide PPLN pumped by an optical injection-locked diode laser," Opt. Express, vol. 18, pp. 10308–10314, May 2010.

Improved Absolute Frequency Measurement of the $^1S_0$–$^3P_0$ Transition of ^{171}Yb at KRISS

Huidong Kim*, Myoung-Sun Heo, Won-Kyu Lee, Chang Yong Park, Hyun-Gue Hong, Sang-Wook Hwang, and Dai-Hyuk Yu

Center for Time and Frequency, Korea Research Institute of Standards and Science
Daejeon, Republic of Korea
*E-mail: khd250@kriss.re.kr

***Abstract*—We measured the absolute frequency of the $^1S_0$–$^3P_0$ transition of ^{171}Yb atom relative to the SI second with an uncertainty reduced by a factor of 14 compared with our previous measurement. The determined frequency was 518 295 836 590 863.38(57) Hz. The experimental setup is being improved for the independent uncertainty evaluation by measuring the frequency shift coefficients of our own system.**

Keywords—Optical lattice clock, uncertainty evaluation, absolute frequency

I. INTRODUCTION

Optical clocks using narrow optical transitions of neutral atoms or ions are promising candidates [1] for the new definition of SI second, which is now defined based on the microwave transition of Cesium. We have developed an ^{171}Yb optical clock using one-dimensional optical lattice with the systematic uncertainty reached 1.8×10^{-16} recently [2]. The determined absolute frequency was 518 295 836 590 863.38(57) Hz, and agreed well with the value recommended by the International Committee for Weights and Measures. The uncertainty was reduced by a factor of 14 compared with our previously reported value in 2013 [3]. Currently, the experimental setup is being modified, aiming at the 10^{-17} uncertainty level using the measured coefficients wholly originated from our system.

II. ABSOLUTE FREQUENCY MEASUREMENT

For the absolute frequency measurement, we prepared about 1,000 atoms confined in 1D optical lattice formed by a power build-up cavity. The temperature of the trapped atoms was 4 μK with the operating trap depth of 163 E_r. To investigate the uncertainty contributions from the systematic effects, we interleaved two different values of the corresponding systematic effect. The stability was $7.5\times10^{-15}/\tau^{1/2}$ and the statistical uncertainty reached 1×10^{-16} at 5,800 s. The measurement was performed during ten days from MJD 57734 to MJD 57743 with the data quasi-homogeneously distributed over the five-day-long TAI grids.

A. Systematic uncertainty evaluation

The systematic uncertainty budget is summarized in Table I with the total fractional uncertainty of 1.8×10^{-16}. The collisional shift and the E1 lattice shift was evaluated by measuring our own coefficients. Determined E1 magic frequency was 394 798 264.7(84) MHz. The nonlinear light shift and the others were evaluated using the known coefficients [4,5]. The frequency shifts; the background gas, the AOM chirp, the fiber noise cancellation, the line pulling, and the lattice tunneling were estimated to be well below 1×10^{-17} and could be neglected in this uncertainty evaluation.

TABLE I. UNCERTAINTY BUDGET FOR THE ABSOLUTE FREQUENCY MEASUREMENT OF THE ^{171}YB CLOCK TRANSITION

Effect	*Relative shift* $\times10^{-16}$	*Relative uncertainty* $\times10^{-16}$
Lattice ac Stark (scalar)	1.6	0.4
Nonlinear lattice shift	0.7	0.4
Collisional shift	-0.7	0.4
Blackbody radiation	-23.3	0.6
Quadratic Zeeman effect	-10.2	1.5
Probe light	0.2	0.04
AOM phase chirp	-	0.03
Servo error	-	0.7
Static Stark shift	-	0.1
Yb total	-31.8	1.8
Statistics	-	4.0
Gravitational red shift	81.4	0.3
H-maser dead-time	-	5.0
H-maser-TAI	945.8	6.5
TAI dead time	-	5.2
TAI-TT	-12.4	2.2
Total	983.0	10.9

B. Absolute frequency measurement relative to the SI second

The clock operation covered 34% of the total ten-day-long measurement duration. The relative frequency offset of the hydrogen maser, which was used as a frequency reference of the optical frequency comb, from TAI (International Atomic Time) was calculated by using BIPM Circular-T No. 348 and the time comparison data between the hydrogen maser and UTC(KRIS). The dead-time uncertainty in calculating the hydrogen maser offset was estimated from the noise characteristics of the hydrogen maser [6]. The frequency offset and the dead-time uncertainty of TAI from the SI second (TT) were calculated by using Circular-T No. 348 and the explanatory supplement.

Also, the measured absolute frequency has been confirmed by a direct comparison with a ^{87}Sr lattice clock at National Institute of Information and Communications Technology (NICT) in Japan via a carrier-phase two-way satellite frequency transfer technique. The measured frequency ratio was in a good agreement with the calculated value using each absolute frequency within the total uncertainty [2,7], the result of which will be presented in EFTF2017 [8].

III. Improvement of the Experiment Setup

A. Quadratic Zeeman Effect

To evaluate the quadratic Zeeman shift, we interleaved two quantization B-field values during the clock interrogation. Preliminary result is shown in Fig. 1. The data is plotted versus the square of the first order Zeeman shift. The measurement time per each point was 8,000 s. Using the conversion value of the first order Zeeman shift versus B-field in ref. [4], the coefficient of the Quadratic Zeeman shift is -6.74(13) Hz/mT^2. The uncertainty of the coefficient is reduced by a factor of 7 compared with that in ref. [4].

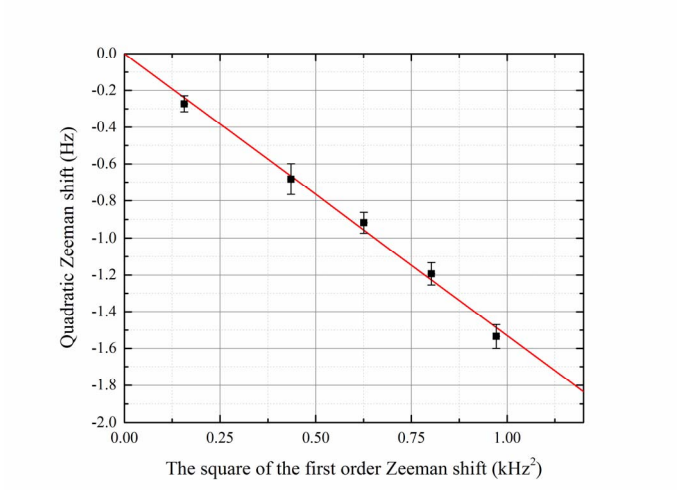


Fig. 1. The Quadratic Zeeman shift vs. the square of the first order Zeeman shift by the interleaved measurement.

B. Non-linear Stark Shifts

Although an optical clock operates at the magic wavelength condition which cancels out the linear light shift, other higher-order effects including multipolar polarizability from E2 or M1 transition and hyper-polarizability from two-photon transition can introduce large light shift even at the 10^{-17} uncertainty level [9]. In case of Yb optical clock, these effects are more dominant problem to reach below 10^{-16} uncertainty level. For a more precise evaluation of the lattice light shift, we need to well define the average vibrational quantum number <n>, for which a sideband cooling technique is usually used to cool down to <n>≈0. Also we need to extend the interleaving leverage of the trap depth, for which reason we built a power build-up cavity and achieved a large trap depth up to ~2000 E_r. Currently, the sideband cooling experiment to control <n> is ongoing.

IV. Conclusion

We report recent status of the ^{171}Yb optical lattice clock at KRISS. We measured the improved value of the absolute frequency of the clock transition of ^{171}Yb atom referenced to the SI second. This result is expected to contribute to the determination of a new recommended value for the secondary representations of the second in 2017. To get better accuracy, we are improving the experimental setup. We expect to reach the systematic uncertainty of 10^{-17} level soon.

Acknowledgment

This work was supported partly by the Korea Research Institute of Standards and Science under the project "Research on Time and Space Measurements," Grant No. 17011005, and also partly by the R&D Convergence Program of NST (National Research Council of Science and Technology) of Republic of Korea (Grant No. CAP-15-08-KRISS)..

References

[1] F. Riehle, "Towards a redefinition of the second based on optical atomic clocks," Comptes Rendus Phys., vol. 16, no. 5, pp. 506–515, 2015.

[2] H. Kim, M.-S. Heo, W.-K. Lee, C. Y. Park, H.-G. Hong, S.-W. Hwang, and D.-H. Yu, "Improved absolute frequency measurement of the ^{171}Yb optical lattice clock at KRISS relative to the SI second," accepted in Jpn. J. Appl. Phys., available at arXiv 1701.04534.

[3] C. Y. Park, D.-H. Yu, W.-K. Lee, S. E. Park, E. B. Kim, S. K. Lee, J. W. Cho, T. H. Yoon, J. Mun, S. J. Park, T. Y. Kwon, and S.-B. Lee, "Absolute frequency measurement of $^1S_0$(F=1/2)–$^3P_0$(F=1/2) transition of ^{171}Yb atoms in a one-dimensional optical lattice at KRISS," Metrologia, vol. 50, pp. 119–128, February 2013.

[4] N. D. Lemke, A. D. Ludlow, Z.W. Barber, T. M. Fortier, S.A. Diddams, Y. Jiang, S. R. Jefferts, T. P. Heavner, T. E. Parker, and C.W. Oates, "Spin-1/2 Optical Latiice Clock," Phys. Rev. Lett. 103, pp. 063001, August 2009.

[5] N. Nemitz, T. Ohkubo, M. Takamoto, I. Ushijima, M. Das, N. Ohmae, and H. Katori, "Frequency ratio of Yb and Sr clocks with 5×10^{-17} uncertainty at 150 seconds averaging time," Nat. Photonics, vol. 10, no. 4, pp. 258–261, Februrary 2016.

[6] D.-H. Yu, M. Weiss and T. E. Parker, "Uncertainty of a frequency comparison with distributed dead time and measurement interval offset," Metrologia, 44, 91-96, February 2007.

[7] H. Hachisu, G. Petit, T. Ido, " Absolute frequency measurement with uncertainty below $1x10^{-15}$ using International Atomic Time," Appl. Phys. B, 123:34, 2017

[8] M. Fujieda, H. Hachisu, R. Tabuchi, T. Gotoh, T. Ido, G. Petit, J. Leute, H. Kim, M.-S. Heo, S.-W. Hwang, S. H. Yang, W.-K. Lee, C. Y. Park, Y. K. Lee, and D.-H. Yu, "NICT-KRISS TWCP link: evaluation and application," to be presented at European Frequency and Time Forum (EFTF), 2017.

[9] H. Katori, V. D. Ovsiannikov, S. I. Marmo, and V. G. Palchikov, "Strategies for reducing the light shift in atomic clocks," Phys. Rev. A - At. Mol. Opt. Phys., vol. 91, no. 5, pp. 1–5, 2015.

A Strontium Optical Lattice Clock Apparatus for Precise Frequency Metrology and Beyond

Marco G. Tarallo, Davide Calonico, Filippo Levi
Istituto Nazionale di Ricerca Metrologica
Strada delle Cacce 91, Torino 10135, Italy
Email: m.tarallo@inrim.it

Matteo Barbiero*, Giacomo Lamporesi, Gabriele Ferrari
CNR–INO Trento
Via Sommarive 13, 38123 Trento, Italy
*(also Politecnico di Torino
Corso Duca degli Abruzzi 24, 10129 Torino, Italy)

***Abstract*—We present the advancement toward the realization of a new optical clock apparatus based on ultracold strontium atoms. The atomic source employs a novel design based on two dimensional magneto optical trapping which is advantageous because of the suppression of thermal atoms in the interrogation volume, and the elimination of hot BBR in the view of the science cell. Compact frequency stabilization of cooling and trapping lasers is achieved via single PDH lock to a three-color ultrastable optical resonator. We also study different lattice topologies to operate the ultracold atomic ensemble in the high-cooperativity regime toward sub-quantum projection noise instability and millihertz-linewidth frequency stabilization by cavity QED.**

***Keywords*—Optical lattice clock, strontium, 2D MOT, cavity QED**

I. Introduction

Optical lattice clocks (OLCs) based on neutral alkali-earth like atoms represent the state of the art in frequency standards [1] both in terms of accuracy and in stability. Among the candidate atomic species, the strontium (Sr) optical clock is the most popular and its clock frequency has shown a reproducibility of uncertainty at the level of 10^{-17}. Frequency comparisons of Sr clocks have been already used to constrain gravitational theories [2] and are foreseen to be used in relativistic geodesy [3].

In first-generation Sr OLCs, the atoms are first loaded from a slowed atomic beam into a MOT operating on the strong $^1S_0$ – $^1P_1$ transition, which is used as a precooling stage to reach mK temperatures. Atoms are then released from the trap and undergo a brief stage of broadband $^1S_0$–$^3P_1$ molasses cooling to reduce the temperature to about 10 μK. Next the atoms are loaded into a single-frequency MOT operating on the 7.4 kHz $^3P_1$ line for direct laser cooling below 1 μK. An optical lattice is typically overlapped with the MOT cloud during the entire cooling sequence to allow loading. The lattice is yielded by either retro-reflecting an intense laser beam [4] or by means of an enhancement Fabry-Perot resonator [5]. This typically results in the capture of between 10^3 and 10^6 atoms for clock spectroscopy.

Here we present the advancement towards the realization of a new Sr optical clock apparatus at INRIM. Our new apparatus simplifies both the atomic source and the laser system, and at the same time eliminates BBR shifts due to the atomic oven currently in the view of the interrogated atomic ensemble. Furthermore, we discuss the potential application of high-finesse optical cavities to both generate the trapping laser and to perform sub-quantum projection noise detection of the collective atomic clock state by means of cavity QED.

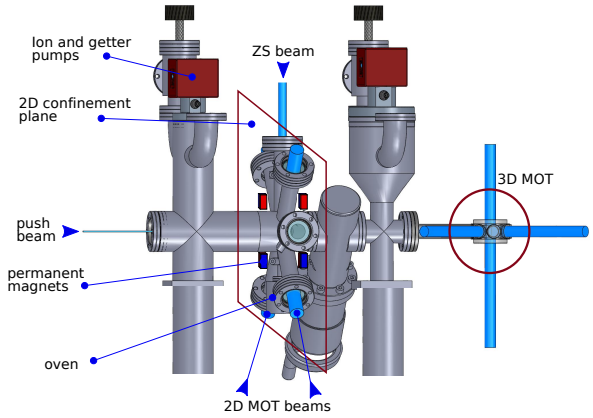


Fig. 1. A 3D drawing (in scale) of experimental apparatus. The 3D MOT chamber here depicted is meant only for visualization.

II. Sr optical clock setup

A. The atomic source

The atomic source employs a novel design based on two dimensional magneto optical trapping (MOT) [6]. This solution offers various advantages related to: (a) the suppression of thermal atoms in the interrogation volume; (b) the elimination of hot elements in the view of the science cell; (c) the possibility to simultaneously load different atomic species in the same science chamber by means of a simple extension of the set-up. A schematic drawing of the vacuum apparatus is shown in Fig.1.

A vertical plane for 2D MOT cooling is created by four stainless steel tubes allowing for atomic and optical access. Four neodymium bar magnets (ECLIPSE N750-RB), surrounding the cross region, generate the static magnetic field that is used for trapping and cooling hot atoms in the 2D MOT and for slowing down them coming from the oven in a ZS-like configuration. The hot flux of Sr atoms is ejected from the oven at a temperature of T_{ov} = 650 K, corresponding to a mean axial velocity of 394 m/s. Along the ejection's direction, a velocity class of atoms is kept on resonance by the residual magnetic field created by the permanent magnets and thus slowed down.

In order to estimate the value of the trapping efficiency we performed numerical simulations of the atoms' dynamics in the

978-1-5386-2916-1/$31.00 ©2017 IEEE

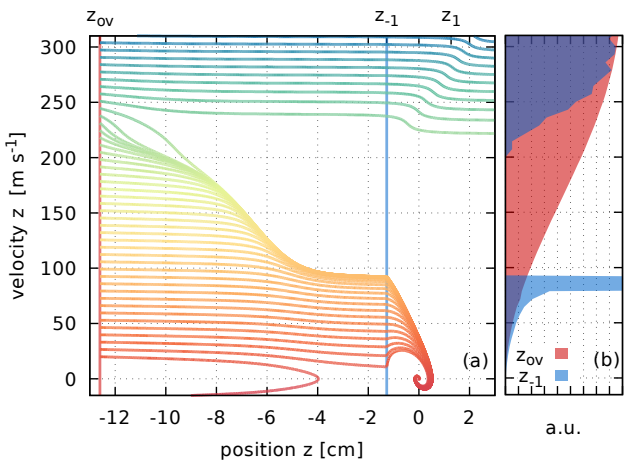


Fig. 2. Numerical simulation of atom's dynamic in the atomic source region. **(a)** Velocity of the atoms in the ZS path and in the 2D MOT trapping region. The ZS path goes from z_{oven}=-12.6 mm to the z_{-1}=-1.27 mm while the 2D MOT trapping region is in between the z_{-1} and z_{+1}. **(b)** Velocity density distribution at the output of the oven and in the final region of the ZS path z_{-1}

atomic source. The result of the simulation is reported in Fig.2. The initial velocity is computed according to the Maxwell-Boltzmann distribution at the temperature T_{ov}. Considering the magnetic field produced by permanent magnets, which we computed by a finite element analysis, and considering a saturation parameter s=1.0 and a detuning Δ/Γ=-16.5 of the Zeeman slower beam, the final maximal velocity in the ZS path is estimated to be 95 m/s. In the 2D-MOT plane, the magnets produce a magnetic gradient of 40 G/cm. In this region the capture velocity is estimated to be 110 m/s. This result is obtained using a saturation of s=0.5 and a detuning Δ/Γ =-2.5 of the 2D-MOT beams. Hence the estimated ratio between the trapped atoms flux and the thermal ones is of the order of 10.

A push beam is aligned in the orthogonal axis to transfer the cold captured atoms through a differential pumping channel (2 mm aperture, 4 cm long) towards a UHV region where a 3D MOT collects the incoming atomic flux. This method allows fast chopping of the atomic beam without any in-vacuum shutters and prevents hot beam atoms to reach the UHV region.

The novel atomic source complies with the requirements set by the employment of science chambers ensuring high temperature-homogeneity, necessary for high-accuracy optical frequency standards.

Currently, the construction of the vacuum system is finalized, with the two vacuum regions both having a background pressure lower than 10^-10 Torr. The Sr oven has been mounted with steel capillaries for further beam collimation toward the 2D MOT region. The vacuum chamber for the 3D MOT is a off-the-shelf titanium octagon with two large viewports (63CF) and seven small viewports with optical aperture of only 16 mm. The whole setup is only 70 cm $\times$ 45 cm $times$ 30 cm large.

B. Laser and interrogation systems

The main laser sources needed for operating a Sr OLC are the blue laser at 461 nm for cooling and probing the atoms on the $^1S_0 - ^1P_1$ strong transition, the second-stage cooling laser at 689 nm on the $^1S_0 - ^3P_1$ intercombination transition, and the lattice laser at the magic wavelength of 813 nm. We will simultaneously stabilize these three laser to an ultrastable ULE *three-color cavity* using the offset sideband locking technique. This approach was recently demonstrated here at INRIM for the Yb clock [7]. In order to reduce heating issues from the mirror coatings, for the blue laser the seed 922 nm laser needed for second-harmonic generation is sent to the cavity. In this way, at a temperature close to 30°C, a drift rate below 22 kHz/h is feasible.

Regarding the clock laser at 698 nm, we plan to build a fiber-coupled external cavity diode laser at 1396 nm, which can be passively narrowed down to 5 kHz [8] and it is more suitable to frequency dissemination through fiber links and single branch stabilization/comparison to/with the 1156 nm Yb clock laser[9], [10], and then frequency doubled for probing the atomic sample.

III. Optical clock and cavity QED

Optical resonators are currently employed in OLCs (mostly outside the vacuum chamber) for power enhancement of the lattice light, ensuring suppression of wavefront aberrations and filtering from residual spontaneous emission. It has been recently proposed and demonstrated shot-noise limited detection of Sr atoms by means of a high-cooperativity cavity resonant to the triplet $^3P_1$ state transition [11].

We are designing and studying a double resonant cavity system which allows both trapping at magic wavelength with a commensurate lattice spacing and entanglement of the atomic collective atomic spin by means of the $^1S_0 - ^3P_1$ intercombination transition. In particular, we envisage the collective strong atom-cavity coupling regime, where the vacuum Rabi splitting $\Omega = 2g_0\sqrt{N_{at}}$ is larger than the cavity photons' decay rate κ, as the most promising for both metrological and fundamental studies. Furthermore, in the case of the Sr intercombination transition, it is almost mandatory to operate in the "bad cavity" regime, i.e. $\Gamma < \kappa$, so that the principal decay channel of the system is via cavity transmission rather than free-space scattering. This system can be engineered by only two parameters in the nearly-confocal geometry: the cavity length L, and the cavity finesse (or the mirrors' transmissivity) $\mathcal{F}$. Constraining the atom-cavity system to be in the strong-coupling regime, it is possible to extract two inequalities for these two parameters:

$$\mathcal{F}^2 > \frac{\pi^3 c}{12\lambda\Gamma N_{at}}$$

$$L < \frac{\pi c}{\mathcal{F}\Gamma}$$

Figure 3 shows how the single atom cooperativity $C_0 = \Omega_0^2/(\kappa\Gamma)$, which describes the ratio between the squared vacuum Rabi splitting the product of the two decay channels of the system, depends on the cavity finesse and the length. We see that for the Sr intercombination transition it is possible

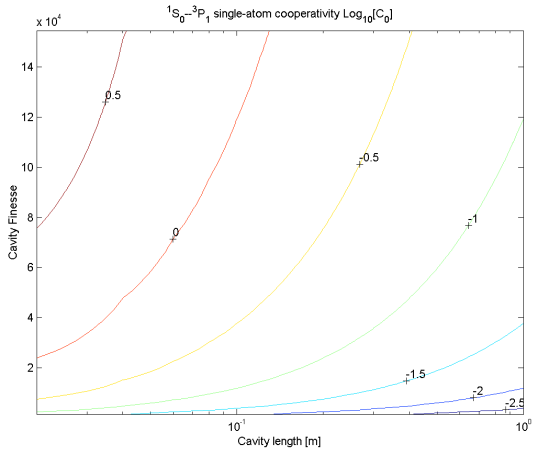


Fig. 3. A 3D drawing (in scale) of experimental apparatus. The 3D MOT chamber here depicted is meant only for visualization.

to get $C_0 \sim 1$, i.e. collective cooperativity $C = N_{at}C_0 \gg 1$ for typical Sr optical clock ensembles, at $L = 6.7$ cm and $\mathcal{F} = 8 \times 10^4$. In this regime of collective cooperativity, it is expected to reach both high degree of spectroscopic enhancement by QND measurement induced entanglement, $\xi^{-1} \simeq 20$ dB [12].

We also expect that this system would probe several other interesting phenomena such as superradiance, Dicke phase transition and optical bistability for direct light squeezing generation.

IV. Conclusion

We have briefly described the design and the progress of the new Sr OLC assembled at INRIM. The new atomic source and the compact laser stabilization system will greatly simplify the Sr OLC structure towards a higher level of transportability. A progressing study on cavity QED setup for the clock transition measurement will be a first step towards a quantum-enhanced atomic clock.

Acknowledgment

We thank M. Mitchell for useful discussions. Funding: European Metrology Program for Innovation and Research (EMPIR) (15SIB03 OC18).

References

[1] A. D. Ludlow, M. M. Boyd, J. Ye, E. Peik, and P.-O. Schmidt, “Optical Atomic Clocks”, Rev. Mod. Phys. 87, 637 (2015)

[2] S. Blatt et al., “New Limits on Coupling of Fundamental Constants to Gravity Using ^{87}Sr Optical Lattice Clocks”, Phys. Rev. Lett. 100, 140801 (2008).

[3] C. Lisdat et al., “A clock network for geodesy and fundamental science”, Nat. Commun. 7, 12443 (2016).

[4] M. Takamoto, F.-L. Hong, R. Higashi, and H. Katori, “An optical lattice clock”, Nature 435, 321 (2005).

[5] A. Brusch, R. Le Targat, X. Baillard, M. Fouché, and P. Lemonde, “Hyperpolarizability Effects in a Sr Optical Lattice Clock”, Phys. Rev. Lett. 96, 103003 (2006)

[6] G. Lamporesi, S. Donadello, S. Serafini, and G. Ferrari, “Compact high-flux source of cold sodium atoms”, Rev. Sci. Instrum. 84, 063102 (2013)

[7] G. Milani, B. Rauf, P. Barbieri, F. Bregolin, M. Pizzocaro, P. Thoumany, F. Levi, and D. Calonico, “Multiple wavelength stabilization on a single optical cavity using the offset sideband locking technique”, Opt. Lett. 42, 1970-1973 (2017)

[8] S. Bennetts, G. D. McDonald, K. S. Hardman, J. E. Debs, C. C. N. Kuhn, J. D. Close, and N. P Robins, “External cavity diode lasers with 5kHz linewidth and 200nm tuning range at 1.55m and methods for linewidth measurement”, Opt. Express 22, 10642-10654 (2014)

[9] M. Pizzocaro, P. Thoumany, B. Rauf, F. Bregolin, G. Milani, C. Clivati, G. A. Costanzo, F. Levi, and D. Calonico, “Absolute frequency measurement of the 1S0 3P0 transition of 171Yb” Metrologia 54, 102112 (2017)

[10] N. Nemitz, T. Ohkubo, M. Takamoto, I. Ushijima, M. Das, N. Ohmae and H. Katori, “Frequency ratio of Yb and Sr clocks with 5x1017 uncertainty at 150 seconds averaging time”, Nature Photonics 10, 258261 (2016)

[11] M. A. Norcia, J. K. Thompson, “Strong coupling on a forbidden transition in strontium and nondestructive atom counting”, Phys. Rev. A 93, 023804 (2016).

[12] Z. Chen, J. G. Bohnet, J. M. Weiner, K. C. Cox, and J. K. Thompson, Phys. Rev. A 89, 043837 (2014).

Production and trapping of Th ions for nuclear frequency standard development.

P.V. Borisyuk[1], S.P. Derevyashkin[1],
K.Yu. Khabarova[4], N.N. Kolachevsky[1,4],
Y.Y. Lebedinskii[1], V.G. Palchikov[1,2], S.S. Poteshin[1],
A.A. Sysoev[1], E.V. Tkalya[1,3], D.O. Tregubov[4],
V.P. Yakovlev[1]

[1] National Research Nuclear University "MEPhI" (Moscow Engineering Physics Institute), Moscow, Russia
[2] National Research Institute for Physical-Technical and Radiotechnical Measurements, Mendeleevo, Russia
[3] Skobeltsyn Institute of Nuclear Physics Lomonosov Moscow State University, Moscow, Russia
[4] The P.N. Lebedev Physical Institute, Moscow, Russia
sp.derevyashkin@gmail.com

***Abstract*— Technique of the production of thorium ions via laser ablation reported. Trapping ions using quadrupole linear trap with trapping time up to 30 s demonstrated.**

Keywords—ion trap; thorium; nuclear frequency standard; laser ablation

I. INTRODUCTION

One of the most promising candidates for development of frequency standards is a unique low-lying nuclear transition in thorium-229 nucleus. This level has an unusually low energy value of 7.8±0.5 eV [1] located in the region of vacuum ultraviolet which is accessible for laser spectroscopy, and therefore it is of special interest due to many potential applications in various areas. Since the nucleus is characterized by extremely low polarizability and shielded by electron cloud, nuclear transitions are less sensitive to external perturbations. The narrowness of the spectral line and the weak oscillator strength of the transition make it a good candidate for frequency standard application. Using this nuclear transition, it is possible to decrease the relative uncertainty down to 10^{-19}. This number is limited by the combination of quadratic and linear Zeeman effects, the Stark effect, the linear Doppler effect, the blackbody radiation, the influence of the gravitational field, and the micromotion of the ion in the trap [2].

This paper describes the techniques of production and trapping of thorium ions required to perform spectroscopic studies of thorium quantum states.

II. PRODUCTION OF IONS

Thorium ions are generated by laser ablation. During short laser pulse plasma plume containing large number of particles ($\sim 10^{14}$) is generated. Large number of ions, inside trap at the same time, allows you to increase number of trapped ions. In addition, the laser ablation provides local evaporation of the target [3], which is good for working with a limited target material. This is important because of ^{229}Th radioactivity. Allowed sample amount of ^{229}Th in laboratory is nanograms of matter..

Due to the high radioactivity of the isotope ^{229}Th initial stages of work were carried out using a model sample of monoisotopic and chemically inert gold ^{197}Au and stable thorium isotope ^{232}Th.

Laser ablation system is based on Q-switched Nd:YAG laser. Laser pulse parameters are following: duration of the laser pulse τ = 25 ns, pulse energy E = 50 mJ, the laser spot radius on the sample r = 100 μm. Thus the obtained power density is about I = 10 GW/cm^2. Mass spectra of gold ions, generated via laser ablation, obtained by quadrupole mass filter is shown in Fig. 1.

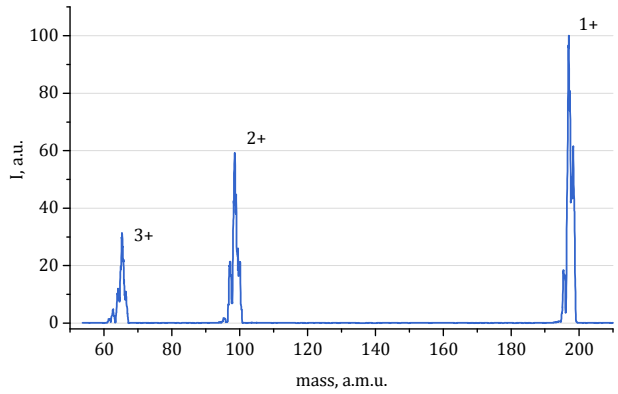


Fig. 1. Mass spectra of gold ions generated by laser ablation.

III. ION TRAPPING

Multisectional quadrupole linear ion trap [4] was used for trapping ions. The trap consists of five separated quadrupole segments (Fig. 2), which makes it possible to vary the potential of each quadrupole individually and thus forming a potential profile for capturing and keeping ions in a wide energy range of 1-500 eV. Each quadrupole section consists of four stainless steel cylindrical rods with a diameter of 8mm mounted at a diagonal distance of 7.1mm between the surfaces of the rods

Trap's rods are supplied with voltage oscillating at a frequency 1.22 MHz. In addition, a DC bias voltage can be applied to one of the sections to perform mass filtering. Power supplies allow mass filtering a range of 2−250 Da, with a resolution ~1 Da.

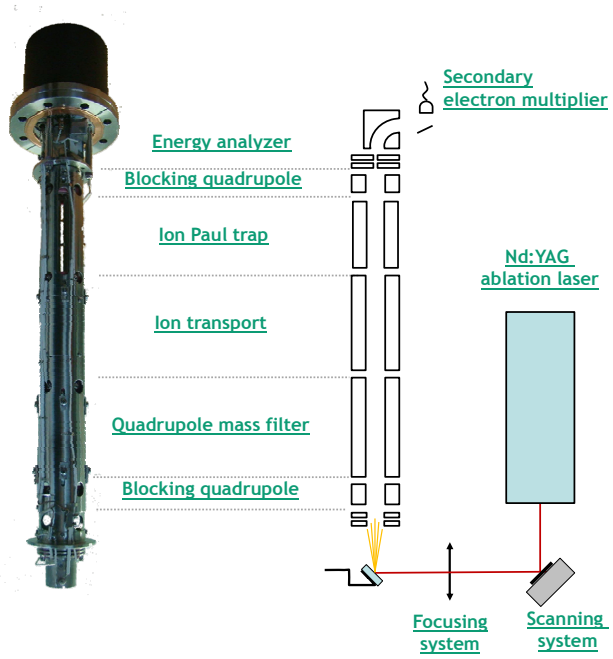


Fig. 2. Scheme of experimental setup and photo of multisectional linear Paul trap.

Trapping process was implemented by supplying DC voltage to end cap electrodes, synchronized (synchronization time 1 μs) with the laser pulse. End cap electrodes have 2mm diameter apertures coaxial with the ion trap axis. Value of "trapping potentials" applied to the electrodes ~100 V.

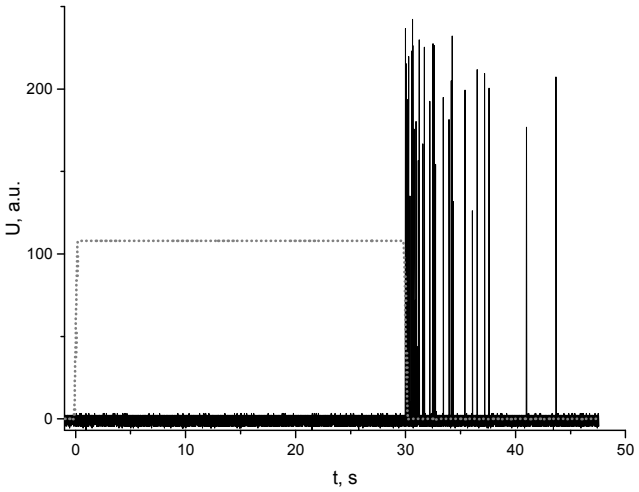


Fig. 3. Demonstration of trapping ions using quadrupole linear trap with trapping time up to 30 s. Peaks correspond to ion signal, obtained by secondary electron multiplier.

Trapping time up to 30 seconds was demonstrated by registration of secondary electron multiplier signal corresponding to ions released from the trap. (Fig 3)

REFERENCES

[1] B.R. Beck, J.A. Becker, P. Beiersdorfer, G.V. Brown, K.J. Moody, J.B.Wilhelmy, F.S. Porter, C.A. Kilbourne, R.L. Kelley, Phys. Rev. Lett.98,142501 (2007).

[2] C. J. Campbell, A. G. Radnaev, A. Kuzmich, V. A. Dzuba, V. V. Flambaum, and A. Derevianko, Physical review letters 108, 120802 (2012).

[3] V.I. Troyan, P.V. Borisyuk, R.R. Khalitov, A.V. Krasavin, Y.Y. Lebedinskii, V.G. Palchikov, S.S. Poteshin, A.A. Sysoev and V.P. Yakovlev, Laser Phys. Lett. 10, 105301 (2013).

[4] V.I. Troyan, P.V. Borisyuk, A.V. Krasavin, O.S. Vasiliev, V.G. Palchikov, I.A. Avdeev, D.M. Chernyshev, S.S. Poteshin, Alexey A. Sysoev, European Journal of Mass Spectrometry, 21, 1-12, (2015).

Polarizability and magic wavelength of Yb^+ clock transition $^2S_{1/2} \rightarrow {}^2D_{3/2}$

A. Roy[1,2], S. De[1,2]
[1]Time and Frequency division, CSIR-NPL, New Delhi, India.
[2]Academy of scientific and innovation research (AcSIR), CSIR-NPL campus, New Delhi,India

Bindiya Arora[3]
[3]Department of physics, Guru Nanak Dev University, Amritsar, India

B. K. Sahoo[4]
[4]Theoretical physics division, Physical Research Laboratory, Ahmedabad, India

***Abstract*—Differential static polarizability and black body radiation (BBR) shift for Ytterbium ion ($^{171}Yb^+$) clock transition from ground state $^2S_{1/2}$ to metastable state $^2D_{3/2}$ corresponding to the wavelength 435.5 nm are calculated accurately for frequency standard applications. The values are found to be -7.5(5) × 10^{-40} Jm^2/V and -0.4(1) Hz, respectively, which are well in agreement with pre-available data and more accurate than the previous theoretical results. We further determine the values of dynamic polarizability of these states to find out the magic and tune-out wavelengths for the above mentioned clock transition.**

Keywords—Static polarizability, BBR shift, magic wavelength, tune-out wavelength

INTRODUCTION

Ytterbium ion ($^{171}Yb^+$) has three forbidden transitions, the wavelengths of which lie in the optical regime and are suitable to be used as frequency standards. These are transitions from the $^2S_{1/2}$ ground state to the $^2D_{3/2}$, $^2D_{5/2}$ states (electric dipole, E2 transition) and to the $^2F_{7/2}$ states (electric octupole E3 transitions) at wavelengths 435.5 nm, 411 nm and 467 nm, respectively as shown in Fig 1. Among these three clock transition 467 nm clock transitions have octupole moment [1], [2] and longest lifetime of excited state greater than 10 year. Other than serving as a precise frequency standard, $^{171}Yb^+$ is suitable for testing some fundamental theories of physical sciences, such as, temporal constancy of the fine structure

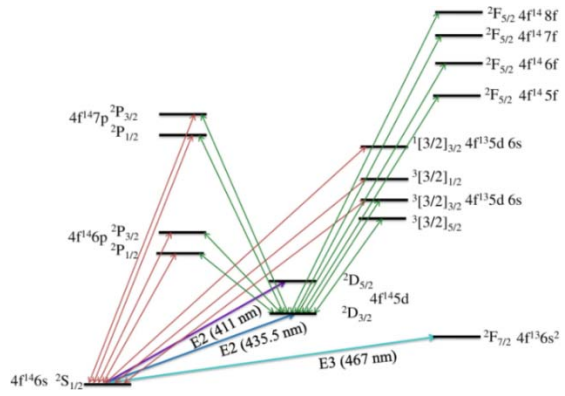


Figure 1. Energy levels of $^{171}Yb^+$ and transitions (green and red lines) that were used to calculate the polarizability of clock states.

constant, electron-to-proton mass ratio, violation of the Lorenz symmetry and parity non-conservation. In order to support these precision measurements we have estimated polarizabilities of the states associated to the clock transition $^2S_{1/2} \rightarrow {}^2D_{3/2}$ which are in better agreement with previous theoretical result and more accurate than the measured values. The black body radiation (BBR) shift and magic wavelength for this clock transition corresponding to wavelength 435.5 nm is also calculated. In general, before probing the clock transition, the ions are trapped in a radio frequency (RF) potential [3], [4], [5], [6] which causes heating of the ions. A probable solution to this problem may be the use of a hybrid trap: combination of both RF and optical lattice to reduce the RF heating problem. This may result in a very precise clock frequency. In this paper, apart from BBR shift and magic wavelength we also present calculations of tune out wavelengths for ground state and the metastable state $^2D_{3/2}$. .At tune out wavelength, λ_T, one of the atomic states involved in the clock transition is inactive or inert. This helps in understanding the behavior of that atomic state at different conditions and interactions when any precision experiment is performed. Tune out wavelength aids to study of several atomic properties like lifetimes, oscillator strength, QED effect on atomic transition etc.

THEORY

When atoms/ions interact with electromagnetic waves, they get polarized and an energy shift (or stark shift) occurs in the atomic states. The stark shift ΔE of a hyperfine state with angular momentum F and polarizability α and in electric field Ɛ is given by

$$\Delta \boldsymbol{E} = \frac{\mathbf{1}}{\mathbf{2}} \alpha_F \, \mathcal{E}^2 \qquad (1)$$

where α is frequency dependent. Polarizability of atomic state is divided into three parts: scalar, vector and tensor polarizability. The equations explaining these polarizabilities can be found in ref [1]. The polarizability of any atomic state corresponding to an applied DC electric field is called static polarizability. Static polarizability is used to calculate BBR shift of atomic states caused by stray DC electric field or very low frequency electromagnetic waves [7] , [8].

Table 1. Scalar polarizability $\alpha_J^{(0)}$ (a.u.) for state 6s $^2S_{1/2}$ for Yb^+, Contribution of each transition and correlation for polarizability of the states are tabulated and errors are giveb in parentheses. E1 matrices are in bold are taken from experimental data [1].

Contribution	**λ_{Res} (nm)**	**E1 (a.u.)**	**$\alpha_J^{(0)}$ (a.u.)**
$[4f^{14}6p]\ ^2P_{1/2}$	369.52	**2.471(3)**	16.51 (4)
$[4f^{13}5d\ 6s]\ ^3[3/2]_{3/2}$	347.73	**1.10(1)**	3.1 (1)
$[4f^{14}6p]\ ^2P_{3/2}$	329.03	**3.36(3)**	27.2(5)
$[4f^{13}5d\ 6s]\ ^3[3/2]_{1/2}$	297.05	**0.81(2)**	1.43 (3)
$[4f^{13}5d\ 6s]\ ^1[3/2]_{3/2}$	289.14	**1.27(2)**	3.45 (3)
$[4f^{14}7p]\ ^2P_{1/2}$	156.97	0.08(1)	0.0008(1)
$[4f^{14}7p]\ ^2P_{3/2}$	152.45	0.11(1)	0.014(2)
α_{core}			7.7 (7)
$\alpha_{core\text{-}valence}$			-0.16(2)
α_{Tail}			0.046 (15)
Total			59.2 (8)

However, when polarizability of atomic state is calculated at non-vanishing wavelength or frequency, it is called dynamic polarizability. The dynamic polarizability is dependent on polarization of light. Vector polarizability goes to zero when linearly polarized light is used. Dynamic polarizability gives the variation in polarizability of atomic states with respect to wavelength of light used. When differential dynamic polarizability between two atomic states goes to zero for a particular value of wavelength, this wavelength is called magic wavelength. When dynamic polarizability is zero for a particular state at a particular wavelength, then this wavelength is termed as tune out wavelength.

METHOD OF CALCULATION

Polarizability of atomic states is calculated by using magnitude of electric dipole E1 transition matrices connecting all other states to $^2S_{1/2}$ and $^2D_{3/2}$ states as shown in Fig 1. In polarizability calculation, in addition to the E1 transitions taking part, some correlation part also plays its role in contributing to the polarizability of atomic states. Polarizability due to the correlations comes into play due to three parts: core, core valence and valence contribution. Among these contributions, core contribution is larger in Yb^+. For calculating E1 matrices, we use both theoretical and experimental data. For theoretical estimation of E1 matrices, we use relativistic couple cluster theory with single and double excitation method (CCSD).We also extract E1 transition matrices using experimental lifetimes and branching ratios of their associated states [2].Using these, we calculate polarizability of the desired states. Further, in the value of the polarizability, we include contribution resulting from the correlation between core and valence electrons in atom. In this calculation, we also use CI method [3] for extracting E1 matrices for $4f^{13}$ 5d 6s type configuration.

Table 2. Scalar polarizability $\alpha_J^{(0)}$ (a.u.) and tensor polarizability $\alpha_J^{(2)}$ (a.u.) for state 5d $^2D_{3/2}$ for Yb^+, Contribution of each transition and correlation for polarizability of the states are tabulated and errors are giveb in parentheses. E1 matrices are in bold are taken from experimental data [7], [9].

Contribution	λ_{Res} (nm)	E1 (a.u.)	$\alpha_J^{(0)}$ (a.u.)	$\alpha_J^{(2)}$ (a.u.)
$[4f^{13}5d\ 6s]\ ^3[3/2]_{5/2}$	2632.81	**0.00075**	0.0	0.0
$[4f^{14}6p]\ ^2P_{1/2}$	2438.42	**2.97(4)**	79(2)	-79(2)
$[4f^{13}5d\ 6s]\ ^3[3/2]_{3/2}$	1724.98	**0.27**	0.46	0.37
$[4f^{14}6p]\ ^2P_{3/2}$	1345.63	1.31(2)	8.45(26)	6.76(21)
$[4f^{14}7p]\ ^2P_{1/2}$	245.42	0.14(2)	0.018(5)	-0.018(5)
$[4f^{14}7p]\ ^2P_{3/2}$	234.56	0.014(5)	0.0002(1)	0.0001(1)
$[4f^{14}5f]\ ^2F_{5/2}$	210.34	2.43(4)	4.54(15)	-0.91(3)
$[4f^{14}6f]\ ^2F_{5/2}$	173.92	1.47(2)	1.38(4)	-0.275(7)
$[4f^{14}7f]\ ^2F_{5/2}$	158.89	0.93(1)	0.503(11)	-0.101(2)
$[4f^{14}8f]\ ^2F_{5/2}$	151.02	0.35(1)	0.068(4)	-0.014(1)
α_{core}			7.7 (7)	0.0
$\alpha_{core\text{-}valence}$			-0.43(3)	-0.08(1)
α_{Tail}			4(2)	-0.83(25)
Total			105(3)	-74(2)

RESULT AND DISCUSSION

Static polarizabilities of ground state, $^2S_{1/2}$ and excited state, $^2D_{3/2}$ of Yb ion, are calculated by considering contribution of E1 transitions shown in Fig.1 in which transitions from ground state $[4f^{14}\ 6s]\ ^2S_{1/2}$ to $[4f^{14}6p]\ ^2P_{1/2}$ and $^2P_{3/2}$ contributes largely. The closed shell orbital configuration $4f^{14}$ too is causing increase in polarizability contribution due to its complete core shell. The remaining E1 transition that we have considered from the ground state to other excited states have minior contributions are shown in Table 1. The calculated value is found to be $9.90(1) \times 10^{-40}$ Jm^2V^{-2}. Tensor polarizability of ground state is zero owing to its angular momentum L= 0. Static polarizability of excited state $^2D_{3/2}$ is calculated in two parts, scalar polarizability and tensor polarizability. Vector polarizability remains zero in static polarization calculations. The major contribution to polarizability comes from the transition $[4f^{14}5d]\ ^2D_{3/2}$ to $[4f^{14}6p]\ ^2P_{1/2}$, and the polarizability due to core contribution and valence shell part for static polarizability as shown in table 2. We added all other minor contributions and obtained value of static polarizaility of state $^2D_{3/2}$ state to be $17.4\ (5) \times 10^{-40} Jm^2V^{-2}$. We also calculated tensor polarizability for state $^2D_{3/2}$ and found it to be $-12.3(3) \times 10^{-40}$ Jm^2V^{-2}. There is no experimental data relating to static polarizability of individual clock states but the same is available for differential static polarizability of these clock states and tensor polarizability of $^2D_{3/2}$ done by PTB Germany. We therefore compare our calculations with the experimental results.

Table 3. Comparison between calculated differential polarizability and BBR shift to experimental values.

Parameters	Experiment (Ref. [10])	Theoretical (Our calculation)
Differential polarizability $\Delta\alpha_s = \alpha_s(^2S_{1/2}) - \alpha_s(^2D_{3/2})$	$-6.9(1.4) \times 10^{-40}$ Jm^2/V	$-7.5(5) \times 10^{-40}$ Jm^2/V
Tensor Polarizability $\alpha_t(^2D_{3/2})$	$-13.6(2.2) \times 10^{-40}$ Jm^2/V	$-12.2(3) \times 10^{-40}$ Jm^2/V
BBR	-0.37(5) Hz	-0.4(1)Hz

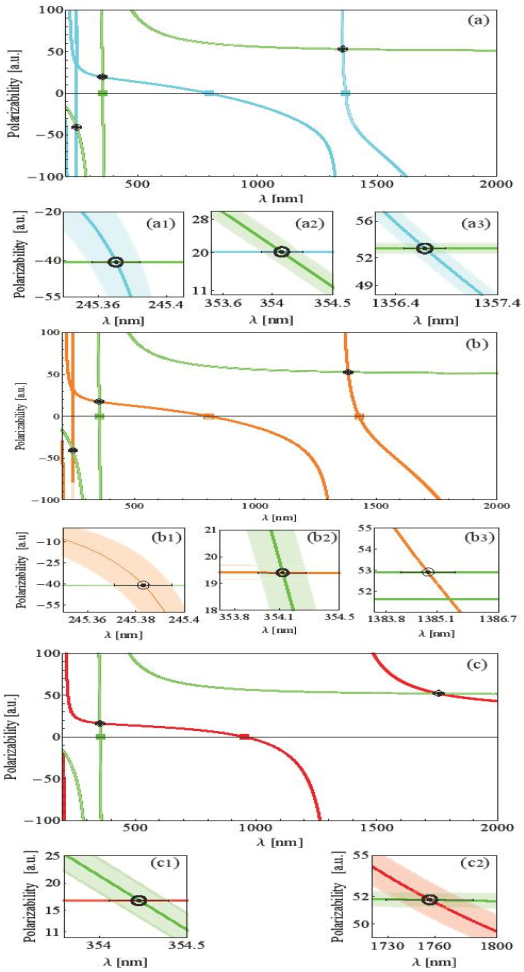


Figure 2.Magic wavelengths and tune out wavelengths are depicted in black and colored dots, respectively for linear polarize light for state $[4f^{14}6s]\ ^2S_{1/2}$ F = 0 (Green) and $[4f^{14}5d]\ ^2D_{3/2}$ F=2 $m_F = 0$ (Cyan) , $m_F = \pm1$ (Orange) and $m_F = \pm2$ (Red).

with this data and conclude that our result is within their experimental error limit. We also calculated BBR shift using our calculated differential polarizability and found that its value is in good agreement with the experimental result, shown in table 3.

Having calculated and compared the static polarizability with available experimental data, we found that the E1 matrices calculated using theoretical methods are correct and reliable. After these calculations, we calculated dynamic polarizability for ground state $^2S_{1/2}$ and excited state $^2D_{3/2}$ state for both circular and linear polarizations of light. In our calculations, we assume the magnetic field to be nearly equal to zero. For different values of m_F, a graph of polarizability vs wavelength is plotted. The corresponding plots for linearly and circularly polarized light are shown in Fig 2 and Fig.3 respectively. In Fig. 2 (a), it is clear that the ground state polarizability curve always intersects the polarizability curve of excited state $^2D_{3/2}$ sharply , which indicates that the lattice for this transition is unable to completely nullify the light shift or in other words,

Table 4. Magic wavelength for all possible m_F transitions of $|5d\ ^2D_{3/2}, F=2\rangle$ to $|6s\ ^2S_{1/2}, F=0\rangle$.

Light Polarization	Excited $\|m_F\rangle$ state	λ_m (nm)	α_m (a.u.)
Linear	±2	1757(32)	51.7(6)
		354.2(2)	16.7(2)
Circular	2	978(48)	56(1)
		352.8	44.7(9)
	-2	1382.4(5)	52.9(6)
		355.3(1)	-6.0(3)
		245.28(4)	-40.7(7)
Linear	±1	1384.8(9)	52.9(6)
		354.1(2)	19.4(3)
		245.38(1)	-35(2)
Circular	1	353.5(2)	30.7(6)
	-1	1422(1)	52.7(6)
		354.8(1)	5.35(9)
		245.3(2)	-40.3(6)
Linear	0	1356.7(2)	53.0(5)
		354.1(2)	20.2(3)
		245.37(2)	-39.7(3)
Circular	0	1500(5)	52.4(5)
		354.2(2)	17.6(2)
		245.41(5)	-41(1)

for this transition we do not get a good magic wavelength. In Fig. 2(b) the intersections for these transitions are smoother compared to previous one. In optical lattice, the ions experience coulombic repulsion resulting in smaller lifetime, so higher wavelength is to be used which may increase the trap lifetime. Hence, the best magic wavelength for trapping is achieved in Fig. 2(c) where the intersections are smooth at higher wavelength, which is good for ion trapping and probing the clock transition. For circularly polarized light, total dynamic polarizability of $^2D_{3/2}$ state includes three parts scalar, vector and tensor polarizability. Due to the vector polarizability, total dynamic polarizability of this state has dependence on the sign of m_F value. In linearly polarized light, m_F = -2 and +2 possess same light shift, but in circularly polarized light, m_F = -2 and +2 have different light shifts due to the vector polarizability. In Fig. 3(a), (b) and (e) the intersection between the clock states are not much smooth which indicates that the magic wavelength for this transition is not good enough to completely nullify the light shift whereas in Fig. 3(c) and (d) we have good magic wavelength where the intersection is comparatively smoother.

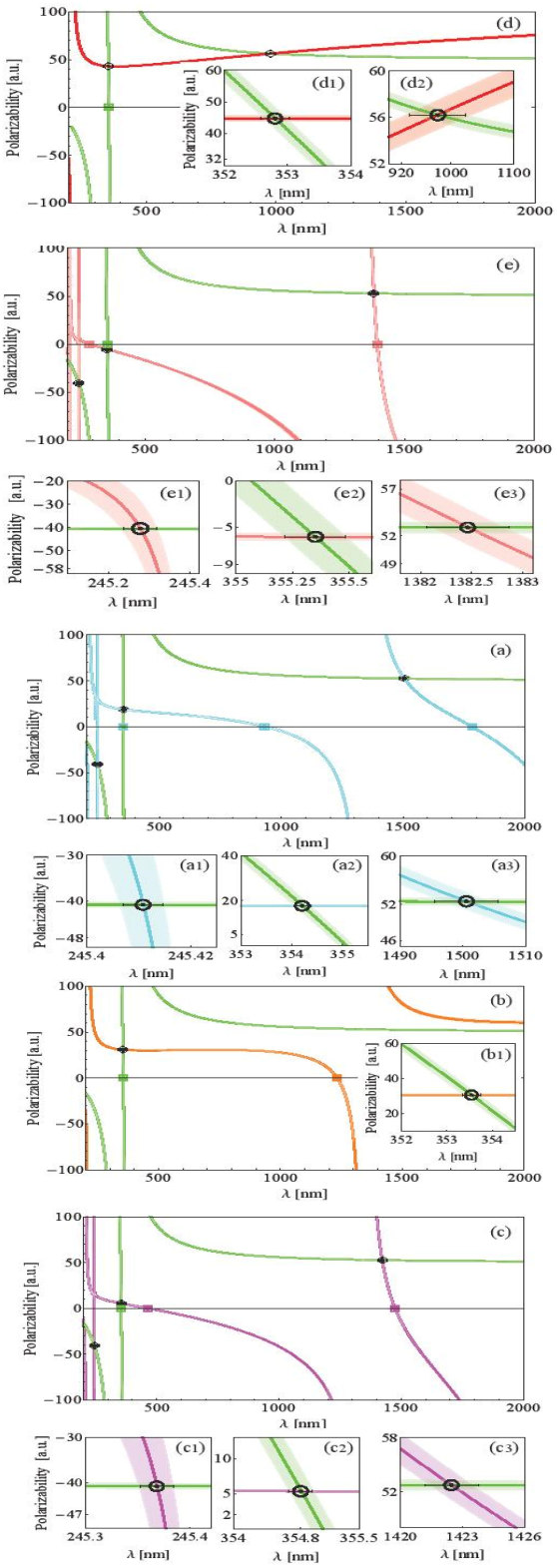


Figure 3. Magic wavelengths and tune out wavelengths are depicted in black and colored dots, respectively, for circularly polarized lightfor state $[4f^{14}6s]\ ^2S_{1/2}$ F = 0 (Green) and $[4f^{14}5d]\ ^2D_{3/2}$ F=2 $m_F = 0$ (Cyan) , $m_F = +1$ (Orange), $m_F = -1$ (magenta), $m_F = 2$(Red) and $m_F = -2$ (Pink).

Table 5. Tune out wavelength for state $[4f^{14}5d]\ ^2D_{3/2}$ state.

Polarization	m_F	λ_T	Polarization	m_F	λ_T
Linear	0	1725.6(1)	Circular	0	1822(7)
		820.2(5)			929.1(5)
	± 1	1727.7(1)		+1	1231.5 (1)
		854.2(7)			
				+2	NA
	± 2	966.2(5)			
				-1	1473.9 (3)
					488.1(7)
				-2	1395.9 (2)
					293.2(4)

Magic wavelengths for all transitions are tabulated in table 4, where the total polarizability (scalar + vector + tensor polarizability) at magic wavelength is in a.u. We also include correlation factors like core, core valence and tail in polarizability calculation.

Other than magic wavelength we also calculated tune out wavelength. At tune out wavelength, polarizability of atomic state goes to zero. When the dynamic polarizability curve of the energy state intersect the x-axis , the intersection points give tune out wavelength , shown in Fig. 2 and 3, represented by color dots. There is only one tune out wavelength for ground state i.e. 357.9(1) nm, where the total polarizability goes to zero.Tune-out wavelengths for excited state are tabulated in Table 5.

Conclusion

In summary, we have conducted a systematic study of the polarizability for the ground state $^2S_{1/2}$ and metastable state $^2D_{3/2}$ state of Yb+. Value of BBR shift was calculated with the help of static polarizablity, unlike in previous theoretical reports. We also present the magic wavelength determined for clock transition $^2S_{1/2} \rightarrow {}^2D_{3/2}$ for circularly and linearly polarized light for all possible m_F values. From our calculations, we propose that the trapping of Yb ion in optical lattice is possible for such a clock transition, which may be used for future commercial optical clocks and also to study the novel physics related to ion-ion/ion-atom interactions.

ACKNOWLEDGMENT

S De and A Roy acknowledges CSIR–NPL, Board of Research in Nuclear Science under Department of Atomic Energy, India (DAE-BRNS) and Department of Science and Technology (DST), India for supporting this work.

References

[1] N. Batra, B. K. Sahoo and S. De*, "An optimized ion trap geometry to measure quadrupole shift of 171Yb+ clocks" –Chin. Phys. B 25, 113703 (2016).

[2] N. Batra, Sukhjit Singh, S. De*, Amisha Arora, Bindiya Arora, A. Sen Gupta. 'Systematic Shifts for Ytterbium-ion Optical Frequency Standards' –Manuscript is communicated, arXiv:1405.5399 (2015).

[3] N. Batra, S. Panja*, S. De, A. Roy, S. Majhi, S. Yadav and A. Sen Gupta, "Design and construction of a helical resonator for delivering radio frequency to an ion trap" MAPAN-J. Metrol. Soc. India, DOI 10.1007/s12647-017-0209-5 (2017)

[4] A. Rastogi, N. Batra, A. Roy, J. Thangjam, V. P. S. Kalsi, S. Panja and S. De*, 'Design of the Ion Trap and Vacuum System for 171Yb-ion Optical Frequency Standard'- MAPAN-J. Metrol. Soc. India 30, 169 (2015).

[5] S. Panja*, S. De, S. Yadav, Sen Gupta. 'Measuring capacitance and inductance of a helical resonator and improving its quality factor by mutual inductance alteration' –Rev. Sci. Instrum. 86, 056104 (2015).

[6] N. Batra, A. Roy, C. Samal, S. Majhi, S. Panja and S. De*,"Automation of an optical frequency standard experiment" IEEE Conf. Proc of 2nd International conference on control, instrumentation, energy and communication, Kolkata. Doi: 10.1109/CIEC.2016.7513823 (2016).

[7] A. Roy, S. De, Bindiya Arora, B. K. Sahoo, "Accurate determination of black-body radiation shift, magic wavelength and tune-out wavelengths for the 6S1/2→ 5D3/2 clock transition in Yb+," unpublished.

[8] Bindiya Arora, D. K. Nandy and B. K. Sahoo., "Multipolar black body radiation shifts for single-ions clocks," Phys. Rev. A 85, 012506 (2012)

[9] S. G. Porsev, M. S. Safronova and M. G. Kozlov, "Correlation effects in Yb+ and implications for parity violation", Phys. Rev. A 86, 022504 (2012).

[10] T. Schneider, E. Peik and Chr.Tamm, "Sub-Hertz optical frequency comparisions between two trapped 171Yb+ ions," Phys. Rev. Lett 94, 230801 (2005).

Preparing a frequency measurement of the first lattice clock based on bosonic magnesium

Steffen Sauer, Steffen Rühmann, Dominika Fim, Klaus Zipfel, Nandan Jha, Waldemar Friesen, Wolfgang Ertmer, and Ernst M. Rasel

Institut für Quantenoptik
Leibniz Universität Hannover
Hannover, Deutschland
sauer@iqo.uni-hannover.de

***Abstract*— We present a magnesium optical lattice clock with the highest Q value of 1.6 x 10^{-13} and an evaluation of its accuracy limitations for an upcoming frequency measurement.**

Keywords—Optical lattice clock, magnesium, tunneling

I. INTRODUCTION

Optical lattice clocks operate in the Lamb Dicke regime and also probe a large number of absorbers. Thus lattice clocks offer the best characteristics of both, ion and neutral clocks. In Hannover, at the Institute of Quantum Optics we work with an optical lattice clock based on bosonic magnesium trapped at the magic wavelength, which matches the theoretical prediction with a high precision [1].

II. CURRENT EXPERIMENTAL STATUS

Even though, we confine the magnesium atoms in the Lamb-Dicke regime at trap depths of 41 E_r, the linewidth of the strictly forbidden clock transition is still dominated by tunnel broadening. The characterization of this broadening and also broadening effects introduced by magnetic field induced spectroscopy [2], resulting in a 42 Hz broad linewidth, will be discussed in this work.

Our ultra-stable laser system interrogating the clock transition consists of a diode laser system at 916 nm stabilized to a high finesse cavity isolated from environmental perturbations. We achieve an instability of 4×10^{-16} in 1 s for the laser itself, which is close to the calculated thermal noise floor level.

For our upcoming frequency comparison against the PTB via a 73 km long fiber, we performed an evaluation of the most dominant systematic frequency shifts influencing our frequency measurement, such as the 2nd order Zeeman shift, AC stark shift due to the lattice laser as well as the clock laser fields. Finally, we will give an insight of our preliminary stability analysis.

This work was supported in part by Deutsche Forschungsgemeinschaft (DFG) within QUEST, Center for Quantum Engineering and Space-Time Research. Moreover we acknowledge financial support from DFG Research Training Group (Graduiertenkolleg) 1729, the Marie Curie Initial Training Network FACT (ITN-FACT) Program, call FP7-PEOPLE-2013-ITN and the Deutsche Zentrum für Luft- und Raumfahrt (DLR) BOOST project.

ACKNOWLEDGMENT

We thank K. Gibble, M. Safranova, U.I. Safranova and S.G. Porsev for the theoretically support. Furthermore we thank O. Prudnikov for helpful discussions and A. Bauch from Physikalisch Technische Bundesanstalt (PTB) for providing a passive H-maser.

REFERENCES

[1] A. P. Kulosa, D. Fim, K. H. Zipfel, S. Rühmann, S. Sauer, N. Jha, K. Gibble, W. Ertmer, E. M. Rasel, M. S. Safronova, U. I. Safronova, and S. G. Porsev, Phys. Rev. Lett. **115**, 240801 (2015)

[2] A. V. Taichenachev, V. I. Yudin, C. W. Oates, C. W. Hoyt, Z. W. Barber, and L. Hollberg, Phys. Rev. Lett. **96**, 083001 (2006)

Optical Sampling Analog-to-Digital Scheme for broadband microwave signal based on atomic resonator

Hongling Meng[1,2], Ruiyuan Liu[1] and Jianye Zhao[1*]
1. School of Electronics Engineering and Computer Science, Peking University, Beijing, China.
2. Beijing Blue Mountains Quantum Technology Co. Ltd, Beijing, China
zhaojianye@pku.edu.cn

***Abstract*—We report a long-term stabilization optical sampling analog-to-digital scheme for broadband microwave signal based on a rubidium coherent population trapping (CPT) atomic resonator. With this scheme, we can realize analog-to-digital conversion with broadband microwave signal based on optical combs with low repetition rate and the optical sampling ADC system also becomes a long-term stabilization system. The frequency stability performance of $8\times10^{-11}\tau^{1/2}$ from 1 s to 10^3 s is obtained and the frequency drift is 1.6×10^{-12} for one day. With this scheme, we could achieve 7 bit ENOB at about tens of GHz carrier frequency over 50MHz bandwidth.**

Keywords—analog-to-digital conversion; optical comb; broadband;

I. INTRODUCTION

Optical sampling analog-to-digital (ADC) conversion system has been greatly advanced ever since the development of optical combs [1-4]. Compared with electronic ADC, optical pulse train generated by optical comb has much short pulse width and ultralow timing jitter. Optical combs can generate pulse train with repetition rate of GHz magnitude easily. So it can fulfill ADC system with GHz sampling rate. But because of the limitation of response time of photodiode and quantization ADC device, traditional optical sampling ADC system has limitation to achieve broadband microwave signal conversion.

In this letter, we demonstrate a new scheme of chip scale atomic clock based optical sampling ADC system for broadband microwave signal conversion. We use two mode-locked fiber lasers with a slight difference in repetition rate. The repetition rate of the mode-locked laser is locked to a 10 MHz atomic resonance-based frequency source. We combine these two optical pulses together as one optical pulse train to sample input microwave with Mach-Zehnder interferometer. The output is then separated and converted to electronic signal and converted to digital signal separately. With this scheme, we could achieve analog-to-digital conversion with microwave which has tens of GHz magnitude carrier frequency with optical combs with low repetition rate. The result shows that the frequency stability reaches $8\times10^{-11}\tau^{1/2}$ from 1 s to 10^3 s.

II. SCHEME OF THE SYSTEM

The traditional optical sampling ADC system is shown as fig. 1. It consists of one optical comb, one electro-optic modulator(EOM), one photodiode and one quantization ADC. The optical pulse train generated by the optical comb is passed through a EOM, and it is modulated with input microwave signal. The output signal is then transferred to electronic signal by a photodiode. The electronic ADC realize quantization. The scheme we use is shown as fig.2. We use two optical combs with slightly offset repetition rates as sampling pulse train. The pulse trains generated by these two combs are combined together. Thus we form a pulse train which has a much shorter pulse-to-pulse interval compared with the original repetition rate of optical comb. After reconstruction of the sampled data, we could conduct optical sampling ADC system with wide bandwidth.

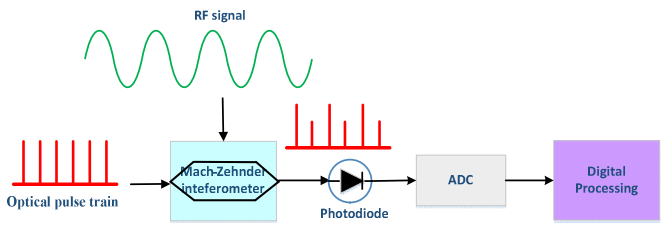


Fig. 1. Optical sampling ADC system

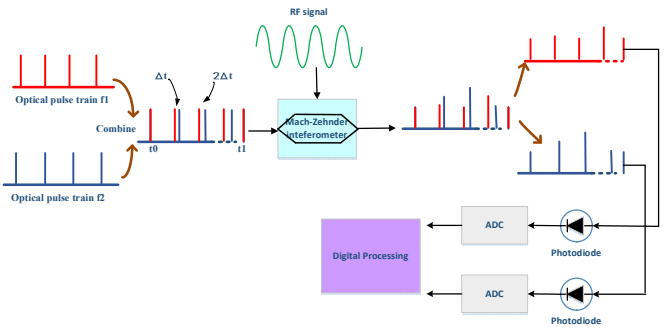


Fig. 2. Optical sampling ADC sytem based on dual optical combs

If we use optical combs with repetition rates of 100MHz and 101MHz. We could generate a pulse train with a pulse-to-pulse interval of 100ps. This scheme could realize optical analog to digital conversion at high carrier frequency.

III. EXPERIMENT AND RESULTS

A scheme of chip-scale atomic resonator based optical sampling ADC system is shown as Fig. 3.

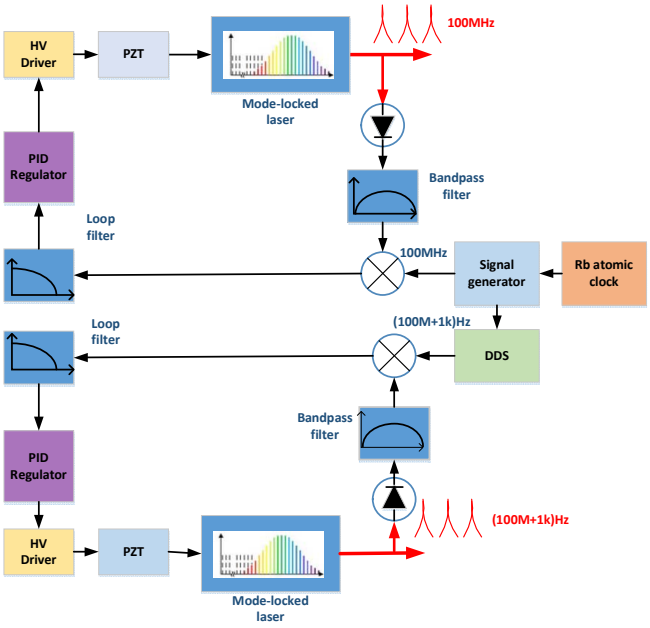


Fig. 3. Optical sampling ADC system based on chip-scale atomic clock[5]

The output of the atomic clock is 10MHz. It is used as a reference for the signal generator. The optical pulse train is converted to electronic signal with photodiode, and then mixed with the reference signal to generate an error signal. The error signal is used to control the high voltage driver to adjust the cavity length of the mode-locked fiber laser to change the repetition rate of it.

The structure of the CSAC is shown as Fig. 4.

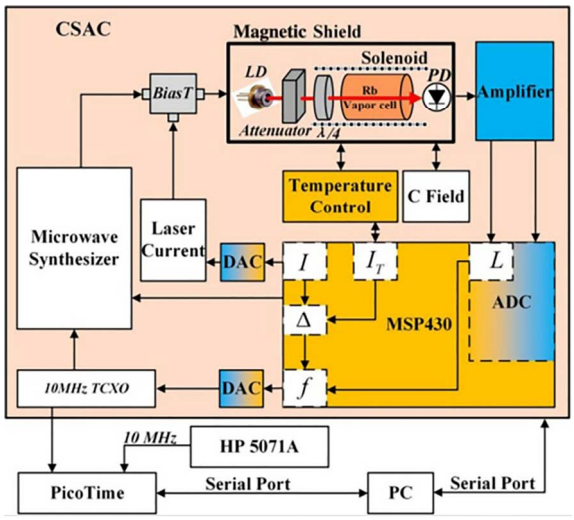


Fig. 4. Structure of the CSAC

The chip-scale atomic clock consists of a physical part and a power servo circuit. The long term frequency stability experiments are carried out on this clock. The Allan deviation of our clock reaches 4×10^{-12}@ 1000s, and the stability shows $8\times10^{-11}\,\tau^{-1/2}$ from 1 s to 10^3 s. The frequency drift of the atomic clock is only $\sim1.6\times10^{-12}$/day.

We conduct the optical sampling ADC based on this scheme. The input signal is 10.021GHz microwave. After sampling this signal with our scheme, we conducted FFT to the output data. Fig. 5 shows the FFT spectrum which is sampled by the 100MHz repetition rate. The ENOB is calculated by $ENOB = (SNDR(dB) - 1.76) / 6.02$. The ENOB is 7 bits.

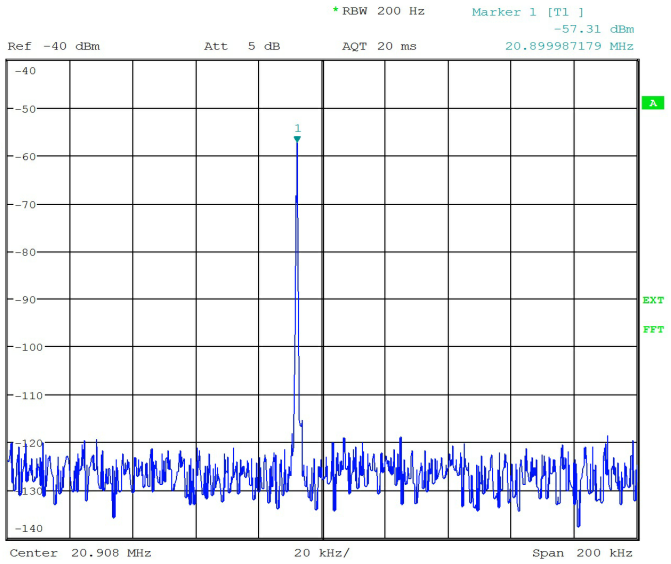


Fig. 5. FFT spectrum of 100MHz microwave signal

According to bandpass sampling theory, we can recovery the input microwave signal precisely with this scheme. The bandwidth of this optical ADC system is 50MHz. we could increase the bandwidth by using mode-locked fiber lasers with high repetition rate. Then we could easily reach optical sampling system with GHz magnitude bandwidth.

IV. CONCLUSTION

In this letter, we demonstrate a new scheme of optical sampling ADC system for broadband microwave signal conversion. We realize 7 bit ENOB. We use two optical combs to generate an optical pulse train which has much short pulse-to-pulse interval. Compared with traditional wavelength interleaving method, this optical source is much easier to get. This scheme is applicable for photonic radar system.

ACKNOWLEDGMENT

This program is funded by National Natural Science Foundation of China (61535001, 61371074,); Program of International S&T Cooperation (No. 2016YFE0100200). We thank Ermeng Hu for useful advice in chip scale atomic clock.

REFERENCES

[1] A. Yariv, and P. G. M. P. Koumans, “Time interleaved optical sampling for ultra-high speed A/D conversion,” Electron. Lett. Vol. 34, pp. 2012-2013, 1998.

[2] J. C. Wwichell, and R. Helkey, “Phase-Encoded Optical Sampling for Analog-to-Digital Converters,” IEEE Photonic Technol. Lett. Vol. 12, pp. 1237-1239, 2000.

[3] J. U. Kang, and R. D. Esman, “Demonstration of time-interweaved photonic four-channel WDM sampler for hybrid analogue-ditital converter,” Electron. Lett. Vol. 25, pp. 60-61, 1999.

[4] 5. A. S. Bhushan, P. Kelkar, and B. Jalali, “30 Gsample/s time-stretch analog-to-digital converter,” Electron. Lett. Vol. 36, pp. 1526-1527, 2000.

[5] Hongling Meng, Jianxiao Leng, Cheng Qian, and Jianye Zhao, "Optical sampling analog-to-digital converter based on two asynchronous mode-locked fiber lasers," J. Opt. Soc. Am. B 34, 824-830 (2017)

Precision Measurement of the Hyperfine Structure of the ^{85}Rb $6P_{3/2}$ State

Shengnan Zhang, Xiaogang Zhang, Zhaojie Jiang, Haosen Shang, Pengyuan Chang, Jingbiao Chen
State Key Laboratory of Advanced Optical Communication, System and Network,
School of Electronics Engineering and Computer Science,
Peking University, Beijing 100871, China
E-mail: zhangsn27@163.com

Jiqing Lian, Jianhui Tu, Shiyu Yang
National Key Laboratory of Science and Technology on Vacuum Technology & Physics,
Lanzhou Institute of Physics, CAST,
Lanzhou, Gansu 730000, China
E-mail: yangshiyu3079@126.com

***Abstract*—Partly subjected to the stability of optical frequency source, the magnetic dipole and electric quadrupole hyperfine constants of the ^{85}Rb $6P_{3/2}$ State have been reported to be 8.163(4) MHz and 8.191(27) MHz, respectively. To pursue the higher precision, here we have constructed two more robust ^{85}Rb spectrometers with a preliminary stability of $2.3\times10^{-13}/\sqrt{\tau}$ based on the modulation transfer spectroscopy technique of ^{85}Rb $5S_{1/2}$ – $6P_{3/2}$ transition. By the heterodyne experiment between the two ^{85}Rb spectrometers, we have measured the hyperfine separations of ^{85}Rb $6P_{3/2}$, and obtained the magnetic dipole constant and the electric quadrupole constant which are 8.220 MHz and 5.148 MHz respectively, not considering the systematic errors yet.**

Keywords—hyperfine structure; precision measure; modulation transfer spectroscopy

I. INTRODUCTION

Within the last few years, the precise measurement and accurate determination of excited-state properties of atomic systems has attracted people's interests for that it can help to further understand the atomic and fundamental physics[1]. The strength of the magnetic dipole, electric quadrupole and magnetic octopole interactions between the nucleus and the orbital electrons can be obtained from the measurement of the hyperfine splitting because it is induced by the electron-nuclear interactions[2]. Additionally, the precise measurements in atomic lines can include the atomic wave function information, which is important while comparing theoretical calculations with experimental data in atomic tests of parity violation.

Recently, lots of work on the precise measurement of atomic hyperfine structure particularly alkali atoms, has been reported[3-7]. In Ref[6], utilizing two ^{87}Rb D_2-saturated-absorption spectrometers with the stability of 3.8×10^{-12} at 1 s, $\pm$3 kHz measurement precision has been achieved. P. V. Kiran Kumar et al. measured the hyperfine splitting for the two-photon transition of both isotopes of potassium by electro-optically modulating the laser beam[7]. Dipankar Das et al. employed the coherent-control spectroscopy technique and measured the hyperfine structure in the first-excited P state of all the naturally-occurring alkali atoms[8].

As for the precision measure of hyperfine structure of $6P_{3/2}$ state of ^{85}Rb, few papers have been reported recently. Bucka, et al. utilized double-resonance experiment and achieved A=8.179(12), B=8.190(49) MHz with a 44% confidence by least-squares fitting[9]. In addition, using the theoretical g_J value of 1.3341, Bucka et al. determined A=8.163(4), B=8.191(27) MHz by a level-crossing measurement[10]. The measurement precision all above was limited at several kHz to tens of kHz, which was determined by the stability and reproducibility of the diode laser.

In this letter, we first utilized the sub-Doppler modulation transfer spectroscopy technique (MTS)[11-15] to achieve two more stable lasers with the stability of 2.3×10^{-13} at 1 s and 1.2×10^{-14} at 1000 s, and then measured the hyperfine splitting of $6P_{3/2}$ state of ^{85}Rb with them. MTS is an excellent frequency stabilization technique for that it has a symmetric sub-Doppler feature free of Doppler background and a high signal-to-noise ratio. We built two identical ^{85}Rb MTS-based spectrometers. One was locked on the hyperfine transition F=3 —F'=4 with the MTS technique, and the other was locked on the other hyperfine transitions of $6P_{3/2}$. The frequency offset between the two systems determines the hyperfine splitting. With the heterodyne experiment, we obtained the hyperfine splittings of $6P_{3/2}$ ^{85}Rb. According to these experimental values, the magnetic dipole and electric quadrupole can also be measured. The current measured precision is mainly subjected to the shift of the reference frequency and the noise of servo circuit. In the next step, we will take some action of precisely controlling the system's temperature to reduce the influence of the ambient temperature's fluctuation. Also, some filters will be added to the servo circuit for filtering the noise.

II. EXPERIMENT

The experimental scheme of the precision measurement of the hyperfine structure of the ^{85}Rb $6P_{3/2}$ State is shown in Fig. 1(a). In this scheme, the two lasers both are locked on different hyperfine transition signals with the MTS technique, respectively. After locking, the frequency beating signal between the two lasers is detected by a photodetector, and then transmitted to the frequency counter. Fig.1(b) shows our MTS-based ^{85}Rb spectrometer. The pump beam is phase modulated by a wideband EOM. A high-speed photodetector detects the modulation-transferred probe beam, and its signal is subsequently demodulated by a double-balanced mixer (DBM). In both systems, the pump and probe beams are spatially overlapped and their polarizations are vertical. The pump power and probe power are around 1 mW and 0.3 mW,

respectively. The modulation frequency is 1.3 MHz approximating to ~0.7 times of spectroscopy linewidth. The error signal from the servo circuit is feedbacked to the current port, PZT port and laser diode. By optimizing the servo loop gain and bandwidth, the diode laser can be stabilized on the atomic hyperfine transition with an excellent stability.

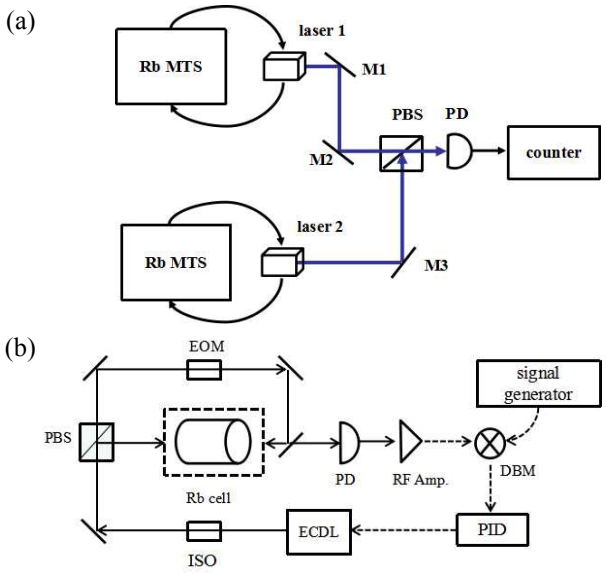


Fig. 1. (a) Experimental scheme of the precision measurement of the hyperfine structure of the Rb $6P_{3/2}$ State with MTS. (b) The MTS-based ^{85}Rb spectrometer. PID, proportional-integral-derivative; PBS, polarization beam splitter; ISO, isolator; PD, photodetector.

III. RESULT

Figure 2 shows the saturated absorption spectroscopy (SAS) of $5S_{1/2}$(F=3) - $6P_{3/2}$(F'=2,3,4) of ^{85}Rb (black curve) and the corresponding MTS signal (blue curve). The various hyperfine components and crossover resonances are clearly resolved and labeled by the value of F'. When the two ^{85}Rb spectrometers are locked on the two different hyperfine transitions, all hyperfine splittings of $6P_{3/2}$ can be obtained.

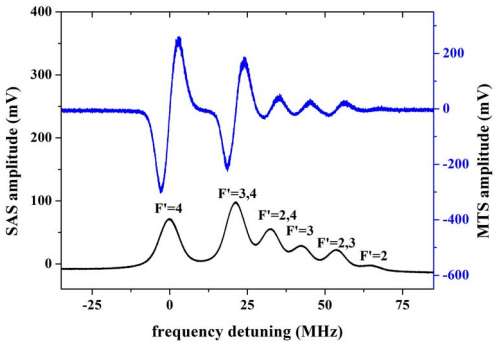


Fig. 2. Frequency scan over the hyperfine components of ^{85}Rb $6P_{3/2}$. The black curve shows the saturated absorption spectroscopy and the blue one shows the corresponding MTS.

Figure 3 shows the recorded frequency fluctuation of the error signal versus time when the ^{85}Rb spectrometer is locked on F=3-F'=4 hyperfine transition and the corresponding Allan deviation. The data are accumulated over 4800 seconds. By the self-evaluation, the Allan deviation of $\sigma(t) = 2.3\times10^{-13}/\sqrt{\tau}$ indicates that the frequency fluctuation is 160 Hz when the averaging time is 1 s. More significantly, the Allan deviation continues to decrease approximately to 1×10^{-14} with increasing averaging time to 1000 s.

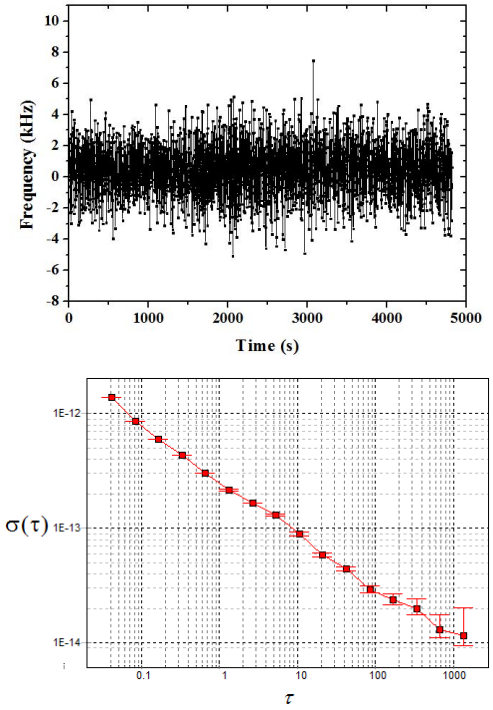


Fig. 3. (a) The frequency fluctuation of the error signal when the laser is locked on F=3-F'=4 hyperfine transition. The frequency fluctuation range is about ±3 kHz. (b) The Allan deviation derived from the fig.3(a). The 1 s stability is about 2.31×10^{-13} and 1000 s stability is near 1×10^{-14}.

By using the two ^{85}Rb spectrometers, we have measured the various hyperfine splittings of ^{85}Rb $6P_{3/2}$, as shown in table 1. With these data, we determine the magnetic dipole constant *A* and the electric quadrupole constant *B*, which are 8.220(3) and 5.148(3) MHz, respectively. The *A* value is close to the Ref[9] and Ref[10], but the *B* value is different from theirs. Figure 4 shows the comparison our measured results with earlier values in Refs[9,10].

TABLE 1. The measured hyperfine separations between the various hyperfine states of the $6P_{3/2}$ in ^{85}Rb.

Hyperfine transition of $6P_{3/2}$ in ^{85}Rb	measured (this work) (MHz)
F'=4 – F'=3	39.059
F'=3 – F'=2	21.186

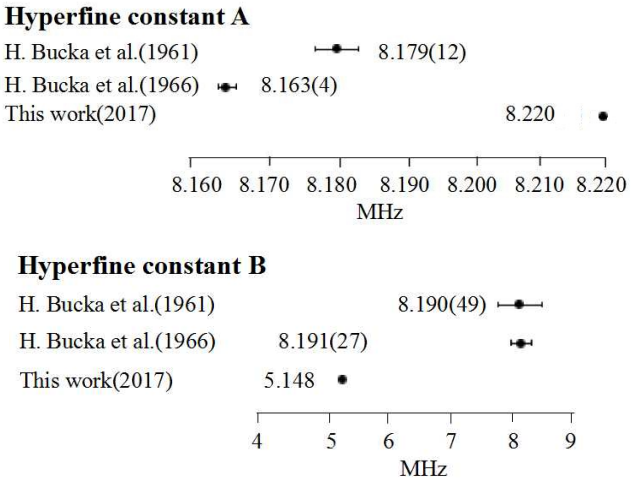


Fig. 4. Comparison between A and B values this work and the earlier results. The earlier results are in Refs[9,10].

In conclusion, we have tried to measure the hyperfine separations of ^{85}Rb $6P_{3/2}$ by using heterodyne experiments between two MTS-based ^{85}Rb spectrometers. By self-evaluation, the stability of our spectrometers have reached $\sigma(t) = 2.3\times10^{-13}/\sqrt{\tau}$. From the measurements of hyperfine separations, we have derived the precise values of the magnetic dipole constant *A* and the electric quadrupole constant *B*, which are 8.220 and 5.148 MHz, respectively. The *A* constant agrees with previous measurements, but the *B* constant is a little different. The systematic shifts caused by the collision and magnetic fields are not considered here. Besides the measured stability is mainly limited by the noise of the servo circuit and the shift of the reference frequency cause by the fluctuation of the ambient temperature. Also, the residual amplitude modulation in EOM can destroy the long-term stability of ^{85}Rb spectrometers. Thus, we will take some steps to precisely control the temperature of the whole system. In addition, noise elimination of the servo circuit will be done.

ACKNOWLEDGMENT

This work is supported by China Academy of Space Technology Foundation (CAST-2015-5-10) and the National Natural Science Foundation of China (NSFC) (91436210).

REFERENCES

[1] P. V. Kiran Kumar, M. Sankari, and M. V. Suryanarayana, "Hyperfine structure of the 7d $^2D_{3/2}$ level in cesium measured by Doppler-free two-photon spectroscopy," Phys. Rev. A, Vol. 87, 012503, 2013.

[2] U. D. Rapol, A. Krishna, and V. Natarajan, "Precise measurement of hyperfine structure in the $5P_{3/2}$ state of ^{85}Rb," Eur. Phys. J. D, Vol. 23, pp. 185-188, 2003.

[3] R. Gupta, W. Happer, L. K. Lam, and S. Svanberg, "Hyperfine-structure measurement of excited S state of the stable isotopes of potassium, rubidium, and cesium by cascade radio-frequency spectroscopy," Phys. Rev. A, Vol. 8, pp. 2792-2810, 1973.

[4] E. Arimondo, M. Inguscio, and P. Violino, "Experimental determinations of the hyperfine structure in the alkali atoms," Rev. Mod. Phys., Vol. 49, pp. 31-75, 1977.

[5] C. E. Tanner and C. Wieman, "Precision measurement of the hyperfine structure of the ^{133}Cs $6P_{3/2}$ state," Phys. Rev. A, Vol. 38, pp. 1616-1617, 1988.

[6] J. Ye, S. Swartz, P. Jungner, and J. L. Hall, "Hyperfine structure and absolute frequency of the ^{87}Rb $5P_{3/2}$ state," Opt. Lett., Vol. 21, pp. 1280-1282, 1996.

[7] P. V. Kiran Kumar and M. V. Suryanarayana, "Isotope shift and hyperfine structure measurements of 4s $^2S_{1/2}$ → 6s $^2S_{1/2}$ two-photon transition of potassium isotopes," J. Phys. B: At. Mol. Opt. Phys. Vol. 44, 055003, 2011.

[8] D. Das and V. Natarajan, "High-precision measurement of hyperfine structure in the D lines of alkali atoms," J. Phys. B: At. Mol. Opt. Phys. Vol. 41, 035001, 2008.

[9] H. Bucka, H. Kopfermann, A. Minor, "Präzisionsmessung der hyperfeinstruktur des $6^2P_{3/2}$-terms des Rb I-spektrums," Zeitschrift für Physik, Vol. 161, pp. 123-131, 1961.

[10] H. Bucka, B. Grosswendt, H. A. Schussler, "Level crossing-experiment in $6P_{3/2}$-term des Rb I-spektrums," Zeitschrift fur Physik, Vol. 194, pp. 193-200, 1966.

[11] R. K. Raj, D. Bloch, J. J. Snyder, G. Camy, and M. Ducloy, "High-frequency optically heterodyned saturation spectroscopy via resonant degenerate four-wave mixing," Phys. Rev. Lett. Vol. 44, pp. 1251-1254, 1980.

[12] L. Hollberg, L. Ma, M. Hohenstatt, and J. L. Hall, "Precision measurements by optical heterodyne techniques," Proc. SPIE, 426, 1983.

[13] N. Ito, "Doppler-free modulation transfer spectroscopy of rubidium 5 $^2S_{1/2}$–6 $^2P_{1/2}$ transitions using a frequency-doubled diode laser blue-light source," Rev. Sci. Instrum. Vol. 71, pp. 2655-2662, 2000.

[14] D. J. McCarron, S. A. King, S. L. Cornish, "Modulation transfer spectroscopy in atomic rubidium," Meas. Sci. Technol. Vol. 19, 105601 2008.

[15] L. Mudarikwa, K. Pahwa and J. Goldwin, "Sub-Doppler modulation spectroscopy of potassium for laser stabilization," J. Phys. B: At. Mol. Opt. Phys. Vol. 45, 065002, 2012.

Frequency Stabilization of 423 nm Laser for Calcium-Beam Optical Frequency Standard

Shengnan Zhang, Xiaogang Zhang, Haosen Shang, Jingbiao Chen
State Key Laboratory of Advanced Optical Communication, System and Network,
School of Electronics Engineering and Computer Science,
Peking University, Beijing 100871, China
E-mail: zhangsn27@163.com

Haijun Chen
National Key Laboratory of Science and Technology on Vacuum Electronics,
Beijing Vacuum Electronics Research Institute,
Beijing 100015, China
E-mail: e1412225@163.com

***Abstract*—The Ca beam optical frequency standard has the potential to be small optical clock like small Cs beam clock in microwave regime. For improving the signal-to-noise ratio of the clock transition spectroscopy, the electron shelving detection, which uses the fast $^1S_0$-$^1P_1$ 423nm transition to detect the narrow $^1S_0$-$^3P_1$ 657nm clock transition, was applied for Ca beam optical frequency standard. Therefore the frequency stability of 423 nm laser to some extent determines the performance of the optical frequency standard. In this paper, we stabilize the 423 nm laser frequency to Ca beam signal with side-band locking technique and estimate the preliminary stability of 423 nm laser which is 1.4×10^{-11} at 1 s and 2×10^{-12} at 100 s.**

Keywords—calcium-beam optical frequency; side-band locking; signal-to-noise ratio; the preliminary stability; fully vacuum-sealed tube

I. INTRODUCTION

The reported Ca beam optical frequency standard with directly detecting the clock transition decay fluorescence has limited low signal-to-noise ratio (SNR)[1], for its less complexity compared with optical lattice clocks[2,3]. For improving the SNR of the clock transition spectroscopy, we first proposed a Ca beam optical frequency standard scheme with the electron-shelving detection, which uses the fast $^1S_0$-$^1P_1$ 423nm transition to detect the narrow $^1S_0$-$^3P_1$ 657nm clock transition[4,5]. With this 423nm shelving detection, John J. McFerran et al achieved a Ca beam optical frequency reference with the fractional frequency instability of 9×10^{-14}[6]. Recently, the stability of Ca optical frequency standard we achieved has reached 3.0×10^{-14} at 1 s and decreased to 2.9×10^{-15} at 200 s[7,8].

In the shelving detection method of Ca optical frequency standard, the 423 nm diode laser locked on the fast $^1S_0$-$^1P_1$ transition acts as the shelved readout of population and detection of the 657 nm clock signal. Therefore, the locking performance of 423 nm laser determines the SNR of the clock signal.

In our Ca beam optical frequency standard system, we employ the side-band locking technique to lock the 423 nm probe laser, which means that the 423 nm fluorescence signal having a Doppler frequency shift is directly used as the error signal without modulation, and lock the 423 nm laser frequency on the calcium atoms. Here the calcium atomic beam tube is fully-sealed and the 423 nm laser is a single diode laser.

II. EXPERIMENT

The experimental scheme of 423 nm side-band locking technique is shown in Fig. 1. Here we use a fully vacuum-sealed calcium atomic beam tube with a small size and light weight, which mainly consists of calcium oven, saturation absorption section, optical Ramsey interaction section, fluorescence detector, and small ion pump. A single home-made 423 nm interference filter configuration external cavity diode laser(ECDL) is used. The measured Lorentz linewidth of the 423 nm diode laser is 21 kHz. The 423 nm laser beam is divided into two parts by mirror1. The rear-window laser beam (the right laser beam) used to detect the clock signal is perpendicular to the direction of calcium atomic beam, while the front-window one (the left one) is not. The photo detectors (PD) are put above the windows to detect the fluorescence signal. The front-window fluorescence signal, which is Doppler shifted, is directly used as the error signal. The 423 nm laser is locked on the atomic transition line.

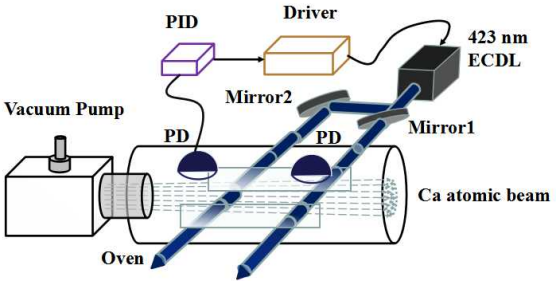


Fig. 1. Experimental scheme of 423 nm side-band locking technique.

III. RESULT

We built two identical 420 nm ECDLs and recorded 47 groups of beating signal data between them. An example beating signal and Lorentzian fitting is shown in Fig. 2. The black dots are the experimental data and the red curve is the Lorentzian fitting. The fitting result shows the linewidth of the beating signal is 28 kHz. The linewidth distribution of 47 groups datum is shown in Fig. 3. While fitted with a

Polynomial 4th function, we obtain the most probable linewidth of the beat signal between two lasers is 30 kHz, corresponding to 21 kHz linewidth of each laser.

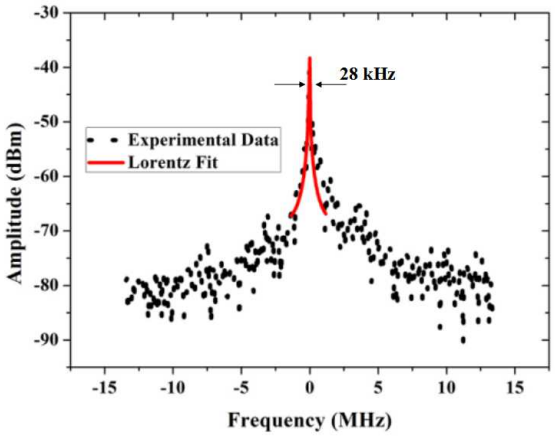


Fig. 2. An example of the spectra of the beat signal between two identical IF diode lasers with black dots and the Lorentzian fitting with red curve.

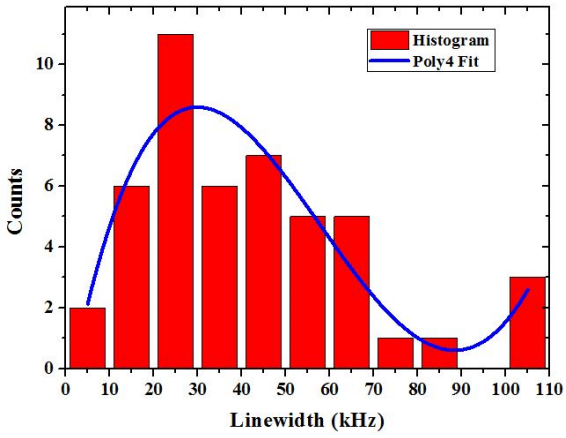


Fig. 3. Linewidth distribution of the beating signal between two identical blue diode lasers and the Polynomial 4th fitting with blue curve.

The narrow-linewidth 423 nm diode laser is used as the light source in this experimental scheme. The continuous tuning range is 15 pm. The power of the rear-window laser and the front-window one can be independently adjusted. Under the condition of the rear-window laser of 3 mW and the front-window one of 5 mW, the amplitudes of rear-window signal and front-window signal are 9 V and 0.6 V, respectively. The 423 nm fluorescence spectrum of front-window section and rear-window section is shown in Fig. 4. The red dashed line shown in Fig. 4 presents the locking point. According to the frequency interval between ^{40}Ca and ^{44}Ca of 773.8 MHz[9,10], the linewidth of the rear-window signal and the front-window signal are both calibrated. The linewidth of the rear-window signal is 120 MHz, and that of front-window signal is 90 MHz. According to the linewidth of rear-window signal, we can deduce the divergence angle of Ca atomic beam by $\Delta\nu = \frac{v}{\lambda}\cdot\sin\theta$, where the $\Delta\nu, v, \theta$ is the Doppler broadening, the velocity and the divergence angle of Ca atomic beam, respectively. Putting these values into the formula, we get the the divergence angle of Ca atomic beam is 64 mrad.

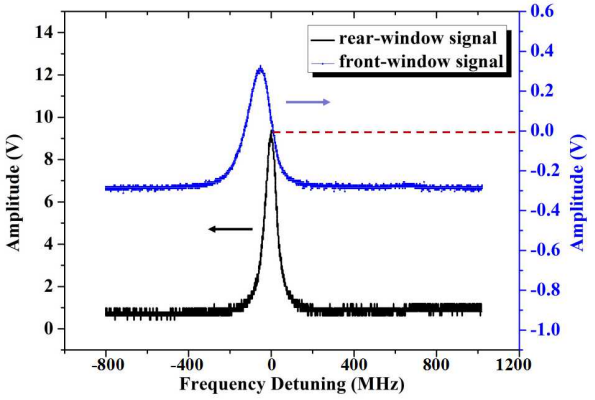


Fig. 4. 423 nm fluorescence signal of rear-window section (black dots) and front-window section (blue dots), respectively.

We also studied the frequency shift of the 423 nm laser when it is free running with the temperature fluctuation of the lab's environment, which is shown in Fig. 5. Here we recorded the lab's temperature fluctuation and the responding laser frequency shift during 70 minutes. From Fig. 5, we can see that the lab's temperature varies between 21.9 □ and 23.5 □ periodically, and the cycle period is about 30 minutes. The change rule of the 423 nm laser frequency shift is similar to that of the temperature fluctuation. During the period, the frequency fluctuation is about 130 MHz. It means that the frequency shift of the 423nm diode laser is 95 MHz/℃. Therefore the temperature of Ca tube and 423 nm diode laser should be precisely controlled to improve the locking performance of 423 nm diode laser.

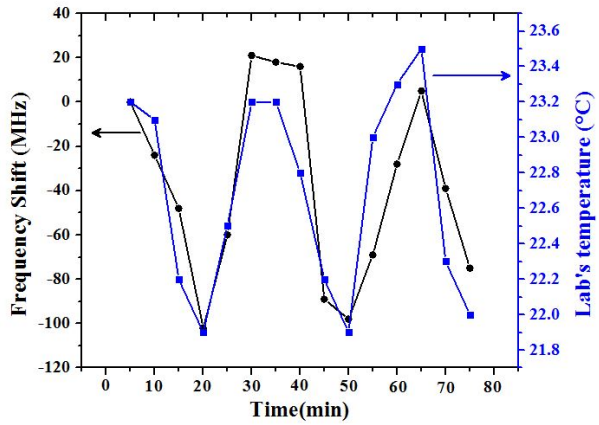


Fig. 5. The change rule of the frequency shift of the 423 nm diode laser and lab's temperature during 70 minutes.

The front-window signal is directly used as the error signal to lock the 423 nm laser frequency to the ^{40}Ca $^1S_0$-$^1P_1$ transition line. The Fig. 6 shows the amplitude fluctuation of the error signal when the laser is locked. The recorded locking time is about 8,300 s. Actually the continuous locking time is largely longer than 8,300 s. Here we unlock the laser frequency artificially. After locking, we estimate the stability of 423 nm laser by the residual error amplitude of locking. Fig. 7 shows

the Allan deviation of the 423 nm laser. From the measured data, we get that the stability is $1.4\times10^{-11}/\sqrt{\tau}$,decreasing to 1.5×10^{-12} at 700 s. It indicates that the signal-to-noise-ratio is 12,000 when the averaging time is 1 s. However, the Allan deviation after 700 s begins to get worse. In the future work, for achieving higher frequency stability, the temperature of Ca tube and 423 nm diode laser would be better controlled.

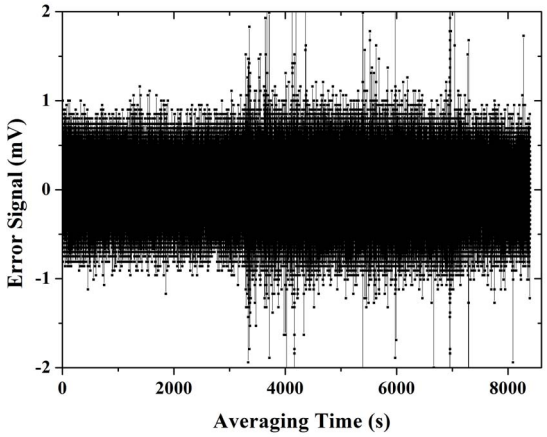


Fig. 6. The fluctuation of the error signal while frequency locking. The locked time is 8,300 seconds.

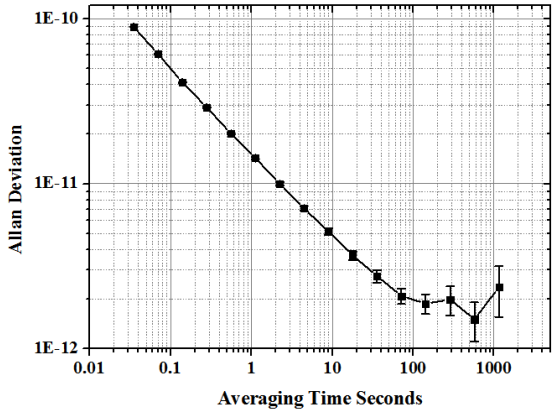


Fig. 7. Self-evaluated Allan deviation of residual error amplitude of 423 nm laser.

IV. CONCLUSION

In this paper, we report the frequency stabilization of 423 nm laser with the side-band locking technique for the calcium atomic optical frequency standard. In this technique, the 423 nm fluorescence signal which is Doppler frequency shifted is directly used as the error signal without frequency modulation, and lock the 423 nm laser frequency on the calcium atoms. Here the linewidth of 423 nm diode laser we used is 21 kHz, and that of the error signal is 120 MHz. The diode laser frequency shift of 95 MHz/□ is obtained. The signal-to-noise-ratio is 12,000 when the averaging time is 1 s. Finally, we estimated the stability of 423 nm laser by the fluctuation of the error signal after locking. The frequency stability is $1.4\times10^{-11}/\sqrt{\tau}$, decreasing to 1.5×10^{-12} at 700 s.

In the future work, the temperature of calcium tube and 423 nm diode laser would be better controlled for improving the frequency stability of the calcium atomic optical frequency standard.

ACKNOWLEDGMENT

This work is supported by the National Hi-Tech Research and Development (863) Program and the National Natural Science Foundation of China (NSFC) (91436210).

REFERENCES

[1] P. Kersten, F. Mensing, U. Sterr, F. Riehle, "A transportable optical calcium frequency standard," Applied Physics B, Vol. 68, pp. 27-38, 1999.

[2] B. J. Bloom, T. L. Nicholson, J. R. Williams, S. L. Campbell, M. Bishof, X. Zhang, S. L. Bromley, J. Ye, "An optical lattice clock with accuracy and stability at the 10^{-18} level," Nature, Vol. 506, 2014, pp. 71-75.

[3] I. Ushijima, M. Takamoto, M. Das, T. Ohkubo, H. Katori, "Cryogenic optical lattice clock," Nature Photonics, Vol. 9, pp. 185-189, 2015.

[4] K. Huang, J. Zhang, D. Yu, Z. Chen, W. Zhuang, J. Chen, "Application of electron-shelving detection via 423nm transition in Calcium-beam optical frequency standard," Chinese Physics Letters, Vol. 23, pp. 3198-3201, 2006.

[5] K. Huang, D. Yang, J. Chen, "Small compact calcium-beam optical frequency standard in Peking university and its new scheme," Proc. Of 20th EFTF, Braunschweig Germany, pp. 376-378, 2006.

[6] J. J. McFerran, A. N. Luiten, "Fractional frequency instability in the 10^{-14} range with a thermal beam optical frequency reference," J. Opt. Soc. Am. B, Vol. 27, pp. 277-285, 2010.

[7] X. Zhang, S. Zhang, Z. Jiang, M. Li, H. Shang, F. Meng, W. Zhuang, A. Wang, J. Chen, "A transportable calcium atomic beam optical clock," IEEE International Frequency Control Symposium (IFCS), pp. 478-481, May, 2016.

[8] H. Chen, Y. Liang, J. Yang, Z. Liu, J. Feng, X. Zhang, S. Zhang, J. Chen, "Study of a fully vacuum-sealed calcium atomic beam tube for optical frequency standard," IEEE International Frequency Control Symposium (IFCS), pp. 482-485, May, 2016.

[9] E. J. Salumbides, V. Maslinskas, I. M. Dildar, A. L. Wolf, E. -J. van Dujin, W. Ubachs, "High-precision frequency measurement of the 423-nm Ca I line," Physical Review A Vol. 83, 012502, 2011.

[10] W. Nortershauser, N. Trautmann, K. Wendt, B. A. Bushaw, "Isotope shifts and hyperfine structure in the $4s^2\ ^1S_0 \rightarrow 4s4p\ ^1P_1 \rightarrow 4s4d\ ^1D_2$ transitions of stable calcium isotopes and calcium-41," Spectrochim. Acta B Vol. 53, 709, 1998.

Spectroscopy of samarium colour centres for a solid-state optical frequency reference

Graham J. A. Edge, Shreyas Potnis and Amar C. Vutha
Department of Physics, University of Toronto, Toronto, Canada M5S 1A7
Email: vutha@physics.utoronto.ca

With the impending redefinition of the SI second based on optical clocks, there is a need for new secondary optical frequency standards. Ideally these secondary standards will offer enhanced robustness, portability and high signal-to-noise ratios (SNR), to enable rapid and precise comparisons against primary standards. A clock based on a narrow optical transition, in atomic ions that are naturally trapped in a solid-state host crystal, offers the technological simplicity and large SNR to satisfy these requirements.

Stabilization of a dye laser to spectral holes in a cryogenically cooled crystal of Eu^{3+}:Y_2SiO_5 has been previously demonstrated [1], with frequency instability $< 10^{-16}$ in 73 s. Here, we present a new system, Sm^{2+} impurities inside a crystal of SrF_2, that could lead to a compact optical frequency reference. Sm^{2+} is isoelectronic with Eu^{3+}, and retains many of the advantages of the Eu^{3+}:Y_2SiO_5 system, including the narrow intra-configuration clock transition and the large number of atoms available in a solid-state system. Importantly, however, many of the Sm^{2+}isotopes possess no nuclear spin, which drastically reduces inhomogeneous broadening of the clock transition due to impurity spins and strains in the crystal – this allows the narrow homogeneously broadened line to be used as a frequency reference. Further, the clock transition in Sm^{2+}:SrF_2 at 684 nm can be conveniently interrogated using a diode laser.

In our poster, we describe the advantages of Sm^{2+}:SrF_2 for realizing a practical portable optical frequency reference, and report on our progress towards direct observation of the Sm^{2+}:SrF_2 clock transition at 4 K.

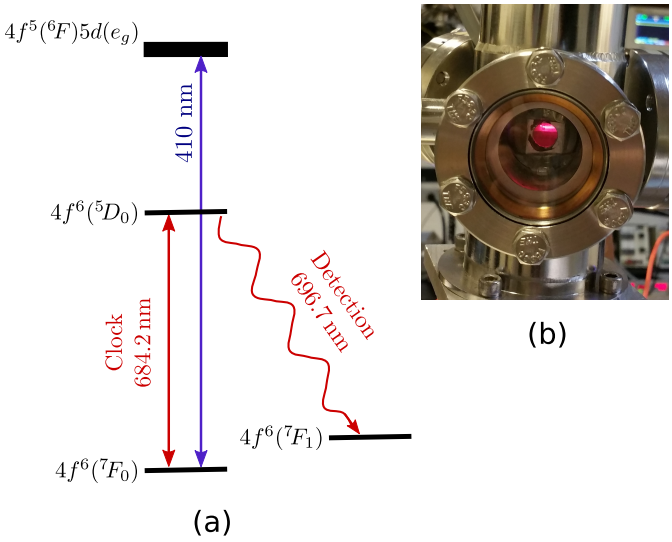


Fig. 1. (a) Energy levels of Sm^{2+}:SrF_2, following [2]. The 684.2 nm $4f^6(^7F_0) \rightarrow 4f^6(^5D_0)$ clock transition can be probed using a diode laser. The $^5D_0$ state has a lifetime $\tau \sim$ 14 ms, and mostly decays to the $^7F_1$ state by an $M1$ transition. Laser-induced fluorescence at 696.7 nm can be used to detect successful excitation of the clock transition. (b) Fluorescence observed on the $^5D_0 \rightarrow {}^7F_1$ detection transition from a Sm:SrF_2 crystal at 77 K, after optical pumping via the broad 410 nm line.

References

[1] S. Cook, T. Rosenband, and D. R. Leibrandt, "Laser-frequency stabilization based on steady-state spectral-hole burning in $Eu^{3+}Y_2SiO_5$," *Physical Review Letters*, vol. 114, no. 25, p. 253902, 2015.

[2] D. Wood and W. Kaiser, "Absorption and fluorescence of Sm^{2+} in CaF_2, SrF_2, and BaF_2," *Physical Review*, vol. 126, no. 6, p. 2079, 1962.

Frequency Stability Transfer by Optical Injection Locking into a Semiconductor Frequency Comb

Amine Chaouche Ramdane, Pierre Grüning , Vincent Roncin, and Frédéric Du-Burck
Laboratoire de Physique des Lasers,
UMR CNRS 7538, Université Paris 13, Sorbonne-Paris-Cité,
99 av. J.-B. Clément, 93430 Villetaneuse, France
frederic.du-burck@univ-paris13.fr

***Abstract*—We present preliminary results on semiconductor frequency comb stabilization via optical injection locking with a frequency stabilized laser. An important mode linewidth reduction is observed all over the comb. A stability better than 5.10^{-12} up to 30s is measured giving to this compact comb a great interest for transportable time and frequency metrology.**

Keywords—Laser stabilization, Semiconductor Mode-locked laser, Frequency comb, Optical Injection Locking.

I. INTRODUCTION

We present new and encouraging results about optical injection locking process of a compact semiconductor frequency comb. The comb is a InGaAs based Quantum-Dash Fabry-Perot Mode Locked Laser Diode (QD-MMLD) at 1.55 µm generating optical pulses with a repetition rate of 10.1 GHz [1,2]. The optical mode linewidth is about 50 MHz. The spectral purity of the self-pulsating frequency resulting in the beating of all modes is 10 kHz. Thanks to injection locking with an External Cavity Laser Diode (ECLD) in one of the QD-MMLD mode, we reduce its linewidth to the one of the master injection laser. Our stable optical injection set-up allows long term frequency stabilization and the measurement of the stability transfer from the master laser to the injected comb. We present the linewidth reduction and the frequency transfer, both achieved with a metrological grid based on two optical cavities referenced onto a metrological optical reference.

II. FREQUENCY COMB OPTICAL INJECTION

Fig. 1 gives the QD-MLLD optical spectrum in a self-pulsating regime. The spectrum is flat into a 12 nm bandwidth corresponding to 150 modes, each spaced each other by 10.1 GHz. The optical power is 3 dBm at the butterfly package fiber's output, corresponding to -19 dBm per mode. We achieved injection locking with a 100 nm tunable Telecom ECLD (Photonetics TUNICS-OM) driven by a home-made low-noise current source. Its linewidth is 50 kHz. Its optical power for the injection which is measured directly at the QD-MLLD input connector is -10 dBm. The injection wavelength is 1547.64 nm towards the low wavelengths of the QD-MLLD spectrum (Fig. 1). Such a high level of injection power leads to a distortion in the spectrum close to the injection wavelength [3,4].

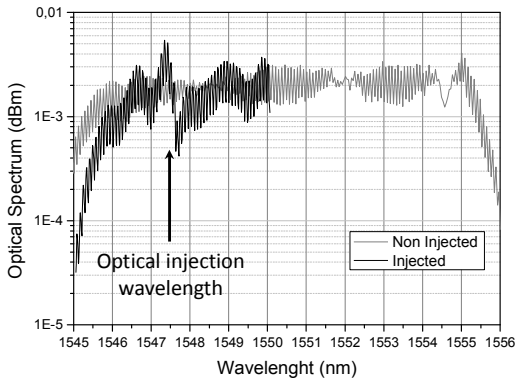


Fig. 1. Impact of the optical injection on the comb spectrum.In grey the non injected spectrum and in black the injected spectrum.

The mode linewidth of the injected QD-MLLD is obtained through the heterodyne beat note between the studied mode and a second stabilized ECLD (A-ECLD for Analysis ECLD). The tunability of the ECLDs allows optical injection and characterization in the entire band of the comb. For this characterization, all lasers are frequency stabilized using the set-up detailed below (Sect. III). Relative frequency fluctuations between them are less than 1 kHz up to 1000 s. The beat notes obtained for different modes are depicted in Fig. 2. The side bands in the spectra result from the current modulation at 1.1 MHz necessary for the QD-MLLD stabilization For the adjacent mode to the injected one (mode N+1), the linewidth is found to be 100 kHz (3 dB). We deduce that this mode has a linewidth of 50 kHz, corresponding to the master laser linewidth. The linewidth increases for modes distant from the injected one. For modes located at 1.8 nm (mode N+1.8 nm) and 5.8 nm (mode N+5.8 nm) from the injected one, it is 400 kHz and 2 MHz respectively.

III. STABILITY RESULTS

A. Experimental set-up

The set-up for stable optical injection of the QD-MLLD and its characterization is summarized in Fig. 3. A metrological frequency grid is implemented by means of two

optical cavities. One mode of each cavity is electronically locked onto an optical reference at 1542.12 nm transmitted to our lab via an optical fiber [5]. This offers a high frequency stability (better than 10^{-13} to 1 s) and a high accuracy (10^{-13}).

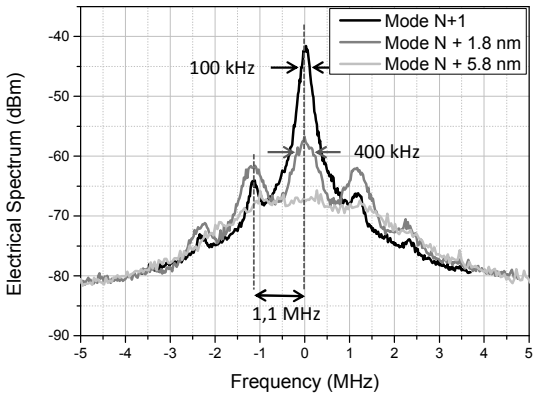


Fig. 2. Reduction of the comb optical mode linewidth induced by the optical injection. The figure shows the mode adjacent to the injection, the mode located at 1.8 nm and the mode at 5.8 nm.

The first cavity is a commercial Fabry-Perot with a Finesse of 300 and a FSR of 1.5 GHz [6] used for correction of the QD-MLLD slow frequency fluctuations (a few MHz/s) induced by thermal effects and excess current noise. The second one is a fiber ring cavity with a FSR of 16 MHz and a linewidth of 800 kHz (finesse of 20) used for frequency stabilization of both ECLDs to the metrological grid [7]. With this set-up, optical injection is assisted by the optoelectronic frequency lock of the QD-MLLD, ensuring stable optical injection, long term frequency stability transfer and characterization.

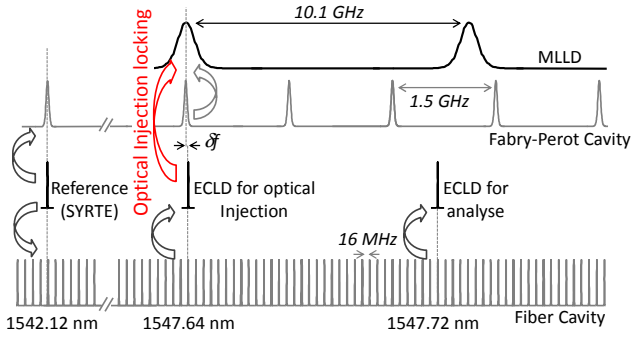


Fig. 3. Experimental set-up for the stability transfer and stability characterization. Two optical cavities are used in the set-up. They are both locked onto the optical reference. Two ECLDs are locked onto the fiber ring cavity, one is used for the optical injection of the QD-MMLD and the other for analysing the modes of the QD-MMLD comb. The injected mode of the QD-MMLD is also electronically locked onto the Fabry-Perot cavity.

B. Stability result

Fig. 4 shows the frequency stability of the optical injection process. The Allan deviation of the beat note between the injected mode and the A-ECLD is drawn and compared to the beat note between the master ECLD and the A-ECLD. For short time (below 1 s), the optical injection allows an efficient stability transfer. Beyond, we observe a degradation of the stability. Nevertheless, the frequency instability is smaller than 1 kHz (5.10^{-12}) between 0.1 s and 30 s.

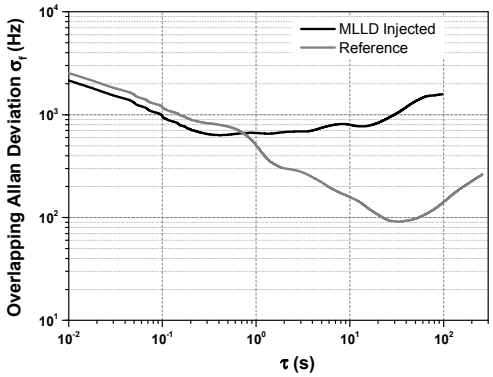


Fig. 4. Frequency stability of one mode of the injected QD-MMLD. Black curve is the beatnote between the QD-MMLD mode N and the A-ECLD. Grey curve is the beatnote between I-ECLD and A-ECLD.

IV. Conclusion

We have presented preliminary results about QD-MLLD frequency stabilization by optical injection locking. For the first time to our knowledge, the mode linewidth reduction over the entire comb is shown (by a factor 1000 close to the injected mode). Moreover, we have demonstrated an effective stability transfer achieved by optical injection locking assisted by optoelectronic long term correction.

V. Acknowledgment

We thank Yenista Optics for providing all ECLS sources, Morgan Advanced Materials for piezoelectric tubes, CNRS FOTON UMR6082 and the GIE 3-5 Lab for providing the QD-MMLD sources, O. Lopez at LPL and P.-E. Pottie et al. at LNE-SYRTE for the optical reference signal at 1542 nm.

References

[1] J. Renaudier et al. "45 GHz self-pulsation with narrow linewidth in quantum dot Fabry-Perot semiconductor lasers at 1.5 µm." Electron. Lett. 41.18 (2005).

[2] E. Sooudi et al. "Optical frequency comb generation using dual-mode injection-locking of quantum-dash mode-locked lasers: Properties and applications." IEEE J. Quantum Electron. 48.10, 1327-1338 (2012).

[3] C. Henry et al. "Locking range and stability of injection locked 1.54 µm InGaAsP semiconductor lasers", IEEE J. Quantum Electron., 21(8), 1152-1156 (1985).

[4] P. Delfyett et al, "Hot carrier thermalization induced self□phase modulation in semiconductor traveling wave amplifiers", Appl. Phys. Lett., 59(1), 10-12 (1991).

[5] H. Jiang et al. "Longdistance frequency transfer over an urban fiber link using optical phase stabilization," J. Opt. Soc. Am. B 25 (12), 2029-2035 (2008).

[6] A. Chaouche-Ramdane et al. "Stability transfer at 1.5 µm for metrological applications using a commercial optical cavity", Appl. Opt., 56(1), 8-14 (2017).

[7] P. Grüning et al., "Frequency Stability Transfer demonstration at 1.55 µm over 80 nm with an All-Fibered Ring Cavity", to be published.

Funding: CNRS; Labex FIRST-TF ; Action Spécifique Gravitation, Références, Astronomie, Métrologie (GRAM).

High Precision Phase and Frequency Measurements in Rare Earth Doped Crystals at Cryogenic Temperatures for Probing Nanoresonators Behavior

N. Galland*†, O. Gobron†, K. Jung†, A. Ferrier‡§, P. Goldner‡, S. Seidelin*¶, Y. Le Coq†
*Univ. Grenoble Alpes and CNRS, Inst. NEEL, F-38042 Grenoble, France
†LNE-SYRTE, Observatoire de Paris, PSL Research University, CNRS, Sorbonne Universités,
UPMC Univ. Paris 06, 61 avenue de l'Observatoire, 75014 Paris, France
Email: yann.lecoq@obspm.fr
‡PSL Research University, Chimie ParisTech, CNRS,
Institut de Recherche de Chimie Paris, 75005, Paris, France
§Sorbonne Universités, UPMC Université Paris 06, 75005, Paris, France
¶Institut Universitaire de France, 103 Boulevard Saint-Michel, F-75005 Paris, France

***Abstract*—High precision spectroscopic measurement using spectral hole burning technique with ultra-stable laser on $Eu^{3+} : Y_2SiO_5$ can be used to measure very small deformations in the crystal such as the ones arising due to quantum motion of nanoresonators. We present an experiment aiming at such high precision characterization.**

A. Spectral Hole Burning

Eu^{3+} atoms in a Y_2SiO_5 host matrix show interesting spectroscopic properties at cryogenic temperatures.

The homogeneous linewidth of the ${}^7F_0 \rightarrow {}^5D_0$ transition can be as low as 1 kHz. Some indication from photon echo measurements shows it should be even possible to reach 100 Hz at 1 K. However, the matrix configuration creates a heterogeneous broadening of several GHz due to heterogeneous constraints applied to each ion. Below 7 K, it is possible to burn a hole in the absorption spectrum whose linewidth depends on the laser used to burn the hole and whose lifetime can reach several hours.

Using a laser prestabilized to a high finesse Fabry-Perot cavity we demonstrate burning narrow holes with a linewidth of 4 kHz.

In addition, there is a coupling, characterized by the piezo-spectroscopic tensor, between mechanical deformation of the crystal and the frequency of the holes in the absorption spectrum. Using the high precision measurement of the frequency of those holes can therefore be used to monitor accurately this deformation.

B. Experimental Setup

In this experiment, we use a two-laser heterodyne detection. The master laser at 1160 nm is stabilized onto a high finesse Fabry-Perot cavity. An offset phase-locked loop is used to servo a second laser (slave), at 1160 nm as well, onto the master laser.

Both lasers are then independently frequency doubled to 580 nm, the absorption wavelength of Eu^{3+} in the Y_2SiO_5 matrix on the ${}^7F_0 \rightarrow {}^5D_0$ narrow transition. The slave laser is further sent to a double pass AOM for fine tuning of the frequency and amplitude. Both lasers are then recombined and sent to the $Eu^{3+} : Y_2SiO_5$ crystal in a 4 K cryostat. (see Fig. 1).

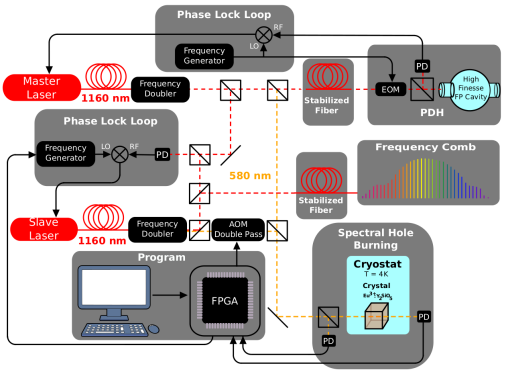


Fig. 1. Experimental Setup

This configuration allows to send the slave laser at the center of the absorption spectrum while the master is away from the inhomogeneously broadened linewidth.

The dispersion due to the burnt hole is monitored by the phase shift of the beatnote between the master and the slave due to propagation in the crystal.

C. Future Implementations

Using the introduced scheme, it is possible to lock the slave laser frequency to the frequency of the hole, which can be used to create a new generation of ultra-stable lasers [1].

Moreover, coupling between hole frequency and mechanical constraints can be a mean to study nanoresonators. Indeed, reaching a high precision on the measurement of the frequency is a mean to measure very small deformations such as the ones that are induced by quatum behavior of a rare-earth

978-1-5386-2916-1/$31.00 ©2017 IEEE

doped crystal nanoresonator [3]. Our current work aims at reaching shot noise limited detection and measuring the piezo-spectroscopic tensor on a bulk crystal. In the future, we will apply this method and obtained information to probe nanoresonator behaviors.

CONCLUSION

Our experimental work relies on high precision frequency measurement to probe nanoresonator behavior down to the quantum level. Our presentation will detail the experimental implementation and preliminary results.

ACKNOWLEDGMENT

This project has received funding from Ville de Paris Emergence Program, First-TF Labex, Rgion Ile de France; European Unions Horizon 2020 research and innovation program under grant agreement No 712721 (NanOQTech); ANR under grant number 14-CE26-0037-01 DISCRYS; EMPIR 15SIB03 OC18 and from the EMPIR program co-financed by the Participating States.

REFERENCES

[1] M. J. Thorpe *et al.* , Nature Photon. **5**, 688-693 (2011)
[2] O. Gobron *et al.* , Optics Express **25**(13), 15539-15548 (2017)
[3] K.Mølmer *et al.* , Phys. Rev. A **94**, 053804 (2016)

Toward an Ultra-Stable Laser Based on Cryogenic Silicon Cavity

B. Maréchal[1], J. Millo[1], A. Didier[2], P.-Y. Bourgeois[1], G. Goavec-Mérou[1], C. Lacroûte[1], E. Rubiola[1], Y. Kersalé[1]

[1] FEMTO-ST, Univ. Bourgogne Franche-Comté, CNRS, ENSMM, 26 Rue de l'Épitaphe, 25030 Besançon cedex, France
[2] *present affiliation* Physikalisch-Technische Bundesanstalt, Bundesallee 100, 38116 Braunschweig, Germany

***Abstract*—We present the development of an ultra-stable laser based on a Fabry-Perot cavity made from single crystal silicon. This cavity is cooled down to 17 K to reach a nulling of the thermal expansion. Thanks to the high mechanical quality factor of silicon and to the low temperature, the expected thermal noise limited fractional frequency instability is 3×10^{-17}.**

I. Introduction

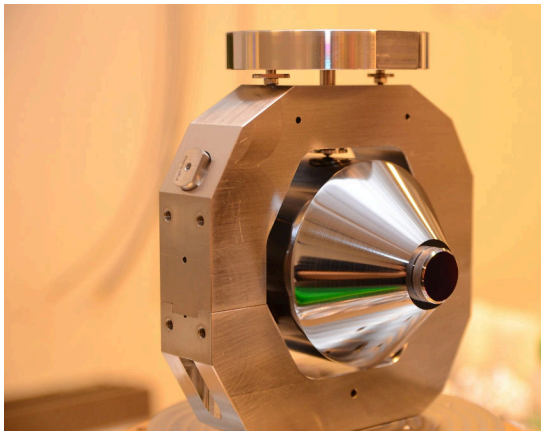
Ultra-stable lasers based on high finesse Fabry-Perot cavity are currently the most stable atomic-transition-free frequency reference [1] and are thus widely used as local oscillators in optical frequency standards [2]. The frequency stability of these lasers is limited by the length fluctuations of the cavity. One can also point out the vibrations-induced deformation and the thermal noise which are the most challenging issues for the improvement of cavities [3].

In order to reduce the thermal noise, we use a mono-crystalline silicon cavity to take advantage of its high mechanical quality factor compared to ULE glass or fused silica. The coefficient of thermal expansion of silicon vanishes for two temperatures 17 K and 124 K [4]. Since the thermal noise scales with the temperature (in terms of power spectrum density), we choose to operate the cavity at the lowest of these two temperatures using a cryocooler. For a cavity with a length of 140 mm, this noise limits the frequency stability at 3×10^{-17} in fractional value. However, the cryocooler is based on a pulsed tube, which is a large source of seismic noise and requires a design of the cavity with a state-of-the-art vibration sensitivity with the strong constrain of the cryogenic environment.

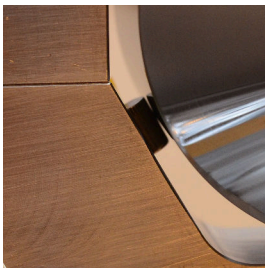
II. Silicon Cavity

The horizontally-oriented optical axis of the cavity is perpendicular to the $\langle 111 \rangle$ plane of the crystalline structure which presents the largest stiffness. The cavity is held in three points included in its $\langle 111 \rangle$ middle plane (see Fig. 1(a)) and the maintaining forces are aligned to specific orientations of the crystalline structure. The simulated sensitivity is about 4.5×10^{-12} $(\mathrm{m.s}^{-2})^{-1}$ or better for each direction.

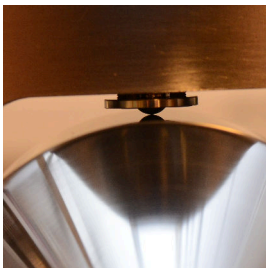
To keep the support independent of the temperature (varying from 300 K to 17 K), the upper contact point is placed under a mass of about 1 kg. The contacts areas are reduced by using a sphere (on the top) and two cylinders made from stainless steel (see Fig. 1(b) and 1(c)).



(a)



(b)



(c)

Fig. 1. 140 mm long silicon cavity (a) with tapered ends held in the support with three contact points (b, c).

III. Crycooler and Mechanical Setup

With the expected vibration sensitivity of the cavity, the acceleration noise must stand below -110 dB $(\mathrm{m.s}^{-2})^2$/Hz at 1 Hz. To meet this specification, a low vibration cryocooler based on a pulsed tube cryogenerator (PT410, Cryomech) has been designed.

The reduction of the vibration level is obtained by minimizing the mechanical coupling between the pulsed tube and the cavity. The head of the pulsed tube is linked to the ground by a rigid frame while the vacuum vessel of the cryocooler is set on an optical breadboard with an active isolation of vibrations. Only two weak mechanical links are needed. The first one is a bellows placed between the head

978-1-5386-2916-1/$31.00 ©2017 IEEE

and the vessel. The second one is a link realized by soft copper braids between the pulsed tube and the experimental part to ensure the extraction of the heat. This experimental part containing the cavity, the support, the thermal shield and the regulation stage is directly set to the bottom of the vacuum chamber through supports with low thermal conductivity.

IV. Temperature Regulation

The temperature of the colder stage of the pulsed tube is 4.2 K after 15 days of cooling. Due to the limited conductivity of copper braid, the equilibrium temperature of the experimental part is at 4.5 K with typically 15 mK short term fluctuations (peak to peak value in few Hertz bandwidth). Using a set of four heating resistances fixed on about 8 kg of copper, the temperature of a thermal shield is regulated around 17 K with a stability below 0.2 mK (estimated with Allan deviation) between 1 s and 10^4 s. The short term is limited by the noise of the sensor and the long term by the influence of the temperature of the laboratory.

V. Optical Setup

The optical set-up is depicted in Fig. 2. On a first optical table (Table 1), there are the tunable laser source at 1550 nm to match the transparency of silicon, the acousto and electro-optic modulators used for the frequency control with a large bandwidth (AOM1 and EOM1). A first Michelson interferometer is needed to measure and compensate the noise of the fiber link, detected on PD1, to the active vibration isolated table (Table 2) where the cryocooler is set. The EOM2, used for the phase modulation which is required to lock the frequency laser to the cavity resonance via the Pound-Drever-Hall technique (PDH), is placed just before the second Michelson interferometer. Its long arm is closed by the reflexion on the entrance mirror of the cavity and the corresponding interference, detected on PD2, allows the monitoring and the cancellation of Doppler shifts. A photodiode (PD3) is used to detect residual amplitude modulations (RAM) of the EOM2 [6] and a second one (PD4) for the detection of the PDH error signal.

One of the challenges is the control of the phase of the laser along the beam path. Such phase noise comes from optical fibers, Doopler effect (due to residual motion of the cavity), fluctuations of refractive index and temperature variations of the optical supports. To compensate these phase noises, two Michelson interferometers are implemented, in which a long arm is phase locked to a short reference arm [5]. A difficulty is the realization of a reference arm with length noise below -194 dB m^2/Hz (slope in f^{-3}) in the Fourier frequencies of interest (0.01 Hz - 1 kHz) that is compatible with the thermal noise of the cavity.

VI. Conclusion

We are developing a laser stabilized to an ultra-stable cavity in silicon at 17 K. The last results of this work will be presented at the conference, specifically the noise of the reference arm used in the Michelson interferometers. We will also show the influence of the cryocooler on the cavity, including the effect of temperature fluctuations, vibration level and its induced residual motion to the cavity.

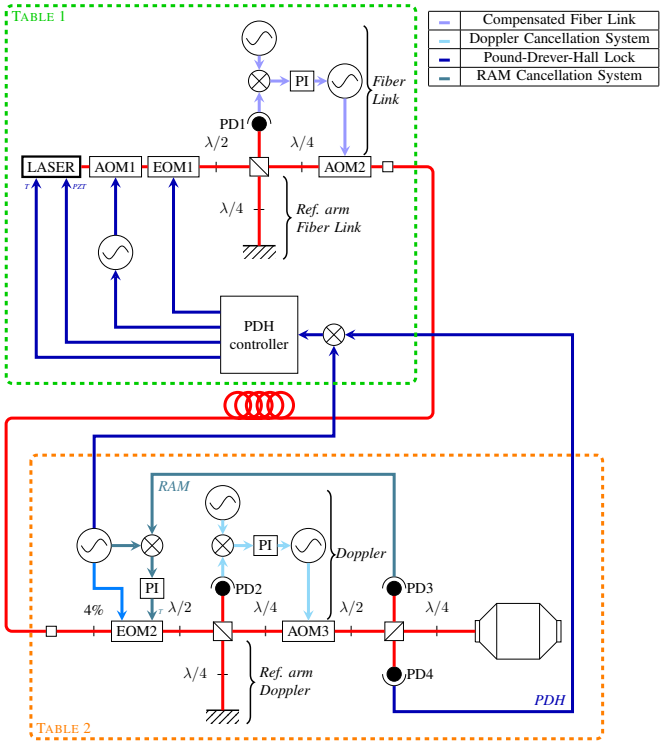


Fig. 2. Principle of the optical setup. AOM: acousto-optic modulator, EOM: electro-optic modulator, PD: photodiode, PI: proportional integrator controller

Acknowledgment

The authors would like to thank the national network for time and frequency Labex FIRST-TF, the Region Franche-Comté and the PIA for funding. The authors also thank A. Bakir, C Rocher, E. Dordor and P. Abbé for electronical and mechanical support.

References

[1] D. G. Matei, T. Legero, S. Häfner, C. Grebing, R. Weyrich, W. Zhang, L. Sonderhouse, J. M. Robinson, J. Ye, F. Riehle, U. Sterr, *1.5μmm lasers with sub 10 mHz linewidth*, arXiv:1702.04669, 2017

[2] A. D. Ludlow, M. M. Boyd, J. Ye, E. Peik, P. Q. Schmidt, *Optical atomic clocks*, Rev. Mod. Phys., vol. 87, 637, 2015

[3] T. Kessler, C. Hagemann, C. Grebing, T. Legero, U. Sterr, F. Riehle, M. J. Martin, L. Chen, J. Ye, *A sub-40-mHz-linewidth laser based on a silicon single-crystal optical cavity*, Nature Photonics, 6, 687, 2012

[4] K. G. Lyon, G. L. Salinger, C. A. Swenson, G. K. White, *Linear thermal expansion measurements on silicon from 6 to 340 K*, J. Appl. Phys. 48, 865, 1977

[5] B. C. Young, F. C. Cruz, W. M. Itano, J. C. Bergquist, *Visible Lasers with Subhertz Linewidths*, Phys. Rev. Lett. 82, 3799, 1999

[6] W. Zhang, M. J. Martin, C. Benko, J. L. Hall, J. Ye, C. Hagemann, T. Legero, U. Sterr, F. Riehle, G. D. Cole, M. Aspelmeyer, *Reduction of residual amplitude modulation to 1×10^{-6} for frequency modulation and laser stabilization*, Optics Letters Vol. 39, Issue 7, pp. 19 80-1983, 2014

Compact Ultra-Stable Laser

A. Didier[2], J. Millo[1], B. Maréchal[1], C. Rocher[1], C. Lacroûte[1], M. Ouisse[1], E. Rubiola[1], Y. Kersalé[1]

[1] FEMTO-ST, Univ. Bourgogne Franche-Comté, CNRS, ENSMM, 26 Rue de l'Épitaphe, 25030 Besançon cedex, France
[2] *present affiliation* Physikalisch-Technische Bundesanstalt, Bundesallee 100, 38116 Braunschweig, Germany

***Abstract*—We present an ultra-stable laser based on a compact Fabry-Perot cavity with a thermal noise limit expected at 2×10^{-15} in trems of fractional frequency stability. The 25 mm long cavity is housed in a cubic vacuum chamber with a volume of about 2.2 L. The measured phase noise is 3 dBrad^2/Hz at 1 Hz with a simple optical set-up at 1542 nm.**

I. Introduction

High finesse Fabry-Perot cavities are widely used as frequency reference to stabilize lasers sources. The improvement of these cavity stabilized lasers are of prime importance for optical frequency standards [1]. Consequently, many laboratories are developping technics to reduce the thermal noise of cavities that is now in the 10^{-17} decade but require complex systems such as cryocoolers [2], [3] and many active controls such as residual amplitude modulation, doopler effect, power stabilisation [4].

Moreover these highly stable lasers are also used to synchronize optical frequency combs for ultra-low phase noise microwave signal generation [5], [6]. High precision spectroscopy is also a field of interest. Such applications do not need state-of-the-art stabilized lasers, but the compactness and the simplicity is an important critera [7]. For such purpose, we are developping a laser based on a 25 mm long cavity with a very compact vacuum chamber and an optical set-up reduced to the quintessential components.

II. Ultra-Stable Cavity

Two high finesse mirrors made of fused silica substrats and cristalyne coatings are optically contacted to a spacer in ULE glass. The high mechanical quality factor of materials used for the mirrors leads to a reduced thermal noise of $1.8 \times 10^{-33} / \left(f\ {L_0}^2\right)$ Hz^{-1}. The length of the spacer made of ULE glass $L_0 = 25$ mm is a compromise between the level of thermal noise and the compactness.

The geometry of the spacer has been optimized using finite element modeling tools to reduce coefficients of sensitivity to vibration to a few $10^{-12}/(\text{m.s}^{-2})$ in order to avoid the use of an active vibration isolation system. The cavity is maintened by three points in the middle plan (perpendicular to the optical axis) and protected by two thermal shields (see Fig. 1). A first one in stainless steel for the high thermal capacitance is also used to support the cavity. Around it, a second shield in copper to reduce gradiant is temperature controlled. The quasi-cubic vacuum chamber ($136 \times 132 \times 128$ mm^3) is placed on an active vibration isolation table that can be used to apply modulation in order to estimate the vibration sensitivity of the cavity.

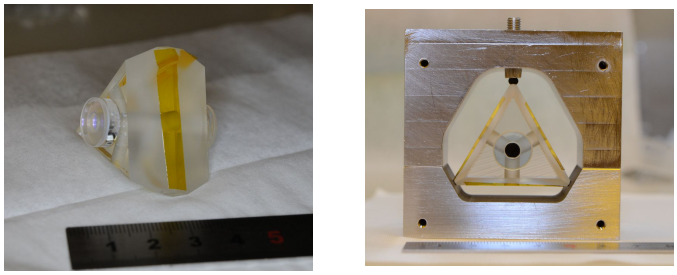


Fig. 1. 25 mm long cavity on the left. The cavity mounted in its support with three contact points on the right.

III. Optical Setup

The optical set-up is based on pigtailed components with polarisation maintening fiber for compactness. The laser source is a compact extented cavity laser diode at 1542 nm showing a phase noise of $6.3 \times 10^7/f^3$ rad^2/Hz from few Hertz to tenth of kilohertz (grey curve on Fig. 2). An optical coupler is used to pick-up the beam for comparison with an other optical reference. The phase modulator for the Pound-Drever-Hall detection is connected just before the output collimator. A free-space part is mandatory to match the mode of the fiber with the mode of the cavity with two lenses. Two mirrors are used to align the beam onto the optical axis of the cavity, and a beam spliter cube sends the reflexion of the cavity to the photodiode for the frequency detuning detection. All these free-space components are mounted on cage systems compatible with half inch optical elements and directly attached to the vacuum chamber.

IV. Results

The phase noise and the frequency stability are measured by comparison with another cavity stabilized laser. This laser has been caracterized using a cryogenic saphire oscillator (with optical frequency division technics) [6]. Its frequency stability is better than that of the compact cavity stabilized laser under test.

We measure a phase noise of 3 dBrad^2/Hz at 1 Hz with a slope in f^{-2} (see Fig. 2). We can see the influence of the active vibration isolation platform between ~ 4 Hz and ~ 60 Hz whereas the noise at 1 Hz is not impacted. The fractional frequency stability measured is at 7.5×10^{-15} at 1 s. This result is consistent with the fractional frequency stability computed from the phase noise measured at 1 Hz (5×10^{-15}).

The phase noise measured at 1 Hz is 13 dB higher than the thermal noise of the cavity. It is important to point out the

978-1-5386-2916-1/$31.00 ©2017 IEEE

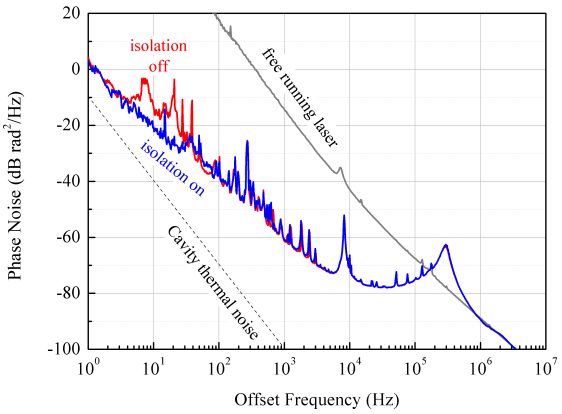


Fig. 2. Phase noise power spectral density of the free runing laser, the laser locked to the cavity with the vibration isolation table on and off.

simplicity of the optical set-up. For example, due to the cage system lenses, waveplates and the photodiode can not be tilted to avoid back reflexions. Furthermore there is no free-space isolator to prevent this problem.

V. Conclusion

We have developed a compact ultra-stable laser with a simple optical set-up that is compatible with a phase noise of 3 dBrad^2/Hz at 1 Hz. The last improvements, and a complete characterization of the cavity and perturbations impacting the frequency stability will be presented at the conference.

Acknowledgment

The authors would like to thank the national network for time and frequency Labex FIRST-TF, the Region Franche-Comté and the PIA for funding. The authors also thank A. Bakir, E. Dordor and P. Abbé for electronical and mechanical support.

References

[1] A. D. Ludlow, M. M. Boyd, J. Ye, E. Peik, P. Q. Schmidt, *Optical atomic clocks*, Rev. Mod. Phys., vol. 87, 637, 2015

[2] T. Kessler, C. Hagemann, C. Grebing, T. Legero, U. Sterr, F. Riehle, M. J. Martin, L. Chen, J. Ye, *A sub-40-mHz-linewidth laser based on a silicon single-crystal optical cavity*, Nature Photonics, 6, 687, 2012

[3] S. Häfner, S. Falke, C. Grebing, S. Vogt, T. Legero, M. Merimaa, C. Lisdat, U. Sterr, 8×10^{-17} *fractional laser frequency instability with a long room-temperature cavity*, Optic Letters, 40, 2112, 2015

[4] W. Zhang, M. J. Martin, C. Benko, J. L. Hall, J. Ye, C. Hagemann, T. Legero, U. Sterr, F. Riehle, G. D. Cole, M. Aspelmeyer, *Reduction of residual amplitude modulation to* 1×10^{-6} *for frequency modulation and laser stabilization*, Optics Letters, Vol. 39, Issue 7, pp. 19 80-1983, 2014

[5] T. M. Fortier, M. S. Kirchner, F. Quinlan, J. Taylor, J. C. Bergquist, T. Rosenband, N. Lemke, A. Ludlow, Y. Jiang, C. W. Oates, S. A. Diddams, *Generation of ultrastable microwaves via optical frequency division*, Nature Photonics, 5, 2011

[6] A. Didier, J. Millo, S. Grop, B. Dubois, E. Bigler, E. Rubiola, C. Lacroûte, Y. Kersalé, *Ultra-low phase noise all-optical microwave generation setup based on commercial devices*, Applied Optics, Vol. 54, 12, 2015

[7] J. Davila-Rodriguez, F. N. Baynes, A. D. Ludlow, T. M. Fortier, H. Leopardi, S. A. Diddams, F. Quinlan, *A compact, thermal noise limited reference cavity for ultra-low noise microwave generation*, to be published in Optics Letters, 2017

Simultaneous spectral purity transfer at three optical clock transitions using an ultra-low noise Er:fiber frequency comb

M. Giunta[1,2], W. Hänsel[1], M. Fischer[1], M. Lezius[1] and R. Holzwarth[1,2]

[1]Menlo Systems GmbH, Martinsried, Germany
[2]Max Planck Institute of Quantum Optics, Garching, Germany
m.giunta@menlosystems.com

***Abstract*— We have performed a multi-branch Er:fiber-based frequency comb comparison for simultaneously address the stability at different spectral regions. The optical beats are synchronously realized for three relevant wavelengths, corresponding to half the Sr, Yb and Hg lattice clock transition frequencies, showing an integrated phase noise below 55 mrad (1 Hz-1 MHz) and modified ADEV of ~6x10^{-18} at 1 s, averaging below 1x10^{-18} in <20 s (Lambda-mode, 1 s gate time).**

Keywords—frequency combs, comb comparison, optical frequency measurement, precision metrology

I. INTRODUCTION

The Optical Frequency Comb (OFC) represents one of the three key components comprised in an optical atomic clock. It is the clockwork capable of down-converting hundreds of THz optical frequencies into the accessible radio frequency domain, where frequency counters or phase meters can provide the read-out. Another use of the OFC is barely in the optical domain. Assuming spectral emission at different frequencies, it allows also comparing different atomic species on which frequency standards are defined.

Nowadays, optical atomic clocks are based on narrowband transitions, showing relative stability and accuracy on the level of 10^{-18} [1,2]. The comb must support such level of stability and frequency uncertainty. In case of comparison between different clocks at this level of performance [3], sufficient optical power on the closest comb line to the optical transition is necessary for generating high contrast beat signals and long-term phase drifts among the different comb branches must be contained. Here we characterize a multi-arm clockwork, equipped with three different peak shifting amplifiers for optimizing the optical power at the spectral regions of interest, in this case half the frequencies of neutral Strontium, Ytterbium and Mercury optical lattice clocks.

II. ULTRA-LOW NOISE OFC COMPARISON

To perform the frequency stability analysis we have compared the multi-branch OFC to a similar system where sufficient light for generating the multi-line comb-comb beat frequencies is usable after the supercontinuum generation, performed in the highly nonlinear fiber for the octave spanning within the f-2f interferometer.

This work was supported by DARPA (Defense Advanced Research Projects Agency) under the PµreComb project and by the European Commission under the Marie Curie Initial Training Network FACT (Future Atomic Clock Technologies).

Fig. 1 shows the optical setup for the long-term frequency stability and short-term phase noise measurements, whereas Fig. 2 shows a schematic of how the two OFCs are set in order to obtain the beat frequencies at the desired spectral regions.

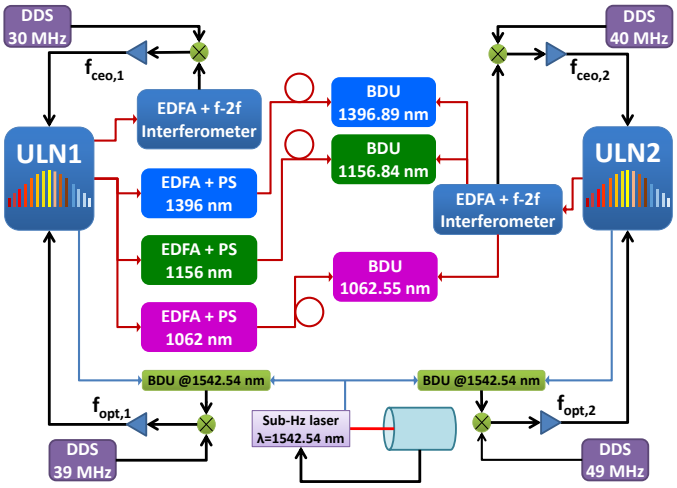


Fig. 1. Experimental setup of the comb-comb comparison

The fiber-based femtosecond lasers are operating at 1.5 µm, passively mode-locked using nonlinear amplifying loop mirror (NALM) [4]. The comb spectra are RF-referenced in carrier-envelope-offset (CEO) frequency and optically referenced to the same 1542 nm high-finesse-cavity stabilized CW-laser (ORS1500, ADEV ~1x10-15 at 1 s). Same mode number is used for both, effectively equalizing the oscillators' repetition rate, at approximately 250 MHz. The reference frequencies for the phase-lock loops are set on the commonly referenced DDSs to obtain an offset of 10 MHz between the two comb spectra, in order to realize three comb-comb optical beats at this nominal radio frequency, specifically at ~1063, 1157 and 1397 nm. The fiber Bragg gratings used for selecting the spectral regions of interest in the beat detection units (BDUs) allows approximately 1500 comb modes to contribute for the beats realization. The first ultra-low noise OFC, indicated as ULN1, comprises six different outputs. One is used for seeding the Er-doped fiber amplifier (EDFA) and f-2f interferometer to detect and stabilize the CEO frequency. A second output is used to optically reference the comb with the common reference laser. The other three outputs are used as seeders for amplifiers and

subsequent wavelength conversion for the three different optical clock transitions. The second comb, ULN2, provides two outputs. One is used for the EDFA and f-2f interferometer, which is optimized to simultaneously provide light with sufficient signal-to-noise ratios for the CEO frequency detection and stabilization as well as for the three different optical beats at 1063 nm, 1157 nm and 1397 nm. In order to simultaneously overlap the pulses for the four different frequencies, fiber links of appropriate lengths are prepared using precision splicing. The fiber lengths between the comb outputs and the beat detection units are similar only up to a few meters for the pairs generating the optical beats, therefore, temperature fluctuations induce changes of differential optical path length on the order of approx. 10^{-5} /m·K, ultimately becoming the limiting factor of the stability and accuracy of the involved OFC.

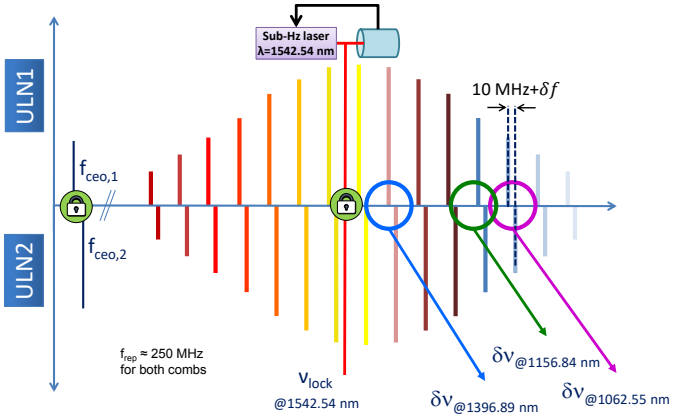


Fig. 2. Representation of the OFCs mode-spacing and relative position for realizing the 10 MHz offset between the two comb spectra.

III. Results

In the direct comparison, the three signals at 10 MHz are analyzed in terms of single-side band (SSB) phase noise, and are counted for assessing the comb lines instability. The integrated phase noise of the optical beats is below 55 mrad (1 Hz–1 MHz) for all frequencies, as shown in Fig. 3. Different spectral powers provided by ULN2 limit the signal-to-noise-ratio for the beat signals at different levels in the range between -110 dBc/Hz and -95 dBc/Hz, all well above the measurement noise floor. We measure a modified ADEV of ~6x10^{-18} at 1 s (Lambda-type counter), dropping below 10^{-18} in less than 20 s, as shown in Fig. 4. The inset represents the phase evolution and the room temperature variation over time. The measurement bandwidth is 1 MHz, defined by the band-pass filters used at the FXE (K+K GmbH) counter channels. A qualitative sensitivity value for such variation can be given as 2π optical phase evolution per 50 mK room temperature variation for the given length of the differential fiber present in the three links.

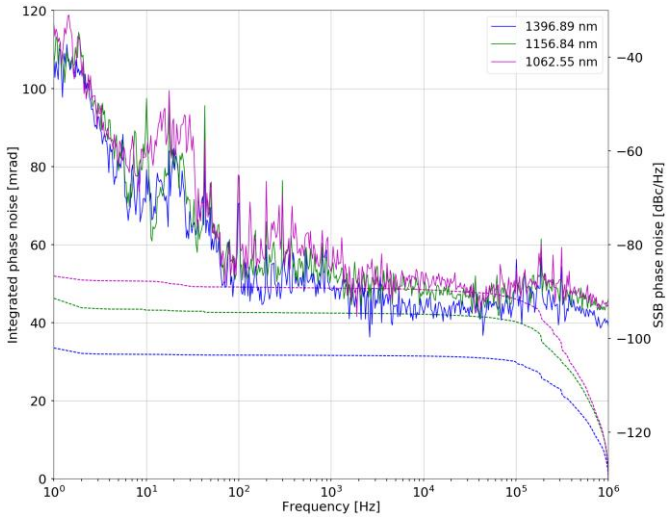


Fig. 3. SSB phase noise of the simultaneously realized beat frequencies.

At the given environmental conditions, all optical frequencies' systematic uncertainties were found to be in the 10^{-19} level.

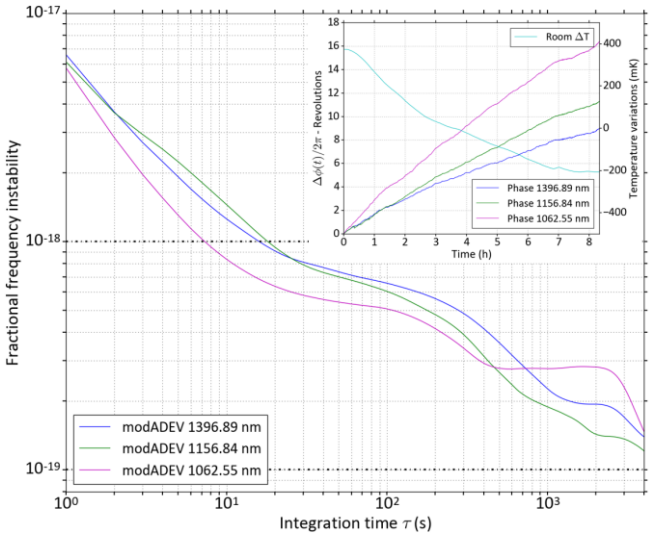


Fig. 4. Modified ADEV and phase-temperature evolution.

References

[1] I. Ushijima, M. Takamoto, M. Das, T. Ohkubo, and H. Katori, "Cryogenic optical lattice clocks," *Nat. Photonics*, vol. 9, no. 3, pp. 185–189, Feb. 2015.

[2] T. L. Nicholson, S. L. Campbell, R. B. Hutson, G. E. Marti, B. J. Bloom, R. L. McNally, W. Zhang, M. D. Barrett, M. S. Safronova, G. F. Strouse, W. L. Tew, and J. Ye, "Systematic evaluation of an atomic clock at 2 × 10−18 total uncertainty," *Nat. Commun.*, vol. 6, p. 6896, Apr. 2015.

[3] N. Nemitz, T. Ohkubo, M. Takamoto, I. Ushijima, M. Das, N. Ohmae, and H. Katori, "Frequency ratio of Yb and Sr clocks with 5 × 10−17 uncertainty at 150 seconds averaging time," *Nat. Photonics*, vol. 10, no. 4, pp. 258–261, Feb. 2016.

[4] W. Hänsel, H. Hoogland, M. Giunta, S. Schmid, T. Steinmetz, R. Doubek, P. Mayer, S. Dobner, C. Cleff, M. Fischer, and R. Holzwarth, "All polarization-maintaining fiber laser architecture for robust femtosecond pulse generation," *Appl. Phys. B*, vol. 123, no. 1, p. 41, Jan. 2017.

Fully-Stabilized 1-GHz Optical Frequency Comb from a Diode-Pumped Solid-State Laser

Sargis Hakobyan, Valentin J. Wittwer, Pierre Brochard, Kutan Gürel, Stéphane Schilt, and Thomas Südmeyer
Laboratoire Temps-Fréquence, Université de Neuchâtel, CH-2000 Neuchâtel, Switzerland
sargis.hakobyan@unine.ch

Aline S. Mayer, and Ursula Keller
Department of Physics, Institute of Quantum Electronics, ETH Zurich, CH-8093 Zurich, Switzerland

***Abstract*—We present the first fully-stabilized optical frequency comb with GHz repetition rate from a diode-pumped solid-state laser emitting at 1 µm. The carrier-envelope offset (CEO) frequency f_{CEO} is tightly locked by fast feedback to the current of the pump diode with a bandwidth of ~150 kHz achieved using a home-built modulation electronics. We present a detailed noise analysis of an optical comb line and compare it to the separately measured noise of the repetition rate f_{rep} and CEO beat to identify their respective contribution. The assessed comb mode linewidth is ~780 kHz (at 1-s observation time), dominated by the residual noise of f_{rep}.**

Keywords—Frequency Comb; Modelocked Laser; Metrology

I. INTRODUCTION

Optical frequency combs from modelocked lasers constitute a versatile tool for various applications and research fields in industry and fundamental science. High repetition rate combs in the GHz range are attractive for several applications, such as low noise microwave generation [1], owing to their lower density of combs lines resulting in a higher power per mode. GHz frequency combs have been demonstrated from ultrafast Ti:Sa lasers [2], however their operation is generally not so user-friendly and they require complex pump sources. On the other side, fiber lasers that are today the most commonly used comb technology are challenging for high repetition rate operation as a result of their limited gain per unit length. Therefore, modelocked diode-pumped solid-state lasers (DPSSL) constitute the most promising solution for GHz frequency combs, as they combine the advantage of simple diode pumping schemes with low loss optical resonators leading to suitable noise properties for comb stabilization, despite their need for highly transverse-mode pump diodes. GHz frequency combs from modelocked DPSSLs based on Yb-doped crystals have been demonstrated with carrier-envelope offset stabilization obtained by direct feedback to the current of the pump diode [3-4]. However, the reported lasers were not fully stabilized.

Here, we present the first demonstration of a fully-stabilized DPSSL comb at 1 µm with GHz repetition rate. We show a detailed characterization of this comb in terms of noise and stability, including the noise analysis of an optical comb line performed by comparison with an ultra-narrow linewidth laser at 1.5 µm using a transfer oscillator scheme.

II. FULLY-STABILIZED MODELOCKED YB:CALGO DPSSL

We have developed a self-starting 1-µm DPSSL oscillator, modelocked with a semiconductor saturable absorber mirror (SESAM). A 2-mm thick Yb:CALGO crystal doped with 5% of Yb is pumped by a commercial highly-multimode pump diode at 980 nm, which can deliver up to 60 W, but a fraction of 7.7 W only was used in the reported experiments. The laser emits short pulses of 89 fs in a 17.6-nm wide optical spectrum. The repetition rate frequency $f_{rep} \approx 1.05$ GHz can be finely tuned using a piezoelectric transducer (PZT) holding the SESAM. The phase stabilization of f_{rep} is implemented by detecting its 8th harmonic at 8.4 GHz using a fast photodiode. This signal is filtered, amplified and compared in a double-balanced mixer to the reference frequency of a synthesizer locked to an H-maser to ensure stable long-term operation. A correction signal processed by a servo-controller is applied to the PZT with a feedback bandwidth of a few kHz.

From the 2.1-W total output power of the laser, a fraction of 870 mW is launched with a coupling efficiency of ~80 % into a photonic crystal fiber (PCF) to generate a supercontinuum (SC) spectrum that spans a full frequency octave, from 660 nm to 1400 nm. The SC spectrum is then launched into a standard *f*-2*f* interferometer to detect the carrier-envelope offset (CEO) beat. This signal is detected at $f_{CEO} \approx 265$ MHz with a signal-to-noise ratio (SNR) of 40 dB in a resolution bandwidth of 10 kHz. It is band-pass filtered, amplified and compared in a digital phase detector to a reference synthesizer locked to the H-maser. The resulting error signal is fed back to a home-built electronics enabling the current of the pump diode to be modulated with a MHz bandwidth.

III. FREQUENCY COMB CHARACTERIZATION

We have characterized the noise properties and the frequency stability of f_{rep} and f_{CEO} in the fully-stabilized GHz comb, as well as the noise of an optical comb line at 1030 nm. Fig. 1(a) shows the performance of the CEO stabilization loop. We have measured the frequency noise power spectral density (FN PSD) of the CEO beat in free-running and locked conditions. A feedback bandwidth of ~150 kHz is assessed from the position of the servo bump in this spectrum, resulting in the collapsing of the ~500-kHz free-running linewidth of the CEO beat (at 1-s observation time) into a coherent peak with a residual integrated phase noise of 1.34 rad. This

978-1-5386-2916-1/$31.00 ©2017 IEEE

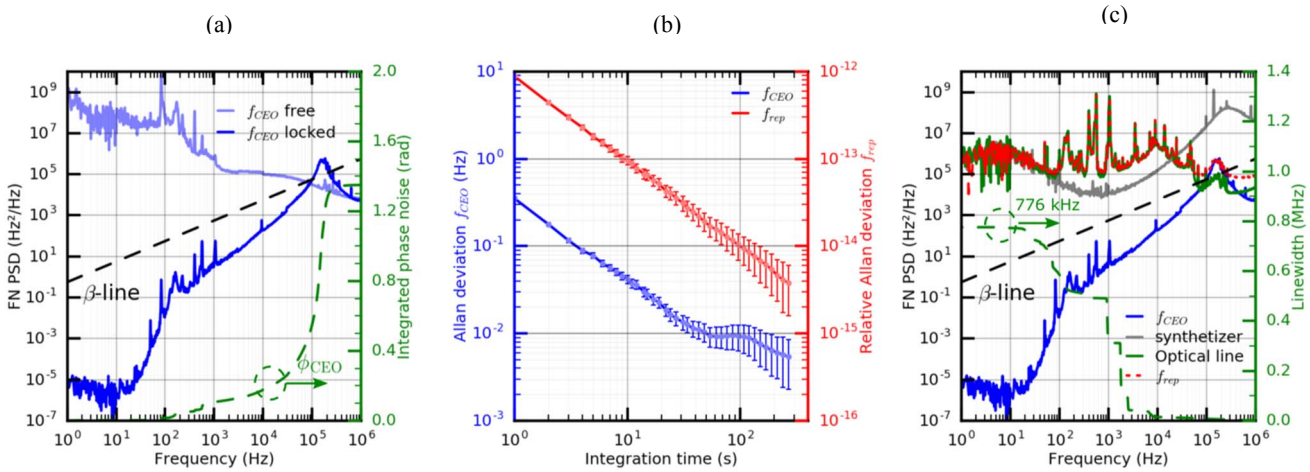


Fig. 1. (a) FN PSD of f_{CEO} in free-running (light blue) and locked (dark blue) conditions and corresponding residual integrated phase noise (green). (b) Frequency stability of the fully-stabilized GHz comb: Allan deviation (ADEV) for f_{CEO} and relative ADEV for f_{rep}. (c) FN PSD of an optical line of the fully-stabilized GHz comb (green) and individual contributions of f_{CEO} (blue) and f_{rep} (red). The corresponding linewidth of the comb line assessed from the FN PSD is shown by the dashed line as a function of the cut-off frequency (inverse of the observation time).

value is partially affected by the stabilization loop of f_{rep}. We previously measured a lower integrated phase noise of ~680 mrad for f_{CEO} in this laser, when using a lower stabilization bandwidth for f_{rep}. However, the optical linewidth of the comb modes was fairly broad in that case, due to the presence of prominent noise peaks in the FN PSD of f_{rep}. To further reduce these peaks, a larger stabilization bandwidth has been implemented for f_{rep} by adding a derivative component in the servo controller. This had an impact on the stabilization of f_{CEO}, probably as a result of a cross influence of the PZT onto f_{CEO} and to the fact that a resonance of the PZT was likely excited. Nevertheless, a narrower comb mode linewidth was observed in that case, at the cost of a slightly reduced CEO lock performance.

The separately measured noise spectrum of f_{rep} showed an integrated timing jitter of 590 fs [1 Hz - 1 MHz]. The frequency stability of the comb has been assessed by simultaneously recording the frequencies f_{rep} and f_{CEO} using a multi-channel Π-type frequency counter without dead-time. Fig. 1(b) shows the resulting Allan deviations, which is limited by the reference synthesizer at the level of 10^{-12} at 1 s for f_{rep}. The sub-Hz Allan deviation observed at 1 s for f_{CEO} contributes at the 10^{-15} level to the relative stability of an optical comb line at 1 µm.

The frequency noise of a comb line of the fully-stabilized GHz comb was assessed from the heterodyne beat with a narrow-linewidth laser. As we did not have a suitable low-noise laser available in the emission spectrum of the GHz comb, we developed a dedicated experimental setup to measure the noise of a comb line in comparison to an ultra-stable laser at 1560 nm locked to an ultra-low thermal expansion (ULE) optical cavity. For this purpose, another fully-stabilized Er-fiber frequency comb was used as a transfer oscillator. An additional SC spectrum extending down to the 1000-nm range was generated from the modelocked Er-fiber oscillator using a highly non-linear fiber. A virtual beat between this SC spectrum and the GHz comb was performed at 1030 nm by combining the beat signal of each of these combs with a distributed feedback (DFB) laser (which was too noisy to enable a direct characterization of the GHz comb line), in order to eliminate the DFB noise. For the GHz comb, this was achieved by slightly broadening the output of the Yb:CALGO oscillator in a few meters of singlemode fiber. As the noise spectrum of the virtual beat between the two combs was partially limited in some spectral regions by the Er-fiber comb, a further virtual beat was implemented between this signal and the 1.56-µm ultra-stable laser, using the Er-fiber comb as a transfer oscillator.

The results of this noise analysis are shown in Fig.1(c), which compares the FN PSD of the virtual beat between the GHz comb line and the ultra-stable laser with the individual FN PSD separately measured for f_{rep} and f_{CEO}. One notices that the comb mode noise is mainly dominated by the noise of f_{rep} at frequencies up to ~100 kHz. This noise matches the noise of the reference synthesizer below 100 Hz, whereas higher noise peaks occur at higher frequencies, probably resulting from mechanical noise in the laser cavity. The CEO has no contribution in the noise of the optical line below 100 kHz, but it has some positive impact at the CEO servo bump (~150 kHz), where it partially compensates the servo bump that also appears in the noise of f_{rep} (resulting from the cross-coupling that generally occurs between f_{rep} and f_{CEO} [5]). As a result, the measured comb line noise at the CEO servo bump is lower than the individual contributions of f_{rep} and f_{CEO}. A linewidth of ~780 kHz (at 1-s observation time) is assessed for the comb mode from the measured FN PSD [6].

IV. Conclusion

We have reported the first full stabilization of a GHz DPSSL frequency comb at 1 µm and have presented a detailed analysis of its noise properties and frequency stability.

Acknowledgment

We acknowledge funding from the Commission for Technology and Innovation (CTI, proj. 17137.1PFNM-NM).

References

[1] T. M. Fortier *et al.*, *Nat. Photonics* **5**(7), 425–429, 2011.
[2] A. Bartels, D. Heinecke, and S. A. Diddams, *Science* **326**, 681, 2009.
[3] A. Klenner *et al.*, *Opt. Express* **22**, 31008, 2014.
[4] A. Klenner *et al.*, *Opt. Express* **24**(10), 11043–11053, 2016.
[5] V. Dolgovskiy *et al.*, *J. Opt. Soc. Am. B* **29**, 2944–2957, 2012.
[6] G. Di Domenico *et al.*, *Appl. Opt.* **49**, 4801–4807, 2010.

Ultra-short optical pulses leading to ultra-stable photonic microwave generation

Xiaopeng Xie, Romain Bouchand,
Daniele Nicolodi, Michel Lours,
Yann Le Coq
LNE-SYRTE, Observatoire de Paris,
PSL Research University, CNRS
Sorbonne Universités, UPMC Univ. Paris 06
Paris, France
Email: yann.lecoq@obspm.fr

Michele Giunta, Wolfgang Hänsel,
Matthias Lezius, Ronald Holzwarth
Menlo Systems GmbH
Martinsried, Germany

Abhay Joshi, Shubhashish Datta
Discovery Semiconductors Inc.
Ewing, New Jersey, USA

Pierre-Alain Tremblin, Giorgio Santarelli
LP2N, IOGS-CNRS-Université de Bordeaux 1
Talence, France

Christophe Alexandre
CNAM, CEDRIC Laboratory
Paris, France

***Abstract*—Microwave signals can be generated by photo-detecting ultra-short optical pulse trains. We demonstrate that the pulse duration, although shorter than the impulse response of photodiode, can greatly limit the phase noise of generated microwave signal.**

***Keywords*—Opto-electronic microwave sources, optical frequency combs, photodiode, ultra-low phase noise.**

I. Introduction

Plenty of applications of optical frequency combs (OFC) have been developed over the past two decades [1-3]. One of them is to generate microwave signals with ultra-low phase noise both close and far from carrier Fourier frequencies [4,5]. As OFC are composed of a series of phase coherent spectral lines, phase locking one of these comb lines to an ultra-stable continue-wave (CW) laser reference allows transferring its spectral purity to all the other comb lines, and the repetition rate of the OFC. Photo-detecting the OFC train of pulses can therefore generate microwave signals with extremely low phase noise.

Here, we demonstrate that for a given optical spectrum bandwidth being photo-detected, the actual pulse duration (related to the spectral phase of the optical spectrum) is critically important for the OFC-based microwave generation scheme. Dispersion changes the relative phase among the comb lines, thus leads to chirped optical pulses, and thereby affecting the optical pulse duration. We observe that the optical pulse duration not only affects the shot-noise limited phase noise floor [6] but also the amplitude to phase noise (AMPM) conversion factor of the photodiode [7]. Furthermore, a linear noise that related to the actual chirped pulse duration is observed. For a 12 GHz microwave signal, this kind of chirp-induced linear noise is decreasing by more than 28 dB when the optical pulse duration is scanned from 19 ps to 0.8 ps while always being shorter than the photodiode response time (approx 50 ps). Similarly, the shot-noise-limited phase noise floor reduces from -166 to -172 dBc/Hz when the optical pulse duration varies from 2.6 to 0.8 ps. Using these effects, we demonstrate a 12 GHz microwave signal with absolute phase noise of -169 dBc/Hz at 10 kHz Fourier frequency by using an ultra-compact commercial laser reference (without a conventional Fabry-Perot cavity as an optical frequency reference). This phase noise result is comparable with the best photonic microwave source [4] for Fourier frequencies 10 kHz and higher.

This work is funded by the DARPA PULSE Program (PμreComb project, under contract No. W31P4Q-14-C-0050); the FIRST-TF Labex and the Eurostar Eureka program (STAMIDOF project).

II. Principle and experimental setup

Fig.1 presents our photonic microwave generation setup. A low noise erbium-doped fiber OFC with 250 MHz repetition rate is phase locked to an ultra-compact commercial CW laser reference. The laser reference has very low phase noise at Fourier frequencies above 10 kHz. This performance is achieved by stabilizing a distributed-feedback laser diode to a high-Q factor crystalline whispering-gallery-mode (WGM) micro-resonator via the self-injection locking [8]. In order to improve the signal to noise ratio of photo-detected microwave signals, an all optical-fiber-based optical pulse repetition rate multiplier is used at the output of OFC system [9], which also introduces some non negligible dispersion. A piece of dispersion compensating fiber (DCF) is following after the

978-1-5386-2916-1/$31.00 ©2017 IEEE

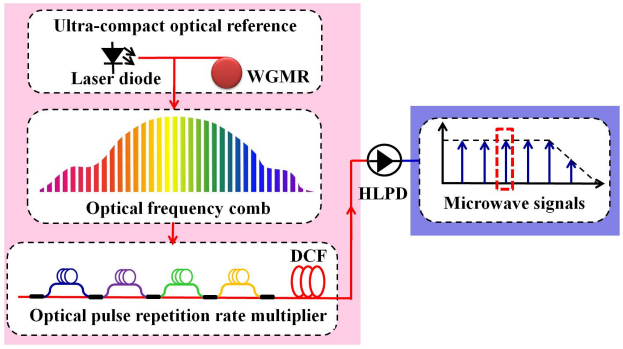


Fig. 1. Schematic diagram of the photonic microwave generation based on an optical frequency comb. WGMR: whispering gallery mode micro-resonator, DCF: dispersion compensating fiber, HLPD: high linear photodiode..

multiplier to recompress the optical pulses. The optical pulse duration impinging the photodiode can be modified by using different lengths of DCF. A 20 GHz high-linear-photodiode is used to convert the stabilized optical pulse trains into a microwave signal. The phase noise of the generated microwave signal is characterized by a cross correlation scheme that we have recently reported in [4].

III. Results and Discussion

Fig.2 shows the phase noise results of 12 GHz for different optical pulse durations. The optical pulse durations are measured by a commercial auto-correlator, the reported value corresponding to a Gaussian fit. As the optical energy per pulse reduces a lot after a four stages multiplier which produces an effective repetition rate of 4 GHz. We therefore operate the photodiode in a non-saturated regime at an average DC photocurrent of 8 mA. AMPM conversion is a key limitation for the OFC-based photonic microwave generation, which can be overcome by carefully choosing the setting and working regime of the photodiode [7]. Here we observe the AMPM conversion is somehow affected by the optical pulse duration. However, what is more important is that a linear noise related the actual pulse is observed. The pink curve in Fig.2(a) is the relative intensity noise (RIN) of the comb laser. The black, red and blue curves show the measured phase noise, as dominated by chirp related linear noise near 10 kHz Fourier frequency. In Fig.2(b), we also show that, as was observed in [6], the shot noise-limited phase noise depends on the optical pulse duration. However, we emphasis that this effect is demonstrated very close to the carrier in this work (tens of kHz instead of several MHz in [6]), which is of paramount importance for real applications. Note that the bump at high Fourier frequencies 700 kHz is here limited by the phase lock loop of the comb.

In conclusion, using state-of-the-art optoelectronic devices and advanced phase noise characterization technology, we showed that the optical pulse duration strongly affects the phase noise of microwave signals generated by photo-detection of the train of pulses of an OFC. In addition, we also demonstrated a system exhibiting ultra-low phase noise at 10 kHz Fourier frequency and above without a reference Fabry-Perot cavity and therefore a very compact system suitable for highly demanding environment in defense and/or transportable applications.

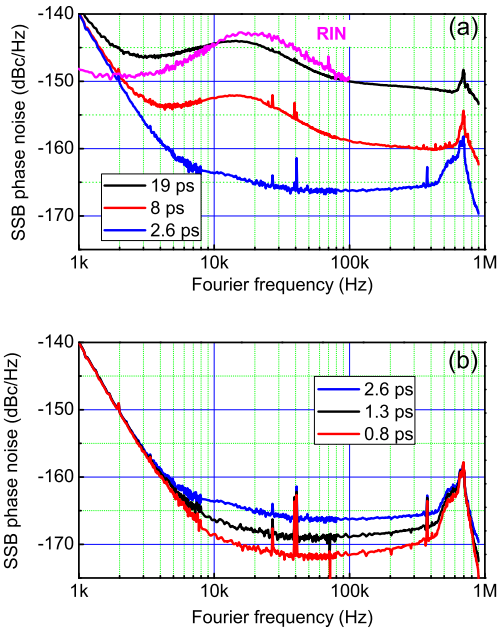


Fig. 2. Absolute single sideband (SSB) phase noise power spectral densities of 12 GHz microwave generated with different optical pulse durations .

Acknowledgment

We thank José Pinto for help with the electronics. Xiaopeng Xie would like to thank Kwangyun Jung for many useful discussions.

References

[1] J. L. Hall,"Nobel lecture: defining and measuring optical frequencies," *Rev. Mod. Phys.*, vol.78, pp.1279-1295, 2006.

[2] T. W. Hänsch, "Nobel lecture: passion for precision," *Rev. Mod. Phys.*, vol.78, pp.1297-1309, 2006.

[3] N. R. Newbury, "Searching for applications with a fine-tooth comb," *Nat. Photon.*, vol.5, pp.186-188, 2011.

[4] X. Xie, R. Bouchand, D. Nicolodi, M. Giunta, W. Hänsel, M. Lezius, A. Joshi, S. Datta, C. Alexandre, M. Lours, P.-A. Tremblin, G. Santarelli, R. Holzwarth, and Y. Le Coq, "Photonic microwave signals with zeptosecond-level absolute timing noise," *Nat. Photon.*, vol.11, pp.44-47, 2017.

[5] T. M. Fortier, M. S. Kirchner, F. Quinlan, J. Taylor, J. C. Bergquist, T. Rosenband, N. Lemke, A. Ludlow, Y. Jiang, C. W. Oates, and S. A. Diddams, "Generation of ultrastable microwaves via optical frequency division," *Nat. Photon.*, vol.5, pp.425-429, 2011.

[6] F. Quinlan, T. M. Fortier, H. Jiang, A. Hati, C. Nelson, Y. Fu, J. C. Campbell, and S. A. Diddams, "Exploiting shot noise correlations in the photodetection of ultrashort optical pulse trains," *Nat. Photon.,* vol. 7, pp. 290-293, 2013.

[7] W. Zhang, T. Li, M. Lours, S. Seidelin, G. Santarelli, and Y. Le Coq, "Amplitude to phase conversion of InGaAs pin photo-diodes for femtosecond lasers microwave signal generation," *Appl. Phys. B*, vol.106, pp.301-308, 2012.

[8] W. Liang, V. S. Ilchenko, D. Eliyahu, A. A. Savchenkov, A. B. Matsko, D. Seidel, and L. Maleki, "Ultralow noise miniature external cavity semiconductor laser," *Nature Commun.*, vol.6, pp.7371, 2015.

[9] A. Haboucha, W. Zhang, T. Li, M. Lours, A. N. Luiten, Y. L. Coq, and G. Santarelli,“Optical-fiber pulse rate multiplier for ultralow phase-noise signal generation”, *Opt. Lett.*, vol.36, pp.3654-3656, 2011.

Sub 10^{-16} frequency transfer with IPPP: Recent results

Gérard Petit, Julia Leute[1]
BIPM
92312 Sèvres, France
gpetit@bipm.org

Sylvain Loyer
CLS, 31520 Ramonville Saint-Agne, France

Félix Perosanz
CNES, 31401 Toulouse, France

[1] Present affiliation : PTB, Braunschweig, Germany

***Abstract*— The Precise Point Positioning (PPP) technique using GPS phase and code observations is widely used to compute time and frequency links. We have shown that a PPP technique where the integer nature of phase ambiguities is preserved provides significant improvement over the classical use of floating ambiguities. We show examples that all indicate that this Integer-PPP (IPPP) technique allows frequency comparisons with $1x10^{-16}$ accuracy in a few days, improving with longer averaging, and can be readily operated with existing products.**

Keywords*— *Frequency comparisons; Carrier phase ambiguities; GPS precise point positioning.

I. INTRODUCTION

Since many years, GPS phase and code observations have provided reliable time and frequency transfer between stations whatever their location on Earth. The technique of choice is Precise Point Positioning (PPP), with a typical uncertainty for frequency comparisons of order $1x10^{-15}$ at 1-day averaging and a few 10^{-16} at 5 to 10 day averaging. It is obvious that the performance of PPP is now a limiting factor in comparing the best frequency standards and a number of techniques are envisioned or already used to provide much better performance. However none is as ubiquitous and simple to operate as GNSS and it is important to push PPP to its limits, which is attempted with integer ambiguity determination (IPPP). In Section II, we recall the main characteristics of the IPPP technique and some earlier results. In Section III, we present several examples where IPPP links are compared to other high-accuracy techniques allowing validation of the achieved performances.

II. THE IPPP TECHNIQUE

One approach to overcome the limitations of "classical PPP" is to consider the integer nature of phase ambiguities. The CNES-GRGS group pioneered this technique and is now an IGS analysis center providing satellite products that allow applying integer ambiguity resolution to PPP [1]. This IPPP technique allows frequency comparison at any distance over long durations and we have shown [2] that a frequency transfer accuracy of $1x10^{-16}$ is reached at ~3 to 5-day averaging for the 270-km link between two time laboratories in Poland: the Astrogeodynamic Observatory of the Space Research Center (AOS, Borowiec) and the Central Office of Measures (GUM, Warsaw), see Fig. 1. A similar performance is likely achievable for long distance links but cannot be tested for lack of an accurate reference. Furthermore the performance of IPPP frequency transfer should continue to improve as the inverse of the integration time as long as the two receiving systems are not perturbed by discontinuities.

A. Basic principles of IPPP

In IPPP, as in classical PPP, the user's clock is determined from dual frequency GPS phase measurements using satellite clock products generated by analysis of a global network. For IPPP, the satellite products are generated by the GRG analysis centre so that the user can determine the ambiguities at the two frequencies N_1/N_2 as integers. This is done in a two-step procedure, first determining the widelane ambiguity $N_w = N_2 - N_1$ and then determining e.g. N_1, see details in [1, 3].

1. In the first step, the zero-difference widelane identification yielding the widelane integer ambiguity N_w constant over a pass is represented, for any receiver and any epoch, by the relation

$$N_w = f(P_1, P_2, L_1, L_2) + \mu_i - \mu^j \quad (1)$$

where f is the Melbourne-Wübenna linear combination of pseudo-range P and phase L measurements at the two frequencies and μ_i and μ^j are the widelane biases for receiver i and satellite j, respectively. The μ^j are taken from the GRG products and the μ_i are solved for together with N_w.

2. In the second step, the zero-difference ionosphere-free phase equation is written as

$$(\gamma\lambda_1 L_1 - \lambda_2 L_2)/(\gamma\text{-}1) = cT_c + W - \lambda_c N_1 + \lambda_2 N_w/(\gamma\text{-}1) + c\Delta h \quad (2)$$

where c is the velocity of light, T_c is the coordinate time of propagation of the signal, including all delays, Δh is the clock difference (station-satellite), the phase measurements L_i are in cycles, and where the wavelengths λ_i and $\lambda_c = (\gamma\lambda_1 - \lambda_2)/(\gamma\text{-}1)$ with $\gamma = (\lambda_2/\lambda_1)^2 = 1.647$ and the wind-up effect W are in meters.

Equation (2) shows that, if the set of widelane ambiguities N_w (one integer value per pass) has been properly determined in the first step, the set of integer ambiguities N_1 can also be determined if the accuracy of the model needed to compute T_c

is well below the narrowlane wavelength λ_c = 10.69 cm. Clock differences are then continuous as long as there is no discontinuity in the set of integer ambiguities.

As shown in [2], the above treatment is performed on a station by station basis independently for each day and the continuity between successive daily batches is sought for by determining an integer number of narrowlane wavelengths. It is simpler to determine this continuity on the difference of two station clocks, i.e. a time link, and two main methods are used: by extrapolation when the clocks instability is such that the extrapolation noise is much lower than one narrowlane wavelength (~350 ps), and by bridging using another independent time transfer solution when the compared clocks are not stable enough. Note that this continuity must be determined also when all ambiguities are reset within the daily batches, e.g. by a short data gap.

In practice, extrapolation is successful when two H-masers are compared and bridging must be used in other cases. In the absence of in independent time transfer solution, a classical PPP solution can be used for bridging, except when a reset of all ambiguities occurs both in IPPP and in PPP, in which case the continuity of IPPP cannot be ensured.

B. Initial assessment of IPPP

In the first reference presenting IPPP [2], we emphasized two possible methods to validate the performance of the IPPP technique (or any new technique) i.e. either by comparing IPPP to another time/frequency transfer technique with known and proven superior performance, or (in absence of a better reference) by showing that IPPP can, better than other techniques, reveal the performance of ultra-stable clocks when comparing them at a given averaging duration.

The first method was used in [2] to show that IPPP reached a frequency transfer accuracy of 1×10^{-16} at ~3 to 5-day averaging for the 270-km link between the two time laboratories in Poland AOS and GUM. These two laboratories are linked by a fibre link using active stabilization and calibration of the propagation delay [4, 5], which was demonstrated on optical paths of several hundred km with an accuracy of order a few tens of ps and a time deviation below 1 ps up to 1-day averaging, i.e. a frequency instability of order 10^{-17}. Measurements for this continuously operating optical time link between two laboratories participating to UTC have been reported to the BIPM since April 2013. Two comparisons IPPP-Fibre where reported in [2] and one is shown in Fig. 1.

The second method was attempted in [2] but did not provide fully satisfactory results. However IPPP was later used to compare optical clocks in European laboratories in the frame of the ITOC project [6]. In this publication it was shown that IPPP allowed comparing the frequencies of Sr lattice clocks between the LNE-SYRTE in Paris and the PTB in Braunschweig with accuracy well below 1×10^{-16}, as confirmed by comparison to the much more accurate fibre link between the two laboratories.

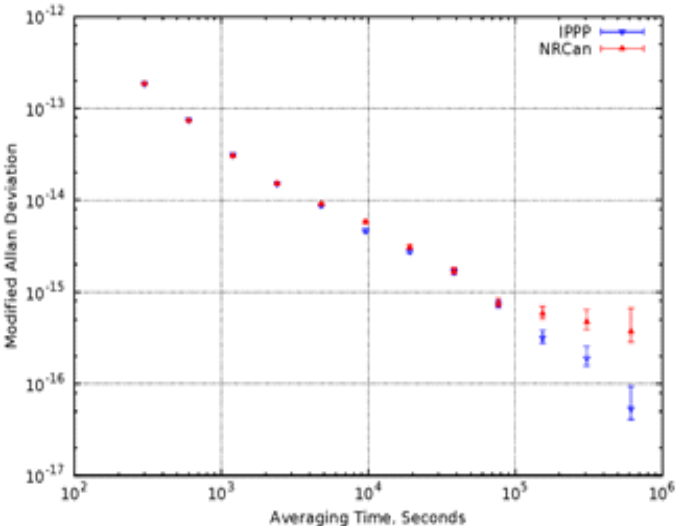


Fig. 1. Stability analysis for the comparison between a 420-km optical fibre link and the results obtained with IPPP (blue) and classical PPP (red) over 41 days.

III. RECENT RESULTS WITH IPPP

As experience is gained, procedures necessary for the IPPP computation are being improved at all stages of the process: the generation of satellite products, the estimation of integer ambiguities on daily batches and the final connection of the links. As IPPP performance is expected to be 1×10^{-16} in a few day averaging, it is challenging to find competitive techniques for comparisons. In the following we present comparisons of IPPP to the continuously operation fiber link AOS-GUM (subsection A), and to novel Two-Way satellite time and frequency transfer (TWSTFT) techniques (subsection B).

A. Long term comparison between IPPP and a fiber link

In late 2015, the BIPM implemented some IPPP computations as an additional technique in its database of link comparisons ftp://ftp2.bipm.org/pub/tai/timelinks/lkc/. This was the case since October 2015 for the link AOS-GUM and the IPPP results are compared to the fibre link and to the classical PPP computation. Accounting for the requirements of quasi continuous GPS phase measurements for IPPP, and on the need for undisturbed environmental conditions to ensure a good behavior of the hardware, it was possible to identify a 104-day period in early 2016 over which a continuous comparison can be performed. For this period, the comparisons PPP-Fibre and IPPP-Fibre are shown in Fig. 2 (top) and the corresponding stability analysis are shown in Fig. 2 (bottom). Note that the classical PPP computation shown on Fig. 2 only covers 99 days as this was a limit set by the analysis software for that run. In principle a continuous PPP solution could be carried out over the exact 104-day interval, with similar results. For the difference IPPP-fiber the achieved frequency instability is found in the low 10^{-17} for an averaging duration above 10 days, and the frequency accuracy over the whole interval is also in the low 10^{-17} as the mean relative frequency difference is $\sim2\times10^{-17}$. Since the fiber link is not a limiting factor at this performance level, this provides a validation of IPPP at the low 10^{-17} level.

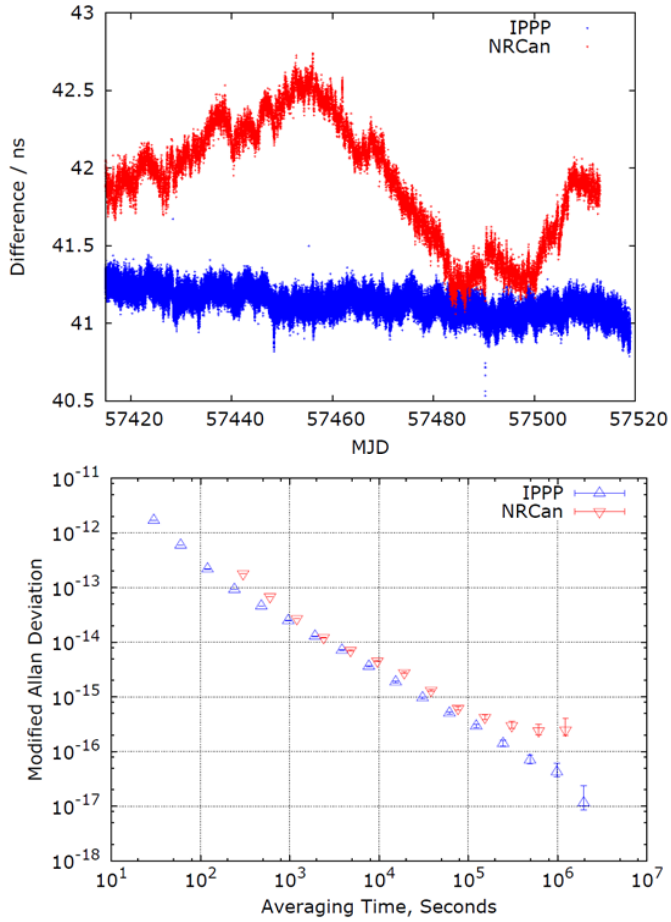


Fig. 2. Time link differences (Top) and Stability analysis (Bottom) for the comparison between a 420-km optical fibre link and the results obtained with IPPP (blue) and classical PPP (red) over 104 days.

B. Comparisonsbetween IPPP and Two Way techniques

Two-way satellite time and frequency transfer, like GPS, uses phase-modulated signals with PRN codes. In recent years, new developments have taken place that promise to further improve the performance of TWSTFT. One is the Software Defined Receiver (SDR) which uses a high-resolution correlator and successive interference cancellation associated with open-loop configuration as the TWSTFT receiver [7] to improve the time stability. Another one uses the Carrier phase of the two-way signal (TWCP) and has been used for frequency comparison over intercontinental links with a performance in the 10^{-15} range over 1000 s, which can be improved by averaging [8].

Comparisons of IPPP have been carried out with SDR over the link between the Telecommunications Laboratory (TL, Chung Li, Chinese Taipei) and the Korea Research Institute of Standards and Science (KRISS, Daejeon). Results for a 37-day comparison are shown in Fig. 3 and it can be seen that IPPP results are more in line with the TW-SDR link than the PPP results. Analyzing the IPPP vs. TW-SDR stability curve, it appears that the measurement noise of TW-SDR may be limiting the short term stability, however this feature could be addressed by denser TW measurements. For the long-term stability, it is not possible to determine whether TW-SDR or IPPP is limiting. We note that $1x10^{-16}$ is reached after averaging ~5 days, slightly more than in the other comparisons presented here, suggesting that TW-SDR somewhat contributes to the instability of the difference. On the other hand, the long-term instability of Classical PPP is limited to ~$2x10^{-16}$.

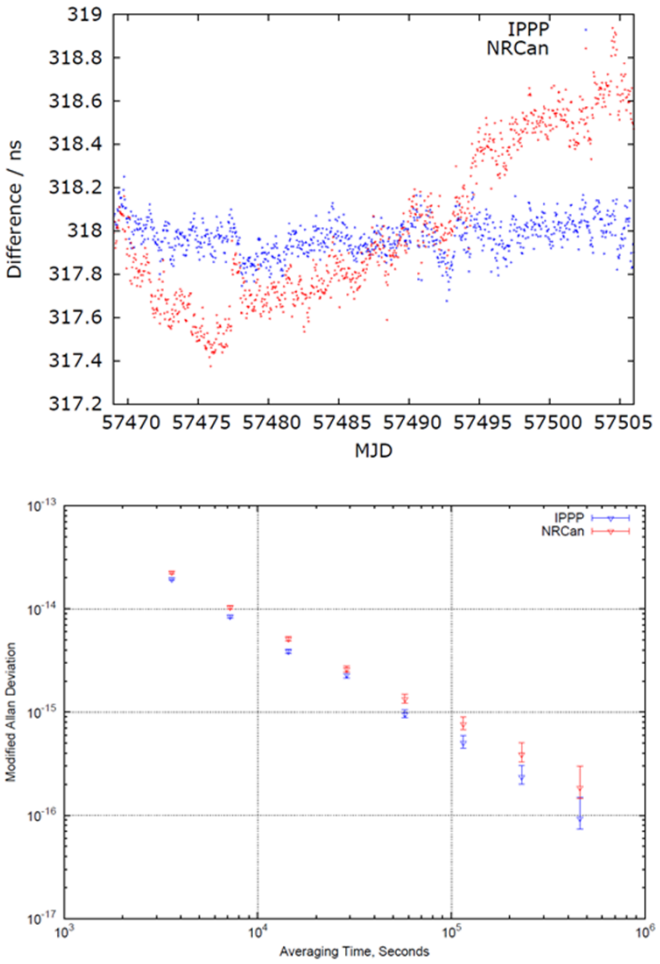


Fig. 3. Time link differences (top) and Stability analysis (bottom) for the comparison between a 1400-km link by TW SDR and the results obtained with IPPP (blue) and classical PPP (red) over 37 days.

Comparisons of IPPP have been carried out with TWCP over the ~1100 km link between the National Institute of Information and Communications Technology (NICT, Tokyo, Japan) and the KRISS over 12 days in January 2017. The resulting stability analysis is shown in Fig.4 for TWCP, Classical PPP and IPPP, and for the comparisons PPP-TWCP and IPPP-TWCP. Analyzing the stability curves, it is clear that TWCP is the most stable until about 20000 s averaging time, then IPPP and TWCP seem to reveal the instability of the compared clocks. Analyzing the differences between techniques, we see that IPPP-TWCP reaches $1x10^{-16}$ after averaging ~2 days, while PPP-TWCP remains at a level of about $2x10^{-16}$. This is in line with all other comparisons and indicates that IPPP (as well as TWCP) reach $1x10^{-16}$ after averaging ~2 days. Because the comparison duration is only 12

days, the uncertainty on the instability (not shown in Fig. 4) should be larger than in the previously shown examples.

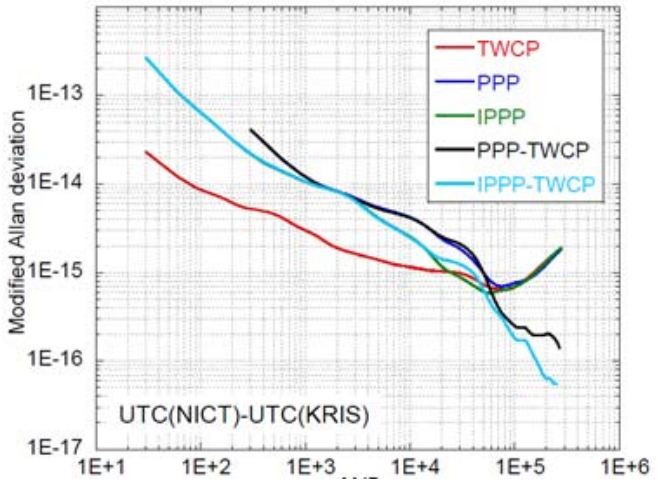


Fig. 4. Stability analysis for several links and link comparisons for NICT-KRISS (~1100 km). The three thechniques TWCP (red), PPP (blue) and IPPP (green) are shown, as well as the comparisons PPP-TWCP (black) and IPPP-TWCP (light blue).

Comparisons of IPPP to both TW-SDR and TWCP provide strong validation of the performance of the two compared techniques.

IV. Conclusions

We show that the IPPP technique, using the CNES-CLS 'grg' products can be put into operation over any link for which continuous Rinex data is available. It is shown that a frequency transfer accuracy of $1x10^{-16}$ is achieved when averaging a few days for regional links and the performance is in the low 10^{-17} for an averaging duration above 10 days. Similar performance is likely achievable for long distance links, although comparisons with techniques of smilar performance remain to be done.

A frequency transfer accuracy of $1x10^{-16}$ at ~3-day averaging represents a significant improvement over the present situation to compare remote frequency standards and it will allow a better characterization of new frequency standards. While regional frequency comparisons will be performed with unprecedented accuracy using fiber links, no simple and perennial technique is on the horizon for long distance links. It is thus important to gain as much as possible from the established GNSS techniques.

Acknowledgment

The NRCan GPSPPP software is provided by Natural Resources Canada, and we thank them for their continuous support. We thank the time laboratories that provided data used in this study, notably the AOS, GUM, KRISS, NICT and TL.

References

[1] Loyer S. et al., Zero-difference GPS ambiguity resolution at CNES–CLS IGS Analysis Center, J Geod 86:991–1003, 2012.

[2] Petit G., Kanj A., Loyer S., Delporte J., Mercier F., Perosanz F., "1x10-16 frequency transfer by GPS PPP with integer ambiguity resolution", Metrologia 52, 301-309, 2015.

[3] J. Delporte, F.Mercier, D. Laurichesse, O. Galy, GPS Carrier Phase Time transfer Using Single Difference Integer Ambiguity Resolution, IJNO, Article ID 273785, 2008.

[4] P. Krehlik, Ł. Sliwczynski, Ł. Buczek, and M. Lipinski, IEEE Trans. on Instr. and Meas., 61 (9), 2573 - 2580, 2012.

[5] Ł. Śliwczyński, P. Krehlik, A. Czubla, Ł. Buczek and M. Lipiński, Metrologia 50 133–145, 2013.

[6] F. Riedel et al., Remote optical and fountain clock comparison using broadband TWSTFT and GPS PPP, Proc. EFTF2016

[7] Y.-J. Huang, M. Fujieda, H. Takiguchi, W.-H. Tseng, and H.-W. Tsao, Stability improvement of an operational two-way satellite time and frequency transfer system, Metrologia, vol, 53, no. 2, pp. 881–890,. 2016.

[8] M. Fujieda, D. Piester, T. Gotoh, J. Becker, M. Aida, and A. Bauch, "Carrier-phase two-way satellite frequency transfer over a very long baseline," Metrologia, 51, pp. 253–262, 2014.

[9] M. Fujieda et al. "NICT-KRISS TWCP link: evaluation and application," these proceedings.

Experimental research on BeiDou time transfer using the NIM made GNSS time and frequency receivers at the BIPM in Euro-Asia link

Kun LIANG, Aimin ZHANG, Zhiqiang YANG
National Institute of Metrology
NIM
Beijing, China
Liangk@nim.ac.cn/kun.liang@bipm.org

Kun LIANG, Laurent Tisserand, Zhiheng Jiang, Gerard Petit, Felicitas Arias
International Bureau of Weights and Measures
BIPM
92312 Sevres Cedex, France

Ye WANG
Beijing Jiaotong University
BJTU
Beijing, China

***Abstract*—A new time and frequency transfer system compatible with BDS has been developed at NIM, and two of them are in operation at the BIPM since Jan 2017. Experiments with this equipment have been implemented to characterize the time and frequency transfer by BDS. This includes analysis of the satellites signal coverage statistics in the BIPM area, the error correction, the measurement noise of the NIM time and frequency transfer receivers, the short and long-term instabilities in the European and Asian baselines, the time transfer link calibration and the accuracy of the time transfer and and AV and CV modes.**

Keywords—BeiDou; time transfer; GNSS; NIM; BIPM

I. INTRODUCTION

Since 27th Dec 2012, BDS (BeiDou Navigation Satellite System) Signal in Space Interface Control Document-Open Service Signal B1I (ICD, Version 1.0) [1] has been released and since then, the developing BDS system with coverage on part of the Asia-Pacific area has provided official service and can be used for time and frequency transfer in this area. After that, several updates of the ICD documents have been produced until its latest version, ICD version 2.1[2]. BDS system is developing fast; 27 navigation satellites have been launched including 8 medium earth orbit (MEO) satellites, 7 geostationary orbit (GEO) satellites, 8 inclined geosynchronous satellite orbit (IGSO) satellites, and 4 experimental satellites. In fact, there are 14 satellites including 5 GEO, 5 IGSO and 4 MEO satellites [3] for use of position, navigation and timing.

Since 2012, at the National Institute of Metrology (NIM, Beijing, China) BDS time and frequency transfer systems have been constructed using two OEM (Original Equipment Manufacturer) boards that are able to receive both BDS and GPS (Global Positioning System) signals. The experiments have been implemented using the BDS observations of a certain 'P3-type' code formed as the iono-free combination of B1 code and so called P2 code, and carrier phase. Compared to GPS P3 code and carrier phase measurements, the performance of time and frequency transfer by BDS has been evaluated and analyzed [3]. Performances equivalent or slightly better than those of GPS time and frequency transfer have been attained most probably due to the good coverage of the BDS signal in Beijing area (see more details in [4]).

A new multi-GNSS (Global Navigation Satellite System) version, NIM-TF-GNSS-3, has been developed at NIM and finished in the middle of 2016, compatible with GPS, GLONASS (GLObal NAvigation Satellite System) and BDS systems. Three of these new systems have been installed at the BIPM in 2017 to investigate the transfer performances over long baselines, in particular, the Euro-Asia link.

II. PRINCIPLE OF TIME TRANSFER BY BDS

BDS is a satellite navigation system performing also functions of a communication satellite. Its navigation system is operated following the similar principles to that of GPS, but with some differences from the GPS system. However, the principle for time and frequency transfer using BDS and GPS are basically the same.

A. BDS System

T The space segment of BDS involves the three types, GEO, IGSO and MEO satellites. GEO and IGSO satellites with one-day cycle around the earth are about more than 36000 kilometers away from the terminal receivers, and MEO satellites, such as the C12 satellite shown in figure 1, which return cycles are 7 days with 13 rounds around the earth, are about more than 20000 kilometers from the terminal receivers.

The time reference for the BDS is the BeiDou navigation satellite system Time (BDT). BDT adopts the international system of units (SI) seconds as the basic unit for the continuous accumulation, without inserting leap seconds. The start epoch of BDT is 00:00:00 on January 1, 2006 of Coordinated Universal Time (UTC). BDT offset with respect to UTC is controlled within 100 nanoseconds (modulo 1 second). The

Supported by Chinese NSFC program 11303024 and the key research program of Chinese MST 2017YFF0212000.

leap seconds are broadcast in navigation (NAV) message [2]. Thus, the difference between TAI and BDT is a constant number of integral seconds (33), while the integral number difference of seconds between BDT and UTC is 4 since 1st Jan, 2017 and until the next insertion of a leap second.

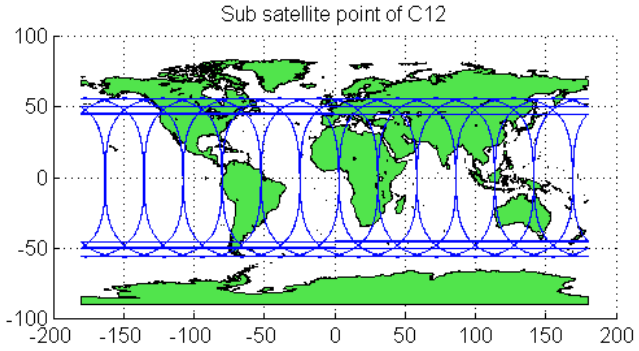


Fig. 1. Path of BDS MEO satellite

B. Principle for Time and Frequency Transfer by BDS

Time and frequency transfer methods by BDS can be of three types that are B1 code, B3 code and carrier phase time and frequency transfer according to the measurement signals. The basic principle is shown in figure 2. In the following sections, we focus on the code measurement, particularly the measurement based on the CGGTTS (CCTF Group on GNSS Time Transfer Standards) data generated by the receivers themselves.

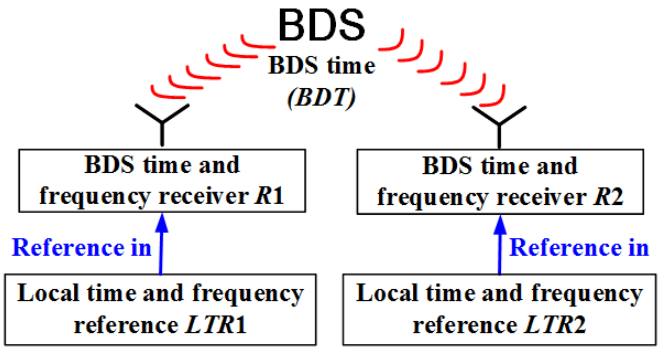


Fig. 2. Time and frequency transfer by BDS

In figure 2, the BDS time and frequency transfer receivers R1 and R2 separately referenced to the corresponding local time and frequency standards $LTR1$ and $LTR2$ are used in the two stations [4]. The reference methods can be different in terms of the operation modes of the receivers. Thus, time and frequency transfer can be realized and the calculation is shown as (1) -(3). First, we can get the time and frequency transfer results $\Delta T1$ and $\Delta T2$ for each station, that is to say, the difference between the local time and frequency standard and BDT. Then the difference between $LTR1$ and $LTR2$ can be calculated by the difference between $\Delta T1$ and $\Delta T2$.

$$\Delta T1 = LTR1 - BDT \quad (1)$$
$$\Delta T2 = LTR2 - BDT \quad (2)$$
$$LTR1 - LTR2 = \Delta T1 - \Delta T2 \quad (3)$$

Those errors, which mainly influence BDS time and frequency transfer will be depicted in section VI.

III. NIM-TF-GNSS-3 Time and Frequency Transfer Receiver

A new type of GNSS time and frequency transfer receiver compatible with GPS, GLONASS and BDS has been developed at NIM, the NIM-TF-GNSS-3. The new features of this receiver, compared to its two previous versions NIM-TF-GNSS-1 [5] and the NIM-TF-GNSS-2 [6] are the automatic measurement of the internal reference delay of the receiver referenced to the different time and frequency sources, the compatibility with BDS system and the file format update towards CGGTTS format v2e [7].

For the evaluation of this kind of receiver, some experiments have been done and the corresponding results will be described in section VII.

A. Scheme of the Receiver

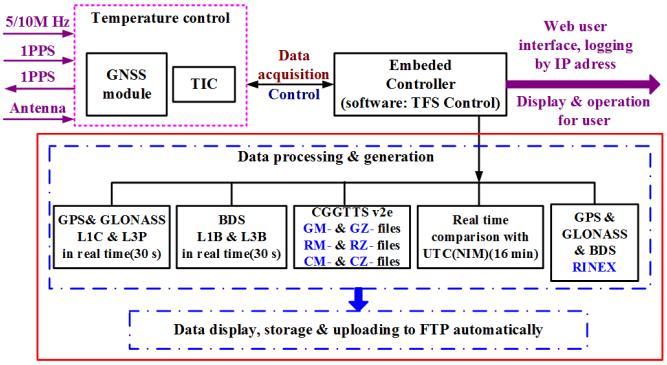


Fig. 3. Scheme of NIM-TF-GNSS-3

The receiver is operated with the operation mode 1 (see operation modes in [8]). The scheme of the receiver described in figure 3 can be divided into two parts. The first part is composed of one GNSS OEM module, one time interval counter (TIC) and one temperature controlling system. Before the receiver starts measuring, the time and frequency signals of the external time reference should be input and after starting GNSS module implements the raw observation together with the TIC. To fulfill the requirement of more precise carrier phase measurement investigated in [8], the temperature controlling system has been installed around the GNSS module and the TIC. The second part is the core of the receiver for data acquisition, processing and system controlling, which consists of one embeded controller and one interface software. The software is network-based and can be used by the webpage logged on through any computer that can be accessed to the receiver. The standard CGGTTS file in accordance with CGGTTS v2e format with the compatibility with Galileo and BDS systems [5] and Rinex files following the format 2.10 or 3.03 could be generated, which includes the measurement types GPS C1 and P3 codes, BDS B1 and B3 codes, and GLONASS C1 and P3 codes, and furthermore the real time measuring and comparison using all the

measurement types in 30 seconds and in 16 minutes is realized by the software.

B. Real Time Measurements

For the convenience of the comparison and monitoring in real time, the function for the generation of the 30-second comparison and its plot is embedded in the receiver, as well the comparison using real-time CGGTTS data, and the real-time comparison to UTC(NIM) in 16 minutes by acquiring the real time CGGTTS data from the NIM data server so that the receiver can link its time reference directly to the precise UTC realization and keep its traceability to UTC.

C. Data Files

The GM and GZ files are generated for GPS C1 and P3 codes, the CM and CZ files are generated for BDS B1 and B3 codes and the RM and RZ files are generated for GLONASS C1 and P3.

The GPS, BDS and GLONASS Rinex files including the formats of v2.10 and v3.03 are generated for mainly carrier phase time and frequency transfer. At present, for daily BDS observations following 2.10 Rinex format, one special single file is generated.

IV. Experimental Setups

In January of 2017, two new self-developed NIM-TF-GNSS-3 receivers (IM15 and IM16) and one compact GNSS receiver compatible with both GPS and BDS systems were sent to BIPM where they had been installed (antenna installation shown in figure 4) in the end of January. All three antennas of BDS time and frequency transfer receivers have been fixed in the NIM antenna holder fastened in the antenna rack located on the roof of the BIPM time laboratory building. The elevation mask has been set to 10-degree in minimum to avoid the possible multipath effect with higher probability below this angle.

A. Scheme of the Experimental Setups

The experiment setups are shown in figure 5. Equipment involved in the experiment includes the three BDS and GPS time transfer receivers of NIM and 6 BIPM receivers all operated at the BIPM, some other GNSS time transfer receivers operational at three sites of two campuses at NIM, hereinto there are six receivers which are compatible with BDS system. However, TF07, TF08 and TF12 were installed during the second half section of the whole experimental period. All the receivers at the same site are referenced to the same time and frequency source. The information on the receivers used for the experiments is listed in Table I.



Fig. 4. Installation of BDS receivers' antennas

TABLE I. Receivers Invovled in the Experiments

Code	Type	Location	Reference	GNSS systems
IM15	NIM-TF-GNSS-3	BIPM	Cs clock	BDS and GPS
IM16	NIM-TF-GNSS-3	BIPM	Cs clock	BDS and GPS
TF06	NIM-TF-GNSS-3	NIM Changping Campus	UTC(NIM)	BDS and GPS
TF07	NIM-TF-GNSS-3	NIM Changping Campus	UTC(NIM)	BDS and GPS
TP01	GTR55	TP	UTC(TP)	BDS and GPS
TP04	GTR50	TP	UTC(TP)	GPS
IM03	NIM-TF-GNSS-1	NIM Changping Campus	UTC(NIM)	GPS
IM05	PolaRx3eTR	NIM Changping Campus	UTC(NIM)	GPS
IM06	GTR50	NIM Changping Campus	UTC(NIM)	GPS
IM13	NIM-TF-GNSS-3	NIM Heingli Campus	Hydrogen maser	BDS and GPS
BP0T	GTR50	BIPM	Cs clock	GPS
BP0R	PolaRx2eTR	BIPM	Cs clock	GPS
BP1B	TTS4	BIPM	Cs clock	GPS
BP1J	PolaRx4eTR	BIPM	Cs clock	GPS
BP1X	GTR51	BIPM	Cs clock	GPS

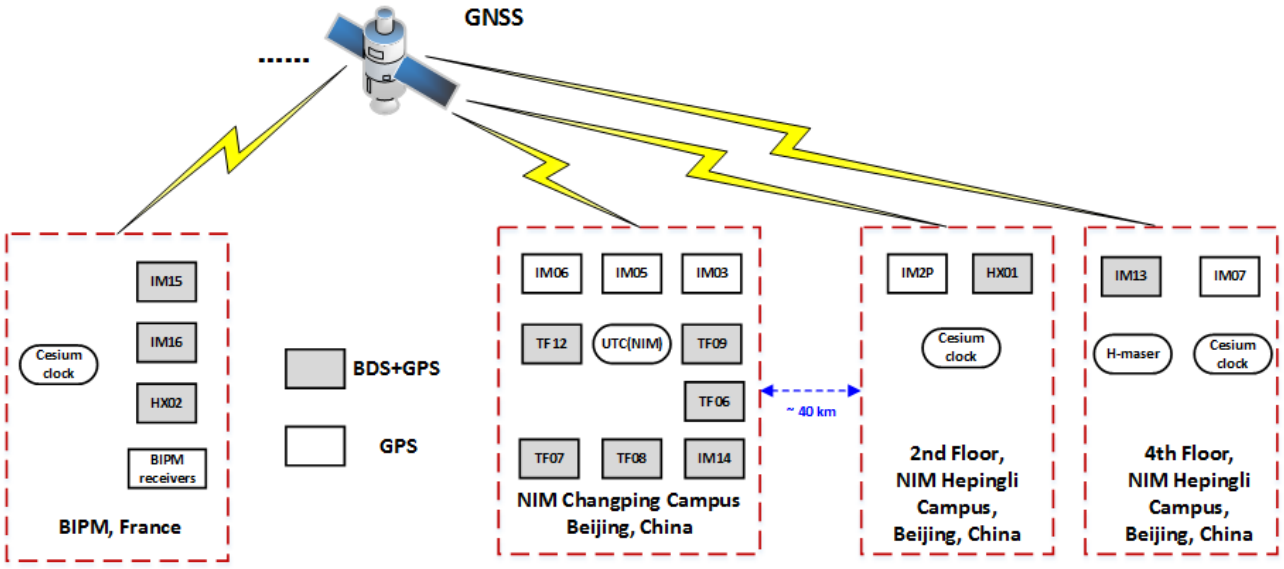


Fig. 5. Scheme of experiment setups

V. SATELLITE SIGNAL COVERAGE STATISTICS

As today, the three NIM receivers have been operated for several months at BIPM. The antenna location is just beside a small hill roughly in the west and northwest direction (partly seen in figure 4), which could block the west and north-west view of the receiver with a natural high elevation mask of about 30 degrees. This effect is visible from the azimuth of the satellites received by the IM15 receiver depicted in figure 6. There are some trees on the hill body, which may cause some additional multipath effects. In figure 6, the satellite view with elevation and azimuth of IM15 at BIPM (on the left) and TF06 at NIM (on the right) has been shown, and certainly because of the 7-day return cycle for MEO satellites, the real elevation statistics for MEO satellites cannot be seen explicitly during one day period.

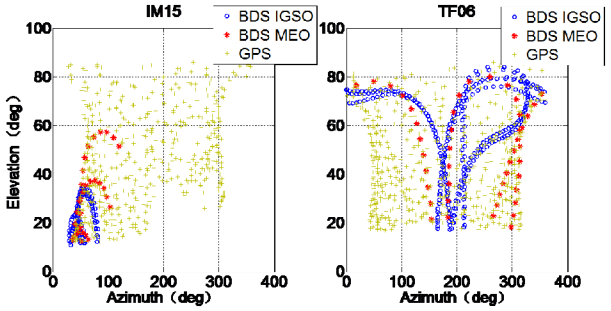


Fig. 6. Elevation and azimuth plot for IM15 and TF06

At the BIPM and NIM antenna positions, the satellite signal coverage has been characterized from the satellite number, satellite elevation, satellite azimuth and satellite signal to noise strength using data from several days to two weeks. Figures 7 and 8 respectively show the statistic results for satellite numbers of BDS and GPS with elevation masks of 10 degrees both at NIM and BIPM; these settings are used as parameters in further experiments and analysis on satellite elevation and signal to noise ratio, as well as in the validation experiments here following.

A. Satellite Number

Satellites with PRN numbers from 1 to 14 are within the view of the receivers at NIM antenna position. The situation at the BIPM is poorer; at the BIPM antenna position, the satellites which PRN numbers are from 5 to 14 are within the view of the receivers. They are one GEO, 3 MEO and 6 IGSO satellites. We got the values of the elevation and the signal to noise ratio (SNR) of one IGSO and one MEO satellite with the lower elevation and lower signal to noise ratio and the GEO satellite which is observed by IM15 in figure 9. Because of the very low elevation and the very low SNR for GEO satellite in this position, we just focus on the IGSO and MEO satellites for the BDS time and frequency transfer. However, from figure 8, at the same time, we can see that BDS satellites in view are quite few, in general, two or three satellites. The number is not highly efficient for the construction of good DOP (Dilution Of Precision) and continuous positioning. In Beijing, this number would be more than 12. Anyway, for time and frequency transfer, one satellite is the lowest limit, allowing to have time and frequency transfer solutions in absolutely most time, as can be concluded from the figure 7.

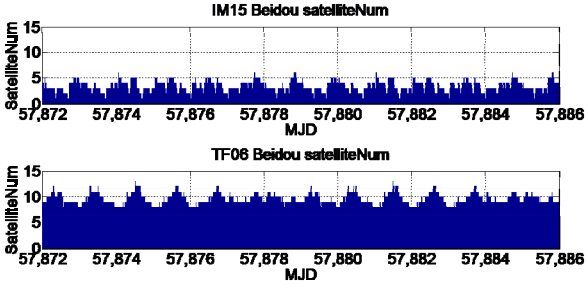


Fig. 7. BDS satellite number statistics of IM15 and TF06

Statistics for the view of the global GPS constellation composed of the more than 30 MEO satellites are presented in figure 8, considering the position and the surroundings of the receivers at BIPM antenna position. Certainly, the number of satellites in view for either GPS or BDS is fewer than those in the open and wide areas without any obstacles, and also at NIM.

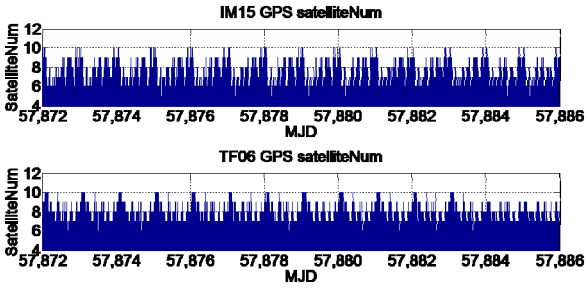


Fig. 8. GPS satellite number statistics of IM15 and TF06

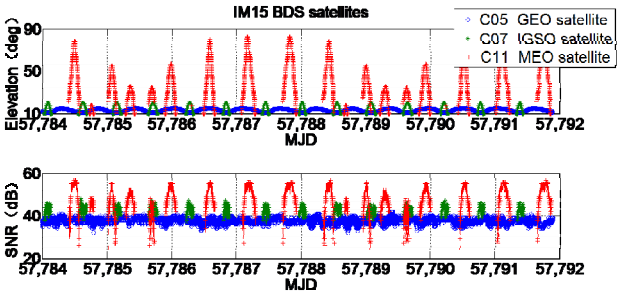


Fig. 9. Elevation and SNR of the different kinds of BDS satellites

B. *Satellite Elevation and Azimuth*

We can defer roughly in which direction the receiver can get the view of BDS and GPS satellites from figure 6 that describes the satellite statistics using one day observation data of IM15 receiver. From figure 10 and 11, at the BIPM antenna position, the elevation angle of the IGSO satellite is between 10 degrees and 35 degrees, and the elevation angle of the MEO satellite has one 7-day cycle and the maximum elevation angle is varying day by day during this 7-day period. Compared to the statistics for TF06 receiver at NIM, IM15 receiver at BIPM has much lower elevation for IGSO satellite, and similar elevation for MEO satellite.

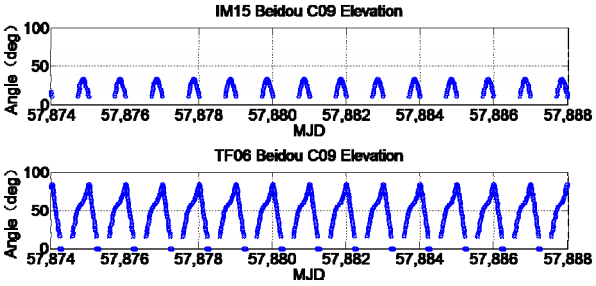


Fig. 10. BDS satellite elevation statistics of IM15 and TF06 for C09

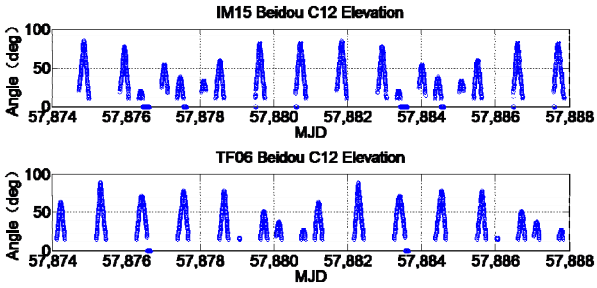


Fig. 11. BDS satellite elevation statistics of IM15 and TF06 for C12

From figure 12, we also validate the narrow azimuth range of IGSO satellite of the receivers at the BIPM antenna position. However, as figure 13 shows, there could be some possibility for MEO satellite coming into the view when the satellite relative to the receiver is at the elevation angle higher than 30 degrees corresponding to figure 11.

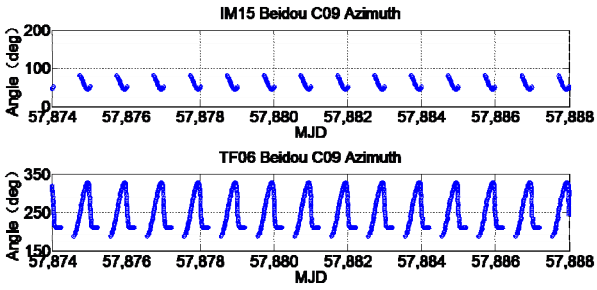


Fig. 12. BDS satellite azimuth statistics of IM15 and TF06 for C09

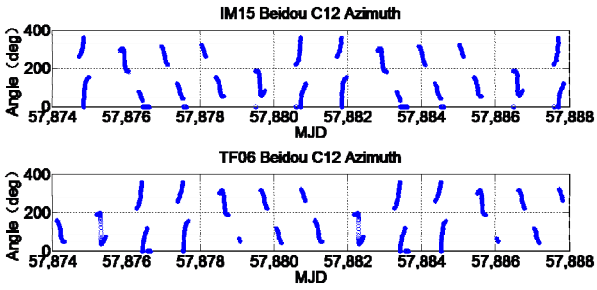


Fig. 13. BDS satellite azimuth statistics of IM15 and TF06 for C12

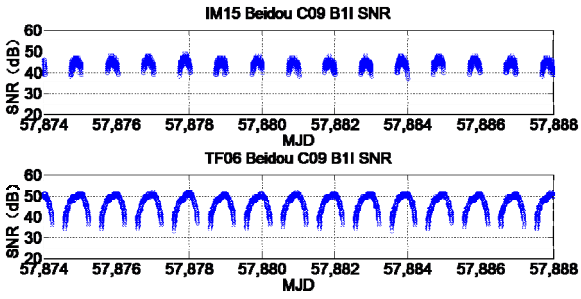


Fig. 14. BDS satellite S/N statistics of IM15 and TF06 for C09

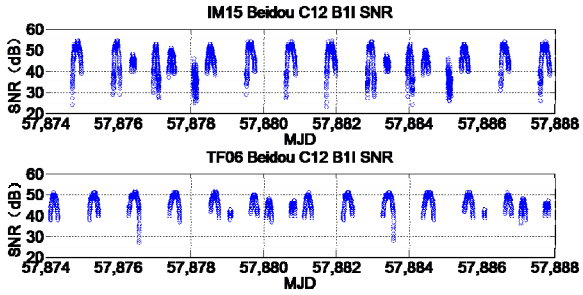


Fig. 15. BDS satellite S/N statistics of IM15 and TF06 for C12

C. Satellite Signal to Noise Ratio

From figure 14, we can see the obvious degradation of signal to noise ration for IGSO satellite at BIPM. From figure 15, for MEO satellite, there might be some kind of degradation with some signal missing because of the natural elevation mask in the north-west direction by the hill, and as well the higher propobility of low signal to noise ratio roughly between 30 dB and 40 dB, which hasn't been explained clearly.

D. Satellite Noise Level by the common clock method

At NIM, the noise level for the different types of satellites has been evaluated by the common clock difference (CCD) experiments in common view mode including BDS IGSO satellites, BDS MEO satellites and GPS MEO satellites, because it is much easier for the receivers at NIM to receive better BDS signals thanks to the better coverage of BDS system signal at NIM antenna position. That is to say, we can get more and better sampling examples for the statistics there. We did the CCD calculation for each satellite in common view using coarse code (B1 for BDS, and C1 for GPS) CGGTTS data. From the statistics of 13 days' data bound during MJD 57897- MJD 57909 used in table II, generally speaking, we could see that BDS satellites and GPS satellites might have the similar noise level. More precisely, in most cases, BDS MEO satellites have the similar noise level to that of BDS IGSO satellites, and a bit better noise level results could be acquired by BDS satellites than by GPS satellites. That could be contributed by the wider bandwidth for BDS B1 signal.

TABLE II. NOISE STATISTICS FOR DIFFERENT SATELLITES

PRN	Satellite type	Mean (ns)	Std (ns)
C06	IGSO	-0.3	0.6
C07	IGSO	-0.3	0.6
C08	IGSO	-0.6	0.6
C09	IGSO	-0.6	0.8
C10	IGSO	-0.2	0.7
C11	MEO	-0.6	0.7
C12	MEO	-0.3	0.8
C13	IGSO	-0.1	0.7
C14	MEO	-0.4	0.6
G09	MEO	0.4	0.8
G12	MEO	-0.1	0.7
G16	MEO	0.4	0.9

VI. ERROR CORRECTIONS

The signal transmitted from the satellites towards the receiver will be influenced by the distance satellites-receiver, the ionospheric and tropospheric delays, relativistic effect, satellite clock bias and satellite group delay and so on. Thus, these corrections should be applied for the precise time and frequency transfer.

The differences from the GPS system depicted in section II might lead to the privilege and advantage of BDS system in the focused areas, such as the Asian-Pacific area, because there are more satellites and better signal coverage in these areas.

Certainly, we should note some parameters related to the earth reference frame, such as the earth's gravitational constant and the earth rotation rate, which are also a bit different from those of GPS system [6].

The two satellite differential group delays, respectively called TGD1 and TGD2, referenced to B3 frequency point separately for the two different frequency points B1 and B2 of BDS systems should be taken into account.

The modeled ionospheric delay can be calculated using the Klobuchar model. Also for the dual frequency BDS measurements, we can compute the ionospheric delay $iono_1$ for B1 code as (4). However, when the measured ionospheric delay through dual frequency measurements is estimated, it should be noted that B1 and B2 code measurements (B_1 and B_2) should be applied after the delay error corrections influenced by the signal frequency are removed from the measurements, such as the satellite differential group delay and the internal delay of the receiver.

$$iono_1 = -\frac{f_2^2}{f_1^2 - f_2^2}(B_1 - B_2) \tag{4}$$

Hereinto, f_1 is the carrier frequency for B1 code and f_2 is the carrier frequency for B2 code.

VII. STABILITY AND ACCURACY

The CCD experiments for the evaluation of the measurement noise level have been fully implemented at the different locations including Beijing and Paris. Time link calibration is also discussed here. We have also implemented time and frequency transfer experiments over long baselines from the several hundreds of kilometers to nearly 9000 kilometers. In addition, the results of GPS and BDS in the Europe-Asia with common view (CV) and All-in view (AV) between BIPM and NIM have been compared and analyzed. All results have been got through averaging of all satellites at the same epoch with either CV or AV.

A. Measurement Noise by the CCD method

From figure 16, a time stability of about 1 ns has been obtained through the CCD results of BDS B1I code using the two new GNSS receivers of the same type (NIM-TF-GNSS-3). About 3 ns instability can be obtained by the iono-free

combination of B1I and B2I codes of BDS, which should in consistence with what we expect in terms of the law of propagation of the uncertainty.

To avoid the influence of the satellite coverage analyzed in section V on the evaluation of the receiver performance, CCD experiments with the two NIM-TF-GNSS-3 receivers at NIM have been implemented. Figure 17 shows that receivers at Beijing are affected by a lower measurement noise level since there is a worse satellite coverage at the BIPM antenna position. In other words, it could be shown that at the IM15 antenna position at BIPM the measurement noise level for the time transfer results is much worse (see the standard deviation, std) due to the few satellites and lower elevation. Results are presented in Table III.

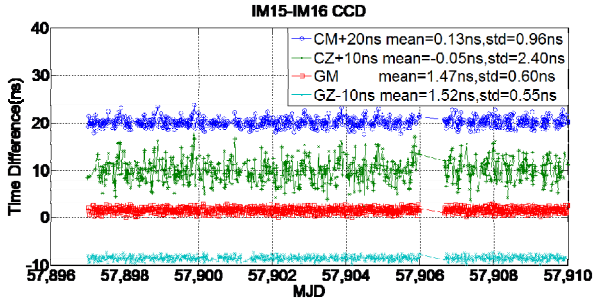


Fig. 16. BDS and GPS CCD results between IM15 and IM16 at BIPM

CM: CGGTTS measurements for BDS B1 code
CZ: CGGTTS measurements for BDS B3 code
GM: CGGTTS measurements for GPS C1 code
GZ: CGGTTS measurements for GPS P3 code
Note: All the above measurement files are in accordance with CGGTTS v2.4 format.

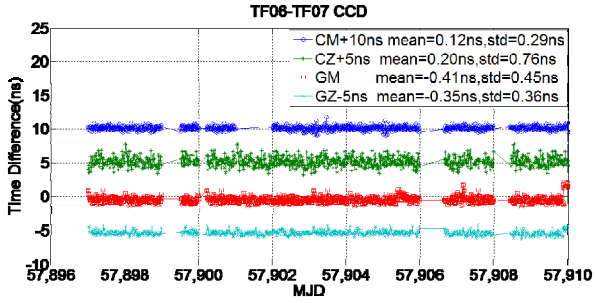


Fig. 17. BDS and GPS CCD results between TF06 and TF07 at NIM

Several BIPM receivers BP0R, BP0T, BP1B, and BP1J, and the three receivers IM03, IM05 and IM06 have been used for the comparison of CCD results, with slightly worse results as can be seen in figures 18 and 19, because almost all the receivers are of different kinds, and only BP0R and BP1J are from the same company (see details in table I). TheB1 code of BDS has a better noise level than the C1 code of GPS due to the double bandwidth of the GPS C1 signal.

TABLE III. MEASUREMENT NOISE BY CCD

Receiver pair	CM (ns)	CZ (ns)	GM (ns)	GZ (ns)
IM15-IM16	1.0	2.4	0.6	0.6
TF06-TF07	0.3	0.8	0.5	0.4

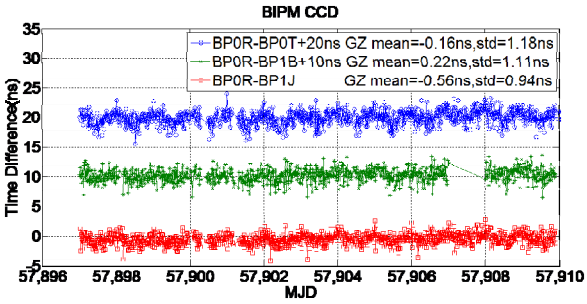


Fig. 18. GPS P3 CCD results among BIPM receivers at BIPM

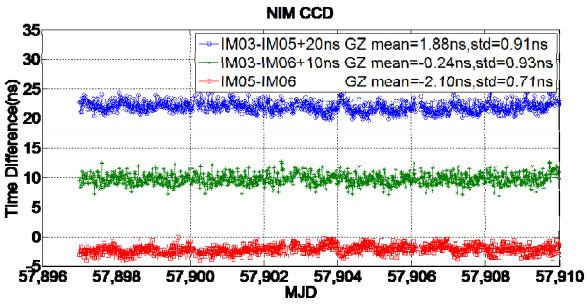


Fig. 19. GPS P3 CCD results among NIM receivers of other types at NIM

B. Time Link Calibration

The time link calibration should be implemented for the accuracy evaluation. There are two methods for this target. One is to calibrate the link by the traveling BDS receiver with closure. The other is just calibrate the whole BDS link by CCD experiments or by aligning the BDS links with other calibrated links, such as GPS time transfer links. And also for the first methods, for making the calibration of each receiver of the time transfer link using the first method, it is necessary to have one BDS reference receiver absolutely calibrated, which is not at present the case. Thus, we calibrated all the links between pairs of receivers and set the receiver TF06 as the pivot receiver for the calibration exercise, and by the CCD experiments we got the calibration values of the other receivers with reference to this receiver, as presented in table IV. For GPS calibration values, we got one for each receiver individually using our reference receiver IM06 calibrated by BIPM. Thus, in this case we can get the time transfer results for the link by BDS and GPS.

As well during the experiments on the BIPM-NIM link, we could verify the BDS calibration values using the calibrated GPS time transfer results.

TABLE IV. CALIBRATION VALUES FOR BDS LINKS AND GPS RECEIVERS

	CM(with TF06) (ns)	CZ(with TF06) (ns)	GM (ns)	GZ (ns)
IM15	-3.2	4.89	-7.1	-10.9
IM16	-3.3	4.80	-5.1	-8.9
TF06	-	-	-12.4	-16.1
TF07	0.3	6.24	-3.8	-6.9
TF08	1.1	4.39	-13.6	-16.9
TF09	0.2	9.88	-4.9	-8.4
TF12	-2.8	3.87	-6.2	-9.7
IM03	-	-	-40.3	-44.4
IM05	-	-	74.0	62.1
IM06	-	-	-30.4	-31.3
IM07	-	-	-24.2	-27.1
IM13	-14.6	139.1	-44.2	-47.0

C. Comparison among the Different Links in Long Baselines

In the experiments on the BIPM-NIM baseline, we have more than 20 days' data for comparison in figure 20 and 21 (Time Deviation (TDEV) plot). From the pair of NIM-TF-GNSS-3 receivers, there is the obvious agreement between the BDS and GPS results. It has been verified through the GPS links using the different receiver pairs as shown in figure 22 and 23. However, the IM06-BP1B link (red line in figure 23) could deviate from the others in TDEV due to the big data gaps of BP1B receiver.

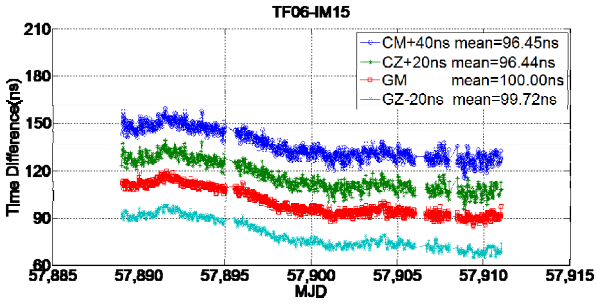


Fig. 20. Latest BDS and GPS results between other receivers at NIM and BIPM

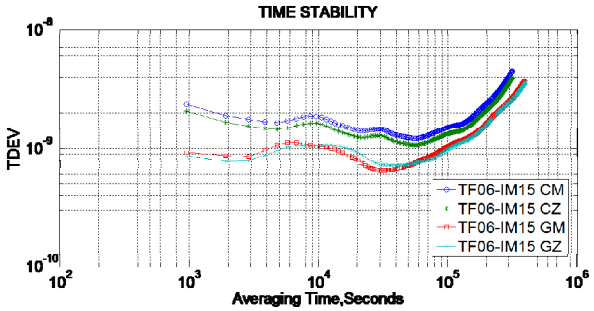


Fig. 21. TDEV for latest BDS and GPS results between TF06 and IM15

The elevation-dependent effect found in the former study [9-11] on BDS measurement evaluation especially for the Geodetic application is not obvious in figure 20. However, the small deviation between the results of BDS and GPS could derive from this effect or worse satellite signal noise level due to worse satellite coverage.

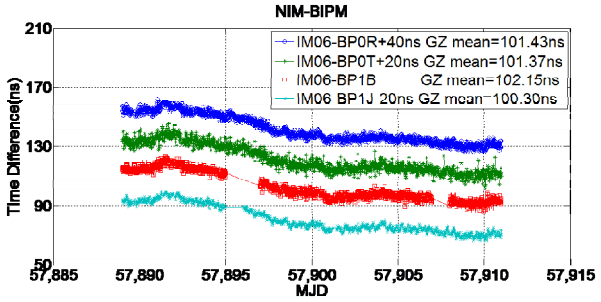


Fig. 22. Lastest GPS P3 results between other receivers at NIM and BIPM

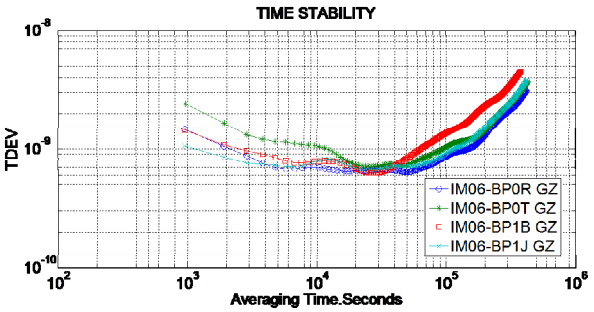


Fig. 23. TDEV for lastest GPS P3 results between other receivers at NIM and BIPM

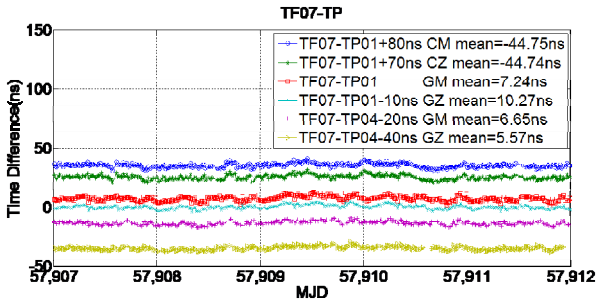


Fig. 24. Results between TF07 and TP receivers

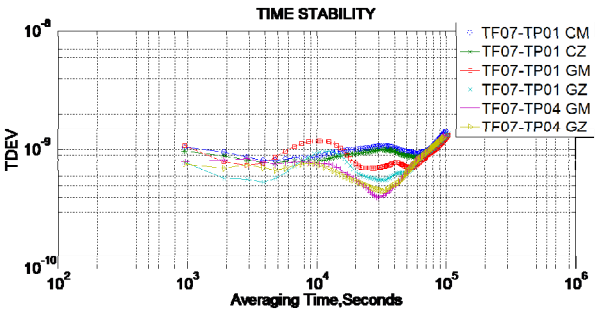


Fig. 25. TDEV for the results between TF07 and TP receivers

Additionally, we implemented the experiments via separately the BIPM-TP (Institute of Photonics and Electronics, Czech Academy of Sciences(IPE/ASCR), Prague, Czech Republic) link and NIM-TP link as shown in figure 24-27. At TP in Prague, there are one time and frequency transfer receiver (Dicom GTR55) compatible with GPS and BDS, and one GPS time and frequency transfer receiver (Dicom GTR50)

for the comparison and verification each other. Finally, the good consistence could be achieved. However, IM15-TP baseline could be worse than TF07-TP baseline because of the satellite coverage reasons. Moreover, we could see the rough consistency between the results of BDS time and frequency transfer and the results of GPS time and frequency transfer either in TF06-TP baselines or in IM15-TP baselines.

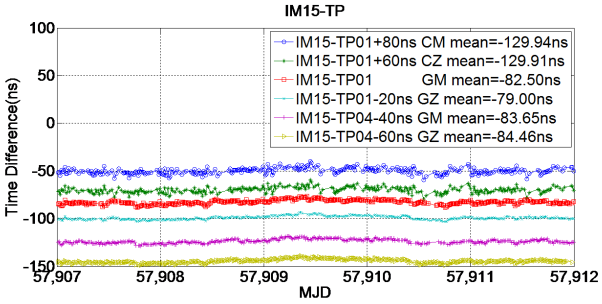


Fig. 26. Results between IM15 and TP receivers

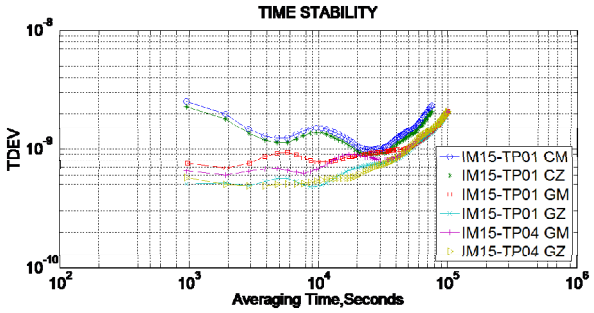


Fig. 27. TDEV fot the results between IM15 and TP receivers

Furthermore, we used two receivers separated about 40 km over the baseline between the two NIM campuses, Changping and Hepingli. One reference is UTC(NIM) based on one hydrogen maser as the master clock and the other reference is one hydrogen maser steered to UTC(NIM) by GPS time and frequency transfer. The comparison results between these two receivers, presented in figures 28 and 29, are similar to the CCD results due to the steering of the hydrogen maser in Hepingli campus. Since there are not so big differences between the elevation angles of the two receivers, the elevation dependent effects are not visible.

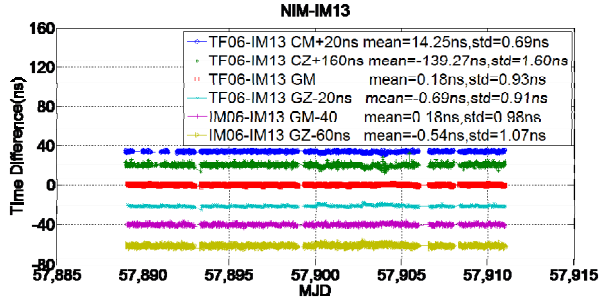


Fig. 28. Results between NIM receivers in Changping campus and IM13

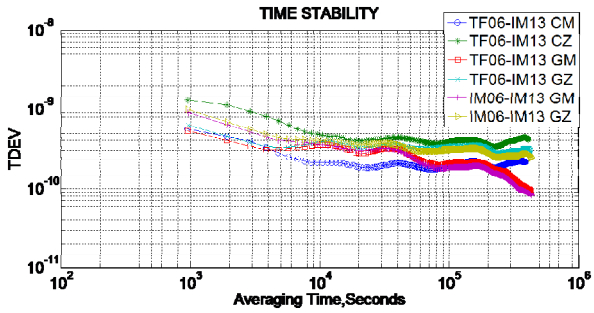


Fig. 29. TDEV for the results between NIM receivers in Changping campus and IM13

Finally, using the data as used in figure 20 and 21, the time transfer results by averaging data of all epochs in each single station and differentiating the average between two stations are presented in Table V. The ones by both GPS and BDS over the long baseline of NIM-BIPM with the references of UTC(NIM) and one cesium clock agree within 2.5 ns even though there were incomplete data in some epochs because of some data gaps. BP0R is the reference receiver for the other BIPM receivers, and the time transfer results between IM06-BP0R and TF06-IM15 receiver pairs are in line within 1.8 ns.

TABLE V. TIME TRANSFER RESULTS FOR THE NIM-BIPM BASELINE EXPERIMENTS

	CM (ns)	CZ (ns)	GM (ns)	GZ (ns)	Calibrated
IM06-BP0R	-	-	-	101.4	IM06 GZ /BP0R GZ
IM06-BP0T	-	-	-	101.4	IM06 GZ /BP0T GZ
IM06-BP1B	-	-	-	102.2	IM06 GZ /BP1B GZ
IM06-BP1J	-	-	-	100.3	IM06 GZ /BP1J GZ
TF06-IM15	99.9	99.9	100.0	99.7	TF06 All / IM15 All

D. All-in View vs Common View

B1 code for BDS and C1 code for GPS have been selected for the comparison of all-in view (AV) and common view (CV).

In CV mode, just a few (less than 4) satellites can be used in either GPS or BDS measurements from figure 30 and 31 because of the super long baseline.

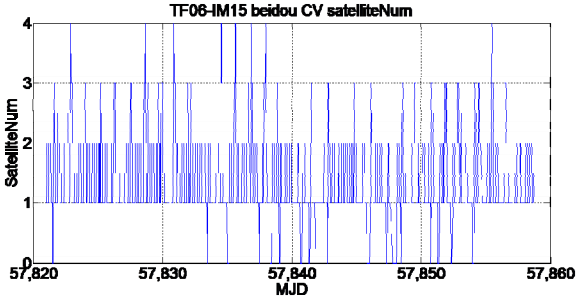


Fig. 30. Elevation differences between IM15 and TF06 for C12

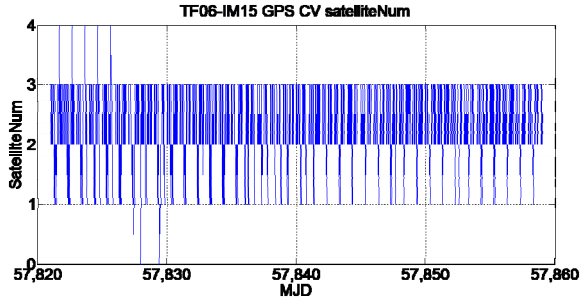


Fig. 31. Elevation differences between IM15 and TF06 for C12

From figure 32 and 33, for BDS, AV mode is not better than CV mode because not so many satellites are visible at the BIPM antenna position, although the baseline is long. In the case of GPS, with more numbers of satellites at both locations in balance, here in general more than 7 satellites, AV mode is clearly advantageous.

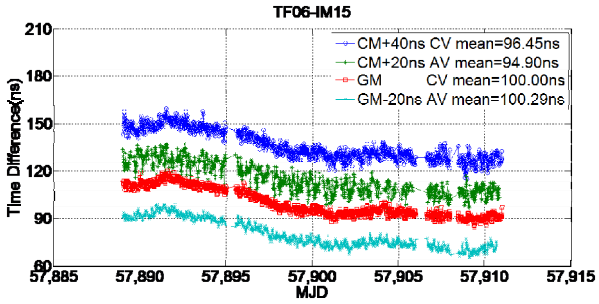


Fig. 32. CV and AV results between TF06 and IM15

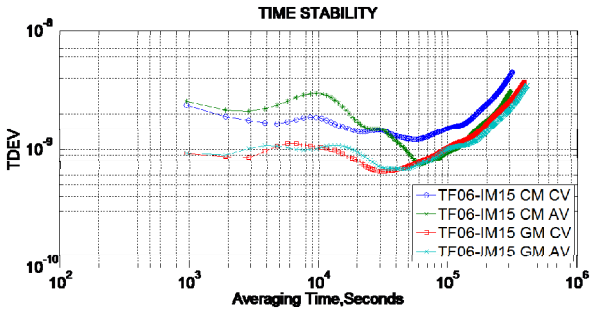


Fig. 33. TDEV for CV and AV results between TF06 and IM15

VIII. SUMMARY AND EXPECTATION

One new time and frequency transfer system compatible with BDS system has been developed, and the measurement noise of the NIM time and frequency transfer receivers has been evaluated as less than 1 ns by CCD experiments. the worse satellites signal coverage statistics in the area at BIPM has been seen with the satellite number, elevation and azimuth and SNR, the error correction for BDS time and frequency transfer is discussed. The short and long-term stabilities and the effects in AV and CV modes by BDS in the European and Asian baselines have been assessed. Agreement between BDS and GPS time and frequency transfer results could be seen. With the time transfer link calibration, the accuracy of the time transfer by BDS has been observed and the difference from the results by GPS is within 2.5 ns. Anyway, the algorithm for the data processing in the receiver is evolving continuously. There is some possibility and potentiality for BDS system to be applied in the Euro-Asia link. Especially in the several years, global coverage of BDS system will be finished probably in 2020, thus the coverage of BDS system in Europe will be much better. As well the new civil BDS signals in better performance with the updated ICD will be published, so we can expect that the performances of time and frequency transfer by BDS would be improved sharply. In principle, the new BDS time and frequency transfer receivers could be firstly applied for the remote comparison, calibration and traceability in Asia-Pacific area and then be used for the construction of the new NIM calibration station compatible BDS system for the BDS time link calibration.

ACKNOWLEDGMENT

We thank TP for the TP01 and TP04 GNSS observation data and thank Xiangwei ZHU from NUDT (National University of Defense Technology, Changsha, China) for some related information of BDS system.

REFERENCES

[1] China Satellite Navigation Office, “BeiDou Navigation Satellite System Signal In Space Interface Control Document Open Service Signal B1I (Version 1.0),” 2012

[2] China Satellite Navigation Office, “BeiDou Navigation Satellite System Signal In Space Interface Control Document Open Service Signal (Version 2.1),” 2016.

[3] China Satellite Navigation Office, “BeiDou Navigation Satellite System Open Service Performance Standard (Version 1.0),” 2013

[4] Liang, Kun; Jinos, Zhaofeng; Pei, Chao; Zuo, Fei; Zhang, Aimin, Preliminary Implementation of Time and Frequency Transfer by BDS, Proceedings of IFCS-EFTF2013.

[5] LIANG Kun, ZHANG Aimin, GAO Xiaoxun, WANG Weibo, NING Dayu , ZHANG Side, Study and Development of a New GNSS Receiver for Time and Frequency Transfer, EFTF 2012.

[6] Liang K, Zhang A, Yang Z, et al. Developing of one time link calibrator with GNSS at NIM[C]//Frequency Control Symposium & the European Frequency and Time Forum (FCS), 2015 Joint Conference of the IEEE International. IEEE, 2015: 545-548.

[7] Defraigne P, Petit G. CGGTTS-Version 2E: an extended standard for GNSS Time Transfer[J]. Metrologia, 2015, 52(6): G1.

[8] Liang K, Feldmann T, Bauch A, et al. Performance evaluation of NIM GPS receivers in use for time transfer with PTB[C]//EFTF-2010 24th European Frequency and Time Forum. IEEE, 2010: 1-8.

[9] Wanninger L, Beer S. BeiDou satellite-induced code pseudorange variations: diagnosis and therapy[J]. GPS solutions, 2015, 19(4): 639-648.

[10] Guo F, Li X, Liu W. Mitigating BeiDou Satellite-Induced Code Bias: Taking into Account the Stochastic Model of Corrections[J]. Sensors, 2016, 16(6): 909.

[11] Huang W, Defraigne P. BeiDou Time Transfer With the Standard CGGTTS[J]. IEEE transactions on ultrasonics, ferroelectrics, and frequency control, 2016, 63(7): 1005-1012.

High-sensitivity cold-atom gyroscope with real-time vibration compensation

D. Savoie, M. Altorio, B. Fang, R. Geiger and A. Landragin

LNE-SYRTE,
Observatoire de Paris, PSL Research University, CNRS, Sorbonne Universités, UPMC Univ. Paris 06,
Paris, France
Email: arnaud.landragin@obspm.fr

***Abstract*— Our cold-atom gyroscope is based on a four-pulse configuration with a very large Sagnac area. Its short-term stability is limited by aliasing effects of the inertial forces (acceleration and rotation). We will show how continuous measurements and real-time compensation of the vibration during the interferometer sequence overcome this limit.**

Keywords—Atom interferometry, gyroscope, Raman transitions

I. INTRODUCTION

We report the operation of a cold-atom gyroscope based on a four-Raman-pulse configuration [1], which enables a very large Sagnac area of 11 cm^2. In such cold-atom inertial sensors, the main limit to the sensitivity comes from aliasing effect linked to the sequential nature of the cold-atom experiments, leading to fluctuations of the inertial phase shift to more than a fringe from shot to shot. In order to resolve this problem and to achieve the intrinsic sensitivity of such sensors, we have demonstrated first the possibility of continuous measurement of the rotation signal, i.e. without dead time between successive measurements, and second the possibility of filtering out the vibration in real time so as to remain at the mid-fringe, where the sensitivity is maximal.

II. CONTINUOUS COLD-ATOM GYROSCOPE

We have demonstrated a joint interrogation scheme, where we simultaneously prepare a cold-atom source and operate an atom interferometer (AI) in order to eliminate dead time [2]. The continuous operation improves the short-term sensitivity of the gyroscope, illustrated by our demonstration of a rotation sensitivity of 100 $nrad.s^{-1}.Hz^{-1/2}$. Moreover, we show that the continuous operation does not affect the long-term sensitivity potential of AIs and report a stability of 1 $nrad.s^{-1}$ after 10^4 s of integration time.

III. REAL TIME COMPENSATION OF THE VIBRATION

The continuous operation will then enable us to quickly reach the quantum projection noise (or Heisenberg) limit in large area AIs, as we should average the inertial noise as τ^{-1}.

If we assume negligible detection noise, observing the τ^{-1} scaling would require to operate the AI within its linear region, i.e., around mid-fringe. Otherwise, the loss of inertial sensitivity, which occurs when approaching the top and bottom of the fringes, prevents us from observing the τ^{-1} scaling. Mid-fringe operation can, for example, be achieved by a real-time compensation of vibrations with a feedback to the Raman laser phase, as demonstrated for acceleration measurements in [3].

We have setup a real-time compensation of the horizontal accelerations using signals from two standard mechanical accelerometers which enable us to estimate the atomic phase shift during the interferometer with a total interrogation time of 800 ms. We apply a jump of the relative phase between the two Raman lasers just before the last light pulse in order to compensate the vibrations. The use of real-time compensation in standard operation (with dead time) has already allowed us to improve the short-term sensitivity to 90 $nrad.s^{-1}.Hz^{-1/2}$, averaging down below 5×10^{-10} $rad.s^{-1}$ in 40 000 s. This demonstrates a record sensitivity among all atom gyroscopes.

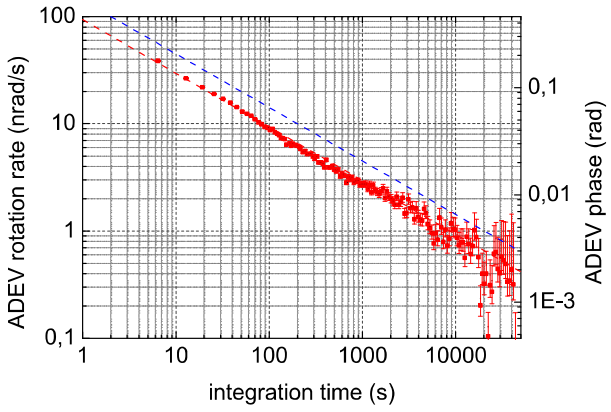


Fig. 1. Allan standard deviation of the rotation rate sensitivity. The blue line represent the sensitivity without real-time compensation and the red points are the data in real-time compensation of the acceleration signal.

Combining real-time compensation and continuous measurement should lead to a vibration noise averaging as τ^{-1}.

With a quantum projection noise limited detection of 10^6 atoms and a 20% interferometer contrast, a rotation sensitivity below 1×10^{-10} rad.s^{-1} in a few 100 s is thus accessible with our setup.

ACKNOWLEDGMENT

We acknowledge the financial support from Direction Générale de l'Armement (DGA Contract No. 2010.34.0005), Centre National d'Etudes Spatiales (CNES), Institut Francilien de Recherche sur les Atomes Froids (IFRAF), the Action Spécifique du CNRS Gravitation, Références, Astronomie et Métrologie (GRAM), and Ville de Paris (project HSENS-MWGRAV). D. S. is supported by DGA, and B.F. by FIRST-TF.

REFERENCES

[1] B. Canuel, F. Leduc, D. Holleville, A. Gauguet, J. Fils, A. Virdis, A. Clairon, N. Dimarcq, Ch. J. Bordé, A. Landragin et P. Bouyer, "Six-axis inertial sensor using cold-atom interferometry", Phys. Rev. Lett. **97**, 2006, 010402.

[2] I. Dutta, D. Savoie, B. Fang, B. Venon, C.L. Garrido Alzar, R. Geiger and A. Landragin, "Continuous Cold-atom Inertial Sensor with 1 nrad.s^{-1} Rotation Stability", Phys. Rev. Lett. **116**, 2016, 183003.

[3] J. Lautier, L. Volodimer, T. Hardin, S. Merlet, M. Lours, F. Pereira dos Santos, and A. Landragin, "Hybridizing matter-wave and classical accelerometers", Applied Physics Letters **105**, 2014, 14410.

Correction of laser wavefronts in an atom interferometer with a deformable mirror

Mehdi Langlois, Azer Trimeche, Sébastien Merlet, and Franck Pereira Dos Santos
SYRTE
Observatoire de Paris, PSL Research University, CNRS, Sorbonne Universités, UPMC Univ. Paris 06, LNE Paris, France
Email: franck.pereira@obspm.fr

***Abstract*—Wavefront aberrations are identified to be an important limit in the accuracy of cold atom interferometers based on two-photon transitions, such as gyroscopes, gravimeters and gradiometers. We used a MEMS deformable mirror to actively control the Raman laser wavefronts in an atom gravimeter and to compensate for the distortions induced by optical elements in a proof of principle experiment.**

I. INTRODUCTION

Atom interferometers, such as gravimeters, gradiometers [1,2,3,4,5] and gyroscopes [6,7], reach nowadays performances comparable, if not better, than classical sensors, which opens for them a large range of applications, ranging from fundamental physics, metrology, and navigation to geosciences [8,9,10]. These light-pulse atom interferometers allow to measure accelerations and rotations from the relative displacement of the atoms compared to the lasers' equiphases. In the best light-pulse atom interferometers, wavefront aberrations are identified and measured [11,12,13] as a major source of biais uncertainty and long term instability.

Similarly, in the field of astronomy, wavefront fluctuations arising from atmospheric turbulence limit the resolution of large area telescope. To overcome this problem deformable mirrors (DM) based on different technologies [14,15,16] have been proposed [17] and developed [18]. They are also used for the control of laser wavefronts [19,20].

In this work, we use for the first time this technology to control the interferometer laser wavefronts in an atom gravimeter, and demonstrate the possibility to efficiently correct for their aberrations.

II. THE EXPERIMENT

Our experiment is a cold atom gravimeter, described in [21] and [22]. The atoms are first trapped from a ^{87}Rb background vapor by a three dimensional magneto-optical trap (3DMOT) and cooled down with far detuned molasses down to 2 µK. They are then dropped in free fall and interrogated by a three Raman pulse sequence $\pi/2 - \pi - \pi/2$ which allows to split, deflect and recombine the atomic wave packets. This realizes a Mach-Zehnder-type interferometer. The gravimeter is obtained by pulsing counter-propagating laser beams in the vertical direction. Two co-propagating vertical laser beams are first overlapped and delivered through a single collimator. The counter-propagating beams are obtained by reflection on a bottom mirror (see figure 1). Due to the Doppler shift induced by the free fall of the atoms, only two counter-propagating beams will drive the stimulated Raman transitions according to the two-photon resonance condition.

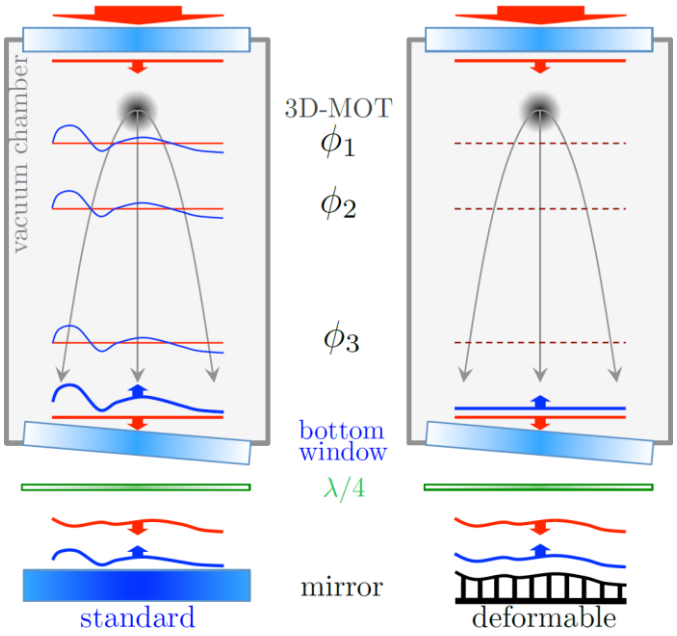


Fig. 1. Raman lasers propagation. We assume a flat descending wavefront (displayed in red), which gets reflected by a mirror. The ascending beam is represented in blue. The expansion of the free falling atomic cloud is represented in grey. Left: Standard mirror. Right: Deformable mirror. The wavefront distortions induced by the bottom optics is corrected by appropriately shaping the DM.

The interferometer phase is given by $\Delta\Phi = \phi_1 + \phi_2 + \phi_3$ [23], with ϕ_i the phase difference between the two Raman lasers, at the position z_i of the center of mass of the wavepacket, at the time of the i-th Raman pulse. For plane wavefronts, $\phi_i^p = k_{eff}.z_i$. This leads to $\Delta\Phi^p = -k_{eff}.g.T^2$ with k_{eff} the effective wave-vector, g the gravity acceleration, and T the free-evolution time between consecutive Raman pulses. Variations of the laser phase with respect to ϕ_i^p lead to bias on the measurement due to the expansion of the atomic cloud across the lasers wavefronts (see Fig. 1).

978-1-5386-2916-1/$31.00 ©2017 IEEE

III. CORRECTION OF WAVEFRONT ABERRATIONS

We demonstrate the possibility to use a DM for wavefront correction in a proof of principle experiment. We inserted a well characterized optical window above the mirror. The effect of this window onto the interferometer phase was first measured, and then corrected for by shaping the DM.

The results are displayed in figure 2. Reference *g* measurements, for T ranging from 20 ms to 50 ms are represented in black squares. They were performed without the additional window and using the DM in flat map (FM) configuration. The observed variation of the g value with T is due to two effects: two photon light shift [24] and aberrations. The same measurements, repeated with the window, are displayed in blue. The contrast decreased from 17% to 10% and the gravity changed by -1040(10) µGal (1µGal = 10^{-8} m/s^2) for T=50 ms. Then, the DM was shaped such as to compensate the distortions of the window, and a new set of measurements was performed (displayed in red). Good agreement was found with the reference g measurements (Fig. 2).

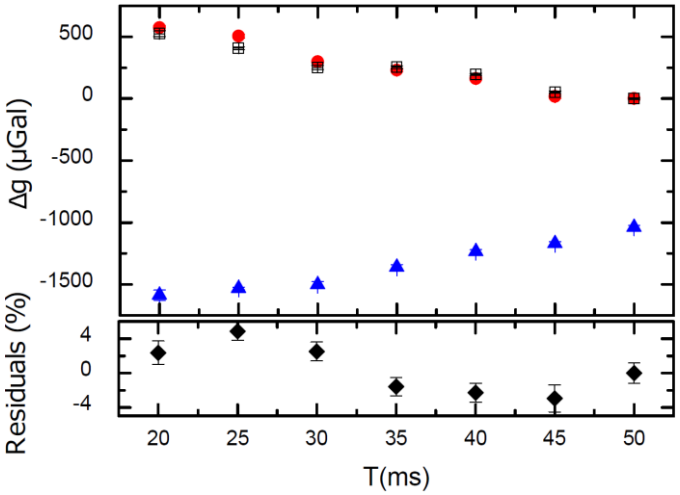


Fig. 2. Gravity measurements. Upper graph: Black open squares: with the deformable mirror (DM) in flat map configuration, without additional window. Blue triangles: with the additional window. Red circles: with the wavefront compensation by the DM. Bottom graph: Relative residuals after the compensation.

IV. CONCLUSION

We demonstrate the ability of a deformable mirror to correct for wavefront aberrations in an atomic gravimeter. This work opens new perspectives in the field of atom interferometry. Deformable mirrors could also be used to compensate for Earth rotation [25] and cancel vibrations [26], thanks to their fast and stable response.

ACKNOWLEDGMENT

This work is supported by CNES (R\&T R-S11/SU-0001-030). M. L. thanks Muquans for financial support. The authors thank A. Landragin for discussions and E. Cocher, C. Janvier, H. Bouchiba and M. Mazet for early contributions.

REFERENCES

[1] Z.-K. Hu, B.-L. Sun, X.-C. Duan, M.-K. Zhou, L.-L. Chen, S. Zhan, Q.-Z. Zhang, and J. Luo, Phys. Rev. A 88, 043610 (2013).

[2] P. Gillot, O. Francis, A. Landragin, F. P. D. Santos, and S. Merlet, Metrologia 51, L15 (2014).

[3] C. Freier, M. Hauth, V. Schkolnik, B. Leykauf, M. Schilling, H. Wziontek, H.-G. Scherneck, J. Müller, and A. Peters, Journal of Physics: Conference Series 723, 012050 (2016).

[4] J. M. McGuirk, G. T. Foster, J. B. Fixler, M. J. Snadden, and M. A. Kasevich, Phys. Rev. A 65, 033608 (2002).

[5] F. Sorrentino, Q. Bodart, L. Cacciapuoti, Y. H. Lien, M. Prevedelli, G. Rosi, L. Salvi, and G. M. Tino, Phys. Rev. A 89, 023607 (2014).

[6] T. L. Gustavson, A. Landragin, and M. A. Kasevich, Classical and Quantum Gravity 17, 2385 (2000).

[7] I. Dutta, D. Savoie, B. Fang, B. Venon, C. L. G. Alzar, R. Geiger, and A. Landragin, Phys. Rev. Lett. 116, 183003 (2016).

[8] J. B. Fixler, G. T. Foster, J. M. McGuirk, and M. A. Kasevich, Science 315, 74 (2007).

[9] G. Rosi, F. Sorrentino, L. Cacciapuoti, M. Prevedelli, and G. M. Tino, Nature 510, 518 (2014).

[10] R. Bouchendira, P. Cladé, S. Guellati-Khélifa, F. Nez, and F. Biraben, Phys. Rev. Lett. 106, 080801 (2011).

[11] A. Louchet-Chauvet, T. Farah, Q. Bodart, A. Clairon, A. Landragin, S. Merlet, and F. P. D. Santos, New Journal of Physics 13, 065025 (2011).

[12] V. Schkolnik, B. Leykauf, M. Hauth, C. Freier, and A. Peters, Appl. Phys. B 120, 311 (2015).

[13] M.-K. Zhou, Q. Luo, L.-L. Chen, X.-C. Duan, and Z.-K. Hu, Phys. Rev. A 93, 043610 (2016).

[14] S. Bonora, Optics Communications 284, 3467 (2011).

[15] D. A. Horsley, H. Park, S. P. Laut, and J. S. Werner, Sensors and Actuators A: Physical 134, 221 (2007).

[16] O. Cugat, S. Basrour, C. Divoux, P. Mounaix, and G. Reyne, Sensors and Actuators A: Physical 89, 1 (2001).

[17] H. W. Babcock, Publications of the Astronomical Society of the Pacific 65, 229 (1953).

[18] F. Merkle, P. Kern, P. L ena, F. Rigaut, J. C. Fontanella, G. Rousset, C. Boyer, J. P. Gaffard, and P. Jagourel, The Messenger 58, 1 (1989).

[19] L. A. Poyneer, B. Bauman, B. A. Macintosh, D. Dillon, and S. Severson, Opt. Lett. 31, 293 (2006).

[20] M. Kasprzack, B. Canuel, F. Cavalier, R. Day, E. Genin, J. Marque, D. Sentenac, and G. Vajente, Appl. Opt. 52, 2909 (2013).

[21] J. L. Gouët, T. E. Mehlstäubler, J. Kim, S. Merlet, A. Clairon, A. Landragin, and F. P. D. Santos, Appl. Phys. B 92, 133 (2008).

[22] S. Merlet, L. Volodimer, M. Lours, and F. P. D. Santos, Appl. Phys. B 117, 749 (2014).

[23] M. Kasevich and S. Chu, Phys. Rev. Lett. 67, 181 (1991).

[24] A. Gauguet, T. E. Mehlstäubler, T. Lévèque, J. L. Gouët, W. Chaibi, B. Canuel, A. Clairon, F. P. D. Santos, and A. Landragin, Phys. Rev. A 78, 043615 (2008).

[25] S.-Y. Lan, P.-C. Kuan, B. Estey, P. Haslinger, and H. Müller, Phys. Rev. Lett. 108, 090402 (2012).

[26] J. M. Hensley, A. Peters, and S. Chu, Rev. Sci. Instrum. 70, 2735 (1999)

Quality Factor and Phase Noise improvements in MEMS Resonators and Oscillators

K.L. Foster, B. Gibson, and K. R. Qalandar
Mechanical Engineering Department
University of California
Santa Barbara, CA
kfoster@engineering.ucsb.edu

G. Piazza, C. Cassella
Electrical Engineering Department
Carnegie Mellon University
Pittsburgh, PA

***Abstract*—Quality factor and phase noise are important figures for any resonator or oscillator. This presentation focuses on studies to address improvements in quality factor in bulk mode resonators, and phase noise in nonlinear flexural mode resonators. In bulk resonators, anchor loss can be a significant limitation on quality factor, especially for resonators in the MHz range. This paper presents an informed study on anchor loss in bulk resonators, and demonstrates how proper anchor design can improve resonator performance. In flexural resonators, nonlinear effects have often been avoided due to amplitude dependence on frequency. However, it has been previously shown that nonlinear effects can improve phase noise performance of resonators. Here, we demonstrate a cascade of parametrically driven resonators that functions as a purely mechanical frequency divider, and also demonstrates improved phase noise performance over identical linear resonators.**

Keywords—nonlinear dynamics; MEMS; microsystems; quality factor; phase noise; oscillator; resonator

I. Introduction (Bulk Mode Resonators)

Piezoelectric contour-mode resonators (CMRs) have shown great promise due to their high electro-mechanical coupling coefficients, their ability to reach frequencies in excess of 2 GHz and the ability to set their frequency in CAD, allowing multiple device frequencies to be fabricated on the same chip [8, 9]. One of the limiting factors for the integration of CMRs is their relatively low quality factors. Quality factors as high as 4000 have been reached [1,2] which is still an order of magnitude lower than traditional quartz crystal-based resonators. In an effort to maximize the device Q of CMRs, extensive research has been conducted in setting the electrode size and placement [3], inactive region dimensions [8], and anchor dimensions [4]–[7]. The latter two areas are particularly relevant in that, [5], [6] have shown that, below 500MHz, anchor loss is a major source of damping in piezoelectric CMRs.

Yet to be considered is how Q is affected by the substrate region beyond the anchor attachment points. In many numerical models, material beyond the anchor is often considered to be rigid. Often, an isotropic etch process is often used to release the device from the substrate [2]. This etch causes additional material to be etched below the anchor, causing a more flexible transition region between the resonator and the substrate (Figure 1).

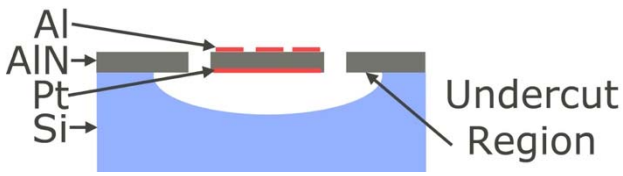


Figure 1. Side view of CMR showing the undercut region created by the isotropic release etch

II. Results (Bulk Mode Resonators)

Systematic measurements of mechanical displacements during bulk mode excitation are possible with a Polytec UHF-120 Laser Doppler Vibrometer (LDV) system. Out of plane velocity measurements are taken with the LDV across the entire resonator, including the anchor. These are compared with COMSOL simulation of the devices. In order to study the effects of the released area anchoring the devices, the release area had to be varied. This was done in the following manner: First, the device was released, and it's displacement was mapped using the LDV. Then, it was etched further, to increase the release area, and measured again. This was repeated for multiple cycles. Measurements included frequency and quality factor.

Figure 2 shows the results of release area on quality factor. Note that there is variation from device to device, but all devices demonstrate the same trend. It is clear that each resonator has an optimal release distance. This effect has been modeled by transmission line theory in [8] and [9]. The talk will explore this effects with modeling and further experimental results.

This work was supported by NSF grant 442550-22031-FGKT10-2 and CMU/DAPPA grant 8-442550-59085-FGKT11-2

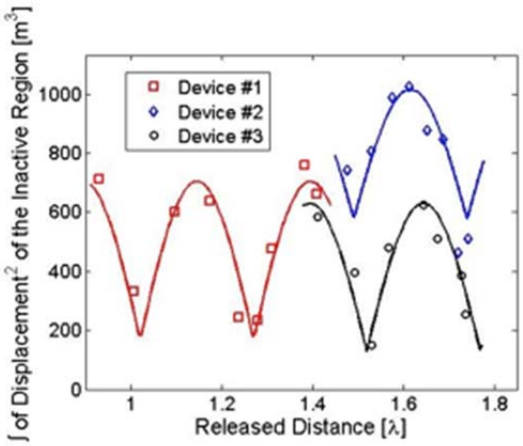


Figure 2. An "energy-like" figure of merit vs. release distance, showing the strong dependence of energy loss vs. release distance.

III. Introduction (Flexural Mode Cascade)

In contrast to the contour mode resonators (CMR) discussed above, which are often extremely stiff and linear, flexural mode resonators can often demonstrate significant nonlinear performance. These nonlinear effects can be both challenging and interesting. In this second half of the presentation, the effects of nonlinearity on phase noise will be discussed in the context of a MEMS frequency converter.

Frequency converters are devices that take an input frequency and change it into another frequency at the output. They are used in spread spectrum communication systems, signal synthesizers, mixers, clock generators, and sensors.

There are several examples in the literature of ways in which to exploit nonlinear phenomenon through novel design of resonator structure to improve the phase noise of MEMS resonators. Other examples of using nonlinear behavior in the resonator to improve phase noise include coupling between resonators [10], internal resonance between modes [11], parametric feedback, operating at a critical point in the nonlinear regime [12], or through appropriate feedback mechanisms. Another approach involves exploiting nonlinearities or the performance enhancement of coupled resonators in arrays. Villanueva et al. show in [12] that it is possible to improve device performance by operating the resonator at special points in the nonlinear regime and thereby reducing the phase noise below that seen in the linear regime.

Parametric resonance, the phenomenon upon which the device in this work is based, has been shown to improve signal from resonators. [13] shows that parametric amplification in a MEMS gyroscope reduces the noise associated with the desired vibrational mode with a greater than twofold increase in the signal to noise ratio. In [14], a high quality factor wine-glass disk array utilizes parametric resonance to generate a 61MHz output signal from a 121MHz input signal, with a 6 dB close-to-carrier phase noise reduction and a 23 dB reduction in far from carrier noise. [15] also uses a parametric actuation scheme to reduce phase noise, and [16] demonstrates a parametrically actuated double-clamped beam which shows improved phase noise characteristics over a traditionally operated device. Evidence from literature suggests that the short-term stability of a particular resonance mode should improve when it is operated in parametric resonance.

IV. Results (Flexural Mode Cascade)

In this work, a 4 stage parametrically driven cascade is presented. A schematic of the device is shown in Figure 3. The phase noise of neighboring stages 2 and 3 were measured. Figure 4 shows the noise performance of two stages in a cascaded frequency divider both when driven individually, and when parametrically cascaded to reduce noise performance.

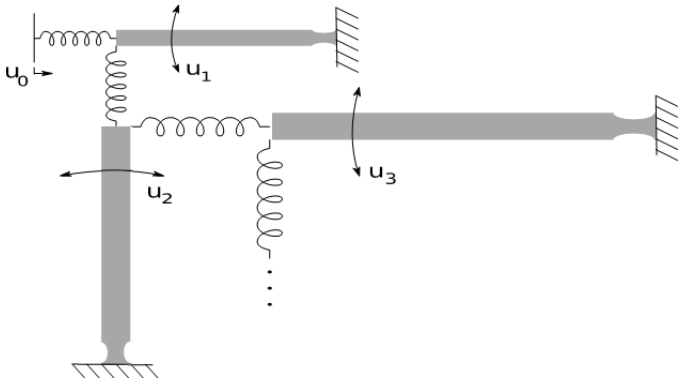


Figure 3. Schematic of a flexural resonant cascade. uo is the input stage, and it's resonance drives u1, u1 drives u2, and u2 drives u3.

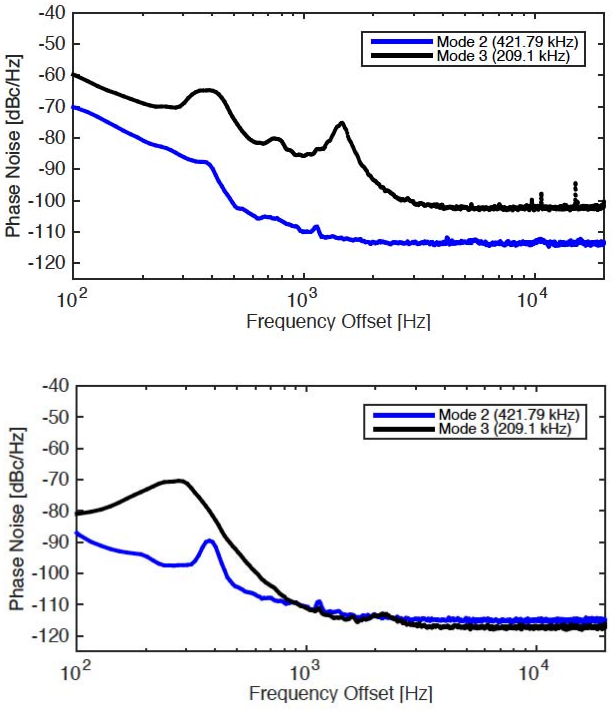


Figure 4. Demonstration of reduction in phase noise in a parametric resonance cascade. The top figure is the phase noise performance of each mode driven linearly, and the bottom figure is the performance when mode 3 is driven by mode 2. Note the reduction in phase noise of mode 3.

References

[1] G. Piazza, P. J. Stephanou, and A. P. Pisano, "One and two port piezoelectric higher order contour-mode MEMS resonators for mechanical signal processing," *Solid-State Electronics*, vol. 51, no.

1112, pp. 1596 – 1608, 2007, special Issue: Papers Selected from the 36th European Solid-State Device Research Conference - ESSDERC06. [Online].http://www.sciencedirect.com/science/article/pii/S0038110107003413

[2] Y. Xu, R. Wang, S. K. Durgam, Z. Hao, and L. Vahala, "Numerical models and experimental investigation of energy loss mechanisms in soi-based tuning-fork gyroscopes," *Sensors and Actuators A: Physical*, vol. 152, no. 1, pp. 63–74, 2009I. S. Jacobs and C. P. Bean, "Fine particles, thin films and exchange anisotropy," in Magnetism, vol. III, G. T. Rado and H. Suhl, Eds. New York: Academic, 1963, pp. 271–350.

[3] M. Giovannini, S. Yazici, N.-K. Kuo, and G. Piazza, "Spurious mode suppression via apodization for 1 GHz AlN contour-mode resonators," in *Frequency Control Symposium (FCS), 2012 IEEE International*. IEEE, 2012, pp. 1–5.

[4] R. Ruby, P. Bradley, J. D. Larson, and Y. Oshmyansky, "PCS 1900 MHz duplexer using thin film bulk acoustic resonators (fbars)," *Electronics Letters*, vol. 35, no. 10, pp. 794–795, May 1999.

[5] K. E. Wojciechowski, B. E. Boser, and A. P. Pisano, "A MEMS resonant strain sensor operated in air," in *Micro Electro Mechanical Systems, 2004. 17th IEEE International Conference on. (MEMS)*, 2004, pp. 841– 845.

[6] C. T. Nguyen, "High-Q micromechanical oscillators and filters for communications," in *Circuits and Systems, 1997. ISCAS'97., Proceedings of 1997 IEEE International Symposium on*, vol. 4, 1997, pp. 2825–2828.

[7] M. Giovannini, S. Yazici, N.-K. Kuo, and G. Piazza, "Spurious mode suppression via apodization for 1 GHz AlN contour-mode resonators," in *Frequency Control Control Symposium (FCS), 2012 IEEE International. IEEE, 2012, pp. 1–5.*

[8] C. Cassella, S. Navab, B. W. Soon, and G. Piazza, "Quality factor dependence on the inactive regions in AlN contour-mode resonators," *Journal of Microelectromechanical Systems*, p. to be published, 2015.

[9] B. Harrington and R. Abdolvand, "In-plane acoustic reflectors for reducing effective anchor loss in lateral extensional MEMS resonators," *Journal of Micromechanics and Microengineering*, vol. 21, no. 8, p. 085021,2011

[10] S. Lee and C. T-C. Nguyen, "Mechanically-coupled micromechanical resonator arrays for improved phase noise," in Frequency Control Symposium and Exposition, 2004, Proceedings of the 2004 IEEE International Frequency Control, PP. 144-150. , 2004.

[11] D. Antonio, D. Zanette, and D. Lopez., "Frequency stabilization in nonlinear micromechanical oscillators," Nature Communications, vol. 3, P. 806, 2012.

[12] L. Villanueva, E. Kenig, R. Karabalin, M. Matheny, R. Lifshitz M. Cross, M. Roukes, "Surpassing Fundamental Limits of Oscillators Using Nonlinear Resonators," Physical Review Letters, vol. 110, P. 177208 2013.

[13] M. Sharma, E. Sarraf, R. Baskaran, E. Cretu, "Parametric Resonance Amplification and Damping in MEMS gyroscopes," Sensors & Actuators A: Physical, vol. 177, pp. 79-86, 2012.

[14] T. Rocheleau, R. Liu, J. Nilchi, T. Naing, and C.-C. Nguyen, \A micromechanical parametric oscillator for frequency division and phase noise reduction," in Micro Electro Mechanical Systems (MEMS), 2014 IEEE 27th International Conference on, pp. 210{213, Jan 2014.

[15] E. Kenig, M. C. Cross, R. Lifshitz, R. B. Karabalin, L. G. Villanueva, M. H. Matheny, and M. L. Roukes, \Passive phase noise cancellation scheme," Phys. Rev. Lett., vol. 108, p. 264102, Jun 2012.

[16] L. G. Villanueva, R. B. Karabalin, M. H. Matheny, E. Kenig, M. C. Cross, and M. L. Roukes, "A nanoscale parametric feedback oscillator," Nano Letters, vol. 11, no. 11, 5054-5059, 2011.

Lowering Motional Resistance by partially HfO_2 gap filling in Double-Ended Tuning Fork MEMS resonators

Mariazel Maqueda López, Emanuele A. Casu, Adrian M. Ionescu and Montserrat Fernández-Bolaños
Nanoelectronic Devices Laboratory (NanoLab)
École Polytechnique Fédérale de Lausanne, EPFL
Lausanne, Switzerland

***Abstract*—This paper reports a 80nm air gap double-ended tuning fork (DETF) resonator partially filled with 20nm of HfO_2. The device operates at 10.7 MHz with a quality *Q*-factor of 7930 and a motional resistance, R_m, x18 better than for the measured counterparts in air-gaps. An enhancement of the S_{21} transmission signal of 6dB in addition to the reduction of the R_m have been achieved thanks to the improvement of the electromechanical coupling factor by partially filling the electrode-to-resonator-gap with an atomic layer deposition (ALD) of 20nm of HfO_2 high-k dielectric (ε_r~19). This result proves an outstanding enhancement in the detection signal while keeping all the desired properties of flexural resonators for future mechanical sensing applications.**

***Keywords*—Microelectromechanical, MEMS, resonators, double-ended tuning fork, quality factor, *Q*-factor, motional resistance, partially-filled gap, Hafnium Oxide, HfO_2, ALD.**

I. Introduction

Silicon-based micro-electro Mechanical Systems (MEMS) resonators have been widely studied thanks to their small size, and CMOS compatibility. Flexural resonators are of greater interest for mixing, filtering and sensing applications (i.e. strain or pressure sensors [1]). Particularly, double-ended tuning fork (DETF) resonators are a desirable approach due to their favorable stress-sensitive dynamically balanced structures [1]. Capacitive transduction has achieved the highest Q's in addition to be most convenient solutions for chip implementation and to drive and detect the mechanical resonance [2]. The electromechanical coupling efficiency in converting velocity to current diminishes inversely with the second power of the gap. In the same way, as the gap thickness is limited by the technology, motional resistance, R_m, usually results very large. Therefore, to overcome the losses due to the mismatch of R_m and the added feedthrough capacitance, extreme narrow gap solutions were reported [3-4] with the drawback of a greater fabrication complexity. On the other hand, in order to reduce the air gap, this could be filled up with a solid high-*k* dielectric [5]. Nevertheless, such an approach was suitable for lateral extensional bulk-mode resonators due to its high mechanical stiffness [2].

In this paper we report for the first time 100nm air-gap DETF resonators partially filled with HfO_2 (20nm). A remarkable improvement in the capacitive coupling is achieved by direct S_{21} transmission measurements as well as a R_m reduction in comparison with their counterparts in air.

This work has been supported by the Swiss National Science Foundation (Grant No. 144268)

II. DETF Design And Characterization

The DETF was designed and fabricated in a SOI wafer (1µm buried oxide) with 40µm length (*l*), 3µm width (*w*), 1µm thickness and different electrodes-to-resonator-gaps (*g*) of 100, 300 and 500nm (Fig. 1).

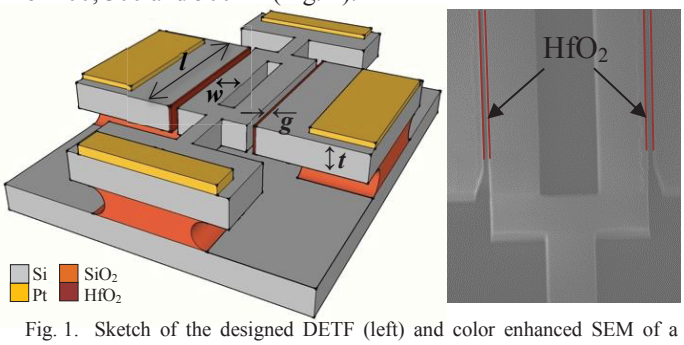


Fig. 1. Sketch of the designed DETF (left) and color enhanced SEM of a DETF after fabrication (l = 40 µm; w = 3 µm; t = 1 µm; g = 500 nm).

The electrical characterization of the DETF resonators before and after ALD was performed in vacuum (<10^{-5}mbar). Fig. 2 shows the frequency characteristics of the 100nm air gap DETF resonator partially filled with 20nm ALD HfO_2 at different RF signal powers. The resonance frequency shifts from 10.95MHz to 10.7MHz. when applying different DC bias. A *Q*-factor of 7930 was achieved at 60V and -30dBm. A capacitive nonlinearity starts to be observable for values over -20dBm, suggesting a spring softening. For strong nonlinear behavior, the transmission peak decreases strongly and shifts towards lower frequencies showing a bifurcation of the frequency-amplitude relation. Fig. 3 gives a comparison of the two-port direct S_{21} transmission measurements for DETF devices with air and air+HfO_2 gaps. The results for the same structures before (top) and after the ALD (bottom) depict that the partially-filled gaps resonators overperform their previous response with air-gaps, showing a detection enhancement of more than 6dB. After the ALD, resonance frequency shift down showing that the HfO_2 loaded mass plays a more

important role in the resonance modulation than the eventual stiffening of the fork coming from the high-*k* HfO_2.

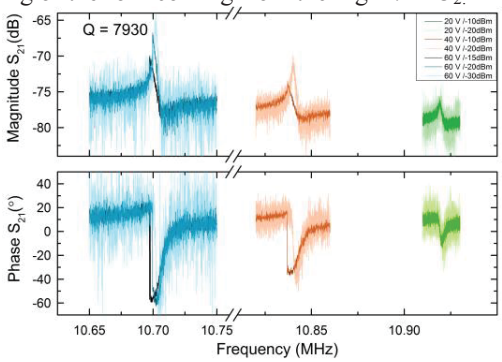


Fig. 2. Frequency characteristics in magnitude and in phase for a DETF 80nm air/ partial-filled 20nm HfO_2 gap at different DC/RF applied signals.

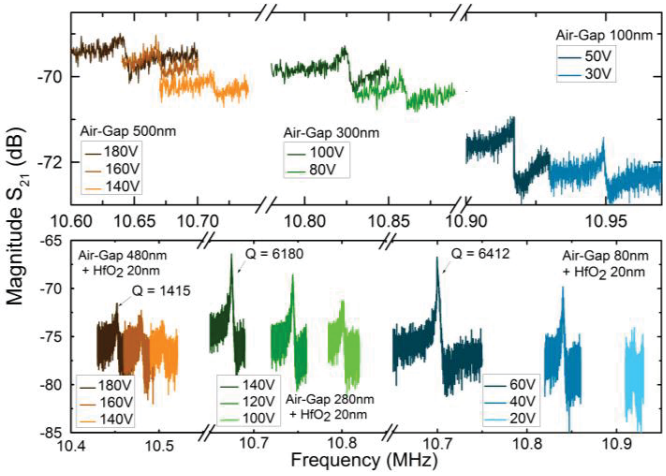


Fig. 3. Comparison of the transmission characteristics for different air-gaps before (top) and after partially fill them with 20nm of ALD HfO_2 (bottom) for different DC bias.

Table 1 shows the extracted parameters of *Q*-factor and R_m for different air and partially filled gaps. R_m was calculated from the effective mass and the extracted spring constant of the structure (k_r = 50.52-52.43N/m). A remarkable reduction in R_m (x18 better) is achieved for the 80nm air+20nm HfO_2 gaps. This outcome results in better impedance matching to the typical 50Ω impedances of electronic systems for eventual applications on chip than their counterparts in air. An apparent enhancenment of the *Q*-factor was observed, nevertheless it will be study more in depth for other consequtive HFO_2 ALD. A comparison between vacuum (<10^{-5} mbar) and ambient conditions was performed (Fig. 4). Partially-filled HfO_2 gaps performs better than air gaps suggesting a potencial enhanced detection for atmospheric operation. In addition, the frequency shift *versus* applied voltage (sensing resolution) remains as good as for air-gap flexural mode DETF (Fig. 5).

TABLE I. COMPARISON OF THE CHARACTERISTIC PARAMETERS

	Gap size (nm)	V_{bias} *(V)*	*Q*	R_m
Air-Gap	500	180	901[a]	1'377 kΩ
	100	50	1459[a]	30'023 Ω
Partially filled gap	80(air)+20(HfO_2)	60	7930	1'638 Ω

a. Extracted from the phase slope approximation $Q = f_r \cdot \pi/360 \cdot d\theta/d\omega$

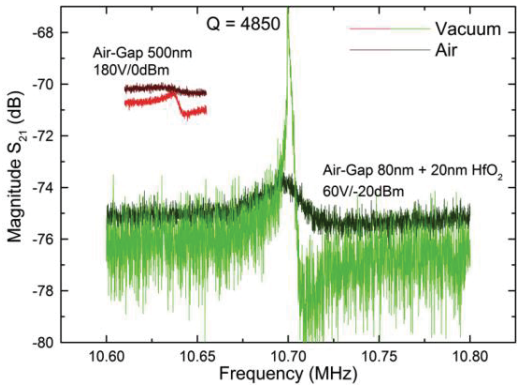


Fig. 4. Frequency characteristics of air-gap versus partially-filled HfO_2 gaps coating both measured in air and vacuum (< 10^{-5}mbar) conditions.

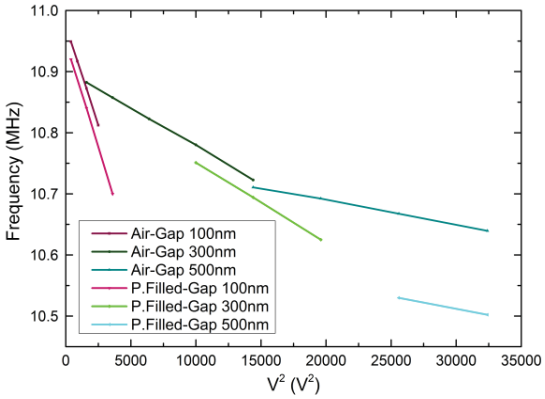


Fig. 5. Frequency versus the square applied voltage for different air and filled gaps thicknesses.

III. CONCLUSIONS

For the first time, capacitively transduced double-ended tuning fork (DETF) resonators operating in lateral flexural mode at 10.7MHz with partially-filled HfO_2 gaps have been reported, featuring amplified signal detection and a reduction 18x of the R_m in comparison with their air counterparts. This improvement enables direct transmission measurement and suggest an interesting solution operating at high frequency for mechanical sensing applications.

REFERENCES

[1] W. Zhang, H. Zhu and J. Lee, *IEEE Trans. Electron Dev.* vol. 62, pp. 1596–602, 2015.

[2] L.-W. Hung, Z. A. Jacobson, Z. Ren, A. Javey, and C. T.-C. Nguyen, *Tech. Digest, Solid-State Sensor, Actuator, and Microsystems Workshop*, pp. 208-211, 2008.

[3] Naghsh Nilchi, R. Liu, and C.T.-C. Nguyen, *IEEE 30th International Conference on Micro Electro Mechanical Systems (MEMS)*, 2017.

[4] J. Kiihamäki, V. Kaajakari, H. Luoto, H. Kattelus, and M. Yli-Koski, in *Proc. 13th Int. Conf. Solid-State Sensors, Acttuat. Microsyst. (TRANSDUCERS)*, pp. 1354-1357, 2005.

[5] M. Maqueda Lopez, E.A. Casu, W.A. Vitale and A.M. Ionescu, *Silicon Nanoelectronics Workshop (SNW)*, 2016.

[6] M. Maqueda Lopez, M. Fernandez-Badia, W.A. Vitale and A.M. Ionescu, *Microelectron. Eng.*, vol. 145, pp. 53-57, 2015.

Orders of Magnitude Reduction in Acoustic Resonator Simulation Times via the Wide-Band Rapid Analytical-FEA Technique

Jonathan M. Puder
OxideMEMS Lab
Cornell University
Ithaca, USA

Jeffrey S. Pulskamp, Ryan Q. Rudy, and Ronald G. Polcawich
Sensors and Electron Devices Directorate
US Army Research Laboratory
Adelphi, USA

Sunil A. Bhave
OxideMEMS Lab
Purdue University
West Lafayette, IN

***Abstract*— Spurious mode excitation is one of the largest obstacles towards the widespread adoption of piezoelectric MEMS resonator technology. This is in large part due to the lack of a wide-band and computationally efficient simulation solution to model the frequency response of complex 3D geometries. This paper presents the results from a solution to this problem: the Rapid Analytical/FEA Technique (RAFT). The RAFT combines the accuracy of FEA with the speed of analytical evaluation. For simulations with similar total degrees of freedom and frequency resolution, the RAFT simulation completes approximately 2,300 times faster than traditional FEA while accurately predicting the behavior of hundreds of spurious modes. The approach of the RAFT allows the use of FEA as an efficient design tool, rather than analysis tool, for in- and far-band spurious modes.**

Keywords— MEMS, Acoustic Resonator, Motional Resistance

I. INTRODUCTION (*Heading 1*)

Contour piezoelectric MEMS resonators are an attractive technology for next generation front-end radio frequency filters. They offer lithographically defined frequencies in an area-efficient footprint. However, contour piezoelectric MEMS resonators have not seen widespread adoption due in large part to spurious mode problems, which degrade resonator response.

Several efforts have been made to address spurious mode problems [1,2,3]. These modeling and design efforts have been restricted to frequencies near the intended mode, or restricted by material, mode type, or geometry. This is primarily due to simulation techniques and limited computational power. Full 3D multiphysics frequency domain sweeps in FEA packages can take a minimum of days to complete. Consequently, many designers resort to 2D simulations. These simulations often miss important out of plane behavior. Clearly, the community requires a 3D, rapid, broad frequency, computationally efficient solution for resonator simulation to enable design for spurious mode mitigation. Accordingly, this paper will present results from the Rapid Analytical/FEA Technique (RAFT). The RAFT simulation accurately predicts the scattering (S) parameters across a wide frequency span orders of magnitude faster than traditional FEA packages. These advantages will enable designers to predict the presence and severity of spurs in a time efficient manner. The devices in this paper are PZT-based, two-port, low frequency, contour mode resonators. However, the RAFT is capable of modeling a variety of resonant systems, such as gyroscopes, oscillators, ultrasonic motors, etc. The systems could be one-port, higher frequency, non-contour (e.g. thin-film bulk acoustic resonators (FBAR)) or non-PZT based.

II. METHOD

The well-known modified Butterworth van-Dyke (mBVD) model is the foundation of this technique. Each "motional" path, consisting of a motional inductance, resistance (R_m), and capacitance, represents the behavior of a single mode. These elements are electrical representations of the lumped resonator mass, spring, and damper. To arrive at the lumped mass and spring, the kinetic and elastic energies of the lumped and continuous resonator systems are compared. The damping is found by assuming or measuring mechanical quality factor (Q_m). Placing motional arms in parallel, as in Fig. 1, superimposes the modes to obtain the frequency response of the resonator.

While the mBVD model is not new, its wide-band design capabilities have not been fully utilized. Until now, a general expression for the modal force, and subsequently the R_m, of the resonator, of an arbitrary mode of an arbitrary resonator did not exist. This is the enabling breakthrough of this simulation technique, and is achieved by comparing elastic energies in the real and lumped systems. By comparing energies, the need for a specific expression for force or strain is eliminated. The closed form expression for R_m separates the simulation of the

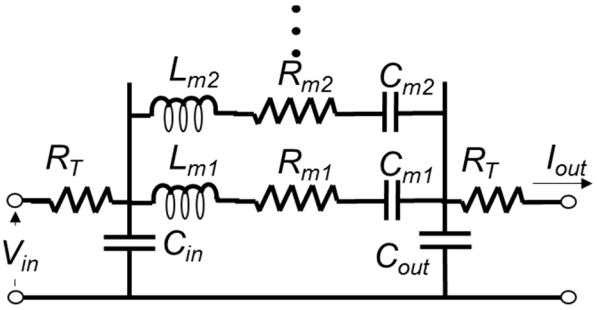


Fig. 1. The mBVD for a single resonator with multiple mechanical modes.

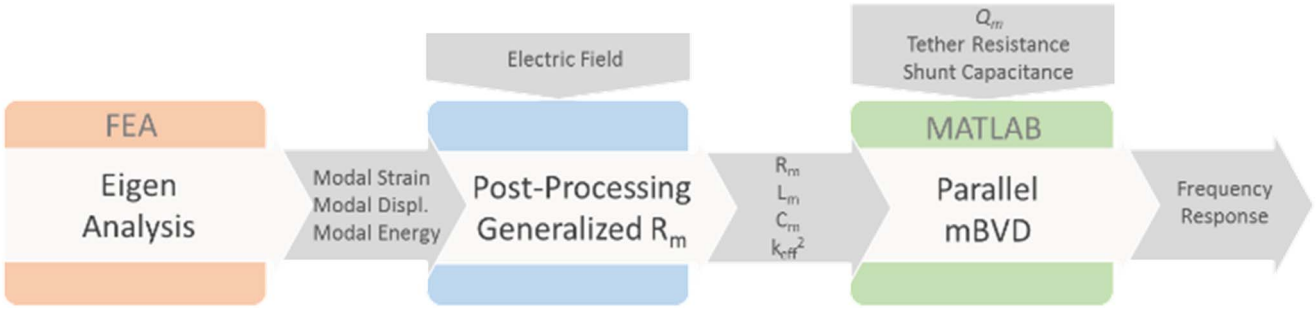


Fig. 2. Overview diagram for the RAFT

mechanical and piezoelectric domains for low-moderate coupling resonators. The complex mode shape, modal energy, and strain may be obtained from relatively fast Eigen frequency simulations. This information is then processed by an analytical software package. After assigning Q_m, the motional parameters of each mode are returned. The full S parameters are then calculated based on R_m, Q_m, and material properties. An overview of this process is presented in Fig. 2.

The closed form expression for R_m is given by

$$R_m = \frac{k_m}{Q_m \omega_n \left| \int_{V_{in}} \boldsymbol{e}^t \cdot \nabla\overline{\phi} \cdot \boldsymbol{S}_n dV \int_{V_{out}} \boldsymbol{e}^t \cdot \nabla\overline{\phi} \cdot \boldsymbol{S}_n \, dV \right|} \quad (1)$$

Where k_m is the modal spring, ω_n is the natural frequency, V_{in} refers to the volume of the piezoelectric material affected by the input port's electric field, e is the piezoelectric coefficient matrix, S_n is the six dimensionalcompressed strain vector in Voigt's notation derived from a unity normalized mode shape, $\overline{\phi}$ is the unity normalized vector field, and A_{out} is the area of the electrode on the output port. For the devices in this paper, the electrodes may be approximated as perfect parallel plate capacitors with electric field in the 3 direction. Additionally, the electrodes are symmetric along the device midplane defined by a vector orthogonal to the tethers and surface of the wafer. Using these assumptions, (1) reduces to

$$R_m = \frac{k_m}{Q_m \omega_n \left(\int_{A_{el}} \boldsymbol{e}_{3i} \cdot \overline{\boldsymbol{S}}_n d\boldsymbol{A} \right)^2} \quad (2)$$

Where $\overline{S}_n$ is the strain in the piezoelectric layer average through the thickness. This is the expression used in the RAFT for resonators with parallel plate electrodes. A mechanical Eigen analysis will return the total energy of the system. After equating the potential energies of the lumped and continuous resonators, a value for k_m is reached. A modal displacement must be chosen to define the modal spring relative to, and is chosen to be the point of largest displacement for each mode. ω_n and the strain may be taken directly from and FEA, and the e matrix is a material property. Finally, a value for the Q_m must be assumed or chosen. Values for L_m and C_m may then be calculated by the definition of Q_m using electrical equivalent parameters, which for parallel plate electrodes are

$$L_m = \frac{m_m}{\left(\int_{A_{el}} \boldsymbol{e}_{3i} \cdot \overline{\boldsymbol{S}}_n d\boldsymbol{A} \right)^2} \quad (3)$$

$$C_m = \frac{\left(\int_{A_{el}} \boldsymbol{e}_{3i} \cdot \overline{\boldsymbol{S}}_n d\boldsymbol{A} \right)^2}{k_m} \quad (4)$$

Where m_m is the modal mass. The parameters for the motional path are now known. The tether resistances and shunt capacitances then must have their values set, and the system may be simulated.

The effective electromechanical coupling factor may be calculated now. Using (1), the most general form is

$$k_{eff}^2 = \frac{1}{\frac{C_0}{C_m} + 1} = \frac{1}{\frac{k_m C_0}{\left| \int_{V_{in}} \boldsymbol{e}^t \cdot \nabla\overline{\phi} \cdot \boldsymbol{S}_n dV \int_{V_{out}} \boldsymbol{e}^t \cdot \nabla\overline{\phi} \cdot \boldsymbol{S}_n \, dV \right|} + 1} \quad (5)$$

Using the parallel plate assumption turns (5) into

$$k_{eff}^2 = \frac{1}{\frac{k_m C_0}{\left| \int_{A_{in}} \boldsymbol{e} \cdot \overline{\boldsymbol{S}}_n \, dA \int_{A_{out}} e \cdot \overline{\boldsymbol{S}}_n dA \right|} + 1} \quad (6)$$

For one port resonators, C_o is the shunt capacitance. For two port resonators, C_o is found by placing the two shunt capacitors in parallel to create an effective one port resonator.

III. Results

The model was validated against resonators fabricated in PZT-on-Silicon process [4]. The material stack consists of 1 µm buried silicon dioxide, 10 µm of silicon, 300 nm of silicon dioxide, 125 nm of platinum, 0.5 µm of PZT, and 50 nm of platinum. A ZVB-8 network analyzer terminated to 50Ω and calibrated using a through, short, open, and load standard (GGB CS-5) was used to measure the resonator's S parameters. One resonator was designed to optimally excite the (1,1) mode of

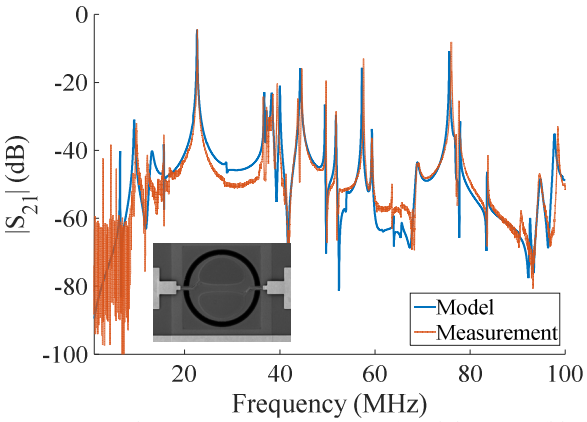


Fig. 3. Agreement between measurement (orange) and the RAFT (blue) for a disk resonator (inset). There were 103 modes in this bandwidth. The plotted resonator data was mathematically terminated to 300 Ω.

transverse disk flexure [5,6] (Fig. 2), which has shown an insertion loss of -1 dB in recent a recent publication[7,8]. The other was designed for beam length extension (Fig. 2), a commonly utilized mode.

Measured properties and designed geometries were used in the model simulations. Elastic moduli of the materials in the PZT-Silicon stack were independently measured [9]. The e_{31} values in the model fell within a range extracted from cross-wafer cantilever test structures. Densities were taken to be bulk values. Geometric dimensions from CAD were decreased for frequency agreement, resulting in a 0.5 µm decrease in disk radius and beam width, which is within fabrication tolerance. mBVD values for the shunt capacitor and tether resistances were extracted from S parameter measurements by analyzing the frequency response away from resonance.

The disk flexure device was measured from 1 to 100 MHz, with the designed mode at 20.65 MHz. The comparison between the measured and predicted S parameters may be seen in Fig. 3. The RAFT model was able to accurately predict the device behavior across the bandwidth. The spurious modes in this simulation had measured and fitted Q_m ranging from 50 to 1700. Some modes had fitted Q_m due to measurement difficulty from loss or frequency spacing. Across the lowest loss modes, the error in predicted S_{21} at resonance was 1.5 dB.

The measurement on the beam extension device was taken from 1-80 MHz, with the designed mode at 20.7 MHz. Agreement between measurements and the results from the analytical-FEA technique is presented in Fig. 2. Fitted and measured Q_m for the beam ranged from 50 to 1500, and average error between measure and model across the lowest loss peaks was 1.8 dB.

The time from simulation start to generation of S parameters for the disk was 11.7 minutes. The total number of degrees of freedom was ~460,000. In this frequency span there were 103 modes. The beam had a total of 345,000 degrees of freedom, which took 9.9 minutes to simulate. There were 247 modes in the frequency range simulated.

To illustrate the speed of this method, a full multiphyics simulation was run in COMSOL. While simulating the same

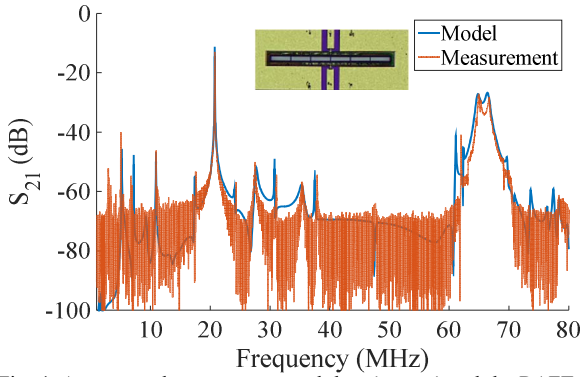


Fig. 4. Agreement between measured data (orange) and the RAFT (blue) for a beam extension resonator (inset). There were a total of 257 modes in this frequency span.

frequency span would take a prohibitively long time, several shorter runs were performed, and the results were linearly extrapolated for comparison. Table 1 compares the time (t_{COMSOL} and t_{RAFT}) to simulate a 99 MHz frequency span with various point densities for models with 460,000 degrees of freedom. For context, a frequency resolution of 1 kHz would place approximately 35 points in the bandwidth of the intended mode of Fig. 1 at 20 MHz.

TABLE I. SIMULATION TIMES FOR 99 MHZ BANDWIDTH

Points	*(Frequency Points/MHz)*	*Frequency Resolution*	*COMSOL Simulation Time*	*RAFT Simulation Time*	t_{COMSOL}/t_{RAFT}
9900	100	10 kHz	~10d 5h 30m	11.7m	1259
49500	500	2 kHz	~54d 10 h	11.7m	6697
99000	1000	1 kHz	~112d 7h	311.7m	13820

IV. DISCUSSION

There are several advantages to this approach to simulation in the context of spurs. First, all simulations may be performed in full 3D with high mesh densities, capturing out of plane behavior and complex behavior such as tether response. Secondly, it may be used as a design tool to parametrically explore how design parameters affect spurs far away from the intended mode. Third, commercially available methods scale linearly with the number of frequency points, since full equations of state must be solved at every point. The RAFT simulation method scales with the number of modes, which is advantageous in contour resonators where there are many modes which are electrically detectable. Additionally, modal information is directly available to analyze the contribution of particular modes to the response. This allows designers to debug spurious modes and intelligently design around them.

The simulations in this paper were low frequency and utilized capacitors that could be approximated as parallel plate. In higher frequency topologies, such as devices with interdigitated electrodes, it may be desirable to simulate t he electrical field in a separately, which would slightly increase the simulation time. However, the R_m equation presented in this paper and the resulting methodology have been generalized for

arbitrary modes in arbitrary geometries and materials, and can provide significant decrease in simulation times. This will decrease reliance on expensive parametric fabrication, make FEA a viable tool for pre-fabrication analysis, enable wide band spurious mode design, allow designers to explore novel high-coupling modes.

REFERENCES

[1] M. Giovannini, et al., "Spurious mode suppression via apodization for 1 GHz AlN Contour-Mode Resonators," *2012 Proc. IEEE Intl. Freq. Cont. Symp.*

[2] R. H. Olsson, et al., "Origins and mitigation of spurious modes in aluminum nitride microresonators," *2010 IEEE Intl. Ultrasonics Symp*.

[3] A. Gao and S. Gong, "Harnessing Mode Conversion for Spurious Mode Suppression in AlN Laterally Vibrating Resonators," in *J. of Microelectromech. Syst.*, vol. 25, no. 3.

[4] Pulskamp, J.S., et. al. (2012). "Electrode-shaping for the excitation and detection of permitted arbitrary modes in arbitrary geometries in piezoelectric resonators." *IEEE Trans. Ultrason., Ferroelect., Freq. Control*.

[5] Pulskamp, Jeffrey S., et al. "Ferroelectric PZT RF MEMS resonators." Frequency Control and the European Frequency and Time Forum (FCS), 2011 Joint Conference of the IEEE International. IEEE, 2011.

[6] Bedair, S. S., et al. "Thin-film piezoelectric transformers operating in harmonics of out-of-plane flexure modes." Solid-State Sensors, Actuators and Microsystems (TRANSDUCERS), 2015 Transducers-2015 18th International Conference on. IEEE, 2015.

[7] Rudy, R.Q, et al.(2016). Piezoelectric Disk Flexure Resonator with 1 dB Loss. *2016 Proc. IEEE Intl. Freq. Cont. Symp*.

[8] Pulskamp, Jeffrey S., et al. "Ferroelectric PZT MEMS HF/VHF resonators/filters." Frequency Control Symposium (IFCS), 2016 IEEE International. IEEE, 2016.

[9] Yagnamurthy, S., et. al. (2011). "Mechanical and Ferroelectric Behavior of PZT-Based Thin Films." *J. of Microelectromech Syst.,* vol. 20, no. 6.

Absolute frequency measurement of the electric quadrupole transition of $^{88}Sr^{+}$

Pierre Dubé, John E. Bernard and Marina Gertsvolf
National Research Council Canada
Ottawa, Ontario, Canada, K1A 0R6
Email: pierre.dube@nrc-cnrc.gc.ca

***Abstract*—We report a new measurement of the 445 THz electric quadrupole transition of the strontium ion made using a GPS link to the SI second. Compared to our previous measurement reported in 2012, the operation of the optical clock has been improved in several ways, especially from a reduction of the micromotion shifts, of the black body radiation shift, and of the servo tracking errors. Moreover, the stability of the clock has been improved three-fold with state-preparation. The uncertainty of the optical clock during the measurement campaign was 7 mHz. The uncertainty of the frequency measurement was 0.75 Hz, limited primarily by the GPS link and to a lesser extent by the measurement statistics. The new frequency measurement is in good agreement with previously reported values.**

Keywords—absolute frequency measurement; single ion clock; optical atomic clock; GPS frequency link

I. Introduction

A number of optical clocks have achieved unprecedented low uncertainties and high frequency stabilities, significantly outperforming Cs fountain clocks that define the SI second [1]. For these reasons, and as further improvements continue to be made, optical atomic clocks are being considered for a re-definition of the SI second [2], [3]. Before this can be achieved, it is essential to measure their absolute frequencies with respect to the current definition of the SI second, and to demonstrate agreement over time and between laboratories. Toward this goal, we made a new absolute frequency measurement of the S–D transition of $^{88}Sr^{+}$ using a GPS link to the SI second. Brief descriptions of the $^{88}Sr^{+}$ ion clock operation and uncertainty evaluation are given in Section II. Details of the frequency measurement are presented in Section III.

II. Strontium ion optical clock

The optical clock developed at the National Research Council of Canada (NRC) is based on the $5s\,^2S_{1/2} - 4d\,^2D_{5/2}$ electric quadrupole transition of a trapped and laser-cooled single ion of $^{88}Sr^{+}$. The S–D transition is interrogated using an ultra-stable 674 nm laser system. The natural linewidth of the S–D transition is 0.4 Hz and its quality factor is $Q \simeq 10^{15}$. The ion is cooled on the strongly allowed $5s\,^2S_{1/2} - 5p\,^2P_{1/2}$ transition at 422 nm, with observed ion kinetic temperatures of typically 2 mK. A repump laser at 1092 nm is required to prevent decay of the $^2P_{1/2}$ state to the metastable $^2D_{3/2}$ state. An additional laser at 1033 nm is used to return the ion to the ground state once the ion state has been detected using the electron shelving method. The clock transition linecenter is determined by independently locking the probe laser to six resonances that connect to all the magnetic sublevels of the $^2D_{5/2}$ state. The lock is performed by cycling through the six resonances and the linecenter frequency is determined from the average of those frequencies. This Zeeman averaging method is used to cancel several shifts and to determine a virtual linecenter that is not affected by the linear Zeeman shift, the electric quadrupole shift (EQS), and the tensor Stark shifts. More details about the experimental setup and operation of the optical clock are given in [4]–[6].

Compared to the absolute frequency measurement reported previously [5], several improvements were implemented in the optical clock. The most important one, from a measurement perspective, was the implementation of a servo algorithm that continuously evaluates and tracks the cavity drift rate. Previously, a constant drift rate of typically 10 mHz/s was used in the servo system. Despite the low average drift rate of the reference ULE cavity, changes of only a few mHz/s yielded significant tracking errors that could only be partially corrected in post-processing [6]. The implemented servo algorithm evaluates the cavity drift rates using an exponential moving average of previously measured values. The tracking errors have been reduced by more than two orders of magnitude to 2×10^{-18} fractional uncertainty with this algorithm and do not necessitate post-processing of the frequency data [7].

Another significant improvement was the implementation of state-preparation that has decreased the instability of the lock to the ion linecenter by a factor of three, to 3×10^{-15} at 1-s averaging time [8]. As a consequence of the higher quantum jump rate, the cycle time through the resonances was reduced by a factor of four, with corresponding reductions of systematic shifts associated with the servo tracking errors and the cancellation of the electric quadrupole shift.

Another advance was a high-accuracy measurement of the differential static scalar polarizability, $\Delta\alpha_0$, of the clock transition [9]. Several benefits to the ion clock accuracy were obtained from a better knowledge of $\Delta\alpha_0$: a reduction of the blackbody radiation (BBR) shift uncertainty by a factor of two, a reduction of the micromotion shifts by a factor of more than 200, and a reduction of the thermal motion shifts by a factor of three [7].

The main sources of uncertainty during the frequency measurement reported here were the evaluation of the BBR shift and an uncertainty caused by acousto-optic modulator

978-1-5386-2916-1/$31.00 ©2017 Crown

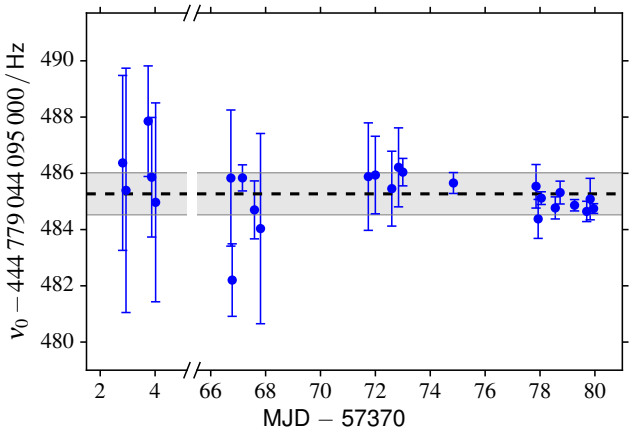


Fig. 1. Absolute frequency measurements of the S–D transition frequency of $^{88}Sr^{+}$ versus the modified Julian date (MJD). The data points are the results of individual measurement runs, with 1σ error bars determined from Allan deviation plots. The dashed line is the average ion frequency and the shaded area indicates the 0.75 Hz uncertainty of the measurement. Note that the determined frequency is not a simple average of the data shown. For more details see [7].

(AOM) frequency chirps. They each contributed approximately 1×10^{-17} to the uncertainty budget. All other shifts contributed 2×10^{-18} or less. The overall uncertainty of the ion clock frequency during the measurement campaign was evaluated at 1.5×10^{-17} in fractional units, which corresponds to 7 mHz at 445 THz.

III. Absolute Frequency Measurement

The frequency of the S–D transition of $^{88}Sr^{+}$ was measured by comparing the probe laser frequency to a reference maser using a fiber-based femto-second laser frequency comb [10]. The maser was itself calibrated using a GPS frequency link to the SI second [7]. The results were combined and corrected for various known shifts to determine the unperturbed ion frequency on the geoid. We have corrected for the offset of the GPS link from the SI second using the monthly BIPM Circular-T reports. The ion frequency was also corrected for the BBR shift, the light shift caused by the repumper laser, the thermal motion shift and the gravitational time-dilation shift. The corrected results are shown in Fig. 1. The measurement campaign resulted in more than 100 h of data.

The uncertainty of the measurement was dominated by the GPS link uncertainty evaluated at 0.67 Hz. The second most important contribution was from the 0.34 Hz statistical uncertainty caused by short-term maser frequency fluctuations and by the dead time in the operation of the optical standard and femto-comb laser link. The ion uncertainty contributed only 7 mHz. The ion frequency determined in the measurement campaign reported here is $444\,779\,044\,095\,485.27(75)$ Hz.

This result is in good agreement with previous results from our laboratory [4], [5] and from the National Physical Laboratories in the United Kingdom (NPL) [11], [12].

IV. Conclusion

We have reported a new measurement of the $^{88}Sr^{+}$ ion electric quadrupole transition at 445 THz. This measurement was obtained with several improvements made to the $^{88}Sr^{+}$ ion clock operation and accuracy. The measurement was made using a GPS link to the SI second and gave a new evaluation of the S–D frequency with an uncertainty of 0.75 Hz, or 1.7×10^{-15} in fractional frequency units. The result is in good agreement with previous measurements.

Future measurements at NRC will be performed using a state-of-the-art cesium fountain clock [13]. We expect to obtain a determination of the $^{88}Sr^{+}$ ion clock frequency with an uncertainty in the mid-10^{-16} level.

Acknowledgment

The authors would like to thank B. Hoger and W. Pakulski for the design and construction of several electronic devices used to operate the single ion clock.

References

[1] A. D. Ludlow, M. M. Boyd, J. Ye, E. Peik, and P. O. Schmidt, "Optical atomic clocks," *Rev. Mod. Phys.*, vol. 87, pp. 637–701, 2015, and references therein.

[2] F. Riehle, "Optical atomic clocks could redefine unit of time," *Physics*, vol. 5, p. 126, 2012.

[3] P. Gill, "Is the time right for a redefinition of the second by optical atomic clocks?" *Journal of Physics: Conference Series*, vol. 723, no. 1, p. 012053, 2016. [Online]. Available: http://stacks.iop.org/1742-6596/723/i=1/a=012053

[4] P. Dubé, A. A. Madej, J. E. Bernard, L. Marmet, J.-S. Boulanger, and S. Cundy, "Electric quadrupole shift cancellation in single-ion optical frequency standards," *Phys. Rev. Lett.*, vol. 95, p. 033001, 2005.

[5] A. A. Madej, P. Dubé, Z. Zhou, J. E. Bernard, and M. Gertsvolf, "$^{88}Sr^{+}$ 445-THz single-ion reference at the 10^{-17} level via control and cancellation of systematic uncertainties and its measurement against the SI second," *Phys. Rev. Lett.*, vol. 109, p. 203002, 2012.

[6] P. Dubé, A. A. Madej, Z. Zhou, and J. E. Bernard, "Evaluation of systematic shifts of the $^{88}Sr^{+}$ single-ion optical frequency standard at the 10^{-17} level," *Phys. Rev.* A, vol. 87, p. 023806, 2013.

[7] P. Dubé, J. E. Bernard, and M. Gertsvolf, "Absolute frequency measurement of the $^{88}Sr^{+}$ clock transition using a GPS link to the SI second," *Metrologia*, vol. 54, no. 3, p. 290, 2017.

[8] P. Dubé, A. A. Madej, A. Shiner, and B. Jian, "$^{88}Sr^{+}$ single-ion optical clock with a stability approaching the quantum projection noise limit," *Phys. Rev. A*, vol. 92, p. 042119, 2015.

[9] P. Dubé, A. A. Madej, M. Tibbo, and J. E. Bernard, "High-accuracy measurement of the differential scalar polarizability of a $^{88}Sr^{+}$ clock using the time-dilation effect," *Phys. Rev. Lett.*, vol. 112, p. 173002, 2014.

[10] J. E. Bernard, P. Dubé, A. A. Madej, S. Cundy, J.-S. Boulanger, J. Jiang, and D. J. Jones, "Fiber-laser-based clockwork for long-term measurements and comparisons of visible optical frequency standards," *Eur. Phys. J. D*, vol. 57, no. 2, pp. 247–252, 2010.

[11] H. S. Margolis, G. P. Barwood, G. Huang, H. A. Klein, S. N. Lea, K. Szymaniec, and P. Gill, "Hertz-level measurement of the optical clock frequency in a single $^{88}Sr^{+}$ ion," *Science*, vol. 306, pp. 1355–1358, 2004.

[12] G. P. Barwood, G. Huang, H. A. Klein, L. A. M. Johnson, S. A. King, H. S. Margolis, K. Szymaniec, and P. Gill, "Agreement between two $^{88}Sr^{+}$ optical clocks to 4 parts in 10^{17}," *Phys. Rev.* A, vol. 89, p. 050501, 2014.

[13] S. Beattie, J. Alcock, B. Jian, M. Gertsvolf, and J. Bernard, "Status of the atomic fountain clock at the National Research Council of Canada," *Journal of Physics: Conference Series*, vol. 723, no. 1, p. 012008, 2016. [Online]. Available: http://stacks.iop.org/1742-6596/723/i=1/a=012008

Absolute frequency measurement of the ^{171}Yb optical lattice clock at INRIM

Marco Pizzocaro*, Pierre Thoumany*, Filippo Bregolin*†, Gianmaria Milani*†, Benjamin Rauf*†, María del Carmen Vélez López‡*, Cecilia Clivati*, Giovanni A. Costanzo*†, Filippo Levi*, Davide Calonico*
* Istituto Nazionale di Ricerca Metrologica (INRIM), Strada delle Cacce 91, 10135 Torino, Italy
Email: m.pizzocaro@inrim.it
† Politecnico di Torino, Corso duca degli Abruzzi 24, 10129 Torino, Italy
‡ Real Instituto y Observatorio de la Armada (ROA), Calle Cecilio Pujazón, 11100 San Fernándo, Spain

***Abstract*—We present the absolute frequency measurement of the transition $^1S_0$ – $^3P_0$ at 578 nm in ytterbium 171 realized in an optical lattice frequency standard relative to the cryogenic caesium fountain ITCsF2. The measurement result is 518 295 836 590 863.59(31) Hz with a relative standard uncertainty of 5.9×10^{-16}. A contribution of 1.6×10^{-16} is coming from the ytterbium clock and we are working to reduce this contribution to the 1×10^{-17} level.**

I. Introduction

We designed and operated an optical lattice frequency standard based on ytterbium 171. We measured the frequency of the unperturbed clock transition $^1S_0$ – $^3P_0$ of ^{171}Yb against the cryogenic caesium fountain ITCsF2 [1] with a relative standard uncertainty of 5.9×10^{-16} [2]. The systematic uncertainty of the Yb optical lattice frequency standard is 1.6×10^{-16}, below that of ITCsF2. The reported result, the first in Europe, is in agreement with previous absolute measurements achieved in North America and Asia [3–5] and measurements from optical ratios [6, 7]. Absolute frequency measurements and ratios of optical frequency standards are important to show confidence in their reproducibility and are a key point for a possible redefinition of the second of the International System of Units based on an optical transition.

II. Yb Optical lattice clock

In our setup we cool and trap ytterbium atoms in a two stage magneto-optical trap (MOT) at 399 nm and 556 nm. Atoms are then transferred in a horizontal, one-dimensional optical lattice at the magic wavelength of 759 nm. The clock transition at 578 nm is probed by a laser stabilized on a high finesse notched ultra-low-expansion-glass cavity. Our system allows for fast loading with 1×10^4 atoms trapped in the lattice in 200 ms.

A small magnetic field is applied during spectroscopy, lifting the degeneracy of the clock transition. The clock laser is independently locked on the two Zeeman π transitions of the fermionic ytterbium 171.

We characterized the systematic effects on the transition as reported in the table. To evaluate the lattice light shift we locked the lattice laser frequency to the optical comb and performed interleaved measurements to work at the magic wavelength. Hyperpolarizability and nonlinear effects have been calculated using values found in the literature [7].

To evaluate the density shift we run interleaved clock measurements varying the number of atoms without changing the trapping conditions. The separation of the two Zeeman π transitions gives a direct measurement of the magnetic field seen by the atoms from which we can calculate the second order Zeeman shift. The BBR shift is calculated by a simple model of the chamber and the known polarizability of ytterbium, keeping into acoount the contribution from the oven tip (400 °C). The uncertainty on the Stark shift is limited by a simple model of our chamber. We observed some phase-noise between the references (mirrors) of the clock laser and of the lattice laser which include noise synchronous with the clock cycle (e.g., MOT coils switching) for which we assign an uncertainty coming from the Doppler effect. Other effects such as probe light shift, background gas shift, fiber links and AOM switching were find to contribute negligibly to the total uncertainty of 16×10^{-17}.

We are now working to improve the stability of the clock and to carry out further measurements and we expect to reduce the uncertainty at the level of 1×10^{-17}.

III. Absolute frequency measurement

We measured the absolute frequency of the ytterbium standard relative to the caesium fountain ITCsF2 using a fiber frequency comb. We took a total of 31 different measurements with a total measurement time of 227 h.

The result is 518 295 836 590 863.59(31) Hz where the total fractional uncertainty is 5.9×10^{-16}. The ytterbium clock contributes an uncertainty of 1.6×10^{-16}, the fountain contributes 4.0×10^{-16} while the statistical uncertainty is 3.9×10^{-16}.

References

[1] F. Levi, D. Calonico, C. E. Calosso, A. Godone, S. Micalizio, and G. A. Costanzo, "Accuracy

978-1-5386-2916-1/$31.00 ©2017 IEEE

Table I
Uncertainty budget for the Yb optical lattice clock.

Effect	Rel. Shift$\times 10^{17}$	Rel. Unc.$\times 10^{17}$
Lattice polarizability	−4	8
Nonlinear lattice shifts	−12	10
Density shift	−2	6
Zeeman shift	−27	4
BBR room	−235.3	2.5
BBR oven	−2.1	0.8
Doppler shift	–	5
Static Stark shift	–	1
Other	–	2
Total	−281	16

evaluation of ITCsF2: a nitrogen cooled caesium fountain," *Metrologia*, vol. 51, no. 3, p. 270, 2014. [Online]. Available: http://stacks.iop.org/0026-1394/51/i=3/a=270

[2] M. Pizzocaro, P. Thoumany, B. Rauf, F. Bregolin, G. Milani, C. Clivati, G. A. Costanzo, F. Levi, and D. Calonico, "Absolute frequency measurement of the $^1S_0$ – $^3P_0$ transition of ^{171}Yb," *Metrologia*, vol. 54, no. 1, p. 102, 2017. [Online]. Available: http://stacks.iop.org/0026-1394/54/i=1/a=102

[3] N. D. Lemke, A. D. Ludlow, Z. W. Barber, T. M. Fortier, S. A. Diddams, Y. Jiang, S. R. Jefferts, T. P. Heavner, T. E. Parker, and C. W. Oates, "Spin-1/2 optical lattice clock," *Phys. Rev. Lett.*, vol. 103, no. 6, p. 063001, Aug 2009.

[4] M. Yasuda, H. Inaba, T. Kohno, T. Tanabe, Y. Nakajima, K. Hosaka, D. Akamatsu, A. Onae, T. Suzuyama, M. Amemiya, and F.-L. Hong, "Improved absolute frequency measurement of the ^{171}yb optical lattice clock towards a candidate for the redefinition of the second," *Applied Physics Express*, vol. 5, no. 10, p. 102401, 2012. [Online]. Available: http://apex.jsap.jp/link?APEX/5/102401/

[5] C. Y. Park, D.-H. Yu, W.-K. Lee, S. E. Park, E. B. Kim, S. K. Lee, J. W. Cho, T. H. Yoon, J. Mun, S. J. Park, T. Y. Kwon, and S.-B. Lee, "Absolute frequency measurement of $^1S_0$ ($f = 1/2$) - $^3P_0$ ($f = 1/2$) transition of ^{171}Yb atoms in a one-dimensional optical lattice at KRISS," *Metrologia*, vol. 50, no. 2, p. 119, 2013. [Online]. Available: http://stacks.iop.org/0026-1394/50/i=2/a=119

[6] D. Akamatsu, M. Yasuda, H. Inaba, K. Hosaka, T. Tanabe, A. Onae, and F.-L. Hong, "Frequency ratio measurement of 171yb and 87sr optical lattice clocks," *Opt. Express*, vol. 22, no. 7, pp. 7898–7905, Apr 2014. [Online]. Available: http://www.opticsexpress.org/abstract.cfm?URI=oe-22-7-7898

[7] N. Nemitz, T. Ohkubo, M. Takamoto, I. Ushijima, M. Das, N. Ohmae, and H. Katori, "Frequency ratio of yb and sr clocks with 5×10^{-17} uncertainty at 150 seconds averaging time," *Nat Photon*, vol. 10, no. 4, pp. 258–261, Apr. 2016. [Online]. Available: http://dx.doi.org/10.1038/nphoton.2016.20

Contributing to TAI with Sr optical lattice clocks

Sławomir Bilicki, Eva Bookjans, Grégoire Vallet, Michel Abgrall, Rodolphe Le Targat and Jérôme Lodewyck
LNE-SYRTE, Observatoire de Paris, PSL Research University, CNRS, Sorbonne Universités, UPMC Univ. Paris 6
61 avenue de l'Observatoire, 75014 Paris
Email: slawomir.bilicki@obspm.fr

***Abstract*—In this paper, we present recent experiments conducted with two ^{87}Sr optical lattice clocks operated at LNE-SYRTE. We report on the first calibrations of TAI with optical clocks, a necessary step towards the redefinition of the SI second. Additionally, we report on the experimental realization of a cavity-assisted non-destructive detection whose improved signal-to-noise ratio can improve the stability of optical clocks by reducing the Dick effect instability contribution, possibly beyond the quantum projection noise. Finally, we discuss the possibility to operate lattice clocks with semi-conductor sources as a lattice trap laser, by evaluating the frequency shift induced by their incoherent background light.**

I. Introduction

Optical lattice clocks (OLCs) have became now more stable and have better systematic uncertainties than cesium microwave fountains currently realizing the SI second ([1], [2]) and their limits are not established yet. OLCs are currently used to explore fundamental physics, astronomy and geo-science. OLCs could make it possible to observe sensitive effects, such as topological-defect dark matter [3], test the special relativity theory ([4], [5]) by observing daily variation of frequency difference between clocks, and measure height difference with centimetre precision [6]. All these applications would benefit from an improved stability and accuracy. In this paper, we report experiments conducted to advance both the stability and accuracy of Sr OLCs. The success of OLCs makes them prime candidates for a possible redefinition of SI second. We report on a decisive step in this direction with a first calibration of TAI with optical clocks.

II. Calibration of TAI with optical clocks

Over the last years, we have repeatedly operated our Sr clocks over long time intervals, ranging from 10 days to 20 days [7]. During these measurement campaigns, the Sr clocks were used to calibrate an H-maser connected to TAI via UTC(OP), which led to five TAI calibrations reports sent to the BIPM. These contributions to TAI show that optical clocks are progressing towards replacing the microwave time and frequency architecture currently realizing the SI second.

III. A lattice with semi-conductor sources

Sr is a possible choice for a compact, transportable and even potentially space optical lattice clocks. For this, a compact and reliable apparatus is required. One of the largest problems is a miniaturized lattice source at 813 nm, given that both a high power and a high spectral purity are required to trap atoms without perturbation. The compactness of semiconductors sources (laser diodes and tapered amplifiers) looks promising, but early tests on clocks show a frequency shift at the Hz level due to the incoherent Amplified Spontaneous Emission (ASE) background inherent to these sources. Therefore, most clocks employ a Titanium Sapphire (TiSa) laser despite its volume and power consumption, because it is shown to have a negligible systematic contribution to the clock. Here, we propose a full characterization of the frequency shifts associated with semi-conductor laser sources including both optical measurement as well as frequency shifts measurements. We propose filtering strategies to reach a frequency shift below 10^{-17}.

IV. Cavity assisted non-destructive detection

Finally, we report on the experimental realization of a non-destructive detection technique of lattice-trapped Sr atoms in a OLC. It based on a bichromatic optical cavity, which is used to build both the optical lattice and the detection beam tuned to the $^1S_0$-$^1P_1$ transition. This detection system can resolve a few atoms in the lattice, while keeping the atoms trapped. Consequently this detection system has the potential to improve the clock frequency stability by reducing the dead-time of the clock cycle used to prepare the atomic sample. Since, its signal-to-noise ratio is significantly below the quantum projection noise, this technique opens the way to atomic spin squeezed states which can potentially allow OLCs to overcome the quantum projection noise.

Acknowledgment

We acknowledge funding support from Centre National d'Études Spatiales (CNES), Conseil Régional Île-de- France (DIM Nano'K), Agence Nationale de la Recherche (Labex First-TF ANR-10-LABX-48-01, ANR-16-CE30-0003-01), European Union under the FP7-PEOPLE-2013-ITN program, GA No. 607493, Future Atomic Clock Technology, project EMPIR 15SIB03 OC18 and EMRP EXL-01 QESOCAS. The EMRP is jointly funded by the EMRP participating countries within EURAMET and the European Union. This project has received funding from the EMPIR programme co-financed by the Participating States and from the European Unions Horizon 2020 research and innovation programme.

References

[1] T.L. Nicholson, S.L. Campbell, R.B. Hutson, G.E. Marti, B.J. Bloom, R.L. McNally, W. Zhang, M.D. Barrett, M.S. Safronova, G.F. Strouse et al. *Systematic evaluation of an atomic clock at* 2×10^{-18} *total uncertainty*, Nature Comm. 6:6896, 2015

978-1-5386-2916-1/$31.00 ©2017 IEEE

[2] I. Ushijima et al. *Cryogenic optical lattice clocks*, Nat. Photon. 9, 185-189 (2015)
[3] P. Wcisło et al. *Experimental constraint on dark matter detection with optical atomic clocks*, Nature Astronomy, 1, 0009 (2016)
[4] P. Delva et al. *Test of special relativity using a fiber network of optical clocks*, in preparation
[5] C. Lisdat et al. *A clock network for geodesy and fundamental science*, Nat. Commun. 7:12443 (2016)
[6] P. Delva, J. Lodewyck *Atomic clocks: new prospects in metrology and geodesy*, Acta Futura 7, 67 78 (2013)
[7] J. Lodewyck et al. *Optical to microwave clock frequency ratios with a nearly continuous strontium optical lattice clock*, Metrologia 53 (2016) 1123-1130

Timing Performance Evaluation of BDS IGSO-6 and GEO-7 Satellite Network

GNSS timing performance evaluation method and characterization

Zhu Feng[1,2], Li Xiao-hui[1,2], Zhang Hui-jun[1,2], Huang Lu-xi[1,2], Xu Long-xia[1,2]
1. National Time Service Center, Chinese Academy of Science, Xi'an 710600, China
2. Key Laboratory of Precision Navigation Positioning and Timing, Chinese Academy of Science,Xi'an 710600, China
E-mail: zhufeng@ntsc.ac.cn

***Abstract*—BeiDou Navigation Satellite System (short for BDS) officially provided service to most parts of Asia since December 27th. 2012[1]. After a year of testing and evaluation work China Satellite Navigation Office published "BeiDou Navigation Satellite System Open Service Performance Standard (Version 1.0)" (hereinafter short for "BDS-OS-PS-1.0") in December 2013[2], which presented each performance index of BDS service. Among 2016 China launched two satellites of IGSO-6 (NO.22, March 30th) and GEO-7 (NO.23, June 12th), and before the formal operation services both of them still needed further testing and evaluation work of satellites network, which obtained the actual testing results of every performance index to provide the basis for network operation and service performance commitment.**

Therefor taking "BDS-OS-PS-1.0" as the basis we undertook the timing evaluation work of each satellite network, which analyzed the satellites timing performance in B1, B3, B1/B2, B1/B3 frequency bands as well as the contribution to the current system. The results showed the timing performance of IGSO-6 and GEO-7 could meet the requirement of timing precision better than 50ns, and either of them adding to BDS would improve the precision and reliability of system service.

Keywords; timing performance; BDS satellite network; evaluation method; performance characterization; Coordinated Universal Time

I. INTRODUCTION

"BDS Interface Control Document (Version 2.1)" regulates the timing performance as follows: BDT is related to the UTC through UTC(NTSC), and BDT offset with respect to UTC is controlled with 100 nanoseconds (modulo 1 second)[3]. According to International Telecommunication Union (ITU) standard broadcasting requirement, the time bias between timing system and UTC must be controlled within 100ns, thus it requires the bias between BDS satellite broadcasting UTC time and actual UTC time less than 100ns, so it is necessary to analyze and test the satellites broadcasting UTC time which evaluates the timing performance of BDS IGSO-6 and GEO-7 satellites network.

II. EVALUATION METHOD

Referring to the characteristic and requirement of satellite timing performance, the paper analyzes the evaluation function, and from the users' characteristic it proposes the concept and method for testing the bias between satellites broadcasting UTC time and actual UTC, with the basic principle showed as follows[4]:

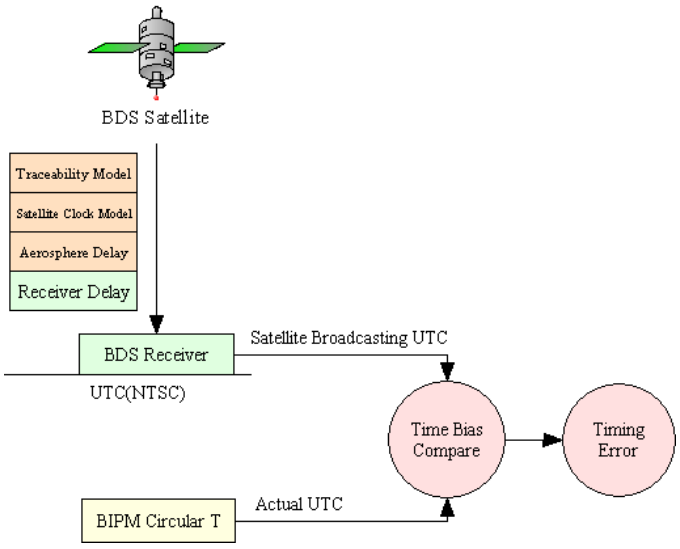


Fig. 1. Evaluation principle of BDS timing performance

1) Calculate the bias $\tau_{S,UTC}(i,j)$ between the satellite broadcasting UTC time and UTC(NTSC) by pseudorange modification:

$$\begin{aligned}\tau_{S,UTC}(i,j) &= UTC(i,j) - UTC(NTSC) \\ &= \frac{\rho(i,j)}{c} - \frac{\rho_0}{c} - \tau_{clk}(i,j) - \tau_{iono}(i,j) - \tau_{tropo}(i) \\ &\quad - \tau_{sagnac}(i) - \tau_{rev}(j) + \tau_{trace}\end{aligned} \quad (1)$$

$UTC(i,j)$ is the prn (i) and frequency band (j) of satellite broadcasting UTC time, $UTC(NTSC)$ is the receiver time as the receiver operating in National Time Service Center, $\rho(i,j)$ is the pseudorange from the receiver, $\tau_{clk}(i,j)$ is the satellite clock bias, $\tau_{iono}(i,j)$ and $\tau_{tropo}(i)$ are relatively the ionosphere delay and troposphere delay, $\tau_{sagnac}(i)$ is the

1. "Light of West China" of Chinese Academy of Science, XAB2016B78
2. "Cooperative Precise Positioning Technology" of 2016 China National Key Research and Development Plan, 2016YFB0501804

Sagnac modification, $\tau_{rev}(j)$ is the receiver group time delay between receiver time and $UTC(NTSC)$, τ_{trace} is the traceability data from navigation message representing $UTC-BDT$, c is the velocity of light, ρ_0 is the geometry path from satellite to receiver showed as below:

$$\rho_0=\sqrt{(x_S-x_R)^2+(y_S-y_R)^2+(z_S-z_R)^2} \tag{2}$$

x_S, y_S, z_S is the satellite position calculated from BDS navigation message, x_R, y_R, z_R is the receiver position measured from survey department;

2) Obtain the bias $\tau_{A,UTC}$ between UTC time and UTC(NTSC) from BIPM Circular T:

$$\tau_{A,UTC}=UTC_{BIPM}-UTC(NTSC) \tag{3}$$

UTC_{BIPM} is the actual UTC time;

3) Calculate the satellite timing error $\sigma_{UTC}(i,j)$:

$$\sigma_{UTC}(i,j)=\tau_{S,UTC}(i,j)-\tau_{A,UTC} \tag{4}$$

The paper utilizes the standard time and frequency resource of UTC(NTSC), thus we can calculate the UTC-UTC(NTSC) representing satellites broadcasting UTC time. Meanwhile we obtain the UTC-UTC(NTSC) representing actual UTC from BIPM Circular T[5]. Through time bias compared the timing error will be evaluated.

From the user perspective, we evaluate the timing performance obtained by each satellite signal instead of the satellite broadcasting errors. Although this evaluation method includes some errors from the signal propagation path, it clears the test object not only making the testing process easy operation but also reflecting the real UTC precision obtained by users. If we share the evaluation result to the users, it will make them easier to master and apply.

III. PERFORMANCE CHARACTERIZATION

Evaluation method is mainly performance characterized by the uncertainty, and the uncertainty contains random error and system error among timing performance, which mainly exists in the middle parts including pseudorange measurement, mathematical model, receiver delay calibration[6] and Circular T data[7]. The uncertainty analysis is showed as table 1:

TABLE I. UNCERTAINTY ANALYSIS OF BDS TIMING EVALUATION METHODS (UNIT:NS)

uncertainty source（ε）	uncertainty
pseudorange measurement	1
mathematical model	2
receiver delay calibration	2
Circular T data	2
combined uncertainty （$\sqrt{\Sigma\varepsilon_i^2}$）	3.61

Analyzing with the uncertainties of these variables, we can get the combined uncertainty of evaluation method (3.61ns). According to this evaluation standard, it reflects the precision of satellites timing performance, which shows the degree of closeness between satellites broadcasting time and UTC time.

Evaluation result is mainly characterized through 95% confidence[8]: taking the absolute value of satellite timing errors under different model and observation time, through ascending order we use the 95% point corresponding to timing error as the satellite timing precision. Whether the timing precision better than 50ns (timing requirement of "BDS-OS-PS-1.0") is considered as the judgement standard of BDS satellites timing performance.

The satellite timing contribution to the BeiDou system is characterized as the pre and post variation of adding the satellite (also through 95% confidence).

$$countribution(i,j)= \frac{\sum_{i=1}^{n-1}\sigma_{UTC}(i,j)}{n-1}(pre)-\frac{\sum_{i=1}^{n}\sigma_{UTC}(i,j)}{n}(post) \tag{5}$$

Equation (5) means calculating the multi-satellite timing error through every meantime satellites timing errors for weighted average, and we respectively compare the pre and post variation of multi-satellite timing precision with adding IGSO-6 or GEO-7.

IV. EVALUATION RESULT

Here are the IGSO-6 and GEO-7 timing evaluation results under different frequency bands. The testing time was respectively from June 1st to July 10st and September 10th to October 30th in 2016 (Fig 2 and 3).

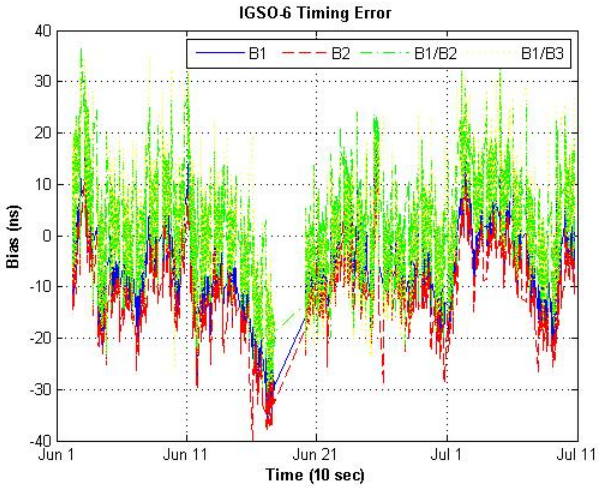


Fig. 2. Evaluation result of IGSO-6 timing performance

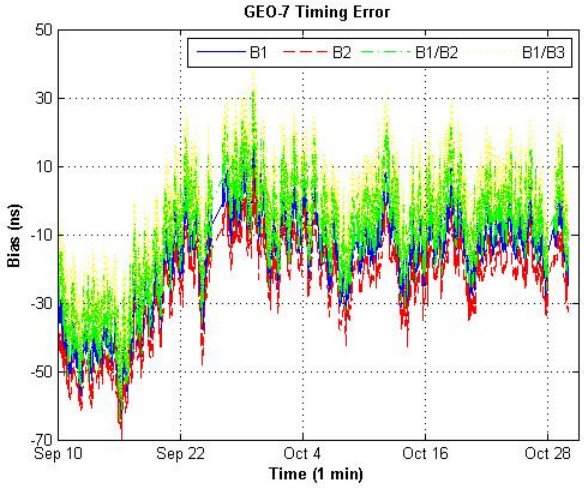


Fig. 3. Evaluation result of GEO-7 timing performance

Table II shows the comparison of IGSO-6 and GEO-7 timing precision under different frequency bands, which also shows the contribution to BDS timing performance. As is can be seen all of them are basically under 50ns with little effect on BDS.

TABLE II. IGSO-6 AND GEO-7 TIMING STATISTICS (UNIT:NS)

Frequency bands	IGSO-6		GEO-7	
	Timing Precision	*Contribution*	*Timing Precision*	*Contribution*
B1	20.55	0.45	46.38	-0.21
B3	23.91	0.38	53.47	-0.61
B1/B2	17.54	-0.15	39.40	-0.44
B1/B3	17.64	-0.16	32.91	0.15

For more intuitively reflecting on the satellites timing performance, we relatively compare IGSO-6 and GEO-7 evaluation results with other 5 same-type BDS satellites under different frequency bands (Fig 4 and 5).

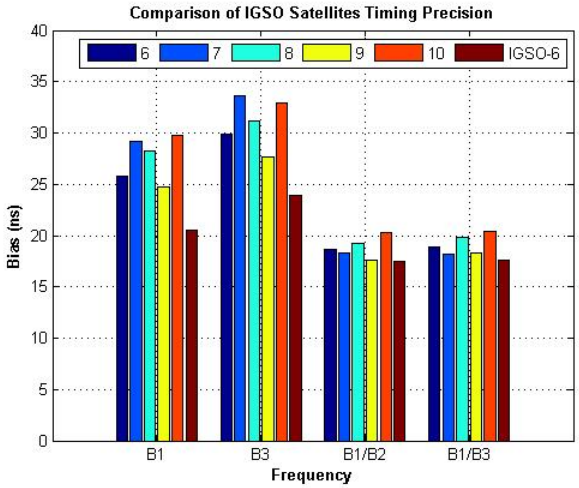


Fig. 4. Comparison of IGSO satellites evaluation result

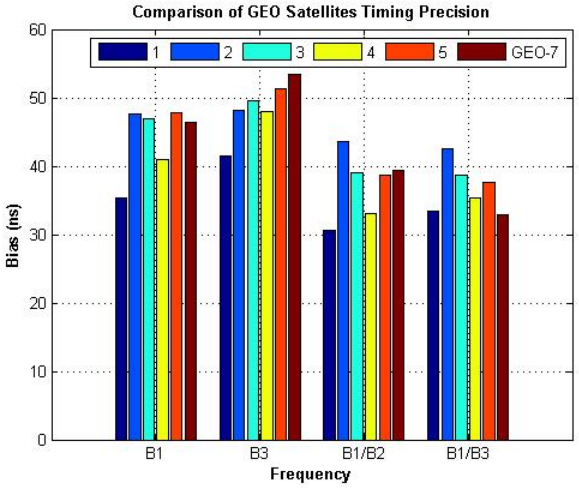


Fig. 5. Comparison of GEO satellites evaluation result

As it can be seen, each frequency band evaluation of IGSO-6 is better than that of other BDS IGSO satellites. GEO-7 evaluation in single-frequency band is less than others but not much in dual-frequency band.

V. CONCLUSION

The testing and evaluation acceptances of BDS IGSO-6 and GEO-7 satellite network were relatively finished at the end of July and November in 2016. From the BeiDou government announcement the IGSO-6 satellite formally provided service with prn (13) on August 5th, 2016, and the GEO-7 satellite formally operated on November 30th, 2016[9].

Through this method we had established the GNSS timing performance evaluation system (including GPS, GLONASS, BDS). The system formally operated in October, 2015 by sending the evaluation results to related users through monthly report, FTP server, etc. Now we have been perfecting this system with Galileo, BDS (BOC signal and S frequency band) adding in the future.

ACKNOWLEDGMENT

The author wishes to thank the IEEE for providing this template and all colleagues who previously provided technical support. The authors also gratefully acknowledge “Light of West China” of Chinese Academy of Science (Grant No.XAB2016B78) and “Cooperative Precise Positioning Technology” of 2016 China National Key Research and Development Plan (Grant No.2016YFB0501804) for the financial support.

REFERENCES

[1] The State Council Information Office of the People’s Republic of China. China' s BeiDou navigation satellite system[M]. Foreign Languages Press Co. Ltd, Jun 2016.

[2] China Satellite Navigation Office. BeiDou Navigation Satellite System Open Service Performance Standard (Version 1.0), Dec 2013.

[3] China Satellite Navigation Office. BeiDou Navigation Satellite System Signal In Space Interface Control Document Open Service Signal (Version 2.1), Nov 2016.

[4] Zhu F, Li X H, Zhang H J, et al. Study on Integrated Testing and Evaluation Method of GNSS Timing Performance[M] China Satellite

Navigation Conference (CSNC) 2016 Proceedings: Volume I. Springer Singapore, 2016.

[5] Arias E F, Panfilo G, Petit G. Timescales at the BIPM[J]. Metrologia, 2011, 48(4): S145.

[6] Zhu F, Zhang H J, Li X H, et al. Influence analysis of the phase difference between the output reference signals on receiver zero-value[J]. Chinese Journal of Scientific Instrument, 2015, 36(7): 1592-1597.

[7] Jiang Z, Lewandowski W. Inter-comparison of the UTC time transfer links[C]. European Frequency and Time Forum(EFTF), 2012. IEEE, 2012: 126-132.

[8] Amirisimkooei A R. Separating receiver noise and multipath effects in time series of GPS baselines using harmonic functions[J]. 2005.

[9] www.beidou.gov.cn.

Validation of the Inter-Frequency calibration of timing GNSS receivers

P. Defraigne, B. Bertrand, W. Huang[1]
Royal Observatory of Belgium
Brussels, Belgium
p.defraigne@oma.be
[1]Now at Politecnico di Torino, Italy

D. Rovera
LNE-SYRTE, Observatoire de Paris PSL Research University, CNRS, Sorbonne Universités, UPMC Univ. Paris 06,
Paris, France

***Abstract*—This paper presents a study of the consistency of the values used as reference for the hardware delays of GPS P1 and P2 for calibration in the TAI network. The inter-signal biases dP1-dP2 are computed from the pseudorange measurements, after applying an ionospheric delay correction, and then compared to the calibrated values. It is shown that the differences between the computed dP1-dP2 and the calibrated values are well inside the expected combined uncertainty. A similar conclusion is reached comparing the computed dP1-dP2 with absolutely calibrated stations. We also show that using a same antenna phase center for the calibration or using different positions for L1 and L2 signals gives maximum differences of 200 ps on the hardware delays of the separate codes P1 and P2, but the final impact on the P3 combination is less than 10 ps.**

The computed dP1-dP2 are then also used to look at the stability of the inter-signal hardware delays of some GPS stations dedicated to time transfer. It is shown that only variations larger than 2 ns can be detected in the computed dP1-dP2 for a particular station, while variations of 200 ps can be detected when differentiating the results between two stations.

Keywords—GPS; calibration; hardware delays.

I. INTRODUCTION

The time laboratories whose clocks participate to the ensemble used in the generation of TAI are equipped with GNSS receiving systems to perform GNSS time transfer as the primary or backup techniques for the realization of TAI/UTC.

The accurate time difference between two remote clocks can only be known if the equipment used for the time transfer has been accurately calibrated, i.e. the hardware delays in the time transfer instruments have been measured, as well as the time offset between the timing reference in the instruments and the clock itself. For GNSS time transfer, the hardware delays have to be determined for each GNSS signal. Either absolute or relative calibration can be used for that purpose. The principle of the absolute calibration is to use simulated signals in order to determine the electric delay of the receiver or antenna (or the complete receiving chain), and determine the hardware delays from the measurements made by the GNSS receiving equipment on the simulated signals. Complete descriptions of the method can be found e.g. in [1] and references therein. This kind of calibration claims a very high accuracy of 0.4 ns [2] but it requires the use of a GNSS simulator and a VNA, as well as an anechoic chamber for the antenna, which do not exist in the major part of the laboratories. More classically used, the relative calibration consists in a comparison of pseudorange measurements collected by the local receiving chain and a reference receiving chain traveling from laboratory to laboratory [3,4]. Once the traveling and the local stations are connected to the same clock, the difference between the hardware delays is obtained from the difference of the pseudoranges measured by the two receiving chains.

Since 2014, the calibration of GNSS equipment for time laboratories participating to TAI is organized by the BIPM in collaboration with the Regional Metrological Organizations (RMO). Calibration trips involving some of the UTC(k) laboratories (named "Group 1") are performed by the BIPM. Then the RMOs organize the calibration of the other laboratories (named "Group 2"), by performing calibration trips where at least one "Group 1" system serves as a reference. The reference is currently defined as the ensemble of the "Group 1", and for each new "Group 1" calibration trip, the delay values are set so as to minimize, for the ensemble of participating "Group 1" systems, the variations of the values with respect to their previous calibration results [5].

A first study proposed in this paper will concern the consistency of the values used as reference for the hardware delays of GPS P1 and P2 for calibration in the TAI network, reference maintained by the Group 1 laboratories. For this, the inter-signal biases dP1-dP2 will be computed from the pseudorange measurements, after applying an ionospheric delay correction, and then compared to the calibrated values. A parallel comparison will also be done with some absolutely calibrated stations. A second investigation will concern the long-term stability of the inter-frequency hardware delays of the GPS stations used for time transfer. Indeed, it was observed that the differences between the clock comparisons based on either GNSS or TWSTFT are not constant but show long term variations [6]. The origin of these differences has not yet been explained; a possible cause is some variation of the GNSS or TWSTFT hardware delays. Looking at the variations of the differences between the P1 and P2 hardware delays will inform on the stability of the ionosphere-free combination P3 [7] which is generally used for the time links either using the all-in-view [8], based on a code-only analysis, or on Precise Point Positioning (PPP) [9]. Finally, we also look at the impact of

frequency-dependent antenna phase centers, presently not taken into account in the calibration.

II. COMPUTATION METHOD

The inter-frequency hardware delay can be obtained from the pseudorange measurements P1 and P2 for each satellite and observation epoch:

$$dP1\text{-}dP2=(P1\text{-}P2)\text{-}(D_1\text{-}D_2)\text{-}(Iono_1\text{-}Iono_2)\text{-}TGD(1\text{-}f_1^2/f_2^2)+\varepsilon \quad (1)$$

where D_1 and D_2 are the distance between the satellite phase center and the local antenna phase center on L1 and L2 respectively, given in the IGS calibration file igs14.atx [10]. $Iono_1$ and $Iono_2$ are the ionospheric delays that effect on L1 and L2 frequencies respectively, and are computed from ionospheric maps [11] provided by the International GNSS Service (IGS). These maps provide the Total Electron Content (TEC) in the ionosphere as a function of latitude, longitude an time, with one map every 2 hours. TGD, the satellite Time Group Delay, is available in the GPS navigation messages, f_1 and f_2 are the frequencies of L1 and L2, and ε is the noise.

At each epoch, the quantity dP1-dP2 is then obtained by averaging the results obtained from all the observed satellites. An elevation weighting is also applied in order to reduce the impact of noisy data from low elevation satellites.

III. LONG-TERM STABILITY

The long-term behavior of dP1-dP2 for three European time laboratories is reproduced in Figure 1 (upper part). Some similar pattern can be observed and are clearly not due to the receiver hardware delay variations, but to some variations in the ionospheric products used. The associated common variations reach 2 ns peak to peak. It can therefore be concluded from this analysis that only large dP1-dP2 variations of more than 1 ns can be detected from this approach. Smaller variations are buried into the noise of the ionospheric products.

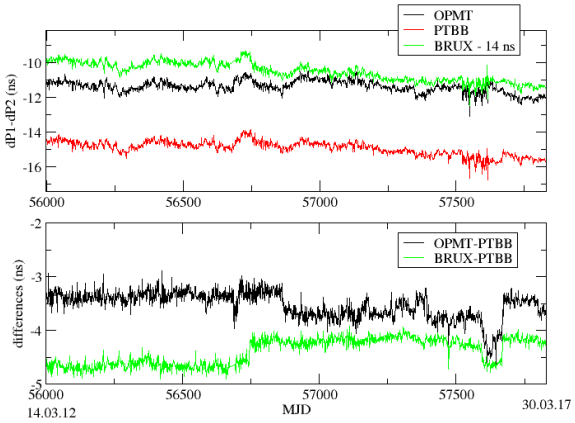


Fig. 1. dP1-dP2 for some timing stations and their differences, computed from the measured pseudoranges using the combined IGS ionospheric maps. The BRUX results were shifted for 14 ns in order to improve the visibility.

As some variations are common to the stations of a same region, the difference between the solutions obtained for two stations can be analyzed more precisely to detect possible dP1-dP2 variations (Figure 1, lower part). From the comparison between BRUX-PTBB and OPMT-PTBB, we can observe a similar variation of about 500 ps around MJD 57600, which can then be attributed to PTBB. Another jump of about 400ps can also be seen in BRUX around MJD 56750. This technique therefore allows studying the stability of dP1-dP2 by comparison with a remote station, when no other station is available in colocation providing the possibility of having a common-clock setup.

IV. CONSISTENCY OF P1 AND P2 REFERENCES FOR CALIBRATION IN GROUP 1 STATIONS

A. Impact of the ionospheric maps

Several IGS analysis centers produce ionospheric TEC maps. A first test consists in looking at the consistency between the results obtained for dP1-dP2 when using different maps. For this comparison, the following maps will be used: COD, EMR, ESA, JPL, UPC and the combined product named IGS. IGS analysis centers: COD, EMR, ESA, JPL, UPC and the combined product named IGS. Figure 2 presents the differential biases than can be obtained between the results obtained with the COD maps and the other maps for several locations over the world: USN0, PTB, SU and NIM (BJNM). Some biases up to 2 ns peak to peak can be observed; note also that these biases are clearly not the same for all the stations, while similar patterns can be observed for nearby stations (not shown here).

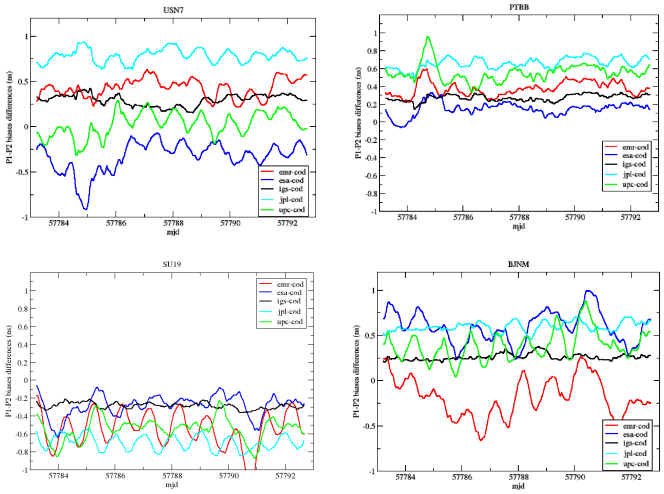


Fig. 2. Differences of dP1-dP2 results computed using COD or another set of ionospheric maps, for different station locations

B. Comparison dP1-dP2 with Group 1 calibrations

In this comparison we only use the combined ionospheric product IGS because it is a kind of average of the others, and therefore is expected to be more accurate. Figure 3 presents the comparison between computed dP1-dP2 and calibrated values for "group 1" laboratories during the calibration campaign of 2014. Each blue line corresponds to the calibration results at the epoch where the calibration took place. The numerical results are presented in Table 1, together with the results of the calibration campaign of 2016. The values indicated in the column "From pseudoranges"

correspond to the average values during the same time period as the calibration campaign.

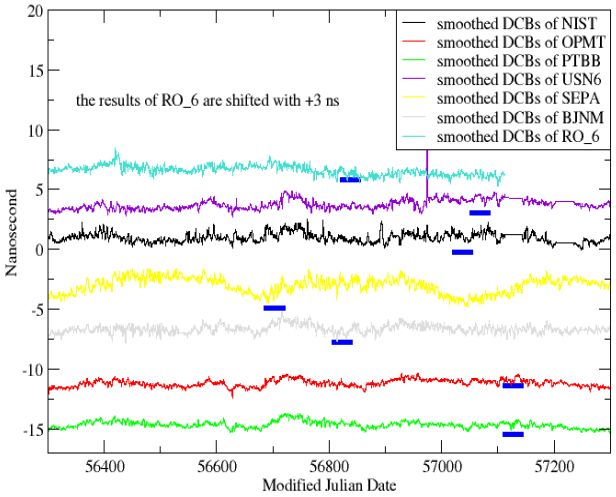


Fig. 3. Comparisons between the computed dP1-dP2 and the calibrated values for the group 1 stations during the calibration campaign of 2014.

Only one station is presented for each Group 1 visited time laboratory. For the calibration campaign 1001-2014, the differences range from 0.2 to 1.8 ns, while for the calibration campaign of 2016, the differences range between -0.1 and +0.6 ns. We estimate the uncertainty on the differences as follows: on one side, due to the possible variable biases between the ionospheric TEC maps, an uncertainty of 1 ns should be given to our dP1-dP2 results computed from pseudoranges. Considering the standard deviations of the differences, the upper bound of the error on the average difference dP1-dP2 of our computations is 0.1 ns. On the other side, the calibration uncertainty of P1-P2 is 1.0 ns as given in the calibration reports [12]. A combined uncertainty on the difference of 1.4 ns can therefore be considered. From the results of Table 1, it appears that the differences obtained are well inside this combined uncertainty of the computed dP1-dP2 and calibrated values. Only the station SEPA shows a difference larger than one sigma in the 2014 campaign; note however that a large annual variation is observed in Figure 3 for this station, probably due to the ionosphere TEC maps.

The last lines of Table 1 provide a comparison with results of absolute calibration. The two stations used were calibrated by the CNES [13] within the frame of DEMETRA, a Demonstrator of EGNSS services based on Time Reference Architecture [13], financed by the Horizon 2020 European Commission Programme (H2020). One of these stations shows a difference of 1.6 ns, i.e. just above the 1-σ uncertainty of the comparison.

The time link for which the difference is the largest among the stations used from the calibration campaign of 2016 is PTBB-TLT1. The combined difference in (dP1-dP2) is 0.7 ns. The impact on the ionospheric free combination can be computed as

$$dP3 = dP1 + 1.545*(dP1-dP2) \quad (2)$$

Considering only the impact of (dP1-dP2), a difference of 0.7 ns gives an effect of 1.0 ns on dP3. This means a difference of 1.0 ns between the calibrated time transfer solutions obtained from either P1 or P3. This difference is well inside the 2.1 ns uB uncertainty of a time transfer link based on GNSS P3 or PPP, when considering the 1.5 ns uncertainty on each calibrated Group 1 station.

TABLE I. COMPARISON BETWEEN COMPUTED AND CALIBRATED VALUES FOR "GROUP 1" LABORATORIES

Station (labo)	dP1-dP2 (ns)		
	From pseudoranges	From calibration	Difference
Calibration Campaign 1001-2014			
SEPA (NICT)	-3.1	-4.9	1.8
BJNM (NIM)	-6.9	-7.7	0.8
NIST (NIST)	1.2	-0.2	1.4
USN6 (USNO)	4.1	3.1	1.0
OPMT (OP)	-11.2	-11.4	0.2
PTBB (PTB)	-14.7	-15.4	0.7
RO_6 (ROA)	3.2	2.8	0.4
Calibration Campaign 1001-2016			
TLT1 (TL)	-8.5	-9.1	0.6
NC01 (NICT)	-4.2	-4.1	-0.1
IMEJ (NIM)	-0.2	-0.2	0.0
NTP1 (NTSC)	1.0	0.6	0.4
OPMT (OP)	-12.0	-11.9	-0.1
PTBB (PTB)	-15.4	-15.3	-0.1
RO_5 (ROA)	0.3	-0.2	0.5
Absolute Calibration			
ORBA (ORB)	0.3	-0.3	0.6
GR01 (IT)	3.8	2.2	1.6

V. CALIBRATION AND ANTENNA PHASE CENTERS

The antenna phase center position differences between the L1 and L2 signals are currently not considered in the BIPM guidelines for calibration [5]. The position to be used for the calculation corresponds to the phase center of the L3 combination. Using a different antenna position (especially in the up component) in the measurement modeling would induce a time bias which will be transferred as an error in the hardware delay determined by relative calibration. We estimate here the possible bias introduced by the use of the antenna phase center of L3 rather than separate L1 and L2 phase centers, for calibration of P1 and P2 signals. Table 2 presents these estimations for different types of antennas when the reference station is OPMT (OP), based on an 3S-02-TSADM antenna, and the traveling station is using a ASH701945C_M antenna. The IGS antenna calibration [e.g. 14] results provided in the file igs14.atx have been used to determine the phase center offsets between L1, L2 and L3. The results proposed in Table 2 show that the differences on the hardware delays of the separate codes reach a maximum of 100 ps for P1 and 200 ps for P2, while the final impact on the P3 combination is always very close to zero.

These results are based on a given reference station, OPMT, but as all type of antennas have been tested, we consider that

the maximum difference cannot be larger than the maximum peak-to-peak difference between the results of Table 2, which correspond to the numerical results provided just before.

TABLE II. IMPACT ON THE HARDWARE DELAYS DETERMINED BY RELATIVE CALIBRATION OF USING THE P3 OR THE SEPARATE P1 AND P2 ANTENNA PHASE CENTERS, WHEN THE REFERENCE STATION IS OPMT (OP), BASED ON AN 3S-02-TSADM ANTENNA, AND THE TRAVELING STATION IS USING A ASH701945C_M ANTENNA.

Station	Antenna	dP1 (ns)	dP2 (ns)	dP3 (ns)
PTBB (PTB)	ASH700936E	-0.001	-0.005	0.005
IENG (IT)	ASH701945C_M	0.001	-0.002	0.006
SP01 (SP)	AOAD\M_T	-0.002	-0.007	0.006
SP02 (SP)	AOAD\M_T	-0.002	-0.007	0.006
RO_5 (ROA)	LEIAR25.R4	-0.105	-0.175	0.003
RO_6 (ROA)	LEIAR25.R4	-0.094	-0.157	0.003
PT07 (PTB)	NOV702GG	-0.097	-0.162	0.003
GTRB (IT)	NOV702	-0.098	-0.164	0.004
INR7 (IT)	SEPCHOKE_MC	-0.043	-0.074	0.005
ORBA (ORB)	SEPCHOKE_MC	-0.042	-0.072	0.004
BRUX (ORB)	JAVRINGANT_DM	-0.006	-0.015	0.008
ZTB1 (ORB)	TRM59800	-0.004	-0.012	0.008

VI. CONCLUSION

This paper presented a study of the consistency between the P1 and P2 reference maintained by the Group 1 laboratories for calibration. The stability of the inter-signal hardware delays dP1-dP2 was also investigated. The dP1-dP2 values were computed from the pseudorange measurement, after applying a correction for the frequency-dependent antenna phase center and the frequency-dependent ionosphere corrections. These values were then compared with the calibrated values.

The differences obtained between calibrated and computed values range from 0.2 to 1.8 ns for the calibration campaign of 2014, from -0.1 to +0.6 ns for the calibration campaign of 2016. The uncertainty on these differences was estimated to 1.4 ns; except for one station in the calibration campaign of 2014, the differences are therefore well inside the one-sigma uncertainty. A comparison was also done with absolutely calibrated stations, and reach 0.6 and 1.6 ns respectively.

Considering the time link for which the difference is the largest among the stations used in the present study, we obtained a difference between the calibrated time transfer solution obtained from either P1 or P3 of 1.0 ns. This difference is well inside the 2.1 ns uB uncertainty of a time transfer link based on GNSS P3 or PPP, when considering the 1.5 ns uncertainty on each calibrated Group 1 station.

Concerning inter-signal hardware delay stability, it was shown that the computed dP1-dP2 for the station allow to detect only variations larger than 2 ns, due to existing variations coming from the ionospheric products used. However, as these ionosphere-induced variations are common to the stations of a same region, the difference between the solutions obtained for two stations can be analysed more precisely to detect possible dP1-dP2 variations at the level of 200 ps. This technique allows studying the stability of inter-signal hardware delays by comparison with a remote station, when no other station is available in colocation providing the possibility of have a common-clock setup.

Finally, the impact of frequency-dependent antenna phase centers on calibration of P1 and P2 was investigated. Our results show that the differences on the hardware delays of the separate codes P1 and P2 reaches a maximum of 100 ps for P1 and 200 ps for P2 when antenna phase centers of L1 and L2 are used or when the antenna phase center of L3 is used for both P1 and P2. However, after applying the ionosphere-free combination, the final impact on the P3 combination is always lower than 10 ps.

ACKNOWLEDGMENT

The authors acknowledge the BIPM and Group 1 laboratories for the calibrations, the time laboratories for the availability of RINEX data and the IGS for the availability of the ionospheric products.

REFERENCES

[1] J. Plumb, K. Larson, J. White, E. Powers: Absolute calibration of a geodetic time transfer system, IEEE Transactions on Ultrasonics, Ferroelectrics, and Frequency Control 52 (11), 1904 – 1911 (2005)

[2] A. Proia, G. Cibiel, L. Yaigre: Time stability and electrical delay comparison of dual frequency GPS receivers, 44th Annual Precise Time and Time Interval (PTTI) Meeting, Reston, VA 26-29 November2012, 297 – 302.

[3] G. Petit, Z. Jiang, P. Uhrich, F. Taris: Differential calibration of Ashtech Z12-T receivers for accurate time comparisons, 14th European Frequency and Time Forum, Torino, Italy March 2000 (Swiss Foundation for Research in Microtechnology, Neuchâtel, Switzerland (2000) 40 – 44

[4] H. Esteban, J. Palacio, F.J. Galindo, T. Feldmann, A. Bauch, D. Piester: Improved GPS-based time link calibration involving ROA and PTB, IEEE Transactions on Ultrasonics, Ferroelectrics, and Frequency Control 57 (3), 714 – 720 (2010)

[5] ftp://ftp2.bipm.org/pub/tai/publication/gnss-calibration/guidelines

[6] Z. Jiang, D. Matsakis and V. Zhang, Long-term instability in UTC time links, Proc. Precise Time and Time Interval, Monterey, 2017.

[7] P. Defraigne, G. Petit: Time transfer to TAI using geodetic receivers, Metrologia 40, 184 – 188 (2003).

[8] M.A.Weiss, G. Petit, Z. Jiang: A comparison of GPS common-view time transfer to all-in-view, IEEE International Frequency Control Symposium and Exposition, Vancouver, Canada 29-31 August 2005 (IEEE International, 2005).

[9] D. Orgiazzi, P. Tavella, F. Lahaye: Experimental assessment of the time transfer capability of precise point positioning (PPP), IEEE International Frequency Control Symposium, Vancouver, Canada 29-31 August 2005 (IEEE International, 2005) 337 – 345Atx

[10] M. Hernández-Pajares, J. M. Juan, J. Sanz, R. Orus, A. Garcia-Rigo, J. Feltens, A. Komjathy, S. C. Schaer, A. KrankowskiIono, The IGS VTEC maps: a reliable source of ionospheric information since 1998, J Geod (2009) 83:263–275

[11] ftp://ftp2.bipm.org/pub/tai/publication/gnss-calibration/group1/1001-2016

[12] J. Delporte, D. Valat, T. Junique, FX Marmet, Progress on absolute calibrations of GNSS reception chains at CNES, Proc of the IEEE

International Frequency Control Symposium, New Orleans, May 9-12, 2016.

[13] P. Tavella, I. Sesia, G. Cerretto, G. Signorile, D. Calonico, R. Costa, C. Clivati, E. Cantoni, C. De Stefano, M. Frittelli, V. Formichella, P. Cerabolini, L. Rotiroti, E. Biserni, V. Leone, E. Zarroli, D. Sormani, P. Defraigne, N. Ozdemir, Q. Baire, M. Gandara, V. Hamoniaux, E. Varriale, Q. Morante, T. Widomski, J. Kaczmarek, J. Uzycki, K. Borgulski, P. Olbrysz, J. Kowalski, A. Cernigliaro, F. Fiasca, A.Perucca, S. Mantero, V. Dhiri, T. Veiga, T. Suárez, J.Diaz, M.Mangiantini, A.E. Wallin, L. Galleani, Time Dissemination Services: The Experimental Results of the European H2020 DEMETRA Project, Proc. IFCS 2016, May 2016, New Orleans.

[14] Görres, B., J. Campbell, M. Becker, M. Siemes (2006). Absolute calibration of GPS Antennas: Laboratory results and comparison with field and robot techniques. GPS Solutions, Volume 10, Number 2, Springer, 136-145.

.

UTC time link calibration in the frame of APMP - Campaigns in 2014-2016

Kun LIANG, Aimin ZHANG, Zhiqiang YANG
National Institute of Metrology
NIM
Beijing, China
Liangk@nim.ac.cn

Jia-lun WANG, Huang-tien Lin
National Time and Frequency Standard
Laboratory, Telecommunication Laboratories
TL
Chunghwa Telecom

Ye WANG
Beijing Jiaotong University
BJTU
Beijing, China

Fan YANG, Jun YANG
Beijing Institute of Radio Metrology and Measurement
BIRM
Beijing, China

Tadahiro Gotoh
National Institute of Information and Communications Technology
NICT
Tokyo, Japan

Zhiwu CAI
Beijing Satellite Navigation Center
BSNC
Beijing, China

Kun LIANG, Zhiheng JIANG
International Bureau of Weights and Measures
BIPM
92312 Sevres Cedex, France

Weihua MOU
National University of Defense Technology
NUDT
Changsha, China

***Abstract*—The experiments and results of these calibation campaigns in the frame of APMP from 2014 to 2016 have been reported and the experiment setups and the corresponding delay measurements have been discussed, and the uncertainty has been evaluated for the campaigns.**

Keywords—UTC, time link, calibration, APMP

I. INTRODUCTION

At present, the TAI (International Atomic Time) corporation organized by BIPM (International Bureau of Weights and Measures) has derived the standard time worldwide, the UTC (Coordinated Universal Time), with the contribution of the seventy-four timekeeping laboratories and moreover the fifty-two ones among the laboratories have contributed to generate the rapid UTC. For this contribution, the time transfer link between TAI laboratory and PTB (Physikalisch-Technische Bundesanstalt, Braunschweig, Germany) is built, which uncertainty is mainly limited by the link calibration uncertainty because of the unbalanced uncertainty construction, thus good calibration is needed for the responsibility of the transfer accuracy, and moreover the link should be calibrated periodically in order to ensure the accuracy variation of time transfer and dissemination. GPS time transfer is one of the most important techniques for TAI time transfer links, and the realization of UTC. For many years, the BIPM organized the calibration of GNSS equipments in UTC-contributing laboratories. Since 2012, BIPM has proposed the new calibration scheme [1] and drawn up the new guideline for GNSS(Global Navigation Satellite System) link calibration [2] and assigned several NMIs (National Metrology Institute) including NIM (National Institute of Metrology, Beijing, China), TL (Telecommunication Laboratories) and NICT (National Institute of Information and Communications Technology, Tokyo, Japan) in APMP (Asia Pacific Metrology Program, depicted in figure 1) as the Group 1 (G1) laboratories to implement the possibility of calibration of Group 2 (G2) laboratories in the local RMO (Regional Metrology Organization) that gives the assist to BIPM, in other words, the laboratories in G2 group participate in calibration trips where at least one G1 system will serve as a reference. During 2014-2016, we have implemented several calibration campaigns including BSNC (Beijing Satellite Navigation Center, Beijing, China), NTSC (National Time Service Center of Chinese Academy of Science, Linton, China) and BIRM (Beijing Institute of Radio Metrology and Measurement, Beijing, China) in China and the G1 calibration tour for exercise and demonstration in APMP area.

Supported by Chinese NSFC program 11303024, the key research program of Chinese MST 2017YFF0212000, APMP TCI 2016-06-TCTF and MEDEA Project supported by PTB



Fig. 1. Rough APMP area(rectangle with rounded corners)

II. CALIBRATION CAMPAIGNS AND THE EXPERIMENTAL SETUPS

The calibration campaigns implemented by NIM in APMP areas during 2014-2016 are shown in table I. Hereinto, the laboratory in BSNC who is planning to contribute to TAI is newly constructed, and there are some basic facilities for the timekeeping system, and the time transfer links of NTSC have not been calibrated since 2008, and the time transfer links of BIRM have never been calibrated.

TABLE I. CALIBRATION CAMPAIGNS

Laboratory	Time	Stations to be calibrated	Calibrator
BSNC	July, 2014	SN58, SN59	IMEU(NIM-TF-GNSS-1)
	May, 2015	SN58, SN59	IMEU(NIM-TF-GNSS-1)
NTSC	March-April, 2016	NTP1, NTP2, NTP4	NIM Cal-001
TL	August-September, 2016	TLT1, TLT3	NIM Cal-001
BIRM	October-November, 2016	BI01, BI02	IM20(NIM-TF-GNSS-2J)
NICT	December, 2016	NC4C, NC5G	NIM Cal-001

The differential calibration with closure [2] is employed, where the calibrator travels from the location of the reference station to the location of the station to be calibrated, and the calibration value of the reference station will be transferred to the station to be calibrated. The common clock difference (CCD) experiments are implemented one after another between the calibrator and the reference station for the keeping of the calibration value of the reference station, and between the calibrator and the station to be calibrated for the transferring of the calibration value of the reference station. Finally, the closure CCD experiments between the calibrator and the reference station must be implemented for the verification of the consistence of the calibration value during this period. Usually, the closure is one of the main contribution sources for the calibration uncertainty.

During the calibration, the NIM calibrator and the local system are connected and the experiment setups are depicted generally in figure 2. The precise positions of the two traveling antennas should be known with an uncertainty of order a few cm and set in the traveling receivers inside the NIM calibrator. Daily CGGTTS (CCTF Group on GNSS Time Transfer Standards) and RINEX (Receiver Independent Exchange Format) files of the traveling receivers and local systems were logged for four to seven successive whole days. All the calibrations are referenced to IMEJ (Dicom GTR50, site name for CGGTTS is IM06), which is the master GPS time and frequency transfer receiver of NIM for TAI contribution has been calibrated in 2012 by NIM and 2014 by BIPM.

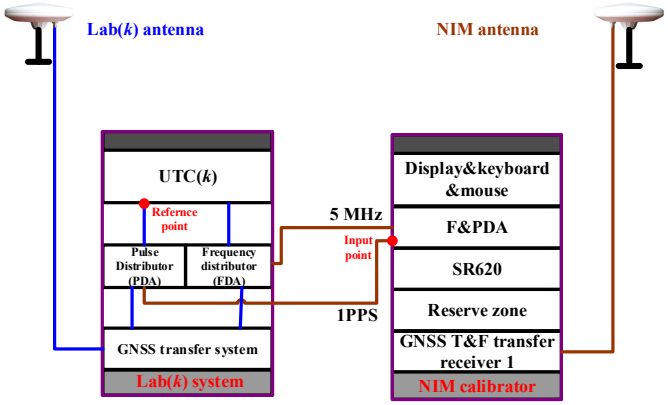


Fig. 2. The schematic of experiment setup

The first NIM calibrator in figure 3 is IMEU (site name for CGGTTS is IM03) that is a NIM-TF-GNSS-1 receiver (made by NIM, see description in [3]), which was evaluated in the performances as a traveling receiver for the link and equipment calibration in [4] and was calibrated separately by NIM in 2012 and by BIPM in 2014. Since 2014, a new calibrator (coded NIM Cal-001, the left one in figure 4) has been developed based on the two time and frequency transfer receivers including IM09 (made by NIM, NIM-TF-GNSS-2) which is described and evaluated in [5] and IM11 (Dicom GTR51), and accordingly a calibration guideline for the calibrator was drawn up (see details in [6]). IM20 (made by NIM, NIM-TF-GNSS-2J) is temporarily for the time transfer link calibration of BIRM.



Fig. 3. IMEU



Fig. 4. NIM and NICT calibrators



Fig. 5. IM20

III. Calibration Operation and Numerical Results

All the CCD experiments and other necessary delay measurements including the reference delays and the antenna cable delays have been implemented. The methodology has been described in section II. Here we focus on the results of these measurements.

A. Calibration Campaigns at BSNC

In 2014, SN58 and SN59 receivers (Septentrio PolaRx4eTR receivers) of BSNC were calibrated using NIM reference receiver IMEU on site at BSNC by NIM. The data of IMEJ and IMEU at NIM from MJD 56840 to 56845 and the data of BC01, BC02 and IMEU at BSNC from MJD 56849 to 56854 were used for computation of the calibration, and the internal delay (INTDLY) values of P3 code were 55.6 ns and 54.2 ns.

In 2015, the calculation of these two receivers have been implemented once again for verification based on the CGGTTS data from 57153 to 57158. The CGGTTS data of Septentrio receivers were generated by the software of rin2cgg.exe using the Rinex data of the receivers and those of IMEU were generated by itself. The common view (CV) method was used for the data processing, and the calibration values 56.1 ns and 54.5 ns.

Below, we just show the CCD results in 2015 for one example in figure 6-8. On MJD 57199, the measurements in BSNC were stopped and IMEU was sent to NIM for the closure experiment with IMEJ. From the one-week data, we can see the good closure in figure 8 after compensating all the delays of IMEU.

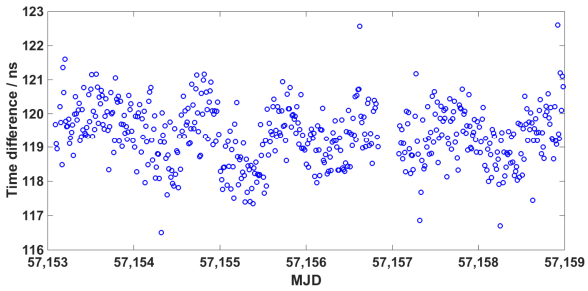


Fig. 6. CCD between SN58 and IMEU

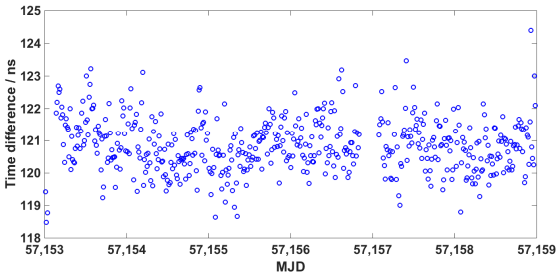


Fig. 7. CCD between SN59 and IMEU

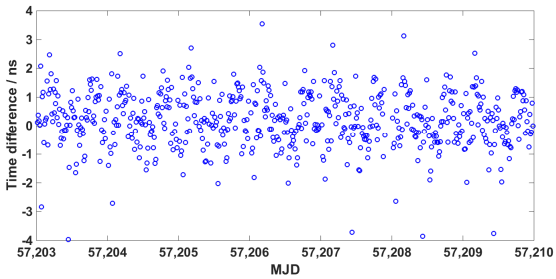


Fig. 8. CCD with IMEJ

In Oct 2013, SN59 receiver was calibrated at NIM using differential calibration through one golden receiver calibrated by BIPM and the INTDLY values of P3 code was 56.1 ns. So, from the three calibration campaigns for BSNC summarized in table II, the consistence among them could be got within 1.9 ns during three years. Especially, for the calibration campaigns in 2014 and 2015, the good agreement between them is within 0.5 ns.

TABLE II. BSNC CALIBRATION VALUES BY NIM

Campaigns	Cal by	P3 INTDLY calibration value (ns)	
		SN58	SN59
2013	NIM	-	56.1
2014	NIM	55.6	54.2
2015	NIM	56.1	54.5
Delta(2014-2013)	NIM	-	-1.9
Delta(2015-2013)	NIM	-	-1.6
Delta(2015-2014)	NIM	0.5	0.3

B. APMP G1 Calibration Trips

After the BIPM proposed the new scheme for GNSS equipment calibration, it's important and pressing to perform a calibration campaign among three G1 labs (NICT, NIM, and TL), to give confidence in the calibrations of currently operating G1 receivers and therefore in any subsequent calibration of G2 receivers. As mentioned in section II, the NIM present calibrator is NIM Cal-001. TL and NICT also have their calibrators prepared for this motivation. Thus in 2016 one APMP TCI (Technical Committee Initiation) project participated by the three G1 laboratories NIM, TL and NICT in APMP was finished for verification and demonstration of UTC time link calibration implementation. This project is to hold a GNSS time link calibration campaign with closure by circulating the NIM calibrator among the G1 laboratories in APMP with the route NIM->TL->NIM->NICT->NIM.

1) Calibration tour to TL

The NIM calibrator has been evaluated and the CCD experiments between it and the NIM main receiver IM06 have been implemented for one long period. In the mid-August in 2016, NIM calibrator was sent to TL and in late August the calibrator arrived at TL. Since early September, the calibrator has been installed at TL in the same environment of the two TL receivers, TLT1 (Astech Z12-T) and TLT3 (Dicom GTR50). The indoor temperature was in control within ±1 ℃. The cable was kept in a temperature-controlled environment as long as possible.

The zero point of UTC(TL) is defined as one output of one PDA (pulse distribution amplifier) at TL. The calibrator PPS input cable is connected to another output of this PDA. Thus, the reference delay of the calibrator between the reference point and the calibration point could be regarded as 0 ns. Accordingly, the reference delays of IM09 and IM11 were both 40.4 ns in terms of the relation between the PPS inputs of the calibrator and the receivers and the known internal delays of the two receivers were 3.37 ns and 7.57 ns, respectively. Thus, using CGGTTS data from MJD 57653 to 57657, the P3 code calibration values could be got. The time interval counter (SRS SR620) inside the NIM calibrator was used for the reference delay measurements and before the measurements SR620 was warmed up for at least one hour. Both TLT1 and TLT3 receivers have been calibrated by BIPM in the first G1 calibration campaign in 2014 and the calibration values have been input in the header of CGGTTS of the two receivers.

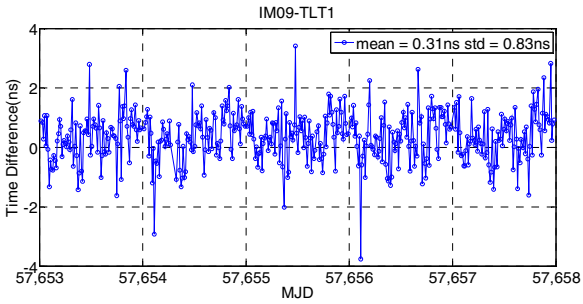


Fig. 9. CCD results 1 at TL

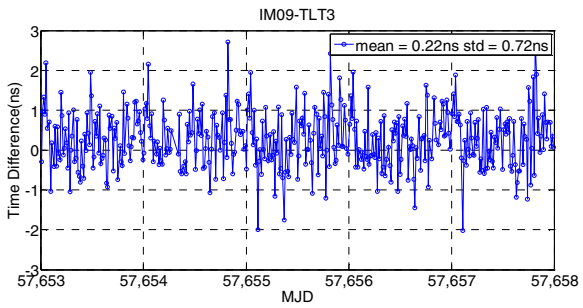


Fig. 10. CCD results 2 at TL

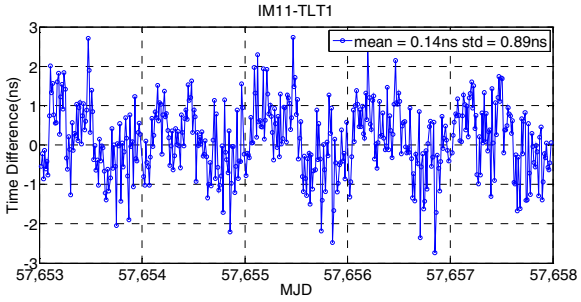


Fig. 11. CCD results 3 at TL

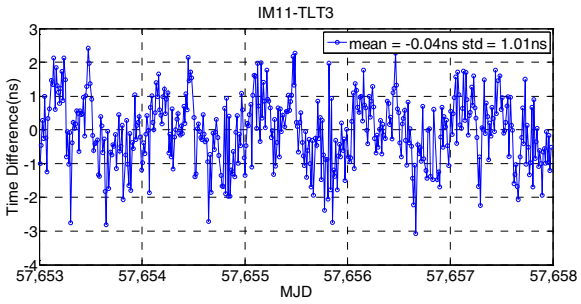


Fig. 12. CCD results 4 at TL

In figure 9-12, we have combined all the reference delays of IM09 and IM11 and the CCD results of the calibrator with IM06 at NIM. Combined with table III, we can see the agreements between the calibration results of TL receivers given separately by BIPM (refer to the calibration results in both 2014 and 2016 in [7] and [8]) and by NIM within 0.4 ns and the standard deviation of the CCD results with reference to the calibrator were about 1 ns. In [8], there is no P3 code calibration values provided by BIPM, and then the P3 code calibration values are calculated through the iono-free combination of P1 and P2 code calibration values. Certainly, at last, the closure experiments were implemented at NIM for the verification of the TL calibration results and uncertainty evaluation. The closure results were within 0.5 ns.

TABLE III. TL CALIBRATION VALUES BY NIM AND BIPM

Campaigns	Cal by	Delta P3 calibration value (ns)	
		TLT1	TLT3
TL(2014)	BIPM	400.8	-41.8
TL(2016)	BIPM	400.9	-42.1
TL(2016)	NIM	401.0	-41.7
Delta(BIPM-NIM 2016)	-	-0.1	-0.4

2) Calibration tour to NICT

The closure experiments for TL calibration experiments were also deemed as the CCD experiments at NIM before the NIM calibrator was sent to NICT. In the end of November in 2016, NIM calibrator was sent to NICT from NIM and in early December, NIM calibrator arrived at NICT. Since the mid-December, the calibrator has been installed at NICT.

The basic principle for the calibration experiment at NICT was the same as that at TL. Thus, the setup for the experiments at NICT was similar to that at TL. In terms of this understanding, the experiments were implemented. When NIM calibrator returned back to NIM in January, the final closure experiments were finished. The final maximum discrepancy in both closure experiments (respectively after TL tour and after NICT tour) was 0.84 ns that should be involved in the uncertainty evaluation.

In the NICT experiments, two receivers, NC4C (Septentrio PolaRx4eTR) and NC5G (Dicom GTR50), included inside the NICT calibrator (the right one in figure 4) and one other receiver, NC01 (Septentrio PolaRx2eTR), have been involved and their agreement with the receivers in NIM calibrator could be observed from figure 13-18. Anyway, for the NICT tour, only two complete days' measurements have been acquired because of not enough time in the end of the year. Both NC01 and NC5G receivers have been calibrated by BIPM in the second round of G1 calibration campaign in 2016. Also, the P3 code calibration values are deferred from the P1 and P2 code calibration values provided in [8] as mentioned in section 1).

Hereinto, the result for NC5G is the change with respect to values entered in the receiver, and the result for NC4C is the total delay because the antenna cable delay and the reference delay are not completely measured.

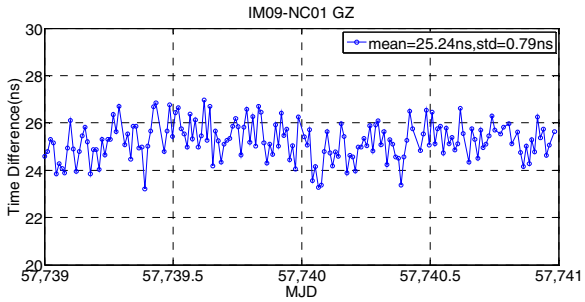


Fig. 13. CCD Results 1 at NICT

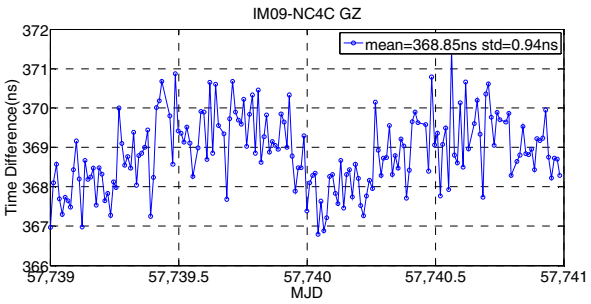


Fig. 14. CCD Results 2 at NICT

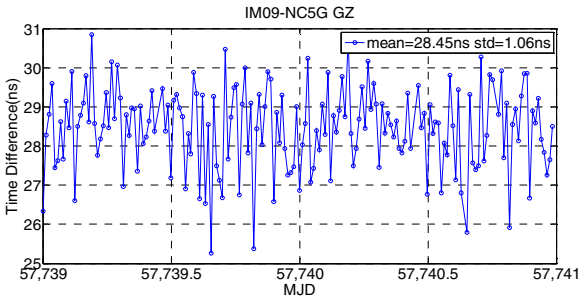


Fig. 15. CCD Results 3 at NICT

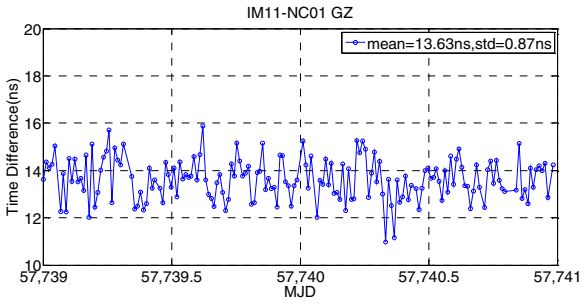


Fig. 16. CCD Results 4 at NICT

All the calibration results and the agreement within 0.7 ns between BIPM and NIM calibration results could be seen in table IV.

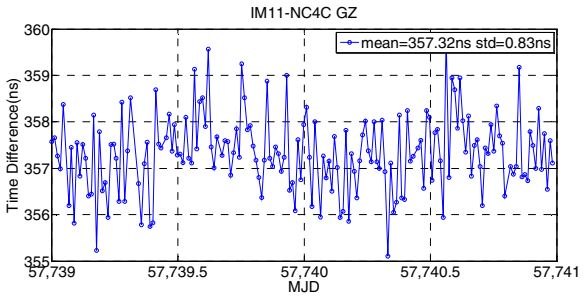


Fig. 17. CCD Results 5 at NICT

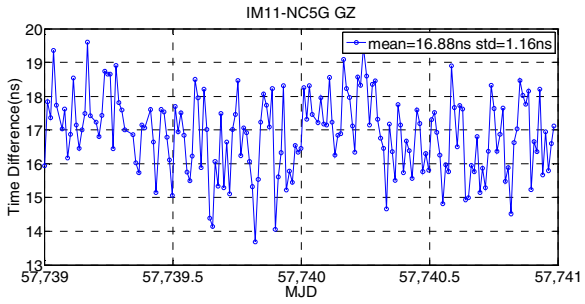


Fig. 18. CCD Resuts 6 at NICT

TABLE IV. NICT CALIBRATION VALUES BY NIM AND BIPM

Campaigns	Cal by	Delta P3 calibration value (ns)		
		NC01	NC5G	NC4C
NICT(2016)	BIPM	212.0	-41.6	-
NICT(2016)	NIM	211.3	-41.3	-346.1(Total delay)
Delta(BIPM-NIM 2016)	-	0.7	-0.3	-

C. Calibration Campaigns at NTSC and BIRM

As well, in late February 2016, NIM received the calibration request from G2 laboratory NTSC. Due to their urgent request, with NIM Cal-001, NIM started GPS time link calibration tour of NTSC in April 2016, which is the first G2 calibration by G1 laboratory in APMP in fact and finished in May. However, the time links of NTSC had been uncalibrated for long time and the calibration values by solution are big, then NIM and BIPM together did the calibration for the second time in July, and the NIM results were verified successfully by BIPM. Also, in March, 2016, BIRM proposed the calibration request and due to the ongoing calibration actions of APMP TCI project with NIM Cal-001 calibrator, the BIRM calibration has been delayed and implemented from October to November 2016 with IM20 as the calibrator.

1) Calibration tour to NTSC

We finished the calibration and made the early version of the calibration report of 1014-2016 and submitted to BIPM, and it happened that BIPM sent its calibrator to NIM for G1 calibration, and then BIPM also sent its calibrator for the double verification of NIM calibration results during the late period of July. During the first calibration by NIM, we found the noisy raw observation of NTP4 at NTSC thus NTSC decided to use NTP3 receiver instead of NTP4. So BIPM has acquired the calibration values of P1 and P2 codes for NTP1, NTP2 and NTP3(see [7] for details).

Finally, the NIM calibration results have been verified by getting the differences of P1 and P2 codes for NTP1 and NTP2 receivers between two calibrations separately by NIM and by BIPM and the maximum differences 1.6 ns are within the combined uncertainty 1.8 ns as shown in table V.

TABLE V. NTSC CALIBRATION VALUES BY NIM AND BIPM

Receiver	Cal by	Calibration value (ns)					
		P1	Delta P1	P2	Delta P2	P3	Delta P3
NTP1	NIM	56.1	0.4	54.8	-0.3	58.2	1.6
	BIPM	55.7		55.1		56.6	
NTP2	NIM	55.9	0.4	53.9	-0.3	59.0	1.5
	BIPM	55.5		54.2		57.5	
NTP3	BIPM	53.1	-	52.2	-	54.5	-
NTP4	NIM	54.9	-	52.8	-	58.3	-

2) Calibration tour to BIRM

IM20 has been operated in a stable status continuously for a long period. We had IM20 installed and operated at BIRM

from MJD 57673, however some interferences transmitted from other experiments made the CCD results very noisy and sometimes the standard deviation approached to 2 ns. The data from MJD 57703 to MJD 57706 after the signal transmitting was closed which looks normal are finally used for computation. Data processing results are divided into the ones by GPS C1 and P3 CGGTTS data of the receivers as shown in table VI.

Due to the very early version of the receiver software and the lack of the factory test cables, the refrence delay (REFDLY) value including the external reference delay and the internal reference delay of BIRM has not been measured completely. The external reference delay between the calibration point and receiver PPS input were separately measured before and after calibration at BIRM. The internal reference delay between the receiver PPS input and the receiver time is difficult to be decided due to its very early version of firmware. Thus the calibration values of this receiver included the present internal reference delay.

TABLE VI. BIRM CALIBRATION VALUES

Receiver	Calibration value (ns)	
	C1	P3
BI01	-54.7	-30.4
BI02	-66.4	-54.7

D. Summary of All the Calibration Results

To summarize, in APMP regional area, six calibration campaigns by NIM for five institutes each of which has been included or will be included in TAI corporation have been finished, and the results are in table VII. The good verification has been implemented.

TABLE VII. CALIBRATION RESULTS OF THE APMP CAMPAIGNS BY NIM IN 2014-2016

Campaign	Receiver	Calibration value (ns)	
		C1	P3
BSNC	SN58(2014)	-	55.6
	SN59(2014)	-	54.2
	SN58(2015)	-	56.1
	SN59(2015)	-	54.5
TL	TLT1(2)	-	401.0
	TLT3	-	-41.7
NICT	NC01	-	211.3
	NC4C(2)	-	-346.1
	NC5G(1)	-	-41.3
NTSC	NTP1	-	58.2
	NTP2	-	59.0
	NTP3	-	54.5
BIRM	BI01	-54.7	-30.4
	BI02	-66.4	-54.7

IV. UNCERTAINTY EVALUATION

Due to the similar methodology and operation in all these calibration campaigns, the uncertainty contributors and evaluations could be nearly the same. Here we make one example using uncertainty evaluation of BIRM calibration in table VIII. We evaluated the uncertainty from the sources as follows and got the combined uncertainty as 1.8 ns conservatively for C1 and P3 codes at BIRM. All the measurements related to the cable and reference delays were done with SR620 on the trigger level 1.0 V. And the uncertainties from position references and multipaths are just referenced to the description of [2]. The u_a values are from TDEV of the corresponding CCD results.

TABLE VIII. UNCERTAINTY BUDGET

Unc.	**Value P1 (ns)**	**Value P2 (ns)**	**Value C1 (ns)**	**Value P3 (ns)**	**Description**
u_a (T-V)	0.5	0.5	0.8	0.9	RAWDIF (traveling-visited)
u_a (T-R)	0.5	0.5	0.7	0.8	RAWDIF (traveling-reference)
u_a	0.7	0.7	1.1	1.2	
Misclosure					
$u_{b,1}$	0.1	0.1	0.3	0.1	observed mis-closure
Systematic components related to RAWDIF					
$u_{b,11}$	0.05	0.05	0.05	0.05	Position error at reference
$u_{b,12}$	0.05	0.05	0.05	0.05	Position error at visited
$u_{b,13}$	0.3	0.3	0.3	0.3	Multipaths at reference
$u_{b,14}$	0.3	0.3	0.3	0.3	Multipaths at visited
Link of the Traveling system to the local UTC(*k*)					

$u_{b,21}$	0.5	0.5	0.5	0.5	$REFDLY_T$ (at ref lab)
$u_{b,22}$	0.5	0.5	0.5	0.5	$REFDLY_T$ (at visited lab)
$u_{b,TOT}$	0.8	0.8	0.8	0.8	
Link of the Reference system to its local UTC(*k*)					
$u_{b,31}$	0.5	0.5	0.5	0.5	$REFDLY_R$ (at ref lab)
Link of the Visited system to its local UTC(*k*)					
$u_{b,32}$	0.5	0.5	0.5	0.5	$REFDLY_V$ (at visited lab)
$u_{b,SYS}$	1.1	1.1	1.1	1.1	Components of equation (2)
u_{CAL}	1.5	1.5	1.7	1.8	Composed of u_a and $u_{b,SYS}$
Antenna cable delays					
$u_{b,41}$	0.5	0.5	0.5	0.5	$CABDLY_R$
$u_{b,42}$	0.5	0.5	0.5	0.5	$CABDLY_V$
Combined Uncertainty: 1.8 ns					

V. STABILITY OF THE CALIBRATORS

The stabilities of the three calibrators use in the above calibration campaigns have been compared using the CCD experiment results for one month as shown in figure 19-21.

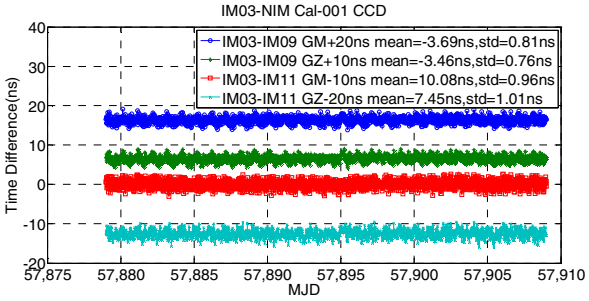


Fig. 19. CCD between IMEU and NIM Cal-001

From table IX as well, the standard deviation within 1.1 ns of the CCD results among these calibrators can be acquired, which could be normal for the noise level for the GNSS time and frequency transfer receivers.

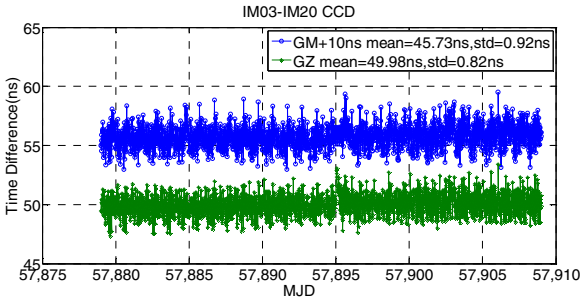


Fig. 20. CCD between IMEU and IM20

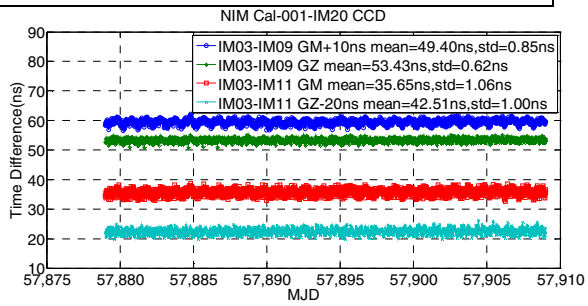


Fig. 21. CCD between NIM Cal-001 and IM20

TABLE IX. STABILITY OF THE CALIBRATORS

Values (ns)	GM		GZ	
	Mean	Std	Mean	Std
IM03-IM09	-3.7	0.8	-3.5	0.8
IM03-IM11	10.1	1.0	7.5	1.0
IM03-IM20	45.7	0.9	50.0	0.8
IM09-IM20	49.4	0.9	53.4	0.6
IM11-IM20	35.7	1.1	42.5	1.0

VI. SUMMARY AND PROSPECTIVES

The experiments and results of these calibration campaigns in the frame of APMP from 2014 to 2016 have been reported and the experiment setups and the corresponding delay measurements have been discussed, and the uncertainty has been demonstrated for the campaigns.

For the more reliability and stability improvement in the future calibration campaigns, maybe more G1 references, such as the different G1 master receivers calibrated by BIPM or the different receivers calibrated by BIPM in one G1 laboratories should be included in the same campaign. It could also be responsible for stabilizing the variation of the calibration values.

ACKNOWLEDGMENT

Thank Dr. Gerard Petit of BIPM for the verification and help during the calibration tours.

REFERENCES

[1] Jiang Z., Arias F., Lewandowski W., Petit G., BIPM Calibration Scheme for UTC Time Links. Proc. EFTF 2011, 2011, 1064-1069.

[2] BIPM. BIPM guidelines for GNSS equipment calibration V2.0. 2014.

[3] LIANG Kun, ZHANG Aimin, GAO Xiaoxun, WANG Weibo, NING Dayu , ZHANG Side, Study and Development of a New GNSS Receiver for Time and Frequency Transfer, EFTF 2012.

[4] Liang K, Feldmann T, Bauch A, et al. Performance evaluation of NIM GPS receivers in use for time transfer with PTB[C]//EFTF-2010 24th European Frequency and Time Forum. IEEE, 2010: 1-8.

[5] Liang K, Zhang A, Yang Z, et al. Developing of one time link calibrator with GNSS at NIM[C]//Frequency Control Symposium & the European Frequency and Time Forum (FCS), 2015 Joint Conference of the IEEE International. IEEE, 2015: 545-548.

[6] BIPM. 2016 Group 1 GPS calibration trip(Cal_Id 1001-2016)-Summary. 2016

[7] BIPM. TM 266: Continuity of GPS “INTDLY” values of Group 1 geodetic receivers in successive Group 1 trips. 2017

Development of a mobile HTS cryogenic oscillator

O. d'Allivy Kelly[1], Y. Lemaître[1], B. Marcilhac[1]
[1]Unité Mixte de Physique, CNRS, Thales, Univ. Paris-Sud, Université Paris-Saclay, 91767, Palaiseau, France
olivier.dallivykelly@thalesgroup.com

D. Chaudy[2,3], J.-M. Hode[2]
[2]Thales Systèmes Aéroportés
75-77 Avenue Marcel Dassault, 33700, Mérignac, France

O. Llopis[3]
[3]LAAS-CNRS, Université de Toulouse, CNRS
7 avenue du Colonel Roche, 31031, Toulouse, France

***Abstract*—High-temperature superconductors (HTS) have shown their potential for analog signal processing at microwave frequencies; they provide high Q resonators, the most critical component of an efficient low phase noise oscillator. Thus, a strategy to outperform state of art quartz oscillators could consist in integrating, in a monolithic block, a planar HTS resonator and a cryo-compatible transistor to build a 1 GHz oscillator.**
However, mobile systems may require reducing hardware size, weight and power consumption while meeting high performances, controlled costs and reliability needs. We discuss these questions and present our approach to validate the integration of HTS based oscillators into embedded systems.

Keywords— Cryogenics; HTS; Oscillators

I. INTRODUCTION

There is a need for high frequency oscillators exceeding quartz performance while meeting mobility constraints of embedded applications (land, naval, airborne systems…). In this respect, HTS technology has many advantages (very high Q factor resonators, reproducibility, frequency accuracy…) that lead now to design high performance HTS oscillators [1].
Even with the very high Q factor of a HTS resonator, the expected phase noise has never been observed on operational oscillators. 3D resonators are vibration sensitive and 2D resonators have been usually tested at too high frequencies.
Our goal is to outperform the specifications of acoustic resonators. To do so, we chose to operate planar resonators at 1 GHz, which has the advantages of a Q higher than 100000, lower multiplication rank and availability of low 1/f noise transistors. Moreover, in order to fully benefit from the low noise floor level at 70 K, we also cool the entire feedback loop including a low-temperature RF amplifier [2].

II. THE TECHNOLOGY PUSH LIMITS

Since the discovery of $YBa_2Cu_3O_{7-\delta}$ (YBCO), more than 30 years ago, the HTS circuits have proven their relevance for high performance RF signal processing. Different circuits (filter banks, multiplexers, …) have already been designed and characterized, presenting very high performances [3.4].
However, there are still many challenges to overcome for this technology to become a product. Indeed, it is not possible to only focus on the HTS circuit without considering the operational requirements, for example a compact cryogenic system is mandatory for embedded applications. Thus, to be developed, an HTS oscillator must be considered as a whole and not only in terms of performance.

III. A GLOBAL APPROACH

Specific applications (military and aerospace), require reducing hardware Size, Weight and Power consumption (SWaP) while meeting high performances, controlled costs, lifetime and reliability needs. Furthermore, due to large R&D costs, HTS devices development requires to address different domains such as RF filters, multiplexers, oscillators but also detectors (bolometers, superconducting quantum interference devices, microwave kinetic inductance detectors, etc.).

1. Cryogenic cooling

HTS devices working temperature (between 60 K and 80 K) is reached and sustained by a cryogenic cooler. It seems difficult to develop from scratch specific cryogenic coolers for each use case. A better idea would consist in re-using coolers employed with infrared sensors as these devices have already shown their performances in terms of reliability and compactness.



Fig 1 Thales Cryogenics coolers
source: www.thales-cryogenics.com

We currently work with cooler devices provided by Thales Cryogenics, one of the European leaders in cryogenic

technology. The best tradeoff between operational constraints and specific needs must be found among the different kinds of coolers: rotary monoblocs, linear split Stirling and pulse tubes [5].
In the case of the oscillator, the vibration noise insulation is critical, therefore we have excluded rotary cooler despite its compactness because the cold finger is directly connected to the motor.
The main advantage of a pulse tube on Stirling machines is that there are no moving parts in the cold finger, so less vibration. On the contrary, Stirling benefit of a smaller size and a better efficiency. An active vibration reduction system can be implemented to these two coolers.

2. Cryopackaging

In order to make mobile devices, standalone dewar (the vacuum chamber that contains HTS circuits) must be developed.
This process has to take into acount many constraints (static vacuum, thermal losses, AC/DC feedthrough, lifetime,…). A standalone compact cryogenic system for RF filter has already been developed by Thales (Fig 2). We are now working to standardize the design and make it compatible with HTS oscillators.



Fig 2 Compact cryogenic system for UHF filter

3. HTS planar resonator circuit

Another key point is the reproducibility of HTS planar resonator performances (Q factor, center frequency).
In this respect, it is necessary to have access to a HTS foundry providing industrial grade YBCO films and stabilized technological processes (lithography, etching, cutting...).
The resonator we use (Fig 3) is designed as a folded half wavelength line. Instead of the classical hairpin shape, we optimized the geometry in a nearly closed C in order to: minimize the size (large pads in the capacitive part of the line), improve the power handling capability (large half circle for the inductive part of the line where the current flows), and minimize the radiated energy (very short electric dipole corresponding to the gap).

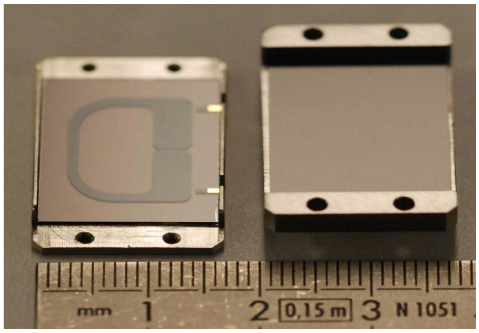


Fig 3 Superconducting resonator: YBCO film (700 nm thick) deposited on a magnesium oxide substrate (500 µm thick)

IV. CONCLUSION

The development of a mobile HTS oscillator is part of a broader framework for the development of HTS technology. It is necessary to adopt a global approach if we want to address use cases. Our goal is to succeed in crossing the innovation gap with a full set of validated industrial processes to build the embedded systems fitting the military and aerospace markets' requirements in terms of quality and quantity.

ACKNOWLEDGMENT

This work is supported by the Direction Générale de l'Armement (DGA).

REFERENCES

[1] Mage J.C, Marcilhac B, Poulain M, Lemaitre Y., Kermorvant J, Lesage J.M., "Low noise oscillator based on 2D superconducting resonator", presented at the IFCS2011, San Fransisco, CA, USA, 2011

[2] D. Chaudy, O. Llopis, B. Marcilhac, Y. Lemaitre, O. d'Allivy Kelly, J.-M. Hode "Active devices choice and design of an all cryogenic superconductor resonator oscillator" submitted to IFCS2017, Besançon, France, 2017

[3] M. J. Lancaster, "Passive Microwave Device Applications of High-Temperature Superconductors", Cambridge University Press, 2006

[4] J-S. Hong, "Recent development in superconducting filters, International Workshop on Microwave Filters", presented at International Workshop on Microwave Filters, France, 2006

[5] D. Willems, J. Mullié, T. Benschop, G. de Jonge "High-reliability and high-efficiency cryocoolers for HTS Applications" presented at the International Workshop on Cooling System for HTS Applications (IWC-HTS), Matsue, Japan, 2015

Latest Results in the Development of an Ultra-Low Phase Noise Rb CPT Vapour Cell Atomic Clock

Tsvetan Burtichelov and Jeremy Everard
Department of Electronics
University of York
York, United Kingdom
tkb502@york.ac.uk, jeremy.everard@york.ac.uk

***Abstract*— This paper describes the latest progress and results, at the University of York, UK, in the development of an atomic clock based on Coherent Population Trapping (CPT). The clock uses Rubidium and a flywheel local oscillator consisting of an ultra-low phase noise Crystal Oscillator (XO), Dielectric Resonator Oscillator (DRO) and Direct Digital Synthesiser. Aspects of the design and construction of the oscillators, phase locked loop, frequency synthesizer and physics package are presented, along with phase noise and stability measurements.**

Keywords—Atomic clocks; CPT; Rubidium; Local Oscillator; Phase Noise; Phase Locked Loops.

I. INTRODUCTION

Recently atomic clocks have been developed to offer high performance in very small packages. See, for example, the chip scale atomic clocks. There is usually a size/performance trade-off in terms of short and long term stability.

The aim of this work is to develop the best performance available in a volume of around a ½ to a full-size shoe box. Both RF (5/10MHz) and Microwave outputs (1.25 to 1.5GHz) should be provided. The key aims here are to produce ultra-low phase noise and excellent long term stability (ADEV).

To achieve this, almost every element of the clock was developed in house from first principles. The key elements are the frequency synthesiser, the physics package and the locking electronics.

This paper will discuss the key aspects of the:

1) Flywheel Local Oscillator
   a) Single/double oven Crystal oscillators
   b) Temperature stabilisation
   c) Dielectric resonator oscillators
   d) Direct Digital Synthesisers
   e) Single sideband mixers
2) Physics Package
   a) Vapour cells:
      i) The Ar/N_2 buffer gas pressures are optimised for low temp. coefficient for the hyperfine lines
      ii) AR coated to minimise reflections
   b) Ultra low noise laser drive electronics and microwave modulation
   c) Magnetic screening and magnetic biasing
3) Laser centre frequency locking
4) Optical sideband/microwave locking to the hyperfine transitions

II. SYTHESISER DESIGN

The LO in the current system uses an ultra-low phase noise crystal oscillator operating at 10 MHz and a DRO operating between 1.25 to 1.5 GHz with a DDS offset loop incorporating a single sideband mixer. Figure 1 shows a block diagram of the configuration.

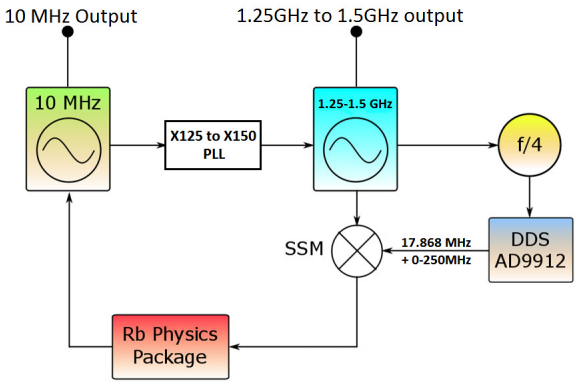


Figure 1: Atomic Clock block diagram.

A. 10 MHz Double Oven Controlled Crystal Oscillator

The Crystal Oscillator (XO) is based on the design described in [1] and [2], but is now constructed in a significantly more compact package and incorporates a two-stage temperature stabilization. Figure 2 shows the layers of temperature stabilization (double oven) and screening.

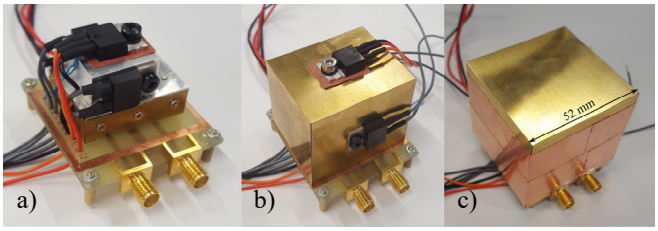


Figure 2: 10 MHz XO. a) Oscillator circuit and resonator enclosure. b) Second enclosure with temperature control. c) Complete oscillator.

The resonator, along with the oscillator circuit is inserted in a custom made aluminium enclosure. A power transistor and resistors are used as heating elements (figure 1.a). The second and outermost enclosures (figures 1.b and 1.c respectively) are made of chemically etched brass plates. The temperature controllers are designed with low-noise voltage regulators and op amps and high-quality passive components.

The circuit diagram of the oscillator is shown in Figure 3. This was presented in [2], but not included as a proceedings paper.

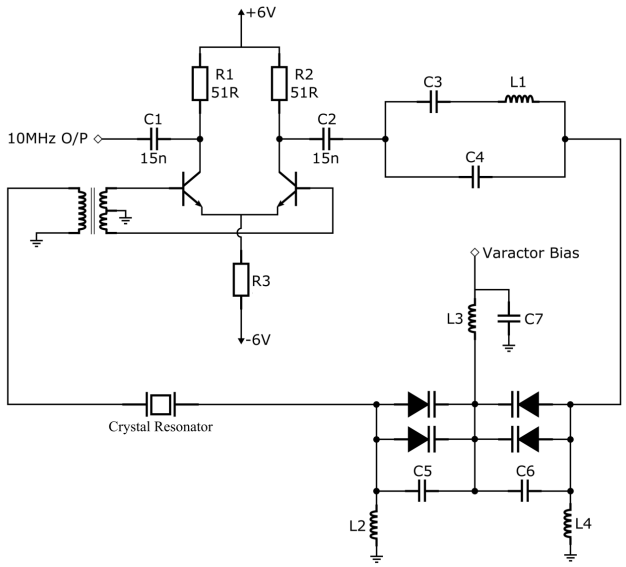


Figure 3: Circuit diagram of the 10 MHz crystal oscillator.

The circuit incorporates:

- A transformer coupled differential amplifier with low flicker noise,
- A notch filter designed to avoid oscillation at the 10.9 MHz mode in the crystal.
- An electronically tuned phase shifter for frequency tuning using varactor diodes.

A full journal paper is currently being written, describing in detail the design and operation of the circuit.

B. 1.5 GHz Dielectric Resonator Oscillator

The design of the DRO is based on the theory and methodology described in [3] and [4]. The microwave output frequency can be preset between 1.25GHz-1.5GHz by changing the Barium Titanite dielectric resonator. The active stage of the oscillator consists of 2 push-pull broadband feedback amplifiers. The output coupler is inserted between the amplifiers to limit saturation effects. An electronic phase shifter is used to phase lock the DRO to the XO. Figure 4 shows the prototype DRO configuration. The resonator enclosure is oversized in this prototype, however the whole oscillator will be made significantly smaller in the final design.

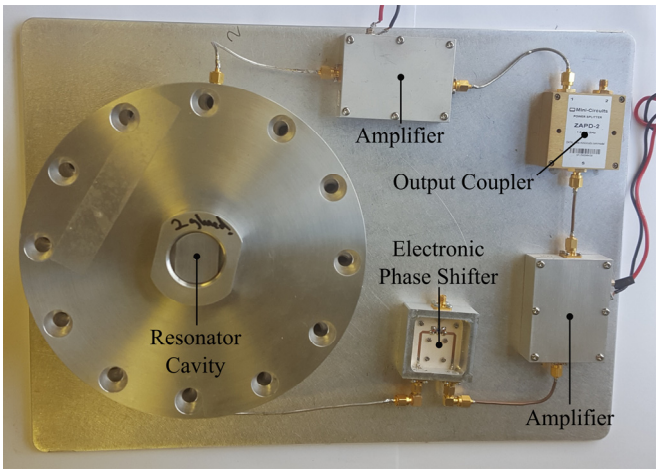


Figure 4: 1.5 GHz Dielectric Resonator Oscillator.

C. Frequency Synthesizer.

Phase locking the DRO to the XO completes the local oscillator, combining the close to carrier phase noise of the XO with the medium and far offset performance of the DRO. Figure 5 shows the phase lock configuration.

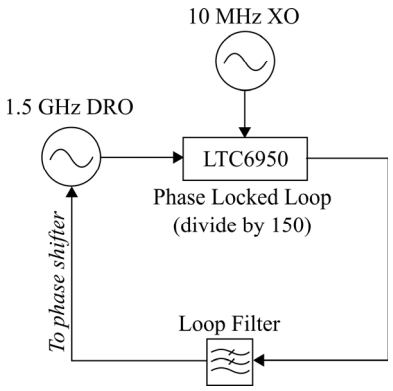


Figure 5: Block Diagram of PLL configuration.

A Direct Digital Synthesizer (DDS) chip is clocked by the DRO and used to produce a 17.868 MHz, tuneable signal. A Single Sideband Mixer (SSM) is then used to upconvert the microwave output to 1.517868 GHz, half the hyperfine

splitting frequency of ^{85}Rb. Figure 6 shows a block diagram of the synthesis chain.

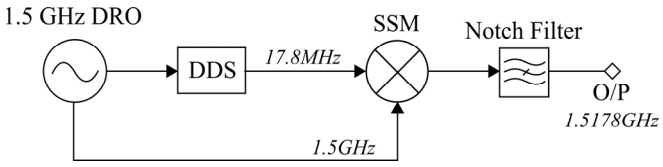


Figure 6: Synthesis chain block diagram.

The SSM uses two double balanced mixers. Lumped element and microstrip quadrature dividers were designed, based on the designs in [5], [6], [7]. The two signals are mixed in phase and with 90° phase difference. This resulting output has a high upper sideband (1.5178 GHz), while the lower sideband is suppressed. There is still significant LO (1.5 GHz) feedthrough, since the isolation of the mixers is not perfect. This is further suppressed using a Notch filter, which is based on the design in [8] and incorporates a high-Q (~3200) coaxial open circuit stub and microstrip transformer. Figures 7 and 8 show photos of the SSM and Notch filter respectively.

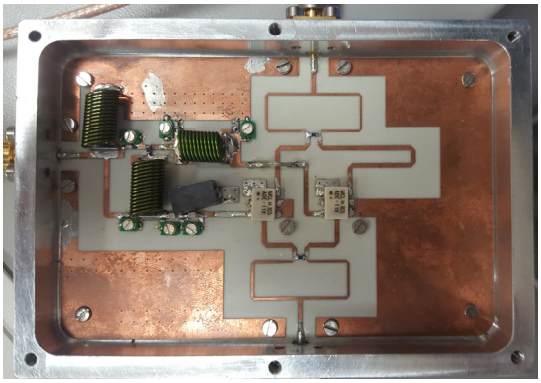


Figure 7: Single Sideband Mixer.

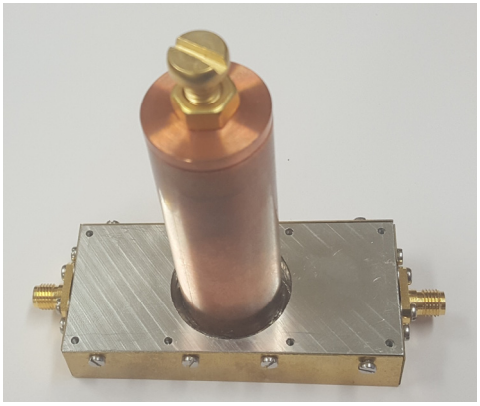


Figure 8: Coaxial open circuit stub notch filter.

The filter can be tuned by adjusting the position of the screw. Figure 9 shows the measured frequency response when the notch was tuned to the LO feedthrough frequency. A 30dB notch is achieved with a single filter, while the loss at ±17 MHz away from the notch is about 1.5dB. A more compact version of this filter can be built using a ceramic resonator.

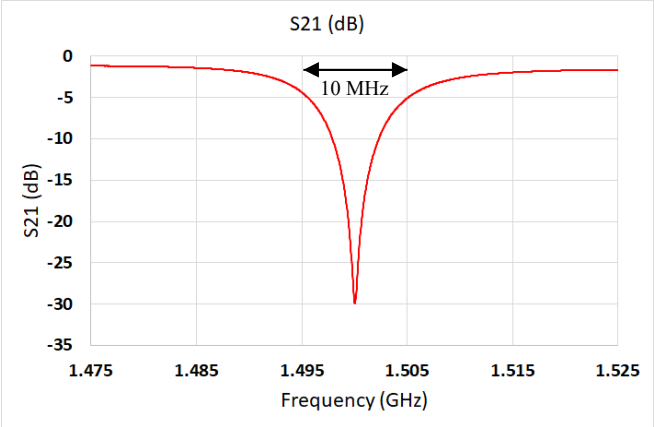


Figure 9: Notch filter frequency response. (-30dB in the stop band, -1.5dB at ±15 MHz)

III. PHASE NOISE MEASUREMENTS

The double oven 10 MHz XO phase noise was measured using the Symmetricom 5120A. The performance is shown in Figure 10.

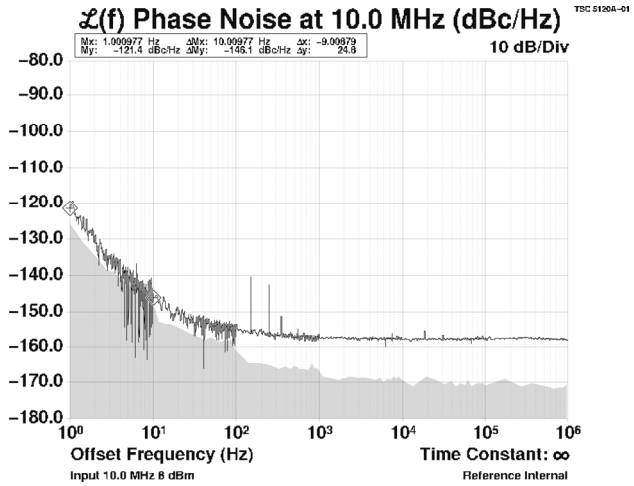


Figure 10: Double oven XO phase noise.

The oscillator exhibits a phase noise of -121.4dBc/Hz at 1Hz offset and -145.1dBc/Hz at 10Hz offset.

A preliminary Allan Deviation measurement was also conducted on the oscillator with the double oven stabilization enabled, however the temperature was not exactly set at the inversion point of the crystal. The plot shows an Allan Deviation of 3×10^{-13} at 100ms as presented in Figure 11.

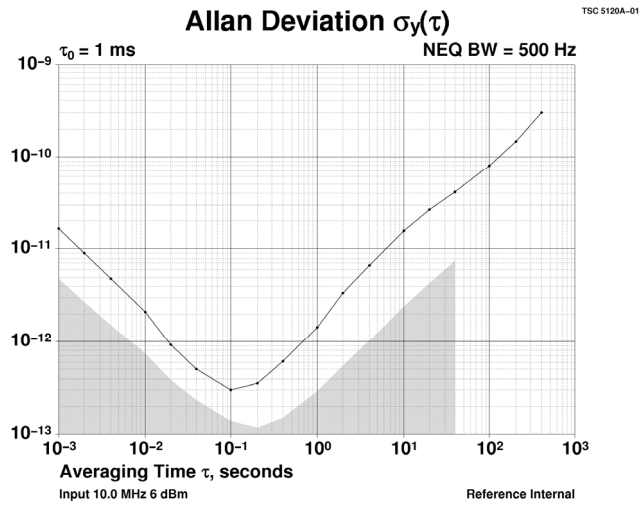


Figure 11: Allan Deviation plot of 10 MHz double oven XO.

The free running DRO was measured by mixing two DROs down to 2.2MHz. The noise floor is set by the measurement system.

The theoretical DRO result is shown in green and based on the following parameters: f_0 = 1.5GHz, Q_0 = 43,000, Q_L = 21,500, P_{AVO} = 200mW, Noise Figure = 11.5dB, fc = 5kHz [3].

The phase locked DRO, shown in blue, was measured directly on an R&S FSWP phase noise analyser. Again, the noise floor is limited by the measurement system.

IV. Phase Noise Performance of a 1.25GHz DRO

The phase noise performance of a 1.25GHz oscillator measured on a low noise floor single channel HP3048 is shown in Figure 13.

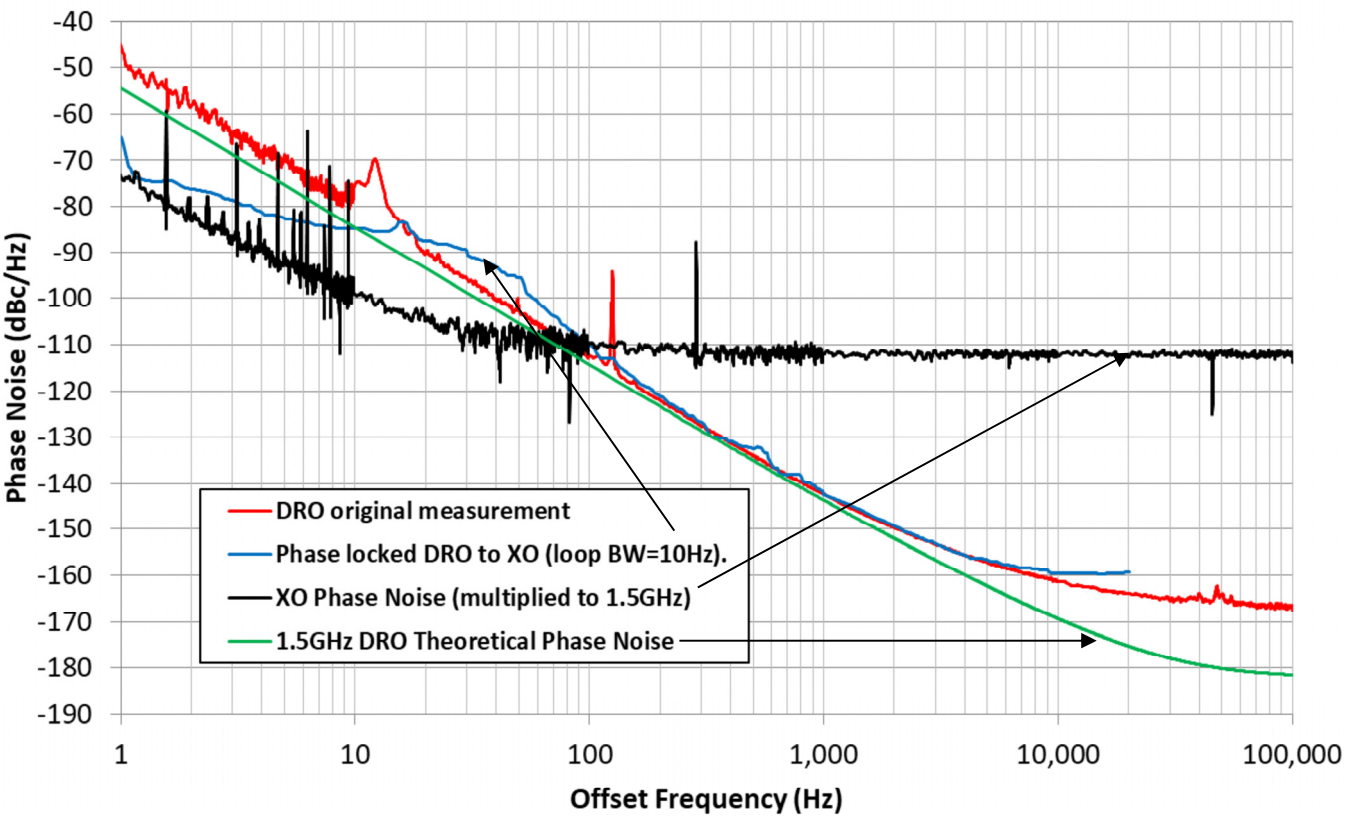


Figure 12: Measured phase noise of free running and phase locked XO and DRO.

Next, the phase locked loop between the XO and DRO was completed and the phase noise of the configuration in Figure 5. This is shown in Figure 12.

The scaled up 10MHz crystal oscillator noise is shown in black.

This demonstrates the low phase noise floor capability of these oscillators. This result is for two oscillators therefore the phase noise performance is -172dBc/Hz at 10kHz offset and < -180dBc/Hz above 50kHz offset.

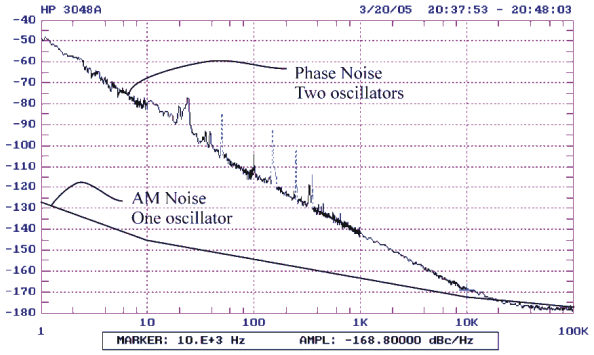


Figure 13: Phase & AM noise for a 1.25GHz DRO

V. PHYSICS PACKAGE

The physics package consists of a Vertical Cavity Surface Emitting Laser (VCSEL) tuned at the D1 line of ^{85}Rb atomic transition (795nm), a custom made 25x25 mm vapour cell containing pure ^{85}Rb and a mixture of buffer gases specified for optimal temperature stability, low noise laser driver electronics and temperature stabilization loops.

A photograph of the AR coated vapour cell with a pair of Helmholtz coils is shown in Firgure 14.

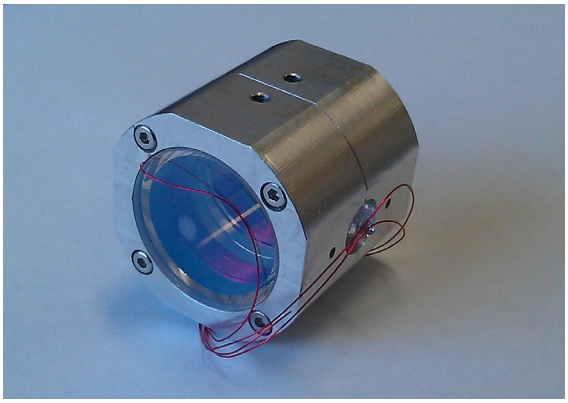


Figure 14: AR coated vapour cell with a pair of Helmholtz coils and optimized Ar/N2 buffer gas pressures.

Figure 15 shows a photo of the prototype physics package with the optical components and control electronics.

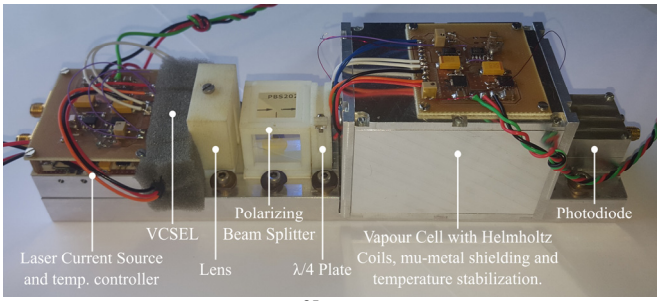


Figure 15: Photo of the ^{85}Rb physics package.

This prototype was made large to enable ease of alignment. For example, the polarizing beam splitter enables optical measurement of the laser centre frequency and modulation sideband levels using a Fabry-Perot spectrometer. All the mounts, enclosures and control circuits of the physics package were developed from first principles.

VI. CONCLUSIONS

An ultra-low noise local oscillator and frequency synthesis chain for a Rb CPT atomic clock were designed, incorporating phase locked loops and frequency synthesizer. The local oscillator exhibits excellent phase noise close to carrier, due to the performance of the 10 MHz double oven controlled crystal oscillator. It also exhibits excellent far from carrier phase noise, due to the performance of the 1.5 GHz DRO. By using a direct digital synthesizer, the phase locked microwave signal was upconverted to half of the hyperfine splitting of ^{85}Rb, which can then be used to detect the CPT resonance. Aspects of the CPT physics package are discussed.

VII. FURTHER WORK

Future work will be focused on completing the loop, locking the local oscillator to the atomic resonance and performing Allan Deviation and phase noise measurements on the completed system. Measurements will also be conducted using multiple clocks to reduce the noise floor of the measurement. Further optimizations will be performed on the control electronics, phase locked loops and oscillator designs.

ACKNOWLEDGMENTS

The authors of this paper would like to thank Leonardo MW Ltd. and EPSRC for funding this research, Professor Robert Lamb, Neil Raphael & Stephen Clark at Leonardo MW Ltd for useful discussions and Dr. David Iddles from Filtronic plc. for his help with the dielectric resonators.

REFERENCES

[1] Jeremy Everard and Keng Ng, “Ultra-Low Phase Noise Crystal Oscillators”, 2007 Joint European Frequency and Time Forum and the IEEE Frequency Control Symposium, Geneva, Switzerland, 29th May to 1st June 2007, pp. 1246-1250.

[2] Tsvetan Burtichelov, Jeremy Everard, “Low Phase Noise 10MHz Crystal Oscillators”, 2016 European Frequency and Time Forum, York, UK, 4th - 7th April 2016

[3] Jeremy K.A. Everard and Konstantinos Theodoropoulos ‘Ultra-Low Phase Noise Ceramic based Dielectric Resonator Oscillators’, IEEE Frequency Control Symposium, Miami USA, June 2006, pp. 869-874.

[4] J. Everard, "Fundamentals of RF Circuit Design with Low Noise Oscillators" ISBN 0 47149793 2, Wiley - December 2000, Reprinted October 2002.

[5] David M. Pozar, "Microwave Engineering", 4th edition, ISBN 978-0-470-63155-3, Wiley - 2012.

[6] Tadashi Kawai, Hiroyuki Mizuno, Isao Ohta, Akira Enokihara "Lumped-Element Quadrature Wilkinson Power Divider", IEEE, 978-1-4244-2802-1/09, 2009, pp. 1012-1015.

[7] Fernando Noriega, Pedro J. González, "Designing LC Wilkinson Power Splitters", eefocus.com [Online], Available: data.eefocus.com/myspace/0/2194/bbs/1190602131/84dbcb80.pdf [Accessed: April 18, 2017]

[8] J.K.A. Everard, J. Bitterling "Low Phase Noise Highly Power Efficient Oscillators", IEEE, International Frequency Control Symposium, 0-7803-3728-X/97, 1997, pp. 919-924.

Active devices choice and design of an all cryogenic superconductor resonator oscillator

D. Chaudy[1,3], O. Llopis[1]
[1]LAAS-CNRS, Université de Toulouse, CNRS
7 avenue du Colonel Roche, 31031, Toulouse, France
dchaudy@laas.fr

B. Marcilhac[2], Y. Lemaitre[2], O. d'Allivy Kelly[2]
[2]Unité Mixte de Physique, CNRS, Thales, Paris-Sud
Université Paris-Saclay, 91767, Palaiseau, France

J.-M. Hode[3]
[3]Thales Systèmes Aéroportés
75-77 Avenue Marcel Dassault, 33700, Mérignac, France

***Abstract*—Several silicon-germanium bipolar transistors have been measured at cryogenic temperature regarding their gain and phase noise performance. The electrical model of the chosen device has been extracted. Using this model, the phase noise performance of a cryogenic superconductor oscillator has been simulated. The results are very promising, with a phase noise level of -155 dBc/Hz at 1 kHz offset from of a 1 GHz carrier.**

Keywords—Microwave oscillator; phase noise; SiGe transistor; nonlinear modeling; superconductors; cryogenics

I. INTRODUCTION

Recent research on high-temperature superconductors (HTS) has led to the development of very high Q planar resonators. Associated with a well-chosen amplifier, those resonators would make a very efficient low phase noise oscillator. This device could outperform the performance of the best quartz referenced oscillators in the low microwave range (near 1 GHz). Indeed, high quality factors of 250 000 have been demonstrated around 1 GHz [1,2,3] with those HTS planar resonators. However, no oscillator with HTS resonators has yet included a low-temperature RF amplifier.

In this paper, the selection and modeling of transistors that can be used to design a low-temperature low phase noise amplifier is described. Then, a fully integrated 1 GHz oscillator working at 60 Kelvin is simulated. The goal is to outperform by 10 dB at least the best commercially available 1 GHz sources, which generally feature a phase noise level in the range of -140 dBc/Hz at 1 kHz offset from 1 GHz carrier.

II. DEVICES SELECTION

Bipolar SiGe-heterojunction transistors are known for their low 1/f noise properties at ambient temperature. Also, contrarily to all-silicon devices, they keep their current and gain performance at low temperature [4,5]. For this reason, four SiGe transistors have been chosen and characterized both at 300 K and at cryogenic temperature. A first test campaign has been conducted at 80 K, using liquid nitrogen, to simplify the experimental procedure. A second campaign at 60 K is scheduled to fully validate the model of the selected transistor. Indeed, the oscillator operation temperature will be 60 K, which ensures an optimized performance of the resonator. All transistors have been measured in common emitter topologies, between two 50 Ω isolators and submitted to a 1 GHz signal. The selection has been based on the combination of two RF parameters: the residual phase noise at the 1-dB compression point and the 50 Ω gain (S_{21}) at 1 GHz.

All measurements have been conducted on a phase noise test bench (Fig. 1) which has been specially optimized for 1 GHz operation. It is based on an ultra-low phase noise 1 GHz source (a multiplied OCXO), uses two phase detectors to benefit from the correlation approach and a search for an optimized rejection of the source AM noise [6] (fine tuning of the quadrature condition).

Specific transistor test fixtures have been used to perform precise RF measurements at low temperature. Indeed, a TRL calibration set for S parameters measurements has been designed with the same test fixtures. Gain (S_{21}) and phase noise results are summarized in Table 1 and 2, for respectively 300 K and 80 K performance.

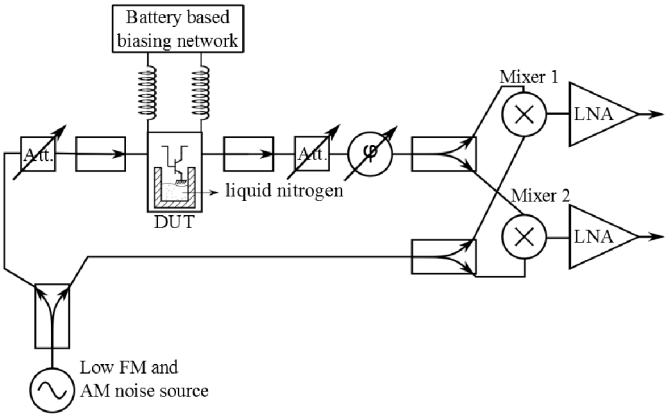


Fig. 1. Test bench for the residual phase noise measurement of a device in liquid nitrogen.

TABLE I. PHASE NOISE AND RF GAIN AT AMBIENT TEMPERATURE.

Phase noise (dBrad²/Hz) and S_{21} at 1 GHz and 300K	***100 Hz***	***1 kHz***	***100 kHz***	**Gain (dB)**
TR-1	-149	-157	-166	21.5
TR-2	-156	-164	-169	20.0
TR-3	-136	-157	-164	21.3
TR-4	-163	-170	-175	14.7

TABLE II. PHASE NOISE AND RF GAIN AT LOW TEMPERATURE.

Phase noise (dBrad²/Hz) and S_{21} at 1 GHz and 80 K	***100 Hz***	***1 kHz***	***100 kHz***	**Gain (dB)**
TR-1	-130	-155	-162	19.0
TR-2	-155	-162	-169	21.4
TR-3	-134	-144	-158	24.4
TR-4	-147	-156	-169	15.6

TR-2 transistor has been chosen among the tested devices. As illustrated in Fig. 2, this transistor features a good residual phase noise level and almost the same performance at ambient and cryogenic temperature.

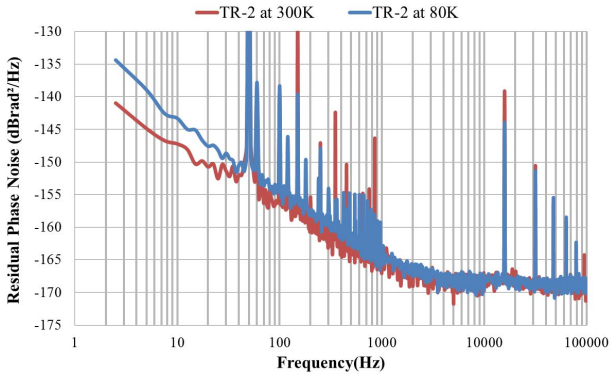


Fig. 2. Measured of TR-2 residual phase noise at 1GHz. Low and ambient temperature measurements with I_C = 30 mA and V_{CE} = 2V.

By using the same test bench, a second investigation has been performed. This time, two silicon phase tuning diodes (varactor diodes) have been tested. Both were measured at ambient and low temperature (60K), and their electrical behavior was unchanged, as illustrated Fig 3. Used in series connected between two 50 Ω loads, these diodes do not add significant phase noise to a 1 GHz RF loop. We tried to measure this phase noise contribution, both at ambient temperature and 80 K, both at low RF input power (0 dBm) or high RF input power (10 dBm), but it was in each case lower than our phase noise measurement bench capabilities, i.e. -171 dBrad²/Hz at 1 kHz offset.

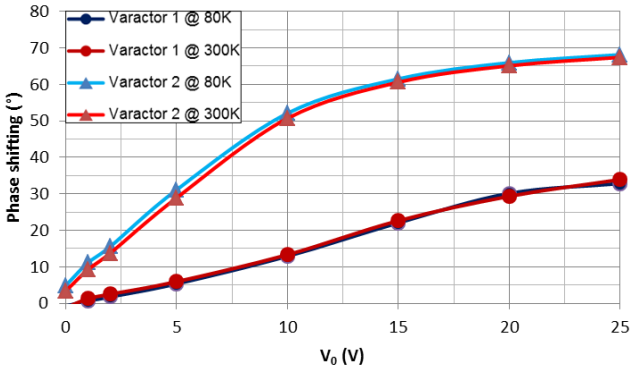


Fig. 3. Phase variation at 1 GHz induced by two in-series connected varactor diodes at low temperature and ambient temperature.

III. LOW-TEMPERATURE NON-LINEAR MODEL

To perform the oscillator design, the physical and electrical characteristics of the active device must be known. Therefore DC, dynamic, low-frequency noise and phase noise measurements have been performed at 80 K. Thanks to those measurements the transistor non-linear model (Gummel-Poon model) has been extracted using Keysight ADS software. Moreover several TR-2 transistors have been tested to validate this model.

This model allows us to fit simulations and measurements for DC-characteristics and S parameters (cf Fig. 4 to Fig. 7 for I(V), S-parameters and output power versus input power). However, concerning the noise, the problem is more complex: an accurate model of the transistor intrinsic noise sources need to be used. Several existing methods and models have already proven their accuracy for SiGe HBT phase noise modeling at ambient temperature. The one we have used is described in the reference [7]. Fig. 8 shows that the implemented model fit the measured residual phase noise.

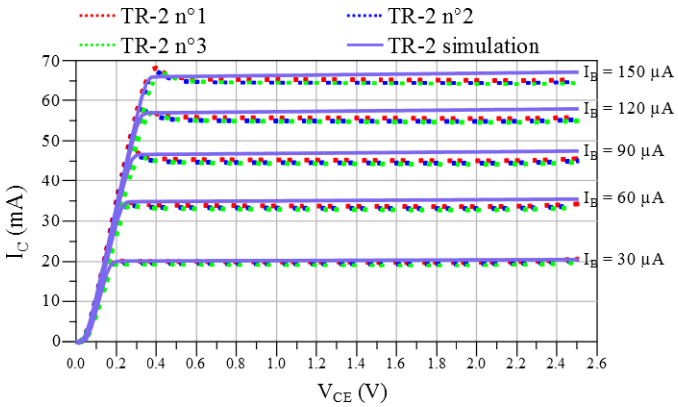


Fig. 4. Simulated and measured DC current-voltage curves at 80 K for 3 different TR-2 transistors.

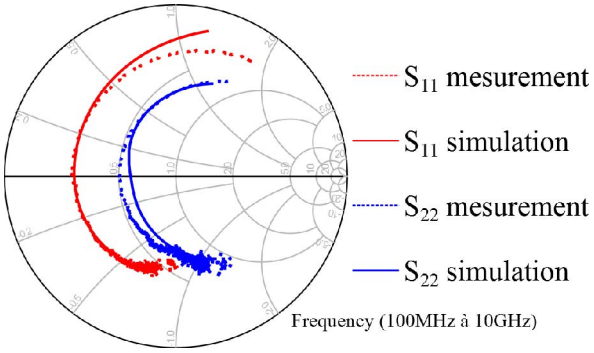


Fig. 5. Simulated and measured S_{11} and S_{22} parameters curves at 80 K for a TR-2 transistor.

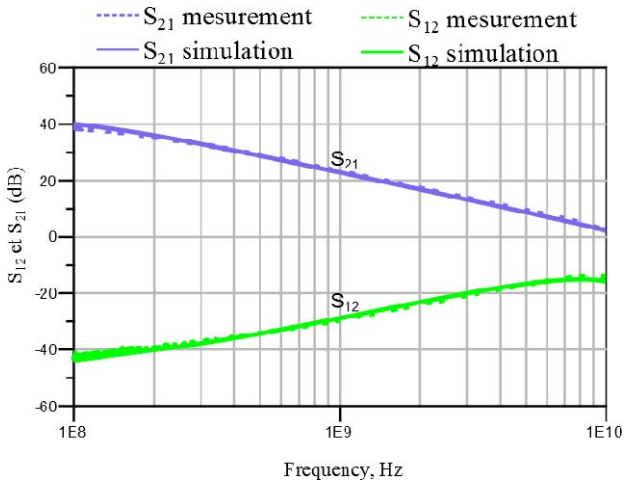


Fig. 6. Simulated and measured S_{21} and S_{12} parameters curves at 80 K for a TR-2 transistor.

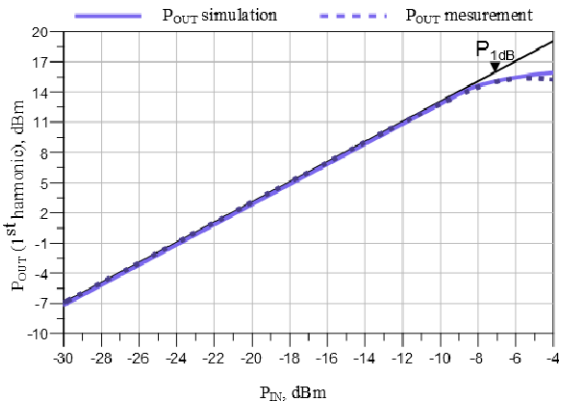


Fig. 7. Simulated and measured power caracteristics at 80 K for a TR-2 transistor.

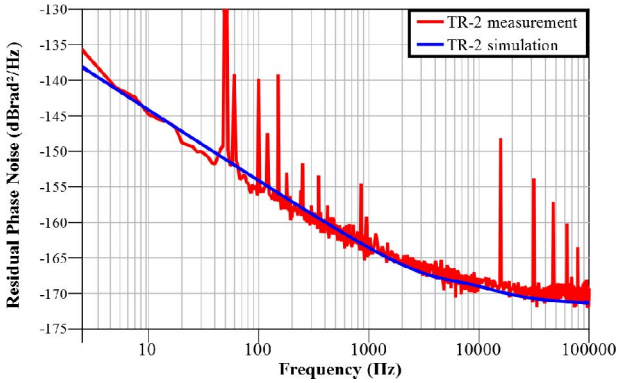


Fig. 8. Simulated and measured TR-2 residual phase noise at 1 GHz. I_C = 30 mA, V_{CE} = 2 V, T = 80 K.

IV. Oscillator Simulation

An oscillator has been designed using TR-2 device and a planar HTS resonator model. The oscillation loop is presented in Fig. 9. The active part of the oscillator is realized on an alumina substrate and link by wire bounding to the HTS-resonator. Apart from the low phase noise amplifier, the coupler, the varactor and the lines that adjust the 2π phase loop are also realized on the alumina substrate. To stabilize, match the amplifier and optimize its residual phase noise, several resistances and capacitors were added (Fig. 10). Then the all integrated oscillator is implemented on the top of the cryocooler's cold finger.

The simulated phase noise is depicted in Fig. 11 and features -155 dBc/Hz at 1 kHz offset. This phase noise level has been obtained with an HTS resonator featuring an unloaded Q of 290 000 at 1 GHz and a loaded Q of 110 000.

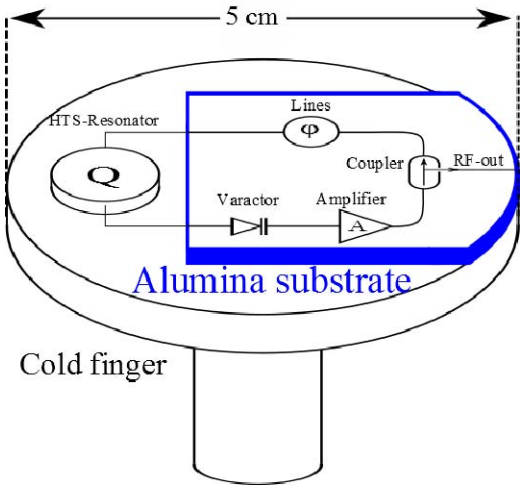


Fig. 9. Picture of the oscillator topology and of its implementation on the cold finger of the cryostat.

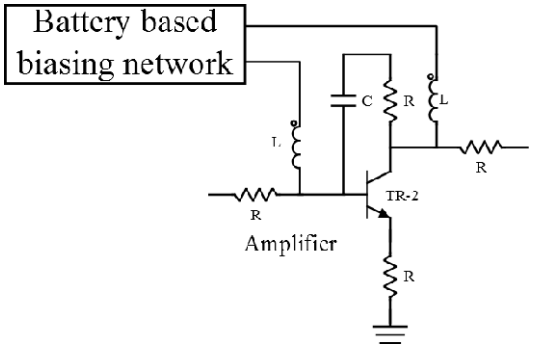


Fig. 10. Amplifier based on TR-2 transistor.

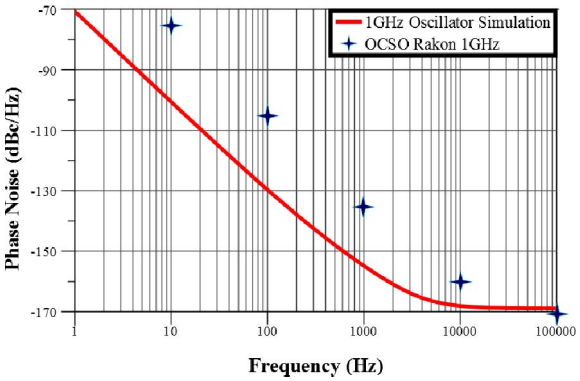


Fig. 11. Simulated 1 GHz oscillator phase noise with TR-2 transistor model and HTS resonator (Q_L = 110000).

V. CONCLUSION

Characterization of SiGe devices at low temperature for oscillator design has been presented. A nonlinear model extraction has been performed on one of these devices at 80 K. The model is able to predict the phase noise performance in amplifier configuration. A superconductor cavity oscillator has been designed using this model and the simulation shows very promising phase noise results. This oscillator will be soon realized on an alumina substrate.

REFERENCES

[1] J. Kermorvant, PhD thesis (in french), Ecole Polytechnique, 2010.

[2] M. Reppel and J. C. Mage, "Superconducting microstrip bandpass filter on $LaAlO_3$ with high out-of-band rejection," in *IEEE Microwave and Guided Wave Letters*, vol. 10, no. 5, pp. 180-182, May 2000.

[3] J.-C. Mage, B. Marcilhac, M. Poulain, Y. Lemaitre, J. Kermorvant, J.-M. Lesage, « Low noise oscillator based on 2D superconducting resonator » 2011 EFTF and IEEE-IFCS conference.

[4] S. Gribaldo, PhD thesis (in french), Toulouse University, 2008.

[5] S. Weinreb, J. C. Bardin and H. Mani, "Design of Cryogenic SiGe Low-Noise Amplifiers," in IEEE Transactions on Microwave Theory and Techniques, vol. 55, no. 11, pp. 2306-2312, Nov. 2007.

[6] G. Cibiel, M. Regis, E. Tournier, O. Llopis, « AM noise impact on low level phase noise measurements » IEEE trans. on Ultrasonics Ferroelect. and Freq. Control, vol. 49, n° 6, Juin 2002, pp. 784-788.

[7] S. Gribaldo, L. Bary, O. Llopis, « SiGe HBT nonlinear phase noise modeling - X band amplifier design », Proc. of the EuMA, 2008, v. 4, pp. 177–182.

This work is supported by the French MoD, Direction Générale de l'Armement (DGA)

Lithium Niobate Phononic Crystals for Radio Frequency SH0 Waves

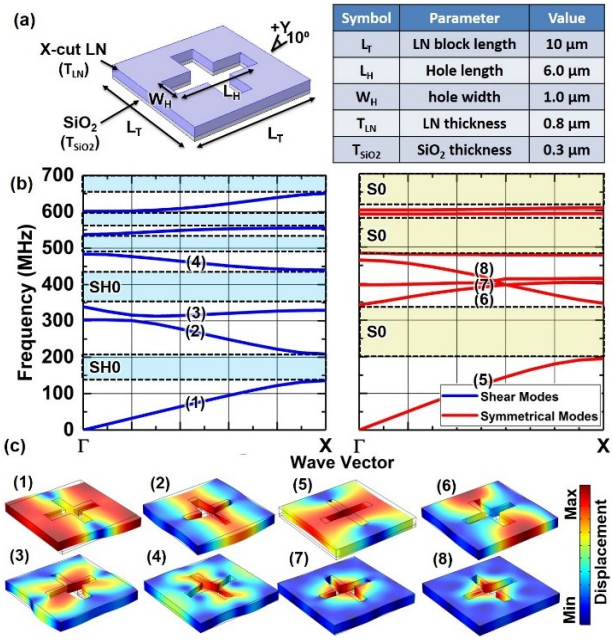
Ruochen Lu, Tomás Manzaneque, Yansong Yang and Songbin Gong
Department of Electrical and Computer Engineering
University of Illinois
Urbana-Champaign, USA

***Abstract*—The first lithium niobate phononic crystals (PnCs) exhibiting band gaps for SH0 modes waves have been designed and demonstrated on X-cut thin films. Transmission properties of PnCs have been experimentally studied in phononic delay lines consisting of wideband input and output transducers separated by PnCs. An equivalent circuit model that incorporates PnCs acoustic scattering matrix and the conventional Mason's model has been constructed to accurately predict the experimental results. The measured devices show 20 dB attenuation for the SH0 mode in the stop-bands with less than 2 dB loss in the pass-bands.**

Keywords*— *Acoustic band gap; acoustic scattering parameters; delay lines; lithium niobate; Mason's model; phononic crystal; piezoelectricity; SH0 mode.

I. Introduction

Phononic crystals (PnCs) are novel artificial materials established by a periodic repetition of an inhomogeneous structure [1]. Desired acoustic wave propagation characteristics in PnC, such as dispersion and phononic bandgaps, can be designed with appropriate choices of the materials, building blocks and arrangement of PnCs. The prospect of manipulating phonon propagation has sparked great interest in engineering PnCs for various potential applications, including wave guiding [2], focusing [3], and energy confinement for enhancing resonator quality factors [4]. However, previous studies on PnCs have so far primarily focused on low frequencies or piezoelectric platforms with moderate electromechanical coupling (k^2) [5] and high propagation loss [6]. Consequently, these demonstrations are not directly applicable to radio frequency (RF) front ends where wideband and low-loss signal processing is typically required. Recently, a new type of delay line structures has been demonstrated in suspended single crystal X-cut lithium niobate ($LiNbO_3$) thin films for the shear horizontal (SH0) mode [7]. The reported device significantly outperforms the surface acoustic wave (SAW) technology for a number of reasons. Frist, the SH0 mode can be excited with high electromechanical coupling exceeding 35% in $LiNbO_3$ thin films [8][9], thus allowing for a much wider transducer bandwidth over which impedance matching can be maintained. Second, the utilization of suspended thin films as acoustic waveguides permits better energy confinement and hence lower propagation loss. Because of the aforementioned advantages, embedding PnCs designed for SH0 waves in suspended $LiNbO_3$ thin films can potentially enable new wide-band and low-loss acoustic functions and signal processing capabilities at RF. This work takes the first step to investigate and demonstrate PnC enabled acoustic stop-bands for the SH0 mode in $LiNbO_3$ with a long-term objective of using PnC stop-bands to enhance $LiNbO_3$ MEMS resonator performance.



Symbol	Parameter	Value
L_T	LN block length	10 μm
L_H	Hole length	6.0 μm
W_H	hole width	1.0 μm
T_{LN}	LN thickness	0.8 μm
T_{SiO2}	SiO_2 thickness	0.3 μm

Figure 1: (a) Schematic illustrations and key parameters of the designed PnC. (b) Simulated dispersion curves for shear modes and symmetrical modes. (c) Mode shape for shear [(1)-(4)] and symmetrical modes [(5)-(8)].

II. Design of Phononic Crystal

Because of our primary focus on SH0 in this work, the PnCs are designed for an orientation of –10° to –Y axis, at which the SH0 mode has been demonstrated with a high electromechanical coupling. Inadvertently, the S0 mode can also be excited with a k^2 of 3.3% and a phase velocity of 6400 m/s at this orientation [10]. Thus, in addition to SH0, the response of PnCs to S0 is also characterized in our investigation.

For studying acoustic stop-bands for the SH0 mode waves, PnCs have been designed [Fig. 1 (a)] with arrays of cross-shape voids in a $LiNbO_3$-SiO_2 film stack. Cross-shape voids are selected as the PnC building blocks because they provide wider acoustic stop-bands in comparison to other shapes. Physical dimensions are listed in the table in Fig. 1 (a). A SiO_2 layer underneath $LiNbO_3$ is included because it is required in fabrication to facilitate film transfer process of $LiNbO_3$.

To study the proposed PnC, we first identify acoustic stop-bands and pass-bands by simulating the dispersion characteristics of SH0 and S0 modes with COMSOL finite element analysis

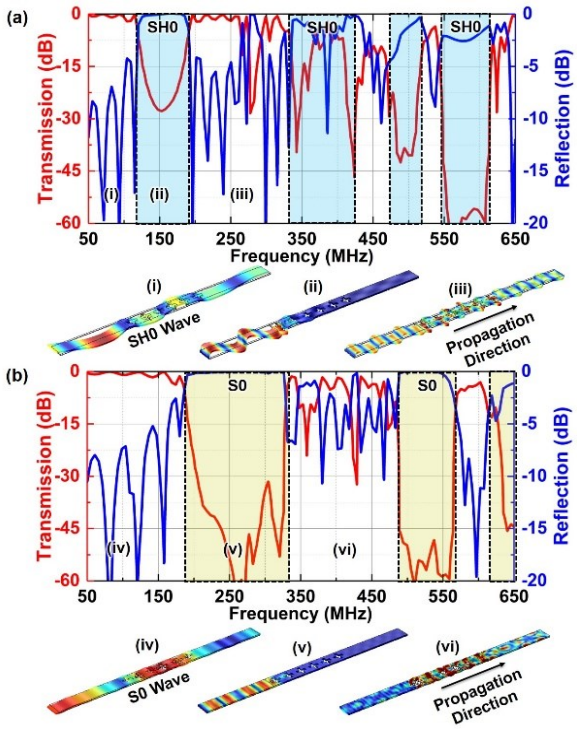
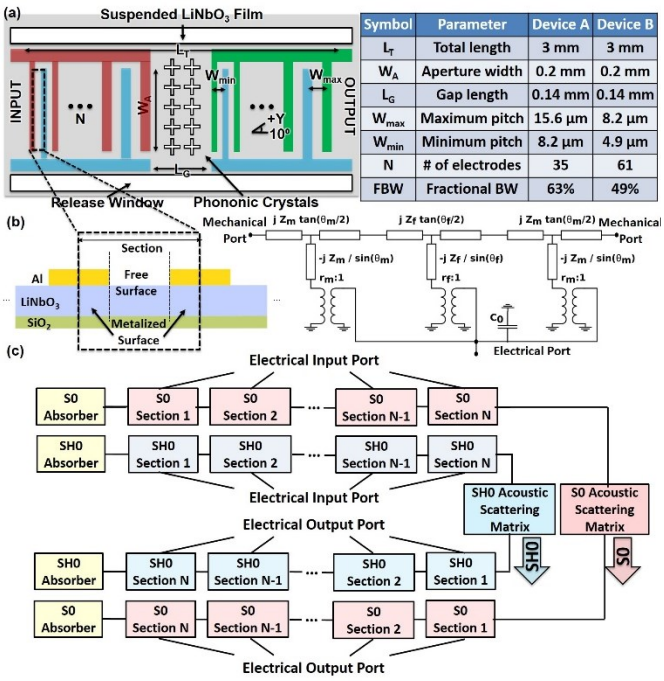


Figure 2: Simulated acoustic scattering parameters of (a) SH0 and (b) S0 waves propagating through 6 columns of PnCs. Simulated displacements of acoustic waves propagating through 6 columns of PnCs at different frequencies [(i)-(vi)] are presented.



Symbol	Parameter	Device A	Device B
L_T	Total length	3 mm	3 mm
W_A	Aperture width	0.2 mm	0.2 mm
L_G	Gap length	0.14 mm	0.14 mm
W_{max}	Maximum pitch	15.6 μm	8.2 μm
W_{min}	Minimum pitch	8.2 μm	4.9 μm
N	# of electrodes	35	61
FBW	Fractional BW	63%	49%

Figure 3: (a) Mocked-up view and physical parameters of PnC delay lines. Physical parameters of the designed PnC delay lines. (b) Sectional equivalent circuit adapted from Mason's model for representing one period of the transducers. (c) PnC delay line model that represents PnC with acoustic scattering matrices and transducers with the conventional Mason's model [9].

(Fig. 1). In the simulations, the horizontal boundaries are set to be free, while the vertical boundaries are set to be periodic. Different modes are classified into shear or symmetrical modes according to the dominant stress field component. The highlighted parts in the dispersive curves respectively indicate acoustic stop-bands for both shear modes and symmetrical modes in the designed structure. From the results, we can conclude that dispersion curves are adequate for qualitatively identifying the existence of acoustic stop-bands and pass-bands for the proposed PnCs. However, a quantitative method is essential to design PnCs with finer-tuned acoustic properties.

To more accurately model the acoustic wave propagation through PnCs, acoustic scattering parameters [11] (reflection and transmission) of both SH0 and S0 modes are simulated with COMSOL (Fig. 2). A 2D array of PnCs with six columns are investigated. In the simulation, low-reflective boundaries are applied to edges of the delay lines on both sides to eliminate reflections caused by the acoustic impedance mismatch at the ports. Periodic conditions are set to the transverse boundaries of the delay line to avoid mode distortion. An external force is applied in the transverse direction and on the left edge of the PnCs to excite SH0 waves, while a force is applied in the longitudinal direction and on the left edge to excite S0 mode waves. The complex reflection coefficient is obtained as the ratio of the sum of the corresponding stress (S_x for S0 wave and S_{xy} for SH0 wave) reflected at the input port to the sum of the stress incident upon the PnCs array. On the other hand, the complex transmission coefficient is calculated as the ratio of the sum of the transmitted stress fields at the output port to the sum of the incident stress fields. The amplitude of transmission and reflection for both modes are presented in Fig. 2. Simulated SH0 wave reflection and transmission through six columns of PnCs over a wide range of frequencies [Fig. 2 (i)-(iii)] are also presented along with S0 counterparts [Fig. 2 (iv)-(vi)].

Both analyses have shown well-defined stop-bands at 120-180 MHz and 330-420 MHz, and pass-bands elsewhere below 450 MHz for SH0 modes. Similarly, the stop-bands for S0 mode waves (180-340 MHz and 480-560 MHz) are also present. One envisioned application for these stop-bands and pass-bands is to surround a conventional $LiNbO_3$ resonator with PnCs, and to create reflective boundaries. Different from etched sidewalls that reflect all modes at all frequencies, PnCs provide frequency-selective reflections, and therefore can suppress spurious resonances that typically plague the response of a conventional resonator.

III. Design of Delay Line Testbeds

In order to validate transmission characteristics of PnCs, low-loss, wideband delay lines seen in Fig. 3(a) are employed as PnC testbeds. The testbeds consist of the designed PnCs embedded between the wideband input and output interdigitated transducers on top of a suspended $LiNbO_3$ thin film waveguide.

The fractional bandwidth (FBW) of the input and output transducers need to be sufficiently large to characterize the response of PnC over the wide frequency range seen in Fig. 2. However, due to the coexistence of SH0 and S0 modes in the chosen orientation, the FBW has to be smaller than 60% to avoid overlapping of emission bands for different modes [7]. As a result, two delay lines are fabricated to collectively cover a wider frequency range, as shown in the table in Fig. 3 (a). The low-

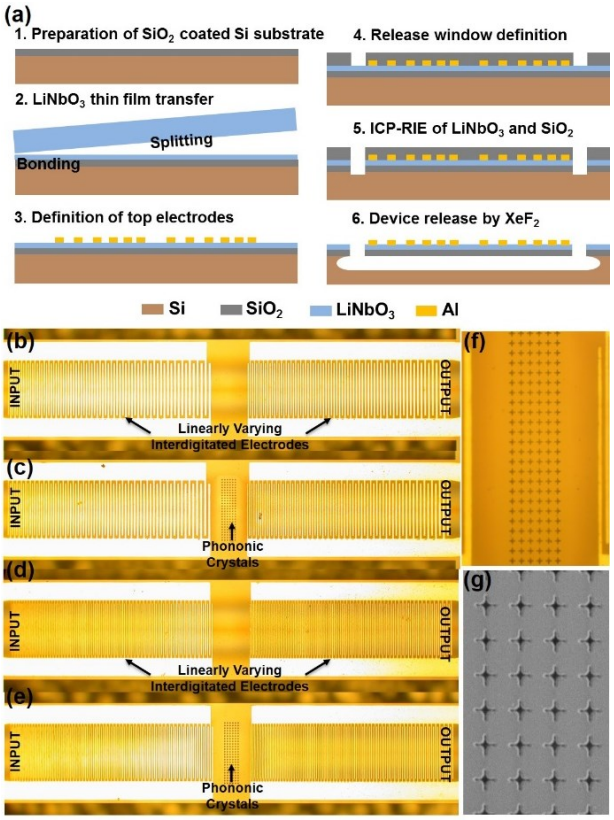


Figure 4: (a) Fabrication flow chart. Optical images of fabricated PnC delay lines of (b) the low frequency reference delay line, (c) the low frequency PnC delay line, (d) the high frequency reference delay line, and (e) the low frequency PnC delay line. Zoomed-in (f) optical image and (g) SEM of the cross-shape PnCs showing good uniformity.

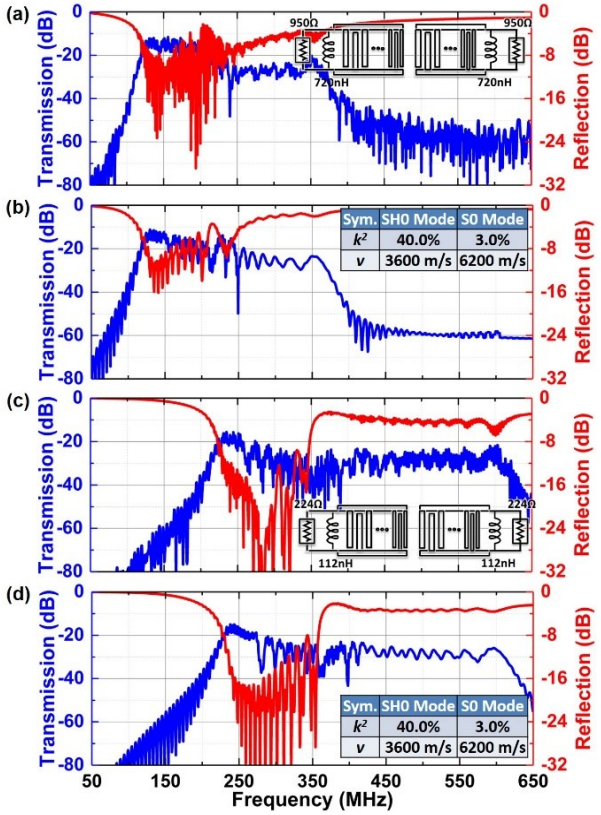


Figure 5: (a) Measured and (b) simulated reflection and transmission of the reference low frequency delay line. (c) Measured and (d) simulated reflection and transmission of the reference high frequency delay line.

frequency delay line, with a bandwidth from 115 to 215 MHz, is attained by linearly varying IDT pitches from 15.6 to 8.2 µm across the length of the transducer. The high-frequency delay line, with a bandwidth from 215 to 360 MHz, is attained by linearly varying IDT pitches from 8.2 to 4.9 µm. IDTs of different pitches are placed with identical separations between the input and output to create the same delay for different frequencies. 6 columns of PnCs were investigated, and benchmarked against reference devices with the identical transducers, delay length, but no PnC. 20 rows of PnCs were chosen to cover the whole acoustic aperture.

An equivalent circuit model shown in Fig. 3(b) has also been constructed to model input and output transducers. The model is based on the Mason's model, of which more details can be found in [12]. In this model, a sectional equivalent circuit is used to represent a pair of half electrodes and the LN thin film in-between and underneath. Each sectional equivalent circuit considers electrostatics using static capacitance, acoustic wave propagation using acoustic transmission lines, and the coupling between electrical and acoustic domains using a transformer. The sectional equivalent circuits are then connected in series with the transformers fed in parallel to model the entire input or output interdigitated transducers. More details on the parameters used to constitute the circuit can be found in [12].

For the chosen orientation of our designed delay lines, both SH0 and S0 modes exist. Thus, two sets of transformers and acoustic transmission lines are connected in parallel to model the transduction of both modes simultaneously. To complete the model for the PnC delay line testbeds, the effects of PnCs on both SH0 and S0 are embedded in the acoustic domain of the model using two parallel two-port scattering matrices. The matrices are introduced and extracted in Section II. Before being incorporated in the model seen in Fig. 3(c), the acoustic scatter matrices are re-normalized with port impedances identical to the impedance of un-metalized acoustic transmission line seen in Fig. 3(b). The reference delay lines can also be modeled in a similar fashion. Instead of embedding scatter matrices, a 60-µm-long acoustic transmission line is inserted between the input and output to represent the short section of $LiNbO_3$ thin film.

Distributed attenuators [omitted in Fig. 3(c)] are also included in the model to emulate the propagation loss in the fabricated devices [12]. Additional loss of the acoustic energy also occurs after the acoustic waves traverse the transducers and are subsequently scattered or absorbed by the substrate. Such effects are captured in the model using acoustic absorbers at the longitudinal ends of the delay line.

IV. Experiment and Discussion

The PnC testbeds were fabricated using a process described in [7] [Fig. 4 (a)]. As shown in Fig. 4(b)-(e), the suspended delay lines remain flat, suggesting an acceptable amount of residue stress. The zoomed-in images [Fig. 4 (f)-(g)] show good uniformity of the fabricated PnCs. However, the fabricated cross-shape patterns show loss of fidelity to the original design due to

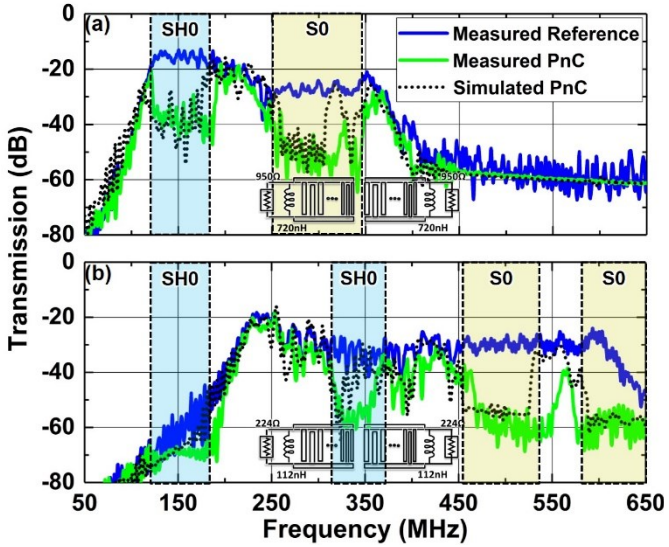


Figure 6: Measured and simulated transmission of the (a) low frequency and (b) high frequency PnC delay lines, benchmarked against the measured responses of the reference delay lines. The predicted stop-bands for both SH0 and S0 are highlighted in the figure.

non-ideal definition of etch-window patterns using contact lithography. Despite the deviation from designed patterns, the measured results, as it will be seen in Figs. 5 and 6, only show a slight deviation from the intended performance.

The transmission and reflection of the reference device were first measured with an Agilent N5249A PNA-X network analyzer. As seen in the insets of Fig. 5, shunt inductors are used at the electrical ports to tune out the acoustic susceptances of the input and output transducers for attaining impedance mismatch. As seen in Fig. 5, the measurements show great agreement with those predicted by our model. The key parameters for the model, namely k^2 and v for both modes are listed in the inset tables of Fig. 5. Next, delay lines with embedded PnCs were measured. The transmission performance, with inductive matching applied at both input and output, is shown in Fig. 6.

Two SH0 stop-bands are observed at 125-185 MHz and 320-360 MHz with other frequencies within the transducer BW exhibiting pass-band characteristics. The results match well with the analyses shown in Figs. 1 and 2. Benchmarked to measured performance of the reference devices, 20 dB attenuation for SH0 mode waves is seen in the stop-bands while less than 2 dB attenuation is observed in the pass-bands. The insertion loss of the reference devices over the BW of transducers is on par with the results seen in [7]. It is primarily limited by the bi-directionality of the transducers and acoustic reflection induced by interdigitated electrodes.

As mentioned in Section III, S0 modes can be inadvertently excited in these devices as well, despite with a lower k^2 and at higher frequencies. Similar to SH0 and as predicted in Figs. 1 and 2, several stop-bands of S0 are also observed in the measurements. Because S0 has a higher phase velocity than SH0, the delay lines with embedded PnCs can be optimized for S0 and higher frequency applications, if an optimal orientation for S0 mode, such as 30° to +Y in X-cut, is selected [13].

V. Conclusion

In this work, $LiNbO_3$ PnCs for the SH0 mode have been theoretically investigated and experimentally demonstrated for the first time. The $LiNbO_3$ thin film platform has been demonstrated to manipulate phonon propagation with unprecedentedly wide bandwidth and low loss, potentially promising a new paradigm of radio frequency signal processing in the acoustic domain.

References

[1] A. Khelif and A. Adibi, *Phononic Crystals: Fundamentals and Applications*. Springer, 2015.

[2] R. H. Olsson, S. X. Griego, I. El-Kady, M. Su, Y. Soliman, D. Goettler, and Z. Leseman, "Ultra high frequency (UHF) phononic crystal devices operating in mobile communication bands," in *Ultrasonics Symposium (IUS), 2009 IEEE International*, 2009, pp. 1150–1153.

[3] N.-K. Kuo and G. Piazza, "Evidence of acoustic wave focusing in a microscale 630 MHz aluminum nitride phononic crystal waveguide," in *Frequency Control Symposium (FCS), 2010 IEEE International*, 2010, pp. 530–533.

[4] C.-M. Lin, J.-C. Hsu, D. G. Senesky, and A. P. Pisano, "Anchor loss reduction in AlN Lamb wave resonators using phononic crystal strip tethers," in *Frequency Control Symposium (FCS), 2014 IEEE International*, 2014, pp. 1–5.

[5] S. Wang, L. C. Popa, and D. Weinstein, "Tapered Phononic Crystal sawresonator in GaN," in *Micro Electro Mechanical Systems (MEMS), 2015 28th IEEE International Conference on*, 2015, pp. 1028–1031.

[6] S. Benchabane, G. Ulliac, O. Gaiffe, R. Salut, Y. Achaoui, and V. Laude, "Hypersonic phononic crystal for surface acoustic waves," in *Ultrasonics Symposium (IUS), 2010 IEEE*, 2010, pp. 158–161.

[7] T. Manzaneque, R. Lu, Y. Yang, and S. Gong, "An SH0 Lithium Niobate Dispersive Delay Line for Chirp Compression-enabled Low Power Radios," in *Micro Electro Mechanical Systems (MEMS), IEEE 29th International Conference on*, 2017.

[8] Y.-H. Song, R. Lu, and S. Gong, "Analysis and removal of spurious response in SH0 lithium niobate MEMS resonators," *IEEE Trans. Electron Devices*, vol. 63, no. 5, pp. 2066–2073, 2016.

[9] R. H. Olsson, K. Hattar, S. J. Homeijer, M. Wiwi, M. Eichenfield, D. W. Branch, M. S. Baker, J. Nguyen, B. Clark, and T. Bauer, "A high electromechanical coupling coefficient SH0 Lamb wave lithium niobate micromechanical resonator and a method for fabrication," *Sensors Actuators A Phys.*, vol. 209, pp. 183–190, 2014.

[10] I. E. Kuznetsova, B. D. Zaitsev, S. G. Joshi, and I. A. Borodina, "Investigation of acoustic waves in thin plates of lithium niobate and lithium tantalate," *IEEE Trans. Ultrason. Ferroelectr. Freq. Control*, vol. 48, no. 1, pp. 322–328, 2001.

[11] M. Åbom, "Measurement of the scattering-matrix of acoustical two-ports," *Mech. Syst. Signal Process.*, vol. 5, no. 2, pp. 89–104, 1991.

[12] T. Manzaneque, R. Lu, Y. Yang, and S. Gong, "An SH0 Lithium Niobate Correlator for Orthogonal Frequency Coded Spread Spectrum Communications," in *Frequency Control Symposium (FCS), 2017 IEEE International,* to appear.

[13] S. Gong and G. Piazza, "Design and analysis of lithium-niobate-based high electromechanical coupling RF-MEMS resonators for wideband filtering," *IEEE Trans. Microw. Theory Tech.*, vol. 61, no. 1, pp. 403–414, 2013.

Backward Acoustic Plate Waves: Features of Properties and Possible Applications in Microelectronic Devices

V. G. Mozhaev
Faculty of Physics
Lomonosov Moscow State University
Moscow, Russia
vgmozhaev@mail.ru

I. A. Nedospasov and I. E. Kuznetsova
Kotel'nikov Institute of Radio-engineering and Electronics
Moscow, Russia
ianedospasov@mail.ru,kuziren@yandex.ru

***Abstract*— An overview is given of the results of recent and new studies by the authors of this work on topics related to backward acoustic waves of pure-shear type and Lamb type in piezoelectric, crystal, and isotropic plates with free and liquid-loaded surfaces. Various physical mechanisms giving rise to such waves are revealed and quantitatively described by the use of asymptotic expansion of the secular equations and the perturbation theory. The peculiarities of properties of leaky backward waves are considered. The possible applications of backward waves in microelectronic devices (such as sensors *et al.*) are discussed.**

Keywords—plate acoustic modes; backward waves; Lamb waves; pure shear waves; crystal plates; piezoelectric plates; isotropic plates; liquid loading; leaky waves; liquid sensors

I. INTRODUCTION

The so-called backward waves, i.e. waves with opposite directions of the phase velocity and the energy flux, continue to attract significant interest of researches due to their very unusual properties. The backward acoustic waves, as is known, can exist in limited bands of spectrum of plate modes. From the point of view of their possible technical applications, as well as from the fundamental point of view, it is of interest to study the peculiarities of these waves caused by piezoelectricity, elastic anisotropy and liquid-loading of the plates. These questions are in the focus of our current and recent studies [1-3]. The aim of this presentation is to give an overview of our new and recent results in this field.

II. THE REASONS FOR ORIGIN OF BACKWARD WAVES

A. Pure Shear Backward Waves in $KNbO_3$ Plates

The relative frequency existence range of pure shear waves in plates of common piezoelectric materials is very small. For ZnO it reaches only $2 \cdot 10^{-5}$ [4]. We have found that for super strong piezoelectric $KNbO_3$ of the *X*-cut (*Y*-propagating) this range is huge in comparison to ZnO. Moreover, such frequency bands corresponding to modes of different order have tendency to overlap each other for higher modes thus forming continuous band of the existence of backward modes, Fig. 1.

The expansions of the secular equations for symmetric and antisymmetric plate modes near the points of thickness resonances confirmed by the independent calculations using the perturbation method [5] allow us to identify and quantitatively describe three factors affecting the appearance of wide frequency bands of the existence of backward waves in the problem under study. They are:

(i) the local concavity of the cross-section of the slowness surface corresponding to pure shear bulk waves near the *x*-axis;

(ii) the negative shift of the energy fluxes of bulk waves reflected at oblique incidence from the surface of piezoelectric plate;

(iii) the involvement into the solution of a uniform electric field of capacitor type for antisymmetric modes.

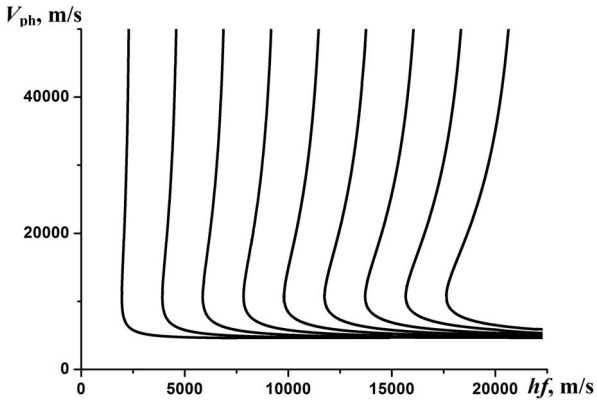


Fig. 1. The dependences of the phase velocities of 9 lower modes of pure shear waves in $KNbO_3$ plate of X-cut on the product of frequency *f* and plate thickness *h*. The parts of curves with abnormal dispersion demonstrating the growth of the phase velocity rather its drop correspond to the backward waves. Zero-order mode is not shown, since it does not exhibit such a behavior.

This study is supported in part by the Russian Foundation for Basic Research, grants 16-07-00629-A and 17-07-00608-A.

The first factor (i) among those described above is dominant but it does not work for the *Y*-cut plate that explains the absence of backward waves for that cut in the same velocity range where they are found for the *X*-cut plate [1].

B. Backward Lamb Waves in Isotropic Plates

Although the proximity, i.e. small frequency separation, of thickness resonances for longitudinal and transverse bulk waves is quite well recognized by researchers as a necessary condition for the occurrence of backward Lamb waves in isotropic plates, nevertheless a simple pictorial explanation of this requirement is still absent in the literature. Fig. 2 provides such an explanation showing how a backward wave loop seen in left is originated from the artificially decoupled modes of longitudinal and transverse bulk waves (Mindlin approximation) by their repulsion at the lower crossing point.

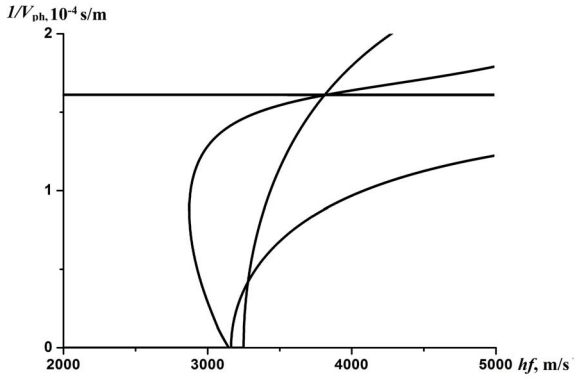


Fig. 2. Origin of the backward Lamb waves (left curve) in isotropic (aluminum) plates as a result of repulsion of crossing curves corresponding to two artificially decoupled longitudinal and transverse plate modes of the same symmetry-type family and close mode numbers.

The additional conclusion from this explanation is that this mechanism can provide the occurrence of backward waves in isotropic plates only if the frequencies of two closely spaced thickness resonances are arranged so that one of them for longitudinal waves does not exceed another one for transverse waves.

C. Backward Lamb Waves in Crystal Plates

One more factor for the occurrence of backward Lamb waves in crystal plates, besides the factor described in the previous section, is the local curvature of the cross-section by the sagittal plane of the slowness surface for bulk waves which are involved into the solution for Lamb waves as partial waves. When the curvature is oriented along the plate surface normal, this factor can become dominant that is demonstrated by calculations for NBBT95/5 and $LiNbO_3$ crystal plates.

III. THE FEAUTERES OF LEAKY BACKWARD WAVES

The main features caused by the leakage of backward waves into surrounding liquid is (i) the inverse arrangement of insonified and shadow zones, (ii) zero total time-averaged energy flux along the plate axis (total means here the sum of fluxes in the plate and liquid), (iii) violation of the Rayleigh's principle of equipartition of kinetic and potential energies, and (iv) inequality of group and energy velocities. Piezoelectricity of plates changes slightly the interpretations of these conclusions without changing their sense.

IV. POSSIBLE APPLICATIONS OF BACKWARD PLATE WAVES

Backward plate waves are characterized by very high phase velocity which is much more than the velocity of surface waves. Therefore these high-velocity plate modes can be excited by an interdigital transducer of a given period at frequency which is much higher than the operational frequency of the same transducer for excitation of surface waves.

The inverse relation occurs between the group velocities of backward plate waves and surface waves. For the first mentioned waves it is much less. This property can be used to construct the delay lines with reduced length if the dispersive properties of the backward waves are acceptable for such applications. On the other hand, these specific dispersion properties can be useful to construct microwave acoustic devices for pulse compression.

Our analytical estimations and numerical calculation show that the sensitivity of propagation characteristics of the backward plate waves to changes of properties of surrounding liquid can be several time higher than for forward waves in the same plate. This property looks to be attractive for possible applications in acoustic sensor devices.

The possibility of using zero-group-velocity Lamb waves to develop high-frequency resonators with high quality factor has been demonstrated in [6]. The results of the present study give insight into the procedure and criteria for optimal search of crystal configurations admitting such specific waves.

REFERENCES

[1] I. E. Kuznetsova, V. G. Mozhaev, and I. A. Nedospasov, "Pure shear backward waves in the X-cut and Y-cut piezoelectric plates of potassium niobate," J. Commun. Technol. Electron., vol. 61, pp. 1305-1313, November 2016.

[2] I. A. Nedospasov, V. G. Mozhaev, and I. E. Kuznetsova, "Leaky backward Lamb waves in various isotropic and anisotropic plate/liquid systems," in 2016 IEEE International Ultrasonics Symposium Proceedings, 2016, pp. 1-4.

[3] I. A. Nedospasov, V. G. Mozhaev, and I. E. Kuznetsova, "Unusual energy properties of leaky backward Lamb waves in a submerged plate," Ultrasonics, vol. 77, pp. 95–99, May 2017.

[4] I. Ya. Kucherov and E. V. Malyarenko, "Energy flows of direct and inverse normal transverse acoustic waves in piezoelectric plates," Akust. Zh., vol. 44, pp. 492-497, July-August 1998 [Sov. Phys. Acoust., vol. 44, pp. 420-425, July-August 1998].

[5] B. A. Auld, Acoustic Fields and Waves in Solids, vol. II. New York: John Wiley, 1973, pp. 271–332.

[6] V. Yantchev, L. Arapan, I. Katardjiev, and V. Plessky, "Thin-film zero-group-velocity Lamb wave resonator," Appl. Phys. Lett., vol. 99, 033505, 2011.

Nonreciprocal reconfigurable zero-transmission filters through nonreciprocal coupling to resonators

Christopher W. Peterson and Jennifer T. Bernhard
Department of Electrical and Computer Engineering
University of Illinois at Urbana-Champaign
Urbana, Illinois, 61801

Gaurav Bahl
Department of Mechanical Science and Engineering
University of Illinois at Urbana-Champaign
Urbana, Illinois, 61801

I. Introduction

Resonators are a common feature of many electromagnetic filters, and when side-coupled to a waveguide can be used as a band-stop or notch filter. The coupling to their resonant modes is extremely important to the function of these devices but is often overlooked as an opportunity for design. It has recently been shown that through spatiotemporal modulation of multiple couplers between a single-mode waveguide and resonator it is possible to couple the resonator only to waves traveling in one direction in the waveguide [1]. This "nonreciprocal coupling" can be used to create nonreciprocal filters, or isolators, that exhibit giant directional contrast and are dynamically reconfigurable. The special case of critical coupling, where the resistive damping of the resonator is equal to the coupling rate between it and the waveguide, results in zero transmission through the waveguide at the resonance frequency since all the energy is dissipated in the resonator.

Due to the bidirectional decay into the coupled waveguide, critical coupling is usually impossible with reflective resonators such as those commonly used in microwave filters. Remarkably, critical coupling can be achieved even in reflective resonators if they are nonreciprocally coupled. This is a direct consequence of the nonreciprocal coupling and is allowed because the reflective path is removed. Here we exploit this property to experimentally demonstrate giant isolation by engaging nonreciprocal critical coupling to a reflective microstrip stub resonator.

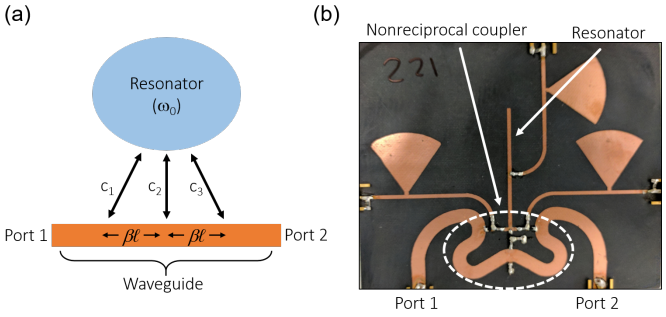


Fig. 1. (a) Schematic of the system under consideration. Two ports are connected by a waveguide which is coupled at three points to a resonator. (b) Photo of the circuit used in the experiment. Three variable capacitors (varactor diodes) couple the waveguide to an open-circuit stub resonator.

II. Nonreciprocal coupling

We consider the system shown in Fig. 1(a), which consists of a waveguide connecting two ports and a resonator coupled to the waveguide through three variable couplers c_1, c_2, and c_3. The couplers are separated by a physical length ℓ in the waveguide such that the phase a wave accumulates traveling between couplers is $\beta\ell \approx 2\pi/3$, where β is the propagation constant of the waveguide near the resonance frequency ω_0. In such a system the coupling between the waveguide and resonator is minimal due to destructive interference between the couplers, i.e. the three signals with phases 0, $2\pi/3$ and $4\pi/3$ that excite the resonator add destructively [1].

If each coupler is then sinusoidally modulated with angular frequency Ω such that $c_n = c_0 + c_M \cos\left(\Omega t - \phi(n-1)\right)$, additional dips in transmission occur at the sidebands $\omega_0 \pm \Omega$ due to frequency shifted coupling from the modulated couplers. The coupling to these sidebands of the original resonance is controlled by both the amplitude c_M and the phase shift ϕ of the applied modulation. The phase of the modulation applied to each coupler adds to the phase of propagation between each coupler in the waveguide and the resulting interference in the resonator becomes dependent on the direction of the incident wave. This direction dependent or nonreciprocal coupling is caused because the propagation phase $\beta\ell$ changes sign with the direction of the wave while the applied phase ϕ remains constant.

A. General case

A complete derivation of the transmission coefficients S_{21} and S_{12} in systems with nonreciprocal coupling can be found in our previous work [1]. Generally, the waveguide-resonator system can be analyzed through temporal coupled mode theory [2]. The simplified expressions for the transmission coefficients in our system are

$$S_{21}[\omega] = e^{(-j2\beta\ell)}\left(1 - \frac{\kappa_{1-}}{j(\omega-(\omega_0-\Omega))+\gamma} - \frac{\kappa_{1+}}{j(\omega-(\omega_0+\Omega))+\gamma}\right), \quad (1)$$

$$S_{12}[\omega] = e^{(-j2\beta\ell)}\left(1 - \frac{\kappa_{2-}}{j(\omega-(\omega_0-\Omega))+\gamma} - \frac{\kappa_{2+}}{j(\omega-(\omega_0+\Omega))+\gamma}\right). \quad (2)$$

978-1-5386-2916-1/$31.00 ©2017 IEEE

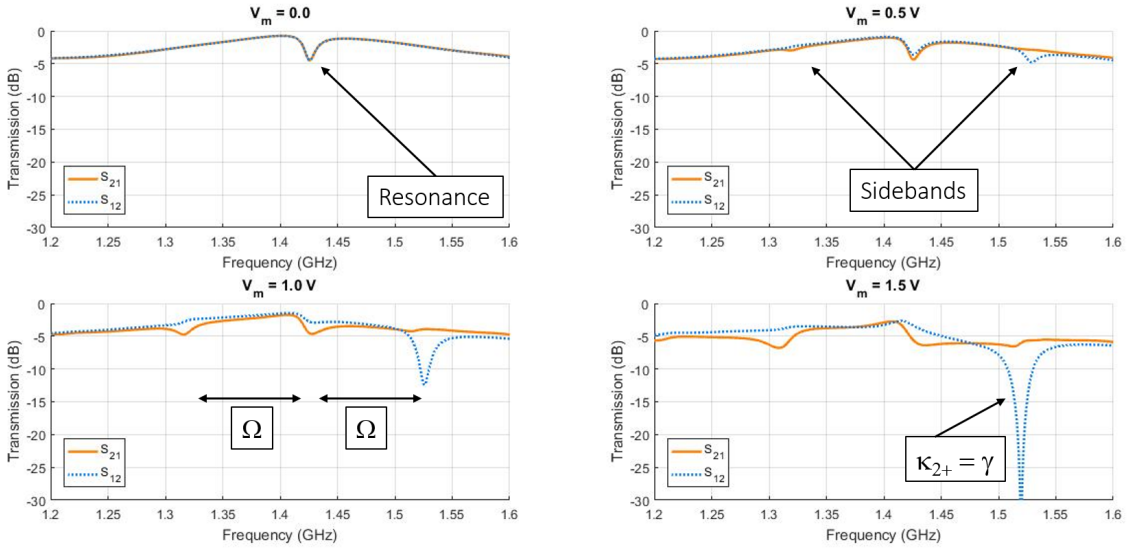


Fig. 2. Transmission coefficients S_{21} and S_{12} for the circuit in Fig. 1(b) for increasing modulation amplitude $V_m \propto c_M$. With no modulation (top left), the resonance is visible but the coupling is severely diminished due to destructive interference from the spacing between couplers ($\kappa_0 \approx 0$). As the modulation amplitude is increased, sidebands of the original resonance appear offset by the modulation frequency. The coupling to these sidebands is controlled by both the magnitude and phase of the applied modulation, resulting in nonreciprocal sidebands that only appear for waves traveling in a certain direction. At very high modulation amplitude (bottom right) the upper sideband becomes critically coupled, resulting in zero transmission through the waveguide at that frequency.

Here $\kappa_{1\pm,2\pm}$ describe the coupling to the upper and lower sidebands for forward and backward propagating waves respectively. These coupling rates are dynamically reconfigurable since they are controlled by the amplitude c_M and phase ϕ of the modulation applied to the couplers. It can be seen in the above equations that the time-modulation of the coupling indeed results in sidebands of the original resonance, offset by $\pm\Omega$. Since the coupling is direction dependent $\kappa_{1\pm} \neq \kappa_{2\pm}$ and transmission becomes nonreciprocal in these sidebands.

B. Critical coupling

Equations (1) and (2) show that for critical coupling, where transmission drops to zero at the sideband frequency, it is necessary that γ is equal to the coupling rate $\kappa_{x\pm}$ in the numerator of whichever sideband is critically coupled. The half-linewidth γ describes the decay rate of the resonance and is the sum of the coupling rates to the waveguide and the intrinsic decay rate κ_i

$$2\gamma = \kappa_{1-} + \kappa_{1+} + \kappa_{2-} + \kappa_{2+} + \kappa_i \ , \qquad (3)$$

In a real system with finite loss ($\kappa_i > 0$) critical coupling is only possible if one of the coupling rates $\kappa_{x\pm}$ is much larger than the other three. We achieve this condition through two methods, first controlling the phase of the applied modulation ϕ to set $\kappa_{1+} = \kappa_{2-} \approx 0$. Additionally, due to Fano resonances which arise from interference pathways between the couplers, the lower sideband coupling κ_{1-} is automatically small in our circuit. This happens because the effective impedance of the resonator becomes very large at $\omega_0 - \Omega$ and the incident waves at that frequency cannot "see" the modulation very well. The result is that κ_{2+} is the only significant coupling rate and the critical coupling condition where $\gamma = \kappa_{2+}$ can be satisfied.

Fig. 2 shows the experimentally measured transmission coefficients for increasing modulation amplitudes when the modulation phase ϕ is set such that κ_{2+} is large and $\kappa_{1+} = \kappa_{2-} \approx 0$. Fig. 2(top left) shows the system with no modulation applied, the resonance is clearly visible but is very weakly coupled to the waveguide. When modulation is applied, nonreciprocal dips in transmission associated with the coupling terms κ_{1-} and κ_{2+} can be seen 104 MHz away from the original resonance, corresponding the modulation frequency $\Omega/2\pi$. Absorption of the upper sideband in the S_{12} measurement is much larger than that of the other sidebands, clearly showing that κ_{2+} is the dominant coupling rate.

In Fig. 2(bottom right) κ_{2+} is equal to γ and nonreciprocal critical coupling is observed ($S_{12} = 0 \neq S_{21}$) at the upper sideband frequency. This is the first experimental demonstration of nonreciprocal critical coupling and the ultra-high isolation that results from it.

REFERENCES

[1] C. W. Peterson, S. Kim, J. T. Bernhard, and G. Bahl, "Reconfigurable arbitrary nonreciprocal transfer functions through nonreciprocal coupling," *arXiv:1702.06476 [physics.optics]*, 2017.

[2] W. Suh, Z. Wang, and S. Fan, "Temporal coupled-mode theory and the presence of non-orthogonal modes in lossless multimode cavities," *IEEE Journal of Quantum Electronics*, vol. 40, no. 10, pp. 1511–1518, 2004.

EFTF-IFCS 2017 Author Index

A

Aarmo, Kjell Arne 385
Abbé, Philippe 567
Abdel Hafiz, Moustafa 169, 278, 614
Abgrall, Michel 468, 707, 815
Ablewski, Piotr 437
Abramzon, Igor 222
Acef, Ouali 471
Achkar, Joseph 705
Adhikari, Pintu 24
Affolderbach, Christoph 57, 63
Ait Mansour, El Houssain 406
Akaike, Kazuo 231
Alcock, John 640
Alexandre, Christophe 781
Ali, Abid 26
Almat, Nil 63
Almirall, Anthony 516
Altorio, Matteo 798
Amy-Klein, Anne 160, 378, 468, 697
Anisimkin, Vladimir I. 343, 345
Arad, Uriel 162
Arafin, Shamsul 534
Argence, Bérengère Argence 468
Arias, Felicitas 788
Armstrong, Jordan 460
Arora, Bindiya 753
Astrua, Milena 462
Aubry, Jean-Pierre 523
Auroux, Vincent 489

B

Bagala, Tomas 575
Bahl, Gaurav 852
Bai, Qingsong 289
Bai, Yan 728
Bailey, Quentin 106
Baili, Ghaya 190, 493
Baire, Q. 475
Bakir, Ahmed 419
Baldy, Michel 136, 324
Balet, Laurent 55
Ballandras, Sylvain 336, 565
Baniulienė, Eglė 241
Bao, Jingfu 538, 547
Barbieri, Piero 446
Barbiero, Matteo 748
Bargiel, Sylwester 636
Barniol, Nuria 506
Baron, Thomas 214, 516
Bartasyte, Ausrine 516
Baryshev, Viacheslav 633
Basalaev, Maksim 307
Basetas, Charis 587, 591, 603
Bassignot, Florent 214
Batagelj, Bostjan 486
Bauch, Andreas 681, 683, 703, 736
Bauernfeind, Roland 385
Baumann, Esther 130
Beattie, Scott 477, 640
Beha, Katja 530
Belfi, Jacopo 462
Belli, Alexandre 72
Bender, Florian 24
Bergeron, Hugo 130
Bergonzi, Giovanni 625
Bernard, John 640, 811
Bernhard, Jennifer 852
Bertacco, Elio 322
Bertrand, Bruno 821
Beverini, Nicolò 462
Bhave, Sunil 139, 554, 558, 807
Bigelow, Matthew 466
Bigler, Emmanuel 419
Bilicki, Sławomir 815
Binczewski, Artur 368, 399, 697
Biserni, E. 475
Bize, Sébastien 106, 317, 498
Blinov, Igor 633
Bober, Marcin 100, 437
Bogacki, Wojbor 368, 399, 697
Bogataj, Luka 486
Boiko, Alexandr 633
Boiko, Dmitri 315
Bon, Jérémy 567
Bookjans, Eva 815
Borgulski, K. 475
Borio, Daniele 385
Borisyuk, P.V. 751
Bortolotti, Paolo 66
Bosse, Stéphane 406
Bouchand, Romain 781
Boucquey, Nicolas 121, 598

Boudot, Rodolphe 169, 278, 322, 419, 614, 636
Bourgeois, Pierre-Yves 419, 578, 773
Bourhill, Jeremey 179
Bourquin, Roger 567
Boursier, Corinne 423
Bowden, William 154
Brazhnikov, Denis 278, 614
Bregolin, Filippo 446, 813
Breitbarth, Jason 108, 261
Bretenaker, Fabien 190, 493
Brochard, Pierre 456, 779
Brown, Roger 32
Buchs, Gilles 315
Burke, John 466
Burtichelov, Tsvetan 837

C

Cahill, James 425
Cai, Zhiwu 826
Calonico, Davide 156, 446, 475, 697, 748, 813
Calosso, Claudio Eligio 169, 322, 638
Calvert, James 498
Camargo, Fabiola 697
Cambier, Valentin 498
Camisard, Emilie 378, 697
Campanella, Mauro 697
Camparo, James 47, 185, 271
Cantin, Etienne 378
Cantoni, E. 475
Canuel, Benjamin 646
Cao, Shiying 302
Cao, Yuanhong 618
Carelli, Giorgio 462
Cassella, Cristian 802
Casu, Emanuele Andrea 805
Catalano, Valeria 385
Cerretto, G. 475
Chang, David 68, 198
Chang, Pengyuan 762
Chaouche Ramdane, Amine 769
Chapellier, Paul 218
Chardonnet, Christian 378
Chastellain, Frederic 136
Chaudy, David 835, 842
Chembo, Yanne 523
Chen, Dawei 132
Chen, Haijun 618, 737, 740, 765
Chen, Huaming 712
Chen, Jiang 292
Chen, Jingbiao 305, 427, 737, 740, 762, 765
Chen, Jingya 690
Chen, Pengfei 607
Chen, Pingping 238
Chen, Qiang 132
Chen, Shijun 132
Chen, Tingting 332
Chen, Weilang 477
Chen, Xuan 656
Chen, Zhangyuan 250
Chen, Ziyu 282
Cheng, Pengfei 294, 481, 616
Cherkaoui, Abdelkarim 77
Chernykh, Dmitriy 452
Chiow, Sheng-Wey 644
Chutani, Ravinder 636
Cibiel, Gilles 176, 595
Číp, Ondřej 697
Ciuryło, Roman 100
Clairet, Alexandre 516
Clement, Marta 353, 519, 561, 662
Clivati, Cecilia 156, 475, 697, 813
Coget, Grégoire 278, 614
Coldren, Larry A. 534
Coppoolse, Willem Walter 136
Cordeau, David 175
Costa, R. 475
Costanzo, Giovanni A. 813
Cranch, Geoffrey 642
Cros, Vincent 66
Cross, Matthew 68
Crozatier, Vincent 190, 493
Cygan, Agata 100
Cyrille, Marie-Claire 66
Czubla, Albin 241, 393, 399

D

Da Silva, Bruno 406
Dai, Shaoyang 302
Dale, Elijah 79
d'Allivy Kelly, Olivier 835, 842

EFTF-IFCS 2017 Author Index

Daniau, William 516
Danielson, Magnus 600
Darquié, Benoît 468
Daryoush, Afshin 484
Das, Pallabi 30
Datta, Shubo 781
de Carlos López, Eduardo 326
de Clercq, Emeric 169, 172, 278, 421
De Sarlo, Luigi 498
De Stefano, C. 475
De, Subhadeep 753
Defay, Emmanuel 514
Defraigne, Pascale 475, 821
Delehaye, Marion 419
Derevyashkin, S.P. 751
Deschênes, Jean-Daniel 130
Desruelle, Bruno 317, 479, 697
Di Virgilio, Angela 462
Diallo, Souleymane 523
Díaz, Javier 186, 410, 683, 697
Didier, Alexandre 773, 775
Dierikx, Erik 385
Djafari-Rouhani, Bahram 22
Do, Cuong 148
Dolfi, Daniel 190, 493
Domnin, Yuri 633
Donchenko, Sergey S. 317, 417
Dong, Jingwen 98
Dong, Richang 267, 332
Dong, ShaoWu 381
Doronin, Ilia 317
Dostal, Jiri 697
Douahi, Adel 136
Dragonja, Uros 486
Droz, Fabien 55
Dubé, Pierre 153, 811
Du-Burck, Frédéric 769
Düllmann, Christoph 1
Dulmet, Bernard 218
Dunst, Piotr 477, 628
Durfee, Dallin 460

E

Ebels, Ursula 66
Eberhardt, C.E. 1
Ebran, Jean-Paul 106
Edge, Graham 768
Eisele, Ignaz 113
Elandaloussi, Hadj 423
El-Hadbi, Assia 77
Elissati, Oussama 77
Eliyahu, Danny 79, 534
Ellinger, Frank 66
Elsayed, Mohannad 203
Ender, Horst 681
Erickson, Christopher 460
Ertmer, Wolfgang 495, 758
Escolano, Jose Miguel 662
Esnault, François-Xavier 176, 595
et. al., - 475, 697
Everard, Jeremy 837
Exertier, Pierre 72

F

Fang, Bess 646, 798
Fang, Fang 302
Fang, Su 439
Favard, Philippe 136
Favier, Maxime 498
Fehrenbacher, David 124
Fernandez, Arnaud 489
Fernández-Bolaños, Montserrat 805
Ferrari, Gabriele 748
Ferreira, Ricardo 66
Ferrier, Alban 771
Fesquet, Laurent 77
Fibich, Adam 575
Fim, Dominika 495, 758
Fischer, Marc 128, 777
Flower, Graeme 179
Folco, Yves 136
Formichella, Valerio 185, 475
Fortier, Tara 32
Foster, Kimberly 802
Fox, Richard 32
François, Bruno 322
Frank, Florian 86
Friedt, Jean-Michel 336, 578
Friesen, Waldemar 495, 758
Frittelli, Matteo 475
Fritze, Holger 193
Fu, Wei 235, 238

Fu, Xiao Hu 439
Furthner, Johann 666
Furuse, Yota 328

G

Galardini, Alessandro 697
Galland, Nicolas 498, 771
Galleani, Lorenzo 34
Gallinet, Benjamin 55
Galliou, Serge 567, 636
Gandara, M. 475
Ganesan, Adarsh 148
Gao, Kelin 4
Gao, Yuan 719
Garcia, Michel 136
Garstecki, Jeffrey 68, 198
Geiger, Remi 646, 798
Gertsvolf, Marina 640, 811
Gharavipour, Mohammadreza 57, 63
Ghatge, Mayur 20, 570
Ghosh, Sagnik 502
Giacomelli, Umberto 462
Gibble, Kurt 477, 640
Gibson, Brian 802
Gill, Patrick 154
Gillot, Jonathan 471
Giordano, Vincent 419
Girela-López, Francisco Jesús 186
Girod, Stéphanie 514
Giunta, Michele 128, 777, 781
Glinsek, Sebastjan 514
Goavec-Mérou, Gwenhaël 578, 773
Gobron, Olivier 771
Godard, Nicolas 514
Gödel, Marion 666
Godone, Aldo 638
Goka, Shigeyoshi 300, 328
Goldfarb, Fabienne 190, 493
Goldner, Philippe 771
Gong, Songbin 143, 846
González, Alejandro 683
Goodlin, Brian 181
Gordillo-Dagallier, Lorena 662
Gorecki, Christophe 636
Gorev, Mikhail 193
Goryachev, Maxim 104, 179
Gotoh, Tadahiro 826
Gozzelino, Michele 322, 638
Granados, Ricardo 388
Griffith, Danielle 181
Grosche, Gesine 697
Groult, Lucas 419
Grudinin, Ivan 126
Gruet, Florian 57, 63
Grüning, Pierre 769
Grupp, Frank 450
Guan, Hua 4
Guan, Yong 292
Gubin, Mikhail 452
Gubin, Sergey P. 345
Guérandel, Stéphane 136, 169, 172
Guerlin, Christine 106
Guo, Changlei 498
Guo, Hong 305
Guo, Lianping 649
Guo, Wenge 458
Gürel, Kutan 779
Gutiérrez-Rivas, José Luis 410

H

Haesler, Jacques 55, 315, 625
Haghighi, Mohammad Hossein 193
Hakobyan, Sargis 779
Hammond, Bob 212
Hamoniaux, V. 475
Han, Runqi 296
Handel, Peter 257
Hänsel, Wolfgang 128, 777, 781
Hanssen, Stefan Blom 347
Hara, Motoaki 277
Hashimoto, Ken-Ya 538, 547
Haslinger, Philipp 104
He, Canbin 611
Hem, Jérôme 66
Hendricks, Richard 477, 628, 640
Heo, Myoung-Sun 622, 629, 744, 746
Herique, Alain 388
Herr, Tobias 84
Hevonkorpi, Ville 55
Hill, Ian 154
Hirai, Yoshikazu 60
Hobson, Richard 154

Hode, Jean-Michel 835, 842
Holleville, David 471, 479, 646
Holzwarth, Ronald 128, 450, 530, 697, 777, 781
Hong, Hyun-Gue..... 622, 629, 746
Hou, Dong 132, 289, 649
Hou, Juan 381
Hou, Shimin 282
Hu, Ermeng 611
Hu, Hongping..... 660
Hu, Jianguo 132, 235, 238, 289
Hu, Weiwei 250
Hu, Yonghui..... 686
Hu, Yuantai..... 660
Hua, Yu 686
Huang, Lu-Xi..... 817
Huang, Wei..... 821
Huang, Wuhuang..... 649
Huang, Xianhe.....132, 235, 238, 289
Huang, Yao..... 4
Huang, Yulin 547
Hudson, Andrew 47
Huillery, Paul 154
Hwang, Sang-Wook..... 746

I

Iborra, Enrique.....353, 519, 561, 662
Ido, Tetsuya..... 277
Ilchenko, Vladimir S. 79, 534
Imaike, Takeshi..... 583
Imbaud, Joël..... 176, 595
Imlau, Helmut 681
Ionescu, Adrian Mihai 805
Ishikawa, Manabu..... 231
Israel, Weiss..... 162
Ito, Manabu..... 231
Ivanov, Eugene..... 104, 179

J

Jackson, Jarom..... 460
Jackson, Shira 448
Jaimes Merazzo, Karla 66
Janssen, Christof..... 423
Jayles, Christian 72
Jelenković, Brana M. 57
Jeseck, Pascal..... 423
Jesorka, Aldo..... 652
Jha, Nandan 495, 758
Jia, Jinsheng..... 282
Jian, Bin..... 477, 640
Jiang, Haifeng..... 444, 458
Jiang, Shan..... 660
Jiang, Songtao..... 227
Jiang, Zhaojie 762
Jiang, Zhiheng 362, 676, 788, 826
Jiang, Zhuangde 253, 656
Jimenez, Erika 66
Jiménez-López, Miguel 410
Jin, Yabin..... 22
Jing, Wenfang..... 6, 728
Jo, Bumkyung 570
Johansson, Leif..... 534
John, František 697
Jones, Matthew..... 154
Joshi, Abhay 781
Josse, Fabien 24
Jost, John 530
Joyce, Richard 68, 198
Juillard, Jerome 506
Jung, Kwangyun 95, 771

K

Kaczmarek, J. 475
Kadota, Michio 206
Kajita, Masatoshi..... 277
Kalaydzhyan, Aram..... 95
Kalinin, Victor..... 347
Kallerud, Torjus..... 181
Kamochkin, Alexey 245
Kang, Sungho 500
Karioja, Pentti 55
Karlen, Sylvain 55, 315, 625
Kärtner, Franz..... 95
Kase, Yuji 328
Kashin, Vitaliy V. 345
Katzmann, Klaus..... 703
Kaur, Namneet..... 86
Kautio, Kari 55
Kazakov, Georgy 430
Keller, Ursula 779
Kersalé, Yann 419, 773, 775
Khabarova, K.Yu..... 751

Khader, Isaac 130
Khan, Elias 106
Khayatzadeh, Ramin 489
Khromov, Maxim 633
Kim, Huidong 744, 746
Kim, Jungwon 95
Kim, Seong-Kyun 534
Kim, Yoonkee 310
Kinali, Attila 38, 121, 408, 598
Kippenberg, Tobias 530
Kirby, Deborah 68, 198
Kirchner, Tom 153
Kireev, Alexey 452
Kirkko-Jaakkola, Martti 385
Klein, Karl-Ludwig 406
Kobayashi, Kaoru 231
Kolachevsky, N.N. 751
Kolesov, Vladimir V. 345
Kolmogorov, Oleg V. 417
Kołodziej, Jacek 399, 681
Konrad, Wolfgang 136
Konyashchenko, Alexander 452
Kopilov, Leonid 633
Kornilov, Aleksei 222
Koskela, Julius 212
Kossek, Tomasz 393
Kotyukov, Aleksandr 245
Kovalenko, Dmitriy 307
Kowalski, J. 475
Krakowski, Michel 136
Krehlik, Przemysław 366, 368, 393, 399, 681, 697, 710
Kreissig, Martin 66
Krmpot, Aleksandar J. 57
Kroemer, Eric 636
Kronjaeger, Jochen 697
Kruger, Justin 179
Kubena, Randall 68, 198
Kubinec, Peter 575
Kupalov, Dmitry 633
Kupalova, Olga 633
Kustanovich, Kiryl 652
Kuznetsova, Iren E. 345, 850
Kwon, Taeg Yong 622, 629

L

Laatiaoui, Mustapha 1
Lacroûte, Clément 419, 773, 775
Lahti, Markku 55
Lahtinen, Ossi 55
Laier English, Elizabeth 697
Lal, Amit 138
Lamporesi, Giacomo 748
Landragin, Arnaud 646, 798
Langlois, Mehdi 800
Laroche, Thierry 336
Lasseri, Raphaël-David 106
Laude, Vincent 660
Laurent, Philippe 707
Lautier-Gaud, Jean 697
Lavenus, Pierre 218
Le Coq, Yann 468, 771, 781
Le Goff, Roland 471
Le Targat, Rodolphe 468, 471, 815
Lebedinskii, Y.Y. 751
Lebrun, Romain 66
Le-Coarer, Etienne 388
Lecomte, Steve 55, 84, 625
Lee, Joshua E.-Y. 26, 502
Lee, Sang-Bum 622, 629
Lee, Sangmin 622
Lee, Won-Kyu 160, 468, 744, 746
Lefevre, Remi 496
Leigh, Arthur 347
Leitenstorfer, Alfred 124
Lelièvre, Oriane 190, 493
Lemaître, Yves 835, 842
Lemański, Dariusz 628
Lemke, Nathan 460, 466
Leone, V. 475
Lesage, Jean-Marc 572
Lessing, Maurice 697
Leute, Julia 736, 784
Lévèque, Thomas 471
Levi, Benny 162
Levi, Chagai 162
Levi, Filippo 156, 446, 638, 697, 748, 813
Lezius, Matthias 128, 530, 777, 781
Li, Bo 699
Li, Dandan 699
Li, Jiang 265

Li, Jianing 565
Li, Sheng-Shian 551
Li, Tang 623
Li, Tianchu 302
Li, Xiaohui 402, 690, 699, 817
Li, Xinyi 538, 547
Lian, Jiqing 762
Liang, Kun 712, 788, 826, 826
Liang, Wei 79, 534
Liehl, Andreas 124
Lim, Jinkang 79
Lin, Chuanfu 607
Lin, Huang-Tien 826
Lin, Jinda 267
Lin, Rui 292
Lin, Shinn Yan 362, 676
Lin, Yige 719
Lipiński, Marcin 393
Lisak, Daniel 100
Liu, Chang 282, 285
Liu, Dandan 292
Liu, Dong 235
Liu, Fengwei 616
Liu, Liang 623
Liu, Nianfeng 302
Liu, Ruiyuan 611, 759
Liu, Ruonan 10
Liu, Shuo 6
Liu, Tao 381, 686
Liu, Ya 402
Liu, Zhongzheng 737
Llopis, Olivier 190, 489, 493, 835, 842
Lodewyck, Jérôme 815
López, Jose Mauricio 326
Lopez, Olivier 160, 378, 468
López-Jiménez, José 410
Lorini, Luca 317
Lou, Janet 642
Lours, Michel 471, 781
Loyer, Sylvain 784
Lü, Desheng 623
Lu, Ruochen 143, 846
Lu, Xiaochun 6, 728
Lucas, Erwan 530
Ludlow, Andrew 32
Lusawa, Marzenna 393

M

Ma, Pei 631
Ma, Rui 66
Määttänen, Antti 55
Maccioni, Enrico 462
Maeda, Ryo 300
Maier, Hans-Jörg 1
Maillard, Antoine 324
Maleki, Lute 79, 534
Man, Rony 162
Manzaneque, Tomas 143, 846
Maqueda López, Mariazel 805
Marcilhac, Bruno 835, 842
Marco-Dufort, Bruno 662
Maréchal, Baptiste 773, 775
Maris Ferreira, Pietro 506
Marmor, Shlomo 162
Marszalec, Michał 393
Martin, Kyle 460, 466
Martinenghi, Romain 523
Mashanovitch, Milan 534
Matic, Alexandre 214
Matsakis, Demetrios 723
Matsko, Andrey B. 79, 534
Mauri, Luca 636
Maurice, Vincent 636
Mayer, Aline S. 779
Mazur, Michal 366
McAlister, Ben 179
McFerran, John 421
Meng, Hongling 611, 759
Meng, Lingda 402
Menyuk, Curtis 425
Merimaa, Mikko 385
Merlet, Sébastien 800
Mertin, Stefan 565
Mestre, Nicole 136
Miao, Peixian 631
Micalizio, Salvatore 169, 322, 638
Mielec, Nicolas 646
Milani, Gianmaria 446, 813
Mileti, Gaetano 57, 63
Millo, Jacques 419, 773, 775
Minissale, Marco 423
Mirea, Teona 353, 519, 561, 662
Mishin, Sergey 542

EFTF-IFCS 2017 Author Index

Miškinis, Rimantas 241
Mokry, Christoph 1
Moraja, Marco 636
Morante, Q. 475
Moreno, William 63
Morrison, Gordon 534
Morvan, Loïc 190, 493
Morzyński, Piotr 100
Mou, Weihua 826
Mozhaev, Vladimir 850
Muller, Holger 104
Mura, Alberto 156, 705
Muralt, Paul 565
Murapaka, Chandrasekhar 66
Mustafazade, Aref 16, 510

N

Nabki, Frederic 203
Nagórny, Bartłomiej 477, 628
Nallatamby, Jean-Christophe 175
Nawrocki, Jerzy 477, 628
Nedospasov, Iliya 850
Neumayr, Jürgen 1
Newbury, Nathan R. 130
Nguyen, Clark T.-C. 10
Nguyen, Hung 68, 198
Nicolodi, Daniele 468, 781
Nikonov, Arkady 245
Nogaś, Paweł 628, 697
Nouchi, Pascale 190, 493
Novoselov, Alex 633

O

Oates, Chris 32
Obrzud, Ewelina 84
Ogawa, Masato 231
Olbrysz, P. 475
Olivares, Jimena 353, 519, 561, 662
Olivera, José Luis 519, 662
Oliveri, Stefania 516
Olson, Judith 32
Omori, Tatsuya 547
Onillon, Emmanuel 315
Ortiz, Carlos Andres 326
Oshmyansky, Yury 542
Osmyk, Roman 393
Ouisse, Morvan 775
Overstolz, Thomas 55, 315, 625
Ozgurluk, Alper 10
Ozimek, Filip 477, 628, 640

P

Paillot, Jean-Marie 175
Palchikov, Vitaly 751
Pan, Duo 305, 427
Pan, Xiaoyan 607
Pandit, Milind 16, 510
Pang, Xiangnan 210
Park, Chang Yong 744, 746
Park, Sang Eon 622, 629, 744
Parker, Stephen 179
Parsapour, Fazel 565
Pashchenko, Vladimir 565
Passilly, Nicolas 636
Pavlenko, Konstantin 317
Pavlenko, Yuri 317
Pei, Yuxian 607
Pellaton, Matthieu 63
Pelle, Bruno 479
Peng, Huanfa 250
Peng, Michael 95
Peng, Xiang 305
Peng, Xiangkai 623
Peng, Xiaofeng 250
Penn, Jean-Francois 572
Pennec, Yan 22
Pereira Dos Santos, Franck 800
Perez, Patrick 136, 324
Perosanz, Félix 784
Peterson, Christopher 852
Petit, Gérard 784, 788
Phelps, Gretchen 466
Philippe, Charles 471
Piazza, Gianluca 802
Piester, Dirk 681, 703, 736
Pihan-Le Bars, Hélène 106
Pillai, Gayathri 551
Píriz, Ricardo 683
Pisani, Marco 462
Pizzocaro, Marco 446, 813
Plessky, Victor 212
Poddar, Ajay 113, 484

Pokharel, Alok 176
Polcawich, Ronald 554, 558, 807
Polewka, Thomas 683, 736
Popović, Zoya 261
Poteshin, S.S. 751
Potnis, Shreyas 448, 768
Pottie, Paul-Eric 86, 160, 378, 468, 697
Prache, Pierre 506
Prazot, Shemi 162
Prigent, Michel 175
Probst, Rafael 450
Prokhorov, Dmitrie V. 417
Prudnikov, Oleg N. 432
Pu, Dong 253, 656
Puder, Jonathan 554, 558, 807
Pulskamp, Jeffrey 554, 558, 807
Purbawati, Anike 66

Q

Qalandar, Kamala 802
Qi, Yi 381
Qian, Zhenyun 500
Qin, Weijin 736
Qiu, Duyu 649
Qu, Lili 381
Qu, Qiuzhi 623
Quintin, Nicolas 378, 697

R

Radil, Jan 697
Radojičić, Ivan S. 57
Rajaram, Vageeswar 500
Ranjita Chanu, Sapam 646
Rasel, Ernst M. 432, 495, 758
Rauf, Benjamin 446, 813
Ren, Juan 253
Ren, Wei 623
Rerucha, Simon 697
Ricco, Antonio 24
Rinaldi, Matteo 500
Riou, Isabelle 646
Rochat, Sylvain 388
Rocher, Cyrus 775
Rodwell, Mark J. 534
Rohde, Ulrich 113, 484
Roldán, Pedro 683
Romer, Andreas 136
Roncin, Vincent 769
Rouillé, Christian 423
Rovera, Giovanni Daniele . 397, 705, 707, 821
Roy, Atish 753
Ruan, Jun 292, 381
Ruan, Yong 296
Rubiola, Enrico 113, 419, 578, 773, 775
Rudy, Ryan 554, 558, 807
Rühmann, Steffen 495, 758
Ruiz Calafora, Ana 66
Runke, J. 1
Rutkowski, Jaroslaw 636
Rydlichowski, Piotr 399

S

Şafak, Kemal 95
Sagnard, Marianne 336
Sahoo, Bijaya Kumar 753
Sakharov, Sergey 193
Salwik, Karol 710
Sangrador, Jesús 353, 519
Santagata, Rosa 468
Santarelli, Giorgio 378, 781
Santiano, Marco 462
Sanz, Diego 683
Sauer, Steffen 495, 758
Savchenkov, Anatoliy A. 79, 534
Savoie, Denis 798
Sbick, Bernhard 703
Schilt, Stéphane 456, 779
Schmeissner, Roman 136, 324
Schmidt, Hagen 193
Schmidt, Tobias 666
Schnatz, Harald 681
Schumm, Thorsten 430
Seidelin, Signe 771
Seiferle, Benedict 1
Seletskiy, Denis 124
Seman, S. E. 68
Seshia, Ashwin 16, 148, 510
Sesia, Ilaria 34, 475, 705
Sette, Daniele 514
Shang, Haosen 737, 740, 762, 765
Sheerin, Todd 32
Shelkovnikov, Alexander 452

Shen, Chao 607
Shepelev, Denis 452
Shi, Junru 292
Shi, Tiantian 305, 427
Shikhabudinov, Alexander M. 345
Shim, Kyu Min 629
Shuai, Tao 607
Si, Hongwei 98
Siccardi, Marco 397
Sierra-Zapata, Maria 561
Signorile, G. 475
Simsek, Arda 534
Sinclair, Laura 130
Śliwczyński, Łukasz ..366, 368, 393, 399, 681, 710
Smirnov, Dimitrij 241
Sobolewski, Łukasz 42
Sobreviela, Guillermo 16, 510
Song, Huijie 381
Sormani, D. 475
Sotiriadis, Paul Peter 587, 591, 603
Sotnikov, Andrei 193
Staliuniene, Egle 703, 736
Stefani, Fabio 160
Steinmetz, Tilo 450
Stern, Avinoam 162
Stern, Guillaume 317
Sthal, Fabrice 176, 595
Stofanik, Vladimir 575
Stopps, Alexander 347
Stratton, Frederic 68, 198
Su, Hang 357
Südmeyer, Thomas 456, 779
Suhak, Yuriy 193
Sulzer, Philipp 124
Sun, Baoqi 357
Sun, Fuyu 132, 289
Sun, Jian Fang 439
Sun, Tianchi 484
Sun, Xiaolin 294, 481, 616
Sun, Yong 282
Suo, Rui 302
Swann, William 130
Sysoev, A.A. 751
Szmuk, Ramon 479
Szterk, Piotr 393
Szymaniec, Krzysztof 477, 628, 640

T

Tabata, Osamu 60
Tabrizian, Roozbeh 20, 570
Tai, Zhaoyang 444, 458
Taichenachev, Alexey V... 102, 278, 307, 432, 496
Tallur, Siddharth 30
Tampellini, Anna 156
Tan, Feng 649
Tanaka, Shuji 206
Tang, Gongbin 547
Tang, Yuanlin 238
Tapkov, Vadim 222
Tarallo, Marco Giacinto 748
Tausenev, Anton 452
Tavella, Patrizia 185, 475
Temenos, Nikos 587, 591, 603
Terashima, Kenta 60
Thai, Tung Thanh 705
Thirolf, Peter 1
Thoumany, Pierre 446, 813
Tinto, Massimo 126
Tisserand, Laurent 788
Tkachev, Sergey V. 345
Tkalya, E.V. 751
Tobar, Michael 104, 179
Tokunaga, Sean K. 468
Torcheboeuf, Nicolas 315
Torres-González, Felipe 186
Torstein Røine, Per 181
Tran, Dang Bao An 468
Tratnik, Jurij 486
Trautmann, N.G. 1
Tregubov, D.O. 751
Tremblin, Pierre-Alain 781
Tricot, François 169, 172
Trimeche, Azer 800
Tsai, Julius Ming-Lin 551
Tsai, Kaichien 181
Tseng, Wen-Hung 676, 723
Tsuchiya, Toshiyuki 60
Tu, Jianhui 631, 762
Tuckey, Philip 86
Turza, Krzysztof 368, 399
Tyurikov, Dmitri 452

EFTF-IFCS 2017 Author Index

U

Udem, Thomas 450
Underhill, Michael 117, 733
Urba, Emilis 241
Uzycki, J. 475

V

Vacheret, Xavier 567
Vahala, Kerry 265
Vaillant, Etienne 595
Vallet, Grégoire 815
Varriale, E. 475
Vélez López, María Del Carmen 813
Verlhac, Béatrice 218
Vernotte, François 72
Verona, Enrico 345
Vila, Laurent 66
von Bandel, Nicolas 136
von der Wense, Lars 1
Vorokhovsky, Yakov 245
Voronova, Natalia 343
Vutha, Amar 153, 448, 768

W

Wallin, Anders 385
Walter, Christopher 310
Wan, Jianhong 285
Wang, Bo 91, 98
Wang, Haifeng 371, 375, 673, 693
Wang, Hongbo 371, 375, 673, 693
Wang, Jia-Lun 826
Wang, Jian 712
Wang, Lijun 98, 294, 481, 616, 631
Wang, Qian 267, 332
Wang, Shuhui 282
Wang, Shuwei 371, 375, 673, 693
Wang, Weibo 719
Wang, Wenli 267, 332
Wang, Wenting 95
Wang, Xiang 381
Wang, Xinliang 292
Wang, Xu 227
Wang, Xueyun 371, 375, 605, 673, 693
Wang, Yanhui 282, 285
Wang, YanPing 381
Wang, Ye 712, 788, 826
Wang, Yuzhu 267, 332, 439
Wang, Yuzhuo 719
Wang, Zhong 611
Watanabe, Koki 647
Wcisło, Piotr 100
Wei, Qiang 618
Wei, Rong 267, 332
Wei, Xueyong 253, 656
Widomski, T. 475
Wiotte, Fabrice 378
Wirth, Hans-Friedrich 1
Wittrock, Steffen 66
Wittwer, Valentin J. 779
Wolf, Peter 106, 471
Wong, Chee Wei 79
Wu, Chenfei 631
Wu, Meifang 357, 686
Wu, Yuanjie 450

X

Xiao, Shunlu 737
Xie, Wei 618
Xie, Xiaopeng 781
Xie, Yonghui 607
Xin, Ming 95
Xu, Dan 160, 468
Xu, Liu 253
Xu, Longxia 690, 699, 817
Xu, Yongchi 250
Xu, Zhen 439
Xue, Biao 427

Y

Yakovlev, V.P. 751
Yamada, Ken 647
Yan, Lulu 444, 458
Yan, Xueshu 631
Yang, Fan 826
Yang, Jun 826
Yang, Lin 618
Yang, Renfu 605
Yang, Shiyu 762
Yang, Wenzhe 371, 375, 673, 693
Yang, Xuhai 357
Yang, Yansong 143, 846

Yang, Zhiqiang 712, 788, 826
Yano, Yuichiro 277
Yantchev, Ventsislav 652
Ye, Peng 649
Yen, Ernest Ting-Ta 181
Yevilevich, Israel 162
Yi, Hang 371, 375, 673, 693
Yim, Sin Hyuk 629
Yong, Yook-Kong 68, 198, 210
You, Zheng 296
Yu, Dai-Hyuk 744, 746
Yu, Fengxiang 292
Yu, Nan 126, 644
Yu, Pen-Li 139
Yuan, Xu 91
Yudin, Valera 496
Yudin, Valeriy 102, 278, 307, 432
Yun, Peter Enxue 169, 172
Yun, Peter 322

Z

Zaitsev, Boris D. 345
Zanon-Willette, Thomas 423, 496
Zarroli, E. 475
Zawada, Michał 100, 437
Zeng, Hao 649
Zhang, Aimin 712, 719, 788, 826
Zhang, Benfeng 547
Zhang, Bingqiang 282
Zhang, Cheng 250
Zhang, Daonong 616
Zhang, Fan 296
Zhang, Hui 292
Zhang, Hui-Jun 817
Zhang, Jianwei 294, 481, 616, 631
Zhang, Ke 728
Zhang, Li 484
Zhang, Pan 458
Zhang, Shengkang 371, 375, 673, 693
Zhang, Shengnan 737, 740, 762, 765
Zhang, Shougang 292, 444, 458, 618
Zhang, Tianyi 656
Zhang, Xiaofei 292, 444, 458
Zhang, Xiaogang 740, 762, 765
Zhang, Yanyan 444, 458
Zhang, Zhenwei 605, 673
Zhao, Chun 16, 510
Zhao, Jianye 611, 759
Zhao, Ru Chen 439
Zhao, Wenyu 444, 458
Zhao, Xingwen 618
Zhao, Yang 607
Zheng, Yajun 660
Zhou, Qi 235, 238
Zhou, Weimin 425
Zhu, Feng 402, 690, 817
Zhu, Lixin 250
Zhu, Xiangwei 712
Zipfel, Klaus 495, 758
Zope, Anurag A. 551
Zuo, Ya'Ni 294, 481

EFTF-IFCS 2017

July 9 –13, 2017 | Micropolis Conference Center |Besançon, France



European Frequency and Time Forum and IEEE International Frequency Control Symposium

FINAL PROGRAM

Table of Contents

Useful Information 5
Conference Exhibitors 10
Special Issue of the T-UFFC 11
IEEE Women in Engineering Special Lunch Workshop 12
Cross-Spectrum L(F) Workshop 13
Student Events 14
Awards 15
Plenary Session 1: Invited Lecture 17
Plenary Session 2: Invited Lecture 18
Plenary Session 3: Invited Lecture 19
Student Paper Competition 20
TUTORIALS – Sunday July 9th 22
Lecture Sessions – Monday July 10th 23
Lecture Sessions – Tuesday July 11th 30
Poster session I – Tuesday 35
Lecture Sessions – Wednesday July 12th 44
Poster session II – Wednesday 50
Lecture Sessions – Thursday July 13th 59
2018 Conferences 64
Conference Center Floorplan 66

2017 European Frequency and Time Forum & IEEE International Frequency Control Symposium

General Chairs

Bernard Dulmet, FEMTO-ST

Lute Maleki, OEwaves

Scientific Chairs

Jérôme Delporte, CNES

Elizabeth Donley, NIST

Conference Secretary and Exhibits Chair

Joël Petetin, SFMC

Finance Chairs

Fabrice Sthal, SFMC, France

Debra Coler, OEwaves

Tutorials Chairs

Gaetano Mileti, University of Neuchatel, Switzerland

Matteo Rinaldi, Northeastern University

Academic Chair

François Vernotte, OSU-THETA, France

Editorial Chair

Greg Weaver, John Hopkins University, APL

Awards Chairs

James Camparo, The Aerospace Corporation

Pierre Waller, ESA, The Netherlands

Welcome from the General Co-Chairs

We are pleased to extend a warm welcome to the attendees and guests of the 2017 Joint Conference of the European Frequency and Time Forum and the IEEE International Frequency Control Symposium. This is the eighth occasion of this event, which over the years has grown both in size and popularity amongst worldwide members of the time and frequency community.

The organizers of this year's Joint Conference agreed early on to strive towards the goal of a strong technical program combined with the optimum environment for technical exchange amongst the attendees. The Technical Program includes three outstanding plenary speakers, four tracks of invited and contributed technical talks, three tutorial tracks, and comprehensive poster sessions to provide an excellent platform for scientific and technical exchange in virtually all areas of interest to the time and frequency community. The Student Poster Competition is our attempt to foster the growth of the number and quality of future members of our community. The volunteers of the Joint Program Committee, under the leadership of our Technical Program Co-chairs, have worked very hard to form a coherent technical program, which represents the latest development and scientific and technical achievements in all areas of work in our field.

We hope that you will savor the hospitality of the city of Besancon, and take some time to walk along the river and appreciate the deep cultural heritage of this city dating back to the Roman era. A very exciting tour is planned to provide the opportunity to gather lasting memories of Besancon and nearby areas. We sincerely hope that you will enjoy all aspects of the conference, including the technical program, the social events, and networking with colleagues.

Welcome to Besançon and the Joint Conference!



Bernard Dulmet



Lute Maleki

Welcome from the Scientific Program Chairs

We are delighted to welcome you to Besançon for the 2017 Joint Meeting of the European Frequency and Time Forum and the IEEE International Frequency Control Symposium.

The program features three exciting plenary lectures. On Monday, Virginie van Wassenhove from CEA will present a lecture titled “How does the human brain make sense of time?” On Tuesday, Terry Quinn, Emeritus Director of the BIPM will present a lecture on “The 50th Anniversary of the atomic definition of the second.” And finally, on Wednesday, Lawrence Krauss from Arizona State University will present a lecture on “Journey to the Beginning of Time: Black Holes, Gravitational Waves, and The Big Bang.”

The four-day technical program consists of 154 lectures, including 25 invited lectures, and 249 posters. The posters can remain on display during both poster sessions, and will be presented by their authors on either Tuesday or Wednesday afternoon. The Student Paper Competition will be part of Tuesday’s poster session, featuring 30 student finalists that were selected from 82 submitted abstracts. The winners will be awarded after the poster session on Wednesday evening.

In addition to the main technical program, we are pleased to offer a day of outstanding tutorials on Sunday that will be presented by 15 world-renowned experts in their fields.

We hope that the scientific program will inspire you to have new ideas and form new relationships with colleagues in the time and frequency community.

Welcome, and enjoy the program!



Jérôme Delporte



Elizabeth Donley

Useful Information

Conference Address

Micropolis, 3 Boulevard Ouest, 25000 Besançon

Local Telephone: 03 81 41 08 09

Emergency Numbers

Medical aid 15

Police 17

Firemen 18

Conference Badge

The conference badge must be worn to all conference events. Attendees without a badge may be denied entrance to the conference site. On Sunday and Monday, the security agents may request you to kindly open your bags at the entrance for a security check. Once you have a badge, the security will let you enter without checking your bag.

Lab Tours

Persons wanting to attend the lab tours organized on Thursday afternoon will have to register at the Conference Desk: availability will be limited, so access being allowed on a first-come first-served basis. ID and e-mail addresses will be requested at the time of registration. The Conference Organization will take care of the transportation to and from the lab sites. Participants will choose one laboratory site from these three options:

- FEMTO-ST Time & Frequency Dept.,
- FEMTO-ST Micro-Nano-Sciences and Systems Dept. and Optics Dept.,
- Observatory of Besançon in cooperation with Time Tech.

No Recording or Job Posting

No unauthorized video or audio recording is allowed on site for the conference duration. No job posting is allowed.

Speakers' Breakfasts

Speakers and Session Chairs for the Oral Sessions are required to attend a complimentary Speakers' Breakfast on the morning of their presentation/session from 8:00 am. The breakfast is limited to one speaker per presentation. The speakers must upload their presentations on the notebook PCs brought by the organization at the Speakers' Breakfast. There will be one PC per parallel track, and one folder per session.

Lunches

Lunches will be provided for all Conference attendees from Monday through Thursday, plus Sunday for the attendees registered for the Tutorials.

Please give any request for a special diet at the time of registration.

People needing to depart before lunch time on Thursday will be provided with a lunch box, to be ordered at the Conference Desk on Saturday evening, Sunday evening or Monday morning.

Conference Dinner

The conference dinner is included with the conference registration and will take place on the conference site on Monday from 7:00 pm-11:00 pm. Guest tickets may be purchased at the registration desk.

Exhibitors Event

Exhibitors awards and winners of the Student Paper Competition will be presented in the exhibits area on Wednesday from 6:00-8:00 pm. Beverages will be served at the event. All conference attendees are welcome to this event.

Transportation

All attendees will be provided with a return ticket for Ginko's local transportation system (bus, tramway). Further tickets are on sale in newspaper shops and most tramway stations. One can buy tickets from the bus drivers. There are no ticket sales in tramway coaches.

IFCS Standing Committee

Elected Members

Mike Driscoll, Consultant
Kurt Gibble, Penn State University
Greg Weaver, John Hopkins University, APL
Aaron Partridge, SiTime
Debra Coler, OEwaves
Elizabeth Donley, NIST
Lute Maleki, OEwaves
Matteo Rinaldi, Northeastern University
James Camparo, The Aerospace Corporation
Jeremy Everard, University of York
Patrizia Tavella, INRIM
Mike Tobar, University of Western Australia
Dana Weinstein, Purdue University
Sarah Bedair, US Army Research Lab
Sheng-Shian Li, NTHU, Taiwan

Ex Officio Members

Ekkehard Peik, PTB
Bernard Dulmet, FEMTO-ST

EFTF Executive Committee

Elected Members

Bernard Dulmet, FEMTO-ST, France
Jeremy Everard, University of York, United Kingdom
Helen Margolis, NPL, United Kingdom
Gaetano Mileti, University of Neuchatel, Switzerland
Ekkehard Peik, PTB, Germany, Chair
Wolfgang Schaefer, TimeTech, Germany
Pascale Defraigne, Royal Observatory, Belgium
Per-Olof Hedekvist, SP-RISE, Sweden
Patrizia Tavella, INRIM, Italy
Philip Tuckey, Paris Observatory, France
François Vernotte, OSU-THETA, France
Pierre Waller, ESA, The Netherlands

Ex Officio Members

Fabrice Sthal, SFMC, France
Elizabeth Donley, NIST, United States of America
Aaron Partridge, SiTime, United States of America
Jérôme Delporte, CNES, France
Lute Maleki, OEwaves, United States of America
Filippo Levi, INRIM, Italy

EFTF-IEEE IFCS 2017 Joint Program Committee

Group 1: Alexandre Reinhardt and Dana Weinstein, Co-Chairs

Thomas Baron, Emmanuel Defay, Marc Faucher, Songbin Gong, Yoonkee Kim, Randy Kubena, Jan H. Kuypers, Olivier Le Traon, Joshua Lee, Sheng-Shian Li, Bernd W. Neubig, Laura Popa, Rick Puccio, Jeffrey Pulskamp, Mina Rais-Zadeh, Matteo Rinaldi, Dan Stevens, Shuji Tanaka, Ji Wang, Max Wang, Ventsi Yantchev, Yook-Kong Yong

Group 2: Jean-Pierre Aubry and Ajay Poddar, Co-Chairs

Claudio Calosso, Gilles Cibiel, Michael Driscoll, Jeremy Everard, Marvin Frerking, Serge Galliou, Wan-Thai Hsu, Xianhe Huang, Eugene Ivanov, Olivier Llopis, Craig Nelson, Ulrich Rohde, Enrico Rubiola, Paul Sotiriadis, Fabrice Sthal, Kia Hock Tan, Michael Tobar, Michael Underhill

Group 3: Scott Crane and Stefan Weyers, Co-Chairs

Marco Belloni, Eric Burt, Francois-Xavier Esnault, Chad Fertig, Kurt Gibble, David Howe, John Kitching, Motohiro Kumagai, Arnaud Landragin, Filippo Levi, Tianchu Li, Salvatore Micalizio, Gaetano Mileti, Bruno Pelle, David Scherer, Tom Swanson, Krzysztof Szymaniec, Qinghua Wang, Steven Wilkinson

Group 4: Svenja Knappe and Ashwin Seshia, Co-Chairs

Jeffrey Andle, Sylvain Ballandras, Sunil Bhave, Alfred Binder, Mark Cheng, Philip Feng, Holger Fritze, Victor Kalinin, Shigeru Kurosawa, Ryszard Lec, Paul Muralt, Clark Nguyen, Mauricio Pereira da Cunha, Victor Plessky, Leonhard Reindl, Sid Tallur, Guillermo Villanueva, Greg Weaver, Ventislav Yantchev

Group 5: Stefania Romisch and Pierre Waller, Co-Chairs

Anne Amy-Klein, Andreas Bauch, Laurent-Guy Bernier, Pascale Defraigne, Miho Fujieda, Gesine Grosche, Per Olof Hedekvist, Jan Johansson, Judah Levine, Huang-Tien Lin, Shinn-Yan Lin (Calvin), XiaoChun LU, Demetrios Matsakis, Nathan Newbury, Vitaly Pal'chikov, Bijunath Patla, Edward Powers, Wolfgang Schaefer, Amitava Sengupta, Jeff Sherman, Patrizia Tavella, Philip Tuckey, Pierre Ulrich, Hongbo Wang, Peter Whibberley, Michael Wouters, Aimin Zhang

Group 6: Dave Leibrandt and Helen Margolis, Co-Chairs

Davide Calonico, Luigi Cacciapuoti, James Chou, Roman Ciuryło, Pierre Dube, Patrick Gill, Feng-Lei Hong, Tetsuya Ido, Jason Jones, Steve Lecomte, Yann LeCoq, Rodolphe Le Targat, Christian Lisdat, Jerome Lodewyck, Andrew Ludlow, Andre Luiten, Long-Sheng Ma, John McFerran, Mikko Merimaa, Jacques Morel, Ekkehard Peik, Franklyn Quinlan, Marianna Safronova, Thomas Südmeyer, Alexey Taichenachev, Masami Yasuda, Lin Yi, Nan Yu

Conference Exhibitors

Booth	Company	Country
01	Stable Laser Systems	USA
02	ITRI Taiwan	Taiwan
03	Vectron Int.	Germany
04	Spectradynamics Inc.	USA
05	NoiseXT	France
06	GuideTech	USA
08	Lange Electronics	Germany
09	PIK Time Systems	Poland
10-11	µQuans	France
12	M Squared Lasers	United Kingdom
13	AR Electronique	France
14	PTF llc	USA
15	Microsemi	USA
16	Menlo Systems	Germany
17	Toptica/Opton Laser	France
18	Holzworth Instrumentation	USA
20	TimeTech GmbH	Germany
21	SAES Getters Spa	Italy
22	Meyer Burger	Germany
23	Spectratime	Switzerland
24	Advanced Modular Systems Inc	USA
25	Syrlinks	France
26	Lanzhou Institute of Physics	China
27	OEwaves	USA
28	SCIA systems GmbH	Germany
29	Anapico AG	Switzerland
30	Morion Inc.	Russia
31	IMRA America Inc.	USA
33	Cristalinnov	France
34	Carmel Instruments	USA

Special Issue of the T-UFFC

DEADLINE FOR PAPER SUBMISSION: SEPTEMBER 30TH, 2017

Following the 2017 Joint EFTF-IFCS conference, select authors will be invited to submit a full manuscript for publication consideration into a 2017 Special Issue of the IEEE Transactions on Ultrasonics, Ferroelectrics and Frequency Control (T-UFFC). It is hoped that the Special Issue serves as a time capsule to represent the state of the art in Time and Frequency to commemorate the 50th Anniversary of the atomic definition of the second. Conference presenters, in particular invited speakers and the student paper finalists, are also encouraged to submit papers.

Of significant note – manuscripts must contain substantial additional technical material from the conference proceedings. This must be justified based on one or more of the following: new theoretical or experimental results, enhanced modeling and characterization, descriptions of new applications, better placing the study in its context, greater depth of discussion, more elaborate analysis of results and additional references.

As a guideline for authors, the Editor-in-Chief of the T-UFFC has set the quantitative threshold for substantial additional technical material to be 40-50% above, not only the conference proceedings, but all previous publicly archived material.

Guest Editors:

Gregory Weaver JHU/APL, gregory.weaver@jhuapl.edu

Jérôme Delporte, CNES

Elizabeth Donley, NIST

Dana Weinstein, Purdue University

Jeremy Everard, University of York

Stefan Weyers, PTB

Ashwin Seshia, University of Cambridge

Stefania Romisch, NIST

Helen Margolis, NPL

IEEE Women in Engineering Special Lunch Workshop

Monday, July 10, 2017, 12:20 – 14:00

"CONFIDENCE THROUGHOUT OUR CAREERS"
Mezzanine Restaurant
Inspiring, thought provoking, and pragmatic!

KNOW YOUR VALUE

Confidence & Assertiveness are two key ingredients to having a fulfilling & satisfying career. Without these elements, we may fall in the trap of feeling frustrated by not having our ideas heard, not advancing in our careers, and ultimately not thriving as much as we should be.

What makes for a fulfilling career? How can we gain more confidence in our careers and within our professional communities? What holds us back? Are we comfortable speaking up? Assertive enough? Daring? Do we know the value we are adding in any given situation? Are we being heard?

Find out how to enhance your self-awareness regarding your own assertiveness, self-confidence, and tips on how to speak up and claim your space within a technical community which may be predominantly male. Boost your acknowledgement of the real value you are adding to any given situation.

Building community! Networking and exchanging on these themes with fellow WIE members in a fun and relaxed way. Each participant will have the opportunity to do their own self-assessment on assertiveness, self-confidence and success storyboard.

Facilitated by **Jody JULIEN:** Born in the USA, holds degrees from universities in Michigan and New York in the areas of International Business and Strategic Human Resources. Trained and certified in both Professional and Life Coaching. Held worldwide leadership positions for over 20 years, has lived in North America, South America, and Europe, and is currently living in France. The founder of J2 Coaching & Consulting since 2011, a global firm specializing in professional development and international organizational effectiveness.

Cross-Spectrum $\mathcal{L}(f)$ Workshop

E. Rubiola, FEMTO-ST & C. W. Nelson, NIST

Tuesday, July 11, 18:00 – 20:00

At The Gallery (Downstairs)

18:00 – Introduction and News after the 2015 Workshop
18:20 – Labs and Industrials Issues
19:20 – Roundtable
19:50 – Conclusions
20:00 – Adjourn

The cross-spectrum method is a standard practice in phase-noise measurement, widely used by manufacturers and users of oscillators, and by academic and public labs as well, including the primary labs.

This workshop follows two previous workshops on the same topic. The first was at the LNE in Paris on December 15, 2014. The second was in Denver on April 15, 2015 as a side event of the EFTF-IFCS Joint Meeting.

The purposes of the 2017 workshop are to:

- Inform the community that measurement errors and inconsistencies are around the corner.
- Summarize the state of the knowledge and the progress since 2015.
- Encourage the participants to communicate their experiences and needs.

The workshop is also intended as an occasion to promote collaboration between manufacturers of oscillators and instruments, users and customers, and Government and International labs.

Conclusions are intended to progressively provide guidelines and recommendations and ultimately to serve as a contribution to updated procedures and standards.

Student Events

Student Pizza Party

Tuesday, July 11 – 20:00 to 23:00

Ristorante-Pizzeria La Vela Azzura, 16 Rue Bersot, Besançon Town Centre

All students are encouraged to attend. Drinks and different kinds of pizza (slices) will be available free of charge.

Student-Exhibitor Networking Event

Wednesday, July 12th – 18:00 to 20:00

Micropolis Exhibition Area

The 2017 EFTF-IFCS in Besançon, will host for the second time a student-networking event. The motivation is to connect students close to graduation with jobs in industry and academia in the areas of time and frequency.

The motivation is to retain the great talent we observe each year attending the annual conference in a related field beyond graduation. The vast job opportunities in the field of time and frequency are often unclear to students, and this event tries to address this by specifically introducing prospective students to the conference exhibitors.

The first part consists of an 80-min slot, in which 20 students will each get four minutes to present their profile to conference exhibitors.

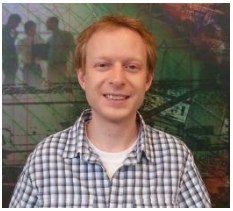
The second part of the event is a 30-min industry panel discussion where exhibitor representatives will talk about their work and students will have a chance to ask questions.

The event will include an awards ceremony for exhibitors to thank them for their contributions to the EFTF-IFCS conference. The student Paper Awards will be presented at the beginning of the event.

Awards

EFTF 2017 Awards

EFTF Young Scientist Award



Dr. Pascal Del'Haye

For outstanding contributions to the development of microresonator–based optical frequency combs.

Marcel Ecabert Award



Prof. Fritz Riehle

For his long-standing and enduring achievements in advancing the development of high accuracy optical atomic clocks within the international time and frequency community, and their implications for a future optical redefinition of the SI second.

IEEE IFCS 2017 Awards

I. I. Rabi Award



Dr. Scott Diddams

For the development and application of optical frequency combs to precision atomic timing.

C. B. Sawyer Memorial



Dr. Ron Stephens

For decades of entrepreneurial leadership in the frequency control industry.

W. G. Cady Award



Prof. Ulrich Rohde

For pioneering research, development, and commercialization of signal generating and processing devices for commercial and scientific applications.

Plenary Session 1: Invited Lecture

Monday July 10th

How does the human brain make sense of time?

Virginie van Wassenhove, CEA

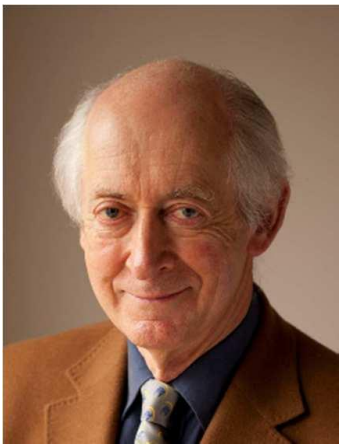


While we are all experts in experiencing time, introspection often provides us with very little intuitions regarding the neural mechanisms underlying how we perceive time. Over the last decades, research in the neurosciences of cognition has shown that different parts of our brain and different neural mechanisms contribute to various mental representations for time perception and cognition. In this talk, I will discuss the idea that time-consciousness is rendering intelligible the non-stationarities of brain activity, and argue that clocking mechanisms are foundational to comprehend the biology of the mind by reframing temporalities from the perspective of the brain as opposed to that of the external observer. These notions will be illustrated with empirical work using psychophysics and functional neuroimaging.

Plenary Session 2: Invited Lecture

Tuesday July 11th

The 50th Anniversary of the atomic definition of the second



Terry Quinn, Emeritus Director of BIPM

At about 4.30 pm in the afternoon of Friday 13 October 1967 the 13th General Conference on Weights and Measures made the historic decision to define the second in terms of a hyperfine transition of the atom of caesium 133, albeit with two votes against. On the occasion of this Conference, bringing together the European Frequency & Time Forum, and the International Frequency Control Symposium, I shall take the opportunity to give a broad sketch of the field of time and frequency metrology. This will include the discussions that took place leading up to the 1967 decision, the structure of the international bodies concerned and developments since then, including perspectives for a definition of the second based on a much higher frequency optical transition or transitions. I shall outline the changing responsibilities for the world's time scale beginning with the Bureau International de l'Heure, which had this responsibility until it was transferred to the BIPM in 1985, by which time it was an atomic time scale, TAI. I shall also describe more recent discussions dealing with the problem of the leap second on the world time reference and proposals for a clearer role for the organs of the Metre Convention whose mission, stated in 1875, remains "to assure the international unification and perfection of the metric system".

Plenary Session 3: Invited Lecture

Wednesday July 12th

Journey to the Beginning of Time: Black Holes, Gravitational Waves, and The Big Bang



Lawrence Krauss, Arizona State University

In Feb 2016 when the LIGO detectors reported the sound of two colliding black holes 1.3 Billion Light Years away, this represented the culmination of a century of exploration made possible by Einstein's remarkable General Theory of Relativity. I will describe how these exotic waves in space and time are everywhere around us, how we can use precision tools to detect them, and the possibility that we might eventually detect a signal from the Big Bang itself, turning metaphysics into physics and revealing insights into our own origins, the nature of gravity, and even the possible existence of other universes.

Student Paper Competition

Tuesday, July 11th, 2017 – Micropolis Poster Area

A strong group of submissions to the Student Paper Competition was reviewed by the Scientific Committee resulting in these finalists. One winner will be chosen for each group. The awards will be presented after the Wednesday poster session. Judging will be based on the quality and content of the work, the interest to our community, the significance of the contribution of the student, and the quality of the presentation.

Group 1:

(300) Ruochen Lu, University of Illinois at Urbana-Champaign – "Lithium Niobate Phononic Crystals for Radio Frequency Sh0 Waves"

(301) Adarsh Ganesan, University of Cambridge – "Observation of Phononic Frequency Comb in a Micromechanical Resonator"

(302) Alper Ozgurluk, University of California, Berkeley – "Q-Boosting of Metal MEMS Resonators via Localized Anneal-Induced Tensile Stress"

(303) Jonathan Puder, Cornell University – "Orders of Magnitude Reduction in Acoustic Resonator Simulation Times via the Wide-Band Rapid Analytical-FEA Technique"

Group 2:

(304) Alok Pokharel, FEMTO-ST Institute – "Investigation on Flicker Noise and Overtone Modes of Ultra-Stables Quartz Crystal Resonators"

(305) Romain Bouchand, Observatoire de Paris – "Accurate Measurement and Control of Amplitude to Phase Conversion for Low-Noise Photonic Microwave Generation"

(306) David Chaudy, Thales Systèmes Aéroportés – "Active Devices Choice and Design of an All Cryogenic Superconductor Resonator Oscillator"

(307) Oriane Lelièvre, Thales Research & Technology – "In-Situ Dispersion Measurement of a Coupled Optoelectronic Oscillator"

(308) Tsvetan Burtichelov, University of York – "Latest Results in the Development of an Ultra-Low Phase Noise Rb CPT Vapour Cell Atomic Clock"

(309) Huanfa Peng, Peking University – "10 GHz Low Timing-Jitter and Broadband Optical Comb Generation Based on an Optoelectronic Oscillator"

Group 3:

(310) Richang Dong, Shanghai Institute of Optics and Fine Mechanics – "Magnetic Field Measurement by Stimulated Raman Transitions and Smoothing by Dynamical Compensation in Rubidium Fountain Clock"

(311) Mohammad Reza Gharavipour, University of Neuchâtel – "Impact of Static-Magnetic-Field-Gradients on Relaxation Times in a Rb Vapor Cell"

(312) Mehdi Langlois, Observatoire de Paris – "Correction of Laser Wavefronts in an Atom Interferometer with a Deformable Mirror"

(313) Hélène Pihan-Le Bars, Observatoire de Paris – "Lorentz-Symmetry Test at Planck-Scale Suppression with a Spin-Polarized ^{133}Cs Cold Atom Clock"

(314) Nil Almat, Université de Neuchâtel – "Cell-Based Stabilized Laser Sources and Light-Shifts in Pulsed Rb Atomic Clocks"

Group 4:

(315) Pallabis Das, IIT Bombay – "Spin-Coated Piezoelectric-Polymer Composite Based Acoustic Resonators and Transducers"

(316) Sagnik Gosh, City University of Hong Kong – "An Ultra-Sensitive Piezoelectric-on-Silicon Flapping Mode MEMS Lateral Field Magnetometer"

(317) Abid Ali, City University of Hong Kong – "Piezoelectric Transduction of a Button-Like Mode Disk Resonator for Enhanced Quality Factor in Water"

(318) Milind Pandit, University of Cambridge – "Closed-Loop Tracking of Amplitude and Frequency in a Mode-Localized Resonant MEMS Sensor"

(319) Zhenyun Qian, Northeastern University – "NEMS Infrared Detectors Based on High Quality Factor 50 nm Thick AlN Nano-Plate Resonators"

Group 5:

(320) Valerio Formichella, Istituto Nazionale di Ricerca Metrologica – "Mitigation of Lamplight-Induced Frequency Variations in Space Rubidium Clocks"

(321) Jingwen Dong, Tsinghua University – "Multichannel Precision Time Delay Measurement in Optical Fibers"

(322) Francisco Girela-Lopez, University of Granada, UGR – "Ethernet Time-Transfer Based on Low Frequency White Rabbit Solution"

(323) Aram Kalaydzhyan, Deutsches Elektronen-Synchrotron DESY – "Ultra-Low Phase Noise Synchronization of Microwave Sources with Fiber-Optic Timing System"

(324) Zeheng Chen, Shanghai Institute of Fine Mechanics and Optics – "Frequency Transfer and Time Synchronization Over Optical Fibre Using Pseudo-Random Noise Ranging"

Group 6:

(325) Andreas Liehl, U. of Konstanz – "Analysis of the Carrier-Envelope Phase Noise of Passively Phase-Locked Er:fiber Frequency Combs Up to the Nyquist Frequency"

(326) William Bowden, National Physical Laboratory – "Rydberg Spectroscopy for DC Stark Shift Characterisation in Optical Lattice Clocks"

(327) Charles Philippe, Observatoire de Paris – "1.5 µm - Optical Frequency Standard Iodine Stabilized in the 10^{-15} Range for Space-Mission Applications"

(328) William McGrew, NIST – "Sources of Uncertainty in an Ytterbium Optical Lattice Clock"

(329) Judith Olson, NIST – "High-Stability Laser Using Ramsey-Borde Interferometry"

	TUTORIALS – Sunday July 9th		
	Tutorials Track 1 Room 3	**Tutorials Track 2 Room 5**	**Tutorials Track 3 Room 7**
8:30–10:00	T1-A *Patrizia Tavella* Precise time scale and navigation systems	T1-B *Eric Burt* Microwave atomic clocks	T1-C *Aaron Partridge* MEMS Oscillators
10:00–10:15	Coffee break		
10:15–11:45	T2-A *Cristian Cassella* Nonlinear techniques for phase noise reduction in micro and nano oscillators	T2-B *Ekkehard Peik* Optical clocks	T2-C *Siddhartha Tallur* The versatile toolbox of cavity opto-mechanics
11:45–13:00	Lunch		
13:00–14:30	T3-A *Craig Nelson* Phase Noise Metrology	T3-B *Yann Le Coq* Femtosecond combs	T3-C *Giacomo Langfelder* MEMS inertial sensors in 2017, with possible future visions
14:30–14:45	Coffee break		
14:45–16:15	T4-A *Enrico Rubiola* Phase noise & jitter in digital electronics	T4-B *Dave Leibrandt* Lasers for optical frequency standards	T4-C *Songbin Gong* Lithium Niobate for MEMS/NEMS
16:15–16:30	Coffee break		
16:30–18:00	T5-A *John Kitching* Atomic Sensors for Navigation	T5-B *Gesine Grosche* Frequency and time transfer using optical fibers	T5-C *Philip Feng* Atomic-Layer Semiconductors for Emerging 2D Devices and Nanosystems
18:00–20:00	**Welcome reception**		

	Lecture Sessions – Monday July 10th			
	Plenary 1 – Amphitheatre			
9:00–10:20	Welcome and Information from the General and Scientific Co-Chairs Presentation of the YSA EFTF Award and the Rabi IFCS Award **Plenary Lecture:** How does the human brain make sense of time? by Virginie van Wassenhove, intr. Jerome Delporte			
10:20–10:40	Coffee Break / Exhibits			
	Amphitheatre	**Room 2**	**Rooms 3+4**	**Rooms 5+6+7**
10:40–12:20	A1L-A (G6) Ekkehard Peik – Optical Clocks I	A1L-B (G5) Andreas Bauch – Space Systems	A1L-C (G1) Dana Weinstein – Resonators I	A1L-D (G4) Ashwin Seshia – Liquid Phase Sensing
10:40–11:20	Direct Detection of the Elusive ^{229}Thorium Isomer: Milestone Towards a Nuclear Clock **(Invited)** *P. Thirolf, B. Seiferle, L. v.d. Wense, J. Neumayr et al.* LMU, München	Navigation and Science with the Deep Space Atomic Clock **(Invited)** *E. Burt* Jet Propulsion Laboratory, Pasadena	Mechanical Resonators Based on Graphene and Other Monolayers **(Invited)** *A. Bachtold* ICFO, Barcelona	Sensing Light and Sound Velocities of Fluids in PhoXonic Crystal **(Invited)** *Y. Pennec, Y. Jin, B. Djafari-Rouhani* Université de Lille

11:20–11:40	Progress Towards a $^{40}Ca^{+}$ Optical Clock with a Fractional Uncertainty at the 10^{-18} Level *Y. Huang, H. Guan, K. Gao* Wuhan Institute of Physics and Mathematics	ACES-Pharao Data Analysis at SYRTE: Status and Tests *F. Meynadier, P. Delva, C. Le Poncin-Lafitte, C. Guerlin et al.* Observatoire de Paris	Q-Boosting of Metal MEMS Resonators via Localized Anneal-Induced Tensile Stress *A. Ozgurluk, R. Liu, C. T.-C. Nguyen* UCB, Berkeley	Design Criteria for Plasticized Polymer Coatings for Long-Term Acoustic-Wave Sensor Measurements in Aqueous Phase *P. Adhikari, F. Bender, A. Ricco, F. Josse* Marquette U., Milwaukee
11:40–12:00	Blackbody Radiation Shifts for $^{171}Yb^{+}$ Optical Clock Transitions *C. Baynham, A. Curtis, R. Godun, J. Jones et al.* NPL, Teddington	NICT-KRISS TWCP Link: Evaluation and Application *M. Fujieda, H. Hachisu, R. Tabuchi, T. Gotoh et al.* NICT, Koganei	Nonlinear Cancellation in Weakly Coupled MEMS Resonators *M. Pandit, C. Zhao, A. Mustafazade, G. Sobreviela et al.* U. of Cambridge	Piezoelectric Transduction of a Button-Like Mode Disk Resonator for Enhanced Quality Factor in Water *A. Ali, J. E.-Y. Lee* City U. of Hong Kong
12:00–12:20	Reducing Time-Dilation Uncertainty in the NIST Al^{+} Quantum-Logic Clock *S. Brewer, J-S. Chen, A. Hankin, E. Clements et al.* NIST, Boulder	Ground-to-Space Time and Frequency Transfer Based on the "Virtual UTC" Method *S. Liu, X. Lu* TimeTech GmbH, Stuttgart	The Effect of Elastic Anharmonicity on the Nonlinear Behavior of Waveguide-Based AlN Resonator *M. Ghatge, R. Tabrizian* U of FL, Gainesville	Spin-Coated Piezoelectric-Polymer Composite Based Acoustic Resonators and Transducers *P. Das, S. Tallur* IIT Bombay, Mumbai

12:20–14:00	Lunch			
	Amphitheatre	**Room 2**	**Rooms 3+4**	**Rooms 5+6+7**
14:00–15:40	A2L-A (G6) Rodolphe Le Targat – Ultrastable Lasers	A2L-B (G5) Gerard Petit – Time Scales	A2L-C (G3) Gaetano Mileti – Compact Atomic Clocks	A2L-D (G2) Fabrice Sthal, Jean-Pierre Aubry – Oscillators Design
14:00–14:20	Ultrastable Lasers with 10 MHz Linewidth **(Invited)** *D. Matei, T. Legero, S. Häfner, Ch. Grebing et al.* PTB, Braunschweig	Estimating the Allan Variance from Frequency Measurements with Missing Data *L. Galleani, I. Sesia* Politecnico di Torino	Mesoscopic Atomic Physics in Vapor-Cell Atomic Clocks *A. Hudson, H. Alexander, J. Camparo* The Aerospace Corporation	SPINTRONIC Based RF Components **(Invited)** *U. Ebels, J. Hem, A. Purbawati, A. Ruiz Calafora et al.* Univ. Grenoble Alpes, Grenoble
14:20–14:40		The Use of Fault-Tolerant Clock Synchronization Algorithms for Time Scales *A. Kinali* Max Planck Institute for Informatics, Saarbrücken	Low-Power and Low-Profile Miniature Atomic Clock: Ceramic Based Flat Form Factor Miniature Atomic Clock Physics Package (C-MAC) *J. Haesler, L. Balet, S. Karlen, T. Overstolz et al.* CSEM SA, Neuchatel	

14:40–15:00	A 25-mm Long Optical Reference Cavity at the Thermal Noise Limit for Optical Frequency Division *J. Davila-Rodriguez, F. Baynes, A. Ludlow, T. Fortier et al.* NIST, Boulder	Realization of a Timescale Based on an Optical Clock *T. Ido, H. Hachisu, F. Nakagawa, Y. Hanado* NICT, Tokyo	Impact of Static-Magnetic-Field-Gradients on Relaxation Times in a Rb Vapor Cell *M. Gharavipour, C. Affolderbach, F. Gruet, G. Mileti et al.* U. of Neuchâtel	A Fully Integrated Quartz MEMS VHF TCXO *R. Kubena, F. Stratton, H. Nguyen, D. Kirby et al.* HRL Laboratories, Malibu
15:00–15:20	Ultrastable Silicon Cavity at 4 Kelvin *J. Robinson, W. Zhang, L. Sonderhouse, E. Oelker et al.* JILA, U. of CO Boulder	Application of GMDH Type Neural Network for Predicting UTC(k) Timescales Realized on the Basis of Hydrogen Masers *Ł. Sobolewski* U. of Zielona Góra	Microfabrication of Cs-Filled MEMS Cell Using Sequential Plasma Activated Bonding *K. Terashima, Y. Hirai, T. Tsuchiya, O. Tabata* Kyoto University	DORIS-Class Oscillator Under Radiations: the Jason Family of Satellites *A. Belli, P. Exertier, C. Jayles, F. Vernotte et al.* CNRS – Géoazur, Valbonne
15:20–15:40	High-Stability Laser Using Ramsey-Borde Interferometry *J. Olson, R. Fox, R. Brown, T. Fortier et al.* NIST, Boulder	New Results and Activities at Russian State Time and Frequency Standard Laboratory *I. Binov, Yu. Domnin, S. Donchenko, I. Ignatenko et al.* VNIIFTRI, Mendeleevo	Cell-Based Stabilized Laser Sources and Light-Shifts in Pulsed Rb Atomic Clocks *N. Almat, W. Moreno, M. Pellaton, M. Gharavip et al.* LTF, Institut de physique, Université de Neuchâtel	High Precision Time Measurement Using a Self-Timed Ring Oscillator Based TDC *A. El-Hadbi, A. Cherkaoui, O. Elissati, L. Fesquet* TIMA Laboratory, Grenoble

15:40–16:00	Coffee Break / Exhibits			
	Amphitheatre	**Room 2**	**Rooms 3+4**	**Rooms 5+6+7**
16:00–18:00	A3L-A (G6) Thomas Südmeyer – Microcombs	A3L-B (G5) Javier Diaz – Network Synchronization and Fiber Optics Timing Systems	A3L-C (G3/6) Kurt Gibble – Fundamental Physics with Atomic Clocks	A3L-D (G2) Enrico Rubiola, Olivier Llopis – Measurement Methods
16:00–16:20	Octave-Spanning Dissipative Kerr Soliton Frequency Combs in Si_3N_4 Microresonators **(Invited)** *M. Pfeiffer, C. Herkommer, J. Liu, H. Guo et al.* EPFL, Lausanne	Applications of Accurate Time in a World of Distributed Compute, Sensing, and/or Actuation **(Invited)** *K. Stanton* Intel, Hillsboro	Measurements of Optical Frequency Ratios for Tests of Fundamental Physics *A. Al-Masoudi, S. Dörscher, N. Huntemann, S. Falke et al.* PTB, Braunschweig	Cross-Spectrum Measurements: Keeping It Honest **(Invited)** *A. Hati, C. Nelson, D. Howe* NIST, Boulder
16:20–16:40			Constraints on Scalar Dark Matter from Six Years of SYRTE Rb/Cs Fountain Data *A. Hees, J. Guéna, M. Abgrall, S. Bize et al.* Observatoire de Paris	

16:40–17:00	Temporal Dissipative Solitons in a 10 GHz Fabry-Pérot Microresonator Driven by Optical Pulses *E. Obrzud, S. Lecomte, T. Herr* CSEM, Neuchatel	Time Transfer Over a Cascaded White Rabbit Network *N. Kaur, F. Frank, P-E. Pottie, P. Tuckey* Observatoire de Paris, PSL Research University, CNRS, Sorbonne Universités, UPMC, Paris	Experimental Constraint on Dark Matter-Standard Model Coupling with Optical Atomic Clocks *P. Wcisło, P. Morzyński, M. Bober, A. Cygan et al.* Nicolaus Copernicus University, Torun	An Additive Phase Noise Measurement Technique for Mixers with Non-DC IF in Large Signal *J. Breitbarth* Holzworth Instrumentation, Boulder
17:00–17:20	Measuring Thermodynamic Noise in Optical WGM Microresonators *J. Lim, C. Wong, L. Maleki, A. A. Savchenkov et al.* OEwaves Inc., Pasadena	A Novel Synchronization Method for WR System *X. Yuan, B. Wang* Tsinghua University, Beijing	Mass Defect Effects in Atomic Clocks *V. Yudin, A. Taichenachev* Novosibirsk State University	Next Generation Radios Communication Networks *U. Rohde, A. Poddar, I. Eisele, E. Rubiola* Brandenburg University of Technology, Cottbus

17:20–17:40	A Kerr-Soliton Microcomb with Electro-Optic Sampling and Absolute Frequency Stabilization *T. Drake, T. Briles, D. Spencer, J. Stone et al.* NIST, Boulder	Ultra-Low Phase Noise Synchronization of Microwave Sources with Fiber-Optic Timing System *A. Kalaydzhyan, M. Xin, K. Şafak, M. Peng, K. Jung et al.* Deutsches Elektronen-Synchrotron DESY, Hamburg	Improving Phonon Sector Tests of Lorentz Invariance *M. Goryachev, E. Ivanov, M. Tobar, P. Haslinger et al.* University of Western Australia, Crawley	The Two-Edge Anti-Jitter Circuit for Phase Noise Reduction on Received Frequency Standards *M. Underhill* Underhill Research Limited, Lingfield
17:40–18:00	In-Fibre Fabry-Pérot Microresonator with 100 Million Q-Factor *E. Obrzud, S. Lecomte, T. Herr* CSEM, Neuchatel	Multichannel Precision Time Delay Measurement in Optical Fibers *J. Dong, B. Wang, H. Si, L. Wang et al.* Tsinghua University, Beijing	Lorentz-Symmetry Test at Planck-Scale Suppression with a Spin-Polarized 133Cs Cold Atom Clock *H. Pihan-Le Bars, C. Guerlin, Raphaël-D. Lasseri, J.P. Ebran et al.* Observatoire de Paris	Damped Sine Based Time Interval Counter *N. Boucquey, A. Kinali* Max Planck Institute for Informatics, Saarbrücken
18:00–19:00	Exhibitors presentations and aperitive			
19:00–23:00	Conference dinner			

	Lecture Sessions – Tuesday July 11th			
	Plenary 2 – Amphitheatre			
9:00–10:20	Presentation of the IFCS Sawyer Award, the IFCS Cady Award, and the EFTF Marcel Ecabert Award **Plenary Lecture:** The 50th Anniversary of the atomic definition of the second by Terry Quinn, intr. Felicitas Arias			
10:20–10:40	Coffee break / Exhibits			
	Amphitheatre	**Room 2**	**Rooms 3+4**	**Rooms 5+6+7**
10:40–12:20	B1L-A (G6) Yann Le Coq – Combs I	B1L-B (G5) Gesine Grosche – Optical Time Transfer	B1L-C (G3) Stephen Wilkinson – Space Clocks	B1L-D (G1) Matteo Rinaldi, Shuji Tanaka – Microacoustic Signal Processing
10:40–11:00	Analysis of the Carrier-Envelope Phase Noise of Passively Phase-Locked Er:fiber Frequency Combs Up to the Nyquist Frequency *A. Liehl, D. Fehrenbacher, P. Sulzer, D. Seletskiy et al.* U. of Konstanz	Doppler-Tolerant Synchronization of Clocks Over Free Space at the Femtosecond Level **(Invited)** *H. Bergeron, J. Deschênes, L. Sinclair, W. Swann et al.* U. Laval, Québec, NIST	Test of Cold Atom Clock in Orbit **(Invited)** *L. Liu, D. Lü, T. Li, Q. Qu et al.* Shanghai Institute of Optics and Fine Mechanics, Chinese Academy of Sciences Shanghai	GHz Ultrasonics for on Chip Delay Lines, Communications, Timing, Memory, and Sensing **(Invited)** *A. Lal* Cornell University, Ithaca

11:00–11:20	Single Branch Er:fiber Optical Frequency Synthesizer with Millihertz Instability *H. Leopardi, J. Davila-Rodriguez, F. Quinlan, S. Diddams, T. Fortier* NIST, U. of CO, Boulder	continued (invited paper)	continued (invited paper)	continued (invited paper)
11:20–11:40	Optical Frequency Stability Transfer Using a Multi-Branch Er:fibre Frequency Comb *A. Rolland, F. Baynes, P. Gill, H. Margolis et al.* NPL, Teddington	Femtosecond Atmospheric Frequency Transfer Using Diode Laser with Electronic Phase Compensation *S. Chen, D. Chen, Q. Chen, F. Sun et al.* U. of Electronic Science & Tech. of China, Chengdu	PHARAO Space Clock: Performance and ACES Mission Scenario **(Invited)** *Ph. Laurent, Ch. Salomon, K. Gibble, P. Peterman et al.* Observatoire de Paris	Acoustic Delay Lines to Measure Piezoelectricity in 4H Silicon Carbide *P.-L. Yu, S. Bhave* Purdue University

11:40–12:00	Optical Frequency Comb Application in Time-Delay Interferometer *N. Yu, I. Grudinin, M. Tinto* JPL, Pasadena	Time Transfer by Laser Link (T2L2) in Non Common View Between Europe and China *E. Samain, P. Exertier, J.M. Torre, C. Courde et al.* Observatoire de la Côte d'Azur, Caussols	continued (invited paper)	An SH0 Lithium Niobate Correlator for Orthorgonal Frequency Coded Spread Spectrum Communications *T. Manzaneque, R. Lu, Y. Yang, S. Gong* U. of IL at Urbana-Champaign
12:00–12:20	Rapid Electro-Optic Control of the Carrier-Envelope-Offset Frequency for Ultra-Low Noise Frequency Combs *W. Hänsel, M. Giunta, M. Fischer, M. Lezius, R. Holzwarth* Menlo Systems GmbH	Sub-*ps* Resolution Optical Time Transfer Over 86 km of Urban Fiber Network *F. Frank, F. Stefani, P. Tuckey, P.-E. Pottie* Observatoire de Paris	Optically Pumped Cs Space Clock Development *R. Schmeissner, P. Favard, A. Douahi, P. Perez et al.* Thales Electron Devices, Velizy	Observation of Phononic Frequency Comb in a Micromechanical Resonator *A. Ganesan, C. Do, A. Seshia* University of Cambridge
12:20–14:00	Lunch			

	Amphitheatre	Room 2	Rooms 3+4	Rooms 5+6+7
14:00–15:40	B2L-A (G6) Jerome Lodewyck – Optical Clocks II	B2L-B (G5) Przemislaw Krehlik – Optical Fiber Links	B2L-C (G3) Christophe Affolderbach – CPT Clocks	B2L-D (G2) Jeremy Everard, Jay Poddard – Noise in Oscillators
14:00–14:40	An Optical Clock Using ^{176}Lu+ **(Invited)** *M. Barrett, K. Arnold, R. Kaewuam, A. Roy, T. Rei Tan* Center for Quantum Technologies, Singapore	The Italian Optical Link for Time and Frequency **(Invited)** *D. Calonico, C. Clivati, A. Mura, A. Tampellini, F. Levi* INRiM, Torino	A High-Performance Cell-Based Microwave Clock Using Push-Pull Optical Pumping **(Invited)** *R. Boudot, M. Abdel Hafiz, B. Francois, G. Coget et al.* FEMTO-ST, Besançon	Noise Sources Characterization and its Compact Modeling Based on Physical Device Simulations for Designing Low Phase Noise Oscillators **(Invited)** *J.-C. Nallatamby, M. Prigent, D. Cordeau, J.-M. Paillot* Université de Limoges
14:40–15:00	Clock Shifts in Coulomb Crystals in an Operational High Precision Ion Trap *A. Didier, J. Keller, T. Burgermeister, D. Kalincev et al.* PTB, Braunschweig	Performance of a Fibre Link Combining Fibre Brillouin Amplification with a Repeater Laser Station *S. Koke, A. Kuhl, O. Lopez, N. Quintin et al.* PTB, Braunschweig	The Medium and Long Term Stability of the NAC Atomic Clock *S. Prazot, A. Stern, W. Israel, C. Levi et al.* AccuBeat Ltd., Jerusalem	Investigation on Flicker Noise and Overtone Modes of Ultra-Stables Quartz Crystal Resonators *A. Pokharel, F. Sthal, J. Imbaud, F.-X. Esnault, G. Cibiel* FEMTO-ST, Besançon

15:00–15:20	The Collisional Frequency Shift of a Trapped-Ion Optical Clock *A. Vutha, T. Kirchner, P. Dubé* University of Toronto	Hybrid Optical Link for Ultra-Stable Frequency Comparison *D. Xu, W-K. Lee, F. Stefani, P.E. Pottie et al.* *Observatoire de Paris, PSL Research University, CNRS, Sorbonne Universités, UPMC, Paris*	Feasibility Toward a Compact High Performance Coherent Population Trapping Clock *P. Yun, F. Tricot, E. de Clercq, S. Guérandel et al.* Observatoire de Paris, INRIM, FEMTO-ST	First Search for Axions of Mass 110 µev Using milliKelvin Cooled 26.6 GHz Microwave Resonator *B. McAlister, J. Kruger, G. Flower, J. Bourhill et al.* University of Western Australia, Crawley
15:20–15:40	Rydberg Spectroscopy for DC Stark Shift Characterisation in Optical Lattice Clocks *W. Bowden, R. Hobson, P. Gill, I. Hill et al.* NPL, Teddington	Regional Multipoint Frequency Dissemination for the Optical Fiber Link PTB - Hanover *T. Waterholter, A. Kuhl, J. Froh, S. Häfner, G. Grösche* *PTB, Braunschweig*	Latest Achievements on the Pulsed CPT Clock *F. Tricot, P. Yun, S. Guerandel, E. de Clercq* Observatoire de Paris	A Crystal-Less Bluetooth Low Energy Radio Using a MEMS-Based Frequency Reference System *D. Griffith, E. T-T. Yen, P. Torstein Røine, T. Kallerud, B. Goodlin* Texas Instruments, Santa Clara
15:40–16:00	Coffee Break / Exhibits			
16:00–18:00	B3P-E Student Poster Competition	B3P-F to B3P-L Poster session 1 - G1 to G6		

Poster session I – Tuesday

July 11th 16:00–18:00

B3PF – Materials, Resonators & Resonator Circuits I – *Ji Wang, Sheng-Shian Li*

1 – Material Parameters of Ca3TaGa3Si2O14 (CTGS) Piezoelectric Single Crystal at Extreme Temperatures, *A. Sotnikov, H. Schmidt, M.H. Haghighi, Yu. Suhak et al.*, IFW Dresden.

3 – Miniaturized VHF Quartz MEMS Resonator Design Methodology, *D. Kirby, R. Kubena, Y.-K. Yong, F. Stratton et al.,* HRL Laboratories, LLC, Malibu, Rutgers University.

5 – Wideband Balanced Fan-Shaped Three-Transducer Low-Loss Leaky SAW Filters on $LiTaO_3$ Substrate, *S. Doberstein,* ONIIP, Omsk.

7 – Capacitive Lamé Mode Resonator with Gap Closing Mechanism for Motional Resistance Reduction, *M. Elsayed, F. Nabki,* Ecole de Technologie Superieure, Montreal.

9 – HAL SAW Resonators Using 42°YX-$LiTaO_3$ Thin Plate on Quartz Substrate, *M. Kadota, S. Tanaka,* Tohoku University, Sendai.

11 – Flexible Mechanical Coupling Scheme in Nanoscale, *Y. Kilinc, B.-E. Alaca, Y. Leblebici*, Koc University, Istanbul, EPFL, Lausanne.

13 – Nonlinear Time Domain-FFT Study of the f – 2f Frequency Response of Lithium Niobate YX-127° SAW Resonators, *Y.-K. Yong, X. Pang*, Rutgers University, Piscataway.

15 – Buried Wave Devices, *V. Plessky, J. Koskela, B. Hammond,* GVR Trade SA, Georgier, Resonant Inc.

17 – Periodically Poled $LiNbO_3$ Transducer on (YXl)\128° Cut for RF Applications, *A. Matic, T. Baron, F. Bassignot,* FEMTO-ST, Besançon.

19 – DRIE of High Q-Factor Length-Extensional Mode Quartz Micro-Resonator, *P. Chapellier, B. Verlhac, P. Lavenus, B. Dulmet,* ONERA, Châtillon, FEMTO-ST, Besançon.

21 – Effects of the LGT Crystal Quality on the Resonance Frequency Stability of Bulk Acoustic Waves Resonators, *M. Allani, J.-J. Boy, N. Batis, T. Laroche et al.,* FEMTO-ST, Besançon, Université de Carthage.

B3PG – Oscillators, Resonators, and Noise – *Joël Imbaud*

23 – Extraordinary OCXO Solutions Based on Advanced IHR Technology, *I. Abramson, V. Tapkov, A. Kornilov,* Magic Xtal Ltd., Omsk, Russia.

25 – The Design of a Novel Low Phase Noise Anti-Vibration OCXO, *S. Jiang, X. Wang,* Chengdu Spaceon Electronics Co., Ltd., Chengdu, China.

27 – High Stability Miniature Size OCXO: Using a SC-Cut Crystal Resonator and Simultaneous Oscillations*, M. Ogawa, M. Ito, K. Kobayashi, M. Ishikawa, K. Akaike,* Nihon Dempa Kogyo Co., Ltd., Saitama, Japan

29 – A Novel Design of Voltage Controlled Temperature Compensated Crystal Oscillator, *J. Hu, X. Huang, D. Liu, X. Huang,* University of Electronic Science and Technology of China, Chengdu.

31 – Limiting Factor for the Performance of High Stability Quartz Crystal Oscillators – the Residual Heat of Crystal Resonators, *X. Huang, Y. Tang, J. Hu, W. Fu, P. Chen,* University of Electronic Science and Technology of China, Chengdu.

33 – Frequency Stabilization of a Quartz Oscillator by Using the Method of Biased Differentiation of Ambient Parameters, *R. Miškinis, D. Smirnov, E. Urba, E. Baniulienė,* Center for Physical Sciences and Technology, Vilius.

35 – Concept and Main Results for Ultraprecise Low Noisy 10 MHz DOCXO Ensuring Allan Deviation of 1…2E-13 for 1…10 S, *Ya. Vorokhovsky, A. Nikonov, A. Kotyukov, A. Kamochkin,* Morion, Inc., St Petersburg.

37 – 10 GHz Low Timing-Jitter and Broadband Optical Comb Generation Based on an Optoelectronic Oscillator, *H. Peng, Y. Xu, X. Peng, C. Zhang et al.,* Peking University, Beijing.

39 – Effect of Joule Heating on the Performance of a Piezoresistive Micromechanical Oscillator, *L. Xu, X. Wei, D. Pu, Z. Jiang et al.,* Xi'an Jiaotong University.

41 – Quantum Theory of 1/F Frequency Fluctuations, *P. Handel,* Univ. of Missouri-St. Louis.

43 – Spectral Performance and Noise Theory of Nonlinear Transmission Line Frequency Multipliers, *J. Breitbarth, Z. Popović,* Holzworth Instrumentation, CTO, University of Colorado, Boulder.

45 – Ultra-Low Phase-Noise Microwave Oscillator Based on Electro-Optical Frequency Division, *J. Li, K. Vahala,* hQphotonics Inc., Pasadena, California Institute of Technology.

B3PH – Microwave Frequency Standards I – *Fang Fang*

47 – Uncertainty Evaluation and Suppression of Atomic Clock Based on Statistical Correlation of Noise, *Q. Wang, R. Wei, R. Dong, T. Chen et al.,* Chinese Academy of Sciences, Shangai.

49 – An Empirical Model of the Alkali RF-Discharge Lamp, *J. Camparo*, The Aerospace Corporation, El Segundo.

51 – Ramsey-CPT Spectroscopy in Buffer-Gas Filled Cs Vapor Micro-Fabricated Cells, *R. Boudot, V. Maurice, E. Kroemer, J. Rutkowki et al.,* FEMTO-ST, Besançon.

53 – Preliminary Results of the Self-Sustaining τ^{-1} Magnetometer, *S. Wang, C. Xu, L. Wang,* Tsinghua University, Beijing.

55 – Theoretical and Experimental Study of Rb Coherent Population Trapping Atomic Clock with Phase Modulation Detection, *Y. Yano, M. Hara, M. Kajita, T. Ido,* National Institute of Information and Communications Technology, Tokyo.

57 – Ultrahigh-Contrast Saturated-Absorption Resonance to Enhance Stability of CPT Atom Clocks, *D. Brazhnikov, A. Taichenachev, V. Yudin, M. Abdel Hafiz et al.,* Institute of Laser Physics SB RAS, Novosibirsk, FEMTO-ST, Besançon.

59 – A Caesium Atomic Beam Microwave Clock Detected by Distributed Feedback Laser Diodes, *C. Liu, S. Wang, Z. Chen, Y. Wang et al.,* Peking University, Beijing.

61 – Compact Vapor Cell Cesium Clock Based on Continuous Wave Optical Pumping, *J. Wan, C. Liu, Y. Wang*, Peking University, Beijing.

63 – Simulation of the Ramsey Cavity Response, *F. Sun, X. Huang, D. Hou, Q. Bai,* University of Electronic Science and Technology of China, Chengdu.

65 – Study of the Phase Transient of the RF Mach-Zehnder Interferometric Switch, *D. Liu, J. Ruan, X. Wang, Y. Guan et al.,* Chinese Academy of Sciences, Xi'an.

67 – Reduction of Dick Effect in a Pulsed CPT Vapor Cell Clock by Interleaving Lock, *X. Sun, P. Cheng, Y. Zuo, J. Zhang*, *L. Wang,* Tsinghua University, Beijing.

69 – Thermal Management of Microfabricated Vapor Cells for Chip Scale Atomic Clocks, *R. Han, Z. You, F. Zhang, Y. Ruan*, Tsinghua University, Beijing.

71 – High Sensitively Coherent Population Trapping Magnetometer with Optically Pumped Degenerate Atoms, *R. Maeda, S. Goka*, Ricoh Co., Ltd., Yokohama, Tokyo Metropolitan University.

73 – The Ultra-Stable Microwave Based on Ultra-Stable Laser by a Er-Doped Fiber Optical Frequency Comb, *S. Dai, F. Fang, S. Cao, T. Li*, NIM, Beijing.

75 – Design of Active All-Optical Magnetometer, *D. Pan, T. Shi, X. Peng, J. Chen, H. Guo,* Peking University, Beijing.

77 – Gravity Sensing with Very Long Baseline Atom Interferometry, *E. Wodey, H. Albers, C. Meiners, L. Richardson et al.*, Leibniz Universität, Hannover.

79 – Optimization of Frequency Modulation Parameters in Atomic Clocks Based on Coherent Population Trapping, *V. Yudin, M. Basalaev, D. Kovalenko, A. Taichenachev*, Novosibirsk State University, Institute of Laser Physics SB RAS.

81 – Pulsed Optically Pumped Rb Clock with AOM in the Anisotropic Bragg Diffraction Regime as a Compact Light Pulse Generator, *V. Baryshev, M. Aleynikov, V. Epikhin, I. Blinov,* FGUP VNIIFTRI, Mendeleevo, Moscow Region.

83 – Current Limits to the Sensitivity of an Atomic Gravimeter Developing at KRISS, *S.-B. Lee, T.-Y. Kwon, S.-E. Park, M.-S. He, H.-G. Hong,* Korea Research Institute of Standard and Science, Dajeon.

85 – Retrace and Disciplining Time Constant Effects on Holdover Clock Drifts in Chip-Scale Atomic Clock, *Y. Kim, C. Walter*, US Army CERDEC.

87 – MEMS Atomic Vapor Cells for Gyroscope Applications, *S. Karlen, G. Buchs, T. Overstolz, N. Torcheboeuf et al.,* CSEM, Neuchatel.

89 – Preliminary Stability Analysis of Rb Fountains for Timescale Generation, *L. Lorini, K. Pavlenko, S. Bize, B. Desruelle et al.*, Observatoire de Paris, PSL research University, CNRS, Sorbonne Universités, UPMC, Paris.

91 – A Portable 12.6 GHz Microwave Atomic Clock Using the Ground State Hyperfine Clock Transition in Cold Trapped Ytterbium Ions, *S. Mulholland, G. Barwood, S. Donellan, G. Huang et al.*, NPL, Teddington.

93 – Generalized Electronics for Compact Atomic Clocks, *C.-E. Calosso, M. Gozzelino, E. Bertacco, S. Micalizio et al.*, INRIM, Torino.

95 – Pin Photodiode Spurious Noise Characterization, *R. Schmeissner, A. Maillard, P. Perez, M. Baldy,* Thales Electron Devices, Vélizy.

97 – Progress in Mexican Cesium Atomic Fountain-CsF1 Using an Ultra-Stable Laser, *C. Ortiz, J. Lopez, E. de Carlos López*, *C. Ortiz,* Cinvestav / CENAM, Santiago de Querétaro.

99 – Frequency Drift Detection Method Using Dual Alkali Gas for Coherent Population Trapping Atomic Clocks, *Y. Furuse, Y. Kase*, *S. Goka,* Tokyo Metroplitan University.

101 – On the Solution of the Problem of Increasing Medium- and Long-Term Stability of Atomic Clock, *E. Pestov,* Geologorazvedka, St Petersburg.

103 – Magnetic Field Measurement by Stimulated Raman Transitions and Smoothing by Dynamical Compensation in Rubidium Fountain Clock, *R. Dong, W. Wang, R. Wei, T. Chen et al.,* Chinese Academy of Sciences, Shanghai.

B3PJ – Sensors & Transducers I – *Sid Tallur*

105 – Impact of the External Environment on a Sensor Response, *M. Sagnard, T. Laroche, J.-M. Friedt, S. Ballandras*, FEMTO-ST, Frec|n|sys, Besançon.

107 – Three-Parameter Liquid Sensor Based on Surface and Plate Acoustic Waves, *N. Voronova, V Anisimkin*, Kotelnikov's Institute of Radioengineering and Electronics Russian Academy of Sciences/IRE RAS, Moscow.

109 – Elastic Properties of Graphene Oxide Films and Changes Due to Gas Phase Adsorption, *E. Verona, I. E. Kuznetsova, V. Anisimkin, S. P. Gubin et al.*, Institute for Photonics and Nanotechnologies, IFN-CNR, Rome, Kotelnikov Institute of Radio Engineering and Electronics of RAS, Moscow.

111 – SAW Torque Sensor for Marine Applications, *V. Kalinin, A. Leigh, A. Stopps, S. B. Hanssen*, Transense Technologies plc, Bicester, Kongsberg Maritime, Norway.

113 – Direct Integration of CNT Forests on Solidly Mounted Resonators and Their Influence on Device Performance, *T. Mirea, J. Olivares, M. Clement, J. Sangrador, E. Iborra*, Universidad Politécnica de Madrid.

B3PK – Timekeeping, Time & Frequency Transfer, GNSS Applications I – *Ann Amy-Klein*

115 – Satellite Clock Offset Estimation and Analysis Based on Arc-Wise Observation Files, *M. Wu, B. Sun, X. Yang, H. Su*, Chinese Academy of Sciences, Xi'an.

117 – Algos-Kalman Combined Time-Scale Algorithm, *J. Zhu, P. Zheng*, Beijing University of Technology.

119 – GPS All in View Time Comparison Using Multi-Receiver Ensemble, *S. Lin, Z. Jiang*, TL, Chunghwa Telecom Co. Ltd, Yangmei, Taoyuan, Taiwan.

121 – High-Precision Joint Time and Frequency Transfer Over a Fiber-Optic Telecom Testbed, *H. Zhang, G. Wu, X. Li, J. Chen*, Shanghai Jiao Tong University.

123 – Delay Compensation of 1 PPS Timetags in Fiber-Optic Time Distribution, *P. Krehlik, M. Mazur, L. Śliwczyński*, AGH University of Science and Technology, Krakow.

125 – Time and Frequency Transfer in Modern DWDM Telecommunication Networks, *K. Turza, A. Binczewski, W. Bogacki, P. Krehlik et al.,* Poznan Supercomputing and Networking Center (PSNC), Poznan.

127 – WAKATI: A Web Application for Time Transfer and Clock Steering, *M. Dyjak, R. Píriz, P. Roldán, J. Nawrocki, P. Waller*, GMV Aerospace, Tres Cantos.

129 – A Novel Real Time Cycle Slip Detection and Repair Method for a Single Dual-Frequency GNSS Receiver, *H. Yi, H. Wang, S. Zhang, X. Wang, H. Wang*, Beijing Institute of Radio Metrology and Measurement.

131 – Three Loops - a Method for Tracking a New TWSTFT Signal FBOC, *H. Wang, X. Wang, H. Wang, H. Yi, S. Zhang*, Beijing Institute of Radio Metrology and Measurement.

133 – Progress on the REFIMEVE Project for Optical Frequency Standard Dissemination, *E. Cantin, N. Quintin, F. Wiotte, C. Chardonnet at al.,* Laboratoire de Physique des Lasers LPL, Villetaneuse.

135 – An Atomic Time Algorithm Based on Predictability Weighting and Wavelet Multi-Scale Threshold Denoising, *H. Song, Y.P. Wang, L. Qu, X. Wang et al*., Chinese Academy of Sciences, Xi'an.

137 – GNSS Based Robust Synchronization Service, *E. Dierikx, A. Wallin, M. Merimaa, R. Bauernfeind et al.*, VSL, Deft, VTT/MIKES, Finland.

139 – Analysis of the Effect of Satellite Motion on TWSTFT, *Y. Jing, J. Yang, H. Peng, X. Wang et al*., Xi'an Aeronautical University, Xian.

141 – Clock Stability for Low Frequency Radar for Tomography of Asteroids: Frequency Stability Impact, *R. Granados, A. Herique, E. Le-Coarer, S. Rochat,* Université Grenoble Alpes, Grenoble.

143 – A New TWSTFT Station in Warsaw, *M. Marszalec, T. Kossek, M. Lusawa, A. Czubla et al.*, National Institute of Telecommunications, Warsaw.

145 – Time Delay Measurements: Estimation of the Error Budget, *M. Siccardi, G. D. Rovera, S. Römisch*, SKK Electronics, Cuneo, Observatoire de Paris LNE - CNRS – UPMC, NIST, Boulder.

147 – A New Long Distance DWDM Optical Fiber Time Transfer Link Between UTC(PL) and UTC(LT), *A. Czubla, P. Krehlik, Ł. Śliwczyński, J. Kołodziej et al.*, Central Office of Measures, Warsaw, AGH University of Science and Technology, Poznan Supercomputing and Networking Center.

149 – Some Approximated Methods of Calculation Sagnac Correction for Optical Fiber Time Transfer, *A. Czubla, P. Krehlik, Ł. Śliwczyński, J. Kołodziej et al.,* Central Office of Measures, Warsaw, AGH University of Science and Technology, PSNCenter.

151 – Analysis of Uncertainty in Time Traceability Links Using GPS Common View and Optical Fiber Techniques, *L. Meng, Y. Liu, F. Zhu, X. Li*, National Time Service Center, Chinese Academy of Sciences, Xi'an.

153 – Global Time Synchronization Mechanism for Radio Interferometer Array, *E.H. Ait Mansour, B. Da Silva, S. Bosse, K.-L. Klein*, Station de Radioastronomie de Nançay, Observatoire de Paris.

155 – Fractional Brownian Motion and its Application in the Simulation of Noise in Atomic Clocks, *A. Kinali*, Max Planck Institute for Informatics, Saarbrücken.

157 – White-Rabbit-Enabled Data Acquisition System, *J. López-Jiménez, J. L. Gutiérrez-Rivas, M. Jiménez-López, J. Diaz*, University of Granada.

159 – One-on-Multi RF Transfer System Using Optical Fibers, *M. Fujieda, T. Gotoh, M. Kumagai*, NICT, Koganei.

161 – Recent Updates of the Revised RINEX-Shift (RRS) Technique, *J. Yao, J. Levine*, NIST, Boulder.

163 – System of Comparison of Time Scales of Distant Objects via Optical Fiber, *O. V. Kolmogorov, S. S. Donchenko, D. V. Prokhorov*, VNIIFTRI, Mendeleevo.

B3PL – Optical Frequency Standards and Applications I – *Nan Yu*

165 – Characterization of the Phase-Noise Induced by an Optical Frequency Doubler, *M. Delehaye, J. Millo, P.-Y. Bourgeois, L. Groult et al.,* FEMTO-ST, Besançon.

167 – Optical Atomic Clock as a Detector of Transient Variations in Fundamental Constants, *M. Bober, P. Morzyński, R. Ciuryło, M. Zawada, P. Wcisło*, Nicolaus Copernicus University, Torun.

169 – Inverted Crossover Resonances with ΔF=0 or 1: Inverted Crossover Resonances from the Zeeman Components of the Intercombination Line of ^{171}Yb, *J. McFerran, E. de Clercq*, University of Western Australia, Crawley.

171 – Towards Doppler-Free Spectroscopy of O_3 Isotopes at 28 THz with a Quantum Cascade Laser Locked to a Stabilized Frequency Comb Reference, *T. Zanon-Willette, M. Minissale, H. Elandaloussi, P. Jecek et al.*, Université Pierre-et-Marie-Curie, Paris.

173 – A Laser System for Single-Photon Interferometry with Strontium Atoms, *L. Hu, R. Pablo del Aguila, T. Mazzoni, L. Salvi et al.*, Università degli Studi di Firenze, Kayser Italia Srl.

175 – Progress of Mercury Ion Optical Frequency Standard in NUDT, *H. Zou, Y. Shen, G. Chen, Q. Liu, H. Guo*, National University of Defense Technology, Shanghai.

177 – Short-Length Homodyne Interferometer for Self-Stabilization of an Optical Frequency Comb, *J. Cahill, W. Zhou, C. Menyuk*, US Army Research Laboratory, Adelphi.

179 – Development of a Micro-Integrated Mode-Locked Extended Cavity Diode Laser for Frequency Comparison Experiments at 780 nm, *H. Christopher, A. Wicht, A. Peters, G. Tränkle,* Ferdinand-Braun-Institut für Höchstfrequenztechnik, Berlin.

181 – Recent Progresses of Dual-Wavelength Good-Bad Cavity Active Optical Clock, *D. Pan, T. Shi, B. Xue, J. Chen*, Peking University, Beijing.

183 – Possibility of Creation of Active Optical Clock on Forbidden Transition in Trapped Ions, *G. Kazakov, T. Schumm*, Technical University of Vienna.

185 – Deep Laser Cooling of Mg in Dipole Trap for Frequency Standard, *O. N. Prudnikov, A. V. Taichenachev, V. I. Yudin, E. M. Rasel*, Institute of Laser Physics, Novosibirsk, Institutur Quantenoptik, Universitat Hannover.

187 – Towards Black Body Radiation Shift Uncertainty in Optical Lattice Clocks at 10^{-18} Level at Room Temperatures, *P. Ablewski, M. Bober, M. Zawada*, Nicolaus Copernicus University, Torun.

189 – Progress on the Yb Clock Laser at ECNU, *L. Jin, Y. Yao, Y. Jiang, H. Yu et al.*, East China Normal University, Shanghai.

191 – Uncertainty Evaluation of ^{171}Yb Optical Lattice Clocks, *Q. Gao, M. Zhou, C. Han, S. Li et al.*, East China Normal University, Shanghai.

193 – Recent Progress of Neutral Mercury Lattice Clock in SIOM, *X. H. Fu, S. Fang, R. C. Zhao, J. F. Sun et al.*, Shanghai Institute of Optics and Fine Mechanics, Chinese Academy of Science.

195 – On-Chip Integrated Zero-Ram Frequency Modulator for Noise Reduction and Linewidth Narrowing in Discrete-Mode Lasers, *S. Kundermann, I. Kjelberg, S. Lecomte, D. Boiko et al.*, CSEM SA, Neuchâtel.

197 – Thermal Noise Limited Ultra-Stable Laser at 1555 nm, *Z. Tai, L. Yan, Y. Zhang, W. Zhao et al.*, Chinese Academy of Sciences, Xi'an.

199 – Multiple Lasers Stabilization on a Single Three Color Optical Cavity, *G. Milani, B. Rauf, P. Barbieri, F. Bregolin et al.*, INRIM, Torino.

201 – Progress Towards a Two-Photon Clock Based on Laser-Cooled Calcium, *S. Potnis, S. Jackson, A. Vutha*, University of Toronto.

203 – A Spectrograph to Characterize Comb Spectra, *R. Probst, T. Steinmetz, Y. Wu, F. Grupp et al.*, Menlo Systems GmbH, Martinsried.

205 – Methane Based Microwave Reference Oscillator, *M. Gubin, A. Kireev, D. Tyurikov, A. Shelkovnikov et al.*, P. N. Lebedev Physical Institute, Russian Academy of Sciences, Moscow.

207 – Revisiting the Relation Between Laser Spectrum and Phase Noise Spectral Density with New Outcomes, *P. Brochard, S. Schilt, T. Südmeyer*, Université de Neuchâtel.

209 – Photonic Microwave Generation at NTSC, *L. Yan, Y. Zhang, Z. Tai, W. Zhao et al.*, National Time Service Center, Chinese Academy of Sciences, Xi'an.

211 – The NIM Sr Optical Lattice Clock, *Y. Lin, Q. Wang, Y. Li, F. Meng et al.*, National Institute of Metrology, Beijing.

213 – Compact Optical Standard Based on the $5S_{1/2}$-$5D_{5/2}$ Two-Photon Transition in Rubidium, *Z. Newman, M. Hummon, L. Stern, V. Maurice et al.*, NIST Boulder.

215 – High-Temperature Calcium Vapor Cell Construction and Spectroscopy, *N. Lemke, C. Erickson, K. Martin, J. Armstrong et al.*, Applied Technology Associates, Albuquerque.

217 – G-LAS: A Ring Laser Goniometer for Angular Metrology, *J. Belfi, N. Beverini, A. Di Virgilio, U. Giacomelli et al.*, Università di Pisa / Istituto Nazionale di Fisica Nucleare, Pisa.

	Lecture Sessions – Wednesday July 12th			
	Plenary 3 – Amphitheatre			
9:00–10:20	General Information and 2018 Conference Announcements **Plenary Lecture:** Journey to the Beginning of Time: Black Holes, Gravitational Waves, and The Big Bang by Lawrence Krauss, intr. Liz Donley			
10:20–10:40	Coffee break / Exhibits			
	Amphitheatre	**Room 2**	**Rooms 3+4**	**Rooms 5+6+7**
10:40–12:20	C1L-A (G6) Steve Lecomte – Transportable Optical Clocks	C1L-B (G5) Pierre Waller – Robust Timing and Synchronization Service	C1L-C (G3) Scott Crane – Cold-Atom Microwave Clocks	C1L-D (G2) Gilles Cibiel, Jean-Pierre Aubry – Microwave Photonics I
10:40–11:00	First Measurement Campaigns with a Transportable Optical Lattice Clock *J. Grotti, S. B. Koller, S. Vogt, S. Häfner et al.* PTB, Braunschweig	The H2020 European Project DEMETRA: Experimental Time Services Based on European GNSS Signals **(Invited)** *P. Tavella* INRIM, Torino	First International Comparison of Fountain Primary Frequency Standards via a Long Distance Optical Fiber Link *J. Guéna, S. Weyers, M. Abgrall, C. Grebing et al.* SYRTE, PSL Research U., CNRS, Sorbonne U., UPMC	High-Resolution Frequency Synthesizers Over X-Band Using SILPLL Opto-Electronic Oscillators *T. Sun, A. Daryoush, A. Poddar, L. Zhang, U. Rohde* Drexel University, Philadelphia

11:00–11:20	Photonically Integrated Compact Atomic Optical Frequency Reference *M. Hummon, S. Kang, A. Dellis, D. Bopp et al.* NIST, Boulder	continued (invited paper)	Design and Performance of Cs Fountain Frequency Standards Constructed for Metrology Laboratories *R. Hendricks, F. Ozimek, K. Szymaniec, P. Dunst et al.* NPL, Teddington	A Highly Stable OEO Using a Multi-Purpose Optical-Delay Stabilization System *L. Bogataj, J. Tratnik, B. Batagelj, J. Tratnik et al.* University of Ljubljana
11:20–11:40	The Optical Rubidium Atomic Frequency Standard at AFRL *N. Lemke, G. Phelps, J. Burke, K. Martin, M. Bigelow* AFRL, Albuquerque	Impact of Adjacent-Band LTE Signals on GPS-Based Precision Time Transfer *B. Patla, N. Ashby, S. Römisch, D. McGillivray et al.* NIST, Boulder	Phase Shifts Evaluation in the TE_{105} FoCS-2 Microwave Cavity *A. Jallageas, L. Devenoges, L.-G. Bernier, J. Morel et al.* METAS, Bern Wabern	COEO Phase Locking and Performance Optimisation *R. Khayatzadeh, V. Auroux, A. Fernandez, O. Llopis* LAAS CNRS, Toulouse
11:40–12:00	Frequency Comb-Assisted QCL Stabilization for High Resolution Molecular Spectroscopy *R. Santagata, D.B.A. Tran, O.Lopez, B. Argence et al.* Lab. de Physique des Lasers, U. Paris 13, CNRS	Defining the Robust Timing Service for Future EGNSS *H. Zelle, H. Veerman, K. A. Aarmo, J.-P. Boyer et al.* Netherlands Aerospace Centre, Marknesse	Cold-Atom-Based Commercial Microwave Clock at the 10^{-15} Level *B. Pelle, B. Desruelle, R. Szmuk, D. Holleville* Muquans, Observatoire de Paris	1.25 GHz Ultra-Low Phase Noise Reference Photonics Oscillator for Space Applications *S. Kundermann, E. Portuondo-Campa, S. Lecomte, A. Perri et al.* CSEM, Neuchatel

12:00–12:20	1.5 µm - Optical Frequency Standard Iodine Stabilized in the 10^{-15} Range for Space-Mission Applications *C. Philippe, R. Le Targat, D. Holleville, M. Lours et al.* Observatoire de Paris	Period for Open Discussion	Investigation of Dual Species Ions Cloud by Molecular-Dynamics Simulation for Microwave Clocks *Y.-N. Zuo, P. Cheng, X. Sun, L. Wang, J. Zhang* Tsinghua University, Beijing	Low Phase Noise 10 GHz Coupled Optoelectronic Oscillator *O. Lelièvre, V. Crozatier, G. Baili, P. Nouchi et al.* Thales Research & Technology, Palaiseau
12:20–14:00	Lunch			

	Amphitheatre	Room 2	Rooms 3+4	Rooms 5+6+7
14:00–15:40	C2L-A (G6) Rachel Godun – Optical Clocks III	C2L-B (G4) Clark Nguyen – MEMS & Advanced Processing	C2L-C (G1) Thomas Baron – Materials	C2L-D (G2) Olivier Llopis, Mike Underhill – Microwave Photonics II
14:00–14:20	Sources of Uncertainty in an Ytterbium Optical Lattice Clock **(Invited)** *W. McGrew, R. Brown, R. Fasano, D. Nicolodi et al.* NIST, Boulder	NEMS Infrared Detectors Based on High Quality Factor 50 nm Thick AlN Nano-Plate Resonators *Z. Qian, V. Rajaram, S. Kang, M. Rinaldi* Northeastern University, Boston	Growth, Characterization and Piezoelectric Applications of Langasite-Type and YCOB Crystals **(Invited)** *Y. Zheng, K. Xiong, X. Tu, E. Shi, B. Neubig et al.* Chinese Academy of Sciences, Jiading	Accurate Measurement and Control of Amplitude to Phase Conversion for Low-Noise Photonic Microwave Generation *R. Bouchand, D. Nicoladi, X. Xie, Y. Le Coq, C. Alexandre* Observatoire de Paris
14:20–14:40		An Ultra-Sensitive Piezoelectric-on-Silicon Flapping Mode MEMS Lateral Field Magnetometer *S. Ghosh, J. E.-Y. Lee* City University of Hong Kong		Brillouin and Kerr-Based Whispering Gallery Mode Crystalline Fluoride-Type Resonators for Low Noise Microwave Source *J.-P. Aubry, S. Diallo, R. Martinenghi, Y. Chembo* FEMTO-ST Institute, UBFC, CNRS, ENSMM, Besançon

14:40–15:00	Towards Magnesium Optical Lattice Clock: Spectroscopy with 40 Hz Linewidth *N. Jha, S. Rühmann, D. Fim, K. Zipfel et al.* Leibniz Universität Hannover	Impact of Output Metric on the Resolution of Mode-Localized MEMS Resonant Sensors *J. Juillard, P. Prache, P. Maris Ferreira, N. Barnio* GEEPS, Gif-sur-Yvette	Characterization of Simple Port SAW Resonators at 3.7GHz on Epitaxial LiNbO3 Layer *A. Clairet, S. Oliveri, A. Almirall, T. Baron, A.Bartasyte* FEMTO-ST Institute, UBFC, CNRS, ENSMM, Besançon	Soliton-Based Optical Kerr Frequency Comb for Low-Noise Microwave Generation *E. Lucas, J. Jost, T. Kippenberg, K. Beha et al.* Ecole Polytechnique Fédérale de Lausanne
15:00–15:20	Optical-Clock Local-Oscillator Universal Interrogation Protocol for Zero Probe-Field-Induced Frequency-Shifts *T. Zanon-Willette, R. Lefevre, A. Taichenachev, V. Yudin* Université Pierre-et-Marie-Curie, Paris	Closed-Loop Tracking of Amplitude and Frequency in a Mode-Localized Resonant MEMS Sensor *M. Pandit, C. Zhao, G. Sobreviela, A. Mustafazade, A. Seshia* University of Cambridge	Achivement of Record Excitation of Hypersonic Acoustic Waves in Diamond-Based HBAR on the Operational Frequencies Up to 20 GHz *B. Sorokin, G. Kvashnin, A. Novoselov* Technological Institute for Superhard and Novel Carbon Materials, Moscow	High Sensitivity Phase Noise Analyzer Using an Electro-Optic Comb *N. Kuse, M. Fermann* IMRA America Inc., Boulder Research Labs

15:20–15:40	A Mercury Optical Lattice Clock with Improved Magic Wavelength Control *C. Guo, M. Favier, J. Calvert, V. Cambier et al.* Observatoire de Paris, CNRS, PSL research University, Sorbonne Universités, UPMC, Paris	Transparent Piezoelectric Transducers for Large Area Ultrasonic Actuators *D. Sette, S. Glinsek, S. Girod, N. Godard, E. Defay* Luxembourg Institute of Science and Technology	AlN-Solidly Mounted Resonators Sustaining Up to 1000°C with TCF Compensation *T. Mirea, J. Olivares, M. Clement, J. L. Olivera et al.* Universidad Politécnica de Madrid	Optical Synthesis Using Kerr Frequency Combs *L. Maleki, W. Liang, V. Ilchenko, A. Savchenkov, et al.* *OEwaves Inc., Pasadena*
15:40–16:00	Coffee break / Exhibits			
16:00–18:00	C3P-F to C3P-L Poster session II – G1 to G6			

Poster session II – Wednesday

July 12th 16:00–18:00

C3P-F – Materials, Resonators & Resonator Circuits II – *Olivier Le Traon, Jeffrey Pulskamp*

2 – Perturbation Analysis of Nonlinear Signal Generation in Radio Frequency Bulk Acoustic Wave Resonators, *K.-Y. Hashimoto, X. Li*, Chiba University, Japan, University of Electronic Science and Technology, China.

4 – Improving Coupling Coefficient Distribution on BAW Filters Manufactured on 200 mm Wafers, *S. Mishin, Yu. Oshmyansky*, Advanced Modular Systems, Inc., Goleta.

6 – Use of Double-Raised-Border Structure for Quality Factor Enhancement of Type II Piston Mode FBAR, *X. Li, J. Bao, Y. Huang, B. Zhang et al.*, University of Electronic Science and Technology of China, Chengdu.

8 – An Apodized 3-GHz Thin Film Piezoelectric on Substrate FBAR, *G. Pillai, A. A. Zope, S.-S. Li, J. Ming-Lin Tsai*, National Tsing Hua University, Hsinchu, InvenSense Inc.

10 – Analytical Modeling of Low Loss Disk Flexure Resonators, *J. Puder, A. Lal, J. Pulskamp, R. Rudy et al.*, Cornell University, Army Research Laboratory.

12 – Fundamental Limits of Disk Flexure Resonators, *J. Puder, J. Pulskamp, R. Rudy, R. Polcawich, S. Bhave*, Cornell University, Army Research Laboratory.

14 – Substrate Texturing for Homogeneous Deposition of Tilted C-Axis AlN Films for Shear Mode Operation, *M. Sierra-Zapata, M. Clement, T. Mirea, J. Olivares, E. Iborra*, Universidad Politécnica de Madrid.

16 – Microwave Tunable SIW Filter with Liquid Crystals, *S. Missaoui, S. Missaoui, M. Kaddour*, University of Tunis El Manar.

18 – Properties of AlScN Thin Films for Hybrid BAW/SAW Resonator Fabrication, *V. Pashchenko, S. Mertin, F. Parsapourkolour, J. Li et al.*, École Polytechnique Fédérale de Lausanne, Frec|n|sys.

20 – Temperature Coefficients of Quartz at Cryogenic Temperature, *J. Bon, R. Bourquin, P. Abbé, X. Vacheret, S. Galliou*, FEMTO-ST Institute, Besançon.

22 – Anti-Symmetric Shear-Extensional AlN Lamb-Wave Resonators with $k_t^2 > 4\%$, *B. Jo, M. Ghatge, R. Tabrizian*, University of Florida, Gainesville.

C3P-G – Digital Methods – *Enrico Rubiola*

24 – Wideband and Low Phase Noise Up-Converted Direct Frequency Synthesis Using High Frequency DAC and Oscillator, *J.-M. Lesage, J.-F. Penn*, DGA, Rennes.

26 – Dynamic Phase Shifting Method Utilized in the Enhanced Frequency Controlled Clock System, *V. Stofanik, A. Fibich, T. Bagala, P. Kubinec*, FEI STU, Bratislava.

28 – A Fully-Digital Realtime SoC FPGA Based Phase Noise Analyzer with Cross-Correlation, *P.-Y. Bourgeois, G. Goavec-Merou, J.-M. Friedt, E. Rubiola,* FEMTO-ST Institute, Besançon.

30 – Full Digital Phase Noise Measurement by Using Two Reference Oscillators and Multichannel ADCs, *T. Imaike*, Nihon University, Funabashi.

32 – Frequency Synthesis Using Low-Pass Single-Bit Multi-Step Look-Ahead Sigma-Delta Modulators in Quadrature Upconversion Scheme, *C. Basetas, P. P. Sotiriadis, N. Temenos*, National Technical University of Athens.

34 – Wide-Band Frequency Synthesis Using Hardware-Efficient Band-Pass Single-Bit Multi-Step Look-Ahead Sigma-Delta Modulators, *C. Basetas, P. P. Sotiriadis, N. Temenos*, National Technical University of Athens.

36 – Phase Noise Measurements of Surface Acoustic Wave Resonators at 2.4 GHz, *E. Vaillant, J. Imbaud, F. Sthal, F-X. Esnault, G. Cibiel*, FEMTO-ST Institute, Besançon, Centre National d'Etudes Spatiales, Toulouse.

38 – Software Defined Radio Platform for Time and Frequency Metrology, *N. Boucquey, A. Kinali*, Institut Supérieur Industriel de Bruxelles, Max Planck Institute for Informatics, Saarbrücken.

40 – Noise Interaction with Time Quantization of TIC, *M. Danielson*, Net Insight AB, Stocksund.

42 – 32-QAM All-Digital RF Signal Generator Based on a Homodyne Sigma-Delta Modulation Scheme, *P. P. Sotiriadis, C. Basetas, N. Temenos*, National Technical University of Athens.

C3P-H – Microwave Frequency Standards II – *Stefan Weyers*

44 – The Portable CPT Atomic Clocks - Recent Developments, *Z. Zhang, R. Yang*, Beijing Institute of Radio Metrology and Measurement.

46 – Characteristics of Space Mini Passive Hydrogen Maser in Shanghai Astronomical Observatory, *Y. Xie, T. Shuai, P. Chen, Y. Pei et al.*, Chinese Academy of Sciences, Shanghai.

48 – Progress Towards Chip-Scale Atomic Clock in Peking University in 2016, *J. Zhao, R. Liu, H. Meng, E. Hu et al.*, Peking University, Beijing.

50 – Analytical Expressions for Parameters of the Dark Resonance in a Vacuum Vapour Cell, *D. Brazhnikov, M. Abdel Hafiz, G. Coget, R. Boudot*, Institute of Laser Physics SB RAS, Novosibirsk, FEMTO-ST Institute, Besançon.

52 – Characterization of 894.6 nm VCSELs and Application to a Microcell-Based Atomic Clock, *R. Vicarini, J. Rutkowski, V. Maurice, E. Kroemer et al.*, FEMTO-ST Institute, Besançon.

54 – An Electronic Controller Based on FPGA for the Ramsey-CPT Atomic Clock, *P. Cheng, X. Sun, L. Wang, J. Zhang et al.*, Tsinghua University, Beijing.

56 – A Merchandized Optically Pumped Cesium Atomic Clock, *Y. Cao, X. Zhao, W. Xie, Q. Wei et al*., Chengdu Spaceon Electronics Co., Ltd., Chengdu.

58 – Mutual Influence of the LF-Microwave Resonances in a System of Two Alkali Vapor Magnetometers with Laser Pumping, *A. Baranov, S. Ermak, V. Semenov, N. Kulachenkov*, Peter the Great St. Petersburg Polytechnic University, St Petersburg, State Research Center of the Russian Federation Concern CSRI Elektropribor, JSC.

60 – Increase of Effective Number of Detected Atoms in KRISS-F1(Cs) Fountain Clock by Optical Pumping, *S. Lee, M.-S. Heo, T.-Y. Kwon, H.-G. Hong et al.*, Korea Research Institute of Standards and Science, Daejeon.

62 – Design of a Space Atomic Clock with Intracavity Cooling, *D. Lü, X. Peng, W. Ren, L. Liu*, Chinese Academy of Sciences, Shanghai.

64 – MEMS Atomic Vapor Cells Sealed by Cu-Cu Thermocompression Bonding, *S. Karlen, J. Haesler, T. Overstolz, G. Bergonzi, S. Lecomte*, CSEM SA, Neuchâtel.

66 – A Vertical MOT – OM to Prepare Cold Atoms for New Fountain NIM6, *F. Fang, W. Chen, K. Liu, N. Liu et al.*, National Institute of Metrology, Beijing.

68 – Preliminary Evaluation of the AOS-CsF1 Primary Frequency Standard, *P. Dunst, B. Nagórny, D. Lemański, P. Nogaś et al.*, Space Research Centre, Warsaw.

70 – Continuous Cold Atomic Beam in a Zerodur Chamber for Atom Interferometry, *M.-S. Heo, T. Y. Kwon, S. E. Park, S.-B. Lee et al.*, KRISS, Daejeon.

72 – A Low Phase Noise Raman Lasers System Based on Optical Injection and an Optical Phase-Lock Loop, *C. Wu, L. Wang, X. Yan, J. Zhang*, Tsinghua University, Beijing.

74 – First Results on Rb Fountain Rb304 Frequency Standard Developed at VNIIFTRI, *D. Kupalov, V. Baryshev, I. Blinov, A. Boiko et al*., VNIIFTRI, Mendeleevo.

76 – Microfabricated Vapor Cells for Miniature Atomic Clocks Based on Post-Sealing Activated Cesium Dispensers, *V. Maurice, J. Rutkowski, E. Kroemer, S. Bargiel et al.*, FEMTO-ST Institute, Besançon.

78 – Development of an Industrial Optically-Pumped Cesium Beam Clock for Ground Applications, *P. Berthoud, M. Haldimann, C. Ducommun, F. Lefebvre et al.*, Oscilloquartz SA, Saint Blaise, Switzerland.

80 – Laser Intensity Noise Transfer for Pulsed Vapor-Cell Clocks with Optical Detection, *M. Gozzelino, S. Micalizio, F. Levi, A. Godone, C. Calosso*, Politecnico di Torino.

82 – The NRC-FCs2 Primary Frequency Standard at the National Research Council Canada, *S. Beattie, B. Jian, J. Alcock, J. Bernard et al.*, National Research Council of Canada, Ottawa.

84 – Off-Resonant Light Shift in CPT Ramsey Spectroscopy of Clock Transitions, *V. Yudin, A. Taichenachev, M. Basalaev, X. Liu et al.*, NIST, Boulder.

86 – Closed-Loop Characterization of Cesium Magnetometers Operating at Ambient Temperature, *J. Lou, G. Cranch*, U.S. Naval Research Laboratory, Washington.

88 – Optimization of a Point Source Atom Interferometer for Compact Devices and Precision Measurement, *A. Hansen, Y.-J. Chen, G. Hoth, B. Pelle et al.*, NIST, Boulder.

90 – Compact Atom Interferometer Using a Single Laser, *S.-W. Chiow, N. Yu*, Jet Propulsion Laboratory, Pasadena.

92 – Progress Towards the Development of a Cold Atomic Beam CPT Clock, *J. Elgin, B. Evers, T. Heavner, J. Kitching, E. Donley*, NIST, Boulder.

94 – Phase Coherent Frequency Detuning in Fountain Clocks, *M. Kazda, C. Hellmann, V. Gerginov, S. Weyers*, PTB, Braunschweig.

96 – Frequency Bandwidth and Sensitivity of Parametric Modulation Magnetometer for Nuclear Spin Precession Measurement, *Z. Wang*, National University of Defense Technology, Changsha.

98 – A Large Mode Optical Resonator for Enhanced Atom Interferometry, *S. R. Chanu, N. Mielec, D. Holleville, B. Fang et al.*, LNE-SYRTE, Observatoire de Paris.

C3P-J – Sensors & Transducers II – *Philip Feng*

100 – Liquid-Level Sensing by a Cylindrical Piezoelectric Resonator Operating in a Trapped-Energy Mode, *K. Yamada, K. Watanabe*, Tohoku-Gakuin University, Tagajo.

102 – A New Method for Measuring Properties of Liquid by Using a Single Quartz Crystal Microbalance, *F. Tan, P. Ye, D. Qiu, L. Guo et al.*, University of Electronic Science and Technology of China, Chengdu.

104 – A Surface Acoustic Wave Resonance (SAR) System for in-Liquid Sensing, *K. Kustanovich, V. Yantchev, A. Jesorka*, Chalmers University of Technology, Goteborg.

106 – A Micromechanical Resonant Optical Power Meter, *X. Chen, T. Zhang, Z. Jiang, X. Wei*, Xi'an Jiaotong University, Xi'an.

108 – Piezoelectric Harvester Scavenges Energy from Cavity of Phononic Crystal, *H. Hu, S. Jiang, Q. Qian, Y. Hu, V. Laude*, Huazhong University of Science and Technology, Wuhan, FEMTO-ST Institute, Besançon.

110 – Integration of Multilayered Graphene on AlN Based Resonators as a Functionalization Platform for Biosensors*, L. Gordillo-Dagallier, J. Olivares, B. Marco-Dufort, J. L. Olivera et al.* Universidad Politécnica de Madrid.

C3P-K – Timekeeping, Time & Frequency Transfer, GNSS Applications II – *Philip Tuckey*

112 – Kalman Filter Approaches for a Mixed Clock Ensemble, *M. Gödel, T. Schmidt, J. Furthner*, German Aerospace Center (DLR), Oberpfaffenhofen.

114 – Two Way Time Comparison via Optical Fiber at BIRMM, *X. Wang, S. Zhang, H. Wang, H. Wang, H. Yi*, Beijing Institute of Radio Metrology and Measurement.

116 – Fully and Optimal Use of the Redundancy in TWSTFT for Accurate Time Transfer, *Z. Jiang, S.-Y. Lin, W.-H. Tseng*, BIPM, Sèvres, Telecommunication Laboratories (TL), Chinese Taipei.

118 – Fibre Optic Time Transfer Between PTB and Deutsche Telekom Using Multi-Link Redundant Topology, *Ł. Śliwczyński, P. Krehlik, J. Kołodziej, H. Imlau et al.*, AGH

120 – A Cost-Efficient Regional Synchronization System, *R. Píriz, P. Roldán, D. Sanz, J. Díaz et al.*, GMV Aerospace, Tres Cantos (Spain), Seven Solution, Spain.

122 – Performance Test and Power-Law Spectrum Analysis of Domestic Cesium Clocks, X.*-L. Wang, Y. Du*, Beijing Satellite Navigation Center, Beijing.

124 – Research on Autonomous High-Precision Time Synchronization Method of UAV Based on Side-Tone Signal, *T. Liu, Y. Hu, Y. Hua, M. Wu,* Chinese Academy of Sciences.

126 – A New Approach of Time Transfer Based on BDS Carrier Phase Observation, *P. Zhang, R. Tu, Y. Gao*, National Time service center, Xi'an.

128 – Coherence Transfer of Subhertz-Linewidth Laser Light via a 50-km-Long Optical Fiber Noise-Compensated by Remote Users, *L. Wu, Y. Jiang, Z. Bi, H. Yu. L. Ma*, East China Normal University, Shanghai.

130 – An Accurate Timing Method Based on Communication Satellite, *L. Xu, F. Zhu, X. Li, J. Chen*, Chinese Academy of Sciences, Xi'an.

132 – The Study of Near Real-Time GPS/BDS Time Transfer, *H. Wang, H. Yi, S. Zhang, H. Wang, X. Wang*, Beijing Institute of Radio Metrology and Measurement.

134 – CLONETS – Clock Network Services: Strategy and Innovation for Clock Services Over Optical-Fibre Networks*: P. Krehlik, Ł. Śliwczyński, J. Dostal, J. Radil et al.*, Observatoire de Paris, PSL research University, CNRS, Sorbonne Universités, UPMC, Paris, Poznan Supercomputing and Networking Center.

136 – Influence of the UTC Parameters Generating Method on BDS Positioning Accuracy, *D. Li, L. Xu, X. Li*, National Time Service Center, Chinese Academy of Sciences, Xi'an.

138 – Monitoring of Time Signals Broadcast by EFR Long-Wave Transmitters at PTB, *B. Sbick, K. Katzmann, E. Staliuniene, D. Piester, A. Bauch*, EFR Europäische Funk-Rundsteuerung GmbH, HKW-Elektronik GmbH, PTB, Braunschweig.

140 – Calibration Method of TWSTFT Stations Equipped with SDR Receivers, *T. T. Thai, A. Mura, I. Sesia, J. Achkar et al.*, INRIM, Torino.

142 – Reference Signal Distribution for the ACES Microwave Link Ground Terminal at SYRTE, *M. Abgrall, Ph. Laurent, D. Rovera*, Observatoire de Paris.

144 – UTC Traceability Through Packet Networks, *P. Whibberley, E. Laier English, C. Langham, D. Hicks, L. Lobo*, NPL, Teddington.

146 – Modeling Time and Frequency Fiber Links with Bi-Directional Amplifiers Using Transmission Matrixes, *Ł. Śliwczyński, P. Krehlik, K. Salwik*, AGH University of Science and Technology, Krakow.

148 – Further Results of Time Transfer Through the Optical Fiber at NIM, *K. Liang, A. Zhang, Z. Yang, Y. Wang et al.*, International Bureau of Weights and Measures / Chinese Academy of Sciences, Beijing.

150 – Recent Experience with Optical Infrastructure for Time and Frequency Transfer, *V. Smotlacha, J. Vojtech*, CESNET, Prague.

152 – GPS Timing Interference Detection and Countermeasures Through Analysis of GPS and Clock Steering Observables, *A. Schultzen, H. Hauglin, T. Dunker, S. Holm*, Justervesenet / University of Oslo.

154 – UTC(NIM) Algorithm Update, *Y. Gao, A. Zhang, W. Wang, Y. Wang et al.*, National Institute of Metrology, Beijing.

156 – The Software Defined Receiver (SDR) as an Enabler for Testing the Einstein Equivalence Principle (EEP) with Two Way Satellite Time and Frequency Transfer (TWSTFT), *W.-H. Tseng, D. Matsakis*, Telecommunication Laboratories, Chunghwa Telecom Co., Ltd, Taoyuan, U.S. Naval Observatory.

158 – Coherence Transfer of an Ultra-Stable Laser Over a 50 km Urban Fiber Link and a Spectral Span of 235 THz, F. Meng, *Y. Lin, Q. Wang, Y. Li et al.*, National Institute of Metrology, Beijing.

160 – Anchor Stations for Inter-Satellite Link and Design for its Time Synchronization, *Y. Bai, X. Lu, W. Jing, K. Zhang et al.*, Chinese Academy of Sciences, Xi'an.

162 – Propagation-Phase/Frequency-Shift Theory for Time/Frequency Transfer, GNSS and Gravity Waves, *M. Underhill*, Underhill Research Limited, Lingfield.

164 – Initial Use of Galileo Signals in PTB, *A. Bauch, J. Leute, T. Polewka, D. Piester et al.*, PTB, Braunschweig, National Time Service Center, Chinese Academy of Sciences, Xi'an.

C3P-L – Optical Frequency Standards and Applications II – *John McFerran*

166 – Experimental Study of a Miniaturized Calcium Atomic Beam Tube for Small Optical Frequency Standard, *H. Chen, Z. Liu, S. Xiao, H. Shang et al.*, Beijing Vacuum Electronics Research Institute, Peking University, Beijing.

168 – A Small Calcium Beam Optical Frequency Standard with Fully-Sealed Vacuum Tube, *H. Shang, X. Zhang, S. Zhang, J. Chen, H. Chen*, Peking University, Beijing, Beijing Vacuum Electronics Research Institute.

170 – New Clock Laser System for the Second Yb Optical Lattice Clock at KRISS, *W.-K. Lee, C. Y. Park, M.-S. Heo, H. Kim et al.*, Korea Research Institute of Standards and Science, Daejeon.

172 – Improved Absolute Frequency Measurement of the $^{1}S_{0}$–$^{3}P_{0}$ Transition of ^{171}Yb at KRISS, *H. Kim, M.-S. Heo, W.-K. Lee, C. Park et al.*, Korea Research Institute of Standards and Science, Daejeon.

174 – A Strontium Optical Lattice Clock Apparatus for Precise Frequency Metrology and Beyond, *M. Tarallo, D. Calonico, F. Levi, M. Barbieri et al.*, INRIM, Torino, CNR-INO, Firenza.

176 – Development of Optical Clocks Based on Strontium Atoms: Systematic Shifts Characterization, *O. Berdasov, S. Strelkin, A. Gribov, G. Belotelov et al.*, All-Russian Research Institute of Physical-Technical and Radiotechnical Measurements, Moscow.

178 – An Optical Absolute Frequency Reference for a Sounding Rocket Mission Based on Iodine, *K. Döringshoff, V. Schkolnik, F. Gutsch, E. Kovalchuk*, Humboldt-Universität zu Berlin, Universität Bremen.

180 – Production and Trapping of Th Ions for Nuclear Frequency Standard Development, *P. Borisyuk, S. Derevyashkin, K. Khabarova, N. Kolachevsky et al.*, National Research Nuclear University "MEPhI", Moscow, The P.N. Lebedev Physical Institute, Moscow.

182 – Space Optical Clocks: Next Generation Optical Frequency Combs on Sounding Rockets, *M. Lezius, B. Pröbster, Ch. Deutsch, R. Holzwarth et al.*, Menlo Systems GmbH, Martinsried.

184 – Polarizability and Magic Wavelength of Yb^+ Clock Transition $^2S_{1/2} \rightarrow {}^2D_{3/2}$, *A. Roy, S. De, B. Arora, B. Sahoo*, CSIR-National Physical Laboratory, New Delhi, Dev University.

186 – Cavity Assisted Non-Destructive Detection for Sr Optical Lattice Clocks, *G. Vallet, E. Bookjans, S. Bilicki, R. Le Targat, J. Lodewyck,* Observatoire de Paris, PSL Research University, CNRS, Sorbonne Universités, UPMC, Paris.

188 – Preparing a Frequency Measurement of the First Lattice Clock Based on Bosonic Magnesium*, S. Sauer, S. Rühmann, D. Fim, K. Zipfel et al.*, Leibniz Universität Hannover, Institut für Quantenoptik.

190 – Higher-Order Non-Linear Effects on Uncertainties of Optical Clocks on Mg Atoms, V. *Ovsiannikov, S. Marmo, S. Mokhnenko, V. Palchikov*, FGUP VNIIFTRI, Mendeleevo.

192 – A High-Precision Strontium Lattice Clock with Cryogenic Silicon Resonators, *R. Schwarz, S. Dörscher, A. Al-Masoudi, S. Herbers et al*., PTB, Braunschweig.

194 – Updated Frequency Measurement of the Clock Transition of In^+, *N. Ohtsubo, Y. Li, K. Matsubara, T. Ido et al.*, National Institute of Information and Communications Technology, Koganei.

196 – On-Site Evaluation of a Portable 100 GHz Microresonator-Based Optical Frequency Comb Generation System*, Y.-C. Chuang, T.-A. Liu, W.-J. Ting, H.-F. Chen et al.*, Center for Measurement Standards, Industrial Technology Research Institute, Hsinchu, Taiwan.

198 – Optical Sampling Analog-to-Digital Scheme for Broadband Microwave Signal, *H. Meng, R. Liu, J. Zhao*, Peking University, Beijing.

200 – New Length Sensor for Optical Absorption Cells Based on Circular Interferometry Yielding Ten Micrometer Accuracy, *H. Elandaloussi, C. Rouillé, P. Marie-Jeanne, C. Janssen*, Université Pierre-et-Marie-Curie, Paris.

202 – Semiconductor-Based, Narrow-Linewidth, Micro-Integrated UV Laser System for Precision Quantum Optical Experiments in the Field*, M. Krüger, A. Bawamia, C. Kürbis, R. Smol et al.*, Ferdinand-Braun-Institut, Leibniz-Institut für Höchstfrequenztechnik, Berlin.

204 – Precision Measurement of the Hyperfine Structure of the Rb $^6P_{3/2}$ State, *S. Zhang, X. Zhang, Z. Jiang, H. Shang et al.*, Peking University, Beijing, Lanzhou Institute of Physics, CAST.

206 – Frequency Stabilization of 423 nm Laser for Calcium-Beam Optical Frequency Standard, *S. Zhang, X. Zhang, H. Shang, J. Chen*, Peking University, Beijing, Beijing Vacuum Electronics Research Institute.

208 – Spectroscopy of Samarium Colour Centres for a Solid-State Optical Frequency Reference, *G. Edge, S. Potnis, A. Vutha*, University of Toronto.

210 – Progresses on the Geometric Scale Factor Stabilization of the GP2 Large Frame Ring Laser Gyroscope, *U. Giacomelli, N. Beverini, G. Carelli, E. Maccioni et al.*, Università di Pisa, Dipartimento di Fisica, Institute of Laser Physics of SB RAS, INFN, sezione di Pisa.

212 – Frequency Stability Transfer by Optical Injection Locking Into a Semiconductor Frequency Comb, *A. Ramdane, P. Grüning, V. Roncin, F. Du-Burck*, Université Paris 13.

214 – High Precision Phase and Frequency Measurements in Rare Earth Doped Crystals at Cryogenic Temperatures for Probing Nanoresonators Behavior, *N. Galland, O. Gobron, K. Jung, S. Seidelin, Y. Le Coq*, Université Grenoble Alpes and CNRS, Institut NEEL, Grenoble, LNE-SYRTE, Observatoire de Paris, PSL research University, CNRS, Sorbonne Universités, UPMC, Paris.

216 – Toward an Ultra-Stable Laser Based on Cryogenic Silicon Cavity, *B. Maréchal, J. Millo, A. Didier, C. Lacroûte et al.*, FEMTO-ST Institute, Besançon, PTB, Braunschweig.

218 – Digitally Controlled Precision Optical Frequency Comb, *A. Rolland, E. Meade, Y. Li, N. Kuse et al.*, IMRA America, Inc., Longmont.

220 – Compact Ultra-Stable Laser, *A. Didier, J. Millo, B. Maréchal, C. Rocher et al.*, FEMTO-ST Institute, Besançon, PTB, Braunschweig.

	Lecture Sessions – Thursday July 13th			
	Amphitheatre	**Room 2**	**Rooms 3+4**	**Rooms 5+6+7**
9:00–10:20	D1L-A (G6) Helen Margolis – Combs II	D1L-B (G5) Pascale Defraigne – GNSS	D1L-C (G3) John Kitching – Atom Interferometry	D1L-D (G1) Songbin Gong – Resonators II
9:00–9:20	All-Polarization-Maintaining Er:fiber Comb for Comparison of Sr, Yb, and Hg Optical Lattice Clocks with Fractional Instability of $< 10^{-17}$ at 1 s *N. Ohmae, N.Kuse, M. Fermann, H. Katori* RIKEN	Using Galileo for Time Synchronization and IEEE 1588 Update: Assessment of the Current State of Galileo **(Invited)** *H. Gerstung* Meinberg Funkuhren GmbH & Co.KG	Atom Interferometry in Microgravity **(Invited)** *Ph. Bouyer* University of Bordeaux	Quality Factor and Phase Noise Improvements in MEMS Resonators and Oscillators **(Invited)** *K. Foster, B. Gibson, K. Qalandar, G. Piazza, C. Casella* UC, Santa Barbara
9:20–9:40	Simultaneous Spectral rity Transfer at Three tical Clock Transitions Using an Ultra-Low Noise Er:fiber Frequency Comb *M. Giunta, W. Hänsel, M. Fischer, M. Lezius et al.* Menlo Systems, MPQ			

9:40–10:00	Fully-Stabilized 1-GHz Optical Frequency Comb from a Diode-Pumped Solid-State Laser *S. Hakobyan, V. Wittwer, P. Brochard, K. Gürel et al.* Université de Neuchâtel	Sub 10^{-16} frequency transfer with IPPP: Recent results *G. Petit, J. Leute, S. Loyer, F. Perosanz* BIPM	High-Sensitivity Cold-Atom Gyroscope with Real-Time Vibration Compensation *D. Savoie, M. Altorio, B. Fang, R. Geiger, A. Landragin* LNE-SYRTE	Lowering Motional Resistance by Partially HfO_2 Gap Filling in Double-Ended Tuning Fork MEMS Resonators *M. Maqueda López, E. Casu, A. Ionescu M. Fernández-Bolaños* EPFL Lausanne
10:00–10:20	Ultra-Short Optical Pulses Leading to Ultra-Stable Photonic Microwave Generation *X. Xie, R. Bouchand, D. Nicolodi, M. Lours et al.* Observatoire de Paris	Experimental Research on Beidou Time Transfer Using the NIM Made GNSS Time and Frequency Receivers at the BIPM in Euro-Asia Link *K. Liang, A. Zhang, Z. Yang, L. Tisserand, Z. Jiang* NIM, BIPM	Correction of Laser Wavefronts in an Atom Interferometer with a Deformable Mirror *M. Langlois, A. Trimeche, S. Merlet, F. Pereira Dos Santos* SYRTE	Orders of Magnitude Reduction in Acoustic Resonator Simulation Times via the Wide-Band Rapid Analytical-FEA Technique *J. Puder, J. Pulskamp, R. Rudy, R. Polcawich, S. Bhave* Cornell University
10:20–10:40	Coffee break			

	Amphitheatre	Room 2	Rooms 3+4	Rooms 5+6+7
10:40–12:20	D2L-A (G6) Dave Leibrandt – Optical Clocks IV	D2L-B (G5) Stefania Romisch – GNSS & Calibration	D2L-C (G2) Serge Galliou, Yann Kersalé – Microwave & Cryogenics	D2L-D (G1/4) Joshua Lee, Alexandre Reinhardt – Wave Propagation
10:40–11:00	Evaluating ^{171}Yb+ Single-Ion Clocks via the E3/E2 Frequency Ratio *N. Huntemann, C. Sanner, R. Lange, B. Lipphardt et al.* PTB	Timing Performance Evaluation of BDS IGSO-6 and GEO-7 Satellite Network: GNSS timing performance evaluation method & characterization *F. Zhu, X.-H. Li, D.-D. Li, H.-J. Zhang, L.-X. Xu* Chinese Academy of Sciences, Xi'an	Development of a Mobile HTS Cryogenic Oscillator **(Invited)** *O. d'Allivy Kelly, Y. Lemaître, B. Marcilhac, D. Chaudy et al.* Thales Research & Technology	Doubly-Resonant Phoxonic Crystal for Enhanced Acousto-Optical Interaction **(Invited)** *V. Laude, M. Addouche, S. Benchabane, A. Khelif et al.* Univ. Bourgogne Franche-Comté
11:00–11:20	Absolute Frequency Measurement of the Electric Quadrupole Transition of ^{88}Sr+ *P. Dubé, J. Bernard, M. Gertsvolf* National Research Council Canada	GPS Calibrations for UTC *G. Petit, F. Arias, Z. Jiang, L. Tisserand* BIPM		

11:20–11:40	Absolute Frequency Measurement of the ^{171}Yb Optical Lattice Clock at INRIM *M. Pizzocaro, P. Thoumany, F. Bregolin, G. Milani et al.* INRIM	Validation of the Inter-Frequency Calibration of Timing GNSS Receivers *P. Defraigne, W. Huang, D. Rovera* Royal Observatory of Belgium	*A Low Power Cryogenic Sapphire Oscillator with Better Than 10^{-15} Short Term Frequency Stability* *C. Fluhr, V. Pétrini, G. Le Tetû, V. Giordano et al.* Institut FEMTO-ST - CNRS	Lithium Niobate Phononic Crystals for Radio Frequency Sh0 Waves *R. Lu, T. Manzaneque, Y. Yang, S. Gong* U. of Illinois at Urbana-Champaign
11:40–12:00	*Estimating the Scale Interval of TAI with an Optical Clock* *H. Hachisu, T. Ido* NICT	Towards an Operational Procedure for Absolute Calibration of GNSS Receivers *P. Waller, D. Schultz, R. Prieto-Cerdeira* ESA/ESTEC	Latest Results in the Development of an Ultra-Low Phase Noise Rb CPT Vapour Cell Atomic Clock *T. Burtichelov, J. Everard* University of York	Backward Acoustic Plate Waves: Features of Properties and Possible Applications in Microelectronic Devices *V. Mozhaev, I. Nedospasov, I. Kuznetsova* Lomonosov Moscow State University

12:00–12:20	Contributing to TAI with Sr Optical Lattice Clocks *S. Bilicki, E. Bookjans, G. Vallet, M. Abgrall et al.* LNE-SYRTE	UTC Time Link Calibration in the Frame of APMP - Campaigns in 2014-2016 *K. Liang, A. Zhang, Z. Yang, Z. Fang et al.* BIPM, Chinese Academy of Sciences	Active Devices Choice and Design of an All Cryogenic Superconductor Resonator Oscillator *D. Chaudy, O. Llopis, B. Marcilhac, Y. Lemaitre et al.* Thales Systèmes Aéroportés	Nonreciprocal Reconfigurable Zero-Transmission Filters Through Nonreciprocal Coupling to Resonators *C. Peterson, J. Bernhard, G. Bahl* University of Illinois at Urbana-Champaign
12:20–14:00	Lunch + Take Away			
14:30–17:00	Laboratory Tours			

2018 Conferences





2018 European Frequency and Time Forum

April 10-12, 2018

National Museum of Automobiles, Torino, Italy.

The European Frequency and Time Forum (EFTF) is an international conference and exhibition, providing information on recent advances and trends of scientific research and industrial development in the fields of Frequency and Time.

In 2018 EFTF will come back to Torino for the second time in its history. The venue of the Forum will be the conference centre of the Automobile Museum, one of the world's most famous museums dedicated to history of motoring (www.museoauto.it). It is few minutes from downtown by metro and few minutes from the Italian Metrological Institute (INRIM), local organizer of the conference.

The website of the conference will be on-line soon (www.eftf2018.it). All members of the local organizing committee are eager to welcome you in Torino for an exciting conference.

Conference Center Floorplan

